October 24, 2016

ORGANISATION EUROPÉENNE POUR LA RECHERCHE NUCLÉAIRE

CERN EUROPEAN ORGANIZATION FOR NUCLEAR RESEARCH

Handbook of LHC Higgs cross sections: 4. Deciphering the nature of the Higgs sector

Report of the LHC Higgs Cross Section Working Group

Editors: D. de Florian
C. Grojean
F. Maltoni
C. Mariotti
A. Nikitenko
M. Pieri
P. Savard
M. Schumacher
R. Tanaka

GENEVA
2016

Conveners

WG1: Higgs XS& BR: B. Mellado, P. Musella, M. Grazzini, R. Harlander

- *BR:* A. Denner, S. Heinemeyer, A. Mück, I. Puljak, D. Rebuzzi
- *ggF:* S. Forte, D. Gilberg, C. Hays, A. Lazopoulos, A. Massironi, G. Petrucciani, G. Zanderighi
- *VBF and WH/ZH:* S. Dittmaier, P. Govoni, B. Jäger, J. Nielsen, L. Perrozzi, E. Pianori, A. Rizzi, F. Tramontano
- *ttH/tH:* S. Guindon, C. Neu, S. Pozzorini, L. Reina

WG2: Higgs properties: M. Chen, M. Dührssen, A. David, A. Falkowski, C. Hays, G. Isidori

WG3: BSM Higgs: N. Rompotis, M. Pelliccioni, I. Low, M. Mühlleitner, R. Wolf

- *MSSM neutral:* R. Lane, S. Liebler, A. McCarn, P. Slavich, M. Spira, D. Winterbottom
- *MSSM charged:* M. Flechl, S. Sekula, M. Ubiali, M. Zaro
- *NMSSM:* U. Ellwanger, M. Mühlleitner, F. Staub, D. Strom, R. Yohay
- *Neutral extended scalars:* R. Gerosa, H. Logan, O. Stål, R. Santos, S. Su, X. Sun
- *Exotic decay:* S. Bressler, S. Gori, A. Mohammadi, J. Shelton

Cross-group task forces:

- *bbH/bH:* M. Beckingham, A. Nikitenko, M. Spira, M. Wiesemann
- *HH:* S. Dawson, C. Englert, M. Gouzevitch, R. Salerno, M. Slawinska
- *Fiducial cross-sections:* F.U. Bernlochner, S. Kraml, P. Milenovic, P. Monni
- *Offshell Higgs:* F. Caola, Y. Gao, N. Kauer, L. Soffi, J. Wang
- *MCnet:* S. Plätzer
- *PDF:* S. Forte, J. Huston, R. Thorne

Abstract

This Report summarizes the results of the activities of the LHC Higgs Cross Section Working Group in the period 2014–2016. The main goal of the working group was to present the state-of-the-art of Higgs physics at the LHC, integrating all new results that have appeared in the last few years. The first part compiles the most up-to-date predictions of Higgs boson production cross sections and decay branching ratios, parton distribution functions, and off-shell Higgs boson production and interference effects. The second part discusses the recent progress in Higgs effective field theory predictions, followed by the third part on pseudo-observables, simplified template cross section and fiducial cross section measurements, which give the baseline framework for Higgs boson property measurements. The fourth part deals with the beyond the Standard Model predictions of various benchmark scenarios of Minimal Supersymmetric Standard Model, extended scalar sector, Next-to-Minimal Supersymmetric Standard Model and exotic Higgs boson decays. This report follows three previous working-group reports: *Handbook of LHC Higgs Cross Sections: 1. Inclusive Observables* (CERN-2011-002), *Handbook of LHC Higgs Cross Sections: 2. Differential Distributions* (CERN-2012-002), and *Handbook of LHC Higgs Cross Sections: 3. Higgs properties* (CERN-2013-004). The current report serves as the baseline reference for Higgs physics in LHC Run 2 and beyond.

We, the authors, would like to dedicate this Report to the memory of

Guido Altarelli (1941 - 2015)

Thomas Kibble (1932 - 2016)

and

Yoichiro Nambu (1921 - 2015)

D. de Florian[1], C. Grojean[2,3,4,5], F. Maltoni[6], C. Mariotti[7], A. Nikitenko[8], M. Pieri[9], P. Savard[10,11], M. Schumacher[12], R. Tanaka[13] (Eds.), R. Aggleton[14,15,16], M. Ahmad[17], B. Allanach[18], C. Anastasiou[19], W. Astill[20], S. Badger[21], M. Badziak[22,23,24], J. Baglio[25], E. Bagnaschi[2], A. Ballestrero[7], A. Banfi[26], D. Barducci[27], M. Beckingham[28], C. Becot[13,29], G. Bélanger[27], J. Bellm[30], N. Belyaev[31], F.U. Bernlochner[32], C. Beskidt[33], A. Biekötter[34], F. Bishara[20], W. Bizon[20], N.E. Bomark[35], M. Bonvini[20], S. Borowka[36], V. Bortolotto[37,38,39], S. Boselli[40], F.J. Botella[41], R. Boughezal[42], G.C. Branco[43], J. Brehmer[44], L. Brenner[45], S. Bressler[46], I. Brivio[47], A. Broggio[48], H. Brun[49], G. Buchalla[50], C.D. Burgard[12], A. Calandri[51], L. Caminada[36], R. Caminal Armadans[52], F. Campanario[53,54], J. Campbell[55], F. Caola[56,30], C.M. Carloni Calame[57], S. Carrazza[56], A. Carvalho[58], M. Casolino[5], O. Cata[50], A. Celis[50], F. Cerutti[24], N. Chanon[59], M. Chen[17], X. Chen[60], B. Chokoufé Nejad[2], N. Christensen[61], M. Ciuchini[62], R. Contino[63,56], T. Corbett[64], D. Curtin[65], M. Dall'Osso[58], A. David[56], S. Dawson[66], J. de Blas[67], W. de Boer[33], P. de Castro Manzano[58], C. Degrande[30], R.L. Delgado[68], F. Demartin[6], A. Denner[69], B. Di Micco[70], R. Di Nardo[56], S. Dittmaier[12], A. Dobado[68], T. Dorigo[58], F.A. Dreyer[71,72,56], M. Dührssen[56], C. Duhr[56,6], F. Dulat[73], K. Ecker[74], K. Ellis[30], U. Ellwanger[75], C. Englert[76], D. Espriu[77], A. Falkowski[75], L. Fayard[13], R. Feger[69], G. Ferrera[78], A. Ferroglia[79,80], N. Fidanza[81,1], T. Figy[82], M. Flechl[83], D. Fontes[43], S. Forte[84], P. Francavilla[85,86], E. Franco[67], R. Frederix[48], A. Freitas[87], F.F. Freitas[26], F. Frensch[33], S. Frixione[88], B. Fuks[71,72], E. Furlan[19], S. Gadatsch[56], J. Gao[42], Y. Gao[89], M.V. Garzelli[90], T. Gehrmann[36], R. Gerosa[9], M. Ghezzi[91], D. Ghosh[46], S. Gieseke[54], D. Gillberg[92], G.F. Giudice[56], E.W.N. Glover[30], F. Goertz[56], D. Gonçalves[30], J. Gonzalez-Fraile[44], M. Gorbahn[93], S. Gori[94], C.A. Gottardo[58], M. Gouzevitch[95], P. Govoni[96], D. Gray[29,97], M. Grazzini[36], N. Greiner[36], A. Greljo[36,98], J. Grigo[99], A.V. Gritsan[100], R. Gröber[62,30], S. Guindon[101], H.E. Haber[102], C. Han[103], T. Han[87], R. Harlander[34], M.A. Harrendorf[33], H.B. Hartanto[34], C. Hays[104], S. Heinemeyer[105,106,107], G. Heinrich[74], M. Herrero[47], F. Herzog[45], B. Hespel[6], V. Hirschi[73], S. Hoeche[73], S. Honeywell[108], S.J. Huber[26], C. Hugonie[109], J. Huston[110], A. Ilnicka[36,111], G. Isidori[36], B. Jäger[25], M. Jaquier[12], S.P. Jones[74], A. Juste[4,5], S. Kallweit[112], A. Kaluza[113], A. Kardos[114], A. Karlberg[20], Z. Kassabov[115,84], N. Kauer[116], D.I. Kazakov[117,33], M. Kerner[74], W. Kilian[118], F. Kling[119,55], K. Köneke[12], R. Kogler[120], R. Konoplich[29,97], S. Kortner[74], S. Kraml[121], C. Krause[50], F. Krauss[30], M. Krawczyk[22], A. Kulesza[122], S. Kuttimalai[30], R. Lane[123], A. Lazopoulos[19], G. Lee[124], P. Lenzi[125], I.M. Lewis[126], Y. Li[55], S. Liebler[2], J. Lindert[36], X. Liu[65], Z. Liu[55], F.J. Llanes-Estrada[68], H.E. Logan[92], D. Lopez-Val[6], I. Low[42,127], G. Luisoni[56], P. Maierhöfer [12], E. Maina[115], B. Mansoulié[128], H. Mantler[53,54], M. Mantoani[129], A.C. Marini[130], V.I. Martinez Outschoorn[52], S. Marzani[131], D. Marzocca[36], A. Massironi[132], K. Mawatari[121], J. Mazzitelli[81,133], A. McCarn[134], B. Mellado[135], K. Melnikov[99], S.B. Menari[136], L. Merlo[47], C. Meyer[137], P. Milenovic[56], K. Mimasu[26], S. Mishima[138], B. Mistlberger[56], S.-O. Moch[90], A. Mohammadi[139], P.F. Monni[20], G. Montagna[40], M. Moreno Llácer[129], N. Moretti[36], S. Moretti[15], L. Motyka[140], A. Mück[34], M. Mühlleitner[54], S. Munir[141], P. Musella[111], P. Nadolsky[142], D. Napoletano[30], M. Nebot[41], C. Neu[143], M. Neubert[112], R. Nevzorov[144,145], O. Nicrosini[57], J. Nielsen[102], K. Nikolopoulos[146], J.M. No[26], C. O'Brien[116], T. Ohl[69], C. Oleari[96], T. Orimoto[132], D. Pagani[6], C.E. Pandini[85], A. Papaefstathiou[56], A.S. Papanastasiou[147], G. Passarino[115], B.D. Pecjak[30], M. Pelliccioni[7], G. Perez[54], L. Perrozzi[111], F. Petriello[148,42], G. Petrucciani[56], E. Pianori[28], F. Piccinini[57], M. Pierini[56], A. Pilkington[136], S. Plätzer[30,136], T. Plehn[44], R. Podskubka[54], C.T. Potter[149], S. Pozzorini[36], K. Prokofiev[39,150], A. Pukhov[151], I. Puljak[152], M. Queitsch-Maitland[136], J. Quevillon[153], D. Rathlev[2], M. Rauch[54], E. Re[27], M.N. Rebelo[43], D. Rebuzzi[40], L. Reina[108], C. Reuschle[108], J. Reuter[2], M. Riembau[5,2], F. Riva[56], A. Rizzi[154], T. Robens[155], R. Röntsch[99], J. Rojo[20], J.C. Romão[43], N. Rompotis[156], J. Roskes[100], R. Roth[54], G.P. Salam[56], R. Salerno[157], R. Santos[158,159], V. Sanz[26], J.J. Sanz-Cillero[47], H. Sargsyan[36], U. Sarica[100], P. Schichtel[30], J. Schlenk[74], T. Schmidt[12], C. Schmitt[113], M. Schönherr[36], U. Schubert[74], M. Schulze[56], S. Sekula[142], M. Sekulla[54], E. Shabalina[129], H.S. Shao[56], J. Shelton[52], C.H. Shepherd-Themistocleous[16], S.Y. Shim[2], F. Siegert[155], A. Signer[160,36], J.P. Silva[43], L. Silvestrini[67], M. Sjodahl[161], P. Slavich[162,72], M. Slawinska[45], L. Soffi[163], M. Spannowsky[30],

C. Speckner[12], D.M. Sperka[164], M. Spira[91], O. Stål[165], F. Staub[56], T. Stebel[140], T. Stefaniak[102], M. Steinhauser[99], I.W. Stewart[130], M.J. Strassler[166], J. Streicher[54], D.M. Strom[149], S. Su[119], X. Sun[17], F.J. Tackmann[2], K. Tackmann[2], A.M. Teixeira[167], R. Teixeira de Lima[132], V. Theeuwes[131], R. Thorne[168], D. Tommasini[169], P. Torrielli[115], M. Tosi[56], F. Tramontano[170], Z. Trócsányi[114], M. Trott[171], I. Tsinikos[6], M. Ubiali[147], P. Vanlaer[49], W. Verkerke[45], A. Vicini[84], L. Viliani[125], E. Vryonidou[6], D. Wackeroth[131], C.E.M. Wagner[172,42], J. Wang[164], S. Wayand[33], G. Weiglein[2], C. Weiss[2,118], M. Wiesemann[36], C. Williams[131], J. Winter[110], D. Winterbottom[8], R. Wolf[33], M. Xiao[100], L.L. Yang[173,174,60], R. Yohay[108], S.P.Y. Yuen[175], G. Zanderighi[56,20], M. Zaro[71,72], D. Zeppenfeld[54], R. Ziegler[72], T. Zirke[74], and J. Zupan[94]

[1] International Center for Advanced Studies, UNSAM, 1650 Buenos Aires, Argentina
[2] DESY, 22607 Hamburg, Germany
[3] Institut für Physik, Humboldt-Universität zu Berlin, 12489 Berlin, Germany
[4] Institució Catalana de Recerca i Estudis Avançats, 08010 Barcelona, Spain
[5] Institut de Física d'Altes Energies, Barcelona Institute of Science and Technology (BIST), 08193 Bellaterra, Barcelona, Spain
[6] Centre for Cosmology, Particle Physics and Phenomenology (CP3), Université catholique de Louvain, 1348 Louvain-la-Neuve, Belgium
[7] INFN Sezione di Torino, 10125 Torino, Italy
[8] High Energy Physics Group, Blackett Lab., Imperial College, SW7 2AZ London, UK
[9] University of California San Diego, CA 92093, USA
[10] University of Toronto, Toronto, ON M5S 1A7, Canada
[11] TRIUMF, Vancouver, BC V6T 2A3, Canada
[12] Physikalisches Institut, Albert-Ludwigs-Universität Freiburg, 79104 Freiburg, Germany
[13] LAL, Université de Paris-Sud, 91405 Orsay, France
[14] University of Bristol, Bristol BS8 1TL, UK
[15] School of Physics and Astronomy, University of Southampton, Highfield SO17 1BJ, UK
[16] Rutherford Appleton Laboratory, Didcot OX110QX, UK
[17] Institute of High Energy Physics, Beijing 100049, China
[18] DAMTP, CMS, University of Cambridge, CB3 0WA Cambridge, UK
[19] Institute for Theoretical Physics, Physics Department, ETH Zürich, 8093 Zurich, Switzerland
[20] Rudolf Peierls Centre for Theoretical Physics, University of Oxford, OX1 3NP Oxford, UK
[21] Higgs Centre for Theoretical Physics, School of Physics and Astronomy, University of Edinburgh, EH9 3JZ Edinburgh, Scotland, UK
[22] Institute of Theoretical Physics, Faculty of Physics, University of Warsaw, 02-093 Warsaw, Poland
[23] Berkeley Center for Theoretical Physics, Department of Physics, University of California, Berkeley, CA 94720, USA
[24] Lawrence Berkeley National Laboratory, Berkeley, CA 94720, USA
[25] Institute for Theoretical Physics, University of Tübingen, 72076 Tübingen, Germany
[26] Department of Physics and Astronomy, University of Sussex, BN1 9QH Brighton, UK
[27] LAPTh, Université Savoie Mont Blanc, CNRS, 74941 Annecy-le-Vieux, France
[28] Department of Physics, University of Warwick, CV4 7AL Warwick, UK
[29] Department of Physics, New York University, New York, NY 10003, USA
[30] Institute for Particle Physics Phenomenology, Department of Physics, Durham University, Durham DH1 3LE, UK
[31] National Research Nuclear University MEPhI (Moscow Engineering Physics Institute), 115409 Moscow, Russia
[32] Physikalisches Institut der Rheinische Friedrich-Wilhelms-Universität Bonn, 53115 Bonn, Germany
[33] Institut für Experimentelle Kernphysik, Karlsruhe Institute of Technology, 76128 Karlsruhe, Ger-

many
[34] Institut für Theoretische Teilchenphysik und Kosmologie, RWTH Aachen University, 52056 Aachen, Germany
[35] University of Agder, 4604 Kristiansand, Norway
[36] Physik-Institut, Universität Zürich, 8057 Zurich, Switzerland
[37] Department of Physics, The Chinese University of Hong Kong, Shatin, Hong Kong
[38] Department of Physics, The University of Hong Kong, Hong Kong
[39] Department of Physics, The Hong Kong University of Science and Technology, Hong Kong
[40] Dipartimento di Fisica, Università di Pavia, and INFN, Sezione di Pavia, 27100 Pavia, Italy
[41] Departamento de Física Teórica and IFIC, Universitat de València-CSIC, 46100 Burjassot, Spain
[42] High Energy Physics Division, Argonne National Laboratory, Argonne, IL 60439, USA
[43] Departamento de Física and CFTP, Instituto Superior Técnico, Universidade de Lisboa, 1049-001 Lisboa, Portugal
[44] Institut für Theoretische Physik, Universität Heidelberg, 69120 Heidelberg, Germany
[45] Nikhef, Science Park 105, 1098 XG Amsterdam, The Netherlands
[46] Department of Particle Physics and Astrophysics, Weizmann Institute of Science, 7610001 Rehovot, Israel
[47] Departamento de Física Teórica and Instituto de Física Teórica, IFT-UAM/CSIC, Universidad Autónoma de Madrid, Cantoblanco, 28049 Madrid, Spain
[48] Technische Universität München, 85748 Garching, Germany
[49] Université Libre de Bruxelles, Service de physique des particules élémentaires, 1050 Bruxelles, Belgium
[50] Ludwig-Maximilians-Universität München, Fakultät für Physik, Arnold Sommerfeld Center for Theoretical Physics, 80333 München, Germany
[51] CPPM, Université Aix-Marseille, 13288 Marseille, France
[52] Department of Physics, University of Illinois at Urbana-Champaign, Urbana, IL 61801, USA
[53] Institute for Nuclear Physics, Karlsruhe Institute of Technology, 76344 Eggenstein-Leopoldshafen, Germany
[54] Institute for Theoretical Physics, Karlsruhe Institute of Technology, 76128 Karlsruhe, Germany
[55] Theoretical Physics Department, Fermilab, Batavia, IL 60510, USA
[56] CERN, 1211 Geneva 23, Switzerland
[57] INFN, Sezione di Pavia, 27100 Pavia, Italy
[58] Dipartimento di Fisica e Astronomia, Università di Padova and INFN, Sezione di Padova, 35131 Padova, Italy
[59] IPHC, Université de Strasbourg, CNRS/IN2P3, 67037 Strasbourg, France
[60] Center for High Energy Physics, Peking University, Beijing 100871, China
[61] Illinois State University, Normal, IL 61790, USA
[62] INFN, Sezione di Roma Tre, 00146 Roma, Italy
[63] Institut de Théorie des Phénomènes Physiques, EPFL, 1015 Lausanne, Switzerland
[64] ARC CoEPP, University of Melbourne, Victoria 3010, Australia
[65] Maryland Center for Fundamental Physics, Department of Physics, University of Maryland, MD 20742, USA
[66] Brookhaven National Laboratory, Upton, NY 11973, USA
[67] INFN, Sezione di Roma, 00185 Roma, Italy
[68] Departamento de Física Teórica I, Universidad Complutense, 28040-Madrid. Spain
[69] Institut für Theoretische Physik und Astrophysik, 97074 Würzburg, Germany
[70] Università degli Studi di Roma Tre and INFN,Sezione di Roma Tre, 00146 Roma, Italy
[71] Sorbonne Universités, Université Pierre et Marie Curie Paris 06, LPTHE, 75005 Paris, France
[72] CNRS, UMR 7589, LPTHE, 75005, Paris France
[73] SLAC National Accelerator Laboratory, Menlo Park, CA 94025, USA

[74] Max-Planck-Institut für Physik, 80805 München, Germany
[75] LPT, UMR 8627, CNRS, Université de Paris-Sud, Université Paris-Saclay, 91405 Orsay, France
[76] SUPA, School of Physics and Astronomy, University of Glasgow, G12 8QQ Glasgow, UK
[77] Institute of Cosmos Sciences, Universitat de Barcelona, 08028 Barcelona, Spain
[78] Dipartimento di Fisica, Universit'a di Milano and INFN, Sezione di Milano, 20133 Milan, Italy
[79] New York City College of Technology, Brooklyn, NY 11201, USA
[80] The Graduate School and University Center, The City University of New York, New York, NY 10016 USA
[81] Departamento de Física, FCEyN, Universidad de Buenos Aires, Capital Federal, Argentina
[82] Department of Mathematics, Statistics, and Physics, Wichita State University, Wichita, KS 67206, USA
[83] Institute of High Energy Physics, Austrian Academy of Sciences, 1050 Wien, Austria
[84] Tif Lab, Dipartimento di Fisica, Università di Milano, and INFN, Sezione di Milano, 20133 Milano, Italy
[85] LPNHE, Université Pierre et Marie Curie and Université Paris-Diderot, 75005 Paris, France
[86] Institut Lagrange de Paris, Université Pierre et Marie Curie, 75005 Paris, France
[87] Department of Physics and Astronomy, University of Pittsburgh, Pittsburgh, PA 15260, USA
[88] INFN, Sezione di Genova, 16146 Genova, Italy
[89] Department of Physics, University of Liverpool, L69 7ZE Liverpool, UK
[90] II. Institut für Theoretische Physik, Universität Hamburg, 22761 Hamburg, Germany
[91] Paul Scherrer Institut, 5323 Villigen PSI, Switzerland
[92] Physics Department, Carleton University, Ottawa, ON K1S 5B6 Canada
[93] Department of Mathematical Sciences, University of Liverpool, L69 7ZL Liverpool, UK
[94] Department of Physics, University of Cincinnati, Cincinnati, OH 45221, USA
[95] Université de Lyon, Université Claude Bernard Lyon 1, CNRS-IN2P3, IPNL, 69622 Villeurbanne, France
[96] Università Milano-Bicocca and INFN, Sezione di Milano-Bicocca, 20126 Milano, Italy
[97] Physics Department, Manhattan College, Riverdale, New York, NY 10471, USA
[98] Faculty of Science, University of Sarajevo, 71000 Sarajevo, Bosnia and Herzegovina
[99] Institute for Theoretical Particle Physics, Karlsruhe Institute of Technology, 76128 Karlsruhe, Germany
[100] Department of Physics and Astronomy, Johns Hopkins University, Baltimore, MD 21218, USA
[101] Physics Department, SUNY Albany, Albany, NY 12222, USA
[102] Santa Cruz Institute for Particle Physics (SCIPP) and Department of Physics, University of California, Santa Cruz, CA 95064, USA
[103] Kavli IPMU (WPI), UTIAS, University of Tokyo, Kashiwa, 277-8583, Japan
[104] Department of Physics, Oxford University, OX1 3RH Oxford, UK
[105] Instituto de Física Teórica, IFT-UAM/CSIC, Universidad Autónoma de Madrid, Cantoblanco, 28049 Madrid, Spain
[106] Campus of International Excellence UAM+CSIC, Cantoblanco, 28049 Madrid, Spain
[107] Instituto de Física de Cantabria (CSIC/UC), 39005 Santander, Spain
[108] Physics Department, Florida State University, Tallahassee, FL 32306, USA
[109] LUPM, UMR 5299, CNRS, Université de Montpellier, 34095 Montpellier, France
[110] Department of Physics and Astronomy, Michigan State University, East Lansing, MI 48824, USA
[111] Institute for Particle Physics, Physics Department, ETH Zürich, 8093 Zurich, Switzerland
[112] PRISMA Cluster of Excellence, Johannes Gutenberg University, 55099 Mainz, Germany
[113] Institut für Physik, Johannes Gutenberg-Universität, 55099 Mainz, Germany
[114] University of Debrecen and MTA-DE Particle Physics Research Group, 4002 Debrecen, Hungary
[115] Dipartimento di Fisica, Università di Torino, INFN Sezione di Torino, 10125 Torino, Italy
[116] Department of Physics, Royal Holloway, University of London, Egham Hill, Egham TW20 0EX,

UK
[117] Bogoliubov Laboratory of Theoretical Physics, Joint Institute for Nuclear Research, 141980 Dubna, Moscow Region, Russia
[118] Department of Physics, University of Siegen, 57068 Siegen, Germany
[119] Department of Physics, University of Arizona, Tucson, AZ 85721, USA
[120] Institut für Experimentalphysik, Universität Hamburg, 22761 Hamburg, Germany
[121] LPSC, Université Grenoble-Alpes, CNRS/IN2P3, 38026 Grenoble, France
[122] Institute for Theoretical Physics, WWU Münster, 48149 Münster, Germany
[123] High Energy Physics Group, Blackett Laboratory, Imperial College, SW7 2AZ London, UK
[124] Physics Department, Technion, Haifa 32000, Israel
[125] Università and INFN, Sezione di Firenze, 50019 Firenze, Italy
[126] Department of Physics and Astronomy, University of Kansas, Lawrence, KS 66045, USA
[127] Department of Physics and Astronomy, Northwestern University, Evanston, IL 60208, USA
[128] CEA IRFU-SPP, 91191 Gif-sur-Yvette, France
[129] II.Physikalisches Institut Universität Goettingen 37077 Germany
[130] CTP, MIT, Cambridge, MA 02139, USA
[131] Department of Physics, University at Buffalo, The State University of New York, Buffalo, NY 14260, USA
[132] Department of Physics, Northeastern University, Boston, MA 02115, USA
[133] International Center for Advanced Studies, UNSAM, 1650 Buenos Aires, Argentina
[134] Department of Physics, The University of Michigan, Ann Arbor, MI 48104, USA
[135] University of the Witwatersrand, School of Physics, Private Bag 3, Wits 2050, South Africa
[136] School of Physics and Astronomy, University of Manchester, Manchester, M13 9PL, UK
[137] Department of Physics, University of Pennsylvania, Philadelphia, PA 19104, USA
[138] Theory Center, Institute of Particle and Nuclear Studies, KEK, Tsukuba, 305-0801, Japan
[139] Kansas State University, Manhattan, KS, 66506, USA
[140] M. Smoluchowski Institute of Physics, Jagiellonian University, Krakow, 30-348 Poland
[141] KIAS, Seoul 130-722, Republic of Korea
[142] Department of Physics, Southern Methodist University, Dallas, TX 75275, USA
[143] University of Virginia, Charlottesville, VA 22903, USA
[144] ARC Centre of Excellence for Particle Physics at the Terascale and CSSM, Department of Physics, The University of Adelaide, Adelaide SA 5005, Australia
[145] Institute for Theoretical and Experimental Physics, Moscow 117218, Russia
[146] University of Birmingham, Birmingham B15 2TT, UK
[147] University of Cambridge, The Cavendish Laboratory, CB3 0HE Cambridge, UK
[148] Department of Physics and Astronomy, Northwestern University, Evanston, IL 60208, USA
[149] Center for High Energy Physics, University of Oregon, Eugene, OR 97403, USA
[150] HKUST Jockey Club Institute for Advanced Study, Hong-Kong
[151] Lomonosov Moscow State University, Skobeltsyn Institute of Nuclear, Moscow 119992, Russia
[152] University of Split, 21000 Split, Croatia
[153] King's College London, WC2R 2LS London, UK
[154] Dipartimento di Fisica Università di Pisa, and INFN, Sezione di Pisa, 56100 Pisa, Italy
[155] Institut für Kern- und Teilchenphysik, TU Dresden, 01069 Dresden, Germany
[156] University of Washington, Physics Department, Seattle WA 98195, USA
[157] LLR, IN2P3-CNRS, École Polytechnique, 91128 Palaiseau, France
[158] ISEL - Instituto Superior de Engenharia de Lisboa, Instituto Politécnico de Lisboa, 1959-007 Lisboa, Portugal
[159] Centro de Física Teórica e Computacional, Faculdade de Ciências, Universidade de Lisboa, 1749-016 Lisboa, Portugal
[160] Paul Scherrer Institut, 5232 Villigen PSI, Switzerland

[161] Department of Astronomy and Theoretical Physics, Lund University, 22362 Lund, Sweden
[162] Sorbonne Universités, UPMC Univ. Paris 06, LPTHE, 75005 Paris, France
[163] Cornell University, Ithaca, NY 14850, USA
[164] University of Florida, Gainesville, FL 32611, USA
[165] The Oskar Klein Centre, Department of Physics, Stockholm University, 106 91 Stockholm, Sweden
[166] Department of Physics, Harvard University, Cambridge, MA 02138, USA
[167] LPC, CNRS/IN2P3 UMR 6533, 63171 Aubière, France
[168] University College London, WC 1E 6BT London, UK
[169] Institute of Nuclear and Particle Physics, NCSR Demokritos, 15310 Agia Paraskevi, Greece
[170] Dipartimento di Fisica "E. Pancini", Università di Napoli Federico II and INFN, Sezione di Napoli, 80126 Napoli, Italy
[171] Niels Bohr International Academy, University of Copenhagen, Blegdamsvej 17, 2100 Copenhagen, Denmark
[172] Enrico Fermi Institute, Kavli Institute for Cosmological Physics, University of Chicago, Chicago, IL 60637, USA
[173] School of Physics and State Key Laboratory of Nuclear Physics and Technology, Peking University, Beijing 100871, China
[174] Collaborative Innovation Center of Quantum Matter, Beijing 100084, China
[175] Physikalisches Institut der Universität Bonn, 53115 Bonn, Germany

Contents

[1] M. Grazzini, R. Harlander, B. Mellado, P. Musella (Eds.)

[2] M. Chen, A. David, M. Dührssen, A. Falkowski, C. Hays, G. Isidori (Eds.)

[3] M. Chen, A. David, M. Dührssen, A. Falkowski, M. Grazzini, R. Harlander, C. Hays, G. Isidori, B. Mellado, P. Musella (Eds.)

[4] I. Low, M. Mühlleitner, M. Pelliccioni, N. Rompotis, R. Wolf (Eds.)

Introduction

D. de Florian, C. Grojean, F. Maltoni, C. Mariotti, A. Nikitenko,
M. Pieri, P. Savard, M. Schumacher, R. Tanaka

The observation by the ATLAS and CMS collaborations in 2012 of a new particle with properties compatible with the Higgs boson predicted by the Standard Model [1,2] was a major breakthrough in particle physics and an unprecedented advance in the understanding of the dynamics at the origin of the breaking of the electroweak symmetry. Following the end of data-taking in 2012, a vast programme aimed at characterizing the new particle was undertaken: the full LHC Run 1 datasets collected by both experiments were reanalysed with updated detector calibrations, and improved reconstruction and analysis techniques. The published Run 1 results cover the main production and decay channels expected of the SM Higgs boson, along with the spin and CP properties of the new particle [3, 4], and precision measurements of its mass [5]. More recently, a combination of the ATLAS and CMS measurements was performed [6]. The combined results feature clear observations of the Higgs boson decay to the bosonic channels, the observation of the decay to tau leptons, and of the weak boson production mode. Overall, the results are consistent with the predictions of the Standard Model, see Figure 1. In parallel, searches for an extended Higgs sector were performed covering many Beyond the Standard Model (BSM) scenarios. No significant evidence of a signal was observed.

In 2015, the LHC started to collide protons at the higher centre of mass energy of 13 TeV. The cross sections for the SM production modes increase by a factor of approximately two to four, depending on the process, and the anticipated integrated luminosity for Run 2 which is scheduled to end in 2018 is of the order of 120 fb^{-1} per experiment. Such a dataset will allow ATLAS and CMS to reduce the current experimental uncertainties significantly, motivating the need for improved theoretical predictions. For BSM Higgs physics, the higher collision energy will increase substantially the reach of searches for BSM Higgs bosons in the high mass regime and the larger dataset will improve the sensitivity of searches for exotic decays of the 125 GeV Higgs boson. New benchmarks and updated calculations will facilitate the exploration of this newly accessible BSM parameter space.

This report presents improved predictions for the production and decay of the Standard Model Higgs boson [7–9]. These include a gluon fusion production cross section at N3LO, updated and improved Parton Distribution Functions and correlation studies following the PDF4LHC prescriptions, fully differential VBF/VH NNLO QCD and NLO electroweak calculations, NLO electroweak corrections to the ttH processes in addition to studies of the ttV backgrounds. Differential NNLO+NNLL QCD calculations for the HH process are now available as well as the first NLO results with full top-quark mass dependence. Also first 2-loop NLO calculations for $gg \to VV$ below top-threshold with a massive quark have been achieved and they will be helpful for the study of the off-shell production of the Higgs boson.

For Higgs boson property measurements, the Interim framework for the analysis of Higgs couplings “kappa framework" [10] was used by the ATLAS and CMS experiments to report Higgs boson coupling related results extracted from the LHC Run 1 data [6]. The update information for Run 2 is provided elsewhere[1]. With the additional statistical power of the Run 2 dataset, the experiments will be able to measure more precisely the kinematic properties of the 125 GeV Higgs and use these measurements to probe for possible deviations induced by new phenomena. To do this, several strategies have been devised to maximize the sensitivity to BSM physics across channels and as a function of the integrated luminosity. These strategies will allow the experiments to extract more information from the data compared to the “kappa framework". To do this, pseudo-observables are defined as a possible alternative to more direct template, fiducial and differential cross section measurements. They will eventually be used as inputs to interpret the data in terms of Effective Field Theories (EFTs). Several Monte Carlo tools necessary to undertake this effort are being developed and made available, as described in this report.

[1] https://twiki.cern.ch/twiki/bin/view/LHCPhysics/LHCHXSWG2KAPPA

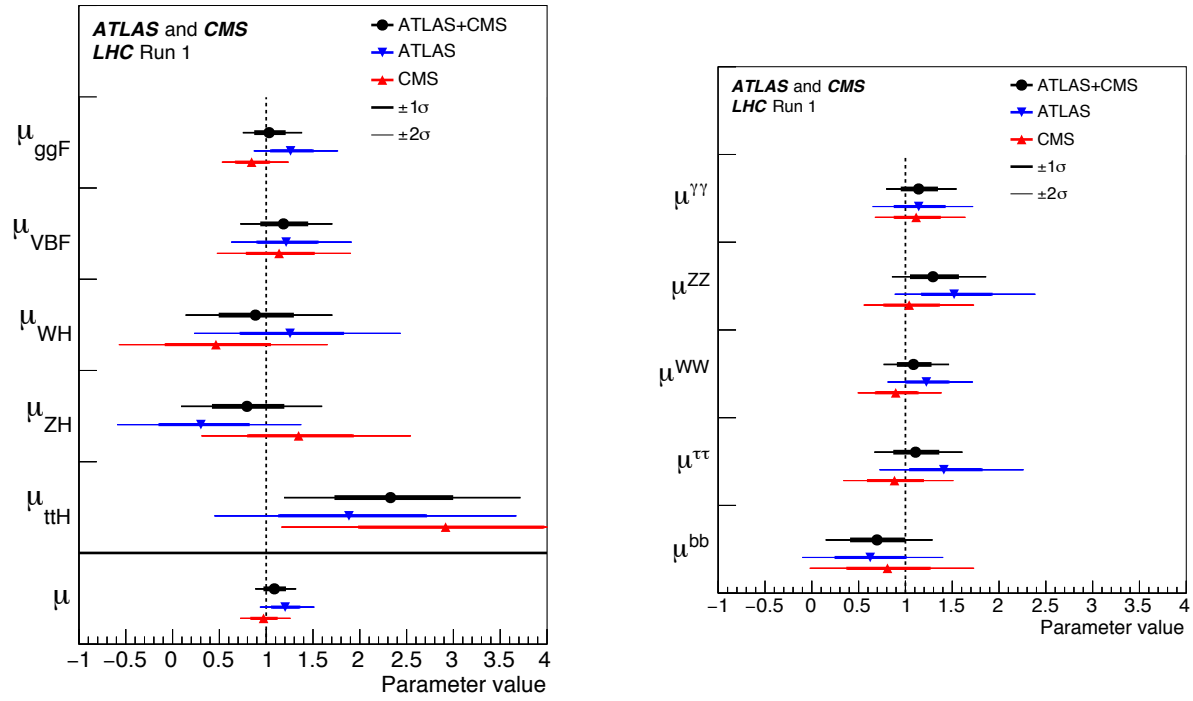

Figure 1: Best fit results for the production (left) and decay (right) signal strengths for the combination of ATLAS and CMS data [6]. The error bars indicate the 1σ (thick lines) and 2σ (thin lines) intervals. The combined results show a remarkable agreement with the SM prediction (normalized to $\mu = 1$).

In the search for new physics in the Higgs sector, this report proposes new benchmarks for the exploration of a BSM Higgs sector along with improved and extended calculations in various scenarios including the MSSM, the NMSSM, and more generic models featuring charged and neutral Higgs bosons. In addition, a new chapter on rare and exotic Higgs boson decays has been added and it covers rare mesonic decays, flavour-violating decays, prompt decays with and without missing energy, and decays into long-lived particles or with displaced vertices, and it provides recommendations on searches for exotic decays of the 125 GeV Higgs boson.

The updated and improved calculations of SM and BSM Higgs boson production and decay processes as reported here provide a solid theoretical reference for experimental studies of the early Run 2 data that are expected to decipher the properties of the 125 GeV Higgs boson and the nature of the full Higgs sector. In addition, they pave the way towards the theoretical developments and improvements in precision that will be needed in the future in order to fully exploit the potential of the complete Run 2 dataset.

Part I

Standard Model Predictions *

*M. Grazzini, R. Harlander, B. Mellado, P. Musella (Eds.)

Chapter I.1

Standard Model Parameters

A. Denner, S. Dittmaier, M. Grazzini, R. Harlander, R. Thorne, M. Spira, M. Steinhauser

We summarize the Standard Model input parameters for Higgs cross section calculations. The same parameters can be used for other SM and BSM processes at the LHC.

I.1.1 Lepton masses

The lepton masses from the PDG [11] are

$$m_e = 0.510998928 \pm 0.000000011 \text{ MeV}\,, \tag{I.1.1}$$
$$m_\mu = 105.6583715 \pm 0.0000035 \text{ MeV}\,, \tag{I.1.2}$$
$$m_\tau = 1776.82 \pm 0.16 \text{ MeV}\,. \tag{I.1.3}$$

I.1.2 Electroweak parameters

The gauge boson masses and widths from the PDG [11] are

$$m_W = 80.385 \pm 0.015 \text{ GeV}\,, \qquad \Gamma_W = 2.085 \pm 0.042 \text{ GeV}\,, \tag{I.1.4}$$
$$m_Z = 91.1876 \pm 0.0021 \text{ GeV}\,, \qquad \Gamma_Z = 2.4952 \pm 0.0023 \text{ GeV}\,. \tag{I.1.5}$$

The Fermi constant is

$$G_F = 1.1663787(6) \cdot 10^{-5} \text{ GeV}^{-2}\,. \tag{I.1.6}$$

These values correspond to the physical on-shell masses. If required, the complex pole masses can be obtained from the well-known relations

$$m_V^{\text{pole}} - i\Gamma_V^{\text{pole}} = \frac{m_V - i\Gamma_V}{\sqrt{1+\Gamma_V^2/m_V^2}}\,, \qquad V \in \{W, Z\}\,. \tag{I.1.7}$$

As for the gauge boson widths, instead of Γ_V^{pole} from (I.1.7), values consistent with the perturbative order can also be used if more appropriate.

I.1.3 QCD parameters and parton densities

The most important QCD parameters are the strong coupling α_s and the quark masses. The default renormalization scheme for these parameters should be the $\overline{\text{MS}}$ scheme. In this scheme, α_s and the quark masses depend on a mass scale μ.

$\alpha_s(\mu)$ and $m_q(\mu)$ are typically determined through their proper renormalization group equations,

$$\mu^2\frac{d}{d\mu^2}\alpha_s(\mu) = \alpha_s(\mu)\beta(\alpha_s)\,, \qquad \mu^2\frac{d}{d\mu^2}m_q(\mu) = m_q(\mu)\gamma_m(\alpha_s)\,, \tag{I.1.8}$$

combined with their numerical value at a reference mass scale, usually $\alpha_s(m_Z)$ and $m_q(m_q)$. The perturbative expansions of the coefficients $\beta(\alpha_s)$ and $\gamma_m(\alpha_s)$ are currently known through order α_s^4 [12, 13] and α_s^5, respectively [14].

Also the parton density functions depend on a mass scale $\mu_{\rm F}$,

$$\mu_{\rm F}^2 \frac{d}{d\mu_{\rm F}^2} \phi_i(x, \mu_{\rm F}) = P_{ij}(\alpha_s) \otimes \phi_j(x, \mu_{\rm F}) \,, \tag{I.1.9}$$

where P_{ij} are the splitting functions, currently known through order α_s^3 [15, 16], and $\otimes$ denotes the usual convolution. Note that in principle also $\mu_{\rm R}$ enters the PDFs implicitly through α_s. However, the available PDF sets assume $\mu_{\rm F} = \mu_{\rm R}$.

If the typical mass scale μ_0 of a process is not equal to the reference mass scale, the input quantities $\alpha_s(\mu_0)$ and $m_q(\mu_0)$ of a perturbative calculation have to be evaluated from their reference values by RG evolution. While 4-loop evolution may result in the most precise currently available results for the input parameters, consistency of the calculation often requires one to use lower order RG evolution.

I.1.3.a Strong coupling constant

The strong coupling α_s enters a typical theory prediction for an LHC observable in many different ways: explicitly as expansion parameter in the partonic calculation, or implicitly through its impact on other input quantities. These sources may be strongly correlated, so that inconsistencies in the input value $\alpha_s(\mu_0)$ have to be avoided. Specifically, the value of α_s used in the partonic process should coincide with the one corresponding to the parton density functions. This means that $\alpha_s(m_Z)$ as well as the RG running of α_s for the evaluation of $\alpha_s(\mu_0)$ have to be adjusted to the parton density functions that are used.

Concerning the default value for $\alpha_s(m_Z)$ and the estimation of the uncertainties resulting from $\alpha_s(m_Z)$ and the PDFs, one should follow the 2015 PDF4LHC recommendation. This amounts to choosing the central value of $\alpha_s(m_Z)$ and the ensuing uncertainty as

$$\alpha_s(m_Z) = 0.118 \pm 0.0015 \,. \tag{I.1.10}$$

I.1.3.b Quark masses

Quark masses (in particular charm and bottom) also enter the PDFs, albeit in a much weaker way as α_s. This releases one from a similar constraint as it was imposed for α_s.

Top-quark mass. The top quark is different from all other known quarks in the sense that it decays before it hadronizes. To a first approximation (i.e., neglecting soft QCD effects), the invariant mass of its decay products may be identified with the on-shell top quark mass. In fact, the agreement with the determination via the top quark pair production cross section justifies this with hindsight.

In order to be consistent with existing ATLAS and CMS analyses, we recommend to use

$$m_t^{\rm OS} = 172.5 \pm 1\,{\rm GeV} \tag{I.1.11}$$

as reference value for the on-shell top quark mass, corresponding to an $\overline{\rm MS}$ value of

$$m_t^{\overline{\rm MS}}(m_t) = 162.7 \pm 1\,{\rm GeV} \,, \tag{I.1.12}$$

where we used the four-loop conversion of Ref. [17]. Note that the recommended uncertainty of ± 1 GeV covers the current world average of $m_t^{\rm OS}\Big|_{\rm world\ ave} = 173.2\,{\rm GeV}$ (notice also Ref. [18]).

The calculation of radiative corrections may require to use the complex pole mass for the top quark. Due to the lack of experimental data for the top width, one should use the theoretical value for the top quark width in the conversion formula (the analogue of Eq. I.1.7), given by [19–25]

$$\Gamma_t = 0.89 \cdot \Gamma_t^{(0)} \,, \tag{I.1.13}$$

where

$$\Gamma_t^{(0)} = \frac{G_F m_t^3}{8\sqrt{2}\pi}\left[1 - 3\left(\frac{m_W^2}{m_t^2}\right)^2 + 2\left(\frac{m_W^2}{m_t^2}\right)^3\right]. \tag{I.1.14}$$

Bottom-quark mass. The situation is much different for the bottom quark mass, because its mass can only be determined indirectly. We recommend to use the current PDG value for the $\overline{\rm MS}$ bottom mass [11]

$$m_b(m_b) = 4.18 \pm 0.03 \text{ GeV} \tag{I.1.15}$$

as reference input value.[I.1] Evolution to the characteristic scale μ_0 of the process should be done through the highest available perturbative order. The inconsistency with the PDF value for the bottom quark mass introduced by this procedure is expected to be small, in particular if no initial-state b-quarks are involved. The uncertainty can be estimated by comparing the results when using PDFs built on different values of the b quark mass.

If the use of the on-shell bottom-quark mass cannot be avoided, the conversion of the $\overline{\rm MS}$ value should be done at the 3-loop level, and the difference to the 4-loop result should be used as the uncertainty. Using $\alpha_s(m_Z) = 0.118$ and $m_b(m_b) = 4.18\,\text{GeV}$, one obtains [17]

$$m_b^{\rm OS}\Big|_{4.18} = (4.18 + 0.40 + 0.20 + 0.14 + 0.13)\,\text{GeV}\,, \tag{I.1.16}$$

where the numbers correspond to consecutive loop orders. Our recommendation for the bottom quark pole mass is therefore obtained by considering the sum of the first four terms in Eq. (I.1.16), and assigning the last term as an uncertainty

$$m_b^{\rm OS} = 4.92 \pm 0.13\,\text{GeV}\,. \tag{I.1.17}$$

Charm-quark mass. The charm quark mass is at the edge of the validity range of perturbation theory. Therefore, using $m_c(m_c)$ as reference input value in order to derive the charm quark mass at a different scale, or its perturbative on-shell mass, would force one to apply perturbation theory at these rather low energies. We therefore recommend to use [26]

$$m_c(3\text{ GeV}) = 0.986 \pm 0.026\text{ GeV} \tag{I.1.18}$$

as overall input value. To be conservative, the error quoted in Ref. [26] has been multiplied by a factor of two here.

Concerning RG evolution and consistency with the charm quark mass in the PDFs, the situation is analogous to the case of the bottom quark (see above).

If the use of the on-shell charm-quark mass cannot be avoided, its mass should be evaluated from the on-shell bottom mass (calculated as described above) through the relation [27]

$$m_c^{\rm OS} = m_b^{\rm OS} - 3.41\,\text{GeV} = 1.51 \pm 0.13\,\text{GeV}\,. \tag{I.1.19}$$

I.1.4 Higgs boson mass

The current combination of the measurements of the Higgs boson mass m_H from ATLAS and CMS is [5]

$$m_H = 125.09 \pm 0.21(\text{stat.}) \pm 0.11(\text{syst.})\text{ GeV}\,. \tag{I.1.20}$$

As a reference value for m_H in theoretical calculations we recommend to use the rounded value

$$m_H = 125\text{ GeV}\,. \tag{I.1.21}$$

[I.1] The dependence of this value on α_s (see Ref. [26]) can usually be neglected.

Chapter I.2

Parton Distribution Functions

S. Forte, J. Huston, R. S. Thorne (Eds.); S. Carrazza, J. Gao, Z. Kassabov, P. Nadolsky, J. Rojo

I.2.1 The PDF4LHC recommendation

Previous Yellow Reports [7–9] have provided snapshots of the state-of-the-art for PDF determination, along with recommendations for PDF use, and for calculations of PDF uncertainties, following the guidance of the PDF4LHC group. In a previous recommendation [28], three PDF sets were used: CT10 [29], MSTW2008 [30] and NNPDF2.3 [31]. These were global PDF fits involving data from a variety of experiments, including collider data from the Tevatron. The uncertainty was provided by the envelope of all three PDF error sets, and the central prediction as mid-point of this envelope. This choice is conservative but not ideal, in that it tends to be dominated by error PDFs at the edge of the uncertainty band; it was adopted because it was felt that the degree of agreement of the PDF sets was not sufficient to warrant their statistical combination. Specifically, agreement was unsatisfactory for the gluon distribution, particularly in the region appropriate for Higgs boson production through gluon-gluon fusion. This disagreement prompted an intensive year-long study by the three global PDF groups, along with HERAPDF [32], but this did not uncover a clear explanation for the differences [33].

Prior to the writing of YR4, the major PDF groups have released updates to their PDF fits, at NLO and NNLO, including in most cases data from the LHC [34]. The new PDF4LHC recommendation [35] uses the updated PDFs from the three global PDF groups included in the previous recommendation: CT14 [36], MMHT14 [37] and NNPDF3.0 [38], respectively. Details as to why this choice was made can be found in the PDF4LHC document. The primary requirements are that the PDFs should be based on global datasets, be carried out in a general-mass variable flavour-number scheme, and have compatible values for the QCD coupling constant $\alpha_s(m_Z)$. As we shall see shortly, these new PDF sets are in good agreement, not only in the quark sector (where the agreement was satisfactory already in the previous generation of PDFs) but also for the gluon. The changes can be ascribed partially to the addition of new data sets used in the PDF fits, but primarily to improvements in the fitting formalisms. This level of agreement may change in detail with future updates, but generally the good level of agreement should stay. An alternative recommendation [39] is that all PDFs (ABM12 [40], CJ15 [41], CT14 [36], HERAPDF2.0 [32], JR14 [42], HERAPDF2.0 [32] MMHT14 [37], NNPDF3.0 [38]) and accompanying coupling and quark mass variation should be used for precision theory predictions and any `LHAPDF6` [43] PDF set for other predictions.

Currently, there are two different representations of PDF uncertainties: the Monte Carlo representation [44, 45] and the Hessian representation [46]. Both provide compatible descriptions of the PDF uncertainties, and recent developments have allowed for the straight-forward conversion of one representation to the other [47–49]. The use of the Monte Carlo representation makes possible a statistical combination of different PDF sets. If different PDF sets can be assured to be equally likely representations of the underlying PDF probability distribution, they can be combined simply by taking their un-weighted average. This can be arrived at by generating equal numbers of Monte Carlo replicas from each input PDF set, and then merging the replica sets. The NNPDF3.0 PDF set is naturally in this format. For the Hessian sets, CT14 and MMHT2014, the Monte Carlo replicas are generated by sampling along the eigenvector directions, assuming a Gaussian distribution.

Combinations in this manner are most appropriate when the PDF sets that are combined are compatible with each other, as CT14, MMHT2014 and NNPDF3.0 are. Such a combination also allows for a direct statistical interpretation of the resulting PDF uncertainties, unlike the envelope method. Monte

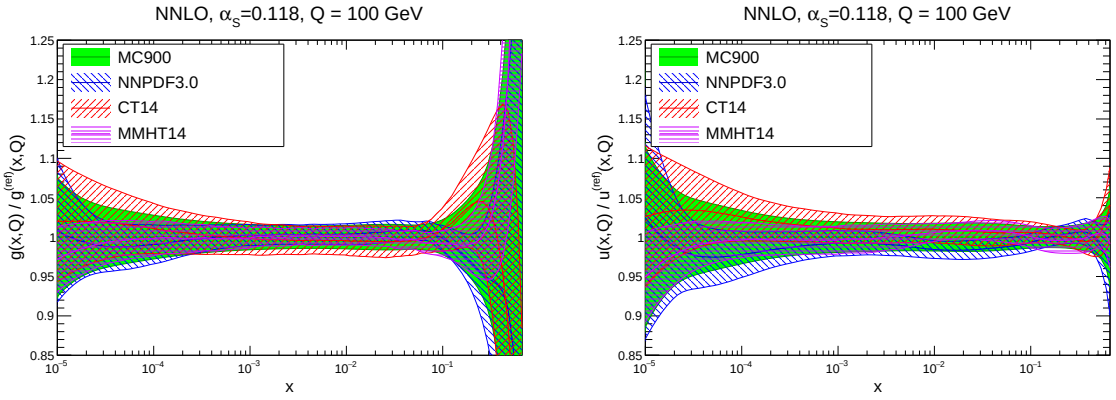

Figure 2: Comparison of the MC900 PDFs with the sets that enter the combination: CT14, MMHT14 and NNPDF3.0 at NNLO. We show the gluon and the up quark at $Q = 100$ GeV. Results are normalized to the central value of the prior set MC900.

Carlo combinations of these three PDFs have been provided at both NLO and NNLO by the PDF4LHC working group. In the following discussion we concentrate on NNLO; similar considerations apply to NLO.

It was determined that $N_{\rm rep} = 900$ Monte Carlo replicas, combining $N_{\rm rep} = 300$ replicas from each of the three individual PDF sets, were sufficient to represent the combined PDF probability distribution. In Figure 2 we show a comparison of the combined PDF4LHC15 NNLO set (indicated by MC900 in the plot) with the three sets that enter the combination, CT14, MMHT14 and NNPDF3.0. We show the gluon and the up quark at $Q = 100$ GeV, normalized to the central value of the PDF4LHC15 combination. In these plots, as in the rest of this chapter, we use a fixed value $\alpha_s(m_Z) = 0.118$.

It can be seen that in the "precision physics" region, roughly from $x \simeq 0.001$ to $x \simeq 0.1$, the PDFs from the three global sets agree reasonably well with each other, with perfect agreement for the gluon, and less good agreement for the up quark. This is reflected in the combined PDF4LHC15 set, constructed from the three input PDF sets. On the other hand, at low and high values of x, the uncertainty bands from the three PDF sets differ, and the uncertainty band for the 900 Monte Carlo replicas is smaller than the envelope of the three PDF uncertainty bands. These are regions in which PDFs are only weakly constrained by data, as seen by the increasingly large size of the uncertainty, and the inflated uncertainty in the combination appears to provides a reasonable estimate.

In Figure 3 we compare the NNLO PDF luminosities at the LHC 13 TeV computed using the prior set PDF4LHC15 NNLO, both to the three sets which were used for the previous PDF4LHC recommendation (CT10, MSTW08 and NNPDF2.3), and the three sets which enter the current combination CT14, MMHT14 and NNPDF3.0 NNLO. We show the gg and $q\bar{q}$ luminosities as a function of the invariant mass of the final state M_X, normalized to the central value of `PDF4LHC15_nnlo_prior`. The improvement in compatibility of the new sets in comparison to the old ones, especially in the gluon sector, is apparent, particularly in the precision mass region, say roughly 50 GeV to 1 TeV (more so for gg than for $q\bar{q}$). Reassuringly, even though uncertainty estimates differ somewhat between current sets, especially for quarks, central values of all sets in this region are in good agreement. Interestingly, they also agree well with the mid-point of the envelope of the old sets. Hence, in practice, in the precision region, the central prediction with the old prescription (the envelope of CT10, MSTW08, and NNPDF2.3) and the new prescription (the PDF4LHC15 combined set) are actually quite close.

There is more disagreement in the low mass region and in the high mass region, and the range of uncertainty for the 900 set Monte Carlo can be less than the envelope of the three PDF groups. This is not surprising, as the combined uncertainty band reflects the common trend of all input PDF ensembles, while the envelope unduly emphasizes extreme behaviour of a few replicas. While the combined

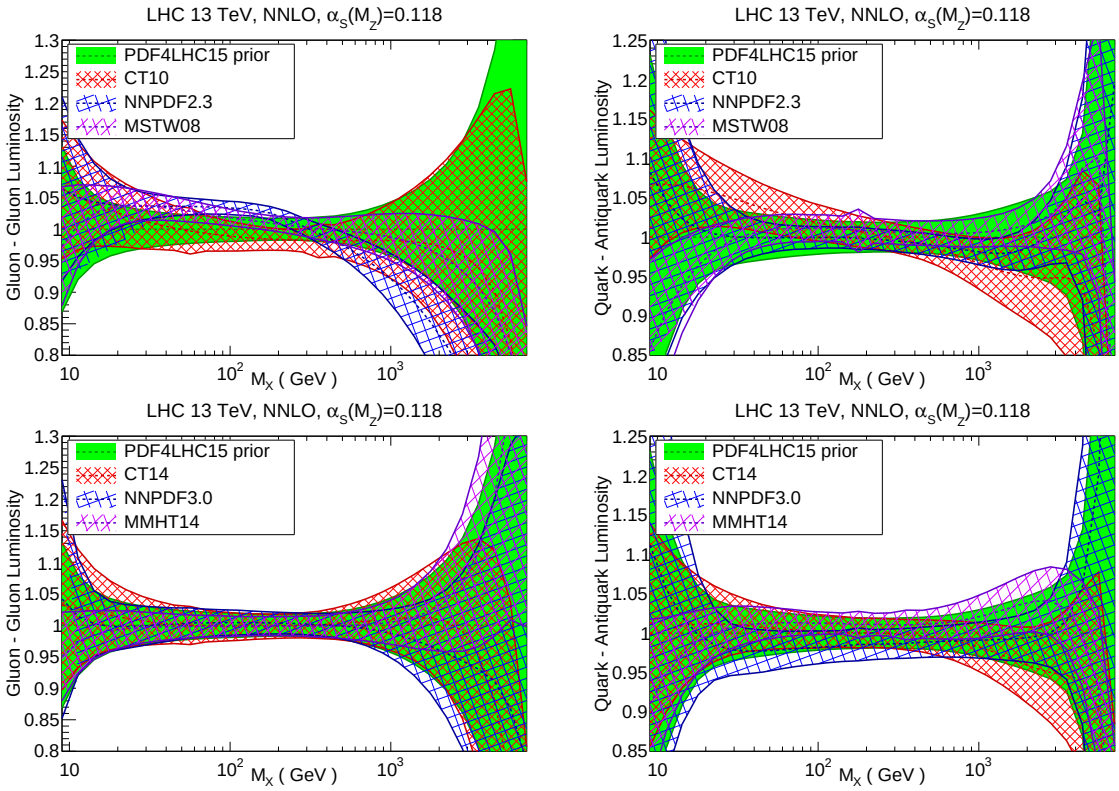

Figure 3: Comparison of NNLO parton luminosities at the LHC 13 TeV. Top: the PDF4LHC15 combined set compared to the CT10, MSTW08, and NNPDF2.3 PDF set whose envelope was used as a previous PDF4LHC recommendation. Bottom: the PDF4LHC15 combined set compared to the three individual sets which enter the combination: CT14, MMHT14 and NNPDF3.0. The gg (left) and the $q\bar{q}$ (right) luminosities are shown as a function of the invariant mass of the final state M_X, normalized to the central value of `PDF4LHC15_nnlo_prior`.

uncertainty appears to be conservative enough, this should be kept in mind especially in discussions of uncertainties of high-mass searches.

I.2.2 The PDF4LHC15 PDF sets

Although the $N_{\rm rep} = 900$ Monte Carlo set itself could be used to determine PDF uncertainties for any LHC process, it suffers from the drawback of having a very large number of PDFs in the set; also, for many applications the non-Hessian framework may be a further drawback. However, the most essential features of the PDF uncertainties can be captured using three techniques that significantly reduce the number of error PDFs needed, especially in view of the fact that there is an uncertainty in the determination of the PDF uncertainties (witness the differences between the PDF groups at low x and high x), and therefore very high precision is not justified in view of the limited accuracy.

Two of these techniques use the Hessian formalism, considering only symmetric PDF uncertainties, while the third technique uses a compressed Monte Carlo technique, which allows for asymmetric uncertainties. Details of the derivations are provided in the PDF4LHC document. Correspondingly, three delivery options are available for the combined sets:

– `PDF4LHC15_mc`: contains 100 PDFs, including non-Gaussian features, constructed using the CMC method [50].
– `PDF4LHC15_30`: contains 30 PDFs in a Hessian framework, determined using the META-PDF technique [48].
– `PDF4LHC15_100`: contains 100 PDFs in a Hessian framework, determined using the MC2H

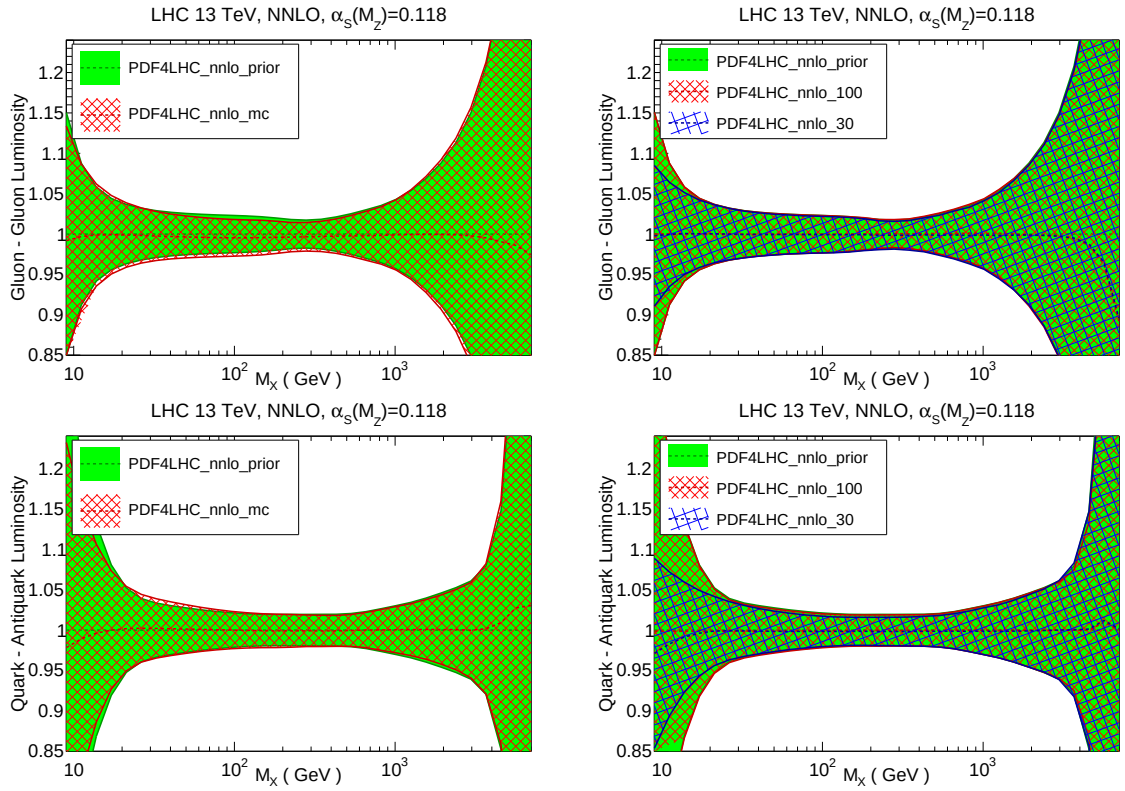

Figure 4: Comparison of parton luminosities at the LHC 13 TeV computed using the prior set `PDF4LHC15_nnlo_prior` with its compressed Monte Carlo representation, `PDF4LHC15_nnlo_mc` (left plots) and with its two Hessian sets, `PDF4LHC15_nnlo_100` and `PDF4LHC15_nnlo_30`. We show the gg (upper plots) and $q\bar{q}$ (lower plots) luminosities as a function of the invariant mass of the final state M_X, normalized to the central value of `PDF4LHC15_nnlo_prior`.

approach [49].

We will henceforth refer to the starting 900 replica Monte Carlo set as the "prior", from which these reduced sets are constructed: `PDF4LHC15_nnlo_prior`.

A central value of $\alpha_s(m_Z) = 0.118$ is used for each of these sets, at both NLO and NNLO, with an uncertainty of $\delta\alpha_s(m_Z) = 0.0015$ as recommended in the chapter on Standard Model parameters of this document. Therefore, for each option, individual error sets using $\alpha_s(m_Z) = 0.1165$ and 0.1195 are provided in order to be able to compute the uncertainty due to $\delta\alpha_s(m_Z)$ in LHC cross-sections, which should be added in quadrature with the PDF uncertainty [35]. It has been verified that addition in quadrature is a good enough approximation (in some cases exact) to the exact recipes for PDF and α_s combination provided by each group [51–53].

The gluon-gluon and quark-antiquark PDF luminosities as a function of the final-state invariant mass M_X at the LHC 13 TeV are shown in Figure 4, where we compare the prior set `PDF4LHC15_nnlo_prior` with its compressed Monte Carlo representation, `PDF4LHC15_nnlo_mc` and with the two Hessian reduced sets, `PDF4LHC15_nnlo_100` and `PDF4LHC15_nnlo_30`. Note that by construction the central values of the two Hessian reduced sets coincide with the central value of the prior, while the central value of the Monte Carlo set reproduces it within the precision of the compression (which is seen to be quite high). All reduced sets correctly reproduce the uncertainty band for the 900 PDF Monte Carlo prior in the precision mass region and as the high mass region, while the `PDF4LHC15_30` shows a certain loss in precision when reproducing uncertainties for the very low mass region.

The three techniques for delivering the PDF4LHC PDF uncertainties are attempts to match the

uncertainty bands produced from the prior, and not the bands from the three PDF groups *per se*. The degree of success is a measure of the precision of the three techniques for this purpose. It is therefore important not to confuse the precision of reproducing the prior with accuracy. The accuracy of the prior is not exactly known, especially at high and low mass, and the quoted PDF uncertainty represents only the best estimate by the PDF4LHC group.

I.2.3 Higgs boson production cross-sections

In Figure 5 we show representative inclusive Higgs boson production cross-sections in the relevant production channels at LHC with $\sqrt{s} = 13$ TeV: gluon-fusion, vector-boson fusion, associated production with a W boson, and associated production with a $t\bar{t}$ pair. These calculations have been performed with NLO matrix elements and NNLO PDFs, using `aMC@NLO` [54] interfaced to `aMCfast` [55] and `applgrid` [56], with the purpose of illustrating PDF uncertainties and also the relative difference between PDF sets. Indeed, since the NNLO/NLO K-factor is to a good approximation independent of PDFs, it should not affect the relative differences between the predictions of individual PDF sets. In this study, the Higgs bosons are left undecayed. No generation cuts are applied to Higgs bosons, jets or top quarks. The only selection cut that is applied is given by the fact that we assume that W and Z bosons decay leptonically, so the corresponding branching fraction is included and we require $p_T^l \geq 10$ GeV and $|\eta_l| \leq 2.5$ for the charged leptons from the weak boson decays. All uncertainties shown are pure PDF uncertainties, not including the uncertainty due to the value of α_s, which is fixed at $\alpha_s(m_Z) = 0.118$ for all cross-sections shown in the plot.

In each case, the predictions of the combined PDF4LHC15 prior and its three reduced versions, all normalized to the central value of the prior set, are shown along with the predictions from the sets which enter the combination, MMHT14, CT14 and NNPDF3.0. Predictions from the older global sets, MSTW08, CT10 and NNPDF2.3, which entered the previous prescription [28] are also shown for comparison. In particular, the better agreement for gluon-gluon fusion prediction using the new generation of PDFs (CT14, MMHT2014 and NNPDF3.0) compared to the older generation (CT10, MSTW08 and NNPDF2.3) is evident. In all cases, predictions using the reduced sets are in excellent agreement with those obtained using the prior.

In Figure 6 we show representative differential distributions for the Higgs boson production in gluon fusion, in particular the transverse momentum and rapidity distributions, at the LHC $\sqrt{s} = 13$ TeV, obtained using the three different deliveries of the combined set. The upper plots show the cross-section per bin, in pico-barns, while the lower plots show the corresponding results normalized to the central value of the PDF4LHC15 NNLO prior set. The three techniques agree well for these kinematic distributions, with a small offset for the predictions of the `PDF4LHC15_mc` set. Note that the transverse momentum distribution shown is a fixed-order result, and thus it is unreliable for $p_t \lesssim 30$ GeV where transverse momentum resummation effects become important.

I.2.4 Strong coupling and heavy quark masses

In order to estimate the further uncertainty due to the choice of α_s value it is useful to plot the cross-sections as a function of the value of $\alpha_s(m_Z)$. This is done in Figure 7, where the total inclusive cross-sections for Higgs boson production at $\sqrt{s} = 13$ TeV in different production channels are shown as a function of α_s for the three sets which enter the combination. In these plots we also include flavour predictions obtained using the ABM12 [40], HERAPDF2.0 [32] and JR14 [42] PDF sets, each at its preferred value of $\alpha_s(m_Z)$. In the case of ABM12, we use the $N_f = 5$ set. For HERAPDF2.0, we consider only the experimental PDF uncertainties. In the case of the JR14 set, we use the version determined in the variable-flavour-number scheme. Note that MMHT14, CT14, NNPDF3.0 and HERAPDF2.0 all use the same central value of the strong coupling, $\alpha_s(m_Z) = 0.118$; in the plot the values corresponding to these sets are slightly offset to improve readability. It is apparent from the figures which PDF sets

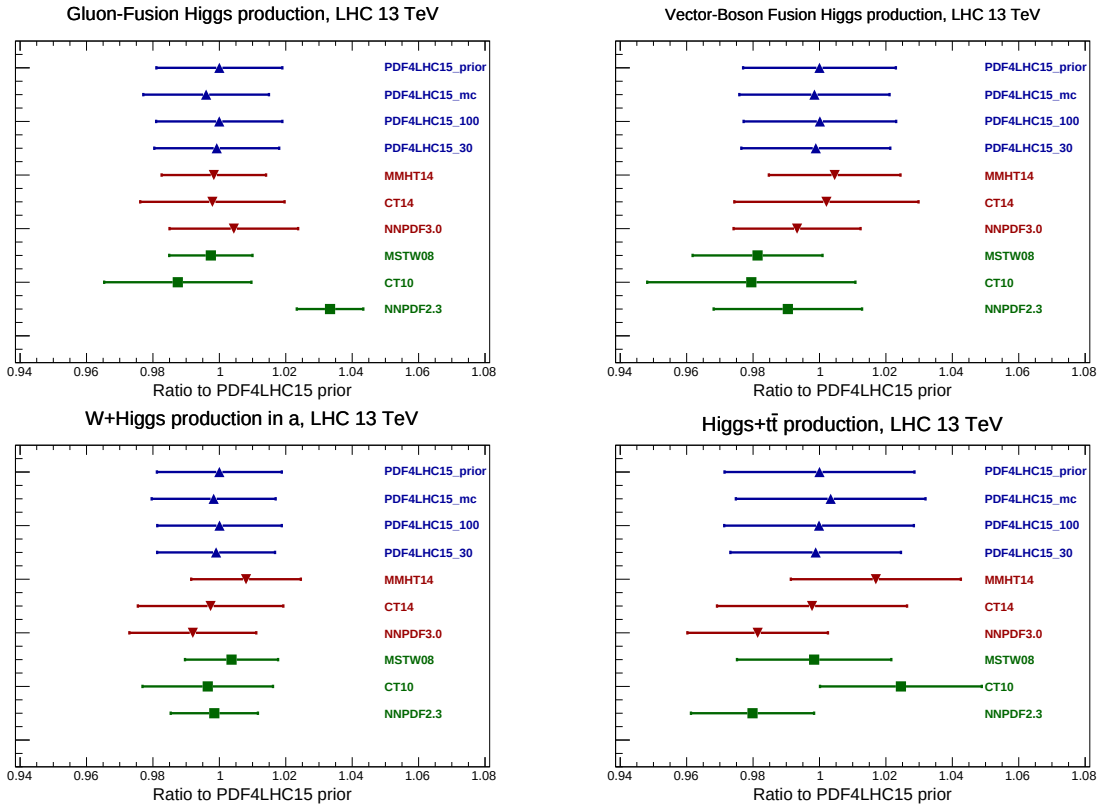

Figure 5: Inclusive Higgs boson production cross-sections at 13 TeV in the gluon-fusion, vector-boson fusion, associated production with W and associated production with a $t\bar{t}$ pair channels. In each case predictions of the three individual sets are shown along with those of the PDF4LHC15 prior and the three reduced sets, normalizing to the central value of the PDF4LHC15 prior set. Predictions obtained using the three older global sets which entered the previous PDF4LHC recommendation are also show. All cross-sections are computed at NLO with NNLO PDFs. The value of the strong coupling is fixed at $\alpha_s(m_Z) = 0.118$; the uncertainties shown are PDF uncertainties (not including the uncertainty due to $\alpha_s(m_Z)$).

can produce predictions that may fall substantially outside of the uncertainties of the three PDF sets that enter the 2015 combination.

Unlike the case for the strong coupling $\alpha_s(M_Z)$, the different PDF groups do not use common values of the charm and bottom masses, and also use different definitions of a general mass variable number scheme (GM-VFN). These are two distinct issues, particularly since each group chooses the quark masses at fixed default values, as opposed to trying to determine them from a best fit, and the values chosen have no relation to the scheme choice.

Let us consider the issue of scheme choices first. Dependence on these has been very thoroughly studied in numerous articles [33, 57–60]. At NLO the variation in LHC cross section predictions for W and Z production due to quite extreme differences in choices of GM-VFN schemes can be of order $2-3\%$; they may be somewhat larger but still moderate especially at high scale for processes which are directly sensitive to charm, such as $Z+c$ or open charm production. However, as with other scheme choices in QCD, the ambiguity at fixed order is always an effect beyond the order of the calculation, and hence diminishes as one goes to higher orders. At NNLO scheme choices lead to changes in LHC cross section predictions of generally no more than 1%, and very often less. This can be appreciated from Figs. 11.6, 11.7 and 11.8 in [33], where differences between groups for the total HERA cross sections calculated using the same PDFs but different schemes can be at most $> 5\%$ at NLO, but never more than $1-2\%$ at NNLO. Differences in $F_2^{\bar{c}c}(x,Q^2)$, an observable which is directly sensitive to charm, which is

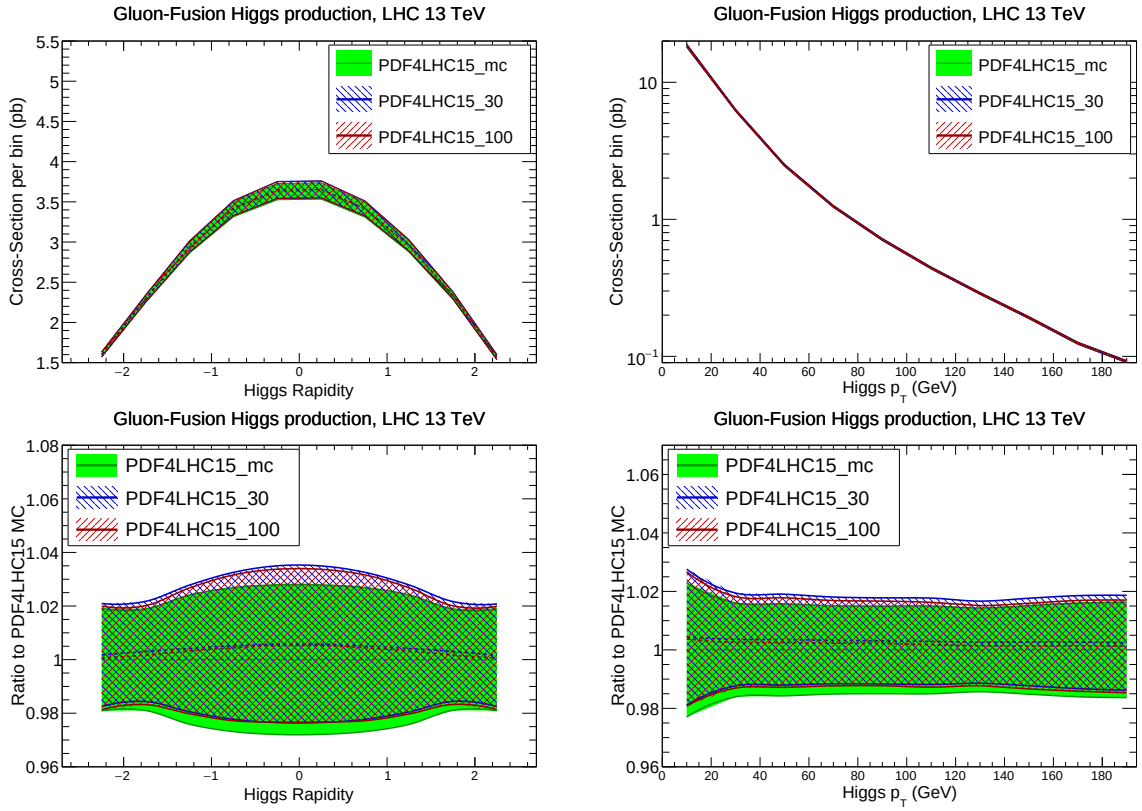

Figure 6: Differential distributions for Higgs boson production at gluon fusion at $\sqrt{s} = 13$ TeV. The Higgs boson rapidity (left) and transverse momentum (right) distributions are shown, using the three different deliveries of the combined PDF4LHC15 set. The upper plots show the absolute distributions, while in the lower plot results are normalized to the central value of the `PDF4LHC15_mc` set. Cross-sections have been computed at NLO with NNLO PDFs.

much less precisely and widely measured at HERA, can be 30% in extreme cases at NLO but are rarely more than 10% at NNLO, and over most of the x, Q^2 range are much less than 5%. Hence, the variation due to the choice of GM-VFN scheme at NNLO is much less than the PDF uncertainty, and the variation between groups due to this can be taken as indicative of part on the theoretical uncertainty at NNLO. The variation due to adopting a FFN scheme would instead be quite large, and outside the PDF uncertainty.

The different PDFs used in the recommendation are all obtained using the heavy quarks defined in the pole mass scheme. However, the values chosen are different, with m_c ranging from 1.275–1.4 GeV and m_b from 4.18–4.75 GeV. The precise determinations of quark masses are performed in the $\overline{\text{MS}}$ scheme, and the conversion to the pole masses is imprecise due to a renormalon ambiguity in the conversion factor. In particular, the series for the charm quark shows essentially no convergence. Using the better behaved expression for the beauty mass, and the fact that $m_b^{\text{pole}} - m_c^{\text{pole}} = 3.4$ GeV with a very small uncertainty [27, 61], it was argued in [62] that a reasonable estimate for pole masses is $m_c^{\text{pole}} = 1.5 \pm 0.2$ GeV and $m_b^{\text{pole}} = 4.9 \pm 0.2$ GeV. Hence, the charm mass values chosen are perhaps slightly low, but not anomalous. The smallest m_b^{pole} value among the three combined sets is somewhat low, but the beauty data (including the contribution to total HERA cross sections) has extremely little constraint on PDFs in the global fit. Moreover, it has been argued that at lower orders a general mass variable flavour number scheme is not very sensitive to the scheme in which the mass is defined [63, 64]. The variation in the quark masses between groups, i.e. the deviations from the mean values, is relatively small compared to the intrinsic uncertainty for m_c, but a bit larger for m_b. As shown in [60, 64, 65], the Higgs cross section via gg fusion can vary by about 1% for m_c changes of about 0.2 GeV, while varia-

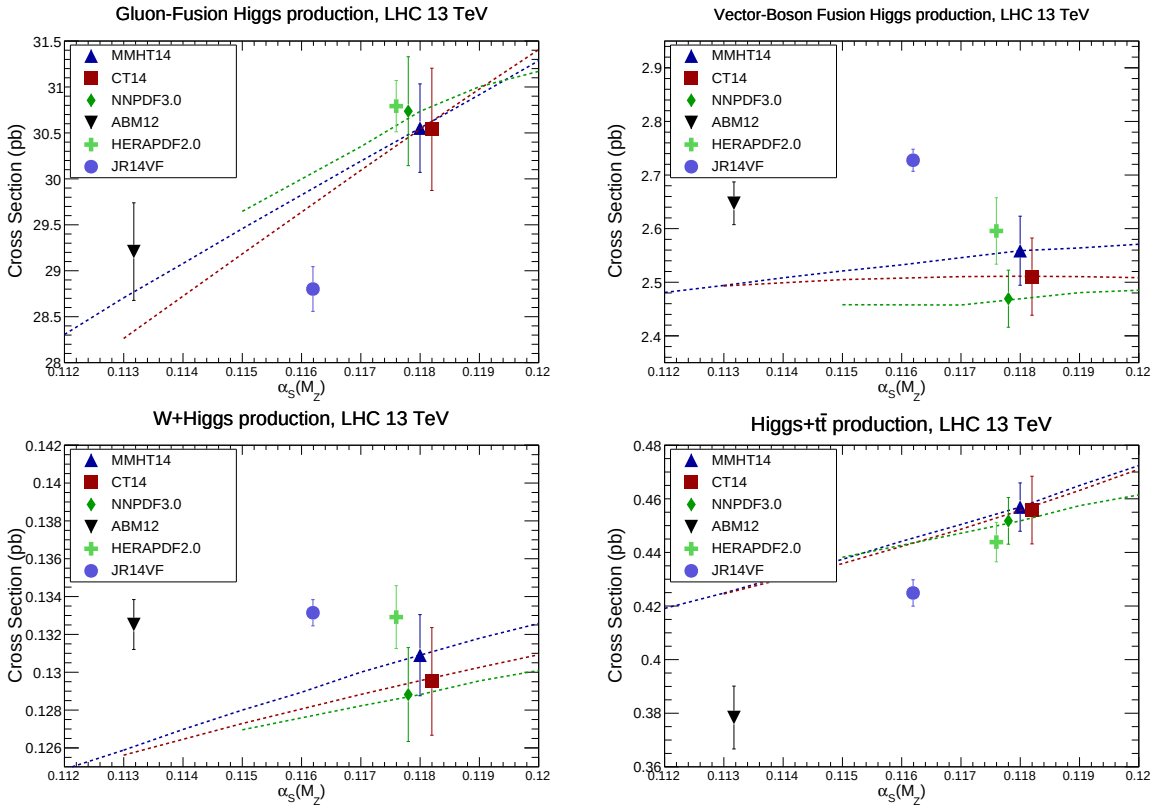

Figure 7: Dependence of the total inclusive cross-sections for Higgs boson production at $\sqrt{s} = 13$ TeV in different production channel on the value of the strong coupling $\alpha_s(m_Z)$ for the PDF sets which enter the combination: MMHT14, CT14, NNPDF3.0. Predictions obtained using ABM12, HERAPDF2.0, JR14VF NNLO sets are also shown at their preferred $\alpha_s(m_Z)$ value. The points shown for MMHT14, CT14, NNPDF3.0 and HERAPDF2.0 all refer to $\alpha_s(m_Z) = 0.118$ and are offset for clarity.

tions with m_b are much smaller than this, even for changes of 0.5 GeV. Hence, the variation in predictions between the groups due to the different quark masses is generally much less than the PDF uncertainty, with the exception of cross sections directly dependent on the b quark distribution, where the mass effect on the distribution is more significant. The uncertainty due to quark masses should ideally be taken into account, and the current variation between groups should achieve this to some extent. However, in the future, it is probably preferable to settle on common mass values, perhaps defined in the $\overline{\rm MS}$ scheme as advocated in [66], and a common uncertainty, as now done for $\alpha_s(M_Z)$.

For LHC calculations that are done in the $\overline{MS}$ scheme with up to 4 active quark flavours in the running α_s and PDFs, three combined PDF4LHC sets determined in this scheme are also provided. The respective PDF4LHC sets are constructed from 900 MC replicas of CT14, MMHT14, and NNPDF3.0 PDFs for $N_f = 4$ using the same combination techniques as for $N_f = 5$. In this case, the initial PDF parameterizations from the $N_f = 5$ fits at initial $Q_0 \sim m_c$ are evolved to higher Q including the lightest 4 flavours only. Contributions from massive bottom and top quarks should be then included in hard matrix elements. The input value $\alpha_s(M_Z, N_f = 4)$ in the $N_f = 4$ scheme is obtained from $\alpha_s(M_Z, N_f = 5) = 0.118$ by applying scheme transformation relations [67] at two or three loops in QCD, and assuming the average $m_b = 4.56$ GeV of the input PDF sets; it is thus rather smaller than the default value 0.118.

Table 1: Correlation coefficient between various Higgs boson production cross-sections and background cross-sections. In each case, the PDF4LHC15 NNLO prior set is compared to the Monte Carlo and with the two Hessian reduced sets. We also show the results from the three individual sets, CT14, MMHT14 and NNPDF3.0.

PDF Set	correlation coefficient					
	$t\bar{t}, Ht\bar{t}$	$t\bar{t}, hW$	$t\bar{t}, hZ$	$ggh, ht\bar{t}$	ggh, hW	ggh, hZ
PDF4LHC15_nnlo_prior	0.87	-0.23	-0.34	-0.13	-0.01	-0.17
PDF4LHC15_nnlo_mc	0.87	-0.27	-0.35	-0.10	0.07	-0.01
PDF4LHC15_nnlo_100	0.87	-0.24	-0.34	-0.13	-0.02	-0.17
PDF4LHC15_nnlo_30	0.87	-0.27	-0.43	-0.13	-0.04	-0.23
CT14	0.09	-0.32	-0.44	-0.26	-0.03	-0.18
MMHT14	0.90	-0.22	-0.52	0.08	-0.18	-0.33
NNPDF3.0	0.90	-0.17	-0.21	0.18	0.52	0.49

PDF Set	correlation coefficient					
	Z, W	$Z, t\bar{t}$	Z, ggh	$Z, ht\bar{t}$	Z, hW	Z, hZ
PDF4LHC15_nnlo_prior	0.89	-0.49	0.08	-0.46	0.56	0.74
PDF4LHC15_nnlo_mc	0.90	-0.44	0.18	-0.42	0.62	0.80
PDF4LHC15_nnlo_100	0.91	-0.48	0.09	-0.46	0.59	0.74
PDF4LHC15_nnlo_30	0.88	-0.63	0.04	-0.61	0.56	0.72
CT14	0.92	-0.69	0.12	-0.69	0.69	0.77
MMHT14	0.76	-0.70	0.12	-0.83	0.15	0.43
NNPDF3.0	0.96	-0.13	0.62	-0.30	0.84	0.85

PDF Set	correlation coefficient					
	$W, t\bar{t}$	W, ggh	$W, ht\bar{t}$	W, hW	W, hZ	$t\bar{t}, ggh$
PDF4LHC15_nnlo_prior	-0.40	0.20	-0.40	0.76	0.77	0.30
PDF4LHC15_nnlo_mc	-0.44	0.26	-0.42	0.81	0.82	0.32
PDF4LHC15_nnlo_100	-0.40	0.20	-0.40	0.76	0.77	0.30
PDF4LHC15_nnlo_30	-0.47	0.19	-0.47	0.77	0.76	0.31
CT14	-0.56	0.22	-0.56	0.80	0.77	0.09
MMHT14	-0.47	0.24	-0.53	0.62	0.63	0.46
NNPDF3.0	-0.08	0.64	-0.26	0.88	0.86	0.51

I.2.5 PDF correlations

Also of importance for Higgs boson predictions and analyses are the PDF correlations, both among Higgs boson production processes and between Higgs boson processes and potential background processes: tables of correlations obtained using various PDF sets were given in the previous Yellow Report [9]. These tables can now be updated using the more recent combined set. In Table 1 we collect the correlation coefficients between different Higgs boson production channels, as well as between representative Higgs boson signal and background processes. We show the results for the PDF4LHC15 NNLO prior and for the three reduced combined PDF sets, and we also include the results for the three individual PDF sets. The cross-sections have been computed at NLO with NNLO PDFs, using the same settings as in previous plots. All of the techniques do reasonably well reproducing the correlations of the prior, with the PDF4LHC15_100 PDFs reproducing the prior to within a per cent.

It should be emphasized that the values of the correlation themselves, however, can be viewed as only having a single digit (or less) accuracy in the sense that the PDF correlations for Higgs processes and backgrounds for the 3 global PDF sets can differ by the order of 0.2 (or more). For example, the spread in correlation coefficients for gluon-gluon fusion production and associated (Zh) production is 0.67. Note that the differences in the correlation coefficients between NNPDF3.0, CT14 and MMHT14 are large in many cases, though there is also good agreement in other cases.

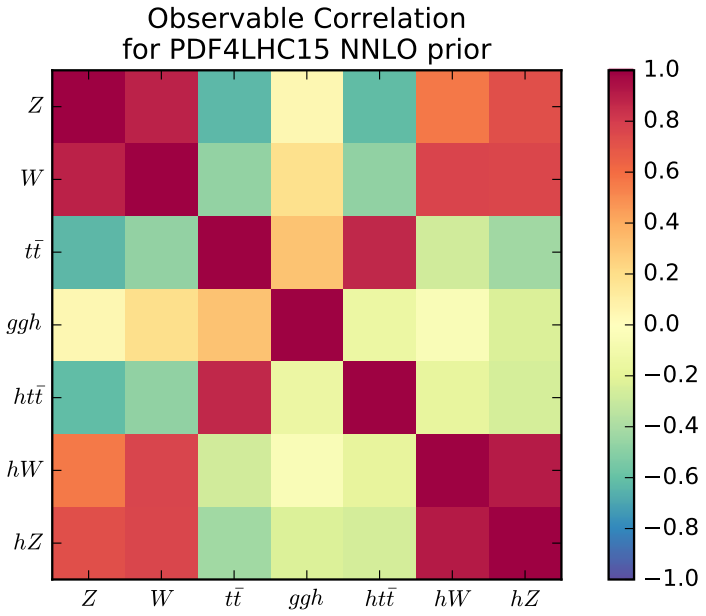

Figure 8: The value of the correlation coefficient between representative Higgs boson signal and background processes at the LHC 13 TeV, using the PDF4LHC15NNLO prior. The colour of each entry of the correlation matrix indicates the absolute size of the correlation coefficient. The processes shown in this figure are ggh, $ht\bar{t}$, hW and hZ (for signal) and Z, W and $t\bar{t}$ (for backgrounds).

In Figure 8 we show the absolute value of the correlation coefficient between representative Higgs boson signal and background processes at the LHC 13 TeV, using the PDF4LHC15NNLO prior. The colour of each entry of the correlation matrix indicates the absolute size of the correlation coefficient, with a granularity of 0.2. The processes shown in this figure are ggh, $ht\bar{t}$, hW and hZ (for signal) and Z, W and $t\bar{t}$ (for backgrounds). Very similar results are obtained if any of the three reduced sets is used.

I.2.6 Acceptance calculations

An important application of the PDF4LHC15 combined sets is the calculation of PDF uncertainties in acceptances. These are defined as the ratio of cross-sections with fiducial selection cuts to the corresponding inclusive cross-section, $\mathcal{A} = (\sigma|_{\rm fid})/(\sigma|_{\rm incl})$. To illustrate this usage, we have computed the acceptances, with the corresponding PDF uncertainties, for two Higgs boson production processes with experimentally realistic selection cuts, namely:

- Higgs boson production in the gluon fusion process, decaying into diphotons, $gg \to h \to \gamma\gamma$,
- Higgs boson production in association with a W boson, with the latter decaying leptonically, $pp \to hW^{\pm} \to hl^{\pm}\nu_l$.

As in the rest of this chapter, the calculations have been performed for the LHC 13 TeV with `aMC@NLO` interfaced to `aMCfast`, using NNLO PDFs with NLO matrix elements.

In the calculation of the fiducial cross-sections, we use similar acceptance requirements as those in the corresponding ATLAS and CMS analyses. For both processes, jets are reconstructed with the anti-k_T algorithm with $R = 0.4$, and they satisfy $p_T \geq 30$ GeV and $|\eta| \leq 4.4$. The additional selection cuts in the case of the $gg \to h \to \gamma\gamma$ are the following: for photons we require $p_T \geq 25$ GeV and $\eta \leq 2.4$, and the invariant mass of the diphotons should satisfy $|m_{\gamma\gamma} - 125\ {\rm GeV}| \leq 15$ GeV. In the case of Higgs associated production, $pp \to hW^{\pm} \to hl^{\pm}\nu_l$, the selection cuts on the charged leptons are $|\eta_l| \leq 2.5$ and $p_T^l \geq 20$ GeV.

Using these kinematical cuts, we have generated `applgrids` for both fiducial and inclusive cross-sections, and computed the resulting acceptance corrections and the corresponding PDF uncertainties. In Table 2 we collect the value of the acceptances $\mathcal{A}$ in each case, together with the corresponding PDF uncertainties computed with the PDF4LHC15 prior and with the three reduced sets. For completeness, we also show the results for the acceptances computed with the individual PDF sets. We observe excellent agreement between the acceptances computed with the prior and with the three reduced sets, both for the central value and for the PDF uncertainties.

Table 2: The acceptance corrections $\mathcal{A}$ for Higgs boson production at the LHC 13 TeV in two different channels with realistic selection cuts, and the corresponding PDF uncertainties. We compare the results of the PDF4LHC15 NNLO prior with the three reduced sets. For completeness, we also show the results for the acceptances computed with the individual PDF sets. See text for more details of the specific selection cuts in each case.

	$\mathcal{A}(gg \to h \to \gamma\gamma)$	$\mathcal{A}(pp \to hW \to hl\nu_l)$
PDF4LHC15 prior	0.728 +- 0.006 (0.9%)	0.7536 +- 0.0014 (0.18%)
`PDF4LHC15_mc`	0.727 +- 0.006 (0.9%)	0.7538 +- 0.0015 (0.20%)
`PDF4LHC15_100`	0.728 +- 0.006 (0.9%)	0.7536 +- 0.0013 (0.17%)
`PDF4LHC15_30`	0.728 +- 0.006 (0.9%)	0.7536 +- 0.0012 (0.15%)
MMHT14	0.728 +- 0.004 (0.6%)	0.7532 +- 0.0012 (0.15%)
CT14	0.725 +- 0.007 (1.0%)	0.7543 +- 0.0014 (0.18%)
NNPDF3.0	0.730 +- 0.005 (0.7%)	0.7534 +- 0.0011 (0.14%)

I.2.7 Summary

To summarize, in Table 3 we collect the available PDF4LHC15 NNLO $N_f = 5$ combined sets. The corresponding sets are also available at NLO, as well as $N_f = 4$ versions. All the combined PDF4LHC14 sets are available through `LHAPDF6` [43], which also includes built-in routines for the calculation of the PDF and PDF+α_s uncertainties for all relevant cases.

Recommendations for the usage of each of these techniques are given in the PDF4LHC 2015 document [35], along with explicit formulae for the calculation of PDF and PDF+$\alpha_s(m_Z)$ uncertainties for each of the techniques. The recommendations can be simply summed up. If asymmetric uncertainties are important, for example at high mass, and Hessian errors are not essential, then `PDF4LHC15_mc` should be used. There are two options for Hessian uncertainties. The `PDF4LHC15_30` set provides a good estimate of the uncertainty of the prior with fewer members, sufficient in many cases, such as for the determination of nuisance parameters or acceptance calculations. To reproduce the uncertainty of the prior exactly, then the `PDF4LHC_100` sets should be used.

Table 3: Summary of the combined NNLO PDF4LHC15 sets with $N_f^{\rm max} = 5$ that are available from LHAPDF6. The corresponding NLO sets are also available. Members 0 and 1 of PDF4LHC15_nnlo_asvar coincide with members 101 and 102 (31 and 32) of PDF4LHC15_nnlo_mc_pdfas and PDF4LHC15_nnlo_100_pdfas (PDF4LHC15_nnlo_30_pdfas). Recall that in LHAPDF6 there is always a zeroth member, so that the total number of PDF members in a given set is always $N_{\rm mem} + 1$. See text for more details.

LHAPDF6 grid	Pert order	ErrorType	$N_{\rm mem}$	$\alpha_s(m_Z^2)$
PDF4LHC15_nnlo_mc	NNLO	replicas	100	0.118
PDF4LHC15_nnlo_100	NNLO	symmhessian	100	0.118
PDF4LHC15_nnlo_30	NNLO	symmhessian	30	0.118
PDF4LHC15_nnlo_mc_pdfas	NNLO	replicas+as	102	mem 0:100 $\to$ 0.118 mem 101 $\to$ 0.1165 mem 102 $\to$ 0.1195
PDF4LHC15_nnlo_100_pdfas	NNLO	symmhessian+as	102	mem 0:100 $\to$ 0.118 mem 101 $\to$ 0.1165 mem 102 $\to$ 0.1195
PDF4LHC15_nnlo_30_pdfas	NNLO	symmhessian+as	32	mem 0:30 $\to$ 0.118 mem 31 $\to$ 0.1165 mem 32 $\to$ 0.1195
PDF4LHC15_nnlo_asvar	NNLO	-	1	mem 0 $\to$ 0.1165 mem 1 $\to$ 0.1195

Chapter I.3

Branching Ratios

A. Denner, S. Heinemeyer, A. Mück, I. Puljak, D. Rebuzzi (Eds.); S. Boselli, C.M. Carloni Calame, S. Dittmaier, G. Montagna, O. Nicrosini, F. Piccinini, M. Spira, M. Mühlleitner

For the accurate study of the properties of the Higgs boson, precise predictions for the various partial decay widths and branching ratios (BRs) along with their theoretical uncertainties are indispensable. In Ref. [7] a first precise prediction of the BRs of the SM Higgs boson was presented. In Refs. [8, 68] the BR predictions were supplemented with an uncertainty estimate including parametric uncertainties as well as the effects of unknown higher-order corrections. In Ref. [9] these predictions were updated with a fine step size around the mass of the Higgs boson discovered by ATLAS [1] and CMS [2]. Moreover, error estimates were presented in a form that is suitable for taking error correlations into account.

In view of the updated parameter set of Chapter I.1 and the improvements in HDECAY [69–71] that reduce theoretical uncertainties, we provide here an update of the predictions on SM Higgs BRs and corresponding uncertainties.

I.3.1 Update of branching ratios and decay width for the Standard Model Higgs boson

In this section we update the SM BR calculations presented in Refs. [7–9, 68]. The strategy for the calculation of BRs and uncertainties is unchanged with respect to Ref. [8] and Ref. [9], respectively. However, the input parameter set has been updated (see Chapter I.1) and some improvements have been made in HDECAY that lead to a reduction of theoretical uncertainties.

I.3.1.a Strategy and input for branching-ratio calculations

We briefly summarize the strategy for the BR calculations for the updates in this report. A detailed description of the methods used can be found in Refs. [8, 9]. We employ HDECAY [69–71] and PROPHECY4F [72–74] to calculate all the partial widths with the highest accuracy available. The higher-order corrections included in HDECAY and PROPHECY4F have been discussed in detail in Section 2.1.3.2 of Ref. [8]. In the meantime, the following improvements have been made in HDECAY: On the one hand, for the Higgs boson decays into fermions the complete NLO electroweak (EW) corrections have been implemented. For small Higgs boson masses, the theoretical uncertainty from missing EW corrections is hence reduced to below 0.5%. This estimate is supported by the recent explicit calculation of the mixed QCD-EW corrections [75]. On the other hand, the input parameters of HDECAY have been moved from the bottom and charm pole masses to the masses $m_{\mathrm{b}}(m_{\mathrm{b}})$ and $m_{\mathrm{c}}(3\ \mathrm{GeV})$ in the $\overline{\mathrm{MS}}$ scheme according to the recommendations of Chapter I.1. Following these recommendations, the corresponding pole masses are calculated internally in HDECAY using the three-loop relation.

The updated estimated relative theoretical uncertainties (THUs) for the different Higgs boson partials widths resulting from missing higher-order corrections (determined as explained in more detail in Section 2.1.3.2 of Ref. [8]) are summarized in Table 4 which replaces Table 2 of Ref. [8]. The corresponding uncertainty for the total width is obtained by adding the uncertainties for the partial widths linearly. In order to determine the uncertainty for a BR, first the variations of this BR are calculated when varying each individual partial width within the corresponding relative error while keeping all other partial widths fixed at their central value. Since each BR depends on all partial widths, scaling a single partial width modifies all BRs. Hence, there is an individual THU of each BR due to the THU of each partial width. We assume the THUs of all partial widths to be uncorrelated except for all $\mathrm{H} \to \mathrm{WW/ZZ} \to 4\mathrm{f}$

Table 4: Estimated theoretical uncertainties from missing higher orders.

Partial width	QCD	electroweak	total
$H \to b\bar{b}/c\bar{c}$	$\sim 0.2\%$	$\sim 0.5\%$ for $M_H < 500$ GeV	$\sim 0.5\%$
$H \to \tau^+\tau^-/\mu^+\mu^-$		$\sim 0.5\%$ for $M_H < 500$ GeV	$\sim 0.5\%$
$H \to t\bar{t}$	$\lesssim 5\%$	$\sim 0.5\%$ for $M_H < 500$ GeV	$\sim 5\%$
$H \to gg$	$\sim 3\%$	$\sim 1\%$	$\sim 3.2\%$
$H \to \gamma\gamma$	$< 1\%$	$< 1\%$	$\sim 1\%$
$H \to Z\gamma$	$< 1\%$	$\sim 5\%$	$\sim 5\%$
$H \to WW/ZZ \to 4f$	$< 0.5\%$	$\sim 0.5\%$ for $M_H < 500$ GeV	$\sim 0.5\%$

Table 5: Input parameters and their relative uncertainties as used for the uncertainty estimation of the branching ratios.

Parameter	Central value	Uncertainty
$\alpha_s(M_Z)$	0.118	± 0.0015
$m_c(3\text{ GeV})$	0.986 GeV	± 0.026 GeV
$m_b(m_b)$	4.18 GeV	± 0.03 GeV
m_t^{pole}	172.5 GeV	± 1 GeV

decays. The THUs of the latter are assumed to be fully correlated and, hence, we only consider the simultaneous scaling of all 4-fermion partial widths. The derived individual THUs for each BR are added linearly to obtain the corresponding total THU.

Also the parametric uncertainties (PUs) have been updated in our calculation. The input-parameter set as defined in Chapter I.1 has been used. From the given PDG values of the gauge-boson masses, we derive the pole masses $M_Z = 91.15348$ GeV and $M_W = 80.35797$ GeV which are used as input. The gauge-boson widths have been calculated at NLO from the other input parameters resulting in $\Gamma_Z = 2.49436$ GeV and $\Gamma_W = 2.08718$ GeV.

Concerning the PUs, we take only those of the input parameters α_s, m_c, m_b, and m_t into account. The values and uncertainties are adopted from Chapter I.1 and are for convenience listed in Table 5 as well. For the masses of the light quarks, we use the masses in the $\overline{\text{MS}}$ scheme $m_b(m_b)$ and $m_c(3\text{ GeV})$ as input,[I.2] while for m_t the pole mass enters. The parametric uncertainties resulting from the gauge-boson masses, the lepton masses, the electromagnetic coupling and the Fermi constant are below one per mille, and the impact of the PUs of the light quark masses on the considered BRs is negligible.

Using these PUs, for each parameter $p = \alpha_s, m_c, m_b, m_t$ we have calculated the Higgs BRs for p, $p + \Delta p$ and $p - \Delta p$ keeping all the other parameters fixed at their central values. The resulting shift on each BR is then given by

$$\begin{aligned} \Delta^p_+ \text{Br} &= \max\{\text{Br}(p+\Delta p), \text{Br}(p), \text{Br}(p-\Delta p)\} - \text{Br}(p), \\ \Delta^p_- \text{Br} &= \text{Br}(p) - \min\{\text{Br}(p+\Delta p), \text{Br}(p), \text{Br}(p-\Delta p)\}, \end{aligned} \tag{I.3.1}$$

which may lead to asymmetric uncertainties. The total PUs have been obtained by adding the calculated shifts due to the four parameters in quadrature. In analogy, the uncertainties of the partial and total decay

[I.2] Since HDECAY version 6.50 it is possible to use directly masses in the $\overline{\text{MS}}$ scheme as input for the light quarks.

widths are given by

$$\begin{aligned}\Delta^p_+\Gamma &= \max\{\Gamma(p+\Delta p),\Gamma(p),\Gamma(p-\Delta p)\}-\Gamma(p),\\ \Delta^p_-\Gamma &= \Gamma(p)-\min\{\Gamma(p+\Delta p),\Gamma(p),\Gamma(p-\Delta p)\},\end{aligned} \tag{I.3.2}$$

where Γ denotes the partial decay width for each considered decay channel or the total width, respectively. The total PUs have been calculated again by adding the individual PUs in quadrature.

The total uncertainties on the BRs, i.e. combinations of PUs and THUs, are derived by adding linearly the total parametric uncertainties and the total theoretical uncertainties, as discussed in detail in Ref. [8]. To allow for taking into account correlations in the errors of the different BRs, we provide also the individual uncertainties for the various partial widths in Section I.3.1.c for selected Higgs boson masses.

For completeness, we repeat that the Higgs boson total width resulting from HDECAY has been modified according to the prescription

$$\Gamma_{\mathrm{H}} = \Gamma^{\mathrm{HD}} - \Gamma^{\mathrm{HD}}_{\mathrm{ZZ}} - \Gamma^{\mathrm{HD}}_{\mathrm{WW}} + \Gamma^{\mathrm{Proph.}}_{\mathrm{4f}}\,, \tag{I.3.3}$$

where Γ_{H} is the total Higgs boson width, Γ^{HD} the Higgs boson width obtained from HDECAY, $\Gamma^{\mathrm{HD}}_{\mathrm{ZZ}}$ and $\Gamma^{\mathrm{HD}}_{\mathrm{WW}}$ stand for the partial widths to $\mathrm{Z}^{(*)}\mathrm{Z}^{(*)}$ and $\mathrm{W}^{(*)}\mathrm{W}^{(*)}$ calculated with HDECAY, while $\Gamma^{\mathrm{Proph.}}_{\mathrm{4f}}$ represents the partial width of $\mathrm{H}\to 4\mathrm{f}$ calculated with PROPHECY4F. The latter can be split into the decays into $\mathrm{Z}^{(*)}\mathrm{Z}^{(*)}$, $\mathrm{W}^{(*)}\mathrm{W}^{(*)}$, and the interference,

$$\Gamma^{\mathrm{Proph.}}_{\mathrm{4f}} = \Gamma_{\mathrm{H}\to\mathrm{W}^{(*)}\mathrm{W}^{(*)}\to 4\mathrm{f}} + \Gamma_{\mathrm{H}\to\mathrm{Z}^{(*)}\mathrm{Z}^{(*)}\to 4\mathrm{f}} + \Gamma_{\mathrm{WW/ZZ-int.}}\,, \tag{I.3.4}$$

where the individual contributions are defined in terms of partial widths with specific final states according to

$$\begin{aligned}\Gamma_{\mathrm{H}\to\mathrm{W}^{(*)}\mathrm{W}^{(*)}\to 4f} &= 9\cdot\Gamma_{\mathrm{H}\to\nu_{\mathrm{e}}\mathrm{e}^+\mu^-\bar{\nu}_\mu} + 12\cdot\Gamma_{\mathrm{H}\to\nu_{\mathrm{e}}\mathrm{e}^+\mathrm{d}\bar{\mathrm{u}}} + 4\cdot\Gamma_{\mathrm{H}\to\mathrm{u}\bar{\mathrm{d}}\mathrm{s}\bar{\mathrm{c}}}\,,\\
\Gamma_{\mathrm{H}\to\mathrm{Z}^{(*)}\mathrm{Z}^{(*)}\to 4f} &= 3\cdot\Gamma_{\mathrm{H}\to\nu_{\mathrm{e}}\bar{\nu}_{\mathrm{e}}\nu_\mu\bar{\nu}_\mu} + 3\cdot\Gamma_{\mathrm{H}\to\mathrm{e}^-\mathrm{e}^+\mu^-\mu^+} + 9\cdot\Gamma_{\mathrm{H}\to\nu_{\mathrm{e}}\bar{\nu}_{\mathrm{e}}\mu^-\mu^+}\\
&\quad + 3\cdot\Gamma_{\mathrm{H}\to\nu_{\mathrm{e}}\bar{\nu}_{\mathrm{e}}\nu_{\mathrm{e}}\bar{\nu}_{\mathrm{e}}} + 3\cdot\Gamma_{\mathrm{H}\to\mathrm{e}^-\mathrm{e}^+\mathrm{e}^-\mathrm{e}^+}\\
&\quad + 6\cdot\Gamma_{\mathrm{H}\to\nu_{\mathrm{e}}\bar{\nu}_{\mathrm{e}}\mathrm{u}\bar{\mathrm{u}}} + 9\cdot\Gamma_{\mathrm{H}\to\nu_{\mathrm{e}}\bar{\nu}_{\mathrm{e}}\mathrm{d}\bar{\mathrm{d}}} + 6\cdot\Gamma_{\mathrm{H}\to\mathrm{u}\bar{\mathrm{u}}\mathrm{e}^-\mathrm{e}^+} + 9\cdot\Gamma_{\mathrm{H}\to\mathrm{d}\bar{\mathrm{d}}\mathrm{e}^-\mathrm{e}^+}\\
&\quad + 1\cdot\Gamma_{\mathrm{H}\to\mathrm{u}\bar{\mathrm{u}}\mathrm{c}\bar{\mathrm{c}}} + 3\cdot\Gamma_{\mathrm{H}\to\mathrm{d}\bar{\mathrm{d}}\mathrm{s}\bar{\mathrm{s}}} + 6\cdot\Gamma_{\mathrm{H}\to\mathrm{u}\bar{\mathrm{u}}\mathrm{s}\bar{\mathrm{s}}} + 2\cdot\Gamma_{\mathrm{H}\to\mathrm{u}\bar{\mathrm{u}}\mathrm{u}\bar{\mathrm{u}}}\\
&\quad + 3\cdot\Gamma_{\mathrm{H}\to\mathrm{d}\bar{\mathrm{d}}\mathrm{d}\bar{\mathrm{d}}}\,,\\
\Gamma_{\mathrm{WW/ZZ-int.}} &= 3\cdot\Gamma_{\mathrm{H}\to\nu_{\mathrm{e}}\mathrm{e}^+\mathrm{e}^-\bar{\nu}_{\mathrm{e}}} - 3\cdot\Gamma_{\mathrm{H}\to\nu_{\mathrm{e}}\bar{\nu}_{\mathrm{e}}\mu^-\mu^+} - 3\cdot\Gamma_{\mathrm{H}\to\nu_{\mathrm{e}}\mathrm{e}^+\mu^-\bar{\nu}_\mu}\\
&\quad + 2\cdot\Gamma_{\mathrm{H}\to\mathrm{u}\bar{\mathrm{d}}\mathrm{d}\bar{\mathrm{u}}} - 2\cdot\Gamma_{\mathrm{H}\to\mathrm{u}\bar{\mathrm{u}}\mathrm{s}\bar{\mathrm{s}}} - 2\cdot\Gamma_{\mathrm{H}\to\mathrm{u}\bar{\mathrm{d}}\mathrm{s}\bar{\mathrm{c}}}\,.\end{aligned} \tag{I.3.5}$$

I.3.1.b Results for partial widths and branching ratios including QCD and EW corrections for Higgs boson masses close to 125 GeV

We provide results for the BRs of the SM Higgs boson using a particularly fine grid of masses close to $M_{\mathrm{H}} = 125$ GeV. The results are generated and presented in analogy to the predictions and error estimates in Ref. [9], taking the improvements mentioned above into account.

Here, we briefly summarize the numerical changes with respect to the results for $M_{\mathrm{H}} = 125$ GeV presented in Ref. [9]. All these changes are well within the error estimates given in Ref. [9]. The partial width for $\mathrm{H}\to\mathrm{b\bar{b}}$ increases by approximately 1.5%, mainly due to the change in α_{s}. The partial widths of the other fermionic decay modes change only at the per mille level due to the inclusion of the full EW corrections and/or the input changes. The partial width for $\mathrm{H}\to\mathrm{gg}$ decreases by approximately 4%. While about half of this shift is due to the change in α_{s}, the remaining part comes from improvements

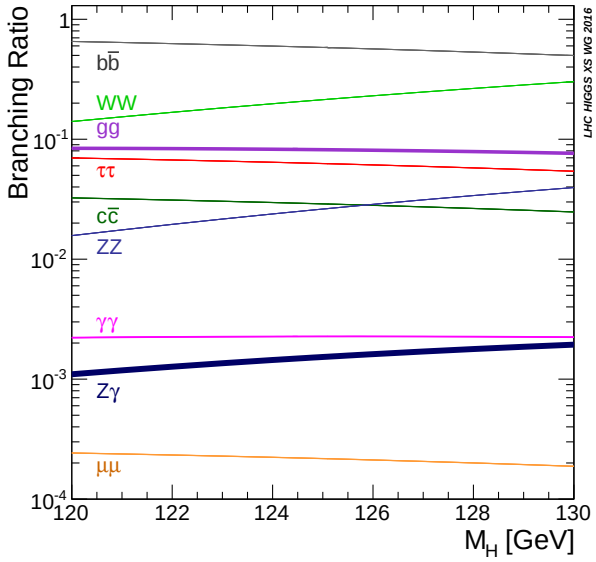

Figure 9: Higgs boson branching ratios and their uncertainties for the mass range around 125 GeV.

in HDECAY, in particular from the inclusion of charm-quark-loop contributions and NLO quark-mass effects. The partial widths for the other bosonic decay modes change at the level of one per mille or below. The total width increases by approximately 0.5%. Correspondingly, the relative increase for the central value of the $\mathrm{H} \to \mathrm{b\bar{b}}$ BR is approximately 1%. The relative decrease in the other fermionic modes is below 1%. For $\mathrm{H} \to \mathrm{gg}$, the relative decrease of the BR is approximately 4%. The relative decrease of the other bosonic BRs is below 1%, only.

The error estimates on the BRs also change as discussed in the following: The total error on the $\mathrm{H} \to \mathrm{b\bar{b}}$ BR decreases to below 2% due to the reduced errors on α_s and the bottom quark mass and the reduced THU. Since the error on $\mathrm{H} \to \mathrm{b\bar{b}}$ is a major source of uncertainty for all the other BRs, their error is reduced by more than 2% due to this improvement alone. In addition, the other fermionic modes benefit from the reduced THU after the inclusion of the full EW corrections, such that the corresponding errors are reduced roughly by a factor of 2 to below 2.5% for the leptonic final states and to below 7% for $\mathrm{H} \to \mathrm{c\bar{c}}$. Also the error estimates for the bosonic decay modes are decreased, mainly due to the improvements in $\mathrm{H} \to \mathrm{b\bar{b}}$. In particular, the error for the decay into massive vector bosons is approximately 2%, i.e. half as big as before. The errors on the partial widths are discussed in Section I.3.1.c.

The BRs for the fermionic decay modes are shown in Tables 174–175. The BRs for the bosonic decay modes together with the total width are given in Tables 176–178. Besides the BRs, the tables list also the corresponding theoretical uncertainties (THU) and parametric uncertainties resulting from the quark masses (PU(m_q)) and the strong coupling (PU(α_s)). The PUs from the different quark masses have been added in quadrature. The BRs (including the full uncertainty) are also presented graphically in Figure 9 for the mass region around the Higgs boson resonance.

Finally, Tables 179–181 list the BRs for the most relevant Higgs boson decays into four-fermion final states. The right-most column in the tables shows the total relative uncertainty of these BRs in per cent, obtained by adding the PUs in quadrature and combining them linearly with the THU. The uncertainty is practically equal for all $\mathrm{H} \to 4\mathrm{f}$ BRs and the same for those for $\mathrm{H} \to \mathrm{WW/ZZ}$. Note that the charge-conjugate final state is not included for $\mathrm{H} \to \ell^+\nu_\mathrm{l}\mathrm{q\bar{q}}$.

I.3.1.c Correlations and uncertainties for branching ratios for Higgs boson masses close to 125 GeV

As in Ref. [9], we provide results and uncertainties resulting from different sources for the partial widths and selected Higgs boson masses. These results can be used to include error correlations for the different BRs. The reason for the correlations is two-fold: Varying the input parameters within their error bands induces shifts of the different partial widths and the resulting BRs in a correlated way. Moreover, there is a trivial correlation because all the BRs have to add up to one. Thus, a shift in a single partial width shifts all BRs in a correlated way.

For the partial widths the THUs are assumed to be uncorrelated (except for the decay to massive gauge bosons). Moreover, the correlated effect on each partial width from varying a parameter within its errors is disentangled from the additional trivial correlation when calculating the BRs. In Table 1 of Ref. [9] we showed the results for the partial widths for $M_{\mathrm{H}} = 122$ GeV, 126 GeV, and 130 GeV including for each partial width the THU and the different PUs.

Using the updated parameter set and the updated THUs we present in Table 182 results for the partial widths and the corresponding uncertainties for $M_{\mathrm{H}} = 124$ GeV, 125 GeV, and 126 GeV. For each partial width, we show the THU evaluated according to (I.3.2). For each input parameter we show the induced shift on each partial width for the maximal and minimal choice of the input parameter as upper and lower entry in the table, respectively. Hence, the table allows to read off the correlation in the variation of the different partial widths. The associated error bands are slightly asymmetric. However, it is a good approximation to symmetrize the error band and assume a Gaussian probability distribution for the corresponding prediction.

The THUs on the partial widths of all the four-fermion final-states can be considered to be fully correlated. All other THUs are considered to be uncorrelated. Hence, for the BRs listed in Tables 174–178 only the trivial correlation is present. However, it should be stressed again that in contrast to the PUs, theory errors cannot be assumed to be Gaussian errors. Assuming a Gaussian distribution and, hence, effectively adding THUs to the PUs in quadrature will in general lead to underestimated errors. According to the recommendations in Section 12 of Ref. [7], the THUs should be considered to have a flat probability distribution within the given range. Alternatively, the envelope of extreme choices for the theory prediction on the partial widths should be used as an error estimate. For all the total errors presented on the BRs, we have added PUs and THUs of the resulting BRs linearly, as discussed in Section I.3.1.a. We thereby provide the envelope for each resulting BR, however, the correlation is lost at the level of BRs.

In total, there are four input parameters to be varied corresponding to the PUs and one has to include eight uncorrelated THUs for the various partial widths. Analysing in detail the interesting region around $M_{\mathrm{H}} = 125$ GeV, the different uncertainties are of different importance. Aiming for a given accuracy, some uncertainties may be safely neglected, as can be inferred from Table 182. Even sizeable uncertainties for a given partial width can be unimportant if the decay mode has a small BR and does not contribute significantly to combined measurements.

Concerning the PUs, the variation of α_{s} and the bottom quark mass impact the BR predictions at the level of $1-2\%$. The charm quark mass is only relevant for $\mathrm{H} \to \mathrm{c\bar{c}}$ and affects other BRs only at the level of $1-2$ per mille. The THU for $\mathrm{H} \to \gamma\gamma$ amounts to 1% and is needed at this level of precision. The THU for $\mathrm{H} \to \mathrm{b\bar{b}}$, $\mathrm{H} \to \mathrm{c\bar{c}}$, $\mathrm{H} \to \mu^+\mu^-$, $\mathrm{H} \to \tau^+\tau^-$, and $\mathrm{H} \to \mathrm{WW/ZZ} \to 4\mathrm{f}$ is estimated at 0.5% and thus also quite small. The THU for $\mathrm{H} \to \mathrm{gg}$ and $\mathrm{H} \to \mathrm{Z}\gamma$ only has sizeable effects if a measurement of the corresponding channel is included or, in the case of $\mathrm{H} \to \mathrm{gg}$, errors of a few per mille are important.

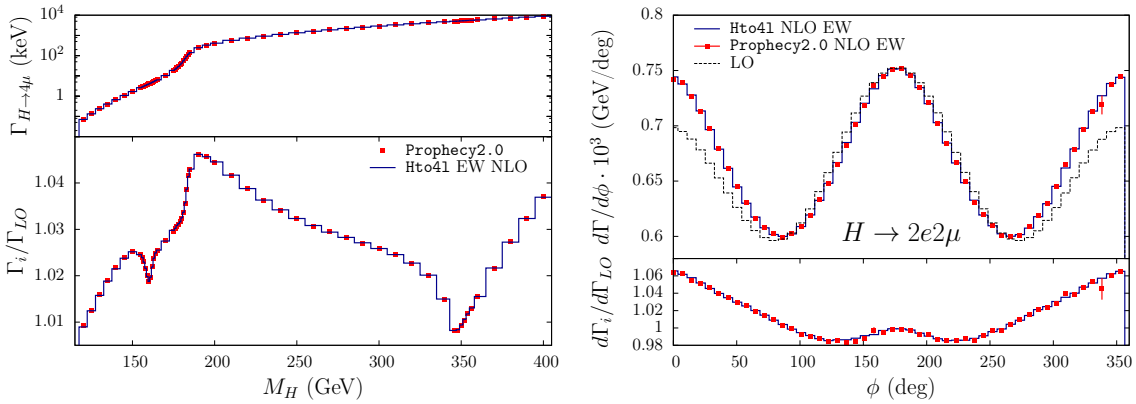

Figure 10: Comparison between HTO4L and PROPHECY4F. On the left, the H $\to$ 4μ partial width is compared as a function of $M_{\rm H}$ together with the relative effect of the NLO EW corrections. On the right, the ϕ-angle distribution for H $\to$ 2e2μ is compared and the NLO EW effect is shown, for $M_{\rm H} = 125$ GeV.

I.3.1.d Benchmark results for partial widths and branching ratios including only QCD corrections for a wide Higgs boson mass range

If the minimal SM is realized, the Higgs boson is light and the best predictions for the corresponding BRs are listed above. However, in extended models additional Higgs bosons might show up. In order to provide a benchmark for such additional Higgs bosons, we list the partial widths calculated in the SM for a wide range of Higgs boson masses. Since the EW corrections become very large and unphysical for Higgs boson masses above $\sim$ 600 GeV, we omit all EW corrections and give results including QCD corrections only. The SM partial widths in this scenario are listed in Tables 183 and 184 for the 2-fermion final states and in Tables 185 and 186 for the 2-boson final states. Without EW corrections the results for the partial widths for H $\to$ WW and H $\to$ ZZ calculated with HDECAY and PROPHECY4F agree within $\sim 1\%$ for Higgs boson masses above 100 GeV. For very light Higgs bosons the differences become bigger owing to interference effects that are included in PROPHECY4F but not in HDECAY. Therefore, we followed our standard procedure and used PROPHECY4F to calculate the numbers presented in Tables 185 and 186.

I.3.1.e HTO4L: a generator for Higgs boson decay into four charged leptons at NLOPS electroweak accuracy

The Monte Carlo event generator HTO4L has been developed for the precise simulation of the SM Higgs boson decay into four charged leptons (H $\to$ $e^+e^-e^+e^-$, $e^+e^-\mu^+\mu^-$, $\mu^+\mu^-\mu^+\mu^-$), including complete NLO EW corrections and multiple-photon effects in a matched-to-NLO Parton Shower (PS) framework. A detailed description of the theoretical approach, the calculation and phenomenological results can be found in Ref. [76] and version 1.0 of the program is publicly available [77].

For inclusive partial widths or at NLO EW accuracy without multi-photon emission, HTO4L and PROPHECY4F (version 2.0) [78,79] should agree for the leptonic final states included in HTO4L. A comparison between the codes has been carried out, both at differential and integrated level. As examples, on the left of Figure 10 we show the partial H $\to$ 4μ decay width as a function of $M_{\rm H}$ (upper panel) and the effect of the NLO EW corrections relative to the LO width (lower panel): the predictions of HTO4L and PROPHECY4F agree in the whole mass range, within the negligible sub-per mille numerical integration error. On the right of Figure 10, the distribution of the angle ϕ (the angle between the decay planes of the virtual Z bosons in the Higgs boson rest frame) in the decay H $\to$ 2e2μ is plotted, showing both the absolute value (upper panel) and the relative effect induced by NLO EW corrections (lower panel): again agreement is found.

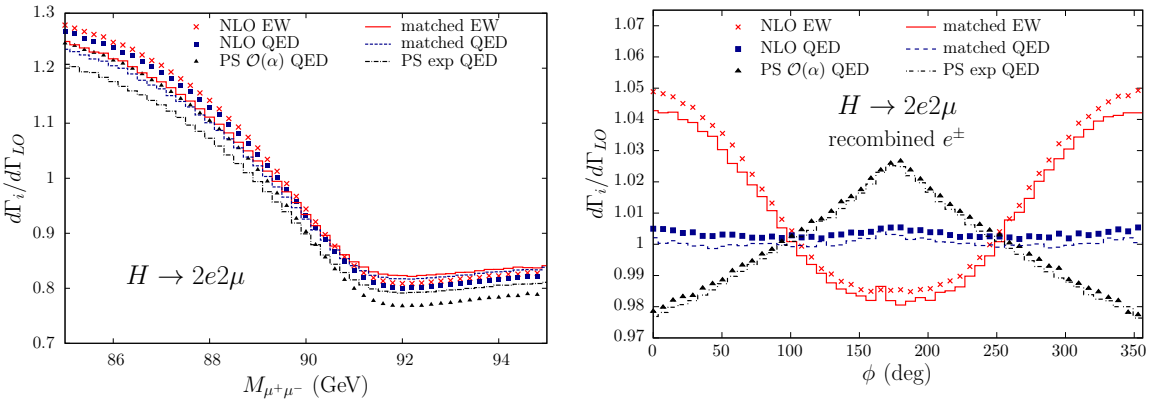

Figure 11: Effects of EW corrections at different level of accuracy on the $M_{\mu^+\mu^-}$ invariant mass (left) and the ϕ-angle (right), with respect to the LO distribution. The decay H $\to$ 2e2μ with $M_{\rm H} = 125$ GeV is considered and, on the right plot, photons with $\Delta R_{e\gamma} < 0.1$ are recombined with the electron. See Ref. [76] for details.

Going beyond the NLO EW accuracy, HTO4L includes also the possibility to simulate multi-photon emissions in a QED PS approach, consistently matched to the NLO calculation [76]. Two examples of the effects induced by multi-photon radiation are shown in Figure 11, where we consider the decay H $\to$ 2e2μ with $M_{\rm H} = 125$ GeV in the Higgs boson rest frame. On the left, the ratio between the $M_{\mu^+\mu^-}$ distribution corrected at different levels of accuracy and the LO one is plotted, emphasizing that multi-photon effects can reach the few per cent level on this distribution. On the right, the size of the corrections is shown on the ϕ-angle distribution: while in this case the impact of QED exponentiation is small, the inclusion of NLO QED and weak corrections is important for studies aiming at accuracies at the level of some per cent. We finally remark that unweighted events are available and, through Les-Houches-Accord (LHA) files, HTO4L can be used in conjunction with any Monte Carlo event generator for (on-shell) Higgs boson production, such as, for instance, POWHEG [80, 81]. An interface, which reads a Higgs boson production LHA file and writes a LHA file with the Higgs momenta replaced by momenta of the decay products (leptons and photons), is provided with the code.

I.3.2 Update on MSSM branching ratios

In the MSSM the evaluation of cross sections and of branching ratios has several common issues as outlined in Sect. 14.1 in Ref. [9] (see also Sect. 12.1 in Ref. [8]). It was discussed that *before* any branching ratio calculation can be performed, the Higgs boson masses, couplings and mixings have to be evaluated from the underlying set of (soft SUSY-breaking) parameters. For the case of real parameters in the MSSM, the code FEYNHIGGS [82–87] was selected for the evaluations in this report. (The case with complex parameters has not been investigated so far.) The results for Higgs boson masses and couplings can be provided to other codes (especially HDECAY [69–71]) via the SUSY Les Houches Accord [88, 89].

In Sect. 2.3 of Ref. [9] it was described how the relevant codes for the calculation of partial decay widths, FEYNHIGGS and HDECAY, are combined to give the most precise result for the Higgs boson branching ratios in the MSSM. The corrections included in these two codes are summarized as follows. The full one-loop corrections in the MSSM (see the discussion in Section IV.1.1) together with resummed SUSY corrections up to the one-loop level and the Z factors up to the two-loop level have been implemented in the code FEYNHIGGS [82–87]. Corrections at and beyond the one-loop level in the MSSM are implemented in the code HDECAY [69–71], including the resummed SUSY corrections up to leading two-loop terms and the O($\alpha_{\rm s}$) corrections to Higgs boson decays to scalar quarks [90]. In Ref. [9] numerical results were shown for all MSSM Higgs bosons (including the charged Higgs) within

the updated benchmark scenarios [91]. Here we briefly describe an update of the branching ratio evaluation, taking into account additional final states (that so far were included in the total width, but not evaluated as individual BRs). The updated numbers can be found in [92].

After the calculation of Higgs boson masses and mixings from the original SUSY input, the branching ratio calculation is performed as follows. We combine the results from HDECAY and FEYNHIGGS (where the decays into massive gauge bosons labelled FH/P4f are based on the SM evaluation taken from PROPHECY4F, see Section IV.1.3) for various decay channels to obtain the most accurate result for the branching ratios currently available. In a first step, all partial widths have been calculated as accurately as possible. Then the branching ratios have been derived from this full set of partial widths. Concretely, we used FEYNHIGGS for the evaluation of the Higgs boson masses and couplings from the original input parameters, including corrections up to the two-loop level. The status of the various evaluations in FEYNHIGGS and HDECAY are detailed in Ref. [8]. The total decay width of the neutral Higgs bosons, $\phi = \mathrm{h}, \mathrm{H}, \mathrm{A}$, is calculated as,

$$\begin{aligned}\Gamma_\phi = {} & \Gamma^{\mathrm{FH}}_{\phi\to\tau^+\tau^-} + \Gamma^{\mathrm{FH}}_{\phi\to\mu^+\mu^-} + \Gamma^{\mathrm{FH/P4f}}_{\phi\to \mathrm{W}^{(*)}\mathrm{W}^{(*)}} + \Gamma^{\mathrm{FH/P4f}}_{\phi\to \mathrm{Z}^{(*)}\mathrm{Z}^{(*)}} \\ & + \Gamma^{\mathrm{HD}}_{\phi\to \mathrm{b\bar{b}}} + \Gamma^{\mathrm{HD}}_{\phi\to \mathrm{t\bar{t}}} + \Gamma^{\mathrm{HD}}_{\phi\to \mathrm{c\bar{c}}} + \Gamma^{\mathrm{HD}}_{\phi\to \mathrm{gg}} + \Gamma^{\mathrm{HD}}_{\phi\to\gamma\gamma} + \Gamma^{\mathrm{HD}}_{\phi\to \mathrm{Z}\gamma} \\ & + \Gamma^{\mathrm{FH}}_{\phi\to \mathrm{Zh}} + \Gamma^{\mathrm{FH}}_{\phi\to \mathrm{hh}} + \Gamma^{\mathrm{FH}}_{\phi\to \mathrm{ZA}} + \Gamma^{\mathrm{FH}}_{\phi\to \mathrm{AA}} + \Gamma^{\mathrm{HD}}_{\phi\to \mathrm{H}^\pm\mathrm{W}^\mp} + \Gamma^{\mathrm{FH}}_{\phi\to \mathrm{SUSY}}\,, \end{aligned} \tag{I.3.6}$$

followed by a corresponding evaluation of the respective branching ratio. With respect to previous evaluations, see Ref. [9], $\Gamma^{\mathrm{FH}}_{\phi\to \mathrm{Zh}}$, $\Gamma^{\mathrm{FH}}_{\phi\to \mathrm{hh}}$, $\Gamma^{\mathrm{FH}}_{\phi\to \mathrm{ZA}}$, $\Gamma^{\mathrm{FH}}_{\phi\to \mathrm{AA}}$ and $\Gamma^{\mathrm{HD}}_{\phi\to \mathrm{H}^\pm\mathrm{W}^\mp}$ are now explicitly included as individual channels. The decays to SUSY particles are not included as individual branching ratios, but of course taken into account in the total width[I.3]. For completeness we also list the evaluation for the charged Higgs boson, which has not changed wrt. Ref. [9]. The total decay width of the charged Higgs boson is calculated as,

$$\begin{aligned}\Gamma_{\mathrm{H}^\pm} = {} & \Gamma^{\mathrm{FH}}_{\mathrm{H}^\pm\to\tau\nu_\tau} + \Gamma^{\mathrm{FH}}_{\mathrm{H}^\pm\to\mu\nu_\mu} + \Gamma^{\mathrm{FH}}_{\mathrm{H}^\pm\to \mathrm{hW}} + \Gamma^{\mathrm{FH}}_{\mathrm{H}^\pm\to \mathrm{HW}} + \Gamma^{\mathrm{FH}}_{\mathrm{H}^\pm\to \mathrm{AW}} \\ & + \Gamma^{\mathrm{HD}}_{\mathrm{H}^\pm\to \mathrm{tb}} + \Gamma^{\mathrm{HD}}_{\mathrm{H}^\pm\to \mathrm{ts}} + \Gamma^{\mathrm{HD}}_{\mathrm{H}^\pm\to \mathrm{td}} + \Gamma^{\mathrm{HD}}_{\mathrm{H}^\pm\to \mathrm{cb}} + \Gamma^{\mathrm{HD}}_{\mathrm{H}^\pm\to \mathrm{cs}} + \Gamma^{\mathrm{HD}}_{\mathrm{H}^\pm\to \mathrm{cd}} \\ & + \Gamma^{\mathrm{HD}}_{\mathrm{H}^\pm\to \mathrm{ub}} + \Gamma^{\mathrm{HD}}_{\mathrm{H}^\pm\to \mathrm{us}} + \Gamma^{\mathrm{HD}}_{\mathrm{H}^\pm\to \mathrm{ud}} + \Gamma^{\mathrm{FH}}_{\mathrm{H}^\pm\to \mathrm{SUSY}}\,, \end{aligned} \tag{I.3.7}$$

followed by a corresponding evaluation of the respective branching ratio.

[I.3] This was also done previously, but not explicitly stated in Refs. [8, 9].

Chapter I.4

Gluon-gluon Fusion

S. Forte, D. Gillberg, C. Hays, A. Lazopoulos, G. Petrucciani, A. Massironi, G. Zanderighi (Eds.); C. Anastasiou, A. Banfi, M. Bonvini, R. Boughezal, F. Caola, X. Chen, B. Di Micco, F.A. Dreyer, C. Duhr, F. Dulat, E. Furlan, T. Gehrmann, E.W.N. Glover, F. Herzog, M. Jaquier, F. Krauss, S. Kuttimalai, A. Lazopoulos, X. Liu, P. Maierhöfer, S. Marzani, B. Mistlberger, P.F. Monni, F. Petriello, E. Re, G.P. Salam, T. Schmidt, M. Schönherr, M. Spira, I.W. Stewart, F.J. Tackmann, K. Tackmann, P. Torrielli

We present here an update of developments since the publication of YR3. First, recent results on the inclusive cross-section are discussed, and we provide recommendations for the computation of its value and uncertainty. Then, jet-binned cross sections are examined: we provide benchmarks for differential transverse-momentum distributions in the effective theory. Finally the effects of heavy-quark masses on these distributions are examined.

I.4.1 The inclusive cross-section

The inclusive gluon fusion Higgs boson production cross-section has a slowly convergent perturbative expansion in QCD with large corrections at NLO and NNLO. Therefore, uncertainties due to missing higher orders have always been large and comparable to PDF uncertainties. Recently, N^{3}LO QCD corrections have been computed in the effective theory as an expansion around threshold in Ref. [93], along with the evaluation of threshold resummation in different schemes. In this section the results of Ref. [93] are reviewed; then, results on threshold resummation at the N^{3}LL matched first with the NNLO (Sect. I.4.1.b) , and then with the N^{3}LO (Sect. I.4.1.c) fixed-order results are presented. fixed or level and its matching to the fixed-order result. Finally, we present the summary for the computation of the central value including all known corrections and the associated total uncertainty.

I.4.1.a The N^{3}LO cross section [I.4]

I.4.1.a.i Ingredients of the computation

This section summarizes our best prediction for the value of the inclusive gluon-fusion cross section and its uncertainties, following Ref. [93]. The main ingredient is the recent computation of gluon-fusion cross section through N^{3}LO in the effective theory where the top-quark is integrated out [94–96].

The master formula that summarizes all the ingredients entering our prediction for the partonic cross-sections is

$$\hat{\sigma}_{ij} \simeq R_{LO}\,\left(\hat{\sigma}_{ij,EFT} + \delta_t\hat{\sigma}^{NNLO}_{ij,EFT} + \delta\hat{\sigma}_{ij,EW}\right) + \delta\hat{\sigma}^{LO}_{ij,ex;t,b,c} + \delta\hat{\sigma}^{NLO}_{ij,ex;t,b,c}\,. \tag{I.4.1}$$

QCD corrections to the production cross-section $\hat{\sigma}_{ij,EFT}$ in the heavy-top limit have been included at NLO [97–99], NNLO [100–102] and N^{3}LO [94–96]. In addition, we also include effects from finite quark masses and electroweak effects, to the extent that they are available. It was already observed at LO and NLO that the validity of the effective theory can be greatly enhanced by rescaling the effective theory by the exact LO result. We therefore rescale the cross-section $\hat{\sigma}_{ij,EFT}$ in the effective theory by the ratio

$$R_{LO} \equiv \frac{\sigma^{LO}_{ex;t}}{\sigma^{LO}_{EFT}}\,, \tag{I.4.2}$$

[I.4] *Author(s): C. Anastasiou, C. Duhr, F. Dulat, E. Furlan, T. Gehrmann, F. Herzog, A. Lazopoulos, B. Mistlberger.*

where $\sigma^{LO}_{ex;t}$ denotes the exact (hadronic) LO cross-section in the SM with a massive top quark and $N_f = 5$ massless quarks. Moreover, at LO and NLO we know the exact result for the production cross-section in the SM, including all mass effects from top, bottom and charm quarks. We include these corrections into our prediction via the terms $\delta\hat{\sigma}^{(N)LO}_{ij,ex;t,b,c}$ in eq. (I.4.1), consistently matched to the contributions from the effective theory to avoid double counting. As a consequence, eq. (I.4.1) agrees with the exact SM cross-section (with massless u, d and s quarks) through NLO in QCD. Beyond NLO, we only know the value of the cross-section in the heavy-top effective theory. We can, however, include subleading corrections at NNLO in the effective theory as an expansion in the inverse top mass [103–106]. These effects are taken into account through the term $\delta_t\hat{\sigma}^{NNLO}_{ij,EFT}$ in eq. (I.4.1), with the factor R_{LO} scaled out. They were originally computed with the top mass at the OS scheme, but their scheme dependence is expected to be at the sub-per mille level, following lower orders, and is hence considered negligible here. We also include electroweak corrections to the gluon-fusion cross-section (normalized to the exact LO cross-section) through the term $\delta\hat{\sigma}_{ij,EW}$ in eq. (I.4.1). Unlike QCD corrections, electroweak corrections have only been computed through NLO in the electromagnetic coupling constant α [107–109]. Moreover, mixed QCD-electroweak corrections, i.e., corrections proportional to $\alpha\,\alpha_s^3$, are known in an effective theory [110] valid in the limit where not only the top quark but also the electroweak bosons are much heavier than the Higgs boson. In this limit the interaction of the Higgs boson with the W and Z bosons is described via a point-like vertex coupling the gluons to the Higgs boson. Higher-order corrections in this limit can thus be included into the Wilson coefficient in front of the dimension-five operator describing the effective interaction of the gluons with the Higgs boson. The validity and limitations of this approximation are discussed in Section I.4.1.a.iii.

I.4.1.a.ii Summary of results

The numerical results quoted in this section are valid for the following set of input parameters:

$\sqrt{S}$	13 TeV
m_h	125 GeV
PDF	`PDF4LHC15_nnlo_100`
$\alpha_s(m_Z)$	0.118
$m_t(m_t)$	162.7 GeV ($\overline{\text{MS}}$)
$m_b(m_b)$	4.18 GeV ($\overline{\text{MS}}$)
$m_c(3GeV)$	0.986 GeV ($\overline{\text{MS}}$)
$\mu = \mu_R = \mu_F$	62.5 GeV ($= m_H/2$)

Using these input parameters, our current best prediction for the production cross section of a Higgs boson with a mass $m_H = 125$ GeV at the LHC with a centre-of-mass energy of 13 TeV is

$$\boxed{\sigma = 48.58\,\text{pb}^{+2.22\,\text{pb}\,(+4.56\%)}_{-3.27\,\text{pb}\,(-6.72\%)}\,(\text{theory}) \pm 1.56\,\text{pb}\,(3.20\%)\,(\text{PDF+}\alpha_s)\,.} \tag{I.4.3}$$

The central value in eq. (I.4.3), computed at the central scale $\mu_F = \mu_R = m_H/2$, is the combination of all the effects considered in eq. (I.4.1). The breakdown of the different effects is:

$$\begin{aligned}
48.58\,\text{pb} = \quad & 16.00\,\text{pb} && (+32.9\%) && (\text{LO, rEFT}) \\
+\,& 20.84\,\text{pb} && (+42.9\%) && (\text{NLO, rEFT}) \\
-\,& 2.05\,\text{pb} && (-4.2\%) && ((t,b,c), \text{exact NLO}) \\
+\,& 9.56\,\text{pb} && (+19.7\%) && (\text{NNLO, rEFT}) \\
+\,& 0.34\,\text{pb} && (+0.7\%) && (\text{NNLO}, 1/m_t) \\
+\,& 2.40\,\text{pb} && (+4.9\%) && (\text{EW, QCD-EW}) \\
+\,& 1.49\,\text{pb} && (+3.1\%) && (\text{N}^3\text{LO, rEFT})
\end{aligned} \tag{I.4.4}$$

where rEFT denotes the cross section in the effective field theory approximation rescaled by R_{LO} of (I.4.2) . We note that the N^{3}LO central value is completely insensitive to threshold resummation effects for $\mu_F = \mu_R = m_H/2$ and the central value obtained from a fixed-order N^{3}LO computation and a resummed computation at N^{3}LO + N^{3}LL are identical for this scale choice. We therefore conclude that threshold resummation does not provide any improvement of the central value, and it is therefore not included in our prediction.

The PDF and α_s uncertainties are computed following the recommendation of the PDF4LHC working group. The remaining theory-uncertainty in eq. (I.4.3) is obtained by adding linearly various sources of theoretical uncertainty, which affect the different contributions to the cross section in eq. (I.4.1). The breakdown of the different theoretical uncertainties whose linear sum produces the theoretical uncertainty in eq. (I.4.3) is

δ(scale)	δ(trunc)	δ(PDF-TH)	δ(EW)	$\delta(t,b,c)$	$\delta(1/m_t)$
$^{+0.10\text{ pb}}_{-1.15\text{ pb}}$	$\pm$0.18 pb	$\pm$0.56 pb	$\pm$0.49 pb	$\pm$0.40 pb	$\pm$0.49 pb
$^{+0.21\%}_{-2.37\%}$	$\pm 0.37\%$	$\pm 1.16\%$	$\pm 1\%$	$\pm 0.83\%$	$\pm 1\%$

In the remainder of this note we address each of the components that enter the final theoretical uncertainty estimate in turn.

I.4.1.a.iii Breakdown of the theoretical uncertainties

Uncertainty from missing higher orders: δ(scale)

The uncertainty δ(scale) captures the impact of missing higher order terms in the perturbative expansion of the cross section in the rEFT. We identify this uncertainty with the scale variation when varying the renormalization and factorization scales simultaneously in the interval $\mu_F = \mu_R \in [m_H/4, m_H]$. The N^{3}LO corrections moderately increase ($\sim 3\%$) the cross-section for renormalization and factorization scales equal to $m_H/2$. In addition, they notably stabilize the scale variation, reducing it almost by a factor of five compared to NNLO. The N^{3}LO scale-variation band is included entirely within the NNLO scale-variation band for scales in the interval $[m_H/4, m_H]$. We note that, while we vary the scales simultaneously, we have checked (see Figure 6 of [93]) that the factorization scale dependence is flat, and the scale dependence at N^{3}LO is driven by the renormalization scale dependence.

It is important to assess how well the scale uncertainty captures the uncertainty due to missing higher orders in the perturbative expansion, given that it failed to capture the shift in the central value due to missing perturbative orders at lower orders. We have found good evidence that the N^{3}LO scale variation captures the effects of missing higher perturbative orders in the EFT. We base this conclusion on the following observations: First, we observe that expanding in α_s separately the Wilson coefficient and matrix-element factors in the cross-section gives results consistent with expanding directly their product through N^{3}LO. Second, a traditional threshold resummation in Mellin space up to N^{3}LL did not contribute significantly to the cross-section beyond N^{3}LO in the range of scales $\mu \in [m_H/4, m_H]$. Although the effects of threshold resummation are in general sensitive to ambiguities due to subleading terms beyond the soft limit, we found that within our preferred range of scales, several variants of the exponentiation formula gave very similar phenomenological results, which are always consistent with fixed-order perturbation theory. Finally, a soft-gluon and π^2-resummation using the SCET formalism also gave consistent results with fixed-order perturbation theory at N^{3}LO. While ambiguities in subleading soft terms limit the use of soft-gluon resummation as an estimator of higher-order effects, and while it is of course possible that some variant of resummation may yield larger corrections, it is encouraging that this does not happen for the mainstream prescriptions studied here.

We conclude this discussion by commenting on the use of resummation to estimate the uncertainty on the cross section. Based on the considerations from the previous paragraph, we are led to conclude

that threshold resummation does not provide any improvement over a fixed-order calculation, and we therefore do not include it into our prediction. We base this conclusion on the following facts. First, we have already observed in the previous section that the central value at N^{3}LO for $\mu \equiv \mu_R = \mu_F = m_H/2$ is insensitive to resummation effects, excluding any need for resummation to improve the fixed order prediction. Second, the scale variation for N^{3}LO + N^{3}LL is contained inside the fixed-order N^{3}LO scale-variation band for $\mu \in [m_H/4, m_H]$ for a variety of different formalisms to perform threshold resummation, indicating that threshold resummation is more likely to underestimate the uncertainty from the variation. Finally, we point out that the resummation program itself is plagued by systematic uncertainties coming from terms that are power suppressed in the threshold variable $(s - m_H^2)$ (or equivalently, in $1/N$ in Mellin space) and are not controlled by the resummation. Although formally of higher order, these uncontrolled terms can have a substantial impact on the cross section, which is in our opinion not physically motivated. Any conclusion based on varying these uncontrolled power-suppressed and constant terms should therefore be discarded in our opinion, and they are not considered in our prediction.

The truncation uncertainty: δ(trunc)

The truncation uncertainty captures the uncertainty introduced by the fact the N^{3}LO corrections are currently only known as an expansion around threshold, i.e., as an expansion in the amount of energy available to QCD radiation, to order 37. We assign an uncertainty due to the truncation of the threshold expansion which is as large as

$$\delta(\text{trunc}) = 10 \times \frac{\sigma^{(3)}_{EFT}(37) - \sigma^{(3)}_{EFT}(27)}{\sigma^{\text{N}^3\text{LO}}_{EFT}} = 0.37\% \,. \tag{I.4.5}$$

The factor 10 is a conservative estimator of the progression of the series beyond the first 37 terms. Note that the complete N^{3}LO cross-section appears in the denominator of eq. (I.4.5), i.e., the uncertainty applies to the complete N^{3}LO result, not just the coefficient of α_s^5.

The uncertainty from missing N^{3}LO PDFs: δ(PDF-TH)

So far, PDFs have only been extracted by comparing data to theory predictions at NNLO in QCD, and so an inconsistency may only arise due to the extraction of the parton densities from data for which there are no N^{3}LO predictions. To assess this uncertainty we resort to the experience from the previous orders and investigate the shift in the NNLO cross section when it is computed with either NLO or NNLO PDFs. We observe that as a function of the factorization scale in the range $\mu_F \in [m_H/4, m_H]$ (with the renormalization scale held fixed) scale) the NNLO cross-section decreases by about $2.2 - 2.4\%$ when NNLO PDFs are used instead of NLO PDFs. Given that N^{3}LO corrections are expected to be milder in general than their counterparts at NNLO, we anticipate that they will induce a smaller shift than at NNLO. Based on these considerations, we assign a conservative uncertainty estimate due to missing higher orders in the extraction of the parton densities obtained as

$$\delta(\text{PDF} - \text{TH}) = \frac{1}{2} \left| \frac{\sigma^{(2),NNLO}_{EFT} - \sigma^{(2),NLO}_{EFT}}{\sigma^{(2),NNLO}_{EFT}} \right| = \frac{1}{2}\, 2.31\% = 1.16\% \,, \tag{I.4.6}$$

where $\sigma^{(2),(N)NLO}_{EFT}$ denotes the NNLO cross-section evaluated with (N)NLO PDFs at the central scale $\mu_F = \mu_R = m_H/2$. In the above, the strong coupling was set to its world-average at the Z pole and evolved using three-loop renormalization group running, and we assumed conservatively that the size of the N^{3}LO corrections is about half of the corresponding NNLO corrections. This estimate is supported by the magnitude of the third-order corrections to the coefficient functions for deep inelastic scattering [111] and a related gluonic scattering process [112], which are the only two coefficient functions that were computed previously to this level of accuracy.

The uncertainty due to missing QCD-EW corrections: δ(EW)

Given the large size of the NLO QCD corrections to the Higgs cross-section, we may expect that also the EW corrections to the NLO QCD cross-section cannot be neglected. Unfortunately, these so-called

mixed QCD-EW corrections are at present unknown, and only the contribution from an EFT approximation where the weak bosons are heavier than the Higgs boson are taken into account. The effective theory method for the mixed QCD-EW corrections is of course not entirely satisfactory, because the computation of the EW Wilson coefficient assumes the validity of the m_H/m_V expansion, $V = W, Z$ while clearly $m_H > m_V$. We thus need to carefully assess the uncertainty on the mixed QCD-EW corrections due to the EFT approximation. In the region $m_H > m_V$, we expect effects from virtual weak bosons going on shell to be important and one should not expect that a naive application of the EFT can give a reliable value for the cross-section. However, the EFT is only used to predict the relative size of QCD radiative corrections with respect to the leading order electroweak corrections, i.e., the dominant electroweak threshold effects from pairs of weak bosons going on shell should already be captured by the leading-order electroweak corrections. This can only vary mildly above and below threshold. For phenomenological purposes, we expect that the rescaling with the exact NLO EW corrections captures the bulk of threshold effects at all perturbative orders. To quantify the remaining uncertainty in this approach, we allow the EW Wilson coefficient C_{1w} to vary by a factor of 3 around its central value. We do this by introducing a rescaling factor y_λ by

$$\lambda_{EW}\,(1 + C_{1w}\,a_s + \ldots) \to \lambda_{EW}\,(1 + y_\lambda\,C_{1w}\,a_s + \ldots)\,, \tag{I.4.7}$$

where $a_s = \alpha_s/\pi$. Varying y_λ in the range $[1/3, 3]$, we see that the cross-section varies by -0.2% to $+0.4\%$. Note that the result obtained by assuming complete factorization of EW and QCD corrections lies in the middle of the variation range, slightly higher than the $y_\lambda = 1$ prediction. Finally, we stress that the choice of the range is largely arbitrary of course. It is worth noting, however, that in order to reach uncertainties of the order of 1%, one needs to enlarge the range to $y_\lambda \in [-3, 6]$.

An alternative way to assess the uncertainty on the mixed QCD-EW corrections is to note that the factorization of the EW corrections is exact in the soft and collinear limits of the NLO phase space. The hard contribution, however, might be badly captured. At NLO in QCD, the hard contribution amounts to $\sim 40\%$ of the $\mathcal{O}(a_s^3)$ contribution to the cross-section, where we define the *hard contribution* as the NLO cross-section minus its soft-virtual contribution, i.e., the NLO contribution that does not arise from the universal exponentiation of soft gluon radiation. The *hard contribution* is defined as the convolution of the parton-level quantity

$$\frac{\hat{\sigma}_{ij}^{(1),\text{hard}}}{z} \equiv \frac{\pi|C_0|^2}{8V}\,a_s^3\,\eta_{ij}^{(1),\text{reg}}(z) \tag{I.4.8}$$

with the PDFs, which receive contributions from the gg, qg and $q\bar{q}$ initial state channels. The mixed QCD-EW corrections are 3.2% of the total cross-section. Even if the uncertainty of the factorization ansatz is taken to be as large as the entire hard contribution, we will obtain an estimate of the uncertainty equal to $0.4 \times 3.2\% = 1.3\%$ with respect to the total cross-section.

An alternative way to define the *hard contribution* is to look at the real emission cross-section regulated by a subtraction term in the FKS scheme [113]. We could then exclude the contribution of the integrated subtraction term, which is proportional to the Born matrix element, and hence of soft-collinear nature. We would then estimate the *hard contribution* as $\sim 10\%$ of the $\mathcal{O}(a_s^3)$ contribution to the cross-section, which would lead to an uncertainty equal to $0.1 \times 3.2\% = 0.32\%$.

We note that the different estimates of the uncertainty range from 0.2% to 1.3%. We therefore assign, conservatively, an uncertainty of 1% due to mixed QCD-EW corrections for LHC energies.

The missing b and c-quark mass effects: $\delta(t, b, c)$

Unlike the case of the top quark, the contributions of the bottom and charm quarks at NNLO are entirely unknown. We estimate the uncertainty of the missing interference between the top and light quarks within the $\overline{\text{MS}}$-scheme as:

$$\delta(t,b,c)^{\overline{\text{MS}}} = \pm \left| \frac{\delta\sigma_{ex;t}^{NLO} - \delta\sigma_{ex;t+b+c}^{NLO}}{\delta\sigma_{ex;t}^{NLO}} \right| (R_{LO}\delta\sigma_{EFT}^{NNLO} + \delta_t\hat{\sigma}_{gg+qg,EFT}^{NNLO}) \simeq \pm 0.31\,\text{pb}\,, \tag{I.4.9}$$

where

$$\delta\sigma_X^{NLO} \equiv \sigma_X^{NLO} - \sigma_X^{LO} \text{ and } \delta\sigma_X^{NNLO} \equiv \sigma_X^{NNLO} - \sigma_X^{NLO} . \tag{I.4.10}$$

Our preferred scheme is the $\overline{\text{MS}}$-scheme (**with** $\mu_R = m_H/2$) due to the bad convergence of the perturbative series for the conversion from an $\overline{\text{MS}}$ mass to a pole mass for the bottom and charm quarks [17, 114]. To account for the difference with the OS scheme, we enlarge the uncertainty on $\sigma_{t+b+c} - \sigma_t$, as estimated via eq. (I.4.9) within the $\overline{\text{MS}}$ scheme, by multiplying it with a factor of 1.3,

$$\delta(t,b,c) = 1.3\,\delta(t,b,c)^{\overline{\text{MS}}} . \tag{I.4.11}$$

Uncertainty from top-mass effects at NNLO: $\delta(1/m_t)$

The corrections due to top-mass effects at NNLO, as an expansion in $1/m_t$, are included through the term $\delta_t\hat{\sigma}_{ij,EFT}^{NNLO}$ in eq. (I.4.1). The $1/m_t$ expansion is in fact an expansion in s/m_t^2, and consequently it needs to be matched to the high-energy limit of the cross-section, known to leading logarithmic accuracy from k_t-factorization. The high-energy limit corresponds to the contribution from small values of z to the convolution integral with the parton luminosities. Since this region is suppressed by the luminosity, a lack of knowledge of the precise matching term is not disastrous and induces an uncertainty of roughly 1%, which is of the order of magnitude of the net contribution. In conclusion, following the analysis of ref. [106], whose conclusions were confirmed by ref. [104], we assign an overall uncertainty of 1% due to the unknown top-quark effects at NNLO.

I.4.1.b N^{3}LL resummation [I.5]

The inclusive gluon-fusion cross section for Higgs boson production can be improved by performing a threshold resummation of soft, virtual and collinear gluon effects [115]. This resummation is performed in Mellin space according to the conventional formalism used before for Higgs boson production [116–123]. The resummed cross section develops a factorized kernel structure in Mellin space

$$\begin{aligned}\tilde{G}_{gg}^{(res)}\left(N;\alpha_s(\mu_R^2),\frac{M_H^2}{\mu_R^2};\frac{M_H^2}{\mu_F^2};\frac{M_H^2}{m_t^2}\right) &= \alpha_s^2(\mu_R^2)C_{gg}\left(\alpha_s(\mu_R^2),\frac{M_H^2}{\mu_R^2};\frac{M_H^2}{\mu_F^2};\frac{M_H^2}{m_t^2}\right)\\ &\quad\times\exp\left\{\tilde{\mathcal{G}}_H\left(\alpha_s(\mu_R^2),\log N;\frac{M_H^2}{\mu_R^2},\frac{M_H^2}{\mu_F^2}\right)\right\}\end{aligned} \tag{I.4.12}$$

We include top mass effects up to the NLL level explicitly in the coefficient function

$$C_{gg}\left(\alpha_s(\mu_R^2),\frac{M_H^2}{\mu_R^2};\frac{M_H^2}{\mu_F^2};\frac{M_H^2}{m_t^2}\right) = 1+\sum_{n=1}^{\infty}\left(\frac{\alpha_s(\mu_R^2)}{\pi}\right)^n C_{gg}^{(n)}\left(\frac{M_H^2}{\mu_R^2},\frac{M_H^2}{\mu_F^2};\frac{M_H^2}{m_t^2}\right) \tag{I.4.13}$$

that contains the finite parts of the virtual corrections. The NLO contribution is given explicitly by ($\tau_Q = 4m_Q^2/M_H^2$) [121]

$$C_{gg}^{(1)} = c_H(\tau_t) + 6\zeta_2 + \frac{33-2N_F}{6}\log\frac{\mu_R^2}{\mu_F^2} + 6(\gamma_E^2+\zeta_2) - 6\gamma_E\log\frac{M_H^2}{\mu_F^2} , \tag{I.4.14}$$

where the function $c_H(\tau_t)$ approaches $11/2$ in the limit of heavy top quarks. The resummed exponential develops the expansion

$$\begin{aligned}\tilde{\mathcal{G}}_H\left(\alpha_s(\mu_R^2),\log N;\frac{M_H^2}{\mu_R^2},\frac{M_H^2}{\mu_F^2}\right) &= \log N\; g_H^{(1)}(\lambda)\\ &\quad+\sum_{n=2}^{\infty}\alpha_s^{n-2}(\mu_R^2)g_H^{(n)}\left(\lambda,\frac{M_H^2}{\mu_R^2};\frac{M_H^2}{\mu_F^2}\right)\Bigg|_{\lambda=b_0\alpha_s(\mu_R^2)\log N}\end{aligned} \tag{I.4.15}$$

[I.5] *Author(s): T. Schmidt, M. Spira.*

with b_0 denoting the leading order term of the QCD beta function,

$$b_0 = \frac{33 - 2N_F}{12\pi} \tag{I.4.16}$$

where N_F is the number of active flavours that we choose as $N_F = 5$ in the following, i.e. the top quark has been decoupled from the strong coupling α_s and the PDFs. The individual functions $g_H^{(i)}$ $(i = 1, \ldots, 4)$ can be found e.g. in [116, 124–126]. The leading and subleading collinear gluon effects have been included by the replacements [115, 116, 127, 128]

$$\begin{aligned} C_{gg}^{(1)} &\rightarrow C_{gg}^{(1)} + 6\,\frac{\tilde{L}}{N} \\ C_{gg}^{(2)} &\rightarrow C_{gg}^{(2)} + (48 - N_F)\,\frac{\tilde{L}^2}{N} \end{aligned} \tag{I.4.17}$$

with the modified logarithm

$$\tilde{L} = \log\frac{N e^{\gamma_E}\mu_F}{M_H} = \log N + \gamma_E - \frac{1}{2}\log\frac{M_H^2}{\mu_F^2}\,. \tag{I.4.18}$$

These replacements reproduce the leading and subleading collinear logarithms up to N^{3}LO.

The general expression for the inclusive cross section can be cast into the form

$$\begin{aligned} &\sigma(s, M_H^2) = \sigma_{tt}^0 \int_{C-i\infty}^{C+i\infty} \frac{dN}{2\pi i}\left(\frac{M_H^2}{s}\right)^{-N+1} \tilde{f}_g(N,\mu_F^2)\tilde{f}_g(N,\mu_F^2) \\ &\times\left\{\tilde{G}_{gg}^{(res)}\left(N;\alpha_s(\mu_R^2),\frac{M_H^2}{\mu_R^2};\frac{M_H^2}{\mu_F^2};0\right) - \left[\tilde{G}_{gg}^{(res)}\left(N;\alpha_s(\mu_R^2),\frac{M_H^2}{\mu_R^2};\frac{M_H^2}{\mu_F^2};0\right)\right]_{(NNLO)}\right\} \\ &+\sigma_{tt}^0 \int_{C-i\infty}^{C+i\infty} \frac{dN}{2\pi i}\left(\frac{M_H^2}{s}\right)^{-N+1} \tilde{f}_g(N,\mu_F^2)\tilde{f}_g(N,\mu_F^2) \\ &\times\left\{\tilde{G}_{gg,NLL}^{(res)}\left(N;\alpha_s(\mu_R^2),\frac{M_H^2}{\mu_R^2};\frac{M_H^2}{\mu_F^2};\frac{M_H^2}{m_t^2}\right) - \tilde{G}_{gg,NLL}^{(res)}\left(N;\alpha_s(\mu_R^2),\frac{M_H^2}{\mu_R^2};\frac{M_H^2}{\mu_F^2};0\right)\right. \\ &\left. - \left[\tilde{G}_{gg,NLL}^{(res)}\left(N;\alpha_s(\mu_R^2),\frac{M_H^2}{\mu_R^2};\frac{M_H^2}{\mu_F^2};\frac{M_H^2}{m_t^2}\right) - \tilde{G}_{gg,NLL}^{(res)}\left(N;\alpha_s(\mu_R^2),\frac{M_H^2}{\mu_R^2};\frac{M_H^2}{\mu_F^2};0\right)\right]_{(NLO)}\right\} \\ &+\sigma_{t+b+c}^{NNLO}(s, M_H^2) \end{aligned} \tag{I.4.19}$$

with σ_{tt}^0 denoting top quark contribution to the LO cross section factor

$$\begin{aligned} \sigma_0 &= \frac{G_F}{288\sqrt{2}\pi}\left|\sum_Q A_Q(\tau_Q)\right|^2 \\ A_Q(\tau) &= \frac{3}{2}\tau[1 + (1-\tau)f(\tau)] \\ f(\tau) &= \begin{cases} \arcsin^2\dfrac{1}{\sqrt{\tau}} & \tau \geq 1 \\ -\dfrac{1}{4}\left[\log\dfrac{1+\sqrt{1-\tau}}{1-\sqrt{1-\tau}} - i\pi\right]^2 & \tau < 1 \end{cases} \end{aligned} \tag{I.4.20}$$

and $\tilde{f}_g$ is the Mellin moment of the gluon density. Moreover, in order to reside to the right of all poles in the complex Mellin plane an offset C is introduced for the integration contour. The Landau singularity at large values of N on the other hand is ensured to lie on the right side of the integration contour [129, 130].

The index '$(NNLO)$' in the second line indicates the fixed-order expansion of the resummed coefficient function $\tilde{G}_{gg}^{(res)}$ in Mellin space up to NNLO while the index '(NLO)' denotes the perturbative expansion of the NLL resummed coefficient function $\tilde{G}_{gg,NLL}^{(res)}$ in Mellin space up to NLO. The first integral has been convolved with N^{3}LO α_s and NNLO PDFs according to the discussion about the non-necessity of N^{3}LO PDFs of Ref. [131] and of resummed PDFs of Ref. [132] for the SM Higgs boson mass, while the second integral has been evaluated with NLO α_s and PDFs consistently. The fixed-order NNLO cross section [100–102] of the last term has been derived as

$$\sigma_{t+b+c}^{NNLO}(s, M_H^2) = \sigma_{\infty}^{NNLO}(s, M_H^2) + \sigma_{t+b+c}^{NLO}(s, M_H^2) - \sigma_{\infty}^{NLO}(s, M_H^2) \tag{I.4.21}$$

with the individual parts

$$\begin{aligned} \sigma_{\infty}^{NNLO}(s, M_H^2) &= \sigma_{tt}^{LO} K_{\infty}^{NNLO} \\ \sigma_{\infty}^{NLO}(s, M_H^2) &= \sigma_{tt}^{LO} K_{\infty}^{NLO} \\ \sigma_{t+b+c}^{NLO}(s, M_H^2) &= \sigma_{t+b+c}^{LO} K_{t+b+c}^{NLO} \end{aligned} \tag{I.4.22}$$

where σ_{tt}^{LO} denotes the full LO cross section including only top loops, σ_{t+b+c}^{LO} the LO cross section including top and bottom/charm loops, $K_{\infty}^{(N)NLO}$ the (N)NLO K-factors obtained in the limit of heavy top quarks and K_{t+b+c}^{NLO} the full NLO K-factor including top and bottom/charm loops. The NNLO parts have been derived with N^{3}LO α_s and NNLO PDFs and the NLO terms with NLO α_s and PDFs consistently as implemented in the programs HIGLU [133, 134] and SusHi [135]. This implementation guarantees that top mass effects are treated at NLL level and bottom/charm contributions at fixed NLO respectively.

Since the virtual coefficient of the bottom contributions behaves in the limit $M_H^2 \gg m_b^2$ as [136] $(C_A = 3, C_F = 4/3)$

$$c_H(\tau_b) \to \frac{C_A - C_F}{12} \log^2 \frac{M_H^2}{m_b^2} - C_F \log \frac{M_H^2}{m_b^2} \tag{I.4.23}$$

if the bottom mass is renormalized on-shell, it contains large logarithms that are not resummed. The resummation of the Abelian part proportional to C_F has been performed in Ref. [137–139] up to the subleading logarithmic level. These logarithms are related to the Sudakov form factor at the virtual $Hb\bar{b}$ vertex that generates these large logarithmic contributions for far off-shell bottom quarks inside the corresponding loop contributions in the Abelian case. The resummation of the non-Abelian part proportional to the Casimir factor C_A has not been considered so far. This type of logarithmic contributions emerges from a different origin than the soft and collinear gluon effects discussed so far and is the main source of the very different size of QCD corrections to the bottom-loop contributions [98, 136, 140–143]. In order to obtain a reliable result for the bottom contributions a resummation of these types of logarithms is mandatory so that we do not include these contributions in our soft and collinear gluon resummation but treat them at fixed NLO. Moreover, according to the discussion presented about Figure 7a in Ref. [136] we prefer to introduce quark pole masses also for the bottom and charm quark, since the finite part of the virtual corrections is then of moderate size due to an (accidental) cancellation of the logarithms present in Eq. (I.4.23), while this contribution is significantly larger if using the running $\overline{\text{MS}}$ masses at the scale $M_H/2$ so that the latter choice is disfavoured.

Following the recommendations of the LHC Higgs Cross Section Working Group [144] our final results for the inclusive cross section at N^{3}LL including NLO electroweak corrections [107–109, 145–149] in factorized form are given in Table 6 for a central renormalization and factorization scale choice $\mu_R = \mu_F = M_H/2$. Compared to our previous work [128] the PDF+α_s uncertainties decreased considerably due to the new PDF4LHC15 sets [35] of recommended parton densities[I.6]. The scale dependence

[1.6] If other PDF sets as ABM12 [40], HERAPDF2.0 [32] or JR14 [42] are included the PDF+α_s uncertainties will increase considerably with a major part originating from sizeable differences in the α_s fits at NNLO and different data sets included in the global fits. Moreover, the proper treatment of higher-twist effects in the global fits is an open aspect in this context.

has been obtained by an independent variation of the renormalization and factorization scales by factors of two up and down avoiding a splitting between these two scales by more than a factor of two. The total uncertainties are evaluated by adding the scale and PDF+α_s uncertainties linearly (to be conservative). They range below the 10%-level. Comparing the resummed numbers with those of the N^{3}LO expansion of our resummed cross section one obtains a resummation effect beyond N^{3}LO of less than two per mille for our central scale choices so that resummation effects are tiny. For different scale choices they can reach a level of about 2%.

Table 6: N^{3}LL Higgs boson production cross sections via gluon fusion for different values of the Higgs boson mass including the individual and total uncertainties due to the renormalization and factorization scale dependence and PDF+α_s uncertainties including electroweak corrections using PDF4LHC15 [35] PDFs for a c.m. energy $\sqrt{s} = 13$ TeV. The renormalization and factorization scales have been chosen as $M_H/2$.

M_H [GeV]	$\sigma(pp \to H + X)$ [pb]	scale	PDF+α_s	total
124	47.53 pb	$^{+4.7\%}_{-5.4\%}$	$\pm 3.3\%$	$^{+8.0\%}_{-8.7\%}$
124.5	47.20 pb	$^{+4.6\%}_{-5.4\%}$	$\pm 3.3\%$	$^{+7.9\%}_{-8.7\%}$
125	46.87 pb	$^{+4.6\%}_{-5.4\%}$	$\pm 3.3\%$	$^{+7.9\%}_{-8.7\%}$
125.5	46.55 pb	$^{+4.6\%}_{-5.4\%}$	$\pm 3.3\%$	$^{+7.8\%}_{-8.7\%}$
126	46.22 pb	$^{+4.5\%}_{-5.4\%}$	$\pm 3.3\%$	$^{+7.8\%}_{-8.7\%}$

Our numbers deviate from the explicit N^{3}LO results given in Ref. [93] due to the different choice of quark mass scheme for the top, bottom and charm contributions. If these are adopted as running $\overline{\rm MS}$ quantities at the scale $M_H/2$ the cross sections increase by 1.4% compared to those with pole masses as shown in Table 7. The numbers with $\overline{\rm MS}$ masses agree with the full N^{3}LO results within about 2 per cent. The differences are due to the omission of NNLO mass effects and the virtual+soft+collinear approximation of our N^{3}LL terms in our results.

Table 7: N^{3}LL Higgs boson production cross sections via gluon fusion for different values of the Higgs boson mass for two different choices of the scheme for the top, bottom and charm quark masses including electroweak corrections using PDF4LHC15 [35] PDFs for a c.m. energy $\sqrt{s} = 13$ TeV. The last column shows the central N^{3}LO numbers of Ref. [93]. The renormalization and factorization scales have been chosen as $M_H/2$.

M_H [GeV]	pole masses	$\overline{m}_Q(M_H/2)$	Ref. [93]
124	47.53 pb	48.19 pb	49.27 pb
124.5	47.20 pb	47.83 pb	48.92 pb
125	46.87 pb	47.51 pb	48.58 pb
125.5	46.55 pb	47.20 pb	48.23 pb
126	46.22 pb	46.86 pb	47.89 pb

The whole framework of our resummation approach to the inclusive gluon-fusion cross sections has also been applied to neutral Higgs boson production within the MSSM, i.e. providing resummed

predictions at N^{3}LL for the scalar Higgs bosons and at NNLL for the pseudoscalar state [128, 150].

I.4.1.c Combined fixed order and resummed results at N^{3}LO+N^{3}LL [I.7]

In this contribution we briefly summarize the impact of threshold resummation on the inclusive Higgs boson production cross-section, both in terms of the shift in the central value, as well as a means to faithfully estimate the theoretical uncertainty from missing higher orders, $\delta(\text{mho})$, as detailed in Ref. [123]. In this context, the proposed best estimate for the Higgs cross section is given by

$$\sigma_{\text{N}^3\text{LO+N}^3\text{LL}} = \sigma_{\text{N}^3\text{LO}} + \Delta_3\sigma_{\text{N}^3\text{LL}}, \tag{I.4.24}$$

where $\sigma_{\text{N}^3\text{LO}}$ is the fixed-order cross section at N^{3}LO, as computed in Refs. [93–96]. The second contribution, $\Delta_3\sigma_{\text{N}^3\text{LL}}$, contains the all-orders resummation of those contributions that are enhanced in the threshold limit to N^{3}LL accuracy [122, 128, 151, 152], minus its expansion to fixed N^{3}LO (so this contribution starts at N^{4}LO). The computation of $\Delta_3\sigma_{\text{N}^3\text{LL}}$ Eq. (I.4.24) is done through the public code `TROLL` [153], formerly `ResHiggs`. `TROLL` does not compute the fixed order, but only the subtracted resummed contribution, $\Delta_3\sigma_{\text{N}^3\text{LL}}$, so the fixed order has to be supplied by an external code. In this section the code `ggHiggs` [154] has been used.

The resummation is performed in a conjugate (Mellin) space, where the threshold limit corresponds to large N. While resummation uniquely determines the coefficients of logarithmically enhanced terms and constants, there is a certain latitude in defining how the soft approximation is constructed, by making choices which differ by terms which vanish as $N \to \infty$. In Refs. [122, 155], this freedom was exploited to construct variants of threshold resummation that have better perturbative properties. In particular, ψ-soft resummation correctly reproduces, order by order in the strong coupling, the analytic properties of fixed-order coefficient functions. Moreover, as pointed out in Ref. [122], ψ-soft can be further improved by including in the calculation more contributions to the soft expansion of the Altarelli-Parisi splitting function. Two options have been considered:

- AP2 (default): P_{gg} is retained to second order in $1 - z$;
- AP1: P_{gg} is retained to first order in $1 - z$.

Varying the order of this soft expansion (AP2 vs. AP1) can be used as an estimate of unknown contributions beyond the threshold limit. Finally, in order to assess the impact of subleading contributions beyond N^{3}LL, one can vary the way we deal with the constant terms, which can be treated in the default setup of Ref. [123] or in two extreme configurations:

- default: those constants coming from the Mellin transform of plus distributions [156] are in the exponent, the others are not;
- all constants in the exponent;
- no constants in the exponent.

Up to the working logarithmic accuracy, the position of the constants does not make any difference. However, beyond the working logarithmic accuracy, moving constants produces, by interference, different subleading contributions. Note that, since constants are known to play an important role for Higgs boson production [157–159], these variations provide a robust way to estimate the perturbative uncertainty. Combining together the different options for subleading logarithmic terms and subleading threshold terms one gets a total of $3 \times 2 = 6$ variants of the resummation.

For simplicity, and for disentangling effects coming from different sources, results are given in the clean environment of the (rescaled) large-m_t effective theory (rEFT), using the top mass $m_t = 172.5$ GeV in the pole scheme, the Higgs boson mass $m_H = 125$ GeV, and the `PDF4LHC15_nnlo_100` PDF set [35–38, 49]. The strong coupling α_s is run from $\alpha_s(m_Z^2) = 0.118$ (from the PDF set) to μ_R at four loops. In order to show the stability of the resummed result, four options for the central common

[I.7] *Author(s): M. Bonvini, S. Marzani.*

Table 8: Fixed-order results and their scale uncertainty together with resummed results and their uncertainty (as given by the envelope of prescription and scale variations) for four choices of the central scale. Results are given in the (rescaled) large-m_t effective theory with pole top mass (see text).

	$\mu_0 = m_H/4$	$\mu_0 = m_H/2$	$\mu_0 = m_H$	$\mu_0 = 2m_H$
LO	$18.6^{+5.8}_{-3.9}$	$16.0^{+4.3}_{-3.1}$	$13.8^{+3.2}_{-2.4}$	$11.9^{+2.5}_{-1.9}$
NLO	$44.2^{+12.0}_{-8.5}$	$36.9^{+8.4}_{-6.2}$	$31.6^{+6.3}_{-4.8}$	$27.5^{+4.9}_{-3.9}$
NNLO	$50.7^{+3.4}_{-4.6}$	$46.5^{+4.2}_{-4.7}$	$42.4^{+4.6}_{-4.4}$	$38.6^{+4.4}_{-4.0}$
N^{3}LO	$48.1^{+0.0}_{-7.5}$	$48.1^{+0.1}_{-1.8}$	$46.5^{+1.6}_{-2.6}$	$44.3^{+2.5}_{-2.9}$
LO+LL	$24.0^{+8.9}_{-6.8}$	$20.1^{+6.2}_{-5.0}$	$16.9^{+4.5}_{-3.7}$	$14.3^{+3.3}_{-2.8}$
NLO+NLL	$46.9^{+15.1}_{-12.6}$	$46.2^{+15.0}_{-13.2}$	$46.7^{+20.8}_{-13.8}$	$47.3^{+26.1}_{-15.8}$
NNLO+NNLL	$50.2^{+5.5}_{-5.3}$	$50.1^{+3.0}_{-7.1}$	$51.9^{+9.6}_{-8.9}$	$54.9^{+17.6}_{-11.5}$
N^{3}LO+N^{3}LL	$47.7^{+1.0}_{-6.8}$	$48.5^{+1.5}_{-1.9}$	$50.1^{+5.9}_{-3.5}$	$52.9^{+13.1}_{-5.3}$

factorization and renormalization scale μ_0 are considered: $\mu_0 = m_H/4$, $\mu_0 = m_H/2$, $\mu_0 = m_H$, $\mu_0 = 2m_H$. Then, the scales μ_R and μ_F are varied about μ_0 by a factor of 2 up and down, keeping the ratio μ_R/μ_F never larger than 2 or smaller than $1/2$ (canonical 7-point scale variation).

In Ref. [123], ψ-soft with AP2 and with the natural choice for the constants is considered as the best option for threshold resummation. However, the other variants of ψ-soft have the same formal accuracy and are used to estimate the uncertainty from $1/N$ terms and subleading logarithmic corrections. Thus, combining these variations with the 7-point scale variation a robust estimate of the uncertainty coming from unknown missing higher orders is proposed:

$\delta(\text{mho})$: envelope of the canonical 7-point scale variations and the 6 variants of ψ-soft resummation

This corresponds to a total of $7 \times 6 = 42$ cross section points from which one takes the highest and the lowest cross sections as the maximum and minimum of the uncertainty band, and provides the most conservative way of including these uncertainties.

Results for the cross section at fixed LO, NLO, NNLO and N^{3}LO accuracy, and its resummed counterpart at LO+LL, NLO+NLL, NNLO+NNLL and N^{3}LO+N^{3}LL accuracy, are reported in Table 8, for the four central scale choices. The same results are shown as plots in Figure 12. For comparison, results for the "standard" threshold resummation (which we call N-soft) are also shown in the plots. For N-soft one only keeps non-vanishing contributions in the large N limit: all the logarithmically enhanced contributions are in the resummed exponent, while the constant terms are not exponentiated. For completeness, we also provide in Table 9 the various results at N^{3}LO+N^{3}LL for individual scales and resummation prescription.

Several comments are in order:

– The uncertainty on the fixed order reduces to the canonical 7-point variation, while at resummed level we have the 42-point variation $\delta(\text{mho})$ detailed above. The fixed-order 7-point variation gives an uncertainty similar to $\delta(\text{scale})$ of Ref. [93], which is based on a 3-point variation of $\mu_0/2 < \mu_R = \mu_F < 2\mu_0$.

– Even ignoring the LO (which contains too few information for being predictive), one can consider the convergence pattern of the fixed-order perturbative expansion when going from NLO to NNLO and to N^{3}LO, relative to the scale uncertainty. The pattern is worse at larger central scales and

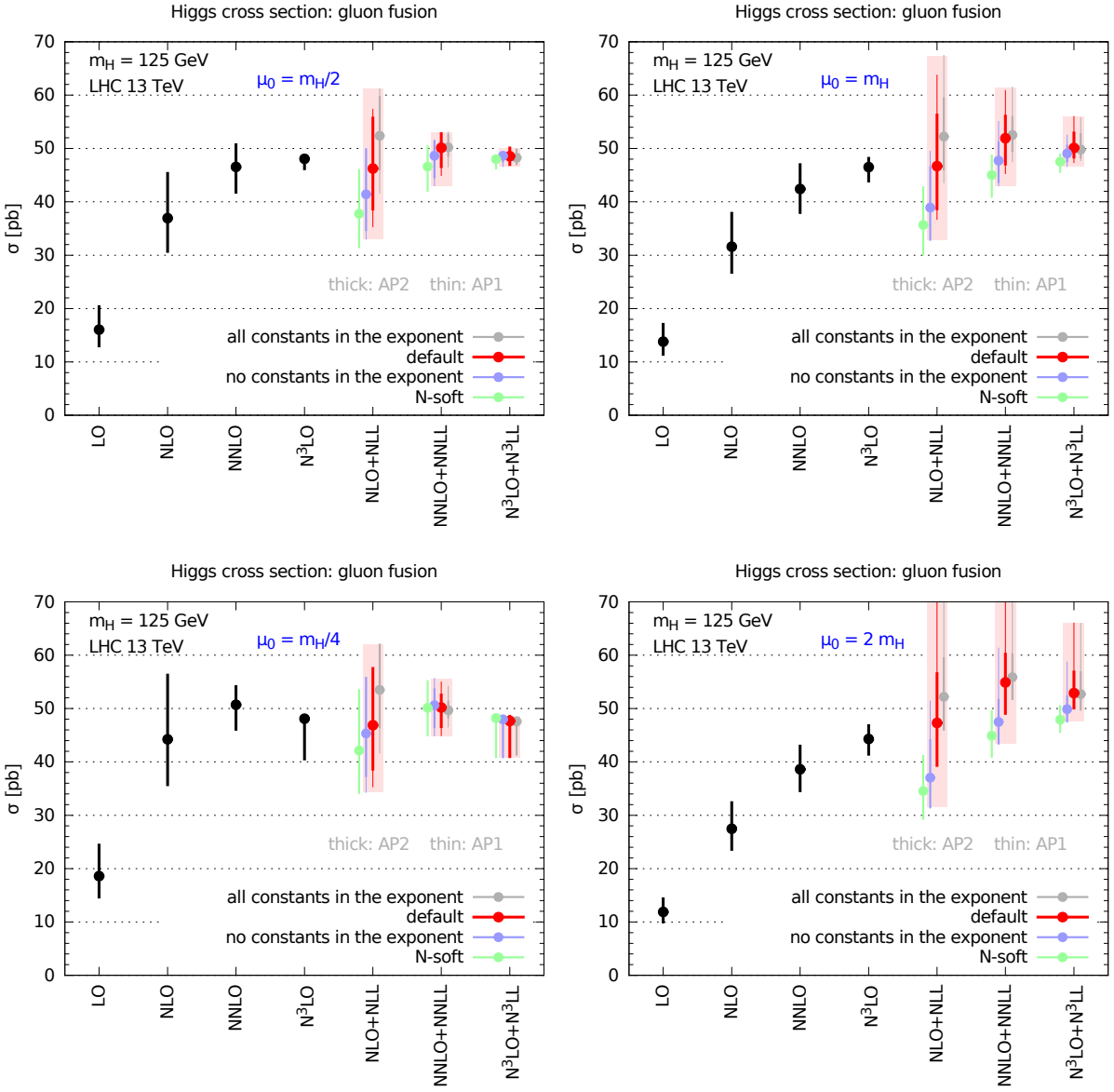

Figure 12: Higgs cross section at 13 TeV in the rescaled effective theory (rEFT), for four different choices of the central scale $\mu_F = \mu_R$: at the top we show $m_H/2$ and m_H, while at the bottom $m_H/4$ and $2m_H$. The uncertainties on the fixed-order predictions and on N-soft come solely from scale variation; for the ψ-soft AP2 results the scale variation is shown as the thick uncertainty band. The thinner bands correspond to the 7-point scale variation envelope on the ψ-soft AP1 instead, whose central value is not shown. The light-red rectangles are the envelope of all ψ-soft variants, corresponding to the 42-point uncertainty described in the text.

Table 9: Resummed cross sections at N^{3}LO+N^{3}LL for the different prescriptions as a function of the scales μ_F and μ_R over a wide range, for $m_H = 125$ GeV and $\sqrt{s} = 13$ TeV in the rEFT.

		ψ-soft						
		default		all constants in exp		no constants in exp		
μ_F/m_H	μ_R/m_H	AP2	AP1	AP2	AP1	AP2	AP1	N-soft
4	4	56.8	66.0	56.8	66.0	51.2	58.7	49.4
4	2	55.1	62.3	54.9	62.0	52.2	58.6	50.5
2	4	53.2	57.2	53.7	57.9	48.2	51.4	46.0
2	2	52.9	56.0	52.7	55.8	49.9	52.5	47.9
2	1	51.2	53.0	50.9	52.6	50.5	52.1	48.9
1	2	50.2	50.4	50.6	50.9	47.6	47.7	45.6
1	1	50.1	50.1	49.8	49.8	49.1	49.0	47.5
1	1/2	48.5	48.3	48.3	48.0	49.1	48.8	48.3
1/2	1	48.4	47.4	48.8	47.7	47.6	46.6	46.3
1/2	1/2	48.5	48.0	48.3	47.8	48.6	48.1	48.0
1/2	1/4	47.0	47.1	47.1	47.2	47.7	47.7	47.9
1/4	1/2	47.8	47.4	48.2	47.7	48.0	47.6	47.6
1/4	1/4	47.7	48.0	47.6	47.9	48.0	48.2	48.2
1/4	1/8	44.7	45.1	45.4	45.7	44.6	45.0	44.9
1/8	1/4	45.5	46.1	46.1	46.6	46.2	46.6	46.5
1/8	1/8	41.0	40.9	41.4	41.2	40.9	40.8	40.9

improves at smaller scales. For instance, at the largest central scale considered ($\mu_0 = 2m_H$), the central result at each order lies outside the band of the previous order; conversely, at the smallest central scale considered ($\mu_0 = m_H/4$), NNLO is contained in the NLO band, and central N^{3}LO in the NNLO band (although the scale error at N^{3}LO is large and very asymmetric). A similar convergence pattern is observed at $\mu_0 = m_H/2$; however, we note that the N^{3}LO band does not overlap with the NLO band. Additionally, the N^{3}LO results at the four central scales shown in Table 8 are barely compatible. This analysis shows that an estimate of the uncertainty from missing higher orders that solely relies on δ(scale), i.e. a canonical 7-point scale variation, is not reliable at fixed order.

– As far as the resummed results and their uncertainty δ(mho) are concerned, one can note that, for each choice of the central scale μ_0, the uncertainty of the resummed results from NLO+NLL onwards covers the central value and at least a portion of the band of the next (logarithmic) order. In fact, with the exception of the choice $\mu_0 = m_H/4$ (the pathological behaviour of which seems to be driven by the N^{3}LO contribution), the NNLO+NNLL band is fully contained in the NLO+NLL band, and the N^{3}LO+N^{3}LL band is fully contained in the NNLO+NNLL band. This, together with the observation of the systematic reduction of the scale uncertainty when going from one logarithmic order to the next, shows that the proposed δ(mho) provides one with a very reliable estimate of the uncertainty from missing higher orders. This is further supported by the observation that resummed results at each order are all compatible among the different choices of the central scale μ_0.
– Note that the different options for the position of the constants, while giving a large spread at NLO+NLL, is of little importance at higher orders, especially at N^{3}LO+N^{3}LL, suggesting a good convergence of the resummed series.
– In many respects, the choice $\mu_0 = m_H/2$ seems optimal, in full agreement with previous analyses, e.g. [93]. The convergence of the fixed-order is already good, and the convergence of the resummed result is very good. The error band at N^{3}LO+N^{3}LL is smaller than for other central scales, but

compatible with the results computed at different values of μ_0. Moreover, given that the way of estimating the uncertainty is very conservative, and successful at previous orders, the uncertainty on the N^{3}LO+N^{3}LL seems reasonably trustful.

The result advocated as best result in Ref. [123] within the rEFT setup considered there is hence

$$\text{rEFT}: \ \sigma_{\text{N}^3\text{LO+N}^3\text{LL}} = \sigma_{\text{N}^3\text{LO}} + \Delta_3\sigma_{\text{N}^3\text{LL}} = 48.5 \pm 1.9\,(4\%)\,\text{pb}, \tag{I.4.25}$$

where, to be even more conservative, the error has been symmetrized. Note that the effect of adding the resummation to the N^{3}LO on the central value is rather small, $+0.4$ pb, corresponding to $+0.8\%$, which, however, is *not* covered by the very asymmetric fixed-order scale uncertainty. The authors of Ref. [123] firmly believe that the uncertainty estimate derived from resummation is much more reliable and trustful than that obtained by simple (asymmetric) scale variation at fixed order.[I.8]

In order to go beyond the rEFT approach, we have to discuss the role of quark mass effects on the resummed contribution. The approach of Ref. [128] consists of including finite m_t effects to NLL, while treating m_b and m_c at fixed-order. Because of the accuracy of the rEFT approach for the top contribution, this leads to a resummed contribution very close to the rEFT one considered so far. In Ref. [122] a more aggressive approach was considered and bottom and charm were included to NLL and the top contribution to NNLL, albeit in the usual $1/m_t$ expansion. However, the interplay between soft logarithms and logarithms of m_b is still to be fully understood (see for instance Ref. [128]). In any case, we believe that the uncertainty $\delta(t,b,c)$ of Ref. [93] likely covers the differences between the two approaches.

In Ref. [123], results from resummation have been compared to different methods for estimating the uncertainty from missing higher orders. First, the Cacciari-Houdeau Bayesian approach [160] has been considered, which employs the known perturbative orders to construct a probability distribution for the subsequent unknown order. In its modified incarnation [131,161], the method gives an uncertainty of ± 2 pb at 95% degree of belief, fully compatible with the estimate obtained from resummation. Second, following an idea by David and Passarino [162], several algorithms to accelerate the convergence of the perturbative series, based on non-linear sequence transformations, have been considered. By performing a survey of different algorithms, it was possible to show that both the fixed-order and resummed series exhibit good convergence properties at $m_H/2$ (and also at $m_H/4$). Noticeably, the mean of each distribution is very close to the N^{3}LO+N^{3}LL prediction.

In conclusion, these tests further support the claim that the N^{3}LO+N^{3}LL calculation, together with its uncertainty $\delta(\text{mho})$, provides the most reliable estimate for the Higgs cross-section in gluon gluon fusion. In terms of relative contributions, which are likely to remain unchanged when quark-mass and electroweak effects are included in the fixed order, the results from this section can be summarized as

$$\boxed{\sigma_{\text{N}^3\text{LO+N}^3\text{LL}} - \sigma_{\text{N}^3\text{LO}} = +0.4\,\text{pb}, \qquad \delta(\text{mho}) = \pm 4\%,} \tag{I.4.26}$$

which are the recommended shift with respect to the N^{3}LO and recommended uncertainty from missing higher orders by the Authors of Ref. [123] for the SM Higgs boson at LHC 13 TeV.

I.4.1.d Summary for the total cross-section [I.9]

We now summarize the working group recommendation for the total cross-section and associated uncertainty for the LHC at 13 TeV.

The recommendation for the central value is to take the pure N^{3}LO result, evaluated at $\mu_R = \mu_f = m_H/2$. This choice of scale is motivated by the observation that the perturbative expansion is more stable

[I.8] If scale variation error at fixed-order is symmetrized the resulting uncertainty becomes more reasonable. However, given that the small uncertainty comes from the vicinity of a stationary point in the scale dependence, it might still underestimate the missing higher order uncertainty.

[I.9] *Author(s): S. Forte, D. Gillberg, C. Hays, A. Lazopoulos, G. Petrucciani, A. Massironi, G. Zanderighi.*

both at fixed order and at the resummed level. With this choice of scale, the effect of the resummation is (at LHC energies) much smaller than the uncertainty related to the choice of resummation prescription, and much smaller than the residual scale uncertainty. Furthermore, the N^{3}LO EFT result should be rescaled by the R_{LO} Eq. (I.4.2); charm, bottom and top contributions should be included exactly up to NLO, and finite top mass effects at NNLO using the expansion in $1/m_t$ from Ref. [103,105,106]. Finally, electroweak corrections [108,109] should be included multiplicatively using complete factorization. The value of the $\overline{\text{MS}}$ heavy quark masses and of α_s given in Chapter I.1 should be used. This leads to the result of Ref. [93], given in Eq. (I.4.3) above. Note that changing from pole (previous recommendation [7]) to $\overline{\text{MS}}$ masses leads to an increase of the cross-section of order 2% [93],

For the treatment of uncertainties, we distinguish parametric uncertainties and theoretical uncertainties.

PDFs and α_s give the parametric uncertainty for this process. For these, we recommend to follow the PDF4LHC15 recommendation [35] summarized in Chapters I.1-I.2. This leads to an absolute uncertainty $\Delta_{\text{PDF}+\alpha_s} = 1.56$ pb, i.e. a relative uncertainty of 3.2 %. This is in agreement with Ref. [93], see also Eq. (I.4.3) of Section I.4.1.a above. This is currently the dominant source of uncertainty. It should be considered Gaussianly distributed, and the above interval provides the standard deviation of the Gaussian, corresponding to a symmetric 68% confidence level.

The estimation of theoretical uncertainties inevitably involves a somewhat subjective component. For these we provide two different procedures, based on two possible different interpretations of theoretical uncertainties.

- In **Procedure F** the final theoretical uncertainty is interpreted as a flat 100% confidence level. This means that if the missing information which provides all the given sources of theoretical uncertainty was supplied, then the result is expected to lie with certainty within the given interval, but not more likely to be in any region within this interval. The interval is constructed as the linear sum of individual sources of theoretical uncertainty, each estimated as explained below. Each individual source of uncertainty should not be endowed with a statistical interpretation and merely concurs to the determination of the final overall range.
- In **Procedure G** each source of theoretical uncertainty is interpreted as a one-sigma range. The final uncertainty is thus obtained by combining in quadrature individual sources of uncertainty. Because there are many sources of uncertainty, the final distribution is expected to be approximately Gaussian, and the final combined uncertainty should thus be interpreted as a symmetric 68% confidence level.

We now provide a list of sources of uncertainty. For each source, we briefly describe and provide the uncertainty estimate to be used in either procedure. It is important to stress that individual uncertainties have a different interpretation in the two procedures: specifically F-uncertainties are merely components of the final uncertainty range, while G-uncertainties are one-sigma ranges. Even when taken to be numerically equal in the two procedures they thus have a different meaning.

The various sources of uncertainty and the corresponding F-uncertainties and G-uncertainties are:

- **missing higher QCD orders** In order to estimate the uncertainty related to missing higher order QCD corrections beyond N^{3}LO various options have been considered:
  - In Ref. [93] it is suggested to perform a scale variation scan of the N^{3}LO result including mass effects, in the range $m_H/4 \leq \mu_R = \mu_F \leq m_H$, (see Section I.4.1.a above).[I.10] This procedure gives $\Delta_{\text{MHOU}} = [-1.2; +0.1]$ pb, i.e. a relative uncertainty of $[-2.4; +0.2]$ %. Note that a three-point scale variation, rather than a scan, would give a vanishing upper uncertainty.
  - A 7-point scale variation can be performed with $m_H/4 \leq \mu_R, \mu_F \leq m_H$ keeping $\frac{1}{2} \leq$

[I.10] The inclusion of mass effects reduces the whole cross section and thus also the uncertainty by a factor of about 0.7 in comparison to what one would obtain performing a scale variation scan with mass effects not included.

$\frac{\mu_R}{\mu_F} \leq 2$. This is a standard procedure used to estimate uncertainties in fixed-order calculations. It turns out to give a result which is similar to the previous one, namely $\Delta_{\rm MHOU} = [-1.4; +0.1]$ pb, i.e. a relative uncertainty of $[-3.0; +0.2]$ %. Note that the lower variation is somewhat larger than that found in the scan, as the latter was performed with fixed ratio $\mu_F/\mu_R = 1$.

- Since scale variation probes only the size of higher-order terms, but not their sign, and the scale-variation uncertainties quoted above are very asymmetric, one can argue that they should be symmetrized while keeping the central value fixed. [I.11] In the case of the 7-point scale variation this gives $\Delta_{\rm MHOU} = \pm 1.4$ pb, i.e. a relative uncertainty of $[-3.0; +3.0]$ %.
- While resummation has a minimal impact at central scale, it provides a more stable perturbative expansion at all previous orders. In Ref. [93] a variety of resummation schemes were examined and it was found that, within an equal scale variation scan, resummation contributions lie within the fixed order scale uncertainty interval in all cases considered. However, one may argue that seven-point scale variation of the resummed result provides a more reliable estimate of the perturbative uncertainty. Taking the default N^{3}LL+N^{3}LO resummation scheme of Ref. [123] (see also Section I.4.1.c above) one gets $\Delta_{\rm MHOU} = [-1.6; +1.5]$ pb, i.e. a relative uncertainty of $[-3.2; +3.2]$ %. Note that the scale variations reported in Table 6 are larger, but the results in that table are at NNLO+N^{3}LL, rather than N^{3}LO+N^{3}LL. This is very close to the symmetrized seven-point scale variation of the fixed order result.[I.12]

The **F-uncertainty** is estimated by performing a scale variation scan in the range $m_H/4 \leq \mu_R = \mu_F \leq m_H$ following the suggestion of Ref. [93], which gives $\Delta_{\rm MHOU} = [-1.2; +0.1]$ pb, corresponding to a relative uncertainty of $[-2.4; +0.2]$ %.

The **G-uncertainty** is estimated by performing a symmetrized seven-point scale uncertainty, which leads to a conservative result that agrees with the uncertainty based on resummation arguments, i.e. $\Delta_{\rm MHOU} = \pm 1.4$ pb, corresponding to a relative uncertainty of $[-3.0; +3.0]$%.

– **missing electroweak corrections** In our recommendation, electroweak (EW) corrections are included assuming complete factorization. This gives rise to a positive 5% correction to the pure QCD result. If instead QCD and EW corrections are combined additively, one gets an enhancement of 1.7%. Finally, mixed QCD-EW corrections computed using an effective field theory (EFT) with m_W, $m_Z \gg m_H$ [110] give an enhancement of 3.2%.

The **F-uncertainty** is estimated as $\Delta_{\rm ew} = 0.5$ pb corresponding to $\pm 1\%$ uncertainty, which is deemed to be conservative enough and it corresponds to an intermediate value between various possible estimates, as seen in Sect. I.4.1.a.iii and Ref. [93].

The **G-uncertainty** is conservatively estimated as the average of the difference between our chosen complete factorization (5%) and either of the alternative possibilities (additive: 1.7%, or EFT: 3.2%). This corresponds to an uncertainty of $\pm 2.5\%$ or ± 1.2 pb.

– **bottom and charm interference with top** Bottom and charm interference with top quark loops are known exactly only up to NLO. At LO and NLO, bottom-top interference leads to a correction which is about the same as the finite top mass correction, but with the opposite sign. At NNLO, including rEFT and $1/m_t$ effects leads to a correction of about 1 pb. Furthermore, the NLO top-bottom and charm interference correction changes by 0.7 pb if $\overline{\rm MS}$ or pole heavy quark masses are used.

The **F-uncertainty** is estimated as $\Delta_{\rm t,bc} = \pm 0.4$ pb, i.e. a relative uncertainty of $\pm 0.8\%$, following Sect. I.4.1.a.iii and Ref. [93].

The **G-uncertainty** is estimated taking the scheme dependence of the NLO interference as a reasonably conservative estimate. This leads to $\Delta_{\rm t,bc} = \pm 0.7$ pb, i.e. a relative uncertainty of $\pm 1.5\%$.

– **finite top mass** Both the **F-uncertainty** and the **G-uncertainty** are estimated as $\Delta_{1/{\rm m_t}} = \pm 0.49$ pb,

[I.11] Yet another alternative would be to keep the scale-uncertainty band and quote as a central value the midpoint.

[I.12] In Ref. [123] it is instead recommended to take the envelope of the seven-point scale variations for a variety of different resummation prescriptions; this leads to a marginally more conservative uncertainty of about $\pm 4\%$.

i.e. a relative uncertainty of $\pm 1\%$, following Sect. I.4.1.a.iii and Ref. [93].

- **missing N^{3}LO PDFs** Both the **F-uncertainty** and the **G-uncertainty** are estimated assigning to lack of knowledge of the N^{3}LO PDFs an uncertainty of $\Delta_{\rm PDF-TH} = \pm 0.56$ pb, i.e. a relative uncertainty of $\pm 1.2\%$, following Sect. I.4.1.a.iii and Ref. [93].
- **truncation of the soft expansion** Both the **F-uncertainty** and the **G-uncertainty** are estimated assigning to the truncation of the soft expansion used to derive the N^{3}LO QCD corrections $\Delta_{\rm soft} = \pm 0.18$ pb, i.e. a relative uncertainty of $\pm 0.4\%$, following Sect. I.4.1.a.iii and Ref. [93].

The total uncertainty is thus:

- **F-uncertainty:** $[-6.7, +4.6]\%$ corresponding to $[-3.3, +2.2]$ pb.
- **G-uncertainty:** $\pm 4.5\%$ corresponding to ± 2.2 pb

We recall that the F-uncertainty is a 100% flat confidence interval, while the G-uncertainty is a one-sigma Gaussian uncertainty. They can be compared by noting that a symmetric flat interval has a variance equal to its half-width divided by $\sqrt{3}$. The symmetrized F-uncertainty hence corresponds to a variance of $6.7/\sqrt{3} = 3.9$, which is not far from the G-uncertainty. The two estimates are thus roughly compatible.

The final recommendation for gluon fusion cross-section at the LHC is presented in Chapter I.9.

I.4.2 Differential and jet-binned cross sections

In some decay channels it is common to perform different analyses depending on the number of jets accompanying the Higgs boson. This is because the Higgs boson signal in different jet multiplicities is affected by different backgrounds. Most notably, when the Higgs boson decays to WW, the dominant top background is significantly suppressed by requiring zero jets in the final state. Jet veto transverse momentum thresholds used by ATLAS and CMS are of order $25-30$ GeV, and thus substantially smaller than the Higgs boson mass m_H. In this case real radiation is suppressed and the imbalance between virtual and real corrections produces logarithms of the form $\ln(p_{\rm t,veto}/m_H)$ which may invalidate the fixed order perturbative expansion. Resummed predictions for the cross section in the 0-jet bin have been obtained both in full QCD [163] and in the framework of Soft Collinear Effective field Theory (SCET) [159, 164]. Several methods for determining the uncertainties and their correlations across jet-bins were proposed in the past, and used in Run 1 measurements. At the end of Run 1 further improvements were proposed. In this section we review different approaches to the treatment of correlated uncertainties in jet bins.

In Section I.4.2.a a general approach to theory uncertainties in kinematic bins is presented. It reduces to the commonly used ST [165] or JVE [163] methods in particular cases and is applicable also to treat simplified template cross sections. In Section I.4.2.b the ST and JVE methods are compared up to NNLO and results for 13 TeV are presented. In Section I.4.2.c an updated calculation of the cross section in the 0-jet, 1-jet and $\geq$ 2-jet bins is presented. This calculation, based on the work of Ref. [159], includes the direct resummation of the logarithmically enhanced terms in the 0-jet bin, and the indirect resummation of the corresponding terms in the 1-jet bin. Heavy quark mass effects are accounted for through an overall rescaling factor.

Recently, the N^{3}LO result for the inclusive cross section (see Section I.4.1.a), and the H+jet cross section at NNLO (see Section I.4.2.f), became available. Both these calculation refer to perturbative corrections at $\mathcal{O}(\alpha_S^5)$ and can be used to improve the computation of the 0-jet cross section. In Section I.4.2.d an updated calculation of the jet vetoed cross section is presented, which consistently includes the above information. The calculation includes the resummation of the $\ln(p_{\rm t,veto}/m_H)$ terms at NNLL and a resummation of the logarithmically enhanced contribution of the jet radius R. Heavy-quark mass effects are included according to the approach of Ref. [166].

When the recoiling QCD radiation is integrated over, the NNLO calculation of H+jet provides an NNLO prediction for the p_T spectrum. In Section I.4.2.e an NNLO calculation of the p_T spectrum is combined with an NNLL resummed computation in momentum space [167] and NNLL+NNLO predic-

tions for the cumulative distribution are presented, together with a comparison of NNLL+NLO results with available reference predictions for this observable.

I.4.2.a General treatment of theory uncertainties in kinematic bins [I.13]

Whenever the experimental measurements are separately performed in different kinematic regions (or bins), the theoretical predictions and their uncertainties must also be evaluated separately for each kinematic region. This is necessary also when the information from all measured bins is eventually combined in the interpretation, since different bins can in general have different sensitivities and therefore contribute with different relative weights to the final result. In this context, the correlations of the theoretical uncertainties for different bins must be taken into account. This is particularly important whenever a binning cut induces an important additional source of perturbative uncertainties that affects each bin but should cancel in their sum. This is precisely what happens in the context of jet binning, and it requires one to treat the uncertainties induced by the binning as anti-correlated between the bins [158, 165]. In general, to properly treat the theoretical uncertainties one should thus try to identify and distinguish different sources of uncertainties and take into account the correlation implied by each source.

I.4.2.a.i Single bin boundary

We first review the case where the cross section is split into two bins by a single perturbatively nontrivial binning cut. To be concrete, we use the 0-jet cross section as an important example.

In this case, the total inclusive cross section, $\sigma_{\text{tot}} \equiv \sigma_{\geq 0}$, is divided into an exclusive 0-jet bin, $\sigma_0(p_T^{\text{cut}})$, where the p_T of the leading jet is restricted to $p_T^{\text{jet}} < p_T^{\text{cut}}$ and the remaining inclusive 1-jet bin, where the leading jet is required to have $p_T^{\text{jet}} \geq p_T^{\text{cut}}$,

$$\sigma_{\geq 0} = \sigma_0(p_T^{\text{cut}}) + \sigma_{\geq 1}(p_T^{\text{cut}})\,. \tag{I.4.27}$$

Typically, the experimentally used p_T^{cut} values are smaller than the hard-interaction scale $\sim m_H$. In this case, the p_T^{cut} restriction induces Sudakov double logarithms [168] $\ln(p_T^{\text{cut}}/m_H)$ at each order in α_s, which grow as p_T^{cut} is lowered. When p_T^{cut} is small enough for $\sigma_{\geq 1}(p_T^{\text{cut}})$ to contain a nonnegligible fraction of the total cross section, this implies that the cut-induced perturbative corrections have a nontrivial influence on the perturbative series of σ_0, corresponding to an additional and a priori nonnegligible source of uncertainty that is not present in $\sigma_{\geq 0}$. (Note that this is irrespective of whether the cut effects are computable in fixed-order or resummed perturbation theory.)

The uncertainties involved in the jet binning can be described in general in terms of fully correlated and fully anticorrelated components, which amounts to parameterizing the uncertainty matrix for $\{\sigma_0, \sigma_{\geq 1}\}$ as

$$C(\{\sigma_0, \sigma_{\geq 1}\}) = \begin{pmatrix} (\Delta_0^{\text{y}})^2 & \Delta_0^{\text{y}}\,\Delta_{\geq 1}^{\text{y}} \\ \Delta_0^{\text{y}}\,\Delta_{\geq 1}^{\text{y}} & (\Delta_{\geq 1}^{\text{y}})^2 \end{pmatrix} + \begin{pmatrix} \Delta_{\text{cut}}^2 & -\Delta_{\text{cut}}^2 \\ -\Delta_{\text{cut}}^2 & \Delta_{\text{cut}}^2 \end{pmatrix}. \tag{I.4.28}$$

While this form was originally utilized in the context of the ST method [165, 169], it is simply a general parameterization of a 2×2 symmetric matrix, and not specific to a particular calculation or framework for determining theory uncertainties. That is, the uncertainties obtained with any prescription can always be written in this form, provided sufficient information or assumptions on the correlations are available.

The parameterization in (I.4.28) proves convenient for two reasons: First, the separation into independent components that are 100% correlated or anticorrelated between the different observables allows for a straightforward implementation in terms of independent nuisance parameters for each component. That is, one has two nuisance parameters κ^{y} and κ_{cut} whose uncertainty amplitudes for $\{\sigma_{\geq 0}, \sigma_0, \sigma_{\geq 1}\}$ are

$$\kappa^{\text{y}}: \quad \{\Delta_{\geq 0}^{\text{y}},\, \Delta_0^{\text{y}},\, \Delta_{\geq 1}^{\text{y}}\} \qquad\qquad \kappa_{\text{cut}}: \quad \{0,\, \Delta_{\text{cut}}, -\Delta_{\text{cut}}\}\,, \tag{I.4.29}$$

[I.13] *Author(s): F.J. Tackmann, K. Tackmann.*

where $\Delta^{\mathrm{y}}_{\geq 0} = \Delta^{\mathrm{y}}_{0} + \Delta^{\mathrm{y}}_{\geq 1}$. Hence, this provides a baseline for the experimental implementation, independent of a particular theoretical prediction. Second, this parameterization admits a simple physical interpretation, which is very useful to identify and estimate each component for a given theory calculation: The first correlated component, denoted with a superscript "y", can be interpreted as an overall yield uncertainty of a common source for all bins. The second anticorrelated component can be interpreted as a migration uncertainty between the two bins, which is introduced by the binning and drops out in their sum.

The existing prescriptions for estimating perturbative uncertainties in jet binning and their justifications have been documented extensively before [8, 9, 165, 169, 170]. Here, we only give a brief summary in order to illustrate the above for the case of the $0/1$-jet boundary. In fixed-order predictions, there is no way to unambiguously identify different sources for Δ^{y} and Δ_{cut}, so one has to make some assumptions. Using a naive correlated scale variation for all jet bins amounts to setting $\Delta^{\mathrm{y}}_{i} \equiv \Delta^{\mathrm{FO}}_{i}$, where Δ^{FO}_{i} are the default perturbative uncertainties estimated by the usual scale variations in the fixed-order predictions, while $\Delta_{\mathrm{cut}} \equiv 0$ is neglected. As mentioned above, once the binning effects become important, the associated migration uncertainty should not be neglected, otherwise this can easily lead to an underestimate. In the ST method [165], this is avoided by taking

$$\text{ST}: \qquad \Delta^{\mathrm{y}}_{0} = \Delta^{\mathrm{y}}_{\geq 0} = \Delta^{\mathrm{FO}}_{\geq 0}\,, \quad \Delta^{\mathrm{y}}_{\geq 1} = 0\,, \qquad \Delta_{\mathrm{cut}} = \Delta^{\mathrm{FO}}_{\geq 1}\,. \tag{I.4.30}$$

That is, the migration uncertainty is approximated by the perturbative uncertainty of $\sigma_{\geq 1}(p_T^{\mathrm{cut}})$, which is motivated by the structure of the perturbative series at small p_T^{cut}. Maintaining as the total uncertainty for $\sigma_{\geq 1}$ its usual fixed-order uncertainty then requires setting $\Delta^{\mathrm{y}}_{\geq 1} = 0$. As a result, one effectively treats the usual fixed-order perturbative uncertainties in $\sigma_{\geq 0}$ and $\sigma_{\geq 1}$ as independent sources. This can also be generalized [169], by using an additional parameter ρ to separate $\Delta^{\mathrm{FO}}_{\geq 1}$ into yield and migration parts, which then effectively determines the correlation between $\Delta^{\mathrm{FO}}_{\geq 0}$ and $\Delta^{\mathrm{FO}}_{\geq 1}$,

$$\text{ST}(\rho): \qquad \Delta^{\mathrm{y}}_{0} = \Delta^{\mathrm{FO}}_{\geq 0}\,, \quad \Delta^{\mathrm{y}}_{\geq 1} = \rho\,\Delta^{\mathrm{FO}}_{\geq 1}\,, \qquad \Delta_{\mathrm{cut}} = \sqrt{1-\rho^2}\,\Delta^{\mathrm{FO}}_{\geq 1}\,. \tag{I.4.31}$$

Another prescription is the JVE method [170], which typically yields similar uncertainties for the same perturbative inputs. It relies on the assumption that the perturbative uncertainty in the 0-jet fraction $\epsilon_0 = \sigma_0(p_T^{\mathrm{cut}})/\sigma_{\geq 0}$ is uncorrelated with that of the inclusive cross section $\sigma_{\geq 0}$, i.e., the perturbative uncertainties in ϵ_0 and $\sigma_{\geq 0}$ are treated as the independent sources. This amounts to taking

$$\text{JVE}: \qquad \Delta^{\mathrm{y}}_{\geq 0} = \Delta^{\mathrm{FO}}_{\geq 0}\,, \quad \Delta^{\mathrm{y}}_{0} = \epsilon_0\,\Delta^{\mathrm{FO}}_{\geq 0}\,, \quad \Delta^{\mathrm{y}}_{\geq 1} = (1-\epsilon_0)\,\Delta^{\mathrm{FO}}_{\geq 0}\,, \qquad \Delta_{\mathrm{cut}} = \sigma_{\geq 0}\,\Delta(\epsilon_0)\,. \tag{I.4.32}$$

This means that the relative yield uncertainties for all bins are equal to the relative uncertainty of the total cross section, $\Delta^{\mathrm{y}}_{i}/\sigma_i = \Delta^{\mathrm{FO}}_{\geq 0}/\sigma_{\geq 0}$. In the migration uncertainty, $\Delta(\epsilon_0)$ is the perturbative uncertainty of ϵ_0, which is obtained by considering its scale variation together with several variations of how to write its perturbative series that differ by higher-order terms. This also means that the total uncertainty for $\sigma_{\geq 1}$ is not just given by the usual $\Delta^{\mathrm{FO}}_{\geq 1}$. When used together with a resummed calculation, the fixed-order estimate of $\Delta(\epsilon_0)$ is replaced by its resummed counterpart, see Section I.4.2.c.

I.4.2.a.ii Multiple bin boundaries

We now move on to discuss the more general case where the total cross section is split into multiple mutually exclusive bins, as is the case in most experimental analyses. Specifically, this applies to the case of the simplified template cross section framework discussed in Section III.2. A full implementation of the theory-independent parameterization discussed here in the simplified template cross sections would allow utilizing theoretical predictions in a very flexible manner. In particular, it would enable easily switching between different theory predictions in the interpretation of the experimental measurements.

With multiple bins, each bin can have more than one boundary and vice versa any given boundary can be shared by different bins. To make this tractable in a systematic fashion, we first note that

Eq. (I.4.28) applies in an obvious way to any single bin boundary and binning cut when all additional subdivisions are removed. That is, a given binning cut, labelled "a/b", separates the cross section as $\sigma_{ab} = \sigma_a + \sigma_b$ with an associated migration uncertainty $\Delta^{a/b}_{\text{cut}}$, which is anticorrelated between σ_a and σ_b. (Note that σ_{ab} is not necessarily the total cross section but can itself correspond to a bin; what is relevant is that the a/b cut does not act outside of σ_{ab}.) Including additional cuts that further subdivide σ_a and σ_b, we have $\sigma_a = \sum_i \sigma_a^i$ and $\sigma_b = \sum_j \sigma_b^j$, where we have labelled the individual sub-bins according to whether they are part of σ_a or σ_b. Since we interpret the a/b boundary as a common uncertainty source, we can consider it as fully correlated among each set of sub-bins and implement it via a single nuisance parameter $\kappa^{a/b}_{\text{cut}}$. The corresponding uncertainty amplitudes for all the bins are given as

$$\kappa^{a/b}_{\text{cut}}: \quad \Delta^{a/b}_{\text{cut}} \times \big\{\{x_a^i\}, -\{x_b^j\}\big\} \qquad \text{with} \qquad \sum_i x_a^i = \sum_j x_b^j = 1\,, \tag{I.4.33}$$

where the parameters x_a^i and x_b^j specify how $\Delta^{a/b}_{\text{cut}}$ gets distributed among the sub-bins. (With this information it is also straightforward to construct a corresponding uncertainty matrix, but this is not actually necessary.)

In this way, we can consider each binning cut (or bin boundary) as a potential source of an uncertainty with an associated nuisance parameter. (Of course, in practice with sufficiently complicated bin boundaries, one has to apply some theoretical judgement in how one chooses the relevant independent binning cuts.) In addition, we can have an overall yield uncertainty correlated among all bins.

To illustrate this for a simple example, consider the case of 3 mutually exclusive jet bins $\{\sigma_0, \sigma_1, \sigma_{\geq 2}\}$. In this case, we can easily identify two bin boundaries as the two relevant sources of migration uncertainties, namely the cut on the leading jet separating $\sigma_{\geq 0} = \sigma_0 + \sigma_{\geq 1}$ and the cut on the 2nd jet separating $\sigma_{\geq 1} = \sigma_1 + \sigma_{\geq 2}$. In addition, we have an overall yield uncertainty. Considering the five (interdependent) observables $\{\sigma_{\geq 0}, \sigma_0, \sigma_{\geq 1}, \sigma_1, \sigma_{\geq 2}\}$, the three nuisance parameters and their respective uncertainty amplitudes are

$$\begin{aligned}
\kappa^{\text{y}}: &\quad \{\Delta^{\text{y}}_{\geq 0},\, \Delta^{\text{y}}_{0},\, \Delta^{\text{y}}_{\geq 1},\, \Delta^{\text{y}}_{1},\, \Delta^{\text{y}}_{\geq 2}\} \quad \text{with} \quad \Delta^{\text{y}}_{\geq 0} = \Delta^{\text{y}}_{0} + \Delta^{\text{y}}_{\geq 1}\,, \qquad \Delta^{\text{y}}_{\geq 1} = \Delta^{\text{y}}_{1} + \Delta^{\text{y}}_{\geq 2}\,,\\
\kappa^{0/1}_{\text{cut}}: &\quad \Delta^{0/1}_{\text{cut}} \times \{0,\, 1,\, -1,\, -(1-x_1),\, -x_1\}\,,\\
\kappa^{1/2}_{\text{cut}}: &\quad \Delta^{1/2}_{\text{cut}} \times \{0,\, x_2,\, -x_2,\, 1-x_2,\, -1\}\,,
\end{aligned} \tag{I.4.34}$$

Here, x_1 determines how $\Delta^{0/1}_{\text{cut}}$ is split between σ_1 and $\sigma_{\geq 2}$, and x_2 determines how $\Delta^{1/2}_{\text{cut}}$ is split between σ_0 and σ_1. For $x_1 \neq 0$, the $0/1$ migration into $\sigma_{\geq 1}$ can affect both σ_1 and $\sigma_{\geq 2}$. For $x_1 = 0$, the $0/1$ migration happens entirely between σ_0 and σ_1, so the binning is effectively treated as $\sigma_{0+1} = \sigma_0 + \sigma_1$. Similarly, for $x_2 = 0$ the $1/2$ migration is contained within $\sigma_{\geq 1} = \sigma_1 + \sigma_{\geq 2}$. On the other hand, allowing for $x_2 \neq 0$ corresponds to the more general case $\sigma_{\geq 0} = \sigma_{<2} + \sigma_{\geq 2}$.

In terms of the uncertainty matrices for the 3 quantities $\{\sigma_0, \sigma_1, \sigma_{\geq 2}\}$, Eq. (I.4.34) corresponds to

$$C(\{\sigma_0, \sigma_1, \sigma_{\geq 2}\}) = C^{\text{y}}(\{\sigma_0, \sigma_1, \sigma_{\geq 2}\}) + C^{0/1}_{\text{cut}}(\{\sigma_0, \sigma_1, \sigma_{\geq 2}\}) + C^{1/2}_{\text{cut}}(\{\sigma_0, \sigma_1, \sigma_{\geq 2}\})\,, \tag{I.4.35}$$

$$C^{\text{y}}(\{\sigma_0, \sigma_1, \sigma_{\geq 2}\}) = \begin{pmatrix} (\Delta^{\text{y}}_0)^2 & \Delta^{\text{y}}_0\Delta^{\text{y}}_1 & \Delta^{\text{y}}_0\Delta^{\text{y}}_{\geq 2} \\ \Delta^{\text{y}}_0\Delta^{\text{y}}_1 & (\Delta^{\text{y}}_1)^2 & \Delta^{\text{y}}_1\Delta^{\text{y}}_{\geq 2} \\ \Delta^{\text{y}}_0\Delta^{\text{y}}_{\geq 2} & \Delta^{\text{y}}_1\Delta^{\text{y}}_{\geq 2} & (\Delta^{\text{y}}_{\geq 2})^2 \end{pmatrix}, \tag{I.4.36}$$

$$C^{0/1}_{\text{cut}}(\{\sigma_0, \sigma_1, \sigma_{\geq 2}\}) = \big(\Delta^{0/1}_{\text{cut}}\big)^2 \begin{pmatrix} 1 & -(1-x_1) & -x_1 \\ -(1-x_1) & (1-x_1)^2 & x_1(1-x_1) \\ -x_1 & x_1(1-x_1) & x_1^2 \end{pmatrix}, \tag{I.4.37}$$

$$C^{1/2}_{\text{cut}}(\{\sigma_0, \sigma_1, \sigma_{\geq 2}\}) = \big(\Delta^{1/2}_{\text{cut}}\big)^2 \begin{pmatrix} x_2^2 & x_2(1-x_2) & -x_2 \\ x_2(1-x_2) & (1-x_2)^2 & -(1-x_2) \\ -x_2 & -(1-x_2) & 1 \end{pmatrix}. \tag{I.4.38}$$

Note that for the most generic case with 3 bins, one could in principle add an analogous third migration component $0/2$ for $\sigma_{\neq 1} = \sigma_0 + \sigma_{\geq 2}$. In this jet-binning example, this is clearly artificial, since σ_0 and $\sigma_{\geq 2}$ do not actually share a boundary and the migration between them is only indirect and already captured by the other two migration components.

The ST method applied to the case of 3 jet bins is equivalent to using $\Delta_0^{\mathrm{y}} = \Delta_{\geq 0}^{\mathrm{FO}}$, $\Delta_1^{\mathrm{y}} = \Delta_{\geq 2}^{\mathrm{y}} = 0$, $\Delta_{\mathrm{cut}}^{0/1} = \Delta_{\geq 1}^{\mathrm{FO}}$, $\Delta_{\mathrm{cut}}^{1/2} = \Delta_{\geq 2}^{\mathrm{FO}}$, and taking $x_1 = x_2 = 0$. This effectively considers $\sigma_{\geq 0}$, $\sigma_{\geq 1}$, and $\sigma_{\geq 2}$ as the independent sources, and in particular one can directly identify the corresponding nuisance parameters $\kappa_{\geq i}$ in existing implementations of the ST method as $\kappa^{\mathrm{y}} \equiv \kappa_{\geq 0}$, $\kappa_{\mathrm{cut}}^{0/1} \equiv \kappa_{\geq 1}$, and $\kappa_{\mathrm{cut}}^{1/2} \equiv \kappa_{\geq 2}$. Section I.4.2.c discusses how estimates for the above parameters can be obtained when both jet boundaries are treated in resummed perturbation theory.

Mathematically speaking, the above generic parameterization has some redundancy, as it has more than the minimal number of six parameters that would be required to describe a general 3x3 symmetric matrix. This is desired and makes it flexible enough to accommodate different scenarios while maintaining the simple physical interpretation in terms of the underlying sources. In contrast, using a mathematically minimal parameterization one would inevitably be forced to reexpress the contributions from several physically independent sources in terms of a minimal number of mathematically independent components and thus lose their physical meaning. In general, there can be several (independent) sources of theory uncertainties that give rise to each type of component. As for any other systematic uncertainty, these should then be implemented via separate nuisance parameters, which preserves their physical origin and in particular allows for the possibility to correlate them with other observables if necessary. For example, when electroweak and QCD corrections are treated as factorized, one could consider separately estimating the perturbative uncertainties of each, with each having their own set of nuisance parameters. (In practice, when the electroweak corrections are applied as an overall correction factor, they give rise to a yield uncertainty and a single nuisance parameter.)

I.4.2.b Exclusive fixed-order cross sections and jet-veto efficiencies at NNLO [I.14]

During Run-1 of LHC data taking at 7 and 8 TeV the two methods reviewed in Sect. I.4.2.a were used to compute uncertainties on the jet bin acceptance for the Higgs boson signal: the so called Stewart-Tackmann method (ST) [165] and the Jet Veto Efficiency method (JVE) [163]. The first method has been used from the Higgs boson discovery paper [1], [2] while the second method has been used in the Run-1 ATLAS paper on the $h \to WW^*$ channel [171]. In the present section we will present results obtained using both methods at 13 TeV, providing all details on the inputs used for the computation of the uncertainties.

I.4.2.b.i The Stewart-Tackmann method

The ST method can be applied to all jet bins and assumes that inclusive jet bin cross sections, that is the cross section to have at least N jets, ($\sigma_{\geq N}$) are uncorrelated for all values of N. In this case the $N-$jet cross section can be written as:

$$\sigma_N = \sigma_{\geq N} - \sigma_{\geq N+1}$$

and the uncertainty on σ_N is computed using the relation:

$$\Delta^2\sigma_N = \Delta^2\sigma_{\geq N} + \Delta^2\sigma_{\geq N+1}$$

The values of $\Delta^2\sigma_{\geq N,\geq N+1}$ are evaluated as the envelope of all cross sections obtained by changing the renormalization (μ_r) and factorization (μ_f) scales by a factor two around the central scale of $\mu = m_H/2$, excluding the values $\mu_f/\mu_r = 4$ and $\mu_f/\mu_r = 1/4$. The values of $\sigma_{\geq 0}$ are computed at NNLO using the HNNLO program [172], and the process $pp \to h \to WW^* \to e^+\nu e^-\bar{\nu}$ is used for the computation of

[I.14] *Author(s): B. Di Micco.*

Table 10: Inclusive cross sections ($\sigma_{\geq 0}$) in pb for the process $pp \to H$ for several renormalization and factorization scale values, the cross section is evaluated with HNNLO at $\sqrt{s} = 13$ TeV, the central value scale is set to $m_H/2$. The Higgs boson mass is set at $m_H = 125.09$ GeV. PDF4LHC15 NNLO MC PDFs are used. The error quoted is the statistical error of the computation. The computation is performed in the infinite top quark mass approximation. The cross section is reported at LO, NLO and NNLO.

		Inclusive cross section (HNNLO)		
μ_F/m_H	μ_R/m_H	LO	NLO	NNLO
1	1	12.697±0.003	30.30±0.15	41.50±0.15
1	1/2	15.519±0.003	36.51±0.26	46.14±0.26
1/4	1/4	16.691±0.003	42.82±0.34	50.16±0.34
1/4	1/2	13.354±0.003	34.38±0.20	45.33±0.20
1/2	1	11.958±0.003	29.43±0.16	40.99±0.16
1/2	1/4	18.267±0.004	43.99±0.35	49.65±0.35
1/2	1/2	14.615±0.003	35.61±0.25	45.64±0.25

Table 11: H+1 jet inclusive cross sections ($\sigma_{\geq 1}$) in pb for the process $pp \to H$ for several renormalization and factorization scale values, the cross section is evaluated with MCFM at $\sqrt{s} = 13$ TeV, the central value scale is set to $m_H/2$. The Higgs boson mass is set at $m_H = 125.09$ GeV. PDF4LHC15 NNLO MC PDFs are used.

		H+1jet inclusive cross section (MCFM)			
		$p_T > 25$ GeV		$p_T > 30$ GeV	
μ_F/m_H	μ_R/m_H	LO	NLO	LO	NLO
1	1	9.303±0.002	16.48±0.05	7.947±0.002	14.11±0.02
1	1/2	12.764±0.002	19.80±0.05	10.900±0.002	16.87±0.03
1/4	1/4	18.373±0.004	22.04±0.08	15.836±0.003	18.96±0.06
1/4	1/2	12.874±0.002	19.18±0.05	11.097±0.002	16.47±0.05
1/2	1	9.398±0.002	16.42±0.02	8.060±0.0016	14.04±0.03
1/2	1/4	18.396±0.003	22.36±0.10	15.777±0.003	19.29±0.06
1/2	1/2	12.893±0.002	19.42±0.10	11.056±0.002	16.77±0.05

the cross section. The branching fraction to W pairs used in HNNLO is $\text{Br}(h \to W^+W^-) = 0.2054$, and it is used, together with the PDG [11] value of $\text{Br}(W \to e\nu) = 0.1070$, to correct the HNNLO cross section by the total branching fraction, in order to extract the h production cross section. The value used is:

$$\text{Br}(h \to W^+W^-)\text{Br}^2(W \to e\nu) = 0.002356$$

The obtained values are tabulated in Table 10.

The $H + 1$ jet and $H + 2$ jet cross sections have been computed at LO and NLO for the $pp \to h \to WW^* \to e^+\nu e^-\bar{\nu}$ process using the MCFM program [173], the branching fraction to W pairs used in MCFM is $\text{Br}(h \to W^+W^-) = 0.214$, and it is used to correct the MCFM cross section by the total branching fraction:

$$\text{Br}(h \to W^+W^-)\text{Br}^2(W \to e\nu) = 0.00245$$

In Table 11 and Table 12 we show the Higgs boson production cross section after having corrected the MCFM results for the branching fraction above. The jet p_T thresholds of 25 GeV and 30 GeV are used.

From Table 10 and Table 11 we can compute $\Delta\sigma_{\geq 0}$, $\Delta\sigma_{\geq 1}$, $\Delta\sigma_{\geq 2}$ and σ_0, σ_1 using the defini-

Table 12: H+2 jet cross-section ($\sigma_{\geq 2}$) in pb for the process $pp \to H$ for several renormalization and factorization scale values. The values are computed with MCFM at $\sqrt{s} = 13$ TeV, R=0.4 for jet thresholds of $p_T > 25$ and $p_T > 30$ GeV. The central value scale is chosen to be $m_H/2$. PDF4LHC15 NNLO MC pdfs are used.

gg→H+2jets cross section (MCFM)			
μ_F/m_H	μ_R/m_H	LO	NLO
		$p_T > 25$ GeV	
1	1	5.250± 0.002	6.96± 0.03
1	1/2	8.003 ±0.003	6.90± 0.06
1/4	1/4	14.565± 0.005	2.26± 0.14
1/4	1/2	9.068± 0.003	4.73± 0.09
1/2	1	5.586 ±0.002	5.67 ±0.05
1/2	1/4	13.679± 0.005	4.10 ±0.11
1/2	1/2	8.514 ±0.003	5.55 ±0.07
		$p_T > 30$ GeV	
1	1	3.980 ±0.001	5.20 ±0.03
1	1/2	6.064 ±0.002	5.27 ±0.04
1/4	1/4	11.192 ±0.004	-1.6 ±0.5
1/4	1/2	6.966 ±0.002	3.52 ±0.05
1/2	1	4.262 ±0.002	4.28 ±0.04
1/2	1/4	10.434 ±0.004	2.81 ±0.10
1/2	1/2	6.496 ±0.002	4.12 ±0.05

tions:[I.15]

$$\sigma_0 = \sigma_{\geq 0} - \sigma_{\geq 1},\ \sigma_1 = \sigma_{\geq 1} - \sigma^{\rm LO}_{\geq 2}.$$

where the cross section corresponding to the scale choice $\mu_F = \mu_R = m_H/2$ is used as central value and the LO value of $\sigma_{\geq 2}$ is used in order to preserve the α_s power counting in σ_1, being $\sigma_{\geq 1}$ computed up to NLO. The central values of the exclusive cross sections and their uncertainties are summarized in Table 13 together with the fractional error on σ_0 and σ_1. The upward and downward fractional errors are obtained using the following formulae:

$$\frac{\Delta^+\sigma_0}{\sigma_0} = \frac{\sqrt{\Delta^{+2}\sigma_{\geq 0} + \Delta^{-2}\sigma_{\geq 1}}}{\sigma_0} \quad \frac{\Delta^-\sigma_0}{\sigma_0} = \frac{\sqrt{\Delta^{-2}\sigma_{\geq 0} + \Delta^{+2}\sigma_{\geq 1}}}{\sigma_0}$$

$$\frac{\Delta^+\sigma_1}{\sigma_1} = \frac{\sqrt{\Delta^{+2}\sigma_{\geq 1} + \Delta^{-2}\sigma_{\geq 2}}}{\sigma_1} \quad \frac{\Delta^-\sigma_1}{\sigma_1} = \frac{\sqrt{\Delta^{-2}\sigma_{\geq 1} + \Delta^{+2}\sigma_{\geq 2}}}{\sigma_1}$$

where the $^+$ sign indicates the upward uncertainty and the $^-$ sign the downward uncertainty. In the same table, the symmetrized number are reported, using the maximum of the upward and downward errors. We recommend to use the symmetrized values as final uncertainties.

I.4.2.b.ii The Jet Veto Efficiency method.

The first version of Jet Veto Efficiency method, presented in Ref. [163], computes the jet veto acceptance uncertainties using three different definitions of the jet veto efficiency. Such definitions differ among each other for terms beyond α_s^2 and the related efficiencies show different behaviour as a function of

[I.15] Note that $\sigma_{\geq 2}$ and its uncertainty are computed here at leading order in order to match the power of α_s with the NLO computation of $\sigma_{\geq 1}$. Alternatively, one could choose to evaluate $\sigma_{\geq 2}$ at the highest known order, namely, NLO.

Table 13: Summary of jet-bin uncertainties on the 0 and 1 jet exclusive cross sections obtained using the ST method. The last two lines show symmetrized uncertainty intervals from the 7^{th} and 8^{th} row.

$\Delta\sigma_{\geq 0}$	$[-4.6, +4.6]$ pb	
	$p_T > 25$ GeV	$p_T > 30$ GeV
$\Delta\sigma_{\geq 1}$	$[-3, +2.9]$ pb	$[-2.7, +2.5$ pb
$\Delta\sigma^{\rm LO}_{\geq 2}$	$[-3.3, +6.0]$ pb	$[-2.5, +4.7]$ pb
σ_0	26.2 pb	28.9 pb
σ_1	10.9 pb	10.3 pb
$\Delta\sigma_0/\sigma_0$ S.T	[-0.22, +0.22]	[-0.18,+0.18]
$\Delta\sigma_1/\sigma_1$ S.T	[-0.62, +0.40]	[-0.53,+0.34]
$\Delta\sigma_0/\sigma_0$ S.T	[-0.22, +0.22]	[-0.18,+0.18]
$\Delta\sigma_1/\sigma_1$ S.T	[-0.62, +0.62]	[-0.53,+0.53]

the vetoed jet p_T. The uncertainty is computed, in this case, by doing the envelope of the naive scale uncertainty of the reference method and the central values obtained with the three jet veto efficiency definitions. The definitions are commonly referred as "schemes" a, b, c and are reported below:

$$\epsilon^a_N = 1 - \frac{\sigma^{\rm NLO}_{\geq N+1}}{\sigma^{\rm NNLO}_{\geq N}} \quad \epsilon^b_N = 1 - \frac{\sigma^{\rm NLO}_{\geq N+1}}{\sigma^{\rm NLO}_{\geq N}} \quad \epsilon^c_N = 1 - \frac{\sigma^{\rm NLO}_{\geq N+1}}{\sigma^{\rm NLO}_{\geq N}} + \left(\frac{\sigma^{\rm NLO}_{\geq N}}{\sigma^{\rm LO}_{\geq N}} - 1\right)\frac{\sigma^{\rm LO}_{\geq N+1}}{\sigma^{\rm LO}_{\geq N}} \tag{I.4.39}$$

The N value represents the number of jets of the exclusive selection.

I.4.2.b.ii.1 The JVE method for zero jet

In the 0-jet case the large logs that are produced by the introduction of the jet p_T threshold can be resummed using the JetVHeto program. Inputs to the JetVHeto computation are the LO, NLO and NNLO inclusive cross sections, that are shown in Table 10 and the $\sigma_{\geq 1}$ cross section shown in Table 11. The resummed computation can be matched to the fixed order result using three different schemes that can be considered equivalent to the three different Jet Veto Efficiency schemes listed above. In the resummed case, all scales, including the resummation scale, are varied by a factor two, and the envelope built using such uncertainty band together with the central value obtained with the three different matching schemes is quoted as final uncertainty. We report results using both the fixed-order computation and the resummed one.

In Table 14 we show the 0-jet JetVHeto efficiencies obtained for the factorization, renormalization and resummation scale considered in the envelope, and the central value of each scheme. The envelope is built using the scale variations of the "scheme a" only, therefore only for this scheme are detailed values for each scale choice shown. The efficiencies are reported for the 25 and 30 GeV p_T threshold using fixed order, resummed only and resummed results matched with the fixed order computation at NNLO+NNLL.

Table 14: $H + 0$ jet efficiencies of the process $pp \to H \to e^+\nu e^-\bar{\nu}$ for several renormalization and factorization scale values, matching schemes and resummation scales. The values are computed with JetVHeto at $\sqrt{s} = 13$ TeV, R=0.4 and $p_T > 25, 30$ GeV. The central value scale is chosen to be $m_H/2$. The Higgs boson mass is set at $m_H = 125.09$ GeV. PDF4LHC15 NNLO MC are used.

0-jet JetVHeto efficiencies for different p_T thresholds									
				$p_T > 25$ GeV			$p_T > 30$ GeV		
μ_F/m_H	μ_R/m_H	$Q_{\rm res}/m_H$	Scheme	NNLO+NNLL	NNLL	NNLO	NNLO+NNLL	NNLL	NNLO
1	1	1/2	a	0.5841	0.5727	0.6028	0.6509	0.6289	0.6600
1	1/2	1/2	a	0.5810	0.5513	0.5708	0.6472	0.6025	0.6344
1/4	1/4	1/2	a	0.5792	0.5176	0.5606	0.6431	0.5642	0.6221
1/4	1/2	1/2	a	0.5549	0.5290	0.5768	0.6248	0.5845	0.6366
1/2	1	1/2	a	0.56790	0.5586	0.5995	0.6379	0.6169	0.6575
1/2	1/4	1/2	a	0.5866	0.5207	0.5495	0.6462	0.5656	0.6114
1/2	1/2	1/2	a	0.5726	0.5413	0.5744	0.6367	0.5940	0.6325
1/2	1/2	1/4	a	0.5650	0.5295	0.5744	0.6273	0.5686	0.6325
1/2	1/2	1	a	0.6336	0.6387	0.5744	0.6987	0.6938	0.6325
1/2	1/2	1/2	b	0.5147	0.5413	0.4544	0.5760	0.5940	0.5289
1/2	1/2	1/2	c	0.7557	0.5413	0.9379	0.8207	0.5940	0.9389

Table 15: H+1 jet efficiency of the process $pp \to H \to e^+\nu e^-\bar{\nu}$ for several renormalization and factorization scale values. The values are computed with MCFM at $\sqrt{s} = 13$ TeV, R=0.4 and and $p_T > 25, 30$ GeV. The central value scale is chosen to be $m_H/2$. The Higgs boson mass is set at $m_H = 125.09$ GeV. PDF4LHC15 NNLO MC are used.

ϵ_1 NLO							
		$p_T > 25$ GeV			$p_T > 30$ GeV		
μ_F/m_H	μ_R/m_H	ϵ_1^b	ϵ_1^c	$(\epsilon_1^b + \epsilon_1^c)/2$	ϵ_1^b	ϵ_1^c	$(\epsilon_1^b + \epsilon_1^c)/2$
1	1	0.5777	0.6874	0.6326	0.6311	0.7335	0.6823
1	1/2	0.6517	0.8054	0.7285	0.6878	0.8215	0.7546
1/4	1/4	0.8976	1.035	0.9665	1.086	1.242	1.164
1/4	1/2	0.7533	0.9776	0.8654	0.7860	0.9865	0.8862
1/2	1	0.6549	0.8411	0.7480	0.6952	0.8615	0.778337
1/2	1/4	0.8167	0.9375	0.8771	0.8543	0.9692	0.9117
1/2	1/2	0.7142	0.9040	0.8091	0.7541	0.9308	0.8424

I.4.2.b.ii.2 The JVE method for one jet

The JVE method in his fixed order form can be easily extended to the 1-jet bin. Such approach has been used by the ATLAS collaboration for the publication of the Run-1 paper on the $h \to WW$ channel [171]. This channels is, at the moment, the decay channel that provides the most accurate measurements of the Higgs boson production cross section and its couplings. Equations (I.4.39) can be used also for the 1-jet bin where ϵ_1 represents the ratio of events with exactly one jet over the number of events with at least one jet. In scheme a the NNLO $H+1$ jet cross section is used. Such value has been nowadays evaluated [174] but software tools are still not publicly available, therefore the same approach of [171] will be followed in the following, assuming that scheme a lies between scheme b and scheme c. Such assumption has been tested up to NLO, and at NNLO for the gg induced process at the $\sqrt{s}$ of 8 TeV. Therefore, the average of schemes b and c is used instead of the scheme a. Using the cross sections reported in Table 10, Table 11 and Table 12 , the ϵ_1 values are computed for schemes b, c and their average and tabulated in Table 15. The uncertainty is evaluated as the envelope of the average of schemes b and c, computed for all renormalization and factorization scales, and the central values of the schemes b and c.

I.4.2.b.ii.3 The JVE method final results

In Table 16 we summarize the jet veto efficiencies and their uncertainties for the 0-jet and 1-jet bin indicating, in the 0-jet case, both the resummed and the fixed order results. We recommend to use the resummed result as reference values.

In order to compare the JVE results with the ST ones, in the same table we report the 0 (σ_0) and 1 (σ_1) jet cross sections with the Jet Veto method. They are computed from the Higgs total cross section and the jet veto efficiencies ϵ_0 and ϵ_1 according to the following formulae:

$$\sigma_0 = \sigma_{\rm tot} \cdot \epsilon_0 \quad \sigma_1 = \sigma_{\rm tot} \cdot (1 - \epsilon_0) \cdot \epsilon_1$$

In this expression, the best available computation of the Higgs total cross section can be used because full factorization between total cross section and acceptance is assumed in this approach. The cross section value computed using the De Florian-Grazzini method for resummation and including the complex pole scheme is:

$$\sigma_{\rm tot} = 43.92 \text{ pb}^{+7.4\%}_{-7.9\%}(\text{scale})^{+7.1\%}_{-6.0\%}(\text{PDF})$$

the PDF error is usually accounted independently in experimental analyses, therefore only the scale

Table 16: Jet veto efficiency, exclusive jet bin cross sections and their uncertainties for the 0 and 1 jet bin using the JVE method. The labels F.O. and RES. refer to the usage of fixed order and resummed inputs, respectively. The last four lines of the table show symmetrized uncertainty intervals.

Summary of JVE related uncertainties.		
	$p_T > 25$ GeV	$p_T > 30$ GeV
ϵ_0 RES.	0.57	0.64
ϵ_0 FO.	0.57	0.63
$\Delta\epsilon_0$ RES.	[- 0.06,+0.18]	[-0.06, +0.18]
$\Delta\epsilon_0$ F.O.	[-0.12, +0.36]	[-0.10, +0.31]
$\Delta\epsilon_0/\epsilon_0$ RES.	[-0.11 , +0.32]	[-0.09, +0.28]
$\Delta\epsilon_0/\epsilon_0$ F.O.	[-0.21 , +0.63]	[-0.16, +0.49]
ϵ_1 F.O.	0.81	0.84
$\Delta\epsilon_1$ F.O.	[-0.18, +0.16]	[-0.16, +0.32]
$\Delta\epsilon_1/\epsilon_1$ F.O.	[-0.22, +0.20]	[-0.19, +0.38]
$\Delta\sigma_0/\sigma_0$ F.O.	[-0.18, +0.37]	[-0.12, +0.33]
$\Delta\sigma_1/\sigma_1$ F.O.	[-0.87, +0.36]	[-0.86, +0.48]
$\Delta\sigma_0/\sigma_0$ RES.	[-0.13, +0.32]	[-0.12, +0.29]
$\Delta\sigma_1/\sigma_1$ RES.	[-0.48, +0.25]	[-0.54, +0.42]
$\Delta\sigma_0/\sigma_0$ F.O.	[-0.37, +0.37]	[-0.33, +0.33]
$\Delta\sigma_1/\sigma_1$ F.O.	[-0.87, +0.87]	[-0.86, +0.86]
$\Delta\sigma_0/\sigma_0$ RES.	[-0.32, +0.32]	[-0.29, +0.29]
$\Delta\sigma_1/\sigma_1$ RES.	[-0.48, +0.48]	[-0.54, +0.54]

variation related error is accounted for. Using simple error propagation, the central values and their uncertainties have been computed and summarized in Table 16.

I.4.2.c Combined resummed predictions for the 0-jet, 1-jet, and $\geq$ 2-jet bins [I.16]

Experimental analyses require a consistent treatment of cross sections and their uncertainties for several jet bins. In the following we discuss predictions for the 0-jet, 1-jet, and $\geq$ 2-jet bins with a resummation of jet-veto logarithms, and provide updated results for 13 TeV. We utilize a theoretical approach that provides flexible control over uncertainties allowing for the identification of different sources of yield and migration uncertainties. It is thus well-suited to provide a theoretical description of jet binning, including multiple jet-bin boundaries.

I.4.2.c.i Jet p_T resummation at NNLL′+NNLO [I.17]

We discuss the resummed predictions for the $H+0$-jet cross section from gluon fusion with a p_T veto on jets and with the resummation of jet-veto logarithms at NNLL′+NNLO order [159]. We place a particular emphasis on a careful estimate of the perturbative uncertainties and include a detailed discussion of how yield and migration uncertainties are determined. The different contributions to the uncertainty are estimated by appropriate variations of the different scales in virtuality and rapidity space appearing in a factorization theorem. This allows us to distinguish between and account for the uncertainties due to higher fixed-order corrections as well as higher-order towers of jet-p_T logarithms.

[I.16] *Author(s): R. Boughezal, X. Liu, F. Petriello, I.W. Stewart, F.J. Tackmann.*
[I.17] *Author(s): I. W. Stewart, F. J. Tackmann.*

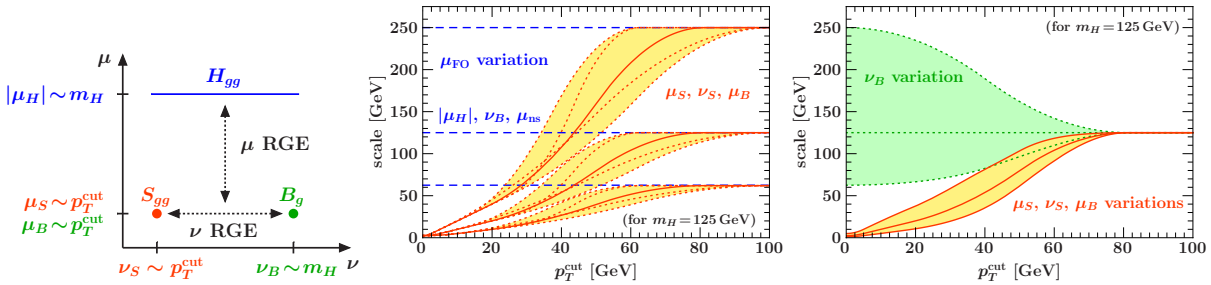

Figure 13: Left panel: Illustration of the RGE in virtuality and rapidity space to resum jet-p_T logarithms. Middle panel: Profile scale variations contributing to the overall fixed-order (yield) uncertainty. Right panel: Profile scale variations whose combinations are used to assess the resummation (migration) uncertainty.

We utilize the framework of soft-collinear effective theory (SCET) [175–178] for jet-veto resummation at hadron colliders [158, 159, 164, 168, 179]. The factorized $pp \to H + 0$-jet cross section with a cut on $p_T^{\rm jet} < p_T^{\rm cut}$ is given by

$$\begin{aligned}\sigma_0(p_T^{\rm cut}) = \frac{\sqrt{2} G_F\, m_H^2}{576\pi E_{\rm cm}^2}\, H_{gg}(m_H^2, \mu_H) \int dY\, B_g\Big(m_H, p_T^{\rm cut}, R, \frac{m_H}{E_{\rm cm}}\, e^{Y}, \mu_B, \nu_B\Big) \\ B_g\Big(m_H, p_T^{\rm cut}, R, \frac{m_H}{E_{\rm cm}}\, e^{-Y}, \mu_B, \nu_B\Big)\, S_{gg}(p_T^{\rm cut}, R, \mu_S, \nu_S)\, U_0(p_T^{\rm cut}, R; \mu_H, \mu_B, \mu_S, \nu_B, \nu_S) \\ + \sigma_0^{R\rm sub}(p_T^{\rm cut}, R) + \sigma_0^{\rm nons}(p_T^{\rm cut}, R, \mu_{\rm ns})\,. \end{aligned} \tag{I.4.40}$$

The first term is the leading contribution containing all the singular logarithmic terms $\alpha_s^i \ln^j(p_T^{\rm cut}/m_H)$. The resummation of the logarithms is performed by renormalization group evolution (RGE) in both virtuality (μ) and rapidity (ν) space, illustrated on the left of Figure 13. The factorized hard (H_{gg}), beam (B_g), and soft (S_g) functions are evaluated at their own natural virtuality scales μ_i and rapidity scales ν_i, where they contain no large logarithms and are calculable at fixed order in α_s. From there they are evolved to a common (arbitrary) scale, yielding the combined evolution factor U_0 which resums the logarithms of the virtuality ratios μ_i/μ_j and rapidity ratios ν_i/ν_j. The resummation is performed to NNLL′ order, which in addition to the NNLL resummation includes the full $\mathcal{O}\left(\alpha_s^2\right)$ corrections to H_{gg}, B_g, and S_{gg} (which includes the $\mathcal{O}\left(\alpha_s^2\right)$ effects from jet clustering). These are formally part of the N^{3}LL resummation for which they provide the correct RGE boundary conditions, and incorporate all dominant (singular) NNLO corrections into the resummed result.

The second term in Eq. (I.4.40), $\sigma_0^{R\rm sub}(p_T^{\rm cut}, R)$, contains $\mathcal{O}\left(R^2\right)$ contributions. For $R = 0.4$ they are numerically very small and are treated as subleading power corrections. The last term in Eq. (I.4.40), $\sigma_0^{\rm nons}(p_T^{\rm cut}, R, \mu_{\rm ns})$, contains $\mathcal{O}\left(p_T^{\rm cut}/m_H\right)$ "nonsingular" corrections, which vanish for $p_T^{\rm cut} \to 0$ but become important at large $p_T^{\rm cut}$. These terms are added to achieve the full NNLL′+NNLO accuracy, which incorporates the complete NNLO cross section for all values of $p_T^{\rm cut}$, including the inclusive NNLO cross section.

The RGE scales $\mu_H, \mu_B, \mu_S, \nu_B$, and ν_S are chosen as functions of $p_T^{\rm cut}$, which are referred to as profile scales [180, 181]. They have to satisfy several constraints and their construction is discussed in detail in Ref. [159]. Essentially, in the resummation region at small $p_T^{\rm cut}$ they have to parametrically follow the canonical scaling dictated by the RGE, while at large $p_T^{\rm cut} \gtrsim m_H/2$ they must approach a common fixed-order scale $\mu_{\rm FO}$ in order to turn off the resummation and avoid unphysical behaviour. The remaining freedom in the choice of the profile scales provides a flexible and powerful way to assess the perturbative uncertainties in the resummed predictions. For this reason, profile scales have been applied by now in a large variety of different contexts and have become an established and reliable method for assessing perturbative uncertainty in resummed predictions. As detailed in Ref. [159], in the context of jet binning the profile scale variations allow us to identify the different uncertainty sources contributing

to the yield and migration uncertainties discussed in Section I.4.2.a.

Before discussing the variations, we stress that the scales are unphysical parameters, and their variations simply provide a convenient way to probe the "typical" size of the associated missing higher-order terms. The observed variations in the results must be interpreted as such. In particular, we do not assign any meaning to accidentally small one-sided scale variations that yield asymmetric uncertainties, which are just the result of nonlinear scale dependence, which is frequently encountered at higher orders and including resummation. Hence, we always consider the maximum absolute deviation from the chosen central scale as the (symmetric) uncertainty. To be explicit, an observed variation of $+|x|$ and $-|y|$ in the cross section is interpreted as uncertainty of $\pm\max\{|x|,|y|\}$.

The first type of variation is a collective variation of all scales by a factor of $1/2$ and 2. This keeps all scale ratios and thus all logarithms fixed, and at large p_T^{cut} reproduces the uncertainty in the fixed-order cross section. Hence, this corresponds to an overall fixed-order uncertainty (within the resummed prediction), and is naturally identified as a common source for all σ_i, giving rise to a yield uncertainty $\Delta_{\mu i}$. A second type of variation included in $\Delta_{\mu i}$ is to the profile shape controlling the transition points where the resummation is turned off. The total of 14 profile variations V_μ contributing to $\Delta_{\mu 0}$ are displayed in the middle panel of Figure 13. For each profile v_i in V_μ we obtain $\Delta_{\mu i}$ as the maximum absolute deviation from the central value,

$$\Delta_{\mu 0}(p_T^{\text{cut}}) = \max_{v_i\in V_\mu} \left|\sigma_0^{v_i}(p_T^{\text{cut}}) - \sigma_0^{\text{central}}(p_T^{\text{cut}})\right|, \qquad \Delta_{\mu\geq 0} = \max_{v_i\in V_\mu} \left|\sigma_{\geq 0}^{v_i} - \sigma_{\geq 0}^{\text{central}}\right|. \tag{I.4.41}$$

For $\Delta_{\mu\geq 0}$, only the variation of μ_{FO} by a factor 2 contributes, and $\Delta_{\mu\geq 1}(p_T^{\text{cut}}) = \Delta_{\mu\geq 0} - \Delta_{\mu 0}(p_T^{\text{cut}})$.

The profile scale variations V_{resum} contributing to the resummation uncertainty, $\Delta_{\text{resum}}^{0/1}$, are shown in the right panel of Figure 13. They separately vary each of the beam and soft scales up and down but keep μ_{FO} fixed. They thus directly probe the intrinsic uncertainty in the resummed logarithmic series. The variation is chosen to approach the conventional factor of 2 for $p_T^{\text{cut}} \to 0$. Out of the 80 possible combinations of all variations, all combinations leading to arguments of logarithms which are more than a factor of 2 different from their central values are not considered. This leaves a total of 35 profile scale variations in V_{resum} that are used to estimate

$$\Delta_{\text{resum}}^{0/1}(p_T^{\text{cut}}) = \max_{v_i\in V_{\text{resum}}} \left|\sigma_0^{v_i}(p_T^{\text{cut}}) - \sigma_0^{\text{central}}(p_T^{\text{cut}})\right|. \tag{I.4.42}$$

The p_T^{cut} logarithms are the primary source of uncertainty caused by the jet binning at small p_T^{cut} and we can therefore identify Δ_{resum} as the corresponding migration uncertainty. Furthermore, $\Delta_{\text{resum}}^{0/1}$ smoothly turns off at large p_T^{cut} where the logarithms become unimportant and the resummation is turned off. This is consistent with the fact that in this limit migration effects become irrelevant since $\sigma_{\geq 1}(p_T^{\text{cut}})$ becomes numerically much smaller than $\sigma_0(p_T^{\text{cut}})$.

Our predictions use a complex hard scale $\mu_H = -i\mu_{\text{FO}}$ with $\mu_{\text{FO}} = m_H$. This is the canonical scale at which the hard function contains no large logarithms and shows a significantly improved perturbative stability compared to $\mu_H = \mu_{\text{FO}}$ (for any value of μ_{FO}). In the transition from small to large p_T^{cut} we keep the hard scale at its complex value. In principle, one could contemplate rotating it to the real axis as a function of p_T^{cut} to turn off the resulting resummation of logarithms of $\ln(\mu_H/|\mu_H|)$. However, this would inevitably lead to an unphysical behaviour of a decreasing cross section with increasing p_T^{cut}. Instead, the improved convergence observed in the small p_T region, where the factorization of the hard virtual corrections into the overall factor H_{gg} is manifest, also translates into the fixed-order cross section at large p_T^{cut}, because the majority of the total cross section comes from the small p_T region. Consequently, as one can see from Table 17, the inclusive cross section for $\mu_H = -im_H$ shows a much better perturbative convergence and as a result is already at NNLO in close agreement with the N^{3}LO result at the default scale $\mu_H = m_H/2$. The uncertainty related to this resummation is estimated by varying the phase of $\mu_H = \mu_{\text{FO}}\exp(-i\varphi)$ as $\varphi = \pi/2 \pm \pi/4$. This phase variation is roughly equivalent

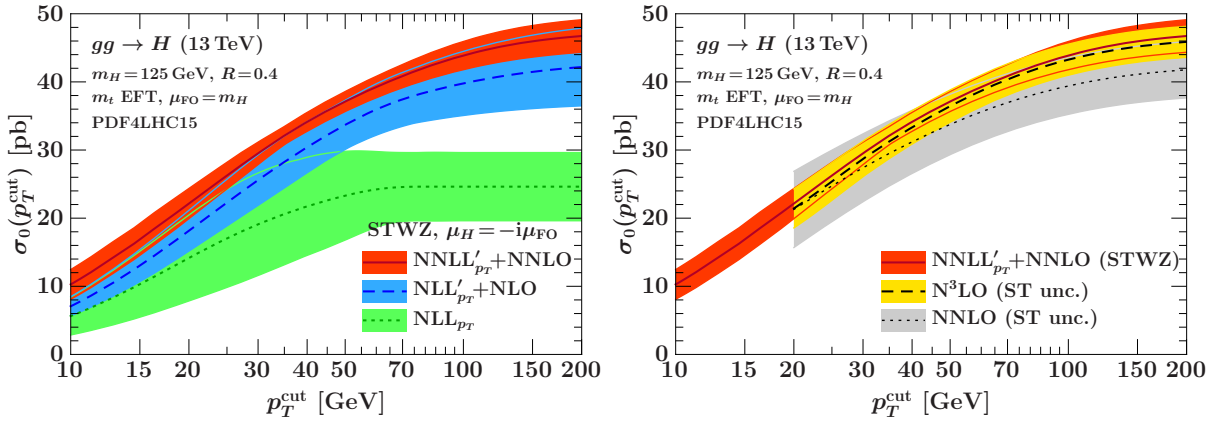

Figure 14: The 0-jet cross section $\sigma_0(p_T^{\rm cut})$, comparing different resummation orders (left) and resummed and fixed-order predictions (right). The N^{3}LO result on the right utilizes the results of Refs. [96, 174].

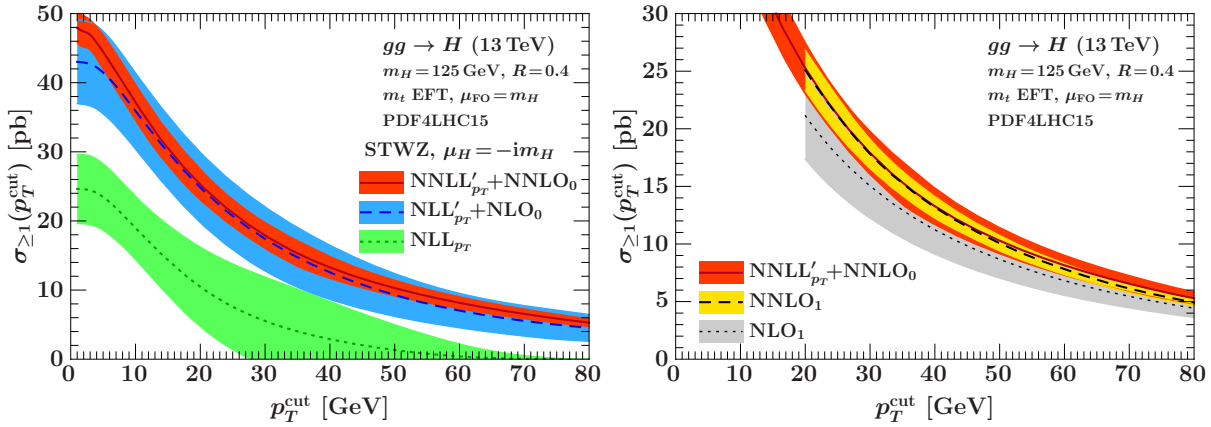

Figure 15: The ≥ 1-jet cross section $\sigma_{\geq 1}(p_T^{\rm cut})$, comparing different resummation orders (left) and resummed and fixed-order predictions (right). The NNLO$_1$ result on the right utilizes the results of Ref. [174].

to the usual factor of 2 since $\pi/4 \simeq \ln 2$. We have

$$\Delta_{\varphi i} = \max_{\varphi \in \{\pi/4, \pi/2, 3\pi/4\}} \left| \sigma_i^{\varphi} - \sigma_i^{\rm central} \right| . \tag{I.4.43}$$

We consider this as an additional independent uncertainty source, and since it affects all cross sections via an overall multiplicative factor, it is treated as a yield uncertainty.

In summary, we have the following three uncertainty amplitudes for $\{\sigma_{\geq 0}, \sigma_0, \sigma_{\geq 1}\}$,

$$\begin{aligned} \kappa_\mu^{\rm y} &: \quad \{\Delta_{\mu \geq 0},\, \Delta_{\mu 0},\, \Delta_{\mu \geq 1}\} , \qquad & \kappa_\varphi^{\rm y} &: \quad \{\Delta_{\varphi \geq 0},\, \Delta_{\varphi 0},\, \Delta_{\varphi \geq 1}\} , \\ \kappa_{\rm cut}^{0/1} &: \quad \Delta_{\rm resum}^{0/1} \times \{0,\, 1,\, -1\} . \end{aligned} \tag{I.4.44}$$

The numerical results we present are obtained in the top EFT limit rescaled with the exact LO m_t dependence. Bottom quark and EW effects are not yet included. Their numerical effects go in opposite directions and largely cancel each other, so they should be included together. Jets are defined with a jet radius of $R = 0.4$ and without any cut on the jet rapidity. We use the PDF4LHC15 PDFs with $\alpha_s(m_Z) = 0.118$. In Table 17 we compare the corresponding results for the inclusive cross section at different hard scales. We also give the corresponding N^{3}LO results, obtained utilizing the results of Ref. [96].

Table 17: The inclusive cross section $\sigma_{\geq 0}$, comparing different orders and the conventional scale choices (columns 2 and 3) and with complex hard scale (columns 4 and 5). The uncertainties are the perturbative uncertainties. The last column corresponds to the default scale choice for μ_H used for the resummed predictions discussed here.

$\sigma_{\geq 0}$/pb	$\mu_H = m_H/2$	$\mu_H = m_H$	$\mu_H = -im_H/2$	$\mu_H = -im_H$
LO	$16.04 \pm 15.8\%$	$13.80 \pm 16.3\%$	$26.70 \pm 12.8\%_\mu \pm 22.9\%_\varphi$	$23.29 \pm 14.6\%_\mu \pm 14.7\%_\varphi$
NLO	$36.94 \pm 19.7\%$	$31.61 \pm 16.9\%$	$47.40 \pm 14.1\%_\mu \pm 10.5\%_\varphi$	$42.18 \pm 12.4\%_\mu \pm 6.8\%_\varphi$
NNLO	$46.55 \pm 9.1\%$	$42.42 \pm 9.7\%$	$48.76 \pm 2.8\%_\mu \pm 1.5\%_\varphi$	$47.41 \pm 4.6\%_\mu \pm 2.0\%_\varphi$
N^{3}LO	$48.03 \pm 3.2\%$	$46.51 \pm 4.9\%$	$47.85 \pm 0.6\%_\mu \pm 0.8\%_\varphi$	$47.96 \pm 1.5\%_\mu \pm 0.5\%_\varphi$

Table 18: Predictions for the 0-jet cross section at $p_T^{\text{cut}} = 25\,\text{GeV}$ (top) and $p_T^{\text{cut}} = 30\,\text{GeV}$ (bottom) corresponding to Figure 14 with a breakdown of the perturbative uncertainties.

	$\sigma_0(25\,\text{GeV})$/pb	$\Delta_{\mu 0}$	$\Delta_{\varphi 0}$	$\Delta^{0/1}_{\text{resum}}$	total pert. unc.
NLL	17.04 ± 7.21	18.7%	12.8%	35.7%	42.3%
NLL′+NLO$_0$	22.29 ± 3.43	7.7%	5.1%	12.3%	15.4%
NNLL′+NNLO$_0$	26.25 ± 1.97	4.7%	0.6%	5.8%	7.5%
	$\sigma_0(30\,\text{GeV})$/pb	$\Delta_{\mu 0}$	$\Delta_{\varphi 0}$	$\Delta^{0/1}_{\text{resum}}$	total pert. unc.
NLL	19.10 ± 7.52	17.4%	12.8%	32.9%	39.4%
NLL′+NLO$_0$	25.59 ± 3.72	7.9%	5.3%	11.0%	14.5%
NNLL′+NNLO$_0$	29.51 ± 1.65	3.8%	0.1%	4.1%	5.6%

In Figure 14 we show our results for the resummed and matched 0-jet cross section, comparing the different consistently matched resummation orders on the left. On the right, we compare our best prediction at NNLL′+NNLO with the pure fixed-order results at the corresponding scale with ST uncertainties at NNLO and N^{3}LO (obtained from the results of Refs. [96, 174]). The NNLL′+NNLO agrees well with the fixed N^{3}LO with ST uncertainties. (The same is also observed for NLL′+NLO compared to NNLO.) Since the typical values of $p_T^{\text{cut}} \simeq 30\,\text{GeV}$ lie in the transition region, it is not unexpected that the resummed result is roughly predicting the next-higher fixed order. This also confirms that the ST method produces reasonably sized uncertainties here. Our resummed predictions still have the advantage of allowing one to separately estimate all types of yield and migration uncertainties, in contrast to the fixed-order predictions where some explicit assumptions on the correlations between cross sections are needed. The corresponding results for the ≥ 1-jet cross section are shown in Figure 15. Here the lowest NLL result is not very meaningful as it does not even contain the correct LO$_1$ result. In the right panel we see that the highest order resummed result agrees well with the corresponding fixed NNLO$_1$ [174, 182, 183] result albeit with larger uncertainties toward larger p_T^{cut}.

At this point we should note that matching to the N^{3}LO$_0$ and NNLO$_1$ results without also going to the corresponding N^{3}LL$^{(\prime)}$ resummation order amounts to including unresummed singular logarithms in the nonsingular matching corrections. Doing so would reduce the overall scale dependence but not necessarily improve the accuracy of the final prediction, because in the resummation region there is no guarantee that this would move the result in the right direction. (Thrust in e^+e^- is a known example where it would not.) It would also come at the cost of reentangling the uncertainties sources, since on the one hand it should not reduce the resummation uncertainties while on the other hand it would impact the dominant p_T^{cut} dependence. Given these potential subtleties and given that our results with a complex hard scale already agree very well with the N^{3}LO$_0$ and NNLO$_1$ results, we do not see sufficient reason to add these terms until the corresponding resummation order is available as well.

The numerical results for $\sigma_0(p_T^{\text{cut}})$ and $\sigma_{\geq 1}(p_T^{\text{cut}})$ for $p_T^{\text{cut}} = 25\,\text{GeV}$ and $p_T^{\text{cut}} = 30\,\text{GeV}$ with a

Table 19: Predictions for the $\geq$ 1-jet cross section at $p_T^{\text{cut}} = 25\,\text{GeV}$ (top) and $p_T^{\text{cut}} = 30\,\text{GeV}$ (bottom) corresponding to Figure 15 with a breakdown of the perturbative uncertainties.

	$\sigma_{\geq 1}(25\,\text{GeV})/\text{pb}$	$\Delta_{\mu\geq 1}$	$\Delta_{\varphi\geq 1}$	$\Delta^{0/1}_{\text{resum}}$	total pert. unc.
NLL′+NLO$_0$	20.69±4.88	17.4%	8.7%	13.3%	23.6%
NNLL′+NNLO$_0$	21.16±1.96	4.5%	3.8%	7.1%	9.3%
	$\sigma_{\geq 1}(30\,\text{GeV})/\text{pb}$	$\Delta_{\mu\geq 1}$	$\Delta_{\varphi\geq 1}$	$\Delta^{0/1}_{\text{resum}}$	total pert. unc.
NLL′+NLO$_0$	17.39±4.63	19.1%	9.1%	16.2%	26.6%
NNLL′+NNLO$_0$	17.90±1.88	6.0%	5.2%	6.8%	10.5%

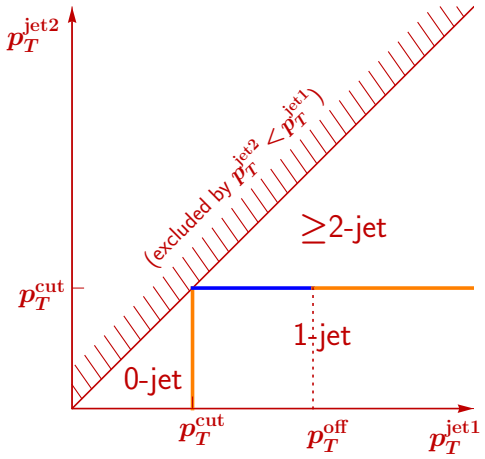

Figure 16: Illustration of the p_T^{jet1}-p_T^{jet2} plane relevant for the $0/1/2$-jet binning. The orange jet boundaries are treated in resummed perturbation theory, while the blue boundary is treated at fixed order. The dependence of the final results on the arbitrary p_T^{off} parameter is negligible compared to the perturbative uncertainties.

full breakdown of the uncertainties are given in Tables 18 and 19. For $p_T^{\text{cut}} = 30\,\text{GeV}$, Δ_μ and $\Delta^{0/1}_{\text{resum}}$ contribute roughly equally at each order, while Δ_φ is subdominant, except at the highest order in $\sigma_{\geq 1}$ where it contributes almost equally. For $p_T^{\text{cut}} = 25\,\text{GeV}$, the picture is roughly similar, except that as expected the uncertainties in σ_0 are somewhat increased compared to $p_T^{\text{cut}} = 30\,\text{GeV}$. Note that for $\sigma_{\geq 1}$ the total uncertainty actually slightly decreases from $p_T^{\text{cut}} = 30\,\text{GeV}$ to $p_T^{\text{cut}} = 25\,\text{GeV}$. The reason is that the cross section increases and the logarithms are resummed which results in the relative size of the remaining overall yield uncertainties to decrease.

I.4.2.c.ii Combining resummed predictions for $0/1/2$-jet bins [I.18]

Here, we discuss resummation-improved predictions for $0/1/2$-jet bins. We provide updated numerical results for 13 TeV and PDF4LHC15 PDFs and include the full breakdown of the uncertainties in terms of the parameterization of Eq. (I.4.34). We follow Ref. [184] for combining the 0-jet resummation of Ref. [159], discussed above, with the 1-jet resummation of Refs. [185, 186], which was documented in Ref. [9], and for the estimation of yield and migration uncertainties.

We denote the p_T of the leading and 2nd leading jet by p_T^{jet1} and p_T^{jet2} and by definition $p_T^{\text{jet2}} < p_T^{\text{jet1}}$. The different jet bins are illustrated in Figure 16. We define

$$\sigma_{\geq 0}: \text{ the inclusive cross section}, \tag{I.4.45}$$

[I.18] *Author(s): R. Boughezal, X. Liu, F. Petriello, F. J. Tackmann.*

$$
\begin{aligned}
\sigma_0(p_T^{\rm cut}):&\ \text{the 0-jet cross section, with } p_T^{\rm jet1} < p_T^{\rm cut}\,,\\
\sigma_{\geq 1}(p_T^{\rm cut}):&\ \text{the inclusive 1-jet cross section, with } p_T^{\rm jet1} \geq p_T^{\rm cut}\,,\\
\sigma_1([p_{Ta},p_{Tb}];p_T^{\rm cut}):&\ \text{the exclusive 1-jet cross section, with } p_{Ta} \leq p_T^{\rm jet1} < p_{Tb}\,,\quad p_T^{\rm jet2} < p_T^{\rm cut}\,,\\
\sigma_{\geq 2}([p_{Ta},p_{Tb}];p_T^{\rm cut}):&\ \text{the inclusive 2-jet cross section, with } p_{Ta} \leq p_T^{\rm jet1} < p_{Tb}\,,\quad p_T^{\rm jet2} \geq p_T^{\rm cut}\,.
\end{aligned}
$$

The exclusive 1-jet bin is theoretically quite nontrivial as it is affected by both the $0/1$-jet and $1/2$-jet boundaries. To construct a resummation-improved expression for it, we introduce a parameter $p_T^{\rm off} > p_T^{\rm cut}$ to separate the low and high $p_T^{\rm jet1}$ regions, shown by the dotted line in Figure 16,

$$
\sigma_1(p_T^{\rm cut}) \equiv \sigma_1([p_T^{\rm cut},\infty];p_T^{\rm cut}) = \sigma_1([p_T^{\rm cut},p_T^{\rm off}];p_T^{\rm cut}) + \sigma_1([p_T^{\rm off},\infty];p_T^{\rm cut})\,. \tag{I.4.46}
$$

In practice, $p_T^{\rm off}$ is taken to be around $m_H/2$. The second term above contains logarithms of $p_T^{\rm cut}/Q$ with $Q \sim p_T^{\rm off} \sim m_H$. These can be resummed to NLL$'$+NLO using the direct resummation of Refs. [185, 186], which is valid for $p_T^{\rm jet1} \sim m_H$ much larger than the $p_T^{\rm cut}$ on the 2nd jet. The first term above contains the $0/1$ jet boundary. To improve it by the corresponding resummation, we can write it as

$$
\sigma_1([p_T^{\rm cut},p_T^{\rm off}];p_T^{\rm cut}) = \big[\sigma_0(p_T^{\rm off}) - \sigma_0(p_T^{\rm cut})\big] - \sigma_{\geq 2}([p_T^{\rm cut},p_T^{\rm off}],p_T^{\rm cut})\,, \tag{I.4.47}
$$

where the first term in brackets is equivalent to $\sigma_0(p_T^{\rm off})-\sigma_0(p_T^{\rm cut}) = \sigma_{\geq 1}(p_T^{\rm cut})-\sigma_{\geq 1}(p_T^{\rm off})$. We can then use the NNLL$'$+NNLO resummation of Ref. [159] for resumming the logarithms of $p_T^{\rm cut}/m_H$ associated with the $0/1$-jet boundary. The additional 2-jet terms in Eq. (I.4.47) are calculated at fixed NLO$_2$. The validity of this indirect resummation approach is discussed and studied in Ref. [184]. It essentially relies on the fact that in the region of interest, the 0-jet terms dominate while the 2-jet terms are numerically small.

The combination of the indirect resummation for $p_T^{\rm jet1} < p_T^{\rm off}$ and the direct resummation for $p_T^{\rm jet1} \geq p_T^{\rm off}$ thus allows for a resummation-improved description of the complete 1-jet bin, i.e.,

$$
\sigma_1([p_T^{\rm cut},\infty];p_T^{\rm cut}) = \sigma_1^{\rm indirect}([p_T^{\rm cut},p_T^{\rm off}];p_T^{\rm cut}) + \sigma_1^{\rm direct}([p_T^{\rm off},\infty];p_T^{\rm cut})\,. \tag{I.4.48}
$$

An important consistency check of this method is that the final result should be largely independent of the precise choice of $p_T^{\rm off}$. More precisely, the residual dependence on $p_T^{\rm off}$ should be much smaller than the estimated perturbative uncertainties. As shown in Ref. [184], by using a complex scale hard scale in the 0-jet resummation as well as including the $H+1$ jet NNLO$_1$ virtual corrections in the direct resummation, the results become practically independent of $p_T^{\rm off}$.

To estimate the perturbative uncertainties, we use profile scale variations in both the 0-jet and 1-jet resummations, using the same physical interpretations to identify the different uncertainties sources. The first is the overall fixed-order uncertainty, $\Delta_{\mu i}$, as discussed above Eq. (I.4.41), which is treated as a yield uncertainty. It is estimated by collectively varying all scales that appear in the resummed predictions and reduces to the usual fixed-order scale variations in the respective limits of large $p_T^{\rm cut}$. The uncertainties for $\{\sigma_{\geq 0},\sigma_0,\sigma_{\geq 1},\sigma_1,\sigma_{\geq 2}\}$ are

$$
\kappa_\mu^{\rm y}:\quad \{\Delta_{\mu\geq 0},\ \Delta_{\mu 0},\ \Delta_{\mu\geq 1},\ \Delta_{\mu 1},\ \Delta_{\mu\geq 2}\}\,, \tag{I.4.49}
$$

where the first three are as in Eqs. (I.4.41) and (I.4.44) and

$$
\begin{aligned}
\Delta_{\mu 1} &\equiv \Delta_{\mu 1}([p_T^{\rm cut},\infty];p_T^{\rm cut}) = \Delta_{\mu 0}(p_T^{\rm off}) - \Delta_{\mu 0}(p_T^{\rm cut}) + \Delta_{\mu 1}([p_T^{\rm off},\infty];p_T^{\rm cut})\,,\\
\Delta_{\mu\geq 2} &\equiv \Delta_{\mu\geq 0} - \Delta_{\mu 0}(p_T^{\rm cut}) - \Delta_{\mu 1}([p_T^{\rm cut},\infty];p_T^{\rm cut})\,.
\end{aligned} \tag{I.4.50}
$$

Since the yield uncertainties are fully correlated, the yield uncertainty in the 1-jet bin is the linear sum from the two regions. For the region below $p_T^{\rm off}$ we use $\Delta_{\mu 0}(p_T^{\rm off})-\Delta_{0\mu}(p_T^{\rm cut})$ from the 0-jet resummation in Eq. (I.4.41). For the region above $p_T^{\rm off}$, $\Delta_{\mu 1}([p_T^{\rm off},\infty];p_T^{\rm cut})$ is determined by the overall profile scale

Table 20: Predictions for the $0/1/2$-jet bins for $p_T^{\text{cut}} = 25\,\text{GeV}$ (top) and $p_T^{\text{cut}} = 30\,\text{GeV}$ (bottom).

$p_T^{\text{cut}} = 25\,\text{GeV}$	σ/pb	Δ_μ	Δ_φ	$\Delta_{\text{cut}}^{0/1}$	$\Delta_{\text{cut}}^{1/2}$	total pert. unc.
$\sigma_{\geq 0}$	47.41 ± 2.40	4.6%	2.0%	-	-	5.1%
σ_0	26.25 ± 1.97	4.7%	0.6%	5.8%	-	7.5%
$\sigma_{\geq 1}$	21.16 ± 1.96	4.5%	3.8%	7.1%	-	9.3%
σ_1	13.28 ± 1.76	4.2%	3.3%	9.8%	7.2%	13.3%
$\sigma_{\geq 2}$	7.88 ± 1.12	5.1%	4.6%	2.7%	12.2%	14.3%
$p_T^{\text{cut}} = 30\,\text{GeV}$	σ/pb	Δ_μ	Δ_φ	$\Delta_{\text{cut}}^{0/1}$	$\Delta_{\text{cut}}^{1/2}$	total pert. unc.
$\sigma_{\geq 0}$	47.41 ± 2.40	4.6%	2.0%	-	-	5.1%
σ_0	29.51 ± 1.65	3.8%	0.1%	4.1%	-	5.6%
$\sigma_{\geq 1}$	17.90 ± 1.88	6.0%	5.2%	6.8%	-	10.5%
σ_1	11.94 ± 1.58	5.5%	4.8%	8.4%	7.2%	13.2%
$\sigma_{\geq 2}$	5.96 ± 1.05	7.1%	6.1%	3.6%	14.5%	17.6%

variations in the 1-jet resummation [186]. The result for $\Delta_{\mu\geq 2}$ then follows from consistency and e.g. ensures that $\Delta_{\mu\geq 1} = \Delta_{\mu 1} + \Delta_{\mu\geq 2}$.

Next, the resummation uncertainties induced by the $0/1$-jet and $1/2$-jet boundaries are used to estimate the respective migration uncertainties. Parameterizing the migration uncertainties by two independent nuisance parameters as in Eq. (I.4.34), the uncertainties for $\{\sigma_{\geq 0}, \sigma_0, \sigma_{\geq 1}, \sigma_1, \sigma_{\geq 2}\}$ are

$$\begin{aligned} \kappa_{\text{cut}}^{0/1}: &\quad \Delta_{\text{cut}}^{0/1} \times \{0,\, 1,\, -1,\, -(1-x_1),\, -x_1\}\,, \\ \kappa_{\text{cut}}^{1/2}: &\quad \Delta_{\text{cut}}^{1/2} \times \{0,\, 0,\, 0,\, 1,\, -1\}\,, \end{aligned} \tag{I.4.51}$$

where we set $x_2 = 0$ and

$$\begin{aligned} \Delta_{\text{cut}}^{0/1} &= \Delta_{\text{resum}}^{0/1}(p_T^{\text{cut}})\,, \qquad x_1 = \Delta_{\text{resum}}^{0/1}(p_T^{\text{off}})/\Delta_{\text{resum}}^{0/1}(p_T^{\text{cut}})\,, \\ \Delta_{\text{cut}}^{1/2} &= \Big\{ \big[\Delta_{\geq 2}^{\text{FO}}([p_T^{\text{cut}}, p_T^{\text{off}}], p_T^{\text{cut}})\big]^2 + \big[\Delta_{\text{resum}}^{1/2}([p_T^{\text{off}}, \infty]; p_T^{\text{cut}})\big]^2 \Big\}^{1/2}. \end{aligned} \tag{I.4.52}$$

Here, $\Delta_{\text{resum}}^{0/1}$ is the 0-jet resummation uncertainty from Eq. (I.4.42) which accounts for the $0/1$-jet boundary (vertical orange line in Figure 16). The nonzero value for x_1 arises from the region below p_T^{off}, which is computed from the difference of the 0-jet cross sections at p_T^{cut} and p_T^{off} as shown in Eq. (I.4.47). Hence, the contribution of the 0-jet resummation uncertainty to σ_1 is $\Delta_{\text{resum}}^{0/1}(p_T^{\text{off}}) - \Delta_{\text{resum}}^{0/1}(p_T^{\text{cut}})$ (where the two are treated as correlated). Comparing this to the parameterization above, this should be equal to $-\Delta_{\text{cut}}^{0/1}(1-x_1)$, which determines x_1.

The $1/2$-jet boundary above p_T^{off} (the horizontal orange line in Figure 16) is accounted for by the 1-jet resummation uncertainty $\Delta_{\text{resum}}^{1/2}([p_T^{\text{off}}, \infty]; p_T^{\text{cut}})$, which is determined by resummation profile scale variations in Ref. [186]. For the $1/2$-jet boundary below p_T^{off} (blue line in Figure 16), we follow the original ST method and use the inclusive 2-jet uncertainty $\Delta_{\geq 2}^{\text{FO}}$, given by the usual scale variation of the 2-jet fixed-order contributions in Eq. (I.4.47). The two are considered independent and added in quadrature.

For our numerical results we use the same input parameters as for the 0-jet resummation in the previous subsubsection. The results are presented in Table 20 for $p_T^{\text{cut}} = 25\,\text{GeV}$ and $p_T^{\text{cut}} = 30\,\text{GeV}$ with a complete breakdown of all uncertainty contributions. The results present a very consistent picture. The underlying parameters entering the migration uncertainties are given by $\Delta_{\text{cut}}^{0/1}(25\,\text{GeV}) = 1.51\,\text{pb}$, $x_1(25\,\text{GeV}) = 0.141$, $\Delta_{\text{cut}}^{1/2}(25\,\text{GeV}) = 0.96\,\text{pb}$, and $\Delta_{\text{cut}}^{0/1}(30\,\text{GeV}) = 1.21\,\text{pb}$, $x_1(30\,\text{GeV}) = 0.175$,

$\Delta^{1/2}_{\rm cut}(30\,{\rm GeV}) = 0.86\,{\rm pb}$. As one might expect, x_1 is small and most of the $0/1$-migration uncertainty enters in σ_1. We also see that σ_1 is dominated by the migration uncertainties with similar contributions from each boundary, while the uncertainty in $\sigma_{\geq 2}$ is dominated by the $1/2$ boundary. However, due to the resummation improvement the total uncertainties in all bins are substantially smaller than in the pure fixed-order predictions.

I.4.2.d Jet-vetoed Higgs cross section in gluon fusion at N^{3}LO+NNLL with small-R resummation[I.19]

In some Higgs boson decay modes (most notably WW^* and $\tau\tau$), it is standard to perform different analyses depending on the number of accompanying jets. This is because different jet multiplicities have different dominant backgrounds. Of particular importance for the WW decay is the zero-jet case, where the dominant top-antitop background is dramatically reduced. For precision studies it is important to predict accurately the fraction of signal events that survive the zero-jet constraint, and to assess the associated theory uncertainty. Jet-veto transverse momentum thresholds used by ATLAS and CMS are relatively soft ($p_{\rm t,veto} \sim 25 - 30$ GeV), hence QCD real radiation is constrained by the cut and the imbalance between virtual and real corrections results in logarithms of the form $\ln(p_{\rm t,veto}/m_H)$ that should be resummed to all orders in the coupling constant. This resummation has been carried out to next-to-next-to-leading logarithmic accuracy (NNLL, i.e. including all terms $\alpha_S^n \ln^k(p_{\rm t,veto}/m_H)$ with $k \geq n-1$ in the logarithm of the cross section) and matched to next-to-next-to-leading order (NNLO) in refs. [159, 163, 187] (some of the calculations also included partial N^{3}LL contributions). At this order one finds that the effect of the resummation is to shift central predictions only moderately, and to reduce somewhat the theoretical uncertainties. Yet, the residual theoretical uncertainty remains sizeable, roughly 10% [163], and the impact of higher-order effects could therefore be significant.

Since the first NNLO+NNLL predictions for the jet-veto, three important theoretical advances happened: firstly, the N^{3}LO calculation of the total gluon-fusion cross section [96]; secondly the calculation of the NNLO corrections to the Higgs plus one-jet cross-section [174, 182, 183]; and finally the LL resummation of logarithms of the jet-radius R [188].

All these recent results were merged together in ref. [189] by extending the matching of the jet-veto cross-section to N^{3}LO+NNLL+LL$_R$. The effect of heavy-quark masses has been considered following the approach of ref. [166]. The code used to produce the following results can be downloaded from [190].

I.4.2.d.i N^{3}LO+NNLL+LL$_R$ cross section and 0-jet efficiency at 13 TeV

In this section we report predictions for the jet-veto efficiency and cross section in Higgs boson production in gluon fusion at the LHC. The results are based on the calculation obtained in ref. [189]. The reader should refer to the latter work for additional information. The various ingredients that we use are summarized below:

- The total N^{3}LO cross section for Higgs boson production in gluon fusion [96], obtained in the heavy-top limit. The Wilson coefficient is expanded out consistently both in the computation of the total and the inclusive one-jet cross section.
- The inclusive one-jet cross section at NNLO taken from the code of ref. [174], in the heavy-top limit. In this computation the qq channel is included only up to NLO, and missing NNLO effects are estimated to be well below scale variation uncertainties [183].
- Exact top- and bottom-mass effects up to NLO in the jet-veto efficiency and cross section [136]. Beyond NLO, we use the heavy-top result, without any modifications.
- Large logarithms $\ln(m_H/p_{\rm t,veto})$ resummed to NNLL accuracy following the procedure of [163], with the treatment of quark-mass effects as described in ref. [166].
- Logarithms of the jet radius resummed to LL accuracy, following the approach of ref. [188].

[I.19] *Author(s): A. Banfi, F. Caola, F.A. Dreyer, P.F. Monni, G.P. Salam, G. Zanderighi, F. Dulat.*

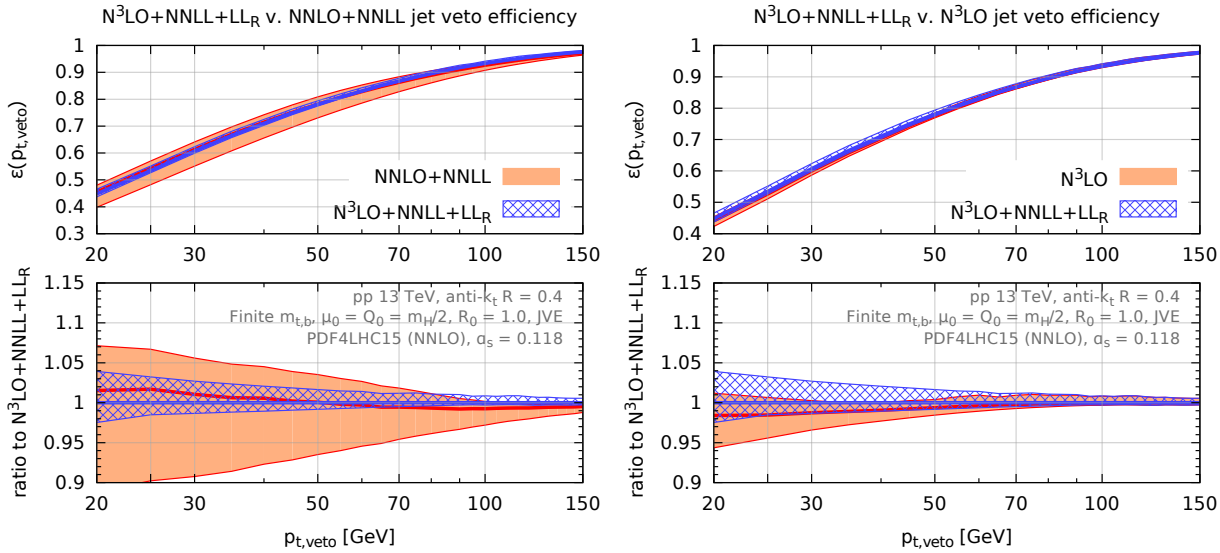

Figure 17: N^{3}LO+NNLL+LL$_R$ best prediction for the jet-veto efficiency (blue/hatched) compared to NNLO+NNLL (left) and fixed-order at N^{3}LO (right).

We consider 13 TeV LHC collisions with a Higgs boson mass of $m_H = 125$ GeV. For the top and bottom pole quark masses, we use $m_t = 172.5$ GeV and $m_b = 4.75$ GeV. Jets are defined using the anti-k_t algorithm [191], as implemented in `FastJet v3.1.2` [192], with radius parameter $R = 0.4$, and perform the momentum recombination in the standard E scheme (i.e. summing the four-momenta of the pseudo-particles). We use PDF4LHC15 parton distribution functions at NNLO with $\alpha_s(m_Z) = 0.118$ (`PDF4LHC15_nnlo_mc`) [35]. The impact of higher-order logarithmic corrections is probed by introducing a resummation scale Q as shown in ref. [163]. The central prediction for the jet-veto efficiency is obtained by using the matching scheme (a) [189], setting the renormalization and factorization scales to $\mu_R = \mu_F = m_H/2$, and the resummation scale relative to both top and bottom contributions to $Q = Q_0 = m_H/2$. To determine the perturbative uncertainties for the jet-veto efficiency we follow the Jet-Veto efficiency (JVE) method as outlined in ref. [189]. This differs from the original method of refs. [163, 170] which has been modified to take into account the excellent convergence observed at the perturbative order considered here [189]. The uncertainty band is determined as described below.

We vary μ_R, μ_F by a factor of 2 in either direction, requiring $1/2 \leq \mu_R/\mu_F \leq 2$. Maintaining central $\mu_{R,F}$ values, we also vary Q in the range $\frac{2}{3} \leq Q/Q_0 \leq \frac{3}{2}$. As far as the small-$R$ effects are concerned, subleading logarithmic effects are estimated by means of a second resummation scale R_0, which acts as the initial radius for the evolution of the gluon-jet fragmentation which gives rise to the $\ln R$ terms. We choose the default value $R_0 = 1.0$,[I.20] and vary it conservatively by a factor of two in either direction. Finally, keeping all scales at their respective central values, we replace the default matching scheme (a) with scheme (b), as defined in ref. [189]. The final uncertainty band is obtained as the envelope of all the above variations. We do not consider here the uncertainties associated with the parton distributions (which mostly affect the cross section, but not the jet-veto efficiency), the value of the strong coupling or the impact of finite quark masses on terms beyond NLO. Moreover, our results do not include electro-weak effects.

In the left plot of Figure 17 we show the comparison between our best prediction for the jet-veto efficiency (N^{3}LO+NNLL+LL$_R$) and the previous NNLO+NNLL accurate prediction, both including mass effects. We see that the impact of the N^{3}LO correction on the central value is in the range 1-2%

[I.20] The initial radius for the small-R evolution differs from the jet radius used in the definition of jets, which is $R = 0.4$.

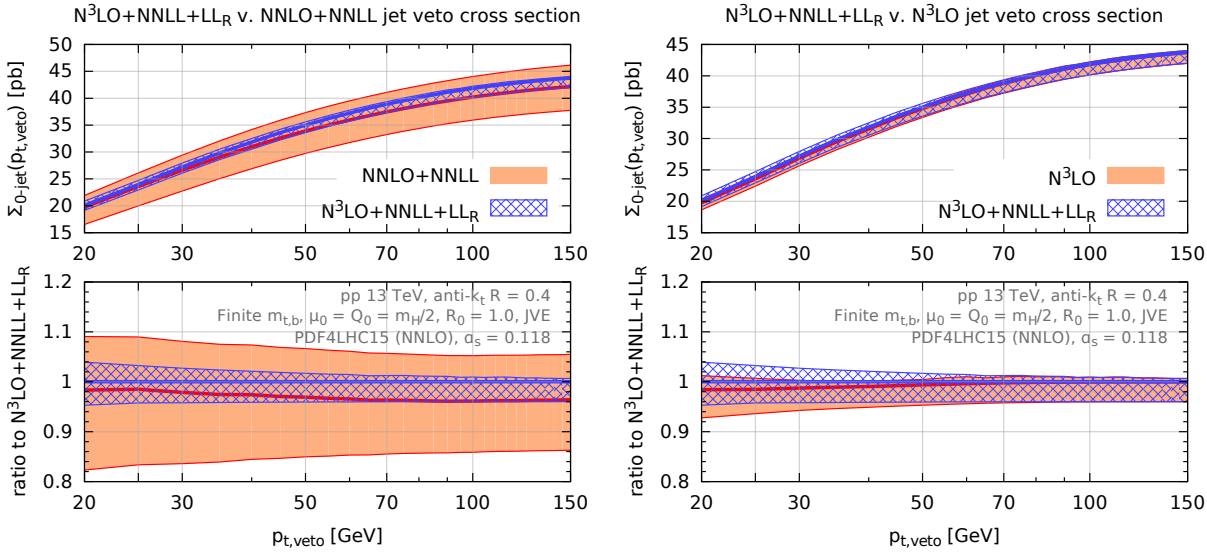

Figure 18: N^{3}LO+NNLL+LL$_R$ best prediction for the jet-veto cross section (blue/hatched) compared to NNLO+NNLL (left) and fixed-order at N^{3}LO (right).

at relevant jet-veto scales. The uncertainty band is significantly reduced when the N^{3}LO corrections are included, going from about 10% at NNLO down to a few per cent at N^{3}LO. Figure 17 (right) shows the comparison between the N^{3}LO+NNLL+LL$_R$ prediction and the pure N^{3}LO result. We observe a shift of the central value of the order of 2% for $p_{\text{t,veto}} > 25\,\text{GeV}$ when the resummation is turned on. In that same $p_{\text{t,veto}}$ region, the uncertainty associated with the N^{3}LO prediction is at the 3% level, comparable with that of the N^{3}LO+NNLL+LL$_R$ prediction. The fact that resummation effects are nearly of the same order as the uncertainties of the fixed order calculation suggests that the latter might be accidentally small. This situation is peculiar to our central renormalization and factorization scale choice, $\mu_R = \mu_F = m_H/2$, and does not occur at, for instance, $\mu_R = \mu_F = m_H$ (see ref. [189] for details).

The zero-jet cross section is obtained as $\Sigma_{\text{0-jet}}(p_{\text{t,veto}}) = \sigma_{\text{tot}}\,\epsilon(p_{\text{t,veto}})$, and the inclusive one-jet cross section is obtained as $\Sigma_{\geq\text{1-jet}}(p_{t,\text{min}}) = \sigma_{\text{tot}}\,(1-\epsilon(p_{t,\text{min}}))$. The associated uncertainties are obtained by combining in quadrature the uncertainty on the efficiency obtained as explained above and that on the total cross section, for which we use plain scale variations. The corresponding results are shown in Figure 18. For this scale choice, we observe that the effect of including higher-order corrections in the zero-jet cross section is quite moderate at relevant $p_{\text{t,veto}}$ scales. This is because the small K factor in the total cross section compensates for the suppression in the jet-veto efficiency. The corresponding theoretical uncertainty is reduced by more than a factor of two.

The predictions for jet-veto efficiency and the zero-jet cross section are summarized in Table 21, for two experimentally relevant $p_{\text{t,veto}}$ choices. Results are reported both at fixed-order, and including the various resummation effects.

Figure 19 shows the inclusive one-jet cross section $\Sigma_{\geq\text{1-jet}}$, for which the state-of-the-art fixed-order prediction is NNLO [174, 182, 183]. The left-hand plot shows the comparison between the best prediction at NNLO+NNLL+LL$_R$, and the fixed-order at NNLO. Both uncertainty bands are obtained with the JVE method outlined in ref. [189]. We observe that the effect of the resummation on the central value at moderately small values of $p_{\text{t,veto}}$ is at the per cent level. Moreover, the inclusion of the resummation leads to a slight increase of the theory uncertainty in the small transverse momentum region.

Table 21: Predictions for the jet-veto efficiency and cross section at N^{3}LO+NNLL+LL$_R$, compared to the N^{3}LO and NNLO+NNLL cross sections. The uncertainty in the fixed-order prediction is obtained using the JVE method. All numbers include the effect of top and bottom quark masses, treated as described in the text, and are for a central scale $\mu_0 = m_H/2$.

LHC 13 TeV	$\epsilon^{\mathrm{N^3LO+NNLL+LL_R}}$	$\Sigma^{\mathrm{N^3LO+NNLL+LL_R}}_{\text{0-jet}}$ [pb]	$\Sigma^{\mathrm{N^3LO}}_{\text{0-jet}}$	$\Sigma^{\mathrm{NNLO+NNLL}}_{\text{0-jet}}$
$p_{\mathrm{t,veto}} = 25\,\mathrm{GeV}$	$0.534^{+0.017}_{-0.008}$	$24.0^{+0.8}_{-1.0}$	$23.6^{+0.5}_{-1.2}$	$23.6^{+2.5}_{-3.6}$
$p_{\mathrm{t,veto}} = 30\,\mathrm{GeV}$	$0.607^{+0.016}_{-0.008}$	$27.2^{+0.7}_{-1.1}$	$26.9^{+0.4}_{-1.2}$	$26.6^{+2.8}_{-3.9}$

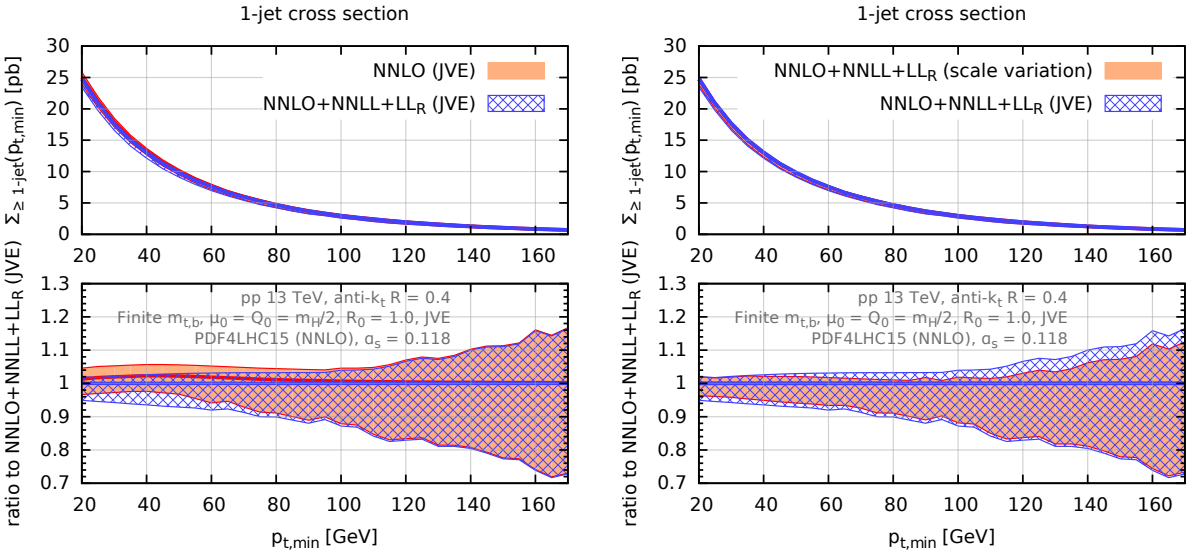

Figure 19: Matched NNLO+NNLL+LL$_R$ prediction for the inclusive one-jet cross section (blue/hatched) compared to fixed-order at NNLO (left) and to the matched result with direct scale variation for the uncertainty (right), as explained in the text.

The right-hand plot of Figure 19 shows our best prediction for the one-jet cross section with uncertainty obtained with the JVE method, compared to the case of just scale (i.e. μ_R, μ_F, Q) variations. We observe a comparable uncertainty both at small and at large transverse momentum, which indicates that the JVE method is not overly conservative in the tail of the distribution. We have observed that the same features persist for the corresponding differential distribution. Table 22 contains the predictions for the inclusive one-jet cross section for two characteristic $p_{t,\mathrm{min}}$ choices.

I.4.2.e Higgs-p_T resummation in momentum space at NNLL+NNLO in gluon fusion [I.21]

In the gluon-fusion production mode, the Higgs boson transverse momentum p_t^{H} is defined as the inclusive vectorial sum of the transverse momenta of the recoiling QCD partons radiated off the incoming gluons. The fixed-order perturbative description of its differential spectrum features large logarithms in the form $\alpha_S^n \ln^m(M_{\mathrm{H}}/p_t^{\mathrm{H}})/p_t^{\mathrm{H}}$, with $m \leq 2n-1$, which spoil the convergence of the series at small p_t^{H}. In order to obtain meaningful predictions in that phase-space region, such terms must be resummed to all orders in α_S, so that the perturbative series can be recast in terms of dominant all-order towers of logarithms. The logarithmic accuracy is commonly defined at the level of the *logarithm* of

[I.21] *Author(s): P.F. Monni, E. Re, P. Torrielli.*

Table 22: Predictions for the inclusive one-jet cross section at NNLO+NNLL+LL$_R$ and NNLO. The uncertainty in the fixed-order prediction is obtained using the JVE method. All numbers include the effect of top and bottom quark masses, treated as described in the text, and are for a central scale $\mu_0 = m_H/2$.

LHC 13 TeV	$\Sigma^{\text{NNLO+NNLL+LL}_\text{R}}_{\geq \text{1-jet}}$ [pb]	$\Sigma^{\text{NNLO}}_{\geq \text{1-jet}}$ [pb]
$p_{\text{t,min}} = 25\,\text{GeV}$	$20.9^{+0.4}_{-1.1}$	$21.2^{+0.7}_{-1.0}$
$p_{\text{t,min}} = 30\,\text{GeV}$	$17.6^{+0.4}_{-1.0}$	$17.9^{+0.6}_{-0.8}$

the cumulative cross section, henceforth referred to as $\Sigma(p_t^{\text{H}})$, where one refers to the dominant terms $\alpha_s^n \ln^{n+1}(M_{\text{H}}/p_t^{\text{H}})$ as leading logarithms (LL), to terms $\alpha_s^n \ln^{n}(M_{\text{H}}/p_t^{\text{H}})$ as next-to-leading logarithms (NLL), to $\alpha_s^n \ln^{n-1}(M_{\text{H}}/p_t^{\text{H}})$ as next-to-next-to-leading logarithms (NNLL), and so on.

The all-order computation of the logarithms of the ratio $M_{\text{H}}/p_t^{\text{H}}$ has been performed up to NNLL order in refs. [193, 194] using the formalism developed in [195, 196], and in ref. [197] using an effective-field-theory approach. These resummed results are usually matched to fixed-order predictions in order to obtain a description of p_t^{H} which gives a reliable coverage of the whole phase space. The recent computations of the differential p_t^{H} distribution at next-to-next-to-leading order (NNLO) [174, 182, 183, 198], and of the inclusive gluon-fusion cross section at next-to-next-to-next-to-leading order (N^{3}LO) in [93, 96], once combined with state-of-the-art resummation, allow to obtain a formal NNLL+NNLO accuracy for $d\sigma/dp_t^{\text{H}}$.

All of the resummation approaches mentioned so far rely on an impact-parameter-space formulation [199, 200], which is motivated by the fact that the observable naturally factorizes in this space as a product of the contributions of each individual emission. Conversely, in p_t^{H} space one is unable to find, at a given order beyond LL, a closed analytic expression for the resummed distribution which is simultaneously free of logarithmically subleading corrections and of singularities at finite p_t^{H} values [201]. This fact has a simple physical origin: the region of small p_t^{H} receives contributions both from configurations in which each of the transverse momenta of the radiated partons is equally small (Sudakov limit), and from configurations where p_t^{H} tends to zero owing to cancellations among non-zero transverse momenta of the emissions. The latter mechanism is in fact the dominant one at small p_t^{H} and, as a result, the cumulative cross section in that region vanishes as $\mathcal{O}(p_t^{\text{H}2})$ rather than being exponentially suppressed [200]. If these effects are neglected in a resummation performed in transverse-momentum space, the latter would feature a geometric singularity at some finite value of p_t^{H}. The same issue is present in an impact-parameter-space formulation whenever one tries to obtain a result in p_t^{H} space free of any contamination from subleading logarithmic terms.

However, it has recently been shown [167] that the problem can be solved also in transverse-momentum space, upon extending the formalism developed in [202, 203] to treat observables that feature such kinematic cancellations.

The method of [167] organizes the computation of the cumulative cross section $\Sigma(p_t^{\text{H}})$ as an ensemble of emissions off the incoming gluons; the amplitude for each emission, characterized by a certain transverse momentum $k_{t,i}$, is then expanded around the largest transverse momentum in the ensemble (denoted as $k_{t,1}$), and one just retains the terms in this expansion that contribute to a given logarithmic accuracy, discarding subleading contributions. The latter expansion is always justified since, by construction, all emissions are softer than $k_{t,1}$ and, owing to the recursive infrared and collinear (rIRC) safety of the observable, emissions with $k_{t,i} \ll k_{t,1}$ that would invalidate the expansion do not contribute to the logarithmic structure of the resummed cross section [202]. The hardest emission is integrated over all of its natural phase space, including the region $k_{t,1} \gg p_t^{\text{H}}$, which is regularized by means of the Sudakov exponential.

This formulation ensures that all kinematic effects that contribute to the $p_t^{\rm H} \to 0$ limit are properly taken into account, and not only is $\Sigma(p_t^{\rm H})$ free of singularities at finite $p_t^{\rm H}$, but it also features the correct $p_t^{\rm H2}$ scaling [200] at low $p_t^{\rm H}$. This procedure can be effectively interpreted as a resummation of the large logarithms $\ln(M_{\rm H}/k_{t,1})$, and the logarithmic order is defined in terms of the latter; the corresponding formal accuracy in terms of the logarithms $\ln(M_{\rm H}/p_t^{\rm H})$ is the same as in terms of $\ln(M_{\rm H}/k_{t,1})$, and the difference amounts to logarithmically-subleading corrections.

In [167] the cumulative cross section is efficiently computed with a fast Monte Carlo method where, for each event, the kinematics of the ensemble of emissions is stochastically generated with weights that take into account all of the physical effects that occur at a given logarithmic accuracy. In particular, at NLL accuracy, all emissions after the hardest can be generated with equal weights obtained in the soft-collinear approximation; at NNLL, one emission weight per event is modified to take into account the corrections which arise when a single parton in the ensemble is either emitted collinearly to the beam with a significant fraction of the emitter's momentum (hard-collinear), or close in rapidity to another parton, and therefore it is sensitive to its correct rapidity bounds. The Sudakov-exponential weight associated with the hardest emission is correspondingly evaluated including terms up to $\mathcal{O}(\alpha_S^n \ln^n(M_{\rm H}/k_{t,1}))$ at NLL, and up to $\mathcal{O}(\alpha_S^n \ln^{n-1}(M_{\rm H}/k_{t,1}))$ at NNLL, and the overall parton luminosity incorporates coefficient functions at the relevant order in the strong coupling – i.e. $\mathcal{O}(\alpha_S^3)$ and $\mathcal{O}(\alpha_S^4)$ for a NLL and NNLL matching, respectively – and is evaluated at a factorization scale of the order of $k_{t,1}$.

The expansion of the cumulative rate, necessary for the matching with fixed-order predictions, is performed in a semi-analytic way, where the contributions to the different orders in α_S are reduced analytically to linear combinations of $p_t^{\rm H}$-dependent master-integral grids that are evaluated numerically with high accuracy once and for all, and interpolated dynamically at runtime, ensuring optimal speed performances.

The computation is entirely carried out in momentum space, without the need to transform the observable and the parton luminosities into impact-parameter space, with benefits in terms of speed. Moreover, in transverse-momentum space a clear physical picture emerges of the effects that determine the low-$p_t^{\rm H}$ region, where all contributions to a given logarithmic accuracy can be systematically tracked down and accounted for.

The approach used to perform the resummation is fully general and it can be straightforwardly extended to the entire class of rIRC-safe [202] observables that feature kinematic cancellations in the infrared.

In the following we report predictions for the Higgs boson transverse momentum distribution in the heavy-top effective theory at the 13 TeV LHC, with $M_{\rm H} = 125\,\text{GeV}$, and `PDF4LHC15` [35] parton densities at NNLO. The central prediction uses $\mu_{\rm R} = \mu_{\rm F} = M_{\rm H}$, and $Q = M_{\rm H}/2$, where Q represents the resummation scale, introduced as usual to estimate the impact on physical results of the neglected higher-order logarithmic contributions. The perturbative uncertainty for all predictions is estimated by varying both $\mu_{\rm R}$ and $\mu_{\rm F}$ by a factor of two in either direction while keeping $1/2 \leq \mu_{\rm R}/\mu_{\rm F} \leq 2$. Moreover, for central $\mu_{\rm R}$ and $\mu_{\rm F}$ scales, the resummation scale Q is varied by a factor of two in either direction.

The matching to the fixed-order prediction is obtained with an additive scheme, according to the formula

$$\Sigma^{\text{NNLL+(N)NLO}}(p_t^{\rm H}) = \Sigma^{\text{(N)NLO}}(p_t^{\rm H}) + \Sigma^{\text{NNLL}}(p_t^{\rm H}) - \Sigma^{\text{EXP}}(p_t^{\rm H}), \tag{I.4.53}$$

where $\Sigma^{\text{EXP}}(p_t^{\rm H})$ represents the expansion of the resummed formula to $\mathcal{O}(\alpha_S^4)$ for a matching to the NLO-accurate differential distribution, or to $\mathcal{O}(\alpha_S^5)$ for a matching to the NNLO-accurate differential distribution. The introduction of modified logarithms of the form $\ln(Q/k_{t,1}) \to \ln\left[(Q/k_{t,1})^p + 1\right]/p$ ensures that the matched cumulative cross section on the left-hand side of (I.4.53) reduces to the fixed-order one at large transverse momentum.

In the main panel of Figure 20 a comparison is shown of the prediction of ref. [167] at NNLL+NLO

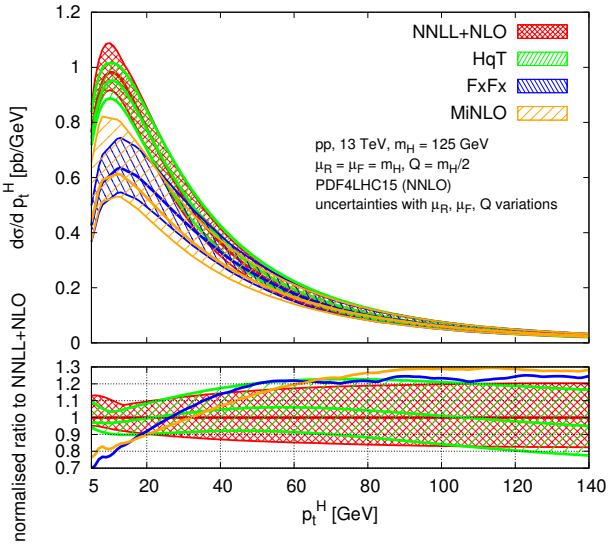

Figure 20: Comparison of the Higgs $p_t^{\rm H}$ NNLL+NLO prediction as obtained in [167] (red) to HqT (green). For reference, the predictions obtained with MiNLO at NLO (orange), and FxFx (blue) are shown. Lower panel: ratio of the various distributions, normalized to their respective central-scale inclusive cross sections, to the central NNLL+NLO prediction [167]. Uncertainty bands are shown only for the resummed results.

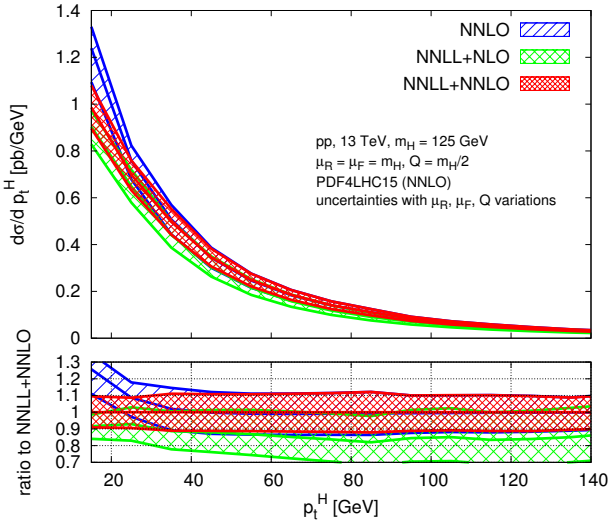

Figure 21: Higgs $p_t^{\rm H}$ at NNLL+NNLO (red), NNLL+NLO (green), and NNLO (blue). Lower panel: ratio of the three predictions to the NNLL+NNLO one.

to that obtained with HqT [194, 204]. As expected, very good agreement over the entire $p_t^{\rm H}$ range is observed between these two results, which have the same perturbative accuracy. The HqT prediction is moderately lower in the peak of the distribution, and higher at intermediate $p_t^{\rm H}$ values, although this pattern may slightly change with different central-scale choices. These small differences have to do with the different treatment of subleading effects in the two resummation methods. The agreement of the two results, both for the central scale and for the uncertainty band, is even more evident in the lower inset of Figure 20, which displays the ratio of the various distributions, each normalized to its central-scale inclusive rate, to the normalized central NNLL+NLO curve of [167].

Figure 20 also reports the $p_t^{\rm H}$ distribution obtained with the NLO version of POWHEG+MiNLO [81, 205], and with the MadGraph5_aMC@NLO+FxFx [54, 206] event generators, using default renormalization and factorization scales for the two methods (in FxFx a merging scale $\mu_Q = M_{\rm H}/2$ has been employed). Both generators are interfaced to Pythia 8.2 [207], without including hadronization, underlying event, and primordial $k_\perp$ (whose impact has been checked to be fully negligible for this observable), and use PDF4LHC15 parton densities at NLO. By inspecting the normalized ratios shown in the lower panel, one observes that the shape of the Monte-Carlo predictions deviates significantly from the NNLL+NLO results at $p_t^{\rm H} \lesssim 60$ GeV. In order to avoid possible misunderstandings between the POWHEG+MiNLO result shown in Figure 20 and the so called "NNLOPS" approach, we recall that the POWHEG+MiNLO generator was further improved to achieve NNLO accuracy for fully inclusive observables in ref. [208]. Although the logarithmic accuracy of the two "POWHEG-based" results is the same, the $p_t^{\rm H}$ spectrum obtained with the NNLOPS approach was found to be, numerically, in very good agreement with the HqT NNLL+NLO result, certainly more than what the POWHEG+MiNLO result does. More details can be found in [208].

Figure 21 shows the comparison of the matched NNLL+NNLO result to the NNLL+NLO and the fixed-order NNLO predictions. The inclusion of the NNLO corrections leads to a $10-15\%$ increase in the matched spectrum for $p_t^{\rm H} > 15$ GeV, and to a consistent reduction in the perturbative uncertainty. The impact of the NNLL resummation on the fixed order becomes increasingly important for $p_t^{\rm H} \lesssim 40$ GeV,

leading to a suppression of the differential spectrum in this phase-space region which reaches about 25% at $p_t^{\mathrm{H}} = 15\,\mathrm{GeV}$. For $p_t^{\mathrm{H}} \gtrsim 40\,\mathrm{GeV}$, the matched prediction reduces to the NNLO one. The final theory uncertainty is at the $\pm 10\%$-level in the phenomenologically relevant p_t^{H} range.

I.4.2.f NNLOJET:: $H + j$ at NNLO using Antenna subtraction [I.22]

The NNLO corrections to $H + j$ receive contributions from processes which, with respect to the leading order, feature two additional external legs (double real emission, [209–211]), one external leg and one internal loop (real virtual, [212–214]) or two additional internal loops (double virtual, [215]). Each of these is separately infrared (IR) divergent, with the divergences cancelling upon integration over the phase space. Since this integration is performed numerically, a procedure is needed to extract the singularities from the various contributions and to achieve their cancellation prior to the phase space integration.

In the integration of the real radiation contributions over their phase space, IR divergences appear in configurations where the momentum of a parton becomes unresolved. In such configurations, a QCD matrix element factorizes into products of universal unresolved factors, which contain the IR singularities, and reduced matrix elements, which depend only on the resolved kinematics. The antenna subtraction formalism [216–218] makes use of this factorization in describing the divergent behaviour of matrix elements in terms of simpler normalized matrix elements involving an adequate set of partons. Using these antenna functions, one can construct subtraction terms which, when added to the corresponding matrix elements, make them well-defined and integrable over the whole phase space, thus allowing for numerical integration.

With the reduced matrix element M_n (possibly with loops) and the jet function J_n, a typical subtraction term has the form:

$$X_m^l(p_a, p_2, \ldots, p_{m-1}, p_b)|M_n(\ldots, \tilde{p}_a, \tilde{p}_b, \ldots)|^2 J_n(\ldots, \tilde{p}_a, \tilde{p}_b, \ldots), \tag{I.4.54}$$

where $X_m^l(p_a, p_2, \ldots, p_{m-1}, p_b)$ is the m-parton l-loop antenna function, which features the full IR divergent behaviour of the partons $p_2, \ldots, p_{m-1}$ in the colour ordering $\{p_a, p_2, \ldots, p_{m-1}, p_b\}$. At NNLO, one is required to consider values of (m, l) up to $(4, 0)$ and $(3, 1)$. The momenta $\tilde{p}_a$ and $\tilde{p}_b$ are given through mappings $\{p_a, p_2, \ldots, p_{m-1}, p_b\} \to \{\tilde{p}_a, \tilde{p}_b\}$ which interpolate between all unresolved configurations of the partons $p_2, \ldots, p_{m-1}$ with the hard radiators p_a and p_b. The subtraction terms can then be integrated analytically over the phase spaces of the unresolved partons to obtain the integrated antenna functions $\mathcal{X}_m^l(p_A, p_B)$, which feature explicit poles up to order $2(m - 2 + l)$ in $D - 4$. Together with the mass factorization counterterms, which originate from the renormalization of the PDFs, they can be shown to fully cancel the pole structure of the virtual loop matrix elements.

We have implemented all subprocesses for $H + j$ at NNLO into the parton-level event generator NNLOJET [198, 219], relying on the antenna subtraction method to cancel the implicit and explicit IR divergences appearing in the matrix elements of the various contributions. This program allows for the computation of all IR-safe observables related to $H + j$ final states to NNLO accuracy. Renormalization and factorization scale can be chosen on an event-by-event basis. In order to stabilize the numerical integration, and to arrive at reliable error estimates on it, we divide the sample of Monte Carlo integration points into sub-samples, on which a weighted average is performed (see [220–222] for details on this procedure). The decay of the Higgs boson to two photons is included, and other decay modes will be added in the future. The program allows us to make predictions for fiducial cross sections taking into account appropriate event selection criteria and Higgs boson decay matrix elements.

The NNLOJET code is used for the fixed order predictions of the observables discussed in Section I.4.3. Besides this, it also provides an independent validation of the fixed-order results described in Section I.4.2.c (JVE method), which use the code of Ref. [174]. For example, the NNLOJET result for the inclusive cross section with scale choice $\mu_F = \mu_R = 1/2 * m_H$ and under infinite top mass

[I.22] *Author(s): X. Chen, E.W.N. Glover, T. Gehrmann, M. Jaquier.*

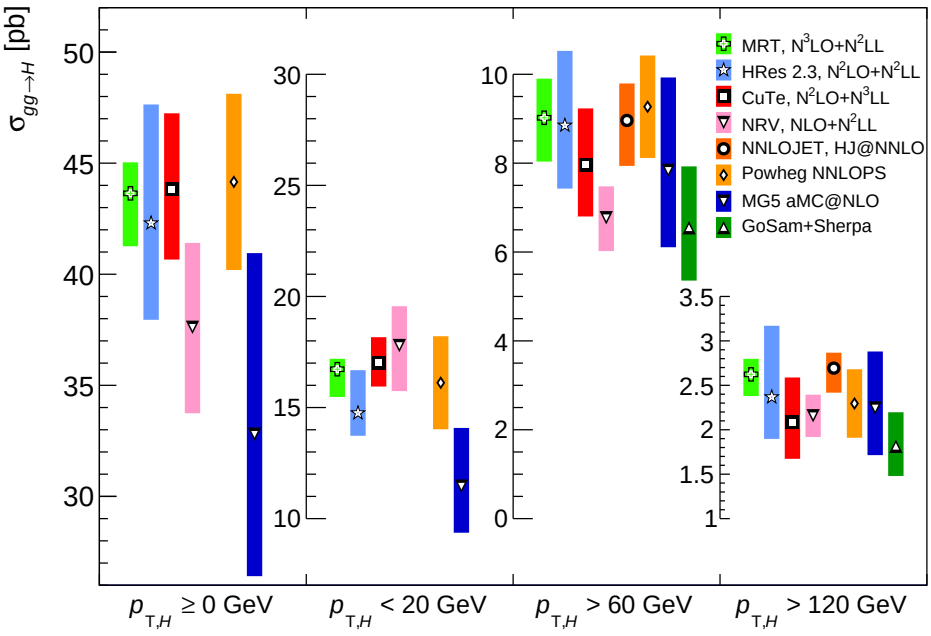

Figure 22: Comparison of cross section in different regions of $p_{T,H}$.

assumption is 17.7 pb for $p_{T,\min} = 30$ GeV. By removing the NNLO contribution from the quark-quark initiated channels and including the finite top quark mass effect at LO (which is the exact setup used for the fixed order results), the NNLOJET result fully agrees with the corresponding NNLO inclusive cross sections quoted in Table 18.

I.4.3 Benchmarks for cross sections and differential distributions[I.23]

An accurate modelling of the differential distributions in gluon fusion production is important since the experimental analyses typically combine measurements in different phase space regions, either to improve the sensitivity to a signal or to target other Higgs boson production modes to which gluon fusion is a background. In this section, comparisons are performed between the predictions of different parton-level computations and hadron-level event generators, to assess their compatibilities and the accuracy of the modelling.

Unless otherwise specified, all the predictions correspond to a Higgs boson mass of 125 GeV, $\sqrt{s} = 13$ TeV, and the choice of SM input parameters and PDFs in Sects. I.1– I.2. We will first list the various codes and calculations used in the benchmarking, and then discuss predictions for several observables in turn.

I.4.3.a Calculations and codes

We list here the calculations and codes used in the following benchmarking, and provide information about settings whenever they differ from our default.

I.4.3.a.i Parton level codes

HRes: A parton-level code [223, 224] to compute differential distributions in gluon fusion production at NNLO QCD accuracy, with NNLL QCD resummation for small $p_{\mathrm{T}}(\mathrm{H})$ and matching to NLO QCD H+1jet at large $p_{\mathrm{T}}(\mathrm{H})$. Finite top, bottom, and charm quark masses are included at NLO QCD accuracy.

[I.23] *Author(s): S. Forte, D. Gillberg, C. Hays, A. Lazopoulos, G. Petrucciani, A. Massironi, G. Zanderighi.*

In this comparison, predictions were computed with a dynamical scale $\mu_R = \mu_F = (\sqrt{m_H^2 + p_t^2})/2$ and with resummation scales $Q_1 = m_H/2$, $Q_2 = 2m_b$. The overall uncertainties are estimated by taking the envelope of a seven-point scale variation of μ_R and μ_F for central Q_1 and Q_2 and a variation of Q_1 and Q_2 one at a time by a factor two about their central value, with central μ_R and μ_F.

CuTe: A parton-level code [225], for the $p_{\mathrm{T}}(\mathrm{H})$ differential distribution, with NNLL QCD resummation at small $p_{\mathrm{T}}(\mathrm{H})$ and matching to NLO QCD H + 1jet at large $p_{\mathrm{T}}(\mathrm{H})$. The resummation is based on Soft Collinear Effective Theory (SCET) and NNLL accuracy is accordingly defined. The finite top quark mass is included at LO QCD accuracy. The scale is chosen as $\mu = p_T + q^* \exp(p_t/q^*)$ with $q^* = 7.83$ GeV. Uncertainties are estimated by varying μ by a factor two about its central value and by varying the unknown coefficient $F^g_{(3,0)}$ of the anomaly exponent F^g in the range $\pm 2(4\pi)F^g_{(2,0)}$, and also by including one-sigma PDF uncertainties and varying α_s in the range $[0.1165, 0.1195]$.

NRV: A parton-level computation to NNLL resummed accuracy matched to the fixed-order $O(\alpha_s^4)$ computation [226]. Resummation is performed using a SCET approach and the logarithmic order is defined accordingly. All quarks but top are assumed massless. Uncertainties are estimated as described in Ref. [226]. The individual NNLO PDF sets MMHT and NNPDF3.0 entering the PDF4LHC recommendations have been used, and uncertainties within and between the sets are included in the error estimation.

MRT: This code was described in Sect. I.4.2.e. It is based on a parton-level computation at NNLL for the Higgs boson p_T distribution matched to the NNLO ($O(\alpha_s^5)$) fixed-order prediction for Higgs+jet. The central prediction uses $\mu_R = \mu_F = m_H$, and $Q = m_H/2$. The perturbative uncertainty for all predictions is estimated by seven-point scale variation of $_R$ and $_F$ with fixed resummation scale, and varying the resummation scale by a factor two for fixed μ_R and μ_F.

BFGLP: A parton-level prediction for H + 1jet at NNLO QCD using jettiness subtraction [183]. The prediction is not matched to inclusive gluon fusion production, and thus the resulting $p_{\mathrm{T}}(\mathrm{H})$ distribution can be directly compared to the other predictions only well above the jet p_{T} threshold used in the computation (30 GeV), but has a higher accuracy because of the extra order in QCD. Predictions shown use the settings of Ref. [9] but with NNPDF2.3 parton distributions.

NNLOJET: This code [198] was described in Sect. I.4.2.f. It has the same perturbative accuracy as BFGLP. A threshold of $p_T = 30$ GeV is adopted for jet counting. Uncertainties are estimated by three-point scale variation about $\mu_r = \mu_F = m_H$. The NNLOJET code was validated extensively against the H+j NNLO calculation of [174] (discussed in Section I.4.2.d), yielding excellent agreement at below one per cent for all distributions.

STWZ-BLPTW This code was described in Sect. I.4.2.c. It is a SCET-based resummation for the jet veto at NNLL′+NNLO. The prescription used for uncertainty estimation was described in detail in Sect. I.4.2.c.

JVE This code was described in Sect. I.4.2.d. It performs a N^{3}LO+NNLL+LLR accurate resummation for the jet veto, including heavy quark mass effects up to NLO. Beyond NLO, the heavy top result is used as explained in Ref. [189]. The prescription used for uncertainty estimation was described in detail in Sect. I.4.2.d.

Gosam + Sherpa: The predictions used in this comparison include up to three additional jets at NLO QCD accuracy [227–229] in the approximation of an infinitely heavy top quark. The predictions presented in this report were computed using sets of Ntuples with generation cuts set to $p_T > 25$ GeV , $|\eta| < 4.5$. The cut on the pseudorapidity can not be removed, but an explicit computation at LO shows that the effect of these cuts is at the per cent level. The renormalization and factorization scales were set to $\frac{\hat{H}'_T}{2} = \frac{1}{2}\left(\sqrt{m_{\mathrm{H}}^2 + p_{T,\mathrm{H}}^2} + \sum_i |p_{T,i}|\right)$, where the sum runs over all partons accompanying the Higgs boson in the event. The theoretical uncertainties were estimated by varying both of them by factors of 0.5 and 2 around this central value. Further details are provided in Ref. [230].

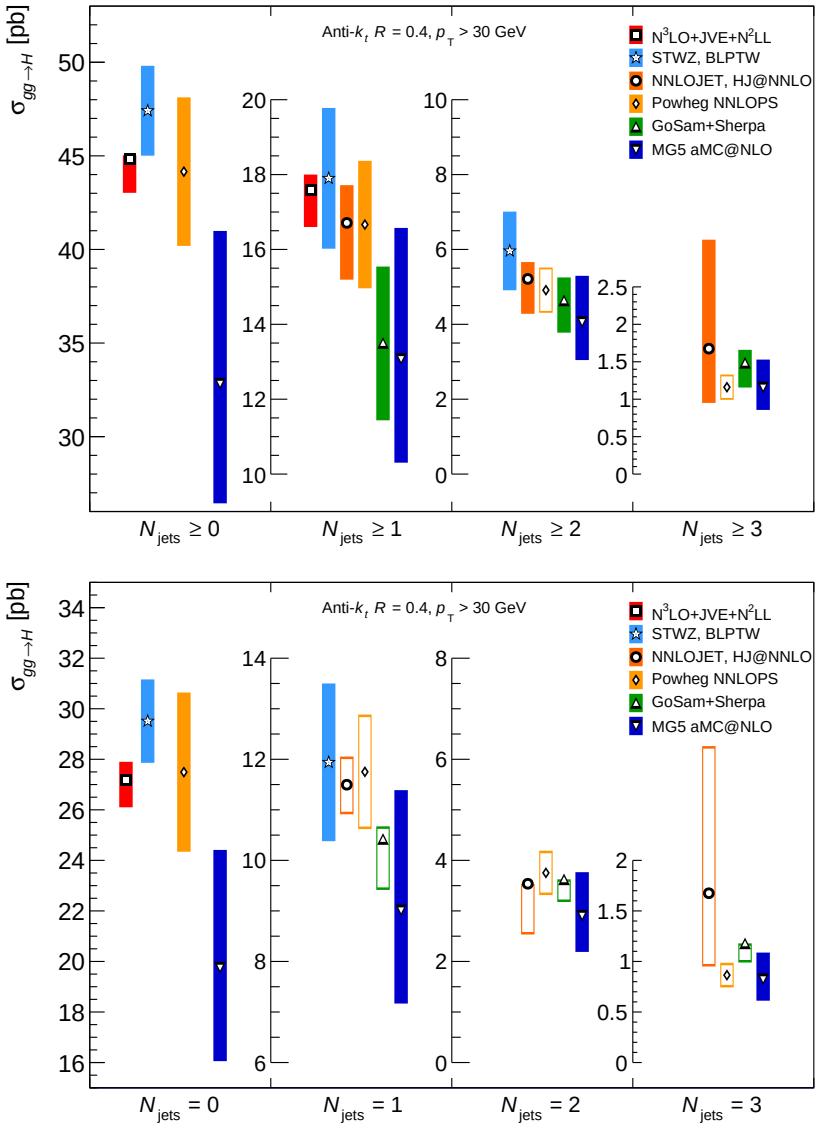

Figure 23: Various predictions for the inclusive and exclusive jet cross section for gluon fusion Higgs boson production.

I.4.3.a.ii Hadron-level event generators

MG5_ aMC@NLO: The predictions used in this comparison include up to two additional jets at NLO QCD accuracy with the FxFx merging scheme, in the Effective Field Theory approach ($m_t \to \infty$). The top quark mass is included via reweighting of the events. The full mass effects are included in all multiplicities in all contributions apart from the two-loop matrix element in the virtual for H + 1jet and H + 2jets NLO matrix elements, for which the correction is approximated using that of the Born contribution. The bottom quark mass and the top-bottom interference are included in H + 0jet at NLO using the resummation scales suggested in [231]. The central value of merging scale is set to 30 GeV, and the deviations from using merging scales of 20 GeV and 50 GeV is taken as an uncertainty. Further details are provided in Ref. [232].

Powheg NNLOPS: Predictions have NNLO QCD accuracy for inclusive events, and NLO+PS for Higgs+one jet. Top and bottom quark mass effects are included up to NLO according to Ref. [233]. The central scale choice is $\mu_F = \mu_R = m_H/2$. Uncertainties are obtained by preforming a three-point

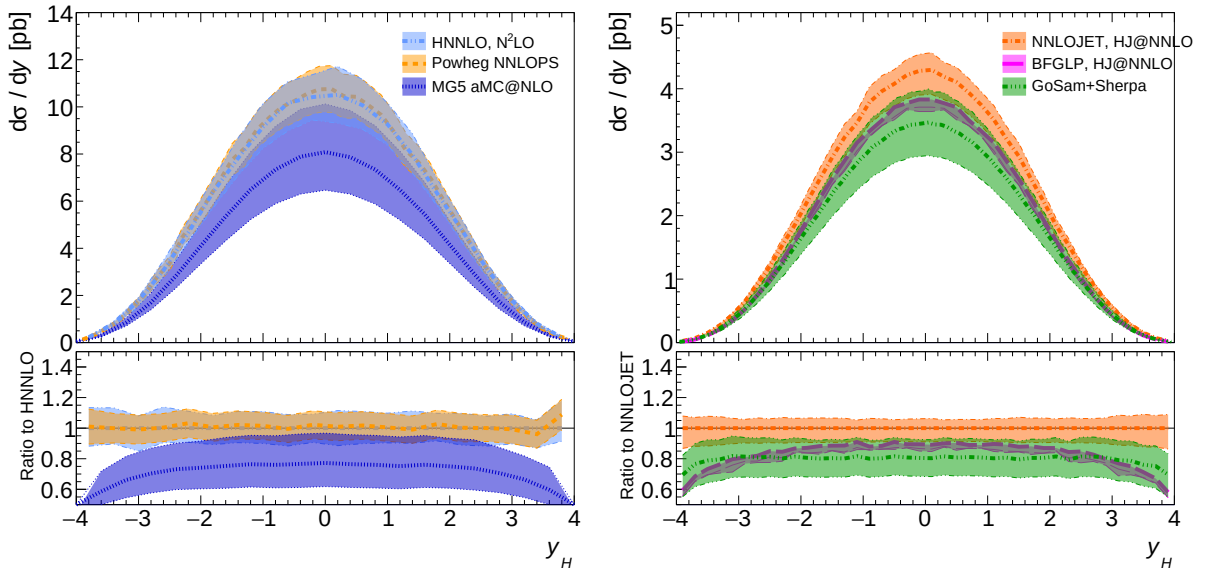

Figure 24: Predictions of the Higgs boson rapidity distribution for gluon fusion production, including both parton-level calculations and hadron-level MC predictions. The spectra are shown at the inclusive level (left) and with a jet cut (right).

scale variation of $\mu_R = \mu_F$ by a factor two about the central value for the NNLO part, and using a 9-point variation for the Powheg scale. These two uncertainties are taken as uncorrelated and are added in quadrature to obtain the total QCD scale variation. Uncertainties are also provided for switching off bottom and top mass effects.

I.4.3.b Observables

We will first discuss results for integrated cross-sections, then consider various differential distributions.

I.4.3.b.i Cross-sections

In Figure 22 we compare predictions for cross-sections in different ranges of the Higgs boson p_T. Cross-sections are obtained integrating differential $p_{T,H}$ distributions separately for each uncertainty variation provided. The uncertainties about the central value are obtained using the prescription associated with each prediction, most commonly quadratic addition of the difference from the nominal for each effect considered.

The QCD scale uncertainty is obtained by integrating the spectrum for each scale choice and taking the envelope around the nominal integral. The exception is NNLOPS, for which two QCD scale uncertainties are considered: one uncertainty from the three-point envelope of the NNLO part, and a separate uncertainty from the nine-point envelope of the Powheg scale. These uncertainties are treated as independent sources and are hence added in quadrature. The former affects the normalization ("yield") while the latter affects the migration between low and high Higgs boson (and jet) p_T.

It should be pointed out that not all predictions include the same set of uncertainties. All include QCD scale variations, which is always the dominant uncertainty. Some also include other uncertainties, for example from choices of PDF set and resummation scale.

For the following discussion we find it useful to take the MRT prediction as a reference, since it has the nominally highest accuracy both at low and high $p_{T,H}$. At low $p_{T,H} < 20$ GeV we see that MRT is in good agreement with all codes which include N^{2}LL resummation (HRes, CuTe and NRV). At high $p_{T,H}$ MRT agrees well with NNLOJET both in central value and (small) uncertainty. We note that POWHEG NNLOPS agrees well with MRT both at low $p_{T,H}$ (even though it does not have formally

Table 23: Fraction of $gg \to H$ events in different kinematic regions from various predictions (central values only). The numbers in italic font have been obtained by using the N^{3}LO cross section with the EW component subtracted $48.58 - 2.4 = 46.18$ pb. GoSam+Sherpa use separate predictions for each jet bin: ggF + 1, 2 and 3 jets at NLO, respectively. In all other cases numbers are normalized to their respective predictions.

	$p_{T,H}$ / GeV			N_{jets}, $p_{T,j} > 30$ GeV			
Prediction	< 20	> 60	> 120	$= 0$	$= 1$	≥ 2	≥ 3
HRes	34.9%	20.9%	5.60%	–	–	–	–
CuTe	38.8%	18.2%	4.76%	–	–	–	–
MRT	38.3%	20.7%	6.00%	–	–	–	–
NRV	47.3%	18.0%	5.74%	–	–	–	–
BLPTW	–	–	–	62.2%	25.2%	12.6%	–
JVE	–	–	–	60.7%	–	–	–
NNLOJET	–	*19.4%*	*5.83%*	*63.8%*	*24.9%*	*11.3%*	*3.63%*
GoSam+Sherpa	–	–	–	–	*22.6%*	*10.0%*	*3.22%*
Powheg NNLOPS	36.5%	21.0%	5.20%	62.3%	26.6%	11.1%	2.63%
aMCNLO MG5	34.9%	23.9%	6.84%	60.2%	27.5%	12.4%	3.52%

NNLL accuracy) and at high $p_{T,H}$ (even if it does not have NNLO corrections to Higgs+1 jet). On the other hand, we observe that MG5_aMC@NLO is lower and with rather larger uncertainty at low p_T since it does not include the NNLO correction to Higgs boson production. The GoSam+Sherpa prediction at high p_T is lower. Finally we remark that the NRV prediction tends to be lower at medium and large $p_{T,H}$, which also reflect on their total cross section. This might be related to the shape function used in the intermediate region by this group in order to switch to the fixed order result at high $p_{T,H}$.

Next, in Figure 23 we compare predictions for inclusive (top) and exclusive (bottom) jet-binned cross sections. The 0-jet inclusive cross-sections obtained integrating the N^{3}LO+JVE+N^{3}LL construction is by definition the recent N^{3}LO result. Furthermore, for the 0-jet inclusive cross-section Powheg NNLOPS is accurate at NNLO; STWZ is formally also NNLO accurate, but it is higher (and with smaller uncertainty) as it includes π^2 resummation; MG5_aMC@NLO is on the other hand lower and with larger uncertainties as it is only accurate to NLO. In the inclusive one-jet bit all predictions which are NNLO accurate (for Higgs+1 jet) are in good agreement with each other, while GoSam+Sherpa and MG5_aMC@NLO are lower. Note that even though Powheg NNLOPS does not include NNLO corrections, it is in good agreement with the NNLO-accurate predictions. In the higher inclusive jet bins all results are in reasonable agreement, with differences most likely due to choices of scale and the treatment of heavy quarks. We note that for the 3-jet cross-section the NNLOJET prediction has a very large uncertainty due to its LO nature. For Powheg NNLOPS the third jet is only provided by parton showering; it is however known that the uncertainty is underestimated in this case.

Exclusive cross sections follow a similar pattern. Note that in this case the uncertainties shown for MG5_aMC@NLO and Powheg NNLOPS are unreliable as jet veto effects are not properly accounted for.

The fractions of events in the various inclusive and exclusive bins are tabulated in Table 23.

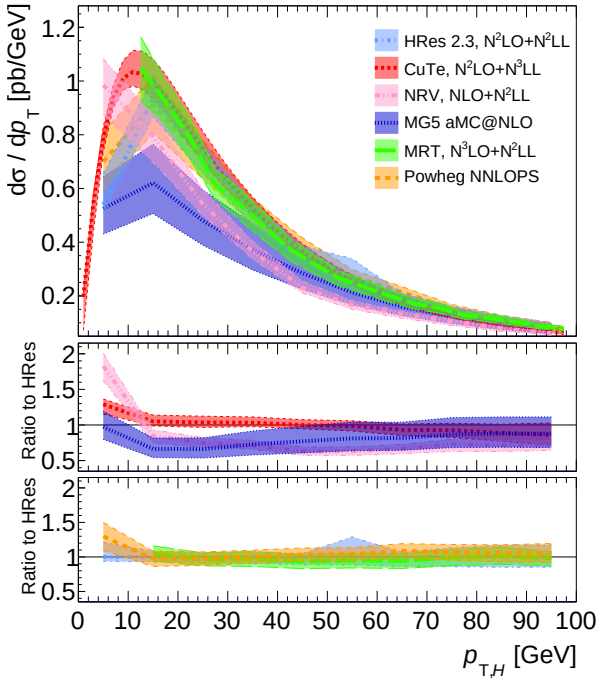

Figure 25: Same as Figure 24, but for the Higgs boson transverse momentum distribution at low p_T.

I.4.3.b.ii Differential distributions

In Figure 24 we compare Higgs boson rapidity distributions, both at the inclusive level (left) and with a jet cut (right) defined as above. At the inclusive level, as before, the NLO MG5_aMC@NLO result undershoots the predictions from HNNLO and Powheg NNLOPS which by construction agree with each other. Note that the K-factor is not flat: NNLO corrections are more important for large rapidity. Also in the presence of a jet the NLO result from GoSam+Sherpa is somewhat low. The BFGLP and NNLOJET results substantially differ in shape, especially at high rapidity, and the BFGLP result seems to have very small scale uncertainties. However, it should be noted that the BFGLP setup is different to the default (see Section I.4.3.a.i), and in particular different PDFs are used.

Next, in Figure 25 we show the Higgs boson transverse momentum distribution at low p_T. Note that all predictions but CuTe have bins with width of 10 GeV. The CuTe, MRT and HRes results are in good agreement throughout the p_T range, with some differences appearing for $p_T \lesssim 10$ GeV. Again the NLO prediction from MG5_aMC@NLO is lower and with a somewhat different shape; similar considerations apply to NRV at high p_T which has the same fixed-order accuracy. At low p_T NRV does not appear to have a Sudakov peak at the same p_T value as other results. NNLOPS follows closely the HRes result, with only minor differences in the smallest p_T bin.

The high p_T region for the same distributions is shown in Figure 26. Note that predictions should be taken with care for $p_T \gtrsim m_T$, as they are all obtained in the infinite top mass approximation. As above, HRes and Powheg NNLOPS agree well within uncertainties for all p_T values. At high p_T MRT and NNLOJET display a somewhat harder spectrum because they include NNLO corrections to the one-jet configuration. The CuTe prediction agrees well with HRes for all p_T values. The NRV prediction appears to have a somewhat different shape, and it overshoots the HRes prediction at the largest p_T despite not including NNLO corrections. Uncertainties are all comparable, with the MRT uncertainty smallest as expected since it includes the N^{3}LO correction to the inclusive result.

We now turn to the leading and subleading jet p_T distributions, shown in Figure 27. For the leading jet (left plot) the NNLOJET result, which is NNLO, is higher and with smaller uncertainty than GoSam+Sherpa and MG5_aMC@NLO, which agree well with each other. The Powheg prediction is af-

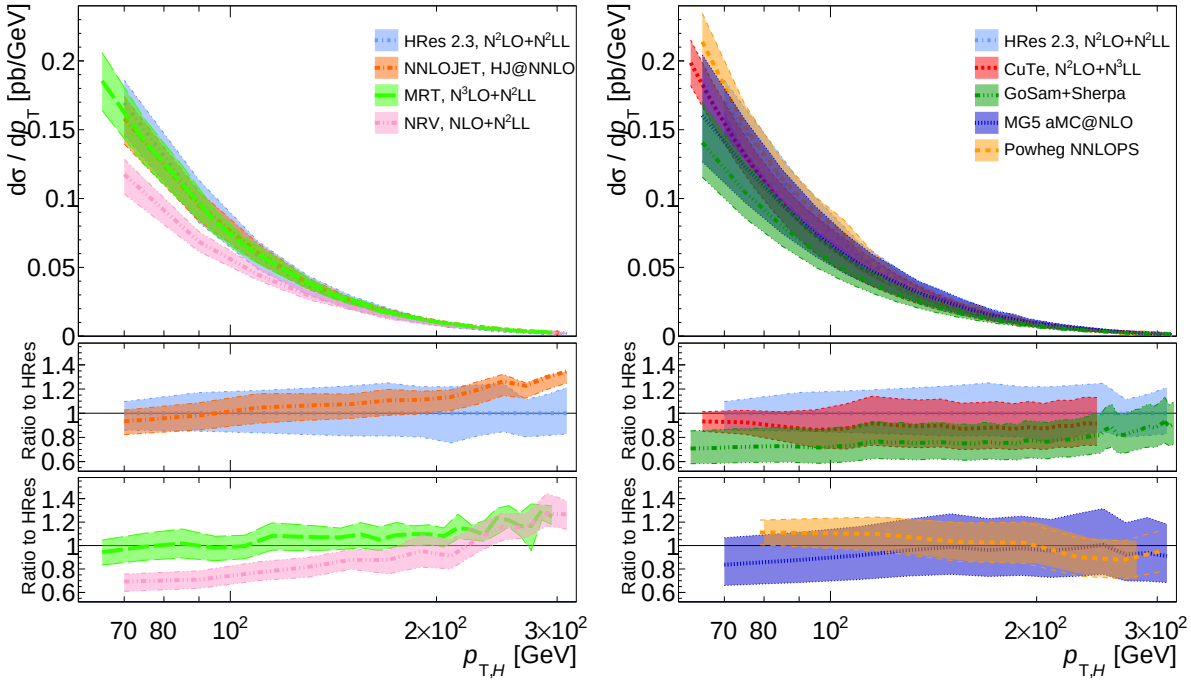

Figure 26: Same as Figure 25 for $p_{T,H} > 60$ GeV.

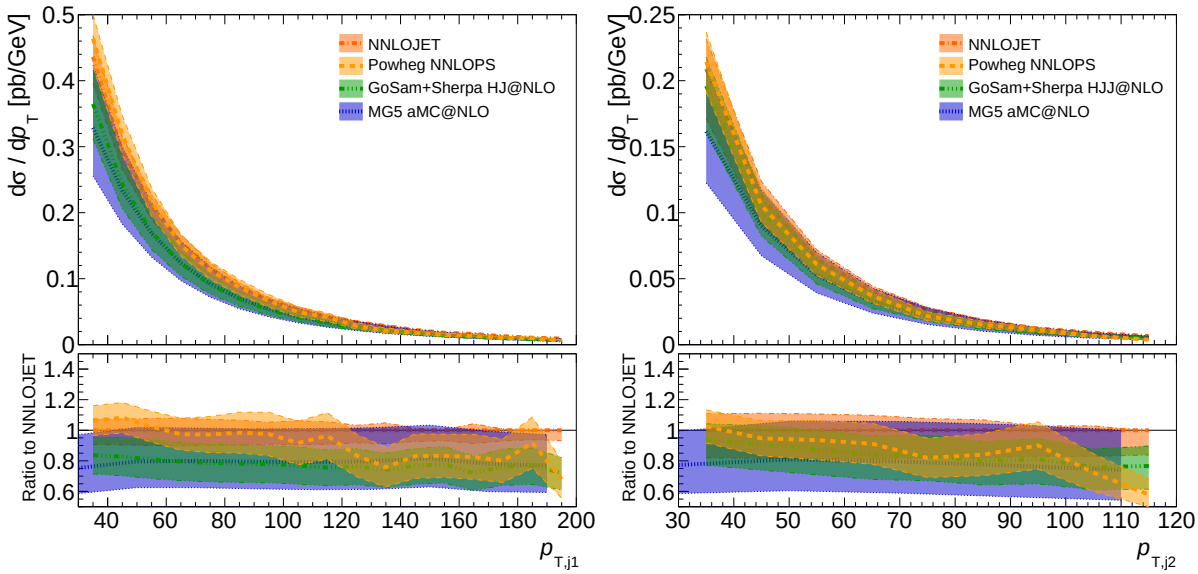

Figure 27: Leading (left) and subleading (right jet p_T distributions.

fected by large statistical fluctuations, but the shape can be understood by noting that at low p_T it agrees with NNLOJET as it includes the NNLO correction to Higgs boson production, while at high p_T it reproduces the behaviour of the other NLO Monte Carlos. For the subleading jet (right plot) all predictions but Powheg NNLOPS have the same NLO accuracy and agree within uncertainties. Powheg NNLOPS on the other hand is leading-order only and its uncertainty is known to be somewhat underestimated, yet it is in reasonable agreement with the other results.

In Figure 28 we show the transverse momentum of the third jet (left) and of the Hjj system (right). These two distributions start at $O(\alpha_s^5)$ and thus they coincide in the NNLOJET computation, which provides a purely leading-order description of these quantities and is thus affected by a large uncertainty. On the other hand, the p_T of the third jet (left plot) is described by GoSam+Sherpa at NLO, and in this

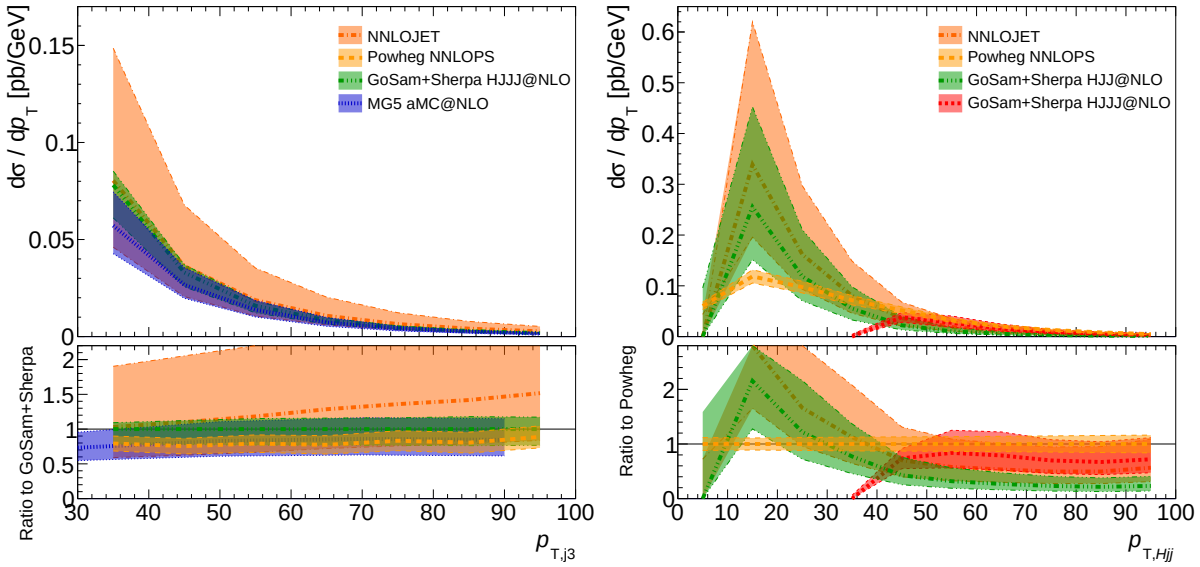

Figure 28: The transverse momentum of the third jet (left) and of the Hjj system (right).

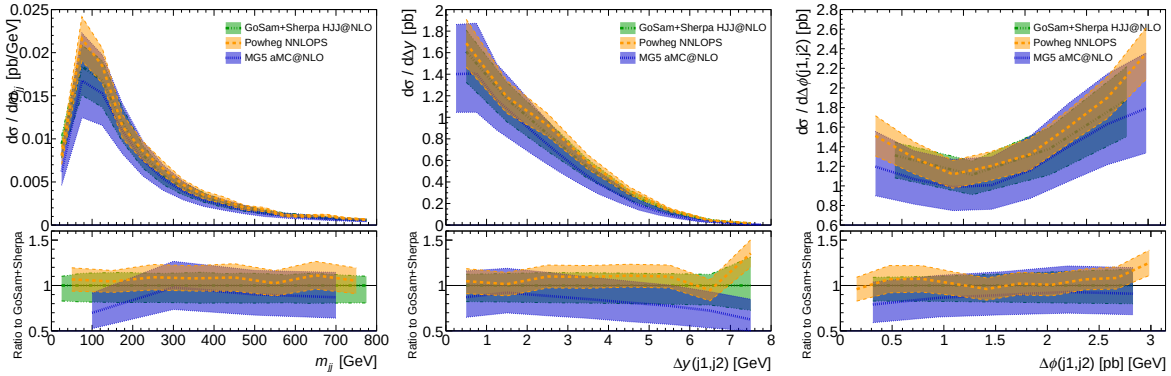

Figure 29: Two-jet variables typically used in VBF studies: from left to right, mass of the dijet system, distance in rapidity, and azimuthal angle between the two jets.

case the uncertainty is reduced. The Powheg NNLOPS result for this distribution agrees well with these computations despite the fact that the third jet is only given by the parton shower. As far as the Hjj p_T is concerned now GoSam+Sherpa HJJ@NLO and NNLOJET both provide a leading-order description while GoSam+Sherpa HJJJ@NLO provides a NLO description at high p_T. The leading order predictions agree well within their large uncertainties. The NLO correction is positive at large p_T but the uncertainty is not significantly reduced [230]. At lower p_T the HJJJ@NLO becomes unreliable as it misses part of the NLO correction since the transverse momentum of all jets, including the third one, is by construction $p_T > 30$ GeV. The Powheg NNLOPS follows, and in fact exceeds HJJJ@NLO at high p_T but it lies below the LO result at lower p_T.

Finally in Figure 29 we show variables relevant for VBF studies. Cross-sections are also tabulated in Table 24. All results agree reasonably well within the large uncertainties.

I.4.4 Effects of heavy-quark masses [I.24]

The Higgs Effective Field Theory (HEFT) framework for perturbative calculations of the gluon fusion Higgs boson production process is a well established tool that allows a significant reduction of complexity in higher-order QCD calculations. In this approach, the heavy-quark-loop induced Higgs-gluon

[I.24] *Author(s): F. Krauss, S. Kuttimalai, P. Maierhöfer, M. Schönherr.*

Table 24: Predicted cross sections for $gg \to H$ with VBF topology. The QCD uncertainties shown for POWHEG NNLOPS are not valid (the third jet is from the showering). Fixed order NLO predictions with two and three jets are provided by GOSAM+SHERPA. The last two rows show results from normalizing the inclusive cross section to 46.18 pb.

	$m_{jj} > 400$ GeV, $\Delta y_{jj} > 2.8$			$m_{jj} > 600$ GeV, $\Delta y_{jj} > 4.0$		
		$p_{T,j3}$ / GeV			$p_{T,j3}$ / GeV	
Prediction	no jet veto	< 30	> 30	no jet veto	< 30	> 30
POWHEG NNLOPS	653^{+86}_{-86} fb	435^{+54}_{-54} fb	218^{+32}_{-32} fb	283^{+36}_{-36} fb	198^{+24}_{-24} fb	85^{+12}_{-12} fb
aMC@NLO MG5	512^{+152}_{-133} fb	329^{+92}_{-84} fb	183^{+67}_{-54} fb	214^{+62}_{-57} fb	142^{+39}_{-37} fb	72^{+29}_{-21} fb
HJJ@NLO	610^{+74}_{-120} fb	435^{+0}_{-70} fb	–	268^{+32}_{-55} fb	195^{+0}_{-31} fb	–
HJJJ@NLO	–	–	240^{+17}_{-54} fb	–	–	97^{+5}_{-22} fb
NNLOPS, $k = 1.05$	683^{+90}_{-90} fb	455^{+57}_{-57} fb	228^{+33}_{-33} fb	296^{+38}_{-38} fb	207^{+25}_{-25} fb	89^{+13}_{-13} fb
MG5, $k = 1.41$	721^{+214}_{-188} fb	463^{+129}_{-118} fb	258^{+94}_{-76} fb	302^{+87}_{-80} fb	200^{+55}_{-52} fb	101^{+41}_{-29} fb

coupling of the Standard Model (SM) is approximated by taking into account only the top quark contribution and by calculating production amplitudes in the limit of an infinite top quark mass. This is typically achieved by deriving the relevant amplitudes from the effective Lagrangian

$$\mathcal{L}_{\text{HEFT}} = -\frac{C_1}{4v} H G_{\mu\nu} G^{\mu\nu} \,, \tag{I.4.55}$$

with the gluon field strength tensor $G_{\mu\nu}$, the Higgs field H, and a perturbatively calculable Wilson coefficient C_1. This Lagrangian gives rise to tree-level couplings that replace the loop-induced SM couplings between gluons and the Higgs boson, effectively reducing the number of loops in any calculation by one.

When considering the total inclusive Higgs boson production cross section, finite top quark mass effects remain very moderate even at higher orders in QCD [103–106, 234, 235]. In the tail of the transverse momentum spectrum of the Higgs boson or for heavy Higgs boson (virtual) masses, however, the corrections can become very large, indicating a complete breakdown of the HEFT approximation [236, 237]. It has also been known for a long time that the bottom quark loops, which are entirely neglected in the HEFT, affect the spectrum in the small-$p_\perp^H$ region [237, 238]. In this region, an all-order resummation of QCD corrections is required. Standard techniques need to be adapted in order to achieve this due to the bottom quark mass that introduces an additional scale into the calculation [224].

Several fully differential Monte Carlo codes have therefore been developed that take into account the full heavy quark mass dependence at NLO [141, 224, 239, 240]. NLO results for Higgs boson production in association with a jet are not available for finite heavy quark masses due to missing two-loop amplitudes for this process.

In this note, we present an approximate treatment of finite top mass effects at NLO based on one-loop amplitudes only. This allows us to calculate Higgs plus n-jet processes at NLO, while retaining finite top mass effects in an approximate way. Using this approximation, we employ multijet merging techniques [241] to merge higher-multiplicity NLO processes matched to a parton shower into one exclusive event sample, extending similar approaches [242–245] in terms of jet multiplicity and α_s accuracy. Based on leading order merging, we also suggest a method to address the issues raised in [224] concerning the inclusion of bottom quark contributions in the low-$p_\perp^H$ region.

I.4.4.a Implementation of quark mass corrections

In order to take into account the full heavy quark mass effects in the hard scattering at leading order, we replace the approximate HEFT tree-level matrix elements provided by Sherpa's matrix element generator Amegic++ [246] with the exact one-loop matrix elements provided by OpenLoops [247] in combination with Collier [248]. This allows the calculation of processes with up to three additional jets in the final state at leading order, with the full top and bottom quark mass dependency taken into account.

At NLO, the cross section for the production of a Higgs boson accompanied by a certain number $m-1$ of jets receives contributions from two integrals of different phase space dimensionality.

$$\sigma = \int (B + V + I) d\phi_m + \int (R - S) d\phi_{m+1} \tag{I.4.56}$$

The born term B and the real emission term R are present already at leading order for processes of the respective jet multiplicity and can be corrected as in the leading order calculation. $I(\phi_m)$ and $S(\phi_{m+1})$ denote the integrated and differential Catani-Seymour subtraction terms, respectively [249]. They render both integrals separately finite and are built up from leading-order m-particle matrix elements dressed with appropriate splitting kernels and can henceforth be corrected by using the full one-loop matrix elements instead of the tree-level HEFT approximation. Note that because we correct R and S with matrix elements of different final state multiplicity, the mere convergence of the corresponding integral already provides a crucial test for our implementation.

The IR-subtracted virtual correction V receives contributions from two-loop diagrams when taking into account the full heavy quark mass dependencies. Since these amplitudes are available only for the Higgs boson plus zero-jet final state, we employ an ad-hoc approximation that only involves one-loop matrix elements (even for the Higgs boson plus zero-jet final state). We assume a factorization of the α_s-corrections from the quark mass corrections and set

$$V = V_{\mathrm{HEFT}} \frac{B}{B_{\mathrm{HEFT}}} \,. \tag{I.4.57}$$

In this approximation, we can straightforwardly apply finite top mass corrections in simulations employing CKKW multi jet merging at NLO in the MEPS@NLO scheme [241].

We expect the approximation (I.4.57) to give reasonable results only if the HEFT-approximation is valid. For any contribution involving the bottom Yukawa coupling y_b , it cannot be used due to the small bottom quark mass. This applies to the interference terms proportional to $y_t y_b$ as well as the squared bottom contributions proportional to y_b^2. We therefore calculate terms that involve y_b as separate processes at leading order. The NLO corrections to the total inclusive cross sections for the $y_t y_b$ contributions and the y_b^2 contributions are only $\mathcal{O}1\%$ and $\mathcal{O}20\%$, respectively [250]. Furthermore, the y_b^2 contributions featuring the slightly larger NLO K-factor are significantly suppressed compared to the $y_t y_b$ terms [250]. We therefore consider a treatment at leading order sufficiently accurate. Any terms proportional to y_t^2 will however be calculated at NLO in the approximation described above.

I.4.4.b Finite top mass effects

As mentioned in the introduction, the total inclusive cross section is only mildly affected by finite top mass effects. The low-$p_\perp^H$ region, where the bulk of the cross section is located, can therefore be expected to exhibit only a moderate dependence on the top quark mass. In kinematic regimes where any invariant significantly exceeds m_t, however, we expect the HEFT approximation to break down. The $p_\perp^H$ distributions in Figure 30 (left) exemplify this picture. We show Higgs boson transverse momentum distributions for final states with one, two, and three jets calculated at fixed leading order. Jets are reconstructed using the anti-k_T algorithm with a radius parameter of $R = 0.4$ and a minimum jet $p_\perp$ of ~ 30 GeV except in the 1-jet case, where we apply only a small minimum $p_\perp$-cut of ~ 1 GeV. The distributions for all three

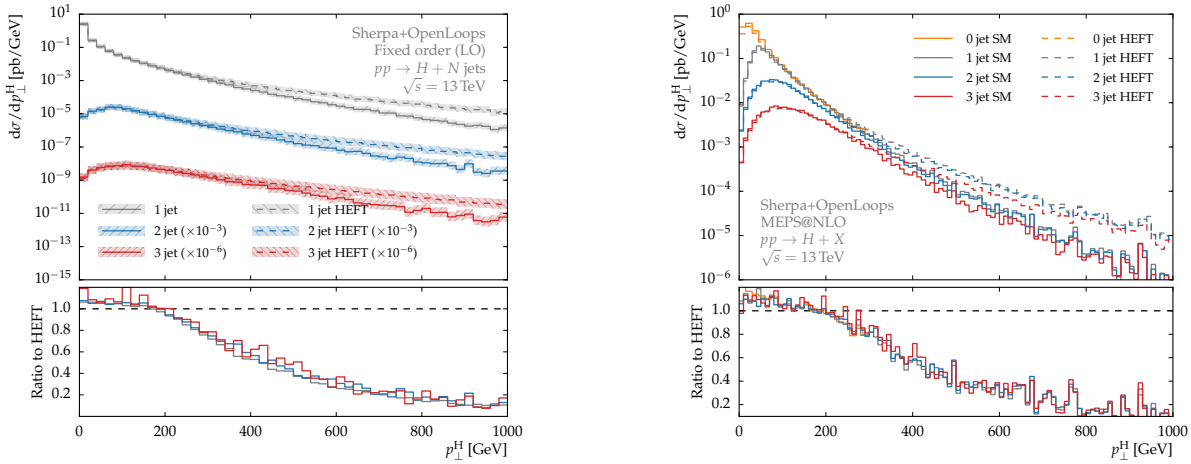

Figure 30: The Higgs boson transverse momentum spectrum in gluon fusion. We show individual curves for the HEFT approximation (dashed) and the full SM result taking into account the mass dependence in the top quark loops. The lower panel shows the ratio of the SM results to the HEFT approximation. Left: LO fixed order calculation for up to three jets. The error bands indicate the uncertainties obtained from variations of the factorization and renormalization scales. Right: Multijet merged calculation. We include the zero and one jet final states at NLO as well as the two jet final state at leading order. The individual curves show inclusive N-jet contributions.

jet multiplicities exhibit a very similar pattern when comparing the full SM result to the HEFT approximation. Below $p_\perp^H \approx m_H$, we observe a flat excess of around $\sim 6\%$ that recovers the correction factor to the total inclusive Higgs boson production cross section at leading order. The deviations become very large when $p_\perp^H$ significantly exceeds m_t, as expected. The similarity of the top mass dependency of the $p_\perp^H$ spectrum for all jet final multiplicities confirms similar findings for one- and two-jet configurations in [251].

In Figure 30 (right), we show analogous results obtained from the MEPS@NLO simulation. We included NLO matrix elements for the zero- and one-jet final states as well as leading order matrix elements for the two-jet final state in the merged setup and set Q_{cut} to $\sim$ 30 GeV. From the ratio plot in Figure 30 it is evident that in our approximation we recover the same suppression patterns as in the respective fixed leading order calculations for all jet multiplicities. This is a nontrivial observation as an m-jet configuration receives corrections from m-jet matrix elements as well as from $m+1$-jet matrix elements through the real emission corrections R in (I.4.57).

I.4.4.c Nonzero bottom mass effects

As pointed out already in [237, 238], the inclusion of the bottom quark in the loops affects the $p_\perp^H$ distribution only at small values of $p_\perp^H$ around m_b. In Figure 31 we reproduce these findings for the process $pp \to H + j$ at fixed order. In the $p_\perp$ range around m_b where the bottom effects are large, a fixed order prediction is of course unreliable due to the large hierarchy of scales between m_H and the transverse momentum. This large separation of scales induces Sudakov logarithms $\ln(m_H/p_\perp)$ that spoil any fixed order expansion and require resummation.

It was argued in [224] that the resummation of these logarithms is complicated by the presence of the bottom quark in loops that couple to the Higgs boson. The bottom quark introduces m_b as an additional scale above which the matrix elements for additional QCD emissions do not factorize. Since a factorization is essential for the applicability of resummation techniques, it was proposed to use a separate resummation scale of the order of m_b for the contributions involving y_b, thereby restricting

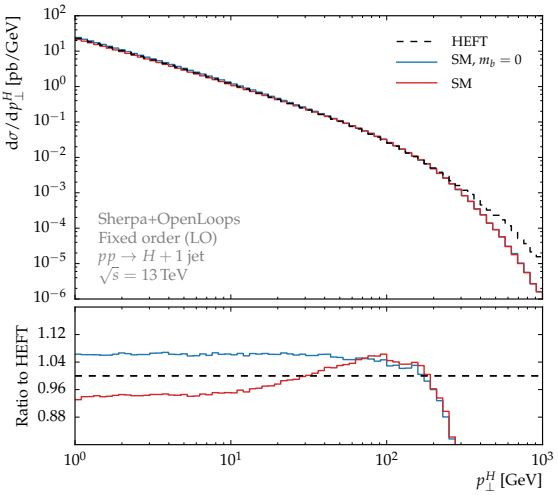

Figure 31: Bottom quark mass effects at fixed leading order. The minimum jet $p_\perp$ is set to ~ 1 GeV in order to display map out the low $p_\perp^H$ region as well.

the range of transverse momenta where resummation is applied to the phase space where factorization is guaranteed. Two quantitative prescriptions have been proposed for the determination of a specific numerical value for the resummation scale of the bottom contributions [231, 252]. These two methods yield numerical values of ~ 9 GeV and ~ 31 GeV [250] for the dominant top-bottom interference terms. In addition to m_b, we will therefore consider these values for our numerical studies. The pure top quark contributions proportional to y_t^2 will be treated as usual, with the resummation scale set to m_H.

While reference [224] was concerned with analytical resummation techniques, similar approaches were studied in the context of NLO-matched parton shower Monte Carlos [231,250,252]. Our discussion will be restricted to the leading order as the approximation used for the NLO calculation of the top quark contributions (I.4.57) is invalid for the bottom quark terms. The equivalent of the resummation scale in analytic calculations is the parton shower starting scale μ_{PS} because it restricts parton shower emissions to the phase space below this scale and because this scale enters as the argument in the Sudakov form factors. Using separate parton shower starting scales for the top and the bottom contributions, respectively, requires to generate and shower them separately as well. A corresponding separation of terms in the one-loop matrix elements can be achieved with OpenLoops. By means of this separation into terms proportional to y_t^2 and the remainder, we can generate an MC@NLO sample for the top quark contributions while calculating the terms involving y_b at leading order. Figure 32 (left) shows the $p_\perp^H$ spectrum obtained this way. We show results with μ_{PS}^b set to m_b, ~ 9 GeV, and ~ 30 GeV as motivated above. The parton shower starting scale for the top quark contributions will be $\mu_{\text{PS}}^t = m_H$ throughout. For small μ_{PS}^b, the suppression in the low $p_\perp$ region below m_b is much more pronounced than in the fixed order result in Figure 31. This is because, pictorially speaking, without changing the cross section of the individual contributions, the parton shower simulation spreads the y_t^2 part over a much wider range, up to $\mathcal{O}(m_H)$, than for the negative $y_t y_b$, up to $\mathcal{O}(m_b)$ only. The spectrum in this region is therefore extremely sensitive to variations of μ_{PS}^b. When varying μ_{PS}^b to sufficiently low values, the differential cross section may even become negative, clearly an unphysical result. We stress, again, that this is not a physical effect but an artefact of the unitary nature of the parton shower. Setting the value of μ_{PS}^b to a small value, the entire leading order bottom cross section contributions will be distributed in a phase space with Higgs boson transverse momenta not significantly exceeding μ_{PS}^b. Since this cross section is negative, the spectrum must become negative at some point when lowering μ_{PS}^b.

We therefore suggest another approach at taking into account the bottom quark contributions in

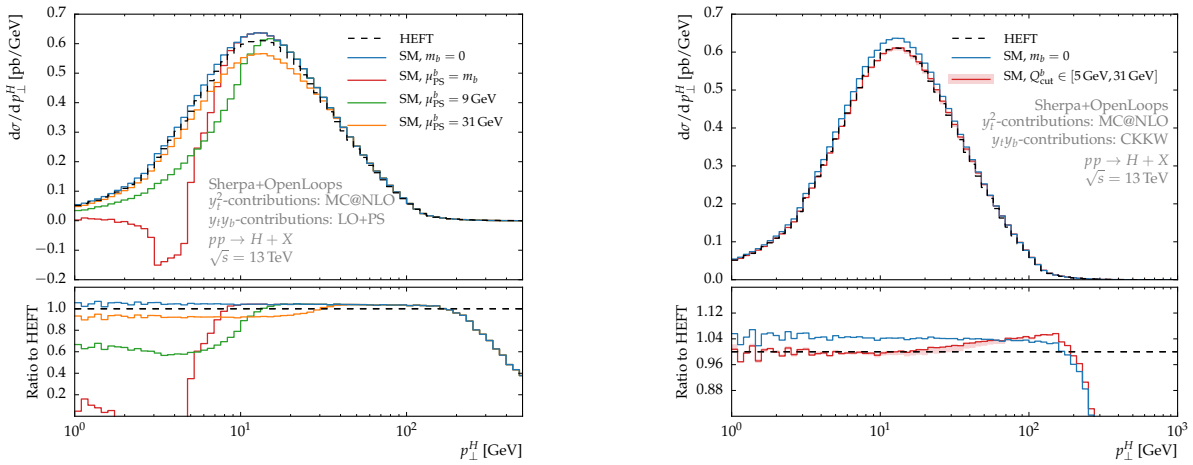

Figure 32: Left: Bottom quark mass effects at LO+PS accuracy with small parton shower starting scales $\mu^b_{\rm PS}$. The specific values chosen for $\mu^b_{\rm PS}$ are motivated in the text. Right: Bottom quark mass effects taken into account by means of CKKW merging with a small merging scale $Q^b_{\rm cut} = \mathcal{O}(m_b)$. The red error band shows variations of this scale as indicated.

a parton shower Monte Carlo simulation. We account for the non-factorization of the real emission matrix elements above some scale $Q^b_{\rm cut}$ by correcting parton shower emissions harder than this scale with the appropriate fixed order matrix elements. This can be done consistently in the CKKW merging scheme [242, 253]. Setting the merging scale for the bottom contributions $Q^b_{\rm cut}$ to m_b allows the correction of the parton shower in the regime where the matrix elements involving m_b do not factorize (without restricting all emissions to the phase space below). Above $Q_{\rm cut}$, the fixed-order accuracy of the real emission matrix elements is thereby retained. Since any NLO prediction of the inclusive process describes the $p_\perp$ spectrum only at leading order, our approach retains the same parametric fixed order accuracy when considering the $p_\perp^H$ distribution. Beyond fixed order, the differences should be small since the NLO corrections to the inclusive cross section are at the per cent level for the $y_t y_b$ interference terms.

In Figure 32 (right) we show the bottom quark effects on the $p_\perp^H$ spectrum in this approach. We include matrix elements with up to one jet in the merging such that a leading order accuracy in α_s is guaranteed for both the top and the bottom contributions to the $p_\perp^H$ spectrum. This allows a comparison to Figure 31. The effects of the bottom quarks lead to a very similar suppression pattern over the entire displayed range of $p_\perp^H$. The large NLO K-factor that appears in the MC@NLO calculations of the top contributions however affects the overall relative normalization of the bottom quark effects. They are correspondingly smaller by roughly $\sim 50\%$ in Figure 32 when compared to Figure 31. The sensitivity to variations of the scale in the calculation that effectively accounts for the presence of the bottom mass in the problem is drastically reduced. Figure 32 includes an error band corresponding to variations of $Q^b_{\rm cut}$ in the large interval between m_b and ~ 31 GeV. On the displayed scale, these variations are hardly visible.

I.4.4.d Conclusions

We presented in this section an implementation of heavy quark mass effects in gluon fusion Higgs boson production that allows to systematically include finite top mass effects in an approximate way at NLO for in principle arbitrary jet multiplicities in the final state. Based on this approximation, we presented results for the Higgs boson transverse momentum distributions obtained from NLO matched and merged samples. When comparing the top quark mass dependence in one-, two-, and three-jet final states, we observed a universal suppression pattern that agrees very well with the corresponding leading order

results.

Our treatment of contributions involving the bottom Yukawa coupling is based on m_b- and m_t-exact leading order matrix elements in combination with tree-level multijet merging techniques. We argued that this approximation is appropriate since it allows to retain leading order accuracy for the corresponding contributions in the $p_\perp^H$-spectrum and it also allows to account for the non-factorization of real emission amplitudes at scales above m_b. In this approach, the uncertainty associated with the appearance of m_b as an additional scale in the calculation is drastically reduced.

Acknowledgements

The editors are grateful to the following people who have provided numbers used for the benchmarks for cross sections and differential distributions presented in Section I.4.3: Thomas Becher, Massimiliano Grazzini, Nicolas Greiner, Thomas Lübbert, Gionata Luisoni, Duff Neill, Matthias Neubert, Hayk Sargsian, Ira Rothstein, Varun Vaidya, Daniel Wilhelm and Jan Winter.

Chapter I.5

VBF and VH

S. Dittmaier, P. Govoni, B. Jäger, J. Nielsen, L. Perrozzi, E. Pianori, A. Rizzi, F. Tramontano (Eds.); W.A. Astill, J. Bellm, W. Bizon, F. Campanario, J. Campbell, A. Denner, F.A. Dreyer, R.K. Ellis, G. Ferrera, T. Figy, P. Francavilla, R. Frederix, S. Frixione, M. Grazzini, R. Harlander, B. Hespel, J. Huston, S. Kallweit, A. Karlberg, F. Krauss, A. Kulesza, G. Luisoni, S.-O. Moch, A. Mück, C. Oleari, C.E. Pandini, A. Papaefstathiou, S. Plätzer, E. Re, G.P. Salam, P. Schichtel, M. Sjödahl, V. Theeuwes, P. Torrielli, E. Vryonidou, C. Williams, G. Zanderighi, M. Zaro, T. Zirke

The production of a Standard Model Higgs boson in association with two hard jets in the forward and backward regions of the detector, frequently quoted as the "vector-boson fusion" (VBF) channel, and the production of a Higgs boson in association with a W or Z boson, known as "VH production" or "Higgs-strahlung", represent cornerstones in a comprehensive study of Higgs boson couplings at the LHC. These production channels do not only provide valuable information on the couplings of Higgs bosons to the massive gauge bosons by themselves, but also allow for the isolation of the Higgs boson decays into τ-lepton or bottom-quark pairs, whose investigation is essential in the Higgs boson couplings analysis.

In the previous reports [7–9], state-of-the-art predictions and error estimates for the total and differential cross sections for $\mathrm{pp} \to \mathrm{H} + 2\,\mathrm{jets}$ and $\mathrm{pp} \to \mathrm{H}V \to \mathrm{H} + 2\,\mathrm{leptons}$ were compiled (with $V = \mathrm{W}, \mathrm{Z}$), but the process of improving and refining predictions is still ongoing, even within the Standard Model. In this contribution we update the cross-section predictions for VBF and VH production, covering integrated total and fiducial cross sections as well as differential distributions. In detail, the presented state-of-the-art predictions include QCD corrections up to next-to-next-to-leading order (NNLO), electroweak (EW) corrections up to next-to-leading order (NLO), and contributions from specific partonic channels that open at higher perturbative orders, such as photon-induced collisions or gluon-fusion contributions. Apart from collecting numerical results, we give recommendations as to how to combine the individual components and to assess conservative estimates of remaining theoretical uncertainties. Moreover, issues connected to the matching and the impact of parton showers (PS) are discussed.

I.5.1 VBF cross-section predictions

I.5.1.a Programs and tools for VBF

I.5.1.a.i HAWK

HAWK [254, 255] is a parton-level event generator for Higgs boson production in vector-boson fusion [256, 257], $\mathrm{pp} \to \mathrm{H} + 2\,\mathrm{jets}$, and Higgs-strahlung [258], $\mathrm{pp} \to \mathrm{H}V \to \mathrm{H} + 2\,\mathrm{leptons}$ (with $V = \mathrm{W}, \mathrm{Z}$). Here we summarize its most important features for the VBF channel.

HAWK includes the complete NLO QCD and EW corrections and all weak-boson fusion and quark–antiquark annihilation diagrams, i.e. t-channel and u-channel diagrams with VBF-like vector-boson exchange and s-channel Higgs-strahlung diagrams with hadronic weak-boson decay, as well as all interferences. HAWK allows for an on-shell Higgs boson or for an off-shell Higgs boson (with optional decay into a pair of gauge singlets). The EW corrections include also the contributions from photon-induced channels, but contributions from effective Higgs–gluon couplings, which are part of the QCD corrections to Higgs boson production via gluon fusion, are not taken into account. External fermion masses are neglected and the renormalization and factorization scales are set to M_{W} by default. Since version 2.0, HAWK includes anomalous Higgs-boson–vector-boson couplings.

I.5.1.a.ii MadGraph5_aMC@NLO

Higgs boson production through VBF, possibly in association with extra jets, can be generated automatically in MADGRAPH5_AMC@NLO, and is thus exactly on the same footing as any other generic process. A phenomenology study of H+2jet VBF production has been presented in Ref. [259], where NLO QCD results matched to different parton showers (HERWIG6, HERWIG++ and virtuality-ordered PYTHIA6) have been compared to fixed-order NLO predictions and the corresponding POWHEG-matched ones. Predictions for VBF matched to PYTHIA8 have been successively presented in Ref. [54]. The code for simulating VBF Higgs boson production at the NLO(+PS) accuracy can be generated and run via the commands

```
generate p p > h j j $$ w+ w- z [QCD]
output VBF-MG5_aMC
launch
```

where the $$ syntax forbids s-channel W and Z bosons. Virtual corrections featuring electroweak bosons in the loop (pentagons) are not included when using the above command lines. Note that diagrams of this class are either zero, or negligible for all practical purposes.[I.25] As the default Standard Model in MADGRAPH5_AMC@NLO assumes a non-vanishing bottom mass, no b quark is included in the definition of the p and j multiparticles. In order to include b quarks, it is sufficient to load the 'loop_sm-no_b_mass' model before generating the code, with the command

```
import model loop_sm-no_b_mass
```

In both cases, a $V_{CKM} = 1$ is assumed and the Higgs boson is kept on its mass shell.
For what concerns Higgs plus three jets production in VBF, predictions for the third and the veto jet at NLO+PS accuracy have been presented in Ref. [54], considering t-channel modes only. The relevant code can be generated and executed with the commands

```
generate p p > h j j j $$ w+ w- z [QCD]
output VBF-MG5_aMC
launch
```

I.5.1.a.iii POWHEG

The POWHEG BOX is a program package that allows for the matching of NLO QCD calculations with parton shower generators using the POWHEG method. VBF-induced Higgs boson production has been implemented in the POWHEG BOX in the factorized approximation, where cross-talk between the fermion lines is neglected, in Ref. [260]. More recently, also an implementation of Higgs boson production in association with three jets via VBF, based on the NLO QCD calculation of Ref. [261], has become available [262].

Both implementations are based on the respective NLO QCD calculations for genuine weak-boson fusion topologies, i.e. the VBF approximation. Quark–antiquark annihilation and interference contributions between t- and u-channel contributions are disregarded. The CKM matrix elements can be assigned by the user. External fermion masses are neglected throughout. For the choice of renormalization and factorization scales, various options are available. For this report, fixed scales, $\mu_{\mathrm{F}} = \mu_{\mathrm{R}} = M_{\mathrm{W}}$, are used, and contributions from external bottom and top quarks are entirely disregarded.

I.5.1.a.iv VBF@NNLO

VBF@NNLO [263,264] computes VBF total Higgs cross sections at LO, NLO, and NNLO in QCD via the structure-function approach. This approach [265] consists in considering VBF process as a double

[I.25] For this reason, the internal check of pole cancellation fails. In order to disable these checks, the parameters `IRPoleCheckThreshold` and `PrecisionVirtualAtRunTime` inside `Cards/FKS_params.dat` must be set to -1.

deep-inelastic scattering (DIS) attached to the colourless pure electroweak vector-boson fusion into a Higgs boson. According to this approach one can include NLO QCD corrections to the VBF process employing the standard DIS structure functions $F_i(x, Q^2)$; $i = 1, 2, 3$ at NLO [266] or similarly the corresponding structure functions at NNLO [267–270].

The effective factorization underlying the structure-function approach does not include all types of contributions. At LO an additional contribution arises from the interferences between identical final-state quarks (e.g., $\mathrm{uu} \to \mathrm{Huu}$) or between processes where either a W or a Z can be exchanged (e.g., $\mathrm{ud} \to \mathrm{Hud}$). These LO contributions have been added to the NNLO results presented here, even if they are very small. Apart from such contributions, the structure-function approach is exact also at NLO. At NNLO, however, several types of diagrams violate the underlying factorization. Their impact on the total rate has been computed or estimated in Ref. [264] and found to be negligible. Some of them are colour suppressed and kinematically suppressed [261,271,272], others have been shown in Ref. [273] to be small enough not to produce a significant deterioration of the VBF signal.

At NNLO QCD, the theoretical QCD uncertainty is reduced to less than 2%. Electroweak corrections, which are at the level of 5%, are not included in VBF@NNLO. The Higgs boson can either be produced on its mass-shell, or off-shell effects can be included in the complex-pole scheme.

I.5.1.a.v proVBFH

`proVBFH` is a parton-level Monte Carlo program for the calculation of differential distributions for VBF Higgs boson production to NNLO QCD accuracy. It is based on POWHEG's fully differential NLO QCD calculation for Higgs boson production in association with three jets via VBF [261, 262], and an inclusive NNLO QCD calculation [263], the latter being taken in the structure-function approximation, which are combined using the projection-to-Born method described in Ref. [274].

`proVBFH` uses a diagonal CKM matrix, Breit–Wigner distributions for the W and Z bosons, and neglects fermion masses. It assumes that there is no cross-talk between the upper and lower hadronic sectors. For this report, the factorization and renormalization scales are set to the W-boson mass, $\mu_\mathrm{R} = \mu_\mathrm{F} = M_\mathrm{W}$.

I.5.1.a.vi VBFNLO

VBFNLO [275] is a parton-level Monte Carlo generator for the simulation of various processes with weak bosons at NLO QCD accuracy. In particular, Higgs boson production in association with two [276] or three jets [261] via VBF is implemented with different options for the decays of the Higgs boson. For VBF Higgs boson production in association with two jets, in addition to the default SM implementation, options are available for the inclusion of anomalous coupling effects [277] and VBF Higgs boson production in the context of the MSSM [278]. NLO EW corrections to VBF can also be computed [278]. Quark–antiquark annihilation and interference contributions between t- and u-channel contributions are not taken into account. In the following we will refer to this setup as "VBF approximation".

I.5.1.b VBF parameters and cuts

The numerical results presented in the next section have been computed using the values of the EW parameters given in Chapter I.1. The electromagnetic coupling is fixed in the G_F scheme,

$$\alpha_{G_F} = \sqrt{2} G_F M_\mathrm{W}^2 (1 - M_\mathrm{W}^2/M_\mathrm{Z}^2)/\pi, \tag{I.5.1}$$

and the weak mixing angle, θ_w, is defined in the on-shell scheme,

$$s_\mathrm{w}^2 \equiv \sin^2\theta_\mathrm{w} = 1 - M_\mathrm{W}^2/M_\mathrm{Z}^2. \tag{I.5.2}$$

The renormalization and factorization scales are set equal to the W-boson mass,

$$\mu = \mu_\mathrm{R} = \mu_\mathrm{F} = M_\mathrm{W}, \tag{I.5.3}$$

and both scales are varied in the range $M_{\mathrm{W}}/2 < \mu < 2M_{\mathrm{W}}$ keeping $\mu_{\mathrm{F}} = \mu_{\mathrm{R}}$, which catches the full scale uncertainty of integrated cross sections (and of differential distributions in the essential regions).

In the calculation of the QCD-based cross sections, we have used the PDF4LHC15_nnlo_100 PDFs [35], for the calculation of the EW corrections we have employed the NNPDF2.3QED PDF set [279], which includes a photon PDF. Note, however, that the relative EW correction factor, which is used in the following, hardly depends on the PDF set, so that the uncertainty due to the mismatch in the PDF selection is easily covered by the other remaining theoretical uncertainties.

For the fiducial cross section and for differential distributions the following reconstruction scheme and cuts have been applied. Jets are constructed according to the anti-k_{T} algorithm [191] with $D = 0.4$, using the default recombination scheme (E scheme). Jets are constructed from partons j with

$$|\eta_j| < 5\,, \tag{I.5.4}$$

where η_j denotes the pseudo-rapidity. Real photons, which appear as part of the EW corrections, are an input to the jet clustering in the same way as partons. Thus, in real photon radiation events, final states may consist of jets only or jets plus a real identifiable photon, depending on whether the photon was merged into a jet or not, respectively. Both events with and without isolated photons are kept.

Jets are ordered according to their p_{T} in decreasing progression. The jet with highest p_{T} is called leading jet (j_1), the one with next highest p_{T} subleading jet (j_2), and both are the tagging jets. Only events with at least two jets are kept. They must satisfy the additional constraints

$$p_{\mathrm{T}\,j} > 20\ \mathrm{GeV}, \qquad |y_j| < 5, \qquad |y_{j_1} - y_{j_2}| > 3\,, \qquad M_{jj} > 130\ \mathrm{GeV}, \tag{I.5.5}$$

where $y_{j_{1,2}}$ are the rapidities of the two leading jets. The cut on the 2-jet invariant mass M_{jj} is sufficient to suppress the contribution of s-channel diagrams to the VBF cross section to the level of $1-2\%$, so that the DIS approximation of taking into account only t- and u-channel contributions is justified. In the cross sections given below, the s-channel contributions will be given for reference, although they are not included in the final VBF cross sections by default.

While the VBF cross sections in the DIS approximation are independent of the CKM matrix, quark mixing has some effect on s-channel contributions. For the calculation of the latter we employed a Cabbibo-like CKM matrix (i.e. without mixing to the third quark generation) with Cabbibo angle, θ_{C}, fixed by $\sin\theta_{\mathrm{C}} = 0.225$. Moreover, we note that we employ complex W- and Z-boson masses in the calculation of s-channel and EW corrections in the standard HAWK approach, as described in Refs. [256, 257].

The Higgs boson is treated as on-shell particle in the following consistently, since its finite-width and off-shell effects in the signal region are suppressed in the SM.

I.5.1.c Integrated VBF cross sections

The final VBF cross section σ^{VBF} is calculated according to:

$$\sigma^{\mathrm{VBF}} = \sigma^{\mathrm{DIS}}_{\mathrm{NNLOQCD}}(1 + \delta_{\mathrm{EW}}) + \sigma_\gamma, \tag{I.5.6}$$

where $\sigma^{\mathrm{DIS}}_{\mathrm{NNLOQCD}}$ is the NNLO QCD prediction for the VBF cross section in DIS approximation, based on the calculation of Ref. [274] with PDF4LHC15_nnlo_100 PDFs. The relative NLO EW correction δ_{EW} is calculated with HAWK, but taking into account only t- and u-channel diagrams corresponding to the DIS approximation. The contributions from photon-induced channels, σ_γ, and from s-channel diagrams, $\sigma_{s\text{-channel}}$ are obtained from HAWK as well, where the latter includes NLO QCD and EW corrections. To obtain σ^{VBF}, the photon-induced contribution is added linearly, but $\sigma_{s\text{-channel}}$ is left out and only shown for reference, since it is not of true VBF origin (like other contributions such as H+2jet production via gluon fusion).

Table 25: Total VBF cross sections including QCD and EW corrections and their uncertainties for different proton–proton collision energies $\sqrt{s}$ for a Higgs boson mass $M_{\mathrm{H}} = 125$ GeV.

$\sqrt{s}$[GeV]	σ^{VBF}[fb]	Δ_{scale}[%]	$\Delta_{\mathrm{PDF}/\alpha_{\mathrm{s}}/\mathrm{PDF}\oplus\alpha_{\mathrm{s}}}$[%]	$\sigma^{\mathrm{DIS}}_{\mathrm{NNLOQCD}}$[fb]	δ_{EW}[%]	σ_γ[fb]	$\sigma_{s\text{-channel}}$[fb]
7	1241.4(1)	$^{+0.19}_{-0.21}$	$\pm 2.1/\pm 0.4/\pm 2.2$	1281.1(1)	-4.4	17.1	584.5(3)
8	1601.2(1)	$^{+0.25}_{-0.24}$	$\pm 2.1/\pm 0.4/\pm 2.2$	1655.8(1)	-4.6	22.1	710.4(3)
13	3781.7(1)	$^{+0.43}_{-0.33}$	$\pm 2.1/\pm 0.5/\pm 2.1$	3939.2(1)	-5.3	51.9	1378.1(6)
14	4277.7(2)	$^{+0.45}_{-0.34}$	$\pm 2.1/\pm 0.5/\pm 2.1$	4460.9(2)	-5.4	58.5	1515.9(6)

Table 26: Fiducial VBF cross sections including QCD and EW corrections and their uncertainties for different proton–proton collision energies $\sqrt{s}$ for a Higgs boson mass $M_{\mathrm{H}} = 125$ GeV.

$\sqrt{s}$[GeV]	σ^{VBF}[fb]	Δ_{scale}[%]	$\Delta_{\mathrm{PDF}/\alpha_{\mathrm{s}}/\mathrm{PDF}\oplus\alpha_{\mathrm{s}}}$[%]	$\sigma^{\mathrm{DIS}}_{\mathrm{NNLOQCD}}$[fb]	δ_{EW}[%]	σ_γ[fb]	$\sigma_{s\text{-channel}}$[fb]
7	602.4(5)	$^{+1.3}_{-1.6}$	$\pm 2.3/\pm 0.3/\pm 2.3$	630.8(5)	-6.1	9.9	8.2
8	795.9(6)	$^{+1.3}_{-1.5}$	$\pm 2.3/\pm 0.3/\pm 2.3$	834.8(7)	-6.2	13.1	11.1
13	1975.4(9)	$^{+1.3}_{-1.2}$	$\pm 2.1/\pm 0.4/\pm 2.2$	2084.2(10)	-6.8	32.3	29.0
14	2236.6(26)	$^{+1.5}_{-1.3}$	$\pm 2.1/\pm 0.4/\pm 2.1$	2362.2(28)	-6.9	36.7	33.1

Tables 25 and 26 summarize the total and fiducial Standard Model VBF cross sections and the corresponding uncertainties for the different proton–proton collision energies for a Higgs boson mass $M_{\mathrm{H}} = 125$ GeV.

The scale uncertainty, Δ_{scale}, results from a variation of the factorization and renormalization scales (I.5.3) by a factor of 2 keeping $\mu_{\mathrm{F}} = \mu_{\mathrm{R}}$, as indicated above, and the combined PDF$\oplus\alpha_{\mathrm{s}}$ uncertainty $\Delta_{\mathrm{PDF}\oplus\alpha_{\mathrm{s}}}$ is obtained following the PDF4LHC recipe [35]. Both Δ_{scale} and $\Delta_{\mathrm{PDF}\oplus\alpha_{\mathrm{s}}}$ are actually obtained from $\sigma^{\mathrm{DIS}}_{\mathrm{NNLOQCD}}$, but this QCD-driven uncertainties can be taken over as uncertainty estimates for σ^{VBF} as well. The theoretical uncertainties of integrated cross sections originating from unknown higher-order EW effects can be estimated by

$$\Delta_{\mathrm{EW}} = \max\{0.5\%, \delta^2_{\mathrm{EW}}, \sigma_\gamma/\sigma^{\mathrm{VBF}}\}. \tag{I.5.7}$$

The first entry represents the generic size of NNLO EW corrections, while the second accounts for potential enhancement effects. Note that the whole photon-induced cross-section contribution σ_γ is treated as uncertainty here, because the PDF uncertainty of σ_γ is estimated to be 100% with the NNPDF2.3QED PDF set. At present, this source, which is about 1.5%, dominates the EW uncertainty of the integrated VBF cross section

Results for the VBF cross sections from a scan over the SM Higgs boson mass M_{H} can be found in Appendix C. In detail the total cross sections are collected in Tables 193–196 and the fiducial cross sections in Tables 197–200. Inclusive cross sections at NNLO QCD computed with the VBF@NNLO code are shown in Tables 201–204 for the SM M_{H}scan, and in Tables 205–206 for the energy scan. No interpolation of results has been performed.

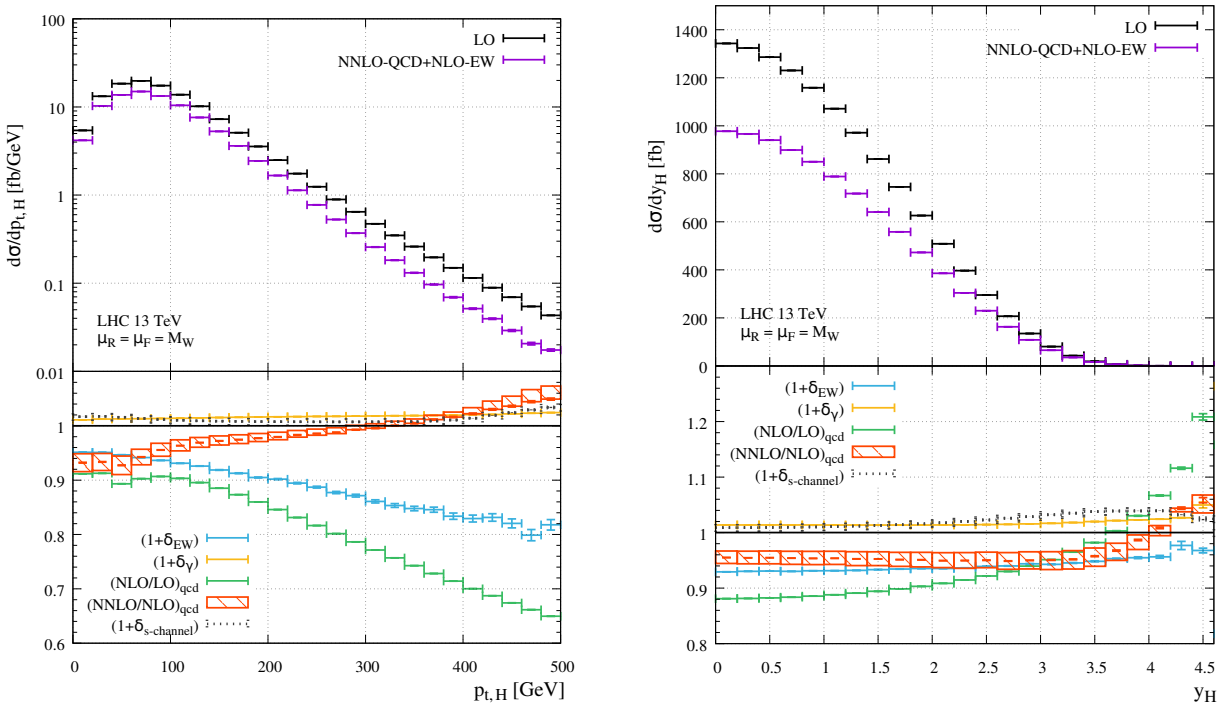

Figure 33: Transverse-momentum and rapidity distributions of the Higgs boson in VBF at LO and including NNLO QCD and NLO EW corrections (upper plots) and various relative contributions (lower plots) for $\sqrt{s} = 13$ TeV and $M_{\mathrm{H}} = 125$ GeV.

I.5.1.d Differential VBF cross sections

Figures 33–37 show the most important differential cross sections for Higgs boson production via VBF in the SM. The upper panels show the LO cross section as well as the best fixed-order prediction, based on the analogue of Eq. (I.5.6) for differential cross sections. The lower panels illustrate relative contributions and the ratios $(\mathrm{NLO}/\mathrm{LO})_{\mathrm{qcd}}$ and $(\mathrm{NNLO}/\mathrm{NLO})_{\mathrm{qcd}}$ of QCD predictions when going from LO to NLO QCD to NNLO QCD. Moreover, the relative EW correction to the (anti)quark–(anti)quark channels ($\delta_{\mathrm{EW}} = \sigma_{\mathrm{EW}}/\sigma_{\mathrm{LO}}$) and the relative correction induced by initial-state photons ($\delta_\gamma = \sigma_\gamma/\sigma_{\mathrm{LO}}$) are shown. Finally, the relative size of the s-channel contribution for Higgs+2jet production ($\delta_{s\text{-channel}} = \sigma_{s\text{-channel}}/\sigma_{\mathrm{LO}}$) is depicted as well, although it is not included in the definition of the VBF cross section. Integrating the differential cross sections shown in the following, and all its individual contributions, results in the fiducial cross sections discussed in the previous section.

The ratio $(\mathrm{NLO}/\mathrm{LO})_{\mathrm{qcd}}$ shows a quite large impact of NLO QCD corrections, an effect that can be traced back to the scale choice $\mu = M_{\mathrm{W}}$, which is on the low side if mass scales such as p_{T} and M_{jj} get large in some distributions. The moderate ratio $(\mathrm{NNLO}/\mathrm{NLO})_{\mathrm{qcd}}$, however, indicates nice convergence of perturbation theory at NNLO QCD. The band around the ratio $(\mathrm{NNLO}/\mathrm{NLO})_{\mathrm{qcd}}$ illustrates the scale uncertainty of the NNLO QCD cross section, which also applies to σ^{VBF}.

The EW corrections δ_{EW} to (pseudo)rapidity and angular distributions are rather flat, resembling the correction to the integrated (fiducial) cross section. In the high-energy tails of the p_{T} and M_{jj} distributions, δ_{EW} increases in size to 10–20%, showing the onset of the well-known large negative EW corrections that are enhanced by logarithms of the form $(\alpha/s_{\mathrm{w}}^2)\ln^2(p_{\mathrm{T}}/M_{\mathrm{W}})$. The impact of the photon-induced channels uniformly stays at the generic level of 1–2%, i.e. they cannot be further suppressed by cuts acting on the variables shown in the distributions.

The contribution of s-channel (i.e. VH-like) production uniformly shows the relative size of about 1.5% observed in the fiducial cross section, with the exception of the M_{jj} and Δy_{jj} distributions, where

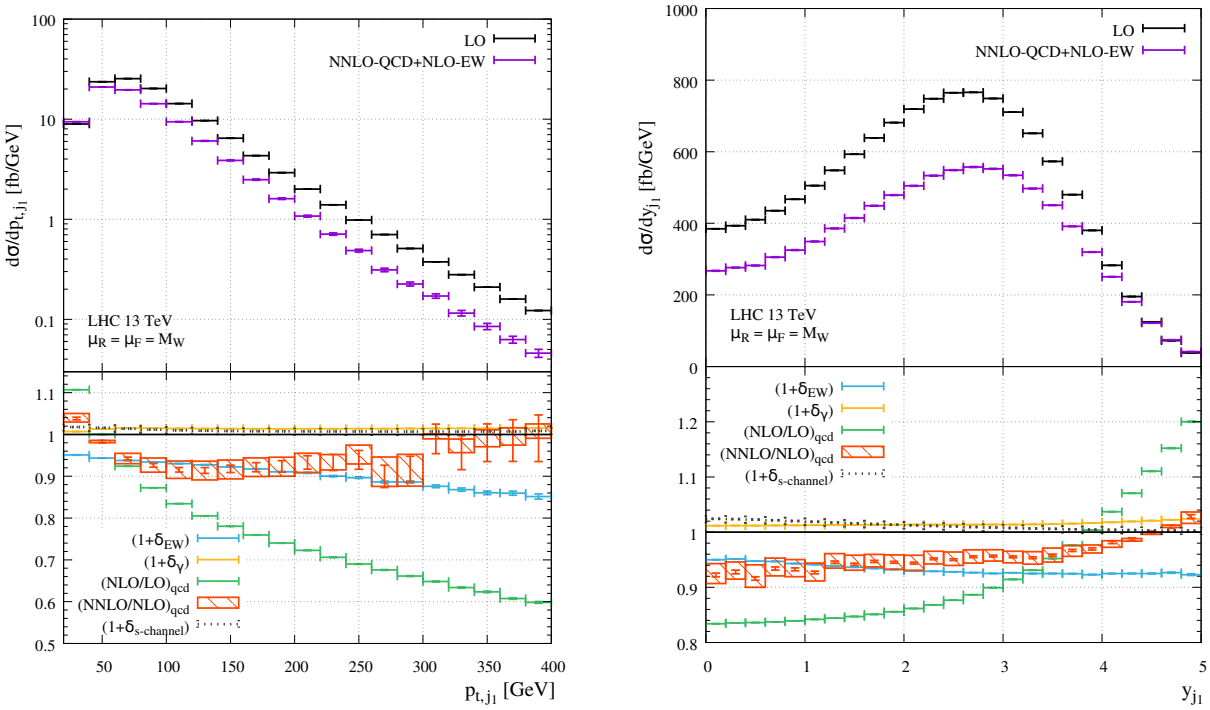

Figure 34: Transverse-momentum and rapidity distributions of the leading jet in VBF at LO and including NNLO QCD and NLO EW corrections (upper plots) and various relative contributions (lower plots) for $\sqrt{s} = 13$ TeV and $M_{\mathrm{H}} = 125$ GeV.

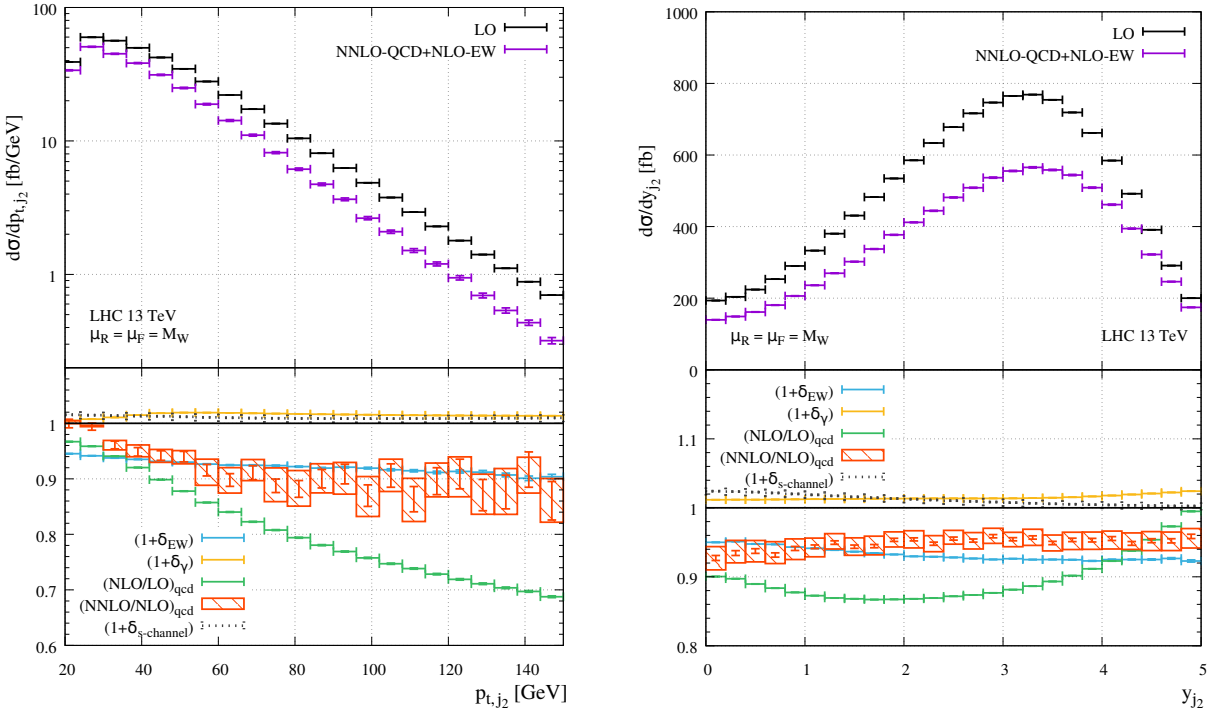

Figure 35: Transverse-momentum and rapidity distributions of the subleading jet in VBF at LO and including NNLO QCD and NLO EW corrections (upper plots) and various relative contributions (lower plots) for $\sqrt{s} = 13$ TeV and $M_{\mathrm{H}} = 125$ GeV.

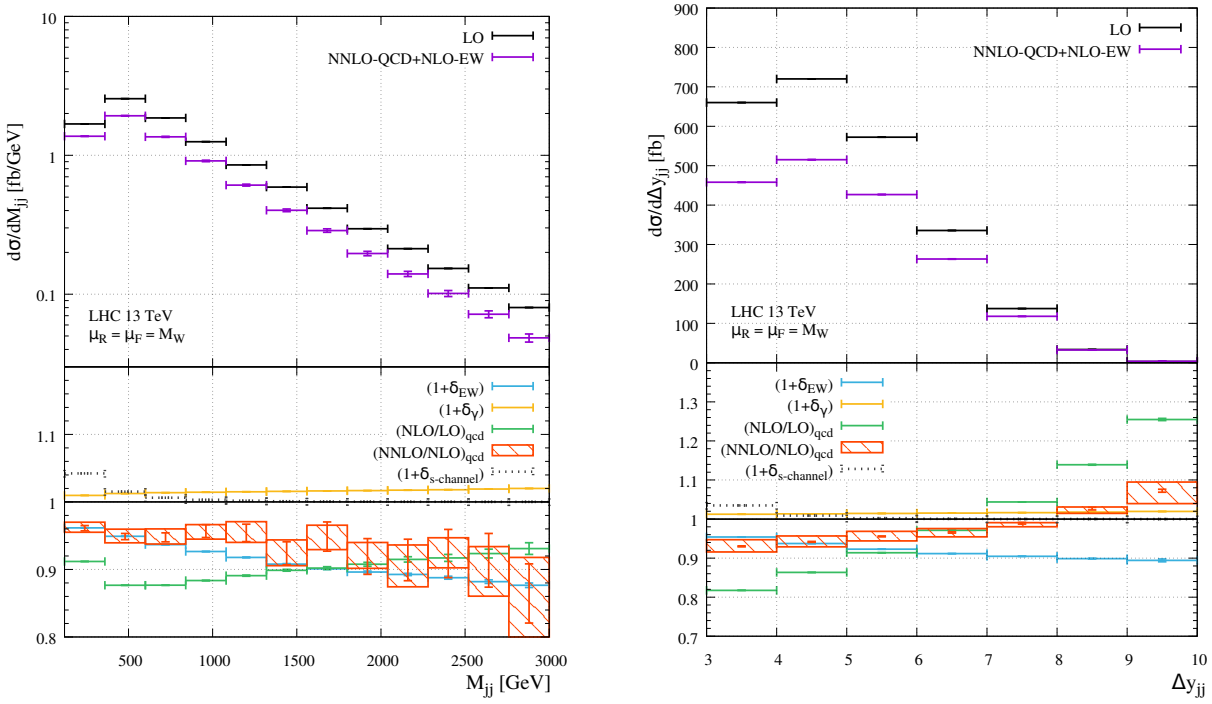

Figure 36: Distributions in the invariant mass and in the rapidity difference of the first two leading jets in VBF at LO and including NNLO QCD and NLO EW corrections (upper plots) and various relative contributions (lower plots) for $\sqrt{s} = 13$ TeV and $M_{\mathrm{H}} = 125$ GeV.

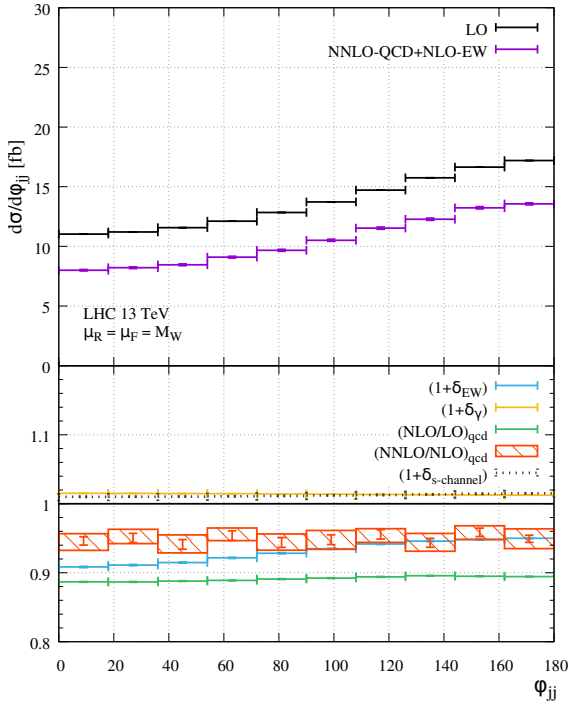

Figure 37: Distribution in the azimuthal-angle difference of the first two leading jets in VBF at LO and including NNLO QCD and NLO EW corrections (upper plots) and various relative contributions (lower plots) for $\sqrt{s} = 13$ TeV and $M_{\mathrm{H}} = 125$ GeV.

this contribution is enhanced at the lower ends of the spectra. Tightening the VBF cuts at theses ends, would further suppress the impact of $\sigma_{s-\text{channel}}$, but reduce the signal at the same time. As an alternative to decreasing $\sigma_{s-\text{channel}}$, a veto on subleading jet pairs with invariant masses around M_W or M_Z may be promising. Such a veto, most likely, would reduce the photon-induced contribution δ_γ, and thus the corresponding uncertainty, as well.

The theoretical uncertainties of differential cross sections originating from unknown higher-order EW effects can be estimated by

$$\Delta_\text{EW} = \max\{1\%, \delta^2_\text{EW}, \sigma_\gamma/\sigma^\text{VBF}\}, \tag{I.5.8}$$

i.e. Δ_EW is taken somewhat more conservative than for integrated cross sections, accounting for possible enhancements of higher-order effects due to a kinematical migration of events in distributions. Note that δ^2_EW, in particular, covers the known effect of enhanced EW corrections at high momentum transfer (EW Sudakov logarithms, etc.). As discussed for integrated cross sections in the previous section, the large uncertainty of the current photon PDF forces us to include the full contribution σ_γ in the EW uncertainties. While the photon-initiated contribution obtained with NNPDF2.3QED or MRST2004QED is currently affected by large PDF uncertainties, it should be noted that those uncertainties are considerably reduced when the more recent LUXqed_plus_PDF4LHC15_nnlo_100 PDF set is instead employed [280].

I.5.2 VH cross-section predictions

I.5.2.a Programs and tools for VH

I.5.2.a.i HAWK

HAWK [254, 255] is a parton-level event generator for Higgs boson production in vector-boson fusion [256, 257], $\text{pp} \to \text{H}jj$, and Higgs-strahlung [258], $\text{pp} \to \text{H}V \to \text{H} + 2\,\text{leptons}$ (with $V = \text{W}, \text{Z}$). Here we summarize its most important features for the VH channel.

HAWK calculates the complete NLO QCD and EW corrections to the processes $\text{pp} \to \text{WH} \to \nu_l\, l\, \text{H}$ and $\text{pp} \to \text{ZH} \to l^- l^+ \text{H}/\nu_l \bar{\nu}_l \text{H}$, i.e. the leptonic decays and all off-shell effects of the W/Z bosons are included. The Higgs boson can be taken as on-shell or off-shell (with optional decay into a pair of gauge singlets). The EW corrections include also the contributions from photon-induced channels, but gluon-fusion contributions ($\text{gg} \to \text{ZH}$) are not taken into account. External fermion masses are neglected, and the renormalization and factorization scales are set to $M_V + M_\text{H}$ ($V = \text{W}, \text{Z}$) by default. Since version 2.0, HAWK includes anomalous Higgs-boson–vector-boson couplings.

I.5.2.a.ii MadGraph5_aMC@NLO

Similar to the generation of any generic process, also Higgs boson production in association with a vector boson can be generated automatically with MADGRAPH5_AMC@NLO. At the NLO QCD accuracy, multiple jets can also be included using the FxFx merging technique [206]. In Ref. [54] the example of $\text{H}\,\text{e}^+\nu_\text{e} + 0, 1$ jets has been presented, and adding a further jet at the NLO is feasible with a small-scale cluster. The situation is entirely similar for the case of ZH (possibly plus jet) production. The commands to generate the corresponding codes are

```
import model loop_sm-no_b_mass
define l+ = e+ mu+ ta+
define l- = e- mu- ta-
define vl~ = ve~ vm~ vt~
define vl = ve vm vt
generate p p > h l+ l- [QCD] @0
add process p p > h l+ vl [QCD] @0
add process p p > h l- vl [QCD] @0
add process p p > h l+ l- j [QCD] @1
```

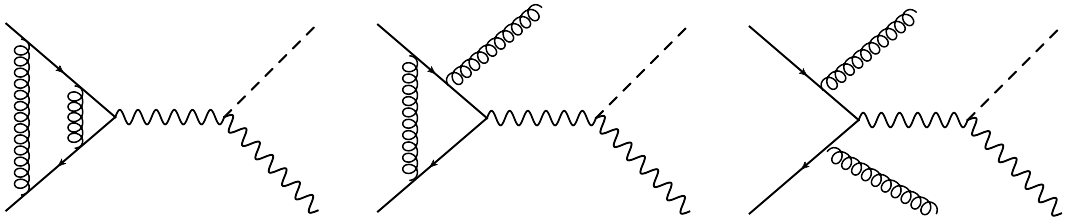

Figure 38: Drell–Yan-like production modes for the associated production of a Higgs boson. Shown are representative Feynman diagrams needed to compute the $\mathcal{O}(\alpha_s^2)$ corrections to the process. Examples are shown for each of the 0-, 1-, and 2-parton phase-space configurations.

```
add process p p > h l+ vl j [QCD] @1
add process p p > h l- vl~ j [QCD] @1
add process p p > h l+ l- j j [QCD] @2
add process p p > h l+ vl j j [QCD] @2
add process p p > h l- vl~ j j [QCD] @2
output VH-MG5_aMC
```

The first command loads a five-flavour scheme model (the MG5_aMC default uses a four-flavour scheme model), which sets the b-quark mass to zero and includes it in the definition of the `p` and `j` multi-particle labels. The next four commands define the multi-particle labels for the leptons and neutrinos used in the `generate` and `add process` commands. After writing the code to disk (with the `output` command) the event generation can be started by executing the command `launch`. The FxFx merging algorithm is available when matching to HERWIG6, PYTHIA8, or HERWIG++ partons showers [206, 281], and can be turned on by setting the `ickkw` parameter to `3` in the file run_card.dat.

I.5.2.a.iii MCFM

The calculation is performed at NNLO QCD and includes the decays of the unstable Higgs and vector bosons. We also include all $\mathcal{O}(\alpha_s^2)$ contributions that occur in production for these processes: those mediated by the exchange of a single off-shell vector boson in the s-channel, and those which arise from the coupling of the Higgs boson to a closed loop of fermions.

Examples of diagrams that contribute at NNLO QCD are shown in Figs. 38 and 39. The first type of contributions has the same structure as single vector-boson production, c.f. Figure 38. Diagrams of the second type, shown in Figure 39, all contain a closed loop of fermions and, in general, represent the Higgs boson coupling directly to a heavy quark (predominantly a top-quark). Note that some of the contributions shown in Figure 39 only occur for the case of ZH production and, for the $\mathrm{gg} \to \mathrm{ZH}$ contributions, not all diagrams are proportional to the top-quark Yukawa coupling. Each of these contributions results in NNLO QCD corrections at the few per cent level for typical cuts, so that inclusion of them all is necessary in order to obtain sufficient theoretical control of this process. A further complication is the inclusion of decays of the Higgs boson into bottom quarks, which we consider. Our calculation also includes the significant impact of NLO QCD corrections in this decay, using the factorized approach described in Refs. [282, 283]. This method takes advantage of improved descriptions of the total decay rate that are available in the HDECAY code [69]. The assembly of a complete calculation at NNLO QCD requires the regularization of infrared singularities, which we handle using the recently-developed "jettiness subtraction" procedure [183, 284–286] that has been implemented in the Monte Carlo program MCFM [287–289]. A detailed description of our calculation can be found in Ref. [290].

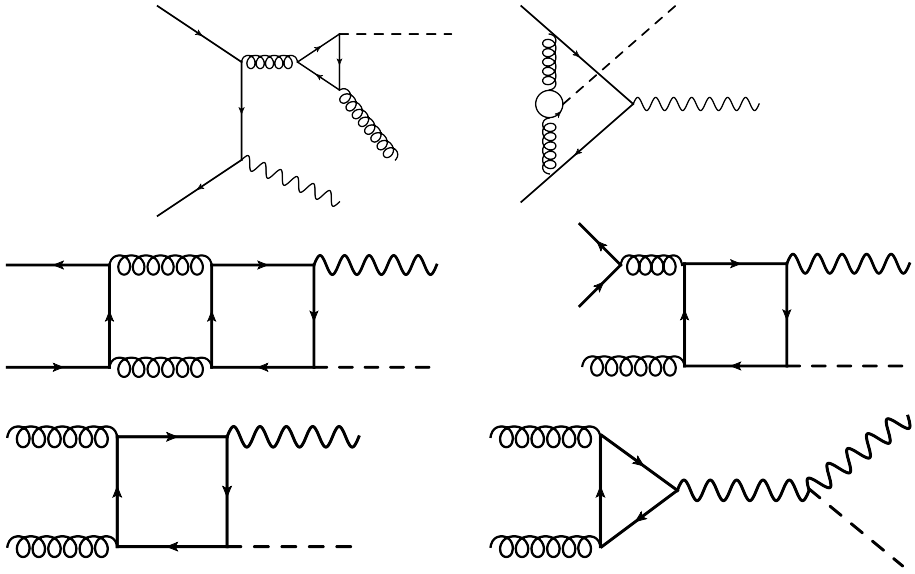

Figure 39: Diagrams representing associated production of a Higgs boson that are sensitive to the top Yukawa coupling y_t. The topologies indicated in the top line occur for either WH or ZH production and interfere with the LO amplitude. The remaining topologies only occur for ZH production. The $gg \to ZH$ contribution represented in the bottom line is not proportional to y_t, as can be seen from the examples on the left (y_t-dependent) and right (no y_t).

I.5.2.a.iv VHNNLO

VHNNLO [282,283,291] is a parton level program for the calculation of fully differential cross sections for $pp \to WH$ and $pp \to ZH$ including up to second order QCD corrections and the decays of the weak bosons to leptons and of the Higgs boson to bottom quarks.

I.5.2.a.v VH@NNLO

VH@NNLO [292, 293] calculates the total inclusive cross section for $pp \to WH$ and $pp \to ZH$ production, including all available QCD corrections through $\mathcal{O}(\alpha_s^2)$, i.e. NNLO.[I.26] Specifically, these are the Drell–Yan-like terms (see Figure 38), given by the process $q\bar{q} \to HV$ (with $V = W, Z$) plus radiative corrections due to virtual and real gluon and/or quark radiation [294, 295], as well as terms involving closed top or bottom loops (see Figure 39). For the latter, we distinguish those that interfere with the lowest-order $q\bar{q} \to HV(g)$ (with $V = W, Z$) amplitude (plus crossings) and which we simply denote as "top-loop" terms $\sigma_{\text{t-loop}}$ [296], and the $gg \to HZ$ process [295, 297–299]. VH@NNLO also includes the NLO corrections for this latter process, which are of order α_s^3 [300]. The NLO+NLL corrections for that process quoted below are not yet included in VH@NNLO [301].

I.5.2.b VH parameters and cuts

The numerical results presented in the next section have been computed using the values of the EW parameters given in Chapter I.1. The electromagnetic coupling is fixed in the G_F scheme,

$$\alpha_{G_F} = \sqrt{2} G_F M_W^2 (1 - M_W^2/M_Z^2)/\pi, \tag{I.5.9}$$

and the weak mixing angle is defined in the on-shell scheme,

$$\sin^2 \theta_w = 1 - M_W^2/M_Z^2. \tag{I.5.10}$$

[I.26] Large parts of VH@NNLO are taken over from ZWPROD by W. van Neerven [294].

In the calculation of the QCD-based cross sections, the renormalization and factorization scales are set equal to the invariant mass of the VH system,

$$\mu = \mu_{\mathrm{R}} = \mu_{\mathrm{F}} = M_{\mathrm{VH}}, \quad M_{VH}^2 \equiv (p_V + p_{\mathrm{H}})^2, \tag{I.5.11}$$

and both scales are varied independently in the range $M_{VH}/3 < \mu < 3M_{VH}$. The PDFs are taken from the set PDF4LHC15_nnlo_mc PDFs.

For the calculation of the EW corrections we employed the NNPDF2.3QED PDF set [279], which includes EW corrections and a photon PDF. For the calculation of photon-induced contributions to the cross sections with a realistic error estimate we took into account the photon PDF of the MRST2004QED PDF set [302] as well. A considerable reduction in the photon PDF uncertainty can be achieved by using the more recent LUXqed_plus_PDF4LHC15_nnlo_100 PDF set [280].

Note, however, that the relative EW correction factor, which is used in the following, hardly depends on the PDF set, so that the uncertainty due to the mismatch in the PDF selection is easily covered by the other remaining theoretical uncertainties. Moreover, the EW corrections show a very small dependence on the factorization scale, so that the use of $\mu_{\mathrm{F}} = M_V + M_{\mathrm{H}}$ is acceptable,[I.27] although full consistency would require to use equal QCD and QED factorization scales.

For the fiducial cross section and for differential distributions the following reconstruction scheme and cuts have been applied. Jets are constructed according to the anti-k_{T} algorithm [191] with $D = 0.4$, using the default recombination scheme (E scheme). Jets are constructed from partons j with

$$|\eta_j| < 5\,, \tag{I.5.12}$$

where y_j denotes the rapidity of the (massive) jet. In the presence of phase-space cuts and in the generation of differential distributions, the treatment of real photons, which appear as part of the NLO EW corrections, has to be specified. In the following we assume perfect isolation of photons from leptons.[I.28] The charged leptons l have to pass the following acceptance cuts,

$$p_{\mathrm{T}l} > 15\ \mathrm{GeV}, \qquad |y_l| < 2.5\,. \tag{I.5.13}$$

For ZH production with $\mathrm{Z} \to \ell^+\ell^-$ the invariant mass of the two leptons should further concentrate around the Z pole,

$$75\ \mathrm{GeV} < M_{ll} < 105\ \mathrm{GeV}. \tag{I.5.14}$$

While the ZH cross sections are independent from the CKM matrix, quark mixing has some effect on WH production. For the calculation of the latter we employed a Cabbibo-like CKM matrix (i.e. without mixing to the third quark generation) with Cabbibo angle θ_{C} fixed by $\sin\theta_{\mathrm{C}} = 0.225$. Moreover, we note that we employ complex W- and Z-boson masses in the calculation of the EW corrections in the standard HAWK approach, as described in Ref. [258].

The Higgs boson is treated as on-shell particle in the following consistently, since its finite-width and off-shell effects in the signal region are suppressed in the Standard Model.

I.5.2.c Total VH cross sections

Tables 27 and 28 summarize the total Standard Model $\mathrm{W}^{\pm}\mathrm{H}$ cross sections with $\mathrm{W}^+ \to l^+\nu_l$ and $\mathrm{W}^- \to l^-\bar{\nu}_l$ as well as the corresponding uncertainties for different proton–proton collision energies for a Higgs boson mass $M_{\mathrm{H}} = 125$ GeV. Tables 29 and 30 likewise show the respective results on the total Standard Model ZH cross sections with $\mathrm{Z} \to \ell^+\ell^-$ and $\mathrm{Z} \to \nu\bar{\nu}$ (summed over three neutrino generations).

[I.27] In its present version, HAWK does not support dynamical scales.

[I.28] Perfect isolation to some extent applies to muons going out into the muon chamber. A simulation of radiation off electrons requires some recombination of collinear electron–photon pairs, mimicking the inclusive treatment of electrons within electromagnetic showers in the detector. The two different treatments were compared in Ref. [258], revealing differences at the 1% level for the relevant physical observables.

Table 27: Total $\mathrm{W}^+(\to l^+\nu_l)\mathrm{H}$ cross sections including QCD and EW corrections and their uncertainties for different proton–proton collision energies $\sqrt{s}$ for a Higgs boson mass $M_\mathrm{H} = 125$ GeV.

$\sqrt{s}$[GeV]	σ[fb]	Δ_scale[%]	$\Delta_{\mathrm{PDF}/\alpha_\mathrm{s}/\mathrm{PDF}\oplus\alpha_\mathrm{s}}$[%]	$\sigma^\mathrm{DY}_\mathrm{NNLOQCD}$[fb]	$\sigma_\text{t-loop}$[fb]	δ_EW[%]	σ_γ[fb]
7	40.99	$^{+0.7}_{-0.9}$	$\pm 1.9/\pm 0.7/\pm 2.0$	42.78	0.42	-7.2	$0.88^{+1.10}_{-0.10}$
8	49.52	$^{+0.6}_{-0.9}$	$\pm 1.8/\pm 0.8/\pm 2.0$	51.56	0.53	-7.3	$1.18^{+1.38}_{-0.14}$
13	94.26	$^{+0.5}_{-0.7}$	$\pm 1.6/\pm 0.9/\pm 1.8$	97.18	1.20	-7.4	$3.09^{+3.33}_{-0.37}$
14	103.63	$^{+0.3}_{-0.8}$	$\pm 1.5/\pm 0.9/\pm 1.8$	106.65	1.36	-7.4	$3.55^{+3.72}_{-0.43}$

Table 28: Total $\mathrm{W}^-(\to l^-\bar{\nu}_l)\mathrm{H}$ cross sections including QCD and EW corrections and their uncertainties for different proton–proton collision energies $\sqrt{s}$ for a Higgs boson mass $M_\mathrm{H} = 125$ GeV.

$\sqrt{s}$[GeV]	σ[fb]	Δ_scale[%]	$\Delta_{\mathrm{PDF}/\alpha_\mathrm{s}/\mathrm{PDF}\oplus\alpha_\mathrm{s}}$[%]	$\sigma^\mathrm{DY}_\mathrm{NNLOQCD}$[fb]	$\sigma_\text{t-loop}$[fb]	δ_EW[%]	σ_γ[fb]
7	23.04	$^{+0.6}_{-0.8}$	$\pm 2.2/\pm 0.6/\pm 2.3$	23.98	0.24	-7.0	$0.51^{+0.69}_{-0.05}$
8	28.62	$^{+0.6}_{-0.8}$	$\pm 2.1/\pm 0.6/\pm 2.1$	29.71	0.31	-7.1	$0.70^{+0.94}_{-0.07}$
13	59.83	$^{+0.4}_{-0.7}$	$\pm 1.8/\pm 0.8/\pm 2.0$	61.51	0.78	-7.3	$2.00^{+2.34}_{-0.22}$
14	66.49	$^{+0.5}_{-0.6}$	$\pm 1.7/\pm 0.9/\pm 1.9$	68.24	0.89	-7.3	$2.32^{+2.65}_{-0.26}$

Table 29: Total ZH cross sections with $\mathrm{Z} \to \ell^+\ell^-$ including QCD and EW corrections and their uncertainties for different proton–proton collision energies $\sqrt{s}$ for a Higgs boson mass $M_\mathrm{H} = 125$ GeV.

$\sqrt{s}$[GeV]	σ[fb]	Δ_scale[%]	$\Delta_{\mathrm{PDF}/\alpha_\mathrm{s}/\mathrm{PDF}\oplus\alpha_\mathrm{s}}$[%]	$\sigma^\mathrm{DY}_\mathrm{NNLOQCD}$[fb]	$\sigma^\mathrm{ggZH}_\mathrm{NLO+NLL}$[fb]	$\sigma_\text{t-loop}$[fb]	δ_EW[%]	σ_γ[fb]
7	11.43	$^{+2.6}_{-2.4}$	$\pm 1.6/\pm 0.7/\pm 1.7$	10.91	0.94	0.11	-5.2	$0.03^{+0.04}_{-0.00}$
8	14.18	$^{+2.9}_{-2.4}$	$\pm 1.5/\pm 0.8/\pm 1.7$	13.36	1.33	0.14	-5.2	$0.04^{+0.05}_{-0.00}$
13	29.82	$^{+3.8}_{-3.1}$	$\pm 1.3/\pm 0.9/\pm 1.6$	26.66	4.14	0.31	-5.3	$0.11^{+0.12}_{-0.01}$
14	33.27	$^{+3.8}_{-3.3}$	$\pm 1.3/\pm 1.0/\pm 1.6$	29.47	4.87	0.36	-5.3	$0.12^{+0.13}_{-0.01}$

Table 30: Total ZH cross sections with $\mathrm{Z} \to \nu\bar{\nu}$ (summed over three neutrino generations) including QCD and EW corrections and their uncertainties for different proton–proton collision energies $\sqrt{s}$ for a Higgs boson mass $M_\mathrm{H} = 125$ GeV.

$\sqrt{s}$[GeV]	σ[fb]	Δ_scale[%]	$\Delta_{\mathrm{PDF}/\alpha_\mathrm{s}/\mathrm{PDF}\oplus\alpha_\mathrm{s}}$[%]	$\sigma^\mathrm{DY}_\mathrm{NNLOQCD}$[fb]	$\sigma^\mathrm{ggZH}_\mathrm{NLO+NLL}$[fb]	$\sigma_\text{t-loop}$[fb]	δ_EW[%]	σ_γ[fb]
7	68.18	$^{+2.6}_{-2.4}$	$\pm 1.6/\pm 0.7/\pm 1.7$	64.70	5.59	0.64	-4.3	-0.00
8	84.56	$^{+2.9}_{-2.4}$	$\pm 1.5/\pm 0.8/\pm 1.7$	79.25	7.89	0.81	-4.3	-0.00
13	177.62	$^{+3.8}_{-3.1}$	$\pm 1.3/\pm 0.9/\pm 1.6$	158.10	24.57	1.85	-4.4	-0.00
14	198.12	$^{+3.8}_{-3.3}$	$\pm 1.3/\pm 1.0/\pm 1.6$	174.77	28.88	2.11	-4.4	-0.00

The total VH cross sections σ^{VH} are calculated according to

$$\sigma^{\mathrm{WH}} = \sigma^{\mathrm{WH,DY}}_{\mathrm{NNLOQCD}}(1+\delta_{\mathrm{EW}}) + \sigma_{\text{t-loop}} + \sigma_{\gamma}, \tag{I.5.15}$$

$$\sigma^{\mathrm{ZH}} = \sigma^{\mathrm{ZH,DY}}_{\mathrm{NNLOQCD}}(1+\delta_{\mathrm{EW}}) + \sigma_{\text{t-loop}} + \sigma_{\gamma} + \sigma^{\mathrm{ggZH}}, \tag{I.5.16}$$

where $\sigma^{\mathrm{VH,DY}}_{\mathrm{NNLOQCD}}$ is the Drell–Yan-like part of the NNLO QCD prediction for the VH cross section, based on the calculation of Ref. [295] with NNLO PDFs. Since we include the leptonic decays of the W/Z bosons, we multiply the cross sections from VH@NNLO with the branching ratios

$$\mathrm{BR}_{\mathrm{LO}}(\mathrm{W}\to\ell\nu_\ell) = 0.108894, \quad \mathrm{BR}_{\mathrm{LO}}(\mathrm{Z}\to\ell^+\ell^-) = 0.0335950, \quad \mathrm{BR}_{\mathrm{LO}}(\mathrm{Z}\to\nu\bar{\nu}) = 0.199218, \tag{I.5.17}$$

which are the ratios of the LO partial widths and the total widths as defined in Chapter I.1. With these branching ratios our combination of QCD and EW corrections results in NNLO QCD + NLO EW accuracy. The relative NLO EW correction δ_{EW} is calculated with HAWK. Note that there is no issue with photon isolation in the calculation of the total cross section, where all mass singularities from collinear photon emission off leptons vanish owing to the KLN theorem. The contributions from photon-induced channels, σ_γ are obtained from HAWK as well and added linearly to the cross section. It is important to notice that σ_γ is based on the average of the median of the cross sections obtained with PDF replicas of NNPDF2.3QED PDFs and the cross section obtained with MRST2004QED PDFs "set 1". The lower error corresponds to the lower limit of all NNPDF2.3QED PDFs, the upper error to the maximum of the 68% smallest cross sections from the NNPDF2.3QED set and the cross section obtained with MRST2004QED "set 0". Since the photon PDF is constrained by data rather loosely, the error on σ_γ is large and non-Gaussian. In fact the mean value of σ_γ calculated with NNPDF2.3QED PDF replicas is larger than the shown median by factors $\sim 2-2.5$.

The contribution σ^{ggZH} of the gluon-fusion channel is calculated through NLO using VH@NNLO [292, 293, 300]; the NLL effects are added on top of that, following Ref. [301]. The scale uncertainty Δ_{scale} results from a variation of the factorization and renormalization scales (I.5.11) by a factor of 3, as indicated above. The errors Δ_{PDF} and $\Delta_{\alpha_\mathrm{s}}$ induced by uncertainties in the PDFs and α_s, respectively, are given separately together with the combined version $\Delta_{\mathrm{PDF}\oplus\alpha_\mathrm{s}}$, which is calculated from the 68% CL interval using the PDF4LHC15_nnlo_mc PDF set. The Δ_{scale} and $\Delta_{\mathrm{PDF}\oplus\alpha_\mathrm{s}}$ are evaluated without taking into account EW effects.

The theoretical uncertainties of integrated cross sections originating from unknown higher-order EW effects can be estimated by

$$\Delta_{\mathrm{EW}} = \max\{0.5\%, \delta^2_{\mathrm{EW}}, \Delta_\gamma\}. \tag{I.5.18}$$

This estimate is based on the maximum of the generic size $\sim 0.5\%$ of the neglected NNLO EW effects, taking into account a possible systematic enhancement $\sim \delta^2_{\mathrm{EW}}$, and the potentially large relative uncertainty $\Delta_\gamma = \Delta\sigma_\gamma/\sigma$ of the photon-induced contribution σ_γ, whose absolute uncertainty $\Delta\sigma_\gamma$ can be read from the tables.

In order to extract the total VH production cross sections without leptonic W/Z decays in NNLO QCD + NLO EW accuracy (neglecting off-shell effects), one should divide the results on total cross sections by the respective leptonic W/Z branching ratios in NLO EW accuracy. These are given by

$$\mathrm{BR}_{\mathrm{NLO}}(\mathrm{W}\to\ell\nu_\ell) = 0.108535, \quad \mathrm{BR}_{\mathrm{NLO}}(\mathrm{Z}\to\ell^+\ell^-) = 0.0335962, \quad \mathrm{BR}_{\mathrm{NLO}}(\mathrm{Z}\to\nu\bar{\nu}) = 0.201030, \tag{I.5.19}$$

calculated from the ratios of the NLO partial widths (calculated in the HAWK setup) and the total widths as defined in Chapter I.1. In this extraction, one should subtract the photon-induced contributions σ_γ from the cross sections before dividing through the branching ratio, since σ_γ receives a significant contribution from incoming photons coupling to the charged leptons of the W or Z decays. Thus, $\sigma_\gamma/\mathrm{BR}$ is an uncertainty of the resulting VH cross section, which is quite significant in the WH case.

Table 31: Fiducial $\mathrm{W}^+(\to l^+\nu_l)\mathrm{H}$ cross sections including QCD and EW corrections and their uncertainties for proton–proton collisions at $\sqrt{s} = 13\mathrm{TeV}$ for a Higgs boson mass $M_\mathrm{H} = 125$ GeV.

$\sqrt{s}$[GeV]	σ[fb]	Δ_scale[%]	Δ_PDF[%]	$\sigma^\mathrm{DY}_\mathrm{NNLOQCD}$[fb]	δ_EW[%]	σ_γ[fb]
13	73.90	$^{+0.3}_{-0.3}$	± 1.4	78.61	-8.3	$1.81^{+1.10}_{-0.23}$

Table 32: Fiducial $\mathrm{W}^-(\to l^-\bar{\nu}_l)\mathrm{H}$ cross sections including QCD and EW corrections and their uncertainties for proton–proton collisions at $\sqrt{s} = 13\mathrm{TeV}$ for a Higgs boson mass $M_\mathrm{H} = 125$ GeV.

$\sqrt{s}$[GeV]	σ[fb]	Δ_scale[%]	Δ_PDF[%]	$\sigma^\mathrm{DY}_\mathrm{NNLOQCD}$[fb]	δ_EW[%]	σ_γ[fb]
13	42.77	$^{+0.2}_{-0.3}$	± 1.8	45.29	-8.0	$1.11^{+0.65}_{-0.12}$

Table 33: Fiducial ZH cross sections with $\mathrm{Z} \to \ell^+\ell^-$ including QCD and EW corrections and their uncertainties for proton–proton collisions at $\sqrt{s} = 13\mathrm{TeV}$ for a Higgs boson mass $M_\mathrm{H} = 125$ GeV.

$\sqrt{s}$[GeV]	σ[fb]	Δ_scale[%]	Δ_PDF[%]	$\sigma^\mathrm{DY}_\mathrm{NNLOQCD}$[fb]	σ^ggZH[fb]	δ_EW[%]	σ_γ[fb]
13	16.08	$^{+2.2}_{-1.4}$	± 1.2	16.21	1.36	-9.2	0.00

Results for the total VH cross sections from a scan over the SM Higgs boson mass M_H can be found in Appendix D. In detail the total cross sections for the production of $\mathrm{W}^+(\to\ell^+\nu_\ell)\mathrm{H}$, $\mathrm{W}^-(\to\ell^-\bar{\nu}_\ell)\mathrm{H}$, $\mathrm{Z}(\to\ell^+\ell^-)\mathrm{H}$, and $\mathrm{Z}(\to\nu\bar{\nu})\mathrm{H}$ final states are summarized in Tables 207–222. The energy scan is presented in Tables 223–226.

I.5.2.d Fiducial and differential VH cross sections

Tables 31 and 32 summarize the fiducial Standard Model $\mathrm{W}^\pm\mathrm{H}$ cross sections with $\mathrm{W}^+\to l^+\nu_l$ and $\mathrm{W}^-\to l^-\bar{\nu}_l$ as well as the corresponding uncertainties for the proton–proton collision at $\sqrt{s} = 13$ TeV for a Higgs boson mass $M_\mathrm{H} = 125$ GeV. Table 33 likewise shows the respective results on the total Standard Model ZH cross sections with $\mathrm{Z} \to \ell^+\ell^-$. The fiducial cross sections are calculated as follows: For QCD corrections we have used VHNNLO with the NNPDF3.0_nnlo_as_0118 PDF set. Renormalization and factorization scales are varied independently by factors of 2 and $1/2$ including 7 combinations, avoiding the cases $(2, 1/2)$ and $(1/2, 2)$. The envelope is taken as a scale uncertainty to parameterize missing higher-order QCD corrections. A representation of the PDF error for the QCD part in VH production has been obtained with SM-PDF [303] starting from a prior of NNPDF3.0 at NNLO. The SM-PDF derived in [303] for VH processes adopted an analysis very close to the one used here and contains in total five symmetric eigenvectors. The EW corrections are again calculated with HAWK in the same way as described for the total cross section. Moreover, the recipe (I.5.18) for estimating the EW uncertainty Δ_EW applies for the fiducial cross section as well.

The combination of QCD and EW corrections has been done following the same procedure as described in Eqs. (I.5.15) and (I.5.16), as far as the corresponding contributions are available (see tables). The Δ_scale and Δ_PDF are evaluated without taking into account EW effects; the uncertainties of the latter can be estimated again following Eq. (I.5.18).

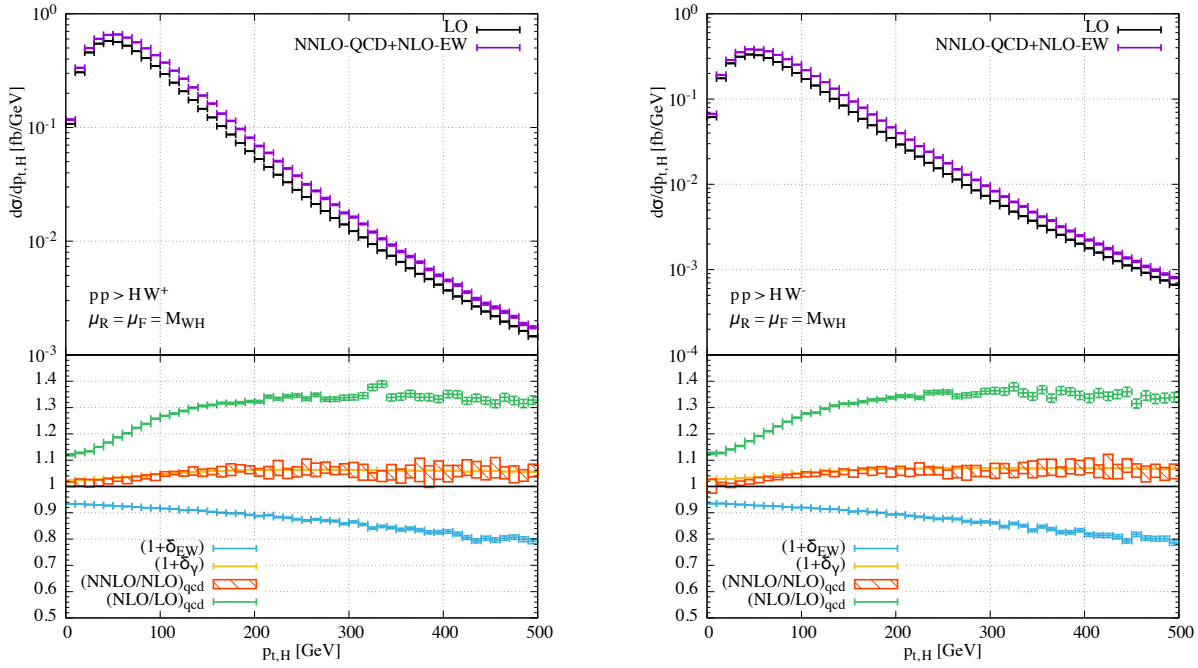

Figure 40: Left: transverse-momentum distributions of the Higgs boson in W^+H production at LO and including NNLO QCD and NLO EW corrections (upper plots) and relative higher-order contributions (lower plots) for $\sqrt{s} = 13$ TeV and $M_H = 125$ GeV. Right: the same for W^-H production. Note that δ_γ is based on the central value of the photon PDF of NNPDF2.3QED, while σ_γ in Tables 27–33 is based on combined results using the median and the photon PDF of MRST2004QED (and smaller by a factor 0.7), see text.

Differential cross section results in NNLO QCD + NLO EW accuracy have been computed following the same procedure as outlined above for the fiducial cross section. QCD corrections are calculated with VHNNLO using the settings reported above for the computation of the fiducial cross sections. The EW corrections are again calculated with HAWK as in the previous section, with the only difference in the calculation of the photon-induced contribution. Instead of working with many PDF replicas we have calculated σ_γ with the central PDF of NNPDF2.3QED. In order to obtain σ_γ in the same setup as for the integrated cross sections of the previous section (for $\sqrt{s} = 13$ TeV), the shown results on σ_γ in WH production should be rescaled by a factor of 0.7. This rescaling is based on the corresponding integrated results for σ_γ. Taking over the relative uncertainty from the integrated cross section as well, we get the estimate $\Delta_\gamma \sim 1.5\%$. For ZH production σ_γ and Δ_γ have a phenomenologically negligible impact.

The theoretical uncertainties of differential cross sections originating from unknown higher-order EW effects can be estimated by

$$\Delta_{\rm EW} = \max\{1\%, \delta^2_{\rm EW}, \Delta_\gamma\}, \tag{I.5.20}$$

i.e. $\Delta_{\rm EW}$ is taken somewhat more conservative than for integrated cross sections, accounting for possible enhancements of higher-order effects due to a kinematical migration of events in distributions. Note that $\delta^2_{\rm EW}$, in particular, covers the known effect of enhanced EW corrections at high momentum transfer (EW Sudakov logarithms, etc.).

Figures 40–44 show the impact of radiative corrections of the most important differential distributions for Higgs boson production via WH mode in the SM, while in Figures 45–47 the same effects are shown for the Higgs boson production in association with a Z boson. The figures generically show the known size of the NLO QCD corrections at the level of $\sim 20-30\%$ in the most important phase-space regions. At NNLO, the QCD corrections amount to some per cent in the dominating regions, but can

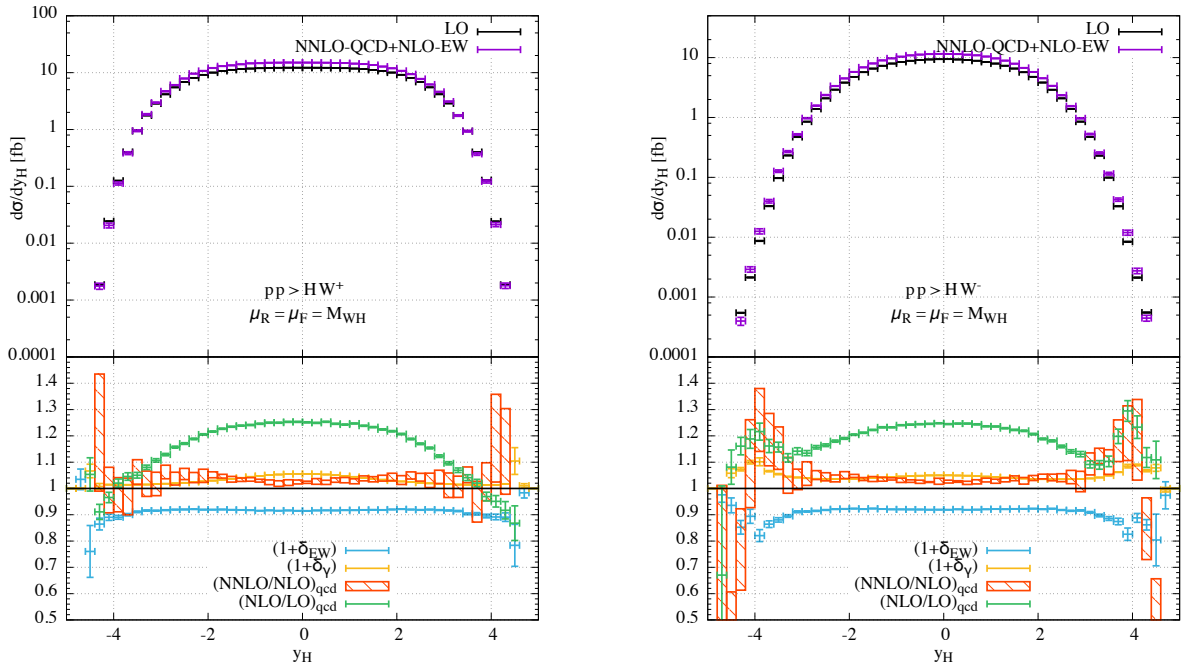

Figure 41: Left: rapidity of the Higgs boson in W^+H production at LO and including NNLO QCD and NLO EW corrections (upper plots) and relative higher-order contributions (lower plots) for $\sqrt{s} = 13$ TeV and $M_H = 125$ GeV. Right: the same for W^-H production. Note that δ_γ is based on the central value of the photon PDF of NNPDF2.3QED, while σ_γ in Tables 27–33 is based on combined results using the median and the photon PDF of MRST2004QED (and smaller by a factor 0.7), see text.

grow to $10-20\%$ in the tails of distributions. In those regions the QCD scale uncertainty accordingly grows to $\sim 5\%$ or more. The EW corrections are generically flat in (pseudo)rapidity distributions, where they resemble the EW corrections to the fiducial cross sections. In transverse-momentum distributions the EW correction grow further negative to $-(10-20)\%$ for p_T of some 100 GeV. The photon-induced corrections turn out to be only significant for WH production. They have a tendency to grow in the tails of distributions as well, but do hardly exceed the 5% level there.

Finally, we emphasize that the contributions $\sigma_{\text{t-loop}}$ are not included in the discussion of fiducial cross sections and differential distributions presented here, while the contribution σ^{ggZH} are included at leading order (α_s^2).

I.5.2.e Cross-section predictions including the decay $H \to b\bar{b}$

We use the Standard Model parameters as recommended by the LHCHXSWG, supplemented by CKM matrix elements $V_{ud} = 0.975$ and $V_{cs} = 0.222$. For the parton distribution functions we use the NNLO CT14 set and associated strong coupling, $\alpha_s(M_Z) = 0.118$ with 3-loop running. Central predictions correspond to the scale choice $\mu_R = \mu_F = \mu_0$ where $\mu_0 = M_V + M_H$ and we consider an envelope of variations around this choice to define the scale uncertainty. For $W^\pm H$ production the extreme choices correspond to $\mu_R = 2\mu_0$, $\mu_F = \mu_0/2$ and $\mu_R = \mu_0/2$, $\mu_F = 2\mu_0$. For ZH production the extrema are instead represented by $\mu_F = \mu_R = 2\mu_0$ and $\mu_F = \mu_R = \mu_0/2$. Our results are obtained for the LHC operating at $\sqrt{s} = 13$ TeV.

We cluster all jets according to the anti-k_T jet algorithm with distance parameter $R = 0.4$. We subsequently require that two of the jets contain the b and $\bar{\text{b}}$ quarks from the Higgs boson decay and that

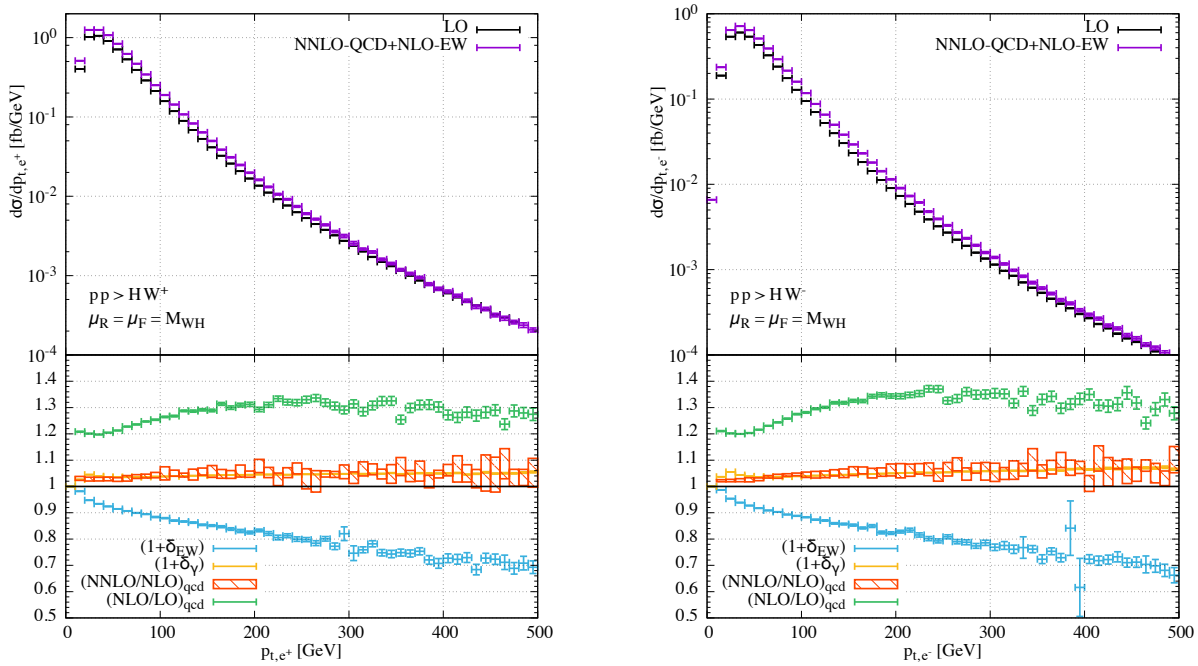

Figure 42: Left: transverse-momentum distribution of the charged lepton in W^+H production at LO and including NNLO QCD and NLO EW corrections (upper plots) and relative higher-order contributions (lower plots) for $\sqrt{s} = 13$ TeV and $M_H = 125$ GeV. Right: the same for W^-H production. Note that δ_γ is based on the central value of the photon PDF of NNPDF2.3QED, while σ_γ in Tables 27–33 is based on combined results using the median and the photon PDF of MRST2004QED (and smaller by a factor 0.7), see text.

these jets satisfy,

$$p_T(\text{b-jet}) > 25 \text{ GeV}, \qquad |\eta(\text{b-jet})| < 2.5\,. \tag{I.5.21}$$

Note that the calculation of the $H \to b\bar{b}$ decay is performed at NLO QCD.

We begin by considering the $W^\pm H$ process, with the W boson decaying to a lepton and a neutrino. The acceptance cuts for the decay products are,

$$p_T(\text{lepton}) > 15 \text{ GeV}, \qquad |\eta(\text{lepton})| < 2.5, \qquad p_T(\text{neutrino}) > 15 \text{ GeV}\,. \tag{I.5.22}$$

The cross sections under these cuts, using NNLO PDFs, are found to be

$$\begin{aligned} \sigma^{\text{NLOQCD}}(W^+H) &= 23.56 \text{ fb}\,, \qquad \sigma^{\text{NNLOQCD}}(W^+H) = 24.18^{+0.36}_{-0.64} \text{ fb}\,, \\ \sigma^{\text{NLOQCD}}(W^-H) &= 15.49 \text{ fb}\,, \qquad \sigma^{\text{NNLOQCD}}(W^-H) = 15.87^{+0.26}_{-0.46} \text{ fb}\,. \end{aligned} \tag{I.5.23}$$

The NNLO QCD corrections under these cuts are small and positive, increasing the NLO QCD cross sections by less than 1%. The scale uncertainty at NNLO QCD is at the 3% level.

For the ZH process we consider the decay of the Z boson into a single family of leptons and apply the cuts,

$$\begin{aligned} &p_T(\text{lepton}) > 15 \text{ GeV}, \qquad |\eta(\text{lepton})| < 2.5, \\ &75 \text{ GeV} < M_{ll} < 105 \text{ GeV}\,. \end{aligned} \tag{I.5.24}$$

These result in the following cross sections,

$$\sigma^{\text{NLOQCD}}(ZH) = 6.041 \text{ fb}\,, \qquad \sigma^{\text{NNLOQCD}}(ZH) = 6.891^{+0.101}_{-0.162} \text{ fb}\,. \tag{I.5.25}$$

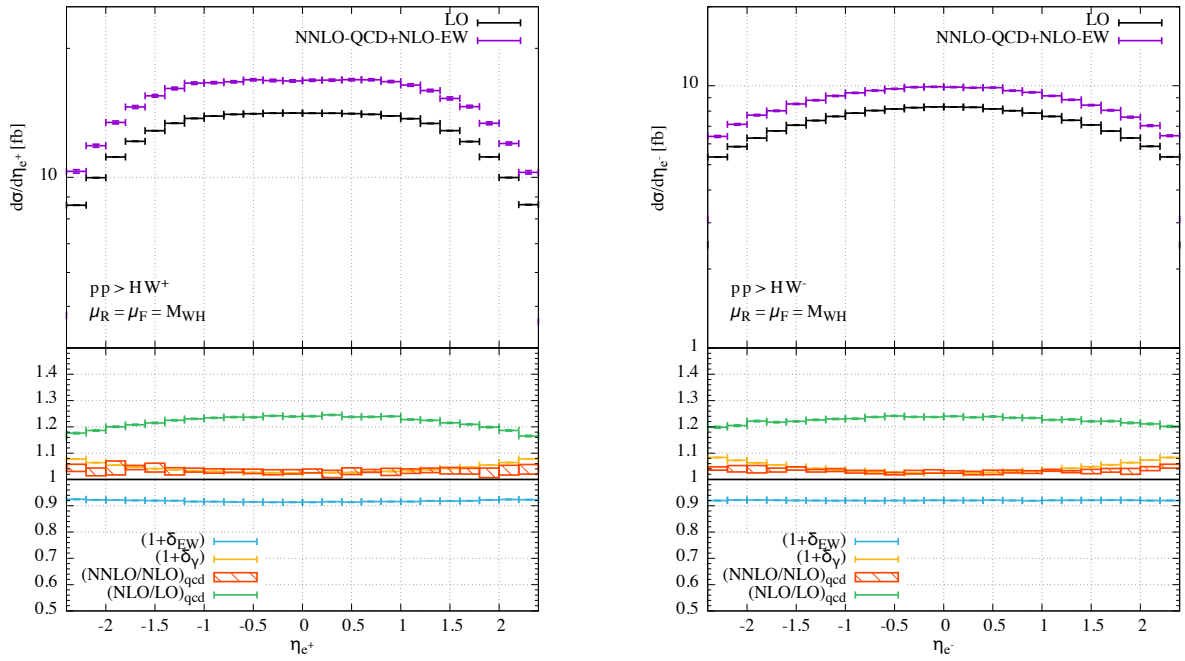

Figure 43: Left: pseudorapidity distribution of the charged lepton in $\mathrm{W}^+\mathrm{H}$ production at LO and including NNLO QCD and NLO EW corrections (upper plots) and relative higher-order contributions (lower plots) for $\sqrt{s} = 13$ TeV and $M_\mathrm{H} = 125$ GeV. Right: the same for $\mathrm{W}^-\mathrm{H}$ production. Note that δ_γ is based on the central value of the photon PDF of NNPDF2.3QED, while σ_γ in Tables 27–33 is based on combined results using the median and the photon PDF of MRST2004QED (and smaller by a factor 0.7), see text.

In this case the NNLO corrections increase the NLO cross section by about 15% and the scale uncertainty at NNLO QCD is around 2%.

Differential predictions for the final state $V(\to l_1 l_2)\mathrm{H}(\to \mathrm{b\bar{b}})$ are presented in Figs. 48-52. For $\mathrm{W}^\pm\mathrm{H}$ production we present the differential observables side-by-side on the same scale, so that the relative suppression of W^- compared to W^+ is readily apparent. Figure 48 presents the p_T of the Higgs boson candidate, whose four-momentum is defined as the sum of those of the identified b-jets. We present predictions for a variety of selection cuts. The red curve corresponds to an "inclusive" p_T^V selection while the remaining curves slice the phase space into various p_T^V bins:

$$\begin{aligned} \text{red:} &\quad p_\mathrm{T}^V \text{ inclusive}\,, \\ \text{blue:} &\quad 0 < p_\mathrm{T}^V < 150 \text{ GeV}\,, \\ \text{green:} &\quad 150 < p_\mathrm{T}^V < 250 \text{ GeV}\,, \\ \text{magenta:} &\quad p_\mathrm{T}^V > 250 \text{ GeV}\,. \end{aligned} \tag{I.5.26}$$

The inclusive curve is thus recovered by summing over all of the remaining curves. At leading order $p_\mathrm{T}^V \equiv p_\mathrm{T}^\mathrm{H}$, with departures from this equality the result of additional radiation that is inherent in the higher-order corrections. The discontinuities that are apparent in the regions of phase space around $p_\mathrm{T}^V = p_\mathrm{T}^\mathrm{H}$, namely at $p_\mathrm{T}^\mathrm{H} = 150, 250$ GeV, are indicators of the fact that perturbation theory is unreliable at such boundaries. The situation is exacerbated by the inclusion of higher-order corrections in the Higgs boson decay, since boundary logarithms also appear due to radiation in the decay [282, 283, 290]. The differences between the $\mathrm{W}^+\mathrm{H}$ and $\mathrm{W}^-\mathrm{H}$ predictions are most clear in the y_H observable (Figure 49). This observable is sensitive to the valence/sea quark distribution inside the proton. The valence u distribution is more favored for $\mathrm{W}^+\mathrm{H}$, and stiffens the y_H distribution by favoring more forward regions of

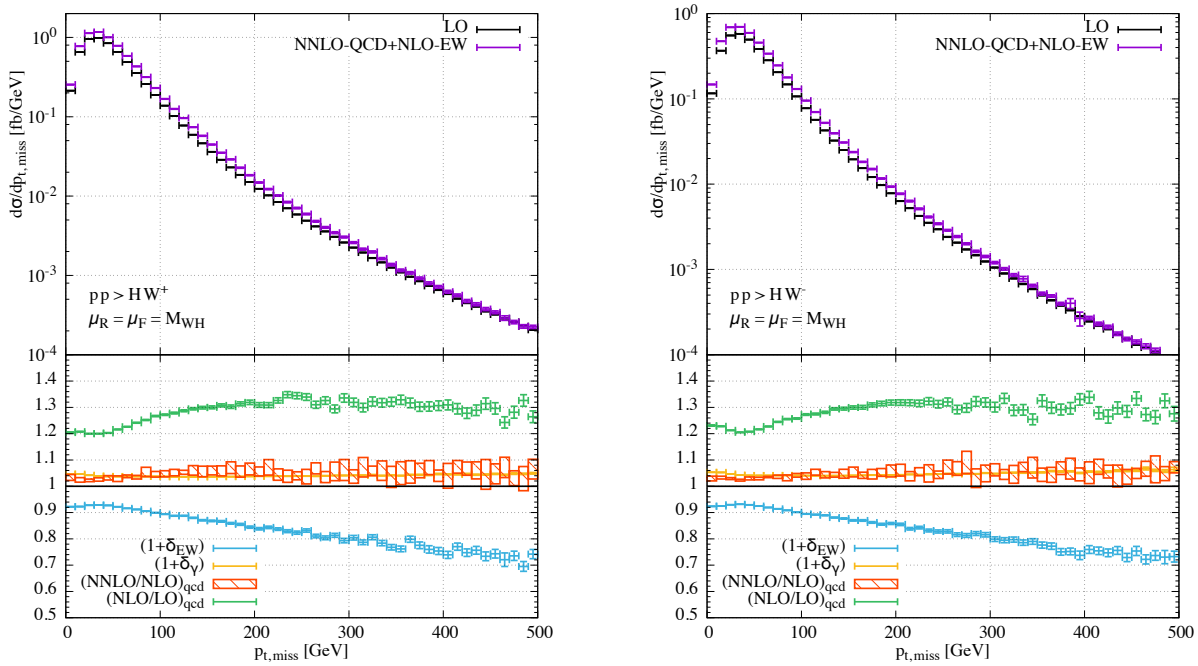

Figure 44: Left: missing transverse momentum in W^+H production at LO and including NNLO QCD and NLO EW corrections (upper plots) and relative higher-order contributions (lower plots) for $\sqrt{s} = 13$ TeV and $M_H = 125$ GeV. Right: the same for W^-H production. Note that δ_γ is based on the central value of the photon PDF of NNPDF2.3QED, while σ_γ in Tables 27–33 is based on combined results using the median and the photon PDF of MRST2004QED (and smaller by a factor 0.7), see text.

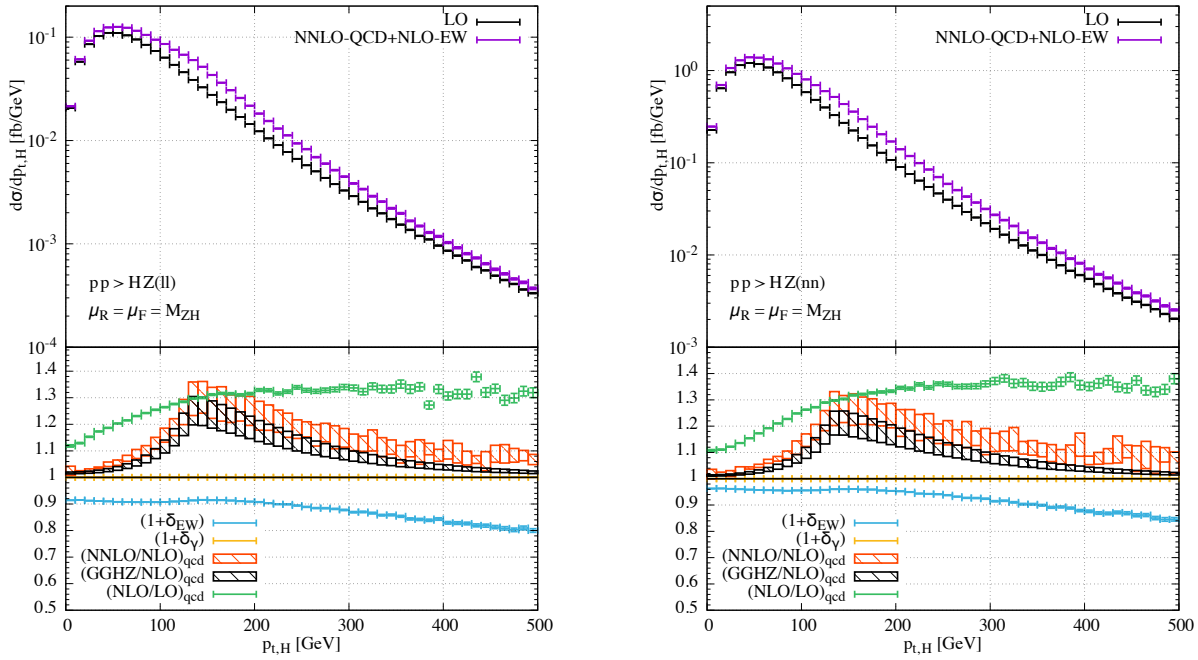

Figure 45: Left: transverse-momentum distributions of the Higgs boson in $Z(\to \ell^+\ell^-)H$ production at LO and including NNLO QCD and NLO EW corrections (upper plots) and relative higher-order contributions (lower plots) for $\sqrt{s} = 13$ TeV and $M_H = 125$ GeV. Right: the same for $Z(\to \nu\bar{\nu})H$ production.

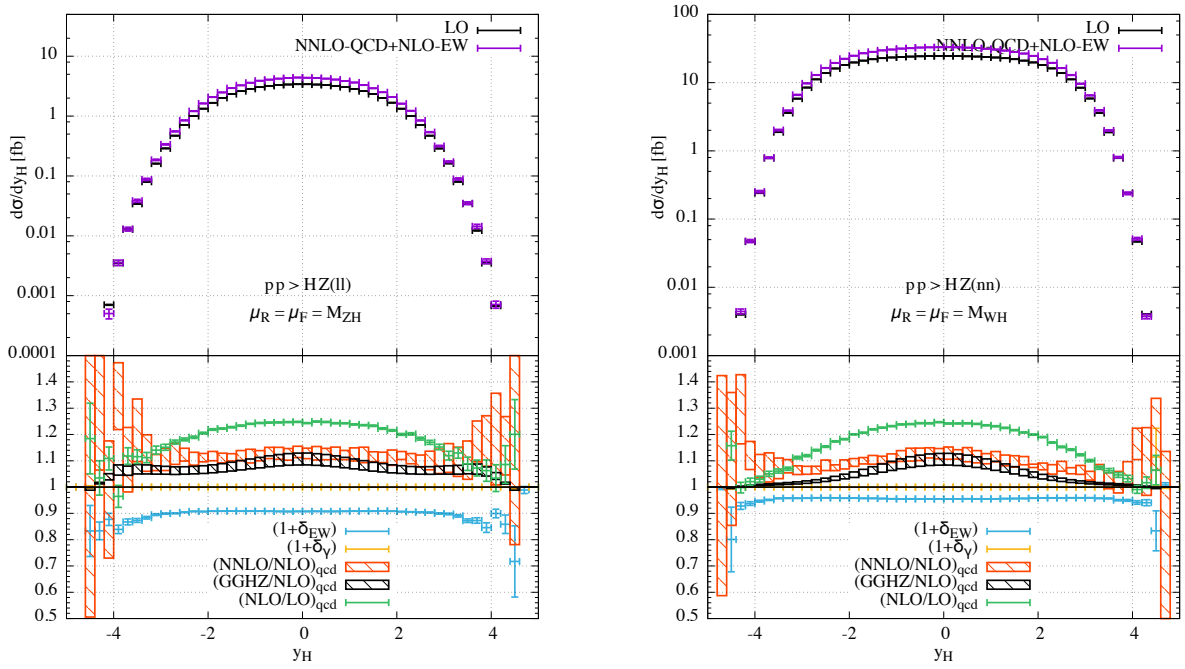

Figure 46: Left: rapidity distributions of the Higgs boson in $\mathrm{Z}(\to l^+l^-)\mathrm{H}$ production at LO and including NNLO QCD and NLO EW corrections (upper plots) and relative higher-order contributions (lower plots) for $\sqrt{s} = 13$ TeV and $M_\mathrm{H} = 125$ GeV. Right: the same for $\mathrm{Z}(\to \nu\bar{\nu})\mathrm{H}$ production.

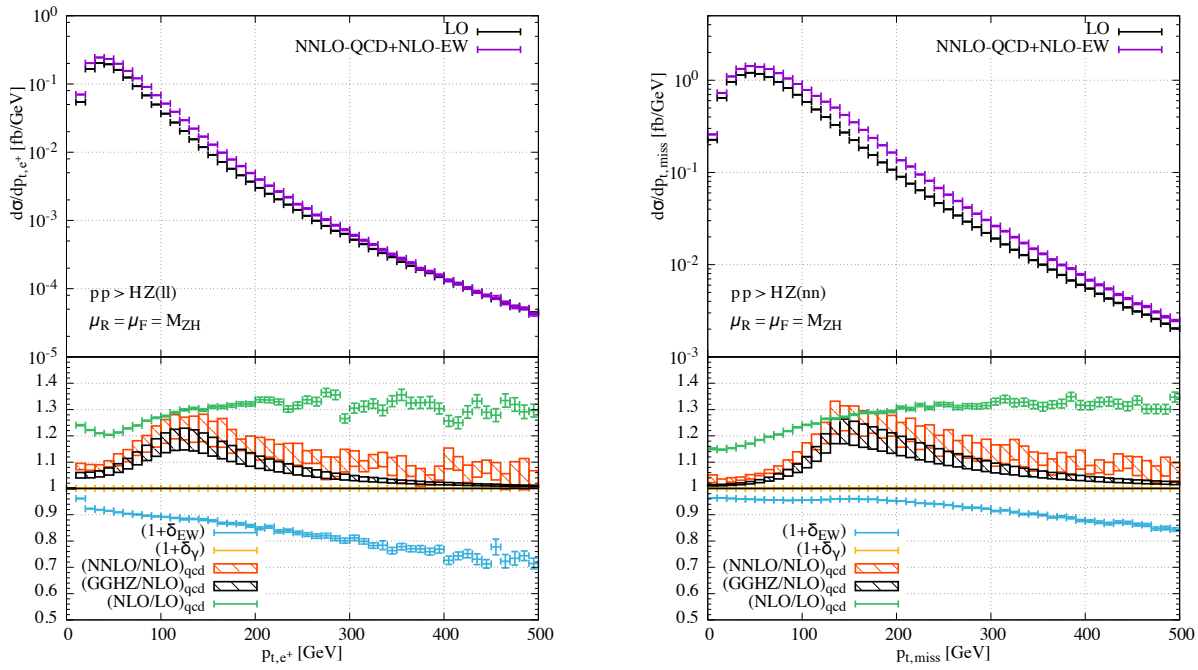

Figure 47: Left: transverse-momentum distributions of the positive charged lepton in $\mathrm{Z}(\to \ell^+\ell^-)\mathrm{H}$ production at LO and including NNLO QCD and NLO EW corrections (upper plots) and relative higher-order contributions (lower plots) for $\sqrt{s} = 13$ TeV and $M_\mathrm{H} = 125$ GeV. Right: the same for the missing-transverse-momentum distribution in $\mathrm{Z}(\to \nu\bar{\nu})\mathrm{H}$ production.

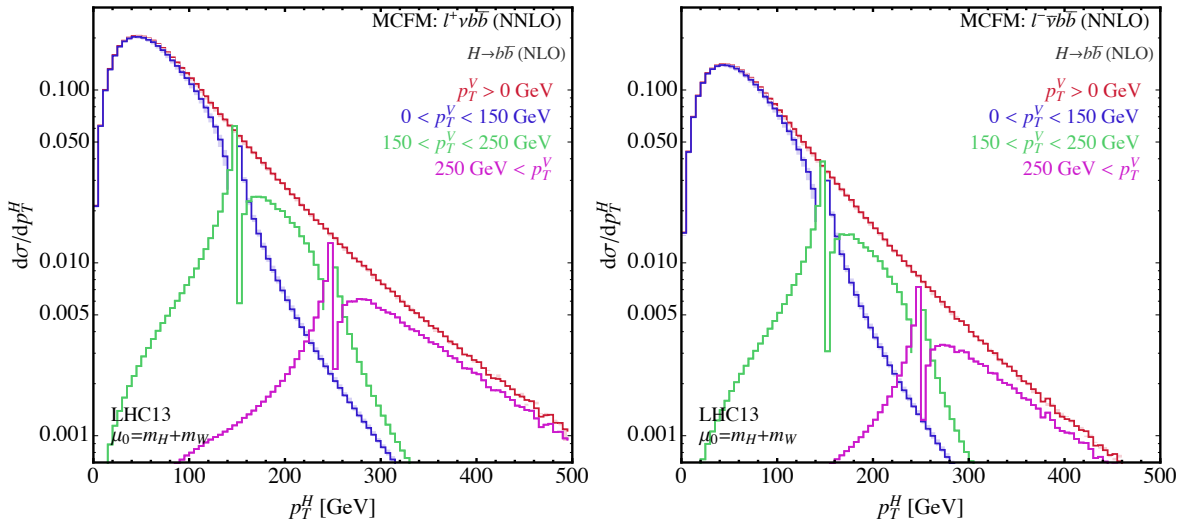

Figure 48: The transverse momentum $p_{\mathrm{T}}^{\mathrm{b\bar{b}}}$ for $\mathrm{W^+H}$ (left) and $\mathrm{W^-H}$ (right) at the 13 TeV LHC, phase space cuts are described in the text.

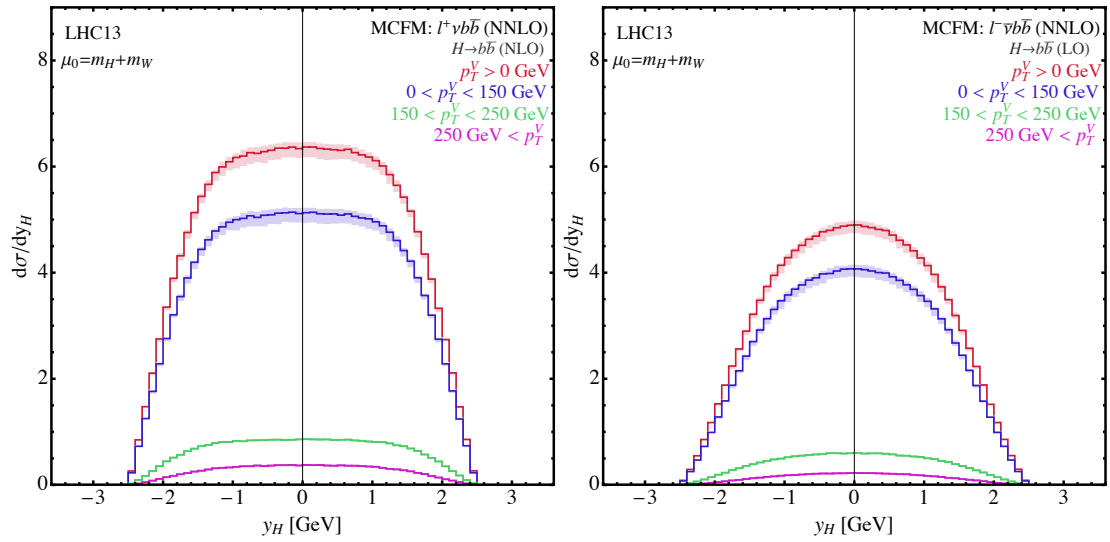

Figure 49: The rapidity of the $\mathrm{b\bar{b}}$ pair for $\mathrm{W^+H}$ (left) and $\mathrm{W^-H}$ (right) at the 13 TeV LHC, phase space cuts are described in the text.

phase space. On the other hand $\mathrm{W^-H}$ production is associated with the production of more central Higgs bosons. We present the leptonic observables in Figure 50. As the p_{T}^V cut is increased the p_{T}^l distribution flattens out. Finally in Figures 51-52 we present the differential predictions for ZH. The conclusions are broadly similar, although the phase-space boundary effects are somewhat damped for this process. This is due to the presence of $\mathrm{gg} \to \mathrm{ZH}$ contributions that provide a sizeable correction to the cross section at NNLO. Since this switches-on in the LO phase space, the large negative bin is partially compensated by the inclusion of these pieces. There is a noticeable inflection in the $p_{\mathrm{T}}^{\mathrm{H}}$ spectrum at around $p_{\mathrm{T}}^{\mathrm{H}} \sim m_t$, which is where these pieces begin to become important.

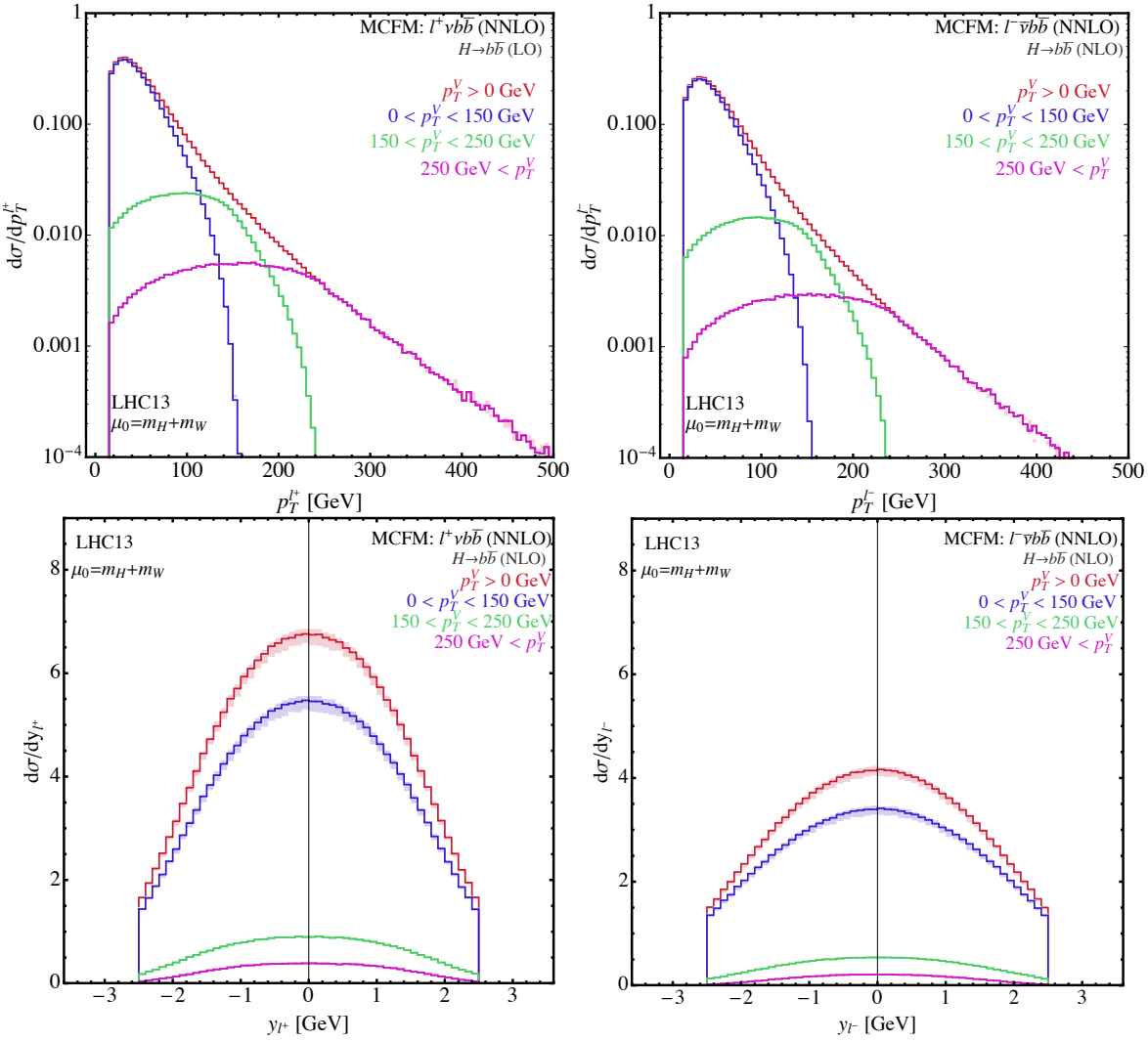

Figure 50: The transverse momentum p_{T}^{l} for $\mathrm{W}^+\mathrm{H}$ (left, upper) and $\mathrm{W}^-\mathrm{H}$ (right, upper) and lepton rapidity $\mathrm{W}^+\mathrm{H}$ (left, lower) and $\mathrm{W}^-\mathrm{H}$ (right, lower) at the 13 TeV LHC, phase space cuts are described in the text.

I.5.3 Electroweak production of H+3jets at NLO+PS

Electroweak production of a Higgs boson in association with three jets has first been considered at NLO-QCD accuracy in Ref. [261] in the VBF approximation. A matching of this calculation to parton shower programs in the framework of the POWHEG BOX has been presented in [262]. In Ref. [304], NLO-QCD corrections have been provided without resorting to the VBF approximation. This latter calculation is based on spinor helicity techniques in combination with the methods developed in the context of [305]. For its implementation, a module has been developed: HJets++is a plugin to HERWIG7's Matchbox [306, 307] module, providing amplitudes for calculating the production of a Higgs boson in association with $n_{\mathrm{jet}} = 2, 3$ jets at next-to-leading order in QCD, *i.e.* at $\mathcal{O}(\alpha^3\alpha_s^{n_{\mathrm{jet}}-1})$[I.29]. The plugin nature of this module enables the amplitudes to be directly used in an NLO-plus-parton shower matched simulation, with both subtractive (MC@NLO-type) and multiplicative (POWHEG-type) matchings being available. Either of the two parton showers available in HERWIG7 can be used in the matching.

[I.29] In this approach, Yukawa couplings are counted as a separate expansion parameter; thus finite heavy quark loop contributions are to be considered separately.

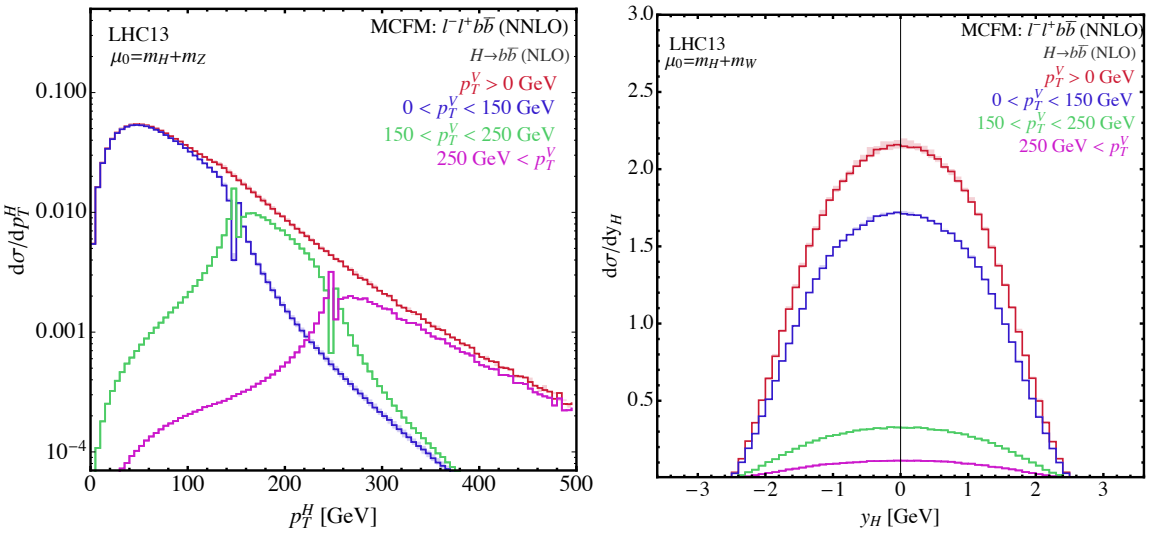

Figure 51: The transverse momentum and rapidity of the $b\bar{b}$ pair for ZH at the 13 TeV LHC, phase space cuts are described in the text.

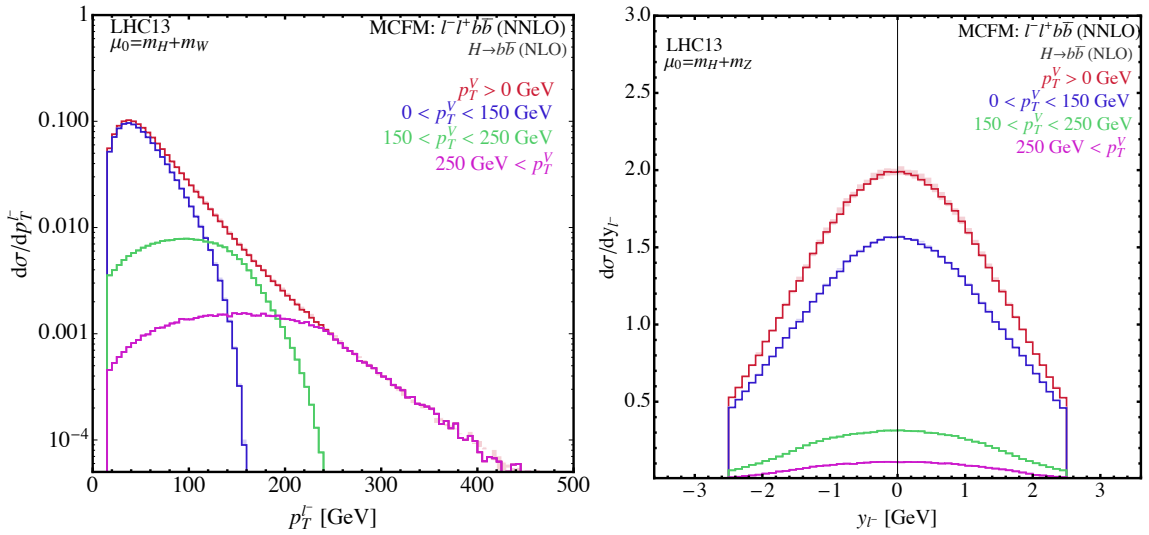

Figure 52: The lepton transverse momentum and rapidity for ZH at the 13 TeV LHC, phase space cuts are described in the text.

Here, results obtained with the HJets++ module matched through the subtractive matching algorithm with the default HERWIG7 angular ordered shower are presented and compared to those obtained with the POWHEG BOX implementation. Multiple partonic interactions and hadronization are disregarded throughout. Contributions from external top- and bottom quarks are neglected and, consistently, the CT10 four-flavour PDF set is used [29]. In addition to the selection cuts of Eqs. (I.5.4)–(I.5.5) a third jet is required with

$$p_{\mathrm{T}\,j} > 20\ \mathrm{GeV}, \qquad |y_j| < 5\,. \tag{I.5.27}$$

Results for the transverse-momentum and rapidity distributions of the Higgs boson and the hardest tagging jet are shown in Figures 53 and 54, respectively. In addition, the respective distributions of the third-hardest jet are illustrated in Figure 55. For the given setup results obtained with the POWHEG BOX code that resorts to the VBF approximation are in good agreement with the full calculation of the

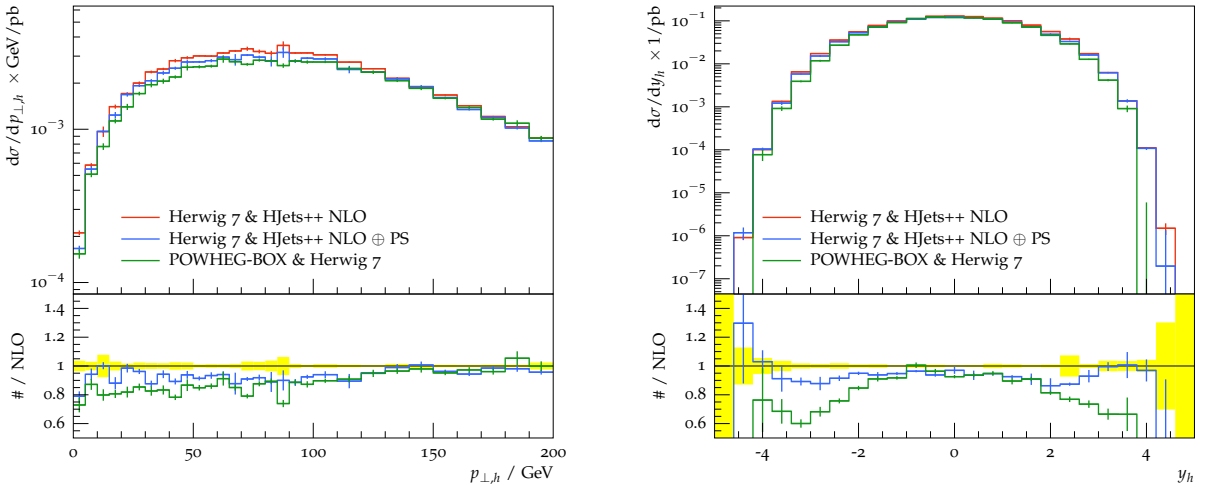

Figure 53: Transverse-momentum and rapidity distributions of the Higgs boson in EW H+3 jet production at NLO QCD (red line) as obtained from using the Matchbox framework of HERWIG7 with the HJets++ plugin, and at NLO QCD matched with the HERWIG7 angular ordered parton shower in the same framework (blue line), and with the POWHEG BOX (green line), respectively. The lower panels show the respective ratios of the NLO+PS to the fixed-order NLO QCD result for $\sqrt{s} = 13$ TeV and $M_{\mathrm{H}} = 125$ GeV. The yellow bands indicate the statistical uncertainty of the NLO result.

HJets++ implementation. A comparison of the HJets++ at NLO QCD and at NLO QCD matched with parton shower reveals that tune effects are moderate for the considered observables.

I.5.4 VH production at NLO+PS

Calculations for the VH process matched to parton shower programs are available at NLO accuracy with the POWHEG BOX [308] and MG5_aMC [54] with FxFx merging [206, 281], for ZH and WH, and at LO for ggZH. Although not used in this report, the gluon gluon fusion contribution can be generated with additional jets that can be merged with MLM merging [309].

Within the POWHEG BOX the computation is carried out using the improved MiNLO prescription [205] applied to HZJ (HWJ-MiNLO) and HWJ (HWJ-MiNLO). The event generation was performed in a similar way as described in ref. [308], but using the NNPDF30_nlo_as_118 [38] PDF set.

A systematic comparison of these calculation for 13 TeV LHC collisions has been carried out in several regions of the phase space making use of several Rivet [310] analyses, differing for the vector boson and Higgs boson candidate selection. The $Z(ll)H(bb)$ process is studied in the Z pT bins: inclusive, [0-100] GeV, (100-200] GeV, >200 GeV. The Z leptons are selected with the cuts $|\eta| < 2.5$, $p_T > 15$ GeV. The dilepton invariant mass m_{ll} in required to be in the range [75-105] GeV. The $Z(\nu\nu)H(bb)$ process is studied in the Z p_T bins: inclusive, [0-150] GeV, (150-250] GeV, >250 GeV. The Z p_T is evaluated through the missing transverse energy of the event. The $W(l\nu)H(bb)$ process is studied in the W p_T bins: inclusive, [0-150] GeV, (150-250] GeV, >250 GeV. The W lepton is required to have $|\eta| < 2.5$, $p_T > 15$ GeV. The neutrino p_T, evaluated through the missing transverse energy of the event, is required to be above 15 GeV.

The processes are studied as a function of the number of additional jets, reconstructed with fastjet [192] with the anti-k_T algorithm and a cone of 0.5, and selected to have $p_T > 20$ GeV and $|\eta| < 4.5$. The jet counting is used to define the exclusive VH+0-jet and VH+1-jet regions and the VH+$\geq$1-jet one, used in the experimental analyses [311, 312].

For each process, the Higgs boson p_T and rapidity, the lepton p_T and rapidity, and the neutrino

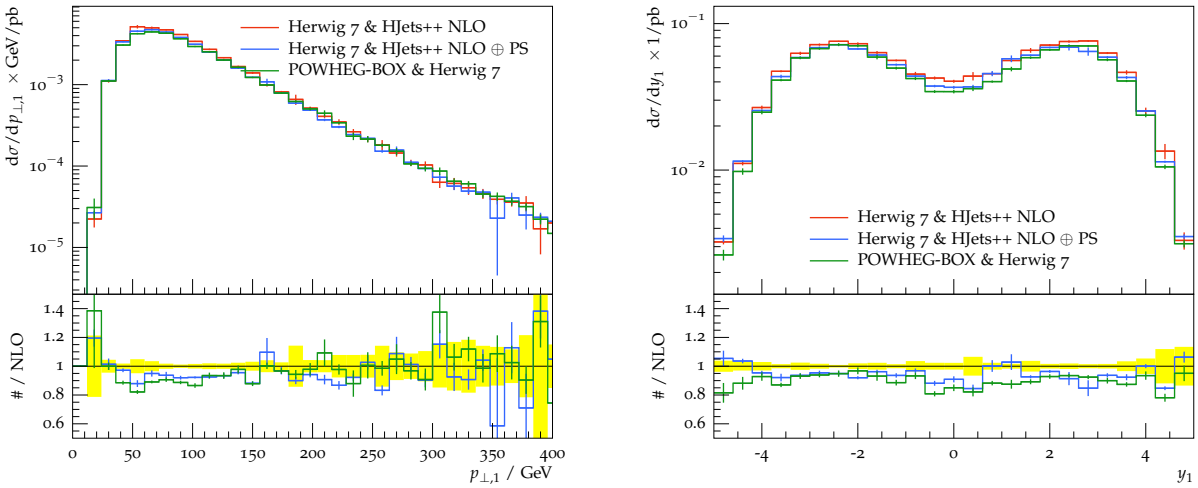

Figure 54: Transverse-momentum and rapidity distributions of the hardest tagging jet in EW H+3 jet production at NLO QCD (red line) as obtained from using the Matchbox framework of HERWIG7 with the HJets++ plugin, and at NLO QCD matched with the HERWIG7 angular ordered parton shower in the same framework (blue line), and with the POWHEG BOX (green line), respectively. The lower panels show the respective ratios of the NLO+PS to the fixed-order NLO QCD result for $\sqrt{s} = 13$ TeV and $M_{\mathrm{H}} = 125$ GeV. The yellow bands indicate the statistical uncertainty of the NLO result.

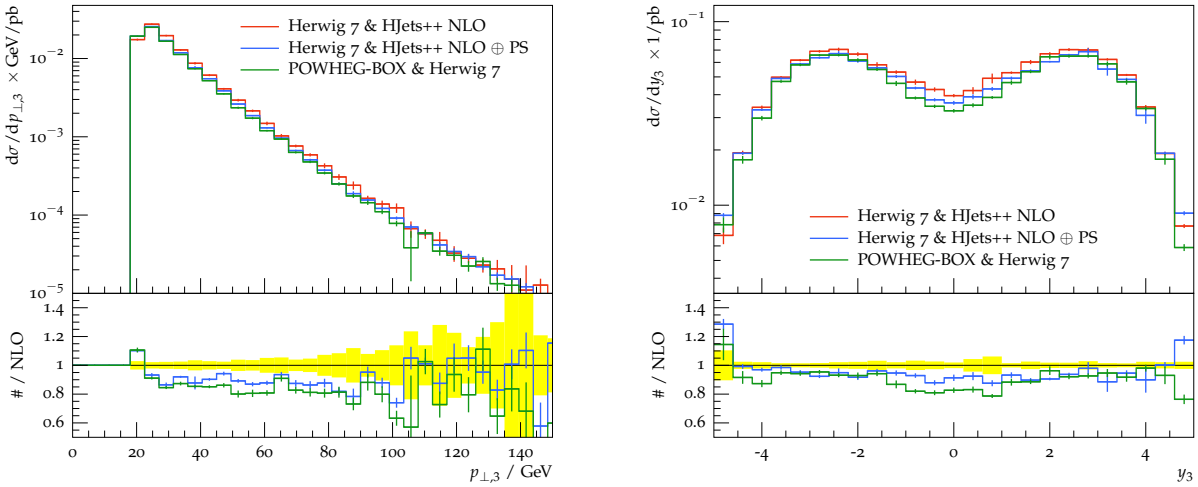

Figure 55: Transverse-momentum and rapidity distributions of the third jet in EW H+3 jet production at NLO QCD (red line) as obtained from using the Matchbox framework of HERWIG7 with the HJets++ plugin, and at NLO QCD matched with the HERWIG7 angular ordered parton shower in the same framework (blue line), and with the POWHEG BOX (green line), respectively. The lower panels show the respective ratios of the NLO+PS to the fixed-order NLO QCD result for $\sqrt{s} = 13$ TeV and $M_{\mathrm{H}} = 125$ GeV. The yellow bands indicate the statistical uncertainty of the NLO result.

p_T are compared in each of the boson p_T bins, for different bins of additional jets after normalizing the inclusive cross section to unity.

The results obtained with POWHEG BOX matched with the default PYTHIA6 (POWHEG+PY6) shower are presented and compared to those obtained with the MG5_aMC implementation matched with both default PYTHIA8 (MG5_aMC+PY8) and default HERWIG7 [306,313] (MG5_aMC+HW7) tune. Comparisons are made keeping the Higgs boson stable. The plots are shown for the ZH case but similar conclusions apply as well to the WH process.

The boson p_T and additional jet multiplicity distributions in the inclusive case are shown in Figure 56. A very small trend is visible in the boson p_T for MG5_aMC+HW7 when compared with POWHEG+PY6 and MG5_aMC+PY8, while the distribution of additional jets for MG5_aMC+PY8 deviates at high multiplicity when compared with the other two cases. The discrepancies highlighted

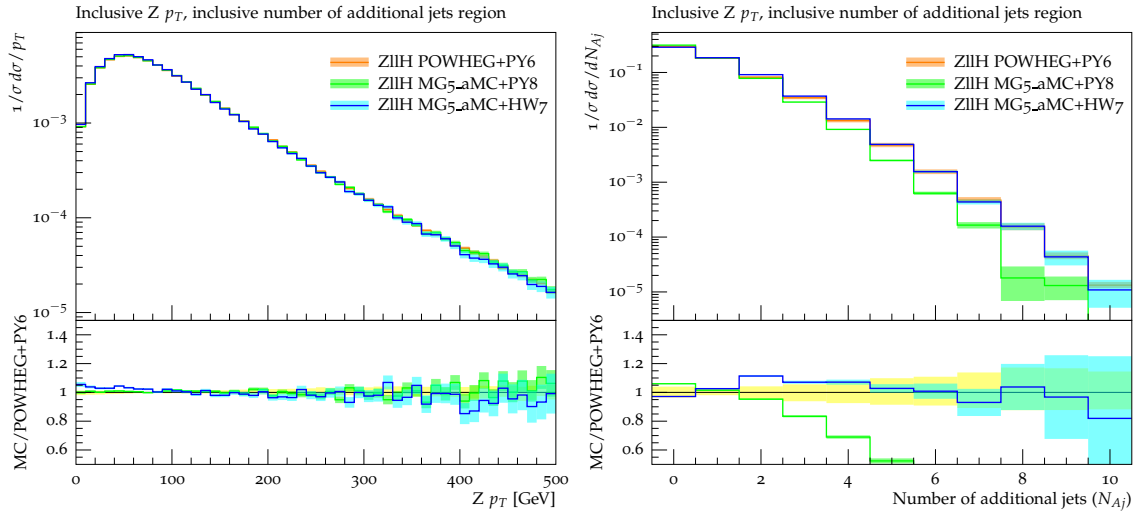

Figure 56: Comparison of the boson p_T (left) and number of additional jets (right) in the inclusive case for $Z(ll)H$.

in the comparison of MG5_aMC+PY8 and MG5_aMC+HW7 clearly indicate the need for a careful choice of the parton shower and underlying event tune when performing analyses which require categories with exclusive number of jets and boson p_T binning.

In the same phase space, characterized by inclusive boson p_T and additional jet selection, the Higgs boson η for MG5_aMC+HW7 exhibits the same trend visible for the boson p_T, while the rapidity shapes are well compatible as shown in Figure 57.

In the phase space characterized by an inclusive boson p_T and the explicit request for 0 additional jets, the Higgs boson p_T and rapidity, the lepton p_T and rapidity, and the neutrino p_T distribution shapes remain well compatible, but a different normalization can be observed as a reflection of the different distribution in the additional jet multiplicity. While requiring exactly 1 additional jet, the lepton and Higgs boson shapes modeled by HW7 tend to deviate slightly, further increasing their discrepancy when requiring the inclusive boson p_T and at least 1 additional jet, as well as the overall normalization due to the aforementioned differences in the additional jet multiplicity. The the boson p_T and rapidity in $Z(\nu\nu)H$ events, and leading lepton p_T and η in $Z(ll)H$ events for the latter case are shown in Figure 58.

Extending the comparison to the low, medium and high boson p_T regions defined above, consistent results are observed. In particular, well compatible shapes are observed for the inclusive jet selection, apart from some minor trend in the low Higgs boson η region, especially for HW7. The same level of agreement is also observed for the 0- and 1-jet phase spaces, as well as when requiring at least 1 jet, with the normalization offset discussed previously. The the boson p_T and rapidity in $Z(\nu\nu)H$ events, and

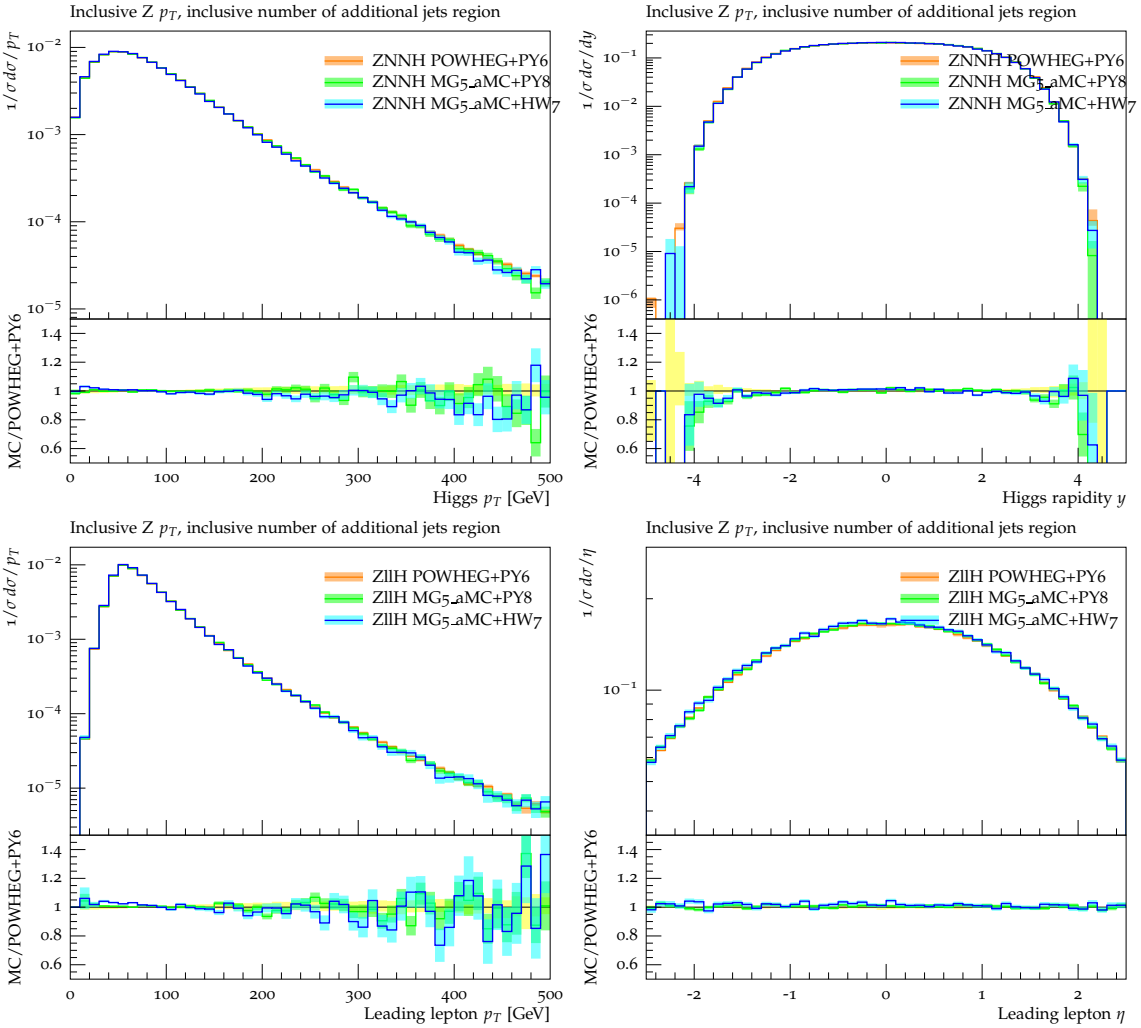

Figure 57: Comparison of the boson p_T and rapidity in $Z(\nu\nu)H$ events, and leading lepton p_T and η in $Z(ll)H$ events in the inclusive jet region.

leading lepton p_T and η in $Z(ll)H$ events for high boson p_T case when requiring exactly 0 additional jets are shown in Figure 59.

Finally, a comparison of the quark-quark (ZH) and gluon-gluon ($ggZH$) initiated processes is performed using MG5_aMC interfaced with a common parton shower, namely PYTHIA8. The plots are shown for the leptonic decay of the Z boson but apply as well to the decay into neutrinos.

The relative cross section of the gluon initiated process is $\sim 15\%$, but a common normalization to unitary cross section is used, to better underline the shape differences. The boson p_T and additional jet multiplicity distributions in the inclusive case are shown in Figure 60 Two correlated features can be observed: both the boson p_T and the multiplicity of additional jets are much harder for the gluon initiated contribution. Therefore in the high boson p_T region, usually regarded as the most sensitive, and in presence of at least 1 jet, the relative contribution of $ggZ(ll)H$ is much higher. The the boson p_T and rapidity, and leading lepton p_T and η in $ggZ(ll)H$ events for high boson p_T case when requiring exactly 0 additional jets are shown in Figure 61 compared to $Z(ll)H$.

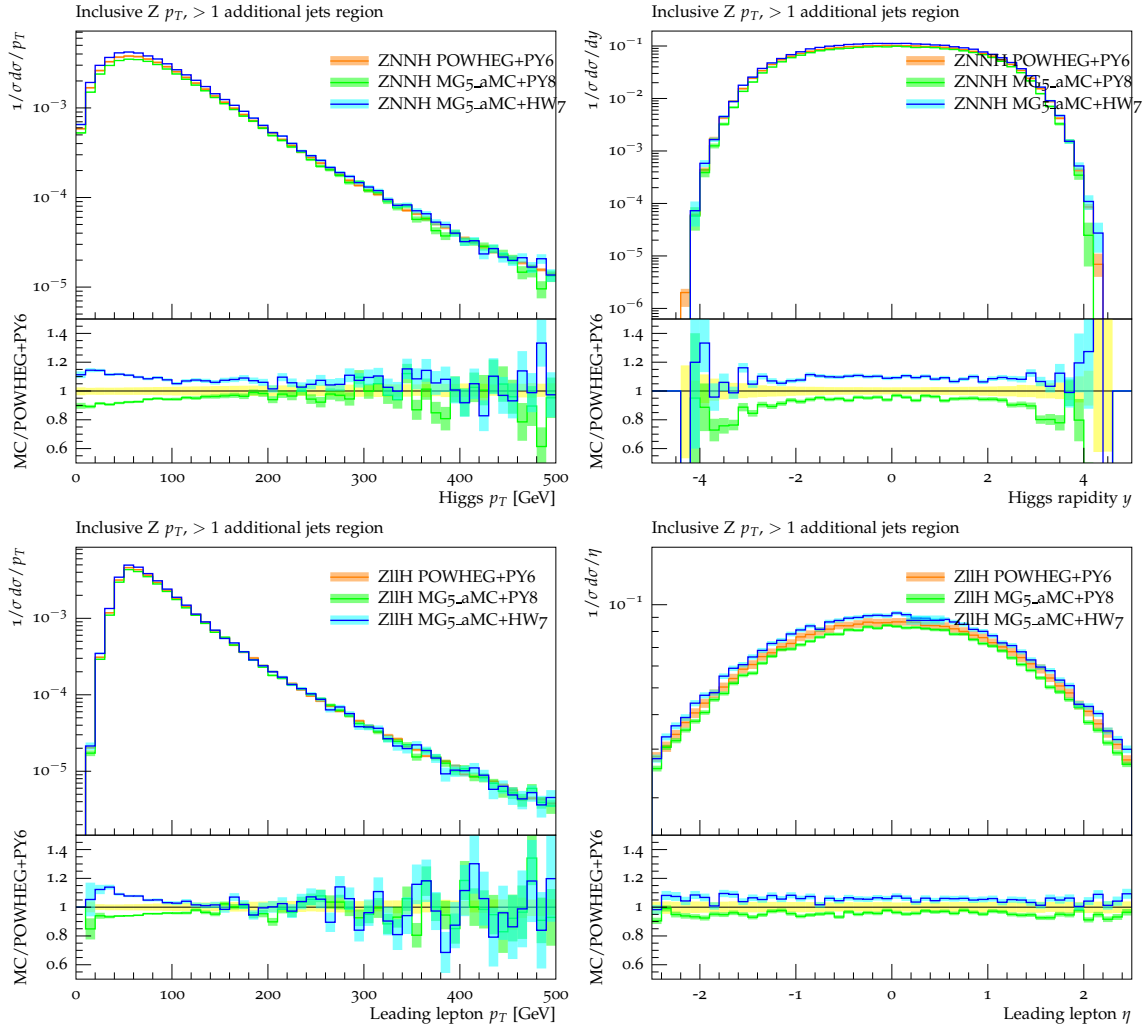

Figure 58: Comparison of the boson p_T and rapidity in $Z(\nu\nu)H$ events, and leading lepton p_T and η in $Z(ll)H$ events in the inclusive the inclusive boson p_T region requiring at least 1 additional jet.

I.5.5 NNLOPS for VH

We report about a study of the Higgs boson production in association with a W^+ boson at next-to-next-to-leading order accuracy including parton shower effects (NNLOPS) [314]

$$pp \to HW^+ \to Hl^+\nu_l\,, \tag{I.5.28}$$

where $l = \{e, \mu\}$. To achieve NNLOPS accuracy we have implemented a reweighting method similar to the one introduced in HNNLOPS [208] and DYNNLOPS [315]. We reweight events obtained with the POWHEG NLO+PS accurate calculation of HW in association with a jet, and upgraded with the MiNLO procedure (HWJ-MiNLO) [308], by a factor:

$$\begin{aligned}\mathcal{W}\left(\Phi_{HW},\, p_{\mathrm{T}}\right) &= h\left(p_T\right) \frac{\int d\sigma^{\mathrm{NNLO}}\ \delta\left(\Phi_{HW} - \Phi_{HW}\left(\Phi\right)\right) - \int d\sigma_B^{\mathrm{MINLO}}\, \delta\left(\Phi_{HW} - \Phi_{HW}\left(\Phi\right)\right)}{\int d\sigma_A^{\mathrm{MINLO}}\, \delta\left(\Phi_{HW} - \Phi_{HW}\left(\Phi\right)\right)} \\ &+ \left(1 - h\left(p_T\right)\right)\,, \end{aligned} \tag{I.5.29}$$

where $d\sigma^{\mathrm{NNLO}}$ and $d\sigma_{A/B}^{\mathrm{MINLO}}$ are multi-differential distributions obtained at pure NNLO level and by analysing produced HWJ-MiNLO events, respectively. The function $h(p_{\mathrm{T}})$ is defined as

$$h(p_{\mathrm{T}}) = \frac{(M_H + M_W)^2}{(M_H + M_W)^2 + p_{\mathrm{T}}^2}\,, \tag{I.5.30}$$

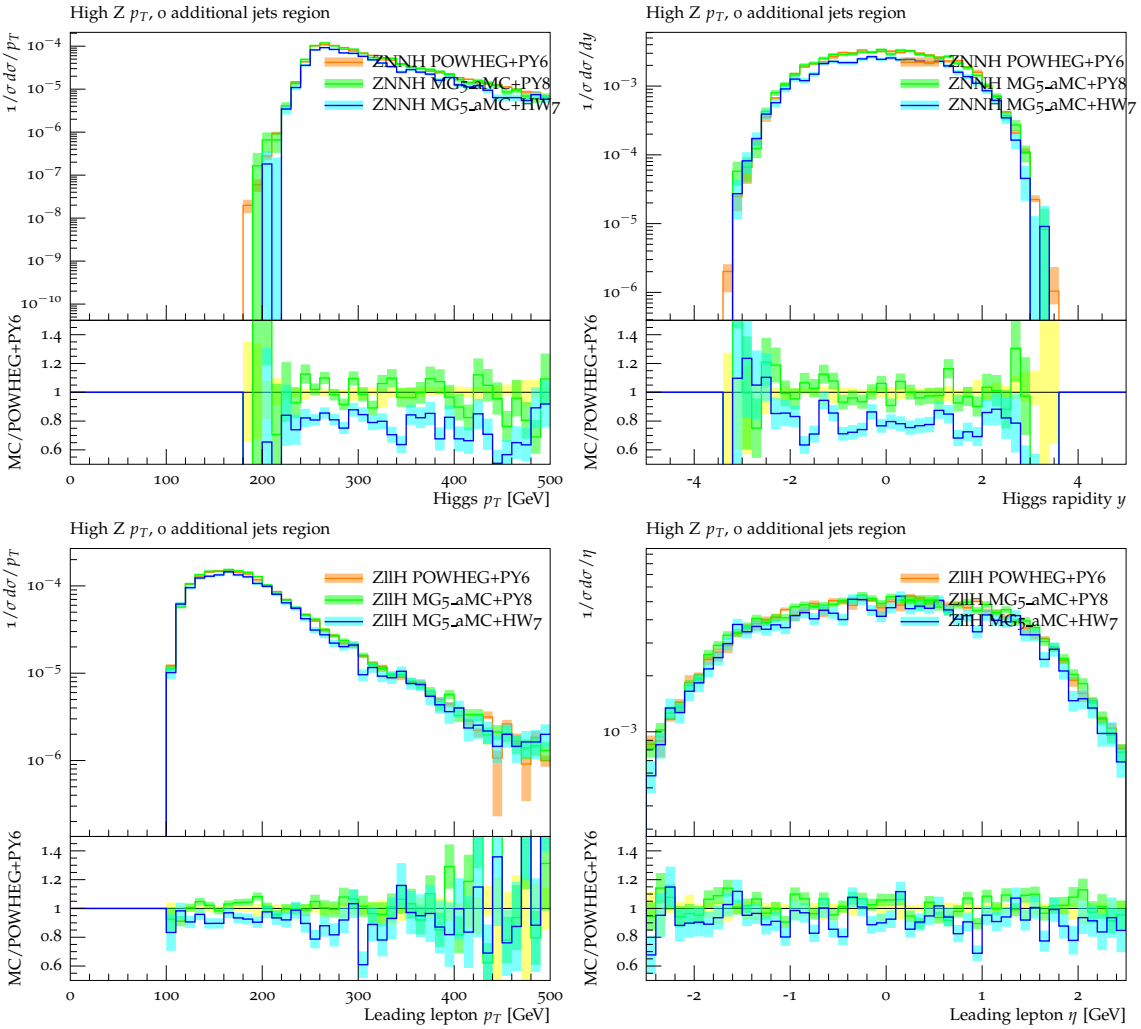

Figure 59: Comparison of the boson p_T and rapidity in $Z(\nu\nu)H$ events, and leading lepton p_T and η in $Z(ll)H$ events in the inclusive the inclusive boson p_T region requiring 0 additional jet.

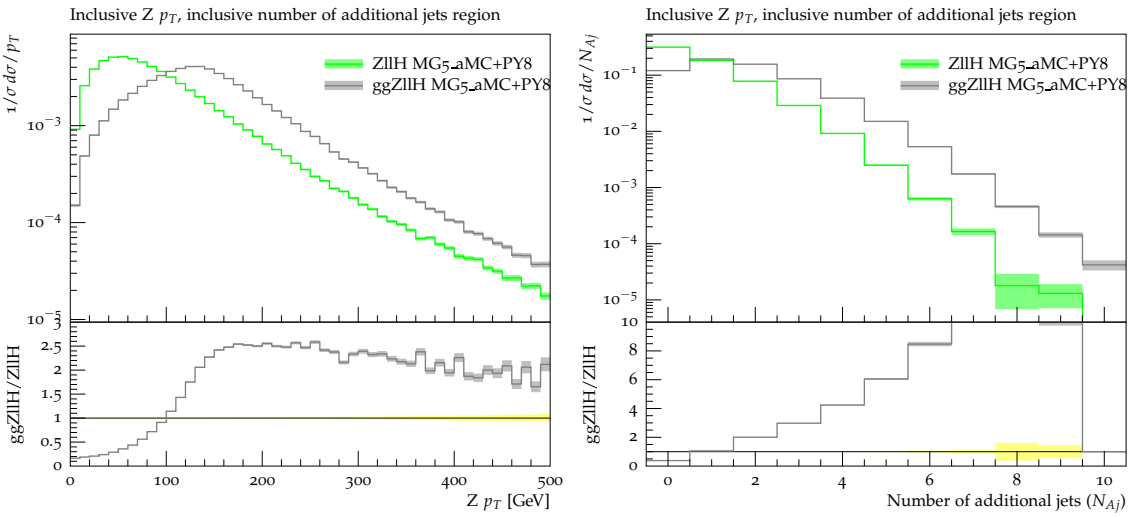

Figure 60: Comparison of the boson p_T (left) and number of additional jets (right) in the inclusive case for $Z(ll)H$.

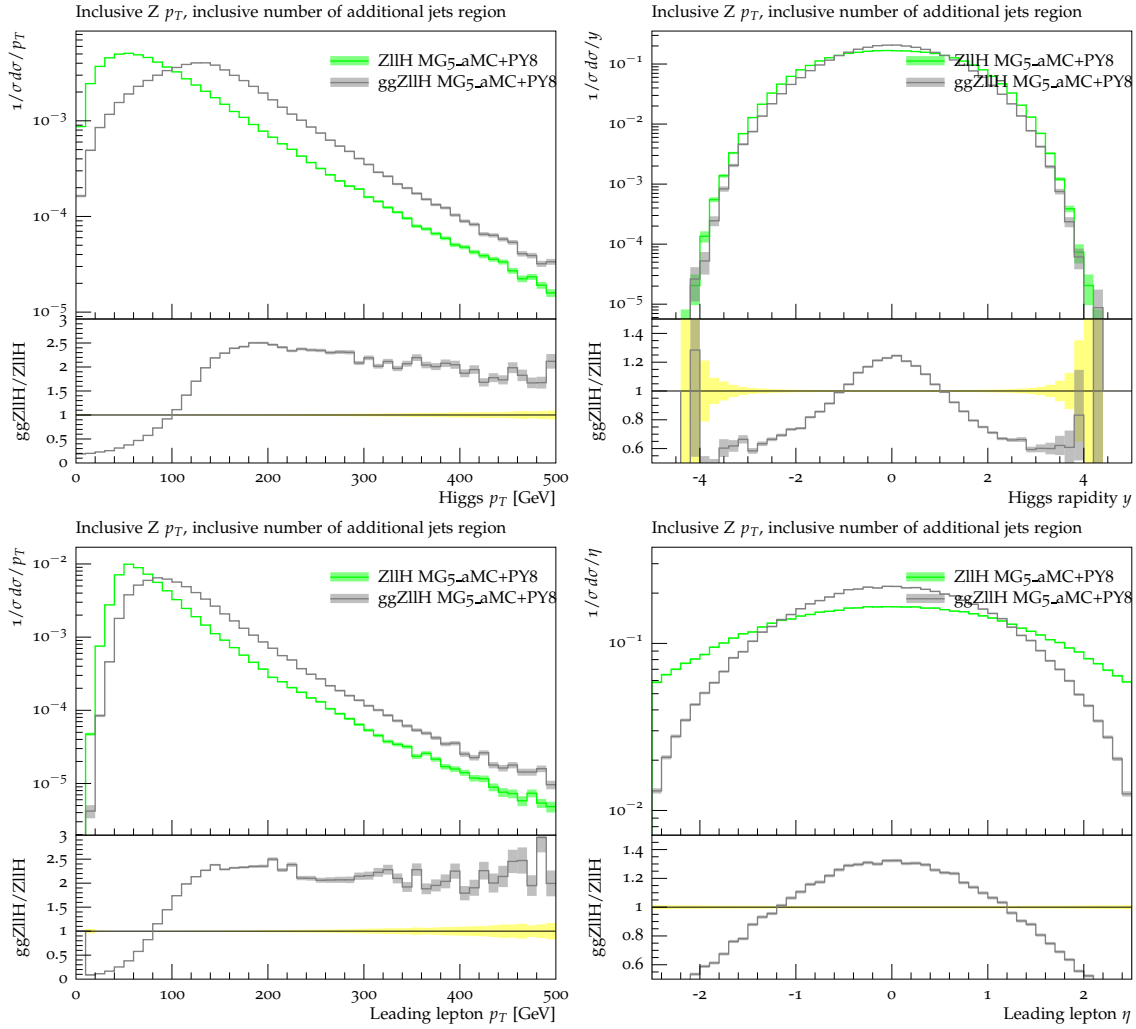

Figure 61: Comparison of the boson p_T and rapidity, and leading lepton p_T and η in $ggZ(ll)H$ $Z(ll)H$ events in the inclusive jet region.

where p_{T} is the transverse momentum of the leading jet, and it is used to split the MINLO cross section into

$$d\sigma_A^{\mathrm{MINLO}} = d\sigma^{\mathrm{MINLO}}\, h(p_{\mathrm{T}})\,, \qquad d\sigma_B^{\mathrm{MINLO}} = d\sigma^{\mathrm{MINLO}}\, (1 - h(p_{\mathrm{T}})\,. \tag{I.5.31}$$

Therefore the function $h(p_{\mathrm{T}})$ ensures that the reweighting is smoothly turned off when the leading jet is hard since in that region the HWJ-MINLO generator is already NLO accurate, as is the NNLO calculation of HW.

For the process in eq. (I.5.28) the Born kinematics is fully specified by 6 independent variables. We have chosen them to be: the transverse momentum of Higgs boson ($p_{\mathrm{T,H}}$); the rapidity of HW system (y_{HW}); the difference of Higgs boson rapidity and the W^+ rapidity (Δy_{HW}); the invariant mass of $e^+\nu_e$ system ($m_{e\nu}$); and the two Collins-Soper angles (θ^*, ϕ^*) [316]:

$$\Phi_B = \{p_{\mathrm{T,H}}, y_{HW}, \Delta y_{HW}, m_{e\nu}, \theta^*, \phi^*\}\,. \tag{I.5.32}$$

In this setup the multi-differential cross-section can be written in the form:

$$\frac{d\sigma}{d\Phi_B} = \frac{d^6\sigma}{dp_{\mathrm{t},H}\, dy_{HW}\, d\Delta y_{HW}\, dm_{e\nu}\, d\theta^* d\phi^*}$$

$$= \frac{3}{16\pi}\left(\frac{d\sigma}{d\Phi_{HW^*}}(1+\cos^2\theta^*)+\sum_{i=0}^{7}A_i(\Phi_{HW^*})f_i(\theta^*,\phi^*)\right), \tag{I.5.33}$$

where $\Phi_{HW^*} = \{p_{\mathrm{T,H}}, y_{HW}, \Delta y_{HW}, m_{e\nu}\}$, and the angular dependence is encoded in the coefficients $A_i(\Phi_{HW^*})$ and the functions:

$$\begin{aligned} f_0(\theta^*,\phi^*) &= \left(1-3\cos^2\theta^*\right)/2\,, & f_1(\theta^*,\phi^*) &= \sin 2\theta^*\cos\phi^*\,,\\ f_2(\theta^*,\phi^*) &= (\sin^2\theta^*\cos 2\phi^*)/2\,, & f_3(\theta^*,\phi^*) &= \sin\theta^*\cos\phi^*\,,\\ f_4(\theta^*,\phi^*) &= \cos\theta^*\,, & f_5(\theta^*,\phi^*) &= \sin\theta^*\sin\phi^*\,,\\ f_6(\theta^*,\phi^*) &= \sin 2\theta^*\sin\phi^*\,, & f_7(\theta^*,\phi^*) &= \sin^2\theta^*\sin 2\phi^*\,. \end{aligned} \tag{I.5.34}$$

Since the angular dependence is fully expressed in terms of the $f_i(\theta^*,\phi^*)$ functions, the coefficients of the expansion $A_i(\Phi_{HW^*})$ depend only on the remaining kinematic variables. Using orthogonality properties of spherical harmonics we can extract these coefficients.

In our work we have simplified our procedure by noting that the $m_{e\nu}$ invariant mass distribution has a flat K-factor. This is true even when examining the $d\sigma/dm_{e\nu}$ distribution in different bins of $\Phi_{HW} = \{p_{\mathrm{T},H}, y_{HW}, \Delta y_{HW}\}$. Therefore, in eq. (I.5.33) we replace the 4-dimensional Φ_{HW^*} with the 3-dimensional Φ_{HW}. This is an approximation, however we believe that it works extremely well as discussed in ref. [314]. In our work we obtain $\frac{d\sigma}{d\Phi_{HW}}$ and $A_i(\Phi_{HW})$ $(i=0,7)$ at pure NNLO level by running the HVNNLO code [282, 291], and we obtain the results at MiNLO level by running HWJ-MiNLO [308]. We store the results in 9 three-dimensional tables. Following this step, we use these tables along with eq. (I.5.33) to obtain the function eq. (I.5.29) to reweight each produced event. The final ensemble of events is NNLO accurate for all observables at Born level and a parton shower can now be applied without affecting the NNLO accuracy.

In the following we show results for 13 TeV LHC collisions applying the lepton cuts reported in Eq. (I.5.13). Jets have been clustered using the anti-k_t algorithm with $R = 0.4$ [191] as implemented in FastJet [192, 317] and count if they fulfil the following conditions:

$$p_{\mathrm{T}}(\text{jet}) > 20\ \text{GeV}, \qquad |\eta(\text{jet})| < 4.5\,. \tag{I.5.35}$$

As for the PDF, we have used the MMHT2014nnlo68cl set [37], corresponding to a value of $\alpha_s(M_Z) = 0.118$. For HWJ-MiNLO events the scale choice is dictated by the MiNLO procedure, while for the NNLO we have used for the central renormalization and factorization scales $\mu_0 = M_H + M_W$. To estimate uncertainties we calculate both the fixed order NNLO and HWJ-MiNLO results at 7 scales, each with renormalization and factorization scale varied independently up and down by a factor of 2. When these results are then used in eq. (I.5.29) this gives 49 combinations for the NNLOPS results. We define our perturbative uncertainty as the envelope of these 49 variations.

To shower partonic events, we have used PYTHIA8 [318] (version 8.185) with the "Monash 2013" [319] tune. We consider events after parton showering and hadronization effects, unless otherwise stated. Underlying event and multiple parton interactions were kept switched off. To define leptons from the boson decays we use the Monte Carlo truth, *i.e.* we assume that if other leptons are present, the ones coming from the W decay can be identified correctly. To obtain the results shown in the following, we have switched on the "doublefsr" option introduced in ref. [320]. The plots shown throughout this study have been obtained keeping the veto scale equal to the default POWHEG prescription. In some figures we also compare our results against HVNNLO, run with $\mu_0 = M_H + M_W$ as central scale choice, and with the same PDF set used for HWJ-MiNLO and HVNNLOPS.

In Figure 62 we show distributions for the transverse momenta of the W boson and the WH system, respectively. NNLO results (from HVNNLO) are compared against those obtained with HWJ-MiNLO and HVNNLOPS. For observables that are fully inclusive over QCD radiation, as $p_{\mathrm{T,W}}$, the agreement among the HVNNLO and NNLOPS predictions is perfect, as expected. One also notices

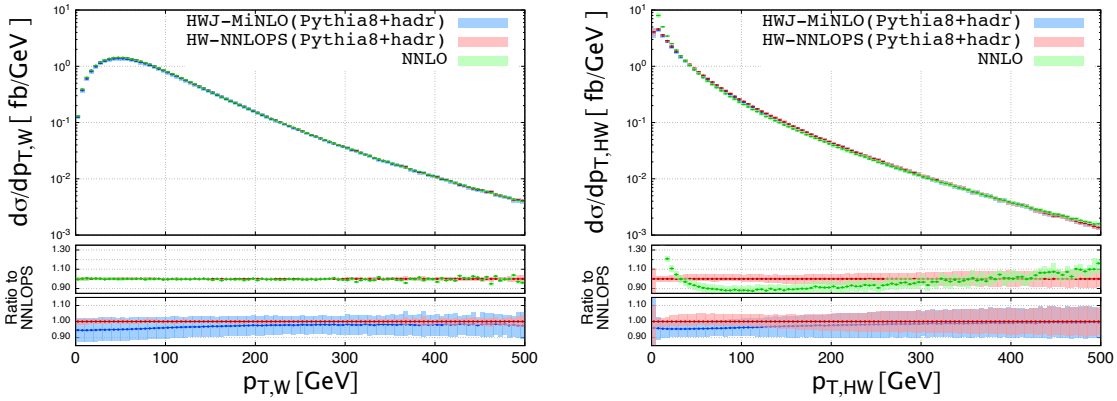

Figure 62: Comparison of HWJ-MiNLO (PYTHIA8+HADR) (blue), NNLO (green), and HW-NNLOPS (PYTHIA8+HADR) (red) for $p_{\mathrm{T,W}}$ (left) and $p_{\mathrm{T,HW}}$ (right).

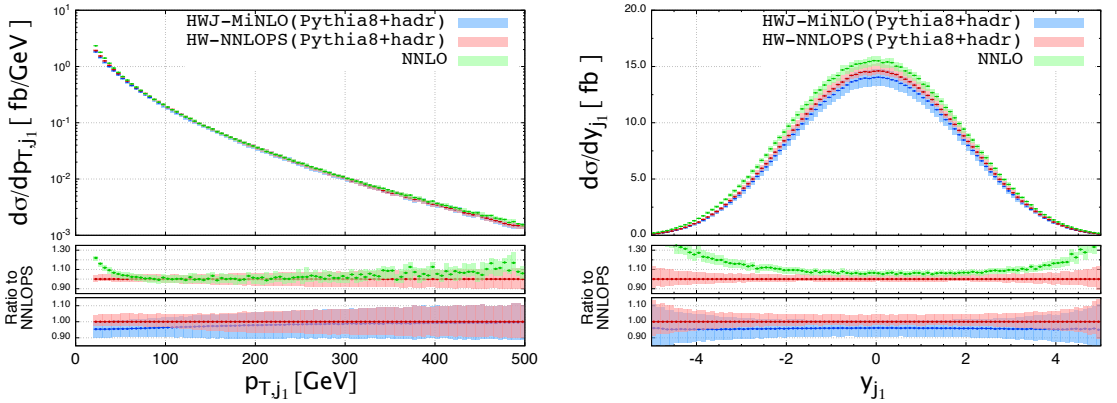

Figure 63: Comparison of HWJ-MiNLO (PYTHIA8+HADR) (blue), NNLO (green), and HW-NNLOPS (PYTHIA8+HADR) (red) for $p_{\mathrm{T,j_1}}$ (left) and $y_{\mathrm{j_1}}$ (right).

the sizeable reduction of the uncertainty band when HWJ-MiNLO results are upgraded to NNLOPS. As no particularly tight cuts are imposed, the NNLO/NLO K-factor is almost exactly flat. The right panel shows instead the effects due to the Sudakov resummation. At small transverse momenta, the NNLO cross section becomes larger and larger due to the singular behaviour of the matrix elements for HW production in association with arbitrarily soft-collinear emissions. The MiNLO method resums the logarithms associated to these emissions, thereby producing the typical Sudakov peak, which for this process is located at $1\text{ GeV} \lesssim p_{\mathrm{T,HW}} \lesssim 4\text{ GeV}$, as expected from the fact that the LO process is Drell-Yan like. It is also interesting to notice here two other features that occur away from the collinear singularity, and which are useful to understand plots to be shown in the following. Firstly, the p_T-dependence of the NNLO reweighting can be explicitly seen in the bottom panel, where one can also appreciate that at very large values not only the NNLOPS and MiNLO results approach each other, but also that the uncertainty band of HVNNLOPS becomes progressively larger (in fact, in this region, the nominal accuracy is NLO). Secondly, in the region $50\text{ GeV} \lesssim p_{\mathrm{T,HW}} \lesssim 300\text{ GeV}$, the NNLO and NNLOPS lines show deviations of up to about 10 %: these are due both to the compensation that needs taking place in order for the two results to integrate to the same total cross section, as well as to the fact that the scale choices are different (fixed for the NNLO line, dynamic and set to $p_{\mathrm{T,HW}}$ in MiNLO). When $p_{\mathrm{T,HW}} \gtrsim 250\text{ GeV}$ the two predictions start to approach, as this is the region of phase space where the MiNLO scale is similar to that used at NNLO ($\mu = M_H + M_W$).

In Figure 63 we show the transverse momentum and the rapidity of the hardest jet. Most of the

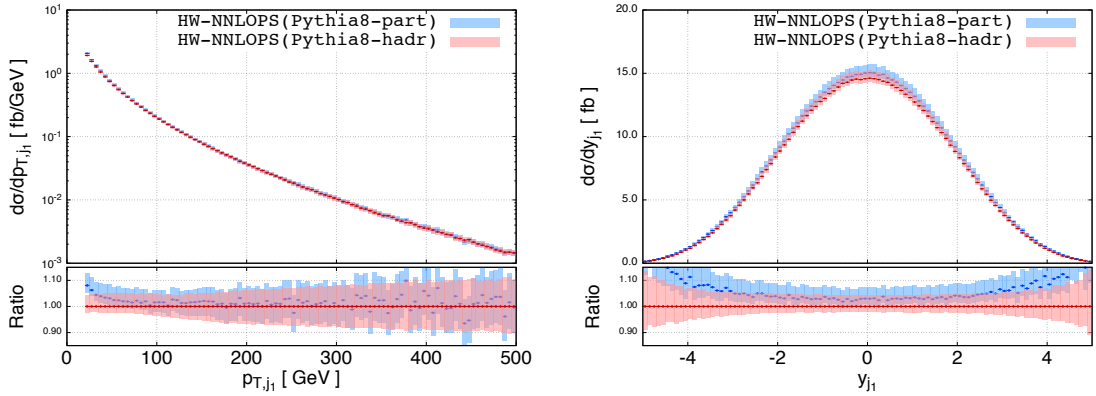

Figure 64: Comparison of HW-NNLOPS with (red) and without (blue) hadronization for $p_{\mathrm{T,j_1}}$ (left) and $y_{\mathrm{j_1}}$ (right).

differences among these three predictions can be easily explained by the considerations made above on the $p_{\mathrm{T,HW}}$ spectrum, although here effects due to multiple radiation as well as hadronization are bound to play some role too. In Figure 63 we notice that, for large values of $|y_{j_1}|$, there are large differences among the NNLO result and those containing Sudakov resummation: this is expected, since a large-rapidity jet has on average a smaller transverse momentum, hence the singular nature of the NNLO result is more evident in these kinematics configurations.

Next we find it interesting to examine the size of non-perturbative effects. As shown in Figure 64, hadronization has a sizeable impact on the shapes of jet distributions: differences up to $7-8$ % can be seen in the jet p_T spectrum at small values, and are still visible at a few per cent level till when relatively hard jets are required ($p_{\mathrm{T,j_1}} > 100$ GeV). Even larger effects can be seen in the rapidity distribution (right panel) at large rapidities. The HVNNLOPS generator allows us to simulate these features in a fully-exclusive way, retaining at the same time all the virtues of an NNLO computation for fully inclusive observables, as well as resummation effects, thanks to the interplay among POWHEG, MINLO and parton showering.

In Figure 65 we show the transverse momentum and rapidity distributions of the Higgs boson and the charged lepton, as predicted by the HVNNLOPS code and by the underlying HWJ-MINLO simulation. No particular feature needs be commented in these plots: since no cuts are applied on extra radiation, the inclusion of higher order corrections just makes the HVNNLO predictions more accurate, as expected. On the other hand it is interesting to see how these distributions are affected by requiring further cuts, like imposing a jet veto or requiring the presence of at least one jet, whilst restricting at the same time the phase space to different windows for $p_{\mathrm{T,W}}$. Figs. 66, 67 and 68 display the Higgs boson transverse momentum and rapidity in the three following cases:

- no jet ("jet veto"), $p_{\mathrm{T,W}} < 150$ GeV
- at least 1 jet, $p_{\mathrm{T,W}} < 150$ GeV
- at least 1 jet, 150 GeV $< p_{\mathrm{T,W}} < 250$ GeV

The first thing to notice is that, in general, the uncertainty band of the NNLOPS-accurate prediction is not as narrow as in Figure 65: this is expected and physically sound, because the phase space is not fully inclusive with respect to the QCD activity, due to the requirements on jets. In the jet-veto case, however, the results show that the inclusion of NNLO corrections within a MINLO-based simulation is important, since the uncertainty band of HVNNLOPS, although larger than in Figure 65, is still narrower than the HWJ-MINLO one.

The second thing to notice is that, when jets are required, the HVNNLOPS predictions display larger uncertainties, a bit smaller but in general similar to those obtained with HWJ-MINLO. This

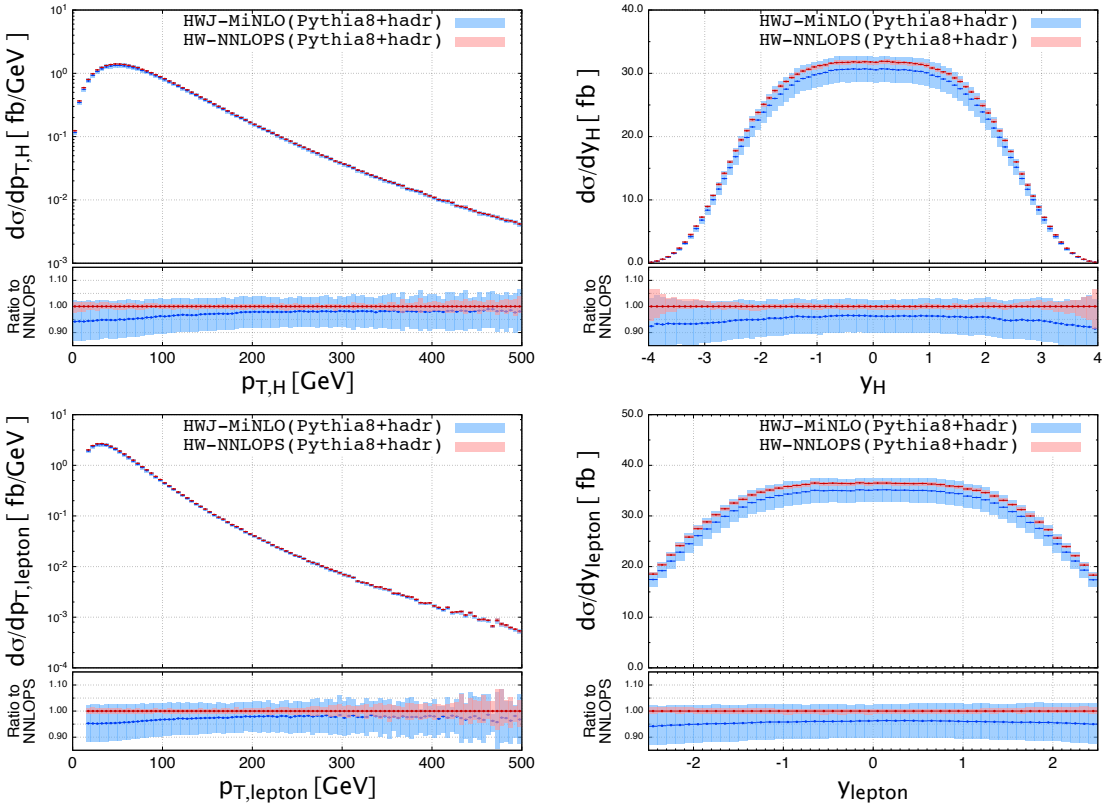

Figure 65: Comparison of HWJ-MiNLO (Pythia8+hadr) (blue) and HW-NNLOPS (Pythia8+hadr) (red) for p_T (left) and rapidity (right) for Higgs (upper) and lepton (lower).

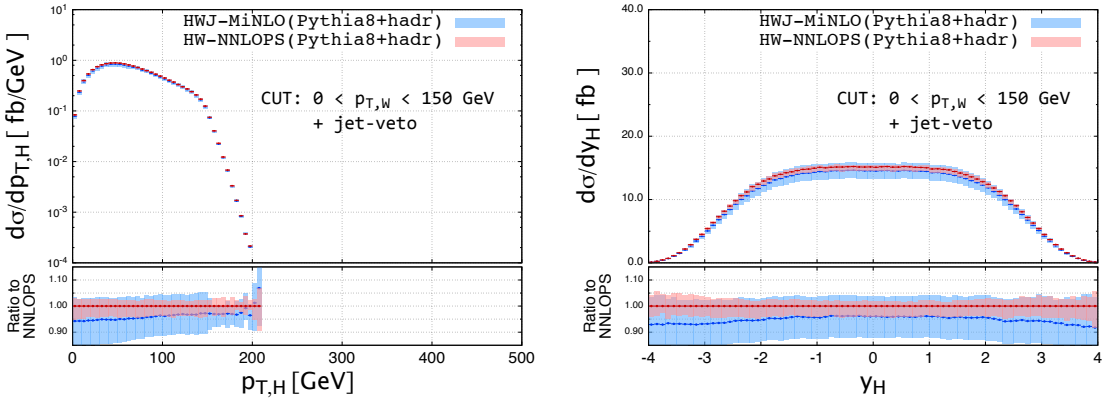

Figure 66: Comparison of HWJ-MiNLO (Pythia8+hadr) (blue) and HW-NNLOPS (Pythia8+hadr) (red) for $p_{\mathrm{T,H}}$ (left) and y_{H} (right) for $p_{\mathrm{T,W}} < 150$ GeV and no jet.

is expected, since this is exactly the phase space region where both computations are formally NLO accurate. The effect of the NNLO/NLO reweighting is still quite visible (both in the overall normalization and in the slightly smaller bands) though, due to the fact that the cut on the jet transverse momentum is relatively small. This also means that the HWJ-MiNLO and HVNNLOPS results are likely to be different from fixed order computations, since the use of dynamic scales in MiNLO and its interplay with resummation has an impact in this phase space region, as shown in Figure 63 for the associated jet distributions.

The final thing to notice, and the one exception to the general trend in the previous observations,

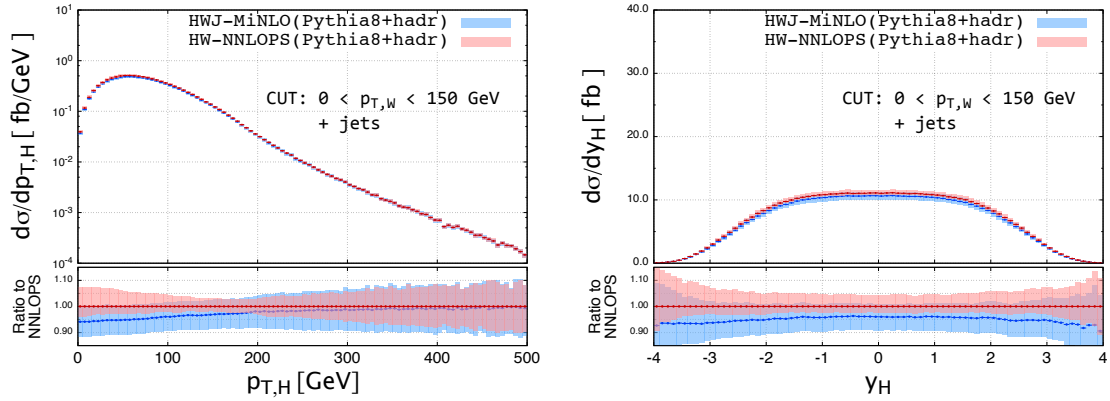

Figure 67: Comparison of HWJ-MiNLO (Pythia8+hadr) (blue) and HW-NNLOPS (Pythia8+hadr) (red) for $p_{\mathrm{T,H}}$ (left) and y_{H} (right) for $p_{\mathrm{T,W}} < 150$ GeV and at least 1 jet.

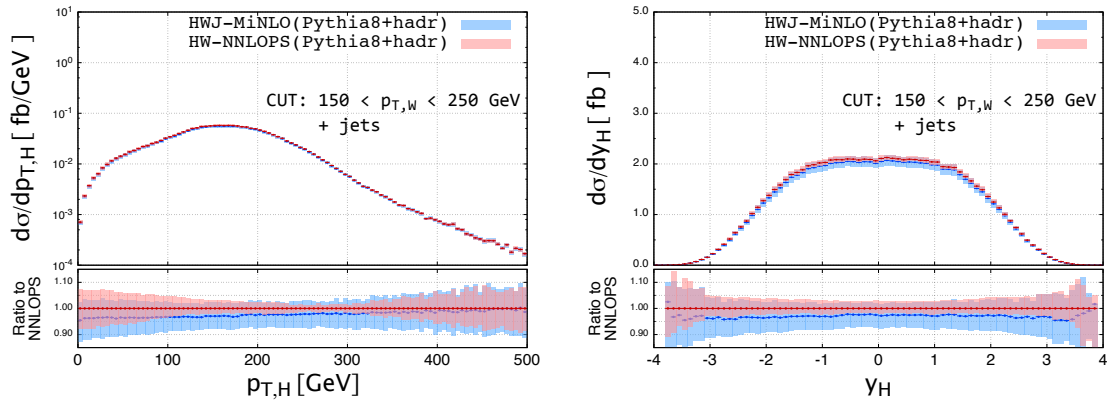

Figure 68: Comparison of HWJ-MiNLO (Pythia8+hadr) (blue) and HW-NNLOPS (Pythia8+hadr) (red) for $p_{\mathrm{T,H}}$ (left) and y_{H} (right) for 150 GeV $< p_{\mathrm{T,W}} < 250$ GeV and at least 1 jet

is the shrinking of the uncertainty band at intermediate values of $p_{\mathrm{T,H}}$ in Figs. 67 and 68, which is even more noticeable in the y_H distributions, the latter being dominated by the kinematics where $p_{\mathrm{T,H}}$ peaks. This feature is due to the requirement on $p_{\mathrm{T,W}}$, and can be explained as follows. For a fully inclusive kinematics, the transverse momenta of the W and H boson are typically balanced, with a value of about 40 GeV (see *e.g.* the peak in Figs. 62 and 65). When jets are required, at least the hardest jet p_T will play a role in the momentum conservation in the transverse plane: its typical value, however, depends on the requirements on the massive bosons kinematics. From this observation the band shrinking in the $p_{\mathrm{T,H}}$ spectrum can be understood. For instance, in Figure 67, when $p_{\mathrm{T,H}}$ approaches values close to the larger values available for $p_{\mathrm{T,W}}$, one enters a region where the jet has to be just above its minimum allowed value: this is the region where the uncertainty band in the jet p_T spectrum is minimal, as shown in Figure 63. As soon as larger $p_{\mathrm{T,H}}$ values are probed whilst keeping $p_{\mathrm{T,W}} < 150$ GeV, harder jets are required by momentum conservation, hence the uncertainty band from HVNNLOPS rapidly approaches the one from HWJ-MiNLO. This effect is even more evident in Figure 68: if $p_{\mathrm{T,H}}$ is relatively small, then momentum conservation doesn't constrain $p_{\mathrm{T,j_1}}$ very strongly, yielding a standard uncertainty band, relatively similar to HWJ-MiNLO. In the region where cuts push $p_{\mathrm{T,W}}$ and $p_{\mathrm{T,H}}$ to similar values, once more the jet must be close to its threshold region, and hence the uncertainty band is reduced.

Chapter I.6

ttH and tH

S. Guindon, C. Neu, S. Pozzorini, L. Reina (Eds.); A. Broggio, M. Casolino, F. Demartin, A. Denner, R. Feger, A. Ferroglia, R. Frederix, S. Frixione, M. V. Garzelli, S. Gieseke, M. Harrendorf, H. B. Hartanto, V. Hirschi, S. Höche, S. Honeywell, B. Jäger, A. Juste, A. Kardos, A. Kulesza, J. Lindert, M. Mantoani, K. Mawatari, M. Moreno Llacer, N. Moretti, L. Motyka, D. Pagani, B. D. Pecjak, S. Plätzer, R. Podskubka, C. Reuschle, E. Shabalina, H. Shao, M. Schönherr, F. Siegert, A. Signer, T. Stebel, V. Theeuwes, Z. Trocsanyi, I. Tsinikos, D. Wackeroth, L. L. Yang, M. Zaro

I.6.1 Introduction

The production of a Higgs boson in association with a top-quark pair ($t\bar{t}H$) or a single top quark (tH) is going to play a very important role in the Higgs boson physics program of Run 2 of the LHC since it can provide a direct measurement of the top-quark Yukawa coupling.

In this context, the $t\bar{t}H/tH$ working group has discussed the current status and future plans of $t\bar{t}H$ and tH experimental analyses and has reviewed the status of theoretical predictions, for both signals and backgrounds. The emphasis has been on identifying and characterizing state-of-the art theoretical predictions and tools for signals and backgrounds in all relevant $t\bar{t}H$ and tH searches, as well as on identifying various theory-related sources of uncertainties and prioritizing them according to both their impact on experimental analyses and the likelihood of theory improvements in the near future.

On top of providing tables of cross sections for both $t\bar{t}H$ and tH production, which include all most up-to-date calculations of QCD and electroweak (EW) corrections, as well as the estimated theoretical uncertainty from scale variations, α_s, and parton distribution functions (PDFs), we review in Section I.6.2 the next-to-leading-order (NLO) QCD+EW predictions for $t\bar{t}H$ inclusive production, and in Section I.6.6 the NLO QCD predictions for tH production. Recent developments in improving the prediction for $t\bar{t}H$ production by either including off-shell effects or subsets of next-to-next-to-leading-order (NNLO) QCD corrections are discussed in Sections I.6.4 and I.6.5, respectively. Dedicated studies of some of the main background processes are presented in Section I.6.7 ($t\bar{t}V$ and $t\bar{t}VV'$ with $V, V' = W^{\pm}, Z$) and Section I.6.8 ($t\bar{t}b\bar{b}$).

One major activity of this working group has been the comparison and validation of state-of-the-art theoretical tools available to calculate both signal and backgrounds including the proper matching of fixed-order NLO QCD corrections and parton-shower evolution. Section I.6.3 presents such comparison for $t\bar{t}H$ production, while Sections I.6.7.b and I.6.8 present analogous studies for the $t\bar{t}V$ ($V = W^{\pm}, Z$) and $t\bar{t}b\bar{b}$ backgrounds.

I.6.2 NLO QCD+EW predictions for $t\bar{t}H$ production

Predictions for inclusive and differential $t\bar{t}H$ production at NLO QCD are available since more than a decade [321–325], while EW corrections have been calculated only recently [326–328]. Although their effect on total rates is usually suppressed with respect to NLO QCD corrections by a factor of order α/α_s, when hard scales are probed they can be enhanced by electroweak Sudakov logarithms [329–332]. For what concerns $t\bar{t}H$ production, in particular for a precise extraction of the top quark Yukawa coupling y_t, EW corrections should be accounted for because of at least two reasons. First, EW corrections, unlike QCD corrections, spoil the trivial dependence of the total cross section on $\sim y_t^2$, introducing also (small) terms where the Higgs couples to $W^{\pm}$ and Z bosons, or to itself. Second, EW corrections show Sudakov effects: in order to suppress backgrounds, many $t\bar{t}H$ searches are performed in a boosted

regime [333–335], where Sudakov logarithms can be important.

This section presents NLO QCD+EW predictions for inclusive $t\bar{t}H$ production. All input parameters are chosen according to [144], and the hadronic cross section is obtained using the PDF4LHC15 [35] and NNPDF2.3QED [279] parton distribution functions as explained in detail below. For the top-quark and Higgs boson masses the on-shell scheme is used, and the top-quark Yukawa coupling[I.30] is related to the top-quark mass and the Fermi constant (G_μ) by

$$y_\mathrm{t} = (\sqrt{2}G_\mu)^{1/2} M_\mathrm{t}\,. \tag{I.6.1}$$

The central value for renormalization and factorization scales is set to

$$\mu = M_\mathrm{t} + M_\mathrm{H}/2\,, \tag{I.6.2}$$

and the scale uncertainty is estimated by independent variations of renormalization (μ_R) and factorization (μ_F) scales in the range $\mu/2 \leq \mu_\mathrm{R}, \mu_\mathrm{F} \leq 2\mu$, with $1/2 \leq \mu_\mathrm{R}/\mu_\mathrm{F} \leq 2$.

The NLO QCD+EW predictions presented in the following,

$$\sigma^\mathrm{NLO}_\mathrm{QCD+EW} = \sigma^\mathrm{NLO}_\mathrm{QCD} + \delta\sigma_\mathrm{EW}\,, \tag{I.6.3}$$

result from the combination of various contributions. The usual NLO QCD cross section,

$$\sigma^\mathrm{NLO}_\mathrm{QCD} = \sigma^\mathrm{LO}_\mathrm{QCD} + \delta\sigma^\mathrm{NLO}_\mathrm{QCD}, \tag{I.6.4}$$

comprises LO terms of $\mathcal{O}(\alpha_\mathrm{s}^2\alpha)$ and NLO terms of $\mathcal{O}(\alpha_\mathrm{s}^3\alpha)$, which involve gg, $q\bar{q}$, and gq partonic channels. The remaining EW corrections, denoted as $\delta\sigma_\mathrm{EW}$, include three types of terms:

1. LO EW terms of $\mathcal{O}(\alpha^3)$ that result from squared EW tree amplitudes in the $q\bar{q}$ and $\gamma\gamma$ channels;
2. LO mixed terms of $\mathcal{O}(\alpha_\mathrm{s}\alpha^2)$ that result from the interference of EW and QCD tree diagrams in the $b\bar{b}$ and γg channels (other $q\bar{q}$ channels do not contribute at this order due to the vanishing interference of the related colour structures);
3. NLO EW corrections of $\mathcal{O}(\alpha_\mathrm{s}^2\alpha^2)$ in the $q\bar{q}$, gg and γg channels. Subleading NLO terms of $\mathcal{O}(\alpha_\mathrm{s}\alpha^3)$ and $\mathcal{O}(\alpha^4)$ are not included as they are expected to be strongly suppressed.

For $\sqrt{s} = 7$–14 TeV and $M_\mathrm{H} = 125$ GeV, the corrections resulting from LO EW, LO mixed and NLO EW effects are all positive and amount, respectively, to 0.5%, 0.8–1.5% and 1.1–1.9% of the NLO QCD cross section.[I.31] Photon-induced partonic channels dominate the LO mixed terms, while their contribution to LO EW and NLO EW terms is almost negligible.

A fully consistent treatment of NLO QCD+EW corrections requires corresponding precision in the employed PDF. In particular, parton distributions should include QED evolution effects and, consequently, a photon density. In order to circumvent the absence of QED effects in the PDF4LHC15 distributions the following approach is adopted:

1. NLO QCD contributions are computed using the PDF4LHC15 set: more precisely, the PDF4LHC15 set with 30+2 members is used for PDF and α_s uncertainty estimates;
2. all EW correction effects resulting form partonic channels with initial-state quarks and/or gluons are computed with the same PDF4LHC15 set;
3. for all γ-induced EW correction effects the NNPDF2.3QED set is used;
4. the missing $\mathcal{O}(\alpha)$ effect due to the QED evolution of quark PDF is estimated from the difference between NNPDF2.3QED parton densities and their NLO QCD counterpart without QED evolution, NNPDF2.3, both with $\alpha_\mathrm{s}(M_\mathrm{Z}) = 0.118$. The relevant $\mathcal{O}(\alpha)$ correction factor is determined as follows by means of a LO QCD calculation,

$$\delta\sigma_\mathrm{EW,PDF} = \sigma^\mathrm{NLO}_\mathrm{QCD}\,(1 + \delta_\mathrm{EW,PDF})\,, \qquad \text{where} \qquad \delta_\mathrm{EW,PDF} = \frac{\sigma^\mathrm{NNPDF\,QED}_\mathrm{LO\ QCD}}{\sigma^\mathrm{NNPDF}_\mathrm{LO\ QCD}} - 1\,. \tag{I.6.5}$$

[I.30] In the adopted convention the Feynman rule of the $t\bar{t}H$ vertex is $(-iy_\mathrm{t})$.

[I.31] Here $\mathcal{O}(\alpha)$ effects related to QED evolution of PDF (see below) are not included.

For $\sqrt{s} = 7$–14 TeV and $M_{\mathrm{H}} = 125$ GeV, the effect of QED PDF evolution ranges from -0.7% to -0.9%. Being negative it compensates in part the effect of LO and NLO EW corrections to the partonic cross sections.

At the same order of $\sigma_{\mathrm{EW}}^{\mathrm{NLO}}$ also the real emission of an extra heavy weak gauge boson can in principle contribute to the cross section for inclusive $t\bar{t}H$ production. Such a contribution from heavy-boson radiation (HBR) is generally not considered as part of EW corrections, owing to the fact that the emission of an extra heavy boson can be distinguished from the corresponding non emission. However, it can contribute to the cross section when the decay products of the heavy boson escape from, *e.g.*, the detector acceptance or the experimental selection cuts. Furthermore, these contributions might compensate the Sudakov logarithms which enhance the NLO EW corrections at large scales. We will not include HBR contributions in the following results. Their impact has been computed for the total cross section and differential observables in [327, 328], where it has been found to be small (less than 1%) on total rates and, unlike NLO EW corrections, only marginally enhanced when large energy scales are probed.

Tables 227–232 present NLO QCD+EW predictions for different collider energies and Higgs boson mass values. The relative impact of QCD and EW corrections is illustrated in the form of a QCD correction factor

$$K_{\mathrm{QCD}} = \frac{\sigma_{\mathrm{QCD}}^{\mathrm{NLO}}}{\sigma_{\mathrm{QCD}}^{\mathrm{LO}}}\,, \tag{I.6.6}$$

and a relative EW correction factor

$$\delta_{\mathrm{EW}} = \delta\sigma_{\mathrm{EW}}/\sigma_{\mathrm{QCD}}^{\mathrm{NLO}}\,. \tag{I.6.7}$$

All result in Tables 227–232 are based on MADGRAPH5_AMC@NLO [54], similarly as in [328]. A cross check against an independent calculation based on SHERPA+OPENLOOPS [336] has confirmed the correctness of NLO QCD+EW predictions for $\sqrt{s} = 7, 8, 13, 14$ TeV and $M_{\mathrm{H}} = 125$ GeV at the per mille level. Predictions for the production of a Higgs boson in the mass range $M_{\mathrm{H}} = 120$–130 GeV are reported in Tables 227–230 for $\sqrt{s} = 7, 8, 13, 14$ TeV respectively. The relative scale and PDF+α_{s} uncertainties are the same for NLO QCD as for NLO QCD+EW cross sections, therefore they can be computed for the former and applied to the latter. Tables 231, 232 list numbers at different $\sqrt{s}$ for $M_{\mathrm{H}} = 125.00$ GeV and $M_{\mathrm{H}} = 125.09$ GeV, respectively. The integration uncertainty affecting results is at 0.1% level for $\sigma_{\mathrm{QCD+EW}}^{\mathrm{NLO}}$. The left and right plots in Figure 69 show the $t\bar{t}H$ cross section as a function of the Higgs boson mass at 13 TeV, for the SM and BSM range respectively. The scale, PDF, and α_{s} uncertainties are also shown, together with the QCD and EW correction factors.

I.6.3 Comparison of NLO QCD+Parton Shower simulations for $t\bar{t}H\,(b\bar{b})$

In recent years fixed-order NLO QCD calculations of $t\bar{t}H$ have been interfaced with parton-shower (PS) Monte-Carlo generators (HERWIG [313, 337, 338], PYTHIA [207, 318, 319, 339], and SHERPA [229]) using one of the methods proposed in the literature, namely MC@NLO [340, 341], POWHEG [342–344], and S-MC@NLO [345, 346], and are nowadays implemented in a variety of tools, from MADGRAPH5_AMC@NLO [54, 347, 348], to POWHEL [349, 350], POWHEG BOX [81, 351], SHERPA+OPENLOOPS [229, 247, 352], and HERWIG7 [306, 313].

The accurate description of the $t\bar{t}H$ signal, from the energy scale of the hard scattering to the hadronization energy scale, crucially relies on these tools and their use in experimental analyses is highly recommended. Due to the prominent role that $t\bar{t}H$ production will play in the Higgs-physics program of Run 2 of the LHC, it is crucial to validate different implementations against each other and verify their compatibility. Given the multiplicity and diversity of NLO QCD parton-shower Monte-Carlo generators available to calculate $t\bar{t}H$ observables (total cross section and distributions), a systematic comparison requires to define a common set-up that takes into account the technical aspects of different matching schemes between fixed-order NLO QCD calculation and parton shower. It is the first necessary step towards a better control of the theoretical accuracy of $t\bar{t}H$ predictions, and has been the purpose of a

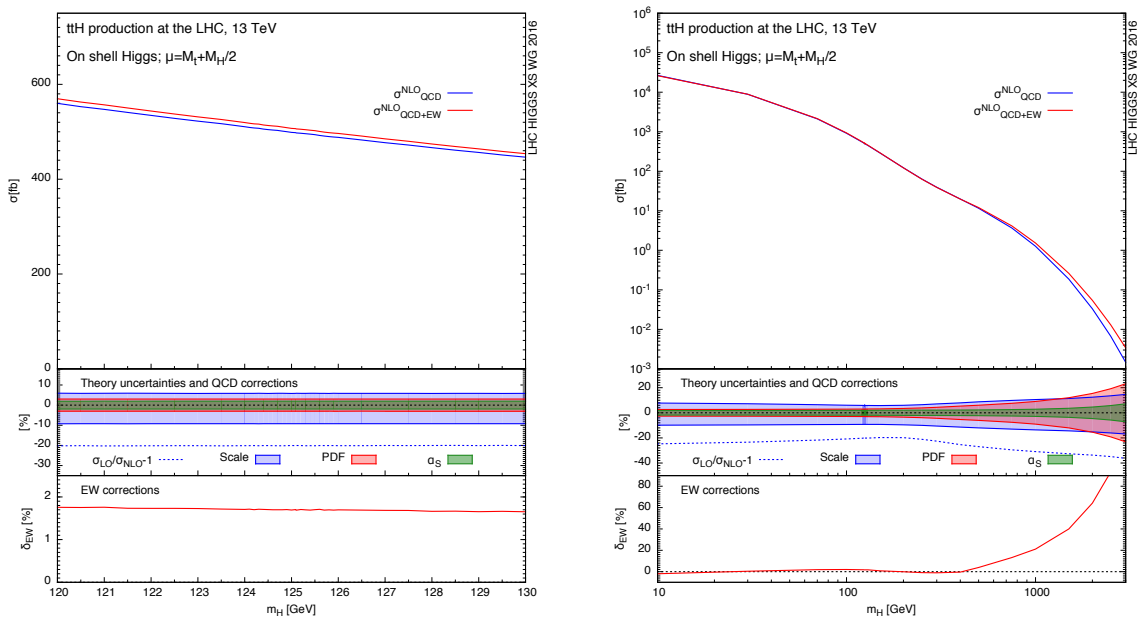

Figure 69: The upper panel shows the $t\bar{t}H$ total cross section as a function of M_{H}, at 13 TeV, including only NLO QCD corrections (blue curve) and both NLO QCD+EW corrections (red curve). The intermediate panel illustrates the estimated theoretical uncertainties from scale, PDF, and α_{s} variation over the same M_{H} ranges. The lower panel shows the size of the electroweak corrections as a function of M_{H}.

dedicated study in the context of the $t\bar{t}H$ working group. Previous studies [8, 33] have shown compatibility among different subsets of these tools, but different choices made in each existing study prevent to derive from them a more uniform comparison.

In this section we present details and outcomes of a new comprehensive comparison of the most up-to-date tools currently available for Run 2 studies, and compare them using a common choice of input parameters for the fixed-order NLO QCD calculation and the PS. Some arbitrariness in the choice of PS-specific parameters can still be present, as will be manifest in the comparison of observables that are more sensitive to regions of phase space that are dominated by the PS. We recommend that the comparison presented in this section serves as the main reference to anybody interested in using any of the NLO QCD+PS tools that will be discussed in the following for the production of official samples of $t\bar{t}H$ showered events.

We have compared five NLO QCD calculations of $t\bar{t}H$ consistently interfaced with either SHERPA, PYTHIA8, or HERWIG7. Namely, we have compared results from:

- S-MC@NLO using OPENLOOPS 1.2.3 + SHERPA 2.2.0,
- MADGRAPH5_AMC@NLO 2.3.2 + PYTHIA8 2.1.0,
- POWHEL + PYTHIA8 2.1.0,
- POWHEG BOX + PYTHIA8 2.1.0,
- HERWIG7 using OPENLOOPS 1.2.4+ MADGRAPH5_AMC@NLO 2.3.0+ HERWIG7.

SHERPA+OPENLOOPS uses OPENLOOPS [247] as a one-loop generator, and relies on the CUTTOOLS library [353] for the numerically stable evaluation of tensor integrals. Real-emission contributions, infrared subtractions based on the Catani-Seymour technique [249, 354], and phase-space integration are handled by SHERPA. The NLO corrections are matched to the SHERPA PS generator [355] using the SHERPA formulation [345, 356] of the MC@NLO [340, 341] method, also dubbed S-MC@NLO.

Within MADGRAPH5_AMC@NLO [54, 348], fixed-order NLO QCD results are obtained by adopting the FKS method [113, 357] for the subtraction of the infrared divergences of the real-emission matrix elements (automated in the module MADFKS [358]), and the OPP integral-reduction procedure [359] for the computation of the one-loop matrix elements (automated in the module MADLOOP [348]). Matching with parton showers is achieved by means of the MC@NLO formalism [340, 341].

The POWHEG BOX framework [81, 342, 343] adopts the FKS subtraction scheme [113, 357] to factor out the infrared singularities of the real-emission cross section, while the the virtual one-loop matrix elements can be provided with different methods. In the public POWHEG BOX (V2) distribution of $t\bar{t}H$, the NLO QCD virtual corrections are implemented using the one-loop routines from the NLO QCD calculation of Ref. [321–323]. The corresponding results are labelled as POWHEG BOX in this section. On the other hand, the POWHEL generator [350] uses the HELAC-NLO package [349] for the computation of all matrix elements provided as input to the POWHEG BOX. Within the POWHEG BOX the matching with parton showers is obtained implementing the POWHEG matching scheme [342–344]. The matched results from the NLO computations are interfaced to PYTHIA8 via Les-Houches event (LHE) files.

HERWIG7, based on extensions of the previously developed MATCHBOX module [306, 307], implements the Catani-Seymour dipole subtraction method [249, 354] for the infrared divergences of the real-emission matrix elements, provides for the final-state phase-space integration, and can interface to a variety of LO and NLO matrix elements providers, either at the level of squared matrix elements, based on extensions of the BLHA standard [33, 360, 361], or at the level of colour–ordered subamplitudes, where the colour bases are provided by an interface to the COLORFULL [362] and CVOLVER [363] libraries. For this study the relevant tree-level matrix elements are provided by MADGRAPH5_AMC@NLO [54, 364] (at the level of colour-ordered subamplitudes), whereas the relevant tree-level/one-loop interference terms are provided by OPENLOOPS [247, 365] (at the level of squared matrix elements). Fully automated NLO matching algorithms are available, henceforth referred to as subtractive (NLO$\oplus$) and multiplicative (NLO$\otimes$) matching – based on the MC@NLO [340] and POWHEG [342] formalism respectively – for the systematic and consistent combination of NLO QCD calculations with both shower variants (an angular–ordered parton shower [366] and a dipole shower [367]) in HERWIG7. For this study the subtractive matching in combination with the angular–ordered parton shower has been chosen.

For the purpose of the comparison presented in this section, the NLO QCD calculation has been performed using $N_{\mathrm{F}} = 5$ light flavours, $\sqrt{s} = 13$ TeV for the centre-of-mass energy, $M_{\mathrm{H}} = 125$ GeV for the Higgs boson mass, and $M_{\mathrm{t}} = 172.5$ GeV for the top-quark mass. The top-quark Yukawa coupling has been defined in terms of the Fermi constant as $y_{\mathrm{t}} = (\sqrt{2}G_F)^{1/2}M_{\mathrm{t}}$. We have followed the recommendation of the Higgs Cross-Section Working Group [144] for all other parameters that are not explicitly given here. We have used a dynamical renormalization (μ_{R}) and factorization (μ_{F}) scale defined as the geometric mean of the transverse energies (E_T) of the final-state particles (t, $\bar{t}$, and H). The central value of both scales is then set to $\mu_0 = (E_{\mathrm{T}}(t)E_{\mathrm{T}}(\bar{t})E_{\mathrm{T}}(H))^{1/3}$, where $E_{\mathrm{T}} = \sqrt{M^2 + p_{\mathrm{T}}^2}$ for M the mass of a given particle and p_{T} its corresponding transverse momentum. Finally, following the Higgs Cross Section Working Group recommendation, we have used the PDF4LHC15 parton distribution functions (PDF) [35], and more specifically the central set of PDF4LHC15_nlo_30, with NLO $\alpha_{\mathrm{s}}(\mu)$ and $\alpha_{\mathrm{s}}(M_{\mathrm{Z}}) = 0.118$.

The different parton-shower generators have all been set up not to include hadronization, underlying events, and QED effects in the shower. The shower resummation scale has been set to $H_T/2$ where

$H_{\rm T}$ is defined as the sum of the $t\bar{t}H$ final-state transverse energies ($H_{\rm T} = E_{\rm T}(t) + E_{\rm T}(\bar{t}) + E_{\rm T}(H)$). In particular, this corresponds to setting $\mu_{\rm Q} = H_{\rm T}/2$ in S-MC@NLO and MADGRAPH5_AMC@NLO, while in POWHEG BOX it is implemented by setting $h = H_{\rm T}/2$ in the definition of $h_{\rm damp} = h^2/(h^2 + p_{\rm T}^2)$, where $p_{\rm T}$ is the transverse momentum of the hardest parton in the $O(\alpha_{\rm s})$ QCD real emission. In the case of HERWIG7 the hard shower scale, similarly to the renormalization and factorization scale, has been set to be the geometric mean of the transverse energies (see above). Internal studies have shown that a different scale choice for the hard shower scale results in only small differences in the distributions.

The theoretical uncertainty bands have been calculated purely from the renormalization and factorization scale dependence, estimated by varying these scales independently by a factor of two about their central value ($\mu_{\rm R} = \xi_{\rm R}\mu_0$ and $\mu_{\rm F} = \xi_{\rm F}\mu_0$, with $\xi_{\rm R,F} = 1/2, 1, 2$). For the purpose of this comparison we have used a common set of PDF and therefore we have not included in the theoretical error any uncertainty from PDF variation (since it would have been the same for all results). No uncertainty from the parton shower has been included. It has been our goal to investigate if, under physically equivalent choices of the parton-shower setup, and having eliminated the differences that can come from different treatment of hadronization and underlying events, all the tools considered in this comparison give results that are compatible within the scale uncertainty for all observables that are not directly affected by parton-shower effects (see discussion of Figs. 70-75). Differences that are observed in regions of phase space dominated by the PS should be resolved by properly including parton-shower uncertainties, and this study should serve as solid ground to investigate these parton-shower specific effects.

Finally, we have considered two scenarios: without and with decays of the $t\bar{t}H$ final-state particles. In the second case, we have let the Higgs boson decay to b quarks, $H \to b\bar{b}$, while the top and antitop quarks decay leptonically to $t \to be^+\nu_{\rm e}$ and $\bar{t} \to \bar{b}\mu^-\bar{\nu}_\mu$, respectively. Notice that, for the purpose of this comparison, the results presented include only this specific decay chain, i.e. correspond to the process $t\bar{t}H \to e^+\mu^-\nu_{\rm e}\bar{\nu}_\mu b\bar{b}b\bar{b}$. Events are required to contain one e^+ and one μ^- with transverse momentum $p_{\rm T}^l > 20$ GeV and pseudorapidity $|\eta^l| < 2.5$ (l=lepton), as well as missing transverse energy $\not{E}_{\rm T} > 30$ GeV, and four b jets. b jets are defined using the anti-k_T jet algorithm with $R = 0.4$, and requiring that the jet contains at least one b or $\bar{b}$ quark and has transverse momentum $p_{\rm T}^{\rm b} > 25$ GeV and pseudorapidity $|\eta^{\rm b}| < 2.5$. Finally, spin-correlation effects have been taken into account using the built-in implementations of each package, like MADSPIN [368] for MADGRAPH5_AMC@NLO, DECAYER [369] for POWHEL, and analogous modules for POWHEG BOX, S-MC@NLO, and HERWIG7, all based on the approach originally proposed in Ref. [370]. The results from the five NLO QCD+PS simulations listed above have been processed through a common R-IVET analysis that implements the selection cuts described above.

In Figs. 70-71 we present results for the comparison of the on-shell case (no decay of t, $\bar{t}$, and H included), while in Figs. 72 -75 we present results for the case of $t\bar{t}H \to e^+\mu^-\nu_{\rm e}\bar{\nu}_\mu b\bar{b}b\bar{b}$. In order to minimize the effect of treating decays at LO the corresponding branching ratios have been normalized to ${\rm Br}(H \to b\bar{b}) = 57.7\%$ (from Ref. [9], for $M_{\rm H} = 125$ GeV), and ${\rm Br}(t \to be^+\nu_{\rm e}) = {\rm Br}(W^+ \to e^+\nu_{\rm e}) = 10.83\%$ (from [11]), and similarly for $\bar{t} \to \bar{b}\mu^-\bar{\nu}_\mu$.

In each case we compare results for various standard differential observables. Each plot shows in the upper window the comparison of results obtained using the five different NLO QCD+PS tools used in our study, as well as the pure NLO QCD fixed-order results (see Table 229) which have been used for validation. The lower windows of each plot illustrate the theoretical uncertainty from renormalization- and factorization-scale dependence calculated as previously explained. More specifically, each lower window shows all results normalized to a particular one, together with the uncertainty band of the latter. For NLO distributions this uncertainty is of the order of 10-15%, but can grow to 20% or more in the tails of distributions. On the other hand, a much larger uncertainty affects distributions like the $p_{\rm T}$ of the hardest light jet since the underlying hard process is LO in nature.

The comparison of both total cross sections and distributions shows in general full compatibility among all sets of results within the theoretical uncertainty considered in this study. This is in particular

true for the on-shell case, when decays of the final-state particles are not considered. This validates the set-up chosen for the comparison, both at the level of the fixed-order NLO QCD calculation and at the level of the matching with the PS.

In the case in which the decays of both top-quarks and Higgs boson are implemented we still see overall very good agreement. We notice some moderate discrepancies in the distribution in the number of b jets ($d\sigma/dN_{\mathrm{b-jets}}$). In the case of POWHEL+PYTHIA8 the excess in the low $N_{\mathrm{b-jets}}$ bins and the deficit in the high $N_{\mathrm{b-jets}}$ bins are mainly due to having considered the bottom quarks as massless in the decays of the top quarks, matched to a parton shower that uses massive bottom quarks. As all other distributions in Figs. 72-75 are obtained from events with exactly four b jets, the difference in the exclusive b-jet multiplicity distribution at $N_{\mathrm{b-jets}} = 4$ affects the normalization of the distributions, but leaves their shapes intact.

On the other hand, the overall discrepancy between most implementations considered for $N_{\mathrm{b-jets}} > 4$ is mainly of parton-shower origin. Indeed, since the $N_{\mathrm{b-jets}} > 4$ bins are mainly populated by b jets originating in the parton shower, these effects depend on the specific set up of the parton-shower algorithm used in each case and should be considered as part of the theoretical uncertainty coming from the parton shower, which we have not explicitly quantified in this study. A dedicated study of parton-shower effects acquires more meaning in the context of specific experimental analyses, if, for instance, observables like $d\sigma/dN_{\mathrm{b-jets}}$ for large numbers of b jets had to become relevant. Having provided a sound comparison of a broad variety of main NLO QCD+PS frameworks, we have laid the foundation for further dedicated studies that will likely happen in the context of specific experimental analyses.

I.6.4 Off-shell effects in $t\bar{t}H$ production

I.6.4.a $t\bar{t}H$ with off-shell top decays: $W^+W^-b\bar{b}H$ production at NLO QCD

In this section predictions for the hadronic production of top–antitop pairs in association with a Higgs boson at next-to-leading-order QCD, including the decay of the top and antitop quark into bottom quarks and leptons, are presented. The computation is based on full leading and next-to-leading-order matrix elements for $\mathrm{e}^+\nu_\mathrm{e}\mu^-\bar{\nu}_\mu\mathrm{b\bar{b}H(j)}$ and includes all non-resonant contributions, off-shell effects and interferences (for more details see Ref. [371]). Besides off-shell effects also NLO corrections to top-quark decays are included, which is not the case in many NLO and NLO + parton shower (PS) $\mathrm{t\bar{t}H}$ calculations on the market.

I.6.4.a.i Method of calculation

The study is based on the tree-level amplitudes at $\mathcal{O}(\alpha_\mathrm{s}\alpha^{5/2})$ for gluon-induced and quark–antiquark-induced processes and the corresponding NLO corrections of order α_s. The bottom quark is considered massless. The corresponding real corrections receive also contributions of quark–gluon- and antiquark–gluon-initiated processes. The Catani–Seymour subtraction formalism [249, 354] is applied for the regularization and analytical cancellation of IR singularities. For the computation of all matrix elements as well as colour- and spin-correlated squared matrix elements needed for the evaluation of subtraction terms, the recursive amplitude generator RECOLA [372] is employed. A consistent description of all resonances is achieved using the complex-mass scheme [373–375]. The top-quark Yukawa coupling is defined in the on-shell scheme.

The matrix elements for the virtual corrections are calculated with RECOLA, which uses the COLLIER [248, 376] library for the numerical evaluation of one-loop scalar [377–380] and tensor integrals [381–383]. The results for the virtual NLO contribution to the squared amplitude, $2\,\mathrm{Re}\,\mathcal{M}_0^*\mathcal{M}_1$, have been successfully compared with MADGRAPH5_AMC@NLO [54]. In addition the Ward identity for the matrix elements of the gluon-initiated process at tree and one-loop level has been checked.

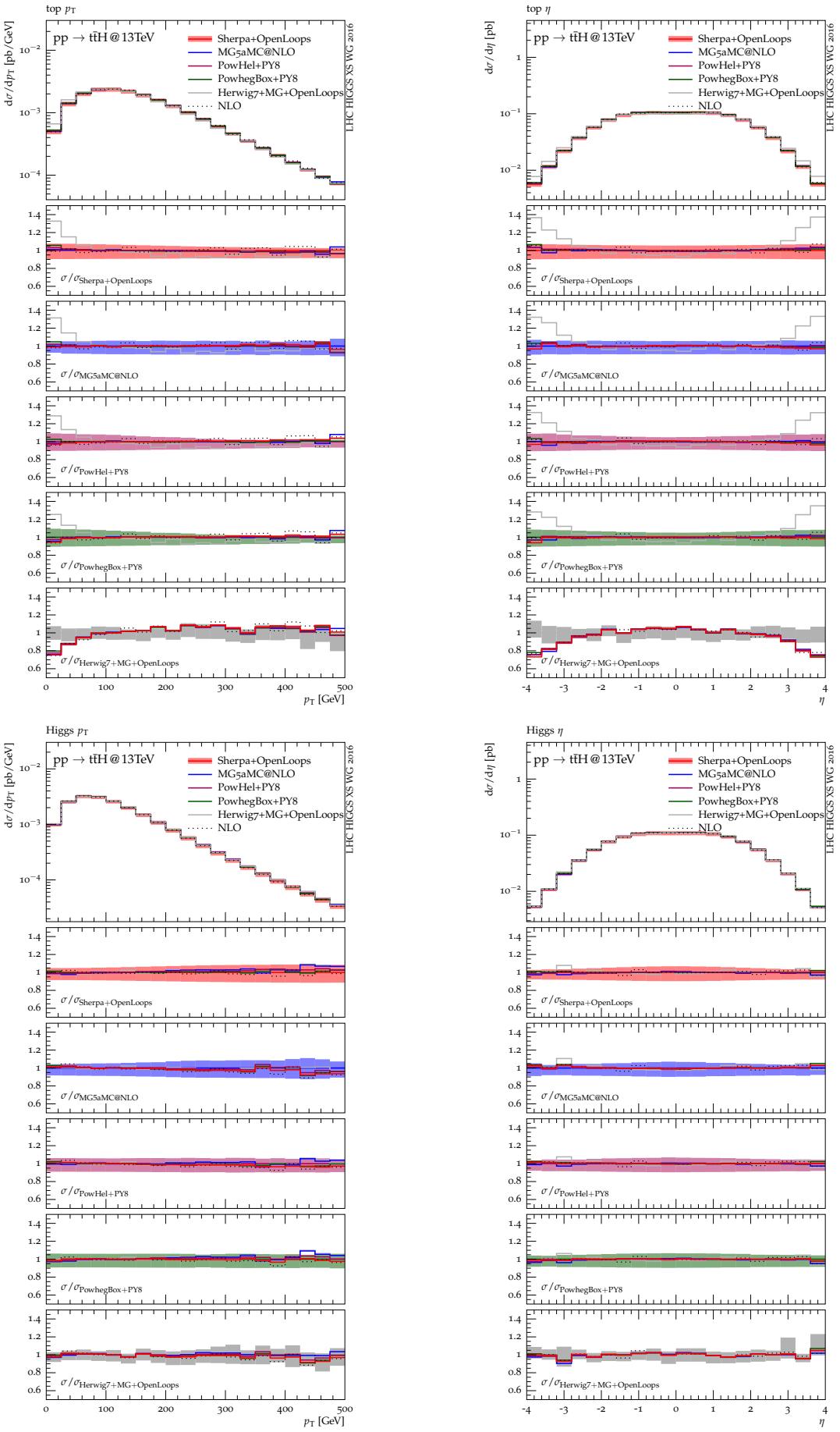

Figure 70: NLO QCD+PS and fixed-order NLO QCD predictions for differential $t\bar{t}H$ observables at 13 TeV. Each ratio plot shows all results normalized to one particular NLO QCD+PS prediction and the scale variation band of the latter.

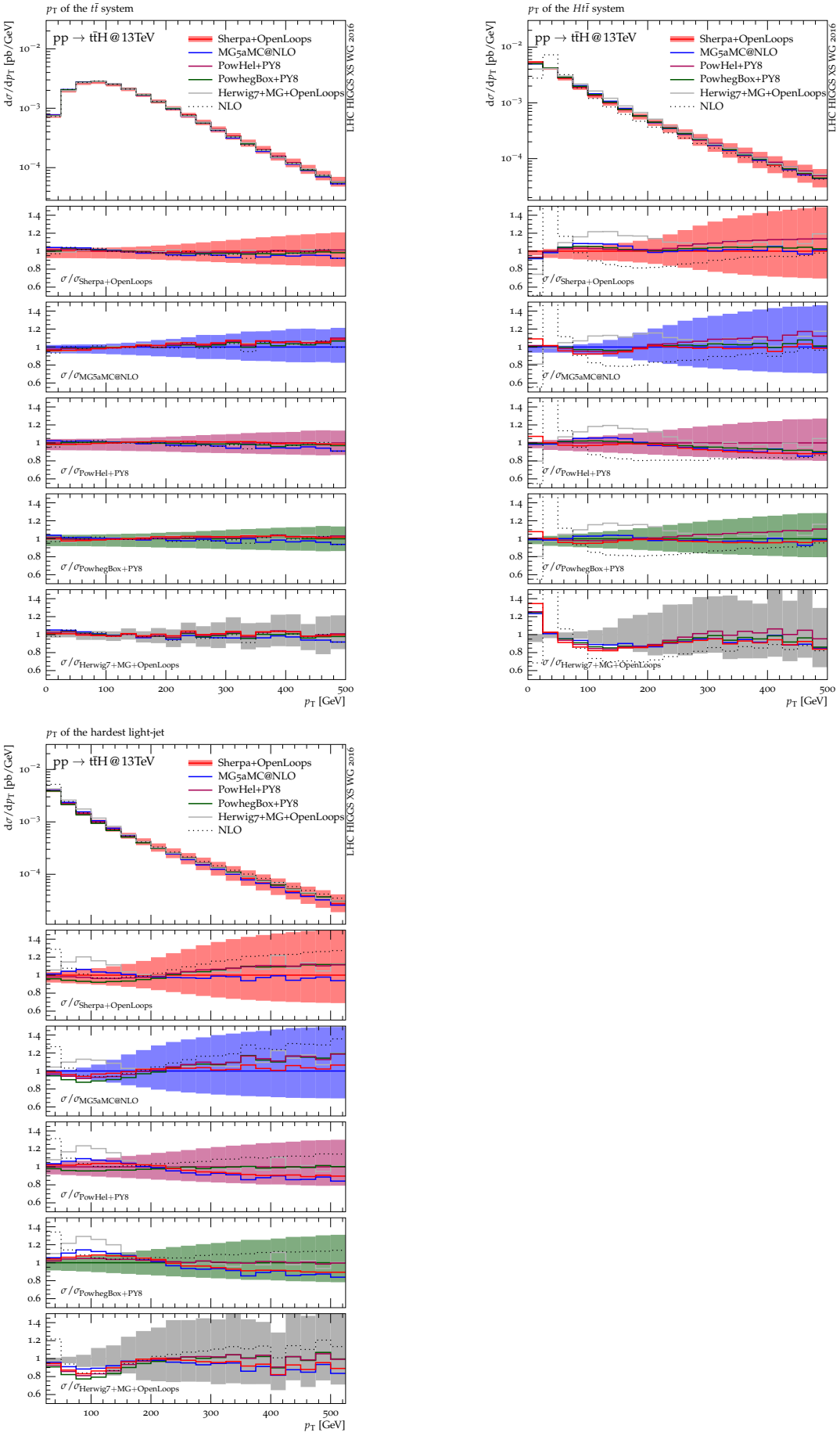

Figure 71: NLO QCD+PS and fixed-order NLO QCD predictions for differential $t\bar{t}H$ observables at 13 TeV. The ratio plots are defined as in Figure 70.

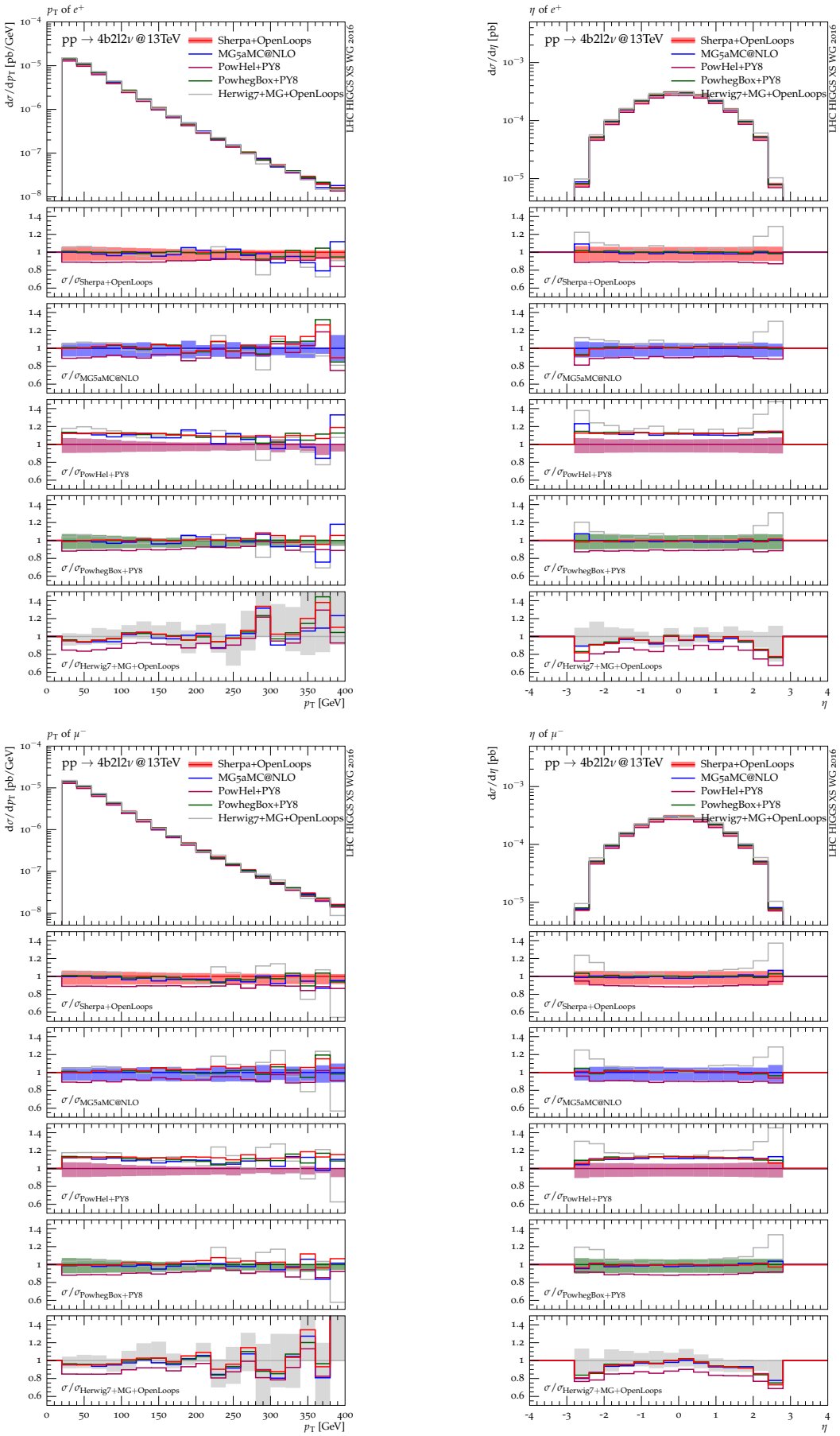

Figure 72: NLO QCD+PS predictions for differential $t\bar{t}H$ observables with $t\bar{t}H \to e^+\mu^-\nu_e\bar{\nu}_\mu + b\bar{b}b\bar{b}$ at 13 TeV. The ratio plots are defined as in Figure 70.

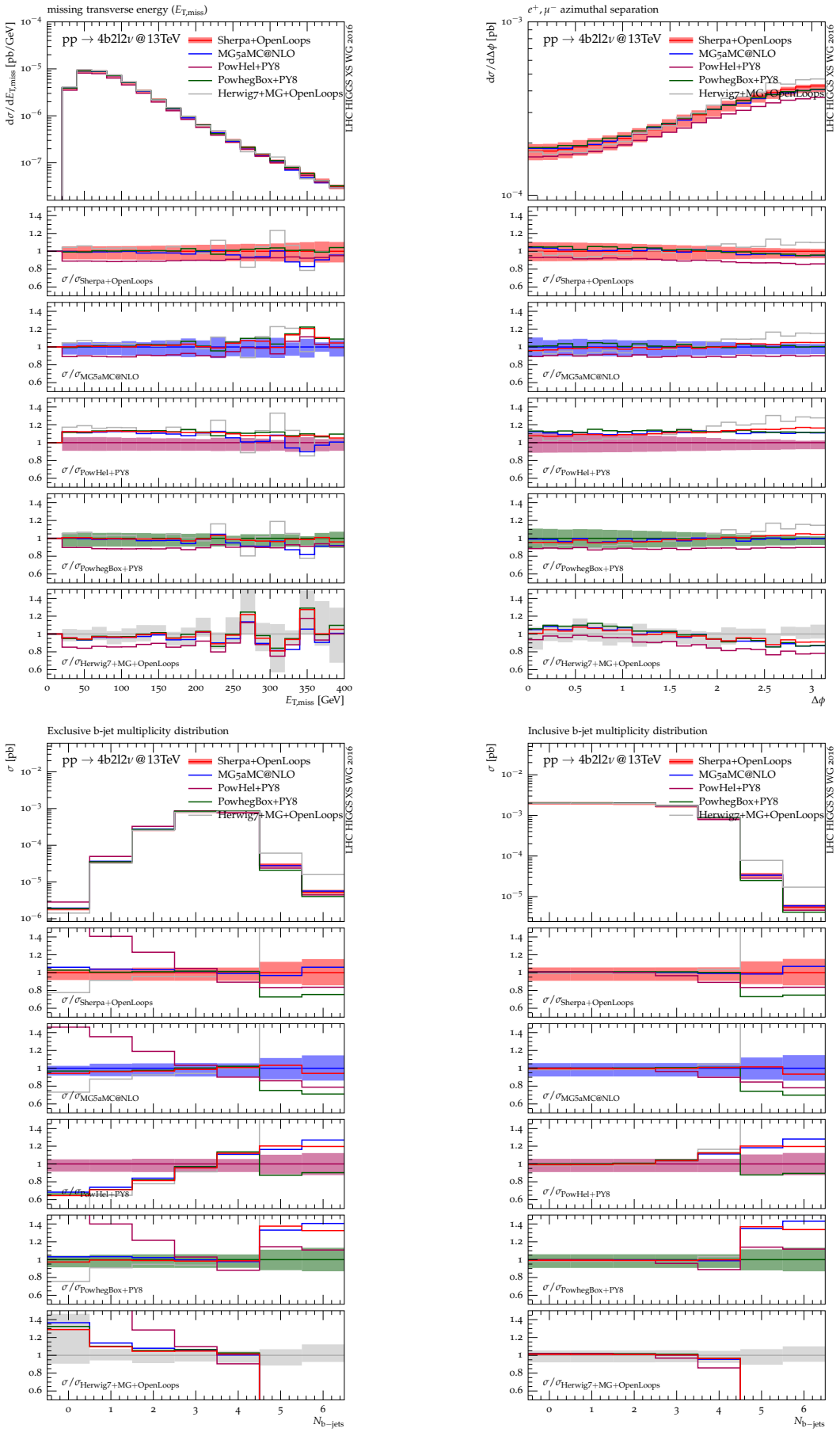

Figure 73: NLO QCD+PS predictions for differential $t\bar{t}H$ observables with $t\bar{t}H \to e^+\mu^-\nu_e\bar{\nu}_\mu + b\bar{b}b\bar{b}$ at 13 TeV. The ratio plots are defined as in Figure 70.

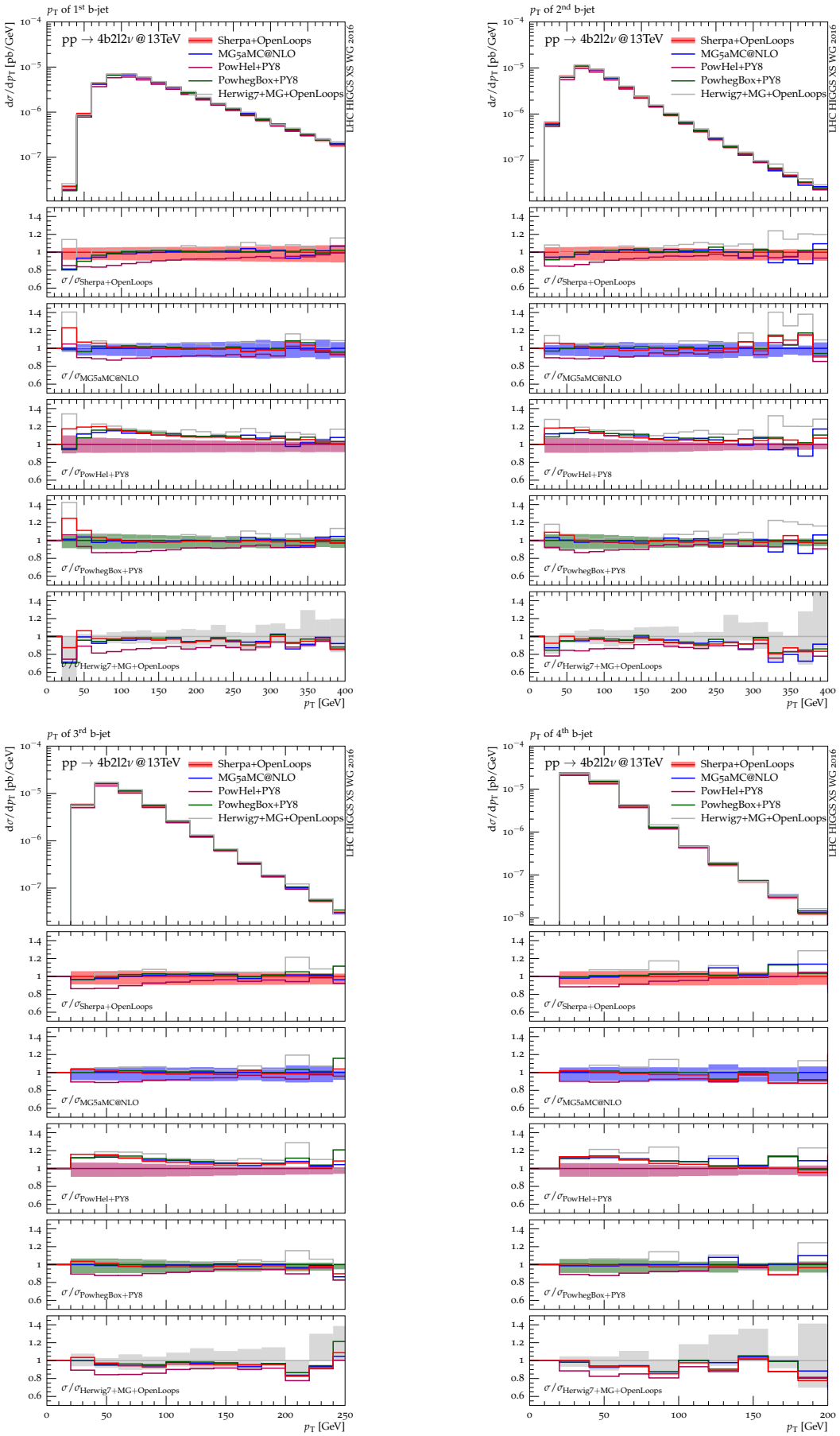

Figure 74: NLO QCD+PS predictions for differential $t\bar{t}H$ observables with $t\bar{t}H \to e^+\mu^-\nu_e\bar{\nu}_\mu + b\bar{b}b\bar{b}$ at 13 TeV. The ratio plots are defined as in Figure 70.

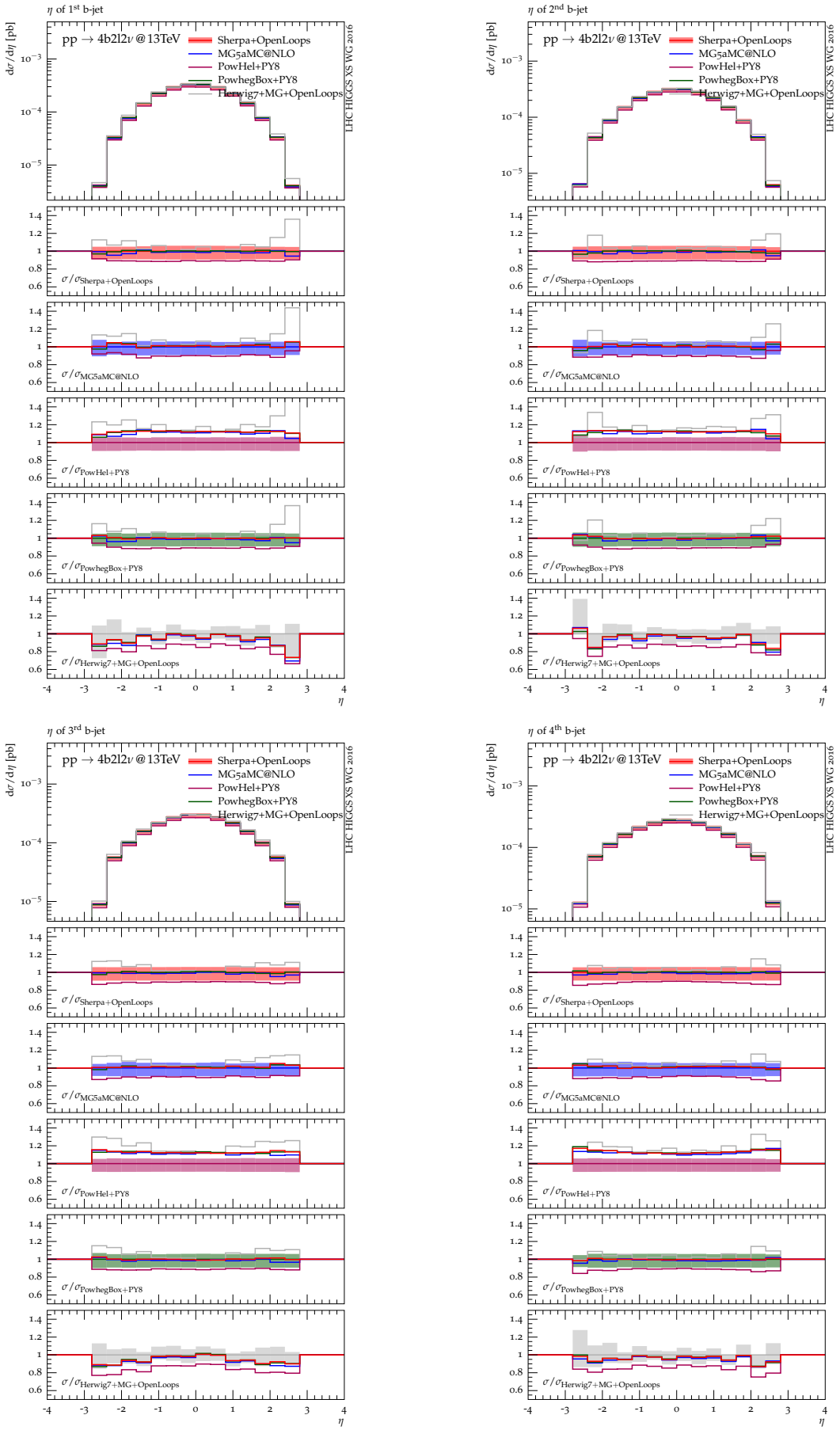

Figure 75: NLO QCD+PS predictions for differential $t\bar{t}H$ observables with $t\bar{t}H \to e^+\mu^-\nu_e\bar{\nu}_\mu + b\bar{b}b\bar{b}$ at 13 TeV. The ratio plots are defined as in Figure 70.

Table 34: Composition of the integrated cross section for $\mathrm{pp} \to \mathrm{e}^+\nu_\mathrm{e}\mu^-\bar{\nu}_\mu \mathrm{b\bar{b}H(j)}$ at the 13 TeV LHC with the dynamical scale. In column one the partonic initial states are listed, where $q = \mathrm{u}, \mathrm{d}, \mathrm{c}, \mathrm{s}$ and $\overline{q} = q, \bar{q}$. The second and third column give the integrated cross sections in fb for LO and NLO, resp., including scale uncertainties. The last column provides the K factor with $K = \sigma_\mathrm{NLO}/\sigma_\mathrm{LO}$.

pp	σ_LO [fb]	σ_NLO [fb]	K
gg	$1.5906(1)^{+33.7\%}_{-23.6\%}$	$2.024(3)^{+8.4\%}_{-16.2\%}$	1.273(2)
$q\bar{q}$	$0.67498(9)^{+24.1\%}_{-18.1\%}$	$0.495(1)^{+17.2\%}_{-39.5\%}$	0.733(2)
$\mathrm{g}\overline{q}$		$0.136(1)^{+295\%}_{-166\%}$	
$\sum$	$2.2656(1)^{+30.8\%}_{-22.0\%}$	$2.656(3)^{+0.9\%}_{-4.6\%}$	1.172(1)

I.6.4.a.ii Setup of the analysis

Cross section and differential distributions for the LHC operating at 13 TeV are investigated. LHAPDF 6.05 with CT10NLO parton distributions are employed for LO and NLO cross sections and contributions from the suppressed bottom-quark parton density and flavour mixing are neglected. The value of the strong coupling constant α_s as provided by LHAPDF based on a two-loop accuracy with $N_\mathrm{F} = 5$ active flavours is used. The electromagnetic coupling α is derived from the Fermi constant in the G_μ scheme. The width of the top quark Γ_t is calculated at LO and NLO QCD including effects of off-shell W bosons according to Ref. [384]. The top-quark width is calculated at the scale M_t, which is kept fixed when studying scale uncertainties.

For the jet reconstruction the anti-k_T algorithm [191] is used with a jet-resolution parameter $R = 0.4$. Only final-state quarks and gluons with rapidity $|y| < 5$ are clustered into infrared-safe jets. After recombination standard selection cuts are imposed on transverse momenta and rapidities of charged leptons and b jets, missing transverse momentum and rapidity–azimuthal-angle distance between b jets. Two b jets and two charged leptons in the final state are required, with bottom quarks in jets leading to b jets, and

$$\begin{aligned} \text{b jets:} \quad & p_{T,\mathrm{b}} > 25\ \text{GeV}, \quad |y_\mathrm{b}| < 2.5, \\ \text{charged lepton:} \quad & p_{T,\ell} > 20\ \text{GeV}, \quad |y_\ell| < 2.5, \\ \text{missing transverse momentum:} \quad & p_{T,\text{miss}} > 20\ \text{GeV}, \\ \text{b-jet–b-jet distance:} \quad & \Delta R_\mathrm{bb} > 0.4. \end{aligned} \tag{I.6.8}$$

As default, a dynamical scale

$$\mu_\text{dyn} = \mu_\mathrm{R} = \mu_\mathrm{F} = \left(M_{\mathrm{T,t}}\, M_{\mathrm{T},\bar{\mathrm{t}}}\, M_{\mathrm{T,H}}\right)^{\frac{1}{3}} \quad \text{with} \quad M_\mathrm{T} = \sqrt{M^2 + p_\mathrm{T}^2} \tag{I.6.9}$$

is used for the renormalization μ_R and factorization scale μ_F following Ref. [347]. Alternatively, a fixed scale according to Ref. [325] is chosen:

$$\mu_\text{fix} = \mu_\mathrm{R} = \mu_\mathrm{F} = \frac{1}{2}\left(2M_\mathrm{t} + M_\mathrm{H}\right) = 236\ \text{GeV}. \tag{I.6.10}$$

Scale uncertainties are determined by computing integrated and differential cross sections at seven scale pairs, $(\mu_\mathrm{R}/\mu_0, \mu_\mathrm{F}/\mu_0) = (0.5, 0.5), (0.5, 1), (1, 0.5), (1, 1), (1, 2), (2, 1), (2, 2)$. The central value corresponds to $(\mu_\mathrm{R}/\mu_0, \mu_\mathrm{F}/\mu_0) = (1, 1)$, and the error band is constructed from the envelope of these seven calculations.

I.6.4.a.iii Results for integrated cross sections

In Table 34 the integrated cross sections for the dynamical scale (I.6.9) is presented. The cross sections for the fixed scale (I.6.10) are lower by only about 1 %, and the K factor for the fixed scale is 1.176(1).

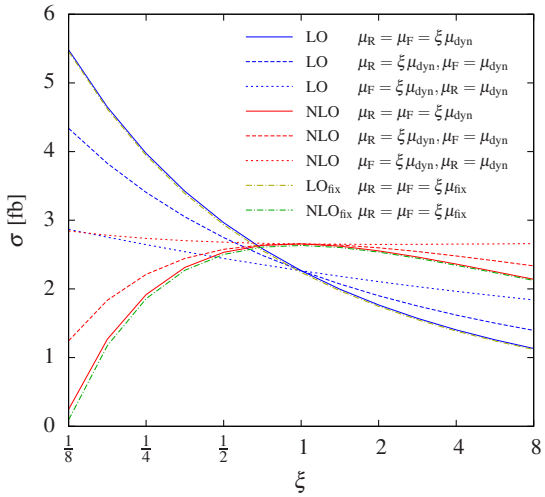

Figure 76: Scale dependence of the LO and NLO integrated cross section at the 13 TeV LHC. The renormalization and factorization scales are varied around the central values of the fixed ($\mu_0 = \mu_{fix}$, dash-dotted lines) and dynamical scale ($\mu_0 = \mu_{dyn}$, solid lines). For the dynamical scale the variation with μ_R while keeping $\mu_F = \mu_{dyn}$ fixed and vice versa is shown with dashed lines.

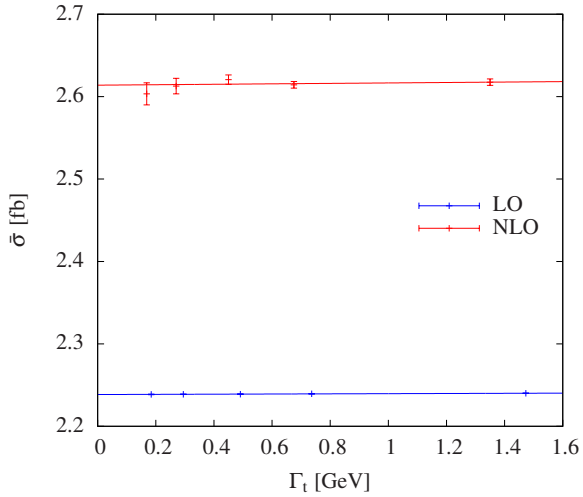

Figure 77: Zero-top-width extrapolation of the LO and NLO cross section at the LHC at $\sqrt{s} = 13$ TeV for fixed scale $\mu_0 = \mu_{fix}$.

The contribution of the dominating gluon-fusion channel increases from about 70 % at LO to 76 % at NLO. The contribution of the quark–antiquark annihilation drops from about 30 % at LO to 19 % at NLO. The gluon–(anti)quark induced real-radiation subprocesses contribute about 5 % at NLO. The inclusion of NLO QCD corrections reduces the scale dependence from 31 % to 5 %. Note that the NLO scale uncertainty band in Table 34 is by a factor 3 smaller than for on-shell $t\bar{t}H$ production at 13 TeV with the PDF4LHC15 prescription. This might be due to the acceptance cuts, the PDFs, or to the fact that scale variations are not applied to the top width.

The dependence of the integrated LO (blue) and NLO (red) cross sections on the values of the fixed and dynamical scale is displayed in Figure 76. Solid lines for the dynamical scale and dash-dotted lines for the fixed scale show the scale dependence for a simultaneous variation of the renormalization and factorization scales and dashed lines the individual variation, where one of the scales is kept fix at the central value, for the dynamical scale only. While the largest scale variation is obtained when both scales are changed simultaneously, the smallest effect results if only the factorization scale is varied. The cross sections for the fixed and dynamical scale choices are uniformly shifted relative to each other by about 1 % as for the central scale μ_0 both for LO and NLO except for $\mu < \mu_0/2$, where the fixed scale leads to a faster decrease of the cross section with μ as the dynamical scale. For the fixed and dynamical scale the maximum of the NLO cross section is near $\mu \simeq \mu_0$, justifying the use of both scale choices to be stable against scale variations. The K factor equals one at the slightly lower scale of about $\mu \simeq 0.7\mu_0$

The effects of the finite top-quark width have been determined via a numerical extrapolation to the zero-top-width limit, $\Gamma_t \to 0$ (see Figure 77). For fixed scale μ_{fix} finite-top-width effects shift the LO and NLO cross section by -0.07 ± 0.01 % and -0.14 ± 0.22 %, respectively, which are within the expected order of Γ_t/M_t.

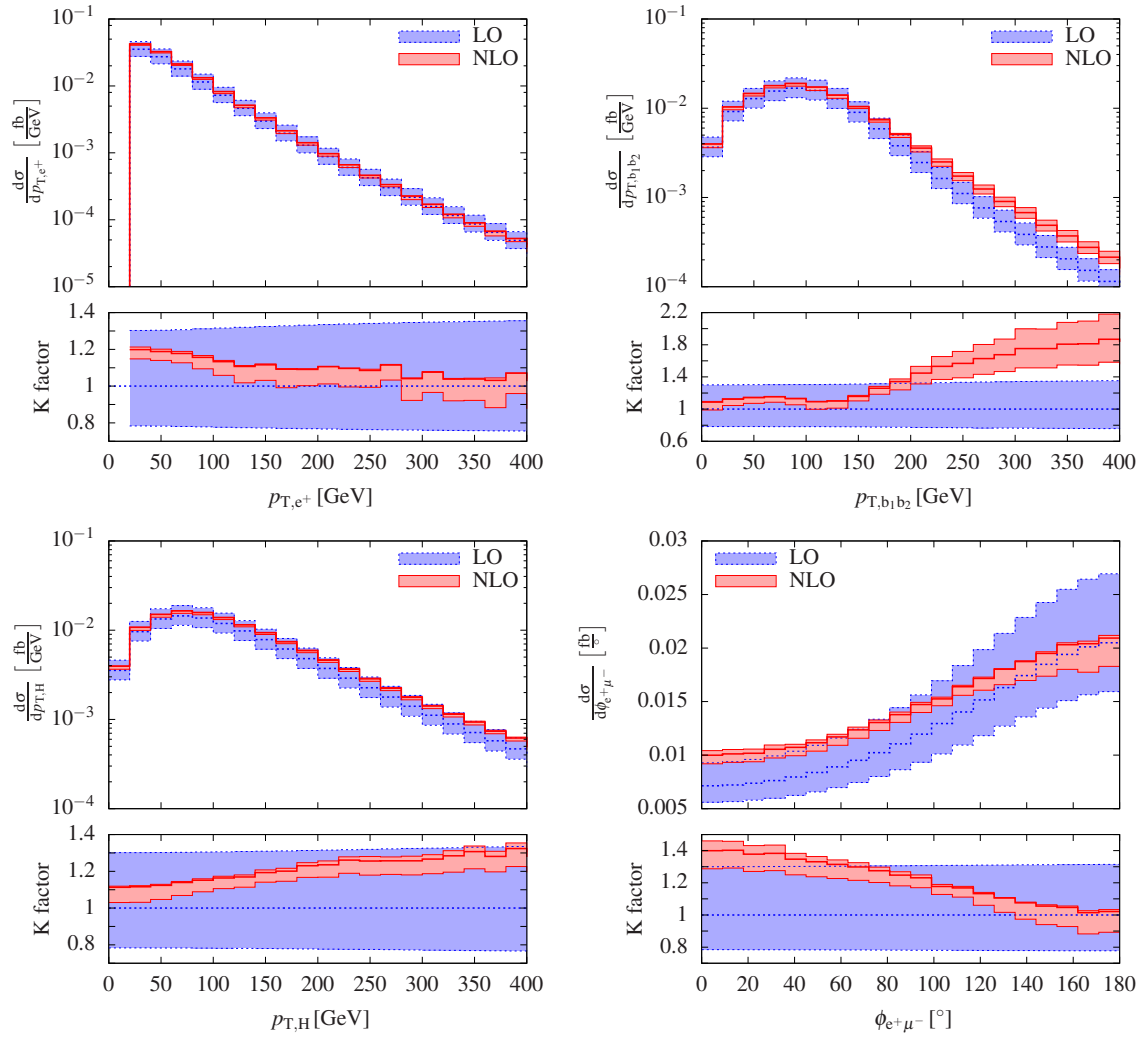

Figure 78: Distributions at the LHC at $\sqrt{s} = 13$ TeV for dynamical scale $\mu_0 = \mu_{\text{dyn}}$: for the transverse momentum of the positron (upper left), for the transverse momentum of the b-jet pair (upper right), for the transverse momentum of the Higgs boson (lower left) and the azimuthal angle between the positron and the muon in the transverse plane (lower right), The lower panels show the K factor.

I.6.4.a.iv Results for distributions

Four differential distributions are shown in Figure 78 for the dynamical scale choice (I.6.9). The upper panels show the LO (blue, dashed) and NLO (red, solid) predictions with uncertainty bands from scale variations. The lower panels display the LO (blue) and NLO (red) predictions with scale uncertainties normalized to the LO results at the central scale, i.e. $K_{\text{LO}} = \mathrm{d}\sigma_{\text{LO}}(\mu)/\mathrm{d}\sigma_{\text{LO}}(\mu_0)$ and $K_{\text{NLO}} = \mathrm{d}\sigma_{\text{NLO}}(\mu)/\mathrm{d}\sigma_{\text{LO}}(\mu_0)$. Thus, the central red curve corresponds to the usual NLO correction factor (K factor), defined as $K = \sigma_{\text{NLO}}(\mu_0)/\sigma_{\text{LO}}(\mu_0)$. The blue band shows the relative scale uncertainty of the LO differential cross section. The scale uncertainties are determined as explained at the end of Section I.6.4.a.ii.

The upper left plot of Figure 78 shows the transverse-momentum distribution of the positron. Using the dynamical scale, the K factor changes only slightly (within 20 %) over the displayed range, and the NLO band lies within the LO band. The residual scale variation is at the level of 10 % at NLO. This behaviour is typical for most other distributions (see Ref. [371]). A notable exception is the distribution in the transverse momentum of the b-jet pair (upper right in Figure 78), where we observe

an increase of the K factor for high transverse momentum to a value of 1.8 at $p_T \simeq 400$ GeV. This originates from the fact that this region is suppressed for on-shell top quarks, an effect known already from $\mathrm{t\bar{t}}$ production, where it is even more pronounced [385]. Using the fixed scale Eq.(I.6.10) instead leads to a much larger variation of the relative corrections and the NLO prediction moves outside the LO band in the high-p_T tails.

The lower left panel in Figure 78 displays the transverse-momentum distribution of the Higgs boson. The average p_T of the Higgs boson is around 70 GeV. The cross section decreases more moderately with p_T in the plotted range than for other transverse-momentum distributions. In the lower right panel of Figure 78 the distributions in the azimuthal angle in the transverse plane between the two charged leptons are presented. It exhibits sizeable NLO effects for small angles and the K factor varies by $40\,\%$. NLO corrections of similar size are found for the distribution in the cosine of the angle between the two charged leptons. Such large NLO effects in the kinematics of top-decay products can be attributed to order α_s radiative corrections to top decays. It would be interesting to compare them against conventional NLO+PS simulations, where such effects are modelled by the parton shower.

To summarize, this study, which includes NLO correction effects to the top–antitop–Higgs-boson production and the top decay processes, showed that for the inclusive investigated set-up, non-resonant and off-shell top-quark effects are below one per cent. Including NLO corrections, the scale uncertainty is reduced to $5\,\%$ for the integrated cross section and to the level of $10\,\%$ for distributions.

I.6.4.b Irreducible background and interference effects: $\ell\nu + \mathrm{jj} + \mathrm{b\bar{b}b\bar{b}}$ production at LO QCD

A LO analysis of Higgs boson production in association with a top-quark pair at the LHC investigating the semi-leptonic final state consisting of four b jets, two jets, one identified charged lepton and missing energy is presented. All the various contributions of order $\alpha_\mathrm{s}^k\alpha^{4-k}$ with $k = 0, 1, 2, 3$ to the LO matrix elements and their interferences are taken into account. The Standard Model predictions in three scenarios are considered: the resonant Higgs boson plus top-quark-pair production, the resonant production of a top-quark pair in association with a b-jet pair and the full process including all non-resonant and interference contributions. By comparing these scenarios the irreducible background for the production rate and several kinematical distributions is examined. More details of this study can be found in Ref. [386].

I.6.4.b.i Setup of the analysis

The full LO process $\mathrm{pp} \to \ell^+\nu_\ell\mathrm{jjb\bar{b}b\bar{b}}$ involves partonic channels with up to 78,000 diagrams. All matrix elements are calculated with RECOLA [372] which provides a fast and numerically stable computation. RECOLA uses recursive methods and allows to specify intermediate particles for a given process. The complex-mass scheme [373–375] is used for the consistent description of all resonances that are not treated in the pole approximation. If resonant particles are required as intermediate states, these are treated in the pole approximation [387–389], i.e. nonresonant contributions are neglected and the momenta are projected such that the corresponding production and decay matrix elements are on shell and gauge invariant.

Cross section and differential distributions are investigated for the LHC operating at 13 TeV. LHAPDF 6.05 with CT10 parton distributions (which is an NLO PDF set) is employed and contributions from the suppressed bottom-quark parton density and flavour mixing are neglected. The strong coupling α_s is taken from the PDF set and the electromagnetic coupling α is derived from the Fermi constant in the G_μ scheme. The width of the top quark Γ_t is calculated at LO QCD including effects of off-shell W bosons according to Ref. [384].

Three scenarios to calculate the process $\mathrm{pp} \to \ell^+\nu_\ell\mathrm{jjb\bar{b}b\bar{b}}$ are considered:

– In the first scenario, the *full process*, all SM contributions to the process $\mathrm{pp} \to \ell^+\nu_\ell\mathrm{jjb\bar{b}b\bar{b}}$ are included. Matrix elements involving external gluons receive contributions of $\mathcal{O}(\alpha_\mathrm{s}\alpha^3)$, $\mathcal{O}(\alpha_\mathrm{s}^2\alpha^2)$

and $\mathcal{O}(\alpha_s^3\alpha)$, whereas amplitudes without external gluons receive an additional $\mathcal{O}(\alpha^4)$ term of pure electroweak origin. In this scenario many different resonant subprocesses contribute, such as ttH, ttZ/γ^*, or ttbb production, as well as single W or W + multiboson production in association with light and/or b jets.

– In the second scenario only those diagrams are taken into account that contain an intermediate top–antitop-quark pair. The resulting amplitude, labelled *$t\bar{t}b\bar{b}$ production* in the following, corresponds to the production of a bottom–antibottom pair and an intermediate top–antitop pair followed by its semileptonic decay, i.e. $\mathrm{pp} \to \mathrm{t\bar{t}b\bar{b}} \to \ell^+\nu_\ell \mathrm{jjb\bar{b}b\bar{b}}$. Note that the pole approximation is used for the top quarks only, hence all off-shell effects of the remaining unstable particles are taken into account. As a consequence of the required top–antitop-quark pair the amplitudes receive no contribution of $\mathcal{O}(\alpha_s^3\alpha)$. In this scenario only the resonant subprocesses $\mathrm{t\bar{t}H}$, $\mathrm{t\bar{t}Z}/\gamma^*$, and $\mathrm{t\bar{t}b\bar{b}}$ production contribute.
– Finally, the signal process $\mathrm{pp} \to \mathrm{t\bar{t}H} \to \ell^+\nu_\ell \mathrm{jjb\bar{b}b\bar{b}}$ is considered and labelled $\mathrm{t\bar{t}H}$ *production*. In addition to the intermediate top–antitop-quark pair an intermediate Higgs boson decaying into a bottom–antibottom-quark pair is required and the pole approximation is used for the top-quark pair and the Higgs boson. The requirement of the Higgs boson eliminates contributions of $\mathcal{O}(\alpha_s^2\alpha^2)$ and all resonant subprocesses other than $\mathrm{t\bar{t}H}$ from the amplitude.

The bottom quarks are taken massive, and a fixed renormalization and factorization scale is used according to Ref. [325],

$$\mu_{\text{fix}} = \mu_{\text{R}} = \mu_{\text{F}} = \frac{1}{2}\left(2M_{\text{t}} + M_{\text{H}}\right) = 236\ \text{GeV}. \tag{I.6.11}$$

While this hard scale choice is appropriate for $\mathrm{t\bar{t}H}$ production, it tends to underestimate $\mathrm{t\bar{t}b\bar{b}}$ production and other QCD contributions by a factor 2 or more [390], leading to a low $\mathrm{t\bar{t}b\bar{b}}/\mathrm{t\bar{t}H}$ ratio. In the future one should consider an improved scale choice for the QCD contributions.

The following analysis requires 4 b jets, 2 jets and one charged lepton within the following acceptance cuts:

$$\begin{aligned}
\text{non-b jets:} &\quad p_{\text{T,j}} > 25\ \text{GeV}, \quad |y_{\text{j}}| < 2.5,\\
\text{b jets:} &\quad p_{\text{T,b}} > 25\ \text{GeV}, \quad |y_{\text{b}}| < 2.5,\\
\text{charged lepton:} &\quad p_{\text{T},\ell^+} > 20\ \text{GeV}, \quad |y_{\ell^+}| < 2.5,\\
\text{missing transverse momentum:} &\quad p_{\text{T,miss}} > 20\ \text{GeV},\\
\text{jet–jet distance:} &\quad \Delta R_{\text{jj}} > 0.4,\\
\text{b-jet–b-jet distance:} &\quad \Delta R_{\text{bb}} > 0.4,\\
\text{jet–b-jet distance:} &\quad \Delta R_{\text{jb}} > 0.4.
\end{aligned} \tag{I.6.12}$$

I.6.4.b.ii Background and interference contributions in integrated cross sections

In Table 35 individual contributions to the integrated cross section for the three scenarios are presented. While the first column specifies the scenario, the following columns contain the contributions resulting from the square of matrix elements of specific orders in the strong and electroweak coupling. The column labelled "Sum" represents the sum of the preceding columns, whereas the column labelled "Total" provides the integrated cross section including in addition all interference effects between different orders in the couplings, and the last column labelled "Int" gives the interference contributions in per cent of the "Total".

For $\mathrm{t\bar{t}H}$ production (2nd row of Table 35), where about 70 % of the events originate from the gluon-fusion process, the bulk of the contributions results from matrix elements of order $\mathcal{O}(\alpha_s\alpha^3)$, quark–antiquark annihilation receives an additional tiny contribution from pure electroweak interactions. Note that there are no interferences between diagrams of $\mathcal{O}(\alpha^4)$ and $\mathcal{O}(\alpha_s\alpha^3)$ in this scenario.

Table 35: Composition of the cross section in fb for $\mathrm{t\bar{t}H}$ production, $\mathrm{t\bar{t}b\bar{b}}$ production and the full process at the LHC at 13 TeV.

scenario	Cross section [fb]						
	$\mathcal{O}((\alpha^4)^2)$	$\mathcal{O}((\alpha_s\alpha^3)^2)$	$\mathcal{O}((\alpha_s^2\alpha^2)^2)$	$\mathcal{O}((\alpha_s^3\alpha)^2)$	Sum	Total	Int
$\mathrm{t\bar{t}H}$	0.014887(2)	7.377(1)	—	—	7.3920(9)	7.3920(9)	—
$\mathrm{t\bar{t}b\bar{b}}$	0.018134(6)	10.311(4)	17.570(9)	—	27.90(1)	26.446(7)	-5.2(3)%
full process	0.02120(3)	10.87(2)	18.69(6)	0.516(2)	30.10 (6)	28.60 (6)	-5.50(5)%

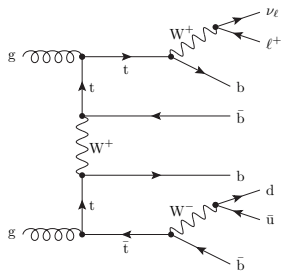

Figure 79: Representative Feynman diagram that gives rise to large interferences with the $\mathrm{t\bar{t}b\bar{b}}$ production diagrams of order $\mathcal{O}(\alpha_s^2\alpha^2)$.

For $\mathrm{t\bar{t}b\bar{b}}$ production (3rd row of Table 35), the production rate is significantly enhanced compared to $\mathrm{t\bar{t}H}$ production, and thus the irreducible background $\sigma_{\mathrm{t\bar{t}b\bar{b}}}^{\mathrm{Irred.}} = \sigma_{\mathrm{t\bar{t}b\bar{b}}}^{\mathrm{Total}} - \sigma_{\mathrm{t\bar{t}H}}^{\mathrm{Total}} = 19.06\,\mathrm{fb}$ exceeds the $\mathrm{t\bar{t}H}$ signal by a factor of 2.6. The major contribution to the irreducible background is due to QCD production of $\mathcal{O}((\alpha_s^2\alpha^2)^2)$. The additional contributions of $\mathcal{O}((\alpha_s\alpha^3)^2)$ in the $\mathrm{t\bar{t}b\bar{b}}$ scenario result from Feynman diagrams involving electroweak interactions with Z bosons, W bosons and photons, where in particular $\mathrm{t\bar{t}Z}$ production contributes 1.01 fb. The difference between the sixth (Sum) and seventh (Total) column in Table 35 is due to interference contributions between matrix elements of different orders in the coupling constants. These cause a reduction of the cross sections by about 5 % with respect to the full cross section. With respect to $\mathrm{t\bar{t}H}$ production or $\mathrm{t\bar{t}b\bar{b}}$ production at order $(\alpha_s^2\alpha^2)^2$ this amounts to 20 % and 8 %, respectively. The dominant effect is due to interferences of diagrams of $\mathcal{O}(\alpha_s\alpha^3)$ where a W boson is exchanged in the t-channel (see Figure 79 for an example) with diagrams of $\mathcal{O}(\alpha_s^2\alpha^2)$ that yield the dominant irreducible background. These kinds of interferences are absent in the $q\bar{q}$ channel. On the other hand, the interference of the $\mathrm{t\bar{t}H}$ signal process with the dominant irreducible background of order $\mathcal{O}(\alpha_s^2\alpha^2)$ is below one per cent.

The results for the full process are listed in the last row of Table 35. Here, additional partonic channels ($\mathrm{g}q$, $\mathrm{g}\bar{q}$, $qq^{(\prime)}$) contribute about 5 %. Nevertheless, the cross section increases by merely 8 % relative to $\mathrm{t\bar{t}b\bar{b}}$ production. With respect to $\mathrm{t\bar{t}H}$ production or $\mathrm{t\bar{t}b\bar{b}}$ production at order $(\alpha_s^2\alpha^2)^2$ this, however, amounts to 30 % and 12 %, respectively. The contributions of order $\mathcal{O}((\alpha_s^3\alpha)^2)$ are below 2 % and the interference pattern is similar to the case of $\mathrm{t\bar{t}b\bar{b}}$ production.

I.6.4.b.iii Background contributions to differential distributions

Turning to differential distributions for the three scenarios, results for the full process are compared with $\mathrm{t\bar{t}b\bar{b}}$ production and $\mathrm{t\bar{t}H}$ production to assess the irreducible background to $\mathrm{t\bar{t}H}$ production. The upper panels in each plot of Figure 80 show the differential distribution of the full process with a black solid line, $\mathrm{t\bar{t}b\bar{b}}$ production with a dashed blue line and $\mathrm{t\bar{t}H}$ production with a dotted red line. The lower panels provide the ratio of $\mathrm{t\bar{t}b\bar{b}}$ production to the full process with a dashed blue line and the ratio of $\mathrm{t\bar{t}H}$ production to the full process with a dotted red line.

Motivated by Ref. [391] the two b jets that most likely originate from the decay of the top quark ($\mathrm{t} \to \mathrm{W}^+\mathrm{b} \to \ell^+\nu_\ell\mathrm{b}$) and antitop quark ($\bar{\mathrm{t}} \to \mathrm{W}^-\bar{\mathrm{b}} \to \bar{u}d\bar{\mathrm{b}}$, with $u = \mathrm{u}, \mathrm{c}$, $d = \mathrm{d}, \mathrm{s}$) are determined and the invariant mass of the remaining b-jet pair is plotted. Since in most events the top quark and antitop quark in $\mathrm{t\bar{t}H}$ production are nearly on-shell, the two b jets maximizing the corresponding propagator contributions are most likely to originate from the top-quark and antitop-quark decay. To determine the maximizing b-jet combination a top-momentum candidate is computed with the charged lepton, neutrino and a b-jet momentum (p_{b_i}),

$$p_{\ell^+\nu_\ell\mathrm{b}_i} = p_{\ell^+} + p_{\nu_\ell} + p_{\mathrm{b}_i} \tag{I.6.13}$$

and an antitop-momentum candidate with the two momenta of the non-b jets and a different b-jet momentum (p_{b_j}),

$$p_{\mathrm{j}_1\mathrm{j}_2\mathrm{b}_j} = p_{\mathrm{j}_1} + p_{\mathrm{j}_2} + p_{\mathrm{b}_j}. \tag{I.6.14}$$

As b jets originating from the top-quark and antitop-quark decay we select those that maximize the likelihood function $\mathcal{L}$ defined as a product of two Breit–Wigner distributions corresponding to the top-quark and antitop-quark propagators:

$$\mathcal{L} \propto \left[\left(p^2_{\ell^+\nu_\ell\mathrm{b}_i} - M_\mathrm{t}^2\right)^2 + \left(M_\mathrm{t}\Gamma_\mathrm{t}\right)^2\right]^{-1} \left[\left(p^2_{\mathrm{j}_1\mathrm{j}_2\mathrm{b}_j} - M_\mathrm{t}^2\right)^2 + \left(M_\mathrm{t}\Gamma_\mathrm{t}\right)^2\right]^{-1}. \tag{I.6.15}$$

Figure 80 upper left presents the b-jet-pair invariant mass that has been identified to originate from the Higgs boson decay by the maximum-likelihood method described above. In the off-shell region the ratio of $\mathrm{t\bar{t}H}$ production to the full process drops considerably below the corresponding ratio for the total cross section of about a fourth. Since this method tags the b jets resulting from the top and antitop quarks, any resonance in the invariant mass of the remaining b-jet pair is resolved, and thus the Z resonance is clearly visible in the plot. Note, however, that this analysis uses an idealized $\mathrm{t\bar{t}b\bar{b}}$ reconstruction. In practice, multi-jet emissions, finite jet-energy resolution, and light-jet mistagging lead to a severe dilution of $\mathrm{b\bar{b}}$ resonances.

In the following distributions that show deviations in the shape between the full process and the $\mathrm{t\bar{t}b\bar{b}}$ and $\mathrm{t\bar{t}H}$ sub-processes are discussed. Figure 80 upper right shows the azimuthal separation of the b-jet pair determined by top–antitop Breit–Wigner maximum likelihood. While $\mathrm{t\bar{t}b\bar{b}}$ production and the full process yield a very similar shape, $\mathrm{t\bar{t}H}$ production exhibits clearly a different shape. This behaviour can be explained by the dominant production mechanisms of bottom–antibottom pairs. In the signal process these result from the Higgs boson and owing to the finite Higgs boson mass tend to have a finite opening angle. In the background processes the bottom–antibottom pairs result mainly from gluons and thus tend to be collinear leading to a peak at small ϕ_{bb} that is cut off by the acceptance function. Thus, this distribution can help to separate bottom–antibottom pairs resulting from Higgs bosons from those of other origin.

Figure 80 lower left displays the transverse-momentum distribution of the third-hardest b jet. Here all three approximations are similar in shape for p_T values below 150 GeV. For higher transverse momenta the distribution for $\mathrm{t\bar{t}H}$ production diverges from those of the full process and $\mathrm{t\bar{t}b\bar{b}}$ production. This behaviour is not found in the transverse momentum distributions of the two harder b jets but to some extent in the one of the fourth-hardest b jet. This results from the fact that in the $\mathrm{t\bar{t}H}$ signal all b jets originate from heavy-particle decays, while in the full process some are directly produced yielding more b jets with high transverse momenta.

Finally, Figure 80 lower right presents the invariant mass of the three hardest b jets. Below the threshold $M_\mathrm{H} + p_{\mathrm{T,b,cut}} \approx 150$ GeV the signal process is strongly suppressed, above its ratio to the full process rises to 36 % at $M_{\mathrm{b_1b_2b_3}} \sim 195$ GeV and then drops slowly to 26 % at $M_{\mathrm{b_1b_2b_3}} \sim 400$ GeV. The ratio of $\mathrm{t\bar{t}b\bar{b}}$ production and the full process on the other hand is roughly constant for $M_{\mathrm{b_1b_2b_3}} \gtrsim 70$ GeV.

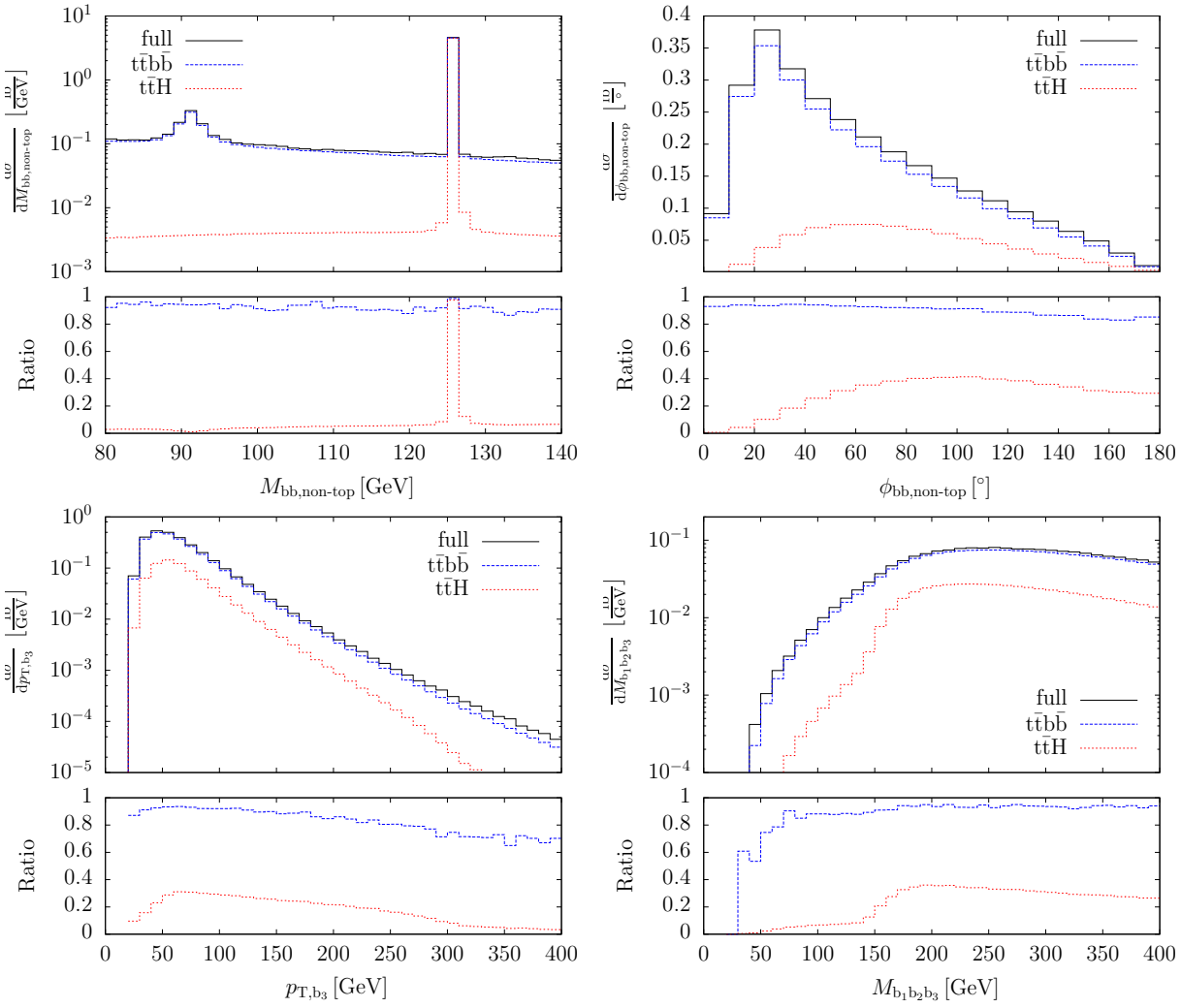

Figure 80: Differential distributions at the LHC at 13 TeV for the three different scenarios: invariant-mass distribution of the b-jet pair determined by top–antitop Breit–Wigner maximum likelihood (upper left), azimuthal separation of this b-jet pair (upper right), transverse momentum of the 3rd-hardest b jet (lower left), and invariant mass of the three hardest b jets (lower right). The lower panels show the relative size of $\mathrm{t\bar{t}b\bar{b}}$ and $\mathrm{t\bar{t}H}$ production normalized to the full process.

I.6.4.b.iv Interference effects in differential distributions

In the following the effects of the interference contributions between matrix elements of different orders in α_s are investigated. For most distributions a uniform shift by roughly the same amount as for the total cross section, i.e. about $5\,\%$ for $\mathrm{t\bar{t}b\bar{b}}$ production and the full process (interference effects are absent in $\mathrm{t\bar{t}H}$ production), is observed. For both scenarios a few kinematical distributions are found that are sensitive to these interference effects. The upper panels of Figure 81 show the results for the full process and the central and lower panels highlight the interference effects. Specifically, the central panels show the relative difference $(\sigma_\mathrm{tot} - \sigma_\mathrm{sum})/\sigma_\mathrm{tot}$ for $\mathrm{t\bar{t}b\bar{b}}$ production with a solid blue line and the lower panels the same relative difference for the full process with a dashed line.

Figure 81 left shows the interference effects on the distribution of the invariant mass of the b-jet pair determined by top–antitop Breit–Wigner maximum likelihood. The suppression of interference in the regions of the Higgs- and Z-boson resonances is clearly visible. For invariant masses above the Higgs threshold the interference effect exceeds $-10\,\%$. As shown in Figure 81 right, the relative

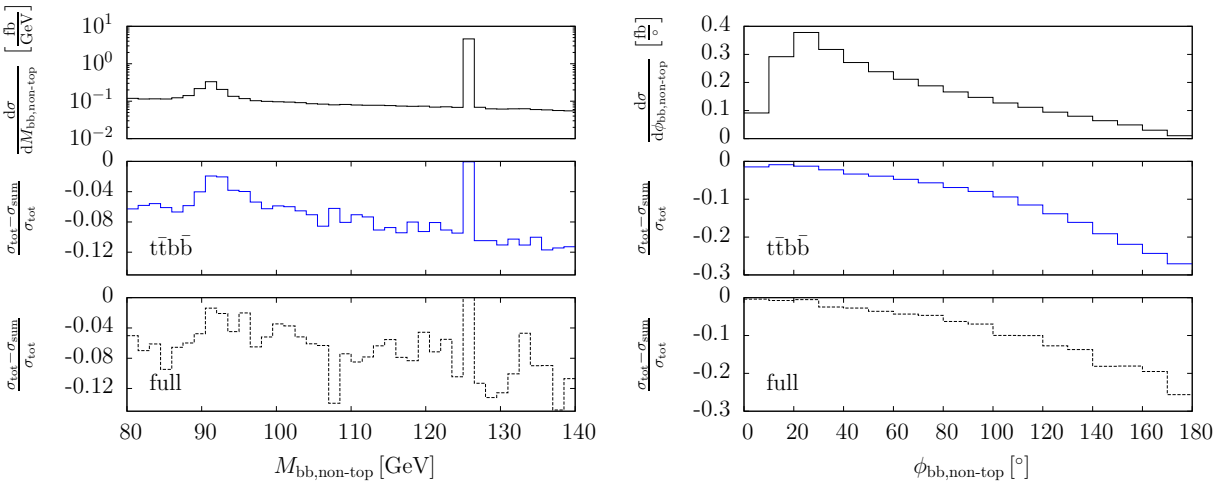

Figure 81: Interference effects versus invariant mass of the b-jet pair determined by top–antitop Breit–Wigner maximum likelihood (left) and azimuthal separation of this b-jet pair (right). The lower panels show the relative interference effects of $t\bar{t}b\bar{b}$ production and the full process, respectively. The upper panel shows the corresponding differential distribution of the full process as reference.

interference effects grow with increasing azimuthal-angle separation of the b-jet pair determined by top–antitop Breit–Wigner maximum likelihood from almost zero at small angles to $-25\,\%$ for $\phi_{\mathrm{bb,non\text{-}top}} = 180°$, while the cross section drops with increasing azimuthal-angle separation.

Finally it should be noted that in Ref. [386] the irreducible background and interference effects for various other distributions have been investigated.

To summarize, the cross section for $t\bar{t}b\bar{b}$ production agrees with the one for the full process within $8\,\%$ and interferences between matrix elements of different orders in the coupling constants contribute about $5\,\%$ of the full process. Note, however, that these effects amount to $30\,\%$ and $20\,\%$ of the Higgs-signal process.

I.6.5 $t\bar{t}H$ production beyond NLO

A fixed-order computation of the NNLO QCD corrections to hadronic $t\bar{t}H$ production is still beyond the technical reach of current higher-order perturbative calculations. Nevertheless, their impact on the theoretical predictions for both total cross sections and distributions can be larger than the first order of EW corrections, and their inclusion could substantially reduce the systematic dependence on renormalization and factorization scales. It is therefore important to investigate the possibility of gaining information on the NNLO QCD corrections to $t\bar{t}H$ production by studying particular sets of higher-order corrections that can be calculated analytically from first principles. Recently two studies [392, 393] have explored the effect of soft-gluon emission beyond NLO. A brief summary of the methods used as well as the results obtained for the LHC at both 13 and 14 TeV are presented in Section I.6.5.a for Ref. [392] and in Section I.6.5.b for Ref. [393].

In spite of the fact that both studies target the same kind of radiative corrections, the two approaches are quite different. In Ref. [392] the soft-gluon corrections are calculated in the absolute threshold limit i.e., in the limit when the partonic centre-of-mass energy approaches the square of the production threshold energy ($2M_{\mathrm{t}} + M_{\mathrm{H}}$), while in Ref. [393] the soft-gluon corrections are calculated in the final-state-invariant-mass threshold limit i.e., in the limit when the partonic centre-of-mass energy approaches the square of the invariant mass of the $t\bar{t}H$ state.

Moreover, while Ref. [392] relies on the classical Mellin resummation technique and performs

an all-order resummation of Next-to-Leading-Logarithms (NLL), Ref. [393] uses techniques of Soft-Collinear Effective Theory (SCET) to obtain approximate NNLO corrections from a truncated expansion of a Next-to-Next-to-Leading-Logarithms (NNLL) resummed formula matched with the full NLO fixed-order calculation.

Given these differences, a comparison of results between the two studies is not obvious. The NLO+NLL results of Section I.6.5.a and Table 36, and the NLO+approximate NNLO results of Section I.6.5.b and Tables 37-38 correspond to different extensions of the NLO QCD results and cannot be directly compared, even when they are evaluated at the same renormalization and factorization scale, because they include different orders of differently-defined soft-gluon corrections. What is however interesting is that within the uncertainty from scale variation and from corrections formally subleading in the soft limit, they both overlap with the NLO QCD fixed-order calculation within its uncertainty range.

It will be interesting to explore directions in which these studies can be used to further improve the theoretical understanding and accuracy of both Mellin and momentum-space resummations, and eventually use them to more systematically control the theoretical uncertainty on $t\bar{t}H$ production at the LHC.

I.6.5.a $t\bar{t}H$ production including NLO+NLL soft-gluon resummation in the partonic centre-of-mass theshold limit

I.6.5.a.i Introduction

In this section we discuss how to improve the NLO QCD calculation of $pp \to t\bar{t}H$ at the LHC by adding the resummation of soft-gluon corrections in the partonic centre-of-mass threshold limit, performed using the Mellin space formalism [392]. This particular type of corrections arises due to soft-gluon emission in the threshold limit i.e., when the production is considered close to the absolute threshold $\hat{s} \sim M^2 = (2M_{\rm t} + M_{\rm H})^2$, where $\hat{s}$ is the partonic centre-of-mass energy, $M_{\rm t}$ the top-quark mass, and $M_{\rm H}$ the Higgs boson mass. In this region, the cross section receives enhancements in the form of logarithmic corrections in $\beta = \sqrt{1 - M^2/\hat{s}}$. The quantity β measures the distance from the absolute production threshold and can be related to the maximal velocity of the $t\bar{t}$ system.

Threshold resummation in Mellin space has been so far well developed and copiously applied only to $2 \to 2$ processes. Its application to the $pp \to t\bar{t}H$ process requires developing the formalism for the case of a $2 \to 3$ process with two coloured massive particles in the final state. While the universality of resummation concepts warrants their applications to scattering processes with many partons in the final state [394, 395], the specifics of the colour structure and kinematics need to be taken into account in the process-dependent terms. In particular, the non-trivial colour flow between four coloured partons at the Born level influences the contributions from wide-angle soft-gluon emissions which have to be included at the next-to-leading-logarithmic (NLL) accuracy. The evolution of the colour exchange at NLL is governed by the one-loop soft anomalous dimension. Correspondingly, the application of the threshold resummation to the $pp \to t\bar{t}H$ process requires the calculation of the one-loop soft anomalous dimension for a $2 \to 3$ process with two coloured massive particles in the final state. An additional improvement of the calculation at the NLL accuracy is the inclusion of the $\mathcal{O}(\alpha_{\rm s})$ non-logarithmic threshold corrections originating from hard off-shell dynamics.

I.6.5.a.ii Resummation at production threshold

At the partonic level, the Mellin moments for the process $ij \to klB$, where i and j denote massless coloured partons, k and l two massive quarks, and B a massive colour-singlet particle, are given by

$$\hat{\sigma}_{ij\to klB,N}(m_k, m_l, m_B, \mu_F^2, \mu_R^2) = \int_0^1 d\hat{\rho}\, \hat{\rho}^{N-1} \hat{\sigma}_{ij\to klB}(\hat{\rho}, m_k, m_l, m_B, \mu_F^2, \mu_R^2)\,, \qquad \text{(I.6.16)}$$

where $\hat{\rho} = 1 - \beta^2 = M^2/\hat{s}$, and $\mu_{\rm R}$ and $\mu_{\rm F}$ denote the renormalization and factorization scales, respectively.

At LO, the $t\bar{t}H$ production process receives contributions from the $q\bar{q}$ and gg channels. Analysing the colour structure of the underlying processes in the s-channel colour bases, $\{c_I^q\}$ and $\{c_I^g\}$, with $c_{\mathbf{1}}^q = \delta^{\alpha_i\alpha_j}\delta^{\alpha_k\alpha_l}$, $c_{\mathbf{8}}^q = T^a_{\alpha_i\alpha_j}T^a_{\alpha_k\alpha_l}$, $c_{\mathbf{1}}^g = \delta^{a_ia_j}\,\delta^{\alpha_k\alpha_l}$, $c_{\mathbf{8S}}^g = T^b_{\alpha_l\alpha_k}d^{ba_ia_j}$, $c_{\mathbf{8A}}^g = iT^b_{\alpha_l\alpha_k}f^{ba_ia_j}$ ($\alpha_{i,j,k,l} = 1,\ldots,N$, and $a,b,a_{i,j} = 1,\ldots,N^2-1$, with $N=3$), the soft anomalous-dimension matrix becomes diagonal in the production threshold limit [396], and the NLL resummed cross section in the N-space has the form [396, 397]

$$\hat{\sigma}^{(\rm res)}_{ij\to klB,N} = \sum_I \hat{\sigma}^{(0)}_{ij\to klB,I,N}\, C_{ij\to klB,I}\, \Delta^i_{N+1}\Delta^j_{N+1}\Delta^{(\rm int)}_{ij\to klB,I,N+1}\,, \tag{I.6.17}$$

where the explicit dependence on the scales is suppressed. The index I in Eq. (I.6.17) distinguishes between contributions from different colour channels. The colour-channel-dependent contributions to the LO partonic cross sections in Mellin-moment space are denoted by $\hat{\sigma}^{(0)}_{ij\to klB,I,N}$. The radiative factors Δ^i_N describe the effect of the soft-gluon radiation collinear to the initial-state partons and are universal, see e.g. [397] . Large-angle soft-gluon emission is accounted for by the factors $\Delta^{(\rm int)}_{ij\to klB,I,N}$ which are directly related to the soft-gluon anomalous dimension calculated in [392]. As indicated by the lower indices, the wide-angle soft emission depends on the partonic process under consideration and the colour configuration of the participating particles. In the limit of absolute threshold production, $\beta \to 0$, the factors $\Delta^{(\rm int)}_{ij\to klB,I,N}$ coincide with the corresponding factors for the $2\to 2$ process $ij\to kl$ [392]. All perturbative functions governing the radiative factors up to the terms needed to obtain NLL accuracy in the resummed expressions are considered.

The coefficients $C_{ij\to klB,I} = 1 + \frac{\alpha_{\rm s}}{\pi}C^{(1)}_{ij\to klB,I} + \ldots$ contain all non-logarithmic contributions to the NLO cross section taken in the threshold limit. More specifically, these consist of Coulomb corrections, N-independent hard contributions from virtual corrections, and N-independent non-logarithmic contributions from soft emissions. Although formally the coefficients $C_{ij\to klB,I}$ begin to contribute at NNLL accuracy, in the numerical studies of the $pp\to t\bar{t}H$ process presented in the following we consider both the case of $C_{ij\to klB,I} = 1$, i.e. with the first-order corrections to the coefficients neglected, as well as the case with these corrections included. In the latter case the Coulomb corrections and the hard contributions are treated additively, i.e. $C^{(1)}_{ij\to klB,I} = C^{(1,\rm hard)}_{ij\to klB,I} + C^{(1,\rm Coul)}_{ij\to klB,I}$. For k,l denoting massive quarks, and more specifically for $kl = t\bar{t}$, the Coulomb corrections are $C^{(1,\rm Coul)}_{ij\to klB,\mathbf{1}} = C_{\rm F}\pi^2/(2\beta_{kl}) = C_{\rm F}\pi^2/(2\beta_{t\bar{t}})$ and $C^{(1,\rm Coul)}_{ij\to klB,\mathbf{8}} = (C_{\rm F} - C_{\rm A}/2)\pi^2/(2\beta_{kl}) = (C_{\rm F} - C_{\rm A}/2)\pi^2/(2\beta_{t\bar{t}})$, with $\beta_{t\bar{t}} = \sqrt{1-4M_{\rm t}^2/\hat{s}_{t\bar{t}}}$, and $\hat{s}_{t\bar{t}} = (p_t + p_{\bar{t}})^2$. As the N-independent non-logarithmic contributions from soft emission are accounted for using the techniques developed for the $2\to 2$ case [398, 399], the problem of calculating the $C^{(1)}_{ij\to t\bar{t}H,I}$ coefficients reduces to the calculation of the $O(\alpha_{\rm s})$ virtual corrections to the $t\bar{t}H$ process. We extract them numerically using the publicly available POWHEG BOX implementation of the $t\bar{t}H$ process [351], based on the calculations developed in [321–323]. The results are then cross-checked using the standalone MADLOOP implementation in AMC@NLO [348]. Since the $q\bar{q}$ channel receives only colour-octet contributions, the extracted value contributing to $C^{(1,\rm hard)}_{q\bar{q}\to t\bar{t}H,\mathbf{8}}$ is exact. In the gg channel, however, both the singlet and octet production modes contribute. We extract the value which contributes to the coefficient $\bar{C}^{(1,\rm hard)}_{gg\to t\bar{t}H}$ averaged over colour channels and use the same value to further calculate $C_{gg\to t\bar{t}H,\mathbf{1}}$ and $C_{gg\to t\bar{t}H,\mathbf{8}}$.

The resummation-improved NLO+NLL cross sections for the $pp\to t\bar{t}H$ process are then obtained through matching the NLL resummed expressions with the full NLO cross sections

$$\sigma^{(\rm NLO+NLL)}_{pp\to t\bar{t}H}(\rho,\mu_{\rm F}^2,\mu_{\rm R}^2) = \sigma^{(\rm NLO)}_{pp\to t\bar{t}H}(\rho,\mu_{\rm F}^2,\mu_{\rm R}^2) + \sigma^{(\rm res-exp)}_{pp\to t\bar{t}H}(\rho,\mu_{\rm F}^2,\mu_{\rm R}^2)$$

with

$$\sigma^{(\mathrm{res-exp})}_{pp\to t\bar{t}H} = \sum_{i,j} \int_{\mathcal{C}} \frac{dN}{2\pi i}\, \rho^{-N} f^{(N+1)}_{i/p}(\mu_{\mathrm{F}}^2)\, f^{(N+1)}_{j/p}(\mu_{\mathrm{F}}^2)$$
$$\times \left[\hat{\sigma}^{(\mathrm{res})}_{ij\to t\bar{t}H,N}(\mu_{\mathrm{F}}^2, \mu_{\mathrm{R}}^2) - \hat{\sigma}^{(\mathrm{res})}_{ij\to t\bar{t}H,N}(\mu_{\mathrm{F}}^2, \mu_{\mathrm{R}}^2)\,|_{(NLO)} \right], \qquad \text{(I.6.18)}$$

where $\hat{\sigma}^{(\mathrm{res})}_{ij\to t\bar{t}H,N}$ is given in Eq. (I.6.17) and $\hat{\sigma}^{(\mathrm{res})}_{ij\to t\bar{t}H,N}\,|_{(NLO)}$ represents its perturbative expansion truncated at NLO. The moments of the parton distribution functions (PDF) $f_{i/p}(x, \mu_{\mathrm{F}}^2)$ are defined in the standard way $f^{(N)}_{i/p}(\mu_{\mathrm{F}}^2) \equiv \int_0^1 dx\, x^{N-1} f_{i/p}(x, \mu_{\mathrm{F}}^2)$. The inverse Mellin transform (I.6.18) is evaluated numerically using a contour $\mathcal{C}$ in the complex N-space according to the "Minimal Prescription" method developed in Ref. [130].

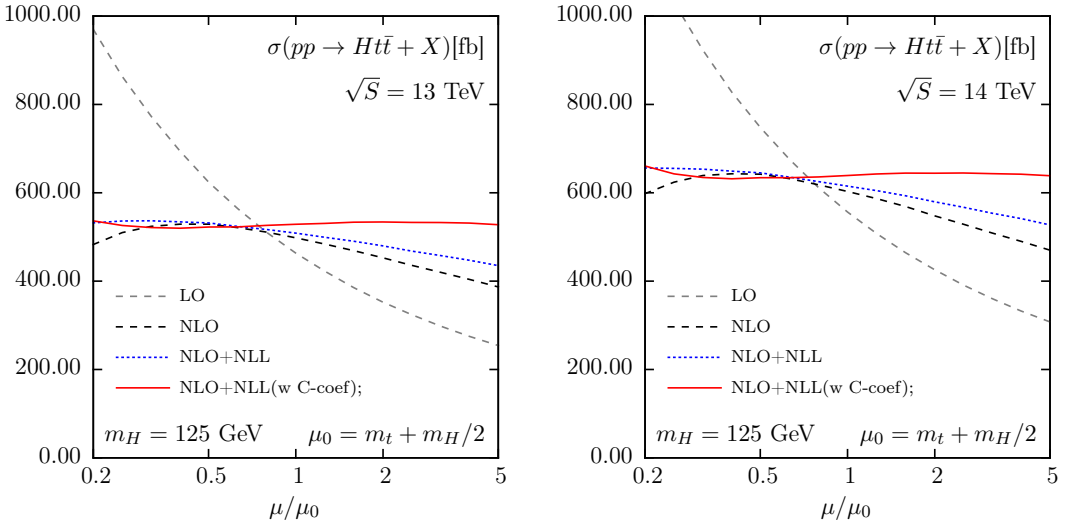

Figure 82: Scale dependence of the LO, NLO, and NLO+NLL cross sections at $\sqrt{s} = 13$ and $\sqrt{s} = 14$ TeV LHC collision energy. The results are obtained by simultaneously varying μ_{F} and μ_{R}, with $\mu = \mu_{\mathrm{F}} = \mu_{\mathrm{R}}$. See Section I.6.5.a.

I.6.5.a.iii Numerical predictions

The numerical results presented in this section are obtained using the parameter values listed in [144], in particular using the PDF4LHC15_100 PDF sets [35] for the NLO and NLO+NLL predictions. The LO results, shown here only for illustration, are obtained with the MMHT14 PDF sets [37]. The NLO cross section is calculated using the aMC@NLO code [54].

In Figure 82 we analyse the scale dependence of the resummed total cross section for $pp \to t\bar{t}H$ at $\sqrt{s} = 13$ and 14 TeV, varying simultaneously the factorization and renormalization scales as $\mu = \mu_{\mathrm{F}} = \mu_{\mathrm{R}}$. As demonstrated in Figure 82, adding the soft-gluon corrections stabilizes the dependence on $\mu = \mu_{\mathrm{F}} = \mu_{\mathrm{R}}$ of the NLO+NLL predictions with respect to NLO. The central values, calculated at $\mu = \mu_0 = M_{\mathrm{t}} + M_{\mathrm{H}}/2$, and the scale error at $\sqrt{s} = 13$ TeV changes from $499^{+5.8\%}_{-9.3\%}$ fb at NLO to $530^{+0.8\%}_{-1.6\%}$ fb at NLO+NLL (with $C^{(1)}_{ij\to t\bar{t}H,I}$ coefficients included) and correspondingly, from $604^{+6.0\%}_{-9.2\%}$ fb to $641^{+0.8\%}_{-1.3\%}$ fb at $\sqrt{s} = 14$ TeV. It is also clear from Figure 82 that the coefficients $C^{(1)}_{ij\to t\bar{t}H}$ strongly impact the predictions, especially at higher scales. In fact, their effect is more important than the effect of the logarithmic corrections alone, in correspondence to the strong suppression $\sim \beta^4$ for the real emission in the $2 \to 3$ process due to the massive three-particle phase space. This observation also indicates the relevance of the contributions originating from the region away from the absolute threshold which need to be known in order to further improve theoretical predictions.

Table 36: NLO+NLL and NLO total cross sections for $pp \to t\bar{t}H$ at $\sqrt{s} = 13$ and 14 TeV. Results have been obtained using $\mu_0 = 235$ GeV, $M_{\rm t} = 172.5$ GeV, $M_{\rm H} = 125$ GeV, and the PDF4LHC15 set of PDF. The error ranges given together with the NLO and NLO+NLL results indicate the scale uncertainty. See Section I.6.5.a.

$\sqrt{s}$ [TeV]	NLO [fb]	NLO+NLL		NLO+NLL with C	
		Value [fb]	K-factor	Value [fb]	K-factor
13	$499^{+5.8\%}_{-9.3\%}$	$509^{+4.2\%}_{-6.5\%}$	1.02	$530^{+7.8\%}_{-5.5\%}$	1.06
14	$604^{+6.0\%}_{-9.2\%}$	$616^{+4.5\%}_{-6.5\%}$	1.02	$641^{+7.9\%}_{-5.5\%}$	1.06

The effect of including NLL corrections is summarized in Table 36 for the LHC collision energy of 13 and 14 TeV. Here we choose to estimate the theoretical uncertainty due to scale variation by varying $\mu_{\rm F}$ and $\mu_{\rm R}$ independently via the 7-point method i.e., by considering the minimum and maximum values obtained with $(\mu_{\rm F}/\mu_0, \mu_{\rm R}/\mu_0) = (0.5, 0.5), (0.5, 1), (1, 0.5), (1, 1), (1, 2), (2, 1), (2, 2)$. The NLO+NLL predictions show a significant reduction of the scale uncertainty, compared to NLO results. The reduction of the positive and negative scale errors amounts to around 25-30% of the NLO error for $\sqrt{s} = 13, 14$ TeV. This general reduction trend is not sustained for the positive error after including the $C^{(1)}_{ij\to t\bar{t}H,I}$ coefficients. More specifically, the negative error is further slightly reduced, while the positive error is increased. The origin of this increase can be traced back to the substantial dependence on μ_F of the resummed predictions with non-zero $C^{(1)}_{ij\to t\bar{t}H,I}$ coefficients, manifesting itself at larger scales. However, even after the redistribution of the error between the positive and negative parts, the overall size of the scale error, corresponding to the size of the error bar, is reduced after resummation by around 12% with respect to the NLO uncertainties. The scale error of the predictions is still larger than the PDF error of the NLO predictions ($\sim$3 %) which is not expected to be significantly influenced by the soft-gluon corrections.

I.6.5.b $t\bar{t}H$ production at approximate NNLO via soft-gluon resummation in the "PIM" limit

I.6.5.b.i Method

A different approach to the estimate of the approximate NNLO QCD corrections to the total and differential $t\bar{t}H$ cross sections was considered in Ref. [393]. In this case, the approximate formulas were obtained by studying soft-gluon corrections in the limit where the partonic centre-of-mass energy approaches the invariant mass of the $t\bar{t}H$ final state, where the latter can be arbitrarily large. The soft limit employed is the exact analogue of the so-called pair-invariant mass (PIM) threshold limit used to study top-quark pair production at NNLL and approximate NNLO in [400]. The approximate NNLO corrections are extracted from the perturbative information contained in a soft-gluon resummation formula valid to NNLL accuracy. The derivation of this formula is based on SCET methods (for a recent review, see [401]). The soft-gluon resummation formula for this process contains three essential ingredients, all of which are matrices in the colour space needed to describe four-parton scattering. These ingredients are 1) a hard function, related to virtual corrections; 2) a soft function, related to real emission corrections in the soft limit; and 3) a soft anomalous dimension, which governs the structure of the all-order soft-gluon corrections through the renormalization group (RG). Of these three ingredients, both the NLO soft function [400, 402] and the NLO soft anomalous dimension [403, 404] needed for NNLL resummation in processes involving two massless and two massive partons can be adapted directly to $t\bar{t}H$ production. The NLO hard function is instead process dependent and it was evaluated in [393] by using a modified version of the one-loop providers GoSam [227, 228], MadLoop [348] and OpenLoops [247] in combination with Collier [248, 380, 382, 383].

Due to the mechanism of dynamical threshold enhancement [400,405], it is often the case that observables receive their dominant contributions from soft-gluon corrections derived in the PIM threshold limit. Obvious examples are the cross section differential in the invariant mass of the $t\bar{t}H$ final state, or the total cross section obtained by integrating this distribution. Furthermore, given that results in the PIM threshold limit are fully differential in the Mandelstam variables characterizing the Born process, it is possible to use them in order to estimate the NNLO corrections to any differential distribution which is non-vanishing at Born level. In [393] an in-house parton-level Monte Carlo was written and employed to study approximate NNLO corrections to the differential cross sections with respect to the p_T of the Higgs boson, the p_T of the top quark, the invariant mass of the $t\bar{t}H$ pair, and the rapidities of the top quark or Higgs boson, in addition to the total cross section and differential cross section with respect to the $t\bar{t}H$ final state. The NNLO approximation was then matched to the complete NLO calculation [321–325,406] obtained from MADGRAPH5_AMC@NLO [54]. This procedure can in principle be extended to include the decays of the final-state particles and by retaining information on the spins of the final-state top quarks, as it was done in [407] for the top-pair production process.

I.6.5.b.ii Approximate NNLO formulas

The fixed-order expansion of the cross section and the resummation of soft-emission effects are two complementary approaches to the precise determination of physical observables. For this reason, one typically wants to match resummed and fixed-order calculations in order to account for all of the known effects when obtaining phenomenological predictions. However, there are situations in which the perturbative expansion in α_s is still justified, but soft-gluon emission effects provide the bulk of the corrections at a given perturbative order. In those cases, one can re-expand the resummed hard scattering kernels in order to obtain approximate formulas which include all of the terms proportional to plus distributions up to a given power of α_s in fixed-order perturbation theory. In PIM kinematics, the hard scattering kernels C depend, among other arguments, on $z \equiv M^2/\hat{s}$, where M indicates the invariant mass of the three heavy particles in the final state (notice that this is different from the M used in Section I.6.5.a) and $\hat{s}$ is the partonic centre-of-mass energy. The PIM soft-emission kinematics corresponds to the limit $z \to 1$. Schematically, the NNLO contribution to the hard-scattering kernels has the following structure

$$C^{(2)}(z,\mu) = \sum_{n=0}^{3} D_n(\mu) \left[\frac{\ln^n(1-z)}{1-z}\right]_+ + C_0(\mu)\delta(1-z) + R(z,\mu) \,, \tag{I.6.19}$$

where several arguments of the functions D_n, C_0, and R in (I.6.19), such as masses and scattering angles have been dropped, and only the μ and z dependence has been kept. The approximate NNLO formulas for the partonic cross sections derived in [393] include the complete set of functions D_i, some of the scale-dependent terms in the function C_0 as well as partial information on the function $R(z)$ which is non singular in the $z \to 1$ limit[I.32]. The information obtained from approximate NNLO formulas can be matched to the complete NLO calculation of a given observable in order to obtain precise predictions for a physical quantity, details can be found in [393]. As an example, for the total cross section the matching operation is straightforward and can be schematically written as,

$$\sigma^{\text{NLO+approxNNLO}} = \sigma^{\text{NLO}} + \sigma^{\text{approx.NNLO}} - \sigma^{\text{approx.NLO}} \,, \tag{I.6.20}$$

where the subtraction of the last term avoids double counting of NLO terms proportional to plus distributions and delta functions, and all of the terms on the r.h.s. of Eq. (I.6.20) are evaluated with NNLO PDF. To avoid lengthy superscripts, in the following the matched NLO + approximate NNLO calculation is denoted as "nNLO".

[I.32] For a detailed description of what is included in the functions C_0 and R in the SCET approach, and how this information improves the agreement between different kinematic schemes in top pair production and stop pair production, the reader can refer to [400, 408, 409].

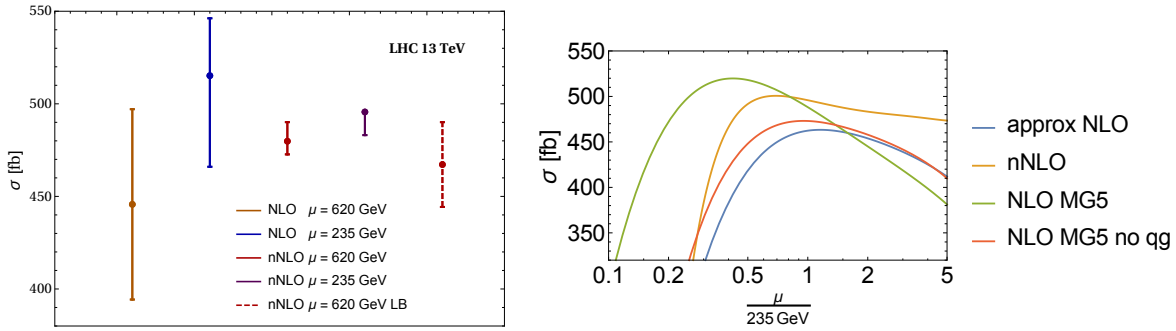

Figure 83: Left panel: Comparison among the NLO and nNLO calculations of the total cross section reported in Table 37 for the LHC at $\sqrt{s} = 13$ TeV. The cross section labelled LB refers to the conservative estimate of the nNLO uncertainty reported in Table 38. Right panel: Scale dependence of the total cross section (from [393]). The curves represent the NLO cross section evaluated with `MG5` by excluding the quark-gluon channel contribution (red line), the complete NLO cross section evaluated with `MG5` (green line), the nNLO cross section (orange line), and the approximate NLO cross section (light blue line). In the right panel, all perturbative orders are evaluated with NNLO MSTW2008 PDF. See Section I.6.5.b.

I.6.5.b.iii Numerical analysis

This section includes results for the total cross section and the final-state invariant mass distribution obtained from the numerical evaluation of the nNLO formulas. In order for corrections in the soft limit to be dominant in observables which are also sensitive to regions of phase space far away from $z \to 1$, the mechanism of dynamical threshold enhancement [400, 405] must occur. This means that the parton luminosities should drop off quickly enough away from the integration region where $z \to 1$ that an expansion under the integral of the partonic cross section in the soft limit is justified. Approximate NLO calculations are obtained by re-expanding the NNLL resummed partonic cross section to NLO; consequently they reproduce completely all of the terms singular in the $z \to 1$ limit in the NLO partonic cross section, but they miss terms which are subleading in the soft limit. In [393] it was checked that the soft approximation works quite well for the NLO total cross section and differential distributions analysed in that work. This fact proves that dynamical threshold enhancement at NLO does take place. This does not immediately imply that the same holds at higher orders, but is an important sanity check nonetheless.

The traditional choice of the factorization and renormalization scale employed in [323–325], namely $\mu_0 = (2M_{\rm t} + M_{\rm H})/2 \sim 235$ GeV is not an ideal choice for the evaluation of approximate formulas obtained from the soft emission limit. While the approximate NLO calculations reproduce very well the exact contribution of the NLO gluon-fusion and quark-annihilation channels also at this scale, the NLO cross section receives a sizeable contribution from the quark gluon channel. In particular, this channel dominates the uncertainty derived from scale variation in the range $[\mu_0/2, 2\mu_0]$. While the contribution of the quark-gluon channel is included in nNLO predictions via NLO matching, the soft gluon emission corrections alone do not provide any information on this channel since it is subleading in the soft limit $z \to 1$. Finally, a steep drop of the gluon-fusion and quark-annihilation channel cross sections occurs for $\mu \sim 100$ GeV (see right panel of Figure 83; all of the curves in that panel are evaluated using NNLO PDF). If one includes the contribution of the quark-gluon channel, the steep decrease of the cross section occurs at smaller values of μ. Consequently, while the choice $\mu_0 = 235$ GeV works well for complete fixed-order calculations at NLO, the same choice makes an evaluation of the theoretical uncertainty affecting nNLO calculations based on scale variation unreliable. For these reasons, the main findings of [393] were obtained for a factorization and renormalization scale fixed at a value $\mu_0 = 620$ GeV, which is close to the peak of the final state invariant mass distribution. The location of

Table 37: Total cross section at $\sqrt{s} = 13$ TeV and $\sqrt{s} = 14$ TeV. Each order is evaluated with the MSTW2008 PDF at the corresponding perturbative order (meaning, e.g. NNLO PDF for the nNLO calculation). The uncertainties reflect scale variation only. The top quark mass is $M_{\rm t} = 172.5$ GeV, the Higgs boson mass is $M_{\rm H} = 125$ GeV. See Section I.6.5.b.

$\sqrt{s}$ [TeV]	μ_0 [GeV]	LO [fb]	NLO MG5 [fb]	nNLO [fb]
13	620	$317.2^{+30.7\ \%}_{-21.8\ \%}$	$445.7^{+11.5\ \%}_{-11.5\ \%}$	$479.8^{+2.1\ \%}_{-1.5\ \%}$
13	235	$464.2^{+35.4\ \%}_{-24.1\ \%}$	$515.2^{+6.0\ \%}_{-9.5\ \%}$	$495.6^{+0.0\ \%}_{-2.5\ \%}$
14	620	$383.2^{+30.6\ \%}_{-21.6\ \%}$	$539.7^{+11.4\ \%}_{-11.4\ \%}$	$580.7^{+2.1\ \%}_{-1.4\ \%}$
14	235	$558.2^{+34.9\ \%}_{-24.0\ \%}$	$623.3^{+6.3\ \%}_{-9.4\ \%}$	$599.5^{+0.0\ \%}_{-2.5\ \%}$

Table 38: Total cross section with an estimate of the error associated to the scale variation and to the formally subleading terms, as explained in the text and in [393]. Each order is evaluated with the MSTW2008 PDF at the corresponding perturbative order. See Section I.6.5.b.

$\sqrt{s}$ [TeV]	μ_0 [GeV]	NLO MG5 [fb]	approx. NLO [fb]	nNLO [fb]
13	620	$445.7^{+11.5\ \%}_{-11.5\ \%}$	$442.4^{+10.0\ \%}_{-10.0\ \%}$	$467.2^{+4.9\ \%}_{-4.9\ \%}$
14	620	$539.7^{+11.4\ \%}_{-11.4\ \%}$	$534.8^{+9.8\ \%}_{-9.8\ \%}$	$565.2^{+4.9\ \%}_{-4.9\ \%}$

this peak is not very sensitive to the LHC energy.

In the calculations reported in the following and in [393], no cuts are applied on the momenta of the final state particles and all of the calculations are carried out with MSTW 2008 PDF. The complete list of input parameters can be found in Table 1 in [393]. The NLO results needed for the matching and for comparison are obtained from the code MADGRAPH5_AMC@NLO [54], which for convenience is indicated by the acronym MG5.

I.6.5.b.iii.1 Total cross section

The total cross section at LO, NLO, and nNLO calculated at $\mu_0 = 620$ GeV can be found in Table 37. If one accounts for the approximate NNLO corrections, the central value of the cross section increases with respect to the NLO calculation carried out at $\mu_0 = 620$ GeV, while the scale uncertainty is significantly reduced. If one compares instead the nNLO prediction at $\mu_0 = 620$ GeV with the NLO cross section evaluated at the standard scale choice $\mu_0 = 235$ GeV (which is also shown in Table 37), one sees that the central value of the nNLO cross section is smaller than the NLO one. However, as shown in the left panel of Figure 83 for the LHC at $\sqrt{s} = 13$ TeV, the nNLO scale uncertainty interval at $\mu_0 = 620$ GeV is completely included in the NLO uncertainty interval evaluated with the standard choice $\mu_0 = 235$ GeV. For completeness we report also the numbers obtained by evaluating the nNLO cross section with the traditional scale choice $\mu_0 = 235$ GeV. In this case the NNLO soft emission corrections are positive and small, however the use of NNLO PDF in the nNLO calculation leads to a result which is smaller than the one found with a NLO calculation employing NLO PDF.

The uncertainty of the nNLO cross sections quoted in Table 37, based on scale variation alone, is likely to underestimate the residual perturbative uncertainty of these results. A more conservative estimate of the residual uncertainty affecting the approximate formulas, which accounts also for the numerical effect of terms which are formally subleading in the soft limit and cannot be determined starting from soft emission resummation formulas, was considered in [393].

This more conservative estimate of the uncertainty leads to the approximate NLO predictions

found in the fourth column of Table 38. The central value of the approximate NLO cross section is placed in the middle of the uncertainty interval. The central value and the uncertainty interval obtained in this way are quite close to the complete NLO results evaluated at $\mu_0 = 620$ GeV, which are shown in the third column of Table 38. While this can be somewhat accidental, it shows that, at least for this choice of the scale μ_0, the terms subleading in the soft limit are numerically of the same size of the quark-gluon channel contributions, which is neglected in approximate NLO calculation. The last column in Table 38 shows the nNLO total cross section calculated by estimating the residual perturbative uncertainty according to the more conservative procedure, as it was done in the next-to-last column for the approximate NLO case. We stress that nNLO results are obtained by matching the NNLO corrections in the soft limit to the complete NLO results. As such, they include the same quark-gluon channel contribution included in the NLO result. By looking at Table 38 one sees that the central value of the nNLO total cross section evaluated at $\mu_0 = 620$ GeV is larger than the NLO one (evaluated at the same scale) and the residual perturbative uncertainty is roughly half the one found at NLO. For both $\sqrt{s} = 13$ TeV and $\sqrt{s} = 14$ TeV, the nNLO results reported in Table 38 are included in the NLO uncertainty interval evaluated at $\mu_0 = 620$ GeV, and their central values are included in the NLO uncertainty interval evaluated with the standard scale choice $\mu_0 = 235$ GeV. For the $\sqrt{s} = 13$ TeV case, this situation is illustrated in the left panel of Figure 83.

I.6.5.b.iii.2 Differential distributions

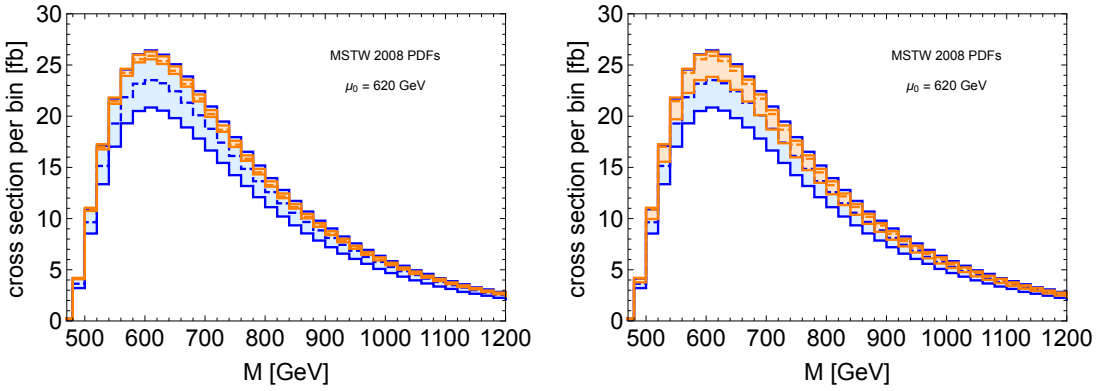

Figure 84: Differential distributions at nNLO (orange band) compared to the NLO calculation carried out with MG5 (blue band) for the LHC at $\sqrt{s} = 13$ TeV. NLO distributions are evaluated with NLO PDF, nNLO distributions with NNLO PDF. The scale is set to $\mu_0 = 620$ GeV in both NLO and nNLO distributions, and it is varied in the range $[\mu_0/2, 2\mu_0]$. The nNLO band in the left panel reflects exclusively the scale variation, while in the right panel it includes also the uncertainty associated with the treatment of subleading terms.

An advantage of the approach followed in [393] is that it can be employed to calculate arbitrary differential cross sections. This can be done by employing standard Monte-Carlo methods. In [393] several differential distributions for the LHC operating at 13 TeV were considered. It was shown in [393] that *i)* the approximate NLO distributions reproduce very well the corresponding NLO calculations carried out by excluding the contribution of the quark-gluon channel, and *ii)* the distributions and their uncertainty, evaluated with the conservative method described above, reproduce well the complete NLO distributions and their scale-variation uncertainty bands obtained from MG5, at least for $\mu_0 = 620$ GeV. A calculation of the differential distributions at nNLO is therefore justified.

Figure 84 shows the invariant-mass distribution at nNLO in comparison with the corresponding complete NLO calculation. In both panels, the NLO perturbative uncertainty band is obtained by varying the scale in the usual range. In the left panel, the nNLO band is obtained by scale variation alone. In the right panel, the band reflecting the residual perturbative uncertainty was obtained by considering

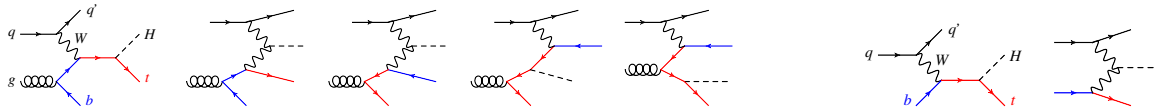

Figure 85: LO Feynman diagrams for t-channel tH production in the 4FS (left) and in the 5FS (right).

both the effect of subleading terms and scale variation, as described above for the total cross section calculation. In [393] it was observed that for all of the distributions considered in that work, including the M distributions, the nNLO predictions at $\mu_0 = 620$ GeV are slightly larger than the NLO ones when the latter are evaluated at the same μ_0 value. The nNLO bands for the differential distribution obtained with the method which considers both the effect of subleading terms and the scale variation are roughly half as large as the ones obtained by evaluating these quantities at NLO.

I.6.6 tH production at NLO in QCD

The production of a Higgs boson in association with a single top quark (tH) at hadron colliders shares important analogies with the electroweak production of a single top quark. At LO one can organize the Feynman diagrams into three independent (non-interfering) sets, based on the virtuality of the W boson coupled to the heavy-quark $b-t$ current: t-channel production features a virtual space-like W, s-channel production a virtual time-like W, and W-associated production an on-shell W boson in the final state. This classification is useful for event generation, but is valid only at LO and in the five-flavour scheme (5FS); when adding higher-order corrections, or when employing the four-flavour scheme (4FS), the picture becomes fuzzy because some amplitudes can interfere.

In the 5FS the separation between t-channel, s-channel and W-associated production is exact up to NLO in QCD (channels start to interfere at NNLO), and calculations are typically simpler than in the 4FS. In the 4FS, instead, the t-channel process can interfere already at NLO in QCD both with (NNLO) s-channel and with W-associated production (only if the W boson decays hadronically); nevertheless, such interference is tiny at NLO and can be neglected if the aim is to compute the dominant t-channel process. Therefore, the separate simulation of t-channel and s-channel tH processes is not a problem up to NLO accuracy in QCD. A detailed study of these two channels at the LHC has been presented recently in Ref. [410], including NLO QCD corrections and addressing many sources of uncertainty (notably the flavour-scheme dependence of the t-channel process). We will review t-channel tH production in Section I.6.6.a, and for s-channel tH production in Section I.6.6.b.

Associated tWH production, on the other hand, interferes also with the much larger $t\bar{t}H$ process starting from NLO in QCD in the 5FS, and this happens already at LO in the 4FS. In general, such interference is large and cannot be neglected, thus NLO simulations of the tWH channel are not straightforward to carry out. For a recent NLO computation of this process in the 5FS, see Ref. [411].

I.6.6.a t-channel tH production

Being a process initiated by bottom quarks, the t-channel tH production can be computed either with the 4FS or with the 5FS approach. In the 4FS the hard matrix element and the phase space are computed taking into account all the bottom-quark (pole) mass effects, but there is no b parton distribution function (PDF), thus b quarks are generated perturbatively in the hard matrix element via initial-state gluon splitting into a $b\bar{b}$ pair (see Figure 85, left). In the 5FS potentially large logarithms associated with such $g \to b\bar{b}$ splitting are resummed to all orders into an initial-state bottom-quark PDF (see Figure 85, right), while all other bottom-quark mass effects are neglected ($M_\mathrm{b} = 0$), and a correct description of the process transverse dynamics is included only at NLO. Both approaches feature advantages and shortcomings at the LHC. Their difference mainly consists of what kind of terms are kept in the perturbative expansion or pushed into missing higher-order corrections, thus it becomes milder when including more

terms in perturbative QCD. Therefore, NLO accuracy is mandatory to reduce the flavour-scheme dependence of theoretical predictions. Moreover, a comparison of 4FS and 5FS results can offer some insights on the relevance of missing higher-order corrections for processes that are more sensitive to large initial-state logarithmic corrections, and should therefore be taken into account in estimating the theoretical uncertainty for a given process.

The results presented in this section have been obtained in the MADGRAPH5_AMC@NLO framework [54], where the NLO simulation can be generated automatically in both the 4FS and 5FS [410]. The top quarks can then be decayed with MADSPIN [368], thereby keeping spin correlations.

I.6.6.a.i Total cross section at NLO

In this section we address the inclusive cross section at NLO accuracy in QCD. The numerical results presented here have been obtained using the input parameters listed below, which follow the prescriptions given in Refs. [35, 144]. The pole mass of the top quark and its Yukawa coupling[I.33] (renormalized on shell) are

$$M_{\rm t} = 172.5\ \text{GeV}\,, \qquad y_{\rm t} = \frac{M_{\rm t}}{v} = \left(\sqrt{2}G_\mu\right)^{1/2} M_{\rm t}\,, \tag{I.6.21}$$

where $v \simeq 246$ GeV is the EW vacuum expectation value. The bottom-quark pole mass in the 4FS (left) and 5FS (right) is set to

$$M_{\rm b}^{(\rm 4FS)} = 4.92\ \text{GeV}\,, \qquad M_{\rm b}^{(\rm 5FS)} = 0\,, \tag{I.6.22}$$

while the bottom-quark Yukawa coupling is always set to zero, $y_{\rm b} = 0$, because its impact on the total cross section amounts to less than 0.1%. Actually, to speed up the 4FS code, the corresponding diagrams are not even generated. The EW parameters are

$$G_\mu = 1.166379 \cdot 10^{-5}\ \text{GeV}^{-2}\,, \qquad M_{\rm Z} = 91.1876\ \text{GeV}\,, \qquad M_{\rm W} = 80.385\ \text{GeV}\,, \tag{I.6.23}$$

which in turn fix the electromagnetic coupling (no running) and the on-shell weak mixing angle to

$$\alpha = \sqrt{2}G_\mu M_{\rm W}^2(1 - M_{\rm W}^2/M_{\rm Z}^2)/\pi \simeq 1/132.233\,, \qquad \sin^2\theta_{\rm W} = 1 - M_{\rm W}^2/M_{\rm Z}^2 \simeq 0.2229\,. \tag{I.6.24}$$

We assume $V_{\rm tb} = 1$ and, for simplicity, the whole CKM matrix to be diagonal[I.34]

$$V_{\rm CKM} = \text{diag}\{V_{\rm ud}, V_{\rm cs}, V_{\rm tb}\} = \text{diag}\{1, 1, 1\}\,. \tag{I.6.25}$$

The proton content in terms of parton distribution functions (PDFs) is evaluated by using the NLO PDF4LHC15 sets in the corresponding flavour-number scheme. The PDFs also determine the reference value of the strong coupling used in the simulation, which then is automatically run at 2-loop accuracy. In the 5FS this value and its uncertainty are

$$\alpha_{\rm s}^{(\rm 5FS)}(M_{\rm Z}) = 0.1180 \pm 0.0015\,, \tag{I.6.26}$$

while in the 4FS $\alpha_{\rm s}(M_{\rm Z})$ is slightly smaller and consistent with a four-flavour running [35]. The combined PDF+$\alpha_{\rm s}$ uncertainty is computed from the Hessian set with 30 (PDF) + 2 ($\alpha_{\rm s}$) members, accordingly to Eq. (28) in Ref. [35]. The renormalization $\mu_{\rm R}$ and factorization $\mu_{\rm F}$ scales are both set equal to the reference value

$$\mu_0^{(t-\text{channel})} = (M_{\rm H} + M_{\rm t})/4\,, \tag{I.6.27}$$

[I.33] In the adopted convention the Feynman rule of the $q\bar{q}H$ vertex is $(-iy_{\rm q})$ for a generic quark q.

[I.34] The only important assumption here is $V_{\rm tb} = 1$; once the third generation is decoupled from the first two, and if one is inclusive over the first two generations, then the result doesn't depend on the mixing between the first two generations (i.e. the Cabibbo angle) due to unitarity.

while the scale dependence in each flavour scheme is estimated from the maximum and minumum variations of the cross section among six scale points with

$$1/2 < \mu_{\rm R,F}/\mu_0 < 2\,, \qquad 1/2 < \mu_{\rm R}/\mu_{\rm F} < 2\,. \tag{I.6.28}$$

The reference scale choice in Eq. (I.6.27) is motivated by physical arguments in the 4FS description [412]. In particular, it ensures that the discrepancy between the 4FS and 5FS results is not unreasonably large, and that the 5FS uncertainty is not underestimated, which might happen when using a very high scale (see Figure 3 in Ref. [410]).

In Tables 233, 234, 235 and 236 we collect the results for the combined t-channel $pp \to tH + \bar{t}H$ production at the LHC, at centre-of-mass energies of $\sqrt{s} = 7, 8, 13$, and 14 TeV, respectively, and for various Higgs boson masses in the range $120-130$ GeV. In the third column we report the reference cross section (in fb), $\sigma_{tH+\bar{t}H}$, computed at NLO and in the 5FS, while in the fourth column we report the NLO $K_{\rm QCD}$ factor, defined as

$$K_{\rm QCD} = \sigma^{\rm NLO\ QCD}_{tH+\bar{t}H}/\sigma^{\rm LO}_{tH+\bar{t}H}\,, \tag{I.6.29}$$

where both the LO and NLO cross sections are computed with the same inputs. In the fifth column we report the combined scale plus flavour-scheme (FS) uncertainty, expressed as upper and lower per cent variations with respect to the reference 5FS prediction. The combined scale+FS uncertainty band is the largest source of theoretical uncertainty, and it is computed from the maximum and minimum variations of the cross section among the 6+6 scale points according to Eqs. (I.6.28) in the two flavour schemes. This translates into the following equations

$$\sigma^+ = \max_{\substack{(\mu_R,\mu_F)\ \text{points}\\ \text{4FS, 5FS}}} \sigma^{\rm (FS)}_{tH+\bar{t}H}(\mu_{\rm R},\mu_{\rm F})\,, \qquad \sigma^- = \min_{\substack{(\mu_{\rm R},\mu_{\rm F})\ \text{points}\\ \text{4FS, 5FS}}} \sigma^{\rm (FS)}_{tH+\bar{t}H}(\mu_R,\mu_F)\,, \tag{I.6.30}$$

$$\text{Scale} + \text{FS}\ [\%] = 100\left(\sigma^+/\sigma^{\rm (5FS)}_{tH+\bar{t}H} - 1\right) \qquad 100\left(\sigma^-/\sigma^{\rm (5FS)}_{tH+\bar{t}H} - 1\right)\,. \tag{I.6.31}$$

In the sixth, seventh, and eighth columns we report the $\alpha_{\rm s}$, PDF, and combined PDF+$\alpha_{\rm s}$ uncertainty in the 5FS, which is the second-largest source of theoretical uncertainty. We recall that it is computed employing the PDF4LHC15 Hessian set with 30 (PDF) + 2 ($\alpha_{\rm s}$) members, with the $\alpha_{\rm s}$ uncertainty given in Eq. (I.6.26), and combining the two uncertainties in quadrature accordingly to the PDF4LHC15 prescription. Finally, in the last two columns we report the separate top (tH) and anti-top ($\bar{t}H$) contributions to the 5FS cross section (in fb). In Table 237 we repeat the exercise, this time keeping the Higgs boson mass fixed to $M_{\rm H} = 125$ GeV and varying instead the collider energy in the range $\sqrt{s} = 6-15$ TeV, to show the gain in the cross section and the reduction of uncertainties. The numbers in Tables 233 to 237, relevant for the SM Higgs boson, are summarized in the plots of Figure 88 where the blue uncertainty band is computed summing the scale+FS and PDF+$\alpha_{\rm s}$ uncertainties.

We conclude the discussion of results relevant for the SM Higgs boson by commenting on two minor uncertainties, namely the ones associated with the bottom-quark and top-quark masses. According to Ref. [144], we take the uncertainty on the bottom-quark mass to be $M_{\rm b} = 4.92 \pm 0.13$ GeV. At 13 TeV, and for a 125 GeV Higgs boson mass, this translates into a 4FS cross section of $\sigma^{\rm (4FS)}_{tH+\bar{t}H} = 67.4^{+0.7}_{-0.5}$ fb, which corresponds to an uncertainty of about 1%. Since no PDF4LHC15 set with heavy-quark mass variations has been published yet, we estimate the impact on the 5FS cross section using the numbers in Ref. [410], where previous-generation PDF sets have been used.

The ± 0.25 GeV bottom-mass uncertainty quoted in Ref. [410] returned an uncertainty in the 5FS cross section of about 2%. A crude rescaling to ± 0.13 GeV results in an uncertainty of roughly 1%, comparable to the one in the 4FS.

Similarly, we consider a top-quark mass uncertainty of $M_{\rm t} = 172.5 \pm 1.0$ GeV, which returns a 5FS cross section of $\sigma^{\rm (5FS)}_{tH+\bar{t}H} = 74.3^{+0.4}_{-0.3}$ fb at 13 TeV. Thus, the $M_{\rm t}$ uncertainty in the total cross section

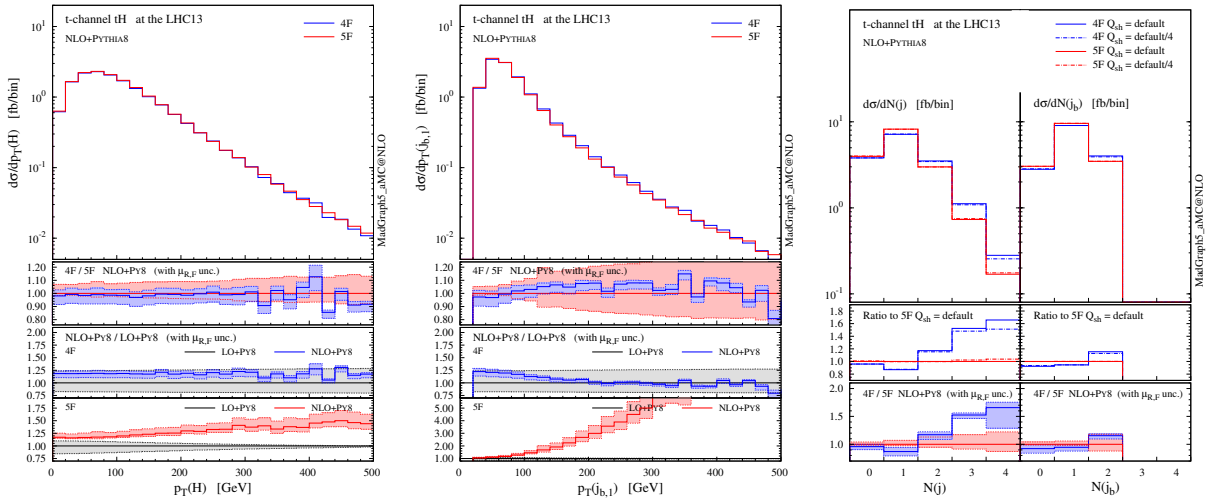

Figure 86: Differential distributions in t-channel $pp \to tH + \bar{t}H$ production at the 13 TeV LHC, computed at NLO matched to PYTHIA8, in the 4FS (blue) and in the 5FS (red). We show the transverse momentum of the Higgs boson $p_{\mathrm{T}}(H)$ on the left, of the hardest b-tagged jet $p_{\mathrm{T}}(j_{\mathrm{b},1})$ in the centre, and the light-jet and b-jet multiplicities on the right. Plots are taken from Ref. [410].

is below 1%, since increasing the top-quark mass causes a reduction of the available phase space which is however partly compensated by the larger top-quark Yukawa coupling.

Associated tH production in the t-channel is known for having maximal destructive interference in the SM between $H-W$ interactions on the one hand, and $H-t$ interactions on the other hand: deviations from the SM top-quark Yukawa coupling can result in a large enhancement of the cross section. This has prompted the LHC experiments to perform searches for the 125 GeV Higgs boson in this process [413, 414] assuming that the sign of the top-quark Yukawa coupling is opposite to the SM coupling in Eq. (I.6.21),

$$y_{\mathrm{t}} = -y_{\mathrm{t}}^{(\mathrm{SM})} = -M_{\mathrm{t}}/v\,, \tag{I.6.32}$$

which results in maximally constructive interference between the two subsets of diagrams. Given the interest in experimental searches, in Table 39 we provide reference cross sections and uncertainties for this scenario at 13 and 14 TeV. For further applications of this process to constrain deviations from the SM interactions of the 125 GeV particle, see also Section II.3.1.

Finally, we extend our investigation to Higgs boson masses in the range $M_{\mathrm{H}} = 10-3000$ GeV keeping the Higgs boson as stable particle and neglecting Higgs boson width effects, which might provide a useful reference for BSM Higgs searches. The results at 13 and 14 TeV are plotted in Figure 89. These results should be taken with care, since an hypothetical BSM Higgs boson may contribute to the same tH final state through different interactions than the ones described by SM-like diagrams.

I.6.6.a.ii Differential distributions at NLO+PS

In this section we briefly address NLO differential distributions matched to a parton shower (NLO+PS). To generate events for distributions, we recommend to use a dynamic event-by-event scale instead of the static one in Eq. (I.6.27). In Ref. [410] we have employed the fraction of transverse energy (restricted to the set of H, t, and b particles) given by the formula

$$\mu_0^{(t-\mathrm{channel,\ dynamic})} = \sum_{\mathrm{i=H,t,b}} M_{\mathrm{T}}(i)/6\,, \qquad \text{where} \quad M_{\mathrm{T}} = \sqrt{M^2 + p_{\mathrm{T}}^2}\,, \tag{I.6.33}$$

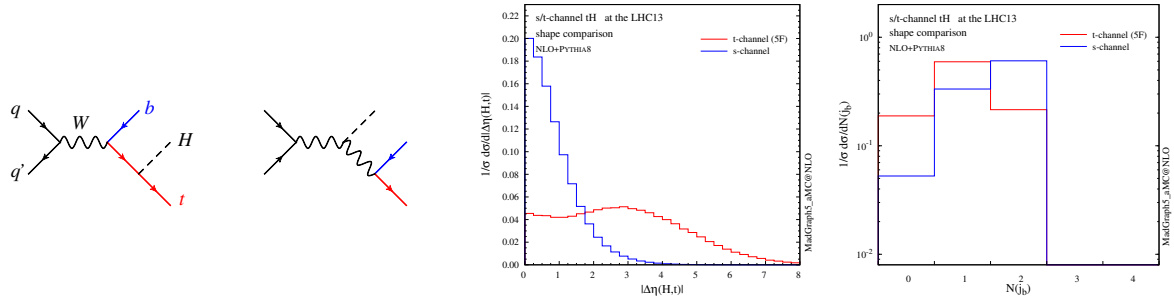

Figure 87: On the left: LO Feynman diagrams for s-channel tH production. At the centre: pseudorapidity distance between the Higgs boson and the top quark $\Delta\eta(H,t)$ in the s-channel process (blue) compared to the t-channel one (red). On the right: multiplicity of b-tagged jets in the s-channel process (blue) compared to the t-channel one (red). Plots are taken from Ref. [410].

is the transverse mass of a particle of mass M. We have found that this choice of dynamic scale returns a total cross section very close to the one computed with the static scale in Eq. (I.6.27). On top of that, there is a remarkable agreement at NLO+PS between the 4FS and 5FS predictions for many observables, such as those related to the Higgs boson (see left plot in Figure 86), the top quark, and the forward jet. This is non trivial, especially in the light of the inadequacy of the 5FS predictions at LO, which can suffer of large differential K factors after the inclusion of bottom-quark transverse dynamics, see central plot in Figure 86. On the other hand, the 4FS gives in general more stable results (flatter K factors, smaller scale dependence in the tails) and is able to provide accurate predictions for a wider set of observables, including those related to the spectator b-quark and the extra jets. Finally, we find the choice of shower starting scale, $Q_{\rm sh}$, to have a tiny impact on NLO+PS results, see right-hand-side plot in Figure 86.

I.6.6.b s-channel tH production

Unlike the t-channel process, s-channel tH production is not affected by flavour-scheme ambiguities, since at LO it is initiated by quark-antiquark annihilation (see left-hand-side of Figure 87). Therefore, one can simply employ the 5FS for simulating this process. Results presented in this section have been obtained in the MADGRAPH5_AMC@NLO framework. Once again, spin correlations can be kept by decaying the top quarks with MADSPIN. The same input parameters as for the t-channel process in the 5FS have been used, with the exception of the reference scale choice, which in this case is

$$\mu_0^{(s-\text{channel})} = (M_{\rm H} + M_{\rm t})/2\,. \tag{I.6.34}$$

In Tables 238, 239, 240 and 241 we collect the results for the combined s-channel $pp \to tH + \bar{t}H$ production at the LHC, at centre-of-mass energies of $\sqrt{s} = 7, 8, 13$, and 14 TeV respectively, and for various Higgs boson masses in the range $120-130$ GeV. These tables are analogous to the ones presented in the previous section for the t-channel process: in the third column we report the reference cross section; in the fourth the QCD K factor, defined in Eq. (I.6.28); in the fifth the scale dependence, computed from the maximum and minimum variations of the cross section among the 6 points listed in Eq. (I.6.28); in the sixth, seventh, and eight the $\alpha_{\rm s}$, PDF, and combined PDF+$\alpha_{\rm s}$ uncertainty, computed employing the 30+2 PDF4LHC15 Hessian set; and finally, in the last two columns we report the separate top and anti-top contributions to the cross section. In Table 242 we show the cross-section results obtained varying the LHC energy in the range $\sqrt{s} = 6-15$ TeV and keeping the Higgs boson mass fixed to $M_{\rm H} = 125$ GeV. All these numbers are summarized in the plots of Figure 90, where the the blue uncertainty band is produced summing the scale and PDF+$\alpha_{\rm s}$ uncertainties.

We also plot in Figure 91 the analogous cross-section results in the extended Higgs boson mass range $10-3000$ GeV, at 13 and 14 TeV. Finally, we remark that even though the s-channel cross section

Table 39: Cross section for t-channel tH and $\bar{t}H$ production at the 13 and 14 TeV LHC, for $y_t = -y_t^{(\mathrm{SM})}$.

$\sqrt{s}$[TeV]	M_{H}[GeV]	$\sigma_{tH+\bar{t}H}$[fb]	K_{QCD}	Scale+FS [%]	α_S [%]	PDF [%]	PDF+α_S [%]	σ_{tH}[fb]	$\sigma_{\bar{t}H}$[fb]
13	125.0	848.0	1.06	$+6.6\ -13.3$	± 1.1	± 3.1	± 3.3	546.7	301.6
14	125.0	1011	1.07	$+6.5\ -13.0$	± 1.1	± 3.0	± 3.2	649	363

is very tiny (around $25-30$ times smaller than the t-channel cross section at $13-14$ TeV), this process features kinematical distributions with shapes rather different than the t-channel ones, see central and right plots in Figure 87.

I.6.7 $t\bar{t}Z$ and $t\bar{t}W^{\pm}$ production

The production of a $t\bar{t}$ pair in association with electroweak vector bosons represent an important source of background to $t\bar{t}H$ production in the $H \to b\bar{b}$, $H \to WW^*$ and $H \to \tau\tau$ channels. In this section we present NLO QCD+EW predictions for inclusive and differential $t\bar{t}Z$ and $t\bar{t}W^{\pm}$ cross sections, a comparison of NLO QCD distributions obtained with various automated tools, as well as NLO QCD predictions for $t\bar{t}$ production in association with two vector bosons.

I.6.7.a NLO QCD+EW predictions for $t\bar{t}Z$ and $t\bar{t}W^{\pm}$ production

Predictions for $t\bar{t}$ production in association with a vector boson $V = Z, W^{\pm}$ at NLO QCD have been presented in [415–417] and matched to the parton shower in [418, 419], while the first calculation of electroweak corrections for this class of processes has been completed more recently [328]. In the following we present NLO QCD+EW predictions for inclusive $t\bar{t}Z$ and $t\bar{t}W^{\pm}$ production at $\sqrt{s} = 13$ TeV and 14 TeV. All input parameters are chosen according to the HXSWG recommendations [144], and the hadronic cross section is obtained using the PDF4LHC15 [35] and NNPDF2.3QED [279] parton distributions as explained below. The top-quark and the electroweak vector bosons are treated as stable particles, and for the renormalization of the respective mass paramaters the on-shell scheme is used. The Higgs boson mass is set to $M_{\mathrm{H}} = 125$ GeV. The electroweak couplings and mixing angle are evaluated in the G_μ-scheme using the Fermi constant and the vector-boson masses as input parameters. The central value for renormalization and factorization scales is set to

$$\mu_0 = M_{\mathrm{t}} + M_{\mathrm{V}}/2\,. \tag{I.6.35}$$

For the NLO QCD part of the calculation scale uncertainties are estimated by independent variations of renormalization and factorization scales in the range $\mu/2 \le \mu_{\mathrm{R}}, \mu_{\mathrm{F}} \le 2\mu$, with $1/2 \le \mu_{\mathrm{R}}/\mu_{\mathrm{F}} \le 2$, while for PDF and α_{s} uncertainties the PDF4LHC15 prescription is used. The resulting uncertainties are applied also to NLO EW correction effects.

The NLO QCD+EW predictions presented in the following,

$$\sigma^{\mathrm{NLO}}_{\mathrm{QCD+EW}} = \sigma^{\mathrm{NLO}}_{\mathrm{QCD}} + \delta\sigma_{\mathrm{EW}}\,, \tag{I.6.36}$$

result from the combination of various contributions. The usual NLO QCD cross section,

$$\sigma^{\mathrm{NLO}}_{\mathrm{QCD}} = \sigma^{\mathrm{LO}}_{\mathrm{QCD}} + \delta\sigma^{\mathrm{NLO}}_{\mathrm{QCD}}, \tag{I.6.37}$$

comprises LO terms of $\mathcal{O}(\alpha_{\mathrm{s}}^2\alpha)$ and NLO QCD corrections of $\mathcal{O}(\alpha_{\mathrm{s}}^3\alpha)$, which involve gg, $q\bar{q}$ and gq partonic channels. Note that the gg channel starts contributing only at NNLO QCD in the case of $t\bar{t}W^{\pm}$ production. The remaining EW corrections, denoted as $\delta\sigma_{\mathrm{EW}}$, include three types of terms:

1. LO EW terms of $\mathcal{O}(\alpha^3)$ that result from squared EW tree amplitudes in the $q\bar{q}$ and $\gamma\gamma$ channels.

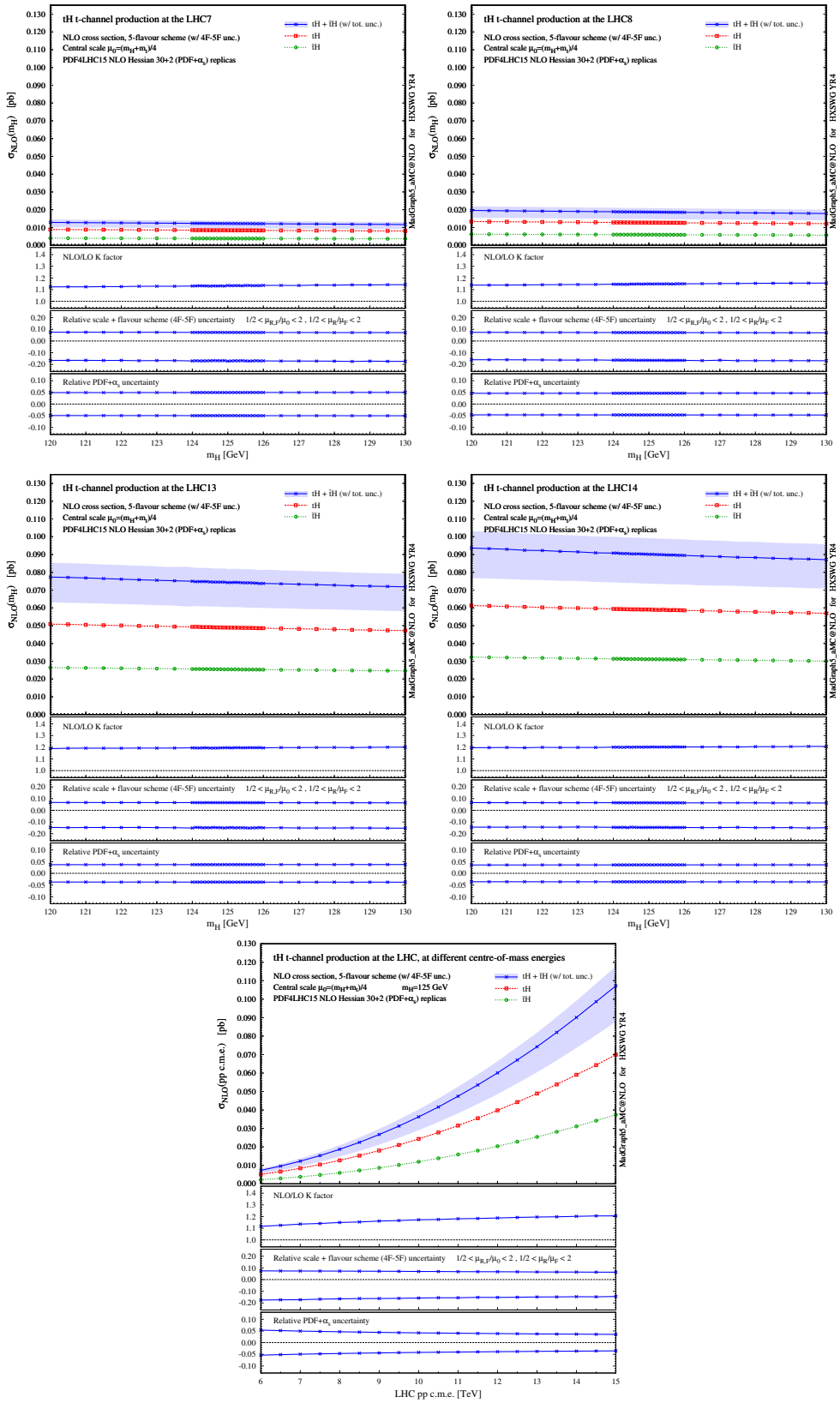

Figure 88: Cross sections for t-channel tH and $\bar{t}H$ production.

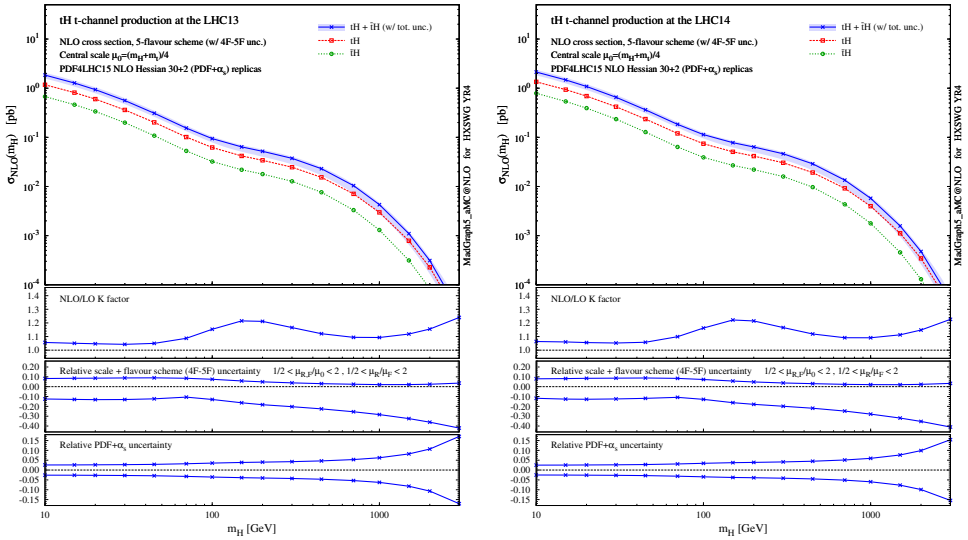

Figure 89: Cross sections for t-channel tH and $\bar{t}H$ production in the extended Higgs boson mass range.

2. LO mixed terms of $\mathcal{O}(\alpha_s\alpha^2)$ that result from the interference of EW and QCD tree diagrams in the $b\bar{b}$ and γg channels. Other $q\bar{q}$ channels do not contribute at this order due to the vanishing interference of the related colour structures. Thus $t\bar{t}W^{\pm}$ production does not receive any $\mathcal{O}(\alpha_s\alpha^2)$ contribution.
3. NLO EW corrections of $\mathcal{O}(\alpha_s^2\alpha^2)$ in the $q\bar{q}$, gg and γg channels. Subleading NLO terms of $\mathcal{O}(\alpha_s\alpha^3)$ and $\mathcal{O}(\alpha^4)$ are not included as they are expected to be strongly suppressed.

At $\sqrt{s} = 13$–14 TeV, LO EW contributions to $t\bar{t}Z$ and $t\bar{t}W^{\pm}$ production correspond to $+1.2\%$ and $+0.6\%$ of the respective NLO QCD cross sections, while LO mixed effects are at the sub-per mille level. Order $\alpha_s^2\alpha^2$ NLO EW corrections to the $t\bar{t}Z$, $t\bar{t}W^+$ and $t\bar{t}W^-$ cross sections amount to -0.9%, -3.3% and -2.6%, respectively.[I.35] Photon-induced channels have a non-negligible impact ($+0.8\%$) only in the $t\bar{t}Z$ cross section at $\mathcal{O}(\alpha_s\alpha^2)$. However their effect is almost completely cancelled by the contribution of the $b\bar{b}$ channel at the same order.

Effects of $\mathcal{O}(\alpha)$ related to the QED evolution of PDF and initial-state photons are included in the same way as discussed in Sect. I.6.2 for $t\bar{t}H$ production: (i) all NLO QCD+EW predictions for partonic channels with initial-state gluons and quarks are computed using the PDF4LHC15 set with 30+2 members; (ii) for γ-induced channels NNPDF2.3QED set (with $\alpha_s(M_Z) = 0.118$) is used; (iii) the effect of the QED evolution of quark PDF is estimated from the difference between NNPDF2.3QED and NNPDF2.3 parton densities as indicated in (I.6.5), and for a more detailed discussion we refer to Sect. I.6.2. Similarly as for $t\bar{t}H$ production, the effect of QED PDF evolution is negative and ranges from -0.6% to -0.8%.

Corrections of order $\alpha^2\alpha_s^2$ resulting from the emission of and extra heavy boson have been discussed in [328]. Although they enter at the same perturbative order as the NLO EW corrections to $t\bar{t}V$ production, such contribution represent separate physics processes, namely $t\bar{t}$ production in associated with two vector bosons. Corresponding predictions at NLO QCD are presented in Sect. I.6.7.c.

Predictions for inclusive $t\bar{t}V$ cross sections at NLO QCD+EW for $\sqrt{s} = 13$ and 14 TeV are listed in Tables 40–41. The impact of QCD and EW corrections is shown in the form of a QCD correction factor

$$K_{\text{QCD}} = \frac{\sigma^{\text{NLO}}_{\text{QCD}}}{\sigma^{\text{LO}}_{\text{QCD}}}, \tag{I.6.38}$$

[I.35] Here $\mathcal{O}(\alpha)$ effects related to the QED evolution of PDF (see below) are not included.

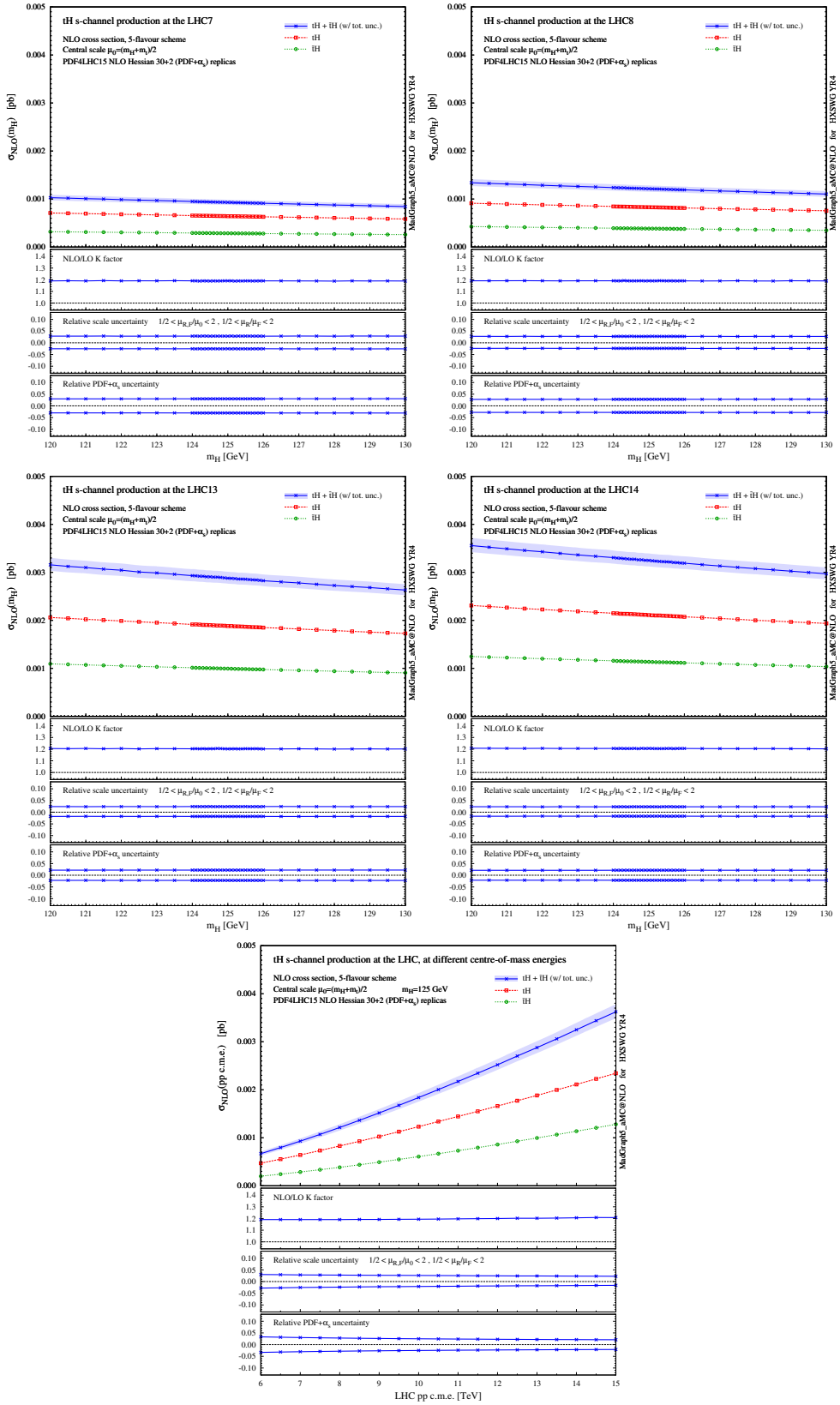

Figure 90: Cross sections for s-channel tH and $\bar{t}H$ production.

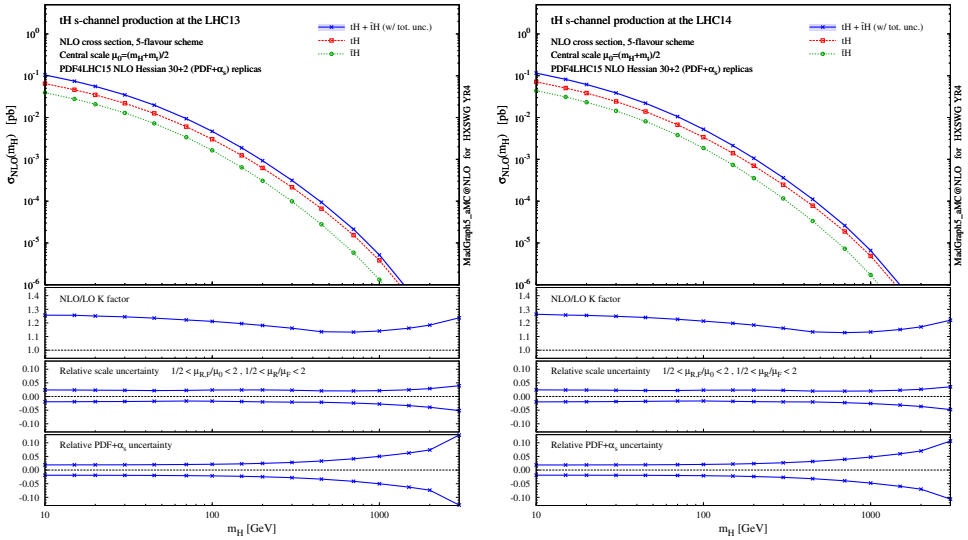

Figure 91: Cross sections for s-channel tH and $\bar{t}H$ production in the extended Higgs boson mass range.

Table 40: Inclusive $t\bar{t}V$ cross sections at NLO QCD and NLO QCD+EW accuracy for $\sqrt{s} = 13$ TeV. NLO QCD+EW results represent the best predictions and should be used in experimental analyses. Scale, PDF, and α_s uncertainties are quoted in per cent. Absolute statistical uncertainties are indicated in parenthesis. We also quote the NLO QCD+EW $t\bar{t}W^- + t\bar{t}W^+$ combined cross sections where correlation effects have been consistently included in the estimate of the corresponding uncertainties. Collider energy and cross sections are in TeV and femtobarn, respectively.

Process	$\sqrt{s}$	$\sigma^{\rm NLO}_{\rm QCD}$	$\sigma^{\rm NLO}_{\rm QCD+EW}$	$K_{\rm QCD}$	$\delta_{\rm EW}$[%]	Scale[%]	PDF[%]	α_S[%]
$t\bar{t}Z$	13	841.3(1.6)	839.3(1.6)	1.39	−0.2	$+9.6\%\ -11.3\%$	$+2.8\%\ -2.8\%$	$+2.8\%\ -2.8\%$
$t\bar{t}W^+$	13	412.0(0.32)	397.6(0.32)	1.49	−3.5	$+12.7\%\ -11.4\%$	$+2.0\%\ -2.0\%$	$+2.6\%\ -2.6\%$
$t\bar{t}W^-$	13	208.6(0.16)	203.2(0.16)	1.51	−2.6	$+13.3\%\ -11.7\%$	$+2.1\%\ -2.1\%$	$+2.9\%\ -2.9\%$
$t\bar{t}W^- + t\bar{t}W^+$	13	620.6(0.36)	600.8(0.36)	1.50	−3.2	$+12.9\%\ -11.5\%$	$+2.0\%\ -2.0\%$	$+2.7\%\ -2.7\%$

Table 41: Inclusive $t\bar{t}V$ cross sections at NLO QCD and NLO QCD+EW accuracy for $\sqrt{s} = 14$ TeV. NLO QCD+EW results represent the best predictions and should be used in experimental analyses. Scale, PDF, and α_s uncertainties are quoted in per cent. Absolute statistical uncertainties are indicated in parenthesis. Collider energy and cross sections are in TeV and femtobarn, respectively.

Process	$\sqrt{s}$	$\sigma^{\rm NLO}_{\rm QCD}$	$\sigma^{\rm NLO}_{\rm QCD+EW}$	$K_{\rm QCD}$	$\delta_{\rm EW}$[%]	Scale[%]	PDF[%]	α_S[%]
$t\bar{t}Z$	14	1018(2.2)	1015(2.2)	1.40	−0.3	$+9.6\%\ -11.2\%$	$+2.7\%\ -2.7\%$	$+2.8\%\ -2.8\%$
$t\bar{t}W^+$	14	474.9(0.36)	458.2(0.36)	1.51	−3.5	$+13.2\%\ -11.6\%$	$+1.9\%\ -1.9\%$	$+2.6\%\ -2.6\%$
$t\bar{t}W^-$	14	244.5(0.17)	238.0(0.17)	1.54	−2.7	$+13.8\%\ -11.8\%$	$+2.0\%\ -2.0\%$	$+2.9\%\ -2.9\%$

and a relative EW correction factor

$$\delta_{\rm EW} = \delta\sigma_{\rm EW}/\sigma^{\rm NLO}_{\rm QCD}\,. \tag{I.6.39}$$

Electroweak corrections include all LO and NLO EW effects discussed above, i.e. also those arising form the QED evolution of PDF. All quantities in (I.6.38)–(I.6.39) are obtained using NLO QCD PDF. Results in Tables 40–41 have been obtained with MADGRAPH5_AMC@NLO [54]. A cross check against an independent calculation based on SHERPA+OPENLOOPS [336] has confirmed the correctness of NLO QCD+EW predictions at the level of the quoted statistical accuracy (0.1–0.2%).

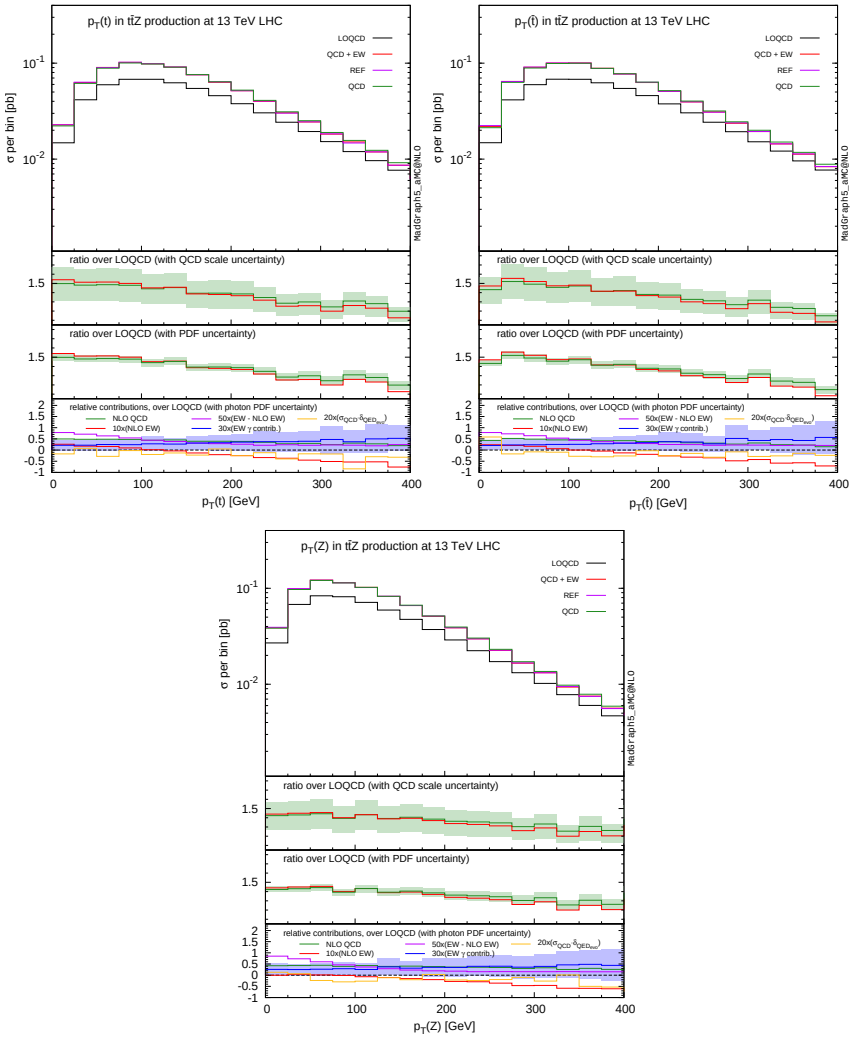

Figure 92: Transverse momentum (p_{T}) distribution of the top quark, anti-top quark, and Z boson.

The size of the corrections as well as the scale and PDF+α_{s} uncertainties vary very little form 13 to 14 TeV. For $t\bar{t}W^{\pm}$ production the QCD and EW corrections as well as the NLO scale uncertainties turn out to be slightly more pronounced as compared to $t\bar{t}Z$ production. Scale variations range from 10 to 13% and represent the dominant source of uncertainty. It was checked that replacing the fixed scale $\mu = M_{\mathrm{t}} + M_{\mathrm{V}}/2$ by a dynamic scale $\mu = H_{\mathrm{T}}/2$ shifts all $t\bar{t}V$ cross sections by -7%, which is consistent with the scale uncertainties quoted in Tables 40–41. The combined PDF+α_{s} uncertainty amounts to 2–3%, and EW correction effects turn out to be similarly small (between -0.2% and -3.5%).

In the tails of transverse-momentum distributions NLO electroweak effects can become more sizeable due to the appearance of Sudakov logarithms. This is illustrated in Figures 92–94, which display differential NLO QCD+EW predictions obtained with MADGRAPH5_AMC@NLO for $t\bar{t}Z$, $t\bar{t}W^{+}$ and $t\bar{t}W^{-}$ production, respectively, using the same setup and fixed scale choice as described above.

I.6.7.b Comparison of NLO QCD predictions for differential distributions

In this section we provide a comparison among fixed-order NLO QCD predictions of differential distributions for $t\bar{t}V$ ($V = Z, W^{\pm}$) production at the LHC with $\sqrt{s} = 13$ TeV, obtained using the following tools:

– SHERPA 2.2.0 + OPENLOOPS 1.2.3,

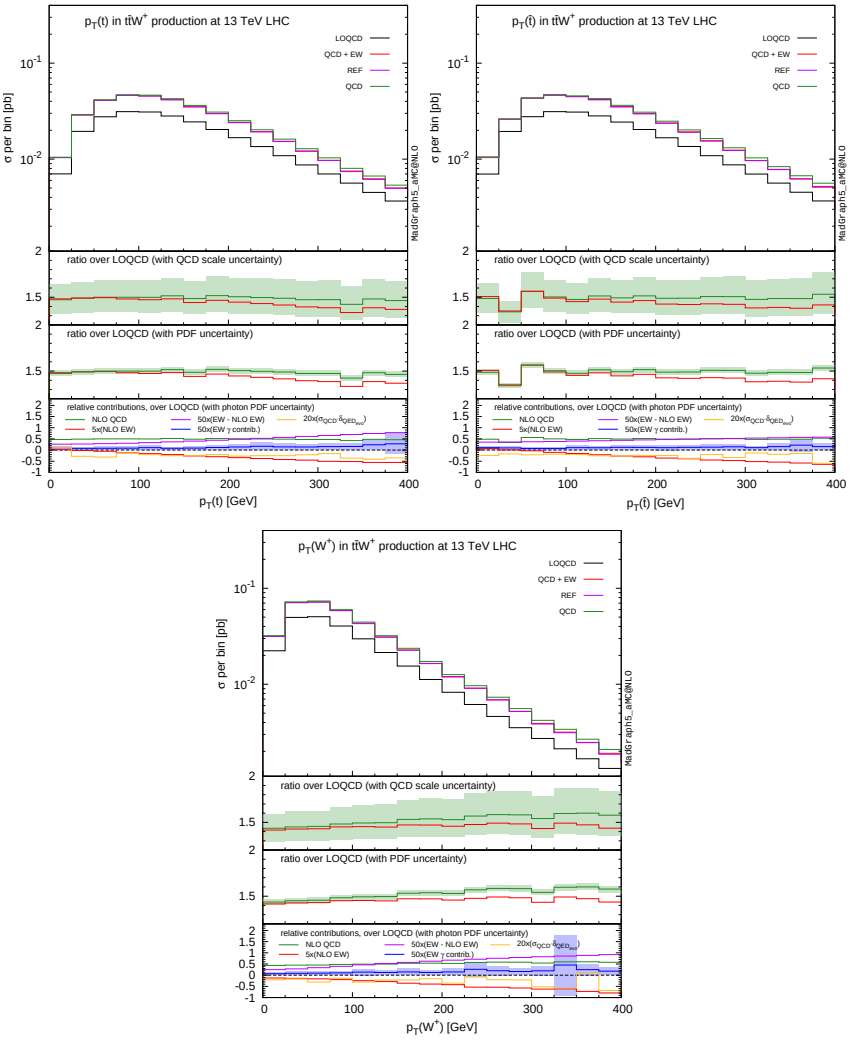

Figure 93: Transverse momentum (p_{T}) distribution of the top quark, anti-top quark, and W^+ boson.

– MADGRAPH5_AMC@NLO 2.3.2,
– POWHEL.

The impact of EW corrections has been discussed in Section I.6.7.a. Here the main goal is only to assess the agreement and compatibility of existing fixed-order NLO QCD calculations at the level of differential cross sections. Future studies will test the compatibility of different implementations of these calculations which also include parton-shower effects. In this context, all the tools listed above have been used as fixed-order QCD Monte Carlo generators.

SHERPA+OPENLOOPS uses OPENLOOPS [247] as a one-loop generator, and relies on the CUTTOOLS library [353] for the numerically stable evaluation of tensor integrals. Real-emission contributions, infrared subtractions based on the Catani-Seymour technique [249, 354], and phase-space integration are handled by SHERPA [345, 355, 356].

In MADGRAPH5_AMC@NLO [54, 348], fixed-order NLO QCD results are obtained by adopting the FKS method [113, 357] for the subtraction of the infrared divergences of the real-emission matrix elements (automated in the module MADFKS [358]), and the OPP integral-reduction procedure [359] for the computation of the one-loop matrix elements (automated in the module MADLOOP [348]).

Finally, the POWHEL generator [419] uses the HELAC-NLO package [349] for the computation of all matrix elements provided as input to the POWHEG BOX. The POWHEG BOX framework [81, 342, 343]

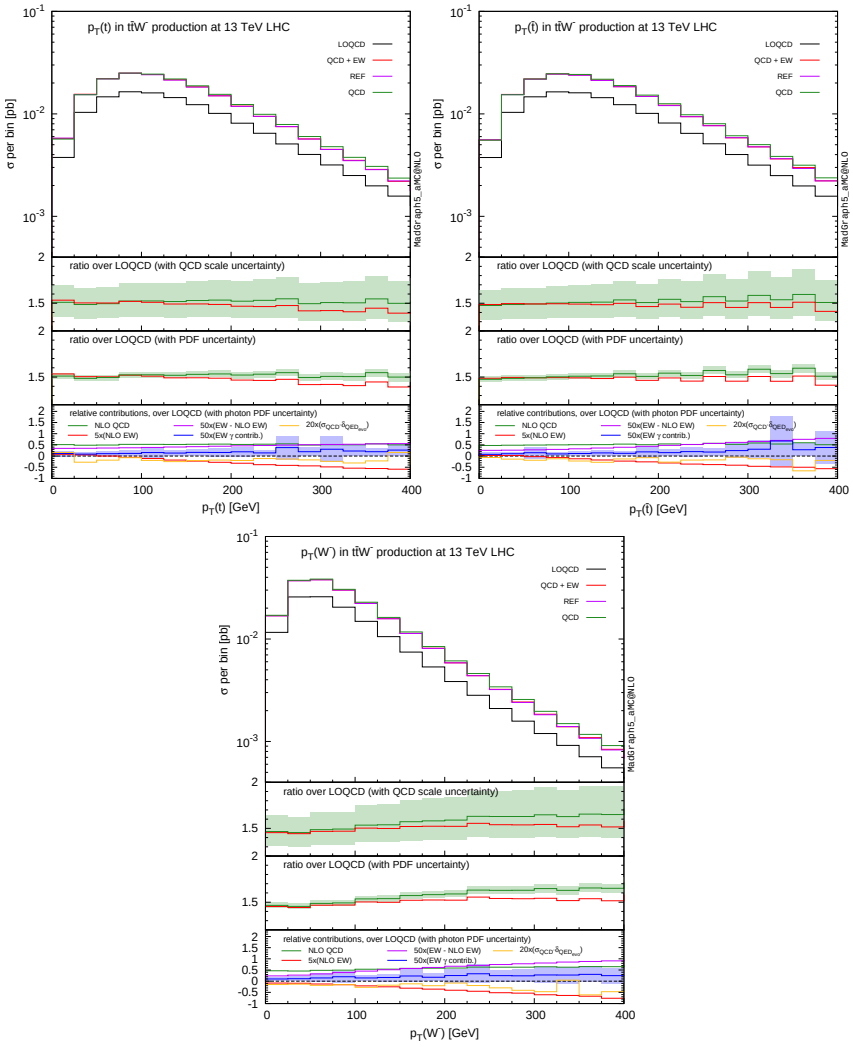

Figure 94: Transverse momentum (p_{T}) distribution of the top quark, anti-top quark, and W^- boson.

adopts the FKS subtraction scheme [113, 357] to factor out the infrared singularities of the real-emission cross section, while the the virtual one-loop matrix elements can be provided with different methods.

For this comparison all input parameters are chosen according to the HXSWG recommendations [144], and the hadronic cross section is obtained using the PDF4LHC15 [35] and a five-flavour scheme (5FS). Renormalization (μ_{R}) and factorization (μ_{F}) scales have been fixed to a dynamical central value $\mu_0 = H_{\mathrm{T}}$, where H_{T} is the sum of the transverse energies of the $t\bar{t}V$ final state ignoring extra jet emission. The theoretical uncertainty has been estimated by varying both μ_{R} and μ_{F} by a factor of 2 about μ_0.

Results for the following distributions:

- transverse momentum (p_{T}) of the top quark, vector boson, $t\bar{t}$ system, and $t\bar{t}V$ system;
- pseudorapidity (η) of the top quark and vector boson,

are presented in Figs. 95-100, for the case of $V = W^+, W^-$, and Z, respectively.

I.6.7.c $t\bar{t}VV$ production ($V = Z, W^{\pm}, H$) at NLO QCD

Besides the dominant contribution from $t\bar{t}Z$ and $t\bar{t}W^{\pm}$, the production of a top-quark pair ($t\bar{t}$) in association with two heavy bosons V with $V = Z, W^{\pm}, H$ can also be a non-negligible component of the

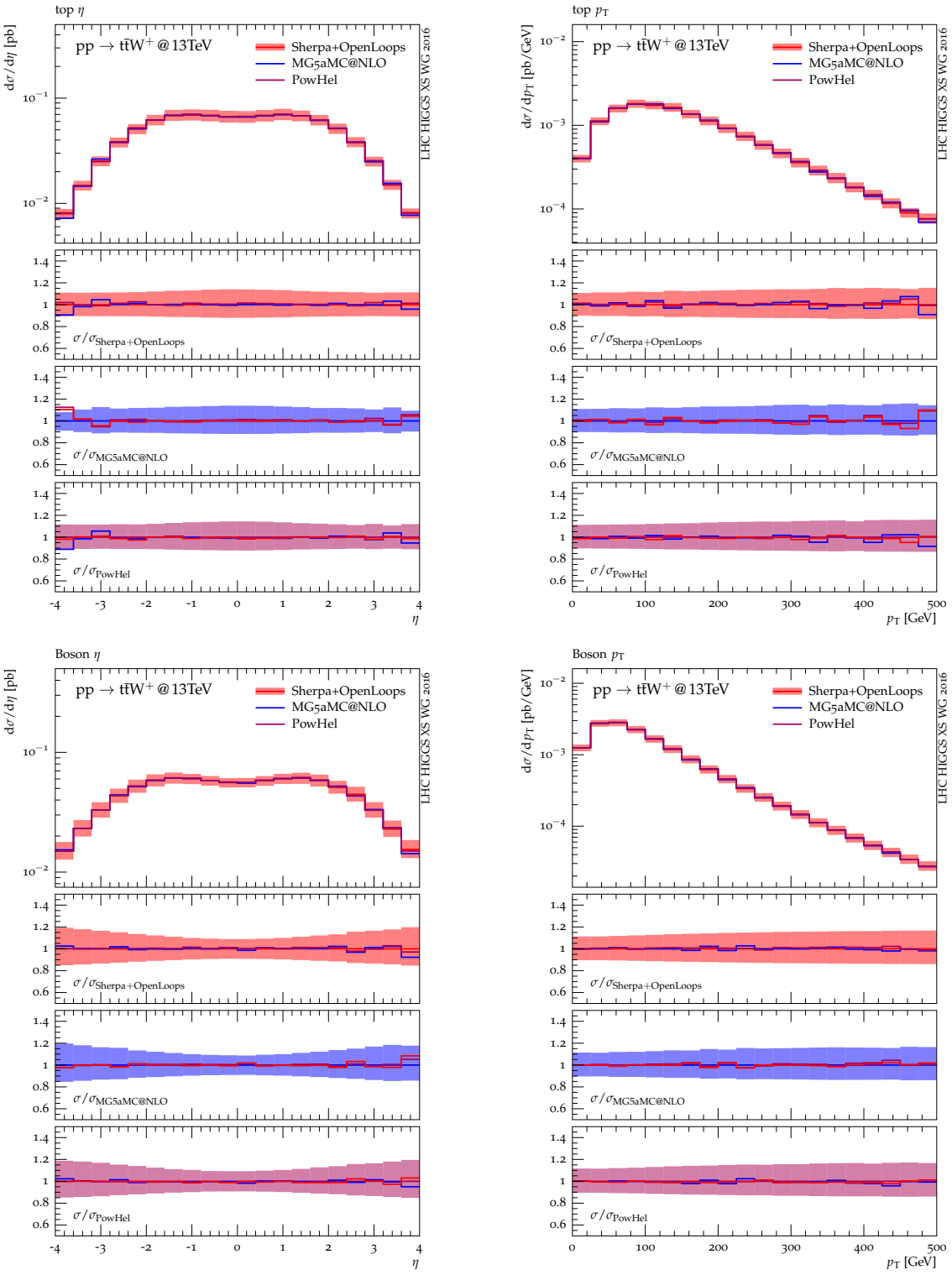

Figure 95: Fixed-order NLO predictions for differential $t\bar{t}W^{+}$ observables at 13 TeV. Each ratio plot shows all results normalized to one particular NLO+PS prediction and the scale variation band of the reference prediction.

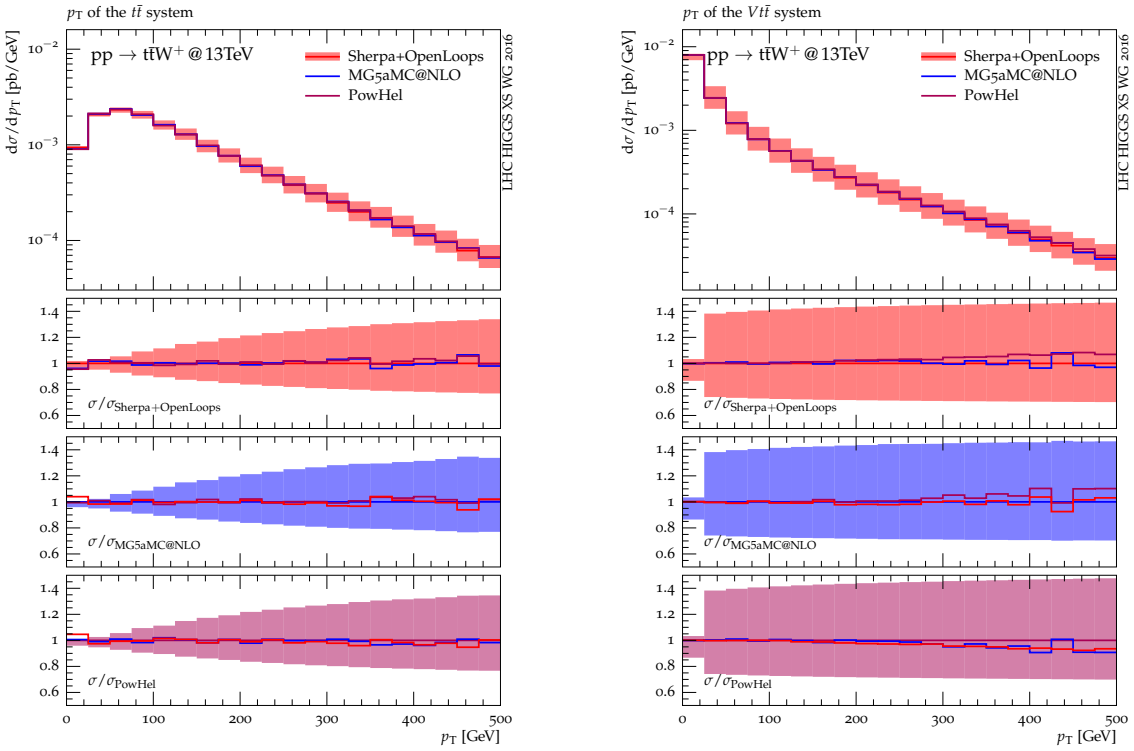

Figure 96: Fixed-order NLO predictions for differential $t\bar{t}W^+$ observables at 13 TeV. Ratio plots as in Figure 95.

Table 42: NLO and LO cross sections for $t\bar{t}VV$ processes ($V = Z, W^{\pm}, H$) at 13 TeV. The renormalization and factorization scales are set equal to half of the sum of the masses of the final-state particles.

13 TeV σ [ab]	$t\bar{t}W^+Z$	$t\bar{t}W^-Z$	$t\bar{t}ZZ$
NLO QCD	$2705(3)^{+9.9\%\ +2.7\%}_{-10.6\%\ -2.7\%}$	$1179(2)^{+11.2\%\ +3.7\%}_{-11.2\%\ -3.7\%}$	$1982(2)^{+5.2\%\ +2.6\%}_{-9.0\%\ -2.6\%}$
LO	$1982(2)^{+28.4\%\ +3.3\%}_{-20.6\%\ -3.3\%}$	$839.4(6)^{+28.2\%\ +4.2\%}_{-20.5\%\ -4.2\%}$	$1611(1)^{+31.4\%\ +2.7\%}_{-22.1\%\ -2.7\%}$
K-factor	1.36	1.40	1.23
13 TeV σ [ab]	$t\bar{t}W^+H$	$t\bar{t}W^-H$	$t\bar{t}ZH$
NLO QCD	$1089(1)^{+1.8\%\ +2.6\%}_{-5.9\%\ -2.6\%}$	$493.0(5)^{+2.6\%\ +3.4\%}_{-6.4\%\ -3.4\%}$	$1535(2)^{+1.9\%\ +3.0\%}_{-6.8\%\ -3.0\%}$
LO	$997.0(9)^{+26.9\%\ +3.0\%}_{-19.8\%\ -3.0\%}$	$440.0(4)^{+26.9\%\ +3.8\%}_{-19.8\%\ -3.8\%}$	$1391(1)^{+32.2\%\ +2.8\%}_{-22.6\%\ -2.8\%}$
K-factor	1.09	1.12	1.10
13 TeV σ [ab]	$t\bar{t}W^+W^-$	$t\bar{t}W^+W^-$ (4f)	$t\bar{t}HH$
NLO QCD	–	$11500(10)^{+8.1\%\ +3.0\%}_{-10.9\%\ -3.0\%}$	$756.5(7)^{+1.1\%\ +3.3\%}_{-4.4\%\ -3.3\%}$
LO	$8380(5)^{+33.2\%\ +3.0\%}_{-23.1\%\ -3.0\%}$	$8357(5)^{+33.3\%\ +3.0\%}_{-23.1\%\ -3.0\%}$	$765.4(5)^{+31.8\%\ +2.9\%}_{-22.4\%\ -2.9\%}$
K-factor	–	1.38	0.99

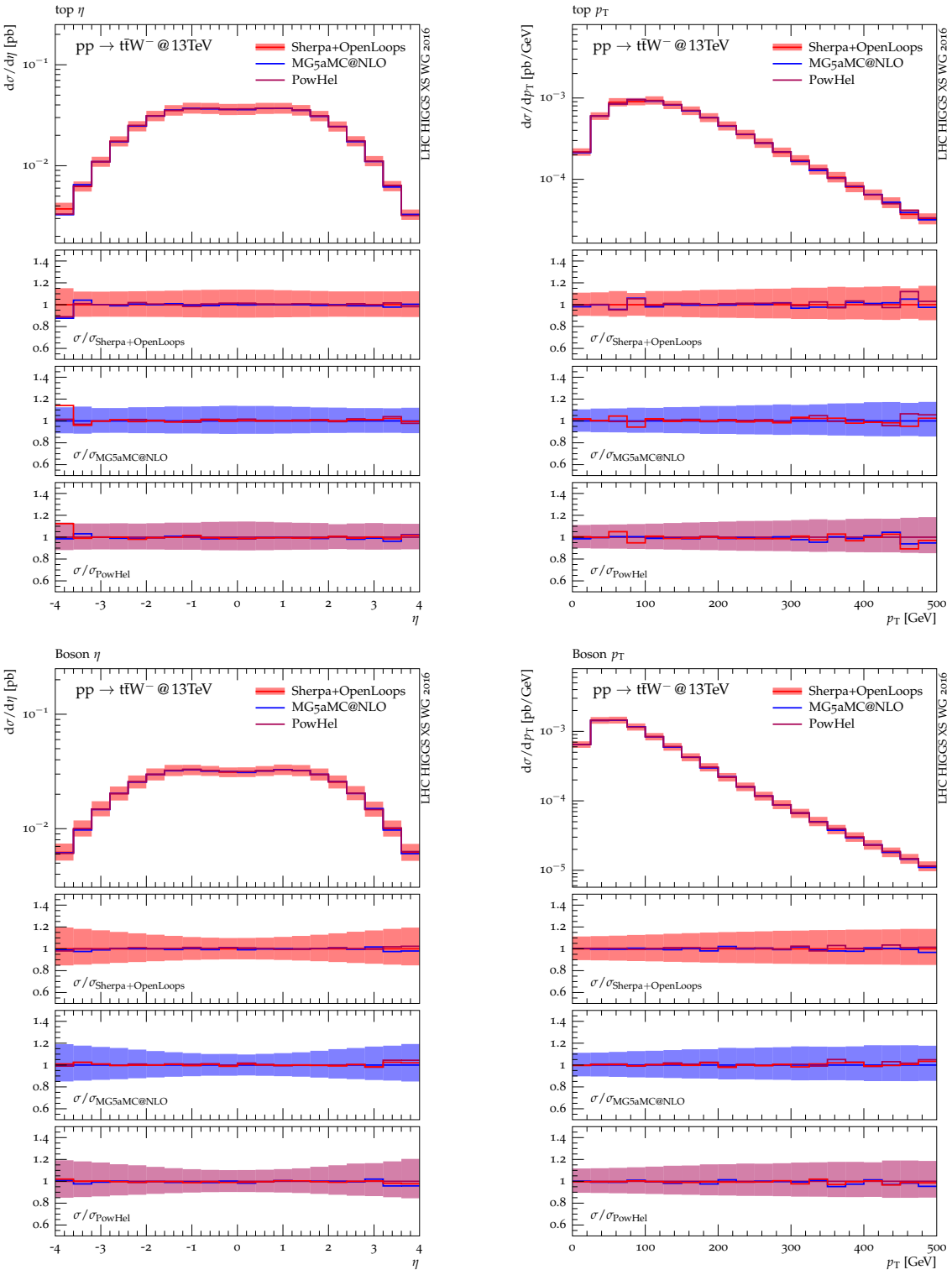

Figure 97: Fixed-order NLO predictions for differential $t\bar{t}W^{-}$ observables at 13 TeV. Each ratio plot shows all results normalized to one particular NLO+PS prediction and the scale variation band of the reference prediction.

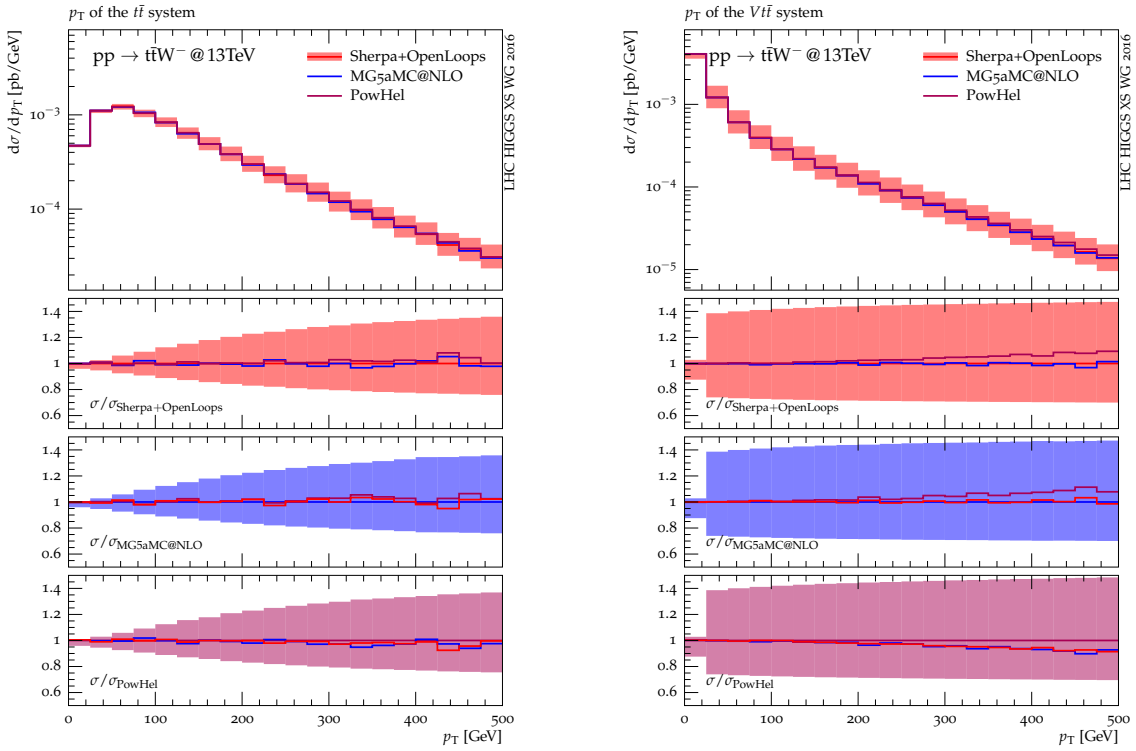

Figure 98: Fixed-order NLO predictions for differential $t\bar{t}W^-$ observables at 13 TeV. Ratio plots as in Figure 97.

background to leptonic signatures emerging from $t\bar{t}H$. In this section we provide LO and NLO QCD results for $t\bar{t}VV$ [I.36] total cross sections at 13 TeV. We set $M_{\rm H} = 125$ GeV and all the other input parameters according to the prescription in Ref. [144]. In order to be consistent with the results at NLO QCD+EW accuracy in Section I.6.2 ($t\bar{t}H$) and Section I.6.7.a ($t\bar{t}Z$ and $t\bar{t}W^{\pm}$), we used as renormalization and factorization scale $\mu_{\rm F} = \mu_{\rm R} = \mu := M_{\rm t} + (M(V_1) + M(V_2))/2$, where V_1 and V_2 are the two heavy bosons in the final states. A detailed study of the dependence on the definition of the scales both for total cross sections and differential distributions for $t\bar{t}VV$ production can be found in Ref. [420]. All the predictions in Ref. [420] and those reported here have been calculated and can be reproduced with the public version of MADGRAPH5_AMC@NLO [54].

LO and NLO QCD cross sections for all the $t\bar{t}VV$ processes are listed in Table 42. All the results include scale uncertainties, obtained by varying independently $\mu_{\rm F}$ and $\mu_{\rm R}$ in the range $\mu/2 < \mu_{\rm F}, \mu_{\rm R} < 2\mu$, and PDF errors evaluated with the LHAPDF set [35]. All the calculations are performed in the five-flavour scheme (5FS), with the exception of $t\bar{t}W^+W^-$ production where we used the four-flavour scheme (4FS) in order to avoid additional resonant top quarks in the matrix elements of the real b-quark radiation. However, also in this case we used the same PDF set with the associate $\alpha_{\rm s}$ in the 5FS. As can be seen in Table 42, the difference between LO results in the two different schemes is of the order of 20 ab, which is negligible for LHC phenomenology, especially below 300 fb^{-1} luminosity.

We want to stress that we did not include in Table 42 results for $t\bar{t}V\gamma$ production, which may be also relevant. However, their LO contribution, without any cut on the photon, is already included in the NLO EW corrections to $t\bar{t}H$, $t\bar{t}Z$ and $t\bar{t}W^{\pm}$ production and consequentially in the best predictions $\sigma^{\rm NLO}_{\rm QCD+EW}$ that are reported in Sections I.6.2 and I.6.7.a. Thus, LO contributions from $t\bar{t}V\gamma$ production must not be reevaluated when $\sigma^{\rm NLO}_{\rm QCD+EW}$ predictions for $t\bar{t}H$, $t\bar{t}Z$ and $t\bar{t}W^{\pm}$ are used. Equivalently, for the same reason, specific cuts on additional photon emission require $t\bar{t}V\gamma$ simulation with the corresponding cuts and the best predictions for $t\bar{t}H$, $t\bar{t}Z$ and $t\bar{t}W^{\pm}$ cannot be used.

[I.36] In this section the symbol V indicates also the Higgs boson.

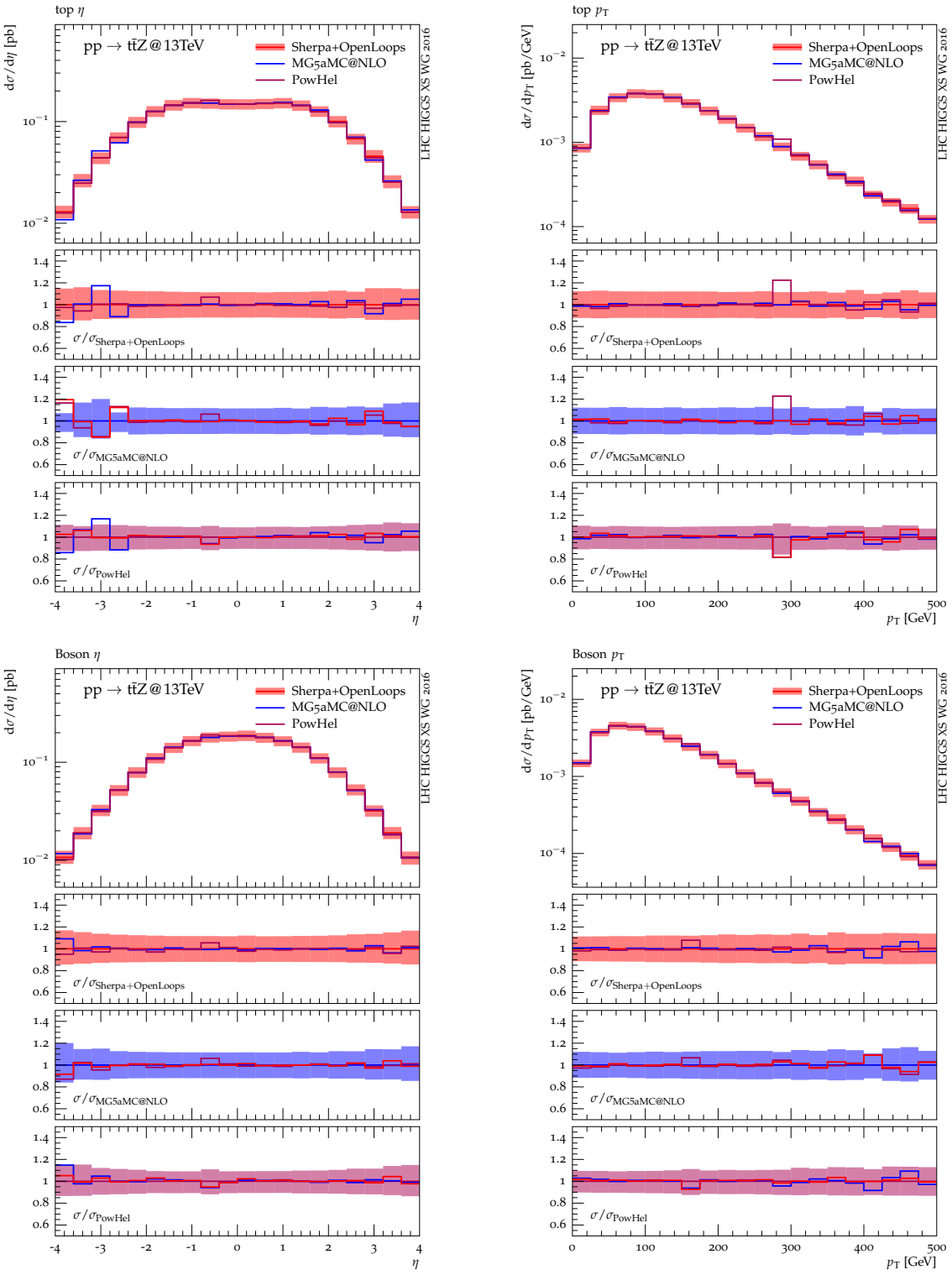

Figure 99: Fixed-order NLO predictions for differential $t\bar{t}Z$ observables at 13 TeV. Each ratio plot shows all results normalized to one particular NLO+PS prediction and the scale variation of the reference prediction.

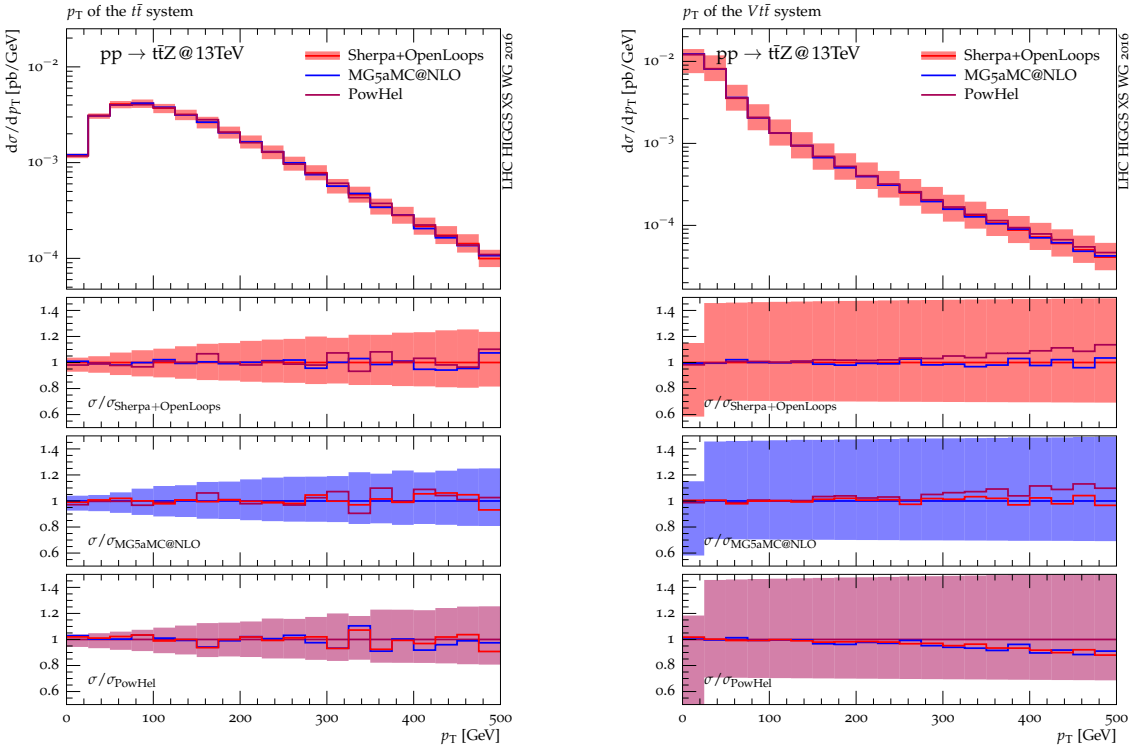

Figure 100: Fixed-order NLO predictions for differential $t\bar{t}Z$ observables at 13 TeV. Ratio plots as in Figure 99.

We want also to point out that, similarly to the case of $t\bar{t}V\gamma$, the LO predictions for $t\bar{t}V_1V_2$ processes may also be classified as part of the NLO EW corrections to $t\bar{t}V_1$ or $t\bar{t}V_2$ production. Indeed, $t\bar{t}VV$ LO cross sections are of $\mathcal{O}(\alpha_s^2\alpha^2)$, *i.e.*, of the same perturbative order of NLO EW corrections to $t\bar{t}H$, $t\bar{t}Z$ and $t\bar{t}W^\pm$ production. The contribution that we denote as Heavy Boson Radiation (HBR) and define as

$$\sigma_{\rm HBR}(t\bar{t}V_1) = \sum_{V_2=H,Z,W^\pm} \sigma_{\rm LO}(t\bar{t}V_1V_2) \tag{I.6.40}$$

can enter the inclusive $\sigma(t\bar{t}V_1)$ at $\mathcal{O}(\alpha_s^2\alpha^2)$. We stress that the HBR contribution has not been included in the best predictions $\sigma^{\rm NLO}_{\rm QCD+EW}$ for $t\bar{t}H$, $t\bar{t}Z$ and $t\bar{t}W^\pm$ production and should not be included whenever the $t\bar{t}V_1V_2$ processes are treated separately. It is nevertheless interesting to evaluate its size, compare it with the corresponding $\sigma^{\rm NLO}_{\rm QCD+EW}$ and verify possible cancellations, which are induced by the partial compensations of the Sudakov logarithms in the $\sigma^{\rm NLO}_{\rm EW}$ component.

Table 43: $\delta_{\rm HBR}$ and $\delta_{\rm EW}$ for all the $t\bar{t}V$ processes.

$t\bar{t}V$	$t\bar{t}H$	$t\bar{t}Z$	$t\bar{t}W^+$	$t\bar{t}W^-$
$\delta_{\rm HBR}$ [%]	1.0	0.9	4.1	7.0
$\delta_{\rm EW}$ [%]	1.7	-0.2	-3.5	-2.6

In Table 43 we list for all the $t\bar{t}V$ processes the value of $\delta_{\rm HBR}$ defined as

$$\delta_{\rm HBR} = \frac{\sigma_{\rm HBR}}{\sigma_{\rm LO}}\,, \tag{I.6.41}$$

together with the values of $\delta_{\rm EW}$ defined in sections I.6.2 and I.6.7.a. As can be seen in Table 43 the HBR contributions are, as expected, of the same order of the electroweak corrections. Here we report only results at the level of the total cross section, in Ref. [328] the impact of HBR contributions has been studied also at differential level.

I.6.8 NLO+PS simulations of $t\bar{t}b\bar{b}$ production

The production of $t\bar{t}$ pairs in association with two b-jets constitutes a large irreducible background to $t\bar{t}H$ production in the $H \to b\bar{b}$ channel, and the rather large uncertainty of Monte Carlo simulations of $t\bar{t}$ + b-jets production is one of the main limitations of current $t\bar{t}H(b\bar{b})$ searches at the LHC. A reliable theoretical description of $t\bar{t}$ production in association with two b-jets requires hard-scattering cross sections for the relevant partonic processes $q\bar{q}/gg \to t\bar{t}b\bar{b}$ at NLO QCD [390, 421, 422]. The inclusion of NLO QCD effects reduces scale uncertainties from the 70–80% level at LO to about 20–30%. To become applicable in the context of experimental analyses, NLO calculations need to be matched to parton showers. A NLO+PS simulation of $t\bar{t}b\bar{b}$ production based on the five flavour number scheme (5FNS), where b-quarks are treated as massless partons, was presented in [423,424], while an alternative NLO+PS simulation that includes b-quark mass effects in the four flavour number scheme (4FNS) was published in [425].

Finite b-quark masses permit to extend $t\bar{t}b\bar{b}$ matrix elements to the full phase space, including regions where b-quark pairs become collinear and matrix elements with $m_b = 0$ would be divergent. Thus, using $t\bar{t}b\bar{b}$ matrix elements with $m_b > 0$ in the 4FNS it is possible to simulate $t\bar{t}+b$-jets production in a fully inclusive way, including also signatures where a b-quark remains unresolved and a single b-jet is observed.[I.37] In contrast, the applicability of 5FNS calculations is limited to phase-space regions where the two b-quarks in $t\bar{t}b\bar{b}$ matrix elements have sufficient transverse momentum and angular separation in order to avoid the breakdown of the $m_b = 0$ approximation in the collinear regions. Such a requirement needs to be imposed at the level of generation cuts, i.e. before matching matrix elements to the parton shower, and one might expect that the resulting NLO+PS predictions for observables with two or more hard b-jets should be insensitive to generation cuts. However, this is not the case, since events with multiple hard b-jets can result from collinear $g \to b\bar{b}$ splittings in $t\bar{t}b\bar{b}$ matrix elements combined with the conversion of hard gluons into b-jets via $g \to b\bar{b}$ parton shower splittings. In fact, as pointed out in [425], this so-called double-splitting mechanism can lead to a sizeable enhancement of the $t\bar{t}b\bar{b}$ background in the Higgs-signal region, $M_{bb} \sim M_H$.

Given the importance of (quasi) collinear $g \to b\bar{b}$ splittings, the choice of the flavour number scheme and the inclusion of b-quark mass effects play a critical role. For what concerns 5FNS calculations, while it is clear that setting $m_b = 0$ and omitting the singular phase-space regions leads to a logarithmic sensitivity to the unphysical generation cuts for observables with a single hard b-jet, double-splitting (or multiple-splitting) contributions imply such a sensitivity also for observables with two or more hard b-jets. Such a logarithmic dependence can naturally be avoided in the framework of NLO merging [206,241,426], where the singular phase space regions, defined in terms of an appropriate merging cut, are populated by the parton shower combined with matrix elements for $t\bar{t} + 0, 1$ jet production. However, applying NLO merging to $t\bar{t} + 0, 1, 2$ jet production [427] is technically much more challenging as compared to NLO+PS simulations of $t\bar{t}b\bar{b}$ production. Moreover, in the merging approach all b-quarks produced via double-splitting contributions would tend to arise from the parton shower, which implies a strong dependence on parton-shower modelling. In contrast, 4FNS simulations with $m_b > 0$ have the advantage that one of the $g \to b\bar{b}$ splittings is entirely described in terms of $t\bar{t}b\bar{b}$ matrix elements at NLO, while the additional hard b-jet arises from $t\bar{t}b\bar{b}g$ tree amplitudes matched to the parton shower via $g \to b\bar{b}$ splittings that can take place at any stage of the shower evolution. In conventional 4FNS calculations as the ones presented in this study, the number of active quark flavours is limited to four

[I.37] Here and in the following we consistently exclude top-decay products from the counting of b jets.

both in the evolution of the PDFs and α_s. Thus, renormalization group logarithms associated with b- and t-quark loops are included only at fixed-order NLO.[I.38] As discussed in [425], such logarithms can be easily resummed by using modified 4FNS PDF sets that include all relevant quark flavours in the running of α_s. At $\sqrt{s} = 8\,\text{TeV}$ it was found that higher-order contributions of this type increase the NLO 4FNS $t\bar{t}b\bar{b}$ cross section by about 9% [425], while in the 5FNS they are naturally included.

Finally, we observe that simulations of $t\bar{t}b\bar{b}$ production in the 4FNS can be combined with fully inclusive $t\bar{t}$+jets samples based on the 5FNS in a rather straightforward way [428]. In fact, in order to avoid the double counting of b-quark production in the $t\bar{t}b\bar{b}$ and $t\bar{t}$+jets sample it is sufficient to veto events that involve b quarks in the $t\bar{t}$+jets sample. This prescription has to be applied after parton showering, and the b-quark veto should be restricted to showered $t\bar{t}$+jets matrix elements before top decays, i.e. it should not be applied to b quarks that arise from (showered) top decays or from the underlying event.

From the above discussion it is clear that the parton shower and the choice of the flavour number scheme play a critical role in the description of $t\bar{t}b\bar{b}$ production, and the thorough understanding of the related uncertainties is of prime importance for the success of $t\bar{t}H(b\bar{b})$ searches. As a first step in this direction, in the following we present a systematic comparison of various NLO+PS simulations of $t\bar{t}b\bar{b}$ production based on different parton showers, matching schemes, and flavour number schemes.

I.6.8.a NLO+PS tools and simulations

Three different NLO+PS simulations of $t\bar{t}b\bar{b}$ production at $\sqrt{s} = 13\,\text{TeV}$ based on SHERPA+OPENLOOPS [229, 247, 352], MADGRAPH5_AMC@NLO+PYTHIA8 [54, 207, 319, 348] and POWHEL+PYTHIA8 [207, 319, 349, 429] have been compared. The various NLO matching methods, parton showers and flavour number schemes employed in the three simulations are summarized in Table 44. The SHERPA+OPENLOOPS and MADGRAPH5_AMC@NLO simulations employ the 4FNS and the MC@NLO matching method[I.39] to combine matrix elements with the SHERPA and PYTHIA8 parton showers, respectively. Therefore possible differences between SHERPA+OPENLOOPS and MADGRAPH5_AMC@NLO predictions can be attributed to parton shower effects or to differences in the two implementations of the MC@NLO approach and related technical parameters. Instead, the POWHEL simulation differs from the other two simulations in at least two aspects: it is performed in the 5FNS and it employs the POWHEG matching method [342, 343]. Moreover, when comparing SHERPA+OPENLOOPS and POWHEL predictions one should keep in mind that also the respective parton showers (SHERPA and PYTHIA8) are different.

Since the POWHEL simulation is performed with massless b quarks,[I.40] in order to avoid collinear $g \to b\bar{b}$ singularities, the hard matrix elements need to be restricted to phase space regions where both b quarks remain resolved. This is achieved through the generation cuts

$$m_{bb} > 2\xi_m m_b, \qquad p_{T,b} > \xi_T m_b. \tag{I.6.42}$$

Technically, in order to guarantee infrared safety, in the case of real emission events the cuts in Eq. (I.6.42) are applied after a projection onto the Born phase space. The above cuts are chosen in a way that mimics, at LO in α_S, the $\log(m_b)$ dependence that arises when one b-quark is integrated out. Thus they can be regarded as an heuristic approach in order to obtain reasonable 5FNS predictions also for $t\bar{t} + b$-jet observables with a single resolved b jet. However, as discussed above, NLO+PS $t\bar{t}b\bar{b}$ predictions in the

[I.38] In the 4FNS, b-quark contributions to the running of α_s are consistently restored at NLO accuracy by including b-quark loops in the matrix elements and renormalizing them via zero-momentum subtraction. Also top-quark loop contributions to α_s have been renormalized via zero-momentum subtraction in the 4FNS.

[I.39] More precisely, MADGRAPH5_AMC@NLO employs the original formulation of MC@NLO matching [340, 341], while SHERPA+OPENLOOPS implements an alternative formulation [345, 356] denoted as S-MC@NLO, which is characterized by an improved treatment of colour correlations but is otherwise equivalent to the method of [340, 341].

[I.40] To be precise, in the POWHEL simulation b-mass effects are neglected at the matrix element level but are taken into account in the parton shower.

Table 44: Employed tools, matching methods, parton showers, flavour number scheme (FNS) and generation cuts in the NLO+PS simulations of $t\bar{t}b\bar{b}$ production. The POWHEL generator implements matrix elements with massless b-quarks but includes b-mass effects through PYTHIA.

Tools	Matching method	Shower	FNS	m_b [GeV]	Generation cuts
SHERPA 2.2.1+OPENLOOPS 1.2.3	S-MC@NLO	SHERPA	4FNS	4.75	fully inclusive
MADGRAPH5_AMC@NLO 2.3.2+PYTHIA8 2.1.0	MC@NLO	PYTHIA8	4FNS	4.75	fully inclusive
POWHEL+PYTHIA8 2.1.0	POWHEG	PYTHIA8	5FNS	0	$m_{bb} > 2m_b,\ p_{T,b} > m_b$

5FNS are sensitive to the generation cuts in Eq. (I.6.42). In particular they depend on the unphysical parameters ξ_m and ξ_T, which have been set to one in the present study.[I.41] Moreover, one should keep in mind that $\log(m_b)$ terms beyond LO and finite terms of order m_b are not consistently included in the 5FNS.

I.6.8.b Parton showers, PDF, and α_s

Full Monte Carlo simulations of $t\bar{t}b\bar{b}$ production involve hard $t\bar{t}b\bar{b}$ cross section at NLO, top-quark decays, parton showering, hadronization, hadron decays, and the underlying event. The main source of theoretical uncertainty in this involved simulation framework is given by the mechanism that governs b-quark production in association with top-quark pairs. Thus, in order to obtain a sufficiently transparent picture of the nontrivial QCD dynamics of b-quark production, it was decided to reduce the complexity that results from the presence of the additional b-quarks that arise from top-quark decays via well-understood weak interactions. To this end, top quarks have been treated as stable particles in the simulations. Moreover, all NLO+PS simulations have been performed at the parton level, including only the perturbative phase of parton shower evolution, and neglecting hadronization as well as any other non-perturbative aspect. The quantitative importance of hadronization and the possible bias that can result from switching off hadronization in the comparison of two $t\bar{t}+b$-jet simulations based on different parton showers was assessed by comparing SHERPA 2.1 and PYTHIA 8.2 LO+PS simulations of $pp \to H+$jets (including b jets) at 14 TeV. Thanks to the colour neutral nature of the Higgs boson, this process allows one to assess the impact of hadronization by turning it on and off. The effects of hadronization increase with decreasing jet transverse momenta. Thus they predominantly arise in the vicinity of the jet-p_T threshold. For the production of b-jets with $p_T > 25$ GeV and $|\eta| < 2.5$ they amount to about $-2\%(-4\%)$ per b jet in PYTHIA8 (SHERPA). This suggests that the bias that results from turning off hadronization should be well below the typical NLO+PS uncertainties in $t\bar{t}b\bar{b}$ production.

In order to reduce uncontrolled sources of bias related to shower modelling in the comparison of NLO+PS simulations based on SHERPA and PYTHIA8, those free parton-shower parameters related to the strong coupling have been chosen in a uniform way. Specifically, the rescaling factors x that are applied to the strong coupling terms $\alpha_S(x\,k_T^2)$ for each shower emission have been set to $x = 1$ both for initial- and final-state radiation. Furthermore the option of resumming subleading logarithms of Catani-Marchesini-Webber kind [430] was deactivated. Note that these choices neither correspond to the SHERPA default nor to the PYTHIA8 default settings. Moreover they are not meant to provide an optimal description of data. They are only aimed at a consistent comparison of the two showers, where simple parametric differences are avoided, and the remaining deviations can be attributed to intrinsic shower features, such as the different definition of the shower evolution variables.

Since parton-shower tunes and PDFs are intimately connected, it is not trivial to identify a common

[I.41] Variations of these parameters will allow to quantify up to which extent, in practice, predictions in conditions typically met in experimental analyses depend on the choice of these technical cuts.

PDF set that is optimal for all parton showers. For the present study the NNPDF3.0 NLO PDF set was adopted, keeping in mind that this choice might bias the comparison of SHERPA against PYTHIA8. The specific PDF set was chosen according to the employed flavour number scheme (4FNS or 5FNS), while the value of $\alpha_s(M_Z)$ in NLO matrix elements and for the first shower emission was chosen consistently with the PDF. The same holds for the running of α_s, whose evolution is implemented at 2-loops both in matrix elements and parton showers. For subsequent shower emissions the 4FNS (5FNS) together with the corresponding value of $\alpha_s(M_Z)$ was used in SHERPA (PYTHIA8).

I.6.8.c Input parameters and scale choices

To simulate $t\bar{t}b\bar{b}$ production at 13 TeV the input parameters $m_t = 172.5$ GeV, $m_b = 4.75$ GeV and $\alpha_s^{(5F)}(M_Z) = 0.118$ have been used together with NNPDF3.0 parton distributions at NLO, as discussed above.[I.42] The central values of the renormalization and factorization scales have been chosen as

$$\mu_{R,0} = \left(\prod_{i=t,\bar{t},b,\bar{b}} E_{T,i} \right)^{1/4}, \qquad \mu_{F,0} = \frac{H_T}{2} = \frac{1}{2} \sum_{i=t,\bar{t},b,\bar{b},j} E_{T,i}, \tag{I.6.43}$$

where $E_{T,i} = \sqrt{M_i^2 + p_{T,i}^2}$ denotes the transverse energy of top and bottom quarks, defined at parton level. Note that also extra parton emissions contribute to the total transverse energy H_T in Eq. (I.6.43). Theoretical uncertainties have been assessed by means of standard variations $\mu_R = \xi_R \mu_{R,0}$, $\mu_F = \xi_F \mu_{F,0}$ with $0.5 < \xi_R, \xi_F < 2$ and $0.5 < \xi_R/\xi_F < 2$.

The CKKW inspired renormalization scale choice in Eq. (I.6.43) is based on [425] and takes into account the fact that top and bottom quarks are produced at widely different scales $E_{T,b} \ll E_{T,t}$. This turns out to improve the perturbative convergence as compared to a hard global scale of order m_t. In particular, in the 4FNS it was checked that using $\mu_R = H_T/2$ instead of $\mu_R = \mu_{R,0}$ increases the K-factor by 0.25 and reduces the NLO cross section by about 40%, which is only barely consistent with the level of uncertainty expected from factor-two scale variations. Moreover, computing LO and NLO cross sections using PDFs and α_s values at NLO throughout[I.43] yields K-factors around 2 with $\mu_R = \mu_{R,0}$ and about 0.25 higher with $\mu_R = H_T/2$. Thus both scale choices seem to be suboptimal, and in order to improve the convergence of the perturbative expansion, a scale even softer than Eq. (I.6.43) should be considered in the future. In any case a hard scale of type $\mu_R = H_T/2$ is not recommended.

In the context of the MC@NLO matching approach, where the resummation scale μ_Q, i.e. the parton shower starting scale, is a free parameter, it is natural to identify this scale with the factorization scale. Thus $\mu_Q = \mu_{F,0} = H_T/2$ was used in the SHERPA+OPENLOOPS simulation. In the case of MADGRAPH5_AMC@NLO a different choice had to be adopted since only resummation scales of the form $\mu_Q = \xi\sqrt{\hat{s}}$ are supported, where the prefactor ξ is randomly distributed in the freely adjustable range $[\xi_{\min}, \xi_{\max}]$ with a distribution that is strongly peaked at $(\xi_{\min} + \xi_{\max})/2$ [54]. Comparing the $H_T/2$ and $\mu_Q = \xi\sqrt{\hat{s}}$ distributions it was observed that the respective peaks lie around 200 GeV and 400 GeV when the default MADGRAPH5_AMC@NLO settings $(\xi_{\min}, \xi_{\max}) = (0.1, 1)$ are used, i.e. the default μ_Q in MADGRAPH5_AMC@NLO is much harder.

Given that MC@NLO predictions for $t\bar{t}b\bar{b}$ production are quite sensitive to μ_Q, it was decided to lower the ξ upper bound to $\xi_{\max} = 0.25$, which brings the μ_Q reasonably close to $H_T/2$. We note that this choice is also supported by the study of an MADGRAPH5_AMC@NLO simulation of $Hb\bar{b}$ production in the 4FNS [431], where it was found that reducing $\xi_{\max}$ from 1 to 0.25 strongly improves the convergence of NLO+PS and NLO distributions at large transverse momenta.

[I.42] Note that the employed NNPDFs and related $\alpha_s(M_Z)$ value in the 4FNS are derived from variable-flavour-number NNPDFs with $\alpha_s^{(5F)}(M_Z) = 0.118$ via appropriate backward and forward evolution with five and four active flavours, respectively.

[I.43] With this approach K-factors are much less dependent on the employed PDF sets and reflect the convergence of the perturbative expansion in a more realistic way as compared to using LO inputs for the LO cross section.

In the POWHEG matching method, the resummation scale is not a freely adjustable parameter, since the first emission on top of $t\bar{t}b\bar{b}$ events is entirely described by matrix elements, and the corresponding transverse momentum scale sets the upper bound for subsequent shower emissions. Nevertheless, POWHEG simulations involve a parameter $h_{\rm damp}$ that separates the first-emission phase space into a singular region, where the first emission is resummed and corrected with a local K-factor, and a remnant region, where it is handled as at fixed-order NLO. Given the analogy with the separation of soft and hard events in the MC@NLO approach, and given that μ_Q represents the upper bound for emissions off soft events, it is natural to chose $h_{\rm damp}$ of the same order of μ_Q. Thus the choice $h_{\rm damp} = H_T/2$ was adopted in the POWHEL simulation.

Variations of the resummation scale and of the $h_{\rm damp}$ parameter have not been considered in this study.

I.6.8.d NLO+PS predictions for $t\bar{t}$ + b-jets cross sections in b-jet bins

In the following we compare integrated and differential NLO+PS predictions for $t\bar{t}$ + b-jets production with a certain minimum number of b jets, $n_b > N_b$. In particular we focus on the bins with $n_b \geq 1$ or $n_b \geq 2$, which are the most relevant ones for $t\bar{t}H(b\bar{b})$ analyses. For the jet definition the anti-k_T algorithm with $R = 0.4$ is adopted, and jets that involve one or more b-quark constituents are classified as b-jets. Note that also jets that result from collinear $g \to b\bar{b}$ splittings are handled as b jets. Moreover no requirement is imposed on the minimum transverse momentum of b quarks inside b jets. Events are categorized according to the number n_b of resolved b jets within the acceptance region,

$$p_{T,b} > 25 \text{ GeV}\,, \qquad |\eta_b| < 2.5\,. \tag{I.6.44}$$

Let us recall that top quarks are treated as stable particles, thus the two b quarks that arise from top decays as well as possible extra b quarks from the showering of top-decay products are not included in n_b. Apart from the requirement $n_b \geq N_b$ no additional cut will be applied.[I.44] In order to illustrate the importance of parton shower effects, the various NLO+PS predictions presented in the following are also compared to fixed-order NLO predictions. The latter are based on SHERPA+OPENLOOPS and are obviously independent of the employed parton shower and matching scheme.

All quoted theoretical uncertainties correspond to factor-two variations of the renormalization and factorization scales. In Figures 101–109 they are shown as bands, and, to improve readability, three different ratio plots are shown, where all results are normalized to one particular NLO QCD+PS prediction and the corresponding scale variation band is shown.

Results for the $t\bar{t}+b$-jets cross sections with $n_b \geq N_b$ b jets for various values of N_b are presented in Table 45 and Figure 101. In the following we will refer to the results for $N_b = 1, 2, 3, 4$ as ttb, ttbb, tt + 3b and tt + 4b cross sections, respectively. For the ttb and ttbb cross sections, which are described at NLO accuracy, the various NLO+PS predictions turn out to be in decent mutual agreement. More precisely, ttb predictions based on the 4FNS (SHERPA+OPENLOOPS and MADGRAPH5_AMC@NLO) agree very well with each other and with fixed-order NLO, and the 5FNS ttb simulation (POWHEL) lies only 20% lower, despite that it was not designed to describe final states with a single b-jet (due to the generation cuts).

For the ttbb cross section one finds excellent agreement between fixed-order NLO, SHERPA+OPENLOOPS and POWHEL. This seems to suggest that this observable has little sensitivity to parton shower effects and to the choice of the flavour number scheme. However this interpretation is challenged by the fact that the MADGRAPH5_AMC@NLO ttbb result lies more than 30% above the other predictions. The only significant differences between MADGRAPH5_AMC@NLO and SHERPA+OPENLOOPS simulations lie in the employed parton showers and details of MC@NLO matching, thus the origin of the observed

[I.44] To be more precise, the SHERPA+OPENLOOPS and MADGRAPH5_AMC@NLO samples are fully inclusive, while in the case of POWHEL the technical cuts Eq. (I.6.42) are applied as discussed above.

Table 45: Fixed-order NLO and NLO+PS predictions for integrated $t\bar{t} + b$-jets cross sections at 13 TeV in bins with $n_b \geq 1$ and $n_b \geq 2$ b jets.

Selection	Tool	σ_{NLO} [fb]	$\sigma_{\text{NLO+PS}}$ [fb]	$\sigma_{\text{NLO+PS}}/\sigma_{\text{NLO}}$
$n_b \geq 1$	SHERPA+OPENLOOPS	$12820^{+35\%}_{-28\%}$	$12939^{+30\%}_{-27\%}$	1.01
	MADGRAPH5_AMC@NLO		$13833^{+37\%}_{-29\%}$	1.08
	POWHEL		$10073^{+45\%}_{-29\%}$	0.79
$n_b \geq 2$	SHERPA+OPENLOOPS	$2268^{+30\%}_{-27\%}$	$2413^{+21\%}_{-24\%}$	1.06
	MADGRAPH5_AMC@NLO		$3192^{+38\%}_{-29\%}$	1.41
	POWHEL		$2570^{+35\%}_{-28\%}$	1.13

discrepancy is likely to lie in the choice of shower starting scale in MADGRAPH5_AMC@NLO combined with the higher intensity of QCD radiation in PYTHIA8 with respect to SHERPA. This is confirmed by the further enhancement of the MADGRAPH5_AMC@NLO cross section in the bins with $n_b \geq 3$ and $n_b \geq 4$ b-jets (see Figure 101), where the additional b quarks arise from $g \to b\bar{b}$ parton-shower splittings, which results in a much stronger sensitivity to shower effects. Note that this kind of uncertainty for $N_b = 3, 4$ is not included in the quoted scale variations. In the SHERPA+OPENLOOPS simulation, the size of scale uncertainties and the difference between NLO and NLO+PS predictions are fairly similar to what observed at $\sqrt{s} = 8$ TeV in [425]. In particular, NLO+PS scale uncertainties range between 20–30% in all b-jet bins and are smaller as compared to the case of fixed-order NLO. Scale variations in MADGRAPH5_AMC@NLO and POWHEL tend to be larger and agree well with each other for $N_b = 2$, while POWHEL features a larger scale dependence in the other bins, especially for $N_b = 3, 4$. These various differences can be attributed to the employed flavour-number schemes and to technical aspects of the implementation of scale variations in the three different NLO+PS Monte Carlo tools.

I.6.8.e ttb differential analysis

Various differential observables for an inclusive ttb analysis with $n_b \geq 1$ b-jets are presented in Figures 102–104. For all distributions that are inclusive with respect to extra light-jet emissions one observes a rather similar behaviour as for the ttb cross section, i.e. SHERPA+OPENLOOPS, MADGRAPH5_AMC@NLO and fixed-order NLO predictions agree well, while POWHEL lies about 20% lower. Only POWHEL features significant shape distortions with respect to fixed-order NLO in the region of low rapidity and/or low p_T for the leading top and bottom quarks and for the $t\bar{t}$ system (Figures 102–103). Observables that explicitly involve the first light-jet emission (Figure 104) turn out to behave differently. While for SHERPA+OPENLOOPS, POWHEL and fixed-order NLO there is mutual agreement within scale variations, the MADGRAPH5_AMC@NLO prediction turns out to lie up to 50% higher at $p_{T,j} \sim 50$ GeV. This enhancement of QCD radiation in MADGRAPH5_AMC@NLO+PYTHIA8 disappears at $p_{T,j} \sim 150$ GeV. It is most likely related to what was observed above in b-jet bin cross sections with $N_b \geq 2$.

I.6.8.f ttbb differential analysis

Various differential observables for an inclusive ttbb analysis with $n_b \geq 2$ b-jets are presented in Figures 105–109 Observables that depend on the top-quark and b-jet kinematics but are inclusive with respect to extra jet emission are presented in Figures 105–107. For all such distributions a fairly good agreement between SHERPA+OPENLOOPS, POWHEL and fixed-order NLO is observed, both at the level of shapes and normalization. The most significant shape differences show up in the p_T of the 2nd b-jet

and do not exceed 20%. In MADGRAPH5_AMC@NLO the matching to the PYTHIA8 shower increases the ttbb rates by about 35% with respect to SHERPA+OPENLOOPS, and turns out to have an non-trivial dependence on the top and b-jet kinematics. In particular it tends to enhance distributions in the the regions with small top-quark and b-jet p_T and at large ΔR separation between the two b-jets.

For the distribution in the invariant mass of the b-jet pairs, which corresponds to the mass of the $H \to b\bar{b}$ candidate, it turns out that all NLO+PS results are in reasonably good mutual agreement. The results also confirm the presence of an NLO+PS distortion of the invariant-mass distribution, which was attributed to double-splitting effects in [425]. More precisely, in the vicinity of the Higgs boson resonance the NLO+PS enhancement w.r.t. NLO is close to 20% and thus less pronounced to what was observed in [425] at $\sqrt{s} = 8\,\text{TeV}$,[I.45] while the POWHEL and MADGRAPH5_AMC@NLO distributions feature an additional enhancement of about 10% and 35%, respectively, w.r.t. SHERPA+OPENLOOPS in the Higgs boson signal region.

Various observables that are directly sensitive to the emission of an additional jet are shown in Figures 108–109. Despite the intrinsic LO nature and stronger shower dependence of such distributions, SHERPA+OPENLOOPS and POWHEL remain in good agreement: the most important deviations, which show up in the p_T tail of the first light jet, do not exceed 40%. In contrast, the excess of MADGRAPH5_AMC@NLO w.r.t. the other predictions grows by about a factor two, reaching about 70% in average, and gives rise to more pronounced shape distortions as compared to the case of inclusive ttbb observables. Similarly as for the ttbb analysis, the enhancement is concentrated at light-jet momenta between 50–150 GeV, where it reaches up to 100%. A similarly strong increase shows up also in the region of central light-jet rapidity, as well as in angular and mass distributions that involve light and b-jets.

I.6.8.g Summary and conclusions

In summary, we have presented a systematic study of Monte Carlo simulations of $pp \to t\bar{t} + b$-jets at 13 TeV that compares various NLO+PS predictions based on different matching methods, parton showers and matching schemes. While the inclusion of b-mass effects is the only fully consistent way of describing inclusive $t\bar{t} + b$-jets production in terms of $t\bar{t}b\bar{b}$ matrix elements, the observed agreement between SHERPA+OPENLOOPS and POWHEL predictions indicates that also simulations with massless b-quarks and appropriate generation cuts provide predictions in agreement well within the scale uncertainties.

The various NLO+PS simulations considered in this study confirm that the invariant mass of the b-jet pair receives significant NLO+PS corrections that can reach 20-30% in the $H \to b\bar{b}$ signal region [425]. Based on standard variations of the renormalization and factorization scales, the expected accuracy of NLO predictions should be at the 25–35% level. However in various phase-space regions the differences between the various NLO+PS simulations tend to be larger.

In particular, some of the distributions generated with MADGRAPH5_AMC@NLO+PYTHIA8 have significantly different shapes, resulting in larger predictions for up to 100%, compared to the other NLO+PS simulations. These are probably related to the high intensity of the QCD radiation in PYTHIA8 and are quite sensitive to the choice of the shower starting scale in the MC@NLO matching framework. These findings should be regarded as a first step towards a thorough investigation of NLO matching and parton shower effects, including all relevant sources of uncertainty, in the Monte Carlo modelling of $t\bar{t} + b$-jets production. In the future also top-quark decays should be investigated.

[I.45] This can be due to the different collider energy and to the different scale choices in this study and in [425].

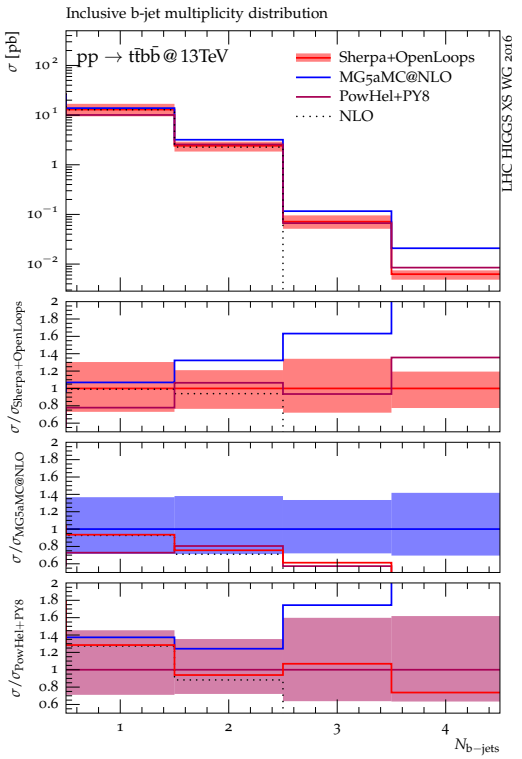

Figure 101: Fixed-order NLO and NLO+PS predictions for integrated $t\bar{t}$+b-jets cross sections at 13 TeV in inclusive bins with $n_b > N_b$ b jets. Each ratio plot shows all results normalized to one particular NLO QCD+PS prediction and the corresponding scale variation band.

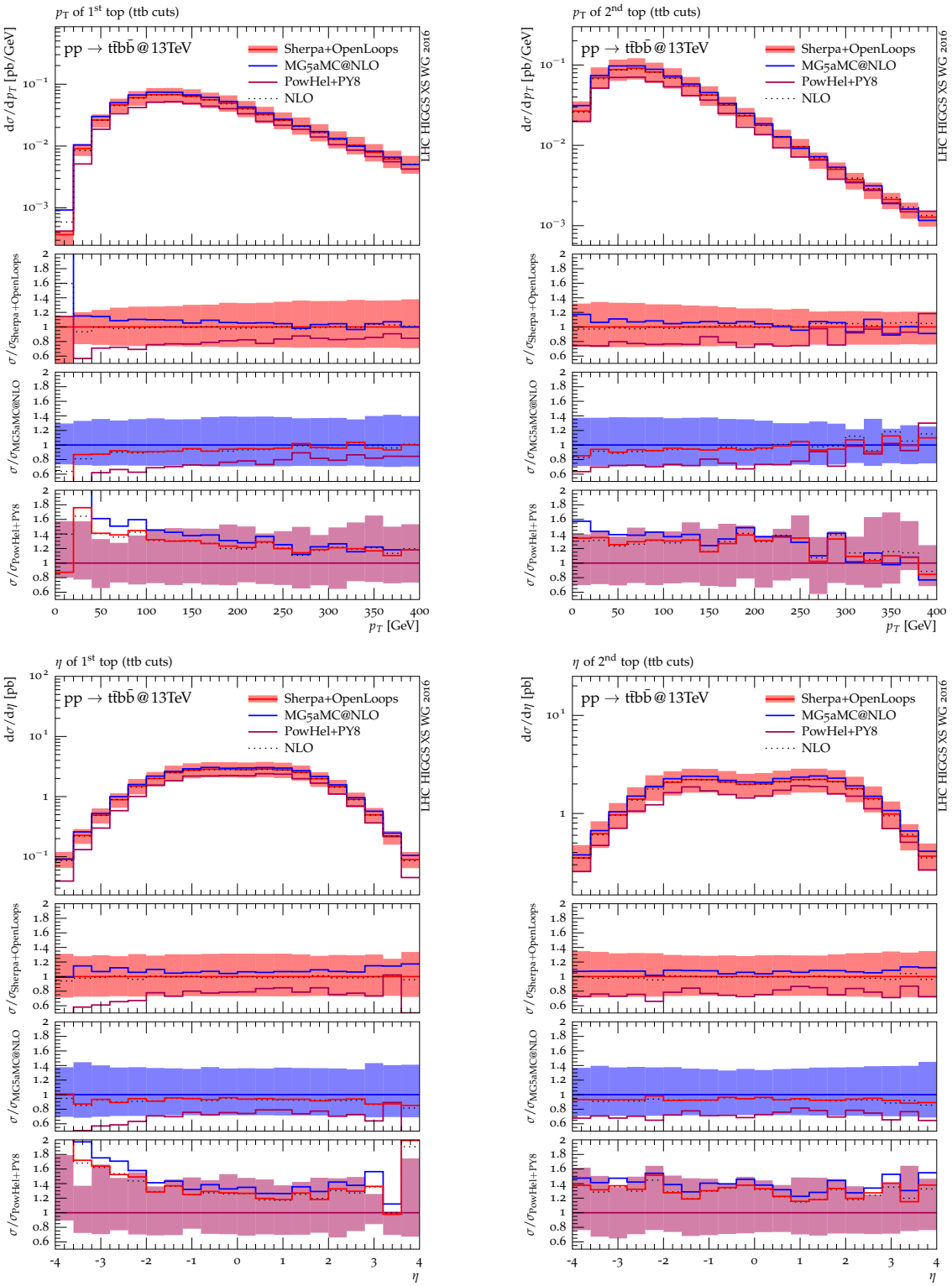

Figure 102: Fixed-order NLO and NLO+PS top-quark distributions for $pp \to t\bar{t} + \geq 1\, b$ jets at 13 TeV. Ratio plots like in Figure 101.

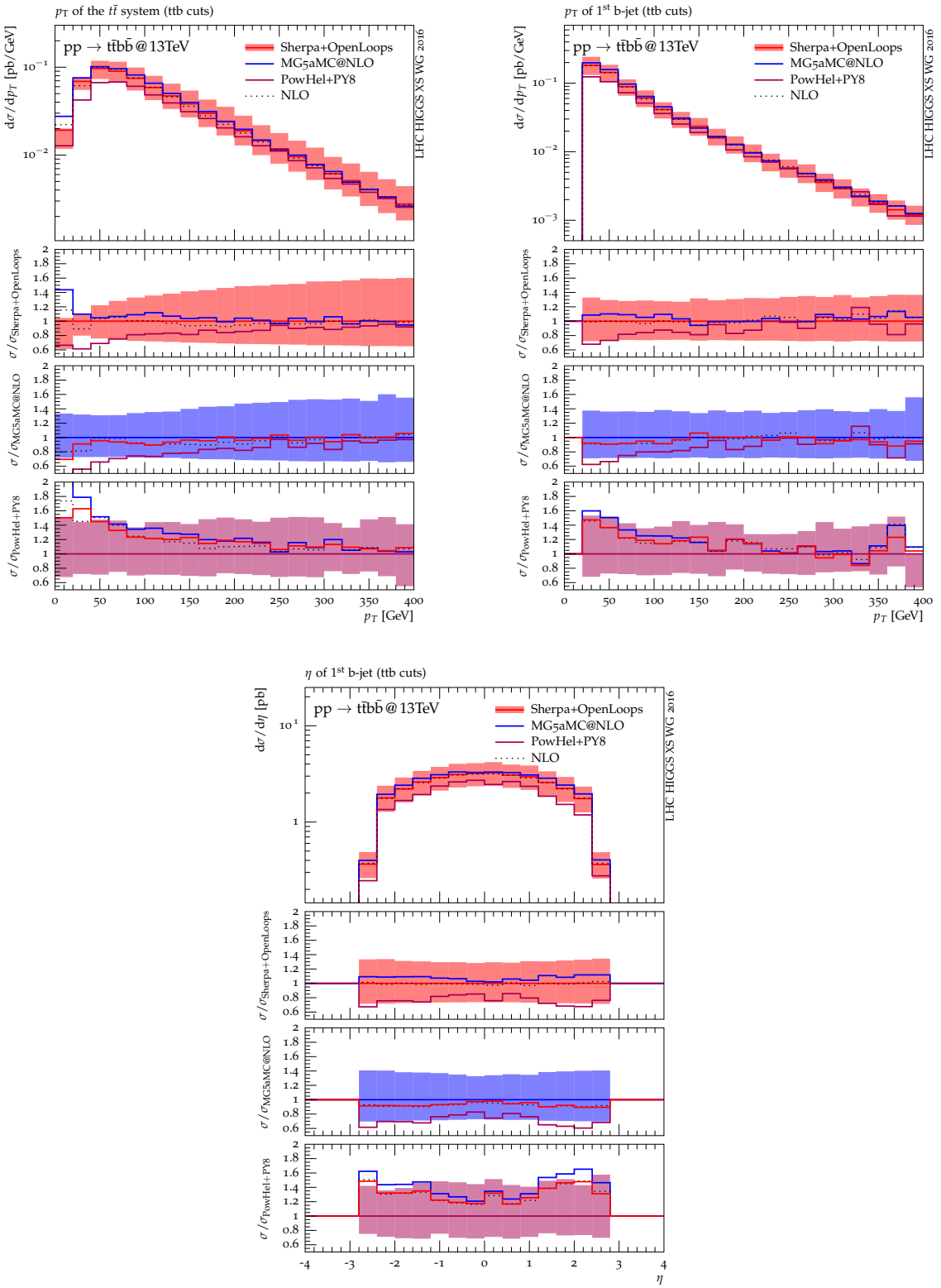

Figure 103: Fixed-order NLO and NLO+PS top-quark and b-jet distributions for $pp \to t\bar{t}+ \geq 1\,b$ jets at 13 TeV. Ratio plots like in Figure 101.

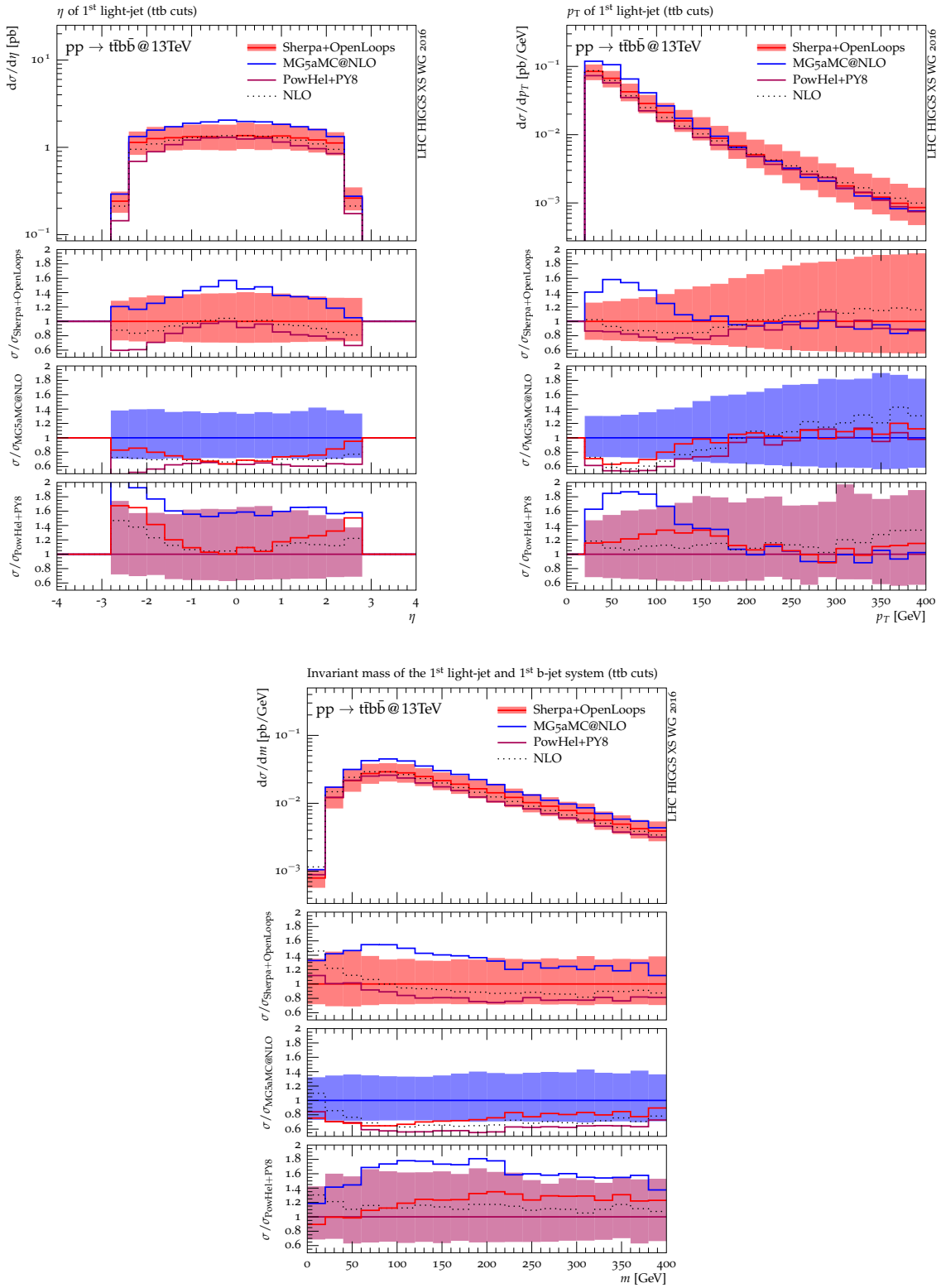

Figure 104: Fixed-order NLO and NLO+PS light-jet distributions for $pp \to t\bar{t}+ \geq 1\,b$ jets at 13 TeV. Ratio plots like in Figure 101.

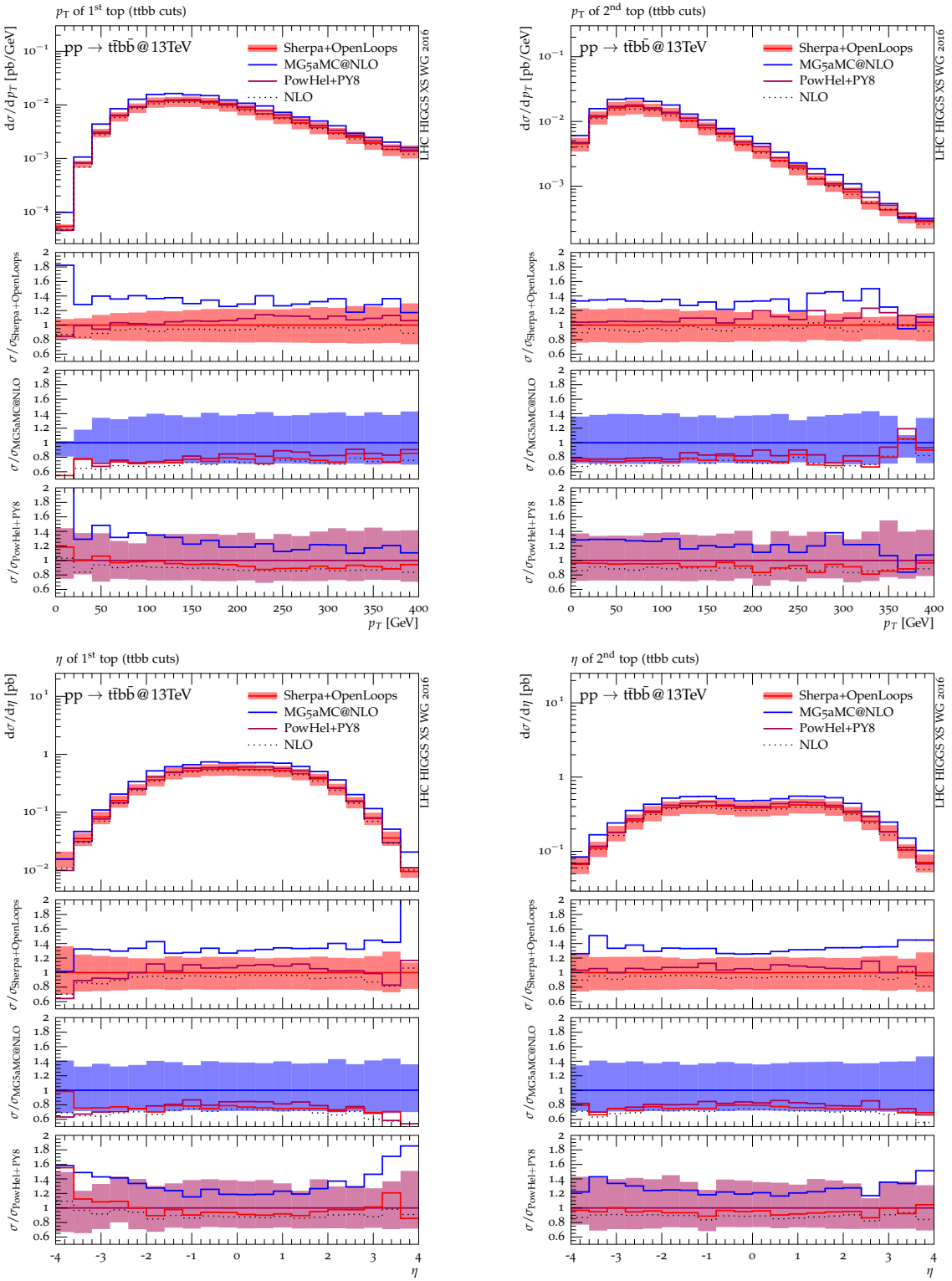

Figure 105: Fixed-order NLO and NLO+PS top-quark distributions for $pp \to t\bar{t}+ \geq 2\,b$ jets at 13 TeV. Ratio plots like in Figure 101.

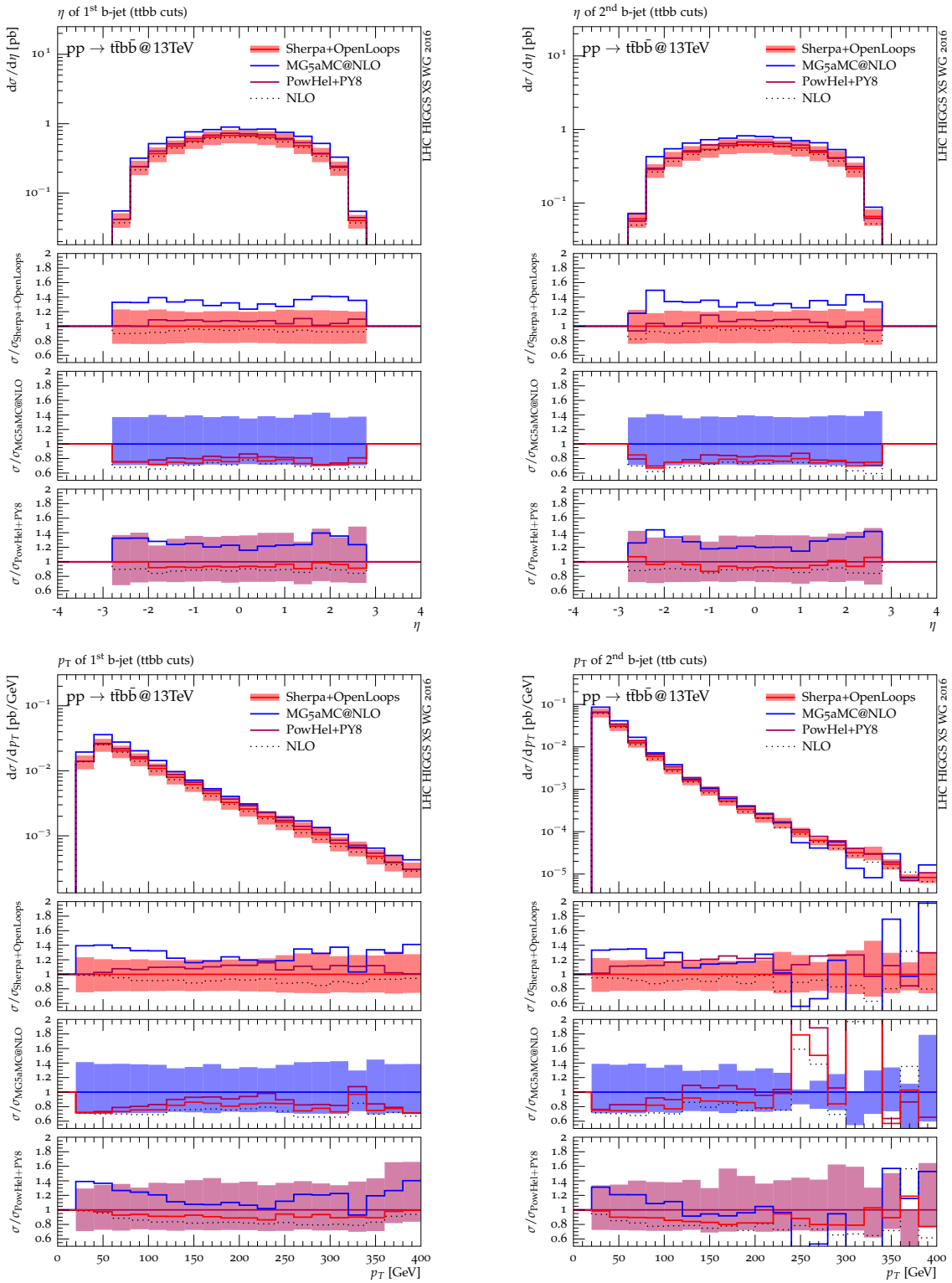

Figure 106: Fixed-order NLO and NLO+PS b-jet distributions for $pp \to t\bar{t}+ \geq 2\,b$ jets at 13 TeV. Ratio plots like in Figure 101.

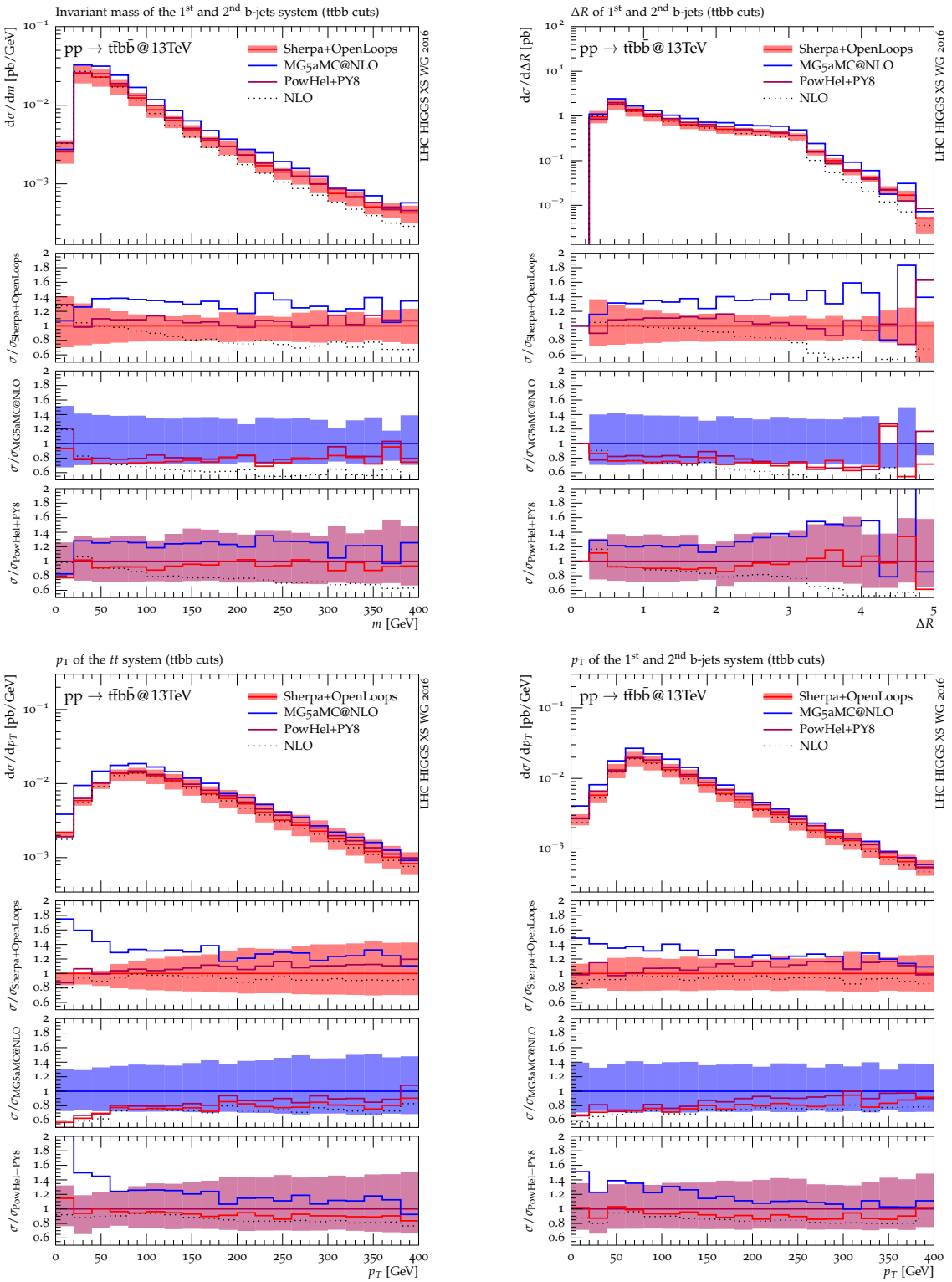

Figure 107: (7) Fixed-order NLO and NLO+PS distributions of the $b\bar{b}$ and $t\bar{t}$ systems for $pp \to t\bar{t}+ \geq 2\,b$ jets at 13 TeV. Ratio plots like in Figure 101.

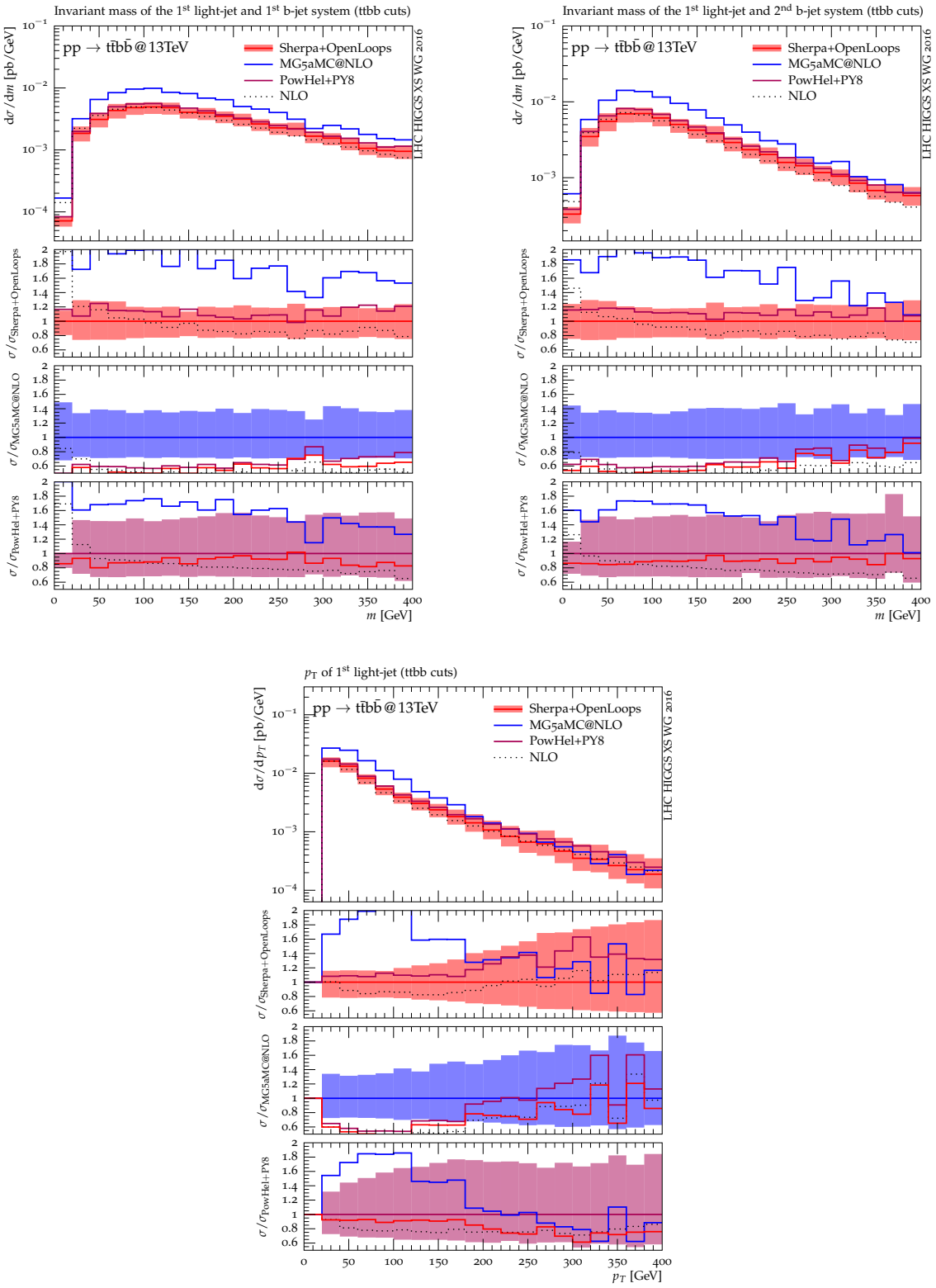

Figure 108: Fixed-order NLO and NLO+PS light-jet mass and transverse momentum distributions for $pp \to t\bar{t}+ \geq 2\,b$ jets at 13 TeV. Ratio plots like in Figure 101.

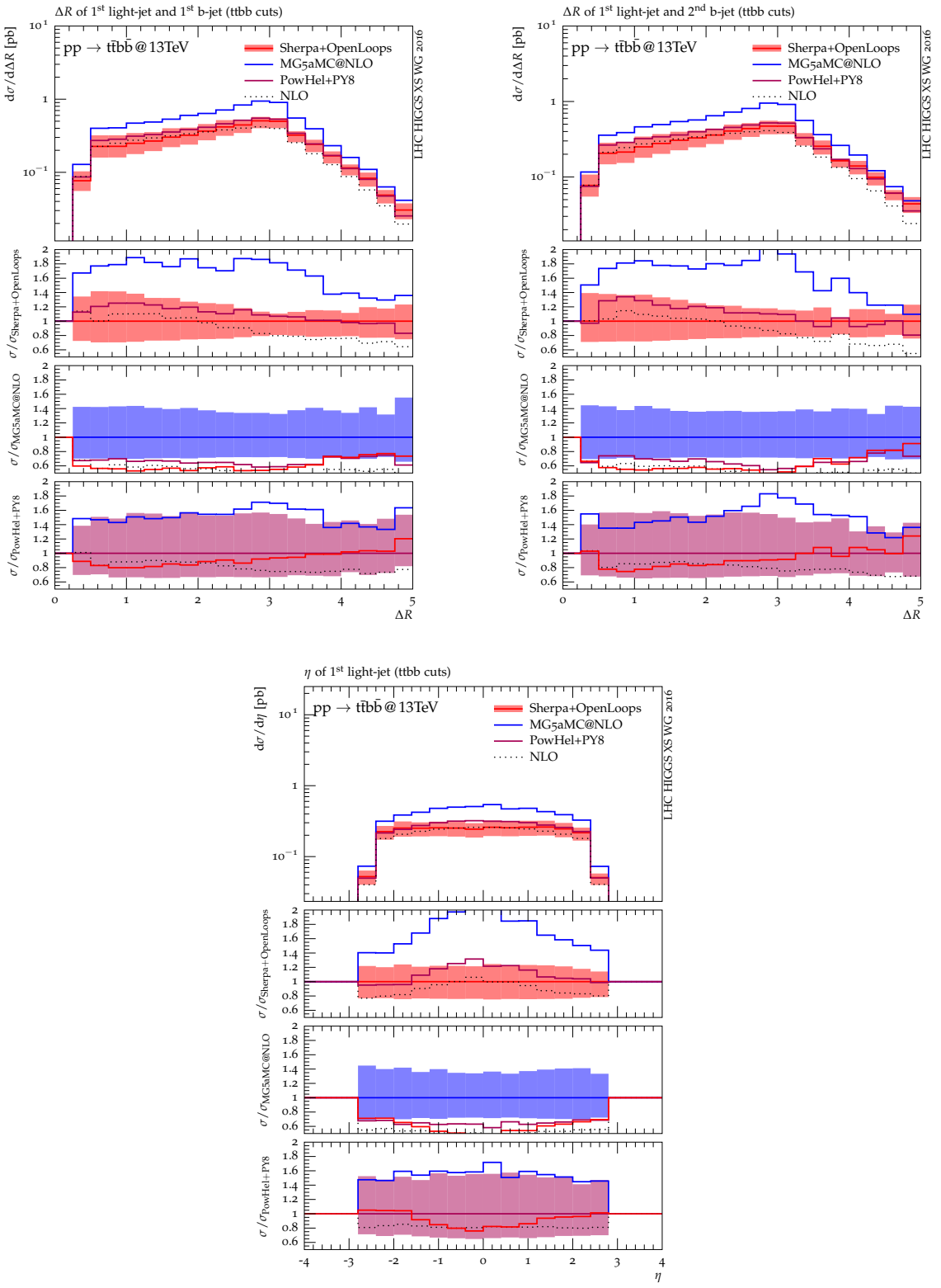

Figure 109: Fixed-order NLO and NLO+PS light-jet angular distributions for $pp \to t\bar{t}+ \geq 2\,b$ jets at 13 TeV. Ratio plots like in Figure 101.

Chapter I.7

Higgs Boson Pair Production

S. Dawson, C. Englert, M. Gouzevitch, R. Salerno, M. Slawinska (Eds.); J. Baglio, S. Borowka, A. Carvalho, M. Dall'Osso, P. de Castro Manzano, D. de Florian, T. Dorigo, F. Goertz, C.A. Gottardo, N. Greiner, J. Grigo, R. Gröber, G. Heinrich, B. Hespel, S. Jones, M. Kerner, I.M. Lewis, J. Mazzitelli, M. Mühlleitner, A. Papaefstathiou, T. Robens, J. Rojo, J. Schlenk, U. Schubert, M. Spannowsky, M. Spira, M. Tosi, E. Vryonidou, M. Zaro, T. Zirke

I.7.1 Introduction

In the SM, the Higgs self-couplings are uniquely determined by the structure of the scalar potential,

$$V = \frac{m_h^2}{2}h^2 + \lambda_3 v h^3 + \frac{\lambda_4}{4}h^4\,, \tag{I.7.1}$$

where $\lambda_3 = \lambda_4 = m_h^2/(2v^2)$. Experimentally measuring λ_3 and λ_4 is thus a crucial test of the mechanism of electroweak symmetry breaking. A measurement of λ_3 requires double Higgs boson production while λ_4 is first probed in the production of 3 Higgs bosons.

The phenomenology of multi-Higgs boson final states will provide complementary information to that found from single Higgs physics at the LHC. Due to generically small inclusive cross sections and a difficult signal vs. background discrimination, the best motivated multi-Higgs final states at the Large Hadron Collider are Higgs boson pair final states, of which gluon fusion $gg \to hh$ is the dominant production mode.

Many models of physics beyond the Standard Model with SM-compatible single Higgs boson signal strengths can exhibit a di-Higgs phenomenology vastly different from the SM expectation. In this sense, a successful discovery of Higgs boson pair production at the LHC and the subsequent measurement of potential deviations from the SM constitutes an important avenue in the search for physics beyond the SM. In particular, modifications of the Higgs trilinear couplings (e.g. via a modified Higgs self interaction) can only be directly observed in Higgs boson pair production. In the gluon fusion process this occurs via the interference of the box and triangle diagrams shown in Figure 110 [432–434].

To facilitate such a measurement, it is crucial to establish the Higgs boson pair production cross section in the SM to the best theoretical accuracy possible and to provide BSM benchmarks that reflect the phenomenology of Higgs boson pairs at the LHC in a consistent and concise fashion.

This report summarizes the results of the HH cross section group of the 2014-2015 LHC Higgs Cross Section working group that aims to establish SM predictions for a range of dominant and subdominant Higgs boson pair production modes at the LHC at the highest available theoretical precision. In

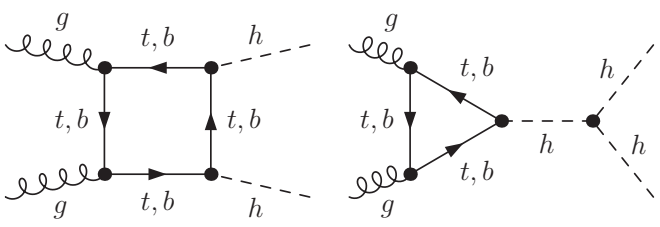

Figure 110: Feynman diagrams contributing to Higgs boson pair production via gluon fusion at leading order.

addition, we provide benchmarks for resonant and non-resonant extensions of the SM phenomenology of Higgs boson pairs in light of current single Higgs property measurements which are aligned with the efforts of other subgroups. This note is structured as follows: In Section I.7.2 we provide an update on the dominant Higgs boson pair production modes at the LHC; special care is devoted to the dominant gluon fusion production mode in Section I.7.2.a. Section I.7.3 contains representative distributions at NLO for the SM gluon fusion pair production channel. Section I.7.4 discusses benchmarks of motivated BSM scenarios. The BSM phenomenology of multi-Higgs final states can be divided into resonant and non-resonant extensions of the SM. The latter is discussed in Section I.7.4.a using the language of Effective Field Theory. Benchmarks for resonant di-Higgs final state searches are discussed using the singlet-extended SM and the 2 Higgs doublet model in Section I.7.4.b, which provide theoretically clean avenues to introduce new resonant physics into Higgs boson pair production.

I.7.2 Total rates in the SM

I.7.2.a Gluon fusion

The NLO [435] and NNLO [436] fixed order corrections to $gg \to hh$ are known in the large top mass limit. Recently, the complete NLO fixed order corrections, including all top quark mass effects, have become available [437, 438]. The QCD corrections are large, typically doubling the cross section from LO to NLO, with another $\sim 20\%$ increase going from NLO to NNLO. The threshold resummation corrections for Higgs boson pair production at NNLL [439] further increase the rate. The NNLL threshold resummed cross sections are combined consistently with the fixed order NNLO results in Table 46, with the rate being weighted by the exact LO finite m_t result normalized to the $m_t \to \infty$ LO result. This is the HEFT approximation. For all the predictions we use the `PDF4LHC15_nnlo_mc` proton PDF set that is recommended by the PDF4LHC group [35].

The scale choice $\mu_0 = M_{hh}/2$ is shown, with the scale variation taken to be $\mu_0/2 < \mu_R, \mu_F < 2\mu_0$, with the restriction $1/2 < \mu_R/\mu_F < 2$. The effect of choosing the central scale to be $\mu_0 = M_{hh}$ is shown in Table 47. The numerical importance of the threshold resummation is minimized for $\mu_0 = M_{hh}/2$, and so we recommend this as our preferred choice. The scale uncertainties are $\sim 4 - 6\%$ and the PDF uncertainties are $\sim 2 - 3\%$ at $\sqrt{s} = 13$ TeV.

For convenience, we define two K factors, computed in $m_t \to \infty$ limit, for the total cross sections, where σ_{NNLL} is the fixed order NNLO rate matched to the NNLL rate,

$$\begin{aligned} K &\equiv \frac{\sigma_{\text{NNLL}}}{\sigma_{\text{NLO}}} \\ K' &\equiv \frac{\sigma_{\text{NNLL}}}{\sigma_{\text{LO}}} . \end{aligned} \tag{I.7.2}$$

The K factors for the scale choices $\mu_0 = M_{hh}$ and $\mu_0 = M_{hh}/2$ are shown in Tabs. 48 and 49, respectively.

I.7.2.a.i Top Quark Mass Uncertainties

Recently, the complete 2-loop reducible contributions have been calculated [440], followed shortly by the full NLO calculation including all top quark mass effects [437, 438], and we can compare with various approximations in the literature,

- An m_t expansion to NNLO estimates uncertainties from top mass effects at $\mathcal{O}(5\%)$ [441–443].
- The exact inclusion of the m_t dependence in the real contributions to the NLO corrections and reweighting the virtual corrections evaluated in the $m_t \to \infty$ approximation with the full LO finite m_t dependence estimates uncertainties to be $\mathcal{O}(-10\%)$. This is the FT_{approx} of Refs. [444, 445].

We provide approximate NLO rates for hh production in Table 52 in the limit in which the top mass effects are retained in the real contributions, the FT_{approx} of Refs. [444] and [445]. These results

$m_h = 124.5$ GeV	$\sigma_{\rm NNLL}(fb)$	Scale Unc. (%)	PDF Unc. (%)	α_s Unc. (%)
$\sqrt{s} = 7$ TeV	7.772	$+4.0 - 5.7$	± 3.4	± 2.8
$\sqrt{s} = 8$ TeV	11.26	$+4.1 - 5.7$	± 3.0	± 2.6
$\sqrt{s} = 13$ TeV	38.20	$+4.3 - 6.0$	± 2.1	± 2.3
$\sqrt{s} = 14$ TeV	45.34	$+4.4 - 6.0$	± 2.1	± 2.2
$\sqrt{s} = 100$ TeV	1760	$+5.0 - 6.7$	± 1.7	± 2.1
$m_h = 125$ GeV	$\sigma_{\rm NNLL}(fb)$	Scale Unc. (%)	PDF Unc. (%)	α_s Unc. (%)
$\sqrt{s} = 7$ TeV	7.718	$+4.0 - 5.7$	± 3.4	± 2.8
$\sqrt{s} = 8$ TeV	11.18	$+4.1 - 5.7$	± 3.1	± 2.6
$\sqrt{s} = 13$ TeV	37.95	$+4.3 - 6.0$	± 2.1	± 2.3
$\sqrt{s} = 14$ TeV	45.05	$+4.4 - 6.0$	± 2.1	± 2.2
$\sqrt{s} = 100$ TeV	1749	$+5.1 - 6.6$	± 1.7	± 2.1
$m_h = 125.09$ GeV	$\sigma_{\rm NNLL}(fb)$	Scale Unc. (%)	PDF Unc. (%)	α_s Unc. (%)
$\sqrt{s} = 7$ TeV	7.708	$+4.0 - 5.7$	± 3.4	± 2.8
$\sqrt{s} = 8$ TeV	11.17	$+4.1 - 5.7$	± 3.1	± 2.6
$\sqrt{s} = 13$ TeV	37.91	$+4.3 - 6.0$	± 2.1	± 2.3
$\sqrt{s} = 14$ TeV	45.00	$+4.4 - 6.0$	± 2.1	± 2.2
$\sqrt{s} = 100$ TeV	1748	$+5.0 - 6.5$	± 1.7	± 2.0
$m_h = 125.5$ GeV	$\sigma_{\rm NNLL}(fb)$	Scale Unc. (%)	PDF Unc. (%)	α_s Unc. (%)
$\sqrt{s} = 7$ TeV	7.663	$+4.0 - 5.7$	± 3.4	± 2.8
$\sqrt{s} = 8$ TeV	11.11	$+4.1 - 5.7$	± 3.1	± 2.6
$\sqrt{s} = 13$ TeV	37.71	$+4.3 - 6.0$	± 2.1	± 2.3
$\sqrt{s} = 14$ TeV	44.76	$+4.4 - 5.9$	± 2.1	± 2.2
$\sqrt{s} = 100$ TeV	1738	$+5.2 - 6.4$	± 1.7	± 2.1

Table 46: NNLL matched to NNLO cross sections for $gg \to hh$ with a central scale $\mu_0 = M_{hh}/2$ with $m_h = 124.5$ GeV, $m_h = 125$ GeV, $m_h = 125.09$ GeV and $m_h = 125.5$ GeV [439] computed in the HEFT approximation. The uncertainties from top quark mass effects are not included in this table. Uncertainties are evaluated using the PDF4LHC recommendation and are based on the `PDF4LHC15_nnlo_mc` set.

can be compared with the NLO results obtained by computing a K factor in the $m_t \to \infty$ limit and re-weighting by the exact LO result (HEFT approximation) as shown in Table 53 [435, 436]. There is good, but not exact, agreement between the two approximations.

The complete NLO results for $m_h = 125$ GeV and $m_t = 173$ GeV, with all top mass effects, are shown in Table 50. The inclusion of the mass effects consistently decreases the NLO cross section from the HEFT result, while the FT_{approx} is a better approximation to the total rate. The inclusion of the mass effects reduces the NLO rate by an energy dependent factor which can be parameterized as ,

$$\sigma(gg \to hh)^{exact}_{NLO} = \sigma(gg \to hh)^{HEFT}_{NLO}(1 + \delta_t)\,, \tag{I.7.3}$$

where (using $m_t = 173$GeV),

$$\delta_t(7\text{ TeV}) = -9.94\% \tag{I.7.4}$$
$$\delta_t(8\text{ TeV}) = -10.88\% \tag{I.7.5}$$
$$\delta_t(13\text{ TeV}) = -13.72\% \tag{I.7.6}$$
$$\delta_t(14\text{ TeV}) = -14.11\%\,. \tag{I.7.7}$$

The top mass effects can be included consistently by writing our final result as,

$$\sigma'_{NNLL} = \sigma_{NNLL} + \delta_t \sigma^{HEFT}_{NLO}\,, \tag{I.7.8}$$

$\mu_0 = M_{hh}$	$\sigma_{NNLL}(fb)$	Scale Unc. (%)	PDF Unc. (%)	α_s Unc.(%)
$\sqrt{s} = 7$ TeV	7.61	$+5.6 - 6.0$	± 3.3	± 2.8
$\sqrt{s} = 8$ TeV	11.0	$+5.5 - 6.0$	± 3.0	± 2.6
$\sqrt{s} = 13$ TeV	37.3	$+5.1 - 6.1$	± 2.1	± 2.3
$\sqrt{s} = 14$ TeV	44.2	$+5.2 - 6.1$	± 2.0	± 2.2
$\sqrt{s} = 100$ TeV	1712	$+5.2 - 6.2$	± 1.7	± 2.0

Table 47: NNLL cross sections for $gg \to hh$ with a central scale $\mu_0 = M_{hh}$ with $m_h = 125$ GeV.The uncertainties from top quark mass effects are not included in this table. Uncertainties are evaluated using the PDF4LHC recommendation and are based on the `PDF4LHC15_nnlo_mc set`.

	$\sqrt{s} = 7$ TeV	$\sqrt{s} = 8$ TeV	$\sqrt{s} = 13$ TeV	$\sqrt{s} = 14$ TeV	$\sqrt{s} = 100$ TeV
K	1.203	1.200	1.193	1.192	1.195
K'	2.299	2.296	2.301	2.304	2.472

Table 48: K factors as defined in Eq. (I.7.2) for $gg \to hh$ with a central scale $\mu_0 = M_{hh}/2$ and $m_h = 125$ GeV [439].

	$\sqrt{s} = 7$ TeV	$\sqrt{s} = 8$ TeV	$\sqrt{s} = 13$ TeV	$\sqrt{s} = 14$ TeV	$\sqrt{s} = 100$ TeV
K	1.426	1.413	1.378	1.373	1.305
K'	2.987	2.949	2.847	2.835	2.699

Table 49: K factors as defined in Eq. (I.7.2) for $gg \to hh$ with a central scale $\mu_0 = M_{hh}$ and $m_h = 125$ GeV [439].

$\sqrt{s}$	NLO HEFT	NLO FT$_{approx}$	NLO^{exact}
7 TeV	$6.44^{+20.1\%}_{-16.9\%}$	$5.95^{+17.3\%}_{-15.7\%}$	$5.80^{+16.3\%}_{-15.2\%}$
8 TeV	$9.37^{+19.8\%}_{-16.5\%}$	$8.61^{+16.7\%}_{-15.1\%}$	$8.35^{+15.7\%}_{-14.6\%}$
13 TeV	$32.22^{+18.2\%}_{-15.1\%}$	$28.90^{+15.0\%}_{-13.4\%}$	$27.80^{+13.8\%}_{-12.8\%}$
14 TeV	$38.32^{+18.1\%}_{-14.9\%}$	$34.26^{+14.7\%}_{-13.2\%}$	$32.91^{+13.6\%}_{-12.6\%}$

Table 50: NLO results for $gg \to hh$. The uncertainty in per cent is from scale variations only. The central scale is $\mu_0 = M_{hh}/2$. We use $m_t = 173$ GeV and $m_h = 125$ GeV. The PDF set is PDF4LHC15_nlo_100_pdfas. [437]

where σ_{NNLL} is given in Table 46. This prescription amounts to subtracting $5.49\ fb$ from the 14 TeV, $4.50\ fb$ from the 13 TeV, $1.02\ fb$ from the 8 TeV and $0.64\ fb$ from the 7 TeV numbers of Table 46 . (We note that Table 46 uses $m_t = 172.5$ GeV, so there is a slight mis-match in the m_t values.) Furthermore, we neglect any possible m_h dependence of δ_t. Our recommended results are given in Table 51 and correspond to the convention of Eq. I.7.8. We arbitrarily assume a top mass uncertainty of $\pm 5\%$ from unknown top quark mass effects at NNLO, and do not include a theoretical error on δ_t.

I.7.2.b Other production channels

There are a number of additional subdominant Higgs boson pair production modes at the LHC [444,446]. In particular, Higgs boson pairs can be produced in association with electroweak bosons ($W^{\pm}hh$, Zhh),

$m_h = 124.5$ GeV	$\sigma'_{\text{NNLL}}(fb)$	Scale Unc. (%)	PDF Unc. (%)	α_s Unc. (%)
$\sqrt{s} = 7$ TeV	7.132	$+4.0 - 5.7$	± 3.4	± 2.8
$\sqrt{s} = 8$ TeV	10.24	$+4.1 - 5.7$	± 3.0	± 2.6
$\sqrt{s} = 13$ TeV	33.78	$+4.3 - 6.0$	± 2.1	± 2.3
$\sqrt{s} = 14$ TeV	39.93	$+4.4 - 6.0$	± 2.1	± 2.2
$m_h = 125$ GeV	$\sigma'_{\text{NNLL}}(fb)$	Scale Unc. (%)	PDF Unc. (%)	α_s Unc. (%)
$\sqrt{s} = 7$ TeV	7.078	$+4.0 - 5.7$	± 3.4	± 2.8
$\sqrt{s} = 8$ TeV	10.16	$+4.1 - 5.7$	± 3.1	± 2.6
$\sqrt{s} = 13$ TeV	33.53	$+4.3 - 6.0$	± 2.1	± 2.3
$\sqrt{s} = 14$ TeV	39.64	$+4.4 - 6.0$	± 2.1	± 2.2
$m_h = 125.09$ GeV	$\sigma'_{\text{NNLL}}(fb)$	Scale Unc. (%)	PDF Unc. (%)	α_s Unc. (%)
$\sqrt{s} = 7$ TeV	7.068	$+4.0 - 5.7$	± 3.4	± 2.8
$\sqrt{s} = 8$ TeV	10.15	$+4.1 - 5.7$	± 3.1	± 2.6
$\sqrt{s} = 13$ TeV	33.49	$+4.3 - 6.0$	± 2.1	± 2.3
$\sqrt{s} = 14$ TeV	39.59	$+4.4 - 6.0$	± 2.1	± 2.2
$m_h = 125.5$ GeV	$\sigma'_{\text{NNLL}}(fb)$	Scale Unc. (%)	PDF Unc. (%)	α_s Unc. (%)
$\sqrt{s} = 7$ TeV	7.023	$+4.0 - 5.7$	± 3.4	± 2.8
$\sqrt{s} = 8$ TeV	10.09	$+4.1 - 5.7$	± 3.1	± 2.6
$\sqrt{s} = 13$ TeV	33.29	$+4.3 - 6.0$	± 2.1	± 2.3
$\sqrt{s} = 14$ TeV	39.35	$+4.4 - 5.9$	± 2.1	± 2.2

Table 51: NNLL matched to NNLO cross sections for $gg \to hh$ including top quark mass effects to NLO [437], as in Eq.I.7.8, with a central scale $\mu_0 = M_{hh}/2$ with $m_h = 124.5$ GeV, $m_h = 125$ GeV, $m_h = 125.09$ GeV and $m_h = 125.5$ GeV [439]. Uncertainties are evaluated using the PDF4LHC recommendation and are based on the `PDF4LHC15_nnlo_mc` set. These are our recommended numbers.

m_h (GeV)	$\sqrt{s} = 7$ TeV	$\sqrt{s} = 8$ TeV	$\sqrt{s} = 13$ TeV	$\sqrt{s} = 14$ TeV	$\sqrt{s} = 100$ TeV
124.5	$6.08^{+17.3\%}_{-15.7\%} \pm 4.0\%$	$8.74^{+16.8\%}_{-15.1\%} \pm 3.6\%$	$29.43^{+15.1\%}_{-13.5\%} \pm 2.7\%$	$35.08^{+14.8\%}_{-13.2\%} \pm 2.6\%$	$1254^{+14.5\%}_{-14.2\%} \pm 2.1\%$
125	$6.01^{+17.2\%}_{-15.6\%} \pm 4.0\%$	$8.62^{+16.8\%}_{-15.2\%} \pm 3.7\%$	$29.26^{+15.0\%}_{-13.4\%} \pm 2.7\%$	$34.59^{+14.6\%}_{-13.1\%} \pm 2.6\%$	$1237^{+14.3\%}_{-14.1\%} \pm 2.1\%$
125.09	$6.03^{+17.2\%}_{-15.6\%} \pm 4.0\%$	$8.70^{+16.7\%}_{-15.1\%} \pm 3.7\%$	$29.27^{+15.1\%}_{-13.5\%} \pm 2.7\%$	$34.59^{+14.7\%}_{-13.2\%} \pm 2.6\%$	$1229^{+14.6\%}_{-14.2\%} \pm 2.1\%$
125.5	$5.99^{+17.4\%}_{-15.7\%} \pm 4.0\%$	$8.64^{+16.9\%}_{-15.2\%} \pm 3.6\%$	$29.28^{+14.9\%}_{-13.4\%} \pm 2.7\%$	$34.41^{+14.9\%}_{-13.2\%} \pm 2.6\%$	$1227^{+14.3\%}_{-14.1\%} \pm 2.1\%$

Table 52: Signal cross section (in fb) for $gg \to hh$ at NLO QCD in the $\text{FT}_{\text{approx}}$ approximation of Ref. [444, 445], with a central scale choice $\mu_0 = M_{hh}/2$. The first uncertainty is the scale uncertainty and the second is the PDF uncertainty based on the `PDF4LHC15_nlo_mc` set. There is an additional uncertainty from top quark mass effects, along with an α_s uncertainty.

m_h (GeV)	$\sqrt{s} = 7$ TeV	$\sqrt{s} = 8$ TeV	$\sqrt{s} = 13$ TeV	$\sqrt{s} = 14$ TeV	$\sqrt{s} = 100$ TeV
125	$6.415^{+20\%}_{-16.8\%}$	$9.318^{+19.5\%}_{-16.4\%}$	$31.81^{+18.2\%}_{-15.0\%}$	$37.79^{+18\%}_{-14.8\%}$	$1464^{+16.1\%}_{-13.8\%}$

Table 53: Signal cross section (in fb) for $gg \to hh$ at NLO QCD in the $m_t \to \infty$ limit, reweighted by the exact LO result, of Ref. [435, 436], with a central scale choice $\mu_0 = M_{hh}/2$. Only the uncertainties due to scale variation are shown. There is an additional uncertainty from top quark mass effects, along with PDF and α_s uncertainties.

top quarks ($t\bar{t}hh$ and $tjhh$,) or jets ($hhjj$). The associated production of hh with vector bosons is known at NNLO QCD [446], where the NNLO corrections to the NLO rate are of order 10%. The NNLO rates are given in Tables 54- 56. The scale choice $\mu_0 = M_{hhV}$ ($V = W, Z$) is shown, with the scale variation taken to be $\mu_0/2 < \mu_R, \mu_F < 2\mu_0$, with the restriction $1/2 < \mu_R/\mu_F < 2$.

While the weak boson fusion configuration (WBF) is reliably known at NLO precision [444, 446] (with NNLO corrections negligible [447]), a LO estimate of the gluon fusion contribution to the WBF configuration [448] suggests that it is non-negligible even for tight WBF selections [449, 450]. The WBF NLO rates are given in Table 57. The WBF cross section is highly stabilized at NLO QCD; electroweak corrections are not available.

The $t\bar{t}hh$ and $t\bar{t}hj$ cross sections are given in Tabs. 58 and 59. The $t\bar{t}hh$ rate is particularly interesting in composite models, where it may be enhanced over the SM rate. The scale variation for $t\bar{t}hh$ and $tjhh$ is chosen as $\mu_0/2 < \mu_R, \mu_F < 2\mu_0$ with $\mu_0 = M_{hh}/2$.

In Table 60 we also provide numbers for $pp \to hhh$ at NLO QCD in the $\text{FT}_{\text{approx}}$ approximation of [444, 445].

m_h (GeV)	$\sqrt{s} = 7$ TeV	$\sqrt{s} = 8$ TeV	$\sqrt{s} = 13$ TeV	$\sqrt{s} = 14$ TeV	$\sqrt{s} = 100$ TeV
124.5	$0.109^{+2.8\%}_{-2.2\%} \pm 2.9\%$	$0.145^{+2.8\%}_{-2.3\%} \pm 2.6\%$	$0.368^{+3.5\%}_{-2.6\%} \pm 1.9\%$	$0.420^{+3.6\%}_{-2.7\%} \pm 1.8\%$	$8.33^{+5.9\%}_{-4.6\%} \pm 1.7\%$
125	$0.108^{+2.6\%}_{-2.2\%} \pm 2.9\%$	$0.143^{+2.8\%}_{-2.2\%} \pm 2.6\%$	$0.363^{+3.4\%}_{-2.7\%} \pm 1.9\%$	$0.415^{+3.5\%}_{-2.7\%} \pm 1.8\%$	$8.23^{+5.9\%}_{-4.6\%} \pm 1.7\%$
125.09	$0.108^{+2.6\%}_{-2.2\%} \pm 2.9\%$	$0.143^{+2.7\%}_{-2.3\%} \pm 2.6\%$	$0.362^{+3.4\%}_{-2.6\%} \pm 1.9\%$	$0.414^{+3.5\%}_{-2.7\%} \pm 1.8\%$	$8.22^{+5.9\%}_{-4.6\%} \pm 1.7\%$
125.5	$0.106^{+2.6\%}_{-2.2\%} \pm 2.9\%$	$0.141^{+2.8\%}_{-2.2\%} \pm 2.6\%$	$0.359^{+3.5\%}_{-2.7\%} \pm 1.9\%$	$0.409^{+3.5\%}_{-2.7\%} \pm 1.9\%$	$8.13^{+5.9\%}_{-4.6\%} \pm 1.7\%$

Table 54: Signal cross section (in fb) for hhZ production at NNLO QCD with the central scale $\mu_0 = \mu_R = \mu_F = M_{hhZ}$ [446]. The first uncertainty is the scale uncertainty and the second is the PDF + α_s uncertainty based on the `PDF4LHC15_nnlo_mc` set.

m_h (GeV)	$\sqrt{s} = 7$ TeV	$\sqrt{s} = 8$ TeV	$\sqrt{s} = 13$ TeV	$\sqrt{s} = 14$ TeV	$\sqrt{s} = 100$ TeV
124.5	$0.0516^{+0.98\%}_{-1.2\%} \pm 4.0\%$	$0.0688^{+1.0\%}_{-1.2\%} \pm 3.7\%$	$0.176^{+1.2\%}_{-1.3\%} \pm 2.8\%$	$0.200^{+1.2\%}_{-1.3\%} \pm 2.7\%$	$3.34^{+3.6\%}_{-4.3\%} \pm 1.9\%$
125	$0.0509^{+0.98\%}_{-1.2\%} \pm 4.0\%$	$0.0679^{+1.0\%}_{-1.2\%} \pm 3.7\%$	$0.173^{+1.2\%}_{-1.3\%} \pm 2.8\%$	$0.198^{+1.2\%}_{-1.3\%} \pm 2.7\%$	$3.30^{+3.5\%}_{-4.3\%} \pm 1.9\%$
125.09	$0.0508^{+0.98\%}_{-1.2\%} \pm 4.0\%$	$0.0677^{+1.0\%}_{-1.2\%} \pm 3.7\%$	$0.173^{+1.2\%}_{-1.3\%} \pm 2.8\%$	$0.197^{+1.2\%}_{-1.3\%} \pm 2.7\%$	$3.30^{+3.5\%}_{-4.3\%} \pm 1.9\%$
125.5	$0.0502^{+0.98\%}_{-1.2\%} \pm 4.0\%$	$0.0670^{+1.0\%}_{-1.2\%} \pm 3.7\%$	$0.171^{+1.2\%}_{-1.3\%} \pm 2.8\%$	$0.195^{+1.2\%}_{-1.3\%} \pm 2.7\%$	$3.27^{+3.5\%}_{-4.3\%} \pm 1.9\%$

Table 55: Signal cross section (in fb) for hhW^- production at NNLO QCD with the central scale $\mu_0 = \mu_R = \mu_F = M_{hhW}$ [446]. The first uncertainty is the scale uncertainty and the second is the PDF + α_s uncertainty based on the `PDF4LHC15_nnlo_mc` set.

m_h (GeV)	$\sqrt{s} = 7$ TeV	$\sqrt{s} = 8$ TeV	$\sqrt{s} = 13$ TeV	$\sqrt{s} = 14$ TeV	$\sqrt{s} = 100$ TeV
124.5	$0.114^{+0.47\%}_{-0.59\%} \pm 3.0\%$	$0.147^{+0.43\%}_{-0.52\%} \pm 2.8\%$	$0.333^{+0.32\%}_{-0.41\%} \pm 2.2\%$	$0.373^{+0.33\%}_{-0.39\%} \pm 2.1\%$	$4.74^{+0.90\%}_{-0.96\%} \pm 1.8\%$
125	$0.113^{+0.47\%}_{-0.59\%} \pm 3.0\%$	$0.145^{+0.43\%}_{-0.52\%} \pm 2.8\%$	$0.329^{+0.32\%}_{-0.41\%} \pm 2.2\%$	$0.369^{+0.33\%}_{-0.39\%} \pm 2.1\%$	$4.70^{+0.90\%}_{-0.96\%} \pm 1.8\%$
125.09	$0.113^{+0.47\%}_{-0.59\%} \pm 3.0\%$	$0.145^{+0.43\%}_{-0.52\%} \pm 2.8\%$	$0.329^{+0.32\%}_{-0.41\%} \pm 2.2\%$	$0.368^{+0.33\%}_{-0.39\%} \pm 2.1\%$	$4.69^{+0.90\%}_{-0.96\%} \pm 1.8\%$
125.5	$0.111^{+0.47\%}_{-0.59\%} \pm 3.0\%$	$0.143^{+0.43\%}_{-0.52\%} \pm 2.8\%$	$0.326^{+0.32\%}_{-0.41\%} \pm 2.2\%$	$0.365^{+0.33\%}_{-0.39\%} \pm 2.1\%$	$4.65^{+0.90\%}_{-0.96\%} \pm 1.8\%$

Table 56: Signal cross section (in fb) for hhW^+ production at NNLO QCD with the central scale $\mu_0 = \mu_R = \mu_F = M_{hhW}$ [446]. The first uncertainty is the scale uncertainty and the second is the PDF + α_s uncertainty based on the `PDF4LHC15_nnlo_mc` set.

m_h (GeV)	$\sqrt{s} = 7$ TeV	$\sqrt{s} = 8$ TeV	$\sqrt{s} = 13$ TeV	$\sqrt{s} = 14$ TeV	$\sqrt{s} = 100$ TeV
124.5	$0.320^{+3.2\%}_{-3.7\%} \pm 2.7\%$	$0.470^{+2.4\%}_{-3.1\%} \pm 2.6\%$	$1.65^{+2.4\%}_{-2.7\%} \pm 2.3\%$	$1.97^{+2.3\%}_{-2.6\%} \pm 2.3\%$	$81.9^{+0.2\%}_{-0.2\%} \pm 1.8\%$
125	$0.316^{+3.7\%}_{-4.1\%} \pm 2.7\%$	$0.468^{+2.8\%}_{-3.3\%} \pm 2.6\%$	$1.64^{+2.0\%}_{-2.5\%} \pm 2.3\%$	$1.94^{+2.3\%}_{-2.6\%} \pm 2.3\%$	$80.3^{+0.5\%}_{-0.4\%} \pm 1.7\%$
125.09	$0.313^{+3.2\%}_{-3.8\%} \pm 2.6\%$	$0.459^{+3.2\%}_{-3.6\%} \pm 2.6\%$	$1.62^{+2.3\%}_{-2.7\%} \pm 2.3\%$	$1.95^{+1.8\%}_{-2.3\%} \pm 2.4\%$	$80.8^{+0.8\%}_{-0.8\%} \pm 1.8\%$
125.5	$0.312^{+3.6\%}_{-4.0\%} \pm 2.7\%$	$0.458^{+2.9\%}_{-3.4\%} \pm 2.6\%$	$1.63^{+2.0\%}_{-2.5\%} \pm 2.3\%$	$1.94^{+1.3\%}_{-1.9\%} \pm 2.3\%$	$80.7^{+0.7\%}_{-0.7\%} \pm 1.8\%$

Table 57: Cross section (in fb) for weak boson fusion $hhjj$ at NLO QCD with the central scale $\mu_0 = M_{hh}/2$ [444]. The first uncertainty is the scale uncertainty and the second is the PDF uncertainty based on the `PDF4LHC15_nlo_mc` set.

m_h (GeV)	$\sqrt{s} = 7$ TeV	$\sqrt{s} = 8$ TeV	$\sqrt{s} = 13$ TeV	$\sqrt{s} = 14$ TeV	$\sqrt{s} = 100$ TeV
124.5	$0.112^{+3.5\%}_{-12.5\%} \pm 4.2\%$	$0.176^{+2.9\%}_{-10.7\%} \pm 3.9\%$	$0.786^{+1.3\%}_{-4.5\%} \pm 3.2\%$	$0.968^{+1.7\%}_{-4.6\%} \pm 3.1\%$	$87.2^{+7.9\%}_{-7.3\%} \pm 1.6\%$
125	$0.110^{+3.5\%}_{-12.5\%} \pm 4.2\%$	$0.174^{+2.9\%}_{-10.6\%} \pm 3.9\%$	$0.775^{+1.5\%}_{-4.3\%} \pm 3.2\%$	$0.949^{+1.7\%}_{-4.5\%} \pm 3.1\%$	$82.1^{+7.9\%}_{-7.4\%} \pm 1.6\%$
125.09	$0.109^{+3.5\%}_{-12.8\%} \pm 4.2\%$	$0.174^{+2.8\%}_{-10.6\%} \pm 3.9\%$	$0.772^{+1.7\%}_{-4.5\%} \pm 3.2\%$	$0.949^{+1.8\%}_{-4.8\%} \pm 3.2\%$	$82.1^{+8.3\%}_{-7.6\%} \pm 1.6\%$
125.5	$0.107^{+3.3\%}_{-12.9\%} \pm 4.2\%$	$0.172^{+2.9\%}_{-10.4\%} \pm 4.0\%$	$0.762^{+1.3\%}_{-4.5\%} \pm 3.2\%$	$0.937^{+1.5\%}_{-4.5\%} \pm 3.1\%$	$81.9^{+8.2\%}_{-7.6\%} \pm 1.6\%$

Table 58: Cross section (in fb) for $t\bar{t}hh$ production at NLO QCD with the central scale $\mu_0 = M_{hh}/2$ [444]. The first uncertainty is the scale uncertainty and the second is the PDF uncertainty based on the `PDF4LHC15_nlo_mc` set.

m_h (GeV)	$\sqrt{s} = 7$ TeV	$\sqrt{s} = 8$ TeV	$\sqrt{s} = 13$ TeV	$\sqrt{s} = 14$ TeV	$\sqrt{s} = 100$ TeV
124.5	$0.00335^{+3.9\%}_{-1.7\%} \pm 6.2\%$	$0.00551^{+5.6\%}_{-3.2\%} \pm 5.8\%$	$0.0289^{+5.4\%}_{-3.4\%} \pm 4.6\%$	$0.0365^{+4.4\%}_{-1.6\%} \pm 4.7\%$	$4.44^{+5.2\%}_{-5.6\%} \pm 2.3\%$
125	$0.00331^{+3.9\%}_{-1.8\%} \pm 6.1\%$	$0.00538^{+5.3\%}_{-3.0\%} \pm 5.6\%$	$0.0289^{+5.5\%}_{-3.6\%} \pm 4.7\%$	$0.0367^{+4.2\%}_{-1.8\%} \pm 4.6\%$	$4.44^{+2.2\%}_{-2.8\%} \pm 2.4\%$
125.09	$0.00331^{+4.3\%}_{-2.1\%} \pm 6.3\%$	$0.00540^{+5.4\%}_{-3.1\%} \pm 5.6\%$	$0.0281^{+5.2\%}_{-3.2\%} \pm 4.5\%$	$0.0364^{+3.7\%}_{-1.3\%} \pm 4.7\%$	$4.43^{+2.0\%}_{-2.6\%} \pm 2.4\%$
125.5	$0.00326^{+3.9\%}_{-1.6\%} \pm 6.1\%$	$0.00521^{+5.5\%}_{-3.4\%} \pm 5.8\%$	$0.0279^{+6.1\%}_{-4.6\%} \pm 6.4\%$	$0.0359^{+3.8\%}_{-1.6\%} \pm 4.7\%$	$4.43^{+2.1\%}_{-2.6\%} \pm 2.4\%$

Table 59: Signal cross section (in fb) for $hhtj$ production at NLO QCD with the central scale $\mu_0 = M_{hh}/2$ [444]. The first uncertainty is the scale uncertainty and the second is the PDF uncertainty based on the `PDF4LHC15_nlo_mc` set.

μ_0	$\sqrt{s} = 7$ TeV	$\sqrt{s} = 8$ TeV	$\sqrt{s} = 13$ TeV	$\sqrt{s} = 14$ TeV	$\sqrt{s} = 100$ TeV
$M_{hhh}/2$	$12.03^{+17.8\%}_{-16.3\%} \pm 5.2\%$	$17.99^{+16.5\%}_{-15.4\%} \pm 4.8\%$	$73.43^{+14.7\%}_{-13.7\%} \pm 3.3\%$	$86.84^{+14.0\%}_{-13.2\%} \pm 3.2\%$	$4732^{+11.9\%}_{-11.6\%} \pm 1.8\%$
M_{hhh}	$9.91^{+19.3\%}_{-16.6\%} \pm 5.3\%$	$15.14^{+18.4\%}_{-16.0\%} \pm 4.7\%$	$63.32^{+16.1\%}_{-14.1\%} \pm 3.4\%$	$76.15^{+15.9\%}_{-14.0\%} \pm 3.2\%$	$4306^{+14.0\%}_{-12.3\%} \pm 1.8\%$

Table 60: Signal cross section (in ab) for $gg \to hhh$ at NLO QCD for $m_h = 125$ GeV with $\mu_R = \mu_F = \mu_0$ [445]. The first uncertainty is the scale uncertainty and the second is the PDF uncertainty based on the `PDF4LHC15_nlo_mc` set.

I.7.3 Differential distributions

The di-Higgs differential mass distribution of the NNLO+NNLL calculation detailed in the previous section is shown in Figure 111. This figure includes the higher order corrections in the $m_t \to \infty$ limit. Due to the intricate destructive interplay of the trilinear and box contributions depicted in Figure 110, however, the top mass threshold significantly impacts the differential distributions for the gluon fusion process, and the invariant di-Higgs boson mass differential cross section in particular. On the one hand, the momentum-dependent distributions of the di-Higgs system are exploited in phenomenological analyses (either implicitly or explicitly), as they exhibit a highly sensitive response to BSM-induced modifications of the SM coupling pattern (see below). On the other hand, experimental characteristics of a particular set of selection cuts motivated from the desire to enhance signal over background strongly depend on the transverse Higgs momentum (and therefore on M_{hh}) selection thresholds; boosted Higgs kinematics [451–454] are a particularly drastic example of this. Both the theoretical appeal and the experimental necessity of studying non-inclusive fiducial cross sections have far-reaching consequences for di-Higgs analyses when we extrapolate the findings of the previous section to realistic selection criteria.

In this section we present some distributions obtained using the $\text{FT}_{\text{approx}}$ approximation for the NLO results to establish to which extent approximate NLO event generators can be used, and to which extent this calculation provides a guideline to relate fiducial cross sections to inclusively modeled quantities. We also comment on the impact of higher order corrections beyond the $\text{FT}_{\text{approx}}$ approximation that have become available [437, 438] while this report was completed. Technically, the $\text{FT}_{\text{approx}}$ calculation is performed using matched `Madgraph5_aMC@NLO + Pythia8` simulations [54, 444]. As already mentioned, this approximation contains exact, full m_t-dependent real emission contributions combined with a finite m_t Born-reweighted $m_t \to \infty$ calculation of the virtual loop corrections to obtain an approximation of the fully differential NLO cross section.

We show in Figs. 112 - 115 the $\text{FT}_{\text{approx}}$ distributions for the hh invariant mass and the leading Higgs boson p_T, including PDF and scale uncertainties for centre-of-mass energies of 8 TeV and 13 TeV. These distributions also rely on the `PDF4LHC15_nlo_mc` sets with 30 replicas. The scale variation dominates over the PDF uncertainty leading to a rather flat $+30\%$, -25% uncertainty over a broad, phenomenologically interesting energy regime, calculated from a scale variation that is again $\mu_0/2 < \mu < 2\mu_0$, for $\mu_0 = M_{hh}/2$. The scale uncertainty is similar when considering the full NLO QCD corrections, see Figs. 116 - 118.

For some observables, for example all rapidity distributions, the differential QCD corrections are simple rescalings of the LO distribution with the total K factor in the $\text{FT}_{\text{approx}}$ scheme. For most distributions, however, the discrepancy between the $\text{FT}_{\text{approx}}$ and the full result moves out of the scale variation uncertainty band in the tail of the distributions. This is shown for the di-Higgs boson invariant

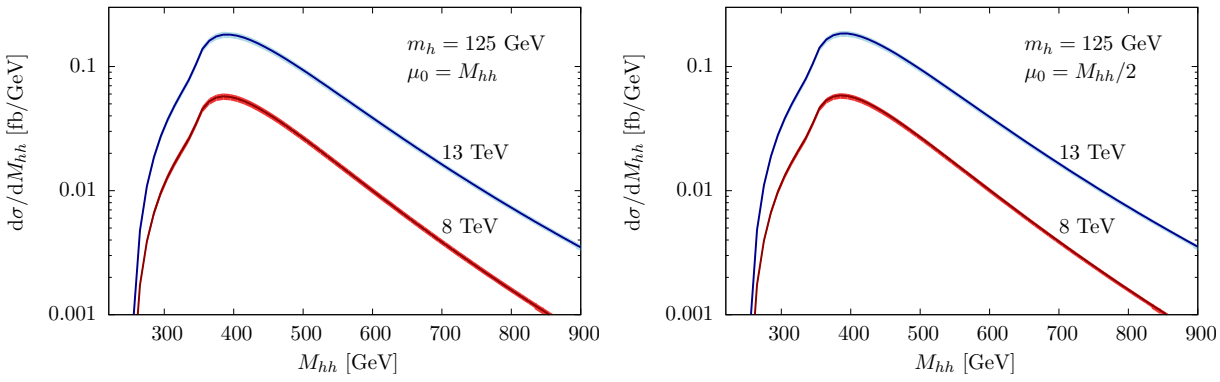

Figure 111: $\sqrt{s} = 8$ TeV and 13 TeV NNLO+NNLL cross section distribution for $m_t \to \infty$ calculation detailed in the previous section, also showing the scale uncertainty [439]. For details see text.

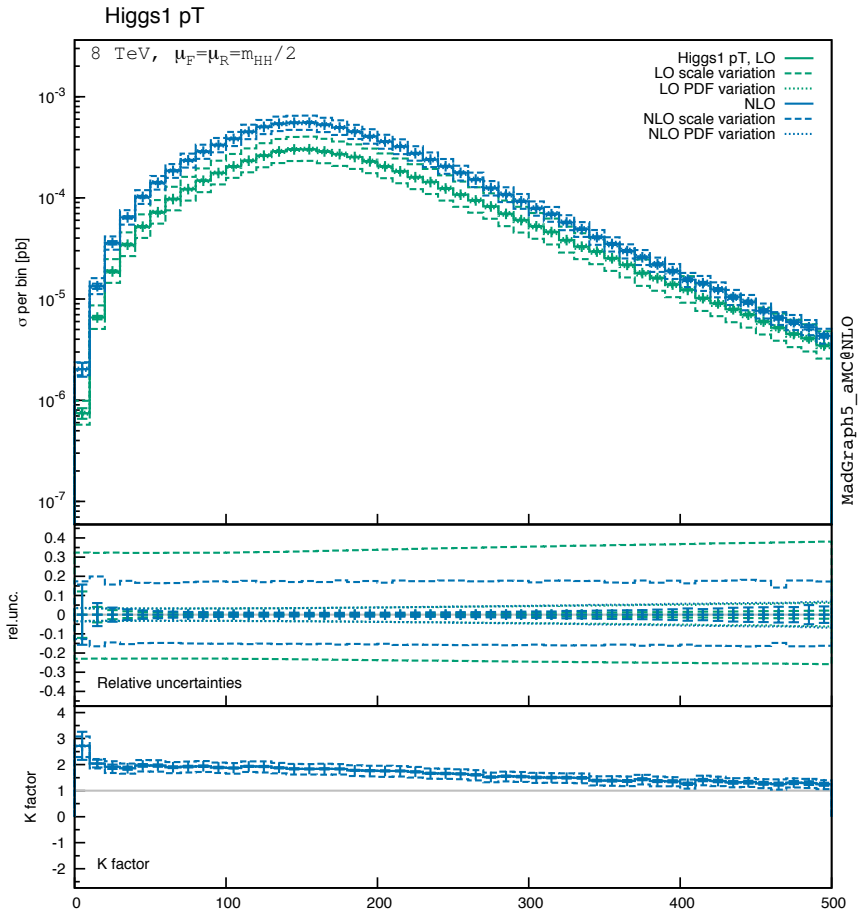

Figure 112: Transverse momentum distribution of the leading Higgs boson in GeVfor $pp \to hh$ using `Madgraph5_aMC@NLO + Pythia8` at NLO with the $\text{FT}_{\text{approx}}$ approximation, for $m_h = 125$ GeV, $m_t = 172.5$ GeV, and $\sqrt{s} = 8$ TeV. The scales are chosen to be $\mu_R = \mu_F = M_{hh}/2$. Scale and PDF uncertainties are added linearly in the distribution. The $K-$factor is defined as the ratio between NLO and LO cross sections.

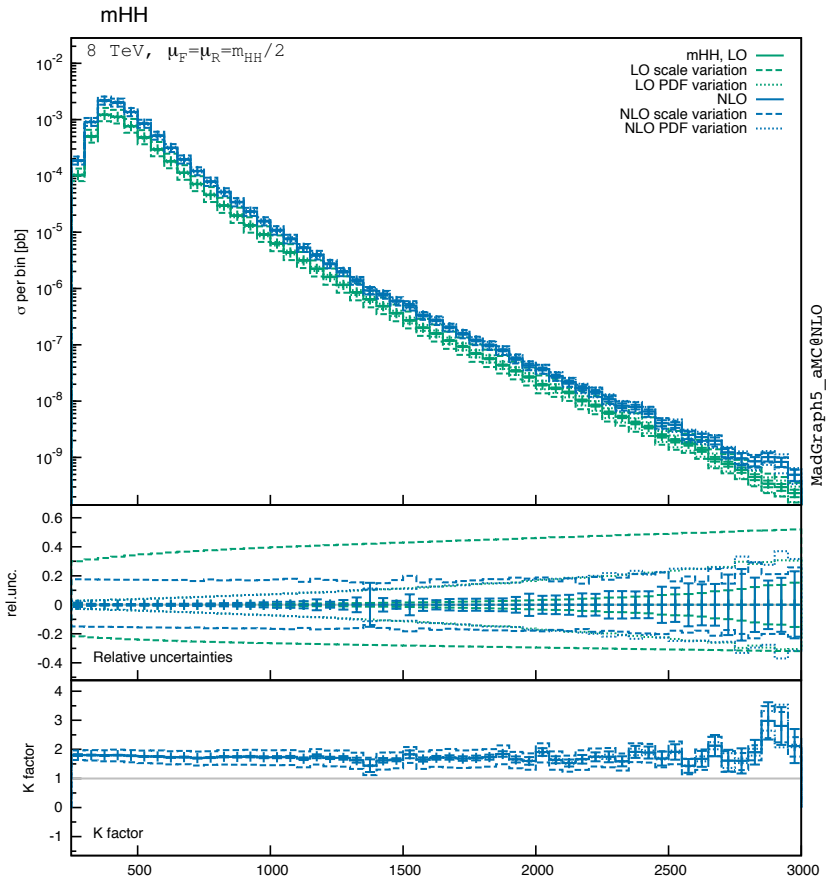

Figure 113: Invariant di-Higgs boson mass differential distribution in GeVfor $pp \to hh$ using `Madgraph5_aMC@NLO + Pythia8` at NLO with the $\text{FT}_{\text{approx}}$ approximation, for $m_h = 125$ GeV, $m_t = 172.5$ GeV, and $\sqrt{s} = 8$ TeV. The scales are chosen to be $\mu_R = \mu_F = M_{hh}/2$. Scale and PDF uncertainties are added linearly in the distribution. The $K-$factor is defined as the ratio between NLO and LO cross sections.

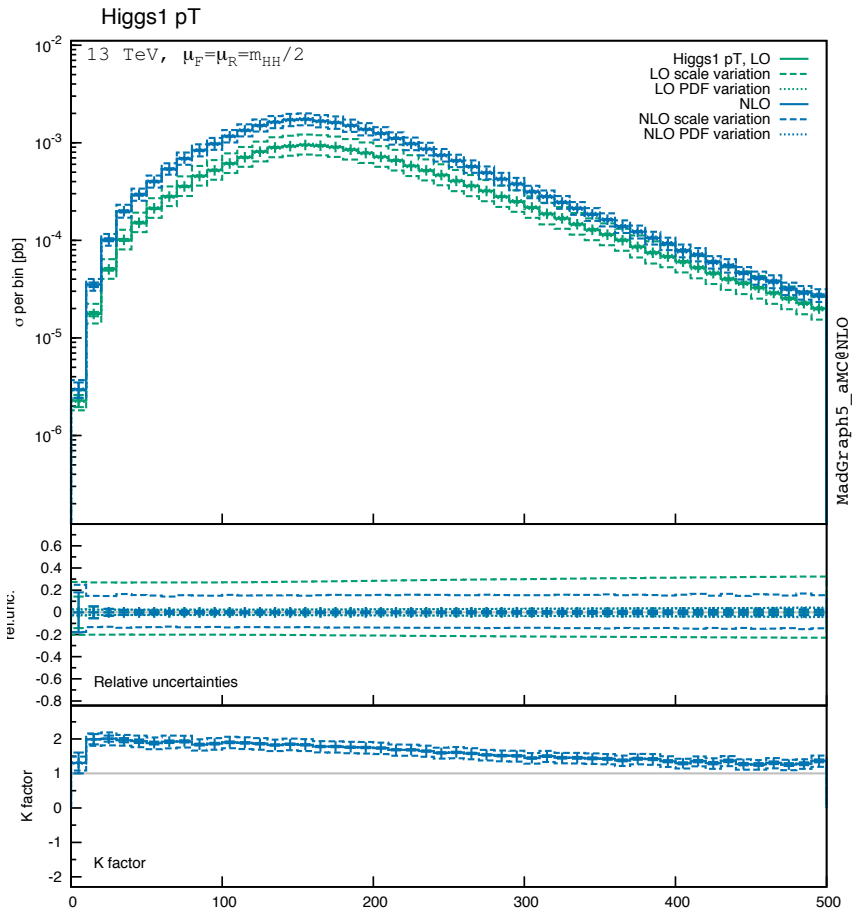

Figure 114: Transverse momentum distribution of the leading Higgs boson in GeVfor $pp \to hh$ using `Madgraph5_aMC@NLO + Pythia8` at NLO with the $\text{FT}_{\text{approx}}$ approximation, for $m_h = 125$ GeV, $m_t = 172.5$ GeV, and $\sqrt{s} = 13$ TeV. The scales are chosen to be $\mu_R = \mu_F = M_{hh}/2$. Scale and PDF uncertainties are added linearly in the distribution. The $K-$factor is defined as the ratio between NLO and LO cross sections.

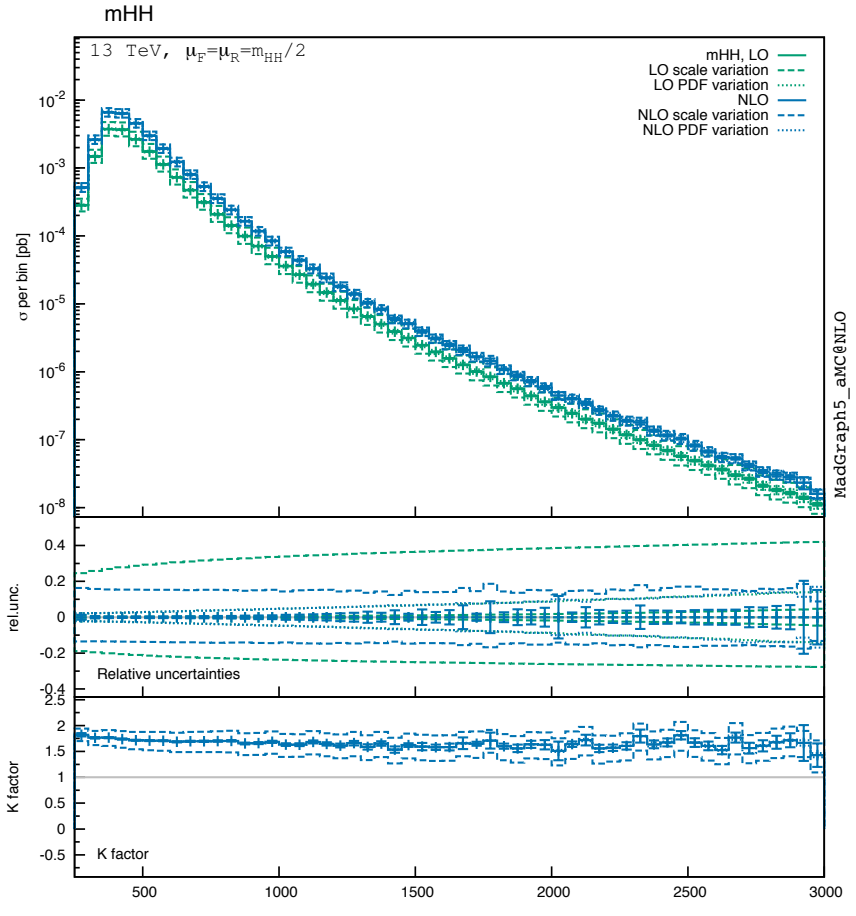

Figure 115: Invariant di-Higgs boson mass differential distribution in GeVfor $pp \to hh$ using `Madgraph5_aMC@NLO + Pythia8` at NLO with the $\text{FT}_{\text{approx}}$ approximation, for $m_h = 125$ GeV, $m_t = 172.5$ GeV, and $\sqrt{s} = 13$ TeV. The scales are chosen to be $\mu_R = \mu_F = M_{hh}/2$. Scale and PDF uncertainties are added linearly in the distribution. The $K-$factor is defined as the ratio between NLO and LO cross sections.

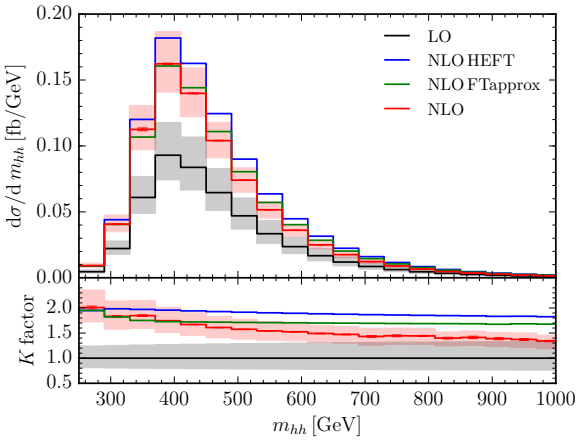

Figure 116: Invariant di-Higgs boson mass distribution for various approximations, taken from [437]. The red curves include the complete m_t dependent NLO calculation. The uncertainty is computed by varying the scales by a factor 2 around $M_{hh}/2$. The Higgs boson mass is chosen to be $m_h = 125$ GeV and $m_t = 173$ GeV, the centre of mass energy is $\sqrt{s} = 14$ TeV.

mass M_{hh}-distribution in Figure 116 and for the leading Higgs boson transverse momentum p_{T,h_1} in Figures 117 and 118.

While the $\mathrm{FT}_{\mathrm{approx}}$ scheme provides a reasonable approximation in the low energy regime within uncertainties, the virtual corrections in the finite m_t limit significantly soften the high energy events compared to the $\mathrm{FT}_{\mathrm{approx}}$ approximation, see Figure 116. These corrections can be as big as 30% and a corresponding reweighting or associated uncertainty needs to be included in analyses that particularly focus on the phase space region $m_{hh} \gtrsim 400$ GeV. The full NLO QCD corrections have a significant effect on the p_T distribution (both the distribution of the leading-p_T Higgs boson, p_{T,h_1}, and the one of any Higgs boson, $p_{T,h}$), as can be seen in Figs. 117 - 119. Both the HEFT and $\mathrm{FT}_{\mathrm{approx}}$approximation fail to reproduce the distribution above the top mass.

The leading jet transverse momentum and the transverse momentum of the di-Higgs system are also not well approximated by a rescaling of the LO results. It should be noted that the leading jet transverse momentum distribution is only known to leading order precision and should be considered with care by including LO uncertainties. For the $p_T(hh)$ distribution, resummed results at NLL+NLO, including the full NLO mass dependence in the $p_T(hh) \to 0$ region, have been obtained recently [455].

Other uncertainties of equal importance become particularly apparent from investigating different shower and matching/merging approaches that we detail in the following. The comparison we detail in the following is based on the MC@NLO calculation that appears in [445] generated using `MadGraph5_aMC@NLO` [54,364] and the merged calculation of [456] using `OpenLoops` matrix elements [247]. All the results use the `HERWIG++` general-purpose Monte Carlo for the parton shower [306,313,457–459]. The Higgs bosons are taken to be stable and hadronization and the underlying event simulation is turned off. The central factorization/renormalization scale for both calculations is chosen to be $\mu_0 = M_{hh}/2$. This scale is varied between $\mu = \mu_0/2$ and $\mu = 2\mu_0$ in the merged calculation. Furthermore, the merging scales used for the MLM procedure were varied in the range 40-90 GeV in steps of 10 GeV and a uniform smooth function, as described in [456], of widths $\epsilon = 10, 20, 30$ GeV is used.

We present comparisons of the MC@NLO samples, labelled 'mc@nlo', the merged calculation, labelled 'mlm' and the pure leading-order calculation, labelled 'shower', all showered with `HERWIG++` in Figs. 120 and 121. We show, respectively, distributions for the transverse momentum and rapidity of (any) single Higgs boson, the transverse momentum of the hardest jet, the invariant mass of the di-Higgs boson pair, the di-Higgs boson transverse momentum and the separation between the Higgs bosons. All

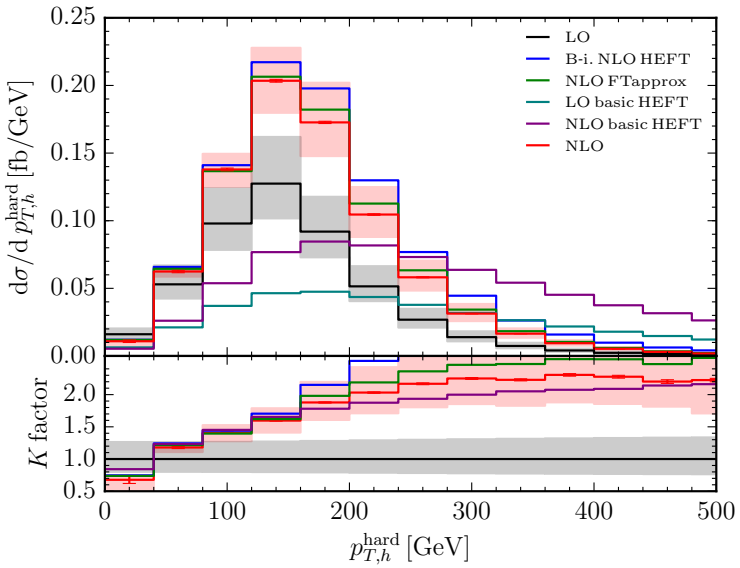

Figure 117: Transverse momentum distribution of the leading Higgs boson in GeVfor $pp \to hh$ at NLO with the full top mass dependence, taken from [438], for $m_h = 125$ GeV, $m_t = 173$ GeV, and $\sqrt{s} = 14$ TeV. The scales are chosen to be $\mu_R = \mu_F = M_{hh}/2$.

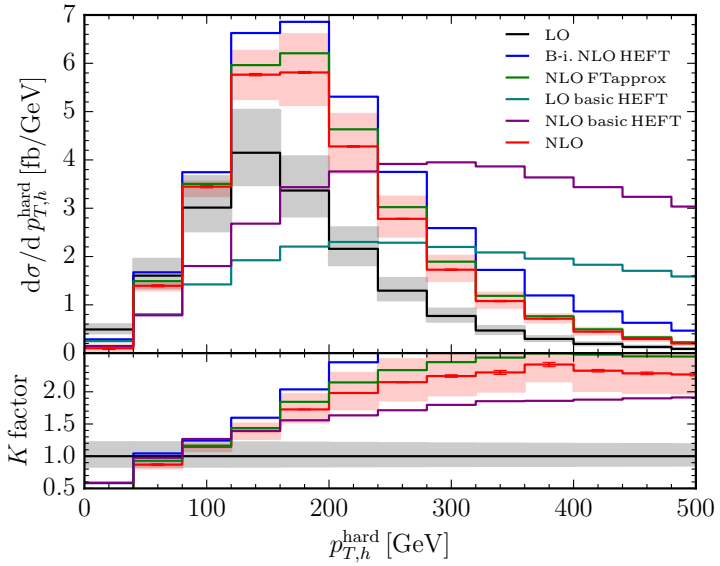

Figure 118: Transverse momentum distribution of the leading Higgs boson in GeVfor $pp \to hh$ at NLO with the full top mass dependence, taken from [438], for $m_h = 125$ GeV, $m_t = 173$ GeV, and $\sqrt{s} = 100$ TeV. The scales are chosen to be $\mu_R = \mu_F = M_{hh}/2$.

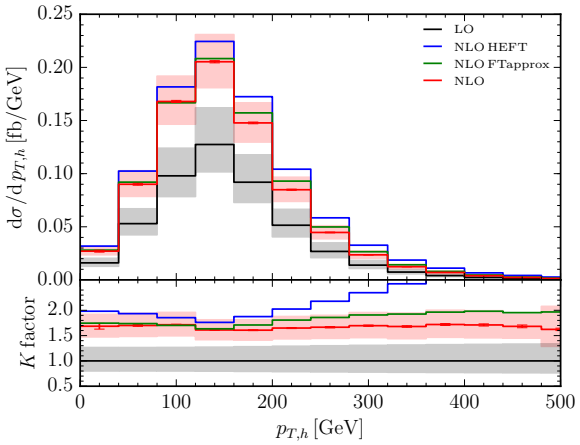

Figure 119: $p_{T,h}$ distribution for various approximations, taken from [437]. The red curves include the complete m_t dependent NLO calculation. The uncertainty is computed by varying the scales by a factor 2 around $M_{hh}/2$. The Higgs boson mass is chosen to be $m_h = 125$ GeV and $m_t = 173$ GeV, the centre of mass energy is $\sqrt{s} = 14$ TeV.

distributions are normalized to unity. The di-Higgs boson invariant mass and separation between the Higgs bosons, as well as the single Higgs observables, are in good agreement within the uncertainties of the merged calculation indicated by the band. There exists a discrepancy in the di-Higgs transverse momentum and the transverse momentum of the hardest jet. One of the reasons that could explain this effect is the difference in the choice of the dynamical starting scale of the shower Q. Figure 122 provides the differential distribution of the hh production cross section as function of Q. We can clearly see that the choice of the scale in the MC@NLO sample differs from MLM sample. This observation suggests that further assessment of the systematics owing to the parton shower should be performed, a task left to future studies.

I.7.4 Benchmark BSM scenarios

In this section we propose BSM models recommended for study in di-Higgs boson production, assuming the two final state Higgs bosons are SM-like. We do not consider the production of two different Higgs particles, such as AH, since these cross sections are highly model-dependent [460–462] and typically suppressed compared to the production of the SM-like Higgs, making generic predictions difficult.

The benchmarks have been chosen based on the following criteria:

- They can by directly related to other (e.g. single Higgs) measurements.
- Their signatures cover resonant and non-resonant production modes and in the former case are distinguishable from each other and from the SM.

We will adopt the Effective Field Theory framework for non-resonant production and advocate the singlet-extended SM and 2HDM for initial studies of resonant di-Higgs final states.

I.7.4.a Effective Field Theory

If no new light particles are observed at the LHC and there are no observable resonances in di-Higgs boson production, then an effective field theory approach is useful and well-motivated. The phenomenologically relevant terms we consider for double Higgs boson production in gg fusion are (written in terms of the physical Higgs boson field, h) [463]

$$L \overset{LO}{=} L_{SM} + \left(c_g \frac{h}{v} + c_{gg} \frac{h^2}{2v^2} \right) \frac{g_s^2}{4} G^A_{\mu\nu} G^{A,\mu\nu} - \frac{h}{v} \Sigma_f \Sigma_{ij} \sqrt{m_{f_i} m_{f_j}} [\delta y_f]_{ij} \overline{f}_i f_j$$

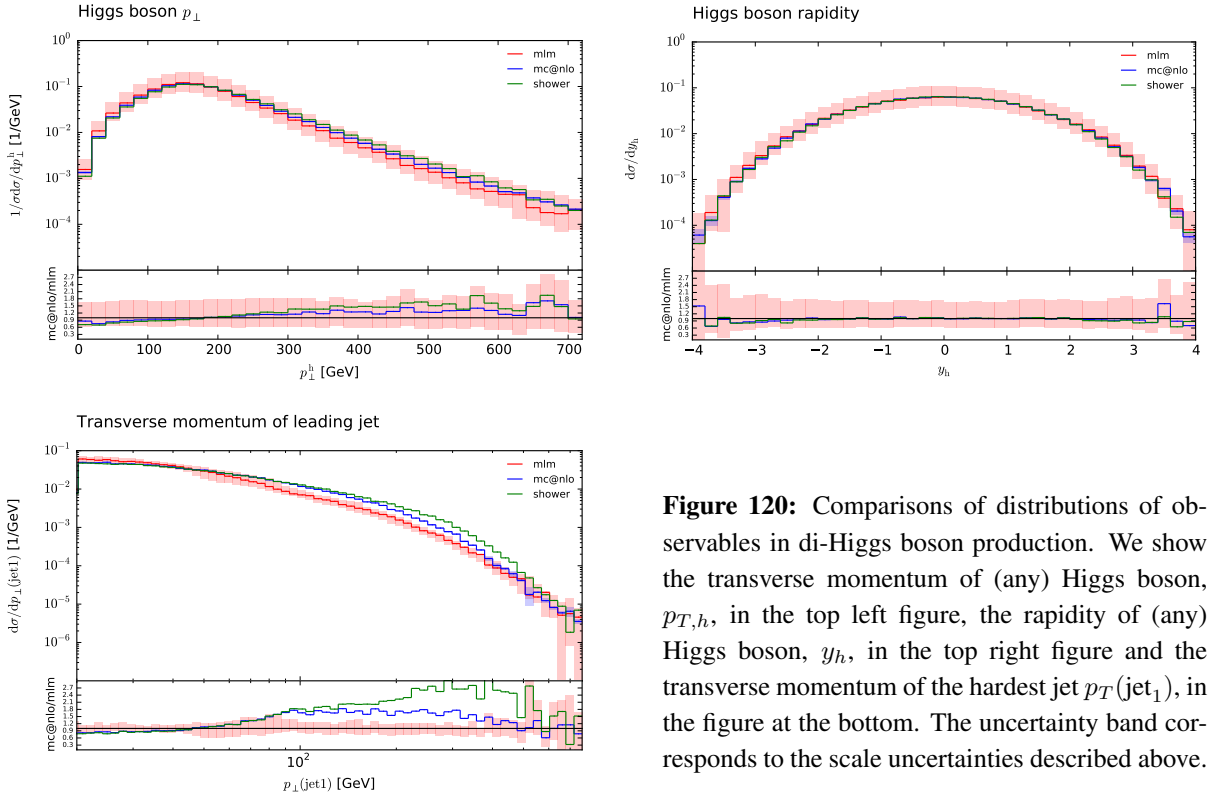

Figure 120: Comparisons of distributions of observables in di-Higgs boson production. We show the transverse momentum of (any) Higgs boson, $p_{T,h}$, in the top left figure, the rapidity of (any) Higgs boson, y_h, in the top right figure and the transverse momentum of the hardest jet $p_T(\text{jet}_1)$, in the figure at the bottom. The uncertainty band corresponds to the scale uncertainties described above.

$$
\begin{aligned}
& -\frac{h^2}{2v^2}\Sigma_f\Sigma_{ij}\sqrt{m_{f_i}m_{f_j}}[y_f^{(2)}]_{ij}\left[\overline{f}_{iR}f_{jL}+hc\right]+\delta\lambda_3 h^3+L_{CPV} \\
L_{CPV} \;=\; & \left(\tilde{c}_g\frac{h}{v}+\tilde{c}_{gg}\frac{h^2}{2v^2}\right)\frac{g_s^2}{4}G^A_{\mu\nu}\tilde{G}^{A,\mu\nu} \\
& -\frac{h}{v}\Sigma_f\Sigma_{ij}\sqrt{m_{f_i}m_{f_j}}[\delta y_f]_{ij}\left\{\left(\cos\phi^f_{ij}-1\right)\overline{f}_i f_j - i\sin\phi^f_{ij}\overline{f}_i\gamma_5 f_j\right\}, \qquad \text{(I.7.9)}
\end{aligned}
$$

where i,j are generation indices, and the sum over f is over all charged fermion species. A hierarchy between CP-violating and CP-conserving interactions has already been established [464, 465] and for simplicity we assume CP conservation and flavour diagonal Higgs boson couplings, leading to the Lagrangian relevant for di-Higgs boson production,

$$
\begin{aligned}
L \;=\; & L_{SM}+\left(c_g\frac{h}{v}+c_{gg}\frac{h^2}{2v^2}\right)\frac{g_s^2}{4}G^A_{\mu\nu}G^{A,\mu\nu}-\frac{h}{v}\Sigma_f\Sigma_i m_{f_i}[\delta y_f]_i\overline{f}_i f_i \\
& -\frac{h^2}{2v^2}\Sigma_f\Sigma_i m_{f_i}[y_f^{(2)}]_i\overline{f}_i f_i+\delta\lambda_3 h^3\,. \qquad \text{(I.7.10)}
\end{aligned}
$$

We do not consider enhanced b couplings, since in order to be relevant for double Higgs boson production, the enhancement must be extremely large[I.46].

The inputs in this realization of the EFT can thus be taken in general as,

– c_g, c_{gg}, δy_t, $y_t^{(2)}$, $\delta\lambda_3$ Non-Linear EFT

which can be reduced to

– c_g, δy_t, $\delta\lambda_3$, $y_t^{(2)}$ Linear EFT

[I.46] See for example, Figure 6 in Ref. [466].

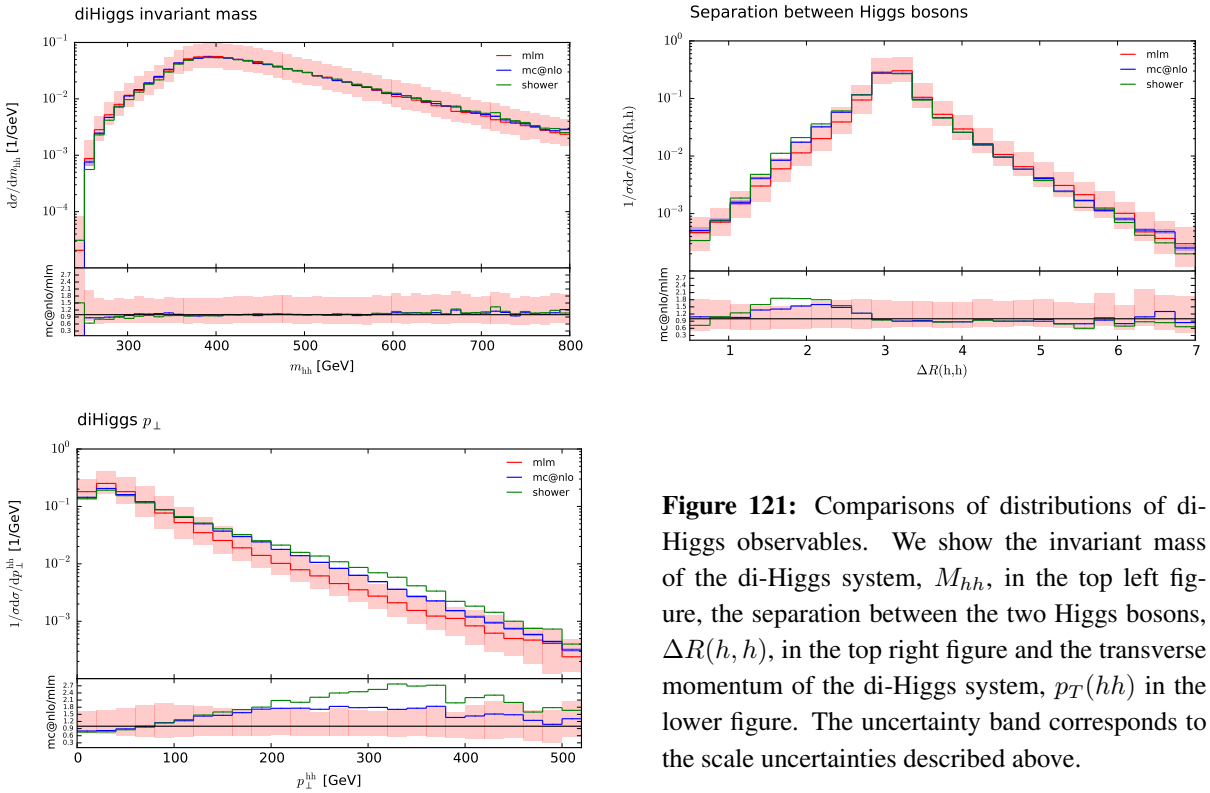

Figure 121: Comparisons of distributions of di-Higgs observables. We show the invariant mass of the di-Higgs system, M_{hh}, in the top left figure, the separation between the two Higgs bosons, $\Delta R(h,h)$, in the top right figure and the transverse momentum of the di-Higgs system, $p_T(hh)$ in the lower figure. The uncertainty band corresponds to the scale uncertainties described above.

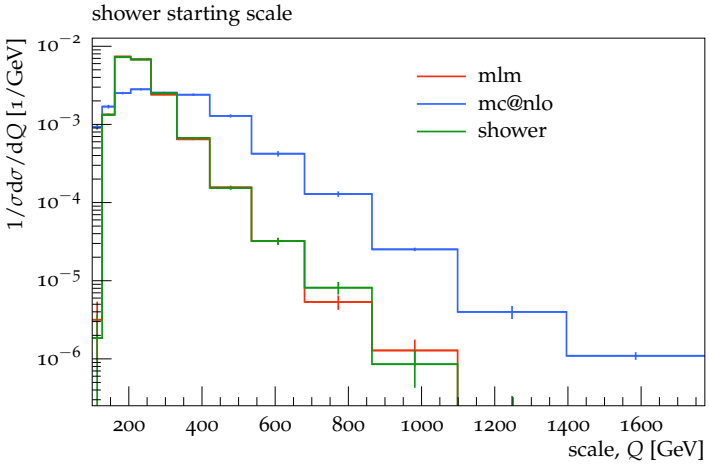

Figure 122: The dynamical starting scale for the HERWIG++ shower used in each of the calculations.

in the linear realization of EWSB, where the Higgs boson is part of a weak doublet, leading to correlations between the couplings.

Note that a combination of c_g and δy_t is fixed by the requirement that single Higgs boson production has the experimentally observed value,

$$R_h \equiv \frac{\sigma(gg \to h)}{\sigma(gg \to h)_{SM}} \sim \left|1 + 12\pi^2 c_g + \delta y_t\right|^2 . \tag{I.7.11}$$

The couplings c_{gg}, $y_t^{(2)}$ and $\delta\lambda_3$ cannot be probed in single Higgs boson production, but require measurement of the di-Higgs rate and distributions [467–470].

A fit to the total cross section in terms of the EFT coefficients shown here has been given in Table 61 and is detailed in a separate note [471], (a similar procedure is performed in Ref. [468]). Those references construct a cross section fit in terms of effective Higgs boson couplings, combining the relevant terms in I.7.10 as:

$$L^{hh} = \frac{1}{2}\partial_\mu h \partial^\mu h - \frac{m_h^2}{2}h^2 - \kappa_\lambda \lambda_{SM} v h^3 \\ - \frac{m_t}{v}\left(v + \kappa_t h + \frac{c_2}{v}hh\right)\left(\bar{t}_L t_R + h.c.\right) + \frac{\alpha_s}{12\pi v}\left(c_{1g}h - \frac{c_{2g}}{2v}hh\right)G^A_{\mu\nu}G^{A,\mu,\nu}\,. \quad \text{(I.7.12)}$$

The SM limit is $\kappa_2 = \kappa_\lambda = 1$ and $c_2 = c_{1g} = c_{2g} = 0$. This fit can be straightforwardly mapped onto the EFT parameters of Eq. (I.7.9) via the identities

$$c_g = \frac{c_{1g}}{12\pi^2}\,, \quad c_{gg} = -\frac{c_{2g}}{12\pi^2}\,, \quad y_t^{(2)} = 2c_2\,, \quad \delta y_t = (\kappa_t - 1)\,, \quad \delta\lambda_3 = -v(\kappa_\lambda - 1)\lambda_{SM}\,. \quad \text{(I.7.13)}$$

Further information on the EFT coefficients can be found from hh production by noting that different EFT operators have different kinematic dependences. The LO box and triangle diagram exactly cancel each other at threshold in the SM. This implies that $d\sigma/dM_{hh}$ is most sensitive to variations in κ_t and κ_λ at threshold, while the dependence on κ_λ is suppressed at high partonic energies. The NLO corrections to the EFT predictions for double Higgs boson production have been investigated in the large m_t limit Ref. [472], with the conclusion that the K factor of the EFT shows little kinematic dependence and little dependence on the effective couplings, however with the same caveats as mentioned in Secs. I.7.2 and I.7.3.

We can take advantage of this property of the K-factors, approximating the ratio between the cross sections obtained for different EFT parameters and the SM cross section with the corresponding LO ratio:

$$R_{hh} \equiv \frac{\sigma_{hh}}{\sigma_{hh}^{SM}} \overset{LO}{=} A_1\kappa_t^4 + A_2 c_2^2 + (A_3\kappa_t^2 + A_4 c_g^2)\kappa_\lambda^2 + A_5 c_{2g}^2 + (A_6 c_2 + A_7\kappa_t\kappa_\lambda)\kappa_t^2 \\ + (A_8\kappa_t\kappa_\lambda + A_9 c_g\kappa_\lambda)c_2 + A_{10}c_2 c_{2g} + (A_{11}c_g\kappa_\lambda + A_{12}c_{2g})\kappa_t^2 \\ + (A_{13}\kappa_\lambda c_g + A_{14}c_{2g})\kappa_t\kappa_\lambda + A_{15}c_g c_{2g}\kappa_\lambda\,. \quad \text{(I.7.14)}$$

The A_i coefficients are extracted from a simultaneous fit, based on the maximization of a likelihood, to the cross sections obtained from a LO simulation and provided in Table 61. A detailed study of theoretical uncertainties was performed in Ref. [471]. The uncertainties related to PDF and α_S variations induces less than a 2% variation in the A_i values.

In general, M_{hh} is a sensitive variable for differentiating the effects of the different EFT coefficients. In the vicinity of the SM limit the utility of this approach, however, is limited by the small di-Higgs rate, although it can nevertheless provide essential additional information on the various effective couplings, in particular in the case of an enhanced cross section. There are large correlations, typically requiring a global fit rather than a fit to a single EFT coefficient [468, 473]. To this end, the analysis of [473] divides kinematic points into 12 clusters, scanning over a range of EFT coefficients, where within the clusters the dependence on the kinematic parameters is similar. The clusters have clear kinematic differences between them, particularly in the peak structure of the M_{hh} distributions. Scanning over a range of EFT coefficients this procedure allows us to formulate a set of benchmark choices that exhibit a particularly interesting di-Higgs phenomenology and to exploit the kinematical particularities of a large portion of the parameter space with a limited number of analyses. These recommendations are given in Table 62. For the particularly interesting case for which the only non-zero EFT coefficient is κ_λ, we have the results in Table 63, that give the relative modification compared to the SM at NNLL [439].

Table 61: Values of A_i parameters for Eq. (I.7.14) [471].

$\sqrt{s}$	7 TeV	8 TeV	13 TeV	14 TeV	100 TeV
A_1	2.21	2.18	2.09	2.08	1.90
A_2	9.82	9.88	10.15	10.20	11.57
A_3	0.33	0.32	0.28	0.28	0.21
A_4	0.12	0.12	0.10	0.10	0.07
A_5	1.14	1.17	1.33	1.37	3.28
A_6	-8.77	-8.70	-8.51	-8.49	-8.23
A_7	-1.54	-1.50	-1.37	-1.36	-1.11
A_8	3.09	3.02	2.83	2.80	2.43
A_9	1.65	1.60	1.46	1.44	3.65
A_{10}	-5.15	-5.09	-4.92	-4.90	-1.65
A_{11}	-0.79	-0.76	-0.68	-0.66	-0.50
A_{12}	2.13	2.06	1.86	1.84	1.30
A_{13}	0.39	0.37	0.32	0.32	0.23
A_{14}	-0.95	-0.92	-0.84	-0.83	-0.66
A_{15}	-0.62	-0.60	-0.57	-0.56	-0.53

Table 62: Coefficient choices of EFT benchmarks.

Benchmark	κ_λ	κ_t	c_2	c_g	c_{2g}
1	7.5	1.0	-1.0	0.0	0.0
2	1.0	1.0	0.5	-0.8	0.6
3	1.0	1.0	-1.5	0.0	-0.8
4	-3.5	1.5	-3.0	0.0	0.0
5	1.0	1.0	0.0	0.8	-1
6	2.4	1.0	0.0	0.2	-0.2
7	5.0	1.0	0.0	0.2	-0.2
8	15.0	1.0	0.0	-1	1
9	1.0	1.0	1.0	-0.6	0.6
10	10.0	1.5	-1.0	0.0	0.0
11	2.4	1.0	0.0	1	-1
12	15.0	1.0	1.0	0.0	0.0
SM	1.0	1.0	0.0	0.0	0.0

The difference between the R_{hh}^{NNLL} found in Table 63 and the R_{hh} calculated by the LO interpolation and the coefficients of Table 61 does not exceed 5% [471]. This variation is inside the theoretical uncertainty of the cross section normalization (Table 46), and slightly larger that the NLO K-factor uncertainty [472].

In summary, to obtain σ_{hh} in the EFT, we recommend the use of the relation $\sigma_{hh} = R_{hh} \cdot \sigma_{hh}^{SM}$. Here σ_{hh}^{SM} is the most up to date calculation based on NNLO+NNLL, with the associated uncertainties, and R_{hh} is found from Eq. I.7.14. The PDF and α_s uncertainties of A_i was found to be well below 1% and can safely be neglected [471]. The missing order uncertainties on R_{hh} are covered by the ones assigned to σ_{hh}^{SM}.

I.7.4.b Higgs Singlet Model

The Higgs singlet model [474–476] is a simple example where double Higgs boson production can receive large contributions from a resonance. The model contains a Higgs doublet, $\Phi^T = (\phi^+, \tilde{\phi}_0 =$

$\frac{\phi_0+v}{\sqrt{2}}$), and Higgs singlet, $S = \frac{s+\langle S\rangle}{\sqrt{2}}$, and is described by 5 parameters in the potential:

$$V = -m^2\Phi^\dagger\Phi - \mu^2 S^2 + \lambda_1(\Phi^\dagger\Phi)^2 + \lambda_2 S^4 + \lambda_3\Phi^\dagger\Phi S^2\,, \tag{I.7.15}$$

where a Z_2 symmetry $S \to -S$ and $\Phi \to \Phi$ has been imposed for simplicity. After electroweak symmetry breaking, both $\tilde{\phi}_0$ and S get vacuum expectation values and the physical fields h, H are mixtures of the original fields

$$\begin{aligned} h &= \cos\alpha\,\phi_0 - \sin\alpha\; s \\ H &= \sin\alpha\,\phi_0 + \cos\alpha\, s\,, \end{aligned} \tag{I.7.16}$$

and we assume $M_H > m_h$ in the following. The LO trilinear Higgs boson couplings are,

$$\lambda_{hhh} = -\frac{3m_h^2}{v}\left(\cos^3\alpha - \tan\beta\sin^3\alpha\right) \tag{I.7.17}$$

$$\lambda_{Hhh} = -\frac{m_h^2}{v}\sin(2\alpha)(\cos\alpha + \sin\alpha\tan\beta)\left(1 + \frac{M_H^2}{2m_h^2}\right). \tag{I.7.18}$$

The NLO relations for the trilinear couplings are in Ref. [477].

The input parameters can be taken as (see e.g. [478]),

– $m_h = 125$ GeV, M_H, $\cos\alpha$, v, $\tan\beta = v/\langle s\rangle$,

and the Higgs boson branching ratios to SM particles, X_{SM}, are:

$$\begin{aligned} \Gamma(h \to X_{SM}X_{SM}) &= \cos^2\alpha\,\Gamma(h \to X_{SM}X_{SM})_{SM} \\ \Gamma(H \to X_{SM}X_{SM}) &= \sin^2\alpha\,\Gamma(H \to X_{SM}X_{SM})_{SM} \\ \Gamma_H &= \sin^2\alpha\,\Gamma_{H,SM}(M_H) + \Gamma(H \to hh) \\ \Gamma_h &= \cos^2\alpha\,\Gamma_{h,SM}(m_h)\,, \end{aligned} \tag{I.7.19}$$

where $\Gamma_{H,SM}(M_H)$ are the Standard Model Higgs boson widths evaluated at M_H which are completely fixed in terms of $\tan\beta, M_H$, and $\cos\alpha$. ATLAS [479] considered the restrictions from Higgs boson coupling measurements on the parameters of the singlet model and found $|\cos\alpha| > 0.94$, where we omit the possibility of the H decaying to some new invisible particles. The heavier Higgs boson contributes to the W mass, which imposes a further limit on $\cos\alpha$ as a function of M_H [480, 481]. The branching ratio, $H \to hh$, can be quite large, $\mathcal{O} \sim 20-30\%$, leading to large effects in di-Higgs boson production. Values of the LO branching ratios and widths for $H \to hh$ for representative values of the parameters are shown in Figures 123 and 124. The maximum and minimum allowed branching ratios, consistent with experimental restrictions, are shown in Table 64 as a function of M_H.

Table 63: Values for $\sigma_{\text{NNLL}}/\sigma_{\text{NNLL},SM}$ for non-SM values of the trilinear Higgs boson coupling, with all other EFT couplings set to their SM values [439].

$R_{hh}^{\text{NNLL}} \equiv \sigma_{\text{NNLL}}/\sigma_{\text{NNLL},SM}(\kappa_\lambda)$					
κ_λ	-1	-0.5	0	0.5	2
$\sqrt{s} = 7$ TeV	4.17	3.12	2.24	1.53	0.452
$\sqrt{s} = 8$ TeV	4.09	3.06	2.21	1.52	0.455
$\sqrt{s} = 13$ TeV	3.85	2.92	2.13	1.49	0.466
$\sqrt{s} = 14$ TeV	3.82	2.90	2.12	1.49	0.467
$\sqrt{s} = 100$ TeV	3.39	2.62	1.97	1.43	0.492

Table 64: Maximal and minimal allowed branching ratios, consistent with experimental restrictions, in the singlet model, taken at the maximal allowed value of $|\sin\alpha|$ for $H \to hh$. Note that the minimal values for the branching ratio stem from $\sin\alpha \leq 0$. Decay branching ratios correspond to the branching ratios of a SM Higgs of the same mass, rescaled by $1 - \text{BR}(H \to h\,h)$ [480, 482].

M_H(GeV)	$\lvert\sin\alpha\rvert_{max}$	$BR(H \to h\,h)_{min}$	$BR(H \to h\,h)_{max}$
255	0.31	0.09	0.27
260	0.34	0.11	0.33
265	0.33	0.13	0.36
280	0.32	0.17	0.40
290	0.31	0.18	0.40
305	0.30	0.20	0.40
325	0.29	0.21	0.40
345	0.28	0.22	0.39
365	0.27	0.21	0.36
395	0.26	0.20	0.32
430	0.25	0.19	0.30
470	0.24	0.19	0.28
520	0.23	0.19	0.26
590	0.22	0.19	0.25
665	0.21	0.19	0.23
770	0.20	0.19	0.23
875	0.19	0.19	0.22
920	0.18	0.19	0.22
≥ 975	0.17	0.19	0.21

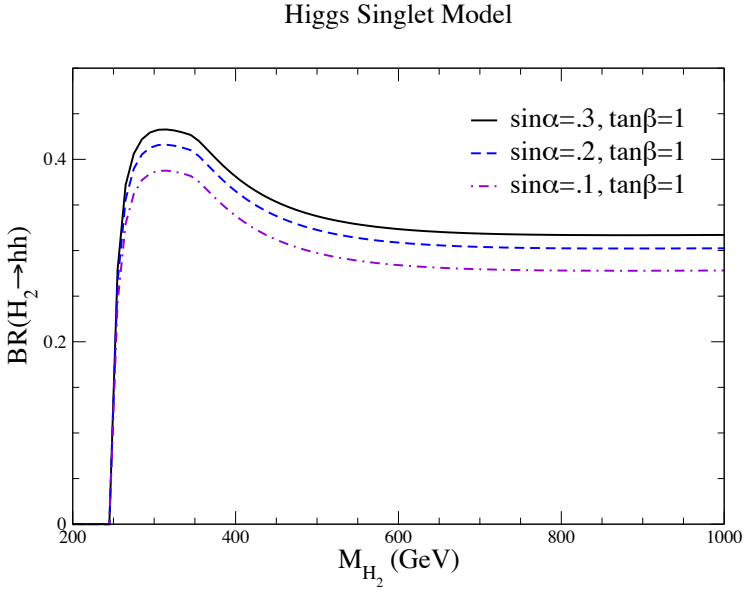

Figure 123: Leading order branching ratio of $H \to hh$ in the singlet model for representative values of the parameters.

The M_{hh} distributions in the singlet model show clear resonance peaks as illustrated in Figure 125. The NLO QCD corrections to double Higgs boson production can be found in the large m_t limit [483]

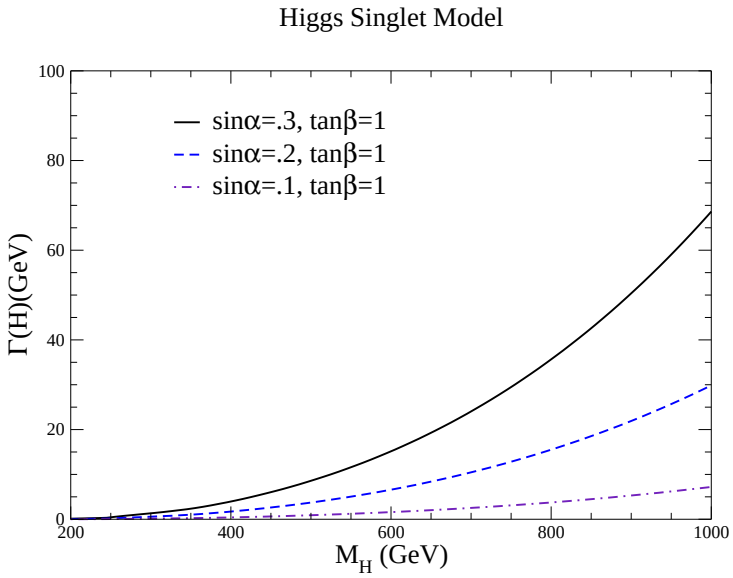

Figure 124: Total leading order width of $H \to hh$ in the singlet model for representative values of the parameters.

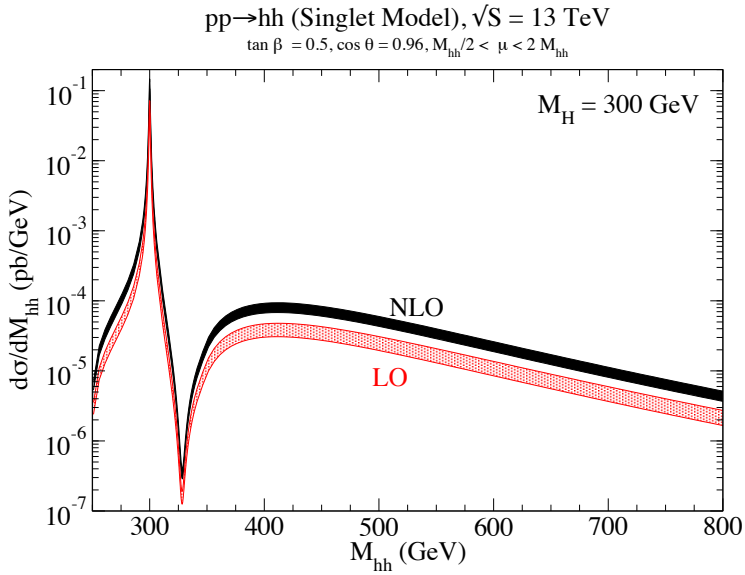

Figure 125: Invariant di-Higgs boson mass differential distribution for $pp \to hh$ in the singlet model with a heavy Higgs with $M_H = 300$ GeV.

and give a K factor which is approximately the same as in the Standard Model. For $M_H \sim 2m_h$, the rate is dominated by the resonance contribution which is implemented in the code sHDECAY [484]. For fixed $\sin\alpha = 0.28$ and $\tan\beta = 0.5$, the predictions for a range of heavy Higgs boson masses are given in Tabs. 65-68.

The enhancements of the di-Higgs cross section in the singlet model can be as large as factors of $\mathcal{O}(10-20)$ and are typical of those which can be obtained in models with a heavy Higgs particle with a mass near $2m_h$ and a large branching ratio to hh, such as the 2HDM, the MSSM, or the NMSSM. It is interesting to tabulate the largest allowed values of the di-Higgs cross section in the singlet model using

Table 65: NLO cross sections in the singlet model for fixed $\sin\theta = 0.28$, $\tan\beta = 0.50$ and $\sqrt{s} = 14$ TeV, with $\mu = M_{hh}/2$ [483].

M_H (GeV)	Cross Section (fb)	PDF (%)	α_s (%)	scale (%)
260	278.06	2.2	2.0	+ 18.9 -14.8
275	311.39	2.2	2.0	+ 18.8 -14.9
300	303.35	2.2	2.0	+ 18.9 -14.9
325	290.68	2.2	2.0	+ 18.7 -14.9
350	307.86	2.3	1.9	+ 18.7 -15.0
400	286.17	2.4	1.9	+ 18.6 -15.0
450	217.24	2.5	1.9	+ 18.4 -15.1
500	163.98	2.7	1.8	+ 18.4 -15.1
600	103.53	2.7	1.8	+ 18.3 -15.1
700	76.07	2.8	1.8	+ 18.2 -15.1
750	68.32	2.8	1.8	+ 18.2 -15.1
800	62.86	2.8	1.8	+ 18.2 -15.1
900	56.04	2.7	1.9	+ 18.3 -15.1
1000	52.28	2.6	1.9	+ 18.3 -15.0
1100	50.06	2.7	1.9	+ 18.3 -15.1
1200	48.71	2.7	1.9	+ 18.3 -15.0
1300	47.84	2.6	1.9	+ 18.3 -15.0
1400	47.22	2.6	1.9	+ 18.3 -15.0
1500	46.81	2.6	1.9	+ 18.3 -15.0
1600	46.48	2.6	1.9	+ 18.3 -15.0
1800	46.03	2.6	1.9	+ 18.3 -15.0
2000	45.71	2.6	1.9	+ 18.3 -15.0
2250	45.37	2.6	1.9	+ 18.3 -15.0
2500	45.03	2.6	1.9	+ 18.3 -15.0
2750	44.67	2.6	1.9	+ 18.3 -15.0
3000	44.25	2.6	1.9	+ 18.3 -15.0

the restrictions of Table 64. These cross sections are shown in Table 69-72.

I.7.4.c 2 Higgs Doublet Model

The 2 Higgs doublet model (2HDM) is a simple extension of the SM which can exhibit large resonance effects. The 2HDM has 5 physical Higgs bosons: 2 neutral scalars, h^0, H^0, a pseudo-scalar, A, and a charged Higgs boson pair $H^\pm$, In general, 2HDMs have Higgs mediated tree level flavour changing neutral currents (FCNCs), which must be suppressed. Most 2HDMs eliminate FCNCs by imposing a discrete Z_2 symmetry in which the fermions of a given charge only couple to one of the Higgs doublets. The two most familiar versions are the type I model, in which all of the fermions couple to the same Higgs doublet, and the type II model, in which the $Q = 2/3$ quarks couple to one doublet and the $Q = -1/3$ quarks and leptons couple to the other. The type II model is the Higgs sector of the MSSM. Two additional versions interchange the lepton assignments. In the “lepton-specific" model, all of the quarks couple to one doublet while the leptons couple to the other, and in the “flipped" model, the $Q = 2/3$ quarks and leptons couple to one doublet and the $Q = -1/3$ quarks couple to the other. All four of these models have been extensively studied [485].

The couplings of the Higgs bosons to fermions are described by two free parameters. The ratio of vacuum expectation values of the two Higgs doublets is $\tan\beta \equiv \frac{v_2}{v_1}$, and the mixing angle which

Table 66: NLO cross sections in the singlet model for fixed $\sin\theta = 0.28$, $\tan\beta = 0.50$ and $\sqrt{s} = 13$ TeV, with $\mu = M_{hh}/2$ [483].

M_H (GeV)	Cross Section (fb)	PDF (%)	α_s (%)	scale (%)
260	240.06	2.2	2.0	+ 19.2 -15.0
275	268.80	2.2	2.0	+ 19.1 -15.1
300	260.78	2.3	2.0	+ 19.1 -15.1
325	248.87	2.3	1.9	+ 18.9 -15.1
350	262.72	2.4	1.9	+ 18.9 -15.2
400	242.67	2.5	1.9	+ 18.8 -15.2
450	183.37	2.7	1.9	+ 18.6 -15.3
500	137.85	2.7	1.9	+ 18.6 -15.3
600	86.49	2.9	1.9	+ 18.4 -15.3
700	63.49	2.9	1.9	+ 18.4 -15.3
750	57.05	2.9	1.8	+ 18.4 -15.3
800	52.49	2.9	1.9	+ 18.4 -15.3
900	46.86	2.9	1.9	+ 18.5 -15.3
1000	43.81	2.8	1.9	+ 18.4 -15.3
1100	42.02	2.8	1.9	+ 18.5 -15.3
1200	40.91	2.7	1.9	+ 18.5 -15.2
1300	40.18	2.6	1.9	+ 18.5 -15.2
1400	39.70	2.6	1.9	+ 18.5 -15.2
1500	39.34	2.6	1.9	+ 18.5 -15.2
1600	39.08	2.6	1.9	+ 18.5 -15.2
1800	38.70	2.6	1.9	+ 18.5 -15.2
2000	38.44	2.7	1.9	+ 18.5 -15.2
2250	38.16	2.7	1.9	+ 18.6 -15.2
2500	37.88	2.7	1.9	+ 18.5 -15.2
2750	37.57	2.7	1.9	+ 18.5 -15.2
3000	37.22	2.7	1.9	+ 18.5 -15.2

diagonalizes the neutral scalar mass matrix is α. The couplings of the light (heavy) CP even Higgs boson, h^0 (H^0), to fermions and gauge bosons relative to the Standard Model couplings are given for all four 2HDMs considered here in Table 73 (Table 74).

2HDMs are significantly limited by experimental data. Higgs boson coupling measurements restrict $\cos(\alpha - \beta)$ to be close to the SM limit, $\cos(\alpha - \beta) \sim 0$, while heavy Higgs searches restrict M_{H^0} as a function of $\cos(\alpha - \beta)$ [479]. A set of benchmarks which respect all experimental limits was found in Refs. [462, 486], and representative benchmarks are given in Table 75. The benchmarks were further chosen such that the total rate for di-Higgs boson production is similar to that of the SM. These benchmarks can exhibit significant resonance effects (B1 and B2), while B7 is almost indistinguishable from the SM. The NLO di-Higgs boson invariant mass distributions for these benchmarks are shown in Figure 126. Note that other benchmarks have been proposed in the literature, such as in Ref. [461], where resonant effects can also be important already at the level of the inclusive rate as in their benchmark H-1.

Table 67: NLO cross sections in the singlet model for fixed $\sin\theta = 0.28$, $\tan\beta = 0.50$ and $\sqrt{s} = 8$ TeV, for $\mu = M_{hh}/2$ [483].

M_H (GeV)	Cross Section (fb)	PDF (%)	α_s (%)	scale (%)
260	85.64	2.7	2.1	+ 20.7 -16.5
275	94.39	2.8	2.1	+ 20.6 -16.5
300	89.08	3.0	2.1	+ 20.6 -16.5
325	82.78	3.1	2.0	+ 20.5 -16.6
350	85.29	3.2	2.0	+ 20.4 -16.6
400	75.37	3.3	2.0	+ 20.2 -16.6
450	54.71	3.6	2.0	+ 20.1 -16.7
500	39.82	3.8	2.0	+ 20.0 -16.7
600	24.07	3.9	2.0	+ 19.9 -16.8
700	17.54	4.0	2.0	+ 19.9 -16.8
750	15.82	3.9	2.0	+ 19.9 -16.7
800	14.64	3.9	2.0	+ 19.9 -16.8
900	13.23	3.8	2.0	+ 20.0 -16.7
1000	12.49	3.8	2.1	+ 19.9 -16.7
1100	12.07	3.7	2.0	+ 20.0 -16.7
1200	11.82	3.7	2.0	+ 20.0 -16.7
1300	11.66	3.7	2.0	+ 20.0 -16.7
1400	11.55	3.7	2.0	+ 20.0 -16.6
1500	11.47	3.7	2.0	+ 19.9 -16.7
1600	11.41	3.7	2.0	+ 20.0 -16.7
1800	11.32	3.7	2.0	+ 20.0 -16.6
2000	11.25	3.7	2.0	+ 20.0 -16.7
2250	11.18	3.7	2.0	+ 20.0 -16.6
2500	11.10	3.7	2.0	+ 19.9 -16.6
2750	11.01	3.6	2.0	+ 20.0 -16.7
3000	10.91	3.6	2.0	+ 20.0 -16.7

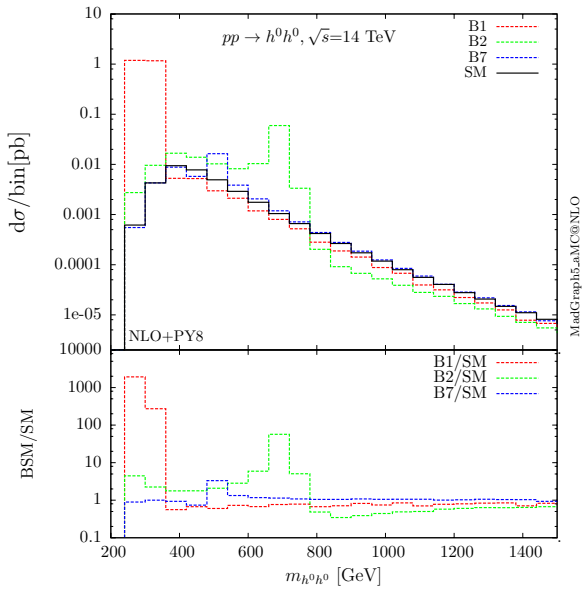

Figure 126: Invariant mass for the $pp \to h^0h^0$ process at NLO using the benchmarks from Table 75 [462] .

Table 68: NLO cross sections in the singlet model for fixed $\sin\theta = 0.28$, $\tan\beta = 0.50$, and $\sqrt{s} = 7$ TeV with $\mu = M_{hh}/2$ [483].

M_H (GeV)	Cross Section (fb)	PDF (%)	α_s (%)	scale (%)
260	62.89	3.0	2.1	+ 21.2 -16.9
275	68.99	3.0	2.1	+ 21.1 -16.9
300	64.40	3.2	2.1	+ 21.0 -16.9
325	59.45	3.2	2.1	+ 20.9 -17.0
350	60.78	3.3	2.1	+ 20.8 -17.0
400	52.85	3.7	2.1	+ 20.7 -17.1
450	37.81	4.0	2.1	+ 20.5 -17.1
500	27.23	4.1	2.1	+ 20.5 -17.2
600	16.28	4.2	2.1	+ 20.3 -17.2
700	11.85	4.2	2.1	+ 20.4 -17.2
750	10.71	4.2	2.1	+ 20.4 -17.2
800	9.93	4.1	2.1	+ 20.3 -17.2
900	9.01	4.1	2.1	+ 20.4 -17.1
1000	8.54	4.0	2.1	+ 20.3 -17.1
1100	8.27	4.0	2.1	+ 20.4 -17.1
1200	8.11	4.0	2.1	+ 20.5 -17.1
1300	8.01	4.0	2.1	+ 20.4 -17.1
1400	7.94	4.0	2.1	+ 20.5 -17.1
1500	7.89	4.0	2.1	+ 20.4 -17.1
1600	7.85	4.0	2.1	+ 20.4 -17.1
1800	7.79	4.0	2.1	+ 20.4 -17.1
2000	7.75	4.0	2.1	+ 20.4 -17.1
2250	7.70	4.0	2.1	+ 20.5 -17.1
2500	7.64	4.0	2.1	+ 20.4 -17.1
2750	7.58	4.0	2.1	+ 20.4 -17.1
3000	7.51	4.0	2.1	+ 20.4 -17.1

Table 69: $\sqrt{s} = 14$ TeV NLO cross sections in the singlet model with parameters chosen to maximize the cross section, with $\mu = M_{hh}/2$ [482].

M_H (GeV)	$\sin\theta$	$\tan\beta$	Cross Section (fb)	PDF (%)	α_s (%)	scale (%)
260	0.31	0.80	365.71	2.1	2.0	+ 19.0 -14.8
275	0.31	0.80	407.56	2.2	2.0	+ 18.9 -14.9
300	0.31	0.80	395.31	2.2	2.0	+ 18.8 -14.9
325	0.27	0.58	279.16	2.2	1.9	+ 18.7 -14.9
350	0.27	0.58	295.73	2.3	1.9	+ 18.7 -14.9
400	0.27	0.58	275.47	2.5	1.9	+ 18.5 -15.1
450	0.24	0.46	169.33	2.5	1.9	+ 18.4 -15.1
500	0.24	0.46	130.40	2.7	1.8	+ 18.3 -15.1
600	0.23	0.37	81.05	2.7	1.8	+ 18.2 -15.1
700	0.21	0.31	58.65	2.7	1.8	+ 18.2 -15.1
750	0.21	0.25	54.15	2.6	1.8	+ 18.3 -15.1
800	0.21	0.25	51.23	2.6	1.9	+ 18.2 -15.1
900	0.19	0.25	45.96	2.6	1.8	+ 18.3 -15.0
1000	0.17	0.23	43.13	2.7	1.9	+ 18.3 -15.0
1100	0.17	0.23	42.39	2.6	1.9	+ 18.3 -15.0
1200	0.17	0.23	41.90	2.6	1.9	+ 18.3 -15.0
1300	0.17	0.23	41.59	2.6	1.9	+ 18.3 -15.0
1400	0.17	0.23	41.38	2.6	1.9	+ 18.3 -15.0
1500	0.17	0.23	41.24	2.6	1.9	+ 18.3 -15.0
1600	0.17	0.23	41.14	2.6	1.9	+ 18.3 -15.0
1800	0.17	0.23	41.00	2.6	1.8	+ 18.3 -15.0
2000	0.17	0.23	40.92	2.6	1.9	+ 18.3 -15.0
2250	0.17	0.23	40.85	2.6	1.9	+ 18.3 -15.0
2500	0.17	0.23	40.81	2.6	1.9	+ 18.3 -15.0
2750	0.17	0.23	40.78	2.6	1.9	+ 18.3 -15.0
3000	0.17	0.23	40.75	2.6	1.9	+ 18.3 -15.0

Table 70: $\sqrt{s} = 13$ TeV NLO cross sections in the singlet model with parameters chosen to maximize the cross section, with $\mu = M_{hh}/2$ [482].

M_H (GeV)	$\sin\theta$	$\tan\beta$	Cross Section (fb)	PDF (%)	α_s (%)	scale (%)
260	0.31	0.80	315.92	2.2	2.0	+ 19.2 -15.0
275	0.31	0.80	351.78	2.2	2.0	+ 19.2 -15.1
300	0.31	0.80	340.05	2.3	2.0	+ 19.1 -15.1
325	0.27	0.58	239.07	2.3	1.9	+ 18.9 -15.1
350	0.27	0.58	252.31	2.4	1.9	+ 18.9 -15.1
400	0.27	0.58	233.65	2.5	1.9	+ 18.7 -15.3
450	0.24	0.46	142.91	2.7	1.9	+ 18.6 -15.3
500	0.24	0.46	109.61	2.7	1.9	+ 18.5 -15.3
600	0.23	0.37	67.81	2.9	1.8	+ 18.4 -15.3
700	0.21	0.31	49.05	2.9	1.9	+ 18.4 -15.3
750	0.21	0.25	45.31	2.9	1.9	+ 18.5 -15.3
800	0.21	0.25	42.90	2.9	1.9	+ 18.4 -15.3
900	0.19	0.25	38.57	2.7	1.9	+ 18.5 -15.3
1000	0.17	0.23	36.24	2.7	1.9	+ 18.4 -15.2
1100	0.17	0.23	35.62	2.7	1.9	+ 18.5 -15.2
1200	0.17	0.23	35.22	2.7	1.9	+ 18.5 -15.2
1300	0.17	0.23	34.96	2.7	1.9	+ 18.5 -15.2
1400	0.17	0.23	34.80	2.7	1.9	+ 18.5 -15.2
1500	0.17	0.23	34.68	2.7	1.9	+ 18.5 -15.2
1600	0.17	0.23	34.60	2.7	1.9	+ 18.5 -15.2
1800	0.17	0.23	34.49	2.7	1.9	+ 18.5 -15.2
2000	0.17	0.23	34.42	2.7	1.9	+ 18.5 -15.2
2250	0.17	0.23	34.37	2.7	1.9	+ 18.5 -15.2
2500	0.17	0.23	34.33	2.7	1.9	+ 18.5 -15.2
2750	0.17	0.23	34.31	2.7	1.9	+ 18.5 -15.2
3000	0.17	0.23	34.29	2.7	1.9	+ 18.5 -15.2

Table 71: $\sqrt{s} = 8$ TeV NLO cross sections in the singlet model with parameters chosen to maximize the cross section, with $\mu = M_{hh}/2$ [482].

M_H (GeV)	$\sin\theta$	$\tan\beta$	Cross Section (fb)	PDF (%)	α_s (%)	scale (%)
260	0.31	0.80	113.38	2.7	2.1	+ 20.8 -16.5
275	0.31	0.80	124.18	2.8	2.1	+ 20.7 -16.5
300	0.31	0.80	116.69	3.0	2.0	+ 20.5 -16.5
325	0.27	0.58	79.42	3.1	2.0	+ 20.4 -16.6
350	0.27	0.58	81.89	3.2	2.0	+ 20.4 -16.6
400	0.27	0.58	72.54	3.3	2.0	+ 20.2 -16.7
450	0.24	0.46	42.59	3.6	2.0	+ 20.1 -16.7
500	0.24	0.46	31.68	3.8	2.0	+ 20.0 -16.7
600	0.23	0.37	19.01	3.9	2.0	+ 19.9 -16.7
700	0.21	0.31	13.79	3.9	2.0	+ 19.9 -16.7
750	0.21	0.25	12.79	3.9	2.0	+ 19.9 -16.7
800	0.21	0.25	12.16	3.8	2.0	+ 19.9 -16.7
900	0.19	0.25	11.07	3.7	2.0	+ 20.0 -16.7
1000	0.17	0.23	10.49	3.7	2.0	+ 19.9 -16.7
1100	0.17	0.23	10.34	3.6	2.0	+ 20.0 -16.6
1200	0.17	0.23	10.26	3.7	2.0	+ 20.0 -16.7
1300	0.17	0.23	10.20	3.7	2.0	+ 19.9 -16.7
1400	0.17	0.23	10.16	3.7	2.0	+ 20.0 -16.6
1500	0.17	0.23	10.14	3.7	2.0	+ 19.9 -16.7
1600	0.17	0.23	10.12	3.7	2.0	+ 20.0 -16.7
1800	0.17	0.23	10.10	3.7	2.0	+ 20.0 -16.7
2000	0.17	0.23	10.08	3.6	2.0	+ 19.9 -16.7
2250	0.17	0.23	10.07	3.7	2.0	+ 20.0 -16.6
2500	0.17	0.23	10.06	3.7	2.0	+ 19.9 -16.7
2750	0.17	0.23	10.05	3.7	2.0	+ 20.0 -16.6
3000	0.17	0.23	10.05	3.7	2.0	+ 20.0 -16.7

Table 72: $\sqrt{s} = 7$ TeV NLO cross sections in the singlet model with parameters chosen to maximize the cross section, with $\mu = M_{hh}/2$ [482].

M_H (GeV)	$\sin\theta$	$\tan\beta$	Cross Section (fb)	PDF (%)	α_s (%)	scale (%)
260	0.31	0.80	83.40	3.0	2.1	+ 21.2 -16.9
275	0.31	0.80	90.93	3.0	2.1	+ 21.1 -16.9
300	0.31	0.80	84.51	3.2	2.1	+ 21.0 -16.9
325	0.27	0.58	57.05	3.2	2.1	+ 20.9 -17.0
350	0.27	0.58	58.34	3.3	2.1	+ 20.8 -17.0
400	0.27	0.58	50.84	3.7	2.1	+ 20.7 -17.1
450	0.24	0.46	29.42	4.0	2.1	+ 20.5 -17.1
500	0.24	0.46	21.68	4.1	2.1	+ 20.4 -17.2
600	0.23	0.37	12.90	4.2	2.1	+ 20.3 -17.2
700	0.21	0.31	9.37	4.1	2.1	+ 20.4 -17.2
750	0.21	0.25	8.71	4.1	2.1	+ 20.4 -17.1
800	0.21	0.25	8.29	4.1	2.1	+ 20.4 -17.1
900	0.19	0.25	7.58	4.0	2.1	+ 20.4 -17.1
1000	0.17	0.23	7.20	4.0	2.1	+ 20.3 -17.1
1100	0.17	0.23	7.11	4.0	2.1	+ 20.4 -17.1
1200	0.17	0.23	7.05	4.0	2.1	+ 20.5 -17.1
1300	0.17	0.23	7.02	4.0	2.1	+ 20.4 -17.1
1400	0.17	0.23	6.99	4.0	2.1	+ 20.4 -17.1
1500	0.17	0.23	6.98	4.0	2.1	+ 20.4 -17.1
1600	0.17	0.23	6.96	4.0	2.1	+ 20.4 -17.1
1800	0.17	0.23	6.95	4.0	2.1	+ 20.4 -17.1
2000	0.17	0.23	6.94	4.0	2.1	+ 20.4 -17.1
2250	0.17	0.23	6.93	4.0	2.1	+ 20.4 -17.1
2500	0.17	0.23	6.92	4.0	2.1	+ 20.4 -17.1
2750	0.17	0.23	6.92	4.0	2.1	+ 20.4 -17.1
3000	0.17	0.23	6.92	4.0	2.1	+ 20.4 -17.1

Table 73: Light Neutral Higgs (h^0) Couplings in the 2HDM

	I	II	Lepton Specific	Flipped
g_{hVV}	$\sin(\beta-\alpha)$	$\sin(\beta-\alpha)$	$\sin(\beta-\alpha)$	$\sin(\beta-\alpha)$
$g_{ht\bar{t}}$	$\frac{\cos\alpha}{\sin\beta}$	$\frac{\cos\alpha}{\sin\beta}$	$\frac{\cos\alpha}{\sin\beta}$	$\frac{\cos\alpha}{\sin\beta}$
$g_{hb\bar{b}}$	$\frac{\cos\alpha}{\sin\beta}$	$-\frac{\sin\alpha}{\cos\beta}$	$\frac{\cos\alpha}{\sin\beta}$	$-\frac{\sin\alpha}{\cos\beta}$
$g_{h\tau^+\tau^-}$	$\frac{\cos\alpha}{\sin\beta}$	$-\frac{\sin\alpha}{\cos\beta}$	$-\frac{\sin\alpha}{\cos\beta}$	$\frac{\cos\alpha}{\sin\beta}$

Table 74: Heavy Neutral CP Even Higgs (H^0) Couplings in the 2HDMs

	I	II	Lepton Specific	Flipped
g_{HVV}	$\cos(\beta-\alpha)$	$\cos(\beta-\alpha)$	$\cos(\beta-\alpha)$	$\cos(\beta-\alpha)$
$g_{Ht\bar{t}}$	$\frac{\sin\alpha}{\sin\beta}$	$\frac{\sin\alpha}{\sin\beta}$	$\frac{\sin\alpha}{\sin\beta}$	$\frac{\sin\alpha}{\sin\beta}$
$g_{Hb\bar{b}}$	$\frac{\sin\alpha}{\sin\beta}$	$\frac{\cos\alpha}{\cos\beta}$	$\frac{\sin\alpha}{\sin\beta}$	$\frac{\cos\alpha}{\cos\beta}$
$g_{H\tau^+\tau^-}$	$\frac{\sin\alpha}{\sin\beta}$	$\frac{\cos\alpha}{\cos\beta}$	$\frac{\cos\alpha}{\cos\beta}$	$\frac{\sin\alpha}{\sin\beta}$

Table 75: Parameter choices for the 2HDM benchmarks. All masses are given in GeV [462].

	$\tan\beta$	α	m_{H^0}	m_{A^0}	$m_{H^\pm}$	m_{12}^2
B1	1.75	-0.5881	300	441	442	38300
B2	1.50	-0.6792	700	701	670	180000
B7	10.00	0.1015	500	500	500	24746

I.7.5 Experimental results

In Run 1 ATLAS and CMS performed searches for BSM di-Higgs boson production in gluon-gluon fusion process assuming resonant and nonresonant hypotheses. Taking in account the Higgs bosons decays, four different final states were explored. One search requires both Higgs bosons to decay to $b\bar{b}$, that is the largest decay branching fraction within the SM. In other two the second Higgs boson decays to $\gamma\gamma$ or $\tau\tau$ final states that helps to reduce the SM background. The fourth channel, explored by ATLAS, features one Higgs boson decaying to WW^* with a subsequent leptonic decay and the other to $\gamma\gamma$. A summary of the searches, obtained assuming a di-Higgs boson production through a spin-0 resonance in s-channel with a negligible natural width, is shown in Figure 127[I.47]. To compare different final states the decays branching fractions of the Higgs boson is assumed to be the SM one. Limits are provided from $m_X^{\text{spin-0}} = 260$ GeV to $m_X^{\text{spin-0}} = 3$ TeV and spans over 3 orders of magnitude from typically 1-10 pb around the lowest edge and 1-10 fb around the highest edge. They are interpreted in the context of two simplified scenarios of the Minimal Supersymmetric Standard Model, 2 Higgs Double Model and Warped Extra Dimensions.

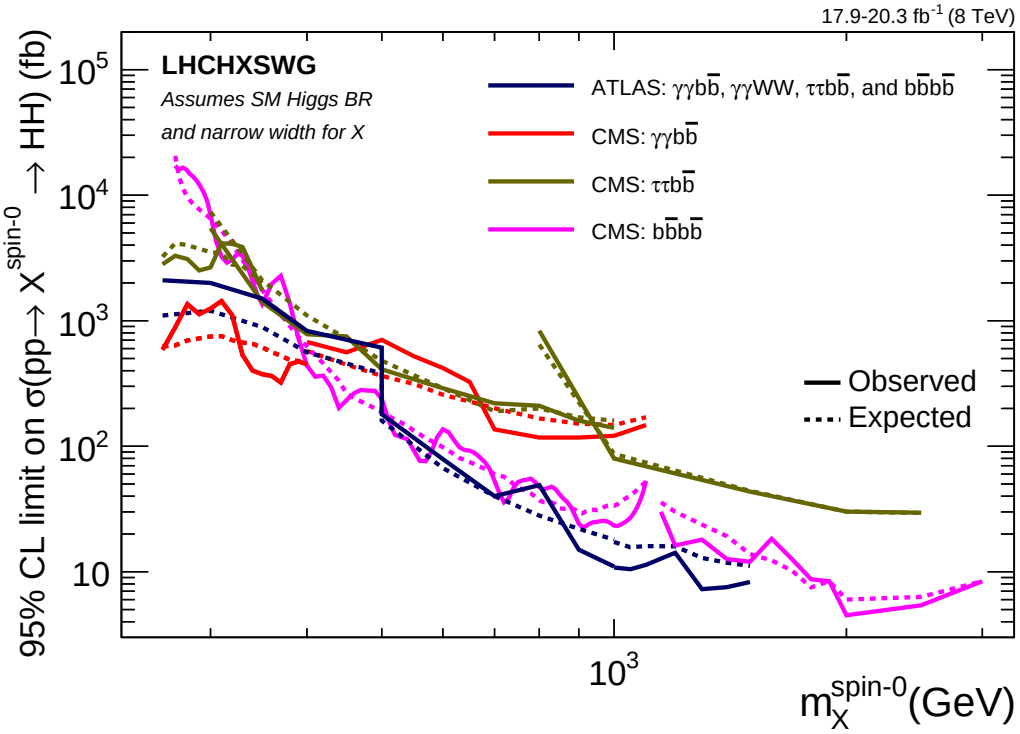

Figure 127: Comparison of the observed and expected 95% confidence level (CL) upper limits on the product of cross section and the branching fraction $\sigma(pp \to X^{\text{spin-0}}) \times \mathcal{B}(X^{\text{spin-0}} \to hh)$. We assuming a narrow width approximation for $X^{\text{spin-0}}$ and SM branching fractions for Higgs boson decay. Results are provided by ATLAS and CMS collaborations based on results from Run 1 data taking period.

ATLAS collaboration performed searches at $\sqrt{s} = 8$ TeV using an integrated luminosity of 20.3 fb^{-1} [487,489,490] and subsequently combined them for $m_X^{\text{spin-0}} < 1$ TeV hypothesis in Ref. [490]. The latter result is shown on Figure 127 complemented with $b\bar{b}b\bar{b}$ results for $m_X^{\text{spin-0}} > 1$ TeV hypothesis.

Similar searches was performed by the CMS collaboration in $\gamma\gamma b\bar{b}$ [491], $\tau\tau b\bar{b}$ [492–494], $b\bar{b}b\bar{b}$ [488, 495] using a data sample of 17.9 to 20.3 fb^{-1} depending on the analysis. The results obtained by different analyses looking in an identical final state are shown in Figure 127 with the same colour. In particular

[I.47] One may notice than for some of the analyses a spin-2 interpretation is also available as well as an interpretation assuming a significant natural width [487, 488].

Table 76: Comparison of the observed and expected 95% CL upper limits on the nonresonant cross section $\sigma(pp \to hh)$ assuming SM-like kinematics.

Channel	Experiment	Observed (pb)	Expected (pb)
$\gamma\gamma b\bar{b}$	ATLAS	2.2	1.0
$\gamma\gamma b\bar{b}$	CMS	0.71	0.60
$\tau\tau b\bar{b}$	ATLAS	1.6	1.3
$\tau\tau b\bar{b}$	CMS	0.59	0.94
$b\bar{b}b\bar{b}$	ATLAS	0.62	0.62
$\gamma\gamma WW^*$	ATLAS	11.0	6.7
Combination	ATLAS	0.69	0.47

in the case of $\tau\tau b\bar{b}$ final state Ref. [492] was optimized to look for low-mass region $m_X^{\text{spin-0}} < 350$ GeV; Ref. [493] concentrate its efforts on middle-mass region $300 < m_X^{\text{spin-0}} < 1000$ GeV using boosted taus; Ref. [494] extends the search up to 2.5 TeV looking on boosted Higgs bosons decaying to nearby taus and jets. Similar logic divides the low-mass [488], $m_X^{\text{spin-0}} < 1100$ GeV, and high-mass [495], $m_X^{\text{spin-0}} > 1150$ GeV, searches in $b\bar{b}b\bar{b}$ final state.

The properties discussed below are valid for the results from both ATLAS and CMS collaborations. In general, we observe that at low mass, $m_X^{\text{spin-0}} \lesssim 350$ GeV, $\gamma\gamma b\bar{b}$ channel is the most sensitive one. It benefits from a good trigger efficiency looking online for a pair of photons, a good reconstruction efficiency of this pair and a low SM background. In contrast, above 500 GeV the most sensitive channel is $b\bar{b}b\bar{b}$. At high mass the trigger efficiency looking for 3 or 4 b-tagged jets with high p_T improves compared to the low mass. Therefore the branching fraction of this channel provides a decisive advantage. The properties of the $\tau\tau b\bar{b}$ channel are intermediate between these two. The sensitivity of different channels crosses around $m_X^{\text{spin-0}} \approx 400 - 500$ GeV depending on the exact details of each analysis. Finally the $\gamma\gamma WW^*$ channel is the less sensitive one since it benefits from all the advantages of $\gamma\gamma b\bar{b}$ channel, but suffers from a significantly lower branching fraction and reconstruction efficiency of $h \to WW^*$ compared to $h \to b\bar{b}$.

The searches for nonresonant Higgs boson pair production assuming SM like kinematics was performed by ATLAS in all four channels followed by a subsequent combination [490] and by CMS in $\gamma\gamma b\bar{b}$ [491] and $\tau\tau b\bar{b}$ [493] channels. The results are shown in Table 76. The observed limits exceeds by at least a factor 40 the total SM cross section provided in Section I.7.2. The CMS collaboration performed also a first generic nonresonant search within the framework of EFT using the $\gamma\gamma b\bar{b}$ final state [491]. This search was designed to exploit the shape properties of the nonresonant m_{hh} spectrum already discussed in Section I.7.4. The limits was interpreted in term of parameters κ_λ, κ_t, and c_2 excluding $|c_2| > 3$ and $\kappa_\lambda < -17.5$ or $\kappa_\lambda > 22.5$.

Although the Run 1 results are still far away from being sensitives to the SM hh production we can already drive interesting conclusions for future analyses. The sensitivity of $\gamma\gamma b\bar{b}$, $\tau\tau b\bar{b}$ and $b\bar{b}b\bar{b}$ is similar for the SM like nonresonant search and for the resonant search with $m_X^{\text{spin-0}} \approx 400$ GeV. This is not a coincidence, indeed the SM m_{hh} spectrum exhibits a broad peak around 400 GeV. This means that a measurement of the SM hh production would equally benefit from a combination of those three channels. This observation confirm the prospect from the ATLAS [496, 497] and CMS [498] collaborations for the HL-LHC program. One shall notice that those prospects includes also $WW^*b\bar{b}$ as a promising channel [498] .

Chapter I.8

Off-shell Higgs Production and Higgs Interference

F. Caola, Y. Gao, N. Kauer, L. Soffi, J. Wang (Eds.); A. Ballestrero, C. Becot, F. Bernlochner, H. Brun, A. Calandri, F. Campanario, F. Cerutti, D. de Florian, R. Di Nardo, L. Fayard, N. Fidanza, N. Greiner, A. V. Gritsan, G. Heinrich, B. Hespel, S. Höche, F. Krauss, Y. Li, S. Liebler, E. Maina, B. Mansoulié, C. O'Brien, S. Pozzorini, M. Rauch, J. Roskes, U. Sarica, M. Schulze, F. Siegert, P. Vanlaer, E. Vryonidou, G. Weiglein, M. Xiao, S. Yuen

I.8.1 Introduction

The Higgs boson measurements in the resonant region (on-peak) are broadly consistent with Standard Model expectations. The observed Higgs boson cross-sections are primarily measured via decays into two electroweak bosons (WW, ZZ and $\gamma\gamma$). However, the measured on-peak cross-sections are affected by an intrinsic scaling ambiguity between the Higgs boson couplings and the total Higgs boson width: $\sigma_{i\to H\to f} \sim g_i^2 g_f^2/\Gamma_H$. Disentangling this ambiguity would make it possible to constrain or even measure the total Higgs boson width at the LHC, which would be highly desirable. The total width of the SM Higgs boson is about 4 MeV, and hence much smaller than the experimental resolution of the Higgs boson mass measurements in the two high-resolution channels $H \to 4\ell$ and $H \to \gamma\gamma$, which is of the order of 1 GeV. For this reason, a direct measurement of the Higgs boson width is not feasible at the LHC.

A novel method has recently been proposed to constrain the Higgs boson width using events away from the on-peak region in the decays into ZZ and WW [499–501]. The off-shell cross-section of $gg \to H^* \to VV$ contributes $\mathcal{O}(15\%)$ due to two threshold effects, near $2M_V$ from the Higgs boson decay and $2m_t$ from the $gg \to H$ production. The electroweak diboson continuum $gg \to VV$ plays an important role in this off-shell region, mainly due to the large destructive interference with the $gg \to H^* \to VV$ signal. At leading order, $gg \to VV$ proceeds through a box diagram, which makes higher order calculations difficult. In this off-shell region, where $M_{VV} \gg M_H$, the cross-section dependence on the total Higgs boson width is negligible, providing a unique opportunity to measure the absolute Higgs boson couplings. The off-shell Higgs boson couplings can then be correlated with the on-shell cross-sections to provide a novel indirect constraint on the total Higgs boson width. It has been pointed out [502, 503] that BSM physics that alters the relation between Higgs cross-sections in the on-peak and off-shell regions could invalidate the method as applied in [500, 501]. Using future LHC data to constrain New Physics affecting the off-shell Higgs boson couplings is therefore important [504, 505].

The method has been promptly adopted by the CMS and ATLAS collaborations. The analyses [506–508] present constraints on the off-shell Higgs boson event yields normalized to the Standard Model prediction (signal strength) in the $ZZ\to 4\ell$, $ZZ\to 2\ell 2\nu$ and $WW\to \ell\nu\ell\nu$ channels. In the ATLAS analysis [507], using the CLs method, the observed 95% confidence level (CL) upper limit on the off-shell signal strength is in the range 5.1–8.6, with an expected range of 6.7–11.0. This range is determined by varying the unknown [I.48] $gg\to ZZ$ and $gg\to WW$ background K-factor from higher-order QCD corrections between half and twice the value of the evaluated signal K-factor. Under the assumption that the Higgs boson couplings are independent of the energy scale of the Higgs boson production, a combination of the off-shell constraint with the on-shell Higgs peak measurement yields an observed (expected) 95% CL upper limit on the Higgs boson total width normalized to the one predicted by the Standard Model, i.e. $\Gamma_{\mathrm{H}}/\Gamma_{\mathrm{SM}}$, in the range of 4.5–7.5 (6.5–11.2) employing the same variation of the

[I.48] cf. Section I.8.4

background K-factor. Assuming that the unknown gg$\to VV$ background K-factor is equal to the signal K-factor, this translates into an observed (expected) 95% CL upper limit on the Higgs boson total width of 22.7 (33.0) MeV.

In the CMS analysis of the ZZ and WW channels combined [508], an observed (expected) upper limit on the off-shell Higgs boson event yield normalized to the Standard Model prediction of 2.4 (6.2) is obtained at the 95% CL for the gluon fusion process and of 19.3 (34.4) for the VBF process. The observed and expected constraints on the Higgs boson total width are 13 MeV and 26 MeV, respectively, at the 95% CL. Concerning the $gg \to VV$ background K-factor, the central values and uncertainties are assumed to be equal to those of the signal K-factor, with an additional 10% uncertainty.

In addition to the off-shell $H^* \to VV$ channels, the $H \to \gamma\gamma$ channel also provides a very clean signature for probing Higgs boson properties, including its mass. However, there is also a large continuum background $gg \to \gamma\gamma$ to its detection in this channel. It is important to study how much the coherent interference between the Higgs boson signal and the background could affect distributions in diphoton observables, and possibly use it to constrain Higgs boson properties. An interesting study [509, 510] showed that this interference can lead to a shift in the Higgs boson mass, which has a strong dependence on the p_T of the diphoton system and the total Higgs boson width. This provides another way to constrain the Higgs boson width.

I.8.2 Overview

This chapter contains selected studies and benchmark results for off-shell Higgs boson production and Higgs interference. In Section I.8.3, theoretical and experimental studies of the SM Higgs boson signal in the off-shell/high-mass region for the gluon-fusion and VBF $\mathrm{H} \to \mathrm{VV}$ channels ($\mathrm{V} = \mathrm{W}, \mathrm{Z}$) including the interference with the background are presented. More specifically, Section I.8.3.a details the used input parameters and gives our recommendations for the QCD scale and the order of the gluon PDF and illustrates the corresponding cross section dependence. Benchmark cross sections and distributions are collected in Section I.8.3.b for the Standard Model, including recommended experimental selections for use in $\mathrm{gg} \to \mathrm{VV}$ calculations, and for the Higgs Singlet Model in Section I.8.3.c. Multi-jet merging and parton shower effects are discussed in Sections I.8.3.d and I.8.3.e. Interference effects for heavy Higgs bosons or Higgs-like resonances in SM extensions are illustrated in Sections I.8.3.f and I.8.3.g. In Section I.8.4, the status of NLO $\mathrm{gg} \to \mathrm{VV}$ calculations is reviewed, and $\mathrm{gg} \to 4\ell$ benchmark results and our recommendation for the treatment of the $\mathrm{gg}(\to \mathrm{H}) \to \mathrm{ZZ}$ interference K-factor are given. In Section I.8.5, the interference in the $\mathrm{H} \to \gamma\gamma$ channel is discussed. A theory overview is given and Monte Carlo interference implementations and related experimental studies are described.

I.8.3 $H \to VV$ modes ($V = W, Z$)

I.8.3.a Input parameters and recommendations for the QCD scale and the order of the gluon PDF

The SM input parameters for Higgs physics given in Ref. [144] are adopted with the G_μ scheme: $M_\mathrm{W} = 80.35797$ GeV, $M_\mathrm{Z} = 91.15348$ GeV, $\Gamma_\mathrm{W} = 2.08430$ GeV, $\Gamma_\mathrm{Z} = 2.49427$ GeV, $m_\mathrm{t} = 172.5$ GeV, $m_\mathrm{b}(m_\mathrm{b}) = 4.18$ GeV and $G_F = 1.1663787 \cdot 10^{-5}$ GeV^{-2}. The CKM matrix is approximated by the identity matrix. Finite top and bottom quark mass effects are included. Lepton and light quark masses are neglected. Results are given for pp collisions at $\sqrt{s} = 13$ TeV unless otherwise noted. The PDF set `PDF4LHC15_nlo_100` [35] is used by default. All PDF sets are used with the default α_s of the set. A fixed-width Breit-Wigner propagator $D(p) \sim (p^2 - M^2 + iM\Gamma)^{-1}$ is employed for W, Z and Higgs bosons, where M and Γ are determined by the complex pole of the amplitude due to unstable particle propagation.[I.49] The SM Higgs boson mass is set to 125 GeV. The SM Higgs boson width parameter is

[I.49] In agreement with HDECAY, the W and Z masses and widths have been changed from physical on-shell masses to the pole values, see Eq. (7) in Ref. [144]. The relative deviation is at the $3 \cdot 10^{-4}$ level.

calculated using HDECAY v6.50 [69]. For $M_{\mathrm{H}} = 125$ GeV one obtains $\Gamma_{\mathrm{H}} = 4.097 \cdot 10^{-3}$ GeV.

For off-shell and high-mass $\mathrm{H} \to \mathrm{VV}$ cross-section and interference calculations, we recommend and employ the QCD scale $\mu_R = \mu_F = M_{\mathrm{VV}}/2$ unless otherwise noted. Next, we elucidate the choice of the PDF order for the $\mathrm{gg} \to \mathrm{VV}$ continuum background and the corresponding Higgs-continuum interference. Combining any n-order PDF fit with a m-order parton-level calculation is theoretically consistent as long as $n \geq m$. Deviations are expected to be of higher order if the same $\alpha_{\mathrm{s}}(M_{\mathrm{Z}})$ is used. But, using a LO gluon PDF with $\alpha_{\mathrm{s}}(M_{\mathrm{Z}})$ obtained in the LO fit is not recommended: The gluon PDF is mostly determined by DIS data, especially in the SM Higgs region. At LO, DIS does not have a gluon channel. It only enters at NLO, with a large K-factor. A LO fit cannot properly account for this $\mathcal{O}(50\%)$ contribution, but incorrectly adjusts the gluon evolution to compensate, which results in an overestimated value of $\alpha_{\mathrm{s}}(M_{\mathrm{Z}})$ of approximately 0.13. We therefore recommend using a NLO PDF set when computing the $\mathrm{gg}\ (\to \mathrm{H}) \to \mathrm{VV}$ interference and the gg continuum background at LO as well as NLO. For consistency, we also use the NLO PDF set for the corresponding signal process.[I.50]

The variation induced by different PDF and QCD scale choices is illustrated in Tables 77, 78, 79 and 80 using the process $\mathrm{gg}\ (\to \mathrm{H}) \to \ell\bar{\ell}\ell'\bar{\ell}'$. The Higgs boson signal (S), gg background (B) and the signal-background interference (I) are displayed at LO for four Higgs boson invariant mass regions:

- *off-shell* (OFS): $M_{\mathrm{VV}} > 140$ GeV
- *off-shell high-mass (interference)* (HM1): $220 < M_{\mathrm{VV}} < 300$ GeV
- *off-shell high-mass (signal enriched)* (HM2): $M_{\mathrm{VV}} > 300$ GeV
- *resonance* (RES): $110 < M_{\mathrm{VV}} < 140$ GeV

Motivated by the Higgs boson width constraints of Refs. [506, 507], the off-shell high-mass region is divided into the interference-sensitive (HM1) and signal-enriched (HM2) regions. Two sets of selection cuts are considered:

- *minimal cuts* (MIN): $M_{\ell\bar{\ell}} > 10$ GeV, $M_{\ell'\bar{\ell}'} > 10$ GeV
- *CMS* $\mathrm{H} \to 4\ell$ *cuts* (CMS): $p_{\mathrm{T1}} > 20$ GeV, $p_{\mathrm{T2}} > 10$ GeV, $p_{\mathrm{T3,4}} > 5$ GeV, $|\eta_{\mathrm{e}}| < 2.5$, $|\eta_{\mu}| < 2.4$, $M_{\mathrm{e\bar{e}}} > 4$ GeV, $M_{\mu\bar{\mu}} > 4$ GeV

The PDF4LHC15 [35] NLO and NNLO sets ($\alpha_{\mathrm{s}}(M_{\mathrm{Z}}) = 0.118$) and the CT14 [36] LO sets with $\alpha_{\mathrm{s}}(M_{\mathrm{Z}}) = 0.130$ and $\alpha_{\mathrm{s}}(M_{\mathrm{Z}}) = 0.118$ (and 1- and 2-loop evolution, respectively) are compared in Tables 77 and 78. As expected, the deviations for PDF sets with $\alpha_{\mathrm{s}}(M_{\mathrm{Z}}) = 0.118$ are of order 10% or less while the LO set with $\alpha_{\mathrm{s}}(M_{\mathrm{Z}}) = 0.130$ yields results that differ by up to 30%. The deviation between the NLO and NNLO sets is at the per cent level. Furthermore, different choices for the QCD scale $\mu = \mu_R = \mu_F$ are compared in Tables 79 and 80. As central scale choices, the dynamic scale $\mu_0 = M_{2\ell 2\ell}/2$ and the fixed scales $M_{\mathrm{H}}/2$ and M_{Z} are considered. The LO scale variation is estimated for μ_0 using the scales $\mu_0/2$ and $2\mu_0$. The results illustrate that using a fixed scale appropriate for resonant signal or background will significantly overestimate the signal, background and interference cross sections in the far off-shell and high-mass regions. With the recommended central scale $M_{2\ell 2\ell}/2$, a factor-two scale variation yields a LO scale uncertainty of 20%−25% for the off-shell signal and signal plus background interference. The results of these comparisons were calculated using GG2VV [499].

I.8.3.b Off-shell and interference benchmark cross sections and distributions: Standard Model

Gluon-fusion SM benchmark results were computed with GG2VV [499] (see also Refs. [511–514]) and MADGRAPH5_AMC@NLO (MG5_AMC) [54,515] (see also Ref. [514]). The GG2VV and MG5_AMC results were found to be in good agreement. Benchmark cross sections for $\mathrm{gg}\ (\to \mathrm{H}) \to \mathrm{VV} \to 4$ leptons processes in pp collisions at $\sqrt{s} = 13$ TeV in the SM are given in Table 81. Results for the Higgs boson signal, the signal including signal-background interference as well as the interfering background without Higgs contribution are displayed for minimal cuts $M_{\ell\bar{\ell}} > 10$ GeV, $M_{\ell'\bar{\ell}'} > 10$ GeV. The cross

[I.50] We note that the LO and NLO VBF results have also been obtained with the NLO PDF set.

Table 77: PDF dependence of off-shell $\mathrm{gg}\ (\to \mathrm{H}) \to \ell\bar{\ell}\ell'\bar{\ell}'$ cross sections at LO in fb for one lepton flavour combination. MIN cuts are applied. R is the ratio of NNLO, LO result to NLO result. The bottom rows show the ratio of OFS, HM1, HM2 to RES result for S and $S + I$. The recommended QCD scale $\mu_R = \mu_F = M_{2\ell 2\ell}/2$ is used. The MC error is given in brackets. See main text for other details.

		PDF set order						
Reg.	Amp.	**NLO**	NNLO	R	LO(0.118)	R	LO(0.130)	R
	S	0.1266(1)	0.1255(1)	0.991(2)	0.1255(1)	0.992(2)	0.1414(2)	1.116(2)
OFS	$S+I$	−0.1313(2)	−0.1298(2)	0.988(2)	−0.1307(2)	0.995(2)	−0.149(1)	1.138(8)
	B	2.988(4)	2.945(5)	0.986(2)	2.960(4)	0.991(2)	3.448(5)	1.154(3)
	S	0.01933(4)	0.01906(4)	0.986(3)	0.01899(4)	0.982(3)	0.02210(5)	1.143(4)
HM1	$S+I$	−0.04550(8)	−0.04475(8)	0.984(3)	−0.04486(7)	0.986(3)	−0.0516(6)	1.13(2)
	B	1.182(3)	1.165(3)	0.985(3)	1.166(3)	0.986(3)	1.354(3)	1.145(4)
	S	0.0981(1)	0.0974(1)	0.993(2)	0.0973(1)	0.992(2)	0.1084(2)	1.105(2)
HM2	$S+I$	−0.0465(1)	−0.04622(9)	0.994(3)	−0.04637(9)	0.997(3)	−0.0522(6)	1.12(2)
	B	0.611(2)	0.605(2)	0.990(4)	0.598(2)	0.980(4)	0.676(2)	1.107(5)
	S	0.800(1)	0.780(1)	0.976(2)	0.843(1)	1.054(2)	1.021(2)	1.276(3)
RES	$S+I$	0.803(2)	0.784(2)	0.976(4)	0.845(4)	1.052(6)	1.023(3)	1.274(5)
	B	0.1092(2)	0.1063(2)	0.974(2)	0.1150(2)	1.053(3)	0.1389(2)	1.272(3)
OFS/	S	0.1583(3)	0.1609(3)		0.1490(3)		0.1385(3)	
RES	$S+I$	−0.1635(4)	−0.1655(5)		−0.1547(7)		−0.146(2)	
HM1/	S	0.02418(6)	0.02443(6)		0.02253(6)		0.02165(5)	
RES	$S+I$	−0.0566(2)	−0.0571(2)		−0.0531(3)		−0.0504(6)	
HM2/	S	0.1227(2)	0.1249(3)		0.1155(2)		0.1062(2)	
RES	$S+I$	−0.0579(2)	−0.0589(2)		−0.0549(3)		−0.0510(6)	

sections are calculated at loop-induced leading order. The recommended next-to-leading order K-factor is discussed in Section I.8.4. Similarly, in Table 82 benchmark cross sections for $\mathrm{gg}\ (\to \mathrm{H}) \to \mathrm{VV} \to$ semileptonic final states in pp collisions at $\sqrt{s} = 13$ TeV in the SM are given. As above, the signal amplitude is calculated at loop-induced leading order. But, for the semileptonic decay modes, the $\mathcal{O}(g_\mathrm{s}^2 e^2)$ tree-level as well as the important loop-induced $\mathcal{O}(g_\mathrm{s}^2 e^4)$ amplitude contributions to the interfering background are taken into account [514]. The following minimal cuts are applied: $M_{\ell\bar{\ell}} > 10$ GeV, $M_{\mathrm{q}\bar{\mathrm{q}}} > 10$ GeV, $p_{\mathrm{T}j} > 25$ GeV. Higgs boson invariant mass distributions corresponding to the cross sections given in Tables 81 and 82 are displayed in Figures 128, 129 and 130.

The following experimental Higgs off-shell search selections are recommended for use in $\mathrm{gg} \to \mathrm{VV}$ calculations:
Jets: ATLAS: $p_{\mathrm{T}j} > 25$ GeV for $|\eta_j| < 2.4$, $p_{\mathrm{T}j} > 30$ GeV for $2.4 < |\eta_j| < 4.5$
Jets: CMS: $p_{\mathrm{T}j} > 30$ GeV for $|\eta_j| < 4.7$
$\mathrm{H} \to \mathrm{ZZ} \to 4\ell$ channel: ATLAS:
$p_{\mathrm{T}\ell,1} > 20$ GeV, $p_{\mathrm{T}\ell,2} > 15$ GeV, $p_{\mathrm{T}\ell,3} > 10$ GeV, $p_{\mathrm{Te},4} > 7$ GeV, $p_{\mathrm{T}\mu,4} > 6$ GeV, $|\eta_\mathrm{e}| < 2.47$, $|\eta_\mu| < 2.7$, $M_{4\ell} > 220$ GeV
$\mathrm{H} \to \mathrm{ZZ} \to 4\ell$ channel: CMS:
$p_{\mathrm{T}\ell,1} > 20$ GeV, $p_{\mathrm{T}\ell,2} > 10$ GeV, $p_{\mathrm{Te},3,4} > 7$ GeV, $p_{\mathrm{T}\mu,3,4} > 5$ GeV, $|\eta_\mathrm{e}| < 2.5$, $|\eta_\mu| < 2.4$, $M_{4\ell} > 220$ GeV
$\mathrm{H} \to \mathrm{ZZ} \to 2\ell 2\nu$ channel: ATLAS:

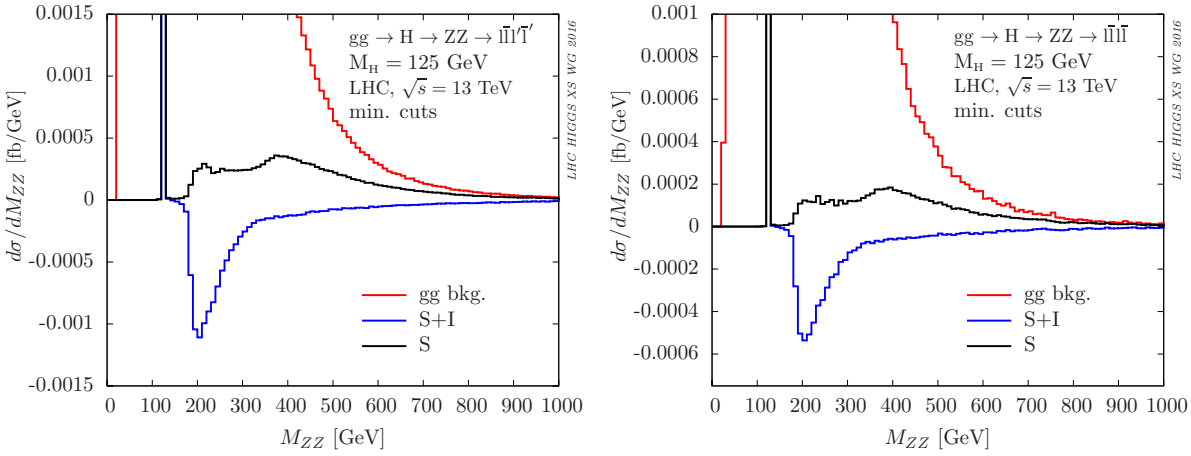

Figure 128: Invariant mass distributions for gg ($\to$ H) $\to$ ZZ $\to \ell\bar{\ell}\ell'\bar{\ell}'$ and gg ($\to$ H) $\to$ ZZ $\to \ell\bar{\ell}\ell\bar{\ell}$. Other details as in Table 81.

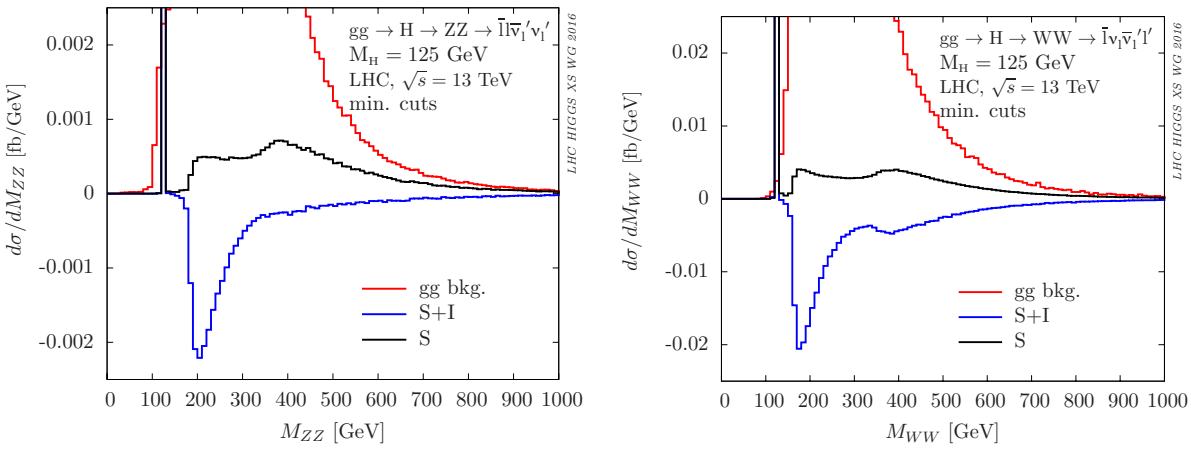

Figure 129: Invariant mass distributions for gg ($\to$ H) $\to$ ZZ $\to \ell\bar{\ell}\nu_{\ell'}\bar{\nu}_{\ell'}$ and gg ($\to$ H) $\to$ WW $\to \bar{\ell}\nu_{\text{l}}\bar{\nu}_{\ell'}\ell'$. Other details as in Table 81.

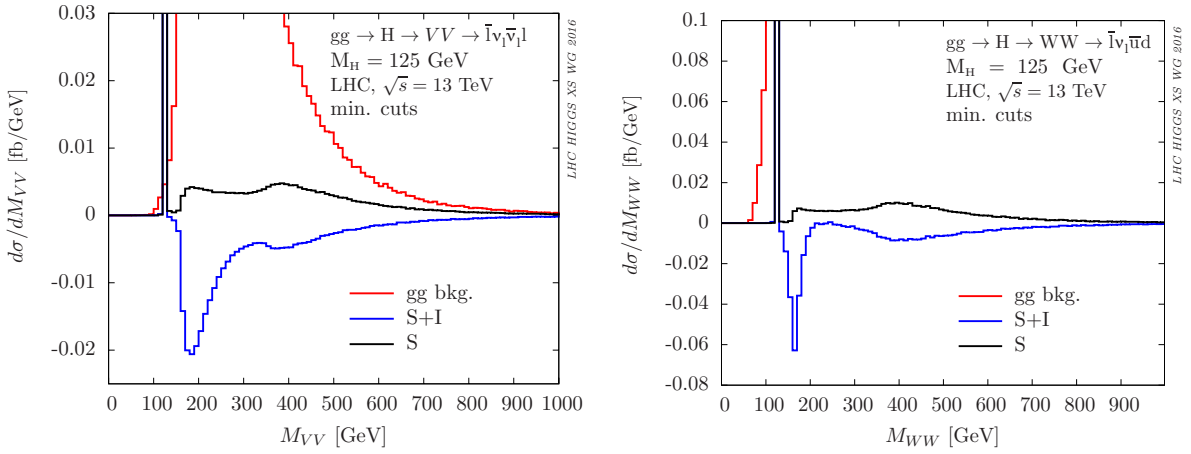

Figure 130: Invariant mass distributions for gg ($\to$ H) $\to$ WW/ZZ $\to \bar{\ell}\nu_{\text{l}}\bar{\nu}_{\text{l}}\ell$ and gg ($\to$ H) $\to$ WW $\to \bar{\ell}\nu_{\text{l}}\bar{\text{u}}\text{d}$. Other details as in Tables 81 and 82.

Table 78: PDF dependence of off-shell gg ($\to$ H) $\to$ $e^-e^+\mu^-\mu^+$ cross sections at LO in fb. CMS cuts are applied. Other details as in Table 77.

		PDF set order						
Reg.	Amp.	**NLO**	NNLO	R	LO(0.118)	R	LO(0.130)	R
OFS	S	0.0952(3)	0.09396(8)	0.986(3)	0.09034(7)	0.949(3)	0.10191(8)	1.070(3)
	$S+I$	−0.0893(3)	−0.0883(1)	0.989(3)	−0.08436(9)	0.944(3)	−0.0973(1)	1.089(4)
	B	1.869(3)	1.841(3)	0.985(2)	1.736(2)	0.928(2)	2.033(3)	1.088(2)
HM1	S	0.01303(9)	0.01278(3)	0.981(7)	0.01200(3)	0.921(7)	0.01402(3)	1.076(8)
	$S+I$	−0.0298(2)	−0.02942(6)	0.986(6)	−0.02759(5)	0.925(5)	−0.03227(6)	1.082(6)
	B	0.738(2)	0.727(2)	0.986(3)	0.679(2)	0.920(3)	0.795(2)	1.079(4)
HM2	S	0.0761(3)	0.07531(8)	0.990(4)	0.07271(7)	0.956(3)	0.08123(8)	1.067(4)
	$S+I$	−0.0349(2)	−0.03471(7)	0.994(6)	−0.03376(6)	0.967(6)	−0.03757(7)	1.076(7)
	B	0.382(2)	0.377(2)	0.987(5)	0.353(1)	0.925(5)	0.403(2)	1.055(5)
RES	S	0.4392(7)	0.4284(7)	0.975(3)	0.4343(7)	0.989(3)	0.5267(8)	1.199(3)
	$S+I$	0.439(2)	0.428(2)	0.975(4)	0.433(2)	0.988(4)	0.527(2)	1.200(5)
	B	0.06294(8)	0.06155(8)	0.978(2)	0.06243(9)	0.992(2)	0.0755(1)	1.200(3)
OFS/	S	0.2169(7)	0.2193(4)		0.2080(4)		0.1935(4)	
RES	$S+I$	−0.2036(8)	−0.2065(6)		−0.1946(6)		−0.1847(6)	
HM1/	S	0.0297(2)	0.02984(8)		0.02762(8)		0.02662(7)	
RES	$S+I$	−0.0680(4)	−0.0688(3)		−0.0637(3)		−0.0613(2)	
HM2/	S	0.1733(6)	0.1758(4)		0.1674(4)		0.1542(3)	
RES	$S+I$	−0.0796(5)	−0.0811(3)		−0.0779(3)		−0.0714(3)	

$p_{\mathrm{T}\ell} > 20$ GeV (electron, muon), $|\eta_{\mathrm{e}}| < 2.47$, $|\eta_{\mu}| < 2.5$, $E_{T,miss} > 180$ GeV, $\Delta\phi_{\ell\ell} < 1.4$, $M_{\mathrm{T,ZZ}} > 380$ GeV
ATLAS transverse mass definition (recommended for $M_{\mathrm{VV}} > 2M_{\mathrm{Z}}$):

$$M_{\mathrm{T,ZZ}} = \sqrt{(M_{\mathrm{T},\ell\ell} + M_{\mathrm{T},miss})^2 - (\mathbf{p}_{T,\ell\ell} + \mathbf{p}_{T,miss})^2}\,, \text{ where } \quad M_{\mathrm{T},X} = \sqrt{p^2_{\mathrm{T},X} + M^2_Z} \qquad \text{(I.8.1)}$$

$\mathrm{H} \to \mathrm{ZZ} \to 2\ell 2\nu$ channel: CMS:
$p_{\mathrm{T}\ell} > 20$ GeV (electron, muon), $E_{T,miss} > 80$ GeV
$M_{\mathrm{T,ZZ}}$ used by CMS: Eq. (I.8.1) with M_Z replaced by $M_{\ell\ell}$
$\mathrm{H} \to \mathrm{WW} \to 2\ell 2\nu$ channel: ATLAS:
$p_{\mathrm{T}\ell,1} > 22$ GeV, $p_{\mathrm{T}\ell,2} > 10$ GeV, $|\eta_{\mathrm{e}}| < 2.47$, $|\eta_{\mu}| < 2.5$, $M_{\ell\ell} > 10$ GeV, $p_{\mathrm{T},miss} > 20$ GeV, $M_{\mathrm{T,WW}} > 200$ GeV
ATLAS transverse mass definition (recommended):

$$M_{\mathrm{T,WW}} = \sqrt{(M_{\mathrm{T},\ell\ell} + p_{\mathrm{T},miss})^2 - (\mathbf{p}_{T,\ell\ell} + \mathbf{p}_{T,miss})^2}\,, \text{ where } \quad M_{\mathrm{T},\ell\ell} = \sqrt{p^2_{\mathrm{T},\ell\ell} + M^2_{\ell\ell}} \qquad \text{(I.8.2)}$$

Vector-boson-fusion SM benchmark results were computed with PHANTOM [516] (see also Ref. [517]) and VBFNLO [275, 518] (see also Refs. [519–523]). Good agreement was achieved for all fully-leptonic Higgs boson decay modes. For VBF, two selection cut sets are applied which have the following selection in common:

- $p_{\mathrm{T}j} > 20$ GeV, $|\eta_j| < 5.0$, $M_{jj} > 60$ GeV for all jets, anti-k_{T} jet clustering with $R = 0.4$
- $p_{\mathrm{T}\ell} > 20$ GeV, $|\eta_\ell| < 2.5$, $M_{\ell\bar{\ell}} > 20$ GeV (same flavour only), $E_{\mathrm{T}}^{\mathrm{miss}} > 40$ GeV
- tagging jets: j_1, j_2, ordered by decreasing $|\eta_j|$

Exception: for the *resonance* (RES) region (see Section I.8.3.a) $M_{\ell\bar{\ell}} > 10$ GeV is applied instead of $M_{\ell\bar{\ell}} > 20$ GeV. With this common selection, we define:

- *loose VBF cuts*: common selection and $M_{j_1 j_2} > 130$ GeV

Table 79: QCD scale $\mu = \mu_R = \mu_F$ dependence and symmetric scale uncertainty of off-shell $\mathrm{gg}\ (\to \mathrm{H}) \to \ell\bar{\ell}\ell'\bar{\ell}'$ cross sections at LO in fb for one lepton-flavour combination. MIN cuts are applied. R is the ratio of the result to the cross section with the recommended scale choice $\mu = M_{2\ell 2\ell}/2$. As recommended, the NLO PDF set is used. Other details as in Table 77.

		Dynamic scale			Fixed scales			
Reg.	Amp.	$M_{2\ell 2\ell}/2$	$\Delta(M_{2\ell 2\ell})$ $\Delta(M_{2\ell 2\ell}/4)$ symmetr. Δ	R R R	$M_{\mathrm{H}}/2$	R	M_{Z}	R
OFS	S		$-0.0258(2)$	$-0.204(2)$				
	S	$0.1266(1)$	$0.0349(2)$	$0.276(2)$	$0.2038(2)$	$1.610(2)$	$0.1760(2)$	$1.390(2)$
	S		$\pm 0.0303(2)$	$\pm 0.240(1)$				
	$S+I$		$0.0251(2)$	$0.182(2)$				
	$S+I$	$-0.1313(2)$	$-0.0328(2)$	$-0.250(2)$	$-0.1831(2)$	$1.394(2)$	$-0.1604(2)$	$1.221(2)$
	$S+I$		$\pm 0.0290(2)$	$\pm 0.221(1)$				
	B		$-0.545(5)$	$-0.182(2)$				
	B	$2.988(4)$	$0.699(7)$	$0.234(3)$	$3.751(4)$	$1.255(3)$	$3.327(4)$	$1.114(2)$
	B		$\pm 0.6225(4)$	$\pm 0.209(2)$				
HM1	S		$-0.00355(4)$	$-0.184(3)$				
	S	$0.01928(3)$	$0.00455(6)$	$0.236(3)$	$0.02406(6)$	$1.248(4)$	$0.02150(5)$	$1.115(3)$
	S		$\pm 0.00405(4)$	$\pm 0.210(2)$				
	$S+I$		$0.0085(1)$	$0.187(3)$				
	$S+I$	$-0.04553(8)$	$-0.0106(2)$	$-0.233(3)$	$-0.0561(1)$	$1.233(3)$	$-0.05002(9)$	$1.099(3)$
	$S+I$		$\pm 0.0096(1)$	$\pm 0.2095(2)$				
	B		$-0.223(4)$	$-0.188(3)$				
	B	$1.186(3)$	$0.273(5)$	$0.230(4)$	$1.462(3)$	$1.232(4)$	$1.302(3)$	$1.098(4)$
	B		$\pm 0.248(2)$	$\pm 0.209(3)$				
HM2	S		$-0.0207(2)$	$-0.211(2)$				
	S	$0.0982(2)$	$0.0284(2)$	$0.289(2)$	$0.1693(2)$	$1.724(3)$	$0.1451(2)$	$1.478(3)$
	S		$\pm 0.0246(2)$	$\pm 0.250(2)$				
	$S+I$		$0.0099(2)$	$0.212(3)$				
	$S+I$	$-0.04651(8)$	$-0.0136(2)$	$-0.293(3)$	$-0.0818(2)$	$1.760(5)$	$-0.0700(2)$	$1.505(4)$
	$S+I$		$\pm 0.0118(1)$	$\pm 0.253(2)$				
	B		$-0.123(2)$	$-0.201(3)$				
	B	$0.610(1)$	$0.167(3)$	$0.275(5)$	$0.929(3)$	$1.524(5)$	$0.807(2)$	$1.323(4)$
	B		$\pm 0.145(2)$	$\pm 0.238(3)$				
RES	S		$-0.115(2)$	$-0.143(2)$				
	S	$0.800(1)$	$0.131(2)$	$0.164(2)$	$0.801(2)$	$1.001(2)$	$0.737(1)$	$0.921(2)$
	S		$\pm 0.123(2)$	$\pm 0.154(2)$				
	$S+I$		$-0.116(3)$	$-0.145(2)$				
	$S+I$	$0.803(2)$	$0.130(3)$	$0.162(3)$	$0.803(2)$	$1.000(3)$	$0.739(2)$	$0.920(3)$
	$S+I$		$\pm 0.123(2)$	$\pm 0.153(2)$				
	B		$-0.0158(3)$	$-0.145(3)$				
	B	$0.1092(2)$	$0.0176(3)$	$0.162(3)$	$0.1089(2)$	$0.998(2)$	$0.1002(2)$	$0.917(2)$
	B		$\pm 0.0167(2)$	$\pm 0.153(2)$				
OFS/ RES	S	$0.1583(3)$			$0.2545(5)$		$0.2389(4)$	
	$S+I$	$-0.1635(4)$			$-0.2279(5)$		$-0.2172(5)$	
HM1/ RES	S	$0.02411(5)$			$0.03005(8)$		$0.02918(8)$	
	$S+I$	$-0.0567(2)$			$-0.0699(2)$		$-0.0677(2)$	
HM2/ RES	S	$0.1228(3)$			$0.2114(4)$		$0.1970(4)$	
	$S+I$	$-0.0579(2)$			$-0.1019(3)$		$-0.0948(3)$	

Table 80: QCD scale $\mu = \mu_R = \mu_F$ dependence and symmetric scale uncertainty of off-shell $\mathrm{gg}\ (\to \mathrm{H}) \to \ell\bar{\ell}\ell'\bar{\ell}'$ cross sections at LO in fb for one lepton-flavour combination. CMS cuts are applied. Other details as in Table 79.

		Dynamic scale			Fixed scales			
Reg.	Amp.	$M_{2\ell 2\ell}/2$	$\Delta(M_{2\ell 2\ell})$ $\Delta(M_{2\ell 2\ell}/4)$ symmetr. Δ	R R R	$M_{\mathrm{H}}/2$	R	M_{Z}	R
OFS	S	0.0952(3)	−0.0196(3) 0.0257(4) ±0.0227(3)	−0.206(4) 0.270(4) ±0.238(3)	0.1545(4)	1.622(6)	0.1338(4)	1.405(5)
	$S+I$	−0.0893(3)	0.0164(4) −0.0223(4) ±0.0194(3)	0.184(4) −0.250(5) ±0.217(3)	−0.1282(4)	1.435(6)	−0.1119(3)	1.253(5)
	B	1.869(3)	−0.331(4) 0.430(4) ±0.381(3)	−0.177(2) 0.230(2) ±0.204(2)	2.341(3)	1.252(3)	2.084(3)	1.115(2)
HM1	S	0.01302(2)	−0.00235(3) 0.00303(3) ±0.00269(2)	−0.181(2) 0.233(3) ±0.207(2)	0.0163(2)	1.25(1)	0.0145(1)	1.115(8)
	$S+I$	−0.02986(5)	0.00536(6) −0.00682(7) ±0.00609(5)	0.179(2) −0.228(3) ±0.204(2)	−0.0370(2)	1.241(7)	−0.0326(2)	1.092(6)
	B	0.739(1)	−0.132(2) 0.168(2) ±0.150(1)	−0.178(2) 0.227(3) ±0.203(2)	0.908(2)	1.229(3)	0.811(2)	1.097(3)
HM2	S	0.0761(1)	−0.0160(2) 0.0218(2) ±0.0189(1)	−0.210(2) 0.286(3) ±0.248(2)	0.1315(4)	1.727(6)	0.1131(4)	1.485(5)
	$S+I$	−0.03505(6)	0.00740(7) −0.01006(9) ±0.0088(1)	0.211(2) −0.287(3) ±0.249(2)	−0.0630(3)	1.798(9)	−0.0537(3)	1.533(8)
	B	0.3822(6)	−0.0768(8) 0.1019(9) ±0.090(1)	−0.201(2) 0.267(3) ±0.234(2)	0.582(2)	1.522(5)	0.506(2)	1.324(4)
RES	S	0.4392(7)	−0.0603(9) 0.066(1) ±0.064(2)	−0.137(2) 0.151(3) ±0.145(2)	0.4389(7)	0.999(3)	0.4044(6)	0.921(2)
	$S+I$	0.439(2)	−0.060(2) 0.067(2) ±0.064(2)	−0.136(4) 0.154(5) ±0.145(3)	0.438(2)	0.999(4)	0.406(2)	0.925(4)
	B	0.06294(8)	−0.0086(2) 0.0097(2) ±0.0092(1)	−0.136(2) 0.155(2) ±0.146(2)	0.06302(9)	1.001(2)	0.05816(8)	0.924(2)
OFS/ RES	S	0.2169(7)			0.352(1)		0.331(1)	
	$S+I$	−0.2036(8)			−0.292(2)		−0.276(2)	
HM1/ RES	S	0.02964(6)			0.0371(3)		0.0359(3)	
	$S+I$	−0.0681(3)			−0.0845(5)		−0.0804(5)	
HM2/ RES	S	0.1734(4)			0.300(1)		0.280(1)	
	$S+I$	−0.0799(3)			−0.1437(8)		−0.1325(7)	

Table 81: Cross sections (fb) for $gg\ (\to H) \to VV \to 4$ leptons processes in pp collisions at $\sqrt{s} = 13$ TeV in the SM. Results for the Higgs boson signal (S), the signal including signal-background interference (S+I) as well as the interfering background without Higgs contribution (gg bkg.) are given. Minimal cuts are applied: $M_{\ell\bar{\ell}} > 10$ GeV, $M_{\ell'\bar{\ell}'} > 10$ GeV. Cross sections are given at loop-induced leading order and for a single lepton flavour (ℓ) or single different-flavour combination (ℓ,ℓ'). γ^* contributions are included in ZZ. The integration error is displayed in brackets.

final state	S	S+I	gg bkg.
$\ell\bar{\ell}\ell'\bar{\ell}'$	0.9284(7)	0.6707(8)	4.264(2)
$\ell\bar{\ell}\ell\bar{\ell}$	0.4739(8)	0.3467(8)	1.723(3)
$\ell\bar{\ell}\nu_{\ell'}\bar{\nu}_{\ell'}$	1.896(2)	1.386(2)	5.730(5)
$\bar{\ell}\nu_l\bar{\nu}_{\ell'}\ell'$	37.95(4)	33.60(4)	45.31(4)
$\bar{\ell}\nu_l\bar{\nu}_l\ell$	36.01(3)	31.19(3)	50.52(4)

Table 82: Cross sections (fb) for $gg\ (\to H) \to VV \to$ semileptonic final states in pp collisions at $\sqrt{s} = 13$ TeV in the SM. Results for the Higgs boson signal (S), the signal including signal-background interference (S+I) as well as the interfering background without Higgs contribution (gg bkg.) are given. The signal amplitude is calculated at loop-induced leading order. For the semileptonic decay modes, the $\mathcal{O}(g_s^2e^2)$ tree-level as well as the important loop-induced $\mathcal{O}(g_s^2e^4)$ amplitude contributions to the interfering background are taken into account [514]. Minimal cuts are applied: $M_{\ell\bar{\ell}} > 10$ GeV, $M_{q\bar{q}} > 10$ GeV, $p_{Tj} > 25$ GeV. Cross sections are given for a single lepton flavour. Other details as in Table 81.

final state	S	S+I	gg bkg.
$\ell\bar{\ell}d\bar{d}$	1.711(3)	0.96(1)	$1.575(6)\cdot10^3$
$\ell\bar{\ell}u\bar{u}$	1.334(3)	0.750(5)	$2.30(5)\cdot10^3$
$\ell\bar{\nu}_l u\bar{d}$	38.66(5)	30.58(8)	$1.111(3)\cdot10^4$
$\bar{\ell}\nu_l\bar{u}d$	38.68(5)	30.59(8)	$1.112(3)\cdot10^4$

– *tight VBF cuts*: common selection and $M_{j_1j_2} > 600$ GeV, $\Delta y_{j_1j_2} > 3.6$, $y_{j_1}y_{j_2} < 0$ (opposite hemispheres)

Benchmark cross sections for $qq'(\to qq'H) \to qq'Z(\gamma^*)Z(\gamma^*) \to qq'\,\ell\bar{\ell}\ell'\bar{\ell}'$ and $qq'(\to qq'H) \to qq'WW \to qq'\,\bar{\ell}\nu_l\bar{\nu}_{\ell'}\ell'$ in pp collisions at $\sqrt{s} = 13$ TeV in the SM with tight and loose VBF cuts are given in Tables 83, 84, 85 and 86. Leading order and next-to-leading order results for the Higgs boson signal, the signal including signal-background interference as well as the interfering background without Higgs contribution are displayed. Corresponding Higgs boson invariant mass (for ZZ) and transverse mass (for WW) distributions are shown in Figures 131 and 132, respectively, for loose and tight VBF cuts.

The full set of SM benchmark cross sections and distributions is available at https://twiki.cern.ch/twiki/bin/view/LHCPhysics/LHCHXSWGOFFSHELL.

I.8.3.c Off-shell and interference benchmarks: 1-Higgs Singlet Model

The simplest extension of the SM Higgs sector is given by the addition of a singlet field which is neutral under the SM gauge groups. We adopt the definition of the 1-Higgs Singlet Model (1HSM), a.k.a.

Table 83: Cross sections for $\mathrm{qq'}(\to \mathrm{qq'\,H}) \to \mathrm{qq'\,Z}(\gamma^*)\mathrm{Z}(\gamma^*) \to \mathrm{qq'}\,\ell\bar{\ell}\ell'\bar{\ell}'$ in pp collisions at $\sqrt{s} = 13$ TeV in the SM. Leading order (LO) and next-to-leading order (NLO) results for the Higgs boson signal (S), the signal including signal-background interference (S+I) as well as the interfering background without Higgs contribution (B) are given. Tight VBF cuts are applied (see main text). Cross sections are given for a single lepton flavour combination. The integration error is displayed in brackets.

σ[fb]		110 GeV $< M_{\mathrm{ZZ}} <$ 140 GeV	$M_{\mathrm{ZZ}} >$ 140 GeV	220 GeV $< M_{\mathrm{ZZ}} <$ 300 GeV	$M_{\mathrm{ZZ}} >$ 300 GeV
S	LO	$6.88(2)\cdot10^{-3}$	$1.2501(9)\cdot10^{-2}$	$1.316(3)\cdot10^{-3}$	$1.0644(9)\cdot10^{-2}$
S+I	LO	$6.92(4)\cdot10^{-3}$	$-1.398(6)\cdot10^{-2}$	$-1.85(3)\cdot10^{-3}$	$-1.126(5)\cdot10^{-2}$
B	LO	$1.0(2)\cdot10^{-4}$	$6.554(4)\cdot10^{-2}$	$1.672(2)\cdot10^{-2}$	$4.126(3)\cdot10^{-2}$
S	NLO	$5.67(4)\cdot10^{-3}$	$1.371(3)\cdot10^{-2}$	$1.234(8)\cdot10^{-3}$	$1.198(3)\cdot10^{-2}$
S+I	NLO	$5.2(6)\cdot10^{-3}$	$-1.55(2)\cdot10^{-2}$	$-1.75(6)\cdot10^{-3}$	$-1.288(9)\cdot10^{-2}$
B	NLO	$5(2)\cdot10^{-5}$	$6.749(9)\cdot10^{-2}$	$1.627(5)\cdot10^{-2}$	$4.400(7)\cdot10^{-2}$

Table 84: Cross sections for $\mathrm{qq'}(\to \mathrm{qq'\,H}) \to \mathrm{qq'\,WW} \to \mathrm{qq'}\,\bar{\ell}\nu_{\mathrm{l}}\bar{\nu}_{\ell'}\ell'$ in pp collisions at $\sqrt{s} = 13$ TeV in the SM. Tight VBF cuts are applied (see main text). Cross sections are given for a single lepton flavour combination, but taking into account both charge assignments, e.g. $(\ell, \ell') = (\mathrm{e}, \mu)$ or (μ, e). Other details as in Table 83.

σ[fb]		110 GeV $< M_{\mathrm{WW}} <$ 140 GeV	$M_{\mathrm{WW}} >$ 140 GeV	220 GeV $< M_{\mathrm{WW}} <$ 300 GeV	$M_{\mathrm{WW}} >$ 300 GeV
S	LO	1.7411(9)	$2.370(6)\cdot10^{-1}$	$3.08(2)\cdot10^{-2}$	$1.783(5)\cdot10^{-1}$
S+I	LO	1.740(3)	$-3.00(4)\cdot10^{-1}$	$-4.9(2)\cdot10^{-2}$	$-0.197(3)$
B	LO	$8(2)\cdot10^{-4}$	3.387(2)	0.8642(6)	1.856(2)
S	NLO	1.453(4)	$2.51(2)\cdot10^{-1}$	$2.96(6)\cdot10^{-2}$	$1.95(2)\cdot10^{-1}$
S+I	NLO	1.45(1)	$-3.0(2)\cdot10^{-1}$	$-3(2)\cdot10^{-2}$	$-0.234(9)$
B	NLO	$6.7(7)\cdot10^{-4}$	3.381(6)	0.825(4)	1.933(4)

Table 85: Cross sections for $\mathrm{qq'}(\to \mathrm{qq'\,H}) \to \mathrm{qq'\,Z}(\gamma^*)\mathrm{Z}(\gamma^*) \to \mathrm{qq'}\,\ell\bar{\ell}\ell'\bar{\ell}'$ in pp collisions at $\sqrt{s} = 13$ TeV in the SM. Loose VBF cuts are applied (see main text). Other details as in Table 83.

σ[fb]		110 GeV $< M_{\mathrm{ZZ}} <$ 140 GeV	$M_{\mathrm{ZZ}} >$ 140 GeV	220 GeV $< M_{\mathrm{ZZ}} <$ 300 GeV	$M_{\mathrm{ZZ}} >$ 300 GeV
S	LO	$1.202(2)\cdot10^{-2}$	$1.662(2)\cdot10^{-2}$	$2.153(5)\cdot10^{-3}$	$1.351(2)\cdot10^{-2}$
S+I	LO	$1.197(7)\cdot10^{-2}$	$-1.95(2)\cdot10^{-2}$	$-3.34(5)\cdot10^{-3}$	$-1.441(8)\cdot10^{-2}$
B	LO	$2.2(2)\cdot10^{-4}$	$1.3535(7)\cdot10^{-1}$	$3.821(3)\cdot10^{-2}$	$7.909(5)\cdot10^{-2}$
S	NLO	$1.035(4)\cdot10^{-2}$	$1.781(3)\cdot10^{-2}$	$1.993(9)\cdot10^{-3}$	$1.495(3)\cdot10^{-2}$
S+I	NLO	$1.02(2)\cdot10^{-2}$	$-2.04(2)\cdot10^{-2}$	$-3.1(1)\cdot10^{-3}$	$-1.58(2)\cdot10^{-2}$
B	NLO	$2.0(4)\cdot10^{-4}$	$1.346(2)\cdot10^{-1}$	$3.651(5)\cdot10^{-2}$	$8.108(9)\cdot10^{-2}$

EW Singlet Model, which is given in Section 13.3 of Ref. [9]. Here, interference benchmark cross sections and distributions in the 1HSM are presented. We employ basis (335) of Ref. [9] and specify four benchmark points:

1. $M_{\mathrm{h2}} = 400$ GeV, $\sin\theta = 0.2$,
2. $M_{\mathrm{h2}} = 600$ GeV, $\sin\theta = 0.2$,
3. $M_{\mathrm{h2}} = 600$ GeV, $\sin\theta = 0.4$,
4. $M_{\mathrm{h2}} = 900$ GeV, $\sin\theta = 0.2$,

Table 86: Cross sections for $\mathrm{qq'}(\to \mathrm{qq'\,H}) \to \mathrm{qq'\,WW} \to \mathrm{qq'}\,\bar{\ell}\nu_{\mathrm{l}}\bar{\nu}_{\ell'}\ell'$ in pp collisions at $\sqrt{s} = 13$ TeV in the SM. Loose VBF cuts are applied (see main text). Other details as in Table 84.

σ[fb]		110 GeV $< M_{\mathrm{WW}} <$ 140 GeV	$M_{\mathrm{WW}} >$ 140 GeV	220 GeV $< M_{\mathrm{WW}} <$ 300 GeV	$M_{\mathrm{WW}} >$ 300 GeV
S	LO	3.271(2)	$3.325(9)\cdot10^{-1}$	$5.10(3)\cdot10^{-2}$	$2.301(8)\cdot10^{-1}$
S+I	LO	3.278(6)	$-4.79(9)\cdot10^{-1}$	$-9.7(3)\cdot10^{-2}$	$-2.61(7)\cdot10^{-1}$
B	LO	$1.8(3)\cdot10^{-3}$	7.449(5)	2.004(2)	3.830(3)
S	NLO	2.836(7)	$3.46(3)\cdot10^{-1}$	$4.75(7)\cdot10^{-2}$	$2.50(3)\cdot10^{-1}$
S+I	NLO	2.85(5)	$-4.4(2)\cdot10^{-1}$	$-7.6(9)\cdot10^{-2}$	$-2.7(2)\cdot10^{-1}$
B	NLO	$1.8(2)\cdot10^{-3}$	7.402(9)	1.928(4)	3.949(7)

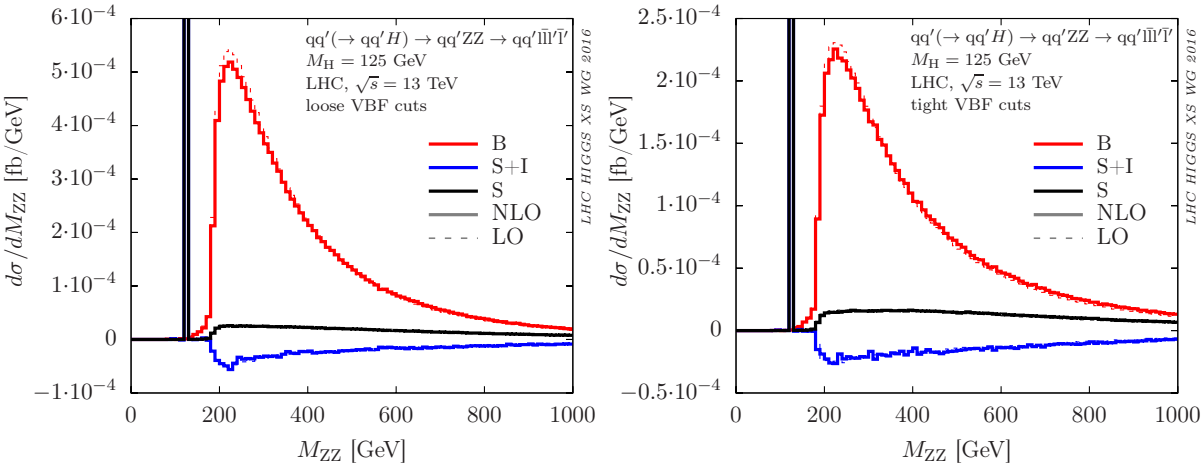

Figure 131: Invariant mass distributions for $\mathrm{qq'}(\to \mathrm{qq'\,H}) \to \mathrm{qq'\,Z}(\gamma^*)\mathrm{Z}(\gamma^*) \to \mathrm{qq'}\,\ell\bar{\ell}\ell'\bar{\ell}'$ in pp collisions at $\sqrt{s} = 13$ TeV in the SM. Loose and tight VBF cuts are applied in the left and right graphs, respectively. Leading order (dashed) and next-to-leading order (solid) results for the Higgs boson signal (S), the signal including signal-background interference (S+I) as well as the interfering background without Higgs contribution (B) are given. Cross sections are given for a single lepton flavour combination.

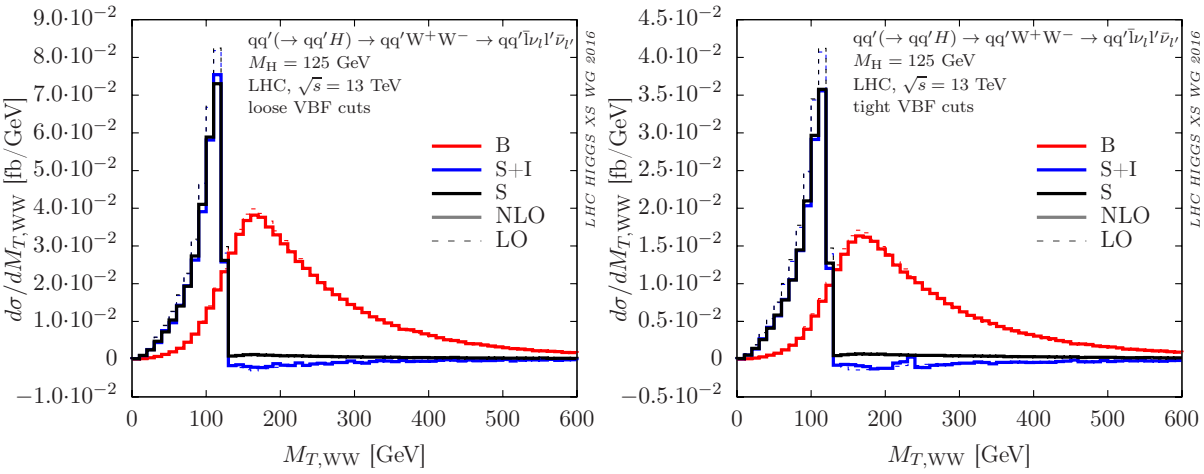

Figure 132: Transverse mass $M_{\mathrm{T,WW}}$ (see Eq. (I.8.2)) distributions for $\mathrm{qq'}(\to \mathrm{qq'\,H}) \to \mathrm{qq'\,WW} \to \mathrm{qq'}\,\bar{\ell}\nu_{\mathrm{l}}\bar{\nu}_{\ell'}\ell'$ in pp collisions at $\sqrt{s} = 13$ TeV in the SM. Cross sections are given for a single lepton flavour combination, but taking into account both charge assignments, e.g. $(\ell, \ell') = (\mathrm{e}, \mu)$ or (μ, e). Other details as in Figure 131.

Table 87: Widths of the physical Higgs bosons h_1 and h_2 in the 1-Higgs-Singlet Extension of the SM with mixing angles $\sin\theta = 0.2$ and $\sin\theta = 0.4$ as well as $\mu_1 = \lambda_1 = \lambda_2 = 0$.

		h_1	h_2		
$\sin\theta$	M [GeV]	125	400	600	900
0.2	Γ [GeV]	$4.34901 \cdot 10^{-3}$	1.52206	5.95419	19.8529
0.4	Γ [GeV]	$3.80539 \cdot 10^{-3}$		22.5016	

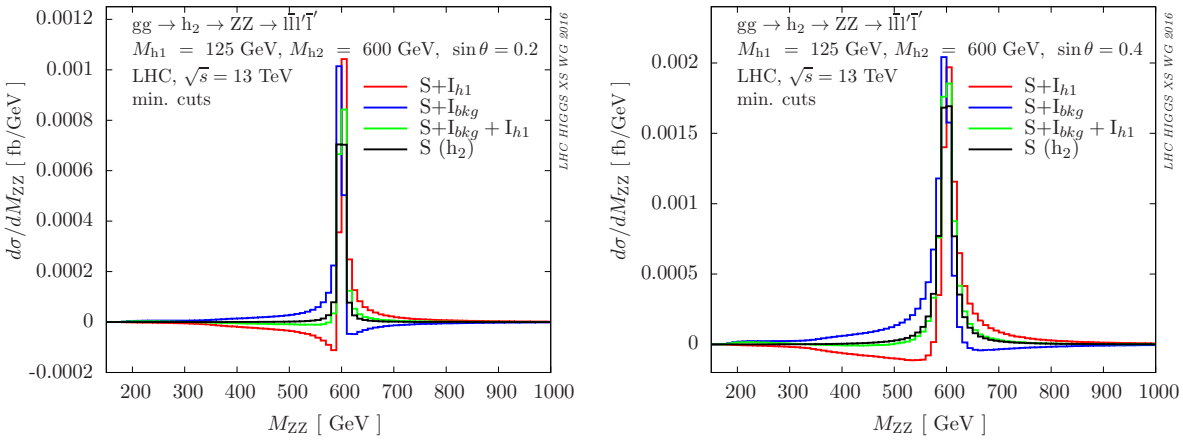

Figure 133: Invariant mass distributions for $gg\ (\to \{h_1, h_2\}) \to Z(\gamma^*)Z(\gamma^*) \to \ell\bar{\ell}\ell'\bar{\ell}'$, other details as in Table 88.

where $M_{h1} = 125$ GeV and $\mu_1 = \lambda_2 = \lambda_1 = 0$ for all points. The corresponding Higgs boson widths are given in Table 87. They have been calculated using FEYNRULES [524].

Gluon-fusion 1HSM benchmark results were computed with GG2VV [499] (see also Ref. [525]). More specifically, cross sections for $gg\ (\to \{h_1, h_2\}) \to Z(\gamma^*)Z(\gamma^*) \to \ell\bar{\ell}\ell'\bar{\ell}'$ for the 13 TeV LHC are given in Tables 88 and 89. The corresponding distributions are shown in Figures 133 and 134, respectively. Results for the heavy Higgs boson signal and its interference with the light Higgs and continuum background and the combined interference are given in Table 88 and Figure 133. In Table 88, the ratio $R_i = (S + I_i)/S$ is used to illustrate the relative change of the heavy Higgs boson signal due to interference with the light Higgs and continuum background amplitude contributions. Heavy-Higgs-light-Higgs interference effects and the coherent sum of all interfering contributions is shown in Table 89 and Figure 134.

Vector-boson-fusion 1HSM benchmark results were computed with PHANTOM [516] (see also Refs. [517,526]) and VBFNLO [275,518] (see also Refs. [519–523]). Good agreement was achieved for all fully-leptonic Higgs boson decay modes. Cross sections for $qq'(\to qq'\{h_1, h_2\}) \to qq'\,Z(\gamma^*)Z(\gamma^*) \to qq'\,\ell\bar{\ell}\ell'\bar{\ell}'$ and $qq'(\to qq'\{h_1, h_2\}) \to qq'\,WW \to qq'\,\ell\bar{\nu}_\ell\ell'\bar{\nu}_{\ell'}$ for the 13 TeV LHC are given in Tables 90 and 92 and Tables 91 and 93 for tight and loose VBF cuts (see Section I.8.3.b), respectively. More specifically, the sum of the light and heavy Higgs contributions including light-heavy interference, the interfering background without Higgs contributions and the sum of the Higgs boson signal and its interference with the background are given. VBF Higgs boson invariant mass distributions in the 1HSM are shown in Figure 135.

The full set of 1HSM benchmark cross sections and distributions is available at https://twiki.cern.ch/twiki/bin/view/LHCPhysics/LHCHXSWGOFFSHELL.

Table 88: Cross sections (fb) for $gg\ (\to \{h_1, h_2\}) \to Z(\gamma^*)Z(\gamma^*) \to \ell\bar{\ell}\ell'\bar{\ell}'$ in pp collisions at $\sqrt{s} = 13$ TeV at loop-induced leading order in the 1-Higgs-Singlet Extension of the SM (1HSM) with $M_{h1} = 125$ GeV, $M_{h2} = 400, 600, 900$ GeV and mixing angle $\sin\theta = 0.2$ or 0.4 as indicated. Results for the heavy Higgs (h_2) signal (S) and its interference with the light Higgs (I_{h1}) and the continuum background (I_{bkg}) and the full interference (I_{full}) are given. The ratio $R_i = (S + I_i)/S$ illustrates the relative change of the heavy Higgs boson signal due to interference with the light Higgs and continuum background amplitude contributions. Cross sections are given for a single lepton flavour combination. Minimal cuts are applied: $M_{\ell\bar{\ell}} > 4$ GeV, $M_{\ell'\bar{\ell}'} > 4$ GeV, $p_{TZ} > 1$ GeV. The integration error is displayed in brackets.

			interference			ratio		
$\sin\theta$	M_{h2} [GeV]	$S(h_2)$	I_{h1}	I_{bkg}	I_{full}	R_{h1}	R_{bkg}	R_{full}
0.2	400	0.07412(6)	0.00682(6)	-0.00171(2)	0.00511(6)	1.092(2)	0.977(1)	1.069(2)
0.2	600	0.01710(2)	-0.00369(3)	0.00384(3)	0.00015(4)	0.784(2)	1.225(2)	1.009(3)
0.2	900	0.002219(2)	-0.003369(9)	0.003058(8)	-0.00031(2)	-0.518(4)	2.378(4)	0.860(6)
0.4	600	0.07065(6)	-0.01191(6)	0.01465(6)	-0.00274(9)	0.831(2)	1.207(2)	1.039(2)

Table 89: Cross sections (fb) for $gg\ (\to \{h_1, h_2\}) \to Z(\gamma^*)Z(\gamma^*) \to \ell\bar{\ell}\ell'\bar{\ell}'$ in pp collisions at $\sqrt{s} = 13$ TeV in the 1HSM with $M_{h1} = 125$ GeV, $M_{h2} = 400, 600, 900$ GeV and mixing angle $\sin\theta = 0.2$ or 0.4 as indicated. Results for the heavy Higgs (h_2) signal (S), light Higgs background (h_1) and continuum background (gg bkg.) are given. Where more than one contribution is included, all interferences are taken into account. Other details as in Table 88.

$\sin\theta$	M_{h2} [GeV]	$S(h_2)$	h_1	gg bkg.	$S + h_1 + I_{h1}$	all
0.2	400	0.07412(6)	0.854(2)	21.18(7)	0.934(2)	21.86(7)
0.2	600	0.01710(2)	0.854(2)	21.18(7)	0.867(2)	21.80(7)
0.2	900	0.002219(2)	0.854(2)	21.18(7)	0.852(2)	21.79(7)
0.4	600	0.07065(6)	0.734(2)	21.18(7)	0.793(2)	21.77(7)

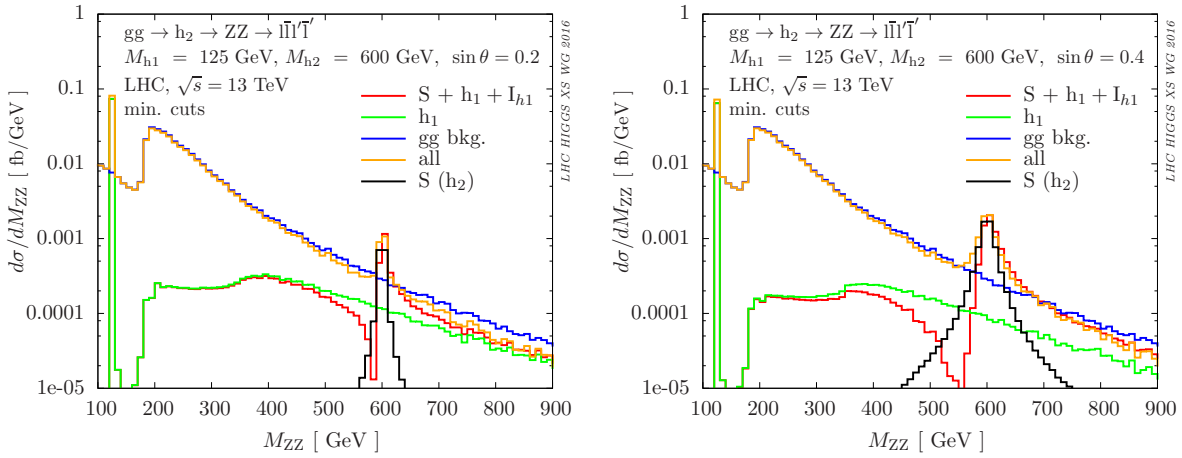

Figure 134: Invariant mass distributions for $gg\ (\to \{h_1, h_2\}) \to Z(\gamma^*)Z(\gamma^*) \to \ell\bar{\ell}\ell'\bar{\ell}'$, other details as in Table 89.

Table 90: Cross sections for $\mathrm{qq}'(\to \mathrm{qq}'\{\mathrm{h}_1, \mathrm{h}_2\}) \to \mathrm{qq}'\,\mathrm{Z}(\gamma^*)\mathrm{Z}(\gamma^*) \to \mathrm{qq}'\,\ell\bar{\ell}\ell'\bar{\ell}'$ in pp collisions at $\sqrt{s} = 13$ TeV in the 1-Higgs-Singlet Extension of the SM (1HSM). Tight VBF cuts (see Section I.8.3.b) are applied. Results are given for the first, second, third and fourth 1HSM benchmark points with $M_{\mathrm{h1}} = 125$ GeV, $\mu_1 = \lambda_2 = \lambda_1 = 0$ and $(M_{\mathrm{h2}}[\mathrm{GeV}], \sin\theta) = (400, 0.2), (600, 0.2), (600, 0.4), (900, 0.2)$, respectively. The sum of the light and heavy Higgs contributions including light-heavy interference (S), the interfering background without Higgs contributions (B) and the sum of the Higgs boson signal and its interference with the background (S+I) are given. Cross sections are given at leading order and for a single lepton flavour combination. The integration error is displayed in brackets.

σ[fb]	1HSM point	$M_{\mathrm{ZZ}} > 140$ GeV	220 GeV $< M_{\mathrm{ZZ}} <$ 300 GeV	$M_{\mathrm{ZZ}} > 300$ GeV
S	1	$1.686(2)\cdot10^{-2}$	$1.185(4)\cdot10^{-3}$	$1.514(2)\cdot10^{-2}$
S+I	1	$-9.69(3)\cdot10^{-3}$	$-1.85(2)\cdot10^{-3}$	$-6.90(2)\cdot10^{-3}$
B	1	$6.725(2)\cdot10^{-2}$	$1.750(1)\cdot10^{-2}$	$4.148(2)\cdot10^{-2}$
S	2	$1.436(1)\cdot10^{-2}$	$1.232(4)\cdot10^{-3}$	$1.259(1)\cdot10^{-2}$
S+I	2	$-1.180(3)\cdot10^{-2}$	$-1.88(2)\cdot10^{-3}$	$-9.00(2)\cdot10^{-3}$
B	2	$6.725(2)\cdot10^{-2}$	$1.750(1)\cdot10^{-2}$	$4.148(2)\cdot10^{-2}$
S	3	$2.025(2)\cdot10^{-2}$	$8.90(4)\cdot10^{-4}$	$1.895(2)\cdot10^{-2}$
S+I	3	$-4.34(3)\cdot10^{-3}$	$-1.74(2)\cdot10^{-3}$	$-1.72(3)\cdot10^{-3}$
B	3	$6.725(2)\cdot10^{-2}$	$1.750(1)\cdot10^{-2}$	$4.148(2)\cdot10^{-2}$
S	4	$1.263(1)\cdot10^{-2}$	$1.238(4)\cdot10^{-3}$	$1.085(1)\cdot10^{-2}$
S+I	4	$-1.309(3)\cdot10^{-2}$	$-1.86(2)\cdot10^{-3}$	$-1.029(2)\cdot10^{-2}$
B	4	$6.725(2)\cdot10^{-2}$	$1.750(1)\cdot10^{-2}$	$4.148(2)\cdot10^{-2}$

I.8.3.d Multijet merging effects in $gg \to \ell\bar{\nu}_\ell\bar{\ell}'\nu_{\ell'}$ using SHERPA

I.8.3.d.i Set-up

In this section, results for the loop–induced process $gg \to \ell\bar{\nu}_\ell\bar{\ell}'\nu_{\ell'}$ obtained with the SHERPA event generation framework [229] will be presented, with the goal to highlight the effect of multijet merging [242] on some critical observables. This is accomplished by directly comparing the results where the leading order processes depicted in Figure 136 have been supplemented with the parton shower (labelled LOOP2+PS) with a sample where an additional jet has been produced, *i.e.* the quark-loop induced processes $gg \to \ell\bar{\nu}_\ell\bar{\ell}'\nu_{\ell'}g$ and $qg \to \ell\bar{\nu}_\ell\bar{\ell}'\nu_{\ell'}q$ (labelled MEPS@LOOP2) as shown in Figure 137. In addition, these two samples are further subdivided into those including a Higgs boson of $m_H = 125$ GeV and those where the Higgs boson has been decoupled with $m_H \to \infty$. Here, the matrix elements are provided from the OPENLOOPS +COLLIER package [247, 248] are being used. For parton showering, the implementation of [355] is employed, with a starting scale

$$\mu_Q^2 = p^2_{\perp,\ell\bar{\nu}_\ell\bar{\ell}'\nu_{\ell'}} + m^2_{\ell\bar{\nu}_\ell\bar{\ell}'\nu_{\ell'}}\,. \tag{I.8.3}$$

A similar analysis, although for centre-of-mass energies of 8 TeV has already been presented in [352]. Here, in addition, the effect of including a Higgs boson with mass $m_H = 125$ GeV is investigated, which was not the case in the previous analysis. Results without the Higgs boson are obtained by effectively decoupling it, pushing its mass to very high values in the calculation, $m_H \to \infty$.

Table 91: Cross sections for $\mathrm{qq}'(\to \mathrm{qq}'\{\mathrm{h}_1,\mathrm{h}_2\}) \to \mathrm{qq}'\,\mathrm{WW} \to \mathrm{qq}'\,\ell\overline{\nu}_l\overline{\ell}'\nu_{\ell'}$ in pp collisions at $\sqrt{s} = 13$ TeV in the 1-Higgs-Singlet Extension of the SM. Tight VBF cuts are applied. Cross sections are given for a single lepton flavour combination, but taking into account both charge assignments, e.g. $(\ell,\ell') = (\mathrm{e},\mu)$ or (μ,e). Other details as in Table 90.

σ[fb]	1HSM point	$M_{\mathrm{WW}} > 140$ GeV	220 GeV $< M_{\mathrm{WW}} <$ 300 GeV	$M_{\mathrm{WW}} > 300$ GeV
S	1	$3.283(3)\cdot10^{-1}$	$2.68(1)\cdot10^{-2}$	$2.758(3)\cdot10^{-1}$
S+I	1	$-1.98(2)\cdot10^{-1}$	$-4.9(1)\cdot10^{-2}$	$-9.8(1)\cdot10^{-2}$
B	1	3.382(2)	$8.63(1)\cdot10^{-1}$	1.854(1)
S	2	$2.727(3)\cdot10^{-1}$	$2.80(1)\cdot10^{-2}$	$2.189(2)\cdot10^{-1}$
S+I	2	$-2.48(2)\cdot10^{-1}$	$-4.9(1)\cdot10^{-2}$	$-1.48(1)\cdot10^{-1}$
B	2	3.382(2)	0.863(1)	1.854(1)
S	3	$3.937(4)\cdot10^{-1}$	$2.01(1)\cdot10^{-2}$	$3.541(4)\cdot10^{-1}$
S+I	3	$-8.4(2)\cdot10^{-2}$	$-4.6(1)\cdot10^{-2}$	$9(1)\cdot10^{-3}$
B	3	3.382(2)	0.863(1)	1.854(1)
S	4	$2.377(2)\cdot10^{-1}$	$2.81(1)\cdot10^{-2}$	$1.836(2)\cdot10^{-1}$
S+I	4	$-2.75(1)\cdot10^{-1}$	$-4.88(1)\cdot10^{-2}$	$-1.74(1)\cdot10^{-1}$
B	4	3.382(2)	0.863(1)	1.854(1)

Table 92: Cross sections for $\mathrm{qq}'(\to \mathrm{qq}'\{\mathrm{h}_1,\mathrm{h}_2\}) \to \mathrm{qq}'\,\mathrm{Z}(\gamma^*)\mathrm{Z}(\gamma^*) \to \mathrm{qq}'\,\ell\overline{\ell}\ell'\overline{\ell}'$ in pp collisions at $\sqrt{s} = 13$ TeV in the 1-Higgs-Singlet Extension of the SM. Loose VBF cuts are applied. Other details as in Table 90.

σ[fb]	1HSM point	$M_{\mathrm{ZZ}} > 140$ GeV	220 GeV $< M_{\mathrm{ZZ}} <$ 300 GeV	$M_{\mathrm{ZZ}} > 300$ GeV
S	1	$2.272(2)\cdot10^{-2}$	$1.94(1)\cdot10^{-3}$	$1.983(2)\cdot10^{-2}$
S+I	1	$-1.34(1)\cdot10^{-2}$	$-3.33(4)\cdot10^{-3}$	$-8.17(5)\cdot10^{-3}$
B	1	$1.3950(5)\cdot10^{-1}$	$4.005(3)\cdot10^{-2}$	$7.964(4)\cdot10^{-2}$
S	2	$1.889(2)\cdot10^{-2}$	$2.00(1)\cdot10^{-3}$	$1.592(2)\cdot10^{-2}$
S+I	2	$-1.68(1)\cdot10^{-2}$	$-3.40(4)\cdot10^{-3}$	$-1.154(5)\cdot10^{-2}$
B	2	$1.3950(5)\cdot10^{-1}$	$4.005(3)\cdot10^{-2}$	$7.964(4)\cdot10^{-2}$
S	3	$2.590(3)\cdot10^{-2}$	$1.45(1)\cdot10^{-3}$	$2.372(2)\cdot10^{-2}$
S+I	3	$-6.9(1)\cdot10^{-3}$	$-3.12(4)\cdot10^{-3}$	$-2.1(1)\cdot10^{-3}$
B	3	$1.3950(5)\cdot10^{-1}$	$4.005(3)\cdot10^{-2}$	$7.964(4)\cdot10^{-2}$
S	4	$1.658(2)\cdot10^{-2}$	$2.02(1)\cdot10^{-3}$	$1.359(2)\cdot10^{-2}$
S+I	4	$-1.85(1)\cdot10^{-2}$	$-3.36(4)\cdot10^{-3}$	$-1.329(5)\cdot10^{-2}$
B	4	$1.3950(5)\cdot10^{-1}$	$4.005(3)\cdot10^{-2}$	$7.964(4)\cdot10^{-2}$

Table 93: Cross sections for $\mathrm{qq}'(\to \mathrm{qq}'\{\mathrm{h}_1, \mathrm{h}_2\}) \to \mathrm{qq}'\,\mathrm{WW} \to \mathrm{qq}'\,\ell\overline{\nu}_\ell\overline{\ell}'\nu_{\ell'}$ in pp collisions at $\sqrt{s} = 13$ TeV in the 1-Higgs-Singlet Extension of the SM. Loose VBF cuts are applied. Other details as in Table 91.

σ[fb]	1HSM point	$M_{\mathrm{WW}} > 140$ GeV	220 GeV $< M_{\mathrm{WW}} <$ 300 GeV	$M_{\mathrm{WW}} > 300$ GeV
S	1	$4.600(5)\cdot10^{-1}$	$4.46(1)\cdot10^{-2}$	$3.692(4)\cdot10^{-1}$
S+I	1	$-3.25(4)\cdot10^{-1}$	$-9.3(2)\cdot10^{-2}$	$-1.23(3)\cdot10^{-1}$
B	1	7.424(3)	2.001(1)	3.815(2)
S	2	$3.733(3)\cdot10^{-1}$	$4.59(1)\cdot10^{-2}$	$2.805(3)\cdot10^{-1}$
S+I	2	$-4.05(4)\cdot10^{-1}$	$-9.2(2)\cdot10^{-2}$	$-2.00(3)\cdot10^{-1}$
B	2	7.424(3)	2.001(1)	3.815(2)
S	3	$5.17(1)\cdot10^{-1}$	$3.33(1)\cdot10^{-2}$	$4.482(5)\cdot10^{-1}$
S+I	3	$-1.88(4)\cdot10^{-1}$	$-8.5(2)\cdot10^{-2}$	$+1(3)\cdot10^{-3}$
B	3	7.424(3)	2.001(1)	3.815(2)
S	4	$3.274(3)\cdot10^{-1}$	$4.65(1)\cdot10^{-2}$	$2.339(3)\cdot10^{-1}$
S+I	4	$-4.43(4)\cdot10^{-1}$	$-9.6(2)\cdot10^{-2}$	$-2.38(3)\cdot10^{-1}$
B	4	7.424(3)	2.001(1)	3.815(2)

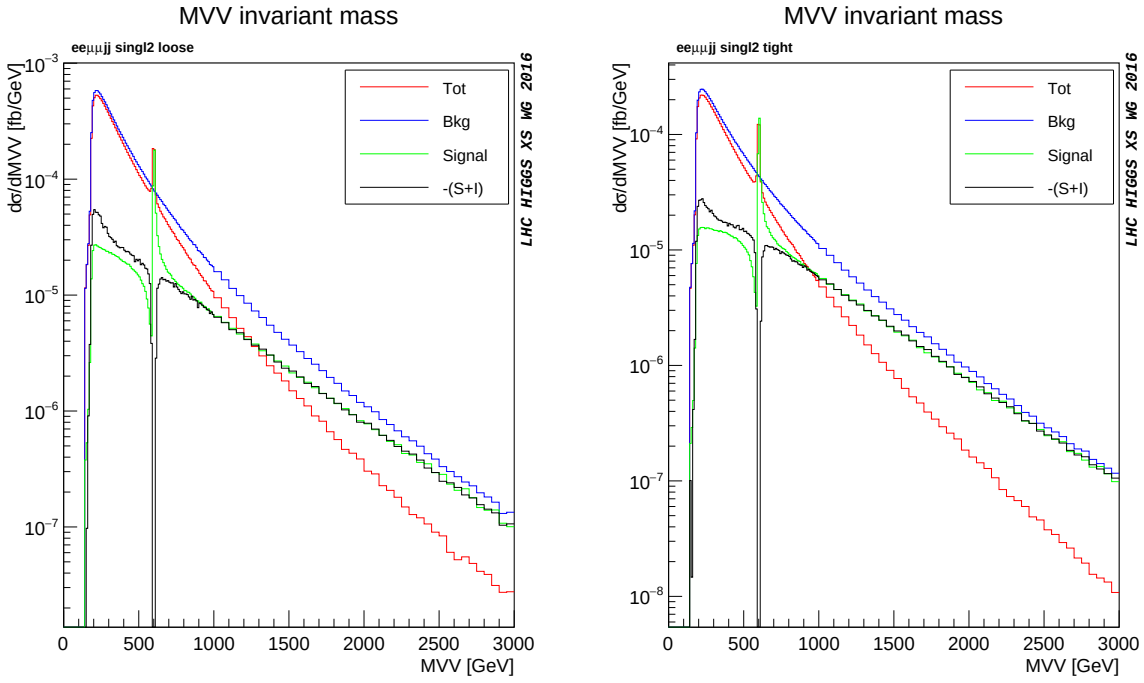

Figure 135: Invariant mass distributions for $\mathrm{qq}'(\to \mathrm{qq}'\{\mathrm{h}_1, \mathrm{h}_2\}) \to \mathrm{qq}'\,\mathrm{Z}(\gamma^*)\mathrm{Z}(\gamma^*) \to \mathrm{qq}'\,\ell\overline{\ell}\ell'\overline{\ell}'$ in pp collisions at $\sqrt{s} = 13$ TeV. Loose and tight VBF cuts are applied in the left and right graphs, respectively. Results for the second 1HSM benchmark point ($M_{\mathrm{h1}} = 125$ GeV, $M_{\mathrm{h2}} = 600$ GeV, $\sin\theta = 0.2$) are shown: the sum of the light and heavy Higgs contributions including light-heavy interference (Signal), the interfering background without Higgs contributions (Bkg), the sum of Signal and Bkg including interference (Tot), and the negative of the sum of Signal and its interference with Bkg (-(S+I)). Other details as in Table 90.

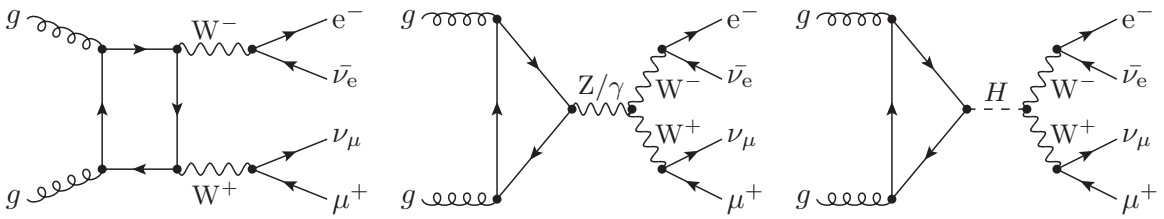

Figure 136: Leading order Feynman diagrams contributing to $gg \to \ell\bar{\nu}_\ell\bar{\ell}'\nu_{\ell'}$.

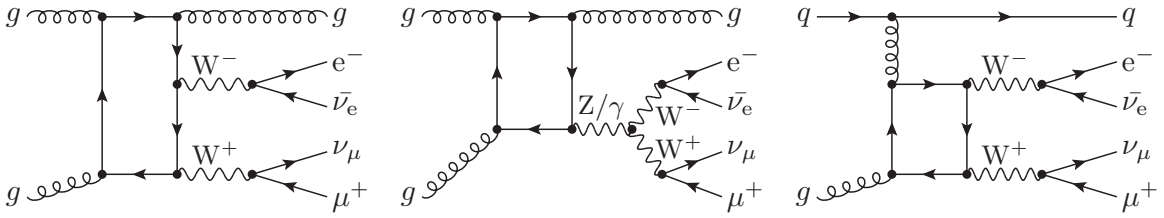

Figure 137: Leading order Feynman diagrams contributing to the background production of final states $\ell\bar{\nu}_\ell\bar{\ell}'\nu_{\ell'}$+jet through a quark loop.

I.8.3.d.ii Results

In this investigation the following cuts have been applied:

$$\begin{aligned} p_{\perp,\ell} &\geq 25\,\text{GeV}\,, & |\eta_\ell| &\leq 2.5 \\ p_{\perp,j} &\geq 30\,\text{GeV}\,, & |\eta_j| &\leq 5\,, \end{aligned}$$

where jets are defined by the anti-k_T algorithm with $R = 0.4$. In addition a cut on the missing transverse momentum has been applied,

$$\not{E}_T \geq 25\,\text{GeV}\,, \tag{I.8.4}$$

which of course is practically given by the combined neutrino momenta.

In Figure 138 inclusive and exclusive jet multiplicities as obtained from the samples described above are displayed. They clearly show that especially for jet multiplicities $N_{\text{jet}} \geq 1$ the impact of multijet merging is sizeable and important. Furthermore, there is a visible difference in the overall rate of about a factor of 2 between the results with and without the Higgs boson. This becomes even more visible when considering cross sections after the application of a jet veto, cf. the right panel of Figure 139. Multijet merging leads to jets that are visibly harder – the LOOP2+PS results fall of very quickly with respect to the merged result, see the left panel of Figure 138. However, since the bulk of the inclusive cross section is related to jet transverse momenta below about 30 GeV, the jet-vetoed cross section saturates relatively quickly and is thus correspondingly independent of the hard tails in transverse momentum. This ultimately leads to effects of the order of about 10% or so from multijet merging. At the same time, in the linear plot of the jet-vetoed cross section the rate difference due to the inclusion of the Higgs boson becomes visible. As expected, these differences manifest themselves in the usual kinematic regions stemming from spin effects in the decay of the W bosons, illustrated in Figure 140. Clearly, the presence of a Higgs boson pushes the leptons closer in phase space. Since the overall rate is dominated by the 0-jet bin, the differences between merged and LO samples are again relatively small, of the order of 10% or below.

To summarize: the application of multijet merging to loop–induced processes $gg \to VV^{(*)}$ leads to visibly harder jet spectra and significantly larger jet multiplicities, irrespective of whether this process is mediated by a Higgs boson or not. It is clearly the overall scale of the process and the fact that the

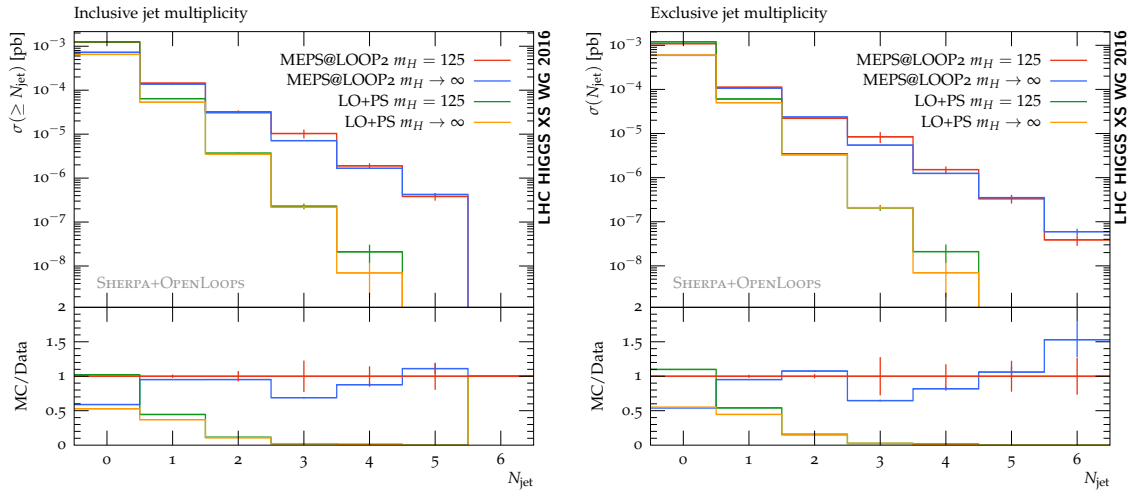

Figure 138: Inclusive (left) and exclusive (right) jet cross sections with and without multijet merging and with ($m_H = 125$ GeV) and without ($m_H \to \infty$) including a Higgs boson, including multijet merging or merely relying on the parton shower to simulate all QCD emissions.

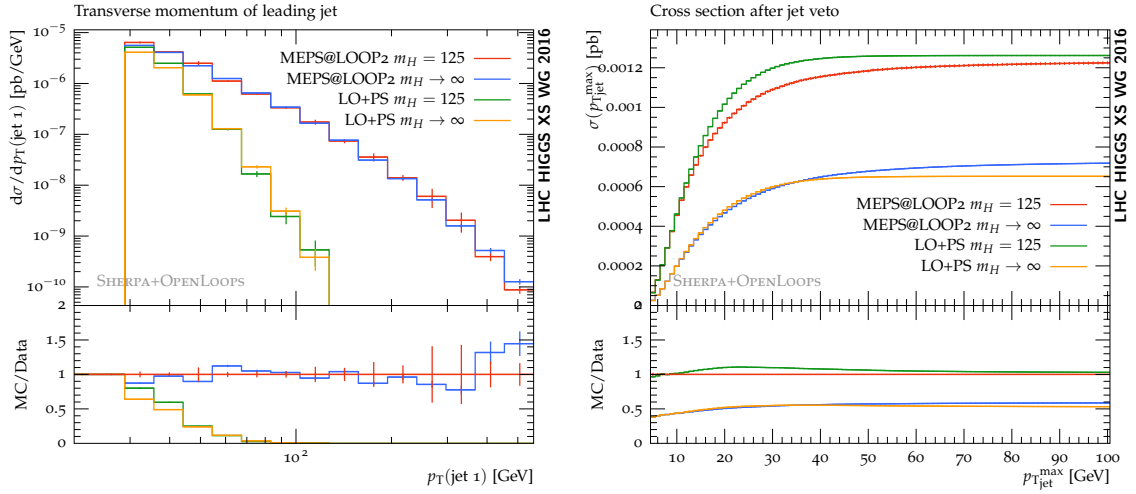

Figure 139: Differential cross section in dependence of the transverse momentum of the leading jet (left) and the cross section after application of a jet veto in dependence of the transverse momentum cut on jets (right).

initial states are identical that is responsible here. The effect on jet-vetoed cross sections in the 0-jet bin is small, 10% or below, since these cross sections essentially appear after integration over the jet-cross section up to the veto scale. Clearly, though, this would be different when asking for exactly one jet and vetoing further jets. The impact of the merging is small on the lepton correlations in the regions that are important for the definition of signal and background regions.

I.8.3.e Study of higher-order QCD corrections in the gg→H→VV process

I.8.3.e.i Introduction

The analysis [507] employed to extract the off-shell signal strength in the high mass ($m_{4\ell}$ >220 GeV) ZZ→4ℓ, ZZ→2ℓ2ν and WW→ $\ell\nu\ell\nu$ final states, is based on two Monte Carlo simulations for gg-initiated processes, namely gg2VV [513] and MCFM [501]. The dominant gg-initiated processes used

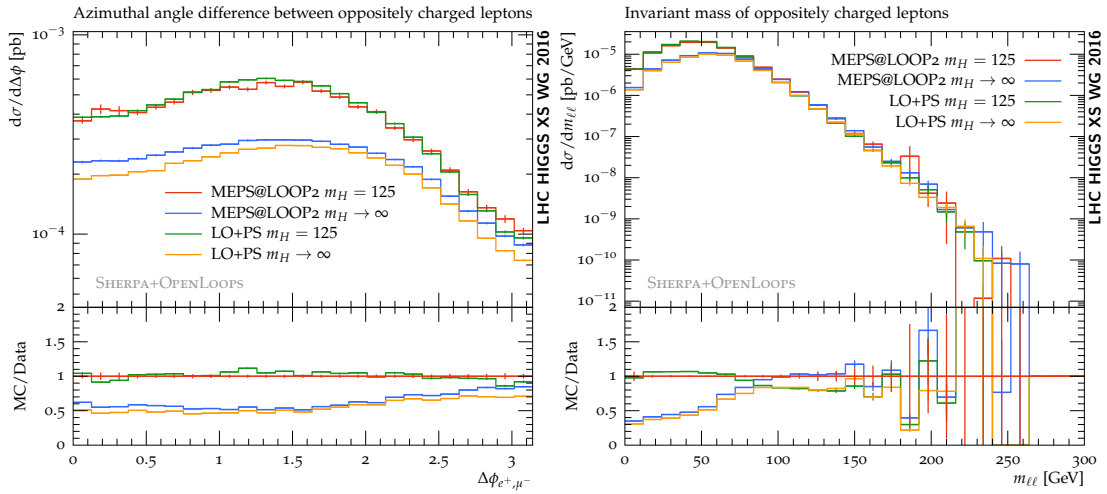

Figure 140: Differential cross section in dependence of the transverse separation of the two leptons (left) and of their invariant mass (right).

in the analysis [507] are listed below:

1. gg→ H → ZZ, the signal (S) comprising both the on-shell peak at m_{H} =125.5 GeV and the off-shell region where the Higgs boson acts as a propagator;
2. gg→ ZZ, the continuum background (B);
3. gg→ (H^*) → ZZ, the signal, continuum background and interference contribution, labelled as SBI in what follows.

However, only Lowest-Order (LO) in QCD Monte Carlo simulations are available, namely gg2VV and MCFM with Pythia8 [318] showering. For this reason, mass-dependent K-factors to higher order accuracy are needed to achieve a better precision.

– For the signal process, higher order QCD corrections are computed: LO to Next-to-Next-to-Leading-Order (NNLO) K-factors are calculated as a function of the diboson invariant mass m_{ZZ}.
– For the background process, the full K-factor from LO to NNLO accuracy is currently not available.

Different approaches exploited in order to take into account the absence of higher order QCD corrections in gg→ (H^*) →VV final states (it is to note that Next-to-Leading Order, NLO, gg→ZZ QCD calculation has been recently performed [527]) and the systematic uncertainties associated to these processes will be detailed in the following sections.

I.8.3.e.ii Parton Shower Scheme Dependence

Given that no higher order matrix element calculations are available for the gg-initiated processes, the only way to simulate QCD radiation is through the parton shower. However, as the generation is done at LO in QCD, there is no clear prescription to evaluate the systematic uncertainties on the QCD scale. According to the maximum jet p_{T} scale emission characterizing the parton showers, two different configurations [528] are exploited, the *power shower* (the emission is allowed up to the kinematical limit) and the *wimpy shower* (the shower is started at the value of the factorization or the renormalization scale). Pythia8 is tuned as default with the power shower option. The comparison is carried out involving the following parton shower schemes at generator level:

– Pythia8 power shower including a matrix element correction on the first jet emission such that information coming from the exact matrix element calculation is exploited for the hardest jet in the shower [318];

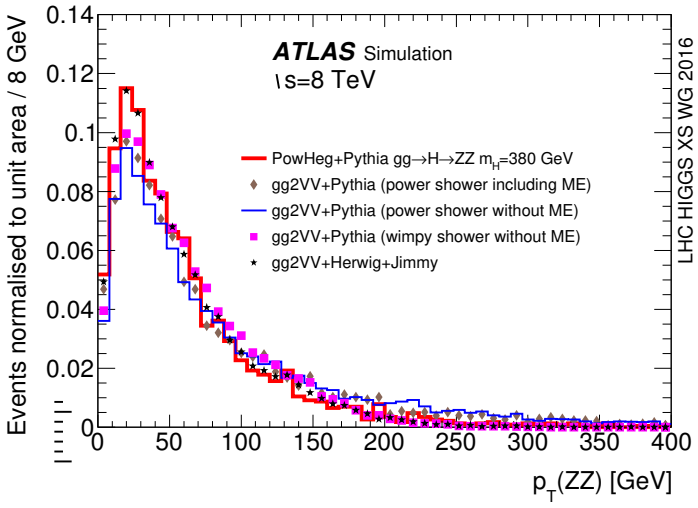

Figure 141: Distribution of p_{T}(ZZ) comparing the NLO generator Powheg showered with Pythia8, the LO generator gg2VV + Pythia (power or wimpy shower), the LO generator gg2VV showered with Jimmy+Herwig. All samples are restricted to the range (345< $m_{4\ell}$ <415) GeV.

– Pythia8 power shower without a matrix element correction;
– Pythia8 wimpy shower without a matrix element correction;
– Herwig6.5 [338] in combination with Jimmy.

The items above are finally compared to high-mass Powheg-Box [80] NLO gg→ H → ZZ event sample with a Higgs boson mass generated with m_{H}=380 GeV, chosen around the most sensitive off-shell invariant mass region for the analysis. The normalized p_{T}(ZZ) distributions, detailed in Figure 141 as reported in Ref. [528] for the sample above in the text are plotted in the same high ZZ mass range (345< $m_{4\ell}$ <415) GeV in order to ensure a compatible mass of the hard interaction system. As the default samples are generated with the LO gg→ (H^*) →ZZ matrix element with Pythia8 using the power shower parton shower option and this sample shows the largest deviation from Powheg, the full difference of the order of 10% is taken as a systematic uncertainty in the ATLAS analysis as in [507].

I.8.3.e.iii Higher order QCD corrections to the transverse momentum and the rapidity of the ZZ system

Higher order QCD corrections for the gg→ ZZ processes are studied using the Sherpa+OpenLoops [229, 247] generator that contains the LO gg→ZZ+1-jet matrix element and merges this with the LO gg→ZZ+ 0-jet matrix element. For the gg→ H → ZZ signal contribution with m_{H}=380 GeV (on-shell signal), the Powheg generator reweighted (as a function of p_{T}) to the HRes2.1 prediction [223] to reach NNLO+NNLL accuracy is also used. Figures 142, 143 and 144 include validation distributions of various comparisons of the variables of interest, namely the transverse momentum, p_{T}(ZZ), and the rapidity, Y(ZZ), of the ZZ system in both on-shell and off-shell mass regions using Powheg+Pythia8, Sherpa+OpenLoops and gg2VV+Pythia8 generators using kinematic variables computed at truth level. The list of cuts applied in the generation level can be found below (p_{T}^{ℓ} is the transverse momentum of each lepton in the final state, $|\eta^{\ell}|$ represents its rapidity [I.51] while m_{Z1} is the Z boson mass closest to the

[I.51] ATLAS uses a right-handed coordinate system with its origin at the nominal interaction point (IP) in the centre of the detector, and the z-axis along the beam line. The x-axis points from the IP to the centre of the LHC ring, and the y-axis points upwards. Cylindrical coordinates (r, ϕ) are used in the transverse plane, ϕ being the azimuthal angle around the beam line. Observables labelled *transverse* are projected into the x-y plane. The pseudorapidity is defined in terms of the polar angle θ as η=-ln tan($\frac{\theta}{2}$).

Z peak, being m_{Z2} the mass of the second lepton pair):

- $m_{4\ell}$ >100 GeV;
- p_{T}^{ℓ} >3 GeV;
- $|\eta^{\ell}|$ <2.8;
- $m_{Z1,Z2}$ > 4 GeV.

Additional selection criteria are applied on the final state quadruplet (the leptons in the quadruplet are ordered in transverse momentum and denoted with the superscript ℓ in what follows) in the Monte Carlo samples in such a way to mimic the standard selection reported in Ref. [507], namely:

- $p_{T}^{\ell 1}$ >20 GeV, $p_{T}^{\ell 2}$ >15 GeV, $p_{T}^{\ell 3}$ >10 GeV, $p_{T}^{\ell 4}$ >5 (6) GeV for muons (electrons);
- $|\eta^{\ell}|$ <2.5;
- (50< m_{Z1} <106) GeV;
- if $m_{4\ell}$ <140 GeV → m_{Z2} >12 GeV, if 140< $m_{4\ell}$ <190 GeV → m_{Z2} >0.76·($m_{4\ell}$-140)+12 GeV, if $m_{4\ell}$ >190 GeV → m_{Z2} >50 GeV.

The errors bars in Figures 142, 143 and 144 indicate the statistical uncertainty related to the finite Monte Carlo statistics only. The systematic uncertainties, when applicable, are drawn as shaded boxes, extracted from scale variations on Sherpa+OpenLoops and HRes2.1 as described in the following Section I.8.3.e.iv. The systematic uncertainties from the HRes2.1 are applicable here as the Powheg generator is directly reweighted to the HRes2.1 prediction. The results and the distributions reported in the following figures refer to Monte Carlo samples generated at a collision energy $\sqrt{s}$=8 TeV.

As highlighted in Figure 142 (a) for what concerns the on-shell and Figure 142 (b) for the off-shell, the lack of higher QCD calculations in gg2VV results in different p_{T} spectra (order of 20% in the relevant kinematic region) compared to the higher order Powheg and Sherpa+OpenLoops Monte Carlo. In the high mass region, the off-shell (generated with m_{H}=125.5 GeV) and on-shell (produced with m_{H}=380 GeV) Higgs boson productions with gg2VV match fairly well as shown in Figure 142 (b).
Figure 143 (a) shows that the differences in p_{T} between Sherpa and gg2VV in the off-shell high mass region are not fully covered by the uncertainties assigned to Sherpa. Since the Sherpa generator has a better treatment of the first hard jet emission, in the H →ZZ→4ℓ analysis, gg2VV is reweighted to the Sherpa prediction in the ATLAS analysis [507]. As for the rapidity distribution reported in Figure 143 (b), no significant difference between gg2VV and Sherpa is present in the high mass region; hence, the reweighting procedure on Y is not necessary.
Figures 143 (c) and (d) stress the fact that the ZZ-transverse momentum and the rapidity of the signal process gg→ (H^{*}) → ZZ differ from the gg→ ZZ background process and the SBI unlike the gg2VV generator as noted in Figures 144 (a) and (b). This is caused by the presence of the additional matrix element correction to the first jet emission included in Sherpa that generates a different treatment of signal and background components. This statement has been explicitly validated by removing the 1-jet matrix element computation in Sherpa: full compatibility is found between signal and background once the 1-jet ME treatment is removed in Sherpa.

In the analysis deployed by ATLAS [507], the LO gg2VV generator, whose p_{T} and y distributions are displayed in Figure 144, is reweighted to Sherpa+OpenLoops in the p_{T} of the VV system to achieve a better description of the p_{T} spectrum: the impact of the reweighting on the acceptance is calculated to be below 1% for the signal and at the level of 4-6% for the background. In the ZZ→4ℓ channel, the reweighting procedure is only used to account for the acceptance effects, as the matrix-element discriminant employed to disentangle signal and background components is insensitive to the p_{T} of the ZZ system. For the ZZ→2ℓ2ν channel, the reweighting is applied in both the transverse mass shape and acceptance as the m_{T} holds dependence on the transverse momentum of the ZZ system.

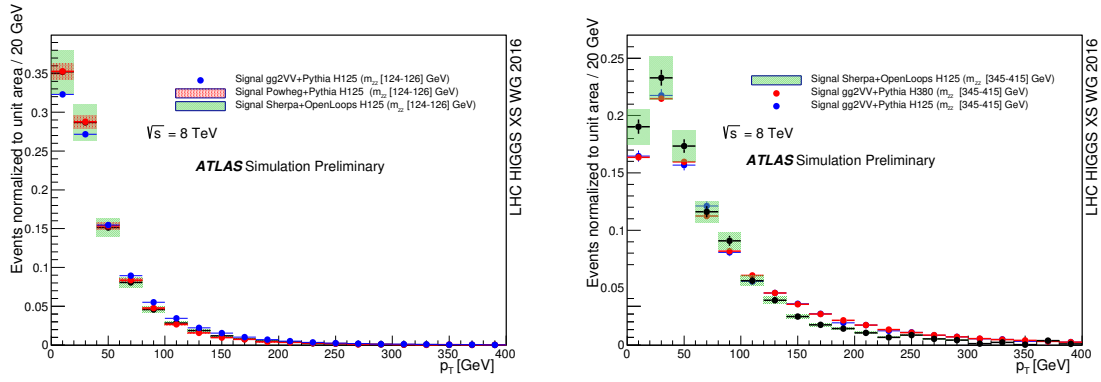

(a) (b)

Figure 142: Comparison of the on-shell gg→ (H^*) → ZZ signal process in p_{T} (a) generated with m_{H}=125.5 GeV in the mass range $m_{\mathrm{ZZ}} \in$ [124,126] GeV for Powheg, Sherpa and gg2VV. Comparison of the gg→ (H^*) → ZZ off-shell signal process in p_{T} (b) with m_{H}=125.5 GeV produced with gg2VV and Sherpa and gg→ (H^*) → ZZ signal process with m_{H}=380 GeV using gg2VV (on-shell) in the region $m_{\mathrm{ZZ}} \in$ [345,415] GeV.

Table 94: Scale variations considered in the evaluation of the theoretical uncertainties related to the p_{T}(ZZ) and Y(ZZ) for the $gg \to H \to$ZZ and $q\bar{q} \to$ZZ processes. The scale variations on Sherpa signal detailed in the second row are also applied on the Sherpa gg→ZZ continuum background as stated in the text. The merging scale for Sherpa has not been modified for this study.

Process	MC	Nominal Scales	Scale variations	# Variations
$gg \to H \to ZZ$	HRes	$\mu_{\mathrm{R}} = \mu_{\mathrm{F}} = \frac{m_{\mathrm{ZZ}}}{2}$	$(\frac{1}{2}\mu_{\mathrm{R/F}}, 2\mu_{\mathrm{R/F}})$, $\frac{1}{2} \leq \mu_{\mathrm{F}}/\mu_{\mathrm{R}} \geq 2$	6
		$\mu_{\mathrm{Q}} = m_{\mathrm{ZZ}}/2$, $\mu_{\mathrm{B}} = m_{\mathrm{b}}$	$(\frac{1}{2}\mu_{\mathrm{Q}}, 2\mu_{\mathrm{Q}})$, $(\frac{1}{4}\mu_{\mathrm{B}}, 4\mu_{\mathrm{B}})$	8
$gg \to H \to ZZ$	Sherpa	$\mu_{\mathrm{R}} = \mu_{\mathrm{F}} = \frac{m_{\mathrm{ZZ}}}{2}$	$(\frac{1}{2}\mu_{\mathrm{R/F}}, 2\mu_{\mathrm{R/F}})$, $\frac{1}{2} \leq \mu_{\mathrm{F}}/\mu_{\mathrm{R}} \geq 2$	6
		$\mu_{\mathrm{Q}} = m_{\mathrm{ZZ}}/2$, $\mu_{\mathrm{B}} = m_{\mathrm{b}}$	$(\frac{1}{\sqrt{2}}\mu_{\mathrm{Q}}, \sqrt{2}\mu_{\mathrm{Q}})$	2
$q\bar{q} \to ZZ$	Powheg	$\mu_{\mathrm{R}} = \mu_{\mathrm{F}} = m_{\mathrm{ZZ}}$	$(\frac{1}{2}\mu_{\mathrm{R/F}}, 2\mu_{\mathrm{R/F}})$	6

I.8.3.e.iv Scale variations on the gg-initiated samples

In order to evaluate the systematic effects on the uncertainties on p_{T} and η in the ZZ frame, the procedure is applied by varying the renormalization scale (μ_{R}), the factorization scale (μ_{F}), the resummation scale (μ_{Q}) and the resummation scale related to the bottom quark mass (μ_{B}).

The impact of the PDF uncertainties is also evaluated: the nominal PDF set, CT10 [529], applied on the Powheg signal sample at m_{H}=125.5 GeV are compared with MSTW2008 [30] and with NNPDF2.3 [31] in bins of ZZ-transverse momentum and rapidity. Its impact is found to be below 3%.

The Monte Carlo simulations employed for these studies and the full scheme of scale variations applied to these samples are listed in Table 94. Assuming that the resummation scales (μ_{Q} and μ_{B}) variations are independent of the normalization and factorization scales (μ_{R} and μ_{F}), we fix the vector pair (μ_{R}, μ_{F}) while varying μ_{Q} or μ_{B}. Similarly we fix the resummation scales, μ_{Q} and μ_{B}, while varying μ_{R} and μ_{F}. Following the usual prescriptions, the nominal scale of the process is set to $m_{\mathrm{ZZ}}/2$ while the nominal value for the resummation scale related to the bottom mass is set to m_{b} and the Powheg nominal values for renormalization and factorization scales are set to m_{ZZ}.

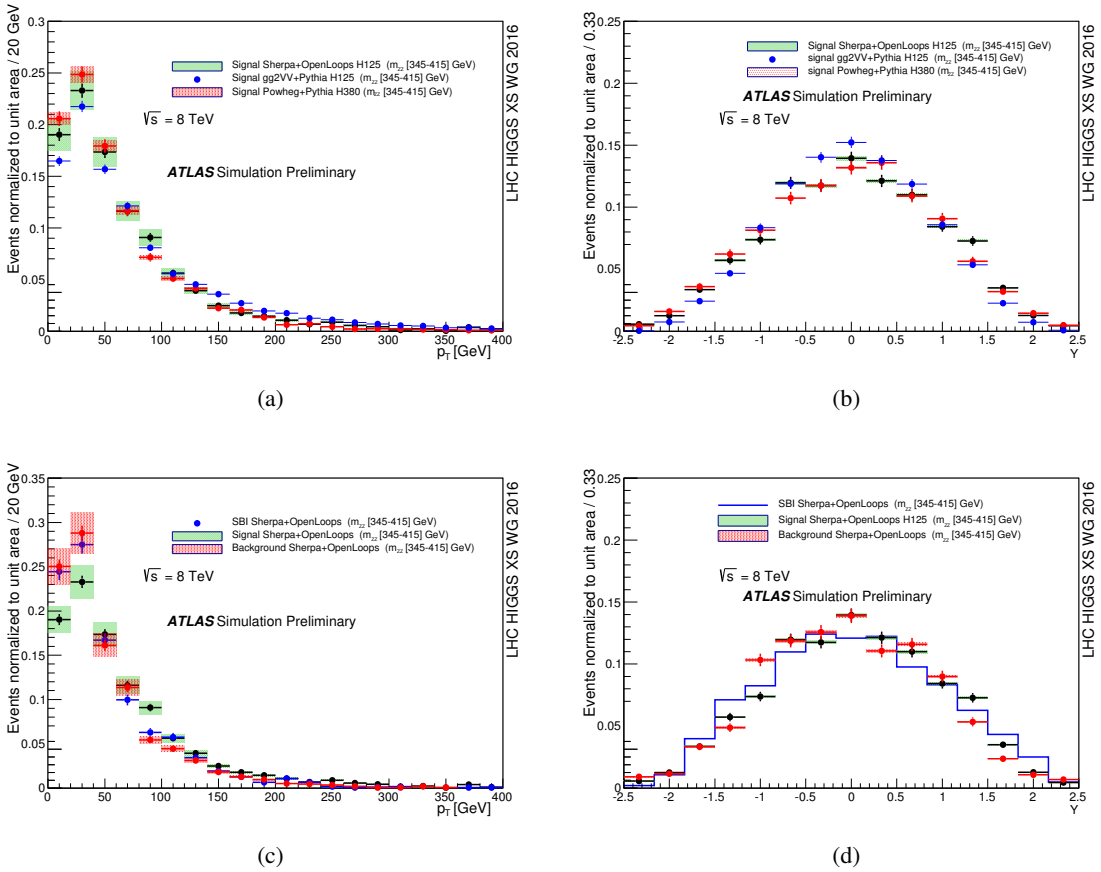

Figure 143: Comparison of the gg→ (H^*) → ZZ off-shell signal process in p_{T} (a) and rapidity (b) generated with m_{H}=125.5 GeV produced with gg2VV and Sherpa and gg→ (H^*) → ZZ signal process with m_{H}=380 GeV using Powheg (on-shell) in the region $m_{\mathrm{ZZ}} \in$ [345,415] GeV. Off-shell comparison in p_{T} (c) and rapidity (d) of the gg→ (H^*) → ZZ signal sample generated with m_{H}=125.5 GeV, the gg→ ZZ background and the SBI contribution using Sherpa in the mass range $m_{\mathrm{ZZ}} \in$ [345,415] GeV.

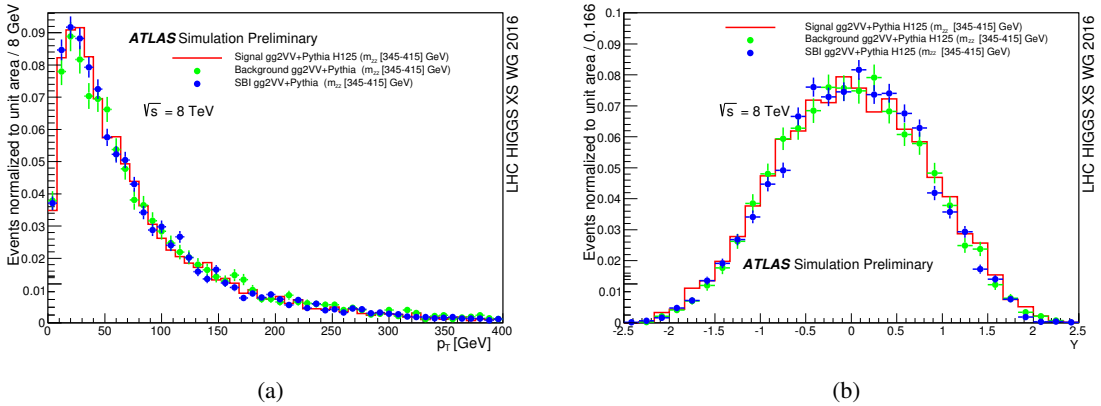

Figure 144: Comparison in p_{T} (a) and rapidity (b) of the three gg2VV contributions (signal generated with m_{H}=125.5 GeV, background and SBI) in the mass region $m_{\mathrm{ZZ}} \in$ [345,415] GeV.

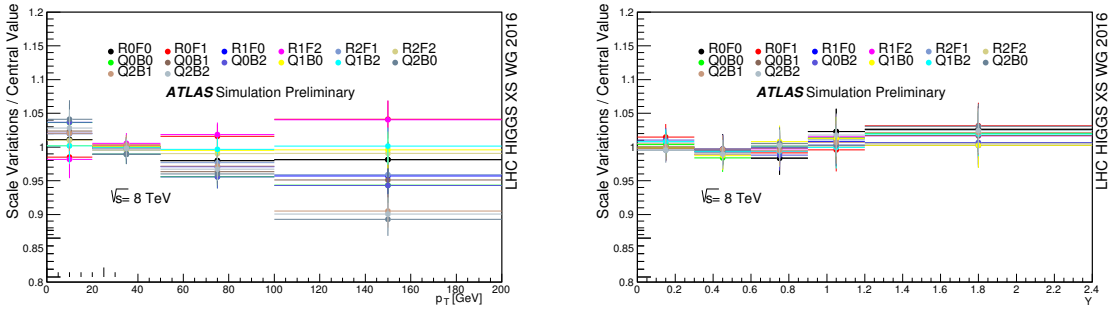

(a) (b)

Figure 145: Relative change of the p_{T} and Y spectra due to the QCD scale variations produced with HRes2.1 signal generated at m_{H}=380 GeV: ratio of the up or down variations p_{T} or rapidity with respect to the nominal distribution. Q labels the resummation scale, B the resummation scale related to the bottom quark mass, R the renormalization scale, F the factorization scale. The numbers coupled with each variation characterize the nominal value (1), the down variation (0) and the up variation (2).

Figure 145 shows the shape-only variations on p_{T}(ZZ) and Y(ZZ) for a high mass m_{H}=380 GeV gg$\to$ H $\to$ ZZ signal process, produced by QCD scale variations evaluated with the HRes2.1 Monte Carlo generator. The scale variations on the rapidity in Figure 145 (b) can be neglected since they are much smaller than those of the transverse momentum, Figure 145 (a). Figure 146 shows the variation of the signal process (a) and the background processes on p_{T}(ZZ) created with the Sherpa+OpenLoops Monte Carlo sample. The envelope of these independent variations on p_{T}(ZZ) is calculated as the maximal up and down contribution for each p_{T} bin for the HRes2.1 case as well as for Sherpa signal and background. Since the contribution of the resummation scale is dominant, a first envelope encompassing renormalization and factorization scales summed it in quadrature with the envelope extracted from the resummation scale provides enough accuracy for this study. Note that the Sherpa variations enclose the variations of HRes2.1 because Sherpa does not contain the full NLO calculations, hence its variations are larger than the typical scales of HRes2.1.The systematic uncertainties reported in Ref. [507] associated with the Sherpa-based reweighting in p_{T} of the VV system are assessed by varying the relevant scales in Sherpa: the larger in value between the scale variations in Sherpa and 50% of the difference between Sherpa and gg2VV+Pythia is assigned as the systematic uncertainty. This conservative approach is chosen to consider potential uncertainties not accounted for by the scale variations. The impact of the PDF uncertainties is found to be negligible.

I.8.3.f Higgs boson off-shell simulation with the MCFM and JHU generator frameworks

The JHU Generator and MELA framework [530–532] is designed for the study of anomalous couplings of a resonance to vector bosons and fermions in various decay and production processes on LHC, and is applicable to either the already discovered boson $H(125)$ or a new resonance $X(m_X)$. In addition to stand-alone generation, the framework is also integrated with the MCFM Monte Carlo package [288, 501, 533] for modelling of the background processes and allows simulation of anomalous couplings in off-shell $H(125)^*$ boson production including interference with continuum diboson production. The simulation of an additional broad resonance X is also included, allowing for the study of a new Higgs-like resonance with arbitrary couplings interfering with the SM processes. The MELA framework allows various likelihood functions either for construction of kinematic discriminants or re-weighting of MC simulation.

The formalism in the JHUGen / MELA framework follows the convention for the tensor structure

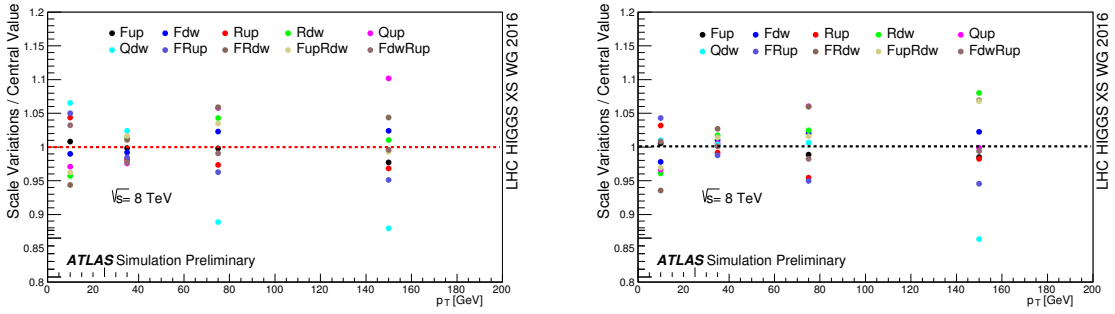

(a) (b)

Figure 146: Relative uncertainties on the p_{T} spectrum for the Sherpa+OpenLoops signal (a) and background (b) samples induced by the QCD scale variations: ratio of the up or down variations with respect to the nominal distribution. Q labels the resummation scale, R the renormalization scale, F the factorization scale.

of HVV couplings

$$A(\mathrm{H}VV) \propto \left[a_1 - e^{i\phi_{\Lambda Q}} \frac{(q_{V1}+q_{V2})^2}{(\Lambda_Q)^2} - e^{i\phi_{\Lambda 1}} \frac{(q_{V1}^2+q_{V2}^2)}{(\Lambda_1)^2}\right] m_V^2 \epsilon_{V1}^* \epsilon_{V2}^* + a_2 f_{\mu\nu}^{*(1)} f^{*(2),\mu\nu} + a_3 f_{\mu\nu}^{*(1)} \tilde{f}^{*(2),\mu\nu}, \tag{I.8.5}$$

where $f^{(i)\mu\nu} = \epsilon_{Vi}^{\mu} q_{Vi}^{\nu} - \epsilon_{Vi}^{\nu} q_{Vi}^{\mu}$ is the field strength tensor of a gauge boson with momentum q_{Vi} and polarization vector ϵ_{Vi}, $\tilde{f}_{\mu\nu}^{(i)} = \frac{1}{2}\epsilon_{\mu\nu\rho\sigma} f^{(i),\rho\sigma}$ is the dual field strength tensor. Spin-one and spin-two resonance couplings, higher-order terms in q^2 expansion, and terms asymmetric in q_{V1}^2 and q_{V2}^2 are supported by the generator but are not shown here, see Refs. [530–532] and generator manual for details. The above q^2 expansion is equivalent to the effective Lagrangian notation with operators up to dimension five [534, 535]

$$\begin{aligned}
L(\mathrm{H}VV) \propto \quad & a_1 \frac{m_Z^2}{2} \mathrm{H} Z^{\mu} Z_{\mu} - \frac{\kappa_1}{(\Lambda_1)^2} m_Z^2 \mathrm{H} Z^{\mu} \Box Z_{\mu} - \frac{\kappa_3}{2\,(\Lambda_Q)^2} m_Z^2 \Box \mathrm{H} Z^{\mu} Z_{\mu} \\
& - \frac{1}{2} a_2 \mathrm{H} Z^{\mu\nu} Z_{\mu\nu} - \frac{1}{2} a_3 \mathrm{H} Z^{\mu\nu} \tilde{Z}_{\mu\nu} \\
& + a_1^{\mathrm{WW}} m_{\mathrm{W}}^2 \mathrm{H} \mathrm{W}^{+\mu} \mathrm{W}_{\mu}^{-} - \frac{1}{\left(\Lambda_1^{\mathrm{WW}}\right)^2} m_{\mathrm{W}}^2 \mathrm{H} \left(\kappa_1^{\mathrm{WW}} \mathrm{W}_{\mu}^{-} \Box \mathrm{W}^{+\mu} + \kappa_2^{\mathrm{WW}} \mathrm{W}_{\mu}^{+} \Box \mathrm{W}^{-\mu}\right) \\
& - \frac{\kappa_3^{\mathrm{WW}}}{(\Lambda_Q)^2} m_{\mathrm{W}}^2 \Box \mathrm{H} \mathrm{W}^{+\mu} \mathrm{W}_{\mu}^{-} - a_2^{\mathrm{WW}} \mathrm{H} \mathrm{W}^{+\mu\nu} \mathrm{W}_{\mu\nu}^{-} - a_3^{\mathrm{WW}} \mathrm{H} \mathrm{W}^{+\mu\nu} \tilde{\mathrm{W}}_{\mu\nu}^{-} \\
& + \frac{\kappa_2^{Z\gamma}}{\left(\Lambda_1^{Z\gamma}\right)^2} m_Z^2 \mathrm{H} Z_{\mu} \partial_{\nu} F^{\mu\nu} - a_2^{Z\gamma} \mathrm{H} F^{\mu\nu} Z_{\mu\nu} - a_3^{Z\gamma} \mathrm{H} F^{\mu\nu} \tilde{Z}_{\mu\nu} \\
& - \frac{1}{2} a_2^{\gamma\gamma} \mathrm{H} F^{\mu\nu} F_{\mu\nu} - \frac{1}{2} a_3^{\gamma\gamma} \mathrm{H} F^{\mu\nu} \tilde{F}_{\mu\nu} - \frac{1}{2} a_2^{\mathrm{gg}} \mathrm{H} G_a^{\mu\nu} G_{\mu\nu}^a - \frac{1}{2} a_3^{\mathrm{gg}} \mathrm{H} G_a^{\mu\nu} \tilde{G}_{\mu\nu}^a,
\end{aligned} \tag{I.8.6}$$

where $V_{\mu\nu} = \partial_{\mu} V_{\nu} - \partial_{\nu} V_{\mu}$, $G_{\mu\nu}^a = \partial_{\mu} A_{\nu}^a - \partial_{\nu} A_{\mu}^a + g f^{abc} A_{\mu}^b A_{\nu}^c$, $\tilde{V}^{\mu\nu} = 1/2 \epsilon^{\mu\nu\alpha\beta} V_{\alpha\beta}$, Z is the Z field, W is the W field, F is the γ field, and G is the g field.

Both on-shell H production and off-shell H^* production are considered. There are no kinematic constraints on either q_{Vi}^2 or $(q_{V1}+q_{V2})^2$, other than the relevant parton luminosities. Since the scale of validity of the nonrenormalizable higher-dimensional operators is *a priori* unknown, effective cut-off scales $\Lambda_{V1,i}, \Lambda_{V2,i}, \Lambda_{H,i}$ are introduced for each term in Eq. (I.8.5) with the form factor scaling the

anomalous contribution $g_i^{\rm BSM}$ as

$$g_i = g_i^{\rm SM} \times \delta_{i1} + g_i^{\rm BSM} \times \frac{\Lambda_{V1,i}^2 \Lambda_{V2,i}^2 \Lambda_{H,i}^2}{(\Lambda_{V1,i}^2 + |q_{V1}^2|)(\Lambda_{V2,i}^2 + |q_{V2}^2|)(\Lambda_{H,i}^2 + |(q_{V1} + q_{V2})^2|)} \,. \tag{I.8.7}$$

The $gg \to ZZ/Z\gamma^*/\gamma^*\gamma^* \to 4f$ process is generated at LO in QCD. In simulation shown in Figure 147, the QCD factorization and renormalization scales are chosen to be running as $m_{4\ell}/2$ and NNPDF30 parton structure functions are adopted. In order to include higher-order QCD corrections, LO, NLO, and NNLO signal cross section calculation is performed using the MCFM and HNNLO programs [172, 224, 536] for a wide range of masses using narrow width approximation. The ratio between the NNLO and LO, or between the NLO and LO, values is used as a weight (k-factor). The NNLO k-factors are applied to simulation as shown in Figure 147. While this calculation is directly applicable for signal, it is approximate for background. However, the NLO calculation is available [527, 537] for background for the mass range $2m_Z < m_{4\ell} < 2m_t$. There is a good agreement between the NLO k-factors calculated for signal and background, and any differences set the scale of systematic uncertainties from this procedure.

Two applications of off-shell $H(125)$ simulation are shown in Figure 147. In one case, anomalous HVV couplings introduce distinct kinematics in the mass range $m_{4\ell} > 2m_Z$. In the other case, a hypothetical $X(m_X)$ resonance interferes with both $H(125)$ off-shell tail and the $gg \to 4\ell$ background. In all cases, most general HVV and XVV couplings discussed above are possible. Anomalous coupling parameterization in terms effective fractions of events follows LHC convention [534, 535] and is equivalent to parameterization in Eq. (I.8.5) with $f_{ai} = |a_i|^2\sigma_i/\Sigma_j|a_j|^2\sigma_j$.

I.8.3.g Interference contributions to gluon-initiated heavy Higgs boson production in the 2HDM using GoSam

I.8.3.g.i GoSam

GoSam [227, 228] is a package for the automated calculation of one-loop (and tree-level) amplitudes. It can be used either in standalone mode or as a *One Loop Provider* (OLP) in combination with a Monte Carlo program, where the interface is automated, based on the standards defined in Refs. [360, 361]. GoSam is not a library of pre-computed processes, but calculates the amplitude for the process specified by the user in a *run card* on the fly. In the OLP version, the information for the code generation is taken from the order file generated by the Monte Carlo program. The amplitudes are evaluated using D-dimensional reduction at integrand level [359, 538, 539], which is available through the reduction procedures and libraries Samurai [540, 541] or Ninja [542, 543]. Alternatively, tensorial reconstruction [544] is also available, based on the library `golem95C` [545–547]. The scalar master integrals can be taken from OneLoop [548] or QcdLoop [549].

The GoSam package comes with the built-in model files `sm`, `smdiag`, `smehc`, `sm_complex`, `smdiag_complex`, where the latter two should be used if complex masses and couplings are present in the amplitude. Complex masses, stemming from the consistent inclusion of decay widths for unstable particles at NLO [374], are particularly important for the inclusion of electroweak corrections, which also can be calculated with GoSam [550]. The model files `smehc` contain the effective Higgs-gluon couplings. It has been used for example in the calculation of the NLO corrections to H+3 jet production in gluon fusion [230, 551] and in the calculation of HH+2 jet production in both the gluon fusion and the vector boson fusion channel [448].

Other models can be imported easily, using the `UFO` (Universal FeynRules Output) [552, 553] format. This feature has been exploited for example in Refs. [554, 555].

Therefore, GoSam comprises all the features which are needed to calculate interference effects, both within and beyond the Standard Model. An example for interference effects within the 2-Higgs-Doublet Model will be given below.

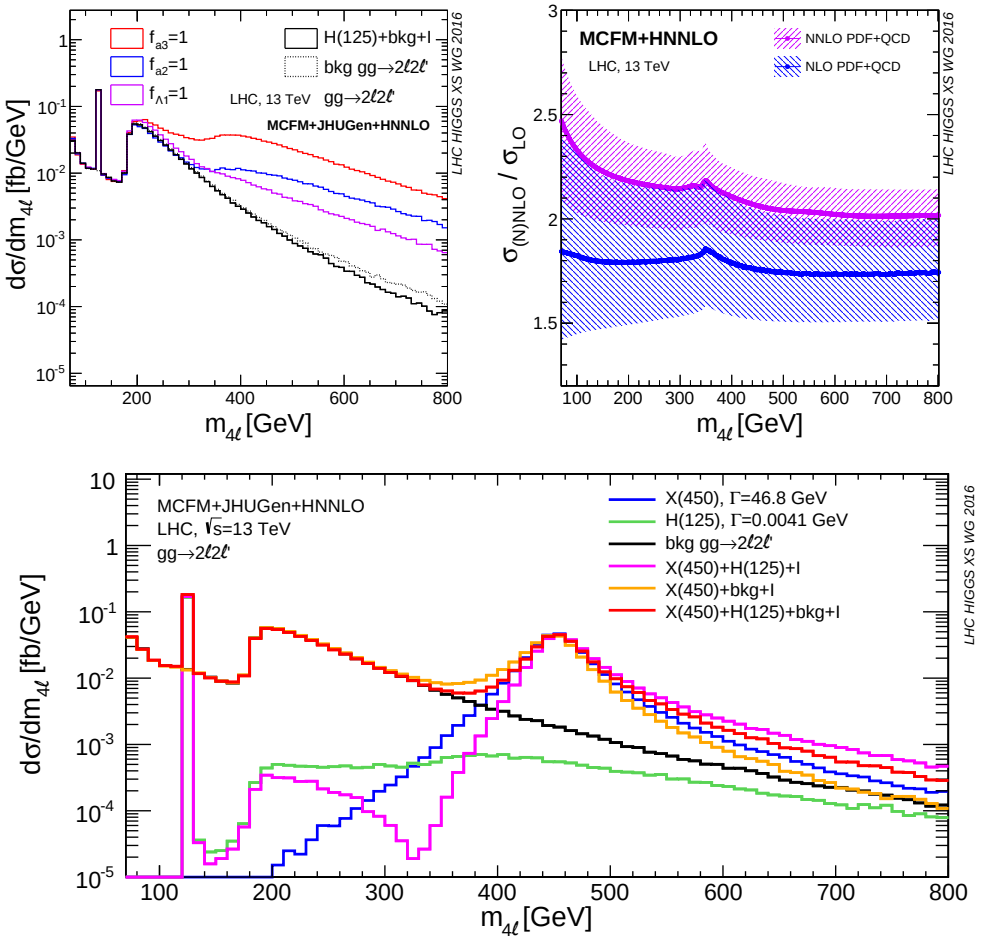

Figure 147: Differential cross section of the process $gg \to ZZ/Z\gamma^*/\gamma^*\gamma^* \to 2\ell 2\ell'$ (where ℓ, $\ell' = e$, μ, or τ) as a function of invariant mass $m_{4\ell}$ generated with the MCFM+JHUGen framework, including the NNLO in QCD weights calculated with MCFM+HNNLO. The NNLO and NLO weights (k-factors) as a function of $m_{4\ell}$ are shown on the top-right plot. The top-left plot shows several scenarios of $H(125)$ anomalous couplings to two weak vector bosons with enhancement in the off-shell region with the a_3, a_2, and Λ_1 terms, as coloured histograms, as well as the a_1 term (SM), as the solid black histogram, from Eq. (I.8.5) in decreasing order of enhancement at high mass. The bottom plot shows distributions in the presence of a hypothetical $X(450)$ resonance with several components either isolated or combined. In all cases interference (I) of all contributing amplitudes is included.

I.8.3.g.ii Interference contributions to gluon-initiated heavy Higgs boson production in the 2HDM

In this section we discuss the loop-induced processes $gg \to ZZ$ and $gg \to VV(\to e^+e^-\mu^+\mu^-/e^+e^-\nu_l\bar{\nu}_l)$ at LO QCD in the context of a CP-conserving Two-Higgs-Doublet-Model (2HDM). In particular, we study the effect of the interference between light and heavy Higgs bosons, and with the background. The 2HDM contains two Higgs doublets, which we name H_1 and H_2. The models can be classified into type I and type II, if we demand no tree-level flavour-changing neutral currents and CP conservation. By convention [485], the up-type quarks couple to H_2. In models of type I, the down-type quarks also couple to H_2, while in type II models, they couple to H_1. The coupling to the leptons can either be through H_1 or H_2, but as our studies are not sensitive to the coupling of the Higgs bosons to leptons, we do not need a further type distinction. The two Higgs doublets form one CP-odd field A and two CP-even Higgs fields h and H due to CP conservation, as well as two charged Higgs bosons $H^\pm$. The 2HDM can be described in different basis representations. We make use of the "physical basis", in which the masses of all physical Higgs bosons, the ratio of the vacuum expectation values $\tan\beta := \tan\beta = v_2/v_1$

Table 95: Relative couplings g_f^ϕ (with respect to the SM coupling) for the two 2HDM types.

Model	g_u^h	g_d^h	g_u^H	g_d^H
Type I	$\cos\alpha/\sin\beta$	$\cos\alpha/\sin\beta$	$\sin\alpha/\sin\beta$	$\sin\alpha/\sin\beta$
Type II	$\cos\alpha/\sin\beta$	$-\sin\alpha/\cos\beta$	$\sin\alpha/\sin\beta$	$\cos\alpha/\cos\beta$

and the Higgs mixing angle in the CP-even sector α, or alternatively $s_{\beta-\alpha} := \sin(\beta-\alpha)$, are taken as input parameters. We choose $\beta-\alpha$ in between $-\pi/2 \le \beta-\alpha \le \pi/2$, such that $-1 \le s_{\beta-\alpha} \le 1$ and $0 \le c_{\beta-\alpha} \le 1$. Our scenarios are thus specified by the two angles α and β, which completely determine the relative couplings (with respect to the couplings of a SM Higgs boson) of the light and the heavy Higgs boson to quarks and the heavy gauge bosons. They are provided in Eq.(I.8.8) and Table 95 (together with Eq.(I.8.9) for a decomposition in terms of $\beta-\alpha$ and β). Moreover, our analysis is sensitive to m_h and m_H, whereas it is rather insensitive to the mass of the pseudoscalar m_A and the heavy charged Higgs boson mass $m_{H^\pm}$, as long as they are heavy enough not to open decay modes of the heavy Higgs H into them and as long as the decay mode $H \to hh$ is sub-dominant. The strengths of the Higgs boson couplings to the gauge bosons $V \in \{W, Z\}$ are given by

$$g_V^h = \sin(\beta-\alpha) =: s_{\beta-\alpha}, \qquad g_V^H = \cos(\beta-\alpha) =: c_{\beta-\alpha} \quad . \tag{I.8.8}$$

The pseudoscalar has no lowest-order couplings to a pair of gauge bosons. It can in principle contribute to the considered processes with four fermions in the final state. Because of the suppression of the Yukawa couplings to leptons, however, these contributions are very small, and thus diagrams involving the pseudoscalar are not of relevance for our discussion. In case of $|s_{\beta-\alpha}| = 1$ the light Higgs boson h couples to the gauge bosons with same strength as the SM Higgs boson. In contrast the coupling of the heavy Higgs boson g_V^H vanishes according to the sum rule $(g_V^h)^2 + (g_V^H)^2 = 1$. Of large relevance for our discussion are the relative couplings of the heavy Higgs boson to bottom-quarks and top-quarks, which are given by

$$\begin{aligned} g_t^H &= \frac{\sin\alpha}{\sin\beta} = -s_{\beta-\alpha}\frac{1}{\tan\beta} + c_{\beta-\alpha}, \\ \text{Type I: } g_b^H &= \frac{\sin\alpha}{\sin\beta} = -s_{\beta-\alpha}\frac{1}{\tan\beta} + c_{\beta-\alpha}, \quad \text{Type II: } g_b^H = \frac{\cos\alpha}{\cos\beta} = s_{\beta-\alpha}\tan\beta + c_{\beta-\alpha} \quad . \end{aligned} \tag{I.8.9}$$

I.8.3.g.ii.1 Details of the calculation

We make use of GoSam [227, 228] to discuss the processes $gg \to e^+e^-\mu^+\mu^-$ and $e^+e^-\nu_l\bar{\nu}_l$ (including all three neutrino flavours). For a study of the relevance of interference contributions we also consider the process $gg \to ZZ$, which we generated with the help of `FeynArts` [556] and `FormCalc` [557] and linked to `LoopTools` [557] for the calculation of the employed one-loop Feynman diagrams. We added its amplitudes to a modified version [293] of `vh@nnlo` [292]. It allows to be linked to `2HDMC` [558] which we need for the calculation of the Higgs boson widths Γ_h and Γ_H. In the case of the four lepton final state we have to sum over all possible intermediate configurations leading to the given final state. This particularly means that depending on the sub-process, also intermediate W-bosons as well as non-resonant contributions and photon exchange have to be taken into account. For the numerical integration over the four particle phase space we have combined the GoSam amplitudes with the integration routines provided by `MadEvent` [559, 560].

It is well-known that the calculation of processes including internal Higgs bosons, in particular if one includes higher orders, needs a gauge invariant formulation of the Higgs boson propagator. Since we are working at LO QCD only, a simplistic Breit-Wigner propagator is sufficient for all our purposes. We

Table 96: 2HDM scenarios considered in our analysis.

Scenario	2HDM type	$\tan\beta$	$s_{\beta-\alpha}$	m_H	Γ_H
S1	II	2	-0.995	200 GeV	0.0277 GeV
S2	II	1	0.990	400 GeV	3.605 GeV
S3	I	5	0.950	400 GeV	2.541 GeV
S4	II	20	0.990	400 GeV	5.120 GeV

checked our modified `vh@nnlo` and our GoSam implementations against each other for $gg \to ZZ$ at the amplitude level and reproduced parts of the results presented in Ref. [525] for the four leptonic final state within the numerical uncertainties.
We consider four benchmark scenarios to cover different aspects of a heavy Higgs boson in the phenomenology of a 2HDM, given in Table 96. All scenarios include a light Higgs boson with mass $m_h = 125\,\text{GeV}$. We keep the couplings of the light Higgs close to the ones of the SM Higgs by a proper choice of $\tan\beta$ and $s_{\beta-\alpha}$. The masses (and widths) of quarks and gauge bosons are set to $m_t = 172.3\,\text{GeV}, m_b(m_b) = 4.16\,\text{GeV}, m_Z = 91.1876\,\text{GeV}, m_W = 80.398\,\text{GeV}, \Gamma_Z = 2.4952\,\text{GeV}, \Gamma_W = 2.085\,\text{GeV}$.

Our studies presented here are carried out for the LHC with a centre-of-mass energy of $\sqrt{s} = 13\,\text{TeV}$. The role of interference effects is a bit less pronounced at $7/8$ TeV compared to 13 TeV. We make use of `CT10nnlo` [529] as PDF set for the gluon luminosities. Since our calculations are purely performed at LO the renormalization scale dependence enters through the strong coupling α_s only, which we take from the employed PDF set. We choose the renormalization and factorization scale to be dynamical, namely half of the invariant mass of the gauge boson system $\mu_R = \mu_F = m_{VV}/2$, i.e. $\mu_R = \mu_F = m_{4l}/2$ in case of the four leptonic final states. It is known to have a small effect on the cross section [501, 561], which we numerically confirm for the processes under consideration. In case of the four lepton or the two lepton and two neutrino final states, we additionally cut on the transverse momentum and the pseudorapidity of each lepton l, $p_T^l > 10\,\text{GeV}$ and $|\eta_l| < 2.7$, the R-separation between individual leptons $R^{ll'} > 0.1$ as well as $m_{ll} > 5\,\text{GeV}$, where ll is an oppositely charged same-flavour dilepton pair. For the neutrinos we ask for a total missing transverse momentum of $E_T^{\text{miss}} > 70\,\text{GeV}$. The cuts are inspired by the recent ATLAS analysis carried out in Ref. [562]. One of the most important observables is certainly the invariant mass distribution of the four leptons as the two Higgs bosons manifest themselves in Breit-Wigner peaks in this distribution. For the process $gg \to e^+e^-\mu^+\mu^-$ this observable m_{4l} is also experimentally easily accessible due to two electrons and two muons in the final state. In the cases with neutrinos in the final state the situation is more involved. The invariant mass is no longer an observable that is experimentally accessible but only a transverse component can be measured. If one is interested in a heavy Higgs boson that will decay into the four leptons via two intermediate electroweak gauge bosons a sensible choice is to consider the transverse mass of the underlying two boson system. In our case the two boson system can be ZZ as well as WW. We therefore define a general transverse mass via [563]

$$m_{VV,T}^2 = \left(E_{T,ll} + E_{T,\nu\nu}\right)^2 - \left|\vec{p}_{T,ll} + \vec{p}_{T,\nu\nu}\right|^2 \,, \tag{I.8.10}$$

with

$$E_{T,ll} = \sqrt{p_{ll}^2 + |\vec{p}_{T,ll}|^2}\,, \quad \text{and} \quad E_T^{\text{miss}} = E_{T,\nu\nu} = |\vec{p}_{T,\nu\nu}| \,. \tag{I.8.11}$$

I.8.3.g.ii.2 Discussion of four fermionic final states

We exemplify the results for the four fermionic final state by discussing the results of scenario S1. Figure 148 shows the invariant mass distribution of the four leptons for $gg \to e^+e^-\mu^+\mu^-$ and the transverse mass distribution using the definition in Eq.(I.8.10) for the processes involving final state neutrinos. We

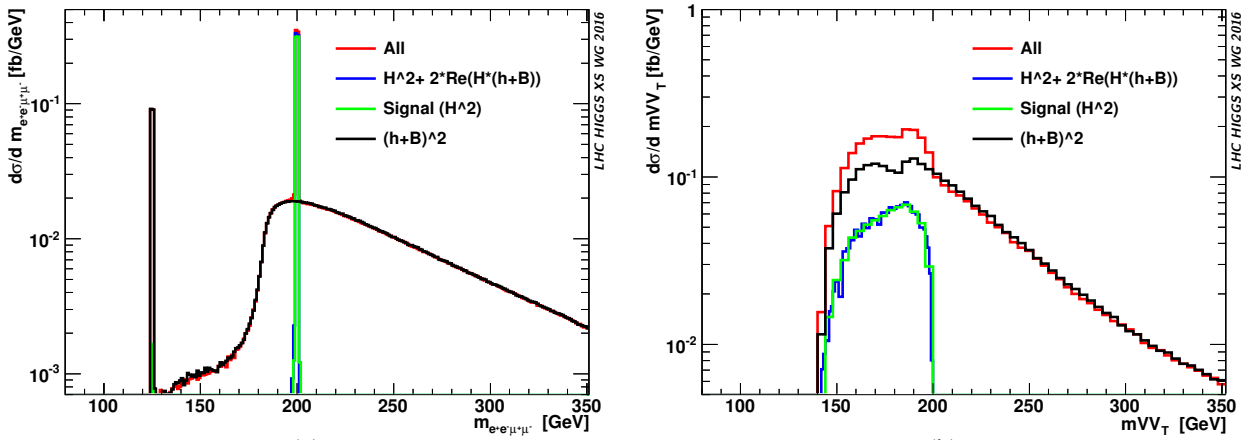

(a) (b)

Figure 148: (a) Invariant mass distribution for $gg \to e^+e^-\mu^+\mu^-$ and (b) transverse mass distribution for $gg \to e^+e^-\nu_l\bar{\nu}_l$ for scenario S1 at $\sqrt{s} = 13\,\text{TeV}$.

distinguish four different contributions. In red, denoted with 'All', we plot all contributions that lead to the given final state in the considered scenario. In green, we only plot the contribution from the heavy Higgs boson, whereas in blue we also add the interference of the heavy Higgs boson with the background and the light Higgs boson. The contribution $|h + B|^2$, plotted in black, contains besides the contributions without any Higgs also contributions of the light Higgs as well as the interference contributions of the light Higgs boson with non-Higgs diagrams.
In the invariant mass plot of $gg \to e^+e^-\mu^+\mu^-$, see Figure 148 (a), the two Higgs boson peaks at $m_{4l} = 125$ and 200 GeV can be clearly seen. Due to the very small width of the heavy Higgs boson there is no distortion of the Breit-Wigner shape visible, and also the impact of the interference contribution to the total height of the peak is rather small. The transverse mass distribution for $gg \to e^+e^-\nu_l\bar{\nu}_l$ shows a quite different pattern. First of all there is no peak from the light Higgs boson. The reason for this are the different cuts compared to the process without neutrinos. The requirement of $E_T^{\text{miss}} > 70\,\text{GeV}$ excludes this region of phase space. Due to the fact that the four momenta of the neutrinos are experimentally not accessible one sets $E_{T,\nu\nu} = |\vec{p}_{T,\nu\nu}|$, which ignores the invariant mass of the neutrino system. This removes the sharp peak of the heavy Higgs boson, which is visible in the invariant mass distribution of the muon process. Instead of a distinguished peak one obtains a broad distribution. But also here the contribution of the interference remains small. A second difference compared to the muon process is the occurrence of a small dip at around $m_{VV,T} = 180\,\text{GeV}$ in both signal and background. This specific shape is due to the fact that the total contribution to the process with neutrino final state consists of the sum of two different sub-processes, namely the one with the electron neutrino and the ones with muon- and tau neutrino in the final state. Whereas the first sub-process also has contributions from intermediate W-bosons, this is not the case for the latter sub-processes. The two sub-processes therefore show a different kinematical behaviour and the sum of the two contributions leads to the given distribution.
For a more detailed discussion of the other scenarios and different observables we refer to Ref. [564].

I.8.3.g.ii.3 Relevance of interference contributions

The interference contributions of the heavy Higgs boson with the light Higgs boson and the background are significantly enhanced in two cases: Naturally small couplings involved in the signal process increase the mentioned interferences. This is either of relevance in the decoupling limit of the 2HDM where $s_{\beta-\alpha} \to 1$ and thus the coupling of the heavy Higgs boson to gauge bosons vanishes or through a small coupling of the heavy Higgs boson to top- and/or bottom-quarks. According to Eq. (2) the top-quark

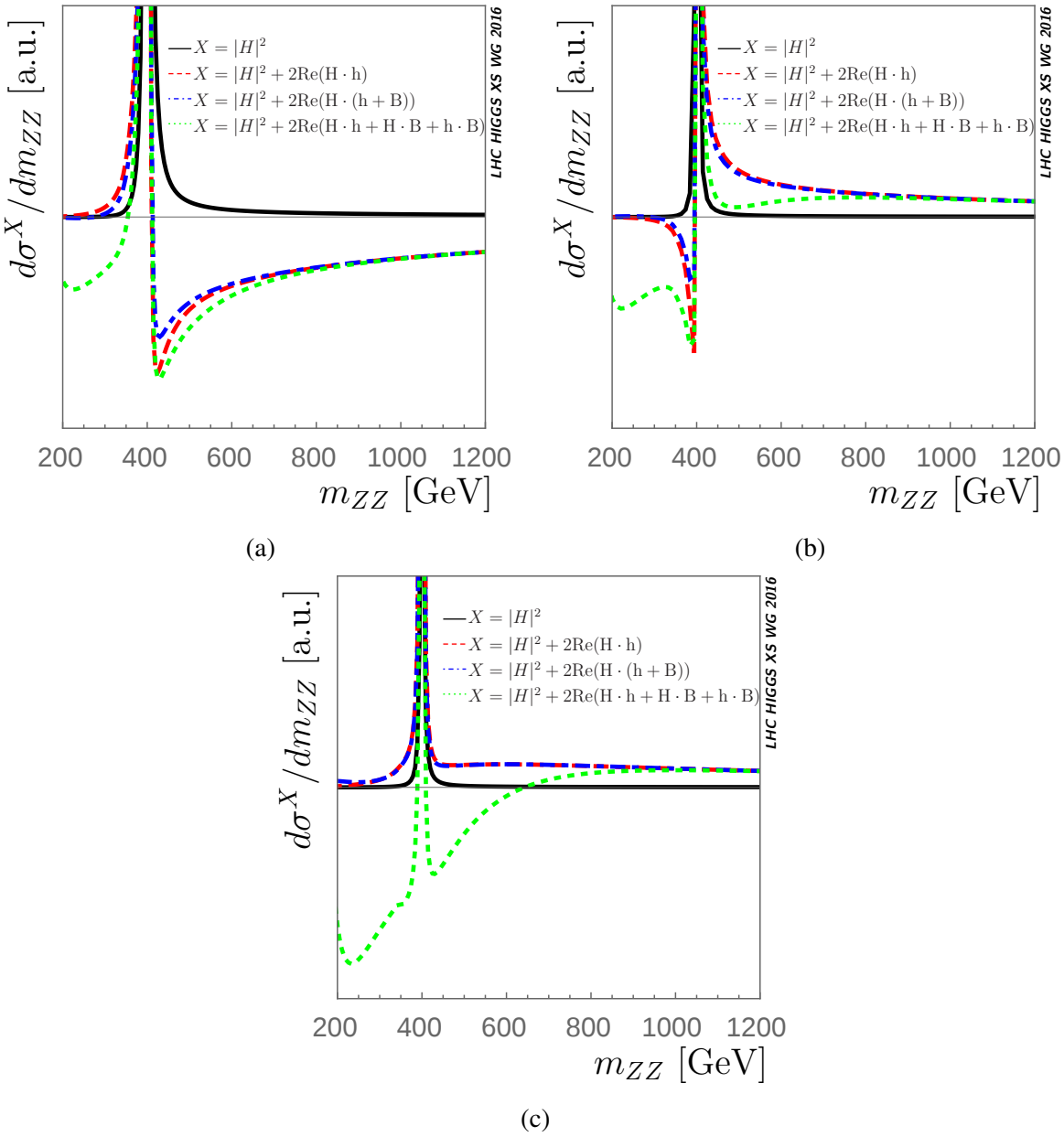

Figure 149: Partonic cross sections $d\sigma^X/dm_{ZZ}$ for $gg \to ZZ$ in arbitrary units as a function of the invariant mass m_{ZZ} in GeV for scenario (a) S2, (b) S3 and (c) S4 (black: $X = |H|^2$; red, dashed: $X = |H|^2 + 2\mathrm{Re}(H \cdot h)$; blue, dot-dashed: $X = |H|^2 + 2\mathrm{Re}(H \cdot h) + 2\mathrm{Re}(H \cdot B)$; green, dotted: $X = |H|^2 + 2\mathrm{Re}(H \cdot h) + 2\mathrm{Re}(H \cdot B) + 2\mathrm{Re}(h \cdot B)$).

coupling vanishes for a specific value of $s_{\beta-\alpha}$ for fixed $\tan\beta$. In a 2HDM type I the bottom-quark coupling vanishes for the same value, such that the cross section $\sigma(gg \to H \to VV)$ gets zero, whereas in a 2HDM type II the cross section is minimal. Moreover the interferences are found to be large for an enhanced bottom-quark Yukawa coupling, i.e. large $\tan\beta$. Again, for further details we refer to Ref. [564]. Interferences in the mentioned two cases can help to lift the signal cross section by more than a factor of 2 and thus enhance the sensitivity of heavy Higgs boson searches.

I.8.3.g.ii.4 Interferences at high invariant masses

So far we focused on the interference effects between the heavy Higgs and the background as well as the heavy Higgs and the light Higgs in the vicinity of the heavy Higgs boson resonance, since the interference between the light Higgs boson and the background can be considered constant in this region. However, at high invariant masses of the diboson system the interplay between all three contributions h and H and the background B is of relevance, to a certain extent related to the unitarization of the cross section. In Figure 149 we plot the differential cross section $gg \to ZZ$ as a function of the invariant mass of the diboson system m_{ZZ} up to high masses beyond the heavy Higgs boson resonance. We exemplify the discussion for the three scenarios S2, S3 and S4. The differences between the coloured curves display the importance of the different interference terms. Since the figures are obtained for the partonic cross section and we are interested in the relative effects of the interferences among each other, we do not display units for $d\sigma/dm_{ZZ}$. At high invariant masses the interference between the heavy Higgs boson and the background is negligible, in contrast to the interference of the light Higgs and the heavy Higgs boson, which remains large and can have either sign. Moreover the smoothly falling interference of the light Higgs boson and the background comes into the game within a certain window of invariant masses below 1 TeV. Figure 149 depicts different cases, where the interference $h \cdot H$ is either negative similar to the interference $h \cdot B$ or leads to a positive contribution to the differential cross section in a region $m_{ZZ} \in [450\,\text{GeV}, 1000\,\text{GeV}]$. The latter case is true for scenarios S3 or S4, where a sign change of the total depicted contribution leads to a dip and a subsequent "peak"-like structure when added to the background. This structure also appears in the total four particle final state, where the gluon luminosities further suppress the cross section at high invariant masses. Thus all interferences need to be taken into account in order to correctly describe the cross section at high invariant masses.

I.8.4 $gg \to VV$ at NLO QCD

I.8.4.a The status of theoretical predictions

A good theoretical control of the off-shell region requires the knowledge of higher order QCD correction for both the signal $pp \to H \to 4l$ and the SM background $pp \to 4l$ processes. At high invariant masses, the signal $gg \to H \to 4l$ and the background $gg \to 4l$ processes individually grow with energy, eventually leading to unitarity violations. In the SM, a strong destructive interference between signal and background restores unitarity in the high energy regime, and its proper modelling is important for reliable predictions in the off-shell tail. At invariant masses larger than the top threshold $m_{4l} > 2m_t$ the effect of virtual top quarks running in the loops is non negligible and must be taken into account.

The state of the art for theoretical predictions of signal, background and interference is very different. For an exhaustive description of the signal cross section we refer the reader to the relevant sections of this report. As far as perturbative QCD is concerned, the signal is known through NLO with exact quark mass dependence [99, 136]. NNLO corrections are known as an expansion around the $m_t \to \infty$ limit [100, 102, 565], matched to the exact high-energy limit [234] to avoid a spurious growth at high energies [104, 106]. Very recently, the N^{3}LO corrections became available [96] in the infinite top mass approximation. They turned out to be moderate, with a best stability of the perturbative expansion reached for central scale $\mu = M_{\rm H}/2$. So far, results are known as an expansion around threshold, which is expected to reproduce the exact result to better than a per cent.

We now briefly discuss the status of theoretical description of the background. In the SM, four-lepton production is dominated by quark fusion processes $q\bar{q} \to VV \to 4l$. Recently, NNLO QCD corrections were computed for both the ZZ [566] and the WW [567] processes, leading to a theoretical uncertainty coming from scale variation of a few per cent. In these prediction, the formally NNLO gluon fusion channel $gg \to 4l$ enters for the first time, i.e. effectively as a LO process. At the LHC, it is enhanced by the large gluon flux and corresponds to roughly 60%(35%) of the total NNLO corrections to the $ZZ(WW)$ process. Despite being sub-dominant for $pp \to 4l$ production, the $gg \to 4l$ sub-channel

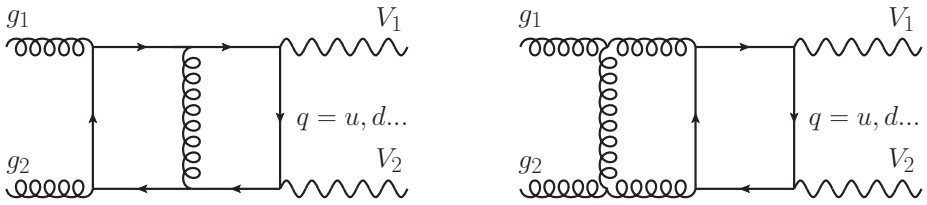

Figure 150: Representative two-loop diagrams for the $gg \to 4l$ process. Leptonic decays of the vector bosons is assumed.

Figure 151: Representative double (left) and single (right) resonant one-loop diagrams for the $gg \to 4l + g$ process.

is of great importance for off-shell studies. First of all, as we already mentioned there is a strong negative interference between $gg \to 4l$ and $gg \to H \to 4l$. Second, the gluon fusion SM background is harder to separate from the Higgs boson signal.

Computing NLO corrections to $gg \to 4l$ is highly non trivial as it involves the knowledge of complicated two-loop amplitudes with both external and internal massive particles. Parton shower studies based on merged $gg \to 4l + 0, 1$ jet have been performed for example in [352]. Very recently, NLO QCD corrections for $gg \to VV \to 4l$ process were computed in the case of massless quark running in the loop [527, 568]. This approximation is expected to hold very well below threshold, $m_{4l} < 2m_t \sim 300$ GeV. As in the Higgs case, finite top quark effects are known as an expansion in $1/m_t$ [537]. Going beyond that would require computing two-loop amplitudes which are currently beyond our technological reach, so the exact result is not expected in the near future.

I.8.4.b Brief description of the NLO computation for $gg \to 4l$

I.8.4.b.i Massless quark contribution

In this section, we briefly report the main details of the $gg \to VV \to 4l$ NLO QCD computations [527, 568]. Despite being NLO calculations, they pose significant technical challenges. First, complicated two-loop amplitude are required, see Figure 150 for a representative sample. These amplitudes were recently computed in [569, 570]. They include decay of the vector bosons and account for full off-shell effects. For the results in [527, 568], the public C++ implementation of Ref. [570] was used. To ensure the result is stable, the code code compares numerical evaluations obtained with different (double, quadruple and, if required, arbitrary) precision settings until the desired accuracy is obtained. For a typical phase space point, the evaluation of all two-loop amplitudes requires about two seconds.

Second, one-loop real emission amplitudes are required, see Figure 151. Despite being only one-loop amplitudes, they must be evaluated in degenerate soft/collinear kinematics, so they must be numerically stable. For the computations in [527, 568], these amplitudes were computed using a mixture of numerical [571] and analytical [572] unitarity. As a cross-check, the obtained amplitudes were compared against OpenLoops [247] for several different kinematic points. Possible numerical instabilities are

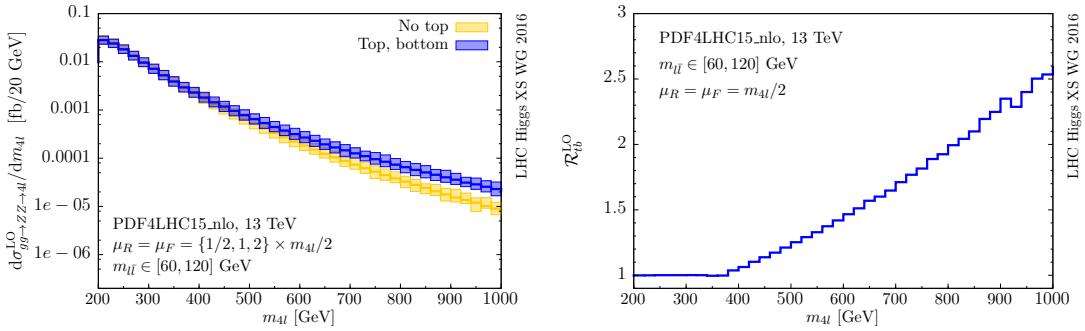

Figure 152: Top quark mass contribution to $gg \to ZZ \to 4l$ at LO. Left: comparison between the exact result (blue) and the approximation where the top quark contribution is omitted and the bottom quark is considered massless (see [527] for details). Right: ratio between the exact and approximate results for the central scale $\mu = m_{4l}/2$. See text for details.

cured by increasing the precision of the computation. The typical evaluation time for a phase space point, summed over colour and helicities, is about 0.1 seconds. Also in this case, full decay of the vector bosons into leptons/neutrinos and off-shell effects are understood. Note that the latter involve single-resonant diagrams, see Figure 151(right). Arbitrary cuts on the final state leptons/neutrinos (and additional jet) are possible. In the computations [527, 568], interference between WW and ZZ mediated processes for $2l2\nu$ final states are neglected. They are expected to be irrelevant in the experimental fiducial regions. Full $ZZ/\gamma\gamma$ interference effects are included.

In [527, 568], contributions coming from $qb \to VVq$ mediated by closed fermion loops were not included. This is because at $\mathcal{O}(\alpha_s^3)$ there are several other contributions to the qg channel other than one-loop squared amplitudes, which in principle are not sub-dominant. Neglecting these channels is fully justified in the large gluon approximation of [527, 568]. Residual factorization scale uncertainties are expected to give an estimate of the impact of neglected channels.

In the ZZ computation [527], the top quark contribution is neglected and the bottom quark is considered massless (see [527] for more details). This approximation is expected to work at the 1% level for the total $gg \to ZZ$ cross-section, but it is not reliable in the high invariant mass regime. To quantify this, in Figure 152 we compare at LO the full massive computation with the approximation [527]. From the figure it is clear that below the top threshold the approximation [527] is essentially exact, while above the top quark contribution becomes rapidly important. The relative size of the top quark contribution is quantified in the right panel of Figure 152, where

$$\mathcal{R}_{tb}^{\rm LO}(m_{4l}) \equiv \left. \frac{{\rm d}\sigma_{t,b}^{\rm LO}/{\rm d}m_{4l}}{{\rm d}\sigma_{{\rm no}-t}^{\rm LO}/{\rm d}m_{4l}} \right|_{\mu_r=\mu_f=m_{4l}/2} . \tag{I.8.12}$$

For the WW case, in the calculation [568] both the top and the bottom quark contributions are omitted. At LO, top/bottom contributions account for $\mathcal{O}(10\%)$ of the total $gg \to WW$ cross section.

I.8.4.b.ii Finite top quark effects

The effect of finite top quark mass in $gg \to ZZ$ at NLO was investigated in [537]. Similar to what is done in the Higgs case, the authors performed the computation as an expansion in the $m_t \to \infty$ limit. The first two non trivial terms in the expansion were kept, which allowed for a reliable description of the top quark contribution up to invariant masses of order $m_{4l} \sim 300$ GeV. In this computation, only the total $gg \to ZZ$ cross-section was considered, although this should be enough to have a rough estimate of the size of the mass effects. The result on the NLO corrections, compared to the signal case, are shown in Figure 153. For these results, the Higgs boson signal is computed in the $m_t \to \infty$ limit as well. Also,

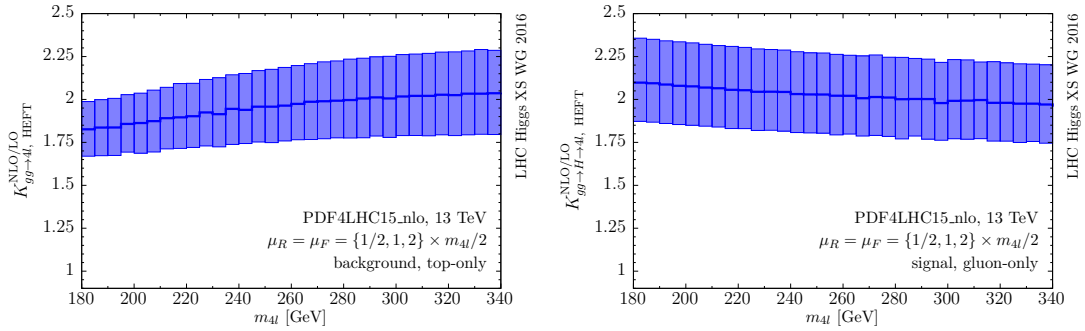

Figure 153: $K-$factors for signal and background, in the heavy top expansion. Both LO and NLO contributions are computed with NLO PDFs and α_s. See text for details.

compared to the K-factor defined in [537], here we used NLO PDFs and α_s evolution for both the LO and the NLO contributions. The band represent scale variation uncertainty, obtained from a factor of two variation around $\mu_0 = m_{4l}/2$.

Close to the ZZ threshold, the background $1/m_t$ expansion is expected to be accurate within $\mathcal{O}(20\%)$ [537]. Signal and $K-$factors are of the same order of magnitude, in agreement with what expected from soft gluon approximations [573]. Below the top threshold, the precision on the approximation [537] can be systematically improved by computing more terms in the $1/m_t$ expansion. Above the top threshold $m_{4l} \sim 300$ GeV, the expansion [537] alone is no longer reliable. Since the full computation is not available, the expansion could be improved along two directions. In principle, it could be matched against the exact high energy behaviour. While this does not pose any conceptual challenge, the computation of the high energy limit is technically more involved than in the Higgs case and it is presently unknown. A second option would be to rescale by the exact LO and hence consider and expansion for the $K-$factor, for which the $1/m_t$ expansion should be better behaved.

I.8.4.c Results and recommendation for the $gg\ (\to H) \to ZZ$ interference K-factor

As explained in the previous section, exact predictions valid up to high ~ 1 TeV invariant masses are only known at NLO for the $gg \to H \to 4l$ signal and LO for the $gg \to 4l$ background. However, several indications point towards sizeable higher order corrections, both for signal and background. In this section we study this issue and present a possible practical recommendation for the signal, background and interference $K-$factors.

We start by describing the setup used for the results presented in this section. LO and NLO results are both obtained with NLO PDFs and α_s. In principle, one could envision using LO PDFs (and α_s) for the LO results, and this would in general lead to smaller corrections, with reduced shape dependence. However, since PDFs fits are still dominated by DIS data, the LO gluon distribution is almost entirely determined by DGLAP evolution. The large LO gluon flux hence is artificially driven by the large NLO DIS $K-$factor and it is not reliable. Until LO gluon PDFs are obtained by fitting hadronic data, using the NLO gluon distribution is preferable, see the PDFs section of this report for more details. NNLO PDFs could be used as well, since the $gg \to 4l$ process enters at NNLO in the $q\bar{q} \to 4l$ computation. However, here we are mostly interested in interference effects, so for consistency with the Higgs case we use NLO PDFs for NLO signal, $gg \to 4l$ background and interference.

Regarding the scale choice, it is well known that for Higgs boson production an optimal choice would be $\mu \sim M_{\rm H}/2$ [100]. Theoretically, it is justified both by all-order analysis of the Hgg form factor and by the fact that the average $p_\perp$ of the Higgs boson is $\sim M_{\rm H}/2$. Empirically, a much better convergence is observed with this scale choice, as well as a reduced impact of resummation effects [93]. For off-shell studies, this translates into choosing as a central scale half of the virtuality of the Higgs

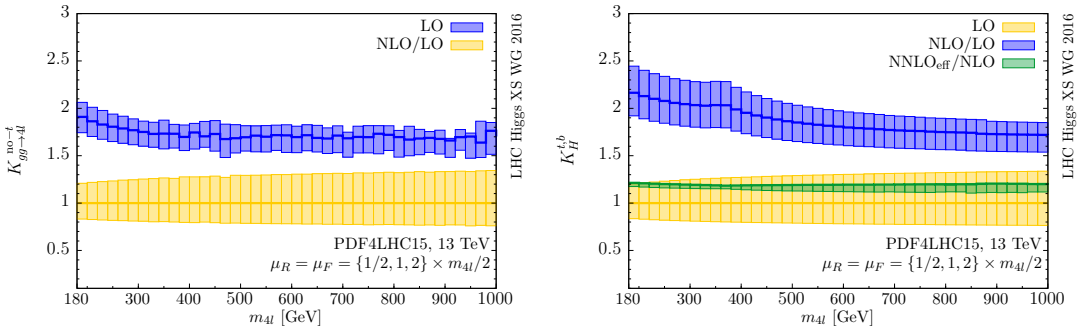

Figure 154: Left: NLO K-factor for $gg \to 4l$ background, massless quark contribution. Right: K-factor for $gg \to H \to 4l$ signal. NLO with full mass dependence, NNLO in the HEFT approximation. See text for details.

boson, i.e. $\mu = m_{4l}/2$. Since most of the above consideration are only based on the colour flow of the process, they also apply for the background and interference scale choice. Incidentally, we note that this was also the preferred choice for the NNLO $pp \to WW/ZZ$ computations [566, 567].

In the region $m_{4l} < 2m_t$, precise results exist for both the signal and the background. In more detail, NNLO results for the signal can be obtained from [104, 106]. For the background, NLO contributions from massless quarks can be obtained using [527][I.52] while top quark contributions can be obtained from [537]. In principle, these results could be used to obtain a NLO prediction for the interference. However, this calculation has not been performed yet. Given the similarity of signal and background $K-$factors, until a better computation is available the interference $K-$ factor can be obtained as the geometric average of the signal and background $K-$ factors. Scale variation uncertainties should account for missing higher order in the perturbative expansion. Alternatively, we note that even with our scale choice the signal still exhibits a non negligible NNLO $K-$factor, and it is not unreasonable to expect a similar $K-$factor also for the background [573]. One may then apply the signal NNLO $K-$factor to the background as well, and take the difference between NNLO and NLO as a conservative estimate of perturbative uncertainties.

In the high invariant mass region $m_{4l} > 2m_t$, it is not possible at this stage to provide a full NNLO (NLO) theoretical prediction for the signal (background), since exact heavy quark mass effects at NLO are unknown. In the following, we investigate signal and background $K-$factors in this region making different assumptions for missing top quark contributions. First, we compare in Figure 154 results for signal – with full top and bottom mass dependence through NLO – and background neglecting top quark contributions, as described in the previous sections and in [527]. For reference, we also show the effect of NNLO QCD corrections (computed with NNLO PDFs and α_s, and in the heavy-top approximation). This figure shows that signal and background K-factors are similar throughout the whole invariant mass spectrum considered here.

To quantify the effect of the missing top quark contribution in the background, we study two extreme approaches. First, we assume that the $K-$factor for massive and massless contributions is identical. Given their similarity in the low-mass region, we believe this assumptions to be reasonable. This leads to the K-factor shown in Figure 154 (see also Eq. I.8.12)

$$K_{gg\to 4l} = \frac{\mathrm{d}\sigma_{t,b}^{\mathrm{LO}}/\mathrm{d}m_{4l} + \mathcal{R}_{t,b}^{\mathrm{LO}}\mathrm{d}\Delta\sigma_{\mathrm{no}-t}^{\mathrm{NLO}}/\mathrm{d}m_{4l}}{\mathrm{d}\sigma_{t,b}^{\mathrm{LO}}/\mathrm{d}m_{4l}} = \frac{\mathrm{d}\sigma_{\mathrm{no}-t}^{\mathrm{LO}}/\mathrm{d}m_{4l} + \mathrm{d}\Delta\sigma_{\mathrm{no}-t}^{\mathrm{NLO}}/\mathrm{d}m_{4l}}{\mathrm{d}\sigma_{\mathrm{no}-t}^{\mathrm{LO}}/\mathrm{d}m_{4l}} = K_{gg\to 4l}^{\mathrm{no}-t}. \tag{I.8.13}$$

Second, we use full mass dependence in the LO contribution and only add NLO corrections for massless quarks[I.53]

[I.52] A numerical code for background predictions should be made public soon.

[I.53] Note that this second approach is rather unrealistic, as it assumes no interference between LO massive amplitudes and

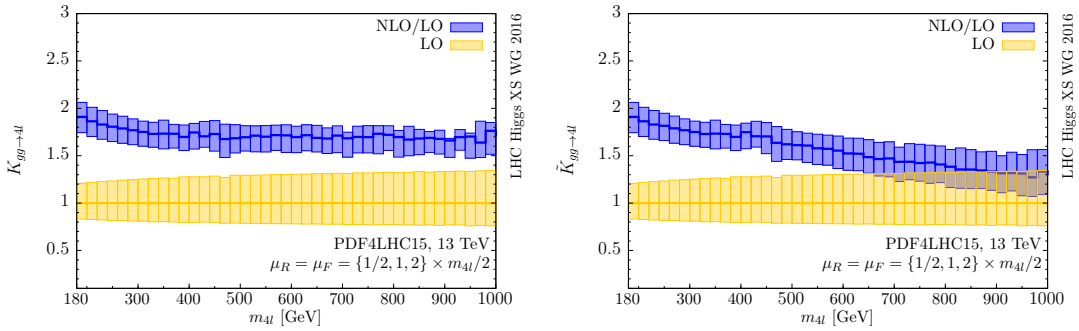

Figure 155: Comparison of different ways of treating quark mass effects at higher orders. Left: assume identical correction to massive and massless contributions. Right: assume zero corrections for massive contributions. See text for details.

$$\tilde{K}_{gg\to 4l} = \frac{\mathrm{d}\sigma^{\mathrm{LO}}_{t,b}/\mathrm{d}m_{4l} + \mathrm{d}\Delta\sigma^{\mathrm{NLO}}_{\mathrm{no}-t}/\mathrm{d}m_{4l}}{\mathrm{d}\sigma^{\mathrm{LO}}_{t,b}/\mathrm{d}m_{4l}}. \tag{I.8.14}$$

A comparison between K Eq. I.8.13 and $\tilde{K}$ Eq. I.8.14 is shown in Figure 155. Up to invariant masses $m_{4l} \sim 500$ GeV the two results are in good agreement, while they differ significantly at higher mass. The spread of these two results is a way to probe the uncertainty due to unknown mass effects.

Summarizing, for background predictions in the high invariant mass region we suggest to use exact LO multiplied by the massless K-factor Eq. I.8.13. The spread shown in Figure 155 may be used as a way to estimate the uncertainty of this procedure until a better computation becomes available. As for low invariant mass region, the interference K-factor is then determined as geometric mean of signal and background K-factors. Alternatively, given the similarity of signal and background $K-$factors and the size of uncertainties a simpler alternative – until more precise theoretical predictions are available – would be to assume the same K-factor for signal and background, and assign to it a systematic uncertainty which covers the effects described above. Note that both these approaches lead to a smooth interference $K-$factor over the whole m_{4l} spectrum, with an uncertainty increasing at large invariant masses to reflect the effect of unknown top quark mass effects. While this report was finalized, Refs. [574, 575] appeared. The results for the NLO corrections to the signal-background interference presented there support the approach advocated in this section.

I.8.5 $H \to \gamma\gamma$ mode

In this section we will review the status of the theoretical and experimental treatments of the interference term between the $gg \to H \to \gamma\gamma$ and $gg \to \gamma\gamma$.

The natural width of the Higgs boson is an important physics property that could reveal new physics in case of disagreement between the prediction and the measured values. Direct measurements of the Higgs boson widths are not possible, as the experimental mass resolution is significantly larger than the expected width. The mass resolution of the $\gamma\gamma$ system is about 1.7 GeV for $m_{\gamma\gamma} = 125$ GeV, 400 times larger than the natural width. Measurements of coupling strengths paired with limits on the invisible branching fraction indirectly constrain the width to close to its SM value [576], but this strategy cannot take into account unobserved (but not truly invisible) decay modes.

A new method as introduced by Dixon, Li, and Martin [509,510], allows to extract an indirect limit on the Higgs boson width using the interference of the $H \to \gamma\gamma$ signal with respect to the continuum diphoton background ($gg \to \gamma\gamma$ box diagrams). This interference has two parts.

NLO massless ones. We consider it here only as a way to estimate possible top quark effects in a conservative way.

1. An imaginary component reduces the total signal yield by $2-3\%$. Because this effect is degenerate with the coupling (signal strength) measurements, it is only measurable using constraints on the production rates from other channels.
2. The real component is odd around the Higgs boson mass and does not change the yield. However, when folded with the experimental resolution, it engenders a negative shift in the apparent mass.

In the SM, this shift was originally estimated using a simplified resolution model to be approximately 80 MeV [510], and for a width 20 times larger than the SM value, the shift was estimated to approximately 400 MeV.

In this section, we will review the latest developments on theoretical calculations, available MC tools, as well as experimental analyses from ATLAS and CMS collaborations.

I.8.5.a Theory overview

The Higgs boson is dominantly produced by gluon fusion through a top quark loop. Its decay to two photons, $H \to \gamma\gamma$, provides a very clean signature for probing Higgs boson properties, including its mass. However, there is also a large continuum background to its detection in this channel. It is important to study how much the coherent interference between the Higgs boson signal and the background could affect distributions in diphoton observables, and possibly use it to constrain Higgs boson properties.

The interference of the resonant process $ij \to X + H(\to \gamma\gamma)$ with the continuum QCD background $ij \to X + \gamma\gamma$ induced by quark loops can be expressed at the level of the partonic cross section as:

$$\begin{aligned} \delta\hat{\sigma}_{ij\to X+H\to\gamma\gamma} &= -2(\hat{s}-m_H^2)\,\frac{\mathrm{Re}\left(\mathcal{A}_{ij\to X+H}\mathcal{A}_{H\to\gamma\gamma}\mathcal{A}^*_{\mathrm{cont}}\right)}{(\hat{s}-m_H^2)^2+m_H^2\Gamma_H^2} \\ &\quad -2m_H\Gamma_H\,\frac{\mathrm{Im}\left(\mathcal{A}_{ij\to X+H}\mathcal{A}_{H\to\gamma\gamma}\mathcal{A}^*_{\mathrm{cont}}\right)}{(\hat{s}-m_H^2)^2+m_H^2\Gamma_H^2}\,, \end{aligned} \tag{I.8.15}$$

where m_H and Γ_H are the Higgs boson mass and decay width, and $\hat{s}$ is the partonic invariant mass. The interference is written in two parts, proportional to the real and imaginary parts of the Higgs Breit-Wigner propagator respectively, to which will be referred to as the real and imaginary part of the interference from now on.

The real part interference is odd in $\hat{s}$ around the Higgs boson mass peak, and thus its effect on the total $\gamma\gamma$ rate is subdominant as pointed out in ref. [577, 578]. The imaginary part of the interference, depending on the phase difference between the signal and background amplitudes, could significantly affect the total cross section. However, for the gluon-gluon partonic subprocess, it was found that the loop-induced background continuum amplitude has a quark mass suppression in its imaginary part for the relevant helicity combinations, making it dominantly real, therefore bearing the same phase as the Higgs boson production and decay amplitudes [578]. As a result, the contribution of the interference to the total cross section in the gluon fusion channel is highly suppressed at leading order (LO). The main contribution of the interference to the total rate comes from the two-loop imaginary part of the continuum amplitude $gg \to \gamma\gamma$, and only amounts to around 3% of the total signal rate [577].

Later, in ref. [509] it was shown that even though the real part of the interference hardly contributes to the total cross section, it has a quantifiable effect on the position of the diphoton invariant mass peak, producing a shift of $\mathcal{O}(100\,\mathrm{MeV})$ towards a lower mass region, once the smearing effect of the detector was taken into account. In ref. [579], the qg and $q\bar{q}$ channels of this process were studied, completing the full $\mathcal{O}(\alpha_S^2)$ computation of the interference effects between the Higgs diphoton signal and the continuum background at the LHC. Note that the extra qg and $q\bar{q}$ channels involve one QCD emission in the final states, but the corresponding background amplitudes start at tree level, and therefore the relevant interference is of the same order as the LO gg channel in which the background amplitude is

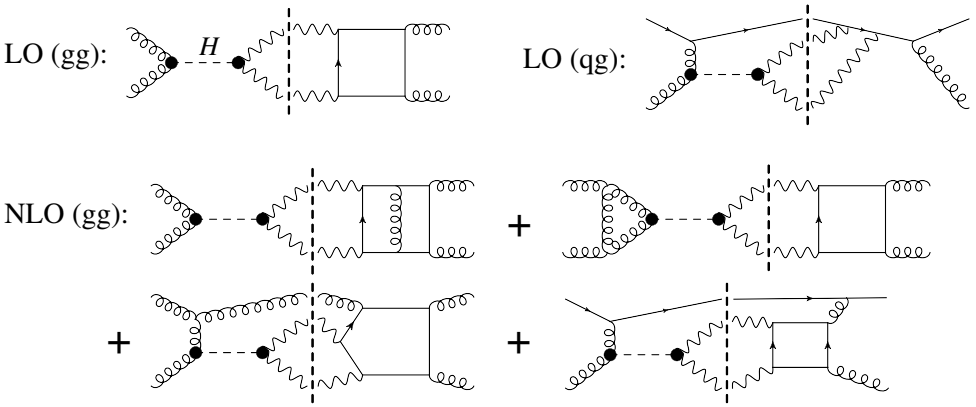

Figure 156: Representative diagrams for interference between the Higgs boson resonance and the continuum in the diphoton channel. The dashed vertical lines separate the resonant amplitudes from the continuum ones.

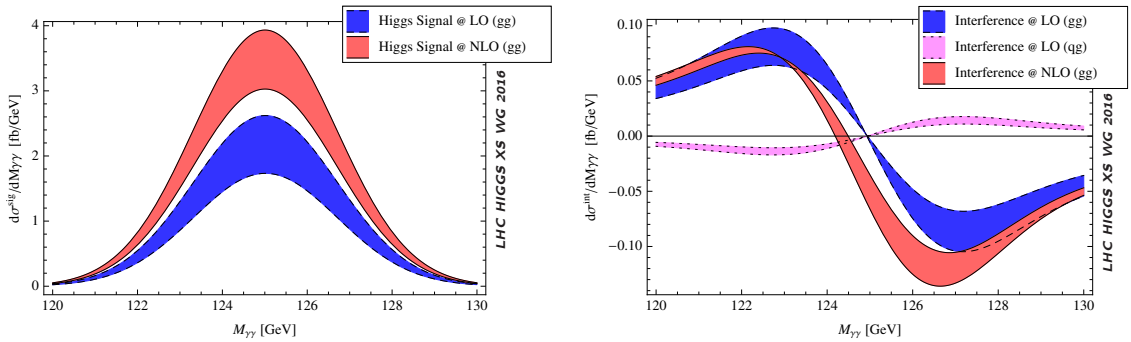

Figure 157: Diphoton invariant mass $M_{\gamma\gamma}$ distribution for pure signal (left panel) and interference term (right panel) after Gaussian smearing.

induced by a quark loop. The extra LO qg interference is depicted by the top right diagram in Figure 156, and the $q\bar{q}$ channel is related by cross symmetry. It was found that the contribution from the $q\bar{q}$ channel is numerically negligible due to the quark PDF suppression.

More recently, the dominant next-to-leading order (NLO) QCD corrections to the interference were calculated in ref. [510], where the dependence of the mass shift on the acceptance cuts was also studied. The left panel of Figure 157 shows the Gaussian-smeared diphoton invariant mass distribution for the pure signal at both LO and NLO in QCD. Standard acceptance cuts were applied to the photon transverse momenta, $p_{T,\gamma}^{\text{hard/soft}} > 40/30$ GeV, and rapidities, $|\eta_\gamma| < 2.5$. In addition, events were discarded when a jet with $p_{T,j} > 3$ GeV was within $\Delta R_{\gamma j} < 0.4$ of a photon. The scale uncertainty bands were obtained by varying $m_H/2 < \mu_F, \mu_R < 2m_H$ independently. For NLO, an additional qg process was included, where the background is induced by a quark loop as shown in the bottom right diagram of Figure 156; this is required as part of NLO gg channel to cancel the quark to gluon splitting in PDF evolution and reduces dependence on the factorization scale μ_F. As a result, the scale uncertainty bands come mostly from varying the renormalization scale μ_R.

The right panel of Figure 157 shows the corresponding Gaussian-smeared interference contributions. Each band is labelled according to Figure 156. The destructive interference from the imaginary part shows up at two-loop order in the gluon channel in the zero mass limit of light quarks [577]. It produces the offset of the NLO gg curve from zero at $M_{\gamma\gamma} = 125$ GeV.

Figure 158 shows the study of the mass shift dependence on a lower cut on the Higgs boson transverse momentum $p_T > p_{T,H}$. This strong dependence could potentially be observed experimentally, completely within the $\gamma\gamma$ channel, without having to compare against a mass measurement using the

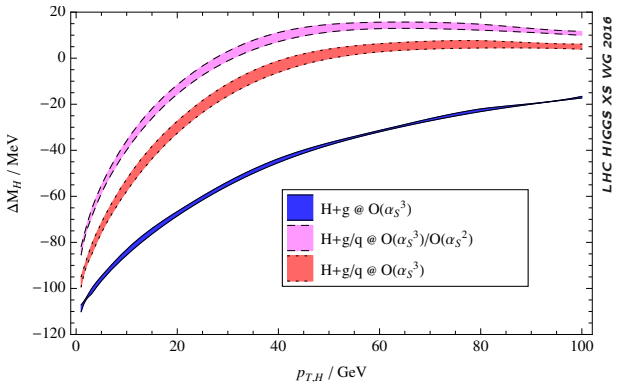

Figure 158: Apparent mass shift for the SM Higgs boson versus the lower cut on the Higgs boson transverse momentum, $p_T > p_{T,H}$.

only other high-precision channel, ZZ^*[I.54]. Using only $\gamma\gamma$ events might lead to reduced experimental systematics associated with the absolute photon energy scale. The $p_{T,H}$ dependence of the mass shift was first studied in ref. [580]. The dotted red band includes, in addition, the continuum process $qg \to \gamma\gamma q$ at one loop via a light quark loop, a part of the full $\mathcal{O}(\alpha_s^3)$ correction as explained above. This new contribution partially cancels against the tree-level qg channel, leading to a larger negative Higgs boson mass shift. The scale variation of the mass shift at finite $p_{T,H}$ is very small, because it is essentially a LO analysis; the scale variation largely cancels in the ratio between interference and signal that enters the mass shift.

Due to large logarithms, the small $p_{T,H}$ portion of Figure 158 is less reliable than the large $p_{T,H}$ portion. In using the $p_{T,H}$ dependence of the mass shift to constrain the Higgs boson width, the theoretical accuracy will benefit from using a wide first bin in p_T. One could take the difference between apparent Higgs boson masses for $\gamma\gamma$ events in two bins, those having p_T above and below, say, 40 GeV.

The Higgs boson width in the SM is $\Gamma_{H,\mathrm{SM}} = 4.07$ MeV, far too narrow to observe directly at the LHC. In global analyses of various Higgs boson decay channels [581–583], it is impossible to decouple the Higgs boson width from the couplings in experimental measurements without a further assumption, because the Higgs boson signal strength is always given by the product of squared couplings for Higgs boson production and for decay, divided by the Higgs boson total width Γ_H. Typically, the further assumption is that the Higgs boson coupling to electroweak vector bosons does not exceed the SM value. However, as was also pointed out in ref. [510], the apparent mass shift could be used to bound the value of the Higgs boson width. This is because the interference effect has different dependence on the Higgs boson width, allowing Γ_H to be constrained independently of assumptions about couplings or new decay modes in a lineshape model. Such a measurement would complement more direct measurements of the Higgs boson width at future colliders such as the ILC [584, 585] or a muon collider [586, 587], but could be accomplished much earlier.

Using $\mu_{\gamma\gamma}$ to denote the ratio of the experimental signal strength in $gg \to H \to \gamma\gamma$ to the SM prediction ($\sigma/\sigma^{\mathrm{SM}}$), the following equation can be set up,

$$\frac{c_{g\gamma}^2 S}{m_H \Gamma_H} + c_{g\gamma} I = \left(\frac{S}{m_H \Gamma_{H,\mathrm{SM}}} + I \right) \mu_{\gamma\gamma} \,, \tag{I.8.16}$$

where $c_{g\gamma} = c_g c_\gamma$ is the rescaling factor to be solved to preserve the signal yield when the Higgs boson width is varied. Once the relation between the $c_{g\gamma}$ and the Higgs boson width Γ_H is obtained, it can be used to determine the size of the apparent mass shift as a function of Γ_H. Neglecting the interference

[I.54] The mass shift for ZZ^* is much smaller than for $\gamma\gamma$, as can be inferred from Figure 17 of ref. [499], because $H \to ZZ^*$ is a tree-level decay, while the continuum background $gg \to ZZ^*$ arises at one loop, the same order as $gg \to \gamma\gamma$.

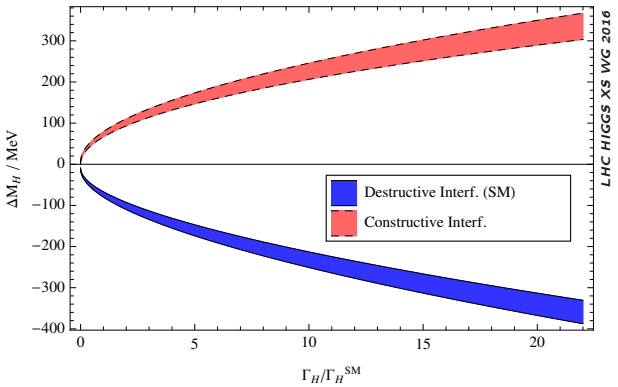

Figure 159: Higgs boson mass shift as a function of the Higgs boson width. The coupling $c_{g\gamma}$ has been adjusted to maintain a constant signal strength, in this case $\mu_{\gamma\gamma} = 1$.

contribution I to the total rate, and assuming $\mu_{\gamma\gamma} = 1$, the mass shift was found to be proportional to the square root of the Higgs boson width, $\delta m_H \propto \sqrt{\Gamma_H/\Gamma_{H,\text{SM}}}$, given that the width is much less than the detector resolution. Figure 159 plots the mass shift with $\mu_{\gamma\gamma} = 1$ and a smearing Gaussian width of 1.7 GeV. It is indeed proportional to $\sqrt{\Gamma_H}$ up to small corrections. If new physics somehow reverses the sign of the Higgs diphoton amplitude, the interference I would become positive.

In ref. [588] it was proposed to use another $\gamma\gamma$ sample to determine the Higgs boson resonance peak, in which the two photons were produced in association with two jets. Although this process is relatively rare, so is the background, making it possible to obtain reasonable statistical uncertainties on the position of the mass peak in this channel despite the lower number of events. The production of a Higgs boson in association with two jets is characteristic of the Vector Boson Fusion (VBF) production mechanism. While, in general terms, VBF is subdominant with respect to GF, it has a very different kinematical signature and can be selected through an appropriate choice of the experimental cuts. From a theoretical point of view, the VBF production mechanism has the additional advantage that perturbative corrections are much smaller than for GF (see e.g. ref. [263]). The effect of the signal-background interference for both the GF and VBF production mechanisms were studied, and the relevant diagrams are given in Figure 160. There are two kinds of backgrounds amplitudes, each of QCD and EW origin. It turns out that the interferences between GF signal and EW background or VBF signal and QCD background are highly suppressed by QCD colour factors, and therefore only the remaining combinations are shown in the first two diagrams of Figure 160. In addition, the interference with loop-induced QCD background, as given in the third diagram of Figure 160, was also considered, since it is enhanced by large gluonic luminosity at the LHC.

In Figure 161 the values of the apparent mass shift δm_H obtained for different cuts on the difference in pseudorapidities between the jets $|\Delta\eta_{jj}|$ are shown. The contributions from VBF and GF are presented separately, as well as the total shift. At the bottom of the plot, the total integrated signal is shown, also separated into VBF and GF contributions for the same cuts. For this plot no cut in $p_{T,H}$ was applied, and only events with the invariant mass of the dijet system $M_{jj} > 400$ GeV were considered. When no cut in $|\Delta\eta_{jj}|$ is applied, the shift in the Higgs boson invariant mass peak position produced by these two main production mechanisms is of the same magnitude, but of opposite sign; hence one observes a partial cancellation between them, with a net shift of around -6 MeV. As the value of $|\Delta\eta_{jj}|_{\text{min}}$ is increased, VBF becomes the dominant contribution, and GF becomes negligible, leading to a shift of around 20 MeV toward lower masses.

Next, the dependence of the mass shift on $p_{T,H}^{\text{min}}$ was studied. In Figure 162 the mass shift and the signal cross section for a range of $p_{T,H}^{\text{min}}$ between 0 GeV and 160 GeV is presented. The curves

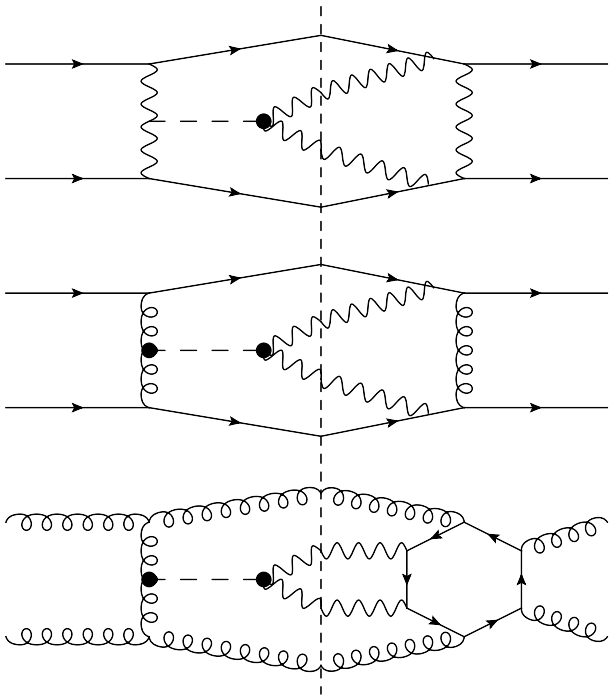

Figure 160: Examples of the Feynman diagrams computed for the calculation. The vertical dotted line separates signal from background. Above, the VBF signal and EW background contributions; in the middle the GF signal with tree level QCD mediated background; below, gluon-initiated signal, with the corresponding loop-induced LO background.

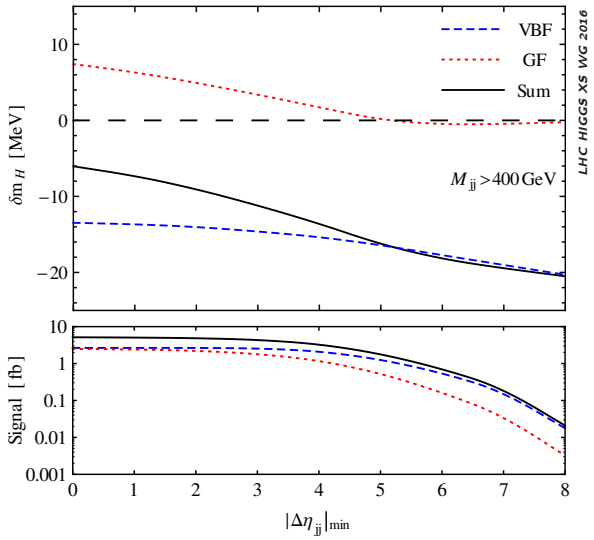

Figure 161: Top: Plot of mass shift δm_H for different values of $|\Delta\eta_{jj}|_{\text{min}}$. The dashed blue line represents the contribution from the VBF mechanism alone, the dotted red line shows GF only, and the solid black line displays the total shift of the Higgs boson invariant mass peak. Bottom: Total integrated signal cross section, also separated into VBF and GF contributions for the same cuts. No cut on $p_{T,H}^{\text{min}}$ was applied, and an additional cut was set of $M_{jj} > 400$GeV.

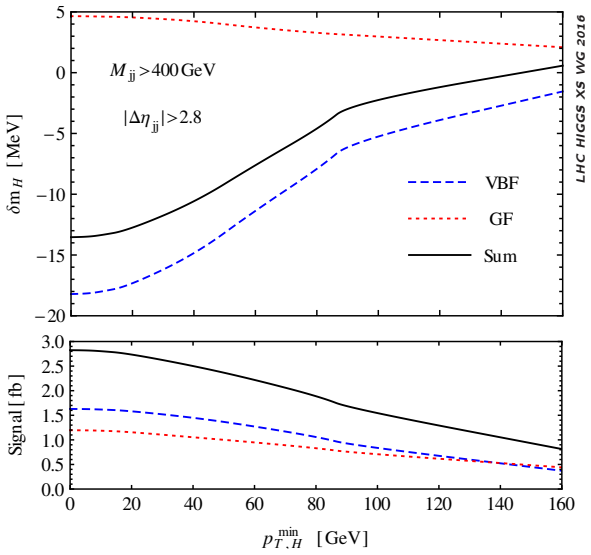

Figure 162: Top: Plot of mass shift δm_H for different values of $p_{T,H}^{\text{min}}$ for VBF, GF and total contributions. The curves are labelled as in Figure 161. Bottom: Total integrated signal, also separated into VBF and GF contributions for the same cuts. The following additional cuts were applied: $M_{jj} > 400$ GeV and $|\Delta\eta_{jj}| > 2.8$.

are labelled in the same way as in Figure 161. Once again, both production mechanisms contribute to the shift in invariant mass with opposite signs. For this plot, additional cuts in $M_{jj} > 400$ GeV and $|\Delta\eta_{jj}| > 2.8$ were applied, enhancing in this way the VBF contributions. However, at higher $p_{T,H}^{\text{min}}$, GF becomes as important as VBF.

As has already been mentioned, the shift in the Higgs boson invariant mass peak in $pp \to H(\to \gamma\gamma) + 2$ jets $+ X$ is considerably smaller than in the inclusive channel $pp \to H(\to \gamma\gamma) + X$. For appropriate cuts it can be almost zero. This makes it useful as a reference mass for experimental measurement of the mass difference,

$$\Delta m_H^{\gamma\gamma} \equiv \delta m_H^{\gamma\gamma,\,\text{incl}} - \delta m_H^{\gamma\gamma,\,\text{VBF}}\,, \tag{I.8.17}$$

where $\delta m_H^{\gamma\gamma,\,\text{incl}}$ is the mass shift in the inclusive channel, as computed at NLO in ref. [510], and $\delta m_H^{\gamma\gamma,\,\text{VBF}}$ is the quantity computed in ref. [588]. In computing $\delta m_H^{\gamma\gamma,\,\text{VBF}}$ for use in eq. (I.8.17) the basic photon and jet p_T and η cuts were imposed, and also $M_{jj} > 400$ GeV, but no additional cuts on $p_{T,H}$ or $\Delta\eta_{jj}$ were applied. This choice of cuts results in a small reference mass shift and a relatively large rate with which to measure it.

The lineshape model of ref. [510], as introduced earlier for the $gg \to \gamma\gamma$ inclusive process, was used in ref. [588] to compute the mass shift for the VBF process. It is in a way relatively independent of the new physics that may increase Γ_H from the SM value. The couplings of the Higgs boson to other SM particles must be modified if the Higgs boson width is varied, in order to be consistent with the Higgs boson signal strength measurements already made by the LHC, and prevent the total cross section from suffering large variations. Here, the deviation from SM coupling is described by a rescaling factor $c_{V\gamma} = c_V c_\gamma$, similar to $c_{g\gamma}$ in the $\gamma\gamma$ inclusive case, which is adjusted for different values of Γ_H to maintain the Higgs boson signal strength near the SM value.

Figure 163 shows how the observable $\Delta m_H^{\gamma\gamma}$ depends on the value of the Higgs boson width. The dependence is proportional to $\sqrt{\Gamma_H/\Gamma_{H,\text{SM}}}$ to a very good accuracy, as dictated by the linearity of the produced shift in $c_{g\gamma}$ or $c_{V\gamma}$ (in the range shown). It is dominated by the mass shift for the inclusive sample [510]. As was stated before, the main theoretical assumption was that the couplings of the Higgs

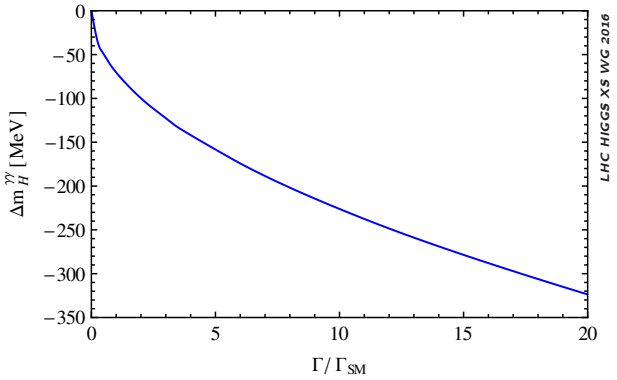

Figure 163: Plot of measurable mass shift $\Delta m_H^{\gamma\gamma}$ defined in eq. (I.8.17), as a function of $\Gamma_H/\Gamma_{H,\mathrm{SM}}$.

rescale by real factors, and the same rescaling for the Higgs boson coupling to gluons as for its coupling to vector boson pairs was assumed; this assumption could easily be relaxed, to the degree allowed by current measurements of the relative yields in different channels. The strong dependence the shift shows on the Higgs boson width might allow LHC experiments to measure or bound the width.

I.8.5.b Monte Carlo interference implementations

An overview of the Monte Carlo tools available to describe the Higgs lineshape and the signal-background interference is presented in this section. A first study using these tools is also presented.

I.8.5.b.i Available Tools: Sherpa 2.2.0 with DIRE parton shower

The calculations of [510, 588] have been implemented in Sherpa 2.2.0. Parton showers have been used for more than three decades to predict the dynamics of multi-particle final states in collider experiments [589, 590]. Recently, a new model was proposed [591], which combines the careful treatment of collinear configurations in parton showers with the correct resummation of soft logarithms in colour dipole cascades [592–595]. Following the basic ideas of the dipole formalism, the ordering variable is chosen as the transverse momentum in the soft limit. The evolution equations are based on the parton picture. Colour-coherence is implemented by partial fractioning the soft eikonal following the approach in [249], and matching each term to the double logarithmically enhanced part of the DGLAP splitting functions. Enforcing the correct collinear anomalous dimensions then determines all splitting kernels to leading order.

I.8.5.b.ii Exercise with DIRE parton shower

This sensitivity study follows the basic search strategy exploited in the past by both the CMS and ATLAS experiments for what concerns the $H \to \gamma\gamma$ search [1, 596]. The study is performed only at generator level assuming only gluon fusion production mode (GGH). The parton shower model assumed is the one described in Section I.8.5.b.i. Two isolated photons fulfiling loose identification criteria are selected and required to be within the the detector acceptance of $|\eta| < 2.5$ and the leading (subleading) photon must have $p_{T1} > 40$ GeV and $p_{T2} > 30$ GeV. The diphoton invariant mass distribution is constructed from these photons and required to be in the $[110 - 150]$ GeV energy range. Figures 164 and 165 show the transverse momentum distributions obtained for the two photons after the selection.

Figures 166 and 167 show the transverse momentum and the pure invariant mass of the diphoton system assuming no interference effect. Finally Figures 168 and 169 show the diphoton mass shapes for only the interference term and for the signal+interference cross–section. Interference effect is considered between the $H \to \gamma\gamma$ resonant process and the non resonant diphoton production. A convolution of

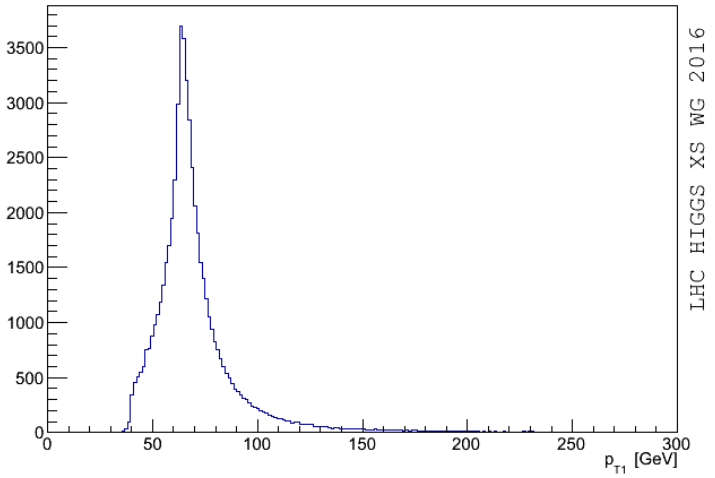

Figure 164: Transverse momentum distribution of the leading photon of the $H \to \gamma\gamma$ process produced via gluon fusion.

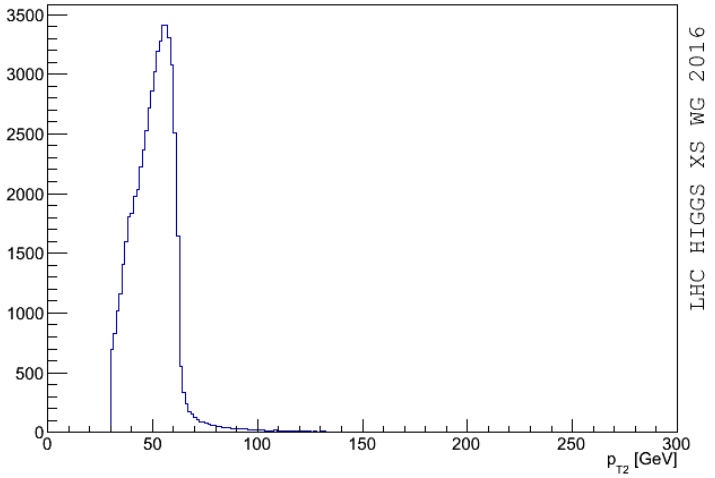

Figure 165: Transverse momentum distribution of the subleading photon of the $H \to \gamma\gamma$ process produced via gluon fusion.

the pure cross–section shape with a gaussian model can be applied to simulate the effects of the limited resolution of the detector in the photon energy measurement. Different values for the energy resolution (the σ of the gaussian function) can be assumed to fold the generator shape. Figure 170 shows the effect of the resolution smearing on the interference term assuming resolution values in the range [1.2-2.2] GeV. A realistic energy resolution value of 1.7 GeV is eventually assumed before comparing the shapes of the pure signal term and of the signal + interference terms in order to evaluate the relative shift introduced by the interference term itself. Figures 171 and 172 show this effect. In this case the shift is evaluated by fitting the two distributions with a gaussian function and taking the difference of the fitted mean values of the two models. The inclusive shift obtained is equal to $\Delta m = -89$ MeV. The trend of this shift varying the assumption on the value of the energy resolution is also shown in Figure 173. The uncertainties associated to the shifts come only from the statistical propagation of the errors on the fit parameters. As outlined in Section I.8.5.a the effect of the shift depends strongly upon the minimum threshold applied on the transverse momentum of the diphoton system. Figure 174 reproduces the results

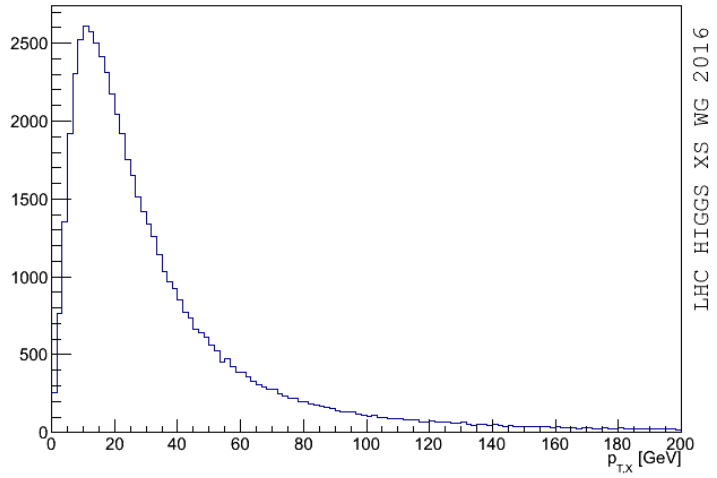

Figure 166: Diphoton transverse momentum distribution for pure $H \to \gamma\gamma$ signal produced via gluon fusion.

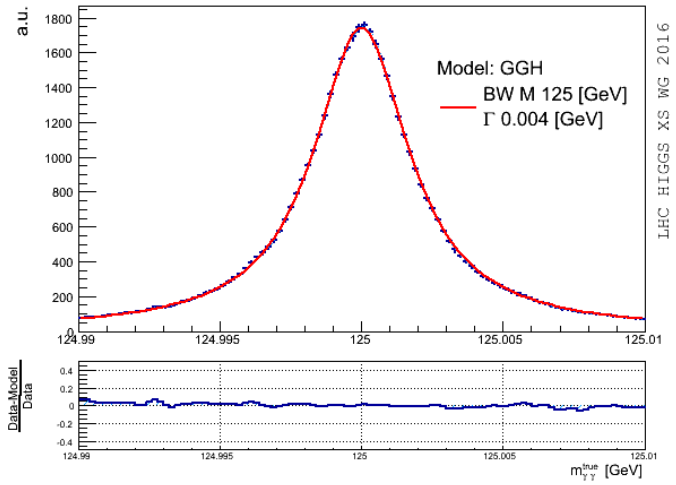

Figure 167: Diphoton invariant mass distribution for pure $H \to \gamma\gamma$ signal produced via gluon fusion.

shown in Section I.8.5.a showing that the greater the requirement on the minimum value of the diphoton momentum, the smaller the shift in the mass peak position. Additional studies are ongoing in order to evaluate the dependence of the shift upon the natural width of the Higgs.

I.8.5.c Studies from ATLAS

This section documents the studies by the ATLAS collaboration [I.55].

I.8.5.c.i Interference impact on the Higgs boson mass

A recent study has been conducted by ATLAS [597] to give a realistic estimate of the impact of the interference term on the Higgs boson mass measured in the $h \to \gamma\gamma$ channel [598]. Sherpa 2.0 is used to generate the $gg \to H \to \gamma\gamma$ signal samples as well as samples corresponding to the interference between this signal and its irreducible background, which is achieved using weighted events. The invariant mass

[I.55] Contact: C. Becot, F. Bernlochner, L. Fayard, S. Yuen

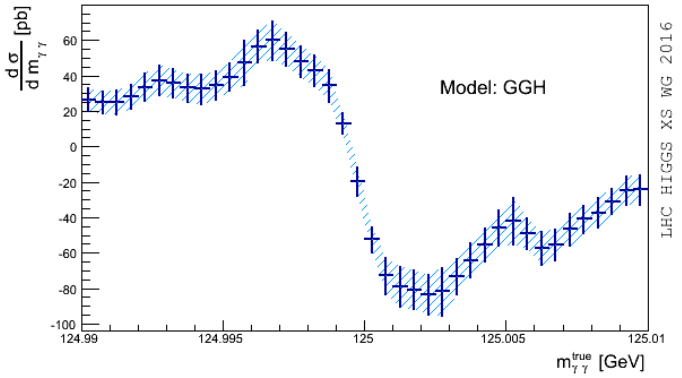

Figure 168: Pure interference term of the diphoton production cross–section.

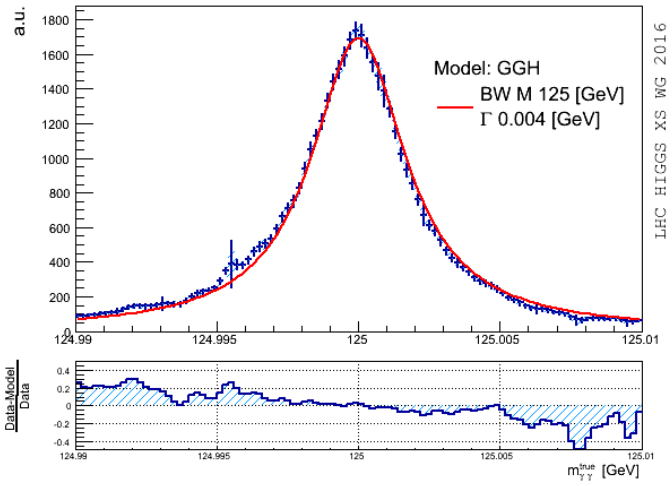

Figure 169: Total cross–section (signal+interference terms) distribution of the diphoton production. Signal refers to the $H \to \gamma\gamma$ process produced via gluon fusion.

spectrum of the di-photon system produced by these samples may be seen in Figure 175 for a specific category used in the ATLAS mass measurement. This generation has been done for a Higgs boson mass of $m_H = 125$ GeV and a Higgs boson width of $\Gamma_H = 4$ MeV. The NLO computation implemented in Sherpa 2 is matched to the CSS parton shower [355], which accounts for additional QCD radiations in the initial state. In order to give the best description of the interference and signal p_T spectra the behaviour of the shower has been tuned so that the Higgs boson signal p_T distribution generated by Sherpa matches the one generated by HRes 2.0 [223] as well as possible. This has been done by modifying the shower parameter CSS_IS_AS_FAC which modifies the energy at which the strong coupling constant is evaluated during the parton-shower evolution. The best agreement between the two distributions is obtained for CSS_IS_AS_FAC = 1.5. This tuning is also applied for the generation of the interference term. After generation, the di-photon mass is smeared according to the signal model derived in [598] which is dominated by a Crystal-Ball component. In order to reproduce the experimental efficiencies, the Monte-Carlo weights are folded by multiplicative weights that have the values of these efficiencies.

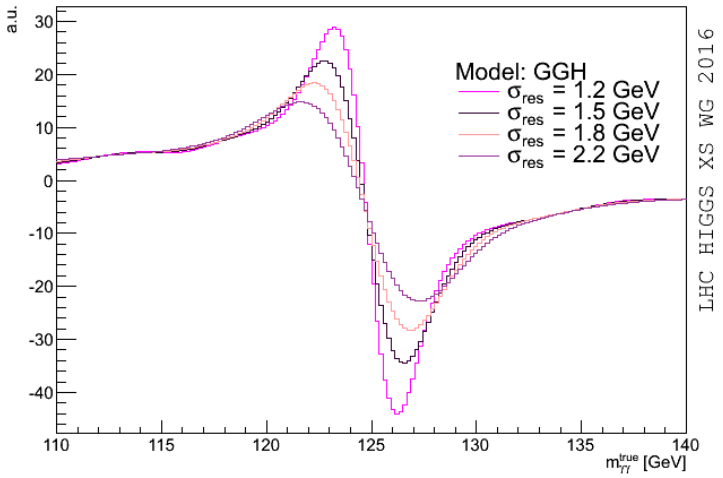

Figure 170: Interference cross–section term smeared assuming different values for the energy resolution in the range [1.2-2.2] GeV.

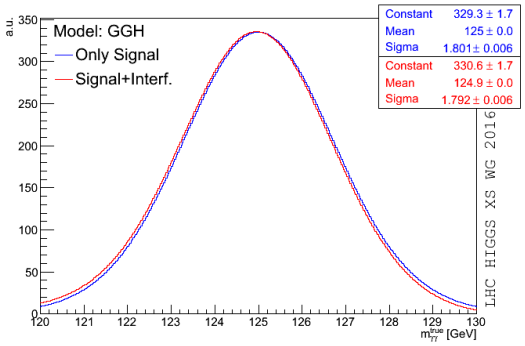

Figure 171: Pure signal and signal + interference shapes after applying a gaussian energy smearing of 1.7 GeV to simulate detector resolution effects. Red distribution corresponds to the pure $H \to \gamma\gamma$ process while the blue distribution includes the interference effect. Cross–section distributions are fitted with a gaussian function. Results of the fit are shown on the plot with the corresponding colours.

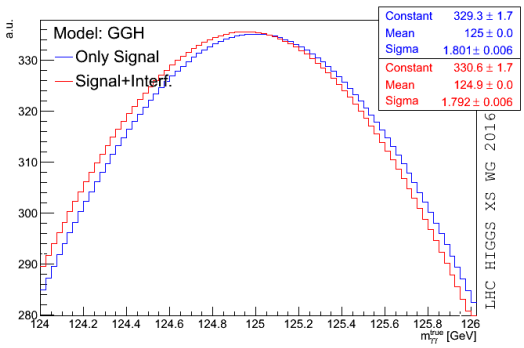

Figure 172: This figure shows the same results of Figure 171 with a zoom around the peak region, applied to better visualize the shift introduced by the interference effect. The inclusive shift obtained is equal to $\Delta m = -89$ MeV.

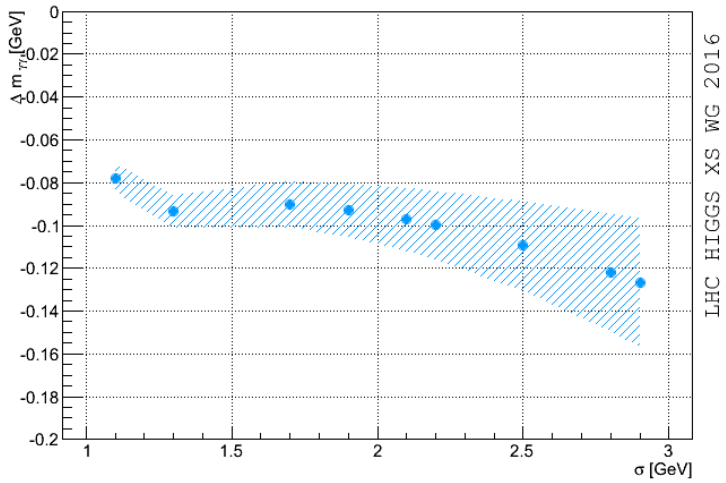

Figure 173: Shift in the mass peak position as a function of the energy mass resolution assumed. The smearing resolution being fixed, both the signal only and the signal+interference cross–section distributions are fitted with a gaussian function. The smearing is evaluated by the difference of the mean values for the two gaussian functions. The uncertainties associated with the shifts comes only from the statistical propagation of the errors on the fit parameters.

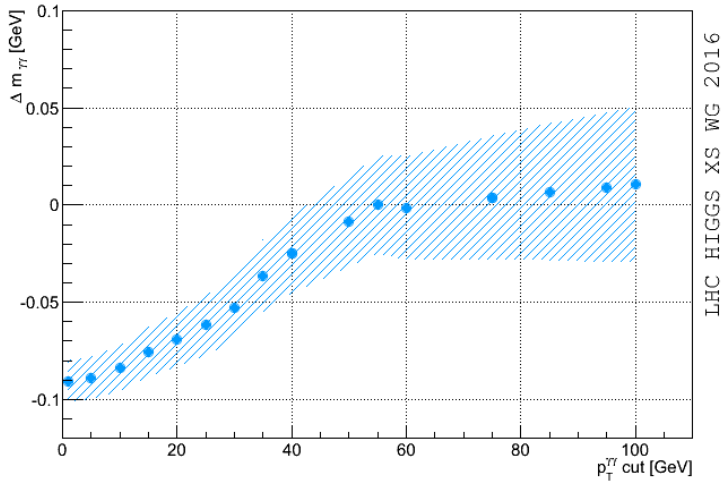

Figure 174: Shift in the mass peak position as a function of the minimum requirement on the diphoton transverse momentum. The smearing resolution being fixed, both the signal only and the signal+interference cross–section distributions are fitted with a gaussian function. The smearing is evaluated by the difference of the mean values for the two gaussian functions. The uncertainties associated to the shifts comes only from the statistical propagation of the errors on the fit parameters.

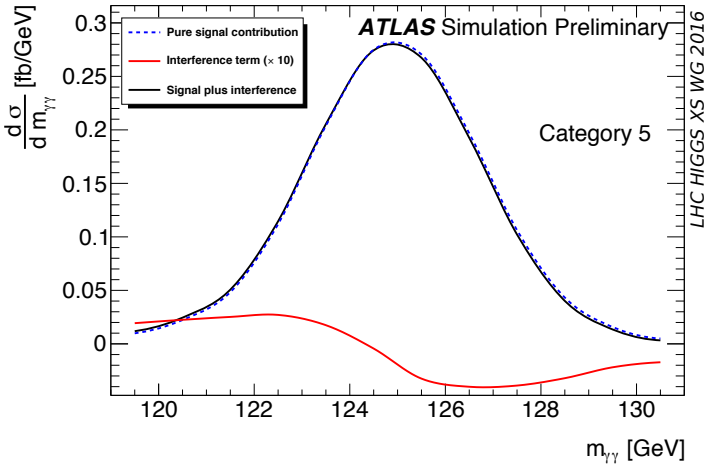

Figure 175: Mass distribution generated by the signal and interference term, as well as their sum, for a specific category of the ATLAS mass measurement (category no. 5). For illustrative purpose the magnitude of the interference-only term has been multiplied by 10.

The background is determined from a fit to data, as is usually done is the construction of the 'Asimov' dataset [599] and is therefore not subject to consideration on the physics modelling. In order to improve the analysis performances the mass measurement is carried out in event categories that are afterwards combined [598], and the actual shape used for this fit of the background depends on the actual category of events and are the same than those used in [598]. The additional production mechanisms with associated objects (vector-boson fusion, Higgs-strahlung and $t\bar{t}H$) are added by a re-scaling of the cross-section of the signal samples. As they have kinematical properties that differ from the main gluon-fusion production mechanism (and especially a different p_T spectrum), the templates determined in each category are rescaled separately using the fraction of gluon-fusion events of this particular category.

Two 'Asimov' datasets are then determined: one that contains only the signal and background templates, and another one that contains the same contributions plus the interference template. Each of these datasets contains one template for each of the ten categories used in [598]. The best-estimate of the Higgs boson mass is obtained separately on each of these datasets with a maximum-likelihood fit that uses the statistical model derived in [598], which is based on the signal and background models described above. The Higgs boson mass shift is then estimated as the signed difference between the two dataset $\Delta m_H = m_H^{S+B+I} - m_H^{S+B}$ and has been estimated to be of $\Delta m_H = -35$ MeV.

In order to assess that the Monte-Carlo samples are sufficiently large to give a negligible statistical uncertainty on Δm_H, four equivalent signal and interference samples have been generated with different random seeds. The mass shift has been determined separately on each of these, giving a variance of less than 1 MeV. The imperfect closure of the estimate of the mass on the signal-plus-background only sample has been added as a systematic uncertainty. The choice the actual background shape used has also been considered and added as an uncertainty. Both of these systematic uncertainties are at the level of 3 MeV.

Theoretical uncertainties have been estimated by varying the signal and background K-factors as well as the QCD scales involved in this problem. For the main result the signal K-factor K_S was set to $K_S = 1.45$, which effectively rescales the signal prediction from Sherpa to the NNLO+NNLL signal cross-section. This factor has been varied by ± 0.1, which accounts for PDF and α_S uncertainties. Ideally the background K-factor K_B would rescale the background cross-section to the same order than the signal (NNLO), however no computation of the $gg \to \gamma\gamma$ background have been performed beyond NLO so far. A conservative uncertainty on k_B has been assessed by varying it from 1 to K_S, using $K_B =$

K_S as a central value. These two factors modify the interference template by rescaling it by a factor $\sqrt{K_S K_B}$. At the end the uncertainty due to the K-factors has been taken has the biggest envelope of all these variations and gave an error of the mass-shift of ± 7 MeV. The three QCD scales (renormalization, factorization and resummation) have been varied, first separately then all at the same time. In spite of having a sizeable impact on the p_T spectrum, the resummation scale has almost no impact on the overall mass-shift estimated from the combined fit to ten categories, as most of the statistical power of this measurement is carried out by low p_T categories on which this scale does not have a big impact. The renormalization and factorization scales are varied by a factor 2, the central value being set to $m_{\gamma\gamma}$. Although the factorization scale has the dominant effect, the scale uncertainty is estimated as the variation that gives the biggest effect, which happens when the three scales are varied at once and gives an uncertainty of ± 5 MeV on the mass-shift.

All these four uncertainties are summed quadratically, which gives an estimate of the mass-shift of $\Delta m_H = -35 \pm 9$ MeV. This is valid only for the mass measurement carried out by ATLAS in the $h \to \gamma\gamma$ channel.

An illustration of the dependence of this shift on the analysis details is provided in [597], where an equivalent number is provided for an 'inclusive' analysis where the events are not split into categories. In this case the shift is estimated to be of $\Delta m_H = -49$ MeV, which is sizeably larger than in the actual measurement combining the ten different categories because of the different resolution. Moreover as the associated production components do not suffer from such large interference effects, their relative weights in the different categories may also give big variations of the actual mass-shift. For instance, it was estimated in [597] that for the inclusive fit and with the associated production removed the mass-shift would be of $\Delta m_H = -54$ MeV. It was also noted in [510] that the mass-shift had a linear dependence on the invariant mass resolution of the detector.

I.8.5.c.ii The choice of $gg \to (H) \to \gamma\gamma$ k-factors

As the most precise computation of the $gg \to \gamma\gamma$ continuum background has been done at NLO [600], the interference term is also limited to a NLO precision. However the signal $gg \to H \to \gamma\gamma$ is known up to NNLO with threshold resummation up to NNLL [223], while the computation provided in Sherpa 2 is only done at NLO. The increase of cross-section due to higher-order effects is usually implemented, for the signal, as a multiplicative k-factor K_S that rescales the cross-section of the signal Monte-Carlo. In this particular case this factor is of $K_S = 1.45$. If the impact of higher orders on the background cross-section was known the same approach could be carried out, using a factor K_B. As these two factors correspond to the impact of additional diagrams in the signal and background amplitudes, they also have an impact on the interference term whose cross-section will then scale as $\sqrt{K_S K_B}$.

Although an exact value for K_B cannot yet be determined, it is possible to determine an interval within which it should be. The dominating contribution to the Higgs boson signal is carried by a loop of top-quarks while for the continuum $gg \to \gamma\gamma$ background it comes from a loop of light quarks. At NLO, it was noticed in [600] that this implied larger short-distance renormalization effects for the signal calculation than for the background, which gave a LO to NLO K-factor larger by $\approx 20\%$ for the signal than for the background. Although no higher-order computations exist for the background yet, it is expected that the same analysis will hold for the NLO to NNLO K-factor, and hence a reasonable interval within which K_B should be is $[1,\ K_S]$.

Chapter I.9

Summary

In this chapter of the Report we have presented the state of the art for the SM Higgs cross-section and branching-ratio calculations.

Here we summarize the Higgs boson production cross sections which are obtained following the new recommendation for the choice of parton distribution functions (PDFs) and their combined uncertainty assessment together with the one for the strong coupling constant α_s (the new PDF4LHC recipe) as described in Chapter I.2. Moreover, we combine this PDF + α_s uncertainty with the theoretical uncertainty (THU). The combination of the two theoretical uncertainties has been discussed at length and while in the vast majority of the cases the theoretical advice is to sum them linearly, the experiments generally sum them in quadrature and assign a gaussian distribution to their density function.

A particular case is the uncertainty assigned to the ggF cross section calculation at N3LO order in QCD (see Section I.4.1.d).

The detailed analysis of the different calculations suggests the following recommendation:
use the F-uncertainty

$$\Delta_{\rm th} = [-6.7, +4.6]\% \tag{I.9.1}$$

which is a 100% flat interval. If it is highly preferred to have Gaussian uncertainties, then symmetrize the flat interval and divide it by $\sqrt{12}$, obtaining

$$\Delta_{\rm th} = \pm 3.9\%. \tag{I.9.2}$$

The corresponding gluon fusion cross-sections expanded to a scan over SM Higgs boson masses are presented in Tables 187–190. Tables 191 and 192 summarize the Standard Model gluon fusion cross-sections and the corresponding uncertainties for the different proton–proton collision energies for a Higgs boson mass $M_{\rm H} = 125$ GeV and $M_{\rm H} = 125.09$ GeV, respectively.

The following figures present the results as described in the above chapter, for a Higgs boson of mass ranging from 120 GeV to 130 GeV for 13 TeV, Figure 176 and 14 TeV, Figure 177, centre-of-mass-energies, with the combined parametric and theoretical uncertainties summed in quadrature and treated as gaussian pdf, illustrated by bands. The labels on the bands briefly indicated the type of radiative corrections that are included in the predictions.

Figure 178, presents the cross section for a Higgs boson of 125 GeV as a function of the centre-of-mass-energies.

The branching ratios for the SM Higgs boson are shown in Figure 179. Tables containing explicit numbers on partial widths, branching ratios, and on the total width can be found in

The results shown in this section will be regularly updated at our webpage[I.56].

Each experiment is recommended to use the common Standard Model input parameters as presented in Chapter I.1, the best known N3LO/NNLO/NLO cross sections and branching ratios reported in this Report as common basis for Higgs physics at LHC.

The SM cross section calculations has been extended to low and to high Higgs boson masses as a basis for Beyond Standard Model analysis and calculations. For these calculation the Narrow Width Approach has been used and Electro-Weak correction have not been included.

[I.56] https://twiki.cern.ch/twiki/bin/view/LHCPhysics/LHCHXSWG

The following figures present the results a function of the Higgs boson mass for 13 TeV (Figure 180) and 14 TeV (Figure 181) centre-of-mass-energies, with the combined parametric and theoretical uncertainties summed in quadrature, illustrated by bands. The labels on the bands briefly indicated the type of radiative corrections that are included in the predictions.

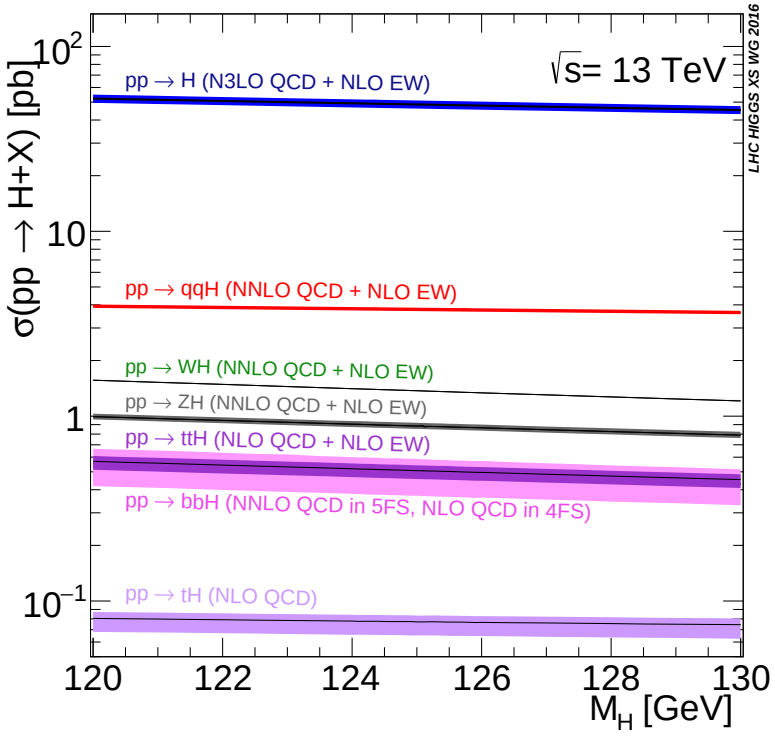

Figure 176: The SM Higgs boson production cross section at $\sqrt{s} = 13$ TeV

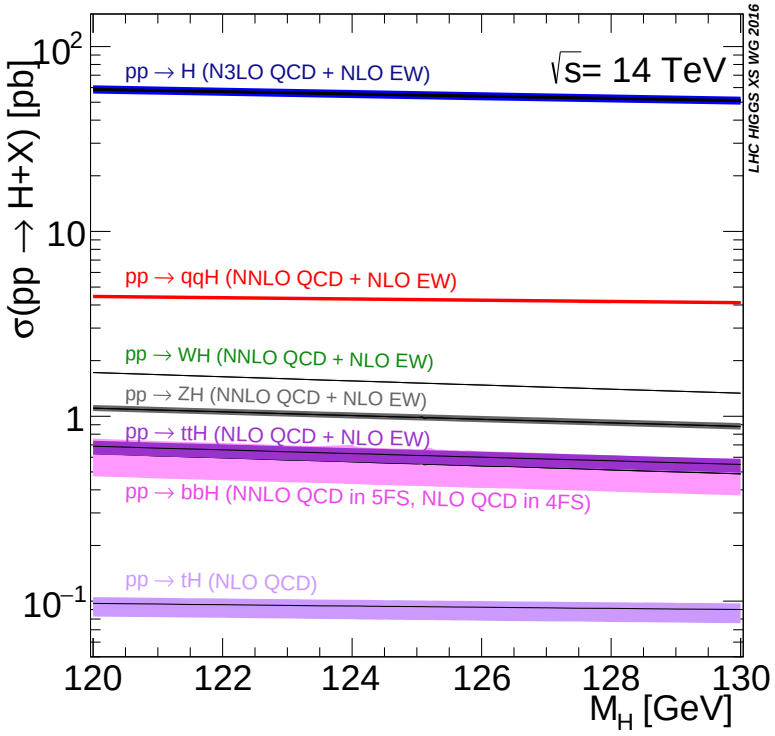

Figure 177: The SM Higgs boson production cross section at $\sqrt{s} = 14$ TeV.

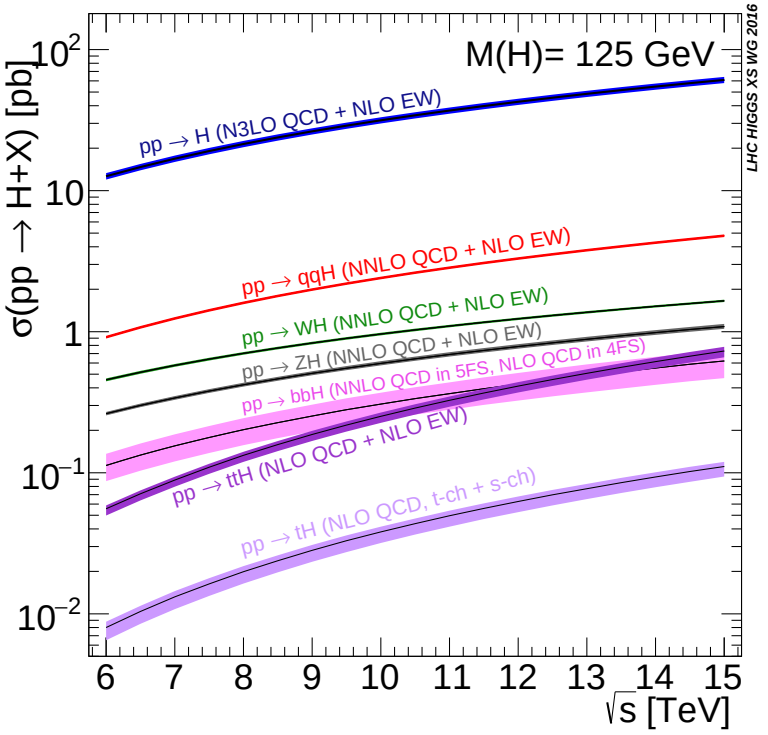

Figure 178: The SM Higgs boson production cross sections as a function of the LHC centre of mass energy.

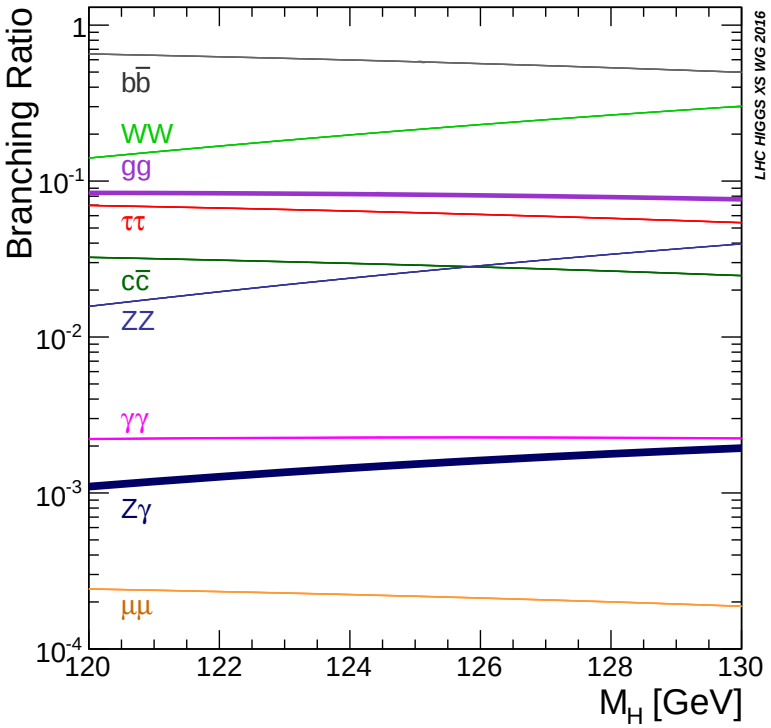

Figure 179: The SM Higgs boson branching ratios as a function of the Higgs boson mass.

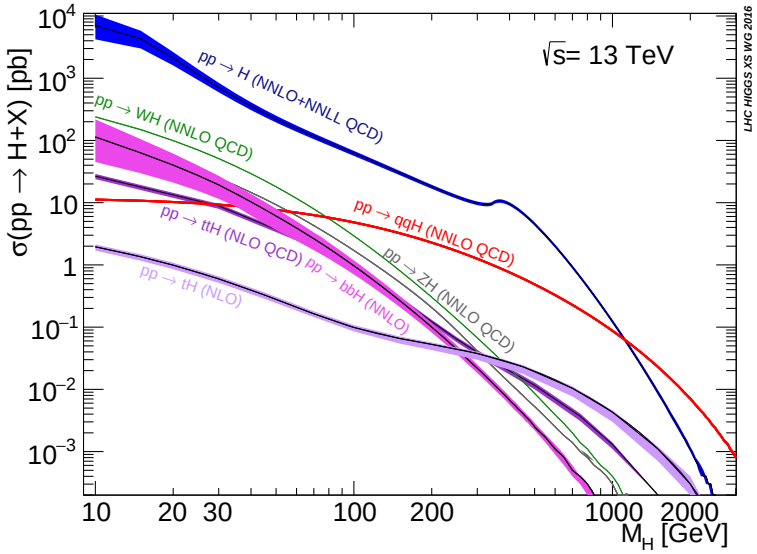

Figure 180: The SM Higgs boson production cross section as a function of the Higgs boson mass at $\sqrt{s} = 13$ TeV

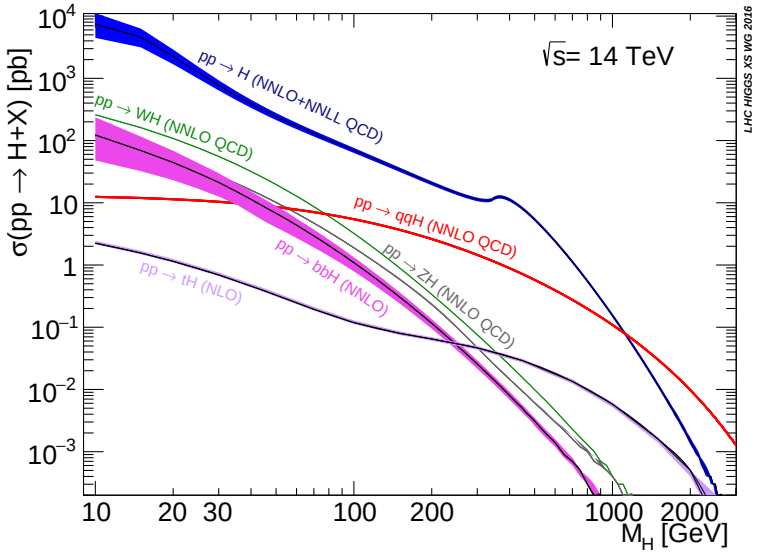

Figure 181: The SM Higgs boson production cross section as a function of the Higgs boson mass at $\sqrt{s} = 14$ TeV.

Part II

Effective Field Theory Predictions *

*M. Chen, A. David, M. Dührssen, A. Falkowski, C. Hays, G. Isidori (Eds.)

Chapter II.1

Executive Summary of Parts II and III

M. Chen, A. David, M. Dührssen, A. Falkowski, C. Hays, G. Isidori

The 2012 discovery of a new particle, subsequently shown by the ATLAS and CMS collaborations to be a Higgs boson, has closed a chapter in particle physics. Not only on the experimental side, putting an end to a decades-long search, but also, and perhaps more sharply, by completing the set of predictions by the standard model (SM) for elementary particles. The challenge that is ahead for the LHC and future machines is now fully in the BSM realm.

The LHC Run 2, which started in 2015, now has a qualitatively different goal in what regards the program for measuring the properties of this Higgs boson and the search for deviations from the SM predictions.

The WG2 contributions to this Yellow Report therefore naturally cluster around two main axes, supplemented by a third aspect:

1. How to expand the palette of measurements that can be performed by the experiments.
2. How to interpret existing measurements to set limits on and constrain new physics and characterize discoveries.
3. Tools with which to proceed in practice.

The two main axes are complementary to and feed off of each other: measurements pave the way for different interpretations, while interpretation frameworks motivate new measurements. This being said, there are caveats to this interaction. For instance, while almost any framework can be used to motivate particular measurements, the interpretation of a measurement and the definition of (pseudo)-observables can only be consistently done in a well-defined theory framework. In other words, much in the same way that finding a significant deviation with the kappa framework would clearly point to BSM physics, its meaning and interpretation would require a well-defined theory, which the kappa framework alone is not.

Complementing the chapters on measurements and interpretation, there are also two chapters describing tools that can be used in the different aspects of the measurement and interpretation steps.

This Executive Summary provides an overview of the WG2 chapters, comprised in Part II and, in collaboration with WG1, in Part III. The goal is not to exhaustively review the contents, but to offer a "lay of the land", providing the reader with the most salient and distinctive features of each chapter and how the different chapters are related and connected with each other.

Measurements

In this Yellow Report, the existing kappa framework for the search of deviations from the SM predictions is substantially expanded in two, complementary, ways: simplified template cross-sections (STXS) and pseudo-observables (PO). This dichotomy arises naturally from the fact that at the LHC the Higgs boson interaction with SM particles is probed at multiple energy scales. For instance, while $H \to 4\ell$ probes the amplitude coupling the Higgs to four fermions in a region of transferred momenta kinematically bounded by m_H, the associated ZH production will probe the same amplitude (or at least part of it) at significantly higher momentum transfer, possibly even in the multi-TeV region. That explains the different approaches presented in this Yellow Report, with some chapters focusing on production properties and others on decay properties.

Chapter III.2 presents a way to partition the phase-spaces of different Higgs boson production

processes into simplified template cross-sections. The goal of the STXS partitioning is two-fold:

1. To separate regions of the phase-space for which theory uncertainties can evolve with time.
2. To single out parts of the production phase-space where BSM physics predicts large deviations from the SM expectation. In this case, rare corners of SM production can be used to probe for BSM-induced deviations.

The STXS are mostly a tool that generalizes the notion of production process into sub-processes and the result of their use is a measurement of fully-extrapolated and unfolded cross-sections that can be also expressed as signal strengths relative to the SM predictions. This allows to recombine the measurements and update total cross section measurements ex post facto. This is for instance the case with jet binning for gluon-fusion cross-sections: measuring the ggH plus 0-jet, 1-jet, and 2-jet sub-processes allows to avoid to commit to a single prescription for jet bin migration that is needed to extract the ggH total cross-section, allowing for the prescription to evolve and be introduced later.

The STXS can be thought of as fully extrapolated and unfolded cross sections that can be inferred differentially in the production properties. As they are extrapolated from a simultaneous fit, this allows for advanced experimental techniques (including multi-variate observables and discriminants) to be employed in the analyses. The use of such techniques is not possible, for instance, when measuring fiducial cross-sections, as it is very hard, if not impossible, to define the fiducial volume for a multi-variate observable.

In a completely complementary way, fiducial cross-section (FXS) measurements provide easy to reproduce phase-spaces. Many practical aspects of FXS measurements are discussed in Chapter III.3, paving the way for common extractions of more model-independent quantities that are easy to collect in persistent form, using the HepData database and the Rivet toolkit. Attention is also paid to the interplay between signal and background processes in a given fiducial volume, as well as to unfolding of experimental effects from the measurements.

Finally, Chapter III.1 discusses how on-shell Higgs boson decays and production cross sections, close to the threshold region, can be parameterized in terms of pseudo-observables. The PO framework builds up on the similar approach introduced for Z-pole observables at LEP. In Higgs physics the formalism is a bit more complicated by the multiple poles involved in Higgs boson decays into 3 and 4 bodies, as well as in Higgs boson production cross sections. This richer kinematical structure is decomposed in terms of independent Lorentz structures, as well as resonant and non-resonant contributions, whose form is dictated by the general analytic properties of the amplitudes under the assumption that no BSM particles appear on-shell. The purpose and the main philosophy of Higgs PO is the same of the Z-pole (pseudo)-observables at LEP: PO are well-defined quantities from the quantum field theory point of view, that can be measured by experiments and then interpreted in generic BSM scenarios, including effective theory approaches.

Interpretation

Given that the SM has been completed, the focus on extending the SM is very strong. There are two fundamentally different ways to go about extending the SM Lagrangian: via concrete BSM alternatives (such as SUSY), for which different predictions are provided in Part IV, or through an effective descriptions of sufficiently high-mass (hence partially decoupled) degrees of freedom, as discussed in Part II. The latter approach, referred to as the effective field theory (EFT) approach to Higgs physics, is the one discussed in the chapters contributed from WG2. In this case, the SM Lagrangian is extended by adding higher-dimension operators written in terms of SM fields. Such a framework can be used to describe the effects of new heavy particles on Higgs physics in a large class of models beyond the SM. The Wilson coefficients of the higher-dimension operators in the EFT encode information about masses and couplings in the UV theory that completes the SM.

The EFT approach to Higgs physics is conceptually different from “top-down” EFT approaches,

such as HQET, where the ultraviolet completion of the theory is known. In the Higgs EFT case, the full theory is unknown and the working conditions are "bottom-up". This means that, a priori, there is a large range for the possible values of the couplings of the higher-dimensional operators. The latter can be restricted employing additional dynamical or symmetry assumptions about the overarching BSM model. This is why different EFT approaches (based on different symmetry hypotheses, and order of the expansion in the various couplings) are discussed in the chapters from WG2.

More generally, two main themes are addressed:

- The definition of the theory frameworks that can be used to extend the SM.
- Discussion of the limitations that such effective descriptions have in describing different BSM physics scenarios (UV completions).

In terms of Lagrangian formulation, two avenues are explored. In Section II.2.4 the chiral Lagrangian relevant to the case of a possible non-linear realization of electroweak symmetry breaking is presented. The largest effort, though, was devoted to the so-called SM EFT where, much as in the SM, the electroweak symmetry is realized linearly and broken spontaneously by the VEV of the Higgs field. Within this framework, Sections II.2.1 and II.2.3 discuss how the Wilson coefficients of dimension-6 operators are related to deformations of the Higgs boson couplings from the SM predictions. Furthermore, Chapter II.2.1 proposes a parameterization of the space of dimension-6 operators, the so-called Higgs basis, that is convenient for calculating Higgs observables at the leading order (LO) in the SM EFT. Section II.2.3 provides NLO results in the SM EFT after performing the renormalization programme. Given the differences between the nonlinear formulation, the SM EFT at the LO, and the NLO formulation, it is important to note that, depending on the exact UV completion realized in nature, there may or may not be a close correspondence between interpretations of the data in these different frameworks. Calculations within the LO EFT are simpler from the theoretical point of view and introduce a minimal number of parameters to describe leading deformations of Higgs observables. However, there may be physical situations where the LO EFT does not provide an adequate description and going beyond the LO is necessary; they are discussed in Sections II.2.2 and II.2.3. EFT with a non-linearly realized electroweak symmetry is less predictive than the SM EFT, but it may be relevant for certain classes of UV completions of the SM.

Sections II.2.2 and II.2.5 then explore the applicability of the SM EFT construction, both concluding that the SM EFT enjoys a broad range of validity in the absence of new particles with masses in the hundreds of GeV. One topic that is particularly difficult to address in interpreting measurements in terms of the underlying theory parameters, Wilson coefficients in this case, is that of theory uncertainties. These studies also shed some light into how operators with dimensions higher than 6 can play a role in the interpretation.

One conclusion arising from the discussion in this chapter is that there isn't a unique EFT approach to be recommended as different EFT approaches have different validity limits. In principle, the more general, the better, as there are fewer implicit assumptions about the ultraviolet completion. However, generality comes at the price of increased complexity and some compromise between generality and simplicity may be necessary, especially in the early phases of the LHC Run 2. This highlights the importance for EFT interpretations of LHC data to always be pursued in parallel to more general (although less predictive) approaches such as FXS, STXS, and POs.

Finally, it should be noted that the SM EFT has overarching implications to electroweak physics and even in other sectors in the sense that in its full generality, it can be constrained not only from precise measurements of Higgs boson properties but also other measurements, ranging from multiboson production, to top quark properties. Global fits of EFT parameters may allow for better constraints on BSM physics and amplify the power of the data. Indeed, the ability to combine distinct measurements within one consistent framework is a great strength of the EFT approach and one of its main motivations.

Tools

Of course none of the concepts above can be put to practice without computational tools that allow for the simulation of the different SM deformations, as well as tools that simplify the practical aspects related to the statistical inference on the parameters of interest.

Section II.3.1 overviews the available frameworks upon which many of the interpretations previously discussed, but also the measurements, can be based on. The effective Lagrangian formulation is widely used in order to make predictions starting from Wilson coefficients, but it is also used without loss of generality for encoding pseudo-observables.

In Section II.3.2 the reader can find a practical proposal to model predictions for different processes in a multidimensional context of SM deformations. The tools provide for continuous interpolation between parameter-space points, are based on commonly use software at the LHC, and may also find use in other applications. By providing smooth and continuous interpolations, they allow for simple application of likelihood ratio methods commonly used by ATLAS and CMS to determine the allowed confidence regions for parameters.

Chapter II.2

EFT Formalism

N. Belyaev, A. Biekötter, J. Brehmer, I. Brivio, G. Buchalla, O. Cata, A. Celis, R. Contino, T. Corbett, R.L. Delgado, A. Dobado, C. Englert, D. Espriu, A. Falkowski, A. Freitas, F. Goertz, D. Gonçalves, J. Gonzalez-Fraile, M. Gorbahn, C. Grojean, M. Herrero, R. Kogler, R. Konoplich, C. Krause, F.J. Llanes-Estrada, D. Lopez-Val, L. Merlo, K. Mimasu, J.M. No, T. Ohl, G. Passarino, T. Plehn, M. Rauch, J. Reuter, M. Riembau, F. Riva V. Sanz, J.J. Sanz-Cillero, M. Spannowsky, M. Trott

II.2.1 Bases for the Standard Model Effective Field Theory [II.1]

II.2.1.a Introduction

For a large class of models beyond the SM, physics at energies below the mass scale Λ of the new particles can be parameterized by an effective field theory (EFT) where the SM Lagrangian is supplemented by new operators with canonical dimensions D larger than 4. The theory has the same field content and the same linearly realized $SU(3) \times SU(2) \times U(1)$ local symmetry as the SM.[II.2] The higher-dimensional operators are organized in a systematic expansion in D, where each consecutive term is suppressed by a larger power of Λ. For a general introduction to the EFT formalism see e.g. [601–605]; for recent review articles about EFT in connection with Higgs physics see e.g. [463, 606–610].

Quite generally, the EFT Lagrangian takes the form:

$$\mathcal{L}_{\text{eff}} = \mathcal{L}_{\text{SM}} + \sum_i \frac{c_i^{(5)}}{\Lambda} \mathcal{O}_i^{(5)} + \sum_i \frac{c_i^{(6)}}{\Lambda^2} \mathcal{O}_i^{(6)} + \sum_i \frac{c_i^{(7)}}{\Lambda^3} \mathcal{O}_i^{(7)} + \sum_i \frac{c_i^{(8)}}{\Lambda^4} \mathcal{O}_i^{(8)} + \cdots , \qquad \text{(II.2.1)}$$

where each $\mathcal{O}_i^{(D)}$ is an $SU(3) \times SU(2) \times U(1)$ invariant operator of dimension D and the parameters $c_i^{(D)}$ multiplying the operators in the Lagrangian are called the *Wilson coefficients*. This EFT is intended to parameterize observable effects of a large class of BSM theories where new particles, with mass of order Λ, are much heavier than the SM ones and much heavier than the energy scale at which the experiment is performed. The main motivation to use this framework is that the constraints on the EFT parameters can be later re-interpreted as constraints on masses and couplings of new particles in many BSM theories. In other words, translation of experimental data into a theoretical framework has to be done only once in the EFT context, rather than for each BSM model separately.

The contribution of each $O_i^{(D)}$ to amplitudes of physical processes at the energy scale of order v scales[II.3] as $(v/\Lambda)^{D-4}$. Since $v/\Lambda < 1$ by construction, the EFT in its validity regime typically describes *small* deviations from the SM predictions, although, under certain conditions, it may be consistent to use this framework to describe large deviations [611, 612].

A complete and non-redundant set of operators that can be constructed from the SM fields is known for D=5 [613], D=6 [614], D=7 [615, 616], and D=8 [616, 617]. All D=5 operators violate the lepton number [613], while all D=7 operators violate $B - L$ (the latter is true for all odd-D operators [618]). Then, experimental constraints dictate that their Wilson coefficients must be suppressed at a level which makes them unobservable at the LHC [619], and for this reason D=5 and 7 operators will not be discussed

[II.1] *Author(s): N. Belyaev, A. Falkowski, F. Goertz, R. Konoplich, K. Mimasu, T. Ohl, J. Reuter, M. Riembau, F. Riva.*

[II.2] The latter assumption can be relaxed, leading to an EFT with a non-linearly realized electroweak symmetry. This framework is discussed in Section II.2.4.

[II.3] Apart from the scaling with Λ, the effects of higher-dimensional operators also scale with appropriate powers of couplings in the UV theory. The latter is important to assess the validity range of the EFT description, as discussed in Section II.2.2 and Ref. [611].

here. Consequently, the leading new physics effects are expected from operators with D=6 [620], whose contributions scale as $(v/\Lambda)^2$. Contributions from operators with $D \geq 8$ are suppressed by at least $(v/\Lambda)^4$, and in most of the following discussion we will assume that they can be neglected.

In this section, we discuss in detail the D=6 operators that can be constructed from the SM fields. We review various possible choices of these operators (the so-called *basis*) and their phenomenological effects. Only the operators that conserve the baryon and lepton numbers are considered. On the other hand, we do not impose a-priori any flavour symmetry. Also, we include CP violating operators in our discussion. One purpose of this section is to propose a common EFT language and conventions that could be universally used in LHC Higgs analyses and be implemented in numerical tools.

In Section II.2.1.b we introduce the SM Lagrangian extended by dimension-6 operators. Two popular bases of dimension-6 operators using the manifestly $SU(2) \times U(1)$ invariant formalism are introduced. In Section II.2.1.c we discuss the interactions of the SM mass eigenstates that arise in the presence of dimension-6 operators beyond the SM, with the emphasis on the Higgs interactions. We also provide a map between the couplings in that effective Lagrangian and Wilson coefficients of dimension-6 operators introduced in Section II.2.1.b. In Section II.2.1.d we define a new basis of D=6 operators, the so-called Higgs basis, which is spanned by a subset of the independent couplings of the mass eigenstate Lagrangian.

II.2.1.b SM EFT with dimension-6 operators

We consider an EFT Lagrangian where the SM is extended by dimension-6 operators:

$$\mathcal{L}_{\rm EFT} = \mathcal{L}_{\rm SM} + \sum_i \bar{c}_i^{(6)} O_i^{(6)}. \tag{II.2.2}$$

Here, the scale Λ has been absorbed in the definition of the Wilson coefficient, $\bar{c}_i^{(6)} = c_i^{(6)}/\Lambda^2$.

To fix our notation and conventions, we first write down the SM Lagrangian:

$$\begin{aligned}
\mathcal{L}_{\rm SM} &= -\frac{1}{4} G^a_{\mu\nu} G^a_{\mu\nu} - \frac{1}{4} W^i_{\mu\nu} W^i_{\mu\nu} - \frac{1}{4} B_{\mu\nu} B_{\mu\nu} + D_\mu H^\dagger D_\mu H + \mu_H^2 H^\dagger H - \lambda (H^\dagger H)^2 \\
&+ \sum_{f \in q,\ell} i \bar{f}_L \gamma_\mu D_\mu f_L + \sum_{f \in u,d,e} i \bar{f}_R \gamma_\mu D_\mu f_R \\
&- \left[q_L \tilde{H} y_u u_R + \bar{q}_L H y_d d_R + \bar{\ell}_L H y_e \ell_R + \text{h.c.} \right].
\end{aligned} \tag{II.2.3}$$

Here, G^a_μ, W^i_μ, and B_μ denote the gauge fields of the $SU(3) \times SU(2) \times U(1)$ local symmetry. The corresponding gauge couplings are denoted by g_s, g, g'; we also define the electromagnetic coupling $e = gg'/\sqrt{g^2 + g'^2}$, and the Weinberg angle $s_\theta = g'/\sqrt{g^2 + g'^2}$. The field strength tensors are defined as $G^a_{\mu\nu} = \partial_\mu G^a_\nu - \partial_\nu G^a_\mu + g_s f^{abc} G^b_\mu G^c_\nu$, $W^i_{\mu\nu} = \partial_\mu W^i_\nu - \partial_\nu W^i_\mu + g \epsilon^{ijk} W^j_\mu W^k_\nu$, $B_{\mu\nu} = \partial_\mu B_\nu - \partial_\nu B_\mu$. The Higgs doublet is denoted as H, and we also define $\tilde{H}_i = \epsilon_{ij} H^*_j$. It acquires the VEV $\langle H^\dagger H \rangle = v^2/2$. In the unitary gauge we have $H = (0, (v+h)/\sqrt{2})$, where h is the Higgs boson field. After electroweak symmetry breaking, the electroweak gauge boson mass eigenstates are defined as $W^\pm = (W^1 \mp i W^2)/\sqrt{2}$, $Z = c_\theta W^3 - s_\theta B$, $A = s_\theta W^3 + c_\theta B$, where $c_\theta = \sqrt{1 - s_\theta^2}$. The tree-level masses of W and Z bosons are given by $m_W = gv/2$, $m_Z = \sqrt{g^2 + g'^2} v/2$. The left-handed Dirac fermions $q_L = (u_L, d_L)$ and $\ell_L = (\nu_L, e_L)$ are doublets of the SU(2) gauge group, and the right-handed Dirac fermions u_R, d_R, e_R are SU(2) singlets. All fermions are 3-component vectors in the generation space, and y_f are 3×3 matrices. The 3 electroweak parameters g, g', v are customarily derived from the Fermi constant G_F measured in muon decays, Z boson mass m_Z, and the low-energy electromagnetic coupling $\alpha(0)$. The Higgs quartic couplings λ can then be fixed from the measured Higgs boson mass.

The tree-level relations between the input observables and the electroweak parameters are given by:

$$G_F = \frac{1}{\sqrt{2}v^2}, \qquad \alpha = \frac{g^2 g'^2}{4\pi(g^2+g'^2)}, \qquad m_Z = \frac{\sqrt{g^2+g'^2}v}{2}, \qquad m_h^2 = 2\lambda v^2. \tag{II.2.4}$$

We demand that the dimension-6 operators $O_i^{(6)}$ in Eq. (II.2.2) form a complete, non-redundant set - a so-called *basis*. Complete means that any dimension-6 operator is either a part of the basis or can be obtained from a combination of operators in the basis using equations of motion, integration by parts, field redefinitions, and Fierz transformations. Non-redundant means it is a minimal such set. Any complete basis leads to the same physical predictions concerning possible new physics effects. Several bases have been proposed in the literature, and they may be convenient for specific applications. Historically, a complete and non-redundant set of D=6 operators was first identified in Ref. [614], and is usually referred to as the *Warsaw basis*. This basis is described in detail in Section II.2.3., and the relevant formulas are summarized in Appendix A of Ref. [621]. Below, we work with another basis choice commonly used in the literature: the so-called SILH basis [464]. Later, in Section. II.2.1.d, we propose a new basis choice that is particularly convenient for leading-order LHC Higgs analyses in the EFT framework.

Table 97: Bosonic D=6 operators in the SILH basis.

Bosonic CP-even		Bosonic CP-odd	
O_H	$\frac{1}{2v^2}\left[\partial_\mu(H^\dagger H)\right]^2$		
O_T	$\frac{1}{2v^2}\left(H^\dagger \overleftrightarrow{D_\mu} H\right)^2$		
O_6	$-\frac{\lambda}{v^2}(H^\dagger H)^3$		
O_g	$\frac{g_s^2}{m_W^2} H^\dagger H\, G^a_{\mu\nu} G^a_{\mu\nu}$	$\widetilde{O}_g$	$\frac{g_s^2}{m_W^2} H^\dagger H\, \widetilde{G}^a_{\mu\nu} G^a_{\mu\nu}$
O_γ	$\frac{g'^2}{m_W^2} H^\dagger H\, B_{\mu\nu} B_{\mu\nu}$	$\widetilde{O}_\gamma$	$\frac{g'^2}{m_W^2} H^\dagger H\, \widetilde{B}_{\mu\nu} B_{\mu\nu}$
O_W	$\frac{ig}{2m_W^2}\left(H^\dagger \sigma^i \overleftrightarrow{D_\mu} H\right) D_\nu W^i_{\mu\nu}$		
O_B	$\frac{ig'}{2m_W^2}\left(H^\dagger \overleftrightarrow{D_\mu} H\right) \partial_\nu B_{\mu\nu}$		
O_{HW}	$\frac{ig}{m_W^2}\left(D_\mu H^\dagger \sigma^i D_\nu H\right) W^i_{\mu\nu}$	$\widetilde{O}_{HW}$	$\frac{ig}{m_W^2}\left(D_\mu H^\dagger \sigma^i D_\nu H\right) \widetilde{W}^i_{\mu\nu}$
O_{HB}	$\frac{ig'}{m_W^2}\left(D_\mu H^\dagger D_\nu H\right) B_{\mu\nu}$	$\widetilde{O}_{HB}$	$\frac{ig}{m_W^2}\left(D_\mu H^\dagger D_\nu H\right) \widetilde{B}_{\mu\nu}$
O_{2W}	$\frac{1}{m_W^2} D_\mu W^i_{\mu\nu} D_\rho W^i_{\rho\nu}$		
O_{2B}	$\frac{1}{m_W^2} \partial_\mu B_{\mu\nu} \partial_\rho B_{\rho\nu}$		
O_{2G}	$\frac{1}{m_W^2} D_\mu G^a_{\mu\nu} D_\rho G^a_{\rho\nu}$		
O_{3W}	$\frac{g^3}{m_W^2} \epsilon^{ijk} W^i_{\mu\nu} W^j_{\nu\rho} W^k_{\rho\mu}$	$\widetilde{O}_{3W}$	$\frac{g^3}{m_W^2} \epsilon^{ijk} \widetilde{W}^i_{\mu\nu} W^j_{\nu\rho} W^k_{\rho\mu}$
O_{3G}	$\frac{g_s^3}{m_W^2} f^{abc} G^a_{\mu\nu} G^b_{\nu\rho} G^c_{\rho\mu}$	$\widetilde{O}_{3G}$	$\frac{g_s^3}{m_W^2} f^{abc} \widetilde{G}^a_{\mu\nu} G^b_{\nu\rho} G^c_{\rho\mu}$

The full set of operators in the SILH basis is given in Tables 97, 98, and 99. We use the normalization and conventions of Ref. [464].[II.4]

[II.4] In Ref. [464] it was assumed that the flavour indices of fermionic D=6 operators are proportional to the unit matrix. Generalizing this to an arbitrary flavour structure, one needs to specify flavour indices of the operators $[O_{H\ell}]$, $[O'_{H\ell}]$, $[O_{\ell\ell}]$ and $[O'_{uu}]$ which are absent in the SILH basis to avoid redundancy. Here, for concreteness, we made a particular though somewhat arbitrary choice of these indices.

Table 98: Two-fermion dimension-6 operators in the SILH basis. They are the same as in the Warsaw basis, except that the operators $[O_{H\ell}]_{11}$, $[O'_{H\ell}]_{11}$ are absent by definition. We define $\sigma_{\mu\nu} = i[\gamma_\mu, \gamma_\nu]/2$. In this table, e, u, d are always right-handed fermions, while ℓ and q are left-handed. For complex operators the complex conjugate operator is implicit.

Vertex	
$[O_{H\ell}]_{ij}$	$\frac{i}{v^2}\bar{\ell}_i\gamma_\mu\ell_j H^\dagger\overleftrightarrow{D_\mu}H$
$[O'_{H\ell}]_{ij}$	$\frac{i}{v^2}\bar{\ell}_i\sigma^k\gamma_\mu\ell_j H^\dagger\sigma^k\overleftrightarrow{D_\mu}H$
$[O_{He}]_{ij}$	$\frac{i}{v^2}\bar{e}_i\gamma_\mu\bar{e}_j H^\dagger\overleftrightarrow{D_\mu}H$
$[O_{Hq}]_{ij}$	$\frac{i}{v^2}\bar{q}_i\gamma_\mu q_j H^\dagger\overleftrightarrow{D_\mu}H$
$[O'_{Hq}]_{ij}$	$\frac{i}{v^2}\bar{q}_i\sigma^k\gamma_\mu q_j H^\dagger\sigma^k\overleftrightarrow{D_\mu}H$
$[O_{Hu}]_{ij}$	$\frac{i}{v^2}\bar{u}_i\gamma_\mu u_j H^\dagger\overleftrightarrow{D_\mu}H$
$[O_{Hd}]_{ij}$	$\frac{i}{v^2}\bar{d}_i\gamma_\mu d_j H^\dagger\overleftrightarrow{D_\mu}H$
$[O_{Hud}]_{ij}$	$\frac{i}{v^2}\bar{u}_i\gamma_\mu d_j \tilde{H}^\dagger D_\mu H$

Yukawa and Dipole	
$[O_e]_{ij}$	$\frac{\sqrt{2m_{e_i}m_{e_j}}}{v^3}H^\dagger H\bar{\ell}_i H e_j$
$[O_u]_{ij}$	$\frac{\sqrt{2m_{u_i}m_{u_j}}}{v^3}H^\dagger H\bar{q}_i \tilde{H} u_j$
$[O_d]_{ij}$	$\frac{\sqrt{2m_{d_i}m_{d_j}}}{v^3}H^\dagger H\bar{q}_i H d_j$
$[O_{eW}]_{ij}$	$\frac{g}{m_W^2}\frac{\sqrt{2m_{e_i}m_{e_j}}}{v}\bar{\ell}_i\sigma^k H\sigma_{\mu\nu}e_j W^k_{\mu\nu}$
$[O_{eB}]_{ij}$	$\frac{g'}{m_W^2}\frac{\sqrt{2m_{e_i}m_{e_j}}}{v}\bar{\ell}_i H\sigma_{\mu\nu}e_j B_{\mu\nu}$
$[O_{uG}]_{ij}$	$\frac{g_s}{m_W^2}\frac{\sqrt{2m_{u_i}m_{u_j}}}{v}\bar{q}_i\tilde{H}\sigma_{\mu\nu}T^a u_j G^a_{\mu\nu}$
$[O_{uW}]_{ij}$	$\frac{g}{m_W^2}\frac{\sqrt{2m_{u_i}m_{u_j}}}{v}\bar{q}_i\sigma^k\tilde{H}\sigma_{\mu\nu}u_j W^k_{\mu\nu}$
$[O_{uB}]_{ij}$	$\frac{g'}{m_W^2}\frac{\sqrt{2m_{u_i}m_{u_j}}}{v}\bar{q}_i\tilde{H}\sigma_{\mu\nu}u_j B_{\mu\nu}$
$[O_{dG}]_{ij}$	$\frac{g_s}{m_W^2}\frac{\sqrt{2m_{d_i}m_{d_j}}}{v}\bar{q}_i H\sigma_{\mu\nu}T^a d_j G^a_{\mu\nu}$
$[O_{dW}]_{ij}$	$\frac{g}{m_W^2}\frac{\sqrt{2m_{d_i}m_{d_j}}}{v}\bar{q}_i\sigma^k H\sigma_{\mu\nu}d_j W^k_{\mu\nu}$
$[O_{dB}]_{ij}$	$\frac{g'}{m_W^2}\frac{\sqrt{2m_{d_i}m_{d_j}}}{v}\bar{q}_i H\sigma_{\mu\nu}d_j B_{\mu\nu}$

II.2.1.c Effective Lagrangian of mass eigenstates

In Section. II.2.1.b we introduced an EFT with the SM supplemented by D=6 operators, using a manifestly $SU(2) \times U(1)$ invariant notation. At that point, the connection between the new operators and phenomenology is not obvious. To relate to high-energy collider observables, it is more transparent to express the EFT Lagrangian in terms of the mass eigenstates after electroweak symmetry breaking (Higgs boson, W, Z, photon, etc.). Once this step is made, only the unbroken $SU(3)_c \times U(1)_{\rm em}$ local symmetry is manifest in the Lagrangian. Moreover, to simplify the interaction vertices, we will make further field transformations that respect only $SU(3)_c \times U(1)_{\rm em}$. Since field redefinitions do not affect physical predictions, the gauge invariance of the EFT we started with ensures that observables calculated using this mass eigenstate Lagrangian are also gauge invariant. This is possible because the full $SU(2) \times U(1)$ electroweak symmetry is still present, albeit in a non-manifest way, in the form of non-trivial relations between different couplings of mass eigenstates. Finally, for the sake of calculating observables beyond the tree-level one needs to specify the gauge fixing terms. Again, the gauge invariance of the starting point ensures that physical observables are independent of the gauge fixing procedure. Below we only present the Lagrangian in the unitary gauge when the Goldstone bosons eaten by W and Z are set to zero, which is completely sufficient to calculate LHC Higgs observables at tree level; see Appendix C of Ref. [621] for a generalization to the R_ξ gauge.

In this section we relate the Wilson coefficients of dimension-6 operators in the SILH basis to the parameters of the tree-level effective Lagrangian describing the interactions of the mass eigenstates. The analogous relations can be derived for any other basis; see Appendix A of [621] for the map from the Warsaw basis. The form of the mass eigenstate Lagrangian obtained directly by inserting the Higgs VEV and eigenstates into Eq. (II.2.2) is not convenient for practical applications. However, at this point one is free to make the following redefinitions of fields and couplings in the Lagrangian:

$$G^a_\mu \;\to\; (1+\delta_G)G^a_\mu, \quad W^\pm_\mu \to (1+\delta_W)W^\pm_\mu, \quad Z_\mu \to (1+\delta_Z)Z_\mu, \quad A_\mu \to (1+\delta_A)A_\mu + \delta_{AZ}Z_\mu,$$

Table 99: Four-fermion operators in the SILH basis. They are the same as in the Warsaw basis [614], except that the operators $[O_{\ell\ell}]_{1221}$, $[O_{\ell\ell}]_{1122}$, $[O_{uu}]_{3333}$ are absent by definition. In this table, e, u, d are always right-handed fermions, while ℓ and q are left-handed. A flavour index is implicit for each fermion field. For complex operators the complex conjugate operator is implicit.

$(\bar{L}L)(\bar{L}L)$ and $(\bar{L}R)(\bar{L}R)$		$(\bar{R}R)(\bar{R}R)$		$(\bar{L}L)(\bar{R}R)$	
$O_{\ell\ell}$	$\frac{1}{v^2}(\bar{\ell}\gamma_\mu\ell)(\bar{\ell}\gamma_\mu\ell)$	O_{ee}	$\frac{1}{v^2}(\bar{e}\gamma_\mu e)(\bar{e}\gamma_\mu e)$	$O_{\ell e}$	$\frac{1}{v^2}(\bar{\ell}\gamma_\mu\ell)(\bar{e}\gamma_\mu e)$
O_{qq}	$\frac{1}{v^2}(\bar{q}\gamma_\mu q)(\bar{q}\gamma_\mu q)$	O_{uu}	$\frac{1}{v^2}(\bar{u}\gamma_\mu u)(\bar{u}\gamma_\mu u)$	$O_{\ell u}$	$\frac{1}{v^2}(\bar{\ell}\gamma_\mu\ell)(\bar{u}\gamma_\mu u)$
O'_{qq}	$\frac{1}{v^2}(\bar{q}\gamma_\mu\sigma^i q)(\bar{q}\gamma_\mu\sigma^i q)$	O_{dd}	$\frac{1}{v^2}(\bar{d}\gamma_\mu d)(\bar{d}\gamma_\mu d)$	$O_{\ell d}$	$\frac{1}{v^2}(\bar{\ell}\gamma_\mu\ell)(\bar{d}\gamma_\mu d)$
$O_{\ell q}$	$\frac{1}{v^2}(\bar{\ell}\gamma_\mu\ell)(\bar{q}\gamma_\mu q)$	O_{eu}	$\frac{1}{v^2}(\bar{e}\gamma_\mu e)(\bar{u}\gamma_\mu u)$	O_{eq}	$\frac{1}{v^2}(\bar{q}\gamma_\mu q)(\bar{e}\gamma_\mu e)$
$O'_{\ell q}$	$\frac{1}{v^2}(\bar{\ell}\gamma_\mu\sigma^i\ell)(\bar{q}\gamma_\mu\sigma^i q)$	O_{ed}	$\frac{1}{v^2}(\bar{e}\gamma_\mu e)(\bar{d}\gamma_\mu d)$	O_{qu}	$\frac{1}{v^2}(\bar{q}\gamma_\mu q)(\bar{u}\gamma_\mu u)$
O_{quqd}	$\frac{1}{v^2}(\bar{q}^j u)\epsilon_{jk}(\bar{q}^k d)$	O_{ud}	$\frac{1}{v^2}(\bar{u}\gamma_\mu u)(\bar{d}\gamma_\mu d)$	O'_{qu}	$\frac{1}{v^2}(\bar{q}\gamma_\mu T^a q)(\bar{u}\gamma_\mu T^a u)$
O'_{quqd}	$\frac{1}{v^2}(\bar{q}^j T^a u)\epsilon_{jk}(\bar{q}^k T^a d)$	O'_{ud}	$\frac{1}{v^2}(\bar{u}\gamma_\mu T^a u)(\bar{d}\gamma_\mu T^a d)$	O_{qd}	$\frac{1}{v^2}(\bar{q}\gamma_\mu q)(\bar{d}\gamma_\mu d)$
$O_{\ell equ}$	$\frac{1}{v^2}(\bar{\ell}^j e)\epsilon_{jk}(\bar{q}^k u)$			O'_{qd}	$\frac{1}{v^2}(\bar{q}\gamma_\mu T^a q)(\bar{d}\gamma_\mu T^a d)$
$O'_{\ell equ}$	$\frac{1}{v^2}(\bar{\ell}^j\sigma_{\mu\nu}e)\epsilon_{jk}(\bar{q}^k\sigma^{\mu\nu}u)$				
$O_{\ell edq}$	$\frac{1}{v^2}(\bar{\ell}^j e)(\bar{d}q^j)$				

$$\begin{aligned} v &\to v(1+\delta v), \qquad g_s \to g_s(1+\delta g_s), \qquad g \to g(1+\delta g), \qquad g' \to g'(1+\delta g'), \\ \lambda &\to \lambda(1+\delta\lambda), \qquad h \to (1+\delta_1)h + \delta_2 h^2/v + \delta_3 h^3/v^2, \end{aligned} \tag{II.2.5}$$

where the free parameters δ_i are $\mathcal{O}(\Lambda^{-2})$ in the EFT expansion. Note that the non-linear transformation of the Higgs boson field does not generate any new interaction terms at $\mathcal{O}(\Lambda^{-2})$ in the effective Lagrangian that cannot be generated by D=6 operators.[II.5] In addition, one is free to add to the Lagrangian a total derivative and/or interactions terms that vanish by equations of motion. These redefinitions of course do not change the physical predictions or symmetries of the theory. However, they allow one to bring the theory to a more convenient form to perform practical calculations.[II.6] We will use this freedom to demand that the mass eigenstate Lagrangian has the following features:

- #1 All kinetic and mass terms are diagonal and canonically normalized. In particular, higher-derivative kinetic terms are absent.
- #2 The non-derivative photon and gluon interactions with fermions are the same as in the SM.
- #3 Tree-level relations between the electroweak parameters and input observables are the same as the SM ones in Eq. (II.2.4).
- #4 Two-derivative self-interactions of the Higgs boson (e.g. $h\partial_\mu h\partial_\mu h$) are absent.
- #5 In the Higgs boson interactions with gauge bosons, the derivative does not act on the Higgs (e.g., there is no $\partial_\mu h V_\nu V_{\mu\nu}$ terms).
- #6 For each fermion pair, the coefficient of the vertex-like Higgs interaction terms $\left(2\frac{h}{v} + \frac{h^2}{v^2}\right) V_\mu \bar{f}\gamma_\mu f$ is equal to the vertex correction to the respective $V_\mu \bar{f}\gamma_\mu f$ interaction.

[II.5] For example, applied to the h^4 self-interaction term in the SM Lagrangian, it generates h^5 and h^6 self-interactions at $\mathcal{O}(\Lambda^{-2})$, which are also generated by the O_6 operator in the SILH basis. Rather than applying the non-linear transformation, one can equivalently use the equations of motion for the Higgs boson field.

[II.6] Editor footnote: Another point of view is expressed in Section II.2.3, where it is argued that this kind of transformations make one-loop calculations harder to develop.

These conditions are a choice of conventions (one among many possible ones) how to represent interactions in the mass eigenstate Lagrangian. It is always possible to implement this choice starting from any D=6 basis: SILH, Warsaw, or any other. The condition #1 simplifies extracting physical predictions of the EFT, and is essential to implement the theory in existing Monte Carlo simulators. The conditions #2-#3 simplify the interpretation of the SM parameters g, g' and v. If the $[G_F,\, \alpha,\, m_Z]$ input is used to determine them (as assumed here), their numerical values should be the same as in the SM, and the input observables are not affected by D=6 operators at the leading order.[II.7] The conditions #4-#6 are conventions commonly used in the literature that allow one to fix the remaining freedom of fields and couplings redefinitions. These particular conventions match the ones used e.g. in the Higgs characterization framework of Ref. [622]. See Appendix D of Ref. [621] for physical examples showing these redefinitions do not change the S-matrix. Other convention choices can be made, leading to the same predictions for observables. For example, the features #3, #4, and #6 are not enforced in Section II.2.3.

In general, dimension-6 operators do induce interaction terms that do not respect the features #1-#6. However, these features can always be achieved, *without any loss of generality*, by using equations of motion, integrating by parts, and redefining the fields and couplings. Starting from the SILH basis, the conditions #1-#6 fix the free parameters in Eq. (II.2.5) as

$$
\begin{aligned}
\delta_G &= \frac{4g_s^2}{g^2}\bar{c}_g, \\
\delta_W &= \bar{c}_W, \\
\delta_Z &= \bar{c}_W + \frac{g'^2}{g^2}\bar{c}_B + \frac{4g'^4}{g^2(g^2+g'^2)}\bar{c}_\gamma, \\
\delta_{AZ} &= \frac{g'}{g}\left(\bar{c}_W - \bar{c}_B\right) - \frac{8g'^3}{g(g^2+g'^2)}\bar{c}_\gamma, \\
\delta_A &= \frac{4g'^2}{g^2+g'^2}\bar{c}_\gamma \\
\delta v &= \frac{[\bar{c}'_{H\ell}]_{22}}{2}, \\
\delta g_s &= -\frac{4g_s^2}{g^2}\bar{c}_g, \\
\delta g &= -\frac{g^2}{g^2-g'^2}\left(\bar{c}_W + \bar{c}_{2W} + \frac{g'^2}{g^2}\bar{c}_B + \frac{g'^2}{g^2}\bar{c}_{2B} - \frac{1}{2}\bar{c}_T + \frac{1}{2}[\bar{c}'_{H\ell}]_{22}\right), \\
\delta g' &= \frac{g'^2}{g^2-g'^2}\left(\bar{c}_W + \bar{c}_{2W} + \frac{g'^2}{g^2}\bar{c}_B + \frac{g'^2}{g^2}\bar{c}_{2B} - \frac{1}{2}\bar{c}_T + \frac{1}{2}[\bar{c}'_{H\ell}]_{22} - 4\frac{g^2-g'^2}{g^2}\bar{c}_\gamma\right), \\
\delta\lambda &= \bar{c}_H - \frac{3}{2}\bar{c}_6 - [\bar{c}'_{H\ell}]_{22}, \\
\delta_1 &= -\frac{\bar{c}_H}{2}, \qquad \delta_2 = -\frac{\bar{c}_H}{2}, \qquad \delta_3 = -\frac{\bar{c}_H}{6}.
\end{aligned}
\tag{II.2.6}
$$

Finally, the Higgs boson mass term in the SM Lagrangian is related by vacuum equations to the other parameters by $\mu_H^2 = \lambda v^2(1 + \delta\lambda + 2\delta v + 3/4\bar{c}_6)$. One can repeat this procedure starting from any other basis than SILH, and find a unique solution to the conditions #1-#6 in terms of the Wilson coefficients in that basis.

We move to discussing the interactions in the mass eigenstate Lagrangian once conditions #1-#6 are satisfied. We will focus on interaction terms that are most relevant for LHC phenomenology. To

[II.7] If other input observables are used, for example $[G_F, m_W, m_Z]$ or $[\alpha, m_W\, m_Z]$, the shift of input observables due to the presence of D=6 operators must be taken into account to correctly derive physical predictions of the theory. Much as in the SM, the input observables $[G_F, \alpha, m_Z]$ are affected by loop corrections, and this has to be taken into account if the framework is used beyond tree level.

organize the presentation, we split the Lagrangian into the following parts,

$$\mathcal{L}_{\rm EFT} = \mathcal{L}_{\rm kinetic} + \mathcal{L}_{\rm aff} + \mathcal{L}_{\rm vertex} + \mathcal{L}_{\rm dipole} + \mathcal{L}_{\rm tgc} + \mathcal{L}_{\rm hff} + \mathcal{L}_{\rm hvv} + \mathcal{L}_{hvff} + \mathcal{L}_{hdvff} + L_{h,\rm self} + \mathcal{L}_{h^2} + \mathcal{L}_{\rm other}. \tag{II.2.7}$$

Below we define each term in order of appearance. We also express the corrections to the SM interactions in $\mathcal{L}_{\rm EFT}$ in terms of linear combinations of Wilson coefficients of D=6 operators in the SILH basis (the analogous formulas for the Warsaw basis are given in Appendix A of Ref. [621]. These corrections start at $\mathcal{O}(1/\Lambda^2)$ in the EFT expansion, and we will ignore all $\mathcal{O}(1/\Lambda^4)$ and higher contributions.

Kinetic Terms

By construction, the kinetic terms of the mass eigenstates are diagonal and canonically normalized:

$$\begin{aligned}\mathcal{L}_{\rm kinetic} &= -\frac{1}{2}W^+_{\mu\nu}W^-_{\mu\nu} - \frac{1}{4}Z_{\mu\nu}Z_{\mu\nu} - \frac{1}{4}A_{\mu\nu}A_{\mu\nu} - \frac{1}{4}G^a_{\mu\nu}G^a_{\mu\nu} \\ &+ \frac{g^2v^2}{4}(1+\delta m)^2 W^+_\mu W^-_\mu + \frac{(g^2+g'^2)v^2}{8}Z_\mu Z_\mu \\ &+ \frac{1}{2}\partial_\mu h \partial_\mu h - \lambda v^2 h^2 + \sum_{f\in q,\ell,u,d,e} \bar f\,(i\gamma_\mu\partial_\mu - m_f)\,f. \end{aligned} \tag{II.2.8}$$

Above, the parameter λ is defined by the tree-level relation $m_h^2 = 2\lambda v^2$. There is no correction to the Z boson mass terms, in accordance with the condition #3. With this convention, the corrections to the W boson mass cannot be in general redefined away, and are parameterized by δm. The relation between δm and the Wilson coefficients in the SILH basis is given by

$$\delta m = -\frac{g'^2}{g^2-g'^2}\left(\bar c_W + \bar c_B + \bar c_{2W} + \bar c_{2B} - \frac{g^2}{2g'^2}\bar c_T + \frac{1}{2}[\bar c'_{H\ell}]_{22}\right). \tag{II.2.9}$$

Gauge boson interactions with fermions

By construction (condition #2), the non-derivative photon and gluon interactions with fermions are the same as in the SM:

$$\mathcal{L}_{aff} = eA_\mu \sum_{f\in u,d,e} \bar f\gamma_\mu Q_f f + g_s G^a_\mu \sum_{f\in u,d} \bar f\gamma_\mu T^a f. \tag{II.2.10}$$

The analogous interactions of the W and Z boson may in general be affected by dimension-6 operators:

$$\begin{aligned}\mathcal{L}_{\rm vertex} &= \frac{g}{\sqrt{2}}\left(W^+_\mu \bar\nu_L\gamma_\mu\left(I_3 + \delta g^{W\ell}_L\right)e_L + W^+_\mu \bar u_L\gamma_\mu\left(I_3+\delta g^{Wq}_L\right)d_L + W^+_\mu \bar u_R\gamma_\mu \delta g^{Wq}_R d_R + \text{h.c.}\right) \\ &+ \sqrt{g^2+g'^2}Z_\mu\left[\sum_{f\in u,d,e,\nu}\bar f_L\gamma_\mu\left(T^3_f - s^2_\theta Q_f + \delta g^{Zf}_L\right)f_L + \sum_{f\in u,d,e}\bar f_R\gamma_\mu\left(-s^2_\theta Q_f + \delta g^{Zf}_R\right)f_R\right].\end{aligned} \tag{II.2.11}$$

Here, I_3 is the 3×3 identity matrix, and the *vertex corrections* δg are 3×3 Hermitian matrices in the generation space, except for δg^{Wq}_R which is a general 3×3 complex matrix. The vertex corrections to W and Z boson couplings to fermions are expressed by the Wilson coefficients in the SILH basis as

$$\begin{aligned}\delta g^{Z\nu}_L &= \frac{1}{2}\bar c'_{H\ell} - \frac{1}{2}\bar c_{H\ell} + \hat f(1/2,0), \\ \delta g^{Ze}_L &= -\frac{1}{2}\bar c'_{H\ell} - \frac{1}{2}\bar c_{H\ell} + \hat f(-1/2,-1), \\ \delta g^{Ze}_R &= -\frac{1}{2}\bar c_{He} + \hat f(0,-1),\end{aligned}$$

$$
\begin{aligned}
\delta g_L^{Zu} &= \frac{1}{2}\bar{c}'_{Hq} - \frac{1}{2}\bar{c}_{Hq} + \hat{f}(1/2, 2/3), \\
\delta g_L^{Zd} &= -\frac{1}{2}V_{\rm CKM}^\dagger \bar{c}'_{Hq} V_{\rm CKM} - \frac{1}{2}V_{\rm CKM}^\dagger \bar{c}_{Hq} V_{\rm CKM} + \hat{f}(-1/2, -1/3), \\
\delta g_R^{Zu} &= -\frac{1}{2}\bar{c}_{Hu} + \hat{f}(0, 2/3), \\
\delta g_R^{Zd} &= -\frac{1}{2}\bar{c}_{Hd} + \hat{f}(0, -1/3), \\
\delta g_L^{W\ell} &= \bar{c}'_{H\ell} + \hat{f}(1/2, 0) - \hat{f}(-1/2, -1), \\
\delta g_L^{Wq} &= \left(\bar{c}'_{Hq} + \hat{f}(1/2, 2/3) - \hat{f}(-1/2, -1/3)\right) V_{\rm CKM}, \\
\delta g_R^{Wq} &= -\frac{1}{2}\bar{c}_{Hud},
\end{aligned}
\tag{II.2.12}
$$

where

$$
\begin{aligned}
\hat{f}(T_f^3, Q_f) &\equiv \left[\bar{c}_{2W} + \frac{g'^2}{g^2}\bar{c}_{2B} + \frac{1}{2}\bar{c}_T - \frac{1}{2}[\bar{c}'_{H\ell}]_{22}\right] T_f^3 \\
&- \frac{g'^2}{(g^2 - g'^2)}\left[\frac{(2g^2 - g'^2)}{g^2}\bar{c}_{2B} + \bar{c}_{2W} + \bar{c}_W + \bar{c}_B - \frac{1}{2}\bar{c}_T + \frac{1}{2}[\bar{c}'_{H\ell}]_{22}\right] Q_f,
\end{aligned}
\tag{II.2.13}
$$

and it is implicit that $[\bar{c}'_{H\ell}]_{11} = [\bar{c}_{H\ell}]_{11} = 0$.

Another type of gauge boson interactions with fermions are the so-called dipole interactions. These do not occur in the tree-level SM Lagrangian, but they in general may appear in the EFT with D=6 operators. We parameterize them as follows:

$$
\begin{aligned}
\mathcal{L}_{\rm dipole} &= -\frac{1}{4v}\left[g_s \sum_{f\in u,d} \frac{\sqrt{m_{f_i} m_{f_j}}}{v} \bar{f}_{L,i}\sigma_{\mu\nu} T^a [d_{Gf}]_{ij} f_{R,j} G^a_{\mu\nu} + e \sum_{f\in u,d,e} \frac{\sqrt{m_{f_i} m_{f_j}}}{v} \bar{f}_{L,i}\sigma_{\mu\nu} [d_{Af}]_{ij} f_{R,j} A_{\mu\nu}\right. \\
&+ \sqrt{g^2 + g'^2} \sum_{f\in u,d,e} \frac{\sqrt{m_{f_i} m_{f_j}}}{v} \bar{f}_{L,i}\sigma_{\mu\nu} [d_{Zf}]_{ij} f_{R,j} Z_{\mu\nu} \\
&+ \sqrt{2} g \frac{\sqrt{m_{u_i} m_{u_j}}}{v} \bar{d}_{L,i}\sigma_{\mu\nu} [d_{Wu}]_{ij} u_{R,j} W^-_{\mu\nu} + \sqrt{2} g \frac{\sqrt{m_{d_i} m_{d_j}}}{v} \bar{u}_{L,i}\sigma_{\mu\nu} [d_{Wd}]_{ij} d_{R,j} W^+_{\mu\nu} \\
&\left. + \sqrt{2} g \frac{\sqrt{m_{e_i} m_{e_j}}}{v} \bar{\nu}_{L,i}\sigma_{\mu\nu} [d_{We}]_{ij} e_{R,j} W^+_{\mu\nu}\right] + \text{h.c.},
\end{aligned}
\tag{II.2.14}
$$

where $\sigma_{\mu\nu} = i[\gamma_\mu, \gamma_\nu]/2$, and d_{Gf}, d_{Af}, d_{Zf}, and d_{Wf} are complex 3×3 matrices. The field strength tensors are defined as $X_{\mu\nu} = \partial_\mu X_\nu - \partial_\nu X_\mu$, and $\tilde{X}_{\mu\nu} = \epsilon_{\mu\nu\rho\sigma}\partial_\rho X_\sigma$. The coefficients d_{vf} are related to the Wilson coefficients in the SILH basis as

$$
\begin{aligned}
d_{Gf} &= -\frac{16}{g^2}\bar{c}_{fG}, \\
d_{Af} &= -\frac{16}{g^2}\left(\eta_f \bar{c}_{fW} + \bar{c}_{fB}\right), \\
d_{Zf} &= -\frac{16}{g^2}\left(\eta_f c_\theta^2 \bar{c}_{fW} - s_\theta^2 \bar{c}_{fB}\right), \\
d_{Wf} &= -\frac{16}{g^2}\bar{c}_{fW},
\end{aligned}
\tag{II.2.15}
$$

where $\eta_u = +1$, $\eta_{d,e} = -1$.

Gauge boson self-interactions

Gauge boson self-interactions are not directly relevant for LHC Higgs searches, however we include them in this presentation because of the important synergy between the triple gauge couplings and Higgs boson couplings measurements [465, 607, 623–627]. The triple gauge interactions in the effective Lagrangian are parameterized by

$$\begin{aligned}
\mathcal{L}_{\rm tgc} &= ie\left(W^+_{\mu\nu}W^-_{\mu} - W^-_{\mu\nu}W^+_{\mu}\right)A_\nu + ie\left[(1+\delta\kappa_\gamma)A_{\mu\nu}\,W^+_\mu W^-_\nu + \tilde\kappa_\gamma \tilde A_{\mu\nu}\,W^+_\mu W^-_\nu\right] \\
&+ igc_\theta\left[(1+\delta g_{1,z})\left(W^+_{\mu\nu}W^-_{\mu} - W^-_{\mu\nu}W^+_{\mu}\right)Z_\nu + (1+\delta\kappa_z)\,Z_{\mu\nu}\,W^+_\mu W^-_\nu + \tilde\kappa_z\,\tilde Z_{\mu\nu}\,W^+_\mu W^-_\nu\right] \\
&+ i\frac{e}{m_W^2}\left[\lambda_\gamma W^+_{\mu\nu}W^-_{\nu\rho}A_{\rho\mu} + \tilde\lambda_\gamma W^+_{\mu\nu}W^-_{\nu\rho}\tilde A_{\rho\mu}\right] + i\frac{gc_\theta}{m_W^2}\left[\lambda_z W^+_{\mu\nu}W^-_{\nu\rho}Z_{\rho\mu} + \tilde\lambda_z W^+_{\mu\nu}W^-_{\nu\rho}\tilde Z_{\rho\mu}\right] \\
&- g_s f^{abc}\partial_\mu G^a_\nu G^b_\mu G^c_\nu + \frac{c_{3g}}{v^2}g_s^3 f^{abc}G^a_{\mu\nu}G^b_{\nu\rho}G^c_{\rho\mu} + \frac{\tilde c_{3g}}{v^2}g_s^3 f^{abc}\widetilde G^a_{\mu\nu}G^b_{\nu\rho}G^c_{\rho\mu}.
\end{aligned} \tag{II.2.16}$$

The couplings of electroweak gauge bosons follow the customary parameterization of Ref. [628]. The anomalous triple gauge couplings of electroweak gauge bosons are related to the Wilson coefficients in the SILH basis as

$$\begin{aligned}
\delta g_{1z} &= -\frac{g^2+g'^2}{g^2-g'^2}\left[\frac{g^2-g'^2}{g^2}\bar c_{HW} + \bar c_W + \bar c_{2W} + \frac{g'^2}{g^2}\bar c_B + \frac{g'^2}{g^2}\bar c_{2B} - \frac{1}{2}\bar c_T + \frac{1}{2}[\bar c'_{H\ell}]_{22}\right], \\
\delta\kappa_\gamma &= -\bar c_{HW} - \bar c_{HB}, \\
\delta\kappa_z &= -\bar c_{HW} + \frac{g'^2}{g^2}\bar c_{HB} - \frac{g^2+g'^2}{g^2-g'^2}\left[\bar c_W + \bar c_{2W} + \frac{g'^2}{g^2}\bar c_B + \frac{g'^2}{g^2}\bar c_{2B} - \frac{1}{2}\bar c_T + \frac{1}{2}[\bar c'_{H\ell}]_{22}\right], \\
\lambda_z &= -6g^2\bar c_{3W}, \qquad \lambda_\gamma = \lambda_z, \\
\delta\tilde\kappa_\gamma &= -\tilde c_{HW} - \tilde c_{HB}, \\
\delta\tilde\kappa_z &= \frac{g'^2}{g^2}\left[\tilde c_{HW} + \tilde c_{HB}\right], \\
\tilde\lambda_z &= -6g^2\tilde c_{3W}, \qquad \tilde\lambda_\gamma = \tilde\lambda_z, \\
c_{3g} &= \frac{4}{g^2}\bar c_{3G}, \qquad \tilde c_{3g} = \frac{4}{g^2}\tilde c_{3G}.
\end{aligned} \tag{II.2.17}$$

The tilded Wilson coefficients refer to the tilded (CP-odd) operators in Table 97.

Single Higgs boson couplings

In this subsection we discuss the terms in the effective Lagrangian that involve a single Higgs boson field h. This part is the most relevant one from the point of view of the LHC Higgs phenomenology.

We first define the Higgs boson couplings to a pair of fermions:

$$\mathcal{L}_{\rm hff} = -\frac{h}{v}\sum_{f\in u,d,e}\sum_{ij}\sqrt{m_{f_i}m_{f_j}}\left(\delta_{ij} + [\delta y_f]_{ij}e^{i[\phi_f]_{ij}}\right)\bar f_{R,i}f_{L,j} + \text{h.c.}, \tag{II.2.18}$$

where $[\delta y_f]_{ij}$ and ϕ_{ij} are general 3×3 matrices with real elements. The corrections to the SM Yukawa interactions are related to the Wilson coefficients in the SILH basis by

$$[\delta y_f]_{ij}e^{i[\phi_f]_{ij}} = -[\bar c_f]_{ij} - \delta_{ij}\frac{1}{2}\left[\bar c_H + [\bar c'_{H\ell}]_{22}\right]. \tag{II.2.19}$$

Next, we define the following single Higgs boson couplings to a pair of the SM gauge fields:

$$\mathcal{L}_{\rm hvv} = \frac{h}{v}\left[(1+\delta c_w)\frac{g^2v^2}{2}W^+_\mu W^-_\mu + (1+\delta c_z)\frac{(g^2+g'^2)v^2}{4}Z_\mu Z_\mu\right.$$

$$
\begin{aligned}
&+c_{ww}\frac{g^2}{2}W^+_{\mu\nu}W^-_{\mu\nu}+\tilde{c}_{ww}\frac{g^2}{2}W^+_{\mu\nu}\tilde{W}^-_{\mu\nu}+c_{w\Box}g^2\left(W^-_\mu\partial_\nu W^+_{\mu\nu}+\text{h.c.}\right)\\
&+c_{gg}\frac{g_s^2}{4}G^a_{\mu\nu}G^a_{\mu\nu}+c_{\gamma\gamma}\frac{e^2}{4}A_{\mu\nu}A_{\mu\nu}+c_{z\gamma}\frac{e\sqrt{g^2+g'^2}}{2}Z_{\mu\nu}A_{\mu\nu}+c_{zz}\frac{g^2+g'^2}{4}Z_{\mu\nu}Z_{\mu\nu}\\
&+c_{z\Box}g^2Z_\mu\partial_\nu Z_{\mu\nu}+c_{\gamma\Box}gg'Z_\mu\partial_\nu A_{\mu\nu}\\
&+\tilde{c}_{gg}\frac{g_s^2}{4}G^a_{\mu\nu}\tilde{G}^a_{\mu\nu}+\tilde{c}_{\gamma\gamma}\frac{e^2}{4}A_{\mu\nu}\tilde{A}_{\mu\nu}+\tilde{c}_{z\gamma}\frac{e\sqrt{g^2+g'^2}}{2}Z_{\mu\nu}\tilde{A}_{\mu\nu}+\tilde{c}_{zz}\frac{g^2+g'^2}{4}Z_{\mu\nu}\tilde{Z}_{\mu\nu}\Bigg],
\end{aligned}
\tag{II.2.20}
$$

where all the couplings above are real. The terms in the first two lines describe corrections to the SM Higgs boson couplings to W and Z, while the remaining terms introduce Higgs boson couplings to gauge bosons with a tensor structure that is absent in the SM Lagrangian. Note that, using equations of motion, we could get rid of certain 2-derivative interactions between the Higgs and gauge bosons: $hZ_\mu\partial_\nu Z_{\nu\mu}$, $hZ_\mu\partial_\nu A_{\nu\mu}$, and $hW^\pm_\mu\partial_\nu W^\mp_{\nu\mu}$. These interactions would then be traded for contact interactions of the Higgs, gauge bosons and fermions in Eq. (II.2.11). However, one of the defining features of our effective Lagrangian is that the coefficients of the latter couplings are equal to the corresponding vertex correction in Eq. (II.2.11). This form can be always obtained, without any loss of generality, starting from an arbitrary dimension-6 Lagrangian provided the 2-derivative $hV_\mu\partial_\nu V_{\nu\mu}$ are kept in the Lagrangian. Note that we work in the limit where the neutrinos are massless and the Higgs boson does not couple to the neutrinos. In the EFT context, the couplings to neutrinos induced by dimension-5 operators are proportional to neutrino masses, therefore they are far too small to have any relevance for LHC phenomenology.

The shifts of the Higgs boson couplings to W and Z bosons are related to the Wilson coefficients in the SILH basis by

$$
\begin{aligned}
\delta c_w &= -\frac{1}{2}\bar{c}_H-\frac{1}{g^2-g'^2}\left[4g'^2(\bar{c}_W+\bar{c}_B+\bar{c}_{2B}+c_{2W})-2g^2\bar{c}_T+\frac{3g^2+g'^2}{2}[\bar{c}'_{H\ell}]_{22}\right],\\
\delta c_z &= -\frac{1}{2}\bar{c}_H-\frac{3}{2}[\bar{c}'_{H\ell}]_{22}.
\end{aligned}
\tag{II.2.21}
$$

The two-derivative Higgs boson couplings to gauge bosons are related to the Wilson coefficients in the SILH basis by

$$
\begin{aligned}
c_{gg} &= \frac{16}{g^2}\bar{c}_g,\\
c_{\gamma\gamma} &= \frac{16}{g^2}\bar{c}_\gamma,\\
c_{zz} &= -\frac{4}{g^2+g'^2}\left[\bar{c}_{HW}+\frac{g'^2}{g^2}\bar{c}_{HB}-4\frac{g'^2}{g^2}s^2_\theta\bar{c}_\gamma\right],\\
c_{z\Box} &= \frac{2}{g^2}\left[\bar{c}_W+\bar{c}_{HW}+\bar{c}_{2W}+\frac{g'^2}{g^2}(\bar{c}_B+\bar{c}_{HB}+\bar{c}_{2B})-\frac{1}{2}\bar{c}_T+\frac{1}{2}[\bar{c}'_{H\ell}]_{22}\right],\\
c_{z\gamma} &= \frac{2}{g^2}\left(\bar{c}_{HB}-\bar{c}_{HW}-8s^2_\theta\bar{c}_\gamma\right),\\
c_{\gamma\Box} &= \frac{2}{g^2}\left(\bar{c}_{HW}-\bar{c}_{HB}\right)+\frac{4}{g^2-g'^2}\left[\bar{c}_W+\bar{c}_{2W}+\frac{g'^2}{g^2}(\bar{c}_B+\bar{c}_{2B})-\frac{1}{2}\bar{c}_T+\frac{1}{2}[\bar{c}'_{H\ell}]_{22}\right],\\
c_{ww} &= -\frac{4}{g^2}\bar{c}_{HW},\\
c_{w\Box} &= \frac{2\bar{c}_{HW}}{g^2}+\frac{2}{g^2-g'^2}\left[\bar{c}_W+\bar{c}_{2W}+\frac{g'^2}{g^2}(\bar{c}_B+\bar{c}_{2B})-\frac{1}{2}\bar{c}_T+\frac{1}{2}[\bar{c}'_{H\ell}]_{22}\right],
\end{aligned}
\tag{II.2.22}
$$

$$
\tilde{c}_{gg} = \frac{16}{g^2}\tilde{c}_g,
$$

$$\begin{aligned}
\tilde{c}_{\gamma\gamma} &= \frac{16}{g^2}\tilde{c}_\gamma, \\
\tilde{c}_{zz} &= -\frac{4}{g^2+g'^2}\left[\tilde{c}_{HW} + \frac{g'^2}{g^2}\tilde{c}_{HB} - 4\frac{g'^2}{g^2}s_\theta^2\tilde{c}_\gamma\right], \\
\tilde{c}_{z\gamma} &= \frac{2}{g^2}\left(\tilde{c}_{HB} - \tilde{c}_{HW} - 8s_\theta^2\tilde{c}_\gamma\right), \\
\tilde{c}_{ww} &= -\frac{4}{g^2}\tilde{c}_{HW}.
\end{aligned} \tag{II.2.23}$$

Next, couplings of the Higgs boson to a gauge field and two fermions (which are not present in the SM Lagrangian) can be generated by dimension-6 operators. The vertex-like contact interactions between the Higgs, electroweak gauge bosons, and fermions are parameterized as:

$$\begin{aligned}
\mathcal{L}_{hvff} &= \sqrt{2}g\frac{h}{v}W_\mu^+\left(\bar{u}_L\gamma_\mu\delta g_L^{hWq}d_L + \bar{u}_R\gamma_\mu\delta g_R^{hWq}d_R + \bar{\nu}_L\gamma_\mu\delta g_L^{hW\ell}e_L\right) + \text{h.}c. \\
&+ 2\frac{h}{v}\sqrt{g^2+g'^2}Z_\mu\left[\sum_{f=u,d,e,\nu}\bar{f}_L\gamma_\mu\delta g_L^{hZf}f_L + \sum_{f=u,d,e}\bar{f}_R\gamma_\mu\delta g_R^{hZf}f_R\right].
\end{aligned} \tag{II.2.24}$$

By construction (condition #6), the coefficients of these interaction are equal to the corresponding vertex correction in Eq. (II.2.11):

$$\delta g^{hZf} = \delta g^{Zf}, \qquad \delta g^{hWf} = \delta g^{Wf}. \tag{II.2.25}$$

The dipole-type contact interactions of the Higgs boson are parameterized as:

$$\begin{aligned}
\mathcal{L}_{hdvff} &= -\frac{h}{4v^2}\left[g_s\sum_{f\in u,d}\frac{\sqrt{m_{f_i}m_{f_j}}}{v}\bar{f}_{L,i}\sigma_{\mu\nu}T^a[d_{hGf}]_{ij}f_{R,j}G^a_{\mu\nu}\right. \\
&+e\sum_{f\in u,d,e}\frac{\sqrt{m_{f_i}m_{f_j}}}{v}\bar{f}_{L,i}\sigma_{\mu\nu}[d_{hAf}]_{ij}f_{R,j}A_{\mu\nu} \\
&+\sqrt{g^2+g'^2}\sum_{f\in u,d,e}\frac{\sqrt{m_{f_i}m_{f_j}}}{v}\bar{f}_{L,i}\sigma_{\mu\nu}[d_{hZf}]_{ij}f_{R,j}Z_{\mu\nu} \\
&+\sqrt{2}g\frac{\sqrt{m_{u_i}m_{u_j}}}{v}\bar{d}_{L,i}\sigma_{\mu\nu}[d_{hWu}]_{ij}u_{R,j}W^-_{\mu\nu} + \sqrt{2}g\frac{\sqrt{m_{d_i}m_{d_j}}}{v}\bar{u}_{L,i}\sigma_{\mu\nu}[d_{hWd}]_{ij}d_{R,j}W^+_{\mu\nu} \\
&\left.+\sqrt{2}g\frac{\sqrt{m_{e_i}m_{e_j}}}{v}\bar{\nu}_{L,i}\sigma_{\mu\nu}[d_{hWe}]_{ij}e_{R,j}W^+_{\mu\nu}\right] + \text{h.c.},
\end{aligned} \tag{II.2.26}$$

where d_{hAf}, , d_{hZf}, and d_{hWf} are general complex 3×3 matrices. The coefficients are simply related to the corresponding dipole interactions in Eq. (II.2.14):

$$d_{hVf} = d_{Vf}. \tag{II.2.27}$$

Dimension-6 operators can also induce single Higgs boson couplings to more than 2 gauge bosons, but we do not display them here.

Higgs boson self-couplings and double Higgs boson couplings

The cubic Higgs boson self-coupling and couplings of two Higgs boson fields to matter play a role in the EFT description of double Higgs boson production [467, 629]. The cubic Higgs boson self-coupling is parameterized as

$$\mathcal{L}_{h,\text{self}} = -(\lambda+\delta\lambda_3)vh^3. \tag{II.2.28}$$

The relation between the cubic Higgs boson coupling correction and the Wilson coefficients in the SILH basis is given by

$$\delta\lambda_3 \;=\; \lambda\left(\bar{c}_6 - \frac{3}{2}\bar{c}_H - \frac{1}{2}[\bar{c}'_{H\ell}]_{22}\right). \tag{II.2.29}$$

In accordance with the condition #4, the 2-derivative Higgs boson self-couplings have been traded for other equivalent interactions and do not occur in the mass eigenstate Lagrangian. Self-interactions terms with 4, 5, and 6 Higgs boson fields may also arise from dimension-6 operators, but we do not display them here.

The interactions between two Higgs bosons and two other SM fields are parameterized as follows:

$$\begin{aligned}
\mathcal{L}_{h^2} \;=\;& h^2\left(1+2\delta c_z^{(2)}\right)\frac{g^2+g'^2}{4}Z_\mu Z_\mu + h^2\left(1+2\delta c_w^{(2)}\right)\frac{g^2}{2}W_\mu^+W_\mu^- \\
-\;& \frac{h^2}{2v^2}\sum_{f;ij}\sqrt{m_{f_i}m_{f_j}}\left[\bar{f}_{i,R}[y_f^{(2)}]_{ij}f_{j,L}+\text{h.}c.\right]. \\
+\;& \frac{h^2}{8v^2}\left(c_{gg}^{(2)}g_s^2G^a_{\mu\nu}G^a_{\mu\nu} + 2c_{ww}^{(2)}g^2W^+_{\mu\nu}W^-_{\mu\nu} + c_{zz}^{(2)}(g^2+g'^2)Z_{\mu\nu}Z_{\mu\nu} + 2c_{z\gamma}^{(2)}gg'Z_{\mu\nu}A_{\mu\nu} + c_{\gamma\gamma}^{(2)}e^2A_{\mu\nu}A_{\mu\nu}\right) \\
+\;& \frac{h^2}{8v^2}\left(\tilde{c}_{gg}^{(2)}g_s^2G^a_{\mu\nu}\tilde{G}^a_{\mu\nu} + 2\tilde{c}_{ww}^{(2)}g^2W^+_{\mu\nu}\tilde{W}^-_{\mu\nu} + \tilde{c}_{zz}^{(2)}(g^2+g'^2)Z_{\mu\nu}\tilde{Z}_{\mu\nu} + 2\tilde{c}_{z\gamma}^{(2)}gg'Z_{\mu\nu}\tilde{A}_{\mu\nu} + \tilde{c}_{\gamma\gamma}^{(2)}e^2A_{\mu\nu}\tilde{A}_{\mu\nu}\right) \\
& -\frac{h^2}{2v^2}\left(g^2c_{w\Box}^{(2)}(W^+_\mu\partial_\nu W^-_{\nu\mu}+W^-_\mu\partial_\nu W^+_{\nu\mu}) + g^2c_{z\Box}^{(2)}Z_\mu\partial_\nu Z_{\nu\mu} + gg'c_{\gamma\Box}^{(2)}Z_\mu\partial_\nu A_{\nu\mu}\right).
\end{aligned} \tag{II.2.30}$$

All double Higgs boson couplings arising from D=6 operators can be expressed by the single Higgs boson couplings:

$$\begin{aligned}
\delta c_z^{(2)} &= \delta c_z, \qquad \delta c_w^{(2)} = \delta c_z + 3\delta m, \\
[y_f^{(2)}]_{ij} &= 3[\delta y_f]_{ij}e^{i\phi_{ij}} - \delta c_z\,\delta_{ij}, \\
c_{vv}^{(2)} &= c_{vv}, \qquad \tilde{c}_{vv}^{(2)} = \tilde{c}_{vv}, \qquad v\in\{g,w,z,\gamma\}, \\
c_{v\Box}^{(2)} &= c_{v\Box}, \qquad v\in\{w,z,\gamma\}.
\end{aligned} \tag{II.2.31}$$

Other interaction terms with two Higgs bosons involve at least 5 fields: e.g the h^2V^3 or h^2ffV contact interactions, and are not displayed here.

Other terms

In this section we have written down the interaction terms of mass eigenstates in the D=6 EFT Lagrangian which are most relevant for LHC Higgs phenomenology. They either enter the single and double Higgs boson production at tree level, or they affect electroweak precision observables that are complementary to Higgs boson couplings measurements. The remaining terms in the mass eigenstate Lagrangian, which are not explicitly displayed in this chapter, are contained in $\mathcal{L}_{\text{other}}$ in Eq. (II.2.7). They include 4-fermion terms, couplings of a single Higgs boson to 3 or more gauge bosons, quartic Higgs and gauge boson self-interactions, dipole-like interactions of two gauge bosons and two fermions, and interaction terms with 5 or more fields. For a future reference, we only comment on two 4-lepton terms involving left-handed electrons and muons and the corresponding neutrinos:

$$\mathcal{L}_{4\ell} \supset \frac{1}{v^2}\left[[c_{\ell\ell}]_{1122}(\bar{\ell}_1\gamma_\mu\ell_1)(\bar{\ell}_2\gamma_\mu\ell_2) + [c_{\ell\ell}]_{1221}(\bar{\ell}_1\gamma_\mu\ell_2)(\bar{\ell}_2\gamma_\mu\ell_1)\right]. \tag{II.2.32}$$

The coefficients of these 4-lepton terms are related to the Wilson coefficients in the SILH basis by

$$[c_{\ell\ell}]_{1122} \;=\; \frac{2g'^2}{g^2}\bar{c}_{2B} - 2\bar{c}_{2W},$$

$$[c_{\ell\ell}]_{1221} \quad = \quad 4\bar{c}_{2W}. \tag{II.2.33}$$

Note that the corresponding 4-fermion operators are absent in the SILH basis. However, in the mass eigenstate Lagrangian, these operators do appear, once the SILH operators O_{2W} and O_{2B} are traded for other interactions terms by using equations of motion. By the same token, the 4-top term $[O_{uu}]_{3333}$ does appear in the mass eigenstate Lagrangian, with the coefficient proportional to $\bar{c}_{2G}$.

II.2.1.d Higgs basis

In the previous section we related the Wilson coefficients in the SILH bases of D=6 operators to the couplings of mass eigenstates in the Lagrangian. With this information at hand, one can proceed to calculating observables at a given order in the EFT as a function of the Wilson coefficients. The information provided above is enough to calculate the leading order EFT corrections to SM predictions for single and double Higgs boson production and decays in all phenomenologically relevant channels.

There is no theoretical obstacle to present the results of LHC Higgs analyses as constraints on the Wilson coefficients in the SILH, Warsaw, or any other basis. However, this procedure may not be the most efficient one from the experimental point of view. The reason is that the relation between the Wilson coefficients in the SILH basis and the relevant couplings of the Higgs boson in the mass eigenstate Lagrangian is somewhat complicated, c.f. Eqs (II.2.12), (II.2.19), (II.2.21), (II.2.22). The situation is similar for the Warsaw basis, see Appendix A of Ref. [621]. In this section we propose another, equivalent parameterization of the EFT with D=6 operators. The idea, put forward in Ref. [630], is to parameterize the space of D=6 operators using a subset of couplings in a mass eigenstate Lagrangian, such as the one defined in Eq. (II.2.7) of Section. II.2.1.c. The parameterization described in this section, which differs slightly from that in Ref. [630], is referred to as the *Higgs basis*.[II.8]

The salient features of the Higgs basis are the following. The goal is to parameterize the space of D=6 operators in a way that can be more directly connected to observable quantities in Higgs physics. The variables spanning the Higgs basis correspond to a subset of the couplings parameterizing interaction terms in the mass eigenstate Lagrangian in Eq. (II.2.7). Since these couplings have been expressed as linear combinations of the SILH basis Wilson coefficients, technically the Higgs basis is defined as a linear transformation from the SILH basis. All couplings in the subset have to be independent, in the sense that none can be expressed by the remaining ones at the level of a general $D = 6$ EFT Lagrangian. It is also a maximal such subset, which implies that their number is the same as the number of independent operators in the Warsaw or SILH basis. We will refer to this set as the *independent couplings*. They parameterize all possible deformations of the SM Lagrangian in the presence of D=6 operators. Therefore, they can be used on par with any other basis to describe the effects of dimension-6 operators on any physical observables (also those unrelated to Higgs physics). By definition of the Higgs basis, the independent couplings will include single Higgs boson couplings to gauge bosons and fermions. Thanks to that, the parameters of the Higgs basis can be connected in a more intuitive way to LHC Higgs observables calculated at leading order in the EFT. Furthermore, the vertex corrections to the Z boson interactions with fermions are chosen to be among the independent couplings. As a consequence, combining experimental information from Higgs and electroweak precision observables is more transparent in the Higgs basis.

Independent couplings

We now describe the choice of independent couplings which defines the Higgs basis.

[II.8] Here, the Higgs basis is introduced in a different manner than how the SILH or Warsaw basis were defined in the literature. Rather than by choosing a set $SU(3) \times SU(2) \times U(1)$ invariant D=6 operators, we introduce the Higgs basis as a parameterization of the space of all possible deformations of the SM mass eigenstate Lagrangian that can arise in the presence of D=6 operators. However, both ways can be shown to be equivalent, which justifies using the term *basis* for our construction. In particular, it is possible to define the Higgs basis as a complete non-redundant set of $SU(3) \times SU(2) \times U(1)$ invariant D=6 operators, see Section II.2.1.d.

The first group of independent couplings parameterizes the interactions of the Higgs boson with itself and with the SM gauge bosons and fermions:

$$c_{gg},\ \delta c_z,\ c_{\gamma\gamma},\ c_{z\gamma},\ c_{zz},\ c_{z\Box},\ \tilde{c}_{gg},\ \tilde{c}_{\gamma\gamma},\ \tilde{c}_{z\gamma},\ \tilde{c}_{zz},\ \delta\lambda_3,$$
$$[\delta y_u]_{ij},\ [\delta y_d]_{ij},\ [\delta y_e]_{ij},\ [\phi_u]_{ij},\ [\phi_d]_{ij},\ [\phi_\ell]_{ij}. \tag{II.2.34}$$

The parameters in the first line are defined by Eq. (II.2.20) and Eq. (II.2.30), and in the second line by Eq. (II.2.18). Overall, there is 65 independent parameters in Eq. (II.2.34), and they all affect Higgs boson production and/or decay at the leading order in the EFT expansion. Therefore they are of crucial importance for LHC Higgs phenomenology. Moreover, at the leading order, they are not constrained at all by LEP-1 electroweak precision tests or low-energy precision observables.

The second group of independent couplings parameterizes the W boson mass and the Z and W boson couplings to fermions:

$$\delta m,\ [\delta g_L^{Ze}]_{ij},\ [\delta g_R^{Ze}]_{ij},\ [\delta g_L^{W\ell}]_{ij},\ [\delta g_L^{Zu}]_{ij},\ [\delta g_R^{Zu}]_{ij},\ [\delta g_L^{Zd}]_{ij},\ [\delta g_R^{Zd}]_{ij},\ [\delta g_R^{Wq}]_{ij},$$
$$[d_{Gu}]_{ij},\ [d_{Gd}]_{ij},\ [d_{Ae}]_{ij},\ [d_{Au}]_{ij},\ [d_{Ad}]_{ij},\ [d_{Ze}]_{ij},\ [d_{Zu}]_{ij},\ [d_{Zd}]_{ij}. \tag{II.2.35}$$

Here the mass correction δm is defined in Eq. (II.2.8), the vertex corrections δg^i are defined in Eq. (II.2.11), and the dipole moments d_i are defined in Eq. (II.2.14). All these parameters also affect the Higgs boson production and/or decay at the leading order in the EFT. However, as opposed to the ones in Eq. (II.2.34), they affect at the same order electroweak and/or low-energy precision observables.

The third group of independent couplings parameterizes the self-couplings of gauge bosons:

$$\lambda_z,\ \tilde{\lambda}_z,\ c_{3G},\ \tilde{c}_{3G}. \tag{II.2.36}$$

They are defined in Eq. (II.2.16). These couplings do not affect Higgs boson production and decay at the leading order in EFT.

To complete the definition of the Higgs basis, one has to select the independent couplings corresponding to 4-fermion operators. We choose to parameterize them by the same set of Wilson coefficients as in the SILH basis, c.f. Table 99:

$$c_{\ell\ell},\ c_{qq},\ c'_{qq},\ c_{\ell q},\ c'_{\ell q},\ c_{quqd},\ c'_{quqd},\ c_{\ell equ},\ c'_{\ell equ},\ c_{\ell edq},$$
$$c_{\ell e},\ c_{\ell u},\ c_{\ell d},\ c_{qe},\ c_{qu},\ c'_{qu},\ c_{qd},\ c'_{qd},\ c_{ee},\ c_{uu},\ c_{dd},\ c_{eu},\ c_{ed},\ c_{ud},\ c'_{ud}. \tag{II.2.37}$$

Each parameter c_{ff} have 4 flavour indices, which are not displayed here. The non-trivial question of which combination of flavour indices constitutes an independent set was worked out in Ref. [631]. In the Higgs basis we take the same choice of independent 4-fermion couplings as in that reference, with one exception. As explained in the next subsection, in a D=6 EFT Lagrangian, the coupling $[c_{\ell\ell}]_{1221}$ multiplying a particular 4-lepton operator can be expressed by δm and δg^i. Therefore $[c_{\ell\ell}]_{1221}$ is not among the independent couplings defining the Higgs basis.

Dependent couplings

The number of parameters characterizing departure from the SM Lagrangian in Eq. (II.2.7) is larger than the number of Wilson coefficients in a basis of D=6 operators. Due to this fact, there must be relations among these parameters. Working in the Higgs basis, some of the parameters in the mass eigenstate Lagrangian can be expressed by the independent couplings; we call them the *dependent* couplings. The relations between dependent and independent couplings can be inferred from the matching between the effective Lagrangian and the Warsaw or SILH basis in Section. II.2.1.c. These relations *hold at the level of the dimension-6 Lagrangian*, and they are in general not respected in the presence of dimension-8 and higher operators.

We start with the dependent couplings in Eq. (II.2.20) parameterizing the single Higgs boson interactions with gauge bosons. They can be expressed in terms of the independent couplings as[II.9]

$$\begin{aligned}
\delta c_w &= \delta c_z + 4\delta m, \\
c_{ww} &= c_{zz} + 2s_\theta^2 c_{z\gamma} + s_\theta^4 c_{\gamma\gamma}, \\
\tilde{c}_{ww} &= \tilde{c}_{zz} + 2s_\theta^2 \tilde{c}_{z\gamma} + s_\theta^4 \tilde{c}_{\gamma\gamma}, \\
c_{w\Box} &= \frac{1}{g^2 - g'^2}\left[g^2 c_{z\Box} + g'^2 c_{zz} - e^2 s_\theta^2 c_{\gamma\gamma} - (g^2 - g'^2) s_\theta^2 c_{z\gamma}\right], \\
c_{\gamma\Box} &= \frac{1}{g^2 - g'^2}\left[2g^2 c_{z\Box} + (g^2 + g'^2) c_{zz} - e^2 c_{\gamma\gamma} - (g^2 - g'^2) c_{z\gamma}\right].
\end{aligned} \tag{II.2.38}$$

The coefficients of W-boson dipole interactions in Eq. (II.2.14) are related to those of the Z and the photon as

$$\eta_f d_{wf} = d_{zf} + s_\theta^2 d_{Af}, \tag{II.2.39}$$

where $\eta_u = 1$ and $\eta_{d,e} = -1$. The coefficients of the dipole-like Higgs boson couplings in Eq. (II.2.26) are simply related to the corresponding dipole moments:

$$d_{hvf} = d_{vf}, \quad \tilde{d}_{hvf} = \tilde{d}_{vf}, \qquad v \in \{g, w, z, \gamma\}. \tag{II.2.40}$$

Coefficients of all interaction terms with two Higgs bosons in Eq. (II.2.30) are dependent couplings. The can be expressed in terms of the independent couplings as:

$$\begin{aligned}
\delta c_z^{(2)} &= \delta c_z, \qquad \delta c_w^{(2)} = \delta c_z + 3\delta m, \\
[y_f^{(2)}]_{ij} &= 3[\delta y_f]_{ij} e^{i\phi_{ij}} - \delta c_z\, \delta_{ij}, \\
c_{vv}^{(2)} &= c_{vv}, \qquad \tilde{c}_{vv}^{(2)} = \tilde{c}_{vv}, \qquad v \in \{g, w, z, \gamma\}, \\
c_{v\Box}^{(2)} &= c_{v\Box}, \qquad v \in \{w, z, \gamma\}.
\end{aligned} \tag{II.2.41}$$

The dependent vertex corrections are expressed in terms of the independent couplings as

$$\delta g_L^{Z\nu} = \delta g_L^{Ze} + \delta g_L^{W\ell}, \qquad \delta g_L^{Wq} = \delta g_L^{Zu} V_{\rm CKM} - V_{\rm CKM} \delta g_L^{Zd}. \tag{II.2.42}$$

All but two triple gauge couplings in Eq. (II.2.16) are dependent couplings expressed in terms of the independent couplings as

$$\begin{aligned}
\delta g_{1,z} &= \frac{1}{2(g^2 - g'^2)}\left[c_{\gamma\gamma} e^2 g'^2 + c_{z\gamma}(g^2 - g'^2) g'^2 - c_{zz}(g^2 + g'^2) g'^2 - c_{z\Box}(g^2 + g'^2) g^2\right], \\
\delta\kappa_\gamma &= -\frac{g^2}{2}\left(c_{\gamma\gamma}\frac{e^2}{g^2 + g'^2} + c_{z\gamma}\frac{g^2 - g'^2}{g^2 + g'^2} - c_{zz}\right), \\
\tilde{\kappa}_\gamma &= -\frac{g^2}{2}\left(\tilde{c}_{\gamma\gamma}\frac{e^2}{g^2 + g'^2} + \tilde{c}_{z\gamma}\frac{g^2 - g'^2}{g^2 + g'^2} - \tilde{c}_{zz}\right), \\
\delta\kappa_z &= \delta g_{1,z} - t_\theta^2 \delta\kappa_\gamma, \qquad \tilde{\kappa}_z = -t_\theta^2 \tilde{\kappa}_\gamma, \\
\lambda_\gamma &= \lambda_z, \quad \tilde{\lambda}_\gamma = \tilde{\lambda}_z.
\end{aligned} \tag{II.2.43}$$

Finally, we discuss how the Wilson coefficient $[c_{\ell\ell}]_{1221}$ is expressed by the independent couplings. One defining feature of the mass eigenstate Lagrangian Eq. (II.2.7) is that the tree-level relations between the SM electroweak parameters and input observables are not affected by D=6 operators (condition # 3). On the other hand, one of the four-fermion couplings in the Lagrangian,

$$\mathcal{L}_{4f}^{D=6} \supset [c_{\ell\ell}]_{1221} (\bar{\ell}_{1,L} \gamma_\rho \ell_{2,L})(\bar{\ell}_{2,L} \gamma_\rho \ell_{1,L}), \tag{II.2.44}$$

[II.9] The relation between c_{ww}, $\tilde{c}_{ww}$ and other parameters can also be viewed as a consequence of the accidental custodial symmetry at the level of the dimension-6 operators [464].

does affect the relation between the parameter v and the muon decay width from which $v = (\sqrt{2}G_F)^{-2}$ is determined:

$$\frac{\Gamma(\mu \to e\nu\nu)}{\Gamma(\mu \to e\nu\nu)_{\rm SM}} \approx 1 + 2[\delta g_L^{We}]_{11} + 2[\delta g_L^{We}]_{22} - 4\delta m - [c_{\ell\ell}]_{1221}. \tag{II.2.45}$$

Therefore, the muon decay width is unchanged with respect to the SM when $[c_{\ell\ell}]_{1221}$ is related to δm and δg as

$$[c_{\ell\ell}]_{1221} = 2\delta[g_L^{We}]_{11} + 2[\delta g_L^{We}]_{22} - 4\delta m. \tag{II.2.46}$$

This relation can be verified using the expressions of these parameters in terms of the SILH Wilson coefficients in Eqs. (II.2.9), (II.2.12), and (II.2.33). In other words, due to the fact that we selected δm and δg selected as an independent coupling in the Higgs basis, $[c_{\ell\ell}]_{1221}$ has to be a dependent coupling. Of course, one could equivalently choose $[c_{\ell\ell}]_{1221}$ to define a basis, and remove e.g. δm from the list of independent couplings. The remaining 4-fermion parameters in Eq. (II.2.37) are independent couplings.

Gauge invariant definition

In summary, in the Higgs basis the parameters spanning the space of D=6 EFT operators are the independent couplings in Eqs. (II.2.34), (II.2.35), (II.2.36), and (II.2.37). In the EFT expansion, the independent couplings are formally of order $\mathcal{O}(\Lambda^{-2})$. These parameters are directly linked to deviations from the SM interactions in the mass eigenstate Lagrangian in Eq. (II.2.7). All other deviations in the mass eigenstate Lagrangian can be expressed by the independent couplings.

In this section, the Higgs basis was introduced by choosing a subset of independent couplings in the mass eigenstate Lagrangian defined in Section II.2.1.c. The latter is not manifestly invariant under the full gauge symmetry of the SM, as the electroweak symmetry $SU(2) \times U(1)$ is broken to $U(1)_{\rm em}$ at the mass eigenstate level. Nevertheless, one can provide an equivalent and manifestly gauge invariant definition of the Higgs basis. To this end, one can introduce the $SU(3) \times SU(2) \times U(1)$ invariant D=6 operators as follows:

$$\begin{aligned}
O_{\delta\lambda_3} &= -\frac{1}{v^2}(H^\dagger H)^3, \\
O_{c_{gg}} &= \frac{g_s^2}{4v^2} H^\dagger H\, G^a_{\mu\nu} G^a_{\mu\nu} \\
O_{\delta c_z} &= -\frac{1}{v^2}\left[\partial_\mu (H^\dagger H)\right]^2 + \frac{3\lambda}{v^2}(H^\dagger H)^3 + \left(\sum_f \frac{\sqrt{2} m_{f_i}}{v^3} H^\dagger H \bar{f}_{L,i} H f_{R,i} + \text{h.c.}\right), \\
O_{c_{z\Box}} &= \frac{ig^3}{v^2(g^2-g'^2)}\left(H^\dagger \sigma^i \overleftrightarrow{D_\mu} H\right) D_\nu W^i_{\mu\nu} - \frac{ig^2 g'}{v^2(g^2-g'^2)}\left(H^\dagger \overleftrightarrow{D_\mu} H\right)\partial_\nu B_{\mu\nu}, \\
O_{c_{zz}} &= \frac{ig(g^2+g'^2)}{2v^2(g^2-g'^2)}\left(H^\dagger \sigma^i \overleftrightarrow{D_\mu} H\right) D_\nu W^i_{\mu\nu} - \frac{ig'(g^2+g'^2)}{2v^2(g^2-g'^2)}\left(H^\dagger \overleftrightarrow{D_\mu} H\right)\partial_\nu B_{\mu\nu} \\
&- \frac{ig}{v^2}\left(D_\mu H^\dagger \sigma^i D_\nu H\right) W^i_{\mu\nu} - \frac{ig'}{v^2}\left(D_\mu H^\dagger D_\nu H\right) B_{\mu\nu}, \\
O_{c_{z\gamma}} &= -\frac{2igg'^2}{v^2(g^2+g'^2)}\left(D_\mu H^\dagger \sigma^i D_\nu H\right) W^i_{\mu\nu} + \frac{2ig'g^2}{v^2(g^2+g'^2)}\left(D_\mu H^\dagger D_\nu H\right) B_{\mu\nu}, \\
O_{c_{\gamma\gamma}} &= -\frac{igg'^4}{2v^2(g^4-g'^4)}\left(H^\dagger \sigma^i \overleftrightarrow{D_\mu} H\right) D_\nu W^i_{\mu\nu} + \frac{ig'^5}{2v^2(g^4-g'^4)}\left(H^\dagger \overleftrightarrow{D_\mu} H\right)\partial_\nu B_{\mu\nu} \\
&- \frac{igg'^4}{v^2(g^2+g'^2)^2}\left(D_\mu H^\dagger \sigma^i D_\nu H\right) W^i_{\mu\nu} + \frac{ig'^3(2g^2+g'^2)}{(g^2+g'^2)^2 v^2}\left(D_\mu H^\dagger D_\nu H\right) B_{\mu\nu} \\
&+ \frac{g'^2}{4v^2} H^\dagger H\, B_{\mu\nu} B_{\mu\nu},
\end{aligned}$$

$$[O_{\delta y_f}]_{ij} \;=\; -\frac{\sqrt{2m_{f_i}m_{f_j}}}{v^3}H^\dagger H \bar{f}_{L,i} H f_{R,j} + \text{h.c.},$$
$$\ldots \tag{II.2.47}$$

The coefficients of the operators on the right-hand side in Eq. (II.2.47) are determined by the linear map relating the SILH Wilson coefficients to those in the Higgs basis, which can be obtained by inverting the relations between the Higgs and SILH coefficients derived earlier in this section. By following this algorithm, a complete and non-redundant set of D=6 operators O_{c_i} defining the Higgs basis can be constructed. Then the Higgs basis Lagrangian can be defined in a manifestly gauge invariant way as $\mathcal{L}_{\rm EFT} = \mathcal{L}_{\rm SM} + \sum_i c_i O_{c_i}$.

Simplified scenarios

In total, the Higgs basis, as any complete basis at the dimension-6 level, is parameterized by 2499 independent real couplings [631]. One should not, however, be intimidated by this number. The point is that a much smaller subset of the independent couplings is relevant for analyses of Higgs data at leading order in EFT. First of all, the coefficients of 4-fermion interactions in Eq. (II.2.37) and triple gauge interactions in Eq. (II.2.36) do not enter Higgs observables at the leading order. At that order, the parameters relevant for LHC Higgs analyses are those in Eqs. (II.2.34) and (II.2.35), which already reduces the number of variables significantly. Furthermore, there are several motivated assumptions about the UV theory underlying the EFT which could be used to further reduce the number of parameters:

- *Minimal flavour violation*, in which case the matrices δy_f, ϕ_f, d_{Vf}, and δg^{Vf}, reduce to a single number for each f.
- *CP conservation*, in which case all CP-odd couplings vanish: $\tilde{c}_i = \phi_f = \text{Im}d_f = 0$.
- *Custodial symmetry*, in which case $\delta m = 0$.[II.10]

We stress that independent couplings should not be arbitrarily set to zero without an underlying symmetry assumption. Furthermore, the relations between the dependent and independent couplings in the mass eigenstate Lagrangian should be consistently imposed, so as to preserve the structure of the D=6 EFT Lagrangian.

Finally, to reduce the number of free parameters in an analysis, one may take advantage of the fact that, in addition to Higgs observables, other measurements are sensitive to the parameters in Eq. (II.2.35). In particular, the parameters in the first line of Eq. (II.2.35) are constrained by electroweak precision tests in LEP-1. These are among the most stringent constraints on EFT parameters, and they have an important impact on possible signals in Higgs searches. Assuming minimal flavour violation, all the vertex corrections in Eq. (II.2.35) are constrained to be smaller than $O(10^{-3})$ (for the leptonic vertex corrections and δm), or $O(10^{-2})$ (for the quark vertex corrections) [623, 625, 632].[II.11] Even when the assumption of minimal flavour violation is not imposed, all the leptonic, bottom and charm quark vertex corrections are still constrained at the level of $O(10^{-2})$ or better [634]. Similarly, many parameters in the second line of Eq. (II.2.35) are strongly constrained by measurements of the magnetic and electric dipole moments. In the LHC environment, experimental sensitivity is often not sufficient to probe these parameters with a comparable accuracy. If that is indeed the case, it is well-motivated to neglect the parameters in Eq. (II.2.35) in LHC Higgs analyses.[II.12]

[II.10] Custodial symmetry implies several relations between Higgs boson couplings to gauge bosons: $\delta c_w = \delta c_z$, $c_{w\Box} = c_\theta^2 c_{z\Box} + s_\theta^2 c_{\gamma\Box}$, $c_{ww} = c_{zz} + 2s_\theta^2 c_{z\gamma} + s_\theta^4 c_\gamma$, and $\tilde{c}_{ww} = \tilde{c}_{zz} + 2s_\theta^2 \tilde{c}_{z\gamma} + s_\theta^4 \tilde{c}_\gamma$. The last three are satisfied automatically at the level of dimension-6 Lagrangian, while the first one is true for $\delta m = 0$, see Eq. (II.2.38).

[II.11] These constraints may be relaxed if the leading-order D=6 EFT does not provide an adequate description of electroweak precision observables [633]. If that is the case, the vertex-like and dipole-like Higgs boson couplings in Eqs. (II.2.24) and (II.2.26) could in principle be sizeable enough to be relevant for the LHC searches without conflict with electroweak precision constraints. However, it is not clear whether there exist explicit BSM models where this concern is relevant.

[II.12] Editor footnote: Another point of view is expressed in Section II.2.3 which argues against neglecting the parameters in Eq. (II.2.35) in EFT analyses of LHC Higgs data.

Once the parameters in Eq. (II.2.35) are neglected, this leaves the parameters collected in Eq. (II.2.34) to describe leading order deformations of Higgs observables. This set consists of 11 bosonic and $2 \times 3 \times 3 \times 3 = 54$ fermionic couplings. While that number is still large, it represents a significant simplification compared to the 2499 Wilson coefficients parameterizing a complete D=6 basis. Further simplifications can be introduced by making more specific assumptions about the high-energy theory that generates D=6 operators in the EFT. For example, if the high-energy theory respects the minimal flavour violation paradigm, the flavour structure of the fermionic parameters in Eq. (II.2.34) is proportional to the unit matrix: $[\delta y_f]_{ij} = \delta_{ij}\delta y_f$ and $[\phi_f]_{ij} = \delta_{ij}\phi_f$. This reduces down to 17 (11 bosonic and 6 fermionic) the number of parameters relevant for LHC Higgs observables. In the Higgs basis, these parameters are:

$$\begin{aligned} \text{CP-even}: &\quad c_{gg},\ \delta c_z,\ c_{\gamma\gamma},\ c_{z\gamma},\ c_{zz},\ c_{z\Box},\ \delta y_u,\ \delta y_d,\ \delta y_e,\ \delta\lambda_3; \\ \text{CP-odd}: &\quad \tilde{c}_{gg},\ \tilde{c}_{\gamma\gamma},\ \tilde{c}_{z\gamma},\ \tilde{c}_{zz},\ \phi_u,\ \phi_d, \phi_e. \end{aligned} \tag{II.2.48}$$

Assuming in addition CP conservation[II.13] in the Higgs sector leaves only 10 CP-even parameters to describe leading order EFT corrections to single and double Higgs boson production and decay.

Providing model-independent constraints on the 17 parameters in Eq. (II.2.48), or at least the 10 CP-even ones, is a realistic target for run-2 LHC Higgs searches. The CP-even parameters are weakly constrained by prior precision experiments, with $\mathcal{O}(0.1)$- $\mathcal{O}(1)$ values allowed by current global fits to Higgs and electroweak data [626]. The CP-odd parameters are even less constrained by Higgs and electroweak data, though they are indirectly constrained by low-energy probes of CP violation [635–638]. Better constraints on this reduced sets of EFT parameters from the ensemble of LHC Higgs measurements would already be a valuable input for constraining a large class of theories beyond the SM.

Relation to other frameworks

The Higgs basis can be used in par with any other basis to describe the effects of dimension-6 operators on physical observables. Other popular SM EFT approaches in the literature use the so-called SILH [464], Warsaw [614], or HISZ [628] bases of D=6 operators. At the leading order in EFT all these approaches are completely equivalent, as there exists a 1-to-1 correspondence between the parameter of the Higgs basis and Wilson coefficients of any other D=6 basis. Therefore, the results of leading order EFT analyses can be always translated from and to the Higgs basis without any loss of generality (see e.g. [626] for the translation of the LHC Higgs and TGC constraints). Formulas necessary for translations between various bases are provided: see Section II.2.1.c for the Higgs-SILH basis translation, and Appendix A of Ref. [621] for the Higgs-Warsaw basis translation. A map between the Higgs basis parameters in Eq. (II.2.48 and the HISZ basis can be found in Appendix B of Ref. [621]. These maps are used by the Rosetta package [639], which provides automated translation between different bases and an interface to Monte Carlo simulations in the MadGraph 5 framework [364].

Using the Higgs basis for leading order Higgs EFT analysis is then simply a matter of convenience. Its usefulness is in the fact that description of Higgs observables and electroweak precision observables at the leading EFT order (tree-level $\mathcal{O}(\Lambda^{-2})$) is more transparent than in other bases. This also implies simplification of Monte Carlo simulation of collider signals, as relevant Higgs observables typically depend on a smaller number of parameters than in other bases. The advantages of the Higgs basis are especially pronounced when simplified approaches to LHC Higgs data are employed. The main point of the Higgs basis is to separate parameters affecting only Higgs observables at leading order from those that also affect electroweak precision observables. If the latter are neglected in an analysis, a small subset of Higgs basis parameters in Eq. (II.2.48 is adequate to describe all leading order effects of D=6

[II.13] The CP-odd parameters affect inclusive Higgs observables only at the quadratic level, ($\mathcal{O}(\Lambda^{-4})$ in the EFT expansion). Therefore they can be neglected in the leading order approximation, even without assuming CP conservation, if one restricts the analysis to inclusive measurements, such as the Higgs boson signal strength measurements at the LHC.

operators on Higgs observables.[II.14]

Beyond tree level, advantages of using the Higgs basis are yet to be demonstrated. Indeed, one-loop corrections will introduce a dependence of the Higgs observables on a larger number of parameters, and the neat separation of parameters affecting precision observables is not maintained. As of this time, no one-loop EFT calculations using the Higgs basis formalism exists in the literature; the existing ones are typically performed in the SILH [472, 640–644] or Warsaw [631, 645–650] basis. Note however that any constraint on a coefficient derived in a certain basis at a given order can be straightforwardly translated to other parametrizations.

We will now comment on the relationship between the Higgs basis and other frameworks that also do not introduce new particles beyond the SM but are *not* equivalent to an EFT. The Higgs basis (and dimension-6 EFT in general) is an extension of the **κ-formalism** [9]. That formalism, widely used in LHC Run1 analyses, assumes that only the Higgs boson couplings already present in the SM receive corrections from new physics. This way, the kinematics of the Higgs boson production and decay in various channels is unchanged with respect to the SM, and only the signal strength is affected. Moreover, the standard approach allows for new effective Higgs boson coupling to gluons and photons, as they lead to subleading modifications of the Higgs kinematics when one restrict experimental analyses to inclusive signal strength observables. Recent applications of the κ-formalism include global fits to the Higgs data with 7 independent coupling modifiers [6]. This is still less general than the dimension-6 EFT, even in its restricted form with the free parameters Eq. (II.2.48). In particular, the D=6 operators may induce Higgs boson couplings with a different Lorentz structure than that present in the SM (see e.g. Eq. (II.2.20)) and thus they my violate the assumptions of the κ-formalism by modifying the Higgs kinematics. Therefore, the results obtained within the κ-formalism cannot be in general translated into the EFT language, whereas the translation is always possible in the opposite direction.[II.15]

A framework more general than the SM EFT discussed in Chapter. III.1 is referred to as **pseudo-observables**. In Refs. [651, 652], pseudo-observables are defined as form factors parameterizing amplitudes of physical processes subject to constraints from Lorentz invariance. These form factors are expanded in powers of kinematical invariants of the process around the known poles of SM particles, assuming poles from BSM particles are absent in the relevant energy regime. Such a framework is more general than SM EFT with D=6 operators and involves a larger number of parameters, as it does not impose relations between different form factors or between amplitudes of different processes that are predicted by D=6 EFT. Constraints on pseudo-observables can always be projected into constraints on the Higgs basis parameters, provided the complete likelihood function (with correlations) is given; see Ref. [651] for a map between observables relevant for $h \to 4f$ decays and EFT parameters. The converse is in general not true: constraints on the Higgs basis parameters cannot always be translated into constraints on pseudo-observables.

In Section II.2.1.c we introduced the effective Lagrangian that arise when D=6 EFT is rewritten in terms of mass eigenstates after electroweak symmetry breaking. The crucial feature of this Lagrangian is that various interaction terms are not independent but are instead related by the formulas summarized in Section II.2.1.d. These relations are required by the SM gauge symmetry realized linearly at the level of operators with $D \leq 6$. However, one could consider the same Lagrangian without imposing the correlations listed in Section II.2.1.d, and treating instead all parameters as independent. Such a construction is referred to as the **Beyond-the-Standard Model Characterization** (BSMC). The BSMC Lagrangian is more general than D=6 EFT, and involves more parameters. At leading order, it can be

[II.14] Editor footnote: Another point of view is expressed in Section II.2.3 which advocates using the Warsaw basis formalism as it is more readily applicable to NLO calculations.

[II.15] Note however that, in the dimension-6 EFT, modifications of the relative Higgs boson coupling strength to $W_\mu W_\mu$ and $Z_\mu Z_\mu$ are always correlated with corrections to the W-boson mass, see Eq. (II.2.38), which is not taken into account in the κ-formalism. Strictly speaking, one can thus project general dim-6 EFT results onto a subset of 6 κ parameters of Ref. [6]: κ_{gZ}, λ_{Zg}, λ_{tg}, $\lambda_{\gamma Z}$, $\lambda_{\tau Z}$, λ_{bZ}, with λ_{WZ} set to zero. In the LO EFT, these 6 κ's are in the 1-to-1 correspondence with a subset of 6 parameters in Eq. (II.2.48): c_{gg}, δc_z, $c_{\gamma\gamma}$, δy_u, δy_d, δy_e.

used to parameterize new physics effects on Higgs and other observables in a manner akin to pseudo-observables. Once the likelihood function for the parameters of the BSMC Lagrangian is provided by experiment, it can be projected into constraints on the Higgs basis parameters by imposing the relations of Section II.2.1.d. At the same time, the BSMC likelihood can be used to constrain some more general theories that do not reduce to a SM EFT at low energies. The BSMC Lagrangian is a part of the Rosetta package [639].

Another well-known framework to describe Higgs observables is the so-called **Higgs Characterization** (HC) [622]. In the HC Lagrangian, one describes the effective Higgs boson couplings to the SM gauge bosons and fermions using 20 new parameters. The HC framework is distinct from the SM EFT. On the one hand, the relations between various 2-derivative Higgs boson couplings to gauge bosons required by D=6 EFT are not imposed. In this aspect HC is more general than the Higgs or other D=6 basis, where these relations follow automatically from the structure of the EFT Lagrangian. On the other hand, the HC Lagrangian does not include all possible deformations of the SM Lagrangian predicted in the presence of D=6 operators. For example, corrections to SM gauge boson couplings to fermions, dipole interactions, or contact Higgs interactions with one gauge boson and 2 fermions are not implemented. In this aspect, the HC framework is less general than the SM EFT.

Thus, it is in general not possible to translate the constraints from the HC framework to the Higgs basis or the other way around. However, it is possible to do so in certain situations when a simplified EFT description is employed. In particular, one can project constraints on the HC parameters onto the subset of the Higgs basis parameters in Eq. (II.2.48, assuming other parameters in the Higgs basis are not relevant for these constraints. For such a special case, the relation between the HC parameters and the Higgs basis parameters is given in Appendix B of Ref. [621].

II.2.2 Comments on the validity of the Effective Field Theory approach to physics beyond the Standard Model [II.16]

II.2.2.a Introduction

We consider an EFT where the SM is extended by a set of higher-dimensional operators, and assume that it reproduces the low-energy limit of a more fundamental UV description. The theory has the same field content and the same linearly-realized $SU(3) \times SU(2) \times U(1)$ local symmetry as the SM. The difference is the presence of operators with canonical dimension D larger than 4. These are organized in a systematic expansion in D, where each consecutive term is suppressed by a larger power of a high mass scale. Assuming baryon and lepton number conservation, the Lagrangian takes the form

$$\mathcal{L}_{\text{eff}} = \mathcal{L}_{\text{SM}} + \sum_i c_i^{(6)} \mathcal{O}_i^{(6)} + \sum_j c_j^{(8)} \mathcal{O}_j^{(8)} + \cdots , \tag{II.2.49}$$

where each $\mathcal{O}_i^{(D)}$ is a gauge-invariant operator of dimension D and $c_i^{(D)}$ is the corresponding coefficient. Each coefficient has dimension $4 - D$ and scales like a given power of the couplings of the UV theory; in particular, for an operator made of n_i fields one has

$$c_i^{(D)} \sim \frac{(\text{coupling})^{n_i - 2}}{(\text{high mass scale})^{D-4}} . \tag{II.2.50}$$

This scaling holds in any UV completion which admits some perturbative expansion in its couplings [653]. An additional suppressing factor $(\text{coupling}/4\pi)^{2L}$ may arise with respect to the naive scaling if the operator is first generated at L loops in the perturbative expansion. If no perturbative expansion is possible in the UV theory because this is maximally strongly coupled, then Eq. (II.2.50) gives a correct estimate of the size of the effective coefficients by replacing the numerator with $(4\pi)^{n_i-2}$ (*i.e.* setting coupling $\sim 4\pi$) [654].

[II.16] *Author(s): N. Belyaev, R. Contino, T. Corbett, A. Falkowski, F. Goertz, C. Grojean, R. Konoplich, T. Ohl, J. Reuter, F. Riva.*

The EFT defined by Eq. (II.2.49) is able to parameterize observable effects of a large class of beyond the SM (BSM) theories. In fact all decoupling $B-L$ conserving BSM physics where new particles are much heavier than the SM ones and much heavier than the energy scale at which the experiment is performed can be mapped to such a Lagrangian. The main motivation to use this framework is that the constraints on the EFT parameters can be later re-interpreted as constraints on masses and couplings of new particles in many BSM theories. In other words, translation of experimental data into a theoretical framework has to be done only once in the EFT context, rather than for each BSM model separately. Moreover, the EFT can be used to establish a consistent picture of deviations from the SM by itself and thus can provide guidance for constructing a UV completion of the SM.

The EFT framework contains higher-dimensional operators (non-renormalizable in the traditional sense). As a consequence, physical amplitudes in general grow with the energy scale of the process, and therefore the EFT inevitably has a limited energy range of validity. In this note we address the question of the validity range at the quantitative level. We will discuss the following points:

- Under what conditions does the EFT give a faithful description of the low-energy phenomenology of some BSM theory?
- When is it justified to truncate the EFT expansion at the level of dimension-6 operators? To what extent can experimental limits on dimension-6 operators be affected by the presence of dimension-8 or higher operators?

It is important to realize that addressing the above questions cannot be done in a completely model-independent way, but requires a number of (broad) assumptions about the new physics. An illustrative example is that of the *Fermi theory*, which is an EFT for the SM degrees of freedom below the weak scale after the W and Z bosons have been integrated out. In this language, the weak interactions of the SM fermions are described at leading order by 4-fermion operators of D=6, such as:

$$\mathcal{L}_{\text{eff}} \supset c^{(6)}\,(\bar{e}\gamma_\rho P_L \nu_e)(\bar{\nu}_\mu \gamma_\rho P_L \mu) + \text{h.c.}\,, \qquad c^{(6)} = -\frac{g^2/2}{m_W^2} = -\frac{2}{v^2}\,. \tag{II.2.51}$$

This operator captures several aspects of the low-energy phenomenology of the SM, including for example the decay of the muon, $\mu \to e\nu\nu$, and the inelastic scattering of neutrinos on electrons $\nu e \to \nu\mu$. It can be used to adequately describe these processes as long as the energy scale involved (*i.e.* the momentum transfer between the electron current and the muon current) is well below m_W. However, the information concerning m_W is *not* available to a low-energy observer. Instead, only the scale $|c^{(6)}|^{-1/2} \sim v = 2m_W/g$ is measurable at low energies, which is not sufficient to determine m_W without knowledge of the coupling g. For example, from a bottom-up viewpoint, a precise measurement of the muon lifetime gives indications on the energy at which some new particle (*i.e.* the W boson) is expected to be produced in a higher-energy process, like the scattering $\nu e \to \nu\mu$, only after making an assumption on the strength of its coupling to electrons and muons. Weaker couplings imply lower scales: for example, the Fermi theory could have ceased to be valid right above the muon mass scale had the SM been very weakly coupled, $g \approx 10^{-3}$. On the other hand, a precise measurement of the muon lifetime sets an upper bound on the mass of the W boson, $m_W \lesssim 1.5$ TeV, corresponding to the limit in which the UV completion is maximally strongly coupled, $g \sim 4\pi$.

This example illustrates the necessity of making assumptions (in this case on the value of the coupling g, see also Section II.2.2.f for another BSM example) when assessing the validity range of the EFT, that is, when estimating the mass scale at which new particles appear. On the other hand, the very interest in the EFT stems from its model-independence, and from the possibility of deriving the results from experimental analyses using Eq. (II.2.49) without any reference to specific UV completions. In this note we identify under which physical conditions Eq. (II.2.49), and in particular its truncation at the level of dimension-6 operators, can be used to set limits on, or determine, the value of the effective coefficients. Doing so, we also discuss the importance that results be reported by the experimental collaborations in a way which makes it possible to later give a quantitative assessment of the validity

range of the EFT approach used in the analysis. As we will discuss below, this entails estimating the energy scale characterizing the physical process under study. Practical suggestions on how experimental results should be reported will be given in this note. A more theoretical discussion of the EFT validity issues and scaling of higher-dimensional operators can be found in Ref. [611].

II.2.2.b General discussion

II.2.2.c Model-independent experimental results

Let us first discuss how an experimental analysis can be performed in the context of the EFT. We start considering Eq. (II.2.49) truncated at the level of $D = 6$ operators, and assume that it gives an approximate low-energy description of the UV theory. Below we discuss the theoretical error associated with this truncation and identify the situations where the truncation is not even possible. Physical observables are computed from the truncated EFT Lagrangian in a perturbative expansion according to the usual rules of effective field theories [655]. The perturbative order to be reached depends on the experimental precision and on the aimed theoretical accuracy, as we discuss in the following. Theoretical predictions obtained in this way depend on the coefficients $c_i^{(6)}$ and can be used to perform a fit to the experimental data. The fit to the coefficients $c_i^{(6)}$ should be performed by correctly including the effect of all the theoretical uncertainties (such as those from the PDFs and missing SM loop contributions [II.17]) not originating from the EFT perturbative expansion. The errors due to the truncation at the $D = 6$ level and higher-loop diagrams involving insertions of different effective operators, on the other hand, are not quantifiable in a model-independent way and should thus be reported separately. Below we discuss how the neglected contributions from $D \geq 8$ operators can be estimated; the effects of EFT loops are discussed elsewhere [NLO note].

Let us consider a situation in which no new physics effect is observed in future data (the discussion follows likewise in the case of observed deviations from the SM). In this case, the experimental results can be expressed into the limits [II.18]

$$c_i^{(6)} < \delta_i^{\rm exp}(M_{\rm cut})\,. \tag{II.2.52}$$

The functions $\delta_i^{\rm exp}$ depend on the upper value, here collectively denoted by $M_{\rm cut}$, of the kinematic variables (such as transverse momenta or invariant masses) that set the typical energy scale characterizing the process and, in general, Eq. (II.2.52) is obtained by imposing cuts on these variables and making use of the differential kinematic distributions of the process. For example, when the EFT is applied to describe inclusive on-shell Higgs boson decays one has $M_{\rm cut} \approx m_h$. Another example is e^+e^- collisions at a fixed centre-of-mass energy $\sqrt{s}$, in which case $M_{\rm cut} \approx \sqrt{s}$. For certain physically important processes these considerations are less trivial, especially in the context of hadron collider experiments. The relevant scale for the production of two on-shell particles in proton-proton collisions, for example, is the centre-of-mass energy of the partonic collision $\sqrt{\hat{s}}$; this varies in each event and may not be fully reconstructed in practice. Important examples of this kind are the vector boson scattering (*e.g.* with final states $WW \to 2\ell 2\nu$ and $ZZ \to 4\ell$), and Higgs production in association with a vector boson (Vh) or a jet (hj). In all these processes the relevant energy is given by the invariant mass of the final pair; when this cannot be fully reconstructed, other correlated variables such as the transverse momentum of the Higgs or a lepton, or the transverse invariant mass can be considered.[II.19] Since the energy scale of the process determines the range of validity of the EFT description, it is extremely important that the experimental limits $\delta_i^{\rm exp}$ are reported by the collaborations for various values of $M_{\rm cut}$. For processes occurring over a wide energy range (unlike Higgs boson decays or e^+e^- collisions), knowledge of only the limit

[II.17] These latter can be estimated as usual by varying the factorization and renormalization scales.

[II.18] In general, the experimental constraints on different $c_i^{(6)}$ may have non-trivial correlations. Depending on a chosen basis, the left-hand-side of Eq. (II.2.52) may contain linear combinations of several Wilson coefficients. If a deviation from the SM is observed, Eq. (II.2.52) turns into a confidence interval, $\delta_i^{\rm d,exp}(M_{\rm cut}) < c_i^{(6)} < \delta_i^{\rm u,exp}(M_{\rm cut})$.

[II.19] However, one needs to be aware that it is the former which determines if one is within the validity range of the EFT.

$\delta_i^{\rm exp}$ obtained by making use of all the events without any restriction on the energy (*i.e.* for $M_{\rm cut} \to \infty$) severely limits the interpretation of the EFT results in terms of constraints on specific BSM models. If the relevant energy of the process cannot be determined (*e.g.* because the kinematics cannot be closed), setting consistent bounds requires a more careful procedure, similar to the one proposed in Ref. [656] in the context of DM searches.

II.2.2.d EFT validity and interpretation of the results

Extracting bounds on (or measuring) the EFT coefficients can be done by experimental collaborations in a completely model-independent way. However, the *interpretation* of these bounds is always model-dependent. In particular, whether or not the EFT is valid in the parameter space probed by the experiment depends on further assumptions about the (unknown) UV theory. These assumptions correspond, in the EFT language, to a choice of power counting, *i.e.* a set of rules to estimate the coefficients of the effective operators in terms of the couplings and mass scales of the UV dynamics.

The simplest situation is when the microscopic dynamics is characterized by a single mass scale Λ and a single new coupling g_* [653]. This particular power counting prescription smoothly interpolates between the naive dimensional analysis ($g_* \sim 4\pi$) [654, 657], the case $g_* \sim 1$ as *e.g.* in the Fermi theory, and the very weak coupling limit $g_* \ll 1$. While this is not a unique prescription, it covers a large selection of popular scenarios beyond the SM. In this class falls the Fermi theory described previously, as well as other weakly coupled models where a narrow resonance is integrated out. Moreover, despite the large number of resonances, also some theories with a strongly-interacting BSM sector belong to this category (*e.g.* the holographic composite Higgs models [658] or, more generally, theories where the strong sector has a large-N description). The scaling of the effective coefficients with g_* is then determined by Eq. (II.2.50) and by symmetries and selection rules.

For a given power counting, it is relatively simple to derive limits on the theoretical parameter space that are automatically consistent with the EFT expansion, provided the relevant energy of the process is known. Consider the case of a single scale Λ and a single coupling strength g_*. Then the bounds (II.2.52) can be recast as limits on these two parameters by using the power counting to estimate $c_i^{(6)} = \tilde{c}_i^{(6)}(g_*)/\Lambda^2$, and setting the maximum relevant energy scale to $M_{\rm cut} = \kappa\Lambda$. Here $\tilde{c}_i^{(6)}(g_*)$ is a (dimensionless) polynomial of g_* and of the SM couplings, while $0 < \kappa < 1$ controls the size of the tolerated error due to neglecting higher-derivative operators (the value of κ can be chosen according to the sensitivity required in the analysis). One finds

$$\frac{\tilde{c}_i^{(6)}(g_*)}{\Lambda^2} < \delta_i^{\rm exp}(\kappa\Lambda)\,. \tag{II.2.53}$$

These inequalities determine the region of the plane (Λ, g_*) which is excluded consistently with the EFT expansion, with a relative error of order κ^2. These are a conservative bounds, since they are obtained by using only a subset of the events (effectively only those with relevant energy up to $M_{\rm cut} = \kappa\Lambda$). They are thus less stringent than the bounds one would obtain in the full theory with the full dataset, but they are by construction consistent with the EFT expansion. They give a useful indication of how effective are the experimental data in constraining the class of theories under consideration (*i.e.* those respecting the assumed power counting). A detailed re-analysis of experimental results based on the $M_{\rm cut}$ technique that we propose here, was performed in Ref. [612] for processes with Vh associated production. The same reasoning can be applied to more complicated theories following a different power counting than the simple g_*-scaling presented above.

The usefulness of power counting stems from a number of reasons. First of all it provides a physically motivated range in which the coefficients $c_i^{(D)}$ are expected to vary. Secondly, and very importantly, it allows one to estimate the relative importance of higher-order terms in the EFT series. As an example, consider a $2 \to 2$ scattering process, where the SM contribution to the amplitude is at most of

order g_{SM}^2 at high energy (g_{SM} denotes a SM coupling). The correction from $D=6$ operators involving derivatives will in general grow quadratically with the energy and can be as large as $g_*^2(E^2/\Lambda^2)$.[II.20] If the coupling strength g_* is much larger than g_{SM}, then the BSM contribution dominates over the SM one at sufficiently high energy (*i.e.* for $\Lambda > E > \Lambda\,(g_{SM}/g_*)$), while the EFT expansion is still valid. The largest contribution to the cross section in this case comes from the square of the $D=6$ term, rather than from its interference with the SM. The best sensitivity to $c_i^{(6)}$ is thus expected to come from the highest value of the relevant energy scale accessible in the experiment. In this example the contribution of $D = 6$ derivative operators is enhanced by a factor $(g_*/g_{SM})^2$ compared to the naive expansion parameter $(E/\Lambda)^2$; such enhancement is a consequence of the fact that the underlying strong coupling g_* only appears at the level of $D=6$ operators, while SM operators mediate weaker interactions. In this example, no further enhancement exists between $D = 6$ and $D = 8$ operators, *i.e.* $D = 8$ operators are subdominant and the EFT series is converging. In other words, although the contributions to the cross section proportional to $(c_i^{(6)})^2$ and $c_i^{(8)}$ are both of order $1/\Lambda^4$, the latter (generated by the interference of $D=8$ operators with the SM) is smaller by a factor $(g_{SM}/g_*)^2$ independently of the energy, and can thus be safely neglected. A well known process where the above situation occurs is the scattering of longitudinally-polarized vector bosons. Depending on the UV dynamics, the same can happen in other $2 \to 2$ scatterings, such as Higgs associated production with a W or Z boson (VH) [612, 661] or dijet searches at the LHC [662]. A simple illustrative example is discussed in the next section. Finally, the domination of $(c_i^{(6)})^2$ terms can also happen when g_* is moderate or small but at the same time g_{SM} is even more suppressed. One possible example concerns flavour-changing neutral current processes which in the SM are strongly suppressed by a loop and CKM factors, see *e.g.* [663]. An even sharper example is lepton-flavour violating processes (*e.g.* $h \to \mu\tau$) for which $g_{\rm SM} = 0$ exactly.

II.2.2.e On the importance of loop corrections

So far our discussion was limited to tree-level effects of $D=6$ operators. The EFT can be consistently extended to an arbitrary loop order by computing observables perturbatively in the SM couplings. The corresponding series is controlled by the expansion parameter $g_{SM}^2/16\pi^2$, which adds to the two EFT parameters $\kappa_v^2 = (g_* v/\Lambda)^2$ (assuming again a simple g_*-scaling of the effective couplings) and $\kappa_E^2 = (E/\Lambda)^2$ controlling the effects of the neglected higher-dimensional operators. One-loop effects of D=6 operators are formally suppressed by $O(g_{SM}^2/16\pi^2)$, and are thus generally subleading compared to the tree-level contributions. Including loop corrections in the EFT context is, at present, less crucial than for a pure SM calculation. This is because the experimental precision is typically better than the magnitude of the SM loop corrections, therefore going beyond tree level in a SM calculation is essential to obtain a correct description of physical processes. In the case of the EFT, on the other hand, we are yet to observe any leading-order effect of higher-dimensional operators.

There do exist situations, however, where including NLO corrections may be important for obtaining an adequate description of physical processes in the EFT (see Refs. [606, 609] for an extended discussion). For example, it is well known that NLO QCD corrections to the SM predictions of certain processes at the LHC can be of order 1, and large k-factors are expected to apply to the EFT corrections as well. Another example is the one-loop Higgs corrections to electroweak precision observables. Since deviations of the Higgs boson couplings due to D=6 operators can be relatively large (up to $O(10\%)$) without conflicting with current experimental data, the 1-loop effects, in spite of the suppression factor, can be numerically important for observables measured with a per mille precision [664–666].

More generally, 1-loop corrections are important if they stem from large coefficients and correct precisely measured observables whose tree-level contribution arises from smaller coefficients. The tree-level contribution of a $D=6$ operator may be suppressed, for example, because its coefficient is generated

[II.20] Effects growing with energy can also be induced by operators without additional derivatives, if they yield new contact interactions relevant for the process, or if they disrupt cancellations between $\mathcal{O}(E^2)$ contribution of different SM diagrams, see *e.g.* [659, 660]. The following discussion is unchanged in these cases.

at the 1-loop level by the UV dynamics. In this case, both the 1-loop and tree-level contributions from $D=6$ operators would correspond to 1-loop processes in the UV theory. An example of this kind is the decay of the Higgs boson to two photons, $h \to \gamma\gamma$, which arises necessarily at the 1-loop level if the UV theory is minimally coupled (see Ref. [653] and the appendix of Ref. [667]) and perturbative. The calculation of NLO effects in the context of the EFT is currently an active field of study. As suggested by the above discussion, it is very important to identify all cases where 1-loop effects of $D=6$ operators can be relevant.[II.21]

Besides one-loop effects, it is sometimes also important to include corrections from real emission processes. In particular, including additional jets may be important when exclusive observables, *i.e.* quantities particularly sensitive to extra radiation, are studied.

II.2.2.f An Explicit Example

In this section we illustrate our general arguments by comparing the predictions of the EFT and of a specific BSM model which reduces to that EFT at low energies. To this end we discuss the $q\bar{q} \to Vh$ process at the LHC, along the lines of Ref. [612]. The purpose of the example presented below is to demonstrate that, as in the Fermi theory, the knowledge of the $D = 6$ coefficients of an effective Lagrangian is not enough to determine the validity range of the EFT approximation. Therefore, the theoretical error incurred as a result of the truncation of the EFT Lagrangian cannot be quantified in a model-independent way.

We consider the SM extended by a triplet of vector bosons V^i_μ with mass M_V transforming in the adjoint representation of the SM $SU(2)_L$ symmetry. Its couplings to the SM fields are described by [668–670]

$$\mathcal{L} \supset i g_H V^i_\mu H^\dagger \sigma^i \overleftrightarrow{D_\mu} H + g_q V^i_\mu \bar{q}_L \gamma_\mu \sigma^i q_L, \tag{II.2.54}$$

where $q_L = (u_L, d_L)$ is a doublet of the 1st generation left-handed quarks. In this model V^i_μ couples to light quarks, the Higgs boson, and electroweak gauge bosons, and it contributes to the $q\bar{q} \to Vh$ process at the LHC. Below the scale M_V, the vector resonances can be integrated out, giving rise to an EFT where the SM is extended by D=6 and higher-dimensional operators. Thus, M_V plays the role of the EFT cut-off scale Λ. Using the language of the Higgs basis introduced in Section II.2.1, at the D=6 leve the EFT l is described by the parameter δc_z (relative correction to the SM Higgs boson couplings to WW and ZZ) and δg_L^{Zq} (relative corrections to the Z and W boson couplings to left-handed quarks), plus other parameters that do not affect the $q\bar{q} \to Vh$ process at tree level. The relevant EFT parameters are matched to those in the UV model as

$$\delta c_z = -\frac{3v^2}{2M_V^2} g_H^2, \qquad [\delta g_L^{Zu}]_{11} = -[\delta g_L^{Zd}]_{11} = -\frac{v^2}{2M_V^2} g_H g_q \,. \tag{II.2.55}$$

When these parameters are non-zero, certain EFT amplitudes grow as the square of the centre-of-mass energy $s \equiv M^2_{Wh}$ of the analysed process, $\mathcal{M} \sim M^2_{Wh}/M^2_V$. Then, for a given value of the parameters, the observable effects of the parameters become larger at higher energies. However, above a certain energy scale, the EFT may no longer approximate correctly the UV theory defined by Eq. (II.2.54), and then experimental constraints on the EFT parameters do not provide any information about the UV theory.

To illustrate this point, we compare the UV and EFT descriptions of $q\bar{q} \to W^+h$ for three benchmark points:

- **Strongly coupled:** $M_V = 7$ TeV, $g_H = -g_q = 1.75$;
- **Moderately coupled:** $M_V = 2$ TeV, $g_H = -g_q = 0.5$;
- **Weakly coupled:** $M_V = 1$ TeV, $g_H = -g_q = 0.25$;

[II.21] Editor footnote: Another point of view is expressed in Section II.2.3 where it is argued that, considering projections for the precision to be reached in LHC RunII analyses, the LO approach may not be sufficient.

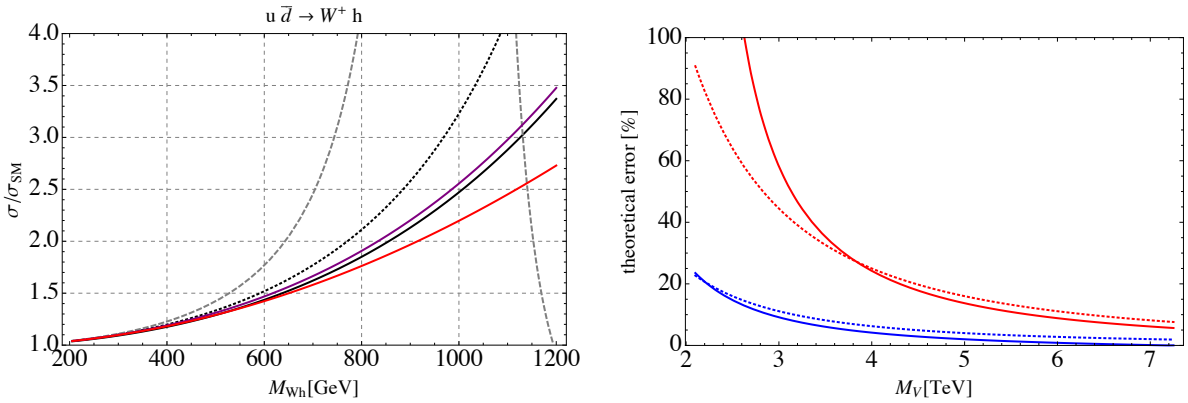

Figure 182: *Left: The partonic $u\bar{d} \to W^+h$ cross section as a function of the centre-of-mass energy of the parton collision. The black lines correspond to the $SU(2)_L$ triplet model with $M_V = 1$ TeV, $g_H = -g_q = 0.25$ (dashed), $M_V = 2$ TeV, $g_H = -g_q = 0.5$ (dotted), and $M_V = 7$ TeV, and $g_H = -g_q = 1.75$ (solid). The corresponding EFT predictions are shown in the linear approximation (solid red), and when quadratic terms in $D=6$ parameters are included in the calculation of the cross section (solid purple). Right: Theory error as a function of M_V (solid line). The error is defined to be the relative difference between the constraints on $g_*^2 \equiv g_H^2 = g_q^2$ obtained by recasting the limits derived in the framework of a $D=6$ EFT and those derived from the resonance model. The limits come from re-interpreting the hypothetical experimental constraints with $M_{\rm cut} = 3$ TeV, as described in the text. The dotted line corresponds to the naive estimate $(M_{\rm cut}/M_V)^2$.*

Clearly, all three benchmarks lead to the same EFT parameters at the $D = 6$ level. However, because $M_V = \Lambda$ varies, these cases imply different validity ranges in the EFT. This is illustrated in Figure 182, where we show (in the left panel) the production cross section as a function of M_{Wh}, for both the full model and the EFT. While, as expected, in all cases the EFT description is valid near the production threshold, above a certain point $M_{Wh}^{\rm max}$ the EFT is no longer a good approximation of the UV theory. Clearly, the value of $M_{Wh}^{\rm max}$ is different in each case. For the moderately coupled case, it coincides with the energy at which the linear and quadratic EFT approximations diverge. From the EFT perspective, this happens because $D = 8$ operators can no longer be neglected. However, for the strongly coupled case, the validity range extends beyond that point. In this case, it is the quadratic approximation that provides a good effective description of the UV theory. As discussed in the previous section, that is because, for strongly-coupled UV completions, the quadratic contribution from $D=6$ operators dominates over that of $D \geq 8$ operators in an energy range below the cutoff scale.

As an illustration of our discussion of setting limits on EFT parameters and estimating associated theoretical errors, consider the following example of an idealized measurement. Suppose an experiment makes the following measurement of the $\sigma(u\bar{d} \to W^+h)$ cross section at different values of M_{Wh}:

M_{Wh}[TeV]	0.5	1	1.5	2	2.5	3
$\sigma/\sigma_{\rm SM}$	1 ± 1.2	1 ± 1.0	1 ± 0.8	1 ± 1.2	1 ± 1.6	1 ± 3.0

This is meant as a simple proxy for more realistic measurements at the LHC, for example measurements of a fiducial $\sigma(pp \to W^+h)$ cross section in several bins of M_{Wh}. For simplicity, we assume that the errors are Gaussian and uncorrelated. These measurements can be recast as constraints on D=6 EFT parameters for different $M_{\rm cut}$ identified in this case with the maximum M_{Wh} bin included in the analysis. For simplicity, in this discussion we only include $\delta g_L^{Wq} \equiv [\delta g_L^{Zu}]_{11} - [\delta g_L^{Zd}]_{11}$ and ignore other EFT parameters (in general, a likelihood function in the multi-dimensional space of EFT parameters

should be quoted by experiments). Then the "measured" observable is related to the EFT parameters as

$$\frac{\sigma}{\sigma_{SM}} \approx \left(1 + 160\,\delta g_L^{Wq} \frac{M_{Wh}^2}{\text{TeV}^2}\right)^2 . \tag{II.2.56}$$

Using this formula, one can recast the measured cross sections as 95% CL confidence intervals on δg_L^{Wq}: Combining the M_{Wh} bins up to $M_{\rm cut}$, one finds the following 95% confidence intervals:

$M_{\rm cut}$[TeV]	0.5	1	1.5	2	2.5	3
$\delta g_L^{Wq} \times 10^3$	[-70, 20]	[-16,4]	[-7,1.6]	[-4.1,1.1]	[-2.7,0.8]	[-2.2,0.7]

Suppose these constraints are quoted by experiment. A theorist may try to interpret them as constraints on the vector resonance model with $g_q = -g_H \equiv g_*$ using the map in Eq. (II.2.55). This way one would obtain the constraints on g_* as a function of M_V: for example, for $M_V = 3$ TeV one would find $g_* \leq 0.80(0.49)$ for $M_{\rm cut,1} = 1$ TeV ($M_{\rm cut,2} = 2$ TeV). Note that, for our (arbitrary) choice of data points, the limits on g_* obtained from the measurement with $M_{\rm cut,2}$ are stronger from the one with $M_{\rm cut,1}$. However, the result for $M_{\rm cut,1}$ is also useful for theorists. First, it can be used also for $M_V \approx 2$ TeV, whereas the one with $M_{\rm cut,2} = 2$ TeV does not have a meaningful interpretation in this mass range. Furthermore, the theory error is smaller for $M_{\rm cut,1}$ ($\sim 10\%$ for $M_V = 3$ TeV) than for $M_{\rm cut,2}$ ($\sim 40\%$ for $M_V = 3$ TeV). Here, we define the theory error as the fractional difference between the bound on g_*^2 interpreted from the EFT constraints, and the true bound obtained by fitting the full resonance model to the experimentally "measured" cross sections using the bins up to a given $M_{\rm cut}$. The theory errors are plotted as solid lines in the right panel of Figure 182. By general arguments discussed in the previous section, one expects the theory error to scale as κ^2 for $M_V \gg M_{\rm cut}$, where $\kappa = M_{\rm cut}/\Lambda = M_{Wh}/M_V$, and this expectation, which is shown as dotted lines in the same plot, is confirmed. While the limits on g_* obviously depend on the experimental central values and errors we assumed, the theory errors as defined here are very weakly dependent on it.

II.2.2.g Summary

In this note we have discussed the validity of an EFT where the SM is extended by D=6 operators. We have emphasized that the validity range cannot be determined using only low-energy information. The reason is that, while the EFT is valid up to energies of order of the mass Λ of the new particles, low-energy observables depend on the combinations $\tilde{c}^{(6)}/\Lambda^2$, where the Wilson coefficients $\tilde{c}^{(6)}$ of D=6 operators are function of the couplings of the UV theory.

The question of a theoretical uncertainty due to the truncation of the EFT at the level of D=6 operators depends on the impact of $D > 6$ operators on the studied processes. The relative size of the contribution of D=8 operators is controlled by $\tilde{c}^{(8)}/\tilde{c}^{(6)}(E_{\rm exp}^2/\Lambda)$, where $E_{\rm exp}$ is the typical energy scale of the process. We have discussed the physical assumptions that lead to a situation with $\tilde{c}^{(8)} \approx \tilde{c}^{(6)}$. In this situation the energy at which the EFT breaks down coincides with the scale at which the contribution of D=8 and higher-dimensional operators is of the same order as that of D=6 operators. Conversely, when the EFT expansion is well convergent at the LHC energies, the effects of D=8 operators can be neglected. We have also shown that the power counting is necessary to estimate the range of variation of the effective coefficients $\tilde{c}_i^{(6)}$, and to identify situations in which departures from the SM can be sizeable (even bigger than the SM itself), compatibly with the EFT expansion. Exceptions from this rule, in the form $\tilde{c}^{(8)} \gg \tilde{c}^{(6)}$, may arise in a controlled way as a consequence of symmetries and selection rules or for certain well-defined classes of processes. The concrete examples where this occurs are discussed in Ref. [611]. The inclusion of D=8 operators in experimental analyses is justified only when dealing with these special cases, and would represent an inefficient strategy in a generic situation.

We have stressed that the ratio $\tilde{c}^{(8)}/\tilde{c}^{(6)}$, which controls the theoretical uncertainty of the EFT predictions, depends on the assumptions about the UV theory that generates the D=6 and D=8 operators. Only when a particular power counting is adopted, for example the g_*-scaling discussed in this note, can the contributions from $D=6$ and $D=8$ relative to the SM be estimated in a bottom-up approach, and the error associated with the series truncation be established. For this reason we suggest to report the estimated uncertainty due to the truncation separately from the other errors, and to clearly state on which assumptions the estimate is based.

If no large deviations from the SM are observed at the LHC Run-2, stronger constraints on $D=6$ operators can be set. As we discussed, this will extend the EFT validity range to a larger class of UV theories (*i.e.* those with smaller $c^{(6)}$) and leave less room for contributions of $D=8$ operators. As a consequence, the internal consistency and the validity range of the LO $D=6$ EFT will increase.[II.22] The validity range can also be improved by means of a global analysis combining different measurements, which often lifts flat directions in the parameter space [623, 632] and leads to stronger constraints on $D=6$ effective coefficients, see *e.g.* [626, 627]. On the other hand, if a deviation from the SM is observed, efforts to include EFT loop corrections and to estimate the effects of $D>6$ operators may be crucial to better characterize the underlying UV theory.

Most of the discussion in this note is relevant at the level of the interpretation of the EFT results, rather than at the level of experimental measurements. However, there are also practical conclusions for experiments. We have proposed a concrete strategy to extract bounds on (or determine) the effective coefficients of $D=6$ operators in a way which is automatically consistent with the EFT expansion. This requires reporting the experimental results as functions of the upper cuts (here collectively denoted by $M_{\rm cut}$) on the kinematic variables, such as transverse momenta or invariant masses, that set the relevant energy scale of the process. This is especially important for hadron collider experiments, such as those performed at the LHC, where collisions probe a wide range of energy scales. In general, knowledge of the experimental results as a function of $M_{\rm cut}$ allows one to constrain a larger class of theories beyond the SM in a larger range of their parameter space. As a quicker (though less complete) way to get an indication on the validity range of the EFT description, it is also useful to present the experimental results both with and without the contributions to the measured cross sections and decay widths that are quadratic in the effective coefficients. This gives an indication on whether the constraints only apply to strongly-interacting UV theories or they extend also to weakly-coupled ones. Notice that even in situations where it makes sense to expand the cross section at linear order in the coefficients of $D=6$ operators, quadratic terms should always be retained in the calculation of the likelihood function. With this way of presentation, the experimental results can be applied to constrain a larger class of theories beyond the SM in a larger range of their parameter space. Other frameworks to present results, for example the template cross-sections or the pseudo-observables discussed elsewhere in this volume, should also be pursued in parallel, as they may address some of the special situations discussed in this note. Finally, given its model-dependency, we suggest to report the estimated uncertainty on the results implied by the EFT truncation separately from the other errors, and to clearly state on which assumptions the estimate is based.[II.23]

Note that even in the case of BSM discoveries in the next LHC runs, the EFT approach and the results presented here remain still useful. For measurements with a characteristic scale $M_{\rm cut}$ considerably below the new physics threshold, the new particle(s) can be integrated out (in analogy to the Fermi Theory) and deviations from the predicted values of the D=6 coefficients can be probed. Such an EFT approach may give a more economical description of the relevant precess, with fewer parameters (the

[II.22] Editor footnote: A different conclusion is presented in Section II.2.3. The discrepancy is due to different assumptions about the underlying UV theory. For example, in a situation in which both Λ and $c^{(6)}$ are small while $c^{(8)}$ is sizeable, the general validity discussion presented in this contribution would not be applicable.

[II.23] Editor footnote: Another point of view is expressed in Section II.2.3 that puts more emphasis on the uncertainty due to the EFT truncation. There it is argued that this uncertainty is an essential part of the theory prediction, to compare to the experimental results.

effective coefficients) that can be directly measured from low-energy data. For processes involving higher scales, an EFT including the BSM degrees of freedom cam be set up and all results generalize straightforwardly.

A concluding comment is in order when it comes to constrain explicit models from the bounds derived in an EFT analysis of the data. Although EFT analyses aim at a global fit with all the operators included, it is important to ensure that the reported results are complete enough to later consider more specific scenarios where one can focus on a smaller set of operators. Reporting the full likelihood function, or at the very least the correlation matrix, would be a way to address this issue.

II.2.3 The Standard Model Effective Field Theory and Next to Leading Order [II.24]

II.2.3.a Overview

In this section we discuss how to interpret data in the Standard Model Effective Field Theory (SMEFT) in a transparent manner at leading order (LO) and explain why a next to leading order (NLO) interpretation of the data is important. The approach presented for LO is the one we consider the most simple to enable the ongoing development of the SMEFT to NLO. The LO approach we present is written in terms of mass eigenstate fields and is trivially connected to Higgs observables and electroweak precision observables. It can be directly used at LO to interpret the data.

Interpreting the data using theoretical results developed beyond LO (in perturbation theory) can often be crucial to do in the SMEFT. NLO calculations should be used if they are available. We discuss the basic issues involved in improving calculations to NLO, and review the advances in this direction that have been achieved to date. These calculations help characterize (and reduce) theoretical errors of a LO result and allow the consistent incorporation of precise measurements, such as the LEP pseudo-observables, in the SMEFT. NLO interpretations of the data are particularly critical in the event that deviations from the Standard Model (SM) emerge over the course of LHC operations. NLO results are being developed in the theoretical community and will become increasingly available over the course of RunII. Experimental analyses can adopt approaches to LO that will allow these results to be incorporated in the future as efficiently as possible. [II.25]

This review provides scientific support for the above statements. The reader who is mostly interested in the LO and NLO summary conclusions can skip directly to the end of this review.

II.2.3.b Introduction to the SMEFT

As exact non-perturbative solutions to quantum field theories are rarely known approximate solutions that expand observables perturbatively in a small coupling constant or in a ratio of scales are generally developed. Such quantum field theories can be regarded as examples of Effective Field Theory (EFT), the treatment of which was pioneered in [671–673]. The predictions of the LO Lagrangian of any EFT are approximations of limited applicability and precision. Developing such predictions beyond leading order is in general extremely useful and straightforward if the LO EFT is well defined. The ability to improve EFTs from LO to NLO largely explains why they have become the standard approach to interpreting data sets of constraints on the SM, as reducing theoretical errors to be below experimental errors is required for a precise interpretation of an experimental measurement.

At LHC it is of interest to treat the Standard Model itself as a general EFT. In this section we briefly outline how the standard straightforward LO formulation of this SMEFT is defined. We then

[II.24] *Author(s): G. Passarino, M. Trott. The present content of this section reflects the initial contribution and also the editing of the WG2 conveners (A. Falkowski, C. Hays, G. Isidori, M. Chen, A. Tinoco).*

[II.25] Editor footnote: Another point of view is expressed in Section II.2.1 which advocates using an operator basis that at leading order simplifies/diagonalizes the relation between the observables and the EFT parameters and focuses the attention on the least constrained directions in the EFT space.

discuss extending the SMEFT approach to NLO in order to incorporate important QCD and Electroweak corrections.

The SMEFT assumes that $\mathrm{SU(2)_L \times U(1)_Y}$ is spontaneously broken to $\mathrm{U(1)_{em}}$ by the vacuum expectation value of the Higgs field (v) and that the observed $J^P = 0^+$ scalar is embedded in the Higgs doublet. The Lagrangian is schematically

$$\mathcal{L}_{SMEFT} = \mathcal{L}_{SM} + \mathcal{L}_5 + \mathcal{L}_6 + \mathcal{L}_7 + \mathcal{L}_8 + \cdots \tag{II.2.57}$$

$\mathcal{L}_5$ has one operator suppressed by one power of the cut off scale (Λ) [613]. $\mathcal{L}_6$ has 76 parameters that preserve Baryon number [613, 614, 620, 674] in the $N_f = 1$ limit[II.26] and four that do not. The baryon preserving operators in $\mathcal{L}_6$ has 2499 parameters in the case $N_f = 3$ [631]. $\mathcal{L}_7$ and $\mathcal{L}_8$ are now known, see Refs. [615, 616]. We label the Wilson coefficients of the operators in $\mathcal{L}_5$ as C_i^5, operators in $\mathcal{L}_6$ as C_i^6 etc., and have implicitly absorbed the appropriate power of $1/\Lambda$ into the definition of the C_i. When $1/\Lambda$ is made explicit, and pulled out of the Wilson coefficient we will use the tilde superscript as a notation to indicate this, for example $\tilde{C}_i/\Lambda^2$.

The SMEFT is a different theory than the SM as it has local contact operators suppressed by powers of $1/\Lambda$. To get a feeling for the nature of the LO and NLO predictions in the SMEFT, consider a (lepton number preserving) amplitude that can be written as

$$\mathcal{A} = \sum_{n=\mathrm{N}}^{\infty} g_{SM}^n \, \mathcal{A}_n^{(4)} + \sum_{n=\mathrm{N_6}}^{\infty} \sum_{l=1}^{n} \sum_{k=1}^{\infty} g_{SM}^n \left[\frac{1}{(\sqrt{2}\, G_F\, \Lambda^2)^k} \right]^l \mathcal{A}_{n\,l\,k}^{(4+2\,k)} \tag{II.2.58}$$

where g_{SM} is a SM coupling. G_F is the Fermi coupling constant and Λ is again the cut off scale. l is an index that indicates the number of SMEFT operator insertions leading to the amplitude, and k indicates the inverse mass dimension of the Lagrangian terms inserted. N is process dependent and indicates the order of the coupling dependence for the leading non-vanishing term in the SM (e.g., $N = 1$ for $\mathrm{H} \to \mathrm{VV}$ etc. but $N = 3$ for $\mathrm{H} \to \gamma\gamma$). $N_6 = N$ for tree initiated processes in the SM. For processes that first occur at loop level in the SM, $N_6 = N - 2$ as operators in the SMEFT can mediate such decays directly thought a contact operator, for example, through a $\mathcal{L}_6$ operator for $\mathrm{H} \to \gamma\gamma$. For instance, the $\mathrm{H}\gamma\gamma$ (tree) vertex is generated by $O_{HB} = H^\dagger H\, B^{\mu\nu}\, B_{\mu\nu}$, by $O_{HW}^8 = H^\dagger B^{\mu\nu}\, B_{\mu\rho}\, \mathrm{D}^\rho \mathrm{D}_\nu\, H$ etc. An example of the Feynman diagrams leading to $\mathcal{A}$ is given in Figure 183.

An example of how the SMEFT orders a double expansion in $1/\Lambda$ and the perturbative expansion in SM couplings is as follows. Consider a tree level 2 body decay of a single field. The double expansion of such a process is given as the following Table [II.27]:

$$\begin{array}{lccc} g_{SM} \,/\, \mathrm{D}im \longrightarrow & & & \\ \downarrow & g_{SM}\, \mathcal{A}_1^{(4)} & + g_{SM}\, g_6\, \mathcal{A}_{1,1,1}^{(6)} & + g_{SM}\, g_8\, \mathcal{A}_{1,1,2}^{(8)} \\ & g_{SM}^3\, \mathcal{A}_3^{(4)} & + g_{SM}^3\, g_6\, \mathcal{A}_{3,1,1}^{(6)} & + g_{SM}^3\, g_6^2\, \mathcal{A}_{3,2,1}^{(6)} \\ & \cdots\cdots & \cdots\cdots & \cdots\cdots \end{array} \tag{II.2.59}$$

The combination of parameters $g_{SM}\, g_6\, \mathcal{A}_{1,1,1}^{(6)}$ defines the LO SMEFT expression for the process, including the leading insertion of a higher dimensional operator, and is generally well known. $g_{SM}^3\, g_6\, \mathcal{A}_{3,1,1}^{(6)}$ defines the NLO SMEFT amplitude in the perturbative expansion, and $g_{SM}\, g_8\, \mathcal{A}_{1,1,2}^{(8)}$ defines the NLO SMEFT Lagrangian expansion contribution to the amplitude. We will refer to these two different NLO effects in this manner in this document. The discussion here generalizes to cases other than two body decays of a single field directly. Currently NLO terms in the double expansion present in the SMEFT are generally unknown, in almost every process that is of interest phenomenologically.

[II.26] Here N_f counts the number of fermion generations.

[II.27] Here we have introduced short hand notation where $g_{4+2\,k} = 1/(\sqrt{2}\, G_F\, \Lambda^2)^k$, so that g_6 denotes a single $\mathcal{O}^{(6)}$ insertion, g_8 denotes a single $\mathcal{O}^{(8)}$ insertion, g_6^2 denotes two, distinct, $\mathcal{O}^{(6)}$ insertions, etc..

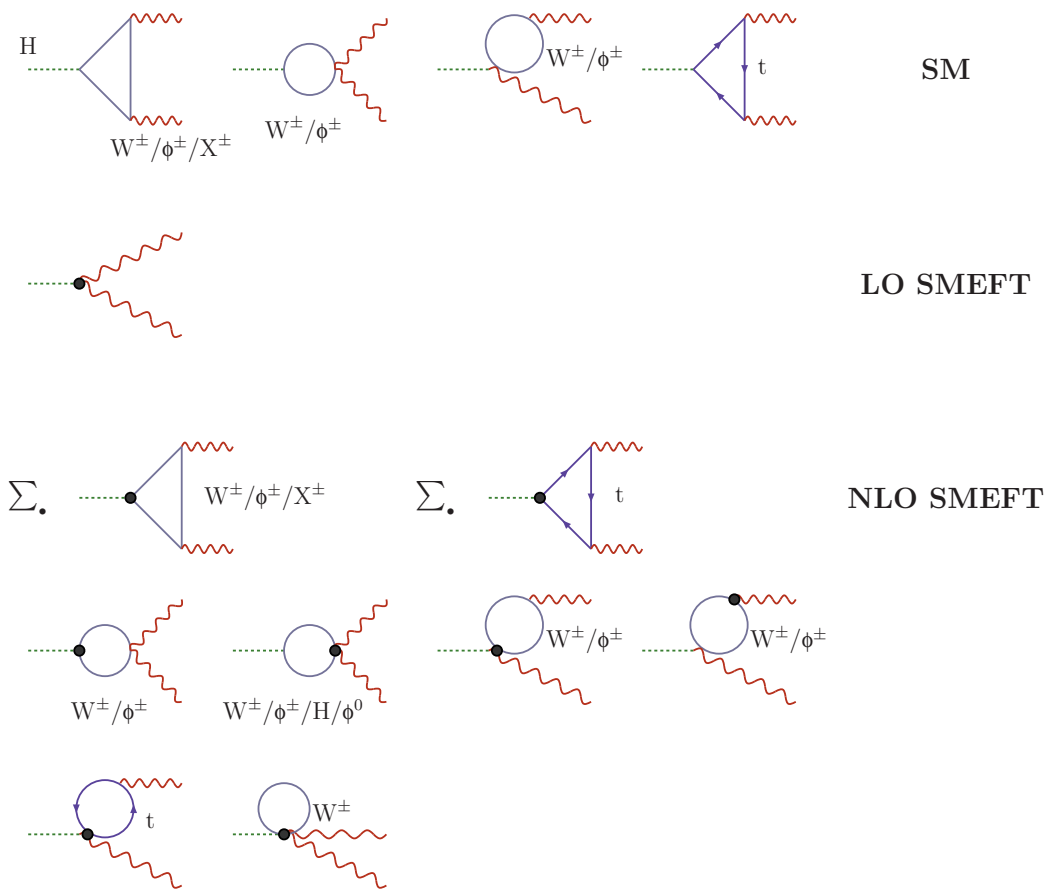

Figure 183: Diagrams contributing to the amplitude for $H \to \gamma\gamma$ in the R_ξ -gauge: SM (first row), LO SMEFT (second row), and NLO SMEFT. Black circles denote the insertion of one $\mathcal{L}_6$ operator. $\sum_\bullet$ implies summing over all insertions in the diagram (vertex by vertex). For triangles with internal charge flow $(t, W^\pm, \phi^\pm, X^\pm)$ only the clockwise orientation is shown. Non-equivalent diagrams obtained by the exchange of the two photon lines are not shown. Higgs and photon wave-function factors are not included. The Fadeev-Popov ghost fields are denoted by X.

The construction of the SMEFT, to all orders, is not based on assumptions on the size of the Wilson coefficients of the higher dimensional operators, although it does assume that a valid perturbative expansion is present. Constructing an NLO SMEFT result means including all operators at a fixed order in the power counting of the theory or performing a complete one loop calculation for a process, including all of the operators in $\mathcal{L}_6$ that can contribute. One must add results for real emission (if present) to get a complete description of a process at NLO in perturbation theory.[II.28]

NLO corrections are a necessary consequence of the SMEFT being a well defined field theory. The *numerical size of the higher order terms* depends upon the high energy (UV) scenario dictating the $\tilde{C}_i$ and Λ, which is unknown. Restricting to a particular UV case is not an integral part of a general SMEFT treatment and various cases can be chosen once the general calculation is performed. All explicit

[II.28] There are different uses of the phrase "NLO" in the literature. This can refer to a fixed-order NLO calculation including non-logarithmic terms not fixed by renormalization group evolution, only an approximate fixed-order NLO calculation, which includes logarithmic terms fixed by renormalization group evolution to NLO, and a genuine leading-log calculation, which uses exact solutions to the RG equations to actually do a resummation. In this work "NLO in the perturbative expansion" refers to a complete perturbative correction due to SM interactions to the operators in $\mathcal{L}_6$.

references to the underlying theory are introduced via the matching procedure in the standard approach to EFTs and power counting, see Refs. [601, 602, 604, 654, 657, 671–673, 675–684] for reviews. Below we briefly summarize the standard definitions of these terms.

II.2.3.b.i Power counting

The size of corrections to SM results due to $\mathcal{L}_{SMEFT}$ interactions are estimated with power counting.[II.29] A naive power counting scheme based on the mass dimensions of the operators simply normalizes an operator by the appropriate power of $1/\Lambda$. Expansions in $(v/\Lambda)^m$ and $(p^2/\Lambda^2)^m$ are then present, where p^2 is a typical invariant momentum flow of a process. Both expansions are relative to the SM interactions.

The Naive Dimensional Analysis (NDA) power counting scheme incorporates the counting of Λ and an estimate of factors of $4\,\pi$ in the normalization of the operators, see Refs. [654, 657, 677, 684] for details. By definition any remaining $4\,\pi$ dependence, coupling dependence, or alternate scales present in the EFT, can be absorbed into the Wilson coefficients in the matching procedure if the naive power counting scheme is used.

II.2.3.b.ii Matching

Wilson coefficients are determined by calculating on-shell amplitudes in the UV theory and in the SMEFT and taking the low energy limit ($E/\Lambda << 1$). The mismatch of the finite terms defines the Wilson coefficient in the matching condition.

If the value of Wilson coefficients in broad UV scenarios could be inferred in general this would be of significant scientific value. An example of a scheme that applies to a fairly large set of UV scenarios is the Artz-Einhorn-Wudka "potentially-tree-generated" (PTG) scheme [685,686]. This approach classifies Wilson coefficients for operators in $\mathcal{L}_6$ as tree or loop level (suppressed by $g^2/16\,\pi^2$) essentially using topological matching arguments. This classification scheme corresponds only to a subset of weakly coupled and renormalizable UV physics cases, as the topologies considered are (effectively) limited by Lorentz invariance and renormalizability. This scheme does not apply to scenarios where any high energy physics is strongly interacting or an EFT itself [680]. This scheme should be only considered with caution, as it is not the result of a precise matching calculation.

One can study the Wilson coefficients using dimensional analysis, by restoring $\hbar \neq 1$ in the Lagrangian, as recently discussed in Refs. [608, 687]. In this note we do not assume any hierarchy among the couplings as discussed in these works. The reasons we do not adopt these claims is that, in our opinion, one cannot unambiguously identify the powers of hypothetical UV couplings present in the $\tilde{C}_i$, as the SM couplings also carry $\hbar$ dimensions and the UV theory is not known. Further, the matching procedure introduces order one constant terms that can be as large as, or dominant over, any such coupling dependence. For these reasons, we adopt an agnostic position and treat the $\tilde{C}_i$ as anything other than parameters to be constrained by experiment. In this approach, by performing the calculations without unnecessary assumptions, it is still possible to study the effect of particular hierarchies and specific UV completions (when they are precisely defined allowing a matching calculation) a posteriori.

II.2.3.b.iii Operator bases for the SMEFT

The Warsaw basis [614] for the SMEFT is given in Table 100. This basis is completely and precisely defined and is fully reduced by the Equations of Motion (EOM). It was the first basis of this form, building upon Ref. [620]. No fully reduced basis was present in the literature prior to 2010 when this result was reported. The Warsaw basis is one of the most (if not the most) standard SMEFT bases in

[II.29] Differences of opinion about the size of NLO corrections exist in the theory community. Our claim is that any differences of opinion regarding NLO analyses are due to different implicit UV assumptions and the data should be reported in a manner that maximizes its potential use in the future, including its use in NLO analyses. This means formalisms that cannot be improved to NLO should be avoided. We return to this point below.

use in the theoretical community. This is the basis we use to define the straightforward LO approach in subsequent sections.

One can make small field redefinitions of $\mathcal{O}(1/\Lambda^2)$ to shift $\mathcal{L}_{SMEFT}$ by operators proportional to the EOM. This procedure can be used to eliminate redundant operators from the Lagrangian to obtain a fully reduced basis or to change to a different operator basis. Operator bases that are related by field redefinitions give equivalent results for physically measured quantities due to the equivalence theorem, see Refs. [688–690] for the proof of this theorem and its conditions. Field redefinitions are a change of variables in a path integral and do not affect S-matrix elements although the source terms in Greens functions can get modified. If a modification of how $\mathcal{L}_{SMEFT}$ is presented uses manipulations that are not gauge independent field redefinitions, it does not directly satisfy the conditions of the equivalence theorem. Any LO Lagrangian construction based on intrinsically gauge dependent manipulations is different from a gauge independent operator basis, like the Warsaw basis, and we believe it would not be referred to as an operator basis in standard EFT literature [601, 602, 604, 654, 657, 671–673, 675–684]. [II.30]

In principle, any well-defined basis (in the sense specified above) can be used. There are very few such bases defined in the literature: the Warsaw basis and various constructions that can be related to the Warsaw basis using the EOM. A notable example is the so-called SILH basis, a later version of which was reported in Ref. [464] in 2013. The different operators that are present in this SILH basis (we adopt here the definition of the basis of Ref. [631]), denoted $\mathcal{O}_i$, are given by

$$\mathcal{O}_{HW} = -i\, g_2\, (D^\mu H)^\dagger\, \tau^I\, (D^\nu H)\, W^I_{\mu\nu}, \qquad \mathcal{O}_{HB} = -i\, g_1\, (D^\mu H)^\dagger\, (D^\nu H)\, B_{\mu\nu}, \tag{II.2.60}$$

$$\mathcal{O}_W = -\frac{i\, g_2}{2}\, (H^\dagger \overleftrightarrow{D}^I_\mu H)\, (D^\nu W^I_{\mu\nu}), \qquad \mathcal{O}_B = -\frac{i\, g_1}{2}\, (H^\dagger \overleftrightarrow{D}^\mu H)\, (D^\nu B_{\mu\nu}), \tag{II.2.61}$$

$$\mathcal{O}_T = (H^\dagger \overleftrightarrow{D}^\mu H)\, (H^\dagger \overleftrightarrow{D}^\mu H). \tag{II.2.62}$$

We use Q_i for the Warsaw basis operators, τ is the Pauli matrix, g_1 is the $U(1)_Y$ coupling and g_2 is the $SU(2)_L$ coupling. See Refs. [614, 631] for more details on notation. All other operators are the same in these bases. The transformation from the Warsaw basis to the $\mathcal{O}_i$ operators is derived using the SM EOM and found[II.31] to be [631]

$$g_1\, g_2\, Q_{HWB} = 4\, \mathcal{O}_B - 4\, \mathcal{O}_{HB} - 2\, \mathsf{y}_H\, g_1^2\, Q_{HB}, \tag{II.2.63}$$

$$g_2^2\, Q_{HW} = 4\, \mathcal{O}_W - 4\, \mathcal{O}_B - 4\, \mathcal{O}_{HW} + 4\, \mathcal{O}_{HB} + 2\, \mathsf{y}_H\, g_1^2\, Q_{HB}, \tag{II.2.64}$$

$$g_1^2\, \mathsf{y}_\ell\, Q^{(1)}_{\substack{Hl\\tt}} = 2\, \mathcal{O}_B + \mathsf{y}_H\, g_1^2\, \mathcal{O}_T - g_1^2 \left[\mathsf{y}_e Q_{\substack{He\\rr}} + \mathsf{y}_q Q^{(1)}_{\substack{Hq\\rr}} + \mathsf{y}_u Q_{\substack{Hu\\rr}} + \mathsf{y}_d Q_{\substack{Hd\\rr}} \right], \tag{II.2.65}$$

$$g_2^2\, Q^{(3)}_{\substack{Hl\\tt}} = 4\, \mathcal{O}_W - 3\, g_2^2\, Q_{H\Box} + 2\, g_2^2 m_h^2\, (H^\dagger H)^2 - 8\, g_2^2\, \lambda\, Q_H - g_2^2\, Q^{(3)}_{Hq}, \tag{II.2.66}$$

$$- 2\, g_2^2 \left([Y_u^\dagger]_{rr} Q_{\substack{uH\\rr}} + [Y_d^\dagger]_{rr} Q_{\substack{dH\\rr}} + [Y_e^\dagger]_{rr} Q_{\substack{eH\\rr}} + h.c. \right). \tag{II.2.67}$$

Here the t subscript is a flavour index and the $(1), (3)$ superscripts are operator labels, see Table 1. In these relations only the flavour singlet component of the operators appears - given by the tt subscript and the notation $Q_{\substack{Hd\\rr}}$ for the Warsaw basis operators. It is necessary to define what flavour components of the operators are removed and retained in this procedure, as first pointed out in Ref. [631].[II.32] Note that these relationships between operators are not gauge dependent as they follow from gauge independent field redefinitions that satisfy the equivalence theorem.

[II.30] Editor footnote: Another point of view is expressed in Section II.2.1 that advocates the use of field transformations to simplify tree level calculations and separate different classes of observables.

[II.31] Operator relations of this form were partially discussed in Refs [691–693] previously.

[II.32] In our opinion, using the SILH basis to describe interactions of vector bosons with fermions, for example in Electroweak Precision Data (EWPD) is less transparent than using the Warsaw basis (see Ref. [694]).

The complete renormalization program for $\mathcal{L}_6$ was only carried out in the Warsaw basis. In the latter basis higher derivative terms are systematically removed using the EOM in favour of other operators without derivatives. This is done for a number of technical reasons which, in our opinion, were crucial to complete the renormalization program in Refs. [631, 645–647]. Only partial renormalization results were derived in the SILH basis. Any LO construction introducing operator normalizations, redefinitions of the SM parameters and EOM manipulations that are intrinsically gauge dependent will, in our opinion, make very hard the use of the results in Refs. [631, 645–647].

II.2.3.b.iv Rotating to mass eigenstate fields

Expanding around the vev in unitary gauge and rotating to mass eigenstate fields, the LO modification of the SM interactions in the SMEFT come about in a straightforward manner.[II.33] Here we list the most phenomenologically relevant terms present for mass eigenstate fields, the remaining interactions unlisted come from Class $1, 3, 5, 6, 8$ operators in Table 1. It is not required in our approach to specify all interactions as we make no assertion that these mass eigenstate interactions listed are an operator basis. As the theory should be canonically normalized, we denote coupling parameters in the canonically normalized SMEFT with bar superscripts. This use of bar notation is distinct from bar superscripts on fermion fields where $\bar{\psi} = \psi^\dagger \gamma^0$. The following section is largely taken from Ref. [631].

II.2.3.b.iv.1 SM Lagrangian

We define the SM Lagrangian as

$$\begin{aligned}\mathcal{L}_{\rm SM} = &-\frac{1}{4} G^A_{\mu\nu} G^{A\mu\nu} - \frac{1}{4} W^I_{\mu\nu} W^{I\mu\nu} - \frac{1}{4} B_{\mu\nu} B^{\mu\nu} + (D_\mu H^\dagger)(D^\mu H) + \sum_{\psi=q,u,d,l,e} \overline{\psi}\, i \not{D}\, \psi \\ &- \lambda \left(H^\dagger H - \frac{1}{2} v^2 \right)^2 - \left[H^{\dagger j} \overline{d}\, Y_d\, q_j + \widetilde{H}^{\dagger j} \overline{u}\, Y_u\, q_j + H^{\dagger j} \overline{e}\, Y_e\, l_j + \text{h.c.} \right], \end{aligned} \tag{II.2.68}$$

which implicitly defines most of our notational conventions. Note $\tilde{H}^j = \epsilon_{jk}\, H^{\dagger k}$. We have suppressed reference to the $\tilde{\theta}$ gauge dual operators of the form $\tilde{\theta}\, F^{\mu\nu}\, \tilde{F}_{\mu\nu}$. These terms are known to be experimentally small. For dual gauge fields we use the convention $\tilde{F}_{\mu\nu} = \epsilon_{\mu\nu\alpha\beta}\, F^{\alpha\beta}$ with $\epsilon_{0123} = +1$. See Ref [631, 646, 647] for more details on notation.

II.2.3.b.iv.2 Higgs boson mass and self-couplings

The potential in the SMEFT is

$$V(H) = \lambda \left(H^\dagger H - \frac{1}{2} v^2 \right)^2 - C_H \left(H^\dagger H \right)^3, \tag{II.2.69}$$

yielding the new minimum

$$\langle H^\dagger H \rangle = \frac{v^2}{2} \left(1 + \frac{3 C_H v^2}{4\lambda} \right) \equiv \frac{1}{2} v_T^2. \tag{II.2.70}$$

The scalar field can be written in unitary gauge as

$$H = \frac{1}{\sqrt{2}} \begin{pmatrix} 0 \\ [1 + c_{H,\rm kin}]\, h + v_T \end{pmatrix}, \tag{II.2.71}$$

[II.33] The operator basis for the SMEFT remains the Warsaw basis when the interaction terms are expanded in terms of mass eigenstate fields in unitary gauge. Operator bases are gauge independent, satisfy the equivalence theorem, and do not change when the SMEFT is improved from LO to NLO.

Table 100: The $\mathcal{L}_6$ operators built from Standard Model fields which conserve baryon number in the Warsaw basis [614]. The flavour labels of the form p, r, s, t on the Q operators are suppressed on the left hand side of the tables.

$1 : X^3$

Q_G	$f^{ABC} G^{A\nu}_{\mu} G^{B\rho}_{\nu} G^{C\mu}_{\rho}$
$Q_{\widetilde{G}}$	$f^{ABC} \widetilde{G}^{A\nu}_{\mu} G^{B\rho}_{\nu} G^{C\mu}_{\rho}$
Q_W	$\epsilon^{IJK} W^{I\nu}_{\mu} W^{J\rho}_{\nu} W^{K\mu}_{\rho}$
$Q_{\widetilde{W}}$	$\epsilon^{IJK} \widetilde{W}^{I\nu}_{\mu} W^{J\rho}_{\nu} W^{K\mu}_{\rho}$

$2 : H^6$

Q_H	$(H^\dagger H)^3$

$3 : H^4 D^2$

$Q_{H\Box}$	$(H^\dagger H)\Box(H^\dagger H)$
Q_{HD}	$\left(H^\dagger D_\mu H\right)^* \left(H^\dagger D_\mu H\right)$

$5 : \psi^2 H^3 + \text{h.c.}$

Q_{eH}	$(H^\dagger H)(\bar{l}_p e_r H)$
Q_{uH}	$(H^\dagger H)(\bar{q}_p u_r \widetilde{H})$
Q_{dH}	$(H^\dagger H)(\bar{q}_p d_r H)$

$4 : X^2 H^2$

Q_{HG}	$H^\dagger H\, G^A_{\mu\nu} G^{A\mu\nu}$
$Q_{H\widetilde{G}}$	$H^\dagger H\, \widetilde{G}^A_{\mu\nu} G^{A\mu\nu}$
Q_{HW}	$H^\dagger H\, W^I_{\mu\nu} W^{I\mu\nu}$
$Q_{H\widetilde{W}}$	$H^\dagger H\, \widetilde{W}^I_{\mu\nu} W^{I\mu\nu}$
Q_{HB}	$H^\dagger H\, B_{\mu\nu} B^{\mu\nu}$
$Q_{H\widetilde{B}}$	$H^\dagger H\, \widetilde{B}_{\mu\nu} B^{\mu\nu}$
Q_{HWB}	$H^\dagger \tau^I H\, W^I_{\mu\nu} B^{\mu\nu}$
$Q_{H\widetilde{W}B}$	$H^\dagger \tau^I H\, \widetilde{W}^I_{\mu\nu} B^{\mu\nu}$

$6 : \psi^2 X H + \text{h.c.}$

Q_{eW}	$(\bar{l}_p \sigma^{\mu\nu} e_r) \tau^I H W^I_{\mu\nu}$
Q_{eB}	$(\bar{l}_p \sigma^{\mu\nu} e_r) H B_{\mu\nu}$
Q_{uG}	$(\bar{q}_p \sigma^{\mu\nu} T^A u_r) \widetilde{H}\, G^A_{\mu\nu}$
Q_{uW}	$(\bar{q}_p \sigma^{\mu\nu} u_r) \tau^I \widetilde{H}\, W^I_{\mu\nu}$
Q_{uB}	$(\bar{q}_p \sigma^{\mu\nu} u_r) \widetilde{H}\, B_{\mu\nu}$
Q_{dG}	$(\bar{q}_p \sigma^{\mu\nu} T^A d_r) H\, G^A_{\mu\nu}$
Q_{dW}	$(\bar{q}_p \sigma^{\mu\nu} d_r) \tau^I H\, W^I_{\mu\nu}$
Q_{dB}	$(\bar{q}_p \sigma^{\mu\nu} d_r) H\, B_{\mu\nu}$

$7 : \psi^2 H^2 D$

$Q^{(1)}_{Hl}$	$(H^\dagger i \overleftrightarrow{D}_\mu H)(\bar{l}_p \gamma^\mu l_r)$
$Q^{(3)}_{Hl}$	$(H^\dagger i \overleftrightarrow{D}^I_\mu H)(\bar{l}_p \tau^I \gamma^\mu l_r)$
Q_{He}	$(H^\dagger i \overleftrightarrow{D}_\mu H)(\bar{e}_p \gamma^\mu e_r)$
$Q^{(1)}_{Hq}$	$(H^\dagger i \overleftrightarrow{D}_\mu H)(\bar{q}_p \gamma^\mu q_r)$
$Q^{(3)}_{Hq}$	$(H^\dagger i \overleftrightarrow{D}^I_\mu H)(\bar{q}_p \tau^I \gamma^\mu q_r)$
Q_{Hu}	$(H^\dagger i \overleftrightarrow{D}_\mu H)(\bar{u}_p \gamma^\mu u_r)$
Q_{Hd}	$(H^\dagger i \overleftrightarrow{D}_\mu H)(\bar{d}_p \gamma^\mu d_r)$
$Q_{Hud} + \text{h.c.}$	$i(\widetilde{H}^\dagger D_\mu H)(\bar{u}_p \gamma^\mu d_r)$

$8 : (\bar{L}L)(\bar{L}L)$

Q_{ll}	$(\bar{l}_p \gamma_\mu l_r)(\bar{l}_s \gamma^\mu l_t)$
$Q^{(1)}_{qq}$	$(\bar{q}_p \gamma_\mu q_r)(\bar{q}_s \gamma^\mu q_t)$
$Q^{(3)}_{qq}$	$(\bar{q}_p \gamma_\mu \tau^I q_r)(\bar{q}_s \gamma^\mu \tau^I q_t)$
$Q^{(1)}_{lq}$	$(\bar{l}_p \gamma_\mu l_r)(\bar{q}_s \gamma^\mu q_t)$
$Q^{(3)}_{lq}$	$(\bar{l}_p \gamma_\mu \tau^I l_r)(\bar{q}_s \gamma^\mu \tau^I q_t)$

$8 : (\bar{R}R)(\bar{R}R)$

Q_{ee}	$(\bar{e}_p \gamma_\mu e_r)(\bar{e}_s \gamma^\mu e_t)$
Q_{uu}	$(\bar{u}_p \gamma_\mu u_r)(\bar{u}_s \gamma^\mu u_t)$
Q_{dd}	$(\bar{d}_p \gamma_\mu d_r)(\bar{d}_s \gamma^\mu d_t)$
Q_{eu}	$(\bar{e}_p \gamma_\mu e_r)(\bar{u}_s \gamma^\mu u_t)$
Q_{ed}	$(\bar{e}_p \gamma_\mu e_r)(\bar{d}_s \gamma^\mu d_t)$
$Q^{(1)}_{ud}$	$(\bar{u}_p \gamma_\mu u_r)(\bar{d}_s \gamma^\mu d_t)$
$Q^{(8)}_{ud}$	$(\bar{u}_p \gamma_\mu T^A u_r)(\bar{d}_s \gamma^\mu T^A d_t)$

$8 : (\bar{L}L)(\bar{R}R)$

Q_{le}	$(\bar{l}_p \gamma_\mu l_r)(\bar{e}_s \gamma^\mu e_t)$
Q_{lu}	$(\bar{l}_p \gamma_\mu l_r)(\bar{u}_s \gamma^\mu u_t)$
Q_{ld}	$(\bar{l}_p \gamma_\mu l_r)(\bar{d}_s \gamma^\mu d_t)$
Q_{qe}	$(\bar{q}_p \gamma_\mu q_r)(\bar{e}_s \gamma^\mu e_t)$
$Q^{(1)}_{qu}$	$(\bar{q}_p \gamma_\mu q_r)(\bar{u}_s \gamma^\mu u_t)$
$Q^{(8)}_{qu}$	$(\bar{q}_p \gamma_\mu T^A q_r)(\bar{u}_s \gamma^\mu T^A u_t)$
$Q^{(1)}_{qd}$	$(\bar{q}_p \gamma_\mu q_r)(\bar{d}_s \gamma^\mu d_t)$
$Q^{(8)}_{qd}$	$(\bar{q}_p \gamma_\mu T^A q_r)(\bar{d}_s \gamma^\mu T^A d_t)$

$8 : (\bar{L}R)(\bar{R}L) + \text{h.c.}$

Q_{ledq}	$(\bar{l}^j_p e_r)(\bar{d}_s q_{tj})$

$8 : (\bar{L}R)(\bar{L}R) + \text{h.c.}$

$Q^{(1)}_{quqd}$	$(\bar{q}^j_p u_r)\epsilon_{jk}(\bar{q}^k_s d_t)$
$Q^{(8)}_{quqd}$	$(\bar{q}^j_p T^A u_r)\epsilon_{jk}(\bar{q}^k_s T^A d_t)$
$Q^{(1)}_{lequ}$	$(\bar{l}^j_p e_r)\epsilon_{jk}(\bar{q}^k_s u_t)$
$Q^{(3)}_{lequ}$	$(\bar{l}^j_p \sigma_{\mu\nu} e_r)\epsilon_{jk}(\bar{q}^k_s \sigma^{\mu\nu} u_t)$

where

$$c_{H,\text{kin}} \equiv \left(C_{H\Box} - \frac{1}{4}C_{HD}\right) v^2, \qquad v_T \equiv \left(1 + \frac{3C_H v^2}{8\lambda}\right) v. \tag{II.2.72}$$

The coefficient of h in Eq. (II.2.71) is no longer unity, in order for the Higgs boson kinetic term to be properly normalized when the dimension-six operators are included. In what follows we can exchange v_T for v when this parameter multiplies a operator in $\mathcal{L}_6$ as the difference is NLO in the lagrangian expansion.The kinetic terms

$$\mathcal{L}^{(6)} = (D_\mu H^\dagger)(D^\mu H) + C_{H\Box}\left(H^\dagger H\right)\Box\left(H^\dagger H\right) + C_{HD}\left(H^\dagger D^\mu H\right)^*\left(H^\dagger D_\mu H\right), \tag{II.2.73}$$

and the potential in Eq. (II.2.69) yield

$$\begin{aligned}\mathcal{L}^{(6)} = {} & \frac{1}{2}(\partial_\mu h)^2 - c_{H,\text{kin}}\left[\frac{h^2}{v^2} + 2\frac{h}{v}\right](\partial_\mu h)^2 - \frac{m_h^2}{2}h^2 - \lambda v_T\left(1 - \frac{5C_H v^2}{2\lambda} + 3c_{H,\text{kin}}\right)h^3 \\ & - \frac{1}{4}\lambda\left(1 - \frac{15C_H v^2}{2\lambda} + 4c_{H,\text{kin}}\right)h^4 + \frac{3}{4}C_H v h^5 + \frac{1}{8}C_H h^6,\end{aligned} \tag{II.2.74}$$

for the h self-interactions. The Higgs boson mass is

$$m_h^2 = 2\lambda v_T^2\left(1 - \frac{3C_H v^2}{2\lambda} + 2c_{H,\text{kin}}\right). \tag{II.2.75}$$

II.2.3.b.iv.3 Yukawa couplings

The Lagrangian terms in the unbroken theory

$$\begin{aligned}\mathcal{L} = & -\left[H^{\dagger j}\overline{d}_r\,[Y_d]_{rs}\,q_{js} + \widetilde{H}^{\dagger j}\overline{u}_r\,[Y_u]_{rs}\,q_{js} + H^{\dagger j}\overline{e}_r\,[Y_e]_{rs}\,l_{js} + \text{h.c.}\right] \\ & + \left[C^*_{\substack{dH\\sr}}\left(H^\dagger H\right)H^{\dagger j}\overline{d}_r q_{js} + C^*_{\substack{uH\\sr}}\left(H^\dagger H\right)\tilde{H}^{\dagger j}\overline{u}_r q_{js} + C^*_{\substack{eH\\sr}}\left(H^\dagger H\right)H^{\dagger j}\overline{e}_r l_{js} + \text{h.c.}\right],\end{aligned} \tag{II.2.76}$$

yield the fermion mass matrices

$$[M_\psi]_{rs} = \frac{v_T}{\sqrt{2}}\left([Y_\psi]_{rs} - \frac{1}{2}v^2 C^*_{\substack{\psi H\\sr}}\right), \qquad \psi = u, d, e \tag{II.2.77}$$

in the broken theory. The coupling matrices of the h boson to the fermions $\mathcal{L} = -h\,\overline{u}\,\mathcal{Y}\,q + h.c + \ldots$ are

$$\begin{aligned}[\mathcal{Y}_\psi]_{rs} &= \frac{1}{\sqrt{2}}[Y_\psi]_{rs}[1 + c_{H,\text{kin}}] - \frac{3}{2\sqrt{2}}v^2 C^*_{\substack{\psi H\\sr}} \\ &= \frac{1}{v_T}[M_\psi]_{rs}[1 + c_{H,\text{kin}}] - \frac{v^2}{\sqrt{2}}C^*_{\substack{\psi H,\\sr}} \qquad \psi = u, d, e.\end{aligned} \tag{II.2.78}$$

The fermion fields can be rotating to diagonal mass eigenstates with 3×3 unitary matrices $\mathcal{U}$ as

$$\psi_L = \mathcal{U}(\psi, L)\,\psi'_L, \qquad \psi_R = \mathcal{U}(\psi, R)\,\psi'_R, \tag{II.2.79}$$

where the measured masses $\hat{m}^i_\psi$ are

$$\mathcal{U}^\dagger(\psi, R)\,[M_\psi]\,\mathcal{U}(\psi, L) = \delta_{ij}\,\hat{m}^i_\psi, \qquad \begin{array}{ll} i = \{u, c, t\}, & \psi = u, \\ i = \{d, s, b\}, & \psi = d, \\ i = \{e, u, \tau\}, & \psi = e. \end{array} \tag{II.2.80}$$

For the complex Yukawa coupling the higgs to the mass eigenstate fermion fields

$$\mathcal{L} = -h\ [\mathcal{Y}_\psi]_{rs}\ \bar{\psi}_r\, P_L\, \psi_s + h.c. \tag{II.2.81}$$

where $P_L = (1-\gamma_5)/2$ and

$$[\mathcal{Y}_\psi]_{rs} = \delta_{rs}\,\frac{\hat{m}^r_\psi}{v_T}\,[1 + c_{H,\text{kin}}] - \frac{v^2}{\sqrt{2}}\left[\mathcal{U}^\dagger(\psi,R)\,C^*_{\psi H}\,\mathcal{U}(\psi,L)\right]_{rs}. \tag{II.2.82}$$

The Yukawa matrices are off diagonal in general and not simply proportional to the fermion mass matrices as in the SM, as indicated by the second term. The CKM and PMNS matrices control flavour violating interactions in the SM and are defined as

$$V_{CKM} = \mathcal{U}(u,L)^\dagger\,\mathcal{U}(d,L), \qquad U_{PMNS} = \mathcal{U}(e,L)^\dagger\,\mathcal{U}(\nu,L), \tag{II.2.83}$$

when the $\mathcal{U}$ matrices only rotate between the weak and mass eigenstates in the SM. The definition of these matrices in the SMEFT is a convention choice. Here we choose to define these matrices so that the masses are taken to diagonal form including the $\mathcal{L}_6$ interactions.

II.2.3.b.iv.4 Gauge boson masses and couplings

The relevant CP even $\mathcal{L}_6$ terms are

$$\begin{aligned}\mathcal{L}^{(6)} = {} & C_{HG}H^\dagger H G^A_{\mu\nu}G^{A\mu\nu} + C_{HW}H^\dagger H W^I_{\mu\nu}W^{I\mu\nu} + C_{HB}H^\dagger H B_{\mu\nu}B^{\mu\nu} \\ & + C_{HWB}H^\dagger\tau^I H W^I_{\mu\nu}B^{\mu\nu} + C_G f^{ABC}G^{A\nu}_\mu G^{B\rho}_\nu G^{C\mu}_\rho + C_W\epsilon^{IJK}W^{I\nu}_\mu W^{J\rho}_\nu W^{K\mu}_\rho\,.\end{aligned} \tag{II.2.84}$$

The gauge fields need to be redefined, so that the kinetic terms are properly normalized and diagonal. The first step is to redefine the gauge fields

$$G^A_\mu = \mathcal{G}^A_\mu\left(1 + C_{HG}v_T^2\right), \qquad W^I_\mu = \mathcal{W}^I_\mu\left(1 + C_{HW}v_T^2\right), \qquad B_\mu = \mathcal{B}_\mu\left(1 + C_{HB}v_T^2\right). \tag{II.2.85}$$

The modified coupling constants are

$$\overline{g}_3 = g_3\left(1 + C_{HG}\,v_T^2\right), \qquad \overline{g}_2 = g_2\left(1 + C_{HW}\,v_T^2\right), \qquad \overline{g}_1 = g_1\left(1 + C_{HB}\,v_T^2\right), \tag{II.2.86}$$

so that the products $g_3G^A_\mu = \overline{g}_3\mathcal{G}^A_\mu$, etc. are unchanged. The mass eigenstate basis is given by [695]

$$\begin{bmatrix}\mathcal{W}^3_\mu \\ \mathcal{B}_\mu\end{bmatrix} = \begin{bmatrix}1 & -\frac{1}{2}\,v_T^2\,C_{HWB} \\ -\frac{1}{2}\,v_T^2\,C_{HWB} & 1\end{bmatrix}\begin{bmatrix}\cos\overline{\theta} & \sin\overline{\theta} \\ -\sin\overline{\theta} & \cos\overline{\theta}\end{bmatrix}\begin{bmatrix}\mathcal{Z}_\mu \\ \mathcal{A}_\mu\end{bmatrix}, \tag{II.2.87}$$

where the rotation angle is

$$\tan\overline{\theta} = \frac{\overline{g}_1}{\overline{g}_2} + \frac{v_T^2}{2}\,C_{HWB}\left[1 - \frac{\overline{g}_1{}^2}{\overline{g}_2{}^2}\right]. \tag{II.2.88}$$

The W and Z masses are

$$\begin{aligned}\bar{M}_W^2 &= \frac{\overline{g}_2{}^2 v_T^2}{4}, \\ \bar{M}_Z^2 &= \frac{v_T^2}{4}(\overline{g}_1{}^2 + \overline{g}_2{}^2) + \frac{1}{8}v_T^4 C_{HD}(\overline{g}_1{}^2 + \overline{g}_2{}^2) + \frac{1}{2}v_T^4\overline{g}_1\overline{g}_2 C_{HWB}.\end{aligned} \tag{II.2.89}$$

The covariant derivative is

$$D_\mu = \partial_\mu + i\,\frac{\overline{g}_2}{\sqrt{2}}\left[\mathcal{W}^+_\mu T^+ + \mathcal{W}^-_\mu T^-\right] + i\overline{g}_Z\left[T_3 - \overline{s}^2 Q\right]\mathcal{Z}_\mu + i\,\overline{e}\,Q\,\mathcal{A}_\mu, \tag{II.2.90}$$

where $Q = T_3 + Y$, and the effective couplings are given by

$$\begin{aligned}
\overline{e} &= \frac{\overline{g}_1\overline{g}_2}{\sqrt{\overline{g}_2{}^2+\overline{g}_1{}^2}}\left[1-\frac{\overline{g}_1\overline{g}_2}{\overline{g}_2{}^2+\overline{g}_1{}^2}v_T^2 C_{HWB}\right] = \overline{g}_2\,\sin\overline{\theta} - \frac{1}{2}\,\cos\overline{\theta}\,\overline{g}_2\,v_T^2\,C_{HWB},\\
\overline{g}_Z &= \sqrt{\overline{g}_2{}^2+\overline{g}_1{}^2} + \frac{\overline{g}_1\overline{g}_2}{\sqrt{\overline{g}_2{}^2+\overline{g}_1{}^2}}v_T^2 C_{HWB} = \frac{\overline{e}}{\sin\overline{\theta}\cos\overline{\theta}}\left[1+\frac{\overline{g}_1{}^2+\overline{g}_2{}^2}{2\overline{g}_1\overline{g}_2}v_T^2 C_{HWB}\right],\\
\overline{s}^2 &= \sin^2\overline{\theta} = \frac{\overline{g}_1{}^2}{\overline{g}_2{}^2+\overline{g}_1{}^2} + \frac{\overline{g}_1\overline{g}_2(\overline{g}_2{}^2-\overline{g}_1{}^2)}{(\overline{g}_1{}^2+\overline{g}_2{}^2)^2}v_T^2 C_{HWB}.
\end{aligned} \tag{II.2.91}$$

The relevant CP odd $\mathcal{L}_6^{\not{CP}}$ terms are

$$\begin{aligned}
\mathcal{L}_6^{\not{CP}} &= C_{H\tilde{G}}H^\dagger H\tilde{G}^A_{\mu\nu}G^{A\mu\nu} + C_{H\tilde{W}}H^\dagger H\tilde{W}^I_{\mu\nu}W^{I\mu\nu} + C_{H\tilde{B}}H^\dagger H\tilde{B}_{\mu\nu}B^{\mu\nu}\\
&+ C_{H\tilde{W}B}H^\dagger\tau^I H\tilde{W}^I_{\mu\nu}B^{\mu\nu} + C_{\tilde{G}}f^{ABC}\tilde{G}^{A\nu}_\mu G^{B\rho}_\nu G^{C\mu}_\rho + C_{\tilde{W}}\epsilon^{IJK}\tilde{W}^{I\nu}_\mu W^{J\rho}_\nu W^{K\mu}_\rho\,.
\end{aligned} \tag{II.2.92}$$

The modified couplings and gauge fields introduced in Eqns.II.2.85, II.2.86 do not cancel the new contribution from these operators suppressed by v_T^2/Λ^2 to the CP violating $\tilde{\theta}$ parameters. These extra contributions strongly indicate that without fine tuning the Wilson coefficients $C_{H\tilde{G}}, C_{H\tilde{W}}, C_{H\tilde{B}}, C_{H\tilde{W}B}$ are suppressed by a large CP violating scale and can be neglected, similar to the treatment of $\mathcal{L}_5$.

II.2.3.b.iv.5 $h \to WW$ and $h \to ZZ$

The relevant CP-even Lagrangian terms are

$$\begin{aligned}
\mathcal{L} &= (D_\mu H)^\dagger(D^\mu H) - \frac{1}{4}\left(W^I_{\mu\nu}W^{I\mu\nu} + B_{\mu\nu}B^{\mu\nu}\right),\\
&+ C_{HW}\,Q_{HW} + C_{HB}\,Q_{HB} + C_{HWB}Q_{HWB} + C_{HD}\,Q_{HD},
\end{aligned} \tag{II.2.93}$$

which lead to the interactions

$$\mathcal{L} = \frac{1}{2}\overline{g}_2{}^2 v_T h\,W^+_\mu\,W^-_\mu\;[1+c_{H,\text{kin}}] + C_{HW}v_T h\,W^+_{\mu\nu}\,W^{-}_{\mu\nu}. \tag{II.2.94}$$

for the W, and

$$\begin{aligned}
\mathcal{L} &= \frac{1}{4}(\overline{g}_2{}^2+\overline{g}_1{}^2)v_T h(\mathcal{Z}_\mu)^2\left[1+c_{H,\text{kin}}+v_T^2 C_{HD}\right] + \frac{1}{2}\overline{g}_1\overline{g}_2 v_T^3 h(\mathcal{Z}_\mu)^2 C_{HWB}\\
&+ v_T h(\mathcal{Z}_{\mu\nu})^2\left(\frac{\overline{g}_2{}^2 C_{HW}+\overline{g}_1{}^2 C_{HB}+\overline{g}_1\overline{g}_2 C_{HWB}}{\overline{g}_2{}^2+\overline{g}_1{}^2}\right)
\end{aligned} \tag{II.2.95}$$

for the Z. Normalizing the SM $\tilde{\theta}$ operators by two powers of the appropriate gauge coupling so that Eqns.II.2.85, II.2.86 do not introduce extra terms, the $\not{CP}$ contributions are

$$\mathcal{L}_6^{\not{CP}} = C_{H\tilde{W}}v_T h\,\tilde{W}^+_{\mu\nu}\,W^-_{\mu\nu} + v_T h(\tilde{\mathcal{Z}}_{\mu\nu}\,\mathcal{Z}^{\mu\nu})\left(\frac{\overline{g}_2{}^2 C_{H\tilde{W}}+\overline{g}_1{}^2 C_{H\tilde{B}}+\overline{g}_1\overline{g}_2 C_{H\tilde{W}B}}{\overline{g}_2{}^2+\overline{g}_1{}^2}\right). \tag{II.2.96}$$

II.2.3.b.iv.6 $h \to \gamma\,\gamma$, $h \to \gamma\,Z$ and $h \to gg$

The CP even and odd couplings of $h \to \gamma\,\gamma$ and $h \to \gamma\,Z$ are given by [696]

$$\mathcal{L} = h\,v_T\,\bar{e}^2\left[C_{\gamma\gamma}\,\mathcal{A}^{\mu\nu}\,\mathcal{A}_{\mu\nu} + \tilde{C}_{\gamma\gamma}\,\tilde{\mathcal{A}}^{\mu\nu}\,\mathcal{A}_{\mu\nu} + C_{\gamma Z}\,\mathcal{A}^{\mu\nu}\,\mathcal{Z}_{\mu\nu} + \tilde{C}_{\gamma Z}\,\tilde{\mathcal{A}}^{\mu\nu}\,\mathcal{Z}_{\mu\nu}\right]. \tag{II.2.97}$$

Here

$$C_{\gamma\gamma} = \frac{C_{HW}}{\bar{g}_2^2} + \frac{C_{HB}}{\bar{g}_1^2} - \frac{C_{HWB}}{\bar{g}_1\,\bar{g}_2}, \tag{II.2.98}$$

$$\tilde{C}_{\gamma\gamma} = \frac{C_{H\tilde{W}}}{\bar{g}_2^2} + \frac{C_{H\tilde{B}}}{\bar{g}_1^2} - \frac{C_{H\tilde{W}B}}{\bar{g}_1\,\bar{g}_2}, \tag{II.2.99}$$

$$C_{\gamma Z} = \frac{1}{\bar{g}_1\,\bar{g}_2}\left(C_{HW} - C_{HB}\right) - \left(\frac{1}{2\,\bar{g}_1^2} - \frac{1}{2\,\bar{g}_2^2}\right) C_{HWB}, \tag{II.2.100}$$

$$\tilde{C}_{\gamma Z} = \frac{1}{\bar{g}_1\,\bar{g}_2}\left(C_{H\tilde{W}} - C_{H\tilde{B}}\right) - \left(\frac{1}{2\,\bar{g}_1^2} - \frac{1}{2\,\bar{g}_2^2}\right) C_{H\tilde{W}B}. \tag{II.2.101}$$

The CP even and odd couplings of $h \to gg$ are trivially

$$\mathcal{L} = h\,v_T\,\left[C_{HG}\,\mathcal{G}^{\mu\,\nu}\,\mathcal{G}_{\mu\,\nu} + C_{H\tilde{G}}\,\tilde{\mathcal{G}}^{\mu\,\nu}\,\mathcal{G}_{\mu\,\nu}\right]. \tag{II.2.102}$$

II.2.3.b.iv.7 Dipoles and Higgs dipole interactions

In the broken phase the dipole interactions with neutral gauge bosons are

$$\begin{aligned}\mathcal{L} = &\frac{\bar{e}\,(v+h)}{\sqrt{2}}\underset{rs}{\mathcal{C}_{\psi\gamma}}\,\overline{\psi}_r\sigma^{\mu\nu}P_R\psi_s\,\mathcal{A}_{\mu\nu} + \frac{\bar{e}\,(v+h)}{\sqrt{2}}\underset{rs}{\mathcal{C}_{\psi\mathcal{Z}}}\,\overline{\psi}_r\sigma^{\mu\nu}P_R\psi_s\,\mathcal{Z}_{\mu\nu},\\ &+\frac{(v+h)}{\sqrt{2}}\underset{rs}{C_{dG}}\,\overline{d}_r\sigma^{\mu\nu}T_A\,P_R d_s\,\mathcal{G}^A_{\mu\nu} + \frac{(v+h)}{\sqrt{2}}\underset{rs}{C_{uG}}\,\overline{u}_r\sigma^{\mu\nu}T_A P_R u_s\,\mathcal{G}^A_{\mu\nu} + h.c.\end{aligned} \tag{II.2.103}$$

where r and s are flavour indices and $\psi = \{e, u, d\}$ so that

$$\begin{aligned}
\underset{rs}{\mathcal{C}_{e\gamma}} &= \left[\mathcal{U}(e,L)^\dagger\left(\frac{C_{eB}}{g_1} - \frac{C_{eW}}{g_2}\right)\mathcal{U}(e,R)\right]_{rs} & \underset{rs}{\mathcal{C}_{eZ}} &= -\left[\mathcal{U}(e,L)^\dagger\left(\frac{C_{eB}}{g_2} + \frac{C_{eW}}{g_1}\right)\mathcal{U}(e,R)\right]_{rs}\\
\underset{rs}{\mathcal{C}_{d\gamma}} &= \left[\mathcal{U}(d,L)^\dagger\left(\frac{C_{dB}}{g_1} - \frac{C_{dW}}{g_2}\right)\mathcal{U}(d,R)\right]_{rs} & \underset{rs}{\mathcal{C}_{dZ}} &= -\left[\mathcal{U}(d,L)^\dagger\left(\frac{C_{dB}}{g_2} + \frac{C_{dW}}{g_1}\right)\mathcal{U}(d,R)\right]_{rs}\\
\underset{rs}{\mathcal{C}_{u\gamma}} &= \left[\mathcal{U}(u,L)^\dagger\left(\frac{C_{uB}}{g_1} + \frac{C_{uW}}{g_2}\right)\mathcal{U}(u,R)\right]_{rs} & \underset{rs}{\mathcal{C}_{uZ}} &= -\left[\mathcal{U}(u,L)^\dagger\left(\frac{C_{uB}}{g_2} - \frac{C_{uW}}{g_1}\right)\mathcal{U}(u,R)\right]_{rs}.
\end{aligned} \tag{II.2.104}$$

C_{uW} has the opposite sign for u-type quarks in Eq. (II.2.104) because of the opposite sign for T_{3L}. Note that $\sigma_{\mu\,\nu} = i\,\left[\gamma_\mu, \gamma_\nu\right]/2$. The dipole interactions with charged gauge bosons are

$$\mathcal{L} = (v+h)\,\left[\overline{\nu}_r\,\sigma^{\mu\nu}\,P_R\,e_s\,\mathcal{W}^+_{\mu\nu}\underset{rs}{\mathcal{C}_{e\,W}} + \overline{u}_r\,\sigma^{\mu\nu}\,P_R\,d_s\,\mathcal{W}^+_{\mu\nu}\,\underset{rs}{\mathcal{C}_{d\,W}} + \overline{d}_r\,\sigma^{\mu\nu}\,P_R\,u_s\,\mathcal{W}^-_{\mu\nu}\,\underset{rs}{\mathcal{C}_{u\,W}}\right] + h.c. \tag{II.2.105}$$

where

$$\begin{aligned}
\underset{rs}{\mathcal{C}_{e\,W}} &= \left[\mathcal{U}(\nu,L)^\dagger\,C_{e\,W}\,\mathcal{U}(e,R)\right]_{rs} & \underset{rs}{\mathcal{C}_{d\,W}} &= \left[\mathcal{U}(u,L)^\dagger\,C_{d\,W}\,\mathcal{U}(d,R)\right]_{rs}\\
\underset{rs}{\mathcal{C}_{u\,W}} &= \left[\mathcal{U}(d,L)^\dagger\,\mathcal{C}_{u\,W}\,\mathcal{U}(u,R)\right]_{rs}.
\end{aligned} \tag{II.2.106}$$

II.2.3.b.iv.8 $(h+v)^2\,V\bar{\psi}\,\psi$ interactions

In the broken phase the interactions of the Higgs with fermions and an associated gauge boson are given by

$$\begin{aligned}\mathcal{L} = &\frac{\sqrt{\bar{g}_1^2+\bar{g}_2^2}}{2}\,(h+v_T)^2\,\mathcal{Z}_\mu\,\bar{\nu}_r\,\gamma^\mu P_L\nu_s\left[\mathcal{U}(\nu,L)^\dagger\,\left(C^{(1)}_{H\ell} - C^{(3)}_{H\ell}\right)\mathcal{U}(\nu,L)\right]_{rs},\\ &+\frac{\sqrt{\bar{g}_1^2+\bar{g}_2^2}}{2}\,(h+v_T)^2\,\mathcal{Z}_\mu\,\bar{e}_r\,\gamma^\mu P_L e_s\left[\mathcal{U}(e,L)^\dagger\,\left(C^{(1)}_{H\ell} + C^{(3)}_{H\ell}\right)\mathcal{U}(e,L)\right]_{rs},\end{aligned}$$

$$
\begin{aligned}
&+\frac{\sqrt{\bar{g}_1^2+\bar{g}_2^2}}{2}(h+v_T)^2\,\mathcal{Z}_\mu\,\bar{u}_r\,\gamma^\mu P_L u_s\left[\mathcal{U}(u,L)^\dagger\left(C_{Hq}^{(1)}-C_{Hq}^{(3)}\right)\mathcal{U}(u,L)\right]_{rs},\\
&+\frac{\sqrt{\bar{g}_1^2+\bar{g}_2^2}}{2}(h+v_T)^2\,\mathcal{Z}_\mu\,\bar{d}_r\,\gamma^\mu P_L d_s\left[\mathcal{U}(d,L)^\dagger\left(C_{Hq}^{(1)}+C_{Hq}^{(3)}\right)\mathcal{U}(d,L)\right]_{rs},\\
&+\frac{\sqrt{\bar{g}_1^2+\bar{g}_2^2}}{2}(h+v_T)^2\,\mathcal{Z}_\mu\,\bar{\psi}_r\,\gamma^\mu P_R\,\psi_s\,\left[\mathcal{U}(\psi,R)^\dagger\,C_{H\psi}\,\mathcal{U}(\psi,R)\right]_{rs},\\
&-\frac{\bar{g}_2}{\sqrt{2}}(h+v_T)^2\,\mathcal{W}_\mu^+\,\bar{\nu}_r\,\gamma^\mu P_L\,e_s\,\left[\mathcal{U}(\nu,L)^\dagger\,C_{H\ell}^{(3)}\,\mathcal{U}(e,L)\right]_{rs}\\
&-\frac{\bar{g}_2}{\sqrt{2}}(h+v_T)^2\,\mathcal{W}_\mu^+\,\bar{u}_r\,\gamma^\mu P_L\,d_s\,\left[\mathcal{U}(u,L)^\dagger\,C_{Hq}^{(3)}\mathcal{U}(d,L)\right]_{rs},\\
&+\frac{i\,\bar{g}_2}{2}(h+v_T)^2\,\mathcal{W}_\mu^+\,\bar{u}_r\,\gamma^\mu P_R\,d_s\,\left[\mathcal{U}(u,R)^\dagger\,C_{Hud}\mathcal{U}(d,R)\right]_{rs}+h.c
\end{aligned}
\tag{II.2.107}
$$

where $\psi=\{u,d,e\}$.

II.2.3.b.iv.9 TGC parameters

The off-shell Triple gauge coupling parameters are given by

$$
\begin{aligned}
\left(-\mathcal{L}_{TGC}\right)/\bar{g}_{VWW}=&\,i\bar{g}_1^V\left(\mathcal{W}^+_{\mu\nu}\mathcal{W}^{-\mu}-\mathcal{W}^-_{\mu\nu}\mathcal{W}^{+\mu}\right)\mathcal{V}^\nu+i\bar{\kappa}_V\mathcal{W}^+_\mu\mathcal{W}^-_\nu\mathcal{V}^{\mu\nu},\\
&+i\frac{\bar{\lambda}_V}{\bar{M}_W^2}\mathcal{V}^{\mu\nu}\mathcal{W}^{+\rho}_\nu\mathcal{W}^-_{\rho\mu}
\end{aligned}
\tag{II.2.108}
$$

where $V=\{\mathcal{Z},\mathcal{A}\}$. In the SM $g_{\mathcal{A}\mathcal{W}\mathcal{W}}=e$ and $g_{\mathcal{Z}\mathcal{W}\mathcal{W}}=g_2\,c_\theta$. In the SMEFT the canonically normalized couplings are modified to $\bar{g}_{\mathcal{A}\mathcal{W}\mathcal{W}}=\bar{e}$ and $\bar{g}_{\mathcal{Z}\mathcal{W}\mathcal{W}}=\bar{g}_2\,\bar{c}_\theta$ and the shifts compared to these normalized couplings are

$$
\delta\bar{g}_1^{\mathcal{A}}=-\delta\bar{\kappa}_{\mathcal{A}}=-\frac{v_T^2}{2}\frac{c_{\bar{\theta}}}{s_{\bar{\theta}}}C_{HWB},\qquad\qquad \delta\bar{g}_1^{\mathcal{Z}}=-\delta\kappa_{\mathcal{Z}}=\frac{v_T^2}{2}\frac{s_{\bar{\theta}}}{c_{\bar{\theta}}}C_{HWB},
\tag{II.2.109}
$$

and

$$
\delta\bar{\lambda}_{\mathcal{A}}=6\,s_{\bar{\theta}}\,C_W\,\frac{\bar{M}_W^2}{\bar{g}_{\mathcal{A}\mathcal{W}\mathcal{W}}},\qquad\qquad \delta\bar{\lambda}_{\mathcal{Z}}=6\,c_{\bar{\theta}}\,C_W\frac{\bar{M}_W^2}{\bar{g}_{\mathcal{Z}\mathcal{W}\mathcal{W}}}.
\tag{II.2.110}
$$

An important check of gauge invariance in TGC shifts is that the relationships

$$
\bar{\kappa}_{\mathcal{Z}}=\bar{g}_1^{\mathcal{Z}}-(\bar{\kappa}_{\mathcal{A}}-1)\,t^2_{\bar{\theta}},\qquad \bar{\lambda}_{\mathcal{Z}}=\bar{\lambda}_{\mathcal{A}},
\tag{II.2.111}
$$

are respected when the shifts in the Lagrangian parameters are expressed in terms of the SM parameters. These shifts respect these relationships.

II.2.3.b.v Summary of mass eigenstate interactions and symmetries

$\mathcal{L}_6$ has 2499 parameters in general [631]. Clearly restricting to a Minimal Flavour Violating (MFV) scenario [697–699], which imposes a $\mathrm{U}(3)^5$ flavour symmetry broken only by the SM Yukawas is desirable. This reduces the number of parameters to 76. Assuming that CP violating effects can also be neglected, the number of parameters is restricted to 53 for $\mathcal{L}_6$ [631]. This is a reasonable symmetry based limit to assume.[II.34] In this symmetric case $[\mathcal{Y}_\psi]_{rs}\in\mathbb{R}$ and

$$
[\mathcal{Y}_\psi]_{rs}=\delta_{rs}\,\frac{\hat{m}^r_\psi}{v_T}\,\left[1+c_{H,\text{kin}}-v^2\,\mathcal{C}_{\psi H}\right],\quad \text{where}\quad \mathcal{C}_{\psi H}[Y_\psi]_{rs}=\mathrm{Re}\left[C^*_{\substack{\psi H\\ rs}}\right].
\tag{II.2.112}
$$

[II.34] Custodial symmetry is broken by gauge interactions in the SM and the mass splitting of fermion doublet fields. The number of parameters removed due to this strongly broken symmetry being assumed are negligible compared to the effects of the CP even and MFV assumptions.

Further all Wilson coefficients for operators with dual fields (denoted with tilde subscripts or superscripts) are neglected. The dipole and Higgs dipole interactions are all flavour diagonal proportional to the corresponding fermion mass and real. The $(h+v)^2\,\mathcal{Z}\bar{\psi}\,\psi$ interactions are flavour diagonal while the $(h+v)^2\,\mathcal{W}^+\bar{\psi}\,\psi$ interactions are proportional to V_{CKM} or $\mathcal{U}^\dagger_{PMNS}$. Finally, flavour violating interactions in the Class 8 operators follow an MFV pattern [697–699].

These symmetries, if assumed in $\mathcal{L}_6$, are broken at least by the SM interactions, which violate these symmetries. NLO calculations are required to define the perturbative breaking of these symmetric limits.

II.2.3.b.vi Input parameters and defining conditions

Differently than in Section II.2.1, we have not imposed the following conditions on the mass eigenstate construction:

- Tree-level relations between the electroweak parameters and a choice of input parameter set (IPS) are the same as the SM ones.
- Two-derivative self-interactions of the Higgs boson are absent.
- For each fermion pair, the coefficients of the $hV\bar{\psi}\,\psi$, $h^2V\bar{\psi}\,\psi$ interaction terms are equal to the vertex correction of $V\bar{\psi}\,\psi$.

These conditions are not required to interpret the data in the SMEFT and, in our view, introduce technical complications in a LO approach that could make NLO calculations harder to develop.

Considering condition one above, we emphasize that an operator basis is IPS independent. If one were to modify the construction of $\mathcal{L}_{SMEFT}$ to make some relationships to a particular IPS the same in the SM and the SMEFT with algebraic manipulations that were only defined classically (i.e. at LO), this would make such a construction an example of a "phenomenological effective Lagrangian" whose advantage is limited to LO. Claims of intuitive connections to LHC Higgs and EWPD observables in such approaches should be considered with great care. We believe it is advantageous not to tie a phenomenological Lagrangian construction to any specific IPS, for a series of reasons:

- Monte Carlo programs do not all use the same IPS. Further, the IPS $\{\alpha_{ew}, G_F, M_Z\}$ is not in common use when automated calculations for the SM beyond LO are generated to define the SM event rate in a measurement. Before any SMEFT implementation is used it must first be checked what IPS set or sets are used to define the SM event rate in the measurement of interest. If a construction tied to the specific IPS $\{\alpha_{ew}, G_F, M_Z\}$ were to be used it must be confirmed that all simulation tools and SM results only use this specific IPS or inconsistent results will be reported.
- When the IPS $\{\alpha_{ew}, G_F, M_Z\}$ is used in the analysis of "high" energy data it is afflicted with hadronic uncertainties entering already at the one loop level and arising because it must be "run up" from low energy, crossing the hadronic resonance region. The Fermi coupling constant, obtained from the muon lifetime, does not suffer from this disadvantage (even in the full SM one loop hadronic effects are mass suppressed) [700].

The parameters v_T, $\bar{g}_1$, $\bar{g}_2$, $\bar{e}$, $s_{\bar{\theta}}$, $c_{\bar{\theta}}$ etc. in the Lagrangian do have to be assigned numerical values consistent with some IPS. This is sometimes known as a "finite renormalization". This is distinct from rotating to the mass eigenstate fields in the canonically normalized SMEFT and does not require the conditions above be imposed in a gauge dependent manner. We now illustrate how a straightforward LO implementation is related to the IPS $\{\alpha_{ew}, G_F, M_Z\}$ in the $\mathrm{U}(3)^5$ limit for tree level gauge boson fermion interactions.

II.2.3.b.vi.1 Input parameters measurements

Define the local effective interaction for muon decay as

$$\mathcal{L}_{G_F} = -\frac{4G_F}{\sqrt{2}}\,(\bar{\nu}_\mu\,\gamma^\mu P_L \mu)\,(\bar{e}\,\gamma_\mu P_L \nu_e)\,. \tag{II.2.113}$$

G_F is defined as the following parameter measured in μ decay, $\mu^- \to e^- + \bar{\nu}_e + \nu_\mu$. In the SMEFT ($e$ and μ are generation indices 1 and 2, and are not summed over)

$$-\frac{4G_F}{\sqrt{2}} = -\frac{2}{v_T^2} + \left(C_{\substack{ll \\ \mu ee \mu}} + C_{\substack{ll \\ e\mu\mu e}} \right) - 2 \left(C^{(3)}_{\substack{Hl \\ ee}} + C^{(3)}_{\substack{Hl \\ \mu\mu}} \right). \tag{II.2.114}$$

The parameter α_{ew} is measured in the Thompson ($p^2 \to 0$) limit and discussed in Section II.2.3.b.vii.5, and M_Z is defined in the resonance pole scan of LEP measurements.

II.2.3.b.vi.2 Gauge boson couplings for the α IPS

Our notational conventions are that shifts due to the SMEFT are denoted as $\delta X = (X)_{SMEFT} - X_{SM}$ for a parameter X.[II.35] Measured input observables or parameters directly defined by combinations of input observables are denoted with hat superscripts. The shifts in the commonly appearing Lagrangian parameters M_Z, M_W, G_F, s^2_θ are

$$\delta M_Z^2 \equiv \frac{1}{2\sqrt{2}} \frac{\hat{m}_Z^2}{\hat{G}_F} C_{HD} + \frac{2^{1/4}\sqrt{\pi}\sqrt{\hat{\alpha}}\,\hat{m}_Z}{\hat{G}_F^{3/2}} C_{HWB}, \tag{II.2.115}$$

$$\delta M_W^2 = -\hat{m}_W^2 \left(\frac{\delta s^2_{\hat{\theta}}}{s^2_{\hat{\theta}}} + \frac{c_{\hat{\theta}}}{s_{\hat{\theta}} \sqrt{2} \hat{G}_F} C_{HWB} + \sqrt{2} \delta G_F \right), \tag{II.2.116}$$

$$\delta G_F = \frac{1}{\sqrt{2}\,\hat{G}_F} \left(\sqrt{2}\, C^{(3)}_{Hl} - \frac{C_{ll}}{\sqrt{2}} \right), \tag{II.2.117}$$

$$\delta s^2_\theta = -\frac{s_{\hat{\theta}}\, c_{\hat{\theta}}}{2\sqrt{2}\,\hat{G}_F (1 - 2 s^2_{\hat{\theta}})} \left[s_{\hat{\theta}}\, c_{\hat{\theta}} \left(C_{HD} + 4\, C^{(3)}_{Hl} - 2\, C_{ll} \right) + 2\, C_{HWB} \right]. \tag{II.2.118}$$

These shifts lead to modifications of the Z couplings with the normalization

$$\mathcal{L}_{Z,eff} = g_{Z,eff} \left(J^{Z\ell}_\mu Z^\mu + J^{Z\nu}_\mu Z^\mu + J^{Zu}_\mu Z^\mu + J^{Zd}_\mu Z^\mu \right), \tag{II.2.119}$$

where $g_{Z,eff} = -\,2\,2^{1/4}\sqrt{\hat{G}_F}\,\hat{m}_Z$, $(J^{Zx}_\mu)^{pr} = \bar{x}_p \gamma_\mu \left[(\bar{g}^x_V)^{pr}_{eff} - (\bar{g}^x_A)^{pr}_{eff} \gamma_5 \right] x_r$ for $x = \{u, d, \ell, \nu\}$. In general, these currents are matrices in flavour space. When we restrict our attention to the case of a MFV scenario $(J^{Zx}_\mu)_{pr} \simeq (J^{Zx}_\mu)\delta_{pr}$. In the Warsaw basis, the effective axial and vector couplings are modified from the SM values by a shift

$$\delta(g^x_{V,A})_{pr} = (\bar{g}^x_{V,A})^{eff}_{pr} - (g^x_{V,A})^{SM}_{pr}, \tag{II.2.120}$$

where

$$\delta(g^\ell_V)_{pr} = \delta\bar{g}_Z\, (g^\ell_V)^{SM}_{pr} - \frac{1}{4\sqrt{2}\hat{G}_F} \left(C_{\substack{He \\ pr}} + C^{(1)}_{\substack{Hl \\ pr}} + C^{(3)}_{\substack{Hl \\ pr}} \right) - \delta s^2_\theta, \tag{II.2.121}$$

$$\delta(g^\ell_A)_{pr} = \delta\bar{g}_Z\, (g^\ell_A)^{SM}_{pr} + \frac{1}{4\sqrt{2}\,\hat{G}_F} \left(C_{\substack{He \\ pr}} - C^{(1)}_{\substack{Hl \\ pr}} - C^{(3)}_{\substack{Hl \\ pr}} \right), \tag{II.2.122}$$

$$\delta(g^\nu_V)_{pr} = \delta\bar{g}_Z\, (g^\nu_V)^{SM}_{pr} - \frac{1}{4\sqrt{2}\,\hat{G}_F} \left(C^{(1)}_{\substack{Hl \\ pr}} - C^{(3)}_{\substack{Hl \\ pr}} \right), \tag{II.2.123}$$

$$\delta(g^\nu_A)_{pr} = \delta\bar{g}_Z\, (g^\nu_A)^{SM}_{pr} - \frac{1}{4\sqrt{2}\,\hat{G}_F} \left(C^{(1)}_{\substack{Hl \\ pr}} - C^{(3)}_{\substack{Hl \\ pr}} \right), \tag{II.2.124}$$

[II.35] See Refs. [623, 695, 701–704] for the development of this approach and Refs. [633, 705] for details.

$$\delta(g_V^u)_{pr} = \delta\bar{g}_Z\,(g_V^u)_{pr}^{SM} + \frac{1}{4\sqrt{2}\,\hat{G}_F}\left(-C^{(1)}_{\substack{Hq\\pr}} + C^{(3)}_{\substack{Hq\\pr}} - C_{\substack{Hu\\pr}}\right) + \frac{2}{3}\delta s^2_{\hat{\theta}}, \tag{II.2.125}$$

$$\delta(g_A^u)_{pr} = \delta\bar{g}_Z\,(g_A^u)_{pr}^{SM} - \frac{1}{4\sqrt{2}\,\hat{G}_F}\left(C^{(1)}_{\substack{Hq\\pr}} - C^{(3)}_{\substack{Hq\\pr}} - C_{\substack{Hu\\pr}}\right), \tag{II.2.126}$$

$$\delta(g_V^d)_{pr} = \delta\bar{g}_Z\,(g_V^d)_{pr}^{SM} - \frac{1}{4\sqrt{2}\,\hat{G}_F}\left(C^{(1)}_{\substack{Hq\\pr}} + C^{(3)}_{\substack{Hq\\pr}} + C_{\substack{Hd\\pr}}\right) - \frac{1}{3}\delta s^2_{\hat{\theta}}, \tag{II.2.127}$$

$$\delta(g_A^d)_{pr} = \delta\bar{g}_Z\,(g_A^d)_{pr}^{SM} + \frac{1}{4\sqrt{2}\,\hat{G}_F}\left(-C^{(1)}_{\substack{Hq\\pr}} - C^{(3)}_{\substack{Hq\\pr}} + C_{\substack{Hd\\pr}}\right), \tag{II.2.128}$$

where

$$\delta\bar{g}_Z = -\frac{\delta G_F}{\sqrt{2}} - \frac{\delta M_Z^2}{2\hat{m}_Z^2} + \frac{s_{\hat{\theta}}\,c_{\hat{\theta}}}{\sqrt{2}\hat{G}_F}\,C_{HWB}, \tag{II.2.129}$$

and similarly the W couplings are defined as

$$\delta(g_V^{W_\pm,\ell})_{rr} = \delta(g_A^{W_\pm,\ell})_{rr} = \frac{1}{2\sqrt{2}\hat{G}_F}\left(C^{(3)}_{\substack{Hl\\rr}} + \frac{1}{2}\frac{c_{\hat{\theta}}}{s_{\hat{\theta}}}\,C_{HWB}\right) + \frac{1}{4}\frac{\delta s^2_{\hat{\theta}}}{s^2_{\hat{\theta}}}, \tag{II.2.130}$$

$$\delta(g_V^{W_\pm,q})_{rr} = \delta(g_A^{W_\pm,q})_{rr} = \frac{1}{2\sqrt{2}\hat{G}_F}\left(C^{(3)}_{\substack{Hq\\rr}} + \frac{1}{2}\frac{c_{\hat{\theta}}}{s_{\hat{\theta}}}\,C_{HWB}\right) + \frac{1}{4}\frac{\delta s^2_{\hat{\theta}}}{s^2_{\hat{\theta}}}. \tag{II.2.131}$$

Here our chosen normalization is $(g_V^x)^{SM} = T_3/2 - Q^x\,s^2_{\hat{\theta}}, (g_A^x)^{SM} = T_3/2$ where $T_3 = 1/2$ for u_i, ν_i and $T_3 = -1/2$ for d_i, ℓ_i and $Q^x = \{-1, 2/3, -1/3\}$ for $x = \{\ell, u, d\}$. The set of δX parameters are not an operator basis for the SMEFT.

II.2.3.b.vii Fitting at LO and NLO: constraints and covariance

The mapping of an experimental constraint to the underlying C_i is based on a linear expansion of a cross section or a pseudo-observable based decomposition of a cross section. A fit at LO to mass eigenstate parameters should include a theoretical covariance matrix and a theoretical error due to neglected higher order effects in the SMEFT [610, 633, 705]. A fit in terms of the underlying weak eigenstate Wilson coefficients is straightforward and we believe it will in general have a much simpler theoretical covariance matrix.

II.2.3.b.vii.1 Digression on theoretical uncertainty

In the SM, when a particular process is calculated, a common practice is that a theoretical error is assigned. For example, for parametric and theoretical uncertainties within the SM, see Table 1 of Ref. [9]. It can be subtle to assign such an error [162] due to the neglect of missing higher order perturbative terms in the SM. The need to include theoretical errors when perturbatively expanding the SMEFT is tied to the fact that different truncations of such expansions can be constructed. Suppose that a given quantity $\mathrm{Q}(a)$ is given in perturbation theory by the following expansion:

$$\mathrm{Q} = a + g\left[a^2 + f_1(a)\right] + g^2\left[a^3 + f_2(a)\right] + \mathcal{O}(g^3) = \bar{a} + g\,f_1(a) + \mathcal{O}(g^2), \tag{II.2.132}$$

where $\bar{a} = a/(1 - ga)$. Suppose that only the f_1 term is actually known. It could be decided that $\bar{a}$ is the effective expansion parameter (or that in the full expression we change variable $a \to \bar{a}$). This is equivalent, in the truncated expansion, to introducing

$$\mathrm{Q} = \bar{a} + g\,f_1(a) = \bar{a} + g\,f_1(\bar{a}), \tag{II.2.133}$$

which gives $\Delta Q = g^2 f_1'(a)$, the difference in the two results due to neglected higher order terms is an estimate of the associated theoretical uncertainty. A fit to observables defined in a perturbative expansion must always include an estimate of the missing higher order terms [706], which specifies a theoretical uncertainty.

II.2.3.b.vii.2 The importance of NLO results for theoretical uncertainty

An excellent example of the importance of theory errors is provided by another effective field theory, NRQED, as discussed in Refs. [27, 707–712]. The Hydrogen hyperfine splitting is measured to fourteen digits, but only computed to seven digits. This introduces a theoretical error when using this measurement. Comparatively, the Positronium hyperfine splitting is measured and computed to eight digits. It would simply be a mistake to give the H hyperfine splitting a weight 10^6 larger than the P_s hyperfine splitting in a global fit to the fundamental constants, and to totally ignore theory errors. A careful consideration of NLO effects can help in avoiding similar errors when using the SMEFT formalism. In our opinion, neglecting such considerations may lead to incorrect conclusions. For example, in Ref. [633, 705] it has been shown that the per mille level due to the LEP experiments projected into the SMEFT might not be as strong as claimed in the previous literature when SMEFT theoretical errors are taken into account. This should not be surprising, as in EWPD the modifications of the W mass, the ρ parameter and the effective weak-mixing angle are loop-induced quantities and a study of their SM deviations requires an analysis at NLO in the SMEFT. As a result of these developments, constraints on parameters in the SMEFT (that are not symmetry based) are not robustly below LHC sensitivity.

For this reason, we believe it is not wise to set parameters that contribute to EWPD to zero in LHC analyses in the SMEFT. The experimental bound should be imposed on these parameters, with a clearly specified theory error. As a rule of thumb when experimental bounds descend below the 10% level SMEFT theory errors should not be neglected in an EFT interpretation of the data. [II.36]

II.2.3.b.vii.3 Covariance due to operator basis in $\mathcal{L}_6$

Consider two mass eigenstate interaction shifts $\delta X_1, \delta X_2$ that contribute to a particular cross section that reports an experimental bound. Several SMEFT Wilson coefficients generally contribute to any one observable through $\delta X_1, \delta X_2$. All such parameters must be retained unless symmetries, or knowledge of the UV theory, allows a reduction. One can directly interpret the data at LO in terms of the underlying Wilson coefficients that are present in $\delta X_1, \delta X_2$ and defined in linear expansions of these parameters, so long as theoretical errors are carefully accounted for.

Alternatively fit results can be reported in terms of $\delta X_1, \delta X_2$. However in this case it is critical that a theoretical covariance matrix is included. As the shifts $\delta X_1, \delta X_2$ are linear in the Wilson coefficients, the bi-linearity property of covariance can be used to obtain the theoretical covariance matrix directly. Schematically the matrix can be build up for $\delta X_1 = aC_1 + bC_2 + \cdots$ and $\delta X_2 = cC_1 + dC_3 + \cdots$ as follows

$$Cov\left[\delta X_1, \delta X_2\right] = a\,c\,Cov[C_1, C_1] + a\,d\,Cov[C_1, C_3] + b\,c\,Cov[C_2, C_1] + b\,d\,Cov[C_2, C_3] + \cdots$$

Assuming that the C_1, C_2, C_3 are independent operators $Cov[C_1, C_1] = Var[C_1]$ and all other entries vanish. The appropriate covariance matrix can be constructed so long as a theoretical error is included for each of the terms in the perturbative expansion of the δX. Estimating a theoretical error for these terms to obtain the individual variances requires an estimate of neglected NLO corrections. A NLO mapping can be carried out in the same manner. The only modification is the use of NLO formula in the expansion of the cross section and smaller theoretical errors, as we illustrate below. Fits to mass eigenstate parameters

[II.36] Editor footnote: Another point of view is expressed in Section II.2.1 which advocates to focus the LHC Higgs analyses, at least in the early phase, on the parameters that are most unconstrained by previous experiments in order to maximize the sensitivity to new physics.

in general have very non trivial covariance matrices (due to gauge invariance of the underlying operator basis) that have to be defined. The required theoretical errors can only be estimated by an understanding of NLO corrections to a LO formalism.

II.2.3.b.vii.4 Fitting at LO or NLO?

A NLO treatment of the data is always advisable if the required theoretical results are available. NLO analyses are required to consistently map lower energy measurements in the SMEFT to the cut off $\mu = \Lambda$, or to consistently combine data sets measured at different effective scales ($\mu_1 \neq \mu_2$). Whether or not a NLO treatment of the data is *required* in the SMEFT is defined by three considerations:

- What is the cut off scale (Λ) and what is the matching pattern of Wilson coefficients into the SMEFT?
- What is the experimental precision that will be reached in a measurement?
- How will a bound projected into the SMEFT formalism at LO be used?

Considering the first question, it is interesting to consider the cases where $1\,\text{TeV} \lesssim \Lambda/\sqrt{\tilde{C}_i} \lesssim 3\,\text{TeV}$. In these cases, deviations in processes measured at the LHC could possibly be observable. If deviations are seen then a NLO analysis is well motivated to learn as precisely as possible about the underlying physics sector through the measured deviation. Cut off scales of this form are not implausible or ruled out. On the contrary they are well motivated by the Hierarchy problem. Further model building exercises for decades have indicated that such cut off scales are not robustly ruled out when considering EWPD. If the ratio $\Lambda/\sqrt{\tilde{C}_i}$ lies in this interesting range, the effect of NLO corrections are clearly not negligible [610, 628, 633, 645, 648–650, 705, 713–718]. Considering the second question, as we have stressed, when experimental precision starts to reach the 10% level a NLO analysis should be pursued. The answer to the third question differs among analyses and authors but in general NLO results will always be useful to authors interested in LO results while the converse is not true.

II.2.3.b.vii.5 Theory errors in a LO formalism on the IPS

As a specific example of a theory error to include in a LO analysis, any LO approach does not take into account that the scales characterizing the measurements of the input parameters α_{ew}, G_F, M_Z differ. Consider the error introduced due to the neglect of this NLO effect in the SMEFT, compared to the errors quoted on α_{ew} in the SM. This parameter is measured at low energies in the $p^2 \to 0$ limit.[II.37] The value of this input parameter is given in Table 2. In the SMEFT, the running of α_{ew} is modified compared to the SM as given in Ref. [646]. As a simple approximation of the error introduced in the SMEFT, one finds that the neglected NLO SMEFT correction to α_{ew} is then

$$\frac{(\Delta\alpha_{ew})_{SMEFT}}{(\Delta\alpha_{ew})_{SM}} \simeq -250 \left(\frac{1\text{TeV}}{\Lambda}\right)^2 \tilde{C}_{HB} - 80 \left(\frac{1\text{TeV}}{\Lambda}\right)^2 \tilde{C}_{HW}, \tag{II.2.134}$$

running from $p^2 \sim 1\,\text{GeV}^2$ to m_h.[II.38] Here $(\Delta\alpha_{ew})_{SM}$ is the SM error quoted in the Table. Depending on $\tilde{C}_{HB}$ and $\tilde{C}_{HW}$ and Λ, which are unknown, the neglected NLO SMEFT effects can lead to an error on this input parameter far larger than in the SM. This should be completely unsurprising. Neglected NLO effects in the SMEFT in this case include corrections of order $g_{1,2}^2 v_T^2/(16\,\pi^2)\,\Lambda^2$. The theoretical errors due to such neglected effects can obviously compete with the SM theoretical errors, introduced in a QED calculation out to *tenth order* in the SM. Similarly, neglected NLO corrections on the other input parameters modify their theoretical error.

[II.37] α_{ew} is frequently extracted in the Thompson limit $p^2 \to 0$ when probing some Coulomb potential of a charged particle, for example in a measurement of $g-2$ for the electron or muon. Recently, extractions with a competitive error budget have emerged where α_{ew} is extracted from the measured ratio of $\hbar/M_{atom}$ via the recoil velocity for a stable atom, such as Rb^{87} [719] or C_s [720]. The important point is to realize that this input parameter differs in the SM and in the SMEFT at NLO.

[II.38] This is only an approximation, as formally all of the SM states with masses $m^2 \gg p^2$ should be integrated out in sequence when running down from the high scale.

Table 101: Current experimental best estimates of α_{ew}, G_F, M_Z.

Parameter	Input Value	Ref.
$\hat{m}_Z$	91.1875 ± 0.0021	[11, 721, 722]
$\hat{G}_F$	$1.1663787(6) \times 10^{-5}$	[11, 722]
$\hat{\alpha}_{ew}$	$1/137.035999074(94)$	[11, 719, 722, 723]

II.2.3.b.vii.6 Approximating unknown SMEFT theory errors

Various ways exist to estimate SMEFT theory errors. One can compute the same observable with different "options", e.g., linearization or quadratization of the squared matrix element, resummation or expansion of the (gauge invariant) fermion part in the wave function factor for the external legs, variation of the renormalization scale, $G_{\rm F}$ renormalization scheme or α -scheme, etc.

A conservative estimate of the associated theoretical uncertainty is obtained by taking the envelope over all "options"; the interpretation of the envelope is a log-normal distribution (commonly done in the experimental community) or a flat Bayesian prior [160, 162] (a solution preferred in a large part of the theoretical community).

In our opinion, to properly characterize the perturbative error, it is essential to calculate at least to one loop order in the SMEFT, including the leading insertion of operators in $\mathcal{L}_6$. Until such calculations are performed, we recommend conservative theoretical errors should be applied to theoretical relations in the SMEFT. Further, the introduction of a "non-perturbative" error, due to $\mathcal{L}_8$ when bounding $\mathcal{L}_6$ should be done. In Eqn.II.2.59, the $g^3\, g_6^2\, \mathcal{A}^{(6)}_{3,2,1}$ terms can be used as estimators of missing higher order non-perturbative terms in the SMEFT. This approach is not particularly novel, but is simply the obvious extension of the widely accepted approach to assigning theoretical error in the SM to the SMEFT. [II.39]

As a specific example, a reasonable approximation of a theoretical error to introduce for an observable i when fitting to the leading parameters in $\mathcal{L}_6$, is given by [633, 705]

$$\Delta^i_{SMEFT}(\Lambda) \simeq \sum_j x_{ij}\, \tilde{C}^8_{ij}\, \frac{v_T^4}{\Lambda^4} + \sum_j \frac{(g^{ij}_{SM})^2}{16\,\pi^2}\, \tilde{C}^6_{ij}\, y_{ij}\, \ln\left[\frac{\Lambda^2}{v_T^2}\right]\, \frac{v_T^2}{\Lambda^2}\,. \tag{II.2.135}$$

Non log dependence in the second term is also present, but is suppressed for a simplifying approximation. Here x_{ij}, y_{ij} label the observable dependence and are $\mathcal{O}(1)$. One can further define

$$x'_i\,\sqrt{N^i_8} = \sum_j \sqrt{x^2_{ij}\,(\tilde{C}^8_{ij})^2}, \qquad y'_i\,\sqrt{N^i_6} = \sum_j \sqrt{y^2_{ij}\,(\tilde{C}^6_{ij})^2} \tag{II.2.136}$$

as the product of $\mathcal{O}(1)$ numbers that characterize the multiplicity of the operators that contribute to a process ($N_{6,8}$) and the typical numerical dependence x'_i, y'_i. The square root is because errors are assumed to add in quadrature. As an alternative, a Bayesian uniform prior for the C_i could be used.

Although the number of operators is large, the relevant number of operators that contribute in a process is far less then the full operator set; in known examples $N_{6,8} \sim \mathcal{O}(10)$. No complete operator basis of $\mathcal{L}_8$ has ever been encoded in a Monte-Carlo program and used to fit the data, and we do not recommend that fits should explicitly include all terms in $\mathcal{L}_8$ and vary corrections in general. Rough error estimates of this form should be sufficient for most purposes.

[II.39] Editor footnote: Another point of view is expressed in Section II.2.2, where it is argued that the validity range of an EFT analysis cannot be determined using only low-energy information or the truncation error of the EFT Lagrangian.

This error is multiplicative and the absolute error is obtained as $\Delta^i_{SMEFT}(\Lambda)$ times the SM prediction for an observable. For cut off scales and Wilson coefficients in the range $1\,\text{TeV} \lesssim \Lambda/\sqrt{\tilde{C}_i} \lesssim 3\,\text{TeV}$ and order one numbers for $x_i, y_i, N_{6,8}$ the value of $\Delta^i_{SMEFT}(\Lambda)$ is in the range of few $\mathcal{O}(\%)$ to $\mathcal{O}(0.1\%)$ [610, 633, 705]. This is the reason we believe that once experimental errors descend to the $\mathcal{O}(10\%)$ level SMEFT theory errors should be considered to be conservative. It is widely considered to be the case that the precision expected in LHC analyses can be expected to approach a few per cent in well measured channels [724, 725].

We believe that a percentage error can be motivated for SMEFT theoretical uncertainties using these approximations and then directly applied (and varied) when reporting a bound.

II.2.3.b.viii NLO SMEFT loop corrections

We believe that including loop corrections in the SMEFT context is somehow even more crucial than for a pure SM calculation.[II.40]

One loop corrections can introduce a dependence on Wilson coefficients that do not contribute at tree level to a particular process and some of these Wilson coefficients are very poorly bounded. This is different from the SM where all of the Lagrangian terms are extremely well known. We will refer to the introduction of such dependence as "non-factorizable" corrections. Such corrections can significantly change the interpretation of a mapping of experimental constraints at NLO in the SMEFT, as we illustrate below. Loop corrections also introduce a perturbative rescaling of the dependence on an operator's Wilson coefficient. These corrections help define the variance discussed Section II.2.3.b.vii.3 for a LO analysis.

Improving the SMEFT to one loop requires a renormalization scheme be defined, a systematic renormalization of the SMEFT be carried out on the new parameters in $\mathcal{L}_6$, and loop corrections be performed in a particular chosen gauge. We now discuss each of these steps in the NLO program in more detail.

II.2.3.b.ix SMEFT: renormalization in practice

In this section we describe a general renormalization procedure in the SMEFT. The results presented have been developed in Refs. [648, 716], based on the conventional formalism widely used in the SM [377, 381, 689, 726]. To perform renormalization in an EFT it is appropriate to use a dimensionless regulator, see Refs. [601] for a review. We work with dimensional regularization and define

$$\Delta_{\rm UV} = \frac{2}{4-d} - \gamma - \ln\pi - \ln\frac{\mu_{\rm R}^2}{\mu^2} \tag{II.2.137}$$

where d is space-time dimension, the loop measure is $\mu^{4-d}\, d^n q$ and $\mu_{\rm R}$ is the renormalization scale; γ is the Euler-Mascheroni constant. Counter-terms for SM parameters and fields are defined by

$$\mathrm{Z}_i = 1 + \frac{g^2}{16\,\pi^2}\left(d\mathrm{Z}_i^{(4)} + g_6\, d\mathrm{Z}_i^{(6)}\right)\,\Delta_{\rm UV}\,. \tag{II.2.138}$$

With field/parameter counter-terms we can make UV finite the self-energies and the corresponding Dyson resummed propagators. However, these counterterm subtractions are not enough to make UV finite the Green's functions with more than two legs (at $\mathcal{O}(g^{\mathrm{N}_6} g_6)$). A mixing matrix among Wilson coefficients is needed:

$$C_i = \sum_j \mathrm{Z}^{\rm W}_{ij}\, C_j^{\rm ren} \qquad \mathrm{Z}^{\rm W}_{ij} = \delta_{ij} + \frac{g^2}{16\,\pi^2}\, d\mathrm{Z}^{\rm W}_{ij}\,\Delta_{\rm UV}\,. \tag{II.2.139}$$

[II.40] Editor footnote: Another point of view is expressed in Section II.2.2 where it is argued that the NLO corrections due to D=6 EFT coefficients are important to include only in particular well-defined situations.

For example, in this way we can renormalize the (on-shell) s -matrix for $\mathrm{H}(P) \to \mathrm{A}_\mu(p_1)\mathrm{A}_\nu(p_2)$ and $\mathrm{H}(P) \to \mathrm{A}_\mu(p_1)\mathrm{Z}_\nu(p_2)$ which have only one (transverse) Lorentz structure. By on-shell s -matrix for an arbitrary process (involving unstable particles) we mean the corresponding (amputated) Green's function supplied with LSZ factors and sources, computed at the (complex) poles of the external lines [727–729]. For processes that involve stable particles this can be straightforwardly transformed into a physical observable.

The connection of the $\mathrm{HVV}, \mathrm{V} = \mathrm{Z}, \mathrm{W}$ (on-shell) s -matrix with the off shell vertex $\mathrm{H} \to \mathrm{VV}$ and the full process $\mathrm{pp} \to 4\,\psi$ is more complicated and is discussed in some detail in Sect. 3 of Ref. [610]. The "on-shell" s -matrix for HVV, being built with the the residue of the $\mathrm{H}-\mathrm{V}-\mathrm{V}$ poles in $\mathrm{pp} \to 4\,\psi$ is gauge invariant by construction (it can be proved by using Nielsen identities [730]) and represents one of the building blocks for the full process: in other words, it is a pseudo-observable [610, 651, 731]. Technically speaking the "on-shell" limit for external legs should be understood "to the complex poles" (for a modification of the LSZ reduction formulas for unstable particles, see Ref. [732]) but, as well known, at one loop we can use on-shell masses (for unstable particles) without breaking the gauge parameter independence of the result. Residues of complex poles are what matters, as far as renormalization is concerned.

The $\mathrm{H}(P) \to \mathrm{Z}_\mu(p_1)\mathrm{Z}_\nu(p_2)$ (on-shell) matrix contains a part of the amplitude proportional to $g^{\mu\nu}$ (referred to as $\mathcal{D}_{HZZ}$ below) and a part of the amplitude proportional to $p_2^\mu\, p_1^\nu$ (referred to as $\mathcal{P}_{HZZ}$ below). Both of these terms get renormalized through a mixing.

Consider now the $\mathrm{H}(P) \to \mathrm{W}^-{}_\mu(p_1)\mathrm{W}^+{}_\nu(p_2)$ (on-shell) matrix: it has the same Lorentz decomposition of $\mathrm{H} \to \mathrm{ZZ}$ and it is UV finite in the $\mathrm{D}im = 4$ part. The $\mathcal{D}_{HWW}$ part at $\mathrm{D}im = 6$ is renormalized through a mixing; however, there are no Wilson coefficients in $\mathcal{P}_{HWW}$ that are not also present in $\mathcal{P}_{HZZ}$, so that the UV finiteness of this term is related by gauge symmetry to the renormalization of $\mathcal{P}_{HZZ}$. This is the first part of the arguments used in Refs. [648, 716] in proving closure of NLO SMEFT under renormalization.

The (on-shell) decays $\mathrm{H}(P) \to \mathrm{b}(p_1)\overline{\mathrm{b}}(p_2)$ and $\mathrm{Z}(P) \to \bar\psi(p_1)\psi(p_2)$ are more involved to improve to NLO in the SMEFT. The SM contribution to these amplitudes are rendered finite by the SM counter-terms, however renormalizing the contributions due to $\mathcal{L}_6$ requires an extensive treatment of this operator mixing. See Ref. [650] for recent results on these decays.

Some structure present in the SM is not preserved when extending an analysis into the SMEFT. Manifestly, processes that first appear at one loop in the SM can occur at tree level in the SMEFT, due to the presence of local contact operators. However, some symmetries of the SM are preserved. For example, consider the universality of the electric charge. In pure QED there is a Ward identity [733] telling us that e can be renormalized in terms of vacuum polarization (which is a way to understand the universality of the coupling), and Ward-Slavnov-Taylor (WST) identities [733–735] allow us to generalize the argument to the full spontaneously broken SM symmetry group. The previous statement means that the contribution from vertices (at zero momentum transfer) in the full SM exactly cancel those from (fermion) wave function renormalization factors. Therefore, by directly computing the vertex $A\,\bar\psi\,\psi$ (at $q^2 = 0$) and the Z_ψ wave function factor in the SMEFT, one can directly prove (or check) that the WST identity is extended to the SMEFT at $\mathcal{L}_6$. This is expected as the corresponding identities are the consequence of symmetries. However, this is technically non-trivial even after the previous steps in the renormalization program discussed above. Once (non-trivial) finiteness of this vertex is established, the finiteness of $\mathrm{e}^+\mathrm{e}^- \to \bar\psi\,\psi$ (including the four-point functions in the non resonant part) follows. This is the second part in proving closure of the NLO SMEFT under renormalization, using the arguments of Refs. [648, 716].

At NLO one first has to render all SM and SMEFT parameters finite. Considering the arguments above, and the complete renormalization results of all the operators in $\mathcal{L}_6$ reported in Refs. [631, 645–647] in the Warsaw basis, this step in the NLO program has been accomplished. This result has not been derived so far in any other basis. We believe that translating these results to other bases may be very

challenging.

II.2.3.b.x Input parameter choices

The detailed fixing of poles and residues that make up precise renormalization conditions require a lengthy discussion. For detailed reviews in the case of the SM, see Refs. [736,737]. Below we summarize the results of the finite renormalization in the relationship to the input observables.

II.2.3.b.x.1 Using a 'G_F-scheme' with G_F, M_W, M_Z

In the 'G_F -scheme', one uses $\{G_F\,,\,M_{\rm W}\,,\,m_Z\}$ to fix terms in the Lagrangian. In this case, we write the following equation for the g finite renormalization

$$g_{\rm ren} = g_{\rm exp} + \frac{g_{\rm exp}^2}{16\,\pi^2}\,\left(d\mathcal{Z}_g^{(4)} + g_6\,d\mathcal{Z}_g^{(6)}\right) \tag{II.2.140}$$

where $g_{\rm exp}$ will be expressed in terms of the Fermi coupling constant G_F. Furthermore, $\mathrm{c}_\theta = M_{\rm W}/m_Z$. The μ -lifetime can be written in the form

$$\frac{1}{\tau_\mu} = \frac{M_\mu^5}{192\,\pi^3}\,\frac{g^4}{32\,M^4}\,(1+\delta_\mu)\;. \tag{II.2.141}$$

The radiative corrections are $\delta_\mu = \delta_\mu^{\rm W} + \delta_{\rm G}$ where $\delta_{\rm G}$ is the sum of vertices, boxes etc and $\delta_\mu^{\rm W}$ is due to the W self-energy. The renormalization equation becomes

$$\frac{G_F}{\sqrt{2}} = \frac{g^2}{8\,M^2}\,\left\{1+\frac{g^2}{16\,\pi^2}\left[\delta_{\rm G}+\frac{1}{M^2}\,\Sigma_{\rm WW}(0)\right]\right\} \tag{II.2.142}$$

where we expand the solution for g

$$g_{\rm ren}^2 = 4\,\sqrt{2}\,G_F\,M_{\rm W\,;\,OS}^2\,\left\{1+\frac{G_F M_{\rm W\,;\,OS}^2}{2\,\sqrt{2}\,\pi^2}\left[\delta_{\rm G}+\frac{1}{M^2}\,\Sigma_{\rm WW\,;\,fin}(0)\right]\right\}\;. \tag{II.2.143}$$

Note that the non universal part of the corrections is given by

$$\delta_{\rm G} = \delta_{\rm G}^{(4)} + g_6\,\delta_{\rm G}^{(6)} \quad \delta_{\rm G}^{(4)} = 6 + \frac{7-4\,\mathrm{S}_\theta^2}{2\,\mathrm{S}_\theta^2}\,\ln \mathrm{c}_\theta s \tag{II.2.144}$$

but the contribution of $\mathcal{L}_6$ to muon decay at NLO is not available yet and has not be included in the calculation. It is worth noting that eq. (II.2.142) defines the finite renormalization in the $\{G_F\,,\,M_{\rm W}\,,\,m_Z\}$ IPS.

II.2.3.b.x.2 The 'α scheme', using $\alpha, G_{\rm F}, M_Z$

This scheme uses the fine structure constant α and is based on using $\{\alpha\,,\,G_F\,,\,m_Z\}$ as the IPS. The new finite-renormalization equation is

$$g^2\,\mathrm{S}_\theta^2 = 4\,\pi\alpha\left[1-\frac{\alpha}{4\,\pi}\,\frac{\Pi_{\rm AA}(0)}{\mathrm{S}_\theta^2}\right] \tag{II.2.145}$$

where $\alpha = \alpha_{\rm QED}(0)$ and $\Pi_{\rm AA}$ defines the vacuum polarization. Therefore, in this scheme, the finite counter-terms are

$$g_{\rm ren}^2 = g_{\rm A}^2\left[1+\frac{\alpha}{4\,\pi}\,d\mathcal{Z}_g\right] \quad \mathrm{c}_\theta r = \hat{\mathrm{c}}_\theta\left[1+\frac{\alpha}{4\,\pi}\,d\mathcal{Z}_{\mathrm{c}_\theta}\right], \quad M_{\rm ren} = M_{\rm Z\,;\,OS}\,\hat{\mathrm{c}}_\theta s\left[1+\frac{\alpha}{8\,\pi}\,d\mathcal{Z}_{M_{\rm W}}\right] \tag{II.2.146}$$

where the parameters $\hat{\mathrm{c}}_\theta$ and g_{A} are defined by

$$g_{\mathrm{A}}^2 = \frac{4\,\pi\,\alpha}{\hat{\mathrm{S}}_\theta^2} \qquad \hat{\mathrm{S}}_\theta^2 = \frac{1}{2}\left[1 - \sqrt{1 - 4\,\frac{\pi\,\alpha}{\sqrt{2}\,G_F\,M_{\mathrm{Z}\,;\,\mathrm{OS}}^2}}\right]. \tag{II.2.147}$$

The reason for introducing this scheme is that the s, T and U parameters Ref. [738] have been originally given in the $\{\alpha\,,\,G_F\,,\,m_Z\}$ scheme, and these input parameters are very well measured in the SM. When calculating processes involving photons final states, this scheme can be transparent to adopt. For other processes, the $\{G_F\,,\,M_{\mathrm{W}}\,,\,m_Z\}$ scheme can be more appropriate, and is in wider use in the SM in higher order calculations. In the α-scheme, after requiring that $M_{\mathrm{Z}\,;\,\mathrm{OS}}^2$ is a zero of the real part of the inverse Z propagator, we are left with one finite counterterm, $d\mathcal{Z}_g$. The latter is fixed by using G_F and requiring that

$$\frac{1}{\sqrt{2}}\,G_F = \frac{g^2}{8\,M^2}\left\{1 + \frac{g^2}{16\,\pi^2}\left[\delta_{\mathrm{G}} + \frac{1}{M^2}\,\Delta_{\mathrm{WW}}(0) - \left(d\mathrm{Z}_{\mathrm{W}} + d\mathrm{Z}_{M_{\mathrm{W}}}\right)\,\Delta_{\mathrm{UV}}\right]\right\} \tag{II.2.148}$$

where we use the following relations for UV and finite renormalization,

$$g = g_{\mathrm{ren}}\left(1 + \frac{g_{\mathrm{ren}}^2}{16\,\pi^2}\,d\mathrm{Z}_g\,\Delta_{\mathrm{UV}}\right) \qquad g_{\mathrm{ren}} = g_{\mathrm{A}}\left(1 + \frac{\alpha}{8\,\pi}\,d\mathcal{Z}_g\right). \tag{II.2.149}$$

Note that SM EW calculations available in literature generally use G_F for the pure weak part or evolve $\alpha(0) \to \alpha(M)$ and use $\alpha(M)$ as the expansion parameter at the scale M. For a comprehensive discussion see Sect. 5.3 of Ref. [360].

II.2.3.b.xi Background field gauge

Any well defined gauge can be used in a calculation, see Ref. [739] for an excellent review on gauge fixing. There can be some advantage to organizing a calculation in a manner that enforces relationships between counter terms due to gauge invariance. A technique that accomplishes this is known as the Background Field (BF) method [740, 741]. The idea is that fields are split into classical and quantum components and a gauge fixing term is added that maintains the gauge invariance of the classical background fields, while breaking the gauge invariance of the quantum fields. Due to the resulting Ward identities, one finds the relations among the SM counter-terms [736]. The gauge fixing in the BF method can be imposed as in Ref. [736, 742]. Use of the background field method can make extending the WST relations between counter-terms manifest and transparent, even when including the effects of $\mathcal{L}_6$. It is worth noting that the WST identities have been explicitly verified in the straightforward LO approach detailed in this note. Proving such identities in any LO approach verifies the gauge-independence of the results.

Extending any gauge fixing procedure to the case of the SMEFT is subtle, due to the order by order redefinition of the fields that are gauged due to terms in $\mathcal{L}_{SMEFT}$. Optimally resolving the technical complications that result is a challenge. These subtleties are some of the reasons it is difficult to directly modify computer programs that have been developed for automatic NLO calculations in the SM, to the case of the SMEFT. The development of NLO SMEFT Monte-Carlo tools is still very much a work in progress.

II.2.3.c Known results in the SMEFT to NLO

Despite all of the challenges to advancing SMEFT results to NLO, progress in this area is rapid and steady. In this section we briefly summarize some of these theoretical developments.

II.2.3.c..1 Renormalization results

The complete renormalization of the Warsaw basis was reported in Refs. [631,645–647]. In the approach outlined in Section II.2.3.b.ix, results for the Warsaw basis operator renormalization were reported in Refs. [648, 716]. Use of SMEFT renormalization results (including a subset of NLO finite terms) to leverage EWPD to bound operators not contributing at tree level was reported in Ref. [743]. Partial results for renormalizing some alternate operator sets in a so called "SILH basis" were given in Refs. [641,665]. A recent study of RGE effects on the oblique parameters, in a subset of UV models, was reported in Ref. [717].

II.2.3.c..2 Advances in one loop matching techniques

Recently, the covariant derivative expansion discussed in Refs. [744–746] has re-emerged in Refs. [609, 747, 748] as a powerful technique to perform matching calculations to underlying UV theories at one loop. The basic idea at work is that, the contribution to the effective action that results when integrating out a heavy field $\mathcal{X}$ at one loop is schematically given by

$$\Delta S \propto i\,\mathrm{Tr}\,\log\left[D^2 + m_{\mathcal{X}}^2 + U(x)\right] \tag{II.2.150}$$

where $m_{\mathcal{X}}$ is the mass of the $\mathcal{X}$ field integrated out, $D^2 = D_\mu\, D^\mu$, D_μ is the covariant derivative, and $U(x)$ depends on the SM field content. The covariant derivative expansion allows this functional trace to be directly evaluated, while keeping gauge covariance manifest. This simplifies and systematizes one loop matching calculations in the SMEFT, in many simple UV physics cases.[II.41]

II.2.3.c..3 Full Lagrangian expansion results to NLO ($\mathcal{L}_8$)

Refs. [615–617,751,752] have developed the theoretical technology (essentially advanced use of Hilbert series techniques) to characterize the number of independent operators present at each order in the SMEFT expansion. This has lead to the complete characterization of the operator sets in $\mathcal{L}_7$ and $\mathcal{L}_8$.

II.2.3.c..4 Perturbative NLO results in the SMEFT

Full results to NLO in the SMEFT have started to appear in the literature. The first pioneering calculations of this form were for the process $\mu \to e\,\gamma$ in Ref. [753] and for the process $\Gamma(\mathrm{H} \to \gamma\,\gamma)$ in Refs. [648, 649, 718]. In [649] the full NLO perturbative SMEFT result for this decay with no assumption in the underlying UV scenario was reported. Ref. [648] also reported NLO results for $\Gamma(\mathrm{H} \to \mathrm{Z}\,\gamma)$, $\mathrm{H} \to \mathrm{Z}\,\mathrm{Z}^\star$, $\mathrm{H} \to \mathrm{W}\,\mathrm{W}^\star$ under the assumption of a PTG scenario and presented results to NLO for the W mass and other EWPD parameters. Recently Ref. [650] also reported NLO perturbative results for $\mathrm{H} \to \bar{\mathrm{b}}\mathrm{b}$ and $\mathrm{H} \to \tau^-\tau^+$ in the general SMEFT, including finite terms, in the large m_{t} limit. NLO QCD results for a set of higher dimensional operators contributing to the Higgs boson pair production process were given in Ref. [472], for the Higgs characterization model in Ref. [622] and for associated Higgs boson production in Ref. [644].

II.2.3.c.i A study of constraints

As a particular example, we discuss the impact of NLO corrections on inferred LO bounds, in the case of $\Gamma(\mathrm{H} \to \gamma\,\gamma)$, using the results of Refs. [649, 718]. We consider the general SMEFT case, consider unknown $\tilde{C}_i \sim 1$ and vary the unknown parameters over $0.8 \leq \Lambda \leq 3$ in TeV units. Note that $\bar{v}_T^2/(0.8\,\mathrm{TeV})^2 \sim 0.1$. Taking κ_γ from Ref. [754] to be $0.93^{+0.36}_{-0.17}$, and neglecting light fermion

[II.41] It is worth noting, that some questions remain about the effect of mixing between the heavy and light field content in this approach [749]. These questions were recently clarified in [750].

($m_{\rm f} < m_{\rm H}$) effects for simplicity, one finds the $1\,\sigma$ range

$$-0.02 \leq \left(\tilde{C}^{1,NP}_{\gamma\gamma} + \frac{\tilde{C}^{NP}_i f_i}{16\,\pi^2} \right) \frac{\bar{v}^2_T}{\Lambda^2} \leq 0.02\,. \tag{II.2.151}$$

Here, the tilde superscript denotes that the scale $1/\Lambda^2$ has been factored out of a Wilson coefficient. The f_i terms correspond to the "nonfactorizable" terms, and $\tilde{C}^{1,NP}_{\gamma\gamma}$ corresponds to the one loop improvement of the Wilson coefficient that gives this decay at tree level – $\tilde{C}^{0,NP}_{\gamma\gamma}$. The difference in the mapping of this constraint to the coefficient of $\tilde{C}^{0,NP}_{\gamma\gamma}$ at tree level, and at one loop, can now be characterized.

To determine this correction we determine the percentage change on the inferred value of the bounds of $\tilde{C}^{0,NP}_{\gamma\gamma}$, while shifting the quoted upper and lower experimental bounds by the NLO SMEFT perturbative correction. The envelope of the two percentage variations on the bounds is quoted in the form $[,]$, for values of Λ varying from $[0.8,\,3]\,\text{TeV}$. For one specific choice of signs for C_i, we find the following characteristic results. The net impact of one-loop corrections (added in quadrature) due to higher dimensional operators on the bound of the tree level Wilson coefficient is

$$\Delta_{\rm quad}\,\tilde{C}^{0,NP}_{\gamma\gamma} \sim [29,\,4]\,\%\,. \tag{II.2.152}$$

Similarly, CMS reports $\kappa_\gamma = 0.98^{+0.17}_{-0.16}$ [755], which gives

$$\Delta_{\rm quad}\,\tilde{C}^{0,NP}_{\gamma\gamma} \sim [52,\,7]\,\%\,. \tag{II.2.153}$$

It is possible that these corrections could add up in a manner that is not in quadrature, as this depends on the unknown $\tilde{C}_i$ values. The impact of the one-loop corrections listed above is on *current* experimental bounds of $\Gamma(\text{H} \to \gamma\gamma)$, following from our conservative treatment of unknown UV effects. As the experimental precision of the measurement of $\Gamma(\text{H} \to \gamma\gamma)$ increases, the impact of the neglected corrections directly scales up. Repeating the exercise above, with a chosen projected RunII value $\kappa_\gamma = 1 \pm 0.045$ which is consistent with projected future bounds (CMS - scenario II [724, 725])

$$(\Delta_{\rm quad}\,\tilde{C}^{0,NP}_{\gamma\gamma})^{\text{proj:RunII}} \sim [167,\,21]\,\%\,. \tag{II.2.154}$$

High luminosity LHC runs are further quoted to have a sensitivity between 2% and 5% in κ_γ [756]. Choosing a value $\kappa_\gamma = 1 \pm 0.03$ for this case, one finds

$$(\Delta_{\rm quad}\,\tilde{C}^{0,NP}_{\gamma\gamma})^{\text{proj:HILHC}} \sim [250,\,31]\,\%\,. \tag{II.2.155}$$

Neglected one loop corrections can have an important effect on the projection of an experimental bound into the LO SMEFT formalism, when measurements become sufficiently precise and the cut off scale is not too high. [II.42]

II.2.3.c.ii A study of SM-deviations

Here the reference process is the off-shell $\text{gg} \to \text{H}$ production. It is important to go off-shell because the correct use of the SMEFT proves that scaling couplings on a resonance pole is not the same thing as scaling them off of a resonance pole, which has important consequences in bounding the Higgs intrinsic width, see Refs. [757–759].

In the κ approach, which was developed out of Refs. [760–762], and formalized in Ref. [10], one writes the amplitude as

$$\text{A}^{\text{gg}} = \sum_{\text{q=t,b}} \kappa^{\text{gg}}_{\text{q}}\,\mathcal{A}^{\text{gg}}_{\text{q}} + \kappa^{\text{gg}}_{c} \tag{II.2.156}$$

[II.42] Editor footnote: A different conclusion is presented in Section II.2.2 that argues that the theoretical uncertainty of the EFT computation decreases when the bounds on the deviations from the SM predictions improve.

$\mathcal{A}_{\rm t}^{\rm gg}$ being the SM t -loop etc. The contact term (which is the LO SMEFT) is given by $\kappa_c^{\rm gg}$. Furthermore $\kappa_{\rm q}^{\rm gg} = 1 + \Delta\,\kappa_{\rm q}^{\rm gg}$ Next we compute the following ratio

$$\mathrm{R} = \sigma\left(\kappa_{\rm q}^{\rm gg}\,,\,\kappa_c^{\rm gg}\right)/\sigma_{\rm SM} - 1 \quad [\%]\,. \tag{II.2.157}$$

In LO SMEFT κ_c is non-zero and $\kappa_{\rm q} = 1$. One measures a deviation and gets a value for κ_c. However, at NLO $\Delta\kappa_{\rm q}$ is non zero and one gets a degeneracy: the interpretation in terms of $\kappa_c^{\rm LO}$ or in terms of $\{\kappa_c^{\rm NLO}, \Delta\kappa_{\rm q}^{\rm NLO}\}$ could be rather different (we show an example in Figure 186). Going interpretational we consider

$$\mathrm{A}_{\rm SMEFT}^{\rm gg} = \frac{g\,g_3}{\pi^2}\sum_{\rm q=t,b}\kappa_{\rm q}^{\rm gg}\,\mathcal{A}_{\rm q}^{\rm gg} + 2\,g_3\,g_6\,\frac{s}{M_{\rm W}^2}\,\tilde{C}_{\rm H\,g} + \frac{g\,g_3\,g_6}{\pi^2}\sum_{\rm q=t,b}\mathcal{A}_{\rm q}^{\rm nfc\,;\,gg}\,\tilde{C}_{\rm qg} \tag{II.2.158}$$

where g_3 is the $SU(3)$ coupling constant. Using eq. (II.2.158) we adopt the Warsaw basis and eventually work in the (PTG) scenario [685, 686]. The following options are available: LO SMEFT: $\kappa_{\rm q} = 1$ and $\tilde{C}_{\rm H\,g}$ is scaled by $1/16\,\pi^2$ being "loop-generated" (LG); NLO PTG-SMEFT: $\kappa_{\rm q} \neq 1$ but only PTG operators inserted in loops (non-factorizable terms absent), $\tilde{C}_{\rm H\,g}$ scaled as above; NLO full-SMEFT: $\kappa_{\rm q} \neq 1$ LG/PTG operators inserted in loops (non-factorizable terms present), LG coefficients scaled as above. Again we note the PTG classification scheme is not valid for all possible UV.

It is worth noting the difference between eq. (II.2.156) and eq. (II.2.158), showing that the original κ-framework can be made consistent at the price of adding "non-factorizable" sub-amplitudes. At NLO, $\Delta\kappa = g_6\,\rho$ and

$$g_6^{-1} = \sqrt{2}\,G_F\,\Lambda^2 \qquad 4\,\pi\,\alpha_{\rm s} = g_3 \tag{II.2.159}$$

$$\rho_{\rm t}^{\rm gg} = \tilde{C}_{\rm H\,W} + \tilde{C}_{\rm tH} + 2\,\tilde{C}_{\rm H\,\Box} - \frac{1}{2}\,\tilde{C}_{\rm H\,D} \qquad \rho_{\rm b}^{\rm gg} = \tilde{C}_{\rm H\,W} - \tilde{C}_{\rm bH} + 2\,\tilde{C}_{\rm H\,\Box} - \frac{1}{2}\,\tilde{C}_{\rm H\,D}\,. \tag{II.2.160}$$

Relaxing the PTG assumption introduces non-factorizable sub-amplitudes proportional to $\tilde{C}_{\rm tH}, \tilde{C}_{\rm bH}$ with a mixing among $\tilde{C}_{\rm H\,g}, \tilde{C}_{\rm tg}, \tilde{C}_{\rm bg}$. Meanwhile, renormalization has made one-loop SMEFT finite, e.g., in the G_F -scheme, with a residual $\mu_{\rm R}$ -dependence.

We allow each Wilson coefficient to vary in some interval $\mathrm{I}_n = [-n\,,\,+n]$ and fix a value for Λ. Next we generate points from I_n for the Wilson coefficients with uniform probability and calculate R. Finally, we calculate the R probability distribution function (pdf), as shown in Figs. 184,185.

As another example, a comparison between the LO pdf and NLO pdf for $\mathrm{H} \to \gamma\gamma$ using the approach of this section, and the results in [648], is shown in Figure 186.

II.2.3.c.iii Comments on Pole observables vs tails of distributions

When analysing data near poles, scaling arguments that apply to the suppression of local contact (non resonant) four fermion operators in $\mathcal{L}_6$ also apply to NLO $\mathcal{L}_8$ corrections. This is fortunate as the very large number of parameters present in $\mathcal{L}_8$ and $\mathcal{L}_6$ are primarily present in four fermion operators. In the case of $\mathcal{L}_6$ 2205 of the 2499 parameters present are due to four fermion operators [631]. NLO power corrections in $\mathcal{L}_8$, higher order in $(v/\Lambda)^m$, are suppressed compared to $\mathcal{L}_6$ by the power counting parameter v^2/Λ^2,which varies from $\sim 6\%$ to $\sim 0.6\%$ for $\Lambda/\sqrt{\tilde{C}_i} = 1, 3\,\mathrm{TeV}$ respectively.

The suppression of NLO terms in the Lagrangian expansion that scale as p^2/Λ^2 can be far less in the tails of distributions[II.43]. Tails of distributions can also have a very large number of SMEFT parameters contributing due to non-resonant fermion pair (and higher multi-body) production background

[II.43] See for example discussion in Ref. [612, 763, 764].

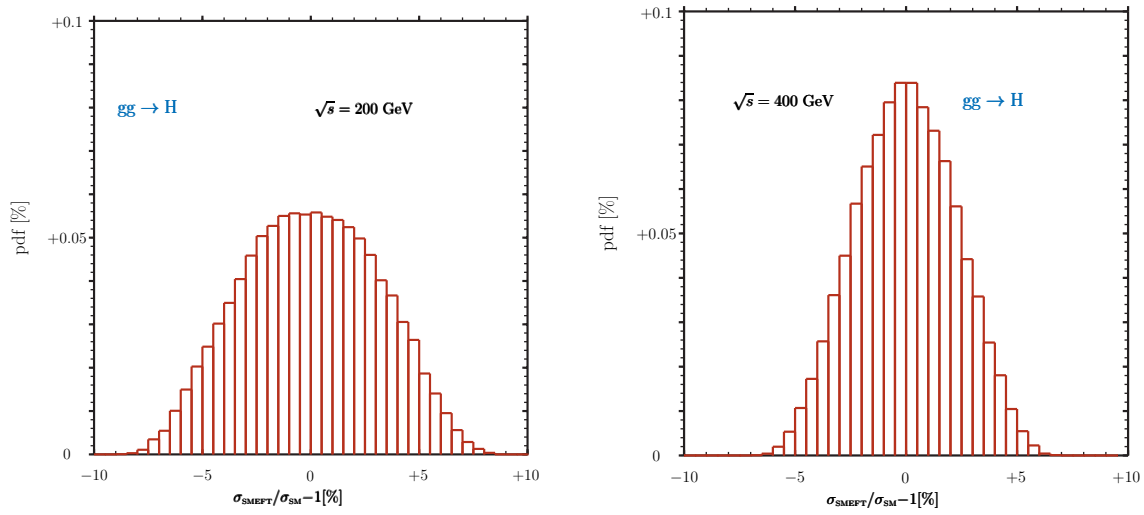

Figure 184: Probability distribution function for the off-shell process $gg \to H$. Support is $C_i \in [-1\,,\,+1]$ with a uniform prior, and we have set $\Lambda = 3\,\mathrm{TeV}$.

processes. The SMEFT expansion breaks down when $p^2/\Lambda^2 \sim 1$, and Pseudo Observable/form factor [610, 651, 731, 764, 765] methods are required to characterize the data in this case. In doing so, it is appropriate to bin the data in a manner that is transparent as to the momentum scale being probed.

It is also worth noting that unlike the case of pole data, NLO corrections to tails of distributions are complicated in their analysis, as the p^2/Λ^2 terms are in general not gauge invariant alone, and need to always be combined with the interference with non-resonant part of the SM, and SMEFT background processes. The requirement for joint analysis including SMEFT corrections on the background that results, further complicates the analysis of non-pole data.

II.2.3.d Summary and comments

We summarize here the main points discussed and advocated in this note.

- NLO results have already had an important impact on the SMEFT physics program. For example, it has been shown that the inclusion of these effects may relax, in some cases, the bounds on some EFT parameters from $\mathcal{O}(10^{-3})$ to $\mathcal{O}(10^{-2})$. This is why we advocate not to use LEP constraints to set to zero effective SMEFT parameters in $\mathcal{L}_6$, or combinations of such parameters for vector boson couplings to fermions in LHC analyses. In general, care should be used when fixing combinations of parameters from EW constraints in LHC analyses. For example, currently, $\mathcal{O}(10^{-3})$ bounds are based on LO SMEFT analyses without any theoretical error assigned.
- It is important to preserve the original data, not just the interpretation results, as the estimate of the missing higher order terms can change over time, modifying the lessons drawn from the data and projected into the SMEFT.
- Overall, the neglect of NLO (perturbative EW) corrections, considering the precision of LHC

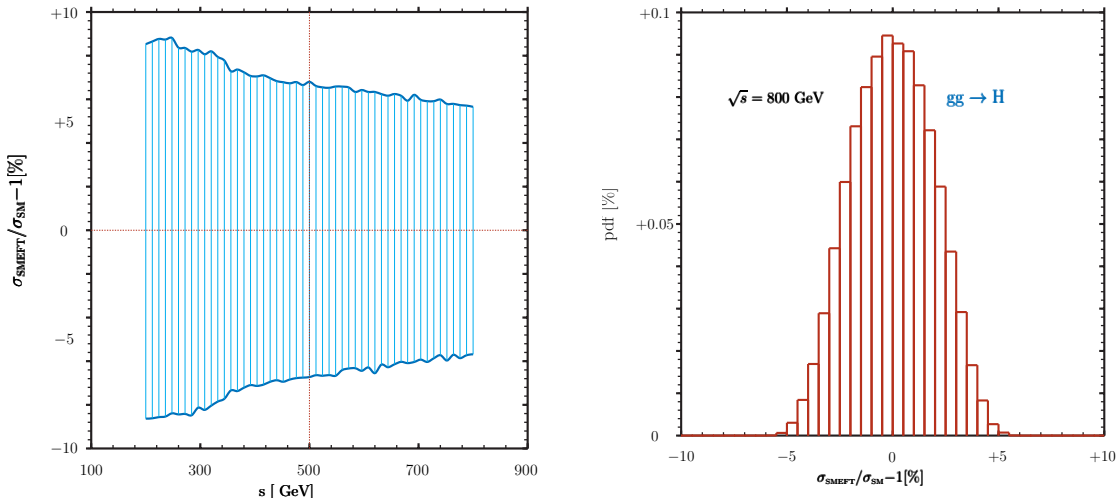

Figure 185: Probability distribution function for the off-shell process $\mathrm{gg} \to \mathrm{H}$. Support is $C_i \in [-1\,,\,+1]$ with a uniform prior, and we have set $\Lambda = 3\,\mathrm{TeV}$.

RunI measurements, is (retrospectively) justified in most channels. On the other hand, NLO QCD corrections are not negligible, even in RunI. However, considering projections for the precision to be reached in LHC RunII analyses, we believe that the LO approach may not be sufficient. This may in particular be the case if the cut off scale is in the few TeV range.

– NLO results are starting to become available in the SMEFT. These results allow the consistent interpretation of the data combining measurements at different scales, and can robustly accommodate the precision projected to be achieved in RunII analyses, even for lower cut off scales.
– In a sense, the SMEFT allow the kappa-framework [10] to be extended/replaced, and NLO results are crucial in this respect. The idea is that interpretations can transition to the linear SMEFT, which is a systematically improvable EFT formalism. NLO results more consistently include kinematic deviations from the SM, and define higher order calculations in relation to a measured observable, in a well defined field theory. A properly formulated SMEFT is not limited to LO and can include QCD and EW corrections.
– The assignment of a theoretical error for LO SMEFT analyses is, in general, important. In our opinion, this is essential if the cut off scale is assumed to be in the "interesting range" $1\,\mathrm{TeV} \lesssim \Lambda/\sqrt{\tilde{C}_i} \lesssim 3\,\mathrm{TeV}$ and the experimental precision of analyses descends below the 10% level. The exact size of NLO corrections depends on the particular UV model, which is unknown, and also the particular channel analysed.
– We do not advocate absorbing the effects of $\mathcal{L}_8$ corrections and/or or absorbing logarithmic NLO perturbative corrections into an "effective" parameter to attempt to incorporate NLO correction. Such a redefinition cannot simultaneously be made in different measurements generally measured at different scales. Correlating different measurements is necessary if the SMEFT is to be used in a predictive fashion for constraints on LHC measurements.
– We think that the experimental collaborations should restrict the bulk of their efforts to defining and reporting clean measurements that can be interpreted in any well defined basis in the SMEFT. The

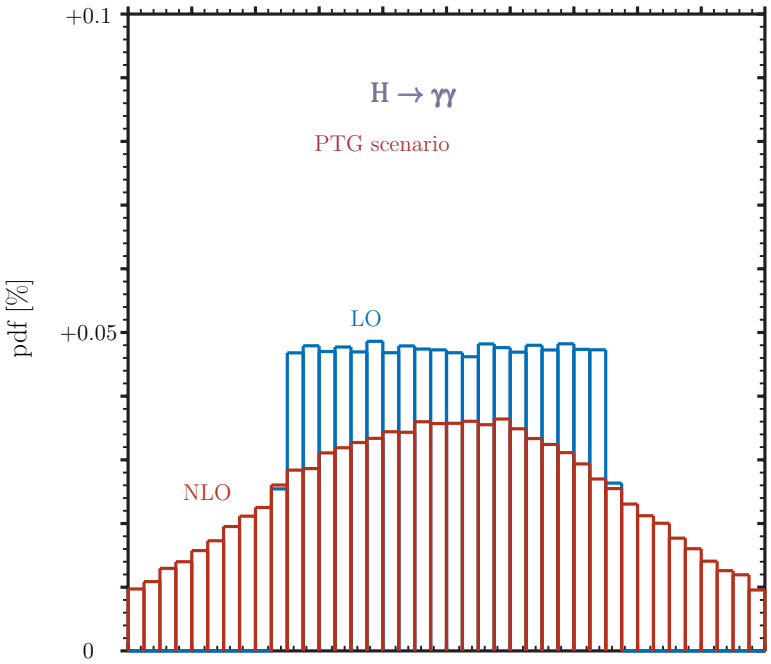

Figure 186: Probability distribution function for the decay $H \to \gamma\gamma$ with a comparison between the LO and the NLO predictions. Here $\Lambda = 3$ TeV and $n = 1$. X axis as in previous figures.

focus for data reporting should be on fiducial cross sections and/or pseudo-observables. If a LO interpretation of the data in the SMEFT is reported there is no barrier to using the straightforward LO formalism of the Warsaw basis discussed in this note. This approach is convenient and well defined.

We have supplied the outline and details of a LO implementation in Section II.2.3.b.iv. We believe that the adoption of this approach for LO fits may be advantageous as it is more readily extendable to NLO. We have sketched out how fits can be pursued at LO and NLO in a consistent fashion using this formalism. The approach presented is well defined, is not intrinsically tied to a particular IPS, can be informed by theoretical errors determined at NLO and can be directly improved to NLO. The gauge invariance of the approach presented has been checked at NLO by explicit confirmation of the WST identities.

We have stressed the standard usage of EFT terminology in this discussion, in particular the definition of an operator basis, to clarify discussion on these issues. EFT is traditionally a very successful paradigm to use to interpret the data because it is implemented as a well defined field theory. Standard EFTs can be systematically improved from LO to NLO and we think that severe caution should be exercised when considering approaches that are that are not constructed in such a standard manner.

II.2.4 Non-linear EFT [II.44]

II.2.4.a Motivation and leading-order Lagrangian

The following section describes the chiral-Lagrangian framework, in which electroweak symmetry breaking is nonlinearly realized, as an effective field theory (EFT) for physics beyond the Standard Model (SM). The motivation for and the main properties of this approach, in particular for describing anoma-

[II.44] *Author(s): I. Brivio, G. Buchalla, O. Cata, A. Celis, R.L. Delgado, A. Dobado, D. Espriu, M. Herrero, C. Krause, F.J. Llanes-Estrada, L. Merlo, J.J. Sanz-Cillero.*

lous Higgs boson couplings, will be reviewed. The connection with the more common EFT based on power counting by canonical dimension (SM + dimension-6 operators, sometimes referred to as SMEFT) will also be discussed. We start with a phenomenologically oriented introduction, which will be followed by a systematic formulation of the nonlinear EFT.

A central goal of the LHC after the discovery of the Higgs boson will be a more comprehensive investigation of its properties in order to test the underlying dynamics of electroweak symmetry breaking. At present, the Higgs boson couplings to gauge bosons and top quarks are compatible with the SM, but deviations of $\mathcal{O}(10\%)$ are still possible [6]. For the couplings to other fermions, or the triple-Higgs boson coupling, even larger effects are not excluded. Anomalous Higgs boson couplings have the potential to give much larger effects than new physics in electroweak gauge interactions, which is typically constrained to the $\mathcal{O}(1\%)$ level by electroweak precision measurements [721].

It then appears natural to focus the attention, in a first step, on the couplings of the Higgs particle. This goal is also well motivated by the foreseeable precision at the LHC with 300 fb^{-1}, projected to reach several per cent accuracy for the Higgs boson couplings to gauge bosons and heavy fermions [724].

Following this line of reasoning, one is led to consider a generalization of the SM, in which the gauge interactions are unchanged (at leading order), but general anomalous couplings are introduced for the physical Higgs boson. To do this in a consistent, gauge-invariant way, the scalar fields have to be decomposed into the three Goldstone fields φ^a, described by

$$U = \exp(2i\varphi^a T^a/v) \tag{II.2.161}$$

where T^a are the generators of $SU(2)$ with normalization $\mathrm{Tr}[T^a T^b] = \delta^{ab}/2$, and the physical Higgs field h. This corresponds to a decomposition of the usual Higgs doublet ϕ_i, $\tilde{\phi}_i = \varepsilon_{ij}\phi_j^*$, into polar coordinates

$$\sqrt{2}(\tilde{\phi}, \phi) \equiv (v + h)U \tag{II.2.162}$$

Under electroweak gauge transformations $SU(2)_L \times U(1)_Y$

$$U \to g_L U g_Y^\dagger, \qquad h \to h \tag{II.2.163}$$

such that h is invariant, and its couplings can be consistently modified.[II.45]

The resulting generalized Lagrangian can be written as

$$\begin{aligned}
\mathcal{L}_2 = &-\frac{1}{2}\langle G_{\mu\nu}G^{\mu\nu}\rangle - \frac{1}{2}\langle W_{\mu\nu}W^{\mu\nu}\rangle - \frac{1}{4}B_{\mu\nu}B^{\mu\nu} + \sum_{\psi=q_L,l_L,u_R,d_R,e_R} \bar{\psi} i \not{D} \psi \\
&+\frac{v^2}{4}\,\langle D_\mu U^\dagger D^\mu U\rangle\,(1 + F_U(h)) + \frac{1}{2}\partial_\mu h \partial^\mu h - V(h) \\
&-v\left[\bar{q}_L\left(Y_u + \sum_{n=1}^{\infty} Y_u^{(n)}\left(\frac{h}{v}\right)^n\right) U P_+ q_R + \bar{q}_L\left(Y_d + \sum_{n=1}^{\infty} Y_d^{(n)}\left(\frac{h}{v}\right)^n\right) U P_- q_R \right. \\
&\left. +\bar{l}_L\left(Y_e + \sum_{n=1}^{\infty} Y_e^{(n)}\left(\frac{h}{v}\right)^n\right) U P_- l_R + \text{h.c.}\right]
\end{aligned} \tag{II.2.164}$$

where

$$D_\mu U = \partial_\mu U + igW_\mu U - ig' B_\mu U T_3, \tag{II.2.165}$$

[II.45] The generic name of "nonlinear" comes from the fact that the scalar sector of the SM has a larger symmetry $SU(2)_L \times SU(2)_R$ (usually called chiral EW symmetry), under which the EW Goldstone bosons φ^a in (II.2.161) transform nonlinearly, in contrast to the usual Higgs doublet field, which transforms linearly. The relevant symmetry breaking pattern in the scalar sector is then given by $SU(2)_L \times SU(2)_R \to SU(2)_{L+R}$, where the $SU(2)_{L+R}$ is usually called the custodial symmetry group.

and $P_\pm = 1/2 \pm T_3$. The trace of a matrix A is denoted by $\langle A \rangle$. The left-handed doublets of quarks and leptons are written as q_L and l_L, the right-handed singlets as u_R, d_R, e_R. Generation indices are omitted. In the Yukawa terms the right-handed quark and lepton fields are collected into $q_R = (u_R, d_R)^T$ and $l_R = (\nu_R, e_R)^T$, respectively. In general, different flavour couplings $Y^{(n)}_{u,d,e}$ can arise at every order in the Higgs field h^n, in addition to the usual Yukawa matrices $Y_{u,d,e}$. The detailed assumptions underlying (II.2.164) are summarized in points (i) – (iii) below.

The first line in (II.2.164) represents the unbroken SM and the remaining lines describe the sector of electroweak symmetry breaking. The h-dependent functions, analytic near zero field, are

$$F_U(h) = \sum_{n=1}^{\infty} f_{U,n} \left(\frac{h}{v}\right)^n, \qquad V(h) = v^4 \sum_{n=2}^{\infty} f_{V,n} \left(\frac{h}{v}\right)^n \tag{II.2.166}$$

In addition to modifying the Higgs boson couplings present in the SM, new couplings with higher powers in the field h are introduced. All these couplings may deviate, in principle, by corrections of $\mathcal{O}(1)$ from their (dimensionless) SM values. For smaller deviations, the Lagrangian in (II.2.164) continues to describe the leading new-physics effects, as long as the anomalous couplings in the Higgs sector dominate over other corrections from physics beyond the SM. (Those would be represented by operators of chiral dimension 4 and higher, see the discussion of power counting below.)

While $\mathcal{L}_2$ in (II.2.164) is gauge invariant, it is no longer renormalizable for general Higgs boson couplings. Renormalizability would be recovered in the SM limit where

$$f_{U,1} = 2, \quad f_{U,2} = 1, \quad f_{V,2} = f_{V,3} = \frac{m_h^2}{2v^2}, \quad f_{V,4} = \frac{m_h^2}{8v^2}, \quad Y_f^{(1)} = Y_f, \tag{II.2.167}$$

and all other couplings $f_{U,n}$, $f_{V,n}$, $Y_f^{(n)}$ equal to zero. In this limit (II.2.164) is just the SM written in somewhat unconventional variables. All S-matrix elements are of course identical to the ones obtained with the familiar linear Lagrangian.

If the deviations of the couplings from their SM values are smaller than unity, it is useful to parameterize them by a quantity $\xi \equiv v^2/f^2$, where $f > v$ represents a new scale (which could be related to a new strongly interacting dynamics). In models of a composite, pseudo-Goldstone Higgs [658, 766–775] f corresponds to the Goldstone-boson decay constant. Experimentally, values of $\xi = \mathcal{O}(10\%)$ are currently still allowed.

For general Higgs boson couplings, the Lagrangian $\mathcal{L}_2$, nonrenormalizable in the traditional sense, is still renormalizable in the modern sense, order by order in a consistent expansion [776]. It therefore continues to serve as a fully consistent effective field theory. This EFT is known as the *electroweak chiral Lagrangian* including a light Higgs boson. For the case without Higgs the electroweak chiral Lagrangian has been formulated and applied in [777–793]. The generalization to include a light Higgs boson has been developed in [683, 785, 794–804].

Having motivated the basic structure of the electroweak chiral Lagrangian, it is useful to summarize the most important assumptions that define it as a systematic EFT. These concern the *particle content* below a certain mass gap, the relevant *symmetries*, and the *power counting*:

(i) SM particle content, where (transverse) gauge bosons and fermions are weakly coupled to the Higgs-sector dynamics.

(ii) SM gauge symmetries; conservation of lepton and baryon number; conservation *at lowest order* of custodial symmetry in the strong sector, CP invariance in the Higgs sector and fermion flavour. The latter symmetries are violated at some level, but this would only affect terms at subleading order. Generalizations may in principle be introduced if necessary.

(iii) Power counting by chiral dimensions [805–808], equivalent to a loop expansion [683], with the simple assignment of 0 for bosons (gauge fields X_μ, Goldstones φ and Higgs h) and 1 for each

derivative, weak coupling (e.g. gauge or Yukawa), and fermion bilinear:

$$[X_\mu, \varphi, h]_\chi = 0\,, \qquad [\partial_\mu, g, y, \psi\bar{\psi}]_\chi = 1 \tag{II.2.168}$$

The loop order L of a term in the Lagrangian is equivalent to its chiral dimension (or chiral order) $2L + 2$.

Under these assumptions the expression in (II.2.164) follows as the most general Lagrangian built from terms of chiral dimension 2 (corresponding to loop-order $L = 0$). This is the systematic basis for the leading-order electroweak chiral Lagrangian.

Functions $F(h)$ multiplying the Higgs or the fermion kinetic terms can be removed by field redefinitions and are therefore omitted in (II.2.164) [653, 801].

Note that the Higgs potential $V(h)$, being related to the light Higgs boson mass $\sim m_h^2$, carries chiral dimension 2. This is explicitly realized in models where the Higgs is a pseudo-Goldstone and its potential is generated at one loop (proportional to two powers of weak coupling, hidden in the coefficients $f_{V,n}$) [658, 770–773].

Expressions of the form $(\bar{\psi}\psi)^2(h/v)^n$, $\bar{\psi}\sigma_{\mu\nu}\psi X^{\mu\nu}(h/v)^n$, $X_{\mu\nu}X^{\mu\nu}(h/v)^{n+1}$, $n \geq 0$, where ψ is a fermion and $X_{\mu\nu}$ a gauge field-strength tensor, might superficially look like terms entering the Lagrangian at chiral dimension 2. However, they represent local interactions arising from the (weak) coupling of ψ and X to the new-physics sector, according to assumption (i) above. The weak coupling associated with $\bar{\psi}\psi$ or $X_{\mu\nu}$ carries chiral dimension. The operators above then acquire a chiral dimension of at least 4, which eliminates them from the leading-order Lagrangian [683].

II.2.4.b Renormalization of the chiral Lagrangian

As the electroweak chiral Lagrangian defines a consistent quantum field theory, loop corrections can be systematically included. For the case without Higgs field this has been discussed in detail in [809–813]. The one-loop divergent parts arising from the scalar sector have recently been also obtained in the chiral Lagrangian including the light Higgs boson [800, 814–818].

At one-loop order, terms up to chiral dimension 4 need to be included and the Lagrangian can be written as $\mathcal{L} = \mathcal{L}_2 + \mathcal{L}_4 + \mathcal{L}_{\rm GF} + \mathcal{L}_{\rm FP}$, including also gauge-fixing and ghost terms. In general, the leading-order approximation is given by the tree-level amplitudes from $\mathcal{L}_2$. The next-to-leading order corrections consist of the one-loop amplitudes with vertices from $\mathcal{L}_2$, together with tree-level contributions to first order in $\mathcal{L}_4$. The latter comprise new interactions, not present in $\mathcal{L}_2$, and act as counterterms for the one-loop divergences. In general, they may get contributions from heavy states with masses of order Λ that are integrated out in the EFT [819–821]. This pattern is known from the chiral perturbation theory of pions. It is typical for the systematics of a nonrenormalizable EFT. Explicit examples are discussed in Section II.2.4.e.

The local operators in $\mathcal{L}_4$ have been discussed for the bosonic sector in [799], a subset of the fermionic terms has been considered in [822]. A systematic presentation of the complete basis of local operators in $\mathcal{L}_4$ can be found in [801]. Concentrating on the electroweak bosonic sector one has (with $2a = f_{U,1}$, $b = f_{U,2}$ in (II.2.166))

$$\begin{aligned}\mathcal{L}_2 = &-\frac{1}{2}\langle W_{\mu\nu}W^{\mu\nu}\rangle - \frac{1}{4}B_{\mu\nu}B^{\mu\nu} \\ &+\frac{v^2}{4}\left[1 + 2a\frac{h}{v} + b\frac{h^2}{v^2} + \dots\right]\langle D^\mu U^\dagger D_\mu U\rangle + \frac{1}{2}\partial^\mu h\,\partial_\mu h + \dots\end{aligned}$$

$$\begin{aligned}\mathcal{L}_4 = &\, a_1 g' g\langle U T_3 B_{\mu\nu} U^\dagger W^{\mu\nu}\rangle + i a_2 g'\langle U T_3 B_{\mu\nu} U^\dagger [V^\mu, V^\nu]\rangle - i a_3 g\langle W_{\mu\nu}[V^\mu, V^\nu]\rangle \\ &+a_4\langle V_\mu V_\nu\rangle\langle V^\mu V^\nu\rangle + a_5\langle V_\mu V^\mu\rangle\langle V_\nu V^\nu\rangle + \frac{e^2}{16\pi^2}c_{\gamma\gamma}\frac{h}{v}F_{\mu\nu}F^{\mu\nu} + \frac{g^{hh}}{v^4}(\partial_\mu h\partial^\mu h)^2\end{aligned}$$

Table 102: Example of the renormalization structure. Running of some NLO coefficients [800, 814, 815].

$\Gamma_{a_1-a_2+a_3}$	$\Gamma_{c_{\gamma\gamma}}$	Γ_{a_1}	$\Gamma_{a_2-a_3}$	Γ_{a_4}	Γ_{a_5}
0	0	$-\frac{1}{6}(1-a^2)$	$-\frac{1}{6}(1-a^2)$	$\frac{1}{6}(1-a^2)^2$	$\frac{1}{8}(b-a^2)^2+\frac{1}{12}(1-a^2)^2$

$$+\frac{d^{hh}}{v^2}(\partial_\mu h\partial^\mu h)\langle D_\nu U^\dagger D^\nu U\rangle+\frac{e^{hh}}{v^2}(\partial_\mu h\partial^\nu h)\langle D^\mu U^\dagger D_\nu U\rangle+\ldots \tag{II.2.169}$$

where $V_\mu\equiv(D_\mu U)U^\dagger$ and $F_{\mu\nu}$ is the photon field strength. Here only a subset of the operators in $\mathcal{L}_4$ has been displayed, corresponding to those needed in the discussion below. All operators that need to be included as counterterms are manifestly custodially preserving, except for the custodial breaking from $U(1)_Y$. This is so because the initial theory is custodially invariant when Yukawas are neglected.

As a simple example for renormalization, consider the oblique S-parameter. The first non-vanishing contribution to S appears at NLO. One finds that the one-loop amplitude is UV–divergent and needs to be renormalized by means of the NLO parameter a_1. In the $\overline{MS}$ scheme one obtains [787, 815, 819]

$$S=-16\pi a_1^r+\frac{(1-a^2)}{12\pi}\left(\frac{5}{6}+\ln\frac{\mu^2}{m_h^2}\right) \tag{II.2.170}$$

In this expression, the oblique parameter is defined with the reference value $m_h^{\rm Ref}$ set to the physical Higgs boson mass [738]. Since fermionic couplings to gauge bosons receive only NLO contributions from new physics, fermion loops do not affect this result. Their impact would be a NNLO effect..

Renormalization leads to a scale dependence of the coefficients. In general, the relation between a given renormalized chiral parameter $C^r(\mu)$ and the corresponding bare parameter $C^{(B)}$ from the $\mathcal{L}_4$ Lagrangian (e.g. a_1), together with the resulting μ-dependence, is given by

$$\frac{dC^r}{d\ln\mu}=-\frac{\Gamma_C}{16\pi^2},\qquad C^r(\mu)=C^{(B)}+\frac{\Gamma_C}{32\pi^2}\frac{1}{\hat\epsilon} \tag{II.2.171}$$

where an $\overline{MS}$ subtraction of the UV divergence has been performed. Here $1/\hat\epsilon=\mu^{-2\epsilon}(1/\epsilon-\gamma_E+\ln 4\pi)$, with $D=4-2\epsilon$.

The running of the $\mathcal{L}_4$ parameters $C=a_1,\,a_2,\,a_3,\,c_{\gamma\gamma}$ [815] (relevant e.g. for $\gamma\gamma\to w^aw^b$) and of $C=a_4,\,a_5$ (contributing to ZZ and W^+W^- scattering [800, 814]) is shown in Table 102. It is apparent that the S-parameter in (II.2.170) is independent of the renormalization scale μ.

II.2.4.c Connection of chiral Lagrangian to κ-formalism

The couplings of the leading-order Lagrangian in (II.2.164), which are non-standard in general, are displayed in Figure 187. They parameterize the leading new-physics effects in tree-level processes.

A further consideration is needed for the application of the chiral Lagrangian to processes that arise only at one-loop level in the SM. Important examples are $h\to gg$, $h\to\gamma\gamma$ and $h\to Z\gamma$. In this case local terms at NLO will also become relevant, in addition to the standard loop amplitudes with modified couplings from (II.2.164). The reason is that both contributions can lead to deviations of the amplitude from the SM at the same order, $\sim\xi/16\pi^2$. The complete list of NLO operators has first been worked out in [801]. The terms that are relevant here are

$$e^2F_{\mu\nu}F^{\mu\nu}h,\qquad eg'F_{\mu\nu}Z^{\mu\nu}h,\qquad g_s^2\langle G_{\mu\nu}G^{\mu\nu}\rangle h \tag{II.2.172}$$

On the other hand, the analogous terms $g'^2Z_{\mu\nu}Z^{\mu\nu}h$ and $g^2W^+_{\mu\nu}W^{-\mu\nu}h$ in the subleading Lagrangian yield only subleading contributions, of $\mathcal{O}(\xi/16\pi^2)$, to the tree-level amplitudes for $h\to ZZ$ and $h\to$

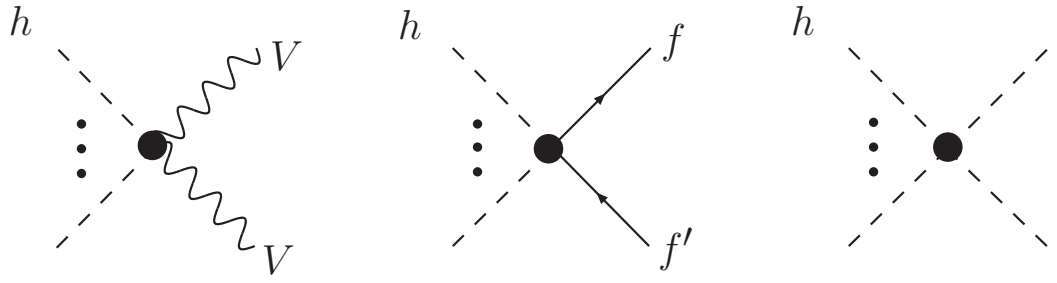

Figure 187: The Higgs vertices from the leading-order Lagrangian $\mathcal{L}_2$ in unitary gauge.They are represented by a black dot and may deviate sizably from the SM. The pair of dashed lines with dots in between signifies any number of Higgs lines. The massive vector bosons are denoted by $V = W, Z$. $f = f'$ if flavour conservation is assumed to hold at leading order. All other couplings are identical to the SM.

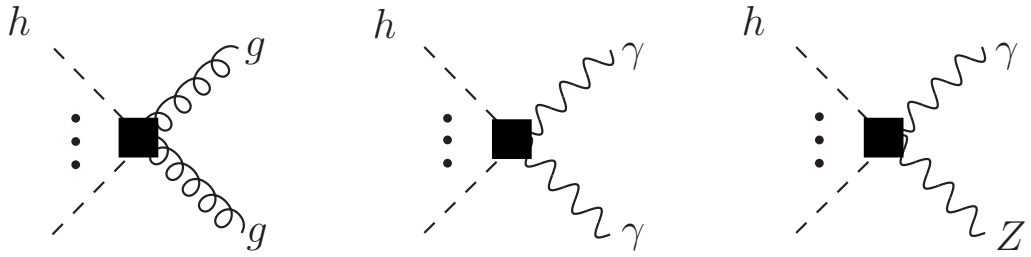

Figure 188: Higgs vertices from the NLO Lagrangian $\mathcal{L}_4$, represented by black squares, that contribute to gg, $\gamma\gamma$ and $Z\gamma$ amplitudes. Since the latter arise only at one-loop order from the interactions of $\mathcal{L}_2$, the NLO couplings give relative corrections of the same order in this case and have to be retained.

W^+W^-, which receive new-physics corrections of $\mathcal{O}(\xi)$ from (II.2.164). They can thus be neglected in a first approximation (see [823] for a discussion of generic NLO effects).

In summary, the Higgs boson couplings from NLO operators that are relevant for a LO analysis of loop-induced processes are shown in Figure 188.

Based on the preceding discussion, one can now define anomalous Higgs boson couplings for specific classes of interactions, corresponding to the leading order approximation within the chiral Lagrangian framework.

An important example are interactions involving a single Higgs field. Focusing on these terms, and working in unitary gauge, (II.2.164) supplemented by the local NLO terms for $h \to \gamma\gamma$, $Z\gamma$ and gg, implies the interaction Lagrangian ($c_V \equiv a$ in (II.2.169))

$$\begin{aligned}\mathcal{L} &= 2c_V \left(m_W^2 W_\mu^+ W^{-\mu} + \tfrac{1}{2} m_Z^2 Z_\mu Z^\mu\right) \frac{h}{v} \\ &\quad - \textstyle\sum_{i,j} (y_{u,ij}^{(1)} \bar{u}_{Li} u_{Rj} + y_{d,ij}^{(1)} \bar{d}_{Li} d_{Rj} + y_{e,ij}^{(1)} \bar{e}_{Li} e_{Rj} + \text{h.c.}) h \\ &\quad + \frac{e^2}{16\pi^2} c_{\gamma\gamma} F_{\mu\nu} F^{\mu\nu} \frac{h}{v} + \frac{eg'}{16\pi^2} c_{Z\gamma} Z_{\mu\nu} F^{\mu\nu} \frac{h}{v} + \frac{g_s^2}{16\pi^2} c_{gg} \langle G_{\mu\nu} G^{\mu\nu} \rangle \frac{h}{v}\end{aligned} \tag{II.2.173}$$

Neglecting flavour violation, the very small Yukawa couplings to light fermions, and concentrating on those Higgs processes that have already become accessible at the LHC, the parameterization reduces to

a set of six anomalous couplings, described by [823, 824]

$$\begin{aligned}\mathcal{L} = 2c_V \left(m_W^2 W_\mu^+ W^{-\mu} + \tfrac{1}{2} m_Z^2 Z_\mu Z^\mu\right) \frac{h}{v} - c_t y_t \bar{t} t h - c_b y_b \bar{b} b h - c_\tau y_\tau \bar{\tau} \tau h \\ + \frac{e^2}{16\pi^2} c_{\gamma\gamma} F_{\mu\nu} F^{\mu\nu} \frac{h}{v} + \frac{g_s^2}{16\pi^2} c_{gg} \langle G_{\mu\nu} G^{\mu\nu} \rangle \frac{h}{v}\end{aligned} \tag{II.2.174}$$

where $y_f = m_f/v$. The SM at tree level is given by $c_V = c_t = c_b = c_\tau = 1$ and $c_{gg} = c_{\gamma\gamma} = 0$. Deviations due to new physics are expected to start at $\mathcal{O}(\xi)$.

A few important points should be emphasized:

(i) The parameterization of anomalous Higgs boson couplings in (II.2.174) essentially corresponds to the *κ-formalism* [9], which is frequently used in experimental analyses. Here, (II.2.174) has been derived from the electroweak chiral Lagrangian.

(ii) The minimal version in (II.2.174) can be generalized to include more of the couplings contained in (II.2.173), such as $h \to Z\gamma$, $h \to \mu\mu$, or the lepton-flavour violating $h \to \tau\mu$.

(iii) The treatment can be further extended, for instance to double-Higgs boson production, where additional couplings with two or three h-fields from (II.2.164) need to be considered (see Section II.2.4.e.iv below).

(iv) The anomalous couplings c_i of the nonlinear EFT at leading order are able to account for deviations of $\mathcal{O}(1)$ from the SM. It is then consistent to retain the terms quadratic in these couplings when computing cross sections and rates. This is in contrast to the linear case, where a linearization in the dimension-6 corrections has to be performed at this level of accuracy.

(v) Eventually the computation of an observable at a given chiral order must incorporate the loop corrections at that order if one wants to perform an accurate determination of the Higgs parameters at the LHC [823].

II.2.4.d Linear vs. nonlinear EFT

In this section the relation between the SMEFT organized by canonical dimensions (often referred to as "linear" EFT) and the one organized by chiral dimensions (usually referred to as "nonlinear" EFT) will be discussed.

SMEFT is the most common approach to the SM as an EFT and starts from the renormalizable, dimension-4 Lagrangian, adding operators of higher canonical dimension to account for the physics at shorter distances. Assuming conservation of baryon and lepton number, the leading corrections come from the terms of dimension 6 [614, 620].

In the case of the electroweak chiral Lagrangian three relevant energy scales may be distinguished: The electroweak scale v, the scale f of the Higgs-sector dynamics, and the cut-off scale $\Lambda = 4\pi f$, where the low-energy description of this dynamics breaks down. These three scales allow for two independent expansion parameters, $\xi = v^2/f^2$ and the loop factor $1/(16\pi^2) = f^2/\Lambda^2$. In full generality, a double expansion can thus be performed on the new-physics effects.

The resulting picture is sketched in Figure 189, where the powers of ξ are plotted on the vertical and the loop order on the horizontal axis [682]. The dots indicate, schematically, (classes of) operators in the effective Lagrangian or, alternatively, terms in a physical amplitude.

Without expanding in ξ, the effective theory takes the form of a loop expansion as in the usual chiral Lagrangians [776]. This amounts to proceeding from left to right in Figure 189, order by order in the loop expansion, resumming at each order all terms along the vertical axis.

Alternatively, the expansion may be organized in powers of ξ, proceeding from bottom to top of Figure 189 and including, in principle, at each power of ξ terms of arbitrary order in the loop expansion. This scheme corresponds to the conventional expansion of the effective theory in terms of the canonical dimension d of operators, where the power of ξ is given by $(d-4)/2$. Since the dimensional expansion

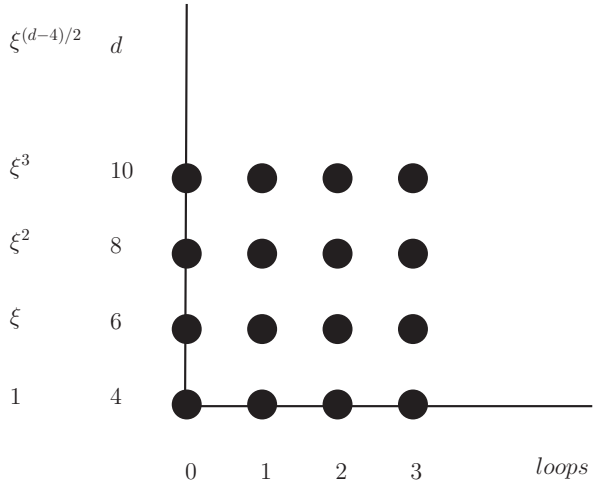

Figure 189: Systematics of the effective theory with sizeable anomalous couplings in the Higgs sector. The dots indicate operators in the effective Lagrangian (or terms in a physical amplitude). In general, they may be organized both in powers of $\xi = v^2/f^2$ (vertical axis) and according to their order L in the loop expansion (horizontal axis). The latter is equivalent to the chiral dimension $2L + 2$.

requires only a hierarchy between v and the new-physics scale f, $\xi \ll 1$, it is not restricted to a pseudo-Goldstone Higgs scenario, typically underlying the chiral Lagrangian.

These observations clarify the relation between an effective theory organized by canonical dimension and the electroweak chiral Lagrangian organized as a loop expansion: The former is constructed row by row, the latter column by column from the terms in Figure 189. In conclusion, both EFTs, the one based on canonical dimension and the one based on chiral dimensions, can in principle account for low-energy deviations from the SM and could in general cover the same correction terms. The difference consists in the way these terms are organized or resummed. It will ultimately depend on the pattern of new-physics effects which of the two formulations will eventually be more appropriate.

Phenomenological implications of linear vs. nonlinear EFT

The essential difference between the EFT with a chiral expansion ('nonlinear') and the one with a dimensional expansion ('linear') consists in a reordering of terms as illustrated in Figure 189. This reordering is dictated by the different dynamics. The chiral framework will be the relevant one if the Higgs-coupling deviations characterized by ξ are parametrically larger than the loop factor, $\xi \gg 1/16\pi^2$, or equivalently $f \ll 4\pi v \approx 3\,\text{TeV}$. This would typically be the case for $\xi = \mathcal{O}(10\%)$, within reach of the precision achievable at the LHC. The experimental program to explore such a scenario will then be the search for anomalous Higgs boson couplings with sizeable deviations from the SM values. Given the precision goal of the LHC in Run 2 and 3, this search should be focussed on the leading-order couplings contained in $\mathcal{L}_2$. Important targets are the hVV, $ht\bar{t}$, $hb\bar{b}$, $h\tau\bar{\tau}$ couplings, but also h^3 from the Higgs potential or $h \to gg$, $h \to \gamma\gamma$, $h \to Z\gamma$ local contributions. Longitudinal gauge-boson scattering, although challenging experimentally, might also yield important information [629, 800, 814]. The same is true for $\gamma\gamma$ scattering and other photon-related observables [815].

Besides the expected size of the deviations, one of the generic features of the chiral Lagrangian is the *decorrelation* between Higgs boson couplings [682, 802], which arises already at leading order. For instance, the quark mass and the Yukawa interaction at LO are controlled by different coefficients (see (II.2.164) above). If an expansion at fixed order in ξ is performed on the Wilson coefficients of the electroweak chiral Lagrangian, then correlations will appear. If ξ is sufficiently small, these correlations

will eventually be the same as in the SMEFT (see for instance [653,682] for a discussion). The distinction between a linear and nonlinear framework therefore depends crucially on the size of ξ.

As another example, the corrections to the oblique parameter a_1 in (II.2.169), or to the triple gauge boson vertex (parameterized by a_2 and a_3), or to longitudinal WW scattering (a_4 and a_5) all appear at chiral dimension 4 in the nonlinear EFT, whereas in the linear realization corrections to the triple gauge boson vertex appear at $D = 6$ while anomalous contribution to the quartic gauge boson vertex appear only at $D = 8$. In the linear case there is thus a strong hierarchy between those corrections. In the nonlinear case $a_1, a_2, a_3 \sim \xi/16\pi^2$ while $a_4, a_5 \sim \xi^2/16\pi^2$, thus their hierarchy depends on the size of ξ and would disappear for $\xi = \mathcal{O}(1)$.

II.2.4.e Sample applications

The following examples illustrate how Higgs-related processes are affected by new physics as described by the electroweak chiral Lagrangian.

II.2.4.e.i $h \to Z\ell^+\ell^-$

The process $h \to Z\ell^+\ell^-$, shown in Figure 190 may serve as a prototype for a tree-level decay of the Higgs boson. At leading order only the rate is affected by an anomalous coupling that modifies

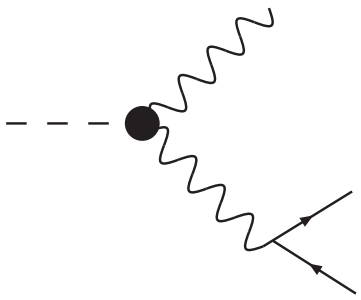

Figure 190: $h \to Z\ell^+\ell^-$ decay at leading order in the chiral Lagrangian. The black dot indicates the (anomalous) hZZ coupling c_V from $\mathcal{L}_2$. The Z-fermion coupling is not modified at this order.

the hZZ vertex. The operators contributing at NLO have been listed in [823, 825]. These give the dominant contributions to the angular distributions. This hierarchy between rates and distributions is a generic feature of the chiral Lagrangian for tree-level processes: in the SMEFT corrections to rates and distributions come at the same (NL) order in the expansion.

The case of $h \to WW^*$ decay is similar. Likewise, the decay of Higgs into a pair of fermions $h \to f\bar{f}$ is modified multiplicatively by a leading-order anomalous coupling.

II.2.4.e.ii $h \to \gamma\gamma$, $h \to Z\gamma$

Further important examples are the decays $h \to \gamma\gamma$ and $h \to Z\gamma$. Based on the chiral Lagrangian, the leading contributions are displayed in Figure 191. Leading-order vertices inside loops contribute at the same level as next-to-leading order local terms at tree level. The (non-Higgs) photon and Z-boson couplings are identical to those in the SM.

II.2.4.e.iii $pp \to h + jet$

The high-p_T distribution of a boosted Higgs in $pp \to h + jet$ has been proposed as a tool to disentangle the contributions from c_t and c_{gg}, which cannot be separated in the $gg \to h$ total rate [826]. The dependence on these couplings in the framework of the electroweak chiral Lagrangian at leading order

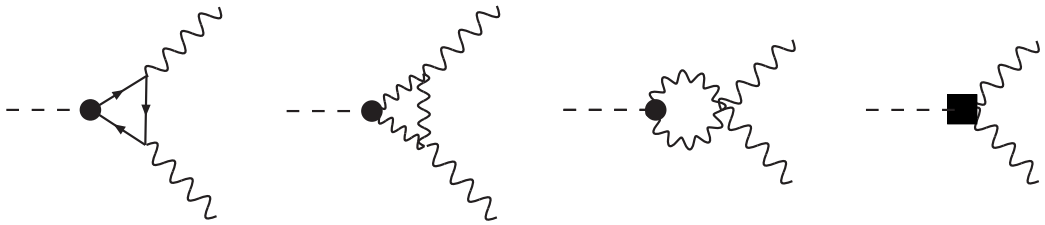

Figure 191: $h \to \gamma\gamma$, $h \to Z\gamma$ decay at leading order in the chiral Lagrangian. The black dots indicate vertices from $\mathcal{L}_2$ (couplings c_V, c_t),the black squares denote local terms from $\mathcal{L}_4$ (couplings $c_{\gamma\gamma}$, $c_{Z\gamma}$).

is illustrated for the partonic process $gg \to gh$ in Figure 192. At high p_T the loop involving c_t can be

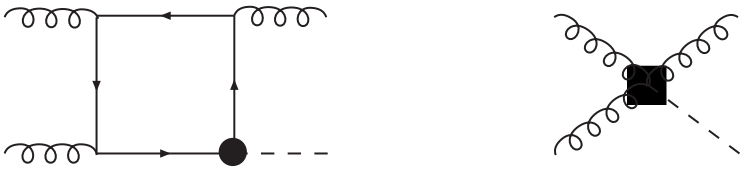

Figure 192: Sample diagrams for $pp \to h + jet$ at leading order in the chiral Lagrangian. The black dot denotes c_t, the black square c_{gg}.

distinguished from the local interaction described by c_{gg}.

II.2.4.e.iv Higgs-pair production in gluon fusion

Another interesting case is Higgs-pair production in gluon-gluon fusion, which has recently been discussed in [472, 827] in the framework of the chiral Lagrangian. NLO QCD effects have been consistently included [472]. The leading-order diagrams are shown in Figure 193. All diagrams are at the same order

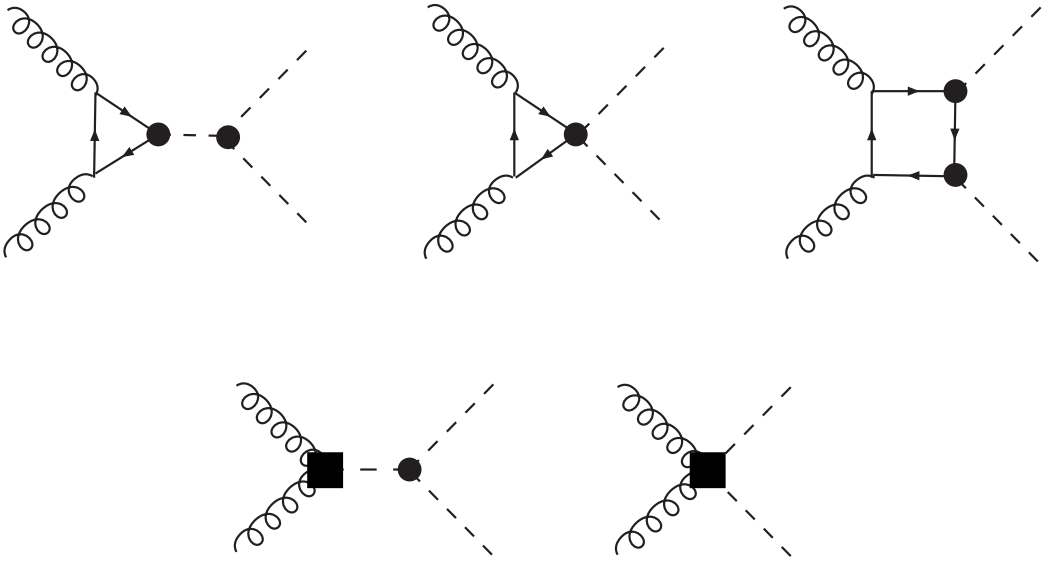

Figure 193: Higgs-pair production in gluon fusion at leading order in the chiral Lagrangian. The black dots indicate vertices from $\mathcal{L}_2$, the black squares denote local terms from $\mathcal{L}_4$.

in the chiral counting. They illustrate again the interplay between leading order anomalous couplings (black dots) within loops, and next-to-leading order terms (black squares) at tree level. Note that five different couplings appear, $ht\bar{t}$, $hht\bar{t}$, hhh from $\mathcal{L}_2$, and hgg, $hhgg$ from $\mathcal{L}_4$.

II.2.4.e.v Photon-photon scattering

The scattering processes $\gamma\gamma \to W_L^+W_L^-$ and $\gamma\gamma \to Z_LZ_L$ have been studied in [815] in the framework of the electroweak chiral Lagrangian with a light Higgs to NLO and by means of the equivalence theorem, where the relevant amplitudes are those for the corresponding Goldstone bosons $\gamma\gamma \to w^+w^-$ and $\gamma\gamma \to zz$, respectively. These Goldstone bosons are introduced via the U-matrix in (II.2.161). Also some related observables like the oblique S-parameter, the electromagnetic form factor $\gamma^* \to w^+w^-$, and the Higgs transition form factor $\gamma^*\gamma^* \to h$ have been studied in [815]. All these photon-related observables are sensitive to the nature and the couplings of the Higgs boson via loops and via internal Higgs propagators, allowing the investigation of a possible dynamical electroweak symmetry breaking and strongly coupled scenarios. This motivates the study of these observables in the context of the LHC and other future colliders, and in particular the photon-photon scattering processes have received increased interest also in the experimental community. The CMS Collaboration has published Run 1 results on the charged channel [828, 829], showing the feasibility of this type of analysis and new forward proton detectors, CMS-TOTEM Precision Proton Spectrometer (CT-PPS) [830, 831] and ATLAS-AFP [832], will be incorporated. The goal would be to search for exclusive or quasi-exclusive W^+W^- production by photon-photon interactions in $pp \to p^{(*)}W^+W^-p^{(*)}$, where the two intermediate photons are radiated collinearly from the protons, which come out undetected along the beam-pipe [828, 829]. Tagging the outgoing $p^{(*)}$ with the CT-PPS and ATLAS-AFP forward detectors will highly increase the efficiency of this type of analyses. On the other hand, a further study could be done if the extra jets, being produced in the deep inelastic regime of these photon mediated processes, are also required to be detected in the forward/backward region. This could also provide interesting additional information on these subprocesses where the photons are virtual.

Within the approximation of the equivalence theorem ($W_L^\pm \to w^\pm$, $Z_L \to z$) considered in [815], the photon-photon scattering amplitudes and the previously mentioned related observables can be described by just a few terms in (II.2.169), parameterized by a in $\mathcal{L}_2$ and a_1, a_2, a_3, $c_{\gamma\gamma}$ in $\mathcal{L}_4$. (Related work on photon-photon processes in the chiral perturbation theory of pions is described in [833–836].)

The results for the scattering amplitudes are presented in terms of the two helicity-independent scalars $A(s,t,u)$ and $B(s,t,u)$, in the form

$$\mathcal{M}(\gamma(k_1,\epsilon_1)\gamma(k_2,\epsilon_2) \to w^a(p_1)w^b(p_2)) \;=\; ie^2(\epsilon_1^\mu\epsilon_2^\nu T^{(1)}_{\mu\nu})A(s,t,u) + ie^2(\epsilon_1^\mu\epsilon_2^\nu T^{(2)}_{\mu\nu})B(s,t,u)$$

which are written in terms of the two independent Lorentz structures and the external photon polarizations ϵ_j,

$$\begin{aligned}(\epsilon_1^\mu\epsilon_2^\nu T^{(1)}_{\mu\nu}) &= \frac{s}{2}(\epsilon_1\epsilon_2) - (\epsilon_1 k_2)(\epsilon_2 k_1), \\ (\epsilon_1^\mu\epsilon_2^\nu T^{(2)}_{\mu\nu}) &= 2s(\epsilon_1\Delta)(\epsilon_2\Delta) - (t-u)^2(\epsilon_1\epsilon_2) - 2(t-u)[(\epsilon_1\Delta)(\epsilon_2 k_1) - (\epsilon_1 k_2)(\epsilon_2\Delta)],\end{aligned} \tag{II.2.175}$$

with the Mandelstam variables defined as usual, $s = (p_1+p_2)^2$, $t = (k_1-p_1)^2$ and $u = (k_1-p_2)^2$, and the relevant momentum combination is defined as $\Delta^\mu \equiv p_1^\mu - p_2^\mu$.

The diagrams contributing to $\gamma\gamma \to ww$ are summarized schematically in Figure 194. The LO amplitudes are provided by tree-level diagrams with vertices from $\mathcal{L}_2$, Figure 194 a) for ww (the diagrams for zz can be found in [815]):

$$A(s,t,u)^{\gamma\gamma\to zz}_{\rm LO} \;=\; B(s,t,u)^{\gamma\gamma\to zz}_{\rm LO} = 0\,,$$

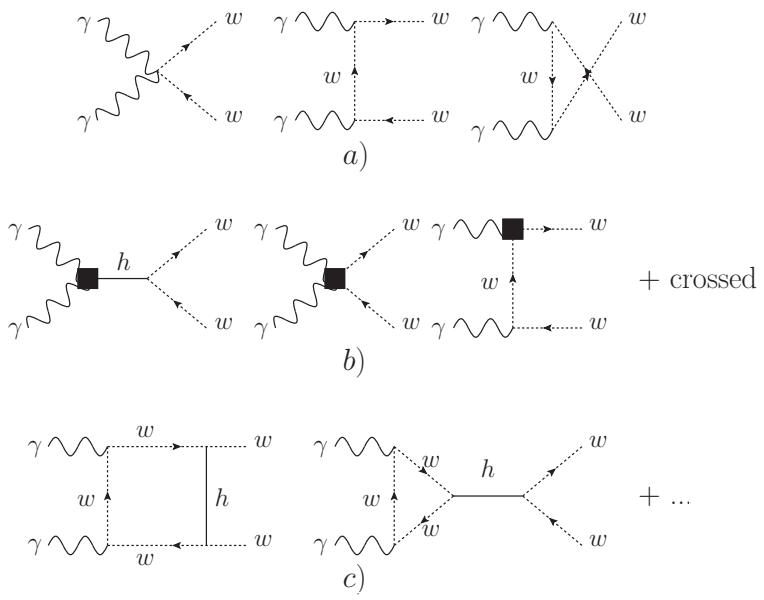

Figure 194: Diagrams contributing to $\gamma\gamma \to ww$ in the nonlinear EFT up to NLO: a) from just $\mathcal{L}_2$ at tree level, b) from both $\mathcal{L}_4$ (in black boxes) and $\mathcal{L}_2$ at tree level, c) from $\mathcal{L}_2$ at one-loop. The full set of diagrams for the two channels $\gamma\gamma \to ww, zz$ can be found in [815].

$$A(s,t,u)^{\gamma\gamma\to w^+w^-}_{\rm LO} = 2sB(s,t,u)^{\gamma\gamma\to w^+w^-}_{\rm LO} = -\frac{1}{t}-\frac{1}{u}\,. \tag{II.2.176}$$

At NLO, there are additional contributions from diagrams of type b) and c) in Figure 194:

$$\begin{aligned} A(s,t,u)^{\gamma\gamma\to zz}_{\rm NLO} &= -\frac{ac^r_{\gamma\gamma}}{4\pi^2v^2}+\frac{(a^2-1)}{4\pi^2v^2}, \\ A(s,t,u)^{\gamma\gamma\to w^+w^-}_{\rm NLO} &= \frac{8(a^r_1-a^r_2+a^r_3)}{v^2}-\frac{ac^r_{\gamma\gamma}}{4\pi^2v^2}+\frac{(a^2-1)}{8\pi^2v^2}, \end{aligned} \tag{II.2.177}$$

and $B(s,t,u)^{\gamma\gamma\to zz}_{\rm NLO} = B(s,t,u)^{\gamma\gamma\to w^+w^-}_{\rm NLO} = 0$. Notice that the last term above coming from the loops with Goldstone bosons cancels for the input value of the SM, i.e for $a = 1$. Fermion loops are missing in this calculation but as the electroweak Goldstones and the Higgs are the only ones coupling derivatively in the LO Lagrangian their contribution is expected to be suppressed by $m^2_{t,b}/E^2$, with $E^2 = s,t,u$.

The above results have been expressed in terms of the renormalized couplings $c^r_{\gamma\gamma}$, a^r_1, a^r_2 and a^r_3. The renormalization of these couplings and their running were first computed in [815] and are summarized in Table 102.

II.2.4.e.vi Electromagnetic form factor $\gamma^* \to w^+w^-$

There are related subprocesses that depend on different combinations of the same effective couplings and can be potentially explored in future collider studies. The electromagnetic transition $\gamma^* \to w^+w^-$ from a deeply virtual photon with momentum $q^\mu = p^\mu_1 + p^\mu_2$ is described through the matrix element

$$\langle w^+(p_1)\, w^-(p_2)|\, J^\mu_{\rm EM}\,|0\rangle = e\,(p^\mu_1 - p^\mu_2)\,\mathbb{F}_{\gamma^*ww}(q^2)\,. \tag{II.2.178}$$

This matrix element is crucial in the production of two longitudinal weak bosons in future e^+e^- colliders. The electromagnetic vector form factor (VFF) can be computed with the chiral Lagrangian up to NLO.

At high momentum-transfer squared (with $q^2 = (p_1 + p_2)^2$), where the equivalence theorem applies, one finds [815]

$$\mathbb{F}_{\gamma^* ww} = \underbrace{1}_{\text{LO}} + \underbrace{\frac{2q^2(a_3^r - a_2^r)}{v^2} + (1-a^2)\frac{q^2}{96\pi^2 v^2}\left(\frac{8}{3} - \ln\frac{-q^2}{\mu^2}\right)}_{\text{NLO}} . \qquad \text{(II.2.179)}$$

The NLO chiral couplings a_2^r and a_3^r are renormalized in the $\overline{MS}$ scheme at the scale μ in dimensional regularization and provide the tree-level NLO contribution to the form factor. They renormalize the UV–divergences that show up in the one-loop NLO contribution, which is given by the term proportional to $(1-a^2)$. Fermion loops are missing in this calculation [815] but their contribution is expected to be suppressed by $m_{t,b}^2/q^2$ for the same reasons previously exposed for $\gamma\gamma$–scattering.

II.2.4.e.vii Higgs transition form factor $\gamma^*\gamma^* \to h$ / associated production

An interesting observable in order to pin down the $h\gamma\gamma$ coupling $c_{\gamma\gamma}$ is the Higgs transition form factor (HTFF), which describes the process $\gamma^*(k_1)\gamma^*(k_2) \to h(p)$ [764, 837, 838]. This transition is given by the matrix element

$$\int d^4x\, e^{-ik_1 x}\, \langle h(p)|\, T\{\, J^\mu_{\rm EM}(x)\, J^\nu_{\rm EM}(0)\,\}\,|0\rangle = i\,e^2\ [\, k_1\cdot k_2\, g^{\mu\nu} - k_2^\mu\, k_1^\nu\,]\ \mathbb{F}_{\gamma^*\gamma^* h}(k_1^2, k_2^2) \qquad \text{(II.2.180)}$$

In the case where one of the photons is on-shell and the other is highly virtual ($k^2 \gg m_h^2$), one finds that the HTFF is zero at LO: $\mathbb{F}_{\gamma^*\gamma h}(k^2, 0)_{\rm LO} = 0$. The first non-zero contribution shows up at NLO [815]:

$$\mathbb{F}_{\gamma^*\gamma h}(k^2, 0)_{\rm NLO} = \frac{c^r_{\gamma\gamma}}{4\pi^2} . \qquad \text{(II.2.181)}$$

We note that the NLO form factor comes exclusively from the renormalized tree-level $h\gamma\gamma$ vertex with $c^r_{\gamma\gamma}$. The one-loop diagrams vanish within the configuration of momenta studied here. Here again we provide the result in the equivalence theorem approximation and neglect corrections due to boson masses. Notice that this result does not correspond to the same kinematical regime as $\Gamma(h \to \gamma\gamma)$, since we are considering $m_h^2 \ll k^2 \ll 16\pi^2 v^2$ in this form factor. For the same reason as in the previous photon observables, fermion loops are expected to be suppressed by powers $m_{t,b}^2/k^2$, as fermions do not couple derivatively in the LO chiral Lagrangian.

As it occurred for the $\gamma\gamma$–scattering, in order to pin down the $\gamma^*\gamma \to h$ process at LHC one should look for events where one of the protons radiates a collinear photon with low virtuality and comes out again undetected, while the other radiates a deeply virtual photon and gives rise to a jet. Again, tagging the outgoing collinear protons $p^{(*)}$ with the forward detectors CT-PPS [830, 831] and ATLAS-AFP [832] will increase the efficiency in LHC analyses. Likewise, electromagnetic subprocesses of this type would be important in future e^+e^- machines or dedicated $e\gamma$ colliders [837].

II.2.4.e.viii TeV-scale particle-pair production at NLO

At the TeV scale, much simplification takes place, in that many couplings become negligible with respect to the sought derivative vertices that grow with $s = E^2_{\rm cm}$. It is then possible to ignore, in first approximation, all SM masses and gauge couplings, and concentrate on the electroweak symmetry breaking sector. The relevant effective Lagrangian follows from (II.2.169) and, even at NLO, contains only seven parameters [839, 840]: the a and b LO parameters coupling the Higgs boson to the longitudinal electroweak $W_L \sim w$ bosons, the classical a_4 and a_5 from the Higgsless electroweak chiral Lagrangian and,

highlighted here, the NLO counterterms to one-loop computations of boson-boson scattering including Higgs in the initial or final state, g^{hh}, d^{hh} and e^{hh}.

The Lagrangian (II.2.169) with these couplings can be used to compute scattering amplitudes between the ww and hh two-body channels, as explained below. Because these amplitudes get strong in the TeV region if there are few per cent level deviations from the SM value couplings, it should be feasible to spot them in experimental diboson production. The reason is Watson's final state rescattering theorem, which corrects the SM production amplitude as implemented, *e.g.* in a Monte Carlo simulation, by a strong rescattering form factor setting the correct phase, as illustrated in Figure 195. Such form

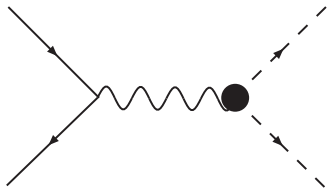

Figure 195: Diboson W_LW_L production with $I = 1$ from a fermion pair via an intermediate W_T. If there are strong interactions in the final state, the production amplitude is multiplied by a universal rescattering form factor, here the thick round blob.

factor needed for the Feynman diagram in Figure 195 can be computed from the scattering amplitudes presented shortly, typically as [839–841] (using the inverse amplitude method (IAM) for unitarization)

$$F_V(s) = F_{11}(s) = \left[1 - \frac{A_{11}^{(1)}(s)}{A_{11}^{(0)}(s)}\right]^{-1} . \tag{II.2.182}$$

Diboson production. Since strong couplings are derivative, their "low energy" ($E \ll 4\pi v \sim 3$ TeV) scattering amplitude $A(s,t)$ can be very economically represented in terms of very few partial waves, because the expansion should quickly converge:

$$A_{i\to j,I}(s,t) = 64\pi \sum_{J=0}^{\infty} (2J+1) P_J(x) A_{i\to j,IJ}(s), \tag{II.2.183}$$

with $x = \cos\theta = 1 - 2t/s$ the cosine of the scattering angle for boson-boson elastic ($i \to i$) or inelastic ($i \to j \neq i$) processes. $P_J(x)$ are the Legendre polynomials.

If the custodial isospin is $I = 1, 2$, the ww scattering is elastic. [II.46] But in the isoscalar case one confronts a $ww \to hh$ coupled-channel problem, so that it is useful to define a reaction matrix for each partial wave,

$$F_{IJ} = \begin{pmatrix} A_{ww\to ww,IJ} & A_{ww\to hh,IJ} \\ A_{hh\to ww,IJ} & A_{hh\to hh,IJ} \end{pmatrix} \equiv \begin{pmatrix} A_{IJ} & A'_{IJ} \\ A'_{IJ} & A''_{IJ} \end{pmatrix} , \tag{II.2.184}$$

whose chiral expansion has the generic form

$$F_{IJ}^{(0)}(s) = K_{IJ} s \tag{II.2.185a}$$

$$F_{IJ}^{(1)}(s) = \left(B_{IJ}(\mu) + D_{IJ} \log \frac{s}{\mu^2} + E_{IJ} \log \frac{-s}{\mu^2} \right) s^2 . \tag{II.2.185b}$$

Here, the constants K_{IJ}, B_{IJ}, D_{IJ}, E_{IJ} are, in general, matrices whose elements depend on the NLO Lagrangian parameters. For elastic $ww \to ww$ scattering in the vector-isovector channel, $I = J = 1$, they are numbers given by

$$K_{11} = \frac{1}{96\pi v^2}(1 - a^2)$$

[II.46] For $I = 1$ the $t\bar{t}$ channel is active, which is more weakly coupled with an amplitude $\sim m_t/\sqrt{s}$.

$$B_{11}(\mu) = \frac{1}{110592\pi^3 v^4}\left[8(1-a^2)^2 - 75(a^2-b)^2 + 4608\{a_4(\mu) - 2a_5(\mu)\}\pi^2\right]$$
$$D_{11} = \frac{1}{9216\pi^3 v^4}\left[(1-a^2)^2 + 3(a^2-b)^2\right],\ E_{11} = -\frac{1}{9216\pi^3 v^4}(1-a^2)^2\,, \quad \text{(II.2.186)}$$

The form factor in Eq. (II.2.182) then modifies SM production, as

$$F_V(s) \sim 1 + \frac{A_{11}^{(1)}(s)}{A_{11}^{(0)}(s)}\,. \quad \text{(II.2.187)}$$

Using the above expressions, the $ww \to ww$ amplitude in the $I = 1$, $J = 1$ (vector) channel is given by

$$A_V(s) = \left[1 - \frac{A_{11}^{(1)}(s)}{A_{11}^{(0)}(s)}\right]^{-1} A_{11}^{(0)}(s)\,, \quad \text{(II.2.188)}$$

from which a fit to the $a_4 - 2a_5$ parameter combination from (II.2.186) can be attempted, for example. The required experimental measurements are, however, rather challenging [629]. The case of resonances and unitarization is discussed in detail in [800, 839–841].

Note that formulae used in this section are derived using the equivalence theorem (ET). By using exact formulae for the tree-level expressions and the optical theorem itself one finds that the ET results are generally reliable, except for the $I = 2$ channel when $a > 1$ where the $I = 2$, $J = 0$ resonance found with the ET disappears [800]. Using "exact" amplitudes also implies that propagation of transverse W and Z needs to be included and this modifies slightly the dependence on the coefficients of chiral order 4 (for instance a_3 enters), although corrections are small.

II.2.4.f Concluding remarks

Assuming that the largest effects of new physics arise in the Higgs sector, and parameterizing the non-standard Higgs boson couplings in a gauge-invariant way, automatically leads to an electroweak chiral Lagrangian as the low-energy EFT.

This EFT represents a consistent quantum field theory framework, in which improvements, through higher-order radiative corrections or by going to next-to-leading order in the new-physics effects, can be systematically included. Focussing first on the leading-order nonstandard couplings has the advantage of reducing the new-physics parameters to a manageable set, in a well-defined and consistent manner. In fact, the formalism essentially corresponds to Higgs-coupling parameterizations routinely used in the experimental analyses of the ATLAS and CMS collaborations (κ-framework).

The electroweak chiral Lagrangian can then be used to systematically improve the κ-formalism, in particular such that differential distributions in general Higgs processes can be studied. However, the detection of such effects will be rather challenging at the LHC, since they are expected to be of $\mathcal{O}(\xi/16\pi^2)$ and therefore rather suppressed.

Consequently, the best strategy to follow at the LHC is to focus the experimental analysis to the leading-order chiral Lagrangian, which matches well the precision goals for Higgs boson properties anticipated for Run 2 and 3. If a deviation is found, the next natural step is to study the differential distributions. This sequential analysis is in contrast with what follows from the SMEFT, where deviations in *both* rates and distributions are expected at NLO and should therefore be studied simultaneously. Additional interesting information on deviations from the Higgs boson couplings and NLO contributions could also be obtained via the study of EW boson scattering (WW, $\gamma\gamma$, etc.).

Acknowledgements

Comments and suggestions from Belen Gavela and Veronica Sanz are gratefully acknowledged.

II.2.5 Fitting EFT parameters and constraining models [II.47]

II.2.5.a The problem

Extending the Higgs boson couplings framework to an effective field theory, usually truncated after including dimension-6 operators [620, 714, 842–845], addresses two short-comings of the classic Higgs boson couplings fit in the κ framework [846, 847]:

1. on the theory side it allows us to systematically include loop corrections, not only in perturbative QCD but also in the weak coupling;
2. on the experimental side it describes modified kinematic distributions, like for example the transverse momentum of the Higgs;
3. on the theory and experimental sides allows us to combine measurements in the Higgs sector for example with anomalous gauge couplings or low-energy precision measurements.

The number of free parameters of the dimension-6 Higgs Lagrangian is an extended set compared to the Higgs boson couplings ansatz. This larger set of free parameters leads to strong correlations when we extract the dimension-6 Wilson coefficients from the usual total cross sections measured at the LHC. If, and only if the measured kinematic distributions can be measured and predicted with similar accuracy as total rates, they will resolve these degeneracies. This also means that the marginalization of the multi-dimensional parameter space will have a sizeable impact on the allowed range for a given dimension-6 Wilson coefficient.

In general, there appear two kinds of operators in the dimension-6 Lagrangian. For example operators simply adding $\phi^\dagger\phi/\Lambda^2$ to the Standard Model do not change the Lorentz structure of interactions, so they do not change kinematic distributions. New operators including a derivative will after a Fourier transformation lead to momentum-dependent Higgs boson couplings. Schematically written the two kinds of operators are

$$\mathcal{O} \propto \frac{g_\Lambda^2 v^2}{\Lambda^2} \qquad \text{and} \qquad \mathcal{O} \propto \frac{g_\Lambda^2 \partial^2}{\Lambda^2} \; . \tag{II.2.189}$$

Only studying total rates at the LHC, we can safely assume that the series of higher-dimensional operators will be ordered by factors $g_\Lambda^2 m_h^2/\Lambda^2$, were g_Λ is the scale of the coupling to new physics. For a reasonably weakly interacting theory with tree-level modifications, an assumed LHC accuracy of 10% directly translates into a new physics reach around

$$\left| \frac{\sigma \times \text{BR}}{(\sigma \times \text{BR})_\text{SM}} - 1 \right| = \frac{g_\Lambda^2 m_h^2}{\Lambda^2} \gtrsim 10\% \qquad \Leftrightarrow \qquad \Lambda < \frac{g_\Lambda \, m_h}{\sqrt{10\%}} < 400 \text{ GeV} \; . \tag{II.2.190}$$

For this estimate we assume $g_\Lambda < 1$, corresponding to a (reasonable) weakly interacting extension of the Standard Model. For momentum-dependent modified Lorentz structures the picture changes. For them the suppression will depend on additional energy scale in LHC processes, for example $g^2 p_{T,h}^2/\Lambda^2$. Taking the above values of $g < 1$ and $\Lambda < 400$ GeV, the experimentally accessible transverse momentum distributions $p_{T,h} > 400$ GeV will then receive order-one corrections through dimension-6 operators. Depending on the sign of the interference term between the Standard Model coupling and the dimension-6 Wilson coefficient, this leading interference correction to the differential rate can even drive the number of predicted events through zero and negative.

II.2.5.b Measuring dimension-6 Wilson coefficients

While there exist many experimental and theoretical challenges to an analysis of LHC Higgs data other than in complete, renormalizable models, the crucial question is if we can sensibly measure dimension-6 Wilson coefficients, and if these results are useful. The aim of this section as well as the following Section II.2.5.c is to illustrate how

[II.47] *Author(s): N. Belyaev, A. Biekötter, J. Brehmer, C. Englert, A. Freitas, D. Gonçalves, J. Gonzalez-Fraile, M. Gorbahn, R. Kogler, D. Lopez-Val, J.M. No, T. Plehn, M. Rauch, V. Sanz, M. Spannowsky.*

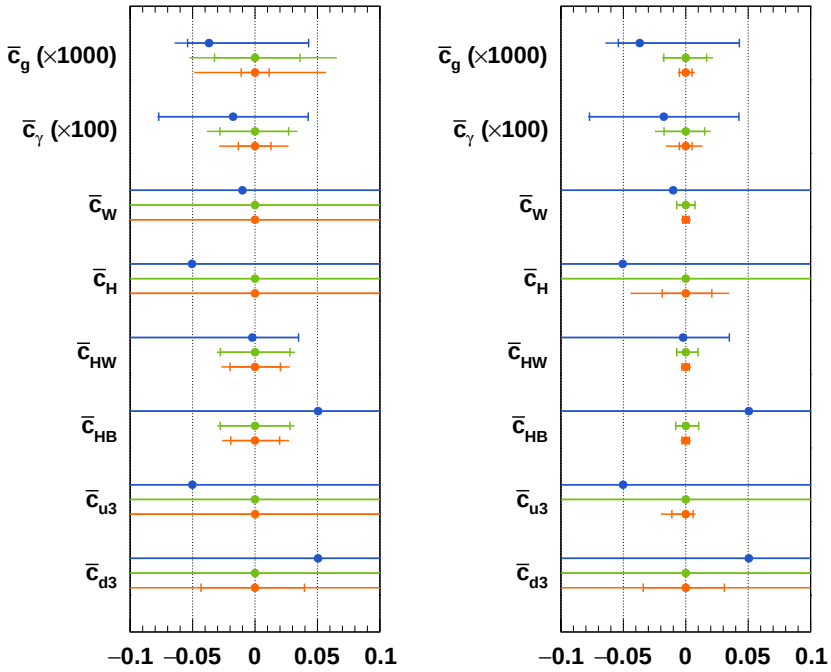

Figure 196: Marginalized 95% confidence level constraints for the dimension-six operator coefficients for current data (blue), the LHC at 14 TeV with 300 fb^{-1} (green), and with 3000 fb^{-1} (orange). The expected constraints are centred around zero by construction. For the left panel we only use signal strengths, while on the right differential $p_{T,h}$ measurements are included. The inner error bar depicts the experimental uncertainty, the outer error bar shows the total uncertainty. Figure from Ref. [848].

– a fit of dimension-6 Wilson coefficients to LHC Higgs data can be done (and has been done for Run I data) by non-members of the ATLAS and CMS collaborations and based on published results;
– kinematic distributions can significantly improve the multi-dimensional parameter fit by resolving strong correlations induced by total rate measurements;
– communicating the relevant information, in particular related to kinematic distributions, is a challenge which needs to be resolved in close collaboration with the fitting projects;
– the results of a dimension-6 fit can be translated into weakly interacting extensions of the Standard Model, and many of the theoretical issues are clearly separated from experimental uncertainties;
– the language of dimension-6 Lagrangians can intuitively be linked to the structure of ultraviolet completions of the Standard Model gauge and Higgs sectors.

Unlike the more general discussion of Section II.2.2 we focus on weakly interacting extensions of the Higgs and gauge sector, and how a dimension-6 Lagrangian approach can be useful in practice.

From the extraordinarily successful and well-established κ framework we know that measurements of Higgs boson couplings at the level of several per cent can be expected from the upcoming LHC run(s) [849]. Towards higher luminosity the Higgs boson couplings to weak bosons will likely be the best-measured parameters, also because the theoretical uncertainties linked to the corresponding LHC production cross sections are under control.

Already in the κ framework, a few select kinematic distributions for example in the gluon fusion production process can be used to collect information on modified Higgs boson couplings. In the top-gluon-Higgs sector we can compare three different analysis strategies: a modified $p_{T,h}$ spectrum of

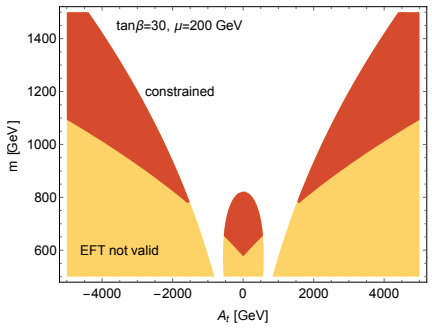

Figure 197: Constraints appearing through $h^\dagger h\, G^{a\mu\nu} G^a_{\mu\nu}$ corresponding to MSSM stops, assuming that no hints for stops exist. The excluded parameter range is indicated by the red region, while the EFT consistency condition removes the orange region. Figure from Ref. [848].

boosted Higgs boson production in gluon fusion [850], off-shell Higgs boson production, and a measurement of the gluon fusion vs $t\bar{t}h$ production rates. Unfortunately, explicit threshold effects in boosted Higgs boson production are too small to be observable in the near future [251]. We can compare the different methods for a simple benchmark model where a 30% reduction in the top Yukawa coupling is compensated in the total rate through an effective Higgs-gluon coupling. Ignoring anything but statistical uncertainties, boosted Higgs boson production can rule out this scenario based on 700 fb^{-1} of LHC data, while off-shell Higgs boson production will require more than 1 ab^{-1} for the same purpose [851]. These numbers are expected to become significantly worse once we include systematic and theoretical uncertainties. Unfortunately, global analyses including kinematic information in all Higgs channels cannot rely on the κ framework, but they can be based on a Higgs EFT. Below, we will describe the potential and the challenges in such analyses.

When focussing on kinematic distributions, the first choice we need to make concerns the the dimension-6 squared terms in our Lagrangian. Writing the Lagrangian as $\mathscr{L} = \mathscr{L}_{\text{SM}} + c/\Lambda^2\, O_c$ we compute the amplitude and the matrix element squared to leading order in the new interactions,

$$\mathcal{M} = \mathcal{M}_{\text{SM}} + \frac{c}{\Lambda^2}\mathcal{M}_{\text{D6}} \qquad \Rightarrow \qquad |\mathcal{M}|^2 = |\mathcal{M}_{\text{SM}}|^2 + \frac{2c}{\Lambda^2}\,\text{Re}\mathcal{M}^*_{\text{D6}}\mathcal{M}_{\text{SM}} \overset{?}{+} \frac{c^2}{\Lambda^4}\,|\mathcal{M}_{\text{D6}}|^2\,. \tag{II.2.191}$$

In the following, we will discuss two analyses choosing different options concerning the dimension-6 squared terms.

Linearized EFT analysis

Following pure power counting, the squared dimension-6 term enters as a dimension-8 contribution. If sizeable, it can signal a breakdown of the systematic EFT approach. Drawing inspiration from fixed-order QCD calculations, where negative event weights are present and are interpreted as a shortcoming of this particular order of the perturbative series expansion, we only include the interference term and require that the differential distributions have positive cross sections for each of the bins. A prediction of negative event rates (or a destructively interfering correction of the same order as the SM expectation) signalizes a breakdown of the perturbative series in a particular Wilson coefficient, so the underlying model should be disregarded. In other words, negative differential cross sections can be used as an estimate of the validity range of a certain Wilson coefficient, unless the symmetries or accidental cancellations render the interference in Eq.(II.2.191) zero or negligibly small.

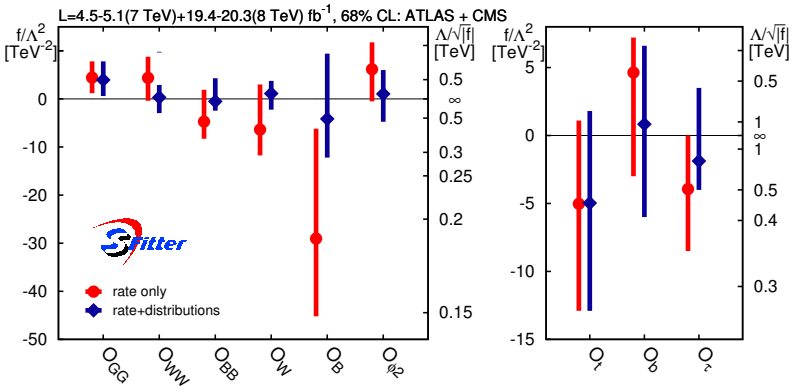

Figure 198: 68% CL error bars on the Wilson coefficients f_x/Λ^2 for the dimension-6 operators. For the Yukawa couplings as well as for $\mathcal{O}_{GG}$ we only show the SM-like solution. Figure from Ref. [849].

For Run I data as well as for different 14 TeV luminosity benchmarks this approach has been adopted in the Higgs EFT fit of Ref. [848]. Its particular emphasis on the question how differential distributions lift degeneracies in a fit to the full set of Higgs-related Wilson coefficients. To this end, $p_{T,h}$ distributions were added to all Higgs boson production and decay signatures. The results shown in Figure 196 indicate that for Run I the EFT approach is in poor shape without this additional information. The EFT energy scales Λ which can be probed lie in the few hundred GeV range, quickly driving constraints on actual TeV-scale models into a non-perturbative regime. Even worse, energy scales in the same range are already resolved in the $p_{T,h}$ distributions, which strictly speaking invalidates the ideal EFT approach. The picture starts to change for Run II at 14 TeV with an assumed 300 fb^{-1}, in which case already the fit to total rates gives more meaningful results. Finally, for the high-luminosity running with 3000 fb^{-1} the kinematic distributions clearly dominate the precision of the expected limits. This conclusion rests on vastly improved experimental systematic uncertainties and good control over theoretical uncertainties. The experimental systematic uncertainties are assumed to scale like statistical uncertainties with the squared root of the number of events. For example, a 50% uncertainty assigned to a signature at 7-8 TeV and 25 fb^{-1} can turn into a $50\%/\sqrt{200} \approx 3.5\%$ uncertainty at 14 TeV assuming 3000 fb^{-1}. The theoretical uncertainties are not reduced for the Run II scenarios, but nevertheless a stringent assumption is made, that they are flat as function of $p_{T,h}$. In that sense the results of Figure 197 support the statement that it might well be possible to rely on a consistent Higgs EFT approach in the long-term of LHC running, if the systematic and theoretical uncertainties are controlled. Interpreting the projections for high-luminosity running in a concrete decoupled stop scenario we obtain Figure 197.

Run I analysis including distributions

Also based on the Run I Higgs measurements, Figure 198 shows the SFITTER analysis [849] of the dimension-6 Lagrangian defined in Refs. [628, 852]. Unlike in the previous analysis, the dimension-6 squared terms indicated in Eq.(II.2.191) are included. The red error bars are only based on total rate measurements, while the blue bars includes the $p_{T,V}$ distribution in Vh production as well the the $\Delta\phi_{jj}$ distribution in weak boson fusion with a decay $h \to \gamma\gamma$. The Higgs-fermion sector is limited to modified Yukawa couplings of the 3rd generation, due to scarce experimental data probing other Yukawa couplings or the structure of the Higgs boson couplings to heavy fermions. Without any information from the distributions the constraints on the Wilson coefficients can be translated into $\Lambda \gtrsim 300$ GeV for $g = 1$. Including kinematic distributions the reach increases to typically $\Lambda \gtrsim 500$ GeV, where the entire improvement comes from the overflow bin of the $p_{T,V}$ distribution defined as $p_{T,V} > 200$ GeV. As discussed before, this limited mass reach implies that the dimension-6 fit should not be viewed as the leading term of an EFT expansion in $1/\Lambda$.

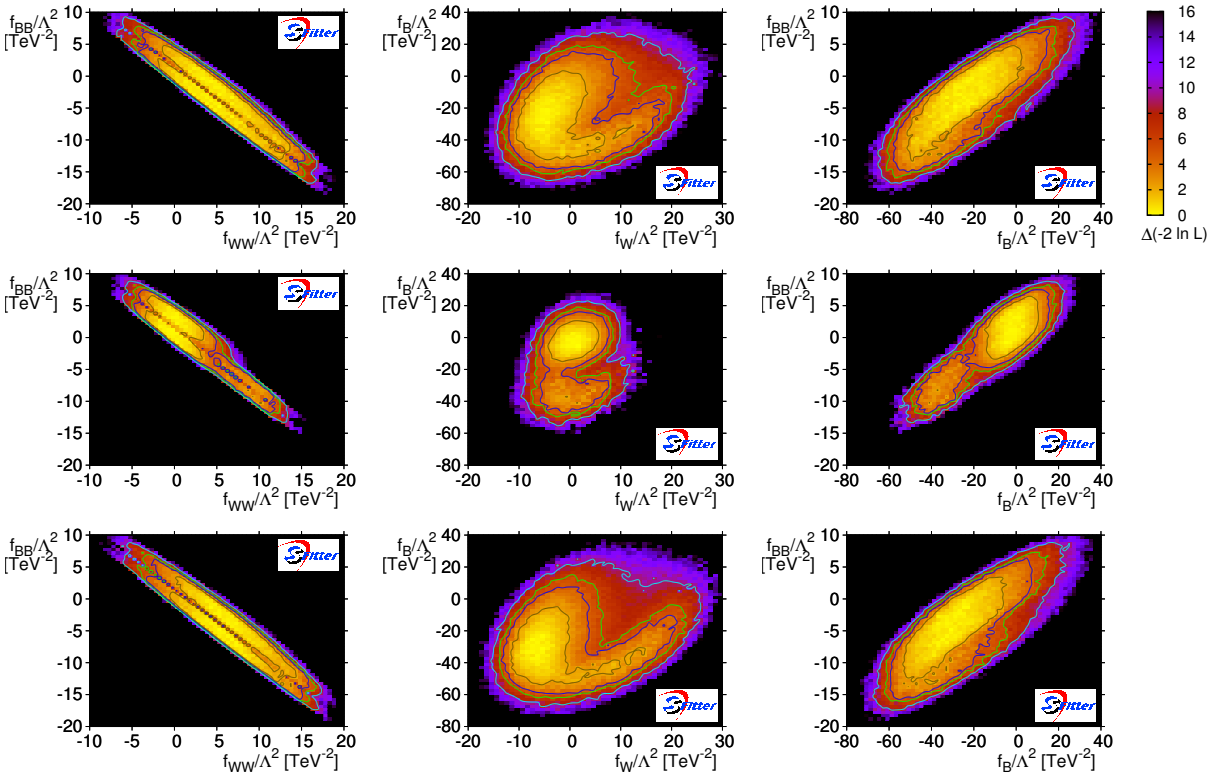

Figure 199: Correlations between different coefficients f_x/Λ^2 after including kinematic distributions. In the top row we only add the $\Delta\phi_{jj}$ distribution; in the second row we also include $p_{T,V}$ from Vh production; in the bottom row we then remove the highest bin associated with large momentum flow through the dimension-6 vertex. Figure from Ref. [849].

Technically, this kinematic information is included based on published kinematic distributions. Looking at future LHC runs there are several ways of making kinematic information available to an independent Higgs operator analysis:

1. kinematic distributions compared to different signal and background predictions shown bin-by-bin. In that case the event counts in each bin are statistically independent measurements;
2. unfolded signal distributions as discussed in Chapter III.3, which are technically simple to include, but might introduce statistical correlations between bins and an additional systematic uncertainty from the unfolding model;
3. fiducial cross sections as discussed in Chapter III.3, which are also technically simple to include, but might provide less information than the full distributions;
4. exclusive likelihood maps, which are highly processed by the experiments and remove the treatment of experimental uncertainties from the operator analysis. Theoretical uncertainties can be decoupled using the procedure presented in Ref. [853].

For the Run I analysis shown here we rely on the first and third of these methods, *i.e.* on published kinematic distributions compared to signal and background predictions. The theoretical predictions for the distributions come from MADGRAPH and can trivially be translated from one operator basis to another. Because the measured total rate in a given Higgs boson production and decay channel does not correspond to the integral under the published distributions, we define ratios of bins such that the measured total rate is not related to the measured distribution. To ensure that kinematic distributions to not develop negative event counts we have to include the dimension-6 squared contribution, even though from a technical perspective we could also find other ways to remove problems in the interpretation of these phase space regions. The technical setup of our fit to a linear representation can easily be extended to

a non-linear representation, where additional degrees of freedom appear in the anomalous gauge sector and the fermionic operators [854]. All operators in the fit are defined and evaluated at the weak scale, but can obviously be renormalization-group evolved to other, experimentally relevant scales of an extended fit.

In Figure 199 we show how kinematic distributions improve the dimension-6 fit because they reduce strong non-Gaussian correlation, for example between $\mathcal{O}_B$ and $\mathcal{O}_W$ or between $\mathcal{O}_{BB}$ and $\mathcal{O}_{WW}$ in model space. Using a profile likelihood analysis leads to poor limits on each of the two operators individually. If we were to vary only one operator at a time, the limit for example on the Wilson coefficients for $\mathcal{O}_{BB}$ or $\mathcal{O}_{WW}$ would improve by an order of magnitude. The top panels show the results after including total rates and the $\Delta\phi_{jj}$ distribution in weak boson fusion. The 1-dimensional profile likelihoods from this setup largely correspond to the red bars in Figure 198. In the second row we show the improvement from the $p_{T,V}$ distribution in Vh production. This includes an overflow bin, where at least the lower end of the bin is not beyond the region of validity of the effective field theory. The corresponding 1-dimensional profile likelihoods are shown as blue bars in Figure 198. The main source of improvement in the 1-dimensional results is an improved control of correlations when we include kinematic distributions as additional observables. It turns out that after including LHC measurements on pair-produced weak bosons these non-trivial correlations essentially vanish [625,627,855]. In the bottom row of Figure 199 we illustrate what happens if we remove the overflow bin of the $p_{T,V}$ distribution from our analysis: this limited scenario is essentially equivalent to not including the $p_{T,V}$ distribution at all.

Finally, we can include off-shell Higgs boson production in a global Higgs analysis, either based on the κ framework or based on a dimension-6 Lagrangian [849]. The tree-level ZZh vertex will only run logarithmically with the relevant momentum scale, and additional operator structures changing the ZZh interaction will hardly modify the $m_{4\ell}$ kinematics. What remains is a combined effect of the gluon-Higgs boson coupling described by $\mathcal{O}_{GG}$ and a modified top Yukawa coupling through $\mathcal{O}_t$. Hence, the main effect of including off-shell Higgs boson production in the SFitter Higgs analysis is to again reduce possible degeneracies in the $\mathcal{O}_{GG}$ vs $\mathcal{O}_t$ plane. The same would be the effect of including a transverse momentum distribution in gluon fusion Higgs boson production. Technically, ATLAS and CMS report off-shell Higgs results in terms of rate measurements in a given phase space region. This approach is related to fiducial cross section measurements on the above list of possible formats. In the future, the same information might be published in the form of $m_{4\ell}$ distributions, which could be easily accommodated by the global analysis tools.

Outlook

Current studies have shown that a dimension-6 analysis of LHC Higgs data is entirely feasible. Only when we try to embed the truncated dimension-6 analysis into a consistent EFT framework we face major issues like theoretical uncertainties due to missing higher-dimensional contributions. One way to test the validity of the EFT description is the treatment of dimension-6 squared terms in Monte Carlo simulations — on the one hand including these terms assures positive event numbers all over phase space, but on the other hand large contributions from these squared terms suggest poor convergence of the underlying framework. As long as we consider a global analysis only in terms of dimension-6 operators the treatment of the dimension-6 terms is part of the underlying hypothesis and only has to be stated clearly. In general, including kinematic distributions makes the EFT analysis more vulnerable to such model assumptions. However, for increased luminosity the hierarchy of scales will be improved at least for inclusive measurements, and the limiting theoretical uncertainties might become smaller with time.

II.2.5.c Weakly interacting new physics to dimension-6

The discussion in the last section shows that an effective theory approach to LHC Higgs data faces serious issues linked to theoretical consistency arguments, triggered by the limited reach of the LHC Run I in terms of the new physics scale. However, these limitations do not necessarily imply that we cannot interpret LHC Higgs data, including kinematic distributions, in terms of a dimension-6 Lagrangian. This has to be tested explicitly for different structures of the new physics model. For pedagogical reviews see *e.g.* Refs [463, 856, 857]. We study weakly interacting modifications of the Higgs sector and the electroweak gauge sector [749],

- singlet extension of the Higgs potential, a so-called Higgs portal with Higgs-scalar mixing;
- two-Higgs-doublet model, including the specific type-2 setup in the MSSM;
- non-Higgs extension of the scalar sector, for example through scalar top partners;
- gauge-triplet extension of the electroweak gauge sector.

For each of these models we construct and match the linear dimension-6 Lagrangian, compute LHC observables, and compare the LHC predictions from the dimension-6 Lagrangian and from the full model. The (dis-)agreement of these predictions determines to what degree we can rely on a dimension-6 analysis at the LHC, without explicitly testing for example dimension-8 operators. The point where our analysis differs from the general consistency arguments of the last section is that for our classes of models we can derive the structure and the size of the dimension-6 Wilson coefficients. Moreover, a specific set of benchmark models allows us to make quantitative statements.

One key ingredient to our analysis is the appropriate matching of models which, to be observable at the LHC, have to feature a low new physics scale M_{heavy} in the extended Lagrangian. In an ideal world, where the effective theory is well defined and we can systematically neglect terms suppressed by $g^2v^2/M^2_{\text{heavy}}$, the matching of the effective field theory is uniquely defined. First, the masses of the new particles will be of the order $m_{\text{heavy}} = M_{\text{heavy}}$ and will serve as the natural matching scale Λ. Second, at this scale $\Lambda = M_{\text{heavy}} \gg v$ we match to the dimension-6 Lagrangian in the unbroken phase and assume $v \to 0$ throughout. For a dimension-6 truncation this also means that we neglect terms of the order $1/\Lambda^4$ in the Wilson coefficients and terms of the order $1/M^4_{\text{heavy}}$ in the full model, which renders the matching condition unique.

For many models we are interested in, the underlying mass scale and the masses of new particles will be linked like

$$m_{\text{heavy}} = M_{\text{heavy}} \pm gv + \cdots \tag{II.2.192}$$

Our choice of Λ is now driven by the phenomenological argument that the effective theory will break down the moment we observe a new resonance. Independent of the hierarchy of the two new physics mass parameters we define a v-improved matching at the scale

$$\Lambda = m_{\text{heavy}} \; . \tag{II.2.193}$$

Similarly, at this scale we want to incorporate as much information of the full model in the Wilson coefficients as possible. This is why we express them in terms of all-order model parameters like masses and mixing angles, *i.e.* we do not truncate them in terms of $1/\Lambda$. This v-improved matching leads to a significant improvement in the comparison of the dimension-6 Lagrangian and the full model in LHC simulations, until actual poles of new particles appear [749].

Because differential information on LHC processes is not described by one single mass scale, we need to test each of our new physics models based on the critical kinematic distributions. For each of these weakly interacting new physics models we therefore study

- Higgs boson decays, where the momentum flow through the vertices is typically smaller than m_h and we can study new physics effects in the $m_{4\ell}$ distribution;

- Vh production, where the momentum flow through the hVV vertex can be reconstructed as m_{Vh}, and where we can search for new gauge resonances in the s-channel;
- weak boson fusion production, where the $2 \to 3$ kinematics with two t-channel propagators complicates the experimental access to momentum flow for example based on the leading $p_{T,j}$;
- Higgs boson pair production, where issues arise not at large energies, but at threshold, and where we are likely to observe new Higgs boson resonances in m_{hh}.

The list of models and the list of observables define a matrix which allows us to systematically study the level of agreement between full models and the dimension-6 Lagrangian at the LHC. More information on such new physics models can be found in Section II.2.5. Unlike in that section, the benchmark point described below are specifically designed to challenge an effective theory description of the LHC features of the full models.

Singlet and doublet extensions

First, we extend the minimal Higgs sector of the Standard Model by a real scalar singlet S,

$$V(\phi, S) = \mu_1^2 \, (\phi^\dagger \, \phi) + \lambda_1 \, |\phi^\dagger \phi|^2 + \mu_2^2 \, S^2 + \lambda_2 \, S^4 + \lambda_3 \, |\phi^\dagger \, \phi| S^2 \, , \tag{II.2.194}$$

where the singlet VEV $v_s \gg v$ induces a Higgs-singlet mixing. All Higgs boson couplings, with the exception of the Higgs self-coupling, are modified as

$$\Delta_x = \frac{g_{xxh}}{g_{xxh}^{\text{SM}}} - 1 = \cos\alpha - 1 \approx -\frac{\alpha^2}{2} \approx -\frac{\lambda_3^2}{8\lambda_2^2} \left(\frac{v}{v_S}\right)^2 \qquad \text{with} \qquad \tan\alpha \approx \frac{\lambda_3}{2\lambda_2} \frac{v}{v_s} \ell^+\ell^- 1 \, . \tag{II.2.195}$$

In our dimension-6 basis the singlet extension only induces the operator $\mathcal{O}_H$ or $\mathcal{O}_{\phi,2} = \partial^\mu(\phi^\dagger\phi)\partial_\mu(\phi^\dagger\phi)$. The matching scale and the corresponding Wilson coefficient from v-improved matching are

$$\Lambda = m_H = \sqrt{2\lambda_2} v_s \qquad \text{and} \qquad \bar{c}_H = 2(1 - \cos\alpha) \, . \tag{II.2.196}$$

This means that a singlet extension of the Higgs potential does not introduce momentum-dependent Higgs boson couplings. The coupling modification to all Standard Model particles is universal and only leads to modified total Higgs rates. In Table 103 we show the parameters of our benchmark points as well as the modification of the Higgs boson couplings and the Higgs rates. In spite of the fact that the mass of the new scalar m_h can be very low, we hardly find visible effect in the Higgs boson couplings. Moreover, the dimension-6 approximation to the modified total rates is by definition fully justified, except for the on-shell contribution from the second scalar shown in Figure 200.

The only exception to this simple structure will be the appearance of the new resonance H, for example in Higgs boson pair production $pp \to hh$. If we do not remove the operator $\mathcal{O}_H$ from our operator basis through equations of motion, it induces a momentum-independent and a momentum-dependent correction to the Higgs self-coupling

$$\mathscr{L} \supset -\frac{m_h^2}{2v} \left(1 - \frac{1}{2}\bar{c}_H\right) h^3 + \frac{g}{2m_W} \bar{c}_H \; h \, \partial_\mu h \, \partial^\mu h \, . \tag{II.2.197}$$

The shift in the SM-like Higgs self-coupling and the 2-derivative term are driven by the same parameter in our model. If, instead, we break the Z_2 symmetry of the Lagrangian in Eq.(II.2.194), there will be an additional contribution to the shift in the self-coupling at tree-level. However, at the LHC we expect the strongly interacting modification in Eq.(II.2.197) to dominate. In the absence of the heavy scalar such a momentum-dependent Higgs self-coupling would indicate the onset of a strongly interacting theory. However, in our case it only describes the onset of a new resonance m_H. Both scalars together lead to a

Table 103: Benchmarks for the singlet extension. We show the model parameters and the universal coupling modification for the complete model, as well as the matching scale Λ, the Wilson coefficient $\bar{c}_H$, and the universal coupling modification for the dimension-6 Lagrangian. m_H and Λ are in GeV. Table from Ref. [749].

	Singlet					
	m_H	$\sin\alpha$	v_s/v	$\Delta_x^{\text{singlet}}$	$\bar{c}_H$	Δ_x^{D6}
S1	500	0.2	10	-0.020	0.040	-0.020
S2	350	0.3	10	-0.046	0.092	-0.046
S3	200	0.4	10	-0.083	0.167	-0.083
S4	1000	0.4	10	-0.083	0.167	-0.092
S5	500	0.6	10	-0.200	0.400	-0.200

well-defined and unitary UV-behaviour of LHC cross sections, as shown in Figure 200. As expected, the dimension-6 description breaks down once we approach the resonance peak above $m_{hh} = 600$ GeV.

Exactly the same analysis we can perform for two-Higgs-doublet models with a potential of the form [858]

$$\begin{aligned} V(\phi_1,\phi_2) = & m_{11}^2\,\phi_1^\dagger\phi_1 + m_{22}^2\,\phi_2^\dagger\phi_2 + \frac{\lambda_1}{2}\,(\phi_1^\dagger\phi_1)^2 + \frac{\lambda_2}{2}\,(\phi_2^\dagger\phi_2)^2 + \lambda_3\,(\phi_1^\dagger\phi_1)\,(\phi_2^\dagger\phi_2) + \lambda_4\,|\phi_1^\dagger\,\phi_2|^2 \\ & + \left[-m_{12}^2\,\phi_1^\dagger\phi_2 + \frac{\lambda_5}{2}\,(\phi_1^\dagger\phi_2)^2 + \text{h.c.}\right] . \end{aligned} \tag{II.2.198}$$

The self-couplings $\lambda_1 \ldots \lambda_5$ are bounded from above only if we require our model to remain perturbative. If they contribute to the light Higgs interactions they can lead to a non-decoupling behaviour. In the conventions of Eq.(II.2.196) the modification of the Higgs boson couplings to weak bosons scales like

$$\Delta_{W,Z} = \sin(\beta-\alpha) \approx \frac{\sin^2(2\beta)}{8}\left(\frac{v}{m_{A^0}}\right)^4 , \tag{II.2.199}$$

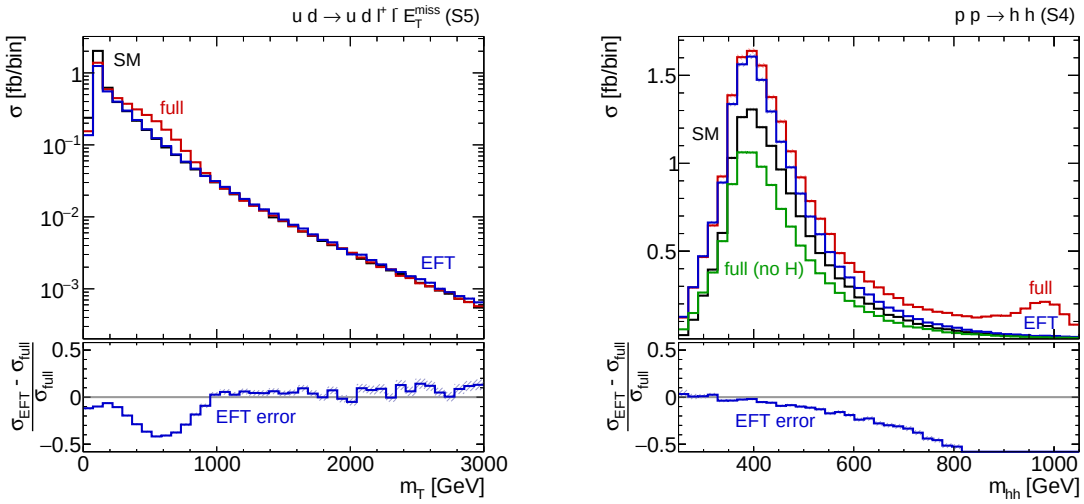

Figure 200: Kinematic distributions for the singlet extension. Left: transverse mass in WBF Higgs boson production. Right: invariant mass m_{hh} linked to the new resonance. Figure from Ref. [749].

Table 104: Scalar top-partner Lagrangian parameters, physical parameters, and selected Wilson coefficient. All masses are in GeV. Table from Ref. [749].

	Top partner							D6		
	M	κ_{LL}	κ_{RR}	κ_{LR}	$m_{\tilde{t}_1}$	$m_{\tilde{t}_2}$	$\theta_{\tilde{t}}$	$\bar{c}_H$	$\bar{c}_W$	$\bar{c}_{HW}$
P1	500	-1.16	2.85	0.147	500	580	-0.15	0.006	$-3.1 \cdot 10^{-7}$	$4.0 \cdot 10^{-7}$
P2	350	-3.16	-2.82	0.017	173	200	-0.10	0.018	$-1.0 \cdot 10^{-3}$	$1.0 \cdot 10^{-3}$
P3	500	-7.51	-7.17	0.012	173	200	-0.10	0.139	$-2.5 \cdot 10^{-3}$	$2.5 \cdot 10^{-3}$

with a suppression in terms of the mass of the heavy pseudoscalar A^0. Through m_{12} it sets the mass scale of the heavy Higgs states, which need to have similar masses to respect custodial symmetry. This degeneracy can be broken by large scalar couplings λ_j and can shift one of the neutral scalar masses with respect to the charged scalar mass. In this situation the v-improved matching at the mass of the lightest new state will be most helpful in the numerical comparison. At tree level the corresponding modifications of the light Higgs rates are as unspectacular as in the Higgs singlet extension. Unlike the dimension-8 effect in the gauge sector, the Yukawa couplings of the light Higgs encounter modifications of the kind $v^2/m^2_{A^0}$, with possible additional powers of $\tan\beta$. For example, in type-II models we find

$$\Delta_b \approx -\tan\beta\,\frac{\sin(2\beta)}{2}\left(\frac{v}{m_{A^0}}\right)^2 . \tag{II.2.200}$$

This dimension-6 effect can already for moderate values of $\tan\beta$ significantly delay the decoupling of the heavy 2HDM states in the Yukawa sector. Generalizing Eq.(II.2.200), we can compute the fermionic corrections which the 2HDM generates at tree level. For the type-I and type-II setups we find

$$\begin{aligned}
\bar{c}_u^{\rm I} = \bar{c}_u^{\rm II} = \bar{c}_d^{\rm I} = \bar{c}_\ell^{\rm I} &= \frac{\sin(2\beta)\cot\beta}{2}\left[\frac{\lambda_1}{2}-\frac{\lambda_2}{2}+\left(\frac{\lambda_1}{2}+\frac{\lambda_2}{2}-\lambda_3-\lambda_4-\lambda_5\right)\cos(2\beta)\right]\left(\frac{v}{m_{A^0}}\right)^2 , \\
\bar{c}_d^{\rm II} = \bar{c}_\ell^{\rm II} &= -\frac{\sin(2\beta)\tan\beta}{2}\left[\frac{\lambda_1}{2}-\frac{\lambda_2}{2}+\left(\frac{\lambda_1}{2}+\frac{\lambda_2}{2}-\lambda_3-\lambda_4-\lambda_5\right)\cos(2\beta)\right]\left(\frac{v}{m_{A^0}}\right)^2 .
\end{aligned} \tag{II.2.201}$$

Unlike for the singlet extension, a new charged Higgs $H^\pm$ induces new features in the loop-induced coupling $g_{h\gamma\gamma}$,

$$\begin{aligned}
\bar{c}_\gamma = \frac{g^2}{11\,520\,\pi^2}\Bigg[&30\left(1-[\cot\beta+\tan\beta]\frac{m_{12}^2}{m_{H^\pm}^2}\right) \\
&+\left(19-4[\cot\beta+\tan\beta]\frac{m_{12}^2}{m_{H^\pm}^2}\right)\frac{m_{h^0}^2}{m_{H^\pm}^2}-30\cot(2\beta)[\cot\beta+\tan\beta]\frac{m_{12}^2}{m_{H^\pm}^2}\,x\Bigg] .
\end{aligned} \tag{II.2.202}$$

Unfortunately, such loop-induced modifications will most likely not be visible at the LHC. In contrast, the heavy additional Higgs particles should appear in LHC Higgs searches as new resonances, provided they are not too heavy. From a dimension-6 perspective the test of two-Higgs-doublet models at the LHC is as little of a challenge as the Higgs singlet extension [858].

Scalar top partners

New scalar particles do not have to be part of the Higgs sector, in the sense that they do not have to participate in electroweak symmetry breaking. We introduce a scalar top partner similar to the stop of

the MSSM. The masses of the additional isospin doublet and singlet in the fundamental representation of $SU(3)_c$ can be different, but for the sake of simplicity we unify them to M. We consider three relatively light new scalars $\tilde{t}_1$, $\tilde{t}_2$ and $\tilde{b}_2 = \tilde{b}_L$. The stop mass matrix reads

$$\begin{pmatrix} \kappa_{LL}\dfrac{v^2}{2} + M^2 & \kappa_{LR}\dfrac{vM}{\sqrt{2}} \\ \kappa_{LR}\dfrac{vM}{\sqrt{2}} & \kappa_{RR}\dfrac{v^2}{2} + M^2 \end{pmatrix} \tag{II.2.203}$$

Through loops the new scalars modify the Higgs boson couplings to gluons, photons, and weak bosons, including new Lorentz structures in the hVV coupling. The SM-like Higgs boson coupling to weak bosons changes in the limit of small stop mixing scales like

$$\Delta_V \approx \frac{\kappa_{LL}^2}{16\pi^2}\left(\frac{v}{m_{\tilde{t}_1}}\right)^2 , \tag{II.2.204}$$

which means we expect loop effects in a dimension-6 Lagrangian. In the v-improved matching scheme we identify $\Lambda = m_{\tilde{t}_1}$. The Wilson coefficients for the induced dimension-6 operators are then

$$\begin{aligned}
\bar{c}_g &= \frac{m_W^2}{24\,(4\pi)^2\,m_{\tilde{t}_1}^2}\left[\kappa_{LL} + \kappa_{RR} - \kappa_{LR}^2\right] & \bar{c}_\gamma &= \frac{m_W^2}{9\,(4\pi)^2\,m_{\tilde{t}_1}^2}\left[\kappa_{LL} + \kappa_{RR} - \kappa_{LR}^2\right] \\
\bar{c}_B &= -\frac{5m_W^2}{12\,(4\pi)^2\,m_{\tilde{t}_1}^2}\left[\kappa_{LL} - \frac{31}{50}\kappa_{LR}^2\right] & \bar{c}_W &= \frac{m_W^2}{4\,(4\pi)^2\,m_{\tilde{t}_1}^2}\left[\kappa_{LL} - \frac{3}{10}\kappa_{LR}^2\right] \\
\bar{c}_{HB} &= \frac{5m_W^2}{12\,(4\pi)^2\,m_{\tilde{t}_1}^2}\left[\kappa_{LL} - \frac{14}{25}\kappa_{LR}^2\right] & \bar{c}_{HW} &= -\frac{m_W^2}{4\,(4\pi)^2\,m_{\tilde{t}_1}^2}\left[\kappa_{LL} - \frac{2}{5}\kappa_{LR}^2\right] \\
\bar{c}_H &= \frac{v^2}{4(4\pi)^2\,m_{\tilde{t}_1}^2}\left[2\kappa_{RR}^2 - \kappa_{LL}^2 - \left(\kappa_{RR} - \frac{1}{2}\kappa_{LL}\right)\kappa_{LR}^2 + \frac{\kappa_{LR}^4}{10}\right] \\
\bar{c}_T &= \frac{v^2}{4(4\pi)^2\,m_{\tilde{t}_1}^2}\left[\kappa_{LL}^2 - \frac{\kappa_{LL}\,\kappa_{LR}^2}{2} + \frac{\kappa_{LR}^4}{10}\right] .
\end{aligned} \tag{II.2.205}$$

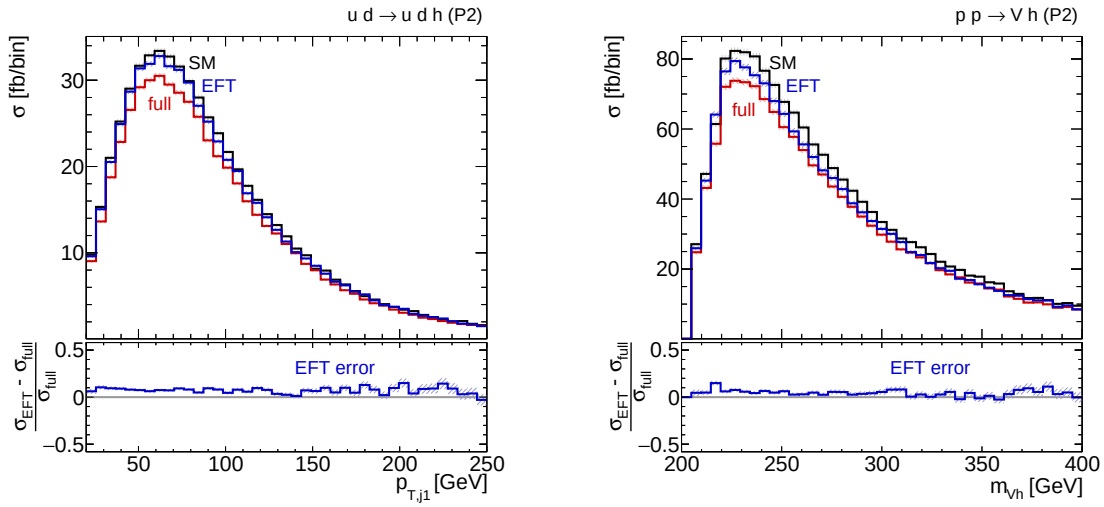

Figure 201: Kinematic distributions for the top partner model. Left: tagging jet properties in WBF Higgs boson production. Right: m_{Vh} distribution in Higgs-strahlung. Figure from Ref. [749].

Table 105: Vector triplet Lagrangian parameters, physical parameters, and selected Wilson coefficient. All masses are in GeV. Table modified from Ref. [749].

	Triplet						D6			
	M_V	g_V	c_H	c_F	c_{VVHH}	m_ξ	$\bar{c}_W$	$\bar{c}_H$	$\bar{c}_6$	$\bar{c}_f$
T1	591	3.0	-0.47	-5.0	2.0	1200	-0.011	0.000	0.000	0.000
T2	946	3.0	-0.47	-5.0	1.0	1200	-0.011	0.000	0.000	0.000
T3	941	3.0	-0.28	3.0	1.0	1200	0.004	0.046	0.061	0.015
T4	1246	3.0	-0.50	3.0	-0.2	1200	0.007	0.111	0.149	0.037
T4'	3738	3.0	-1.50	9.0	-1.8	3600	0.007	0.111	0.149	0.037
T5	846	1.0	-0.56	-1.32	0.08	849	-0.007	-0.020	-0.027	-0.007
T5'	2538	1.0	-1.68	-3.96	0.72	2547	-0.007	-0.020	-0.027	-0.007

We can evaluate these corrections for the most optimistic benchmark point, *i.e.* $m_{\tilde{t}_1} \approx m_t$ and $\kappa_{ij} \gg 1$ as shown in Table 104. The problem is that typical pre-factors of loop-induced Wilson coefficients are still at most

$$\frac{v^2 \kappa_{ij}^2}{4(4\pi)^2\, m_{\tilde{t}_1}^2} < 0.16 \qquad \text{for} \quad \kappa_{ij} < 5\,, \tag{II.2.206}$$

leading to mild rate modifications at the LHC. In Figure 201 we show a case where rate modifications in the 10% range might be large enough to be seen. However, the kinematic distributions in weak boson fusion and in Vh production are hardly modified. The matched dimension-6 Lagrangian follows the full model only for Vh production, exposing the underlying problem that we have to push the benchmarks for top partner models aggressively towards small masses to find possibly relevant deviations from the Standard Model.

A more promising place to look for modification through scalar top partners at the LHC might be Higgs plus jet production at large $p_{T,h}$, as described in Section II.2.5.b Altogether, this means that even though they in principle generate the corresponding momentum-dependent operators, scalar top partners are well described by the dimension-6 Lagrangian. This is because the new structures are loop-induced, and the corresponding suppression renders them hardly visible at the LHC, not even talking about an agreement between the full model and the dimension-6 Lagrangian in the relevant kinematic distributions.

Vector triplet model

Given scalar extensions of the Standard Model do not challenge the dimension-6 approach to LHC Higgs data we now assume a modification of the weak gauge sector. It consists of a massive vector field V_μ^a forming an $SU(2)$ triplet. To allow for large, tree-level modifications of LHC observables we assume that the new fields mix with the weak bosons,

$$\begin{aligned}\mathscr{L} \supset & -\frac{1}{4}\, V^a_{\mu\nu}\, V^{\mu\nu\, a} + \frac{M_V^2}{2}\, V^a_\mu\, V^{\mu\, a} \\ & + i\,\frac{g_V}{2}\, c_H\, V^a_\mu \left[\phi^\dagger \sigma^a \overleftrightarrow{D}^\mu \phi\right] + \frac{g_w^2}{2 g_V}\, V^a_\mu \sum_{\text{fermions}} c_F \overline{F}_L\, \gamma^\mu\, \sigma^a\, F_L + g_V^2\, c_{VVHH}\, V^a_\mu\, V^{\mu a}\, \phi^\dagger \phi + \cdots\end{aligned} \tag{II.2.207}$$

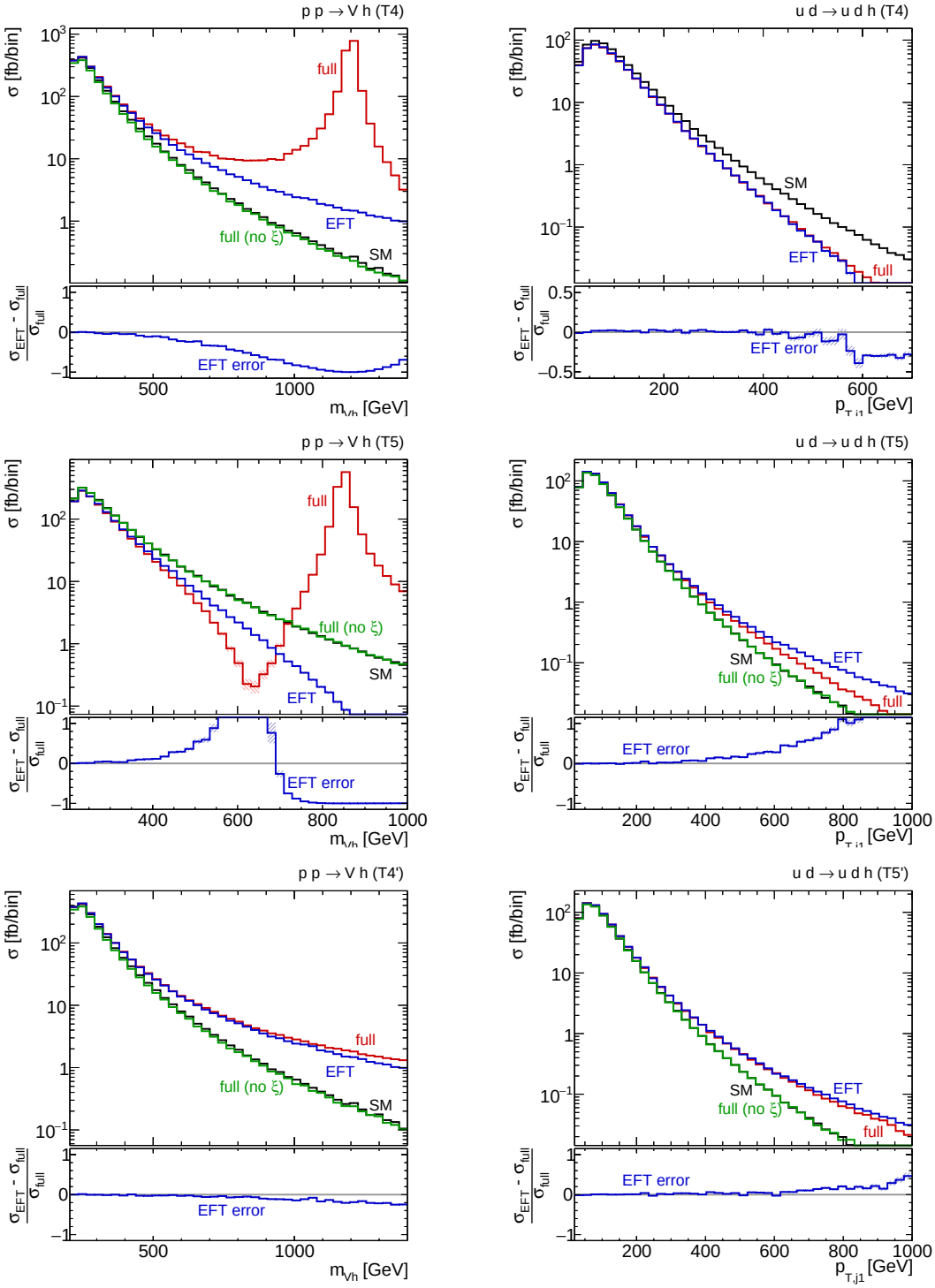

Figure 202: Distributions for WBF production and Higgs-strahlung in the vector triplet model. Figure modified from Ref. [749].

After mixing with the W and Z bosons we denote the new heavy states as ξ^0 and $\xi^\pm$. The masses of these particles define the matching scale $\Lambda = m_\xi$ in our v-improved matching. Integrating out the vector triplet leaves us with a set of dimension-6 Wilson coefficients generated at tree level

$$\bar{c}_H = \frac{3\,g^2\,v^2}{4\,m_\xi^2}\left[c_H^2\frac{g_V^2}{g^2} - 2\,c_F\,c_H\right] \qquad \bar{c}_6 = \frac{g^2\,v^2}{m_\xi^2}\left[c_H^2\frac{g_V^2}{g^2} - 2\,c_F\,c_H\right]$$

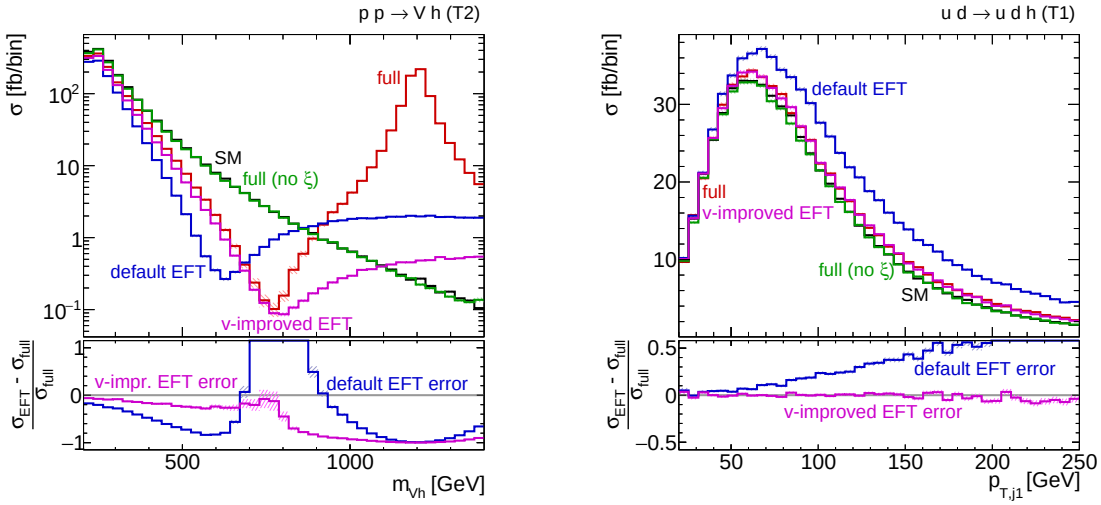

Figure 203: Distributions for WBF Higgs boson production and Higgs-strahlung in the vector triplet model for both the default and v-improved matching conditions. Figure modified from Ref. [749].

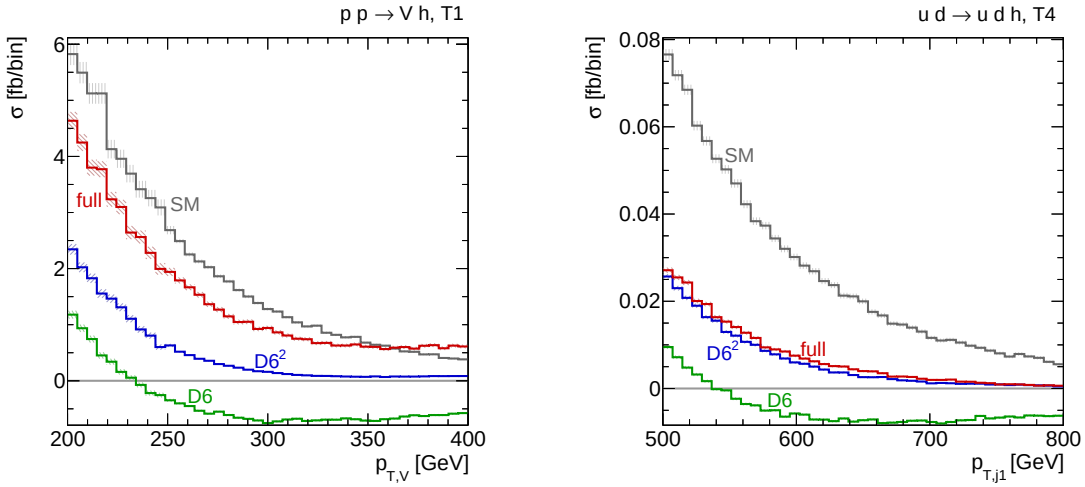

Figure 204: Distributions for WBF Higgs boson production and Higgs-strahlung in the vector triplet model with and without the dimension-6 squared contribution. Figure from Ref. [661].

$$\bar{c}_f = \frac{g^2\, v^2}{4\, m_\xi^2}\left[c_H^2\,\frac{g_V^2}{g^2} - 2\, c_F\, c_H\right] \qquad \bar{c}_W = -\frac{m_W^2}{m_\xi^2}\, c_F c_H\ . \tag{II.2.208}$$

This universal structure implies that along a line in c_F vs c_H all Wilson coefficients except for the operator $\mathcal{O}_W$ vanish. Following the argument from the scalar top partners we neglect further, loop-induced contributions. The Wilson coefficients induced at tree level are shown together with the model parameters for a set of benchmarks in Table 105. In the definition of these benchmarks we ignore experimental constraints on those models as well as open questions concerning their ultraviolet completions. They are merely chosen to test the agreement between the full model predictions and the dimension-6 Lagrangian at the LHC. Moreover, the notion of weakly interacting new particles might not really apply, given the size of the couplings defined in Eq.(II.2.207).

In Figure 202 we show a set of sample distributions for the vector triplet model. In the upper panel

for the Vh channel we immediately see what the limitations in matching the dimension-6 Lagrangian are: the benchmark points include new states at 1.2 TeV. The invariant mass distribution m_{Vh} develops a pole with tails reaching down to around $m_{Vh} = 600$ GeV. Below this, at least the v-improved dimension-6 Lagrangian follows the full model description to around 20 %. What is remarkable is that the description of the full model without the heavy ξ state deviates significantly from the complete model and from the dimension-6 Lagrangian. Far below the mass shell the latter indeed describes the effect of the s-channel ξ exchange, while it obviously fails to reproduce the pole region. The WBF distribution shows less dramatic effects, because the new states occur in the t-channel and there is no on-set of a resonance peak. Moreover, for the same benchmark model we observe a different sign of the (interference) effects; now the full model as well as the dimension-6 approximation stay below the Standard Model curve. Over the entire p_{T,j_1} range the agreement between the full model and the dimension-6 Lagrangian with v-improved matching is excellent even in regions where deviations from the Standard Model are due to new particle exchange.

In the second row of Figure 202 we show another benchmark point, where the new resonance peak in m_{Vh} appears around 850 GeV, and the interference effects between the Standard Model continuum and the developing pole above $m_{Vh} = 500$ GeV are destructive. The full model and its dimension-6 agree well into the range where the extended model deviates from the Standard Model. For WBF production the new particles in the t-channel lead to a significant enhancement of the $p_{T,j}$ distribution, which is described by the dimension-6 approximation to transverse momenta around 500 GeV.

In the lower panels of Figure 202 we show the same distributions for modified benchmark points where the masses of the new particles are heavier and this decoupling effect is compensated by larger couplings, so that the Wilson coefficients are the same as in the scenarios shown in the upper panels. In the absence of new resonances the agreement between the full vector triplet model and the dimension-6 description improves to an almost perfect match, reflecting the fact that higher-dimensional operators are still most appropriate in describing strongly interacting models at the LHC.

While for the generic high-mass scenarios shown in Figure 202 the choice of default and v-improved matching does not make a big difference, we demonstrate in Figure 203 that this question can be crucial for other benchmarks. Here the dimension-6 description based on the default matching fails to reproduce the full model already in the bulk of the distributions. The large discrepancies are caused by low masses of the new states as shown in Eq.(II.2.192). The v-improved matching, designed to include such effects, leads to impressive agreement up to large energies.

Finally, an open question is if in the dimension-6 approach we want to include the squared dimension-6 term in the combination $|\mathcal{M}_{\text{SM}} + \mathcal{M}_{\text{D6}}|^2$. For our strictly dimension-6 approach this is an entirely practical question, as long as it is clearly stated what is done. One issue of the truncation without the dimension-6 squared terms is that the matrix element squared is not guaranteed to be positive; this is true even if the effective theory is valid and dimension-8 operators are negligible, but the new physics effects dominate over the Standard Model and the bulk contribution stems from the dimension-6 structures.

In Figure 204 we show two distributions for the vector triplet model in an extreme benchmark point and based on v-improved matching. For Vh production and WBF production we choose a benchmark point with large new physics contributions, negatively interfering with the Standard Model contribution. For the Vh process we show the $p_{T,V}$ distribution, which is strongly correlated with m_{Vh}. In spite of the fact that the new particles only occur at $m_\xi = 1.2$ TeV the predictions without the dimension-6 squared term become negative for $p_{T,V} > 230$ GeV for Vh production and for $p_{T,j} > 550$ GeV for WBF. In particular the former is within reach of early LHC analyses.

Outlook

In view of the limited precision of early LHC data, and the typical size of new physics deviations, it is often assumed that a consistent EFT framework is of little practical use in LHC Higgs analyses. The reason is that models with a clear hierarchy of scales will only predict small deviations in LHC observables. For many key observables, the situation will get better with more LHC data being analysed, until all relevant observables become systematics-limited or theory-limited. The crucial question then become how well an ad-hoc truncated dimension-6 Lagrangian describes LHC observables for example compared to a weakly interacting full model.

Our first finding is that weakly interacting new physics models usually do not generate a large number of dimension-6 operators with non-negligible Wilson coefficients. This is particularly true for extended scalar sectors and all operators affecting associated Higgs boson production and Higgs boson production in weak boson fusion. Tree-level effects tend to be structurally simple, numerically small, and well described by a dimension-6 Lagrangian. Loop-induced effects for example induced by scalar top partners will be very hard to measure, and possible deviations between the full model and the dimension-6 approximation will not cause any problem. Effects on the gluon fusion process can be larger, but actual model predictions are known to agree well with the dimension-6 framework. This line of argument becomes stronger for more realistic new physics scenarios, compatible with all current constraints. If instead we want to generate large deviations from the Standard Model we should turn to extensions of the weak gauge sector. Here we can test how well a properly matched dimension-6 Lagrangian described the sizeable changes in the LHC kinematics.

Second, we find very good agreement between the full models extending the gauge and Higgs sector and the respective dimension-6 approximation for the relevant LHC observables. In cases where the standard matching procedure reaches its limitations, a v-improved matching procedure leads to excellent agreement between the full model and the dimension-6 approximation for our set of models. Note that our comparison between the full model and the dimension-6 approximation does not necessarily imply that all individual dimension-8 operators are negligible, because towers of higher-dimensional operators can cancel due to an unknown structure or even symmetry. We illustrate our findings in Table 106.

Finally, we confirm that the dimension-6 approximation typically breaks down when we become sensitive to new particles, often visible as poles in the s-channel. Unless we start observing such new

Table 106: Possible sources of failure of dimension-6 Lagrangian at the LHC. We use parentheses where deviations in kinematic distributions appear, but are unlikely to be observed in realistic scenarios.

Model	Process	EFT failure		
		resonance	kinematics	matching
singlet	on-shell $h \to 4\ell$, WBF, Vh, ...			$\times$
	off-shell WBF, ...		$(\times)$	$\times$
	hh	$\times$	$\times$	$\times$
2HDM	on-shell $h \to 4\ell$, WBF, Vh, ...			$\times$
	off-shell $h \to \gamma\gamma$, ...		$(\times)$	$\times$
	hh	$\times$	$\times$	$\times$
top partner	WBF, Vh			$\times$
vector triplet	WBF		$(\times)$	$\times$
	Vh	$\times$	$(\times)$	$\times$

resonances the dimension-6 approach seems valid to describe large classes of weakly interacting new physics at the LHC. The consistent effective field theory as well as the dimension-6 Lagrangian allow us to describe kinematic distributions and to include electroweak quantum corrections. The fundamental difference between the two approaches is that a consistent effective theory allows us to assign a theoretical uncertainty to the truncated operator basis in the model hypothesis we are testing at the LHC. In contrast, the dimension-6 Lagrangian does not include such a theoretical uncertainty. On the other hand, in most searches for new physics at the LHC we do not account for theoretical uncertainties beyond the perturbative QCD description, either. This means that the missing, most likely sizeable, theoretical uncertainty in the dimension-6 approach only has to be accounted for when we translate our findings into full weakly interacting models. This implies that from an experimental perspective a dimension-6 Lagrangian can be used in LHC Higgs physics as long as we do not observe an obvious breakdown through new resonances.

Chapter II.3

EFT Application

N. Belyaev, V. Bortolotto, L. Brenner, C.D. Burgard, F. Campanario, B. Chokoufé Nejad, M. Ciuchini, R. Contino, T. Corbett, J. de Blas, F. Demartin, A. Denner, S. Dittmaier, M. Dührssen, K. Ecker, A. Falkowski, E. Franco, B. Fuks, S. Gadatsch, M. Ghezzi, D. Ghosh, D. Gray, A. Greljo, A. Gritsan, R. Gröber, C. Grojean, G. Isidori, S. Kallweit, A. Kaluza, W. Kilian, K. Köneke, R. Konoplich, S. Kortner, D. Marzocca, K. Mawatari, K. Mimasu, S. Mishima, A. Mück, M. Mühlleitner, T. Ohl, A. Papaefstathiou, G. Perez, M. Pierini, K. Prokofiev, M. Rauch, L. Reina, J. Reuter, F. Riva, R. Röntsch, J. Roskes, R. Roth, V. Sanz, U. Sarica, C. Schmitt, M. Schulze, M. Sekulla, S. Shim, L. Silvestrini, C. Speckner, M. Spira, J. Streicher, W. Verkerke, C. Weiss, M. Xiao, M. Zaro, D. Zeppenfeld

II.3.1 High-energy physics tools for the study of the Higgs boson properties in Effective Field Theories [II.48]

II.3.1.a Introduction

The discovery by the ATLAS and CMS collaborations of a Higgs boson boson with a mass of about 125 GeV [1, 2] has marked an important step forward in the study and the understanding of the electroweak symmetry breaking mechanism. Although the currently measured properties of this newly discovered boson seem to be compatible with the Standard Model expectation, the recent start of the second LHC experimental run has risen new hopes to detect phenomena beyond the Standard Model. In this context, present and future LHC data could be interpreted in an effective field theory framework where departures from the Standard Model are organized as a series expansion in the new physics energy scale Λ that is assumed to be large.

The leading effects implied by such an effective field theory description usually consist of dimension-six operators that are supplemented to the Standard Model Lagrangian, each of these being associated with a new interaction strength. The number of independent coefficients is usually large, but important classes of observables turn to only depend on a much smaller subset of parameters. The effective field theory approach is therefore testable and the results could be reinterpreted to constrain explicit new physics models. Consequently, the development of high-energy physics tools able to perform computations in the effective field theory context has been a very active field during the last years. The recent progress described in the document addresses total and differential cross section precision calculations for the production of a single Higgs boson (see Section II.3.1.b for the gluon fusion channel and Section II.3.1.c for the vector boson fusion and the Higgs-strahlung channels) and of a pair of Higgs bosons (see Section II.3.1.d), as well as precision predictions for Higgs boson decays (see Section II.3.1.e). In addition, several machineries have been built so that we are now able to characterize the Higgs boson properties on the basis of Monte Carlo event generators. These include a description of the Higgs boson decays by means of pseudo-observables (see Section II.3.1.f), as well as all Higgs boson properties in full generality within the MADGRAPH5_aMC@NLO (see Section II.3.1.g) or JHUGEN/MELA (see Section II.3.1.h) platforms. Monte Carlo simulations can also be performed with the HERWIG (see Section II.3.1.i), VBFNLO (see Section II.3.1.j) and WHIZARD (see Section II.3.1.k) packages. As all codes are using different conventions, we review the notation in each case. Constraints on effective opera-

[II.48] *Author(s): B. Fuks (Ed.); F. Campanario, B. Chokoufé Nejad, M. Ciuchini, R. Contino, T. Corbett, J. de Blas, F. Demartin, A. Denner, S. Dittmaier, A. Falkowski, E. Franco, M. Ghezzi, D. Ghosh, A. Greljo, A. Gritsan, R. Gröber, C. Grojean, G. Isidori, S. Kallweit, W. Kilian, D. Marzocca, K. Mawatari, K. Mimasu, S. Mishima, A. Mück, M. Mühlleitner, T. Ohl, A. Papaefstathiou, G. Perez, M. Pierini, M. Rauch, L. Reina, J. Reuter, F. Riva, R. Roentsch, J. Roskes, R. Roth, V. Sanz, U. Sarica, M. Schulze, M. Sekulla, S. Shim, L. Silvestrini, C. Speckner, M. Spira, J. Streicher, C. Weiss, M. Xiao. M. Zaro, D. Zeppenfeld.*

tors can also be extracted by fitting the experimental results, which can be achieved for instance via the HEPFIT package (see Section II.3.1.l).

An important aspect of the effective field theory approach is the freedom in the choice of the operator basis, so that a given effect could be modeled by several different combinations of operators at a fixed order in the effective energy scale expansion. This is related to the possibility of redefining the Standard Model fields in such a way that the Standard Model Lagrangian is unaltered (or more precisely the scattering amplitudes), while certain combinations of dimension-six operators proportional to the Standard Model equations of motion can be eliminated up to subleading higher-dimensional effects. Different complete operator bases have been proposed in the past, and although each of them yields the same predictions, they present specific and different advantages. Existing calculations or tools are however often bound to a given basis choice, and it is desirable to be able to reuse results derived in the context of one basis in another basis. The ROSETTA platform (see Section II.3.1.m) has been very recently released to close this gap.

II.3.1.b HIGLU: Higgs boson production via gluon fusion

The program HIGLU [133,134], that is available at http://tiger.web.psi.ch/higlu/ calculates the Higgs boson production cross section via gluon-fusion up to the next-to-next-to-leading order (NNLO) accuracy in QCD in the large top mass limit [97–102, 127, 136, 140, 141, 859] and includes next-to-leading order (NLO) electroweak corrections [107–110, 145–149] within the Standard Model, and up to the NNLO in QCD and in the large top mass limit [97–102, 127, 136, 140–143, 859–867] for the minimal supersymmetric extension of the Standard Model. The genuine supersymmetric corrections are not included in the program, although the supersymmetric QCD ones are known [868–878]. Starting from the Standard Model Higgs results, the contributions of dimension-six operators beyond the Standard Model are included up to the NNLO in QCD. The latter extension is based on the effective Lagrangian (in the heavy top limit for the Standard Model part) [70, 115, 879, 880],

$$\mathcal{L}_{\text{eff}} = \frac{\alpha_s}{\pi}\left[\frac{c_t}{12}(1+\delta) + c_g\right] G_a^{\mu\nu} G^a_{\mu\nu} \frac{H}{v}, \tag{II.3.1}$$

where H denotes the Standard Model physical Higgs boson and v the vacuum expectation value of the neutral component of the Higgs field Φ. Moreover, the gluon field strength tensor is denoted by $G_a^{\mu\nu}$ and the strong coupling constant by α_s. The contributions of dimension-six operators are absorbed in the rescaling factor c_t for the top Yukawa coupling and the point-like coupling c_g. In other words, deviations of c_t and c_g from their Standard Model values $c_t = 1$ and $c_g = 0$ are understood to originate from dimension-six operators. The contribution of the chromomagnetic dipole operator [881, 882] is not included. The Lagrangian above includes QCD corrections via the δ parameter,

$$\delta = \delta_1 \frac{\alpha_s}{\pi} + \delta_2 \left(\frac{\alpha_s}{\pi}\right)^2 + \delta_3 \left(\frac{\alpha_s}{\pi}\right)^3, \tag{II.3.2}$$

whose three components read

$$\begin{aligned}
\delta_1 &= \frac{11}{4}, \qquad \delta_2 = \frac{2777}{288} + \frac{19}{16} L_t + N_F\left(\frac{L_t}{3} - \frac{67}{96}\right), \\
\delta_3 &= \frac{897943}{9216}\zeta_3 - \frac{2761331}{41472} + \frac{209}{64} L_t^2 + \frac{2417}{288} L_t + N_F\left(\frac{58723}{20736} - \frac{110779}{13824}\zeta_3 + \frac{23}{32} L_t^2 + \frac{91}{54} L_t\right) \\
&\quad + N_F^2\left(-\frac{L_t^2}{18} + \frac{77}{1728} L_t - \frac{6865}{31104}\right),
\end{aligned} \tag{II.3.3}$$

where $L_t = \log(\mu_R^2/m_t^2)$ with μ_R denoting the renormalization scale, N_F the number of active quark flavours and m_t the top quark pole mass.

The leading order (LO) cross section extended by the new physics contributions induced by the above effective Lagrangian is given by

$$\sigma_{LO}(pp \to H) = \sigma_0 \tau_H \frac{\mathrm{d}\mathcal{L}^{gg}}{\mathrm{d}\tau_H}, \tag{II.3.4}$$

where $\mathcal{L}^{gg}$ stands for the gluon-gluon partonic luminosity and where $\tau_H = m_h^2/S$, m_h being the Higgs boson mass and S the hadronic centre-of-mass energy. The σ_0 prefactor can be computed either in the non-linear case ($\sigma_0^{\rm NL}$) or in the SILH (strongly interacting light Higgs) framework ($\sigma_0^{\rm SILH}$) [653],

$$\begin{aligned}
\sigma_0^{\rm NL} &= \frac{G_F \alpha_s^2}{288\sqrt{2}\pi} \left| \sum_Q c_Q A_{1/2}(\tau_Q) + 12 c_g \right|^2, \\
\sigma_0^{\rm SILH} &= \sigma_0^{\rm NL} - \frac{G_F \alpha_s^2}{288\sqrt{2}\pi} \left| \sum_Q (c_Q - 1) A_Q(\tau_Q) + 12 c_g \right|^2,
\end{aligned} \tag{II.3.5}$$

where $\tau_Q = 4m_Q^2/m_h^2$ with m_Q being a generic quark mass, and where $G_F = (\sqrt{2}v^2)^{-1}$ stands for the Fermi constant. The LO form factors depend on the $A_{1/2}$ function that is given by

$$A_{1/2}(\tau) = \frac{3}{2}\tau\Big[1 + (1-\tau) f(\tau)\Big] \qquad \text{with} \qquad f(\tau) = \begin{cases} \arcsin^2 \dfrac{1}{\sqrt{\tau}} & \text{for } \tau \geq 1 \\ -\dfrac{1}{4}\left[\ln \dfrac{1+\sqrt{1-\tau}}{1-\sqrt{1-\tau}} - i\pi \right]^2 & \text{for } \tau < 1\,. \end{cases} \tag{II.3.6}$$

Rescaling factors c_Q have been introduced in Eq. (II.3.5) for all contributing quarks, *i.e.*, the top (c_t), bottom (c_b) and charm (c_c) quarks.

The Wilson coefficient c_g does not receive QCD corrections within the effective Lagrangian, but develops a scale dependence according to the renormalization group equation

$$\mu^2 \frac{\partial c_g(\mu^2)}{\partial \mu^2} = -\left\{ \beta_1 \Big(\frac{\alpha_s(\mu^2)}{\pi} \Big)^2 + 2\beta_2 \Big(\frac{\alpha_s(\mu^2)}{\pi} \Big)^3 \right\} c_g(\mu^2), \tag{II.3.7}$$

with

$$\beta_0 = \frac{33 - 2N_F}{12}, \qquad \beta_1 = \frac{153 - 19N_F}{24} \qquad \text{and} \qquad \beta_2 = \frac{1}{128}\Big(2857 - \frac{5033}{9} N_F + \frac{325}{27} N_F^2 \Big). \tag{II.3.8}$$

This renormalization group equation can be derived either from the scale-invariant trace anomaly term $\beta(\alpha_s)/\alpha_s G_a^{\mu\nu} G^a_{\mu\nu}$ [883–888], or from the scale dependence of the factor $(1+\delta)$ of the effective Lagrangian of Eq. (II.3.1), since both coefficients, $c_t(1+\delta)$ and c_g, have to develop the same scale dependence. The solution of the RGE for c_g up to the next-to-next-to-leading logarithmic (NNLL) level can be cast into the form

$$c_g(\mu^2) = c_g(\mu_0^2) \, \frac{\beta_0 + \beta_1 \frac{\alpha_s(\mu^2)}{\pi} + \beta_2 \Big(\frac{\alpha_s(\mu^2)}{\pi} \Big)^2}{\beta_0 + \beta_1 \frac{\alpha_s(\mu_0^2)}{\pi} + \beta_2 \Big(\frac{\alpha_s(\mu_0^2)}{\pi} \Big)^2}. \tag{II.3.9}$$

In order to compute the modified cross section up to NNLO, the mismatch of the individual terms of the effective Lagrangian of Eq. (II.3.1) with respect to the δ terms have been taken into account, the NNLL scale dependence of the Wilson coefficient c_g being properly included. In addition, the finite NLO quark mass term effects have been added at fixed NLO to the Standard Model contributions. This yields a consistent determination of the gluon-fusion cross section up to NNLO including the dimension-six operators that imply a rescaling of the top, bottom and charm Yukawa couplings and the point-like Hgg coupling parameterized by $c_g(\mu_R^2)$.

The present version 4.34 of HIGLU is linked to HDECAY (version 6.51) [69, 71] and allows one to choose the usual Standard Model Higgs input values in the separate input files `higlu.in` and `hdecay.in`. In addition, the rescaling factors $c_{t,b,c}$ and the point-like Wilson coefficient $c_g(\mu_0^2)$ can be set, together with the corresponding input scale μ_0, in the `higlu.in` file. In this way, HIGLU provides a consistent calculation of the gluon-fusion cross section up to NNLO QCD including dimension-six operator effects. More detailed information about the input files `higlu.in` and `hdecay.in` can be found as comment lines at the beginning of the main FORTRAN files `higlu.f` and `hdecay.f` shipped with the program. Finally, we note that the pole masses of the bottom and charm quarks are computed from the $\overline{\rm MS}$ input values $\overline{m}_b(\overline{m}_b)$ and $\overline{m}_c(3\ {\rm GeV})$ with N^{3}LO accuracy internally.

II.3.1.c HAWK: Precision predictions for Higgs boson production in the vector boson fusion and the Higgs-strahlung channels

HAWK is a parton-level Monte Carlo program providing precision predictions for Higgs boson production in the vector-boson fusion and Higgs-strahlung modes. For the Higgs-strahlung case, *i.e.*, VH production with $V = W$ or Z, HAWK includes the leptonic decays of the vector bosons, while contributions stemming from VH production with an hadronically decaying vector boson can be included in the vector-boson-fusion calculation optionally. In the Standard Model context, HAWK provides fully differential predictions that include QCD and electroweak next-to-leading-order corrections, and the results are returned as binned distributions for important hadron-collider observables. A detailed description of the program, that can be obtained at `http://hawk.hepforge.org`, can be found in Ref. [254], while details concerning the underlying calculations are given in Refs. [256–258].

Concerning the inclusion of higher-dimensional operators, HAWK supports anomalous HVV couplings which correspond to the Feynman rule

$$\mathrm{i}\, a_1^{\rm hvv}\, g_{\mu\nu} + \mathrm{i}\, a_2^{\rm hvv}\, (-k_1\cdot k_2\, g_{\mu\nu} + k_{1\nu}k_{2\mu}) + \mathrm{i}\, a_3^{\rm hvv}\, \epsilon_{\rho\sigma\mu\nu}\, k_1^\rho k_2^\sigma\ , \tag{II.3.10}$$

where k_1 and k_2 are the four-momenta of the gauge bosons and the a_i parameters are real quantities. One can either directly specify the coupling factors $a_1^{\rm hvv}$, $a_2^{\rm hvv}$ and $a_3^{\rm hvv}$ in the input file or the coefficients of the corresponding higher-dimensional operators, where a (modified) parameterization of the one introduced in Ref. [277] is used. The correspondence of the coefficients and the coupling factors is given in Ref. [254]. Anomalous coupling effects on the predictions can be calculated by including QCD corrections. However, for the vector-boson fusion case, the dressing of the anomalous amplitudes with QCD corrections is restricted to the embedding of 'diagonal QCD contributions' which correspond to corrections in the t-channel (or DIS-like) approximation where colour exchange between the two protons does not take place. In the Standard Model, the remaining 'non-diagonal' contributions are suppressed to a phenomenologically irrelevant level, and the introduction of anomalous coupling diagrams into those corrections would require an application of the effective-field-theory approach including a renormalization of the anomalous couplings. Moreover, the anomalous couplings related to the neutral gauge bosons are switched off for small momentum transfer by means of a form factor,

$$F_1 = |s_1||s_2|/(m_0^2+|s_1|)/(m_0^2+|s_2|)\ , \tag{II.3.11}$$

to avoid infrared singularities induced by the anomalous couplings. In this expression, s_1 and s_2 denote the virtualities of the two intermediate W and Z bosons and $m_0 = 1$ GeV is used. The code also allows one to use a form factor

$$F_2 = \Lambda_{\rm hvv}^4/(\Lambda_{\rm hvv}^2+|s_1|)/(\Lambda_{\rm hvv}^2+|s_2|)\ , \tag{II.3.12}$$

to control the anomalous coupling effects at large momentum transfer.

The HAWK implementation of anomalous HVV has been used, *e.g.*, in the ATLAS analysis [889] that focuses on the anomalous effects on vector-boson scattering via the reweighting of Standard Model predictions.

II.3.1.d HPAIR: Higgs boson pair production via gluon fusion

The program HPAIR, available at http://tiger.web.psi.ch/hpair/, calculates the Higgs boson pair production cross section via gluon fusion up to the NLO in QCD [435] in the limit of heavy top quarks within the Standard Model and the quark-loop induced contributions in the minimal supersymmetric extension of the Standard Model. While genuine supersymmetric QCD (in the general case) and electroweak corrections are unknown, known subleading NLO top mass effects [441,443–445], NNLO QCD corrections [436,439,442] and NLO supersymmetric QCD corrections in the limit of heavy superpartner masses [890] are not included in the program. Starting from the Standard Model Higgs result in the heavy top mass limit, the contributions of dimension-six operators beyond the Standard Model are included up to the NLO in QCD [472]. The latter extension is based on an effective phenomenological Lagrangian given by

$$\mathcal{L}_{\text{eff}} = -m_t \bar{t}t\left[c_t \frac{H}{v} + c_{tt}\frac{H^2}{2v^2}\right] - \frac{1}{6}c_3\left[\frac{3m_h^2}{v}\right]H^3 + \frac{\alpha_s}{\pi}G_a^{\mu\nu}G^a_{\mu\nu}\left[c_g\frac{H}{v} + c_{gg}\frac{H^2}{2v^2}\right], \tag{II.3.13}$$

As in Section II.3.1.b, the contributions of the dimension-six operators are absorbed in the rescaling factors c_t for the top Yukawa coupling and c_3 for the trilinear Higgs boson coupling, *i.e.*, deviations of c_t and c_3 from the Standard Model expectation of $c_t = c_3 = 1$ originate from dimension-six operators. The remaining couplings c_{tt}, c_g and c_{gg} are novel contributions purely arising from dimension-six operators and not present in the Standard Model Lagrangian. Integrating out the heavy top quark loops one arrives at the effective Lagrangian

$$\mathcal{L}_{\text{eff}} = \frac{\alpha_s}{\pi}G_a^{\mu\nu}G^a_{\mu\nu}\left\{\frac{H}{v}\left[\frac{c_t}{12}\left(1+\frac{11}{4}\frac{\alpha_s}{\pi}\right)+c_g\right] + \frac{H^2}{v^2}\left[\frac{c_{tt}-c_t^2}{24}\left(1+\frac{11}{4}\frac{\alpha_s}{\pi}\right)+\frac{c_{gg}}{2}\right]\right\}, \tag{II.3.14}$$

describing the Higgs boson couplings to gluons when only the leading QCD corrections for the single Higgs interactions are kept (compared to Eq. (II.3.1)).

The partonic LO cross section extended by beyond the Standard Model contributions induced by the above Lagrangian is given by

$$\hat{\sigma}_{LO}(gg\to HH) = \int_{\hat{t}_-}^{\hat{t}_+} \mathrm{d}\hat{t}\,\frac{G_F^2\alpha_s^2(\mu_R)}{512(2\pi)^3}\left[|C_\Delta F_1 + F_2|^2 + |c_t^2 G_\Box|^2\right], \tag{II.3.15}$$

where the Mandelstam variables are defined by

$$\hat{s} = Q^2\,, \qquad \hat{t} = m_h^2 - \frac{Q^2(1-\beta\cos\theta)}{2} \qquad \text{and} \qquad \hat{u} = m_h^2 - \frac{Q^2(1+\beta\cos\theta)}{2}, \tag{II.3.16}$$

with $\beta = \sqrt{1-4m_h^2/Q^2}$ and with Q denoting the invariant mass of the Higgs boson pair. Moreover, the integration bounds at $\cos\theta = \pm 1$ read

$$\hat{t}_\pm = m_h^2 - \frac{Q^2(1\mp\beta)}{2}. \tag{II.3.17}$$

The form factors F_1 and F_2 can be cast into the form

$$F_1 = c_t F_\Delta + \frac{2}{3}c_\Delta \qquad \text{and} \qquad F_2 = c_t^2 F_\Box + c_{tt}F_\Delta - \frac{2}{3}c_\Box, \tag{II.3.18}$$

with the explicit expressions of F_Δ, $F_\Box$ and $G_\Box$ being available in Ref. [432,434]. In the limit of heavy top quarks they simplify to

$$F_1^{\text{lim}} = \frac{2}{3}\Big(c_t + c_\Delta\Big)\,, \qquad F_2^{\text{lim}} = \frac{2}{3}\Big(-c_t^2 + c_{tt} - c_\Box\Big), \tag{II.3.19}$$

after introducing the abbreviations c_Δ and $c_\Box$. The latter read, together with the C_Δ variable of Eq. (II.3.15),

$$C_\Delta \equiv \lambda_{hhh} \frac{m_Z^2}{Q^2 - m_h^2 + i m_h \Gamma_h} , \qquad c_\Delta \equiv 12 c_g \qquad \text{and} \qquad c_\Box \equiv -12 c_{gg}, \tag{II.3.20}$$

with m_Z denoting the Z-boson mass, Γ_h the Higgs boson width, and the trilinear Higgs boson coupling being normalized as

$$\lambda_{hhh} = \frac{3 m_h^2 c_3}{m_Z^2}. \tag{II.3.21}$$

The partonic cross section has then to be convoluted with the gluon density in the proton in order to obtain the hadronic cross section.

The present version 2.00 of HPAIR needs the usual Standard Model Higgs input values that are provided in a separate input file `hpair.in`. In addition, this file also allows one for choosing the anomalous dimension-six factors c_t, c_{tt}, c_g, c_{gg} and c_3. Alternatively the dimension-six coefficients $\bar{c}_H$, $\bar{c}_u$, $\bar{c}_6$ and $\bar{c}_g$ can be provided within the usual SILH basis [653], starting from the effective SILH Lagrangian

$$\Delta\mathcal{L}_6^{\rm SILH} \supset \frac{\bar{c}_H}{2v^2}\partial_\mu(\Phi^\dagger\Phi)\partial^\mu(\Phi^\dagger\Phi) + \frac{\bar{c}_u}{v^2} y_t \Big(\Phi^\dagger\Phi \bar{q}_L \Phi^c t_R + \text{h.c.}\Big) - \frac{\bar{c}_6}{6v^2}\frac{3m_h^2}{v^2}\Big(\Phi^\dagger\Phi\Big)^3 + \bar{c}_g \frac{g_s^2}{m_W^2}\Phi^\dagger\Phi G^a_{\mu\nu} G_a^{\mu\nu}, \tag{II.3.22}$$

where $y_t = \sqrt{2} m_t/v$ denotes the top quark Yukawa coupling, g_s the strong coupling constant and m_W the W-boson mass. The connection to the Lagrangian of Eq. (II.3.13) is given by

$$c_t = 1 - \frac{\bar{c}_H}{2} - \bar{c}_u , \qquad c_{tt} = -\frac{1}{2}(\bar{c}_H + 3\bar{c}_u) , \qquad c_3 = 1 - \frac{3}{2}\bar{c}_H + \bar{c}_6 , \qquad c_g = c_{gg} = \bar{c}_g \frac{4\pi}{\alpha_2}, \tag{II.3.23}$$

with $\alpha_2 = \sqrt{2} G_F m_W^2/\pi$. Contrary to the strongly interacting non-linear case, in the SILH case products of dimension-six coefficients are not taken into account in accordance with a consistent expansion of the physical observable up to linear dimension-six terms. In the SILH case, this also requires the expansion of the LO cross section of Eq. (II.3.15) up to linear dimension-six terms. The NLO terms are treated accordingly in the HPAIR program that allows for both options, *i.e.*, the non-linear and SILH cases. In this way, HPAIR provides a consistent calculation of the gluon-fusion cross section up to NLO QCD including the effects of dimension-six operators. More detailed information about the input file `hpair.in` can be found as comment lines at the beginning of the main FORTRAN file `hpair.f` shipped with the program.

II.3.1.e eHDECAY, Higgs boson decays in the effective Lagrangian approach

Ref. [642] has presented the program eHDECAY, a FORTRAN code based on a modification of the program HDECAY [69, 71], and discussed the relation between the non-linear and the linear effective Lagrangian approaches. The program can be downloaded from `http://www.itp.kit.edu/~maggie/eHDECAY/`. In eHDECAY, the full list of leading bosonic operators of the Higgs effective Lagrangian has been implemented, both for a linear and a non-linear realization of the electroweak symmetry and for two benchmark composite Higgs models called MCHM4 [658] and MCHM5 [770]. All the relevant QCD corrections have been included and we detail in the following the importance of higher-order QCD corrections and of mass effects on the corrections. We also show how to consistently include electroweak corrections whenever it is possible, focusing on the example of the Higgs boson decay into two gluons. As the leading part of the QCD corrections in general factorizes with respect to the expansion in the number of fields and derivatives of the effective Lagrangian, they can be included by taking over the results from the Standard Model. The electroweak corrections, on the contrary, require dedicated computations that are only partly available at present. They are consequently only implemented up to higher orders in a v^2/f^2 expansion in the framework of the linear Lagrangian, where $f = \Lambda/g_\star$ with $g_\star$ being a typical new physics coupling strength. They are valid, for instance, in the SILH framework [653] in which the

deviations from the Standard Model are small. On different lines, higher-order QCD corrections and mass effects are included also in the non-linear implementation.

Denoting by c_ψ the modifications of the Higgs boson couplings to fermions with respect to the Standard Model and by c'_{gg} the effective Higgs boson coupling to gluons, the related non-linear effective Lagrangian reads

$$\Delta\mathcal{L}_{\rm NL} = -\sum_{\psi=u,d,\ell} c_\psi m_\psi \bar\psi\psi \frac{H}{v} + \frac{c'_{gg}}{2} G^a_{\mu\nu} G_a^{\mu\nu} \frac{H}{v} \,. \tag{II.3.24}$$

The decay rate into gluons implemented in EHDECAY in the framework of the non-linear Lagrangian is then given by

$$\begin{aligned}\Gamma_{gg}^{\rm NL} =& \frac{G_F \alpha_s^2 m_h^3}{4\sqrt{2}\pi^3}\left[\left|\sum_{q=t,b,c}\frac{c_q}{3}\,A_{1/2}(\tau_q)\right|^2 c_{\rm eff}^2\,\kappa_{\rm soft} + 2\,{\rm Re}\left\{\sum_{q=t,b,c}\frac{c_q}{3}\,A^*_{1/2}(\tau_q)\frac{2\pi c_{gg}}{\alpha_s}\right\} c_{\rm eff}\,\kappa_{\rm soft}\right.\\ &\left. + \left|\frac{2\pi c'_{gg}}{\alpha_s}\right|^2 \kappa_{\rm soft} + \frac{1}{9}\sum_{q,q'=t,b} c_q\,A^*_{1/2}(\tau_q) c_{q'}\,A_{1/2}(\tau_{q'})\kappa^{\rm NLO}(\tau_q,\tau_{q'})\right].\end{aligned} \tag{II.3.25}$$

On the other hand, the part of the linear Lagrangian that contributes to the Higgs boson decay into two gluons reads, in the SILH basis,

$$\Delta\mathcal{L}_6^{\rm SILH} \supset \frac{\bar c_H}{2v^2}\partial^\mu(\Phi^\dagger\Phi)\partial_\mu(\Phi^\dagger\Phi) + \frac{\bar c_g g_s^2}{m_W^2}\Phi^\dagger\Phi G^a_{\mu\nu}G_a^{\mu\nu} + \left(\frac{\bar c_u y_u}{v^2}\Phi^\dagger\Phi\bar q_L\Phi^c u_R + \frac{\bar c_d y_d}{v^2}\Phi^\dagger\Phi\bar q_L\Phi d_R + {\rm h.c.}\right), \tag{II.3.26}$$

where $\bar c_H$, $\bar c_g$, $\bar c_u$ and $\bar c_d$ are the Wilson coefficients of the corresponding dimension-six effective operators and $y_{u,d}$ the Yukawa couplings of the up- and down-type quarks, respectively. In this case, the Higgs boson decay rate into gluons implemented in EHDECAY is given by

$$\begin{aligned}\Gamma_{gg}^{\rm SILH} =& \frac{G_F\alpha_s^2 m_h^3}{4\sqrt{2}\pi^3}\left[\frac{1}{9}\sum_{q,q'=t,b,c}(1-\bar c_H-\bar c_q-\bar c_{q'})A^*_{1/2}(\tau_{q'})A_{1/2}(\tau_q)c_{\rm eff}^2\,\kappa_{\rm soft}\right.\\ &+ 2\,{\rm Re}\left\{\sum_{q=t,b,c}\frac{1}{3}\,A^*_{1/2}(\tau_q)\frac{16\pi\bar c_g}{\alpha_2}\right\} c_{\rm eff}\,\kappa_{\rm soft} + \left|\sum_{q=t,b,c}\frac{1}{3}\,A_{1/2}(\tau_q)\right|^2 c_{\rm eff}^2\,\kappa_{\rm ew}\,\kappa_{\rm soft}\\ &\left.+\frac{1}{9}\sum_{q,q'=t,b}(1-\bar c_H-\bar c_q-\bar c_{q'})A^*_{1/2}(\tau_q)A_{1/2}(\tau_{q'})\kappa^{\rm NLO}(\tau_q,\tau_{q'})\right].\end{aligned} \tag{II.3.27}$$

In both Eq. (II.3.25) and Eq. (II.3.27), $\tau_q = 4m_q^2/m_h^2$ and the loop function $A_{1/2}(\tau)$ is defined as in Eq. (II.3.6). We use the pole masses for the top, bottom and charm quark masses and α_s is computed up to N^{3}LO at a scale fixed to m_h and for $N_F = 5$ active flavours. The QCD corrections have been taken into account up to N^{3}LO in QCD in the limit of heavy loop-particle masses so that the effect from low-energy gluon radiation, given by the coefficient $\kappa_{\rm soft}$, factorizes in this limit. The corrections from high-energy gluon and quark exchange (with virtuality $q^2 \gg m_t^2$) are encoded in the coefficient $c_{\rm eff}$. Namely, for $m_h \ll 2m_t$, the top quark can be integrated out, leading to the effective five-flavour Lagrangian

$$\mathcal{L}_{\rm eff} = -2^{1/4} G_F^{1/2} C_1 G^a_{\mu\nu} G_a^{\mu\nu} H \,, \tag{II.3.28}$$

where the dependence on the top quark mass m_t is included in the coefficient function C_1. We then have

$$\kappa_{\rm soft} = \frac{\pi}{2m_h^4}\,{\rm Im}\left\{\Pi^{GG}(q^2=m_h^2)\right\} \qquad \text{and} \qquad c_{\rm eff} = -\frac{12\pi\,C_1}{\alpha_s(m_h)}\,, \tag{II.3.29}$$

with the vacuum polarization $\Pi^{GG}(q^2)$ being induced by the gluon operator. The N^{3}LO expressions for C_1 and for $\mathrm{Im}\{\Pi^{GG}\}$ have been given in Refs. [67, 115, 880, 891] and Ref. [892], respectively. In particular, the NLO expressions for $\kappa_{\rm soft}$ and $c_{\rm eff}$ read [99, 893, 894]

$$\kappa_{\rm soft}^{\rm NLO} = 1 + \frac{\alpha_s}{\pi}\left(\frac{73}{4} - \frac{7}{6}N_F\right) \qquad \text{and} \qquad c_{\rm eff}^{\rm NLO} = 1 + \frac{\alpha_s}{\pi}\frac{11}{4}\,, \tag{II.3.30}$$

in agreement with the low-energy theorem [895–897]. The additional mass effects at NLO [136] in the top and bottom quark loops are taken into account by the function $\kappa^{\rm NLO}(\tau_q, \tau_{q'})$ in the last lines of Eqs. (II.3.25) and (II.3.27). This function quantifies the difference between the NLO QCD corrections for the top (bottom) contribution taking into account finite mass effects in the loop, and the result for the top (bottom) contribution in the limit of a large loop-particle mass.

Higher order corrections are large, with in particular the N^{3}LO QCD corrections increasing the total width by almost up to 90%. The mass effects at NLO QCD are relevant for the bottom loop where they amount to 8%, while they are negligible for the top loop. To be consistent with the non-linear approach, no electroweak corrections have been included in the non-linear parameterization, as a perturbative expansion in powers of v^2/f^2 is not possible in the general case. In contrast, in the linear parameterization, both QCD and electroweak corrections are included. The treatment of the QCD corrections is in accordance with the non-linear case, while the electroweak corrections [107–109, 145–149] are taken into account by the factor $\kappa_{\rm ew}$ of Eq. (II.3.27). In the Standard Model, they can be factorized in the particular case of the Higgs boson decaying into two gluons. However, this factorization is not valid in the general case. In particular, when the contributions from the effective Lagrangian are taken into account, modified Higgs boson couplings absent at the leading order can appear and spoil the factorization. Hence, a consistent inclusion of the electroweak corrections is only possible in the linear-Lagrangian case and up to higher orders in v^2/f^2. More precisely, the Standard Model electroweak corrections can be added to get a result that includes the leading $\mathcal{O}(v^2/f^2)$ and the next-to-leading $\mathcal{O}(\alpha/4\pi)$ corrections as well as the mixed $\mathcal{O}[(\alpha_s/4\pi)^5(\alpha/4\pi)]$ contributions, but that neglects terms of $\mathcal{O}[(\alpha/4\pi)(v^2/f^2)]$, $\mathcal{O}[((v^2/f^2)^2]$ and $\mathcal{O}[(\alpha/4\pi)^2]$, where α is generically meant as the electroweak expansion parameter.

For the future it is planned to add to EHDECAY contributions from the fermionic effective operators and those from the effective Lagrangian to the set of input observables m_W, m_Z and G_F. Moreover, in accordance with the Higgs Cross Section Working Group Internal Note of Ref. [144], a switch from the pole-mass scheme to the $\overline{\rm MS}$ scheme for the fermionic masses is under consideration, as well as the implementation of an interface for the so-called Higgs basis parameterization of the effective Lagrangian (see Section II.2.1 and Section II.3.1.m).

II.3.1.f Implementation of Higgs Pseudo-Observables in the universal FEYNRULES output

With the LHC Run-II, Higgs physics is entering a precision era. This would allow us to look for new physics effects not only in the overall signal strengths, but also in kinematical distributions. In this perspective, the so called 'κ-framework' [10] is insufficient and needs to be extended. The natural extension is the so-called Higgs pseudo-observables framework introduced in Refs. [651,652]. A detailed discussion about this formalism is presented in Chapter III.1. Here we limit ourself to summarize its main features in order to illustrate its implementation via the Universal FEYNRULES Output model HIGGSPO that is available at http://www.physik.uzh.ch/data/HiggsPO.

The pseudo-observables are a finite set of parameters that are experimentally accessible, well-defined from the point of view of a quantum field theory, and that characterize possible deviations from the Standard Model in processes involving the Higgs boson in great generality. More precisely, the Higgs pseudo-observables are defined from a general decomposition (based on analyticity, unitarity, and crossing symmetry) of on-shell amplitudes involving the Higgs boson and a momentum expansion following the assumption of no new light particles in the kinematical regime where the decomposition

is assumed to be valid. A further key assumption of the pseudo-observables formalism is that the Higgs boson is a spin zero resonance with a narrow width, such that new physics effects in production and decay factorize.

For the convenience of the reader, let us stress the difference between a pseudo-observable approach, such as the one summarized here, and an effective field theory one. On the one hand, pseudo-observables are defined from on-shell properties of the relevant scattering amplitudes and are thus well-defined at all orders in perturbation theory. On the other hand, effective field theory coefficients are Lagrangian parameters and, as such, not observable quantities. Pseudo-observables can be computed in an effective field theory approach at a given order in perturbation theory and, doing this at the tree-level, it is possible to derive a one-to-one correspondence between the two setups. However, this correspondence would change, and become more complex, if the computation is performed at higher orders: the physical meaning of the pseudo-observable would not change while the operator coefficients would loose the direct connection to observable quantities which was obtained at the tree-level. In other words, the difference between pseudo-observables and effective field theory coefficients is the same as the one between the pole mass of a particle (a pseudo-observable) and the mass parameters in the Lagrangian.

Due to their simple kinematics, two-body Higgs boson decays (into a $\gamma\gamma$ and an $\bar{f}f$ pair) can be parameterized by only two pseudo-observables each, one describing the CP-conserving amplitude and another for the CP-violating one. Unless the polarization of the final states can be measured, only a combination of the two is experimentally accessible. Three-body and four-body Higgs boson decays (such as into $2\ell\gamma$, 4ℓ and $2\ell2\nu$ systems) have a more complicated kinematics. In this case the pseudo-observables are defined from the expansion of the on-shell amplitudes around the known physical poles due to the propagation of intermediate Standard Model electroweak gauge bosons. General amplitude decomposition and pseudo-observables definitions can be found in Ref. [651] for the Higgs boson decays and in Ref. [652] for Higgs boson production in the vector-boson fusion mode and in association with a gauge boson.

The pseudo-observables are defined directly at the amplitude level. As such, on the one hand they can be computed from a specific Lagrangian (to a specific order in perturbation theory), and on the other hand the pseudo-observables are directly connected to S-matrix elements, providing a direct link to physical observables [651]. They are thus particularly well suited for the analysis of experimental data with the matrix-element method [898]. In order to use the pseudo-observable decomposition for precision studies, it is important to account for the long-distance contributions due to soft and collinear photon emission (*i.e.*, the leading QED radiative corrections). These represent a universal correction factor that can be implemented, by means of appropriate convolution functions or, equivalently, by showering algorithms in Monte Carlo simulations, irrespective of the specific short-distance structure of the amplitude. It has been shown that inclusion of such correction in $H \to 2e2\mu$ decays recovers the complete NLO Standard Model predictions within an accuracy of about 1% [899].

In order to use the pseudo-observable framework in experimental analyses, it is convenient to have a tool capable of generating signal events for specific values of the pseudo-observables. Such a tool has been developed in the context of the Higgs boson decays and is publicly available on the above webpage that also includes a detailed user manual. The implementation of pseudo-observables in electroweak Higgs boson production including NLO QCD corrections is underway and will be available at the same Internet link. We have implemented into FEYNRULES [524] (version 2.3.1) a HIGGSPO model, whose source file is named `HPO.fr`, by means of an effective Lagrangian generating the corresponding vertices at the tree level. We stress that such a Lagrangian should not be considered as a specific model or an effective field theory description, but rather as an auxiliary tool to be used (at tree level only) in order to reproduce the correct Higgs boson decay amplitude decomposition in terms of pseudo-observables that is valid beyond the tree level.

The HIGGSPO FEYNRULES model as implemented in the `HPO.fr` file is exported to the Universal FeynRules Output (UFO) format [552], which can then be used within the MADGRAPH5_aMC@NLO [54]

Process	$H \to bb$	$H \to \tau\tau$	$H \to cc$	$H \to \mu\mu$
Pseudo-observables	$\kappa_b,\ \delta_b^{\rm CP}$	$\kappa_\tau,\ \delta_\tau^{\rm CP}$	$\kappa_c,\ \delta_c^{\rm CP}$	$\kappa_\mu,\ \delta_\mu^{\rm CP}$

Table 107: Pseudo-observables relevant for Higgs boson decays into two fermions.

Process	Pseudo-observables
$H \to \gamma\gamma$	$\kappa_{\gamma\gamma},\ \delta_{\gamma\gamma}^{\rm CP}$
$H \to Z\gamma$	$\kappa_{Z\gamma},\ \delta_{Z\gamma}^{\rm CP}$
$H \to \gamma 2\nu$	$\kappa_{Z\gamma},\ \delta_{Z\gamma}^{\rm CP}$
$H \to \gamma 2\ell$	$\kappa_{\gamma\gamma},\ \delta_{\gamma\gamma}^{\rm CP},\ \kappa_{Z\gamma},\ \delta_{Z\gamma}^{\rm CP}$
$H \to Z 2\ell$	$\kappa_{ZZ},\ \epsilon_{ZZ},\ \epsilon_{ZZ}^{\rm CP},\ \kappa_{Z\gamma},\ \delta_{Z\gamma}^{\rm CP},\ \epsilon_{Z\ell_L},\ \epsilon_{Z\ell_R}$
$H \to 2\ell 2\ell'$	$\kappa_{ZZ},\ \epsilon_{ZZ},\ \epsilon_{ZZ}^{\rm CP},\ \kappa_{Z\gamma},\ \delta_{Z\gamma}^{\rm CP},\ \kappa_{\gamma\gamma},\ \delta_{\gamma\gamma}^{\rm CP},\ \epsilon_{Z\ell_L},\ \epsilon_{Z\ell_R},\ \epsilon_{Z\ell'_L},\ \epsilon_{Z\ell'_R}$
$H \to 4\ell$	$\kappa_{ZZ},\ \epsilon_{ZZ},\ \epsilon_{ZZ}^{\rm CP},\ \kappa_{Z\gamma},\ \delta_{Z\gamma}^{\rm CP},\ \kappa_{\gamma\gamma},\ \delta_{\gamma\gamma}^{\rm CP},\ \epsilon_{Z\ell_L},\ \epsilon_{Z\ell_R}$
$H \to \bar{\ell}\ell 2\nu$	$\begin{cases}\kappa_{ZZ},\ \epsilon_{ZZ},\ \epsilon_{ZZ}^{\rm CP},\ \kappa_{Z\gamma},\ \delta_{Z\gamma}^{\rm CP},\ \epsilon_{Z\ell_L},\ \epsilon_{Z\ell_R},\ \epsilon_{Z\nu} \\ \kappa_{WW},\ \epsilon_{WW},\ \epsilon_{WW}^{\rm CP},\ \epsilon_{W\ell},\ \phi_{W\ell}\end{cases}$
$H \to \bar{\ell}\ell' 2\nu$	$\kappa_{WW},\ \epsilon_{WW},\ \epsilon_{WW}^{\rm CP},\ \epsilon_{W\ell},\ \phi_{W\ell},\ \epsilon_{W\ell'},\ \phi_{W\ell'}$

Table 108: Pseudo-observables relevant for Higgs boson decays into a gauge-boson pair, and into a three-body or four-body system. We denote by ℓ an electron, a muon or a tau and ν indicates any of the three neutrino species.

and SHERPA [229] event generators. The general idea is that after simulating Higgs boson production with a dedicated Monte Carlo generator, the Higgs boson can be decayed at the parton-level with the HIGGSPO model and the partonic events can then be passed to a general purpose event generator for subsequent parton showering and hadronization (such as PYTHIA [318]). This last step will automatically account for the important radiative corrections [899]. We note that it is very practical to use the MADSPIN module [368] of MADGRAPH5_aMC@NLO to decay the Higgs boson with the HIGGSPO model on the fly. We stress again that our FEYNRULES implementation only consists of a set of effective interactions that generate exactly the scattering amplitude of interest at the tree level and is supposed to be used for this purpose only. It should not be used as a Lagrangian for arbitrary process and beyond the tree level.

All the Higgs boson decay processes implemented in the HIGGSPO model, together with the associated Higgs pseudo-observables accessible in the parameter card, are summarized in Table 107 and Table 108. The Higgs pseudo-observables relevant for describing the Higgs boson decays into two fermions are shown in Table 107. The coupling strengths have been assigned an interaction order `YUK` $= 1$. The pseudo-observables relevant for all other Higgs boson decays are presented in Table 108 and the coupling strengths have been related to an interaction order `HPO` $= 1$. Translation of the pseudo-observable language to the Higgs basis defined in Section II.2.1 is also available in Refs. [651, 652].

II.3.1.g Higgs and beyond the Standard Model characterization in the MADGRAPH5_aMC@NLO framework

The HIGGS CHARACTERIZATION (HC) implementation provides a complete framework, based on an effective field theory description, that allows for the study of the Higgs boson properties in a consistent, systematic and accurate way. The HC [622] follows the general strategy outlined in Ref. [900], and has been implemented in a complete simulation chain from Lagrangian to hadron-level events, especially in the FEYNRULES/MADGRAPH5_aMC@NLO framework. The HC effective Lagrangian fea-

tures bosons $X(J^P)$ with various spin-parity assignments ($J^P = 0^+$, 0^-, 1^+, 1^- and 2^+) and has been implemented in terms of mass eigenstates into FEYNRULES [524], whose output files are interfaced [552, 901] with various event generators. The HC model files are publicly available online, http://feynrules.irmp.ucl.ac.be/wiki/HiggsCharacterisation.

Later on, the HC framework has been extended as a BEYOND THE STANDARD MODEL CHARACTERIZATION (BSMC) framework [639] where the effective Lagrangian has been constructed as above, but starting from the Higgs basis Lagrangian in Section II.2.1 where all possible effective operators of dimension up to six are written in terms of mass eigenstates. In particular, fermionic operators different from the Yukawa interactions are now included. However, instead of imposing the realization of the electroweak symmetry that relates the Wilson coefficients, the latter have been kept independent. Due to the lack of manifest $SU(2)_L \times U(1)_Y$ invariance, the BSMC Lagrangian is associated with a larger number of independent coefficients compared to more traditional bases such as the Warsaw [614] or SILH [464,653] bases. Therefore, the BSMC model can be used in many contexts, not only in the case of linear effective field theories but also in the non-linear case or in the pseudo-observable parameterization (see Section II.3.1.f). As introduced in Section II.3.1.m, the ROSETTA package allows for the translation of the Wilson coefficients given in a particular basis of non-redundant dimension-six operators (such as the Warsaw or SILH basis) to the BSMC parameterization coefficients by including constraints that render the Lagrangian invariant under the full electroweak symmetry group. Extensions to other translations are foreseen. As for the HC case, the BSMC Lagrangian has been implemented into FEYNRULES and is available online, http://feynrules.irmp.ucl.ac.be/wiki/BSMCharacterisation. A corresponding implementation of the dimension-six Lagrangian above the weak scale, where $SU(2)_L \times U(1)_Y$ is an exact symmetry, has been also achieved [838] and has overlapping as well as complementary features with respect to the HC and BSMC Lagrangians. It is available at http://feynrules.irmp.ucl.ac.be/wiki/HEL. In this case, the implementation has been performed in the SILH basis.

There are several advantages in having a first principle implementation in terms of an effective Lagrangian which can be automatically interfaced to event generators. First and most important, all relevant production and decay modes can be studied within the same model, and the corresponding processes automatically generated within minutes. Second, it is straightforward to modify the model implementation to extend it further in case of need, by adding further interactions, for example of higher dimensions in energy. Finally, higher-order effects can be easily accounted for, by generating multi-jet merged samples or computing NLO corrections within automatic frameworks. As accumulated data has been increasing, the last point became more and more important. The detailed demonstrations and analyses for all the main production modes of the Higgs boson (gluon fusion, vector boson fusion, VH associated production and $t\bar{t}H$ production) as well as tH production at NLO accuracy in QCD have been done recently [410, 902, 903], within the MADGRAPH5_aMC@NLO program [54]. In the following, we focus, for the sake of the example, on a spin-0 (Higgs) boson that is denoted by X_0, and compute several differential distributions for some production processes and for different benchmark scenarios.

In the HC framework, the only assumptions are that the 125 GeV resonance found at the LHC corresponds to a spin-0 state, that no other new state coupled to such a resonance exists below the cutoff scale Λ and that new physics is dominantly described by the lowest dimensional operators. We thus include all effects stemming from the complete set of dimension-six operators allowed by the Standard

Scenario	HC parameter choice	Scenario	HC parameter choice
0^+(GF, SM)	$\kappa_{Hgg/Htt} = 1$ $(c_\alpha = 1)$	0^+(VBF, SM)	$\kappa_{SM} = 1$ $(c_\alpha = 1)$
0^-(GF)	$\kappa_{Agg/Att} = 1$ $(c_\alpha = 0)$	0^+(VBF, HD)	$\kappa_{HZZ,HWW} = 1$ $(c_\alpha = 1)$
$0^\pm$(GF)	$\kappa_{Hgg,Agg/Htt,Att} = 1$ $(c_\alpha = 1/\sqrt{2})$	0^-(VBF, HD)	$\kappa_{AZZ,AWW} = 1$ $(c_\alpha = 0)$
		$0^\pm$(VBF, HD)	$\kappa_{HZZ,HWW,AZZ,AWW} = 1$ $(c_\alpha = 1/\sqrt{2})$

Table 109: Benchmark scenarios for X_0 production in the gluon fusion and $t\bar{t}H$ (GF) and in the vector boson fusion (VBF) channel.

Model gauge symmetry. The effective interaction Lagrangian is given by

$$\begin{aligned}\mathcal{L}_0 =& \Big\{ -\sum_{f=t,b,\tau} \bar{\psi}_f \big(c_\alpha \kappa_{Htt} g_{Htt} + i s_\alpha \kappa_{Att} g_{Att}\, \gamma_5\big)\psi_f + c_\alpha \kappa_{\rm SM} \big[\frac{1}{2} g_{HZZ}\, Z_\mu Z^\mu + g_{HWW}\, W^+_\mu W^{-\mu}\big] \\ & - \frac{1}{4}\big[c_\alpha \kappa_{H\gamma\gamma} g_{H\gamma\gamma}\, A_{\mu\nu}A^{\mu\nu} + s_\alpha \kappa_{A\gamma\gamma} g_{A\gamma\gamma}\, A_{\mu\nu}\widetilde{A}^{\mu\nu}\big] - \frac{1}{2}\big[c_\alpha \kappa_{HZ\gamma} g_{HZ\gamma}\, Z_{\mu\nu}A^{\mu\nu} + s_\alpha \kappa_{AZ\gamma} g_{AZ\gamma}\, Z_{\mu\nu}\widetilde{A}^{\mu\nu}\big] \\ & - \frac{1}{4}\big[c_\alpha \kappa_{Hgg} g_{Hgg}\, G^a_{\mu\nu}G^{a,\mu\nu} + s_\alpha \kappa_{Agg} g_{Agg}\, G^a_{\mu\nu}\widetilde{G}^{a,\mu\nu}\big] - \frac{1}{4}\frac{1}{\Lambda}\big[c_\alpha \kappa_{HZZ}\, Z_{\mu\nu}Z^{\mu\nu} + s_\alpha \kappa_{AZZ}\, Z_{\mu\nu}\widetilde{Z}^{\mu\nu}\big] \\ & - \frac{1}{2}\frac{1}{\Lambda}\big[c_\alpha \kappa_{HWW}\, W^+_{\mu\nu}W^{-\mu\nu} + s_\alpha \kappa_{AWW}\, W^+_{\mu\nu}\widetilde{W}^{-\mu\nu}\big] \\ & - \frac{1}{\Lambda} c_\alpha \big[\kappa_{H\partial\gamma}\, Z_\nu \partial_\mu A^{\mu\nu} + \kappa_{H\partial Z}\, Z_\nu \partial_\mu Z^{\mu\nu} + \kappa_{H\partial W}\big(W^+_\nu \partial_\mu W^{-\mu\nu} + h.c.\big)\big]\Big\}\, X_0\,, \end{aligned} \tag{II.3.31}$$

where $A_{\mu\nu}$ ($\widetilde{A}_{\mu\nu}$), $Z_{\mu\nu}$ ($\widetilde{Z}_{\mu\nu}$) and $W^\pm_{\mu\nu}$ ($\widetilde{W}^\pm_{\mu\nu}$) represent the field strength tensors of the physical electroweak bosons, and $G^a_{\mu\nu}$ and $\widetilde{G}^a_{\mu\nu}$ the gluon field strength tensor and its dual. This parameterization allows for the easy recovery of the Standard Model case by fixing the dimensionless parameters κ_i to appropriate values, since the dimensionful couplings $g_{Xyy'}$ are set to their Standard Model values. For instance, we enforce that $g_{H\gamma\gamma} = 47\alpha/18\pi v$ and $g_{Hgg} = -\alpha_s/3\pi v$, two values that can be obtained in the limit of large W-boson and top-quark masses. Moreover, the model description includes the interactions of a 0^- state typical of supersymmetry or of generic two Higgs doublet models, and enables the CP-mixing between the 0^+ and 0^- states via a mixing angle α whose sine and cosine are denoted by s_α and c_α. In the Standard Model, $c_\alpha = 1$ and $s_\alpha = 0$.

We then make use of MADGRAPH5_aMC@NLO to generate both a numerical code and events, at the NLO accuracy in QCD. In practice, for the production of an X_0 state plus two jets in the gluon fusion channel, this is achieved by issuing the following commands (with the `/ t` syntax forbidding diagrams containing top loops),

```
> import model HC_NLO_X0-heft
> generate p p > x0 j j / t [QCD]
> output
> launch
```

where the `-heft` suffix in the model name refers to the corresponding model restriction. As a result, all the amplitudes featuring the Higgs–gluon effective vertices in the heavy-top limit are generated, including corrections up to the NLO in QCD. Analogous commands can be issued to generate events related to the production of an X_0 state plus zero and one jet. After the `launch` command, one can modify the `param_card.dat` file to change the values of the Λ, κ and c_α parameters. Similarly, a code and events can be generated in the vector boson fusion case (left, with the $$ sign forbidding diagrams with $W^\pm$ or Z bosons in the s-channel as they are included in Higgs-strahlung production) and in the Higgs-strahlung production mode (right) by typing in

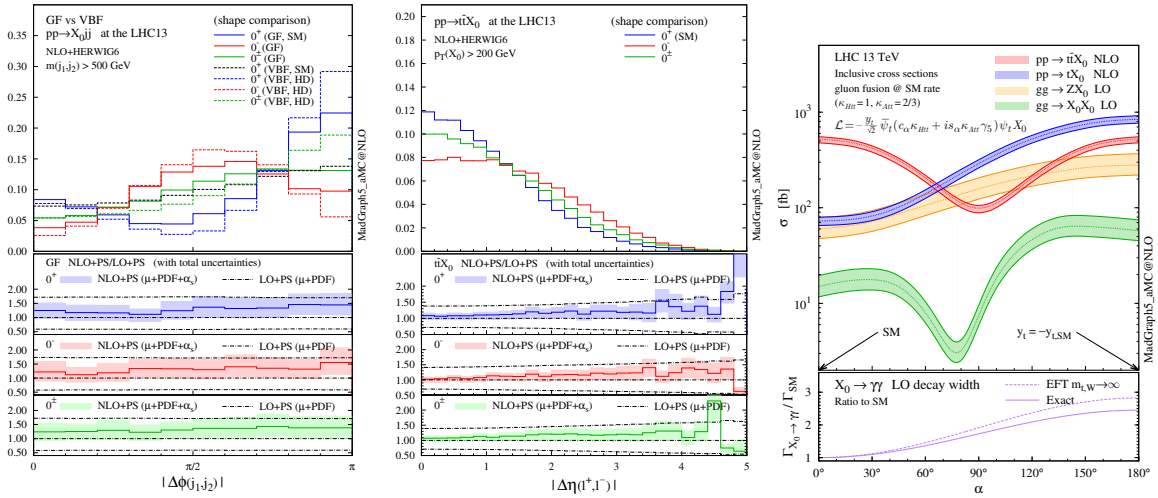

Figure 205: Normalized kinematical distributions at the LHC, running at a centre-of-mass energy of 13 TeV. We show the azimuthal difference between the two tagging jets for $pp \to X_0 jj$ after imposing a $m_{jj} > 500$ GeV selection (left) and the rapidity separation between the leptons (centre) for the dileptonic decay channel in $pp \to t\bar{t}X_0$ after enforcing a $p_T(X_0) > 200$ GeV selection. For each scenario, the lower panels give the ratio of the NLO results matched to parton showers to the LO results matched to parton showers, together with the total theoretical uncertainties. In the right panel of the figure, we show NLO (or loop-induced LO) cross sections, presented with the associated scale uncertainties, for $t\bar{t}H$ and t-channel tH (ZH and HH) production as a function of the CP-mixing angle α. The κ_{Htt} and κ_{Att} parameters have been set to reproduce the Standard Model gluon-fusion cross section for every value of α. The ratio of the $X_0 \to \gamma\gamma$ partial decay width to the corresponding Standard Model value is also shown in the lower panel of the figure.

```
> import model HC_NLO_X0
> generate p p > x0 l+ vl [QCD]
> generate p p > x0 j j $$ w+ w- z / a [QCD]
> add process p p > x0 l- vl~ [QCD]
> add process p p > x0 l+ l- / a [QCD]
```

as well as in the $t\bar{t}H$ production mode with the command

```
> generate p p > x0 t t~ [QCD]
```

Furthermore, the X_0 and the top quark decays are subsequently performed starting from the event files generated as above with the help of the MADSPIN [368] package, following the procedure described in Ref. [370] that allows one to keep spin correlations.

We show in Figure 205 (left and central panels) a few kinematical distributions, including theoretical uncertainties, for the benchmark scenarios presented in Table 109. The parton densities are evaluated by using the NNPDF2.3 (LO/NLO) parameterization [31] and the central value μ_0 for the renormalization (μ_R) and factorization (μ_F) scales is set to $H_T/2$, m_W and $\sqrt[3]{m_T(t)\, m_T(\bar{t})\, m_T(X_0)}$ in the gluon fusion, vector boson fusion and $t\bar{t}H$ production channel respectively. Uncertainties have been automatically calculated within the MADGRAPH5_aMC@NLO framework and consist of the linear sum of two components respectively related to the scale and the parton density (plus α_s) dependence. Scale uncertainties have been obtained by varying independently the unphysical scales by a factor of two up and down with respect to the reference scale μ_0, and parton densities and α_s uncertainties have been derived following the PDF4LHC recommendations.

Finally, in the right panel of the figure, we present the dependence of the $t\bar{t}H$ and tH production cross sections on the CP-mixing angle α. The nature of the top quark Yukawa coupling also affects the loop-induced Higgs coupling to gluons and photons. In order to maintain the Standard Model gluon-

fusion production cross section, the rescaling parameters are set to $\kappa_{Htt} = 1$ and $\kappa_{Att} = 2/3$. The LO cross sections for the loop-induced ZH [309] and HH [462] production processes via gluon fusion are also shown as references.

II.3.1.h Higgs boson properties with the JHUGEN / MELA framework

The JHU GENERATOR and MELA framework [530–532], available at http://www.pha.jhu.edu/spin/, is designed for the study of anomalous couplings of a resonance to vector bosons and fermions in various processes. A wide range of production and decay channels are supported for either spin-zero, spin-one, or spin-two resonances and for the most general Lorentz structures of the HVV and Hff interaction vertices, with the focus on the spin-zero case. These processes include the hadronic production of the resonances in association with zero, one, or two jets, their production via vector boson fusion, their associated production with a vector boson (ZH, WH), and their production in association with heavy flavour quarks (such as $t\bar{t}H$, tH and $b\bar{b}H$). The supported decay modes include $H \to ZZ$ / $Z\gamma^*$ / $\gamma^*\gamma^* \to 4f$, $H \to WW \to 4f$, $H \to Z\gamma$ / $\gamma^*\gamma \to 2f\gamma$, $H \to \gamma\gamma$, $H \to \tau\tau$, and generally $H \to f\bar{f}$, with a complete modelling of the spin correlations including the interference effects related to identical particles. In the case of a resonance carrying a non-zero spin or of the associated production of a spin-zero resonance, spin correlations between the initial and final states are also fully modeled.

While the JHUGEN / MELA framework can be used in a standalone mode, it is also integrated with the MCFM Monte Carlo package [288,501,533] that allows for the modelling of all necessary background processes and for the simulation of off-shell Higgs boson production (including anomalous coupling effects) after accounting for the interferences with the continuum arising from diboson production. The simulation of the impact of an additional broad resonance is also possible, allowing for the study of a new Higgs-like state with arbitrary couplings and interfering with the Standard Model contributions. The program can be interfaced to parton showers, as well as full detector simulators, through the Les Houches Event file (LHE) format [904]. The JHU generator also allows for the simulation of the decay of a spin-zero particle when its production is taking care of by other codes (or by the JHU generator itself) via an interface through LHE files. As an example, this allows for the production of a spin-zero boson through the NLO QCD accurate POWHEG [343] package, and further decay this boson with the JHU generator.

Additionally, the MELA framework allows to construct various likelihood functions in order to distinguish between different hypotheses concerning the Lorentz structure of the HVV and Hff interaction vertices. These likelihood functions are obtained from kinematic probability distributions that can be either computed analytically or numerically. Analytical parameterizations are currently available for the gg or $q\bar{q} \to H \to VV(\to 4f)$ and $q\bar{q}' \to VH$ processes and an arbitrary spin of the H-boson. On the other hand, numerical matrix element computations are provided by the JHU and MCFM generators. Both the analytical and numerical options are implemented as separate functions within the MELA package and can be accessed by an end-user directly. These matrix elements can then be used for Monte Carlo reweighting techniques and the construction of kinematic discriminants for an optimal analysis of the considered processes. The JHU generator and MELA package have been in this way extensively used in many LHC analyses by both the CMS [2, 4, 506, 534, 535, 596, 905–907] and ATLAS [3, 908] collaborations, including analyses that include the discovery [2] of the Higgs boson and the first measurement of its spin-parity properties [4].

The implemented formalism uses equivalent formulations of the effective field theory scattering amplitudes, in which the dependence on the virtualities of the weak and Higgs bosons is additionally tested by means of form factors. The general couplings of a spin-zero particle H to two fermions is hence given by the amplitude

$$A(Hff) = -\frac{m_f}{v}\bar{f}\left(\kappa_f + i\tilde{\kappa}_f\gamma_5\right)f\,, \tag{II.3.32}$$

where m_f denotes a generic fermion mass and f and $\bar{f}$ are the related Dirac spinors, and where the

coupling strengths κ_f ($= 1$ in the Standard Model) and $\tilde{\kappa}_f$ are respectively connected to a scalar and pseudoscalar H-boson. Anomalous HVV couplings are described by the amplitude

$$A(HVV) \propto \left[a_1 - e^{i\phi_{\Lambda 1}} \frac{\left(q_{V1}^2 + q_{V2}^2\right)}{\left(\Lambda_1\right)^2} - e^{i\phi_{\Lambda Q}} \frac{\left(q_{V1} + q_{V2}\right)^2}{\left(\Lambda_Q\right)^2}\right] m_V^2 \epsilon_{V1}^* \epsilon_{V2}^* + a_2 f_{\mu\nu}^{*(1)} f^{*(2),\mu\nu} + a_3 f_{\mu\nu}^{*(1)} \tilde{f}^{*(2),\mu\nu}, \tag{II.3.33}$$

where $f^{(i)\mu\nu} = \epsilon_{Vi}^{\mu} q_{Vi}^{\nu} - \epsilon_{Vi}^{\nu} q_{Vi}^{\mu}$ is the field strength tensor of a gauge boson with momentum q_{Vi} and polarization vector ϵ_{Vi}, and $\tilde{f}_{\mu\nu}^{(i)} = \frac{1}{2}\epsilon_{\mu\nu\rho\sigma} f^{(i)\rho\sigma}$ is its dual field strength tensor. For spin-one and spin-two resonance couplings, higher-order terms in the momentum expansion, and terms asymmetric in q_{V1}^2 and q_{V2}^2 that are supported by the JHU generator, we refer to Refs. [530–532] and the program manual for details. The q^2-expansion of Eq. (II.3.33) can be equivalently rewritten as an effective Lagrangian containing operators with a mass-dimension up to five [534],

$$\begin{aligned}
L(HVV) \propto\ & a_1 \frac{m_Z^2}{2} H Z^{\mu} Z_{\mu} - \frac{\kappa_1}{\left(\Lambda_1\right)^2} m_Z^2 H Z^{\mu} \Box Z_{\mu} - \frac{\kappa_3}{2\left(\Lambda_Q\right)^2} m_Z^2 \Box H Z^{\mu} Z_{\mu} \\
& - \frac{1}{2} a_2 H Z^{\mu\nu} Z_{\mu\nu} - \frac{1}{2} a_3 H Z^{\mu\nu} \tilde{Z}_{\mu\nu} \\
& + a_1^{\mathrm{WW}} m_{\mathrm{W}}^2 H \mathrm{W}^{+\mu} \mathrm{W}_{\mu}^{-} - \frac{1}{\left(\Lambda_1^{\mathrm{WW}}\right)^2} m_{\mathrm{W}}^2 H \left(\kappa_1^{\mathrm{WW}} \mathrm{W}_{\mu}^{-} \Box \mathrm{W}^{+\mu} + \kappa_2^{\mathrm{WW}} \mathrm{W}_{\mu}^{+} \Box \mathrm{W}^{-\mu}\right) \\
& - \frac{\kappa_3^{\mathrm{WW}}}{\left(\Lambda_Q\right)^2} m_{\mathrm{W}}^2 \Box H \mathrm{W}^{+\mu} \mathrm{W}_{\mu}^{-} - a_2^{\mathrm{WW}} H \mathrm{W}^{+\mu\nu} \mathrm{W}_{\mu\nu}^{-} - a_3^{\mathrm{WW}} H \mathrm{W}^{+\mu\nu} \tilde{\mathrm{W}}_{\mu\nu}^{-} \\
& - a_2^{Z\gamma} H A^{\mu\nu} Z_{\mu\nu} - a_3^{Z\gamma} H A^{\mu\nu} \tilde{Z}_{\mu\nu} - \frac{1}{2} a_2^{\gamma\gamma} H A^{\mu\nu} A_{\mu\nu} - \frac{1}{2} a_3^{\gamma\gamma} H A^{\mu\nu} \tilde{A}_{\mu\nu} \\
& - \frac{1}{2} a_2^{\mathrm{gg}} H G_a^{\mu\nu} G_{\mu\nu}^a - \frac{1}{2} a_3^{\mathrm{gg}} H G_a^{\mu\nu} \tilde{G}_{\mu\nu}^a \,.
\end{aligned} \tag{II.3.34}$$

Both on-shell H production and off-shell H^* production are considered and there is no kinematic limit neither on $q_{V_i}^2$ nor on $(q_{V1}+q_{V2})^2$ other than the one due to the energy of the colliding beams and the relevant partonc luminosities. Since the scale of validity of the non-renormalizable higher-dimensional operators is *a priori* unknown, effective cut-off scales $\Lambda_{V1,i}$, $\Lambda_{V2,i}$ and $\Lambda_{H,i}$ are introduced for each term in Eq. (II.3.33) with a form factor scaling the anomalous contribution a_i^{BSM} as

$$a_i = a_i^{\mathrm{SM}} \times \delta_{i1} + a_i^{\mathrm{BSM}} \times \frac{\Lambda_{V1,i}^2 \Lambda_{V2,i}^2 \Lambda_{H,i}^2}{(\Lambda_{V1,i}^2 + |q_{V1}^2|)(\Lambda_{V2,i}^2 + |q_{V2}^2|)(\Lambda_{H,i}^2 + |(q_{V1}+q_{V2})^2|)} \,. \tag{II.3.35}$$

In Figure 206, representative distributions of HVV observables are shown for the $H \to VV$ decay channel (left), and for the VH (centre) and VBF (right) production modes. The anomalous coupling parameterization in terms of the effective fractions of events follows the LHC conventions [534] and is equivalent to start from Eq. (II.3.33) and fix $f_{ai} = |a_i|^2 \sigma_i / \Sigma_j |a_j|^2 \sigma_j$ and $\phi_{ai} = \arg(a_i/a_1)$, where σ_i denotes the cross section for a given process with $a_i = 1$ [534].

II.3.1.i Higgs boson pair production in HERWIG 7

The general-purpose event generator HERWIG 7 [306, 313, 457–459], that is available at https://herwig.hepforge.org, contains the HIGGSPAIR and HIGGSPAIROL packages that offer the generation of exclusive events for Higgs boson pair production via gluon fusion. The former uses code from HPAIR [435, 909] (see Section II.3.1.d), whereas the latter uses the OPENLOOPS one-loop generator for the matrix elements [247]. HIGGSPAIR describes leading-order Higgs boson pair production with the option of either including an additional scalar as an intermediate or final state particle, or including

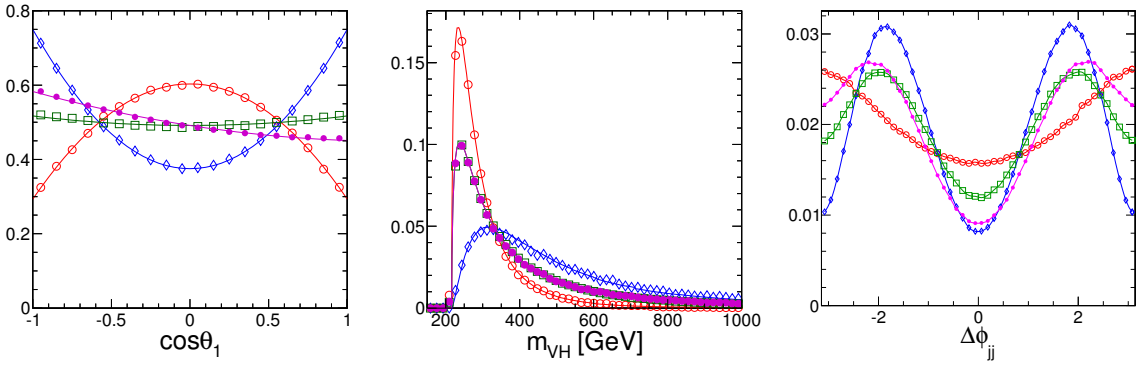

Figure 206: Representative distributions of observables depending on HVV anomalous couplings as generated with JHUGEN (dots) shown together with the analytical results obtained with MELA likelihood projections (smooth curves on the left and middle panels) in the context of a Higgs boson of 125 GeV and proton-proton collisions at a centre-of-mass energy of 14 TeV. Left: distribution of the helicity angle of a Z boson in the decay $H \to ZZ \to 4\ell$; middle: spectrum of the VH invariant-mass in the case of $q\bar{q} \to ZH$ production; right: distribution in the azimuthal angle between the two jets in VBF production. Four scenarios are shown: the Standard Model case (0^+, red open circles), a case with a pseudoscalar boson (0^-, blue diamonds), and two mixed cases corresponding to $f_{a3} = 0.5$ with $\phi_{a3} = 0$ (green squares) and $\pi/2$ (magenta points).

the effects of dimension-six effective field theory operators that could extend the Standard Model. The validation of the implementation has been performed using an equivalent MADGRAPH5_AMC@NLO model [54], implemented in a similar (but independent) way using functions taken from the HPAIR package. Comparisons of several distributions and the total cross section between the two implementations have been performed, and the total cross section output obtained by using HERWIG was confirmed to match that obtained using HPair at leading order for various parton density sets and the scale choice $\mu = \sqrt{\hat{s}}$. The dimension-six effective field theory extension was examined in detail in Ref. [467]. The relevant Lagrangian terms affecting Higgs boson pair production whose effects can be included at the time of event generation is given, using the SILH basis conventions and mass eigenstates, by

$$\begin{aligned}\mathcal{L}_{hh} = &-\frac{m_h^2}{2v}\left[1-\frac{3}{2}c_H+c_6\right]H^3-\frac{m_h^2}{8v^2}\left[1-\frac{25}{3}c_H+6c_6\right]H^4+\frac{\alpha_s}{4\pi}\left[c_g\frac{h}{v}+c_{2g}\frac{H^2}{2v^2}\right]G^a_{\mu\nu}G_a^{\mu\nu}\\ &-\left[\frac{m_t}{v}\left(1-\frac{c_H}{2}+c_t\right)\bar{t}_L t_R H+\frac{m_b}{v}\left(1-\frac{c_H}{2}+c_b\right)\bar{b}_L b_R H+\text{h.c.}\right]\\ &-\left[\frac{m_t}{v^2}\left(\frac{3c_{2t}}{2}-\frac{c_H}{2}\right)\bar{t}_L t_R H^2+\frac{m_b}{v^2}\left(\frac{3c_{2b}}{2}-\frac{c_H}{2}\right)\bar{b}_L b_R H^2+\text{h.c.}\right],\end{aligned} \tag{II.3.36}$$

where the Wilson coefficients c_H, c_6, c_g, c_{2g}, c_t, c_b, c_{2t} and c_{2b} can be varied independently through the input file. Note that in the case of a single Higgs boson doublet, we have the relations $c_g = c_{2g}$, $c_t = c_{2t}$ and $c_b = c_{2b}$.

The HIGGSPAIROL package describes Standard Model Higgs boson pair production, with the optional use of Higgs-pair plus one jet matrix elements merged to the parton shower via the MLM method. We refer to Ref. [456] for a detailed description of this procedure. The implementation of the effects of higher dimensional operators in this framework is foreseen in the near future.

II.3.1.j Anomalous couplings in VBFNLO

NLO QCD predictions including anomalous coupling effects can be studied for several processes with the flexible Monte Carlo program VBFNLO [275, 518], available at https://www.itp.kit.edu/vbfnlo. The ensemble of implemented processes includes Higgs, single and double vector boson production via

vector boson fusion (VBF), WH production, as well as double and triple vector boson (plus jet) production. The Standard Model QCD-induced background for double vector boson production in association with two jets is also available at the NLO accuracy. Furthermore, anomalous HVV coupling effects are also included in the gluon-induced contributions to diboson (plus jet) production as well as in the gluon fusion processes $gg \to Hjj \to VVjj$. Although these processes are all one-loop induced and hence computed at the leading-order accuracy, the full top- and bottom-quark mass dependence is retained.

In the VBFNLO-3.0 β release, an interface compliant with the Binoth Les Houches Accord (BLHA) [360, 361] has been added for all VBF processes including fully leptonic decays, which allows for Monte Carlo studies at NLO in QCD including the full functionality of event generators like HERWIG 7 [306, 313]. The K-matrix unitarization procedure has been implemented for the two dimension-eight operators $\mathcal{O}_{S,0} + \mathcal{O}_{S,2}$ and $\mathcal{O}_{S,1}$ that are defined in Eq. (II.3.40) below. The strength of the anomalous triple and quartic gauge boson couplings can be set in the file `anomV.dat`. They are parameterized using an effective Lagrangian, as described in Refs. [620, 628, 910, 911],

$$\mathcal{L}_{\text{eff}} = \sum_i \frac{f_i}{\Lambda^n} \mathcal{O}_i^{n+4} \,, \tag{II.3.37}$$

where $n+4$ signifies the dimension of the operator $\mathcal{O}_i$. VBFNLO then defines anomalous gauge couplings in terms of the coefficients f_i/Λ^n of the dimension-six and dimension-eight operators. The full list of implemented operators can be found in the Appendix 1 of the VBFNLO manual [912]. The explicit form of the included CP-even dimension-six operators is given by

$$\begin{aligned} &\mathcal{O}_W = (D_\mu\Phi)^\dagger \widehat{W}^{\mu\nu}(D_\nu\Phi), \qquad \mathcal{O}_B = (D_\mu\Phi)^\dagger \widehat{B}^{\mu\nu}(D_\nu\Phi), \qquad \mathcal{O}_{WWW} = \mathrm{Tr}\Big[\widehat{W}_{\mu\nu}\widehat{W}^{\nu\rho}\widehat{W}_\rho{}^\mu\Big], \\ &\mathcal{O}_{WW} = \Phi^\dagger \widehat{W}_{\mu\nu}\widehat{W}^{\mu\nu}\Phi, \qquad \mathcal{O}_{BB} = \Phi^\dagger \widehat{B}_{\mu\nu}\widehat{B}^{\mu\nu}\Phi. \end{aligned} \tag{II.3.38}$$

The building blocks for these operators (following the notation of Refs. [628, 714]) are defined by

$$\widehat{W}_{\mu\nu} = igT_a W^a_{\mu\nu}, \qquad \widehat{B}_{\mu\nu} = ig'Y B_{\mu\nu}, \qquad D_\mu = \partial_\mu + igT_a W^a_\mu + ig'Y B_\mu, \tag{II.3.39}$$

where g and g' are the $SU(2)_L$ and $U(1)_Y$ gauge couplings, and T_a and Y the generators of the $SU(2)$ group in the fundamental representation and the hypercharge operator, respectively. The CP-odd part of the Lagrangian is obtained replacing the field strength tensor with the corresponding dual field strength tensors. The dimension-eight operators that are supported are taken from Ref. [910] although slightly different normalizations for the field strength tensors are employed in this work, $\widehat{W}_{\mu\nu} = T_a W^a_{\mu\nu}$ and $\widehat{B}_{\mu\nu} = B_{\mu\nu}$. The conversion factors for the coupling strengths f_i relating Ref. [910] to our implementation can be found in the Appendix 1 of the VBFNLO manual. The dimension-eight operators that are supported can be split into three categories, namely operators depending on the gauge-covariant derivative $D_\mu\Phi$ only,

$$\begin{aligned} &\mathcal{O}_{S,0} = \Big[(D_\mu\Phi)^\dagger D_\nu\Phi\Big]\Big[(D^\mu\Phi)^\dagger D^\nu\Phi\Big], \qquad \mathcal{O}_{S,1} = \Big[(D_\mu\Phi)^\dagger D^\mu\Phi\Big]\Big[(D_\nu\Phi)^\dagger D^\nu\Phi\Big], \\ &\mathcal{O}_{S,2} = \Big[(D_\mu\Phi)^\dagger D_\nu\Phi\Big]\Big[(D^\nu\Phi)^\dagger D^\mu\Phi\Big], \end{aligned} \tag{II.3.40}$$

operators depending on both $D_\mu\Phi$ and the electroweak field strength tensors $\widehat{W}_{\mu\nu}$ and $\widehat{B}_{\mu\nu}$, *e.g.*,

$$\mathcal{L}_{M,0} = \mathrm{Tr}\Big[\widehat{W}_{\mu\nu}\widehat{W}^{\mu\nu}\Big]\Big[(D_\rho\Phi)^\dagger D^\rho\Phi\Big], \tag{II.3.41}$$

and operators depending only on the electroweak field strength tensors $\widehat{W}_{\mu\nu}$ and $\widehat{B}_{\mu\nu}$, such as,

$$\mathcal{L}_{T,0} = \mathrm{Tr}\Big[\widehat{W}_{\mu\nu}\widehat{W}^{\mu\nu}\Big]\mathrm{Tr}\Big[\widehat{W}_{\rho\sigma}\widehat{W}^{\rho\sigma}\Big]. \tag{II.3.42}$$

Anomalous Higgs boson HVV coupling parameters are controlled in VBFNLO via the file named `anom_HVV.dat`, where three different parameterizations are available. The latter consist of the Wilson coefficients associated with the subset of dimension-six operators introduced above that contribute to the Higgs boson couplings, the parameterization used by the L3 collaboration that is defined in Ref. [913], and a parameterization based on anomalous couplings in the mass basis that is thus expressed in terms of the field strength and dual field strength tensors of the W and Z bosons [914]. The relationships between these three parameterizations are discussed in more detail on the VBFNLO webpage.

Since the pure operators for anomalous gauge boson couplings might lead to a violation of tree-level unitarity within the energy range of the LHC, special care has to be taken to avoid this unphysical behaviour. Within VBFNLO, we have opted for using the following form factors, all of them depending on Λ, the characteristic scale where the form factor effects become relevant. Equivalently, introducing these form factors is like restricting the validity range of the effective field theory rather than implementing a sharp cutoff. For HVV vertices, two different form factors can be chosen as described in Refs. [277,914].

$$F_1 = \frac{\Lambda^2}{|q_1|^2+\Lambda^2}\,\frac{\Lambda^2}{|q_2|^2+\Lambda^2}, \qquad F_2 = -2\,\Lambda^2\,C_0\Big(q_1^2, q_2^2, (q_1+q_2)^2, \Lambda^2\Big). \tag{II.3.43}$$

where q_i are the momenta of the vector bosons and C_0 is the scalar one-loop three point function in the notation of Ref. [381]. For triple and quartic gauge couplings the form factor takes the form

$$F = \left(1+\frac{s}{\Lambda^2}\right)^{-p}, \tag{II.3.44}$$

for each phase space point, where s is a universal scale identified with the invariant mass squared of the produced bosons. Finally, for γjj production in VBF, the form factor reads

$$F = \left(1+\frac{|q_1|^2}{\Lambda^2}+\frac{|q_2|^2}{\Lambda^2}+\frac{|q_3|^2}{\Lambda^2}\right)^{-p}, \tag{II.3.45}$$

with q_1^2, q_2^2 and q_3^2 as the invariant masses squared of the three vector bosons involved in the VVV vertex. On the VBFNLO webpage, we provide the 'Formfactor Calculation Tool for aGC' which gives the maximum value of the scale Λ which is allowed by unitarity. The value is determined by calculating on-shell VV scattering and computing the zeroth partial wave of the amplitude. As unitarity criterion, the absolute value of the real part of the zeroth partial wave has to be below 0.5 [915]. Each channel in $VV \to VV$ scattering (with $V = W/Z/\gamma$) is checked individually, while additionally channels with the same electrical charge for the VV system are combined [916]. We recall that the definition of the partial wave expansion in Ref. [916] differs from ours by a factor of 2.

Finally, the K-matrix unitarization procedure has been implemented for the two dimension-eight operators $\mathcal{O}_{S,0} + \mathcal{O}_{S,2}$ and $\mathcal{O}_{S,1}$ by using the relations to the operators $\mathcal{O}_4$ and $\mathcal{O}_5$ of the electroweak chiral Lagrangian and the procedure worked out in Ref. [917]. This method guarantees the preservation of unitarity when either of these operators is used in the study of anomalous quartic gauge couplings. In contrast to using form factors, no additional input parameters need to be set. The anomalous contributions are automatically suppressed at the energy scale where unitarity would be violated without unitarization. After this energy scale is reached, the anomalous contributions are kept at a finite value, representing the maximally possible anomalous contribution. We refer to Refs. [911,917,918] for details of the K-matrix unitarization procedure and its implementation.

II.3.1.k Event generation with WHIZARD

WHIZARD [919] is a multipurpose event generator for hadron and lepton colliders that can be obtained from `https://whizard.hepforge.org`. It has a highly optimized internal matrix element generator, O'MEGA, for the recursive computing of tree-level amplitudes for almost arbitrary theories [920]. In the QCD case, it additionally uses the colour flow formalism [921]. WHIZARD has its own parton shower

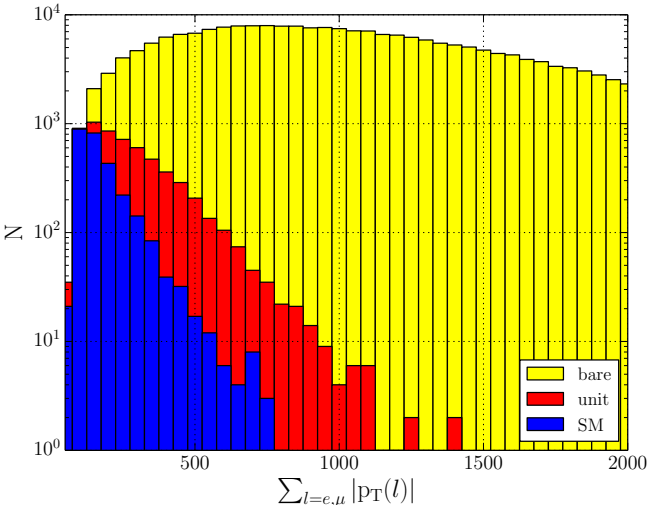

Figure 207: Events generated by WHIZARD when a dimension-eight coupling $F_{S,0} = 480$ TeV^{-4} (the Wilson coefficient associated with the $\mathcal{O}_{S,0}$ operator of Eq. (II.3.40)) is added to the Standard Model and for the process $pp \to e^+\mu^+\nu_e\nu_\mu jj$ at a centre-of-mass energy of 14 TeV and for an integrated luminosity of $\mathcal{L} = 1000$ fb^{-1}. Event selection requires a dijet invariant mass $M_{jj} > 500$ GeV, a rapidity separation between the jets of $\Delta y_{jj} > 2.4$, and the two jets must have a transverse momentum $p_T^j > 20$ GeV and a pseudorapidity $|\eta_j| < 4.5$. In addition, leptons are required to have a transverse momentum $p_T^l > 20$ GeV. Red and yellow histograms represent the naive and unitarized effective field theory predictions, respectively, while the pure Standard model expectation is shown as a blue histogram for comparison.

implementation [922], with both a p_T-ordered shower and an analytic shower. Recently, automated FKS subtraction and POWHEG matching for NLO QCD corrections (using external virtual matrix elements) have been implemented [923, 924]. For external theories beyond the Standard Model, interfaces to the packages SARAH and FEYNRULES [925] are available, and support for the UFO file format allowing for arbitrary Lorentz and colour structures is currently under way.

With respect to Higgs Effective Field Theories and higher-dimensional operators, WHIZARD supports the whole set of bosonic dimension-six operators in the Warsaw basis [614]. For vector-boson scattering at the LHC, usually dimension-eight operators in the coupled system of electroweak gauge and Higgs bosons are as important as dimension-six operators as they can be generated at tree-level in some new physics models. These electroweak dimension-eight operators have been implemented in WHIZARD, both as plain operators and also with their interplay with new resonances in the electroweak sector. The description of new physics contributions with a low energy effective energy is however only valid up to an a priori unknown scale Λ. At energies above Λ, the effective field theory will lead to unphysical predictions. As an example, the sum of the norm of the transverse momenta of all leptons produced in the process $pp \to e^+\mu^+\nu_e\nu_\mu$ is shown on Figure 207 when the dimension-eight operator $\mathcal{O}_{S,0}$ of Eq. (II.3.40) is included. The number of events generated with a naive effective field theory description (yellow histogram) will largely overshoot a physically possible distribution, because S-matrix unitarity is violated within the experimental energy reach. A selection to avoid energy regions where the theoretical description breaks down is not possible in general, due to the inability to reconstruct the invariant mass for some final states. Using the T-matrix scheme, a unitarization prescription for high-energy regions of the phase space [917, 918, 926], avoid the unphysical high number of generated events by WHIZARD. Instead, the number of events are saturated in every isospin-spin channel to satisfy S-matrix unitarity (red histogram). In order to simplify unitarization, WHIZARD does not use the basis of Ref. [927] as this basis does not respect isospin symmetry which makes calculation of the channels in

need for unitarization much easier.

On different lines, fermionic dimension-six operators are implemented for the top quark sector as (form-factor regularized) anomalous couplings [928, 929].

II.3.1.l Model-independent constraints on non-standard Higgs boson couplings with HEPFIT

The HEPFIT package (formerly SUSYFIT) is a general tool to combine direct and indirect constraints on the Standard Model and its extensions and is available under the GNU General Public License (GPL) from http://hepfit.roma1.infn.it. The HEPFIT code can be extended to include any observables and new physics models (supersymmetric theories, Two-Higgs-Doublet Models, ...) which can be added to the main core as external modules. Exploiting the Markov Chain Monte Carlo implementation of the Bayesian Analysis Toolkit [930], HEPFIT can be used as a standalone program to perform Bayesian statistical analyses. Alternatively, it can be used in library mode to compute observables in any implemented model, allowing for phenomenological analyses in any statistical framework. The interested reader can find more details on HEPFIT in Refs. [931, 932].

In particular, HEPFIT has been used to perform statistical analyses of electroweak precision data, including Higgs boson signal-strength measurements, in the Standard Model and beyond. Most importantly, these analyses have obtained constraints on possible deviations of the Higgs boson couplings to both gauge bosons and fermions from the Standard Model predictions. Results from the initial stages of this project were presented in Refs. [933, 934] and recently updated in Refs. [935, 936] to reflect all the most recent developments in theoretical calculations and experimental measurements.

Within HEPFIT, new physics effects on electroweak precision observables and on Higgs boson couplings can also be systematically studied in the context of an effective field theory that adds to the Lagrangian of the Standard Model new interactions of the Standard Model fields in the form of higher-dimension (of dimension $d > 4$) local operators that preserve the Standard Model gauge symmetry, namely

$$\mathcal{L}_{\rm eff} = \mathcal{L}_{\rm SM} + \sum_{d>4} \frac{1}{\Lambda^{d-4}} \mathcal{L}_d, \quad \text{with} \quad \mathcal{L}_d = \sum_i C_i \mathcal{O}_i, \quad [\mathcal{O}_i] = d\,. \tag{II.3.46}$$

In this equation, the dependence on Λ, the scale at which direct evidence of the new physics degrees of freedom is expected, has been made explicit. In particular, the current public version of HEPFIT implements as a *model* the $d = 6$ extension of the Standard Model Lagrangian using the basis of $d = 6$ operators proposed in Ref. [614], which is quite easy to relate to electroweak precision data and Higgs observables by means of shifts of the couplings to the Standard Model bosons. Through a global fit of electroweak-data and Higgs boson signal-strengths measurements HEPFIT provides constraints on the individual Wilson coefficients C_i at the electroweak scale. At the moment HEPFIT does not include effects of operator mixing induced by renormalization-group scale evolution, waiting for more insight on the new physics theory that determines the initial condition of the renormalization group running. Results have been presented in [933], where the subset of relevant to Higgs boson observables have been considered and constraints on the corresponding coefficients have been derived by switching on one operator at a time, for a fixed scale $\Lambda = 1$ TeV. *Vice versa*, for values of the individual coefficients $C_i = \pm 1$, lower bounds on the scale Λ have been found.

II.3.1.m ROSETTA

Different complete and non-redundant operator bases of dimension-six effective operators have been proposed in the literature, the most popular choices including the Warsaw basis [614], the SILH basis [464, 653] and the beyond the Standard Model primaries basis [607, 608, 630]. It is however cumbersome to express any experimental result in a basis-independent manner. Different bases may be convenient for particular applications, either because they facilitate the comparison with a given class of theories or simply because different experimental analyses look more transparent in a specific basis. The

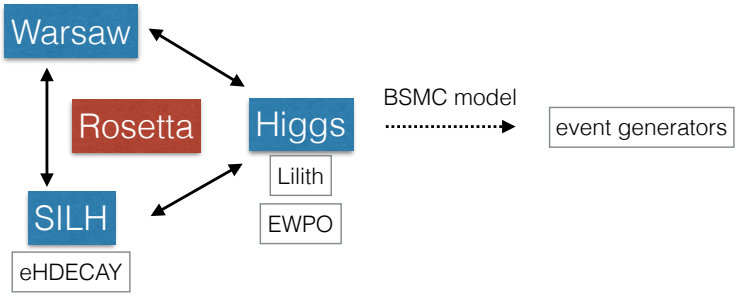

Figure 208: Description of the way the ROSETTA package works and is interfaced to other high-energy physics tools and connect different effective field theory operator basis choice. We moreover indicate tools or calculations that exist for a specific basis.

ROSETTA package [639] has been designed to explicitly solve such problems by allowing for a straightforward translation between different effective field theory languages. In addition to translating, another important goal of the ROSETTA program is to provide a platform for communication with Monte Carlo event generators, no matter which basis is chosen. To achieve this, ROSETTA contains an implementation of the Higgs basis defined in Section II.2.1 and is connected to the BSMC Lagrangian introduced in Section II.3.1.g. More precisely, the output format of ROSETTA has been tuned so that the translation maps an effective field theory Lagrangian given in a specific basis to the BSMC Lagrangian and generates an output file that is compatible with the BSMC implementation into FEYNRULES [524]. As a consequence, any high-energy physics tool that is interfaced to FEYNRULES can be employed within the context of any basis of dimension-six operators that is included in ROSETTA, as illustrated on Figure 208. A full description of the program including detailed example usage and information on how to create a user-defined basis class can be found in the manual [639].

The most basic functionality of ROSETTA is to map a chosen set of input parameters (the Wilson coefficients in a specific basis choice) onto the BSMC coefficients such that the output can be employed within tools relying on a BSMC Lagrangian description. In addition, the user may define his/her own map to the BSMC coefficients (or to any other basis implementation) and proceed with event generation using the related FEYNRULES implementation. This highlights one of the key features of ROSETTA, the possibility to easily define one's own input basis and directly use it in the context of many programs via the translation functionality. An example of this would be the EHDECAY program (see Ref. [464] and Section II.3.1.e) for which ROSETTA provides an interface to calculate the Higgs boson width and branching fractions including effective field theory effects in any basis. The strength of this approach is that it is much simpler than developing from scratch new modules for existing tools in the context of a new basis. Moreover, ROSETTA not only enables translation into the BSMC Lagrangian, but also allows for translations into any of the other bases included in the package that are currently the Higgs, Warsaw and SILH bases. Translations between these three bases in any direction are possible, so that the addition of a new basis by the user only requires the specification of translation rules to any one of the three core bases. One is subsequently able to indirectly translate the new basis into any of the other two bases, as well as into the BSMC Lagrangian.

The latest release of ROSETTA can be obtained from `http://rosetta.hepforge.org`. The package contains a PYTHON executable named `translate`, an information file named `README` and two directories, a first folder (named `Cards`) collecting example input files and a second folder (named `Rosetta`) including the source code of ROSETTA. Each basis is implemented as a class in its own PYTHON module, where the coefficients and the required inputs are declared. Moreover, the input format must respect conventions inspired by the Supersymmetry Les Houches Accord (SLHA) [88, 89] and the related SLHA block structure is defined in the class. Translations are defined as member functions

of the class with a special syntax to identify the target basis. Several utility functions may also be implemented to either calculate the values of parameters declared as dependent as a function of those declared as independent or modify the values of the Standard Model input parameters as a function of the effective operator coefficients.

The `translate` executable takes as input an SLHA-style parameter file with the coefficients of the dimension-six operators associated with a particular basis. Information on the format of such an input file can be found in the manual [639]. Depending on the basis implementation, some basic input quantities, such as Standard Model input constants and particle masses may be required in addition to the effective field theory coefficients. The execution of the `translate` script from a shell yields the generation of an output parameter file where all parameters are this time the coefficients of the dimension-six operators associated with a specified new basis, the default choice being the BSMC Lagrangian. The tool can be used by typing in

```
./translate PARAMCARD.dat OPTION
```

where `PARAMCARD.dat` is the name of the SLHA-style input file and `OPTIONS` stands for optional arguments. These can range from specifying the output file name (`-output`, `-o`) or target basis into which to translate (`-target`, `-t`) to invoking the EHDECAY (`-ehdecay`, `-e`) interface to additionally generate an SLHA decay block for the Higgs as part of the output file. A particularly useful option is the `-flavour` or `-f` one which allows users to specify the treatment of the flavour structure relevant for fermionic operators. This can take the values `general`, `diagonal` and `universal` depending on the desired degree of simplicity. A more complicated example of usage might read

```
./translate myinput.dat -t warsaw -f universal -e -o myoutput.dat
```

which would read the `myinput.dat` file and translate it to the Warsaw basis, assuming the universal flavour structure which is designed to map easily to the Minimal Flavour Violation assumption [698]. The EHDECAY interface will also be called, writing in the output file, specified to be `myoutput.dat` an additional SLHA block containing Higgs boson decay information.

With the advent of NLO-accurate Monte Carlo event generation software, it is important that ROSETTA remains flexible enough to eventually provide compatibility with this new generation of tools. The future development plans of the program are connected to the recent progresses that have been made on the theory side both in implementing the linear dimension-six description in the FEYNRULES framework [937] and in calculating the renormalization group evolution of the full set of operators and their mutual mixing [609,631,646,647,938]. In the former case, ROSETTA can simply be extended to provide an output compatible with the eventual NLO model implementation, analogously to the BSMC Lagrangian. The latter case of evaluating the renormalization group running effects, while being a slightly separate issue, highlights a key feature of ROSETTA, given that the calculation of these effects has only been performed in the Warsaw basis and that ROSETTA could allow for the application of these results in any desired basis.

II.3.2 Morphing implementation [II.49]

The properties of the newly discovered Higgs boson have been extensively probed by the ATLAS and CMS experiments using LHC Run 1 proton-proton collision data at $\sqrt{s} = 7$ and 8 TeV [5, 6, 534, 908]. The studies of the tensor structure of the Higgs boson couplings to gauge bosons were based on signal models including at most one or two Beyond the Standard Model coupling parameters at a time, with all remaining Beyond the Standard Model (BSM) parameters set to zero. For Run 2, it is envisioned to have signal models which depend on a larger number of coupling parameters, in order to account for possible correlations among them. Additional coupling parameters in the Higgs boson coupling to Standard Model (SM) particles change the predicted cross section, as well as the shape of differential distributions. In this context, it is necessary to revise the existing signal modelling methods and provide

[II.49] *Author(s): N. Belyaev, V. Bortolotto, L. Brenner, C.D. Burgard, M. Dührssen, K. Ecker, S. Gadatsch, D. Gray, A. Kaluza, K. Köneke, R. Konoplich, S. Kortner, K. Prokofiev, C. Schmitt, W. Verkerke.*

alternatives which are better suited for such a multidimensional parameter space.

For this purpose, a morphing method has been developed and implemented. It provides a continuous description of arbitrary physical signal observables such as cross sections or differential distributions in a multidimensional space of coupling parameters. The morphing-based signal model is a linear combination of a minimal set of orthogonal base samples (templates) spanning the full coupling parameter space. The weight of each template is derived from the coupling parameters appearing in the signal matrix element.

Morphing is more than a simple interpolation technique, in that it is not limited to the points in the range spanned by the input samples. In fact, the choice of the input samples is arbitrary, and any set of input samples satisfying the required conditions to build the morphing function will span the entire space, independent of their precise coordinates.

A full explanation and validation of this method is shown in reference [939].

II.3.2.a Morphing principles

The morphing procedure is based on the concepts of the morphing of (possibly multi-dimensional) histograms described in Ref [940]. It is introduced to describe the dependence of a given physical observable T on an arbitrary configuration of a set of non-SM Higgs boson couplings $\vec{g}_{\text{target}} \equiv \{g_{\text{SM}}, g_{\text{BSM},1}, .., g_{\text{BSM},n}\}$ to known particles. This dependence is described by a morphing function

$$T_{\text{out}}(\vec{g}_{\text{target}}) = \sum_i w_i(\vec{g}_{\text{target}}; \vec{g}_i) T_{\text{in}}(\vec{g}_i), \tag{II.3.47}$$

which linearly combines the values or differential distributions T_{in} at a number of selected discrete coupling configurations $\vec{g}_i = \{\tilde{g}_{\text{SM},i}, \tilde{g}_{\text{BSM},1}, .., \tilde{g}_{\text{BSM},n}\}$. The input distributions T_{in} are normalized to their expected cross sections such that T_{out} includes not only the correct shape, but also the correct cross section prediction. Here, g_{SM} denotes the Higgs boson coupling predicted by the Standard Model. Morphing only requires that any differential cross section can be expressed as a polynomial in coupling parameters. For calculation at lowest order and using the narrow-width approximation for a resonance, this yields a second order polynomial each in production and decay.

In practice, the template distributions T_{in} are obtained from the Monte Carlo (MC) simulation of the signal process for a given coupling configuration $\vec{g}_i$. The minimal number N of Monte Carlo samples needed to describe the signal at all possible coupling configurations, depends on the number n of studied non-SM coupling parameters. The contribution of each sample T_{in} is weighted by a weight w_i based on the assumption that the value of a physical observable is proportional to the squared matrix element for the studied process

$$T \propto |\mathcal{M}|^2 . \tag{II.3.48}$$

The weights w_i can therefore be expressed as functions of the coupling parameters in the matrix element $\mathcal{M}$. In this case T can be anything derived from the Matrix element, for example a whole MC sample.

The described procedure allows for a continuous description in an n-dimensional parameter space. A feature-complete implementation has been developed within the RooFit package [941], making use of HistFactory [942]. The provided signal model can therefore be used in commonly used RooFit workspaces in a straightforward, black-box-like way. A visual representation of the idea for a simple case is shown in Figure 209.

II.3.2.b General procedure to construct morphing function

A step-by-step explanation on how to construct the morphing function for processes with an arbitrary number of free coupling parameters in two vertices is outlined below.

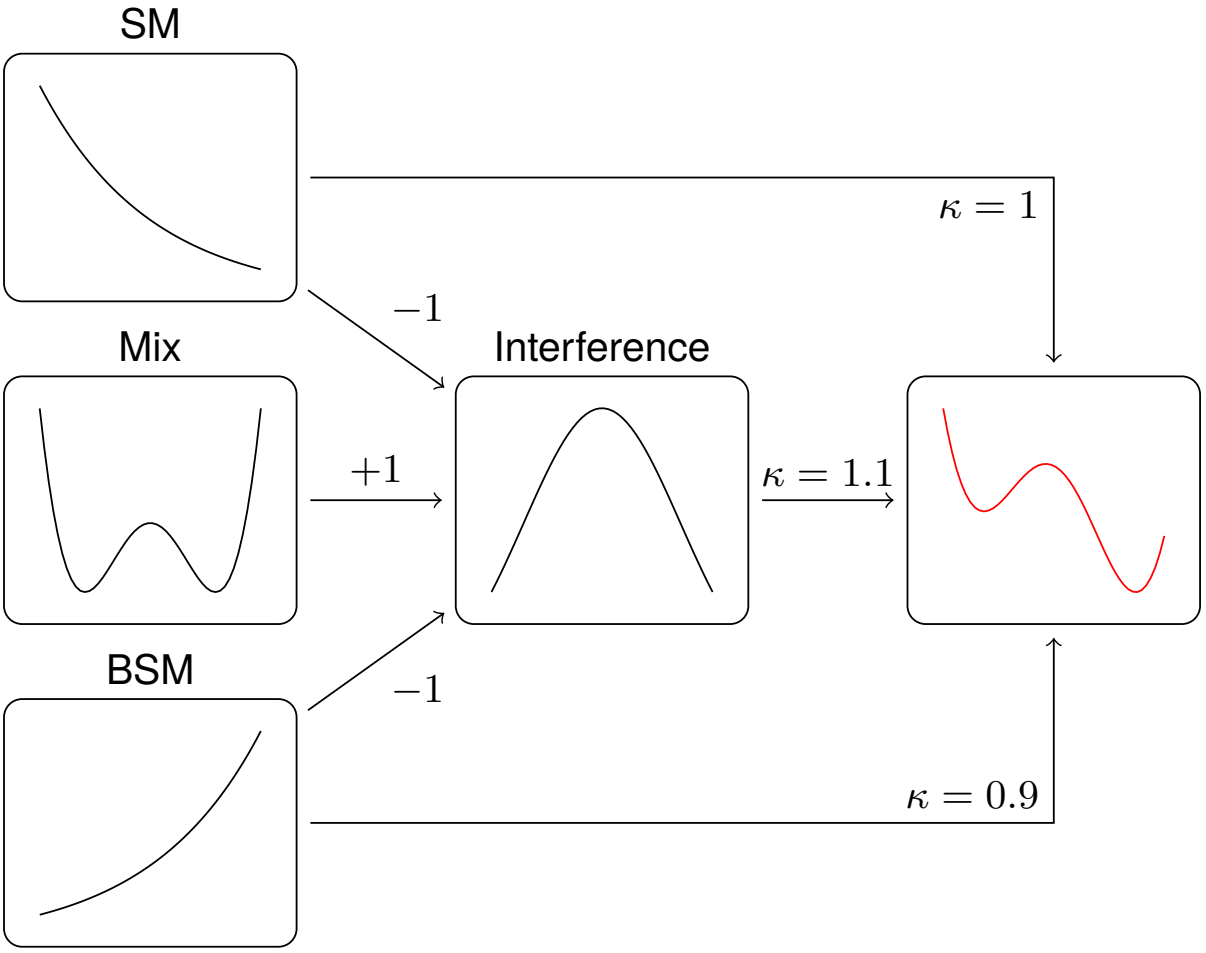

Figure 209: Illustration of the morphing procedure in a simple showcase.

1. Construct a general matrix element squared

$$|\mathrm{ME}(\vec{g})|^2 = \underbrace{\left(\sum_{x\in p,s} g_x \mathcal{O}(g_x)\right)^2}_{\text{production}} \cdot \underbrace{\left(\sum_{x\in d,s} g_x \mathcal{O}(g_x)\right)^2}_{\text{decay}}, \tag{II.3.49}$$

   denoting operators appearing only in the production vertex with p, such only appearing in the decay vertex with d, and such shared between both vertices with s, and assuming that production and decay vertices are uncorrelated, which is the case for a scalar intermediate particle.
2. Expand the matrix element squared to a 4th degree polynomial in the coupling parameters

$$|\mathrm{ME}(\vec{g})|^2 = \sum_{i=1}^{N} X_i \cdot P_i\left(\vec{g}\right), \tag{II.3.50}$$

   X_i is a prefactor, which will be represented by an input distribution. In the 4th degree polynomial $P_i\left(\vec{g}\right) = g_a g_b g_c g_d$ of the coupling parameters $\vec{g}$, the same coupling can occur multiple times (e.g. g_{SM}^4 or $g_{\mathrm{BSM},1} g_{\mathrm{BSM},2} g_{\mathrm{BSM},3}^2$). The number of different expressions in the polynomial N is equal to the number of samples needed for the morphing.
3. Next generate input distributions at arbitrary but fixed parameter points $\vec{g}_i$

$$T_{\mathrm{in},i} \propto |\mathrm{ME}(\vec{g}_i)|^2 . \tag{II.3.51}$$

4. Construct the morphing function with an ansatz

$$T_{\text{out}}(\vec{g}) = \sum_{i=1}^{N} \underbrace{\left(\sum_{j=1}^{N} A_{ij} P_j\left(\vec{g}\right) \right)}_{w_i(\vec{g})} T_{\text{in},i}. \tag{II.3.52}$$

$$= \vec{P}\left(\vec{g}\right) \cdot A\vec{T}, \tag{II.3.53}$$

   where the second line is the first one recast in matrix notation. The matrix A has to be calculated to obtain the full morphing function.
5. Thus, exploit that the output distribution should be equal to the input distribution at the respective input parameters

$$T_{\text{out}}\left(\vec{g}_i\right) = T_{\text{in},i} \qquad \text{for} \qquad i = 1, \ldots, N. \tag{II.3.54}$$

   which can also be cast in matrix notation as

$$\begin{aligned} & A \cdot \left(P_j\left(\vec{g}_i\right)\right)_{ij} = \mathbb{1} \\ \Leftrightarrow \qquad & A \cdot G = \mathbb{1}. \end{aligned} \tag{II.3.55}$$

6. The unique solution $A = G^{-1}$ requires the input parameters to fulfil the condition $\det(G) \neq 0$.

When the aim is to perform a likelihood fit on some (pseudo-)data T_d, the minimization condition is

$$\widehat{\vec{g}}\left(T_d\right) = \text{argmin}_{\vec{g}} - 2 \ln P\left(T_d \mid \mu = \sum_{i=1}^{N} \left(\sum_{j=1}^{N} A_{ij} P_j\left(\vec{g}\right) \right) T_{\text{in},i} \right). \tag{II.3.56}$$

From this it becomes apparent that only the polynomials $P_j\left(\vec{g}\right)$ need to be recalculated during the minimization process, while the non-trivial quantities A_{ij} and $T_{\text{in},i}$ stay fixed.

The error propagation of statistical uncertainties to the output T_{out} is conceptually straightforward. Since the $\vec{g}_i$ are free parameters, the matrix A carries no uncertainty besides numerical fluctuations. Thus, uncertainties only propagate via linear combinations. The question of how the input parameters $\vec{g}_i$ need to be chosen such that the expected uncertainty of the output is minimal, within some parameter region of interest, is non-trivial and will be addressed in future studies.

The number N of input base samples depends on how many of coupling parameters enter the production and/or the decay vertex. However, the general morphing principle remains the same and the method can be generalized to a higher-dimensional coupling parameter space.

A general expression for the number of input samples N with n_p couplings appearing only in production, n_d couplings appearing only in decay and n_s couplings shared in production and decay is given by

$$N = \quad \frac{n_p\left(n_p+1\right)}{2} \cdot \frac{n_d\left(n_d+1\right)}{2} + \binom{4+n_s-1}{4} \tag{II.3.57}$$

$$+ \left(n_p \cdot n_s + \frac{n_s\left(n_s+1\right)}{2} \right) \cdot \frac{n_d\left(n_d+1\right)}{2} \tag{II.3.58}$$

$$+ \left(n_d \cdot n_s + \frac{n_s\left(n_s+1\right)}{2} \right) \cdot \frac{n_p\left(n_p+1\right)}{2} \tag{II.3.59}$$

$$+ \frac{n_s\left(n_s+1\right)}{2} \cdot n_p \cdot n_d + \left(n_p + n_d\right) \binom{3+n_s-1}{3}. \tag{II.3.60}$$

In this expression the counting is split for (II.3.57) terms pure in production and decay, or pure in shared, (II.3.58) terms pure in decay and mixed in production and shared or purely shared, (II.3.59) terms pure in production and mixed in decay and shared or purely shared, and (II.3.60 terms mixed in both, and terms mixed in one and purely shared in the other.

This is a general definition of the number of samples N in terms of number of coupling parameters n_p, n_d, and n_s. In case of the gluon fusion process with subsequent decays to vector bosons, the production and decay will have a completely disjoint set of couplings, and the number of input samples will be given by Eq. II.3.57 by setting $n_s = 0$. For the VBF Higgs boson production with subsequent decay into vector bosons, when considering the same set of couplings in the production and the decay vertex, the number of samples is given by Eq. II.3.57 with $n_p = 0$ and $n_d = 0$.

II.3.2.c Conclusions

This note describes a method for modelling signal parameters and distributions in a multidimensional space of coupling parameters. This method is capable of continuously morphing signal distributions and rates based on a minimal orthogonal set of independent base samples. Therefore it allows to directly fit for the coupling parameters that describe the SM and possibly non-SM interaction of the Higgs boson with fermions and bosons of the SM.

This method can be utilized to test the properties of the Higgs boson during the LHC Run 2 data-taking period and beyond and has already been tested successfully [939].

Part III

Measurements and Observables *

*M. Chen, A. David, M. Dührssen, A. Falkowski, M. Grazzini, R. Harlander, C. Hays, G. Isidori, B. Mellado, P. Musella (Eds.)

Chapter III.1

Pseudo-observables

A. David, A. Greljo, G. Isidori, J. Lindert, D. Marzocca, G. Passarino

III.1.1 Introduction

The idea of PO has been formalized the first time in the context of electroweak observables around the Z pole [706]. A generalization of this concept to describe possible deformations from the SM in Higgs boson production and decay processes has been discussed in Refs. [610, 648, 651, 652, 731, 943]. The basic idea is to identify a set of quantities that are

I. experimentally accessible,
II. well-defined from the point of view of QFT,

and capture all relevant New Physics (NP) effects (or all relevant deformations from the SM) without losing information and with minimum theoretical bias. The last point implies that changes in the underlying NP model should not require any new processing of raw experimental data. In the same spirit, the PO should be independent from the theoretical precision (e.g. LO, NLO, ...) at which NP effects are computed. Finally, the PO are obtained after removing (via a proper deconvolution) the effect of the soft SM radiation (both QED and QCD radiation), that is assumed to be free from NP effects. In the case of observables around the Z pole, the $\Gamma(Z \to f\bar{f})$ partial decay rates provide good examples of PO.

The independence from NP models can not be fulfilled in complete generality. However, it can be fulfilled under very general assumptions. In particular, we require the PO to

III. capture all relevant NP effects in the limit of no new (non-SM) particles propagating on-shell (in the amplitudes considered) in the kinematical range where the decomposition is assumed to be valid.

Under this additional hypothesis, the PO provide a bridge between the fiducial cross-section measurements and the determination of NP couplings in explicit NP frameworks.

On a more theoretical footing, the Higgs PO are defined from a general decomposition of on-shell amplitudes involving the Higgs boson – based on analyticity, unitarity, and crossing symmetry – and a momentum expansion following from the dynamical assumption of no new light particles (hence no unknown physical poles in the amplitudes) in the kinematical regime where the decomposition is assumed to be valid. These conditions ensure the generality of this approach and the possibility to match it to a wide class of explicit NP model, including the determination of Wilson coefficients in the context of Effective Field Theories.

The old κ framework [9, 10] satisfied the conditions I and II, but not the condition III, since the framework was not general enough to describe modifications in $(n > 2)$-body Higgs boson decays resulting in non-SM kinematics. Similarly, the old κ framework could not describe modifications of the Higgs-cross sections that cannot be reabsorbed into a simple overall re-scaling with respect to the SM.

Similarly to the case of electroweak observables, it is convenient to introduce two complementary sets of Higgs PO:

– a set of *physical* PO, namely a set of (idealized) partial decay rates and asymmetries;
– a set of *effective-couplings* PO, parameterizing the on-shell production and decay amplitudes.

The two sets are in one-to-one correspondence: by construction, the effective-couplings PO are directly related to the *physical* PO after properly working out the decay kinematics. The effective-couplings PO are particularly useful to build tools to simulate data, taking into account the effect of soft QCD and

QED radiation.[III.1] This is why, from the practical point of view, the effective-couplings PO are first extracted from data in the LHC Higgs analysis, and from these the *physical* PO are indirectly derived. As we discuss below, the latter provide a more intuitive and effective presentation of the measurements performed.

The note is organized as follows: the PO for Higgs boson decays are discussed in Section III.1.2-III.1.4, separating two, three, and four-body decay modes. General aspects of PO in electroweak production processes are discussed in Section III.1.5, whereas the specific implementation for VH and VBF is presented in Section III.1.6. The total number of PO to discuss both production and decay processes is summarized in Section III.1.7, where we also address the reduction of the number of independent terms under specify symmetry assumptions (in particular CP conservation and flavour universality). Finally, a discussion about the matching between the PO approach and the SM Effective Field Theory (SMEFT) is presented in Sections III.1.8. The latter section is not needed to discuss the PO implementation in data analyses, but it provides a bridge between this chapter of the YR (Measurements and Observables) and the one devoted to the EFT approaches.

III.1.2 Two-body decay modes

In the case of two-body Higgs boson decays into on-shell SM particles, namely $h \to f\bar{f}$ and $h \to \gamma\gamma$, the natural *physical PO* for each mode are the partial decay widths, and possibly the polarization asymmetry if the spin of the final state is accessible.

In the $h \to f\bar{f}$ case the main issue to be addressed is the optimal definition of the partial decay width taking into account the final state QED and QCD radiation.

In the $h \to \gamma\gamma$ case the point to be addressed is the extrapolation to real photons of electromagnetic showers with non-vanishing invariant mass.

III.1.2.a $h \to f\bar{f}$

For each fermion species we can decompose the on-shell $h \to f\bar{f}$ amplitude in terms of two effective couplings ($y^f_{S,P}$), defined by

$$\mathcal{A}(h \to f\bar{f}) = -\frac{i}{\sqrt{2}}\left(y^f_S \bar{f} f + i y^f_P \bar{f}\gamma_5 f\right) , \tag{III.1.1}$$

where f, $\bar{f}$ in the right hand side are spinor wave functions. These couplings are real in the limit where we neglect re-scattering effects, that is an excellent approximation (also beyond the SM if we assume no new light states), for all the accessible $h \to f\bar{f}$ channels. If h is a CP-even state (as in the SM), then y^f_P is a CP-violating coupling.

In order to match our notation with the κ framework [9], we define the two *effective couplings* PO of the $h \to f\bar{f}$ decays as follows:

$$\kappa_f = \frac{y^f_S}{y^{f,\mathrm{SM}}_S} , \qquad \delta^{\mathrm{CP}}_f = \frac{y^f_P}{y^{f,\mathrm{SM}}_S} . \tag{III.1.2}$$

Here $y^{f,\mathrm{SM}}_S$ is the SM effective coupling that provides the best SM prediction in the $\kappa_f \to 1$ and $\delta^{\mathrm{CP}}_f \to 0$ limit.

The measurement of $\Gamma(h \to f\bar{f})_{(\mathrm{incl})}$ determines the combination $|\kappa_f|^2 + |\delta^{\mathrm{CP}}_f|^2$, while the $\delta^{\mathrm{CP}}_f/\kappa_f$ ratio can be determined only if the fermion polarization is experimentally accessible. With this notation, the inclusive decay rates, computed assuming a pure bremsstrahlung spectrum can be written as

$$\Gamma(h \to f\bar{f})_{(\mathrm{incl})} = \left[|\kappa_f|^2 + |\delta^{\mathrm{CP}}_f|^2\right] \Gamma(h \to f\bar{f})^{(\mathrm{SM})}_{(\mathrm{incl})} , \tag{III.1.3}$$

[III.1] A first public tool for Higgs PO is available in Ref. [944].

where fermion-mass effects, of per-mil level even for the b quark, have been neglected. In experiments $\Gamma(h \to f\bar{f})_{(\rm incl)}$ cannot be directly accessed, given tight cuts on the $f\bar{f}$ invariant mass to suppress the background: $\Gamma(h \to f\bar{f})_{(\rm incl)}$ is extrapolated from the experimentally accessible $\Gamma(h \to f\bar{f})_{(\rm cut)}$ assuming a pure bremsstrahlung spectrum, both as far as QED and as far as QCD (for the $q\bar{q}$ channels only) radiation is concerned.

The SM decay width is given by

$$\Gamma(h \to f\bar{f})^{(\rm SM)}_{(\rm incl)} = N_c^f \frac{|y_{\rm eff}^{f,\rm SM}|^2}{16\pi} m_H^2 \,, \tag{III.1.4}$$

where the colour factor N_c^f is 3 for quarks and 1 for leptons. Using the best SM prediction of the branching ratios in these channels [9], for $m_H = 125.0$ GeV and $\Gamma_H^{\rm tot} = 4.07 \times 10^{-3}$ GeV, we extract the values of the $|y_{\rm eff}^{f,\rm SM}|$ couplings in Eq. (III.1.4):

	$\bar{b}b$	$\bar{\tau}\tau$
$\mathcal{B}(h \to \bar{f}f)$	5.77×10^{-1}	6.32×10^{-2}
$\lvert y_{\rm eff}^{f,\rm SM}\rvert$	1.77×10^{-2}	1.02×10^{-2}

,

	$\bar{c}c$	$\bar{\mu}\mu$
$\mathcal{B}(h \to \bar{f}f)$	2.91×10^{-2}	2.19×10^{-4}
$\lvert y_{\rm eff}^{f,\rm SM}\rvert$	3.98×10^{-3}	5.99×10^{-4}

,

As anticipated, the *physical* PO sensitive to $\delta_f^{\rm CP}/\kappa_f$ necessarily involve a determination (direct or indirect) of the fermion spins. Denoting by $\vec{k}_f$ the 3-momentum of the fermion f in the Higgs centre of mass frame, and with $\{\vec{s}_f, \vec{s}_{\bar{f}}\}$ the two fermion spins, we can define the following CP-odd asymmetry [945]

$$\mathcal{A}_f^{\rm CP} = \frac{1}{|\vec{k}_f|}\langle \vec{k}_f \cdot (\vec{s}_f \times \vec{s}_{\bar{f}})\rangle = -\frac{\delta_f^{\rm CP}\kappa_f}{\kappa_f^2 + (\delta_f^{\rm CP})^2} \tag{III.1.5}$$

As pointed out in Ref. [946], in the $h \to \tau^+\tau^- \to X_{\tau^+}X_{\tau^-}$ decay chains asymmetries proportional to $\mathcal{A}_f^{\rm CP}$ are accessible through the measurement of the angular distribution of the $\tau^\pm$ decay products.

Note that, by construction, the effective couplings PO depend on the SM normalization. This imply an intrinsic theoretical uncertainty in their determination related to the theory error on the SM reference value. On the other hand, the *physical* PO are independent of any reference to the SM. Indeed the (conventional) SM normalization of κ_f cancels in Eq. (III.1.3).

III.1.2.b $h \to \gamma\gamma$

The general decomposition for the $h \to \gamma\gamma$ amplitude is

$$\mathcal{A}\left[h \to \gamma(q,\epsilon)\gamma(q',\epsilon')\right] = i\frac{2}{v_F}\epsilon'_\mu\epsilon_\nu\left[\epsilon_{\gamma\gamma}(g^{\mu\nu}\, q{\cdot}q' - q^\mu q'^\nu) + \epsilon_{\gamma\gamma}^{\rm CP}\varepsilon^{\mu\nu\rho\sigma}q_\rho q'_\sigma\right] \,, \tag{III.1.6}$$

where $\epsilon^{\mu\nu\rho\sigma}$ is the fully antisymmetric tensor and $\epsilon^{0123} = 1$ in our convention. From this we identify the two effective couplings $\epsilon_{\gamma\gamma}$ and $\epsilon_{\gamma\gamma}^{\rm CP}$ that, similarly to $y_{S,P}^f$, can be assumed to be real in the limit where we assume no new light states and small deviations from the SM limit. Here $v_F = (\sqrt{2}G_F)^{-1/2}$, and G_F is the Fermi constant extracted from the muon decay. We define the effective couplings PO for this channels as

$$\kappa_{\gamma\gamma} = \frac{\rm Re(\epsilon_{\gamma\gamma})}{\rm Re(\epsilon_{\gamma\gamma}^{SM})} \,, \qquad \delta_{\gamma\gamma}^{\rm CP} = \frac{\rm Re(\epsilon_{\gamma\gamma}^{CP})}{\rm Re(\epsilon_{\gamma\gamma}^{SM})} \,, \tag{III.1.7}$$

where $\epsilon^{\gamma\gamma}_{\rm SM}$ is the value of the PO which reproduces the best SM prediction of the decay width. By construction, the SM expectation for the two PO is $\kappa^{\rm SM}_{\gamma\gamma} = 1$ and $(\delta^{\rm CP}_{\gamma\gamma})^{\rm SM} = 0$.

If the photon polarization is not accessible, the only *physical* PO for this channel is $\Gamma(h \to \gamma\gamma)$. Starting from realistic observables, where the electromagnetic showers have non-vanishing invariant mass, $\Gamma(h \to \gamma\gamma)$ is defined as the extrapolation to the limit of zero invariant mass for the electromagnetic showers. The relation between $\Gamma(h \to \gamma\gamma)$ and the two effective couplings PO is

$$\Gamma(h \to \gamma\gamma) = \left[\kappa^2_{\gamma\gamma} + (\delta^{\rm CP}_{\gamma\gamma})^2\right] \Gamma(h \to \gamma\gamma)^{\rm (SM)} \,, \tag{III.1.8}$$

where

$$\Gamma(h \to \gamma\gamma)^{\rm (SM)} = \frac{|\epsilon^{\rm SM,eff}_{\gamma\gamma}|^2}{16\pi} \frac{m_H^3}{v_F^2}. \tag{III.1.9}$$

Using the SM prediction for the branching ratios in two photons [9], for $v_F = 246.22$ GeV, $m_H = 125.0$ GeV and $\Gamma^{\rm tot}_H = 4.07 \times 10^{-3}$ GeV, we obtain

$$\mathcal{B}(h \to \gamma\gamma)^{\rm SM} = 2.28 \times 10^{-3} \quad \to \quad \epsilon^{\gamma\gamma}_{\rm SM} = 3.8 \times 10^{-3} \,. \tag{III.1.10}$$

This value corresponds to the 1-loop contribution in the SM, which also fixes the relative sign. Similarly to the $f\bar{f}$ case, the SM normalization cancels in the definition of the *physical* PO.

The *physical* PO linear in the CP-violating coupling $\delta^{\rm CP}_{\gamma\gamma}$ necessarily involves the measurement of the photon polarization and is therefore hardly accessible at the LHC (at least in a direct way, see for example [947]). Denoting by $\vec{q}_{1,2}$ the 3-momenta of the two photons in the centre of mass frame, and with $\vec{\epsilon}_{1,2}$ the corresponding polarization vectors, we can define:

$$\mathcal{A}^{\rm CP}_{\gamma\gamma} = \frac{1}{m_h} \langle (\vec{q}_1 - \vec{q}_2) \cdot (\vec{\epsilon}_1 \times \vec{\epsilon}_2) \rangle \propto \frac{\delta^{\rm CP}_{\gamma\gamma} \kappa_{\gamma\gamma}}{\kappa^2_{\gamma\gamma} + (\delta^{\rm CP}_{\gamma\gamma})^2} \,. \tag{III.1.11}$$

III.1.3 Three-body decay modes

The guiding principle for the definition of PO in multi-body channels is the decomposition of the decay amplitudes in terms of contributions associated to a specific single-particle pole structure. In the absence of new light states, such poles are generated only by the exchange of the SM electroweak bosons (γ, Z, and W) or by hadronic resonances (whose contribution appears only beyond the tree level and is largely suppressed). Since positions and residues on the poles are gauge-invariant quantities, this decomposition satisfies the general requirements for the definitions of PO.

III.1.3.a $h \to f\bar{f}\gamma$

The general form factor decomposition for these channels is

$$\begin{aligned}\mathcal{A}\left[h \to f(p_1)\bar{f}(p_2)\gamma(q,\epsilon)\right] = i\frac{2}{v_F} \sum_{f=f_L,f_R} (\bar{f}\gamma_\mu f)\epsilon_\nu \times \\ \times\Big[F^{f\gamma}_T(p^2)(p\cdot q\, g^{\mu\nu} - q^\mu p^\nu) + F^{f\gamma}_{CP}(p^2)\varepsilon^{\mu\nu\rho\sigma} q_\rho p_\sigma\Big] \,,\end{aligned} \tag{III.1.12}$$

where $p = p_1 + p_2$. The form factors can be further decomposed as

$$F^{f\gamma}_T(p^2) = \epsilon_{Z\gamma} \frac{g^f_Z}{P_Z(p^2)} + \epsilon_{\gamma\gamma} \frac{eQ_f}{p^2} + \Delta^{\rm SM}_{f\gamma}(p^2) \,, \tag{III.1.13}$$

$$F^{f\gamma}_{CP}(p^2) = \epsilon^{\rm CP}_{Z\gamma} \frac{g^f_Z}{P_Z(p^2)} + \epsilon^{\rm CP}_{\gamma\gamma} \frac{eQ_f}{p^2} \,. \tag{III.1.14}$$

Here g_Z^f are the effective PO describing on-shell $Z \to f\bar{f}$ decays[III.2] and $P_Z(q^2) = q^2 - m_Z^2 + im_Z\Gamma_Z$. In other words, we decompose the form factors identifying the physical poles associated to the Z and γ propagators.

The term $\Delta_{f\gamma}^{\rm SM}(p^2)$ denotes the remnant of the SM $h \to f\bar{f}\gamma$ loop function that is regular both in the limit $p^2 \to 0$ and in the limit $p^2 \to m_Z^2$. This part of the amplitude is largely subdominant (being not enhanced by a physical single-particle pole) and cannot receive non-standard contributions from operators of dimension up to 6 in the EFT approach to Higgs physics. For this reason it is fixed to its SM value.

In this channel we thus have four effective couplings PO, related to the four ϵ_X terms in Eqs. (III.1.13) and (III.1.14), two of which are accessible also in $h \to 2\gamma$.[III.3]

Similarly to the $h \to 2\gamma$ case, it is convenient to define the PO normalizing them the corresponding reference SM values of the amplitudes. We thus define

$$\kappa_{Z\gamma} = \frac{{\rm Re}(\epsilon_{Z\gamma})}{{\rm Re}(\epsilon_{Z\gamma}^{\rm SM})}\,, \qquad \delta_{Z\gamma}^{\rm CP} = \frac{{\rm Re}(\epsilon_{Z\gamma}^{\rm CP})}{{\rm Re}(\epsilon_{Z\gamma}^{\rm SM})}\,, \tag{III.1.15}$$

where the numerical value of the SM contribution $\epsilon_{Z\gamma}^{\rm SM}$ is obtained from the best SM prediction for the $h \to Z\gamma$ decay width.

The simplest *physical* PO that can be extracted from this channel is $\Gamma(h \to Z\gamma)$, where both the Z boson and the photon are on-shell. By construction, this can be written as

$$\Gamma(h \to Z\gamma) = \left[\kappa_{Z\gamma}^2 + (\delta_{Z\gamma}^{\rm CP})^2\right]\Gamma(h \to Z\gamma)^{\rm (SM)}\,, \tag{III.1.16}$$

where

$$\Gamma(h \to Z\gamma)^{\rm (SM)} = \frac{|\epsilon_{Z\gamma}^{\rm SM,eff}|^2}{8\pi}\frac{m_H^3}{v^2}\left(1 - \frac{m_Z^2}{m_H^2}\right)^3\,. \tag{III.1.17}$$

The SM prediction for this decay rate [9] provides the value of $\epsilon_{\rm SM}^{Z\gamma}$:

$$\mathcal{B}(h \to Z\gamma)^{\rm (SM)} = 1.54 \times 10^{-3} \quad \to \quad \epsilon_{Z\gamma}^{\rm SM} = 6.9 \times 10^{-3}\,. \tag{III.1.18}$$

The independent *physical* PO linear in the coupling $\delta_{Z\gamma}^{\rm CP}$ is the following CP-odd asymmetry at the Z peak:

$$\mathcal{A}_{Z\gamma}^{\rm CP} = \frac{1}{|\vec{p}||\vec{q}|}\langle\vec{p}\cdot(\vec{q}\times\vec{\epsilon_\gamma})\rangle\Big|_{(p^2=m_Z^2)} \propto \frac{\delta_{Z\gamma}^{\rm CP}\kappa_{Z\gamma}}{\kappa_{Z\gamma}^2 + (\delta_{Z\gamma}^{\rm CP})^2}\,, \tag{III.1.19}$$

where all 3-momenta are defined in the Higgs centre of mass frame.

This channel is also sensitive to $\Gamma(h \to \gamma\gamma)$ and $\mathcal{A}_{\gamma\gamma}^{\rm CP}$ via the effective couplings $\kappa_{\gamma\gamma}$ (or $\epsilon_{\gamma\gamma}$) and $\delta_{\gamma\gamma}^{\rm CP}$ (or $\epsilon_{\gamma\gamma}^{\rm CP}$). Determining such couplings from a fit to the from factors in the low p^2 region, one can indirectly determine $\Gamma(h \to \gamma\gamma)$ and $\mathcal{A}_{\gamma\gamma}^{\rm CP}$ by means of Eq. (III.1.8) and Eq. (III.1.11), respectively.

[III.2] We have absorbed a factor $g/\cos(\theta_W)$ with respect to the definition of the effective Z couplings adopted at LEP-1, see Eq. (III.1.24).

[III.3] In the decomposition (III.1.12) we have also neglected possible dipole-type (helicity-suppressed) amplitudes. The latter necessarily give a strongly suppressed contribution to the decay rate since the interference with the leading $h \to f\bar{f}\gamma$ amplitude vanishes in the limit $m_f \to 0$. There is no obstacle, in principle, to add a corresponding set of PO for these suppressed amplitudes. However, for all light fermions they will be un-measurable in realistic scenarios even in the high-luminosity phase of the LHC (see e.g. [948] for a numerical discussion in the $h \to 2\mu\gamma$ case).

III.1.4 Four-fermion decay modes

Similarly to the three-body modes, also in this case the guiding principle for the definition of PO is the decomposition of the decay amplitudes in terms of contributions associated to a specific pole structure. Such decomposition for the $h \to 4f$ channels has been presented in Ref. [651]. The effective coupling PO that appear in these channels consist of four sets:

- 3 flavour-universal charged-current PO: $\{\kappa_{WW}, \epsilon_{WW}, \epsilon^{\rm CP}_{WW}\}$;
- 7 flavour-universal neutral-current PO, 4 of which are appearing already in $h \to \gamma\gamma$ and $h \to f\bar{f}\gamma$: $\{\kappa_{\gamma\gamma}, \delta^{\rm CP}_{\gamma\gamma}, \kappa_{Z\gamma}, \delta^{\rm CP}_{Z\gamma}\}$, and another 3 which are specific for $h \to 4f$: $\{\kappa_{ZZ}, \epsilon_{ZZ}, \epsilon^{\rm CP}_{ZZ}\}$;
- the set of flavour non-universal charged-current PO: $\{\epsilon_{Wf}\}$;
- the set of flavour non-universal neutral-current PO: $\{\epsilon_{Zf}\}$.

While the number of flavour-universal PO is fixed, the number of flavour non-universal PO depend on the fermion species we are interested in. For instance, looking only at light leptons ($\ell = e, \mu$), we have 4 flavour non-universal PO contributing to $h \to 4\ell$ modes (ϵ_{Zf}, with $f = e_L, e_R, \mu_L, \mu_R$) and 4 PO contributing to $h \to 2\ell 2\nu$ modes ($\epsilon_{We_L}, \epsilon_{W\mu_L}, \epsilon_{Ze_\nu}, \epsilon_{Z\nu_\mu}$). The definition of these PO is done at the amplitude level, separating neutral-current and charged-current contributions to the $h \to 4f$ processes, as discussed below.

Starting from each of the effective couplings PO we can define a corresponding *physical* PO. In particular, $\Gamma(h \to ZZ)$ is defined as the (ideal) rate extracted from the full $\Gamma(h \to 4f)$, extrapolating the result in the limit $\kappa_{ZZ} \neq 0$ and all the other effective couplings set to zero. Similarly $\Gamma(h \to Zf\bar{f})$ is defined from the extrapolation in the limit $\epsilon_{Zf} \neq 0$ and all the other effective couplings set to zero (see extended discussion below).

III.1.4.a $h \to 4f$ neutral currents

Let us consider the case of two different (light) fermion species: $h \to f\bar{f} + f'\bar{f}'$. Neglecting helicity-violating terms (yielding contributions suppressed by light fermion masses in the rates), we can decompose the neutral-current contribution to the amplitude in the following way

$$\begin{aligned}
\mathcal{A}_{n.c.}\left[h \to f(p_1)\bar{f}(p_2)f'(p_3)\bar{f}'(p_4)\right] &= i\frac{2m_Z^2}{v_F}\sum_{f=f_L,f_R}\sum_{f'=f'_L,f'_R}(\bar{f}\gamma_\mu f)(\bar{f}'\gamma_\nu f')\mathcal{T}^{\mu\nu}_{n.c.}(q_1,q_2)\\
\mathcal{T}^{\mu\nu}_{n.c.}(q_1,q_2) &= \left[F_L^{ff'}(q_1^2,q_2^2)g^{\mu\nu} + F_T^{ff'}(q_1^2,q_2^2)\frac{q_1\cdot q_2\, g^{\mu\nu} - q_2{}^\mu q_1{}^\nu}{m_Z^2}\right.\\
&\qquad \left. + F_{CP}^{ff'}(q_1^2,q_2^2)\frac{\varepsilon^{\mu\nu\rho\sigma}q_{2\rho}q_{1\sigma}}{m_Z^2}\right], \qquad \text{(III.1.20)}
\end{aligned}$$

where $q_1 = p_1 + p_2$ and $q_2 = p_3 + p_4$. The form factor F_L describes the interaction with the longitudinal part of the current, as in the SM, the F_T term describes the interaction with the transverse part, while F_{CP} describes the CP-violating part of the interaction (if the Higgs is assumed to be a CP-even state).

We can further expand the form factors in full generality around the poles, providing the definition of the neutral-current PO [651]:

$$F_L^{ff'}(q_1^2,q_2^2) = \kappa_{ZZ}\frac{g_Z^f g_Z^{f'}}{P_Z(q_1^2)P_Z(q_2^2)} + \frac{\epsilon_{Zf}}{m_Z^2}\frac{g_Z^{f'}}{P_Z(q_2^2)} + \frac{\epsilon_{Zf'}}{m_Z^2}\frac{g_Z^f}{P_Z(q_1^2)} + \Delta_L^{\rm SM}(q_1^2,q_2^2)\,, \qquad \text{(III.1.21)}$$

$$\begin{aligned}
F_T^{ff'}(q_1^2,q_2^2) &= \epsilon_{ZZ}\frac{g_Z^f g_Z^{f'}}{P_Z(q_1^2)P_Z(q_2^2)} + \epsilon_{Z\gamma}\left(\frac{eQ_{f'}g_Z^f}{q_2^2P_Z(q_1^2)} + \frac{eQ_f g_Z^{f'}}{q_1^2P_Z(q_2^2)}\right) + \epsilon_{\gamma\gamma}\frac{e^2Q_fQ_{f'}}{q_1^2q_2^2}\\
&\quad + \Delta_T^{\rm SM}(q_1^2,q_2^2), \qquad \text{(III.1.22)}
\end{aligned}$$

$$F_{CP}^{ff'}(q_1^2,q_2^2) = \epsilon_{ZZ}^{\rm CP}\frac{g_Z^f g_Z^{f'}}{P_Z(q_1^2)P_Z(q_2^2)} + \epsilon_{Z\gamma}^{\rm CP}\left(\frac{eQ_{f'}g_Z^f}{q_2^2 P_Z(q_1^2)} + \frac{eQ_f g_Z^{f'}}{q_1^2 P_Z(q_2^2)}\right) + \epsilon_{\gamma\gamma}^{\rm CP}\frac{e^2 Q_f Q_{f'}}{q_1^2 q_2^2} \quad \text{(III.1.23)}$$

Here g_Z^f are Z-pole PO extracted from Z decays at LEP-I, the translation to the notation used at LEP being very simple

$$g_Z^f = \frac{2m_Z}{v_F} g_f^{\rm LEP}\,, \qquad \text{and} \qquad (g_Z^f)_{\rm SM} = \frac{2m_Z}{v_F}(T_3^f - Q_f s^2_{\theta_W})\,. \quad \text{(III.1.24)}$$

As anticipated, all the parameters but ϵ_{Zf} and g_Z^f are flavour universal, i.e. they do not depend on the fermion species. In fact, flavour non-universal effects in g_Z^f have been very tightly constrained at LEP-I [721], however, sizeable effects in ϵ_{Zf} are possible and should be tested at the LHC. In the limit where we neglect re-scattering effects, both κ_{ZZ} and ϵ_X are real. The functions $\Delta_{L,T}^{\rm SM}(q_1^2,q_2^2)$ denote subleading non-local contributions that are regular both in the limit $q_{1,2}^2 \to 0$ and in the limit $q_{1,2}^2 \to m_Z^2$. As in the 3-body decay case, this part of the amplitude is largely subdominant and not affected by operators with dimension up to 6, therefore it is fixed it to its SM value.

III.1.4.b $h \to 4f$ charged currents

Let us consider the $h \to \ell\bar\nu_\ell\bar\ell'\nu_{\ell'}$ process.[III.4] Employing the same assumptions used in the neutral current case, we can decompose the amplitude in the following way:

$$\begin{aligned}\mathcal{A}_{c.c.}\left[h\to\ell(p_1)\bar\nu_\ell(p_2)\nu_{\ell'}(p_3)\bar\ell'(p_4)\right] &= i\frac{2m_W^2}{v_F}(\bar\ell_L\gamma_\mu\nu_{\ell L})(\bar\nu_{\ell' L}\gamma_\nu\ell'_L)\mathcal{T}_{c.c.}^{\mu\nu}(q_1,q_2)\\ \mathcal{T}_{c.c.}^{\mu\nu}(q_1,q_2) &= \left[G_L^{\ell\ell'}(q_1^2,q_2^2)g^{\mu\nu} + G_T^{\ell\ell'}(q_1^2,q_2^2)\frac{q_1\cdot q_2\, g^{\mu\nu} - q_2{}^\mu q_1{}^\nu}{m_W^2}\right.\\ &\quad \left. + G_{CP}^{\ell\ell'}(q_1^2,q_2^2)\frac{\varepsilon^{\mu\nu\rho\sigma}q_{2\rho}q_{1\sigma}}{m_W^2}\right]\,, \end{aligned} \quad \text{(III.1.25)}$$

where $q_1 = p_1 + p_2$ and $q_2 = p_3 + p_4$. The decomposition of the form factors, that allows us to define the charged-current PO, is [651]

$$G_L^{\ell\ell'}(q_1^2,q_2^2) = \kappa_{WW}\frac{(g_W^\ell)^* g_W^{\ell'}}{P_W(q_1^2)P_W(q_2^2)} + \frac{(\epsilon_{W\ell})^*}{m_W^2}\frac{g_W^{\ell'}}{P_W(q_2^2)} + \frac{\epsilon_{W\ell'}}{m_W^2}\frac{(g_W^\ell)^*}{P_W(q_1^2)}\,, \quad \text{(III.1.26)}$$

$$G_T^{\ell\ell'}(q_1^2,q_2^2) = \epsilon_{WW}\frac{(g_W^\ell)^* g_W^{\ell'}}{P_W(q_1^2)P_W(q_2^2)}\,, \quad \text{(III.1.27)}$$

$$G_{CP}^{\ell\ell'}(q_1^2,q_2^2) = \epsilon_{WW}^{\rm CP}\frac{(g_W^\ell)^* g_W^{\ell'}}{P_W(q_1^2)P_W(q_2^2)}\,, \quad \text{(III.1.28)}$$

where $P_W(q^2)$ is the W propagator defined analogously to $P_Z(q^2)$ and g_W^f are the effective couplings describing on-shell W decays (we have absorbed a factor of g compared to standard notations). In the SM,

$$(g_W^{ik})_{\rm SM} = \frac{g}{\sqrt{2}}V_{ik}\,, \quad \text{(III.1.29)}$$

where V is the CKM mixing matrix.[III.5] In absence of rescattering effects, the Hermiticity of the underlying effective Lagrangian implies that κ_{WW}, ϵ_{WW} and $\epsilon_{WW}^{\rm CP}$ are real couplings, while $\epsilon_{W\ell}$ can be complex.

[III.4] The analysis of a process involving quarks is equivalent, with the only difference that the ϵ_{Wf} coefficients are in this case non-diagonal matrices in flavour space, as the g_{ud}^W effective couplings.

[III.5] More precisely, $(g_W^{ik})_{\rm SM} = \frac{g}{\sqrt{2}}V_{ik}$ if i and k refers to left-handed quarks, otherwise $(g_W^{ik})_{\rm SM} = 0$.

III.1.4.c $h \to 4f$ complete decomposition

The complete decomposition of a generic $h \to 4f$ amplitude is obtained combining neutral- and charged-current contributions depending on the nature of the fermions involved. For instance $h \to 2e2\mu$ and $h \to \ell\bar{\ell}q\bar{q}$ decays are determined by a single neutral current amplitude, while the case of two identical lepton pairs is obtained from Eq. (III.1.20) taking into account the proper (anti-)symmetrization of the amplitude:

$$\begin{aligned}\mathcal{A}\left[h \to \ell(p_1)\bar{\ell}(p_2)\ell(p_3)\bar{\ell}(p_4)\right] &= \mathcal{A}_{n.c.}\left[h \to f(p_1)\bar{f}(p_2)f'(p_3)\bar{f}'(p_4)\right]_{f=f'=\ell} \\ &- \mathcal{A}_{n.c.}\left[h \to f(p_1)\bar{f}(p_4)f'(p_3)\bar{f}'(p_2)\right]_{f=f'=\ell} .\end{aligned} \tag{III.1.30}$$

The $h \to e^{\pm}\mu^{\mp}\nu\bar{\nu}$ decays receive contributions from a single charged-current amplitude, while in the $h \to \ell\bar{\ell}\nu\bar{\nu}$ case we have to sum charged and neutral-current contributions:

$$\begin{aligned}\mathcal{A}\left[h \to \ell(p_1)\bar{\ell}(p_2)\nu(p_3)\bar{\nu}(p_4)\right] &= \mathcal{A}_{n.c.}\left[h \to \ell(p_1)\bar{\ell}(p_2)\nu(p_3)\bar{\nu}(p_4)\right] \\ &- \mathcal{A}_{c.c.}\left[h \to \ell(p_1)\bar{\nu}(p_4)\nu(p_3)\bar{\ell}(p_2)\right] .\end{aligned} \tag{III.1.31}$$

III.1.4.d *Physical* PO for $h \to 4\ell$

To define the idealized *physical* PO we start with the quadratic terms for each of the form factors in Eqs. (III.1.21-III.1.23), and compute their contribution to the double differential decay rate for $h \to e^+e^-\mu^+\mu^-$ (for κ_{ZZ}, ϵ_{ZZ} and $\epsilon_{ZZ}^{\rm CP}$) and for $h \to Z\ell^+\ell^-$ (for the contact terms $\epsilon_{Z\ell}$). It is important to stress that *physical* PO as defined here, are extracted from the *effective-coupling* PO, and represent a more intuitive presentation of the experimental measurements.

Decay channel $h \to e^+e^-\mu^+\mu^-$

We choose this particular decay channel for the (conventional) definition of the *physical* PO because it depends on all the PO relevant for $h \to 4\ell$ and because it does not contain interference between the two fermion currents as in Eq. (III.1.30). The independent contributions of the three form factors to the decay rate are:

$$\begin{aligned}\frac{d\Gamma^{\rm LL}}{dm_1 dm_2} &= \frac{\lambda_p \beta_{10}}{2304\pi^5}\frac{m_Z^4 m_h^3}{v_F^2} m_1 m_2 \sum_{f,f'}\left|F_{\rm L}^{ff'}\right|^2 , \\ \frac{d\Gamma^{\rm TT}}{dm_1 dm_2} &= \frac{\lambda_p \beta_4}{1152\pi^5}\frac{m_h^3}{v_F^2} m_1^3 m_2^3 \sum_{f,f'}\left|F_{\rm T}^{ff'}\right|^2 , \\ \frac{d\Gamma^{\rm CP}}{dm_1 dm_2} &= \frac{\lambda_p \beta_2}{1152\pi^5}\frac{m_h^3}{v_F^2} m_1^3 m_2^3 \sum_{f,f'}\left|F_{\rm CP}^{ff'}\right|^2 ,\end{aligned} \tag{III.1.32}$$

where $f = e_L, e_R$, $f' = \mu_L, \mu_R$, $m_{1(2)} \equiv \sqrt{q_{1(2)}^2}$ and

$$\lambda_p = \sqrt{1 + \left(\frac{m_1^2 - m_2^2}{m_h^2}\right)^2 - 2\frac{m_1^2 + m_2^2}{m_h^2}} , \qquad \beta_N = 1 + \frac{m_1^4 + N m_1^2 m_2^2 + m_2^4}{m_h^4} - 2\frac{m_1^2 + m_2^2}{m_h^2} . \tag{III.1.33}$$

By integrating over m_1 and m_2 we obtain the partial decay rate as

$$\Gamma(h \to 2e2\mu) = \Gamma(h \to 2e2\mu)^{\rm SM} \times \sum_{j \geq i} X_{ij}^{2e2\mu}\kappa_i\kappa_j , \tag{III.1.34}$$

where $X_{ij}^{2e2\mu}$ are the numerical coefficients reported in Ref. [943], while κ_i are the corresponding *effective-coupling* PO. We define the *physical PO* as the specific contribution to the partial decay rate.

Namely, *physical PO* is the partial decay rate due to a single PO, while setting other PO to zero. In particular,

$$\begin{aligned}\Gamma(h\to 2e2\mu)[\kappa_{ZZ}] &= 4.929\times 10^{-2}(|g_{Ze_L}|^2+|g_{Ze_R}|^2)(|g_{Z\mu_L}|^2+|g_{Z\mu_R}|^2)\,|\kappa_{ZZ}|^2\ \text{MeV}\\ \Gamma(h\to 2e2\mu)[\epsilon_{ZZ}] &= 4.458\times 10^{-3}(|g_{Ze_L}|^2+|g_{Ze_R}|^2)(|g_{Z\mu_L}|^2+|g_{Z\mu_R}|^2)\,|\epsilon_{ZZ}|^2\ \text{MeV}\\ \Gamma(h\to 2e2\mu)[\epsilon^{\rm CP}_{ZZ}] &= 1.884\times 10^{-3}(|g_{Ze_L}|^2+|g_{Ze_R}|^2)(|g_{Z\mu_L}|^2+|g_{Z\mu_R}|^2)\,|\epsilon^{\rm CP}_{ZZ}|^2\ \text{MeV}\end{aligned} \tag{III.1.35}$$

The numerical coefficients in Eq. (III.1.35) have been obtained neglecting QED corrections. The latter must be included at the simulation level by appropriate QED showering programs, such as PHOTOS [949]. As shown in Ref. [899]: the impact of such corrections is negligible after integrating over the full phase space, hence in the overall normalization of the partial rates in Eq. (III.1.35), while they can provide sizeable distortions of the spectra in specific phase-space regions.

Since each effective coupling PO correspond to a well-defined pole contribution to the amplitude (with one or two poles of the Z boson), and a well-defined Lorentz and flavour structure, we can associate to those contributions to partial rates an intuitive physical meaning. In particular, we define the following *physical PO* for the $h\to 4\ell$ decays:

$$\begin{aligned}\Gamma(h\to Z_LZ_L) &\equiv \frac{\Gamma(h\to 2e2\mu)[\kappa_{ZZ}]}{\mathcal{B}(Z\to 2e)\mathcal{B}(Z\to 2\mu)} = 0.209\,|\kappa_{ZZ}|^2\ \text{MeV}\\ \Gamma(h\to Z_TZ_T) &\equiv \frac{\Gamma(h\to 2e2\mu)[\epsilon_{ZZ}]}{\mathcal{B}(Z\to 2e)\mathcal{B}(Z\to 2\mu)} = 0.0189\,|\epsilon_{ZZ}|^2\ \text{MeV}\\ \Gamma^{\rm CPV}(h\to Z_TZ_T) &\equiv \frac{\Gamma(h\to 2e2\mu)[\epsilon^{\rm CP}_{ZZ}]}{\mathcal{B}(Z\to 2e)\mathcal{B}(Z\to 2\mu)} = 0.00799\,|\epsilon^{\rm CP}_{ZZ}|^2\ \text{MeV}\end{aligned} \tag{III.1.36}$$

where, due to the double pole structure of the amplitude, we have removed the (physical) branching ratios of the $Z\to e^+e^-$ and $Z\to\mu^+\mu^-$ decays. Here

$$\mathcal{B}(Z\to 2\ell) = \frac{\Gamma_0}{\Gamma_Z}R^\ell\left((g_Z^{\ell_L})^2+(g_Z^{\ell_R})^2\right)\approx 0.4856\left((g_Z^{\ell_L})^2+(g_Z^{\ell_R})^2\right)\,, \tag{III.1.37}$$

where $\Gamma_0=\frac{m_Z}{24\pi}$, Γ_Z is the total decay width and $R^\ell=\left(1+\frac{3}{4\pi}\alpha(m_Z)\right)$ describes final state QED radiation. The relative uncertainty in the numerical coefficients in Eqs. (III.1.36,III.1.37), due to the experimental error on Γ_Z and m_Z [11], is at the $\sim 10^{-3}$ level, thus negligible even given the expected long-term sensitivity in these Higgs measurements.

Decay channel $h\to Z\ell^+\ell^-$

The idealized *physical* PO related to the contact terms can be defined directly from the on-shell decay $h\to Z\ell^+\ell^-$, where $\ell=e_L,e_R,\mu_L,\mu_R$ and the Z boson is assumed to be on-shell (narrow width approximation). We compute this decay rate, neglecting QED corrections and light lepton masses, in presence of the contact terms $\epsilon_{Z\ell}$ only. The Dalitz double differential rate in $s_{12}\equiv(p_{\ell^+}+p_{\ell^-})^2$ and $s_{23}\equiv(p_{\ell^-}+p_Z)^2$ is

$$\frac{d\Gamma}{ds_{12}ds_{23}} = \frac{1}{(2\pi)^3}\frac{1}{32m_h^2}\frac{4|\epsilon_{Z\ell}|^2}{v^2}\left(s_{12}+\frac{(s_{23}-m_Z^2)(m_h^2-s_{12}-s_{23})}{m_Z^2}\right)\,, \tag{III.1.38}$$

The allowed kinematical region is $0<s_{12}<(m_h-m_Z)^2$ and, for any given value of s_{12}, $s_{23}^{\rm min}<s_{23}<s_{23}^{\rm Max}$ with

$$s_{23}^{\rm min(Max)} = (E_2^*+E_Z^*)^2-\left(E_2^*\pm\sqrt{(E_Z^*)^2-m_Z^2}\right)^2\,, \tag{III.1.39}$$

where $E_2^* = \sqrt{s_{12}}/2$ and $E_Z^* = \frac{m_h^2 - s_{12} - m_Z^2}{2\sqrt{s_{12}}}$. The decay rate defines the relation between the *physical* PO and the effective couplings PO as:

$$\Gamma(h \to Z\ell^+\ell^-) = 0.0366 |\epsilon_{Z\ell}|^2 \text{ MeV} \,. \tag{III.1.40}$$

As before, the *physical* PO is defined as the contribution to partial decay rate from the relevant PO, assuming others are set to zero. The only inputs in the numerical coefficient in Eq. (III.1.40) are the Z and Higgs boson masses, as well as the Higgs vev, therefore the relative uncertainty is at the 10^{-3} level. Together with the *physical* PO already defined for $h \to \gamma\gamma$ and $h \to Z\gamma$, we have thus established a complete mapping between the effective couplings PO and the *physical* PO appearing in $h \to 4\ell$ decays.

III.1.4.e *Physical* PO for $h \to 2\ell 2\nu$

Physical PO for charged-current processes can be defined in a very similar way as the neutral-current ones. In particular, we use the $h \to e^+\nu_e\mu^-\bar{\nu}_\mu$ process for the *physical* PO corresponding to k_{WW}, ϵ_{WW}, and $\epsilon_{WW}^{\rm CP}$, and $h \to W^+\ell\bar{\nu}_\ell$ for the contact terms.

Decay channel $h \to e^+\nu_e\mu^-\bar{\nu}_\mu$

Integrating the differential distributions analogous to Eq. (III.1.32) we obtain the expression of the partial decay rate in this channel, in the limit where only one PO is turned on:

$$\begin{aligned}
\Gamma(h \to e\mu 2\nu)[\kappa_{WW}] &= 2.20 \times 10^{-4} |g_{We_L}|^2 |g_{W\mu_L}|^2 \, |\kappa_{WW}|^2 \text{ MeV} \\
\Gamma(h \to e\mu 2\nu)[\epsilon_{WW}] &= 4.27 \times 10^{-5} |g_{We_L}|^2 |g_{W\mu_L}|^2 \, |\epsilon_{WW}|^2 \text{ MeV} \\
\Gamma(h \to e\mu 2\nu)[\epsilon_{WW}^{\rm CP}] &= 1.77 \times 10^{-5} |g_{We_L}|^2 |g_{W\mu_L}|^2 \, |\epsilon_{WW}^{\rm CP}|^2 \text{ MeV}
\end{aligned} \tag{III.1.41}$$

As in the neutral channel, the *physical PO* are defined from these quantities by factorizing the W branching ratios:

$$\begin{aligned}
\Gamma(h \to W_L W_L) &\equiv \frac{\Gamma(h \to e\mu 2\nu)[\kappa_{WW}]}{\mathcal{B}(W \to e\bar{\nu}_e)\mathcal{B}(W \to \mu\bar{\nu}_\mu)} = (0.841 \pm 0.016) \, |\kappa_{WW}|^2 \text{ MeV} \\
\Gamma(h \to W_T W_T) &\equiv \frac{\Gamma(h \to e\mu 2\nu)[\epsilon_{WW}]}{\mathcal{B}(W \to e\bar{\nu}_e)\mathcal{B}(W \to \mu\bar{\nu}_\mu)} = (0.1634 \pm 0.0030) \, |\epsilon_{WW}|^2 \text{ MeV} \\
\Gamma^{\rm CPV}(h \to W_T W_T) &\equiv \frac{\Gamma(h \to e\mu 2\nu)[\epsilon_{WW}^{\rm CP}]}{\mathcal{B}(W \to e\bar{\nu}_e)\mathcal{B}(W \to \mu\bar{\nu}_\mu)} = (0.0677 \pm 0.0012) \, |\epsilon_{WW}^{\rm CP}|^2 \text{ MeV} \,,
\end{aligned} \tag{III.1.42}$$

where the uncertainty has been obtained from the experimental error on Γ_W [11] that, as recently pointed out in [950], it has a non-neglible impact in the prediction of $h \to 2\ell 2\nu$ branching ratios. The W branching ratios are given by

$$\mathcal{B}(W \to \ell\bar{\nu}_\ell) = \frac{\Gamma_0}{\Gamma_W} (g_{W\ell_L})^2 \approx 0.511 (g_{W\ell_L})^2 \,, \tag{III.1.43}$$

where $\Gamma_0 = \frac{m_W}{24\pi}$, Γ_W is the total decay width.

Decay channel $h \to W^+\ell\bar{\nu}_\ell$

Also in this case the *physical* PO corresponding to the charged-current contact terms are defined in complete analogy to the neutral-current case, starting from the 3-body decay $h \to W^+\ell\bar{\nu}_\ell$. The partial decay width computed in the limit where only the contact term PO is switched on defines the relation between the *physical* PO and the effective couplings PO as:

$$\Gamma(h \to W^+\ell\bar{\nu}_\ell) = 0.143 |\epsilon_{W\ell}|^2 \text{ MeV} \,, \tag{III.1.44}$$

where the relative uncertainty in the coefficient due to the experimental error on m_W [11] is below $\sim 2 \times 10^{-3}$.

Table 110: Summary of the *effective coupling* PO and the corresponding *physical* PO. The parameter N_c^f is 1 for leptons and 3 for quarks. In the case of the charged-current contact term, f' is the $SU(2)_L$ partner of the fermion f. See the main text for a discussion about the errors on the numerical coefficient in the table and the reference values of $\{\kappa_X, \delta_X, \epsilon_X\}$ within the SM.

PO	*Physical* PO	Relation to the eff. coupl.
$\kappa_f,\ \delta_f^{\rm CP}$	$\Gamma(h \to f\bar{f})$	$= \Gamma(h \to f\bar{f})^{(\rm SM)}[(\kappa_f)^2 + (\delta_f^{\rm CP})^2]$
$\kappa_{\gamma\gamma},\ \delta_{\gamma\gamma}^{\rm CP}$	$\Gamma(h \to \gamma\gamma)$	$= \Gamma(h \to \gamma\gamma)^{(\rm SM)}[(\kappa_{\gamma\gamma})^2 + (\delta_{\gamma\gamma}^{\rm CP})^2]$
$\kappa_{Z\gamma},\ \delta_{Z\gamma}^{\rm CP}$	$\Gamma(h \to Z\gamma)$	$= \Gamma(h \to Z\gamma)^{(\rm SM)}[(\kappa_{Z\gamma})^2 + (\delta_{Z\gamma}^{\rm CP})^2]$
κ_{ZZ}	$\Gamma(h \to Z_L Z_L)$	$= (0.209\ \text{MeV}) \times \lvert\kappa_{ZZ}\rvert^2$
ϵ_{ZZ}	$\Gamma(h \to Z_T Z_T)$	$= (1.9 \times 10^{-2}\ \text{MeV}) \times \lvert\epsilon_{ZZ}\rvert^2$
$\epsilon_{ZZ}^{\rm CP}$	$\Gamma^{\rm CPV}(h \to Z_T Z_T)$	$= (8.0 \times 10^{-3}\ \text{MeV}) \times \lvert\epsilon_{ZZ}^{\rm CP}\rvert^2$
ϵ_{Zf}	$\Gamma(h \to Zf\bar{f})$	$= (3.7 \times 10^{-2}\ \text{MeV}) \times N_c^f\ \lvert\epsilon_{Zf}\rvert^2$
κ_{WW}	$\Gamma(h \to W_L W_L)$	$= (0.84\ \text{MeV}) \times \lvert\kappa_{WW}\rvert^2$
ϵ_{WW}	$\Gamma(h \to W_T W_T)$	$= (0.16\ \text{MeV}) \times \lvert\epsilon_{WW}\rvert^2$
$\epsilon_{WW}^{\rm CP}$	$\Gamma^{\rm CPV}(h \to W_T W_T)$	$= (6.8 \times 10^{-2}\ \text{MeV}) \times \lvert\epsilon_{WW}^{\rm CP}\rvert^2$
ϵ_{Wf}	$\Gamma(h \to Wf\bar{f}')$	$= (0.14\ \text{MeV}) \times N_c^f\ \lvert\epsilon_{Wf}\rvert^2$
κ_g	$\sigma(pp \to h)_{gg-\rm fusion}$	$= \sigma(pp \to h)^{\rm SM}_{gg-\rm fusion}\kappa_g^2$
κ_t	$\sigma(pp \to t\bar{t}h)_{\rm Yukawa}$	$= \sigma(pp \to t\bar{t}h)^{\rm SM}_{\rm Yukawa}\kappa_t^2$
κ_H	$\Gamma_{\rm tot}(h)$	$= \Gamma^{\rm SM}_{\rm tot}(h)\kappa_H^2$

III.1.5 PO in Higgs electroweak production: generalities

The PO decomposition of $h \to 4f$ amplitude discussed above can naturally be generalized to describe electroweak Higgs-production processes, namely Higgs-production via vector-boson fusion (VBF) and Higgs-production in association with a massive SM gauge boson (VH).

The interest of such production processes is twofold. On the one hand, they are closely connected to the $h \to 4\ell, 2\ell 2\nu$ decay processes by crossing symmetry, and by the exchange of lepton currents into quark currents. As a result, some of the Higgs PO necessary to describe the $h \to 4\ell, 2\ell 2\nu$ decay kinematics appear also in the description of the VBF and VH cross sections (independently of the Higgs boson decay mode). This facts opens the possibility of combined analyses of production cross sections and differential decay distributions, with a significant reduction on the experimental error on the extraction of the PO. On the other hand, the production cross sections allow to explore different kinematical regimes compared to the decays. By construction, the momentum transfer appearing in the Higgs boson decay amplitudes is limited by the Higgs boson mass, while such limitation is not present in the production amplitudes. The higher energies probed in the production processes provide an increased sensitivity to new physics effects. This fact also allows to test the momentum expansion that is intrinsic in the PO decomposition, as well as in any effective field theory approach to physics beyond the SM.

Despite the similarities at the fundamental level, the phenomenological description of VBF and VH in terms of PO is significantly more challenging compared to that of Higgs boson decays. On the

one hand, QCD corrections plays a non-negligible role in the production processes. Although technically challenging, this fact does not represent a conceptual problem for the PO approach: the leading QCD corrections factorize in VBF and VH, similarly to the factorization of QED corrections in $h \to 4\ell$. This implies that NLO QCD corrections can be incorporated in general terms with suitable modifications of the existing Montecarlo tools. On the other hand, the relation between the kinematical variables at the basis of the PO decomposition (i.e. the momentum transfer of the partonic currents, q^2) and the kinematical variables accessible in pp collisions is not straightforward, especially in the VBF case. This problem finds a natural solution in the VBF case due to strong correlation between q^2 and the p_T of the VBF tagged jets, while in the VH case invariant mass of the VH system is correlated to the vector p_T.

III.1.5.a Amplitude decomposition

Neglecting the light fermion masses, the electroweak production processes VH and VBF or, more precisely, the electroweak partonic amplitudes $f_1 f_2 \to h + f_3 f_4$, can be completely described by the three-point correlation function of the Higgs boson and two (colour-less) fermion currents

$$\langle 0|\mathcal{T}\left\{J^\mu_f(x), J^\nu_{f'}(y), h(0)\right\}|0\rangle\ , \tag{III.1.45}$$

where all the states involved are on-shell. The same correlation function controls also the four-fermion Higgs boson decays discussed above. In the $h \to 4\ell, 2\ell 2\nu$ case both currents are leptonic and all fermions are in the final state. In case of VH associate production one of the currents describes the initial state quarks, while the other describes the decay products of the (nearly on-shell) vector boson. Finally, in VBF production the currents are not in the s-channel as in the previous cases, but in the t-channel. Strictly speaking, in VH and VBF the quark states are not on-shell; however, their off-shellness can be neglected compared to the electroweak scale characterizing the process (both within and beyond the SM).

As in the $h \to 4f$ case, we can expand the correlation function in Eq. (III.1.45) around the known physical poles due to the propagation of intermediate SM electroweak gauge bosons. The PO are then defined by the residues on the poles and by the non-resonant terms in this expansion. By construction, terms corresponding to a double pole structure are independent from the nature of the fermion current involved. As a result, the corresponding PO are universal and can be extracted from any of the above mention processes, both in production and in decays [652].

III.1.5.a.i Vector boson fusion Higgs boson production

Higgs boson production via vector boson fusion (VBF) receives contribution both from neutral- and charged-current channels. Also, depending on the specific partonic process, there could be two different ways to construct the two currents, and these two terms interfere with each other. For example, for $uu \to uuh$ one has the interference between two neutral-current processes, while in $ud \to udh$ the interference is between neutral and charged currents. In this case it is clear that one should sum the two amplitudes with the proper symmetrization, as done in the case of $h \to 4e$.

We now proceed describing how each of these amplitudes can be parameterized in terms of PO. Let us start with the neutral-current one. The amplitude for the on-shell process $q_i(p_1)q_j(p_2) \to q_i(p_3)q_j(p_4)h(k)$ can be parameterized by

$$\mathcal{A}_{n.c}(q_i(p_1)q_j(p_2) \to q_i(p_3)q_j(p_4)h(k)) = i\frac{2m_Z^2}{v}\bar{q}_i(p_3)\gamma_\mu q_i(p_1)\bar{q}_j(p_4)\gamma_\nu q_j(p_2)\mathcal{T}^{\mu\nu}_{n.c.}(q_1,q_2), \tag{III.1.46}$$

where $q_1 = p_1 - p_3$, $q_2 = p_2 - p_4$ and $\mathcal{T}^{\mu\nu}_{n.c.}(q_1,q_2)$ is the same tensor structure appearing in $h \to 4f$ decays. Indeed, proceeding as in Eq. (III.1.20), using Lorentz invariance we decompose this tensor

structure in term of three from factors:

$$\mathcal{T}^{\mu\nu}_{n.c.}(q_1,q_2) = \left[F_L^{q_iq_j}(q_1^2,q_2^2) g^{\mu\nu} + F_T^{q_iq_j}(q_1^2,q_2^2) \frac{q_1{\cdot}q_2\; g^{\mu\nu} - q_2{}^\mu q_1{}^\nu}{m_Z^2} \right.$$
$$\left. + F_{CP}^{q_iq_j}(q_1^2,q_2^2) \frac{\varepsilon^{\mu\nu\rho\sigma} q_{2\rho} q_{1\sigma}}{m_Z^2} \right] . \qquad \text{(III.1.47)}$$

Similarly, the charged-current contribution to the amplitude for the on-shell process $u_i(p_1)d_j(p_2) \to d_k(p_3)u_l(p_4)h(k)$ can be parameterized by

$$\mathcal{A}_{c.c}(u_i(p_1)d_j(p_2) \to d_k(p_3)u_l(p_4)h(k)) = i\frac{2m_W^2}{v} \bar{d}_k(p_3)\gamma_\mu u_i(p_1)\bar{u}_l(p_4)\gamma_\nu d_j(p_2)\mathcal{T}^{\mu\nu}_{c.c.}(q_1,q_2), \qquad \text{(III.1.48)}$$

where, again, $\mathcal{T}^{\mu\nu}_{c.c.}(q_1,q_2)$ is the same tensor structure appearing in the charged-current $h \to 4f$ decays:

$$\mathcal{T}^{\mu\nu}_{c.c.}(q_1,q_2) = \left[G_L^{ijkl}(q_1^2,q_2^2) g^{\mu\nu} + G_T^{ijkl}(q_1^2,q_2^2) \frac{q_1{\cdot}q_2\; g^{\mu\nu} - q_2{}^\mu q_1{}^\nu}{m_W^2} \right.$$
$$\left. + G_{CP}^{ijkl}(q_1^2,q_2^2) \frac{\varepsilon^{\mu\nu\rho\sigma} q_{2\rho} q_{1\sigma}}{m_W^2} \right] \qquad \text{(III.1.49)}$$

The amplitudes for the processes with initial anti-quarks can easily be obtained from the above ones.

The next step is to perform a momentum expansion of the form factors around the physical poles due to the propagation of SM electroweak gauge bosons (γ, Z and $W^\pm$), and to define the PO (i.e. the set $\{\kappa_i, \epsilon_i\}$) from the residues of such poles. We stop this expansion neglecting terms which can be generated only by local operators with dimension higher than six. A discussion about limitations and consistency checks of this procedure will be presented later on. The decomposition of the form factors closely follows the procedure already introduced for the decay amplitudes and will not be repeated here. We report explicitly only expression of the longitudinal form factors, where the contact terms not accessible in the leptonic decays appear:

$$F_L^{q_iq_j}(q_1^2,q_2^2) = \kappa_{ZZ} \frac{g_Z^{q_i} g_Z^{q_j}}{P_Z(q_1^2)P_Z(q_2^2)} + \frac{\epsilon_{Zq_i}}{m_Z^2}\frac{g_Z^{q_j}}{P_Z(q_2^2)} + \frac{\epsilon_{Zq_j}}{m_Z^2}\frac{g_Z^{q_i}}{P_Z(q_1^2)} + \Delta^{\rm SM}_{L,n.c.}(q_1^2,q_2^2) \,,$$
$$G_L^{ijkl}(q_1^2,q_2^2) = \kappa_{WW} \frac{g_W^{ik} g_W^{jl}}{P_W(q_1^2)P_W(q_2^2)} + \frac{\epsilon_{Wik}}{m_W^2}\frac{g_W^{jl}}{P_W(q_2^2)} + \frac{\epsilon_{Wjl}}{m_W^2}\frac{g_W^{ik}}{P_W(q_1^2)} + \Delta^{\rm SM}_{L,c.c}(q_1^2,q_2^2) \,. \qquad \text{(III.1.50)}$$

Here $P_V(q^2) = q^2 - m_V^2 + i m_V \Gamma_V$, while g_Z^f and g_W^{ik} are the PO characterizing the on-shell couplings of Z and W boson to a pair of fermions, see Eqs. (III.1.24) and (III.1.29). The functions $\Delta^{\rm SM}_{L,n.c.(c.c.)}(q_1^2,q_2^2)$ denote non-local contributions generated at the one-loop level (and encoding multi-particle cuts) that cannot be re-absorbed in the definition of κ_i and ϵ_i. At the level of precision we are working, taking into account also the high-luminosity phase of the LHC, these contributions can be safely fixed to their SM values.

As anticipated, the crossing symmetry between $h \to 4f$ and $2f \to h\,2f$ amplitudes ensures that the PO are the same in production and decay (if the same fermions species are involved). The amplitudes are explored in different kinematical regimes in the two type of processes (in particular the momentum-transfers, $q_{1,2}^2$, are space-like in VBF and time-like in $h \to 4f$). However, this does not affect the definition of the PO. This implies that the fermion-independent PO associated to a double pole structure, such as κ_{ZZ} and κ_{WW} in Eq. (III.1.50), are expected to be measured with higher accuracy in $h \to 4\ell$ and $h \to 2\ell 2\nu$ rather than in VBF. On the contrary, VBF is particularly useful to constrain the fermion-dependent contact terms ϵ_{Zq_i} and $\epsilon_{Wu_id_j}$, that appear only in the longitudinal form factors.

III.1.5.a.ii Associated vector boson plus Higgs boson production

The VH production process denote the production of a Higgs boson with a nearly on-shell massive vector boson (W or Z). For simplicity, in the following we will assume that the vector boson is on-shell and that the interference with the VBF amplitude can be neglected. However, we stress that the PO formalism clearly allow to describe both these effects (off-shell V and interference with VBF in case of $V \to \bar{q}q$ decay) simply applying the general decomposition of neutral- and charged-current amplitudes as outlined above.

Similarly to VBF, Lorentz invariance allows us to decompose the amplitudes for the on-shell processes $q_i(p_1)\bar{q}_i(p_2) \to h(p)Z(k)$ and $u_i(p_1)\bar{d}_j(p_2) \to h(p)W^+(k)$ in three possible tensor structures: a longitudinal one, a transverse one, and a CP-odd one,

$$\begin{aligned}\mathcal{A}(q_i(p_1)\bar{q}_i(p_2) \to h(p)Z(k)) &= i\frac{2m_Z^2}{v}\bar{q}_i(p_2)\gamma_\nu q_i(p_1)\epsilon_\mu^{Z*}(k)\times \\ &\times \left[F_L^{q_iZ}(q^2)g^{\mu\nu} + F_T^{q_iZ}(q^2)\frac{-(q\cdot k)g^{\mu\nu}+q^\mu k^\nu}{m_Z^2} + F_{CP}^{q_iZ}(q^2)\frac{\epsilon^{\mu\nu\alpha\beta}q_\alpha k_\beta}{m_Z^2}\right] ,\end{aligned} \tag{III.1.51}$$

$$\begin{aligned}\mathcal{A}(u_i(p_1)\bar{d}_j(p_2) \to h(p)W^+(k)) &= i\frac{2m_W^2}{v}\bar{d}_j(p_2)\gamma_\nu u_i(p_1)\epsilon_\mu^{W*}(k)\times \\ &\times \left[G_L^{q_{ij}W}(q^2)g^{\mu\nu} + G_T^{q_{ij}W}(q^2)\frac{-(q\cdot k)g^{\mu\nu}+q^\mu k^\nu}{m_W^2} + G_{CP}^{q_{ij}W}(q^2)\frac{\epsilon^{\mu\nu\alpha\beta}q_\alpha k_\beta}{m_W^2}\right] ,\end{aligned} \tag{III.1.52}$$

where $q = p_1 + p_2 = k + p$. In the limit where we neglect the off-shellness of the final-state V, the form factors depend only on q^2. Already from this decomposition of the amplitude it is clear the importance of providing measurements of the differential cross-section as a function of q^2, as well as differential measurements in terms of the angular variables that allow to disentangle the different tensor structures.

Performing the momentum expansion of the form factors around the physical poles, and defining the PO as in Higgs boson decays and VBF, we find

$$\begin{aligned} F_L^{q_iZ}(q^2) &= \kappa_{ZZ}\tfrac{g_{Zq_i}}{P_Z(q^2)} + \tfrac{\epsilon_{Zq_i}}{m_Z^2} \qquad G_L^{q_{ij}W}(q^2) = \kappa_{WW}\tfrac{(g_W^{u_id_j})^*}{P_W(q^2)} + \tfrac{\epsilon^*_{Wu_id_j}}{m_W^2} \\ F_T^{q_iZ}(q^2) &= \epsilon_{ZZ}\tfrac{g_{Zq_i}}{P_Z(q^2)} + \epsilon_{Z\gamma}\tfrac{eQ_q}{q^2} \; G_T^{q_{ij}W}(q^2) = \epsilon_{WW}\tfrac{(g_W^{u_id_j})^*}{P_W(q^2)} \\ F_{CP}^{q_iZ}(q^2) &= \epsilon_{ZZ}^{\rm CP}\tfrac{g_{Zq_i}}{P_Z(q^2)} - \epsilon_{Z\gamma}^{\rm CP}\tfrac{eQ_q}{q^2} \; G_{CP}^{q_{ij}W}(q^2) = \epsilon_{WW}^{\rm CP}\tfrac{(g_W^{u_id_j})^*}{P_W(q^2)} \end{aligned} \tag{III.1.53}$$

where we have omitted the indication of the (tiny) non-local terms, fixed to their corresponding SM values. As in the VBF case, only the longitudinal form factors F_L and G_L contain PO not accessible in the leptonic decays, namely the quark contact terms ϵ_{Zq_i} and $\epsilon_{Wu_id_j}$.

III.1.6 PO in Higgs electroweak production: phenomenology

III.1.6.a Vector Boson Fusion

At the parton level (i.e. in the $qq \to hqq$ hard scattering) the ideal observable relevant to extract the momentum dependence of the factor factors would be the double differential cross section $d^2\sigma/dq_1^2dq_2^2$, where $q_1 = p_1 - p_3$ and $q_2 = p_2 - p_4$ are the momenta of the two fermion currents entering the process (here p_1, p_2 (p_3, p_4) are the momenta of the initial (final) state quarks). The q_i^2 are also the key variables to test and control the momentum expansion at the basis of the PO decomposition.

A first nontrivial task is to choose the proper pairing of the incoming and outgoing quarks, given we are experimentally blind to their flavour. For partonic processes receiving two interfering contributions when the final-state quarks are exchanged, such as $uu \to huu$ or $ud \to hud$, the definition of $q_{1,2}$ is even less transparent since a univocal pairing of the momenta can not be assigned, in general, even if one knew the flavour of all partons. This problem can be simply overcome at a practical level

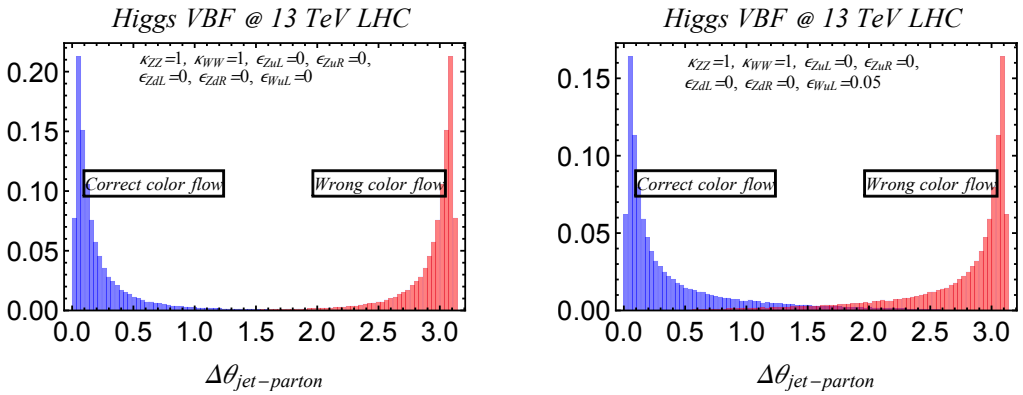

Figure 210: Leading order parton level simulation of the Higgs VBF production at 13 TeV pp c.m. energy (from Ref. [652]). Show in blue is the distribution in the opening angle of the colour connected incoming and outgoing quarks $\measuredangle(\vec{p}_3, \vec{p}_1)$, while in red is the distribution for the opposite pairing, $\measuredangle(\vec{p}_3, \vec{p}_2)$. The left plot is for the SM, while the plot on the right is for a specific NP benchmark.

by making use of the VBF kinematics, in particular the fact that the two jets are always very forward. This implies one can always pair the momenta of the jet going, for example, on the $+z$ direction with the initial parton going in the same direction, and vice versa. The same argument can be used to argue that the interference between different amplitudes (e.g. neutral current and charged current) is negligible in VBF. In order to check this, we have performed a leading order parton level simulation of the VBF Higgs boson production ($pp \to hjj$) using MADGRAPH [54] (version 2.2.3) at 13 TeV c.m. energy. We have imposed the basic set of cuts,

$$p_{\mathrm{T,j_{1,2}}} > 30 \text{ GeV}, \quad |\eta_{\mathrm{j_{1,2}}}| < 4.5, \quad \text{and} \quad m_{\mathrm{j_1 j_2}} > 500 \text{ GeV}. \tag{III.1.54}$$

In Figure 210, we show the distribution in the opening angle of the incoming and outgoing quark momenta for the two different pairings. The left plot is for the SM, while the right plot is for a specific NP benchmark point. Shown in blue is the pairing based on the leading colour connection using the colour flow variable while in red is the opposite pairing. The plot shows that the momenta of the colour connected quarks tend to form a small opening angle and the overlap between the two curves, i.e. where the interference effects might be sizeable, is negligible. This implies that in the experimental analysis the pairing should be done based on this variable. Importantly, the same conclusions can be drawn in the presence of new physics contributions to the contact terms.

There is a potential caveat to the above argument: the colour flow approximation ignores the interference terms that are higher order in $1/N_C$, where N_C is number of colours. Let us consider a process with two interfering amplitudes with the final state quarks exchanged, for example in $uu \to uuh$. The differential cross section receives three contributions proportional to

$$|F_L^{ff'}(t_{13}, t_{24})|^2, \quad |F_L^{ff'}(t_{13}, t_{24}) F_L^{ff'}(t_{14}, t_{23})| \,, \quad \text{and} \quad |F_L^{ff'}(t_{14}, t_{23})|^2 \,,$$

where $t_{ij} = (p_i - p_j)^2 = -2E_iE_j(1 - \cos\theta_{ij})$. For the validity of the momentum expansion it is important that the momentum transfers (t_{ij}) remain smaller than the hypothesized scale of new physics. On the other hand, imposing the VBF cuts, the interference terms turns out to depend on one small and one large momentum transfer. However, thanks to the pole structure of the form factors, these interference effects turns out to give a very small contribution. Therefore, we can safely state that the momentum transfers marked with the leading colour flow are reliable control variables of the momentum expansion validity.

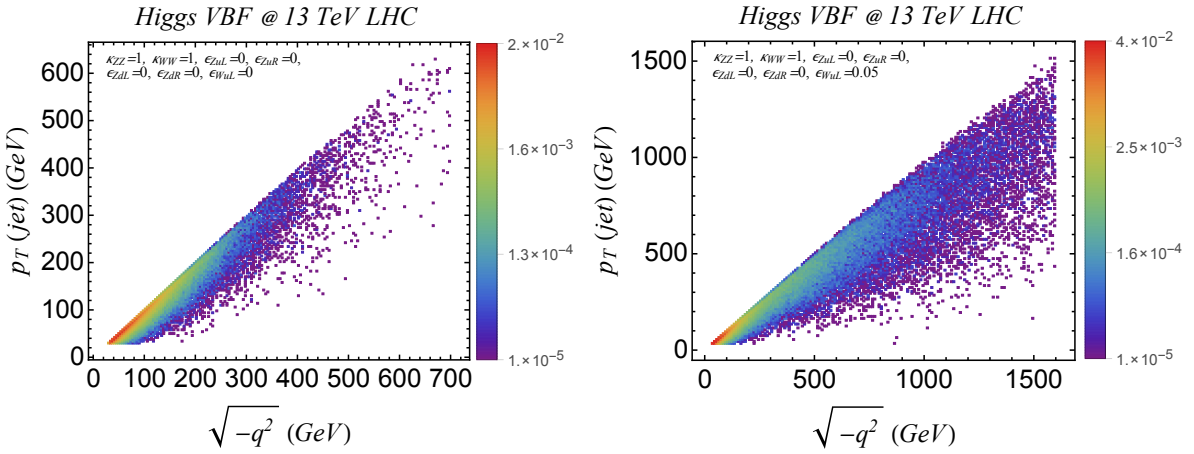

Figure 211: Leading order parton level simulation of the Higgs VBF production at 13 TeV pp c.m. energy [652]. Shown here is the density histogram in two variables; the outgoing quark p_T and the momentum transfer $\sqrt{-q^2}$ with the initial "colour-connected" quark. The left plot is for the SM, while the plot on the right is for a specific NP benchmark.

In some realistic experimental analyses, after reconstructing the momenta of the two VBF tagged jets and the Higgs boson, one can compute the relevant momentum transfers q_1 and q_2, adopting the pairing based on the opening angle. However, for some interesting Higgs boson decays modes, such as $h \to 2\ell 2\nu$, it is not possible to reconstruct the Higgs boson momentum. In this case, a good approximation of the momentum transfer is the jet p_T. This can be understood by explicitly computing the momentum transfer $q^2_{1,2}$ in the limit $|p_T| \ll E_{jet}$ and for a Higgs produced close to threshold. Let us consider the partonic momenta in c.o.m. frame for the process: $p_1 = (E, \vec{0}, E)$, $p_2 = (E, \vec{0}, -E)$, $p_3 = (E'_1, \vec{p}_{T1}, \sqrt{E'^2_1 - p^2_{T1}})$ and $p_4 = (E'_2, \vec{p}_{T2}, \sqrt{E'^2_2 - p^2_{T2}})$. Conservation of energy for the whole process dictates $2E = E'_1 + E'_2 + E_h$, where E^2_h is the Higgs energy, usually of order m_h if the Higgs is not strongly boosted. In this case $E - E'_i = \Delta E_i \ll E$ since the process is symmetric for $1 \leftrightarrow 2$. For each leg, energy and momentum conservation (along the z axis) give

$$\begin{cases} q^z_i = E - \sqrt{E'^2_i - p^2_{Ti}} \\ q^0_i = E - E'_i \end{cases} \quad \to \quad \begin{cases} q^0_i - q^z_i = \sqrt{E'^2_i - p^2_{Ti}} - E'_i \approx -\frac{p^2_{Ti}}{2E'_i} \\ q^0_i + q^z_i \approx 2\Delta E_i + \frac{p^2_{Ti}}{2E'_i} \end{cases} . \tag{III.1.55}$$

Putting together these two relations one gets

$$q^2_i = (q^0_i)^2 - p^2_{Ti} - (q^z_i)^2 = -p^2_{Ti} + (q^0_i - q^z_i)(q^0_i + q^z_i) \approx -p^2_{Ti} - \frac{p^2_{Ti}\Delta E_i}{2E'_i} + \mathcal{O}(p^4_{Ti}/E'^2) . \tag{III.1.56}$$

We can thus conclude that, for a Higgs produced near threshold ($\Delta E_i << E'$), $q^2 \approx -p^2_T$.

To illustrate the above conclusion, in Figure 211 we show a density histogram in two variables: the outgoing quark p_T and the momentum transfer $\sqrt{-q^2}$ obtained from the correct colour flow pairing (the left and the right plots are for the SM and for a specific NP benchmark, respectively). The plots indicate the strong correlation of the jet p_T with the momentum transfer $\sqrt{-q^2}$ associated with the correct colour pairing. We stress that this conclusion holds both within and beyond the SM.

Given the strong $q^2 \leftrightarrow p^2_T$ correlation, we strongly encourage the experimental collaborations to report the unfolded measurement of the double differential distributions in the two VBF tagged jet p_T's: $\tilde{F}(p_{Tj_1}, p_{Tj_2})$. This measurable distribution is closely related to the form factor entering the amplitude decomposition, $F_L(q^2_1, q^2_2)$, and encode (in a model-independent way) the dynamical information about

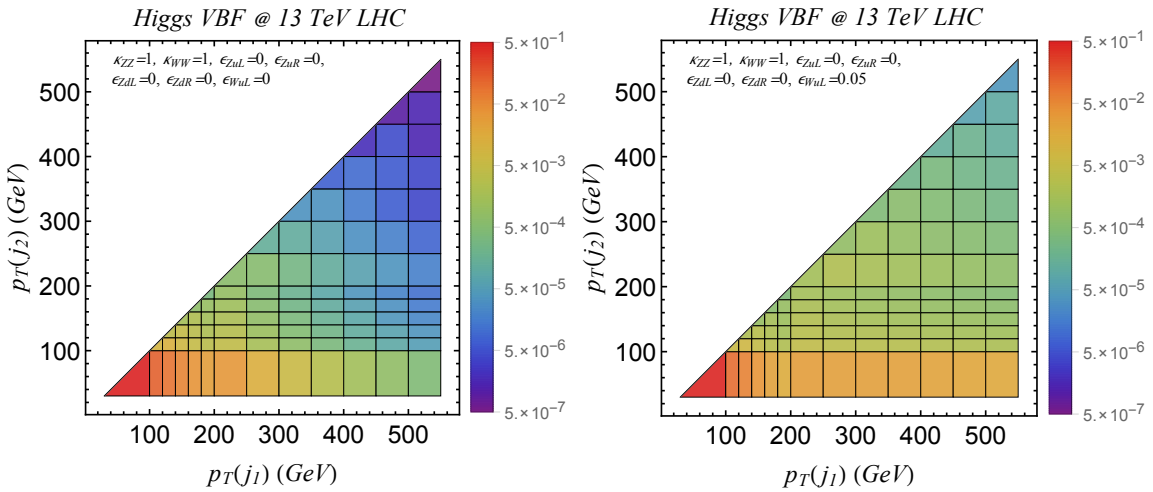

Figure 212: Double differential distribution in the two VBF-tagged jet p_T for VBF Higgs boson production at 13 TeV LHC [652]. The distribution is normalized such that the total sum of events in all bins is 1. (Left) Prediction in the SM. (Right) Prediction for NP in $\epsilon_{Wu_L} = 0.05$.

the high-energy behaviour of the process. Moreover, the extraction of the PO in VBF must be done preserving the validity of the momentum expansion: the latter can be checked and enforced setting appropriate upper cuts on the p_T distribution. As an example, in Figure 212, we show the prediction in the SM (left plot) and in the specific NP benchmark (right plot) of the normalized p_T-ordered double differential distribution.

III.1.6.b Associated vector boson plus Higgs boson production

Higgs boson production in association with a W or Z boson are respectively the third and fourth Higgs boson production processes in the SM, by total cross section. Combined with VBF studies, they offer other important handles to disentangle the various Higgs PO. Due to the lower cross section, this process is mainly studied in the highest-rate Higgs boson decay channels, such as $h \to b\bar{b}$ and WW^*. The drawback of these channels is the background, which is overwhelming in the $b\bar{b}$ case and of the same order as the signal in the WW^* channels. Nonetheless, kinematical cuts, such as the Higgs boson p_T in the $b\bar{b}$ case, and the use of multivariate analysis allow the experiments to precisely extract the the signal rates from these measurements.

An important improvement for future studies of these channels with the much higher luminosity which will be available, is to study differential distributions in some specific kinematical variables. In Section III.1.5.a.ii we showed that the invariant mass of the Vh system is the most important observable in this process, since the form factors directly depend on it. In those channels where the Vh invariant mass can not be reconstructed due to the presence of neutrinos, another observable which shows some correlation with the q^2 is the p_T of the vector boson, or equivalently of the Higgs, as can be seen in the Figure 213. Even though this correlation is not as good as the one between the jet p_T and the momentum transfer in the VBF channel, a measurement of the vector boson (or Higgs) p_T spectrum, i.e. of some form factor $\tilde{F}^{Vh}(p_{TV})$ would still offer important information on the underlying structure of the form factors appearing in Eq. (III.1.53), $F_L^{q_i Z}(q^2)$ or $G_L^{q_{ij} W}(q^2)$. The invariant mass of the Vh system is given by $m_{Vh}^2 = q^2 = (p_V + p_h)^2 = m_V^2 + m_h^2 + 2p_V \cdot p_h$. Going in the centre of mass frame, we have $p_V = (E_V, \vec{p}_T, p_z)$ and $p_h = (E_h, -\vec{p}_T, -p_z)$, where $E_i = \sqrt{m_i^2 + p_T^2 + p_z^2}$ $(i = V, h)$. Computing

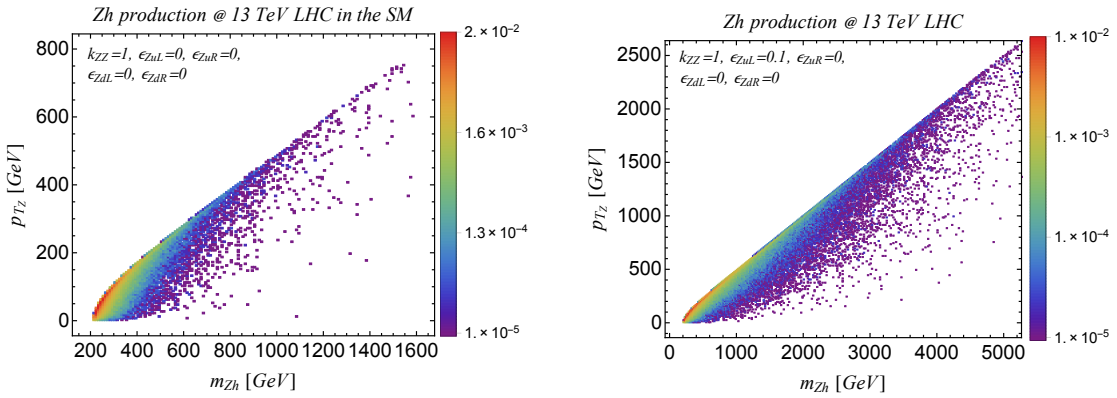

Figure 213: The correlation between the Zh invariant mass and the p_T of the Z boson in Zh associate production at the 13TeV LHC in the SM (left plot) and for a BSM point $\kappa_{ZZ} = 1$, $\epsilon_{Zu_L} = 0.1$ (right plot) [652]. A very similar correlation is present in the Wh channel.

m^2_{Vh} explicitly:

$$m^2_{Vh} = m^2_V + m^2_h + 2p^2_T + 2p^2_z + 2\sqrt{m^2_V + p^2_T + p^2_z}\sqrt{m^2_h + p^2_T + p^2_z} \overset{|p_T|\to\infty}{\longrightarrow} 4p^2_T \,. \qquad \text{(III.1.57)}$$

For $p_z = 0$ this equation gives the minimum q^2 for a given p_T, which can be seen as the left edge of the distributions in the Figure 213. This is already a valuable information, for example the boosted Higgs regime used in some $b\bar{b}$ analysis implies a lower cut on the q^2: a bin with $p_T > 300$ GeV implies $\sqrt{q^2} \gtrsim 630$ GeV, which could be a problem for the validity of the momentum expansion.

In the Wh process, if the W decays leptonically its p_T can not be reconstructed independently of the Higgs boson decay channel. One could think that the p_T of the charged lepton from the W decay would be correlated with the Wh invariant mass, but we checked that there is no significant correlation between the two observables.

III.1.6.c Validity of the momentum expansion

In order to control the momentum expansion at the basis of the PO composition, it is necessary to set an upper cut on appropriate kinematical variables. These are the p_T of the leading VBF-tagged jet in VBF, and the Vh invariant mass (or the p_T of the massive gauge boson) in VH.

The momentum expansion of the form factors in Eq. (III.1.50) makes sense only if the higher order terms in $q^2_{1,2}$ are suppressed. Comparing the first two terms in this expansion, this leads to the consistency condition,

$$\epsilon_{X_f}\, q^2_{\rm max} \lesssim m^2_Z\, g^f_X \,, \qquad \text{(III.1.58)}$$

where $q^2_{\rm max}$ is the largest momentum transfer in the process. A priori we don't know which is the size of the ϵ_{X_f} or, equivalently, the effective scale of new physics. However, a posteriori we can verify by means of Eq. (III.1.58) if we are allowed to truncate the momentum expansion to the first non-trivial terms. In VBF, setting a cut-off on p_T we implicitly define a value of $q_{\rm max}$. Extracting the ϵ_{X_f} for $p^j_T < (p^j_T)^{\rm max} \approx q_{\rm max}$ we can check if Eq. (III.1.58) is satisfied. Ideally, the experimental collaborations should perform the extraction of the ϵ_{X_f} for different values of $(p^j_T)^{\rm max}$ optimizing the range according to the results obtained. The issue is completely analog in VH, where the $q^2_{\rm max}$ is controlled by m^2_{Vh}.

It must be stressed that if data indicate non-vanishing values for the ϵ_{X_f}, and the condition (III.1.58) is falsified, this does not necessarily imply a break down of the momentum expansion.[III.6] However, in

[III.6] The break-down of the momentum expansion occurs only when we approach, with a given kinematical variable, a new

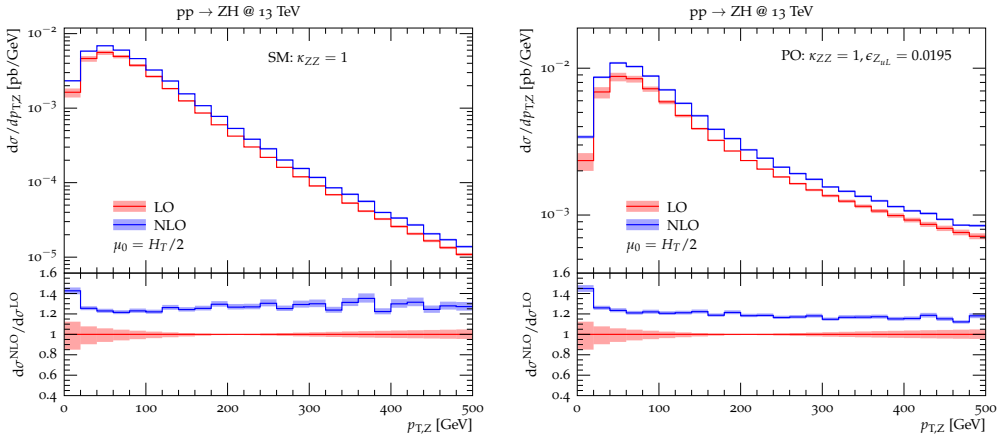

Figure 214: Differential $p_{\mathrm{T},Z}$ distributions in the process $pp \to ZH$ in the SM (left) and including an example of NP within the PO framework with $\kappa_{ZZ} = 1, \epsilon_{ZuL} = 0.0195$ (right). Shown are LO (red) and NLO (blue) predictions and corresponding (7-pt) scale variations employing a central scale $\mu_0 = H_{\mathrm{T}}/2$.

such case it is important to check with data the size of additional terms in this expansion. From this point of view, it is very important to complement the PO approach with the differential measurements of the cross-section as function of p_T^j that could be achieved via the so-called *template-cross-section* method. In such distributions a possible break-down of the momentum expansion at the basis of the PO decomposition could indeed be seen (or excluded) directly by data.

A further check to assess the validity of the momentum expansion is obtained comparing the fit performed including the full quadratic dependence of the distributions, as function on the PO, with the fit in which such distributions are linearized in $\delta\kappa_X \equiv \kappa_X - \kappa_X^{\mathrm{SM}}$ and ϵ_X. The idea behind this procedure is that the quadratic corrections to physical observable in $\delta\kappa_X$ and ϵ_X are formally of the same order as the interference of the first neglected term in Eq. (III.1.50) with the leading SM contribution. If the two fits yields significantly different results, the difference can be used as an estimate of the uncertainty due to the neglected higher-order terms in the momentum expansion. However, as discussed in detail in Ref. [652], such procedure naturally leads to a large overestimate of the uncertainty. This is because in the linearized fit only a few linear combinations of the PO enter the observables, and thus the number of independent constraints derived from data is effectively reduced. On general grounds, the fit obtained with the full quadratic dependence should be considered as the most reliable result, provided that the obtained PO satisfy the consistency condition in Eq. (III.1.58).

III.1.6.d Illustration of NLO QCD effects

Higgs boson production via Higgs-strahlung and VBF are very stable with respect to NLO QCD corrections. At the inclusive level NLO scale uncertainties are as small as a few per cent [7–9, 265, 276] and further reduced at NNLO [263, 264, 274, 282, 283, 291]. Given an appropriate scale choice similar conclusion also hold at the differential level with residual NLO scale uncertainties at the 10% level.

As already discussed above, similar to the factorization in QED, the dominant QCD corrections are universal and factorize from any new physics effects in EW Higgs boson production. Consequently, with respect to possible small deformations from the SM, parameterized via effective form factor contributions in the PO framework, we expect a very limited sensitivity to QCD effects assuming a similar stabilization of higher order corrections as observed for the SM. In order to verify this assumption (and

pole in the amplitude due to the exchange of a NP particle. On the other hand, the dominance of the contact terms leading to a violation of the condition (III.1.58) could also occur far from the NP poles in case of strongly interacting theories (see e.g. Ref. [611]).

to make a corresponding tool available), the PO framework has been implemented in the `Sherpa + OpenLoops` [229, 247, 951, 952] framework, where the implementation within `Sherpa` is based on a model independent `UFO` interface [953]. As in illustration, in Figure 214 we compare the NLO QCD corrections to the p_T distribution of the Z-boson in $pp \to ZH$ between the SM and a NP point with $\kappa_{ZZ} = 1, \epsilon_{ZuL} = 0.0195$. Despite the very different shape of the two distributions, higher order QCD corrections are very similar and do only show a very mild shape dependence. Detailed studies for VBF and VH including parton shower matching are under way.

After the inclusion of NLO QCD corrections the dominant theoretical uncertainties to Higgs observables in VBF and VH are of EW type and dominated by large EW Sudakov logarithms at large energies [254, 257, 258]. The dominant NLO EW effects are factorizable corrections which can be reabsorbed into a future redefinition of the PO.

III.1.7 Parameter counting and symmetry limits

We are now ready to identify the number of independent pseudo-observables necessary to describe various sets of Higgs boson decay amplitudes and productions cross sections. We list them below separating four set of observables:

i) the Yukawa decay modes ($h \to f\bar{f}$);
ii) the EW decays ($h \to \gamma\gamma, f\bar{f}\gamma, 4f$);
iii) the EW production production cross sections (VBF and VH);
iv) the non-EW production cross sections (gluon fusion and $t\bar{t}H$) and the total Higgs boson decay width.

We list the PO needed for a completely general analysis, and the reduction of the number of independent PO obtained under well-defined symmetry hypotheses, such as CP invariance or flavour universality. The latter can be more efficiently tested considering specific sub-sets of observables.

III.1.7.a Yukawa modes

As discussed in Section III.1.2.a the $h \to f\bar{f}$ amplitudes are characterized by two independent PO (κ_f and $\delta_f^{\rm CP}$) for each fermion species. Considering only the decay channels relevant for LHC, the full set of 8 parameters is:

$$\kappa_b, \kappa_c, \kappa_\tau, \kappa_\mu, \delta_b^{\rm CP}, \delta_c^{\rm CP}, \delta_\tau^{\rm CP}, \delta_\mu^{\rm CP} \ . \tag{III.1.59}$$

Assuming CP conservation (that implies $\delta_f^{\rm CP} = 0$ for each f) the number of PO is reduced to 4. This is also the number of independent PO effectively measurable if the spin polarization of the final-state fermions is not accessible. The corresponding *physical* PO are the $\Gamma(h \to f\bar{f})$ partial widths (see Table 110).

III.1.7.b Higgs EW decays

The category of EW decays includes a long list of channels; however, not all of them are accessible at the LHC. The clean neutral current processes $h \to e^+e^-\mu^+\mu^-$, $h \to e^+e^-e^+e^-$ and $h \to \mu^+\mu^-\mu^+\mu^-$, together with the photon channels $h \to \gamma\gamma$ and $h \to \ell^+\ell^-\gamma$, can be described in terms of 11 real parameters:

$$\kappa_{ZZ}, \kappa_{Z\gamma}, \kappa_{\gamma\gamma}, \epsilon_{ZZ}, \epsilon_{ZZ}^{CP}, \delta_{Z\gamma}^{CP}, \delta_{\gamma\gamma}^{CP}, \epsilon_{Ze_L}, \epsilon_{Ze_R}, \epsilon_{Z\mu_L}, \epsilon_{Z\mu_R} \tag{III.1.60}$$

(of which only the subset $\{\kappa_{\gamma\gamma}, \kappa_{Z\gamma}, \delta_{\gamma\gamma}^{CP}, \delta_{Z\gamma}^{CP}\}$ is necessary to describe $h \to \gamma\gamma$ and $h \to \ell^+\ell^-\gamma$). The charged-current process $h \to \bar{\nu}_e e \bar{\mu} \nu_\mu$ needs 7 further independent real parameters to be completely specified:

$$\kappa_{WW}, \epsilon_{WW}, \epsilon_{WW}^{CP} \ (\text{real}) \quad + \quad \epsilon_{We_L}, \epsilon_{W\mu_L} \ (\text{complex}) \ . \tag{III.1.61}$$

Finally, the mixed processes $h \to e^+e^-\nu\bar{\nu}$ and $h \to \mu^+\mu^-\nu\bar{\nu}$ can be described by a subset of the coefficients already introduced plus 2 further real contact interactions coefficients:

$$\epsilon_{Z\nu_e}\,, \epsilon_{Z\nu_\mu}\,. \tag{III.1.62}$$

This brings the total number of (real) parameters to 20 for all the (EW) decays involving muons, electrons, and photons.

The extension to discuss $h \to 4f$ or $h \to f\bar{f}\gamma$ decays with one or two pairs of tau leptons is straightforward: it requires the introduction of the corresponding set of contact terms ($\epsilon_{Z\tau_L}, \epsilon_{Z\tau_R}$, $\epsilon_{W\tau_L}, \epsilon_{Z\nu_\tau}$). Similarly, quark contact terms need to be introduced if one or two lepton pairs are replaced by a quark pair.

A first simple restriction in the number of parameters is obtained by assuming flavour universality. This hypothesis imply that the contact terms are the same for all flavours. In particular, for muon and electron modes, this implies

$$\epsilon_{Ze_L} = \epsilon_{Z\mu_L}\,, \qquad \epsilon_{Ze_R} = \epsilon_{Z\mu_R}\,, \qquad \epsilon_{Z\nu_e} = \epsilon_{Z\nu_\mu}\,, \qquad \epsilon_{We_L} = \epsilon_{W\mu_L}\,. \tag{III.1.63}$$

Technically, this correspond to assume an underlying $U(N_\ell)^2$ flavour symmetry, for the N_ℓ generations of leptons considered (namely the maximal flavour symmetry compatible with the SM gauge group).

Since the $\epsilon_{W\ell_L}$ parameters are complex in general, the relations (III.1.63) allow to reduce the total number of parameters to 15. This assumption can be tested directly from data by comparing the extraction of the contact terms from $h \to 2e2\mu$, $h \to 4e$ and $h \to 4\mu$ modes.

The assumption that CP is a good approximate symmetry of the BSM sector and that the Higgs is a CP-even state, allows us to set to zero six independent (real) coefficients:

$$\epsilon_{ZZ}^{CP} = \delta_{Z\gamma}^{CP} = \delta_{\gamma\gamma}^{CP} = \epsilon_{WW}^{CP} = \mathrm{Im}\epsilon_{We_L} = \mathrm{Im}\epsilon_{W\mu_L} = 0\,. \tag{III.1.64}$$

Assuming, at the same time, flavour universality, the number of free real parameters reduces to 10.

The various cases are prorated in the upper panel of Table 111: in the second column we list the 10 PO needed assuming both CP invariance and flavour universality, while in the third and fourth column we list the additional PO needed if these hypotheses are relaxed (for the clean modes involving only muons and electrons). The corresponding *physical* PO are the partial widths reported in Table 110.

III.1.7.c EW production processes

The fermion-independent PO present in Higgs boson decays appear also in EW production processes. The additional PO appearing only in production (assuming Higgs boson decays to quark are not detected) are the contact terms for the light quarks. In a four-flavour scheme, in absence of any symmetry assumption, the number of independent parameters for the neutral currents contact terms is 16 ($\epsilon_{Zq^{ij}}$, where $q = u_L, u_R, d_L, d_R$, and $i, j = 1, 2$): 8 real parameters for flavour diagonal terms and 4 complex flavour-violating parameters. Similarly, there are 16 independent parameters in charged currents, namely the 8 complex terms $\epsilon_{Wu_L^i d_L^j}$ and $\epsilon_{Wu_R^i d_R^j}$. However, we can safely reduce the number of independent PO under neglecting the terms that violates the $U(1)_f$ flavour symmetry acting on each of the light fermion species, u_R, d_R, s_R, c_R, $q_L^{(d)}$, and $q_L^{(s)}$, where $q_L^{(d,s)}$ denotes the two quark doublets in the basis where down quarks are diagonal. This symmetry is an exact symmetry of the SM in the limit where we neglect light quark masses. Enforcing it at the PO level is equivalent to neglecting terms that do not interfere with SM amplitudes in the limit of vanishing light quark masses. Under this (rather conservative) assumption, the number of independent neutral currents contact terms reduces to 8 real parameters,

$$\epsilon_{Zu_R},\ \epsilon_{Zc_R},\ \epsilon_{Zd_R},\ \epsilon_{Zs_R},\ \epsilon_{Zd_L},\ \epsilon_{Zs_L},\ \ \epsilon_{Zu_L},\ \epsilon_{Zc_L}, \tag{III.1.65}$$

and only 2 complex parameters appear in the charged-current case:

$$\epsilon_{Wu_L^i d_L^j} \equiv V_{ij}\epsilon_{Wu_L^j}\,, \qquad \epsilon_{Wu_R^i d_R^j} = 0\,. \tag{III.1.66}$$

Similarly to the decays, a further interesting reduction of the number of parameters is obtained assuming flavour universality or, more precisely, under the assumption of an $U(2)^3$ symmetry acting on the first two generations of quarks. The latter is the the maximal flavour symmetry for the light quarks compatible with the SM gauge group. In this case the independent parameters in this case reduces to six:

$$\epsilon_{Zu_L},\ \epsilon_{Zu_R},\ \epsilon_{Zd_L},\ \epsilon_{Zd_R},\ \epsilon_{Wu_L}\,, \tag{III.1.67}$$

where ϵ_{Wu_L} is complex, or five if we further neglect CP-violating contributions (in such case ϵ_{Wu_L} is real). This case is listed in the second column of Table 111 (middle panel), where the terms between brackets denote the PO appearing also in decays.

Custodial symmetry and the combination of EW production and decay modes

Assuming flavour universality and CP conservation, the number of independent PO necessary to describe all EW decays and production cross sections is 15. These are the terms listed in the second column of the first two panels of Table 111.

A further reduction of the number of independent PO is obtained under the hypothesis of custodial symmetry, that relates charged and neutral current modes. The complete list of custodial symmetry relations can be found in Refs. [651, 652]. Here we only mention the one between κ_{WW} and κ_{ZZ}, noting that the presence of contact terms modify it with respect to the one known in the context of the kappa-framework:

$$\kappa_{WW} - \kappa_{ZZ} = -\frac{2}{g}\left(\sqrt{2}\epsilon_{W\ell_L} + 2\frac{m_W}{m_Z}\epsilon_{Z\ell_L}\right)\,, \tag{III.1.68}$$

where $\ell = e, \mu$. After imposing flavour and CP conservation, custodial symmetry allow a reduction of the number of independent PO from 15 down to 11, as shown in the lower panel of Table 111.

III.1.7.d Additional PO

The remaining PO needed for a complete description of Higgs physics at the LHC are those related to the non-EW production processes (gluon fusion and $t\bar{t}H$) and to the total Higgs boson decay width (i.e. NP effects in invisible or undetected decay modes).

A detailed formalism, similar to the one developed for EW production and decay process, has not been developed yet for gluon fusion and $t\bar{t}H$ production process. However, it should be stressed that the latter are on a very different footing compared to EW processes since they involve a significantly smaller number of observables. Moreover, a smaller degrees of modellization is required in order to analyse the corresponding data in generic NP frameworks. As a result, the combination of PO for the total cross sections, and template-cross-section analyses of the kinematical distributions, provide an efficient way to report data in a sufficiently general and unbiased way.

More precisely, for the time being we suggest to introduce the following two PO

$$\kappa_g^2 = \left.\frac{\sigma(pp\to h)}{\sigma^{\rm SM}(pp\to h)}\right|_{gg-\rm fusion}\,, \qquad \kappa_t^2 = \left.\frac{\sigma(pp\to t\bar{t}h)}{\sigma^{\rm SM}(pp\to t\bar{t}h)}\right|_{\rm Yukawa}\,, \tag{III.1.69}$$

in close analogy to what it is presently done within the κ formalism. As far as the gluon fusion is concerned, it is well known that the Higgs boson p_T distribution carries additional dynamical information about the underlying process. However, such distribution can be efficiently reported via the template-cross-section method. Moreover, the steep fall of the p_T spectrum (that is a general consequence of the

infrared structure of QCD) implies that the determination of κ_{gg} is practically unaffected by possible NP effects in this distribution.

Finally, as far as the Higgs boson width is concerned, we need to introduce a single effective *physical* PO to account for all the invisible or undetected Higgs boson decay modes. This additional partial width must be added to the various visible partial widths in order to determine the total Higgs boson width. Alternatively, it is possible to define an effective coupling PO as the ratio

$$\kappa_H^2 = \frac{\Gamma_{\rm tot}(h)}{\Gamma_{\rm tot}^{\rm SM}(h)} \,. \tag{III.1.70}$$

III.1.8 PO meet SMEFT

One of the main goals of the LHC is to perform high-precision studies of possible deviations from the SM. Ideally, this would require the following four steps: i) for each process write down some (QFT-compatible) amplitude allowing for SM-deviations, both for the main signal analysed (e.g. a given Higgs cross-section, close to the resonance) as well as for the background (non-resonant signal); ii) compute fiducial observables; iii) fit the signal (SM+NP) via an appropriate set of conventionally-defined PO, without subtracting the SM background; iv) using the PO thus obtained to derive information on the Wilson coefficients of an appropriate Lagrangian allowing for deviations from the SM.

In the previous sections we have discussed a convenient choice for the definition of the PO relevant to resonant Higgs physics (steps i and iii). In this section we outline how to address the last step in the case of the so-called SM Effective Field Theory (SMEFT), i.e. how to extract the Wilson coefficients of the SMEFT from the measured PO.

Before starting, it is worth stressing that PO are *not* Wilson coefficients, despite one can derive a linear relation between the two sets of parameters when working at the lowest-order (LO) in a given Lagrangian framework. The distinction between PO and Wilson coefficients is quite clear from their different "status" in QFT: the PO provide a general parameterization a given set of on-shell scattering amplitudes and are not Lagrangian parameters. Once a PO is observed to deviate from its SM value we cannot, without further theoretical assumptions, predict deviations in other amplitudes. The latter can be obtained only using a given Lagrangian and after extracting from data (or better from PO) the corresponding set of Wilson coefficients. Conversely, Wilson coefficients are scale and scheme dependent parameters that require specific theoretical prescriptions to be extracted from physical observables. This is why the PO can be measured including only the SM THU[III.7], while the extraction of SMEFT Wilson coefficients require also an estimate of the corresponding SMEFT THU[III.8].

There is a line of thought where the Wilson coefficients in any LO EFT approach to physics beyond the SM are not actual Wilson coefficients, but parameters encoding deformation possibilities. According to this line of though, PO and and Wilson coefficients are somehow the same object. But this way of proceeding has a limited applicability, especially if a deviations from the SM is found. Proceeding along this line one could write an ad-hoc effective Lagrangian, do some calculations at LO (deviation parameters at tree-level), interpret the data, and limit the considerations to answer the question "are there deviations from the SM?". If we want to go a step further, viz. answering the question "What do the deviations from the SM mean?" then it is important to separate the role of PO and Wilson coefficients. Indeed after extracting the PO, two possibilities appear: i) *top-down*, namely employ a specific UV model, compute the PO and try to figure out if it matches or not with the observed deviation; in such case there will be an uncertainty in projecting down the UV model to the parameters and in the choice of the input parameter set (IPS); ii) *bottom-up*, namely do a SMEFT analysis to extract from the PO conclusions

[III.7] By THU we mean theoretical uncertainty which has two components, parametric (PU) and missing higher order uncertainties (MHOU)

[III.8] Although SMEFT converges to SM in the limit of zero Wilson coefficients, SMEFT and SM are different theories in the UV.

on the actual Wilson coefficients; here there will be an uncertainty from the order at which the calculation is done, as well as a parametric uncertainty. In the following we illustrate the basic strategy of for the latter (bottom-up) approach.

III.1.8.a SMEFT summary

To establish our notations we observe that in the SMEFT a (lepton number preserving) amplitude can be written as

$$\mathcal{A} = \sum_{n=\mathrm{N}}^{\infty} g^n \, \mathcal{A}_n^{(4)} + \sum_{n=\mathrm{N}_6}^{\infty} \sum_{l=1}^{n} \sum_{k=1}^{\infty} g^n \left[\frac{1}{(\sqrt{2}\, G_\mathrm{F}\, \Lambda^2)^k}\right]^l \mathcal{A}_{n\,l\,k}^{(4+2\,k)} \,, \tag{III.1.71}$$

where g is a SM coupling. G_F is the Fermi coupling constant and Λ is the cut off scale. l is an index that indicates the number of SMEFT operator insertions leading to the amplitude, and k indicates the inverse mass dimension of the Lagrangian terms inserted. N is a label for each individual process, that indicates the order of the coupling dependence for the leading non vanishing term in the SM (e.g., $N = 1$ for $h \to VV$ etc. but $N = 3$ for $h \to \gamma\gamma$). $N_6 = N$ for tree initiated processes in the SM. For processes that first occur at loop level in the SM, $N_6 = N - 2$ when operators in the SMEFT can mediate such decays directly thought a contact operator, for example, through a $\dim = 6$ operator for $h \to \gamma\gamma$. For instance, the $h\gamma\gamma$ (tree) vertex is generated by $O_{HB} = \Phi^\dagger \, \Phi \, B^{\mu\nu} \, B_{\mu\nu}$, by $O_{HW}^8 = \Phi^\dagger \, B^{\mu\nu} \, B_{\mu\rho} \, \mathrm{D}^\rho \, \mathrm{D}_\nu \, \Phi$ etc. Therefore, SMEFT is a double expansion: in g and $g_6 = \mathrm{v}_\mathrm{F}^2/\Lambda^2$ for pole observables and in g, g_6 $E^2/\mathrm{v}_\mathrm{F}^2$ for off-shell ones; furthermore, the combination of parameters $g\, g_6\, \mathcal{A}_{1,1,1}^{(6)}$ defines the LO SMEFT expression for the process while $g^3\, g_6\, \mathcal{A}_{3,1,1}^{(6)}$ defines the NLO SMEFT amplitude in the perturbative expansion.

To summarize, LO SMEFT refers to $\dim = 6$ operators in tree diagrams, sometimes called "contact terms" while NLO SMEFT refers to one loop diagrams with a single insertion of $\dim = 6$ operators. One can make additional assumptions by introducing classification schemes in SMEFT. One example of a classification scheme is the Artz-Einhorn-Wudka "potentially-tree-generated" (PTG) scenario [685,686]. In this scheme, it is argued that classes of Wilson coefficients for operators of $\dim = 6$ can be argued to be tree level, or loop level (suppressed by $g^2/16\,\pi^2$)[III.9]. In these cases the expansion in eq. (III.1.71) is reorganized in terms of TG (we assume a BSM model where PTG is actually TG) and LG insertions, i.e., LG contact terms and one loop TG insertions, one loop LG insertions and two loop SM etc. It is clear that LG contact terms alone do not suffice.

Strictly speaking we are considering here the virtual part of SMEFT, under the assumptions that LHC PO are defined à la LEP, i.e., when QED and QCD corrections are deconvoluted. Otherwise, the real (emission) part of SMEFT should be included and it can be shown that the infrared/collinear part of the one-loop virtual corrections and of the real ones respect factorization: the total = virtual + real is IR/collinear finite at $\mathcal{O}(g^4\, g_6)$.

It is worth nothing that SMEFT has limitations, obviously the scale should be such that $E \ll \Lambda$. Understanding SM deviations in tails of distributions requires using SMEFT, but only up to the point where it stops to be valid, or using the kappa–BSM-parameters connection, i.e., replace SMEFT with BSM models, optimally matching to SMEFT at lower scales.

In any process, the residues of the poles corresponding to unstable particles (starting from maximal degree) are numbers while the non-resonant part is a multivariate function that requires some basis, i.e., a less model independent, underlying, theory of SM deviations. That is to say, residue of the poles can be PO by themselves, expressing them in terms of Wilson coefficients is an operation the can be eventually postponed. The very end of the chain, the non-resonant part, may require model dependent BSM interpretation. Numerically speaking, it depends on the impact of the non-resonant part which is

[III.9] This classification scheme corresponds only to a subset of weakly coupled and renormalizable UV physics cases.

small in gluon-fusion but not in Vector Boson Scattering. Therefore, the focus for data reporting should always be on real observables, fiducial cross sections and pseudo-observables.

To explain SMEFT in a nutshell consider a process described by some SM amplitude

$$\mathcal{A}_{\rm SM} = \sum_{i=1,n} \mathcal{A}^{(i)}_{\rm SM}\,, \tag{III.1.72}$$

where i labels gauge-invariant sub-amplitudes. In general, the same process is given by a contact term or a collection of contact terms of $\dim = 6$; for instance, direct coupling of h to $VV(V = \gamma, Z, W)$. In order to construct the theory one has to select a set of higher-dimensional operators and to start the complete procedure of renormalization. Of course, different sets of operators can be interchangeable as long as they are closed under renormalization. It is a matter of fact that renormalization is best performed when using the so-called Warsaw basis, see Ref. [614]. Moving from SM to SMEFT we obtain

$$\mathcal{A}^{\rm LO}_{\rm SMEFT} = \sum_{i=1,n} \mathcal{A}^{(i)}_{\rm SM} + i\, g_6\, \hat{\kappa}_{\rm c}\,, \qquad \mathcal{A}^{\rm NLO}_{\rm SMEFT} = \sum_{i=1,n} \hat{\kappa}_i\, \mathcal{A}^{(i)}_{\rm SM} + i\, g_6\, \hat{\kappa}_{\rm c} + g_6 \sum_{i=1,\rm N} a_i\, \mathcal{A}^{(i)}_{\rm nfc}\,, \tag{III.1.73}$$

where $g_6^{-1} = \sqrt{2}\, G_{\rm F}\, \Lambda^2$. The last term in eq. (III.1.73) collects all loop contributions that do not factorize and the coefficients a_i are Wilson coefficients. The $\hat{\kappa}_i$ are linear combinations of Wilson coefficients.[III.10] We conclude that eq. (III.1.73) gives a consistent and convenient generalization of the original κ-framework at the price of introducing additional, non-factorizable, terms in the amplitude.

There are several reasons why loops should not be neglected in SMEFT, one is as follows: consider the "off-shell"$\rm gg \to h$ fusion [499, 757, 759, 954], the "contact" term is real while the SM amplitude crosses normal thresholds, e.g., at $s = 4\, m_{\rm t}^2$, where s is the Higgs virtuality. Therefore, in the interference one misses the large effect induced by the SM imaginary part while this effect (of the order of 5% above the $\rm \bar{t}t$ -threshold) is properly taken into account by the inclusion of SMEFT loops, also developing an imaginary part after crossing the same normal threshold. To summarize, the LO part (contact term) alone shows large deviations from the SM around the $\rm \bar{t}t$ -threshold while the one-loop part reproduces, with the due rescaling, the SM lineshape in a case where there is no reason to neglect the insertion of PTG operators in loops. Only the formulation including loops gives an accurate result, with deviations of $\mathcal{O}(5\%)$ wrt tree (uncritical as long as experimental precision is $\gg 10\%$ but experiments are getting close).

III.1.8.b Theoretical uncertainty

A theoretical uncertainty arises when the value of the Wilson coefficients in the PO scenario is inferred. A fit defined in a perturbative expansion must always include an estimate of the missing higher order terms (MHOU) [706]. Various ways exist to estimate this uncertainty, at any order in perturbation theory. One can compute the same observable with different "options", e.g., linearization or quadratization of the squared matrix element, resummation or expansion of the (gauge invariant) fermion part in the wave function factor for the external legs (does not apply at tree level), variation of the renormalization scale, $G_{\rm F}$ renormalization scheme or α -scheme, etc.

A conservative estimate of the associated theoretical uncertainty is obtained by taking the envelope over all "options"; the interpretation of the envelope is a log-normal distribution (this is the solution preferred in the experimental community) or a flat Bayesian prior [160, 162] (a solution preferred in a large part of the theoretical community). It is clear that MHOU for the SM should always be included.

The notion of MHOU has a long history but it is worth noting that there is no statistical foundation and that it cannot be derived from a set of consistent (incomplete) principles. Ideally, calculations should

[III.10] We denote these combinations of Wilson coefficients $\hat{\kappa}_i$, rather than κ_i, in order to distinguish them from the PO defined in the previous sections.

be repeated using a well defined (and definable) set of options, results from different calculations should be compared and their MHOU assumptions subjectable to falsification. Therefore, no estimate of the theoretical errors is general enough and it is clear that there are several ways to approach the problem with conceptual differences between the bottom-up and the top-down scenarios.

III.1.8.c Examples

In this section we provide a number of examples connecting PO to Wilson coefficients; results are based on the work of Refs. [648, 716], and of Refs. [649, 694, 705, 718]. For simplicity we will confine the presentation to CP-even couplings.

– $\underline{h \to \bar{b}b}$ At tree level this amplitude is given by

$$\mathcal{A}_{\mathrm{H}\bar{\mathrm{b}}\mathrm{b}} = -\frac{1}{2}\, g\, \frac{m_{\mathrm{b}}}{m_W}\left[\mathrm{A}^{\mathrm{SM}}_{\mathrm{H}\bar{\mathrm{b}}\mathrm{b}} + g_6\,\left(a_{\phi\,\mathrm{W}} - \frac{1}{4}\,a_{\phi\,\mathrm{D}} + a_{\phi\,\Box} - a_{\mathrm{b}\,\phi}\right)\right], \tag{III.1.74}$$

giving the following connection with Eq. (III.1.1) (note that all deviations are real):

$$y^{\mathrm{b}}_{\mathrm{S}} = -\frac{i}{\sqrt{2}}\, g\, \frac{m_{\mathrm{b}}}{m_W}\left[\mathrm{A}^{\mathrm{SM}}_{\mathrm{H}\bar{\mathrm{b}}\mathrm{b}} + g_6\,\left(a_{\phi\,\mathrm{W}} - \frac{1}{4}\,a_{\phi\,\mathrm{D}} + a_{\phi\,\Box} - a_{\mathrm{b}\,\phi}\right)\right]. \tag{III.1.75}$$

– $\underline{h \to \gamma\gamma}$ The amplitude for the process $h(P) \to \gamma_\mu(p_1)\gamma_\nu(p_2)$ can be written as

$$\mathrm{A}^{\mu\nu}_{\mathrm{HAA}} = i\,\mathcal{T}_{\mathrm{HAA}}\,\mathrm{T}^{\mu\nu}\,, \quad m_h^2\,\mathrm{T}^{\mu\nu} = p_2^\mu\,p_1^\nu - p_1\cdot p_2\,g^{\mu\nu}\,. \tag{III.1.76}$$

The S-matrix element follows from eq. (III.1.76) when we multiply the amplitude by the photon polarizations $e_\mu(p_1)\,e_\nu(p_2)$; in writing eq. (III.1.76) we have used $p\cdot e(p) = 0$. A convenient way for writing the amplitude is the following: after renormalization we neglect all fermion masses but $m_{\mathrm{t}}, m_{\mathrm{b}}$ and write

$$\mathcal{T}_{\mathrm{HAA}} = \frac{g_{\mathrm{F}}^3\,\mathrm{s}_{\mathrm{W}}^2}{8\,\pi^2}\sum_{\mathrm{I}=W,\mathrm{t},\mathrm{b}}\rho_{\mathrm{I}}^{\mathrm{HAA}}\,\mathcal{T}^{\mathrm{I}}_{\mathrm{HAA\,;\,LO}} + g_{\mathrm{F}}\,g_6\,\frac{m_h^2}{m_W}\,a_{\mathrm{AA}} + \frac{g_{\mathrm{F}}^3\,g_6}{\pi^2}\,\mathcal{T}^{\mathrm{nfc}}_{\mathrm{HAA}}\,, \tag{III.1.77}$$

where $g_{\mathrm{F}}^2 = 4\,\sqrt{2}\,G_{\mathrm{F}}\,m_W^2$ and $\mathrm{c}_{\mathrm{W}} = m_W/m_Z$. Note that, at this point we have selected the $\{G_{\mathrm{F}}\,,\,m_Z\,,\,m_W\}$ IPS, alternatively one could use the $\{\alpha\,,\,G_{\mathrm{F}}\,,\,m_Z\}$ IPS where

$$g_{\mathrm{A}}^2 = \frac{4\,\pi\,\alpha}{\hat{\mathrm{s}}_\theta^2} \qquad \hat{\mathrm{s}}_\theta^2 = \frac{1}{2}\left[1 - \sqrt{1 - 4\,\frac{\pi\,\alpha}{\sqrt{2}\,G_{\mathrm{F}}\,m_Z^2}}\right], \tag{III.1.78}$$

with a numerical difference that enters the MHOU. Referring to eq. (III.1.73) we have

$$\hat{\kappa}_{\mathrm{I}}^{\mathrm{HAA}} = \frac{g_{\mathrm{F}}^3\,\mathrm{s}_{\mathrm{W}}^2}{8\,\pi^2}\,\rho_{\mathrm{I}}^{\mathrm{HAA}}\,, \qquad \hat{\kappa}_{\mathrm{c}}^{\mathrm{HAA}} = g_{\mathrm{F}}\,\frac{m_h^2}{m_W}\,a_{\mathrm{AA}}\,. \tag{III.1.79}$$

In writing deviations in terms of Wilson coefficients we introduce the following combinations:

$$\begin{aligned} a_{\mathrm{ZZ}} &= \mathrm{s}_{\mathrm{W}}^2\,a_{\phi\,\mathrm{B}} + \mathrm{c}_{\mathrm{W}}^2\,a_{\phi\,\mathrm{W}} - \mathrm{s}_{\mathrm{W}}\,\mathrm{c}_{\mathrm{W}}\,a_{\phi\,\mathrm{WB}}\,, \qquad a_{\mathrm{AA}} = \mathrm{c}_{\mathrm{W}}^2\,a_{\phi\,\mathrm{B}} + \mathrm{s}_{\mathrm{W}}^2\,a_{\phi\,\mathrm{W}} + \mathrm{s}_{\mathrm{W}}\,\mathrm{c}_{\mathrm{W}}\,a_{\phi\,\mathrm{WB}}\,, \\ a_{\mathrm{AZ}} &= 2\,\mathrm{c}_{\mathrm{W}}\,\mathrm{s}_{\mathrm{W}}\,\left(a_{\phi\,\mathrm{W}} - a_{\phi\,\mathrm{B}}\right) + \left(2\,\mathrm{c}_{\mathrm{W}}^2 - 1\right)\,a_{\phi\,\mathrm{WB}} \end{aligned} \tag{III.1.80}$$

The process dependent ρ-factors are given by

$$\rho_{\mathrm{I}}^{\mathrm{proc}} = 1 + g_6\,\Delta\rho_{\mathrm{I}}^{\mathrm{proc}}\,, \tag{III.1.81}$$

and there are additional, non-factorizable, contributions. For $h \to \gamma\gamma$ the $\Delta\rho$ factors are as follows:

$$\Delta\rho_{\mathrm{t}}^{\mathrm{HAA}} = \frac{3}{16}\,\frac{m_h^2}{\mathrm{s}_{\mathrm{W}}\,m_W^2}\,a_{\mathrm{t\,WB}} + (2 - \mathrm{s}_{\mathrm{W}}^2)\,\frac{\mathrm{c}_{\mathrm{W}}}{\mathrm{s}_{\mathrm{W}}}\,a_{\mathrm{AZ}} + (6 - \mathrm{s}_{\mathrm{W}}^2)\,a_{\mathrm{AA}}$$

$$
\begin{aligned}
&- \frac{1}{2}\left[a_{\phi\,\mathrm{D}} + 2\,\mathrm{s}_\mathrm{W}^2\,(\mathrm{c}_\mathrm{W}^2\,a_{\mathrm{ZZ}} - a_{\mathrm{t}\,\phi} - 2\,a_{\phi\,\Box})\right]\frac{1}{\mathrm{s}_\mathrm{W}^2}\,,\\
\Delta\rho_\mathrm{b}^{\mathrm{HAA}} &= -\frac{3}{8}\,\frac{m_h^2}{\mathrm{s}_\mathrm{W}\,m_W^2}\,a_{\mathrm{b\,WB}} + (2-\mathrm{s}_\mathrm{W}^2)\,\frac{\mathrm{c}_\mathrm{W}}{\mathrm{s}_\mathrm{W}}\,a_{\mathrm{AZ}} + (6-\mathrm{s}_\mathrm{W}^2)\,a_{\mathrm{AA}}\\
&- \frac{1}{2}\left[a_{\phi\,\mathrm{D}} + 2\,\mathrm{s}_\mathrm{W}^2\,(\mathrm{c}_\mathrm{W}^2\,a_{\mathrm{ZZ}} + a_{\mathrm{b}\,\phi} - 2\,a_{\phi\,\Box})\right]\frac{1}{\mathrm{s}_\mathrm{W}^2}\,,\\
\Delta\rho_W^{\mathrm{HAA}} &= (2+\mathrm{s}_\mathrm{W}^2)\,\frac{\mathrm{c}_\mathrm{W}}{\mathrm{s}_\mathrm{W}}\,a_{\mathrm{AZ}} + (6+\mathrm{s}_\mathrm{W}^2)\,a_{\mathrm{AA}} - \frac{1}{2}\left[a_{\phi\,\mathrm{D}} - 2\,\mathrm{s}_\mathrm{W}^2\,(2\,a_{\phi\,\Box} + \mathrm{c}_\mathrm{W}^2\,a_{\mathrm{ZZ}})\right]\frac{1}{\mathrm{s}_\mathrm{W}^2}
\end{aligned}
\tag{III.1.82}
$$

In the PTG scenario we only keep $a_{\mathrm{t}\,\phi}, a_{\mathrm{b}\,\phi}, a_{\phi\,\mathrm{D}}$ and $a_{\phi\,\Box}$ in eq. (III.1.82). The advantage of eq. (III.1.77) is to establish a link between the EFT and the κ-framework, which has a validity restricted to LO. As a matter of fact eq. (III.1.77) tells us that appropriate $\hat{\kappa}$-factors can be introduced also at the loop level; they are combinations of Wilson coefficients but we have to extend the scheme with the inclusion of process dependent, non-factorizable, contributions.

We also derive the following result for the non-factorizable part of the amplitude:

$$
\mathcal{T}_{\mathrm{HAA}}^{\mathrm{nfc}} = m_W \sum_{a\,\in\,\{A\}} \mathcal{T}_{\mathrm{HAA}}^{\mathrm{nfc}}(a)\,a\,, \quad \{A\} = \{a_{\mathrm{t\,WB}}, a_{\mathrm{b\,WB}}, a_{\mathrm{AA}}, a_{\mathrm{AZ}}, a_{\mathrm{ZZ}}\}\,. \tag{III.1.83}
$$

In the PTG scenario all non-factorizable amplitudes for $h \to \gamma\gamma$ vanish. Comparing with Eq. (III.1.6) we obtain

$$
\epsilon_{\gamma\gamma} = -\frac{1}{2}\,\frac{\mathrm{v_F}}{m_h^2}\,\mathcal{T}_{\mathrm{HAA}}\,, \quad \mathcal{T}_{\mathrm{HAA}}^{\mathrm{LO}} = \mathcal{T}_{\mathrm{HAA}}^{\mathrm{SM}} + g_\mathrm{F}\,g_6\,\frac{m_h^2}{m_W}\,a_{\mathrm{AA}}\,. \tag{III.1.84}
$$

– $\underline{h \to 4\,f}$

Few additional definitions are needed: by on-shell S-matrix for an arbitrary process (involving external unstable particles) we mean the corresponding (amputated) Green's function supplied with LSZ factors and sources, computed at the (complex) poles of the external lines [727, 729]. For processes that involve stable particles this can be straightforwardly transformed into a *physical* PO.

The connection of the $hVV, V = Z, W$ (on-shell) S-matrix with the off shell vertex $h \to VV$ and the full process $\mathrm{pp} \to 4\,\psi$ is more complicated and is discussed in some detail in Sect. 3 of Ref. [610]. The "on-shell" S-matrix for hVV, being built with the the residue of the $h{-}V{-}V$ poles in $\mathrm{pp} \to 4\,\psi$ is gauge invariant by construction (it can be proved by using Nielsen identities) and represents one of the building blocks for the full process: in other words, it is a PO. Technically speaking the "on-shell" limit for external legs should be understood "to the complex poles" (for a modification of the LSZ reduction formulas for unstable particles see Ref. [732]) but, as well known, at one loop we can use on-shell masses (for unstable particles) without breaking the gauge parameter independence of the result. In order to understand the connection with Eqs. (III.1.21)–(III.1.23), defining neutral current PO we consider the process

$$
h(P) \to e^-(p_1) + e^+(p_2) + f(p_3) + f(p_4) \tag{III.1.85}
$$

where $f \neq \mathrm{e}, \nu_\mathrm{e}$, and introduce the following invariants: $s_\mathrm{H} = P^2$, $s_1 = q_1^2 = (p_1+p_2)^2$ and $s_2 = q_2^2 = (p_3+p_4)^2$, while $s_i, i = 3, \ldots, 5$ denote the remaining invariants describing the process. We also introduce s_Z, the Z complex pole. Propagators are

$$
\Delta_\mathrm{A}(i) = \frac{1}{s_i}\,, \qquad \Delta_\mathrm{Z}(i) = \mathrm{P}_Z^{-1}(s_i) = \frac{1}{s_i - s_\mathrm{Z}}\,. \tag{III.1.86}
$$

The total amplitude for process eq. (III.1.85) is given by the sum of different contributions, doubly Z resonant etc.

$$
\mathcal{A}\left(h \to e^-e^+ff\right) = \mathrm{A}_{\mathrm{ZZ}}\left(s_\mathrm{H}\,,\,s_1\,,\,s_2\right)\,\Delta_\mathrm{Z}(s_1)\,\Delta_\mathrm{Z}(s_2)
$$

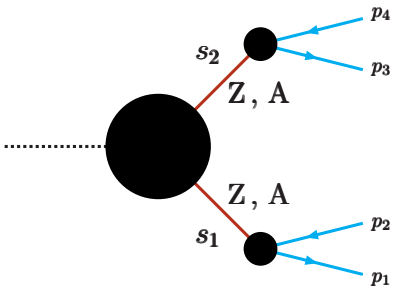

Figure 215: Doubly-resonant (ZZ, AA or AZ) part of the amplitude for the process of eq. (III.1.85).

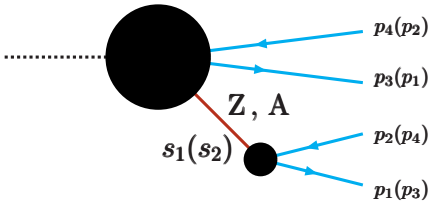

Figure 216: Singly-resonant (Z or A) part of the amplitude for the process of eq. (III.1.85).

$$
\begin{aligned}
&+ \mathrm{A}_{\mathrm{AA}}\left(s_{\mathrm{H}}\,,\,s_1\,,\,s_2\right)\,\Delta_{\mathrm{A}}(s_1)\,\Delta_{\mathrm{A}}(s_2) + \mathrm{A}_{\mathrm{AZ}}\left(s_{\mathrm{H}}\,,\,s_1\,,\,s_2\right)\,\Delta_{\mathrm{A}}(s_1)\,\Delta_{\mathrm{Z}}(s_2)\\
&+ \mathrm{A}_{\mathrm{AZ}}\left(s_{\mathrm{H}}\,,\,s_2\,,\,s_1\right)\,\Delta_{\mathrm{Z}}(s_1)\,\Delta_{\mathrm{A}}(s_2) + \mathrm{A}_{\mathrm{Z}}\left(s_{\mathrm{H}}\,,\,s_1\,,\,s_2\right)\,\Delta_{\mathrm{Z}}(s_1)\\
&+ \mathrm{A}_{\mathrm{Z}}\left(s_{\mathrm{H}}\,,\,s_2\,,\,s_1\right)\,\Delta_{\mathrm{Z}}(s_2) + \mathrm{A}_{\mathrm{A}}\left(s_{\mathrm{H}}\,,\,s_1\,,\,s_2\right)\,\Delta_{\mathrm{A}}(s_1)\\
&+ \mathrm{A}_{\mathrm{A}}\left(s_{\mathrm{H}}\,,\,s_2\,,\,s_1\right)\,\Delta_{\mathrm{A}}(s_2) + \mathrm{A}_{\mathrm{NR}}\,.
\end{aligned}
\tag{III.1.87}
$$

To describe in details the various terms in eq. (III.1.87) we introduce fermion currents defined by

$$
\begin{aligned}
J^{\mu}_{Z\,f}\,(p\,;\,q,k) &= \bar{\mathrm{u}}_f(q)\,\gamma^{\mu}\left[\mathcal{V}_f(p^2) + \mathcal{A}_f(p^2)\,\gamma^5\right]\mathrm{v}_f(k)\\
&= \mathcal{V}^{+}_f(p^2)\,\bar{\mathrm{u}}_{f\,\mathrm{L}}(q)\,\gamma^{\mu}\;\mathrm{v}_{f\,\mathrm{L}}(k) + \mathcal{V}^{-}_f(p^2)\,\bar{\mathrm{u}}_{f\,\mathrm{R}}(q)\,\gamma^{\mu}\;\mathrm{v}_{f\,\mathrm{R}}(k)\,,\\
J^{\mu}_{A\,f}\,(p\,;\,q,k) &= \mathcal{Q}_f(p^2)\,\bar{\mathrm{u}}_f(q)\,\gamma^{\mu}\,\mathrm{v}_f(k)\,,
\end{aligned}
\tag{III.1.88}
$$

where $p = q + k$. At tree level we have

$$
\mathcal{V}^{+}_f = \frac{g}{\mathrm{c_W}}\left(\mathrm{I}^{(3)}_f - \mathrm{Q}_f\,\mathrm{s}^2_{\mathrm{W}}\right)\,,\qquad \mathcal{V}^{-}_f = -g\,\mathrm{Q}_f\,\frac{\mathrm{s}^2_{\mathrm{W}}}{\mathrm{c_W}}\,,\qquad \mathcal{Q}_f = g\,\mathrm{Q}_f\,\mathrm{s_W}\,.
\tag{III.1.89}
$$

The amplitude for $h(P) \to \gamma(q_1) + \gamma(q_2)$ is

$$
\mathrm{A}_{\mathrm{AA}}\left(s_{\mathrm{H}}\,,\,s_1\,,\,s_2\right) = \mathcal{T}_{\mathrm{HAA}}\left(s_{\mathrm{H}}\,,\,s_1\,,\,s_2\right)\,\mathrm{T}_{\mu\nu}\left(q_1\,,\,q_2\right)\,J^{\mu}_{A\,\mathrm{e}}\left(q_1\,;\,p_1,p_2\right)\,J^{\nu}_{A\,f}\left(q_2\,;\,p_3,p_4\right)\,,
\tag{III.1.90}
$$

with $q_1^2 = s_1$ and $q_2^2 = s_2$. Similarly, the amplitude for $h(P) \to Z(q_1) + Z(q_2)$ is

$$
\begin{aligned}
\mathrm{A}_{\mathrm{ZZ}}\left(s_{\mathrm{H}}\,,\,s_1\,,\,s_2\right) = &\left[\mathcal{P}_{\mathrm{HZZ}}\left(s_{\mathrm{H}}\,,\,s_1\,,\,s_2\right)\,q_{2\mu}\,q_{1\nu} - \mathcal{D}_{\mathrm{HZZ}}\left(s_{\mathrm{H}}\,,\,s_1\,,\,s_2\right)\,g_{\mu\nu}\right]\\
&\times J^{\mu}_{Z\,\mathrm{e}}\left(q_1\,;\,p_1,p_2\right)\,J^{\nu}_{Z\,f}\left(q_2\,;\,p_3,p_4\right)\,.
\end{aligned}
\tag{III.1.91}
$$

The ZZ, AA or AZ, doubly-resonant parts of the amplitude are shown in Figure 215 while the singly, Z or A, parts are shown in Figure 216. For the singly-resonant amplitudes we write

$$
\mathrm{A}_{\mathrm{Z}}\left(s_{\mathrm{H}}\,,\,s_1\,,\,s_2\right) = \bar{\mathrm{u}}_f(p_3)\,\mathcal{F}_{\mathrm{HZ}\,\mu}\left(s_{\mathrm{H}}\,,\,s_1\,,\,s_2\right)\,\mathrm{v}_f(p_4)\,J^{\mu}_{Z,\mathrm{e}}\left(q_1\,;\,p_1,p_2\right)\,,
\tag{III.1.92}
$$

where the form factor $\mathcal{F}$ is again decomposed as follows:

$$\begin{aligned}\bar{\mathrm{u}}_f(p_3)\,\mathcal{F}_{\mathrm{HZ}\,\mu}\,\mathrm{v}_f(p_4) &= \textstyle\sum_i\, \mathcal{F}^i_{\mathrm{HZ}}\,\mathcal{C}_{i\,\mu} \qquad\qquad ,\\ \mathcal{C}_{i\,\mu} &= \{\,\bar{\mathrm{u}}_f(p_3)\,\gamma_\mu\,\mathrm{v}_f(p_4)\;,\;\bar{\mathrm{u}}_f(p_3)\,\gamma_\mu\,\gamma^5\,\mathrm{v}_f(p_4)\;,\;\ldots\}\;. \end{aligned} \tag{III.1.93}$$

Having the full amplitude we start expanding, e.g.,

$$\begin{aligned}\mathrm{A}_{\mathrm{ZZ}}\left(s_{\mathrm{H}}\,,\,s_1\,,\,s_2\right) &= \mathrm{A}_{\mathrm{ZZ}}\left(s_{\mathrm{H}}\,,\,s_{\mathrm{Z}}\,,\,s_2\right) + \left(s_1 - s_{\mathrm{Z}}\right)\,\mathrm{A}^{(1)}_{\mathrm{ZZ}}\left(s_{\mathrm{H}}\,,\,s_1\,,\,s_2\right)\,,\\ \mathrm{A}^{(1)}_{\mathrm{ZZ}}\left(s_{\mathrm{H}}\,,\,s_1\,,\,s_2\right) &= \mathrm{A}^{(1)}_{\mathrm{ZZ}}\left(s_{\mathrm{H}}\,,\,s_1\,,\,s_{\mathrm{Z}}\right) + \left(s_2 - s_{\mathrm{Z}}\right)\,\mathrm{A}^{(12)}_{\mathrm{ZZ}}\left(s_{\mathrm{H}}\,,\,s_1\,,\,s_2\right)\,, \end{aligned} \tag{III.1.94}$$

etc. The total amplitude of eq. (III.1.87) can be split into several components, Z doubly resonant (DR) ... Z singly resonant (SR) ... non resonant (NR). Note that NR includes multi-leg functions, up to pentagons:

$$\begin{aligned}\mathcal{A}_{\mathrm{DR}\,;\,\mathrm{ZZ}} &= \mathrm{A}_{\mathrm{ZZ}}\left(s_{\mathrm{H}}\,,\,s_{\mathrm{Z}}\,,\,s_{\mathrm{Z}}\right)\,\Delta_{\mathrm{Z}}(s_1)\,\Delta_{\mathrm{Z}}(s_2)\,,\\ \mathcal{A}_{\mathrm{DR}\,;\,\mathrm{AA}} &= \mathrm{A}_{\mathrm{AA}}\left(s_{\mathrm{H}}\,,\,0\,,\,0\right)\,\Delta_{\mathrm{A}}(s_1)\,\Delta_{\mathrm{A}}(s_2)\,,\\ \mathcal{A}_{\mathrm{SR}\,;\,\mathrm{Z}} &= \Big[\mathrm{A}_{\mathrm{Z}}\left(s_{\mathrm{H}}\,,\,s_{\mathrm{Z}}\,,\,s_2\right) + \mathrm{A}^{(2)}_{\mathrm{AZ}}\left(s_{\mathrm{H}}\,,\,s_2\,,\,s_{\mathrm{Z}}\right) + \mathrm{A}^{(2)}_{\mathrm{ZZ}}\left(s_{\mathrm{H}}\,,\,s_{\mathrm{Z}}\,,\,s_2\right)\Big]\,\Delta_{\mathrm{Z}}(s_1)\,,\\ &+ \Big[\mathrm{A}_{\mathrm{Z}}\left(s_{\mathrm{H}}\,,\,s_{\mathrm{Z}}\,,\,s_1\right) + \mathrm{A}^{(1)}_{\mathrm{AZ}}\left(s_{\mathrm{H}}\,,\,s_1\,,\,s_{\mathrm{Z}}\right) + \mathrm{A}^{(1)}_{\mathrm{ZZ}}\left(s_{\mathrm{H}}\,,\,s_1\,,\,s_{\mathrm{Z}}\right)\Big]\,\Delta_{\mathrm{Z}}(s_2)\,,\\ \mathcal{A}_{\mathrm{SR}\,;\,\mathrm{A}} &= \Big[\mathrm{A}_{\mathrm{A}}\left(s_{\mathrm{H}}\,,\,0\,,\,s_2\right) + \mathrm{A}^{(2)}_{\mathrm{AA}}\left(s_{\mathrm{H}}\,,\,0\,,\,s_2\right) + \mathrm{A}^{(2)}_{\mathrm{AZ}}\left(s_{\mathrm{H}}\,,\,0\,,\,s_2\right)\Big]\,\Delta_{\mathrm{A}}(s_1)\\ &+ \Big[\mathrm{A}_{\mathrm{A}}\left(s_{\mathrm{H}}\,,\,0\,,\,s_1\right) + \mathrm{A}^{(1)}_{\mathrm{AA}}\left(s_{\mathrm{H}}\,,\,s_1\,,\,0\right) + \mathrm{A}^{(1)}_{\mathrm{AZ}}\left(s_{\mathrm{H}}\,,\,0\,,\,s_1\right)\Big]\,\Delta_{\mathrm{A}}(s_2)\\ \mathcal{A}_{\mathrm{DR}\,;\,\mathrm{AZ}} &= \mathrm{A}_{\mathrm{AZ}}\left(s_{\mathrm{H}}\,,\,s_{\mathrm{Z}}\,,\,s_1\right)\,\Big[\Delta_{\mathrm{Z}}(s_1)\,\Delta_{\mathrm{A}}(s_2) + \Delta_{\mathrm{A}}(s_1)\,\Delta_{\mathrm{Z}}(s_2)\Big]\\ \mathcal{A}_{\mathrm{NR}} &= \mathrm{A}^{(1,2)}_{\mathrm{DR}\,;\,\mathrm{ZZ}}\left(s_{\mathrm{H}}\,,\,s_1\,,\,s_2\right) + \mathrm{A}^{(2,1)}_{\mathrm{DR}\,;\,\mathrm{ZZ}}\left(s_{\mathrm{H}}\,,\,s_1\,,\,s_2\right) + \mathrm{A}^{(1,2)}_{\mathrm{DR}\,;\,\mathrm{AZ}}\left(s_{\mathrm{H}}\,,\,s_2\,,\,s_1\right)\\ &+ \mathrm{A}^{(2,1)}_{\mathrm{DR}\,;\,\mathrm{AZ}}\left(s_{\mathrm{H}}\,,\,s_1\,,\,s_2\right) + \mathrm{A}^{(1,2)}_{\mathrm{DR}\,;\,\mathrm{AA}}\left(s_{\mathrm{H}}\,,\,s_1\,,\,s_2\right) + \mathrm{A}^{(2,1)}_{\mathrm{DR}\,;\,\mathrm{AA}}\left(s_{\mathrm{H}}\,,\,s_1\,,\,s_2\right)\\ &+ \mathrm{A}^{(1)}_{\mathrm{SR}\,;\,\mathrm{Z}}\left(s_{\mathrm{H}}\,,\,s_1\,,\,s_2\right) + \mathrm{A}^{(2)}_{\mathrm{SR}\,;\,\mathrm{Z}}\left(s_{\mathrm{H}}\,,\,s_2\,,\,s_1\right) + \mathrm{A}^{(1)}_{\mathrm{SR}\,;\,\mathrm{A}}\left(s_{\mathrm{H}}\,,\,s_1\,,\,s_2\right)\\ &+ \mathrm{A}^{(2)}_{\mathrm{SR}\,;\,\mathrm{A}}\left(s_{\mathrm{H}}\,,\,s_2\,,\,s_1\right) + \mathrm{A}_{\mathrm{NR}}\,. \end{aligned} \tag{III.1.95}$$

Each $\mathcal{A}$ amplitude is gauge parameter independent. Let us consider SMEFT at tree level, so that

$$\mathrm{A}_{\mathrm{AA}}\left(s_{\mathrm{H}}\,,\,s_1\,,\,s_2\right) = \mathrm{A}^{\mathrm{SM}}_{\mathrm{AA}}\left(s_{\mathrm{H}}\,,\,s_1\,,\,s_2\right) + \Delta\mathrm{A}_{\mathrm{AA}}\left(s_{\mathrm{H}}\,,\,s_1\,,\,s_2\right)\,, \tag{III.1.96}$$

etc.. In $\Delta\mathrm{A}$ we do not include loops with $\dim = 6$ insertions. Taking $f = \mu^-$ and neglecting fermion masses we obtain the following result

$$\begin{aligned}\Delta\mathcal{A}\left(h \to e^-e^+\mu^-\mu^+\right) &= -\,i\,g^3\,g_6\,J^\mu_{\mathrm{L}}\left(q_1\,;\,p_1,p_2\right)\,J_{\mu\,\mathrm{L}}\left(q_2\,;\,p_3,p_4\right)\,\Delta\mathcal{A}_{\mathrm{L}}\\ &- i\,\frac{g^3\,g_6}{m_W}\,\left(q_{2\mu}\,q_{1\nu} - q_1\cdot q_2\,g_{\mu\nu}\right)\,J^\mu_{\mathrm{L}}\left(q_1\,;\,p_1,p_2\right)\,J^\nu_{\mathrm{L}}\left(q_2\,;\,p_3,p_4\right)\Big]\,\Delta\mathcal{A}_{\mathrm{T}}\,, \end{aligned} \tag{III.1.97}$$

where J^μ_{L} is the left-handed fermion current (fermion masses are neglected) and $\Delta\mathcal{A}_{\mathrm{L}\,,\,\mathrm{T}}$ are the longitudinal and transverse parts of the LO SMEFT deviations. We obtain

$$\begin{aligned}\Delta\mathcal{A}_{\mathrm{T}} &= 2\,\mathrm{s}^2_{\mathrm{W}}\,a_{\mathrm{AA}}\,\Delta_{\mathrm{A}}(s_1)\,\Delta_{\mathrm{A}}(s_2) + \frac{1}{2}\,\mathrm{v}_\ell\,\frac{\mathrm{s}_{\mathrm{W}}}{\mathrm{c}_{\mathrm{W}}}\,a_{\mathrm{AZ}}\,\Big[\Delta_{\mathrm{A}}(s_1)\,\Delta_{\mathrm{Z}}(s_2) + \Delta_{\mathrm{A}}(s_2)\,\Delta_{\mathrm{Z}}(s_1)\Big]\\ &- \frac{1}{2}\,\mathrm{v}^2_\ell\,\frac{a_{\mathrm{ZZ}}}{\mathrm{c}^2_{\mathrm{W}}}\,\Delta_{\mathrm{Z}}(s_1)\,\Delta_{\mathrm{Z}}(s_2)\,, \end{aligned} \tag{III.1.98}$$

$$\Delta\mathcal{A}_{\mathrm{L}} = \frac{1}{4}\,\frac{\mathrm{v}_\ell}{\mathrm{c}^2_{\mathrm{W}}}\,\frac{1}{m_W}\,\left(a_{\phi\,\ell\,\mathrm{V}} + a_{\phi\,\ell\,\mathrm{A}}\right)\,\Big[\Delta_{\mathrm{Z}}(s_1) + \Delta_{\mathrm{Z}}(s_2)\Big]$$

$$
\begin{aligned}
&- \frac{1}{16}\left[\left(7 - 20\,\mathrm{s}_\mathrm{W}^2 + 12\,\mathrm{s}_\mathrm{W}^4\right)\frac{a_{\phi\,\mathrm{D}}}{\mathrm{c}_\mathrm{W}^4} + 4\,\mathrm{v}_\ell^2\,\frac{a_{\phi\,\Box}}{\mathrm{c}_\mathrm{W}^4} + 8\,\frac{\mathrm{v}_\ell}{\mathrm{c}_\mathrm{W}^4}\,\left(a_{\phi\,\ell\,\mathrm{V}} + a_{\phi\,\ell\,\mathrm{A}}\right)\right.\\
&\left. + 4\left(3 - 7\,\mathrm{s}_\mathrm{W}^2 + 4\,\mathrm{s}_\mathrm{W}^6\right)\frac{a_{\mathrm{ZZ}}}{\mathrm{c}_\mathrm{W}^4} - 4\left(5 - 12\,\mathrm{s}_\mathrm{W}^2 + 4\,\mathrm{s}_\mathrm{W}^4\right)\frac{\mathrm{s}_\mathrm{W}}{\mathrm{c}_\mathrm{W}^4}\left(\mathrm{s}_\mathrm{W}\,a_{\mathrm{AA}} + \mathrm{c}_\mathrm{W}\,a_{\mathrm{AZ}}\right)\right]\\
&\times m_W\,\Delta_\mathrm{Z}(s_1)\,\Delta_\mathrm{Z}(s_2)\,,
\end{aligned}
\tag{III.1.99}
$$

where $\mathrm{v}_\ell = 1 - 2\,\mathrm{s}_\mathrm{W}^2$. With the help of eqs. (III.1.98) and (III.1.99) it is straightforward to establish the relation between the PO of Sect. 4 and the SMEFT Wilson coefficients (when the complex poles are identified with on-shell masses). It is worth noting that we have not included dipole operators.

It is worth noting that there are subtleties when the h is off-shell, they are described in Appendix C.1 of Ref. [729]. Briefly, there is a difference between performing an analytical continuation (h virtuality $\to h$ on-shell mass) in the off-shell decay width and using leading-pole approximation (LPA) of Ref. [955], i.e., the DR part, where the matrix element (squared) is projected but not the phase-space. Analytical continuation is a unique, gauge invariant procedure, the advantage of LPA is that it allows for a straightforward implementation of cuts.

In order to extend the SMEFT-PO connection to loop-level SMEFT we have to consider various ingredients separately.

– $\underline{h \to ZZ}$ The amplitude for $h(P) \to Z_\mu(p_1) Z_\nu(p_2)$ can be written as

$$
\mathrm{A}_{\mathrm{HZZ}}^{\mu\nu} = i\left(\mathcal{P}_{\mathrm{HZZ}}^{11}\,p_1^\mu\,p_1^\nu + \mathcal{P}_{\mathrm{HZZ}}^{12}\,p_1^\mu\,p_2^\nu + \mathcal{P}_{\mathrm{HZZ}}^{21}\,p_2^\mu\,p_1^\nu + \mathcal{P}_{\mathrm{HZZ}}^{22}\,p_2^\mu\,p_2^\nu - \mathcal{D}_{\mathrm{HZZ}}\,g^{\mu\nu}\right). \tag{III.1.100}
$$

The result in eq. (III.1.100) is fully general and can be used to prove Ward-Slavnov-Taylor identities (WSTI). As far as the partial decay width is concerned only $\mathcal{P}_{\mathrm{HZZ}}^{21} \equiv \mathcal{P}_{\mathrm{HZZ}}$ will be relevant, due to $p \cdot e(p) = 0$ where e is the polarization vector. Note that computing WSTI requires additional amplitudes, i.e., $h \to \phi^0\gamma$ and $h \to \phi^0\phi^0$. The result can be written as follows:

$$
\begin{aligned}
\mathcal{D}_{\mathrm{HZZ}} &= -g_\mathrm{F}\,\frac{m_W}{\mathrm{c}_\mathrm{W}^2}\,\rho_{\mathrm{D\,;\,LO}}^{\mathrm{HZZ}} + \frac{g_\mathrm{F}^3}{\pi^2}\left[\sum_{\mathrm{I=t,b},W}\rho_{\mathrm{I\,;\,D\,;\,NLO}}^{\mathrm{HZZ}}\,\mathcal{D}_{\mathrm{HZZ\,;\,NLO}}^{\mathrm{I}} + \mathcal{D}_{\mathrm{HZZ}}^{(4)\,;\,\mathrm{nfc}} + g_6\sum_{\{a\}}\mathcal{D}_{\mathrm{HZZ}}^{(6)\,;\,\mathrm{nfc}}(a)\right],\\
\mathcal{P}_{\mathrm{HZZ}} &= 2\,g_\mathrm{F}\,g_6\,\frac{a_{\mathrm{ZZ}}}{m_W} + \frac{g_\mathrm{F}^3}{\pi^2}\left[\sum_{\mathrm{I=t,b},W}\rho_{\mathrm{I\,;\,P\,;\,NLO}}^{\mathrm{HZZ}}\,\mathcal{P}_{\mathrm{HZZ\,;\,NLO}}^{\mathrm{I}} + g_6\sum_{\{a\}}\mathcal{P}_{\mathrm{HZZ}}^{(6)\,;\,\mathrm{nfc}}(a)\right].
\end{aligned}
\tag{III.1.101}
$$

$$
\Delta\rho_{\mathrm{D\,;\,LO}}^{\mathrm{HZZ}} = \mathrm{s}_\mathrm{W}^2\,a_{\mathrm{AA}} + \left[4 + \mathrm{c}_\mathrm{W}^2\left(1 - \frac{m_h^2}{m_W^2}\right)\right]a_{\mathrm{ZZ}} + \mathrm{c}_\mathrm{W}\,\mathrm{s}_\mathrm{W}\,a_{\mathrm{AZ}} + 2\,a_{\phi\,\Box}\,, \tag{III.1.102}
$$

$$
\begin{aligned}
\Delta\rho_{\mathrm{q\,;\,D\,;\,NLO}}^{\mathrm{HZZ}} &= \Delta\rho_{\mathrm{q\,;\,P\,;\,NLO}}^{\mathrm{HZZ}} = 2\,\mathrm{I}_\mathrm{q}^{(3)}\,a_{\mathrm{q}\,\phi} + 2\,a_{\phi\,\Box} - \frac{1}{2}\,a_{\phi\,\mathrm{D}} + 2\,a_{\mathrm{ZZ}} + \mathrm{s}_\mathrm{W}^2\,a_{\mathrm{AA}}\,,\\
\Delta\rho_{W\,;\,\mathrm{D\,;\,NLO}}^{\mathrm{HZZ}} &= \frac{1}{12}\left(4 + \frac{1}{\mathrm{c}_\mathrm{W}^2}\right)a_{\phi\,\mathrm{D}} + 2\,a_{\phi\,\Box} + \mathrm{s}_\mathrm{W}^2\,a_{\mathrm{AA}}\\
&\quad + \mathrm{s}_\mathrm{W}^2\left(3\,\mathrm{c}_\mathrm{W} + \frac{5}{3}\,\frac{1}{\mathrm{c}_\mathrm{W}}\right)a_{\mathrm{AZ}} + \left(4 + \mathrm{c}_\mathrm{W}^2\right)a_{\mathrm{ZZ}}\,,\\
\Delta\rho_{W\,;\,\mathrm{P\,;\,NLO}}^{\mathrm{HZZ}} &= 4\,a_{\phi\,\Box} + \frac{5}{2}\,a_{\phi\,\mathrm{D}} + 12\,a_{\mathrm{ZZ}} + 3\,\mathrm{s}_\mathrm{W}^2\,a_{\mathrm{AA}}
\end{aligned}
\tag{III.1.103}
$$

It is convenient to define sub-amplitudes; however, to respect a factorization into t, b and bosonic components, we have to introduce the following quantities:

$$\begin{aligned}
&\mathrm{W}_h = \mathrm{W}_{h\ W} + \mathrm{W}_{h\ \mathrm{t}} + \mathrm{W}_{h\ \mathrm{b}} && \mathrm{W}_Z = \mathrm{W}_{Z\ W} + \mathrm{W}_{Z\ \mathrm{t}} + \mathrm{W}_{Z\ \mathrm{b}} + \overline{\sum}_{\text{gen}} \mathrm{W}_{Z\,;f} \\
&\mathrm{d}\mathcal{Z}_g = \mathrm{d}\mathcal{Z}_{g\,;W} + \sum_{\text{gen}} \mathrm{d}\mathcal{Z}_{g\,;f} && \mathrm{d}\mathcal{Z}_{\mathrm{c_W}} = \mathrm{d}\mathcal{Z}_{\mathrm{c_W}\,;W} + \mathrm{d}\mathcal{Z}_{\mathrm{c_W}\,;\mathrm{t}} + \mathrm{d}\mathcal{Z}_{\mathrm{c_W}\,;\mathrm{b}} + \overline{\sum}_{\text{gen}} \mathrm{d}\mathcal{Z}_{\mathrm{c_W}\,;f} \\
&\mathrm{d}\mathcal{Z}_{m_W} = \mathrm{d}\mathcal{Z}_{m_W\,;W} + \sum_{\text{gen}} \mathrm{d}\mathcal{Z}_{m_W\,;f}
\end{aligned} \tag{III.1.104}$$

where $\mathrm{W}_{\phi\,;\phi}$ denotes the ϕ component of the ϕ (LSZ) wave-function factor etc. By $\mathrm{d}\mathcal{Z}_{\mathrm{par}}$ we denote the (UV finite) counterterm that is needed in connecting the renormalized parameters to an input parameter set (IPS). In the actual calculation we use IPS = $\{G_\mathrm{F}\,,\, m_Z\,,\, m_W\}$. Furthermore, $\sum_{\text{gen}}$ implies summing over all fermions and all generations, while $\overline{\sum}_{\text{gen}}$ excludes t and b from the sum.

$$\mathcal{D}^{(4)\,;\,\mathrm{nfc}}_{\mathrm{HZZ}} = \frac{1}{32}\,\frac{m_W}{\mathrm{c}^2_\mathrm{W}}\,\left(2\,\overline{\sum}_{\text{gen}}\,\mathrm{W}_{Z\,;f} - \sum_{\text{gen}}\,\mathrm{dZ}_{m_W\,;f} + 4\,\overline{\sum}_{\text{gen}}\,\mathrm{dZ}_{\mathrm{c_W}\,;f} - 2\sum_{\text{gen}}\,\mathrm{dZ}_{g\,;f}\right)\,. \tag{III.1.105}$$

The connection to Eqs. (20)–(24) is given by

$$\mathrm{v_F}\,g^f_Z\,g^{f'}_Z\,\mathcal{P}_{\mathrm{HZZ}} = -2\,\epsilon_{ZZ}\,, \qquad \mathrm{v_F}\,g^f_Z\,g^{f'}_Z\,\left(p_1\cdot p_2\,\mathcal{P}_{\mathrm{HZZ}} - \mathcal{D}_{\mathrm{HZZ}}\right) = 2\,m^2_Z\,\kappa_{ZZ}\,. \tag{III.1.106}$$

– $\underline{h \to WW}$ The derivation of the amplitude for $h \to WW$ follows closely the one for $h \to ZZ$.

$$\begin{aligned}
\mathcal{D}_{\mathrm{HWW}} &= -g_\mathrm{F}\,m_W\,\rho^{\mathrm{HWW}}_{\mathrm{D}\,;\,\mathrm{LO}} + \frac{g^3_\mathrm{F}}{\pi^2}\Big[\sum_{\mathrm{I=q},W}\rho^{\mathrm{HWW}}_{\mathrm{I}\,;\,\mathrm{D}\,;\,\mathrm{NLO}}\,\mathcal{D}^{\mathrm{I}}_{\mathrm{HWW}\,;\,\mathrm{NLO}} + \mathcal{D}^{(4)\,;\,\mathrm{nfc}}_{\mathrm{HWW}} + g_6\sum_{\{a\}}\mathcal{D}^{(6)\,;\,\mathrm{nfc}}_{\mathrm{HWW}}(a)\Big]\,, \\
\mathcal{P}_{\mathrm{HWW}} &= 2\,g_\mathrm{F}\,g_6\,\frac{1}{m_W}\,a_{\phi\,\mathrm{W}} + \frac{g^3_\mathrm{F}}{\pi^2}\Big[\sum_{\mathrm{I=q}}\rho^{\mathrm{HWW}}_{\mathrm{I}\,;\,\mathrm{P}\,;\,\mathrm{NLO}}\,\mathcal{P}^{\mathrm{I}}_{\mathrm{HWW}\,;\,\mathrm{NLO}} + g_6\sum_{\{a\}}\mathcal{P}^{(6)\,;\,\mathrm{nfc}}_{\mathrm{HWW}}(a)\Big]\,,
\end{aligned} \tag{III.1.107}$$

where we have introduced

$$\mathcal{D}^{(4)\,;\,\mathrm{nfc}}_{\mathrm{HWW}} = \frac{1}{32}\,m_W\,\overline{\sum}_{\text{gen}}\,\left(2\,\mathrm{W}_{W\,;f} - \mathrm{d}\mathcal{Z}_{m_W\,;f} - 2\,\mathrm{d}\mathcal{Z}_{g\,;f}\right)\,. \tag{III.1.108}$$

$$\Delta\rho^{\mathrm{HWW}}_{\mathrm{D}\,;\,\mathrm{LO}} = \mathrm{s}^2_\mathrm{W}\,\left(\frac{m^2_h}{m_W} - 5\,m_W\right)\,\left(a_{\mathrm{AA}} + a_{\mathrm{AZ}} + a_{\mathrm{ZZ}}\right) + \frac{1}{2}\,m_W\,a_{\phi\,\mathrm{D}} - 2\,m_W\,a_{\phi\,\Box}\,, \tag{III.1.109}$$

$$\begin{aligned}
\Delta\rho^{\mathrm{HWW}}_{\mathrm{q}\,;\,\mathrm{D}\,;\,\mathrm{NLO}} &= \Delta\rho^{\mathrm{HWW}}_{\mathrm{q}\,;\,\mathrm{P}\,;\,\mathrm{NLO}} = a_{\phi\,\mathrm{t\,V}} + a_{\phi\,\mathrm{t\,A}} + a_{\phi\,\mathrm{b\,V}} + a_{\phi\,\mathrm{b\,A}} - a_{\mathrm{b}\,\phi} + 2\,a_{\phi\,\Box} - \frac{1}{2}\,a_{\phi\,\mathrm{D}} \\
&\quad + \mathrm{s_W}\,a_{\mathrm{b\,WB}} + \mathrm{c_W}\,a_{\mathrm{b\,BW}} + 5\,\mathrm{s}^2_\mathrm{W}\,a_{\mathrm{AA}} + 5\,\mathrm{c_W}\,\mathrm{s_W}\,a_{\mathrm{AZ}} + 5\,\mathrm{c}^2_\mathrm{W}\,a_{\mathrm{ZZ}}\,, \\
\Delta\rho^{\mathrm{HWW}}_{W\,;\,\mathrm{D}\,;\,\mathrm{NLO}} &= \frac{1}{96}\,\frac{\mathrm{s}^2_\mathrm{W}}{\mathrm{c}^2_\mathrm{W}}\,a_{\phi\,\mathrm{D}} + \frac{23}{12}\,a_{\phi\,\Box} - \frac{35}{96}\,a_{\phi\,\mathrm{D}} \\
&\quad + 4\,\mathrm{s}^2_\mathrm{W}\,a_{\mathrm{AA}} + \frac{1}{12}\,\mathrm{s_W}\,\left(3\,\frac{1}{\mathrm{c_W}} + 49\,\mathrm{c_W}\right)\,a_{\mathrm{AZ}} + \frac{1}{2}\,\left(9\,\mathrm{c}^2_\mathrm{W} + \mathrm{s}^2_\mathrm{W}\right)\,a_{\mathrm{ZZ}}\,, \\
\Delta\rho^{\mathrm{HWW}}_{W\,;\,\mathrm{P}\,;\,\mathrm{NLO}} &= 7\,a_{\phi\,\Box} - 2\,a_{\phi\,\mathrm{D}} + 5\,\mathrm{s}^2_\mathrm{W}\,a_{\mathrm{AA}} + 5\,\mathrm{c_W}\,\mathrm{s_W}\,a_{\mathrm{AZ}} + 5\,\mathrm{c}^2_\mathrm{W}\,a_{\mathrm{ZZ}}\,.
\end{aligned} \tag{III.1.110}$$

These results allow us to write ϵ_{WW} and κ_{WW} of Eqs. (25)–(27) in terms of Wilson coefficients.

– $\underline{Z \to ff}$ Let us consider the $Zf\mathrm{F}$ vertex, entering the process $h \to 4\,f$:

$$J^{\mu}_{Z\,f}\,(p\,;\,q,k) = \bar{\mathrm{u}}_f(q)\left\{\gamma^{\mu}\left[\mathcal{V}_f(p^2) + \mathcal{A}_f(p^2)\,\gamma^5\right] + \mathcal{T}_f(p^2)\,\sigma^{\mu\nu}\,p_\nu\,\mathrm{v}_f(k)\right\}. \tag{III.1.111}$$

At lowest order we have deviations defined by

$$\mathcal{V}_f = i\,\mathrm{I}^{3)}_f\,\frac{g}{\mathrm{c_W}}\,\left(\mathrm{v}_f + g_6\,\Delta\mathcal{V}_f\right)\,,\quad \mathcal{A}_f = i\,\mathrm{I}^{(3)}_f\,\frac{g}{\mathrm{c_W}}\,\left(\frac{1}{2} + g_6\,\Delta\mathcal{A}_f\right)\,,\quad \mathcal{T}_f = -\frac{g}{2}\,g_6\,\frac{m_f}{m_W}\,a_{\mathrm{f\,WB}}\,, \tag{III.1.112}$$

$$\begin{aligned}\Delta\mathcal{V}_f &= a_{\phi\,\mathrm{f\,V}} + \left[\mathrm{v}_f + \mathrm{c}^2_{\mathrm{W}}\,\left(\mathrm{v}_f - 1\right)\right]\left(a_{\mathrm{AA}} + \frac{\mathrm{c_W}}{\mathrm{s_W}}\,a_{\mathrm{AZ}} - \frac{1}{4\,\mathrm{s}^2_{\mathrm{W}}}\,a_{\phi\,\mathrm{D}}\right) + (1-\mathrm{v}_f)\,\mathrm{c}^2_{\mathrm{W}}\,a_{\mathrm{ZZ}}\,,\\ \Delta\mathcal{A}_f &= a_{\phi\,\mathrm{f\,A}} + \frac{1}{2}\left(a_{\phi\,\mathrm{W}} - \frac{1}{4}\,a_{\phi\,\mathrm{D}}\right)\,.\end{aligned} \tag{III.1.113}$$

where the vector couplings are $\mathrm{v_u} = 1/2 - 2\,Q_{\mathrm{u}}\,\mathrm{s}^2_{\mathrm{W}}$, $\mathrm{v_d} = 1/2 + 2\,Q_{\mathrm{d}}\,\mathrm{s}^2_{\mathrm{W}}$ and u, d are generic up, down fermions. When loops are included the decomposition in gauge invariant sub-amplitudes is not as simple as in the previous case, fermion loops and boson loops. Here the decomposition is given in terms of abelian and non-abelian (Z and W) parts, Q -components (those proportional to γ^μ) and L -parts (those proportional to $\gamma^\mu\,\gamma_+$). Details can be found in Sect. 6.15 of Ref. [956]. The general expression in SMEFT will not be reported here. It is worth noting that

$$\mathrm{A}_{Zff}(P^2) = \mathrm{A}^{\mathrm{inv}}_{Zff}(m^2_Z) + \left(P^2 - m^2_Z\right)\,\mathrm{A}^{\xi}_{Zff}(P^2)\,, \tag{III.1.114}$$

where ξ denotes the collection of gauge parameters.

– $\underline{W \to \mathbf{ud}}$ Similarly to the Z vertex we obtain

$$i\,\frac{g}{2\,\sqrt{2}}\,\gamma^\mu\left[\mathrm{V}^{(+)}_{\mathrm{F}}\,\gamma^+ + \mathrm{V}^{(-)}_{\mathrm{F}}\,\gamma^-\right] + \frac{g}{4}\,g_6\,\left(\frac{m^2_{\mathrm{U}}}{m_W}\,a_{\mathrm{U\,W}} - \frac{m^2_{\mathrm{D}}}{m_W}\,a_{\mathrm{D\,W}}\right)\,\sigma^{\nu\mu}\,p_\nu\,, \tag{III.1.115}$$

$$\mathrm{V}^{(+)}_{\mathrm{F}} = 1 + \sqrt{2}\,g_6\,\left(a^{(3)}_{\phi\,\mathrm{F}} + \frac{1}{2}\,a_{\phi\,\mathrm{W}}\right)\,,\qquad \mathrm{V}^{(-)}_{\mathrm{F}} = \sqrt{2}\,g_6\,a_{\phi\,\mathrm{U\,D}}\,. \tag{III.1.116}$$

Here F is a generic doublet of components $\mathrm{U} = \mathrm{u}$ or ν_{l} and $\mathrm{D} = \mathrm{d}$ or ℓ. Note that $a_{\phi\,\mathrm{U\,D}} = 0$ for leptons. The general expression in SMEFT will not be reported here.

– $\underline{Z \to WW}$ Triple gauge boson couplings are dscribed by the following deviations (all momenta flowing inwards):

$$\begin{aligned}&\mathrm{V}^{\mu\nu\rho}_{\mathrm{ZWW}}\,(p_1\,,\,p_2\,,\,p_3) = g\,\mathrm{c_W}\,\mathrm{F}^{\mu\nu\rho}\,(p_1\,,\,p_2\,,\,p_3) + \frac{3}{2}\,g\,g_6\,\mathrm{H}^{\mu\nu\rho}\,(p_1\,,\,p_2\,,\,p_3)\,\frac{a_{\mathrm{QW}}}{m^2_W}\\ &+ g\,g_6\mathrm{c_W}\,\mathrm{F}^{\mu\nu\rho}\,(p_1\,,\,p_2\,,\,p_3)\,\left[\left(1 - 2\,\mathrm{s}^2_{\mathrm{W}}\right)\,\left(\frac{\mathrm{s_W}}{\mathrm{c_W}}\,a_{\phi\,\mathrm{WB}} - a_{\phi\,\mathrm{W}}\right) + 2\,\mathrm{s}^2_{\mathrm{W}}\,a_{\phi\,\mathrm{B}} + \frac{1}{4}\,a_{\phi\,\mathrm{D}}\right]\\ &+ g\,g_6\mathrm{c_W}\,\mathrm{s_W}\,\mathrm{G}^{\mu\nu\rho}\,(p_1\,,\,p_2\,,\,p_3)\,\left[\left(1 - 2\,\mathrm{s}^2_{\mathrm{W}}\right)\,\frac{\mathrm{s_W}}{\mathrm{c_W}} + 2\,\mathrm{c_W}\right]a_{\phi\,\mathrm{WB}}\,,\end{aligned} \tag{III.1.117}$$

$$\begin{aligned}&\mathrm{F}^{\mu\nu\rho}\,(p_1\,,\,p_2\,,\,p_3) = p^\rho_1\,p^\mu_2\,p^\nu_3 - p^\nu_1\,p^\rho_2\,p^\mu_3 + g^{\nu\rho}\,\left(p^\mu_3\,p_1\cdot p_2 - p^\mu_2\,p_1\cdot p_3\right)\\ &+ g^{\nu\mu}\,\left(p^\rho_2\,p_1\cdot p_3 - p^\rho_1\,p_2\cdot p_3\right) + g^{\rho\mu}\,\left(p^\nu_1\,p_2\cdot p_3 - p^\nu_3\,p_1\cdot p_2\right)\,,\\ &\mathrm{G}^{\mu\nu\rho}\,(p_1\,,\,p_2\,,\,p_3) = g^{\nu\rho}\,\left(p^\mu_2 - p^\mu_3\right) + g^{\nu\mu}\,\left(p^\rho_1 - p^\rho_2\right) + g^{\rho\mu}\,\left(p^\nu_3 - p^\nu_1\right)\,,\\ &\mathrm{H}^{\mu\nu\rho}\,(p_1\,,\,p_2\,,\,p_3) = g^{\nu\rho}\,\left(p^\mu_3 - p^\mu_2\right) + g^{\nu\mu}\,\left(p^\rho_2 - p^\nu_3\right)\,.\end{aligned} \tag{III.1.118}$$

– VBF The process that we want to consider is

$$\mathrm{u}(p_1) + \mathrm{u}(p_2) \to \mathrm{u}(p_3) + e^-(p_4) + e^+(p_5) + \mu^-(p_6) + \mu^+(p_7) + \mathrm{u}(p_8)\,. \tag{III.1.119}$$

At LO SMEFT we introduce the triply-resonant (TR) part of the amplitude (t-channel propagators are never resonant):

$$J^\mu_\pm(p_i\,,\,p_j) = \bar{\mathrm{u}}_{p_i}\,\gamma^\mu\,\gamma_\pm\,\mathrm{u}_{p_j}\,, \qquad \Delta^{-1}_\Phi(p) = s - M^2_\Phi\,, \quad s = p^2\,, \tag{III.1.120}$$

$$\begin{aligned}\mathcal{A}^{\mathrm{TR}}_{\mathrm{LO}} = &\Big[J^\mu_-(p_4\,,\,p_5)\,(1-v_\ell) + J^\mu_+(p_4\,,\,p_5)\,(1+v_\ell)\Big]\Big[J^-_\mu(p_6\,,\,p_7)\,(1-v_\ell) + J^+_\mu(p_6\,,\,p_7)\,(1+v_\ell)\Big]\\ &\times\Big[J^\nu_-(p_3\,,\,p_2)\,(1-v_{\mathrm{u}}) + J^\nu_+(p_3\,,\,p_2)\,(1+v_{\mathrm{u}})\Big]\Big[J^-_\nu(p_8\,,\,p_1)\,(1-v_{\mathrm{u}}) + J^+_\nu(p_8\,,\,p_1)\,(1+v_{\mathrm{u}})\Big]\,,\end{aligned} \tag{III.1.121}$$

$$\begin{aligned}\mathcal{A}^{\mathrm{TR}}_{\mathrm{SMEFT}} &= -\frac{g^6}{4096}\,\Delta_h(q_1+q_2)\prod_{i=1,4}\Delta_Z(q_i)\,\frac{m_W^2}{c_\theta^8}\,\rho_{\mathrm{LO}}\,\mathcal{A}^{\mathrm{TR}}_{\mathrm{LO}} + g^6\,g_6\,\mathcal{A}^{\mathrm{TR\,;\,nfc}}_{\mathrm{SMEFT}}\\ \Delta\rho_{\mathrm{LO}} &= 2\,a_{\phi\,\Box} - \frac{2\,m_Z^2 - 2\,m_h^2 + q_1\cdot q_2 + q_2\cdot q_2}{m_W^2}\,\mathrm{c}^2_{\mathrm{W}}\,a_{\mathrm{ZZ}}\,,\end{aligned} \tag{III.1.122}$$

where $q_1 = p_8 - p_1,\ q_2 = p_3 - p_2$ are the incoming momenta in VBF and $q_3 = p_4 + p_5,\ q_4 = p_6 + p_7$ are the outgoing ones. Furthermore, $\gamma_\pm = 1 \pm \gamma^5$.

III.1.8.d SMEFT and *physical* PO

In this section we describe the connection between a possible realization of *physical* PO and SMEFT.

Multi pole expansion (MPE) has a dual role: as we mentioned, poles and their residues are intimately related to the gauge invariant splitting of the amplitude (Nielsen identities); residues of poles (after squaring the amplitude and after integration over residual variables) can be interpreted as *physical* PO, which requires factorization into subprocesses. However, gauge invariant splitting is not the same as "factorization" of the process into sub-processes, indeed phase space factorization requires the pole to be inside the physical region. For all technical details we refer to the work in Sect. 3 of Ref. [610] which is based on the following decomposition of the square of a propagator

$$\Delta = \frac{1}{\left(s - M^2\right)^2 + \Gamma^2\,M^2} = \frac{\pi}{M\,\Gamma}\,\delta\left(s - M^2\right) + \mathrm{PV}\left[\frac{1}{\left(s - M^2\right)^2}\right]\,. \tag{III.1.123}$$

and on the n-body decay phase space

$$d\Phi_n\left(P, p_1 \ldots p_n\right) = \frac{1}{2\,\pi}\,dQ^2\,d\Phi_{n-j+1}\left(P, Q, p_{j+1} \ldots p_n\right)\,d\Phi_j\left(Q, p_1 \ldots p_j\right)\,. \tag{III.1.124}$$

To "complete" the decay ($d\Phi_j$) we need the δ-function in eq. (III.1.124). We can say that the δ-part of the resonant (squared) propagator opens the corresponding line allowing us to define *physical* PO (t-channel propagators cannot be cut). Consider the process $\mathrm{qq} \to f_1 f_1 f_2 f_2 jj$, according to the structure of the resonant poles we have different options in extracting *physical* PO, e.g.,

$$\begin{aligned}\sigma(\mathrm{qq} \to f_1 f_1 f_2 f_2 jj) &\overset{PO}{\longmapsto} \sigma(\mathrm{qq} \to hjj)\,\mathrm{Br}(h \to Z f_1 f_1)\,\mathrm{Br}(Z \to f_2 f_2)\,,\\ \sigma(\mathrm{qq} \to f_1 f_1 f_2 f_2 jj) &\overset{PO}{\longmapsto} \sigma(\mathrm{qq} \to ZZjj)\,\mathrm{Br}(Z \to f_1 f_1)\,\mathrm{Br}(Z \to f_2 f_2)\,.\end{aligned} \tag{III.1.125}$$

There are fine points when factorizing a process into "physical" sub-processes (PO): extracting the δ from the (squared) propagator, eq. (III.1.123), does not necessarily factorize the phase space; if cuts are not introduced, the interference terms among different helicities oscillate over the phase space and drop out, i.e., we achieve factorization, see Refs. [957]. Furthermore, MPE should be understood as "asymptotic expansion", see Refs. [958, 959], not as Narrow-Width-Approximation (NWA). The phase space decomposition obtains by using the two parts in the propagator expansion of eq. (III.1.124): the δ-term is what we need to reconstruct PO, the PV-term (understood as a distribution [958]) gives the remainder and PO are extracted without making any approximation. It is worth noting that, in extracting PO, analytic continuation (on-shell masses into complex poles) is performed only after integrating over residual variables [729].

We can illustrate the SMEFT - MPE - PO connection by using a simple but non-trivial example: Dalitz decay of the Higgs boson, see Refs. [610, 960]. Consider the process

$$h(P) \to f(p_1) + f(p_2) + \gamma(p_3)\,, \tag{III.1.126}$$

and introduce invariants $s_{\rm H} = -P^2$, $s = -(p_1+p_2)^2$ and propagators, $\Delta_{\rm A}(i) = 1/s_i$, $\Delta_{\rm Z}(i) = 1/(s_i - s_{\rm Z})$. With $s_{\rm H} = \mu_{\rm H}^2 - i\,\mu_{\rm H}\,\gamma_{\rm H}$ we denote the h complex pole etc. In the limit $m_f \to 0$ the total amplitude for process eq. (III.1.126) is given by the sum of three contributions, Z, A-resonant and non-resonant:

$$\mathcal{A}\,(h \to f f \gamma) = \left[{\rm A}_{\rm Z}^{\mu}\left(s_{\rm H}\,,\,s\right)\,\Delta_{\rm Z}(s) + {\rm A}_{\rm A}^{\mu}\left(s_{\rm H}\,,\,s\right)\,\Delta_{\rm A}(s)\right] e_{\mu}\,(p_3, l) + {\rm A}_{\rm NR}\,, \tag{III.1.127}$$

where e_μ is the photon polarization vector. The two resonant components are given by

$${\rm A}_{\rm V}^{\mu}\left(s_{\rm H}\,,\,s\right) = \mathcal{T}_{\rm HAV}\left(s_{\rm H}\,,\,s\right)\,{\rm T}_{\nu}^{\mu}\,(q\,,\,p_3)\;J_{V\,f}^{\nu}\,(q\,;\,p_1, p_2)\;, \tag{III.1.128}$$

where $J_{V\,f}^{\mu}$ is the V fermion (f) current, $V = A, Z$, $q = p_1 + p_2$ and ${\rm T}^{\mu\nu}\,(k_1\,,\,k_2) = k_1\cdot k_2\,g^{\mu\nu} - k_1^{\nu}\,k_2^{\mu}$. Having the full amplitude we start expanding (MPE) according to

$$\mathcal{T}_{\rm HAZ}\left(s_{\rm H}\,,\,s\right) = \mathcal{T}_{\rm HAZ}\left(s_{\rm H}\,,\,s_{\rm Z}\right) + \left(s - s_{\rm Z}\right)\,\mathcal{T}_{\rm HAZ}^{(1)}\left(s_{\rm H}\,,\,s\right) \qquad \text{etc.} \tag{III.1.129}$$

Derivation continues till we define physical PO:

$$\begin{aligned}
\Gamma_{\rm PO}\,(h \to Z\gamma) &= \frac{1}{16\,\pi}\,\frac{1}{M_{\rm H}}\left(1 - \frac{\mu_{\rm Z}^2}{m_h^2}\right)\,{\rm F}_{h\to Z\gamma}\left(s_{\rm Z}\,,\,\mu_{\rm Z}^2\right)\,,\\
\Gamma_{\rm PO}\,(Z \to f f) &= \frac{1}{48\,\pi}\,\frac{1}{\mu_{\rm Z}}\,{\rm F}_{Z\to ff}\left(s_{\rm Z}\,,\,\mu_{\rm Z}^2\right)\,.\\
\Gamma_{\rm SR}\,(h \to f f\gamma) &= \frac{1}{2}\,\Gamma_{\rm PO}\,(h\to Z\gamma)\,\frac{1}{\gamma_{\rm Z}}\,\Gamma_{\rm PO}\,(Z\to ff) + \quad \text{remainder}\,.
\end{aligned} \tag{III.1.130}$$

In the NWA the remainder is neglected while we keep it in our formulation where the goal is extracting PO without making approximations. The interpretation in terms of SMEFT is based on $\mathcal{T}_{\rm HAZ}\left(s_{\rm H}\,,\,s_{\rm Z}\right)$. A convenient way for writing $\mathcal{T}_{\rm HAZ}$ is the following:

$$\mathcal{T}_{\rm HAZ} = \frac{g_{\rm F}^3}{\pi^2 m_Z}\sum_{{\rm I}=W,{\rm t},{\rm b}}\rho_{\rm I}^{\rm HAZ}\,\mathcal{T}_{{\rm HAZ}\,;\,{\rm LO}}^{\rm I} + g_{\rm F}\,g_6\,\frac{m_h^2}{M}\,a_{\rm AZ} + \frac{g_{\rm F}^3\,g_6}{\pi^2}\,\mathcal{T}_{\rm HAZ}^{\rm nfc}\,. \tag{III.1.131}$$

The factorizable part is defined in terms of ρ-factors

$$\Delta\rho_{\rm q}^{\rm HAZ} = \left(2\,{\rm I}_{\rm q}^{(3)}\,a_{{\rm q}\,\phi} + 2\,a_{\phi\,\Box} - \frac{1}{2}\,a_{\phi\,{\rm D}} + 3\,a_{\rm AA} + 2\,a_{\rm ZZ}\right)\,,$$

$$\Delta\rho_W^{\rm HAZ} = \frac{1+6\,c_W^2}{c_W^2}\,a_{\phi\,\Box} - \frac{1}{4}\,\frac{1+4\,c_W^2}{c_W^2}\,a_{\phi\,D} - \frac{1}{2}\,\frac{1+c_W^2-24\,c_W^4}{c_W^2}\,a_{AA}\,,$$
$$+\,\frac{1}{4}\left(1+12\,c_W^2-48\,c_W^4\right)\frac{s_W}{c_W^3}\,a_{AZ} + \frac{1}{2}\,\frac{1+15\,c_W^2-24\,c_W^4}{c_W^2}\,a_{ZZ}\,. \qquad \text{(III.1.132)}$$

In the PTG scenario we only keep $a_{t\,\phi}, a_{b\,\phi}, a_{\phi\,D}$ and $a_{\phi\,\Box}$ in eq. (III.1.132). We also derive the following result for the non-factorizable part of the amplitude:

$$\mathcal{T}^{\rm nfc}_{\rm HAZ} = \sum_{a\,\in\,\{A\}} \mathcal{T}^{\rm nfc}_{\rm HAZ}(a)\,a\,, \qquad \text{(III.1.133)}$$

where $\{A\} = \{a_{\phi\,t\,V}, a_{t\,BW}, a_{t\,WB}, a_{\phi\,b\,V}, a_{b\,WB}, a_{b\,BW}, a_{\phi\,D}, a_{AZ}, a_{AA}, a_{ZZ}\}$. In the PTG scenario there are only 3 non-factorizable amplitudes for $h \to \gamma Z$, those proportional to $a_{\phi\,t\,V}, a_{\phi\,b\,V}$ and $a_{\phi\,D}$.

III.1.8.e Summary on the PO-SMEFT matching

As we have shown, there are different layers of measurable parameters that can be extracted from LHC data. An external layer, where the kinematics is kept exact, is represented by *physical PO* such as $\Gamma_{\rm SR}\,(h \to f f\gamma)$ of eq. (III.1.130): these are similar to the $\sigma_f^{\rm peak}$ measured at LEP and, similarly to the LEP case, can be extracted from data via a non-trivial NWA. A first intermediate inner layer is represented by the *effective-couplings PO* introduced in Sections III.1.2–sec:PO-phen (and summarized in Section III.1.7): these are similar to effective Z-boson couplings ($g^{\rm e}_{V\,A}$) measured at LEP and control the parameterization of on-shell amplitudes. A further internal layer is represented by the $\hat\kappa_i$ introduced in this section, that are appropriate combinations of Wilson coefficients in the SMEFT. Finally, the innermost layer is represented by the Wilson coefficients (or the Lagrangian couplings) of the specific EFT (or explicit NP model) employed to analyse the data. When moving to the innermost layer in the SMEFT context we still have the option of performing the tree-level translation, which is well defined and should be integrated with the corresponding estimate of MHOU, or we can go to SMEFT at the loop level, again with its own MHOU.

III.1.9 Conclusions

The experimental precision on the kinematical distributions of Higgs boson decays and production cross sections is expected to significantly improve in the next few years. This will allow us to investigate in depth a wide class of possible extensions of the SM. To reach this goal, an accurate and sufficiently general parameterization of possible NP effects in such distributions is needed.

The Higgs PO presented in this note are conceived exactly to fulfil this goal: they provide a general decomposition of on-shell amplitudes involving the Higgs boson, based on analyticity, unitarity, and crossing symmetry. A further key assumption is the absence of new light particles in the kinematical regime of interest, or better no unknown physical poles in theses amplitudes. These conditions ensure the generality of this approach and the possibility to match it to a wide class of explicit NP models, including the determination of Wilson coefficients in the context of Effective Field Theories.

As we have shown, the PO can be organized in two complementary sets: the so-called physical PO, that are nothing but a series of idealized Higgs boson partials decay widths, and the effective-couplings PO, that are particularly useful for the developments of simulation tools. The two sets are in one-to-one correspondence, and their relation is summarized in Table 110. The complete set of effective-couplings PO that can be realistically accessed in Higgs-related measurements at the LHC, both in production and in decays, is summarized in Section III.1.7. The reduction of independent PO obtained under specific symmetry assumptions (in particular flavour universality and CP invariance) is also discussed in Section III.1.7. In two-body processes the effective-couplings PO are in one-to-one correspondence with the

parameters of the original κ framework. A substantial difference arises in more complicated processes, such as $h \to 4f$ or VBF and VH production. Here, in order to take into account possible kinematical distortions in the decay distributions and/or in the production cross-sections, the PO framework requires the introduction of a series of additional terms. These terms encode generic NP effects in the $hVf\bar{f}$ amplitudes and their complete list is summarized in Table 111.

The PO framework can be systematically improved to include the effect of higher-order QCD and QED corrections, recovering the best up-to-date SM predictions in absence of new physics. The effective-couplings PO should not be confused with EFT Wilson coefficients. However, their measurement can facilitate the extraction of Wilson coefficients in any EFT approach to Higgs physics, as briefly illustrated in Section III.1.8 in the context of the so-called SMEFT. The physical and the effective-couplings PO can be considered as the most general and external layers in the characterization of physics beyond the SM, whose innermost layer is represented by the couplings of some explicit NP model.

Table 111: Summary of the effective couplings PO appearing in EW Higgs boson decays and in the VBF and VH production cross-sections (see main text). The terms between square brakes in the middle table are the PO present both in production and decays. The last table denote the PO needed to describe both production and decays under the assumption of custodial symmetry.

Higgs (EW) decay amplitudes

Amplitudes	Flavour + CP	Flavour Non Univ.	CPV
$h \to \gamma\gamma, 2e\gamma, 2\mu\gamma$ $4e, 4\mu, 2e2\mu$	$\kappa_{ZZ}, \kappa_{Z\gamma}, \kappa_{\gamma\gamma}, \epsilon_{ZZ}$ $\epsilon_{Ze_L}, \epsilon_{Ze_R}$	$\epsilon_{Z\mu_L}, \epsilon_{Z\mu_R}$	$\epsilon^{CP}_{ZZ}, \delta^{CP}_{Z\gamma}, \delta^{CP}_{\gamma\gamma}$
$h \to 2e2\nu, 2\mu2\nu, e\nu\mu\nu$	$\kappa_{WW}, \epsilon_{WW}$ $\epsilon_{Z\nu_e}$, Re(ϵ_{We_L})	$\epsilon_{Z\nu_\mu}$, Re($\epsilon_{W\mu_L}$) Im($\epsilon_{W\mu_L}$)	ϵ^{CP}_{WW}, Im(ϵ_{We_L})

Higgs (EW) production amplitudes

Amplitudes	Flavour + CP	Flavour Non Univ.	CPV
VBF neutral curr. and Zh	$[\ \kappa_{ZZ}, \kappa_{Z\gamma}, \kappa_{\gamma\gamma}, \epsilon_{ZZ}\ ]$ $\epsilon_{Zu_L}, \epsilon_{Zu_R}, \epsilon_{Zd_L}, \epsilon_{Zd_R}$	$\epsilon_{Zc_L}, \epsilon_{Zc_R}$ $\epsilon_{Zs_L}, \epsilon_{Zs_R}$	$\left[\ \epsilon^{CP}_{ZZ}, \delta^{CP}_{Z\gamma}, \delta^{CP}_{\gamma\gamma}\ \right]$
VBF charged curr. and Wh	$[\ \kappa_{WW}, \epsilon_{WW}\ ]$ Re(ϵ_{Wu_L})	Re(ϵ_{Wc_L}) Im(ϵ_{Wc_L})	$[\epsilon^{CP}_{WW}]$, Im(ϵ_{Wu_L})

EW production and decay modes, with custodial symmetry

Amplitudes	Flavour + CP	Flavour Non Univ.	CPV
production & decays	$\kappa_{ZZ}, \kappa_{Z\gamma}, \kappa_{\gamma\gamma}, \epsilon_{ZZ}$		$\epsilon^{CP}_{ZZ}, \delta^{CP}_{Z\gamma}, \delta^{CP}_{\gamma\gamma}$
VBF and VH only	$\epsilon_{Zu_L}, \epsilon_{Zu_R}, \epsilon_{Zd_L}, \epsilon_{Zd_R}$	$\epsilon_{Zc_L}, \epsilon_{Zc_R}$ $\epsilon_{Zs_L}, \epsilon_{Zs_R}$	
decays only	$\epsilon_{Ze_L}, \epsilon_{Ze_R}$, Re($\epsilon_{We_L}$)	$\epsilon_{Z\mu_L}, \epsilon_{Z\mu_R}$	

Chapter III.2

Simplified Template Cross Sections

M. Dührssen, P. Francavilla, F.J. Tackmann, K. Tackmann

We acknowledge discussions in Les Houches 2015 and WG2 and contributions and feedback from Aaron Armbruster, Josh Bendavid, Fawzi Boudjema, André David, Marco Delmastro, Dag Gillberg, Admir Greljo, Thibault Guillemin, Chris Hays, Gino Isidori, Sabine Kraml, Kirtimaan Mohan, James Lacey, Carlo Pandini, Elisabetta Pianori, Tilman Plehn, Michael Rauch, Chris White, and many others.

III.2.1 Overview

After the successful Higgs boson coupling measurements during the LHC Run1, which had as their main results measured signal strength and multiplicative coupling modifiers, it is important to discuss in which way the experiments should present and perform Higgs boson coupling measurements in the future. Simplified template cross sections were developed to provide a natural way to evolve the signal strength measurements used during Run1. Compared to the Run1 measurements, the simplified template cross section framework allows one to reduce in a systematic fashion the theory dependences that must be directly folded into the measurements. This includes both the dependence on the theoretical uncertainties in the SM predictions as well as the dependence on the underlying physics model (i.e. the SM or BSM models). In addition, they provide more finely-grained measurements (and hence more information for theoretical interpretations), while at the same time allowing and benefitting from the global combination of the measurements in all decay channels.

The primary goals of the simplified template cross section framework are to maximize the sensitivity of the measurements while at the same time to minimize their theory dependence. This means in particular

- combination of all decay channels
- measurement of cross sections instead of signal strengths, in mutually exclusive regions of phase space
- cross sections are measured for specific production modes (with the SM production serving as kinematic template)
- measurements are performed in abstracted/simplified fiducial volumes
- allow the use of advanced analysis techniques such as event categorization, multivariate techniques, etc.

The measured exclusive regions of phase space, called "bins" for simplicity, are specific to the different production modes. Their definitions are motivated by

- minimizing the dependence on theoretical uncertainties that are directly folded into the measurements
- maximizing experimental sensitivity
- isolation of possible BSM effects
- minimizing the number of bins without loss of experimental sensitivity

These will of course be competing requirements in some cases and some compromise has to be achieved. The implementation of these basic design principles is discussed in more detail below.

A schematic overview of the simplified template cross section framework is shown in Figure 217. The experimental analyses shown on the left are very similar to the Run1 coupling measurements. For each decay channel, the events are categorized in the analyses, and there are several motivations for the

precise form of the categorization. Typically, a subset of the experimental event categories is designed to enrich events of a given Higgs boson production mode, usually making use of specific event topologies. This is what eventually allows the splitting of the production modes in the global fit. Another subset of event categories is defined to increase the sensitivity of the analysis by splitting events according to their expected signal-to-background ratio and/or invariant-mass resolution. In other cases, the categories are motivated by the analysis itself, e.g. as a consequence of the backgrounds being estimated specifically for certain classes of events. While these are some of the primary motivations, in the future the details of the event categorization can also be optimized in order to give good sensitivity to the simplified template cross sections to be measured.

The centre of Figure 217 shows a sketch of the simplified template cross sections, which are determined from the experimental categories by a global fit that combines all decay channels and which represent the main results of the experimental measurements. They are cross sections per production mode, split into mutually exclusive kinematic bins for each of the main production modes. In addition, the different Higgs boson decays are treated by fitting the partial decay widths. Note that as usual, without additional assumptions on the total width, only ratios of partial widths and ratios of simplified template cross sections are experimentally accessible.

The measured simplified template cross sections together with the partial decay widths then serve as input for subsequent interpretations, as illustrated on the right of Figure 217. Such interpretations could for example be the determination of signal strength modifiers or coupling scale factors κ (providing compatibility with earlier results), EFT coefficients, tests of specific BSM models, and so forth. For this purpose, the experimental results should quote the full covariance among the different bins. By aiming to minimize the theory dependence that is folded into the first step of determining the simplified template cross sections from the event categories, this theory dependence is shifted into the second interpretation step, making the measurements more long-term useful. For example, the treatment of theoretical uncertainties can be decoupled from the measurements and can be dealt with at the interpretation stage. In this way, propagating improvements in theoretical predictions and their uncertainties into the measurements itself, which is a very time-consuming procedure and unlikely to be feasible for older datasets, becomes much less important. Propagating future theoretical advances into the interpretation, on the other hand, is generally much easier.

To increase the sensitivity to BSM effects, the simplified template cross sections can be interpreted together with e.g. POs in Higgs boson decays. To make this possible, the experimental and theoretical correlations between the simplified template cross sections and the decay POs would need to be evaluated and taken into account in the interpretation. This point will not be expanded on further in this section, but would be interesting to investigate in the future.

While the simplified template cross section bins have some similarity to a differential cross section measurement, they aim to combine the advantages of the signal strength measurements and fiducial and differential measurements. In particular, they are complementary to full-fledged fiducial and differential measurements and are neither designed nor meant to replace these. Fully fiducial differential measurements are of course essential but can only be carried out in a subset of decay channels in the foreseeable future. They are explicitly optimized for maximal theory independence. In practice, this means that in the measurements acceptance corrections are minimized, typically, simple selection cuts are used, and the measurements are unfolded to a fiducial volume that is as close as possible to the fiducial volume measured for a particular Higgs boson decay channel. In contrast, simplified template cross sections are optimized for sensitivity while reducing the dominant theory dependence in the measurement. In practice, this means that simplified fiducial volumes are used and larger acceptance corrections are allowed in order to maximally benefit from the use of event categories and multivariate techniques. They are also inclusive in the Higgs boson decay to allow for the combination of the different decay channels. The fiducial and differential measurements are designed to be agnostic to the production modes as much as possible. On the other hand, the separation into the production modes is an essential aspect of the

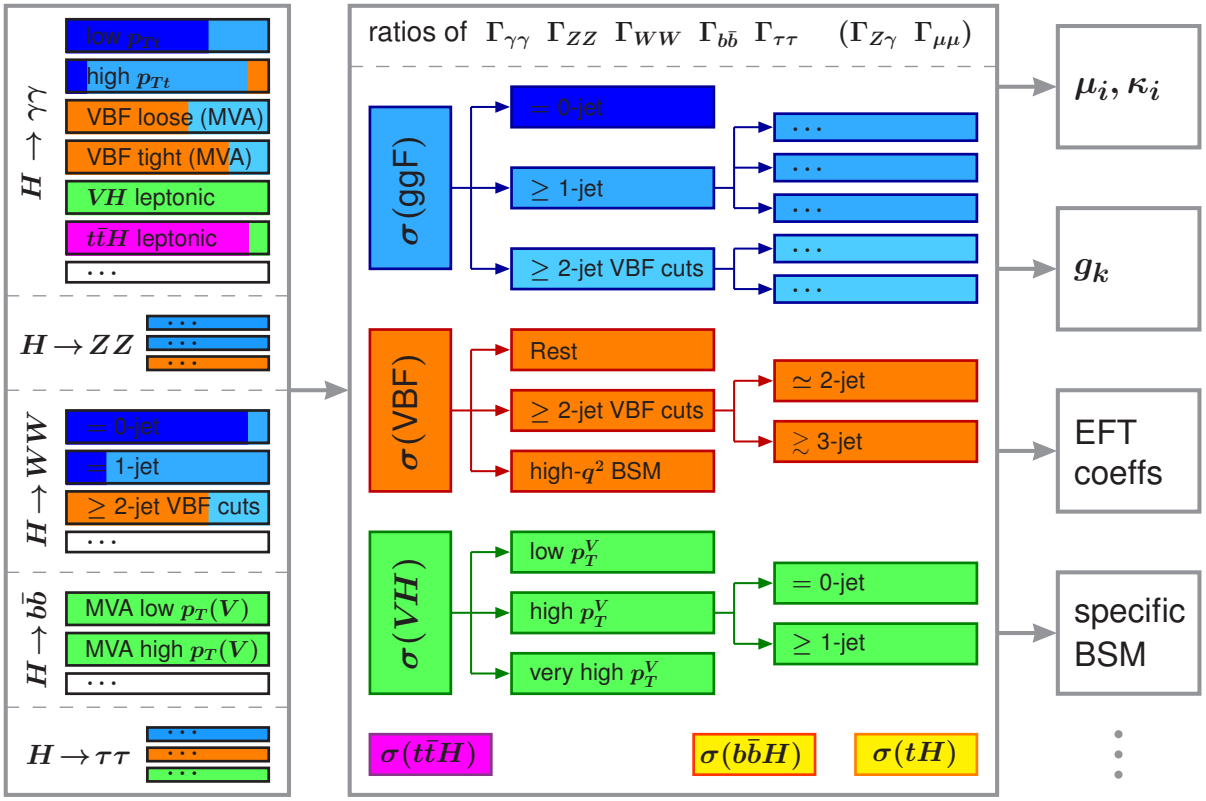

Figure 217: Schematic overview of the simplified template cross section framework.

simplified template cross sections to reduce their model dependence.

III.2.2 Guiding principles in the definition of simplified template cross section bins

As outlined above, several considerations have been taken into account in the definition of the simplified template cross section bins.

One important design goal is to reduce the dependence of the measurements on theoretical uncertainties in SM predictions. This has several aspects. First, this requires avoiding that the measurements have to extrapolate from a certain region in phase space to the full (or a larger region of) phase space whenever this extrapolation carries nontrivial or sizeable theoretical uncertainties. A example is the case where an event category selects an exclusive region of phase space, such as an exclusive jet bin. In this case, the associated theoretical uncertainties can be largely avoided in the measurement by defining a corresponding truth jet bin. The definition of the bins is preferably in terms of quantities that are directly measured by the experiments to reduce the needed extrapolation.

There will of course always be residual theoretical uncertainties due to the experimental acceptances for each truth bin. Reducing the theory dependence thus also requires to avoid cases with large variation in the experimental acceptance within one truth bin, as this would introduce a direct dependence on the underlying theoretical distribution in the simulation. If this becomes an issue, the bin can be further split into two or more smaller bins, which reduces this dependence in the measurement and moves it to the interpretation step.

To maximize the experimental sensitivity, the analyses should continue to use event categories primarily optimized for sensitivity, while the definition of the truth bins should take into consideration the experimental requirements. However, in cases where multivariate analyses are used in the analyses,

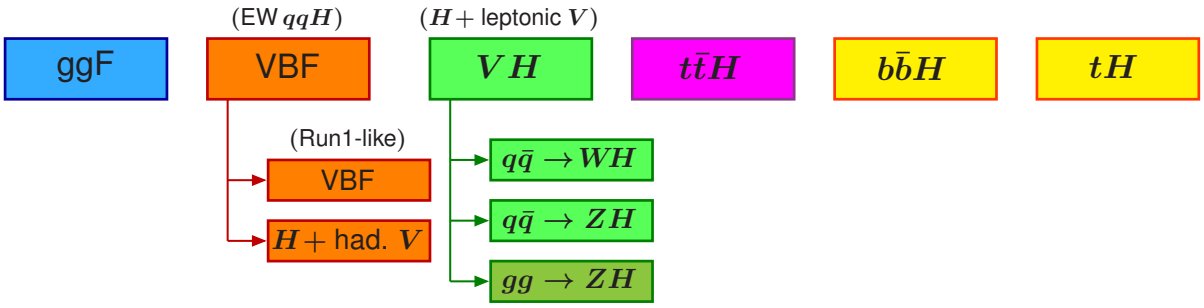

Figure 218: Stage 0 bins.

it has to be carefully checked and balanced against the requirement to not introduce theory dependence, e.g., by selecting specific regions of phase space.

Another design goal is to isolate regions of phase space, typically at large kinematic scales, where BSM effects could be potentially large and visible above the SM background. Explicitly separating these also reduces the dependence of the measurements on the assumed SM kinematic distribution.

In addition, the experimental sensitivity is maximized by allowing the combination of all decay channels, which requires the framework to be used by all analyses. To facilitate the experimental implementation, the bins should be mutually exclusive to avoid introducing statistical correlations between different bins. In addition, the number of bins should be kept minimal to avoid technical complications in the individual analyses as well as the global fit, e.g. in the evaluation of the full covariance matrix. For example, each bin should typically have some sensitivity from at least one event category in order to avoid the need to statistically combine many poorly constrained or unconstrained measurements. On the other hand, in BSM sensitive bins experimental limits are already very useful for the theoretical interpretation.

III.2.2.a Splitting of production modes

The definition of the production modes has some notable differences compared to Run1 to deal with the fact that the naive distinction between the $q\bar{q} \to VH$ and VBF processes, and similarly between $gg \to VH$ and gluon-fusion production, becomes ambiguous at higher order when the V decays hadronically. For this reason, the VH production mode is explicitly defined as Higgs boson production in association with a leptonically decaying V boson. The $q\bar{q} \to VH$ process with a hadronically decaying V boson is considered to be part of what is called "VBF production", which is defined as electroweak qqH production. Similarly, the $gg \to ZH$ process with hadronically decaying Z boson is included in what is called "gluon-fusion production".

In principle, also the separation of ZH production with a leptonic Z into $q\bar{q}$ or gg initial states becomes ambiguous at higher order. For present practical purposes, on the experimental side the split can be defined according to the separate MC samples for $q\bar{q} \to ZH$ and $gg \to ZH$ used in the analyses.

III.2.2.b Staging

In practice, it will be impossible to define a set of bins that satisfies all of the above requirements for every analysis. Some analyses will only be able to constrain a subset of all bins or only constrain the sum of a set of bins. In addition, the number of bins that will be possible to measure increases with increasing amount of available data. For this reason, several stages with an increasing number of bins are defined. The evolution from one stage to the next can take place independently for each production mode.

III.2.2.b.i Stage 0

Stage 0 is summarized in Figure 218 and corresponds most closely to the measurement of the production mode μ in Run1. At this stage, each main production mode has a single inclusive bin, with associated Higgs boson production separated into $q\bar{q} \to WH$, $q\bar{q} \to ZH$ and $gg \to ZH$ channels.

As discussed in Section III.2.2.a, VBF production is defined as electroweak qqH production. For better compatibility with Run1 measurements, the VBF production is split into a Run1-like VBF and Run1-like $V(\to jj)H$ bin, where the splitting is defined by the conventional Feynman diagrams included in the simulations. In practice, most decay channels will only provide a measurement for the Run1-like VBF bin.

III.2.2.b.ii Stage 1

Stage 1 defines a binning that is targeted to be used by all analyses on an intermediate time scale. In principle, all analyses should aim to eventually implement the full stage 1 binning. If necessary, intermediate stages to reach the full stage 1 binning can be implemented by a given analysis by merging bins that cannot be split. In this case, the analysis should ensure that the merged bins have similar acceptances, such that the individual bins can still be determined in an unbiased way in the global combination of all channels. In the diagrams presented below, the possibilities for merging bins are indicated by "(+)".

III.2.2.b.iii Stage 2

Defining the stage 2 binning in full detail is very difficult before having gained experience with the practical implementation of the framework with the stage 1 binning. Therefore, instead of giving a detailed proposal for the stage 2 binning, we only give indications of interesting further separation of bins that should be considered for the stage 2 binning.

III.2.3 Definition of leptons and jets

The measured event categories in all decay channels are unfolded by the global fit to the simplified template cross sections bins. For this purpose, and for the comparison between the measured bins and theoretical predictions from either analytic calculations or MC simulations, the truth final state particles need to be defined unambiguously. The definition of the final state particles, leptons, jets, and in particular also the Higgs boson are explicitly kept simpler and more idealized than in the fiducial cross section measurements. Treating the Higgs boson as a final state particle is what allows the combination of the different decay channels.

For the moment, the definitions are adapted to the current scope of the measurements. Once a finer binning is introduced for $t\bar{t}H$ or processes such as VBF with the emission of a hard photon are added, some of the definitions below might have to be adapted or refined.

III.2.3.a Higgs boson

The simplified template cross sections are defined for the production of an on-shell Higgs boson, and the unfolding should be done accordingly. A global cut on the Higgs boson rapidity at $|Y_H| < 2.5$ is included in all bins. As the current measurements have no sensitivity beyond this rapidity range, this part of phase space would only be extrapolated by the MC simulation. On the other hand, it is in principle possible to use forward electrons (up to $|\eta|$ of 4.9) in $H \to ZZ^* \to 4\ell$ and extend the accessible rapidity range. For this purpose, an additional otherwise inclusive bin for $|Y_H| > 2.5$ can be included.

III.2.3.b Leptons

Electrons and muons from decays of signal vector bosons, e.g. from VH production, are defined as dressed, i.e. FSR photons should be added back to the electron or muon. τ leptons are defined from the

sum of their decay products (for any τ decay mode). There should be no restriction on the transverse momentum or the rapidity of the leptons. That is, for a leptonically decaying vector boson the full decay phase space is included.

III.2.3.c Jets

Truth jets are defined as anti-k_t jets with a jet radius of $R = 0.4$, and are built from all stable particles (exceptions are given below), including neutrinos, photons and leptons from hadron decays or produced in the shower. Stable particles here have the usual definition, having a lifetime greater than 10 ps, i.e. those particles that are passed to GEANT in the experimental simulation chain. All decay products from the Higgs boson decay are removed as they are accounted for by the truth Higgs boson. Similarly, leptons (as defined above) and neutrinos from decays of the signal V bosons are removed as they are treated separately, while decay products from hadronically decaying signal V bosons are included in the inputs to the truth jet building.

By default, truth jets are defined without restriction on their rapidity. A possible rapidity cut can be included in the bin definition. A common p_{T} threshold for jets should be used for all truth jets. A lower threshold would in principle have the advantage to split the events more evenly between the different jet bins. Experimentally, a higher threshold at 30 GeV is favored due to pile up and is therefore used for the jet definition to limit the amount of phase-space extrapolation in the measurements.

III.2.4 Bin definitions for the different production modes

In the following, the bin definitions for the different production modes in each stage are given. The bins are easily visualized through cut flow diagrams. In the diagrams, the bins on each branch are defined to be mutually exclusive and sum up to the preceding parent bin. For simplicity, sometimes not all cuts are explicitly written out in the diagrams, in which case the complete set of cuts are specified in the text. In case of ambiguities, a more specific bin is excluded from a more generic bin. As already mentioned, for the stage 1 binning the allowed possibilities for merging bins at intermediate stages are indicated by a "(+)" between two bins.

III.2.4.a Bins for $gg \to H$ production

III.2.4.a.i Stage 0

Inclusive gluon fusion cross section within $|Y_H| < 2.5$. Should the measurements start to have acceptance beyond 2.5, an additional bin for $|Y_H| > 2.5$ can be included.

III.2.4.a.ii Stage 1

Stage 1 refines the binning for $|Y_H| < 2.5$. The stage 1 binning is depicted in Figure 219 and summarized as follows:

- Split into jet bins: $N_j = 0$, $N_j = 1$, $N_j \geq 2$, $N_j \geq 2$ with VBF topology cuts (defined with the same cuts as the corresponding bin in VBF production). For the $N_j \geq 2$ with VBF topology cuts, $p_{\mathrm{T}}^H < 200$ GeV is required, which gives priority to the $p_{\mathrm{T}}^H > 200$ GeV bin for $N_j \geq 2$. Otherwise, the $N_j \geq 2$ with VBF topology cuts is excluded from the $N_j \geq 2$ bins. The jet bins are motivated by the use of jet bins in the experimental analyses. Introducing them also for the simplified template cross sections avoids folding the associated theoretical uncertainties into the measurement. The separation of the $N_j \geq 2$ with VBF topology cuts is motivated by the wish to separately measure the gluon fusion contamination in the VBF selection. If the fit has no sensitivity to determine the gluon fusion and the VBF contributions with this topology, the sum of the two contributions can be quoted as result.

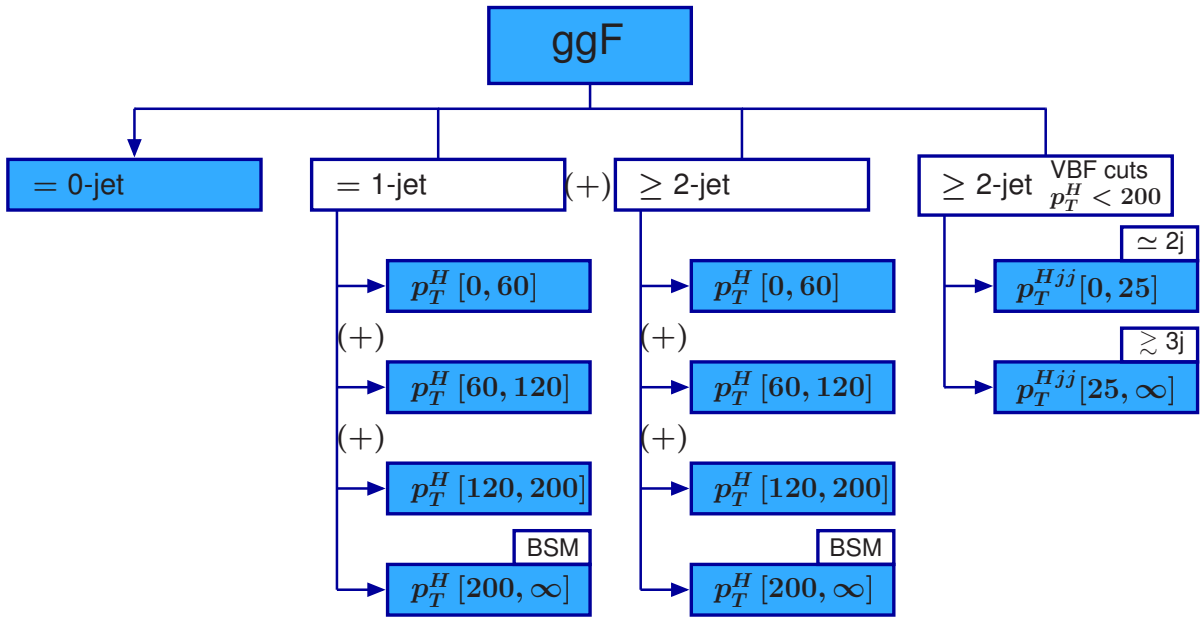

Figure 219: Stage 1 binning for gluon fusion production.

- The $N_j \geq 2$ with VBF topology bin is split further into an exclusive 2-jet-like and inclusive 3-jet-like bin. The split is implemented by a cut on $p_{\mathrm{T}}^{Hjj} = |\vec{p}_{\mathrm{T}}^{\,H} + \vec{p}_{\mathrm{T}}^{\,j1} + \vec{p}_{\mathrm{T}}^{\,j2}|$ at 25 GeV. See the corresponding discussion for VBF for more details. This split is explicitly included here since it induces nontrivial theory uncertainties in the gluon-fusion contribution.
- The $N_j = 1$ and $N_j \geq 2$ bins are further split into p_{T}^H bins.
  - 0 GeV $< p_{\mathrm{T}}^H <$ 60 GeV: The boson channels have most sensitivity in the low p_{T}^H region. The upper cut is chosen as low as possible to give a more even split of events but at the same time high enough that no resummation effects are expected. The cut should also be sufficiently high that the jet p_{T} cut introduces a negligible bias.
  - 60 GeV $< p_{\mathrm{T}}^H <$ 120 GeV: This is the resulting intermediate bin between the low and high p_{T}^H regions. The lower cut here is high enough that this bin can be safely treated as a hard $H + j$ system in the theoretical description.
  - 120 GeV $< p_{\mathrm{T}}^H <$ 200 GeV: The boosted selection in $H \to \tau\tau$ contributes to the high p_{T}^H region. Defining a separate bin avoids large extrapolations for the $H \to \tau\tau$ contribution. For $N_j = 2$, this bin likely provides a substantial part of the gluon-fusion contribution in the hadronic VH selection.
  - $p_{\mathrm{T}}^H >$ 200 GeV: Beyond the top-quark mass, the top-quark loop gets resolved and top-quark mass effects become relevant. Splitting off the high-p_{T}^H region ensures the usability of the heavy-top expansion for the lower-p_{T}^H bins. At the same time, the high p_{T}^H bin in principle offers the possibility to distinguish a pointlike ggH vertex induced by heavier BSM particles in the loop from the resolved top-quark loop.

At intermediate stages, all lower three p_{T}^H bins, or any two adjacent bins, can be merged. Alternatively or in addition the $N_j = 1$ and $N_j \geq 2$ bins can be merged by individual analyses as needed, and potentially also when the combination is performed at an intermediate stage.

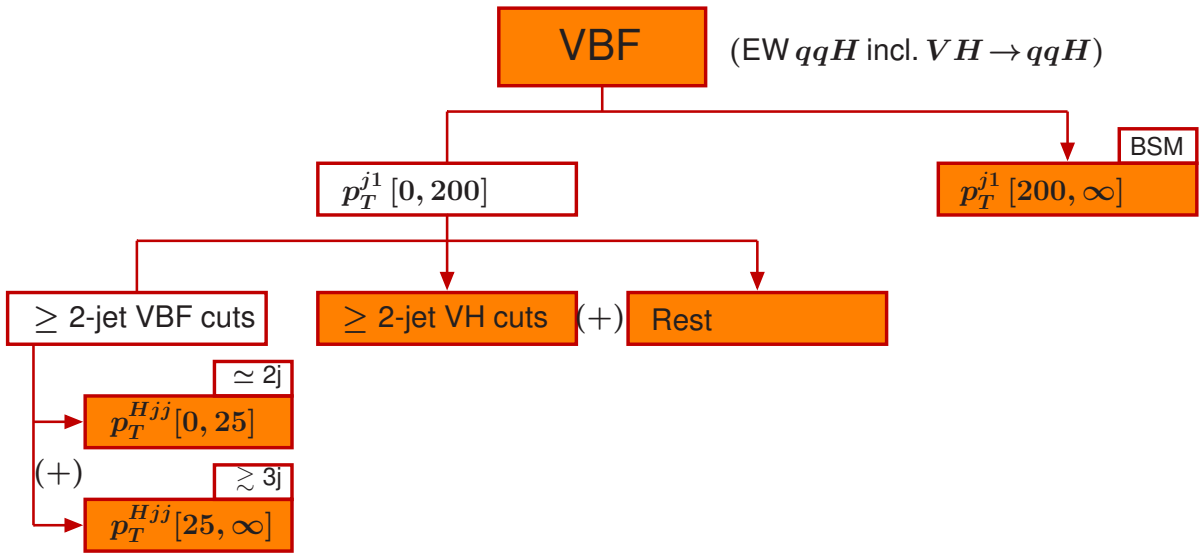

Figure 220: Stage 1 binning for vector boson fusion production.

III.2.4.a.iii Stage 2

In stage 2, the high p_{T}^{H} bin should be split further, in particular if evidence for new heavy particles arises. In addition, the low p_{T}^{H} region can be split further to reduce any theory dependence there. If desired by the analyses, another possible option is to further split the $N_j \geq 2$ bin into $N_j = 2$ and $N_j \geq 3$.

III.2.4.b Bins for VBF production

At higher order, VBF production and VH production with hadronically decaying V become ambiguous. Hence, what we refer to as VBF in this section, is defined as as electroweak $qq'H$ production, which includes both VBF and VH with hadronic V decays.

III.2.4.b.i Stage 0

Inclusive vector boson fusion cross section within $|Y_H| < 2.5$. Should the measurements start to have acceptance beyond 2.5, an additional bin for $|Y_H| > 2.5$ can be included.

III.2.4.b.ii Stage 1

Stage 1 refines the binning for $|Y_H| < 2.5$. The stage 1 binning is depicted in Figure 220 and summarized as follows:

- VBF events are split by p_{T}^{j1}, the transverse momentum of the highest-p_{T} jet. The lower p_{T}^{j1} region is expected to be dominated by SM-like events, while the high-p_{T}^{j1} region is sensitive to potential BSM contributions, including events with typical VBF topology as well as boosted $V(\to jj)H$ events where the V is reconstructed as one jet. The suggested cut is at 200 GeV, to keep the fraction of SM events in the BSM bin small. Note that events with $N_j = 0$, corresponding to $p_{\mathrm{T}}^{j1} < 30$ GeV, is included in the $p_{\mathrm{T}}^{j1} < 200$ GeV bin.
- The $p_{\mathrm{T}}^{j1} < 200$ GeV bin is split further:
  - Typical VBF topology: The adopted VBF topology cuts are $m_{jj} > 400$ GeV, $\Delta\eta_{jj} > 2.8$ (and without any additional rapidity cuts on the signal jets). This should provide a good intermediate compromise among the various VBF selection cuts employed by different channels.

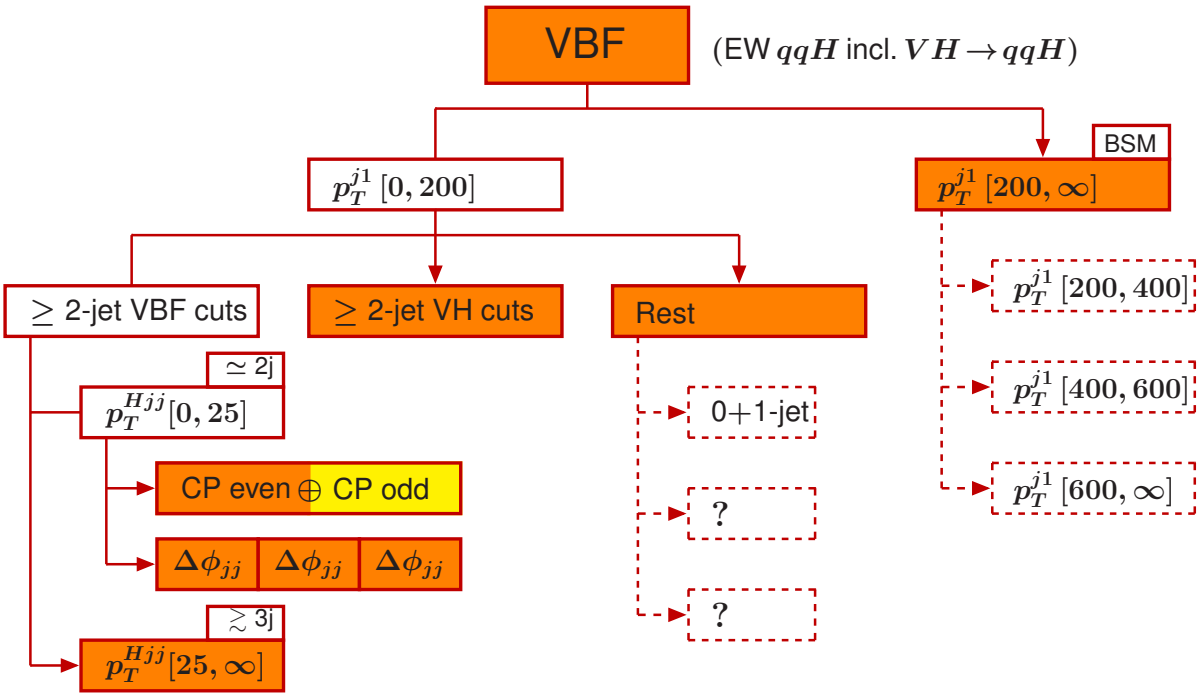

Figure 221: Possible stage 2 binning for vector boson fusion production.

* The bin with typical VBF topology is split into an exclusive 2-jet-like and inclusive 3-jet-like bin using a cut on p_{T}^{Hjj} at 25 GeV, where the cut value is a compromise between providing a good separation of gluon fusion and VBF and the selections used in the measurements. p_{T}^{Hjj} as quantity to define this split is chosen as a compromise between the different kinematic variables used by different channels to enrich VBF production. (In particular the kinematic variables $\Delta\phi_{H-jj}$ and p_{T}^{j3} are both correlated with p_{T}^{Hjj}).

– Typical $V(\to jj)H$ topology: events with at least two jets and 60 GeV $< m_{jj} <$ 120 GeV.
– Rest: all remaining events, including events with zero or one jet. The "rest" bin can be sensitive to certain BSM contributions that do not follow the typical SM VBF signature with two forward jets.

III.2.4.b.iii Stage 2

More splits are introduced at stage 2 as illustrated in Figure 221. While the details require more discussion and cannot be finalized at the present, this could include

– The high-p_{T}^{j1} bin can be split further by separating out very high-p_{T}^{j1} events for example with additional cuts at 400 GeV and 600 GeV.
– The "rest" bin can be split further, e.g., by explicitly separating out a looser VBF selection, and/or by separating out events with zero or one jets.
– The $N_j \simeq 2$ VBF topology bin can be split further to gain sensitivity to CP odd contributions, e.g. by splitting it into subbins of $\Delta\phi_{jj}$ or alternatively by measuring a continuous parameter.

III.2.4.c Bins for VH production

In this section, VH is defined as Higgs boson production in association with a leptonically decaying V boson.

Note that $q\bar{q} \to VH$ production with a hadronically decaying V boson is considered part of VBF

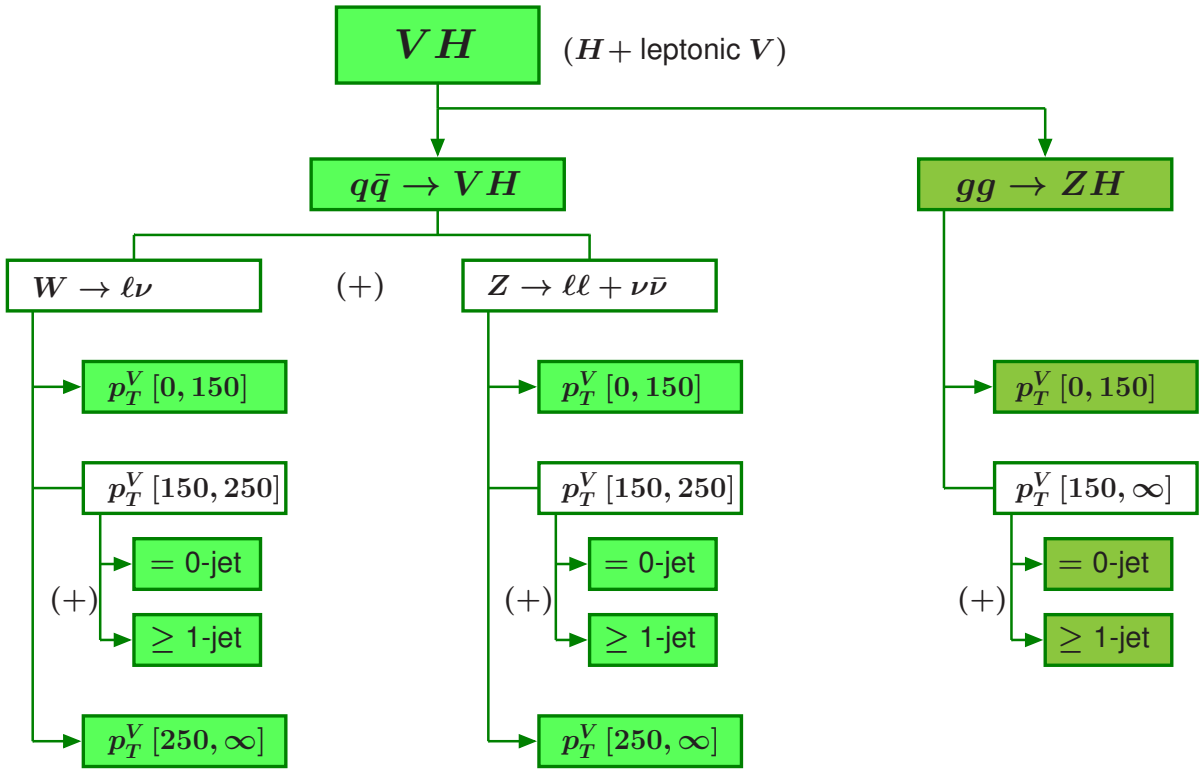

Figure 222: Stage 1 binning for associated production with vector bosons.

production. Similarly, $gg \to VH$ production with hadronically decaying V boson is considered part of gluon fusion production.

III.2.4.c.i Stage 0

Inclusive associated production with vector bosons cross section within $|Y_H| < 2.5$. Should the measurements start to have acceptance beyond 2.5, an additional bin for $|Y_H| > 2.5$ can be included.

III.2.4.c.ii Stage 1

Stage 1 refines the binning for $|Y_H| < 2.5$. The stage 1 binning is depicted in Figure 222 and summarized as follows:

- VH production is first split into the production via a $q\bar{q}$ or gg initial state. This split becomes ambiguous at higher order. For practical purposes, on the experimental side the split can be defined according to the MC samples used in the analyses, which are split by $q\bar{q}$ and gg.
  - The production via $q\bar{q} \to VH$ is split according to the vector boson: $W \to \ell\nu$ and $Z \to \ell\ell + \nu\bar{\nu}$.
  - $W \to \ell\nu$ and $Z \to \ell\ell + \nu\bar{\nu}$ are split further into bins of p_{T}^V, aligned with the quantity used in the $H \to b\bar{b}$ analysis, which is one of the main contributors to the VH bins.
    * $p_{\mathrm{T}}^V < 150$ GeV receives contributions from the bosonic decay channels and from $H \to b\bar{b}$ with $W \to \ell\nu$ and $Z \to \ell\ell$, which do not rely on $E_{\mathrm{T}}^{\mathrm{miss}}$ triggers.
    * 150 GeV $< p_{\mathrm{T}}^V <$ 250 GeV receives contributions from $H \to b\bar{b}$ with $Z \to \nu\bar{\nu}$ due to the high threshold of the $E_{\mathrm{T}}^{\mathrm{miss}}$ trigger, as well as from $H \to b\bar{b}$ with $W \to \ell\nu$ and $Z \to \ell\ell$.

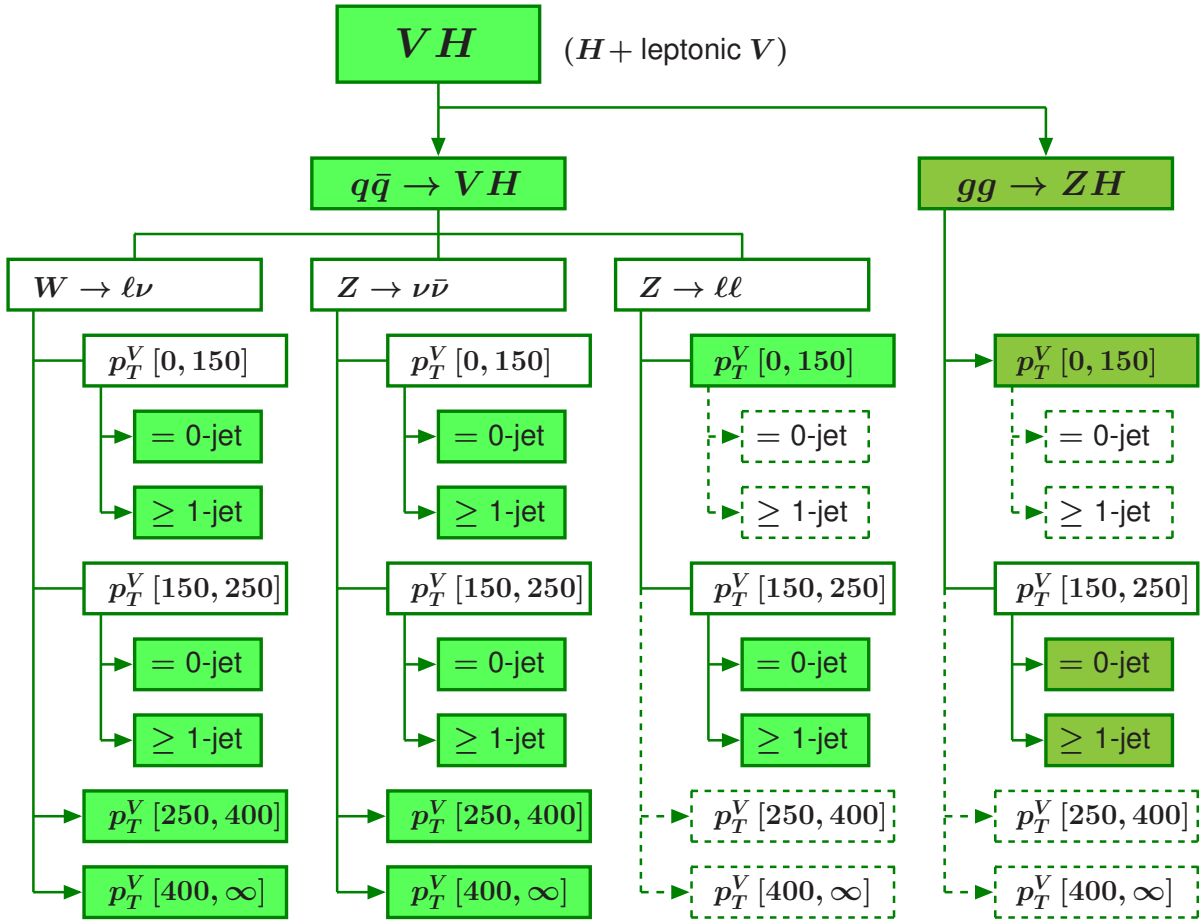

Figure 223: Possible Stage 2 binning for associated production with vector bosons.

· This bin is split further into a $N_j = 0$ and a $N_j \geq 1$ bin, reflecting the different experimental sensitivity and to avoid the corresponding theory dependence.

* $p_{\mathrm{T}}^V > 250$ GeV is sensitive to BSM contributions.

– The production via $gg \to ZH$ is split in analogy to production from the $q\bar{q}$ initial state, apart from the $p_{\mathrm{T}}^V > 250$ GeV bin, which is not split out.

III.2.4.c.iii Stage 2

More splits are introduced at stage 2 as illustrated in Figure 221. While the details need more discussion, this could include

– Split of the $Z \to \ell\ell + \nu\bar{\nu}$ into $Z \to \ell\ell$ and $Z \to \nu\bar{\nu}$.
– Split of the $p_{\mathrm{T}}^V < 150$ GeV into a $N_j = 0$ and a $N_j \geq 1$ bin, except maybe for the $Z \to \ell\ell$ channel, which will suffer from the low $Z \to \ell\ell$ branching ratio.
– Split of the $p_{\mathrm{T}}^V > 250$ GeV bin into $p_{\mathrm{T}}^V < 400$ GeV and $p_{\mathrm{T}}^V > 400$ GeV, to increase the sensitivity to BSM contributions with very high p_{T}^V, potentially apart from the $Z \to \ell\ell$.
– Potentially analogous splits for $gg \to ZH$ production.

III.2.4.d Treatment of $t\bar{t}H$ production

III.2.4.d.i Stage 0

Inclusive $t\bar{t}H$ production with $|Y_H| < 2.5$. Should the measurements start to have acceptance beyond 2.5, an additional bin for $|Y_H| > 2.5$ can be included.

III.2.4.d.ii Stage 1

Currently no additional splits beyond stage 0 are foreseen. One option might be to separate different top decay channels for $|Y_H| < 2.5$.

III.2.4.d.iii Stage 2

In the long term it could be useful to split into bins with 0 and ≥ 1 additional jets or one or more bins tailored for BSM sensitivity.

III.2.4.e Treatment of $b\bar{b}H$ and tH production

In the foreseeable future, there will only be one inclusive bin for $b\bar{b}H$ production and only one inclusive bin for tH production for $|Y_H| < 2.5$. Should the measurements start to have acceptance beyond 2.5, an additional bin for $|Y_H| > 2.5$ can be included.

III.2.5 Practical considerations

To facilitate the combination of the results from ATLAS and CMS, the same bin definitions need to be used by the two collaborations. As for the Run1 Higgs boson coupling measurements, a combination of results from ATLAS and CMS will also require that the two collaborations estimate systematic and residual theoretical uncertainties in a compatible way. This might be facilitated for example by the use of the same Monte Carlo generators in the measurements.

After first experience with the measurement and interpretation has been collected, the stage 1 bin definitions should be reviewed. This should in particular include the definition of the VBF topology cuts as well as the p_{T}^{Hjj} split. In cases where the bin definitions are clearly inadequate, they should be improved for future measurements. The stage 2 bins will be defined in detail taking into account the experience gained during the measurements based on the stage 1 definitions.

A reference implementation of the bin definitions in Rivet has been developed [961]. This will facilitate a consistent treatment in both experiments as well as in theoretical studies.

III.2.6 Summary

Simplified template cross sections provide a way to evolve the signal strength measurements that were performed during LHC Run1, by reducing the theoretical uncertainties that are directly folded into the measurements and by providing more finely-grained measurements, while at the same time allowing and benefitting from the combination of measurements in many decay channels. Several stages are proposed: stage 0 essentially corresponds to the production mode measurements of Run1 and stage 1 defines a first complete setup, with indications for potential bin merging when a given channel cannot yet afford the full stage 1 granularity. A complete proposal for the stage 2 binning will need to be based on experience of using the simplified template cross section framework in real life, but some indications of what could be interesting are already given here.

Chapter III.3

Higgs Fiducial Cross Sections

F.U. Bernlochner, S. Kraml, P. Milenovic, P.F. Monni (Eds.); M. Ahmad, F. Caola, N. Chanon, D. de Florian, G. Ferrera, F.F. Freitas, M. Grazzini, D. Gonçalves, J. Huston, S. Kallweit, P. Lenzi, A.C. Marini, K. Melnikov, S. Menary, C. Meyer, A. Pilkington, T. Plehn, M. Queitsch-Maitland, D. Rathlev, V. Sanz, H. Sargsyan, M. Schönherr, M. Schulze, D.M. Sperka, D. Tommasini, L. Viliani

III.3.1 Introduction

Over the past years fiducial measurements, both differential and total, became standard practice for characterizing Standard Model (SM) processes at the LHC. The advantage of quoting such results over inclusive cross section measurements lies in the almost complete factorization of experimental and theoretical uncertainty sources: whereas for inclusive cross section measurements one extrapolates back to account for acceptance and phase-space regions not measured by the detector or removed by the analysis, fiducial cross sections are defined within an experiment dependent fiducial volume of acceptance and phase space. The large extrapolation from the measured subset to the entirety of phase space is reduced to account solely for reconstruction efficiencies and to revert resolution effects and migrations inside and outside the fiducial region. If one now wishes to confront the measured fiducial cross section with a new SM or beyond the SM (BSM) theory, one can readily do so once one accounted for the acceptance and no repetition of the analysis of the original data is needed. This helps preserve the measured results and allow for a comparison even in a scenario of a new theory being developed years after an original measurement has been carried out.

The measurement of differential or total fiducial cross sections offers an alternative approach to study the properties of the Higgs boson: a range of physical phenomena are accessible, such as the theoretical modelling of different Higgs boson production mechanism or BSM contributions, by measuring kinematic distributions constructed from the Higgs boson decay products or other objects produced in association with the Higgs boson. The fiducial or differential cross sections may be split into four categories based on what underlying physical aspect they are probing:

1. Higgs boson kinematics: In Higgs boson decay final states with no undetectable particles, such as neutrinos, the transverse momentum of the Higgs boson, $p_{\mathrm{T}}^{\mathrm{H}}$, and the absolute rapidity, $\left|y^{\mathrm{H}}\right|$, can be measured with good experimental precision. Inclusive Higgs boson production is dominated by gluon fusion for which the transverse momentum is largely balanced by the emission of QCD radiation. Measuring p_T^H probes the perturbative QCD modelling of this production mechanism. The rapidity distribution of the Higgs boson is sensitive to the gluon fusion production mechanism as well as to the parton distribution functions (PDFs) of the colliding protons.

2. Jet activity: The jet multiplicity, N_{jets} and the transverse momentum and rapidity distributions of the leading and subleading jets are sensitive to the theoretical modelling and relative contributions of different Higgs boson production mechanisms. In the SM events with zero and one jet are dominated by gluon fusion production of the Higgs boson and the transverse momentum and rapidity of the leading jet probes the theoretical modelling of hard quark and gluon radiation in this process. The contribution from vector boson fusion and associated production with vector bosons becomes more important for two-jet events. The contribution from Higgs boson production in association with top-antitop production becomes more relevant in the highest jet multiplicities.

3. Spin and CP quantum numbers: Angular observables, such as the angle between the Higgs boson decay products and the beam axis or the azimuthal angle between the two leading jets in events containing two or more jets are sensitive to the spin and charge conjugation and parity properties of the Higgs boson, respectively.

4. Higgs boson production mechanisms: Specific fiducial regions may be constructed which target certain Higgs boson production mechanism. For instance in events with two or more jets, one may look at the subset of events with jets with a large rapidity separation between the two leading jets and a large dijet mass. This selects events with suppressed colour flow between the two jets, which is expected for Higgs boson production from the vector boson fusion process, but not from gluon fusion. Using similar criteria Higgs boson production associated with vector bosons or top-antitop pairs can be targeted and fiducial cross sections enriched with such can be studied.

For BSM contributions some regions are more interesting than others: in some scenarios large contributions near kinematic corners of phase space are expected. The purpose of this chapter is to review the state of the art of predicting fiducial cross sections inside the SM and provide a summary of interesting observables and fiducial regions that can be used to search for physics beyond the SM. In addition a summary of the experimental aspects of fiducial measurements are reviewed and a range of suggestions for future measurements is given. The rest of this chapter is organized as follows: Section III.3.2 provides a brief summary of fiducial measurements carried out in Run 1 of the LHC. Section III.3.3 reviews the state-of-the-art of predicting fiducial cross sections for the SM and discusses the current limitations. These studies are carried out using template fiducial regions with acceptance and kinematic cuts close to the expected definition for Run 2 for the ATLAS and CMS experiments. Section III.3.4 reviews the effects that can arise from new physics contributions. In particular, a range of suggestions is presented which kinematic regions might be probed in future measurements. Section III.3.5 provides a review of the necessary experimental methods and prerequisites to carry out fiducial measurements. Among the aspects discussed is a brief review of what points should be considered when reverting migrations inside the fiducial region or in and outside the fiducial region. The combination of several measurements, as well as the implications of different treatments of the Higgs boson mass is discussed as well. The chapter concludes with Section III.3.6 with a list of recommendations on how future measurements should be presented.

III.3.2 Review of Run 1 and early Run 2 results

In the first running period of the LHC, several measurements of fiducial cross sections have been carried out by the ATLAS and CMS experiments. These measurements mark the transition from the discovery of the Higgs boson, and first measurement characterizing its quantum numbers, to less statistical powerful but more model independent statements about its properties. Such measurements were first carried out in the channels with high mass resolution, $\mathrm{H} \to \gamma\gamma$ [962, 963] and $\mathrm{H} \to \mathrm{ZZ}^* \to 4\ell$ [964, 965], More recently, the first measurements of the differential fiducial cross sections in $H \to WW$ decay channel also appeared [966]. First combinations of total and differential information from $\mathrm{H} \to \gamma\gamma$ and $\mathrm{H} \to \mathrm{ZZ}^* \to 4\ell$ also were carried out, extrapolating into the inclusive phase space and correcting for the difference in branching fraction, cf. Ref. [967]. A variety of results were reported, ranging from inclusive and exclusive jet multiplicities to differential information characterizing the Higgs boson, its decay products, or objects produced in association with it: the Higgs boson p_T distribution and absolute rapidity has been measured, the number of jets as well as the p_T and rapidity distributions of the leading and sub-leading jets. Angular observables from jets and jets plus the Higgs boson decay products have been reported. Figure 224 shows a summary of the fiducial regions measured by ATLAS in the $\mathrm{H} \to \gamma\gamma$ channel and the measured Higgs boson p_T spectrum reported by CMS using $\mathrm{H} \to \mathrm{ZZ}^* \to 4\ell$ events. The precision of the probed fiducial regions and differential observables are all statistically limited at this point.

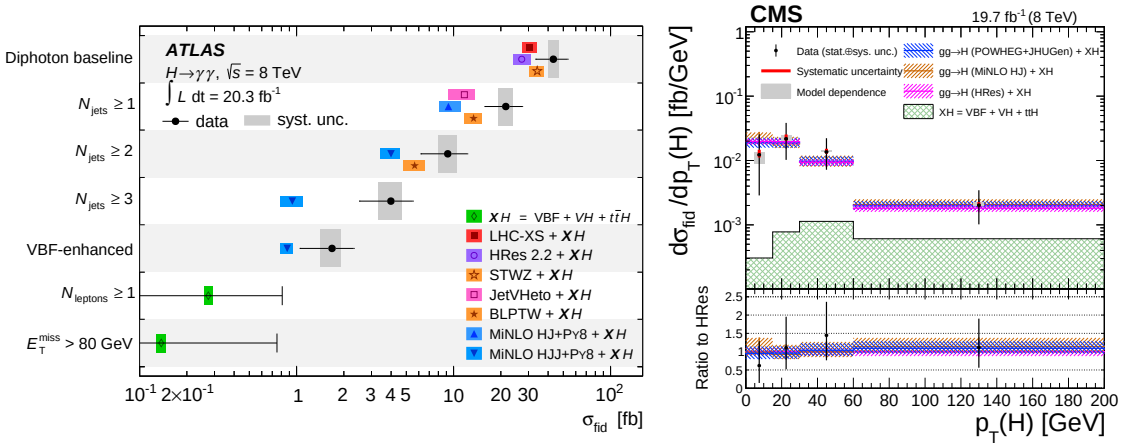

Figure 224: (left) Various fiducial regions measured by Ref. [962] using $\mathrm{H} \to \gamma\gamma$ decays: the data points show measured cross sections of total, inclusive jet multiplicities as well as VBF and VH enhanced regions. The coloured bands show several theory predictions for the different fiducial regions for gluon fusion and other SM Higgs boson production. (right) The measured differential Higgs boson p_{T} spectrum is shown from Ref. [965] using $\mathrm{H} \to \mathrm{ZZ}^* \to 4\ell$ events. The data points show the measured cross section and the different shaded bands theory predictions from gluon fusion and other SM Higgs boson production.

The reported cross sections are unfolded to the particle level, defined by particles that have lifetimes such that $c\tau > 10$ mm. The reported fiducial volumes differ for each final state and between experiments. The defining criteria of the fiducial volumes were chosen to be very similar to the criteria applied at detector level to ensure minimal model dependence in the final measurements. In both experiments, leptons are identified using an isolation criterion by summing over energetic clusters in a cone around the charged track trajectory. This can be mimicked at particle level by requiring a similar isolation in a cone around the particle-level lepton. For photons a similar requirement can be imposed to closely match the experimental selection. Other requirements that enter the fiducial acceptance is the overall detector acceptance, trigger threshold energies, and analysis selection cuts. Once defined, selection related efficiencies can be reverted to convert fitted yields into fiducial cross sections. Migrations inside the fiducial volumes from finite resolution are reverted as well, what allows direct comparison with theory predictions. Two different methods to accomplish this are used right now: the ATLAS $\mathrm{H} \to \gamma\gamma$ and $\mathrm{H} \to \mathrm{ZZ}^* \to 4\ell$ results chose to use correction factors, while the CMS $\mathrm{H} \to \mathrm{ZZ}^* \to 4\ell$ and the CMS $\mathrm{H} \to \gamma\gamma$ results directly inverted the migration matrix. Several results [962, 964] are already published on HEPDATA [968] along with example RIVET routines [310] to apply the corresponding particle level fiducial selection of each analysis, while the others are expected to follow [963, 965, 966].

The ATLAS experiment reported in a follow up publication to Ref. [962] also the statistical correlations between five measured differential distributions in Ref. [969]. This allows the simultaneous analysis of several differential distributions and the result of a proof-of-concept analysis constraining BSM physics is shown in Figure 225 along with the determined statistical correlations between exclusive jet bins and the Higgs boson p_{T}. Finally, ATLAS reported fiducial cross sections of $\mathrm{pp} \to \mathrm{ZZ}^{(*)} \to 4\ell$ in which the Higgs boson contribution from $\mathrm{H} \to \mathrm{ZZ}^* \to 4\ell$ was included as part of the signal definition [970].

Fiducial cross sections results using early Run 2 data were reported by both ATLAS and CMS for the $\mathrm{H} \to \gamma\gamma$ and $\mathrm{H} \to \mathrm{ZZ}^* \to 4\ell$ channels. Figure 226 shows preliminary results of the total fiducial cross section for centre-of-mass energies at 7, 8 and 13 TeV from Refs. [971, 972].

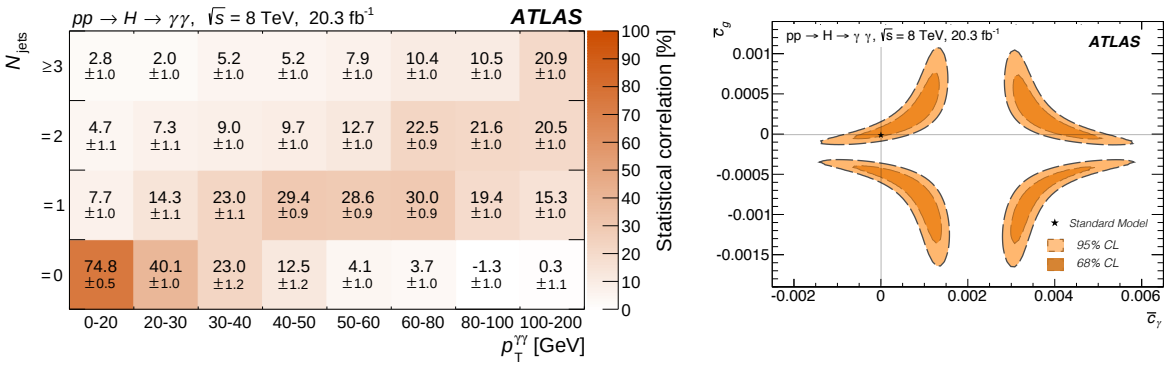

Figure 225: (left) Statistical correlations between exclusive jet bins and Higgs boson p_T. (right) Proof-of-concept analysis using five differential distributions: allowed 95% and 68% CL for two Wilson coefficients which add additional point-like interactions for Higgs boson production via gluon fusion (c_g) and Higgs boson decay into two photons (c_γ) are shown.

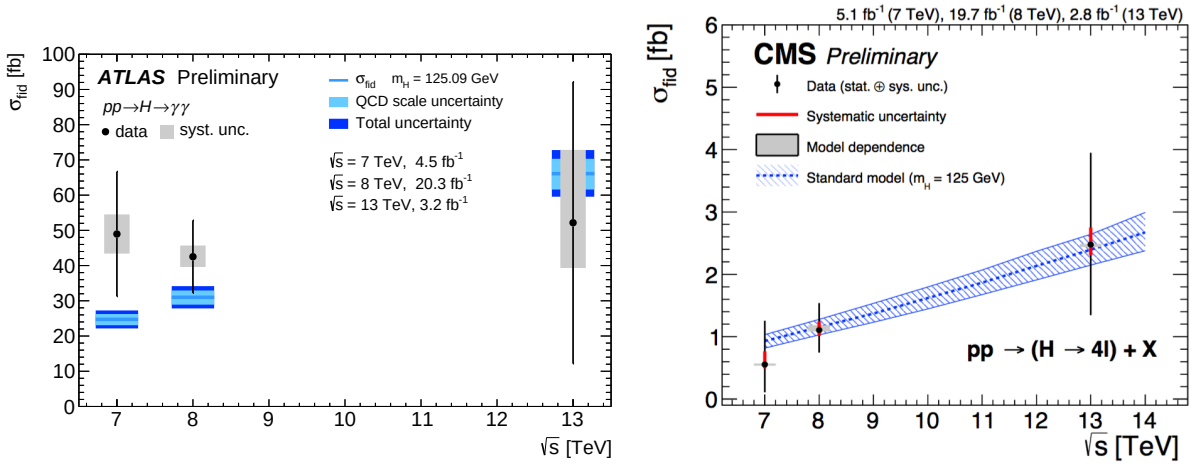

Figure 226: (left) Fiducial cross sections from H $\to \gamma\gamma$ for $\sqrt{s} = 7$, 8 and 13 TeV. The fiducial volumes were extrapolated so that there is an identical definition between all centre-of-mass energies. The hatched theory band shows the prediction from the SM. (right) Fiducial cross sections from H $\to$ ZZ* $\to 4\ell$ for $\sqrt{s} = 7$, 8 and 13 TeValso with matching fiducial volume definitions.

III.3.3 State-of-the-art Standard Model predictions

Sometimes in the experimental analyses the fiducial cross sections are extrapolated onto the full phase space by simulating the relevant geometric acceptances by means of various Monte Carlo generators in order to quote a total cross section for the underlying process (cf. Ref. [967] and Section III.3.5.e). In view of the high precision expected in Run 2 fiducial measurements, it is of primary relevance to provide the experiments with accurate theory predictions for two reasons. On the one hand, it is necessary to perform an comparison to data at the fiducial level, before extrapolating to the inclusive phase space, and to quote the relative measurement publicly. On the other hand, it is important to study how the tools used in the comparison and in the extrapolation behave in the presence of the fiducial cuts, in order to avoid the propagation of unwanted generator-dependent effects into the quoted total cross sections. In order to have a robust control over the extrapolation procedure, it is in fact necessary to assess precisely the performance of the event generators as well as the theoretical uncertainties associated with such simulations, both at the perturbative and non-perturbative level.

The ultimate and future goal of this section of the Task Force is to perform a comprehensive comparison and validation of the predictions obtained with the event generators currently used in experimental analyses to the best available results.

The development of several computational techniques in the past few years considerably improved the known perturbative accuracy of many of the relevant signal and background processes. In the rest of this section we provide templates for the fiducial volumes relative to the three final states $\gamma\gamma$, $\mathrm{WW}^* \to 2\ell 2\nu$, $\mathrm{ZZ}^* \to 4\ell$, followed by the state-of-the-art predictions for the signal and, whenever possible, background processes. As far as the signal is concerned, since the template fiducial volumes that will be given below are dominated by the gluon fusion production mode, we limit ourselves to considering the latter in this section. A comprehensive review of the available predictions and public tools can be found in Chapter I.4 of this volume. The contribution of additional production modes, notably VBF and VH associate production, should be also taken into account when considering the fiducial template volumes presented here. A review of the available results for both QCD and EW effects can be found in the Chapter I.5 of the present volume. However, considering the moderate size of the latter production channels in comparison to the gluon-fusion mode, it is necessary to define different sets of fiducial cuts which enhance their contribution. This study is addressed in Chapter I.5 of this report, and it will be considered in the future by this Task Force. Analogously, the precise study of subdominant contributions to a given fiducial volume may require the definition of multiple specific fiducial sub-categories, with the goal of enhancing different kinematic regimes and increasing the experimental sensitivity. Examples of these regions are the tails of the differential distributions, or the off-shell production regime.

In the rest of this section, we classify the signal predictions into two categories, according to their jet multiplicity: totally inclusive in the number of QCD jets, and with at least one jet. For such processes NNLO QCD predictions for the fiducial cross sections and distributions will be reported in Sections III.3.3.b, III.3.3.c below. Since some analyses use the theory calculations to perform the background subtraction, the same type of validation is necessary for the relevant background processes. As far as the irreducible background reactions are concerned, while in $\gamma\gamma$ production a data-driven fit is used to estimate the background, in the ZZ^* and WW^* final states a precise theoretical calculation is necessary. Section III.3.3.d reports NNLO QCD predictions for $\mathrm{ZZ}^* \to 4\ell$ production, while the WW^* case is left for future work.

A similar comprehensive benchmarking in the presence of exclusive cuts on the QCD activity accompanying Higgs boson production is being conducted within the context of the Les Houches 2015 Workshop [973]. We conclude this section with a summary of the detailed comparisons which have been carried out. The future validation of tools in the presence of realistic fiducial cuts should benefit from the interaction and coordination of activities between the two working groups.

III.3.3.a Template fiducial regions for benchmark

In this section we report the definitions of the template fiducial volumes for Higgs boson production. These templates do not serve as a reference for the fiducial definitions that will be used in Run 2 analyses, but rather as a plausible set of cuts that will be used in the benchmarking process. Kinematic cuts are listed according to the Higgs boson decay mode, for the three final states $\mathrm{H} \to \mathrm{ZZ}^* \to 4\ell$, $\mathrm{H} \to \gamma\gamma$, and $\mathrm{H} \to \mathrm{WW}^* \to 2\ell 2\nu$. As mentioned in the introduction to this chapter, the definition of the fiducial regions should have as little impact as possible on the phase space available for BSM searches in Higgs signatures, and should be defined mainly in order to minimize the model dependence. Therefore, fiducial regions will be largely defined by the detector coverage and by trigger performances, rather than by theoretical prejudice.

III.3.3.a.i Fiducial volume for $H \to ZZ^* \to 4\ell$

Muons (electrons) are required to have a transverse momentum larger than 5 GeV(7 GeV) and rapidity $|\eta| \leq 2.5$. The leading lepton pair is defined as the same-flavoured-opposite-signed (SFOS) lepton pair with the smallest $|m_{\mathrm{Z}} - m_{\ell\ell}|$. The leading-lepton-pair invariant mass is denoted by m_{12}. The subleading lepton pair is the remaining pair of SFOS leptons with smallest $|m_{\mathrm{Z}} - m_{\ell\ell}|$. Its invariant mass is denoted by m_{34}. Jets are reconstructed using the anti-k_t algorithm [191] with a radius parameter of 0.4. All jets with a transverse momentum larger than 30 GeVand rapidity $|\eta| \leq 4.4$ are used in the selection criteria. Neutrinos are not considered in the jet definition.

The fiducial volume for the $\mathrm{H} \to \mathrm{ZZ}^* \to 4\ell$ channel is reported in Table 112

Table 112: Template fiducial cuts for the $\mathrm{H} \to \mathrm{ZZ}^* \to 4\ell$ channel.

Template fiducial region for $\mathrm{H} \to \mathrm{ZZ}^* \to 4\ell$
Leading lepton: $p_t > 20$ GeV
1^{st} subleading lepton: $p_t > 10$ GeV
2^{nd} subleading lepton: $p_t > 7\,(5)$ GeVfor electrons (muons)
3^{rd} subleading lepton: $p_t > 7\,(5)$ GeVfor electrons (muons)
All leptons are required to be isolated: ratio of the sum of p_t's of all charged particles within $\Delta R = [(\Delta\phi)^2 + (\Delta\eta)^2]^{1/2} < 0.4$ from the lepton to the lepton's p_t must be smaller than 0.4
Mass requirements: $40\,\mathrm{GeV} \leq m_{12} \leq 120$ GeV; 12 GeV $\leq m_{34} \leq 120$ GeV
Lepton separation: $\Delta R(i,j) > 0.1$ for all leptons i, j
J/Ψ invariant mass veto: $m_{ij} > 4$ GeVfor all SFOS leptons i, j
Invariant mass cut: 120 GeV $\leq m_{4\ell} \leq 130$ GeV

III.3.3.a.ii Fiducial volume for $H \to \gamma\gamma$

Photons are requested to have a transverse momentum larger than 25 GeVand rapidity $|\eta| \leq 2.5$. The photon pair with the largest transverse momentum is denoted as the leading photon pair. Its invariant mass is denoted by $m_{\gamma\gamma}$. Jets are reconstructed using the anti-k_t algorithm [191] with a radius parameter of 0.4. All jets with a transverse momentum larger than 30 GeVand rapidity $|\eta| \leq 4.4$ are used in the selection criteria. Neutrinos are not considered in the jet definition.

The fiducial volume for the $H \to \gamma\gamma$ channel is reported in Table 113

Table 113: Template fiducial cuts for the $H \to \gamma\gamma$ channel.

Fiducial region for $H \to \gamma\gamma$
Leading photon: $p_t/m_{\gamma\gamma} > 0.35$
Subleading photon: $p_t/m_{\gamma\gamma} > 0.25$
All photons are required to be isolated: ratio of the sum of E_t's of all charged particles within $\Delta R = [(\Delta\phi)^2 + (\Delta\eta)^2]^{1/2} < 0.2$ from the photon to the photon's E_t must be smaller than 0.2
Invariant mass cut: 105 GeV $\leq m_{\gamma\gamma} \leq$ 160 GeV

III.3.3.a.iii Fiducial volume for $H \to W^+W^- \to 2\ell 2\nu$

The leading (subleading) lepton is required to have a transverse momentum larger than 20 GeV(10 GeV), and rapidity $|\eta| \leq 2.5$. Jets are reconstructed using the anti-k_t algorithm [191] with $R = 0.4$. All jets with a transverse momentum larger than 30 GeVand rapidity $|\eta| \leq 4.4$ are used in the selection criteria. Neutrinos are not considered in the jet definition.

The fiducial volume for the $H \to W^+W^- \to 2\ell 2\nu$ channel is reported in Table 114

III.3.3.b Fiducial cross sections for Higgs boson production in association with $n_{\text{jet}} \geq 1$ jets

In this section we present results at 13 TeV for the fiducial cross sections and some kinematic distributions for Higgs boson production, inclusive in the number of QCD jets. The calculation is performed with the `HRes` [223, 224] program, which computes the cross section for SM Higgs boson (H) production by gluon-gluon fusion. `HRes`[III.11] combines the fixed-order calculation of the cross section up to NNLO with the resummation of the logarithmically-enhanced contributions at small transverse momentum (q_T) up to NNLL accuracy in QCD. The method that is used to perform the resummation is presented in Ref. [196].

The produced Higgs boson subsequently decays into the three final states $H \to \gamma\gamma$, $H \to WW^* \to 2\ell 2\nu$ or $H \to ZZ^* \to 4\ell$. In the case of $H \to WW^*$ and $H \to ZZ^*$ decays, finite-width effects of the vector bosons and the appropriate interference contributions are also included. The results below are generally obtained in the large-m_t approximation, and the effects of top- and bottom-quarks in the production are included following ref. [224]. The calculation retains the full kinematics of the Higgs boson and of its decay products, allowing the user to apply arbitrary cuts on these final-state kinematical variables, and to plot the corresponding distributions in the form of bin histograms. Given that the Higgs boson transverse momentum resummation is fully inclusive in the QCD initial-state radiation, we

[III.11] The program can be downloaded from Ref. [974], together with some accompanying notes.

Table 114: Template fiducial cuts for the $\mathrm{H} \to W^+W^- \to 2\ell 2\nu$ channel.

Fiducial region for $\mathrm{H} \to W^+W^- \to 2\ell 2\nu$
Lepton invariant mass: $m(ll) > 12$ GeV
Lepton transverse momentum: $p_{t,\ell\ell} > 30$ GeV
All leptons are required to be isolated: ratio of the sum of p_t's of all charged particles within $\Delta R = [(\Delta\phi)^2 + (\Delta\eta)^2]^{1/2} < 0.4$ from the lepton to the lepton's p_t must be smaller than 0.4
Lepton transverse mass: $m_T(ll, \nu\nu) > 50$ GeV
where $m_T(ll, \nu\nu) = \sqrt{(E_{t,\ell\ell} + p_{t,\nu\nu})^2 - \lvert\vec{p}_{t,\ell\ell} + \vec{p}_{t,\nu\nu}\rvert^2}$, and $E_{t,\ell\ell} = \sqrt{p^2_{t,\ell\ell} + m^2_{\ell\ell}}$
Missing transverse energy: $E_T^{\mathrm{miss}} > 15$ GeV

consider the sets of fiducial volumes presented in the previous subsection, ignoring the cuts on QCD jets. This in particular affects the isolation requirements on photons and charged leptons.

The parton distribution functions are chosen according to the PDF4LHC15 recommendation [35], with densities and α_S evaluated at each corresponding perturbative order. As for the electroweak parameters, we follow the LHCHXSWG recommendations [9], in particular we set the Higgs boson mass at $M_{\mathrm{H}} = 125$ GeV. The renormalization and factorization scales are fixed to the value $\mu_R = \mu_F = M_{\mathrm{H}}$ while the resummation scale is fixed at the value $Q = M_{\mathrm{H}}/2$.

We start by considering the diphoton decay channel $\mathrm{H} \to \gamma\gamma$. The cuts on final state photons are reported in Table 113, and QCD jets are not considered in the isolation criterion. The corresponding fiducial cross sections are shown in Table 115, which reports the resummed results at NLL+NLO and NNLL+NNLO level, and we compare them with the NNLO fixed order predictions obtained with the `HNNLO` code. [172].

We recall that at large values of q_T the resummed calculation implements a perturbative unitarity constraint [196], that guarantees to exactly reproduce the NNLO value of the total cross section for the Higgs boson production after integration over q_T. However, kinematic cuts affects in a different way fixed order and resummed predictions, leading to small differences in the fiducial cross sections, as shown in Table 115.

Figures 227 and 228 show some relevant differential distributions. The left plot of Figure 227 shows the diphoton transverse-momentum $p_T^{\gamma\gamma}$ distribution, and the right plot shows the $p_T^{t,\gamma\gamma}$ distribution defined as the magnitude of the transverse momentum of the diphoton system perpendicular to the diphoton thrust axis $\hat{t}$. The transverse momentum distributions for the leading and subleading photons are shown in Figure 228. By inspecting these plots we see that the resummed calculations are essential to restore the predictivity of perturbation theory in the small-transverse-momentum region. Moreover, NNLL resummation gives a sizeable effect, with respect to the NNLO calculations, in a wide intermediate region up to the chosen resummation scale $q_T \lesssim M_{\mathrm{H}}/2$. Finally in the large-$q_T$ region ($q_T \sim M_{\mathrm{H}}$), where the resummation does not improve the accuracy of the fixed-order expansion, the NNLL+NNLO predictions obtained with `HRes` show perfect agreement with the NNLO ones.

Next we consider the decay channels $\mathrm{H} \to ZZ \to 4\ell$ and $\mathrm{H} \to W^+W^- \to 2\ell 2\nu$ with the cuts on the final state leptons as in tabs. 112, 114. The corresponding fiducial cross sections at NLL+NLO,

Table 115: Fiducial cross sections for $pp \to \mathrm{H} + X \to \gamma\gamma + X$, $pp \to \mathrm{H} + X \to W^+W^- + X \to 2\ell 2\nu + X$ and $pp \to \mathrm{H} + X \to \mathrm{ZZ} + X \to 4\ell + X$ at the LHC ($\sqrt{s} = 13$ TeV): fixed-order results at NNLO and corresponding resummed results at NLL+NLO and NNLL+NNLO. The result in the W^+W^- channel refers to a single lepton family. The uncertainties are obtained by varying the scales $\mu_R = \mu_F$ by a factor of two around the central value. For the resummed calculations, in addition, the resummation scale Q is varied by a factor of two in either direction by keeping $\mu_R = \mu_F = 2Q$.

Cross section [fb]	NLL+NLO	NNLL+NNLO	NNLO
$\mathrm{H} \to \gamma\gamma$	$41.63^{+9\%}_{-8\%}$	$54.2^{+9\%}_{-8\%}$	$54.6^{+9\%}_{-8\%}$
$\mathrm{H} \to W^+W^- \to 2\ell 2\nu$	$34.99^{+9\%}_{-8\%}$	$45.4^{+9\%}_{-8\%}$	$46.0^{+9\%}_{-8\%}$
$\mathrm{H} \to \mathrm{ZZ} \to e^+e^-\mu^+\mu^-$	$0.792^{+9\%}_{-8\%}$	$1.042^{+9\%}_{-8\%}$	$1.042^{+9\%}_{-8\%}$
$\mathrm{H} \to \mathrm{ZZ} \to e^+e^-e^+e^-$	$0.441^{+9\%}_{-8\%}$	$0.581^{+9\%}_{-8\%}$	$0.583^{+9\%}_{-8\%}$
$\mathrm{H} \to \mathrm{ZZ} \to \mu^+\mu^-\mu^+\mu^-$	$0.521^{+9\%}_{-8\%}$	$0.685^{+9\%}_{-8\%}$	$0.687^{+9\%}_{-8\%}$

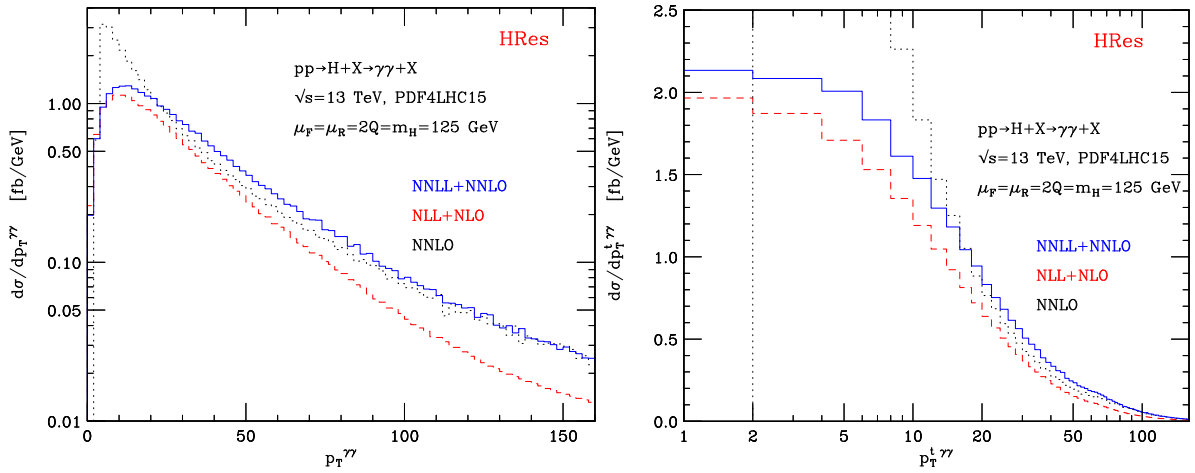

Figure 227: Higgs boson production and diphoton decay at the LHC. Transverse-momentum distribution $p_T^{\gamma\gamma}$ (left) and $p_T^{t,\gamma\gamma}$ distribution (right) obtained by resummed NLL+NLO and NNLL+NNLO and fixed-order NNLO calculations. Selection cuts on the final-state photons are described in the text.

NNLL+NNLO and NNLO are reported in Table 115. In the left plot of Figure 229 we show the transverse-momentum spectrum of the $e^+e^-\mu^+\mu^-$ system relative to the $\mathrm{H} \to ZZ \to 4\ell$ channel. Regarding the $\mathrm{H} \to W^+W^- \to 2\ell 2\nu$ final state, the right plot of Figure 229 shows the transverse momentum of the $2\ell 2\nu$ (right plot) system, while the leading- and subleading-lepton transverse momentum distributions are displayed in Figure 230.

From the above results we observe that resummation effects on top of the exclusive NNLO prediction tend to be very sizeable in specific kinematic configurations. It is therefore important to validate the Monte-Carlo event generators used in experimental analyses for a complete set of kinematic distributions in the presence of realistic fiducial cuts. This validation should be carried out over the whole spectrum - both in the multijet region and in the regime where the radiation is mainly unresolved - by comparing with the state-of-the-art perturbative predictions.

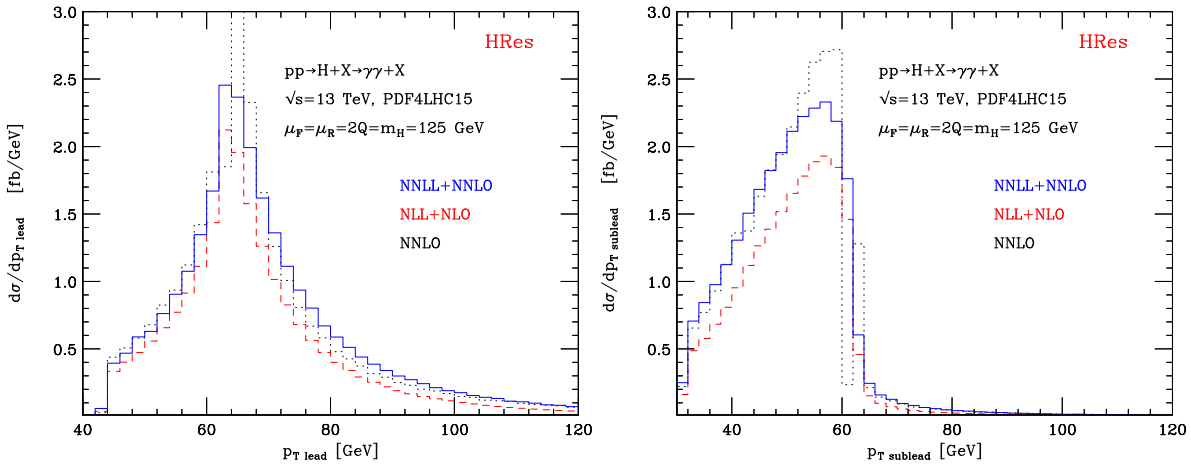

Figure 228: Higgs boson production and diphoton decay at the LHC. Transverse-momentum distributions for the leading $p_{T,\mathrm{lead}}$ (left) and subleading $p_{T,\mathrm{sublead}}$ (right) photon obtained by resummed NLL+NLO and NNLL+NNLO and fixed-order NNLO calculations. Selection cuts on the final-state photons are described in the text.

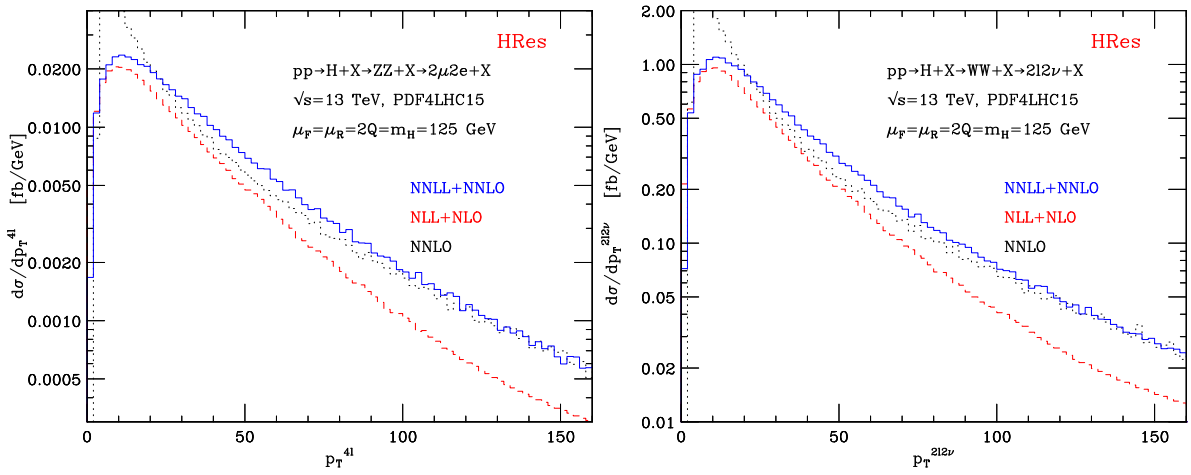

Figure 229: Transverse-momentum distributions $p_T^{4\ell}$ for the $\mathrm{H} \to \mathrm{ZZ} \to e^+e^-\mu^+\mu^-$ signal (left) and $p_T^{2\ell 2\nu}$ for the $\mathrm{H} \to W^+W^- \to 2\ell 2\nu$ signal (right) at the LHC. Prediction for NNLL+NNLO, NLL+NLO and NNLO calculations. Selection cuts on the final-state leptons are described in the text.

III.3.3.c Fiducial cross sections for Higgs boson production in association with $n_{\mathrm{jet}} \geq 1$ jets

In this section we present results for fiducial cross section and differential observables obtained from the NNLO QCD computation of Higgs boson production in association with one hard jet at the LHC [174]. First, we briefly describe the setup of the computation. We work in a Higgs Effective Theory where the massive top quark is integrated out. This approximation is parametric in $\frac{q^2}{m_t}$ where q is a typical scale of the process, and it is known to work well up to $q \sim m_t$ [975]. In principle, the exact top quark mass dependence is known at LO [236, 237] and could be included in our predictions. However, for simplicity we refrain from including them in the results presented here. In our computation we include all partonic channels at NLO. For the NNLO corrections we include the gg and qg channels which are the only ones relevant for phenomenology within the p_T range considered here. The effect of the missing channels is expected to be much smaller than the residual scale uncertainty and probably comparable to finite top quark mass corrections. We treat the Higgs boson on-shell and include all relevant decays to $\gamma\gamma$ and four lepton final states. We neglect interference effects in the case of identical fermions and

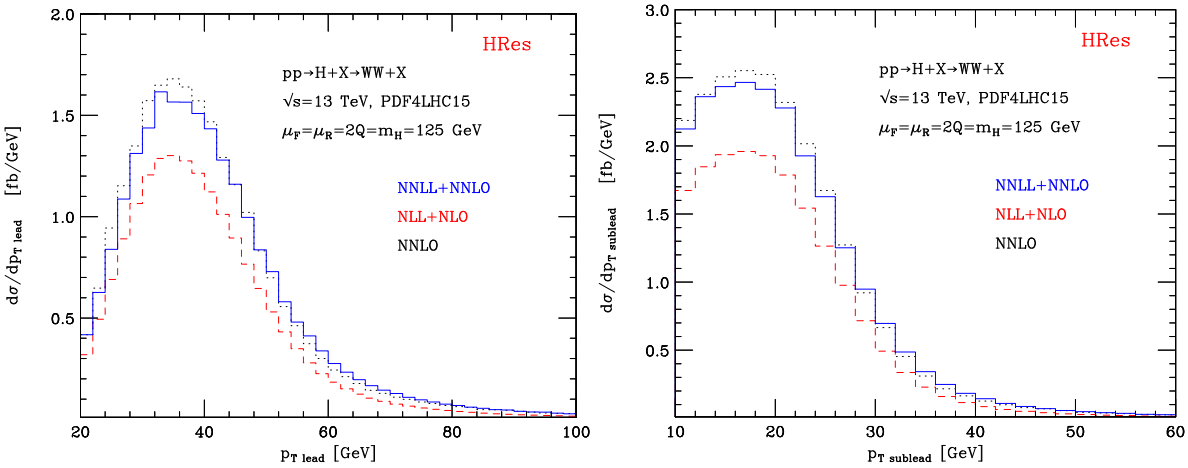

Figure 230: Transverse-momentum distributions for the leading $p_{T,\text{lead}}$ (left) and subleading $p_{T,\text{sublead}}$ (right) charged lepton obtained by resummed NLL+NLO and NNLL+NNLO and fixed-order NNLO calculations in the $\text{H} \to W^+W^- \to 2\ell 2\nu$ channel. Selection cuts on the final-state photons are described in the text.

$W - Z$ interference for $2\ell\,2\nu$ final states. All these effects are expected to be small in the fiducial region considered in this section, with the exception of off-shell production in the WW channel. Indeed, the fiducial region studied in this section does not include any cut on the WW transverse mass, m_T. As it is well known [499], this leads to a sizeable off-shell and signal/background effects on the Higgs cross-section[III.12]. One should carefully take this into account when performing any study in the fiducial region defined in this section. As we said, our numbers are for on-shell Higgs and do not include $pp \to 2l2\nu$ signal/background interference, so by construction they don't account for such (potentially large) effects. As a consequence, they lead to reliable predictions only in a region where off-shell effects are negligible. Finally, we use $\mu = \mu_{\text{fact}} = \mu_{\text{ren}} = m_H$ as the central scale and vary by a factor of two upwards and downwards. We believe that this choice gives a more conservative estimate of residual theoretical uncertainty while not changing much (at NNLO) the central value compared to the more traditional choice $\mu = m_H/2$. Also, we note that the stability w.r.t. scale variation of the NNLO results presented in this section makes the use of dynamical scales unnecessary at this order.

Our results show that NNLO corrections lead to a stabilization of fiducial cross sections and shapes of differential distributions. The unphysical scale dependence of the NNLO result is reduced by a factor of more than two with respect to NLO[III.13]. In general, we find that applying fiducial cuts does not spoil the convergence of the perturbative expansion. Acceptances are found to be stable when moving from NLO to NNLO, in agreement to our results in Ref. [174]. To illustrate this, and to explore the validity range of pure fixed order computations, in Figure 231, we present the cumulative leading jet $p_\perp$ distribution as a function of the lower cut on $p_\perp$, for the $\gamma\gamma$ channel in the fiducial region. In the lower pane we plot the NLO and NNLO K-factors and observe very stable corrections to p_{cut} as low as 30 GeV[III.14]. There is no indication of a breakdown of perturbation theory for these values of transverse momentum. Hence, it appears, that also in the fiducial region the NNLO result already captures the dominant logarithmic enhancements and additional resummation effects are small [189] for $p_\perp \geq 30$ GeV. This is in contrast to NLO predictions where missing higher logarithmic terms still lead to sizeable corrections. A similar behaviour is observed also in the WW and ZZ channels.

Next, we show in Table 116 the NLO and NNLO cross-sections in the fiducial region for the $\gamma\gamma$, WW and ZZ channel. Note that since all leptons are massless in our computation, there is no

[III.12] Note that in the the ZZ fiducial region off-shell effects are negligible thanks to the m_{4l}.
[III.13] Our results do not include PDFs uncertainties which are estimated to be at the level of 5% [182].
[III.14] In this section, both NLO and the NNLO results are computed with NNLO PDFs and α_s.

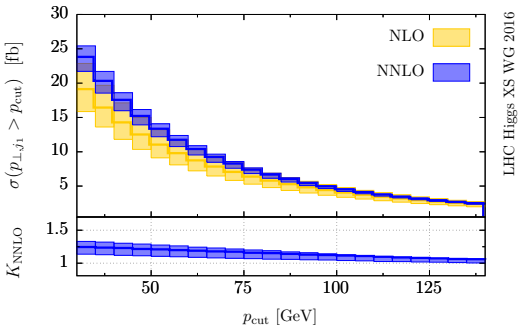

Figure 231: Cumulative jet $p_\perp$ Distribution in the fiducial volume at NLO (yellow) and NNLO (blue) for $H \to \gamma\gamma$. Both NLO and NNLO curves obtained with NNLO PDFs and α_s. Solid line: value for $\mu_r = \mu_f = m_H$. Filled band: scale uncertainty. In the lower pane the ratio of NNLO to the NLO central $\mu_r = \mu_f$ value is shown. See text for details.

distinction between $2e2\nu$ and $2\mu2\nu$ predictions for the fiducial region considered here. Our result show that the $K-$factor is similar for all the three channels, and similar to the inclusive $K-$factor.

Table 116: The NLO and NNLO cross-sections in the fiducial region for the $\gamma\gamma$, WW and ZZ channel.

	$\gamma\gamma$	$WW \to e\mu\nu\nu$	$ZZ \to 4l$		
			4μ	$2e2\mu$	$4e$
NLO (fb)	$19.1^{+3.8}_{-3.2}$	$14.9^{+3.0}_{-2.5}$	$0.336^{+0.065}_{-0.057}$	$0.611^{+0.120}_{-0.103}$	$0.282^{+0.055}_{-0.048}$
NNLO (fb)	$22.7^{+1.4}_{-1.9}$	$17.9^{+1.0}_{-1.6}$	$0.388^{+0.010}_{-0.030}$	$0.707^{+0.020}_{-0.055}$	$0.327^{+0.008}_{-0.026}$

Finally, we present result for selected differential distributions in the fiducial region, for the $\gamma\gamma$ (Figs. 232,233,234,235), WW (Figs. 236,237,238) and ZZ (Figs. 239,240). Note that for the ZZ channel we only show results for the 4μ sub-channel and for lepton observables. Results for other sub-channels are very similar to these ones, and results for jet observables are very similar to the WW case already shown.

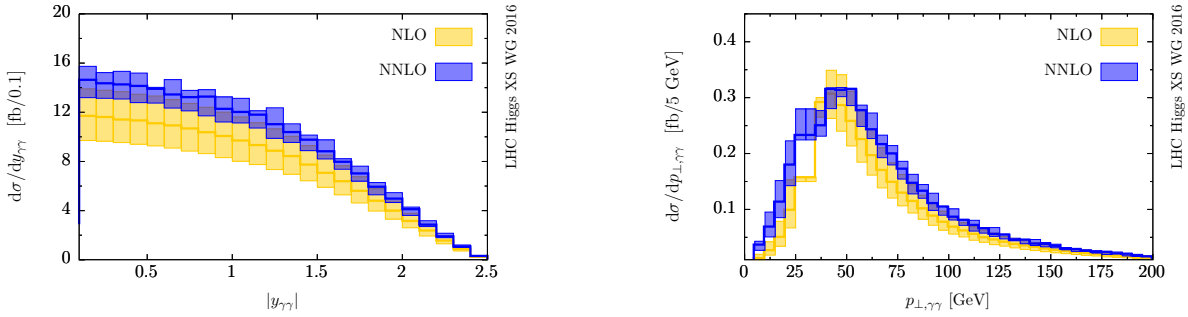

Figure 232: Distribution in the fiducial volume at NLO (yellow) and NNLO (blue) for $H \to \gamma\gamma$. Left: di-photon rapidity. Right: di-photon $p_\perp$. Both NLO and NNLO curves obtained with NNLO PDFs and α_s. Solid line: value for $\mu_r = \mu_f = m_H$. Filled band: scale uncertainty. See text for details.

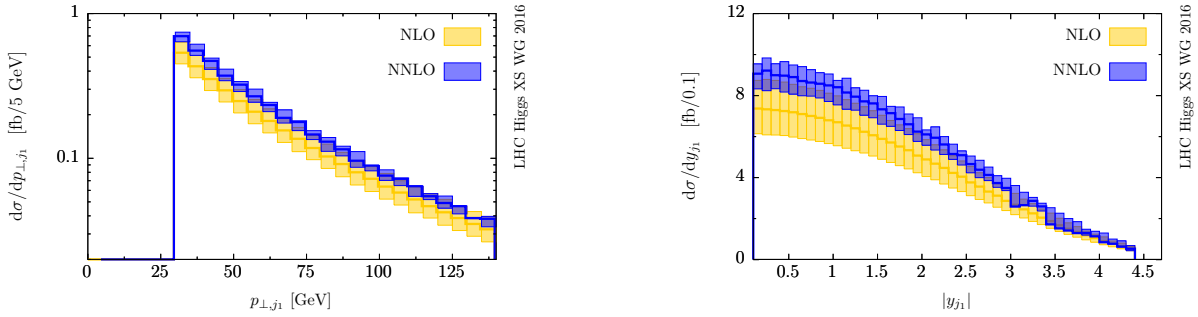

Figure 233: Distribution in the fiducial volume at NLO (yellow) and NNLO (blue) for $H \to \gamma\gamma$. Left: leading jet $p_\perp$. Right: leading jet rapidity. Both NLO and NNLO curves obtained with NNLO PDFs and α_s. Solid line: value for $\mu_r = \mu_f = m_H$. Filled band: scale uncertainty. See text for details.

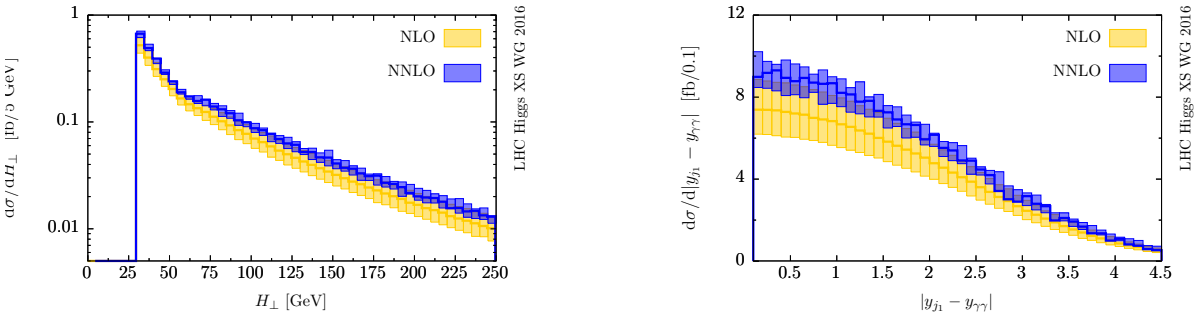

Figure 234: Distribution in the fiducial volume at NLO (yellow) and NNLO (blue) for $H \to \gamma\gamma$. Left: $H_\perp$. Right: rapidity difference between the di-photon system and the leading jet. Both NLO and NNLO curves obtained with NNLO PDFs and α_s. Solid line: value for $\mu_r = \mu_f = m_H$. Filled band: scale uncertainty. See text for details.

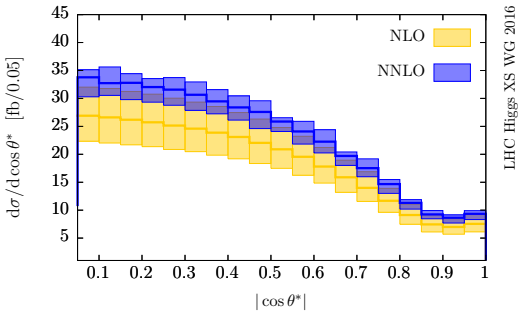

Figure 235: $\cos\theta^*$ distribution in the fiducial volume at NLO (yellow) and NNLO (blue) for $H \to \gamma\gamma$. Both NLO and NNLO curves obtained with NNLO PDFs and α_s. Solid line: value for $\mu_r = \mu_f = m_H$. Filled band: scale uncertainty. See text for details.

III.3.3.d Fiducial cross section and distribution for the irreducible background

In this contribution we present NNLO predictions for four-lepton production in the Higgs background region. The calculation includes the leptonic decays of the vector bosons together with spin correlations and off-shell effects. Contributions from $Z\gamma^*$ and $\gamma^*\gamma^*$ production as well as from $pp \to Z/\gamma^* \to 4$ leptons topologies are also consistently included with all interference terms. The corresponding results for the $ZZ \to 4l$ signal region have been presented in [976].

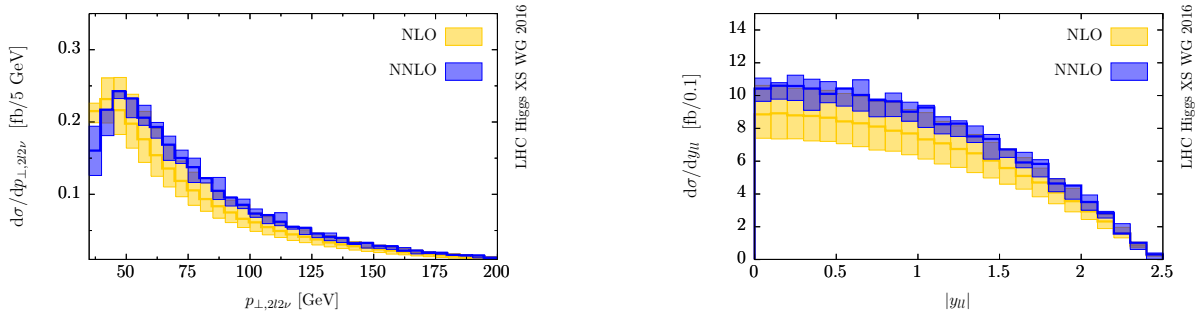

Figure 236: Distribution in the fiducial volume at NLO (yellow) and NNLO (blue) for $H \to WW \to e\mu\nu\nu$. Left: Higgs boson $p_\perp$. Right: di-lepton rapidity. Both NLO and NNLO curves obtained with NNLO PDFs and α_s. Solid line: value for $\mu_r = \mu_f = m_H$. Filled band: scale uncertainty. See text for details.

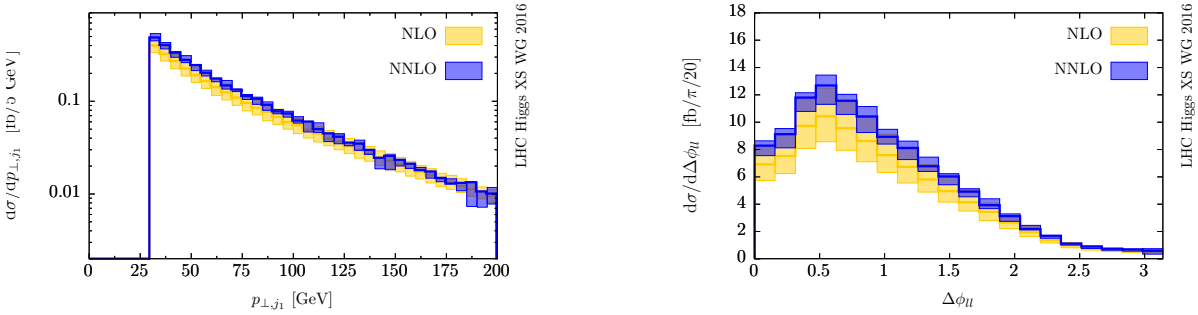

Figure 237: Distribution in the fiducial volume at NLO (yellow) and NNLO (blue) for $H \to WW \to e\mu\nu\nu$. Left: leading jet $p_\perp$. Right: di-lepton azimuthal separation. Both NLO and NNLO curves obtained with NNLO PDFs and α_s. Solid line: value for $\mu_r = \mu_f = m_H$. Filled band: scale uncertainty. See text for details.

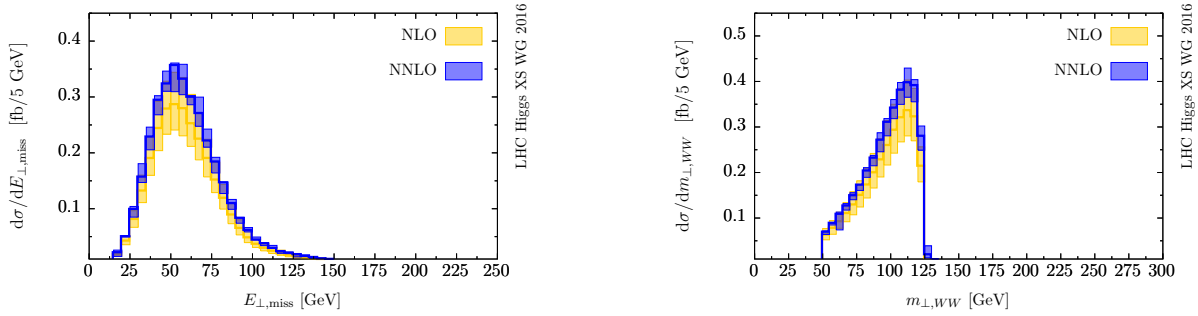

Figure 238: Distribution in the fiducial volume at NLO (yellow) and NNLO (blue) for $H \to WW \to e\mu\nu\nu$. Left: $E_{\perp,\mathrm{miss}}$. Right: WW transverse mass $m_\perp$. Both NLO and NNLO curves obtained with NNLO PDFs and α_s. Solid line: value for $\mu_r = \mu_f = m_H$. Filled band: scale uncertainty. See text for details.

The calculation is performed with the numerical program MATRIX[III.15], which combines the q_T-subtraction [172] and -resummation [194] formalisms with the MUNICH Monte Carlo framework [977]. MUNICH provides a fully automated implementation of the Catani–Seymour dipole subtraction method [249, 978], an efficient phase-space integration, as well as an interface to the one-loop generator OPENLOOPS [247] to obtain all required (spin- and colour-correlated) tree-level and one-loop amplitudes. The two-loop he-

[III.15] MATRIX is the abbreviation of "MUNICH Automates qT subtraction and Resummation to Integrate X-sections", by M. Grazzini, S. Kallweit, D. Rathlev, M. Wiesemann. In preparation.

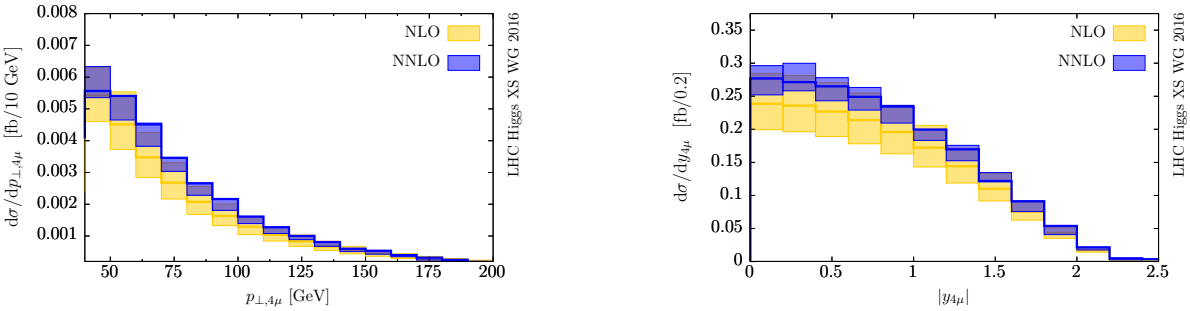

Figure 239: Distribution in the fiducial volume at NLO (yellow) and NNLO (blue) for $H \to ZZ \to 4\mu$. Left: Higgs boson $p_\perp$. Right: Higgs boson rapidity. Both NLO and NNLO curves obtained with NNLO PDFs and α_s. Solid line: value for $\mu_r = \mu_f = m_H$. Filled band: scale uncertainty. See text for details.

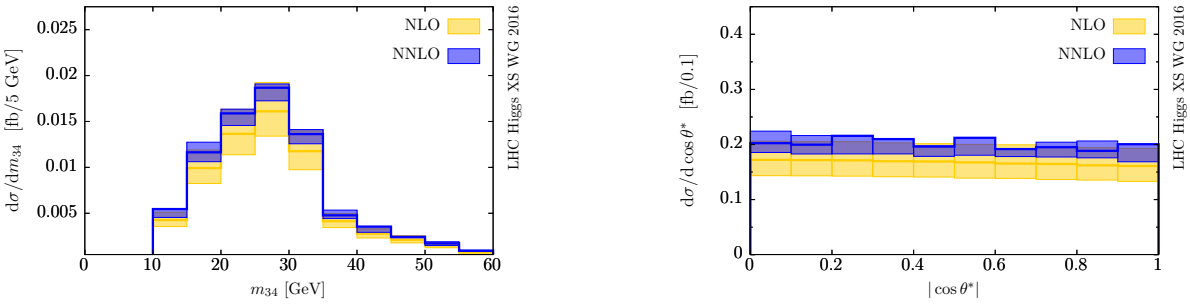

Figure 240: Distribution in the fiducial volume at NLO (yellow) and NNLO (blue) for $H \to ZZ \to 4\mu$. Left: sub-leading di-lepton invariant mass. Right: $\cos\theta^*$. Both NLO and NNLO curves obtained with NNLO PDFs and α_s. Solid line: value for $\mu_r = \mu_f = m_H$. Filled band: scale uncertainty. See text for details.

licity amplitudes for this process have been computed in Refs. [979, 980].

Our calculation allows us to apply arbitrary cuts on the final-state leptons and the associated QCD radiation. The central values for the factorization and renormalization scales are fixed to the invariant mass of the four-lepton system, i.e. $\mu_F = \mu_R = \mu_0 = m_{ZZ}$. Perturbative uncertainties are estimated as usual by varying μ_F and μ_R in the range $0.5\mu_0 \leq \mu_F, \mu_R \leq 2\mu_0$ with the constraint $0.5 \leq \mu_F/\mu_R \leq 2$.

In Table 117 we report the fiducial cross sections at LO, NLO and NNLO in the three decay channels. We also compare our result with the approximation in which only the loop-induced gg contribution is included.

Table 117: Fiducial cross sections and scale uncertainties at LO, NLO and NNLO in the three channels. The NLO+gg result is also shown for comparison.

Channel	σ_{LO} (fb)	σ_{NLO} (fb)	σ_{NLO+gg} (fb)	σ_{NNLO} (fb)
$e^+e^-e^+e^-$	$0.1347(1)^{+10\%}_{-11\%}$	$0.1485(2)^{+2.4\%}_{-3.6\%}$	$0.1584(2)^{+2.4\%}_{-3.6\%}$	$0.159(1)^{+0.7\%}_{-0.9\%}$
$\mu^+\mu^-\mu^+\mu^-$	$0.1946(2)^{+10\%}_{-11\%}$	$0.2150(2)^{+2.4\%}_{-3.6\%}$	$0.2291(2)^{+2.4\%}_{-3.6\%}$	$0.230(1)^{+0.9\%}_{-0.8\%}$
$e^+e^-\mu^+\mu^-$	$0.3165(3)^{+10\%}_{-11\%}$	$0.3457(3)^{+2.4\%}_{-3.6\%}$	$0.3677(2)^{+2.3\%}_{-3.5\%}$	$0.3690(6)^{+0.5\%}_{-0.8\%}$

The NNLO effect increases the NLO result by about 7%. By using NNLO PDFs throughout,

the loop-induced gluon-fusion contribution provides about $83\% - 85\%$ of the full NNLO result. The impact of the gluon fusion contribution is thus higher than what was found in Ref. [976] in the case of the ZZ analysis, in which the ZZ bosons are essentially produced on shell. This is due to the selection cuts, which suppress the impact of genuine radiative corrections to the $q\bar{q}$ channel. This effect is visible already at NLO, where the impact of radiative corrections is reduced from $+23\%$ in the case of inclusive on shell ZZ production to $+9\% - 10\%$.

In Figure 241 we present our LO, NLO and NNLO predictions for the invariant mass (left) and the rapidity (right) of the four leptons. The lower panels show the NNLO results normalized to the NLO predictions. The NLO+gg prediction is also shown. We see that the impact of NNLO corrections is rather stable for these distributions.

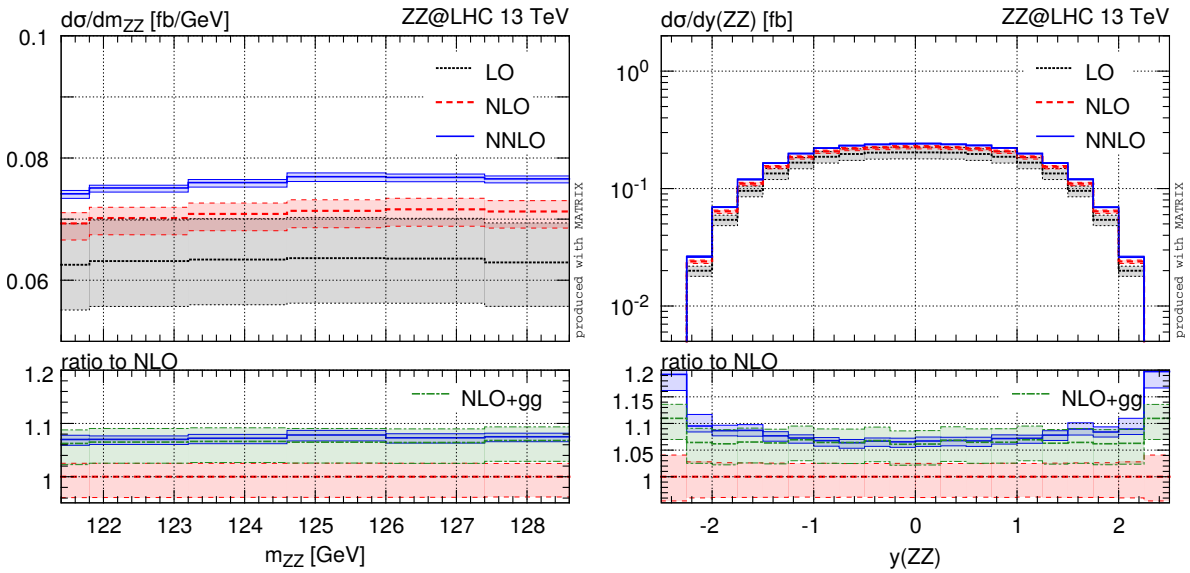

(a) (b)

Figure 241: The invariant mass (left) and rapidity (right) distributions of the four-lepton system at LO, NLO and NNLO. The lower panel shows the NNLO result normalized to NLO. The NLO+gg result is also shown for comparison.

In Figure 242 we show the distributions in the invariant mass of the subleading lepton pair (left) and in $\cos\theta_{12}$ (right). Here we notice that the NNLO corrections are larger at large m_{34} and small $\cos\theta_{12}$.

In Figure 243 we show the p_T distributions of the four-lepton system (left) and of the leading jet (right). These distributions are identical at NLO, when only one parton recoils against the four-lepton system, and show significant corrections at NNLO. This is not unexpected since the NNLO calculation is effectively NLO in this case.

Analogous comments apply to Figure 244, which shows our results for the rapidity distribution of the leading jet (left) and for the rapidity difference between the leading jet and the four-lepton system (right).

III.3.3.e Comparison of the description of QCD activity associated with Higgs production in gluon fusion

In this section we present a brief summary of the extensive comparison of the description of QCD activity in association with Higgs boson production in gluon fusion, undertaken within the context of the Les Houches 2015 workshop [973]. It aims at comparing the description of the QCD activity accom-

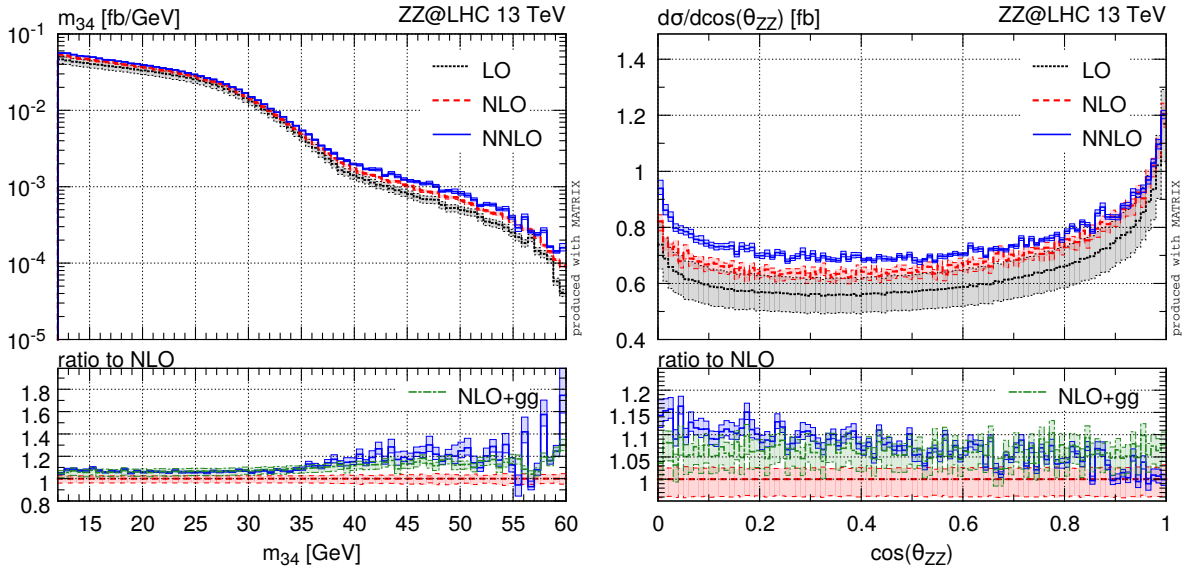

(a) (b)

Figure 242: As in Figure 241, but for the invariant mass of the subleading lepton pair (left) and the $\cos\theta_{12}$ distributions.

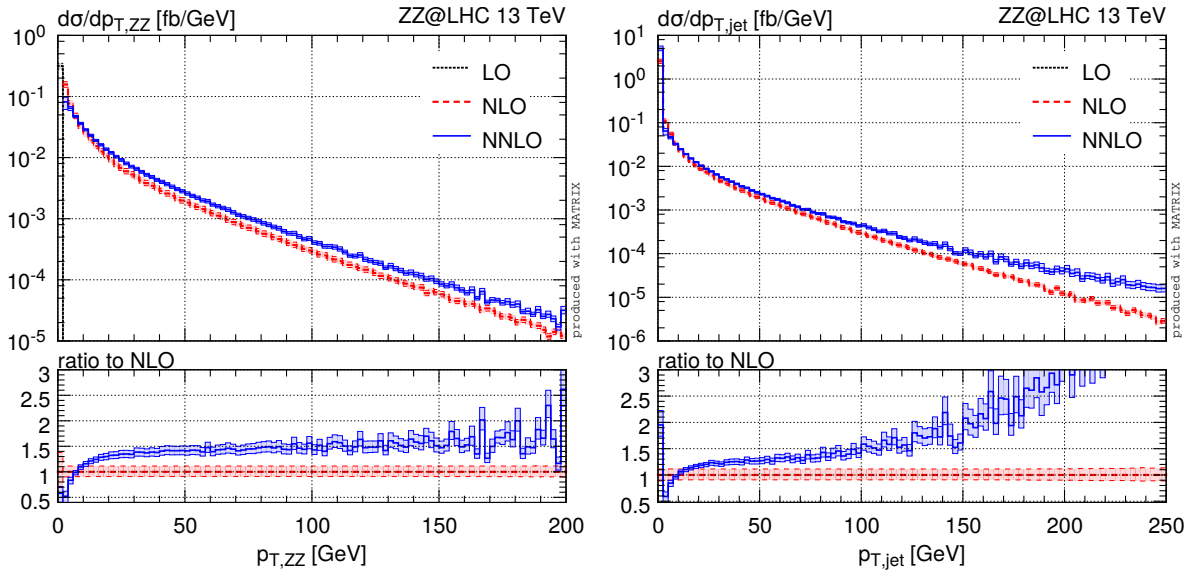

(a) (b)

Figure 243: As in Figure 241, but for the p_T distributions of the four-lepton system (left) and of the leading jet (right).

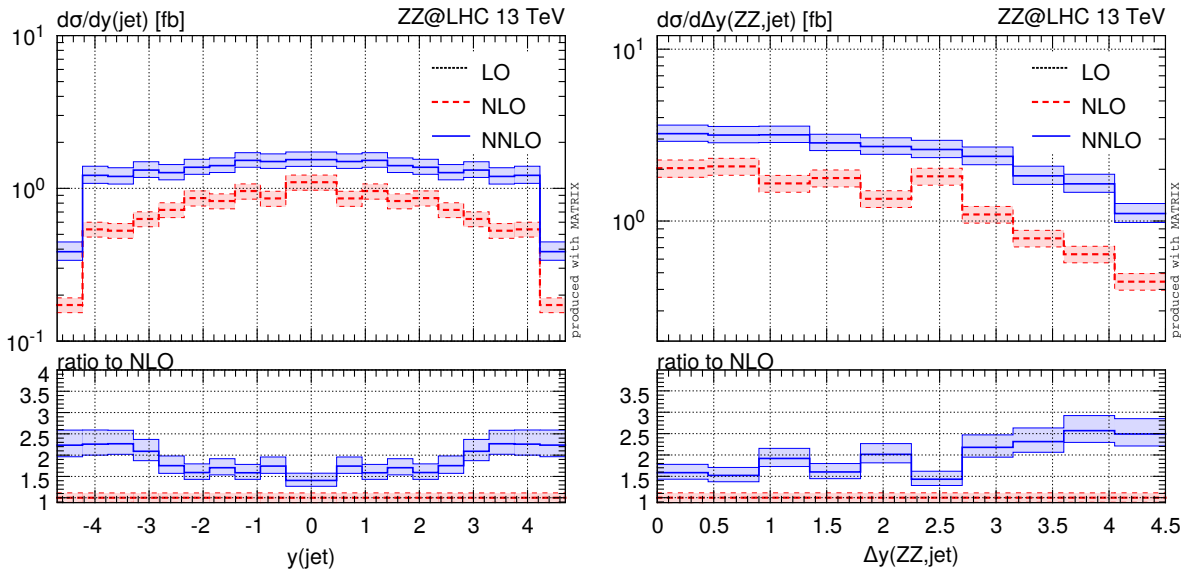

(a) (b)

Figure 244: As in Figure 241, but for the rapidity distribution of the leading jet (left) and the rapidity difference of the leading jet and the four-lepton system (right).

panying the production of a Higgs boson in gluon fusion. To this end contributions obtained from from a multitude of authors applying different approximations and calculational schemes were subjected to a comprehensive list of inclusive and successively exclusive observables. To facilitate the comparison a common setup was adopted. Beside working in the pure Higgs effective theory (HEFT) in the $m_t \to \infty$ limit, scales reducing to $\frac{1}{2} M_{\mathrm{H}}$ in the zero jet limit were adopted along with the common PDF sets `MMHT2014nlo68clas0118/MMHT2014nnlo68cl` [37], as appropriate, with $\alpha_s(M_{\mathrm{Z}}) = 0.118$ were used where possible. It is important to stress that for many tools this does not necessarily constitute their respective best setup, but was adopted for the sake of the comparison.

The contributions comprise the analytical resummations of

- HQT [194, 204] for the Higgs boson transverse momentum,
- STWZ [159] for the jet veto cross sections, the leading jet transverse momentum, the inclusive cross section and the exclusive zero jet cross section,
- RESBOS 2 [981, 982] for inclusive zero and one jet observables,

the fixed-order computations of

- SHERPA NNLO [229, 983] calculation of $pp \to h + X$,
- BFGLP [182, 183] NNLO calculation of $pp \to h + j + X$,
- GOSAM+SHERPA [227–229, 984] NLO calculation of $pp \to h + 1, 2, 3j + X$ [230, 551], here also a MINLO [985] and LOOPSIM [986] (labelled nNLO) calculation are available

the NNLOPS matched computations of

- `Powheg` NNLOPS [208], showered with PYTHIA 8.253 [207],
- SHERPA NNLOPS [229, 983],

the NLO multijet merged computations of

- `MadGraph5_aMC@NLO` in the FxFx scheme [54, 206], showered with PYTHIA 8.210 [207]
- SHERPA in the MEPS@NLO scheme [229, 241, 345, 356, 987] using one-loop matrix elements from GOSAM [227, 228, 230, 551],
- HERWIG 7.1 in the unitarized merging scheme [306, 426, 988] using its dipole shower [367] and

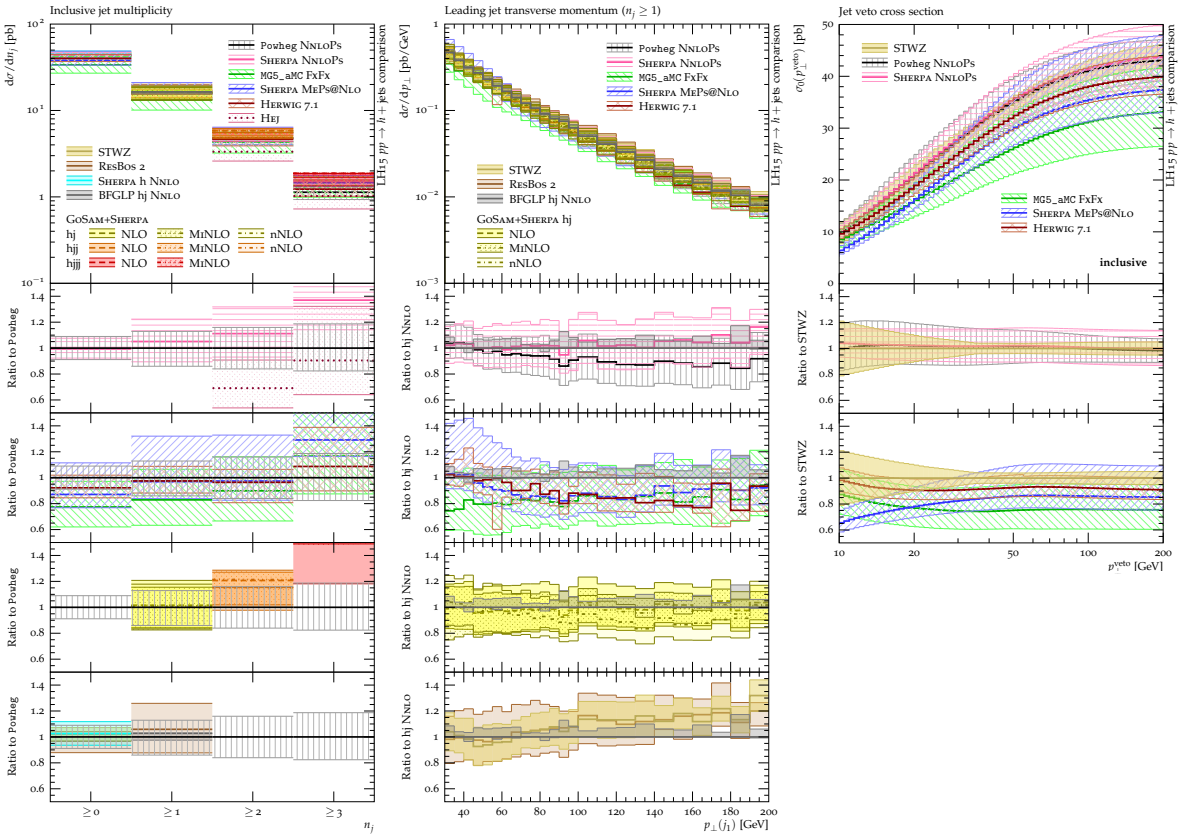

Figure 245: Example comparisons of the description of QCD activity accompanying Higgs boson production in gluon fusion, taken from [973]. The inclusive jet multiplicity (top left), the leading jet transverse momentum (right) and the jet vetoed inclusive cross section (bottom left) are shown. The ratio panels compare to the appropriate reference as indicated. See text for details.

matrix elements from `MadGraph5_aMC@NLO` [54] and OPENLOOPS [247],

and the BFKL resummation of

– HEJ [989–991] describing $pp \to h + 2j + X$,

and therefore cover a large space of calculations available. Uncertainties are determined varying the appropriate scales, cf. [973] for details.

To facilitate comparisons with as diverse calculations as possible we consider inclusive Higgs boson production with no restriction on its decay products. Jets are identified using the anti-k_T algorithm [191] with $R = 0.4$ and are required to have $p_T > 30\,\text{GeV}$ and $|\eta| < 4.4$. An implementation in RIVET [992] exists. Figure 245 displays exemplary results of this comparison for three observables of interest out of the 79 observables considered: the inclusive jet multiplicity, the leading jet transverse momentum, and the jet vetoed inclusive cross section. All plots show a main plot accompanied by multiple ratio plots, grouping the individual contributions to ease the comparison. Noteworthy in the observables exhibited here are the agreement in the inclusive $n_j \geq 1$ cross section between all tools considered which possess at least NLO accuracy in this observable. While for $n_j \geq 2$ all predictions including parton showering agree well, for $n_j \geq 3$ the spread is larger. However, it has to be kept in mind that the NNLOPS matched calculations revert leading order accuracy for $n_j \geq 2$ and to pure parton shower accuracy for $n_j \geq 3$ while `MadGraph5_aMC@NLO` and HERWIG 7.1 are NLO and LO accurate there, respectively. Only, the GOSAM+SHERPA and the SHERPA MEPS@NLO prediction possess NLO accuracy in both cases. HEJ, being LO accurate for $n_j \geq 2, 3$, predicts slightly different inclusive jet multiplicities. The leading jet transverse momentum spectrum shows a consensus between (almost) all

parton shower matched and/or multijet merged calculations exhibiting NLO accuracy for this observable: Powheg NNLOPS, SHERPA NNLOPS, MadGraph5_aMC@NLO, SHERPA MEPS@NLO and HERWIG 7.1. The parton level calculations deviate mostly due to the individual scales set. However, the pure fixed order NLO and NNLO calculation, employing the same scale, agree very well, indicating a K-factor very close to unity. Finally, the degree of congruence in the jet vetoed inclusive cross section between the NNLOPS matched calculations and the STWZ dedicated resummation is remarkable. Here, the NLO multijet merged tools primarily suffer from their NLO normalization in the $p_{\mathrm{T}}^{\mathrm{veto}} \to \infty$ limit. Generally, a remarkable level of agreement is found between the individual calculations throughout most observables.

III.3.4 Beyond the Standard Model effects

New physics beyond the SM could affect Higgs physics in total rates (including differences in efficiencies of selection cuts) and differential distributions. While one can attempt to isolate effects in either production or decay processes, a full BSM scenario typically affects both simultaneously. (Differential) fiducial cross sections are an appropriate complementary tool for scrutinizing the Lagrangian structure of the Higgs boson interactions, for instance through tests for new tensorial couplings, non-standard production modes, and effective form factors. In addition to the measurement of specific fiducial regions, the combined analysis of all available fiducial measurements in a global fit seems a promising approach.

Below we address the effects that can be expected in a variety of BSM scenarios and we discuss interesting distributions and fiducial regions that can be used to target them. Unless otherwise specified, we will not consider any generic fiducial cuts on the results shown below. The eventual feasibility to measure such regions in a model independent way needs though to be scrutinized by experimentalists, since in some cases the poor resolution for some of the observable used to define the fiducial volumes could lead to non-negligible migration effects, cf. Section III.3.5.a. We also note that a parallel effort is required from the theory community, in obtaining predictions with adequate precision, and a robust determination of the associated uncertainties, and their correlations, within the theoretical framework used in the comparison to the measurements, be it specific BSM models or effective Lagrangian descriptions. The status of the presently existing tools is discussed in the various other sections of this report.

III.3.4.a Higgs boson production in gluon fusion

Higgs boson production in gluon fusion has one specific feature which allows us to test to what degree the observed Higgs is described by the SM: its production amplitude at one loop is mediated by virtual top quarks, which means that any new, strongly interacting particle can lead to order-one corrections to the effective Higgs-gluon coupling. The relevant Lagrangian describing this channel is

$$\mathcal{L} = \mathcal{L}\Big|_{\kappa_j=0} + \left[\kappa_{\mathrm{t}}\, g_{\mathrm{ggH}} + \kappa_{\mathrm{g}} \frac{\alpha_s}{12\pi}\right] \frac{\mathrm{H}}{v}\, G_{\mu\nu}G^{\mu\nu} - \kappa_{\mathrm{t}}\, \frac{m_{\mathrm{t}}}{v}\mathrm{H}\left(\bar{\mathrm{t}}_R \mathrm{t}_L + \mathrm{h.c.}\right) \,. \tag{III.3.1}$$

In combination with a second measurement of the top Yukawa coupling, for example in $t\bar{t}\mathrm{H}$ production, already a total rate measurement in this largest Higgs boson production channel can constrain particles like light top partners.

While the Lagrangian of eq. (III.3.1) only features shifts in SM-like Higgs boson couplings, the interplay between the renormalizable top Yukawa coupling and the dimension-6 Higgs-gluon coupling can affect kinematic distributions. For example, the reach for new particles contributing to the effective Higgs-gluon coupling can be enhanced by adding off-shell Higgs boson production to the set of measurements [499, 500, 993]. Strictly speaking, off-shell Higgs production with a subsequent decay $\mathrm{H} \to 4\ell$ is best described by a shape analysis of the $m_{4\ell}$ distribution. Based on the Lagrangian of eq. (III.3.1) we can write the complete gluon-induced amplitude $\mathrm{gg} \to \mathrm{ZZ}$ as

$$\mathcal{M}_{\mathrm{ZZ}} = \kappa_{\mathrm{t}}\mathcal{M}_{\mathrm{t}} + \kappa_{\mathrm{g}}\mathcal{M}_{\mathrm{g}} + \mathcal{M}_c \,, \tag{III.3.2}$$

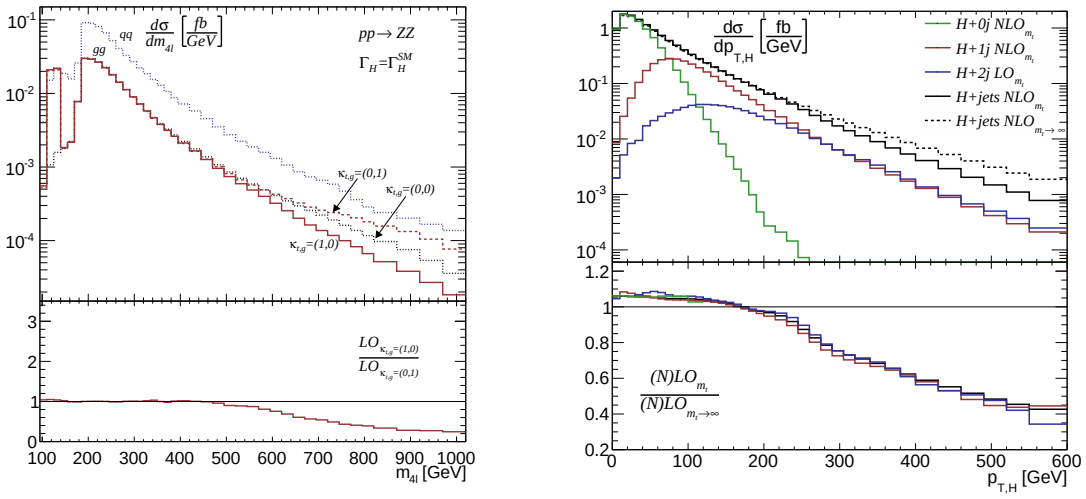

Figure 246: (left) Invariant $m_{4\ell}$ distributions for the process $\mathrm{q\bar{q}(gg)} \to \mathrm{ZZ}$ at 13 TeV, obtained with MCFM [290] (right) $p_{\mathrm{T}}^{\mathrm{H}}$ including jets recoiling against the on-shell Higgs. We merge 0-jet and 1-jet production to NLO with the full top mass dependence, 2-jet production to LO with the full top mass dependence, and parton shower effects. Figure from Ref. [851].

where the last term arises from the Higgs-independent continuum diagram. Numerically, the interference between the Higgs and continuum diagrams is one of the key features in the measurement of off-shell Higgs effects at the LHC. While this phase space region is not included in the template fiducial regions in Section III.3.3.a, considering it is extremely beneficial [970].[III.16] The longitudinal components to the different contributions feature different dependences on $m_{4\ell}$, namely

$$\begin{aligned}
\mathcal{M}_{\mathrm{g}}^{++00} &\approx -\frac{m_{4\ell}^2}{2M_{\mathrm{Z}}^2} && \text{with } m_{\mathrm{t}} \gg m_{4\ell} \gg M_{\mathrm{H}}, M_{\mathrm{Z}} \\
\mathcal{M}_{\mathrm{t}}^{++00} &\approx +\frac{m_{\mathrm{t}}^2}{2M_{\mathrm{Z}}^2} \log^2 \frac{m_{4\ell}^2}{m_{\mathrm{t}}^2} && \text{with } m_{4\ell} \gg m_{\mathrm{t}} \gtrsim M_{\mathrm{H}}, M_{\mathrm{Z}} \\
\mathcal{M}_{c}^{++00} &\approx -\frac{m_{\mathrm{t}}^2}{2M_{\mathrm{Z}}^2} \log^2 \frac{m_{4\ell}^2}{m_{\mathrm{t}}^2} && \text{with } m_{4\ell} \gg m_{\mathrm{t}} \gtrsim M_{\mathrm{Z}} \,. \qquad \text{(III.3.3)}
\end{aligned}$$

In the proper limit a logarithmic dependence on $m_{4\ell}/m_{\mathrm{t}}$ develops far above the Higgs boson mass shell. The ultraviolet logarithm cancels between the correct Higgs amplitude and the continuum, ensuring the proper ultraviolet behaviour of the full amplitude. The sensitivity due to this logarithmic dependence on $m_{4\ell}/m_{\mathrm{t}}$, as shown in the left panel of Figure 246, should allow us to extract the top mass dependence of the observed signal from the $m_{4\ell}$ distribution. This means Higgs boson production is a good example of a process where it is not clear where we can expect to best find BSM effects: on the one hand, a precise measurement of the total rates of inclusive Higgs boson production and $\mathrm{t\bar{t}H}$ production can be expected to constrain the Lagrangian if eq. (III.3.1). On the other hand, off-shell Higgs production, or better the $m_{4\ell}$ distribution might well benefit from its known dependence on the ratio $m_{4\ell}/m_{\mathrm{t}}$ in the Standard Model, in that case relying on the tails of a momentum-related kinematic distribution.

III.3.4.b Boosted Higgs boson production in gluon fusion

An alternative way to search for BSM effects in gluon-fusion Higgs boson production is to require a large boost of the Higgs to generate a large momentum flow through its production vertex. The leading

[III.16] Off-shell Higgs boson production and Higgs interference are discussed in detail in Chapter I.8 of this report.

partonic signal process is $gg \to Hg$, where the $2 \to 2$ kinematics defines the momentum flow through the Higgs vertex for example in terms of p_T^H or, equivalently, $p_{T,j}$. When a second jet is considered, the p_T^H spectrum provides the information about this production mode. Following the Lagrangian given in eq. (III.3.1) we can again compute the leading $\mathcal{O}(\alpha_s)$ dependence on the ratio p_T^H/m_t [251, 851],

$$|\mathcal{M}_{Hj(j)}|^2 \propto m_t^4 \, \log^4 \frac{(p_T^H)^2}{m_t^2} \, . \tag{III.3.4}$$

The effect of the different partonic sub-processes is shown in the right panel of Figure 246. In this observable, sizeable top mass effects already appear for $p_T^H > 250$ GeV. In the tail of the distributions, where for $p_T^H > 500$ GeV the SM expectations have dropped below a per mille of all events, the corrections from the new dimension-6 Higgs-gluon operator dominate the distribution. The sensitivity of off-shell Higgs boson production and boosted Higgs boson production in terms of the modified Lagrangian of eq. (III.3.1) can be compared. Because both methods rely on a small number of events in the tail of the kinematic distribution, large luminosities will be needed to detect sizeable deviations from the SM.

Going beyond the description in terms of dimension-6 operators, benchmarks for searches in this channel are coloured partners to the top, which participate in gluon fusion but whose contribution cancels at leading order. In this case, the $H + j$ channel provides the best handle on BSM. Examples of this situation– cancellation of effects at LO Higgs boson production– are fermionic top-partners in Composite Higgs models [850, 994] and stops in the so-called *funnel region* [826, 995].

In the right plot of Figure 247 we show the $p_{T,j}$ distribution in the SM case (blue), and the effect of introducing top-partners of different masses (M_T) and mixing angles ($\sin\theta$). This distribution has been obtained using a modified version of MCFM [290] including the effect of top partners, see Ref. [850] for details. Note that the lowest order effect in gluon fusion of these top-partners is exactly cancelled by the top, due to a low-energy theorem [895–897], hence information on these new particles is delegated to the H+jets channel, or parametrically small finite-mass effects.

III.3.4.c VH associated production

In this channel, the Higgs recoils against a vector boson, and thus it has an inherent boost. This boost enhances the momentum-dependent effects of New Physics with respect to the SM production, where the VVH interaction has no momentum dependence. Because the signal process has a simple $2 \to 2$ kinematic structure, the description of these effects in terms of p_T^H or p_T^V, or m_{VH} is, from a theory perspective, essentially equivalent. The relevant question is for which observable the experimental boundary conditions allow for the best coverage of phase space.

Generally speaking, the higher the momentum of the Higgs and vector boson one has access to, the higher the sensitivity to BSM effects [763,996]. In the left plot of Figure 247 we show this dependence in the context of an EFT approach to BSM performed at NLO QCD accuracy in POWHEG and showered through PYTHIAv8 [644]. The selection criteria applied to produce this plot are jets using k_T algorithm of $\Delta R = 0.4$, $p_T > 25$ GeV and $|\eta_j| < 2.5$, 2 b-jets with $p_T > 25$ GeV and $|\eta_b| < 2.5$, and 1 lepton (ℓ = e or μ) with $p_T > 25$ GeV, and $|\eta_\ell| < 2.5$. Needless to say, in this channel there is a strong correlation between the distributions in p_T^H (or p_T^V) and the invariant mass of the system, m_{VH} for resolved final states or m_T in the channels with missing energy, see Figure 10 in [855] and Figure 3 in [661].

In Run 1, the best limit on BSM phenomena using this channel was obtained by looking at the last reported bin, the overflow bin, which typically contains a low number of events. Despite this, one can use the estimate of SM background to set limits on new physics [849, 855]. This procedure is analogous to searches for anomalous trilinear gauge couplings in WW by looking at the overflow bin in the leading lepton p_T distribution performed at LEP and now at the LHC [997–999]. The combination of both sets of measurements would in fact be useful to enhance the sensitivity to anomalous trilinear couplings.

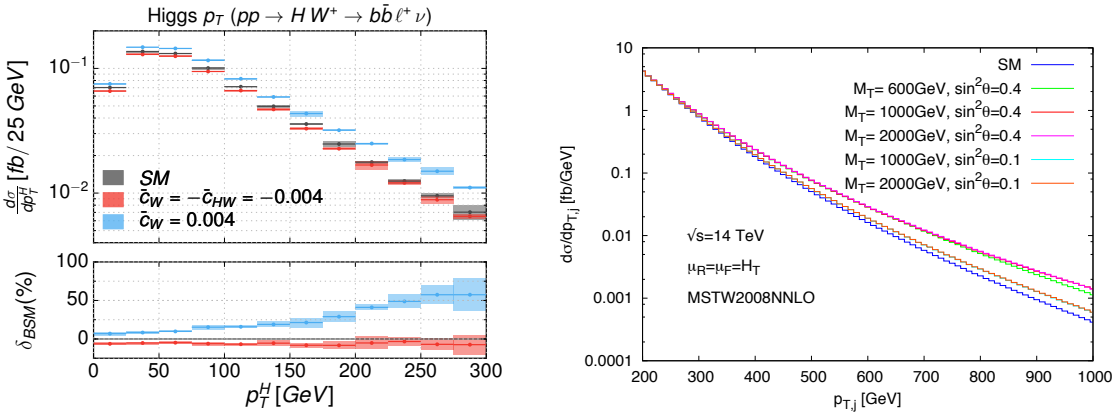

Figure 247: (left) Comparison of differential distribution of the Higgs p_{T} in the SM and the two EFT benchmarks of $\bar{c}_W = 0.004$ and $\bar{c}_W = -\bar{c}_{HW} = -0.004$ using POWHEG + PYTHIA8 in the process $\mathrm{pp} \to \mathrm{W^+H} \to \ell^+\nu b\bar{b}$. The lower panel show the percentage deviation of the EFT benchmarks from the SM prediction, δ_{BSM}. Figure taken from Ref. [644]. (right) Jet p_{T} differential distribution in the channel $\mathrm{H} + j$, with the SM case in blue, and the effect of introducing top-partners of different masses (M_T) and mixing angles ($\sin\theta$) shown in other colours. Figure from Ref. [850].

The sensitivity to BSM obtained via the last bin raises questions on the validity of the EFT approach at high-momentum transfer, as in this region one *could* be able to resolve new physics effects. This question is discussed in Sections II.2.2 and II.2.5. Tools incorporating BSM (incl. EFT) effects at higher order in precision are discussed in Section II.3.1.

III.3.4.d Vector boson fusion

In several ways, vector boson fusion is the most prolific of the usual Higgs boson production channels when it comes to measuring the properties of the Higgs boson. The first reason is that its $2 \to 3$ kinematics allows us to test a sizeable number of observables, including pure tagging jet correlations; second, we can test modifications of the gauge sector as well as modifications of the scalar or Higgs sector as long as they affect the central VVH coupling; third, it allows us to separate the very specific Lorentz structure of the VVH coupling in the SM from many modified structures induced by BSM physics; and finally, as an electroweak process with further suppressed QCD corrections we expect theoretical uncertainties to be under better control than in the gluon-fusion process.

A prime example for a general test of the SM nature of the Higgs boson is the direct test of the Lorentz structure of the VVH coupling which can be performed via the measurement of the azimuthal angle between the tagging jets [1000]. While the SM predicts a rather flat distributions, the typical CP-even and CP-odd structures could be identified with essentially zero events at 90 degrees or for back-to-back configurations, respectively. Similarly, the transverse momentum spectra of the tagging jets in the SM show a strong peak below $p_{\mathrm{T},j} \sim M_{\mathrm{W}}/2$. Generally, the longitudinal or transverse polarization of the gauge bosons affects this spectrum [1001], as originally computed in the effective W approximation [1002]. Finally, the rapidity difference of the two tagging jets is particularly large for SM Higgs boson production, and the tagging jets should become significantly more central if we change the VVH coupling in any way [1003–1005]. The important aspect of all these measurements (illustrated in Figure 248) is that they do not require a reconstructed Higgs 4-momentum, provided that global cuts ensure that we are working with a Higgs-rich event sample. This implies that it is secondary how we modify the VVH coupling, *i.e.* through a modification of the Higgs quantum numbers or through higher-

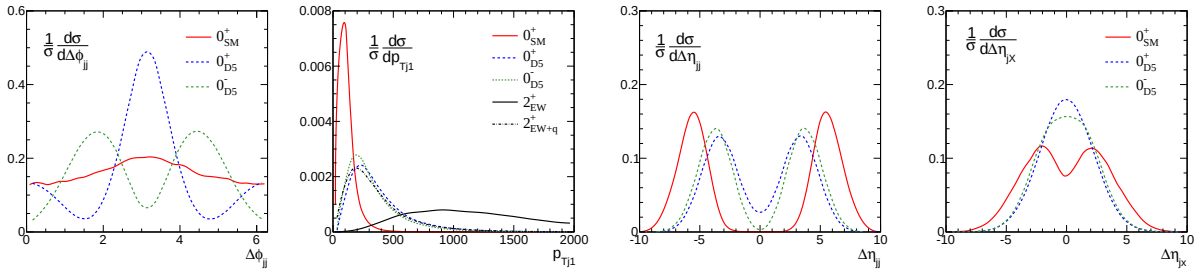

Figure 248: Normalized correlations between the two tagging jets in VBF production of a SM-like Higgs and a CP-even or CP-odd scalar coupled through a higher-dimensional operator. We show the difference in the azimuthal angle $\Delta\phi_{jj}$, the tagging jet p_T, the rapidity difference between the tagging jets $\Delta\eta_{jj}$, and the rapidity difference between the tagging jet and the Higgs-like resonance X. Figure from Ref. [1004].

dimensional operators for a SM-like Higgs. On the other hand, adding information from the Higgs boson decay will of course enhance the power of these measurements, for example re-formulating all questions originally asked in the framework of WW $\to$ WW scattering at high energies [918, 1001, 1006].

In the spirit of the discussion of gluon fusion Higgs boson production and VH associated production we focus on experimental tests enhanced by the momentum flow through the Higgs boson production vertex. We can link the transverse momenta of the two tagging jets or the Higgs to the virtuality of the weak bosons. Obviously, all of them are strongly correlated, so it becomes a theoretical as well as experimental question which of these observables to include in an analysis [661]. The only key requirement is that we do not bias these distributions for example by cutting on the tagging jet correlations discussed before. In Figure 249 we present the p_T of the Higgs, as a function of CP-violating operators in an EFT approach to BSM. Basic cuts applied to these events are $m_{jj} > 400$ GeV, $\Delta\eta_{jj} > 2.8$ and $|\eta_j| < 4.5$.

III.3.4.e Invisible Higgs boson decays

Once it is possible to experimentally target a specific Higgs production mechanism in terms of fiducial cross sections, we can focus on specific Higgs boson decay modes in this production mechanism. Arguably the hardest Higgs boson decay mode to search for the LHC are invisible Higgs boson decays. The SM predicts a very small invisible Higgs boson branching ratio through H $\to$ ZZ* $\to 4\nu$, but for example in Higgs portal models [1007] or in supersymmetry [1008] this decay can be an observable effect of weakly interacting dark matter. To date, searches for invisible Higgs boson decays in weak boson fusion, *i.e.* two tagging jets combined with missing transverse momentum [1009], appear to be the most promising strategy. The key feature of this signature are two tagging jets with exactly the same kinematics as in other VBF Higgs boson production channels. This means that fiducial volumes are related to other VBF studies by replacing the central Higgs boson decay products by missing transverse momentum.

Current projections for different LHC luminosities are shown in Table 118. The main background is Z+jets production, with an invisible Z decay. Two production mechanisms contribute to the background, one at the order $\alpha_s^2\alpha$ and one at the order $\alpha_s\alpha^2$. The QCD-like channel can be strongly reduced by a central jet veto, while weak boson fusion Z-production is essentially irreducible, with some kinematic differences for example in the azimuthal correlation of the tagging jets reflecting the Lorentz structures of the Z and H production vertices. For a success of this channel it is crucial to understand the central jet activity, so the right columns of Table 118 should be considered a challenge to the experimental performance of jet and particle-flow-like algorithms. In general, weak boson fusion signatures might also be extracted just based on one tagging jet [1010], a channel which has not (yet) been studied for invisible Higgs boson decays.

Table 118: Exclusion reach in $\mathrm{BR_{inv}} = \Gamma_{\mathrm{inv}}/\Gamma_H$ at 95% CLs to an invisible Higgs boson width at various luminosities and different combinations of cuts and multivariate analyses. Here, Γ_H is defined to be the width of the Higgs boson in the SM without the additional invisible component due to new physics. Table from Ref. [1011].

	$p_{\mathrm{T},j} > 20$ GeV				$p_{\mathrm{T},j} > 10$ GeV	
$\mathcal{L}[\mathrm{fb}^{-1}]$	VBF cuts	+ jet veto	+ $\Delta\phi_{jj}$	BDT 2-jets	BDT 2-jets	+ BDT 3-jets
10	1.02	0.49	0.47	0.28	0.18	0.16
100	0.49	0.20	0.18	0.10	0.07	0.061
3000	0.25	0.094	0.069	0.035	0.025	0.021

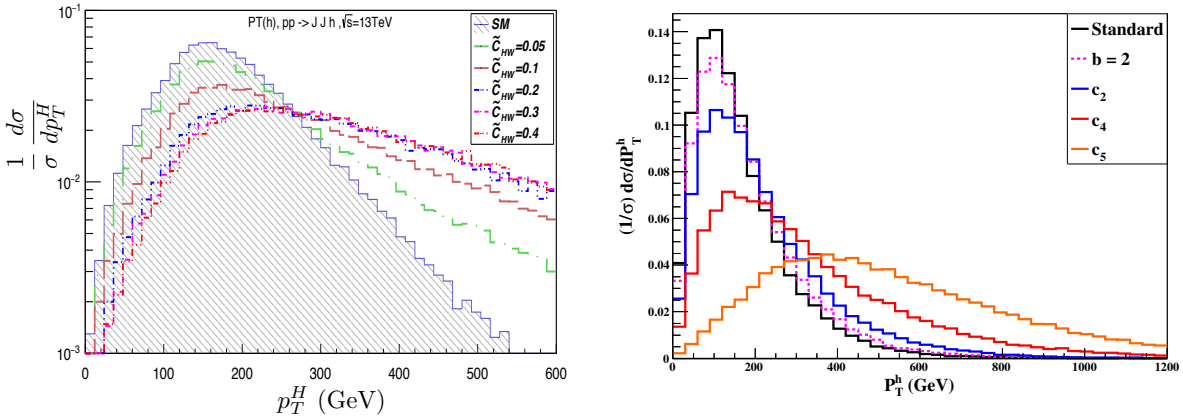

Figure 249: Distributions of the Higgs p_{T} in two channels. (left) Vector boson fusion, with the SM case represented by the solid distribution, and the SM plus additional modifications due to different values for the possible CP-violating operator $\tilde{c}_{HW}$ [838] are given by the coloured lines. (right) The production of the Higgs boson in association with a pair of Dark Matter scalar particles of mass 500 GeV [1013] at LHC13. The black line corresponds to the standard portal coupling h^2S^2, and the other lines represent different contributions due to a non-linear nature of electroweak symmetry breaking.

III.3.4.f Mono-Higgs signatures

An alternative way to probe the connection between the Higgs and Dark Matter are channels where the Higgs recoils against missing energy, *i.e.* mono-Higgs signatures. Again, fiducial measurements are closely linked to a SM signatures, $\mathrm{pp} \to \nu\bar{\nu}\mathrm{H}$ arising in the VH topology. Unlike for invisible Higgs boson decays, the kinematical structure of BSM mono-Higgs events will not resemble that in VH production. Instead, we expect significant deviations for example in the distributions of the reconstructed Higgs. Nevertheless, we would be able to utilize fiducial volumes defined for associated VH production with only a transverse reconstruction of the gauge boson.

Studies at Run 1 on the mono-Higgs signature have been done in the context of the Higgs portal [1012], and other extensions of the SM are now being considered. Particularly interesting distributions are the transverse mass of the system or the p_{T} distribution of the Higgs. In Figure 249, we show the Higgs p_{T} distribution in events where the Higgs is produced in association with a pair of Dark Matter particles of mass 500 GeV at LHC13. The labels correspond to different assumptions of the coupling of Dark Matter to the Higgs sector with the blacks line the benchmark of standard Higgs portal coupling $\lambda_{hs}h^2S^2$. Note that to produce this distribution, no cuts at generation level have been applied.

III.3.5 Experimental aspects

In this section a brief overview of the experimental aspects important for the fiducial cross section measurements is given. It includes the criteria for the particle level fiducial volume definition, a brief review of the unfolding procedures, estimation of the remaining model dependence, treatment of the Higgs boson mass parameter, aspects related to the statistical combination of the fiducial measurements between different processes and/or different experiments, and also recommends the points that should be carefully studied when designing the fiducial measurements. It primarily focuses on the measurement that are deemed feasible in the short and medium term of the LHC running.

III.3.5.a Definition of the fiducial phase space

The acceptance and selection efficiency for the particular Higgs boson decay channel can vary significantly between different Higgs boson production mechanisms and different exotic models of Higgs boson properties. In processes with large jet activity such as the $t\bar{t}\phi$ production or those with the kinematics of the decay products very different from the SM prediction (such as in case of the exotic Higgs-like spin-one models), the acceptance of signal events within a certain part of the phase space can significantly differ from the acceptance for the SM Higgs boson decays. In order to minimize the dependence of the measurement on the specific theoretical model assumption, the fiducial phase space for the Higgs boson cross section measurements should be defined to match as closely as possible the experimental acceptance in terms of the kinematics of the decay products and topological reconstruction-level event selection.

The fiducial phase space is typically defined using the stable particles or more complex objects built out of them (leptons, photons, jets, missing transverse momentum, etc.) at the hard scattering level, before their interaction with the detector material. In order to minimize the model dependence, fiducial-level particles and objects are typically defined to be as close as possible to the particles and objects used at the reconstruction level. In case of the leptons, it is typical that fiducial-level leptons are defined as the leptons "dressed" with the photons from the final state radiation (the photons that are within certain distance ΔR from the lepton), as at the reconstruction level those photons are typically recovered by the experimental methods. In case of differential measurements as a function of jet-related observables, it is recommended that jets are reconstructed from the individual stable particles, excluding neutrinos, using the anti-k_t clustering algorithm with a distance parameter identical to the one used at the reconstruction level.

III.3.5.a.i Isolation requirement in the definition of the fiducial volume [III.17]

The inclusion of isolation of photons and leptons can be important in the fiducial phase space definition whenever object isolation is used at the reconstruction level, as it can reduce the differences in signal selection efficiency between different models. It has been verified in simulation that this difference can be significant if the lepton isolation requirement is included at the reconstruction but not at the fiducial level [964, 965]. This can be especially pronounced in case of large associated jet activity such as in the $t\bar{t}\phi$ production mode. Exclusion of neutrinos from the computation of the isolation sum typically brings the definition of the fiducial phase space closer to the reconstruction level selection, and can additionally improve the model independence of the signal selection efficiency. It is recommended that these effects are studied in each particular analysis separately.

The experimental analyses measuring fiducial cross sections in the $H \to \gamma\gamma$ channel typically require two isolated photons with a p_T above a certain threshold. In order to minimize the extrapolation when correcting experimental yields to particle level fiducial cross sections, it is useful to impose a similar criterion which duplicates a similar requirement using stable particles. Imposing such drastically reduces the underlying model dependence: this can be readily understood if one compares for example

[III.17] *Author(s): S. Menary, A. Pilkington.*

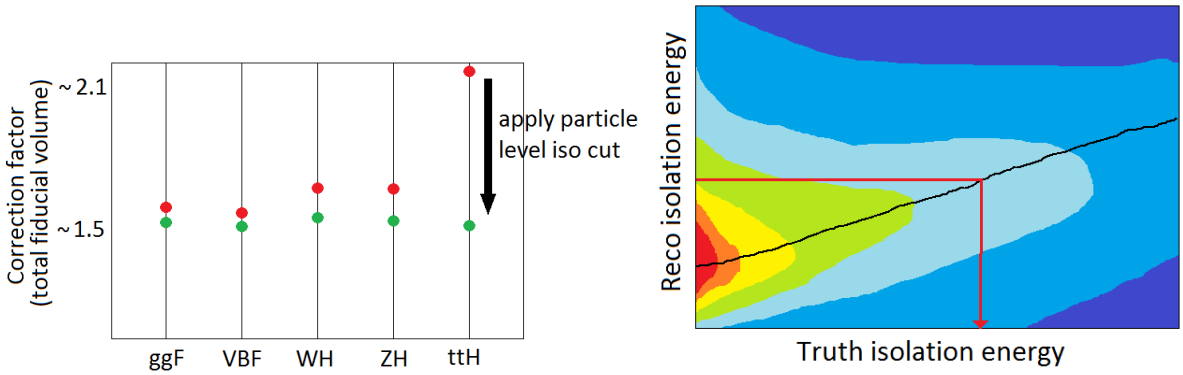

Figure 250: (left) Illustration for correction factor which maps reconstructed yields to fiducial cross sections without (red) and with (green) imposing a particle level isolation criterion are shown. Imposing particle level isolation significantly reduces the differences between different Higgs boson production modes which minimizes the model dependence. (right) The procedure to map a reconstructed isolation criterion to a particle level isolation criterion using profiles is illustrated.

Higgs boson production with gluon fusion versus in association with a top quark pair: $H \to \gamma\gamma$ photons from the latter fail more often the isolation criterion due to the large hadronic activity and thus have a lower reconstruction efficiency. Figure 250 shows the correction factors mapping reconstructed yields into fiducial cross sections with and without imposing a similar particle level isolation cut. A particle level isolation criterion can be imposed by summing around a fixed cone the energies of all stable particles and events are similarly rejected when the isolation energy is larger than a certain threshold. The exact cut can be tuned such that the model dependence becomes minimal, i.e. that the efficiency difference between rejecting a reconstructed event and a true event is very similar: In Figure 250 the correlation between true and reco isolation is shown, and an illustrative reconstruction cut is mapped to a given true value using a profile of both observables. The effect of imposing this criterion is illustrated as well, resulting in near matching correction factors for all Higgs boson production processes.

III.3.5.a.ii Signal contributions from outside of the fiducial phase space

At the reconstruction level, additional signal contribution from events that do not originate from the fiducial phase space can arise due to detector resolution effects that cause differences between the quantities used for the fiducial phase space definition (such as the lepton or photon isolation, jet transverse momentum, missing transverse momentum etc.) and the analogous quantities used for the event selection. This contribution should be treated as background and subtracted before the unfolding procedure is applied. Hereafter we refer to this contribution as the "nonfiducial signal" contribution. It has been shown in simulation that the shape of these events is typically very similar to the shape of the fiducial signal. In order to minimize the model dependence of the measurement - it should be studied how to optimize fiducial phase space definition to minimize the effect that arises from nonfiducial signal' contribution, and how to experimentally treat this contribution in the measurement. Studies in simulation have shown that this component can vary from just few per cent e.g. for the $\mathrm{gg} \to \mathrm{H}$ production mode to several per cent for the $t\bar{t}\phi$ production mode [964, 965]. The variation of this fraction between different signal models can be included in the model dependence estimation.

The nonfiducial signal contribution deserves special attention when the observables used to define the signal region have poor experimental resolution (such as missing transverse energy, transverse momentum of jets, etc.). In those cases effects of migration of the signal events can be large, and it might be worth studying if the measurement can benefit (in terms of the overall model dependence) from relaxing the requirements on such observables at the fiducial level with respect to the reconstruction level.

These effects have been discussed in the light of the fiducial measurements of the Higgs boson transverse momentum in the $H \to WW$ decay channel [966].

The fraction of signal events within the fiducial phase space $\mathcal{A}_{\text{fid}}$, the reconstruction efficiency ϵ for signal events within the fiducial phase space for individual SM production modes and exotic signal models, as well as the fraction of signal events outside of the fiducial phase space f_{nonfid} are listed in Table 119. Values are given for characteristic signal models assuming $m_{\text{H}} = 125.0$ GeV, $\sqrt{s} = 8$ TeV, and the overall picture is similar in case of the pp collision at $\sqrt{s} = 13$ TeV.

Table 119: The fraction of signal events within the fiducial phase space (acceptance $\mathcal{A}_{\text{fid}}$), reconstruction efficiency (ϵ) for signal events from within the fiducial phase space, and ratio of reconstructed events which are from outside the fiducial phase space to reconstructed events which are from within the fiducial phase space (f_{nonfid}). Values are given for characteristic signal models assuming $m_{\text{H}} = 125.0$ GeV, $\sqrt{s} = 8$ TeV, and the uncertainties include only the statistical uncertainties due to the finite number of events in MC simulation.

Signal process	$\mathcal{A}_{\text{fid}}$	ϵ	f_{nonfid}	$(1 + f_{\text{nonfid}})\epsilon$
Individual Higgs boson production modes				
$\text{gg} \to \text{H}$ (POWHEG+JHUGEN)	0.422 ± 0.001	0.647 ± 0.002	0.053 ± 0.001	0.681 ± 0.002
VBF (POWHEG)	0.476 ± 0.003	0.652 ± 0.005	0.040 ± 0.002	0.678 ± 0.005
WH (PYTHIA)	0.342 ± 0.002	0.627 ± 0.003	0.072 ± 0.002	0.672 ± 0.003
ZH (PYTHIA)	0.348 ± 0.003	0.634 ± 0.004	0.072 ± 0.003	0.679 ± 0.005
$t\bar{t}\phi$ (PYTHIA)	0.250 ± 0.003	0.601 ± 0.008	0.139 ± 0.008	0.685 ± 0.010
Some characteristic models of a Higgs-like boson with exotic decays and properties				
$\text{q}\bar{\text{q}} \to \text{H}(J^{CP} = 1^-)$ (JHUGEN)	0.238 ± 0.001	0.609 ± 0.002	0.054 ± 0.001	0.642 ± 0.002
$\text{q}\bar{\text{q}} \to \text{H}(J^{CP} = 1^+)$ (JHUGEN)	0.283 ± 0.001	0.619 ± 0.002	0.051 ± 0.001	0.651 ± 0.002
$\text{gg} \to \text{H} \to \text{Z}\gamma^*$ (JHUGEN)	0.156 ± 0.001	0.622 ± 0.002	0.073 ± 0.001	0.667 ± 0.002
$\text{gg} \to \text{H} \to \gamma^*\gamma^*$ (JHUGEN)	0.188 ± 0.001	0.629 ± 0.002	0.066 ± 0.001	0.671 ± 0.002

III.3.5.a.iii Signal definition

The requirement on the invariant masses of the Higgs boson decay products is also important as the off-shell production cross section in the dominant gluon fusion production mode can be sizeable and can amount up to a few per cent of the total cross section [499].

III.3.5.b Unfolding of experimental data

Dealing with experimental resolutions will become a major aspect of differential fiducial measurements in Run 2: the large increase in integrated luminosity will mark the transition of the total uncertainties being statistically dominated to becoming systematically limited. This will offer new challenges to reverting experimental resolutions. A summary about the caveats and various approaches of unfolding can be found for instance in Ref. [1014], which this overview follows.

III.3.5.b.i Introduction

In measurements of differential cross sections, one often faces the problem of non-negligible migrations due to the finite resolution of the experimental apparatus. The reversion of such resolution migrations is typically called 'unfolding' or 'deconvolution' and compromises an essential ingredient that allows

the easy comparison of theory predictions with measured fiducial cross sections. Mathematically the problem can be formulated in finding an inversion to the function

$$f_{\text{meas}}(x) = \int R(x|y| f_{\text{true}}(y)\,\mathrm{d}y\,, \tag{III.3.5}$$

where $f_{\text{meas}}(x)$ is the PDF of the measured values x, and $f_{\text{true}}(y)$ the PDF of true (but unknown) values y, smeared out by a detector response $R(x|y)$. In practice measurements are carried out in bins of observables, reducing Eq. III.3.5, to a matrix multiplication

$$x_i = \sum_{j=1}^{N} R_{ij} y_j\,. \tag{III.3.6}$$

and the response matrix R_{ij} can be interpreted as a conditional probability

$$R_{ij} = \mathcal{P}(\text{reconstructed in bin } i \,|\, \text{true value in bin } j) \tag{III.3.7}$$

with the sum

$$\sum_{i=1}^{N} R_{ij} = \mathcal{P}(\text{observed anywhere} \,|\, \text{true value in bin } j) = \epsilon_j\,, \tag{III.3.8}$$

resulting in the the reconstruction efficiency. The task of unfolding is now to revert Eq. III.3.6 to convert measured values to true values. There exist several approaches for this, each with different strengths and caveats.

III.3.5.b.ii Inverting the response matrix and correction factors

The most straightforward approach of unfolding involves the inversion of the matrix Eq. III.3.7 and construct R_{ij}^{-1}. This is generally often possible, but has some drawbacks: if the response matrix has large off-diagonal elements, e.g. if the chosen bin size is too small compared to the measurement resolution or one tries to measure an observable with an intrinsic poor resolution, such as jet multiplicities, the resulting expression for the true value

$$y = R_{ij}^{-1}\, x \tag{III.3.9}$$

can have extremely large variances and strong negative correlations between neighbouring bins. If the measured values x themselves are affected by large statistical fluctuations, these get amplified as one tries to revert migrations in a given bin using the estimated bin content of neighbouring bins with large variances themselves. In scenarios with small measured variances the resulting variances also can get amplified, if a high degree of fine structure is present, cf. Ref. [1014]. Technically the inversion of R_{ij} can be implemented using least square estimators and in case the inversion is not possible, a pseudo-inverse may be constructed. The advantage of this inversion approach is that the resulting values for y, albeit in generally affected by large variances are in fact unbiased and the variance itself has the smallest possible value for any unbiased estimator. Thus any other method that aims to reduce the variance will necessarily introduce a bias. Thus the strategy that is followed is to accept a small bias in exchange for a large reduction in variance, i.e. trading statistical for systematic errors.

III.3.5.b.iii Correction factor method

A relative simple method, often used in low statistics situation, is based on multiplicative correction factors derived from Monte Carlo simulations. The estimator for y in a given bin i is constructed as

$$y_i = C_i x_i \tag{III.3.10}$$

where the correction factor C_i is

$$C_i = \frac{y_i^{\mathrm{MC}}}{x_i^{\mathrm{MC}}}\,, \tag{III.3.11}$$

where y_i^{MC} and x_i^{MC} are the expected true and reco yields from the simulation. This inversion has a much smaller variance than the inversion of the migration matrix, but has a potential bias of the size

$$b_i = \left(\frac{y_i^{\mathrm{MC}}}{x_i^{\mathrm{MC}}} - \frac{y_i^{\mathrm{true}}}{x_i^{\mathrm{true}}}\right) x_i^{\mathrm{obs}} \tag{III.3.12}$$

which has to be carefully estimated. In Eq. III.3.12 the quantities y_i^{true} and x_i^{true} are the true underlying mean population of the bin. The bias is zero in case the model is correct, which is not something that can be inferred prior a measurement. Typically the size of the bias is estimated with respect to some baseline scenario (e.g. the SM) and a maximal deviation one expects (e.g. a certain amount of new physics). One is satisfied when b_i is small with respect to the variance and the size of the estimated bias is added to the systematic error of the measurement. This maximal deviation can also be composed by an entire of ensemble of scenarios.

III.3.5.b.iv Regularized unfolding

Regularized unfolding tries to find some middle ground between these two approaches: inverting the migration matrix assumes that all the relevant information on how to revert migrations comes from the neighbouring bins of a measured distributions. The correction factor method excludes all the information from neighbouring bins to revert migrations. In regularized unfolding the information from both is used, and the weighting of either piece of information is typically controlled by one or many regularization parameters. There exist a range of different methods following different philosophies, often used are for example Refs. [1015, 1016]. It is important to note, that regularized unfolding also has to carefully control and estimate the size of a potential bias. Here, as for the correction factor method, the found bias using a baseline scenario and a scenario for the largest to be expected deviation is added to the systematic error of the unfolded spectrum. In addition special attention has to be payed to not 'over-regularize' the unfolded distributions, that is to impose a too strong dampening of statistical fluctuations. This is usually achieved by careful tuning of the regularization parameter(s).

A priori any method for unfolding is fine to use, as long as the bias is properly estimated. Even the combination of information gained via different unfolding methods is not a priori a problem, as long as the bias is negligible with respect to the statistical precision and is included into the error budget properly. With the expected large data sets of Run 2 of the LHC, it is expected that experiments will shift away from simpler methods and follow suit what is standard practice in SM measurements.

III.3.5.c Model dependence

The underlying assumptions on the signal model used to extract the fiducial cross sections unavoidably introduce some remaining systematic effects on the final measurement. The size of these effects can be estimated by extracting the fiducial cross sections from data assuming a range of alternative signal models, and by comparing them to the fiducial cross sections obtained assuming the SM Higgs boson. The range of alternative models to consider can include models with an arbitrary fraction of different SM Higgs boson production modes, models of Higgs-like resonances with anomalous interactions with a pair of neutral gauge bosons, models of Higgs-like resonances with some exotic decays to the final state of interest, and similar.

After the comparison is performed, the largest deviation between the fiducial cross section measured assuming any of the models from a particular range of alternative signal models, and the fiducial

cross section measured under the SM Higgs boson assumption, should be reported as the systematic effect associated with the model dependence.

Given the fact that a wide range of exotic signal models has been excluded using the LHC Run 1 data at the 95% C.L. or better [Ref.], it is recommended to impose those existing experimental constraints to narrow the range of the considered exotic signal models, and to report the model dependence computed using this reduced range of models. Naturally, in cases when it is considered useful, analyses are welcome to report also the model dependence computed from some wider range of alternative models (e.g. obtained by completely neglecting the existing experimental constraints).

III.3.5.d Treatment of the Higgs boson mass in fiducial and differential measurements

All fiducial and differential cross section measurements rely on knowledge of the Higgs boson mass and analyses typically face two choices:

1. To extract the Higgs boson mass simultaneously along with the desired cross section parameters.
2. To fix the Higgs boson mass to the current world average and treat it as an external parameter.

A simultaneous extraction of the Higgs boson mass and cross section is not always possible due to poor mass resolution, as for instance in $H \to WW \to 2\ell 2\nu$ cross section measurements. Both approaches are justifiable and have a number of advantages and disadvantages.

III.3.5.d.i Simultaneous extraction of Higgs boson mass and cross section

In channels with good mass resolution, the simultaneous extraction of the Higgs boson mass and the fiducial cross sections is possible. Carrying out such a simultaneous analysis has the benefit that one avoids using information twice, once in the fiducial measurement and once from the Higgs boson mass measurement or average it might enter. In addition, one could argue that such measurements are less prone to possible systematic biases due to an accidental miscalibration of object energy scales, which relate the measured invariant mass with the physical Higgs boson mass. The clear disadvantage of the approach is that knowledge on the Higgs boson mass from complementary channels is completely discarded.

III.3.5.d.ii Treating the Higgs boson mass as an external parameter

Treating the Higgs boson mass as an external parameter allows one to incorporate such external knowledge from other centre-of-mass energies or channels. The apparent complication that enters the analyses though is the double use of data events in high resolution channels, such as $H \to \gamma\gamma$ and $H \to 4\ell$, which might have been used to determine the Higgs boson mass world averages in the first place. In practice, this is not an issue as the extracted quantities of interest, the Higgs boson mass and the reconstructed cross section yields, are uncorrelated entities and as such can be extracted individually from the same dataset without introducing a bias or error under-coverage.

III.3.5.d.ii.1 Updating the Higgs boson mass

The knowledge of the Higgs boson mass is bound to improve in the future. In order to update existing and future measurements which treat the Higgs boson mass as an external parameter, the impact of shifting the Higgs boson mass within its experimental error on the measured fiducial and differential cross sections should be determined and quoted along with other systematic shifts.

III.3.5.e Combination of inclusive cross sections for Higgs boson production

III.3.5.e.i Introduction

This section discusses the combination of measured Higgs boson cross sections across multiple decay channels. The combination is only possible in the inclusive phase space, where the effects of the Higgs

boson decay products have been removed. This introduces some model dependence: namely, the correction for the acceptance of the fiducial selection, and the assumption of Standard Model decay branching fractions for each decay channel. Although measurements of cross sections within a fiducial phase space offer a more model-independent way of probing the properties of the Higgs boson, measurements at the LHC are currently statistically limited [962–966]. It is therefore beneficial to combine the data across several channels, and maximize its potential. This has been performed in Run-1 by the ATLAS Collaboration in the diphoton and four-lepton decay channels [967].

Both total and differential cross sections can be combined, provided that there is a consistent definition of the observable of interest between the different decay channels. If only the shape of the differential distribution is of interest, the uncertainties from the combination can be reduced further as the assumptions of the SM decay branching fractions for each decay channel can be neglected.

III.3.5.e.ii Combination method

III.3.5.e.ii.1 Extrapolation to the total phase space

The inclusive phase space must be carefully defined such that all observables of interest are independent of the Higgs boson decay products. It is preferable to retain the philosophy of the fiducial cross-section measurements and keep the theoretical predictions and measurement as disentangled as possible, to maximize the longevity of the data. The data should therefore ideally be corrected to the particle level in the inclusive phase space. In order to compare theoretical predictions at the parton level to measurements, non-perturbative corrections accounting for the impact of underlying event, multi-parton interactions and hadronization can be provided separately. The central values and uncertainties should be evaluated using a range of generators with different tunes for showering, hadronization and underlying event, such as in Refs. [1017–1019].

III.3.5.e.ii.2 Jets in the inclusive phase space

When measuring differential cross sections, it is important that all observables of interest are independent of the decay products of the Higgs boson, in particular when considering jets. Generally the inputs to jet finding at the particle level are all final state particles with lifetimes $c\tau > 10$ mm, preferably excluding neutrinos, electrons, and muons that do not originate from hadronic decays (as suggested in Ref. [1020]). Using this method, some of the resulting particle-level jets will contain decay products of the Higgs boson. It is then possible for jets to veto – or be vetoed by – nearby decay products, due to overlap removal between physics objects. This creates an inconsistency in the definition of a jet between different decay channels, such as diphoton (two decay products in the final state) and four-lepton (four decay products in the final state).

The effect of the Higgs boson decay can be effectively removed by reconstructing jets at the particle level and explicitly excluding the decay products of the Higgs boson. This is possible in generators that retain the history of the Higgs boson decay on the event record. The effects of final-state radiation from the Higgs boson decay products can also be removed. For example, photons can be excluded from jet finding if they lie inside a cone of radius $\Delta\mathrm{R} < 0.1$ of an electron or muon, where neither the photon nor lepton originate from a hadron decay.

Optimally, a similar definition can be used when reconstructing detector-level jets. This can be done using the so-called particle-flow method, which reconstructs individual leptons and photons before using them as inputs to the jet finding algorithm.

III.3.5.e.ii.3 Binning of differential observables

In order to carry out a statistical combination of differential observables, matching bin boundaries are helpful. This reduces the combination in the inclusive phase space to a statistical problem of statistically combining coarse cross sections which hold information about the sum of more fine cross section

sums. In case no matching bin boundaries are present, a combination requires additional theory input to approximate such matching bin boundaries. For the Run 1 results, a range of criteria have been used to justify the binning of a given observable: binning choices aiming to have equal (expected) statistical significance in each bin or identical expected purities for example, offer a first rough guideline but no unique choice. In analyses which rely on extracting signal yields by subtracting non-resonant production, a certain given binning choice cannot introduce a bias. Thus future measurements should be encouraged to use matching bin boundaries wherever possible and practical to facilitate the possibility of a later inclusive combination.

III.3.5.e.iii Treatment of uncertainties

Care must be taken to appropriately correlate shared uncertainty sources (both experimental and theoretical) between the different decay channels. In particular, the uncertainties on the corrections for acceptance and branching fractions need to be assessed appropriately.

The branching fraction uncertainties for Run-1 are described in the LHC HXSWG YR3 [9]. For example, in Ref. [967] five nuisance parameters were used to describe the branching fraction uncertainties; three fully correlated and two uncorrelated between the diphoton and four-lepton decay channels.

Since the acceptance corrections are largely driven by the Higgs boson rapidity distribution, which is shaped by the phase space of the PDF, the choice of PDF set is one of the largest contributions to the acceptance factor uncertainty. In Run-1 this uncertainty was assessed by following the PDF4LHC recommendations [28]. Uncertainties associated with missing higher-order corrections are evaluated by varying the renormalization and factorization scales, also following the PDF4LHC recommendations.

The acceptance may also be sensitive to the choice of the assumed mass of the Higgs boson, if for example a mass window around the peak is chosen [964]. In this case the mass of the Higgs boson in the Monte Carlo samples used to calculate the fiducial acceptance should be varied within the current uncertainties. In order to cover a range of different event topologies and modest deviations from the SM couplings, the composition of the SM signal should also be varied within current experimental constraints. Finally, uncertainties in the MC simulation of underlying event, multi-parton interactions and hadronization should be included. This can be done using different MC tunes, preferably the "systematic variation" eigentunes which give more accurate variations of the perturbative effects [1017].

III.3.5.e.iii.1 Statistical procedure

Provided that the uncertainties are normal distributed, a weighted average between the two measurements may be performed. However, because channels are often statistically limited the use of Poisson statistics is frequently necessary. In this case a combined likelihood fit that accounts for common theoretical and experimental uncertainties can be used.

III.3.5.e.iv Summary

Combining different Higgs boson decay channels to reduce the large statistical uncertainty will continue to be important until a larger data sample is available. For example, the combination of the diphoton and four-lepton final states reduced the total uncertainty on the ATLAS 8 TeV inclusive measurement by on average $25-30\%$. While special care must be taken to unify the object definitions and to account for appropriate correlations between decay channels, the recommendations given here should provide a useful starting point for future combined measurements.

III.3.6 Summary and recommendations for future measurements

Fiducial measurements will play an important role in characterizing the Higgs boson in Run 2 and beyond: differential and total fiducial cross sections allow the study of a wide range of physical phenomena,

such as for example the accuracy of the theoretical model of different Higgs boson production mechanisms or the presence of beyond the SM contributions. To take full opportunity of these measurements further advancements in certain theory and experimental questions should be prioritized. In the following a list of such prioritized areas is given, which is based on the contributions of this report and the discussions inside our working group:

1. Fiducial definitions: The particle-level fiducial phase space should be designed with the goal to minimize the underlying model dependence. Often this leads to particle-level fiducial phase space definitions which closely follow the reconstruction level definition. In Run 1 such model errors contributed only negligible ot the total error budget for most observables, but with an expected integrated luminosity of 100/fb in Run 2 such aspects will become more important. Section III.3.5 discussed several experimental aspects on how such model dependence can be minimized. Among the most important ones is the use of particle-level isolation, which does mimic the reconstruction level requirements of isolated objects. If tuned right the ratio of reconstruction level and particle level fiducial efficiency can be brought close to be near production process independent. Both experiments should continue such studies and explore alternative fiducial regions and definitions, as there is no need to stay in sync with past definitions or other experiments.

2. Unfolding of detector effects: Reverting migrations induced by the finite resolution of the detectors is an important aspect of how measured differential cross sections are presented. Without such an unfolding a direct comparison of the measured fiducial cross sections with particle-level differential theory predictions cannot be made. In Run 1 both experiments followed a slightly different philosophy in unfolding, briefly summarized in Section III.3.5. In principle any method of unfolding is fine to use and combine as long as underlying model biases are properly estimated and included in the error budget. Besides making the unfolded results available (cf. recommendation 3), it became clear that it would be useful to also publish the migration matrices and the folded yield. One core aspect of fiducial measurements is the preservation of results, such that measured differential information can be confronted with new theory ideas even many years after the original measurement was carried out. As it is difficult to forsee the needs of future analyses, we recommend to provide the full array of information which lead to unfolded results: that is the original yields, the migration and efficiency matrix, as well as the full experimental on either such that the published results can be reproduced.

3. Preservation of data: An important trend, which is already very much being prioritized for SM measurements, is the publication of experimental information on HEPDATA [968], an online archive which allows easy access of many experimental results. The remaining Run 1 measurements which are not published there, should follow suit and for Run 2 a full summary of the experimental result of a paper should be made available there. In addition, experiments should provide validated RIVET routines [310] to apply the corresponding particle level fiducial selection of each analysis, as done in some cases in Run 1 already. This will allow phenomenologists or other interested parties to make maximal use of the measurements and minimize the possibility for errors. This is particular important if non-trivial fiducial definitions are used (cf. recommendation 1).

4. Higgs boson mass shifts: In Run 1 the experiments followed two different approaches when dealing with the Higgs boson mass: some either assumed that this is external knowledge and fixed the mass at the current best known world average. Although this implied a double use of the same data, the near complete decorrelation of cross section yields and resonance mass value, justified such an approach, as then both properties can be measured independently from each other. The alternative approach was to determine the Higgs boson mass using the available data and neglecting any other information from other channels. Both approaches are fine and could be used in the

future. As the knowledge on the Higgs boson mass will improve with Run 2, we recommend that measurements which fix the Higgs boson mass at its world average value provide the necessary information to allow updating their cross sections if our knowledge there improves. This information is contained completely in the shifts in cross sections within the current experimental bounds of the Higgs boson mass.

5. Additional object definitions and bin boundaries: Albeit not mandatory, the harmonization of object definitions (such as jets or of additional particles in the event) and bin boundaries would simplify comparisons between the experiments and theory considerably. In addition, it would allow both experiments to provide inclusive averages of their results. Such are more model independent, but will provide interesting future input to probe SM properties such as the modelling of hard and soft quark and gluon radiation or help constraining PDFs. In Run 1 such a combination between channels was carried out in Ref. [967] and experiments are encouraged to discuss a full combination of all experimental information to provide differential information of inclusive Higgs boson production. A review of some crucial points which need to be taken into account is provided in Section III.3.5.e.

6. Continued benchmarking of fiducial acceptance: An important aspect of fiducial measurements as well as for a combination between several channels outlined in point 5, is the understanding of the fiducial acceptance. In Section III.3.3 a first set of public results of differential Higgs boson p_T spectra are provided for a benchmark fiducial region. Such studies should continue to better understand the accuracy of the range of tools used to calculate such factors in an experimental context. A first contribution in this direction on the object level was carried out by Ref. [973], but future studies will be needed.

7.a Signal definitions: In Ref. [970] a first fiducial cross section measurement of $\mathrm{pp} \to \mathrm{ZZ}^{(*)} \to 4\ell$ was reported which absorbs the Higgs boson signal into its cross section definition. Such measurements are very interesting and should be pursuit also in Run 2, as they allow for a simultaneous analysis of resonant and non-resonant production: if for instance new physics would alter the coupling of the Higgs boson to the Weak bosons, the non-resonant background also would be modified what in turn would change the extracted yield. In addition, the maximal sensitivity to probe for such scenarios would involve the simultaneous analysis of resonant and non-resonant $\mathrm{pp} \to \mathrm{ZZ}^{(*)} \to 4\ell$ production.

7.b Signal definitions: In Ref. [1021] a value for the gluon fusion fiducial cross section is provided from $\mathrm{H} \to \mathrm{WW}^{(*)} \to 2\ell 2\nu$ decays. Albeit in terms of this measurement it is natural to subtract non-gluon Higgs boson production, we advocate a fiducial cross section definition which is inclusive over the Higgs boson production mechanism. Albeit this complicates the eventual analysis (as migration patterns are more complicated), such results allow for a wider range of interpretations. In particular, they do not make weaker assumptions of non-gluon fusion Higgs boson production, which is then subtracted. By providing inclusive measurements in all channels, the information is complementary to the information provided in the $\mathrm{H} \to \mathrm{ZZ}^{*} \to 4\ell$ and $\mathrm{H} \to \gamma\gamma$ channels, where no such subtractions are carried out and is left to an additional interpretation step.

8. Global beyond the SM analyses: A combined global analysis of several fiducial observables offers a unique probe to constrain beyond the SM physics. Such an analysis can either happen inside a given BSM model or in an effective field theory framework (cf. Section III.3.4 and the EFT review inside this report). This approach is complementary and more model independent to the simplified template cross sections, but also more limited as only channels can be included which allow for fiducial measurements. To maximize the sensitivity of such an analysis, the experimental and

theory communities should both work together to create the necessary tools and identity the necessary measurements that maximize the sensitivity. This for example requires theory predictions which match the experimental sensitivity and the determination of statistical correlations between observables. A proof-of-concept global analysis which could serve as a template for future global analyses was carried out in Ref. [962] using Run 1 data, where Wilson coefficients of dimension six operators were constrained using the differential information of five differential observables and their experimental correlations.

9. Targeted beyond the SM analyses: Complementary to global analyses, which use a broad collection of differential or fiducial regions to constrain beyond the SM physics, is the Ansatz of targeting regions with a specific sensitivity for a given model. If for example one wishes to constrain a dark matter scenario in association with a Higgs boson, that produces a lepton and missing transverse energy, most sensitivity will come from a matching fiducial region. Theorists are encouraged to enter a dialogue with their experimental colleagues if they have specific suggestions. Section III.3.4 provides a first discussion and specific regions targeting VBF, VH, and dark matter associated production seem among the most promising suggestions.

Part IV

Beyond the Standard Model Predictions *

*I. Low, M. Mühlleitner, M. Pelliccioni, N. Rompotis, R. Wolf (Eds.)

Chapter IV.1

Neutral MSSM

R. Lane, S. Liebler, A. McCarn, P. Slavich, M. Spira, D. Winterbottom (Eds.) E. Bagnaschi, F. Frensch, R. Harlander, S. Heinemeyer, G. Lee, H. Mantler, M. Mühlleitner, J. Quevillon, N. Rompotis, A. Vicini, C. Wagner, M. Wiesemann, R. Wolf

IV.1.1 Introduction

In contrast to the SM, the *Minimal Supersymmetric Standard Model* (MSSM) requires the introduction of two complex Higgs doublets, H_u and H_d, to provide masses for up- and down-type fermions via the spontaneous breaking of the $SU(2)_L \times U(1)_Y$ gauge symmetry. If the MSSM Lagrangian does not contain new sources of CP violation, the presence of two complex Higgs doublets implies the existence of two charged Higgs bosons, $\mathrm{H}^\pm$, and three neutral Higgs bosons: a CP-odd (i.e., pseudoscalar) state A, and two CP-even (i.e., scalar) states, h and H, with $M_\mathrm{h} < M_\mathrm{H}$. At the tree level in the MSSM, the masses of these five Higgs bosons and their mixing can be expressed in terms of the gauge-boson masses M_W and M_Z plus two additional parameters, which can be chosen as the pseudoscalar mass M_A and the ratio of the vacuum expectation values of the neutral components of the two Higgs doublets, $\tan\beta \equiv v_u/v_d$. The tree-level mass of the charged states is given by $M^2_{\mathrm{H}^\pm} = M^2_\mathrm{A} + M^2_\mathrm{W}$, and the tree-level masses of the neutral CP-even states are:

$$M^2_{\mathrm{h,H}} = \frac{1}{2}\left(M^2_\mathrm{A} + M^2_\mathrm{Z} \mp \sqrt{\left(M^2_\mathrm{A} + M^2_\mathrm{Z}\right)^2 - 4\,M^2_\mathrm{A}\,M^2_\mathrm{Z}\,\cos^2 2\beta}\right) . \tag{IV.1.1}$$

In the MSSM the role of the SM Higgs boson is shared between the scalars h and H. In particular, the couplings of the neutral scalars to pairs of massive vector bosons (VV) and of SM fermions (uu, dd and $\ell\ell$), relative to the corresponding SM couplings, are:

$$\begin{array}{cccc} & g_{\mathrm{VV}} & g_{uu} & g_{dd,\ell\ell} \\ \mathrm{A} & 0 & \cot\beta & \tan\beta \\ \mathrm{H} & \cos(\beta-\alpha) & \sin\alpha/\sin\beta & \cos\alpha/\cos\beta \\ \mathrm{h} & \sin(\beta-\alpha) & \cos\alpha/\sin\beta & -\sin\alpha/\cos\beta \end{array} \tag{IV.1.2}$$

where α is the angle that diagonalizes the CP-even mass matrix, given at tree level by:

$$\tan\alpha = \frac{-(M^2_\mathrm{A} + M^2_\mathrm{Z})\,\sin 2\beta}{(M^2_\mathrm{Z} - M^2_\mathrm{A})\cos 2\beta + \sqrt{\left(M^2_\mathrm{A} + M^2_\mathrm{Z}\right)^2 - 4\,M^2_\mathrm{A}\,M^2_\mathrm{Z}\,\cos^2 2\beta}} . \tag{IV.1.3}$$

In addition, there are non-SM couplings of the neutral scalars to ZA and to $\mathrm{W}^\mp\mathrm{H}^\pm$. These are proportional to $\cos(\beta-\alpha)$ in the case of h and to $\sin(\beta-\alpha)$ in the case of H, while the ZAA coupling vanishes and the $\mathrm{W}^\mp\mathrm{H}^\pm\mathrm{A}$ coupling does not depend on α or β. Also relevant for the discussion in Section IV.1.2 is the trilinear coupling of one heavy scalar to two light scalars, whose tree-level value reads, in units of M^2_Z/v where $v \equiv (v_u^2 + v_d^2)^{1/2} \approx 246$ GeV,

$$\lambda_{\mathrm{Hhh,\,tree}} = 2\,\sin 2\alpha\,\sin(\beta+\alpha) - \cos 2\alpha\,\cos(\beta+\alpha) . \tag{IV.1.4}$$

In the *decoupling limit*, $M_A \gg M_Z$, the mixing angle in the CP-even sector simplifies to $\alpha \approx \beta - \pi/2$. As a result, the tree-level mass of the light neutral scalar h becomes $M_h \approx M_Z\,|\cos 2\beta|$, and its couplings to gauge bosons, quarks and leptons in Eq. (IV.1.2) become SM-like. The masses of H and $H^\pm$ become approximately degenerate with M_A, the couplings of H to two massive gauge bosons vanish, the couplings of H to two up-type (down-type) SM fermions are suppressed (enhanced) for large $\tan\beta$, and the coupling of H to two light neutral scalars is suppressed for large $\tan\beta$. Therefore, in this limit, the Higgs sector of the MSSM reduces to an SM-like Higgs boson with tree-level mass $M_h < M_Z$, and a heavy and mass-degenerate multiplet $(H, A, H^\pm)$ with vanishing couplings to two massive gauge bosons. In contrast, for low values of M_A there is a crossing point where H and h swap their roles, i.e. the heavy neutral scalar is the one whose mass is independent of M_A and whose couplings approach SM strength. For $\tan\beta \gtrsim 10$, the decoupling behaviour of the tree-level scalar masses is rather sharp, with a clear crossing point around $M_A \approx M_Z$. For lower values of $\tan\beta$, the onset of the decoupling behaviour at $M_A \gg M_Z$ (or $M_A \ll M_Z$) is delayed to larger (or smaller) values of M_A. Indeed, for $\tan\beta = 3$ a heavy scalar H of mass around 300 GeV can still have non-negligible couplings to two massive gauge bosons (as well as to two light scalars, due to the reduced $\tan\beta$ suppression). However, for low $\tan\beta$ the upper bound on the tree-level mass of the light scalar can be considerably lower than M_Z, with $\tan\beta = 1$ corresponding to a vanishing tree-level mass.

As is well known, the tree-level predictions for the masses of the MSSM Higgs bosons are subject to substantial radiative corrections, which can lift the lightest-scalar mass well above the tree-level bound and introduce a dependence on several other parameters of the MSSM. The dominant one-loop contribution to the lightest-scalar mass arises from loops of top quarks and their scalar superpartners, the top squarks (stops), and in the decoupling limit takes the approximate form

$$\left(\Delta M_h^2\right)_{1\ell}^{t/\tilde{t}} \;\approx\; \frac{3\,m_t^4}{2\,\pi^2\,v^2}\left(\log\frac{M_{SUSY}^2}{m_t^2} + \frac{X_t^2}{M_{SUSY}^2} - \frac{X_t^4}{12\,M_{SUSY}^4}\right)\,, \tag{IV.1.5}$$

where $M_{SUSY} = \sqrt{M_{\tilde{t}_1}\,M_{\tilde{t}_2}}$ is an average scale for the stop masses, and $X_t = A_t - \mu\cot\beta$ is the stop mixing term, where A_t is the soft SUSY-breaking Higgs-stop coupling and μ is the higgsino mass parameter. The one-loop top/stop contribution to M_h is maximized for large values of M_{SUSY} (due to the logarithmic term) and for the *maximal mixing* condition $|X_t| = \sqrt{6}\,M_{SUSY}$. A smaller negative contribution from sbottom loops, not shown in the equation above, can be relevant only for large values of $\tan\beta$.

Due to the crucial role of radiative corrections in pushing the prediction for the lightest-scalar mass above the tree-level bound, an impressive theoretical effort has been devoted over a quarter-century to the precise determination of the Higgs sector of the MSSM.[IV.1] After the first computations of the one-loop top/stop contributions [1022–1027], full one-loop computations of the MSSM Higgs boson masses have become available [1028–1033], leading logarithmic corrections beyond one loop have been included via renormalization-group (RG) methods [1034–1041], and the genuine two-loop corrections have been evaluated in the limit of vanishing external momentum in the Higgs self-energies [83, 1042–1055]. The external-momentum dependence of the dominant two-loop corrections involving the strong gauge coupling or the third-family Yukawa couplings has subsequently been computed [1056–1059], and some of the dominant three-loop corrections to the lightest-scalar mass have also been obtained, both via RG methods [87, 1060, 1061] and by explicit calculation of the Higgs self-energy at zero external momentum [1062, 1063].

As in the SM, one of the most important production mechanisms for the neutral Higgs bosons in the MSSM is gluon fusion [1064], mediated by loops involving the top and bottom quarks and their superpartners. However, for intermediate to large values of $\tan\beta$ bottom-quark annihilation can be-

[IV.1] We focus here on the MSSM with real parameters. Significant efforts have also been devoted to the Higgs boson mass calculation in the presence of CP-violating phases, as well as in non-minimal supersymmetric extensions of the SM.

come the dominant production mechanism for the neutral Higgs bosons that have enhanced couplings to down-type fermions. For what concerns gluon fusion, the knowledge of the contributions of diagrams involving only quarks and gluons includes: NLO-QCD contributions [97–99, 136, 140, 142, 143, 862, 865] with full dependence on the Higgs boson and quark masses; NNLO-QCD contributions in the heavy-top limit [70, 100–102, 115, 127, 859, 866, 867, 879, 880, 1065, 1066] and including finite top-mass effects [103–106, 234, 235, 1067, 1068]; partial NNNLO-QCD contributions [94, 95, 117, 119, 155, 1069]; soft-gluon resummation effects [115, 116, 1070–1072]. The NLO-QCD contributions of diagrams involving only squarks and gluons are fully known [142, 863–865]. For the NLO-QCD contributions of diagrams involving quarks, squarks and gluinos, approximate analytic results assuming different hierarchies between the Higgs, quark and superparticle masses are available [868, 870–875, 1073], and exact results relying on a combination of analytic and numerical methods have been presented [876, 877]. Approximate results, in the limit of vanishing Higgs boson mass, also exist for the NNLO-QCD contributions of diagrams involving superparticles [869, 1074, 1075]. Finally, the effects of non-decoupling, $\tan\beta$-enhanced corrections to the Higgs-bottom coupling can be taken into account via an effective-Lagrangian approach [1076–1083], and the subset of electroweak (EW) contributions involving loops of light quarks and gauge bosons can be adapted to the MSSM from the corresponding SM calculation [107, 1084]. For Higgs boson production in bottom-quark annihilation, the cross section is known in the four-flavour scheme at NLO-QCD [1085, 1086] and in the five-flavour scheme up to NNLO-QCD [565, 1087, 1088]. As in the case of gluon fusion, the $\tan\beta$-enhanced contributions from diagrams involving superpartners can be taken into account by means of an effective Higgs-bottom coupling. The remaining one-loop contributions from superpartners have been found to be small [1089–1091].

The kinematic distributions of the Higgs bosons of the MSSM can exhibit different properties with respect to the corresponding ones of an SM-like Higgs boson of equal mass [224, 231, 239, 240, 252, 826, 850, 994, 1092–1095]. In the case of gluon fusion, these effects are due to the modified relative importance of the top and bottom amplitudes and to the additional contributions from SUSY particles that mediate the interaction between the Higgs and the gluons. To understand the size of these effects and to estimate the discriminating power in distinguishing them from the SM behaviour, it is important to compute precise predictions where all theoretical uncertainties are under control [1096].

The decays of the MSSM Higgs bosons should also be calculated including higher-order corrections. Decays to SM fermions have been evaluated at the full one-loop level in the MSSM [1097, 1098] (see also Ref. [1099]), where higher-order SUSY corrections can be included via resummation [1076–1083]. Decays to (lighter) Higgs bosons have been evaluated at the full one-loop level in the MSSM in Refs. [1098, 1100] (see also Refs. [1101, 1102]). Decays to SM gauge bosons have been evaluated at the full one-loop level in Ref. [1103], but no corresponding computer code is available. In an approximative way they can be evaluated using the full SM one-loop result [72, 73] rescaled with the appropriate effective LO coupling factors. The latter are available in the form of radiatively corrected effective couplings and Z factors up to the two-loop level [85] and ensure, also in the other decay modes, the on-shell properties of the decaying Higgs boson. The (heavy) MSSM Higgs bosons can (if kinematically allowed) also decay to SUSY particles, i.e. to charginos, neutralinos and scalar fermions, where these modes can dominate the heavy Higgs boson decays. The lightest neutral Higgs boson, on the other hand, can have a substantial branching ratio into the lightest neutralino, i.e. the Dark Matter candidate in the MSSM [1104, 1105]. Higher-order contributions to the decays of the MSSM Higgs bosons to scalar fermions have been evaluated at the full one-loop level in Refs. [1106, 1107]. In Ref. [90] the $\mathcal{O}(\alpha_s)$ corrections to Higgs boson decays to scalar quarks were re-analysed. Full one-loop corrections to the decays to charginos and neutralinos can be found in Refs. [1108–1110].

The discovery of an approximately SM-like Higgs boson with mass around 125 GeV – and the non-observation of SUSY particles or of additional (neutral or charged) Higgs bosons – in the first few years of operation of the LHC have led to strong constraints on the allowed parameter space of the MSSM. For low values of the parameter $\tan\beta$, the direct bounds on the masses of the additional Higgs

bosons are still relatively weak, but very heavy top squarks are required to reproduce the observed mass of the SM-like Higgs boson. In Section IV.1.2 we discuss two approaches, proposed in Refs. [1111–1114] and [1115], for predicting the properties of the Higgs bosons in the region with low $\tan\beta$ and heavy SUSY particles. We also compare the predictions of the two approaches with those of a recent calculation based on the effective-field-theory (EFT) method [1116].

In Section IV.1.3 we discuss the content and structure of the ROOT files which are provided on the webpages of the subgroup for various MSSM benchmark scenarios. They contain crucial information about Higgs boson masses, cross sections and branching ratios relevant for the experimental analysis. We also describe a comparison between the ROOT files for the two above-mentioned MSSM scenarios with low $\tan\beta$.

In Section IV.1.4 we turn our attention to the Higgs transverse-momentum distribution. In the context of the matching between resummed and fixed-order computations, we investigate the main sources of matching ambiguities by means of a twofold comparison. On the one hand, we present a comparison of two recently introduced algorithms for determining the matching scale [231, 252], an auxiliary parameter of these matched-resummed computations, whose variation can be used as a probe of the theoretical uncertainties akin to what is usually done with the renormalization and factorization scales in the case of fixed-order results. On the other hand, we compare the predictions of two NLO+PS frameworks, MC@NLO [340] (in its implementation aMCSusHi [54,135,1117,1118]) and POWHEG [342] (using the POWHEG-BOX [81,240,1119]), and of the NLO+NLL code MoRe-SusHi [1120,1121] based on collinear analytic resummation [194, 195]. We consider for simplicity the process of heavy Higgs boson production in a type-II Two-Higgs-Doublet Model (THDM).

We remark that Section IV.1.2 and part of Section IV.1.3 summarize the content of a recent LHC-HXSWG public note, Ref. [1122]. Section IV.1.4 summarizes another recent study, Ref. [250].

IV.1.2 Benchmark scenarios for low $\tan\beta$ in the MSSM

The Run 1 data taken at the LHC in 2011 and 2012 have led to strong constraints on the allowed parameter space of the MSSM. [IV.2] These constraints are imposed by (i) the discovery of a scalar particle with a mass of 125.09 ± 0.24 GeV [1, 2, 5] and couplings compatible with the predictions for the SM Higgs boson within an experimental accuracy of $\pm(10-20)\%$ [6, 754, 755]; (ii) the non-observation so far of additional neutral or charged Higgs bosons in direct searches [1123–1126]; and (iii) the non-observation so far of SUSY particles.

Within the MSSM, the newly discovered particle is usually interpreted as the light neutral scalar h, while the interpretation as the heavy neutral scalar H is disfavored by the data [1125, 1126]. For the set-up and testing of benchmark scenarios, the light-scalar mass is usually treated as a constraint on the unknown SUSY parameters, with the requirement

$$M_{\rm h} = 125 \pm 3 \text{ GeV} , \tag{IV.1.6}$$

where the ± 3 GeV variation corresponds to an approximate estimate of the theoretical uncertainty of the MSSM prediction for $M_{\rm h}$, due to the unknown effect of higher-order corrections [84, 1127].

For $\tan\beta \gtrsim 10$ and $M_{\rm A}$ in the decoupling region, the tree-level mass of the light scalar saturates the bound $M_{\rm h} < M_{\rm Z}$; values of $M_{\rm SUSY}$ around 1 TeV are then necessary to reproduce the observed $M_{\rm h}$ in the maximal mixing case, whereas multi-TeV stop masses are necessary for smaller $|X_t|$. However, the $\tan\beta$-enhancement of the couplings of the heavy Higgs bosons to bottom quarks and to τ leptons leads to significant constraints on the $(M_{\rm A}, \tan\beta)$ plane from direct searches by ATLAS and CMS [1123–1126].

[IV.2] Additional constraints on the MSSM parameter space arise, e.g., from cold dark matter density, $(g-2)_\mu$ and B-physics observables. In particular, the latter can exclude regions of the $(M_{\rm A}, \tan\beta)$ plane in scenarios where all SUSY contributions decouple. However, such indirect constraints are independent of – and complementary to – those arising from Higgs phenomenology at the LHC, and will not be discussed further here.

For example, in the benchmark MSSM scenario $M_{\rm H}^{\rm mod+}$, described in Ref. [91], values of $\tan\beta \gtrsim 10$ (20) are directly excluded for $M_{\rm A} \lesssim 300$ (500) GeV. For Run 2 of the LHC the allowed parameter space is expected to shrink further, unless a discovery is made.

For lower values of $\tan\beta$, heavy Higgs bosons with masses as low as 200 GeV are not yet excluded by direct searches at the LHC. Moreover, thanks to the delayed approach to the decoupling limit and to the reduced $\tan\beta$-suppression of the three-scalar coupling, the decays

$$\mathrm{H} \to \mathrm{WW}\,, \qquad \mathrm{H} \to \mathrm{ZZ}\,, \qquad \mathrm{H} \to \mathrm{hh}\,, \qquad \mathrm{A} \to \mathrm{Zh}\,, \tag{IV.1.7}$$

may still have significant branching ratios, especially below the threshold for the decay to a top-quark pair (see, e.g., Refs. [1111, 1128]). However, as mentioned above, lower values of $\tan\beta$ imply a reduced tree-level mass for the lightest scalar, and hence require larger values of $M_{\rm SUSY}$ entering the radiative corrections to satisfy the mass constraint in Eq. (IV.1.6). For $\tan\beta$ in the low single digits, the required hierarchy between $M_{\rm SUSY}$ and $m_{\rm t}$ is so large that a fixed-order result such as the one in Eq. (IV.1.5) would be inadequate even if extended to two- or three-loop order, because the unknown higher-order corrections contain higher powers of the large logarithm of $M_{\rm SUSY}/m_{\rm t}$. In this case, the large logarithmic corrections to the Higgs boson masses should be *resummed* to all orders via an EFT approach: the heavy SUSY particles are integrated out at the scale $M_{\rm SUSY}$, where appropriate boundary conditions, free of logarithmic enhancements, are imposed on the quartic Higgs boson couplings; the latter are evolved down to the weak scale with the corresponding renormalization group equations (RGE); finally, the Higgs boson masses are computed from the quartic Higgs boson couplings, including the radiative corrections due to the contributions of the remaining light particles at the weak scale.

An EFT calculation of the MSSM Higgs boson masses in scenarios where all the SUSY particles (except possibly charginos and neutralinos) are far above the TeV scale, while all Higgs bosons are below it, has recently been completed [1116], extending the earlier work in Ref. [1061] to the case of two light Higgs doublets. The boundary conditions on the quartic couplings are computed at two loops, and the RG evolution is performed at two or three loops (the latter only in the region where the relevant effective theory is the SM). However, no public code implementing the results of such a calculation is currently available. For the analysis of low-$\tan\beta$ scenarios by ATLAS and CMS, this limitation has been circumvented in two ways: (i) in the phenomenological `hMSSM` approach of Refs. [1111–1114], which will be briefly described in Section IV.1.2.a, the experimental knowledge of $M_{\rm h}$ can be traded – under certain assumptions – with the calculation of the radiative corrections, and used to predict the remaining masses and couplings of the MSSM Higgs bosons; (ii) in an alternative approach [1115], the accurate fixed-order calculation of the MSSM Higgs boson masses provided by the code FeynHiggs [82–85] has been supplemented with a partial resummation of the large logarithmic corrections [87], and used to produce a new benchmark scenario with $M_{\rm A} \leq 500$ GeV, $\tan\beta \leq 10$ and sufficiently heavy SUSY particles, whose predictions for $M_{\rm h}$ are compatible with the requirement of Eq. (IV.1.6). This scenario, referred to as `low-tb-high`, will be briefly described in Section IV.1.2.b.

IV.1.2.a The hMSSM approach

In the hMSSM approach [1111–1114], the Higgs sector of the MSSM is described in terms of just the parameters entering the tree-level expressions for masses and mixing, Eqs. (IV.1.1) and (IV.1.3), plus the experimentally known value of $M_{\rm h}$. In this sense, the hMSSM approach can be considered "model independent", because the predictions for the properties of the MSSM Higgs bosons do not depend – with some caveats which will be discussed below – on the details of the unobserved SUSY sector.

The mass matrix for the neutral CP-even states can be decomposed into a tree-level part and radiative corrections as

$$\mathcal{M}_\Phi^2 = \begin{pmatrix} M_{\rm A}^2 \sin^2\beta + M_{\rm Z}^2 \cos^2\beta & -(M_{\rm A}^2 + M_{\rm Z}^2)\sin\beta\cos\beta \\ -(M_{\rm A}^2 + M_{\rm Z}^2)\sin\beta\cos\beta & M_{\rm A}^2 \cos^2\beta + M_{\rm Z}^2 \sin^2\beta \end{pmatrix} + \begin{pmatrix} \Delta\mathcal{M}_{11}^2 & \Delta\mathcal{M}_{12}^2 \\ \Delta\mathcal{M}_{12}^2 & \Delta\mathcal{M}_{22}^2 \end{pmatrix}. \tag{IV.1.8}$$

The hMSSM approach is based on the following assumptions: (i) the observed Higgs boson is the light scalar h; (ii) of the radiative corrections in Eq. (IV.1.8), only the element $\Delta\mathcal{M}^2_{22}$, which contains the leading logarithmic terms arising from top and stop loops, needs to be taken into account; (iii) all SUSY particles are heavy enough to escape detection at the LHC, and their effects on the Higgs sector other than those on the mass matrix, e.g. via direct loop corrections to the Higgs boson couplings or via modifications of the total decay widths, can be neglected.

With these assumptions $\Delta\mathcal{M}^2_{22}$ can be traded for the known value of M_h, inverting the relation that gives the lightest eigenvalue of the mass matrix in Eq. (IV.1.8):

$$\Delta\mathcal{M}^2_{22} = \frac{M_\mathrm{h}^2\,(M_\mathrm{A}^2 + M_\mathrm{Z}^2 - M_\mathrm{h}^2) - M_\mathrm{A}^2\,M_\mathrm{Z}^2\,\cos^2 2\beta}{M_\mathrm{Z}^2\cos^2\beta + M_\mathrm{A}^2\sin^2\beta - M_\mathrm{h}^2}\,, \tag{IV.1.9}$$

which leads to the following expressions for the heavy-scalar mass and for the mixing angle

$$M_\mathrm{H}^2 = \frac{(M_\mathrm{A}^2 + M_\mathrm{Z}^2 - M_\mathrm{h}^2)(M_\mathrm{Z}^2\cos^2\beta + M_\mathrm{A}^2\sin^2\beta) - M_\mathrm{A}^2\,M_\mathrm{Z}^2\cos^2 2\beta}{M_\mathrm{Z}^2\cos^2\beta + M_\mathrm{A}^2\sin^2\beta - M_\mathrm{h}^2}\,, \tag{IV.1.10}$$

$$\tan\alpha = -\frac{(M_\mathrm{Z}^2 + M_\mathrm{A}^2)\cos\beta\sin\beta}{M_\mathrm{Z}^2\cos^2\beta + M_\mathrm{A}^2\sin^2\beta - M_\mathrm{h}^2}\,. \tag{IV.1.11}$$

The mass of the charged scalars coincides with the tree-level value $M^2_{\mathrm{H}^\pm} = M_\mathrm{A}^2 + M_\mathrm{W}^2$ in this approximation. The couplings of the neutral Higgs bosons to fermions and to gauge bosons are fixed to their tree-level form as in Eq. (IV.1.2), but they are expressed in terms of the effective (i.e., loop-corrected) angle α obtained in Eq. (IV.1.11). In contrast, the triple and quartic Higgs self-couplings receive additional contributions. In particular, the effective Hhh coupling in the hMSSM reads

$$\lambda_\mathrm{Hhh} \;=\; \lambda_{\mathrm{Hhh,\,tree}} \;+\; 3\,\frac{\Delta\mathcal{M}^2_{22}}{M_\mathrm{Z}^2}\,\frac{\sin\alpha}{\sin\beta}\,\cos^2\alpha\,, \tag{IV.1.12}$$

where the tree-level coupling, see Eq. (IV.1.4), is also expressed in terms of the effective α, and the correction $\Delta\mathcal{M}^2_{22}$ is given in Eq. (IV.1.9). Under the assumptions that characterize the hMSSM, the information encoded in Eqs. (IV.1.10)–(IV.1.12) is sufficient to determine the production cross sections and the decay branching ratios of all the MSSM Higgs bosons, as function of only M_A and $\tan\beta$ for a fixed value of the light-scalar mass (which we can take as $M_\mathrm{h} = 125$ GeV). The precise calculation of these observables will be described in Section IV.1.3 below.

It should be noted that the hMSSM approach is well defined only in the region of the $(M_\mathrm{A},\,\tan\beta)$ plane where the denominator in Eqs. (IV.1.9)–(IV.1.11) is greater than zero (indeed, as the denominator approaches zero $\Delta\mathcal{M}^2_{22}$ diverges, and we get $\alpha \to -\pi/2$ and $M_\mathrm{H} \to \infty$). In other words, for any given value of $\tan\beta$ there is a minimum value $M_\mathrm{A}^\mathrm{min}$ below which it is not possible to reproduce the desired M_h with only a correction to the $(2,2)$ element of the Higgs boson mass matrix. For large $\tan\beta$ one has $M_\mathrm{A}^\mathrm{min} \approx M_\mathrm{h}$, while for decreasing $\tan\beta$ the minimum value of M_A increases, up to $M_\mathrm{A}^\mathrm{min} = (2\,M_\mathrm{h}^2 - M_\mathrm{Z}^2)^{1/2}$ for $\tan\beta = 1$ (for $M_\mathrm{h} = 125$ GeV, this corresponds to $M_\mathrm{A}^\mathrm{min} \approx 151$ GeV). However, in Ref. [1114] it is argued that the region where the hMSSM approach breaks down is already excluded, both by direct searches for $\mathrm{H}^\pm$ and A at the LHC and by the requirement that the couplings of h be approximately SM-like.

The validity of the assumption (ii), that $\Delta\mathcal{M}^2_{11}$ and $\Delta\mathcal{M}^2_{12}$ can be neglected, is also discussed in Refs. [1113, 1114]. Direct inspection of the dominant one-loop contributions from top/stop loops shows that the corrections to the $(1,1)$ and $(1,2)$ elements of the Higgs boson mass matrix are proportional to powers of the ratio $\mu\,X_t/M^2_\mathrm{SUSY}$. Since the sbottom contributions to those matrix elements are not enhanced at the moderate $\tan\beta$ values of interest here, the assumption (ii) is satisfied as soon as

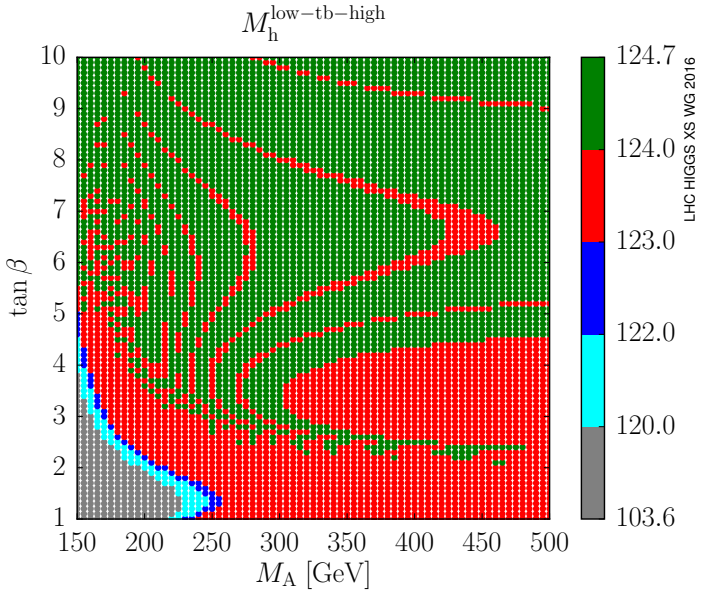

Figure 251: Mass of the light scalar h as computed by FEYNHIGGS 2.10.4 in the "low-tb-high" scenario, as a function of M_A and $\tan\beta$.

$\mu X_t/M_{\text{SUSY}}^2$ is suppressed. In MSSM scenarios with M_{SUSY} up to a few TeV, the inclusion of the full one-loop contributions and of the known two-loop contributions does not alter this picture. This was shown in Refs. [1113, 1114] via numerical comparisons between the predictions for M_H and α obtained with the codes SUSPECT [1129] and FEYNHIGGS [82–85, 87] and those obtained with the hMSSM approximations, Eqs. (IV.1.10) and (IV.1.11), using the values of M_h produced by the codes as input. To extend this check to the very large values of M_{SUSY} required to obtain the observed value of M_h at low $\tan\beta$, a comparison against the proper EFT calculation becomes necessary. The studies in Ref. [1116] indicate that, even in such heavy-SUSY scenarios, the predictions of Eqs. (IV.1.10)–(IV.1.12) agree within a few per cent with the exact results for M_H, α and λ_{Hhh}, as long as $\mu X_t/M_{\text{SUSY}}^2 \lesssim 1$.

Concerning the assumption (iii), i.e. the absence of direct SUSY corrections to the Higgs boson couplings, we recall that the couplings to bottom quarks are subject to potentially large, $\tan\beta$-enhanced SUSY corrections – often called Δ_b corrections – which do not decouple in the limit of heavy superparticles. However, those corrections are not particularly relevant at the values of $\tan\beta$ considered here, and in addition they scale like μ/M_{SUSY}, i.e. they could be suppressed by the same choices of SUSY parameters that guarantee the validity of the assumption (ii).

IV.1.2.b The "low-tb-high" scenario

The second approach [1115] to the study of low-$\tan\beta$ scenarios in the MSSM is essentially orthogonal to the one outlined in the previous section. Instead of treating M_h as an input, and using it to obtain a simple but approximate description of the Higgs sector which is largely independent of the underlying SUSY parameters, one looks for choices of SUSY parameters that, using a high-precision calculation of the Higgs boson masses and mixing, allow to obtain the desired value of M_h in most of the $(M_A, \tan\beta)$ plane.

As discussed in Section IV.1.1, for low $\tan\beta$ the values of M_{SUSY} required to obtain $M_h \approx 125$ GeV are so large that a fixed-order calculation of the Higgs boson masses becomes inadequate, and a resummation of the large logarithmic corrections is unavoidable. Starting from version 2.10.0, the public code FEYNHIGGS [82–85] does include such resummation [87], with some limitations that

will be discussed below. The so-called "low-tb-high" scenario is defined for $0.5 \leq \tan\beta \leq 10$ and $150\text{ GeV} \leq M_\text{A} \leq 500\text{ GeV}$, and the masses and mixing of all the MSSM Higgs bosons are computed with version 2.10.4 of FEYNHIGGS.

To obtain values of M_h in the desired range, the SUSY parameters – in the on-shell scheme adopted by FEYNHIGGS – are chosen as follows: (i) all soft SUSY-breaking masses for the sfermions (both squarks and sleptons) as well as the gluino mass are set equal to M_SUSY; (ii) M_SUSY is varied between few TeV (for large values of M_A or $\tan\beta$) and up to 100 TeV (for small values of M_A or $\tan\beta$), keeping the following relations between X_t, M_SUSY and $\tan\beta$:

$$\begin{aligned} \tan\beta \leq 2 \quad &: \quad X_t/M_\text{SUSY} = 2; \\ 2 < \tan\beta \leq 8.6 \quad &: \quad X_t/M_\text{SUSY} = 0.0375\,\tan^2\beta - 0.7\,\tan\beta + 3.25; \\ 8.6 < \tan\beta \quad &: \quad X_t/M_\text{SUSY} = 0; \end{aligned}$$

(iii) for what concerns the remaining SUSY parameters, all Higgs-sfermion trilinear couplings other than A_t are set to 2 TeV, μ is set to = 1.5 TeV and the $SU(2)$ gaugino mass M_2 is set to 2 TeV (this fixes also the $U(1)$ gaugino mass M_1 via the GUT relation $M_1/M_2 = 5/3\,\tan^2\theta_W$). With these choices of SUSY parameters, the prediction of FEYNHIGGS for the light-scalar mass M_h is shown in Figure 251 as a function of M_A and $\tan\beta$. As can be seen, the requirement of Eq. (IV.1.6) can be met over most of the parameter space, with the exception of the lower-left corner corresponding to very low values of both M_A and $\tan\beta$. However, it has not been tested whether the predictions for the production cross section and the branching ratios of the light scalar are in full agreement with the latest results of the ATLAS and CMS collaborations [754, 755], which indicate an SM-like Higgs boson with uncertainties in the $(10-20)\%$ range. For the heavy Higgs bosons, the chosen values of μ and M_2 ensure that all decays to charginos and neutralinos (henceforth, electroweakinos or EW-inos) are kinematically forbidden, thus maximizing the branching ratios for the decays in Eq. (IV.1.7).

A limitation of the "low-tb-high" scenario should be taken into account. The resummation procedure currently implemented in FEYNHIGGS – which accounts only for the leading and next-to-leading logarithmic corrections to the Higgs boson masses controlled by the strong gauge coupling and by the top Yukawa coupling – relies on the assumption that all SUSY masses as well as the heavy-Higgs boson masses are of the order of M_SUSY. However, in the "low-tb-high" scenario the parameters μ and $M_{1,2}$ are fixed to $\mathcal{O}$(TeV), and M_A is below 500 GeV. To assess the adequacy of FEYNHIGGS in an MSSM scenario with heavy sfermions and gluinos but relatively light EW-inos and additional Higgs bosons, a comparison with a proper EFT calculation – where the effective theory below M_SUSY is a THDM augmented with EW-inos – would be necessary.

The studies in Ref. [1116] indicate that, with the choices of SUSY parameters of the "low-tb-high" scenario, the EFT predictions for M_h can be considerably lower than those of the current FEYNHIGGS implementation. In particular, for $\tan\beta > 5.5$ the EFT calculation yields values of M_h that are about 2 GeV lower than those obtained by FEYNHIGGS. For lower values of $\tan\beta$, the disagreement is more severe: the difference is greater than 5 GeV (10 GeV) for $\tan\beta < 3.5$ ($\tan\beta < 2$). When one looks at the minimal value of M_SUSY required to obtain M_h in the desired range, the logarithmic dependence of M_h on M_SUSY amplifies the discrepancy. For $\tan\beta = 2$, the EFT calculation requires $M_\text{SUSY} > 10^8$ TeV ($M_\text{SUSY} > 200$ TeV) to obtain $M_\text{h} > 122$ GeV with $M_\text{A} = 200$ GeV ($M_\text{A} = 500$ GeV). This should be compared with the maximal value $M_\text{SUSY} = 100$ TeV adopted in the "low-tb-high" scenario for the lowest values of M_A and $\tan\beta$. Discrepancies up to $(10-12)\%$ between FEYNHIGGS and the EFT calculation can also be found in the predictions for M_H and α at very small values of M_A and $\tan\beta$. Further investigation will be required to ascertain how these discrepancies are related to the presence of a light THDM, to the presence of light EW-inos, and to other aspects of the calculation such as the determination of the top Yukawa coupling.

On the other hand, the fact that $\mu \ll M_\text{SUSY}$ over the whole parameter space ensures that the dominant top/stop corrections to the elements other than $(2,2)$ of the CP-even Higgs boson mass matrix

Table 120: Benchmark scenarios provided on the webpage of the MSSM subgroup of the LHC-HXSWG [1130] in the form of new ROOT files for Run 1 and Run 2 of the LHC. We give information about the ranges of M_A and $\tan\beta$, and the centre-of-mass energies $\sqrt{s}$. The $M_H^{\text{mod+}}$ scenario is delivered for different values of $\mu \in \mu^{\text{val}} = \{-1000, -500, -200, 200, 500, 1000\}$ GeV with the restriction $\tan\beta < 40$ for $\mu = -1000$ GeV. In the light-stop scenario the gaugino and higgsino mass parameters are fixed as $M_1 = 350$ GeV, $M_2 = \mu = 400$ GeV to avoid the bounds from direct stop searches.

scenario	M_A [GeV]	$\tan\beta$	$\sqrt{s}$ [TeV]
"low-tb-high" [1122]	$150 - 500$	$0.5 - 10$	$8, 13$
hMSSM [1111–1114]	$130 - 1000$	$1 - 60$	$8, 13$
M_H^{max} [91]	$90 - 2000$	$0.5 - 60$	$13, 14$
$M_H^{\text{mod+}}$ [91], $\mu \in \mu^{\text{val}}$	$90 - 2000$	$0.5 - 60$	$8, 13, 14$
$M_H^{\text{mod}-}$ [91]	$90 - 2000$	$0.5 - 60$	$13, 14$
light stau [91]	$90 - 2000$	$0.5 - 60$	$13, 14$
light stop [91]	$90 - 650$	$0.5 - 60$	$13, 14$
τ-phobic [91]	$90 - 2000$	$0.5 - 50$	$13, 14$

are suppressed. Therefore, a meaningful comparison with the results obtained in the hMSSM approach can be performed, as will be discussed in Section IV.1.3.c.

IV.1.3 ROOT files for cross sections and branching ratios

For Run 1 of the LHC, benchmark scenarios for the MSSM were delivered by the LHC-HXSWG in the form of ROOT files, which contain masses, inclusive production cross sections and branching ratios of the Higgs bosons. The files can be downloaded from the webpages of the MSSM subgroup [1130]. Their structure and content were significantly updated for Run 2 of the LHC, and in this section we describe the changes in some detail. We first focus on the content of the files, including a description of how the relevant quantities were calculated. Afterwards the structure of the files and the possible ways to access the included data are explained. Finally we describe a comparison of the ROOT files for the hMSSM and the "low-tb-high" scenario.

IV.1.3.a Content of the ROOT files

All ROOT files contain the Higgs boson masses, cross sections (including estimates of the theoretical uncertainties via scale variations) and branching ratios for a grid of M_A and $\tan\beta$ values. Table IV.1.3.a provides an overview of the delivered benchmark scenarios, including the ranges of M_A and $\tan\beta$ and the centre-of-mass energies for which the cross sections were produced. In the following we describe how the quantities included in the ROOT files were obtained. We detail the calculations of the Higgs boson masses, cross sections, and decay widths and branching ratios, and then we describe the SM input parameters used by the codes.

For the benchmark scenarios already presented in the third report of the LHC-HXSWG [9], which are based on Ref. [91], the neutral-scalar masses, the Higgs mixing angle α and the charged Higgs boson

mass are computed with FEYNHIGGS 2.10.2. In contrast, for the "low-tb-high" scenario the masses and mixing are computed with FEYNHIGGS 2.10.4, activating the option to resum large logarithms due to the heavy SUSY scale. Finally, in the ROOT files for the hMSSM the mass of the light neutral scalar is fixed to $M_{\mathrm{h}} = 125$ GeV, M_{H} and α are computed as function of M_{A} and $\tan\beta$ using Eqs. (IV.1.10) and (IV.1.11), and the charged Higgs boson mass is obtained from the tree-level relation $M^2_{\mathrm{H}^\pm} = M^2_{\mathrm{A}} + M^2_{\mathrm{W}}$.

We use SUSHI 1.5.0 [135] to obtain the inclusive cross sections for the production of the neutral Higgs bosons $\phi \equiv (\mathrm{h}, \mathrm{H}, \mathrm{A})$ via gluon fusion, $\mathrm{gg} \to \phi$, and bottom annihilation, $\mathrm{b\bar{b}} \to \phi$. In preparation for Run 2 of the LHC the ROOT files are produced for centre-of-mass energies of 13 TeV and 14 TeV, with the exception of the scenarios for the low-$\tan\beta$ studies, available for 8 and 13 TeV, and the $M_{\mathrm{H}}^{\mathrm{mod}+}$ scenario with different values of μ, available for 8, 13 and 14 TeV. In the calculation of the gluon-fusion cross section, SUSHI implements the NLO-QCD top and bottom contributions from Refs. [136, 140]. Moreover, NNLO-QCD top contributions from Refs. [101, 866] are taken into account in the heavy-top limit, and the electroweak contributions by light quarks from Refs. [107, 1084] are added. In the benchmark scenarios of Ref. [91], the squark contributions are taken into account in different limits: For the heavy scalar and the pseudoscalar, SUSHI employs the NLO virtual corrections in the limit of heavy SUSY masses from Refs. [873–875]. For the light scalar, SUSHI employs the results implemented in EVALCSUSY [868, 870, 871], which were obtained in the limit of vanishing Higgs boson mass, for the NLO corrections involving stops, and the results of Ref. [873] for those involving sbottoms. In addition, SUSHI takes into account the resummation of $\tan\beta$-enhanced SUSY corrections in the Higgs-bottom coupling, with a correction factor Δ_b computed by FEYNHIGGS. In the "low-tb-high" scenario, characterized by very heavy squarks, the squark-loop contributions to gluon fusion are negligible and are omitted, but the non-decoupling Δ_b corrections are included. Finally, in the case of the hMSSM SUSHI is Run with a THDM input file providing the Higgs boson masses and the Higgs mixing angle, thus no SUSY contributions to the cross section are included.

For bottom annihilation, SUSHI calculates the inclusive cross section at NNLO-QCD in the five-flavour scheme (5F), based on Ref. [565]. For each neutral Higgs boson ϕ, the amplitude for the production of a SM Higgs boson with mass M_ϕ is reweighted with the effective Higgs-bottom coupling. As for gluon fusion, the Δ_b corrections are included in all scenarios except the hMSSM. The ROOT files also include reweighted four-flavour scheme (4F) cross sections for bottom-quark associated production, $\mathrm{gg} \to \mathrm{b\bar{b}}\,\phi$, based on Refs. [1085, 1086]. These 4F cross sections now also include a mixed top- and bottom-quark induced contribution, which is reweighted with effective up- and down-type quark couplings, taken from SUSHI. Finally, the 4F and 5F descriptions can be combined into the "Santander matched" cross sections [1131] by the output routines delivered for the ROOT files.

The ROOT files also include estimates for the theoretical uncertainties of the cross sections. The central values of the renormalization scale μ_R and the factorization scale μ_F are set to $\mu_R = \mu_F = M_\phi/2$ for gluon fusion and to $\mu_R = 4\,\mu_F = M_\phi$ for bottom annihilation. Scale uncertainties are then determined from the envelope of seven independent variations of μ_R and μ_F by factors of 2, with the additional constraint $1/2 \leq \mu_R/\mu_F \leq 2$ for gluon fusion and $2 \leq \mu_R/\mu_F \leq 8$ for bottom annihilation. For the parton distribution functions the MSTW2008 [30] set has been used, and the residual uncertainties on the parton distribution functions and on the strong coupling constant, α_s, are obtained from the corresponding relative uncertainties for a SM Higgs boson of mass M_ϕ, evaluated as proposed in Ref. [1132]. Note however that PDF and α_s uncertainties are only available for gluon fusion and bottom annihilation (5F), not for bottom associated production (4F).

For the calculation of branching ratios and their inclusion in the ROOT files there is a substantial difference between standard MSSM benchmark scenarios and the hMSSM. For the standard MSSM benchmark scenarios, including the "low-tb-high" scenario, the branching ratios are computed as recommended by the LHC-HXSWG [9]. They are thus a combination of the results of HDECAY for the decays to quark pairs with the results of FEYNHIGGS for the remaining decays. In particular, for the decays to massive gauge bosons FEYNHIGGS approximates the MSSM results by reweighting the SM

results from the code PROPHECY4F [72, 73] with the appropriate Higgs-gauge boson coupling. For the decays to Higgs bosons, FEYNHIGGS implements a full one-loop calculation within the (complex) MSSM [1098], improved – starting from version 2.10.4 – with the resummation of potentially large logarithmic corrections to the decay $\mathrm{H} \to \mathrm{hh}$ that are relevant for the "low-tb-high" scenario. Finally, the ROOT files for the standard MSSM benchmark scenarios also include the branching ratios for the decays of the charged Higgs boson, as well as the branching ratio for the decay $\mathrm{t} \to \mathrm{H}^+\mathrm{b}$ (relevant for low masses of the charged Higgs boson), all obtained from FEYNHIGGS. In contrast, in the ROOT files for the hMSSM the branching ratios for the decays of the neutral and charged Higgs bosons, as well as for $\mathrm{t} \to \mathrm{H}^+\mathrm{b}$, are solely computed with the code HDECAY [69–71], which starting from version 6.40 allows for hMSSM input. HDECAY implements N^{4}LO-QCD corrections to the decays to quark pairs [1133–1146]; LO results for the decays to lepton pairs and for the decays involving massive gauge bosons, both on-shell and off-shell; a LO calculation of the decays to Higgs boson pairs, both on-shell and off-shell, using effective hMSSM couplings.

The SM parameters used as input by the codes that compute the Higgs boson masses, production and decays mostly coincide with the recommendations of the LHC-HXSWG, see Ref. [144] and Chapter I.1, with the following exceptions: for the calculation of Higgs boson masses in FEYNHIGGS and the calculation of branching ratios in FEYNHIGGS and HDECAY $\alpha_s(M_\mathrm{Z}) = 0.119$ is used. The cross sections are calculated by SUSHI with the strong coupling constant α_s taken from the PDF set employed. In both FEYNHIGGS and SUSHI, the $\overline{\mathrm{MS}}$ masses of the bottom and charm quarks are set to $m_\mathrm{b}^{\overline{\mathrm{MS}}}(m_\mathrm{b}) = 4.16$ GeV and $m_\mathrm{c}^{\overline{\mathrm{MS}}}(m_\mathrm{c}) = 1.28$ GeV, respectively, and the W boson mass is set to $M_\mathrm{W} = 80.398$ GeV. In addition, SUSHI requires the pole bottom mass, set to $m_\mathrm{b}^\mathrm{pole} = 4.75$ GeV, and FEYNHIGGS requires the widths of the massive gauge bosons, set to $\Gamma_\mathrm{W} = 2.118$ GeV and $\Gamma_\mathrm{Z} = 2.4952$ GeV, and the τ lepton mass, set to $m_\tau = 1777.03$ MeV. In contrast, HDECAY employs $m_\mathrm{b}^\mathrm{pole} = 4.49$ GeV, $m_\mathrm{c}^\mathrm{pole} = 1.42$ GeV, $M_\mathrm{Z} = 91.15349$ GeV, $M_\mathrm{W} = 80.36951$ GeV, $\Gamma_\mathrm{Z} = 2.49581$ GeV and $\Gamma_\mathrm{W} = 2.08856$ GeV, corresponding to the on-shell parameters in the complex-mass scheme.

IV.1.3.b Technical details and data access

The setup to combine Higgs boson masses, cross sections and branching ratios into two-dimensional ROOT histograms for MSSM benchmark scenarios was reorganized in 2015. We will now summarize the procedure to access the data stored in the ROOT files. The user can download the `C++` class `mssm_xs_tools.C` and the header file `mssm_xs_tools.h` from the webpage of the MSSM subgroup. Together with a scenario, here named "`scenario.root`", the class is initialized within ROOT through

$$\texttt{mssm\_xs\_tools} \quad \texttt{mssm}(\text{“}\texttt{scenario.root}\text{”}, \texttt{INT}, 0).$$

Setting `INT` to `true` enables linear interpolation between the grid points in M_A and $\tan\beta$, providing results for intermediate values of M_A or $\tan\beta$. The last argument with default setting `0` controls the printout level for debugging. After the initialization, data can be accessed either through the predefined routines listed in the header file or through the commands

$$\texttt{mssm.COMMAND}(\texttt{STRING}, M_\mathrm{A}, \tan\beta) \qquad ,$$

where `COMMAND` can be one of the member functions `mass`, `width`, `br` or `xsec` for the Higgs boson masses, the total decay widths, branching ratios or cross sections, respectively. Examples for `STRING` are

$$\begin{aligned}
&\texttt{mssm.mass}(\text{“}\texttt{H}\text{”}, M_\mathrm{A}, \tan\beta)\\
&\texttt{mssm.br}(\text{“}\texttt{A} \to \texttt{tautau}\text{”}, M_\mathrm{A}, \tan\beta)\\
&\texttt{mssm.xsec}(\text{“}\texttt{gg} \to \texttt{H} :: \texttt{scaleUp}\text{”}, M_\mathrm{A}, \tan\beta) \quad ,
\end{aligned}$$

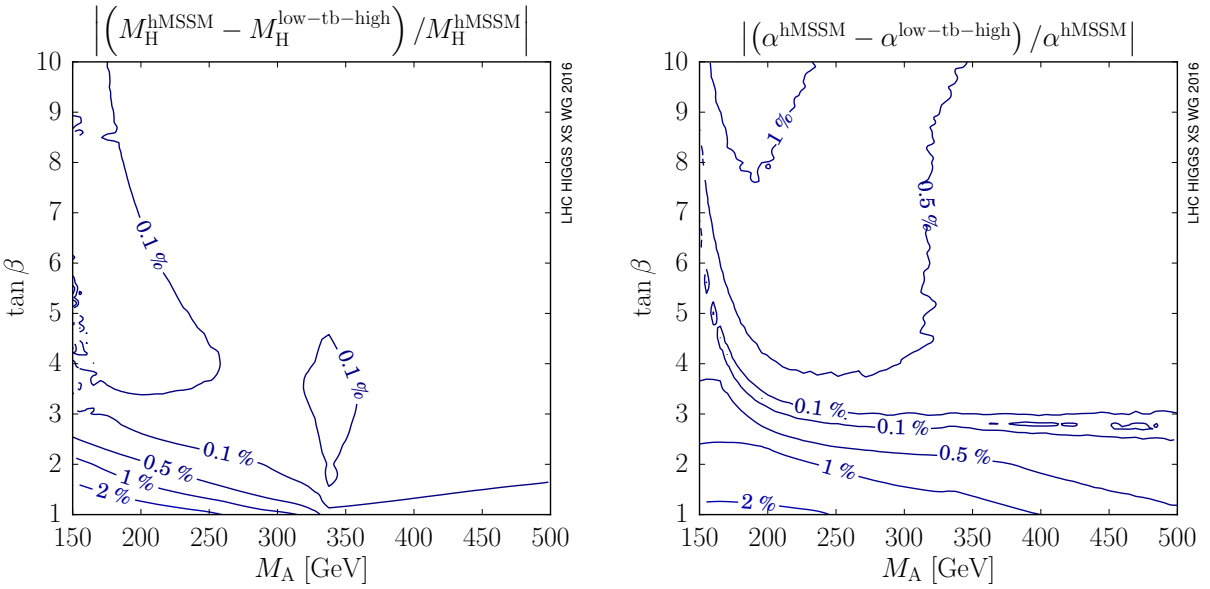

Figure 252: Relative differences in $M_{\rm H}$ (left) and α (right) between the predictions of FEYNHIGGS for the "low-tb-high" scenario and the corresponding predictions obtained in the hMSSM approach via Eqs. (IV.1.10) and (IV.1.11), starting from the values of $M_{\rm h}$ computed by FEYNHIGGS.

where the latter provides the upper bound of the uncertainty of the gluon fusion cross section $\rm gg \to H$ obtained from the variation of the renormalization and factorization scales. A complete list of possible strings can again be deduced from the class description in the header file. Alternatively, a PYTHON wrapper is available on the webpage. An example for its usage is included at the end of the PYTHON file.

IV.1.3.c Comparison of benchmark scenarios for low $\tan\beta$

As mentioned in Section IV.1.2.b, the choices of SUSY parameters in the "low-tb-high" scenario satisfy all of the assumptions that underlie the hMSSM, thus inviting a comparison between the predictions for the Higgs boson properties obtained within the two approaches. However, a direct comparison between the two sets of ROOT files is hindered by the fact that the light-scalar mass is fixed as $M_{\rm h} = 125$ GeV in the hMSSM files, whereas it varies with $M_{\rm A}$ and $\tan\beta$ in the "low-tb-high" files. To circumvent this problem, the predictions of the "low-tb-high" scenario for $M_{\rm H}$, α and the branching ratios were compared with the corresponding results obtained in the hMSSM approach taking as input the values of $M_{\rm h}$ from the "low-tb-high" scenario and computing all branching ratios with HDECAY.

In the left and right panels of Figure 252 we show the relative differences between the predictions of the "low-tb-high" scenario and those of the hMSSM for $M_{\rm H}$ and α, respectively, on the $(M_{\rm A}, \tan\beta)$ plane with $150\ \text{GeV} \le M_{\rm A} \le 500\ \text{GeV}$ and $1 \le \tan\beta \le 10$. The figure shows that, for the SUSY parameters that characterize the "low-tb-high" scenario, the results of FEYNHIGGS for $M_{\rm H}$ and α and the approximate results obtained via Eqs. (IV.1.10) and (IV.1.11) differ by less than 1% over most of the parameter space. Larger discrepancies, up to a few per cent, occur only in the lower-left corner at very low $M_{\rm A}$ and $\tan\beta$. In view of this good accord, we can expect any significant discrepancy in the predictions for cross sections and branching ratios to be due to differences in the calculation of the physical observables themselves, rather than to the approximation in Eqs. (IV.1.10) and (IV.1.11). While the production cross sections are computed with SUSHI in both cases, discrepancies can arise in the widths for the decays $\rm H \to WW, ZZ, hh$ and $\rm A \to Zh$, which in the "low-tb-high" and hMSSM files are computed with FEYNHIGGS+PROPHECY4F and with HDECAY, respectively.

The left and right panels in Figure 253 show the branching ratio for the decay $\rm H \to hh$ in the

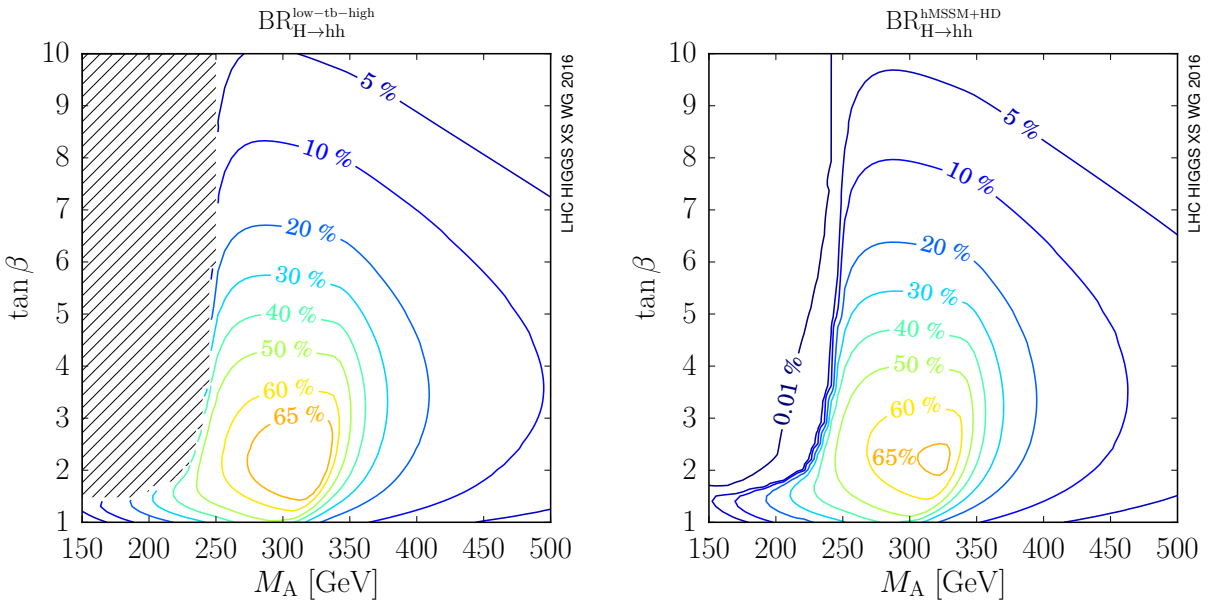

Figure 253: Left: Branching ratio for the decay $\mathrm{H} \to \mathrm{hh}$ as computed in the "low-tb-high" scenario following the LHC-HXSWG recommendations for the decay widths (in particular, $\Gamma(\mathrm{H} \to \mathrm{hh})$ is computed with FeynHiggs). Right: The same branching ratio obtained with the hMSSM+HDECAY combination – namely, starting from the values of M_{h} computed by FeynHiggs in the "low-tb-high" scenario, then computing the branching ratio with HDECAY, which obtains M_{H}, α and λ_{Hhh} from the hMSSM prescriptions in Eqs. (IV.1.10)–(IV.1.12).

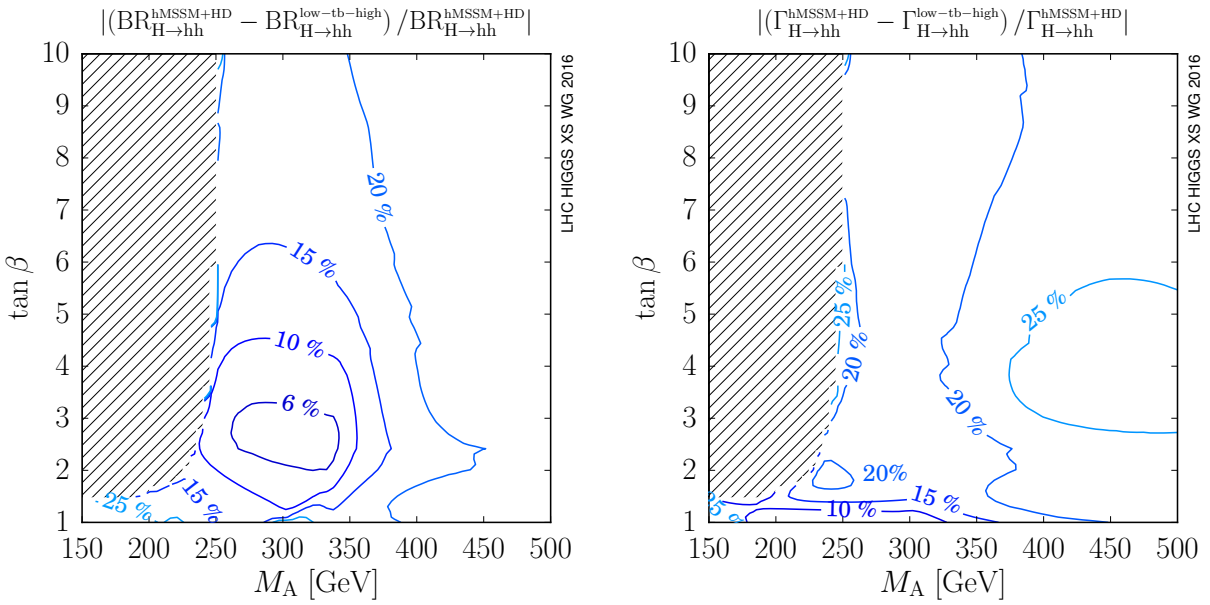

Figure 254: Relative differences in $\mathrm{BR}(\mathrm{H} \to \mathrm{hh})$ (left) and $\Gamma(\mathrm{H} \to \mathrm{hh})$ (right) between the predictions of the "low-tb-high" scenario (where $\Gamma(\mathrm{H} \to \mathrm{hh})$ is computed with FeynHiggs) and the corresponding predictions obtained with the hMSSM+HDECAYcombination. For the latter we start from the values of M_{h} computed by FeynHiggs in the "low-tb-high" scenario, then we compute width and branching ratio with HDECAY, which obtains M_{H}, α and λ_{Hhh} from the hMSSM prescriptions in Eqs. (IV.1.10)–(IV.1.12).

"low-tb-high" scenario and in the hMSSM+HDECAY combination, respectively. Again, in the hMSSM plot the mass $M_{\rm h}$ used to compute $M_{\rm H}$ and α via Eqs. (IV.1.10) and (IV.1.11) in a given point of the $(M_{\rm A},\,\tan\beta)$ plane has been adjusted to the value computed by FEYNHIGGS in the corresponding point of the "low-tb-high" scenario. In the hatched region on the left plot the decay is below threshold, and the corresponding width is set to zero by FEYNHIGGS (in contrast, in the right plot HDECAY computes also the small width to off-shell scalars). The plots show that, in this scenario, $\mathrm{BR}(\mathrm{H}\to\mathrm{hh})$ can be larger than 50% for $\tan\beta\lesssim 4$ and for values of $M_{\rm A}$ such that $M_{\rm H}$ sits between the kinematic threshold for the decay to a light-scalar pair and the one for the decay to a top-quark pair. A visual comparison of the left and right plots also shows that the qualitative dependence of $\mathrm{BR}(\mathrm{H}\to\mathrm{hh})$ on $M_{\rm A}$ and $\tan\beta$ is the same in both approaches, but the branching ratio takes on somewhat larger values in the "low-tb-high" plot than it does in the hMSSM plot.

To quantify the previous statement, the left plot in Figure 254 shows the relative difference between the values of $\mathrm{BR}(\mathrm{H}\to\mathrm{hh})$ computed in the "low-tb-high" scenario and those computed in the hMSSM with HDECAY. The plot shows that the discrepancy in the branching ratio is less than 10% in the region where the decay $\mathrm{H}\to\mathrm{hh}$ is dominant, and exceeds 20% for larger values of $M_{\rm A}$ and, hence, $M_{\rm H}$. However, in the region where a decay channel is dominant a comparison between branching ratios can mask the true extent of a discrepancy. The right plot of Figure 254 shows instead the relative difference between the corresponding values of the decay width $\Gamma(\mathrm{H}\to\mathrm{hh})$. It appears that, at the level of the decay width, the discrepancy between the results obtained in the two approaches is above 15% in most of the relevant parameter space, and exceeds 25% for large $M_{\rm A}$ and intermediate $\tan\beta$. The size of the discrepancy can be understood in view of the different accuracy of the $\Gamma(\mathrm{H}\to\mathrm{hh})$ calculation in the two approaches. Indeed, while in the hMSSM the effect of the top/stop contributions is included via the effective coupling in Eq. (IV.1.12), FEYNHIGGS implements a full calculation of the one-loop corrections to the decay width, supplemented with the resummation of large logarithmic terms. Thus, the FEYNHIGGS result accounts for potentially large threshold effects in diagrams with loops of SM particles, which are not captured by using an effective coupling alone.

In Figures 255 and 256 we show plots analogous to those in Figure 254 for the decays $\mathrm{H}\to\mathrm{WW}$ and $\mathrm{A}\to\mathrm{Zh}$. For what concerns the decays of H to W-boson pairs, the relative differences between the two calculations of the widths are – over most of the $(M_{\rm A},\tan\beta)$ plane – smaller than 15%. In the case of the decays to Z-boson pairs, not shown here, we find differences smaller than 10%. Again, such discrepancies can be explained by the fact that, in the "low-tb-high" files, the MSSM results for the $\mathrm{H}\to\mathrm{VV}$ decay widths are approximated by reweighting the state-of-the-art SM results of PROPHECY4F with the appropriate Higgs-gauge boson couplings, whereas in the hMSSM files those widths are computed at LO with HDECAY. For the decay $\mathrm{A}\to\mathrm{Zh}$, Figure 256 shows that – in the region with $M_{\rm A}>M_{\rm Z}+M_{\rm h}$ where the decay is kinematically open – the relative differences between the two calculations of the widths are smaller than 10% unless $\tan\beta$ is very close to 1. For lower values of $M_{\rm A}$, where the pseudoscalar must decay to off-shell bosons, large discrepancies appear, due to differences in both the implementation of the calculations and the input value of α. However, the decay width is extremely suppressed in that region, and the process is not relevant to the low-$\tan\beta$ analysis.

Finally, we performed analogous comparisons for all the remaining decay channels of H and A, but we discuss here only the decays to pairs of third-family SM fermions, which can reach sizeable branching ratios in the considered scenario. The widths for the decays to top and bottom pairs are computed with HDECAY in both approaches, therefore any discrepancy must be due to different input values for $M_{\rm H}$ and α. For the decays to top quarks, we find discrepancies of $\mathcal{O}(1\%)$ in the region where the relevant Higgs boson mass is above the threshold for the production of a real-top pair and the decay is unsuppressed. For the decays to bottom quarks, the discrepancies for $\tan\beta\gtrsim 3$, where the branching ratio becomes significant, are also of $\mathcal{O}(1\%)$. In contrast, the decays to tau leptons are computed at LO with HDECAY in the hMSSM files, and at one loop with FEYNHIGGS in the "low-tb-high" files. In this case, the discrepancies for $\tan\beta\gtrsim 3$ are smaller than 5% for $\Gamma(\mathrm{H}\to\tau\tau)$, and smaller than 8% for

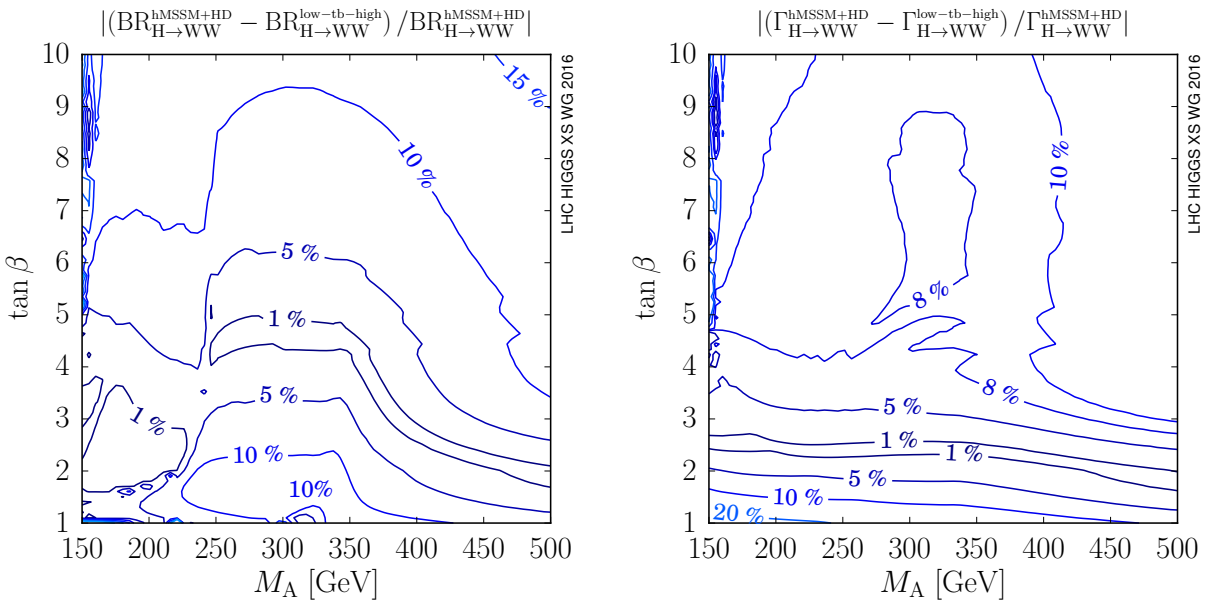

Figure 255: Relative differences in $\mathrm{BR}(\mathrm{H}\to\mathrm{WW})$ (left) and $\Gamma(\mathrm{H}\to\mathrm{WW})$ (right) between the predictions of the "low-tb-high" scenario (where $\Gamma(\mathrm{H}\to\mathrm{WW})$ is computed with FeynHiggs+Prophecy4F) and the corresponding predictions obtained with the hMSSM+HDECAYcombination. For the latter we start from the values of M_{h} computed by FeynHiggs in the "low-tb-high" scenario, then we compute width and branching ratio with HDECAY, which obtains M_{H}, α and λ_{Hhh} from the hMSSM prescriptions in Eqs. (IV.1.10)–(IV.1.12).

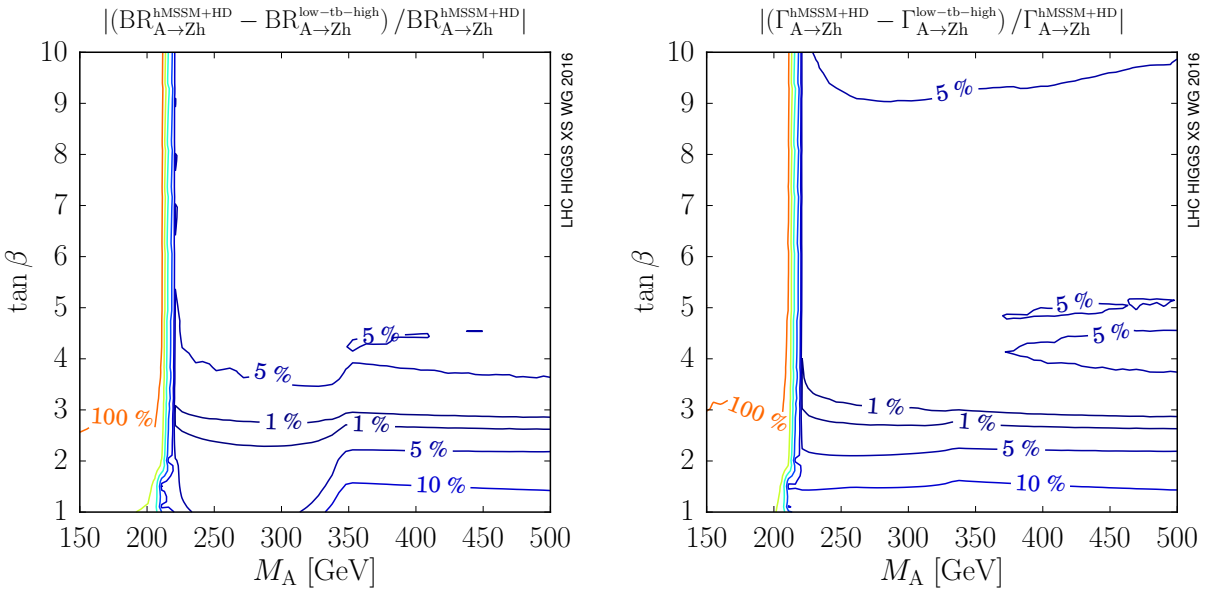

Figure 256: Relative differences in $\mathrm{BR}(\mathrm{A}\to\mathrm{Zh})$ (left) and $\Gamma(\mathrm{A}\to\mathrm{Zh})$ (right) between the predictions of the "low-tb-high" scenario (where $\Gamma(\mathrm{A}\to\mathrm{Zh})$ is computed with FeynHiggs) and the corresponding predictions obtained with the hMSSM+HDECAYcombination. For the latter we start from the values of M_{h} computed by FeynHiggs in the "low-tb-high" scenario, then we compute width and branching ratio with HDECAY, which obtains M_{H}, α and λ_{Hhh} from the hMSSM prescriptions in Eqs. (IV.1.10)–(IV.1.12).

$\Gamma(\mathrm{A} \to \tau\tau)$.

In summary, this comparison shows that – in an MSSM scenario where its underlying assumptions are satisfied – the hMSSM approach provides a good approximation to the results of a direct calculation of the Higgs boson properties. The observed discrepancies of order $(10-20)\%$ in the decays of Eq. (IV.1.7) originate from the different accuracy in the calculations of the decay widths, and could be reduced by including in HDECAY the effect of EW corrections from loops involving SM particles or additional Higgs bosons. However, we stress again that a direct comparison between the ROOT files for the hMSSM and those for the "low-tb-high" scenario would yield larger discrepancies than those shown in Figures 253–256, due to the different values of M_{h} used in the two sets of files.

IV.1.4 Description of the transverse momentum of the Higgs boson in gluon fusion

The transverse momentum distribution of the Higgs boson at fixed order exhibits a logarithmic divergence in the limit of $p_T^{\phi} \to 0$. To obtain meaningful predictions, it is necessary to resum the logarithmically enhanced terms to all orders in α_s. The resummed result is then matched to the fixed-order result by avoiding double counting. Various matching approaches have been proposed; common to all of them is the introduction of an auxiliary momentum scale (from now on generically referred to as "matching scale"), which indicates the transverse-momentum region of the transition from the resummed to the fixed-order result. The dependence of the distribution on this matching scale is of higher logarithmic order. Variations of the theoretical prediction with the matching scale may be used as estimates of the residual uncertainty due to the resummation/matching procedure.

Assuming that the dominant contributions to Higgs boson production are dominated by top- and bottom-quark mediated Higgs-gluon coupling, the process is characterized by three scales, namely M_{ϕ}, m_{t} and m_{b}. The wide separation of these scales prohibits an intuitive choice of the resummation scale, in particular in BSM models (see, e.g., Refs. [224, 240, 1120]). In the following sections we will try to address this issue (for a more detailed discussion, see Ref. [250]). At first we will compare two possible determinations of the matching parameter and then, using these values, we will compare the predictions of three different resummation frameworks.

IV.1.4.a Determination of the matching scale

In this section we describe and compare two recently proposed algorithms to determine the matching scales, defined in Ref. [231] and Ref. [252] and referred to as HMW and BV, respectively, in what follows. In both approaches, the matching scale μ_i ($i = \mathrm{t}, \mathrm{b}, \mathrm{int}$) is determined separately for the component of the cross section involving only the top- or the bottom-quark loop (μ_{t}, μ_{b}), and for the top-bottom interference contribution (μ_{int}). The resummed results for each of these terms are then added in order to yield the best prediction for the p_T^{ϕ} distribution:

$$\frac{\mathrm{d}\sigma}{\mathrm{d}p_T^{\phi}} = \frac{\mathrm{d}\sigma_{\mathrm{t}}}{\mathrm{d}p_T^{\phi}}\bigg|_{\mu_{\mathrm{t}}} + \frac{\mathrm{d}\sigma_{\mathrm{b}}}{\mathrm{d}p_T^{\phi}}\bigg|_{\mu_{\mathrm{b}}} + \frac{\mathrm{d}\sigma_{\mathrm{int}}}{\mathrm{d}p_T^{\phi}}\bigg|_{\mu_{\mathrm{int}}} . \tag{IV.1.13}$$

The interference term, at variance with the first two, is not positive definite; in particular, it may vanish for a specific value of the Higgs boson mass. Note that, due to the fact that the scales are determined separately for each component, it is possible to use them in any model with arbitrary relative strength of the couplings of the Higgs boson to the top and bottom quarks.

IV.1.4.a.i Matching scale determination à la HMW and BV

In the HMW method, one first defines, for each different contribution (top, bottom and interference), $Q_{\mathrm{res}}^{\mathrm{max}}$ as the maximum value of Q_{res} for which the analytically resummed p_T^{ϕ}-distribution stays within the interval $[0,2]\cdot[\mathrm{d}\sigma/\mathrm{d}p_T^{\phi\,2}]_{\mathrm{f.o.}}$ of the fixed-order distribution, for $p_T^{\phi} \geq M_{\phi}$. The default matching scale

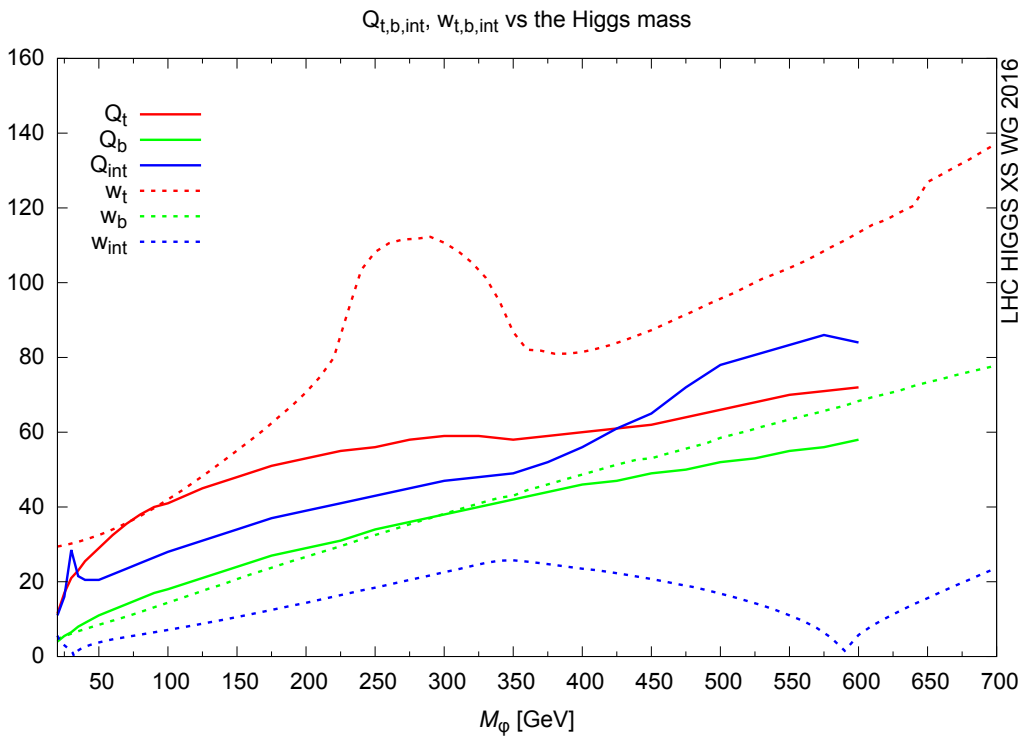

Figure 257: Comparison of the matching scales in the BV and the HMW approach for a scalar Higgs. Solid (dashed) curves correspond to the HMW (BV) scales. The scale corresponding to the top (bottom) quark squared matrix element is shown in red (green), while the values to be used for the interference term are in blue.

Q is then defined to be half of that maximum value. As it turns out, for the results based on analytic resummation this choice of the central matching scale indeed leads to a behaviour of the matched result in the large p_T^ϕ region that is very close to the fixed-order result.

In the BV approach, the exact squared matrix elements of the subprocesses $\mathrm{gg} \to \mathrm{gH}$ and $\mathrm{qg} \to \mathrm{qH}$ are compared to their collinear approximation, again separately for each different contribution. A deviation by more than 10% from the exact result is interpreted as a breakdown of the latter. The upper limit w of the range of Higgs boson transverse momenta where the collinear approximation is accurate is chosen as the value for the matching scale. The two partonic subprocesses initiated by gg and by qg have a different collinear behaviour, which leads to two different scales w^{gg} and w^{qg}; the final scale w is computed as the average of the two previous values, weighted differentially by their relative importance to the transverse momentum distribution of the Higgs, in the p_T^ϕ range between w^{gg} and w^{qg}.

IV.1.4.a.ii Comparison of the two approaches

Since the matching scale is unphysical, its choice is formally arbitrary, and any prescription for its determination is necessarily heuristic. The BV and the HMW approach are complementary in at least two aspects. While BV works at the *partonic* level and considers the *low-p_T^ϕ* region, the HMW approach uses the *large-p_T^ϕ* region of the *hadronic* distribution in order to choose a value for the matching scale. It is thus not surprising that the numerical values of the resulting scales are different. The spread of the results is likely to cover in a quite conservative way the ambiguities of this scale determination.

In Figure 257 we compare the BV scales w_i and the HMW scales Q_i $(i = t, b, \mathrm{int})$. The numerical results of Figure 257 exhibit a moderate agreement between the BV and the HMW scale for the top

contribution, and a very good agreement for the bottom contribution. Concerning the former, we notice that the largest deviation between the approaches appears to be close to the $t\bar{t}$ threshold, around which the BV scales exhibit a non-trivial structure, while it has no effect on the HMW scale determination. The difference between the scales of BV and HMW is largest in cases where the LO term is much smaller than the NLO term. This only happens for the interference contribution which is not required to be positive definite. The collinear approximation is proportional to the LO term, which is why the BV scale will be very small in these cases. On the contrary, since the matched curve becomes almost identical to the fixed-order one, and since the HMW algorithm looks for the largest scale that fulfils the HMW criteria, the resulting matching scale will tend to be very large. This explains the respective behaviours of the two blue curves around $M_\phi \simeq 30$ and $M_\phi \simeq 590$ GeV.

IV.1.4.b Resummation frameworks

We consider the following three representative theoretical approaches for the resummation of the collinear logarithms, indicating the specific software implementations ("codes") used in this study[IV.3]

- analytic resummation (AR) as formulated in Refs. [194, 195]
  (code: MoRe-SuSHi [231, 1120, 1121]);
- the POWHEG method, described in Refs. [342, 343]
  (code: GG_H_QUARK-MASS-EFFECTS and GG_H_2HDM [240] of the POWHEG-BOX [81, 1119]);
- the MC@NLO method of Ref. [340]
  (code: aMCSuSHi [1117, 1118]).

All codes work at NLO-QCD accuracy in the prediction of the Higgs boson production total cross section, i.e., $\mathcal{O}(\alpha_s^3)$. The differences in the p_T^ϕ distribution are formally subleading,[IV.4] but can be numerically sizeable, as we will see later on. In order to assess the impact of these differences, we compare their numerical results using the same values of the matching scales for all of them. On the other hand, we compare the results of a single code for the two different strategies of setting the matching scale proposed in Refs. [231, 252]. As we will see, both the intrinsic difference in the formulation of the codes as well as the dependence on their matching scales are a source of sizeable ambiguities in the theoretical prediction of the Higgs p_T^ϕ distribution, in particular at intermediate and large p_T^ϕ.

IV.1.4.c Phenomenological analysis in the THDM

In order to compare the predictions of the three codes, we compute the uncertainty band obtained varying only the resummation scale in a range $[1/2, 2]$ times the central value (chosen either with the BV or HMW procedure), while keeping the renormalization and factorization scales fixed. Moreover, specifically for AR, which consistently matches the fixed-order results at large transverse momenta, we follow Ref. [231] and apply a suppression factor to the error band which damps it towards large values of p_T^ϕ. For our phenomenological study, we construct two theoretical scenarios (i.e., not necessarily compatible with current experimental constraints), defined on the basis of a type-II THDM, with parameters and NLO total cross sections reported in Table 121; we discuss in these two examples the production of the heavy neutral Higgs boson with mass $M_\mathrm{H} = 300$ GeV (other scenarios have been considered in Ref. [250]).

In the first scenario, dubbed *large-t* in what follows, the production cross section is top-loop dominated. The results for the p_T^ϕ distribution are shown in Figure 258. Within uncertainties (which are based solely on resummation scale variation), the three predictions are compatible with each other for

[IV.3] Note that all approaches feature NLO accuracy (up to α_s^3) on the total Higgs boson production cross section, which implies, however, a formally LO accurate prediction at large p_T^ϕ.

[IV.4] Note that the meaning of "subleading terms" is somewhat different for AR and the MC generators. AR consistently resums NLL terms to all orders, while the PS in the Monte Carlo approaches strictly includes only the leading logarithms, but resums also some logarithms beyond the leading ones.

Table 121: Mixing angle values specific of the large-t and large-b THDM scenarios considered in Section IV.1.4.c. The cross sections for the production of a heavy scalar and a pseudoscalar Higgs boson have been obtained with SusHi (the integration error at NLO is of the order of 0.1%, and negligible at LO).

scenario	$\tan\beta$	$\sin(\beta-\alpha)$	ϕ	σ_t/pb		σ_b/pb		$-\sigma_{int}$/pb	
				LO	NLO	LO	NLO	LO	NLO
large-t	1.0	0.999	H	3.715	6.788	0.002	0.003	-0.132	-0.168
			A	12.844	23.832	0.004	0.005	0.334	0.428
large-b	50	0.999	H	0.002	0.005	5.085	7.089	0.163	0.199
			A	0.005	0.010	9.984	13.408	0.334	0.412

$p_T^\phi \lesssim 200$ GeV. Using HMW scales, the central value of AR merges into the fixed-order NLO prediction (fNLO) at about $p_T^\phi = 200$ GeV; for MC@NLO, this transition is a bit slower, while POWHEG's asymptotic value towards large p_T^ϕ appears to be about $40-50\%$ above fNLO. This overshooting of fNLO at large p_T^ϕ is a general feature of the default POWHEG matching; its origin will be discussed in more detail below.

Using BV scales, one notices that AR deviates quite significantly ($\sim 50\%$) from the fNLO result already at $p_T^\phi = 400$ GeV; this deviation tends to further increase towards larger p_T^ϕ values. This is not unexpected since the HMW scales are designed to guarantee similarity between the resummed and the fNLO curve at large p_T^ϕ. Scale choices larger than the values determined by HMW will therefore necessarily lead to a deviation from the fNLO predictions in that region. The agreement between the two Monte Carlos turns out to be excellent, at least up to p_T^ϕ values as large as the Higgs boson mass. Despite the large deviations of AR in the tail and the much softer AR spectrum, all approaches are compatible within uncertainties at small to intermediate transverse momenta ($p_T^\phi \lesssim 200$ GeV). It should be noted that this is partly due to the fact that the uncertainty bands are significantly larger (almost by a factor of two) than in the SM.

In the second scenario, dubbed *large-b* in what follows, the production cross section for the heavy Higgs is bottom-loop dominated. Since the associated matching scales w_b and Q_b are very close to each other, any difference in the p_T^ϕ distributions are due to the conceptional variants of the matching in the three codes under consideration.

Let us first discuss the left plot of Figure 259. The large-p_T^ϕ behaviour is similar to the large-b scenario, when using HMW scales, discussed above. Apparently, the specific matching procedure of POWHEG has a significant impact on the large-p_T^ϕ region, where the Parton Shower, based on the soft/collinear approximation, is outside its region of validity. Note that the size of the error bands is very different in the two Monte Carlo approaches: the MC@NLO band blows up to $\mathcal{O}(100\%)$ around $p_T^\phi \sim 125$ GeV; the POWHEG band remains very narrow over the whole range.

It turns out that both the enhanced high-p_T^ϕ tail of the POWHEG curve and its small uncertainty band can be tackled by the same modification of the matching procedure. In the original POWHEG approach, the starting scale of the shower (t_1) for each event is identified with the transverse momentum of the first emission. If the latter is very large, the shower will act up to scales which are way beyond the validity range of the underlying approximations. In the mPOWHEG modification [250], on the other hand, t_1 is defined to remain below the matching scale for all "remnant events" (i.e., events which are described by the pure fixed-order real emission matrix element; this restriction ensures that the formal accuracy of the original POWHEG approach remains unaffected). This results in the magenta, solid

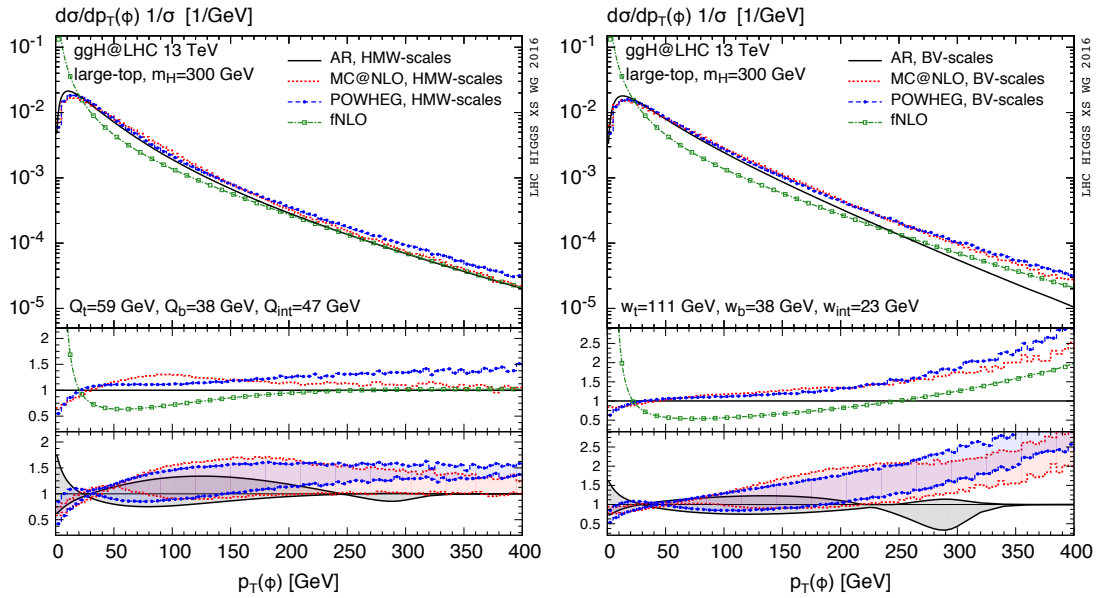

Figure 258: Shapes of the transverse-momentum distributions (i.e., normalized such that the integral yields one) for the heavy Higgs boson with $M_{\mathrm{H}} = 300$ GeV in the large-t scenario. The distributions are computed with AR (black, solid), MC@NLO (red, dotted), and POWHEG (blue, dashed overlaid by points), by setting the matching scales to the HMW values (left) and the BV values (right). For reference, we also show the fixed-order NLO (fNLO) prediction (green, dash-dotted with open boxes). The main frame shows the absolute distributions, the first inset the shape-ratio of the central values to the AR distribution, and the second inset the uncertainty bands, normalized again to the central AR value.

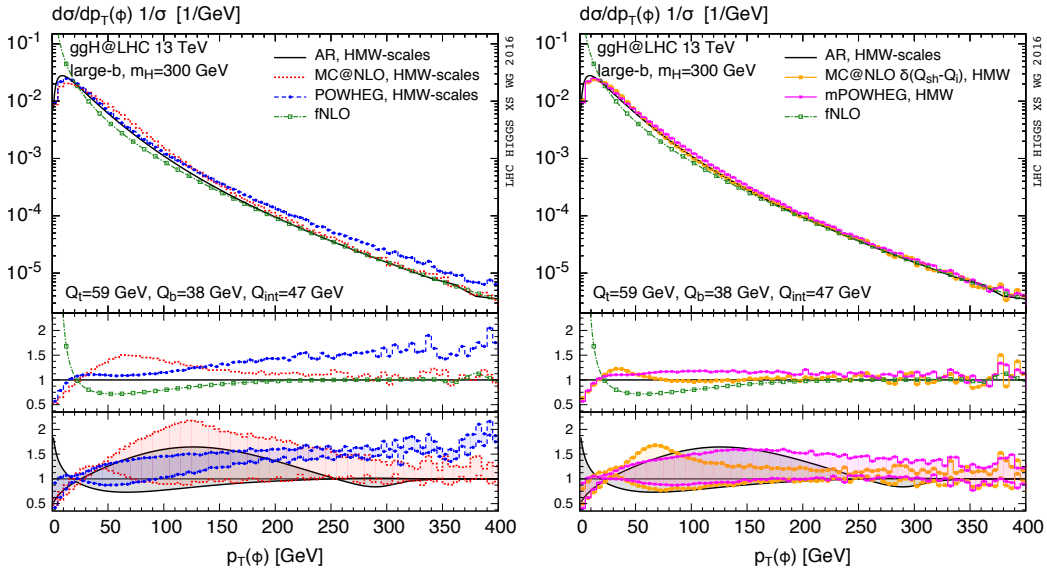

Figure 259: Left: Same as left plot in Figure 258, but for the large-b scenario. Right: Same, but using a fixed shower scale for the soft events in MC@NLO, and mPOWHEG (see main text). (HMW scales are assumed here; the plots for BV scales are identical for all practical purposes.)

curve in the right plot of Figure 259, which exhibits a fNLO-like high-p_T^ϕ behaviour; also the uncertainty band appears to describe the matching uncertainty more realistically.

In the MC@NLO implementation the choice of the shower scale $Q_{\rm sh}$ of soft events follows a distribution peaking at the value of the matching scale Q_i. Restricting the range of that distribution has a significant effect on the central MC@NLO prediction: in particular, in the limit where this distribution turns into a delta function $\delta(Q_{\rm sh} - Q_i)$, also the size of the uncertainty band is strongly reduced, as can be observed from the orange curve in the right plot of Figure 259.

This study simply shows that the predictions in bottom-quark dominated scenarios, both in the POWHEG and in the MC@NLO approaches, strongly depend on the details of the matching procedure; this feature is reflected in the large associated uncertainties.

The distributions for the pseudo-scalar Higgs in the large-b scenario largely resemble the ones of the heavy Higgs shown in Figure 259, and we do not need to discuss them separately.

Chapter IV.2

Neutral Higgs Boson Production in Association with Bottom Quarks

M. Beckingham, A. Nikitenko, M. Spira, M. Wiesemann (Eds.) M. Bonvini, S. Forte, H.B. Hartanto, B. Jäger, S. Liebler, D. Napoletano, A. Papanastasiou, F.J. Tackmann, M. Ubiali

IV.2.1 Introduction

Higgs boson production modes that feature a $b\bar{b}\phi$ vertex at tree level are a viable alternative to determine the Higgs-bottom Yukawa coupling (y_b), since the $H \to b\bar{b}$ decay is problematic from an experimental viewpoint: it suffers from the huge b-quark QCD background; the absolute value of the total width is extremely small; and the $H \to b\bar{b}$ branching ratio is large, which renders the determination of the relative partial decay widths at a certain accuracy difficult. Besides loop-induced Higgs boson production through gluon fusion, that receives a contribution from both top- and bottom-quark loops, the direct production of a Higgs boson in association with bottom quarks (i.e., tree-level processes that contain a b-quark radiating a Higgs boson) gives access to the $b\bar{b}\phi$ coupling.

The associated production of a Higgs boson with bottom quarks ($b\bar{b}\phi$ production) is suppressed in the SM by almost two orders of magnitude with respect to the gluon-fusion process. Furthermore, this inclusive rate strongly decreases when requiring realistic b-tagging (i.e., minimal transverse momentum and centrality requirements on the b jets) in order to render it distinguishable from other production mechanisms. However, in theories with extended Higgs sector, such as a generic THDM or the MSSM, the Higgs boson coupling to bottom quarks can be significantly enhanced and the $b\bar{b}\phi$ process can, in fact, become the dominant production mode. Since experimentally a scalar sector richer than the one of the SM has not been ruled out so far, this constitutes a strong motivation for precision computations of the total rate (see Section IV.2.2), a proper modelling of the $b\bar{b}\phi$ signal in Monte Carlo (MC) generators (see Section IV.2.3) and the study of uncertainties related to the experimental acceptance (see Section IV.2.4). We will further report total inclusive cross sections for the $c\bar{c}\phi$ production mode (see Section IV.2.5) which may become relevant in specific models with enhanced charm Yukawa coupling. Although all presented predictions are in the SM, they are directly applicable to all neutral Higgs bosons ($\phi = h, H, A$) in a THDM, by a proper rescaling of the bottom Yukawa; for the MSSM this has been shown [1089–1091] to be a good approximation of the full result.

As for all processes that feature b quarks at the level of the hard-scattering process, there are two viable approaches to compute the $b\bar{b}\phi$ cross section. In the four-flavour scheme (4FS), bottom quarks are treated as massive particles, hence no bottom quarks can appear in the initial state of the partonic scattering process. This is relevant for those cases where the physical mass of the b quark is considered as a hard scale and implies that observables with tagged final-state b quarks are well defined (and thus can be computed) at fixed α_S order in perturbation theory. The leading-order (LO) partonic processes in

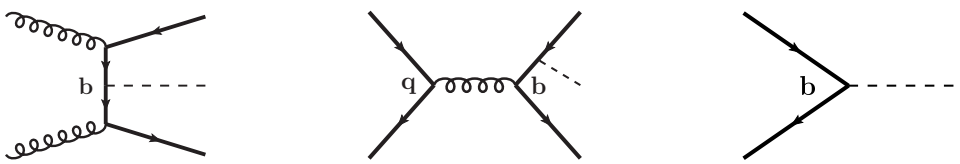

Figure 260: Sample of LO Feynman diagrams for $b\bar{b}\phi$ production in the four-flavour scheme (left, centre) and the five-flavour scheme (right).

the 4FS are (see left and centre diagrams in Figure 260)

$$gg \to b\bar{b}H\,, \qquad q\bar{q} \to b\bar{b}H\,, \tag{IV.2.1}$$

where q denotes a light quark.

At any order in perturbation theory the 4FS involves terms $\sim \alpha_S^k \log^k(m_b/Q)$, where Q is the characteristic scale of the $g \to b\bar{b}$ splitting. These logarithmically enhanced terms remain small as long as $Q \sim m_b$, but can spoil the perturbative convergence when $Q \gg m_b$. Such terms are generally dealt with by re-organizing the perturbative series while resumming them to all orders in α_S. This is precisely achieved by working in second viable approaches to compute the $b\bar{b}\phi$ cross section, the five-flavour scheme (5FS), which is particularly important when the characteristic of an observable is that of being dominated by such logarithms. In this scheme, one assumes massless b quarks ($m_b \equiv 0$) at the level of the short-distance cross section, which are therefore treated at equal footing as the other light quarks and may appear as initial state particles; the potentially large logarithms are effectively resummed through the DGLAP evolution of the b-quark PDFs. Hence, the LO cross section in the 5FS is simply given by (see right diagram of Figure 260)

$$b\bar{b} \to H\,. \tag{IV.2.2}$$

It is clear from the discussion above that 4FS computations do not account for logarithmic terms beyond the first few, while 5FS results lack power-suppressed terms $(m_b/Q)^n$. If either of these properties is important the other scheme must be preferred. Being highly observable dependent[IV.5], at least for inclusive quantities neither resummation nor mass effects are dominant and the two approaches lead to generally similar results. One must bear in mind, however, that reasonable agreement is found only by judicious choices of hard scales, i.e., the resummation and factorization scales, which must be chosen significantly smaller than m_H [412, 565, 1088, 1147]—the hardness one would naively associate with $b\bar{b}\phi$ production. [IV.6]

For inclusive observables the 5FS process in Eq. (IV.2.2) has the technical advantage of being much simpler ($2 \to 1$ at the LO), which renders feasible radiative corrections beyond the NLO (and even beyond the NNLO with current technology), while the $2 \to 3$ Born-level processes of Eq. (IV.2.1) in the 4FS limit perturbative computations in this scheme to NLO.

Considering more exclusive observables, in particular regarding the final-state b quarks, which are relevant for a realistic description of the $b\bar{b}\phi$ signal, the 5FS loses its advantage mentioned above: The process in Eq. (IV.2.2) has much more limited information on the final-state kinematics than the one in Eq. (IV.2.1). Only higher orders in the 5FS recover such information, e.g., 1-b and 2-b tag observables can be described in the 5FS only starting from NLO and NNLO, respectively, while the 4FS tree-level process in Eq. (IV.2.1) describes observables involving 0-, 1-, or 2-b tags formally already with leading perturbative accuracy. Furthermore, b-tagged objects in the 5FS can not be consistently defined at any order in perturbation theory, because the corresponding cross section becomes infinite beyond the LO, when the massless b quarks are not considered as (and clustered into) jets or integrated over. The massive b quarks in the 4FS, on the other hand, can be associated with physical objects, allowing for realistic b tagging with arbitrary selection cuts on the b quark kinematics[IV.7], whereas too small p_T cuts directly lead to a divergence in the 5FS. The problems related to a consistent definition of b-tagged objects in the 5FS can be alleviated by matching the fixed-order computation to parton showers (PS). Due to the backward evolution of the initial-state b quarks the shower will generate b-flavoured hadrons already at the LO, rendering realistic any b-tagging requirements. However, one must not forget that the backward

[IV.5] This receives an additional complication from the fact that an observable may be associated with different powers of α_S in the four- and five-flavour schemes.

[IV.6] This is also supported by arguments based on collinear dominance [412] and the small upper p_T limit of the factorizing part in the p_T distribution [1148].

[IV.7] Note that fragmentation effects when turning the b quarks into B hadrons are assumed to be moderate and neglected in general at fixed order.

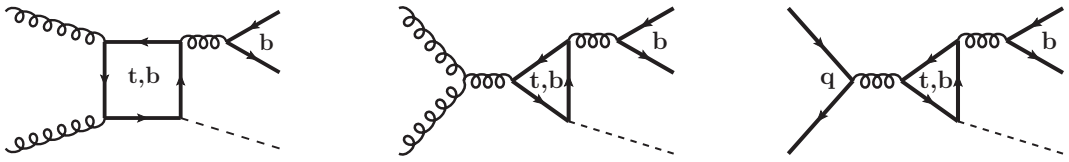

Figure 261: Sample of one-loop Feynman diagrams for $b\bar{b}\phi$ production in the four-flavour scheme featuring a y_t coupling.

evolution in the Monte Carlos is not trivial and has only leading logarithmic (LL) accuracy. Furthermore, the kinematic reshuffling of massless into massive b quarks can have sizeable effects on the B hadron kinematics. Both come at the price of an additional uncertainty. As far as the 4FS is concerned, the PS matching particularly improves the Sudakov-suppressed small-p_T initial-state radiation, although the impact of the PS is less crucial than in the 5FS. In both schemes, the PS introduces additional power-suppressed contributions due to long-distance phenomena.

Before considering phenomenological predictions, let us discuss the general coupling structure in the two schemes. Being a $2 \to 3$ process the lowest order cross section in the 4FS starts at $\mathcal{O}(\alpha_S^2)$. In the 5FS each bottom PDF can be considered as being of $\mathcal{O}(\alpha_S)$ with respect to the gluon and hence the LO features no power of α_S. In both schemes the LO cross section is proportional to y_b^2, since the Higgs boson is always coupled to a b quark. Considering higher order corrections, the coupling structure becomes more involved, in particular in the 4FS. In this case virtual diagrams with a $b\bar{b}\phi$ final state may involve a top quark circulating in the loop, which couples to the Higgs boson (e.g., see Figure 261), and thus are proportional to the Higgs-top coupling (y_t). Such diagrams are generally attributed to the gluon-fusion Higgs boson production mode (their square enters the NNLO gluon-fusion cross section), but their interference with diagrams proportional to y_b must be carefully accounted for in the cross section of the $b\bar{b}\phi$ production mode. Such contributions will be generically referred to as $y_b y_t$ terms. Including such interference effects, but neglecting all contributions that already appear in the gluon-fusion process, we may thus express the $b\bar{b}\phi$ cross section in the two schemes as follows:

$$\sigma_{b\bar{b}\phi}^{\text{4FS}} = \underbrace{\alpha_S^2\, y_b^2\, \Delta_{y_b^2}^{(0)} + \alpha_S^3 \left(y_b^2\, \Delta_{y_b^2}^{(1)} \right.}_{\equiv \sigma_{y_b^2}} + \underbrace{\left. y_b\, y_t\, \Delta_{y_b y_t}^{(1)} \right)}_{\equiv \sigma_{y_b y_t}/\alpha_S^3} + \alpha_S^4 \left(y_b^2\, \Delta_{y_b^2}^{(2)} + y_b\, y_t\, \Delta_{y_b y_t}^{(2)} \right) + \mathcal{O}(\alpha_s^5)\,. \quad \text{(IV.2.3)}$$

$$\sigma_{b\bar{b}\phi}^{\text{5FS}} = y_b^2 \left(\Delta_{y_b^2}^{(0)} + \alpha_S\, \Delta_{y_b^2}^{(1)} + \alpha_S^2\, \Delta_{y_b^2}^{(2)} + \alpha_S^3 \Delta_{y_b^2}^{(3)} + \mathcal{O}(\alpha_s^4) \right). \quad \text{(IV.2.4)}$$

The 4FS cross section at NLO (being the current state-of-the-art) can be decomposed in terms proportional to y_b^2 ($\sigma_{y_b^2}$) and $y_b y_t$ ($\sigma_{y_b y_t}$). Any component with a $b\bar{b}\phi$ final state, but proportional to y_t^2, must originate from a squared gluon-fusion amplitude (i.e., with a Higgs radiated from a closed top-quark loop) and can be incoherently added to the $b\bar{b}\phi$ cross section above.[IV.8] In the 5FS, on the other hand, interference terms (proportional to $y_b y_t$) between the gluon-fusion and $b\bar{b}\phi$ processes exactly vanish order by order in perturbative QCD, since they involve a helicity flip of the bottom quarks that leads to a vanishing interference term with the generic 5FS amplitudes in the massless limit.

IV.2.2 Total inclusive cross section

In this section, we study and compare the state-of-the-art predictions for the total inclusive $b\bar{b}\phi$ cross section within the 4FS, within the 5FS and matched predictions of the two schemes.

[IV.8] Note that starting from the NNLO in both schemes such squared gluon-fusion diagrams contribute also to the y_b^2 and $y_b y_t$ components of the $b\bar{b}\phi$ cross section, which, as stated above and being common practice, are not attributed to the $b\bar{b}\phi$ cross section, but to the gluon-fusion one.

Before introducing the features of the different matched computations under consideration, let us summarize the available total cross section computations for $b\bar{b}\phi$-production in the literature. The 4FS cross section is known through NLO QCD in the SM [431, 1085, 1086]; MSSM-type couplings have been studied in Ref. [1149]; and the SUSY-QCD corrections in the MSSM were computed in Refs. [1091, 1150]. Owing to its technically simpler process structure, radiative corrections in the 5FS are known through NLO [1087, 1151] and NNLO QCD [565]. Even the relevant matrix elements for the full N^{3}LO prediction are already available [1152, 1153] (their combination being far from trivial though).

Matched four- and five-flavour scheme computations will be discussed and their phenomenological results compared in the following sections. The Santander matching [1131] has been introduced as an empirical approach to combine 4FS and 5FS predictions by a weighted average with respect to the Higgs boson mass. More recently, two consistent flavour-scheme matching procedures have been applied to the $b\bar{b}\phi$ production process. In Ref. [1154] the formally NLO+NLL accurate (NLO in the 4FS, and NLL refers to the logarithms resummed through the 5FS) cross section is presented, while Ref. [1155] works in the FONLL approach, but includes only the LO 4FS cross section.

IV.2.2.a Choice of bottom PDFs in the 5FS

The resummation of potentially large collinear logarithms due to initial-state gluons splitting into b quark pairs is achieved through their factorization into the definition of the PDFs, and consequently through DGLAP evolution. Once this is done, the partonic coefficients do not contain collinear b-quark logarithms,[IV.9] so the detail of their resummation resides entirely in the PDFs. Therefore, the choice and usage of the PDF set in resummed computations must be regarded as a (fundamental) part of the computation itself. It is the purpose of this section to briefly review how the resummation in PDFs works and to describe the choice of PDFs adopted in this Chapter for $b\bar{b}\phi$ production.

Since splittings involving bottom quarks are finite (the bottom mass regulates the collinear limit), factorizing or not the collinear logarithms generated by these splittings gives rise to two factorization schemes, denoted by 5FS and 4FS respectively. In the 5FS, a bottom PDF exists and the DGLAP evolution involves 5 active flavours, while in the 4FS there is no bottom PDF and DGLAP evolution involves only 4 active flavours. The PDFs in the two schemes can be related by matching conditions, obtained imposing scheme invariance, possibly up to power corrections in the bottom mass (for a recent review, see Ref. [1156]). The matching conditions at the generic scale μ_b read

$$f_i^{[5]}(\mu_b) = \sum_{j=g,u,\bar{u},d,\bar{d},s,\bar{s},c,\bar{c}} \mathcal{K}_{ij}(m_b,\mu_b) \otimes f_j^{[4]}(\mu_b), \qquad i = g,u,\bar{u},d,\bar{d},s,\bar{s},c,\bar{c},b,\bar{b}, \tag{IV.2.5}$$

($\otimes$ denotes Mellin convolution) where $\mathcal{K}_{ij}(m_b,\mu_b)$ are matching functions fully known to $O(\alpha_S^2)$ [1157, 1158] and partially to $O(\alpha_S^3)$ [1159–1162]. Since resumming bottom mass logarithms is useful only at large scales, where phase space constraints allow gluon splittings into b quark pairs, the factorization scheme adopted in standard PDF sets changes dynamically: for scales below the "bottom threshold" μ_b the 4FS is used, at the threshold scale μ_b 5FS PDFs are generated from the 4FS ones through Eq. (IV.2.5), and for scales higher than μ_b 5FS evolution is used.

The value of μ_b is in principle arbitrary, however its value should be chosen to be close to the bottom mass m_b, so that the collinear logarithms of μ_b/m_b factorized in $\mathcal{K}_{ij}(m_b,\mu_b)$ are not large and a fixed-order expression for $\mathcal{K}_{ij}$ is reliable. The standard choice adopted in PDF sets is $\mu_b = m_b$. However, it is useful to let μ_b vary to estimate the theoretical uncertainty due to missing higher orders in the matching procedure. The remaining potentially large logarithms of μ_b/μ_F, where $\mu_F \sim m_H$ is the typical hard scale of the process, are then resummed via DGLAP evolution with 5 active flavours from the scale μ_b to the factorization scale μ_F.

[IV.9] In the massless 5FS, the partonic coefficients do not contain any bottom mass dependence, while in the matched computations only power suppressed mass contribution are present.

The values of the bottom mass, m_b, and bottom threshold, μ_b, as well as the mass-renormalization scheme are therefore entirely contained in the PDF set one uses for resummed computation. Therefore, when computing a cross section, one must either set the input parameters to be consistent with the PDF set used, or refit the PDFs using the desired input parameters. For instance, in matched computations, it is important to ensure that the value of the mass adopted in the computation of power-suppressed contributions is equal (perhaps modulo mass-renormalization scheme conversion) to the one present in the PDF set.

In practice, the effect of the choice of the bottom mass value on PDF fits is very mild for all PDFs, barring the bottom-quark PDF [64]. Hence, one can expect that refitting the PDFs with different values of the bottom mass and threshold should not significantly affect light PDFs at scales below the bottom threshold. Therefore, taking any PDF set with a given bottom mass, and re-evolving it from a low scale ($< \mu_b$) using a different bottom mass, threshold and even renormalization scheme should yield virtually the same resulting PDF set as refitting with the same setting. This "approximate" approach is very useful because it opens up the possibility of using any desired setting with any input PDF.

We now discuss the settings used for the resummed calculations (5FS and matched) presented in this report. Since the bottom mass is most precisely determined in the $\overline{\text{MS}}$ scheme, it seems most correct to use this scheme for the mass renormalization in the PDF matching. However, current PDF fits have been performed with pole-scheme masses, and, to date, no fits with $\overline{\text{MS}}$-scheme masses are publicly available. Furthermore, existing computations of the $b\bar{b}\phi$ cross section assumed pole-scheme masses in the PDFs [1154, 1155]. In order to be consistent with existing fits and computations it is convenient at this stage to use the pole scheme. However, since the bottom pole mass is not very well determined and is additionally affected by the renormalon ambiguity [1163, 1164], the choice of the value of the pole mass is a delicate point. We argue that the pole mass which can better reproduce a hypothetical NNLO $\overline{\text{MS}}$ fit with $\overline{m_b}(\overline{m_b}) = 4.18$ GeV is obtained from a 1-loop conversion, which gives

$$m_b^{\text{pole}} = 4.58 \text{ GeV}. \tag{IV.2.6}$$

The reason for this is that the bottom mass first enters the matching functions $\mathcal{K}_{ij}$ at $O(\alpha_S)$. This means that an NNLO fit, which employs the $\mathcal{K}_{ij}$ at $O(\alpha_S^2)$, is only affected by the 1-loop pole to $\overline{\text{MS}}$ conversion. We have verified that evolving the same initial PDF set using either the pole scheme with $m_b^{\text{pole}} = 4.58$ GeV or the $\overline{\text{MS}}$ scheme with $\overline{m_b}(\overline{m_b}) = 4.18$ GeV gives very similar results.

Taking Eq. (IV.2.6), together with $\mu_b = m_b^{\text{pole}}$, as the central choice for the resummed $b\bar{b}\phi$ computations, we can now discuss how to compute theoretical uncertainties. As already mentioned, the uncertainty due to missing higher order terms in the matching procedure can be probed by varying μ_b. Following Ref. [1154], we propose to use a canonical factor of 2 around the central value $\mu_b = m_b^{\text{pole}}$. In addition to this, one can consider a parametric uncertainty on the value of the bottom mass itself. A reasonable variation, which should be sufficient to cover the uncertainties on both the determination of $\overline{m_b}(\overline{m_b})$ and in the conversion to the pole scheme, is ± 0.14 GeV. Therefore, we recommend that uncertainties are estimated according to

$$4.44 \text{ GeV} \leq m_b^{\text{pole}} \leq 4.72 \text{ GeV}, \qquad 2.29 \text{ GeV} \leq \mu_b \leq 9.16 \text{ GeV}. \tag{IV.2.7}$$

For m_b^{pole} variations, the bottom threshold is kept fixed at $\mu_b = 4.58$ GeV.

As far as the initial PDF set is concerned, we use the `PDF4LHC15_nnlo_mc` set. All the 101 PDF members are re-evolved from an initial scale of 2 GeV, using all the possible variations of settings mentioned above. This is done using the latest version (≥ 2.8) of `APFEL` [1165], which can now handle heavy quark thresholds that are different from the mass. The new re-evolved PDF sets[IV.10] are publicly available for download from `http://www.ge.infn.it/~bonvini/bbh`.

[IV.10] We acknowledge V. Bertone who cross-checked the sets and S. Liebler who tested them against the original PDF4LHC15 set.

The settings used here differ from the LHCHXSWG default [35], which in particular includes PDF4LHC15 PDFs. Specifically, the bottom pole mass value used in the PDF sets included in the PDF4LHC15 combination differ from each other. This is supposed to give a rough estimate of the PDF uncertainty associated to the choice of m_b in the PDF fit, but it contrasts with the needs of the more detailed estimate of the uncertainties related to the bottom mass in our calculation, as discussed above. A fully consistent treatment of the bottom mass, such as the one adopted here, is of crucial importance for processes such as $b\bar{b}\phi$ production, which are very sensitive to the bottom PDF: as stated in the PDF4LHC15 recommendation, such cases require special care.

IV.2.2.b Santander matching

The 5FS result is obtained with the help of SUSHI [135] which includes the NNLO QCD corrections to the process $b\bar{b}\phi$ [565]. The bottom Yukawa coupling is renormalized in the $\overline{\text{MS}}$ scheme. It is evaluated according to the prescription of Chapter I.1 by running $m_b(\mu)$ from $\mu = 4.18\,\text{GeV}$ to m_H at 4-loop level, which corresponds to our central choice of the renormalization scale. The central factorization scale is $\mu_F = m_H/4$ [565, 1088, 1147, 1148]. The scale uncertainties are determined by taking the minimum and the maximum of the seven values for the cross section, corresponding to the choices $\mu_R, 4\,\mu_F \in \{m_H/2, m_H, 2\,m_H\}$ while $1/2 \leq 4\mu_F/\mu_R < 2$. The Yukawa coupling at μ_R is obtained from its previously determined value at m_H by 3-loop evolution.

The 4FS result uses the implementation of the $b\bar{b}\phi$ processes by means of MADGRAPH5_AMC@NLO at NLO [431].[IV.11] The bottom Yukawa coupling has been adopted according to the 5FS, while for the PDFs 4-flavour PDF4LHC15 densities are used consistently with the appropriate choice of a 4-flavour coupling α_s. The central renormalization and factorization scales have been chosen as $\mu_R = \mu_F = (M_H + 2m_b)/4$. The renormalization scales of α_s and the bottom Yukawa coupling have been identified. This implementation has been cross checked against the published 4FS results of Refs. [431, 1085, 1086].

In the asymptotic limits $m_H/m_b \to 1$ and $m_H/m_b \to \infty$, the 4FS and 5FS results tend to provide the unique description of the inclusive $b\bar{b}\phi$ cross section, respectively. In the Santander matching prescription [1131], the 4FS and 5FS are thus combined in such a way that they are given variable weight, depending on the value of the Higgs boson mass. Since the difference between the two approaches is formally logarithmic, the dependence of their relative importance on the Higgs boson mass should be controlled by a logarithmic term, i.e.

$$\sigma^{\text{matched}} = \frac{\sigma^{\text{4FS}} + w\,\sigma^{\text{5FS}}}{1+w}\,, \tag{IV.2.8}$$

with the weight w defined as

$$w = \ln\frac{m_H}{m_b} - 2\,. \tag{IV.2.9}$$

The theoretical errors are combined according to

$$\Delta\sigma_\pm = \frac{\Delta\sigma_\pm^{\text{4FS}} + w\,\Delta\sigma_\pm^{\text{5FS}}}{1+w}\,, \tag{IV.2.10}$$

where $\Delta\sigma_\pm^{\text{4FS}}$ and $\Delta\sigma_\pm^{\text{5FS}}$ are the upper/lower uncertainty limits of the 4FS and the 5FS, respectively.

The corresponding $b\bar{b}\phi$ cross-sections expanded to a scan over SM Higgs boson masses are presented in Tables 243–246. Tables 247 and 248 summarize the Standard Model $b\bar{b}\phi$ cross-sections and the corresponding uncertainties for the different proton–proton collision energies for a Higgs boson mass $M_{\text{H}} = 125$ GeV and $M_{\text{H}} = 125.09$ GeV, respectively.

[IV.11] See also Section IV.2.3.a for details on the dedicated $b\bar{b}\phi$ implementation in MADGRAPH5_AMC@NLO.

IV.2.2.c NLO+NLL matching

This section summarizes the approach of Ref. [1154] which combines the virtues of the 4F and 5F schemes into a fully consistent fixed-order + resummation matched result, which is valid for any parametric scale hierarchy between m_b and m_H. The updated results for LHC 13 TeV together with the estimate for the perturbative and parametric uncertainties are discussed in detail in Ref. [1166]. The code for the NLO+NLL matched predictions will be available at `http://www.ge.infn.it/~bonvini/bbh`.

To describe the matched result, it is instructive to first briefly recall the 4FS and 5FS results. The 4FS calculation of the bbH cross section is formally valid in the $m_b \sim m_H$ limit. In this scheme, bottom quarks do not appear in the initial-state, but rather via gluon splitting into b-quark pairs. The 4FS cross section includes both power corrections in the bottom-quark mass, $O(m_b^2/m_H^2)$, and logarithmic terms $\sim \ln(m_b^2/m_H^2)$ at fixed order in α_s that arise from collinear gluon splittings into b-quark pairs.

The 4FS (fixed-order) result is given by the Mellin convolution of coefficient functions $D_{ij}(m_H, m_b, \mu_F)$, which depend explicitly on m_b, and evolved 4FS PDFs,

$$\begin{aligned}\sigma^{\text{FO}} &= \sum_{i,j=g,q,\bar{q}} D_{ij}(m_H, m_b, \mu_F) \otimes f_i^{[4]}(\mu_F) \otimes f_j^{[4]}(\mu_F) \\ &= \sum_{i,j,k,l=g,q,\bar{q}} D_{ij}(m_H, m_b, \mu_F) \otimes \left[U_{ik}^{[4]}(\mu_F, \mu_0) \otimes f_k^{[4]}(\mu_0)\right] \otimes \left[U_{jl}^{[4]}(\mu_F, \mu_0) \otimes f_l^{[4]}(\mu_0)\right].\end{aligned} \tag{IV.2.11}$$

The sum is restricted to gluons and light quarks and antiquarks ($q = d, u, s, c$), μ_F is the hard (factorization) scale of the process, μ_0 is the scale at which PDFs are fitted,[IV.12] and $U^{[4]}$ are DGLAP evolution factors with $n_f = 4$ active quark flavours. The 4FS predictions for the inclusive cross section are most accurate at small values of the Higgs boson masses (parametrically $m_H \sim m_b$), where power corrections are important and the logarithms are small.

The 5FS is formally valid in the limit $m_b \ll m_H$. In this scheme, bottom quarks do appear in the initial state. The large collinear logarithms are resummed through DGLAP evolution by the introduction of a bottom-quark PDF, as described in Sect. IV.2.2.a. In this scheme, the bottom quark mass is set to zero in the partonic cross section and therefore the power-corrections $O(m_b^2/m_H^2)$ are not included. The cross section is given by the convolution of coefficient functions $C_{ij}(m_H, \mu_F)$, which contain no m_b dependence, with evolved 5FS PDFs,

$$\begin{aligned}\sigma^{\text{Resum}} &= \sum_{i,j=g,q,\bar{q},b,\bar{b}} C_{ij}(m_H, \mu_F) \otimes f_i^{[5]}(m_b, \mu_F) \otimes f_j^{[5]}(m_b, \mu_F) \\ &= \sum_{i,j=g,q,\bar{q},b,\bar{b}} C_{ij}(m_H, \mu_F) \otimes \left[\sum_{\substack{k=g,q,\bar{q},b,\bar{b} \\ l,p=g,q,\bar{q}}} U_{ik}^{[5]}(\mu_F, \mu_b) \otimes \mathcal{K}_{kl}(m_b, \mu_b) \otimes U_{lp}^{[4]}(\mu_b, \mu_0) \otimes f_p^{[4]}(\mu_0)\right] \\ &\qquad \otimes \left[\sum_{\substack{k=g,q,\bar{q},b,\bar{b} \\ l,p=g,q,\bar{q}}} U_{jk}^{[5]}(\mu_F, \mu_b) \otimes \mathcal{K}_{kl}(m_b, \mu_b) \otimes U_{lp}^{[4]}(\mu_b, \mu_0) \otimes f_p^{[4]}(\mu_0)\right].\end{aligned} \tag{IV.2.12}$$

In the second equation we explicitly wrote out how the 5FS PDFs at $\mu = \mu_F$ are perturbatively constructed from the fitted 4FS PDFs at the initial scale μ_0, the 4-flavour evolution from μ_0 to the bottom matching scale μ_b, the matching Eq. (IV.2.5) at μ_b and the 5-flavour evolution from μ_b to μ_F.

To facilitate the matching of the two results, it is advantageous to bring the 5FS result into a form that is consistent with the logarithms present in the fixed-order result. To do so, the perturbative counting

[IV.12] We consider the charm quark as fitted light-quark PDF; in most PDF fits, the charm PDF is generated perturbatively similar to the bottom PDF, but this is not of relevance for the present discussion.

assigned to the resummed cross section is revisited. Usually, the PDFs are treated as external $O(1)$ objects and one assigns a perturbative counting to the cross section based on a perturbative counting of the coefficient functions alone. For the b-quark PDF, this would be justified in the limit where the off-diagonal evolution factor $U_{bg}^{[5]}(\mu_F,\mu_b) \sim 1$. However, $U_{bg}^{[5]}$ is $\alpha_s \ln(\mu_F/\mu_b)$-suppressed relative to the diagonal evolution factors, and therefore this only holds for scales $\mu_F \ggg \mu_b$. Numerically, for $\mu_b \sim O(m_b)$ this is only attained for scales $\mu_F \gtrsim 1$ TeV. Hence, for the relevant scales of interest here it is more appropriate to count $U_{bg}^{[5]}$ as $O(\alpha_s)$, and therefore also count $f_b^{[5]}$ as $O(\alpha_s)$. We refer to the 5FS result reorganized with this counting as the resummed result. For a more detailed discussion we refer to Ref. [1154].

This counting has the important property that it provides a perturbative treatment of the b-quark PDF that is consistent between the fixed-order (4FS) and resummed results. The 5FS cross section in Eq. (IV.2.12) is expanded in α_s by counting $U_{bg}^{[5]} \sim \alpha_s$ and expanding the coefficient functions C_{ij} *together* with the b-quark matching coefficients $\mathcal{K}$. The key feature is that order by order in α_s the limit $\mu_b \to \mu_F$ in the resummed cross section then exactly reproduces *all* the logarithmic terms (and nothing more) that are present in the $m_b \to 0$ limit of the fixed-order cross section. (Or in other words, the reexpansion of the resummed result to fixed order is simply given by setting $\mu_b \to \mu_F$.) This in turn means that for $\mu_b < \mu_F$ the evolution factors $U^{[5]}$ in this expansion precisely resum the singular logarithms present in the fixed-order result.

With this re-arrangement of the resummed cross section, all that is missing in the latter compared to the fixed-order result are purely nonsingular terms (i.e. terms that do vanish in the limit $m_b \to 0$). Therefore, matching the two results becomes completely straightforward. All that is required is to add to the purely resummed result the remaining nonsingular fixed-order terms. The matched cross section is given by

$$\sigma^{\text{FO+Resum}} = \sigma^{\text{Resum}} + \big(\sigma^{\text{FO}} - \sigma^{\text{Resum}}\big|_{\mu_b=\mu_F}\big). \tag{IV.2.13}$$

By construction, it satisfies $\sigma^{\text{FO+Resum}} \to \sigma^{\text{FO}}$ in the limit $\mu_b \to \mu_F$, as required for a consistently matched prediction. The terms in brackets are precisely the nonsingular terms. For the practical implementation, they can be conveniently absorbed into modified gluon and light-quark coefficient functions, $\bar{C}_{ij}(m_H, m_b, \mu_F)$, which now carry an explicit dependence on m_b, convolved with 5F PDFs.[IV.13] The final matched result is then written as

$$\begin{aligned}
\sigma^{\text{FO+Resum}} = &\sum_{i,j=b,\bar{b}} C_{ij}(m_H,\mu_F) \otimes f_i^{[5]}(m_b,\mu_F) \otimes f_j^{[5]}(m_b,\mu_F) \\
&+ \sum_{\substack{i=b,\bar{b}\\ j=g,q,\bar{q}}} \Big[C_{ij}(m_H,\mu_F) \otimes f_i^{[5]}(m_b,\mu_F) \otimes f_j^{[5]}(m_b,\mu_F) + (i \leftrightarrow j)\Big] \\
&+ \sum_{i,j=g,q,\bar{q}} \bar{C}_{ij}(m_H,m_b,\mu_F) \otimes f_i^{[5]}(m_b,\mu_F) \otimes f_j^{[5]}(m_b,\mu_F),
\end{aligned} \tag{IV.2.14}$$

where $f_{i,b}^{[5]}$ are perturbative objects, and an expansion of C_{ij} and $\bar{C}_{ij}$ against $f_{i,b}^{[5]}$ as discussed above is implicit. It was explicitly checked that for values of $m_b/m_H \lesssim 0.1$ a strict expansion of the square brackets in Eq. (IV.2.12) against the expansion of C_{ij} gives practically the same numerical results as expanding C_{ij} but keeping the square brackets unexpanded, as in the first line of Eq. (IV.2.12), under the condition that one counts $f_b^{[5]} \sim \alpha_s$. This allows for a significant simplification in the implementation of the matched cross section, as it avoids having to split up the b-quark PDF into its pieces but allows working with a common b-quark PDF.[IV.14]

[IV.13] Moving the nonsingular corrections underneath the 5F resummation corresponds to including some resummation effects for power-suppressed terms, which is beyond the order one is working in either the 4FS or 5FS.

[IV.14] This applies to all Higgs boson mass values considered in this report except for $m_H = 25$ GeV, for which the strict expansion would be necessary.

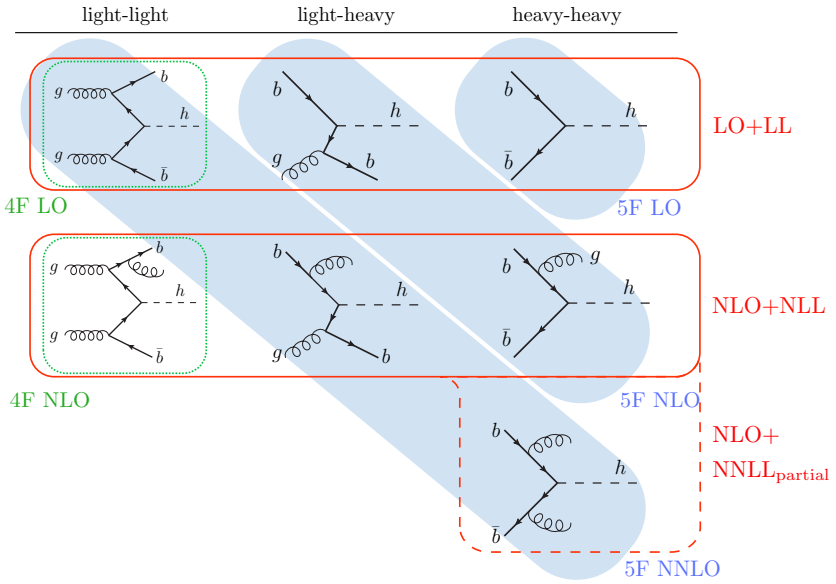

Figure 262: Pictorial representation with sample diagrams appearing in the computation of the bbH cross section, grouped according to the different perturbative countings adopted in the 4FS (green), 5FS (blue areas) and the matched resummed result of Ref. [1154] (red).

With this simplification, expanding the all-orders result for the matched cross section in powers of $\alpha_s = \alpha_s(\mu_F)$, the following perturbative expansion is obtained

$$\begin{aligned}
\text{LO+LL} \quad \sigma = \quad & \alpha_s^2 \bar{C}_{ij}^{(2)} \otimes f_i^{[5]} \otimes f_j^{[5]} + \alpha_s 4 C_{bg}^{(1)} \otimes f_b^{[5]} \otimes f_g^{[5]} + \quad 2 C_{b\bar{b}}^{(0)} \otimes f_b^{[5]} \otimes f_b^{[5]} \\
\text{NLO+NLL} \quad & + \alpha_s^3 \bar{C}_{ij}^{(3)} \otimes f_i^{[5]} \otimes f_j^{[5]} + \alpha_s^2 4 C_{bk}^{(2)} \otimes f_b^{[5]} \otimes f_k^{[5]} + \alpha_s 2 C_{b\bar{b}}^{(1)} \otimes f_b^{[5]} \otimes f_b^{[5]} \\
\text{NNLO+NNLL} \quad & + \alpha_s^4 \bar{C}_{ij}^{(4)} \otimes f_i^{[5]} \otimes f_j^{[5]} + \alpha_s^3 4 C_{bk}^{(3)} \otimes f_b^{[5]} \otimes f_k^{[5]} + \alpha_s^2 (2 C_{b\bar{b}}^{(2)} + 2 C_{bb}^{(2)}) \otimes f_b^{[5]} \otimes f_b^{[5]} \\
& + \dots . \qquad \text{(IV.2.15)}
\end{aligned}$$

The factors of two and four account for the exchange of partons among the two protons and (to a first approximation) the equality $f_b^{[5]} = f_{\bar{b}}^{[5]}$. A sum over *light* quark and gluons is implicitly assumed when latin indices $i, j, k, ...$ are repeated. The superscripts on the coefficient functions indicate the order in α_s to which these are computed. In Figure 262 the counting of Eq. (IV.2.15) is pictorially summarized and compared to the 4FS and 5FS counting.

At this point, it is important to point out that the construction of the coefficient functions $\bar{C}_{ij}$ is formally the same as the corresponding construction in the the FONLL approach [1155] (and to a hypothetical S-ACOT construction). There are however, two main differences between these approaches. Firstly, the matched NLO+NLL result of Refs. [1154, 1166] counts the effective b-quark PDF as an $O(\alpha_s)$ perturbative object, which follows from including all perturbative ingredients in the perturbative counting, as explained above. Secondly, the results of Refs. [1154, 1166] and those provided here, explicitly include an estimate of the resummation uncertainty associated with the 5F resummation by varying the (in principle arbitrary) matching scale μ_b.

At present, all coefficient functions in Eq. (IV.2.15) except $\bar{C}_{ij}^{(4)}$ and $C_{bk}^{(3)}$ are known [565, 1085, 1086, 1167]. Therefore, the highest possible accuracy that can be currently achieved is NLO+NLL and it is not yet possible to produce full NNLO+NNLL results, which would require knowledge of the full NNLO 4FS result. However, the two-loop coefficients $C_{b\bar{b}}^{(2)}$ and $C_{bb}^{(2)}$ are known [565], and can in principle be added to the NLO+NLL result. In our counting this provides a partial NNLL result, denoted as

NLO+NNLL$_{\rm partial}$ in Figure 262.[IV.15] Including these higher-order terms at low/intermediate Higgs boson masses would include part of the resummation of some NNLL logarithms that are not present in the NLO fixed-order result (i.e. in the matched result the resummation is no longer consistent with the fixed order). This could potentially bias the result and/or lead to underestimating the perturbative uncertainty. For this reason, we do not recommend this as the default result. Nevertheless, we also provide it here, as it gives a good indication of the size of the next-order correction, thus providing a useful additional cross check on the estimated perturbative uncertainties of the NLO+NLL result, which indeed fully cover the NLO+NNLL$_{\rm partial}$ result. In the limit of very large m_H, including these terms may be beneficial, once the size of the resummed logarithms grows, $\alpha_s \log(\mu_F^2/\mu_b^2) \sim 1$, and the original strict 5FS counting applies.

Regarding the nonsingular terms, at LO there is only a contribution proportional to y_b^2. At NLO there are terms proportional to y_b^2 as well as terms $\sim y_b y_t$ due to the interference of the Born-level diagrams diagrams with diagrams involving a top-quark loop, see eq. (IV.2.3). These interference terms can lead to a noticeable correction. For the scale setup chosen, the $y_b y_t$ terms reduce the cross section for $m_H \lesssim 300$ GeV and increase it for $m_H \gtrsim 300$ GeV. They were not yet included in Ref. [1154] but are straightforward to add as they correspond to purely nonsingular corrections, and their effect was studied in Ref. [1166]. Here, we provide the results both with and without the interference terms included.

Next, we turn to the discussion of how to estimate the theoretical uncertainties. The approach taken in Ref. [1154], and summarized in Sect. IV.2.2.a is that perturbative uncertainties are most realistically estimated by varying both the hard scale μ_F as well as the scale μ_b that resides in the PDFs. In this report we further explore the dependence on the renormalization scale μ_R at which α_s is computed, and on the renormalization scale μ_Y at which the Yukawa coupling is evaluated. For the parametric uncertainty on the bottom mass, the prescription of Sect. IV.2.2.a, Eq. (IV.2.7), is used. It is important of course that we consistently change the value of the pole mass in the coefficient functions $\bar{C}_{ij}$ when varying its value in the PDFs.

The Yukawa coupling is computed according to the prescription of Sect. I.1, namely evolving from $\overline{m}_b(\overline{m}_b) = 4.18$ GeV to the central Yukawa scale μ_Y with 4-loop evolution, while μ_Y variations are computed using 2-loop evolution. The strong coupling α_s in the coefficient functions is evaluated at the renormalization scale μ_R. While both μ_R and μ_Y are renormalization scales, they do not necessarily need to be the same; it is always possible to evolve α_s and the Yukawa coupling to different scales using their own renormalization group evolution, compensating in the partonic coefficients with the appropriate fixed-order logarithms. We have found that varying μ_R and μ_Y together gives the maximal uncertainty and we therefore set $\mu_Y = \mu_R$ in all our results and variations.

The factorization scale μ_F is taken to be $\mu_F = (m_H + 2m_b)/4$, and varied by a factor of two up and down. The choice is motivated by the well-known fact that in bbH such a small factorization scale leads to improved perturbative convergence. This choice is also consistent with the scale adopted in the 4FS and 5FS computations, but we emphasize that the matched NLO+NLL result is significantly less sensitive to the central value of μ_F [1154]. The value of m_b in the definition of μ_F is taken to be the central pole mass value $m_b = 4.58$ GeV, and is kept fixed under m_b variations. While varying μ_F, the threshold scale μ_b is varied by the same factor of two up and down. As discussed in Ref. [1154], this enables us to interpret the μ_F variation as an overall fixed-order uncertainty. In addition, we estimate a resummation uncertainty by separately varying μ_b by a factor of two while keeping all other scales and m_b fixed.

In Ref. [1154], the central value for μ_R ($= \mu_Y$) was taken to be the same as μ_F, and all scales were varied together. This choice leads to an excellent perturbative convergence. Despite this, here an even more conservative approach is taken whereby μ_R and μ_F are varied independently. In addition, we use a larger central value for the renormalization scale, namely $\mu_R = m_H/2$. This is motivated by the fact

[IV.15] In Ref. [1154], this result was called NLO+NLL+$C^{(2)}_{b\bar{b}}$.

that the primary reason for a small scale $\sim m_H/4$ is related to the collinear factorization (μ_F) and not the renormalization (μ_R). On the other hand, choosing $\mu_R = m_H$ produces somewhat artificial leftover $\ln 4$ terms in the cross section, so $\mu_R = m_H/2$ seems a sensible compromise and also lies between the 4FS and the 5FS choices for μ_R. This choice has the additional advantage that the NLO+NNLL$_{\text{partial}}$ turns out to be a tiny correction over the NLO+NLL.

For each of the fixed-order (envelope of individual μ_F and μ_R variations omitting cases where the product of the variations from their respective central values exceeds a factor of two), resummation (μ_b), and parametric m_b uncertainties we take the maximum deviation from the central result as the symmetrized uncertainty. The total perturbative uncertainty is obtained by adding the $\mu_F + \mu_R$ and the μ_b uncertainties in quadrature. We have checked that this includes the envelope of the individual variations of the three scales. The total parametric uncertainty emerges from the quadratic sum of the m_b and the asymmetric PDF+α_s (computed according to the PDF4LHC15 prescription) uncertainties. The full uncertainty band is then obtained by adding the perturbative and parametric uncertainties linearly. For a detailed discussion of the different uncertainties in the cross section see Ref. [1166].

IV.2.2.d FONLL matching

The FONLL method is based on the observation that the four- and the five-flavour scheme perturbative series are made up, although formally at different orders, by the same type of terms with the difference that perturbative coefficients in the four-flavour expansion exhibit full mass dependence. The idea is therefore to replace in the five-flavour scheme expansion those terms, that are known in the four-flavour scheme, with their counterpart calculated in the four-flavour scheme. This procedure can thus be seen as including fixed-order (of the order of the four-flavour scheme calculation) mass effects to a resummed calculation (of the order of the five-flavour scheme).

In the case of Higgs boson production in bottom-quark fusion the five-flavour scheme total cross section is known up to NNLL, $\mathcal{O}(\alpha_S^2)$, while the four-flavour one is known up to NLO, $\mathcal{O}(\alpha_s^3)$. The FONLL matching can thus be performed in two different ways: one could either match the NNLL five-flavour with the LO four-flavour which we refer to as FONLL-A [1155], or the NNLL five-flavour to the NLO four-flavour scheme calculation, which we will refer to as FONLL-B [1168].

In order to perform the matching procedure in either of the mentioned schemes, we need to have comparable perturbative series. This means in particular that both the four- and the five-flavour scheme have to be expressed in terms of the same scheme couplings and PDFs. To achieve this, one needs to compute matching conditions in both schemes. In the four-flavour scheme, one has to express the value of $\alpha_S(\mu_R^2)$ calculated with four active flavour to that evolved with five active flavour up to the desired order. The same must be done for the PDFs evolution kernel as well. This can be done by using the following relations

$$\alpha_S^{4F}(\mu^2) = \alpha_S(\mu^2)\left[1 + \sum_{p=1}^{\infty} c_i\left(\log\frac{\mu^2}{m_b^2}\right)\alpha_S^p(\mu^2)\right]; \tag{IV.2.16}$$

$$f_i^{4F}(x,\mu^2) = \sum_{j=q,\bar{q},g}\int_x^1 \frac{\mathrm{d}y}{y}\left[\delta_{ij}\,\delta(1-y) + \sum_{p=1}^{\infty}\alpha_S^p(\mu^2)\,K_{ij}^{(p)}(y,\mu^2)\right] f_j\left(\frac{x}{y},\mu^2\right). \tag{IV.2.17}$$

Quantities were the flavour number scheme is not explicit are intended as to be computed in the five-flavour scheme. In order to perform the FONLL-A type matching we don't need any of these formulae, however we need the $\mathcal{O}(\alpha_S)$ expression for both in the FONLL-B case.

Likewise, in the five-flavour scheme one also has to compute some matching conditions. In particular, to make the two scheme comparable, one needs to re-express the bottom-quark PDF in terms of the light-quarks and gluon PDFs. In both cases only the terms of the needed order have to be kept into

account. Thus we need respectively the $\mathcal{O}(\alpha_S)$ and $\mathcal{O}(\alpha_S^2)$ of:

$$f_b(x,\mu^2) = \sum_{j=q,\bar{q},g} \int_x^1 \frac{\mathrm{d}y}{y} \left[\sum_{p=1}^{\infty} \alpha_S^p(\mu^2) \mathcal{A}_{bj}^{(p)}(y,\mu^2) f_j\left(\frac{x}{y},\mu^2\right) \right] \tag{IV.2.18}$$

for the FONLL-A and -B matching.

We need then to subtract from the five-flavour scheme those terms which are computed with exact mass dependence in the four-flavour scheme. The terms that we need for this purpose are those terms which are either logarithmic or constant in m_b, *i.e* all non-vanishing terms in the four-flavour scheme when we take the limit of $m_b \to 0$. Clearly those terms must also be present in the five-flavour scheme and can be computed from the five-flavour scheme as well. Critically, we choose this latter method to compute the massless limit up to $\mathcal{O}(\alpha_S^2)$ and $\mathcal{O}(\alpha_S^3)$ respectively for the FONLL-A and -B scheme. This enables us to perform the subtraction in the five-flavour scheme of those terms that are known, in the four-flavour scheme, with full mass dependence up to the desired order in α_S.

To obtain numerical results we use the bbh@nnlo code for both the five-flavour scheme partonic cross-section and those terms needed to compute the massless limit of the four-flavour scheme. The NLO four-flavour scheme is obtained with a modified version of the SHERPA code such as to accommodate for the described change of scheme, and NLO matrix elements are obtained from the OpenLoops matrix element generator. As we stated, the four-flavour scheme has to be computed with a five-flavour scheme α_S, bottom Yukawa coupling y_b and PDFs (plus all the corrections needed to express four-flavour scheme quantities in the five-flavour scheme). The running coupling constant, as well as parton distribution functions, are obtain from the NNLO, five-flavour, PDF4LHC combined PDF set through the LHAPDF interface. The running of the bottom Yukawa coupling is computed at two-loop in the five-flavour scheme with $m_b(m_b) = 4.18$ GeV and a pole mass $m_b = 4.58$ GeV. The four-flavour scheme calculation includes both y_b^2 proportional terms and $y_b y_t$ ones. Scale variations bands are obtained by varying μ_R and μ_F separately in the range $K_\mu \in [1/2, 2]$ excluding the two extrema $(\mu_R = 1/2, \mu_F = 2)$ and $(\mu_R = 2, \mu_F = 1/2)$. The central scale is chosen to be $\mu = (m_H + 2\,m_b)/4$.

IV.2.2.e Comparison of different matching approaches

First we compare the results of the 4FS, 5FS and the Santander matching in Figure 263 including the total uncertainty bands. The blue band displays the 5FS, the red one the 4FS and the green band the Santander-matched result. For small Higgs boson masses the 4FS and 5FS overlap considerably and the Santander-matched result overlaps with both of them by construction. Only for small Higgs boson masses below 50 GeV the 5FS develops an ill-defined uncertainty due to the fact that the central scale choices determined in terms of the Higgs boson mass become too small to give sense to a sophisticated definition of the bottom PDFs. For the Santander-matched result this is also reflected by a negative value of the weight w of Eq. IV.2.9. Thus for Higgs boson masses below 50 GeV the Santander-matched result has been defined as the 4FS one. This procedure guarantees that for small Higgs boson masses the 4FS is singled out for the matched result, while for large Higgs boson masses the Santander matching follows the 5FS. From the lower plot of Figure 263 one can infer that the deviations between all central predictions are less than about 30% for larger Higgs boson masses.

In Figure 264 we compare the Santander matching with the two consistent matching procedures FONLL-B and NLO+NNLL$_{\mathrm{partial}}$+ybyt as discussed in the previous sections. The green band represents the uncertainty band of the Santander matching, the blue one the FONLL-B matching and the red band the NLO+NNLL$_{\mathrm{partial}}$+ybyt approach. It is clearly visible that all three approaches overlap over the full Higgs boson mass range which means that also the systematic resummation approach tends to favor the 4FS results for small Higgs boson masses and the 5FS one for large Higgs boson masses. It should be noted that for larger Higgs boson masses both approaches, FONLL-B and NLO+NNLL$_{\mathrm{partial}}$+ybyt, show that resummation effects are indeed important, while finite bottom mass effects on top of resummation

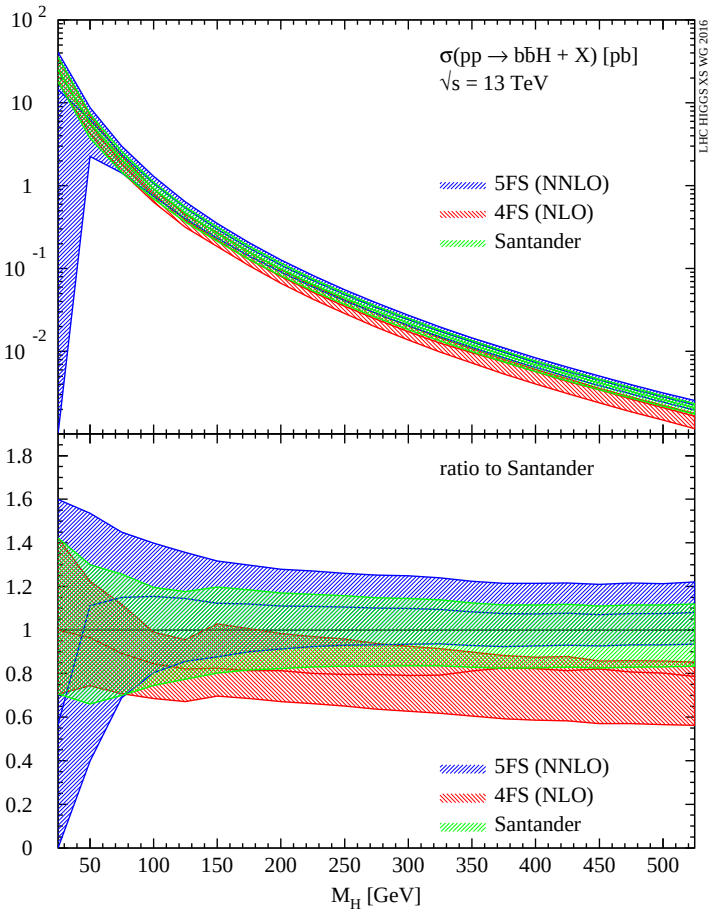

Figure 263: Comparison of the inclusive $b\bar{b}\phi$ production cross sections in the 4FS and 5FS with the Santander-matched result. The lower plot displays the ratios to the central Santander-matched prediction.

effects turn out to be tiny. The two systematic matching procedure provide comparable results provided the renormalization and factorization scales are set to the same values. The residual differences in the plot are due to the different choice of renormalization scale ($M_H/2$ in NLO+NNLL$_{\text{partial}}$ and $(M_H + 2m_b)/4$ in FONLL-B) and to a different way of computing the error associated to the final prediction. In particular, in the FONLL-B matching procedure the threshold μ_b is kept fixed to m_b, while it is varied independently of m_b in the NLO+NNLL$_{\text{partial}}$ approach and the scale variation is symmetrized in the latter, while it is kept asymmetric in the former. The matched results instead are systematically away from the Santander matched results. The matched results are about 15% higher than the Santander-matched ones for all values of M_H, although mostly within its uncertainty band. For large Higgs boson masses the FONLL-B and NLO+NNLL$_{\text{partial}}$+ybyt results tend towards the 5FS as expected. The uncertainty bands of the matched calculations increase for small Higgs boson masses due to the problems to define reasonable bottom PDFs for small scales.

In total the consistent NLO+NNLL$_{\text{partial}}$+ybyt and FONLL-B matched results follow the expected pattern, i.e. a clear tendency towards the 5FS for larger Higgs boson masses. For a unique procedure to provide a single prediction for the inclusive $b\bar{b}\phi$ cross section we recommend to use the envelope of both predictions for the uncertainty band and the central values inside as the central prediction. The consistently matched results should be used when available and can be seen as an important cross-check of the empirical Santander central values in case a matched result is not available.

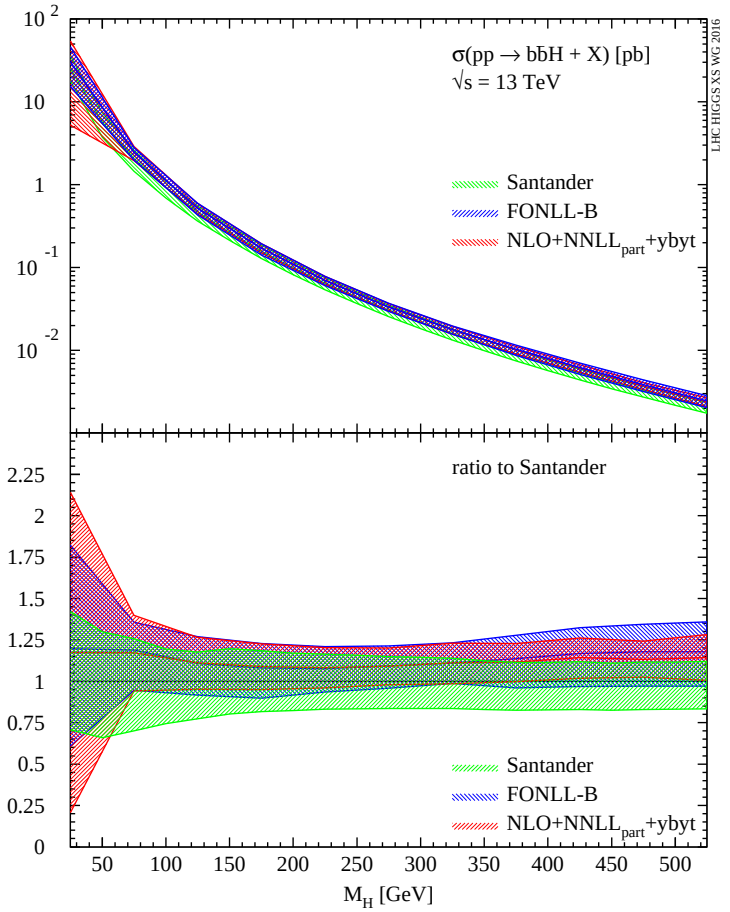

Figure 264: Comparison of the inclusive $b\bar{b}\phi$ production cross sections for the different matching procedures, i.e. Santander matching, FONLL-B and NLO+NNLL$_{\rm partial}$+ybyt. The lower plot displays the ratios to the central Santander-matched prediction.

IV.2.3 Differential Monte-Carlo predictions

In this section, we present Monte-Carlo predictions at the 13 TeV LHC for both total rates with and without cuts, and several differential distributions, reconstructed from the final-state momenta in $b\bar{b}\phi$ production, and compare them among the different generators under consideration.

Before introducing the different Monte Carlo generators under consideration, let us summarize the available computations for differential $b\bar{b}\phi$-production in the literature. The first distributions in the 4FS cross section have been presented (to a very limited extent though) through NLO QCD in Refs. [1085, 1086]. A more comprehensive study of differential quantities in the 4FS and the first matching of the NLO cross section to the PS has later been performed in Ref. [431] within the MC@NLO approach [340]. Recently, the corresponding computation in the POWHEG framework [342, 343] was done in Ref. [1169]. The number of differential computations in the 5FS is considerably larger. At parton-level NLO corrections are known for the $H + b$ and H+jet processes [1170, 1171], as well as NNLO corrections for the jet-vetoed rate [1172] and the fully-differential cross section [1167]. The transverse momentum distribution of the Higgs boson was studied analytically at NNLO [1173] and including resummation at NLO+NLL [1174] and NNLO+NNLL [1175]. NLO+PS predictions in the 5FS were computed in Ref. [431].

IV.2.3.a $b\bar{b}\phi$ in MADGRAPH5_AMC@NLO

The first NLO simulation matched to parton showers of the $b\bar{b}\phi$ signal in the 4FS has been performed in Ref. [431]. This computation has been treated as a special case in the automated framework of MADGRAPH5_AMC@NLO due to the necessity of a $\overline{\text{MS}}$ renormalization of the bottom-quark Yukawa coupling, which can not be handled by the public version so far. Therefore, dedicated process folders have been provided[IV.16], which were also used for all NLO+PS simulations with MADGRAPH5_AMC@NLO throughout this chapter.

MADGRAPH5_AMC@NLO allows for the computation of LO and NLO cross sections both with and without matching to parton showers. NLO results not matched to parton showers are obtained by adopting the FKS method [113, 357] automated in the module MADFKS [358], and the OPP integral-reduction procedure [359] for the computation of the one-loop matrix elements (automated in the module MADLOOP [348], which makes use of CUTTOOLS [353] and of an in-house implementation of the optimizations proposed in Ref. [247] (OPENLOOPS)). Matching with parton showers is achieved by means of the MC@NLO formalism [340]. MADGRAPH5_AMC@NLO is maximally automated.

The default treatment of Yukawa couplings in the MADGRAPH5_AMC@NLO code, however, is that of an on-shell scheme renormalization, which is not optimal in the case of $b\bar{b}\phi$ production, where the $\overline{\text{MS}}$ scheme has to be preferred [1133]. The advantage of an $\overline{\text{MS}}$ renormalized bottom Yukawa $\overline{y}_b(\mu_\text{R})$ is the resummation of potentially large logarithms of m_H/m_b, when $\mu_\text{R} \sim m_H$ is chosen. An additional complication emerges from the fact that y_b enters at different powers in the $\sigma_{y_b^2}$ and $\sigma_{y_b y_t}$ terms introduced in eq. (IV.2.3). At the moment the implementation does not warrant a completely general and automated solution. However, since such complication is recurrent in the mixed-coupling expansion as for EW corrections, we have included a general $\overline{y}_b(\mu_\text{R})$ implementation applicable not only to $b\bar{b}\phi$ production in this context, which will be made available in the future. This will allow any user to generate the $b\bar{b}\phi$ process in the general MADGRAPH5_AMC@NLO interface and replace the current necessity of using the dedicated process folders.

The inputs are coordinated to be the same as the ones for the POWHEG BOX described in the upcoming section to warrant a consistent comparison of the results, starting from a reasonable agreement in the normalization, i.e., the total rate. We set the renormalization and factorization scales to the sum of the transverse masses of all Born-level particles, divided by a factor of four, which in the soft/collinear limit is in keeping with the scales used for the total 4FS rate (see Sect. IV.2.2.b):

$$\mu_\text{R} = \mu_\text{F} = \mu_0 = \frac{H_T^\text{Born}}{4} \equiv \frac{1}{4} \sum_{i \in \{b,\bar{b},\phi\}} \sqrt{m_i^2 + p_T^2(i)}\,. \tag{IV.2.19}$$

The respective scale uncertainties are estimated by the independent variation $0.5\,\mu_0 \leq \mu_\text{R}, \mu_\text{F} \leq 2\,\mu_0$ with the constraint $0.5 \leq \mu_\text{R}/\mu_\text{F} \leq 2$.

The additional factor of $1/4$ in the scale settings of the 4FS reflects the fact that the optimal values for the hard scales that enter the $b\bar{b}\phi$ calculation appear to be significantly smaller than the hardness of the process would suggest. As pointed out in Ref. [431] another hard scale is affected by this choice, when considering simulations matched to parton showers, namely the shower scale Q_sh, which loosely speaking can be identified with the largest hardness accessible to the shower. It is the MC that determines, event-by-event, the value of Q_sh, by choosing it so as to maximize the kinematic population of the phase-space due to shower radiation, without overstretching the approximations upon which the MC is based.

In MADGRAPH5_AMC@NLO one is given the possibility of setting the upper value[IV.17] of Q_sh; this value is actually picked up at random in a user-defined range:

$$\alpha f_1 \sqrt{s_0} \leq Q_\text{sh} \leq \alpha f_2 \sqrt{s_0}\,, \tag{IV.2.20}$$

[IV.16] See https://cp3.irmp.ucl.ac.be/projects/madgraph/wiki/bbH.

[IV.17] If the MC-determined Q_sh value is lower than that set by the user, the latter is ignored. Also bear in mind that the physical meaning of Q_sh depends on the specific MC employed – see Ref. [54].

so as to avoid possible numerical inaccuracies due to the presence of sharp thresholds.[IV.18] s_0 is the Born-level partonic centre of mass energy squared, and α, f_1, and f_2 are numerical constants whose default inputs are 1, 0.1, and 1, respectively. The way, in which $Q_{\rm sh}$ is generated, results in a distribution peaked at values slightly larger than $\alpha(f_1+f_2)\sqrt{\langle s_0\rangle}/2$. As argued in Ref. [431] the typical shower scales in the default setup are rather large as compared to the factorization scale, even though their origin is quite similar being both based on the soft/collinear approximation. By setting $\alpha = 1/4$ the two scales become significantly closer. Ref. [431] further studied the distribution of the Born-level "system" ($p_T^{\rm syst}$), which showed a strongly improved matching behaviour of the NLO+PS curve with the NLO curve in the high-$p_T^{\rm syst}$ tail for smaller values of α. In conclusion a reduced shower scale by setting $\alpha = 1/4$ has to be preferred over the default choice in MADGRAPH5_AMC@NLO and will be the default choice fo all numerical results produced with MADGRAPH5_AMC@NLO throughout this section.

Additionally, we assign a theoretical uncertainty to the shower scale choice by varying $\alpha \in [1/(4\sqrt{2}), \sqrt{2}/4]$, which is added linearly to the $\mu_{\rm R}$-$\mu_{\rm F}$ scale uncertainties.

IV.2.3.b $b\bar{b}\phi$ in the POWHEG BOX

In Ref. [1169] an implementation of the NLO-QCD calculation of Ref. [1086] in the framework of the POWHEG BOX [81, 342, 343] has been presented. While the virtual corrections to the $pp \to b\bar{b}\phi$ process have been extracted from the fixed-order calculation of Ref. [1086], the tree-level amplitudes were generated with a tool based on `MadGraph 4` [560, 1176]. The process-independent ingredients of the implementation are provided internally by the POWHEG BOX. All building blocks have been implemented in the 4FS, i.e. no contributions from incoming bottom quarks have been taken into account, and the bottom-quark was always assumed to be massive.

In the virtual corrections, not only diagrams including a $b\bar{b}\phi$ coupling emerge, but also loop diagrams with a $t\bar{t}\phi$ coupling. Both contributions are fully taken into account in the implementation. However, a switch is provided that allows the user to deactivate the contributions involving a $t\bar{t}\phi$ coupling.

By default, the renormalization of the bottom-quark Yukawa coupling is defined in the $\overline{\rm MS}$ renormalization scheme [1085, 1086, 1149]. In addition, an option for defining the bottom-quark Yukawa coupling in the on-shell renormalization scheme is provided.

In its default version, the POWHEG BOX code for $pp \to b\bar{b}\phi$ provides three different options for the renormalization and factorization scales: a fixed scale, $\mu_0 = (m_H + 2m_b)/2$, as used for total rates, a dynamical scale defined via the transverse masses $m_T(f) = (m_f^2 + p_{T,f}^2)^{1/2}$ of the born-level final state particles f in an event, $\mu_0 = m_T(H) + m_T(b) + m_T(\bar{b})$, or the geometrical mean of the transverse masses, $\mu_0 = \left(m_T(H)\, m_T(b)\, m_T(\bar{b})\right)^{1/3}$; the latter two being particularly relevant as far as tails of kinematical distributions are concerned. Scaling factors, ξ_R and ξ_F, can be set individually for the factorization and renormalization scales, μ_R and μ_F, such that the relevant scales are given by $\mu_R = \xi_R\mu_0$ and $\mu_F = \xi_F\mu_0$. Throughout this section we use the second scale setting in the list above with $\xi_R = \xi_F = 1/4$, in keeping with the settings quoted for MADGRAPH5_AMC@NLO in the previous section.

In order to assess the intrinsic uncertainties associated with the matching of the NLO-QCD calculation with parton shower programs, the POWHEG BOX offers the possibility to vary the so-called `hdamp` parameter, defined as [81]

$$D_h = \frac{h^2}{h^2 + p_T^2}\,. \tag{IV.2.21}$$

Here, p_T denotes the transverse momentum of the hardest parton in the real emission contributions, and h is a parameter that can be chosen by the user. If no explicit choice is made, the `hdamp` parameter

[IV.18] More details can be found in Sect. 2.4.4 of Ref. [54] (see in particular Eq. (2.113) and the related discussion).

is set to one. In general, this parameter determines the separation of the cross section in a part at low transverse momentum of the extra emission, generated mainly with the Sudakov form factor, and a part at high transverse momentum, generated mainly with the real-emission diagrams only. The uncertainty of observables simulated at NLO+PS level associated with a variation of the h parameter provides an estimate of the intrinsic matching uncertainty of the POWHEG BOX. We choose $h = 1/4\,(m_H + 2\,m_b)$, consistent with the shower scale setting proposed in Ref. [431] and used in MADGRAPH5_AMC@NLO throughout.

Residual uncertainties are estimated by performing a seven-point variation of the renormalization and factorization scales by a factor of two with respect to their central values. We then combine these uncertainties linearly with the variation of D_h in the same range.

IV.2.3.c $b\bar{b}\phi$ in SHERPA

In this section, the setup of the SHERPA event generation framework [229] is presented. Two classes of results are considered for SHERPA:

- 4FS using the MC@NLO matching:
  One set of results is in the 4FS, and based on the MC@NLO technique [340], as implemented in SHERPA [345]. At tree-level the simulation thus starts from processes such as $gg \to b\bar{b}H$ and $q\bar{q} \to b\bar{b}H$, where no specific cuts are applied on the b quarks. Their finite mass regulates collinear divergences that would appear in the massless case. In most cases, therefore, a b jet actually originates from the parton shower evolution and hadronization of a b quark. At the NLO, our computation involves contributions proportional to y_b^2 and $y_b y_t$, see Eq. (IV.2.3).
- 5FS using the MEPS@NLO multi-jet merging:
  Alternatively, we employ the 5FS with massless b quarks. In order to account for bins with zero and one b jets, multi-jet merging is being employed. In SHERPA, the well-established mechanism for combining into one inclusive sample towers of matrix elements with increasing jet multiplicity at tree level [242] has recently been extended to next-to leading order matrix elements, in a technique dubbed MEPS@NLO [241]. This is the technique chosen here. Merging rests on a jet criterion, applied to the matrix elements. As a result, jets are being produced by the fixed-order matrix elements and further evolved by the parton shower. As a consequence, the jet criterion separating the two regimes is typically chosen such that the jets produced by the matrix elements are softer than the jets entering the analysis. This is realized here by a cut-off of $\mu_{\text{jet}} = 20$ GeV. In the MEPS@NLO simulation matrix elements for $b\bar{b}\phi$ production in the 5FS up to 2 jets at NLO accuracy have been included, i.e. final states for ϕ, $\phi + j$, and $\phi + jj$ with ϕ emitted from a massless bottom-quark line are calculated using the MC@NLO technique, while $\phi + jjj$ matrix elements are accounted for only at the LO, where the jets can be light jets or b jets. For the former, it is of course always possible that a light jet originating from, e.g., a gluon, can turn into a b jet through a $g \to b\bar{b}$ splitting during the parton shower. We note that only contributions proportional to y_b^2 do not vanish in the 5FS computation, see Eq. (IV.2.4).

In SHERPA, tree-level cross sections are provided by two matrix element generators, AMEGIC++ [246] and COMIX [984], which also implement the automated infrared subtraction [951] through the Catani-Seymour scheme [249, 354]. For parton showering, the implementation of [355] is employed with the difference that for $g \to b\bar{b}$ splitting the invariant mass instead of the transverse momentum are being used as scale. One-loop matrix elements are instead obtained from OPENLOOPS [247, 365].

Our central scales, both of perturbative origin (μ_R, μ_F) and relevant to the shower (μ_Q), are computed according to the so-called reverse clustering algorithm; for further details we refer the reader to Ref. [241]. The residual uncertainties are computed through variations by a factor of two from the central scales, where we combine the seven-point variation of the renormalization and factorization scales linearly with the uncertainties related to μ_Q. We adopt these scale settings and variations for both our 4FS and 5FS setups, introduced above.

IV.2.3.d Comparison of the Monte-Carlo tools

We compare predictions of the different Monte Carlo generators for the simulation of a $b\bar{b}\phi$ signal introduced in the preceding section in four- and five-flavour schemes which are at least NLO accurate and matched to PS. Higgs boson decays are not considered. In the MADGRAPH5_AMC@NLO and POWHEG BOX computations we employ PYTHIA8 [318] for the parton-shower matching. Throughout this section we consider Higgs boson production in association with bottom quarks for a SM Higgs boson with mass $M_\phi = 125\,\text{GeV}$ at the 13 TeV LHC. We use a top-quark pole mass of $m_t = 172.5\,\text{GeV}$ relevant to the $y_b y_t$ contribution, see Eq. (IV.2.3). The internal bottom-quark mass is set to its pole value of $m_b = 4.92\,\text{GeV}$, while the bottom-quark mass in the Yukawa is renormalized in the $\overline{\text{MS}}$ scheme and set to $m_b(\mu_R)$. The central value $m_b(\mu_R \equiv \mu_0)$ is evaluated with $n_f = 4$ ($n_f = 5$) four-loop running from $m_b(m_b) = 4.18\,\text{GeV}$ in the 4FS (5FS); scale variations are done from that central value with two-loop accuracy (which is consistent with the NLO order of the computations). Finally, we use the PDF4LHC15 sets of parton distribution functions in its four and five flavour versions where applicable.

In Table 122 and Table 123 we report predictions of the various tools (MADGRAPH5_AMC@NLO, POWHEG BOX, SHERPA4FS, SHERPA5FS) for total rates with requirements on the final-state b-jets and jets, respectively. In Table 122 we also give the total inclusive cross section. The three 4FS predictions for the inclusive rate are in rather good agreement at the 1-2% level, which is roughly of the order of the numerical accuracy. Also the uncertainties are similarly large, bearing in mind that the central scale for the Sherpa prediction differs from the other two 4FS results. We recall that all uncertainties quoted for the predictions of each code are given by a 7-point μ_R-μ_F variation combined linearly with the uncertainties coming from the scale related to the respective shower matching procedure of each code. The latter of course should not have any impact on the total inclusive cross section, although unexpectedly the bulk of the Sherpa 4FS uncertainties on this quantity originates from variations of the shower starting scale. This issue could not be resolved in the course of this comparison. The 5FS prediction is significantly larger than the 4FS ones and quite far beyond the quoted uncertainties owing to the positive effect due to the merging of higher multiplicities. In a full 5FS NNLO computation the cross section is usually reduced by the additional two-loop contribution, leading to a far better agreement at the level of the total inclusive cross section. In any case, the focus throughout this section is on the kinematics and distributions of the final-state particles, which is why we will rescale the 5FS result, once we consider distributions below.

For the total rates with requirements on the b jets, we define a b jets as any jet that contains a B hadron, using the anti-k_T algorithm [191] with $R = 0.4$, a minimal transverse momentum of 25 GeV and a rapidity of $|y| < 2.5$. We consider the cross section with a b-jet veto ($0j_b$), one or more b jets ($\geq 1j_b$), two or more b jets ($\geq 2j_b$), exactly one b jet ($1j_b$), and exactly two b jets ($2j_b$). To allow a comparison with the 5FS prediction we also show the respective acceptances for each code, i.e., the ratio of the prediction within cuts with respect to the total rate. The general conclusions that can be drawn from the table are the following:

- The cross section without any b-tagged object in the final state (b-jet veto) has the smallest value with the MADGRAPH5_AMC@NLO generator, being roughly 20% below POWHEG and 10% below the 4FS result of Sherpa. Given the well-known fact that $b\bar{b}\phi$ production in the 4FS comes with rather large ($\sim$20%) uncertainties even at NLO, due to the logarithmic structure, the mutual agreement among the codes is still well within scale uncertainties for the jet-vetoed rate.
- As pointed out before the 5FS is significantly larger due to the different normalization. Looking at the acceptances, however, we see that the 5FS result is just in between the 4FS predictions by POWHEG and Sherpa. Due to the very similar total rates the conclusions among the 4FS results for the acceptances are, by construction, identical to the ones for the absolute cross sections. Overall, a large fraction (of the order of 70%) of the events have no b-tagged objects in the final state.
- Since the cross section with the requirement of one or more b-jets is fully determined by the total and the jet-vetoed rate, the general conclusions are identical to the ones for the latter. The

uncertainties are, however, larger (except for POWHEG), in particular for the 5FS prediction. Let us point out again that tagging at least one of the b jets reduces the total rate by about a factor of 3–4, which is rather large. Requiring a second b jet further reduces the cross section by one order of magnitude. This is consistent with the findings of Ref. [431].

– The various predictions become increasingly different for higher b-jet multiplicities starting at two b jets. While POWHEG and Sherpa 4FS are still quite close to each other, the 5FS results and the MADGRAPH5_AMC@NLO prediction are rather different; the former predicting generally a smaller jet activity and the latter a larger one. Still, there is by and large agreement within the respective uncertainties, in particular because the 5FS uncertainties are quite sizeable.

Considering total rates with requirements on the jets in Table 123, we define a jet with the anti-k_T algorithm [191] with $R = 0.4$ and a minimal transverse momentum of 25 GeV. We consider the same types of rates as in the case of b jets for jets without any flavour tagging, and also report the corresponding acceptances in the table. The general conclusions are very similar as compared to the b-jet case and can by summarized as follows:

– The 0-jet rates in the 4FS are quite different. In particular the POWHEG prediction is rather large, which is 25% larger than Sherpa and 45% than MADGRAPH5_AMC@NLO, having only barely overlapping uncertainties with the latter. As expected, the 5FS rate is significantly larger, but the acceptance is quite similar to the one predicted in by Sherpa in the 4FS.
– The 1-jet exclusive bin agrees very well among the three 4FS codes and also the acceptances are very close among all four predictions.
– The biggest difference emerges again from higher jet multiplicities (two and more), which is largest in the case of MADGRAPH5_AMC@NLO and smallest for POWHEG. The uncertainties become quite sizeable for the high multiplicities though.

We turn now to kinematical distribution of the final-state particles both generated already at the hard-matrix element level and by the shower. The figures are all organized according to the same pattern: In the main frame the relevant predictions for the different codes are shown as cross section per bin (namely, the sum of the contents of the bins is equal to the total cross section, possibly within cuts), with MADGRAPH5_AMC@NLO+PYTHIA8 (black, solid), POWHEG+PYTHIA8 (red, dotted), SHERPA 4FS (blue, dashed with dots) and SHERPA 5FS (green, dash-dotted with open boxes). In the first inset we display the bin-by-bin ratio of all the histograms which appear in the main frame over the black solid curve, chosen as a reference. Finally, in a second inset the bands that represent the fractional scale dependence are given by taking the bin-by-bin ratios of the maximum and the minimum of a given simulation over the same central prediction that has been used as reference for the ratios of the first inset. We recall that the SHERPA 5FS normalization is generally much larger than 4FS results and that therefore its curve is rescaled to have the identical normalization as the MADGRAPH5_AMC@NLO+PYTHIA8 result, since we use it as reference also in the ratios.

In Figure 265 we consider the transverse-momentum distribution of the Higgs boson $p_T(\phi)$ with different requirements on the b jets: inclusive (upper left), no b-jets (upper right), one or more b jets (lower left) and two or more b jets (lower right). Considering the inclusive case first, it is clear that overall there is a reasonable agreement among the predictions of the different codes. This conclusion can be drawn from the nicely overlapping uncertainty bands in the second inset. The size of the uncertainties are also very similar with POWHEG having a slightly smaller scale dependence than the other results. Considering only the shape of the curves while ignoring the bands for the moment, as shown in the first inset, some differences emerge even though they are not too severe. In the low-$p_T(\phi)$ region the agreement of the two Sherpa predictions and POWHEG is quite remarkable in terms of shape, with MADGRAPH5_AMC@NLO being a bit harder than the other predictions. Around $p_T(\phi) \sim 100$ GeV the 5FS SHERPA prediction departs from the other two predictions and gets closer to the MADGRAPH5_AMC@NLO curve, while POWHEG and the 4FS SHERPA result staying rather close to each other over the whole $p_T(\phi)$ range that is displayed. One should note, however, that apart from

$p_T(\phi) \lesssim 50\,\text{GeV}$ all three 4FS results are very similar in terms of shape.

The $p_T(\phi)$ distribution with a veto on b jets in the upper right panel of Figure 265, shows a quite similar pattern as in the inclusive case, with the relative size of the differences among the curves being amplified though. Except for the first bin the POWHEG and SHERPA 4FS results are again in very good agreement, while the MADGRAPH5_AMC@NLO prediction is quite much harder and up to $\sim 40\%$ away for $p_T(\phi) \lesssim 100\,\text{GeV}$. In that region also the SHERPA 5FS prediction is very close to the POWHEG and SHERPA 4FS results, but gets significantly harder than all the 4FS predictions in the tail of the distribution. Due to the considerably increased size of the uncertainty bands, however, the predictions agree by and large within their respective uncertainties.

The picture essentially reverses when considering one or more b-tagged objects in the final state: the MADGRAPH5_AMC@NLO result now featuring the softest spectrum and SHERPA 5FS the hardest. In this case, from $p_T(\phi) \gtrsim 30\,\text{GeV}$ all four predictions (in particular the 4FS ones) are in excellent agreement in terms of both normalization and shape, with entirely overlapping uncertainty bands.

Finally, in the case with two or more observed b jets, the biggest difference comes from the fact, that the overall normalization, i.e. the rate, is larger for MADGRAPH5_AMC@NLO as already pointed out in the discussion of Table 122. Still, the predictions agree largely within the given uncertainty bands. Considering only the shape, the MADGRAPH5_AMC@NLO result is in very good agreement with the SHERPA 5FS curve and also quite similar to the one of POWHEG. The SHERPA 4FS shape in this case is a bit harder than all the other curves.

In conclusion, we find a decent agreement among the various predictions for the Higgs boson transverse-momentum spectrum with and without cuts, once the respective uncertainties are taken into consideration.

Let us move now to distributions relevant to the associated jets and b jets shown in Figure 266. We start by discussing the transverse-momentum $p_T(b_1)$ (left panel) and rapidity distributions $y(b_1)$ (right panel) of the hardest b jet in the upper panel of Figure 266. We first notice that the mutual agreement of the central predictions for $p_T(b_1)$ among all the codes is very good; none of the curves differs by more than $\sim 20\%$ from the others. Hence, we observe well overlapping uncertainty bands, which, however, turn out to be rather large in the case of MADGRAPH5_AMC@NLO and the SHERPA 5FS prediction. The agreement is even better in terms of shape. In particular the shapes of POWHEG, SHERPA 5FS and MADGRAPH5_AMC@NLO are essentially identical up to statistical fluctuations. For the rapidity $y(b_1)$ the situation is pretty much the same. In this case, however, all predictions are in perfect agreement apart from the slightly different normalization of POWHEG and SHERPA 5FS being roughly 25% lower than MADGRAPH5_AMC@NLO as already pointed out in the discussion of Table 122. Furthermore, the MADGRAPH5_AMC@NLO uncertainty is much lower in case of the $y(b_1)$ distribution and quite similar to the SHERPA 4FS band, while POWHEG still has the smallest uncertainty band.

Finally, we can draw similar conclusion for the hardest jet distributions in the lower panel of Figure 266: The residual uncertainties are rather large in case of the $p_T(j_1)$ distribution and all predictions agree well within uncertainties. The central predictions are quite quite similar in terms of their shape, where again the SHERPA 5FS and the MADGRAPH5_AMC@NLO result are essentially identical up to statistical fluctuations. For the rapidity of the hardest jet the shapes are quite similar to each other except for the one of MADGRAPH5_AMC@NLO which is slightly enhanced in the forward region. Nevertheless, we find agreement within the quoted uncertainties for the predictions of all codes.

Table 122: Predictions for the total rates (in pb) of the various Monte-Carlo tools under consideration inclusive and within cuts on the final-state b jets. For comparison, also the respective acceptances are given.

		inclusive	$0j_b$	$\geq 1j_b$	$\geq 2j_b$	$1j_b$	$2j_b$
σ[pb]	MG5_aMC	$0.369^{+19.7\%}_{-18.8\%}$	$0.243^{+22.5\%}_{-23.0\%}$	$0.126^{+32.5\%}_{-28.3\%}$	$0.0160^{+47.2\%}_{-39.8\%}$	$0.110^{+30.4\%}_{-26.7\%}$	$0.0154^{+46.0\%}_{-38.9\%}$
	POWHEG	$0.375^{+20.3\%}_{-17.9\%}$	$0.281^{+21.8\%}_{-18.6\%}$	$0.0943^{+16.6\%}_{-16.5\%}$	$0.00761^{+15.0\%}_{14.8\%}$	$0.0867^{+16.8\%}_{-16.7\%}$	$0.00754^{+14.0\%}_{-14.9\%}$
	SHERPA 4FS	$0.370^{+15.4\%}_{-26.8\%}$	$0.264^{+11.8\%}_{-26.0\%}$	$0.105^{+26.9\%}_{-28.8\%}$	$0.00955^{+74.9\%}_{-45.4\%}$	$0.0952^{+22.2\%}_{-28.6\%}$	$0.00934^{+70.9\%}_{-44.1\%}$
	SHERPA 5FS	$0.586^{+30.4\%}_{-22.7\%}$	$0.423^{+20.6\%}_{-15.7\%}$	$0.162^{+56.1\%}_{-40.7\%}$	$0.00773^{+68.9\%}_{-59.7\%}$	$0.155^{+55.5\%}_{-40.4\%}$	$0.00746^{+68.7\%}_{-59.0\%}$
acceptance	MG5_aMC	1	0.659	0.342	0.0432	0.298	0.0417
	POWHEG	1	0.749	0.251	0.0203	0.231	0.0201
	SHERPA 4FS	1	0.717	0.283	0.0258	0.258	0.0253
	SHERPA 5FS	1	0.723	0.277	0.0132	0.264	0.0127

Table 123: Predictions for the total rates (in pb) of the various Monte-Carlo tools under consideration within cuts on the final-state jets. For comparison, also the respective acceptances are given.

		$0j$	$\geq 1j$	$\geq 2j$	$1j$	$2j$
σ[pb]	MG5_aMC	$0.163^{+27.5\%}_{-25.8\%}$	$0.206^{+31.0\%}_{-30.5\%}$	$0.102^{+44.4\%}_{-41.3\%}$	$0.104^{+18.5\%}_{-19.9\%}$	$0.0613^{+37.9\%}_{-36.5\%}$
	POWHEG	$0.239^{+21.6\%}_{-19.3\%}$	$0.136^{+23.0\%}_{-20.2\%}$	$0.0347^{+41.7\%}_{-26.7\%}$	$0.101^{+17.3\%}_{-18.2\%}$	$0.0299^{+38.7\%}_{-26.2\%}$
	SHERPA 4FS	$0.192^{+11.7\%}_{-15.5\%}$	$0.177^{+32.6\%}_{-48.6\%}$	$0.0637^{+73.2\%}_{-77.2\%}$	$0.113^{+9.9\%}_{-38.3\%}$	$0.0428^{+41.6\%}_{-68.4\%}$
	SHERPA 5FS	$0.328^{+34.6\%}_{-28.6\%}$	$0.258^{+94.2\%}_{-69.4\%}$	$0.0851^{+93.2\%}_{-68.6\%}$	$0.173^{+94.7\%}_{-69.7\%}$	$0.068^{+90.0\%}_{-65.3\%}$
acceptance	MG5_aMC	0.442	0.558	0.276	0.283	0.166
	POWHEG	0.637	0.363	0.0927	0.270	0.0798
	SHERPA 4FS	0.521	0.479	0.172	0.307	0.116
	SHERPA 5FS	0.559	0.440	0.145	0.295	0.116

Due to the limited statistics of the samples under consideration, we refrain from showing results relevant to the second hardest jets or b jets. The general conclusions in these cases should be rather similar though to what has been observed so far.

IV.2.3.e Recommendations for $b\bar{b}\phi$ signal simulation

Let us conclude this section by formulating recommendations for the simulation of Higgs boson production in association with bottom quarks at the LHC Run 2. In summary of the preceding section, all the Monte-Carlo tools under consideration provide decent predictions for the simulation of a $b\bar{b}\phi$ signal, with the agreement among the different codes being reasonably well within their respective uncertainties. As pointed out in the introduction, the 5FS has the disadvantage of being less accurate in the perturbative prescription of observables exclusive in the degrees of freedom of the final-state bottom quarks, which are most relevant in the context of the $b\bar{b}\phi$ process. This is alleviated to some extent by the merging of higher multiplicities, but the prescription of the bottom kinematics does still rely, in part, on the poorly described $g \to b\bar{b}$ splittings in the backward evolution of the shower. This fact is also reflected in the very large uncertainties of the merged 5FS results, see Table 122 and the related discussion. Nevertheless, the agreement of the 5FS with the 4FS predictions is overall quite satisfactory within their respective uncertainties and the 5FS computation serves as a crucial consistency check.

In conclusion, we recommend the use of fully-differential 4FS predictions for any realistic $b\bar{b}\phi$ signal simulation in experimental searches. We further point out that in NLO calculations matched to parton showers precaution must be taken for the choice of a suitable matching scale. As pointed out in Ref. [431] such a scale must be chosen of the order of the other unphysical scales (in particular the factorization scale), which assume generally much lower values than m_ϕ, the scale naively associated with the hardness of the $b\bar{b}\phi$ process. As far as theoretical systematics are concerned, the variation of all unphysical scales must be taken into account as well as PDF+α_S uncertainties.

As pointed out before, all three 4FS Monte-Carlo codes provide valid predictions. At least two of them should be used in order to assess the systematic differences among them. The SHERPA $b\bar{b}\phi$ simulation develops a dependence of the total inclusive cross section on the shower starting scale, while its factorization- and renormalization-scale uncertainties is four time smaller than expected from from other computations of that quantity; a cross check of the SHERPA with fixed scales $\mu_{\rm R} = \mu_{\rm F} = (m_H + 2\,m_b)/4$ showed an unexpected decrease of the total cross section with respect to the default dynamical scale settings; these issues still have to be resolved. The use of two different Monte Carlos comes with the potential advantage of using two complementary matching schemes, i.e., MC@NLO and POWHEG.

IV.2.4 Acceptance uncertainties

The $b\bar{b}\phi,\ \phi \to \tau\tau$ process is the most sensitive one in the searches for the Higgs bosons, $\phi = {\rm h}, {\rm H}, {\rm A}$ in the MSSM at large values of tanβ. The final state with two τ–jets ($\tau_{\rm h}\tau_{\rm h}$) has the largest sensitivity compared to $\tau_\ell\tau_{\rm h}$ or $\tau_\ell\tau_\ell$ in the searches for the heavy Higgs bosons, A or H with $m_{\rm A/H} \geq 400$ GeV (ATLAS 13 TeV reference).

The parton level acceptance and its uncertainties of the $\tau_{\rm h}\tau_{\rm h}$ final state have been evaluated with MADGRAPH5_AMC@NLO using the selection criteria of the recent ATLAS and CMS analyses with 13 TeV data. We take a Higgs boson mass of $m_{\rm H} = 700$ GeV and $\sqrt{s} = 13$ TeV at the LHC. The selection criteria for the $\tau_{\rm h}\tau_{\rm h}$ final state in the CMS analysis are:

- two τ–jets with $p_{\rm T}^{\tau_{\rm h}} > 40$ GeV, $|\eta^{\tau_{\rm h}}| < 2.1$
- at least one b–jet with $p_{\rm T} > 20$ GeV, $|\eta| < 2.4$
- no more than one jet with $p_{\rm T} > 30$ GeV, $|\eta| < 4.7$

In the ATLAS analysis the $\tau_{\rm h}\tau_{\rm h}$ final state is selected requiring two τ–jets with the leading jet $p_{\rm T}^{\tau_{\rm h1}} > 135$ GeV and the sub–leading jet $p_{\rm T}^{\tau_{\rm h2}} > 55$ GeV in the pseudo–rapidity region of $|\eta^{\tau_{\rm h}}| < 2.5$. The τ–jets are required to be back-to-back in the transverse plane of the detector, $\Delta\phi(\tau_{\rm h1}, \tau_{\rm h2}) > 2.7$.

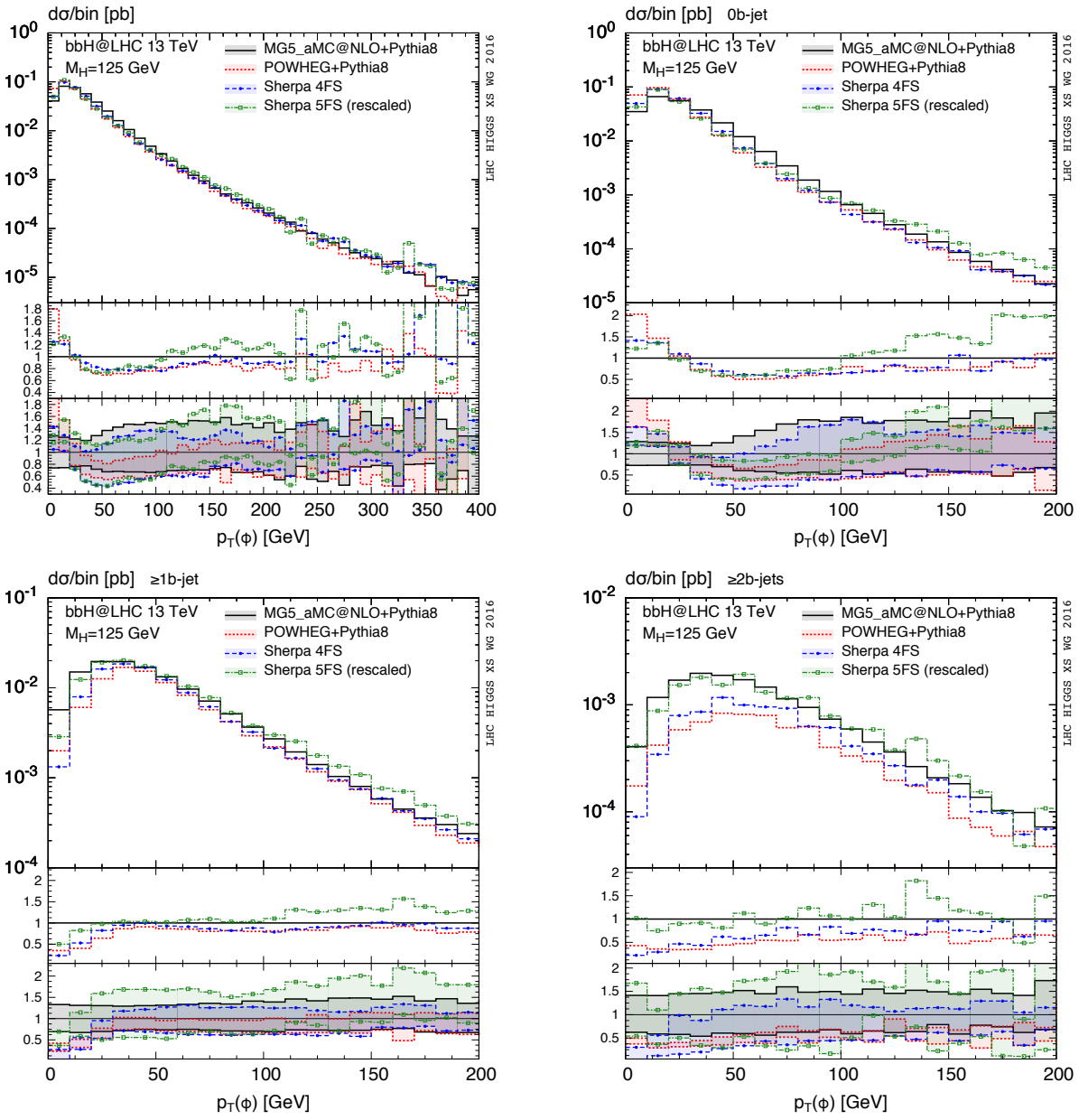

Figure 265: Transverse-momentum distribution of the Higgs boson as predicted by the various codes with requirements on the final-state b jets; upper left panel: inclusive; upper right panel: with a veto on b-tagged jets; lower left panel: with one or more b jets; lower right panel: with at least two observed b jets; see text for details.

The parton jets are reconstructed from the gluons and quarks after PYTHIA8 showering using the anti–k_T algorithm with $R = 0.4$. The parton jet is identified as a b–jet if it has a b–quark as a jet constituent. The p_{T} of τ_{h} is a vector sum p_{T} of the hadronic τ decay products.

The acceptance uncertainties are separated into the uncertainties due to the QCD scale choice, due to the PDF uncertainty and due to the shower scale, Q_{sh} choice in MADGRAPH5_AMC@NLO (see Section IV.2.3.e). The PDF4LHC15_nlo_nf4_30 set is used.

The QCD scale is varied as $0.5\mu_0 \leq \mu_{\mathrm{R}}, \mu_{\mathrm{F}} \leq 2\mu_0$ with the constraint $0.5 \leq \mu_{\mathrm{R}}/\mu_{\mathrm{F}} \leq 2$. The shower scale, Q_{sh} is varied by varying the parameter $\alpha \in [1/(4\sqrt{2}), \sqrt{2}/4]$ as described in Section IV.2.3.e.

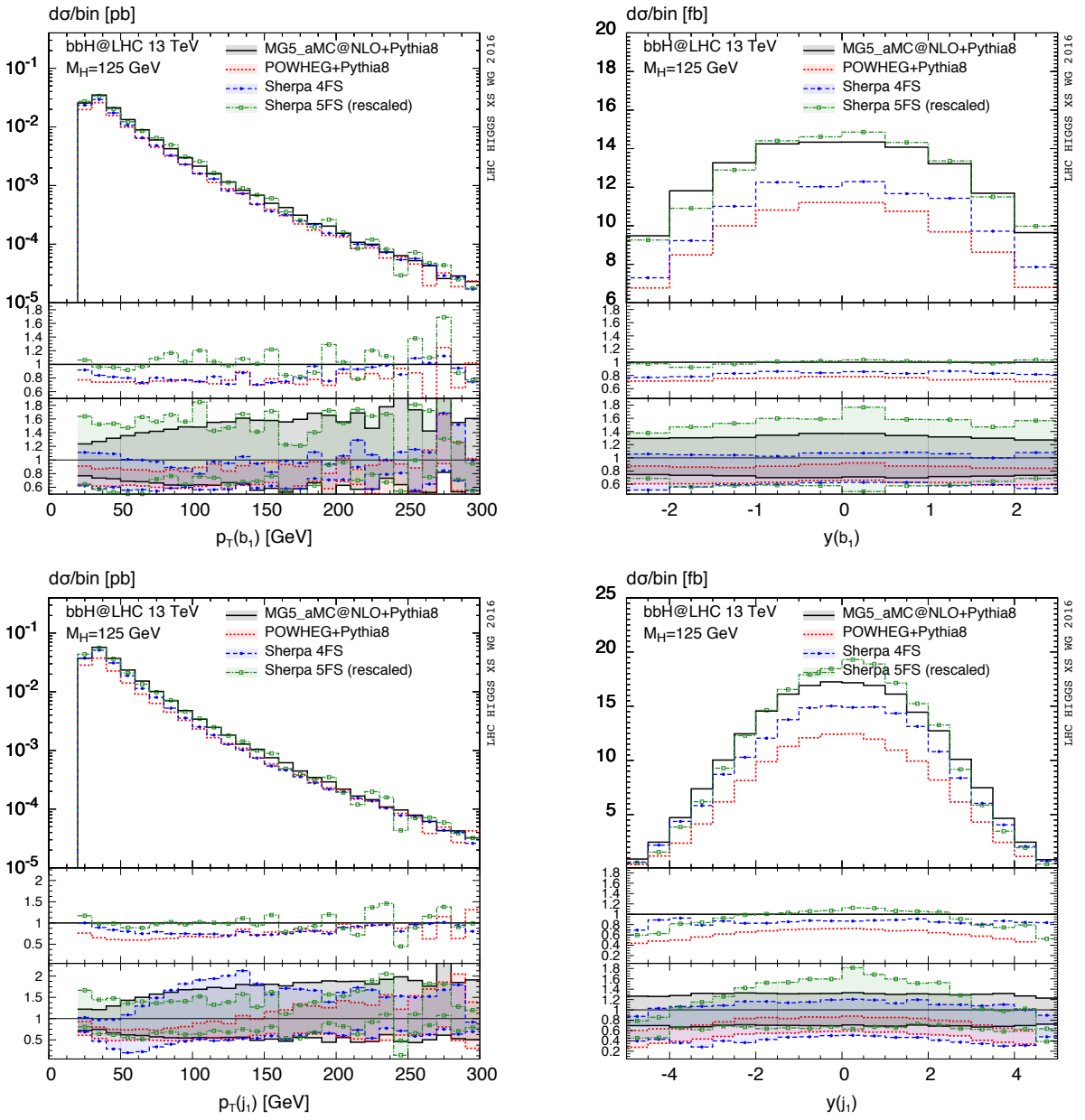

Figure 266: Transverse-momentum (left) and rapidity distributions (right) of the hardest b jet (upper) and hardest jet without requirements on its flavour (lower); see text for details.

Table 124 shows the parton level acceptance and its uncertainties for ATLAS and CMS analysis selections evaluated with MADGRAPH5_AMC@NLO. One can see that the uncertainty is dominated by the choice of the shower scale.

IV.2.5 Total cross sections for $c\bar{c}\phi$ production

As shown in Ref. [1177], the partonic 5FS results for $b\bar{b}\phi$ production allow for the calculation of other quark-initiated cross sections by simply changing the parton density flavour. Amplitudes with different Yukawa couplings do not interfere with each other if kinematical quark masses and terms which involve a loop-induced Higgs-gluon coupling are neglected.

Of particular interest in certain extended theories may be the $c\bar{c}\phi$ cross section. Table 125 shows

Table 124: The parton level acceptance of ATLAS and CMS $\tau_{\rm h}\tau_{\rm h}$ analysis selections and its uncertainties evaluated with MADGRAPH5_AMC@NLO for $m_{\rm H} = 700$ GeV and $\sqrt{s} =$ 13TeV LHC.

	ATLAS	CMS
selections	acceptance	
$\tau_{\rm h}$ kinematics	0.671	0.816
jet selections	no jet selections	0.161
source of uncertainty	acceptance uncertainty in %	
QCD scale	+2.6, –1.4	+3.0, -2.0
PDF	+0.2, -0.9	+0.4, –0.9
shower scale, $Q_{\rm sh}$	+1.0, -7.2	+4.4, -10.9

the total inclusive $c\bar{c}\phi$ cross section through NNLO. To obtain these numbers, the parton `PDF4LHC15` parton densities have been used. The Yukawa coupling has been set to its SM value, with the charm quark mass $m_c(\mu_R)$ derived from $m_c(3\ {\rm GeV}) = 0.986\,{\rm GeV}$ by running it at four-loop order to $m_c(M_H)$, and from there at three-loop order to $m_c(\mu_R)$.

These numbers have been obtained with version 1.6 of the program `SusHi` [135].

Table 125: Total inclusive cross section for $c\bar{c}\phi$ production at $\sqrt{s} = 13\,\text{TeV}$.

M_H[GeV]	$\sigma_{c\bar{c}\phi}$[pb]	Δ_scale[%]	Δ_PDF[%]
25	$8.120 \cdot 10^{0}$	$^{+22.6}_{-44.1}$	± 8.0
45	$1.890 \cdot 10^{0}$	$^{+10.5}_{-21.9}$	± 5.7
65	$6.657 \cdot 10^{-1}$	$^{+6.8}_{-14.3}$	± 5.1
85	$2.944 \cdot 10^{-1}$	$^{+5.0}_{-10.4}$	± 5.1
105	$1.500 \cdot 10^{-1}$	$^{+4.0}_{-8.1}$	± 4.9
125	$8.429 \cdot 10^{-2}$	$^{+3.3}_{-6.5}$	± 4.9
145	$5.082 \cdot 10^{-2}$	$^{+2.8}_{-5.4}$	± 4.9
165	$3.234 \cdot 10^{-2}$	$^{+2.4}_{-4.6}$	± 4.9
185	$2.148 \cdot 10^{-2}$	$^{+2.1}_{-3.9}$	± 5.1
205	$1.476 \cdot 10^{-2}$	$^{+1.9}_{-3.4}$	± 5.2
225	$1.044 \cdot 10^{-2}$	$^{+1.7}_{-3.0}$	± 5.2
245	$7.562 \cdot 10^{-3}$	$^{+1.6}_{-2.7}$	± 5.1
265	$5.591 \cdot 10^{-3}$	$^{+1.4}_{-2.4}$	± 5.0
285	$4.207 \cdot 10^{-3}$	$^{+1.3}_{-2.1}$	± 5.2
305	$3.215 \cdot 10^{-3}$	$^{+1.2}_{-1.9}$	± 5.3
325	$2.491 \cdot 10^{-3}$	$^{+1.2}_{-1.7}$	± 5.4
345	$1.953 \cdot 10^{-3}$	$^{+1.1}_{-1.6}$	± 5.6
365	$1.549 \cdot 10^{-3}$	$^{+1.0}_{-1.4}$	± 5.6
385	$1.240 \cdot 10^{-3}$	$^{+1.0}_{-1.3}$	± 5.6
405	$1.001 \cdot 10^{-3}$	$^{+0.9}_{-1.2}$	± 5.6
425	$8.150 \cdot 10^{-4}$	$^{+0.9}_{-1.1}$	± 5.7
445	$6.684 \cdot 10^{-4}$	$^{+0.8}_{-1.0}$	± 5.7
465	$5.518 \cdot 10^{-4}$	$^{+0.8}_{-0.9}$	± 5.7
485	$4.585 \cdot 10^{-4}$	$^{+0.7}_{-0.8}$	± 5.8
505	$3.831 \cdot 10^{-4}$	$^{+0.7}_{-0.8}$	± 6.0
525	$3.218 \cdot 10^{-4}$	$^{+0.7}_{-0.8}$	± 6.0

Chapter IV.3

Charged Higgs Bosons

M. Flechl, S. Sekula, M. Ubiali, M. Zaro (Eds.) C. Degrande, H.E. Haber, M. Spira, M. Wiesemann

IV.3.1 Introduction

Charged Higgs bosons $\mathrm{H}^{\pm}$ appear in many extensions of the Standard Model, in particular when adding additional doublets or triplets to its scalar sector. Here, the focus is on charged Higgs bosons in 2-Higgs-doublet models (2HDM) including the special case of the Higgs sector of the minimal supersymmetric extension of the standard model (MSSM). The dominant production mode for a charged Higgs boson depends on its mass. In particular, for masses below the top quark mass, the charged Higgs boson is dominantly produced in top-quark decays. Therefore, the production cross section corresponds to the top pair production times the branching ratio $\mathrm{t} \to \mathrm{H}^{+}\mathrm{b}$. For values of the mass close to the top quark mass ($160 - 180$ GeV), both contributions with resonant and non-resonant top quarks are equally important, and the full $\mathrm{W}^{-}\mathrm{H}^{+}\mathrm{b}\bar{\mathrm{b}}$ has to be simulated. Finally, heavy charged Higgs bosons are dominantly produced in association with a top quark. Most of the parameter space for a light charged Higgs boson has already been excluded at the LHC Run 1 [1126, 1178]. For what concerns the intermediate mass region $m_{\mathrm{H}^{\pm}} \sim m_{\mathrm{t}}$, no search has been performed to date due to the lack of accurate predictions for the signal. In fact, NLO predictions for the total cross section have been made available only recently [1179]. Further theoretical developments in this direction are encouraged. In this chapter we will focus on the heavy mass range, up to masses of 2 TeV, which is being probed at the Run 2.
In the following, we present updated NLO predictions for heavy charged Higgs boson production in a type-II 2HDM. These cross sections can also be translated into predictions for a type-I, type-III or type-IV 2HDM according to the recipe in Ref. [1180]. We continue by showing differential cross sections for this production process with an emphasis on the comparisons of the 4-flavour scheme (4FS) and 5-flavour scheme (5FS) predictions. We conclude the chapter providing some recommendations for the signal simulation in experimental searches.

IV.3.2 Inclusive production cross sections

The dominant charged Higgs boson production mode for $m_{\mathrm{H}^{\pm}} > m_t$ in a 2HDM is via the process

$$\mathrm{pp} \to \mathrm{tH}^{\pm} + X.$$

The cross section for associated $\mathrm{tH}^{\pm}$ production can be computed in the 4FS or the 5FS. In the 4FS there are no b quarks in the initial state, hence the lowest-order QCD production processes are gluon-gluon fusion and quark-antiquark annihilation, $\mathrm{gg} \to \mathrm{tbH}^{\pm}$ and $\mathrm{q\bar{q}} \to \mathrm{tbH}^{\pm}$, respectively. Potentially large logarithms of the ratio between the hard scale of the process and the mass of the bottom quark, which arise from the splitting of incoming gluons into nearly collinear $\mathrm{b\bar{b}}$ pairs, can be summed to all orders in perturbation theory by introducing bottom parton densities. This defines the five-flavour scheme (5FS). The use of bottom quark distribution functions is based on the approximation that the outgoing b quark is at small transverse momentum and massless, and the virtual b quark has a vanishing virtuality ($m \approx 0$). In this scheme, the LO process for the inclusive top-quark-associated production cross section is gluon-bottom fusion, $\mathrm{gb} \to \mathrm{tH}^{\pm}$. The NLO cross section in the 5FS scheme includes $\mathcal{O}(\alpha_{\mathrm{s}})$ corrections to $\mathrm{gb} \to \mathrm{tH}^{\pm}$, including the tree-level processes $\mathrm{gg} \to \mathrm{tbH}^{\pm}$ and $\mathrm{q\bar{q}} \to \mathrm{tbH}^{\pm}$. To all orders in perturbation theory the two schemes are identical, but the way of ordering the perturbative expansion is different, and the results do not match exactly at finite order.

Here, we present cross-section predictions for this process by following the methodology described in more detail in Refs. [9, 1180]. The main differences are the usage of the most recent combination of PDF sets provided by PDF4LHC15, the centre-of-mass energy of $\sqrt{s} = 13$ TeV, and the parameters which are set according to the conventions adopted in this report. In addition, we have significantly extended the mass range up to $m_{\mathrm{H}^\pm} = 2$ TeV and we explicitly calculate the $\tan\beta$ dependence, by computing separately the contributions to the cross section proportional to y_b^2 and y_t^2 and rescaling each of them by the corresponding overall $\tan\beta$ factor. In the previous analysis [1180] the central value of the cross section was computed for all points in the $\tan\beta$ scan, the approximation was made that the size of the relative theoretical uncertainty is independent of the value of $\tan\beta$. The present analysis goes beyond this approximation by taking into account the theoretical uncertainty associated to the running of the bottom Yukawa coupling up to the renormalization scale: the uncertainties for all considered values of $\tan\beta$ are computed explicitly.

For a type-II 2HDM, the $\mathrm{t\bar{b}H^-}$ coupling is given by $\sqrt{2}\left(y_\mathrm{t}\, P_R \cot\beta + y_\mathrm{b}\, P_L \tan\beta\right)$. We separately evaluate the y_t^2 and y_b^2 terms. The size of the interference term, $y_\mathrm{t} y_\mathrm{b}$, is proportional to m_b and will be neglected in the following. In the 5FS, this contribution is exactly zero, while in the 4FS, it has been shown [1181] that neglecting this term leads to an overestimate of the cross section by at most 5% for $m_{\mathrm{H}^\pm} = 200$ GeV and less than 1% for $m_{\mathrm{H}^\pm} > 600$ GeV. This estimate refers to $\tan\beta = 8$; for all other values of $\tan\beta$, the size of this contribution is further suppressed by $\tan^2\beta$ ($1/\tan^2\beta$) for large (small) $\tan\beta$ values. In all cases, the impact of this term remains much smaller than the size of the theoretical uncertainties. For what concerns supersymmetric corrections, effects due to virtual supersymmetric particles in the loop have to be taken into account. Such corrections are finite and can be simply added to the total cross section. Among these corrections the dominant ones are those that modify the relation between the b quark mass and its Yukawa coupling. This class of corrections are enhanced at large $\tan\beta$ and can be summed up to all orders through a modification of the b quark Yukawa coupling [1033, 1076, 1080–1083, 1182, 1183]. The remaining SUSY-QCD effects are negligible at large $\tan\beta$ but can be of order 10% at small $\tan\beta$.
We present results for the 4FS and 5FS schemes, including the theoretical uncertainty, and combine the two schemes according to the Santander matching [1131]. Fully-matched computations have been presented for bottom-fusion initiated Higgs boson production in this report [1154, 1155], but are not available for charged Higgs boson production. Throughout this report we present results for the $\mathrm{tH^-}$ final state. The charge-conjugated final state can be included by simply multiplying the results by a factor two.

To estimate the theoretical uncertainty due to missing higher-order contributions, we vary the renormalization scale μ_R, the factorization scale μ_F and the scale μ_b (which determines the running bottom quark mass in the Yukawa coupling and is set to μ_R) by a factor two about their central values. In addition to the scale uncertainties, we have computed the PDF and α_s uncertainties following the PDF4LHC15 recommendation. We stress that the PDF uncertainty computed with the PDF4LHC15 set also accounts for the parametric uncertainty associated to the value of m_b used in PDF fits. PDF uncertainties are given at 68% confidence level (CL).

The results for heavy charged Higgs boson production within the 4FS are based on the calculation presented in Ref. [1183] and implemented in MadGraph5_aMC@NLO [54, 1181], interfaced to the LHAPDF library [43, 1184]. The renormalization and factorization scales are set to $\mu = (m_{\mathrm{H}^\pm} + m_\mathrm{t} + m_\mathrm{b})/3$. The resulting 4FS cross section and uncertainties are shown in Figure 267.

For the calculation in the 5FS, the program Prospino [1185] has been employed, interfaced to the LHAPDF library [1184]. The renormalization scale is set to $\mu_\mathrm{R} = (m_{\mathrm{H}^\pm} + m_\mathrm{t})/2$, while the factorization scale $\mu_\mathrm{F} = \tilde{\mu}$ is chosen according to the method proposed in [412]. The effective factorization scale entering the initial state logarithms is proportional to the hard scale, but modified by a phase space factor which tends to reduce the size of the logarithms for processes at hadron colliders. A table with $\tilde{\mu}$ values for the various charged Higgs boson masses is provided on the Twiki

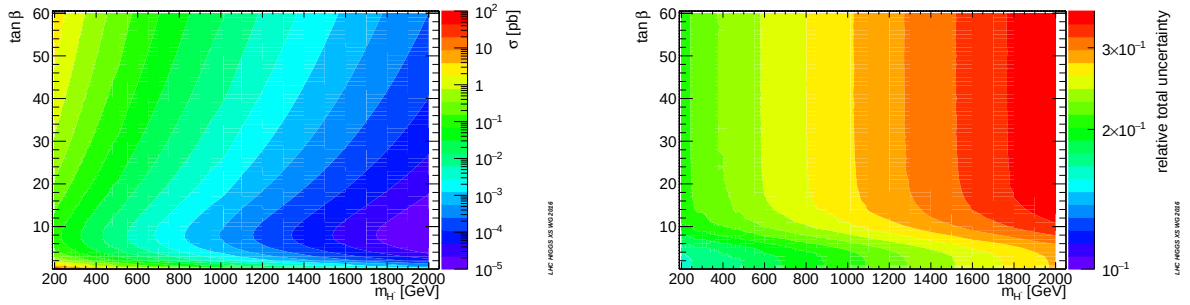

Figure 267: Cross section (left) and average relative uncertainty (right) for $\mathrm{tH}^{\pm} + X$ production in the 4FS, as a function of $m_{\mathrm{H}^{\pm}}$ and $\tan\beta$.

page https://twiki.cern.ch/twiki/bin/view/LHCPhysics/LHCHXSWGMSSMCharged. The resulting 5FS cross section and uncertainties are shown in Figure 268. Before presenting matched predictions,

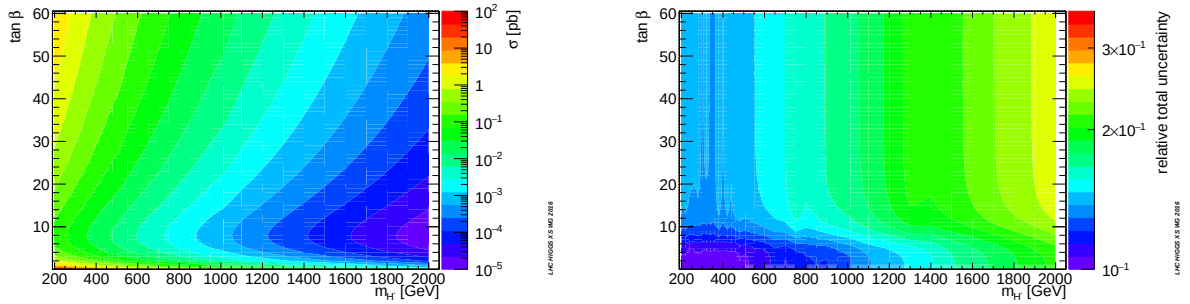

Figure 268: Cross section (left) and average relative uncertainty (right) for $\mathrm{tH}^{\pm} + X$ production in the 5FS, as a function of $m_{\mathrm{H}^{\pm}}$ and $\tan\beta$.

we would like to make some comments on the numbers, see Table 126. The central values of the four- and five-flavour predictions are compatible within uncertainties, as observed also in Ref. [1180], although the agreement is worse. This is mostly due to the different way of computing the bottom Yukawa coupling compared to previous predictions. As far as uncertainties are concerned, the 4FS numbers are affected by a total uncertainty which is about 50% larger than the one of the 5FS. Furthermore, in the 5FS the largest contribution to the total uncertainty comes from PDFs, in particular for heavy Higgs bosons $m_{\mathrm{H}^{\pm}} > 1TeV$, while scale uncertainties remain around or below 10% also at higher values of the masses. In the 4FS, the situation is reversed, as scale uncertainties are dominant and reach up to 20% for $m_{\mathrm{H}^{\pm}} \sim 1TeV$. PDF uncertainties on the other hand are smaller, about half the PDF uncertainty of the 5FS calculation. The smaller scale uncertainty of the 5FS calculation is also observed in the case of $b\bar{b}\phi$: in particular, in Ref. [1155] it has been suggested that this fact may be associated with theoretical uncertainties coming from mass terms included only in the 4FS powers of m_{b}. Overall the total theoretical uncertainty is smaller in the 5FS calculation by about 30%.

To provide a final prediction for heavy charged Higgs boson production we combine the NLO 4FS and 5FS cross sections according to Santander matching [1131]. We note that the 4FS and 5FS calculations provide the unique description of the cross section in the asymptotic limits $M_{\phi}/m_{\mathrm{b}} \to 1$ and $M_{\phi}/m_{\mathrm{b}} \to \infty$, respectively (here and in the following M_{ϕ} denotes a generic Higgs boson mass). The 4FS and 5FS are thus combined in such a way that they are given variable weight, depending on

Table 126: Comparison of $pp \to tH^+ + X$ cross sections (in units of pb) and percentage uncertainties for the 4FS, the 5FS, and when matching both.

$m_{\mathrm{H}^\pm}$	$\tan\beta$	4FS				5FS				matched	
[GeV]		σ	$\Delta\sigma^{\mathrm{scale}}$	$\Delta\sigma^{\mathrm{pdf}}$	$\Delta\sigma^{\mathrm{tot}}$	σ	$\Delta\sigma^{\mathrm{scale}}$	$\Delta\sigma^{\mathrm{pdf}}$	$\Delta\sigma^{\mathrm{tot}}$	σ	$\Delta\sigma^{\mathrm{tot}}$
200	1	2.90	13.1	3.1	16.6	3.63	4.1	6.6	11.8	3.36	12.5
200	8	0.0961	15.7	3.2	18.9	0.1194	6.4	5.9	13.8	0.1109	14.4
200	30	0.718	18.0	3.2	21.2	0.886	8.5	5.6	15.7	0.825	16.2
600	1	0.143	13.3	4.9	18.9	0.186	2.7	8.1	12.9	0.175	12.6
600	8	0.00461	16.7	5.0	21.9	0.00602	5.1	7.8	15.1	0.00566	14.8
600	30	0.0336	19.6	5.1	24.7	0.0440	7.3	7.7	17.0	0.0413	16.9
1000	1	0.0162	14.2	6.8	21.0	0.0217	2.3	10.6	14.7	0.0204	14.2
1000	8	0.000516	17.4	7.0	24.4	0.000697	5.2	10.0	16.6	0.000655	16.8
1000	30	0.00371	20.8	7.0	27.8	0.00506	7.9	9.7	18.8	0.00475	19.4

the value of the Higgs boson mass. The difference between the two approaches is formally logarithmic. Therefore, the dependence of their relative importance on the Higgs boson mass should be controlled by a logarithmic term, i.e.

$$\sigma^{\mathrm{matched}} = \frac{\sigma^{\mathrm{4FS}} + w\,\sigma^{\mathrm{5FS}}}{1+w} \quad \text{with} \quad w = \ln\frac{\mathrm{M}_\phi}{m_{\mathrm{b}}} - 2\,. \tag{IV.3.1}$$

The theoretical uncertainties are combined according to

$$\Delta\sigma_\pm^{\mathrm{matched}} = \frac{\Delta\sigma_\pm^{\mathrm{4FS}} + w\Delta\sigma_\pm^{\mathrm{5FS}}}{1+w} \tag{IV.3.2}$$

where $\Delta\sigma_\pm^{\mathrm{4FS}}$ and $\Delta\sigma_\pm^{\mathrm{5FS}}$ are the upper/lower uncertainty limits of the 4FS and the 5FS, respectively.

The resulting matched cross section is shown in Figure 269. We observe that the NLO 4FS and 5FS predictions are in fair mutual agreement, with differences of the central values of roughly 20%. The dynamical choice for μ_{F} in the 5FS used here improves the matching of the predictions in the two schemes. The overall theoretical uncertainty of the matched NLO prediction is about 10%. Cross sections and uncertainties for a two-dimensional grid, $m_{\mathrm{H}^\pm} = 200$ GeV $-$ 2000 GeV and $\tan\beta = 0.1 - 60$, can be retrieved online[IV.19].

In contrast to the type-II 2HDM, for type-I the bottom Yukawa coupling is not enhanced by $\tan\beta$, so that $g_{\mathrm{t\bar{b}H^-}}|_{\mathrm{type-I}} = \sqrt{2}\,m_{\mathrm{t}}/v\,P_R\cot\beta + \mathcal{O}(m_{\mathrm{b}}/m_{\mathrm{t}})$. Up to corrections suppressed by $\mathcal{O}(m_{\mathrm{b}}/m_{\mathrm{t}})$, the cross section for heavy charged Higgs boson production in the type-I 2HDM, $\sigma|_{\mathrm{type-I}} \propto g^2_{\mathrm{t\bar{b}H^-}}|_{\mathrm{type-I}} \propto 2(m_{\mathrm{t}}/v)^2\cot^2\beta + \mathcal{O}(m_{\mathrm{b}}/m_{\mathrm{t}})$, can thus be obtained from the type-II cross section, $\sigma|_{\mathrm{type-II},\tan\beta=1} \propto g^2_{\mathrm{t\bar{b}H^-}}|_{\mathrm{type-II},\tan\beta=1} \propto 2(m_{\mathrm{t}}/v)^2 + \mathcal{O}(m_{\mathrm{b}}/m_{\mathrm{t}})$, evaluated at $\tan\beta = 1$ and rescaled by $\cot^2\beta$. This relation is correct to all orders in QCD, but *not* to all orders in the electroweak corrections. Given the overall theoretical uncertainty of the cross section prediction it is, however, an excellent approximation and sufficient for all practical purposes. Note that the charged Higgs boson cross section predictions for the type-I and type-II 2HDMs also hold for the so-called lepton-specific and flipped 2HDMs, respectively, see e.g. Ref. [485].

[IV.19] https://twiki.cern.ch/twiki/bin/view/LHCPhysics/LHCHXSWGMSSMCharged

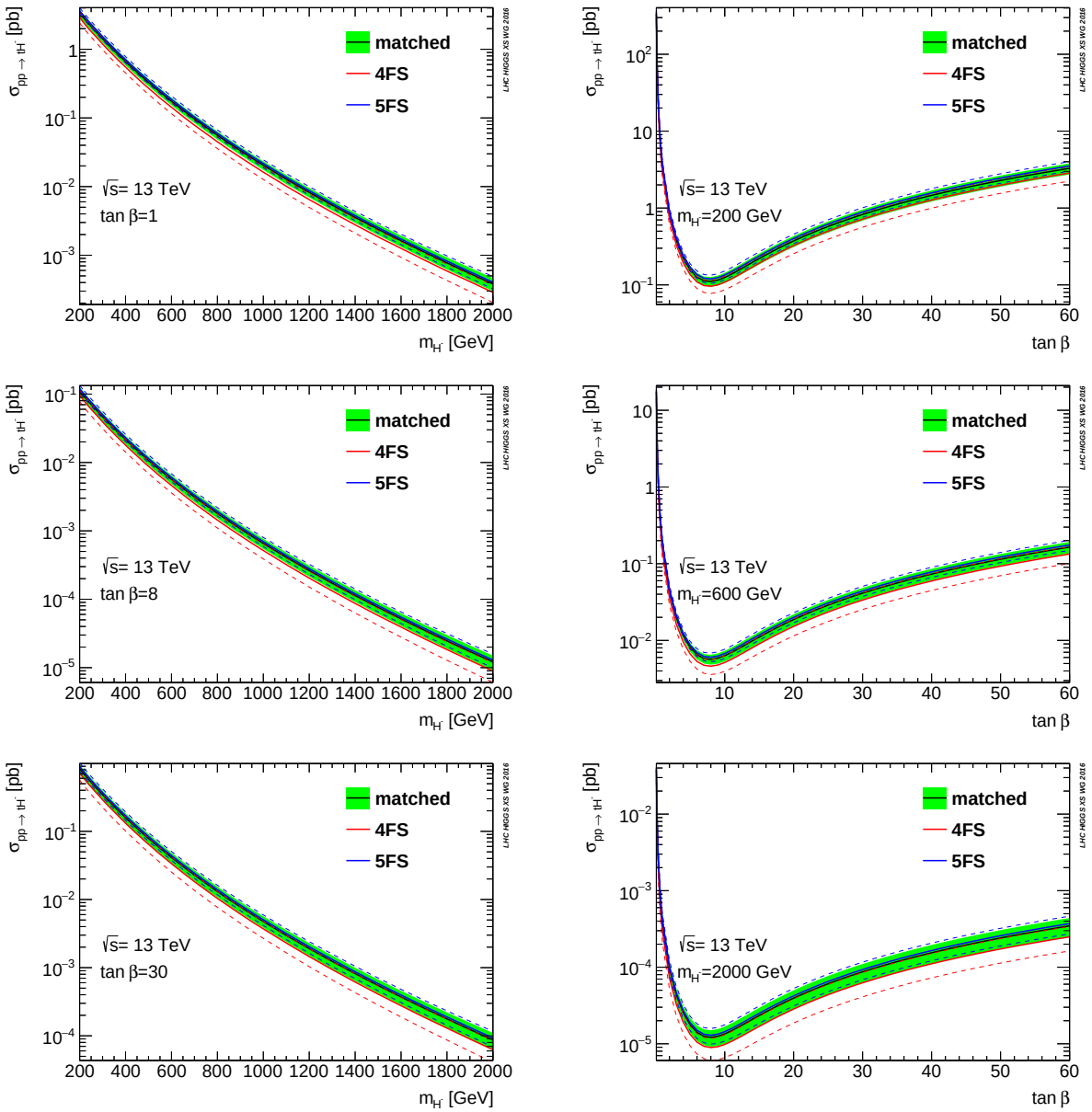

Figure 269: Cross section for $\mathrm{tH}^{\pm} + X$ production, after matching the 4FS and 5FS results. The result is given for three different values of $\tan\beta$ (left) and of $m_{\mathrm{H}^{\pm}}$ (right).

IV.3.3 Differential production cross sections

We now present differential distributions for the production of a heavy charged Higgs boson in association with a top quark in a type-II 2HDM. We present results in the 4FS and 5FS up to NLO accuracy and including matching to parton shower Monte Carlos. Fully differential results in the 5FS have been available for some years [1186, 1187], while 4FS results have been presented only recently [1181]. In this chapter, we follow the methodology presented in Ref. [1181], where fully-differential results in the 4FS were presented for the first time using MADGRAPH5_AMC@NLO [54] together with HERWIG++ [313] or PYTHIA8 [318]. In particular, we use a reduced shower scale (generated in the range $0.025\sqrt{s_0} < \mu^2_{sh} < \times 0.25\sqrt{s_0}$, s_0 being the born-level partonic centre of mass energy) with respect to the default one in MADGRAPH5_AMC@NLO which improves the matching between NLO+PS and

NLO predictions at large transverse momentum. In the results shown here, we adapt relevant input parameters to match the recommendations followed throughout this report. In particular, differences in the setup with respect to Ref. [1181] include the running of the bottom Yukawa up to the renormalization scale using four loops for the central predictions and two loops for the renormalization scale variations and the usage of the PDF4LHC15 parton distributions [35]. We employ 4FS and 5FS PDFs consistently with the flavour scheme of the computation. In both cases (and also for LO predictions) PDFs are evolved at NLO. As in Ref. [1181], we assume that the top quark decays leptonically while the charged Higgs remains stable. Therefore, b jets in the final state will typically come from the top quark and from the matrix element.

In Figs. 270-273, we present a comparison between the two schemes at LO and NLO matched with PYTHIA8, for several differential observables. All figures refer to the case of a $m_{\mathrm{H}^\pm} = 200$ GeV Higgs boson and $\tan\beta = 8$. For the sake of generality, the y_{t}^2 and y_{b}^2 contributions to the cross section are shown separately, omitting the negligible interference term. Predictions for different values of $\tan\beta$ can be obtained by a trivial rescaling of the shown histograms. All figures have the same layout, namely: a main frame with the absolute predictions in the two schemes, at LO and NLO, and five smaller frames below. In the first four of these frames, the ratio of histograms in the main frame over the 5FS NLO prediction is shown, together with scale (first and third frames, respectively for the y_{b}^2 and y_{t}^2 contributions) and PDF uncertainties (second and fourth frames). The last frame shows the differential K-factors (NLO/LO).

Before looking at the various observables, we outline some general features: the first one is that, as expected, the inclusion of NLO corrections brings predictions in the two schemes much closer than at LO. The second is about the size of uncertainties at NLO, which follows the same pattern as the inclusive cross section described in the previous section: for observables which are described with the same accuracy in the two schemes (e.g. top and Higgs boson p_T, b-jet rates for zero and one jet), scale uncertainties in the 4FS are usually larger than in the 5FS ($\pm 10 - 12\%$ vs$\pm 4 - 6\%$). PDF uncertainties display instead an opposite behaviour (at least for this value of the charged Higgs boson mass): they are larger in the 5FS, with a similar size as scale uncertainties, and smaller in the 4FS, where they are negligible with respect to scale variations. Finally, due to the additional running of the bottom Yukawa, the y_{b}^2 contribution has a broader scale uncertainty band than the y_{t}^2 one.

We now turn to compare the two schemes for a number of differential observables: in Figure 270 we observe that for the transverse momentum of the top quark (reconstructed using Monte Carlo truth information) and the Higgs boson the difference between the two schemes can be compensated by a simple overall rescaling of the total rates at NLO (similar to the one observed in the previous section) while LO predictions in the two schemes have quite different shapes (in particular for the top quark). The same level of agreement is expected to be found also for observables related to the decay products of the top quark (and of the charged Higgs boson). Indeed, the p_T spectrum of the hardest b jet (left plot in Figure 271) displays a flat ratio between the 4FS and 5FS at NLO up to ≈ 120 GeV. While below 120 GeV the hardest b jet essentially coincides with the b jet from the top quark, above 120 GeV secondary $\mathrm{g} \to \mathrm{b\bar{b}}$ splitting from hard gluons becomes relevant. This fact is reflected in the growth of the 5FS scale uncertainty band and of the k factor. Larger differences between the two schemes appear for the second-hardest b jet, see right plot in Figure 271. This distribution is expected to be poorly described in the 5FS. In particular, its kinematics in the 5FS at LO is determined by the shower, while at NLO it is driven by a tree-level matrix element (therefore being formally only LO accurate). As expected, the 5FS develops larger k factors. The 4FS calculation thus describes these observables significantly better, both because of its more robust perturbative behaviour and because of the proper modelling of the final-state b jets.

The effect of the different treatment of the bottom quark in the two schemes is even more visible for the transverse momentum of the hardest and second hardest B hadron (left and right plot in Figure 272).

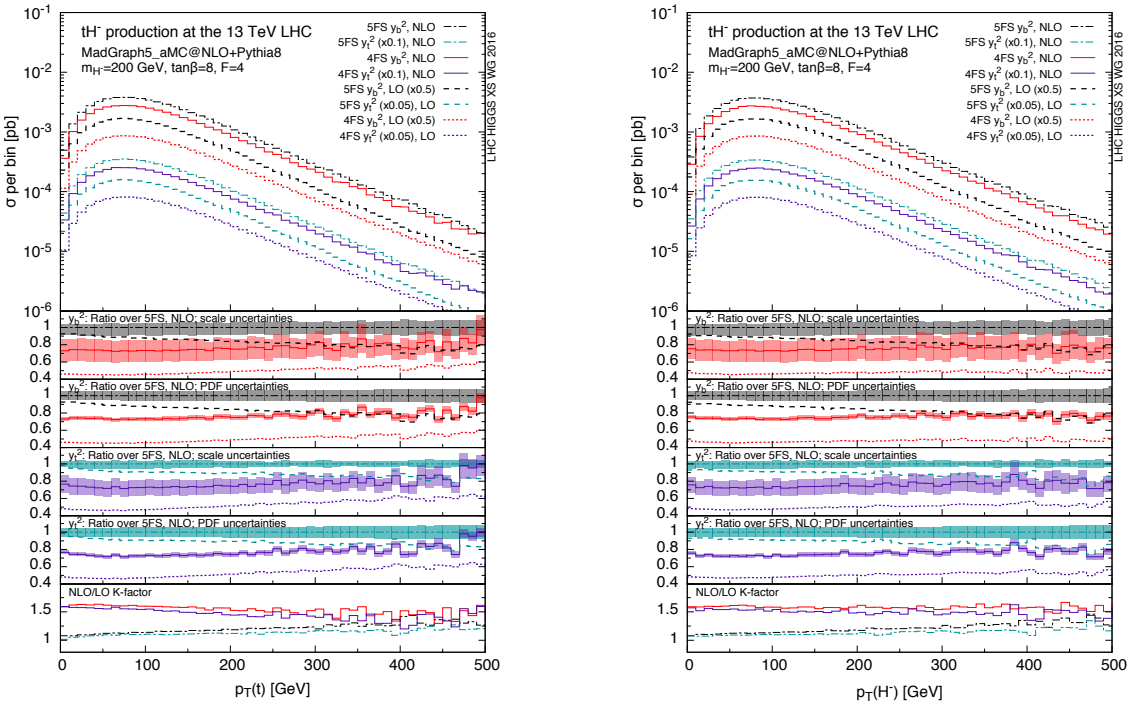

Figure 270: LO and NLO predictions matched with PYTHIA8 in the 4FS and 5FS, separately for the the y_{b}^2 and y_{t}^2 terms, for the transverse momentum of the top quark (left) and of the charged Higgs boson (right). Rescaling factors are introduced in the main frame for better visibility. The first four smaller frames at the bottom show the ratio over the NLO prediction in the 5FS for the y_b^2 and y_t^2 terms, and the scale and PDF uncertainty bands for the NLO curves. The bottom frame shows the differential K factor (NLO/LO) for the four predictions. A charged Higgs boson mass of $m_{\mathrm{H}^\pm} = 200$ GeV is assumed.

At medium and large p_{T} of the hardest B hadron similar effects as for the hardest b jet are observed. At low momentum, the 4FS prediction is suppressed with respect to the 5FS . This is most likely due to mass effects as these kinematical regions correspond to one b quark being collinear to the beam. In the 5FS these configurations are enhanced because of the collinear singularities, while in the 4FS such singularities are screened by the b quark mass. Therefore, even after the parton shower, the 5FS is reminiscent of the collinear enhancement. In the case of the second-hardest B such effects are further enhanced.

Finally, looking at jet (Figure 273 left) and b-jet multiplicities (Figure 273 right), we observe again that the effect of NLO corrections is very different in the two schemes: while in the 5FS NLO corrections make the jet spectrum moderately harder, in the 4FS they tend to make it softer, with greater enhancements in the low multiplicity bins. Despite this fact, at NLO the 4FS still shows a slightly harder spectrum than the 5FS. Irrespective of whether b-tagged jets are required or not, the overall effect of NLO QCD corrections is to bring the two schemes in much better agreement in the zero- and one-jet bin. The two-jet bin is only described at LO accuracy by the 5FS NLO prediction, therefore for this bin the 4FS prediction is expected to be more reliable. Higher multiplicities are described with rather poor accuracy (LO or even LL) by both schemes.

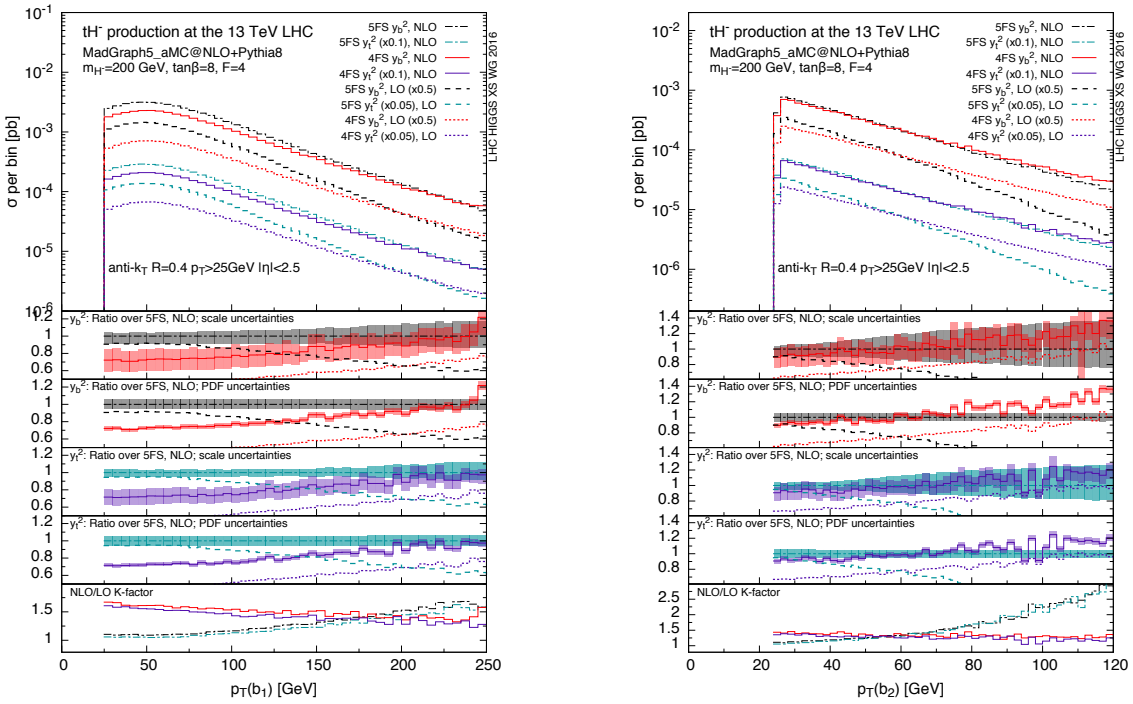

Figure 271: LO and NLO predictions matched with PYTHIA8 in the 4FS and 5FS, separately for the the y_{b}^2 and y_{t}^2 terms, for the transverse momentum of the hardest (left) and second hardest b jet (right). Rescaling factors are introduced in the main frame for better visibility. The first four smaller frames at the bottom show the ratio over the NLO prediction in the 5FS for the y_b^2 and y_t^2 terms, and the scale and PDF uncertainty bands for the NLO curves. The bottom frame shows the differential K factor (NLO/LO) for the four predictions. A charged Higgs boson mass of $m_{\mathrm{H}^\pm} = 200$ GeV is assumed.

All in all, the global behaviour of predictions closely follows what has been observed in Ref. [1181]. The interested reader can find more details in that paper, in particular for what concerns the comparison of matched and fixed-order computations and the usage of different parton showers.

IV.3.4 Recommendations for signal simulation

We conclude this chapter by providing some recommendations for the simulation of heavy charged Higgs boson production at the LHC Run 2. The use of 4FS fully-differential predictions is recommended for any realistic fully-differential signal simulation for experimental searches. This recommendation is backed by two sets of evidences: first, for a large number of observables, the 4FS prediction provides a better description of the final state kinematics; second, it reduces the systematic error related to the usage of a given parton shower. Moreover, when matching the NLO calculation to the shower, we recommend to use a lower shower scale by reducing the current default value from MADGRAPH5_AMC@NLO by a factor four. This corresponds to a shower scale generated in the range $0.025\sqrt{s_0} < \mu_{sh}^2 < \times 0.25\sqrt{s_0}$, s_0 being the born-level partonic centre of mass energy. This choice provides a better matching to the fixed-order computation at large transverse momenta, slightly reduces the parton shower dependence and also improves the agreement of four- and five-flavour scheme computations.

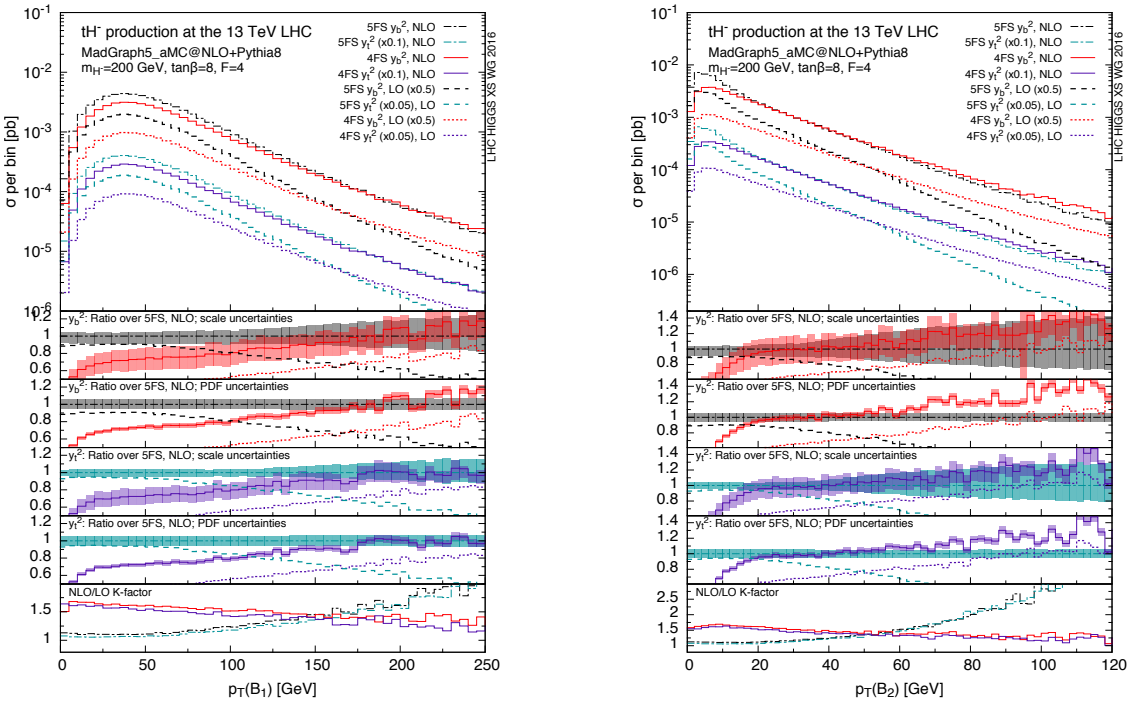

Figure 272: LO and NLO predictions matched with PYTHIA8 in the 4FS and 5FS, separately for the the y_{b}^2 and y_{t}^2 terms, for the transverse momentum of the hardest (left) and second hardest b hadron (right). Rescaling factors are introduced in the main frame for better visibility. The first four smaller frames at the bottom show the ratio over the NLO prediction in the 5FS for the y_b^2 and y_t^2 terms, and the scale and PDF uncertainty bands for the NLO curves. The bottom frame shows the differential K factor (NLO/LO) for the four predictions. A charged Higgs boson mass of $m_{\mathrm{H}^\pm} = 200$ GeV is assumed.

For what concerns the normalization of the signal total cross-section, the Santander-matched prediction provided in this section should be employed as central value.

As far as the estimate of theoretical uncertainties is concerned, the most obvious choice would be to use the scale and PDF uncertainties coming from the 4FS fully-differential computation. For observables inclusive in the b kinematics, this choice results into a slightly larger theoretical uncertainty than the one associated with the matched prediction (suggested for the normalization). On the other hand, for more exclusive observables, the 4FS uncertainty is smaller and more reliable than the 5FS one.

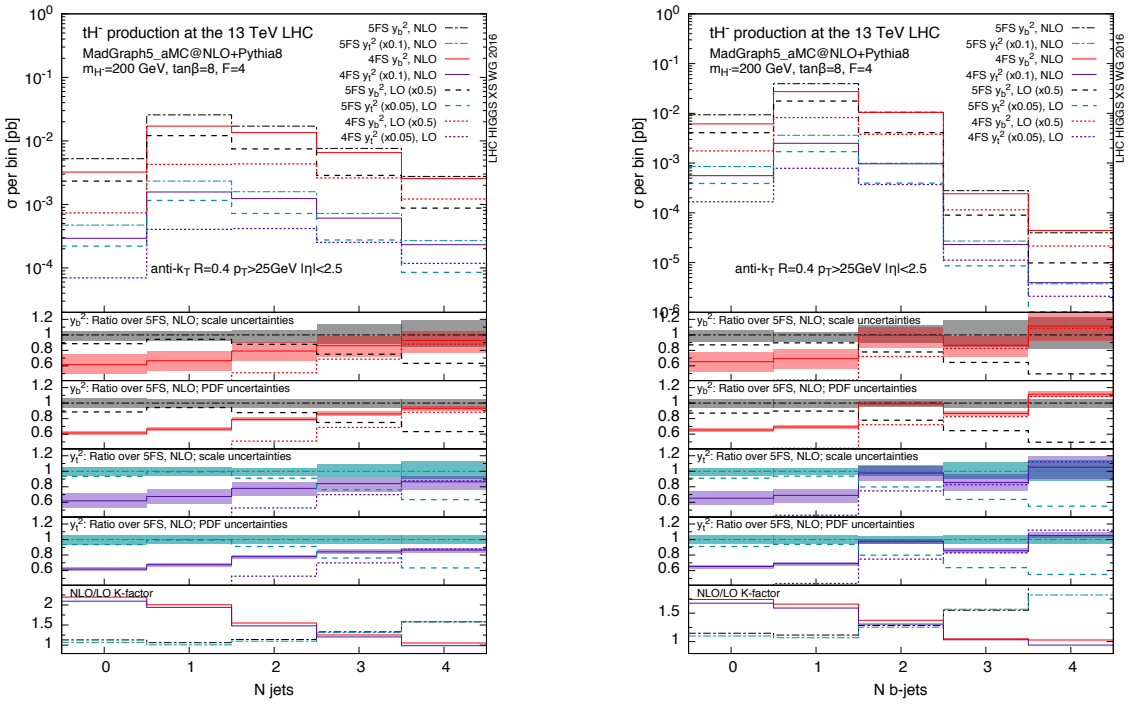

Figure 273: LO and NLO predictions matched with PYTHIA8 in the 4FS and 5FS, separately for the the y_{b}^2 and y_{t}^2 terms, for for jet (left) and b jet (right) multiplicity. Rescaling factors are introduced in the main frame for better visibility. The first four smaller frames at the bottom show the ratio over the NLO prediction in the 5FS for the y_b^2 and y_t^2 terms, and the scale and PDF uncertainty bands for the NLO curves. The bottom frame shows the differential K factor (NLO/LO) for the four predictions. A charged Higgs boson mass of $m_{\mathrm{H}^\pm} = 200$ GeV is assumed.

Chapter IV.4

Extended Scalar Sector

R. Gerosa, H. Logan, R. Santos, O. Stål, S. Su, X. Sun (Eds.) R. Aggleton, D. Barducci, F.J. Botella, G.C. Branco, D. Fontes, G.F. Giudice, H.E. Haber, S. Huber, A. Ilnicka, F. Kling, M. Krawczyk, D. Lopez-Val, K. Mimasu, S. Moretti, M. Nebot, J.M. No, M. Pelliccioni, M.N. Rebelo, T. Robens, J.C. Romão, N. Rompotis, C.H. Shepherd-Themistocleous, J.P. Silva, T. Stefaniak, M. Zaro

IV.4.1 Introduction

The two-Higgs doublet model (2HDM) is one of the simplest extensions of the Standard Model (SM) and is build by simply adding one more scalar doublet to the SM field content while keeping the Lagrangian invariant under the same symmetries. It was first proposed by T.D. Lee [1188] as a means to provide an extra source of CP-violation thus helping to explain the observed matter anti-matter asymmetry of the Universe. In recent years the 2HDM has been used as a benchmark model helping to identify possible directions to minimal changes with respect to the SM. These changes can lead to the inclusion of a dark matter candidate, new sources of CP-violation, baryogenesis and even a more elaborate flavour structure. Even in its minimal $\mathbb{Z}_2$ symmetric and CP-conserving version, it has been used by the ATLAS and CMS collaborations, to perform phenomenological studies involving extra scalars production and decay. In its CP-conserving versions the model has three neutral states - two CP-even (h and H) and one CP-odd (A) - and two charged states ($\mathrm{H}^{\pm}$) while the remaining three degrees of freedom are the longitudinal components of the gauge bosons. In its CP-violating versions the three neutral states have no definite CP numbers and are usually denoted by h_1, h_2 and h_3. A thorough description of the different versions of two-Higgs doublet models can be found in [485, 1189].

In order to avoid flavour changing neutral currents (FCNC) at tree-level, a $\mathbb{Z}_2$ symmetry is imposed on the fields ($\Phi_1 \to \Phi_1$ and $\Phi_2 \to -\Phi_2$). The Higgs potential invariant under $\mathbb{Z}_2$, softly broken by a dimension-two term, can be written as

$$\begin{aligned}\mathcal{V} = m_{11}^2 \Phi_1^\dagger \Phi_1 + m_{22}^2 \Phi_2^\dagger \Phi_2 - \left(m_{12}^2 \Phi_1^\dagger \Phi_2 + \mathrm{h.c.}\right) + \tfrac{1}{2}\lambda_1 \left(\Phi_1^\dagger \Phi_1\right)^2 + \tfrac{1}{2}\lambda_2 \left(\Phi_2^\dagger \Phi_2\right)^2 \\ + \lambda_3 \Phi_1^\dagger \Phi_1 \Phi_2^\dagger \Phi_2 + \lambda_4 \Phi_1^\dagger \Phi_2 \Phi_2^\dagger \Phi_1 + \left[\tfrac{1}{2}\lambda_5 \left(\Phi_1^\dagger \Phi_2\right)^2 + \mathrm{h.c.}\right] . \end{aligned} \tag{IV.4.1}$$

Since $\mathcal{V}$ has to be hermitian, m_{12}^2 and λ_5 can be complex while all other parameters have to be real. Choosing the two vacuum expectation values (VEVs) to be real we end up with a model that is either CP-conserving or explicitly CP-violating. This particular version of the CP-violating 2HDM, where both m_{12}^2 and λ_5 are complex and the VEVs are real, was first analysed in [1190]. In the following, the CP-conserving model is denoted by "2HDM" while the CP-violating model is denoted by "C2HDM".

Since the VEVs are real we can define $\tan\beta = v_2/v_1$ for both models. The remaining independent parameters for the 2HDM are the four masses M_{h}, M_{H}, M_{A} and $M_{\mathrm{H}^{\pm}}$, the rotation angle α that diagonalizes the CP-even mass matrix, and m_{12}^2. For the C2HDM the remaining free parameters are the two lighter neutral states masses M_1 and M_2, $M_{\mathrm{H}^{\pm}}$, the three rotation angles that diagonalize the neutral mass matrix α_1, α_2 and α_3 and $\mathrm{Re}[\mathrm{m}_{12}^2]$. If $\sin\alpha_2 = 0$, h_1 is a pure scalar and if $\sin\alpha_2 = 1$ h_1 is a pure pseudoscalar. The 2HDM Higgs boson couplings to massive gauge bosons are given by

$$g_{\mathrm{2HDM}}^{\mathrm{hVV}} = \sin(\beta-\alpha)\, g_{\mathrm{SM}}^{\mathrm{hVV}} \qquad\qquad g_{\mathrm{2HDM}}^{\mathrm{HVV}} = \cos(\beta-\alpha) g_{\mathrm{SM}}^{\mathrm{hVV}} \tag{IV.4.2}$$

while the lightest Higgs boson couplings in the CP-violating case can be written as

$$g_{\mathrm{C2HDM}}^{\mathrm{h}_1\mathrm{VV}} = \cos\alpha_2 \; g_{\mathrm{2HDM}}^{\mathrm{hVV}}. \tag{IV.4.3}$$

In order to avoid FCNCs at tree level, the simple solution of coupling fermions of a given electric charge to no more than one Higgs doublet [1191, 1192] is used. In practice, a $\mathbb{Z}_2$ symmetry is imposed to all fields and invariance of the Lagrangian under that symmetry is enforced. The $\mathbb{Z}_2$ charge assignments (Φ_1 is even and Φ_2 is odd) lead to four independent combinations [1193]: only Φ_2 couples to all fermions (type I); Φ_2 couples to up-type quarks while Φ_1 couples to charged leptons and down-type quarks (type II); Φ_2 couples to charged leptons and up-type quarks while Φ_1 couples to down-type quarks (type Flipped or Y); Φ_2 couples to quarks while Φ_1 couples to charged leptons (type Lepton Specific or X). The Yukawa couplings for the CP-conserving model, relative to the SM ones, are shown in Table 127.

Table 127: Yukawa couplings to the scalars h, H and A normalized to the SM Higgs Yukawa couplings. Notation is $c(s)_\alpha = \cos(\sin)\alpha$, $c(s)_\beta = \cos(\sin)\beta$.

	$y^{\rm u}_{\rm h}$	$y^{\rm d}_{\rm h}$	$y^{\ell}_{\rm h}$	$y^{\rm u}_{\rm H}$	$y^{\rm d}_{\rm H}$	$y^{\ell}_{\rm H}$	$y^{\rm u}_{\rm A}$	$y^{\rm d}_{\rm A}$	$y^{\ell}_{\rm A}$
Type-I	$\frac{c_\alpha}{s_\beta}$	$\frac{c_\alpha}{s_\beta}$	$\frac{c_\alpha}{s_\beta}$	$\frac{s_\alpha}{s_\beta}$	$\frac{s_\alpha}{s_\beta}$	$\frac{s_\alpha}{s_\beta}$	$\cot\beta$	$-\cot\beta$	$-\cot\beta$
Type-II	$\frac{s_\alpha}{s_\beta}$	$-\frac{s_\alpha}{c_\beta}$	$-\frac{s_\alpha}{c_\beta}$	$\frac{s_\alpha}{s_\beta}$	$\frac{c_\alpha}{c_\beta}$	$\frac{c_\alpha}{c_\beta}$	$\cot\beta$	$\tan\beta$	$\tan\beta$
Flipped (Y)	$\frac{c_\alpha}{s_\beta}$	$-\frac{s_\alpha}{c_\beta}$	$\frac{c_\alpha}{s_\beta}$	$\frac{s_\alpha}{s_\beta}$	$\frac{s_\alpha}{s_\beta}$	$\frac{s_\alpha}{s_\beta}$	$\cot\beta$	$\tan\beta$	$-\cot\beta$
Lepton Specific (X)	$\frac{c_\alpha}{s_\beta}$	$\frac{c_\alpha}{s_\beta}$	$-\frac{s_\alpha}{c_\beta}$	$\frac{s_\alpha}{s_\beta}$	$\frac{c_\alpha}{c_\beta}$	$\frac{s_\alpha}{s_\beta}$	$\cot\beta$	$-\cot\beta$	$\tan\beta$

The Yukawa couplings for the the lightest Higgs boson in the C2HDM can be obtained from the respective 2HDM h couplings via

$$y^{\rm C2HDM}_{\rm h_1} = \cos\alpha_2\, y^{\rm 2HDM}_{\rm h} \pm \sin\alpha_2\, F(\tan\beta)\,\gamma_5 \tag{IV.4.4}$$

where the sign of the pseudoscalar term and the function $F(\tan\beta)$ (that can be either $\tan\beta$ or $\cot\beta$) depend on the model type considered (see details in [1194]).

We will now briefly discuss some properties of the models. When $\cos(\beta-\alpha)=0$ there is no mixing of the two-Higgs-doublet fields in the Higgs basis which is the basis where the Goldstone bosons are all in one of the doublets. For this reason it is called the alignment limit and h has SM-like couplings to the fermions and to the gauge bosons [IV.20]. The decoupling limit [1195] is defined by the previous condition plus having all scalar masses well above the electroweak scale. Finally the wrong sign Yukawa coupling [1196–1198] regime is defined as the region of 2HDM parameter space in which at least one of the couplings of h to down-type and up-type fermion pairs is opposite in sign to the corresponding coupling of h to V V. In the convention followed here ($|\alpha| \leq \pi/2$), the limit appears only in Type II and Flipped versions of the 2HDM for the down-type quarks and is obtained by setting $\sin(\beta+\alpha)=1$. Other wrong sign limits are also possible as discussed in [1197, 1198].

There are two particular cases of the 2HDM that will also be discussed. These are the *Inert Model* and a *Fermiophobic Model* which are particular cases of a type I 2HDM. The potential of the Inert Model [1199–1208] is obtained from the one in equation (IV.4.1) by setting $m^2_{12}=0$ and by taking the VEV of the second doublet to be zero. In the Yukawa Lagrangian, only the doublet that generates a VEV, Φ_1, couples to all fermions. Φ_2 is usually called the dark doublet, since it contains the dark matter candidate. The scalars from the dark doublet couple to gauge bosons via the covariant derivative term, but because the $\mathbb{Z}_2$ symmetry is exact, they always come in pairs in their interactions, that is the $\mathbb{Z}_2$ charge is conserved. The Fermiophobic Model [1209–1211] is obtained form the usual type I 2HDM. By setting $\cos\alpha = 0$, the lightest CP-even scalar decouples from all fermions and becomes fermiophobic. The discovery of the Higgs boson and subsequent measurement of Higgs rates has excluded the possibility

[IV.20] If $\sin(\beta-\alpha)=0$ it is the heaviest Higgs boson H that acquires SM-like couplings.

of a 125 GeV fermiophobic Higgs boson by more than 3σ [1212] at the end of Run 1. There is however the possibility of having a heavier fermiophobic CP-even Higgs boson, which implies setting $\sin\alpha = 0$. In this scenario the lightest CP-even scalar is the SM-like Higgs boson while the heavy CP-even scalar decouples from the fermions.

There are other versions of 2HDMs where the $\mathbb{Z}_2$ symmetry is not imposed to the scalar doublets. These models either have tree-level FCNCs or are not stable under the renormalization group [1213] (see also [485]). However, there are ways to force the neutral flavour changing currents to be small at tree-level. One such example is a class of models known as BGL [1214] models, where the tree-level FCNC couplings are proportional to the elements of the CKM matrix. Therefore, the off-diagonal CKM elements naturally suppress the neutral scalars flavour changing couplings. BGL models were first proposed for the quark sector in [1214] and later generalized in [1215]. The extension to the leptonic sector was presented in [1216].

There are several versions of the BGL models and the first was obtained by imposing the following symmetry on the quark and scalar sector of the Lagrangian,

$$\mathrm{Q}^0_{Lj} \to \exp(i\tau)\,\mathrm{Q}^0_{Lj}\,, \qquad \mathrm{u}^0_{Rj} \to \exp(i2\tau)\mathrm{u}^0_{Rj}\,, \qquad \Phi_2 \to \exp(i\tau)\Phi_2\,, \tag{IV.4.5}$$

where $\tau \neq 0, \pi$, with all other quark fields transforming trivially under the symmetry. The index j can be fixed as either 1, 2 or 3. Alternatively the symmetry may be chosen as

$$\mathrm{Q}^0_{Lj} \to \exp(i\tau)\,\mathrm{Q}^0_{Lj}\,, \qquad \mathrm{d}^0_{Rj} \to \exp(i2\tau)\mathrm{d}^0_{Rj}\,, \quad \Phi_2 \to \exp(-i\tau)\Phi_2\,. \tag{IV.4.6}$$

The symmetry given by Eq. (IV.4.5) leads to Higgs FCNC in the down sector and the models are known as BGL up-type models, whereas the symmetry specified by Eq. (IV.4.6) leads to Higgs FCNC in the up sector and to the BGL down-type models. These two alternative choices of symmetries combined with the three possible ways of fixing the index j give rise to six different realizations of the model with the flavour structure, in the quark sector, controlled by the CKM matrix. In the leptonic sector, with Dirac type neutrinos, there is a perfect analogy with the quark sector. There are thirty six different models corresponding to the combinations of the six possible different implementations in each sector.

This symmetry constrains the Higgs potential in such a way that it does not violate CP neither explicitly nor spontaneously. As a result, once in the Higgs basis, the fields H^+ and A are already physical and only H^0 and R (real and imaginary neutral fields respectively) are allowed to mix such that they are combined into the two CP-even states h and H via the rotation

$$\mathrm{h} = s_{\beta-\alpha}\mathrm{H} + c_{\beta-\alpha}R, \qquad \mathrm{H} = c_{\beta-\alpha}\mathrm{H}^0 - s_{\beta-\alpha}R \tag{IV.4.7}$$

In the case of $s_{\beta-\alpha} \neq 1$ all neutral scalars mediate flavour changing neutral currents.

For a general 2HDM the Yukawa couplings in terms of quark mass eigenstates for H^+, H^0, R and A are given by

$$\begin{aligned}\mathcal{L}_Y(\text{quark, Higgs}) = &-\frac{\sqrt{2}\mathrm{H}^\pm}{v}\overline{\mathrm{u}}\left(VN_\mathrm{d}\gamma_R - N_\mathrm{u}^\dagger V\gamma_L\right)\mathrm{d} + \text{h.c.} - \frac{H^0}{v}\left(\bar{u}D_u u + \bar{d}D_d\, d\right)\\ &-\frac{R}{v}\left[\overline{\mathrm{u}}(N_\mathrm{u}\gamma_R + N_\mathrm{u}^\dagger\gamma_L)\mathrm{u} + \overline{\mathrm{d}}(N_\mathrm{d}\gamma_R + N_\mathrm{d}^\dagger\gamma_L)\,\mathrm{d}\right]\\ &+i\frac{\mathrm{A}}{v}\left[\overline{\mathrm{u}}(N_\mathrm{u}\gamma_R - N_\mathrm{u}^\dagger\gamma_L)\mathrm{u} - \overline{\mathrm{d}}(N_\mathrm{d}\gamma_R - N_\mathrm{d}^\dagger\gamma_L)\,\mathrm{d}\right].\end{aligned} \tag{IV.4.8}$$

In BGL up-type models the matrices N_d and N_u have the following simple form

$$\left(N_\mathrm{d}^{(\mathrm{u}_j)}\right)_{rs} = \left[t_\beta\delta_{rs} - (t_\beta + t_\beta^{-1})V^*_{jr}V_{js}\right](D_\mathrm{d})_{ss} \tag{IV.4.9}$$

where no sum in j is implied and t_β stands for $\tan\beta$. The upper index (u_j) indicates that the BGL is of the up-type form, with index j, thus leading to FCNC in the down-sector. Note that all FCNC are

proportional to the factor $(t_\beta + t_\beta^{-1})$ and to a product of elements of one single row of the $V_{\rm CKM}$. The corresponding $N_{\rm u}$ matrix is given by

$$\left(N_{\rm u}^{({\rm u}_j)}\right)_{rs} = \left[t_\beta - (t_\beta + t_\beta^{-1})\delta_{rj}\right](D_{\rm u})_{ss}\delta_{rs}\,. \tag{IV.4.10}$$

$N_{\rm u}$ is a diagonal matrix, the t_β dependence is not the same for all diagonal entries. It is proportional to $(-t_\beta^{-1})$ for the (jj) element and to t_β for all other elements. The index j fixes the row of the $V_{\rm CKM}$ matrix which suppresses the flavour changing neutral currents. Since for each up-type BGL model a single row of $V_{\rm CKM}$ participates in these couplings, one may choose a phase convention where all elements of $N_{\rm u}$ and $N_{\rm d}$ are real.

In BGL down-type models the matrices $N_{\rm d}$ and $N_{\rm u}$ exchange rôle,

$$\left(N_{\rm u}^{({\rm d}_j)}\right)_{rs} = \left[t_\beta\delta_{rs} - (t_\beta + t_\beta^{-1})V_{rj}V_{sj}^*\right](D_{\rm u})_{ss} \tag{IV.4.11}$$

$$\left(N_{\rm d}^{({\rm d}_j)}\right)_{rs} = \left[t_\beta - (t_\beta + t_\beta^{-1})\delta_{rj}\right](D_{\rm d})_{ss}\delta_{rs} \tag{IV.4.12}$$

In down-type models the flavour changing neutral currents are suppressed by the columns of the $V_{\rm CKM}$ matrix. Since the flavour structure of these scalar currents results from a symmetry of the Lagrangian, each BGL model is natural and stable under the renormalization group. Furthermore, the resulting number of free parameters is very small and therefore BGL models are very predictive.

IV.4.1.a Input parameters

- 2HDM
  The set of input parameters are the four masses $M_{\rm h}$, $M_{\rm H}$, $M_{\rm A}$, $M_{\rm H^\pm}$, $\tan\beta$, α and m_{12}^2.
- Inert Model
  The input parameters are the four masses $M_{\rm h}$, $M_{\rm H}$, $M_{\rm A}$, $M_{\rm H^\pm}$, λ_2 and $\lambda_{345} = \lambda_3 + \lambda_4 + \lambda_5$. The h boson is taken to be the SM-like Higgs boson discovered at the LHC.
- Fermiophobic Model
  The input parameters are the four masses $M_{\rm h}$, $M_{\rm H}$, $M_{\rm A}$, $M_{\rm H^\pm}$, $\tan\beta$ and m_{12}^2. The fermiophobic limit is attained with the condition $\sin\alpha = 0$. The fermiophobic scalar is denoted by H and the charged Higgs boson mass is chosen such that $M_{\rm A} = M_{\rm H^\pm}$. The free parameters are then $M_{\rm H}$, $\Delta M = M_{\rm H} - M_{\rm A}$ and $\tan\beta$.
- C2HDM
  The input parameters are three masses M_1, M_2, $M_{\rm H^\pm}$, $\tan\beta$, $Re[m_{12}^2]$ and the three rotation angles of the neutral sector α_1, α_2 α_3. With this choice the heavier state has a mass defined by

$$M_3^2 = \frac{M_1^2\, R_{13}(R_{12}\tan\beta - R_{11}) + M_2^2\, R_{23}(R_{22}\tan\beta - R_{21})}{R_{33}(R_{31} - R_{32}\tan\beta)}. \tag{IV.4.13}$$

  and the parameter space will be restricted to values which obey $M_3 > M_2$.
- BGL
  The set of input parameters are the four masses $M_{\rm h}$, $M_{\rm H}$, $M_{\rm A}$, $M_{\rm H^\pm}$, $\tan\beta$ and $\cos(\beta-\alpha)$.

IV.4.2 Tools and constraints

At present there are only two public codes that allows one to perform scans in the 2HDM parameter space: 2HDMC [558,1217] - 2-Higgs Doublet Model Calculator and ScannerS [1198,1218]. These codes can only be used for CP-conserving versions of the 2HDM. Several codes have been compared [1219] regarding the neutral scalar production in gluon fusion and the decay of all scalars in the 2HDM.

IV.4.2.a Vacuum stability and theoretical constraints

The CP-conserving minimum of any 2HDM is stable against tunnelling to both CP-violating and charge breaking minima [1220, 1221]. However, the potential invariant under $\mathbb{Z}_2$ and softly broken by the term m_{12}^2, can still have two simultaneous CP-conserving minima [1222–1225]. In this case, choosing the global minimum is easily achieved by imposing a simple condition on the parameters of the potential [1226, 1227].

The two codes 2HDMC and ScannerS have in-built the following theoretical constraints: tree-level vacuum stability [1199, 1223], that is, the potential is forced to be bounded from below at tree-level, and perturbative unitarity [1228, 1229] is enforced to the quartic couplings of the potential as proposed by Lee, Quigg and Thacker [1230] for the SM. In 2HDMC a further perturbativity constraint is imposed on the quartic couplings of the mass eigenstates fields ($|\lambda_{ijkl}| \leq 4\pi$) where the indices run over all allowed quartic vertices. In ScannerS one can opt for having a global minimum at tree-level by imposing the condition proposed in [1226, 1227] to the parameters of the potential. For all other benchmarks proposed, the points produced comply to the respective vacuum stability and perturbative unitarity (or/and perturbativity) constraints.

IV.4.2.b Experimental constraints

The parameter space of the models that is used to produce benchmarks satisfies a number of experimental constraints described in this section. If for a given benchmark one or more constraints are not taken into account it will be explicitly stated. This section is intended to give an overview of the most relevant experimental constraints for all benchmark points presented. It should be noted that, for instance, the constraints for the charged Higgs boson mass from LEP do not apply to the Inert Model as it does not couple to fermions. Conversely, dark matter constraints only apply to the Inert Model.

The main experimental constraints are

- The parameter space complies with S and T parameters [1231–1235] as derived from electroweak precision observables [1236].
- Collider constraints are taken into account. In most cases and in particular in 2HDMC and ScannerS these bounds are considered via an interface with the HIGGSBOUNDS [1237] and HIGGSSIGNALS [1238] codes that include all LHC data published so far by the ATLAS and CMS collaboration and that are updated regularly. The codes also include the LEP bounds and in particular the only bound on the charged Higgs boson mass that only assumes that $BR(\mathrm{H}^\pm \to \mathrm{cs}) + BR(\mathrm{H}^\pm \to \tau\nu) + BR(\mathrm{H}^\pm \to \mathrm{AW}^\pm) = 1$ [1239]. This leads us to roughly consider for the four type of 2HDMs (and C2HDMs) $M_{\mathrm{H}^\pm} \geq 90$ GeV.
- There are indirect constraints on the $(M_{\mathrm{H}^\pm}, \tan\beta)$ plane stemming mainly from loop processes involving charged Higgs bosons but also from direct measurements at the LHC. Indirect bounds come mainly from B-physics observables [1240–1244] and $R_{b\bar{b}} = \Gamma(\mathrm{Z} \to \mathrm{b\bar{b}})/\Gamma(\mathrm{Z} \to \text{hadrons})$/ [1245–1247]. When considering all experimental results a rough bound of $\tan\beta \geq 1$ is obtained. Of particular importance is the bound coming from the charged Higgs loop contribution to $\mathrm{b} \to \mathrm{s}\gamma$ that applies only to Type II and Flipped (Y) and is at present $M_{\mathrm{H}^\pm} \geq 480$ GeV [1248]. Direct constraints in the $(M_{\mathrm{H}^\pm}, \tan\beta)$ plane were obtained during the LHC Run 1 in the process $\mathrm{pp} \to \mathrm{t\bar{t}}(\mathrm{H}^+\mathrm{W}^-\mathrm{b\bar{b}})$ [1249, 1250].
  Except for $\mathrm{B} \to \tau^\pm\nu_\tau$ and $\overline{\mathrm{B}} \to \mathrm{D}^{(*)}\tau^-\bar{\nu}_\tau$ the 2HDM contributions to B-physics arise via one-loop radiative corrections. For such observables, cancellations could occur in the loops if other sources of new physics are considered. This would lead to cancellations in the loop from other sources of new physics and a consequent relaxation of the respective bounds.
- The CP-violating phase of the C2HDM is also constrained by electric dipole moment (EDM) measurements. The most stringent bound [1251] comes from the ACME [1252] results on the ThO molecule EDM. Points are rejected if the calculated EDMs, with Barr-Zee diagrams with

fermions in the loop, are not of the order of magnitude of ACME result. The ACME limit can only be evaded by either going to the limit of the CP-conserving 2HDM or in scenarios where cancellations [1253, 1254] among the neutral scalars occur. It should be noted that ref. [1253] argues that the extraction of the electron EDM from the data is filled with uncertainties and an order of magnitude larger EDM than that claimed by ACME should be allowed for.

– Regarding astrophysical constraints on the dark matter part of the Inert Doublet Model, relic density limits are required to respect the results obtained by the Planck experiment [1255]:

$$\Omega_c h^2 = 0.1197 \pm 0.0022, \tag{IV.4.14}$$

where an upper limit of

$$\Omega_c h^2 \leq 0.1241, \tag{IV.4.15}$$

is imposed, which corresponds to not over closing the universe at $\sim 95\,\%$ confidence level. Direct detection limits are taken into account by using an approximation function (cf. [1203] for details) to compare with limits from the LUX experiment [1256], where multicomponent dark matter scenarios are discarded. The dark matter properties are calculated by processing through MicrOmegas (version 4.2.3) [1257], where [1258] provides explicit details about the calculation of nucleon-dark matter cross sections.

IV.4.2.c Calculation of cross sections and decay widths

A detailed study of the various tools and their accuracy has been performed in [1219]. For the CP-conserving case it includes both production via gluon and $\mathrm{b\bar{b}}$ fusion and decay of the 2HDM scalars. For the production the tools compared were SUSHI [135] and HIGLU [133]. Regarding the scalar decays the two codes compared were 2HDMC [558, 1217] and HDECAY [69, 71] with a very good agreement. The remaining cross sections were just rescaled from the SM ones.

In the particular cases of the Inert and Fermiophobic models, the cross sections cannot be obtained from the SM ones and were calculated at LO with MadGraph 5 [364]. The new decays in the BGL were calculated at LO.

IV.4.3 Benchmark points

In this section benchmark points for the 2HDM are presented. For each point, plane or scenario physical motivation is given together with their main features, cross sections and branching ratios. In same cases only scenarios were proposed.

A quick summary of the points before their detailed presentation is shown in the following:

$\mathrm{BP1_A}$ 2HDM, non-alignment, h approximately SM-like; plane: $1 < \tan\beta < 60$, $150 < M_{\mathrm{H}} < 600$ GeV
signatures: type-I $\mathrm{H} \to \mathrm{hh}$, $\mathrm{t\bar{t}}$, WW, ZZ; type-II: $\mathrm{H} \to \mathrm{b\bar{b}}$, $\mathrm{t\bar{t}}$

$\mathrm{BP1_B}$ 2HDM, H is SM-like; line of $65 < M_{\mathrm{h}} < 120$ GeV; signatures: $\mathrm{h} \to \mathrm{b\bar{b}}$, $\tau\tau$

$\mathrm{BP1_C}$ 2HDM, $M_{\mathrm{h}} = M_{\mathrm{A}} = 125$ GeV; line $1 < \tan\beta < 10$ for $M_{\mathrm{H}} = M_{\mathrm{H}^\pm} = 300$ GeV
large deviations from the SM value of $\tau\tau$ for the 125 GeV Higgs boson

$\mathrm{BP1_D}$ 2HDM short cascades, $M_{\mathrm{h}} = 125$ GeV, exact alignment; line $250 < M_{\mathrm{H}} < 500$ GeV
signatures: $\mathrm{H} \to \mathrm{ZA}$, $\mathrm{W^\pm H^\pm}$, $\mathrm{H^\pm H^\mp}$, AA

$\mathrm{BP1_E}$ 2HDM long cascades, $M_{\mathrm{h}} = 125$ GeV, exact alignment; line $200 < M_{\mathrm{H}} < 300$ GeV
signatures: $\mathrm{H^\pm} \to \mathrm{W^\pm A} \to \mathrm{W^\pm ZH}$, $\mathrm{A} \to \mathrm{W^\pm H^\mp} \to \mathrm{W^\pm W^\mp H}$

$\mathrm{BP1_F}$ 2HDM, $M_{\mathrm{h}} = 125$ GeV, opposite sign coupling to down-type fermions;
plane: $5 < \tan\beta < 50$, $150 < M_{\mathrm{H}} < 600$ GeV; signatures: $\mathrm{H} \to \mathrm{WW}$, ZZ

BP1$_{\rm G}$ 2HDM, $M_{\rm h} = 125$ GeV, with an MSSM-like Higgs sector;
signatures $\rm H \to hh$ and $\rm H, A \to t\bar{t}$ or $\rm H, A \to \tau\tau$ for large $\tan\beta$

BP2 Exotic decays in the 2HDM alignment limit; planes provided

BP3 2HDM, $M_{\rm h} = 125$ GeV, large mass splitting between H and A for electroweak baryogenesis
signatures: $\rm A \to ZH$ with $\rm H \to WW, b\bar{b}, t\bar{t}$

BP4 2HDM, $M_{\rm h} = 125$ GeV, A is very light ($M_{\rm A} \lesssim M_{\rm Z}$); signatures: $\rm h \to ZA$ with $\rm A \to b\bar{b}$, $\tau\tau$, $\mu\mu$

BP5 Inert 2HDM, $M_{\rm h} = 125$ GeV and SM-like, H dark matter candidate, $M_{\rm H} > 45$ GeV
signatures: $\rm A \to ZH$, $\rm H^{\pm} \to W^{\pm}H$; H will give missing transverse energy in the event

BP6 Fermiophobic 2HDM, $M_{\rm h} = 125$ GeV and SM-like, H fermiophobic; various planes are suggested
signatures: $\rm pp \to HA, HH^{\pm}$, and has large branching ratios to $\rm H \to WW, ZZ$

BP7 C2HDM, $M_{\rm h} = 125$ GeV and SM-like, CP-violation detected by the simultaneous existence of 3 decay channels signatures: e.g. $\rm h_3 \to h_2 Z$, $\rm h_2 \to h_1 Z$, $\rm h_3 \to h_1 Z$ simultaneously

BP8 BGL models: Higgs bosons with flavour changing decays; plane: $\tan\beta$ versus $\cos(\beta-\alpha)$
signatures: $\rm t \to hc$, $\rm h \to \tau\tau, b\bar{b}, bs, \mu\tau$

A detailed description of the benchmark points follows in the next sections.

IV.4.3.a Benchmark points $BP1$

Scenario $BP1_A$: 2HDM non-alignment	
Howard E. Haber and Oscar Stål from Eur. Phys. J. C **75** (2015) 491, arXiv:1507.04281 [hep-ph]	
Main Features	Departures from the alignment limit with h SM-like. Scan over values of $1 < \tan\beta < 50$.
Type-I Scenarios $BP1_{A1.1}$ with $\cos(\beta-\alpha) = 0.1$, and $BP1_{A1.2}$ with $\cos(\beta-\alpha) = 0.1 \times (150\ \text{GeV}/M_{\rm H})^2$	
Spectrum	$M_{\rm h} = 125$ GeV, 150 GeV $< M_{\rm H} < 600$ GeV, $M_{\rm H} < M_{\rm H^{\pm}} = M_{\rm A}$
Production cross sections and branching fractions	
h	SM-like cross-sections and decays with small deviations from SM predictions.
H	gg fusion cross sections are largest at low $\tan\beta$ values. At low $\tan\beta$, $\rm H \to hh$ dominant for $2M_{\rm h} < M_{\rm H} < 2m_{\rm t}$ and $\rm H \to t\bar{t}$ dominates for $M_{\rm H} > 2m_{\rm t}$. At higher $\tan\beta$ values, $\rm t\bar{t}$ is suppressed and hh is dominant for $M_{\rm H} > 2M_{\rm h}$ and the WW and ZZ modes are more relevant.
A and $\rm H^{\pm}$	Assumed to be very heavy with little impact on LHC Higgs phenomenology
Type-II Scenarios $BP1_{A2.1}$ with $\cos(\beta-\alpha) = 0.1$, and $BP1_{A2.2}$ with $\cos(\beta-\alpha) = 0.1 \times (150\ \text{GeV}/M_{\rm H})^2$	
Spectrum	$M_{\rm h} = 125$ GeV, 150 GeV $< M_{\rm H} < 600$ GeV, $M_{\rm H} < M_{\rm H^{\pm}} = M_{\rm A}$
Production cross sections and branching fractions	

h	SM-like cross-sections and decays with small deviations from SM predictions.
H	gg fusion cross sections are largest either at low $\tan\beta$ values or at high $\tan\beta$ values for moderate values of $M_{\rm H}$. $\rm b\bar{b}$ fusion cross sections relevant at larger $\tan\beta$. At low $\tan\beta$, $\rm H \to b\bar{b}$ dominant for $M_{\rm H} < 2m_{\rm t}$ and $\rm H \to t\bar{t}$ dominates for $M_{\rm H} > 2m_{\rm t}$. At higher $\tan\beta$, $\rm t\bar{t}$ is somewhat suppressed above threshold and $\rm b\bar{b}$ is dominant.
A and $\rm H^{\pm}$	Assumed to be very heavy with little impact on LHC Higgs phenomenology

Scenario $BP1_B$: 2HDM with a SM-like H

Howard E. Haber and Oscar Stål
from Eur. Phys. J. C **75** (2015) 491, arXiv:1507.04281 [hep-ph]

Main Features	The heavier of the two CP-even Higgs bosons, H is SM-like. Scan over values of $\frac{1}{2}M_{\rm H} < M_{\rm h} < M_{\rm H}$, with $\tan\beta = 1.5$.
Type-I Scenarios $BP1_{B1.1}$ with $\cos(\beta-\alpha) = 1.0$, and $BP1_{B1.2}$ with $\cos(\beta-\alpha) = 0.9$	
Spectrum	$M_{\rm H} = 125$ GeV, 65 GeV $< M_{\rm h} <$ 120 GeV, $M_{\rm H} < M_{\rm H^{\pm}} = M_{\rm A}$
Production cross sections and branching fractions	
H	SM-like cross-sections and decays with small deviations from SM predictions.
h	$\mathrm{BR}(\rm h \to b\bar{b}) \sim 75{-}80\%$ and $\mathrm{BR}(\rm h \to \tau\tau) \sim 8\%$.
A and $\rm H^{\pm}$	very heavy and difficult to detect at the LHC
Type-II Scenario $BP1_{B2}$ with $\cos(\beta-\alpha) = 1.0$	
Spectrum	$M_{\rm h} = 125$ GeV, 150 GeV $< M_{\rm H} <$ 600 GeV, $M_{\rm H} < M_{\rm H^{\pm}} = M_{\rm A}$
Production cross sections and branching fractions	
H	SM cross-sections and decays with no deviations from SM predictions.
h	$\mathrm{BR}(\rm h \to b\bar{b}) \sim 75{-}80\%$ and $\mathrm{BR}(\rm h \to \tau\tau) \sim 8\%$.
A and $\rm H^{\pm}$	Assumed to be very heavy with little impact on LHC Higgs phenomenology

Scenario $BP1_C$: 2HDM with degenerate h and A

Howard E. Haber and Oscar Stål
from Eur. Phys. J. C **75** (2015) 491, arXiv:1507.04281 [hep-ph]

Main Features	The CP-even h and the CP-odd A are roughly mass-degenerate and both contribute to the observed scalar at 125 GeV. H and $\rm H^{\pm}$ are assumed heavy. Exact alignment limit of $\cos(\beta-\alpha) = 0$ taken. Scan over values of $1 < \tan\beta < 10$.
Type-I Scenario $BP1_{C1}$	
Spectrum	$M_{\rm h} = M_{\rm A} = 125$ GeV, $M_{\rm H} = M_{\rm H^{\pm}} = 300$ GeV
Production cross sections and branching fractions	
h, A	Combined $\sigma \times \mathrm{BR}$ of $\rm h,\ A \to \tau\tau$ deviates significantly from SM for $\tan\beta < 2$. At large $\tan\beta$, the combined signal approaches that of the SM.

H and $H^{\pm}$	Assumed to be very heavy with little impact on LHC Higgs phenomenology
Type-II Scenario $BP1_{C2}$	
Spectrum	$M_{\rm H} = M_{\rm A} = 125$ GeV, $M_{\rm H} = M_{\rm H^{\pm}} = 300$ GeV
Production cross sections and branching fractions	
h, A	Combined $\sigma \times$ BR of h, A $\to \tau\tau$ deviates significantly from SM over the entire $\tan\beta$ range (with a minimum enhancement of about 1.5 at at $\tan\beta = 3.5$.
H and $H^{\pm}$	Assumed to be very heavy with little impact on LHC Higgs phenomenology

Scenario $BP1_D$: - short cascade of Higgs-to-Higgs boson decay

Howard E. Haber and Oscar Stål
from Eur. Phys. J. C **75** (2015) 491, arXiv:1507.04281 [hep-ph]

Main Features	h has SM couplings in the exact alignment limit, $\cos(\beta-\alpha) = 0$. The Higgs boson mass spectrum is chosen such that either one or both decay modes, $H \to ZA$ and/or $H \to W^{\pm}H^{\mp}$ are open, resulting in a short cascade of Higgs-to-Higgs boson decay. Scan over 250 GeV $< M_{\rm H} <$ 500 GeV.
Type-I Scenario $BP1_{D1.1}$ or Type-II Scenario $BP1_{D1.2}$ with $\tan\beta = 2$	
Spectrum	$M_{\rm h} = 125$ GeV and $M_{\rm H}^2 = M_{\rm H^{\pm}}^2 = M_{\rm A}^2 + v^2$, where $v \equiv 246$ GeV.
Production cross sections and branching fractions	
$M_{\rm h}$	Cross sections and branching ratios are SM-like. Small corrections to $M_{\rm h} \to \gamma\gamma$ due to $H^{\pm}$-loop.
H	$H \to ZA$ kinematically allowed and dominant below $t\bar{t}$ threshold. $H \to AA$ can be significant if kinematically allowed.
$H^{\pm}$	$H^{\pm} \to W^{\pm}A$ is kinematically allowed, but may have a small BR.
Type-I Scenario $BP1_{D2.1}$ or Type-II Scenario $BP1_{D2.2}$ with $\tan\beta = 2$	
Spectrum	$M_{\rm h} = 125$ GeV and $M_{\rm H}^2 = M_{\rm A}^2 = M_{\rm H^{\pm}}^2 + v^2$, where $v \equiv 246$ GeV.
Production cross sections and branching fractions	
h	Cross sections and branching ratios are SM-like. Small corrections to $h \to \gamma\gamma$ due to $H^{\pm}$-loop.
H	$H \to W^{\pm}H^{\mp}$ kinematically allowed and dominant below $t\bar{t}$ threshold. $H \to H^{+}H^{-}$ can be significant if kinematically allowed.
A	$A \to W^{\pm}H^{\mp}$ is kinematically allowed, but may have a small BR.
Type-I Scenario $BP1_{D3.1}$ or Type-II Scenario $BP1_{D3.2}$ with $\tan\beta = 2$	
Spectrum	$M_{\rm h} = 125$ GeV and $M_{\rm A}^2 = M_{\rm H^{\pm}}^2 = M_{\rm H}^2 - v^2$, where $v \equiv 246$ GeV.
Production cross sections and branching fractions	
h	Cross sections and branching ratios are SM-like. Small corrections to $h \to \gamma\gamma$

	due to $\mathrm{H}^{\pm}$-loop.
H	$\mathrm{H} \to \mathrm{ZA}$ and $H \to \mathrm{W}^{\pm}\mathrm{H}^{\mp}$ are both kinematically allowed and significant below $\mathrm{t\bar{t}}$ threshold. $\mathrm{H} \to \mathrm{AA}$ and/or $\mathrm{H} \to \mathrm{H}^{+}\mathrm{H}^{-}$ can be significant if kinematically allowed.

Scenario $BP1_E$: Long cascade of Higgs-to-Higgs boson decays

Howard E. Haber and Oscar Stål
from Eur. Phys. J. C **75** (2015) 491, arXiv:1507.04281 [hep-ph]

Main Features	h has SM couplings in the exact alignment limit, $\cos(\beta-\alpha)=0$. The Higgs boson mass spectrum is chosen such that a long cascade of Higgs-to-Higgs boson decays, $\mathrm{H}^{\pm} \to \mathrm{W}^{\pm}\mathrm{A} \to \mathrm{W}^{\pm}\mathrm{ZH}$ or $\mathrm{A} \to \mathrm{W}^{\pm}\mathrm{H}^{\mp} \to \mathrm{W}^{\pm}\mathrm{W}^{\mp}\mathrm{H}$, are kinematically allowed. The former will compete with $\mathrm{H}^{\pm} \to \mathrm{W}^{\pm}\mathrm{H}$ and the latter will compete with $\mathrm{A} \to \mathrm{ZH}$. Scan over 200 GeV $< M_{\mathrm{H}} <$ 300 GeV.
Type-I Scenario $BP1_{E1}$ with $\tan\beta = 2$	
Spectrum	$M_{\mathrm{h}} = 125$ GeV and $M_{\mathrm{H}} < M_{\mathrm{A}} < M_{\mathrm{H}^{\pm}}$
Production cross sections and branching fractions	
h	Cross sections and branching ratios are SM-like.
H	Decays dominantly into the heaviest kinematically accessible fermion pairs.
$\mathrm{H}^{\pm}$	BR($\mathrm{H}^{\pm} \to \mathrm{W}^{\pm}\mathrm{H}$) $\sim$ 0.74–0.79. BR for the long cascade of order a few per cent.
A	BR($\mathrm{A} \to \mathrm{ZH}$) $\sim$ 0.39–0.62.
Type-I Scenario $BP1_{E2}$ with $\tan\beta = 2$	
Spectrum	$M_{\mathrm{h}} = 125$ GeV and $M_{\mathrm{H}} < M_{\mathrm{H}^{\pm}} < M_{\mathrm{A}}$.
Production cross sections and branching fractions	
h	Cross sections and branching ratios are SM-like.
H	Decays dominantly into the heaviest kinematically accessible fermion pairs.
A	BR($\mathrm{A} \to \mathrm{ZH}$) $\sim$ 0.50–0.56. BR for the long cascade of order a few per cent.
$\mathrm{H}^{\pm}$	BR($\mathrm{H}^{\pm} \to \mathrm{W}^{\pm}\mathrm{H}$) $\sim$ 0.03–0.27.

Scenario $BP1_{F1}$: Type-II 2HDM with the opposite sign Higgs boson coupling to down-type fermions.

Howard E. Haber and Oscar Stål
from Eur. Phys. J. C **75** (2015) 491, arXiv:1507.04281 [hep-ph]

Main Features	The couplings of h to vector boson pairs ($\mathrm{W}^{\pm}\mathrm{W}^{-}$ and ZZ) and to up-type fermions are SM-like (close to the alignment limit). The magnitude of the coupling of h to down-type fermions is also SM-like but the sign of this coupling is flipped. The latter occurs in the Type-II 2HDM when $\cos(\beta-\alpha) = \sin 2\beta$. Scan over 150 GeV $< M_{\mathrm{H}} <$ 600 GeV and $5 < \tan\beta < 50$.
Type-II Scenario $BP1_{F2}$	
Spectrum	$M_{\mathrm{h}} = 125$ GeV, 150 GeV $< M_{\mathrm{H}} <$ 600 GeV, $M_{\mathrm{H}} < M_{\mathrm{H}^{\pm}} = M_{\mathrm{A}}$

Production cross sections and branching fractions	
h	Cross sections and branching ratios are mostly SM-like. The ggh and $\gamma\gamma M_{\mathrm{h}}$ effective couplings exhibit small modifications due to the change of sign of the b-quark loop contribution.
H	BR into vector boson pairs can be sizeable over a large part of the parameter space, since the departure from the alignment limit of $\cos(\beta-\alpha)=0$ can be significant.
A and $\mathrm{H}^{\pm}$	Assumed to be very heavy with little impact on LHC Higgs phenomenology

Scenario $BP1_{G1}$: 2HDM with an MSSM-like Higgs sector	
Howard E. Haber and Oscar Stål from Eur. Phys. J. C **75** (2015) 491, arXiv:1507.04281 [hep-ph]	
Main Features	The Higgs scalar potential of the MSSM is employed, with one modification. The coefficient λ_2 of the scalar potential is modified, $\lambda_2=\frac{1}{4}(g^2+g'^2)+\delta\lambda_2$, to accommodate the observed Higgs boson at 125 GeV in mass. Scan over 90 GeV $< M_{\mathrm{A}} <$ 1000 GeV and $1<\tan\beta<60$.
Type-II Scenario $BP1_{G2}$	
Spectrum	$M_{\mathrm{h}}=125$ GeV; tree-level MSSM relations $M_{\mathrm{H}}^2=M_{\mathrm{A}}^2+M_{\mathrm{Z}}^2-M_{\mathrm{h}}^2$ and $M_{\mathrm{H}^{\pm}}^2=M_{\mathrm{A}}^2+M_{\mathrm{W}}^2$ hold approximately.
Production cross sections and branching fractions	
h	Cross sections and branching ratios are very SM-like in the decoupling regime, where A is heavy. Present precision Higgs data requires that $M_{\mathrm{A}}>360$ GeV, almost independently of the value of $\tan\beta$.
H, A and $\mathrm{H}^{\pm}$	These states are heavy in the decoupling regime, presenting a challenge for LHC Higgs phenomenology. For low values of $\tan\beta$, $\mathrm{H}\to\mathrm{hh}$ may provide a viable signal. Otherwise, one may have to rely on $\mathrm{H},\mathrm{A}\to\mathrm{t\bar{t}}$. At very large $\tan\beta$, $\mathrm{H},\mathrm{A}\to\tau\tau$ and $\mathrm{H}^{\pm}\to\tau^{\pm}\nu$ provide the most useful final states for discovery.

IV.4.3.b Benchmark points $BP2$

BP2	
F. Kling, J. M. No and S. Su [1259]	
$BP2_1$: Exotic Decays in the Alignment Limit	
Fixed Param.	$M_{\mathrm{h}}=125$ GeV, $c_{\beta-\alpha}=0$, $\lambda_6=\lambda_7=0$
Benchmark Planes	
$BP2_{1A}$	Mass Hierarchy: $M_{\mathrm{H}}=M_{\mathrm{H}^{\pm}}<M_{\mathrm{A}}$, $m_{12}^2=M_{\mathrm{H}}^2 s_\beta c_\beta$ for $t_\beta=1.5,7,30$ and $m_{12}^2=0$ for $t_\beta=1.5$. Open Decays: $\mathrm{A}\to\mathrm{HZ}/\mathrm{H}^{\pm}\mathrm{W}$.

	See Figure 274 for $\tan\beta = 1.5$ and $m_{12}^2 = M_{\mathrm{H}}^2 s_\beta c_\beta$.
Example BP:	$M_{\mathrm{H}} = \mathrm{H}^\pm = 200$ GeV, $M_{\mathrm{A}} = 500$ GeV, $t_\beta = 1.5$, $m_{12} = 135$ GeV, $\sigma(\mathrm{gg} \to \mathrm{A}) = 3.7$ pb, BR$(\mathrm{A} \to \mathrm{HZ}) = 28\%$, BR$(\mathrm{A} \to \mathrm{H}^\pm\mathrm{W}) = 58\%$, BR$(\mathrm{h} \to \mathrm{bb}) = 83\%$, BR$(\mathrm{H} \to \tau\tau) = 9\%$, BR$(\mathrm{H}^\pm \to \mathrm{tb}) = 99\%$.
$BP2_{1B}$	Mass Hierarchy: $M_{\mathrm{H}} < M_{\mathrm{A}} = M_{\mathrm{H}^\pm}$, $m_{12}^2 = M_{\mathrm{H}}^2 s_\beta c_\beta$ for $t_\beta = 1.5, 7, 30$ and $m_{12}^2 = 0$ for $t_\beta = 1.5$. Open Decays: $\mathrm{A} \to \mathrm{HZ}, \mathrm{H}^\pm \to \mathrm{HW}$. See Figure 275 for $\tan\beta = 1.5$ and $m_{12}^2 = M_{\mathrm{H}}^2 s_\beta c_\beta$.
Example BP:	$M_{\mathrm{H}} = 200$ GeV, $M_{\mathrm{A}} = M_{\mathrm{H}^\pm} = 500$ GeV, $t_\beta = 1.5$, $m_{12} = 135$ GeV, $\sigma(\mathrm{gg} \to \mathrm{A}) = 3.7$ pb, $\sigma(\mathrm{gg} \to \mathrm{H}^\pm tb) = 0.2$ pb, BR$(\mathrm{A} \to \mathrm{HZ}) = 66\%$, BR$(\mathrm{H}^\pm \to \mathrm{HW}) = 70\%$, BR$(\mathrm{H} \to \mathrm{bb}) = 83\%$, BR$(\mathrm{H} \to \tau\tau) = 9\%$.
$BP2_{1C}$	Mass Hierarchy: $M_{\mathrm{A}} = M_{\mathrm{H}^\pm} < M_{\mathrm{H}}$, $m_{12}^2 = 0$ for $t_\beta = 1.5$. Open Decays: $\mathrm{H} \to \mathrm{AZ}/\mathrm{H}^\pm\mathrm{W}/\mathrm{AA}/\mathrm{H}^+\mathrm{H}^-$.
Example BP:	$M_{\mathrm{H}} = 400$ GeV, $M_{\mathrm{A}} = M_{\mathrm{H}^\pm} = 225$ GeV, $t_\beta = 1.5$, $m_{12} = 0$ GeV, $\sigma(\mathrm{gg} \to \mathrm{H}) = 4.2$ pb, BR$(\mathrm{H} \to \mathrm{AZ}) = 27\%$, BR$(\mathrm{H} \to \mathrm{H}^\pm\mathrm{W}) = 60\%$, BR$(\mathrm{A} \to \mathrm{bb}) = 75\%$, BR$(\mathrm{A} \to \tau\tau) = 8\%$, BR$(\mathrm{H}^\pm \to \mathrm{tb}) = 99\%$.
$BP2_{1D}$	Mass Hierarchy: $M_{\mathrm{A}} < M_{\mathrm{H}} = M_{\mathrm{H}^\pm}$, $m_{12}^2 = 0$ for $t_\beta = 1.5$. Open Decays: $\mathrm{H} \to \mathrm{AZ}/\mathrm{AA}, \mathrm{H}^\pm \to \mathrm{AW}$. See Figure 276 for $\tan\beta = 1.5$ and $m_{12}^2 = 0$.
Example BP:	$M_{\mathrm{H}} = M_{\mathrm{H}^\pm} = 400$ GeV, $M_{\mathrm{A}} = 100$ GeV, $t_\beta = 1.5$, $m_{12} = 0$ GeV, $\sigma(\mathrm{gg} \to \mathrm{H}) = 4.2$ pb, $\sigma(\mathrm{gg} \to \mathrm{H}^\pm\mathrm{tb}) = 0.4$ pb, BR$(\mathrm{H} \to \mathrm{AA}) = 28\%$, BR$(\mathrm{H} \to \mathrm{AZ}) = 63\%$, BR$(\mathrm{H}^\pm \to \mathrm{AW}) = 70\%$.
$BP2_2$: Exotic Decays for Non-Alignment	
Fixed Param.	$M_{\mathrm{h}} = 125$ GeV, $\lambda_6 = \lambda_7 = 0$
Benchmark Planes	
$BP2_{2A}$	Mass Hierarchy: $M_{\mathrm{h}} < M_{\mathrm{H}} = M_{\mathrm{A}} = M_{\mathrm{H}^\pm}$, $c_{\beta-\alpha} \in (-1, 1)$, $m_{12}^2 = M_{\mathrm{H}}^2 s_\beta c_\beta$ for $t_\beta = 1.5, 7, 30$ and $m_{12}^2 = 0$ for $t_\beta = 1.5$. Open Decays: $\mathrm{H} \to \mathrm{hh},\ \mathrm{A} \to \mathrm{hZ},\ \mathrm{H}^\pm \to \mathrm{hW}$. See Figure 277 for $\tan\beta = 7$ and $m_{12}^2 = M_{\mathrm{H}}^2 s_\beta c_\beta$
Example BP:	$M_{\mathrm{H}} = M_{\mathrm{H}^\pm} = M_{\mathrm{A}} = 500$ GeV, $s_{\beta-\alpha} = 0.96$, $t_\beta = 7$, $m_{12} = 187$ GeV, $\sigma(\mathrm{gg} \to \mathrm{H}) = 97$ fb, $\sigma(\mathrm{gg} \to \mathrm{A}) = 205$ fb, $\sigma(\mathrm{gg} \to \mathrm{H}^\pm\mathrm{tb}) = 10$ fb, BR$(\mathrm{H} \to \mathrm{hh}) = 4\%$, BR$(\mathrm{A} \to \mathrm{hZ}) = 65\%$, BR$(\mathrm{H}^\pm \to \mathrm{hW}) = 70\%$.

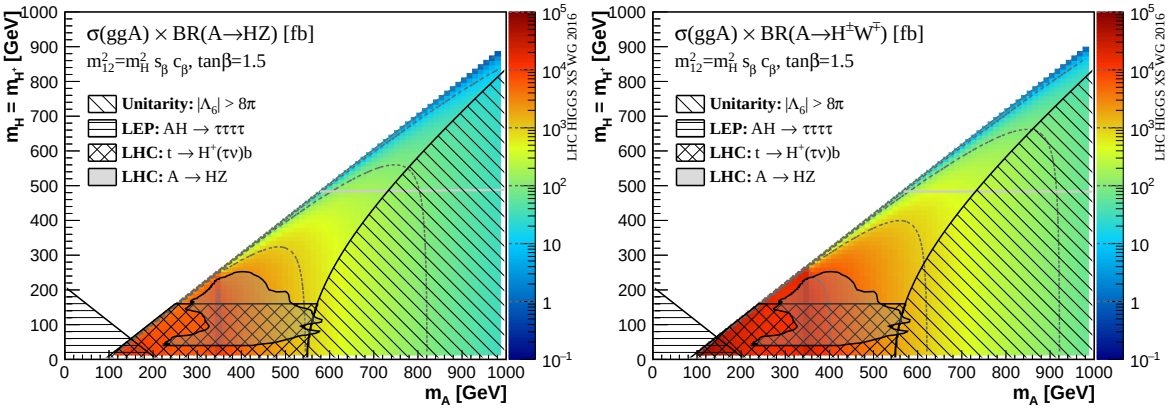

Figure 274: $\sigma \times$ BR for $\mathrm{gg} \to \mathrm{A} \to \mathrm{HZ}$ (left) and $\mathrm{gg} \to \mathrm{A} \to \mathrm{H}^{\pm}\mathrm{W}^{\mp}$ (right) for the mass hierarchy $M_{\mathrm{H}} = M_{\mathrm{H}^{\pm}} < M_{\mathrm{A}}$. We consider the alignment limit at $\tan\beta = 1.5$ and $m_{12}^2 = M_{\mathrm{H}}^2 s_\beta s_\beta$. We show contours in $\sigma \times$ BR (dashed lines) and excluded regions (hatched and shaded area). The solid horizontal or vertical grey line indicates the flavour constraints.

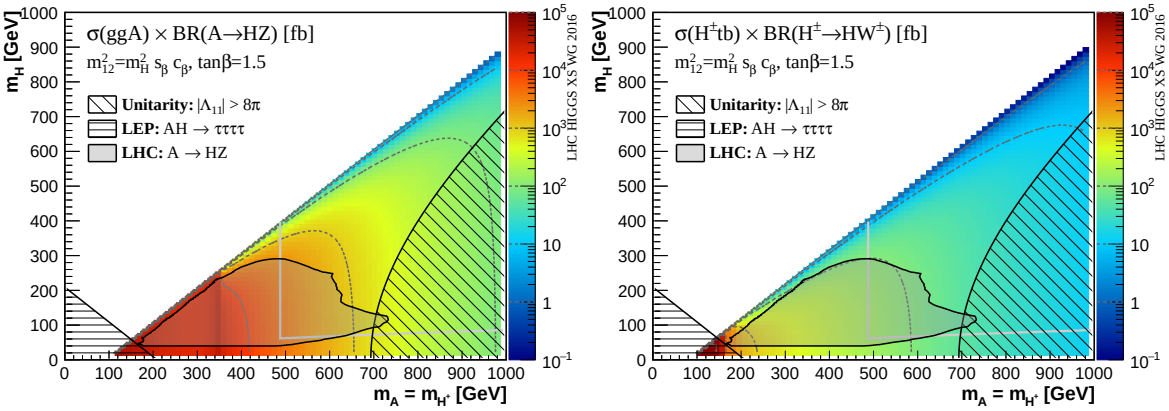

Figure 275: $\sigma \times$ BR for $\mathrm{gg} \to \mathrm{A} \to \mathrm{HZ}$ (left) and $\mathrm{gg} \to \mathrm{H}^{+}\mathrm{tb} \to \mathrm{HWtb}$ (right) for the mass hierarchy $M_{\mathrm{H}} < M_{\mathrm{A}} = M_{\mathrm{H}^{\pm}}$. We consider the alignment limit at $\tan\beta = 1.5$ and $m_{12}^2 = M_{\mathrm{H}}^2 s_\beta s_\beta$. Lines and hatched areas are the same as in Figure 274.

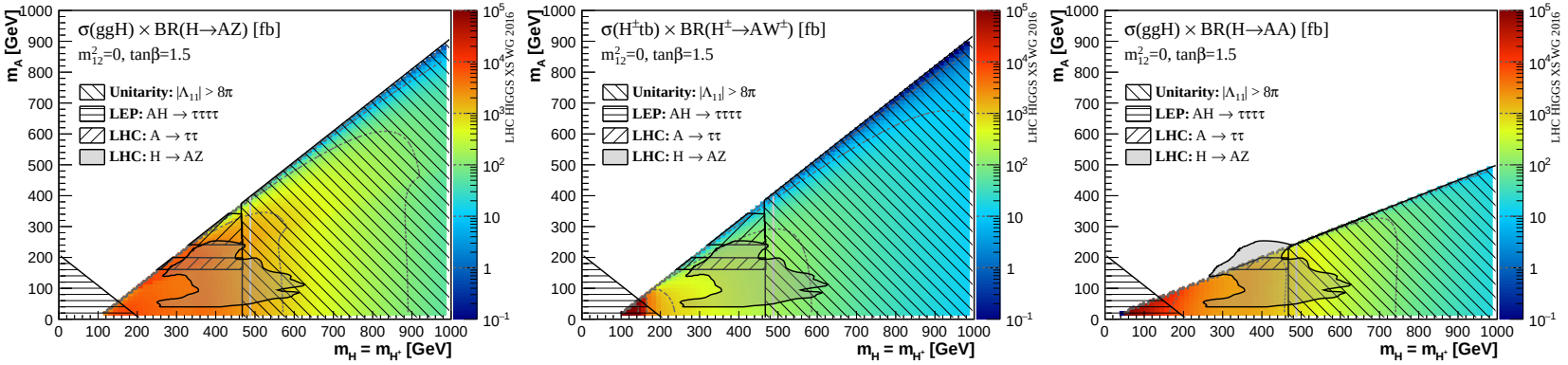

Figure 276: $\sigma \times$ BR for $gg \to H \to AZ$ (left), $gg \to H^+tb \to AWtb$ (centre) and $gg \to H \to AA$ (right) for the mass hierarchy $M_A < M_H = M_{H^\pm}$. We consider the alignment limit at $\tan\beta = 1.5$ and $m_{12}^2 = 0$. Lines and hatched areas are the same as in Figure 274.

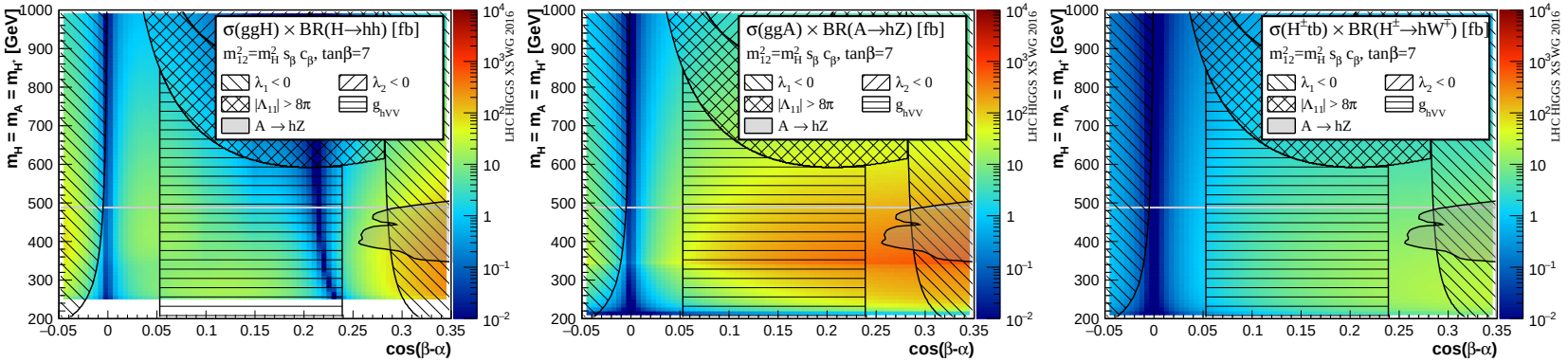

Figure 277: $\sigma \times$ BR for $gg \to H \to hh$ (left), $gg \to A \to hZ$ (centre) and $gg \to H^+tb \to hWtb$ (right) for the mass hierarchy $M_h < M_H = M_A = M_{H^\pm}$. We consider the non-alignment case at $\tan\beta = 1.5$ and $m_{12}^2 = M_H^2 s_\beta s_\beta$. Lines and hatched areas are the same as in Figure 274.

IV.4.3.c Benchmark points $BP3$

$BP3$: **EW Cosmology Benchmarks for A $\to$ H Z Decays**	
G. C. Dorsch, S. J. Huber, K. Mimasu and J. M. No [1260]	
Physical Motivation	$M_{\rm A} - M_{\rm H} > M_{\rm Z}$ is a primary signature of a strong EW Phase Transition in the 2HDM, potentially leading to successful EW Baryogenesis
$BP3_A$	
Main Features	Type I and II 2HDM, alignment limit $c_{\beta-\alpha} = 0$ $\lambda_6 = \lambda_7 = 0$, no impact from μ_{12}^2
Spectrum	$M_{\rm H} + M_{\rm Z} < M_{\rm A} = M_{\rm H^\pm}$
Particular Signatures	A $\to$ ZH, H $\to \rm b\bar{b}$ (for $M_{\rm H} < 340$ GeV); H $\to \rm t\bar{t}$ (for $M_{\rm H} > 340$ GeV) See Figure 278(a) for Type I 2HDM with $t_\beta = 3$
Example: $BP3_{A1}$	$M_{\rm A} = M_{\rm H^\pm} = 420$ GeV, $M_{\rm H} = 180$ GeV, $t_\beta = 3$, $\mu = 100$ GeV Type I: $\sigma(\rm gg \to A) = 2.369$ pb, BR(A $\to$ ZH) = 0.843, BR(H $\to \rm b\bar{b}$) = 0.711 Type II: $\sigma(\rm gg \to A) = 2.405$ pb, BR(A $\to$ ZH) = 0.838, BR(H $\to \rm b\bar{b}$) = 0.899
Example: $BP3_{A2}$	$M_{\rm A} = M_{\rm H^\pm} = 550$ GeV, $M_{\rm H} = 400$ GeV, $t_\beta = 3$, $\mu = 210$ GeV Type I: $\sigma(\rm gg \to A) = 0.548$ pb, BR(A $\to$ ZH) = 0.498, BR(H $\to \rm t\bar{t}$) = 0.992 Type II: $\sigma(\rm gg \to A) = 0.570$ pb, BR(A $\to$ ZH) = 0.486, BR(H $\to \rm t\bar{t}$) = 0.866
$BP3_B$	
Main Features	Type I 2HDM, non-alignment $\lvert c_{\beta-\alpha}\rvert > 0.1$ Type II 2HDM, non-alignment $s_{\beta+\alpha} \sim 1$ ($t_\beta \geq 3$) $\lambda_6 = \lambda_7 = 0$, $\mu^2 = M_{\rm H}^2 s_\beta c_\beta$
Spectrum	$M_{\rm H} + M_{\rm Z} < M_{\rm A} = M_{\rm H^\pm}$
Particular Signatures	A $\to$ ZH, H $\to \rm W^+W^-$ See Figure 278(b) for Type II 2HDM with $t_\beta = 3$
Example: $BP3_{B1}$	$M_{\rm A} = M_{\rm H^\pm} = 420$ GeV, $M_{\rm H} = 200$ GeV, $t_\beta = 3$, $c_{\beta-\alpha} = 0.3$, $\mu = 110$ GeV Type I: $\sigma(\rm gg \to A) = 2.369$ pb BR(A $\to$ ZH) = 0.697, BR(H $\to \rm W^+W^-$) = 0.742
Example: $BP3_{B2}$	$m_{A_0} = m_{H^\pm} = 420$ GeV, $m_{\rm H} = 200$ GeV, $t_\beta = 3$, $c_{\beta-\alpha} = 0.5$, $\mu = 110$ GeV Type II: $\sigma(\rm gg \to A_0) = 2.405$ pb BR(A $\to$ ZH) = 0.517, BR(H $\to \rm W^+W^-$) = 0.662

IV.4.3.d Benchmark points $BP4$

$BP4$: **Light Pseudoscalars**
R. Aggleton, D. Barducci, S. Moretti, A. Nikitenko and C. Shepherd-Themistocleous

$BP4_1$	
Main Features	2HDM Type I: light pseudoscalar (~ 20 GeV) and substantial $\mathrm{h} \to \mathrm{ZA}$ decay rate
Spectrum	$M_{\mathrm{h}} \approx 126$ GeV, $M_{\mathrm{A}} \approx 20$ GeV, $M_{\mathrm{H}} \approx 165$ GeV, $M_{\mathrm{H}^\pm} \approx 444$ GeV
Production cross sections and branching fractions	
$\mathrm{h} \to \mathrm{ZA}$	ggF(h) ≈ 38 pb (at 13 TeV), $BR(\mathrm{h} \to \mathrm{Za}) \approx 10\%$ BR$(\mathrm{A} \to \mathrm{bb}) \approx 85\%$, BR$(\mathrm{A} \to \tau\tau) \approx 6\%$, BR$(\mathrm{A} \to \mu\mu) \approx 0.02\%$
Particular signatures	On shell Z from $\mathrm{h} \to \mathrm{ZA}$ decay
Model Parameters	$M_{\mathrm{h}} = 126.0$ GeV, $M_{\mathrm{H}} = 165.5$ GeV, $M_{\mathrm{A}} = 20.2$ GeV, $M_{\mathrm{H}^\pm} = 444.7$ GeV $\tan\beta = 1.9$, $\lambda_{6,7} = 0$, $m_{12}^2 = 3891.5$ GeV^2, $\sin(\beta - \alpha) = -0.99$

$BP4_2$	
Main Features	2HDM Type I: light pseudoscalar (~ 60 GeV) and substantial $\mathrm{h} \to \mathrm{ZA}$ decay rate
Spectrum	$M_{\mathrm{h}} \approx 126$ GeV, $M_{\mathrm{A}} \approx 63$ GeV, $M_{\mathrm{H}} \approx 153$ GeV, $M_{\mathrm{H}^\pm} \approx 258$ GeV
Production cross sections and branching fractions	
$\mathrm{h} \to \mathrm{ZA}$	ggF(h) ≈ 26 pb (at 13 TeV), BR$(\mathrm{h} \to \mathrm{Za}) \approx 3\%$ BR$(\mathrm{A} \to \mathrm{bb}) \approx 79\%$, BR$(\mathrm{A} \to \tau\tau) \approx 7\%$, BR$(\mathrm{A} \to \mu\mu) \approx 0.02\%$
Particular signatures	Off shell Z from $\mathrm{h} \to \mathrm{ZA}$ decay
Model Parameters	$M_{\mathrm{h}} = 126.0$ GeV, $M_{\mathrm{H}} = 153.4$ GeV, $M_{\mathrm{A}} = 63.4$ GeV, $M_{\mathrm{H}^\pm} = 257.7$ GeV $\tan\beta = 6.2$, $\lambda_{6,7} = 0$, $m_{12}^2 = 2793.3$ GeV^2, $\sin(\beta - \alpha) = -0.85$

$BP4_3$	
Main Features	2HDM Type II: light pseudoscalar (~ 6 GeV) and substantial $\mathrm{h} \to \mathrm{ZA}$ decay rate
Spectrum	$M_{\mathrm{h}} \approx 126$ GeV, $M_{\mathrm{A}} \approx 6$ GeV, $M_{\mathrm{H}} \approx 264$ GeV, $M_{\mathrm{H}^\pm} \approx 308$ GeV
Production cross sections and branching fractions	
$\mathrm{h} \to \mathrm{ZA}$	ggF(h) ≈ 51 pb (at 13 TeV), BR$(\mathrm{h} \to \mathrm{Za}) \approx 31\%$ BR$(\mathrm{A} \to \mathrm{bb}) = 0\%$, BR$(\mathrm{A} \to \tau\tau) \approx 78\%$, BR$(\mathrm{A} \to \mu\mu) \approx 0.3\%$
Particular signatures	On shell Z from $\mathrm{h} \to \mathrm{ZA}$ decay. Extremely light A, decay products will be very boosted
Model Parameters	$M_{\mathrm{h}} = 126.0$ GeV, $M_{\mathrm{H}} = 263.7$ GeV, $M_{\mathrm{A}} = 6.3$ GeV, $M_{\mathrm{H}^\pm} = 308.3$ GeV $\tan\beta = 1.9$, $\lambda_{6,7} = 0$, $m_{12}^2 = 2737.4$ GeV^2, $\sin(\beta - \alpha) = 0.99$

$BP4_4$

Main Features	2HDM Type II: light pseudoscalar (~ 25 GeV) and substantial $\mathrm{h} \to \mathrm{ZA}$ decay rate
Spectrum	$M_{\mathrm{h}} \approx 126$ GeV, $M_{\mathrm{A}} \approx 25$ GeV, $M_{\mathrm{H}} \approx 227$ GeV, $M_{\mathrm{H}^\pm} \approx 227$ GeV
Production cross sections and branching fractions	
$\mathrm{h} \to \mathrm{ZA}$	ggF(h) $\approx$ 52 pb (at 13 TeV), BR($\mathrm{h} \to \mathrm{Za}$) $\approx 15\%$ BR($\mathrm{A} \to \mathrm{bb}$) $\approx 92\%$, BR($\mathrm{A} \to \tau\tau$) $\approx 6\%$, BR($\mathrm{A} \to \mu\mu$) $\approx 0.02\%$
Particular signatures	On shell Z from $\mathrm{h} \to \mathrm{ZA}$ decay.
Model Parameters	$M_{\mathrm{h}} = 126.2$ GeV, $M_{\mathrm{H}} = 227.1$ GeV, $M_{\mathrm{A}} = 24.7$ GeV, $M_{\mathrm{H}^\pm} = 226.8$ GeV $\tan\beta = 1.8$, $\lambda_{6,7} = 0$, $m_{12}^2 = 3406.8$ GeV^2, $\sin(\beta - \alpha) = 0.99$

$BP4_5$	
Main Features	2HDM Type II: light pseudoscalar (~ 63 GeV) and substantial $\mathrm{h} \to \mathrm{ZA}$ decay rate
Spectrum	$M_{\mathrm{h}} \approx 126$ GeV, $M_{\mathrm{A}} \approx 63$ GeV, $M_{\mathrm{H}} \approx 210$ GeV, $M_{\mathrm{H}^\pm} \approx 333$ GeV
Production cross sections and branching fractions	
$\mathrm{h} \to \mathrm{ZA}$	ggF(h) $\approx$ 57 pb (at 13 TeV), BR($\mathrm{h} \to \mathrm{Za}$) $\approx 4\%$ BR($\mathrm{A} \to \mathrm{bb}$) $\approx 92\%$, BR($\mathrm{A} \to \tau\tau$) $\approx 7\%$, BR($\mathrm{A} \to \mu\mu$) $\approx 0.03\%$
Particular signatures	Off shell Z from $\mathrm{h} \to \mathrm{ZA}$ decay.
Model Parameters	$M_{\mathrm{h}} = 125.2$ GeV, $M_{\mathrm{H}} = 210.2$ GeV, $M_{\mathrm{A}} = 63.06$ GeV, $M_{\mathrm{H}^\pm} = 333.5$ GeV $\tan\beta = 2.4$, $\lambda_{6,7} = 0$, $m_{12}^2 = 4791.9$ GeV^2, $\sin(\beta - \alpha) = 0.7$

IV.4.3.e Benchmark points $BP5$

$BP5$**: Benchmarks for the Inert Doublet Model**	
Agnieszka Ilnicka, Maria Krawczyk, Tania Robens [1203]	
Main Features	IDM, two $\mathrm{SU}(2) \times \mathrm{U}(1)$ doublet model with SM-like Higgs boson h and dark matter candidate H
Floating parameters	masses of scalars M_{H}, M_{A}, $M_{\mathrm{H}^\pm}$ $M_{\mathrm{H}} > 45$ GeV, mass degeneracy
Fixed parameters Irrelevant parameters	$M_{\mathrm{h}} = 125.1$ GeV λ_2; λ_{345} (if kept within allowed ranges); $\lambda_2 \in [0; 4.2]$
BR ($\mathrm{A} \to \mathrm{ZH}$) BR ($\mathrm{H}^\pm \to \mathrm{W}^\pm\mathrm{H}$)	1 dominant
comment	dark scalars (H, A, $\mathrm{H}^\pm$) have to be produced in pairs

	signature: always $E_{\mathrm{T}}^{\mathrm{miss}}$ from H H in final states
	Production cross sections and branching fractions
$BP5_A$	
Main Features	Low mass H [$M_{\mathrm{H}} < M_{\mathrm{h}}/2$]
Spectrum	M_{H}=57.5 GeV, M_{A}=113.0 GeV, $M_{\mathrm{H}^\pm}$=123.0 GeV, $\|\lambda_{345}\| \in [0.002, 0.015]$
$\sigma(\mathrm{pp} \to \mathrm{HA})$	0.371(4) [pb]
$\sigma(\mathrm{pp} \to \mathrm{H^+H})$	0.3071(4) [pb]
$\sigma(\mathrm{pp} \to \mathrm{H^+A})$	0.1267(1) [pb]
$\sigma(\mathrm{pp} \to \mathrm{H^+H^-})$	0.097(1) [pb]
BR($\mathrm{H^+} \to \mathrm{W^+H}$)	>0.99
BR($\mathrm{H^+} \to \mathrm{W^+A}$)	<0.01
$BP5_B$	
Main Features	Low mass H [$M_{\mathrm{h}}/2 < M_{\mathrm{H}} < M_{\mathrm{h}}$]
Spectrum	M_{H}=85.5 GeV, M_{A}=111.0 GeV, $M_{\mathrm{H}^\pm}$=140.0 GeV, $\|\lambda_{345}\| < 0.015$
$\sigma(\mathrm{pp} \to \mathrm{HA})$	0.226(2) [pb]
$\sigma(\mathrm{pp} \to \mathrm{H^+H})$	0.1439(2) [pb]
$\sigma(\mathrm{pp} \to \mathrm{H^+A})$	0.1008(1) [pb]
$\sigma(\mathrm{pp} \to \mathrm{H^+H^-})$	0.0605(9) [pb]
BR($\mathrm{H^+} \to \mathrm{W^+H}$)	0.96
BR($\mathrm{H^+} \to \mathrm{W^+A}$)	0.04
$BP5_C$	
Main Features	Low mass H [$M_{\mathrm{H}} \sim M_{\mathrm{h}}$]
Spectrum	M_{H}=128.0 GeV, M_{A}=134.0 GeV, $M_{\mathrm{H}^\pm}$=176.0 GeV, $\|\lambda_{345}\| < 0.05$
$\sigma(\mathrm{pp} \to \mathrm{HA})$	0.0765(7) [pb]
$\sigma(\mathrm{pp} \to \mathrm{H^+H})$	0.04985(5) [pb]
$\sigma(\mathrm{pp} \to \mathrm{H^+A})$	0.04653(5) [pb]
$\sigma(\mathrm{pp} \to \mathrm{H^+H^-})$	0.0259(3) [pb]
BR($\mathrm{H^+} \to \mathrm{W^+H}$)	0.66
BR($\mathrm{H^+} \to \mathrm{W^+A}$)	0.34
$BP5_D$	
Main Features	High mass H [$M_{\mathrm{H}} > M_{\mathrm{h}}$]; degeneracy
Spectrum	M_{H}=363.0 GeV, M_{A}=374.0 GeV, $M_{\mathrm{H}^\pm}$=374.0 GeV, $\|\lambda_{345}\| < 0.25$
$\sigma(\mathrm{pp} \to \mathrm{HA})$	0.00122(1) [pb]
$\sigma(\mathrm{pp} \to \mathrm{H^+H})$	0.001617(2) [pb]
$\sigma(\mathrm{pp} \to \mathrm{H^+A})$	0.001518(2) [pb]
$\sigma(\mathrm{pp} \to \mathrm{H^+H^-})$	0.00124(1) [pb]
BR($\mathrm{H^+} \to \mathrm{W^+H}$)	1
$BP5_E$	
Main Features	High mass H [$M_{\mathrm{H}} > M_{\mathrm{h}}$]

Spectrum	$M_{\rm H}$=311.0 GeV, $M_{\rm A}$=415.0 GeV, $M_{\rm H^\pm}$=447.0 GeV, $\|\lambda_{345}\| < 0.19$
$\sigma(\rm pp \to HA)$	0.00129(1) [pb]
$\sigma(\rm pp \to H^+H)$	0.001402(2) [pb]
$\sigma(\rm pp \to H^+A)$	0.0008185(8) [pb]
$\sigma(\rm pp \to H^+H^-)$	0.000553(7) [pb]
BR($\rm H^+ \to W^+H$)	>0.99
BR($\rm H^+ \to W^+A$)	<0.01

IV.4.3.f Benchmark points $BP6$

$BP6$: **Fermiophobic heavy Higgs**	
D. López-Val [462]	
Benchmark setup	
Main Features	• SM-like light Higgs boson • Fermiophobic heavy neutral Higgs boson • ⇒ Relatively light, yet very elusive Higgs companion • ⇒ Warning sign: lack of signal should not rule out the model too early
Spectrum	$M_{\rm h}$= 125 GeV, $M_{\rm H} = 200$ GeV, $M_{\rm A} = 500$ GeV, $M_{\rm H^\pm} = 500$ GeV
Model parameters (physical basis)	Type I Yukawas, $\sin\alpha = 0$, $\tan\beta = 20$, $m_{12}^2 = 2000$ GeV^2
Production cross sections and branching fractions	
leading signatures	Light Higgs phenomenology essentially unaffected Heavy Higgs sharp resonance into WW/ZZ $\sigma(\rm pp \to HA) \simeq 1.91$ fb (13 TeV) $\sigma(\rm pp \to HH^\pm) \simeq 0.88$ fb (13 TeV)
Heavy Higgs boson total width	$\Gamma(\rm H) = 3.39 \times 10^{-3}$ GeV
Heavy Higgs boson branching fractions	BR($\rm H \to ZZ$) = 0.742 BR($\rm H \to WW$) = 0.258 BR($\rm H \to \gamma\gamma$) < 10^{-4} BR($\rm H \to Z\gamma$) < 10^{-4} BR($\rm H \to f\bar{f}$) = 0
Benchmark planes	
Floating parameters	$M_{\rm H}$, mass splitting ΔM
Fixed parameters	$\sin\alpha = 0$ (by construction) $M_{\rm A} = M_{\rm H} + \Delta M$, $M_{\rm H^\pm} = M_{\rm H} + \Delta M$, $m_{12}^2 = M_{\rm H}^2/\tan\beta$
Fiducial $\tan\beta$ choices	$\tan\beta = 40$ (mild departure from alignment, coupling shifts of $\mathcal{O}(2\%)$) $\tan\beta = 20$ (moderate departure, coupling shifts of $\mathcal{O}(5\%)$)

	$\tan\beta = 10$ (large departure, coupling shifts of $\mathcal{O}(10\%)$)

IV.4.3.g Benchmark points $BP7$

As proposed in [1262,1263], CP-violation in the scalar sector can be found in the interactions with gauge bosons in a very simple way. Assuming CP is conserved, any decay $\mathrm{h_i} \to \mathrm{h_j Z}$ would imply opposite CP parities for $\mathrm{h_i}$ and $\mathrm{h_j}$. Moreover, assuming only Lagrangian terms up to dimension four, any scalar $\mathrm{h_i}$ decaying into ZZ would be CP even [IV.21].

In Table 135 we define five classes of CP-violation with the respective decays. Classes C_1-C_4 represent CP-violation, regardless of the origin of the neutral scalars. Class C_5 does not represent necessarily CP-violation in models other than the 2HDM. There are other classes of decays that constitute a

Table 135: Classes of combined measurements guaranteed to probe CP-violation in 2HDMs.

Classes	C_1	C_2	C_3	C_4	C_5
Decays	$\mathrm{h_3} \to \mathrm{h_2 Z}$	$\mathrm{h_2} \to \mathrm{h_1 Z}$	$\mathrm{h_3} \to \mathrm{h_1 Z}$	$\mathrm{h_3} \to \mathrm{h_2 Z}$	$\mathrm{h_3} \to \mathrm{ZZ}$
	$\mathrm{h_2} \to \mathrm{h_1 Z}$	$\mathrm{h_1} \to \mathrm{ZZ}$	$\mathrm{h_1} \to \mathrm{ZZ}$	$\mathrm{h_2} \to \mathrm{ZZ}$	$\mathrm{h_2} \to \mathrm{ZZ}$
	$\mathrm{h_3} \to \mathrm{h_1 Z}$	$\mathrm{h_2} \to \mathrm{ZZ}$	$\mathrm{h_3} \to \mathrm{ZZ}$	$\mathrm{h_3} \to \mathrm{ZZ}$	$\mathrm{h_1} \to \mathrm{ZZ}$

sign of CP-violation with at least one process where a scalar decays to two other scalars. Some of them involve the decay $\mathrm{h_3} \to \mathrm{h_2 h_1}$ which is not present in the CP-conserving version of the 2HDM. The two remaining classes are presented in table 136.

Table 136: Classes of combined measurements guaranteed to probe CP-violation.

Classes	C_6	C_7
Decays	$\mathrm{h_3} \to \mathrm{h_2 h_1}$	$\mathrm{h_{2,3}} \to \mathrm{h_1 h_1}$
	$\mathrm{h_3} \to \mathrm{h_2 Z}$	$\mathrm{h_{2,3}} \to \mathrm{h_1 Z}$
	$\mathrm{h_1} \to \mathrm{ZZ}$	$\mathrm{h_1} \to \mathrm{ZZ}$

Finally, other combinations like $\mathrm{h_3} \to \mathrm{h_1 h_1 (h_2 h_2)}$, $\mathrm{h_2} \to \mathrm{h_1 h_1}$ and $\mathrm{h_1} \to \mathrm{ZZ}$ are not possible in a CP-conserving 2HDM but are possible in the C2HDM and can also serve to determine the CP-quantum numbers of other extensions of the scalar sector.

$BP7_1$ **Benchmarks for the Complex Two Higgs Doublet Model**	
D. Fontes, J.C. Romão, R. Santos, João P. Silva [1265]	
Benchmark setup	
Main Features	• lightest Higgs boson at 125 GeV • CP violation through scalar-pseudoscalar mixing

[IV.21] There are CP conserving terms of dimension higher than four that can mediate the decay of a pseudoscalar into two vector bosons. A calculation performed in the framework of the 2HDM has shown [1264] that the loop mediated decays of the type $\mathrm{h_i} \to \mathrm{ZZ}$ are several orders of magnitude smaller than the tree-level ones.

	• CP violation detected by the simultaneous existence of three decay channels (see classes C_1-C_7 in the text)

Benchmark point 1_{C2HDM}

Model Type	Type II
Higgs boson masses	M_{h_1}= 125 GeV, $M_{\mathrm{h}_2} = 288$ GeV, $M_{\mathrm{h}_3} = 445$ GeV, $M_{\mathrm{H}^\pm} = 481$ GeV
Other point parameters	$\mathrm{Re}m_{12}^2 = 1.2 \times 10^4$ GeV^2, $\tan\beta = 1.66$, $\alpha_1 = 0.986$, $\alpha_2 = -0.008$, $\alpha_3 = 0.006$

Production cross sections times branching ratios

Class C_1	C_1: $\sigma_3 \times \mathrm{BR}(\mathrm{h}_3 \to \mathrm{h}_2\mathrm{Z}) = 1844$ fb C_1: $\sigma_2 \times \mathrm{BR}(\mathrm{h}_2 \to \mathrm{h}_1\mathrm{Z}) = 20$ fb C_1: $\sigma_3 \times \mathrm{BR}(\mathrm{h}_3 \to \mathrm{h}_1\mathrm{Z}) = 18$ fb
Class C_2	C_2: $\sigma_2 \times \mathrm{BR}(\mathrm{h}_2 \to \mathrm{h}_1\mathrm{Z}) = 20$ fb C_2: $\sigma_1 \times \mathrm{BR}(\mathrm{h}_1 \to \mathrm{ZZ}) = 971$ fb C_2: $\sigma_2 \times \mathrm{BR}(\mathrm{h}_2 \to \mathrm{ZZ}) = 611$ fb
Class C_6	C_6: $\sigma_3 \times \mathrm{BR}(\mathrm{h}_3 \to \mathrm{h}_2\mathrm{h}_1) = 0.024$ fb C_6: $\sigma_3 \times \mathrm{BR}(\mathrm{h}_3 \to \mathrm{h}_2\mathrm{Z}) = 1844$ fb C_6: $\sigma_1 \times \mathrm{BR}(\mathrm{h}_1 \to \mathrm{ZZ}) = 971$ fb
Class C_{7a}	C_{7a}: $\sigma_2 \times \mathrm{BR}(\mathrm{h}_2 \to \mathrm{h}_1\mathrm{h}_1) = 0.441$ fb C_{7a}: $\sigma_2 \times \mathrm{BR}(\mathrm{h}_2 \to \mathrm{h}_1\mathrm{Z}) = 20$ fb C_{7a}: $\sigma_1 \times \mathrm{BR}(\mathrm{h}_1 \to \mathrm{ZZ}) = 971$ fb
Class C_{7b}	C_{7b}: $\sigma_3 \times \mathrm{BR}(\mathrm{h}_3 \to \mathrm{h}_1\mathrm{h}_1) = 0.142$ fb C_{7b}: $\sigma_3 \times \mathrm{BR}(\mathrm{h}_3 \to \mathrm{h}_1\mathrm{Z}) = 18$ fb C_{7b}: $\sigma_1 \times \mathrm{BR}(\mathrm{h}_1 \to \mathrm{ZZ}) = 971$ fb
Heavy Higgs boson total width	$\Gamma(\mathrm{h}_2) = 2.85 \times 10^{-2}$ GeV $\quad$ $\Gamma(\mathrm{h}_3) = 10.87$ GeV
Heavy Higgs boson branching fractions	$\mathrm{BR}(\mathrm{h}_2 \to \tau\tau) = 5.38 \times 10^{-2}$ $\quad$ $\mathrm{BR}(\mathrm{h}_3 \to \tau\tau) = 2.36 \times 10^{-4}$ $\mathrm{BR}(\mathrm{h}_2 \to \mathrm{b\bar{b}}) = 4.55 \times 10^{-1}$ $\quad$ $\mathrm{BR}(\mathrm{h}_3 \to \mathrm{b\bar{b}}) = 1.97 \times 10^{-3}$ $\mathrm{BR}(\mathrm{h}_2 \to \mathrm{WW}) = 2.91 \times 10^{-1}$ $\quad$ $\mathrm{BR}(\mathrm{h}_3 \to \mathrm{WW}) = 1.36 \times 10^{-4}$ $\mathrm{BR}(\mathrm{h}_2 \to \mathrm{ZZ}) = 1.27 \times 10^{-1}$ $\quad$ $\mathrm{BR}(\mathrm{h}_3 \to \mathrm{ZZ}) = 6.44 \times 10^{-5}$ $\mathrm{BR}(\mathrm{h}_2 \to \gamma\gamma) = 1.49 \times 10^{-4}$ $\quad$ $\mathrm{BR}(\mathrm{h}_2 \to \gamma\gamma) = 8.81 \times 10^{-6}$

$BP7_2$ Benchmarks for the Complex Two Higgs Doublet Model

D. Fontes, J.C. Romão, R. Santos, João P. Silva [1265]

Benchmark setup

Main Features	• lightest Higgs boson at 125 GeV • CP violation through scalar-pseudoscalar mixing • CP violation detected by the simultaneous existence of three decay channels (see classes C_1-C_7 in the text)

Benchmark point 2_{C2HDM}

Model Type	Type II
Higgs boson masses	M_{h_1}= 125 GeV, $M_{\mathrm{h}_2} = 442$ GeV, $M_{\mathrm{h}_3} = 446$ GeV, $M_{\mathrm{H}^\pm} = 484$ GeV
Other point parameters	Re$m_{12}^2 = 4.85 \times 10^4$ GeV^2, $\tan\beta = 3.49$,
	$\alpha_1 = -1.349$, $\alpha_2 = -0.0007$, $\alpha_3 = 0.772$
Production cross sections times branching ratios	
Class C_2	C_2: $\sigma_2 \times \mathrm{BR}(\mathrm{h}_2 \to \mathrm{h}_1\mathrm{Z}) = 254$ fb
	C_2: $\sigma_1 \times \mathrm{BR}(\mathrm{h}_1 \to \mathrm{ZZ}) = 1274$ fb
	C_2: $\sigma_2 \times \mathrm{BR}(\mathrm{h}_2 \to \mathrm{ZZ}) = 156$ fb
Class C_3	C_3: $\sigma_3 \times \mathrm{BR}(\mathrm{h}_3 \to \mathrm{h}_1\mathrm{Z}) = 265$ fb
	C_3: $\sigma_1 \times \mathrm{BR}(\mathrm{h}_1 \to \mathrm{ZZ}) = 1274$ fb
	C_3: $\sigma_3 \times \mathrm{BR}(\mathrm{h}_3 \to \mathrm{ZZ}) = 146$ fb
Class C_3	C_5: $\sigma_3 \times \mathrm{BR}(\mathrm{h}_3 \to \mathrm{ZZ}) = 146$ fb
	C_5: $\sigma_2 \times \mathrm{BR}(\mathrm{h}_2 \to \mathrm{ZZ}) = 156$ fb
	C_5: $\sigma_1 \times \mathrm{BR}(\mathrm{h}_1 \to \mathrm{ZZ}) = 1274$ fb
Class C_{7a}	C_{7a}: $\sigma_2 \times \mathrm{BR}(\mathrm{h}_2 \to \mathrm{h}_1\mathrm{h}_1) = 24$ fb
	C_{7a}: $\sigma_2 \times \mathrm{BR}(\mathrm{h}_2 \to \mathrm{h}_1\mathrm{Z}) = 254$ fb
	C_{7a}: $\sigma_1 \times \mathrm{BR}(\mathrm{h}_1 \to \mathrm{ZZ}) = 1274$ fb
Class C_{7b}	C_{7b}: $\sigma_3 \times \mathrm{BR}(\mathrm{h}_3 \to \mathrm{h}_1\mathrm{h}_1) = 25$ fb
	C_{7b}: $\sigma_3 \times \mathrm{BR}(\mathrm{h}_3 \to \mathrm{h}_1\mathrm{Z}) = 265$ fb
	C_{7b}: $\sigma_1 \times \mathrm{BR}(\mathrm{h}_1 \to \mathrm{ZZ}) = 1274$ fb
Heavy Higgs boson total width	$\Gamma(\mathrm{h}_2) = 7.49$ GeV $\quad$ $\Gamma(\mathrm{h}_3) = 7.71$ GeV
Heavy Higgs boson branching fractions	BR($\mathrm{h}_2 \to \tau\tau$) $= 1.52 \times 10^{-3}$ $\quad$ BR($\mathrm{h}_3 \to \tau\tau$) $= 1.49 \times 10^{-3}$
	BR($\mathrm{h}_2 \to \mathrm{b\bar{b}}$) $= 1.27 \times 10^{-2}$ $\quad$ BR($\mathrm{h}_3 \to \mathrm{b\bar{b}}$) $= 1.25 \times 10^{-2}$
	BR($\mathrm{h}_2 \to \mathrm{WW}$) $= 3.67 \times 10^{-1}$ $\quad$ BR($\mathrm{h}_3 \to \mathrm{WW}$) $= 3.51 \times 10^{-4}$
	BR($\mathrm{h}_2 \to \mathrm{ZZ}$) $= 1.73 \times 10^{-1}$ $\quad$ BR($\mathrm{h}_3 \to \mathrm{ZZ}$) $= 1.66 \times 10^{-1}$
	BR($\mathrm{h}_2 \to \gamma\gamma$)$= 3.15 \times 10^{-6}$ $\quad$ BR($\mathrm{h}_2 \to \gamma\gamma$) $= 3.04 \times 10^{-6}$

$BP7_3$ Benchmarks for the Complex Two Higgs Doublet Model

D. Fontes, J.C. Romão, R. Santos, João P. Silva [1265]

Benchmark setup	
Main Features	• lightest Higgs boson at 125 GeV
	• CP violation through scalar-pseudoscalar mixing
	• CP violation detected by the simultaneous existence
	of three decay channels (see classes C_1-C_7 in the text)
Benchmark point 3_{C2HDM}	
Model Type	Flipped
Higgs boson masses	M_{h_1}= 125 GeV, $M_{\mathrm{h}_2} = 278$ GeV, $M_{\mathrm{h}_2} = 475$ GeV, $M_{\mathrm{H}^\pm} = 483$ GeV
Other point parameters	Re$m_{12}^2 = 3.44 \times 10^4$ GeV^2, $\tan\beta = 4.27$,
	$\alpha_1 = -1.353$, $\alpha_2 = -0.007$, $\alpha_3 = 0.832$

Production cross sections times branching ratios	
Class C_1	C_1: $\sigma_3 \times \mathrm{BR}(\mathrm{h}_3 \to \mathrm{h}_2\mathrm{Z}) = 187$ fb C_1: $\sigma_2 \times \mathrm{BR}(\mathrm{h}_2 \to \mathrm{h}_1\mathrm{Z}) = 313$ fb C_1: $\sigma_3 \times \mathrm{BR}(\mathrm{h}_3 \to \mathrm{h}_1\mathrm{Z}) = 69$ fb
Class C_2	C_2: $\sigma_2 \times \mathrm{BR}(\mathrm{h}_2 \to \mathrm{h}_1\mathrm{Z}) = 313$ fb C_2: $\sigma_1 \times \mathrm{BR}(\mathrm{h}_1 \to \mathrm{ZZ}) = 1062$ fb C_2: $\sigma_2 \times \mathrm{BR}(\mathrm{h}_2 \to \mathrm{ZZ}) = 267$ fb
Class C_3	C_3: $\sigma_3 \times \mathrm{BR}(\mathrm{h}_3 \to \mathrm{h}_1\mathrm{Z}) = 69$ fb C_3: $\sigma_1 \times \mathrm{BR}(\mathrm{h}_1 \to \mathrm{ZZ}) = 1062$ fb C_3: $\sigma_3 \times \mathrm{BR}(\mathrm{h}_3 \to \mathrm{ZZ}) = 50$ fb
Class C_4	C_4: $\sigma_3 \times \mathrm{BR}(\mathrm{h}_3 \to \mathrm{h}_2\mathrm{Z}) = 187$ fb C_4: $\sigma_2 \times \mathrm{BR}(\mathrm{h}_2 \to \mathrm{ZZ}) = 267$ fb C_4: $\sigma_3 \times \mathrm{BR}(\mathrm{h}_3 \to \mathrm{ZZ}) = 50$ fb
Class C_5	C_5: $\sigma_3 \times \mathrm{BR}(\mathrm{h}_3 \to \mathrm{ZZ}) = 50$ fb C_5: $\sigma_2 \times \mathrm{BR}(\mathrm{h}_2 \to \mathrm{ZZ}) = 267$ fb C_5: $\sigma_1 \times \mathrm{BR}(\mathrm{h}_1 \to \mathrm{ZZ}) = 1062$ fb
Class C_{7a}	C_{7a}: $\sigma_2 \times \mathrm{BR}(\mathrm{h}_2 \to \mathrm{h}_1\mathrm{h}_1) = 32$ fb C_{7a}: $\sigma_2 \times \mathrm{BR}(\mathrm{h}_2 \to \mathrm{h}_1\mathrm{Z}) = 313$ fb C_{7a}: $\sigma_1 \times \mathrm{BR}(\mathrm{h}_1 \to \mathrm{ZZ}) = 1062$ fb
Class C_{7b}	C_{7b}: $\sigma_3 \times \mathrm{BR}(\mathrm{h}_3 \to \mathrm{h}_1\mathrm{h}_1) = 33$ fb C_{7b}: $\sigma_3 \times \mathrm{BR}(\mathrm{h}_3 \to \mathrm{h}_1\mathrm{Z}) = 69$ fb C_{7b}: $\sigma_1 \times \mathrm{BR}(\mathrm{h}_1 \to \mathrm{ZZ}) = 1062$ fb
Heavy Higgs boson total width	$\Gamma(\mathrm{h}_2) = 0.81$ GeV $\quad \Gamma(\mathrm{h}_3) = 14.36$ GeV
Heavy Higgs boson branching fractions	$\mathrm{BR}(\mathrm{h}_2 \to \tau\tau) = 3.67 \times 10^{-5}$ $\quad \mathrm{BR}(\mathrm{h}_3 \to \tau\tau) = 3.71 \times 10^{-6}$ $\mathrm{BR}(\mathrm{h}_2 \to \mathrm{b\bar{b}}) = 1.11 \times 10^{-1}$ $\quad \mathrm{BR}(\mathrm{h}_3 \to \mathrm{b\bar{b}}) = 1.05 \times 10^{-2}$ $\mathrm{BR}(\mathrm{h}_2 \to \mathrm{WW}) = 4.44 \times 10^{-1}$ $\quad \mathrm{BR}(\mathrm{h}_3 \to \mathrm{WW}) = 2.18 \times 10^{-1}$ $\mathrm{BR}(\mathrm{h}_2 \to \mathrm{ZZ}) = 1.93 \times 10^{-1}$ $\quad \mathrm{BR}(\mathrm{h}_3 \to \mathrm{ZZ}) = 1.04 \times 10^{-1}$ $\mathrm{BR}(\mathrm{h}_2 \to \gamma\gamma) = 1.45 \times 10^{-5}$ $\quad \mathrm{BR}(\mathrm{h}_2 \to \gamma\gamma) = 1.16 \times 10^{-6}$

$BP7_4$ **Benchmarks for the Complex Two Higgs Doublet Model**	
D. Fontes, J.C. Romão, R. Santos, João P. Silva [1265]	
Benchmark setup	
Main Features	• lightest Higgs boson at 125 GeV • CP violation through scalar-pseudoscalar mixing • CP violation detected by the simultaneous existence of three decay channels (see classes C_1-C_7 in the text)
Benchmark point $4_{\mathbf{C2HDM}}$	
Model Type	Type I
Higgs boson masses	$M_{\mathrm{h}_1} = 125$ GeV, $M_{\mathrm{h}_2} = 259$ GeV, $M_{\mathrm{h}_3} = 364$ GeV, $M_{\mathrm{H}^\pm} = 409$ GeV

Other point parameters	$\mathrm{Re}m_{12}^2 = 4.18 \times 10^3$ GeV^2, $\tan\beta = 2.45$, $\alpha_1 = 1.167$, $\alpha_2 = -0.139$, $\alpha_3 = 0.247$
Production cross sections times branching ratios	
Class C_1	C_1: $\sigma_3 \times \mathrm{BR}(\mathrm{h_3} \to \mathrm{h_2 Z}) = 724$ fb C_1: $\sigma_2 \times \mathrm{BR}(\mathrm{h_2} \to \mathrm{h_1 Z}) = 1252$ fb C_1: $\sigma_3 \times \mathrm{BR}(\mathrm{h_3} \to \mathrm{h_1 Z}) = 66$ fb
Class C_2	C_2: $\sigma_2 \times \mathrm{BR}(\mathrm{h_2} \to \mathrm{h_1 Z}) = 1252$ fb C_2: $\sigma_1 \times \mathrm{BR}(\mathrm{h_1} \to \mathrm{ZZ}) = 1093$ fb C_2: $\sigma_2 \times \mathrm{BR}(\mathrm{h_2} \to \mathrm{ZZ}) = 271$ fb
Class C_3	C_3: $\sigma_3 \times \mathrm{BR}(\mathrm{h_3} \to \mathrm{h_1 Z}) = 66$ fb C_3: $\sigma_1 \times \mathrm{BR}(\mathrm{h_1} \to \mathrm{ZZ}) = 1093$ fb C_3: $\sigma_3 \times \mathrm{BR}(\mathrm{h_3} \to \mathrm{ZZ}) = 304$ fb
Class C_4	C_4: $\sigma_3 \times \mathrm{BR}(\mathrm{h_3} \to \mathrm{h_2 Z}) = 724$ fb C_4: $\sigma_2 \times \mathrm{BR}(\mathrm{h_2} \to \mathrm{ZZ}) = 271$ fb C_4: $\sigma_3 \times \mathrm{BR}(\mathrm{h_3} \to \mathrm{ZZ}) = 304$ fb
Class C_5	C_5: $\sigma_3 \times \mathrm{BR}(\mathrm{h_3} \to \mathrm{ZZ}) = 304$ fb C_5: $\sigma_2 \times \mathrm{BR}(\mathrm{h_2} \to \mathrm{ZZ}) = 271$ fb C_5: $\sigma_1 \times \mathrm{BR}(\mathrm{h_1} \to \mathrm{ZZ}) = 1093$ fb
Class C_{7a}	C_{7a}: $\sigma_2 \times \mathrm{BR}(\mathrm{h_2} \to \mathrm{h_1 h_1}) = 417$ fb C_{7a}: $\sigma_2 \times \mathrm{BR}(\mathrm{h_2} \to \mathrm{h_1 Z}) = 1252$ fb C_{7a}: $\sigma_1 \times \mathrm{BR}(\mathrm{h_1} \to \mathrm{ZZ}) = 1093$ fb
Class C_{7b}	C_{7b}: $\sigma_3 \times \mathrm{BR}(\mathrm{h_3} \to \mathrm{h_1 h_1}) = 303$ fb C_{7b}: $\sigma_3 \times \mathrm{BR}(\mathrm{h_3} \to \mathrm{h_1 Z}) = 66$ fb C_{7b}: $\sigma_1 \times \mathrm{BR}(\mathrm{h_1} \to \mathrm{ZZ}) = 1093$ fb
Heavy Higgs boson total width	$\Gamma(\mathrm{h_2}) = 3.4 \times 10^{-2}$ GeV $\quad$ $\Gamma(\mathrm{h_3}) = 2.15$ GeV
Heavy Higgs boson branching fractions	$\mathrm{BR}(\mathrm{h_2} \to \tau\tau) = 3.29 \times 10^{-3}$ $\quad$ $\mathrm{BR}(\mathrm{h_3} \to \tau\tau) = 5.46 \times 10^{-5}$ $\mathrm{BR}(\mathrm{h_2} \to \mathrm{b\bar{b}}) = 2.79 \times 10^{-2}$ $\quad$ $\mathrm{BR}(\mathrm{h_3} \to \mathrm{b\bar{b}}) = 4.59 \times 10^{-4}$ $\mathrm{BR}(\mathrm{h_2} \to \mathrm{WW}) = 2.34 \times 10^{-1}$ $\quad$ $\mathrm{BR}(\mathrm{h_3} \to \mathrm{WW}) = 9.37 \times 10^{-2}$ $\mathrm{BR}(\mathrm{h_2} \to \mathrm{ZZ}) = 9.98 \times 10^{-2}$ $\quad$ $\mathrm{BR}(\mathrm{h_3} \to \mathrm{ZZ}) = 4.3 \times 10^{-2}$ $\mathrm{BR}(\mathrm{h_2} \to \gamma\gamma) = 3.09 \times 10^{-5}$ $\quad$ $\mathrm{BR}(\mathrm{h_2} \to \gamma\gamma) = 1.80 \times 10^{-5}$
$BP7_5$ **Benchmarks for the Complex Two Higgs Doublet Model**	
D. Fontes, J.C. Romão, R. Santos, João P. Silva [1265]	
Benchmark setup	
Main Features	• lightest Higgs boson at 125 GeV • CP violation through scalar-pseudoscalar mixing • CP violation detected by the simultaneous existence of three decay channels (see classes C_1-C_7 in the text)
Benchmark point $5_{\mathbf{C2HDM}}$	

Model Type	Lepton Specific
Higgs boson masses	M_{h_1}= 125 GeV, $M_{\mathrm{h}_2} = 276$ GeV, $M_{\mathrm{h}_3} = 277$ GeV, $M_{\mathrm{H}^\pm} = 338$ GeV
Other point parameters	$\mathrm{Re}m_{12}^2 = 3.19 \times 10^4$ GeV^2, $\tan\beta = 1.82$,
	$\alpha_1 = 1.016$, $\alpha_2 = -0.0095$, $\alpha_3 = 0.863$
Production cross sections times branching ratios	
Class C_2	C_2: $\sigma_2 \times \mathrm{BR}(\mathrm{h}_2 \to \mathrm{h}_1\mathrm{Z}) = 385$ fb
	C_2: $\sigma_1 \times \mathrm{BR}(\mathrm{h}_1 \to \mathrm{ZZ}) = 1080$ fb
	C_2: $\sigma_2 \times \mathrm{BR}(\mathrm{h}_2 \to \mathrm{ZZ}) = 636$ fb
Class C_3	C_3: $\sigma_3 \times \mathrm{BR}(\mathrm{h}_3 \to \mathrm{h}_1\mathrm{Z}) = 653$ fb
	C_3: $\sigma_1 \times \mathrm{BR}(\mathrm{h}_1 \to \mathrm{ZZ}) = 1080$ fb
	C_3: $\sigma_3 \times \mathrm{BR}(\mathrm{h}_3 \to \mathrm{ZZ}) = 487$ fb
Class C_5	C_5: $\sigma_3 \times \mathrm{BR}(\mathrm{h}_3 \to \mathrm{ZZ}) = 487$ fb
	C_5: $\sigma_2 \times \mathrm{BR}(\mathrm{h}_2 \to \mathrm{ZZ}) = 636$ fb
	C_5: $\sigma_1 \times \mathrm{BR}(\mathrm{h}_1 \to \mathrm{ZZ}) = 1080$ fb
Class C_{7a}	C_{7a}: $\sigma_2 \times \mathrm{BR}(\mathrm{h}_2 \to \mathrm{h}_1\mathrm{h}_1) = 3661$ fb
	C_{7a}: $\sigma_2 \times \mathrm{BR}(\mathrm{h}_2 \to \mathrm{h}_1\mathrm{Z}) = 385$ fb
	C_{7a}: $\sigma_1 \times \mathrm{BR}(\mathrm{h}_1 \to \mathrm{ZZ}) = 1080$ fb
Class C_{7b}	C_{7b}: $\sigma_3 \times \mathrm{BR}(\mathrm{h}_3 \to \mathrm{h}_1\mathrm{h}_1) = 2780$ fb
	C_{7b}: $\sigma_3 \times \mathrm{BR}(\mathrm{h}_3 \to \mathrm{h}_1\mathrm{Z}) = 653$ fb
	C_{7b}: $\sigma_1 \times \mathrm{BR}(\mathrm{h}_1 \to \mathrm{ZZ}) = 1080$ fb
Heavy Higgs boson total width	$\Gamma(\mathrm{h}_2) = 3.7 \times 10^{-2}$ GeV $\quad$ $\Gamma(\mathrm{h}_3) = 2.8 \times 10^{-2}$ GeV
Heavy Higgs boson branching fractions	$\mathrm{BR}(\mathrm{h}_2 \to \tau\tau) = 5.04 \times 10^{-2}$ $\quad$ $\mathrm{BR}(\mathrm{h}_3 \to \tau\tau) = 6.55 \times 10^{-2}$
	$\mathrm{BR}(\mathrm{h}_2 \to \mathrm{b\bar{b}}) = 4.39 \times 10^{-2}$ $\quad$ $\mathrm{BR}(\mathrm{h}_3 \to \mathrm{b\bar{b}}) = 5.67 \times 10^{-2}$
	$\mathrm{BR}(\mathrm{h}_2 \to \mathrm{WW}) = 2.00 \times 10^{-1}$ $\quad$ $\mathrm{BR}(\mathrm{h}_3 \to \mathrm{WW}) = 1.78 \times 10^{-1}$
	$\mathrm{BR}(\mathrm{h}_2 \to \mathrm{ZZ}) = 8.67 \times 10^{-2}$ $\quad$ $\mathrm{BR}(\mathrm{h}_3 \to \mathrm{ZZ}) = 7.73 \times 10^{-2}$
	$\mathrm{BR}(\mathrm{h}_2 \to \gamma\gamma) = 1.96 \times 10^{-4}$ $\quad$ $\mathrm{BR}(\mathrm{h}_2 \to \gamma\gamma) = 2.21 \times 10^{-4}$

IV.4.3.h Benchmark points $BP8$

$BP8$**: Controlled Higgs flavour changing couplings**	
F. Botella, G.C. Branco, M. Nebot & M.N. Rebelo [1266]	
Main Features	Higgs flavour changing decays, can be probed at the 14 TeV LHC
$BP8_1$ BGL model (b, τ)	
Spectrum:	$M_{\mathrm{h}} = 125$ GeV, $M_{\mathrm{H}} \approx M_{\mathrm{A}} \approx M_{\mathrm{H}^\pm} \gtrsim 600$ GeV
$\cos(\alpha - \beta)$	≤ 0.17
$\tan\beta$	$25 - 100$

Flavour changing Higgs boson decay branching fractions	
BR($\mathrm{t} \to \mathrm{hc}$)	up to 10^{-2}
Non-SM flavour conserving Higgs boson decay branching fractions	
BR($\mathrm{h} \to \tau\tau$)	0.06 to 0.10
BR($\mathrm{h} \to \mathrm{b\bar{b}}$)	0.46 to 0.64
$BP8_2$ BGL model (t, ν_2)	
Spectrum:	$M_\mathrm{h} = 125$ GeV, $M_\mathrm{H} \approx M_\mathrm{A} \approx M_{\mathrm{H}^\pm} \gtrsim 250$ GeV
$\cos(\alpha - \beta)$	≤ 0.5
$\tan\beta$	$0.5 - 3.5$
Flavour changing Higgs boson decay branching fractions	
BR($\mathrm{h} \to \mathrm{bs}$)	up to 10^{-3}
BR($\mathrm{h} \to \mu\tau$)	up to 10^{-2}
Non-SM flavour conserving Higgs boson decay branching fractions	
BR($\mathrm{h} \to \tau\tau$)	0.06 to 0.10
BR($\mathrm{h} \to \mathrm{b\bar{b}}$)	0.42 to 0.66
$BP8_3$ BGL model (b, ν_2)	
Spectrum:	$M_\mathrm{h} = 125$ GeV, $M_\mathrm{H} \approx M_\mathrm{A} \approx M_{\mathrm{H}^\pm} \approx 600$ GeV
$\cos(\alpha - \beta)$	≤ 0.17
$\tan\beta$	$1 - 25$
Flavour changing Higgs boson decay branching fractions	
BR($\mathrm{t} \to \mathrm{hc}$)	up to 10^{-3}
BR($\mathrm{h} \to \mu\tau$)	up to 10^{-2}
Non-SM flavour conserving Higgs boson decay branching fractions	
BR($\mathrm{h} \to \tau\tau$)	0.06 to 0.10
BR($\mathrm{h} \to \mathrm{b\bar{b}}$)	0.42 to 0.66

IV.4.4 Georgi-Machacek model

Extensions of the Standard Model (SM) Higgs sector that contain scalars in triplet or larger isospin representations and that preserve the custodial symmetry in the scalar sector generically contain fermiophobic scalars that transform as a fiveplet under the custodial symmetry. These custodial-fiveplet scalars play an essential role in the unitarity of vector boson scattering amplitudes [1267–1269]. The coupling strength of the custodial-fiveplet scalars to VV is proportional to the vacuum expectation value (vev) carried by the higher-isospin representation(s). While many scenarios with scalars in larger isospin representations are severely constrained by the electroweak ρ parameter, preservation of the custodial symmetry renders these models viable.

The experiments at the CERN Large Hadron Collider (LHC) have sensitivity to the production

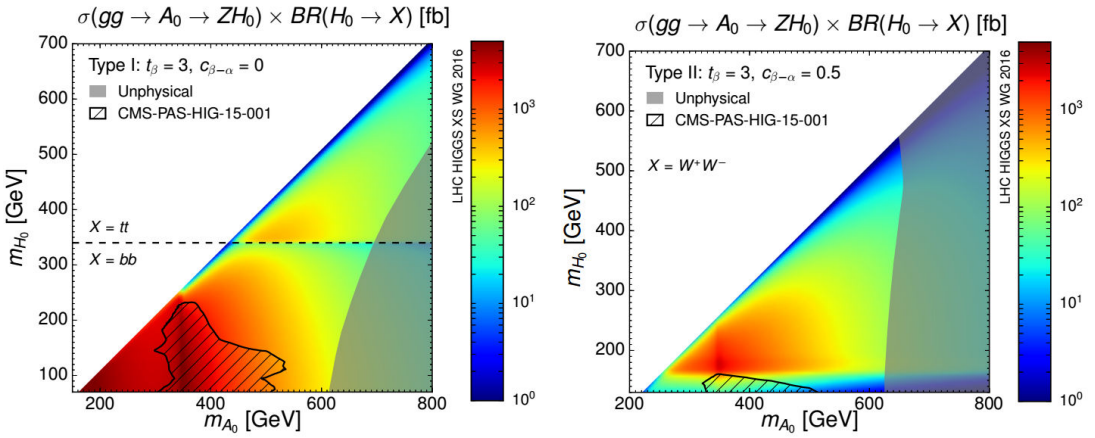

Figure 278: Example planes for BP3. (a) (left) $\sigma\times$ BR for $\mathrm{gg} \to \mathrm{A} \to \mathrm{ZH}$ ($\mathrm{H} \to \mathrm{f\bar{f}}$) in 2HDM Type I for $t_\beta = 3$ and the alignment limit $c_{\beta-\alpha} = 0$. For $M_\mathrm{H} < 340$ GeV (> 340 GeV), $\mathrm{f\bar{f}} = \mathrm{b\bar{b}}$ ($= \mathrm{t\bar{t}}$). The black-hatched region corresponds to the exclusion from CMS-PAS-HIG-15-001 [1261]. (b) (right) $\sigma\times$ BR for $\mathrm{gg} \to \mathrm{A} \to \mathrm{ZH}$ ($\mathrm{H} \to \mathrm{W^+W^-}$) in 2HDM Type II for $t_\beta = 3$ away from the alignment limit ($s_{\beta+\alpha} \sim 1$). See Table IV.4.3.c for more details.

and decay of the fermiophobic custodial-fiveplet states,

$$\mathrm{H_5^{++}}, \mathrm{H_5^{+}}, \mathrm{H_5^{0}}, \mathrm{H_5^{-}}, \mathrm{H_5^{--}}, \tag{IV.4.16}$$

through their tree-level couplings to W and Z boson pairs. This states offer several interesting features, including a tree-level $\mathrm{H_5^{\pm}W^{\mp}Z}$ interaction, $\mathrm{H_5^{\pm\pm}}$ decays to like-sign W bosons, and $\mathrm{H_5^0}$ decays to $\mathrm{W^+W^-}$ and ZZ in a different ratio than appears in the SM. The production of $\mathrm{H_5^{\pm}}$ via vector boson fusion (VBF) followed by decays to $\mathrm{W^{\pm}Z}$ has already been studied by ATLAS in Run 1 of the LHC [1270].

As a prototype model containing a custodial fiveplet of scalars, we consider the Georgi-Machacek (GM) model [1271, 1272], in which the SM Higgs sector is extended by two isospin triplets while preserving custodial SU(2) symmetry. The phenomenology of these scalars is dramatically different from that of the additional Higgs bosons found in two Higgs doublet models (2HDMs) or singlet extensions of the SM. They do not couple to fermions and hence cannot be produced in gluon fusion or in association with a top quark. The singly-charged scalars $\mathrm{H_5^{\pm}}$ couple to $\mathrm{W^{\pm}Z}$ at tree level, in contrast to the charged scalar of the 2HDM for which this coupling appears only at one loop. The relative coupling strengths of $\mathrm{H_5^0}$ to $\mathrm{W^+W^-}$ and ZZ are different than those of the SM Higgs boson, leading to $\Gamma(\mathrm{H_5^0} \to \mathrm{WW})/\Gamma(\mathrm{H_5^0} \to \mathrm{ZZ}) \to 1/2$ in the high-mass limit in contrast to the SM relation $\Gamma(\mathrm{h_{SM}} \to \mathrm{WW})/\Gamma(\mathrm{h_{SM}} \to \mathrm{ZZ}) \to 2$. The presence of a doubly-charged Higgs boson with decays to like-sign W bosons is a dramatic indication of isospin representations larger than doublets that contribute to electroweak symmetry breaking. A comprehensive tree-level phenomenological study of the production of $\mathrm{H_5^0}$, $\mathrm{H_5^{\pm}}$, and $\mathrm{H_5^{\pm\pm}}$ at the LHC via VBF with decays to $\mathrm{W^+W^-/ZZ}$, $\mathrm{W^{\pm}Z}$, and $\mathrm{W^{\pm}W^{\pm}}$ respectively, with the gauge bosons decaying leptonically, was performed in [1273].

In this section we define the H5plane benchmark for the GM model, in which the two free parameters most relevant for $\mathrm{H_5^0}$ searches can be varied. The benchmark plane specification is designed to be compatible with the spectrum calculator GMCALC [1274]. We also provide tables of cross sections for $\mathrm{H_5^0}$, $\mathrm{H_5^{\pm}}$, and $\mathrm{H_5^{\pm\pm}}$ production in VBF for the 13 TeV LHC, and well as their decay widths to vector boson pairs. The cross section recommendations include QCD corrections at next-to-next-to-leading order (NNLO) and were generated using the VBF@NNLO code [263,264]. The decay widths were calculated at tree level using the code GMCALC 1.2.0 [1274], and include doubly-offshell effects. We concentrate

on H_5^0 masses in the range 200–2000 GeV. For H_5^0 masses below 200 GeV, decays to off-shell vector bosons and other final states need to be considered, which changes the experimental analysis.

A fully differential study including next-to-leading order (NLO) QCD matrix elements interfaced to the parton shower has recently been undertaken in [1275] using the MADGRAPH5_AMC@NLO technology [54, 553], and the corresponding model file made public. The largest remaining theoretical uncertainties in the cross section and decay width predictions are due to NLO electroweak corrections. A calculation of these corrections would require the full one-loop electroweak renormalization of the Georgi-Machacek model. This is unlikely to be undertaken by hand in the few-years timescale, but might become feasible using automated NLO technology [553].

In the next subsection we give a brief summary of the GM model. We specify the H5plane benchmark in Section IV.4.4.b. The VBF production cross sections are tabulated in Section IV.4.4.c and the total widths of the H_5^0 states are tabulated in Section IV.4.4.d.

IV.4.4.a Model parameterization

The scalar sector of the GM model [1271, 1272] consists of the usual complex isospin doublet (ϕ^+, ϕ^0) with eHcharge[IV.22] $Y = 1$, a real triplet (ξ^+, ξ^0, ξ^-) with $Y = 0$, and a complex triplet $(\chi^{++}, \chi^+, \chi^0)$ with $Y = 2$. The doublet is responsible for the fermion masses as in the SM.

The scalar potential is chosen by hand to preserve a global $SU(2)_L \times SU(2)_R$ symmetry. This ensures $\rho = 1$ at tree level. In order to make the global $SU(2)_L \times SU(2)_R$ symmetry explicit, we write the doublet in the form of a bidoublet Φ and combine the triplets to form a bitriplet X:

$$\Phi = \begin{pmatrix} \phi^{0*} & \phi^+ \\ -\phi^{+*} & \phi^0 \end{pmatrix}, \qquad X = \begin{pmatrix} \chi^{0*} & \xi^+ & \chi^{++} \\ -\chi^{+*} & \xi^0 & \chi^+ \\ \chi^{++*} & -\xi^{+*} & \chi^0 \end{pmatrix}. \tag{IV.4.17}$$

The vacuum expectation values (vevs) are defined by $\langle \Phi \rangle = \frac{v_\phi}{\sqrt{2}} \mathbf{I}_{2\times 2}$ and $\langle X \rangle = v_\chi \mathbf{I}_{3\times 3}$, where $\mathbf{I}$ is the unit matrix. The Fermi constant G_F fixes the combination of vevs,

$$v_\phi^2 + 8 v_\chi^2 \equiv v^2 = \frac{1}{\sqrt{2} G_F} \approx (246 \text{ GeV})^2. \tag{IV.4.18}$$

The most general gauge-invariant scalar potential involving these fields that conserves custodial SU(2) is given, in the conventions of Ref. [1276], by

$$\begin{aligned} V(\Phi, X) = {} & \frac{\mu_2^2}{2} \mathrm{Tr}(\Phi^\dagger \Phi) + \frac{\mu_3^2}{2} \mathrm{Tr}(X^\dagger X) + \lambda_1 [\mathrm{Tr}(\Phi^\dagger \Phi)]^2 + \lambda_2 \mathrm{Tr}(\Phi^\dagger \Phi) \mathrm{Tr}(X^\dagger X) \\ & + \lambda_3 \mathrm{Tr}(X^\dagger X X^\dagger X) + \lambda_4 [\mathrm{Tr}(X^\dagger X)]^2 - \lambda_5 \mathrm{Tr}(\Phi^\dagger \tau^a \Phi \tau^b) \mathrm{Tr}(X^\dagger t^a X t^b) \\ & - M_1 \mathrm{Tr}(\Phi^\dagger \tau^a \Phi \tau^b)(U X U^\dagger)_{ab} - M_2 \mathrm{Tr}(X^\dagger t^a X t^b)(U X U^\dagger)_{ab}. \end{aligned} \tag{IV.4.19}$$

Here the SU(2) generators for the doublet representation are $\tau^a = \sigma^a/2$ with σ^a being the Pauli matrices, the generators for the triplet representation are

$$t^1 = \frac{1}{\sqrt{2}} \begin{pmatrix} 0 & 1 & 0 \\ 1 & 0 & 1 \\ 0 & 1 & 0 \end{pmatrix}, \qquad t^2 = \frac{1}{\sqrt{2}} \begin{pmatrix} 0 & -i & 0 \\ i & 0 & -i \\ 0 & i & 0 \end{pmatrix}, \qquad t^3 = \begin{pmatrix} 1 & 0 & 0 \\ 0 & 0 & 0 \\ 0 & 0 & -1 \end{pmatrix}, \tag{IV.4.20}$$

[IV.22] We normalize the hypercharge operator such that $Q = T^3 + Y/2$.

and the matrix U, which rotates X into the Cartesian basis, is given by [1277]

$$U = \begin{pmatrix} -\frac{1}{\sqrt{2}} & 0 & \frac{1}{\sqrt{2}} \\ -\frac{i}{\sqrt{2}} & 0 & -\frac{i}{\sqrt{2}} \\ 0 & 1 & 0 \end{pmatrix}. \tag{IV.4.21}$$

We decompose the neutral fields into real and imaginary parts according to

$$\phi^0 \to \frac{v_\phi}{\sqrt{2}} + \frac{\phi^{0,r} + i\phi^{0,i}}{\sqrt{2}}, \qquad \chi^0 \to v_\chi + \frac{\chi^{0,r} + i\chi^{0,i}}{\sqrt{2}}, \qquad \xi^0 \to v_\chi + \xi^0. \tag{IV.4.22}$$

The physical fields can then be organized by their transformation properties under the custodial SU(2) symmetry into a fiveplet, a triplet, and two singlets. The custodial-fiveplet states are given by

$$\mathrm{H}_5^{++} = \chi^{++}, \qquad \mathrm{H}_5^{+} = \frac{\left(\chi^+ - \xi^+\right)}{\sqrt{2}}, \qquad \mathrm{H}_5^{0} = \sqrt{\frac{2}{3}}\xi^0 - \sqrt{\frac{1}{3}}\chi^{0,r}. \tag{IV.4.23}$$

Because the states in the custodial fiveplet contain no doublet field content, they do not couple to fermions.

The custodial-triplet states are given by

$$\mathrm{H}_3^{+} = -s_\mathrm{H}\phi^+ + c_\mathrm{H}\frac{\left(\chi^+ + \xi^+\right)}{\sqrt{2}}, \qquad \mathrm{H}_3^{0} = -s_\mathrm{H}\phi^{0,i} + c_\mathrm{H}\chi^{0,i}, \tag{IV.4.24}$$

where the vevs are parameterized by

$$c_\mathrm{H} \equiv \cos\theta_\mathrm{H} = \frac{v_\phi}{v}, \qquad s_\mathrm{H} \equiv \sin\theta_\mathrm{H} = \frac{2\sqrt{2}\,v_\chi}{v}. \tag{IV.4.25}$$

The quantity s_H^2 represents the fraction of the gauge boson masses-squared M_W^2 and M_Z^2 that is generated by the vev of the triplets, while c_H^2 represents the fraction generated by the usual Higgs doublet.

The states of the custodial fiveplet ($\mathrm{H}_5^{\pm\pm}$, $\mathrm{H}_5^{\pm}$, H_5^{0}) have a common mass m_5 and the states of the custodial triplet ($\mathrm{H}_3^{\pm}$, H_3^{0}) have a common mass m_3. These masses can be written (after eliminating μ_2^2 and μ_3^2 in favor of the vevs) as[IV.23]

$$m_5^2 = \frac{M_1}{4v_\chi}v_\phi^2 + 12M_2v_\chi + \frac{3}{2}\lambda_5 v_\phi^2 + 8\lambda_3 v_\chi^2, \tag{IV.4.27}$$

$$m_3^2 = \frac{M_1}{4v_\chi}(v_\phi^2 + 8v_\chi^2) + \frac{\lambda_5}{2}(v_\phi^2 + 8v_\chi^2) = \left(\frac{M_1}{4v_\chi} + \frac{\lambda_5}{2}\right)v^2. \tag{IV.4.28}$$

The two custodial-singlet mass eigenstates are given by

$$\mathrm{h} = \cos\alpha\,\phi^{0,r} - \sin\alpha\,\mathrm{H}_1^{0\prime}, \qquad \mathrm{H} = \sin\alpha\,\phi^{0,r} + \cos\alpha\,\mathrm{H}_1^{0\prime}, \tag{IV.4.29}$$

where

$$\mathrm{H}_1^{0\prime} = \sqrt{\frac{1}{3}}\xi^0 + \sqrt{\frac{2}{3}}\chi^{0,r}. \tag{IV.4.30}$$

[IV.23] Note that the ratio M_1/v_χ can be written using the minimization condition $\partial V/\partial v_\chi = 0$ as

$$\frac{M_1}{v_\chi} = \frac{4}{v_\phi^2}\left[\mu_3^2 + (2\lambda_2 - \lambda_5)v_\phi^2 + 4(\lambda_3 + 3\lambda_4)v_\chi^2 - 6M_2v_\chi\right], \tag{IV.4.26}$$

which is finite in the limit $v_\chi \to 0$.

The mixing angle and masses are given by

$$\sin 2\alpha = \frac{2\mathcal{M}_{12}^2}{M_{\rm H}^2 - M_{\rm h}^2}, \qquad \cos 2\alpha = \frac{\mathcal{M}_{22}^2 - \mathcal{M}_{11}^2}{M_{\rm H}^2 - M_{\rm h}^2}, \tag{IV.4.31}$$

$$m_{\rm h,H}^2 = \frac{1}{2}\left[\mathcal{M}_{11}^2 + \mathcal{M}_{22}^2 \mp \sqrt{\left(\mathcal{M}_{11}^2 - \mathcal{M}_{22}^2\right)^2 + 4\left(\mathcal{M}_{12}^2\right)^2}\right], \tag{IV.4.32}$$

where we choose $M_{\rm h} < M_{\rm H}$, and

$$\begin{aligned}
\mathcal{M}_{11}^2 &= 8\lambda_1 v_\phi^2, \\
\mathcal{M}_{12}^2 &= \frac{\sqrt{3}}{2} v_\phi \left[-M_1 + 4\left(2\lambda_2 - \lambda_5\right) v_\chi\right], \\
\mathcal{M}_{22}^2 &= \frac{M_1 v_\phi^2}{4 v_\chi} - 6 M_2 v_\chi + 8\left(\lambda_3 + 3\lambda_4\right) v_\chi^2.
\end{aligned} \tag{IV.4.33}$$

The fiveplet states couple to vector bosons according to the following Feynman rules [1189, 1273, 1276]:

$$\begin{aligned}
{\rm H_5^0 W^+}_\mu {\rm W^-}_\nu &: \sqrt{\frac{2}{3}} i g^2 v_\chi g_{\mu\nu} = 2i \frac{M_{\rm W}^2}{v}\left(\frac{s_{\rm H}}{\sqrt{3}}\right) g_{\mu\nu} = 2(\sqrt{2}G_F)^{1/2} M_{\rm W}^2 \left(-\frac{s_{\rm H}}{\sqrt{3}}\right)(-i g_{\mu\nu}), \\
{\rm H_5^0 Z}_\mu {\rm Z}_\nu &: -\sqrt{\frac{8}{3}} i \frac{g^2 v_\chi}{c_W^2} g_{\mu\nu} = 2i \frac{M_{\rm Z}^2}{v}\left(-\frac{2 s_{\rm H}}{\sqrt{3}}\right) g_{\mu\nu} = 2(\sqrt{2}G_F)^{1/2} M_{\rm Z}^2 \left(\frac{2 s_{\rm H}}{\sqrt{3}}\right)(-i g_{\mu\nu}), \\
{\rm H_5^+ W^-}_\mu {\rm Z}_\nu &: -\sqrt{2} i \frac{g^2 v_\chi}{c_W} g_{\mu\nu} = 2i \frac{M_{\rm W} M_{\rm Z}}{v}\left(-s_{\rm H}\right) g_{\mu\nu} = 2(\sqrt{2}G_F)^{1/2} M_{\rm W} M_{\rm Z}\left(s_{\rm H}\right)(-i g_{\mu\nu}), \\
{\rm H_5^{++} W^-}_\mu {\rm W^-}_\nu &: 2 i g^2 v_\chi g_{\mu\nu} = 2i \frac{M_{\rm W}^2}{v}\left(\sqrt{2} s_{\rm H}\right) g_{\mu\nu} = 2(\sqrt{2}G_F)^{1/2} M_{\rm W}^2 \left(-\sqrt{2} s_{\rm H}\right)(-i g_{\mu\nu}),
\end{aligned} \tag{IV.4.34}$$

where we write the coupling in multiple forms to make contact with the notation of Refs. [264, 1273]. The triplet vev v_χ is called v' in [1273], and the factors $F_{\rm VV}$ in Eq. (5.2) of Ref. [264] correspond in this model to

$$\begin{aligned}
F_{\rm W^+W^-} &= -\frac{s_{\rm H}}{\sqrt{3}} \qquad ({\rm H_5^0 \text{ production}}), \\
F_{\rm ZZ} &= \frac{2 s_{\rm H}}{\sqrt{3}} \qquad ({\rm H_5^0 \text{ production}}), \\
F_{\rm W^\pm Z} &= s_{\rm H} \qquad ({\rm H_5^\pm \text{ production}}), \\
F_{\rm W^\pm W^\pm} &= -\sqrt{2} s_{\rm H} \qquad ({\rm H_5^{\pm\pm} \text{ production}}).
\end{aligned} \tag{IV.4.35}$$

Note in particular that, for $\rm H_5^0$, one cannot simply rescale the vector boson fusion cross section of the SM Higgs boson because the ratio of WW to ZZ couplings is different than in the SM (for SM Higgs boson production, $F_{\rm W^+W^-} = F_{\rm ZZ} = -1$).

The VBF production cross sections for a single $\rm H_5^0$ state depend only on the two parameters m_5 and $s_{\rm H}$. If the spectrum is such that decays of $\rm H_5^0$ to $\rm H_3 V$ or $\rm H_3 H_3$ are kinematically inaccessible, the total decay widths of the $\rm H_5^0$ states to vector boson pairs also depend only on m_5 and $s_{\rm H}$.

IV.4.4.b H5plane benchmark

The purpose of the H5plane benchmark is to facilitate searches for the $\rm H_5$ states over the m_5–$s_{\rm H}$ plane. The other parameters are chosen so that $m_3 > m_5$ (thereby forbidding decays of $\rm H_5 \to H_3 V$ or $\rm H_3 H_3$)

Table 139: Specification of the H5plane benchmark for the Georgi-Machacek model. These input parameters correspond to INPUTSET = 4 in GMCALC [1274].

Fixed parameters	Variable parameters	Dependent parameters
$G_F = 1.1663787 \times 10^{-5}$ GeV^{-2}	$m_5 \in [200, 3000]$ GeV	$\lambda_2 = 0.4(m_5/1000\text{ GeV})$
$M_{\rm h} = 125$ GeV	$s_{\rm H} \in (0, 1)$	$M_1 = \sqrt{2}s_{\rm H}(m_5^2 + v^2)/v$
$\lambda_3 = -0.1$		$M_2 = M_1/6$
$\lambda_4 = 0.2$		

and so that the largest possible parameter region is allowed by theoretical constraints for 200 GeV $< m_5 <$ 3000 GeV.

The benchmark is defined as follows. The nine parameters of the GM model scalar potential in Eq. (IV.4.19) are fixed in terms of the input parameters G_F, $M_{\rm h}$, m_5, $s_{\rm H}$, λ_2, λ_3, λ_4, M_1, and M_2, i.e., the input parameters of INPUTSET = 4 in GMCALC. The values are given in Table 139.

Perturbative unitarity of VV $\to$ VV scattering amplitudes constrains [1278]

$$s_{\rm H}^2 < \frac{3}{5}\frac{(16\pi v^2 - 5M_{\rm h}^2)}{(4m_5^2 + 5M_{\rm h}^2)}, \qquad \text{or} \qquad s_{\rm H}^2 \lesssim \left(\frac{667\text{ GeV}}{m_5}\right)^2, \tag{IV.4.36}$$

for $m_5 \gg M_{\rm W}, M_{\rm Z}, M_{\rm h}$. This implies that $\Gamma({\rm H}_5 \to {\rm VV}) \lesssim 0.15\, m_5$ for each of the ${\rm H}_5$ states. The full set of perturbative unitarity constraints [1276, 1277] constrain the model a little more tightly, leading to $\Gamma({\rm H}_5 \to {\rm VV}) \lesssim 0.10\, m_5$. These constraints are implemented in GMCALC, which will return an error message if they are violated.

The H5plane benchmark has the following features:

- It populates nearly all of the theoretically-allowed region of the m_5–$s_{\rm H}$ plane for $m_5 \in [200, 3000]$ GeV, except for a small corner at low m_5 and high $s_{\rm H}$ which is already excluded by the cross section for like-sign W boson pair production in VBF [1279] (this limits the maximum allowed production cross section for VBF$\to {\rm H}_5^{\pm\pm} \to {\rm W}^\pm{\rm W}^\pm$, and hence sets an upper bound on $s_{\rm H}$ as a function of m_5).
- Constraints from ${\rm b} \to {\rm s}\gamma$ (see Ref. [1280]) eliminate only points that are already excluded by the cross section for like-sign W boson pair production in VBF [1279].
- The benchmark is not unreasonably constrained by coupling measurements of the 125 GeV Higgs boson: the region of the m_5–$s_{\rm H}$ plane in which $|\kappa_i^{\rm h} - 1| < 0.1$, with $i = {\rm f}, {\rm V}, \gamma$, is essentially the same in the H5plane benchmark as in a full parameter scan.
- It has $m_3 \gtrsim m_5 + 10$ GeV over the whole benchmark plane, so that the Higgs-to-Higgs boson decays ${\rm H}_5 \to {\rm H}_3{\rm H}_3$ and ${\rm H}_5 \to {\rm H}_3{\rm V}$ are kinematically forbidden, leaving only the decays ${\rm H}_5 \to$ VV at tree level; i.e., to a very good approximation,

$$\text{BR}({\rm H}_5^0 \to {\rm W}^+{\rm W}^-, {\rm ZZ}) = \text{BR}({\rm H}_5^\pm \to {\rm W}^\pm{\rm Z}) = \text{BR}({\rm H}_5^{\pm\pm} \to {\rm W}^\pm{\rm W}^\pm) = 1. \tag{IV.4.37}$$

- It has $M_{\rm H} \gtrsim m_5 + 12$ GeV over the whole benchmark plane, except for a few points at $s_{\rm H} > 0.7$ which are already excluded by the cross section for like-sign W boson pair production in VBF [1279]. However, there is a large region of parameter space covering $m_5 \gtrsim 600$ GeV and $0.07 \lesssim s_{\rm H} \lesssim 0.6$ in which the total decay widths of ${\rm H}_5^0$ and H are larger than the mass splitting between these two states. In this region, a dedicated study of the lineshape and interference effects of the two resonances in VBF$\to ({\rm H}_5^0,\ {\rm H}) \to {\rm WW}, {\rm ZZ}$ will be required.

IV.4.4.c Vector boson fusion production cross sections of the H_5 states

The total cross sections for production of H_5^0, $H_5^\pm$, and $H_5^{\pm\pm}$ in VBF can be computed up to NNLO accuracy using the VBF@NNLO code [263, 264, 1281], via the structure-function approach. This approach [265] consists in considering the VBF process as a double deep-inelastic scattering (DIS) attached to the colourless pure electroweak vector-boson fusion into a Higgs boson. According to this approach one can include next-to-leading order (NLO) QCD corrections to the VBF process employing the standard DIS structure functions $F_i(x, Q^2)$; $i = 1, 2, 3$ at NLO [266] or similarly the corresponding structure functions at NNLO [267–270].

Although the effective factorization underlying the structure-function approach holds to a very good approximation up to NNLO, it formally does not include all types of contributions. At leading order (LO) an additional contribution arises from the interference between identical final-state quarks (e.g., $\mathrm{uu} \to \mathrm{Huu}$) or between processes where either a W or a Z boson can be exchanged (e.g., $\mathrm{ud} \to \mathrm{Hud}$). These LO contributions are known to be extremely small (less than 0.1% of the total cross-section). Apart from such contributions, the structure-function approach is exact up to NLO. At NNLO, however, several types of diagrams violate the underlying factorization. Their impact on the total rate has been computed or estimated in [264] and found to be negligible. Some of them are colour and kinematically suppressed [261, 271, 272], and others have been shown in [273] to be small enough not to produce a significant deterioration of the VBF signal.

NLO electroweak corrections are known for SM Higgs boson production in VBF [256, 257], but not for any beyond-the-SM scenario, and therefore are not included in the numbers shown here.

To produce the numbers shown in this chapter, we have used the following electroweak parameters:

$$G_F = 1.1663787 \cdot 10^{-5}\ \mathrm{GeV}^{-2}, \quad M_\mathrm{W} = 80.385\ \mathrm{GeV}, \quad M_\mathrm{Z} = 91.1876\ \mathrm{GeV},$$
$$\Gamma_\mathrm{W} = 2.085\ \mathrm{GeV}, \quad \Gamma_\mathrm{Z} = 2.4952\ \mathrm{GeV}. \qquad \text{(IV.4.38)}$$

The H_5VV vertices have the form given in Eq. (IV.4.34), and we have set $s_\mathrm{H} = 1$. The production cross sections for other values of s_H are conveniently obtained using the relation

$$\sigma^\mathrm{NNLO}(\mathrm{VBF} \to \mathrm{H}_5) = s_\mathrm{H}^2 \sigma_1^\mathrm{NNLO}(\mathrm{VBF} \to \mathrm{H}_5), \qquad \text{(IV.4.39)}$$

where σ_1^NNLO represents the NNLO cross section for $s_\mathrm{H} = 1$. The values of σ_1^NNLO computed for the 13 TeV LHC for H_5^0, H_5^+, and H_5^- are shown in Tables 140–141, and for H_5^{++} and H_5^{--} are shown in Tables 142–143.

We have employed the PDF4LHC NNLO parton distribution function [35] with 30 sets (Hessian error estimate) plus 2 sets to estimate the α_s systematic uncertainties. For the NNLO PDF set, $\alpha_s(M_\mathrm{Z}) = 0.118$. As is the case of the SM, the systematic uncertainty from α_s is rather small for VBF. The renormalization and factorization scales have been set to M_W. Scale uncertainties have been computed by varying the two scales independently by a factor in the range $[1/2, 2]$.

As for SM Higgs boson production in VBF, the impact of QCD corrections is well under control: with our setup, and using PDF sets with QCD evolution consistent with the perturbative order of the cross-section, NLO QCD corrections increase the LO cross-section by $6-7\%$ and NNLO corrections contribute at most another 1% to the cross-section. The inclusion of NNLO corrections reduces the QCD scale uncertainties to the 1% level or below, while PDF uncertainties are at the level of 2% of the cross-section.

For the uncertainty due to uncalculated NLO electroweak corrections, we suggest to adopt a fractional uncertainty of $\pm 7\%$. This encompasses the size of the NLO electroweak correction to the SM Higgs VBF cross section [9] for SM Higgs boson masses below 700 GeV, where tree-level perturbative unitarity constraints in $2 \to 2$ gauge and Higgs boson scattering are satisfied. This same tree-level perturbativity requirement results in the upper bound on s_H given in Eq. (IV.4.36).

Table 140: VBF production cross sections for H_5^0, H_5^+ and H_5^- in the GM model, computed for $s_H = 1$ at the $\sqrt{s} = 13$ TeV LHC. The first (asymmetric) uncertainties are the QCD scale uncertainty, the second is the PDF uncertainty, and the third is the α_s uncertainty. The uncertainty from uncalculated NLO electroweak corrections should be taken as $\pm 7\%$. The relative Monte Carlo numerical integration error is below 5×10^{-4} in all cases.

m_5 [GeV]	$\sigma_1^{\rm NNLO}(H_5^0)$ [fb]	$\sigma_1^{\rm NNLO}(H_5^+)$ [fb]	$\sigma_1^{\rm NNLO}(H_5^-)$ [fb]
200.	$1375._{-0.20\%}^{+0.35\%} \pm 1.8\% \pm 0.51\%$	$1770._{-0.18\%}^{+0.30\%} \pm 1.6\% \pm 0.46\%$	$1148._{-0.21\%}^{+0.36\%} \pm 2.2\% \pm 0.54\%$
210.	$1288._{-0.19\%}^{+0.33\%} \pm 1.8\% \pm 0.49\%$	$1662._{-0.17\%}^{+0.28\%} \pm 1.7\% \pm 0.45\%$	$1073._{-0.21\%}^{+0.34\%} \pm 2.2\% \pm 0.53\%$
220.	$1209._{-0.18\%}^{+0.30\%} \pm 1.8\% \pm 0.48\%$	$1564._{-0.17\%}^{+0.26\%} \pm 1.7\% \pm 0.44\%$	$1004._{-0.20\%}^{+0.32\%} \pm 2.2\% \pm 0.52\%$
230.	$1136._{-0.17\%}^{+0.28\%} \pm 1.8\% \pm 0.47\%$	$1473._{-0.16\%}^{+0.25\%} \pm 1.7\% \pm 0.43\%$	$940.9_{-0.19\%}^{+0.31\%} \pm 2.2\% \pm 0.51\%$
240.	$1069._{-0.17\%}^{+0.26\%} \pm 1.8\% \pm 0.46\%$	$1388._{-0.15\%}^{+0.25\%} \pm 1.7\% \pm 0.42\%$	$883.0_{-0.18\%}^{+0.29\%} \pm 2.3\% \pm 0.50\%$
250.	$1006._{-0.16\%}^{+0.27\%} \pm 1.8\% \pm 0.46\%$	$1311._{-0.14\%}^{+0.25\%} \pm 1.7\% \pm 0.41\%$	$829.6_{-0.17\%}^{+0.27\%} \pm 2.3\% \pm 0.49\%$
260.	$948.9_{-0.15\%}^{+0.27\%} \pm 1.8\% \pm 0.45\%$	$1239._{-0.14\%}^{+0.25\%} \pm 1.7\% \pm 0.40\%$	$780.4_{-0.17\%}^{+0.27\%} \pm 2.3\% \pm 0.48\%$
270.	$895.7_{-0.15\%}^{+0.27\%} \pm 1.8\% \pm 0.44\%$	$1172._{-0.13\%}^{+0.25\%} \pm 1.7\% \pm 0.39\%$	$734.9_{-0.16\%}^{+0.27\%} \pm 2.3\% \pm 0.48\%$
280.	$846.3_{-0.14\%}^{+0.27\%} \pm 1.8\% \pm 0.43\%$	$1110._{-0.13\%}^{+0.25\%} \pm 1.7\% \pm 0.38\%$	$692.8_{-0.15\%}^{+0.28\%} \pm 2.3\% \pm 0.47\%$
290.	$800.5_{-0.14\%}^{+0.27\%} \pm 1.8\% \pm 0.42\%$	$1052._{-0.12\%}^{+0.26\%} \pm 1.7\% \pm 0.37\%$	$653.8_{-0.14\%}^{+0.28\%} \pm 2.3\% \pm 0.46\%$
300.	$757.8_{-0.13\%}^{+0.27\%} \pm 1.8\% \pm 0.41\%$	$997.7_{-0.11\%}^{+0.26\%} \pm 1.7\% \pm 0.37\%$	$617.5_{-0.14\%}^{+0.28\%} \pm 2.3\% \pm 0.45\%$
310.	$718.0_{-0.12\%}^{+0.28\%} \pm 1.8\% \pm 0.40\%$	$947.3_{-0.10\%}^{+0.26\%} \pm 1.7\% \pm 0.36\%$	$583.9_{-0.13\%}^{+0.28\%} \pm 2.4\% \pm 0.45\%$
320.	$680.9_{-0.12\%}^{+0.28\%} \pm 1.8\% \pm 0.40\%$	$900.3_{-0.10\%}^{+0.26\%} \pm 1.7\% \pm 0.35\%$	$552.6_{-0.13\%}^{+0.28\%} \pm 2.4\% \pm 0.44\%$
330.	$646.3_{-0.11\%}^{+0.28\%} \pm 1.8\% \pm 0.39\%$	$856.2_{-0.09\%}^{+0.27\%} \pm 1.7\% \pm 0.34\%$	$523.4_{-0.13\%}^{+0.28\%} \pm 2.4\% \pm 0.43\%$
340.	$614.0_{-0.11\%}^{+0.28\%} \pm 1.9\% \pm 0.38\%$	$815.0_{-0.09\%}^{+0.27\%} \pm 1.7\% \pm 0.33\%$	$496.1_{-0.12\%}^{+0.28\%} \pm 2.4\% \pm 0.42\%$
350.	$583.7_{-0.10\%}^{+0.28\%} \pm 1.9\% \pm 0.37\%$	$776.3_{-0.08\%}^{+0.27\%} \pm 1.7\% \pm 0.32\%$	$470.7_{-0.12\%}^{+0.28\%} \pm 2.4\% \pm 0.42\%$
360.	$555.2_{-0.10\%}^{+0.28\%} \pm 1.9\% \pm 0.37\%$	$739.9_{-0.08\%}^{+0.27\%} \pm 1.7\% \pm 0.31\%$	$446.9_{-0.11\%}^{+0.28\%} \pm 2.4\% \pm 0.41\%$
370.	$528.6_{-0.09\%}^{+0.28\%} \pm 1.9\% \pm 0.36\%$	$705.8_{-0.08\%}^{+0.27\%} \pm 1.7\% \pm 0.31\%$	$424.6_{-0.10\%}^{+0.28\%} \pm 2.5\% \pm 0.41\%$
380.	$503.6_{-0.09\%}^{+0.28\%} \pm 1.9\% \pm 0.35\%$	$673.7_{-0.07\%}^{+0.27\%} \pm 1.7\% \pm 0.30\%$	$403.7_{-0.10\%}^{+0.28\%} \pm 2.5\% \pm 0.40\%$
390.	$480.0_{-0.08\%}^{+0.28\%} \pm 1.9\% \pm 0.34\%$	$643.4_{-0.06\%}^{+0.27\%} \pm 1.7\% \pm 0.29\%$	$384.1_{-0.09\%}^{+0.28\%} \pm 2.5\% \pm 0.39\%$
400.	$457.9_{-0.07\%}^{+0.28\%} \pm 1.9\% \pm 0.34\%$	$614.9_{-0.06\%}^{+0.27\%} \pm 1.7\% \pm 0.28\%$	$365.7_{-0.09\%}^{+0.28\%} \pm 2.5\% \pm 0.39\%$
410.	$437.1_{-0.07\%}^{+0.28\%} \pm 1.9\% \pm 0.33\%$	$588.0_{-0.05\%}^{+0.27\%} \pm 1.7\% \pm 0.28\%$	$348.4_{-0.08\%}^{+0.28\%} \pm 2.5\% \pm 0.38\%$
420.	$417.4_{-0.06\%}^{+0.28\%} \pm 1.9\% \pm 0.32\%$	$562.6_{-0.05\%}^{+0.27\%} \pm 1.7\% \pm 0.27\%$	$332.1_{-0.07\%}^{+0.28\%} \pm 2.5\% \pm 0.38\%$
430.	$398.9_{-0.06\%}^{+0.28\%} \pm 1.9\% \pm 0.32\%$	$538.5_{-0.04\%}^{+0.27\%} \pm 1.7\% \pm 0.26\%$	$316.8_{-0.06\%}^{+0.29\%} \pm 2.5\% \pm 0.37\%$
440.	$381.4_{-0.06\%}^{+0.28\%} \pm 1.9\% \pm 0.31\%$	$515.8_{-0.06\%}^{+0.27\%} \pm 1.7\% \pm 0.25\%$	$302.3_{-0.06\%}^{+0.29\%} \pm 2.6\% \pm 0.36\%$
450.	$364.9_{-0.05\%}^{+0.28\%} \pm 1.9\% \pm 0.30\%$	$494.3_{-0.07\%}^{+0.27\%} \pm 1.7\% \pm 0.24\%$	$288.7_{-0.06\%}^{+0.28\%} \pm 2.6\% \pm 0.36\%$
460.	$349.2_{-0.05\%}^{+0.28\%} \pm 1.9\% \pm 0.30\%$	$473.9_{-0.08\%}^{+0.27\%} \pm 1.7\% \pm 0.24\%$	$275.9_{-0.06\%}^{+0.28\%} \pm 2.6\% \pm 0.35\%$
470.	$334.4_{-0.06\%}^{+0.28\%} \pm 1.9\% \pm 0.29\%$	$454.6_{-0.09\%}^{+0.27\%} \pm 1.7\% \pm 0.23\%$	$263.7_{-0.06\%}^{+0.28\%} \pm 2.6\% \pm 0.35\%$
480.	$320.4_{-0.07\%}^{+0.28\%} \pm 1.9\% \pm 0.28\%$	$436.3_{-0.10\%}^{+0.28\%} \pm 1.7\% \pm 0.22\%$	$252.2_{-0.07\%}^{+0.28\%} \pm 2.6\% \pm 0.34\%$
490.	$307.1_{-0.08\%}^{+0.28\%} \pm 1.9\% \pm 0.28\%$	$418.9_{-0.12\%}^{+0.28\%} \pm 1.7\% \pm 0.22\%$	$241.4_{-0.08\%}^{+0.28\%} \pm 2.6\% \pm 0.34\%$
500.	$294.5_{-0.10\%}^{+0.28\%} \pm 2.0\% \pm 0.27\%$	$402.4_{-0.13\%}^{+0.28\%} \pm 1.7\% \pm 0.21\%$	$231.1_{-0.09\%}^{+0.28\%} \pm 2.7\% \pm 0.33\%$
550.	$240.4_{-0.15\%}^{+0.28\%} \pm 2.0\% \pm 0.24\%$	$331.0_{-0.18\%}^{+0.28\%} \pm 1.8\% \pm 0.18\%$	$187.0_{-0.15\%}^{+0.28\%} \pm 2.7\% \pm 0.31\%$
600.	$198.0_{-0.20\%}^{+0.28\%} \pm 2.0\% \pm 0.21\%$	$274.8_{-0.24\%}^{+0.28\%} \pm 1.8\% \pm 0.14\%$	$152.9_{-0.21\%}^{+0.28\%} \pm 2.8\% \pm 0.29\%$
650.	$164.5_{-0.26\%}^{+0.28\%} \pm 2.1\% \pm 0.19\%$	$230.0_{-0.29\%}^{+0.28\%} \pm 1.8\% \pm 0.11\%$	$126.1_{-0.26\%}^{+0.28\%} \pm 2.9\% \pm 0.27\%$
700.	$137.7_{-0.32\%}^{+0.29\%} \pm 2.1\% \pm 0.16\%$	$193.8_{-0.34\%}^{+0.28\%} \pm 1.8\% \pm 0.08\%$	$104.8_{-0.32\%}^{+0.28\%} \pm 3.0\% \pm 0.25\%$
750.	$115.9_{-0.36\%}^{+0.29\%} \pm 2.1\% \pm 0.14\%$	$164.3_{-0.39\%}^{+0.29\%} \pm 1.8\% \pm 0.05\%$	$87.64_{-0.37\%}^{+0.28\%} \pm 3.1\% \pm 0.23\%$
800.	$98.20_{-0.41\%}^{+0.29\%} \pm 2.2\% \pm 0.11\%$	$140.1_{-0.43\%}^{+0.29\%} \pm 1.8\% \pm 0.02\%$	$73.75_{-0.42\%}^{+0.29\%} \pm 3.2\% \pm 0.21\%$
850.	$83.60_{-0.46\%}^{+0.29\%} \pm 2.2\% \pm 0.09\%$	$120.0_{-0.48\%}^{+0.29\%} \pm 1.8\% \pm 0.00\%$	$62.39_{-0.47\%}^{+0.29\%} \pm 3.2\% \pm 0.20\%$
900.	$71.50_{-0.51\%}^{+0.29\%} \pm 2.2\% \pm 0.07\%$	$103.3_{-0.53\%}^{+0.29\%} \pm 1.9\% \pm 0.03\%$	$53.03_{-0.52\%}^{+0.29\%} \pm 3.3\% \pm 0.18\%$

Table 141: Continuation of Table 140.

m_5 [GeV]	$\sigma_1^{\rm NNLO}(\mathrm{H}_5^0)$ [fb]	$\sigma_1^{\rm NNLO}(\mathrm{H}_5^+)$ [fb]	$\sigma_1^{\rm NNLO}(\mathrm{H}_5^-)$ [fb]
950.	$61.41^{+0.29\%}_{-0.55\%} \pm 2.3\% \pm 0.05\%$	$89.21^{+0.29\%}_{-0.57\%} \pm 1.9\% \pm 0.06\%$	$45.27^{+0.29\%}_{-0.57\%} \pm 3.4\% \pm 0.17\%$
1000.	$52.94^{+0.30\%}_{-0.60\%} \pm 2.3\% \pm 0.03\%$	$77.35^{+0.29\%}_{-0.62\%} \pm 1.9\% \pm 0.08\%$	$38.80^{+0.29\%}_{-0.62\%} \pm 3.5\% \pm 0.16\%$
1050.	$45.79^{+0.30\%}_{-0.64\%} \pm 2.4\% \pm 0.01\%$	$67.28^{+0.30\%}_{-0.66\%} \pm 1.9\% \pm 0.11\%$	$33.38^{+0.29\%}_{-0.67\%} \pm 3.6\% \pm 0.15\%$
1100.	$39.74^{+0.30\%}_{-0.69\%} \pm 2.4\% \pm 0.00\%$	$58.70^{+0.30\%}_{-0.71\%} \pm 1.9\% \pm 0.13\%$	$28.81^{+0.30\%}_{-0.72\%} \pm 3.7\% \pm 0.14\%$
1150.	$34.58^{+0.31\%}_{-0.74\%} \pm 2.4\% \pm 0.02\%$	$51.34^{+0.30\%}_{-0.75\%} \pm 1.9\% \pm 0.15\%$	$24.93^{+0.30\%}_{-0.77\%} \pm 3.8\% \pm 0.13\%$
1200.	$30.17^{+0.30\%}_{-0.79\%} \pm 2.5\% \pm 0.04\%$	$45.03^{+0.30\%}_{-0.80\%} \pm 2.0\% \pm 0.17\%$	$21.64^{+0.30\%}_{-0.81\%} \pm 3.9\% \pm 0.12\%$
1250.	$26.39^{+0.31\%}_{-0.83\%} \pm 2.5\% \pm 0.05\%$	$39.58^{+0.33\%}_{-0.84\%} \pm 2.0\% \pm 0.20\%$	$18.83^{+0.32\%}_{-0.86\%} \pm 4.0\% \pm 0.11\%$
1300.	$23.13^{+0.34\%}_{-0.87\%} \pm 2.6\% \pm 0.07\%$	$34.86^{+0.35\%}_{-0.88\%} \pm 2.0\% \pm 0.22\%$	$16.43^{+0.33\%}_{-0.91\%} \pm 4.1\% \pm 0.11\%$
1350.	$20.32^{+0.36\%}_{-0.92\%} \pm 2.6\% \pm 0.08\%$	$30.77^{+0.37\%}_{-0.92\%} \pm 2.0\% \pm 0.24\%$	$14.36^{+0.36\%}_{-0.95\%} \pm 4.2\% \pm 0.10\%$
1400.	$17.88^{+0.38\%}_{-0.96\%} \pm 2.7\% \pm 0.09\%$	$27.20^{+0.39\%}_{-0.97\%} \pm 2.0\% \pm 0.26\%$	$12.58^{+0.38\%}_{-1.00\%} \pm 4.3\% \pm 0.10\%$
1450.	$15.77^{+0.40\%}_{-1.00\%} \pm 2.7\% \pm 0.11\%$	$24.09^{+0.41\%}_{-1.01\%} \pm 2.1\% \pm 0.28\%$	$11.04^{+0.40\%}_{-1.04\%} \pm 4.4\% \pm 0.10\%$
1500.	$13.92^{+0.43\%}_{-1.05\%} \pm 2.7\% \pm 0.12\%$	$21.37^{+0.43\%}_{-1.05\%} \pm 2.1\% \pm 0.30\%$	$9.704^{+0.43\%}_{-1.09\%} \pm 4.5\% \pm 0.09\%$
1550.	$12.32^{+0.45\%}_{-1.09\%} \pm 2.8\% \pm 0.13\%$	$18.98^{+0.45\%}_{-1.10\%} \pm 2.1\% \pm 0.32\%$	$8.545^{+0.46\%}_{-1.14\%} \pm 4.6\% \pm 0.09\%$
1600.	$10.91^{+0.47\%}_{-1.14\%} \pm 2.8\% \pm 0.14\%$	$16.89^{+0.47\%}_{-1.14\%} \pm 2.1\% \pm 0.34\%$	$7.536^{+0.48\%}_{-1.19\%} \pm 4.7\% \pm 0.09\%$
1650.	$9.677^{+0.50\%}_{-1.18\%} \pm 2.9\% \pm 0.15\%$	$15.04^{+0.50\%}_{-1.19\%} \pm 2.1\% \pm 0.36\%$	$6.656^{+0.50\%}_{-1.23\%} \pm 4.8\% \pm 0.09\%$
1700.	$8.594^{+0.51\%}_{-1.23\%} \pm 2.9\% \pm 0.16\%$	$13.41^{+0.52\%}_{-1.23\%} \pm 2.2\% \pm 0.37\%$	$5.886^{+0.53\%}_{-1.28\%} \pm 4.9\% \pm 0.09\%$
1750.	$7.641^{+0.54\%}_{-1.28\%} \pm 3.0\% \pm 0.17\%$	$11.97^{+0.54\%}_{-1.28\%} \pm 2.2\% \pm 0.39\%$	$5.211^{+0.55\%}_{-1.33\%} \pm 5.0\% \pm 0.09\%$
1800.	$6.802^{+0.56\%}_{-1.33\%} \pm 3.0\% \pm 0.18\%$	$10.70^{+0.55\%}_{-1.33\%} \pm 2.2\% \pm 0.41\%$	$4.620^{+0.57\%}_{-1.38\%} \pm 5.1\% \pm 0.09\%$
1850.	$6.061^{+0.58\%}_{-1.38\%} \pm 3.1\% \pm 0.19\%$	$9.571^{+0.58\%}_{-1.37\%} \pm 2.2\% \pm 0.43\%$	$4.100^{+0.60\%}_{-1.43\%} \pm 5.3\% \pm 0.09\%$
1900.	$5.405^{+0.61\%}_{-1.41\%} \pm 3.1\% \pm 0.20\%$	$8.568^{+0.60\%}_{-1.42\%} \pm 2.2\% \pm 0.44\%$	$3.642^{+0.62\%}_{-1.48\%} \pm 5.4\% \pm 0.10\%$
1950.	$4.826^{+0.64\%}_{-1.46\%} \pm 3.2\% \pm 0.20\%$	$7.678^{+0.63\%}_{-1.47\%} \pm 2.2\% \pm 0.46\%$	$3.239^{+0.65\%}_{-1.53\%} \pm 5.5\% \pm 0.10\%$
2000.	$4.312^{+0.67\%}_{-1.51\%} \pm 3.3\% \pm 0.21\%$	$6.885^{+0.66\%}_{-1.51\%} \pm 2.3\% \pm 0.47\%$	$2.883^{+0.67\%}_{-1.58\%} \pm 5.7\% \pm 0.11\%$
2050.	$3.856^{+0.69\%}_{-1.55\%} \pm 3.3\% \pm 0.22\%$	$6.179^{+0.68\%}_{-1.56\%} \pm 2.3\% \pm 0.49\%$	$2.568^{+0.71\%}_{-1.63\%} \pm 5.8\% \pm 0.11\%$
2100.	$3.450^{+0.71\%}_{-1.60\%} \pm 3.4\% \pm 0.22\%$	$5.549^{+0.70\%}_{-1.61\%} \pm 2.3\% \pm 0.50\%$	$2.289^{+0.73\%}_{-1.68\%} \pm 5.9\% \pm 0.12\%$
2150.	$3.090^{+0.73\%}_{-1.65\%} \pm 3.4\% \pm 0.23\%$	$4.986^{+0.73\%}_{-1.65\%} \pm 2.3\% \pm 0.52\%$	$2.043^{+0.75\%}_{-1.72\%} \pm 6.1\% \pm 0.13\%$
2200.	$2.769^{+0.76\%}_{-1.70\%} \pm 3.5\% \pm 0.23\%$	$4.484^{+0.76\%}_{-1.71\%} \pm 2.3\% \pm 0.53\%$	$1.824^{+0.78\%}_{-1.78\%} \pm 6.2\% \pm 0.13\%$
2250.	$2.483^{+0.79\%}_{-1.75\%} \pm 3.6\% \pm 0.24\%$	$4.034^{+0.78\%}_{-1.76\%} \pm 2.4\% \pm 0.55\%$	$1.629^{+0.80\%}_{-1.83\%} \pm 6.4\% \pm 0.14\%$
2300.	$2.228^{+0.82\%}_{-1.80\%} \pm 3.6\% \pm 0.24\%$	$3.632^{+0.81\%}_{-1.80\%} \pm 2.4\% \pm 0.56\%$	$1.457^{+0.83\%}_{-1.88\%} \pm 6.5\% \pm 0.15\%$
2350.	$2.000^{+0.85\%}_{-1.85\%} \pm 3.7\% \pm 0.24\%$	$3.271^{+0.83\%}_{-1.86\%} \pm 2.4\% \pm 0.58\%$	$1.303^{+0.86\%}_{-1.92\%} \pm 6.7\% \pm 0.16\%$
2400.	$1.796^{+0.87\%}_{-1.90\%} \pm 3.8\% \pm 0.25\%$	$2.947^{+0.86\%}_{-1.90\%} \pm 2.4\% \pm 0.59\%$	$1.166^{+0.88\%}_{-1.98\%} \pm 6.9\% \pm 0.17\%$
2450.	$1.614^{+0.90\%}_{-1.95\%} \pm 3.8\% \pm 0.25\%$	$2.656^{+0.88\%}_{-1.94\%} \pm 2.5\% \pm 0.60\%$	$1.044^{+0.91\%}_{-2.03\%} \pm 7.0\% \pm 0.18\%$
2500.	$1.451^{+0.92\%}_{-2.00\%} \pm 3.9\% \pm 0.25\%$	$2.395^{+0.91\%}_{-1.99\%} \pm 2.5\% \pm 0.62\%$	$0.9357^{+0.94\%}_{-2.08\%} \pm 7.2\% \pm 0.20\%$
2550.	$1.305^{+0.95\%}_{-2.05\%} \pm 4.0\% \pm 0.25\%$	$2.161^{+0.93\%}_{-2.03\%} \pm 2.5\% \pm 0.63\%$	$0.8387^{+0.97\%}_{-2.13\%} \pm 7.4\% \pm 0.21\%$
2600.	$1.174^{+0.97\%}_{-2.10\%} \pm 4.1\% \pm 0.25\%$	$1.950^{+0.95\%}_{-2.09\%} \pm 2.5\% \pm 0.64\%$	$0.7522^{+1.00\%}_{-2.18\%} \pm 7.6\% \pm 0.22\%$
2650.	$1.057^{+1.00\%}_{-2.15\%} \pm 4.2\% \pm 0.25\%$	$1.760^{+0.98\%}_{-2.14\%} \pm 2.5\% \pm 0.66\%$	$0.6748^{+1.03\%}_{-2.24\%} \pm 7.8\% \pm 0.24\%$
2700.	$0.9512^{+1.03\%}_{-2.19\%} \pm 4.2\% \pm 0.25\%$	$1.590^{+1.00\%}_{-2.18\%} \pm 2.6\% \pm 0.67\%$	$0.6057^{+1.05\%}_{-2.29\%} \pm 8.0\% \pm 0.25\%$
2750.	$0.8566^{+1.06\%}_{-2.24\%} \pm 4.3\% \pm 0.25\%$	$1.436^{+1.03\%}_{-2.24\%} \pm 2.6\% \pm 0.68\%$	$0.5437^{+1.09\%}_{-2.33\%} \pm 8.2\% \pm 0.27\%$
2800.	$0.7718^{+1.08\%}_{-2.30\%} \pm 4.4\% \pm 0.25\%$	$1.297^{+1.06\%}_{-2.29\%} \pm 2.6\% \pm 0.69\%$	$0.4883^{+1.12\%}_{-2.38\%} \pm 8.4\% \pm 0.29\%$
2850.	$0.6955^{+1.11\%}_{-2.35\%} \pm 4.5\% \pm 0.25\%$	$1.172^{+1.10\%}_{-2.34\%} \pm 2.6\% \pm 0.70\%$	$0.4387^{+1.14\%}_{-2.45\%} \pm 8.6\% \pm 0.30\%$
2900.	$0.6268^{+1.14\%}_{-2.39\%} \pm 4.6\% \pm 0.25\%$	$1.059^{+1.13\%}_{-2.39\%} \pm 2.7\% \pm 0.71\%$	$0.3943^{+1.18\%}_{-2.49\%} \pm 8.8\% \pm 0.32\%$
2950.	$0.5652^{+1.17\%}_{-2.45\%} \pm 4.7\% \pm 0.25\%$	$0.9579^{+1.14\%}_{-2.45\%} \pm 2.7\% \pm 0.73\%$	$0.3543^{+1.21\%}_{-2.54\%} \pm 9.0\% \pm 0.34\%$
3000.	$0.5096^{+1.19\%}_{-2.50\%} \pm 4.8\% \pm 0.25\%$	$0.8662^{+1.18\%}_{-2.51\%} \pm 2.7\% \pm 0.74\%$	$0.3186^{+1.22\%}_{-2.59\%} \pm 9.3\% \pm 0.36\%$

Table 142: VBF production cross sections for H_5^{++} and H_5^{--} in the GM model, computed for $s_H = 1$ at the $\sqrt{s} = 13$ TeV LHC. The first (asymmetric) uncertainties are the QCD scale uncertainty, the second is the PDF uncertainty, and the third is the α_s uncertainty. The uncertainty from uncalculated NLO electroweak corrections should be taken as $\pm 7\%$. The relative Monte Carlo numerical integration error is below 5×10^{-4} in all cases.

m_5 [GeV]	$\sigma_1^{\rm NNLO}(H_5^{++})$ [fb]	$\sigma_1^{\rm NNLO}(H_5^{--})$ [fb]
200.	$2511.^{+0.24\%}_{-0.14\%} \pm 1.9\% \pm 0.40\%$	$1070.^{+0.33\%}_{-0.21\%} \pm 2.9\% \pm 0.54\%$
210.	$2364.^{+0.24\%}_{-0.14\%} \pm 1.9\% \pm 0.39\%$	$997.0^{+0.31\%}_{-0.20\%} \pm 2.9\% \pm 0.53\%$
220.	$2229.^{+0.23\%}_{-0.13\%} \pm 1.9\% \pm 0.38\%$	$930.3^{+0.29\%}_{-0.19\%} \pm 3.0\% \pm 0.52\%$
230.	$2104.^{+0.24\%}_{-0.13\%} \pm 1.9\% \pm 0.37\%$	$869.2^{+0.27\%}_{-0.19\%} \pm 3.0\% \pm 0.51\%$
240.	$1988.^{+0.24\%}_{-0.12\%} \pm 1.9\% \pm 0.35\%$	$813.3^{+0.25\%}_{-0.18\%} \pm 3.0\% \pm 0.51\%$
250.	$1881.^{+0.24\%}_{-0.11\%} \pm 1.9\% \pm 0.34\%$	$762.0^{+0.25\%}_{-0.18\%} \pm 3.1\% \pm 0.50\%$
260.	$1781.^{+0.24\%}_{-0.10\%} \pm 1.9\% \pm 0.33\%$	$714.8^{+0.25\%}_{-0.18\%} \pm 3.1\% \pm 0.49\%$
270.	$1689.^{+0.25\%}_{-0.09\%} \pm 1.9\% \pm 0.32\%$	$671.3^{+0.25\%}_{-0.17\%} \pm 3.1\% \pm 0.49\%$
280.	$1602.^{+0.25\%}_{-0.09\%} \pm 1.9\% \pm 0.31\%$	$631.2^{+0.25\%}_{-0.16\%} \pm 3.1\% \pm 0.48\%$
290.	$1522.^{+0.24\%}_{-0.09\%} \pm 1.9\% \pm 0.30\%$	$594.1^{+0.26\%}_{-0.15\%} \pm 3.2\% \pm 0.47\%$
300.	$1447.^{+0.25\%}_{-0.08\%} \pm 1.9\% \pm 0.29\%$	$559.8^{+0.26\%}_{-0.14\%} \pm 3.2\% \pm 0.47\%$
310.	$1377.^{+0.25\%}_{-0.07\%} \pm 1.9\% \pm 0.28\%$	$527.9^{+0.26\%}_{-0.14\%} \pm 3.2\% \pm 0.46\%$
320.	$1311.^{+0.25\%}_{-0.06\%} \pm 1.9\% \pm 0.28\%$	$498.4^{+0.26\%}_{-0.13\%} \pm 3.3\% \pm 0.45\%$
330.	$1249.^{+0.25\%}_{-0.06\%} \pm 1.9\% \pm 0.27\%$	$471.0^{+0.26\%}_{-0.13\%} \pm 3.3\% \pm 0.45\%$
340.	$1192.^{+0.25\%}_{-0.06\%} \pm 1.9\% \pm 0.26\%$	$445.4^{+0.26\%}_{-0.12\%} \pm 3.3\% \pm 0.44\%$
350.	$1137.^{+0.25\%}_{-0.05\%} \pm 1.9\% \pm 0.25\%$	$421.6^{+0.26\%}_{-0.12\%} \pm 3.3\% \pm 0.44\%$
360.	$1086.^{+0.25\%}_{-0.05\%} \pm 1.9\% \pm 0.24\%$	$399.4^{+0.26\%}_{-0.11\%} \pm 3.4\% \pm 0.43\%$
370.	$1038.^{+0.25\%}_{-0.07\%} \pm 1.9\% \pm 0.23\%$	$378.7^{+0.26\%}_{-0.10\%} \pm 3.4\% \pm 0.43\%$
380.	$992.6^{+0.25\%}_{-0.08\%} \pm 2.0\% \pm 0.22\%$	$359.3^{+0.26\%}_{-0.10\%} \pm 3.4\% \pm 0.42\%$
390.	$949.8^{+0.25\%}_{-0.09\%} \pm 2.0\% \pm 0.21\%$	$341.1^{+0.25\%}_{-0.10\%} \pm 3.5\% \pm 0.42\%$
400.	$909.3^{+0.25\%}_{-0.11\%} \pm 2.0\% \pm 0.21\%$	$324.1^{+0.26\%}_{-0.09\%} \pm 3.5\% \pm 0.41\%$
410.	$871.1^{+0.25\%}_{-0.12\%} \pm 2.0\% \pm 0.20\%$	$308.1^{+0.26\%}_{-0.09\%} \pm 3.5\% \pm 0.41\%$
420.	$835.0^{+0.25\%}_{-0.13\%} \pm 2.0\% \pm 0.19\%$	$293.1^{+0.26\%}_{-0.08\%} \pm 3.6\% \pm 0.41\%$
430.	$800.8^{+0.25\%}_{-0.14\%} \pm 2.0\% \pm 0.18\%$	$279.0^{+0.26\%}_{-0.07\%} \pm 3.6\% \pm 0.40\%$
440.	$768.4^{+0.26\%}_{-0.16\%} \pm 2.0\% \pm 0.17\%$	$265.8^{+0.26\%}_{-0.07\%} \pm 3.6\% \pm 0.40\%$
450.	$737.7^{+0.26\%}_{-0.17\%} \pm 2.0\% \pm 0.16\%$	$253.3^{+0.26\%}_{-0.08\%} \pm 3.6\% \pm 0.39\%$
460.	$708.5^{+0.26\%}_{-0.18\%} \pm 2.0\% \pm 0.16\%$	$241.5^{+0.27\%}_{-0.10\%} \pm 3.7\% \pm 0.39\%$
470.	$680.9^{+0.26\%}_{-0.19\%} \pm 2.0\% \pm 0.15\%$	$230.5^{+0.27\%}_{-0.11\%} \pm 3.7\% \pm 0.39\%$
480.	$654.5^{+0.26\%}_{-0.20\%} \pm 2.0\% \pm 0.14\%$	$220.0^{+0.27\%}_{-0.13\%} \pm 3.7\% \pm 0.38\%$
490.	$629.5^{+0.26\%}_{-0.21\%} \pm 2.0\% \pm 0.13\%$	$210.2^{+0.26\%}_{-0.14\%} \pm 3.8\% \pm 0.38\%$
500.	$605.7^{+0.26\%}_{-0.22\%} \pm 2.0\% \pm 0.13\%$	$200.8^{+0.27\%}_{-0.15\%} \pm 3.8\% \pm 0.38\%$
550.	$502.4^{+0.26\%}_{-0.27\%} \pm 2.0\% \pm 0.09\%$	$161.1^{+0.27\%}_{-0.21\%} \pm 3.9\% \pm 0.36\%$
600.	$420.3^{+0.26\%}_{-0.33\%} \pm 2.0\% \pm 0.05\%$	$130.6^{+0.27\%}_{-0.28\%} \pm 4.1\% \pm 0.35\%$
650.	$354.3^{+0.27\%}_{-0.38\%} \pm 2.0\% \pm 0.02\%$	$106.9^{+0.26\%}_{-0.33\%} \pm 4.3\% \pm 0.34\%$
700.	$300.7^{+0.27\%}_{-0.43\%} \pm 2.1\% \pm 0.01\%$	$88.12^{+0.26\%}_{-0.39\%} \pm 4.4\% \pm 0.33\%$
750.	$256.7^{+0.27\%}_{-0.48\%} \pm 2.1\% \pm 0.05\%$	$73.17^{+0.27\%}_{-0.45\%} \pm 4.6\% \pm 0.32\%$
800.	$220.3^{+0.27\%}_{-0.53\%} \pm 2.1\% \pm 0.08\%$	$61.13^{+0.27\%}_{-0.50\%} \pm 4.7\% \pm 0.31\%$
850.	$189.9^{+0.27\%}_{-0.57\%} \pm 2.1\% \pm 0.11\%$	$51.36^{+0.27\%}_{-0.56\%} \pm 4.9\% \pm 0.31\%$
900.	$164.4^{+0.28\%}_{-0.62\%} \pm 2.1\% \pm 0.14\%$	$43.37^{+0.27\%}_{-0.61\%} \pm 5.0\% \pm 0.30\%$

Table 143: Continuation of Table 142.

m_5 [GeV]	$\sigma_1^{\rm NNLO}(\mathrm{H}_5^{++})$ [fb]	$\sigma_1^{\rm NNLO}(\mathrm{H}_5^{--})$ [fb]
950.	$142.8^{+0.28\%}_{-0.67\%} \pm 2.2\% \pm 0.17\%$	$36.79^{+0.28\%}_{-0.66\%} \pm 5.2\% \pm 0.30\%$
1000.	$124.5^{+0.28\%}_{-0.71\%} \pm 2.2\% \pm 0.20\%$	$31.33^{+0.28\%}_{-0.72\%} \pm 5.4\% \pm 0.30\%$
1050.	$108.9^{+0.28\%}_{-0.76\%} \pm 2.2\% \pm 0.23\%$	$26.79^{+0.29\%}_{-0.78\%} \pm 5.5\% \pm 0.30\%$
1100.	$95.49^{+0.30\%}_{-0.80\%} \pm 2.2\% \pm 0.25\%$	$22.98^{+0.27\%}_{-0.84\%} \pm 5.7\% \pm 0.30\%$
1150.	$83.95^{+0.32\%}_{-0.84\%} \pm 2.3\% \pm 0.28\%$	$19.78^{+0.30\%}_{-0.88\%} \pm 5.9\% \pm 0.30\%$
1200.	$73.98^{+0.34\%}_{-0.89\%} \pm 2.3\% \pm 0.31\%$	$17.07^{+0.33\%}_{-0.93\%} \pm 6.0\% \pm 0.31\%$
1250.	$65.33^{+0.36\%}_{-0.94\%} \pm 2.3\% \pm 0.34\%$	$14.77^{+0.34\%}_{-0.98\%} \pm 6.2\% \pm 0.31\%$
1300.	$57.81^{+0.38\%}_{-0.98\%} \pm 2.3\% \pm 0.36\%$	$12.81^{+0.37\%}_{-1.04\%} \pm 6.4\% \pm 0.32\%$
1350.	$51.24^{+0.39\%}_{-1.02\%} \pm 2.4\% \pm 0.39\%$	$11.14^{+0.40\%}_{-1.09\%} \pm 6.6\% \pm 0.32\%$
1400.	$45.50^{+0.42\%}_{-1.07\%} \pm 2.4\% \pm 0.41\%$	$9.706^{+0.43\%}_{-1.14\%} \pm 6.8\% \pm 0.33\%$
1450.	$40.46^{+0.44\%}_{-1.11\%} \pm 2.4\% \pm 0.44\%$	$8.474^{+0.45\%}_{-1.19\%} \pm 6.9\% \pm 0.34\%$
1500.	$36.04^{+0.46\%}_{-1.16\%} \pm 2.4\% \pm 0.46\%$	$7.412^{+0.48\%}_{-1.24\%} \pm 7.1\% \pm 0.35\%$
1550.	$32.14^{+0.48\%}_{-1.21\%} \pm 2.5\% \pm 0.48\%$	$6.493^{+0.50\%}_{-1.29\%} \pm 7.3\% \pm 0.36\%$
1600.	$28.70^{+0.50\%}_{-1.25\%} \pm 2.5\% \pm 0.51\%$	$5.698^{+0.53\%}_{-1.34\%} \pm 7.5\% \pm 0.38\%$
1650.	$25.66^{+0.52\%}_{-1.30\%} \pm 2.5\% \pm 0.53\%$	$5.008^{+0.55\%}_{-1.40\%} \pm 7.7\% \pm 0.39\%$
1700.	$22.97^{+0.54\%}_{-1.34\%} \pm 2.5\% \pm 0.56\%$	$4.408^{+0.57\%}_{-1.45\%} \pm 8.0\% \pm 0.41\%$
1750.	$20.57^{+0.57\%}_{-1.39\%} \pm 2.6\% \pm 0.58\%$	$3.885^{+0.60\%}_{-1.50\%} \pm 8.2\% \pm 0.42\%$
1800.	$18.45^{+0.59\%}_{-1.43\%} \pm 2.6\% \pm 0.60\%$	$3.428^{+0.62\%}_{-1.56\%} \pm 8.4\% \pm 0.44\%$
1850.	$16.56^{+0.62\%}_{-1.48\%} \pm 2.6\% \pm 0.62\%$	$3.028^{+0.65\%}_{-1.61\%} \pm 8.6\% \pm 0.46\%$
1900.	$14.88^{+0.64\%}_{-1.53\%} \pm 2.7\% \pm 0.65\%$	$2.678^{+0.68\%}_{-1.66\%} \pm 8.9\% \pm 0.48\%$
1950.	$13.37^{+0.66\%}_{-1.58\%} \pm 2.7\% \pm 0.67\%$	$2.371^{+0.70\%}_{-1.72\%} \pm 9.1\% \pm 0.50\%$
2000.	$12.03^{+0.69\%}_{-1.63\%} \pm 2.7\% \pm 0.69\%$	$2.101^{+0.73\%}_{-1.77\%} \pm 9.4\% \pm 0.52\%$
2050.	$10.83^{+0.71\%}_{-1.67\%} \pm 2.8\% \pm 0.71\%$	$1.863^{+0.76\%}_{-1.83\%} \pm 9.6\% \pm 0.54\%$
2100.	$9.756^{+0.74\%}_{-1.72\%} \pm 2.8\% \pm 0.73\%$	$1.654^{+0.79\%}_{-1.87\%} \pm 9.9\% \pm 0.57\%$
2150.	$8.793^{+0.76\%}_{-1.77\%} \pm 2.8\% \pm 0.75\%$	$1.469^{+0.82\%}_{-1.93\%} \pm 10.2\% \pm 0.59\%$
2200.	$7.930^{+0.78\%}_{-1.82\%} \pm 2.9\% \pm 0.77\%$	$1.306^{+0.85\%}_{-1.99\%} \pm 10.4\% \pm 0.62\%$
2250.	$7.155^{+0.80\%}_{-1.88\%} \pm 2.9\% \pm 0.80\%$	$1.162^{+0.88\%}_{-2.04\%} \pm 10.7\% \pm 0.64\%$
2300.	$6.459^{+0.83\%}_{-1.92\%} \pm 2.9\% \pm 0.82\%$	$1.035^{+0.90\%}_{-2.09\%} \pm 11.0\% \pm 0.67\%$
2350.	$5.833^{+0.86\%}_{-1.98\%} \pm 3.0\% \pm 0.84\%$	$0.9221^{+0.94\%}_{-2.15\%} \pm 11.3\% \pm 0.70\%$
2400.	$5.270^{+0.89\%}_{-2.03\%} \pm 3.0\% \pm 0.86\%$	$0.8222^{+0.96\%}_{-2.21\%} \pm 11.6\% \pm 0.73\%$
2450.	$4.763^{+0.92\%}_{-2.08\%} \pm 3.1\% \pm 0.88\%$	$0.7334^{+0.99\%}_{-2.26\%} \pm 11.9\% \pm 0.76\%$
2500.	$4.306^{+0.95\%}_{-2.12\%} \pm 3.1\% \pm 0.90\%$	$0.6545^{+1.02\%}_{-2.32\%} \pm 12.3\% \pm 0.80\%$
2550.	$3.895^{+0.96\%}_{-2.18\%} \pm 3.1\% \pm 0.92\%$	$0.5844^{+1.05\%}_{-2.37\%} \pm 12.6\% \pm 0.83\%$
2600.	$3.524^{+1.00\%}_{-2.23\%} \pm 3.2\% \pm 0.94\%$	$0.5221^{+1.08\%}_{-2.43\%} \pm 12.9\% \pm 0.86\%$
2650.	$3.189^{+1.02\%}_{-2.28\%} \pm 3.2\% \pm 0.96\%$	$0.4666^{+1.12\%}_{-2.47\%} \pm 13.3\% \pm 0.90\%$
2700.	$2.886^{+1.05\%}_{-2.33\%} \pm 3.3\% \pm 0.98\%$	$0.4172^{+1.14\%}_{-2.53\%} \pm 13.6\% \pm 0.94\%$
2750.	$2.613^{+1.07\%}_{-2.38\%} \pm 3.3\% \pm 1.00\%$	$0.3732^{+1.18\%}_{-2.57\%} \pm 14.0\% \pm 0.97\%$
2800.	$2.367^{+1.10\%}_{-2.44\%} \pm 3.3\% \pm 1.02\%$	$0.3340^{+1.22\%}_{-2.63\%} \pm 14.4\% \pm 1.01\%$
2850.	$2.144^{+1.14\%}_{-2.49\%} \pm 3.4\% \pm 1.04\%$	$0.2990^{+1.24\%}_{-2.69\%} \pm 14.8\% \pm 1.05\%$
2900.	$1.942^{+1.17\%}_{-2.54\%} \pm 3.4\% \pm 1.06\%$	$0.2677^{+1.27\%}_{-2.74\%} \pm 15.2\% \pm 1.09\%$
2950.	$1.760^{+1.19\%}_{-2.61\%} \pm 3.5\% \pm 1.07\%$	$0.2398^{+1.30\%}_{-2.80\%} \pm 15.6\% \pm 1.14\%$
3000.	$1.594^{+1.21\%}_{-2.65\%} \pm 3.5\% \pm 1.09\%$	$0.2149^{+1.33\%}_{-2.86\%} \pm 16.0\% \pm 1.18\%$

IV.4.4.d Decay widths of the H_5 states

We computed the tree-level decay partial widths $\Gamma(H_5^{\pm\pm} \to W^{\pm}W^{\pm})$, $\Gamma(H^{\pm} \to W^{\pm}Z)$, $\Gamma(H_5^0 \to W^+W^-)$, and $\Gamma(H_5^0 \to ZZ)$ using GMCALC 1.2.0 [1274]. In the H5plane benchmark, $\mathrm{BR}(H_5 \to VV) = 1$, so that these partial widths correspond to the total widths of the H_5 scalars. The decay calculation includes the effects of both of the final-state gauge bosons off-shell. The numerical calculation has been benchmarked against HDECAY 6.42 [69] with agreement to within 1%. We use the electroweak input parameters given in Eq. (IV.4.38) and scale all decay widths to $s_H = 1$. For $H_5^{\pm\pm}$ and $H_5^{\pm}$, the decay width is the same for the charge-conjugate process. The total widths of the H_5 states are given in Tables 144–145 for $H_5^{\pm\pm}$, $H_5^{\pm}$ and H_5^0 in the H5plane benchmark, for which $\mathrm{BR}(H_5 \to VV) = 1$. We also give $\mathrm{BR}(H_5^0 \to W^+W^-)$. The branching ratio $\mathrm{BR}(H_5^0 \to ZZ)$ is then equal to $1 - \mathrm{BR}(H_5^0 \to W^+W^-)$. So long as $\mathrm{BR}(H_5 \to VV) = 1$, these decay widths depend only on m_5 and s_H. The branching ratios of H_5^0 to WW and ZZ depend only on m_5.

The decay widths for other values of s_H are conveniently obtained using the relation

$$\Gamma(H_5 \to VV) = s_H^2 \Gamma_1(H_5 \to VV), \tag{IV.4.40}$$

where Γ_1 represents the decay width for $s_H = 1$ as given in Tables 144–145.

The widths given here were computed at tree level. For the uncertainty due to uncalculated NLO electroweak corrections, we suggest to adopt a fractional uncertainty on each partial width of $\pm 12\%$. This encompasses the size of the NLO electroweak correction to the SM Higgs boson decay partial widths to WW and ZZ [72] for SM Higgs boson masses below 700 GeV, where tree-level perturbative unitarity constraints in $2 \to 2$ gauge and Higgs boson scattering are satisfied. This same tree-level perturbativity requirement results in the upper bound on s_H given in Eq. (IV.4.36).

For H_5^0 we take the electroweak uncertainty on the total width to be also $\pm 12\%$, corresponding to fully correlated variations of $\Gamma(H_5^0 \to W^+W^-)$ and $\Gamma(H_5^0 \to ZZ)$. We compute the electroweak uncertainty on $\mathrm{BR}(H_5^0 \to W^+W^-)$ by assuming fully anticorrelated variations of $\Gamma(H_5^0 \to W^+W^-)$ and $\Gamma(H_5^0 \to ZZ)$; we give these latter uncertainties in Tables 144–145. This is the maximally conservative approach to combining the theory uncertainties on the two contributing decay widths.

IV.4.5 Singlet

IV.4.5.a Introduction

The simplest extension of the SM where a resonant di-Higgs final state would be detectable is the one where an extra real or complex spin-zero gauge singlet is added to its field content. This is also the minimal model for dark matter [1282–1292] and for electroweak baryogenesis by allowing a strong first-order phase transition during the era of EWSB [1293–1297]. Although minimal, this extension provides a rich collider phenomenology leading to some distinctive signatures that can be tested at the LHC [475, 1298–1304]. There is also some discussion about the singlet model in Chapter I.7 of this document.

In this section we present the real (RxSM) and the complex (CxSM) singlet extensions of the SM. The minimal versions of these models that we will discuss can have at least two phases. A $\mathbb{Z}_2$-symmetric phase, with one dark matter candidate, and a broken phase, where the singlet component(s) mix with the neutral Higgs field fluctuation of the SM Higgs doublet. Both models can be used as simple benchmarks for resonant double Higgs boson production $pp \to H \to hh$, with $M_H > 2M_h$. Furthermore, the CxSM is the simplest extension that also provides a scenario where a heavy scalar h_3 may decay into two other scalars h_1, h_2 with different masses, $h_3 \to h_2 h_1$.

The CxSM is an extension of the SM where a complex singlet field

$$\mathbb{S} = S + iA\ , \tag{IV.4.41}$$

Table 144: Tree-level total decay widths for $H_5^{\pm\pm}$, $H_5^{\pm}$, and H_5^0 in the GM model, rescaled to $s_H = 1$ and assuming that $BR(H_5 \to VV) = 1$. The uncertainty on the total widths from uncalculated NLO electroweak corrections should be taken as $\pm 12\%$. We also give $BR(H_5^0 \to W^+W^-)$, assuming that $BR(H_5^0 \to W^+W^-) + BR(H_5^0 \to ZZ) = 1$, and its uncertainty from the uncalculated NLO electroweak corrections.

m_5 [GeV]	$\Gamma_1^{tot}(H_5^{\pm\pm})$ [GeV]	$\Gamma_1^{tot}(H_5^{\pm})$ [GeV]	$\Gamma_1^{tot}(H_5^0)$ [GeV]	$BR(H_5^0 \to W^+W^-)$
200.	1.006	0.8608	0.8008	$0.4187^{+14.\%}_{-14.\%}$
210.	1.275	1.118	1.071	$0.3969^{+15.\%}_{-14.\%}$
220.	1.578	1.410	1.362	$0.3863^{+15.\%}_{-14.\%}$
230.	1.921	1.737	1.686	$0.3799^{+15.\%}_{-14.\%}$
240.	2.307	2.105	2.051	$0.3749^{+15.\%}_{-15.\%}$
250.	2.739	2.516	2.459	$0.3714^{+16.\%}_{-15.\%}$
260.	3.219	2.975	2.912	$0.3685^{+16.\%}_{-15.\%}$
270.	3.750	3.484	3.414	$0.3661^{+16.\%}_{-15.\%}$
280.	4.333	4.045	3.968	$0.3640^{+16.\%}_{-15.\%}$
290.	4.972	4.660	4.577	$0.3621^{+16.\%}_{-15.\%}$
300.	5.666	5.332	5.241	$0.3604^{+16.\%}_{-15.\%}$
310.	6.420	6.063	5.965	$0.3588^{+16.\%}_{-15.\%}$
320.	7.235	6.854	6.748	$0.3574^{+16.\%}_{-15.\%}$
330.	8.112	7.708	7.595	$0.3560^{+16.\%}_{-15.\%}$
340.	9.054	8.627	8.506	$0.3548^{+16.\%}_{-15.\%}$
350.	10.06	9.612	9.483	$0.3537^{+16.\%}_{-15.\%}$
360.	11.14	10.67	10.53	$0.3526^{+16.\%}_{-15.\%}$
370.	12.29	11.79	11.65	$0.3517^{+16.\%}_{-15.\%}$
380.	13.51	12.99	12.83	$0.3508^{+16.\%}_{-15.\%}$
390.	14.80	14.26	14.10	$0.3499^{+16.\%}_{-15.\%}$
400.	16.17	15.60	15.44	$0.3491^{+16.\%}_{-15.\%}$
410.	17.62	17.03	16.85	$0.3484^{+16.\%}_{-15.\%}$
420.	19.14	18.53	18.35	$0.3477^{+16.\%}_{-15.\%}$
430.	20.75	20.12	19.93	$0.3471^{+16.\%}_{-15.\%}$
440.	22.45	21.79	21.59	$0.3465^{+16.\%}_{-15.\%}$
450.	24.23	23.55	23.34	$0.3459^{+16.\%}_{-15.\%}$
460.	26.09	25.39	25.18	$0.3454^{+16.\%}_{-15.\%}$
470.	28.05	27.33	27.10	$0.3449^{+16.\%}_{-15.\%}$
480.	30.09	29.35	29.12	$0.3445^{+16.\%}_{-15.\%}$
490.	32.24	31.47	31.23	$0.3440^{+16.\%}_{-15.\%}$
500.	34.47	33.68	33.44	$0.3436^{+16.\%}_{-15.\%}$
550.	47.15	46.25	45.97	$0.3419^{+16.\%}_{-15.\%}$
600.	62.49	61.48	61.16	$0.3406^{+16.\%}_{-15.\%}$
650.	80.74	79.63	79.27	$0.3395^{+16.\%}_{-15.\%}$
700.	102.1	100.9	100.5	$0.3387^{+17.\%}_{-15.\%}$
750.	126.9	125.6	125.2	$0.3380^{+17.\%}_{-15.\%}$
800.	155.4	153.9	153.5	$0.3375^{+17.\%}_{-15.\%}$
850.	187.7	186.1	185.6	$0.3370^{+17.\%}_{-15.\%}$
900.	224.1	222.4	221.9	$0.3367^{+17.\%}_{-15.\%}$

Table 145: Continuation of Table 144.

m_5 [GeV]	$\Gamma_1^{\rm tot}(H_5^{\pm\pm})$ [GeV]	$\Gamma_1^{\rm tot}(H_5^{\pm})$ [GeV]	$\Gamma_1^{\rm tot}(H_5^0)$ [GeV]	$\mathrm{BR}(H_5^0 \to W^+W^-)$
950.	264.9	263.1	262.5	$0.3363^{+17.\%}_{-15.\%}$
1000.	310.3	308.4	307.8	$0.3361^{+17.\%}_{-15.\%}$
1050.	360.5	358.5	357.8	$0.3358^{+17.\%}_{-15.\%}$
1100.	415.8	413.7	413.0	$0.3356^{+17.\%}_{-15.\%}$
1150.	476.5	474.2	473.4	$0.3355^{+17.\%}_{-15.\%}$
1200.	542.7	540.3	539.5	$0.3353^{+17.\%}_{-15.\%}$
1250.	614.7	612.2	611.3	$0.3352^{+17.\%}_{-15.\%}$
1300.	692.7	690.1	689.2	$0.3350^{+17.\%}_{-15.\%}$
1350.	777.1	774.3	773.4	$0.3349^{+17.\%}_{-15.\%}$
1400.	868.0	865.1	864.1	$0.3348^{+17.\%}_{-15.\%}$
1450.	965.7	962.6	961.6	$0.3347^{+17.\%}_{-15.\%}$
1500.	1070.	1067.	1066.	$0.3347^{+17.\%}_{-15.\%}$
1550.	1182.	1179.	1178.	$0.3346^{+17.\%}_{-15.\%}$
1600.	1302.	1298.	1297.	$0.3345^{+17.\%}_{-15.\%}$
1650.	1429.	1425.	1424.	$0.3345^{+17.\%}_{-15.\%}$
1700.	1564.	1560.	1559.	$0.3344^{+17.\%}_{-15.\%}$
1750.	1708.	1704.	1702.	$0.3344^{+17.\%}_{-15.\%}$
1800.	1860.	1855.	1854.	$0.3343^{+17.\%}_{-15.\%}$
1850.	2020.	2016.	2014.	$0.3343^{+17.\%}_{-15.\%}$
1900.	2190.	2185.	2184.	$0.3342^{+17.\%}_{-15.\%}$
1950.	2369.	2364.	2362.	$0.3342^{+17.\%}_{-15.\%}$
2000.	2557.	2552.	2550.	$0.3342^{+17.\%}_{-15.\%}$
2050.	2755.	2750.	2748.	$0.3341^{+17.\%}_{-15.\%}$
2100.	2962.	2957.	2956.	$0.3341^{+17.\%}_{-15.\%}$
2150.	3180.	3175.	3173.	$0.3341^{+17.\%}_{-15.\%}$
2200.	3409.	3403.	3401.	$0.3341^{+17.\%}_{-15.\%}$
2250.	3648.	3642.	3640.	$0.3340^{+17.\%}_{-15.\%}$
2300.	3898.	3892.	3890.	$0.3340^{+17.\%}_{-15.\%}$
2350.	4159.	4153.	4151.	$0.3340^{+17.\%}_{-15.\%}$
2400.	4431.	4425.	4423.	$0.3340^{+17.\%}_{-15.\%}$
2450.	4716.	4709.	4707.	$0.3340^{+17.\%}_{-15.\%}$
2500.	5011.	5005.	5002.	$0.3339^{+17.\%}_{-15.\%}$
2550.	5319.	5312.	5310.	$0.3339^{+17.\%}_{-15.\%}$
2600.	5640.	5633.	5630.	$0.3339^{+17.\%}_{-15.\%}$
2650.	5973.	5965.	5963.	$0.3339^{+17.\%}_{-15.\%}$
2700.	6319.	6311.	6308.	$0.3339^{+17.\%}_{-15.\%}$
2750.	6678.	6669.	6667.	$0.3339^{+17.\%}_{-15.\%}$
2800.	7050.	7041.	7039.	$0.3339^{+17.\%}_{-15.\%}$
2850.	7435.	7427.	7424.	$0.3338^{+17.\%}_{-15.\%}$
2900.	7835.	7826.	7823.	$0.3338^{+17.\%}_{-15.\%}$
2950.	8249.	8239.	8236.	$0.3338^{+17.\%}_{-15.\%}$
3000.	8676.	8667.	8664.	$0.3338^{+17.\%}_{-15.\%}$

with hypercharge zero, is added to the SM field content. The most general renormalizable scalar potential with a $U(1)$ global symmetry that is softly broken by terms with mass dimension up to two, is given by

$$V_{\rm CxSM} = \frac{m^2}{2}\mathrm{H}^\dagger\mathrm{H} + \frac{\lambda}{4}(\mathrm{H}^\dagger\mathrm{H})^2 + \frac{\delta_2}{2}\mathrm{H}^\dagger\mathrm{H}|\mathbb{S}|^2 + \frac{b_2}{2}|\mathbb{S}|^2 + \frac{d_2}{4}|\mathbb{S}|^4 + \left(\frac{b_1}{4}\mathbb{S}^2 + a_1\mathbb{S} + c.c.\right) \ . \quad \text{(IV.4.42)}$$

The soft breaking terms in Eq. (IV.4.42) are shown in parenthesis. The doublet and the complex singlet are

$$\mathrm{H} = \frac{1}{\sqrt{2}}\begin{pmatrix} \mathrm{G}^+ \\ v + \mathrm{h} + i\mathrm{G}^0 \end{pmatrix} \quad \text{and} \quad \mathbb{S} = \frac{1}{\sqrt{2}}\left[v_{\rm S} + \mathrm{s} + i(v_{\rm A} + \mathrm{a})\right] \ , \quad \text{(IV.4.43)}$$

respectively. Here $v \approx 246$ GeV and $v_{\rm S}$ and $v_{\rm A}$ are the real and imaginary parts of the complex singlet field VEV, respectively.

The various phases of the model were discussed in [1218]. A number of models can be obtained with the same field content by imposing extra symmetries on the potential. For example the exact $U(1)$-symmetric potential has $a_1 = b_1 = 0$, leading to either one or to two dark matter candidates depending on the pattern of symmetry breaking. Here we will focus on the version of the model where the potential is symmetric under $\mathbb{S} \to \mathbb{S}^*$, or, equivalently symmetric under a $\mathbb{Z}_2$ symmetry for the imaginary component A. In this case both the soft breaking terms, $\{a_1, b_1\}$, and the other parameters, $\{m, \lambda, \delta_2, b_2, d_2\}$, have to be real. Under these conditions there are two phases, namely,

- $v_{\rm A} = 0$ and $v_{\rm S} \neq 0$ - mixing between the doublet field h and the real component s of the singlet; the imaginary component $\mathrm{A} \equiv \mathrm{a}$ becomes a dark matter candidate. We call it the symmetric or *dark matter phase*.
- $v_{\rm S} \neq 0$ and $v_{\rm A} \neq 0$ - no dark matter candidate and mixing among all scalars. We call it the *broken phase*.

The model phases are summarized in table 146.

Table 146: Phase classification for the version of the CxSM with the $\mathbb{S} \to \mathbb{S}^*$ symmetry.

Phase	Scalar content	VEVs at global minimum
Symmetric (dark)	2 mixed + 1 dark	$\langle S\rangle \neq 0$ and $\langle A\rangle = 0$
Broken ($\mathbb{Z}_2$)	3 mixed	$\langle S\rangle \neq 0$ and $\langle A\rangle \neq 0$

In order to obtain the couplings of the scalars to the SM particles one first defines the mass eigenstates $\mathrm{h_i}$ (i$=1,2,3$). These are obtained from the gauge eigenstates h, s and a through the mixing matrix R

$$\begin{pmatrix} \mathrm{h}_1 \\ \mathrm{h}_2 \\ \mathrm{h}_3 \end{pmatrix} = R \begin{pmatrix} \mathrm{h} \\ \mathrm{s} \\ \mathrm{a} \end{pmatrix} \ , \quad \text{(IV.4.44)}$$

with

$$R\,\mathcal{M}^2\,R^T = \mathrm{diag}\left(m_1^2, m_2^2, m_3^2\right) \ . \quad \text{(IV.4.45)}$$

Here $m_1 \leq m_2 \leq m_3$ are the masses of the neutral Higgs particles. The mixing matrix R is parameterized as

$$R = \begin{pmatrix} c_1c_2 & s_1c_2 & s_2 \\ -(c_1s_2s_3 + s_1c_3) & c_1c_3 - s_1s_2s_3 & c_2s_3 \\ -c_1s_2c_3 + s_1s_3 & -(c_1s_3 + s_1s_2c_3) & c_2c_3 \end{pmatrix} \quad \text{(IV.4.46)}$$

with $s_i \equiv \sin\alpha_i$ and $c_i \equiv \cos\alpha_i$ $(i = 1, 2, 3)$ and

$$-\pi/2 < \alpha_i \leq \pi/2 \,. \tag{IV.4.47}$$

All scalar couplings to the SM particles are modified by the same matrix element R_{i1}, which is independent of the SM particle. This means that for any SM coupling $\lambda^{(p)}_{\mathrm{h}_{SM}}$, where p runs over all SM fermions and gauge bosons, the corresponding coupling in the singlet model, for the scalar h_i, is given by

$$\lambda^{(p)}_i = R_{i1}\lambda^{(p)}_{h_{SM}} \,. \tag{IV.4.48}$$

The self interactions are presented in [484] and in the code `sHDECAY`. In the particular case of the dark matter phase, $R_{i1} = (R_{11}, R_{21}, 0)$. The state $i = 3$ (i.e. A) then corresponds to the dark matter candidate which does not couple to any of the remaining SM particles. The model has seven free parameters which are chosen to be $\{\alpha_1, \alpha_2, \alpha_3, v, v_{\mathrm{S}}, m_1, m_3\}$ for the broken phase and $\{\alpha_1, v, v_{\mathrm{S}}, a_1, m_1, m_2, m_3 \equiv M_{\mathrm{A}}\}$ for the dark matter phase.

The real singlet model, RxSM, is obtained with the addition of a real singlet S with a $\mathbb{Z}_2$ symmetry ($\mathrm{S} \to -\mathrm{S}$) to the SM. The most general renormalizable potential then reads

$$V_{\mathrm{RxSM}} = \frac{m^2}{2}\mathrm{H}^\dagger\mathrm{H} + \frac{\lambda}{4}(\mathrm{H}^\dagger\mathrm{H})^2 + \frac{\lambda_{\mathrm{HS}}}{2}\mathrm{H}^\dagger\mathrm{H}\mathrm{S}^2 + \frac{m_{\mathrm{S}}^2}{2}\mathrm{S}^2 + \frac{\lambda_{\mathrm{S}}}{4!}\mathrm{S}^4 \,, \tag{IV.4.49}$$

where $m,\ \lambda,\ \lambda_{\mathrm{HS}},\ m_{\mathrm{S}}$ and λ_{S} are real and

$$\mathrm{H} = \frac{1}{\sqrt{2}}\begin{pmatrix} \mathrm{G}^+ \\ v + \mathrm{h} + i\mathrm{G}^0 \end{pmatrix} \quad \text{and} \quad \mathrm{S} = v_{\mathrm{S}} + \mathrm{s} \,. \tag{IV.4.50}$$

Here, again, $v \approx 246$ GeV is the SM Higgs VEV, and v_{S} is the singlet VEV. The benchmarks presented for this model are for the broken phase, $v_{\mathrm{S}} \neq 0$, where m_1 and m_2 are the mass-ordered scalar states. The mixing matrix has the same form as the sub-block responsible for the mixing in the dark phase of the CxSM, i.e. when $\alpha_1 \equiv \alpha$ and $\alpha_2 = \alpha_3 = 0$. In the symmetric phase of the RxSM, which we will not discuss here, one of the scalars is the SM-like Higgs boson while the other is the dark matter candidate.

The model has five independent parameters. Two different sets of parameters were proposed. Common to both sets are the particle masses, $\{m_1, m_2\}$, the angle $\alpha_1 \equiv \alpha$ (or $\sin\alpha$) and the SM VEV v, which is determined from the Fermi constant G_F. The remaining independent parameter is chosen to be v_{S} or $\tan\beta = v/v_{\mathrm{S}}$.

The renormalization of the RxSM has recently been addressed in [477, 1305]. It was found [1305] that the electroweak corrections to Higgs bosons decays to gauge bosons and fermions are at most of the order of 1% and this maximal value is attained in the limit where the theory becomes indistinguishable from the SM. In [477] it was found that the corrections to the triple scalar vertex (Hhh) are small, typically of a few per cent, once all theoretical and experimental constraints are taken into account.

The issue of interference in beyond the SM scenarios has been raised in [526] for the particular case of a real singlet extension of the SM. Although these interference effects can be large, it was shown in [525] for the process $\mathrm{gg} \to \mathrm{h}^*, \mathrm{H}^{(*)} \to \mathrm{ZZ} \to 4\ell$ at 8 TeV, that judicious kinematical cuts can be used in the analysis to reduce the interference effects to $\mathcal{O}(10\%)$. Interference effects were also studied for $\mathrm{gg} \to \mathrm{h}^*, \mathrm{H}^{(*)} \to \mathrm{hh}$ at next-to-leading order (NLO) in QCD [483]. It was found that the interference effects distort the double Higgs boson invariant mass distributions. Depending on the heavier Higgs boson mass value, they can either decrease by 30% or increase by 20%. Furthermore, it was shown that the NLO QCD corrections are large and can significantly distort kinematic distributions near the resonance peak. This means that any experimental analysis to be performed in the future should take these effects into account.

IV.4.5.a.i Constraints Applied to the Singlet Models

To restrict the parameter space of the singlet models various theoretical and phenomenological constraints have been applied. These have been described in detail in [480–482, 1306] for the first set of benchmarks and in [1218, 1307] for the second set. Here we will only discuss them briefly.

Theoretical constraints

The following theoretical constraints are applied both to the CxSM and to the RxSM: : i) the potential must be bounded from below; ii) the vacuum is the global minimum and iii) perturbative unitarity holds.

The first set of benchmarks also demands perturbativity of the couplings. These are imposed using one-loop RGEs [1308]. The perturbativity and minimization conditions i), ii) are required to hold at a scale of $\sim 10^{10}$ GeV.

For the second set of benchmarks, the conditions that the potential is bounded from below and that the couplings remain perturbative were required to hold at higher scales with the two-loop RGE evolution of the couplings, as discussed in [1307].

Dark matter constraints

In the dark phase of the CxSM, the relic density $\Omega_A h^2$ is computed using MICROMEGAS [1309] and points in parameter space are excluded if $\Omega_A h^2$ is larger than $\Omega_c h^2 + 3\sigma$. Here $\Omega_c h^2 = 0.1199 \pm 0.0027$ is the combined result from the WMAP and Planck satellites [1310, 1311] and σ is the standard deviation. Direct detection bounds are imposed with the spin-independent scattering cross section of weakly interacting massive particles (WIMPs) on nucleons also with MICROMEGAS with the procedure described in [1218]. Points are rejected if the cross section is larger than the upper bound obtained by the LUX2013 collaboration [1256].

Electroweak precision observables

A 95% exclusion limit is applied from the electroweak precision observables S, T, U [1231, 1312]. The first set of benchmarks also takes explicit limits from a higher order calculation of the W-boson mass [481] into account.

Collider constraints

The strongest phenomenological constraints come from collider data and in particular from the the LHC data. Whichever the model or phase under discussion, one of the scalars has to match the observed signal for a Higgs boson with a mass of $\simeq 125$ GeV. The remaining scalars must be compatible with the exclusion limits set by the Tevatron, LEP and LHC searches. 95% C.L. exclusion limits were applied using HIGGSBOUNDS [1237]. As for consistency with the Higgs boson signal measurements, we test the global signal strength of the 125 GeV Higgs boson with the latest combination of the ATLAS and the CMS LHC Run 1 datasets, i.e. $\mu_{125} = 1.09 \pm 0.11$ [6].

In the first set of benchmark points HIGGSSIGNALS [1238] is used to explore the Higgs boson signal rate constraints in the mass range $100-150$ GeV. This way a potential signal overlap of the two Higgs states in the LHC signal rate measurement can approximately be taken into account.

HIGGSBOUNDS [1313–1315] computes internally various experimental quantities such as the signal rates

$$\mu_{\mathrm{h_i}} = \frac{\sigma_{\mathrm{New}}(\mathrm{h_i})\mathrm{BR}_{\mathrm{New}}\left(\mathrm{h_i} \to \mathrm{X_{SM}}\right)}{\sigma_{\mathrm{SM}}(\mathrm{h_i})\mathrm{BR}_{\mathrm{SM}}\left(\mathrm{h_i} \to \mathrm{X_{SM}}\right)} \quad . \tag{IV.4.51}$$

Here σ_{New} denotes the production cross section of the Higgs boson $\mathrm{h_i}$ in the new model under consideration and σ_{SM} the SM production cross section of a Higgs boson with the same mass. Similarly, $\mathrm{BR}_{\mathrm{New}}$ is the branching ratio in the new model for $\mathrm{h_i}$ to decay into a final state with SM particles $\mathrm{X_{SM}}$. $\mathrm{BR}_{\mathrm{SM}}$

is the corresponding SM quantity for a Higgs boson with the same mass. In singlet models, at leading order (and also at higher order in QCD), the cross section ratios are all simply given by the suppression factor squared, R^2_{i1}, see Eq. (IV.4.48).

IV.4.5.b Tools

Cross sections for Higgs boson production via gluon fusion were calculated with the programs SUSHI [135] and HIGLU [133] at next-to-next-to-leading order (NNLO) QCD and with higher order electroweak corrections consistently turned off. All other cross sections were rescaled from the SM ones by `HiggsBounds` using its internal tables.

The points for the first set are all obtained from the rescaled SM ones except for the width for $\mathrm{H} \to \mathrm{hh}$ which was calculated at LO.

The points for the second set of benchmarks were obtained with the SCANNERS code [1218, 1316] where all the constraints previously described are either in-built or interfaced with other codes. The branching ratios for the new scalars were calculated with the new implementation of the CxSM and RxSM in HDECAY [69, 71] called SHDECAY[IV.24] [484].

IV.4.5.c Benchmarks

In this section benchmark points for the real and complex singlet extensions are presented. For each set of points, plane or scenario a physical motivation is given together with the main features of the benchmark.

IV.4.5.c.i Benchmark Points and Planes for the RxSM

IV.4.5.c.i.1 Benchmark Points $BP1$

See Tables 147-149.

IV.4.5.c.i.2 Benchmark planes

See Tables 150 and 151.

As input parameters, we have three independent parameters,

$$m \equiv m_{H/h},\ \sin\alpha,\ \tan\beta$$

where the latter affects the collider phenomenology only via the additional decay channel $\mathrm{H} \to \mathrm{hh}$. Note that from a collider perspective, for cases where the decay mode $\mathrm{H} \to \mathrm{hh}$ is kinematically allowed, the *third* input variable could be replaced by either the total width of the heavier state, the branching ratio $\mathrm{BR}\,(\mathrm{H} \to \mathrm{hh})$, or the partial decay width into this channel respectively, such that

$$\left\{m \equiv M_{\mathrm{H/h}},\ \sin\alpha,\ \tan\beta\right\};\ \left\{m \equiv M_{\mathrm{H/h}},\ \sin\alpha,\ \Gamma(\mathrm{H})\right\};\ \left\{m \equiv M_{\mathrm{H/h}},\ \sin\alpha,\ \mathrm{BR}(\mathrm{H} \to \mathrm{hh})\right\}$$

are all viable parameter choices.

IV.4.5.d Benchmark points for the CxSM and RxSM

In the numbers presented we have set the SM-like Higgs boson mass to 125.1 GeV which is the central value[IV.25] of the ATLAS/CMS combination reported in [5].

[IV.24] The code SHDECAY is available at `http://www.itp.kit.edu/~maggie/sHDECAY/`.

[IV.25] The reported value with the experimental errors is $M_{\mathrm{h}} = 125.09 \pm 0.21(\mathrm{stat}) \pm 0.11(\mathrm{syst})$ GeV.

IV.4.5.d.i Benchmark Points for the CxSM and RxSM

The benchmark points to be presented were chosen as to cover different physical situations. The first goal is to maximize the number of scalars being produced while preserving consistency with the LHC Run 1 measurements. Hence we require to be consistent with the global signal strength obtained by the combination of the ATLAS and CMS data from the LHC Run 1, within at most 3σ. In most scenarios we find points satisfying the required properties within 2σ.

Besides phenomenological requirements, whenever possible, we choose points for which the model remains stable up to a large cutoff scale μ, where the theory reaches a Landau pole or the scalar potential develops a runaway direction (a detailed two-loop analysis can be found in [1307]). In the dark matter phase, we require that the dark matter relic density predicted by the model, $\Omega_A h^2$, is within 3σ of the central value for the WMAP and Planck combination quoted in Section IV.4.5.a.i.

IV.4.5.d.ii CxSM Broken Phase

In Tables 152 and 153 we show a sample of various kinematically allowed set-ups for the three mixing scalars of the broken phase of the CxSM. The first, Table 152, contains the parameters which define the chosen benchmark points and the production rates of the lightest and next-to-lightest Higgs bosons h_1 and h_2 in the various final states. The corresponding values for h_3 are listed in Table 153. For h_2 and h_3 the tables contain, in particular, the Higgs-to-Higgs boson decay rates. We also give the signal rates M_{h_i} (i$=1,2,3$) as defined in Eq. (IV.4.51). An interesting feature is that there are points which stabilize the model up to a large cutoff scale, $\log_{10}(\mu/\text{ GeV})$, as shown for example for CxSM.B3 and CxSM.B4 in Table 153. Most points are such that the cross sections for the indirect decay channels of the new scalars can compete with the direct decays. In particular, in most cases, we have tried to maximize $\mathrm{h}_3 \to \mathrm{h}_2\mathrm{h}_1$ where all three scalars could be observed at once. We have furthermore chosen points with large cross sections for the new scalars, so that they can also be detected directly in their decays.

Regarding the various kinematical possibilities, we have chosen:

- *Two points where the SM-like Higgs boson is the lightest scalar (CxSM.B1 and CxSM.B2)*: For CxSM.B1 all Higgs-to-Higgs boson decay channels are open apart from $\mathrm{h}_3 \to \mathrm{h}_2\mathrm{h}_2$.[IV.26] and it has a large ratio $\mu^C_{\mathrm{h}_{125}}/\mu^T_{\mathrm{h}_{125}}$. The latter measures the importance of the production of the SM-like Higgs boson in the chain decay of a heavier scalar, $\mu^C_{\mathrm{h}_{125}}$, compared to the total rate $\mu^T_{\mathrm{h}_{125}}$ – see also [484]. The additional Higgs-to-Higgs boson decays, e.g. $\mathrm{h}_{2,3} \to \mathrm{h}_1\mathrm{h}_1 \to \mathrm{bb}\tau\tau$, have rates of a few fb, suggesting that all new scalars are expected to be observed. On the other hand, CxSM.B2 has a lighter Higgs boson mass spectrum since only the $\mathrm{h}_3 \to \mathrm{h}_{125}\mathrm{h}_{125}$ Higgs-to-Higgs boson decay is open. This has a large branching ratio of $\sim 48\%$ and allows for the largest fraction of chain decays, $\mu^C_{\mathrm{h}_{125}}/\mu^T_{\mathrm{h}_{125}} \simeq 4\%$, of all the five benchmark points. In addition to the direct decays to SM particles (mostly into massive vector bosons), the scalar h_3 should also be accessible in the chain decays into a pair of h_{125} bosons (4b, 2b2τ or 2b2W final states), whereas h_2 would be visible in its direct decays (also mostly into massive vector bosons).
- *Two points where the SM-like Higgs boson is the next-to-lightest scalar (CxSM.B3 and CxSM.B4)*: For CxSM.B3 all kinematic situations for the scalar decays are available while the spectrum remains light. Both the Higgs-to-Higgs boson decays for $\mathrm{h}_{2,3}$ and the direct decays of h_1 have been maximized so that all scalars may be discovered either in chain decays (where the cross-sections can be of the order of $10-100$ [fb]) or through their direct decays. The most significant difference in CxSM.B4 is the larger h_1 mass so that the channel $\mathrm{h}_2 \to \mathrm{h}_1\mathrm{h}_1$ is kinematically closed.
- *One point where the SM-like Higgs boson is the heaviest scalar (CxSM.B5)*: This does not allow for SM-like Higgs boson production through chain decays and, since $\mathrm{h}_3 \equiv \mathrm{h}_{125}$, the overall spectrum is very light. This point was chosen to have large branching fractions for the Higgs-to-Higgs boson

[IV.26] In this scenario we do not present a case with all channels open because the spectrum would be even heavier and more difficult to be tested.

decays $\mathrm{h}_3 \to \mathrm{h}_1\mathrm{h}_1$ or $\mathrm{h}_3 \to \mathrm{h}_1\mathrm{h}_2$ ($\mathrm{h}_2 \to \mathrm{h}_1\mathrm{h}_1$ is closed), which can reach up to ~ 500 fb and ~ 100 fb respectively, in the $\mathrm{bb}\tau\tau$ final state. The lightest Higgs boson h_1 can also be observed directly, for example in decays to bb or $\tau\tau$, and so can h_2 (though with smaller rates).

IV.4.5.d.iii CxSM Dark Phase

For the first two points, CxSM.D1 and CxSM.D2, the lightest of the two visible scalars is the SM-like Higgs boson and, except for h_1 in CxSM.D2, all visible scalars have large invisible decay branching ratios. The branching ratios for the Higgs-to-Higgs boson decays $\mathrm{h}_2 \to \mathrm{h}_1\mathrm{h}_1$ are large with 18.4% for CxSM.D1 and 28% for CxSM.D2, and the cross sections for the direct production of h_2 are also large, so that it can be discovered in its direct decays into SM particles. An attractive feature of these two points is that the new heavy scalar h_2 can stabilize the theory up to a high scale as can be inferred from $\log_{10}(\mu/\ \mathrm{GeV})$ in the last row of the table.

In the scenarios CxSM.D3 and CxSM.D4 the SM-like Higgs boson is the heaviest of the two visible Higgs bosons. The overall spectrum is lighter and the theory must have a UV completion above $\sim 10^3$ TeV. Point CxSM.D3 represents a case with no invisible decays, and in CxSM.D4 decays of the SM-like Higgs boson h_2 into a lighter Higgs boson pair are forbidden while allowing for a large invisible decay into the dark matter state A. In CxSM.D3 μ_{h_2} is at the edge of compatibility with the LHC data, while allowing for the light Higgs state h_1 to be discovered in the chain decay of the SM-like Higgs boson h_2 into an h_1 pair or through its direct production (compare for example the $4b$ and the $\mathrm{bb}\tau\tau$ final state with the direct production).

CxSM.D4, represents the challenging case where the non-SM-like light h_1 has a mass close to the SM-like Higgs boson and a very large invisible decay. This point is only accessible in its direct decays into SM particles with largest rates in the bb and $\tau\tau$ final states.

IV.4.5.d.iv RxSM Broken Phase

Table 155 contains four benchmark points for the two possible kinematic configurations in this model.

For the points RxSM.B1 and RxSM.B2 the SM-like Higgs boson is the lightest of the two scalar states. Benchmark RxSM.B1 allows a relatively large $\sigma_2 \times \mathrm{BR}(\mathrm{h}_2 \to \mathrm{h}_1\mathrm{h}_1)$, comparable to the direct h_2 production cross section, and in particular the $\mathrm{bb}\tau\tau$ final state reaches 72 fb. For RxSM.B2 the decay into scalars is kinematically closed, but instead various direct decay channels of h_2 are enhanced compared to RxSM.B1, most notably the WW final state but also bb, $\tau\tau$ and $\gamma\gamma$.

The points RxSM.B3 and RxSM.B4 feature a SM-like Higgs boson which is the heaviest of the two scalars. RxSM.B3 is such that the non-SM-like Higgs boson h_1 can be found directly or in the decay $\mathrm{h}_2 \to \mathrm{h}_1\mathrm{h}_1$. One should note the large rates for the direct h_1 production and decay into the bb and also $\tau\tau$ final states and compare with the indirect processes $\mathrm{h}_2 \to \mathrm{h}_1\mathrm{h}_1 \to \mathrm{bb} + \mathrm{bb}$ and $\mathrm{bb} + \tau\tau$, where the magnitude of the latter two is comparable to the former two. RxSM.B4 represents the situation where the indirect channel is closed but the cross section for direct h_1 production is larger. While this allows for larger rates into the bb and $\tau\tau$ final states its discovery would be challenging since its mass is very close to the Z boson resonance.

Table 147: Benchmarks for fixed masses and $|\sin\alpha|$, floating $\tan\beta$ (between scenarios a and b)

Benchmarks for the Real Singlet	
Tania Robens, Tim Stefaniak Reference: Eur.Phys.J. C76 (2016) no.5, 268 [482]	
Main Features	real singlet extension, with two VEVs and no hidden sector interaction with heavy Higgs boson H and light Higgs boson h
Fixed parameters	$M_{\rm h}$ = 125.1 GeV or $M_{\rm H}$ = 125.1 GeV
Irrelevant parameters	$\tan\beta$ when channel $\rm H \to hh$ not accessible (LO, factorized production and decay)
additional comments	a,b signify maximal and minimal BR for $\rm H \to hh$ decay; for b, $\sin\alpha < 0$. any values for $\tan\beta$ between scenario a and b are allowed BR $(\rm H \to \mathit{SM})$ needs to be rescaled by $1 -$ BR $(\rm H \to hh)$ for SM final states.
Production cross sections at 14 TeV [pb] and branching fractions	
BHM300 a,b	
Spectrum	$M_{\rm H}$=300 GeV, $\lvert\sin\alpha\rvert = 0.31$, $\tan\beta(a) = 0.79$, $\tan\beta(b) = 0.79$
$\sigma(\rm gg \to h)$	44.91
$\sigma(\rm gg \to H)$	1.09
BR($\rm H \to hh$)	0.41 (a), 0.17 (b)
BR($\rm H \to WW$)	0.41 (a), 0.57 (b)
BR($\rm H \to ZZ$)	0.18 (a), 0.25 (b)
BHM400a,b	
Spectrum	$M_{\rm H}$=400 GeV, $\lvert\sin\alpha\rvert = 0.26$, $\tan\beta(a) = 0.58$, $\tan\beta(b) = 0.59$
$\sigma(\rm gg \to \mathit{h})$	46.32
$\sigma(\rm gg \to \mathit{H})$	0.76
BR($\rm H \to hh$)	0.32 (a), 0.20 (b)
BR($\rm H \to WW$)	0.40 (a), 0.47 (b)
BR($\rm H \to ZZ$)	0.18 (a), 0.22 (b)
BR($\rm H \to t\bar{t}$)	0.10 (a), 0.12 (b)
BHM500a,b	
Spectrum	$M_{\rm H}$=500 GeV, $\lvert\sin\alpha\rvert = 0.24$, $\tan\beta(a) = 0.46$, $\tan\beta(b) = 0.47$
$\sigma(\rm gg \to \mathit{h})$	46.82
$\sigma(\rm gg \to \mathit{H})$	0.31
BR($\rm H \to hh$)	0.26 (a), 0.19 (b)
BR($\rm H \to WW$)	0.41 (a), 0.44 (b)
BR($\rm H \to ZZ$)	0.19 (a), 0.21 (b)
BR($\rm H \to t\bar{t}$)	0.14 (a), 0.16 (b)

Table 148: Benchmarks for fixed masses and $|\sin\alpha|$, floating $\tan\beta$ (between scenarios a and b)

BHM600a,b	
Spectrum	$M_{\rm H}$=600 GeV, $\lvert\sin\alpha\rvert = 0.22$, $\tan\beta(a) = 0.38$, $\tan\beta(b) = 0.38$
$\sigma(\rm gg \to h)$	47.28
$\sigma(\rm gg \to H)$	0.12
BR($\rm H \to hh$)	0.25 (a), 0.19 (b)
BR($\rm H \to WW$)	0.41 (a), 0.45 (b)
BR($\rm H \to ZZ$)	0.21 (a), 0.22 (b)
BR($\rm H \to t\bar{t}$)	0.13 (a), 0.14 (b)
BHM700a,b	
Spectrum	$M_{\rm H}$=700 GeV, $\lvert\sin\alpha\rvert = 0.21$, $\tan\beta(a) = 0.31$, $\tan\beta(b) = 0.32$
$\sigma(\rm gg \to h)$	47.49
$\sigma(\rm gg \to H)$	0.050
BR($\rm H \to hh$)	0.24 (a), 0.19 (b)
BR($\rm H \to WW$)	0.44 (a), 0.47 (b)
BR($\rm H \to ZZ$)	0.22 (a), 0.23 (b)
BR($\rm H \to t\bar{t}$)	0.10 (a), 0.11 (b)
BHM800a,b	
Spectrum	$M_{\rm H}$=800 GeV, $\lvert\sin\alpha\rvert = 0.2$, $\tan\beta(a) = 0.25, \tan\beta(b) = 0.27$
$\sigma(\rm gg \to h)$	47.46
$\sigma(\rm gg \to H)$	0.022
BR($\rm H \to hh$)	0.23 (a), 0.19 (b)
BR($\rm H \to WW$)	0.46 (a), 0.48 (b)
BR($\rm H \to ZZ$)	0.23 (a), 0.24 (b)
BR($\rm H \to t\bar{t}$)	0.08 (a), 0.09 (b)
BHM200	
Spectrum	$M_{\rm H}$=200 GeV, $\lvert\sin\alpha\rvert = 0.29$, $\tan\beta = 1.19$
$\sigma(\rm gg \to h)$	45.50
$\sigma(\rm gg \to H)$	1.74
BR($\rm H \to$ SM)	as a 200 GeV SM Higgs boson

Table 149: Benchmarks for fixed masses and $|\sin\alpha|$, floating $\tan\beta$ (between scenarios a and b). In scenario b $\tan\beta = -\cot\alpha$. Low mass cross sections are courtesy of M. Grazzini

BHM60a,b	
Spectrum	$M_{\rm h}$=60 GeV, $\lvert\sin\alpha\rvert = 0.9997$, $\tan\beta(a) = 3.48$, $\tan\beta(b) = 0.025$
$\sigma(\rm gg \to h)$	0.10
$\sigma(\rm gg \to H)$	49.65
BR($\rm H \to hh$)	0.26 (a), 0. (b)
BR($\rm H \to$ SM)	rescaled by 0.74 (a), as in SM (b)
BHM50a,b	
Spectrum	$M_{\rm h}$=50 GeV, $\lvert\sin\alpha\rvert = 0.9998$, $\tan\beta(a) = 3.25$, $\tan\beta(b) = 0.020$
$\sigma(\rm gg \to h)$	0.098
BR($\rm H \to hh$)	0.26 (a), 0. (b)
BR($\rm H \to$ SM)	rescaled by 0.74 (a), as in SM (b)
BHM40a,b	
Spectrum	$M_{\rm h}$=40 GeV, $\lvert\sin\alpha\rvert = 0.9998$, $\tan\beta(a) = 3.13$, $\tan\beta(b) = 0.020$
$\sigma(\rm gg \to h)$	0.16
BR($\rm H \to hh$)	0.26 (a), 0. (b)
BR($\rm H \to$ SM)	rescaled by 0.74 (a), as in SM (b)
BHM30a,b	
Spectrum	$M_{\rm h}$=30 GeV, $\lvert\sin\alpha\rvert = 0.9998$, $\tan\beta(a) = 3.16$, $\tan\beta(b) = 0.020$
$\sigma(\rm gg \to h)$	0.31
BR($\rm H \to hh$)	0.26 (a), 0. (b)
BR($\rm H \to$ SM)	rescaled by 0.74 (a), as in SM (b)
BHM20a,b	
Spectrum	$M_{\rm h}$=20 GeV, $\lvert\sin\alpha\rvert = 0.9998$, $\tan\beta(a) = 3.23$, $\tan\beta(b) = 0.020$
$\sigma(\rm gg \to h)$	0.90
BR($\rm H \to hh$)	0.26 (a), 0. (b)
BR($\rm H \to$ SM)	rescaled by 0.74 (a), as in SM (b)
BHM10a,b	
Spectrum	$M_{\rm h}$=10 GeV, $\lvert\sin\alpha\rvert = 0.9998$, $\tan\beta(a) = 3.29$, $\tan\beta(b) = 0.020$
$\sigma(\rm gg \to h)$	2.98
BR($\rm H \to hh$)	0.26 (a), 0. (b)
BR($\rm H \to$ SM)	rescaled by 0.74 (a), as in SM (b)

Table 150: Benchmark points for mass ranges where the onshell decay $\mathrm{H} \rightarrow \mathrm{hh}$ is kinematically forbidden. Maximal values of $\tan\beta$ were calculated at the maximal mixing angle, and should be applied for consistency reasons. H decays the same way a SM-like Higgs boson of the same mass would decay, and the production cross sections need to be rescaled by $\sin^2\alpha$ with respect to SM predictions for the heavy and $\cos^2\alpha$ for the light Higgs boson. Production cross sections range from 8.21 pb (for $M_{\mathrm{H}} = 130$ GeV) to 1.8 pb (for $M_{\mathrm{H}} = 245$ GeV).

M_{H} [GeV]	$\lvert\sin\alpha\rvert_{\mathrm{max}}$	$\tan\beta_{\mathrm{max}}$	M_{H}[GeV]	$\lvert\sin\alpha\rvert_{\mathrm{max}}$	$\tan\beta_{\mathrm{max}}$
130	0.42	1.79	195	0.28	1.22
135	0.38	1.73	200	0.29	1.19
140	0.36	1.69	210	0.28	1.14
145	0.35	1.62	215	0.33	1.12
150	0.34	1.57	220	0.34	1.10
160	0.36	1.49	230	0.35	1.05
180	0.30	1.32	235	0.34	1.03
185	0.27	1.28	240	0.31	1.00
190	0.29	1.26	245	0.28	0.98

Table 151: Maximal and minimal allowed branching ratios, taken at the maximal allowed value of $|\sin\alpha|$. Note that minimal values for the BR stem from $\sin\alpha \leq 0$. Decay branching ratios correspond to the BRs of a SM Higgs boson of the same mass, rescaled by $1 - \text{BR}(H \to \text{hh})$. Production cross sections range from 1.71 pb (for $M_{\text{H}} = 250$ GeV) to 0.004 pb (for $M_{\text{H}} = 1$ TeV).

M_{H}[GeV]	$\lvert\sin\alpha\rvert_{\text{max}}$	$\text{BR}(\text{H} \to \text{hh})_{\text{min}}$	$\text{BR}(\text{H} \to \text{hh})_{\text{max}}$
255	0.31	0.09	0.27
260	0.34	0.11	0.33
265	0.33	0.13	0.36
280	0.32	0.17	0.40
290	0.31	0.18	0.40
305	0.30	0.20	0.40
325	0.29	0.21	0.40
345	0.28	0.22	0.39
365	0.27	0.21	0.36
395	0.26	0.20	0.32
430	0.25	0.19	0.30
470	0.24	0.19	0.28
520	0.23	0.19	0.26
590	0.22	0.19	0.25
665	0.21	0.19	0.24
770	0.20	0.19	0.23
875	0.19	0.19	0.22
920	0.18	0.19	0.22
975	0.17	0.19	0.21
1000	0.17	0.19	0.21

Table 152: *Benchmark points for the CxSM broken phase:* The parameters of the theory that we take as input values are denoted with a star ($\star$). The cross sections are for $\sqrt{s} \equiv 13$ TeV.

Benchmarks for the CxSM – Broken phase					
Raul Costa, Margarete Mühlleitner, Marco O. P.Sampaio, Rui Santos Reference: [484] (see also [1307])					
	CxSM.B1	CxSM.B2	CxSM.B3	CxSM.B4	CxSM.B5
$\star\, M_{h1}$ (GeV)	125.1	125.1	57.83	86.79	33.17
M_{h_2} (GeV)	260.6	228	125.1	125.1	64.99
$\star\, M_{\mathrm{h}_3}$ (GeV)	449.6	311.3	299	291.8	125.1
$\star\, \alpha_1$	-0.04375	0.05125	-1.102	-1.075	1.211
$\star\, \alpha_2$	0.4151	-0.4969	1.136	0.8628	-1.319
$\star\, \alpha_3$	-0.6983	-0.5059	-0.02393	-0.0184	1.118
$\star\, v_{\mathrm{S}}$ (GeV)	185.3	52.3	376.9	241.9	483.2
v_{A} (GeV)	371.3	201.6	236.3	286.1	857.8
λ	1.148	1.018	0.869	0.764	0.5086
δ_2	-0.9988	1.158	-0.4875	-0.4971	0.01418
d_2	1.819	3.46	0.6656	0.9855	0.003885
m^2 (GeV^2)	5.118×10^4	-5.597×10^4	2.189×10^4	1.173×10^4	-2.229×10^4
b_2 (GeV^2)	-3.193×10^4	-5.147×10^4	-3.484×10^4	-3.811×10^4	1362
b_1 (GeV^2)	9.434×10^4	5.864×10^4	1.623×10^4	1.599×10^4	3674
a_1 (GeV^3)	-1.236×10^7	-2.169×10^6	-4.325×10^6	-2.735×10^6	-1.255×10^6
$\mu^C_{\mathrm{h}_1}/\mu^T_{\mathrm{h}_1}$	0.0127	0.0407	0.365	0.117	0.687
μ_{h_1}	0.836	0.771	0.0362	0.0958	0.00767
$\sigma_1 \equiv \sigma(\mathrm{gg} \to \mathrm{h}_1)$	36.1 [pb]	33.3 [pb]	6.42 [pb]	8.03 [pb]	4.61 [pb]
$\sigma_1 \times \mathrm{BR}(\mathrm{h}_1 \to \mathrm{WW})$	7.55 [pb]	6.96 [pb]	0.345 [fb]	10.3 [fb]	< 0.01 [fb]
$\sigma_1 \times \mathrm{BR}(\mathrm{h}_1 \to \mathrm{ZZ})$	944 [fb]	871 [fb]	0.106 [fb]	2.44 [fb]	< 0.01 [fb]
$\sigma_1 \times \mathrm{BR}(\mathrm{h}_1 \to \mathrm{bb})$	21.3 [pb]	19.6 [pb]	5.48 [pb]	6.6 [pb]	4.01 [pb]
$\sigma_1 \times \mathrm{BR}(\mathrm{h}_1 \to \tau\tau)$	2.29 [pb]	2.11 [pb]	501 [fb]	659 [fb]	323 [fb]
$\sigma_1 \times \mathrm{BR}(\mathrm{h}_1 \to \gamma\gamma)$	83.7 [fb]	77.2 [fb]	2.87 [fb]	9.13 [fb]	0.617 [fb]
$\mu^C_{\mathrm{h}_2}/\mu^T_{\mathrm{h}_2}$	0.0958	0	0.0128	0.0104	0.353
μ_{h_2}	0.0752	0.0759	0.782	0.785	0.0106
$\mathrm{BR}(\mathrm{h}_2 \to \mathrm{X}_{\mathrm{SM}})$ %	87.9	100	96.2	100	100
$\sigma_2 \equiv \sigma(\mathrm{gg} \to \mathrm{h}_2)$	1.01 [pb]	1.11 [pb]	35.1 [pb]	33.9 [pb]	1.51 [pb]
$\sigma_2 \times \mathrm{BR}(\mathrm{h}_2 \to \mathrm{WW})$	618 [fb]	784 [fb]	7.06 [pb]	7.09 [pb]	0.185 [fb]
$\sigma_2 \times \mathrm{BR}(\mathrm{h}_2 \to \mathrm{ZZ})$	265 [fb]	319 [fb]	883 [fb]	887 [fb]	0.0553 [fb]
$\sigma_2 \times \mathrm{BR}(\mathrm{h}_2 \to \mathrm{bb})$	0.83 [fb]	1.66 [fb]	19.9 [pb]	20 [pb]	1.27 [pb]
$\sigma_2 \times \mathrm{BR}(\mathrm{h}_2 \to \tau\tau)$	0.103 [fb]	0.201 [fb]	2.14 [pb]	2.15 [pb]	120 [fb]
$\sigma_2 \times \mathrm{BR}(\mathrm{h}_2 \to \gamma\gamma)$	0.0189 [fb]	0.0373 [fb]	78.3 [fb]	78.6 [fb]	0.873 [fb]
$\mathrm{BR}(\mathrm{h}_2 \to \mathrm{h}_1\mathrm{h}_1)$ %	12.1	0	3.82	0	0
$\sigma_2 \times \mathrm{BR}(\mathrm{h}_2 \to \mathrm{h}_1\mathrm{h}_1)$	122 [fb]	0	1.34 [pb]	0	0
$\sigma_2 \times \mathrm{BR}(\mathrm{h}_2 \to \mathrm{h}_1\mathrm{h}_1 \to \mathrm{bbbb})$	42.5 [fb]	0	977 [fb]	0	0
$\sigma_2 \times \mathrm{BR}(\mathrm{h}_2 \to \mathrm{h}_1\mathrm{h}_1 \to \mathrm{bb}\tau\tau)$	9.13 [fb]	0	179 [fb]	0	0
$\sigma_2 \times \mathrm{BR}(\mathrm{h}_2 \to \mathrm{h}_1\mathrm{h}_1 \to \mathrm{bbWW})$	30.1 [fb]	0	0.123 [fb]	0	0
$\sigma_2 \times \mathrm{BR}(\mathrm{h}_2 \to \mathrm{h}_1\mathrm{h}_1 \to \mathrm{bb}\gamma\gamma)$	0.334 [fb]	0	1.02 [fb]	0	0
$\sigma_2 \times \mathrm{BR}(\mathrm{h}_2 \to \mathrm{h}_1\mathrm{h}_1 \to \tau\tau\tau\tau)$	0.491 [fb]	0	8.16 [fb]	0	0

Table 153: *CxSM broken phase benchmarks (continuation of Table 152)*

	CxSM.B1	CxSM.B2	CxSM.B3	CxSM.B4	CxSM.B5
μ_{h_3}	0.0558	0.0791	0.0788	0.0491	0.855
$BR(h_3 \to X_{SM})$ %	71	51.6	52.2	41.2	87.1
$\sigma_3 \equiv \sigma(gg \to h_3)$	520 [fb]	1.46 [pb]	1.48 [pb]	1.2 [pb]	42.4 [pb]
$\sigma_3 \times BR(h_3 \to WW)$	201 [fb]	519 [fb]	536 [fb]	344 [fb]	7.72 [pb]
$\sigma_3 \times BR(h_3 \to ZZ)$	95 [fb]	232 [fb]	238 [fb]	152 [fb]	966 [fb]
$\sigma_3 \times BR(h_3 \to bb)$	0.0569 [fb]	0.401 [fb]	0.468 [fb]	0.323 [fb]	21.8 [pb]
$\sigma_3 \times BR(h_3 \to \tau\tau)$	< 0.01 [fb]	0.0513 [fb]	0.0594 [fb]	0.0408 [fb]	2.34 [pb]
$\sigma_3 \times BR(h_3 \to \gamma\gamma)$	< 0.01 [fb]	< 0.01 [fb]	0.0105 [fb]	< 0.01 [fb]	85.6 [fb]
$BR(h_3 \to h_1h_1)$ %	8.53	48.4	29.5	35.4	11.0
$\sigma_3 \times BR(h_3 \to h_1h_1)$	44.3 [fb]	706 [fb]	438 [fb]	426 [fb]	4.66 [pb]
$\sigma_3 \times BR(h_3 \to h_1h_1 \to bbbb)$	15.4 [fb]	246 [fb]	319 [fb]	289 [fb]	3.52 [pb]
$\sigma_3 \times BR(h_3 \to h_1h_1 \to bb\tau\tau)$	3.32 [fb]	52.8 [fb]	58.2 [fb]	57.6 [fb]	567 [fb]
$\sigma_3 \times BR(h_3 \to h_1h_1 \to bbWW)$	10.9 [fb]	174 [fb]	0.0401 [fb]	0.897 [fb]	0.011 [fb]
$\sigma_3 \times BR(h_3 \to h_1h_1 \to bb\gamma\gamma)$	0.121 [fb]	1.93 [fb]	0.334 [fb]	0.798 [fb]	1.08 [fb]
$\sigma_3 \times BR(h_3 \to h_1h_1 \to \tau\tau\tau\tau)$	0.178 [fb]	2.84 [fb]	2.66 [fb]	2.88 [fb]	22.9 [fb]
$BR(h_3 \to h_1h_2)$ %	20.5	0	5.98	17.2	1.93
$\sigma_3 \times BR(h_3 \to h_1h_2)$	107 [fb]	0	88.8 [fb]	207 [fb]	820 [fb]
$\sigma_3 \times BR(h_3 \to h_1h_2 \to bbbb)$	0.0518 [fb]	0	43 [fb]	100 [fb]	603 [fb]
$\sigma_3 \times BR(h_3 \to h_1h_2 \to bb\tau\tau)$	0.012 [fb]	0	8.55 [fb]	20.8 [fb]	105 [fb]
$\sigma_3 \times BR(h_3 \to h_1h_2 \to bbWW)$	38.6 [fb]	0	15.2 [fb]	35.8 [fb]	0.0883 [fb]
$\sigma_3 \times BR(h_3 \to h_1h_2 \to bb\gamma\gamma)$	< 0.01 [fb]	0	0.191 [fb]	0.534 [fb]	0.506 [fb]
$\sigma_3 \times BR(h_3 \to h_1h_2 \to \tau\tau\tau\tau)$	< 0.01 [fb]	0	0.422 [fb]	1.08 [fb]	4.56 [fb]
$BR(h_3 \to h_2h_2)$ %	0	0	12.3	6.24	0
$\sigma_3 \times BR(h_3 \to h_2h_2)$	0	0	182 [fb]	75.2 [fb]	0
$\sigma_3 \times BR(h_3 \to h_2h_2 \to bbbb)$	0	0	58.7 [fb]	26.2 [fb]	0
$\sigma_3 \times BR(h_3 \to h_2h_2 \to bb\tau\tau)$	0	0	12.6 [fb]	5.63 [fb]	0
$\sigma_3 \times BR(h_3 \to h_2h_2 \to bbWW)$	0	0	41.6 [fb]	18.5 [fb]	0
$\sigma_3 \times BR(h_3 \to h_2h_2 \to bb\gamma\gamma)$	0	0	0.462 [fb]	0.206 [fb]	0
$\sigma_3 \times BR(h_3 \to h_2h_2 \to \tau\tau\tau\tau)$	0	0	0.679 [fb]	0.303 [fb]	0
$\log_{10}\left(\frac{\mu}{\text{GeV}}\right)$	9.40	6.05	19.3	15.7	6.64

Table 154: *Benchmark points for the CxSM dark phase:* The parameters of the theory that we take as input values are denoted with a star ($\star$). The cross-sections are for $\sqrt{s} \equiv 13$ TeV.

Benchmarks for the CxSM – Dark phase				
Raul Costa, Margarete Mühlleitner, Marco O. P.Sampaio, Rui Santos, Reference: [484] (see also [1307])				
	CxSM.D1	CxSM.D2	CxSM.D3	CxSM.D4
$\star\, M_{\mathrm{h}_1}$ (GeV)	125.1	125.1	56.12	121.2
$\star\, M_{\mathrm{h}_2}$ (GeV)	335.2	341.4	125.1	125.1
$\star\, M_{\mathrm{A}}$ (GeV)	52.46	93.97	139.3	51.96
$\star\, \alpha$	0.4587	-0.4156	1.507	1.358
$\star\, v_{\mathrm{S}}$ (GeV)	812.5	987.5	177.9	909.7
λ	1.142	1.059	0.5146	0.5149
δ_2	-0.3839	0.3066	-0.0362	-0.001764
d_2	0.2669	0.164	0.1653	0.03508
m^2 (GeV^2)	9.21×10^4	-1.816×10^5	-1.503×10^4	-1.488×10^4
b_2 (GeV^2)	-6.838×10^4	-6.027×10^4	1.848×10^4	-1.154×10^4
b_1 (GeV^2)	2570	1.132×10^4	-1.883×10^4	-2479
$\star\, a_1$ (GeV^3)	-3.057×10^6	-1.407×10^7	-7.362×10^4	-1.418×10^5
$\mu^C_{\mathrm{h}_1}/\mu^T_{\mathrm{h}_1}$	0.019	0.0235	0.97	0
μ_{h_1}	0.804	0.837	0.00404	0.0444
$\mathrm{BR}(\mathrm{h}_1 \to \mathrm{X_{SM}})$ %	70.5	100	100	1.56
$\sigma_1 \equiv \sigma(\mathrm{gg} \to \mathrm{h}_1)$	34.7 [pb]	36.2 [pb]	759 [fb]	2.03 [pb]
$\sigma_1 \times \mathrm{BR}(\mathrm{h}_1 \to \mathrm{WW})$	5.12 [pb]	7.56 [pb]	0.0331 [fb]	4.81 [fb]
$\sigma_1 \times \mathrm{BR}(\mathrm{h}_1 \to \mathrm{ZZ})$	640 [fb]	945 [fb]	0.0103 [fb]	0.561 [fb]
$\sigma_1 \times \mathrm{BR}(\mathrm{h}_1 \to \mathrm{bb})$	14.4 [pb]	21.3 [pb]	649 [fb]	20.4 [fb]
$\sigma_1 \times \mathrm{BR}(\mathrm{h}_1 \to \tau\tau)$	1.55 [pb]	2.29 [pb]	58.9 [fb]	2.18 [fb]
$\sigma_1 \times \mathrm{BR}(\mathrm{h}_1 \to \gamma\gamma)$	56.8 [fb]	83.8 [fb]	0.317 [fb]	0.0723 [fb]
$\sigma_1 \times \mathrm{BR}(\mathrm{h}_1 \to AA)$	10.2 [pb]	0	0	2.00 [pb]
μ_{h_2}	0.138	0.108	0.710	0.834
$\mathrm{BR}(\mathrm{h}_2 \to \mathrm{X_{SM}})$ %	70.3	66.1	71.3	87.3
$\sigma_2 \equiv \sigma(\mathrm{gg} \to \mathrm{h}_2)$	1.83 [pb]	1.55 [pb]	43 [pb]	41.3 [pb]
$\sigma_2 \times \mathrm{BR}(\mathrm{h}_2 \to \mathrm{WW})$	886 [fb]	704 [fb]	6.41 [pb]	7.54 [pb]
$\sigma_2 \times \mathrm{BR}(\mathrm{h}_2 \to \mathrm{ZZ})$	402 [fb]	320 [fb]	802 [fb]	943 [fb]
$\sigma_2 \times \mathrm{BR}(\mathrm{h}_2 \to \mathrm{bb})$	0.553 [fb]	0.417 [fb]	18.1 [pb]	21.3 [pb]
$\sigma_2 \times \mathrm{BR}(\mathrm{h}_2 \to \tau\tau)$	0.0717 [fb]	0.0542 [fb]	1.95 [pb]	2.29 [pb]
$\sigma_2 \times \mathrm{BR}(\mathrm{h}_2 \to \gamma\gamma)$	0.012 [fb]	< 0.01 [fb]	71.1 [fb]	83.6 [fb]
$\mathrm{BR}(\mathrm{h}_2 \to \mathrm{h}_1\mathrm{h}_1)$ %	18.4	28	28.7	0
$\sigma_2 \times \mathrm{BR}(\mathrm{h}_2 \to \mathrm{h}_1\mathrm{h}_1)$	337 [fb]	436 [fb]	12.3 [pb]	0
$\sigma_2 \times \mathrm{BR}(\mathrm{h}_2 \to \mathrm{h}_1\mathrm{h}_1 \to \mathrm{bbbb})$	58.3 [fb]	152 [fb]	9.02 [pb]	0
$\sigma_2 \times \mathrm{BR}(\mathrm{h}_2 \to \mathrm{h}_1\mathrm{h}_1 \to \mathrm{bb}\tau\tau)$	12.5 [fb]	32.6 [fb]	1.64 [pb]	0
$\sigma_2 \times \mathrm{BR}(\mathrm{h}_2 \to \mathrm{h}_1\mathrm{h}_1 \to \mathrm{bbWW})$	41.3 [fb]	107 [fb]	0.92 [fb]	0
$\sigma_2 \times \mathrm{BR}(\mathrm{h}_2 \to \mathrm{h}_1\mathrm{h}_1 \to \mathrm{bb}\gamma\gamma)$	0.458 [fb]	1.19 [fb]	8.81 [fb]	0
$\sigma_2 \times \mathrm{BR}(\mathrm{h}_2 \to \mathrm{h}_1\mathrm{h}_1 \to \tau\tau\tau\tau)$	0.675 [fb]	1.75 [fb]	74.3 [fb]	0
$\sigma_2 \times \mathrm{BR}(\mathrm{h}_2 \to \mathrm{AA})$	207 [fb]	91.3 [fb]	0	5.23 [pb]
$\Omega_A h^2$	0.118	0.123	0.116	0.125
$\log_{10}\left(\frac{\mu}{\mathrm{GeV}}\right)$	14.9	17.1	6.69	6.69

Table 155: *Benchmark points for the RxSM broken phase:* The parameters of the theory that we take as input values are denoted with a star ($\star$). The cross sections are for $\sqrt{s} \equiv 13$ TeV.

Benchmarks for the RxSM – Broken phase				
Raul Costa, Margarete Mühlleitner, Marco O. P.Sampaio, Rui Santos Reference: [484]				
	RxSM.B1	RxSM.B2	RxSM.B3	RxSM.B4
$\star\, M_{\mathrm{h}_1}$ (GeV)	125.1	125.1	55.26	92.44
$\star\, M_{\mathrm{h}_2}$ (GeV)	265.3	172.5	125.1	125.1
$\star\, \alpha$	-0.4284	-0.4239	1.376	1.156
$\star\, v_{\mathrm{S}}$ (GeV)	140.3	94.74	591	686.1
λ	0.828	0.595	0.5007	0.4782
λ_{HS}	0.599	0.2268	-0.01646	-0.01552
λ_{S}	9.294	9.149	0.03029	0.06182
m^2 (GeV^2)	-3.688×10^4	-2.007×10^4	-9426	-7190
m_{S}^2 (GeV^2)	-4.863×10^4	-2.056×10^4	-1265	-4380
$\mu^C_{\mathrm{h}_1}/\mu^T_{\mathrm{h}_1}$	0.051	0	0.557	0
μ_{h_1}	0.827	0.831	0.0376	0.163
$\sigma_1 \equiv \sigma(\mathrm{gg} \to \mathrm{h}_1)$	35.7 [pb]	35.9 [pb]	7.26 [pb]	12.2 [pb]
$\sigma_1 \times \mathrm{BR}(\mathrm{h}_1 \to \mathrm{WW})$	7.47 [pb]	7.5 [pb]	0.285 [fb]	35.4 [fb]
$\sigma_1 \times \mathrm{BR}(\mathrm{h}_1 \to \mathrm{ZZ})$	935 [fb]	938 [fb]	0.0887 [fb]	6.17 [fb]
$\sigma_1 \times \mathrm{BR}(\mathrm{h}_1 \to \mathrm{bb})$	21.1 [pb]	21.2 [pb]	6.21 [pb]	9.9 [pb]
$\sigma_1 \times \mathrm{BR}(\mathrm{h}_1 \to \tau\tau)$	2.27 [pb]	2.28 [pb]	562 [fb]	1 [pb]
$\sigma_1 \times \mathrm{BR}(\mathrm{h}_1 \to \gamma\gamma)$	82.8 [fb]	83.2 [fb]	2.93 [fb]	16.1 [fb]
μ_{h_2}	0.0887	0.169	0.857	0.837
$\sigma_2 \equiv \sigma(\mathrm{gg} \to \mathrm{h}_2)$	1.97 [pb]	4.06 [pb]	41.6 [pb]	36.2 [pb]
$\sigma_2 \times \mathrm{BR}(\mathrm{h}_2 \to \mathrm{WW})$	708 [fb]	3.9 [pb]	7.73 [pb]	7.56 [pb]
$\sigma_2 \times \mathrm{BR}(\mathrm{h}_2 \to \mathrm{ZZ})$	305 [fb]	112 [fb]	967 [fb]	946 [fb]
$\sigma_2 \times \mathrm{BR}(\mathrm{h}_2 \to \mathrm{bb})$	0.897 [fb]	30.5 [fb]	21.8 [pb]	21.3 [pb]
$\sigma_2 \times \mathrm{BR}(\mathrm{h}_2 \to \tau\tau)$	0.111 [fb]	3.48 [fb]	2.35 [pb]	2.29 [pb]
$\sigma_2 \times \mathrm{BR}(\mathrm{h}_2 \to \gamma\gamma)$	0.0204 [fb]	0.582 [fb]	85.8 [fb]	83.9 [fb]
$\mathrm{BR}(\mathrm{h}_2 \to \mathrm{h}_1\mathrm{h}_1)$ %	48.6	0	11	0
$\sigma_2 \times \mathrm{BR}(\mathrm{h}_2 \to \mathrm{h}_1\mathrm{h}_1)$	960 [fb]	0	4.57 [pb]	0
$\sigma_2 \times \mathrm{BR}(\mathrm{h}_2 \to \mathrm{h}_1\mathrm{h}_1 \to \mathrm{bbbb})$	334 [fb]	0	3.35 [pb]	0
$\sigma_2 \times \mathrm{BR}(\mathrm{h}_2 \to \mathrm{h}_1\mathrm{h}_1 \to \mathrm{bb}\tau\tau)$	71.8 [fb]	0	605 [fb]	0
$\sigma_2 \times \mathrm{BR}(\mathrm{h}_2 \to \mathrm{h}_1\mathrm{h}_1 \to \mathrm{bbWW})$	237 [fb]	0	0.307 [fb]	0
$\sigma_2 \times \mathrm{BR}(\mathrm{h}_2 \to \mathrm{h}_1\mathrm{h}_1 \to \mathrm{bb}\gamma\gamma)$	2.62 [fb]	0	3.16 [fb]	0
$\sigma_2 \times \mathrm{BR}(\mathrm{h}_2 \to \mathrm{h}_1\mathrm{h}_1 \to \tau\tau\tau\tau)$	3.86 [fb]	0	27.4 [fb]	0

Chapter IV.5

NMSSM

U. Ellwanger, M. Mühlleitner, F. Staub, D. Strom, R. Yohay (Eds.) R. Aggleton, B. Allanach, M. Badziak, D. Barducci, G. Bélanger, C. Beskidt, N.E. Bomark, N. Christensen, W. de Boer, H.E. Haber, C. Han, T. Han, C. Hugonie, D. Kazakov, S. Liebler, Z. Liu, S. Moretti, S. Munir, R. Nevzorov, C.T. Potter, A. Pukhov, C.H. Shepherd-Themistocleous, A.M. Teixeira, S. Wayand, G. Weiglein, R. Ziegler

IV.5.1 Introduction

The Next-to-Minimal Supersymmetric Standard Model (NMSSM) [1317–1331] shares the benefits of supersymmetric extensions of the Standard Model (SM) with the MSSM: the hierarchy problem can be strongly reduced, the presence of dark matter can be explained, and the running gauge couplings are automatically consistent with a Grand Unified Theory (GUT).

In addition, the $\mathbb{Z}_3$-invariant version of the NMSSM (with a scale invariant superpotential) solves the μ-problem of the MSSM [1332]. Both, the general and the $\mathbb{Z}_3$-invariant versions of the NMSSM, render more natural the mass of $\sim$ 125 GeV of the SM-like Higgs boson [1333–1343] and the non-observation of sparticles like squarks and gluinos at the Run 1 of the LHC [1344]. For these reasons the NMSSM has become more and more appealing in the recent years.

The field content of the NMSSM differs from the MSSM by an additional gauge singlet superfield $\hat{S}$ which contains a Majorana fermion (the singlino), a CP-even, and a CP-odd scalar. The couplings of the components of $\hat{S}$ to the MSSM-like Higgs fields H_u, H_d and sparticles are proportional to a dimensionless coupling λ, and the self couplings of the components of $\hat{S}$ are proportional to a dimensionless coupling κ. With these conventions, the general, renormalizable and R-parity conserving superpotential for the model reads

$$\mathcal{W}_S = \mathcal{W}_{\rm Yukawa} + \frac{1}{3}\kappa\hat{S}^3 + (\mu + \lambda\hat{S})\hat{H}_u\hat{H}_d + \frac{1}{2}\mu_s\hat{S}^2 + t_s\hat{S}\ . \tag{IV.5.1}$$

Here, $\mathcal{W}_{\rm Yukawa}$ contains the Yukawa part which is the same as in the MSSM, and the superfields containing the Higgs doublets are called $\hat{H}_u$, $\hat{H}_d$. In the scale invariant version of the model, $\mu = \mu_s = t_s = 0$ holds. Assuming the absence of a Landau singularity for the running coupling λ up to the GUT scale imposes $\sqrt{\kappa^2 + \lambda^2} \lesssim 0.7$ at the weak (SUSY) scale, and κ satisfies typically $\kappa \lesssim \lambda$. The soft SUSY breaking terms in the Higgs and singlet sector are

$$\begin{aligned} V_{\rm soft} =& m_s^2|S|^2 + m_{H_u}^2|H_u|^2 + m_{H_d}^2|H_d|^2 + \\ & \left(B_\mu H_u H_d + \frac{1}{2}B_s SS + \chi_s S + A_\lambda \lambda S H_u H_d + \frac{1}{3}A_\kappa \kappa S^3 + h.c.\right)\ , \end{aligned} \tag{IV.5.2}$$

where S is the scalar component of $\hat{S}$, and $B_\mu = B_s = \chi_s = 0$ in the scale invariant version.

After electroweak symmetry breaking the components of S mix with the neutral components of H_u, H_d. If CP is conserved, the CP-even sector of the NMSSM contains three states H_i, $i = 1, 2, 3$, which are ordered in mass. Typically, two of them have the properties of the MSSM-like states h (mostly SM-like) and H, and a third state H_S is mostly singlet-like. The CP-odd sector of the NMSSM contains two states A_i, $i = 1, 2$, ordered in mass, one of which has typically the properties of the MSSM-like state A, and a second state A_S is mostly singlet-like. Past and present searches for Higgs bosons at LEP, the Tevatron and the LHC do not exclude masses of H_S and/or A_S below 125 GeV. These masses depend on unknown parameters, like the NMSSM couplings λ and κ, soft SUSY breaking mass terms, the trilinear

couplings A_λ and A_κ and $\tan\beta$, the ratio of the two vacuum expectation values (VEVs) of the Higgs doublets, as well as on the VEV of the singlet, [1330]. A charged Higgs boson $\mathrm{H}^\pm$ remains present as in the MSSM, but with slightly modified relations among the masses of $\mathrm{H}^\pm$, H and A.

The singlino Majorana fermion mixes after electroweak symmetry breaking with the four neutralinos (bino, neutral wino and two Higgsinos) of the MSSM. Like in the scalar sector, the mixing angle is proportional to the coupling λ. The mostly singlet-like neutralino can well be the lightest supersymmetric particle (LSP) and a good candidate for dark matter with a relic density consistent with present results from Planck and WMAP, with a mass from below a GeV to hundreds of GeV depending on the unknown parameters.

The NMSSM with an enlarged Higgs sector and an additional singlino-like neutralino leads to a plethora of interesting signatures. On the one hand these can be more challenging for the discovery of physics beyond the SM (BSM). This is because the components of $\hat{S}$ have no couplings to the SM so that all states in the Higgs and neutralino sectors which mix with components of $\hat{S}$ have reduced production cross sections compared to the MSSM. On the other hand there may be exotic signatures like Higgs-to-Higgs cascade decays e.g. with striking BSM signatures of multi-fermion and/or photon final states [1345, 1346]. It is the target of this document to point out, which signatures allow to test which regions of the parameter space of the NMSSM in future runs of the LHC, which ones are clear signs of BSM physics and which may serve to distinguish between different new physics models. In fact, in the decoupling limit of the NMSSM $\lambda \to 0$ (with a fixed ratio $\kappa/\lambda \lesssim 1$), the phenomenology of the NMSSM turns into the phenomenology of the MSSM up to a possible additional singlino-like LSP. The solution of the μ-problem can be maintained in the decoupling limit, but not the naturalness of the mass of the SM-like Higgs boson.

In order to test the NMSSM, in a first step its parameters have to be translated into physical quantities: the masses, couplings, production cross sections, and decay branching fractions of all states. Including the presently known radiative corrections, this task can be undertaken only with the help of numerical codes. In Section IV.5.2 we present the currently publicly available codes (tools) which allow to compute the physical quantities in terms of the parameters in the Lagrangian for different versions of the NMSSM: the $\mathbb{Z}_3$-invariant NMSSM, the general NMSSM, the NMSSM without or with explicit CP violation, the NMSSM with general soft SUSY breaking terms at the SUSY scale, or high-scale scenarios as minimal supergravity (mSUGRA) or gauge mediated SUSY breaking (GMSB). Some of these tools allow, in addition, to verify present constraints on the Higgs, heavy flavour and/or dark matter sectors.

With these tools at hand NMSSM-specific signatures can be searched for that are in accordance with present data and can be tested during future runs of the LHC. Ideally, in the case of a discovery, these should also allow to distinguish the NMSSM from the MSSM (outside the decoupling limit). In Section IV.5.3 we present such signatures and a list of benchmark points in the parameter space of the NMSSM. Some of these points lead to NMSSM mass spectra, that could be discovered via different processes. Practically, all of these processes involve an NMSSM specific scalar or pseudoscalar. Production cross sections and branching fractions are provided, while more details can be found in the indicated original publications. In some cases these references include proposals for cuts and estimates of SM backgrounds. Of course, the masses, production cross sections and branching fractions of the involved particles can vary sometimes over wide ranges, but the benchmark points represent useful targets for desirable sensitivities to BSM signatures.

IV.5.2 Tools for the NMSSM

IV.5.2.a Calculation of the spectrum and of the branching fractions

A precise determination of the full SUSY and Higgs spectrum in the NMSSM is a difficult task. In particular, for the Higgs state which is associated with the SM-like boson with a mass of about 125 GeV, it is very well known that radiative corrections are crucial. Today, full one-loop corrections of the Higgs

boson masses including the contributions from all states and the momentum dependence are known in the $\overline{\rm DR}$ [1347, 1348] and on-shell (OS) scheme [1349–1351]. At the two-loop level the dominant corrections involving the strong coupling constant are known: For the real case [1347] results for the corrections $\mathcal{O}(\alpha_{\rm s}(\alpha_{\rm b}+\alpha_{\rm t}))$ exist , while for complex parameters the corrections $\mathcal{O}(\alpha_{\rm s}\alpha_{\rm t})$ have been calculated [1352]. Other two-loop corrections involving only superpotential couplings such as Yukawa and singlet interactions have been derived in Ref. [1353].

There are several numerical codes available which calculate the mass spectrum for different versions of the NMSSM making use of these results. A detailed comparison of the calculations of the NMSSM Higgs boson masses in the $\overline{\rm DR}$ scheme is given in Ref. [1354]. We summarize in the following the main features of the codes in the order in which the tools became available[IV.27].

IV.5.2.a.i `NMSSMTools`

`NMSSMTools` is a collection of the codes `NMHDECAY` [1355, 1356], `NMSPEC` [1357] and `NMGMSB` and can be downloaded from `http://www.th.u-psud.fr/NMHDECAY/nmssmtools.html`. `NMSSMTools` allows to study the NMSSM with or without $\mathbb{Z}_3$ symmetry, without or with Grand Unification of its gauge couplings and soft SUSY breaking terms. So far `NMSSMTools` is restricted to the real NMSSM, but a version to support also CP violation at one-loop level is under construction [1358].

`NMSSMTools` allows to calculate the Higgs boson masses for a parameter point with three different options. The most precise calculation makes use of the NMSSM corrections of Ref. [1347]. This provides a full one-loop calculation of the Higgs boson masses including all contributions and the momentum dependence. At two-loop the corrections $\mathcal{O}(\alpha_{\rm s}(\alpha_{\rm b}+\alpha_{\rm t}))$ and the corrections known from the MSSM at $\mathcal{O}((\alpha_{\rm t}+\alpha_{\rm b})^2+\alpha_\tau(\alpha_\tau+\alpha_{\rm b}))$ [1050–1053, 1359] are included.

Other calculations performed by `NMSSMTools` are the SUSY spectrum at the one-loop level, Higgs and sparticle decay branching fractions ([1360], based on HDECAY [69] and `SDECAY` [1361], respectively). B-physics observables and the muon anomalous magnetic moment $(g-2)_\mu$ are computed following Refs. [1362, 1363]. An NMSSM-version of MicrOmegas [1364] is included which allows to determine the dark matter relic density, direct and indirect detection rates. All these can be compared to present constraints. Bounds on the Higgs boson couplings from LEP [1365] and on the signal rates of the SM-like Higgs boson from the LHC Run 1 (from Ref. [1366]) are implemented.

IV.5.2.a.ii `SPheno` *and* `SARAH`

A `SPheno` [1367, 1368] version for the NMSSM can be generated by the `Mathematica` code `SARAH` [1369–1373]. Both tools are available at `hepforge`: `http://spheno.hepforge.org/` and at `http://sarah.hepforge.org/`. By default, `SPheno` has included a GUT scenario based on minimal supergravity, but other SUSY breaking mechanism can be implemented via the `SARAH` interface.

`SPheno` calculates the full one-loop corrections to all Higgs and SUSY masses, including the entire momentum dependence [1348]. At two-loop all corrections in the gaugeless limit with vanishing external momenta are calculated for the real and complex NMSSM [1374, 1375], including the NMSSM-specific corrections of $\mathcal{O}(\alpha_\lambda(\alpha_\lambda+\alpha_\kappa+\alpha_{\rm t}))$ even in the case of CP violation [1353, 1376]

`SPheno` also computes the most important quark-flavour violating observables (B and K decays, $\Delta M_{B_{d,s}}/\Delta M_K$, ϵ_K) at one-loop using the `FlavourKit` functionality [1377], and calculations for $(g-2)_l$, $\delta\rho$ as well as electromagnetic dipole moments are included. Moreover, all two- and three-body decays of SUSY particles, and two-body decays of the Higgs scalars are calculated. The sparticle decays are purely tree-level, while for the Higgs bosons the next-to-leading order (NLO) QCD corrections to decays in two quarks, photons and gluons are included. Also decays in virtual vector bosons are taken into account. `SPheno` writes all necessary input files to test points with `HiggsBounds` [1237, 1313, 1314]

[IV.27] A public version of `FeynHiggs` for the NMSSM, based on Ref. [1351], is in preparation.

and HiggsSignals [1238].

IV.5.2.a.iii NMSSMCALC

The Fortran code NMSSMCALC [1378] allows the computation of the Higgs boson masses and branching fractions both in the CP-conserving and CP-violating NMSSM. It can be downloaded from http://www.itp.kit.edu/~maggie/NMSSMCALC/ and comes together with an NMSSM extension of HDECAY [69, 71, 1379] for the Higgs boson decays.

NMSSMCALC makes use of mixed $\overline{\text{DR}}$–OS renormalization conditions for the computation of the Higgs boson masses. The Higgs boson mass calculation at one-loop level is performed including the full momentum dependence and all possible contributions [1349, 1350]. At the two-loop level the $\mathcal{O}(\alpha_s\alpha_t)$ corrections are included [1352]. They include the $\mathcal{O}(\alpha_s\alpha_t)$ part relating the vacuum expectation value to physical observables, which is missing so far in the other spectrum generators.

Decays are calculated in the CP-conserving and CP-violating NMSSM including the dominant higher-order QCD, SUSY-QCD and SUSY-electroweak (EW) corrections: The neutral Higgs boson decays into quarks include the fully massive NLO corrections near threshold [1133–1137] and massless $\mathcal{O}(\alpha_s^4)$ corrections far above threshold [1138–1146]. Large logarithms are resummed by taking into account the running of the quark masses and the strong coupling constant. The charged Higgs boson decay into a heavy quark pair includes the QCD corrections given in [1380–1382] and taken over to the NMSSM case. By adapting the results from the MSSM, the decays of the neutral Higgs bosons into a bottom pair include SUSY-QCD [1033, 1076–1080, 1383, 1384] and the approximate SUSY-EW corrections [1081–1083]. For the decays into gluons the QCD corrections to quark loops have been included up to N^{3}LO in the limit of heavy quark masses [67, 99, 115, 136, 862, 880, 891, 892, 892–894] and NLO QCD corrections to the squark loops in the heavy squark mass limit [863, 1385]. In the photon decays the QCD corrections to quark [136, 861, 864, 1386–1390] and squark loops have been taken into account including the full mass dependence both for the quarks and the squarks. All two-body decays into SUSY particles have been implemented [1391, 1392]. For the CP-conserving case the decays into stop and sbottom pairs come with the SUSY-QCD corrections [90, 1393–1396]. Finally, all relevant off-shell decays into two massive gauge boson final states [1397], into gauge and Higgs boson final states [70, 1398–1400], into Higgs boson pairs as well as into heavy quark pairs are included [1398, 1399].

Recently, the electric dipole moments (EDMs) with NMSSM contributions [654, 1401–1418] have been implemented in NMSSMCALC [1419] allowing to check for the compatibility of CP-violating phases with the experimental constraints on the EDMs [1252, 1420–1422]. The output file contains furthermore the necessary couplings to test points with HiggsBounds.

IV.5.2.a.iv SoftSUSY

The NMSSM version of SoftSUSY includes different high-scale scenarios like mSUGRA-inspired semi-constrained NMSSM and a general high-scale boundary condition which allows one to set all soft parameters independently. The users may also easily create their own boundary conditions. For the determination of the parameters at the SUSY/weak scale, SoftSUSY uses the full three-family one- and two-loop RGEs for the NMSSM.

The homepage of SoftSUSY is http://softsusy.hepforge.org/.

The one-loop self-energies and tadpole corrections for the Higgs boson masses were extended to the NMSSM using the expressions in Refs. [1347, 1348]. The NMSSM extension also includes the two-loop corrections at order $\mathcal{O}(\alpha_s(\alpha_t+\alpha_b))$ from Ref. [1347] and uses the MSSM results from Refs. [1050–1053, 1359].

Higgs and sparticle decays may be obtained by interfacing SoftSUSY with NMHDECAY [1355, 1356] and NMSDECAY [1360], which is based upon Ref. [1361]. These are both distributed as part of the

NMSSMTools package, and SoftSUSY provides a script to do the interface with this package automatically.

IV.5.2.a.v FlexibleSUSY

FlexibleSUSY [1423] is a Mathematica and C++ package, which also makes use of SARAH to obtain model-dependent details. It can be downloaded from http://flexiblesusy.hepforge.org/. The boundary conditions on the model parameters at different scales, as well as spectrum-generator specific configuration details can be specified in a FlexibleSUSY model file.

FlexibleSUSY computes the Higgs spectrum employing the full two-loop RGEs and one-loop corrections. At the two-loop level it makes use of Higgs boson mass corrections available in the literature. In the case of the NMSSM FlexibleSUSY uses the $\alpha_s(\alpha_t + \alpha_b)$ corrections given in Ref. [1347]. In addition, the MSSM two-loop corrections can be used as SoftSUSY does.

IV.5.2.b Check for the vacuum stability

A valid spectrum obtained with one of the mentioned spectrum generators necessarily has a local minimum of the scalar potential where the electroweak symmetry is broken such that the electroweak data like the Z boson mass are fulfilled. However, none of the above described codes performs an exhaustive check if this is also the global minimum. Possible scenarios where deeper minima arise are given in the following situations: (i) In the case of light stops and a large mixing to accommodate the Higgs boson mass as in the MSSM, it can happen that at the global minimum charge and colour are broken by VEVs for the stops [1424–1428]. (ii) In the case of large A_λ and A_κ deeper minima with different numerical values for the singlet and the two doublet VEVs can exist [1429–1431]. Both possibilities are disastrous and the corresponding parameter points are ruled out if the local minimum with correct EWSB is short-lived on cosmological times scales.
The software package Vevacious [1432] addresses these issues and performs a numerical check of the vacuum stability. Given a model file and a parameter point in the SLHA format, Vevacious checks for the global minimum of the one-loop effective potential including also finite temperature effects. If necessary, it calculates the life-time for the input minimum using Cosmotransitions [1433]. Vevacious includes model files not only to check the possibility of stop, but also of stau VEVs in addition to the Higgs and singlet VEVs. Model files for other scenarios can be generated with SARAH.

IV.5.2.c Calculation of the neutral Higgs boson production cross sections

The essential features of Higgs boson production in the NMSSM can directly be adapted from the ones of the MSSM which were broadly analysed in the previous reports [7–9]. Thus, when we subsequently discuss the production of the five neutral Higgs bosons we mainly elaborate on the most prominent differences with respect to the MSSM.

The dominant production mechanism for neutral Higgs bosons is gluon fusion (ggF) [97, 99, 136, 1064] mediated through loops involving the third generation quarks, top and bottom, as in the SM. In SUSY also the squarks of the third generation, stops and sbottoms, contribute, but are typically suppressed by the ratio $m_Z^2/m_{\tilde{q}}^2$ at leading order (LO) QCD. The NLO QCD contributions are important and have been provided with full quark mass dependence [136, 140]. The next-to-next-to leading order (NNLO) QCD corrections to the top quark loops have been calculated in the heavy top quark mass limit [100–102, 866, 867, 1067] and with finite top-quark mass effects [103–106, 234, 235, 1067, 1068]. Partial NNNLO QCD corrections to the top-quark contribution were provided in Refs. [94, 95, 117, 119, 155, 1069]. The QCD corrections to top- and bottom-quark loops can be taken over to the NMSSM case. Moreover, even though $\tan\beta$ is mostly chosen small in the NMSSM, non-decoupling Δ_b terms [1079–1083], i.e. the $\tan\beta$-enhanced resummed SUSY corrections to the Higgs-bottom coupling, are known in the NMSSM [1378] and can be included in the NMSSM Higgs Yukawa coupling to the bottom quarks.

The code SusHi [135], starting with version 1.5.0, allows for the inclusion of the above mentioned higher order quark contributions for the NMSSM Higgs bosons as well [1434], but additionally takes into account genuine SUSY contributions, namely stop and sbottom contributions up to NLO QCD in the expansion of heavy SUSY masses [871,874,875]. Furthermore, for the Higgs bosons of the NMSSM there exists a private version of the code HIGLU [133, 1340, 1346]. It takes into account the NLO QCD corrections to the quark and squark loops including the full mass dependence, see Refs. [136, 140] and Refs. [142, 143, 864], respectively.

Electroweak contributions mediated by light quarks [107,1084] can be added in SusHi for the CP-even Higgs bosons of the NMSSM, while they are absent for the CP-odd Higgs bosons. They are known to capture the dominant fraction of the full SM electroweak correction factor [107, 108, 145, 149, 1084] for the SM-like Higgs boson with a mass of ~ 125 GeV.

The discussion of theory uncertainties for the gluon fusion process applies to large extent to the case of the MSSM. We therefore refer to the detailed discussion of theory uncertainties in Refs. [9,1096]. In order to mimic next-to-next-to-leading-log (NNLL) resummation [116–118] of large logarithms for the top-quark induced contributions, central scales of $m_\phi/2$ for the renormalization and factorization scale are advisable, where m_ϕ generically denotes the mass of the Higgs boson under consideration. The scale uncertainties can then be obtained through a combination of five different scale choices, as presented in Refs. [1096, 1434]. PDF+α_s uncertainties were found to be mostly a function of the mass m_ϕ of the Higgs boson involved [1096,1434]. Thus, the relative PDF+α_s uncertainties can be taken from the ggF cross section of a SM Higgs boson with mass m_ϕ. Since $\tan\beta$ is usually chosen small in the NMSSM, the uncertainties which stem from missing contributions to Δ_b and from the renormalization prescription taken for the bottom-quark Yukawa coupling are not as relevant as in the MSSM. In contrast, the negligence of NNLO stop contributions to Higgs boson production can be important for pseudo-scalars, where the couplings to quarks can vanish for a CP-odd singlet-like state [1434].

The other production mechanisms can be treated in a similar fashion as in the MSSM. Thus, vector-boson fusion (VBF) [1435–1437] and top-quark associated production ($\mathrm{t\bar{t}H}$) [1438–1442] can be reweighted with the effective couplings of the Higgs boson under consideration to the heavy gauge bosons Z, W and the top quark, respectively. In the MSSM SUSY-QCD corrections are known to be small for vector-boson fusion [1443, 1444] and moderate for top-quark associated production [1445–1448], and thus - as a first approximation - are neglected in the NMSSM. Similarly, bottom-quark associated production ($\mathrm{b\bar{b}H}$), which is relevant for large values of $\tan\beta$ and can either be described in the four-flavour scheme [1085, 1086] at NLO QCD accuracy or the five-flavour scheme [565, 1087, 1151] at NNLO QCD accuracy, can be adjusted to the NMSSM by reweighting the SM predictions with the effective coupling of the Higgs boson under consideration to the bottom quark. Again non-decoupling Δ_b terms should be added to the effective Higgs-bottom coupling. SusHi provides the effective coupling to bottom quarks and also the bottom-quark annihilation cross sections (5FS) directly. As a first approximation Higgs-strahlung (VH) [1449, 1450] can be adjusted from the SM to the NMSSM through a proper reweighting with the Higgs to gauge boson couplings. However gluon induced contributions to Higgs-strahlung, which contribute $\mathcal{O}(10\%)$ [300] to the inclusive cross section and are mediated through top-quark or bottom-quark loops, need to be treated differently. Moreover s-channel Higgs induced contributions can arise in Higgs sectors with more than one Higgs doublet. SUSY-QCD corrections to Higgs-strahlung in the MSSM are known to be small [1443]. A code, which reweights the individual contributions to VH according to the quark and gauge boson couplings in the NMSSM and which adds s-channel Higgs induced contributions, is desirable.

The relative couplings of the Higgs boson under consideration to quarks, the heavy gauge bosons, gluons and photons with respect to an SM Higgs boson of identical mass can also be obtained with the different spectrum generators presented in Section IV.5.2.a: In NMSSMTools the relative coupling to a pair of bottom quarks includes Δ_b corrections and the relative coupling to gluons and photons take into account the LO one-loop induced contributions with the full NMSSM particle spectrum. SPheno

includes in addition the NLO QCD corrections in the coupling of the scalars to a pair of gluons.

Of large relevance for the phenomenology of Higgs bosons are their transverse momentum (p_T) distributions in gluon fusion. We refer to the MSSM section, see Section IV.1.4, for a detailed discussion of their knowledge in the SM and beyond. Neglecting squark contributions, the top-quark, bottom-quark and the top-bottom-interference contributions can be reweighted from the SM to the NMSSM as depicted in the MSSM section for the example of a 2HDM. For this purpose the 2HDM/MSSM implementations [240] of the gluon fusion process in the `POWHEG-BOX` [81] or the two codes `MoRe-SusHi` [231,1120] and `aMCSusHi` [1117] can be used, which all allow to extract the three mentioned quark contributions individually and reweight them with the corresponding Yukawa couplings of the NMSSM Higgs boson under consideration. An extension of the codes `MoRe-SusHi` and `aMCSusHi` from the MSSM to the NMSSM to directly obtain p_T distributions for the five neutral Higgs bosons in gluon fusion is planned.

IV.5.3 NMSSM benchmark points

IV.5.3.a NMSSM specific processes

The benchmark points presented here cover various possible NMSSM specific processes to be searched for during the ongoing and future runs of the LHC. The focus is on possible discovery scenarios, as adequate at the present and foreseen LHC energies and luminosities. Additionally, the benchmark points can also be exploited to test specific features of the NMSSM Higgs bosons and be used to distinguish the NMSSM from other SUSY extensions like e.g. the MSSM.

The production mechanisms for NMSSM Higgs bosons are given by the same mechanisms as for an SM-like Higgs boson, i.e. ggF, VBF, VH and associated production $\mathrm{b\bar{b}H}$ or $\mathrm{t\bar{t}H}$ with, however, reduced cross sections[IV.28]. Alternatively, NMSSM specific Higgs states can appear in decay cascades of heavier (MSSM-like or NMSSM-like) Higgs states, or in sparticle decay cascades. Likewise, NMSSM specific Higgs states can decay into the same final states as an SM-like Higgs boson and additionally, if kinematically allowed, into pairs of other Higgs states, other Higgs states and a Z or W boson, or pairs of SUSY particles.

With the here presented benchmark points designed to be potential search and discovery modes for the NMSSM Higgs states, it is useful to start with their classification according to production mechanisms and decay chains. This is summarized in Tables 156–160 below, together with the corresponding combinations that appear for the various benchmark points described in the next subsection. We choose the following notation: the mostly SM-like Higgs boson is denoted by H_{125}, the dominantly MSSM-like CP-even and CP-odd scalars are given by H and A, respectively, and the mostly NMSSM-like CP-even and CP-odd scalars by H_S and A_S each. Note that the latter two can be lighter or heavier than all other scalars. Neutralinos are indicated by $\widetilde{\chi}^0_i$ ($i = 1, ..., 5$) where, in most considered cases, $\widetilde{\chi}^0_1$ is mostly singlino-like and can have a very small mass. The c.m. energy $\sqrt{s}$ used by the authors of the various benchmark points has been set to either 13 or 14 TeV, namely we have $\sqrt{s} = 13$ TeV in BP1, BP2 ,BP3, BP4, BP5, BP7 and $\sqrt{s} = 14$ TeV in BP6, BP8, BP9. Note that the gluon fusion cross section increases, depending on the Higgs boson mass value, by ∼10-20% when increasing the c.m. energy from 13 to 14 TeV.

Direct H_{125} Production and Decays

The set I of signatures given in Table 156 summarizes scenarios that feature a directly produced SM-like Higgs boson H_{125} that decays into lighter singlet-like Higgs boson pair or neutralino final states. The branching fractions corresponding to the NMSSM-specific H_{125} decays listed in Table 156 are (or will be) limited by the presently (or prospectively) measured signal rates of H_{125} decays into SM channels. These indirect constraints on NMSSM-specific H_{125} decays can be stronger than the limits from direct

[IV.28] With the exception of production processes where $\tan\beta$ enhanced couplings to b-quarks are involved.

Table 156: Summary of NMSSM-specific H_{125} decays and their signatures. The last column indicates the benchmark points in which the scenarios are realized.

I	Direct H_{125} production and decays			
	Process	Signatures	Comments	BM points
a	$H_{125} \to H_S + H_S$ or $H_{125} \to A_S + A_S$	Combinations of decays into $\mathrm{b\bar{b}}$, $\tau^+\tau^-$, $\mu^+\mu^-$, $\gamma\,\gamma$	Notably A_S can be very light	BP2_1, BP4_1,2, BP9_1
b	$H_{125} \to H_S + H_S$ $\to 4A_S$	Combinations of decays into $\mathrm{b\bar{b}}$, $\tau^+\tau^-$, $\mu^+\mu^-$, $\gamma\,\gamma$	A_S can be very light	BP4_2
c	$H_{125} \to \widetilde{\chi}_1^0 + \widetilde{\chi}_2^0$, $\widetilde{\chi}_2^0 \to \widetilde{\chi}_1^0 + H_S$	H_S decay products $+E_{\mathrm{T}}^{\mathrm{miss}}$		Not necessary

Table 157: NMSSM-specific H_S/A_S production and decays as well as the corresponding collider signatures. The last column indicates the benchmark points in which the scenarios are realized.

II	Direct H_S/A_S production and decays			
	Process	Signatures	Comments	BM points
a	ggF(H_S/A_S)	$\mathrm{b\bar{b}}$, $\tau^+\tau^-$, $\mu^+\mu^-$, $\gamma\,\gamma$		BP1_1,2, BP4_1,2, BP7_1,2, BP8_1,2, BP9_1,2
b	ggF(H_S) $\to A_S A_S$	Combinations of decays into $\mathrm{b\bar{b}}$, $\tau^+\tau^-$, $\mu^+\mu^-$, $\gamma\,\gamma$	A_S can be very light	BP2_1,2, BP3, BP4_2, BP7_2, BP9_2
c	ggF(H_S) $\to H_{125} H_{125}$			BP9_2
d	ggF(A_S) $\to \mathrm{Z}H_S$	$\mathrm{Z} + \mathrm{b\bar{b}}$		BP8_1,2
e	ggF(H_S/A_S) $\to \widetilde{\chi}_1^0\widetilde{\chi}_1^0$			BP4_1,2, BP8_2, BP9_2

searches of the corresponding final states. Some benchmark points lead also to MSSM-like decays $H_{125} \to$ invisible. Here and in the following MSSM-like decays have been omitted for simplicity.

Direct Light H_S/A_S Production and Decays

In set II, *cf.* Table 157, we collect signatures stemming from direct production of singlet-like CP-even Higgs boson H_S and A_S. These may decay into SM particle final states, into lighter NMSSM Higgs boson pairs, among which also the H_{125} is possible, into a gauge boson and an NMSSM Higgs boson or into a lightest neutralino pair. The production cross sections for H_S/A_S in Table 157 are proportional to the singlet-doublet mixing angles (squared) and can be very small.

Table 158: NMSSM-specific H/A production and decays as well as the corresponding collider signatures. The last column indicates the benchmark points in which the scenarios are realized.

III	Direct H/A production and decays			
	Process	Signatures	Comments	BM points
a	$\mathrm{ggF}(H) \to H_S + H_S$ $\mathrm{ggF}(H) \to A_S + A_S$ $\mathrm{ggF}(A) \to H_S + A_S$	$\mathrm{b\bar{b}} + \mathrm{b\bar{b}}$, $\mathrm{b\bar{b}} + \tau^+\tau^-$, $\mathrm{b\bar{b}} + \gamma\gamma$, 4γ	A_S can be very light	BP7_1,2, BP8_2
b	$\mathrm{ggF}(H) \to H_{125} + H_S$ $\mathrm{ggF}(A) \to H_{125} + A_S$	$\mathrm{b\bar{b}} + \mathrm{b\bar{b}}$, $\mathrm{b\bar{b}} + \tau^+\tau^-$, $\mathrm{b\bar{b}} + \gamma\gamma$, 4γ	A_S can be very light	BP7_1,2, BP8_1,2
c	$\mathrm{ggF}(H) \to H_{125} + H_{125}$	$\mathrm{b\bar{b}} + \mathrm{b\bar{b}}$, $\mathrm{b\bar{b}} + \gamma\gamma$, $\tau^+\tau^- + \gamma\gamma$		BP7_2
d	$\mathrm{ggF}(H) \to H_{125} + H_S$ $\to H_{125} + A_S + A_S$ $\mathrm{ggF}(A) \to A_S + H_S$ $\to A_S + A_S + A_S$	$\mathrm{b\bar{b}} + \mathrm{b\bar{b}} + \mathrm{b\bar{b}}$, $\mathrm{b\bar{b}} + \mathrm{b\bar{b}} + \tau^+\tau^-$, $\mathrm{b\bar{b}} + \mathrm{b\bar{b}} + \gamma\gamma$, $\mathrm{b\bar{b}} + \tau^+\tau^- + \gamma\gamma$, $\mathrm{b\bar{b}} + 4\gamma$, $\tau^+\tau^- + 4\gamma$		BP7_2
e	$\mathrm{ggF}(H) \to \mathrm{Z} + A_S$ $\mathrm{ggF}(A) \to \mathrm{Z} + H_S$	$\ell^+\ell^- + \mathrm{b\bar{b}}$, $\ell^+\ell^- + \tau^+\tau^-$, $\ell^+\ell^- + \gamma\gamma$	$\ell^+\ell^-$ from Z decays	BP2_2, BP7_1, BP8_1,2
f	$\mathrm{ggF}(A) \to \mathrm{Z} + H_S$ $\to \mathrm{Z} + A_S + A_S$	$\ell^+\ell^- + \mathrm{b\bar{b}} + \mathrm{b\bar{b}}$	$\ell^+\ell^-$ from Z decays	BP7_2

Direct H / A Production and Decays

The production cross sections of set III for direct MSSM-like Higgs boson, H, A, production in Table 158 are dominated by ggF for low values of $\tan\beta$, which are typical for the NMSSM. Some benchmark points lead also to MSSM-like decays $\mathrm{H}/A \to H_{125} + H_{125}$, $\mathrm{H}/A \to$ invisible, $\mathrm{H}/A \to \mathrm{t\bar{t}}$, $\mathrm{H}/A \to \widetilde{\chi}^+\widetilde{\chi}^-$, $\mathrm{H}/A \to \widetilde{\chi}^0{}_i\widetilde{\chi}^0{}_j$, which have been omitted. The decays IIIe), IIIf) including Z bosons occur only if H_S/A_S have doublet components through mixing, and if other channels are suppressed.

Higgs Bosons in Squark/Chargino/Neutralino decays, Singlino-Like LSP

Set IV is dedicated to NMSSM Higgs boson production through squark/chargino/neutralino decay cascades. They are given in Table 159 and the NMSSM-specific features consist in the appearance of the 5th singlino-like lightest SUSY particle (LSP), which couples weakly to all other sparticles. Hence sparticle decay cascades end up provisionally in the next-to-lightest SUSY particle (NLSP), e.g. the one that is mostly bino-like, which finally decays into the LSP plus H_{125} or H_S, depending on M_{H_S} and the available phase space. If the LSP is light and the phase space is narrow, the LSP carries little energy and the $E_{\mathrm{T}}^{\mathrm{miss}}$ can become very small.

Displaced vertices

Displaced vertices as given by set V in Table 160 can occur as in the MSSM in models with light Gravitinos, like in gravity mediated SUSY breaking (GMSB) for instance, but also for very weakly

Table 159: NMSSM-specific squark/chargino/neutralino decay cascades as well as the corresponding collider signatures. The last column indicates the benchmark points in which the scenarios are realized.

IV	Higgs bosons in squark/chargino/neutralino decays, singlino-like LSP			
	Process	Signatures	Comments	BM points
a	$\widetilde{\chi}_2^0 \to \widetilde{\chi}_1^0 + H_{125}$	Jets + $H_{125} + H_{125}$ + $E_{\mathrm{T}}^{\mathrm{miss}}$ $H_{125} \to \mathrm{b\bar{b}}$, $\tau^+\tau^-$ or $\gamma\,\gamma$		BP1_2
b	$\widetilde{\chi}_2^0 \to \widetilde{\chi}_1^0 + H_{125}$	Jets + $H_{125} + H_{125}$ $H_{125} \to \mathrm{b\bar{b}}$, $\tau^+\tau^-$ or $\gamma\,\gamma$	$\widetilde{\chi}_1^0$ very light, little $E_{\mathrm{T}}^{\mathrm{miss}}$	BP5_1,2
c	$\widetilde{\chi}_2^0 \to \widetilde{\chi}_1^0 + H_S$	Jets + $H_S + H_S$ + $E_{\mathrm{T}}^{\mathrm{miss}}$ $H_S \to \mathrm{b\bar{b}}$, $\tau^+\tau^-$ or $\gamma\,\gamma$		BP1_2
d	$\widetilde{\chi}_3^0 \to \widetilde{\chi}_1^0 + H_S$, $H_S \to A_S + A_S$	Jets + $E_{\mathrm{T}}^{\mathrm{miss}}$ + up to $4A_S$		BP3
e	$\widetilde{\chi}^0{}_i \to \widetilde{\chi}_1^0 + A_S$	Trileptons + $E_{\mathrm{T}}^{\mathrm{miss}}$	A_S very light	BP6

Table 160: Processes which can cause displaced vertices, their collider signatures and corresponding benchmark points

V	Displaced vertices		
	Process	Signatures	BM points
a	Squark/gluino production	Jets + displaced vertices	BP1_1,2
b	chargino/slepton production	Leptons + displaced vertices	BP1_1,2

coupled singlino-like LSPs.

IV.5.3.b Benchmark points

In this section we present (pairs of) benchmark points which are aimed to cover most of the NMSSM-specific processes and final states, that have been presented in Tables 156–160. The benchmark points BP1–9_1,2 have been provided by different author groups and are classified accordingly.

For better readability and easy identification of the striking features and signatures, we give only the main features, i.e. the relevant parts of the spectra and the signatures. For more information we refer the reader to the publications, on which the points are based and which are given in the following tables, as well as to the TWiki page: https://twiki.cern.ch/twiki/bin/view/LHCPhysics/LHCHXSWGNMSSM. Here detailed information on the benchmark spectra, the production cross sections, the branching ratios and the rates to be expected can be found. Furthermore, the program codes with which the benchmark points have been generated are specified, so that they can be reproduced. Since, in contrast to other BSM theories like the MSSM or the 2HDM, there is no official recommendation for NMSSM tools yet, the various authors of the benchmark points chose different tools. Note, that the numbers presented here and on the TWiki page sometimes differ from the ones of the originally proposed points in

the given references. This is due to the following reasons: (i) The SM input parameters have been unified according to the official proposal of Ref. [144]. (ii) Some benchmarks use `NMSSMTools` to calculate the Higgs boson mass spectrum. If not done before, the highest precision available in `NMSSMTools` is now used throughout. (iii) Parameters were tweaked to resurrect scenarios ruled out by previous LHC runs.

The corresponding publications contain typically more benchmark points with similar features and sometimes proposals for search strategies including cuts and estimates of the background.

All benchmark points have been chosen such that they are not in conflict with previous searches at the Run 1 of the LHC, and use the SM parameters recommended by the LHC-HXSWG, see Ref. [144] and Chapter I.1.

BP1: GMSB combined with $\mathbb{Z}_3$-invariant NMSSM	
B. Allanach, M. Badziak, C. Hugonie and R. Ziegler from Phys.Rev. D92 (2015) 1, 015006, arXiv:1502.05836 [1451]	
Main Features	GMSB combined with $\mathbb{Z}_3$-invariant NMSSM (gravitino $\tilde{G}$ LSP) $\widetilde{\chi}_1^0$: singlino-like NLSP
BP1_1	
Spectrum	$M_{H_{125}} \approx 123$ GeV, $M_{A_S} \approx 26$ GeV, $M_{H_S} \approx 93$ GeV, $M_H \approx 895$ GeV, $M_A \approx 895$ GeV, $M_{\widetilde{\chi}_1^0} \approx 103$ GeV, $M_{\widetilde{\tau}_1^-} \approx 332$ GeV (NNLSP)
Production cross sections (at 13 TeV) and branching fractions	
H_S	via ggF ≈ 16 pb, $BR(H_S \to \mathrm{b\bar{b}}) \approx 83\%$, $BR(H_S \to \tau^+\tau^-) \approx 8\%$
A_S	via ggF ≈ 11 fb, $BR(A_S \to \mathrm{b\bar{b}}) \approx 91\%$, $BR(A_S \to \tau^+\tau^-) \approx 8\%$
$\widetilde{\chi}_1^0$	$BR(\widetilde{\chi}_1^0 \to \tilde{G} + A_S) = 100\%$, displaced vertex (mostly inside the detector)
$\widetilde{\tau}_1^-$	$BR(\widetilde{\tau}_1^- \to \tau^- + \widetilde{\chi}_1^0) = 100\%$
Particular signatures	A_S appears at the end of every sparticle decay chain H_S potentially observable via direct production
BP1_2	
Spectrum	$M_{H_{125}} \approx 124$ GeV, $M_{A_S} \approx 32$ GeV, $M_{H_S} \approx 94$ GeV, $M_H \approx 1.4$ TeV, $M_A \approx 1.4$ TeV, $M_{\widetilde{\chi}_1^0} \approx 105$ GeV, $M_{\widetilde{\chi}_2^0} \approx 397$ GeV (NNLSP)
Production cross sections (at 13 TeV) and branching fractions	
H_S	via ggF ≈ 17 pb, $BR(H_S \to \mathrm{b\bar{b}}) \approx 83\%$, $BR(H_S \to \tau^+\tau^-) \approx 8\%$
A_S	via ggF ≈ 0.1 fb, $BR(A_S \to \mathrm{b\bar{b}}) \approx 91\%$, $BR(A_S \to \tau^+\tau^-) \approx 9\%$
$\widetilde{\chi}_1^0$	$BR(\widetilde{\chi}_1^0 \to \tilde{G} + A_S) = 100\%$, displaced vertex (mostly outside the detector)
$\widetilde{\chi}_2^0$	$BR(\widetilde{\chi}_2^0 \to \widetilde{\chi}_1^0 + H_S) \approx 24\%$, $BR(\widetilde{\chi}_2^0 \to \widetilde{\chi}_1^0 + H_{125}) \approx 76\%$
Particular signatures	H_S or H_{125} appear at the end of every sparticle decay chain H_S potentially observable via direct production
BP2: Light Pseudoscalars	
R. Aggleton, D. Barducci, N-E. Bomark, S. Moretti,	

A. Nikitenko, C. Shepherd-Themistocleous, L. Roszkowski
from JHEP 1502 (2015) 044, arXiv:1409.8393 [1452], and arXiv:1503.04228 [1453]

BP2_1	
Main Features	A light pseudoscalar with $M_{A_S} \approx 9$ GeV
Spectrum	$M_{H_{125}} \approx 123.3$ GeV, $M_{A_S} \approx 8.6$ GeV, $M_{H_S} \approx 480$ GeV, $M_H \approx 2254$ GeV, $M_A \approx 2255$ GeV
Production cross sections (at 13 TeV) and branching fractions	
$H_S \to A_S A_S$	ggF$(H_S) \approx 43.2$ pb, $BR(H_S \to A_S + A_S) \approx 9.7\%$ $BR(A_S \to \tau^+\tau^-) \approx 88.4\%$, $BR(A_S \to \mu^+\mu^-) \approx 0.34\%$ ggF$(H_S) \to A_S + A_S \to 4\tau \approx 3.27$ pb, ggF$(H_S) \to A_S + A_S \to 2\tau + 2\mu \approx 0.0254$ pb
Particular signatures	Considerable cross-section for very light pseudoscalar boson production with 4τ final signature state, with possibility for $2\tau + 2\mu$ final state, free from Upsilon contamination
BP2_2	
Main Features	GMSB, lightest scalar SM-like, light pseudoscalar just above $M_{H_{125}}/2$.
Spectrum	$M_{H_{125}} \approx 125.9$ GeV, $M_{H_S} \approx 201$ GeV, $M_{A_S} \approx 65$ GeV, $M_H \approx 448$ GeV, $M_A \approx 440$ GeV
Production cross sections (at 13 TeV) and branching fractions	
$H_S \to A_S A_S$	ggF$(H_S) \approx 0.86$ pb, $BR(H_S \to A_S + A_S) \approx 91\%$ $BR(A_S \to \mathrm{b\bar{b}}) \approx 91\%$, $BR(A_S \to \tau^+\tau^-) \approx 8.8\%$ ggF$(H_S) \to A_S + A_S \to 4\mathrm{b} \approx 0.641$ pb ggF$(H_S) \to A_S + A_S \to 2\mathrm{b} + 2\tau \approx 0.124$ pb ggF$(H_S) \to A_S + A_S \to 4\tau \approx 6$ fb
$\mathrm{H} \to \mathrm{Z} + A_S$	ggF$(H) \approx 1.254$ pb(at 13 TeV), $BR(H \to \mathrm{Z} + A_S) \approx 3.8\%$ ggF$(H) \to \mathrm{Z} + A_S \to \ell^+\ell^- + \mathrm{b\bar{b}} \approx 2.88$ fb
Particular signatures	$\mathrm{H} \to \mathrm{Z} + A_S$ of particular interest, could potentially use fat b-jet techniques for $A_S \to \mathrm{b\bar{b}}$

BP3: Discovery Through Stop to Electroweakinos

C.T. Potter
from Eur.Phys.J. C76 (2016) 1, 44, arXiv:1505.05554v3 [1454]

Main Features	Natural NMSSM with discovery potential at LHC13 via stop $\widetilde{\mathrm{t}}_1$ to electroweakinos: light H_S, A_S, singlino-like $\widetilde{\chi}_1^0$, wino-like $\widetilde{\chi}_3^0$
Spectrum	$M_{H_{125}} \approx 123$ GeV, $M_{H_S} \approx 55.7$ GeV, $M_{A_S} \approx 10.0$ GeV, $M_H \approx 1062$ GeV, $M_A \approx 1061$ GeV $M_{\widetilde{\mathrm{t}}_1} \approx 336$ GeV, $M_{\widetilde{\chi}_3^0} \approx 122$ GeV
Production cross sections (at 13 TeV) and branching fractions	

Stop pair production	$pp \to \bar{\tilde{t}}_1 \tilde{t}_1 \approx 5$ pb, $BR(\tilde{t}_1 \to \tilde{\chi}_2^+ + b) \approx 75\%$, $BR(\tilde{\chi}_2^+ \to \tilde{\chi}_3^0 + W^+) \approx 38\%$ $BR(\tilde{t}_1 \to \tilde{\chi}_3^0 + t) \approx 15\%$, $BR(\tilde{\chi}_3^0 \to \tilde{\chi}_1^0 + H_S) \approx 80\%$ $BR(H_S \to A_S + A_S) \approx 72\%$ $BR(A_S \to \tau^+\tau^-) \approx 80\%$, $BR(A_S \to \mu^+\mu^-) \approx 0.3\%$
Particular signatures	At least two tops and up to $4A_S$ as final states

BP4: nMSSM Scenarios

D. Barducci, G. Belanger, C. Hugonie and A. Pukhov
from JHEP 1601 (2016) 050, arXiv:1510.00246 [1455]

Main Features	nMSSM ($\kappa = 0$, not $\mathbb{Z}_3$-invariant), very light singlino-like LSP
BP4_1	
Spectrum	$M_{H_{125}} \approx 122$ GeV, $M_{H_S} \approx 37$ GeV, $M_{A_S} \approx 7$ GeV, $M_H \approx 2.1$ TeV, $M_A \approx 2.1$ TeV, $M_{\tilde{\chi}_1^0} \approx 3$ GeV
Production cross sections (at 13 TeV) and branching fractions	
A_S	ggF$(A_S) \approx 117$ pb, $BR(A_S \to \tilde{\chi}_1^0\tilde{\chi}_1^0) \approx 73\%$, $BR(A_S \to \tau^+\tau^-) \approx 25\%$
H_S	ggF$(H_S) \approx 13$ pb, $BR(H_S \to b\bar{b}) \approx 85\%$, $BR(H_S \to \tau^+\tau^-) \approx 7\%$, $BR(H_S \to \tilde{\chi}_1^0\tilde{\chi}_1^0) \approx 7\%$
H_{125}	$BR(H_{125} \to A_S A_S) \approx 9\%$, $BR(H_{125} \to \tilde{\chi}_1^0\tilde{\chi}_1^0) \approx 12\%$
Particular signatures	Two additional light Higgs states A_S and H_S can be visible A_S potentially visible in H_{125} decays
BP4_2	
Spectrum	$M_{H_{125}} \approx 122$ GeV, $M_{H_S} \approx 44$ GeV, $M_H \approx 2.4$ TeV, $M_{A_S} \approx 7$ GeV, $M_A \approx 2.4$ TeV, $M_{\tilde{\chi}_1^0} \approx 3$ GeV
Production cross sections (at 13 TeV) and branching fractions	
A_S	ggF$(A_S) \approx 116$ pb, $BR(A_S \to \tilde{\chi}_1^0\tilde{\chi}_1^0) \approx 73\%$, $BR(A_S \to \tau^+\tau^-) \approx 25\%$
H_S	ggF$(H_S) \approx$1.7 pb, $BR(H_S \to b\bar{b}) \approx 66\%$, $BR(H_S \to \tau^+\tau^-) \approx 6\%$, $BR(H_S \to A_S A_S) \approx 26\%$
H_{125}	$BR(H_{125} \to H_S H_S) \approx 8\%$, $BR(H_{125} \to \tilde{\chi}_1^0\tilde{\chi}_1^0) \approx 13\%$
Particular signatures	Two additional light Higgs states A_S and H_S can be visible H_S potentially visible in H_{125} decays

BP5: Light Singlino LSPs

U. Ellwanger and A. M. Teixeira
from JHEP 1410 (2014) 113, arXiv:1406.7221 [1344] and JHEP 1504 (2015) 172, arXiv:1412.6394 [1456]

BP5_1	

Main Features	Light singlino-like LSP, all sparticle decay cascades end with $\widetilde{\chi}_2^0 \to \widetilde{\chi}_1^0 + H_{125}$, the LSP carries little $E_{\mathrm{T}}^{\mathrm{miss}}$
Spectrum	$M_{H_{125}} \approx 125$ GeV, $M_{H_S} \approx 91.8$ GeV, $M_{\widetilde{\chi}_1^0} \approx 3.3$ GeV, $M_{\widetilde{\chi}_2^0} \approx 130$ GeV, $M_{\mathrm{squarks}} \approx 1.5$ TeV, $M_{\widetilde{\mathrm{g}}} \approx 1.3$ TeV, $M_{\widetilde{\mathrm{t}}} \approx 2$ TeV
Production cross sections (at 13 TeV) and branching fractions	
Squark + gluino production	Jets + $H_{125} + H_{125} \to$ Jets + $2\mathrm{b\overline{b}}$: 63.1 fb Jets + $H_{125} + H_{125} \to$ Jets + $\mathrm{b\overline{b}} + \tau^+\tau^-$: 13.9 fb Jets + $H_{125} + H_{125} \to$ Jets + $\gamma\gamma + X$: 0.8 fb
Particular signatures	Hard jets, little $E_{\mathrm{T}}^{\mathrm{miss}}$, invariant masses of $\mathrm{b\overline{b}}$, $\tau^+\tau^-$, $\gamma\,\gamma$ peak at 125 GeV
BP5_2	
Main Features	Light singlino-LSP, all sparticle decay cascades end with $\widetilde{\chi}_2^0 \to \widetilde{\chi}_1^0 + H_S$, the LSP carries little $E_{\mathrm{T}}^{\mathrm{miss}}$
Spectrum	$M_{H_{125}} \approx 125$ GeV, $M_{H_S} \approx 82.3$ GeV, $M_{\widetilde{\chi}_1^0} \approx 5.3$ GeV, $M_{\widetilde{\chi}_2^0} \approx 88.7$ GeV, $M_{\mathrm{squarks}} \approx 1.1$ TeV, $M_{\widetilde{\mathrm{g}}} \approx 900$ GeV, $M_{\widetilde{\mathrm{t}}} \approx 2$ TeV
Production cross sections (at 13 TeV) and branching fractions	
Squark + gluino production	Jets + $H_S + H_S \to$ Jets + $2\mathrm{b\overline{b}}$: 1.341 pb Jets + $H_S + H_S \to$ Jets + $\mathrm{b\overline{b}} + \tau^+\tau^-$: 272 fb Jets + $H_S + H_S \to$ Jets + $\gamma\gamma + X$: 3.7 fb
Particular signatures	Hard jets, little $E_{\mathrm{T}}^{\mathrm{miss}}$, invariant masses of $\mathrm{b\overline{b}}$, $\tau^+\tau^-$, $\gamma\,\gamma$ peak at ≈ 82 GeV

BP6: Light Singlino LSP and Singlet-like Pseudoscalar, good Relic Density

C. Han, D. Kim, S. Munir and M. Park
from JHEP 1507 (2015) 002, arXiv:1504.05085 [1457]

Main Features	Good relic density, light singlino-like LSP, singlet-like pseudoscalar, can be probed at the 14 TeVLHC in the di-muon decay channel
Spectrum	$M_{H_{125}} \approx 123.7$ GeV, $M_{H_S} \approx 14.8$ GeV, $M_{A_S} \approx 3.0$ GeV, $M_H \approx 1504$ GeV, $M_A \approx 1504$ GeV, $M_{\widetilde{\chi}_1^0} \approx 1.34$ GeV, $M_{\widetilde{\chi}_2^0} \approx 131.7$ GeV, $M_{\widetilde{\chi}_3^0} \approx 166.8$ GeV, $M_{\widetilde{\chi}_1^\pm} \approx 147.2$ GeV
Production cross sections (at 14 TeV) and branching fractions	
$\widetilde{\chi}^0{}_{2,3} + \widetilde{\chi}_1^\pm$ production	$\mathrm{pp} \to \widetilde{\chi}^0{}_{2,3} + \widetilde{\chi}_1^\pm \to A_S + \widetilde{\chi}_1^0 + \mathrm{W}^\pm + \widetilde{\chi}_1^0$ $\to \mu^+\mu^- + \widetilde{\chi}_1^0 + \ell^\pm + \nu_l + \widetilde{\chi}_1^0$: 3.16 fb After cuts: 0.126 fb, 38 events/300 fb^{-1}, S/B ≈ 8
Particular signatures	significance via A_S much larger than in standard trilepton channel

BP7: Natural NMSSM and Cascade Higgs-to-Higgs Decays	
S.F. King, M. Muhlleitner, R. Nevzorov and K. Walz from N.P. B870 (2013) 323, arXiv:1211.5074 [1340] and Phys.Rev. D90 (2014) 9, 095014, arXiv:1408.1120 [1346]	
BP7_1	
Main Features	natural NMSSM: overall light Higgs spectrum testable at LHC13
Spectrum	$M_{H_{125}} \approx 124.4$ GeV, $M_{H_S} \approx 95.6$ GeV, $M_{A_S} \approx 108$ GeV, $M_H \approx 299$ GeV, $M_A \approx 298$ GeV
Production cross sections (at 13 TeV) and branching fractions	
ggF(H_S):	3.34 pb, $H_S \to b\bar{b}$: 2.5 pb, $H_S \to \tau^+\tau^-$: 0.26 pb, $H_S \to \gamma\gamma$: 13 fb
ggF(H):	4.63 pb, H $\to W^+W^-$: 54.5 fb, H $\to$ ZZ: 24.2 fb
ggF(H) $\to$ ZA_S	$\to$ Z + $b\bar{b}$: 614 fb, $\to$ Z + $\tau^+\tau^-$: 64.2 fb, $\to$ Z + $\gamma\gamma$: 0.48 fb
ggF(H) $\to H_S H_S$	$\to 4b$: 310 fb, $\to b\bar{b} + \tau\tau$: 63.7 fb, $\to 4\tau$: 3.27 fb, $\to b\bar{b} + \gamma\gamma$: 3.21 fb
ggF(H) $\to H_{125} H_S$	$\to 4b$: 187 fb, $\to b\bar{b} + \tau\tau$: 39.4 fb, $\to 4\tau$: 2.08 fb, $\to b\bar{b} + \gamma\gamma$: 1.63 fb
ggF(H) $\to \tilde{\chi}\tilde{\chi}$	$\to \tilde{\chi}_1^0\tilde{\chi}_1^0$: 1662 fb, $\to \tilde{\chi}_1^0\tilde{\chi}_2^0$: 336 fb, $\to \tilde{\chi}_2^0\tilde{\chi}_2^0$: 575 fb, $\to \tilde{\chi}_1^+\tilde{\chi}_1^-$: 195 fb
ggF(A_S)	2.41 pb, $A_S \to b\bar{b}$: 2.1 pb, $H_S \to \tau^+\tau^-$: 0.22 pb, $H_S \to \gamma\gamma$: 1.63 fb
ggF(A)	11.18 pb, A $\to b\bar{b}$: 57.5 fb, A $\to \tau^+\tau^-$: 7.43 fb
ggF(A) $\to H_S A_S$	$\to 4b$: 878 fb, $\to b\bar{b} + \tau\tau$: 182 fb, $\to 4\tau$: 9.44 fb, $\to b\bar{b} + \gamma\gamma$: 5.23 fb
ggF(A) $\to H_{125} A_S$	$\to 4b$: 703 fb, $\to b\bar{b} + \tau\tau$: 149 fb, $\to 4\tau$: 7.93 fb, $\to b\bar{b} + \gamma\gamma$: 3.04 fb
ggF(A) $\to$ ZH_S	$\to$ Z + $b\bar{b}$: 392 fb, $\to$ Z + $\tau\tau^+$: 40.3 fb, $\to$ Z + $\gamma\gamma$: 2.03 fb
ggF(A) $\to \tilde{\chi}\tilde{\chi}$	$\to \tilde{\chi}_1^0\tilde{\chi}_1^0$: 3.7 pb, $\to \tilde{\chi}_1^0\tilde{\chi}_2^0$: 2.8 pb, $\to \tilde{\chi}_2^0\tilde{\chi}_2^0$: 1.0 pb, $\to \tilde{\chi}_1^+\tilde{\chi}_1^-$: 3.1 pb
Particular signatures	Large Higgs-to-Higgs, Higgs-to-gauge+Higgs boson decay rates
BP7_2	
Main Features	cascade Higgs-to-Higgs boson decays, spectacular signatures
Spectrum	$M_{H_{125}} \approx 126.6$ GeV, $M_{H_S} \approx 172$ GeV, $M_{A_S} \approx 85.9$ GeV, $M_H \approx 316.8$ GeV, $M_A \approx 306.7$ GeV
Production cross sections (at 13 TeV) and branching fractions	
ggF(H_S)	90 fb, $\to b\bar{b}$: 6.15 fb, $\to \tau^+\tau^-$: 0.69 fb, $\to$ WW: 61.5 fb, $\to$ ZZ: 1.7 fb
ggF(H_S) $\to A_S A_S$	$\to 4b$: 13.3 fb, $\to b\bar{b} + \tau\tau$: 1.82 fb, $\to b\bar{b} + \gamma\gamma$: 4.12 fb, $\to 4\gamma$: 0.32 fb
ggF(H)	3 pb, $\to b\bar{b}$: 165 fb, $\to \tau^+\tau^-$: 21.4 fb, $\to$ WW: 91.6 fb, $\to$ ZZ: 41.1 fb
ggF(H) $\to \tilde{\chi}\tilde{\chi}$	$\to \tilde{\chi}_1^0\tilde{\chi}_1^0$: 391 fb, $\to \tilde{\chi}_1^+\tilde{\chi}_1^-$: 337 fb
ggF(H) $\to H_{125} H_S$	$\to b\bar{b} + 4\gamma$: 2.41 fb, $\to 4b + 2\gamma$: 29.7 fb, $\to \tau\tau + 4\gamma$: 0.25 fb,

$\to H_{125} + A_S + A_S$	$\to 4\tau + \gamma\gamma$: 0.21 fb, $\to 6\gamma$: 0.012 fb, $\to b\bar{b} + \tau\tau + \gamma\gamma$: 5.15 fb
ggF(H) $\to H_{125}H_{125}$	$\to 4b$: 203.7 fb, $\to b\bar{b} + \gamma\gamma$: 2.14 fb, $\to \tau\tau + \gamma\gamma$: 0.23 fb
ggF(H) $\to A_S A_S$	$\to 4b$: 6.78 fb, $\to b\bar{b} + \gamma\gamma$: 2.10 fb, $\to 4\gamma$: 0.16 fb
ggF(A_S)	7.71 fb, $\to b\bar{b}$: 6.25 fb, $\to \tau^+\tau^-$: 0.43 fb, $\to \gamma\gamma$: 0.97 fb
ggF(A)	8.80 pb, $\to b\bar{b}$: 289.4 fb, $\to \tau^+\tau^-$: 36.9 fb
ggF(A) $\to \widetilde{\chi}\widetilde{\chi}$	$\to \widetilde{\chi}_1^0\widetilde{\chi}_1^0$: 3.46 pb, $\to \widetilde{\chi}_1^+\widetilde{\chi}_1^-$: 997 fb
ggF(A) $\to H_S A_S$ $\to A_S A_S A_S$	$\to 6\gamma$: 0.68 fb, $\to b\bar{b} + 4\gamma$: 13.1 fb, $\to 4b + \gamma\gamma$: 84.8 fb $\to \tau\tau + 4\gamma$: 0.90 fb, $\to b\bar{b} + \tau\tau + \gamma\gamma$: 11.6 fb, $\to 4\tau + \gamma\gamma$: 0.40 fb
ggF(A) $\to H_{125}A_S$	$\to 4b$: 210 fb, $\to b\bar{b} + \gamma\gamma$: 33.6 fb, $\to \tau\tau + \gamma\gamma$: 3.51 fb
ggF(A) $\to$ ZH_S $\to b\bar{b} + A_S + A_S$	$\to b\bar{b} + 4\gamma$: 0.97 fb, $\to 4b + \gamma\gamma$: 12.5 fb, $\to b\bar{b} + \tau\tau + \gamma\gamma$: 0.85 fb
ggF(A) $\to$ ZH_S $\to \ell\ell/\tau\tau + A_S + A_S$	$\to \ell\ell/\tau\tau + 4\gamma$: 0.21 fb, $\to \ell\ell/\tau\tau + b\bar{b} + \gamma\gamma$: 2.78 fb, $\to \ell\ell/\tau\tau + \tau\tau + \gamma\gamma$: 0.19 fb
Particular signatures	Cascade Higgs-to-Higgs boson decays lead to multi-photon and multi-fermion final states

BP8: Light Higgs Spectrum, Higgs-to-Higgs Decays

C. Beskidt, W. de Boer, D. Kazakov and S. Wayand
from Phys.Lett. B759 (2016) 141-148, arXiv:1602.08707 [1458]

BP8_1

Main Features	Light Higgs spectrum with heavier Higgs bosons just above $t\bar{t}$ threshold, so main decay into $t\bar{t}$ (absent in CMSSM)
Spectrum	$M_{H_{125}} \approx 125.2$ GeV, $M_{H_S} \approx 100.0$ GeV, $M_{A_S} \approx 300.0$ GeV, $M_H \approx 450.0$ GeV, $M_A \approx 444.9$ GeV
Production cross sections (at 14 TeV) and branching fractions	
ggF(H_S)	0.42 pb, $\to b\bar{b}$: 0.38 pb, $\to \tau^+\tau^-$: 0.040 pb
ggF(H)	1.44 pb, $\to t\bar{t}$: 0.79 pb, $\to$ WW: 2.20 fb, $\to$ ZZ: 1.04 fb
ggF(H) $\to H_{125}H_S$	366 fb
ggF(H) $\to A_S$Z	18.7 fb
ggF(H) $\to \widetilde{\chi}\widetilde{\chi}$	$\to \widetilde{\chi}_1^0\widetilde{\chi}_1^0$: 117 fb, $\to \widetilde{\chi}_1^0\widetilde{\chi}_2^0$: 10.6 fb, $\to \widetilde{\chi}_1^0\widetilde{\chi}_3^0$: 59.9 fb, $\to \widetilde{\chi}_1^+\widetilde{\chi}_1^-$: 26.7 fb
ggF(A_S)	102 fb, $\to b\bar{b}$: 14.6 fb, $\to \tau^+\tau^-$: 1.86 fb
ggF(A_S) $\to H_S$Z	85 fb
ggF(A)	3.38 pb, $\to t\bar{t}$: 2.16 pb, $\to b\bar{b}$: 20.7 fb, $\to \tau^+\tau^-$: 2.72 fb
ggF(A) $\to H_S$Z	436 fb
ggF(A) $\to \widetilde{\chi}\widetilde{\chi}$	$\to \widetilde{\chi}_1^0\widetilde{\chi}_1^0$: 407 fb, $\to \widetilde{\chi}_1^+\widetilde{\chi}_1^-$: 111 fb

Particular signatures	H, A produced simultaneously, decay mostly into $\mathrm{t\bar{t}} \rightarrow$ large fraction of $\mathrm{t\bar{t}}$ final states, $\rightarrow$ search for broad bump around 450 GeV in tail of $\mathrm{t\bar{t}}$ invariant mass spectrum, A_S decays largely into $\mathrm{Z} + H_S$ $\rightarrow$ events with two Z bosons and H_S of 100 GeV with practically SM decay modes

BP8_2

Main Features	Light Higgs spectrum, can be tested at LHC14, Higgs-to-Higgs boson decays
Spectrum	$M_{H_{125}} \approx 125.2$ GeV, $M_{H_S} \approx 100.0$ GeV, $M_{A_S} \approx 300$ GeV, $M_H \approx 350$ GeV, $M_A \approx 342$ GeV
Production cross sections (at 14 TeV) and branching fractions	
ggF(H_S)	0.55 pb, $\rightarrow \mathrm{b\bar{b}}$: 0.50 pb, $\rightarrow \tau^+\tau^-$: 0.052 pb
ggF(H)	2.77 pb, $\rightarrow \mathrm{b\bar{b}}$: 97 fb, $\rightarrow \tau^+\tau^-$: 12.7 fb, $\rightarrow$ WW: 29.8 fb, $\rightarrow$ ZZ: 13.7 fb
ggF(H) $\rightarrow H_{125}H_S$	1.88 pb
ggF(H) $\rightarrow H_SH_S$	169 fb
ggF(H) $\rightarrow \widetilde{\chi}\widetilde{\chi}$	$\rightarrow \widetilde{\chi}_1^0\widetilde{\chi}_1^0$: 205 fb, $\rightarrow \widetilde{\chi}_1^+\widetilde{\chi}_1^-$: 147.6 fb
ggF(A_S)	61 fb
ggF(A_S) $\rightarrow H_S$Z	0.2 fb
ggF(A_S) $\rightarrow \widetilde{\chi}\widetilde{\chi}$	$\rightarrow \widetilde{\chi}_1^0\widetilde{\chi}_1^0$: 60.8 fb
ggF(A)	11.14 pb, $\rightarrow \mathrm{b\bar{b}}$: 325 fb, $\rightarrow \tau^+\tau^-$: 41.0 fb,
ggF(A) $\rightarrow H_S$Z	5.50 pb
ggF(A) $\rightarrow \widetilde{\chi}\widetilde{\chi}$	$\rightarrow \widetilde{\chi}_1^0\widetilde{\chi}_1^0$: 3.97 pb, $\rightarrow \widetilde{\chi}_1^0\widetilde{\chi}_2^0$: 40.1 fb, $\rightarrow \widetilde{\chi}_1^+\widetilde{\chi}_1^-$: 1.17 fb
Particular signatures	H, A produced simultaneously, H decays mostly (68%) into $H_{125}H_S$, A decays (49%) into $H_S + \mathrm{Z}$ remaining decay modes mostly into gauginos

BP9: Singlino-Like and Bino-Like LSP Scenario

N. Christensen, T. Han, Z. Liu and S. Su

from JHEP 1308 (2013) 019, arXiv:1303.2113 [1459] and JHEP 1408 (2014) 093, arXiv:1406.1181 [1460]

BP9_1

Main Features	≈ 30 GeV singlino-like LSP (good DM candidate), two singlet-like Higgs states below 100 GeV decay mainly into $\mathrm{b\bar{b}}$, H_{125} can decay into H_SH_S with $\gtrsim 10\%$ BR
Spectrum	$M_{H_{125}} \approx 126$ GeV, $M_{H_S} \approx 19.1$ GeV, $M_{A_S} \approx 73.2$ GeV, $M_{\widetilde{\chi}_1^0} \approx 36.7$ GeV, $M_H \approx 2340$ GeV, $M_A \approx 2340$ GeV
Production cross sections and branching fractions	

H_{125}	$BR(H_{125} \to H_S H_S) \approx 13\%$, $BR(H_{125} \to \widetilde{\chi}_1^0 \widetilde{\chi}_1^0) \approx 1\%$
H_S	$BR(H_S \to b\bar{b}) \approx 89\%$, $BR(H_S \to \tau^+\tau^-) \approx 7.7\%$
A_S	$BR(A_S \to b\bar{b}) \approx 90\%$, $BR(A_S \to \tau^+\tau^-) \approx 9.4\%$
BP9_2	
Main Features	≈ 30 GeV bino-like LSP (good DM candidate), one singlet-like Higgs state below 100 GeV, decays mainly into $b\bar{b}$. H_{125} can decay into $\widetilde{\chi}_1^0 \widetilde{\chi}_1^0$ with $\approx 10\%$ BR
Spectrum	$M_{H_{125}} \approx 125$ GeV, $M_{H_S} \approx 430$ GeV, $M_{A_S} \approx 65.7$ GeV, $M_{\widetilde{\chi}_1^0} \approx 32.3$ GeV, $M_H \approx 2480$ GeV, $M_A \approx 2480$ GeV
Production cross sections (at 14 TeV) and branching fractions	
H_{125}	$BR(H_{125} \to \widetilde{\chi}_1^0 \widetilde{\chi}_1^0) \approx 10\%$
H_S	ggF$(H_S) \approx 0.90$ fb, $BR(H_S \to t\bar{t}) \approx 1.8\%$, $BR(H_S \to WW) \approx 5.7\%$, $BR(H_S \to ZZ) \approx 2.7\%$
$H_S \to A_S\, A_S$	$BR(H_S \to A_S\, A_S) \approx 85\%$
$H_S \to H_{125}\, H_{125}$	$BR(H_S \to H_{125}\, H_{125}) \approx 3.5\%$
A_S	$BR(A_S \to b\bar{b}) \approx 88\%$, $BR(A_S \to \tau^+\tau^-) \approx 9.0\%$, $BR(A_S \to \widetilde{\chi}_1^0 \widetilde{\chi}_1^0) \approx 2.7\%$

Chapter IV.6

Exotic Higgs Decays

S. Bressler, S. Gori, A. Mohammadi, J. Shelton (Eds.) F. Bishara, L. Caminada, R. Caminal Armadans, D. Curtin, G. Isidori, Z. Liu, V.I. Martinez Outschoorn, M. Neubert, K. Nikolopoulos, T. Orimoto, M. Pelliccioni, F. Petriello, M.J. Strassler, R. Teixeira de Lima, M. Trott, J. Zupan

IV.6.1 Introduction and motivation

As the program to characterize the properties of the observed Standard Model (SM)-like Higgs boson advances, one of the major new discovery opportunities it offers is potential new physics (NP) revealed in the Higgs boson's rare and exotic decays. For any newly-discovered particle, a comprehensive characterization of its decay modes is imperative; rare decays of SM particles are prime places to search for signs of new physics, and the Higgs boson is no exception. It is worth emphasizing, however, that among the SM particles the Higgs is unique in its sensitivity to new physics. The tiny SM width of the Higgs, $\Gamma(h) = 4.08\,\mathrm{MeV} \pm 3.9\%$ [9] for a $m_h = 125.09$ GeV Higgs boson [6], combined with the ease with which the Higgs can couple to physics beyond the SM (BSM), make exotic decays of the SM Higgs a natural and often leading signature of a broad class of theories of physics beyond the SM. Within the SM, the observation of rare exclusive decay modes involving mesons would provide either confirmation or disproof of the SM origin of mass for light quarks, which would otherwise remain out of reach at the LHC. This chapter discusses both these *rare* decays to exclusive mesonic final states as well as *exotic* decays involving on-shell BSM particles.

Run 1 measurements of the discovered Higgs boson properties limit the exotic branching fraction of the Higgs boson to be $\mathrm{Br}(h \to \mathrm{BSM}) < 34\%$ at 95% confidence level [6] assuming that $\kappa_V \leq 1$, but allowing for the potential influence of new physics on the Higgs boson couplings with gluons and photons, κ_g, κ_γ. Thus substantial potential branching fractions of the Higgs to new BSM particles are allowed by current data. The anticipated LHC data set, 3000 fb^{-1} at 13 TeV, will contain $\mathcal{O}(10^8)$ Higgs bosons, allowing branching ratios as small as $\lesssim 10^{-7}$ to be probed, given a sufficient detection efficiency as well as sufficient separation between the signal and the standard model background. For exotic decays, this enormous sample of Higgs bosons translates into potential sensitivity to very small Higgs-BSM couplings: e.g., for a fermionic state, an effective Yukawa coupling of order 10^{-3} smaller than the bottom Yukawa, and for a vector boson, a loop-induced coupling of order 10^{-2} times the effective coupling of the Higgs to gluon pairs. For rare SM Higgs boson decays, this data set offers the prospect of measuring many exclusive decay modes such as $h \to J/\Psi\gamma$, $h \to \rho\gamma$, and $h \to \phi\gamma$, for which the predicted SM branching fractions are $\mathcal{O}(10^{-5} - 10^{-6})$. This program builds on the pioneering Run 1 searches for $h \to J/\Psi\gamma$ [1461, 1462], which were for the first time able to exclude couplings of the Higgs to charm quarks at the level of 220 times the SM charm Yukawa coupling [1463], and extends it to yield insights into the strange, up, and down Yukawas, which have remained almost entirely untested to date.

Exotic Higgs boson decays are a generic prediction of many well-motivated theories of physics beyond the SM. They occur frequently in theories with extended Higgs sectors, as demanded by (e.g.) the NMSSM [1464–1469] or theories with a first-order electroweak phase transition [1295, 1470]; in models of dark matter [1282, 1471–1474]; in theories of neutral naturalness [1475–1477]; and, more broadly, represent a generic signature of physics beyond the Standard Model [1478, 1479]. In many cases, e.g. [1471, 1474, 1476–1478], exotic Higgs boson decays together with $\mathcal{O}(5\%)$ deviations in Higgs boson properties may be the *only* observable signal of new physics at the LHC.

In this chapter, we first cover rare exclusive mesonic decays of the Higgs boson in Section IV.6.2.

We give recommendations for predicted SM branching ratios for these modes, present the predictions of a broad set of NP models that give rise to enhanced mesonic branching ratios, and discuss experimental prospects. Next, we present our overarching recommendations for a successful search program for exotic Higgs boson decays at the LHC in Section IV.6.3. In Section IV.6.4, we discuss the decay topology $h \to XX \to 2Y2Y'$ where X is a NP particle and Y, Y' are SM particles. In particular, we study the kinematics of this final state as realized in the prototypical decay $h \to aa \to 4b$, compare predictions from different Monte Carlo generators, and highlight the relatively low p_T objects in the final state; these studies provide a guide for trigger and analysis strategies for decays with this overall topology. In Section IV.6.5, we focus on prompt Higgs boson decays containing missing energy, and perform a sensitivity study for Higgs boson decays into two (resonant or non-resonant) photons plus missing energy. This study provides a careful examination of the interplay of different possible trigger and reconstruction strategies for decays of the Higgs to electroweak objects in combination with missing energy. Finally, in Section IV.6.6, we discuss theoretical motivations and experimental prospects for searches for displaced Higgs boson decays, together with recommendations for presenting results in such searches.

IV.6.2 Exclusive mesonic and flavour-violating Higgs boson decays

Rare exclusive decays of the SM-like Higgs boson to mesonic final states provide a unique window onto light quark Yukawa couplings. We discuss the SM predictions for the branching ratio for Higgs boson decays into a meson plus a photon in Section IV.6.2.a and for Higgs boson decay to a meson plus a massive gauge boson in Section IV.6.2.b. In Section IV.6.2.c we summarize the impact of different frameworks for physics beyond the SM on these exclusive branching ratios, and in Section IV.6.2.d we discuss prospects for their detection at the LHC.

IV.6.2.a Theoretical predictions: photon plus a meson [IV.29]

The SM predictions that the Higgs boson couplings to heavy gauge bosons and fermions are given by $2m_{W,Z}^2/v$ and m_f/v, where $v \approx 246\,\text{GeV}$ is the Higgs vacuum expectation value, have been confirmed within experimental uncertainties for the W and Z bosons and for the third-generation fermions. However, no direct measurements of the Higgs boson couplings to the light fermions of the first two generations are available at present. As discussed in Section IV.6.2.c of this report, in several BSM models these couplings can deviate significantly from those predicted in the SM. Indeed, this is a generic prediction in many models trying to explain the hierarchies seen in the spectrum of fermion masses and mixing angles. Probing the Higgs boson couplings to light fermions is thus of paramount importance. This includes both flavour-diagonal and flavour-changing interactions.

The measurement of the rare exclusive decays $h \to M\gamma$, where M denotes a vector meson, would allow a unique probe of the Higgs boson coupling to light quarks at the LHC. While the absolute value of the bottom-quark Yukawa coupling can be accessed by measuring b-tagged jets in the associated production of the Higgs boson with a W or Z boson, this method becomes progressively more difficult for the lighter-quark couplings. Advanced charm-tagging techniques may allow some access to the charm-quark Yukawa coupling [1480], but no other way of directly measuring even lighter-quark couplings is currently known. The tiny branching ratios for these exclusive decays renders them inaccessible at future e^+e^- colliders. The program of measuring these decay modes is therefore only a possibility for the LHC and future hadron-collider facilities.

The possibility of measuring rare exclusive Higgs boson decays was first pointed out in [1481, 1482] and in more modern discussions in [1483, 1484], and the theoretical framework for their prediction was further developed in [1485–1487]. Our discussion follows closely the techniques introduced in Refs. [1483–1487], and we only summarize the salient features here. We begin our discussion of the

[IV.29] *Author(s): M. Neubert, F. Petriello.*

theoretical predictions for these modes by introducing the effective Yukawa Lagrangian

$$\mathcal{L} = -\sum_q \kappa_q \frac{m_q}{v} H\,\bar{q}_L q_R - \sum_{q\neq q'} \frac{y_{qq'}}{\sqrt{2}} H\,\bar{q}_L q'_R + h.c.\,, \tag{IV.6.1}$$

where in the SM $\kappa_q = 1$ while the flavour-changing Yukawa couplings $y_{qq'}$ vanish. The effective Lagrangian leads to two categories of exclusive Higgs boson decays: flavour-conserving decays involving the κ_q couplings, where $M = \rho, \omega, \phi, J/\psi, \Upsilon(nS)$, and flavour-violating decays involving the $y_{qq'}$ couplings, where $M = B_s^{*0}, B_d^{*0}, K^{*0}, D^{*0}$. In view of the very strong indirect bounds on flavour off-diagonal Higgs boson couplings to light quarks [1488], the flavour-violating decays $h \to M\gamma$ are bound to be very strongly suppressed. We will therefore restrict our discussion here to flavour-conserving processes.

The exclusive decays $H \to M\gamma$ are mediated by two distinct mechanisms, which interfere destructively.

- In the *indirect process*, the Higgs boson decays (primarily through loops involving heavy top quarks or weak gauge bosons) to a real photon γ and a virtual γ^* or Z^* boson, which then converts into the vector meson M. This contribution only occurs for the flavour-conserving decay modes. The effect of the off-shellness of the photon and the contribution involving the $h\gamma Z^*$ coupling are suppressed by m_M^2/m_h^2, with m_M the mass of the meson, and hence are very small [1487].
- In the *direct process*, the Higgs boson decays into a quark and an antiquark, one of which radiates off a photon. This process introduces the dependence of the decay amplitude on the κ_q parameters. The formation of the vector meson out of the quark-antiquark pair involves some non-trivial hadronic dynamics.

The relevant lowest-order Feynman diagrams contributing to the direct and indirect processes are shown in Figure 279 (left-middle and right panel, respectively).

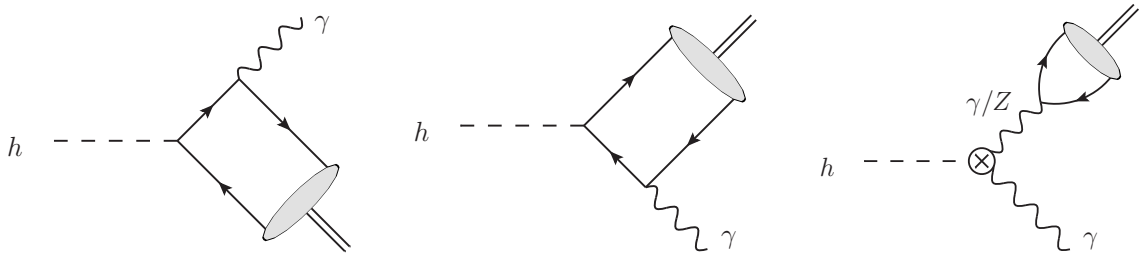

Figure 279: Direct (left and centre) and indirect (right) contributions to the $h \to M\gamma$ decay amplitude. The blob represents the non-perturbative meson wave function. The crossed circle in the third diagram denotes the off-shell $h \to \gamma\gamma^*$ and $h \to \gamma Z^*$ amplitudes, which in the SM arise first at one-loop order.

We begin by outlining the calculation of the indirect amplitude. The virtual photon or Z boson couples to the vector meson through the matrix element of a local current, which can be parameterized in terms of a single hadronic parameter: the vector-meson decay constant f_M. This quantity can be obtained directly from experimental data. In particular, the leptonic decay rate of the vector meson can be written as

$$\Gamma(M \to l^+ l^-) = \frac{4\pi Q_M^2 f_M^2}{3m_M} \alpha^2(m_M)\,, \tag{IV.6.2}$$

where Q_M is the relevant combination of quark electric charges. The effective $h\gamma\gamma^*$ and $H\gamma Z^*$ vertices, which appear in the indirect amplitude, can be calculated with high accuracy in the SM. The by far dominant contributions involve loop diagrams containing heavy top quarks or W bosons. The two-loop electroweak and QCD corrections to this amplitude are known, and when combined shift the leading one-loop expression by less than 1% for the measured value of the Higgs boson mass [1489]. However,

Table 162: Theoretical predictions for the $h \to M\gamma$ branching ratios in the SM, obtained using different theoretical approaches.

Mode	Branching Fraction $[10^{-6}]$		
Method	NRQCD [1485]	LCDA LO [1484]	LCDA NLO [1487]
$\mathrm{Br}(h \to \rho\gamma)$	–	19.0 ± 1.5	16.8 ± 0.8
$\mathrm{Br}(h \to \omega\gamma)$	–	1.60 ± 0.17	1.48 ± 0.08
$\mathrm{Br}(h \to \phi\gamma)$	–	3.00 ± 0.13	2.31 ± 0.11
$\mathrm{Br}(h \to J/\psi\,\gamma)$	–	$2.79\,^{+0.16}_{-0.15}$	2.95 ± 0.17
$\mathrm{Br}(h \to \Upsilon(1S)\,\gamma)$	$(0.61\,^{+1.74}_{-0.61}) \cdot 10^{-3}$	–	$(4.61\,^{+1.76}_{-1.23}) \cdot 10^{-3}$
$\mathrm{Br}(h \to \Upsilon(2S)\,\gamma)$	$(2.02\,^{+1.86}_{-1.28}) \cdot 10^{-3}$	–	$(2.34\,^{+0.76}_{-1.00}) \cdot 10^{-3}$
$\mathrm{Br}(h \to \Upsilon(3S)\,\gamma)$	$(2.44\,^{+1.75}_{-1.30}) \cdot 10^{-3}$	–	$(2.13\,^{+0.76}_{-1.13}) \cdot 10^{-3}$

physics beyond the SM could affect these couplings in a non-trivial way, either through modifications of the $ht\bar{t}$ and hW^+W^- couplings or by means of loops containing new heavy particles. The measurement of the light-quark couplings to the Higgs should therefore be considered together with the extraction of the effective $h\gamma\gamma$ coupling. As pointed out in [1487], by taking the ratio of the $h \to M\gamma$ and $h \to \gamma\gamma$ branching fractions one can remove this sensitivity to unknown new contributions to the $h\gamma\gamma$ coupling.

We now consider the theoretical prediction for the direct amplitude. This quantity cannot be directly related to data, unlike the indirect amplitude. Two theoretical approaches have been used to calculate this contribution. The hierarchy $m_h \gg m_M$ implies that the vector meson is emitted at very high energy $E_M \gg m_M$ in the Higgs boson rest frame. The partons making up the vector meson can thus be described by energetic particles moving collinear to the direction of M. This kinematic hierarchy allows the QCD factorization approach [1490, 1491] to be utilized. Up to corrections of order $(\Lambda_{\mathrm{QCD}}/m_h)^2$ for light mesons, and of order $(m_M/m_h)^2$ for heavy vector mesons, this method can be used to express the direct contribution to the $h \to M\gamma$ decay amplitude as a perturbatively calculable hard-scattering coefficient convoluted with the leading-twist light-cone distribution amplitude (LCDA) of the vector meson. This approach was pursued in [1487], where the full next-to-leading order (NLO) QCD corrections were calculated and large logarithms of the form $[\alpha_s \ln(m_h/m_M)]^n$ were resummed at NLO, and in [1484], where an initial LO analysis was performed. The dominant theoretical uncertainties remaining after this calculation are parametric uncertainties associated with the non-perturbative LCDAs of the vector mesons. Thanks to the high value $\mu \sim m_h$ of the factorization scale, however, the LCDAs are close to the asymptotic form $\phi_M(x,\mu) = 6x(1-x)$ attained for $\mu \to \infty$, and hence the sensitivity to not yet well-known hadronic parameters turns out to be mild. For the heavy vector mesons $M = J/\psi, \Upsilon(nS)$, the quark and antiquark which form the meson are slow-moving in the M rest frame. This allows the non-relativistic QCD framework (NRQCD) [709] to be employed to facilitate the calculation of the direct amplitude. This approach was pursued in [1485], where the NLO corrections in the velocity v of the quarks in the M rest frame, the next-to-leading order corrections in α_s, and the leading-logarithmic resummation of collinear logarithms were incorporated into the theoretical predictions. The dominant theoretical uncertainties affecting the results for $h \to J/\psi\,\gamma$ and $h \to \Upsilon(nS)\,\gamma$ after the inclusion of these corrections are the uncalculated $\mathcal{O}(v^4)$ and $\mathcal{O}(\alpha_s v^2)$ terms in the NRQCD expansion.

Table 162 collects theoretical predictions for the various $h \to M\gamma$ branching fractions in the SM. The inclusion of NLO QCD corrections and resummation help to reduce the theoretical uncertainties. There is in general good agreement between the results obtained by different groups. The $h \to \phi\gamma$

branching ratio obtained in [1487] is lower than that found in [1484] because of an update of the ϕ-meson decay constant performed in the former work. Also, in [1487] the effects of ρ–ω–ϕ mixing are taken into account. One observes that the $h \to M\gamma$ branching fractions are typically of order few times 10^{-6}, which makes them very challenging to observe. The most striking feature of the results shown in the table concerns the $h \to \Upsilon(nS)\,\gamma$ modes, whose branching fractions are very strongly suppressed. This suppression results from an accidental and almost perfect cancellation between the direct and indirect amplitudes. In the case of $h \to \Upsilon(1S)\,\gamma$ the cancellation is so perfect that the small imaginary part of the direct contribution induced by one-loop QCD corrections gives the leading contribution to the decay amplitude. The fact that this imaginary part was neglected in [1485] explains why a too small branching fraction for this mode was obtained there.

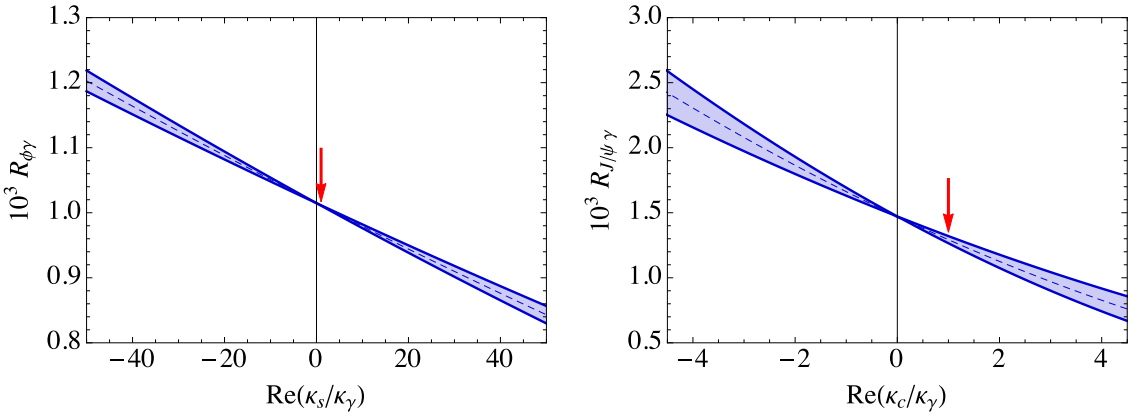

Figure 280: $h \to \phi\gamma$ and $H \to J/\psi\,\gamma$ branching ratios, normalized to the $h \to \gamma\gamma$ branching fraction, as functions of the real part of $\kappa_{s,c}/\kappa_\gamma$. The SM values are indicated by the red arrows.

The main purpose of searching for the decays $h \to M\gamma$ is to use them for probing the light-quark Yukawa couplings. In order to eliminate possible new physics effects in the $h \to \gamma\gamma$ rate, it is of advantage to consider the ratio $R_{M\gamma} = \mathrm{Br}(h \to M\gamma)/\mathrm{Br}(h \to \gamma\gamma)$ [1487], where in the SM $\mathrm{BR}(h \to \gamma\gamma) = (2.28 \pm 0.11) \cdot 10^{-3}$ [9]. In the limit where the CP-violating contributions to the $h \to \gamma\gamma$ amplitude are neglected (the dominant such contributions would likely arise from the top-quark loop, but Electric Dipole Moment (EDM) constraints limit the imaginary part of κ_t to be less than 1% [635]), one finds [1487]

$$R_{M\gamma} = \frac{8\pi\alpha^2(m_M)}{\alpha}\,\frac{Q_M^2 f_M^2}{m_M^2}\left(1 - \frac{m_M^2}{m_h^2}\right)^2 \left(\left|1 - \Delta_M\right|^2 + \left|\tilde{\Delta}_M\right|^2\right). \tag{IV.6.3}$$

The parameters Δ_M ($\tilde{\Delta}_M$) are proportional to the real (imaginary) part of the relevant κ_q parameter and can be calculated using the QCD factorization approach, as described earlier. For all mesons other than the $\Upsilon(nS)$ states the interference of the direct amplitude with the dominant indirect one is a small effect, and hence the ratio $R_{M\gamma}$ is to excellent approximation a linear function of the real part of the ratio κ_q/κ_γ, where κ_γ is the new physics modification of the entire $h \to \gamma\gamma$ matrix element. This quantity is known to be close to its SM value 1. Figure 280 shows theoretical predictions for the ratios $R_{\phi\gamma}$ and $R_{J/\psi\,\gamma}$ (times 10^3) obtained in [1487]. The width of the bands reflects the theoretical uncertainties. The corresponding predictions for the lighter mesons ρ and ω suffer from significant hadronic uncertainties due to ρ–ω–ϕ mixing.

In the case of the $h \to \Upsilon(nS)\,\gamma$ decay modes the SM branching ratios are so small that a discovery at the LHC (or any other conceivable collider) is all but elusive. The direct contributions are no longer a small correction, and hence the quadratic terms in κ_b are important. On the other hand, the almost perfect cancellation between the direct and indirect amplitudes no longer holds in the presence of new physics.

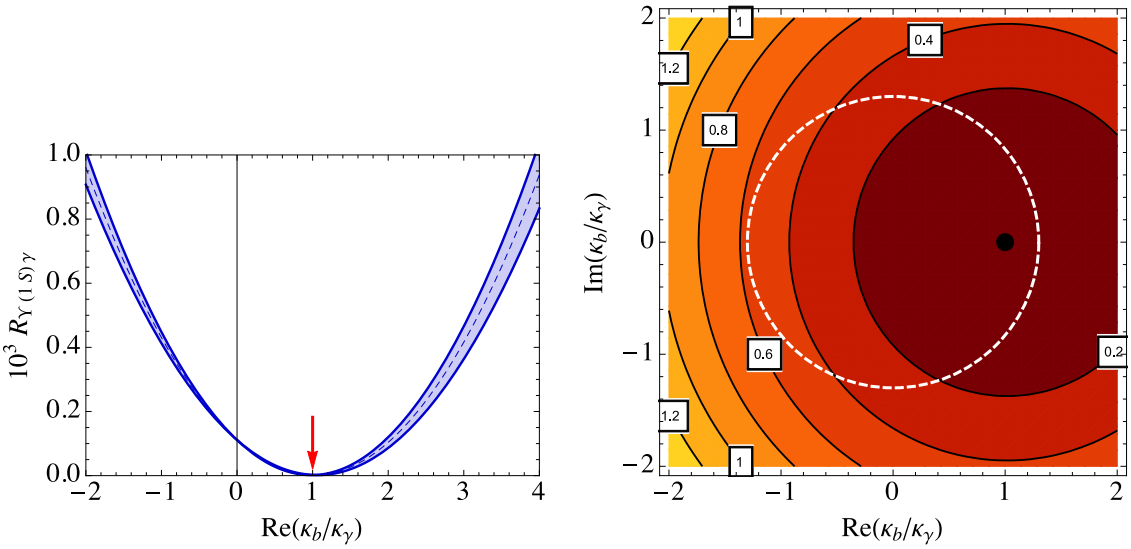

Figure 281: Ratio $R_{\Upsilon(1S)\gamma}$ as a function of the real and imaginary parts of κ_b/κ_γ. In the left plot the imaginary part is set to zero. The right plot shows contour lines of $10^3\, R_{\Upsilon(1S)\gamma}$ in the complex κ_b/κ_γ plane. The black dot and the arrow indicate the SM values. Coupling parameters inside the dashed white circle are preferred by the current LHC data on $h \to b\bar{b}$.

The left plot in Figure 281 shows the dependence of the ratio $R_{\Upsilon(1S)\gamma}$ on the real part of κ_b/κ_γ, assuming that the CP-violating imaginary part vanishes. It is evident that the SM value accidentally coincides with the minimum of the curve, while significantly larger branching fractions are possible when new physics alters the value of κ_b. As an interesting benchmark for LHC experiments, we consider the case where $\kappa_b = -1$, while κ_γ takes its SM value of 1. This benchmark is and will be in great agreement with LHC Higgs boson coupling fits, since Higgs boson coupling measurements cannot probe the sign of κ_b. We then obtain the branching fractions

$$\begin{aligned} \mathrm{Br}(h \to \Upsilon(1S)\,\gamma) &= (0.98 \pm 0.06) \cdot 10^{-6}\,, \\ \mathrm{Br}(h \to \Upsilon(2S)\,\gamma) &= (0.45 \pm 0.03) \cdot 10^{-6}\,, \qquad (\kappa_b = -1) \\ \mathrm{Br}(h \to \Upsilon(3S)\,\gamma) &= (0.33 \pm 0.03) \cdot 10^{-6}\,, \end{aligned} \tag{IV.6.4}$$

more than two orders of magnitude larger than in the SM. The right plot in Figure 281 shows contours of $10^3\, R_{\Upsilon(1S)\gamma}$ in the complex κ_b/κ_γ plane. The dashed white circle indicates the current upper bound on the combination $\lambda_{b\gamma} = |\kappa_b/\kappa_\gamma|$, which to an excellent approximation measures the deviation of the ratio $\mathrm{Br}(h \to b\bar{b})/\mathrm{Br}(h \to \gamma\gamma)$ from its SM value. The Higgs bosons must be produced via the same production mechanism in both cases, so that possible new physics effects in Higgs boson production cancel out. Since the $h \to b\bar{b}$ mode is measured at the LHC in the rare VH and $t\bar{t}H$ associated-production channels, at present no accurate direct measurements of $\lambda_{b\gamma}$ are available. However, from the model-independent global analyses of Higgs boson couplings, in which all couplings to SM particles (including the effective couplings to photons and gluons) are rescaled by corresponding κ_i parameters and also invisible Higgs boson decays are allowed, one obtains $\lambda_{b\gamma} = 0.63 \pm 0.27$ for CMS [755] and $\lambda_{b\gamma} = 0.67 \pm 0.32$ for ATLAS [754]. At 95% CL this implies $\lambda_{b\gamma} < 1.3$. Within this allowed region, the $h \to \Upsilon(1S)$ branching ratio varies by more than two orders of magnitude and can take values as large as $1.3 \cdot 10^{-6}$, which may be within reach of the high-luminosity run at the LHC.

The decays $h \to \Upsilon(nS)\,\gamma$ provide a golden opportunity to probe new-physics effects on the bottom-quark Yukawa couplings. Any measurement of such a decay would be a clear signal of new physics. A combined measurement of the two ratios $\mathrm{Br}(h \to \Upsilon(nS)\,\gamma)/\mathrm{Br}(h \to \gamma\gamma)$ and $\mathrm{BR}(h \to b\bar{b})/\mathrm{Br}(h \to \gamma\gamma)$ can provide complementary information on the real and imaginary parts of the b-quark

Yukawa coupling. We can think of no other way in which one can probe the magnitudes and signs of the real and imaginary parts of κ_b separately.

IV.6.2.b $h \to VP$ and $h \to VP^\star$ [IV.30]

In this section, we discuss decays of the form $h \to VM$ where V is a massive on-shell SM vector boson ($V = Z, W$) and M is an associated meson (vector or pseudoscalar) produced in the decay of the h particle.

We will focus on the decay of the Higgs, assuming a narrow width approximation to factorize the decay and production mechanisms. The decays we will discuss are very rare decays in the SM, with extremely small branching ratios. Despite these small rates, it is still important to search for such rare decays, to learn experimentally about the properties of the discovered h state robustly. It was pointed out in Ref. [765] that such rare exclusive decays of the h particle with an associated massive vector boson offer complementary information about the properties of this state, and how it couples to the SM fields. This information is complementary to what can be determined experimentally from more inclusive h decay modes. Reaching the experimental sensitivity required to observe such extremely rare decays, with *any* associated $V = \{\gamma, Z, W\}$, is extremely challenging but worth the effort.

Given the strong suppression of such exclusive decay modes, the theoretical predictions of the corresponding decay rates are subject to an irreducible uncertainty due to the limited knowledge of the h dominant decay modes, both within and, especially, beyond the SM. In particular, the total uncertainty in the width of the h particle (Γ_h) feeds into the uncertainty in the predicted $\mathrm{Br}(h \to i)$ as

$$\delta BR(h \to i) = \mathrm{BR(h \to i)} \left(\frac{\delta\Gamma_{h\to i}}{\Gamma_{h\to i}} + \frac{\delta\Gamma_h}{\Gamma_h} - 2\frac{\Delta_{i\,\Gamma_h}}{\Gamma_{h\to i}\Gamma_h} \right)^{1/2}, \tag{IV.6.5}$$

using simple Gaussian error propagation, where δ indicates a 1σ error. Here $\Delta_{i\,\Gamma_h}$ is the covariance of the total width and the decay channel $h \to i$. Although possible tests of the decay width—within the SM—have been proposed in the literature [499–501] and carried out by the experimental collaborations [506, 507], the corresponding constraint on the decay width does not hold in an EFT generalization of the SM [502]. Indeed, as emphasized in Ref. [502], the uncertainty in μ_{ggF} and μ_{ZZ} directly feeds into such a measurement. When we discuss theoretical uncertainties for the rare modes in Tables 163 and 164, we report theoretical uncertainties of the form $\delta\Gamma_{h\to i}/\Gamma_{h\to i}$ for the SM, added in quadrature to the total theoretical width defined as $\Gamma_h = 4.08\ \mathrm{MeV}$ with a $\pm 3.9\%$ relative error. We neglect the unknown $\Delta_{i\,\Gamma_h}$ in this estimate.

IV.6.2.b.i SM predictions, dominant electroweak dependence

The SM prediction for the decay proceeds dominantly through the diagrams shown in Figure 282. Defining the SM currents coupling to the massive vector bosons as

$$\mathcal{L}_J = \frac{e}{\sqrt{2}\,\sin\theta_W} J^\pm_\mu W^\mu_\pm + \frac{e}{\sin\theta_W \cos\theta_W} J^0_\mu Z^\mu, \tag{IV.6.6}$$

and the pseudoscalar (P) and vector meson ($P^\star$) decay constants with the following normalizations

$$\langle P(q)|J_\mu(q)|0\rangle 0 = \frac{1}{2} F_P\, q_\mu, \qquad \langle P^\star(q)|J_\mu(q)|0\rangle = \frac{1}{2} F^\star_P\, m^\star_p\, \epsilon_\mu, \tag{IV.6.7}$$

then the tree-level (Figure 282a) SM contribution is [765],

$$\mathcal{B}^{\mathrm{SM}}(h \to VP) = \frac{m_h^3\, G_F^2}{8\,\pi} \frac{|C_V F_P|^2}{(\Gamma_h)_{SM}} \lambda^3(1, \rho, \hat{q}^2), \tag{IV.6.8}$$

[IV.30] *Author(s): G. Isidori, M. Trott.*

where $C_V = \{1/\sqrt{2}, 1\}$ for the cases W and Z respectively. Here $\rho = m_V^2/m_h^2$ and $\hat{q}^2 = m_P^2/m_h^2$ and $\lambda(a,b,c) = \sqrt{a^2+b^2+c^2-2(ab+ac+bc)}$. G_F is the fermi constant and $(\Gamma_h)_{SM}$ is the SM Higgs boson decay width. The case of a decay to a vector meson through a $Z^\star$, for example $h \to J/\psi Z$, through Figure 282a gives a branching ratio [948]

$$\mathcal{B}^{\rm SM}(h \to V J/\Psi) = \frac{m_h^3\, G_F^2}{8\,\pi} \frac{\left|F^\star_{J/\Psi}\right|^2}{(\Gamma_h)_{SM}} \frac{\sqrt{\lambda(1,\rho,\hat{q}^2)}}{(1-\hat{q}^2/\rho)^2} \left[(1-\rho)^2 \left(1 - \frac{\hat{q}^2}{1-\rho}\right)^2 + 8\,\hat{q}^2\,\rho\right]. \quad \text{(IV.6.9)}$$

The tree-level contribution in Figure 282a is usually largely dominant but for the case of charmonium vector resonances (J/ψ, ψ', ...). In the latter case the accidental suppression of the Z-boson vector coupling to charm makes the formally subleading (one-loop induced) $h \to Z\,\gamma$ amplitude (Figure 282b) compete with the tree-level one [1483, 1492]. The full SM expression including this contribution and the interference term can be found in Ref. [1492][IV.31]. The SM predictions of pseudoscalar decays are given in Table 163. We use the value $C_{Z\gamma}^{SM} = -5.540$ for the Wilson coefficient of this operator, consistent with the normalization of the operator defined in Ref. [1492, 1494].

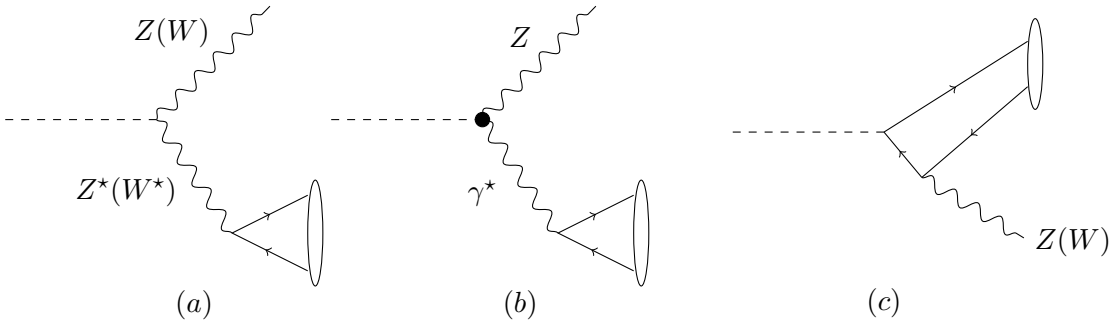

Figure 282: Direct contributions to exclusive decay modes of the form $h \to VP$ and $h \to VP^\star$. Diagram (a) is generally the dominant contribution in the SM, while diagram (b) can also contribute significantly for narrow light vector mesons. Diagram (c) is generally negligible in the SM, but can be significantly enhanced in beyond the SM scenarios.

IV.6.2.b.ii SM predictions, subdominant Yukawa dependence

In the SM branching ratios reported in Tables 163 and 164 the contribution from Figure 282c is neglected, being suppressed by a small Yukawa coupling. This is always a good approximation in the SM if the associated vector meson is a Z or a W, i.e. when there is a tree-level contribution not suppressed by small Yukawa couplings.

The Yukawa amplitude is not necessarily negligible in the radiative modes ($V = \gamma$), when the tree-level amplitude is absent. The possibility of determining this contribution in the modes $V = \gamma$ has been already discussed in. Section IV.6.2.a. However, as we briefly illustrate below, this goal is extremely challenging for the SM values of $\kappa_q = 1$, given that the Yukawa contribution is typically subleading.

New physics in the Higgs sector at some high scale can induce large deviations of the light-quark Yukawa couplings from their SM values even when the cut-off scale is parametrically greater than the electroweak scale. Indeed the corresponding amplitudes scale as

$$A(\bar{\psi}\,\psi \to W_L\,W_L) = \frac{m_\psi \sqrt{s}}{v^2}(1 - \kappa_\psi\,\kappa_W). \quad \text{(IV.6.10)}$$

[IV.31] See Ref. [1493] for the latest computation using the QCD factorization approach. A future LHC HXSWG note will contain updated predictions.

Due to the presence of a small fermion (ψ) mass scale, large deviations in κ_ψ still allow the cut-off scale of the theory to remain parametrically separated from the scale v. While such enhancements would generally occur along with other deviations in Higgs phenomenology, including deviations in the electroweak couplings present in Figure 282a and Figure 282b, some classes of BSM models can predict parametrically large enhancements to κ_ψ while leaving other Higgs boson couplings largely unaffected, as discussed in SectionIV.6.2.c. It is important to bear in mind that in BSM models which do yield large deviations in other Higgs boson couplings, the extraction of any information on the sub-leading Yukawa contribution could be out of reach.

As a specific example, consider the results quoted in Ref. [1484], and discussed in Section IV.6.2.a, for the γ-tagged decays:

$$\begin{aligned}
\frac{\mathrm{Br}(h\to\phi\,\gamma)}{\mathrm{Br}(h\to b\bar{b})} &\simeq \frac{\kappa_\gamma\left[(3.0\pm0.13)\,\kappa_\gamma-0.02\,\kappa_s\right]}{0.57\,\kappa_b^2}\times10^{-6},\\
\frac{\mathrm{Br}(h\to\rho\,\gamma)}{\mathrm{Br}(h\to b\bar{b})} &\simeq \frac{\kappa_\gamma\left[(1.9\pm0.15)\,\kappa_\gamma-1\times10^{-4}\,\kappa_u-1\times10^{-4}\,\kappa_d\right]}{0.57\,\kappa_b^2}\times10^{-5},\\
\frac{\mathrm{Br}(h\to\omega\,\gamma)}{\mathrm{Br}(h\to b\bar{b})} &\simeq \frac{\kappa_\gamma\left[(1.6\pm0.17)\,\kappa_\gamma-3\times10^{-4}\,\kappa_u-3\times10^{-4}\kappa_d\right]}{0.57\,\kappa_b^2}\times10^{-6}.
\end{aligned}\qquad \text{(IV.6.11)}$$

The only modification here compared to Ref. [1484] is to utilize κ_q factors normalized to the light quark masses, consistent with standard usage. Recall that currently $\kappa_\gamma = 0.92^{+0.12}_{-0.11}$ when Br_{BSM} is assumed to be 0 in the ATLAS/CMS coupling fit combination [6]. While enhancements of $\kappa_{s,u,d}$ by $\mathcal{O}(100)$ may thus be measurable (see Section IV.6.2.a), Eq. IV.6.11 demonstrates that a very large reduction in the uncertainties of the tree-level couplings of the h state, and the effective one-loop couplings of this state (i.e. κ_γ), would be required for these rare decays to be sensitive to light quark Yukawa couplings of $\mathcal{O}(10)$ their SM values or smaller.

IV.6.2.b.iii SM Theory errors

The dominant theoretical errors in the branching ratios are due to the lattice (or experimental) errors on the meson decay constants F_P (ranging between few % and 10%), which are combined in quadrature with the uncertainties on the elements of the Cabibbo-Kobayashi-Maskawa mixing matrix (V_{CKM}). This uncertainty is given in column three of the branching ratio tables. This theoretical error, combined with the theoretical error on the Higgs boson total width ($\sim 4\%$ [1495]) dictates the error given in the fifth column of the tables.

IV.6.2.c NP benchmarks for enhanced branching ratios [IV.32]

The Higgs boson couplings to the SM fermions, f, can differ from their SM values due to NP. We describe the size of the modification using a generalized κ framework,

$$\mathcal{L}_{\text{eff}} = -\kappa_f\frac{m_f}{v}\bar{f}fh - i\tilde{\kappa}_f\frac{m_f}{v}\bar{f}\gamma_5 fh - \left[\left(\kappa_{ff'}+i\tilde{\kappa}_{ff'}\right)\bar{f}_L f'_R h + \text{h.c.}\right], \qquad \text{(IV.6.12)}$$

where a sum over $f = t, b, c, s, d, u, \tau, \mu, e$ is understood. The first two terms are flavour-diagonal with the first term CP-conserving and the second CP-violating. The terms in square brackets are flavour violating. The real (imaginary) part of the coefficient is CP conserving (violating). In the SM, we have $\kappa_f = 1$ while $\tilde{\kappa}_f = \kappa_{ff'} = \tilde{\kappa}_{ff'} = 0$.

The Higgs boson production and decay strengths measured at the LHC constrain the flavour-diagonal CP-conserving Yukawa couplings to be [6, 1463, 1484] (for future prospects see also [1461, 1480, 1483, 1485, 1487, 1501])

$$\kappa_t = 1.43\pm0.23, \qquad \kappa_b = 0.60\pm0.18, \qquad \kappa_c \lesssim 6.2, \qquad \text{(IV.6.13)}$$

[IV.32] *Author(s): F. Bishara, J. Zupan.*

Table 163: SM branching ratios $\mathcal{B}^{\rm SM}$ for selected $h \to VP$ decays. The decay constants are defined as $F_{\pi^0} = f_\pi/\sqrt{2}$, $F_{K^\pm} = V_{us}\, f_K$ $F_{\pi^\pm} = V_{ud} f_\pi$, $F_{D^\pm} = V_{cd} f_D$, $F_{D_s} = V_{cs} f_{D_s}$, $F_{B^\pm} = V_{ub} f_B$, $F_{B_c^\pm} = V_{cb} f_B$, and $F_{\eta_c} = f_{\eta_c}/2$, where f_P are the standard meson decay constants reported in [1495–1497] for $N_f = 2+1$ (when available) and the CKM parameters are PDG values [1495]. The theoretical errors quoted are 1σ values.

VP mode	P mass	F_P	$\mathcal{B}^{\rm SM}$	Th. Error
$W^-\pi^+$	139.57018 ± 0.00035 MeV	126.6 ± 1.4 MeV	0.42×10^{-5}	±5%
W^-K^+	493.677 ± 0.016 MeV	35.2 ± 0.3 MeV	0.33×10^{-6}	±4%
$W^-D_s^+$	1968.30 ± 0.11 MeV	248.6 ± 2.4 MeV	1.6×10^{-5}	±4%
W^-D^+	1869.61 ± 0.09 MeV	47.07 ± 2.4 MeV	0.58×10^{-6}	±11%
W^-B^+	5279.29 ± 0.15 MeV	0.79 ± 0.10 MeV	1.6×10^{-10}	±26%
$W^-B_c^+$	6275.1 ± 1.0 MeV	7.82 ± 0.42 MeV	1.6×10^{-8}	±11%
$Z\pi^0$	134.9766 ± 0.0006 MeV	92.1 ± 1.0 MeV	0.23×10^{-5}	±5%
$Z\eta_c$	2984.3 ± 0.84 MeV	197.4 ± 0.30 MeV	1.0×10^{-5}	±5%

Table 164: SM branching ratios for selected $h \to VP^\star$ decays. The normalizations are defined as in the case of the pseudoscalar mesons. We use $F_B^\star/F_B = 1.02 \pm 0.08$ [1498]. The theoretical errors quoted are 1σ values. Total errors quoted at $\gtrsim 4\%$ do not have a decay constant theoretical error assigned.

$VP^\star$ mode	$P^\star$ mass	$F_P^\star/2$	$\mathcal{B}^{\rm SM}$	Th. Error
$W^-\rho^+$	775.26 ± 0.25 MeV	210 ± 5.5 MeV [1499]	1.5×10^{-5}	±6%
$W^-K^{\star+}$	891.66 ± 0.026 MeV	35.8 ± 0.3 MeV	4.3×10^{-7}	±4%
W^-D^+	2010.26 ± 0.07 MeV	61.1 ± 0.6 MeV	1.3×10^{-6}	±6%
$W^-D_s^{\star+}$	2112.1 ± 0.4 MeV	320.5 ± 3.1 MeV	3.5×10^{-5}	±6%
$W^-B^{\star+}$	5325.2 ±0.4 MeV	194.3 ± 15.8 MeV [1498]	1.3×10^{-5}	±17%
$ZJ/\Psi(1S)$	3096.916 ± 0.011 MeV	405 ± - MeV	3.2×10^{-6}	$\gtrsim 4\%$
$ZJ/\Psi(2S)$	3686.109 ± 0.013 MeV	290 ± - MeV	1.5×10^{-6}	$\gtrsim 4\%$
$Z\Upsilon(1S)$	9460.30 ± 0.26 MeV	680 ± - MeV	1.7×10^{-5}	$\gtrsim 4\%$
$Z\Upsilon(2S)$	10023.26 ± 0.31 MeV	485 ± - MeV	8.9×10^{-6}	$\gtrsim 4\%$
$Z\Upsilon(3S)$	10355.2 ± 0.5 MeV	420 ± - MeV	6.7×10^{-6}	$\gtrsim 4\%$
$Z\rho^0$	775.26 ± 0.25 MeV	216 ± 5.5 MeV [1499]	1.4×10^{-5}	±6%
$Z\omega^0$	782.65 ± 0.12 MeV	216 ± 5.5 MeV	1.6×10^{-6}	±6%
$Z\phi^0$	1019.461 ± 0.019 MeV	233 ± 5 MeV [1500]	4.2×10^{-6}	±6%

$$\kappa_s < 65, \qquad \kappa_d < 1.4 \cdot 10^3, \qquad \kappa_u < 3.0 \cdot 10^3, \tag{IV.6.14}$$

$$\kappa_\tau = 0.88 \pm 0.13, \qquad \kappa_\mu = 0.2^{+1.2}_{-0.2}, \qquad \kappa_e \lesssim 630. \tag{IV.6.15}$$

Here, $\kappa_{t,b,c,s,d,u,\tau}$ constraints have been obtained by allowing BSM particles to modify the $h \to gg$ and $h \to \gamma\gamma$ couplings, i.e. $\delta\kappa_{g,\gamma}$ were floated, while assuming that there are no new decay channels, $BR_{\rm BSM} = 0$. The $\kappa_{\mu,e}$ were required to be non-negative and, in addition, when obtaining the respective bounds, $\delta\kappa_{g,\gamma}$ were set to zero. The upper bounds on $\kappa_{c,s,d,u}$ roughly correspond to the size of the SM bottom Yukawa coupling and are thus much bigger than the corresponding SM Yukawa couplings. The upper bounds can be saturated only if one allows for large cancellations between the contribution to fermion masses from the Higgs vev and an equally large but opposite in sign contribution from NP. We will show that in models of NP motivated by the hierarchy problem, the effects of NP are generically well below these bounds.

The CP-violating flavour-diagonal Yukawa couplings, $\tilde{\kappa}_f$, are well constrained from bounds on the electric dipole moments (EDMs) [635–637] under the assumption of no other contribution to EDMs beyond the Higgs contributions. The flavour violating Yukawa couplings are well constrained by the low-energy flavour-changing neutral current measurements [1488, 1502, 1503]. A notable exception are the flavour-violating couplings involving a tau lepton. The strongest constraints on $\kappa_{\tau\mu}, \kappa_{\mu\tau}, \kappa_{\tau e}, \kappa_{e\tau}$ are thus from direct searches of flavour-violating Higgs boson decays at the LHC [1504, 1505]. This is especially interesting in light of a potential hint of a signal in $h \to \tau\mu$ [1505, 1506].

In the rest of the section we review the expected sizes of κ_i in popular models of weak scale NP, some of them motivated by the hierarchy problem. At the end of the section we also discuss the implications of a potential nonzero $\mathrm{Br}(h \to \tau\mu)$ close to the present experimental upper bound.

IV.6.2.c.i Modified Yukawa couplings and electroweak New Physics

Tables 165, 166, and 167, adapted from [1507–1511], summarize the predictions for the effective Yukawa couplings, κ_f, in the Standard Model, multi-Higgs-doublet models (MHDM) with natural flavour conservation (NFC) [1191, 1192], the MSSM at tree level, a single Higgs doublet with a Froggat-Nielsen mechanism (FN) [1512], the Giudice-Lebedev model of quark masses modified to 2HDM (GL2) [1513], NP models with minimal flavour violation (MFV) [698], Randall-Sundrum models (RS) [1514], and models with a composite Higgs where Higgs is a pseudo-Nambu-Goldstone boson (pNGB) [766, 767, 769, 1515]. The flavour-violating couplings in the above set of NP models are collected in Tables 168 and 169. Next, we briefly discuss each of the above models, and show that the effects are either suppressed by $1/\Lambda^2$, where Λ is the NP scale, or are proportional to the mixing angles with the extra scalars.

Dimension-Six Operators with Minimal Flavour Violation (MFV). We first assume that there is a mass gap between the SM and NP. Integrating out the NP states leads to dimension six operators (after absorbing the modifications of kinetic terms using equations of motion [1516]),

$$\mathcal{L}_{\rm EFT} = \frac{Y'_u}{\Lambda^2}\bar{Q}_L H^c u_R (H^\dagger H) + \frac{Y'_d}{\Lambda^2}\bar{Q}_L H d_R (H^\dagger H) + \frac{Y'_\ell}{\Lambda^2}\bar{L}_L H \ell_R (H^\dagger H) + \text{h.c.}\,, \tag{IV.6.16}$$

which correct the SM Yukawa interactions, $Y_u\bar{Q}_L H^c u_R + Y_d\bar{Q}_L H d_R + Y_\ell \bar{L}_L H \ell_R$. Here Λ is the NP scale and $H^c = i\sigma_2 H^*$. The fermion mass matrices and Yukawa couplings after EWSB are

$$M_f = \frac{v}{\sqrt{2}}\left(Y_f + Y'_f\frac{v^2}{2\Lambda^2}\right), \qquad y_f = Y_f + 3Y'_f\frac{v^2}{2\Lambda^2}\,, \qquad f = u, d, \ell\,. \tag{IV.6.17}$$

Because Y_f and Y'_f appear in two different combinations in M_f and in the physical Higgs Yukawa couplings, y_f, the two, in general, cannot be made diagonal in the same basis and will lead to flavour-violating Higgs boson couplings.

In Tables 165-168 we show the resulting κ_f assuming MFV, i.e., that the flavour breaking in the NP sector is only due to the SM Yukawas [697, 698, 1517–1521]. This gives $Y'_u = a_u Y_u + b_u Y_u Y_u^\dagger Y_u +$

Table 165: Predictions for the flavour-diagonal up-type Yukawa couplings in a sample of NP models (see text for details).

Model	κ_t	$\kappa_{c(u)}/\kappa_t$	$\tilde{\kappa}_t/\kappa_t$	$\tilde{\kappa}_{c(u)}/\kappa_t$
SM	1	1	0	0
MFV	$1+\frac{\mathrm{Re}(a_u v^2+2b_u m_t^2)}{\Lambda^2}$	$1-\frac{2\,\mathrm{Re}(b_u)m_t^2}{\Lambda^2}$	$\frac{\mathrm{Im}(a_u v^2+2b_u m_t^2)}{\Lambda^2}$	$\frac{\mathrm{Im}(a_u v^2)}{\Lambda^2}$
NFC	$V_{hu}\,v/v_u$	1	0	0
MSSM	$\cos\alpha/\sin\beta$	1	0	0
FN	$1+\mathcal{O}\left(\frac{v^2}{\Lambda^2}\right)$	$1+\mathcal{O}\left(\frac{v^2}{\Lambda^2}\right)$	$\mathcal{O}\left(\frac{v^2}{\Lambda^2}\right)$	$\mathcal{O}\left(\frac{v^2}{\Lambda^2}\right)$
GL2	$\cos\alpha/\sin\beta$	$\simeq 3(7)$	0	0
RS	$1-\mathcal{O}\left(\frac{v^2}{m_{KK}^2}\bar{Y}^2\right)$	$1+\mathcal{O}\left(\frac{v^2}{m_{KK}^2}\bar{Y}^2\right)$	$\mathcal{O}\left(\frac{v^2}{m_{KK}^2}\bar{Y}^2\right)$	$\mathcal{O}\left(\frac{v^2}{m_{KK}^2}\bar{Y}^2\right)$
pNGB	$1+\mathcal{O}\left(\frac{v^2}{f^2}\right)+\mathcal{O}\left(y_*^2\lambda^2\frac{v^2}{M_*^2}\right)$	$1+\mathcal{O}\left(y_*^2\lambda^2\frac{v^2}{M_*^2}\right)$	$\mathcal{O}\left(y_*^2\lambda^2\frac{v^2}{M_*^2}\right)$	$\mathcal{O}\left(y_*^2\lambda^2\frac{v^2}{M_*^2}\right)$

Table 166: Same as Table 165 but for down-type Yukawa couplings.

Model	κ_b	$\kappa_{s(d)}/\kappa_b$	$\tilde{\kappa}_b/\kappa_b$	$\tilde{\kappa}_{s(d)}/\kappa_b$
SM	1	1	0	0
MFV	$1+\frac{\mathrm{Re}(a_d v^2+2c_d m_t^2)}{\Lambda^2}$	$1-\frac{2\,\mathrm{Re}(c_d)m_t^2}{\Lambda^2}$	$\frac{\mathrm{Im}(a_d v^2+2c_d m_t^2)}{\Lambda^2}$	$\frac{\mathrm{Im}(a_d v^2+2c_d\lvert V_{ts(td)}\rvert^2 m_t^2)}{\Lambda^2}$
NFC	$V_{hd}\,v/v_d$	1	0	0
MSSM	$-\sin\alpha/\cos\beta$	1	0	0
FN	$1+\mathcal{O}\left(\frac{v^2}{\Lambda^2}\right)$	$1+\mathcal{O}\left(\frac{v^2}{\Lambda^2}\right)$	$\mathcal{O}\left(\frac{v^2}{\Lambda^2}\right)$	$\mathcal{O}\left(\frac{v^2}{\Lambda^2}\right)$
GL2	$-\sin\alpha/\cos\beta$	$\simeq 3(5)$	0	0
RS	$1-\mathcal{O}\left(\frac{v^2}{m_{KK}^2}\bar{Y}^2\right)$	$1+\mathcal{O}\left(\frac{v^2}{m_{KK}^2}\bar{Y}^2\right)$	$\mathcal{O}\left(\frac{v^2}{m_{KK}^2}\bar{Y}^2\right)$	$\mathcal{O}\left(\frac{v^2}{m_{KK}^2}\bar{Y}^2\right)$
pNGB	$1+\mathcal{O}\left(\frac{v^2}{f^2}\right)+\mathcal{O}\left(y_*^2\lambda^2\frac{v^2}{M_*^2}\right)$	$1+\mathcal{O}\left(y_*^2\lambda^2\frac{v^2}{M_*^2}\right)$	$\mathcal{O}\left(y_*^2\lambda^2\frac{v^2}{M_*^2}\right)$	$\mathcal{O}\left(y_*^2\lambda^2\frac{v^2}{M_*^2}\right)$

$c_u Y_d Y_d^\dagger Y_u + \cdots$, and similarly for Y_d' with $u \leftrightarrow d$, while $a_q, b_q, c_q \sim \mathcal{O}(1)$ and are in general complex. For leptons we follow [1510] and assume that the SM Y_ℓ is the only flavour-breaking spurion even for the neutrino mass matrix (see also [699]). Then Y_ℓ' and Y_ℓ are diagonal in the same basis and there are no flavour-violating couplings. The flavour-diagonal κ_ℓ are given in Table 167.

Multi-Higgs-doublet model with natural flavour conservation (NFC). Natural flavour conservation in multi-Higgs-doublet models is an assumption that only one doublet, H_u, couples to the up-type quarks, only one Higgs doublet, H_d, couples to the down-type quarks, and only one doublet, H_ℓ couples to leptons (it is possible that any of these coincide, as in the SM where $H = H_u = H_d = H_\ell$) [1191, 1192]. The neutral scalar components of H_i are $(v_i + h_i)/\sqrt{2}$, where $v^2 = \sum_i v_i^2$. The dynamical fields h_i are a linear combination of the neutral Higgs boson mass eigenstates (and include h_u and h_d). We thus have $h_i = V_{hi} h + \ldots$, where V_{hi} are elements of the unitary matrix V that diagonalizes the neutral-Higgs boson mass terms and we only write down the contribution of the lightest Higgs, h. NFC means that there are no tree-level Flavour Changing Neutral Currents (FCNCs) and no CP violation in the Yukawa

Table 167: Same as Table 165 but for lepton Yukawa couplings. NP effects in the pNGB model are negligible and therefore we do not report them here.

Model	κ_τ	$\kappa_{\mu(e)}/\kappa_\tau$	$\tilde{\kappa}_\tau/\kappa_\tau$	$\tilde{\kappa}_{\mu(e)}/\kappa_\tau$
SM	1	1	0	0
MFV	$1+\frac{\mathrm{Re}(a_\ell)v^2}{\Lambda^2}$	$1-\frac{2\,\mathrm{Re}\,(b_\ell)m_\tau^2}{\Lambda^2}$	$\frac{\mathrm{Im}(a_\ell)v^2}{\Lambda^2}$	$\frac{\mathrm{Im}(a_\ell)v^2}{\Lambda^2}$
NFC	$V_{h\ell}\,v/v_\ell$	1	0	0
MSSM	$-\sin\alpha/\cos\beta$	1	0	0
FN	$1+\mathcal{O}\left(\frac{v^2}{\Lambda^2}\right)$	$1+\mathcal{O}\left(\frac{v^2}{\Lambda^2}\right)$	$\mathcal{O}\left(\frac{v^2}{\Lambda^2}\right)$	$\mathcal{O}\left(\frac{v^2}{\Lambda^2}\right)$
GL2	$-\sin\alpha/\cos\beta$	$\simeq 3(5)$	0	0
RS	$1+\mathcal{O}\left(\bar{Y}^2\frac{v^2}{m_{KK}^2}\right)$	$1+\mathcal{O}\left(\bar{Y}^2\frac{v^2}{m_{KK}^2}\right)$	$\mathcal{O}\left(\bar{Y}^2\frac{v^2}{m_{KK}^2}\right)$	$\mathcal{O}\left(\bar{Y}^2\frac{v^2}{m_{KK}^2}\right)$

Table 168: Same as Table 165 but for flavour-violating up-type Yukawa couplings. In the SM, NFC and the tree-level MSSM the Higgs Yukawa couplings are flavour diagonal. The CP-violating $\tilde{\kappa}_{ff'}$ are obtained by replacing the real part, Re, with the imaginary part, Im. All the other models predict a zero contribution to these flavour changing couplings.

Model	$\kappa_{ct(tc)}/\kappa_t$	$\kappa_{ut(tu)}/\kappa_t$	$\kappa_{uc(cu)}/\kappa_t$
MFV	$\frac{\mathrm{Re}\left(c_u m_b^2 V_{cb}^{(*)}\right)}{\Lambda^2}\frac{\sqrt{2}m_{t(c)}}{v}$	$\frac{\mathrm{Re}\left(c_u m_b^2 V_{ub}^{(*)}\right)}{\Lambda^2}\frac{\sqrt{2}m_{t(u)}}{v}$	$\frac{\mathrm{Re}\left(c_u m_b^2 V_{ub(cb)}V_{cb(ub)}^*\right)}{\Lambda^2}\frac{\sqrt{2}m_{c(u)}}{v}$
FN	$\mathcal{O}\left(\frac{vm_{t(c)}}{\Lambda^2}\lvert V_{cb}\rvert^{\pm 1}\right)$	$\mathcal{O}\left(\frac{vm_{t(u)}}{\Lambda^2}\lvert V_{ub}\rvert^{\pm 1}\right)$	$\mathcal{O}\left(\frac{vm_{c(u)}}{\Lambda^2}\lvert V_{us}\rvert^{\pm 1}\right)$
GL2	$\epsilon(\epsilon^2)$	$\epsilon(\epsilon^2)$	ϵ^3
RS	$\sim\lambda^{(-)2}\frac{m_{t(c)}}{v}\bar{Y}^2\frac{v^2}{m_{KK}^2}$	$\sim\lambda^{(-)3}\frac{m_{t(u)}}{v}\bar{Y}^2\frac{v^2}{m_{KK}^2}$	$\sim\lambda^{(-)1}\frac{m_{c(u)}}{v}\bar{Y}^2\frac{v^2}{m_{KK}^2}$
pNGB	$\mathcal{O}(y_*^2\frac{m_t}{v}\frac{\lambda_{L(R),2}\lambda_{L(R),3}m_W^2}{M_*^2})$	$\mathcal{O}(y_*^2\frac{m_t}{v}\frac{\lambda_{L(R),1}\lambda_{L(R),3}m_W^2}{M_*^2})$	$\mathcal{O}(y_*^2\frac{m_c}{v}\frac{\lambda_{L(R),1}\lambda_{L(R),2}m_W^2}{M_*^2})$

interactions $\kappa_{qq'}=\tilde{\kappa}_{qq'}=0\,,\tilde{\kappa}_q=0$.

There is a universal shift in all up-quark Yukawa couplings, $\kappa_u=\kappa_c=\kappa_t=V_{hu}v/v_u$. Similarly there is a (different) universal shift in all down-quark Yukawa couplings and in all lepton Yukawa couplings, see Tables 165 - 167.

Higgs sector of the MSSM at tree level. The MSSM tree-level Higgs potential and the couplings to quarks are the same as in the type-II two-Higgs-doublet model, see, e.g., [1522]. This is an example of a 2HDM with natural flavour conservation in which $v_u=\sin\beta\,v$, $v_d=\cos\beta\,v$. The mixing of $h_{u,d}$ into the Higgs boson mass-eigenstates h and H is given by $h_u=\cos\alpha h+\sin\alpha H$, $h_d=-\sin\alpha h+\cos\alpha H$, where h is the observed SM-like Higgs. The up-quark Yukawa couplings are rescaled universally, $\kappa_u=\kappa_c=\kappa_t=\cos\alpha/\sin\beta$, and similarly the down-quark Yukawas, $\kappa_d=\kappa_s=\kappa_b=-\sin\alpha/\cos\beta$. The flavour-violating and CP-violating Yukawas are zero[IV.33]. In Tables 165-167 we limit ourselves to the tree-level expectations, which are a good approximation for a large part of the MSSM parameter space.

In the alignment limit, $\beta-\alpha=\pi/2$ [486, 1195, 1524–1528], the Yukawa couplings tend toward

[IV.33] Note that beyond the tree level, in fine-tuned regions of parameter space the loops of sfermions and gauginos can lead to substantial corrections to these expressions [1523].

Table 169: Same as Table 168 but for flavour-violating down-type Yukawa couplings.

Model	$\kappa_{bs(sb)}/\kappa_b$	$\kappa_{bd(db)}/\kappa_b$	$\kappa_{sd(ds)}/\kappa_b$
MFV	$\frac{\mathrm{Re}\left(c_d m_t^2 V_{ts}^{(*)}\right)}{\Lambda^2}\frac{\sqrt{2}m_{s(b)}}{v}$	$\frac{\mathrm{Re}\left(c_d m_t^2 V_{td}^{(*)}\right)}{\Lambda^2}\frac{\sqrt{2}m_{d(b)}}{v}$	$\frac{\mathrm{Re}\left(c_d m_t^2 V_{ts(td)}^{*} V_{td(ts)}\right)}{\Lambda^2}\frac{\sqrt{2}m_{s(d)}}{v}$
FN	$\mathcal{O}\left(\frac{v m_{b(s)}}{\Lambda^2}\lvert V_{cb}\rvert^{\pm 1}\right)$	$\mathcal{O}\left(\frac{v m_{b(d)}}{\Lambda^2}\lvert V_{ub}\rvert^{\pm 1}\right)$	$\mathcal{O}\left(\frac{v m_{s(d)}}{\Lambda^2}\lvert V_{us}\rvert^{\pm 1}\right)$
GL2	$\epsilon^2(\epsilon)$	ϵ	$\epsilon^2(\epsilon^3)$
RS	$\sim \lambda^{(-)2}\frac{m_{b(s)}}{v}\bar{Y}^2\frac{v^2}{m_{KK}^2}$	$\sim \lambda^{(-)3}\frac{m_{b(d)}}{v}\bar{Y}^2\frac{v^2}{m_{KK}^2}$	$\sim \lambda^{(-)1}\frac{m_{s(d)}}{v}\bar{Y}^2\frac{v^2}{m_{KK}^2}$
pNGB	$\mathcal{O}(y_*^2\frac{m_b}{v}\frac{\lambda_{L(R),2}\lambda_{L(R),3}m_W^2}{M_*^2})$	$\mathcal{O}(y_*^2\frac{m_b}{v}\frac{\lambda_{L(R),1}\lambda_{L(R),3}m_W^2}{M_*^2})$	$\mathcal{O}(y_*^2\frac{m_s}{v}\frac{\lambda_{L(R),1}\lambda_{L(R),2}m_W^2}{M_*^2})$

Table 170: Same as Table 168 but for flavour-violating lepton Yukawa couplings.

Model	$\kappa_{\tau\mu(\mu\tau)}/\kappa_\tau$	$\kappa_{\tau e(e\tau)}/\kappa_\tau$	$\kappa_{\mu e(e\mu)}/\kappa_\tau$
FN	$\mathcal{O}\left(\frac{v m_{\mu(\tau)}}{\Lambda^2}\lvert U_{23}\rvert^{\mp 1}\right)$	$\mathcal{O}\left(\frac{v m_{e(\tau)}}{\Lambda^2}\lvert U_{13}\rvert^{\mp 1}\right)$	$\mathcal{O}\left(\frac{v m_{e(\mu)}}{\Lambda^2}\lvert U_{12}\rvert^{\mp 1}\right)$
GL2	$\epsilon^2(\epsilon)$	ϵ	$\epsilon^2(\epsilon^3)$
RS	$\sim \sqrt{\frac{m_{\mu(\tau)}}{m_{\tau(\mu)}}}\bar{Y}^2\frac{v^2}{m_{KK}^2}$	$\sim \sqrt{\frac{m_{e(\tau)}}{m_{\tau(e)}}}\bar{Y}^2\frac{v^2}{m_{KK}^2}$	$\sim \sqrt{\frac{m_{e(\mu)}}{m_{\mu(e)}}}\bar{Y}^2\frac{v^2}{m_{KK}^2}$

their SM value, $\kappa_i = 1$. The global fits to Higgs data in type-II 2HDM already constrain $\beta - \alpha$ to be not to far from $\pi/2$ [1529–1531] so that the couplings of the light Higgs are also constrained to be close to their SM values. Note that the decoupling limit of the 2HDM, where the heavy Higgs bosons become much heavier than the SM Higgs, implies the alignment limit while the reverse is not necessarily true [1524].

A single Higgs doublet with Froggatt-Nielsen mechanism (FN). The Froggatt-Nielsen [1512] mechanism provides a simple explanation of the size and hierarchy of the SM Yukawa couplings. In the simplest realization this is achieved by a $U(1)_H$ horizontal symmetry under which different generations of fermions carry different charges. The $U(1)_H$ is broken by a spurion, ϵ_H. The entries of the SM Yukawa matrix are then parametrically suppressed by powers of ϵ_H as, for example, in the lepton sector

$$\left(Y_\ell\right)_{ij} \sim \epsilon_H^{H(L_i)-H(e_j)}, \tag{IV.6.18}$$

where $H(e, L)$ are the FN charges of the right- and left-handed charged lepton, respectively. The dimension 6 operators in (IV.6.16) due to electroweak NP have similar flavour suppression, $\left(Y'_\ell\right)_{ij} \sim \epsilon_H^{H(e_j)-H(L_i)} v^2/\Lambda^2$ [1508, 1510]. After rotating to the mass eigenbasis, the lepton masses and mixing angles are then given by [1532, 1533]

$$m_{\ell_i}/v \sim \epsilon_H^{|H(L_i)-H(e_i)|}, \quad |U_{ij}| \sim \epsilon_H^{|H(L_i)-H(L_j)|}, \tag{IV.6.19}$$

giving the Higgs Yukawa couplings in Tables 167 and 170 in the row labelled 'FN' [1508]. Similarly for the quarks, after rotating to the mass eigenbasis, the masses and the mixings are given by [1532]

$$m_{u_i(d_i)}/v \sim \epsilon_H^{|H(Q_i)-H(u_i(d_i))|}, \quad |V_{ij}| \sim \epsilon_H^{|H(Q_i)-H(Q_j)|}, \tag{IV.6.20}$$

where V is the Cabibbo-Kobayashi-Maskawa (CKM) mixing matrix and $H(u,d,Q)$ are the FN charges of the right-handed up and down and the left-handed quark fields, respectively.

Higgs-dependent Yukawa couplings (GL2) In the model of quark masses introduced by Giudice and Lebedev [1513], the quark masses, apart from the top mass, are small because they arise from higher dimensional operators. The original GL proposal is ruled out by data, while the straightforward modification to a 2HDM (GL2) is

$$\begin{aligned}\mathcal{L}_f = c^u_{ij}\left(\frac{H_1^\dagger H_1}{M^2}\right)^{n^u_{ij}} \bar{Q}_{L,i} u_{R,j} H_1 + c^d_{ij}\left(\frac{H_1^\dagger H_1}{M^2}\right)^{n^d_{ij}} \bar{Q}_{L,i} d_{R,j} H_2 + \\ c^\ell_{ij}\left(\frac{H_1^\dagger H_1}{M^2}\right)^{n^\ell_{ij}} \bar{L}_{L,i} e_{R,j} H_2 + \text{h.c.}\,,\end{aligned} \tag{IV.6.21}$$

where M is the mass scale of the mediators. In the original GL model H_2 is identified with the SM Higgs, $H_2 = H$, while $H_1 = H^c$. Taking $c^{u,d}_{ij} \sim \mathcal{O}(1)$, the ansatz $n^{u,d}_{ij} = a_i + b^{u,d}_j$ with $a = (1,1,0)$, $b^d = (2,1,1)$, and $b^u = (2,0,0)$ then reproduces the hierarchies of the observed quark masses and mixing angles for $\epsilon \equiv v^2/M^2 \approx 1/60$. The Yukawa couplings are of the form $y^{u,d}_{ij} = (2n^{u,d}_{ij}+1)(y^{u,d}_{ij})_{\rm SM}$. The SM Yukawas are diagonal in the same basis as the quark masses, while the $y^{u,d}_{ij}$ are not. Because the bottom Yukawa is largely enhanced, $\kappa_b \simeq 3$, this simplest version of the GL model is already excluded by the Higgs data. Its modification, GL2, is still viable, though [1507]. For $v_1/v_2 = \tan\beta \sim 1/\epsilon$ one can use the same ansatz for $n^{u,d}_{ij}$ as before, modifying only b^d, so that $b^d = (1,0,0)$, with the results shown in Tables 165-170. For leptons we use the same scalings as for right-handed quarks. Note that the $H_1^\dagger H_1$ is both a gauge singlet and a flavour singlet. From symmetry point of view it is easier to build flavour models, if $H_1 H_2$ acts as a spurion in (IV.6.21), instead of $H_1^\dagger H_1$. This possibility is severely constrained phenomenologically, though [1511, 1534].

Randall-Sundrum models (RS). The Randall-Sundrum warped extra-dimensional model has been proposed to address the hierarchy problem and simultaneously explain the hierarchy of the SM fermion masses [1514, 1535–1538]. Integrating out the Kaluza-Klein (KK) modes of mass m_{KK}, and working in the limit of a brane-localized Higgs, keeping only terms of leading order in v^2/m^2_{KK}, the SM quark mass matrices are given by [1539] (see also [1540–1548], and Ref. [1549] for a bulk Higgs scenario)

$$M^{d(u)}_{ij} = \left[F_q Y^{5D}_{1(2)} F_{d(u)}\right]_{ij} v\,. \tag{IV.6.22}$$

The $F_{q,u,d}$ are 3×3 matrices of fermion wave-function overlaps with the Higgs and are diagonal and hierarchical. Assuming flavour anarchy, the 5D Yukawa matrices, $Y^{5D}_{1,2}$, are general 3×3 complex matrices with $\bar{Y} \sim \mathcal{O}(1)$ entries, but usually $\bar{Y} \lesssim 4$, see, e.g., [1543]. At leading order in v^2/m^2_{KK} the Higgs Yukawas are aligned with the quark masses, i.e., $M_{u,d} = y_{u,d} v/\sqrt{2} + \mathcal{O}(v^2/m^2_{KK})$. The misalignments are generated by tree-level KK quark exchanges, giving

$$\left[y_{u(d)}\right]_{ij} - \frac{\sqrt{2}}{v}\left[M_{u,d}\right]_{ij} \sim -\frac{1}{3} F_{q_i} \bar{Y}^3 F_{u_j(d_j)} \frac{v^2}{m^2_{KK}}\,. \tag{IV.6.23}$$

For the charged leptons, there are two choices for generating the hierarchy in the masses [1539]. If left- and right-handed fermion profiles are both hierarchical (and taken to be similar) then the misalignment between the masses and Yukawas is $\sim \sqrt{m_i m_j/v^2} \times \mathcal{O}\big(\bar{Y}^2 v^2/m^2_{KK}\big)$. If only the right-handed profiles are hierarchical the misalignment is given by (see also Tables 167 and 170)

$$\left[y_\ell\right]_{ij} - \frac{\sqrt{2}}{v}\left[M_\ell\right]_{ij} \sim -\frac{1}{3}\bar{Y}^2 \frac{v^2}{m^2_{KK}} \frac{m^\ell_j}{v}\,. \tag{IV.6.24}$$

The Higgs mediated FCNCs are suppressed by the same zero-mode wave-function overlaps that also suppress the quark masses, (IV.6.22), giving rise to the RS GIM mechanism [1550–1552]. Using the

fact that the CKM matrix elements are given by $V_{ij} \sim F_{q_i}/F_{q_j}$ for $i < j$, Eq. (IV.6.23), one can rewrite the κ_i as in Tables 165-169. The numerical analysis of Ref. [1539] found that for diagonal Yukawas typically $\kappa_i < 1$, with deviations in $\kappa_{t(b)}$ up to $30\%(15\%)$, and in $\kappa_{s,c(u,d)}$ up to $\sim 5\%(1\%)$. For the charged leptons one obtains deviations in $\kappa_{\tau\mu(\mu\tau)} \sim 1(5) \times 10^{-5}$ [1539]. These estimates were obtained fixing the mass of the first KK gluon excitation to 3.7 TeV, above the present ATLAS bound [1553].

Composite pseudo-Goldstone Higgs (pNGB). Finally, we assume that the Higgs is a pseudo-Goldstone boson arising from the spontaneous breaking of a global symmetry in a strongly coupled sector, and couples to the composite sector with a typical coupling y_* [766,767,769,1515] (for a review, see [687]). Assuming partial compositeness, the SM fermions couple linearly to composite operators $O_{L,R}$, $\lambda^q_{L,i}\bar{Q}_{L,i}O^i_R + \lambda^u_{R,j}\bar{u}_{R,j}O^j_L + h.c.$, where i, j are flavour indices [1554]. This is the 4D dual of fermion mass generation in 5D RS models. The SM masses and Yukawa couplings arise from expanding the two-point functions of the $O_{L,R}$ operators in powers of the Higgs field [1555].

The new ingredient compared to the EFT analysis in (IV.6.16) is that the shift symmetry due to the pNGB nature of the Higgs dictates the form of the higher-dimensional operators. The flavour structure and the composite Higgs coset structure completely factorize if the SM fields couple to only one composite operator. The general decomposition of Higgs boson couplings then becomes [1555] (see also [469, 1556, 1557])

$$Y_u \bar{Q}_L H u_R + Y'_u \bar{Q}_L H u_R \frac{(H^\dagger H)}{\Lambda^2} + \ldots \quad \to \quad c^u_{ij}\, P(h/f)\, \bar{Q}^i_L H u^j_R\,, \tag{IV.6.25}$$

and similarly for the down quarks. Here $f \gtrsim v$ is the equivalent of the pion decay constant, while $P(h/f) = a_0 + a_2(H^\dagger H/f^2) + \ldots$ is an analytic function whose form is fixed by the pattern of the spontaneous breaking and the embedding of the SM fields in the global symmetry of the strongly coupled sector. In (IV.6.25) the flavour structure of Y_u and Y'_u is the same. The resulting corrections to the quark Yukawa couplings are therefore strictly diagonal,

$$\kappa_q \sim 1 + \mathcal{O}\big(v^2/f^2\big). \tag{IV.6.26}$$

For example, for the models based on the breaking of $SO(5)$ to $SO(4)$, the diagonal Yukawa couplings can be written as $\kappa_q = (1 + 2m - (1 + 2m + n)(v/f)^2)/\sqrt{1-(v/f)^2}$, where n, m are positive integers [1558]. The MCHM4 model corresponds to $m = n = 0$, while MCHM5 is given by $m = 0, n = 1$.

The flavour-violating contributions to the quark Yukawa couplings arise only from corrections to the quark kinetic terms [1555],

$$\bar{q}_L i\not{D} q_L \frac{H^\dagger H}{\Lambda^2},\ \bar{u}_R i\not{D} u_R \frac{H^\dagger H}{\Lambda^2}, \ldots\,, \tag{IV.6.27}$$

due to the exchanges of composite vector resonances with typical mass $M_* \sim \Lambda$. After using the equations of motion these give (neglecting relative $\mathcal{O}(1)$ contributions in the sum) [1555, 1557, 1559],

$$\kappa^u_{ij} \sim 2y_*^2 \frac{v^2}{M_*^2}\left(\lambda^q_{L,i}\lambda^q_{L,j}\frac{m_{u_j}}{v} + \lambda^u_{R,i}\lambda^u_{R,j}\frac{m_{u_i}}{v}\right), \tag{IV.6.28}$$

and similarly for the down quarks. If the strong sector is CP violating, then $\tilde{\kappa}^{u,d}_{ij} \sim \kappa^{u,d}_{ij}$.

The exchange of composite vector resonances also contributes to the flavour-diagonal Yukawa couplings, shifting the estimate (IV.6.26) by $\Delta\kappa_{q_i} \sim 2y_*^2 \frac{v^2}{M_*^2}\left[\left(\lambda^q_{L,i}\right)^2 + \left(\lambda^u_{R,i}\right)^2\right]$. This shift can be large for the quarks with a large composite component if the Higgs is strongly coupled to the vector resonances, $y_* \sim 4\pi$, and these resonances are relatively light, $M_* \sim 4\pi v \sim 3$ TeV. The left-handed top and bottom, as well as the right-handed top, are expected to be composite, explaining the large top

mass (i.e., $\lambda^q_{L,3} \sim \lambda^u_{R,3} \sim 1$). In the anarchic flavour scenario, one expects the remaining quarks to be mostly elementary (so the remaining $\lambda_i \ll 1$). If there is some underlying flavour alignment, it is also possible that the light quarks are composite. This is most easily achieved in the right-handed sector [1556, 1560, 1561].

In the case of the lepton sector, if we assume that there are no hierarchies in the composite sector [1562] (see also [1563–1566]), then the NP effects in the flavour diagonal and off-diagonal Yukawas are negligible. For this reason, we do not report them in Tabs. 167 and 170.

IV.6.2.c.ii Models with large flavour-violating Higgs boson decays

In Section IV.6.2.c.i we explored the modifications of Higgs Yukawa couplings in a number of popular NP models, some of which are motivated by the hierarchy problem. The deviations from the SM predictions share several common features. If the scale of NP is well above the weak scale, $\Lambda \gg v$, the deviations from the SM expectations become increasingly small.

Flavour-violating Higgs Yukawa couplings to quarks are significantly constrained by meson mixing constraints [1488, 1502]. If the tree-level Higgs exchange is the dominant NP contribution, the constraints from $D-\bar{D}$, $B_d-\bar{B}_d$, $B_s-\bar{B}_s$ and $K-\bar{K}$ mixing translate to $\mathrm{Br}(h\to c\bar{u}+u\bar{c})<3.7\times10^{-6}$, $\mathrm{Br}(h\to b\bar{d}+d\bar{b})<1.7\times10^{-5}$, $\mathrm{Br}(h\to b\bar{s}+s\bar{b})<1.3\times10^{-3}$, and $\mathrm{Br}(h\to s\bar{d}+d\bar{s})<4.2\times10^{-7}$ at 95% C.L., respectively. These branching ratios are too small to be experimentally searched for, with the possible exception of $h\to\bar{b}s+b\bar{s}$. The indirect bounds can be relaxed to per-cent-level branching ratios only if there is substantial cancellation between the flavour-violating Higgs exchange and other NP contributions to the mixing amplitude.

The flavour-violating couplings of the Higgs involving top quarks, $\kappa_{tc,tu}$ and $\kappa_{ct,ut}$, are more loosely constrained experimentally. The most important constraints come from direct searches for the flavour-violating top decays at the LHC, $t\to hc, hu$, giving $\sqrt{\kappa^2_{tc}+\kappa^2_{ct}}<0.13$ and $\sqrt{\kappa^2_{tu}+\kappa^2_{ut}}<0.13$ [1567–1569].The $D-\bar{D}$ mixing also constrains combinations of the couplings, $|\kappa_{ut}\kappa_{ct}|, |\kappa_{tu}\kappa_{tc}| < 7.6\times10^{-3}$, $|\kappa_{tu}\kappa_{ct}|, |\kappa_{ut}\kappa_{tc}| < 2.2\times10^{-3}$, $|\kappa_{ut}\kappa_{ct}\kappa_{tu}\kappa_{tc}|^{1/2}<0.9\times10^{-3}$ [1488].

Similarly, the flavour-violating Yukawa couplings involving the τ lepton are relatively loosely constrained. The most stringent constraints come from direct searches for $h\to\tau\mu,\tau e$ at the LHC [1504–1506], giving $\sqrt{\kappa^2_{\tau\mu}+\kappa^2_{\mu\tau}}<3.6\times10^{-3}$ [1506], $\sqrt{\kappa^2_{\tau e}+\kappa^2_{e\tau}}<2.4\times10^{-3}$ [1504]. These numbers should be compared to the indirect constraints from searches for $\tau\to\mu\gamma$ and $\tau\to e\gamma$: $\sqrt{\kappa^2_{\tau\mu}+\kappa^2_{\mu\tau}}<0.016$, $\sqrt{\kappa^2_{\tau e}+\kappa^2_{e\tau}}<0.014$ [1488, 1502].

In contrast, the most stringent constraint on $\kappa_{\mu e}$ is due to $\mu\to e\gamma$, giving $\sqrt{\kappa^2_{\mu e}+\kappa^2_{e\mu}}<3.6\times10^{-6}$ [1488] to be compared with the bound from the direct search $h\to e\mu$ which is two orders of magnitude less stringent, $\sqrt{\kappa^2_{\tau e}+\kappa^2_{e\tau}}<5.4\times10^{-4}$ [1504].

The bounds from indirect constraints also limit the relative sizes of $h\to\tau\mu$ and $h\to\tau e$ branching ratios. Since $\mu\to e\gamma$ and $\mu\to e$ conversion provide complementary information on the relevant Yukawa couplings, it is possible to write a relation [1570]

$$\mathrm{Br}(h\to\tau\mu)\times\mathrm{Br}(h\to\tau e)=7.95\times10^{-10}\left(\frac{\mathrm{Br}(\mu\to e\gamma)}{10^{-13}}\right)+3.15\times10^{-4}\left(\frac{\mathrm{Br}(\mu\to e)_{\mathrm{Au}}}{10^{-13}}\right), \quad \text{(IV.6.29)}$$

where the present experimental limits are $\mathrm{Br}(\mu\to e\gamma)<5.7\times10^{-13}$ [1571] and $\mathrm{Br}(\mu\to e)_{\mathrm{Au}}<7\times10^{-13}$ [1572]. This relation will become phenomenologically interesting once the sensitivity of the $\mu\to e$ conversion experiments is improved. Using the central value of the experimental hint for nonzero $h\to\tau\mu$, $\mathrm{BR}(h\to\tau\mu)=(0.84\pm0.38)\%$ [1506], Eq. (IV.6.29) gives at present only a very loose bound, $\mathrm{Br}(h\to\tau e)<26\%$ compared to the direct constraint $\mathrm{BR}(h\to\tau e)<0.69\%$.

An interesting question is what kind of models could explain the relatively large $\mathrm{BR}(h\to\tau\mu)=(0.84\pm0.38)\%$, if this hint were to become statistically significant. In terms of Yukawa couplings this

hint is $\sqrt{|\kappa_{\tau\mu}|^2 + |\kappa_{\mu\tau}|^2} = (2.6 \pm 0.6) \cdot 10^{-3}$. For $\kappa_{\mu\tau} \sim \kappa_{\tau\mu}$ this measurement would imply that the product of off-diagonal Yukawa couplings is of the same order of magnitude as the product of the diagonal ones, $\kappa_{\mu\tau} \sim \sqrt{m_\tau m_\mu}/v$. In particular, the off-diagonal couplings should not be additionally suppressed by powers of v^2/Λ^2, unlike what we found for the models considered in Section IV.6.2.c.i.

A potential obstacle to any viable model of large $\kappa_{\tau\mu}$ couplings is that the same type of NP that generates $\kappa_{\tau\mu,\mu\tau}$ will also generate $\tau \to \mu\gamma$. Let us take for instance a model for which $\kappa_{\tau\mu}$ is generated at one-loop, with NP particles running in the loop. Attaching a photon anywhere in the loop will then produce the $\tau \to \mu\gamma$ transition. It is instructive to attempt a naive dimensional analysis (NDA) estimate of this transition, assuming that the Higgs is the only source of electroweak symmetry breaking generating the charged lepton masses, i.e. that in the limit $v \to 0$ also $m_\tau, m_\mu \to 0$. The NDA then gives a $\mathrm{Br}(\tau \to \mu\gamma)$ that is four orders above the experimental bound, if one is to explain the present central value of $\mathrm{Br}(h \to \tau\mu)$ [1573]. One is therefore led to conclude that an observation of $h \to \tau\mu$ at the present level would strongly suggest that there is an additional source of charged lepton masses (another option is that the NDA estimate is badly violated, for instance by large slepton mass hierarchies in the MSSM [1523] or by ad-hoc cancellations [1570]).

A well-motivated possibility is that the Higgs is predominantly responsible for the masses of the third generation charged fermions, while the masses of the first two generations fermions are generated from a new source of electroweak symmetry breaking [1573, 1574]. This second contribution is a subleading correction, explaining the approximate $U(2)$ symmetry of the charged fermion masses (i.e. that $m_{\mu,e} \ll m_\tau$) [1574]. The lepton mass matrix is then of the form

$$\mathcal{M}^\ell = \mathcal{M}_0^\ell + \Delta\mathcal{M}^\ell, \tag{IV.6.30}$$

where a rank 1 matrix $\mathcal{M}_0^\ell$ is due to the vev of a scalar doublet Φ_1 (the primary component of the Higgs), and accounts for the bulk of the third generation mass, m_τ. The matrix $\Delta\mathcal{M}_\ell$ is due to an additional source of EWSB, can be rank 2 or 3, and accounts for first and second generation masses, m_e and m_μ. Note that the above mass matrix $\mathcal{M}^\ell$ in general does not imply anything about the texture of neutrino masses, which can still come from the see-saw at or close to the GUT scale.

The simplest example is a 2HDM where $\mathcal{M}_0^\ell$ is due to Φ_1 and $\Delta\mathcal{M}^\ell$ due to an extra doublet Φ_2 [1573, 1574] (for other considerations in the context of 2HDM see [1575–1578]). This version of 2HDM is quite different from type II 2HDM covered in Section IV.6.2.c.i.

Note that the off-diagonal entries in $\Delta\mathcal{M}^\ell$ can lead to the current central value for $\mathrm{BR}(h \to \tau\mu)$ without violating the $\tau \to \mu\gamma$ bound (the above mentioned NDA scaling fails since one always pays an extra charged lepton Yukawa insertion). Scans over a reasonable range of $\Delta\mathcal{M}^\ell$ entries predict that $|\kappa_\mu/\kappa_\tau| < 1$ is preferred, with $\kappa_\tau - 1 \sim \mathcal{O}(\text{few } 10\%)$ typical [1573].

Another realization of (IV.6.30) are models in which $\Delta\mathcal{M}^\ell$ comes from strong dynamics, and is due to a condensate of a new set of strongly interacting fermions that also carry electroweak quantum numbers [1573, 1574]. In that case the $\tau \to \mu\gamma$ constraint is avoided if the NP scale is $\gtrsim 8$ TeV. In both examples it is straightforward to construct the correct texture of the mass matrix using flavour models, e.g. using the FN mechanism, so that a large enough $\mathrm{Br}(h \to \tau\mu)$ is obtained [1573]. It is also possible to apply the same principle to the quark sector, so that the bottom and top quark masses are due to the Higgs, while the light quark masses are due to a new source of EWSB. In that case a deviation in $B_s \to \mu\mu$, as well as signals in $\mathrm{BR}(B_s \to \tau\mu)$, $\mathrm{BR}(B \to K^{(*)}\tau\mu) \sim \mathcal{O}(10^{-7})$ are expected [1573].

IV.6.2.d Experimental status and prospects [IV.34]

In the SM, the charged fermions obtain mass (m_f) via a direct Yukawa coupling to the Higgs field, which, following electroweak symmetry breaking, results in fermion mass terms and a fermion-Higgs boson interaction with a strength proportional to m_f. This is the most economic way to generate fermion

[IV.34] *Author(s): L. Caminada, K. Nikolopoulos.*

masses, but it is not imposed by any fundamental symmetry principle. Several viable models of physics beyond the SM predict modifications of these couplings, as discussed in Section IV.6.2.c.

To date, the only direct experimental evidence of the Yukawa mechanism for fermion mass generation is the Higgs boson coupling to third generation fermions. The ATLAS and CMS Collaborations have reported evidence for the observation of the Higgs boson decays to a pair of τ-leptons, $h \to \tau^+\tau^-$, in line with the SM expectation [1579, 1580]. For Higgs boson decays to b-quark pairs, $h \to b\bar{b}$, the Tevatron experiments have reported evidence [1581], complemented by indications at the LHC [311, 312]. CMS has also reported the strong evidence for the direct coupling of the 125 GeV Higgs boson to down-type fermions (combining Higgs boson decays to pair of tau leptons and b-quark) [1582]. Higgs boson decays to top-quark pairs are kinematically forbidden, thus the associated production of a Higgs boson with a top-quark pair, $t\bar{t}h$, is exploited: several final states have been analysed [754, 1583], and the sensitivity begins to approach the SM expectation. The muon Yukawa coupling is probed through the $h \to \mu^+\mu^-$ decay, yielding 95% confidence level upper limits of 7-10 times the predicted SM rate [1584, 1585]. Higgs boson decays to an electron-positron pair have been also searched for [1585], although the resulting bound is many orders of magnitude larger than the predicted SM value, which is anticipated to remain out of reach even at the HL-LHC [636]. Flavour-violating Higgs boson interactions have been searched for in top-quark decays [1567, 1586] and via $h \to e^\pm\mu^\mp$, $h \to \tau^\pm e^\mp$ $h \to \tau^\pm\mu^\mp$ [1505, 1506], yielding an intriguing excess in the latter.

The Yukawa couplings of the first and second generation quarks are among the most challenging of the SM couplings to test experimentally. Indirect constraints are sparse, with some specifically derived for flavour-violating interactions via meson-anti-meson mixing [1488, 1502]. These Yukawa couplings have been, generally, considered beyond the reach of the LHC experiments. Recently, the possibility to probe these couplings using rare exclusive decays of the Higgs boson to a vector meson and a photon has resurfaced[IV.35], initially for the charm quark, and subsequently for all the light quarks, including flavour-violation (see Section IV.6.2.a for details). The rare exclusive decays of a Higgs boson to a meson and massive vector boson, $h \to MV$, and their potential in clarifying the nature of the Higgs boson have also been considered (see Section IV.6.2.b). These developments prompted significant interest, with theoretical investigations towards precise estimates of the relevant SM predictions, as detailed in Sections IV.6.2.a–IV.6.2.b, and phenomenological sensitivity studies, e.g. Ref. [1480].

Currently, these exclusive decays constitute the only available method to probe the Higgs boson interactions with first and second generation quarks. Recently, charm-quark specific suggestions regarding the feasibility of the $h \to c\bar{c}$ channel [1559], using charm-tagging techniques [1587], and of the associated production of a Higgs boson with a charm quark [1501], were made and are under investigation.

Similar exclusive decays of the $W^\pm$ and Z bosons have also attracted interest [1486, 1588, 1589], offering a physics programme in precision quantum chromodynamics (QCD), electroweak physics, and physics beyond the SM.

Using 20.3 fb^{-1} of 8 TeV proton-proton collision data, the ATLAS Collaboration has performed a search for Higgs and Z boson decays to $J/\psi\,\gamma$ or and $\Upsilon(nS)\,\gamma$ ($n = 1, 2, 3$) [1461]. No significant excess has been observed and 95% confidence level upper limits where placed on the respective branching ratios. In the $J/\psi\,\gamma$ final state the limits are 1.5×10^{-3} and 2.6×10^{-6} for the Higgs and Z boson decays, respectively, while in the $\Upsilon(1S, 2S, 3S)\,\gamma$ final states the limits are $(1.3, 1.9, 1.3) \times 10^{-3}$ and $(3.4, 6.5, 5.4) \times 10^{-6}$, respectively. The CMS Collaboration has placed a 95% C.L. upper limit of 1.5×10^{-3} on the $h \to J/\psi\,\gamma$ branching ratio [1462]. In all cases, an SM production rate for the observed Higgs boson is assumed. Currently, no other direct experimental constraint on these decays is available.

Looking to the future, the ATLAS Collaboration estimated the expected sensitivity for Higgs and

[IV.35] Such rare decays were considered as a discovery channel for a light Higgs boson [1481] but then abandoned.

Z boson decays to a J/ψ and a photon, assuming up to 3000 fb^{-1} of data collected with the ATLAS detector at the centre-of-mass energy of 14 TeV [1590], during the operation of the High Luminosity LHC. The expected sensitivity for the $h \to J/\psi\,\gamma$ branching ratio, assuming 300 and 3000 fb^{-1} at 14 TeV, is 153×10^{-6} and 44×10^{-6}, respectively [1590]. The corresponding sensitivities for the $Z \to J/\psi\,\gamma$ branching ratios are 7×10^{-7} and 4.4×10^{-7}, respectively [1590]. In this analysis, the same overall detector performance as in LHC Run 1 is assumed, while an analysis optimization has been performed and a multivariate discriminant using the same kinematic information as the published analysis [1461] has been introduced. As the search sensitivity approaches the SM expectation for the $h \to J/\psi\,\gamma$ branching ratio, the contribution from $h \to \mu\mu\gamma$ decays, with a non-resonant dimuon pair, needs to be included. These can be separated statistically from the $h \to J/\psi\,\gamma$ signal using dimuon mass information.

Regarding the Higgs boson coupling to the strange-quark, the $h \to \phi\gamma$ decay is a potential probe. The subsequent $\phi \to K^+K^-$ decay features a large branching ratio of about 49% and gives access to a simple final state of a hard photon recoiling against two collimated high transverse momentum tracks, as can be seen in Figure 283. With the SM branching ratio prediction presented in Table 162, about 6.5 events are expected to be produced with 100 fb^{-1} at 14 TeV. For the first generation quarks, the $h \to \omega\gamma$ and $h \to \rho\gamma$ are being considered, followed by the $\omega \to \pi^+\pi^-\pi^0$ and $\rho \to \pi^+\pi^-$ decays, both with large branching ratios of about 89% and 100%, respectively. The corresponding expected number of events, assuming the SM branching ratios for these decays, are about 7.6 and 96, respectively. The experimental acceptance for these decays, assuming reasonable geometrical acceptance and transverse momentum requirements, is expected to range between 40 and 70% [1591].

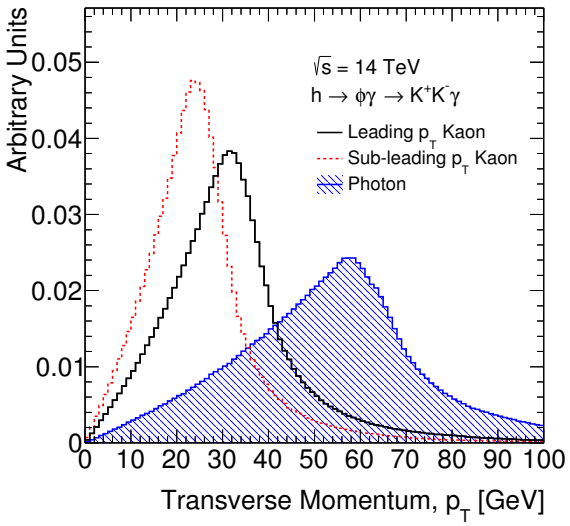

Figure 283: Transverse momentum distribution of decay products in $h \to \phi\gamma \to K^+K^-\gamma$ decays [1591].

These rare decays to a vector meson and a photon feature very interesting and experimentally challenging boosted topologies. The signature is distinct, but the QCD backgrounds require careful consideration. A primary challenge arises from the trigger availability to collect the required datasets. In the considered cases, the decay signature is a photon of large transverse momentum that is isolated from hadronic activity, recoiling against a narrow hadronic jet. Triggering on such signatures, especially under pile-up, will benefit from the upcoming detector upgrades, such as the ATLAS Fast TracKer (FTK) [1592] that will provide rapid track finding and reconstruction in the inner detector for every event that passes the level-1 trigger. The search for the final states $\omega\gamma$ and $\rho\gamma$ is complicated further due to the large natural width of the ρ meson and the ω-ρ interference.

In the following, as an example of a potentially interesting target rare decay for the high-statistics proton-proton collision data at a centre-of-mass energy of 14 TeV, the search for the Higgs boson decay to WD is presented in some detail. This is an interesting experimental target due to its clean experimental signature. The decay signature includes a high transverse momentum lepton from the W-boson decay, which gives the trigger for the event, and a displaced vertex from the charmed meson decay. Since the branching ratio of the Higgs boson decay to $WD_s^{(*)}$ is more than an order of magnitude larger than the branching ratio to $WD^{(*)}$ (see Table 163), the discussion here focuses on the former.

The search for this rare Higgs boson decay utilizes the dominant Higgs boson production mechanisms at the LHC, namely gluon-gluon fusion (ggF) and vector boson fusion (VBF). The cross section

for VBF Higgs boson production is about an order of magnitude smaller compared to ggF, but features distinct event kinematics, with two jets in the forward regions of the detector that can be used to tag the event. The main challenge in the search for $H \to W D_s^{(*)}$ is to suppress the large background from W bosons produced in association with charm quarks fragmenting into D_s mesons. In order to estimate the sensitivity of the search signal and background events have been produced using the PYTHIA event generator. The W-boson is required to decay leptonically to either an electron or a muon. Based on the detector acceptance and trigger requirements, the fiducial region is defined by lepton $p_{\mathrm{T}} > 30\,\mathrm{GeV}$, $|\eta| < 2.5$ and neutrino $p_{\mathrm{T}} > 25\,\mathrm{GeV}$. Since the transverse momentum of the D_s meson in signal events peaks at higher values compared to background events, a requirement of D_s $p_{\mathrm{T}} > 30\,\mathrm{GeV}$, $|\eta| < 2.1$ is applied. The acceptance of these requirements is 18% and 22% for ggF and VBF Higgs boson production, respectively, while 0.6% of the background events fulfil these requirements.

The $D_s^{(*)}$ meson is identified by reconstructing displaced vertices from its hadronic decay to charged pions or kaon, in particular $D_s \to K^+K^-\pi^+(\pi_0)$. The excited D_s^* state decays almost exclusively to $D_s + \gamma/\pi_0$ and is tagged by the subsequent D_s decay. The measurements of the SM $W + c$ production at the LHC [1593, 1594] demonstrate that hadronic charm decay signatures can be reconstructed in the detector with reasonable efficiency of 30% to 40%. Combinatorial background in the charm reconstruction is largely rejected by exploiting the charge correlation between the W boson and the charmed meson. However, the major background from $W + c$ production also predominantly yields opposite sign signatures and therefore is not reduced by this requirement.

The main discriminating variable against the non-resonant $W + D_s$ background is the Higgs boson mass as reconstructed from the W-boson and D_s meson four-momenta. Since an excellent mass resolution of about 1% is achieved for the D_s meson, the Higgs boson mass resolution is dominated by the measurement of the missing transverse energy in the detector which has a resolution of about 10% to 30% in the kinematic region relevant for this study. Requiring the reconstructed mass to be within a window of 20 GeV centred around the Higgs boson mass reduces the background by about a factor of 6.

A further distinct characteristic of the signal events is the isolation of the D_s meson. In background events the D_s meson originates from charm-quark fragmentation and is thus seen within a particle jet in the detector. By applying isolation criteria in the reconstruction of the D_s meson about 80% of the background events are rejected. In order to tag VBF events, two jets with an invariant mass of $m_{jj} > 500\,\mathrm{GeV}$ and separated by $\Delta\eta > 3$ are required.

About 12 signal events and 16000 background events can be expected in the ggF channel assuming an integrated luminosity of $\mathcal{L} = 3000\,\mathrm{fb}^{-1}$ and the Standard Model branching ratio for $H \to W D_s^{(*)}$. For the VBF channel predicted numbers of 1 signal event and 120 background events are obtained. Since the branching ratio of this decay can be significantly enhanced in many scenarios beyond the Standard Model (see Section IV.6.2.c of this report for a review), setting upper limits on the decay branching ratio is of considerable interest in exploring the phase space of these models. Based on these results an upper limit of 7×10^{-4} on the branching ratio of $H \to W D_s^{(*)}$ can be achieved.

IV.6.3 Recommendations for searches for exotic Higgs boson decays

In Run 2 of the LHC, the programmatic search for exotic Higgs boson decays will increasingly become an important topic of study. To help guide this experimental program, in this section we provide a set of recommendations for searches for the production of exotic particles in the decays of the Higgs boson.

A signature-based search program for exotic decays:

We recommend that the search program for exotic Higgs boson decays take a signature-based approach, targeting individual signatures rather than specific BSM models. A model that gives rise to exotic decays of the Higgs boson will typically lead to many different possible final states. For instance, a model containing a light pseudo-scalar with Yukawa-weighted decays will yield, in addition to the dominant

$h \to aa \to 4b$ decay, the much rarer but cleaner $h \to aa \to bb\mu\mu$ decay [1595]. Combining the results of searches for both exotic modes can substantially boost overall sensitivity to the overall exotic branching fraction $h \to aa$ [1479]. On the other hand, a single given final state, such as $h \to 4b$, may be predicted by a wide range of different theories; for a detailed discussion of this point, see Ref. [1479].

Presentation of results:

We recommend that searches for specific signatures quote their results in terms of $\sigma \times \mathrm{Br}$. This model-independent prescription allows for more flexible interpretation of results in a broad range of theories, and facilitates the ultimate combination of results obtained in different final states to achieve the best sensitivity to a specific model.

Production cross-sections:

The SM Higgs boson width is dominated by the small b-quark Yukawa coupling and is accidentally small, which means that even small couplings of the Higgs to BSM physics can generate exotic branching fractions of order the current upper bound, $\mathrm{BR}(h \to \mathrm{BSM}) \sim 30\%$. However, Higgs boson production cross-sections are controlled by the much larger electroweak and top couplings, and are thus substantially less affected by small couplings of the Higgs to new physics. As a simple example, consider the case of a real scalar s which mixes with the SM Higgs boson through a small Higgs portal interaction, $\mathcal{L}_{int} = -\epsilon/2\,|H|^2 s^2$, after both H and s acquire vacuum expectation values, v and $\langle s \rangle$, respectively. The Higgs boson production cross-section then receives corrections at the order $\mathcal{O}(\theta^2)$, where $\theta = \epsilon\langle s \rangle v/(m_h^2 - m_s^2)$ is the s-h mixing angle. However, the values of θ that induce $\mathrm{Br}(h \to ss) \sim 20\%$ are $\mathcal{O}(10^{-2})$ [IV.36]. Thus, *corrections to Higgs boson production cross-sections are subleading* in theories yielding exotic Higgs boson decays consistent with Run 1 data. As these corrections are model-dependent, and as many different models can yield the same Higgs boson decay final states, to maximize the flexibility and utility of experimental searches for exotic decays we recommend that searches for exotic Higgs boson decays assume SM Higgs boson production cross-sections. In the event that an exotic decay mode is discovered, it will then be of high interest to consider how possible effects of specific related new physics models would affect Higgs boson properties and production cross-sections. However, to institute and support a broad program of searches for direct production of exotic particles in Higgs boson decays, we recommend that SM Higgs boson production be used as the baseline for generating signal events and performing searches.

Signal event generation:

Apart from the special cases of decays with detector-stable or highly-displaced objects, exotic Higgs boson decays result in at least three objects in the final state. Since the Higgs itself is not heavy with respect to the LHC's centre-of-mass (CM) energy, one generic feature of exotic Higgs boson decays is thus that the particles in the final state tend to be soft. The spectrum of the Higgs boson decay products is a major factor in determining signal acceptance. Consequently, in carrying out searches for exotic Higgs boson decays, it is important to model Higgs boson production and in particular the Higgs boson p_T spectrum with some degree of care. On the other hand, the ease and flexibility with which BSM models can be implemented in `MadGraph` is also of practical importance to support a broad search program capable of covering the vast number of possible BSM decays.

Our baseline recommendation for signal event generation in searches for BSM particles produced in exotic Higgs boson decays is to use `MadGraph5` [364], followed by showering and hadronization in `Pythia` [318]. This recommendation is supported by the studies in the following section, where we compare kinematic distributions for the Higgs and its decay products in the prototypical decay $h \to aa \to 4b$

[IV.36] In this model, a given exotic branching fraction does not uniquely determine the mixing angle; these numbers are obtained in the generic regime $\langle s \rangle \sim m_s$.

as predicted by MadGraph+Pythia to those predicted by POWHEG [81,342,343]+Pythia, demonstrating good agreement overall. For gluon fusion production in MadGraph, Higgs boson production should be matched to at least one jet; see Section IV.6.4 for further relevant settings. For VBF and VH production, Higgs boson production is well-modeled in MadGraph without matching. In all cases the inclusive Higgs boson production cross-section should be normalized to the predictions from I.4.1.a. For searches that dominantly rely on gluon fusion production, the Higgs boson p_T spectrum should be reweighted according to the (N)NLO predictions following the recommendations of I.4.1.a.

Mass ranges:

While the primary focus of searches for exotic Higgs boson decays is and should remain the decays of the discovered 125 GeV SM-like Higgs boson, analyses should keep in mind the possibility of extending the search to cover other possible masses for the parent particle, particularly but not exclusively lower masses. This extends the sensitivity of searches to include cases where the originating 125 GeV Higgs boson decay includes small amounts of missing energy [1479] as well as the potential direct production of BSM Higgs bosons.

IV.6.4 Partonic distributions for the prompt decay topology $h \to XX \to 2Y2Y'$ [IV.37]

IV.6.4.a Introduction

In this section we study the decay topology where the Higgs boson decays to two exotic particles of the same mass, each of which then undergoes a prompt two-body decay to visible SM particles Y, Y': $h \to XX \to 2Y2Y'$. This decay topology is naturally realized in many well-motivated BSM frameworks. In particular, extensions of the Higgs sector by an additional, possibly complex, singlet scalar can naturally have Higgs boson decays to (pseudo-)scalars as one of their leading signatures. These (pseudo-)scalars decay mainly to fermions, with preference for heavy flavour. Signals of this class of models, SM+S and 2HDM+S, are described in detail in [1479]. The NMSSM is one of the best-studied examples of this type of extended Higgs sector. It has a large portion of parameter space where an approximate R-symmetry yields a SM-like Higgs boson with appreciable branching ratio into a pair of light pseudo-scalars a [1464–1466, 1468, 1469]. Other motivations for singlet-extended Higgs sectors include models of first-order electroweak phase transitions [1295, 1470] and thermal dark matter [1282, 1471, 1473, 1474]. In composite Higgs models, a symmetry-protected light pseudo-scalar in the spectrum may be fermiophobic, with dominant decays to gluon or photon pairs, thus yielding the exotic decay modes $h \to aa \to 4g, 2\gamma 2g, 4\gamma$ [1596–1600]. Another well-studied extension of the SM is a Higgsed dark $U(1)$ that kinetically mixes with SM hypercharge [1601–1603], in which case the Higgs boson decay $h \to Z_D Z_D \to 2f2f'$ yields final states weighted by gauge couplings, rather than Yukawa couplings, giving relatively leptophilic signatures [1604–1608]. All these exotic decays have very similar parton-level kinematics [IV.38].

As discussed in Section IV.6.3, exotic Higgs boson decays are characterized by low p_T objects in the final state. Thus, object acceptance becomes one of the main limiting factors in recording and reconstructing many exotic Higgs boson decays. Consequently, a good understanding of the parent Higgs boson and resulting decay product kinematics is necessary to assess realistic triggering opportunities and analysis strategies.

Here we study the (parton-level) kinematics of the final state particles in the prototypical exotic decay $h \to aa \to 4b$ in depth, considering gluon fusion, VBF, and WH associated production modes. In addition, we compare the predictions of LO and NLO generators, showing results for Higgs boson production using both MadGraph [364] and POWHEG [81, 342, 343].

[IV.37] *Author(s): R. Caminal Armadans, Z. Liu, V. Martinez Outschoorn.*

[IV.38] Angular correlations present in the decay $h \to Z_D Z_D \to 4f$ will modify the final state fermion distributions relative to the decay $h \to ss(aa) \to 4f$, but the (pseudo-)scalar decays are still a good guide to the overall kinematics.

IV.6.4.b Signal model and event generation

We consider augmenting the SM with a singlet pseudo-scalar a, which obtains interactions with SM fermions through mixing with the pseudo-scalar state A^0 in a 2HDM. After electroweak symmetry breaking, the relevant interaction terms are

$$\mathcal{L}^{\text{BSM}} \supset i y_b^a a \bar{b} \gamma_5 b + \frac{1}{2}\lambda_{aH} h a^2 + \frac{1}{2} m_a^2 a^2, \tag{IV.6.31}$$

where $m_a < m_h/2$ is the mass of the pseudo-scalar, the effective Yukawa coupling y_b^a controls the singlet's decay into $b\bar{b}$ pairs, and the trilinear coupling λ_{aH} determines the partial width for the Higgs boson decay into pairs of pseudo-scalars. A discussion of how these parameters depend on the couplings in the full 2HDM+S Lagrangian can be found in [1479]. The trilinear coupling and the pseudo-scalar mass can be independently adjusted, making the pseudo-scalar mass and the Higgs boson branching fraction $\text{Br}(h \to aa)$ independent parameters. We assume that y_b^a is large enough to yield prompt decays; displaced decays are discussed in Section IV.6.6.

The exotic Higgs boson decay mode $h \to aa(ss) \to b\bar{b}b\bar{b}$ will be the leading signature of a broad class of SM+S, 2HDM+S theories. Here we explore the kinematics of the final state b-partons in this decay for a range of pseudo-scalar masses $m_a = 20, 30, 40, 50$ and 60 GeV. The kinematics for a scalar field s decaying to bottom quark pairs are identical. We consider three Higgs boson production channels: gluon fusion (ggF); W-boson associated (WH) production; and weak vector-boson-fusion (VBF) production. In each production channel, we compare the differential predictions from events generated at LO (`Madgraph5+ Pythia`) to those generated at NLO (`Powheg+Pythia`). We find that predictions for the b-parton kinematics from `Madgraph` and `Powheg` event generators agree very well overall, justifying the use of LO signal event generation for BSM signal models.

We use the `CTEQ6L1` [1609] PDF set for `MadGraph 5` [54] signal samples, with the factorization and renormalization scales set to `MadGraph` default. The signal model is implemented using a modification of `MadGraph`'s `heft` model to include an additional pseudo-scalar. For ggF production we match events to one jet using the MLM matching scheme [1610] with matching parameters `xqcut` = 15 GeV and `QCUT` = 20 GeV; `Pythia6` [339] is used for showering. In all three production modes, the final state is generated inclusively except for the forward tagging jets in VBF, where cuts of $|\eta| < 5$ and $p_T > 20$ GeV are applied.

In `Powheg-Box` v2 [81, 342–344], signal samples for all three production modes are generated using the CT10 PDF set [29]. The events are interfaced with `Pythia` 8.186 which is used to decay the Higgs boson into a pair of pseudo-scalars a, which are themselves decayed to a pair of b-quarks with $\text{Br}(a \to b\bar{b})$ = 1. Event generation is fully inclusive for all three production modes.

IV.6.4.c Results

We begin with the Higgs boson p_T distribution for ggF, WH and VBF Higgs boson production at the 13 TeV LHC, shown in the left panels of Figure 284. For VBF production, we show the Higgs boson p_T distribution in events containing two jets with $p_T > 20$ GeV and $|\eta| < 5$. The Higgs boson p_T spectrum is a key quantity that affects all subsequent decay product distributions. Overall we find good agreement between the predictions of the two event generators, `MadGraph` and `Powheg`. For VBF and WH, the p_T spectra from the two generators are in excellent agreement. The greatest differences are seen in ggF, where `Powheg` predicts a slightly harder spectrum than does `MadGraph`; however, even here the p_T distributions are quite similar, with good agreement in the tail and in the peak. As discussed in Section IV.6.3, we recommend that searches that rely on ggF for the bulk of their sensitivity reweight the Higgs boson p_T distribution according to the recommendations of WG1. In the right panels of Figure 284, we compare predictions for the p_T spectrum of the leading b-parton in the same set of events, for the case $m_a = 60$ GeV. Good agreement is shown for VBF and WH production modes, while in ggF the spectrum predicted by `MadGraph` is slightly softer than the spectrum predicted by `Powheg`.

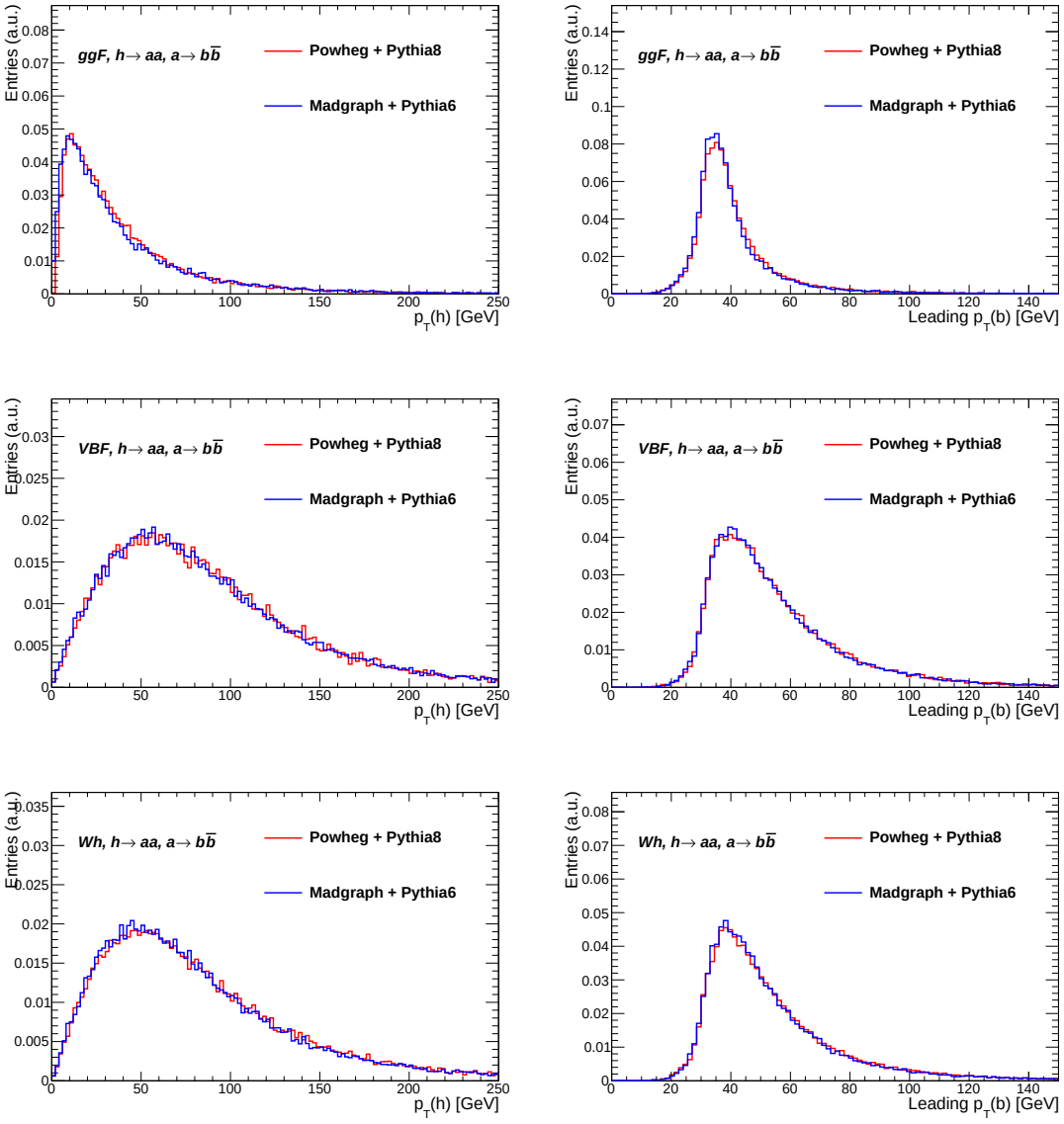

Figure 284: Left panels: the p_T distribution of the Higgs boson at LHC 13 TeV from different production modes: ggF (top), VBF (centre) and WH (bottom) using `MadGraph 5` (blue) and `Powheg` (red). Right panels: same, but for the p_T distribution of the leading b-parton, for the pseudo-scalar mass $m_a = 60$ GeV.

We further show various parton-level differential distributions, as generated in `Powheg`, for masses of the pseudo-scalar a ranging between 20 to 60 GeV in steps of 10 GeV. In these plots no cuts are applied to the final state particles; in particular, no cuts on VBF jets have been imposed. In Figure 285 we show the angular separation ΔR between the two pseudo-scalars a and between the $b\bar{b}$ pair originating from the same pseudo-scalar a decay for various Higgs boson production modes. From the left panels of this figure, we can see that heavy a's are less separated than lighter a's, as they are less boosted in the Higgs rest frame. Similarly, from the right panels we can see that the $b\bar{b}$ pairs from heavier a's are more back-to-back. The higher average Higgs boson p_Ts in the VBF and WH production channels result in more collimated decay products. We have checked that the `MadGraph` samples agree well with the `Powheg` samples in modelling these distributions. Figure 286 shows the p_T spectrum of the leading b-parton for various Higgs boson production modes. The broader distributions for lighter a masses reflect the bigger boost of those a's in the Higgs rest frame. Again, we have checked that the `MadGraph` samples agree

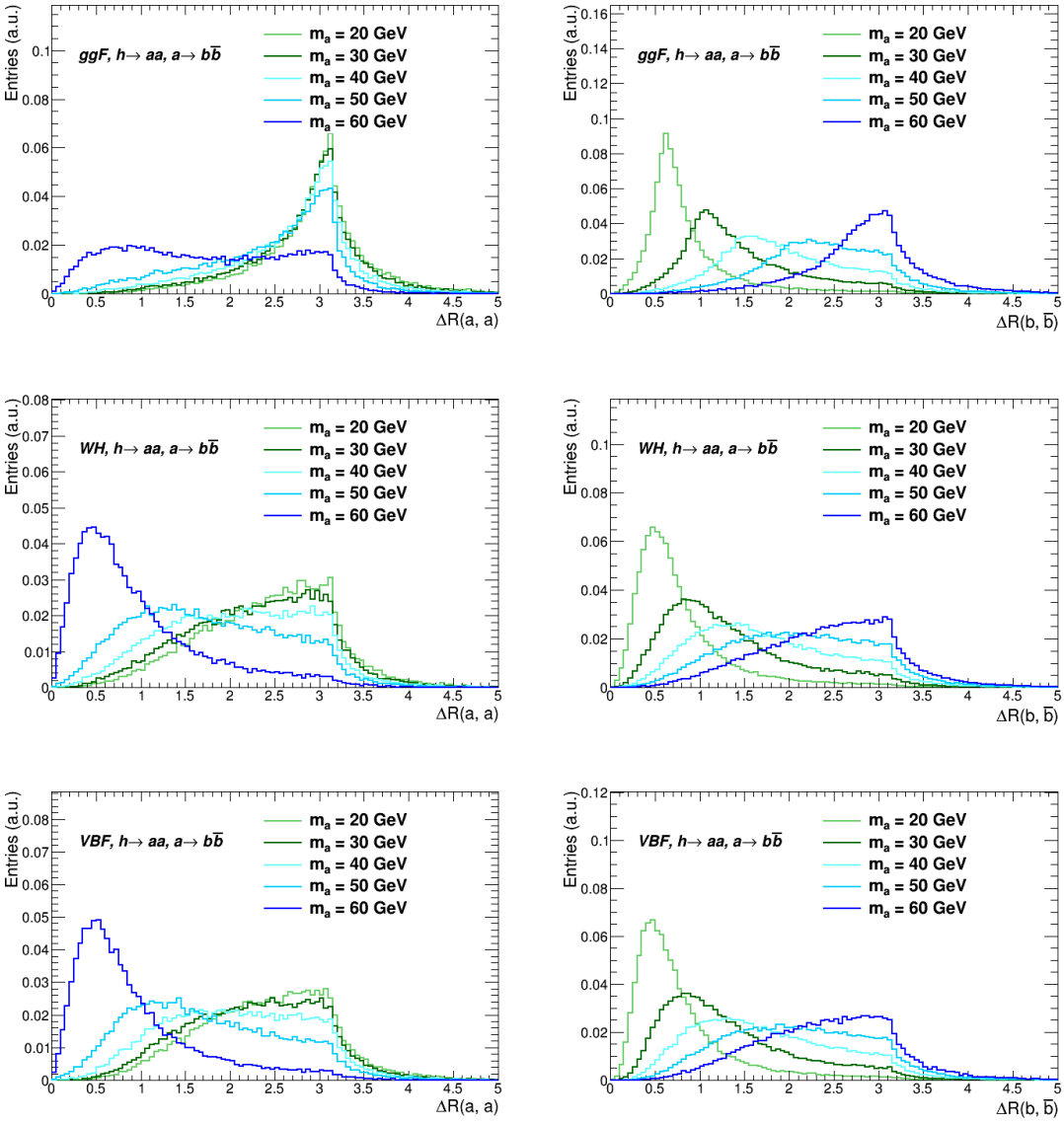

Figure 285: The angular separation ΔR between the two pseudo-scalars from Higgs boson decay (left panels), and between the $b\bar{b}$ pairs from a pseudo-scalar a decay (right panels) as computed by Powheg at LHC 13 TeV, normalized to unity. The upper, middle and lower panels correspond to Higgs boson production modes of ggF, WH and VBF, respectively.

well with the Powheg samples in modelling these distributions in VBF and WH production modes, while in ggF there are minor differences comparable to those in Figure 284.

In Figure 287 we show the fraction of events which have $N_b = 2, 3, 4$ partons above a given p_T for models with heavy ($m_a = 60$ GeV) and light ($m_a = 20$ GeV) pseudoscalars. Here the b-quarks are required to have $|\eta| < 2.5$, but no further cuts are applied. These plots quantify the overall softness of the final state particles. In all three production modes, the efficiency drops quickly with the p_T threshold. For the light (heavy) pseudoscalar, the efficiency reaches the level of 30% around a threshold of $\sim$ 10 (17) GeV for $N_b = 4$, $\sim$ 20(25) GeV for $N_b = 3$, and 35(35) GeV for $N_b = 2$. Again, ggF gives rise to an overall softer b spectrum. The broader p_T distribution produced by the lighter pseudo-scalar results in a more rapid falloff of efficiency with increasing p_T.

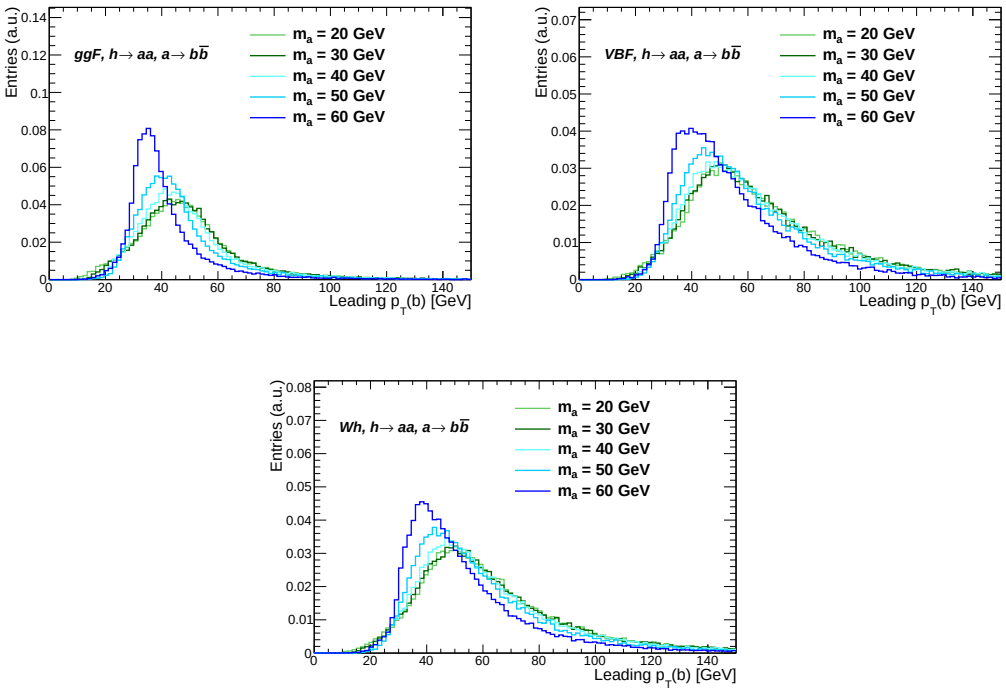

Figure 286: The p_T spectrum of the leading b-parton, as computed by `Powheg` at LHC 13 TeV, normalized to unity, for ggF (left, upper panel), VBF (right upper panel), and WH (lower panel).

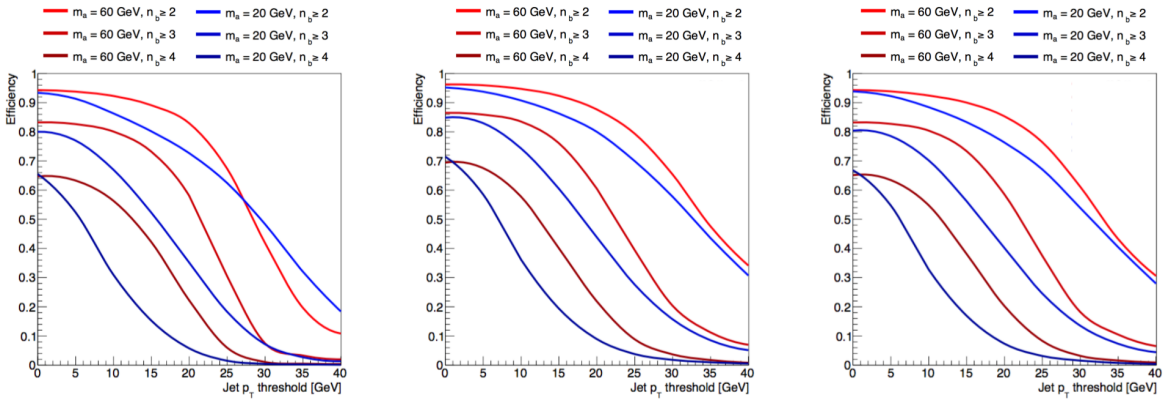

Figure 287: Fraction of events having $N_b = 2, 3, 4$ partons above a given p_T threshhold and $|\eta| < 2.5$, as computed by `Powheg` at LHC 13 TeV, for ggF (left), VBF (centre), and WH (right). No other cuts are applied. Results are shown for both $m_a = 20$ GeV and $m_a = 60$ GeV.

IV.6.5 Prospects for prompt decays with MET: $h \to 2\gamma + \not{E}_T$ test case [IV.39]

IV.6.5.a Introduction

In this section, we discuss exotic Higgs boson decays to two photons together with missing transverse energy ($E_{\mathrm{T}}^{\mathrm{miss}}$). This decay is an example of an interesting class of *semi-invisible* decays, where visible objects in the final state are accompanied by one or more detector-stable particles. Decays featuring multiple electroweak objects together with $E_{\mathrm{T}}^{\mathrm{miss}}$ generally have good prospects at the LHC [1479], and present an obvious target for Run 2. However, this class of signatures poses some questions for analysis

[IV.39] *Author(s): T. Orimoto, R. Teixeira De Lima.*

design. First, the multiple possible topologies that can contribute to any specific final state raise the question of how to design an analysis strategy capable of providing good coverage to more than one signal model. Second, such decays offer several possible trigger strategies. The presence of electroweak objects in the final state can potentially make it possible to trigger on the large population of Higgs bosons produced through gluon fusion, significantly enhancing the statistical reach. On the other hand, the relative softness of these electroweak objects can mean that weak vector boson-associated or vector boson fusion production modes offer better sensitivity given realistic trigger thresholds. Which trigger strategy offers the best sensitivity to a given decay mode is generally not immediately obvious, and will depend in detail on the mass spectrum of the BSM particles produced in the Higgs boson decay.

Here, to illustrate these general points and to begin to answer these questions, we consider two simplified models yielding Higgs boson decays to a final state consisting of two photons and $E_{\mathrm{T}}^{\mathrm{miss}}$. In the first, non-resonant, case, the photons arise from opposite sides of an initial two-body decay: $h \to XX, X \to \gamma Y$, where Y is a stable neutral particle. Such a decay can occur for instance within gauge-mediated supersymmetry breaking (GMSB) SUSY models, in which the X corresponds to a neutralino next-to-lightest supersymmetric particle (NLSP) with mass less than half the Higgs boson mass, and the Y corresponds to a gravitino LSP [1611–1613]. In the second, resonant, case, the photons are produced through an intermediate resonance: $h \to S_1 S_2$, with $S_1 \to \gamma\gamma$ on one side of the decay, while S_2 escapes detection, appearing as $E_{\mathrm{T}}^{\mathrm{miss}}$ in the detector. This signal can arise in e.g. hidden valley scenarios [1478]. The resonant signal benefits from a peak in the diphoton invariant mass spectrum. The Feynman diagrams for the non-resonant and resonant decays can be seen in Figure 288.

Previous searches for the $\gamma\gamma + E_{\mathrm{T}}^{\mathrm{miss}}$ final state in the low energy regime include searches for the non-resonant Higgs boson decay in the supersymmetric scenario described above. The current bounds on this decay mode come from searches using both gluon fusion and ZH production for CMS [1614], and using vector boson fusion for ATLAS [1615]. Both the CMS and ATLAS analyses directly search for the decay $h \to \gamma + \not{E}_T$, which can be sensitive to the decay $h \to 2\gamma + \not{E}_T$ when one of the photons is not reconstructed. The CMS search sets a 95% CL limit on branching ratios larger than 8%-10% on this decay, with the neutralino mass ranging between 1 and 60 GeV, and assuming SM Higgs boson production and depending on the assumed topology of the decay; ATLAS sets a 95% CL limit of 20%-30% under the same assumptions.

In this study, we devise a search strategy for the $\gamma\gamma + E_{\mathrm{T}}^{\mathrm{miss}}$ final state, motivated by the exotic decays of the Higgs described above. We estimate the sensitivity of this search for 100 fb^{-1} of $\sqrt{s} = 14$ TeV pp data from the LHC.

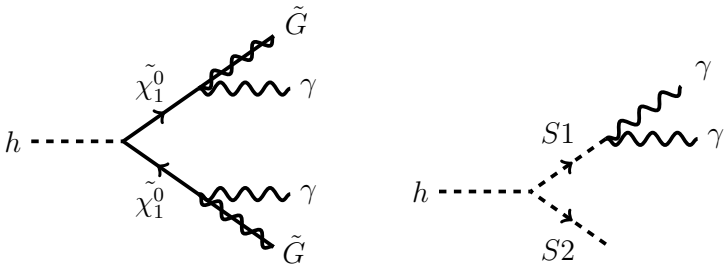

Figure 288: Feynman diagrams for (left) the non-resonant and (right) the resonant signal scenarios.

IV.6.5.b Methodology

IV.6.5.b.i Simulation Samples

Signal and background Monte Carlo (MC) samples were generated with `MadGraph 5` [364] and hadronized with `Pythia 8` [318], with the detector simulation provided by `DELPHES 3` [1616]. The samples were produced at $\sqrt{s} = 14$ TeV. The object reconstruction and identification are performed with `DELPHES`,

according to the information provided in the detector configuration card. For photon reconstruction and identification, we assume an efficiency of 95% in the electromagnetic calorimeter barrel ($|\eta| < 1.5$) and 85% in the endcap ($1.5 < |\eta| < 2.5$). We also impose an isolation cut on the photons by requiring all tracks, neutral hadrons and photons reconstructed by DELPHES within a cone of $\Delta R < 0.3$ of the photon candidate to have an energy ratio less than 0.1 with respect to the photon candidate. For muons, we assume an efficiency of 95% for the whole detector acceptance ($|\eta| < 2.5$). An isolation cut similar to the photons is also applied. Jets are reconstructed with the anti-k_T algorithm with jet radius $R = 0.4$.

Signal Monte Carlo. The signal for the non-resonant case was based on the supersymmetric cascade decay of the Higgs boson into two neutralinos, which subsequently decay into two gravitinos and two photons (Figure 288, left). This class of models has been implemented in FeynRules [1617] and generated using MadGraph. We assume a gravitino mass close to zero, which is consistent with gauge mediated low-scale SUSY breaking models with $\sqrt{f} \approx$ TeV [1613]. We simulate neutralino masses in the range $10\,\text{GeV} \leq m_\chi \leq 60$ GeV in steps of 5 GeV, with 100,000 events per mass point.

For the resonant case, we assume the Higgs boson decays into two scalar particles, S_1 and S_2 (Figure 288, right). One of the scalars then decays into two photons, while the other escapes detection. For this study, we assume the masses of these two particles are the same; this choice was made for simplicity, but for detailed studies, more combinations should be investigated. We generate samples with $M_1 = M_2$ in the range $10\,\text{GeV} \leq M_1 \leq 60$ GeV, in steps of 5 GeV, with 100,000 events per mass point.

We investigate the production of the Higgs boson through both gluon fusion (ggF) and associated production with a Z boson (ZH), with the Z boson decaying to two muons. The inclusion of the di-electron decay of the Z can also be considered for future studies. A branching ratio of $\text{Br}(h \to \gamma\gamma + E_\text{T}^\text{miss}) = 10\%$ is assumed for the signal. This value of the branching ratio was chosen to be within the current bounds on the Higgs boson width, yet close to the 8 TeV limits from the search for Higgs boson decays to the monophoton final state ($h \to \gamma + E_\text{T}^\text{miss}$) [1614].

Background Monte Carlo. Although this analysis is not guaranteed to be entirely free from QCD multi-jet backgrounds, it has been shown in similar analyses primarily targeting $h \to \gamma + E_\text{T}^\text{miss}$ (such as [1614]) that it is possible to reduce QCD backgrounds to a sub-dominant contribution. As we require two photons for most aspects of this analysis, we expect that multi-jet backgrounds will typically be less important than in Ref. [1614]. For this reason, no pure QCD sample was produced for this study. As such, the remaining backgrounds for this analysis arise predominantly from single boson ($\gamma/Z/W$) plus jets and diboson processes.

Backgrounds were modeled using the Snowmass LHE simulation samples [1618]. These consist of single boson samples ($\gamma/Z/W$) with at least one jet and inclusive diboson ($\gamma\gamma/Z\gamma/W\gamma/\ WW/ZZ/WZ$) samples. The samples include both hadronic and leptonic decays of the W and Z bosons. The cross sections used for normalizing the single boson samples were estimated with MCFM [533], assuming an efficiency of 15% for the one jet requirement (as obtained with MadGraph). For the diboson samples, the cross sections used were estimated from Ref. [288]. The cross sections and number of events in the samples are shown in Table 172.

IV.6.5.b.ii Event Selection

Trigger Projections.

For the ZH channel, the trigger strategy is expected to be straightforward and can be based on the decay of the Z to two muons. On the other hand, triggering is one of the main challenges for the ggF channel, since the final state consists of two soft photons plus (a relatively small amount of) missing energy. The standard triggers used for $h \to \gamma\gamma$ analyses in CMS typically have a diphoton invariant mass cut which makes it incompatible with the low energy spectrum of this analysis. However, we have identified three possible trigger strategies for this channel, based on unprescaled triggers used by the

Table 171: Analysis selection for the ggF channel (for each trigger scenario) and the ZH channel.

	ggF			ZH
Variable	Asymmetric $\gamma\gamma$	Symmetric $\gamma\gamma$	$\gamma + E_{\mathrm{T}}^{\mathrm{miss}}$	
Number of photons	> 1	> 1	> 1	> 1
$p_T(\gamma_1)$	> 45 GeV	> 40 GeV	> 55 GeV	> 20 GeV
$\lvert\eta(\gamma_1)\rvert$	< 2.5	< 2.5	< 1.4	< 2.5
$p_T(\gamma_2)$	> 30 GeV	> 40 GeV	> 20 GeV	> 20 GeV
$\lvert\eta(\gamma_2)\rvert$	< 2.5	< 2.5	< 2.5	< 2.5
$M(\gamma\gamma)$	$\in [15, 100]$ GeV	< 100 GeV	< 100 GeV	< 100 GeV
$E_{\mathrm{T}}^{\mathrm{miss}}$	> 90 GeV	> 90 GeV	> 90 GeV	> 60 GeV
$M_T(\gamma\gamma, E_{\mathrm{T}}^{\mathrm{miss}})$	< 140 GeV	< 140 GeV	< 140 GeV	< 140 GeV
$\Delta\phi(\gamma\gamma, E_{\mathrm{T}}^{\mathrm{miss}})$	< 1.5	< 1.5	< 1.5	< 1.5
Number of leptons	< 1	< 1	< 1	2 muons
$p_T(\mu_{1,2})$	-	-	-	> 20 GeV
$\lvert\eta(\mu_{1,2})\rvert$	-	-	-	< 2.5
$M(\mu\mu)$	-	-	-	$\in [75, 115]$ GeV
$M_T(\gamma\gamma + E_{\mathrm{T}}^{\mathrm{miss}}, \mu\mu)$	-	-	-	> 400 GeV

CMS experiment in Run 2:

- Asymmetric Diphoton Trigger: This trigger requires two photons with different E_T and trigger-level identification requirements, plus a diphoton invariant mass cut. This type of trigger usually has a non-negligible turn-on curve in the leading and subleading photon E_T.
- Symmetric Diphoton Trigger: This trigger requires two photons with the same E_T requirement, without any extra requirements.
- $\gamma + E_{\mathrm{T}}^{\mathrm{miss}}$ Trigger: This trigger requires only one barrel photon passing identification requirements and a E_T requirement that is usually higher than the previous two triggers. In addition, there is a calorimetric $E_{\mathrm{T}}^{\mathrm{miss}}$ requirement. We expect non-negligible turn-on curves with respect to both photon and $E_{\mathrm{T}}^{\mathrm{miss}}$ for this trigger.

The three triggers described here represent different selection strategies that were investigated and will be described below.

Offline Selection. In the ggF analysis, events are triggered based on the properties of the photons, and the selection cuts must reflect the chosen trigger strategy, while maintaining a good signal efficiency. The ZH-produced signal events are tagged through the decay of the Z boson to muons, minimizing the largest backgrounds. The photon selection is chosen to maximize the signal acceptance in the ZH case, with E_T thresholds as low as possible. The final event selection requirements for the ggF and ZH channels are summarized in Table 171. In this table, we use the following definitions for transverse mass:

$$M_T(\gamma\gamma, E_{\mathrm{T}}^{\mathrm{miss}}) = \sqrt{2E_T(\gamma\gamma)E_{\mathrm{T}}^{\mathrm{miss}}(1 - \cos(\Delta\phi(\gamma\gamma, E_{\mathrm{T}}^{\mathrm{miss}}))}, \tag{IV.6.32}$$

$$M_T(\gamma\gamma + E_{\mathrm{T}}^{\mathrm{miss}}, \mu\mu) = \sqrt{2E_T(\gamma\gamma + E_{\mathrm{T}}^{\mathrm{miss}})p_T(\mu\mu)(1 - \cos(\Delta\phi(\gamma\gamma + E_{\mathrm{T}}^{\mathrm{miss}}, \mu\mu))}. \tag{IV.6.33}$$

To exploit the topology of the resonant signature, we apply an additional requirement of a ± 10 GeV mass window, in the diphoton invariant mass distribution ($M(\gamma\gamma)$), around the signal mass (M_1).

Table 172: Cross-sections, numbers of events generated per process, and selection efficiencies for background processes and signal points, for ggF and ZH production mechanisms. Signal cross-sections are quoted for a 10% branching ratio.

Process	σ (pb)	$N_{\text{Generated}}$	ggF			ZH
			Asymmetric $\gamma\gamma$	Symmetric $\gamma\gamma$	$\gamma + E_{\text{T}}^{\text{miss}}$	
Backgrounds						
γ + Jets	1.0×10^5	5425448	1.9×10^{-6}	4.7×10^{-7}	8.9×10^{-7}	≈ 0
Z + Jets	0.94×10^4	1888446	5.6×10^{-4}	1.5×10^{-4}	5.0×10^{-5}	≈ 0
W + Jets	2.96×10^4	5263872	6.2×10^{-4}	1.9×10^{-4}	2.7×10^{-5}	≈ 0
$\gamma\gamma$	10.8×10^1	4268781	3.1×10^{-5}	1.0×10^{-5}	1.1×10^{-5}	≈ 0
$Z\gamma$	6.30×10^2	3406151	4.3×10^{-4}	1.4×10^{-4}	5.7×10^{-5}	≈ 0
$W\gamma$	1.03×10^3	5258034	1.4×10^{-4}	4.6×10^{-5}	5.4×10^{-5}	≈ 0
WW	1.24×10^2	8059829	2.6×10^{-1}	8.4×10^{-2}	9.8×10^{-5}	8.2×10^{-8}
ZZ	1.8×10^1	1101611	1.4×10^{-2}	4.7×10^{-3}	6.7×10^{-4}	7.3×10^{-6}
WZ	5.1×10^1	3319770	3.6×10^{-1}	1.2×10^{-1}	2.5×10^{-4}	2.9×10^{-6}
Signals						
Res., M = 10 GeV	10.8×10^1	4268781	2.5×10^{-4}	2.2×10^{-4}	1.7×10^{-4}	5.7×10^{-4}
Res., M = 40 GeV	6.30×10^2	3406151	8.7×10^{-3}	5.7×10^{-3}	5.0×10^{-3}	6.9×10^{-3}
Res., M = 60 GeV	1.03×10^3	5258034	1.6×10^{-2}	1.1×10^{-2}	1.1×10^{-2}	9.2×10^{-3}
Non-Res., M = 10 GeV	1.24×10^2	8059829	1.5×10^{-3}	9.5×10^{-4}	1.1×10^{-3}	1.1×10^{-3}
Non-Res., M = 40 GeV	1.8×10^1	1101611	8.0×10^{-3}	5.5×10^{-3}	5.2×10^{-3}	6.3×10^{-3}
Non-Res., M = 60 GeV	5.1×10^1	3319770	1.1×10^{-2}	7.6×10^{-3}	6.9×10^{-3}	8.1×10^{-3}

The efficiencies for each individual process and the different searches, after the full selection (without the $M(\gamma\gamma)$ mass window requirement), are shown in Table 172.

For the ZH case, we also explore the strategy performed by CMS in their Run 1 result [1614], in which one or more photons are required in the event, instead of two or more. In this case, we gain back the efficiency that is lost due to the inefficiency in reconstructing the subleading photon, which can have very low E_T. The selection is similar to what is described in Table 171, but without the $M(\gamma\gamma)$ cut or the mass window requirement for the non-resonant topology. The other variables that use the diphoton information are instead reconstructed using only the leading photon in the event. Plots of some of the discriminating variables are available at `https://twiki.cern.ch/twiki/bin/view/LHCPhysics/LHCHXSWGExoticDecayYR4ExtraMaterials`.

IV.6.5.b.iii Background Estimation for Misidentified Photons

Background processes with misidentified (or "fake") photons, such as jets and electrons erroneously reconstructed as photons, that pass the final selection generally have very low efficiency at the LHC. Nonetheless, such backgrounds may be non-negligible since the production cross-sections can be large. Such mis-identification rates are typically measured with data-driven methods at the LHC. Although this study was limited by MC statistics in measuring fake photon backgrounds, a method was developed to mitigate this problem, which we describe below.

The object reconstruction and selection is done at `DELPHES` level, where, given the photon identification requirements described in Section IV.6.5.b.i, we obtain an associated fake rate. These fake rates

are accounted for in the overall efficiencies in Table 172. In order to bypass the efficiency loss due to the small fake rates, we select jets and electrons to be redesignated as fake photon candidates. For the background processes with one prompt photon (γ+jets, $W\gamma$ and $Z\gamma$), we select one fake photon candidate. For the processes with no prompt photons (W/Z+jets, WW, WZ and ZZ), we select two fake photon candidates. No fake photon selection is done for the $\gamma\gamma$+jets sample.

With the assumption of a flat fake rate for both jets and electrons, the fake photon candidates are randomly selected from the jets and electrons that passed the photon acceptance requirements. One extra assumption is that the electron-to-photon fake rate is set to be one order of magnitude larger than the jets-to-photon fake rate. Therefore, electrons are set to have a probability of being selected to be redesignated as a photon that is ten times higher than for jets.

After the choice of fake photon candidates, we calculate weights for the individual samples based on the E_T spectrum of the selected photons (prompt and fake) to match the spectrum found with the photon candidates reconstructed directly from DELPHES. This reweighting is done on the sum of E_T of the two leading photons for samples with at least one prompt photon, and on the E_T of the leading photon for samples with no prompt photon. An independent reweighting is also done in η. Both reweightings reflect the different reconstruction efficiencies and energy resolutions of objects that are not reconstructed as photons (i.e., electrons and jets). After applying the weights, we observe good agreement between the kinematic distributions of interest arising from photons reconstructed by DELPHES, and in particular from events with two photons reconstructed by DELPHES in samples containing only one prompt photon at truth level, and from our fake photon candidates.

IV.6.5.c Results

We present the expected sensitivity of this search in terms of the necessary $h \to \gamma\gamma + E_{\mathrm{T}}^{\mathrm{miss}}$ branching ratio to reach a 5σ sensitivity for an assumed integrated luminosity of 100 fb^{-1} at $\sqrt{s} = 14$ TeV, with the sensitivity defined as:

$$\mathcal{S} = \frac{N_{\mathrm{Signal}}}{\sqrt{N_{\mathrm{Background}}}}. \tag{IV.6.34}$$

In Figure 289, we show the sensitivity plot for the different trigger scenarios of the ggF case. This plot shows that, after the full selection, the performance of the different trigger strategies is comparable. Although it is safe to assume that a diphoton trigger with a low $M(\gamma\gamma)$ cut will be present in the future trigger menus of CMS and ATLAS, we choose to perform the analysis in the $\gamma + E_{\mathrm{T}}^{\mathrm{miss}}$ case. We make this choice as an effort to make the case for the existence of such a trigger strategy for the future LHC runs. While the diphoton triggers are designed with specific usages that are already well established, the $h \to \gamma\gamma + E_{\mathrm{T}}^{\mathrm{miss}}$ analysis could be viewed as a benchmark for the $\gamma + E_{\mathrm{T}}^{\mathrm{miss}}$ trigger for three reasons:

- It is a trigger that is already present at the LHC experiments, but can be retuned with a specific analysis as benchmark;
- A dedicated trigger for this analysis requiring two photons might not be as efficient at trigger level, given the soft spectrum of the second photon;
- This trigger can also be used for other exotic searches, such as the extension to low energies of the dark matter searches in the monophoton channel.

In Figure 290, on the left, we show the branching ratio of $h \to \gamma\gamma + E_{\mathrm{T}}^{\mathrm{miss}}$ needed for a significance of 5σ, assuming the Standard Model Higgs cross section, for the ggF analysis (assuming the $\gamma + E_{\mathrm{T}}^{\mathrm{miss}}$ trigger strategy and selection). On the right, we show the branching ratio $h \to \gamma\gamma + E_{\mathrm{T}}^{\mathrm{miss}}$ needed for a significance of 2σ, which represents the 95% confidence level for exclusion, assuming SM ZH production. For the ZH case, we show the results for the strategies requiring at least one ($N_\gamma \geq 1$) and at least two ($N_\gamma \geq 2$) photons.

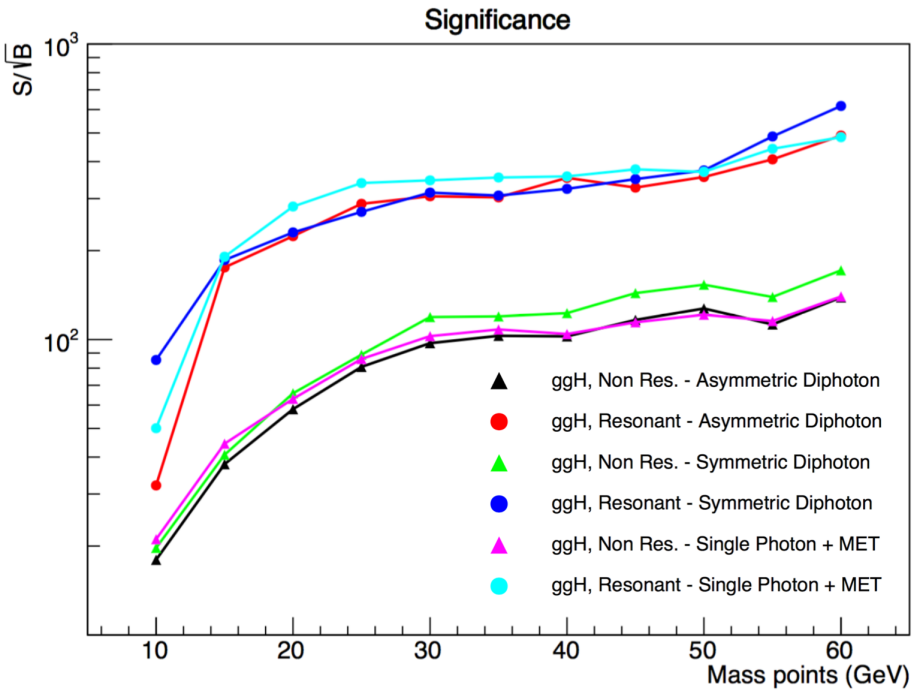

Figure 289: Statistical significance corresponding to different trigger scenarios in the gluon fusion analysis, for a reference signal branching ratio of $\mathrm{Br}(h \to \gamma\gamma + E_{\mathrm{T}}^{\mathrm{miss}}) = 10\%$.

IV.6.5.c.i Systematic Uncertainties

While the uncertainties in the ZH channel are expected to be dominated by statistics, the ggF channel is very sensitive to the systematic uncertainties associated with the background predictions. We estimate the effect of these uncertainties by parameterizing the sensitivity as:

$$\mathcal{S}_{sys} = \frac{N_{\text{Signal}}}{\sqrt{N_{\text{Background}}} + \sigma_{sys} \times N_{\text{Background}}}, \tag{IV.6.35}$$

with σ_{sys} representing a source of uncertainty that does not scale with the amount of statistics. Figure 290 shows the effect on the 5σ branching ratios due to the addition of a 10% systematic uncertainty according to Eq. (IV.6.35).

IV.6.6 Long lived particles from Higgs boson decays [IV.40]

IV.6.6.a Overview and motivation

Long-lived particles (LLPs), specifically meta-stable particles with proper lifetimes $c\tau \gtrsim \mu$m, arise in a large variety of BSM scenarios. Such particles, once produced at the LHC or other colliders, can decay within the detector volume with measurable displacement from the interaction point. For experimental searches, this represents both a challenge and an opportunity. On the one hand, the ATLAS and CMS detectors were not specifically optimized for displaced decays, which can make triggering and reconstruction challenging. On the other hand, events with displaced decays are spectacular and relatively background-free. This makes LLP searches enticing discovery avenues for new physics, especially in light of null results from prompt BSM searches at the LHC Run 1.

LLP's often arise as a part of hidden sectors, which make exotic Higgs boson decays a very promising production mechanism [1479]. One simple toy model that realizes this possibility involves

[IV.40] *Author(s): D. Curtin, M. Strassler.*

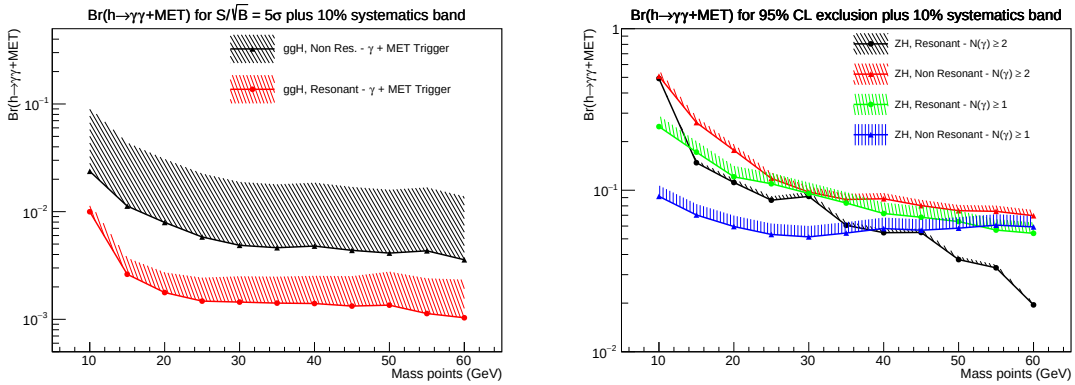

Figure 290: (Left) 5σ branching ratios for the ggF channel, for resonant (in red) and non-resonant (in black) final states, using the $\gamma + E_{\mathrm{T}}^{\mathrm{miss}}$ trigger. (Right) Branching ratios for 95% confidence level exclusion in the ZH case, resonant and non-resonant topologies, requiring at least one photon ($N_\gamma \geq 1$, in green and blue, respectively) and at least two photons ($N_\gamma \geq 2$ in black and red, respectively). The shaded areas correspond to a variation in systematic uncertainties up to 10%.

the Higgs boson coupling to two (pseudo)scalars X which decay back to the SM, resulting in the decay chain $h \to XX \to \mathrm{SM}$. The X couplings to SM particles may be inherited from mixing with the SM-like Higgs (and with any additional doublets, if present), which gives them Yukawa-weighted branching fractions that prefer third-generation fermion final states like $X \to \bar{b}b$ or $\tau^+\tau^-$. Due to this preference for heavy-flavour final states, we will call this scenario "hXX-HF." For prompt X-decays this toy model arises as part of the NMSSM [1466] or more generally the SM+S or 2HDM+S models described in [1595]. This toy model is also commonly relevant in Hidden Valley models [1478, 1619–1621]. Perhaps the most compelling motivation for this type of decay is the connection to *Neutral Naturalness*, where models like the Fraternal Twin Higgs [1476] or Folded SUSY [1475] give rise to this decay (as well as others) through the structure of their hidden sectors.

Although we will not address most of them here, there are many other possible scenarios for LLPs arising from exotic Higgs boson decays. For example, the Higgs might decay to spin-one bosons with displaced decays [1619]. Ref. [1608] studied the well-motivated scenario where the Higgs boson decays to two dark photons via mixing with a dark Higgs. The dark photons can then decay with long-lifetimes via a small kinetic mixing with SM hypercharge. This also realizes a $h \to XX \to \mathrm{SM}$ signal model, but now with *gauge-ordered* branching fractions of X, yielding lepton-rich final states. This scenario (hXX-GO) may be even easier to discover, and is already more constrained [1622, 1623] than is hXX-HF.[IV.41] Other examples can arise naturally within weak-scale extensions of the SM. For instance, models with weak-scale right-handed (RH) neutrinos can feature Higgs boson decays into RH neutrino pairs, with the RH neutrinos generically long-lived and decaying via $W^{(*)}\ell$ or $Z^{(*)}\nu$ [1624–1627]. The MSSM offers many ways to obtain LLPs, which can result in displaced Higgs boson decays. For instance, the Higgs can decay to a pair of bino-like neutralinos with a displaced R-parity-violating decay [1628, 1629]. Another example, which we study in Section IV.6.6.c, occurs in models with gauge-mediated SUSY-breaking, where the initial Higgs boson decay to neutralinos is followed by the displaced decay of the neutralino to a gravitino and a photon [1468, 1612].

The simplicity and motivation of the hXX-HF scenario makes it an obvious starting point to explore this class of signals. In fact, several experimental searches looking for hXX-HF have already been conducted [1630, 1631], and these kinds of analyses will have significant power to probe scenarios like Neutral Naturalness at LHC Run 2. The success of these studies is highly encouraging, and prompts us to examine how to improve and broaden their reach for new physics.

In the course of this discussion, we find it useful to carefully define the following:

- *Associated Object* (AO): Any conventional detector object, such as leptons, VBF jets, or a hard initial state radiation (ISR) jet, that is produced in the same event as the LLP(s).
- *Displaced Object* (DO): An LLP decaying into visible SM particles in the detector with a *potentially measurable displacement* from the primary interaction point. Importantly, a DO is a "truth-level" definition, and does not necessarily imply the object can be detected or reconstructed.
- *Triggerable Displaced Object* (tDO): A DO which can, in principle, *be triggered upon*, either by itself or in conjunction with an AO.
- *Displaced Vertex* (DV): an *off-line reconstructed* displaced vertex in the tracker or the ATLAS muon system.

The most obvious strategy for improving the experimental reach is to include searches which only require a *single* DO, but have a low trigger threshold. In this context, background reduction and triggering usually require the presence of an AO arising from Higgs boson production. Compared to what is possible in current searches, these searches would give access to long-lived Higgs daughters that have shorter lifetimes (and thus decay only in the tracker) or lower masses (where the LLP's decay products are insufficient to pass trigger thresholds). They may also in some cases increase trigger efficiencies.

[IV.41] There is some overlap of the issues that displaced dilepton searches [1622, 1623] and searches for the hXX-HF scenario have to contend with. However, since triggering on displaced leptons, especially muons, is generally much easier than triggering on displaced jets, we do not discuss the case of displaced dileptons further.

Crucially, such searches are also sensitive to more general classes of signals, e.g. $h \to XX'$ where only X decays in the detector. Timing may also be an important search strategy for heavier X.

Below, in Section IV.6.6.b we consider displaced objects arising in the hXX-HF scenario from exotic Higgs boson decays. In Section IV.6.6.c we consider signals that give rise to displaced photons.

IV.6.6.b Displaced objects

We now consider DOs produced in Higgs boson decays. For brevity we consider only the hXX-HF scenario. In Section IV.6.6.b.i we define a simplified model for this scenario, and show how to simulate this signal in `Madgraph`. Section IV.6.6.b.ii gives a review of Neutral Naturalness and how it generates the hXX-HF scenario. An overview of present experimental searches is given in Section IV.6.6.b.iii. Finally, we suggest new searches for the future years of the LHC in Section IV.6.6.b.iv, and supply some benchmark points to aid in the design of DO searches that cover the most theoretically motivated parameter space of the hXX-HF scenario.

IV.6.6.b.i A simplified model for the hXX-HF scenario

The easiest way to parameterize the hXX-HF scenario is by introducing a small mixing between a scalar X and the Higgs. (For the purpose of signal event generation the distinction between scalar and pseudoscalar X is immaterial). However, the coupling which controls the $h \to XX$ decay does not arise from this mixing, so that the exotic Higgs boson decay branching fraction $\mathrm{Br}(h \to XX)$ and the X decay length $c\tau_X$ are independently adjustable. A simple Lagrangian to realize this possibility after electroweak symmetry breaking is the following:

$$\mathcal{L} \supset \frac{1}{2}(\partial_\mu X)^2 - \frac{1}{2}m_X^2 X^2 - g_X v h X X - \epsilon_v v^2\, h X \,, \tag{IV.6.36}$$

The three important parameters are

(a) the mass m_X of the long-lived particle,
(b) $\mathrm{Br}(h \to XX)$, which is controlled by the effective coupling g_X, and
(c) the decay length $c\tau_X = 1/\Gamma_X$, which is controlled by the small mixing parameter ϵ_v. (Displaced decays of X require $\epsilon_v \lesssim 10^{-4}$, and so ϵ_v has a negligible effect on m_h and on h branching fractions to SM particles.)

Madgraph implementation

The hXX-HF scenario can be realized by repurposing the SM + dark vector + dark Higgs `MadGraph` model of [1608] available at `http://insti.physics.sunysb.edu/~curtin/hahm_mg.html`. In this model, X is identified with the dominantly singlet scalar state `hs`, with m_X corresponding to the model parameter `MHSinput`. The singlet `hs` decays to SM fermions via its mixing with the SM-like Higgs `h`, which is controlled by the model parameter `kap`. This `MadGraph` model includes the couplings between the Higgs and SM gauge bosons, including the gluons via an effective operator. X therefore inherits the same couplings, and decays like $X \to V^{(*)}V^{(*)}$ can also be generated.

For a given $\mathrm{Br}(h \to XX)$, $\Gamma_X = 1/(c\tau_X)$ and m_X, the procedure for generating $h \to XX \to$ SM events is the following:

1. Switch off dark photon effects (by setting the `epsilon` and `mZDinput` parameters to, say, `10e-09` and `1000e+00` respectively.)
2. Set the parameter `MHSinput` to the desired m_X.
3. Event generation will depend on how LLPs are handled, specifically whether X is decayed in `MadGraph` or *e.g.* in `Pythia`. In the former case, one could generate the processes
   `p p > hs hs, hs > b b~`
   `p p > hs hs, hs > ta+ ta-`

`p p > hs hs, hs > ta+ ta-, hs > b b~`
separately (for the most important $b\bar{b}$ and $\tau^+\tau^-$ final states), then manually displace the decays. In the latter case, X can be left undecayed in `MadGraph`. The lifetime can then be written to the LHE file before running through `Pythia`.
Another possibility is to produce events with the X decay implemented directly in `Pythia`. In that case the lifetime can be written to the SLHA file.

4. Each sample can then be rescaled to the desired $\sigma_h \times \mathrm{Br}(h \to XX) \times \mathrm{BR}(XX \to f\bar{f}f'\bar{f}')$. Here σ_h is the inclusive Higgs boson production cross section, and $\mathrm{BR}(X \to f\bar{f})$ can be computed for a SM-like Higgs boson of mass m_X using HDECAY 6.42 [69]. This method ensures that important NLO QCD and threshold effects are handled accurately, which is not guaranteed if using LO branching fractions generated internally by `Madgraph` or `Pythia`. Higher-order differential effects in Higgs boson production can be taken into account by reweighing events using Higgs boson p_T spectra according to the recommendations of Secs. IV.6.3 and IV.6.4.

IV.6.6.b.ii Neutral naturalness

Perturbative solutions to the hierarchy problem introduce top partners that cancel the quadratically divergent one-loop Higgs boson mass contribution of the top quark. In most theories, this top partner is related to the top quark by a continuous symmetry like supersymmetry, and carries SM colour charge. In models of Neutral Naturalness the symmetry relating the top to its partner includes a discrete group like $\mathbb{Z}_2$, and does not commute with SM colour. This leads to the possibility of colour-neutral top partners.

Moreover, a hidden QCD gauge group is usually required in Neutral Naturalness theories. Without it, the top partner's coupling to the Higgs and the SM top Yukawa coupling will run differently, ruining the cancellation between the top loop and the top partner loop. Neutral Naturalness therefore realizes a Hidden Valley scenario, where hidden gluons couple to the Higgs via top partner loops. This allows hidden hadrons to be produced in exotic Higgs boson decays, as shown in Figure 291. The same coupling then allows hidden glueballs and hidden quarkonia to decay back to the SM via an off-shell Higgs, producing DO signatures. Neutral Naturalness is therefore one of the best motivated scenarios producing the $h \to XX \to \mathrm{SM}$ displaced vertex signature [1476].

Here we describe two archetypal examples of Neutral Naturalness. The first is *Folded SUSY* (FSUSY) [1475] which features a hidden sector of sparticles carrying SM electroweak quantum numbers but charged under the hidden QCD. The hidden QCD confines at a (few–10) GeV, and since LEP limits generically forbid EW-charged particles below $\sim$ 100 GeV, the lightest new particles are always hidden glueballs.

The second example is the *Twin Higgs* [1632] featuring SM-singlet fermionic top partners which are part of a hidden sector containing copies of all SM particles and gauge forces. The original mirror Twin Higgs model has several cosmological problems due to an abundance of light invisible hidden states. A simple modification which satisfies all cosmological constraints is the Fraternal Twin Higgs (FTH) model [1476], which only duplicates the third generation in the hidden sector. In that case, the hadrons of hidden QCD can be made up of hidden glueballs, hidden quarkonia, or a mixture of both.

We now discuss Higgs boson decays to hidden hadrons, following [1476] and [1477], with additional results from [1633].

Hidden Glueballs

In the absence of light hidden matter, the lightest states in the hidden sector are glueballs. A pure $SU(3)$ gauge theory has $\sim$12 stable low-energy states [1634], which can decay on detector timescales when Higgs portal interactions [1635] are present. The lightest state is the 0^{++} state, G_0, with mass $m_0 \approx 7\Lambda_{\mathrm{QCD}}$; the heaviest has order twice this mass. We concentrate on G_0 since it has a potentially

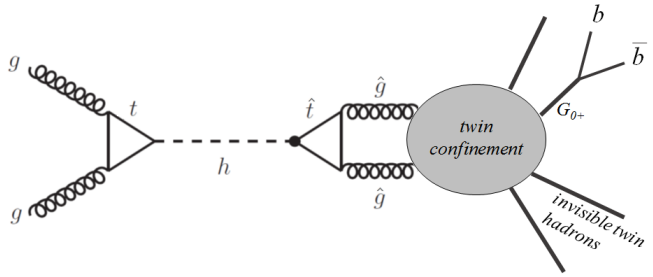

Figure 291: Production of hidden hadrons in exotic Higgs boson decays, and their decay back to the SM, in the Fraternal Twin Higgs model. Figure from [1476].

detectable lifetime and is kinematically the easiest to produce.[IV.42] One can show using RG arguments [1476, 1477] that FSUSY and FTH prefer glueballs in the $\sim (10-60)$GeV mass range. This motivates the study of hidden glueball production in exotic Higgs boson decays.

Hidden gluons couple to $|H|^2$ via a dimension-6 operator, allowing G_0 to decay via its mixing with h. For $m_0 \gtrsim 2m_b$ and top partner mass m_T, the decay length is approximately

$$c\tau \;\approx\; \left(\frac{m_T}{400\text{ GeV}}\right)^4 \left(\frac{20\text{ GeV}}{m_0}\right)^7 \times \begin{cases} (35\text{cm}) & \text{[FSUSY]} \\ (8.8\text{cm}) & \text{[FTH]} \end{cases} \tag{IV.6.37}$$

where we assume $m_T \gg m_t/2$ for FTH and degenerate unmixed stops for FSUSY. As shown in Figure 292 (left) for FSUSY, these decay lengths can range from $\mathcal{O}(10\mu\text{m})$ to $\mathcal{O}(\text{km})$ and more, motivating searches for displaced vertices in all detector subsystems.

The rate for *inclusive* production of hidden glueballs from exotic Higgs boson decays can be estimated by rescaling the $\text{Br}(h \to \text{gluons})$ which is of the order of $\sim 8\%$ in the SM

$$\text{Br}(h \to \text{hidden glue}) \;\approx\; 10^{-3} \left(\frac{400\text{ GeV}}{m_T}\right)^4 \times \begin{cases} 1 & \text{[FSUSY]} \\ 4 & \text{[FTH]} \end{cases} \tag{IV.6.38}$$

Nonperturbative effects could in some regimes reduce or enhance this by a factor of order one [1476]; meanwhile RG effects on the hidden QCD coupling at scale m_h can increase the branching ratio by a factor of two [1477].

In the FTH model this branching fraction can be greatly enhanced if the hidden bottom quark B has a mass in the range $m_0 \lesssim m_B < m_h/2$. In this case $h \to \bar{B}B$ is possible, but any hidden bottomonium states annihilate to hidden glueballs. The effect is to enhance the inclusive twin glueball rate to

$$\text{Br}(h \to \text{hidden glue}) \approx (h \to \bar{B}B) \;\approx\; 0.15 \left(\frac{m_B}{12\text{ GeV}}\right)^2 \left(\frac{400\text{ GeV}}{m_T}\right)^4 \quad , \; (m_B < m_h/2) \tag{IV.6.39}$$

which can be as large as current limits on the branching ratio into exotics. From Eq. (IV.6.38) and Eq. (IV.6.39), we expect at least 10^4 and up to 10^6 such decays at Run 2 with 300 fb^{-1} data, giving the LHC experiments an attractive target.

[IV.42] There is a second 0^{++} state, heavier and shorter-lived, which may be phenomenologically relevant. In Folded SUSY, the 0^{-+} state can also decay through mixing with the SM Z-boson; the lifetime and branching fractions of this state are still under study [1636]. Note also that all formulas in this section have order-one uncertainties due to RG effects, lattice uncertainties, etc.

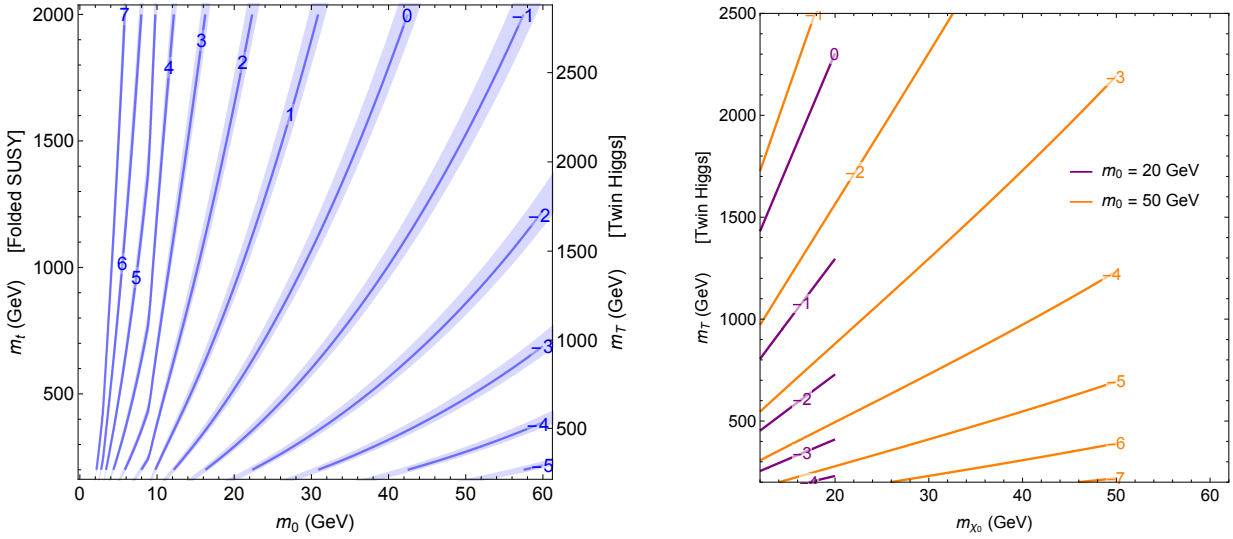

(a) (b)

Figure 292: (a) Contours show $\log_{10}(c\tau/1\mathrm{m})$, where $c\tau$ is the proper decay length of the lightest hidden glueball state G_0. The blue bands correspond to the shift of the contours resulting from the 25% uncertainty in the total G_0 width [1477]. (b) Estimate of the decay length of the hidden bottomonium χ_0 state, Eq. (IV.6.41), for $m_0 = 20$ (in purple) and 50GeV (in orange). Uncertainties are not shown.

Since only a fraction of hidden glueballs may be G_0 states, explicit signal estimates for DO searches require an estimate of *exclusive* G_0 production, and thus of G_0 production in hidden hadronization. A conservative assumption is that G_0 are produced only in two-body decays $h \to G_0 G_0$, which is the hXX-HF scenario. This probably underestimates the signal, since light glueballs (which are very long-lived) are likely produced at greater multiplicities and lower boost, effects which increase the number of observable DOs. Introducing κ as a nuisance parameter that encapsulates our uncertainty of hidden hadronization, we can write the exclusive branching ratio as

$$\mathrm{Br}(h \to G_0 G_0) \;=\; \mathrm{Br}(h \to \text{hidden glue}) \;\cdot\; \kappa \;\cdot \sqrt{1 - \frac{4m_0^2}{m_h^2}}\,, \tag{IV.6.40}$$

where the phase space factor ensures the branching ratio goes to zero for $m_0 \to m_h/2$. We adopt two benchmark values for κ which bracket the range of likely physical outcomes. The most optimistic estimate is that all glueballs produced are G_0 pairs, giving $\kappa_{\max} = 1$. Conversely, a reasonable lower bound on κ is to assume democratic production of the light C-even glueballs $0^{++}, 2^{++}, 0^{-+}, 2^{-+}$ with masses m_i, $i = 1, \ldots, 4$. In terms of phase space factors $\mathcal{P}(m_i) \equiv \sqrt{1 - 4m_i^2/m_h^2}$, we then define $\kappa_{\min} = \mathcal{P}(m_0)/\sum_i n_i \mathcal{P}(m_i)$ with $n_i = 1, 4$ for spin 0, 2 glueballs, which ranges from $\kappa_{\min} \approx 1/12$ for light glueballs to 1 for heavier glueballs.

The authors of [1477] performed signal estimates for displaced glueballs from exotic Higgs boson decay for the two benchmark values $\kappa = 1, \frac{1}{12}$, which are reproduced in Section IV.6.6.b.iv. The LHC can probe G_0 lifetimes corresponding to values of m_T up to the TeV scale with a variety of DO searches.

We should emphasize that there are certain non-perturbative effects and special regimes where this minimal parameterization may not be sufficient, or where $1 > \kappa > 1/12$ may not be broad enough. For the near term, however, we recommend these subtleties be ignored in designing searches.

Additional complications may arise when many DO's are clustered in the same region of the detector, or are not isolated from prompt objects. That being said, these difficulties are unlikely to be prohibitive for DO's decaying in the tracker.

Hidden Bottomonia

In the FTH, if $m_B < m_0/2$, then G_0 (and all other hidden glueballs) will decay to hidden bottomonium. The hidden bottomonium spectrum also contains a 0^{++} state, χ_0, which can decay via mixing with the SM-like Higgs. The lifetime of this state is

$$\Gamma_{\chi_0 \to YY} \sim 2 \times 10^{-3} \left(\frac{v}{f}\right)^4 \frac{m_{\chi_0}^{11/3} m_0^{10/3}}{v^2 m_h (m_h^2 - m_{\chi_0}^2)^2} \Gamma_{h \to YY}(m_h) \,, \tag{IV.6.41}$$

assuming there are no light twin neutrinos which could short-circuit this decay mode. The corresponding proper lifetime for $m_0 = 20$ and 50 GeV is shown in the (m_{χ_0}, m_T) - plane in Figure 292 (b). The phenomenology of exotic Higgs boson decays and resulting search strategies are broadly similar to the glueball case discussed above, with two notable differences:

1. The rate of hidden bottomonium production is approximately given by the exotic Higgs boson decay rate to $\bar{B}B$, see Eq. (IV.6.39), and can be much larger than the direct Higgs boson decay to glueballs; however, χ_0 itself may not be commonly produced in the subsequent hadronization of the mirror bottom quark pair.
2. Hidden bottomonia can have much shorter decay lengths at low masses $m_{\chi_0} \ll m_h/2$ than glueballs of the same mass. (In some cases the decay can be prompt, which makes the decay harder to detect.) This motivates searches for low mass DOs at small displacement.

IV.6.6.b.iii Experimental analyses

At the time of writing, two experimental searches by the ATLAS collaboration have significant sensitivity to the hXX-HF scenario discussed here. Ref. [1631] used a dedicated trigger sensitive to tDOs in the muon system (MS). In addition to the triggered decay, an additional DV in *either* the muon system or the inner tracker (IT) was required. This stringent requirement made the search effectively background-free, giving it good sensitivity for X's which live long enough to reach the MS. An earlier search using the HCAL utilized a similar strategy [1630] but is not as sensitive as the search in the MS.

CMS conducted a search [1637] for heavy particles decaying to at least one long-lived daughter, as arises in e.g. SUSY with R-parity violation (RPV). A $H_T > 300$ GeV preselection requirement makes this search inefficient to the DOs arising from decays of the relatively light Higgs. A recast of this search [1633] estimates hXX-HF limits on $\mathrm{Br}(h \to XX)$ of order 10%. This is considerably better than indirect constraints from coupling fits. However, it is only marginally sensitive to Neutral Naturalness, see Eq. (IV.6.38), though it does encroach upon the parameter space for the Higgs boson decaying to mirror bottomonia, see Eq. (IV.6.39). As we discuss below, a different version of this search, with a trigger on VBF jets plus a displaced or trackless jet, could potentially be much more sensitive.

IV.6.6.b.iv Suggested searches and benchmarks

Suggested searches

In the context of this discussion we carefully use the terms DO, tDO and DV as defined at the end of Section IV.6.6.a.

The above existing searches can be categorized into two classes. The ATLAS searches require a tDO in the Muon System or HCAL for triggering, as well as an additional DV or tDO in offline reconstruction. The CMS search triggers on a high-threshold associated object (AO) at L1 (H_T) and on a (tDO + high-threshold AO) at higher trigger level, where the tDO refers to the displaced jets in the tracker.

Our central recommendation is that, in addition to existing methods, searches be added that require only a *single* DO across all lifetimes, with thresholds that maintain sensitivity to production of LLPs in exotic Higgs boson decays.

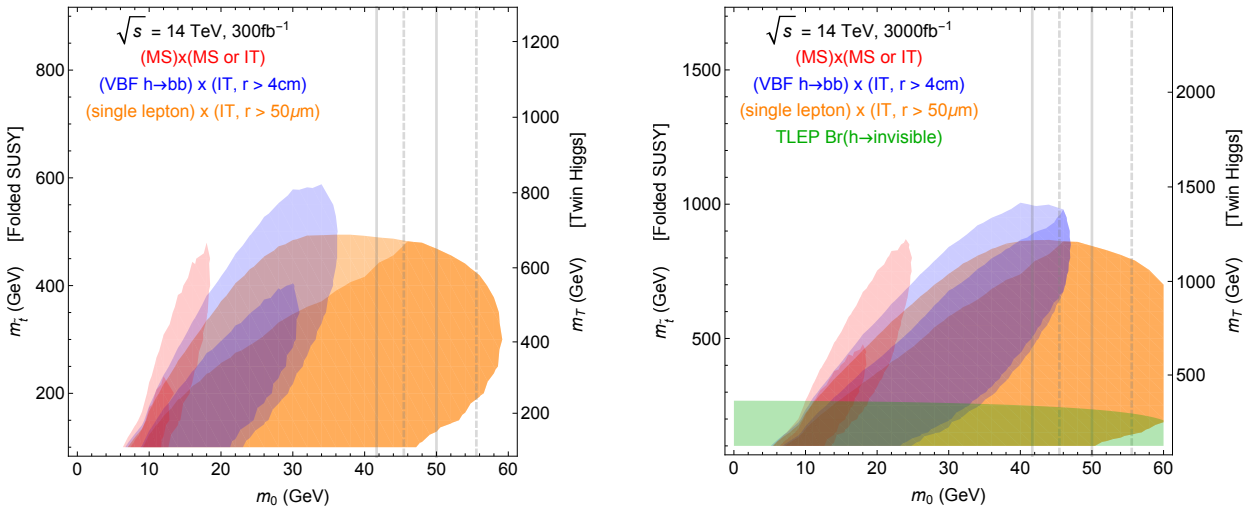

Figure 293: Summary of discovery potential at LHC14 with 300 fb^{-1} (left panel) and HL-LHC (right panel) from looking for (i) one DV in the muon system and one additional DV in either the MS or the inner tracker, (ii) one DV at least 4 cm from beam line and VBF jets (blue) and (iii) one DV with at least 50 μm from beam line and a single lepton (orange). Assuming negligible backgrounds and 10 events for discovery, which is likely more realistic for the MS search with two DVs than the IT searches with one DV. Electroweak top partners (Folded SUSY, Quirky Little Higgs) motivate glueball masses in the 10–60 GeV range. See [1477] for details. Note different scaling of vertical axes. For comparison, the inclusive TLEP $h \to$ invisible limit, as applied to the perturbative prediction for $\text{Br}(h \to \text{all glueballs})$, is shown for future searches as well, which serves as a pessimistic estimate of TLEP sensitivity. Lighter and darker shading correspond to the optimistic (pessimistic) signal estimates $\kappa = \kappa_{\max}$, $(\kappa_{\min})$, under the assumption that h decays dominantly to two glueballs, see Eq. (IV.6.40). The effect of glueball lifetime uncertainty is small and not shown. m_0 is the mass of the lightest glueball G_0; the vertical axes correspond to hidden stop mass in FSUSY and hidden top mass in FTH and Quirky Little Higgs. Vertical solid (dashed) lines show where κ might be enhanced (suppressed) due to non-perturbative mixing effects, see [1477] for details and [1476] for additional discussion.

For longer lifetimes, recent progress has been made in demonstrating how existing ATLAS triggers could be used to search for exotic Higgs boson decay events with a single DO in the Muon System [1638]. The data-driven methods used in that work to control backgrounds in searches featuring a *single* DO are general and may be of use for other searches as well. For shorter lifetimes, triggering and background suppression may require the presence of an AO that accompanies the Higgs, namely VBF jets or an associated Z/W. This allows the probing of shorter lifetimes and lower masses for X, while making the searches more inclusive to other final states outside the hXX-HF framework. In the short term, progress can be achieved by some very simple extensions of current analyses.

Specifically, we suggest searches which at off-line reconstruction level look for AO + tDO or AO + DV (since the tracker is crucial to detect shorter lifetimes). The most useful AO's for Higgs boson production are VBF jets, ISR jets, ISR jet plus MET, and leptons. These searches can utilize the following trigger strategies:

- a pure AO trigger, in particular VBF jets, leptons, or jets + MET (where MET comes from an undecayed or partially invisibly decaying LLP, and the jet arises from ISR);
- a tDO + AO trigger, such as the VBF + displaced dijet trigger explored for CMS in [1633];
- a pure tDO trigger, which though not currently possible for decays in the tracker, has been used by ATLAS for decays in the HCAL and muon system.

Furthermore, all existing searches focus on lifetimes longer than about a mm. In many scenarios, espe-

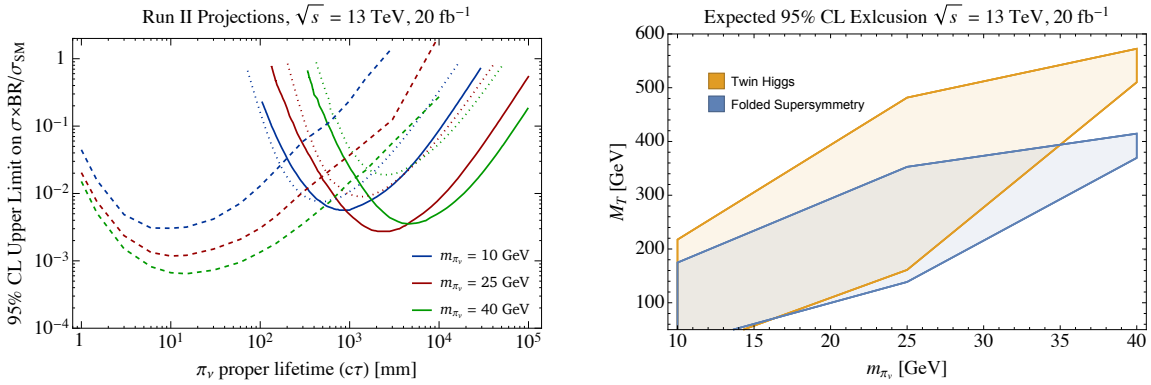

(a) (b)

Figure 294: (a) Projected bounds for the 13 TeV LHC with 20 fb^{-1} of data, from [1633]. The dashed lines represent CMS searches for single displaced vertices in the tracker, where different search and trigger strategies were separately considered. The best sensitivities are achieved using VBF or (VBF + displaced jet) triggers. The solid lines are projections of the ATLAS searches for displaced decays in the HCAL and muon systems [1630, 1631]. (b) Application of those bounds to Neutral Naturalness theories, shown in the same top partner mass (m_T) vs. lightest glueball mass $m_0 = m_{\pi_v}$ as in Figure 293. This assumes $\kappa = \kappa_{\max} = 1$, i.e. all exotic Higgs boson decays to hidden glue give $h \to G_0 G_0$, and so may not be accurate at low m_0.

cially for relatively heavy LLP's, the lifetime can be much shorter. Therefore, in order to cover the entire naturally motivated parameter space, we also suggest study of

– DVs at very short displacements from the interaction point, as low as $\sim 50\mu$m if possible.

Implementing these search strategies may give much greater coverage of Neutral Naturalness scenarios. In [1477] it was demonstrated that such a search program, even with pessimistically extrapolated signal yields using current ATLAS DV reconstruction efficiencies, allows discovery for colourless top partners with mass of $\mathcal{O}(\text{TeV})$: see Figure 293 for the LHC14 ATLAS reach with 300 and 3000 fb^{-1} of data.[IV.43] These projections are consistent with recasts of [1637], which suggest that reach can be improved by including a VBF + displaced dijet trigger [1633]. The projected sensitivities with just 20 fb^{-1} of 13 TeV data are shown in Figure 294, and cover uncoloured top partner masses of several hundred GeV. These searches will have even greater reach if the Higgs boson decays directly to mirror bottomonia, which increases the exotic branching fraction as shown in Eq. (IV.6.39).

We now elaborate on the reasoning behind these suggestions. First, triggering on an AO is relatively independent of the Higgs boson decay final state, and certain tDO trigger thresholds can be lowered if an AO is also present in the trigger path, in compensation for events lost because they lack an AO.

An important motivation for DO + AO searches is their sensitivity to regions of the hXX-HF model, and to other models, in which the typical exotic h decay has only one observable DO. Single DO events may be common because it is rare for two LLPs to be produced together (in some regimes of Neutral Naturalness models, the probability to produce one G_0 in hadronization may be much larger than to produce two). They may also be common because the LLPs are very long-lived, and so it is rare for two of them to decay before exiting the detector. This particularly motivates the use of an ISR jet + MET as the AO.

Another important motivation is that low-mass DO's in the tracker can not currently be triggered on. This is unfortunate because offline reconstruction of tracker DVs can be efficient. By triggering on an AO (and perhaps the DO as well), the overall efficiency for signal events will increase. Backgrounds

[IV.43] This study used a slightly different definition of $\kappa_{\min}$ than used here, but this does not significantly affect the results.

Table 173: Displaced $h \to XX \to$ SM simplified model benchmarks to give efficient coverage of Neutral Naturalness. Recall that X decays via its mixing with the SM-like Higgs, and thus dominantly to $\bar{b}b$ and $\tau^+\tau^-$.

		$c\tau_X$ (m)		
		$5 \cdot 10^{-5}$	10^{-1}	10
m_X (GeV)	7	`short7`	`medium7`	`long7`
	15	`short15`	`medium15`	`long15`
	40	`short40`	`medium40`	`long40`
	55	`short55`	`medium55`	`long55`

may also be controllable, since one may employ a standard "matrix" or "ABCD" method, examining events with and without an AO, and with and without a DV.

Finally, of course, requiring two reconstructed DOs reduces signal efficiency sharply. Efficient searches that require only one should have better reach, as long as backgrounds are under control and the price of requiring an AO is not too high.

No matter what search strategy is adopted, there are also significant challenges to be overcome on the level of reconstructing any single DV.

- Existing searches focus on $m_X \gtrsim 15$ GeV. It is important to understand how light X can be while still being efficiently reconstructed as a DV in different detector systems. Small opening angles and small numbers of tracks from the DV can make reconstruction challenging, though [1623] was able to study displaced photons with masses of a few 100 MeV. (An extreme case was studied in [1639], where long-lived dark photons with masses below 100 MeV were considered.) DV or AO reconstruction criteria could be loosened for $m_X \lesssim 15$ GeV to maintain efficiency, but backgrounds would have to be carefully studied. In principle, there is no qualitative obstacle to the reconstruction of lower-mass DVs [1630, 1631, 1633].
- When m_X is fairly heavy (close to half the Higgs boson mass, or more for asymmetric Higgs boson decays), the slow-moving X may have to be reconstructed out-of-time with the rest of the event. This can make analyses more complicated, but could also provide a handle to reject backgrounds.
- Independent of triggering issues, what is the shortest lifetime that could be reconstructed and distinguished from prompt background? Going below cm or mm decay lengths opens up very well-motivated parameter space in theories of Neutral Naturalness. Maximizing the rejection of B-meson related backgrounds will be a high priority for such a search.

Benchmarks

In order to help develop these searches with full coverage we suggest 12 benchmark points, given in Table 173. They span the range of well-motivated X masses that yield the $\bar{b}b$ and $\tau^+\tau^-$ final states, and the range of lifetimes that can be realized in Neutral Naturalness and potentially reconstructed as a displaced decay. Of the light benchmarks, `long7` is most motivated for hidden glueballs, since their lifetime increases sharply above the $b\bar{b}$ threshold; `short7` and `medium7` can be realized for hidden bottomonia, which have potentially much shorter lifetimes. Each lifetime requires a different search strategy to optimally constrain $\mathrm{Br}(h \to XX)$. Dealing with time-of-flight issues may be particularly challenging (or fruitful) for the `long55` benchmark point, while short decay length reconstruction is yet to be demonstrated for the `short` benchmarks. The sensitivity of LHCb to these decays also deserves future

study – in some cases it might be superior to ATLAS or CMS, despite the reduced luminosity available for analysis, because of its special triggering and reconstruction capabilities.

Presentation of limits

Conventionally, in searches for DOs from exotic Higgs boson decays, results are represented by plotting excluded $\sigma_h \times \mathrm{Br}/\sigma_{\mathrm{SM}}$, as a function of decay length $c\tau_X$, for different discrete benchmark values of the long-lived particle mass m_X. This is shown, for example, in Figure 294 (a). We strongly recommend continuation of this model-independent presentation.

We also recommend an additional means of presenting results for the hXX-HF signal model. This method of presentation would allow constraints to be directly applied to the Neutral Naturalness scenario where the Higgs can decay to mirror glueballs, which decay back to the SM via Higgs mixing. This is the case for FSUSY, and can occur in Twin Higgs models.

Consider a search that is sensitive to LLPs X produced in the decay $h \to XX$, setting bounds on $\mathrm{Br}(h \to XX)$ as a function of m_X and $c\tau_X$. In the above scenario where X is the glueball G_0, its lifetime is almost uniquely determined in the (m_0, m_T) plane, where m_0, m_T are the G_0 and top partner masses. Therefore, the search gives a constraint on $\mathrm{Br}(h \to G_0G_0)$ as a function of m_0 and m_T.[IV.44]

We can now make use of the known *inclusive* exotic Higgs boson decay branching fraction $\mathrm{Br}(h \to \text{hidden glue})$, see Eq. (IV.6.38), even if the *exclusive* branching fraction to a given number of G_0's cannot be computed. Clearly, if the limit on $\mathrm{Br}(h \to G_0G_0)$ is much larger than $\mathrm{Br}(h \to \text{hidden glue})$ then the search has no sensitivity to this Neutral Naturalness scenario. Similarly, since we expect a sizeable fraction of the produced glueballs to be the lightest G_0, if the limit on $\mathrm{Br}(h \to G_0G_0)$ is orders of magnitude smaller than $\mathrm{Br}(h \to \text{hidden glue})$, then this scenario can effectively be excluded for a given (m_0, m_T). This reasoning can be most easily articulated by defining the parameter

$$\kappa^{G_0G_0}(m_0, m_T) \equiv \frac{\sigma_h \times \mathrm{Br}(h \to G_0G_0)}{\sigma_{\mathrm{SM}} \times \mathrm{Br}(h \to \text{hidden glue})}. \tag{IV.6.42}$$

The denominator is completely determined in the (m_0, m_T) plane, while the numerator can be constrained by the search. Bounds on $\kappa^{G_0G_0}$ can therefore be shown in the (m_0, m_T) plane and constrain the fraction of glueballs that are in the G_0 state. Regions with $\kappa^{G_0G_0} < 0.1$ (> 1) are likely (not) excluded. In regions with intermediate values of κ^{ex}, the bounds are sensitive to pure-glue hadronization assumptions.

IV.6.6.c Higgs boson decays to displaced photons and missing energy from Supersymmetry [IV.45]

Here we discuss one realization of displaced Higgs boson decays within the MSSM, consistent with current experimental constraints. In models of gauge-mediated supersymmetry breaking (GMSB), the next-to-lightest Standard Model superpartner (NLSP) will decay to a gravitino LSP, which is stable in the presence of R-parity, together with one or more SM states. This decay becomes displaced as the supersymmetry-breaking scale is raised. In particular, in generalized GMSB models, for gauge messenger masses of $\mathcal{O}(100)$ TeV, it is possible to have the decay $h \to \tilde{\chi}_1\tilde{\chi}_1 \to \gamma\tilde{G}\ \gamma\tilde{G}$ with a long-lived Bino-like lightest neutralino, $\tilde{\chi}_1$. While the first stage of this decay is prompt with a possibly sizeable branching ratio, the second decay occurs with a branching ratio of one, and the lifetime of the neutralino can be evaluated as [1612]

$$c\tau = 48\,\pi \frac{m_{3/2}^2 M_{\mathrm{Pl}}^2}{m_{\tilde{\chi}_1^5}} \frac{1}{|P_{1\gamma}|^2} \tag{IV.6.43}$$

with $P_{1\gamma} = N_{11}\cos\theta_W + N_{12}\sin\theta_W$ given in terms of the neutralino mixing matrix N. Here N_{11} and N_{12} are the Bino and Wino $\tilde{\chi}_1$ components, respectively. The gravitino mass $m_{3/2}$ is at or below

[IV.44] Similar reasoning applies to searches for one LLP that set bounds on $\mathrm{Br}(h \to X + \ldots)$.

[IV.45] *Author(s): S. Heinemeyer.*

the level of eV, and $M_{\rm Pl}$ is the Planck mass. Thus neutralino decay lengths of up to one meter or even more can be obtained, depending on the choice of parameters and in particular on the neutralino mass $m_{\tilde{\chi}_1}$. As an illustrative example, in Figure 295, we present the branching ratio for this process, i.e. BR($h \to \tilde{\chi}_1\tilde{\chi}_1 \to \gamma\gamma + \tilde{G}\tilde{G}$) and the lifetime of the neutralino as a function of the Bino mass M_1 and $\tan\beta$, having fixed the μ parameter, as well as the Wino mass, M_2, to 400 GeV. The other parameters are chosen as in the $m_h^{\rm mod+}$ scenario [91]. We note that this benchmark has not been probed by multi-lepton searches for electroweak production of Higgsinos and Winos at Run 1 LHC (see for example [1640–1642]). One can see that the branching ratio depends mainly on $\tan\beta$, and can reach $\sim \mathcal{O}(10\%)$ or larger at small values of $\tan\beta$. The lifetime, on the other hand, depends mainly on M_1. The smallest values of $M_1 \lesssim 10$ GeV lead to decay lengths of 1 m or more, while values larger than ~ 25 GeV lead to decay lengths below 1 cm. This shows that this particular scenario, depending on choice of parameters, offers the full spectrum of collider-relevant decay lengths and the corresponding phenomenological opportunities and challenges.

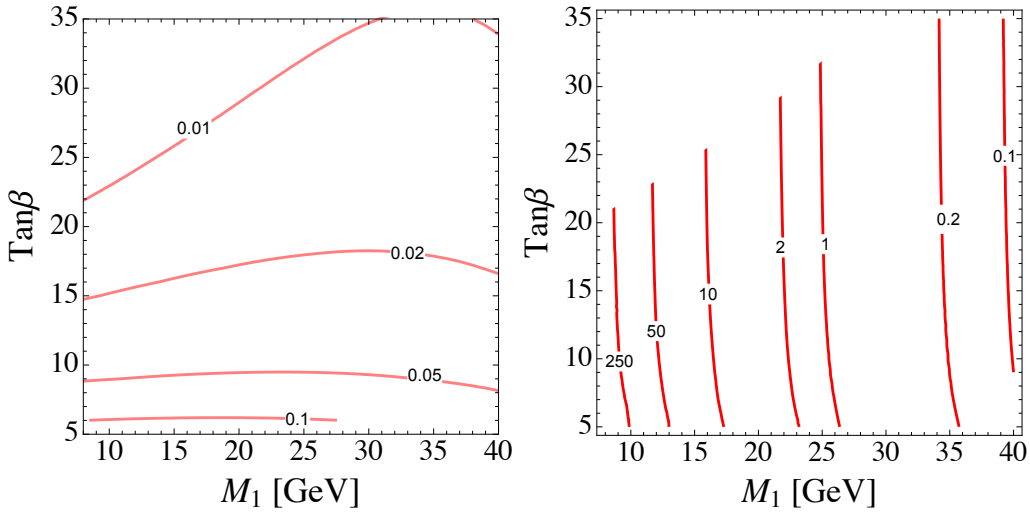

Figure 295: Branching ratio for $h \to \tilde{\chi}_1\tilde{\chi}_1 \to \tilde{G}\tilde{G}\gamma\gamma$ (left) and neutralino $\tilde{\chi}_1$ lifetime in cm (right), as a function of the Bino mass parameter M_1 and $\tan\beta$. The benchmark model used is the $m_h^{\rm mod+}$ scenario [91], with $\mu = M_2 = 400$ GeV.

Acknowledgements

We are obliged to CERN, in particular to the IT Department and to the Theory Unit and the LPCC for the support with logistics and technical assistance.

Fermilab is operated by Fermi Research Alliance, LLC under grant DE-AC02-07CH11359 with the US Department of Energy.

R. Aggleton, F. Bishara and C.H. Shepherd-Themistocleous are supported by the Science and Technology Facilities Council (STFC).

B. Allanach has been partially supported by STFC grant ST/L000385/1.

W. Astill, W. Bizon, S. Carrazza, B. Mistlberger, E. Re and G. Zanderighi are partly supported by the ERC Consolidator grant "HICCUP" (614577). W. Astill and W. Bizon thank CERN and the Mainz Institute of Theoretical Physics (MITP) for their hospitality while part of this work was carried out.

S. Badger is supported by an STFC Rutherford Fellowship ST/L004925/1.

M. Badziak has been supported in part by the Polish Ministry of Science and Higher Education (decision 1266/MOB/IV/2015/0), the US Department of Energy under Contract DE-AC02-05CH11231, the National Science Foundation under grant PHY-1316783 and by the Foundation for Polish Science through its programme HOMING PLUS.

J. Baglio is supported in part by the Institutional Strategy of the University of Tübingen (DFG, ZUK 63) and by the DFG grant JA 1954/1.

D. Barducci, G. Bélanger, S. Forte, E.W.N. Glover, M. Grazzini, G. Heinrich, A. Ilnicka, S.P. Jones, Z. Kassabov, F. Krauss, E. Maina, C. Mariotti, D. Napoletano, G. Passarino, P. Slavich, M. Spannowsky, M. Spira, U. Ellwanger, A. Vicini and G. Weiglein are partly supported by the 7th Framework Programme of the European Commission through the Initial Training Network "HiggsTools" (PITN-GA-2012-316704).
D. Barducci, G. Bélanger and S. Kraml are partly supported by the "Investissements d'avenir, Labex ENIGMASS", by the French ANR Project "DMAstroLHC" (ANR-12-BS05-006).

J. Bellm, S. Gieseke, A. Papaefstathiou, P. Schichtel and E. Vryonidou are supported in part by the 7th Framework Programme of the European Commission through the Initial Training Network "MCnetITN" (PITN-GA-2012-315877).

N. Belyaev's work was performed within the framework of the Center for Fundamental Research and Particle Physics supported by MEPhI Academic Excellence Project (contract 02.a03.21.0005).

A. Biekötter acknowledges support from the German Research Foundation (DFG) through the Forschergruppe "New Physics at the LHC" (FOR 2239)..

N.E. Bomark is grateful to NCBJ for access to the CIS computer cluster.

M Bonvini and J. Rojo have been partly supported by the ERC Starting grant "PDF4BSM".

S. Borowka and E.W.N. Glover acknowledge financial support by the ERC Advanced grant "MC@NNLO" (340983).

V. Bortolotto and K. Prokofiev are partially supported by a grant from the Research Grant Council of the Hong Kong Special Administrative Region, China (project CUHK4/CRF/13G).

S. Boselli, G. Montagna, O. Nicrosin and F. Piccinini were partially supported by the Research Executive Agency (REA) of the European Union under the Grant Agreement number PITN-GA-2010-264564 (LHCPhenoNet) and by the Italian Ministry of University and Research under the PRIN project 2010YJ2NYW.

F.J. Botella is supported by Spanish MINECO under grants FPA2015-68318-R and SEV-2014-0398, and by Generalitat Valenciana under grant GVPROMETEOII 2014-049.

R. Boughezal is supported by the DOE grant DE-AC02-06CH11357. Her research used resources of: the National Energy Research Scientific Computing Center, a DOE Office of Science User Facility supported by the DOE under contract DE-AC02-05CH11231; the Argonne Leadership Computing Facility, which is supported under DOE contract DE-AC02-06CH11357. R. Boughezal and F. Petriello thank the KITP, Santa Barbara, supported by the National Science Foundation under grant NSF PHY11-25915

for hospitality.

G.C. Branco and M.N. Rebelo were partially supported by Fundação para a Ciência e a Tecnologia (FCT, Portugal) through the projects CERN/FIS/NUC/0010/2015 and CFTP-FCT Unit 777 (UID/FIS/00777/2013) which are partially funded through POCTI (FEDER), COMPETE, QREN and EU.

J. Brehmer is supported by the German Research Foundation (DFG) through the research training group GRK 1940.

S. Bressler is supported by the I-CORE Program of the Planning and Budgeting Committee and The Israel Science Foundation (grant 1937/12). S. Bressler, S. Gori, A. Mohammadi and J. Shelton thank Fermilab for its hospitality and support.

I. Brivio, M. Herrero, U. Ellwanger and L. Merlo were supported by the EU networks FP7 ITN INVISIBLES (PITN-GA-2011-289442), FP10 ITN ELUSIVES (H2020-MSCA-ITN-2015-674896) and INVISIBLES-PLUS (H2020- MSCA-RISE-2015-690575). I. Brivio, M. Herrero, L. Merlo and J.J. Sanz-Cillero acknowledge partial support of the Spanish MINECO's "Centro de Excelencia Severo Ochoa" Programme under grant SEV-2012-0249.

H. Brun thanks the FRS-FNRS IISN for financial support.

G. Buchalla and O. Cata acknowledge support by the ERC Advanced grant "FLAVOUR" (267104) and by the DFG Cluster of Excellence "Origin and Structure of the Universe" (EXC 153).

F. Campanario thanks support to the Spanish Government and ERDF funds from the European Commission (FPA2014-53631-C2-1-P and FPA2014-54459-P).

C.M. Carloni Calame and A. Ballestrero have been supported by the MIUR-PRIN project 2010YJ2NYW.

A. Carvalho is supported by MIUR-FIRB RBFR12H1MW grant.

M. Casolino and A. Juste are supported in part by the Spanish Ministerio de Economía y Competitividad under projects FPA2012-38713 and Centro de Excelencia Severo Ochoa SEV-2012-0234.

A. Celis is supported by the Alexander von Humboldt Foundation.

M. Chen is supported by the Hundred Talents Program of Chinese Academy of Sciences.

X. Chen thanks the IPPP at the University of Durham for hospitality, and T. Morgan, A. Huss, A. Gehrmann-De Ridder, J. Pires, J. Currie and J. Niehues for useful discussions and their many contributions to the NNLOJET code.

R. Contino and L. Silvestrini have been partly supported by the ERC Advanced grant "DaMeSyFla" (267985).

T. Corbett was supported in part by the Australian Research Council.

D. Curtin is supported by National Science Foundation grant PHY-1315155 and the Maryland Center for Fundamental Physics. He thanks C. Csáki, E. Kuflik, S. Lombardo, O. Slone for helpful conversation and collaboration.

M. Dall'Osso is supported by grant CPDR155582 of Padua University.

S. Dawson is supported by the United States Department of Energy under grant DE-SC0012704.

J. de Blas, D. Ghosh and L. Silvestrini have been partly supported by the ERC grant "NPFlavour" (279972).

W. de Boer warmly acknowledges support from the Heisenberg-Landau program and the Deutsche Forschungsgemeinschaft (DFG grant BO 1604/3-1).

D. de Florian and J. Mazzitelli are partially supported by CONICET and ANPCyT (Argentina). J. Mazzitelli also acknowledges support by UBACYT.

C. Degrande is a Durham International Junior Research Fellow.

R.L. Delgado, A. Dobado and F.J. Llanes-Estrada have been supported by grants BES-2012-056054, UCM:910309 and MINECO:FPA2014-53375-C2-1-P and by the Spanish Excellence Network on Hadronic Physics FIS2014-57026-REDT.

F. Demartin is supported by the IISN "MadGraph" convention 4.4511.10 and the IISN "Fundamental interactions" convention 4.4517.08.

A. Denner, R. Feger and T. Ohl acknowledge support by the Bundesministerium für Bildung und Forschung (BMBF) under contract 05H12WWE.

S. Dittmaier is supported by the Research Training Group GRK 2044 of the German Science Foundation (DFG).

F.A. Dreyer, P. Francavilla, P. Slavich, M. Zaro and R. Ziegler are supported by the ILP LABEX (ANR-10-LABX-63) supported by French state funds managed by the ANR within the Investissements d'Avenir programme under reference ANR-11-IDEX-0004-02.

C. Duhr is supported by the ERC Starting Grant "MathAm".

F. Dulat acknowledges the support of the US Department of Energy under grant DE-AC02-76SF00515.

U. Ellwanger, G.P. Salam and P. Slavich are supported in part by ERC Advanced grant "Higgs@LHC" (321133). U. Ellwanger and S. Moretti are supproted in part by he EU project "NonMinimalHiggs" (H2020-MSCA-RISE-2014 645722). U. Ellwanger also acknowledges support from the Défi InPhyNiTi project N2P2M-SF .

C. Englert is supported in part by the IPPP Associateship scheme.

D. Espriu is supported by the grants FPA2013-46570 and 2014-SGR-104.

A. Ferroglia is supported in part by the National Science Foundation grant PHY-1417354.

T. Figy used the Extreme Science and Engineering Discovery Environment (XSEDE), which is supported by National Science Foundation grant ACI-1053575. He thanks Mats Rynge for his assistance with implementing workflows on the Open Science Grid, which was made possible through the XSEDE Extended Collaborative Support Service (ECSS) program.

M. Flechl is supported by the Austrian Science Fund (FWF), project P 28857-N36.

S. Forte thanks M. Bonvini, A. De Roeck, S. Marzani, C. Muselli and P. Nason for discussions. He is supported in part by an Italian PRIN2010 grant, by a European Investment Bank EIBURS grant.

P. Francavilla is supported by the ILP LABEX (under reference ANR-10-LABX-63 and ANR-11-IDEX-0004-02).

R. Frederix is supported by the Alexander von Humboldt Foundation, in the framework of the Sofja Kovaleskaja Award Project "Event Simulation for the Large Hadron Collider at High Precision".

F.F. Freitas work is supported by the Brazilian program "Ciencia sem fronteras".

B. Fuks, S. Kraml and K. Mawatari acknowledges partial support by the Théorie-LHC France initiative of the CNRS (INP.IN2P3).

M.V. Garzelli, R. Kogler, S. Liebler, J. Reuter, K. Tackmann and G. Weiglein are supported by the German Research Foundation (DFG) in the Collaborative Research Centre (SFB) 676 "Particles, Strings and the Early Universe".

E.W.N. Glover is supported in part by the UK Science and Technology Facilities Council through grant ST/G000905/1.

F. Goertz is supported by a Marie Curie Intra European Fellowship within the 7th European Community Framework Programme (PIEF-GA-2013-628224)..

D. Gonçalves is supported by STFC through the IPPP grant.

M. Gorbahn is supported by STFC under grant ST/L000431/1.

S. Gori thanks the Galileo Galilei Institute for Theoretical Physics for the hospitality and the INFN for partial support during some part of this work.

D. Gray and R. Konoplich are partially supported by the US National Science Foundation under grant PHY-1402964.

M. Grazzini was supported in part by the Swiss National Science Foundation (SNF) under contracts CRSII2-141847, 200021-156585.

N. Greiner was supported by the Swiss National Science Foundation under contract PZ00P2-154829.

A. Greljo, G. Isidori and D. Marzocca are supported by the Swiss National Science Foundation under contract 200021-159720.

A.V. Gritsan, J. Roskes, U. Sarica and M. Xiao are partially supported by US NSF under grant PHY-1404302 while their calculations were performed on the Maryland Advanced Research Computing Center (MARCC).

C. Grojean is supported by the European Commission through the Marie Curie Career Integration Grant 631962, by the Helmholtz Association and in part by the Spanish Ministerio de Economía y Competitividad under projects FPA2014-55613-P and Centro de Excelencia Severo Ochoa SEV-2012-0234 and by the Generalitat de Catalunya grant 2014-SGR-1450.

S. Guindon is supported by the National Science Foundation.

H.E. Haber is supported in part by the US Department of Energy under grant DE-FG02-04ER41286. He gratefully acknowledges the hospitality and support of S. Heinemeyer during the Higgs Days meeting in Santander, Spain where the work on 2HDM benchmarks was initiated, and to the Theory Group at CERN, where this work was completed.

C. Han is supported by World Premier International Research Center Initiative (WPI), MEXT, Japan.

T. Han was supported in part by the US DOE and in part by the PITT PACC.

R. Harlander, K. Köneke, M. Moreno Llácer, C. Schmidtt and E. Shabalina are supported by Bundesministerium für Bildung und Forschung (BMBF) under contract 05H15PACC1.

M.A. Harrendorf's work was funded by the DFG Research Training Group 1694 and by the German BMBF under the contract 05H15VKCCA.

H.B. Hartanto is supported by the German Research Foundation (DFG).

S. Heinemeyer is supported in part by CICYT (grant FPA 2013-40715-P) and by the Spanish MICINN's Consolider-Ingenio 2010 Program under grant MultiDark CSD2009-00064.

M. Herrero is supported by CICYT through Grant No. FPA2012-31880.

F. Herzog is supported by the ERC grant "HEPGAME" (320651).

B. Hespel is supported by the National Fund for Scientific Research (FRS-FNRS Belgium) under a FRIA grant.

V. Hirschi is supported by the Swiss National Science Foundation grant PBELP2-146525. He thanks the CP3 IT team for the computational resources put at his disposal.

S. Hoeche was supported by the US Department of Energy under grant DE-AC02-76SF00515.

S. Honeywell, L. Reina, and C. Reuschle are supported in part by the US Department of Energy under grant DE-FG02-13ER41942.

S. Huberand K. Mimasu is supported by STFC under grant ST/L000504/1.

C. Hugonie acknowledges the support of France Grilles for providing cloud computing resources on the French National Grid Infrastructure.

J. Huston is supported by the National Science Foundation under grant PHY-1410972.

B. Jäger was supported in part by the Institutional Strategy of the University of Tübingen (DFG, ZUK 63) and in part by the German Federal Ministry for Education and Research (BMBF) under contract number 05H2015.

A. Kardos gratefully acknowledges financial support from the Post Doctoral Fellowship programme of the Hungarian Academy of Sciences and the Research Funding Program ARISTEIA, HOC-Tools (co-financed by the European Union (European Social Fund ESF).

A. Karlberg is supported by STFC and by the Buckee Scholarship at Merton College.

N. Kauer and C. O'Brien are supported by the STFC grants ST/J000485/1, ST/J005010/1 and ST/L000512/1.

F. Kling thanks the Munich Institute for Astro- and Particle Physics (MIAPP) of the DFG cluster of excellence "Origin and Structure of the Universe" for hospitality. He is supported by US Department of Energy under grant DE-FG02-04ER-41298 also acknowledges support from the Fermilab Graduate Student Research Program in Theoretical Physics operated by Fermi Research Alliance, LLC under contract DE-AC02-07CH11359 with the US Department of Energy.

C. Krause is supported by the DFG grant BU 1391/2-1 and in part by the DFG cluster of excellence "Origin and Structure of the Universe".

F. Krauss is supported by the 7th Framework Programme of the European Commission through the Initial Training Network "MCnetITN" (PITN-GA-2012-315877).

M. Krawczyk is partly supported by the Polish National Science Centre within an OPUS research project under grant 2012/05/B/ST2/03306.

A. Kulesza is supported by the German Research Foundation DFG grant KU 3103/1.

G. Lee is supported by the Israel Science Foundation (grant 720/15), by the United-States-Israel Binational Science Foundation (BSF) (grant 2014397), and by the ICORE Program of the Israel Planning and Budgeting Committee (grant 1937/12).

H.E. Logan and P. Savard are supported by the Natural Sciences and Engineering Research Council of Canada.

D. Lopez-Val acknowledges the support of the FRS-FNRS “Fonds de la Recherche Scientifique”.

I. Low is supported in part by the US Department of Energy under grant DE-SC0010143.

E. Maina has been supported by MIUR (Italy) under contract 2010YJ2NYW006, by the Compagnia di San Paolo under contract ORTO11TPXK.

F. Maltoni is supported by the Fonds de la Recherche Scientifique (FNRS).

S. Marzani and V. Theeuwes are supported in by the US National Science Foundation under grant PHY-0969510 “LHC Theory Initiative".

A. McCarn is supported by the US Department of Energy under grant DE-SC0007859.

L. Merlo acknowledges partial support of CiCYT through the project FPA2012-31880.

N. Moretti and S. Pozzorini are supported by the Swiss National Science Foundation under contracts PP00P2-153027 and BSCGI0157722.

S. Moretti is financed in part through the NExT Institute.

L. Motyka gratefully acknowledges support of the Polish National Science Centre grant DEC-2014/13/B/ST2/02486.

S. Munir was in part supported by the Swedish Research Council under contracts 2007-4071 and 621-2011-5107.

P. Musella is supported by the Swiss National Science Foundation.

P. Nadolsky is supported by the US Department of Energy under grant DE-SC0013681.

M. Nebot acknowledges support from Spanish MINECO under grants FPA2015-68318-R and SEV-2014-0398, and from Generalitat Valenciana under grant PROMETEOII/2013/017.

M. Neubert is supported by the ERC Advanced grant “EFT4LHC", the DFG Cluster of Excellence “Precision Physics, Fundamental Interactions and Structure of Matter" (PRISMA, EXC 1098) and grant 05H12UME of the German Federal Ministry for Education and Research (BMBF).

R. Nevzorov is supported by the University of Adelaide and the Australian Research Council through the ARC Center of Excellence in Particle Physics at the Terascale.

J. Nielsen is supported by the US Department of Energy under grant DE-SC0010107.

K. Nikolopoulos is supported by the European Union’s 7th Framework Programme for research, technological development and demonstration under grant agreement 334034 “EWSB".

J.M. No is supported by a Marie Curie Intra European Fellowship within the 7th European Community Framework Programme (PIEF-GA-2013-625809).

T. Orimoto is supported by the US Department of Energy.

D. Pagani and H.S. Shao are supported by the ERC Advanced grant “LHCtheory" (291377).

C.E. Pandini is supported by the PhD program of the UPMC and Université Paris-Diderot (Paris, France).

A. Papaefstathiou is supported by a Marie Curie Intra European Fellowship within the 7th European Community Framework Programme (PIEF-GA-2013-622071).

A.S. Papanastasiou is supported by STFC under grant ST/L002760/1.

M. Pelliccioni is supported by the Istituto Nazionale di Fisica Nucleare.

G. Perez, R. Podskubka and R. Roth are supported by “Graduiertenkolleg" of Karlsruhe Institute of Technology.

F. Petriello is supported by the DOE grants DE-FG02-91ER40684 and DE-AC02-06CH11357. His research used resources of: the National Energy Research Scientific Computing Center, a DOE Of-

fice of Science User Facility supported by the DOE under contract DE-AC02-05CH11231; the Argonne Leadership Computing Facility, which is supported under DOE contract DE-AC02-06CH11357.

A. Pilkington is supported in the UK by the Royal Society.

S. Plätzer is supported by a Marie Curie Intra European Fellowship within the 7th European Community Framework Programme (PIEF-GA-2013-628739).

C.T. Potter thanks the Alder Institute for High Energy Physics (AIHEP) for financial support.

A. Pukhov thanks LAPTH for his hospitality.

I. Puljak is supported by Croatian Science Foundation under project 7118.

J. Quevillon is supported by STFC under grant ST/L000326/1.

T. Robens thanks CERN-TH and the University of Warsaw for their hospitality while parts of this work were completed, and G. Challons, D. Lopez-Val, and G.M. Pruna for fruitful collaboration on related work.

J. Rojo is supported by an STFC Rutherford Fellowship and grant ST/K005227/1 ST/M003787.

J.C. Romão was partially supported by Fundação para a Ciência e a Tecnologia (FCT, Portugal) through the projects CERN/FP/123580/2011 and CFTP-FCT Unit 777 (UID/FIS/00777/2013) which are partially funded through POCTI (FEDER), COMPETE, QREN and EU.

V. Sanz is supported by STFC under grant ST/J000477/1.

J.J. Sanz-Cillero is partially supported by the Spanish Ministry MINECO under grant FPA2013-44773-P.

M. Schönherr acknowledges support by the Swiss National Science Foundation under contract PP00P2-128552.

U. Schubert is supported by the Alexander von Humboldt Foundation, in the framework of the Sofja Kovalevskaja Award 2010, “Advanced Mathematical Methods for Particle Physics".

S. Sekula is supported by the US Department of Energy under grant DE-SC0010129. He gratefully acknowledges SMU’s Center for Scientific Computation for their support and for the use of the SMU ManeFrame Tier 3 ATLAS System.

J. Shelton is partially supported by US Department of Energy under grant DE-SC0015655.

F. Siegert is supported by the German Research Foundation (DFG) under grant SI 2009/1-1.

J.P. Silva is supported in part by the Portuguese Fundacao para a Ciencia e Tecnologia under contract UID/FIS/00777/2013.

M. Sjodahl is supported by the Swedish Research Council under contract 621-2012-2744.

P. Slavich is supported in part by the French ANR Young Researchers project “HiggsAutomator” (ANR-15-CE31-0002-01).

M. Slawinska is supported by the research programme of the Foundation for Fundamental Research on Matter (FOM), which is part of the Netherlands Organisation for Scientific Research (NWO).

T. Stebel acknowledges support of Marian Smoluchowski Research Consortium Matter Energy Future from KNOW funding and Polish National Science Centre grant DEC-2014/13/B/ST2/02486.

T. Stefaniak is supported by US Department of Energy grant number DESC0010107 and a Feodor-Lynen research fellowship sponsored by the Alexander von Humboldt foundation.

I.W. Stewart is supported by the US Department of Energy under grant DE-SC0011090 and by the Simons Foundation through the Investigator grant 327942.

M.J. Strassler thanks Harvard University’s theory group for its hospitality.

S. Su is supported by US Department of Energy under grant DE-FG02-04ER-41298.

X. Sun is supported by NSFC China.

F.J. Tackmann is supported by the German Science Foundation (DFG) through the Emmy-Noether Grant No. TA 867/1-1.

R. Teixeira De Lima is supported by the US Department of Energy.

R.S. Thorne is supported by STFC under grant ST/L000377/1 and and he thanks the members of the MMHT group and PDF4LHC working group for many helpful discussions.

P. Torrielli has received funding from the European Union 7th Framework programme for research

and innovation under the Marie Curie grant agreement 609402-2020 researchers: Train to Move (T2M).

M. Tosi thanks Josh Bandavid.

F. Tramontano is partially supported by the INFN Iniziativa Specifica PhenoLNF.

Z. Trócsányi is supported by the Hungarian Scientific Research Fund grant K-101482 and the Swiss National Science Foundation SCOPES-JRP grant IZ73Z0-152601.

M. Trott thanks the Villum Foundation for support.

I. Tsinikos is supported by the FRS-FNRS "Fonds de la Recherche Scientifique" and in part by the Belgian Federal Science Policy Office through the Interuniversity Attraction Pole P7/37.

A. Vicini was supported in part by an Italian PRIN2010 grant, by a European Investment Bank EIBURS grant.

D. Wackeroth is supported in part by the US National Science Foundation under grant PHY-1417317.

C.E.M. Wagner is supported by the US Department of Energy under grant DE-FG02-13ER41958. His work at ANL is supported in part by the US Department of Energy under grant DE-AC02-06CH11357.

M. Wiesemann is supported in part by the Swiss National Science Foundation under contract 200021-156585.

C. Williams acknowledges support provided by the Center for Computational Research at the University at Buffalo.

L.L. Yang is supported in part by the National Natural Science Foundation of China under grant 11575004.

M. Zaro is supported by the European Union's Horizon 2020 research and innovation programme under the Marie Sklodovska-Curie grant agreement No 660171.

J. Zupan is supported in part by the US National Science Foundation under CAREER grant PHY-1151392.

Appendices

Appendix A

Tables of branching ratios

In this appendix we complete the listing of the branching fractions of the Standard Model Higgs boson discussed in Section I.3.1.a

Table 174: SM Higgs boson branching ratios for $\mathrm{H} \to \mathrm{b\overline{b}}$ and $\mathrm{H} \to \tau^+\tau^-$, corresponding theoretical uncertainties (THU) and parametric uncertainties from the quark masses (PU(m_q)) and the strong coupling (PU(α_s)) (expressed in percentage). Mass range around the Higgs boson resonance.

M_H [GeV]	$\mathrm{H} \to \mathrm{b\overline{b}}$	THU [%]	PU(m_q) [%]	PU(α_s) [%]	$\mathrm{H} \to \tau^+\tau^-$	THU [%]	PU(m_q) [%]	PU(α_s) [%]
120.0	$6.536{\cdot}10^{-1}$	+0.58 -0.58	+0.60 -0.63	+0.67 -0.68	$6.981{\cdot}10^{-2}$	+1.16 -1.16	+1.10 -1.09	+0.71 -0.69
120.5	$6.472{\cdot}10^{-1}$	+0.59 -0.59	+0.60 -0.64	+0.68 -0.70	$6.918{\cdot}10^{-2}$	+1.17 -1.16	+1.09 -1.09	+0.71 -0.68
121.0	$6.406{\cdot}10^{-1}$	+0.59 -0.59	+0.62 -0.65	+0.69 -0.71	$6.854{\cdot}10^{-2}$	+1.17 -1.16	+1.07 -1.09	+0.68 -0.68
121.5	$6.338{\cdot}10^{-1}$	+0.60 -0.60	+0.63 -0.66	+0.70 -0.72	$6.787{\cdot}10^{-2}$	+1.17 -1.16	+1.06 -1.07	+0.68 -0.67
122.0	$6.269{\cdot}10^{-1}$	+0.61 -0.61	+0.64 -0.67	+0.71 -0.73	$6.718{\cdot}10^{-2}$	+1.17 -1.16	+1.07 -1.06	+0.68 -0.65
122.5	$6.198{\cdot}10^{-1}$	+0.61 -0.61	+0.66 -0.68	+0.72 -0.74	$6.648{\cdot}10^{-2}$	+1.17 -1.16	+1.04 -1.06	+0.66 -0.65
123.0	$6.126{\cdot}10^{-1}$	+0.62 -0.62	+0.67 -0.69	+0.73 -0.75	$6.576{\cdot}10^{-2}$	+1.17 -1.16	+1.02 -1.04	+0.66 -0.64
123.5	$6.052{\cdot}10^{-1}$	+0.63 -0.63	+0.68 -0.70	+0.75 -0.75	$6.502{\cdot}10^{-2}$	+1.17 -1.16	+1.02 -1.02	+0.64 -0.65
124.0	$5.978{\cdot}10^{-1}$	+0.63 -0.63	+0.68 -0.72	+0.75 -0.78	$6.427{\cdot}10^{-2}$	+1.17 -1.16	+1.02 -1.00	+0.63 -0.62
124.1	$5.962{\cdot}10^{-1}$	+0.63 -0.63	+0.69 -0.72	+0.76 -0.77	$6.411{\cdot}10^{-2}$	+1.17 -1.16	+1.01 -1.00	+0.64 -0.63
124.2	$5.947{\cdot}10^{-1}$	+0.64 -0.64	+0.69 -0.72	+0.75 -0.78	$6.396{\cdot}10^{-2}$	+1.17 -1.16	+1.00 -1.00	+0.63 -0.62
124.3	$5.932{\cdot}10^{-1}$	+0.64 -0.64	+0.70 -0.72	+0.76 -0.77	$6.381{\cdot}10^{-2}$	+1.17 -1.16	+1.00 -1.00	+0.63 -0.61
124.4	$5.916{\cdot}10^{-1}$	+0.64 -0.64	+0.70 -0.73	+0.76 -0.79	$6.366{\cdot}10^{-2}$	+1.17 -1.16	+0.99 -1.00	+0.62 -0.63
124.5	$5.901{\cdot}10^{-1}$	+0.64 -0.64	+0.70 -0.73	+0.76 -0.79	$6.349{\cdot}10^{-2}$	+1.17 -1.16	+1.00 -0.99	+0.63 -0.61
124.6	$5.886{\cdot}10^{-1}$	+0.64 -0.64	+0.71 -0.73	+0.77 -0.78	$6.335{\cdot}10^{-2}$	+1.17 -1.16	+0.98 -1.00	+0.62 -0.62
124.7	$5.870{\cdot}10^{-1}$	+0.64 -0.64	+0.70 -0.73	+0.76 -0.79	$6.318{\cdot}10^{-2}$	+1.17 -1.16	+0.99 -0.98	+0.63 -0.61
124.8	$5.855{\cdot}10^{-1}$	+0.64 -0.64	+0.71 -0.74	+0.77 -0.79	$6.303{\cdot}10^{-2}$	+1.17 -1.16	+0.99 -0.99	+0.63 -0.60
124.9	$5.839{\cdot}10^{-1}$	+0.65 -0.64	+0.71 -0.75	+0.77 -0.79	$6.286{\cdot}10^{-2}$	+1.17 -1.16	+1.00 -0.97	+0.64 -0.60
125.0	$5.824{\cdot}10^{-1}$	+0.65 -0.65	+0.72 -0.74	+0.78 -0.80	$6.272{\cdot}10^{-2}$	+1.17 -1.16	+0.98 -0.99	+0.62 -0.62
125.09	$5.809{\cdot}10^{-1}$	+0.65 -0.65	+0.72 -0.74	+0.77 -0.79	$6.256{\cdot}10^{-2}$	+1.17 -1.16	+0.98 -0.98	+0.62 -0.60
125.1	$5.807{\cdot}10^{-1}$	+0.65 -0.65	+0.72 -0.74	+0.78 -0.79	$6.256{\cdot}10^{-2}$	+1.17 -1.16	+0.98 -0.98	+0.61 -0.61
125.2	$5.792{\cdot}10^{-1}$	+0.65 -0.65	+0.72 -0.74	+0.78 -0.79	$6.240{\cdot}10^{-2}$	+1.17 -1.16	+0.96 -0.98	+0.60 -0.61
125.3	$5.776{\cdot}10^{-1}$	+0.65 -0.65	+0.72 -0.75	+0.77 -0.80	$6.223{\cdot}10^{-2}$	+1.17 -1.16	+0.98 -0.97	+0.61 -0.60
125.4	$5.760{\cdot}10^{-1}$	+0.65 -0.65	+0.73 -0.75	+0.78 -0.80	$6.208{\cdot}10^{-2}$	+1.17 -1.16	+0.97 -0.99	+0.61 -0.61
125.5	$5.744{\cdot}10^{-1}$	+0.65 -0.65	+0.73 -0.75	+0.79 -0.80	$6.192{\cdot}10^{-2}$	+1.17 -1.16	+0.95 -0.97	+0.60 -0.61
125.6	$5.728{\cdot}10^{-1}$	+0.66 -0.65	+0.73 -0.75	+0.79 -0.81	$6.175{\cdot}10^{-2}$	+1.17 -1.16	+0.98 -0.96	+0.62 -0.59
125.7	$5.713{\cdot}10^{-1}$	+0.66 -0.66	+0.73 -0.76	+0.79 -0.81	$6.159{\cdot}10^{-2}$	+1.17 -1.16	+0.96 -0.96	+0.60 -0.60
125.8	$5.696{\cdot}10^{-1}$	+0.66 -0.66	+0.73 -0.76	+0.79 -0.81	$6.143{\cdot}10^{-2}$	+1.17 -1.16	+0.95 -0.96	+0.60 -0.60
125.9	$5.681{\cdot}10^{-1}$	+0.66 -0.66	+0.74 -0.77	+0.79 -0.82	$6.126{\cdot}10^{-2}$	+1.17 -1.16	+0.97 -0.95	+0.60 -0.59
126.0	$5.664{\cdot}10^{-1}$	+0.66 -0.66	+0.74 -0.76	+0.79 -0.82	$6.109{\cdot}10^{-2}$	+1.17 -1.16	+0.97 -0.94	+0.60 -0.57
126.5	$5.583{\cdot}10^{-1}$	+0.67 -0.67	+0.76 -0.77	+0.81 -0.82	$6.027{\cdot}10^{-2}$	+1.17 -1.16	+0.93 -0.96	+0.58 -0.58
127.0	$5.501{\cdot}10^{-1}$	+0.68 -0.67	+0.77 -0.79	+0.82 -0.84	$5.943{\cdot}10^{-2}$	+1.17 -1.16	+0.92 -0.92	+0.57 -0.57
127.5	$5.417{\cdot}10^{-1}$	+0.68 -0.68	+0.78 -0.79	+0.83 -0.85	$5.857{\cdot}10^{-2}$	+1.17 -1.16	+0.90 -0.92	+0.57 -0.56
128.0	$5.332{\cdot}10^{-1}$	+0.69 -0.69	+0.79 -0.82	+0.84 -0.87	$5.770{\cdot}10^{-2}$	+1.17 -1.16	+0.90 -0.89	+0.57 -0.53
128.5	$5.246{\cdot}10^{-1}$	+0.70 -0.70	+0.82 -0.82	+0.86 -0.87	$5.681{\cdot}10^{-2}$	+1.17 -1.16	+0.89 -0.89	+0.56 -0.52
129.0	$5.160{\cdot}10^{-1}$	+0.70 -0.70	+0.83 -0.85	+0.86 -0.89	$5.592{\cdot}10^{-2}$	+1.16 -1.16	+0.86 -0.88	+0.54 -0.51
129.5	$5.073{\cdot}10^{-1}$	+0.71 -0.71	+0.84 -0.86	+0.87 -0.90	$5.502{\cdot}10^{-2}$	+1.16 -1.16	+0.86 -0.86	+0.52 -0.51
130.0	$4.985{\cdot}10^{-1}$	+0.72 -0.72	+0.86 -0.87	+0.90 -0.90	$5.411{\cdot}10^{-2}$	+1.16 -1.16	+0.84 -0.85	+0.51 -0.51

Table 175: SM Higgs boson branching ratios for $\mathrm{H} \to \mu^+\mu^-$ and $\mathrm{H} \to c\bar{c}$, corresponding theoretical uncertainties (THU) and parametric uncertainties from the quark masses (PU(m_q)) and the strong coupling (PU(α_s)) (expressed in percentage). Mass range around the Higgs boson resonance.

M_H [GeV]	$\mathrm{H} \to \mu^+\mu^-$	THU [%]	PU(m_q) [%]	PU(α_s) [%]	$\mathrm{H} \to c\bar{c}$	THU [%]	PU(m_q) [%]	PU(α_s) [%]
120.0	$2.423 \cdot 10^{-4}$	+1.23 -1.23	+1.07 -1.09	+0.69 -0.70	$3.244 \cdot 10^{-2}$	+1.20 -1.20	+5.27 -1.08	+1.14 -1.18
120.5	$2.401 \cdot 10^{-4}$	+1.23 -1.23	+1.09 -1.10	+0.71 -0.70	$3.212 \cdot 10^{-2}$	+1.20 -1.20	+5.26 -1.06	+1.17 -1.19
121.0	$2.378 \cdot 10^{-4}$	+1.23 -1.23	+1.10 -1.07	+0.71 -0.67	$3.180 \cdot 10^{-2}$	+1.20 -1.20	+5.25 -1.05	+1.17 -1.20
121.5	$2.355 \cdot 10^{-4}$	+1.23 -1.23	+1.06 -1.08	+0.68 -0.68	$3.147 \cdot 10^{-2}$	+1.20 -1.20	+5.23 -1.06	+1.15 -1.21
122.0	$2.331 \cdot 10^{-4}$	+1.23 -1.23	+1.08 -1.04	+0.68 -0.64	$3.112 \cdot 10^{-2}$	+1.20 -1.20	+5.26 -1.03	+1.20 -1.20
122.5	$2.307 \cdot 10^{-4}$	+1.23 -1.23	+1.05 -1.06	+0.64 -0.69	$3.077 \cdot 10^{-2}$	+1.20 -1.20	+5.26 -1.01	+1.18 -1.21
123.0	$2.282 \cdot 10^{-4}$	+1.23 -1.23	+1.01 -1.07	+0.66 -0.65	$3.041 \cdot 10^{-2}$	+1.20 -1.20	+5.28 -0.99	+1.23 -1.22
123.5	$2.256 \cdot 10^{-4}$	+1.23 -1.23	+1.02 -1.04	+0.66 -0.62	$3.005 \cdot 10^{-2}$	+1.20 -1.20	+5.23 -1.00	+1.20 -1.24
124.0	$2.230 \cdot 10^{-4}$	+1.23 -1.23	+0.99 -1.01	+0.62 -0.63	$2.968 \cdot 10^{-2}$	+1.20 -1.20	+5.22 -1.02	+1.21 -1.25
124.1	$2.224 \cdot 10^{-4}$	+1.23 -1.23	+1.05 -1.00	+0.67 -0.63	$2.960 \cdot 10^{-2}$	+1.20 -1.20	+5.24 -0.98	+1.22 -1.25
124.2	$2.219 \cdot 10^{-4}$	+1.23 -1.23	+1.00 -1.00	+0.63 -0.62	$2.953 \cdot 10^{-2}$	+1.20 -1.20	+5.23 -0.98	+1.20 -1.26
124.3	$2.214 \cdot 10^{-4}$	+1.23 -1.23	+0.99 -1.02	+0.62 -0.63	$2.945 \cdot 10^{-2}$	+1.20 -1.20	+5.26 -1.00	+1.22 -1.27
124.4	$2.208 \cdot 10^{-4}$	+1.23 -1.23	+1.00 -0.96	+0.63 -0.59	$2.937 \cdot 10^{-2}$	+1.20 -1.20	+5.28 -0.95	+1.23 -1.24
124.5	$2.203 \cdot 10^{-4}$	+1.23 -1.23	+1.00 -1.01	+0.63 -0.63	$2.930 \cdot 10^{-2}$	+1.20 -1.20	+5.26 -0.99	+1.24 -1.27
124.6	$2.198 \cdot 10^{-4}$	+1.23 -1.23	+0.96 -1.03	+0.59 -0.64	$2.922 \cdot 10^{-2}$	+1.20 -1.20	+5.24 -0.97	+1.24 -1.27
124.7	$2.192 \cdot 10^{-4}$	+1.23 -1.23	+1.01 -0.97	+0.64 -0.58	$2.914 \cdot 10^{-2}$	+1.20 -1.20	+5.25 -0.96	+1.25 -1.24
124.8	$2.187 \cdot 10^{-4}$	+1.23 -1.23	+0.96 -1.03	+0.59 -0.64	$2.907 \cdot 10^{-2}$	+1.20 -1.20	+5.23 -0.97	+1.21 -1.28
124.9	$2.181 \cdot 10^{-4}$	+1.23 -1.23	+0.98 -0.97	+0.64 -0.59	$2.899 \cdot 10^{-2}$	+1.20 -1.20	+5.24 -0.97	+1.26 -1.28
125.0	$2.176 \cdot 10^{-4}$	+1.23 -1.23	+0.97 -0.99	+0.59 -0.64	$2.891 \cdot 10^{-2}$	+1.20 -1.20	+5.26 -0.98	+1.25 -1.25
125.09	$2.171 \cdot 10^{-4}$	+1.23 -1.23	+0.97 -0.99	+0.60 -0.64	$2.884 \cdot 10^{-2}$	+1.20 -1.20	+5.27 -0.94	+1.26 -1.25
125.1	$2.170 \cdot 10^{-4}$	+1.23 -1.23	+0.98 -0.99	+0.65 -0.60	$2.883 \cdot 10^{-2}$	+1.20 -1.20	+5.28 -0.95	+1.25 -1.25
125.2	$2.165 \cdot 10^{-4}$	+1.23 -1.23	+0.97 -1.00	+0.59 -0.65	$2.876 \cdot 10^{-2}$	+1.20 -1.20	+5.23 -0.98	+1.22 -1.30
125.3	$2.159 \cdot 10^{-4}$	+1.23 -1.23	+0.99 -0.98	+0.60 -0.59	$2.868 \cdot 10^{-2}$	+1.20 -1.20	+5.26 -0.97	+1.23 -1.29
125.4	$2.153 \cdot 10^{-4}$	+1.23 -1.23	+0.98 -0.95	+0.65 -0.60	$2.860 \cdot 10^{-2}$	+1.20 -1.20	+5.24 -0.95	+1.23 -1.26
125.5	$2.148 \cdot 10^{-4}$	+1.23 -1.23	+0.93 -0.99	+0.61 -0.61	$2.852 \cdot 10^{-2}$	+1.20 -1.20	+5.25 -0.95	+1.27 -1.27
125.6	$2.142 \cdot 10^{-4}$	+1.23 -1.23	+0.99 -0.95	+0.61 -0.60	$2.844 \cdot 10^{-2}$	+1.20 -1.20	+5.28 -0.96	+1.28 -1.27
125.7	$2.137 \cdot 10^{-4}$	+1.23 -1.23	+0.94 -1.01	+0.60 -0.61	$2.836 \cdot 10^{-2}$	+1.20 -1.20	+5.25 -0.92	+1.27 -1.28
125.8	$2.131 \cdot 10^{-4}$	+1.23 -1.23	+0.94 -0.96	+0.61 -0.61	$2.828 \cdot 10^{-2}$	+1.20 -1.20	+5.26 -0.93	+1.28 -1.28
125.9	$2.125 \cdot 10^{-4}$	+1.23 -1.23	+0.95 -0.96	+0.60 -0.57	$2.820 \cdot 10^{-2}$	+1.20 -1.20	+5.28 -0.93	+1.28 -1.29
126.0	$2.119 \cdot 10^{-4}$	+1.23 -1.23	+1.01 -0.91	+0.61 -0.55	$2.812 \cdot 10^{-2}$	+1.20 -1.20	+5.27 -0.93	+1.30 -1.29
126.5	$2.092 \cdot 10^{-4}$	+1.23 -1.22	+0.91 -0.99	+0.56 -0.57	$2.772 \cdot 10^{-2}$	+1.20 -1.20	+5.21 -0.95	+1.27 -1.32
127.0	$2.061 \cdot 10^{-4}$	+1.23 -1.22	+0.93 -0.88	+0.58 -0.54	$2.731 \cdot 10^{-2}$	+1.20 -1.20	+5.26 -0.91	+1.28 -1.32
127.5	$2.032 \cdot 10^{-4}$	+1.23 -1.22	+0.88 -0.97	+0.53 -0.59	$2.690 \cdot 10^{-2}$	+1.20 -1.20	+5.22 -0.91	+1.27 -1.36
128.0	$2.002 \cdot 10^{-4}$	+1.22 -1.22	+0.85 -0.91	+0.55 -0.59	$2.648 \cdot 10^{-2}$	+1.20 -1.19	+5.26 -0.87	+1.30 -1.33
128.5	$1.971 \cdot 10^{-4}$	+1.22 -1.22	+0.87 -0.89	+0.55 -0.55	$2.606 \cdot 10^{-2}$	+1.20 -1.19	+5.18 -0.89	+1.31 -1.35
129.0	$1.940 \cdot 10^{-4}$	+1.22 -1.22	+0.88 -0.90	+0.56 -0.51	$2.563 \cdot 10^{-2}$	+1.20 -1.19	+5.23 -0.87	+1.34 -1.38
129.5	$1.909 \cdot 10^{-4}$	+1.22 -1.22	+0.84 -0.86	+0.52 -0.52	$2.520 \cdot 10^{-2}$	+1.19 -1.19	+5.20 -0.84	+1.32 -1.40
130.0	$1.877 \cdot 10^{-4}$	+1.22 -1.21	+0.86 -0.82	+0.52 -0.47	$2.476 \cdot 10^{-2}$	+1.19 -1.19	+5.25 -0.82	+1.35 -1.39

Table 176: SM Higgs boson branching ratios for $\mathrm{H} \to \mathrm{gg}$ and $\mathrm{H} \to \gamma\gamma$, corresponding theoretical uncertainties (THU) and parametric uncertainties from the quark masses (PU(m_q)) and the strong coupling (PU(α_s)) (expressed in percentage). Mass range around the Higgs boson resonance.

M_H [GeV]	$\mathrm{H} \to \mathrm{gg}$	THU [%]	PU(m_q) [%]	PU(α_s) [%]	$\mathrm{H} \to \gamma\gamma$	THU [%]	PU(m_q) [%]	PU(α_s) [%]
120.0	$8.409{\cdot}10^{-2}$	+3.39 -3.40	+1.24 -1.26	+3.80 -3.72	$2.218{\cdot}10^{-3}$	+1.73 -1.73	+1.08 -1.10	+0.71 -0.72
120.5	$8.401{\cdot}10^{-2}$	+3.39 -3.40	+1.23 -1.24	+3.80 -3.70	$2.226{\cdot}10^{-3}$	+1.73 -1.73	+1.08 -1.05	+0.72 -0.71
121.0	$8.390{\cdot}10^{-2}$	+3.39 -3.40	+1.23 -1.23	+3.81 -3.69	$2.235{\cdot}10^{-3}$	+1.73 -1.73	+1.03 -1.05	+0.71 -0.72
121.5	$8.376{\cdot}10^{-2}$	+3.39 -3.40	+1.21 -1.22	+3.79 -3.68	$2.242{\cdot}10^{-3}$	+1.73 -1.73	+1.03 -1.05	+0.71 -0.71
122.0	$8.358{\cdot}10^{-2}$	+3.39 -3.40	+1.22 -1.19	+3.78 -3.66	$2.248{\cdot}10^{-3}$	+1.73 -1.73	+1.03 -1.04	+0.71 -0.71
122.5	$8.339{\cdot}10^{-2}$	+3.39 -3.41	+1.18 -1.20	+3.75 -3.66	$2.253{\cdot}10^{-3}$	+1.73 -1.73	+1.03 -0.99	+0.70 -0.66
123.0	$8.315{\cdot}10^{-2}$	+3.39 -3.41	+1.18 -1.19	+3.75 -3.64	$2.258{\cdot}10^{-3}$	+1.73 -1.73	+1.02 -0.99	+0.67 -0.65
123.5	$8.288{\cdot}10^{-2}$	+3.39 -3.41	+1.16 -1.16	+3.74 -3.64	$2.262{\cdot}10^{-3}$	+1.73 -1.72	+0.97 -0.99	+0.65 -0.66
124.0	$8.258{\cdot}10^{-2}$	+3.40 -3.41	+1.15 -1.16	+3.72 -3.63	$2.266{\cdot}10^{-3}$	+1.73 -1.72	+0.98 -0.99	+0.66 -0.66
124.1	$8.251{\cdot}10^{-2}$	+3.40 -3.41	+1.17 -1.14	+3.73 -3.62	$2.266{\cdot}10^{-3}$	+1.73 -1.72	+0.98 -0.99	+0.66 -0.66
124.2	$8.244{\cdot}10^{-2}$	+3.40 -3.41	+1.17 -1.14	+3.73 -3.60	$2.266{\cdot}10^{-3}$	+1.73 -1.72	+0.98 -0.98	+0.66 -0.65
124.3	$8.238{\cdot}10^{-2}$	+3.40 -3.41	+1.14 -1.16	+3.71 -3.63	$2.268{\cdot}10^{-3}$	+1.73 -1.72	+0.96 -1.00	+0.61 -0.66
124.4	$8.231{\cdot}10^{-2}$	+3.40 -3.41	+1.14 -1.15	+3.72 -3.62	$2.268{\cdot}10^{-3}$	+1.73 -1.72	+0.97 -0.99	+0.66 -0.66
124.5	$8.224{\cdot}10^{-2}$	+3.40 -3.41	+1.14 -1.13	+3.71 -3.61	$2.267{\cdot}10^{-3}$	+1.73 -1.72	+0.97 -0.94	+0.66 -0.61
124.6	$8.217{\cdot}10^{-2}$	+3.40 -3.41	+1.14 -1.14	+3.71 -3.62	$2.269{\cdot}10^{-3}$	+1.73 -1.72	+0.97 -1.00	+0.66 -0.66
124.7	$8.209{\cdot}10^{-2}$	+3.40 -3.41	+1.14 -1.12	+3.72 -3.60	$2.268{\cdot}10^{-3}$	+1.73 -1.72	+0.98 -0.94	+0.66 -0.61
124.8	$8.203{\cdot}10^{-2}$	+3.40 -3.41	+1.13 -1.13	+3.71 -3.62	$2.269{\cdot}10^{-3}$	+1.73 -1.72	+0.97 -0.94	+0.66 -0.62
124.9	$8.194{\cdot}10^{-2}$	+3.40 -3.41	+1.14 -1.12	+3.72 -3.60	$2.270{\cdot}10^{-3}$	+1.73 -1.72	+0.94 -0.99	+0.62 -0.65
125.0	$8.187{\cdot}10^{-2}$	+3.40 -3.41	+1.12 -1.13	+3.69 -3.61	$2.270{\cdot}10^{-3}$	+1.73 -1.72	+0.93 -0.99	+0.61 -0.62
125.09	$8.180{\cdot}10^{-2}$	+3.40 -3.41	+1.12 -1.14	+3.70 -3.59	$2.270{\cdot}10^{-3}$	+1.73 -1.72	+0.97 -0.94	+0.66 -0.61
125.1	$8.179{\cdot}10^{-2}$	+3.40 -3.41	+1.12 -1.13	+3.70 -3.60	$2.270{\cdot}10^{-3}$	+1.73 -1.72	+0.98 -0.94	+0.66 -0.62
125.2	$8.172{\cdot}10^{-2}$	+3.40 -3.41	+1.12 -1.12	+3.70 -3.61	$2.270{\cdot}10^{-3}$	+1.73 -1.72	+0.97 -0.94	+0.65 -0.62
125.3	$8.163{\cdot}10^{-2}$	+3.40 -3.41	+1.12 -1.11	+3.70 -3.59	$2.270{\cdot}10^{-3}$	+1.73 -1.72	+0.98 -0.93	+0.66 -0.61
125.4	$8.154{\cdot}10^{-2}$	+3.40 -3.41	+1.12 -1.11	+3.70 -3.59	$2.270{\cdot}10^{-3}$	+1.73 -1.72	+0.97 -0.94	+0.66 -0.62
125.5	$8.147{\cdot}10^{-2}$	+3.40 -3.41	+1.11 -1.11	+3.69 -3.59	$2.271{\cdot}10^{-3}$	+1.73 -1.72	+0.93 -0.99	+0.62 -0.66
125.6	$8.139{\cdot}10^{-2}$	+3.40 -3.41	+1.10 -1.12	+3.68 -3.59	$2.271{\cdot}10^{-3}$	+1.72 -1.72	+0.93 -0.95	+0.62 -0.66
125.7	$8.130{\cdot}10^{-2}$	+3.40 -3.41	+1.10 -1.12	+3.68 -3.59	$2.271{\cdot}10^{-3}$	+1.72 -1.72	+0.93 -0.95	+0.61 -0.66
125.8	$8.121{\cdot}10^{-2}$	+3.40 -3.41	+1.10 -1.10	+3.69 -3.58	$2.271{\cdot}10^{-3}$	+1.72 -1.72	+0.93 -0.95	+0.62 -0.66
125.9	$8.112{\cdot}10^{-2}$	+3.40 -3.41	+1.11 -1.11	+3.69 -3.58	$2.270{\cdot}10^{-3}$	+1.72 -1.72	+0.98 -0.90	+0.65 -0.62
126.0	$8.102{\cdot}10^{-2}$	+3.40 -3.42	+1.12 -1.09	+3.68 -3.56	$2.270{\cdot}10^{-3}$	+1.72 -1.72	+0.94 -0.89	+0.66 -0.60
126.5	$8.056{\cdot}10^{-2}$	+3.40 -3.42	+1.08 -1.10	+3.65 -3.57	$2.269{\cdot}10^{-3}$	+1.72 -1.72	+0.92 -0.92	+0.60 -0.57
127.0	$8.006{\cdot}10^{-2}$	+3.41 -3.42	+1.08 -1.06	+3.66 -3.56	$2.267{\cdot}10^{-3}$	+1.72 -1.72	+0.94 -0.89	+0.62 -0.58
127.5	$7.953{\cdot}10^{-2}$	+3.41 -3.42	+1.05 -1.08	+3.63 -3.55	$2.265{\cdot}10^{-3}$	+1.72 -1.72	+0.88 -0.92	+0.56 -0.62
128.0	$7.896{\cdot}10^{-2}$	+3.41 -3.42	+1.04 -1.04	+3.63 -3.54	$2.261{\cdot}10^{-3}$	+1.72 -1.72	+0.89 -0.85	+0.57 -0.57
128.5	$7.836{\cdot}10^{-2}$	+3.41 -3.43	+1.03 -1.03	+3.61 -3.53	$2.257{\cdot}10^{-3}$	+1.72 -1.71	+0.85 -0.91	+0.53 -0.57
129.0	$7.774{\cdot}10^{-2}$	+3.42 -3.43	+1.01 -1.01	+3.60 -3.52	$2.251{\cdot}10^{-3}$	+1.72 -1.71	+0.85 -0.86	+0.57 -0.53
129.5	$7.707{\cdot}10^{-2}$	+3.42 -3.43	+0.99 -1.01	+3.59 -3.50	$2.245{\cdot}10^{-3}$	+1.71 -1.71	+0.85 -0.83	+0.53 -0.53
130.0	$7.638{\cdot}10^{-2}$	+3.42 -3.43	+0.98 -0.99	+3.57 -3.48	$2.238{\cdot}10^{-3}$	+1.71 -1.71	+0.81 -0.82	+0.52 -0.53

Table 177: SM Higgs boson branching ratios for $\mathrm{H} \to \mathrm{Z}\gamma$ and $\mathrm{H} \to \mathrm{WW}$, corresponding theoretical uncertainties (THU) and parametric uncertainties from the quark masses (PU(m_q)) and the strong coupling (PU(α_s)) (expressed in percentage). Mass range around the Higgs boson resonance.

M_H [GeV]	$\mathrm{H} \to \mathrm{Z}\gamma$	THU [%]	PU(m_q) [%]	PU(α_s) [%]	$\mathrm{H} \to \mathrm{WW}$	THU [%]	PU(m_q) [%]	PU(α_s) [%]
120.0	$1.100 \cdot 10^{-3}$	+5.72 -5.72	+1.09 -1.01	+0.72 -0.64	$1.405 \cdot 10^{-1}$	+1.08 -1.08	+1.11 -1.11	+0.73 -0.73
120.5	$1.143 \cdot 10^{-3}$	+5.72 -5.72	+1.05 -1.07	+0.70 -0.69	$1.470 \cdot 10^{-1}$	+1.07 -1.07	+1.10 -1.09	+0.73 -0.71
121.0	$1.186 \cdot 10^{-3}$	+5.72 -5.72	+1.10 -1.04	+0.76 -0.67	$1.537 \cdot 10^{-1}$	+1.06 -1.06	+1.09 -1.08	+0.72 -0.71
121.5	$1.229 \cdot 10^{-3}$	+5.72 -5.72	+1.06 -1.08	+0.73 -0.65	$1.606 \cdot 10^{-1}$	+1.05 -1.05	+1.07 -1.07	+0.70 -0.70
122.0	$1.272 \cdot 10^{-3}$	+5.72 -5.72	+1.11 -1.03	+0.70 -0.63	$1.677 \cdot 10^{-1}$	+1.05 -1.04	+1.04 -1.07	+0.69 -0.69
122.5	$1.316 \cdot 10^{-3}$	+5.72 -5.72	+0.99 -1.10	+0.60 -0.68	$1.750 \cdot 10^{-1}$	+1.04 -1.04	+1.04 -1.06	+0.69 -0.68
123.0	$1.359 \cdot 10^{-3}$	+5.72 -5.72	+1.03 -1.04	+0.67 -0.65	$1.824 \cdot 10^{-1}$	+1.03 -1.03	+1.03 -1.05	+0.69 -0.69
123.5	$1.402 \cdot 10^{-3}$	+5.72 -5.72	+1.00 -1.01	+0.63 -0.64	$1.900 \cdot 10^{-1}$	+1.02 -1.02	+1.01 -1.03	+0.66 -0.66
124.0	$1.447 \cdot 10^{-3}$	+5.72 -5.71	+0.97 -1.07	+0.62 -0.69	$1.977 \cdot 10^{-1}$	+1.01 -1.01	+1.02 -0.99	+0.68 -0.65
124.1	$1.454 \cdot 10^{-3}$	+5.72 -5.71	+1.04 -0.97	+0.69 -0.62	$1.993 \cdot 10^{-1}$	+1.01 -1.01	+1.00 -1.01	+0.66 -0.65
124.2	$1.464 \cdot 10^{-3}$	+5.72 -5.71	+0.97 -0.97	+0.62 -0.61	$2.008 \cdot 10^{-1}$	+1.01 -1.00	+0.99 -1.00	+0.66 -0.64
124.3	$1.472 \cdot 10^{-3}$	+5.72 -5.71	+1.01 -0.97	+0.67 -0.61	$2.024 \cdot 10^{-1}$	+1.00 -1.00	+1.00 -1.01	+0.64 -0.65
124.4	$1.481 \cdot 10^{-3}$	+5.72 -5.71	+1.02 -0.96	+0.67 -0.61	$2.040 \cdot 10^{-1}$	+1.00 -1.00	+1.01 -0.99	+0.67 -0.65
124.5	$1.490 \cdot 10^{-3}$	+5.72 -5.71	+0.94 -1.03	+0.60 -0.66	$2.056 \cdot 10^{-1}$	+1.00 -1.00	+1.00 -0.99	+0.67 -0.63
124.6	$1.498 \cdot 10^{-3}$	+5.72 -5.71	+1.01 -0.95	+0.67 -0.60	$2.072 \cdot 10^{-1}$	+1.00 -1.00	+1.00 -1.00	+0.65 -0.64
124.7	$1.507 \cdot 10^{-3}$	+5.72 -5.71	+1.00 -1.01	+0.60 -0.59	$2.089 \cdot 10^{-1}$	+1.00 -0.99	+0.98 -0.99	+0.64 -0.63
124.8	$1.516 \cdot 10^{-3}$	+5.72 -5.71	+0.93 -1.02	+0.59 -0.66	$2.104 \cdot 10^{-1}$	+0.99 -0.99	+0.99 -0.99	+0.66 -0.64
124.9	$1.524 \cdot 10^{-3}$	+5.72 -5.71	+1.00 -0.93	+0.66 -0.58	$2.121 \cdot 10^{-1}$	+0.99 -0.99	+1.00 -0.98	+0.64 -0.63
125.0	$1.533 \cdot 10^{-3}$	+5.71 -5.71	+0.98 -1.01	+0.58 -0.65	$2.137 \cdot 10^{-1}$	+0.99 -0.99	+0.99 -0.98	+0.66 -0.63
125.09	$1.541 \cdot 10^{-3}$	+5.71 -5.71	+0.91 -1.00	+0.58 -0.64	$2.152 \cdot 10^{-1}$	+0.99 -0.99	+0.98 -0.98	+0.64 -0.62
125.1	$1.541 \cdot 10^{-3}$	+5.71 -5.71	+0.98 -0.92	+0.65 -0.59	$2.154 \cdot 10^{-1}$	+0.99 -0.99	+0.96 -0.98	+0.64 -0.63
125.2	$1.550 \cdot 10^{-3}$	+5.71 -5.71	+0.97 -0.98	+0.64 -0.64	$2.170 \cdot 10^{-1}$	+0.99 -0.98	+0.98 -0.98	+0.63 -0.63
125.3	$1.558 \cdot 10^{-3}$	+5.71 -5.71	+0.98 -0.90	+0.64 -0.57	$2.186 \cdot 10^{-1}$	+0.98 -0.98	+0.99 -0.96	+0.64 -0.61
125.4	$1.567 \cdot 10^{-3}$	+5.71 -5.71	+0.96 -0.97	+0.64 -0.57	$2.203 \cdot 10^{-1}$	+0.98 -0.98	+0.97 -0.97	+0.63 -0.62
125.5	$1.576 \cdot 10^{-3}$	+5.71 -5.71	+0.95 -0.98	+0.57 -0.63	$2.219 \cdot 10^{-1}$	+0.98 -0.98	+0.97 -0.97	+0.63 -0.62
125.6	$1.584 \cdot 10^{-3}$	+5.71 -5.71	+0.95 -0.96	+0.63 -0.56	$2.236 \cdot 10^{-1}$	+0.98 -0.98	+0.95 -0.97	+0.63 -0.64
125.7	$1.593 \cdot 10^{-3}$	+5.71 -5.71	+0.94 -0.97	+0.56 -0.63	$2.253 \cdot 10^{-1}$	+0.98 -0.97	+0.96 -0.96	+0.65 -0.62
125.8	$1.601 \cdot 10^{-3}$	+5.71 -5.71	+0.94 -0.95	+0.63 -0.56	$2.270 \cdot 10^{-1}$	+0.97 -0.97	+0.96 -0.96	+0.62 -0.62
125.9	$1.610 \cdot 10^{-3}$	+5.71 -5.71	+0.94 -0.96	+0.55 -0.62	$2.286 \cdot 10^{-1}$	+0.97 -0.97	+0.96 -0.95	+0.64 -0.62
126.0	$1.618 \cdot 10^{-3}$	+5.71 -5.71	+0.94 -0.93	+0.62 -0.60	$2.303 \cdot 10^{-1}$	+0.97 -0.97	+0.94 -0.97	+0.62 -0.62
126.5	$1.660 \cdot 10^{-3}$	+5.71 -5.71	+0.96 -0.94	+0.59 -0.54	$2.388 \cdot 10^{-1}$	+0.96 -0.96	+0.93 -0.95	+0.61 -0.61
127.0	$1.702 \cdot 10^{-3}$	+5.71 -5.71	+0.95 -0.90	+0.59 -0.59	$2.475 \cdot 10^{-1}$	+0.95 -0.95	+0.93 -0.93	+0.60 -0.59
127.5	$1.744 \cdot 10^{-3}$	+5.71 -5.71	+0.92 -0.89	+0.56 -0.57	$2.563 \cdot 10^{-1}$	+0.94 -0.93	+0.90 -0.92	+0.60 -0.58
128.0	$1.785 \cdot 10^{-3}$	+5.71 -5.70	+0.90 -0.91	+0.56 -0.55	$2.652 \cdot 10^{-1}$	+0.92 -0.92	+0.91 -0.90	+0.60 -0.56
128.5	$1.825 \cdot 10^{-3}$	+5.70 -5.70	+0.89 -0.90	+0.54 -0.54	$2.743 \cdot 10^{-1}$	+0.91 -0.91	+0.87 -0.90	+0.56 -0.58
129.0	$1.864 \cdot 10^{-3}$	+5.70 -5.70	+0.86 -0.87	+0.52 -0.53	$2.835 \cdot 10^{-1}$	+0.90 -0.90	+0.87 -0.87	+0.57 -0.55
129.5	$1.903 \cdot 10^{-3}$	+5.70 -5.70	+0.84 -0.86	+0.52 -0.52	$2.927 \cdot 10^{-1}$	+0.89 -0.89	+0.86 -0.86	+0.55 -0.54
130.0	$1.941 \cdot 10^{-3}$	+5.70 -5.70	+0.83 -0.85	+0.50 -0.51	$3.021 \cdot 10^{-1}$	+0.87 -0.87	+0.84 -0.84	+0.53 -0.54

Table 178: SM Higgs boson branching ratios for $\mathrm{H} \to \mathrm{ZZ}$ and Higgs boson total width Γ_{H}, corresponding theoretical uncertainties (THU) and parametric uncertainties from the quark masses (PU(m_q)) and the strong coupling (PU(α_{s})) (expressed in percentage). Mass range around the Higgs boson resonance.

M_{H} [GeV]	$\mathrm{H} \to \mathrm{ZZ}$	THU [%]	PU(m_q) [%]	PU(α_{s}) [%]	Γ_{H} [GeV]	THU [%]	PU(m_q) [%]	PU(α_{s}) [%]
120.0	$1.572 \cdot 10^{-2}$	+1.08 -1.08	+1.11 -1.11	+0.73 -0.73	$3.527 \cdot 10^{-3}$	+0.73 -0.73	+1.12 -1.10	+0.71 -0.70
120.5	$1.662 \cdot 10^{-2}$	+1.07 -1.07	+1.10 -1.09	+0.73 -0.71	$3.574 \cdot 10^{-3}$	+0.73 -0.73	+1.10 -1.09	+0.69 -0.70
121.0	$1.755 \cdot 10^{-2}$	+1.06 -1.06	+1.09 -1.08	+0.72 -0.71	$3.622 \cdot 10^{-3}$	+0.73 -0.73	+1.09 -1.07	+0.69 -0.69
121.5	$1.851 \cdot 10^{-2}$	+1.05 -1.05	+1.07 -1.07	+0.71 -0.70	$3.673 \cdot 10^{-3}$	+0.73 -0.73	+1.08 -1.06	+0.67 -0.68
122.0	$1.951 \cdot 10^{-2}$	+1.05 -1.04	+1.04 -1.07	+0.69 -0.69	$3.725 \cdot 10^{-3}$	+0.73 -0.73	+1.09 -1.03	+0.67 -0.66
122.5	$2.055 \cdot 10^{-2}$	+1.04 -1.04	+1.04 -1.06	+0.68 -0.67	$3.779 \cdot 10^{-3}$	+0.73 -0.73	+1.08 -1.03	+0.65 -0.65
123.0	$2.161 \cdot 10^{-2}$	+1.03 -1.03	+1.03 -1.05	+0.68 -0.69	$3.836 \cdot 10^{-3}$	+0.73 -0.73	+1.06 -1.02	+0.66 -0.65
123.5	$2.270 \cdot 10^{-2}$	+1.02 -1.02	+1.01 -1.03	+0.66 -0.66	$3.896 \cdot 10^{-3}$	+0.73 -0.73	+1.04 -1.00	+0.64 -0.63
124.0	$2.383 \cdot 10^{-2}$	+1.01 -1.01	+1.02 -0.99	+0.68 -0.65	$3.957 \cdot 10^{-3}$	+0.73 -0.73	+1.00 -1.01	+0.63 -0.65
124.1	$2.406 \cdot 10^{-2}$	+1.01 -1.01	+1.00 -1.01	+0.66 -0.65	$3.969 \cdot 10^{-3}$	+0.73 -0.73	+1.02 -0.99	+0.63 -0.63
124.2	$2.429 \cdot 10^{-2}$	+1.01 -1.00	+0.99 -1.00	+0.66 -0.64	$3.982 \cdot 10^{-3}$	+0.73 -0.73	+1.01 -0.98	+0.62 -0.63
124.3	$2.452 \cdot 10^{-2}$	+1.00 -1.00	+1.00 -1.01	+0.64 -0.65	$3.995 \cdot 10^{-3}$	+0.73 -0.73	+1.02 -0.99	+0.62 -0.61
124.4	$2.476 \cdot 10^{-2}$	+1.00 -1.00	+1.01 -0.99	+0.67 -0.65	$4.008 \cdot 10^{-3}$	+0.73 -0.73	+1.00 -1.00	+0.62 -0.64
124.5	$2.499 \cdot 10^{-2}$	+1.00 -1.00	+1.00 -0.99	+0.67 -0.63	$4.021 \cdot 10^{-3}$	+0.73 -0.73	+1.00 -0.99	+0.61 -0.64
124.6	$2.523 \cdot 10^{-2}$	+1.00 -1.00	+1.00 -1.00	+0.65 -0.64	$4.034 \cdot 10^{-3}$	+0.73 -0.73	+1.01 -0.99	+0.62 -0.62
124.7	$2.547 \cdot 10^{-2}$	+1.00 -0.99	+0.98 -0.99	+0.65 -0.63	$4.047 \cdot 10^{-3}$	+0.73 -0.73	+1.00 -0.97	+0.61 -0.61
124.8	$2.571 \cdot 10^{-2}$	+0.99 -0.99	+0.99 -0.99	+0.66 -0.64	$4.061 \cdot 10^{-3}$	+0.73 -0.73	+1.00 -0.98	+0.61 -0.63
124.9	$2.595 \cdot 10^{-2}$	+0.99 -0.99	+1.00 -0.98	+0.64 -0.63	$4.074 \cdot 10^{-3}$	+0.73 -0.73	+0.99 -0.99	+0.60 -0.61
125.0	$2.619 \cdot 10^{-2}$	+0.99 -0.99	+0.99 -0.98	+0.66 -0.63	$4.088 \cdot 10^{-3}$	+0.73 -0.73	+0.99 -0.98	+0.61 -0.63
125.09	$2.641 \cdot 10^{-2}$	+0.99 -0.99	+0.98 -0.98	+0.64 -0.62	$4.100 \cdot 10^{-3}$	+0.73 -0.73	+0.99 -0.97	+0.60 -0.61
125.1	$2.643 \cdot 10^{-2}$	+0.99 -0.99	+0.96 -0.98	+0.64 -0.63	$4.101 \cdot 10^{-3}$	+0.73 -0.73	+0.99 -0.95	+0.61 -0.61
125.2	$2.667 \cdot 10^{-2}$	+0.99 -0.98	+0.98 -0.98	+0.63 -0.63	$4.115 \cdot 10^{-3}$	+0.73 -0.73	+0.99 -0.97	+0.60 -0.60
125.3	$2.692 \cdot 10^{-2}$	+0.98 -0.98	+0.99 -0.96	+0.63 -0.62	$4.129 \cdot 10^{-3}$	+0.73 -0.73	+0.97 -0.98	+0.59 -0.60
125.4	$2.716 \cdot 10^{-2}$	+0.98 -0.98	+0.97 -0.97	+0.63 -0.63	$4.143 \cdot 10^{-3}$	+0.73 -0.73	+0.98 -0.96	+0.60 -0.60
125.5	$2.741 \cdot 10^{-2}$	+0.98 -0.98	+0.97 -0.97	+0.63 -0.62	$4.156 \cdot 10^{-3}$	+0.73 -0.73	+0.97 -0.96	+0.60 -0.60
125.6	$2.766 \cdot 10^{-2}$	+0.98 -0.98	+0.95 -0.97	+0.63 -0.64	$4.170 \cdot 10^{-3}$	+0.73 -0.73	+0.97 -0.94	+0.61 -0.60
125.7	$2.790 \cdot 10^{-2}$	+0.98 -0.97	+0.96 -0.96	+0.64 -0.62	$4.185 \cdot 10^{-3}$	+0.73 -0.73	+0.97 -0.95	+0.59 -0.61
125.8	$2.816 \cdot 10^{-2}$	+0.97 -0.97	+0.96 -0.96	+0.62 -0.62	$4.199 \cdot 10^{-3}$	+0.73 -0.73	+0.97 -0.95	+0.59 -0.59
125.9	$2.840 \cdot 10^{-2}$	+0.97 -0.97	+0.96 -0.95	+0.64 -0.62	$4.214 \cdot 10^{-3}$	+0.73 -0.73	+0.96 -0.95	+0.59 -0.61
126.0	$2.866 \cdot 10^{-2}$	+0.97 -0.97	+0.94 -0.97	+0.62 -0.62	$4.228 \cdot 10^{-3}$	+0.73 -0.73	+0.98 -0.93	+0.60 -0.59
126.5	$2.993 \cdot 10^{-2}$	+0.96 -0.96	+0.93 -0.95	+0.62 -0.60	$4.303 \cdot 10^{-3}$	+0.73 -0.73	+0.96 -0.92	+0.58 -0.59
127.0	$3.124 \cdot 10^{-2}$	+0.95 -0.95	+0.93 -0.93	+0.60 -0.59	$4.381 \cdot 10^{-3}$	+0.72 -0.72	+0.94 -0.92	+0.57 -0.57
127.5	$3.257 \cdot 10^{-2}$	+0.94 -0.93	+0.90 -0.92	+0.60 -0.58	$4.463 \cdot 10^{-3}$	+0.72 -0.72	+0.92 -0.89	+0.56 -0.57
128.0	$3.392 \cdot 10^{-2}$	+0.92 -0.92	+0.91 -0.89	+0.60 -0.56	$4.548 \cdot 10^{-3}$	+0.72 -0.72	+0.90 -0.90	+0.54 -0.56
128.5	$3.530 \cdot 10^{-2}$	+0.91 -0.91	+0.88 -0.90	+0.56 -0.58	$4.635 \cdot 10^{-3}$	+0.72 -0.72	+0.91 -0.87	+0.55 -0.53
129.0	$3.670 \cdot 10^{-2}$	+0.90 -0.90	+0.87 -0.87	+0.57 -0.55	$4.728 \cdot 10^{-3}$	+0.72 -0.72	+0.88 -0.86	+0.52 -0.54
129.5	$3.811 \cdot 10^{-2}$	+0.89 -0.89	+0.86 -0.86	+0.56 -0.54	$4.824 \cdot 10^{-3}$	+0.72 -0.72	+0.87 -0.85	+0.51 -0.53
130.0	$3.955 \cdot 10^{-2}$	+0.87 -0.87	+0.84 -0.84	+0.53 -0.54	$4.923 \cdot 10^{-3}$	+0.72 -0.72	+0.85 -0.83	+0.52 -0.49

Table 179: SM Higgs boson branching ratios for $\mathrm{H} \to 4\ell$ and corresponding total uncertainty (expressed in percentage). Mass range around the Higgs boson resonance.

M_{H} [GeV]	$\mathrm{H} \to \ell^+\ell^-\ell^+\ell^-$ $\ell = \mathrm{e}, \mu, \tau$	$\mathrm{H} \to \ell^+\ell^-\ell^+\ell^-$ $\ell = \mathrm{e}, \mu$	$\mathrm{H} \to \mathrm{e}^+\mathrm{e}^-\mathrm{e}^+\mathrm{e}^-$	$\mathrm{H} \to \mathrm{e}^+\mathrm{e}^-\mu^+\mu^-$	Δ BR[%]
120.0	$1.659 \cdot 10^{-4}$	$7.524 \cdot 10^{-5}$	$1.995 \cdot 10^{-5}$	$3.533 \cdot 10^{-5}$	± 2.41
120.5	$1.753 \cdot 10^{-4}$	$7.950 \cdot 10^{-5}$	$2.107 \cdot 10^{-5}$	$3.735 \cdot 10^{-5}$	± 2.40
121.0	$1.850 \cdot 10^{-4}$	$8.387 \cdot 10^{-5}$	$2.221 \cdot 10^{-5}$	$3.946 \cdot 10^{-5}$	± 2.37
121.5	$1.950 \cdot 10^{-4}$	$8.837 \cdot 10^{-5}$	$2.337 \cdot 10^{-5}$	$4.162 \cdot 10^{-5}$	± 2.34
122.0	$2.054 \cdot 10^{-4}$	$9.304 \cdot 10^{-5}$	$2.458 \cdot 10^{-5}$	$4.388 \cdot 10^{-5}$	± 2.32
122.5	$2.161 \cdot 10^{-4}$	$9.785 \cdot 10^{-5}$	$2.581 \cdot 10^{-5}$	$4.622 \cdot 10^{-5}$	± 2.30
123.0	$2.271 \cdot 10^{-4}$	$1.028 \cdot 10^{-4}$	$2.708 \cdot 10^{-5}$	$4.863 \cdot 10^{-5}$	± 2.28
123.5	$2.385 \cdot 10^{-4}$	$1.079 \cdot 10^{-4}$	$2.839 \cdot 10^{-5}$	$5.110 \cdot 10^{-5}$	± 2.24
124.0	$2.502 \cdot 10^{-4}$	$1.131 \cdot 10^{-4}$	$2.974 \cdot 10^{-5}$	$5.365 \cdot 10^{-5}$	± 2.24
124.1	$2.526 \cdot 10^{-4}$	$1.142 \cdot 10^{-4}$	$3.002 \cdot 10^{-5}$	$5.417 \cdot 10^{-5}$	± 2.21
124.2	$2.549 \cdot 10^{-4}$	$1.153 \cdot 10^{-4}$	$3.029 \cdot 10^{-5}$	$5.469 \cdot 10^{-5}$	± 2.20
124.3	$2.574 \cdot 10^{-4}$	$1.164 \cdot 10^{-4}$	$3.057 \cdot 10^{-5}$	$5.522 \cdot 10^{-5}$	± 2.20
124.4	$2.598 \cdot 10^{-4}$	$1.174 \cdot 10^{-4}$	$3.085 \cdot 10^{-5}$	$5.575 \cdot 10^{-5}$	± 2.21
124.5	$2.622 \cdot 10^{-4}$	$1.185 \cdot 10^{-4}$	$3.112 \cdot 10^{-5}$	$5.628 \cdot 10^{-5}$	± 2.21
124.6	$2.646 \cdot 10^{-4}$	$1.196 \cdot 10^{-4}$	$3.140 \cdot 10^{-5}$	$5.681 \cdot 10^{-5}$	± 2.19
124.7	$2.671 \cdot 10^{-4}$	$1.207 \cdot 10^{-4}$	$3.169 \cdot 10^{-5}$	$5.735 \cdot 10^{-5}$	± 2.17
124.8	$2.695 \cdot 10^{-4}$	$1.218 \cdot 10^{-4}$	$3.197 \cdot 10^{-5}$	$5.788 \cdot 10^{-5}$	± 2.19
124.9	$2.720 \cdot 10^{-4}$	$1.229 \cdot 10^{-4}$	$3.225 \cdot 10^{-5}$	$5.843 \cdot 10^{-5}$	± 2.18
125.0	$2.745 \cdot 10^{-4}$	$1.240 \cdot 10^{-4}$	$3.254 \cdot 10^{-5}$	$5.897 \cdot 10^{-5}$	± 2.18
125.09	$2.768 \cdot 10^{-4}$	$1.251 \cdot 10^{-4}$	$3.280 \cdot 10^{-5}$	$5.947 \cdot 10^{-5}$	± 2.16
125.1	$2.771 \cdot 10^{-4}$	$1.252 \cdot 10^{-4}$	$3.283 \cdot 10^{-5}$	$5.953 \cdot 10^{-5}$	± 2.16
125.2	$2.796 \cdot 10^{-4}$	$1.263 \cdot 10^{-4}$	$3.312 \cdot 10^{-5}$	$6.007 \cdot 10^{-5}$	± 2.15
125.3	$2.821 \cdot 10^{-4}$	$1.274 \cdot 10^{-4}$	$3.340 \cdot 10^{-5}$	$6.062 \cdot 10^{-5}$	± 2.16
125.4	$2.846 \cdot 10^{-4}$	$1.286 \cdot 10^{-4}$	$3.370 \cdot 10^{-5}$	$6.118 \cdot 10^{-5}$	± 2.14
125.5	$2.872 \cdot 10^{-4}$	$1.297 \cdot 10^{-4}$	$3.399 \cdot 10^{-5}$	$6.174 \cdot 10^{-5}$	± 2.14
125.6	$2.898 \cdot 10^{-4}$	$1.309 \cdot 10^{-4}$	$3.429 \cdot 10^{-5}$	$6.230 \cdot 10^{-5}$	± 2.13
125.7	$2.923 \cdot 10^{-4}$	$1.320 \cdot 10^{-4}$	$3.458 \cdot 10^{-5}$	$6.285 \cdot 10^{-5}$	± 2.13
125.8	$2.949 \cdot 10^{-4}$	$1.332 \cdot 10^{-4}$	$3.488 \cdot 10^{-5}$	$6.342 \cdot 10^{-5}$	± 2.12
125.9	$2.974 \cdot 10^{-4}$	$1.343 \cdot 10^{-4}$	$3.517 \cdot 10^{-5}$	$6.398 \cdot 10^{-5}$	± 2.13
126.0	$3.001 \cdot 10^{-4}$	$1.355 \cdot 10^{-4}$	$3.548 \cdot 10^{-5}$	$6.455 \cdot 10^{-5}$	± 2.12
126.5	$3.133 \cdot 10^{-4}$	$1.414 \cdot 10^{-4}$	$3.699 \cdot 10^{-5}$	$6.743 \cdot 10^{-5}$	± 2.08
127.0	$3.268 \cdot 10^{-4}$	$1.475 \cdot 10^{-4}$	$3.854 \cdot 10^{-5}$	$7.038 \cdot 10^{-5}$	± 2.05
127.5	$3.405 \cdot 10^{-4}$	$1.536 \cdot 10^{-4}$	$4.010 \cdot 10^{-5}$	$7.338 \cdot 10^{-5}$	± 2.02
128.0	$3.544 \cdot 10^{-4}$	$1.599 \cdot 10^{-4}$	$4.171 \cdot 10^{-5}$	$7.644 \cdot 10^{-5}$	± 2.01
128.5	$3.687 \cdot 10^{-4}$	$1.662 \cdot 10^{-4}$	$4.333 \cdot 10^{-5}$	$7.956 \cdot 10^{-5}$	± 1.98
129.0	$3.830 \cdot 10^{-4}$	$1.726 \cdot 10^{-4}$	$4.497 \cdot 10^{-5}$	$8.270 \cdot 10^{-5}$	± 1.94
129.5	$3.976 \cdot 10^{-4}$	$1.792 \cdot 10^{-4}$	$4.664 \cdot 10^{-5}$	$8.590 \cdot 10^{-5}$	± 1.91
130.0	$4.124 \cdot 10^{-4}$	$1.858 \cdot 10^{-4}$	$4.832 \cdot 10^{-5}$	$8.914 \cdot 10^{-5}$	± 1.88

Table 180: SM Higgs boson branching ratios for $H \to 2\ell 2\nu$ and corresponding total uncertainty (expressed in percentage). Mass range around the Higgs boson resonance.

M_H [GeV]	$H \to \ell^+\ell^-\nu\bar{\nu}$ $\ell = e, \mu, \tau$ ν =any	$H \to \ell^+\ell^-\nu\bar{\nu}$ $\ell = e, \mu$ ν = any	$H \to e^+\nu_e e^-\bar{\nu}_e$	$H \to e^+\nu_e \mu^-\bar{\nu}_\mu$	Δ BR[%]
120.0	$1.526 \cdot 10^{-2}$	$6.864 \cdot 10^{-3}$	$1.634 \cdot 10^{-3}$	$1.656 \cdot 10^{-3}$	± 2.41
120.5	$1.598 \cdot 10^{-2}$	$7.190 \cdot 10^{-3}$	$1.712 \cdot 10^{-3}$	$1.733 \cdot 10^{-3}$	± 2.40
121.0	$1.673 \cdot 10^{-2}$	$7.528 \cdot 10^{-3}$	$1.793 \cdot 10^{-3}$	$1.812 \cdot 10^{-3}$	± 2.37
121.5	$1.749 \cdot 10^{-2}$	$7.874 \cdot 10^{-3}$	$1.876 \cdot 10^{-3}$	$1.894 \cdot 10^{-3}$	± 2.34
122.0	$1.828 \cdot 10^{-2}$	$8.230 \cdot 10^{-3}$	$1.962 \cdot 10^{-3}$	$1.977 \cdot 10^{-3}$	± 2.32
122.5	$1.908 \cdot 10^{-2}$	$8.594 \cdot 10^{-3}$	$2.049 \cdot 10^{-3}$	$2.063 \cdot 10^{-3}$	± 2.30
123.0	$1.990 \cdot 10^{-2}$	$8.967 \cdot 10^{-3}$	$2.138 \cdot 10^{-3}$	$2.150 \cdot 10^{-3}$	± 2.28
123.5	$2.074 \cdot 10^{-2}$	$9.349 \cdot 10^{-3}$	$2.230 \cdot 10^{-3}$	$2.240 \cdot 10^{-3}$	± 2.24
124.0	$2.160 \cdot 10^{-2}$	$9.739 \cdot 10^{-3}$	$2.324 \cdot 10^{-3}$	$2.331 \cdot 10^{-3}$	± 2.24
124.1	$2.178 \cdot 10^{-2}$	$9.819 \cdot 10^{-3}$	$2.343 \cdot 10^{-3}$	$2.350 \cdot 10^{-3}$	± 2.21
124.2	$2.195 \cdot 10^{-2}$	$9.898 \cdot 10^{-3}$	$2.362 \cdot 10^{-3}$	$2.368 \cdot 10^{-3}$	± 2.20
124.3	$2.213 \cdot 10^{-2}$	$9.978 \cdot 10^{-3}$	$2.381 \cdot 10^{-3}$	$2.387 \cdot 10^{-3}$	± 2.20
124.4	$2.230 \cdot 10^{-2}$	$1.006 \cdot 10^{-2}$	$2.400 \cdot 10^{-3}$	$2.405 \cdot 10^{-3}$	± 2.21
124.5	$2.248 \cdot 10^{-2}$	$1.014 \cdot 10^{-2}$	$2.420 \cdot 10^{-3}$	$2.424 \cdot 10^{-3}$	± 2.21
124.6	$2.266 \cdot 10^{-2}$	$1.022 \cdot 10^{-2}$	$2.439 \cdot 10^{-3}$	$2.443 \cdot 10^{-3}$	± 2.19
124.7	$2.284 \cdot 10^{-2}$	$1.030 \cdot 10^{-2}$	$2.459 \cdot 10^{-3}$	$2.462 \cdot 10^{-3}$	± 2.17
124.8	$2.302 \cdot 10^{-2}$	$1.038 \cdot 10^{-2}$	$2.478 \cdot 10^{-3}$	$2.481 \cdot 10^{-3}$	± 2.19
124.9	$2.320 \cdot 10^{-2}$	$1.046 \cdot 10^{-2}$	$2.498 \cdot 10^{-3}$	$2.500 \cdot 10^{-3}$	± 2.18
125.0	$2.338 \cdot 10^{-2}$	$1.055 \cdot 10^{-2}$	$2.518 \cdot 10^{-3}$	$2.519 \cdot 10^{-3}$	± 2.18
125.09	$2.354 \cdot 10^{-2}$	$1.062 \cdot 10^{-2}$	$2.536 \cdot 10^{-3}$	$2.537 \cdot 10^{-3}$	± 2.16
125.1	$2.356 \cdot 10^{-2}$	$1.063 \cdot 10^{-2}$	$2.538 \cdot 10^{-3}$	$2.539 \cdot 10^{-3}$	± 2.16
125.2	$2.374 \cdot 10^{-2}$	$1.071 \cdot 10^{-2}$	$2.558 \cdot 10^{-3}$	$2.558 \cdot 10^{-3}$	± 2.15
125.3	$2.393 \cdot 10^{-2}$	$1.080 \cdot 10^{-2}$	$2.578 \cdot 10^{-3}$	$2.578 \cdot 10^{-3}$	± 2.16
125.4	$2.411 \cdot 10^{-2}$	$1.088 \cdot 10^{-2}$	$2.598 \cdot 10^{-3}$	$2.597 \cdot 10^{-3}$	± 2.14
125.5	$2.429 \cdot 10^{-2}$	$1.096 \cdot 10^{-2}$	$2.618 \cdot 10^{-3}$	$2.617 \cdot 10^{-3}$	± 2.14
125.6	$2.448 \cdot 10^{-2}$	$1.105 \cdot 10^{-2}$	$2.638 \cdot 10^{-3}$	$2.636 \cdot 10^{-3}$	± 2.13
125.7	$2.466 \cdot 10^{-2}$	$1.113 \cdot 10^{-2}$	$2.658 \cdot 10^{-3}$	$2.656 \cdot 10^{-3}$	± 2.13
125.8	$2.485 \cdot 10^{-2}$	$1.122 \cdot 10^{-2}$	$2.679 \cdot 10^{-3}$	$2.676 \cdot 10^{-3}$	± 2.12
125.9	$2.504 \cdot 10^{-2}$	$1.130 \cdot 10^{-2}$	$2.699 \cdot 10^{-3}$	$2.695 \cdot 10^{-3}$	± 2.13
126.0	$2.523 \cdot 10^{-2}$	$1.139 \cdot 10^{-2}$	$2.720 \cdot 10^{-3}$	$2.716 \cdot 10^{-3}$	± 2.12
126.5	$2.618 \cdot 10^{-2}$	$1.182 \cdot 10^{-2}$	$2.824 \cdot 10^{-3}$	$2.816 \cdot 10^{-3}$	± 2.08
127.0	$2.714 \cdot 10^{-2}$	$1.226 \cdot 10^{-2}$	$2.929 \cdot 10^{-3}$	$2.918 \cdot 10^{-3}$	± 2.05
127.5	$2.812 \cdot 10^{-2}$	$1.270 \cdot 10^{-2}$	$3.036 \cdot 10^{-3}$	$3.022 \cdot 10^{-3}$	± 2.02
128.0	$2.912 \cdot 10^{-2}$	$1.316 \cdot 10^{-2}$	$3.145 \cdot 10^{-3}$	$3.127 \cdot 10^{-3}$	± 2.01
128.5	$3.013 \cdot 10^{-2}$	$1.362 \cdot 10^{-2}$	$3.256 \cdot 10^{-3}$	$3.235 \cdot 10^{-3}$	± 1.98
129.0	$3.115 \cdot 10^{-2}$	$1.408 \cdot 10^{-2}$	$3.367 \cdot 10^{-3}$	$3.342 \cdot 10^{-3}$	± 1.94
129.5	$3.218 \cdot 10^{-2}$	$1.455 \cdot 10^{-2}$	$3.480 \cdot 10^{-3}$	$3.452 \cdot 10^{-3}$	± 1.91
130.0	$3.323 \cdot 10^{-2}$	$1.503 \cdot 10^{-2}$	$3.595 \cdot 10^{-3}$	$3.562 \cdot 10^{-3}$	± 1.88

Table 181: SM Higgs boson branching ratios for $H \to 2\ell 2q$, $\ell\nu 2q$, $2\nu 2q$, $4q, 4f$ and corresponding total uncertainty (expressed in percentage). Mass range around the Higgs boson resonance.

M_H [GeV]	$H \to \ell^+\ell^- q\bar{q}$ $\ell = e, \mu, \tau$ $q = u, d, c, s, b$	$H \to \ell^+\ell^- q\bar{q}$ $\ell = e, \mu$ $q = u, d, c, s, b$	$H \to \ell^+\bar{\nu}_l q\bar{q}$ $\ell = e, \mu$ $q = u, d, c, s, b$	$H \to \nu\nu q\bar{q}$ ν = any $q = u, d, c, s, b$	$H \to 4q$ $q = u, d, c, s, b$	$H \to 4f$ f=any fermion	Δ BR[%]
120.0	$2.200 \cdot 10^{-3}$	$1.466 \cdot 10^{-3}$	$2.060 \cdot 10^{-2}$	$4.390 \cdot 10^{-3}$	$7.076 \cdot 10^{-2}$	$1.553 \cdot 10^{-1}$	± 2.41
120.5	$2.325 \cdot 10^{-3}$	$1.550 \cdot 10^{-3}$	$2.155 \cdot 10^{-2}$	$4.641 \cdot 10^{-3}$	$7.413 \cdot 10^{-2}$	$1.626 \cdot 10^{-1}$	± 2.40
121.0	$2.456 \cdot 10^{-3}$	$1.637 \cdot 10^{-3}$	$2.254 \cdot 10^{-2}$	$4.902 \cdot 10^{-3}$	$7.762 \cdot 10^{-2}$	$1.703 \cdot 10^{-1}$	± 2.37
121.5	$2.591 \cdot 10^{-3}$	$1.727 \cdot 10^{-3}$	$2.355 \cdot 10^{-2}$	$5.172 \cdot 10^{-3}$	$8.119 \cdot 10^{-2}$	$1.781 \cdot 10^{-1}$	± 2.34
122.0	$2.732 \cdot 10^{-3}$	$1.821 \cdot 10^{-3}$	$2.459 \cdot 10^{-2}$	$5.452 \cdot 10^{-3}$	$8.488 \cdot 10^{-2}$	$1.862 \cdot 10^{-1}$	± 2.32
122.5	$2.877 \cdot 10^{-3}$	$1.918 \cdot 10^{-3}$	$2.565 \cdot 10^{-2}$	$5.742 \cdot 10^{-3}$	$8.866 \cdot 10^{-2}$	$1.944 \cdot 10^{-1}$	± 2.30
123.0	$3.026 \cdot 10^{-3}$	$2.017 \cdot 10^{-3}$	$2.674 \cdot 10^{-2}$	$6.039 \cdot 10^{-3}$	$9.254 \cdot 10^{-2}$	$2.029 \cdot 10^{-1}$	± 2.28
123.5	$3.179 \cdot 10^{-3}$	$2.120 \cdot 10^{-3}$	$2.785 \cdot 10^{-2}$	$6.345 \cdot 10^{-3}$	$9.650 \cdot 10^{-2}$	$2.115 \cdot 10^{-1}$	± 2.24
124.0	$3.337 \cdot 10^{-3}$	$2.225 \cdot 10^{-3}$	$2.898 \cdot 10^{-2}$	$6.661 \cdot 10^{-3}$	$1.005 \cdot 10^{-1}$	$2.204 \cdot 10^{-1}$	± 2.24
124.1	$3.370 \cdot 10^{-3}$	$2.247 \cdot 10^{-3}$	$2.921 \cdot 10^{-2}$	$6.726 \cdot 10^{-3}$	$1.014 \cdot 10^{-1}$	$2.222 \cdot 10^{-1}$	± 2.21
124.2	$3.402 \cdot 10^{-3}$	$2.268 \cdot 10^{-3}$	$2.944 \cdot 10^{-2}$	$6.790 \cdot 10^{-3}$	$1.022 \cdot 10^{-1}$	$2.240 \cdot 10^{-1}$	± 2.20
124.3	$3.435 \cdot 10^{-3}$	$2.290 \cdot 10^{-3}$	$2.967 \cdot 10^{-2}$	$6.855 \cdot 10^{-3}$	$1.030 \cdot 10^{-1}$	$2.258 \cdot 10^{-1}$	± 2.20
124.4	$3.467 \cdot 10^{-3}$	$2.312 \cdot 10^{-3}$	$2.991 \cdot 10^{-2}$	$6.920 \cdot 10^{-3}$	$1.039 \cdot 10^{-1}$	$2.276 \cdot 10^{-1}$	± 2.21
124.5	$3.500 \cdot 10^{-3}$	$2.333 \cdot 10^{-3}$	$3.014 \cdot 10^{-2}$	$6.986 \cdot 10^{-3}$	$1.047 \cdot 10^{-1}$	$2.294 \cdot 10^{-1}$	± 2.21
124.6	$3.534 \cdot 10^{-3}$	$2.356 \cdot 10^{-3}$	$3.038 \cdot 10^{-2}$	$7.052 \cdot 10^{-3}$	$1.055 \cdot 10^{-1}$	$2.313 \cdot 10^{-1}$	± 2.19
124.7	$3.567 \cdot 10^{-3}$	$2.378 \cdot 10^{-3}$	$3.061 \cdot 10^{-2}$	$7.119 \cdot 10^{-3}$	$1.064 \cdot 10^{-1}$	$2.331 \cdot 10^{-1}$	± 2.17
124.8	$3.601 \cdot 10^{-3}$	$2.401 \cdot 10^{-3}$	$3.085 \cdot 10^{-2}$	$7.186 \cdot 10^{-3}$	$1.072 \cdot 10^{-1}$	$2.349 \cdot 10^{-1}$	± 2.19
124.9	$3.635 \cdot 10^{-3}$	$2.423 \cdot 10^{-3}$	$3.108 \cdot 10^{-2}$	$7.253 \cdot 10^{-3}$	$1.081 \cdot 10^{-1}$	$2.368 \cdot 10^{-1}$	± 2.18
125.0	$3.668 \cdot 10^{-3}$	$2.445 \cdot 10^{-3}$	$3.132 \cdot 10^{-2}$	$7.320 \cdot 10^{-3}$	$1.089 \cdot 10^{-1}$	$2.386 \cdot 10^{-1}$	± 2.18
125.09	$3.699 \cdot 10^{-3}$	$2.466 \cdot 10^{-3}$	$3.154 \cdot 10^{-2}$	$7.381 \cdot 10^{-3}$	$1.097 \cdot 10^{-1}$	$2.403 \cdot 10^{-1}$	± 2.16
125.1	$3.703 \cdot 10^{-3}$	$2.468 \cdot 10^{-3}$	$3.157 \cdot 10^{-2}$	$7.389 \cdot 10^{-3}$	$1.098 \cdot 10^{-1}$	$2.406 \cdot 10^{-1}$	± 2.16
125.2	$3.737 \cdot 10^{-3}$	$2.491 \cdot 10^{-3}$	$3.181 \cdot 10^{-2}$	$7.456 \cdot 10^{-3}$	$1.106 \cdot 10^{-1}$	$2.424 \cdot 10^{-1}$	± 2.15
125.3	$3.771 \cdot 10^{-3}$	$2.514 \cdot 10^{-3}$	$3.204 \cdot 10^{-2}$	$7.525 \cdot 10^{-3}$	$1.115 \cdot 10^{-1}$	$2.443 \cdot 10^{-1}$	± 2.16
125.4	$3.806 \cdot 10^{-3}$	$2.537 \cdot 10^{-3}$	$3.229 \cdot 10^{-2}$	$7.593 \cdot 10^{-3}$	$1.124 \cdot 10^{-1}$	$2.462 \cdot 10^{-1}$	± 2.14
125.5	$3.840 \cdot 10^{-3}$	$2.560 \cdot 10^{-3}$	$3.253 \cdot 10^{-2}$	$7.662 \cdot 10^{-3}$	$1.132 \cdot 10^{-1}$	$2.481 \cdot 10^{-1}$	± 2.14
125.6	$3.875 \cdot 10^{-3}$	$2.583 \cdot 10^{-3}$	$3.277 \cdot 10^{-2}$	$7.732 \cdot 10^{-3}$	$1.141 \cdot 10^{-1}$	$2.500 \cdot 10^{-1}$	± 2.13
125.7	$3.909 \cdot 10^{-3}$	$2.606 \cdot 10^{-3}$	$3.302 \cdot 10^{-2}$	$7.800 \cdot 10^{-3}$	$1.150 \cdot 10^{-1}$	$2.519 \cdot 10^{-1}$	± 2.13
125.8	$3.945 \cdot 10^{-3}$	$2.630 \cdot 10^{-3}$	$3.327 \cdot 10^{-2}$	$7.871 \cdot 10^{-3}$	$1.159 \cdot 10^{-1}$	$2.538 \cdot 10^{-1}$	± 2.12
125.9	$3.980 \cdot 10^{-3}$	$2.653 \cdot 10^{-3}$	$3.351 \cdot 10^{-2}$	$7.940 \cdot 10^{-3}$	$1.167 \cdot 10^{-1}$	$2.557 \cdot 10^{-1}$	± 2.13
126.0	$4.016 \cdot 10^{-3}$	$2.677 \cdot 10^{-3}$	$3.376 \cdot 10^{-2}$	$8.012 \cdot 10^{-3}$	$1.176 \cdot 10^{-1}$	$2.577 \cdot 10^{-1}$	± 2.12
126.5	$4.196 \cdot 10^{-3}$	$2.797 \cdot 10^{-3}$	$3.501 \cdot 10^{-2}$	$8.368 \cdot 10^{-3}$	$1.221 \cdot 10^{-1}$	$2.674 \cdot 10^{-1}$	± 2.08
127.0	$4.379 \cdot 10^{-3}$	$2.920 \cdot 10^{-3}$	$3.628 \cdot 10^{-2}$	$8.733 \cdot 10^{-3}$	$1.266 \cdot 10^{-1}$	$2.774 \cdot 10^{-1}$	± 2.05
127.5	$4.565 \cdot 10^{-3}$	$3.044 \cdot 10^{-3}$	$3.757 \cdot 10^{-2}$	$9.104 \cdot 10^{-3}$	$1.313 \cdot 10^{-1}$	$2.875 \cdot 10^{-1}$	± 2.02
128.0	$4.756 \cdot 10^{-3}$	$3.170 \cdot 10^{-3}$	$3.887 \cdot 10^{-2}$	$9.482 \cdot 10^{-3}$	$1.360 \cdot 10^{-1}$	$2.978 \cdot 10^{-1}$	± 2.01
128.5	$4.950 \cdot 10^{-3}$	$3.300 \cdot 10^{-3}$	$4.021 \cdot 10^{-2}$	$9.868 \cdot 10^{-3}$	$1.408 \cdot 10^{-1}$	$3.082 \cdot 10^{-1}$	± 1.98
129.0	$5.145 \cdot 10^{-3}$	$3.430 \cdot 10^{-3}$	$4.154 \cdot 10^{-2}$	$1.026 \cdot 10^{-2}$	$1.456 \cdot 10^{-1}$	$3.187 \cdot 10^{-1}$	± 1.94
129.5	$5.344 \cdot 10^{-3}$	$3.563 \cdot 10^{-3}$	$4.290 \cdot 10^{-2}$	$1.065 \cdot 10^{-2}$	$1.505 \cdot 10^{-1}$	$3.294 \cdot 10^{-1}$	± 1.91
130.0	$5.545 \cdot 10^{-3}$	$3.697 \cdot 10^{-3}$	$4.428 \cdot 10^{-2}$	$1.106 \cdot 10^{-2}$	$1.554 \cdot 10^{-1}$	$3.402 \cdot 10^{-1}$	± 1.88

Table 182: SM Higgs boson partials widths and their relative parametric (PU) and theoretical (THU) uncertainties for a selection of Higgs boson masses. For PU, all the single contributions are shown. For these four columns, the upper percentage value (with its sign) refers to the positive variation of the parameter, while the lower one refers to the negative variation of the parameter.

Channel	M_{H} [GeV]	Γ [MeV]	$\Delta\alpha_{\mathrm{s}}$	Δm_{b}	Δm_{c}	Δm_{t}	THU
$\mathrm{H} \to \mathrm{b\bar{b}}$	124	2.37	$^{-1.4\%}_{+1.4\%}$	$^{+1.7\%}_{-1.7\%}$	$^{+0.0\%}_{-0.0\%}$	$^{+0.0\%}_{-0.0\%}$	$^{+0.5\%}_{-0.5\%}$
	125	2.38	$^{-1.4\%}_{+1.4\%}$	$^{+1.7\%}_{-1.7\%}$	$^{+0.0\%}_{-0.0\%}$	$^{+0.0\%}_{-0.0\%}$	$^{+0.5\%}_{-0.5\%}$
	126	2.40	$^{-1.4\%}_{+1.4\%}$	$^{+1.7\%}_{-1.7\%}$	$^{+0.0\%}_{-0.0\%}$	$^{+0.0\%}_{-0.0\%}$	$^{+0.5\%}_{-0.5\%}$
$\mathrm{H} \to \tau^+\tau^-$	124	$2.54{\cdot}10^{-1}$	$^{+0.0\%}_{-0.0\%}$	$^{+0.0\%}_{-0.0\%}$	$^{+0.0\%}_{-0.0\%}$	$^{+0.0\%}_{-0.0\%}$	$^{+0.5\%}_{-0.5\%}$
	125	$2.56{\cdot}10^{-1}$	$^{+0.0\%}_{-0.0\%}$	$^{+0.0\%}_{-0.0\%}$	$^{+0.0\%}_{-0.0\%}$	$^{+0.0\%}_{-0.0\%}$	$^{+0.5\%}_{-0.5\%}$
	126	$2.58{\cdot}10^{-1}$	$^{+0.0\%}_{-0.0\%}$	$^{+0.0\%}_{-0.0\%}$	$^{+0.0\%}_{-0.0\%}$	$^{+0.0\%}_{-0.0\%}$	$^{+0.5\%}_{-0.5\%}$
$\mathrm{H} \to \mu^+\mu^-$	124	$8.83{\cdot}10^{-4}$	$^{+0.0\%}_{-0.0\%}$	$^{+0.0\%}_{-0.0\%}$	$^{+0.0\%}_{-0.0\%}$	$^{+0.0\%}_{-0.0\%}$	$^{+0.5\%}_{-0.5\%}$
	125	$8.90{\cdot}10^{-4}$	$^{+0.0\%}_{-0.0\%}$	$^{+0.0\%}_{-0.0\%}$	$^{+0.0\%}_{-0.0\%}$	$^{+0.0\%}_{-0.0\%}$	$^{+0.5\%}_{-0.5\%}$
	126	$8.96{\cdot}10^{-4}$	$^{+0.0\%}_{-0.0\%}$	$^{+0.0\%}_{-0.0\%}$	$^{+0.0\%}_{-0.0\%}$	$^{+0.0\%}_{-0.0\%}$	$^{+0.5\%}_{-0.5\%}$
$\mathrm{H} \to \mathrm{c\bar{c}}$	124	$1.17{\cdot}10^{-1}$	$^{-1.9\%}_{+1.9\%}$	$^{-0.0\%}_{-0.0\%}$	$^{+5.3\%}_{-5.2\%}$	$^{+0.0\%}_{-0.0\%}$	$^{+0.5\%}_{-0.5\%}$
	125	$1.18{\cdot}10^{-1}$	$^{-1.9\%}_{+1.9\%}$	$^{-0.0\%}_{-0.0\%}$	$^{+5.3\%}_{-5.2\%}$	$^{+0.0\%}_{-0.0\%}$	$^{+0.5\%}_{-0.5\%}$
	126	$1.19{\cdot}10^{-1}$	$^{-1.9\%}_{+1.9\%}$	$^{-0.0\%}_{-0.0\%}$	$^{+5.3\%}_{-5.2\%}$	$^{+0.0\%}_{-0.0\%}$	$^{+0.5\%}_{-0.5\%}$
$\mathrm{H} \to \mathrm{gg}$	124	$3.27{\cdot}10^{-1}$	$^{+3.0\%}_{-3.0\%}$	$^{-0.2\%}_{+0.1\%}$	$^{+0.0\%}_{-0.0\%}$	$^{-0.1\%}_{+0.1\%}$	$^{+3.2\%}_{-3.2\%}$
	125	$3.35{\cdot}10^{-1}$	$^{+3.0\%}_{-3.0\%}$	$^{-0.1\%}_{+0.1\%}$	$^{+0.0\%}_{-0.0\%}$	$^{-0.1\%}_{+0.1\%}$	$^{+3.2\%}_{-3.2\%}$
	126	$3.43{\cdot}10^{-1}$	$^{+3.1\%}_{-3.0\%}$	$^{-0.1\%}_{+0.2\%}$	$^{+0.0\%}_{-0.0\%}$	$^{-0.1\%}_{+0.1\%}$	$^{+3.2\%}_{-3.2\%}$
$\mathrm{H} \to \gamma\gamma$	124	$8.97{\cdot}10^{-3}$	$^{+0.0\%}_{-0.0\%}$	$^{+0.0\%}_{-0.0\%}$	$^{+0.0\%}_{-0.0\%}$	$^{+0.0\%}_{-0.0\%}$	$^{+1.0\%}_{-1.0\%}$
	125	$9.28{\cdot}10^{-3}$	$^{+0.0\%}_{-0.0\%}$	$^{+0.0\%}_{-0.0\%}$	$^{+0.0\%}_{-0.0\%}$	$^{+0.0\%}_{-0.0\%}$	$^{+1.0\%}_{-1.0\%}$
	126	$9.60{\cdot}10^{-3}$	$^{+0.0\%}_{-0.0\%}$	$^{+0.0\%}_{-0.0\%}$	$^{+0.0\%}_{-0.0\%}$	$^{+0.0\%}_{-0.0\%}$	$^{+1.0\%}_{-1.0\%}$
$\mathrm{H} \to \mathrm{Z}\gamma$	124	$5.72{\cdot}10^{-3}$	$^{+0.0\%}_{-0.0\%}$	$^{+0.0\%}_{-0.0\%}$	$^{+0.0\%}_{-0.0\%}$	$^{+0.0\%}_{-0.0\%}$	$^{+5.0\%}_{-5.0\%}$
	125	$6.27{\cdot}10^{-3}$	$^{+0.0\%}_{-0.0\%}$	$^{+0.0\%}_{-0.0\%}$	$^{+0.0\%}_{-0.0\%}$	$^{+0.0\%}_{-0.0\%}$	$^{+5.0\%}_{-5.0\%}$
	126	$6.84{\cdot}10^{-3}$	$^{+0.0\%}_{-0.0\%}$	$^{+0.0\%}_{-0.0\%}$	$^{+0.0\%}_{-0.0\%}$	$^{+0.0\%}_{-0.0\%}$	$^{+5.0\%}_{-5.0\%}$
$\mathrm{H} \to \mathrm{WW}$	124	$7.82{\cdot}10^{-1}$	$^{+0.0\%}_{-0.0\%}$	$^{+0.0\%}_{-0.0\%}$	$^{+0.0\%}_{-0.0\%}$	$^{+0.0\%}_{-0.0\%}$	$^{+0.5\%}_{-0.5\%}$
	125	$8.74{\cdot}10^{-1}$	$^{+0.0\%}_{-0.0\%}$	$^{+0.0\%}_{-0.0\%}$	$^{+0.0\%}_{-0.0\%}$	$^{+0.0\%}_{-0.0\%}$	$^{+0.5\%}_{-0.5\%}$
	126	$9.74{\cdot}10^{-1}$	$^{+0.0\%}_{-0.0\%}$	$^{+0.0\%}_{-0.0\%}$	$^{+0.0\%}_{-0.0\%}$	$^{+0.0\%}_{-0.0\%}$	$^{+0.5\%}_{-0.5\%}$
$\mathrm{H} \to \mathrm{ZZ}$	124	$9.43{\cdot}10^{-2}$	$^{+0.0\%}_{-0.0\%}$	$^{+0.0\%}_{-0.0\%}$	$^{+0.0\%}_{-0.0\%}$	$^{+0.0\%}_{-0.0\%}$	$^{+0.5\%}_{-0.5\%}$
	125	$1.07{\cdot}10^{-1}$	$^{+0.0\%}_{-0.0\%}$	$^{+0.0\%}_{-0.0\%}$	$^{+0.0\%}_{-0.0\%}$	$^{+0.0\%}_{-0.0\%}$	$^{+0.5\%}_{-0.5\%}$
	126	$1.21{\cdot}10^{-1}$	$^{+0.0\%}_{-0.0\%}$	$^{+0.0\%}_{-0.0\%}$	$^{+0.0\%}_{-0.0\%}$	$^{+0.0\%}_{-0.0\%}$	$^{+0.5\%}_{-0.5\%}$

Table 183: SM Higgs boson partials widths (in GeV) for 2-fermion decay channels, predictions without electroweak corrections. Low and intermediate mass range.

M_{H} [GeV]	$\Gamma_{\mathrm{H}\to\mathrm{b\bar{b}}}$	$\Gamma_{\mathrm{H}\to\tau^+\tau^-}$	$\Gamma_{\mathrm{H}\to\mu^+\mu^-}$	$\Gamma_{\mathrm{H}\to\mathrm{c\bar{c}}}$
20	$5.244\cdot10^{-4}$	$3.949\cdot10^{-5}$	$1.465\cdot10^{-7}$	$2.936\cdot10^{-5}$
25	$6.568\cdot10^{-4}$	$5.024\cdot10^{-5}$	$1.831\cdot10^{-7}$	$3.437\cdot10^{-5}$
30	$7.709\cdot10^{-4}$	$6.086\cdot10^{-5}$	$2.198\cdot10^{-7}$	$3.921\cdot10^{-5}$
35	$8.754\cdot10^{-4}$	$7.139\cdot10^{-5}$	$2.563\cdot10^{-7}$	$4.390\cdot10^{-5}$
40	$9.752\cdot10^{-4}$	$8.193\cdot10^{-5}$	$2.932\cdot10^{-7}$	$4.851\cdot10^{-5}$
45	$1.070\cdot10^{-3}$	$9.234\cdot10^{-5}$	$3.296\cdot10^{-7}$	$5.297\cdot10^{-5}$
50	$1.163\cdot10^{-3}$	$1.028\cdot10^{-4}$	$3.663\cdot10^{-7}$	$5.738\cdot10^{-5}$
55	$1.253\cdot10^{-3}$	$1.132\cdot10^{-4}$	$4.029\cdot10^{-7}$	$6.172\cdot10^{-5}$
60	$1.342\cdot10^{-3}$	$1.237\cdot10^{-4}$	$4.397\cdot10^{-7}$	$6.601\cdot10^{-5}$
65	$1.430\cdot10^{-3}$	$1.341\cdot10^{-4}$	$4.763\cdot10^{-7}$	$7.025\cdot10^{-5}$
70	$1.516\cdot10^{-3}$	$1.445\cdot10^{-4}$	$5.129\cdot10^{-7}$	$7.442\cdot10^{-5}$
75	$1.600\cdot10^{-3}$	$1.549\cdot10^{-4}$	$5.494\cdot10^{-7}$	$7.851\cdot10^{-5}$
80	$1.684\cdot10^{-3}$	$1.653\cdot10^{-4}$	$5.862\cdot10^{-7}$	$8.258\cdot10^{-5}$
85	$1.767\cdot10^{-3}$	$1.756\cdot10^{-4}$	$6.227\cdot10^{-7}$	$8.662\cdot10^{-5}$
90	$1.849\cdot10^{-3}$	$1.860\cdot10^{-4}$	$6.592\cdot10^{-7}$	$9.063\cdot10^{-5}$
95	$1.931\cdot10^{-3}$	$1.964\cdot10^{-4}$	$6.961\cdot10^{-7}$	$9.460\cdot10^{-5}$
100	$2.011\cdot10^{-3}$	$2.068\cdot10^{-4}$	$7.325\cdot10^{-7}$	$9.852\cdot10^{-5}$
105	$2.092\cdot10^{-3}$	$2.172\cdot10^{-4}$	$7.694\cdot10^{-7}$	$1.024\cdot10^{-4}$
110	$2.170\cdot10^{-3}$	$2.275\cdot10^{-4}$	$8.058\cdot10^{-7}$	$1.063\cdot10^{-4}$
115	$2.250\cdot10^{-3}$	$2.379\cdot10^{-4}$	$8.425\cdot10^{-7}$	$1.101\cdot10^{-4}$
120	$2.328\cdot10^{-3}$	$2.483\cdot10^{-4}$	$8.791\cdot10^{-7}$	$1.140\cdot10^{-4}$
125	$2.406\cdot10^{-3}$	$2.587\cdot10^{-4}$	$9.159\cdot10^{-7}$	$1.178\cdot10^{-4}$
125.09	$2.407\cdot10^{-3}$	$2.589\cdot10^{-4}$	$9.166\cdot10^{-7}$	$1.179\cdot10^{-4}$
130	$2.483\cdot10^{-3}$	$2.690\cdot10^{-4}$	$9.526\cdot10^{-7}$	$1.216\cdot10^{-4}$
135	$2.560\cdot10^{-3}$	$2.794\cdot10^{-4}$	$9.890\cdot10^{-7}$	$1.253\cdot10^{-4}$
140	$2.637\cdot10^{-3}$	$2.898\cdot10^{-4}$	$1.025\cdot10^{-6}$	$1.290\cdot10^{-4}$
145	$2.712\cdot10^{-3}$	$3.002\cdot10^{-4}$	$1.062\cdot10^{-6}$	$1.327\cdot10^{-4}$
150	$2.787\cdot10^{-3}$	$3.105\cdot10^{-4}$	$1.099\cdot10^{-6}$	$1.364\cdot10^{-4}$
160	$2.938\cdot10^{-3}$	$3.313\cdot10^{-4}$	$1.172\cdot10^{-6}$	$1.438\cdot10^{-4}$
170	$3.088\cdot10^{-3}$	$3.521\cdot10^{-4}$	$1.246\cdot10^{-6}$	$1.511\cdot10^{-4}$
180	$3.233\cdot10^{-3}$	$3.728\cdot10^{-4}$	$1.319\cdot10^{-6}$	$1.582\cdot10^{-4}$
190	$3.376\cdot10^{-3}$	$3.935\cdot10^{-4}$	$1.392\cdot10^{-6}$	$1.652\cdot10^{-4}$
200	$3.519\cdot10^{-3}$	$4.144\cdot10^{-4}$	$1.466\cdot10^{-6}$	$1.723\cdot10^{-4}$
210	$3.659\cdot10^{-3}$	$4.349\cdot10^{-4}$	$1.539\cdot10^{-6}$	$1.790\cdot10^{-4}$
220	$3.798\cdot10^{-3}$	$4.557\cdot10^{-4}$	$1.612\cdot10^{-6}$	$1.859\cdot10^{-4}$
230	$3.938\cdot10^{-3}$	$4.765\cdot10^{-4}$	$1.685\cdot10^{-6}$	$1.927\cdot10^{-4}$
240	$4.636\cdot10^{-3}$	$5.657\cdot10^{-4}$	$2.000\cdot10^{-6}$	$2.269\cdot10^{-4}$
250	$4.214\cdot10^{-3}$	$5.178\cdot10^{-4}$	$1.832\cdot10^{-6}$	$2.062\cdot10^{-4}$

Table 184: SM Higgs boson partials widths (in GeV) for 2-fermion decay channels, predictions without electroweak corrections. High mass range.

M_{H} [GeV]	$\Gamma_{\mathrm{H}\to\mathrm{b\bar{b}}}$	$\Gamma_{\mathrm{H}\to\tau^+\tau^-}$	$\Gamma_{\mathrm{H}\to\mu^+\mu^-}$	$\Gamma_{\mathrm{H}\to\mathrm{c\bar{c}}}$	$\Gamma_{\mathrm{H}\to\mathrm{t\bar{t}}}$
260	$4.351\cdot10^{-3}$	$5.384\cdot10^{-4}$	$1.905\cdot10^{-6}$	$2.129\cdot10^{-4}$	$1.946\cdot10^{-7}$
270	$4.487\cdot10^{-3}$	$5.592\cdot10^{-4}$	$1.978\cdot10^{-6}$	$2.195\cdot10^{-4}$	$1.235\cdot10^{-5}$
280	$4.689\cdot10^{-3}$	$5.885\cdot10^{-4}$	$2.081\cdot10^{-6}$	$2.294\cdot10^{-4}$	$7.015\cdot10^{-5}$
290	$4.756\cdot10^{-3}$	$6.008\cdot10^{-4}$	$2.125\cdot10^{-6}$	$2.328\cdot10^{-4}$	$2.247\cdot10^{-4}$
300	$4.890\cdot10^{-3}$	$6.215\cdot10^{-4}$	$2.198\cdot10^{-6}$	$2.393\cdot10^{-4}$	$5.767\cdot10^{-4}$
310	$5.023\cdot10^{-3}$	$6.423\cdot10^{-4}$	$2.271\cdot10^{-6}$	$2.458\cdot10^{-4}$	$1.317\cdot10^{-3}$
320	$5.155\cdot10^{-3}$	$6.629\cdot10^{-4}$	$2.345\cdot10^{-6}$	$2.522\cdot10^{-4}$	$2.862\cdot10^{-3}$
330	$5.288\cdot10^{-3}$	$6.838\cdot10^{-4}$	$2.418\cdot10^{-6}$	$2.588\cdot10^{-4}$	$6.306\cdot10^{-3}$
340	$5.420\cdot10^{-3}$	$7.046\cdot10^{-4}$	$2.492\cdot10^{-6}$	$2.653\cdot10^{-4}$	$1.617\cdot10^{-2}$
350	$5.549\cdot10^{-3}$	$7.250\cdot10^{-4}$	$2.564\cdot10^{-6}$	$2.715\cdot10^{-4}$	$2.420\cdot10^{-1}$
360	$5.680\cdot10^{-3}$	$7.459\cdot10^{-4}$	$2.637\cdot10^{-6}$	$2.780\cdot10^{-4}$	$9.160\cdot10^{-1}$
370	$5.810\cdot10^{-3}$	$7.667\cdot10^{-4}$	$2.711\cdot10^{-6}$	$2.843\cdot10^{-4}$	$1.705\cdot10^{0}$
380	$5.939\cdot10^{-3}$	$7.873\cdot10^{-4}$	$2.784\cdot10^{-6}$	$2.907\cdot10^{-4}$	$2.550\cdot10^{0}$
390	$6.067\cdot10^{-3}$	$8.080\cdot10^{-4}$	$2.856\cdot10^{-6}$	$2.969\cdot10^{-4}$	$3.426\cdot10^{0}$
400	$6.195\cdot10^{-3}$	$8.288\cdot10^{-4}$	$2.931\cdot10^{-6}$	$3.032\cdot10^{-4}$	$4.315\cdot10^{0}$
410	$6.324\cdot10^{-3}$	$8.495\cdot10^{-4}$	$3.004\cdot10^{-6}$	$3.094\cdot10^{-4}$	$5.206\cdot10^{0}$
420	$6.449\cdot10^{-3}$	$8.700\cdot10^{-4}$	$3.077\cdot10^{-6}$	$3.156\cdot10^{-4}$	$6.093\cdot10^{0}$
430	$6.578\cdot10^{-3}$	$8.909\cdot10^{-4}$	$3.150\cdot10^{-6}$	$3.218\cdot10^{-4}$	$6.975\cdot10^{0}$
440	$6.703\cdot10^{-3}$	$9.118\cdot10^{-4}$	$3.224\cdot10^{-6}$	$3.280\cdot10^{-4}$	$7.843\cdot10^{0}$
450	$6.829\cdot10^{-3}$	$9.322\cdot10^{-4}$	$3.297\cdot10^{-6}$	$3.342\cdot10^{-4}$	$8.701\cdot10^{0}$
460	$6.954\cdot10^{-3}$	$9.531\cdot10^{-4}$	$3.370\cdot10^{-6}$	$3.403\cdot10^{-4}$	$9.545\cdot10^{0}$
470	$7.082\cdot10^{-3}$	$9.741\cdot10^{-4}$	$3.444\cdot10^{-6}$	$3.464\cdot10^{-4}$	$1.038\cdot10^{1}$
480	$7.204\cdot10^{-3}$	$9.945\cdot10^{-4}$	$3.517\cdot10^{-6}$	$3.526\cdot10^{-4}$	$1.119\cdot10^{1}$
490	$7.327\cdot10^{-3}$	$1.015\cdot10^{-3}$	$3.590\cdot10^{-6}$	$3.586\cdot10^{-4}$	$1.199\cdot10^{1}$
500	$7.452\cdot10^{-3}$	$1.036\cdot10^{-3}$	$3.663\cdot10^{-6}$	$3.648\cdot10^{-4}$	$1.278\cdot10^{1}$
550	$8.070\cdot10^{-3}$	$1.139\cdot10^{-3}$	$4.029\cdot10^{-6}$	$3.948\cdot10^{-4}$	$1.651\cdot10^{1}$
600	$8.677\cdot10^{-3}$	$1.243\cdot10^{-3}$	$4.395\cdot10^{-6}$	$4.245\cdot10^{-4}$	$1.994\cdot10^{1}$
650	$9.281\cdot10^{-3}$	$1.347\cdot10^{-3}$	$4.764\cdot10^{-6}$	$4.542\cdot10^{-4}$	$2.314\cdot10^{1}$
700	$9.874\cdot10^{-3}$	$1.450\cdot10^{-3}$	$5.128\cdot10^{-6}$	$4.831\cdot10^{-4}$	$2.613\cdot10^{1}$
750	$1.046\cdot10^{-2}$	$1.554\cdot10^{-3}$	$5.493\cdot10^{-6}$	$5.118\cdot10^{-4}$	$2.898\cdot10^{1}$
800	$1.105\cdot10^{-2}$	$1.658\cdot10^{-3}$	$5.861\cdot10^{-6}$	$5.406\cdot10^{-4}$	$3.169\cdot10^{1}$
850	$1.163\cdot10^{-2}$	$1.761\cdot10^{-3}$	$6.229\cdot10^{-6}$	$5.691\cdot10^{-4}$	$3.430\cdot10^{1}$
900	$1.221\cdot10^{-2}$	$1.865\cdot10^{-3}$	$6.594\cdot10^{-6}$	$5.971\cdot10^{-4}$	$3.681\cdot10^{1}$
950	$1.278\cdot10^{-2}$	$1.969\cdot10^{-3}$	$6.962\cdot10^{-6}$	$6.250\cdot10^{-4}$	$3.926\cdot10^{1}$
1000	$1.334\cdot10^{-2}$	$2.072\cdot10^{-3}$	$7.326\cdot10^{-6}$	$6.528\cdot10^{-4}$	$4.163\cdot10^{1}$

Table 185: SM Higgs boson partials widths (in GeV) for 2-boson decay channels, predictions without electroweak corrections. Low and intermediate mass range.

M_{H} [GeV]	$\Gamma_{\mathrm{H}\to\mathrm{gg}}$	$\Gamma_{\mathrm{H}\to\gamma\gamma}$	$\Gamma_{\mathrm{H}\to\mathrm{Z}\gamma}$	$\Gamma_{\mathrm{H}\to\mathrm{WW}}$	$\Gamma_{\mathrm{H}\to\mathrm{ZZ}}$
20	$1.895\cdot10^{-5}$	$2.861\cdot10^{-8}$	$0.000\cdot10^{0}$	$3.560\cdot10^{-11}$	$3.100\cdot10^{-12}$
25	$1.604\cdot10^{-5}$	$5.592\cdot10^{-8}$	$0.000\cdot10^{0}$	$1.753\cdot10^{-10}$	$3.760\cdot10^{-11}$
30	$1.522\cdot10^{-5}$	$9.586\cdot10^{-8}$	$0.000\cdot10^{0}$	$6.432\cdot10^{-10}$	$1.586\cdot10^{-10}$
35	$1.647\cdot10^{-5}$	$1.512\cdot10^{-7}$	$0.000\cdot10^{0}$	$1.956\cdot10^{-9}$	$5.108\cdot10^{-10}$
40	$1.939\cdot10^{-5}$	$2.246\cdot10^{-7}$	$0.000\cdot10^{0}$	$5.186\cdot10^{-9}$	$1.407\cdot10^{-9}$
45	$2.355\cdot10^{-5}$	$3.191\cdot10^{-7}$	$0.000\cdot10^{0}$	$1.236\cdot10^{-8}$	$3.456\cdot10^{-9}$
50	$2.879\cdot10^{-5}$	$4.380\cdot10^{-7}$	$0.000\cdot10^{0}$	$2.720\cdot10^{-8}$	$7.734\cdot10^{-9}$
55	$3.523\cdot10^{-5}$	$5.850\cdot10^{-7}$	$0.000\cdot10^{0}$	$5.623\cdot10^{-8}$	$1.594\cdot10^{-8}$
60	$4.305\cdot10^{-5}$	$7.642\cdot10^{-7}$	$0.000\cdot10^{0}$	$1.103\cdot10^{-7}$	$3.129\cdot10^{-8}$
65	$5.234\cdot10^{-5}$	$9.800\cdot10^{-7}$	$0.000\cdot10^{0}$	$2.086\cdot10^{-7}$	$5.954\cdot10^{-8}$
70	$6.318\cdot10^{-5}$	$1.237\cdot10^{-6}$	$0.000\cdot10^{0}$	$3.839\cdot10^{-7}$	$1.080\cdot10^{-7}$
75	$7.570\cdot10^{-5}$	$1.541\cdot10^{-6}$	$0.000\cdot10^{0}$	$6.900\cdot10^{-7}$	$1.889\cdot10^{-7}$
80	$9.002\cdot10^{-5}$	$1.898\cdot10^{-6}$	$0.000\cdot10^{0}$	$1.227\cdot10^{-6}$	$3.257\cdot10^{-7}$
85	$1.062\cdot10^{-4}$	$2.316\cdot10^{-6}$	$0.000\cdot10^{0}$	$2.222\cdot10^{-6}$	$5.504\cdot10^{-7}$
90	$1.245\cdot10^{-4}$	$2.805\cdot10^{-6}$	$0.000\cdot10^{0}$	$4.509\cdot10^{-6}$	$9.188\cdot10^{-7}$
95	$1.449\cdot10^{-4}$	$3.373\cdot10^{-6}$	$1.053\cdot10^{-8}$	$1.076\cdot10^{-5}$	$1.551\cdot10^{-6}$
100	$1.674\cdot10^{-4}$	$4.035\cdot10^{-6}$	$1.226\cdot10^{-7}$	$2.67\cdot10^{-5}$	$2.775\cdot10^{-6}$
105	$1.924\cdot10^{-4}$	$4.804\cdot10^{-6}$	$4.539\cdot10^{-7}$	$6.218\cdot10^{-5}$	$5.627\cdot10^{-6}$
110	$2.198\cdot10^{-4}$	$5.699\cdot10^{-6}$	$1.114\cdot10^{-6}$	$1.327\cdot10^{-4}$	$1.234\cdot10^{-5}$
115	$2.499\cdot10^{-4}$	$6.746\cdot10^{-6}$	$2.215\cdot10^{-6}$	$2.613\cdot10^{-4}$	$2.688\cdot10^{-5}$
120	$2.827\cdot10^{-4}$	$7.977\cdot10^{-6}$	$3.881\cdot10^{-6}$	$4.826\cdot10^{-4}$	$5.536\cdot10^{-5}$
125	$3.185\cdot10^{-4}$	$9.428\cdot10^{-6}$	$6.266\cdot10^{-6}$	$8.489\cdot10^{-4}$	$1.066\cdot10^{-4}$
125.09	$3.191\cdot10^{-4}$	$9.460\cdot10^{-6}$	$6.313\cdot10^{-6}$	$8.573\cdot10^{-4}$	$1.078\cdot10^{-4}$
130	$3.572\cdot10^{-4}$	$1.116\cdot10^{-5}$	$9.555\cdot10^{-6}$	$1.442\cdot10^{-3}$	$1.933\cdot10^{-4}$
135	$3.992\cdot10^{-4}$	$1.326\cdot10^{-5}$	$1.403\cdot10^{-5}$	$2.399\cdot10^{-3}$	$3.335\cdot10^{-4}$
140	$4.445\cdot10^{-4}$	$1.584\cdot10^{-5}$	$2.007\cdot10^{-5}$	$3.963\cdot10^{-3}$	$5.531\cdot10^{-4}$
145	$4.933\cdot10^{-4}$	$1.911\cdot10^{-5}$	$2.832\cdot10^{-5}$	$6.623\cdot10^{-3}$	$8.900\cdot10^{-4}$
150	$5.459\cdot10^{-4}$	$2.347\cdot10^{-5}$	$3.998\cdot10^{-5}$	$1.159\cdot10^{-2}$	$1.403\cdot10^{-3}$
160	$6.629\cdot10^{-4}$	$4.336\cdot10^{-5}$	$9.587\cdot10^{-5}$	$7.105\cdot10^{-2}$	$3.402\cdot10^{-3}$
170	$7.975\cdot10^{-4}$	$5.812\cdot10^{-5}$	$1.518\cdot10^{-4}$	$3.466\cdot10^{-1}$	$8.791\cdot10^{-3}$
180	$9.509\cdot10^{-4}$	$6.441\cdot10^{-5}$	$1.864\cdot10^{-4}$	$5.603\cdot10^{-1}$	$3.694\cdot10^{-2}$
190	$1.125\cdot10^{-3}$	$7.011\cdot10^{-5}$	$2.195\cdot10^{-4}$	$7.758\cdot10^{-1}$	$2.093\cdot10^{-1}$
200	$1.325\cdot10^{-3}$	$7.535\cdot10^{-5}$	$2.512\cdot10^{-4}$	$1.013\cdot10^{0}$	$3.521\cdot10^{-1}$
210	$1.549\cdot10^{-3}$	$8.011\cdot10^{-5}$	$2.810\cdot10^{-4}$	$1.280\cdot10^{0}$	$4.879\cdot10^{-1}$
220	$1.804\cdot10^{-3}$	$8.450\cdot10^{-5}$	$3.093\cdot10^{-4}$	$1.584\cdot10^{0}$	$6.319\cdot10^{-1}$
230	$2.093\cdot10^{-3}$	$8.855\cdot10^{-5}$	$3.360\cdot10^{-4}$	$1.928\cdot10^{0}$	$7.904\cdot10^{-1}$
240	$2.754\cdot10^{-3}$	$1.050\cdot10^{-4}$	$4.108\cdot10^{-4}$	$2.317\cdot10^{0}$	$9.673\cdot10^{-1}$
250	$2.792\cdot10^{-3}$	$9.572\cdot10^{-5}$	$3.849\cdot10^{-4}$	$2.750\cdot10^{0}$	$1.166\cdot10^{0}$

Table 186: SM Higgs boson partials widths (in GeV) for 2-boson decay channels, predictions without electroweak corrections. High mass range.

M_{H} [GeV]	$\Gamma_{\mathrm{H}\to\mathrm{gg}}$	$\Gamma_{\mathrm{H}\to\gamma\gamma}$	$\Gamma_{\mathrm{H}\to\mathrm{Z}\gamma}$	$\Gamma_{\mathrm{H}\to\mathrm{WW}}$	$\Gamma_{\mathrm{H}\to\mathrm{ZZ}}$
260	$3.215\cdot10^{-3}$	$9.890\cdot10^{-5}$	$4.072\cdot10^{-4}$	$3.232\cdot10^{0}$	$1.386\cdot10^{0}$
270	$3.699\cdot10^{-3}$	$1.018\cdot10^{-4}$	$4.282\cdot10^{-4}$	$3.765\cdot10^{0}$	$1.632\cdot10^{0}$
280	$4.315\cdot10^{-3}$	$1.061\cdot10^{-4}$	$4.545\cdot10^{-4}$	$4.351\cdot10^{0}$	$1.904\cdot10^{0}$
290	$4.894\cdot10^{-3}$	$1.071\cdot10^{-4}$	$4.665\cdot10^{-4}$	$4.992\cdot10^{0}$	$2.202\cdot10^{0}$
300	$5.644\cdot10^{-3}$	$1.094\cdot10^{-4}$	$4.840\cdot10^{-4}$	$5.690\cdot10^{0}$	$2.529\cdot10^{0}$
310	$6.529\cdot10^{-3}$	$1.116\cdot10^{-4}$	$5.004\cdot10^{-4}$	$6.446\cdot10^{0}$	$2.885\cdot10^{0}$
320	$7.597\cdot10^{-3}$	$1.137\cdot10^{-4}$	$5.157\cdot10^{-4}$	$7.264\cdot10^{0}$	$3.271\cdot10^{0}$
330	$8.934\cdot10^{-3}$	$1.157\cdot10^{-4}$	$5.304\cdot10^{-4}$	$8.147\cdot10^{0}$	$3.689\cdot10^{0}$
340	$1.073\cdot10^{-2}$	$1.177\cdot10^{-4}$	$5.438\cdot10^{-4}$	$9.091\cdot10^{0}$	$4.139\cdot10^{0}$
350	$1.363\cdot10^{-2}$	$1.156\cdot10^{-4}$	$5.537\cdot10^{-4}$	$1.010\cdot10^{1}$	$4.623\cdot10^{0}$
360	$1.649\cdot10^{-2}$	$1.072\cdot10^{-4}$	$5.575\cdot10^{-4}$	$1.118\cdot10^{1}$	$5.140\cdot10^{0}$
370	$1.908\cdot10^{-2}$	$9.822\cdot10^{-5}$	$5.587\cdot10^{-4}$	$1.233\cdot10^{1}$	$5.694\cdot10^{0}$
380	$2.146\cdot10^{-2}$	$8.922\cdot10^{-5}$	$5.584\cdot10^{-4}$	$1.356\cdot10^{1}$	$6.285\cdot10^{0}$
390	$2.367\cdot10^{-2}$	$8.052\cdot10^{-5}$	$5.567\cdot10^{-4}$	$1.485\cdot10^{1}$	$6.910\cdot10^{0}$
400	$2.573\cdot10^{-2}$	$7.226\cdot10^{-5}$	$5.545\cdot10^{-4}$	$1.623\cdot10^{1}$	$7.574\cdot10^{0}$
410	$2.764\cdot10^{-2}$	$6.451\cdot10^{-5}$	$5.516\cdot10^{-4}$	$1.769\cdot10^{1}$	$8.278\cdot10^{0}$
420	$2.943\cdot10^{-2}$	$5.730\cdot10^{-5}$	$5.484\cdot10^{-4}$	$1.922\cdot10^{1}$	$9.022\cdot10^{0}$
430	$3.112\cdot10^{-2}$	$5.064\cdot10^{-5}$	$5.450\cdot10^{-4}$	$2.084\cdot10^{1}$	$9.808\cdot10^{0}$
440	$3.271\cdot10^{-2}$	$4.447\cdot10^{-5}$	$5.411\cdot10^{-4}$	$2.254\cdot10^{1}$	$1.064\cdot10^{1}$
450	$3.420\cdot10^{-2}$	$3.885\cdot10^{-5}$	$5.369\cdot10^{-4}$	$2.432\cdot10^{1}$	$1.150\cdot10^{1}$
460	$3.561\cdot10^{-2}$	$3.373\cdot10^{-5}$	$5.327\cdot10^{-4}$	$2.620\cdot10^{1}$	$1.242\cdot10^{1}$
470	$3.694\cdot10^{-2}$	$2.911\cdot10^{-5}$	$5.287\cdot10^{-4}$	$2.816\cdot10^{1}$	$1.338\cdot10^{1}$
480	$3.820\cdot10^{-2}$	$2.495\cdot10^{-5}$	$5.241\cdot10^{-4}$	$3.022\cdot10^{1}$	$1.438\cdot10^{1}$
490	$3.938\cdot10^{-2}$	$2.126\cdot10^{-5}$	$5.196\cdot10^{-4}$	$3.236\cdot10^{1}$	$1.544\cdot10^{1}$
500	$4.052\cdot10^{-2}$	$1.802\cdot10^{-5}$	$5.151\cdot10^{-4}$	$3.460\cdot10^{1}$	$1.654\cdot10^{1}$
550	$4.539\cdot10^{-2}$	$7.930\cdot10^{-6}$	$4.925\cdot10^{-4}$	$4.734\cdot10^{1}$	$2.280\cdot10^{1}$
600	$4.921\cdot10^{-2}$	$7.031\cdot10^{-6}$	$4.707\cdot10^{-4}$	$6.274\cdot10^{1}$	$3.039\cdot10^{1}$
650	$5.243\cdot10^{-2}$	$1.429\cdot10^{-5}$	$4.508\cdot10^{-4}$	$8.110\cdot10^{1}$	$3.945\cdot10^{1}$
700	$5.497\cdot10^{-2}$	$2.905\cdot10^{-5}$	$4.325\cdot10^{-4}$	$1.026\cdot10^{2}$	$5.010\cdot10^{1}$
750	$5.711\cdot10^{-2}$	$5.099\cdot10^{-5}$	$4.173\cdot10^{-4}$	$1.275\cdot10^{2}$	$6.245\cdot10^{1}$
800	$5.896\cdot10^{-2}$	$7.996\cdot10^{-5}$	$4.051\cdot10^{-4}$	$1.561\cdot10^{2}$	$7.663\cdot10^{1}$
850	$6.050\cdot10^{-2}$	$1.159\cdot10^{-4}$	$3.961\cdot10^{-4}$	$1.886\cdot10^{2}$	$9.276\cdot10^{1}$
900	$6.179\cdot10^{-2}$	$1.587\cdot10^{-4}$	$3.911\cdot10^{-4}$	$2.252\cdot10^{2}$	$1.110\cdot10^{2}$
950	$6.293\cdot10^{-2}$	$2.087\cdot10^{-4}$	$3.899\cdot10^{-4}$	$2.662\cdot10^{2}$	$1.314\cdot10^{2}$
1000	$6.392\cdot10^{-2}$	$2.660\cdot10^{-4}$	$3.932\cdot10^{-4}$	$3.118\cdot10^{2}$	$1.541\cdot10^{2}$

Appendix B

SM gluon-gluon-fusion cross sections

In this appendix the recommended gluon-gluon fusion cross-sections are presented.

Table 187: Inclusive ggF cross sections for a LHC CM energy of $\sqrt{s} = 7$ TeV, at N^{3}LO QCD, together with their uncertainties. The TH uncertainty is interpreted as a flat 100% confidence level. $\Delta_{\rm TH}^{\rm Gaussian}$ uncertainty is interpreted as a one-sigma range.

$M_{\rm H}$[GeV]	σ^{ggF}[fb]	$\Delta_{\rm TH}$[%]	$\Delta_{\rm TH}^{\rm Gaussian}$[%]	$\Delta_{\rm PDF\oplus\alpha_s}$[%]	$\Delta_{\rm PDF}$[%]	Δ_{α_s}[%]
120.0	18.31	$^{+4.5}_{-7.1}$	$\pm$4.1	$\pm$3.3	$\pm$1.9	$\pm$2.7
120.5	18.16	$^{+4.5}_{-7.1}$	$\pm$4.1	$\pm$3.3	$\pm$1.9	$\pm$2.7
121.0	18.00	$^{+4.5}_{-7.1}$	$\pm$4.1	$\pm$3.3	$\pm$1.9	$\pm$2.7
121.5	17.85	$^{+4.5}_{-7.1}$	$\pm$4.1	$\pm$3.3	$\pm$1.9	$\pm$2.7
122.0	17.71	$^{+4.5}_{-7.1}$	$\pm$4.1	$\pm$3.3	$\pm$1.9	$\pm$2.7
122.5	17.56	$^{+4.5}_{-7.0}$	$\pm$4.1	$\pm$3.3	$\pm$1.9	$\pm$2.7
123.0	17.41	$^{+4.5}_{-7.0}$	$\pm$4.1	$\pm$3.3	$\pm$1.9	$\pm$2.7
123.5	17.27	$^{+4.4}_{-7.0}$	$\pm$4.0	$\pm$3.3	$\pm$1.9	$\pm$2.7
124.0	17.13	$^{+4.4}_{-7.0}$	$\pm$4.0	$\pm$3.3	$\pm$1.9	$\pm$2.7
124.1	17.10	$^{+4.4}_{-7.0}$	$\pm$4.0	$\pm$3.3	$\pm$1.9	$\pm$2.7
124.2	17.07	$^{+4.4}_{-7.0}$	$\pm$4.0	$\pm$3.3	$\pm$1.9	$\pm$2.7
124.3	17.04	$^{+4.4}_{-7.0}$	$\pm$4.0	$\pm$3.3	$\pm$1.9	$\pm$2.7
124.4	17.02	$^{+4.4}_{-7.0}$	$\pm$4.0	$\pm$3.3	$\pm$1.9	$\pm$2.7
124.5	16.99	$^{+4.4}_{-7.0}$	$\pm$4.0	$\pm$3.3	$\pm$1.9	$\pm$2.7
124.6	16.96	$^{+4.4}_{-7.0}$	$\pm$4.0	$\pm$3.3	$\pm$1.9	$\pm$2.7
124.7	16.93	$^{+4.4}_{-7.0}$	$\pm$4.0	$\pm$3.3	$\pm$1.9	$\pm$2.7
124.8	16.90	$^{+4.4}_{-7.0}$	$\pm$4.0	$\pm$3.3	$\pm$1.9	$\pm$2.7
124.9	16.88	$^{+4.4}_{-7.0}$	$\pm$4.0	$\pm$3.3	$\pm$1.9	$\pm$2.7
125.0	16.85	$^{+4.4}_{-7.0}$	$\pm$4.0	$\pm$3.3	$\pm$1.9	$\pm$2.7
125.1	16.82	$^{+4.4}_{-7.0}$	$\pm$4.0	$\pm$3.3	$\pm$1.9	$\pm$2.7
125.09	16.82	$^{+4.4}_{-7.0}$	$\pm$4.0	$\pm$3.3	$\pm$1.9	$\pm$2.7
125.2	16.79	$^{+4.4}_{-7.0}$	$\pm$4.0	$\pm$3.3	$\pm$1.9	$\pm$2.7
125.3	16.77	$^{+4.4}_{-7.0}$	$\pm$4.0	$\pm$3.3	$\pm$1.9	$\pm$2.7
125.4	16.74	$^{+4.4}_{-7.0}$	$\pm$4.0	$\pm$3.3	$\pm$1.9	$\pm$2.7
125.5	16.71	$^{+4.4}_{-7.0}$	$\pm$4.0	$\pm$3.3	$\pm$1.9	$\pm$2.7
125.6	16.68	$^{+4.4}_{-7.0}$	$\pm$4.0	$\pm$3.3	$\pm$1.9	$\pm$2.7
125.7	16.66	$^{+4.4}_{-6.9}$	$\pm$4.0	$\pm$3.3	$\pm$1.9	$\pm$2.7
125.8	16.63	$^{+4.4}_{-6.9}$	$\pm$4.0	$\pm$3.3	$\pm$1.9	$\pm$2.7
125.9	16.60	$^{+4.4}_{-6.9}$	$\pm$4.0	$\pm$3.3	$\pm$1.9	$\pm$2.7
126.0	16.58	$^{+4.4}_{-6.9}$	$\pm$4.0	$\pm$3.3	$\pm$1.9	$\pm$2.7
126.5	16.44	$^{+4.4}_{-6.9}$	$\pm$4.0	$\pm$3.3	$\pm$1.9	$\pm$2.7
127.0	16.31	$^{+4.4}_{-6.9}$	$\pm$4.0	$\pm$3.3	$\pm$1.9	$\pm$2.7
127.5	16.18	$^{+4.4}_{-6.9}$	$\pm$4.0	$\pm$3.3	$\pm$1.9	$\pm$2.7
128.0	16.05	$^{+4.4}_{-6.9}$	$\pm$4.0	$\pm$3.3	$\pm$1.9	$\pm$2.7
128.5	15.92	$^{+4.3}_{-6.9}$	$\pm$4.0	$\pm$3.3	$\pm$1.9	$\pm$2.7
129.0	15.80	$^{+4.3}_{-6.8}$	$\pm$3.9	$\pm$3.3	$\pm$1.9	$\pm$2.7
129.5	15.67	$^{+4.3}_{-6.8}$	$\pm$3.9	$\pm$3.3	$\pm$1.9	$\pm$2.7
130.0	15.55	$^{+4.3}_{-6.8}$	$\pm$3.9	$\pm$3.3	$\pm$1.9	$\pm$2.7

Table 188: Inclusive ggF cross sections for a LHC CM energy of $\sqrt{s} = 8$ TeV, at N^{3}LO QCD, together with their uncertainties. The TH uncertainty is interpreted as a flat 100% confidence level. $\Delta_{\rm TH}^{\rm Gaussian}$ uncertainty is interpreted as a one-sigma range.

$M_{\rm H}$[GeV]	σ^{ggF}[fb]	$\Delta_{\rm TH}[\%]$	$\Delta_{\rm TH}^{\rm Gaussian}[\%]$	$\Delta_{\rm PDF\oplus\alpha_s}[\%]$	$\Delta_{\rm PDF}[\%]$	$\Delta_{\alpha_s}[\%]$
120.0	23.22	$^{+4.5}_{-7.1}$	±4.1	±3.3	±1.9	±2.7
120.5	23.03	$^{+4.5}_{-7.0}$	±4.1	±3.2	±1.9	±2.7
121.0	22.85	$^{+4.5}_{-7.0}$	±4.1	±3.2	±1.9	±2.7
121.5	22.66	$^{+4.5}_{-7.0}$	±4.0	±3.2	±1.9	±2.6
122.0	22.48	$^{+4.5}_{-7.0}$	±4.0	±3.2	±1.9	±2.6
122.5	22.30	$^{+4.5}_{-7.0}$	±4.0	±3.2	±1.9	±2.6
123.0	22.12	$^{+4.5}_{-7.0}$	±4.0	±3.2	±1.9	±2.6
123.5	21.94	$^{+4.5}_{-6.9}$	±4.0	±3.2	±1.9	±2.6
124.0	21.77	$^{+4.5}_{-6.9}$	±4.0	±3.2	±1.9	±2.6
124.1	21.73	$^{+4.5}_{-6.9}$	±4.0	±3.2	±1.9	±2.6
124.2	21.70	$^{+4.5}_{-6.9}$	±4.0	±3.2	±1.9	±2.6
124.3	21.66	$^{+4.5}_{-6.9}$	±4.0	±3.2	±1.9	±2.6
124.4	21.63	$^{+4.5}_{-6.9}$	±4.0	±3.2	±1.9	±2.6
124.5	21.59	$^{+4.4}_{-6.9}$	±4.0	±3.2	±1.9	±2.6
124.6	21.56	$^{+4.4}_{-6.9}$	±4.0	±3.2	±1.9	±2.6
124.7	21.53	$^{+4.4}_{-6.9}$	±4.0	±3.2	±1.9	±2.6
124.8	21.49	$^{+4.4}_{-6.9}$	±4.0	±3.2	±1.9	±2.6
124.9	21.46	$^{+4.4}_{-6.9}$	±4.0	±3.2	±1.9	±2.6
125.0	21.42	$^{+4.4}_{-6.9}$	±4.0	±3.2	±1.9	±2.6
125.1	21.39	$^{+4.4}_{-6.9}$	±4.0	±3.2	±1.9	±2.6
125.09	21.39	$^{+4.4}_{-6.9}$	±4.0	±3.2	±1.9	±2.6
125.2	21.36	$^{+4.4}_{-6.9}$	±4.0	±3.2	±1.9	±2.6
125.3	21.32	$^{+4.4}_{-6.9}$	±4.0	±3.2	±1.9	±2.6
125.4	21.29	$^{+4.4}_{-6.9}$	±4.0	±3.2	±1.9	±2.6
125.5	21.26	$^{+4.4}_{-6.9}$	±4.0	±3.2	±1.9	±2.6
125.6	21.22	$^{+4.4}_{-6.9}$	±4.0	±3.2	±1.9	±2.6
125.7	21.19	$^{+4.4}_{-6.9}$	±4.0	±3.2	±1.9	±2.6
125.8	21.16	$^{+4.4}_{-6.9}$	±4.0	±3.2	±1.9	±2.6
125.9	21.12	$^{+4.4}_{-6.9}$	±4.0	±3.2	±1.9	±2.6
126.0	21.09	$^{+4.4}_{-6.9}$	±4.0	±3.2	±1.9	±2.6
126.5	20.92	$^{+4.4}_{-6.9}$	±4.0	±3.2	±1.9	±2.6
127.0	20.76	$^{+4.4}_{-6.8}$	±3.9	±3.2	±1.9	±2.6
127.5	20.60	$^{+4.4}_{-6.8}$	±3.9	±3.2	±1.9	±2.6
128.0	20.44	$^{+4.4}_{-6.8}$	±3.9	±3.2	±1.9	±2.6
128.5	20.28	$^{+4.4}_{-6.8}$	±3.9	±3.2	±1.9	±2.6
129.0	20.13	$^{+4.4}_{-6.8}$	±3.9	±3.2	±1.9	±2.6
129.5	19.98	$^{+4.4}_{-6.8}$	±3.9	±3.2	±1.9	±2.6
130.0	19.82	$^{+4.3}_{-6.7}$	±3.9	±3.2	±1.9	±2.6

Table 189: Inclusive ggF cross sections for a LHC CM energy of $\sqrt{s} = 13$ TeV, at N^{3}LO QCD, together with their uncertainties. The TH uncertainty is interpreted as a flat 100% confidence level. $\Delta_{\rm TH}^{\rm Gaussian}$ uncertainty is interpreted as a one-sigma range.

$M_{\rm H}$[GeV]	σ^{ggF}[fb]	$\Delta_{\rm TH}[\%]$	$\Delta_{\rm TH}^{\rm Gaussian}[\%]$	$\Delta_{\rm PDF\oplus\alpha_s}[\%]$	$\Delta_{\rm PDF}[\%]$	$\Delta_{\alpha_s}[\%]$
120.0	52.22	$^{+4.7}_{-6.9}$	±4.0	±3.2	±1.9	±2.6
120.5	51.84	$^{+4.7}_{-6.9}$	±4.0	±3.2	±1.9	±2.6
121.0	51.46	$^{+4.6}_{-6.9}$	±4.0	±3.2	±1.9	±2.6
121.5	51.08	$^{+4.6}_{-6.8}$	±3.9	±3.2	±1.9	±2.6
122.0	50.71	$^{+4.6}_{-6.8}$	±3.9	±3.2	±1.9	±2.6
122.5	50.35	$^{+4.6}_{-6.8}$	±3.9	±3.2	±1.9	±2.6
123.0	49.98	$^{+4.6}_{-6.8}$	±3.9	±3.2	±1.9	±2.6
123.5	49.63	$^{+4.6}_{-6.8}$	±3.9	±3.2	±1.9	±2.6
124.0	49.27	$^{+4.6}_{-6.8}$	±3.9	±3.2	±1.9	±2.6
124.1	49.20	$^{+4.6}_{-6.8}$	±3.9	±3.2	±1.9	±2.6
124.2	49.13	$^{+4.6}_{-6.8}$	±3.9	±3.2	±1.9	±2.6
124.3	49.06	$^{+4.6}_{-6.7}$	±3.9	±3.2	±1.9	±2.6
124.4	48.99	$^{+4.6}_{-6.7}$	±3.9	±3.2	±1.9	±2.6
124.5	48.92	$^{+4.6}_{-6.7}$	±3.9	±3.2	±1.9	±2.6
124.6	48.85	$^{+4.6}_{-6.7}$	±3.9	±3.2	±1.9	±2.6
124.7	48.78	$^{+4.6}_{-6.7}$	±3.9	±3.2	±1.9	±2.6
124.8	48.71	$^{+4.6}_{-6.7}$	±3.9	±3.2	±1.9	±2.6
124.9	48.64	$^{+4.6}_{-6.7}$	±3.9	±3.2	±1.9	±2.6
125.0	48.58	$^{+4.6}_{-6.7}$	±3.9	±3.2	±1.9	±2.6
125.1	48.52	$^{+4.6}_{-6.7}$	±3.9	±3.2	±1.9	±2.6
125.09	48.51	$^{+4.6}_{-6.7}$	±3.9	±3.2	±1.9	±2.6
125.2	48.44	$^{+4.6}_{-6.7}$	±3.9	±3.2	±1.9	±2.6
125.3	48.37	$^{+4.6}_{-6.7}$	±3.9	±3.2	±1.9	±2.6
125.4	48.30	$^{+4.6}_{-6.7}$	±3.9	±3.2	±1.9	±2.6
125.5	48.23	$^{+4.6}_{-6.7}$	±3.9	±3.2	±1.9	±2.6
125.6	48.16	$^{+4.6}_{-6.7}$	±3.9	±3.2	±1.9	±2.6
125.7	48.10	$^{+4.6}_{-6.7}$	±3.9	±3.2	±1.9	±2.6
125.8	48.03	$^{+4.6}_{-6.7}$	±3.9	±3.2	±1.9	±2.6
125.9	47.96	$^{+4.5}_{-6.7}$	±3.9	±3.2	±1.9	±2.6
126.0	47.89	$^{+4.5}_{-6.7}$	±3.9	±3.2	±1.9	±2.6
126.5	47.56	$^{+4.5}_{-6.7}$	±3.9	±3.2	±1.9	±2.6
127.0	47.23	$^{+4.5}_{-6.7}$	±3.8	±3.2	±1.9	±2.6
127.5	46.90	$^{+4.5}_{-6.6}$	±3.8	±3.2	±1.9	±2.6
128.0	46.58	$^{+4.5}_{-6.6}$	±3.8	±3.2	±1.9	±2.6
128.5	46.25	$^{+4.5}_{-6.6}$	±3.8	±3.2	±1.9	±2.6
129.0	45.94	$^{+4.5}_{-6.6}$	±3.8	±3.2	±1.9	±2.6
129.5	45.62	$^{+4.5}_{-6.6}$	±3.8	±3.2	±1.9	±2.6
130.0	45.31	$^{+4.5}_{-6.6}$	±3.8	±3.2	±1.8	±2.6

Table 190: Inclusive ggF cross sections for a LHC CM energy of $\sqrt{s} = 14$ TeV, at N^{3}LO QCD, together with their uncertainties. The TH uncertainty is interpreted as a flat 100% confidence level. $\Delta_{\rm TH}^{\rm Gaussian}$ uncertainty is interpreted as a one-sigma range.

$M_{\rm H}$[GeV]	σ^{ggF}[fb]	$\Delta_{\rm TH}$[%]	$\Delta_{\rm TH}^{\rm Gaussian}$[%]	$\Delta_{\rm PDF\oplus\alpha_s}$[%]	$\Delta_{\rm PDF}$[%]	Δ_{α_s}[%]
120.0	58.71	$^{+4.7}_{-6.9}$	±4.0	±3.2	±1.9	±2.6
120.5	58.29	$^{+4.7}_{-6.9}$	±4.0	±3.2	±1.9	±2.6
121.0	57.87	$^{+4.7}_{-6.8}$	±3.9	±3.2	±1.9	±2.6
121.5	57.45	$^{+4.7}_{-6.8}$	±3.9	±3.2	±1.9	±2.6
122.0	57.04	$^{+4.7}_{-6.8}$	±3.9	±3.2	±1.9	±2.6
122.5	56.64	$^{+4.6}_{-6.8}$	±3.9	±3.2	±1.9	±2.6
123.0	56.24	$^{+4.6}_{-6.8}$	±3.9	±3.2	±1.9	±2.6
123.5	55.84	$^{+4.6}_{-6.8}$	±3.9	±3.2	±1.9	±2.6
124.0	55.45	$^{+4.6}_{-6.7}$	±3.9	±3.2	±1.9	±2.6
124.1	55.37	$^{+4.6}_{-6.7}$	±3.9	±3.2	±1.9	±2.6
124.2	55.29	$^{+4.6}_{-6.7}$	±3.9	±3.2	±1.9	±2.6
124.3	55.21	$^{+4.6}_{-6.7}$	±3.9	±3.2	±1.9	±2.6
124.4	55.14	$^{+4.6}_{-6.7}$	±3.9	±3.2	±1.9	±2.6
124.5	55.06	$^{+4.6}_{-6.7}$	±3.9	±3.2	±1.9	±2.6
124.6	54.98	$^{+4.6}_{-6.7}$	±3.9	±3.2	±1.9	±2.6
124.7	54.90	$^{+4.6}_{-6.7}$	±3.9	±3.2	±1.9	±2.6
124.8	54.83	$^{+4.6}_{-6.7}$	±3.9	±3.2	±1.9	±2.6
124.9	54.75	$^{+4.6}_{-6.7}$	±3.9	±3.2	±1.9	±2.6
125.0	54.67	$^{+4.6}_{-6.7}$	±3.9	±3.2	±1.9	±2.6
125.1	54.61	$^{+4.6}_{-6.7}$	±3.9	±3.2	±1.9	±2.6
125.09	54.60	$^{+4.6}_{-6.7}$	±3.9	±3.2	±1.9	±2.6
125.2	54.52	$^{+4.6}_{-6.7}$	±3.9	±3.2	±1.9	±2.6
125.3	54.45	$^{+4.6}_{-6.7}$	±3.9	±3.2	±1.9	±2.6
125.4	54.37	$^{+4.6}_{-6.7}$	±3.9	±3.2	±1.9	±2.6
125.5	54.29	$^{+4.6}_{-6.7}$	±3.9	±3.2	±1.9	±2.6
125.6	54.22	$^{+4.6}_{-6.7}$	±3.9	±3.2	±1.9	±2.6
125.7	54.14	$^{+4.6}_{-6.7}$	±3.9	±3.2	±1.9	±2.6
125.8	54.07	$^{+4.6}_{-6.7}$	±3.9	±3.2	±1.9	±2.6
125.9	53.99	$^{+4.6}_{-6.7}$	±3.9	±3.2	±1.9	±2.6
126.0	53.92	$^{+4.6}_{-6.7}$	±3.9	±3.2	±1.9	±2.6
126.5	53.55	$^{+4.6}_{-6.7}$	±3.8	±3.2	±1.9	±2.6
127.0	53.18	$^{+4.6}_{-6.6}$	±3.8	±3.2	±1.9	±2.6
127.5	52.82	$^{+4.5}_{-6.6}$	±3.8	±3.2	±1.9	±2.6
128.0	52.46	$^{+4.5}_{-6.6}$	±3.8	±3.2	±1.9	±2.6
128.5	52.10	$^{+4.5}_{-6.6}$	±3.8	±3.2	±1.9	±2.6
129.0	51.75	$^{+4.5}_{-6.6}$	±3.8	±3.2	±1.9	±2.6
129.5	51.40	$^{+4.5}_{-6.6}$	±3.8	±3.2	±1.9	±2.6
130.0	51.05	$^{+4.5}_{-6.6}$	±3.8	±3.2	±1.9	±2.6

Table 191: Energy scan of Inclusive ggF cross sections for a Higgs boson mass of 125 GeV, at N^{3}LO QCD, together with their uncertainties. The TH uncertainty is interpreted as a flat 100% confidence level. $\Delta_{\rm TH}^{\rm Gaussian}$ uncertainty is interpreted as a one-sigma range.

$\sqrt{s}$ [TeV]	σ^{ggF}[fb]	$\Delta_{\rm TH}$[%]	$\Delta_{\rm TH}^{\rm Gaussian}$[%]	$\Delta_{\rm PDF\oplus\alpha_s}$[%]	$\Delta_{\rm PDF}$[%]	Δ_{α_s}[%]
6.0	12.65	$^{+4.4}_{-7.1}$	±4.1	±3.3	±1.9	±2.7
6.5	14.70	$^{+4.4}_{-7.0}$	±4.0	±3.3	±1.9	±2.7
7.0	16.85	$^{+4.4}_{-7.0}$	±4.0	±3.3	±1.9	±2.7
7.5	19.09	$^{+4.4}_{-6.9}$	±4.0	±3.3	±1.9	±2.7
8.0	21.42	$^{+4.4}_{-6.9}$	±4.0	±3.2	±1.9	±2.7
8.5	23.84	$^{+4.5}_{-6.9}$	±4.0	±3.2	±1.9	±2.6
9.0	26.33	$^{+4.5}_{-6.8}$	±3.9	±3.2	±1.9	±2.6
9.5	28.89	$^{+4.5}_{-6.8}$	±3.9	±3.2	±1.9	±2.6
10.0	31.53	$^{+4.5}_{-6.8}$	±3.9	±3.2	±1.9	±2.6
10.5	34.22	$^{+4.5}_{-6.8}$	±3.9	±3.2	±1.9	±2.6
11.0	36.97	$^{+4.5}_{-6.8}$	±3.9	±3.2	±1.9	±2.6
11.5	39.79	$^{+4.5}_{-6.8}$	±3.9	±3.2	±1.9	±2.6
12.0	42.66	$^{+4.6}_{-6.8}$	±3.9	±3.2	±1.9	±2.6
12.5	45.59	$^{+4.6}_{-6.8}$	±3.9	±3.2	±1.9	±2.6
13.0	48.57	$^{+4.6}_{-6.7}$	±3.9	±3.2	±1.9	±2.6
13.5	51.59	$^{+4.6}_{-6.7}$	±3.9	±3.2	±1.9	±2.6
14.0	54.67	$^{+4.6}_{-6.7}$	±3.9	±3.2	±1.9	±2.6
14.5	57.79	$^{+4.6}_{-6.7}$	±3.9	±3.2	±1.9	±2.6
15.0	60.95	$^{+4.6}_{-6.7}$	±3.9	±3.2	±1.9	±2.6

Table 192: Energy scan of Inclusive ggF cross sections for a Higgs boson mass of 125.09 GeV, at N^{3}LO QCD, together with their uncertainties. The TH uncertainty is interpreted as a flat 100% confidence level. $\Delta_{\rm TH}^{\rm Gaussian}$ uncertainty is interpreted as a one-sigma range.

$\sqrt{s}$ [TeV]	σ^{ggF}[fb]	$\Delta_{\rm TH}[\%]$	$\Delta_{\rm TH}^{\rm Gaussian}[\%]$	$\Delta_{\rm PDF\oplus\alpha_s}[\%]$	$\Delta_{\rm PDF}[\%]$	$\Delta_{\alpha_s}[\%]$
6.0	12.63	$^{+4.4}_{-7.1}$	±4.1	±3.3	±1.9	±2.7
6.5	14.68	$^{+4.4}_{-7.0}$	±4.0	±3.3	±1.9	±2.7
7.0	16.83	$^{+4.4}_{-7.0}$	±4.0	±3.3	±1.9	±2.7
7.5	19.07	$^{+4.4}_{-6.9}$	±4.0	±3.3	±1.9	±2.7
8.0	21.39	$^{+4.4}_{-6.9}$	±4.0	±3.2	±1.9	±2.7
8.5	23.80	$^{+4.5}_{-6.9}$	±4.0	±3.2	±1.9	±2.6
9.0	26.29	$^{+4.5}_{-6.8}$	±3.9	±3.2	±1.9	±2.6
9.5	28.85	$^{+4.5}_{-6.8}$	±3.9	±3.2	±1.9	±2.6
10.0	31.48	$^{+4.5}_{-6.8}$	±3.9	±3.2	±1.9	±2.6
10.5	34.18	$^{+4.5}_{-6.8}$	±3.9	±3.2	±1.9	±2.6
11.0	36.93	$^{+4.5}_{-6.8}$	±3.9	±3.2	±1.9	±2.6
11.5	39.75	$^{+4.5}_{-6.8}$	±3.9	±3.2	±1.9	±2.6
12.0	42.61	$^{+4.6}_{-6.8}$	±3.9	±3.2	±1.9	±2.6
12.5	45.53	$^{+4.6}_{-6.8}$	±3.9	±3.2	±1.9	±2.6
13.0	48.51	$^{+4.6}_{-6.7}$	±3.9	±3.2	±1.9	±2.6
13.5	51.53	$^{+4.6}_{-6.7}$	±3.9	±3.2	±1.9	±2.6
14.0	54.60	$^{+4.6}_{-6.7}$	±3.9	±3.2	±1.9	±2.6
14.5	57.72	$^{+4.6}_{-6.7}$	±3.9	±3.2	±1.9	±2.6
15.0	60.87	$^{+4.6}_{-6.7}$	±3.9	±3.2	±1.9	±2.6

Appendix C

SM vector-boson-fusion cross sections

In this appendix the cross-section Tables 25 and 26 for the SM VBF cross sections shown in Section I.5.1.c are expanded to a scan over SM Higgs boson masses.

Table 193: Total VBF cross sections in the SM for a LHC CM energy of $\sqrt{s} = 7$ TeV, including QCD and EW corrections and their uncertainties for different Higgs boson masses M_{H}. For more details see Section I.5.1.c.

M_{H}[GeV]	σ^{VBF}[fb]	Δ_{scale}[%]	$\Delta_{\mathrm{PDF}/\alpha_{\mathrm{s}}/\mathrm{PDF}\oplus\alpha_{\mathrm{s}}}$[%]	$\sigma^{\mathrm{DIS}}_{\mathrm{NNLOQCD}}$[fb]	δ_{EW}[%]	σ_{γ}[fb]	$\sigma_{s\text{-channel}}$[fb]
120.0	1301.6(2)	$^{+0.20}_{-0.22}$	$\pm 2.1/\pm 0.4/\pm 2.2$	1344.0(2)	-4.5	17.6	668.7(2)
120.5	1295.5(2)	$^{+0.20}_{-0.22}$	$\pm 2.1/\pm 0.4/\pm 2.2$	1337.6(2)	-4.5	17.5	659.7(2)
121.0	1289.3(2)	$^{+0.20}_{-0.22}$	$\pm 2.1/\pm 0.4/\pm 2.2$	1331.2(2)	-4.5	17.5	650.9(2)
121.5	1283.2(2)	$^{+0.20}_{-0.22}$	$\pm 2.1/\pm 0.4/\pm 2.2$	1324.8(2)	-4.5	17.5	642.1(2)
122.0	1277.2(2)	$^{+0.20}_{-0.22}$	$\pm 2.1/\pm 0.4/\pm 2.2$	1318.5(2)	-4.5	17.4	633.5(2)
122.5	1271.1(2)	$^{+0.20}_{-0.22}$	$\pm 2.1/\pm 0.4/\pm 2.2$	1312.2(2)	-4.4	17.4	624.9(2)
123.0	1265.1(2)	$^{+0.19}_{-0.21}$	$\pm 2.1/\pm 0.4/\pm 2.2$	1305.9(2)	-4.4	17.3	616.7(2)
123.5	1259.2(2)	$^{+0.19}_{-0.21}$	$\pm 2.1/\pm 0.4/\pm 2.2$	1299.7(2)	-4.4	17.3	608.4(2)
124.0	1253.2(2)	$^{+0.19}_{-0.21}$	$\pm 2.1/\pm 0.4/\pm 2.2$	1293.5(2)	-4.4	17.2	600.1(2)
124.1	1252.1(2)	$^{+0.19}_{-0.21}$	$\pm 2.1/\pm 0.4/\pm 2.2$	1292.3(2)	-4.4	17.2	598.6(2)
124.2	1250.9(2)	$^{+0.19}_{-0.21}$	$\pm 2.1/\pm 0.4/\pm 2.2$	1291.0(2)	-4.4	17.2	597.0(2)
124.3	1249.7(2)	$^{+0.19}_{-0.21}$	$\pm 2.1/\pm 0.4/\pm 2.2$	1289.8(2)	-4.4	17.2	595.4(2)
124.4	1248.5(1)	$^{+0.19}_{-0.21}$	$\pm 2.1/\pm 0.4/\pm 2.2$	1288.6(2)	-4.4	17.2	593.8(2)
124.5	1247.3(1)	$^{+0.19}_{-0.21}$	$\pm 2.1/\pm 0.4/\pm 2.2$	1287.3(2)	-4.4	17.2	592.2(2)
124.6	1246.2(1)	$^{+0.19}_{-0.21}$	$\pm 2.1/\pm 0.4/\pm 2.2$	1286.1(2)	-4.4	17.2	590.8(2)
124.7	1245.0(1)	$^{+0.19}_{-0.21}$	$\pm 2.1/\pm 0.4/\pm 2.2$	1284.9(2)	-4.4	17.2	589.0(2)
124.8	1243.8(1)	$^{+0.19}_{-0.21}$	$\pm 2.1/\pm 0.4/\pm 2.2$	1283.7(2)	-4.4	17.1	587.6(2)
124.9	1242.6(1)	$^{+0.19}_{-0.21}$	$\pm 2.1/\pm 0.4/\pm 2.2$	1282.5(2)	-4.4	17.1	586.0(2)
125.0	1241.5(1)	$^{+0.19}_{-0.21}$	$\pm 2.1/\pm 0.4/\pm 2.2$	1281.2(2)	-4.4	17.1	584.5(2)
125.09	1240.3(1)	$^{+0.19}_{-0.21}$	$\pm 2.1/\pm 0.4/\pm 2.2$	1280.0(2)	-4.4	17.1	582.8(2)
125.1	1240.3(1)	$^{+0.19}_{-0.21}$	$\pm 2.1/\pm 0.4/\pm 2.2$	1280.0(2)	-4.4	17.1	582.9(2)
125.2	1239.1(1)	$^{+0.19}_{-0.21}$	$\pm 2.1/\pm 0.4/\pm 2.2$	1278.8(2)	-4.4	17.1	581.2(2)
125.3	1238.0(1)	$^{+0.19}_{-0.21}$	$\pm 2.1/\pm 0.4/\pm 2.2$	1277.6(2)	-4.4	17.1	579.7(2)
125.4	1236.8(1)	$^{+0.19}_{-0.21}$	$\pm 2.1/\pm 0.4/\pm 2.2$	1276.4(2)	-4.4	17.1	578.1(2)
125.5	1235.7(1)	$^{+0.19}_{-0.21}$	$\pm 2.1/\pm 0.4/\pm 2.2$	1275.2(2)	-4.4	17.1	576.6(2)
125.6	1234.5(1)	$^{+0.19}_{-0.21}$	$\pm 2.1/\pm 0.4/\pm 2.2$	1273.9(2)	-4.4	17.1	575.2(2)
125.7	1233.3(1)	$^{+0.19}_{-0.21}$	$\pm 2.1/\pm 0.4/\pm 2.2$	1272.7(2)	-4.4	17.1	573.7(2)
125.8	1232.2(1)	$^{+0.19}_{-0.21}$	$\pm 2.1/\pm 0.4/\pm 2.2$	1271.5(2)	-4.4	17.1	572.1(2)
125.9	1231.0(1)	$^{+0.19}_{-0.21}$	$\pm 2.1/\pm 0.4/\pm 2.2$	1270.3(2)	-4.4	17.0	570.5(2)
126.0	1229.9(1)	$^{+0.19}_{-0.21}$	$\pm 2.1/\pm 0.4/\pm 2.2$	1269.1(2)	-4.4	17.0	569.1(2)
126.5	1224.1(1)	$^{+0.18}_{-0.21}$	$\pm 2.1/\pm 0.4/\pm 2.2$	1263.1(2)	-4.4	17.0	561.5(2)
127.0	1218.4(1)	$^{+0.18}_{-0.21}$	$\pm 2.1/\pm 0.4/\pm 2.2$	1257.2(2)	-4.4	16.9	554.2(2)
127.5	1212.7(1)	$^{+0.18}_{-0.21}$	$\pm 2.1/\pm 0.4/\pm 2.2$	1251.2(2)	-4.4	16.9	546.8(2)
128.0	1207.1(1)	$^{+0.18}_{-0.21}$	$\pm 2.1/\pm 0.4/\pm 2.2$	1245.3(2)	-4.4	16.9	539.9(2)
128.5	1201.4(1)	$^{+0.18}_{-0.20}$	$\pm 2.1/\pm 0.4/\pm 2.2$	1239.5(2)	-4.4	16.8	532.9(2)
129.0	1195.9(1)	$^{+0.18}_{-0.20}$	$\pm 2.1/\pm 0.4/\pm 2.2$	1233.7(2)	-4.4	16.8	526.0(2)
129.5	1190.3(1)	$^{+0.17}_{-0.20}$	$\pm 2.1/\pm 0.4/\pm 2.2$	1227.9(1)	-4.4	16.7	519.1(2)
130.0	1184.8(1)	$^{+0.17}_{-0.20}$	$\pm 2.1/\pm 0.4/\pm 2.2$	1222.1(1)	-4.4	16.7	512.2(2)

Table 194: Total VBF cross sections in the SM for a LHC CM energy of $\sqrt{s} = 8$ TeV, including QCD and EW corrections and their uncertainties for different Higgs boson masses M_{H}. For more details see Section I.5.1.c.

M_{H}[GeV]	σ^{VBF}[fb]	Δ_{scale}[%]	$\Delta_{\mathrm{PDF}/\alpha_{\mathrm{s}}/\mathrm{PDF}\oplus\alpha_{\mathrm{s}}}$[%]	$\sigma^{\mathrm{DIS}}_{\mathrm{NNLOQCD}}$[fb]	δ_{EW}[%]	σ_{γ}[fb]	$\sigma_{s\text{-channel}}$[fb]
120.0	1675.7(2)	$^{+0.26}_{-0.25}$	$\pm 2.1/\pm 0.4/\pm 2.2$	1733.7(2)	-4.7	22.7	811.7(3)
120.5	1668.1(2)	$^{+0.26}_{-0.25}$	$\pm 2.1/\pm 0.4/\pm 2.2$	1725.8(2)	-4.7	22.6	800.5(3)
121.0	1660.5(2)	$^{+0.26}_{-0.25}$	$\pm 2.1/\pm 0.4/\pm 2.2$	1717.8(2)	-4.7	22.6	790.0(3)
121.5	1652.9(2)	$^{+0.26}_{-0.25}$	$\pm 2.1/\pm 0.4/\pm 2.2$	1709.9(2)	-4.6	22.5	779.3(3)
122.0	1645.4(2)	$^{+0.26}_{-0.25}$	$\pm 2.1/\pm 0.4/\pm 2.2$	1702.1(2)	-4.6	22.5	768.7(3)
122.5	1637.9(2)	$^{+0.26}_{-0.24}$	$\pm 2.1/\pm 0.4/\pm 2.2$	1694.3(2)	-4.6	22.4	759.0(3)
123.0	1630.5(2)	$^{+0.25}_{-0.24}$	$\pm 2.1/\pm 0.4/\pm 2.2$	1686.5(2)	-4.6	22.3	748.9(2)
123.5	1623.2(2)	$^{+0.25}_{-0.24}$	$\pm 2.1/\pm 0.4/\pm 2.2$	1678.8(2)	-4.6	22.3	739.2(2)
124.0	1615.8(2)	$^{+0.25}_{-0.24}$	$\pm 2.1/\pm 0.4/\pm 2.2$	1671.1(2)	-4.6	22.2	729.3(3)
124.1	1614.4(2)	$^{+0.25}_{-0.24}$	$\pm 2.1/\pm 0.4/\pm 2.2$	1669.6(2)	-4.6	22.2	727.3(3)
124.2	1612.9(2)	$^{+0.25}_{-0.24}$	$\pm 2.1/\pm 0.4/\pm 2.2$	1668.1(2)	-4.6	22.2	725.5(3)
124.3	1611.4(2)	$^{+0.25}_{-0.24}$	$\pm 2.1/\pm 0.4/\pm 2.2$	1666.6(2)	-4.6	22.2	723.5(2)
124.4	1610.0(2)	$^{+0.25}_{-0.24}$	$\pm 2.1/\pm 0.4/\pm 2.2$	1665.0(2)	-4.6	22.2	721.8(3)
124.5	1608.5(2)	$^{+0.25}_{-0.24}$	$\pm 2.1/\pm 0.4/\pm 2.2$	1663.5(2)	-4.6	22.2	719.9(3)
124.6	1607.1(2)	$^{+0.25}_{-0.24}$	$\pm 2.1/\pm 0.4/\pm 2.2$	1662.0(2)	-4.6	22.2	717.9(3)
124.7	1605.6(2)	$^{+0.25}_{-0.24}$	$\pm 2.1/\pm 0.4/\pm 2.2$	1660.5(2)	-4.6	22.1	716.1(2)
124.8	1604.2(2)	$^{+0.25}_{-0.24}$	$\pm 2.1/\pm 0.4/\pm 2.2$	1659.0(2)	-4.6	22.1	714.2(3)
124.9	1602.8(2)	$^{+0.25}_{-0.24}$	$\pm 2.1/\pm 0.4/\pm 2.2$	1657.5(2)	-4.6	22.1	712.4(3)
125.0	1601.3(2)	$^{+0.25}_{-0.24}$	$\pm 2.1/\pm 0.4/\pm 2.2$	1656.0(2)	-4.6	22.1	710.4(3)
125.09	1599.8(2)	$^{+0.25}_{-0.24}$	$\pm 2.1/\pm 0.4/\pm 2.2$	1654.4(2)	-4.6	22.1	708.7(3)
125.1	1599.8(2)	$^{+0.25}_{-0.24}$	$\pm 2.1/\pm 0.4/\pm 2.2$	1654.4(2)	-4.6	22.1	708.7(3)
125.2	1598.4(2)	$^{+0.25}_{-0.24}$	$\pm 2.1/\pm 0.4/\pm 2.2$	1652.9(2)	-4.6	22.1	706.5(2)
125.3	1597.0(2)	$^{+0.25}_{-0.24}$	$\pm 2.1/\pm 0.4/\pm 2.2$	1651.4(2)	-4.6	22.1	704.8(3)
125.4	1595.5(2)	$^{+0.25}_{-0.24}$	$\pm 2.1/\pm 0.4/\pm 2.2$	1649.9(2)	-4.6	22.1	703.0(3)
125.5	1594.1(2)	$^{+0.25}_{-0.24}$	$\pm 2.1/\pm 0.4/\pm 2.2$	1648.4(2)	-4.6	22.1	701.2(3)
125.6	1592.7(2)	$^{+0.25}_{-0.24}$	$\pm 2.1/\pm 0.4/\pm 2.2$	1646.9(2)	-4.6	22.0	699.3(3)
125.7	1591.2(2)	$^{+0.25}_{-0.24}$	$\pm 2.1/\pm 0.4/\pm 2.2$	1645.4(2)	-4.6	22.0	697.5(3)
125.8	1589.8(2)	$^{+0.25}_{-0.24}$	$\pm 2.1/\pm 0.4/\pm 2.2$	1643.9(2)	-4.6	22.0	695.6(3)
125.9	1588.4(2)	$^{+0.25}_{-0.24}$	$\pm 2.1/\pm 0.4/\pm 2.2$	1642.4(2)	-4.6	22.0	693.7(3)
126.0	1587.0(2)	$^{+0.24}_{-0.24}$	$\pm 2.1/\pm 0.4/\pm 2.2$	1640.9(2)	-4.6	22.0	692.0(3)
126.5	1579.8(2)	$^{+0.24}_{-0.24}$	$\pm 2.1/\pm 0.4/\pm 2.2$	1633.5(2)	-4.6	21.9	683.1(3)
127.0	1572.8(2)	$^{+0.24}_{-0.24}$	$\pm 2.1/\pm 0.4/\pm 2.2$	1626.1(2)	-4.6	21.9	674.2(3)
127.5	1565.7(2)	$^{+0.24}_{-0.24}$	$\pm 2.1/\pm 0.4/\pm 2.2$	1618.7(2)	-4.6	21.8	665.4(2)
128.0	1558.7(2)	$^{+0.24}_{-0.24}$	$\pm 2.1/\pm 0.4/\pm 2.2$	1611.4(2)	-4.6	21.8	656.9(2)
128.5	1551.7(2)	$^{+0.24}_{-0.24}$	$\pm 2.1/\pm 0.4/\pm 2.2$	1604.2(2)	-4.6	21.7	648.5(2)
129.0	1544.8(2)	$^{+0.24}_{-0.23}$	$\pm 2.1/\pm 0.4/\pm 2.2$	1596.9(2)	-4.6	21.7	640.2(2)
129.5	1537.9(2)	$^{+0.24}_{-0.23}$	$\pm 2.1/\pm 0.4/\pm 2.2$	1589.8(2)	-4.6	21.6	631.9(2)
130.0	1531.1(2)	$^{+0.23}_{-0.23}$	$\pm 2.1/\pm 0.4/\pm 2.2$	1582.6(2)	-4.6	21.5	623.7(2)

Table 195: Total VBF cross sections in the SM for a LHC CM energy of $\sqrt{s} = 13$ TeV, including QCD and EW corrections and their uncertainties for different Higgs boson masses M_{H}. For more details see Section I.5.1.c.

M_{H}[GeV]	σ^{VBF}[fb]	Δ_{scale}[%]	$\Delta_{\mathrm{PDF}/\alpha_{\mathrm{s}}/\mathrm{PDF}\oplus\alpha_{\mathrm{s}}}$[%]	$\sigma^{\mathrm{DIS}}_{\mathrm{NNLOQCD}}$[fb]	δ_{EW}[%]	σ_{γ}[fb]	$\sigma_{s\text{-channel}}$[fb]
120.0	3935.2(7)	$^{+0.44}_{-0.33}$	$\pm 2.1/\pm 0.5/\pm 2.1$	4100.8(7)	-5.3	53.0	1567.0(6)
120.5	3919.4(7)	$^{+0.44}_{-0.33}$	$\pm 2.1/\pm 0.5/\pm 2.1$	4084.2(7)	-5.3	52.9	1546.0(7)
121.0	3903.9(7)	$^{+0.44}_{-0.33}$	$\pm 2.1/\pm 0.5/\pm 2.1$	4067.8(7)	-5.3	52.8	1525.7(6)
121.5	3888.3(7)	$^{+0.44}_{-0.33}$	$\pm 2.1/\pm 0.5/\pm 2.1$	4051.5(7)	-5.3	52.7	1506.7(6)
122.0	3873.0(7)	$^{+0.44}_{-0.33}$	$\pm 2.1/\pm 0.5/\pm 2.1$	4035.2(7)	-5.3	52.5	1487.6(6)
122.5	3857.6(7)	$^{+0.43}_{-0.33}$	$\pm 2.1/\pm 0.5/\pm 2.1$	4019.0(7)	-5.3	52.4	1468.2(6)
123.0	3842.3(7)	$^{+0.43}_{-0.33}$	$\pm 2.1/\pm 0.5/\pm 2.1$	4003.0(7)	-5.3	52.3	1449.3(5)
123.5	3827.0(7)	$^{+0.43}_{-0.33}$	$\pm 2.1/\pm 0.5/\pm 2.1$	3987.0(7)	-5.3	52.2	1430.8(5)
124.0	3811.9(7)	$^{+0.43}_{-0.33}$	$\pm 2.1/\pm 0.5/\pm 2.1$	3971.1(7)	-5.3	52.1	1412.9(5)
124.1	3808.9(7)	$^{+0.43}_{-0.33}$	$\pm 2.1/\pm 0.5/\pm 2.1$	3967.9(7)	-5.3	52.1	1409.4(5)
124.2	3805.9(7)	$^{+0.43}_{-0.33}$	$\pm 2.1/\pm 0.5/\pm 2.1$	3964.7(7)	-5.3	52.0	1405.8(5)
124.3	3802.9(7)	$^{+0.43}_{-0.33}$	$\pm 2.1/\pm 0.5/\pm 2.1$	3961.6(7)	-5.3	52.0	1401.9(5)
124.4	3799.9(7)	$^{+0.43}_{-0.33}$	$\pm 2.1/\pm 0.5/\pm 2.1$	3958.4(7)	-5.3	52.0	1398.4(5)
124.5	3796.9(7)	$^{+0.43}_{-0.33}$	$\pm 2.1/\pm 0.5/\pm 2.1$	3955.2(7)	-5.3	52.0	1395.1(5)
124.6	3793.9(7)	$^{+0.43}_{-0.33}$	$\pm 2.1/\pm 0.5/\pm 2.1$	3952.1(7)	-5.3	51.9	1391.5(5)
124.7	3790.9(7)	$^{+0.43}_{-0.33}$	$\pm 2.1/\pm 0.5/\pm 2.1$	3948.9(7)	-5.3	51.9	1388.0(5)
124.8	3788.0(6)	$^{+0.43}_{-0.33}$	$\pm 2.1/\pm 0.5/\pm 2.1$	3945.8(7)	-5.3	51.9	1384.9(5)
124.9	3785.0(6)	$^{+0.43}_{-0.33}$	$\pm 2.1/\pm 0.5/\pm 2.1$	3942.7(7)	-5.3	51.9	1381.5(5)
125.0	3782.0(6)	$^{+0.43}_{-0.33}$	$\pm 2.1/\pm 0.5/\pm 2.1$	3939.5(7)	-5.3	51.9	1378.1(5)
125.09	3779.0(6)	$^{+0.43}_{-0.33}$	$\pm 2.1/\pm 0.5/\pm 2.1$	3936.4(7)	-5.3	51.8	1374.5(5)
125.1	3779.1(6)	$^{+0.43}_{-0.33}$	$\pm 2.1/\pm 0.5/\pm 2.1$	3936.4(7)	-5.3	51.8	1373.9(5)
125.2	3775.9(6)	$^{+0.43}_{-0.33}$	$\pm 2.1/\pm 0.5/\pm 2.1$	3933.2(7)	-5.3	51.8	1370.5(5)
125.3	3773.0(6)	$^{+0.43}_{-0.33}$	$\pm 2.1/\pm 0.5/\pm 2.1$	3930.1(7)	-5.3	51.8	1367.2(5)
125.4	3769.9(6)	$^{+0.43}_{-0.33}$	$\pm 2.1/\pm 0.5/\pm 2.1$	3927.0(7)	-5.3	51.8	1364.0(5)
125.5	3767.0(6)	$^{+0.43}_{-0.33}$	$\pm 2.1/\pm 0.5/\pm 2.1$	3923.9(7)	-5.3	51.7	1360.0(5)
125.6	3764.2(6)	$^{+0.43}_{-0.33}$	$\pm 2.1/\pm 0.5/\pm 2.1$	3920.7(7)	-5.3	51.7	1356.7(5)
125.7	3761.1(6)	$^{+0.43}_{-0.33}$	$\pm 2.1/\pm 0.5/\pm 2.1$	3917.6(7)	-5.3	51.7	1353.3(5)
125.8	3758.1(6)	$^{+0.43}_{-0.33}$	$\pm 2.1/\pm 0.5/\pm 2.1$	3914.5(7)	-5.3	51.7	1349.8(5)
125.9	3755.1(6)	$^{+0.43}_{-0.32}$	$\pm 2.1/\pm 0.5/\pm 2.1$	3911.4(7)	-5.3	51.6	1346.5(5)
126.0	3752.2(6)	$^{+0.43}_{-0.32}$	$\pm 2.1/\pm 0.5/\pm 2.1$	3908.3(7)	-5.3	51.6	1343.2(5)
126.5	3737.5(6)	$^{+0.42}_{-0.32}$	$\pm 2.1/\pm 0.5/\pm 2.1$	3892.8(7)	-5.3	51.5	1326.4(5)
127.0	3723.0(6)	$^{+0.42}_{-0.32}$	$\pm 2.1/\pm 0.5/\pm 2.1$	3877.4(7)	-5.3	51.4	1310.2(5)
127.5	3708.4(6)	$^{+0.42}_{-0.32}$	$\pm 2.1/\pm 0.5/\pm 2.1$	3862.1(7)	-5.3	51.3	1293.4(5)
128.0	3693.9(6)	$^{+0.42}_{-0.32}$	$\pm 2.1/\pm 0.5/\pm 2.1$	3846.8(7)	-5.3	51.2	1277.6(5)
128.5	3679.5(6)	$^{+0.42}_{-0.32}$	$\pm 2.1/\pm 0.5/\pm 2.1$	3831.7(7)	-5.3	51.0	1261.8(5)
129.0	3665.1(6)	$^{+0.42}_{-0.32}$	$\pm 2.1/\pm 0.5/\pm 2.1$	3816.6(7)	-5.3	50.9	1246.4(5)
129.5	3650.8(6)	$^{+0.42}_{-0.32}$	$\pm 2.1/\pm 0.5/\pm 2.1$	3801.6(7)	-5.3	50.8	1231.0(5)
130.0	3636.7(6)	$^{+0.42}_{-0.32}$	$\pm 2.1/\pm 0.5/\pm 2.1$	3786.7(7)	-5.3	50.7	1216.1(5)

Table 196: Total VBF cross sections in the SM for a LHC CM energy of $\sqrt{s} = 14$ TeV, including QCD and EW corrections and their uncertainties for different Higgs boson masses M_{H}. For more details see Section I.5.1.c.

M_{H}[GeV]	σ^{VBF}[fb]	Δ_{scale}[%]	$\Delta_{\mathrm{PDF}/\alpha_{\mathrm{s}}/\mathrm{PDF}\oplus\alpha_{\mathrm{s}}}$[%]	$\sigma^{\mathrm{DIS}}_{\mathrm{NNLOQCD}}$[fb]	δ_{EW}[%]	σ_{γ}[fb]	$\sigma_{s\text{-channel}}$[fb]
120.0	4448.4(8)	$^{+0.46}_{-0.34}$	$\pm 2.1/\pm 0.5/\pm 2.1$	4640.4(8)	−5.4	59.8	1722.3(6)
120.5	4430.8(8)	$^{+0.46}_{-0.34}$	$\pm 2.1/\pm 0.5/\pm 2.1$	4622.1(8)	−5.4	59.7	1700.5(7)
121.0	4413.6(8)	$^{+0.46}_{-0.34}$	$\pm 2.1/\pm 0.5/\pm 2.1$	4603.8(8)	−5.4	59.5	1678.6(6)
121.5	4396.3(8)	$^{+0.46}_{-0.34}$	$\pm 2.1/\pm 0.5/\pm 2.1$	4585.6(8)	−5.4	59.4	1657.0(6)
122.0	4379.0(8)	$^{+0.46}_{-0.34}$	$\pm 2.1/\pm 0.5/\pm 2.1$	4567.6(8)	−5.4	59.3	1636.0(6)
122.5	4362.0(8)	$^{+0.46}_{-0.34}$	$\pm 2.1/\pm 0.5/\pm 2.1$	4549.6(8)	−5.4	59.2	1615.1(6)
123.0	4345.0(8)	$^{+0.46}_{-0.34}$	$\pm 2.1/\pm 0.5/\pm 2.1$	4531.8(8)	−5.4	59.0	1594.4(6)
123.5	4328.3(8)	$^{+0.46}_{-0.34}$	$\pm 2.1/\pm 0.5/\pm 2.1$	4514.0(8)	−5.4	58.9	1574.4(6)
124.0	4311.4(8)	$^{+0.45}_{-0.34}$	$\pm 2.1/\pm 0.5/\pm 2.1$	4496.3(8)	−5.4	58.8	1554.3(6)
124.1	4308.0(8)	$^{+0.45}_{-0.34}$	$\pm 2.1/\pm 0.5/\pm 2.1$	4492.8(8)	−5.4	58.7	1550.3(6)
124.2	4304.8(8)	$^{+0.45}_{-0.34}$	$\pm 2.1/\pm 0.5/\pm 2.1$	4489.3(8)	−5.4	58.7	1546.8(6)
124.3	4301.4(8)	$^{+0.45}_{-0.34}$	$\pm 2.1/\pm 0.5/\pm 2.1$	4485.8(8)	−5.4	58.7	1542.9(6)
124.4	4298.2(8)	$^{+0.45}_{-0.34}$	$\pm 2.1/\pm 0.5/\pm 2.1$	4482.2(8)	−5.4	58.7	1538.9(6)
124.5	4294.8(8)	$^{+0.45}_{-0.34}$	$\pm 2.1/\pm 0.5/\pm 2.1$	4478.7(8)	−5.4	58.6	1535.2(6)
124.6	4291.4(8)	$^{+0.45}_{-0.34}$	$\pm 2.1/\pm 0.5/\pm 2.1$	4475.2(8)	−5.4	58.6	1531.4(6)
124.7	4288.2(8)	$^{+0.45}_{-0.34}$	$\pm 2.1/\pm 0.5/\pm 2.1$	4471.7(8)	−5.4	58.6	1527.4(6)
124.8	4284.9(8)	$^{+0.45}_{-0.34}$	$\pm 2.1/\pm 0.5/\pm 2.1$	4468.2(8)	−5.4	58.6	1524.0(6)
124.9	4281.4(8)	$^{+0.45}_{-0.34}$	$\pm 2.1/\pm 0.5/\pm 2.1$	4464.7(8)	−5.4	58.5	1519.7(6)
125.0	4278.0(8)	$^{+0.45}_{-0.34}$	$\pm 2.1/\pm 0.5/\pm 2.1$	4461.2(8)	−5.4	58.5	1515.9(6)
125.09	4274.8(8)	$^{+0.45}_{-0.34}$	$\pm 2.1/\pm 0.5/\pm 2.1$	4457.8(8)	−5.4	58.5	1512.5(6)
125.1	4274.9(8)	$^{+0.45}_{-0.34}$	$\pm 2.1/\pm 0.5/\pm 2.1$	4457.8(8)	−5.4	58.5	1512.2(6)
125.2	4271.5(8)	$^{+0.45}_{-0.34}$	$\pm 2.1/\pm 0.5/\pm 2.1$	4454.3(8)	−5.4	58.5	1508.0(6)
125.3	4268.2(8)	$^{+0.45}_{-0.34}$	$\pm 2.1/\pm 0.5/\pm 2.1$	4450.8(8)	−5.4	58.4	1504.3(6)
125.4	4264.9(8)	$^{+0.45}_{-0.34}$	$\pm 2.1/\pm 0.5/\pm 2.1$	4447.3(8)	−5.4	58.4	1500.8(6)
125.5	4261.6(7)	$^{+0.45}_{-0.34}$	$\pm 2.1/\pm 0.5/\pm 2.1$	4443.8(8)	−5.4	58.4	1497.0(6)
125.6	4258.2(7)	$^{+0.45}_{-0.34}$	$\pm 2.1/\pm 0.5/\pm 2.1$	4440.4(8)	−5.4	58.4	1493.7(6)
125.7	4255.0(7)	$^{+0.45}_{-0.34}$	$\pm 2.1/\pm 0.5/\pm 2.1$	4436.9(8)	−5.4	58.3	1489.5(6)
125.8	4251.6(7)	$^{+0.45}_{-0.34}$	$\pm 2.1/\pm 0.5/\pm 2.1$	4433.4(8)	−5.4	58.3	1485.8(6)
125.9	4248.5(7)	$^{+0.45}_{-0.34}$	$\pm 2.1/\pm 0.5/\pm 2.1$	4430.0(8)	−5.4	58.3	1481.7(5)
126.0	4245.1(7)	$^{+0.45}_{-0.34}$	$\pm 2.1/\pm 0.5/\pm 2.1$	4426.5(8)	−5.4	58.3	1478.5(6)
126.5	4228.8(7)	$^{+0.45}_{-0.33}$	$\pm 2.1/\pm 0.5/\pm 2.1$	4409.3(8)	−5.4	58.1	1459.8(6)
127.0	4212.6(7)	$^{+0.45}_{-0.33}$	$\pm 2.1/\pm 0.5/\pm 2.1$	4392.2(8)	−5.4	58.0	1441.8(6)
127.5	4196.4(7)	$^{+0.45}_{-0.33}$	$\pm 2.1/\pm 0.5/\pm 2.1$	4375.2(8)	−5.4	57.9	1424.0(6)
128.0	4180.4(7)	$^{+0.44}_{-0.33}$	$\pm 2.1/\pm 0.5/\pm 2.1$	4358.2(8)	−5.4	57.8	1406.6(5)
128.5	4164.4(7)	$^{+0.44}_{-0.33}$	$\pm 2.1/\pm 0.5/\pm 2.1$	4341.3(8)	−5.4	57.6	1389.1(6)
129.0	4148.4(7)	$^{+0.44}_{-0.33}$	$\pm 2.1/\pm 0.5/\pm 2.1$	4324.6(8)	−5.4	57.5	1371.7(6)
129.5	4132.5(7)	$^{+0.44}_{-0.33}$	$\pm 2.1/\pm 0.5/\pm 2.1$	4307.9(8)	−5.4	57.4	1355.1(5)
130.0	4116.8(7)	$^{+0.44}_{-0.33}$	$\pm 2.1/\pm 0.5/\pm 2.1$	4291.3(8)	−5.4	57.3	1338.8(6)

Table 197: Fiducial VBF cross sections in the SM for a LHC CM energy of $\sqrt{s} = 7$ TeV, including QCD and EW corrections and their uncertainties for different Higgs boson masses $M_{\rm H}$. For more details see Section I.5.1.c. The numbers in the $\sigma^{\rm DIS}_{\rm NNLOQCD}$ column have been obtained from a linear interpolation. The interpolation was performed by fitting the cross section for $M_{\rm H} = \{120.0,\ 122.5,\ 125.0,\ 127.5,\ 130.0\}$ GeV to a linear function. The scale uncertainty in the column $\Delta_{\rm scale}$ was only computed for $M_{\rm H} = 125.0$ GeV.

$M_{\rm H}$[GeV]	$\sigma^{\rm VBF}$[fb]	$\Delta_{\rm scale}$[%]	$\Delta_{\rm PDF/\alpha_s/PDF\oplus\alpha_s}$[%]	$\sigma^{\rm DIS}_{\rm NNLOQCD}$[fb]	$\delta_{\rm EW}$[%]	σ_γ[fb]	$\sigma_{s\text{-chan}}$[fb]
120.0	625.8(9)	$^{+1.3}_{-1.6}$	$\pm 2.3/\pm 0.3/\pm 2.3$	655.7(10)	-6.1	10.1	9.3
120.5	623.5(8)	$^{+1.3}_{-1.6}$	$\pm 2.3/\pm 0.3/\pm 2.3$	653.2(9)	-6.1	10.1	9.2
121.0	621.2(8)	$^{+1.3}_{-1.6}$	$\pm 2.3/\pm 0.3/\pm 2.3$	650.7(8)	-6.1	10.1	9.1
121.5	618.8(7)	$^{+1.3}_{-1.6}$	$\pm 2.3/\pm 0.3/\pm 2.3$	648.2(8)	-6.1	10.1	9.0
122.0	616.4(7)	$^{+1.3}_{-1.6}$	$\pm 2.3/\pm 0.3/\pm 2.3$	645.7(7)	-6.1	10.0	8.8
122.5	614.1(6)	$^{+1.3}_{-1.6}$	$\pm 2.3/\pm 0.3/\pm 2.3$	643.2(6)	-6.1	10.0	8.7
123.0	611.7(6)	$^{+1.3}_{-1.6}$	$\pm 2.3/\pm 0.3/\pm 2.3$	640.7(6)	-6.1	10.0	8.6
123.5	609.4(5)	$^{+1.3}_{-1.6}$	$\pm 2.3/\pm 0.3/\pm 2.3$	638.3(6)	-6.1	10.0	8.5
124.0	607.1(5)	$^{+1.3}_{-1.6}$	$\pm 2.3/\pm 0.3/\pm 2.3$	635.8(5)	-6.1	9.9	8.4
124.1	606.6(5)	$^{+1.3}_{-1.6}$	$\pm 2.3/\pm 0.3/\pm 2.3$	635.3(5)	-6.1	9.9	8.4
124.2	606.2(5)	$^{+1.3}_{-1.6}$	$\pm 2.3/\pm 0.3/\pm 2.3$	634.8(5)	-6.1	9.9	8.4
124.3	605.7(5)	$^{+1.3}_{-1.6}$	$\pm 2.3/\pm 0.3/\pm 2.3$	634.3(5)	-6.1	9.9	8.4
124.4	605.2(5)	$^{+1.3}_{-1.6}$	$\pm 2.3/\pm 0.3/\pm 2.3$	633.8(5)	-6.1	9.9	8.3
124.5	604.8(5)	$^{+1.3}_{-1.6}$	$\pm 2.3/\pm 0.3/\pm 2.3$	633.3(5)	-6.1	9.9	8.3
124.6	604.3(5)	$^{+1.3}_{-1.6}$	$\pm 2.3/\pm 0.3/\pm 2.3$	632.8(5)	-6.1	9.9	8.3
124.7	603.8(5)	$^{+1.3}_{-1.6}$	$\pm 2.3/\pm 0.3/\pm 2.3$	632.3(5)	-6.1	9.9	8.3
124.8	603.4(5)	$^{+1.3}_{-1.6}$	$\pm 2.3/\pm 0.3/\pm 2.3$	631.8(5)	-6.1	9.9	8.2
124.9	602.9(5)	$^{+1.3}_{-1.6}$	$\pm 2.3/\pm 0.3/\pm 2.3$	631.3(5)	-6.1	9.9	8.2
125.0	602.4(5)	$^{+1.3}_{-1.6}$	$\pm 2.3/\pm 0.3/\pm 2.3$	630.8(5)	-6.1	9.9	8.2
125.09	602.0(5)	$^{+1.3}_{-1.6}$	$\pm 2.3/\pm 0.3/\pm 2.3$	630.3(5)	-6.1	9.9	8.2
125.1	602.0(5)	$^{+1.3}_{-1.6}$	$\pm 2.3/\pm 0.3/\pm 2.3$	630.3(5)	-6.1	9.9	8.2
125.2	601.5(5)	$^{+1.3}_{-1.6}$	$\pm 2.3/\pm 0.3/\pm 2.3$	629.8(5)	-6.1	9.9	8.2
125.3	601.1(5)	$^{+1.3}_{-1.6}$	$\pm 2.3/\pm 0.3/\pm 2.3$	629.3(5)	-6.1	9.9	8.2
125.4	600.5(5)	$^{+1.3}_{-1.6}$	$\pm 2.3/\pm 0.3/\pm 2.3$	628.8(5)	-6.1	9.9	8.1
125.5	600.1(5)	$^{+1.3}_{-1.6}$	$\pm 2.3/\pm 0.3/\pm 2.3$	628.3(5)	-6.1	9.9	8.1
125.6	599.7(5)	$^{+1.3}_{-1.6}$	$\pm 2.3/\pm 0.3/\pm 2.3$	627.8(5)	-6.1	9.9	8.1
125.7	599.2(5)	$^{+1.3}_{-1.6}$	$\pm 2.3/\pm 0.3/\pm 2.3$	627.3(5)	-6.1	9.9	8.1
125.8	598.7(5)	$^{+1.3}_{-1.6}$	$\pm 2.3/\pm 0.3/\pm 2.3$	626.8(5)	-6.1	9.9	8.1
125.9	598.2(5)	$^{+1.3}_{-1.6}$	$\pm 2.3/\pm 0.3/\pm 2.3$	626.3(5)	-6.1	9.9	8.0
126.0	597.8(5)	$^{+1.3}_{-1.6}$	$\pm 2.3/\pm 0.3/\pm 2.3$	625.8(5)	-6.1	9.9	8.0
126.5	595.4(5)	$^{+1.3}_{-1.6}$	$\pm 2.3/\pm 0.3/\pm 2.3$	623.3(6)	-6.1	9.8	7.9
127.0	593.1(6)	$^{+1.3}_{-1.6}$	$\pm 2.3/\pm 0.3/\pm 2.3$	620.8(6)	-6.0	9.8	7.8
127.5	590.8(6)	$^{+1.3}_{-1.6}$	$\pm 2.3/\pm 0.3/\pm 2.3$	618.4(6)	-6.0	9.8	7.7
128.0	588.5(7)	$^{+1.3}_{-1.6}$	$\pm 2.3/\pm 0.3/\pm 2.3$	615.9(7)	-6.0	9.8	7.6
128.5	586.1(7)	$^{+1.3}_{-1.6}$	$\pm 2.3/\pm 0.3/\pm 2.3$	613.4(8)	-6.0	9.7	7.5
129.0	583.8(8)	$^{+1.3}_{-1.6}$	$\pm 2.3/\pm 0.3/\pm 2.3$	610.9(8)	-6.0	9.7	7.5
129.5	581.5(8)	$^{+1.3}_{-1.6}$	$\pm 2.3/\pm 0.3/\pm 2.3$	608.4(9)	-6.0	9.7	7.4
130.0	579.1(9)	$^{+1.3}_{-1.6}$	$\pm 2.3/\pm 0.3/\pm 2.3$	605.9(10)	-6.0	9.7	7.3

Table 198: Fiducial VBF cross sections in the SM for a LHC CM energy of $\sqrt{s} = 8$ TeV, including QCD and EW corrections and their uncertainties for different Higgs boson masses M_{H}. For more details see Section I.5.1.c. The numbers in the $\sigma^{\mathrm{DIS}}_{\mathrm{NNLOQCD}}$ column have been obtained from a linear interpolation. The interpolation was performed by fitting the cross section for $M_{\mathrm{H}} = \{120.0, 122.5, 125.0, 127.5, 130.0\}$ GeV to a linear function. The scale uncertainty in the column Δ_{scale} was only computed for $M_{\mathrm{H}} = 125.0$ GeV.

M_{H}[GeV]	σ^{VBF}[fb]	Δ_{scale}[%]	$\Delta_{\mathrm{PDF}/\alpha_{\mathrm{s}}/\mathrm{PDF}\oplus\alpha_{\mathrm{s}}}$[%]	$\sigma^{\mathrm{DIS}}_{\mathrm{NNLOQCD}}$[fb]	δ_{EW}[%]	σ_{γ}[fb]	$\sigma_{s\text{-chan}}$[fb]
120.0	824.9(11)	$^{+1.3}_{-1.5}$	$\pm 2.3/\pm 0.3/\pm 2.3$	865.7(12)	−6.3	13.4	12.4
120.5	821.9(11)	$^{+1.3}_{-1.5}$	$\pm 2.3/\pm 0.3/\pm 2.3$	862.6(11)	−6.3	13.3	12.3
121.0	819.1(10)	$^{+1.3}_{-1.5}$	$\pm 2.3/\pm 0.3/\pm 2.3$	859.5(11)	−6.3	13.3	12.2
121.5	816.2(9)	$^{+1.3}_{-1.5}$	$\pm 2.3/\pm 0.3/\pm 2.3$	856.4(10)	−6.2	13.3	12.0
122.0	813.3(8)	$^{+1.3}_{-1.5}$	$\pm 2.3/\pm 0.3/\pm 2.3$	853.3(9)	−6.2	13.2	11.9
122.5	810.4(8)	$^{+1.3}_{-1.5}$	$\pm 2.3/\pm 0.3/\pm 2.3$	850.2(8)	−6.2	13.2	11.7
123.0	807.5(7)	$^{+1.3}_{-1.5}$	$\pm 2.3/\pm 0.3/\pm 2.3$	847.1(8)	−6.2	13.2	11.6
123.5	804.7(7)	$^{+1.3}_{-1.5}$	$\pm 2.3/\pm 0.3/\pm 2.3$	844.1(7)	−6.2	13.1	11.4
124.0	801.6(6)	$^{+1.3}_{-1.5}$	$\pm 2.3/\pm 0.3/\pm 2.3$	841.0(7)	−6.2	13.1	11.3
124.1	801.1(6)	$^{+1.3}_{-1.5}$	$\pm 2.3/\pm 0.3/\pm 2.3$	840.3(7)	−6.2	13.1	11.3
124.2	800.6(6)	$^{+1.3}_{-1.5}$	$\pm 2.3/\pm 0.3/\pm 2.3$	839.7(7)	−6.2	13.1	11.2
124.3	799.9(6)	$^{+1.3}_{-1.5}$	$\pm 2.3/\pm 0.3/\pm 2.3$	839.1(7)	−6.2	13.1	11.2
124.4	799.4(6)	$^{+1.3}_{-1.5}$	$\pm 2.3/\pm 0.3/\pm 2.3$	838.5(7)	−6.2	13.1	11.2
124.5	798.9(6)	$^{+1.3}_{-1.5}$	$\pm 2.3/\pm 0.3/\pm 2.3$	837.9(7)	−6.2	13.1	11.2
124.6	798.2(6)	$^{+1.3}_{-1.5}$	$\pm 2.3/\pm 0.3/\pm 2.3$	837.2(7)	−6.2	13.1	11.1
124.7	797.6(6)	$^{+1.3}_{-1.5}$	$\pm 2.3/\pm 0.3/\pm 2.3$	836.6(7)	−6.2	13.1	11.1
124.8	797.1(6)	$^{+1.3}_{-1.5}$	$\pm 2.3/\pm 0.3/\pm 2.3$	836.0(7)	−6.2	13.1	11.1
124.9	796.6(6)	$^{+1.3}_{-1.5}$	$\pm 2.3/\pm 0.3/\pm 2.3$	835.4(7)	−6.2	13.1	11.1
125.0	795.9(6)	$^{+1.3}_{-1.5}$	$\pm 2.3/\pm 0.3/\pm 2.3$	834.8(7)	−6.2	13.1	11.1
125.09	795.4(6)	$^{+1.3}_{-1.5}$	$\pm 2.3/\pm 0.3/\pm 2.3$	834.1(7)	−6.2	13.1	11.0
125.1	795.3(6)	$^{+1.3}_{-1.5}$	$\pm 2.3/\pm 0.3/\pm 2.3$	834.1(7)	−6.2	13.1	11.0
125.2	794.8(6)	$^{+1.3}_{-1.5}$	$\pm 2.3/\pm 0.3/\pm 2.3$	833.5(7)	−6.2	13.0	11.0
125.3	794.3(6)	$^{+1.3}_{-1.5}$	$\pm 2.3/\pm 0.3/\pm 2.3$	832.9(7)	−6.2	13.0	11.0
125.4	793.6(6)	$^{+1.3}_{-1.5}$	$\pm 2.3/\pm 0.3/\pm 2.3$	832.3(7)	−6.2	13.0	10.9
125.5	793.0(6)	$^{+1.3}_{-1.5}$	$\pm 2.3/\pm 0.3/\pm 2.3$	831.7(7)	−6.2	13.0	10.9
125.6	792.4(6)	$^{+1.3}_{-1.5}$	$\pm 2.3/\pm 0.3/\pm 2.3$	831.1(7)	−6.2	13.0	10.9
125.7	791.8(6)	$^{+1.3}_{-1.5}$	$\pm 2.3/\pm 0.3/\pm 2.3$	830.4(7)	−6.2	13.0	10.8
125.8	791.2(6)	$^{+1.3}_{-1.5}$	$\pm 2.3/\pm 0.3/\pm 2.3$	829.8(7)	−6.2	13.0	10.8
125.9	790.7(6)	$^{+1.3}_{-1.5}$	$\pm 2.3/\pm 0.3/\pm 2.3$	829.2(7)	−6.2	13.0	10.8
126.0	790.1(6)	$^{+1.3}_{-1.5}$	$\pm 2.3/\pm 0.3/\pm 2.3$	828.6(7)	−6.2	13.0	10.8
126.5	787.1(7)	$^{+1.3}_{-1.5}$	$\pm 2.3/\pm 0.3/\pm 2.3$	825.5(7)	−6.2	13.0	10.7
127.0	784.3(7)	$^{+1.3}_{-1.5}$	$\pm 2.3/\pm 0.3/\pm 2.3$	822.4(8)	−6.2	12.9	10.5
127.5	781.5(8)	$^{+1.3}_{-1.5}$	$\pm 2.3/\pm 0.3/\pm 2.3$	819.3(8)	−6.2	12.9	10.4
128.0	778.5(8)	$^{+1.3}_{-1.5}$	$\pm 2.3/\pm 0.3/\pm 2.3$	816.2(9)	−6.2	12.9	10.3
128.5	775.7(9)	$^{+1.3}_{-1.5}$	$\pm 2.3/\pm 0.3/\pm 2.3$	813.1(10)	−6.2	12.8	10.2
129.0	772.8(10)	$^{+1.3}_{-1.5}$	$\pm 2.3/\pm 0.3/\pm 2.3$	810.0(11)	−6.2	12.8	10.0
129.5	769.8(11)	$^{+1.3}_{-1.5}$	$\pm 2.3/\pm 0.3/\pm 2.3$	806.9(11)	−6.2	12.8	9.9
130.0	766.9(11)	$^{+1.3}_{-1.5}$	$\pm 2.3/\pm 0.3/\pm 2.3$	803.8(12)	−6.2	12.8	9.8

Table 199: Fiducial VBF cross sections in the SM for a LHC CM energy of $\sqrt{s} = 13$ TeV, including QCD and EW corrections and their uncertainties for different Higgs boson masses M_{H}. For more details see Section I.5.1.c. The numbers in the $\sigma^{\mathrm{DIS}}_{\mathrm{NNLOQCD}}$ column have been obtained from a linear interpolation. The interpolation was performed by fitting the cross section for $M_{\mathrm{H}} = \{120.0, 122.5, 125.0, 127.5, 130.0\}$ GeV to a linear function. The scale uncertainty in the column Δ_{scale} was only computed for $M_{\mathrm{H}} = 125.0$ GeV.

M_{H}[GeV]	σ^{VBF}[fb]	Δ_{scale}[%]	$\Delta_{\mathrm{PDF}/\alpha_{\mathrm{s}}/\mathrm{PDF}\oplus\alpha_{\mathrm{s}}}$[%]	$\sigma^{\mathrm{DIS}}_{\mathrm{NNLOQCD}}$[fb]	δ_{EW}[%]	σ_{γ}[fb]	$\sigma_{s\text{-chan}}$[fb]
120.0	2038.9(45)	$^{+1.3}_{-1.2}$	$\pm 2.1/\pm 0.4/\pm 2.2$	2152.8(48)	−6.8	33.0	32.4
120.5	2032.3(41)	$^{+1.3}_{-1.2}$	$\pm 2.1/\pm 0.4/\pm 2.2$	2145.9(44)	−6.8	32.9	32.1
121.0	2026.3(36)	$^{+1.3}_{-1.2}$	$\pm 2.1/\pm 0.4/\pm 2.2$	2139.1(39)	−6.8	32.8	31.7
121.5	2020.0(32)	$^{+1.3}_{-1.2}$	$\pm 2.1/\pm 0.4/\pm 2.2$	2132.2(35)	−6.8	32.8	31.3
122.0	2013.4(28)	$^{+1.3}_{-1.2}$	$\pm 2.1/\pm 0.4/\pm 2.2$	2125.4(30)	−6.8	32.7	30.9
122.5	2007.1(24)	$^{+1.3}_{-1.2}$	$\pm 2.1/\pm 0.4/\pm 2.2$	2118.5(26)	−6.8	32.6	30.6
123.0	2000.5(20)	$^{+1.3}_{-1.2}$	$\pm 2.1/\pm 0.4/\pm 2.2$	2111.7(21)	−6.8	32.6	30.2
123.5	1994.5(16)	$^{+1.3}_{-1.2}$	$\pm 2.1/\pm 0.4/\pm 2.2$	2104.8(17)	−6.8	32.5	29.9
124.0	1987.9(13)	$^{+1.3}_{-1.2}$	$\pm 2.1/\pm 0.4/\pm 2.2$	2097.9(14)	−6.8	32.4	29.6
124.1	1986.9(12)	$^{+1.3}_{-1.2}$	$\pm 2.1/\pm 0.4/\pm 2.2$	2096.6(13)	−6.8	32.4	29.5
124.2	1985.3(12)	$^{+1.3}_{-1.2}$	$\pm 2.1/\pm 0.4/\pm 2.2$	2095.2(12)	−6.8	32.4	29.5
124.3	1984.2(11)	$^{+1.3}_{-1.2}$	$\pm 2.1/\pm 0.4/\pm 2.2$	2093.8(12)	−6.8	32.4	29.4
124.4	1982.7(11)	$^{+1.3}_{-1.2}$	$\pm 2.1/\pm 0.4/\pm 2.2$	2092.5(11)	−6.8	32.4	29.3
124.5	1981.4(10)	$^{+1.3}_{-1.2}$	$\pm 2.1/\pm 0.4/\pm 2.2$	2091.1(11)	−6.8	32.4	29.2
124.6	1980.4(10)	$^{+1.3}_{-1.2}$	$\pm 2.1/\pm 0.4/\pm 2.2$	2089.7(11)	−6.8	32.4	29.2
124.7	1979.2(10)	$^{+1.3}_{-1.2}$	$\pm 2.1/\pm 0.4/\pm 2.2$	2088.4(10)	−6.8	32.4	29.1
124.8	1977.6(9)	$^{+1.3}_{-1.2}$	$\pm 2.1/\pm 0.4/\pm 2.2$	2087.0(10)	−6.8	32.3	29.0
124.9	1976.4(9)	$^{+1.3}_{-1.2}$	$\pm 2.1/\pm 0.4/\pm 2.2$	2085.6(10)	−6.8	32.3	29.0
125.0	1975.4(9)	$^{+1.3}_{-1.2}$	$\pm 2.1/\pm 0.4/\pm 2.2$	2084.2(10)	−6.8	32.3	29.0
125.09	1974.0(9)	$^{+1.3}_{-1.2}$	$\pm 2.1/\pm 0.4/\pm 2.2$	2082.9(10)	−6.8	32.3	28.9
125.1	1974.1(9)	$^{+1.3}_{-1.2}$	$\pm 2.1/\pm 0.4/\pm 2.2$	2082.9(10)	−6.8	32.3	28.9
125.2	1972.8(9)	$^{+1.3}_{-1.2}$	$\pm 2.1/\pm 0.4/\pm 2.2$	2081.5(10)	−6.8	32.3	28.8
125.3	1971.4(10)	$^{+1.3}_{-1.2}$	$\pm 2.1/\pm 0.4/\pm 2.2$	2080.1(10)	−6.8	32.3	28.7
125.4	1970.1(10)	$^{+1.3}_{-1.2}$	$\pm 2.1/\pm 0.4/\pm 2.2$	2078.8(11)	−6.8	32.3	28.7
125.5	1968.8(10)	$^{+1.3}_{-1.2}$	$\pm 2.1/\pm 0.4/\pm 2.2$	2077.4(11)	−6.8	32.2	28.6
125.6	1967.6(11)	$^{+1.3}_{-1.2}$	$\pm 2.1/\pm 0.4/\pm 2.2$	2076.0(11)	−6.8	32.2	28.5
125.7	1966.2(11)	$^{+1.3}_{-1.2}$	$\pm 2.1/\pm 0.4/\pm 2.2$	2074.6(12)	−6.8	32.2	28.5
125.8	1965.1(12)	$^{+1.3}_{-1.2}$	$\pm 2.1/\pm 0.4/\pm 2.2$	2073.3(12)	−6.8	32.2	28.4
125.9	1963.6(12)	$^{+1.3}_{-1.2}$	$\pm 2.1/\pm 0.4/\pm 2.2$	2071.9(13)	−6.8	32.2	28.4
126.0	1962.6(13)	$^{+1.3}_{-1.2}$	$\pm 2.1/\pm 0.4/\pm 2.2$	2070.5(14)	−6.8	32.2	28.3
126.5	1956.2(16)	$^{+1.3}_{-1.2}$	$\pm 2.1/\pm 0.4/\pm 2.2$	2063.7(17)	−6.8	32.1	27.9
127.0	1949.7(20)	$^{+1.3}_{-1.2}$	$\pm 2.1/\pm 0.4/\pm 2.2$	2056.8(21)	−6.8	32.1	27.6
127.5	1943.5(24)	$^{+1.3}_{-1.2}$	$\pm 2.1/\pm 0.4/\pm 2.2$	2050.0(26)	−6.8	32.0	27.4
128.0	1937.2(28)	$^{+1.3}_{-1.2}$	$\pm 2.1/\pm 0.4/\pm 2.2$	2043.1(30)	−6.7	31.9	27.1
128.5	1930.7(32)	$^{+1.3}_{-1.2}$	$\pm 2.1/\pm 0.4/\pm 2.2$	2036.3(35)	−6.7	31.9	26.8
129.0	1924.4(36)	$^{+1.3}_{-1.2}$	$\pm 2.1/\pm 0.4/\pm 2.2$	2029.4(39)	−6.7	31.8	26.5
129.5	1917.7(41)	$^{+1.3}_{-1.2}$	$\pm 2.1/\pm 0.4/\pm 2.2$	2022.6(44)	−6.8	31.7	26.2
130.0	1911.5(45)	$^{+1.3}_{-1.2}$	$\pm 2.1/\pm 0.4/\pm 2.2$	2015.7(48)	−6.7	31.7	25.9

Table 200: Fiducial VBF cross sections in the SM for a LHC CM energy of $\sqrt{s} = 14$ TeV, including QCD and EW corrections and their uncertainties for different Higgs boson masses M_{H}. For more details see Section I.5.1.c. The numbers in the $\sigma^{\mathrm{DIS}}_{\mathrm{NNLOQCD}}$ column have been obtained from a linear interpolation. The interpolation was performed by fitting the cross section for $M_{\mathrm{H}} = \{120.0, 122.5, 125.0, 127.5, 130.0\}$ GeV to a linear function. The scale uncertainty in the column Δ_{scale} was only computed for $M_{\mathrm{H}} = 125.0$ GeV.

M_{H}[GeV]	σ^{VBF}[fb]	Δ_{scale}[%]	$\Delta_{\mathrm{PDF}/\alpha_{\mathrm{s}}/\mathrm{PDF}\oplus\alpha_{\mathrm{s}}}$[%]	$\sigma^{\mathrm{DIS}}_{\mathrm{NNLOQCD}}$[fb]	δ_{EW}[%]	σ_{γ}[fb]	$\sigma_{s\text{-chan}}$[fb]
120.0	2301.6(48)	$^{+1.5}_{-1.3}$	$\pm 2.1/\pm 0.4/\pm 2.1$	2432.4(51)	−6.9	37.4	37.0
120.5	2294.9(45)	$^{+1.5}_{-1.3}$	$\pm 2.1/\pm 0.4/\pm 2.1$	2425.4(48)	−6.9	37.3	36.6
121.0	2288.6(41)	$^{+1.5}_{-1.3}$	$\pm 2.1/\pm 0.4/\pm 2.1$	2418.3(44)	−6.9	37.2	36.2
121.5	2282.0(38)	$^{+1.5}_{-1.3}$	$\pm 2.1/\pm 0.4/\pm 2.1$	2411.3(41)	−6.9	37.1	35.8
122.0	2275.5(35)	$^{+1.5}_{-1.3}$	$\pm 2.1/\pm 0.4/\pm 2.1$	2404.3(38)	−6.9	37.1	35.4
122.5	2269.1(33)	$^{+1.5}_{-1.3}$	$\pm 2.1/\pm 0.4/\pm 2.1$	2397.3(35)	−6.9	37.0	35.0
123.0	2262.8(31)	$^{+1.5}_{-1.3}$	$\pm 2.1/\pm 0.4/\pm 2.1$	2390.3(33)	−6.9	36.9	34.6
123.5	2256.0(29)	$^{+1.5}_{-1.3}$	$\pm 2.1/\pm 0.4/\pm 2.1$	2383.2(31)	−6.9	36.9	34.2
124.0	2249.8(27)	$^{+1.5}_{-1.3}$	$\pm 2.1/\pm 0.4/\pm 2.1$	2376.2(29)	−6.9	36.8	33.8
124.1	2248.5(27)	$^{+1.5}_{-1.3}$	$\pm 2.1/\pm 0.4/\pm 2.1$	2374.8(29)	−6.9	36.8	33.7
124.2	2247.3(27)	$^{+1.5}_{-1.3}$	$\pm 2.1/\pm 0.4/\pm 2.1$	2373.4(29)	−6.9	36.8	33.7
124.3	2245.9(27)	$^{+1.5}_{-1.3}$	$\pm 2.1/\pm 0.4/\pm 2.1$	2372.0(29)	−6.9	36.7	33.6
124.4	2244.2(26)	$^{+1.5}_{-1.3}$	$\pm 2.1/\pm 0.4/\pm 2.1$	2370.6(28)	−6.9	36.7	33.5
124.5	2243.1(26)	$^{+1.5}_{-1.3}$	$\pm 2.1/\pm 0.4/\pm 2.1$	2369.2(28)	−6.9	36.7	33.4
124.6	2241.9(26)	$^{+1.5}_{-1.3}$	$\pm 2.1/\pm 0.4/\pm 2.1$	2367.8(28)	−6.9	36.7	33.4
124.7	2240.5(26)	$^{+1.5}_{-1.3}$	$\pm 2.1/\pm 0.4/\pm 2.1$	2366.4(28)	−6.9	36.7	33.3
124.8	2239.0(26)	$^{+1.5}_{-1.3}$	$\pm 2.1/\pm 0.4/\pm 2.1$	2365.0(28)	−6.9	36.7	33.2
124.9	2237.5(26)	$^{+1.5}_{-1.3}$	$\pm 2.1/\pm 0.4/\pm 2.1$	2363.6(28)	−6.9	36.7	33.1
125.0	2236.6(26)	$^{+1.5}_{-1.3}$	$\pm 2.1/\pm 0.4/\pm 2.1$	2362.2(28)	−6.9	36.7	33.1
125.09	2235.3(26)	$^{+1.5}_{-1.3}$	$\pm 2.1/\pm 0.4/\pm 2.1$	2360.8(28)	−6.9	36.6	33.0
125.1	2235.2(26)	$^{+1.5}_{-1.3}$	$\pm 2.1/\pm 0.4/\pm 2.1$	2360.8(28)	−6.9	36.6	33.0
125.2	2233.8(26)	$^{+1.5}_{-1.3}$	$\pm 2.1/\pm 0.4/\pm 2.1$	2359.4(28)	−6.9	36.6	32.9
125.3	2232.6(26)	$^{+1.5}_{-1.3}$	$\pm 2.1/\pm 0.4/\pm 2.1$	2358.0(28)	−6.9	36.6	32.9
125.4	2231.4(26)	$^{+1.5}_{-1.3}$	$\pm 2.1/\pm 0.4/\pm 2.1$	2356.6(28)	−6.9	36.6	32.8
125.5	2230.0(26)	$^{+1.5}_{-1.3}$	$\pm 2.1/\pm 0.4/\pm 2.1$	2355.2(28)	−6.9	36.6	32.7
125.6	2228.6(26)	$^{+1.5}_{-1.3}$	$\pm 2.1/\pm 0.4/\pm 2.1$	2353.8(28)	−6.9	36.6	32.6
125.7	2227.5(27)	$^{+1.5}_{-1.3}$	$\pm 2.1/\pm 0.4/\pm 2.1$	2352.4(29)	−6.9	36.6	32.6
125.8	2226.1(27)	$^{+1.5}_{-1.3}$	$\pm 2.1/\pm 0.4/\pm 2.1$	2351.0(29)	−6.9	36.5	32.5
125.9	2224.7(27)	$^{+1.5}_{-1.3}$	$\pm 2.1/\pm 0.4/\pm 2.1$	2349.6(29)	−6.9	36.5	32.4
126.0	2223.5(27)	$^{+1.5}_{-1.3}$	$\pm 2.1/\pm 0.4/\pm 2.1$	2348.2(29)	−6.9	36.5	32.3
126.5	2217.0(29)	$^{+1.5}_{-1.3}$	$\pm 2.1/\pm 0.4/\pm 2.1$	2341.1(31)	−6.9	36.4	32.0
127.0	2210.3(31)	$^{+1.5}_{-1.3}$	$\pm 2.1/\pm 0.4/\pm 2.1$	2334.1(33)	−6.9	36.4	31.6
127.5	2204.0(33)	$^{+1.5}_{-1.3}$	$\pm 2.1/\pm 0.4/\pm 2.1$	2327.1(35)	−6.9	36.3	31.3
128.0	2197.6(35)	$^{+1.5}_{-1.3}$	$\pm 2.1/\pm 0.4/\pm 2.1$	2320.1(38)	−6.8	36.2	30.9
128.5	2190.9(38)	$^{+1.5}_{-1.3}$	$\pm 2.1/\pm 0.4/\pm 2.1$	2313.1(41)	−6.8	36.2	30.6
129.0	2184.5(41)	$^{+1.5}_{-1.3}$	$\pm 2.1/\pm 0.4/\pm 2.1$	2306.0(44)	−6.8	36.1	30.3
129.5	2177.9(45)	$^{+1.5}_{-1.3}$	$\pm 2.1/\pm 0.4/\pm 2.1$	2299.0(48)	−6.8	36.0	29.9
130.0	2171.5(48)	$^{+1.5}_{-1.3}$	$\pm 2.1/\pm 0.4/\pm 2.1$	2292.0(51)	−6.8	35.9	29.6

Table 201: Inclusive VBF cross sections for a LHC CM energy of $\sqrt{s} = 7$ TeV, at NNLO QCD, with an on shell Higgs or with off-shell effects included in the complex-pole scheme, together with their uncertainties. For more details see Section I.5.1.a.iv.

$M_{\rm H}$[GeV]	$\sigma^{\rm VBF}_{\rm OS}$[fb]	$\sigma^{\rm VBF}_{\rm CPS}$[fb]	$\delta_{\rm CPS}$	$\Delta_{\rm scale}$[%]	$\Delta_{\rm PDF}$[%]	$\Delta_{\alpha_{\rm s}}$[%]	$\Delta_{\rm PDF\oplus\alpha_{\rm s}}$[%]
120.0	1339	1353	1.0	$^{+0.2}_{-0.2}$	±1.9	±0.4	±1.9
120.5	1332	1346	1.1	$^{+0.2}_{-0.2}$	±1.9	±0.4	±1.9
121.0	1326	1340	1.1	$^{+0.2}_{-0.2}$	±1.9	±0.4	±1.9
121.5	1320	1334	1.1	$^{+0.2}_{-0.2}$	±1.9	±0.4	±1.9
122.0	1313	1327	1.1	$^{+0.2}_{-0.2}$	±1.9	±0.4	±1.9
122.5	1307	1321	1.1	$^{+0.2}_{-0.2}$	±1.9	±0.4	±1.9
123.0	1301	1315	1.1	$^{+0.2}_{-0.2}$	±1.9	±0.4	±1.9
123.5	1295	1309	1.1	$^{+0.2}_{-0.2}$	±1.9	±0.4	±1.9
124.0	1288	1303	1.2	$^{+0.2}_{-0.2}$	±1.9	±0.4	±1.9
124.1	1287	1302	1.2	$^{+0.2}_{-0.2}$	±1.9	±0.4	±1.9
124.2	1286	1301	1.2	$^{+0.2}_{-0.2}$	±1.9	±0.4	±1.9
124.3	1285	1299	1.1	$^{+0.2}_{-0.2}$	±1.9	±0.4	±1.9
124.4	1283	1298	1.2	$^{+0.2}_{-0.2}$	±1.9	±0.4	±1.9
124.5	1282	1297	1.2	$^{+0.2}_{-0.2}$	±1.9	±0.4	±1.9
124.6	1281	1296	1.2	$^{+0.2}_{-0.2}$	±1.9	±0.4	±1.9
124.7	1280	1295	1.2	$^{+0.2}_{-0.2}$	±1.9	±0.4	±1.9
124.8	1279	1293	1.1	$^{+0.2}_{-0.2}$	±1.9	±0.4	±1.9
124.9	1277	1292	1.2	$^{+0.2}_{-0.2}$	±1.9	±0.4	±1.9
125.0	1276	1291	1.2	$^{+0.2}_{-0.2}$	±1.9	±0.4	±1.9
125.09	1275	1290	1.2	$^{+0.2}_{-0.2}$	±1.9	±0.4	±1.9
125.1	1275	1290	1.2	$^{+0.2}_{-0.2}$	±1.9	±0.4	±1.9
125.2	1274	1289	1.2	$^{+0.2}_{-0.2}$	±1.9	±0.4	±1.9
125.3	1272	1288	1.3	$^{+0.2}_{-0.2}$	±1.9	±0.4	±1.9
125.4	1271	1286	1.2	$^{+0.2}_{-0.2}$	±1.9	±0.4	±1.9
125.5	1270	1285	1.2	$^{+0.2}_{-0.2}$	±1.9	±0.4	±1.9
125.6	1269	1284	1.2	$^{+0.2}_{-0.2}$	±1.9	±0.4	±1.9
125.7	1268	1283	1.2	$^{+0.2}_{-0.2}$	±1.9	±0.4	±1.9
125.8	1266	1282	1.3	$^{+0.2}_{-0.2}$	±1.9	±0.4	±1.9
125.9	1265	1280	1.2	$^{+0.2}_{-0.2}$	±1.9	±0.4	±1.9
126.0	1264	1279	1.2	$^{+0.2}_{-0.2}$	±1.9	±0.4	±1.9
126.5	1258	1273	1.2	$^{+0.2}_{-0.2}$	±1.9	±0.4	±1.9
127.0	1252	1268	1.3	$^{+0.2}_{-0.2}$	±1.9	±0.4	±1.9
127.5	1247	1262	1.2	$^{+0.2}_{-0.2}$	±1.9	±0.4	±1.9
128.0	1240	1256	1.3	$^{+0.2}_{-0.2}$	±1.9	±0.4	±1.9
128.5	1235	1250	1.2	$^{+0.2}_{-0.2}$	±1.9	±0.4	±1.9
129.0	1229	1244	1.2	$^{+0.2}_{-0.2}$	±1.9	±0.4	±1.9
129.5	1223	1239	1.3	$^{+0.2}_{-0.2}$	±1.9	±0.4	±1.9
130.0	1217	1233	1.3	$^{+0.2}_{-0.2}$	±1.9	±0.4	±1.9

Table 202: Inclusive VBF cross sections for a LHC CM energy of $\sqrt{s} = 8$ TeV, at NNLO QCD, with an on shell Higgs or with off-shell effects included in the complex-pole scheme, together with their uncertainties. For more details see Section I.5.1.a.iv.

M_{H}[GeV]	$\sigma^{\mathrm{VBF}}_{\mathrm{OS}}$[fb]	$\sigma^{\mathrm{VBF}}_{\mathrm{CPS}}$[fb]	δ_{CPS}	Δ_{scale}[%]	Δ_{PDF}[%]	$\Delta_{\alpha_{\mathrm{s}}}$[%]	$\Delta_{\mathrm{PDF}\oplus\alpha_{\mathrm{s}}}$[%]
120.0	1727	1748	1.2	$^{+0.3}_{-0.2}$	±1.9	±0.5	±1.9
120.5	1719	1741	1.3	$^{+0.2}_{-0.2}$	±1.9	±0.5	±1.9
121.0	1711	1733	1.3	$^{+0.3}_{-0.2}$	±1.9	±0.5	±1.9
121.5	1704	1725	1.2	$^{+0.2}_{-0.2}$	±1.9	±0.5	±1.9
122.0	1695	1717	1.3	$^{+0.3}_{-0.2}$	±1.9	±0.5	±1.9
122.5	1688	1710	1.3	$^{+0.2}_{-0.2}$	±1.9	±0.5	±1.9
123.0	1680	1702	1.3	$^{+0.3}_{-0.2}$	±1.9	±0.5	±1.9
123.5	1673	1695	1.3	$^{+0.2}_{-0.2}$	±1.9	±0.5	±1.9
124.0	1665	1687	1.3	$^{+0.3}_{-0.2}$	±1.9	±0.5	±1.9
124.1	1663	1685	1.3	$^{+0.3}_{-0.2}$	±1.9	±0.5	±1.9
124.2	1662	1684	1.3	$^{+0.3}_{-0.2}$	±1.9	±0.5	±1.9
124.3	1660	1682	1.3	$^{+0.3}_{-0.2}$	±1.9	±0.5	±1.9
124.4	1659	1681	1.3	$^{+0.3}_{-0.2}$	±1.9	±0.5	±1.9
124.5	1657	1679	1.3	$^{+0.3}_{-0.2}$	±1.9	±0.5	±1.9
124.6	1656	1678	1.3	$^{+0.3}_{-0.2}$	±1.9	±0.5	±1.9
124.7	1654	1676	1.3	$^{+0.3}_{-0.2}$	±1.9	±0.5	±1.9
124.8	1653	1675	1.3	$^{+0.3}_{-0.2}$	±1.9	±0.5	±1.9
124.9	1651	1673	1.3	$^{+0.3}_{-0.2}$	±1.9	±0.5	±1.9
125.0	1650	1672	1.3	$^{+0.3}_{-0.2}$	±1.9	±0.5	±1.9
125.09	1648	1670	1.3	$^{+0.3}_{-0.2}$	±1.9	±0.5	±1.9
125.1	1648	1670	1.3	$^{+0.3}_{-0.2}$	±1.9	±0.5	±1.9
125.2	1647	1669	1.3	$^{+0.3}_{-0.2}$	±1.9	±0.5	±1.9
125.3	1645	1667	1.3	$^{+0.3}_{-0.2}$	±1.9	±0.5	±1.9
125.4	1644	1666	1.3	$^{+0.3}_{-0.2}$	±1.9	±0.5	±1.9
125.5	1642	1664	1.3	$^{+0.3}_{-0.2}$	±1.9	±0.5	±1.9
125.6	1641	1663	1.3	$^{+0.3}_{-0.2}$	±1.9	±0.5	±1.9
125.7	1639	1661	1.3	$^{+0.3}_{-0.2}$	±1.9	±0.5	±1.9
125.8	1638	1660	1.3	$^{+0.3}_{-0.2}$	±1.9	±0.5	±1.9
125.9	1636	1659	1.4	$^{+0.3}_{-0.2}$	±1.9	±0.5	±1.9
126.0	1635	1657	1.3	$^{+0.3}_{-0.2}$	±1.9	±0.5	±1.9
126.5	1628	1650	1.4	$^{+0.2}_{-0.2}$	±1.9	±0.5	±1.9
127.0	1620	1643	1.4	$^{+0.2}_{-0.2}$	±1.9	±0.4	±1.9
127.5	1613	1635	1.4	$^{+0.2}_{-0.2}$	±1.9	±0.4	±1.9
128.0	1605	1629	1.5	$^{+0.2}_{-0.2}$	±1.9	±0.4	±1.9
128.5	1599	1621	1.4	$^{+0.2}_{-0.2}$	±1.9	±0.4	±1.9
129.0	1591	1614	1.4	$^{+0.2}_{-0.2}$	±1.9	±0.4	±1.9
129.5	1584	1607	1.5	$^{+0.2}_{-0.2}$	±1.9	±0.4	±1.9
130.0	1577	1600	1.5	$^{+0.2}_{-0.2}$	±1.9	±0.4	±1.9

Table 203: Inclusive VBF cross sections for a LHC CM energy of $\sqrt{s} = 13$ TeV, at NNLO QCD, with an on shell Higgs or with off-shell effects included in the complex-pole scheme, together with their uncertainties. For more details see Section I.5.1.a.iv.

$M_{\rm H}$[GeV]	$\sigma^{\rm VBF}_{\rm OS}$[fb]	$\sigma^{\rm VBF}_{\rm CPS}$[fb]	$\delta_{\rm CPS}$	$\Delta_{\rm scale}$[%]	$\Delta_{\rm PDF}$[%]	$\Delta_{\alpha_{\rm s}}$[%]	$\Delta_{\rm PDF\oplus\alpha_{\rm s}}$[%]
120.0	4086	4162	1.9	$^{+0.5}_{-0.2}$	±1.8	±0.6	±1.9
120.5	4072	4148	1.9	$^{+0.4}_{-0.3}$	±1.8	±0.6	±1.9
121.0	4053	4130	1.9	$^{+0.5}_{-0.2}$	±1.8	±0.6	±1.9
121.5	4039	4110	1.8	$^{+0.4}_{-0.3}$	±1.8	±0.6	±1.9
122.0	4020	4098	1.9	$^{+0.5}_{-0.2}$	±1.8	±0.6	±1.9
122.5	4007	4082	1.9	$^{+0.4}_{-0.3}$	±1.8	±0.6	±1.9
123.0	3988	4068	2.0	$^{+0.5}_{-0.2}$	±1.8	±0.6	±1.9
123.5	3975	4054	2.0	$^{+0.4}_{-0.3}$	±1.8	±0.6	±1.9
124.0	3957	4041	2.1	$^{+0.5}_{-0.2}$	±1.8	±0.6	±1.9
124.1	3953	4038	2.2	$^{+0.5}_{-0.2}$	±1.8	±0.6	±1.9
124.2	3950	4034	2.1	$^{+0.5}_{-0.2}$	±1.8	±0.6	±1.9
124.3	3947	4029	2.1	$^{+0.5}_{-0.2}$	±1.8	±0.6	±1.9
124.4	3944	4026	2.1	$^{+0.5}_{-0.2}$	±1.8	±0.6	±1.9
124.5	3941	4024	2.1	$^{+0.5}_{-0.2}$	±1.8	±0.6	±1.9
124.6	3938	4021	2.1	$^{+0.5}_{-0.2}$	±1.8	±0.6	±1.9
124.7	3935	4021	2.2	$^{+0.5}_{-0.2}$	±1.8	±0.6	±1.9
124.8	3931	4017	2.2	$^{+0.5}_{-0.2}$	±1.8	±0.6	±1.9
124.9	3928	4015	2.2	$^{+0.5}_{-0.2}$	±1.8	±0.6	±1.9
125.0	3925	4013	2.2	$^{+0.5}_{-0.2}$	±1.8	±0.6	±1.9
125.09	3922	4006	2.1	$^{+0.5}_{-0.2}$	±1.8	±0.6	±1.9
125.1	3922	4005	2.1	$^{+0.5}_{-0.2}$	±1.8	±0.6	±1.9
125.2	3919	4005	2.2	$^{+0.5}_{-0.2}$	±1.8	±0.6	±1.9
125.3	3916	4000	2.1	$^{+0.5}_{-0.2}$	±1.8	±0.6	±1.9
125.4	3913	4000	2.2	$^{+0.5}_{-0.2}$	±1.8	±0.6	±1.9
125.5	3910	3997	2.2	$^{+0.5}_{-0.2}$	±1.8	±0.6	±1.9
125.6	3906	3994	2.3	$^{+0.5}_{-0.2}$	±1.8	±0.6	±1.9
125.7	3903	3991	2.3	$^{+0.5}_{-0.2}$	±1.8	±0.6	±1.9
125.8	3900	3988	2.3	$^{+0.5}_{-0.2}$	±1.8	±0.6	±1.9
125.9	3897	3985	2.3	$^{+0.5}_{-0.2}$	±1.8	±0.6	±1.9
126.0	3894	3982	2.3	$^{+0.5}_{-0.2}$	±1.8	±0.6	±1.9
126.5	3881	3968	2.2	$^{+0.4}_{-0.3}$	±1.8	±0.6	±1.9
127.0	3863	3954	2.4	$^{+0.5}_{-0.2}$	±1.8	±0.6	±1.9
127.5	3851	3939	2.3	$^{+0.4}_{-0.3}$	±1.8	±0.6	±1.9
128.0	3833	3924	2.4	$^{+0.5}_{-0.2}$	±1.8	±0.6	±1.9
128.5	3820	3911	2.4	$^{+0.4}_{-0.3}$	±1.8	±0.6	±1.9
129.0	3803	3895	2.4	$^{+0.5}_{-0.2}$	±1.8	±0.6	±1.9
129.5	3790	3882	2.4	$^{+0.4}_{-0.3}$	±1.8	±0.6	±1.9
130.0	3773	3868	2.5	$^{+0.4}_{-0.2}$	±1.8	±0.6	±1.9

Table 204: Inclusive VBF cross sections for a LHC CM energy of $\sqrt{s} = 14$ TeV, at NNLO QCD, with an on shell Higgs or with off-shell effects included in the complex-pole scheme, together with their uncertainties. For more details see Section I.5.1.a.iv.

M_{H}[GeV]	$\sigma^{\mathrm{VBF}}_{\mathrm{OS}}$[fb]	$\sigma^{\mathrm{VBF}}_{\mathrm{CPS}}$[fb]	δ_{CPS}	Δ_{scale}[%]	Δ_{PDF}[%]	$\Delta_{\alpha_{\mathrm{s}}}$[%]	$\Delta_{\mathrm{PDF}\oplus\alpha_{\mathrm{s}}}$[%]
120.0	4623	4718	2.1	$^{+0.5}_{-0.2}$	±1.8	±0.6	±1.9
120.5	4608	4700	2.0	$^{+0.4}_{-0.3}$	±1.8	±0.6	±1.9
121.0	4587	4687	2.2	$^{+0.5}_{-0.2}$	±1.8	±0.6	±1.9
121.5	4572	4673	2.2	$^{+0.4}_{-0.3}$	±1.8	±0.6	±1.9
122.0	4551	4651	2.2	$^{+0.5}_{-0.2}$	±1.8	±0.6	±1.9
122.5	4536	4634	2.2	$^{+0.4}_{-0.3}$	±1.8	±0.6	±1.9
123.0	4515	4605	2.0	$^{+0.5}_{-0.2}$	±1.8	±0.6	±1.9
123.5	4501	4590	2.0	$^{+0.4}_{-0.3}$	±1.8	±0.6	±1.9
124.0	4480	4577	2.2	$^{+0.5}_{-0.2}$	±1.8	±0.6	±1.9
124.1	4476	4572	2.1	$^{+0.5}_{-0.2}$	±1.8	±0.6	±1.9
124.2	4473	4569	2.1	$^{+0.5}_{-0.2}$	±1.8	±0.6	±1.9
124.3	4469	4563	2.1	$^{+0.5}_{-0.2}$	±1.8	±0.6	±1.9
124.4	4466	4562	2.1	$^{+0.5}_{-0.2}$	±1.8	±0.6	±1.9
124.5	4462	4561	2.2	$^{+0.5}_{-0.2}$	±1.8	±0.6	±1.9
124.6	4459	4559	2.2	$^{+0.5}_{-0.2}$	±1.8	±0.6	±1.9
124.7	4455	4556	2.3	$^{+0.5}_{-0.2}$	±1.8	±0.6	±1.9
124.8	4452	4552	2.2	$^{+0.5}_{-0.2}$	±1.8	±0.6	±1.9
124.9	4448	4549	2.3	$^{+0.5}_{-0.2}$	±1.8	±0.6	±1.9
125.0	4445	4547	2.3	$^{+0.5}_{-0.2}$	±1.8	±0.6	±1.9
125.09	4442	4543	2.3	$^{+0.5}_{-0.2}$	±1.8	±0.6	±1.9
125.1	4441	4542	2.3	$^{+0.5}_{-0.2}$	±1.8	±0.6	±1.9
125.2	4438	4540	2.3	$^{+0.5}_{-0.2}$	±1.8	±0.6	±1.9
125.3	4434	4538	2.3	$^{+0.5}_{-0.2}$	±1.8	±0.6	±1.9
125.4	4431	4536	2.4	$^{+0.5}_{-0.2}$	±1.8	±0.6	±1.9
125.5	4428	4533	2.4	$^{+0.5}_{-0.2}$	±1.8	±0.6	±1.9
125.6	4424	4531	2.4	$^{+0.5}_{-0.2}$	±1.8	±0.6	±1.9
125.7	4421	4528	2.4	$^{+0.5}_{-0.2}$	±1.8	±0.6	±1.9
125.8	4417	4525	2.4	$^{+0.5}_{-0.2}$	±1.8	±0.6	±1.9
125.9	4414	4522	2.4	$^{+0.5}_{-0.2}$	±1.8	±0.6	±1.9
126.0	4410	4519	2.5	$^{+0.5}_{-0.2}$	±1.8	±0.6	±1.9
126.5	4396	4505	2.5	$^{+0.4}_{-0.3}$	±1.8	±0.6	±1.9
127.0	4376	4488	2.6	$^{+0.5}_{-0.2}$	±1.8	±0.6	±1.9
127.5	4362	4472	2.5	$^{+0.4}_{-0.3}$	±1.8	±0.6	±1.9
128.0	4342	4454	2.6	$^{+0.5}_{-0.2}$	±1.8	±0.6	±1.9
128.5	4329	4438	2.5	$^{+0.4}_{-0.3}$	±1.8	±0.6	±1.9
129.0	4309	4423	2.6	$^{+0.5}_{-0.2}$	±1.8	±0.6	±1.9
129.5	4295	4407	2.6	$^{+0.4}_{-0.3}$	±1.8	±0.6	±1.9
130.0	4276	4388	2.6	$^{+0.5}_{-0.2}$	±1.8	±0.6	±1.9

Table 205: Inclusive VBF cross sections for a Higgs boson mass of $M_{\rm H} = 125$ GeV, at NNLO QCD, with an on shell Higgs or with off-shell effects included in the complex-pole scheme, together with their uncertainties. For more details see Section I.5.1.a.iv.

$M_{\rm H}$[GeV]	$\sigma^{\rm VBF}_{\rm OS}$[fb]	$\sigma^{\rm VBF}_{\rm CPS}$[fb]	$\delta_{\rm CPS}$	$\Delta_{\rm scale}$[%]	$\Delta_{\rm PDF}$[%]	$\Delta_{\alpha_{\rm s}}$[%]	$\Delta_{\rm PDF\oplus\alpha_{\rm s}}$[%]
6.0	938	947	0.9	$^{+0.2}_{-0.1}$	±1.9	±0.4	±2.0
6.5	1102	1114	1.1	$^{+0.2}_{-0.1}$	±1.9	±0.4	±1.9
7.0	1276	1291	1.2	$^{+0.2}_{-0.2}$	±1.9	±0.4	±1.9
7.5	1459	1477	1.2	$^{+0.2}_{-0.2}$	±1.9	±0.4	±1.9
8.0	1650	1672	1.3	$^{+0.3}_{-0.2}$	±1.9	±0.5	±1.9
8.5	1848	1873	1.4	$^{+0.3}_{-0.2}$	±1.9	±0.5	±1.9
9.0	2054	2083	1.4	$^{+0.3}_{-0.2}$	±1.8	±0.5	±1.9
9.5	2267	2300	1.5	$^{+0.3}_{-0.2}$	±1.8	±0.5	±1.9
10.0	2487	2529	1.7	$^{+0.4}_{-0.2}$	±1.8	±0.5	±1.9
10.5	2713	2758	1.7	$^{+0.4}_{-0.2}$	±1.8	±0.5	±1.9
11.0	2944	2997	1.8	$^{+0.4}_{-0.2}$	±1.8	±0.5	±1.9
11.5	3182	3240	1.8	$^{+0.4}_{-0.2}$	±1.8	±0.5	±1.9
12.0	3424	3486	1.8	$^{+0.4}_{-0.2}$	±1.8	±0.6	±1.9
12.5	3672	3740	1.9	$^{+0.4}_{-0.2}$	±1.8	±0.6	±1.9
13.0	3925	4013	2.2	$^{+0.5}_{-0.2}$	±1.8	±0.6	±1.9
13.5	4183	4276	2.2	$^{+0.5}_{-0.2}$	±1.8	±0.6	±1.9
14.0	4445	4547	2.3	$^{+0.5}_{-0.2}$	±1.8	±0.6	±1.9
14.5	4711	4823	2.4	$^{+0.5}_{-0.2}$	±1.8	±0.6	±1.9
15.0	4982	5079	1.9	$^{+0.5}_{-0.3}$	±1.8	±0.6	±1.9

Table 206: Inclusive VBF cross sections for a Higgs boson mass of $M_{\rm H} = 125.09$ GeV, at NNLO QCD, with an on shell Higgs or with off-shell effects included in the complex-pole scheme, together with their uncertainties. For more details see Section I.5.1.a.iv.

$M_{\rm H}$[GeV]	$\sigma^{\rm VBF}_{\rm OS}$[fb]	$\sigma^{\rm VBF}_{\rm CPS}$[fb]	$\delta_{\rm CPS}$	$\Delta_{\rm scale}$[%]	$\Delta_{\rm PDF}$[%]	$\Delta_{\alpha_{\rm s}}$[%]	$\Delta_{\rm PDF\oplus\alpha_{\rm s}}$[%]
6.0	937	946	0.9	$^{+0.2}_{-0.1}$	±1.9	±0.4	±2.0
6.5	1101	1113	1.1	$^{+0.2}_{-0.1}$	±1.9	±0.4	±1.9
7.0	1275	1290	1.2	$^{+0.2}_{-0.2}$	±1.9	±0.4	±1.9
7.5	1457	1476	1.3	$^{+0.2}_{-0.2}$	±1.9	±0.4	±1.9
8.0	1648	1670	1.3	$^{+0.3}_{-0.2}$	±1.9	±0.5	±1.9
8.5	1847	1872	1.4	$^{+0.3}_{-0.2}$	±1.9	±0.5	±1.9
9.0	2052	2081	1.4	$^{+0.3}_{-0.2}$	±1.8	±0.5	±1.9
9.5	2265	2299	1.5	$^{+0.3}_{-0.2}$	±1.8	±0.5	±1.9
10.0	2485	2527	1.7	$^{+0.4}_{-0.2}$	±1.8	±0.5	±1.9
10.5	2710	2759	1.8	$^{+0.4}_{-0.2}$	±1.8	±0.5	±1.9
11.0	2942	2992	1.7	$^{+0.4}_{-0.2}$	±1.8	±0.5	±1.9
11.5	3179	3232	1.7	$^{+0.4}_{-0.2}$	±1.8	±0.5	±1.9
12.0	3422	3480	1.7	$^{+0.4}_{-0.2}$	±1.8	±0.6	±1.9
12.5	3670	3740	1.9	$^{+0.4}_{-0.2}$	±1.8	±0.6	±1.9
13.0	3922	4006	2.1	$^{+0.5}_{-0.2}$	±1.8	±0.6	±1.9
13.5	4180	4267	2.1	$^{+0.5}_{-0.2}$	±1.8	±0.6	±1.9
14.0	4442	4543	2.3	$^{+0.5}_{-0.2}$	±1.8	±0.6	±1.9
14.5	4708	4813	2.2	$^{+0.5}_{-0.2}$	±1.8	±0.6	±1.9
15.0	4979	5093	2.3	$^{+0.5}_{-0.3}$	±1.8	±0.6	±1.9

Appendix D

SM Higgs-strahlung cross sections

Here we expand Tables 27–30, which contain predictions for total and fiducial Higgs-strahlung cross sections in the SM for $M_{\mathrm{H}} = 125$ GeV, to a scan over SM Higgs boson masses.

Table 207: Total $W^+(\to \ell^+\nu_\ell)H$ cross sections including QCD and EW corrections and their uncertainties for a proton–proton collision energy $\sqrt{s} = 7$ TeV.

M_H [GeV]	σ [fb]	Δ_{scale} [%]	$\Delta_{PDF/\alpha_s/PDF\oplus\alpha_s}$ [%]	$\sigma^{DY}_{NNLOQCD}$ [fb]	$\sigma_{t\text{-loop}}$ [fb]	δ_{EW} [%]	σ_γ [fb]
120.0	46.85	$^{+0.6}_{-0.9}$	$\pm 1.8/\pm 0.6/\pm 1.9$	48.90	0.47	-7.0	$0.91^{+1.13}_{-0.11}$
120.5	46.22	$^{+0.6}_{-1.0}$	$\pm 1.8/\pm 0.6/\pm 1.9$	48.24	0.46	-7.0	$0.90^{+1.12}_{-0.11}$
121.0	45.57	$^{+0.7}_{-0.9}$	$\pm 1.9/\pm 0.6/\pm 1.9$	47.56	0.46	-7.0	$0.90^{+1.12}_{-0.10}$
121.5	44.95	$^{+0.7}_{-0.9}$	$\pm 1.9/\pm 0.6/\pm 2.0$	46.92	0.45	-7.1	$0.90^{+1.12}_{-0.10}$
122.0	44.38	$^{+0.7}_{-0.9}$	$\pm 1.9/\pm 0.6/\pm 2.0$	46.32	0.45	-7.1	$0.90^{+1.12}_{-0.10}$
122.5	43.80	$^{+0.6}_{-0.9}$	$\pm 1.9/\pm 0.6/\pm 2.0$	45.72	0.44	-7.1	$0.89^{+1.11}_{-0.10}$
123.0	43.22	$^{+0.7}_{-0.9}$	$\pm 1.9/\pm 0.6/\pm 2.0$	45.11	0.44	-7.1	$0.89^{+1.11}_{-0.10}$
123.5	42.63	$^{+0.7}_{-0.9}$	$\pm 1.9/\pm 0.6/\pm 2.0$	44.50	0.43	-7.2	$0.89^{+1.11}_{-0.10}$
124.0	42.07	$^{+0.7}_{-0.8}$	$\pm 1.9/\pm 0.7/\pm 2.0$	43.91	0.43	-7.2	$0.88^{+1.11}_{-0.10}$
124.1	41.96	$^{+0.7}_{-0.8}$	$\pm 1.9/\pm 0.7/\pm 2.0$	43.80	0.43	-7.2	$0.88^{+1.10}_{-0.10}$
124.2	41.84	$^{+0.7}_{-0.8}$	$\pm 1.9/\pm 0.7/\pm 2.0$	43.67	0.42	-7.2	$0.88^{+1.10}_{-0.10}$
124.3	41.75	$^{+0.7}_{-0.9}$	$\pm 1.9/\pm 0.7/\pm 2.0$	43.58	0.42	-7.2	$0.88^{+1.10}_{-0.10}$
124.4	41.65	$^{+0.7}_{-0.9}$	$\pm 1.9/\pm 0.7/\pm 2.0$	43.47	0.42	-7.2	$0.88^{+1.10}_{-0.10}$
124.5	41.54	$^{+0.6}_{-0.9}$	$\pm 1.9/\pm 0.7/\pm 2.0$	43.36	0.42	-7.2	$0.88^{+1.10}_{-0.10}$
124.6	41.45	$^{+0.6}_{-1.0}$	$\pm 1.9/\pm 0.7/\pm 2.0$	43.26	0.42	-7.2	$0.88^{+1.10}_{-0.10}$
124.7	41.32	$^{+0.7}_{-0.9}$	$\pm 1.9/\pm 0.7/\pm 2.0$	43.13	0.42	-7.2	$0.88^{+1.10}_{-0.10}$
124.8	41.21	$^{+0.7}_{-0.9}$	$\pm 1.9/\pm 0.7/\pm 2.0$	43.01	0.42	-7.2	$0.88^{+1.10}_{-0.10}$
124.9	41.10	$^{+0.7}_{-0.9}$	$\pm 1.9/\pm 0.7/\pm 2.0$	42.90	0.42	-7.2	$0.88^{+1.10}_{-0.10}$
125.0	40.99	$^{+0.7}_{-0.9}$	$\pm 1.9/\pm 0.7/\pm 2.0$	42.78	0.42	-7.2	$0.88^{+1.10}_{-0.10}$
125.09	40.88	$^{+0.7}_{-0.8}$	$\pm 1.9/\pm 0.7/\pm 2.0$	42.68	0.42	-7.2	$0.88^{+1.10}_{-0.10}$
125.1	40.89	$^{+0.7}_{-0.9}$	$\pm 1.9/\pm 0.7/\pm 2.0$	42.67	0.42	-7.2	$0.88^{+1.10}_{-0.10}$
125.2	40.79	$^{+0.6}_{-0.9}$	$\pm 1.9/\pm 0.7/\pm 2.0$	42.57	0.42	-7.2	$0.88^{+1.10}_{-0.10}$
125.3	40.68	$^{+0.6}_{-0.9}$	$\pm 1.9/\pm 0.7/\pm 2.0$	42.46	0.42	-7.2	$0.88^{+1.10}_{-0.10}$
125.4	40.56	$^{+0.7}_{-0.9}$	$\pm 1.9/\pm 0.7/\pm 2.0$	42.34	0.42	-7.2	$0.88^{+1.10}_{-0.10}$
125.5	40.47	$^{+0.6}_{-0.9}$	$\pm 1.9/\pm 0.7/\pm 2.0$	42.24	0.41	-7.2	$0.88^{+1.10}_{-0.10}$
125.6	40.36	$^{+0.6}_{-0.9}$	$\pm 1.9/\pm 0.7/\pm 2.0$	42.13	0.41	-7.3	$0.87^{+1.10}_{-0.10}$
125.7	40.26	$^{+0.6}_{-0.9}$	$\pm 1.9/\pm 0.7/\pm 2.0$	42.02	0.41	-7.3	$0.87^{+1.10}_{-0.10}$
125.8	40.15	$^{+0.7}_{-0.9}$	$\pm 1.9/\pm 0.7/\pm 2.0$	41.90	0.41	-7.3	$0.87^{+1.10}_{-0.10}$
125.9	40.03	$^{+0.7}_{-0.9}$	$\pm 1.9/\pm 0.7/\pm 2.0$	41.78	0.41	-7.3	$0.87^{+1.10}_{-0.10}$
126.0	39.93	$^{+0.7}_{-0.9}$	$\pm 1.9/\pm 0.7/\pm 2.0$	41.68	0.41	-7.3	$0.87^{+1.10}_{-0.10}$
126.5	39.41	$^{+0.7}_{-0.9}$	$\pm 1.9/\pm 0.7/\pm 2.0$	41.14	0.40	-7.3	$0.87^{+1.09}_{-0.10}$
127.0	38.91	$^{+0.7}_{-0.9}$	$\pm 1.9/\pm 0.7/\pm 2.0$	40.61	0.40	-7.3	$0.87^{+1.09}_{-0.10}$
127.5	38.40	$^{+0.6}_{-0.9}$	$\pm 1.9/\pm 0.7/\pm 2.0$	40.08	0.40	-7.3	$0.86^{+1.09}_{-0.10}$
128.0	37.91	$^{+0.7}_{-0.9}$	$\pm 1.9/\pm 0.6/\pm 2.0$	39.57	0.39	-7.4	$0.86^{+1.09}_{-0.10}$
128.5	37.42	$^{+0.7}_{-0.9}$	$\pm 1.9/\pm 0.6/\pm 2.0$	39.06	0.39	-7.4	$0.86^{+1.08}_{-0.10}$
129.0	36.94	$^{+0.7}_{-0.9}$	$\pm 1.9/\pm 0.6/\pm 2.0$	38.56	0.38	-7.4	$0.86^{+1.08}_{-0.10}$
129.5	36.48	$^{+0.6}_{-1.0}$	$\pm 1.9/\pm 0.6/\pm 2.0$	38.08	0.38	-7.4	$0.85^{+1.08}_{-0.10}$
130.0	36.01	$^{+0.6}_{-0.9}$	$\pm 1.9/\pm 0.6/\pm 2.0$	37.59	0.37	-7.5	$0.85^{+1.08}_{-0.09}$

Table 208: Total $\mathrm{W}^+(\to\ell^+\nu_\ell)\mathrm{H}$ cross sections including QCD and EW corrections and their uncertainties for a proton–proton collision energy $\sqrt{s} = 8$ TeV.

M_H	σ	Δ_scale	$\Delta_{\mathrm{PDF}/\alpha_\mathrm{s}/\mathrm{PDF}\oplus\alpha_\mathrm{s}}$	$\sigma^\mathrm{DY}_\mathrm{NNLOQCD}$	$\sigma_\text{t-loop}$	δ_EW	σ_γ
[GeV]	[fb]	[%]	[%]	[fb]	[fb]	[%]	[fb]
120.0	56.46	$^{+0.6}_{-0.8}$	$\pm1.8/\pm0.7/\pm2.0$	58.79	0.59	-7.0	$1.21^{+1.44}_{-0.15}$
120.5	55.73	$^{+0.5}_{-0.9}$	$\pm1.8/\pm0.7/\pm2.0$	58.04	0.59	-7.1	$1.21^{+1.43}_{-0.15}$
121.0	54.97	$^{+0.6}_{-0.8}$	$\pm1.8/\pm0.7/\pm2.0$	57.24	0.58	-7.1	$1.21^{+1.43}_{-0.15}$
121.5	54.24	$^{+0.6}_{-0.8}$	$\pm1.8/\pm0.7/\pm2.0$	56.48	0.58	-7.1	$1.20^{+1.42}_{-0.14}$
122.0	53.52	$^{+0.6}_{-0.8}$	$\pm1.8/\pm0.7/\pm2.0$	55.73	0.56	-7.1	$1.20^{+1.41}_{-0.14}$
122.5	52.84	$^{+0.6}_{-0.8}$	$\pm1.8/\pm0.7/\pm2.0$	55.02	0.56	-7.2	$1.20^{+1.41}_{-0.14}$
123.0	52.14	$^{+0.6}_{-0.9}$	$\pm1.8/\pm0.8/\pm2.0$	54.29	0.55	-7.2	$1.19^{+1.40}_{-0.14}$
123.5	51.46	$^{+0.6}_{-0.9}$	$\pm1.8/\pm0.8/\pm2.0$	53.58	0.55	-7.2	$1.19^{+1.39}_{-0.14}$
124.0	50.79	$^{+0.7}_{-0.8}$	$\pm1.8/\pm0.8/\pm2.0$	52.88	0.54	-7.2	$1.19^{+1.39}_{-0.14}$
124.1	50.67	$^{+0.6}_{-0.8}$	$\pm1.8/\pm0.8/\pm2.0$	52.75	0.54	-7.2	$1.19^{+1.39}_{-0.14}$
124.2	50.54	$^{+0.6}_{-0.9}$	$\pm1.8/\pm0.8/\pm2.0$	52.63	0.54	-7.2	$1.18^{+1.39}_{-0.14}$
124.3	50.42	$^{+0.6}_{-0.9}$	$\pm1.8/\pm0.8/\pm2.0$	52.50	0.54	-7.2	$1.18^{+1.38}_{-0.14}$
124.4	50.32	$^{+0.5}_{-0.9}$	$\pm1.8/\pm0.8/\pm2.0$	52.38	0.54	-7.2	$1.18^{+1.38}_{-0.14}$
124.5	50.17	$^{+0.6}_{-0.9}$	$\pm1.8/\pm0.8/\pm2.0$	52.23	0.54	-7.2	$1.18^{+1.38}_{-0.14}$
124.6	50.02	$^{+0.6}_{-0.9}$	$\pm1.8/\pm0.8/\pm2.0$	52.09	0.53	-7.3	$1.18^{+1.38}_{-0.14}$
124.7	49.87	$^{+0.7}_{-0.8}$	$\pm1.8/\pm0.8/\pm2.0$	51.92	0.53	-7.3	$1.18^{+1.38}_{-0.14}$
124.8	49.77	$^{+0.6}_{-0.9}$	$\pm1.8/\pm0.8/\pm2.0$	51.82	0.53	-7.3	$1.18^{+1.38}_{-0.14}$
124.9	49.65	$^{+0.6}_{-0.9}$	$\pm1.8/\pm0.8/\pm2.0$	51.69	0.53	-7.3	$1.18^{+1.38}_{-0.14}$
125.0	49.52	$^{+0.6}_{-0.9}$	$\pm1.8/\pm0.8/\pm2.0$	51.56	0.53	-7.3	$1.18^{+1.38}_{-0.14}$
125.09	49.40	$^{+0.7}_{-0.9}$	$\pm1.8/\pm0.8/\pm2.0$	51.44	0.53	-7.3	$1.18^{+1.38}_{-0.14}$
125.1	49.40	$^{+0.6}_{-0.9}$	$\pm1.8/\pm0.8/\pm2.0$	51.43	0.53	-7.3	$1.18^{+1.37}_{-0.14}$
125.2	49.25	$^{+0.7}_{-0.9}$	$\pm1.8/\pm0.8/\pm2.0$	51.28	0.53	-7.3	$1.18^{+1.37}_{-0.14}$
125.3	49.11	$^{+0.7}_{-0.9}$	$\pm1.8/\pm0.8/\pm2.0$	51.14	0.53	-7.3	$1.18^{+1.37}_{-0.14}$
125.4	48.98	$^{+0.7}_{-0.9}$	$\pm1.8/\pm0.8/\pm2.0$	51.00	0.53	-7.3	$1.18^{+1.37}_{-0.14}$
125.5	48.84	$^{+0.7}_{-0.8}$	$\pm1.8/\pm0.8/\pm2.0$	50.85	0.52	-7.3	$1.18^{+1.37}_{-0.14}$
125.6	48.73	$^{+0.6}_{-0.8}$	$\pm1.8/\pm0.8/\pm2.0$	50.73	0.53	-7.3	$1.18^{+1.37}_{-0.14}$
125.7	48.61	$^{+0.6}_{-0.9}$	$\pm1.8/\pm0.7/\pm2.0$	50.62	0.52	-7.3	$1.17^{+1.37}_{-0.14}$
125.8	48.47	$^{+0.7}_{-0.8}$	$\pm1.8/\pm0.7/\pm2.0$	50.47	0.52	-7.3	$1.17^{+1.37}_{-0.14}$
125.9	48.36	$^{+0.6}_{-0.9}$	$\pm1.8/\pm0.7/\pm2.0$	50.35	0.52	-7.3	$1.17^{+1.37}_{-0.14}$
126.0	48.23	$^{+0.6}_{-0.9}$	$\pm1.8/\pm0.7/\pm2.0$	50.21	0.52	-7.3	$1.17^{+1.37}_{-0.14}$
126.5	47.59	$^{+0.7}_{-0.8}$	$\pm1.8/\pm0.7/\pm2.0$	49.55	0.52	-7.3	$1.17^{+1.37}_{-0.14}$
127.0	47.00	$^{+0.6}_{-0.9}$	$\pm1.8/\pm0.7/\pm2.0$	48.93	0.51	-7.4	$1.17^{+1.36}_{-0.14}$
127.5	46.39	$^{+0.7}_{-0.8}$	$\pm1.8/\pm0.7/\pm2.0$	48.29	0.50	-7.4	$1.16^{+1.36}_{-0.14}$
128.0	45.83	$^{+0.6}_{-0.8}$	$\pm1.8/\pm0.7/\pm2.0$	47.70	0.50	-7.4	$1.16^{+1.36}_{-0.14}$
128.5	45.26	$^{+0.6}_{-0.9}$	$\pm1.8/\pm0.7/\pm2.0$	47.11	0.49	-7.4	$1.16^{+1.35}_{-0.14}$
129.0	44.67	$^{+0.6}_{-0.9}$	$\pm1.9/\pm0.7/\pm2.0$	46.51	0.49	-7.5	$1.15^{+1.35}_{-0.13}$
129.5	44.12	$^{+0.6}_{-0.9}$	$\pm1.9/\pm0.7/\pm2.0$	45.93	0.48	-7.5	$1.15^{+1.35}_{-0.13}$
130.0	43.57	$^{+0.6}_{-1.0}$	$\pm1.9/\pm0.7/\pm2.0$	45.36	0.48	-7.5	$1.15^{+1.34}_{-0.13}$

Table 209: Total $W^+(\to \ell^+\nu_\ell)H$ cross sections including QCD and EW corrections and their uncertainties for a proton–proton collision energy $\sqrt{s} = 13$ TeV.

M_H [GeV]	σ [fb]	Δ_{scale} [%]	$\Delta_{PDF/\alpha_s/PDF\oplus\alpha_s}$ [%]	$\sigma^{DY}_{NNLOQCD}$ [fb]	$\sigma_{t\text{-loop}}$ [fb]	δ_{EW} [%]	σ_γ [fb]
120.0	106.94	$^{+0.6}_{-0.6}$	$\pm 1.6/\pm 0.9/\pm 1.8$	110.37	1.33	−7.2	$3.16^{+3.39}_{-0.38}$
120.5	105.60	$^{+0.5}_{-0.7}$	$\pm 1.6/\pm 0.9/\pm 1.8$	108.99	1.32	−7.2	$3.15^{+3.39}_{-0.38}$
121.0	104.30	$^{+0.5}_{-0.7}$	$\pm 1.6/\pm 0.9/\pm 1.8$	107.63	1.30	−7.2	$3.15^{+3.38}_{-0.38}$
121.5	103.03	$^{+0.4}_{-0.8}$	$\pm 1.6/\pm 0.9/\pm 1.8$	106.32	1.29	−7.3	$3.14^{+3.37}_{-0.38}$
122.0	101.77	$^{+0.3}_{-0.8}$	$\pm 1.6/\pm 0.9/\pm 1.8$	105.00	1.27	−7.3	$3.13^{+3.37}_{-0.37}$
122.5	100.48	$^{+0.5}_{-0.8}$	$\pm 1.6/\pm 0.9/\pm 1.8$	103.65	1.26	−7.3	$3.13^{+3.36}_{-0.37}$
123.0	99.10	$^{+0.6}_{-0.7}$	$\pm 1.6/\pm 0.9/\pm 1.8$	102.20	1.25	−7.3	$3.12^{+3.35}_{-0.37}$
123.5	97.81	$^{+0.6}_{-0.7}$	$\pm 1.6/\pm 0.9/\pm 1.8$	100.87	1.23	−7.3	$3.11^{+3.35}_{-0.37}$
124.0	96.57	$^{+0.6}_{-0.6}$	$\pm 1.6/\pm 0.9/\pm 1.8$	99.58	1.22	−7.4	$3.11^{+3.34}_{-0.37}$
124.1	96.34	$^{+0.5}_{-0.6}$	$\pm 1.6/\pm 0.9/\pm 1.8$	99.34	1.22	−7.4	$3.10^{+3.34}_{-0.37}$
124.2	96.10	$^{+0.5}_{-0.6}$	$\pm 1.6/\pm 0.9/\pm 1.8$	99.07	1.22	−7.4	$3.10^{+3.34}_{-0.37}$
124.3	95.88	$^{+0.6}_{-0.7}$	$\pm 1.6/\pm 0.9/\pm 1.8$	98.86	1.21	−7.4	$3.10^{+3.34}_{-0.37}$
124.4	95.65	$^{+0.6}_{-0.7}$	$\pm 1.6/\pm 0.9/\pm 1.8$	98.61	1.22	−7.4	$3.10^{+3.34}_{-0.37}$
124.5	95.36	$^{+0.6}_{-0.6}$	$\pm 1.6/\pm 0.9/\pm 1.8$	98.31	1.22	−7.4	$3.10^{+3.33}_{-0.37}$
124.6	95.21	$^{+0.5}_{-0.7}$	$\pm 1.6/\pm 0.9/\pm 1.8$	98.15	1.21	−7.4	$3.10^{+3.33}_{-0.37}$
124.7	94.94	$^{+0.6}_{-0.7}$	$\pm 1.6/\pm 0.9/\pm 1.8$	97.88	1.20	−7.4	$3.10^{+3.33}_{-0.37}$
124.8	94.71	$^{+0.6}_{-0.8}$	$\pm 1.6/\pm 0.9/\pm 1.8$	97.64	1.21	−7.4	$3.09^{+3.33}_{-0.37}$
124.9	94.47	$^{+0.6}_{-0.7}$	$\pm 1.6/\pm 0.9/\pm 1.8$	97.38	1.21	−7.4	$3.09^{+3.33}_{-0.37}$
125.0	94.26	$^{+0.5}_{-0.7}$	$\pm 1.6/\pm 0.9/\pm 1.8$	97.18	1.20	−7.4	$3.09^{+3.33}_{-0.37}$
125.09	94.04	$^{+0.5}_{-0.7}$	$\pm 1.6/\pm 0.9/\pm 1.8$	96.94	1.20	−7.4	$3.09^{+3.33}_{-0.37}$
125.1	94.01	$^{+0.6}_{-0.7}$	$\pm 1.6/\pm 0.9/\pm 1.8$	96.91	1.20	−7.4	$3.09^{+3.33}_{-0.37}$
125.2	93.77	$^{+0.6}_{-0.7}$	$\pm 1.6/\pm 0.9/\pm 1.8$	96.66	1.19	−7.4	$3.09^{+3.33}_{-0.37}$
125.3	93.54	$^{+0.6}_{-0.8}$	$\pm 1.6/\pm 0.9/\pm 1.8$	96.42	1.20	−7.4	$3.09^{+3.32}_{-0.37}$
125.4	93.31	$^{+0.6}_{-0.7}$	$\pm 1.6/\pm 0.9/\pm 1.8$	96.18	1.19	−7.4	$3.09^{+3.32}_{-0.37}$
125.5	93.08	$^{+0.6}_{-0.7}$	$\pm 1.6/\pm 0.9/\pm 1.8$	95.94	1.19	−7.4	$3.09^{+3.32}_{-0.37}$
125.6	92.84	$^{+0.5}_{-0.6}$	$\pm 1.6/\pm 0.9/\pm 1.8$	95.70	1.18	−7.4	$3.08^{+3.32}_{-0.36}$
125.7	92.54	$^{+0.6}_{-0.6}$	$\pm 1.6/\pm 0.9/\pm 1.8$	95.37	1.19	−7.4	$3.08^{+3.32}_{-0.36}$
125.8	92.34	$^{+0.7}_{-0.7}$	$\pm 1.6/\pm 0.9/\pm 1.8$	95.18	1.17	−7.5	$3.08^{+3.32}_{-0.36}$
125.9	92.20	$^{+0.6}_{-0.8}$	$\pm 1.6/\pm 0.9/\pm 1.8$	95.02	1.19	−7.5	$3.08^{+3.32}_{-0.36}$
126.0	91.91	$^{+0.6}_{-0.8}$	$\pm 1.6/\pm 0.9/\pm 1.8$	94.74	1.17	−7.5	$3.08^{+3.32}_{-0.36}$
126.5	90.77	$^{+0.6}_{-0.7}$	$\pm 1.6/\pm 0.9/\pm 1.8$	93.56	1.16	−7.5	$3.07^{+3.31}_{-0.36}$
127.0	89.75	$^{+0.5}_{-0.7}$	$\pm 1.6/\pm 0.9/\pm 1.8$	92.48	1.16	−7.5	$3.06^{+3.31}_{-0.36}$
127.5	88.58	$^{+0.6}_{-0.7}$	$\pm 1.6/\pm 0.9/\pm 1.8$	91.26	1.14	−7.5	$3.06^{+3.30}_{-0.36}$
128.0	87.54	$^{+0.5}_{-0.7}$	$\pm 1.6/\pm 0.9/\pm 1.8$	90.18	1.13	−7.6	$3.05^{+3.30}_{-0.36}$
128.5	86.47	$^{+0.6}_{-0.7}$	$\pm 1.6/\pm 0.9/\pm 1.8$	89.07	1.12	−7.6	$3.04^{+3.29}_{-0.35}$
129.0	85.45	$^{+0.5}_{-0.7}$	$\pm 1.6/\pm 0.9/\pm 1.8$	88.00	1.11	−7.6	$3.04^{+3.29}_{-0.35}$
129.5	84.44	$^{+0.5}_{-0.7}$	$\pm 1.6/\pm 0.9/\pm 1.8$	86.96	1.10	−7.6	$3.03^{+3.28}_{-0.35}$
130.0	83.49	$^{+0.4}_{-0.8}$	$\pm 1.6/\pm 0.9/\pm 1.8$	85.97	1.09	−7.7	$3.02^{+3.28}_{-0.35}$

Table 210: Total $\mathrm{W}^+(\to\ell^+\nu_\ell)\mathrm{H}$ cross sections including QCD and EW corrections and their uncertainties for a proton–proton collision energy $\sqrt{s} = 14$ TeV.

M_H [GeV]	σ [fb]	Δ_scale [%]	$\Delta_{\mathrm{PDF}/\alpha_\mathrm{s}/\mathrm{PDF}\oplus\alpha_\mathrm{s}}$ [%]	$\sigma^\mathrm{DY}_\mathrm{NNLOQCD}$ [fb]	$\sigma_\text{t-loop}$ [fb]	δ_EW [%]	σ_γ [fb]
120.0	117.37	$^{+0.5}_{-0.6}$	$\pm1.5/\pm0.9/\pm1.8$	120.96	1.48	−7.2	$3.63^{+3.80}_{-0.43}$
120.5	115.95	$^{+0.4}_{-0.7}$	$\pm1.5/\pm0.9/\pm1.8$	119.46	1.48	−7.2	$3.62^{+3.79}_{-0.43}$
121.0	114.51	$^{+0.5}_{-0.7}$	$\pm1.5/\pm0.9/\pm1.8$	117.96	1.47	−7.2	$3.61^{+3.78}_{-0.43}$
121.5	112.91	$^{+0.5}_{-0.6}$	$\pm1.5/\pm0.9/\pm1.8$	116.32	1.44	−7.3	$3.60^{+3.77}_{-0.43}$
122.0	111.56	$^{+0.4}_{-0.6}$	$\pm1.5/\pm0.9/\pm1.8$	114.90	1.44	−7.3	$3.60^{+3.77}_{-0.43}$
122.5	110.21	$^{+0.4}_{-0.8}$	$\pm1.5/\pm0.9/\pm1.8$	113.50	1.42	−7.3	$3.59^{+3.76}_{-0.43}$
123.0	108.86	$^{+0.5}_{-0.8}$	$\pm1.5/\pm0.9/\pm1.8$	112.10	1.40	−7.3	$3.58^{+3.75}_{-0.43}$
123.5	107.39	$^{+0.6}_{-0.6}$	$\pm1.5/\pm0.9/\pm1.8$	110.56	1.39	−7.4	$3.57^{+3.74}_{-0.43}$
124.0	106.19	$^{+0.5}_{-0.7}$	$\pm1.5/\pm0.9/\pm1.8$	109.32	1.38	−7.4	$3.56^{+3.73}_{-0.43}$
124.1	105.94	$^{+0.5}_{-0.7}$	$\pm1.5/\pm0.9/\pm1.8$	109.06	1.38	−7.4	$3.56^{+3.73}_{-0.43}$
124.2	105.73	$^{+0.3}_{-0.7}$	$\pm1.5/\pm0.9/\pm1.8$	108.84	1.37	−7.4	$3.56^{+3.73}_{-0.43}$
124.3	105.47	$^{+0.3}_{-0.8}$	$\pm1.5/\pm0.9/\pm1.8$	108.56	1.37	−7.4	$3.56^{+3.73}_{-0.43}$
124.4	105.12	$^{+0.4}_{-0.6}$	$\pm1.5/\pm0.9/\pm1.8$	108.20	1.37	−7.4	$3.56^{+3.73}_{-0.43}$
124.5	104.93	$^{+0.4}_{-0.8}$	$\pm1.5/\pm0.9/\pm1.8$	108.01	1.36	−7.4	$3.55^{+3.73}_{-0.43}$
124.6	104.62	$^{+0.5}_{-0.7}$	$\pm1.5/\pm0.9/\pm1.8$	107.70	1.36	−7.4	$3.55^{+3.72}_{-0.43}$
124.7	104.44	$^{+0.4}_{-0.8}$	$\pm1.5/\pm0.9/\pm1.8$	107.51	1.36	−7.4	$3.55^{+3.72}_{-0.43}$
124.8	104.10	$^{+0.4}_{-0.7}$	$\pm1.5/\pm0.9/\pm1.8$	107.15	1.35	−7.4	$3.55^{+3.72}_{-0.43}$
124.9	103.93	$^{+0.3}_{-0.8}$	$\pm1.5/\pm0.9/\pm1.8$	106.97	1.35	−7.4	$3.55^{+3.72}_{-0.43}$
125.0	103.63	$^{+0.3}_{-0.8}$	$\pm1.5/\pm0.9/\pm1.8$	106.65	1.36	−7.4	$3.55^{+3.72}_{-0.43}$
125.09	103.40	$^{+0.4}_{-0.8}$	$\pm1.5/\pm0.9/\pm1.8$	106.42	1.35	−7.4	$3.54^{+3.72}_{-0.43}$
125.1	103.37	$^{+0.4}_{-0.8}$	$\pm1.5/\pm0.9/\pm1.8$	106.39	1.35	−7.4	$3.54^{+3.72}_{-0.43}$
125.2	103.06	$^{+0.5}_{-0.7}$	$\pm1.5/\pm0.9/\pm1.8$	106.06	1.34	−7.4	$3.54^{+3.71}_{-0.43}$
125.3	102.91	$^{+0.3}_{-0.9}$	$\pm1.5/\pm0.9/\pm1.8$	105.91	1.34	−7.4	$3.54^{+3.71}_{-0.43}$
125.4	102.56	$^{+0.4}_{-0.7}$	$\pm1.5/\pm0.9/\pm1.8$	105.56	1.33	−7.5	$3.54^{+3.71}_{-0.43}$
125.5	102.31	$^{+0.4}_{-0.7}$	$\pm1.5/\pm0.9/\pm1.8$	105.27	1.34	−7.5	$3.54^{+3.71}_{-0.43}$
125.6	101.97	$^{+0.6}_{-0.6}$	$\pm1.5/\pm0.9/\pm1.8$	104.91	1.34	−7.5	$3.53^{+3.71}_{-0.42}$
125.7	101.78	$^{+0.6}_{-0.7}$	$\pm1.5/\pm0.9/\pm1.8$	104.73	1.33	−7.5	$3.53^{+3.70}_{-0.42}$
125.8	101.60	$^{+0.4}_{-0.7}$	$\pm1.5/\pm0.9/\pm1.8$	104.54	1.33	−7.5	$3.53^{+3.70}_{-0.42}$
125.9	101.32	$^{+0.4}_{-0.7}$	$\pm1.5/\pm0.9/\pm1.8$	104.27	1.32	−7.5	$3.53^{+3.70}_{-0.42}$
126.0	101.08	$^{+0.5}_{-0.7}$	$\pm1.5/\pm0.9/\pm1.8$	104.01	1.33	−7.5	$3.53^{+3.70}_{-0.42}$
126.5	99.82	$^{+0.5}_{-0.7}$	$\pm1.5/\pm0.9/\pm1.8$	102.70	1.31	−7.5	$3.52^{+3.69}_{-0.42}$
127.0	98.61	$^{+0.5}_{-0.7}$	$\pm1.5/\pm0.9/\pm1.8$	101.44	1.30	−7.5	$3.51^{+3.68}_{-0.42}$
127.5	97.44	$^{+0.4}_{-0.7}$	$\pm1.5/\pm0.9/\pm1.8$	100.23	1.28	−7.6	$3.50^{+3.67}_{-0.42}$
128.0	96.21	$^{+0.5}_{-0.7}$	$\pm1.5/\pm0.9/\pm1.8$	98.95	1.27	−7.6	$3.49^{+3.66}_{-0.42}$
128.5	95.11	$^{+0.4}_{-0.8}$	$\pm1.5/\pm0.9/\pm1.8$	97.81	1.26	−7.6	$3.48^{+3.65}_{-0.41}$
129.0	94.00	$^{+0.5}_{-0.8}$	$\pm1.5/\pm0.9/\pm1.8$	96.67	1.25	−7.6	$3.47^{+3.64}_{-0.41}$
129.5	92.83	$^{+0.5}_{-0.7}$	$\pm1.5/\pm0.9/\pm1.8$	95.44	1.24	−7.7	$3.46^{+3.63}_{-0.41}$
130.0	91.71	$^{+0.5}_{-0.7}$	$\pm1.5/\pm0.9/\pm1.8$	94.30	1.22	−7.7	$3.46^{+3.63}_{-0.41}$

Table 211: Total $\mathrm{W}^-(\to\ell^-\bar{\nu}_\ell)\mathrm{H}$ cross sections including QCD and EW corrections and their uncertainties for a proton–proton collision energy $\sqrt{s} = 7$ TeV.

M_H	σ	Δ_scale	$\Delta_{\mathrm{PDF}/\alpha_\mathrm{s}/\mathrm{PDF}\oplus\alpha_\mathrm{s}}$	$\sigma^\mathrm{DY}_\mathrm{NNLOQCD}$	$\sigma_\text{t-loop}$	δ_EW	σ_γ
[GeV]	[fb]	[%]	[%]	[fb]	[fb]	[%]	[fb]
120.0	26.48	$^{+0.6}_{-0.8}$	$\pm2.2/\pm0.6/\pm2.3$	27.56	0.27	−6.8	$0.52^{+0.72}_{-0.05}$
120.5	26.10	$^{+0.6}_{-0.8}$	$\pm2.2/\pm0.6/\pm2.3$	27.17	0.27	−6.8	$0.52^{+0.72}_{-0.05}$
121.0	25.74	$^{+0.6}_{-0.8}$	$\pm2.2/\pm0.6/\pm2.3$	26.80	0.26	−6.9	$0.52^{+0.72}_{-0.05}$
121.5	25.38	$^{+0.6}_{-0.9}$	$\pm2.2/\pm0.6/\pm2.3$	26.42	0.26	−6.9	$0.52^{+0.71}_{-0.05}$
122.0	25.03	$^{+0.7}_{-0.9}$	$\pm2.2/\pm0.6/\pm2.3$	26.06	0.26	−6.9	$0.52^{+0.71}_{-0.05}$
122.5	24.68	$^{+0.6}_{-0.8}$	$\pm2.2/\pm0.6/\pm2.3$	25.69	0.25	−6.9	$0.52^{+0.71}_{-0.05}$
123.0	24.35	$^{+0.6}_{-0.8}$	$\pm2.2/\pm0.6/\pm2.3$	25.34	0.25	−7.0	$0.51^{+0.70}_{-0.05}$
123.5	24.02	$^{+0.6}_{-0.9}$	$\pm2.2/\pm0.6/\pm2.3$	25.00	0.25	−7.0	$0.51^{+0.70}_{-0.05}$
124.0	23.69	$^{+0.5}_{-0.9}$	$\pm2.2/\pm0.6/\pm2.3$	24.66	0.25	−7.0	$0.51^{+0.70}_{-0.05}$
124.1	23.63	$^{+0.5}_{-0.9}$	$\pm2.2/\pm0.6/\pm2.3$	24.59	0.25	−7.0	$0.51^{+0.70}_{-0.05}$
124.2	23.57	$^{+0.5}_{-0.9}$	$\pm2.2/\pm0.6/\pm2.3$	24.53	0.24	−7.0	$0.51^{+0.69}_{-0.05}$
124.3	23.49	$^{+0.6}_{-0.8}$	$\pm2.2/\pm0.6/\pm2.3$	24.45	0.24	−7.0	$0.51^{+0.69}_{-0.05}$
124.4	23.42	$^{+0.6}_{-0.8}$	$\pm2.2/\pm0.6/\pm2.3$	24.38	0.24	−7.0	$0.51^{+0.69}_{-0.05}$
124.5	23.38	$^{+0.5}_{-0.9}$	$\pm2.2/\pm0.6/\pm2.3$	24.33	0.24	−7.0	$0.51^{+0.69}_{-0.05}$
124.6	23.30	$^{+0.6}_{-0.9}$	$\pm2.2/\pm0.6/\pm2.3$	24.25	0.24	−7.0	$0.51^{+0.69}_{-0.05}$
124.7	23.24	$^{+0.6}_{-0.9}$	$\pm2.2/\pm0.6/\pm2.3$	24.18	0.24	−7.0	$0.51^{+0.69}_{-0.05}$
124.8	23.17	$^{+0.6}_{-0.9}$	$\pm2.2/\pm0.6/\pm2.3$	24.12	0.24	−7.0	$0.51^{+0.69}_{-0.05}$
124.9	23.11	$^{+0.6}_{-0.9}$	$\pm2.2/\pm0.6/\pm2.3$	24.05	0.24	−7.0	$0.51^{+0.69}_{-0.05}$
125.0	23.04	$^{+0.6}_{-0.8}$	$\pm2.2/\pm0.6/\pm2.3$	23.98	0.24	−7.0	$0.51^{+0.69}_{-0.05}$
125.09	22.98	$^{+0.6}_{-0.8}$	$\pm2.2/\pm0.6/\pm2.3$	23.92	0.24	−7.0	$0.51^{+0.69}_{-0.05}$
125.1	22.97	$^{+0.6}_{-0.8}$	$\pm2.2/\pm0.6/\pm2.3$	23.91	0.24	−7.1	$0.51^{+0.69}_{-0.05}$
125.2	22.90	$^{+0.7}_{-0.9}$	$\pm2.2/\pm0.6/\pm2.3$	23.84	0.24	−7.1	$0.51^{+0.69}_{-0.05}$
125.3	22.85	$^{+0.6}_{-0.9}$	$\pm2.2/\pm0.6/\pm2.3$	23.78	0.24	−7.0	$0.51^{+0.69}_{-0.05}$
125.4	22.78	$^{+0.6}_{-0.9}$	$\pm2.2/\pm0.6/\pm2.3$	23.71	0.24	−7.1	$0.51^{+0.69}_{-0.05}$
125.5	22.72	$^{+0.6}_{-0.9}$	$\pm2.2/\pm0.6/\pm2.3$	23.65	0.24	−7.1	$0.51^{+0.69}_{-0.05}$
125.6	22.66	$^{+0.6}_{-0.9}$	$\pm2.2/\pm0.6/\pm2.3$	23.58	0.24	−7.1	$0.51^{+0.69}_{-0.05}$
125.7	22.59	$^{+0.6}_{-0.8}$	$\pm2.2/\pm0.6/\pm2.3$	23.51	0.24	−7.1	$0.50^{+0.69}_{-0.05}$
125.8	22.54	$^{+0.6}_{-0.8}$	$\pm2.3/\pm0.6/\pm2.3$	23.46	0.23	−7.1	$0.50^{+0.68}_{-0.05}$
125.9	22.48	$^{+0.6}_{-0.9}$	$\pm2.3/\pm0.6/\pm2.3$	23.40	0.23	−7.1	$0.50^{+0.68}_{-0.05}$
126.0	22.41	$^{+0.7}_{-0.8}$	$\pm2.3/\pm0.6/\pm2.3$	23.32	0.23	−7.1	$0.50^{+0.68}_{-0.05}$
126.5	22.11	$^{+0.6}_{-0.9}$	$\pm2.3/\pm0.6/\pm2.3$	23.01	0.23	−7.1	$0.50^{+0.68}_{-0.05}$
127.0	21.82	$^{+0.6}_{-1.0}$	$\pm2.3/\pm0.6/\pm2.3$	22.71	0.23	−7.1	$0.50^{+0.68}_{-0.05}$
127.5	21.52	$^{+0.6}_{-0.9}$	$\pm2.3/\pm0.6/\pm2.4$	22.40	0.23	−7.2	$0.50^{+0.68}_{-0.05}$
128.0	21.22	$^{+0.7}_{-0.9}$	$\pm2.3/\pm0.6/\pm2.4$	22.08	0.22	−7.2	$0.50^{+0.67}_{-0.05}$
128.5	20.94	$^{+0.7}_{-0.9}$	$\pm2.3/\pm0.6/\pm2.4$	21.79	0.22	−7.2	$0.49^{+0.67}_{-0.05}$
129.0	20.65	$^{+0.6}_{-0.9}$	$\pm2.3/\pm0.6/\pm2.4$	21.49	0.22	−7.2	$0.49^{+0.67}_{-0.05}$
129.5	20.39	$^{+0.6}_{-0.9}$	$\pm2.3/\pm0.6/\pm2.4$	21.22	0.22	−7.2	$0.49^{+0.66}_{-0.05}$
130.0	20.10	$^{+0.7}_{-0.9}$	$\pm2.3/\pm0.6/\pm2.4$	20.92	0.21	−7.3	$0.49^{+0.66}_{-0.05}$

Table 212: Total $\mathrm{W}^-(\to\ell^-\bar{\nu}_\ell)\mathrm{H}$ cross sections including QCD and EW corrections and their uncertainties for a proton–proton collision energy $\sqrt{s} = 8$ TeV.

M_H	σ	Δ_scale	$\Delta_{\mathrm{PDF}/\alpha_\mathrm{s}/\mathrm{PDF}\oplus\alpha_\mathrm{s}}$	$\sigma^\mathrm{DY}_\mathrm{NNLOQCD}$	$\sigma_\text{t-loop}$	δ_EW	σ_γ
[GeV]	[fb]	[%]	[%]	[fb]	[fb]	[%]	[fb]
120.0	32.88	$^{+0.5}_{-0.9}$	$\pm2.1/\pm0.6/\pm2.2$	34.15	0.35	-6.9	$0.72^{+0.98}_{-0.07}$
120.5	32.41	$^{+0.5}_{-0.8}$	$\pm2.1/\pm0.6/\pm2.2$	33.66	0.35	-6.9	$0.72^{+0.98}_{-0.07}$
121.0	31.96	$^{+0.6}_{-0.8}$	$\pm2.1/\pm0.6/\pm2.2$	33.20	0.34	-6.9	$0.72^{+0.97}_{-0.07}$
121.5	31.51	$^{+0.5}_{-0.8}$	$\pm2.1/\pm0.6/\pm2.2$	32.73	0.34	-6.9	$0.72^{+0.97}_{-0.07}$
122.0	31.09	$^{+0.5}_{-0.8}$	$\pm2.1/\pm0.6/\pm2.2$	32.29	0.34	-7.0	$0.71^{+0.97}_{-0.07}$
122.5	30.67	$^{+0.5}_{-0.8}$	$\pm2.1/\pm0.6/\pm2.2$	31.85	0.33	-7.0	$0.71^{+0.96}_{-0.07}$
123.0	30.23	$^{+0.6}_{-0.8}$	$\pm2.1/\pm0.6/\pm2.2$	31.39	0.33	-7.0	$0.71^{+0.96}_{-0.07}$
123.5	29.81	$^{+0.6}_{-0.8}$	$\pm2.1/\pm0.6/\pm2.2$	30.96	0.32	-7.0	$0.70^{+0.95}_{-0.07}$
124.0	29.44	$^{+0.5}_{-0.8}$	$\pm2.1/\pm0.6/\pm2.2$	30.57	0.32	-7.1	$0.70^{+0.95}_{-0.07}$
124.1	29.34	$^{+0.5}_{-0.8}$	$\pm2.1/\pm0.6/\pm2.2$	30.48	0.32	-7.1	$0.70^{+0.95}_{-0.07}$
124.2	29.27	$^{+0.5}_{-0.9}$	$\pm2.1/\pm0.6/\pm2.2$	30.40	0.32	-7.0	$0.70^{+0.95}_{-0.07}$
124.3	29.20	$^{+0.5}_{-0.9}$	$\pm2.1/\pm0.6/\pm2.2$	30.32	0.32	-7.1	$0.70^{+0.95}_{-0.07}$
124.4	29.12	$^{+0.5}_{-0.9}$	$\pm2.1/\pm0.6/\pm2.2$	30.24	0.32	-7.1	$0.70^{+0.95}_{-0.07}$
124.5	29.03	$^{+0.5}_{-0.8}$	$\pm2.1/\pm0.6/\pm2.2$	30.14	0.32	-7.1	$0.70^{+0.95}_{-0.07}$
124.6	28.96	$^{+0.5}_{-0.8}$	$\pm2.1/\pm0.6/\pm2.2$	30.07	0.32	-7.1	$0.70^{+0.95}_{-0.07}$
124.7	28.87	$^{+0.6}_{-0.8}$	$\pm2.1/\pm0.6/\pm2.2$	29.98	0.32	-7.1	$0.70^{+0.95}_{-0.07}$
124.8	28.79	$^{+0.6}_{-0.8}$	$\pm2.1/\pm0.6/\pm2.2$	29.90	0.31	-7.1	$0.70^{+0.94}_{-0.07}$
124.9	28.70	$^{+0.6}_{-0.8}$	$\pm2.1/\pm0.6/\pm2.1$	29.80	0.31	-7.1	$0.70^{+0.94}_{-0.07}$
125.0	28.62	$^{+0.6}_{-0.8}$	$\pm2.1/\pm0.6/\pm2.1$	29.71	0.31	-7.1	$0.70^{+0.94}_{-0.07}$
125.09	28.55	$^{+0.6}_{-0.7}$	$\pm2.1/\pm0.6/\pm2.1$	29.64	0.31	-7.1	$0.70^{+0.94}_{-0.07}$
125.1	28.55	$^{+0.6}_{-0.7}$	$\pm2.1/\pm0.6/\pm2.1$	29.64	0.31	-7.1	$0.70^{+0.94}_{-0.07}$
125.2	28.48	$^{+0.6}_{-0.8}$	$\pm2.1/\pm0.6/\pm2.2$	29.57	0.31	-7.1	$0.70^{+0.94}_{-0.07}$
125.3	28.41	$^{+0.5}_{-0.8}$	$\pm2.1/\pm0.6/\pm2.2$	29.50	0.31	-7.1	$0.70^{+0.94}_{-0.07}$
125.4	28.32	$^{+0.6}_{-0.8}$	$\pm2.1/\pm0.6/\pm2.2$	29.40	0.31	-7.1	$0.69^{+0.94}_{-0.07}$
125.5	28.24	$^{+0.6}_{-0.7}$	$\pm2.1/\pm0.6/\pm2.2$	29.33	0.31	-7.1	$0.69^{+0.94}_{-0.07}$
125.6	28.16	$^{+0.6}_{-0.8}$	$\pm2.1/\pm0.6/\pm2.2$	29.24	0.31	-7.1	$0.69^{+0.94}_{-0.07}$
125.7	28.09	$^{+0.6}_{-0.8}$	$\pm2.1/\pm0.6/\pm2.2$	29.17	0.31	-7.1	$0.69^{+0.94}_{-0.07}$
125.8	28.01	$^{+0.6}_{-0.7}$	$\pm2.1/\pm0.6/\pm2.2$	29.08	0.31	-7.1	$0.69^{+0.94}_{-0.07}$
125.9	27.94	$^{+0.6}_{-0.7}$	$\pm2.1/\pm0.6/\pm2.2$	29.00	0.31	-7.1	$0.69^{+0.94}_{-0.07}$
126.0	27.87	$^{+0.6}_{-0.8}$	$\pm2.1/\pm0.6/\pm2.2$	28.93	0.31	-7.1	$0.69^{+0.94}_{-0.07}$
126.5	27.52	$^{+0.5}_{-0.8}$	$\pm2.1/\pm0.6/\pm2.2$	28.57	0.30	-7.2	$0.69^{+0.94}_{-0.07}$
127.0	27.14	$^{+0.6}_{-0.8}$	$\pm2.1/\pm0.6/\pm2.2$	28.18	0.30	-7.2	$0.69^{+0.93}_{-0.07}$
127.5	26.79	$^{+0.5}_{-0.8}$	$\pm2.1/\pm0.6/\pm2.2$	27.81	0.30	-7.2	$0.69^{+0.93}_{-0.07}$
128.0	26.43	$^{+0.6}_{-0.9}$	$\pm2.1/\pm0.6/\pm2.2$	27.44	0.29	-7.2	$0.68^{+0.93}_{-0.07}$
128.5	26.06	$^{+0.6}_{-0.8}$	$\pm2.1/\pm0.6/\pm2.2$	27.06	0.29	-7.3	$0.68^{+0.92}_{-0.07}$
129.0	25.74	$^{+0.6}_{-0.8}$	$\pm2.1/\pm0.6/\pm2.2$	26.71	0.29	-7.3	$0.68^{+0.92}_{-0.06}$
129.5	25.39	$^{+0.5}_{-0.8}$	$\pm2.1/\pm0.6/\pm2.2$	26.36	0.28	-7.3	$0.68^{+0.92}_{-0.06}$
130.0	25.05	$^{+0.6}_{-0.8}$	$\pm2.1/\pm0.6/\pm2.2$	26.01	0.28	-7.3	$0.68^{+0.92}_{-0.06}$

Table 213: Total $\mathrm{W}^-(\to\ell^-\bar{\nu}_\ell)\mathrm{H}$ cross sections including QCD and EW corrections and their uncertainties for a proton–proton collision energy $\sqrt{s} = 13$ TeV.

M_H	σ	Δ_scale	$\Delta_{\mathrm{PDF}/\alpha_\mathrm{s}/\mathrm{PDF}\oplus\alpha_\mathrm{s}}$	$\sigma^\mathrm{DY}_\mathrm{NNLOQCD}$	$\sigma_\text{t-loop}$	δ_EW	σ_γ
[GeV]	[fb]	[%]	[%]	[fb]	[fb]	[%]	[fb]
120.0	68.17	$^{+0.4}_{-0.6}$	$\pm1.7/\pm0.9/\pm1.9$	70.18	0.86	−7.0	$2.05^{+2.38}_{-0.23}$
120.5	67.25	$^{+0.5}_{-0.6}$	$\pm1.7/\pm0.8/\pm1.9$	69.22	0.85	−7.0	$2.05^{+2.37}_{-0.23}$
121.0	66.35	$^{+0.5}_{-0.6}$	$\pm1.8/\pm0.8/\pm1.9$	68.29	0.85	−7.1	$2.04^{+2.37}_{-0.23}$
121.5	65.48	$^{+0.5}_{-0.6}$	$\pm1.8/\pm0.8/\pm1.9$	67.39	0.83	−7.1	$2.04^{+2.37}_{-0.23}$
122.0	64.60	$^{+0.6}_{-0.6}$	$\pm1.8/\pm0.8/\pm1.9$	66.46	0.83	−7.1	$2.03^{+2.36}_{-0.23}$
122.5	63.82	$^{+0.4}_{-0.7}$	$\pm1.8/\pm0.8/\pm2.0$	65.66	0.82	−7.1	$2.03^{+2.36}_{-0.23}$
123.0	62.99	$^{+0.5}_{-0.6}$	$\pm1.8/\pm0.8/\pm2.0$	64.80	0.81	−7.2	$2.02^{+2.36}_{-0.23}$
123.5	62.19	$^{+0.5}_{-0.7}$	$\pm1.8/\pm0.8/\pm2.0$	63.96	0.80	−7.2	$2.02^{+2.35}_{-0.22}$
124.0	61.33	$^{+0.6}_{-0.6}$	$\pm1.8/\pm0.8/\pm2.0$	63.08	0.79	−7.2	$2.01^{+2.35}_{-0.22}$
124.1	61.22	$^{+0.5}_{-0.7}$	$\pm1.8/\pm0.8/\pm2.0$	62.96	0.80	−7.2	$2.01^{+2.35}_{-0.22}$
124.2	61.04	$^{+0.5}_{-0.6}$	$\pm1.8/\pm0.8/\pm2.0$	62.76	0.79	−7.2	$2.01^{+2.35}_{-0.22}$
124.3	60.93	$^{+0.5}_{-0.6}$	$\pm1.8/\pm0.8/\pm2.0$	62.65	0.78	−7.2	$2.01^{+2.35}_{-0.22}$
124.4	60.78	$^{+0.4}_{-0.7}$	$\pm1.8/\pm0.8/\pm2.0$	62.49	0.79	−7.2	$2.01^{+2.35}_{-0.22}$
124.5	60.57	$^{+0.6}_{-0.6}$	$\pm1.8/\pm0.8/\pm2.0$	62.27	0.78	−7.2	$2.01^{+2.35}_{-0.22}$
124.6	60.47	$^{+0.4}_{-0.7}$	$\pm1.8/\pm0.8/\pm2.0$	62.17	0.79	−7.2	$2.01^{+2.35}_{-0.22}$
124.7	60.31	$^{+0.4}_{-0.7}$	$\pm1.8/\pm0.8/\pm2.0$	62.00	0.78	−7.2	$2.01^{+2.35}_{-0.22}$
124.8	60.18	$^{+0.4}_{-0.7}$	$\pm1.8/\pm0.8/\pm2.0$	61.87	0.78	−7.2	$2.01^{+2.34}_{-0.22}$
124.9	60.02	$^{+0.3}_{-0.7}$	$\pm1.8/\pm0.8/\pm2.0$	61.71	0.78	−7.2	$2.01^{+2.34}_{-0.22}$
125.0	59.83	$^{+0.4}_{-0.7}$	$\pm1.8/\pm0.8/\pm2.0$	61.51	0.78	−7.3	$2.00^{+2.34}_{-0.22}$
125.09	59.67	$^{+0.4}_{-0.6}$	$\pm1.8/\pm0.8/\pm2.0$	61.33	0.78	−7.2	$2.00^{+2.34}_{-0.22}$
125.1	59.66	$^{+0.4}_{-0.6}$	$\pm1.8/\pm0.8/\pm2.0$	61.34	0.77	−7.3	$2.00^{+2.34}_{-0.22}$
125.2	59.50	$^{+0.5}_{-0.6}$	$\pm1.8/\pm0.8/\pm2.0$	61.16	0.77	−7.3	$2.00^{+2.34}_{-0.22}$
125.3	59.33	$^{+0.5}_{-0.6}$	$\pm1.8/\pm0.8/\pm2.0$	60.99	0.77	−7.3	$2.00^{+2.34}_{-0.22}$
125.4	59.22	$^{+0.5}_{-0.8}$	$\pm1.8/\pm0.8/\pm2.0$	60.88	0.77	−7.3	$2.00^{+2.34}_{-0.22}$
125.5	59.08	$^{+0.4}_{-0.7}$	$\pm1.8/\pm0.8/\pm2.0$	60.74	0.77	−7.3	$2.00^{+2.34}_{-0.22}$
125.6	58.91	$^{+0.4}_{-0.7}$	$\pm1.8/\pm0.8/\pm2.0$	60.56	0.77	−7.3	$2.00^{+2.33}_{-0.22}$
125.7	58.76	$^{+0.3}_{-0.7}$	$\pm1.8/\pm0.8/\pm2.0$	60.41	0.77	−7.3	$2.00^{+2.33}_{-0.22}$
125.8	58.62	$^{+0.4}_{-0.8}$	$\pm1.8/\pm0.8/\pm2.0$	60.25	0.77	−7.3	$2.00^{+2.33}_{-0.22}$
125.9	58.45	$^{+0.4}_{-0.7}$	$\pm1.8/\pm0.8/\pm2.0$	60.07	0.76	−7.3	$1.99^{+2.33}_{-0.22}$
126.0	58.29	$^{+0.5}_{-0.7}$	$\pm1.8/\pm0.8/\pm2.0$	59.91	0.76	−7.3	$1.99^{+2.33}_{-0.22}$
126.5	57.59	$^{+0.5}_{-0.7}$	$\pm1.8/\pm0.8/\pm2.0$	59.18	0.75	−7.3	$1.99^{+2.32}_{-0.22}$
127.0	56.80	$^{+0.5}_{-0.6}$	$\pm1.8/\pm0.8/\pm1.9$	58.36	0.74	−7.3	$1.98^{+2.32}_{-0.22}$
127.5	56.12	$^{+0.5}_{-0.6}$	$\pm1.8/\pm0.8/\pm1.9$	57.66	0.74	−7.4	$1.98^{+2.31}_{-0.22}$
128.0	55.41	$^{+0.4}_{-0.6}$	$\pm1.8/\pm0.8/\pm1.9$	56.91	0.73	−7.4	$1.97^{+2.30}_{-0.22}$
128.5	54.74	$^{+0.4}_{-0.7}$	$\pm1.8/\pm0.8/\pm1.9$	56.22	0.72	−7.4	$1.97^{+2.29}_{-0.22}$
129.0	54.07	$^{+0.4}_{-0.7}$	$\pm1.8/\pm0.8/\pm1.9$	55.53	0.71	−7.4	$1.96^{+2.29}_{-0.21}$
129.5	53.38	$^{+0.5}_{-0.7}$	$\pm1.8/\pm0.8/\pm1.9$	54.81	0.71	−7.5	$1.96^{+2.28}_{-0.21}$
130.0	52.70	$^{+0.5}_{-0.6}$	$\pm1.8/\pm0.8/\pm1.9$	54.10	0.70	−7.5	$1.95^{+2.27}_{-0.21}$

Table 214: Total $\mathrm{W}^-(\to\ell^-\bar{\nu}_\ell)\mathrm{H}$ cross sections including QCD and EW corrections and their uncertainties for a proton–proton collision energy $\sqrt{s} = 14$ TeV.

M_H	σ	Δ_scale	$\Delta_{\mathrm{PDF}/\alpha_\mathrm{s}/\mathrm{PDF}\oplus\alpha_\mathrm{s}}$	$\sigma^\mathrm{DY}_\mathrm{NNLOQCD}$	$\sigma_\text{t-loop}$	δ_EW	σ_γ
[GeV]	[fb]	[%]	[%]	[fb]	[fb]	[%]	[fb]
120.0	75.77	$^{+0.4}_{-0.6}$	$\pm1.7/\pm0.8/\pm1.9$	77.89	0.97	-7.0	$2.39^{+2.74}_{-0.26}$
120.5	74.76	$^{+0.4}_{-0.6}$	$\pm1.7/\pm0.8/\pm1.9$	76.82	0.98	-7.1	$2.38^{+2.73}_{-0.26}$
121.0	73.78	$^{+0.4}_{-0.6}$	$\pm1.7/\pm0.8/\pm1.9$	75.82	0.96	-7.1	$2.37^{+2.72}_{-0.26}$
121.5	72.89	$^{+0.3}_{-0.7}$	$\pm1.7/\pm0.8/\pm1.9$	74.91	0.95	-7.1	$2.37^{+2.71}_{-0.26}$
122.0	71.93	$^{+0.4}_{-0.7}$	$\pm1.7/\pm0.8/\pm1.9$	73.90	0.94	-7.1	$2.36^{+2.70}_{-0.26}$
122.5	71.01	$^{+0.5}_{-0.7}$	$\pm1.7/\pm0.8/\pm1.9$	72.94	0.93	-7.1	$2.35^{+2.69}_{-0.26}$
123.0	70.10	$^{+0.4}_{-0.7}$	$\pm1.7/\pm0.8/\pm1.9$	71.99	0.92	-7.2	$2.35^{+2.69}_{-0.26}$
123.5	69.18	$^{+0.4}_{-0.7}$	$\pm1.7/\pm0.8/\pm1.9$	71.04	0.91	-7.2	$2.34^{+2.68}_{-0.26}$
124.0	68.29	$^{+0.4}_{-0.6}$	$\pm1.7/\pm0.8/\pm1.9$	70.12	0.90	-7.2	$2.33^{+2.67}_{-0.26}$
124.1	68.11	$^{+0.4}_{-0.6}$	$\pm1.7/\pm0.8/\pm1.9$	69.94	0.90	-7.2	$2.33^{+2.67}_{-0.26}$
124.2	67.91	$^{+0.5}_{-0.6}$	$\pm1.7/\pm0.8/\pm1.9$	69.72	0.90	-7.2	$2.33^{+2.67}_{-0.26}$
124.3	67.76	$^{+0.5}_{-0.6}$	$\pm1.7/\pm0.8/\pm1.9$	69.57	0.90	-7.2	$2.33^{+2.67}_{-0.26}$
124.4	67.60	$^{+0.5}_{-0.6}$	$\pm1.7/\pm0.8/\pm1.9$	69.40	0.89	-7.2	$2.33^{+2.66}_{-0.26}$
124.5	67.42	$^{+0.4}_{-0.7}$	$\pm1.7/\pm0.8/\pm1.9$	69.22	0.89	-7.2	$2.33^{+2.66}_{-0.26}$
124.6	67.31	$^{+0.3}_{-0.8}$	$\pm1.7/\pm0.9/\pm1.9$	69.10	0.89	-7.2	$2.33^{+2.66}_{-0.26}$
124.7	67.07	$^{+0.4}_{-0.6}$	$\pm1.7/\pm0.9/\pm1.9$	68.85	0.89	-7.3	$2.33^{+2.66}_{-0.26}$
124.8	66.84	$^{+0.5}_{-0.6}$	$\pm1.7/\pm0.9/\pm1.9$	68.61	0.89	-7.3	$2.32^{+2.66}_{-0.26}$
124.9	66.67	$^{+0.5}_{-0.5}$	$\pm1.7/\pm0.9/\pm1.9$	68.44	0.89	-7.3	$2.32^{+2.66}_{-0.26}$
125.0	66.49	$^{+0.5}_{-0.6}$	$\pm1.7/\pm0.9/\pm1.9$	68.24	0.89	-7.3	$2.32^{+2.65}_{-0.26}$
125.09	66.33	$^{+0.5}_{-0.5}$	$\pm1.7/\pm0.9/\pm1.9$	68.09	0.88	-7.3	$2.32^{+2.65}_{-0.26}$
125.1	66.31	$^{+0.5}_{-0.5}$	$\pm1.7/\pm0.9/\pm1.9$	68.07	0.88	-7.3	$2.32^{+2.65}_{-0.26}$
125.2	66.23	$^{+0.4}_{-0.7}$	$\pm1.7/\pm0.9/\pm1.9$	67.98	0.88	-7.3	$2.32^{+2.65}_{-0.26}$
125.3	66.02	$^{+0.5}_{-0.6}$	$\pm1.7/\pm0.9/\pm1.9$	67.75	0.88	-7.3	$2.32^{+2.65}_{-0.26}$
125.4	65.86	$^{+0.4}_{-0.6}$	$\pm1.7/\pm0.9/\pm1.9$	67.60	0.88	-7.3	$2.32^{+2.65}_{-0.26}$
125.5	65.72	$^{+0.4}_{-0.6}$	$\pm1.7/\pm0.9/\pm1.9$	67.46	0.87	-7.3	$2.32^{+2.65}_{-0.26}$
125.6	65.55	$^{+0.3}_{-0.6}$	$\pm1.7/\pm0.9/\pm1.9$	67.28	0.87	-7.3	$2.32^{+2.65}_{-0.26}$
125.7	65.42	$^{+0.3}_{-0.7}$	$\pm1.7/\pm0.9/\pm1.9$	67.13	0.87	-7.3	$2.31^{+2.65}_{-0.26}$
125.8	65.22	$^{+0.4}_{-0.7}$	$\pm1.7/\pm0.9/\pm1.9$	66.92	0.87	-7.3	$2.31^{+2.65}_{-0.26}$
125.9	65.07	$^{+0.3}_{-0.7}$	$\pm1.7/\pm0.9/\pm1.9$	66.77	0.87	-7.3	$2.31^{+2.65}_{-0.25}$
126.0	64.93	$^{+0.3}_{-0.7}$	$\pm1.7/\pm0.9/\pm1.9$	66.62	0.87	-7.3	$2.31^{+2.65}_{-0.25}$
126.5	64.09	$^{+0.3}_{-0.7}$	$\pm1.7/\pm0.9/\pm1.9$	65.76	0.85	-7.3	$2.31^{+2.64}_{-0.25}$
127.0	63.21	$^{+0.4}_{-0.6}$	$\pm1.7/\pm0.9/\pm1.9$	64.84	0.85	-7.4	$2.30^{+2.64}_{-0.25}$
127.5	62.50	$^{+0.3}_{-0.7}$	$\pm1.7/\pm0.9/\pm1.9$	64.10	0.84	-7.4	$2.30^{+2.63}_{-0.25}$
128.0	61.68	$^{+0.5}_{-0.7}$	$\pm1.7/\pm0.9/\pm1.9$	63.25	0.83	-7.4	$2.29^{+2.63}_{-0.25}$
128.5	60.85	$^{+0.5}_{-0.7}$	$\pm1.7/\pm0.9/\pm1.9$	62.39	0.82	-7.4	$2.29^{+2.63}_{-0.25}$
129.0	60.11	$^{+0.5}_{-0.6}$	$\pm1.7/\pm0.9/\pm1.9$	61.62	0.82	-7.5	$2.28^{+2.62}_{-0.24}$
129.5	59.39	$^{+0.5}_{-0.7}$	$\pm1.7/\pm0.9/\pm1.9$	60.87	0.80	-7.5	$2.28^{+2.62}_{-0.24}$
130.0	58.70	$^{+0.4}_{-0.7}$	$\pm1.7/\pm0.9/\pm1.9$	60.16	0.80	-7.5	$2.27^{+2.61}_{-0.24}$

Table 215: Total $\mathrm{Z}(\to\ell^+\ell^-)\mathrm{H}$ cross sections including QCD and EW corrections and their uncertainties for a proton–proton collision energy $\sqrt{s} = 7$ TeV.

M_H	σ	Δ_scale	$\Delta_{\mathrm{PDF}/\alpha_\mathrm{s}/\mathrm{PDF}\oplus\alpha_\mathrm{s}}$	$\sigma^\mathrm{DY}_\mathrm{NNLOQCD}$	$\sigma^\mathrm{ggZH}_\mathrm{NLO+NLL}$	$\sigma_\text{t-loop}$	δ_EW	σ_γ
[GeV]	[fb]	[%]	[%]	[fb]	[fb]	[fb]	[%]	[fb]
120.0	12.97	$^{+2.5}_{-2.2}$	$\pm1.6/\pm0.7/\pm1.7$	12.46	1.00	0.12	−5.1	$0.03^{+0.04}_{-0.00}$
120.5	12.81	$^{+2.4}_{-2.2}$	$\pm1.6/\pm0.7/\pm1.7$	12.29	0.99	0.12	−5.1	$0.03^{+0.04}_{-0.00}$
121.0	12.65	$^{+2.5}_{-2.2}$	$\pm1.6/\pm0.7/\pm1.7$	12.13	0.99	0.12	−5.1	$0.03^{+0.04}_{-0.00}$
121.5	12.48	$^{+2.5}_{-2.2}$	$\pm1.6/\pm0.7/\pm1.7$	11.96	0.98	0.12	−5.1	$0.03^{+0.04}_{-0.00}$
122.0	12.32	$^{+2.6}_{-2.1}$	$\pm1.6/\pm0.7/\pm1.7$	11.80	0.98	0.11	−5.1	$0.03^{+0.04}_{-0.00}$
122.5	12.17	$^{+2.6}_{-2.2}$	$\pm1.6/\pm0.7/\pm1.7$	11.65	0.97	0.11	−5.1	$0.03^{+0.04}_{-0.00}$
123.0	12.00	$^{+2.7}_{-2.1}$	$\pm1.6/\pm0.7/\pm1.7$	11.49	0.96	0.11	−5.1	$0.03^{+0.04}_{-0.00}$
123.5	11.85	$^{+2.6}_{-2.2}$	$\pm1.6/\pm0.7/\pm1.7$	11.34	0.96	0.11	−5.1	$0.03^{+0.04}_{-0.00}$
124.0	11.72	$^{+2.6}_{-2.3}$	$\pm1.6/\pm0.7/\pm1.7$	11.20	0.96	0.11	−5.1	$0.03^{+0.04}_{-0.00}$
124.1	11.69	$^{+2.6}_{-2.3}$	$\pm1.6/\pm0.7/\pm1.7$	11.17	0.95	0.11	−5.1	$0.03^{+0.04}_{-0.00}$
124.2	11.66	$^{+2.5}_{-2.3}$	$\pm1.6/\pm0.7/\pm1.7$	11.14	0.95	0.11	−5.1	$0.03^{+0.04}_{-0.00}$
124.3	11.63	$^{+2.6}_{-2.3}$	$\pm1.6/\pm0.7/\pm1.7$	11.11	0.95	0.11	−5.1	$0.03^{+0.04}_{-0.00}$
124.4	11.60	$^{+2.5}_{-2.3}$	$\pm1.6/\pm0.7/\pm1.7$	11.09	0.95	0.11	−5.1	$0.03^{+0.04}_{-0.00}$
124.5	11.57	$^{+2.7}_{-2.3}$	$\pm1.6/\pm0.7/\pm1.7$	11.05	0.95	0.11	−5.2	$0.03^{+0.04}_{-0.00}$
124.6	11.54	$^{+2.6}_{-2.3}$	$\pm1.6/\pm0.7/\pm1.7$	11.03	0.95	0.11	−5.2	$0.03^{+0.04}_{-0.00}$
124.7	11.51	$^{+2.6}_{-2.3}$	$\pm1.6/\pm0.7/\pm1.7$	11.00	0.95	0.11	−5.2	$0.03^{+0.04}_{-0.00}$
124.8	11.48	$^{+2.6}_{-2.3}$	$\pm1.6/\pm0.7/\pm1.7$	10.97	0.94	0.11	−5.2	$0.03^{+0.04}_{-0.00}$
124.9	11.46	$^{+2.6}_{-2.3}$	$\pm1.6/\pm0.7/\pm1.7$	10.94	0.94	0.11	−5.2	$0.03^{+0.04}_{-0.00}$
125.0	11.43	$^{+2.6}_{-2.4}$	$\pm1.6/\pm0.7/\pm1.7$	10.91	0.94	0.11	−5.2	$0.03^{+0.04}_{-0.00}$
125.09	11.40	$^{+2.6}_{-2.3}$	$\pm1.6/\pm0.7/\pm1.7$	10.88	0.94	0.11	−5.2	$0.03^{+0.04}_{-0.00}$
125.1	11.40	$^{+2.6}_{-2.3}$	$\pm1.6/\pm0.7/\pm1.7$	10.88	0.94	0.11	−5.2	$0.03^{+0.04}_{-0.00}$
125.2	11.37	$^{+2.6}_{-2.3}$	$\pm1.6/\pm0.7/\pm1.7$	10.85	0.94	0.11	−5.2	$0.03^{+0.04}_{-0.00}$
125.3	11.34	$^{+2.7}_{-2.3}$	$\pm1.6/\pm0.7/\pm1.7$	10.82	0.94	0.11	−5.2	$0.03^{+0.04}_{-0.00}$
125.4	11.31	$^{+2.7}_{-2.3}$	$\pm1.6/\pm0.7/\pm1.7$	10.80	0.94	0.11	−5.2	$0.03^{+0.04}_{-0.00}$
125.5	11.28	$^{+2.6}_{-2.3}$	$\pm1.6/\pm0.7/\pm1.7$	10.76	0.94	0.11	−5.2	$0.03^{+0.04}_{-0.00}$
125.6	11.25	$^{+2.6}_{-2.3}$	$\pm1.6/\pm0.7/\pm1.7$	10.73	0.94	0.11	−5.2	$0.03^{+0.04}_{-0.00}$
125.7	11.23	$^{+2.6}_{-2.3}$	$\pm1.6/\pm0.7/\pm1.7$	10.71	0.94	0.11	−5.2	$0.03^{+0.04}_{-0.00}$
125.8	11.20	$^{+2.6}_{-2.3}$	$\pm1.6/\pm0.7/\pm1.7$	10.68	0.94	0.11	−5.2	$0.03^{+0.04}_{-0.00}$
125.9	11.17	$^{+2.6}_{-2.3}$	$\pm1.6/\pm0.7/\pm1.7$	10.65	0.93	0.11	−5.2	$0.03^{+0.04}_{-0.00}$
126.0	11.14	$^{+2.6}_{-2.3}$	$\pm1.6/\pm0.7/\pm1.7$	10.63	0.93	0.10	−5.2	$0.03^{+0.04}_{-0.00}$
126.5	11.00	$^{+2.7}_{-2.3}$	$\pm1.6/\pm0.7/\pm1.7$	10.48	0.93	0.10	−5.2	$0.03^{+0.04}_{-0.00}$
127.0	10.87	$^{+2.7}_{-2.3}$	$\pm1.6/\pm0.7/\pm1.7$	10.35	0.92	0.10	−5.2	$0.03^{+0.04}_{-0.00}$
127.5	10.73	$^{+2.7}_{-2.3}$	$\pm1.6/\pm0.7/\pm1.7$	10.22	0.92	0.10	−5.2	$0.03^{+0.04}_{-0.00}$
128.0	10.60	$^{+2.7}_{-2.3}$	$\pm1.6/\pm0.7/\pm1.7$	10.08	0.91	0.10	−5.2	$0.03^{+0.04}_{-0.00}$
128.5	10.48	$^{+2.7}_{-2.3}$	$\pm1.6/\pm0.7/\pm1.7$	9.96	0.91	0.10	−5.2	$0.03^{+0.04}_{-0.00}$
129.0	10.35	$^{+2.7}_{-2.3}$	$\pm1.6/\pm0.7/\pm1.7$	9.84	0.90	0.10	−5.2	$0.03^{+0.04}_{-0.00}$
129.5	10.22	$^{+2.7}_{-2.4}$	$\pm1.6/\pm0.7/\pm1.7$	9.71	0.89	0.10	−5.2	$0.03^{+0.04}_{-0.00}$
130.0	10.10	$^{+2.7}_{-2.4}$	$\pm1.6/\pm0.7/\pm1.7$	9.59	0.89	0.10	−5.2	$0.03^{+0.04}_{-0.00}$

Table 216: Total $\mathrm{Z}(\to\ell^+\ell^-)\mathrm{H}$ cross sections including QCD and EW corrections and their uncertainties for a proton–proton collision energy $\sqrt{s} = 8$ TeV.

M_{H}	σ	Δ_{scale}	$\Delta_{\mathrm{PDF}/\alpha_{\mathrm{s}}/\mathrm{PDF}\oplus\alpha_{\mathrm{s}}}$	$\sigma^{\mathrm{DY}}_{\mathrm{NNLOQCD}}$	$\sigma^{\mathrm{ggZH}}_{\mathrm{NLO+NLL}}$	$\sigma_{\text{t-loop}}$	δ_{EW}	σ_γ
[GeV]	[fb]	[%]	[%]	[fb]	[fb]	[fb]	[%]	[fb]
120.0	16.06	$^{+2.6}_{-2.4}$	$\pm1.5/\pm0.8/\pm1.7$	15.24	1.41	0.15	−5.1	$0.04^{+0.05}_{-0.00}$
120.5	15.85	$^{+2.7}_{-2.3}$	$\pm1.5/\pm0.8/\pm1.7$	15.03	1.40	0.15	−5.1	$0.04^{+0.05}_{-0.00}$
121.0	15.66	$^{+2.7}_{-2.3}$	$\pm1.5/\pm0.8/\pm1.7$	14.84	1.39	0.15	−5.1	$0.04^{+0.05}_{-0.00}$
121.5	15.47	$^{+2.7}_{-2.3}$	$\pm1.5/\pm0.8/\pm1.7$	14.65	1.38	0.15	−5.1	$0.04^{+0.05}_{-0.00}$
122.0	15.28	$^{+2.8}_{-2.4}$	$\pm1.5/\pm0.8/\pm1.7$	14.46	1.38	0.15	−5.1	$0.04^{+0.05}_{-0.00}$
122.5	15.09	$^{+2.7}_{-2.4}$	$\pm1.5/\pm0.8/\pm1.7$	14.27	1.37	0.14	−5.2	$0.04^{+0.05}_{-0.00}$
123.0	14.90	$^{+2.8}_{-2.4}$	$\pm1.5/\pm0.8/\pm1.7$	14.08	1.36	0.14	−5.2	$0.04^{+0.05}_{-0.00}$
123.5	14.71	$^{+2.8}_{-2.4}$	$\pm1.5/\pm0.8/\pm1.7$	13.90	1.35	0.14	−5.2	$0.04^{+0.05}_{-0.00}$
124.0	14.54	$^{+2.8}_{-2.4}$	$\pm1.5/\pm0.8/\pm1.7$	13.72	1.35	0.14	−5.2	$0.04^{+0.05}_{-0.00}$
124.1	14.50	$^{+2.8}_{-2.4}$	$\pm1.5/\pm0.8/\pm1.7$	13.68	1.34	0.14	−5.2	$0.04^{+0.05}_{-0.00}$
124.2	14.46	$^{+2.8}_{-2.4}$	$\pm1.5/\pm0.8/\pm1.7$	13.65	1.34	0.14	−5.2	$0.04^{+0.05}_{-0.00}$
124.3	14.43	$^{+2.7}_{-2.4}$	$\pm1.5/\pm0.8/\pm1.7$	13.62	1.34	0.14	−5.2	$0.04^{+0.05}_{-0.00}$
124.4	14.40	$^{+2.8}_{-2.5}$	$\pm1.5/\pm0.8/\pm1.7$	13.58	1.34	0.14	−5.2	$0.04^{+0.05}_{-0.00}$
124.5	14.36	$^{+2.7}_{-2.5}$	$\pm1.5/\pm0.8/\pm1.7$	13.55	1.34	0.14	−5.2	$0.04^{+0.05}_{-0.00}$
124.6	14.32	$^{+2.8}_{-2.5}$	$\pm1.5/\pm0.8/\pm1.7$	13.51	1.34	0.14	−5.2	$0.04^{+0.05}_{-0.00}$
124.7	14.28	$^{+2.9}_{-2.4}$	$\pm1.5/\pm0.8/\pm1.7$	13.47	1.33	0.14	−5.2	$0.04^{+0.05}_{-0.00}$
124.8	14.25	$^{+2.9}_{-2.4}$	$\pm1.5/\pm0.8/\pm1.7$	13.43	1.33	0.14	−5.2	$0.04^{+0.05}_{-0.00}$
124.9	14.21	$^{+2.9}_{-2.4}$	$\pm1.5/\pm0.8/\pm1.7$	13.40	1.33	0.14	−5.2	$0.04^{+0.05}_{-0.00}$
125.0	14.18	$^{+2.9}_{-2.4}$	$\pm1.5/\pm0.8/\pm1.7$	13.36	1.33	0.14	−5.2	$0.04^{+0.05}_{-0.00}$
125.09	14.15	$^{+2.8}_{-2.4}$	$\pm1.5/\pm0.8/\pm1.7$	13.34	1.33	0.14	−5.2	$0.04^{+0.05}_{-0.00}$
125.1	14.15	$^{+2.8}_{-2.5}$	$\pm1.5/\pm0.8/\pm1.7$	13.34	1.33	0.14	−5.2	$0.04^{+0.05}_{-0.00}$
125.2	14.11	$^{+2.8}_{-2.5}$	$\pm1.5/\pm0.8/\pm1.7$	13.30	1.33	0.14	−5.2	$0.04^{+0.05}_{-0.00}$
125.3	14.07	$^{+2.9}_{-2.4}$	$\pm1.5/\pm0.8/\pm1.7$	13.26	1.33	0.14	−5.2	$0.04^{+0.05}_{-0.00}$
125.4	14.04	$^{+2.8}_{-2.4}$	$\pm1.5/\pm0.8/\pm1.7$	13.23	1.32	0.14	−5.2	$0.04^{+0.05}_{-0.00}$
125.5	14.01	$^{+2.8}_{-2.5}$	$\pm1.5/\pm0.8/\pm1.7$	13.20	1.32	0.14	−5.2	$0.04^{+0.05}_{-0.00}$
125.6	13.98	$^{+2.8}_{-2.5}$	$\pm1.5/\pm0.8/\pm1.7$	13.16	1.32	0.13	−5.2	$0.04^{+0.05}_{-0.00}$
125.7	13.94	$^{+2.8}_{-2.5}$	$\pm1.5/\pm0.7/\pm1.7$	13.13	1.32	0.14	−5.2	$0.04^{+0.05}_{-0.00}$
125.8	13.91	$^{+2.7}_{-2.6}$	$\pm1.5/\pm0.7/\pm1.7$	13.10	1.32	0.14	−5.2	$0.04^{+0.05}_{-0.00}$
125.9	13.88	$^{+2.8}_{-2.6}$	$\pm1.5/\pm0.7/\pm1.7$	13.07	1.32	0.14	−5.2	$0.04^{+0.05}_{-0.00}$
126.0	13.84	$^{+2.8}_{-2.5}$	$\pm1.5/\pm0.7/\pm1.7$	13.03	1.32	0.13	−5.2	$0.04^{+0.05}_{-0.00}$
126.5	13.67	$^{+2.9}_{-2.5}$	$\pm1.5/\pm0.7/\pm1.7$	12.86	1.31	0.13	−5.2	$0.04^{+0.05}_{-0.00}$
127.0	13.51	$^{+2.9}_{-2.5}$	$\pm1.5/\pm0.7/\pm1.7$	12.70	1.30	0.13	−5.2	$0.04^{+0.05}_{-0.00}$
127.5	13.35	$^{+2.8}_{-2.6}$	$\pm1.5/\pm0.7/\pm1.7$	12.54	1.29	0.13	−5.2	$0.04^{+0.05}_{-0.00}$
128.0	13.19	$^{+2.9}_{-2.6}$	$\pm1.5/\pm0.7/\pm1.7$	12.38	1.29	0.13	−5.2	$0.04^{+0.05}_{-0.00}$
128.5	13.02	$^{+3.0}_{-2.5}$	$\pm1.5/\pm0.7/\pm1.7$	12.22	1.28	0.13	−5.2	$0.04^{+0.05}_{-0.00}$
129.0	12.87	$^{+2.9}_{-2.6}$	$\pm1.5/\pm0.7/\pm1.7$	12.07	1.27	0.13	−5.2	$0.04^{+0.05}_{-0.00}$
129.5	12.72	$^{+2.9}_{-2.6}$	$\pm1.5/\pm0.7/\pm1.7$	11.92	1.26	0.13	−5.2	$0.04^{+0.05}_{-0.00}$
130.0	12.56	$^{+3.0}_{-2.6}$	$\pm1.5/\pm0.7/\pm1.7$	11.77	1.25	0.12	−5.3	$0.04^{+0.05}_{-0.00}$

Table 217: Total $\mathrm{Z}(\to\ell^+\ell^-)\mathrm{H}$ cross sections including QCD and EW corrections and their uncertainties for a proton–proton collision energy $\sqrt{s} = 13$ TeV.

M_H	σ	Δ_scale	$\Delta_{\mathrm{PDF}/\alpha_\mathrm{s}/\mathrm{PDF}\oplus\alpha_\mathrm{s}}$	$\sigma^\mathrm{DY}_\mathrm{NNLOQCD}$	$\sigma^\mathrm{ggZH}_\mathrm{NLO+NLL}$	$\sigma_\text{t-loop}$	δ_EW	σ_γ
[GeV]	[fb]	[%]	[%]	[fb]	[fb]	[fb]	[%]	[fb]
120.0	33.52	$^{+3.4}_{-3.0}$	$\pm1.3/\pm1.0/\pm1.6$	30.24	4.38	0.35	−5.2	$0.11^{+0.13}_{-0.01}$
120.5	33.15	$^{+3.4}_{-3.0}$	$\pm1.3/\pm1.0/\pm1.6$	29.89	4.36	0.34	−5.2	$0.11^{+0.13}_{-0.01}$
121.0	32.73	$^{+3.5}_{-3.0}$	$\pm1.3/\pm1.0/\pm1.6$	29.49	4.32	0.34	−5.2	$0.11^{+0.13}_{-0.01}$
121.5	32.35	$^{+3.6}_{-3.0}$	$\pm1.3/\pm1.0/\pm1.6$	29.14	4.28	0.34	−5.2	$0.11^{+0.13}_{-0.01}$
122.0	31.99	$^{+3.6}_{-3.0}$	$\pm1.3/\pm1.0/\pm1.6$	28.75	4.29	0.33	−5.2	$0.11^{+0.13}_{-0.01}$
122.5	31.61	$^{+3.6}_{-3.0}$	$\pm1.3/\pm0.9/\pm1.6$	28.38	4.27	0.33	−5.2	$0.11^{+0.12}_{-0.01}$
123.0	31.25	$^{+3.6}_{-3.1}$	$\pm1.3/\pm0.9/\pm1.6$	28.05	4.23	0.33	−5.2	$0.11^{+0.12}_{-0.01}$
123.5	30.89	$^{+3.5}_{-3.1}$	$\pm1.3/\pm0.9/\pm1.6$	27.69	4.22	0.33	−5.2	$0.11^{+0.12}_{-0.01}$
124.0	30.53	$^{+3.6}_{-3.1}$	$\pm1.3/\pm0.9/\pm1.6$	27.34	4.19	0.32	−5.2	$0.11^{+0.12}_{-0.01}$
124.1	30.48	$^{+3.7}_{-3.2}$	$\pm1.3/\pm0.9/\pm1.6$	27.29	4.19	0.32	−5.3	$0.11^{+0.12}_{-0.01}$
124.2	30.39	$^{+3.8}_{-3.0}$	$\pm1.3/\pm0.9/\pm1.6$	27.20	4.19	0.32	−5.3	$0.11^{+0.12}_{-0.01}$
124.3	30.32	$^{+3.7}_{-3.1}$	$\pm1.3/\pm0.9/\pm1.6$	27.14	4.18	0.32	−5.3	$0.11^{+0.12}_{-0.01}$
124.4	30.24	$^{+3.7}_{-3.0}$	$\pm1.3/\pm0.9/\pm1.6$	27.06	4.17	0.32	−5.3	$0.11^{+0.12}_{-0.01}$
124.5	30.17	$^{+3.8}_{-3.0}$	$\pm1.3/\pm0.9/\pm1.6$	27.00	4.17	0.32	−5.3	$0.11^{+0.12}_{-0.01}$
124.6	30.10	$^{+3.8}_{-3.0}$	$\pm1.3/\pm0.9/\pm1.6$	26.93	4.16	0.32	−5.3	$0.11^{+0.12}_{-0.01}$
124.7	30.03	$^{+3.8}_{-3.1}$	$\pm1.3/\pm0.9/\pm1.6$	26.86	4.17	0.32	−5.3	$0.11^{+0.12}_{-0.01}$
124.8	29.97	$^{+3.7}_{-3.1}$	$\pm1.3/\pm0.9/\pm1.6$	26.81	4.15	0.32	−5.3	$0.11^{+0.12}_{-0.01}$
124.9	29.88	$^{+3.9}_{-3.1}$	$\pm1.3/\pm0.9/\pm1.6$	26.72	4.14	0.31	−5.3	$0.11^{+0.12}_{-0.01}$
125.0	29.82	$^{+3.8}_{-3.1}$	$\pm1.3/\pm0.9/\pm1.6$	26.66	4.14	0.31	−5.3	$0.11^{+0.12}_{-0.01}$
125.09	29.77	$^{+3.8}_{-3.0}$	$\pm1.3/\pm0.9/\pm1.6$	26.60	4.14	0.31	−5.3	$0.11^{+0.12}_{-0.01}$
125.1	29.75	$^{+3.9}_{-3.0}$	$\pm1.3/\pm0.9/\pm1.6$	26.59	4.14	0.32	−5.3	$0.11^{+0.12}_{-0.01}$
125.2	29.69	$^{+3.8}_{-3.1}$	$\pm1.3/\pm0.9/\pm1.6$	26.53	4.13	0.32	−5.3	$0.11^{+0.12}_{-0.01}$
125.3	29.63	$^{+3.8}_{-3.1}$	$\pm1.3/\pm0.9/\pm1.6$	26.47	4.13	0.31	−5.3	$0.11^{+0.12}_{-0.01}$
125.4	29.57	$^{+3.8}_{-3.1}$	$\pm1.3/\pm0.9/\pm1.6$	26.42	4.13	0.31	−5.3	$0.11^{+0.12}_{-0.01}$
125.5	29.50	$^{+3.7}_{-3.1}$	$\pm1.3/\pm0.9/\pm1.6$	26.34	4.12	0.31	−5.3	$0.11^{+0.12}_{-0.01}$
125.6	29.44	$^{+3.8}_{-3.1}$	$\pm1.3/\pm0.9/\pm1.6$	26.28	4.13	0.31	−5.3	$0.11^{+0.12}_{-0.01}$
125.7	29.36	$^{+3.8}_{-3.0}$	$\pm1.3/\pm0.9/\pm1.6$	26.22	4.11	0.31	−5.3	$0.11^{+0.12}_{-0.01}$
125.8	29.32	$^{+3.7}_{-3.2}$	$\pm1.3/\pm0.9/\pm1.6$	26.17	4.11	0.31	−5.3	$0.11^{+0.12}_{-0.01}$
125.9	29.24	$^{+3.8}_{-3.1}$	$\pm1.3/\pm0.9/\pm1.6$	26.09	4.11	0.31	−5.3	$0.11^{+0.12}_{-0.01}$
126.0	29.18	$^{+3.8}_{-3.1}$	$\pm1.3/\pm0.9/\pm1.6$	26.03	4.11	0.31	−5.3	$0.11^{+0.12}_{-0.01}$
126.5	28.84	$^{+3.7}_{-3.2}$	$\pm1.3/\pm0.9/\pm1.6$	25.70	4.09	0.31	−5.3	$0.11^{+0.12}_{-0.01}$
127.0	28.50	$^{+3.7}_{-3.2}$	$\pm1.3/\pm0.9/\pm1.6$	25.38	4.06	0.30	−5.3	$0.11^{+0.12}_{-0.01}$
127.5	28.17	$^{+3.8}_{-3.2}$	$\pm1.3/\pm0.9/\pm1.6$	25.05	4.04	0.30	−5.3	$0.11^{+0.12}_{-0.01}$
128.0	27.85	$^{+3.9}_{-3.1}$	$\pm1.3/\pm0.9/\pm1.6$	24.75	4.02	0.30	−5.3	$0.11^{+0.12}_{-0.01}$
128.5	27.54	$^{+3.9}_{-3.2}$	$\pm1.3/\pm0.9/\pm1.6$	24.46	3.98	0.29	−5.3	$0.11^{+0.12}_{-0.01}$
129.0	27.24	$^{+3.8}_{-3.2}$	$\pm1.3/\pm0.9/\pm1.6$	24.16	3.97	0.29	−5.3	$0.10^{+0.12}_{-0.01}$
129.5	26.93	$^{+3.9}_{-3.2}$	$\pm1.3/\pm0.9/\pm1.6$	23.85	3.95	0.29	−5.3	$0.10^{+0.12}_{-0.01}$
130.0	26.65	$^{+3.9}_{-3.2}$	$\pm1.3/\pm0.9/\pm1.6$	23.59	3.93	0.29	−5.3	$0.10^{+0.12}_{-0.01}$

Table 218: Total $\mathrm{Z}(\to\ell^+\ell^-)\mathrm{H}$ cross sections including QCD and EW corrections and their uncertainties for a proton–proton collision energy $\sqrt{s} = 14$ TeV.

M_{H}	σ	Δ_{scale}	$\Delta_{\mathrm{PDF}/\alpha_{\mathrm{s}}/\mathrm{PDF}\oplus\alpha_{\mathrm{s}}}$	$\sigma^{\mathrm{DY}}_{\mathrm{NNLOQCD}}$	$\sigma^{\mathrm{ggZH}}_{\mathrm{NLO+NLL}}$	$\sigma_{\text{t-loop}}$	δ_{EW}	σ_γ
[GeV]	[fb]	[%]	[%]	[fb]	[fb]	[fb]	[%]	[fb]
120.0	37.31	$^{+3.6}_{-3.0}$	$\pm1.3/\pm1.0/\pm1.7$	33.39	5.14	0.39	−5.2	$0.13^{+0.14}_{-0.01}$
120.5	36.90	$^{+3.7}_{-3.1}$	$\pm1.3/\pm1.0/\pm1.7$	32.99	5.12	0.39	−5.2	$0.13^{+0.14}_{-0.01}$
121.0	36.46	$^{+3.6}_{-3.1}$	$\pm1.3/\pm1.0/\pm1.7$	32.57	5.08	0.38	−5.2	$0.13^{+0.14}_{-0.01}$
121.5	36.06	$^{+3.5}_{-3.1}$	$\pm1.3/\pm1.0/\pm1.7$	32.17	5.07	0.38	−5.2	$0.13^{+0.14}_{-0.01}$
122.0	35.64	$^{+3.6}_{-3.1}$	$\pm1.3/\pm1.0/\pm1.7$	31.77	5.03	0.38	−5.2	$0.13^{+0.14}_{-0.01}$
122.5	35.25	$^{+3.6}_{-3.2}$	$\pm1.3/\pm1.0/\pm1.7$	31.39	5.00	0.37	−5.2	$0.13^{+0.14}_{-0.01}$
123.0	34.82	$^{+3.8}_{-3.1}$	$\pm1.3/\pm1.0/\pm1.6$	30.97	4.97	0.37	−5.2	$0.13^{+0.14}_{-0.01}$
123.5	34.41	$^{+3.7}_{-3.1}$	$\pm1.3/\pm1.0/\pm1.6$	30.58	4.94	0.37	−5.3	$0.13^{+0.14}_{-0.01}$
124.0	34.03	$^{+3.8}_{-3.2}$	$\pm1.3/\pm1.0/\pm1.6$	30.20	4.93	0.36	−5.3	$0.12^{+0.13}_{-0.01}$
124.1	33.95	$^{+3.7}_{-3.2}$	$\pm1.3/\pm1.0/\pm1.6$	30.13	4.92	0.36	−5.3	$0.12^{+0.13}_{-0.01}$
124.2	33.86	$^{+3.7}_{-3.1}$	$\pm1.3/\pm1.0/\pm1.6$	30.04	4.91	0.36	−5.3	$0.12^{+0.13}_{-0.01}$
124.3	33.80	$^{+3.7}_{-3.2}$	$\pm1.3/\pm1.0/\pm1.6$	29.97	4.92	0.36	−5.3	$0.12^{+0.13}_{-0.01}$
124.4	33.70	$^{+3.8}_{-3.2}$	$\pm1.3/\pm1.0/\pm1.6$	29.89	4.90	0.36	−5.3	$0.12^{+0.13}_{-0.01}$
124.5	33.65	$^{+3.7}_{-3.3}$	$\pm1.3/\pm1.0/\pm1.6$	29.84	4.90	0.36	−5.3	$0.12^{+0.13}_{-0.01}$
124.6	33.55	$^{+3.8}_{-3.2}$	$\pm1.3/\pm1.0/\pm1.6$	29.75	4.89	0.36	−5.3	$0.12^{+0.13}_{-0.01}$
124.7	33.49	$^{+3.8}_{-3.3}$	$\pm1.3/\pm1.0/\pm1.6$	29.68	4.89	0.36	−5.3	$0.12^{+0.13}_{-0.01}$
124.8	33.40	$^{+3.8}_{-3.2}$	$\pm1.3/\pm1.0/\pm1.6$	29.61	4.87	0.36	−5.3	$0.12^{+0.13}_{-0.01}$
124.9	33.32	$^{+3.8}_{-3.2}$	$\pm1.3/\pm1.0/\pm1.6$	29.52	4.87	0.36	−5.3	$0.12^{+0.13}_{-0.01}$
125.0	33.27	$^{+3.8}_{-3.3}$	$\pm1.3/\pm1.0/\pm1.6$	29.47	4.87	0.36	−5.3	$0.12^{+0.13}_{-0.01}$
125.09	33.19	$^{+3.8}_{-3.2}$	$\pm1.3/\pm1.0/\pm1.6$	29.39	4.87	0.36	−5.3	$0.12^{+0.13}_{-0.01}$
125.1	33.18	$^{+3.9}_{-3.3}$	$\pm1.3/\pm1.0/\pm1.6$	29.39	4.86	0.36	−5.3	$0.12^{+0.13}_{-0.01}$
125.2	33.11	$^{+3.8}_{-3.2}$	$\pm1.3/\pm1.0/\pm1.6$	29.31	4.87	0.35	−5.3	$0.12^{+0.13}_{-0.01}$
125.3	33.04	$^{+3.8}_{-3.3}$	$\pm1.3/\pm1.0/\pm1.6$	29.25	4.86	0.35	−5.3	$0.12^{+0.13}_{-0.01}$
125.4	32.96	$^{+3.9}_{-3.2}$	$\pm1.3/\pm1.0/\pm1.6$	29.17	4.85	0.35	−5.3	$0.12^{+0.13}_{-0.01}$
125.5	32.88	$^{+3.9}_{-3.2}$	$\pm1.3/\pm1.0/\pm1.6$	29.10	4.84	0.35	−5.3	$0.12^{+0.13}_{-0.01}$
125.6	32.82	$^{+3.8}_{-3.3}$	$\pm1.3/\pm1.0/\pm1.6$	29.04	4.84	0.35	−5.3	$0.12^{+0.13}_{-0.01}$
125.7	32.73	$^{+3.9}_{-3.3}$	$\pm1.3/\pm1.0/\pm1.6$	28.95	4.84	0.35	−5.3	$0.12^{+0.13}_{-0.01}$
125.8	32.65	$^{+3.9}_{-3.2}$	$\pm1.3/\pm1.0/\pm1.6$	28.87	4.83	0.35	−5.3	$0.12^{+0.13}_{-0.01}$
125.9	32.58	$^{+3.9}_{-3.2}$	$\pm1.3/\pm1.0/\pm1.6$	28.81	4.82	0.35	−5.3	$0.12^{+0.13}_{-0.01}$
126.0	32.48	$^{+4.0}_{-3.2}$	$\pm1.3/\pm1.0/\pm1.6$	28.71	4.82	0.35	−5.3	$0.12^{+0.13}_{-0.01}$
126.5	32.14	$^{+4.0}_{-3.3}$	$\pm1.3/\pm1.0/\pm1.6$	28.39	4.79	0.35	−5.3	$0.12^{+0.13}_{-0.01}$
127.0	31.79	$^{+4.1}_{-3.3}$	$\pm1.3/\pm1.0/\pm1.6$	28.04	4.77	0.34	−5.3	$0.12^{+0.13}_{-0.01}$
127.5	31.44	$^{+4.0}_{-3.3}$	$\pm1.3/\pm1.0/\pm1.6$	27.71	4.74	0.34	−5.3	$0.12^{+0.13}_{-0.01}$
128.0	31.07	$^{+4.1}_{-3.2}$	$\pm1.3/\pm1.0/\pm1.6$	27.36	4.71	0.34	−5.3	$0.12^{+0.13}_{-0.01}$
128.5	30.76	$^{+4.0}_{-3.4}$	$\pm1.3/\pm1.0/\pm1.6$	27.06	4.69	0.34	−5.3	$0.12^{+0.13}_{-0.01}$
129.0	30.44	$^{+3.9}_{-3.4}$	$\pm1.3/\pm1.0/\pm1.6$	26.75	4.66	0.33	−5.3	$0.12^{+0.13}_{-0.01}$
129.5	30.08	$^{+3.9}_{-3.4}$	$\pm1.3/\pm1.0/\pm1.6$	26.41	4.64	0.33	−5.3	$0.12^{+0.14}_{-0.01}$
130.0	29.72	$^{+4.1}_{-3.4}$	$\pm1.3/\pm1.0/\pm1.6$	26.07	4.60	0.32	−5.4	$0.12^{+0.14}_{-0.01}$

Table 219: Total $Z(\to\nu\bar{\nu})H$ cross sections including QCD and EW corrections and their uncertainties for a proton–proton collision energy $\sqrt{s} = 7$ TeV.

M_H	σ	Δ_{scale}	$\Delta_{\text{PDF}/\alpha_s/\text{PDF}\oplus\alpha_s}$	$\sigma^{\text{DY}}_{\text{NNLOQCD}}$	$\sigma^{\text{ggZH}}_{\text{NLO+NLL}}$	$\sigma_{\text{t-loop}}$	δ_{EW}	σ_γ
[GeV]	[fb]	[%]	[%]	[fb]	[fb]	[fb]	[%]	[fb]
120.0	77.40	$^{+2.5}_{-2.2}$	$\pm1.6/\pm0.7/\pm1.7$	73.87	5.92	0.71	−4.2	0.00
120.5	76.43	$^{+2.4}_{-2.2}$	$\pm1.6/\pm0.7/\pm1.7$	72.90	5.89	0.70	−4.2	0.00
121.0	75.46	$^{+2.5}_{-2.2}$	$\pm1.6/\pm0.7/\pm1.7$	71.93	5.86	0.69	−4.2	0.00
121.5	74.48	$^{+2.5}_{-2.2}$	$\pm1.6/\pm0.7/\pm1.7$	70.95	5.83	0.69	−4.2	0.00
122.0	73.51	$^{+2.6}_{-2.1}$	$\pm1.6/\pm0.7/\pm1.7$	70.00	5.78	0.68	−4.2	0.00
122.5	72.59	$^{+2.6}_{-2.2}$	$\pm1.6/\pm0.7/\pm1.7$	69.08	5.76	0.67	−4.2	0.00
123.0	71.62	$^{+2.7}_{-2.1}$	$\pm1.6/\pm0.7/\pm1.7$	68.12	5.72	0.66	−4.2	0.00
123.5	70.73	$^{+2.6}_{-2.2}$	$\pm1.6/\pm0.7/\pm1.7$	67.24	5.68	0.66	−4.2	0.00
124.0	69.90	$^{+2.6}_{-2.3}$	$\pm1.6/\pm0.7/\pm1.7$	66.40	5.67	0.65	−4.2	0.00
124.1	69.73	$^{+2.6}_{-2.3}$	$\pm1.6/\pm0.7/\pm1.7$	66.23	5.66	0.65	−4.2	0.00
124.2	69.58	$^{+2.5}_{-2.3}$	$\pm1.6/\pm0.7/\pm1.7$	66.08	5.66	0.65	−4.2	0.00
124.3	69.37	$^{+2.6}_{-2.3}$	$\pm1.6/\pm0.7/\pm1.7$	65.88	5.64	0.65	−4.2	0.00
124.4	69.23	$^{+2.5}_{-2.3}$	$\pm1.6/\pm0.7/\pm1.7$	65.74	5.64	0.64	−4.2	0.00
124.5	69.01	$^{+2.7}_{-2.3}$	$\pm1.6/\pm0.7/\pm1.7$	65.52	5.63	0.64	−4.2	0.00
124.6	68.88	$^{+2.6}_{-2.3}$	$\pm1.6/\pm0.7/\pm1.7$	65.39	5.63	0.64	−4.2	0.00
124.7	68.69	$^{+2.6}_{-2.3}$	$\pm1.6/\pm0.7/\pm1.7$	65.21	5.61	0.64	−4.2	0.00
124.8	68.50	$^{+2.6}_{-2.3}$	$\pm1.6/\pm0.7/\pm1.7$	65.03	5.60	0.64	−4.3	0.00
124.9	68.35	$^{+2.6}_{-2.3}$	$\pm1.6/\pm0.7/\pm1.7$	64.87	5.60	0.64	−4.3	0.00
125.0	68.18	$^{+2.6}_{-2.4}$	$\pm1.6/\pm0.7/\pm1.7$	64.70	5.59	0.64	−4.3	0.00
125.09	68.02	$^{+2.6}_{-2.3}$	$\pm1.6/\pm0.7/\pm1.7$	64.53	5.60	0.63	−4.3	0.00
125.1	68.00	$^{+2.6}_{-2.3}$	$\pm1.6/\pm0.7/\pm1.7$	64.51	5.59	0.64	−4.3	0.00
125.2	67.82	$^{+2.6}_{-2.3}$	$\pm1.6/\pm0.7/\pm1.7$	64.34	5.59	0.64	−4.3	0.00
125.3	67.65	$^{+2.7}_{-2.3}$	$\pm1.6/\pm0.7/\pm1.7$	64.17	5.58	0.63	−4.3	0.00
125.4	67.49	$^{+2.7}_{-2.3}$	$\pm1.6/\pm0.7/\pm1.7$	64.02	5.57	0.63	−4.3	0.00
125.5	67.28	$^{+2.6}_{-2.3}$	$\pm1.6/\pm0.7/\pm1.7$	63.81	5.56	0.63	−4.3	0.00
125.6	67.13	$^{+2.6}_{-2.3}$	$\pm1.6/\pm0.7/\pm1.7$	63.65	5.56	0.63	−4.3	0.00
125.7	66.97	$^{+2.6}_{-2.3}$	$\pm1.6/\pm0.7/\pm1.7$	63.50	5.56	0.63	−4.3	0.00
125.8	66.83	$^{+2.6}_{-2.3}$	$\pm1.6/\pm0.7/\pm1.7$	63.35	5.55	0.63	−4.3	0.00
125.9	66.62	$^{+2.6}_{-2.3}$	$\pm1.6/\pm0.7/\pm1.7$	63.16	5.54	0.62	−4.3	0.00
126.0	66.48	$^{+2.6}_{-2.3}$	$\pm1.6/\pm0.7/\pm1.7$	63.02	5.53	0.62	−4.3	0.00
126.5	65.62	$^{+2.7}_{-2.3}$	$\pm1.6/\pm0.7/\pm1.7$	62.17	5.50	0.62	−4.3	0.00
127.0	64.82	$^{+2.7}_{-2.3}$	$\pm1.6/\pm0.7/\pm1.7$	61.38	5.47	0.61	−4.3	0.00
127.5	64.03	$^{+2.7}_{-2.3}$	$\pm1.6/\pm0.7/\pm1.7$	60.58	5.44	0.61	−4.3	0.00
128.0	63.24	$^{+2.7}_{-2.3}$	$\pm1.6/\pm0.7/\pm1.7$	59.80	5.40	0.60	−4.3	0.00
128.5	62.48	$^{+2.7}_{-2.3}$	$\pm1.6/\pm0.7/\pm1.7$	59.06	5.37	0.59	−4.3	0.00
129.0	61.72	$^{+2.7}_{-2.3}$	$\pm1.6/\pm0.7/\pm1.7$	58.32	5.33	0.59	−4.3	0.00
129.5	60.97	$^{+2.7}_{-2.4}$	$\pm1.6/\pm0.7/\pm1.7$	57.57	5.31	0.58	−4.3	0.00
130.0	60.22	$^{+2.7}_{-2.4}$	$\pm1.6/\pm0.7/\pm1.7$	56.84	5.27	0.58	−4.3	0.00

Table 220: Total $Z(\to\nu\bar{\nu})H$ cross sections including QCD and EW corrections and their uncertainties for a proton–proton collision energy $\sqrt{s} = 8$ TeV.

M_H [GeV]	σ [fb]	Δ_{scale} [%]	$\Delta_{\text{PDF}/\alpha_s/\text{PDF}\oplus\alpha_s}$ [%]	$\sigma^{\text{DY}}_{\text{NNLOQCD}}$ [fb]	$\sigma^{\text{ggZH}}_{\text{NLO+NLL}}$ [fb]	$\sigma_{\text{t-loop}}$ [fb]	δ_{EW} [%]	σ_γ [fb]
120.0	95.81	$^{+2.6}_{-2.4}$	$\pm1.5/\pm0.8/\pm1.7$	90.37	8.35	0.90	−4.2	0.00
120.5	94.56	$^{+2.7}_{-2.3}$	$\pm1.5/\pm0.8/\pm1.7$	89.13	8.30	0.89	−4.2	0.00
121.0	93.41	$^{+2.7}_{-2.3}$	$\pm1.5/\pm0.8/\pm1.7$	87.99	8.26	0.88	−4.2	0.00
121.5	92.27	$^{+2.7}_{-2.3}$	$\pm1.5/\pm0.8/\pm1.7$	86.87	8.21	0.87	−4.2	0.00
122.0	91.12	$^{+2.8}_{-2.4}$	$\pm1.5/\pm0.8/\pm1.7$	85.72	8.17	0.86	−4.2	0.00
122.5	90.01	$^{+2.7}_{-2.4}$	$\pm1.5/\pm0.8/\pm1.7$	84.62	8.12	0.86	−4.2	0.00
123.0	88.85	$^{+2.8}_{-2.4}$	$\pm1.5/\pm0.8/\pm1.7$	83.48	8.07	0.85	−4.3	0.00
123.5	87.74	$^{+2.8}_{-2.4}$	$\pm1.5/\pm0.8/\pm1.7$	82.40	8.02	0.84	−4.3	0.00
124.0	86.69	$^{+2.8}_{-2.4}$	$\pm1.5/\pm0.8/\pm1.7$	81.35	7.98	0.83	−4.3	0.00
124.1	86.47	$^{+2.8}_{-2.4}$	$\pm1.5/\pm0.8/\pm1.7$	81.13	7.97	0.83	−4.3	0.00
124.2	86.27	$^{+2.8}_{-2.4}$	$\pm1.5/\pm0.8/\pm1.7$	80.94	7.96	0.82	−4.3	0.00
124.3	86.07	$^{+2.7}_{-2.4}$	$\pm1.5/\pm0.8/\pm1.7$	80.74	7.96	0.82	−4.3	0.00
124.4	85.87	$^{+2.8}_{-2.5}$	$\pm1.5/\pm0.8/\pm1.7$	80.54	7.94	0.83	−4.3	0.00
124.5	85.65	$^{+2.7}_{-2.5}$	$\pm1.5/\pm0.8/\pm1.7$	80.33	7.93	0.82	−4.3	0.00
124.6	85.42	$^{+2.8}_{-2.5}$	$\pm1.5/\pm0.8/\pm1.7$	80.09	7.92	0.83	−4.3	0.00
124.7	85.19	$^{+2.9}_{-2.4}$	$\pm1.5/\pm0.8/\pm1.7$	79.88	7.91	0.82	−4.3	0.00
124.8	84.97	$^{+2.9}_{-2.4}$	$\pm1.5/\pm0.8/\pm1.7$	79.66	7.90	0.81	−4.3	0.00
124.9	84.76	$^{+2.9}_{-2.4}$	$\pm1.5/\pm0.8/\pm1.7$	79.46	7.89	0.81	−4.3	0.00
125.0	84.56	$^{+2.9}_{-2.4}$	$\pm1.5/\pm0.8/\pm1.7$	79.25	7.89	0.81	−4.3	0.00
125.09	84.40	$^{+2.8}_{-2.4}$	$\pm1.5/\pm0.8/\pm1.7$	79.09	7.89	0.81	−4.3	0.00
125.1	84.40	$^{+2.8}_{-2.5}$	$\pm1.5/\pm0.8/\pm1.7$	79.08	7.89	0.81	−4.3	0.00
125.2	84.16	$^{+2.8}_{-2.5}$	$\pm1.5/\pm0.8/\pm1.7$	78.86	7.87	0.81	−4.3	0.00
125.3	83.94	$^{+2.9}_{-2.4}$	$\pm1.5/\pm0.8/\pm1.7$	78.64	7.86	0.81	−4.3	0.00
125.4	83.73	$^{+2.8}_{-2.4}$	$\pm1.5/\pm0.8/\pm1.7$	78.44	7.85	0.81	−4.3	0.00
125.5	83.56	$^{+2.8}_{-2.5}$	$\pm1.5/\pm0.8/\pm1.7$	78.26	7.84	0.81	−4.3	0.00
125.6	83.36	$^{+2.8}_{-2.5}$	$\pm1.5/\pm0.8/\pm1.7$	78.07	7.84	0.80	−4.3	0.00
125.7	83.13	$^{+2.8}_{-2.5}$	$\pm1.5/\pm0.7/\pm1.7$	77.84	7.83	0.80	−4.3	0.00
125.8	82.98	$^{+2.7}_{-2.6}$	$\pm1.5/\pm0.7/\pm1.7$	77.70	7.82	0.80	−4.3	0.00
125.9	82.79	$^{+2.8}_{-2.6}$	$\pm1.5/\pm0.7/\pm1.7$	77.49	7.82	0.80	−4.3	0.00
126.0	82.54	$^{+2.8}_{-2.5}$	$\pm1.5/\pm0.7/\pm1.7$	77.26	7.80	0.80	−4.3	0.00
126.5	81.53	$^{+2.9}_{-2.5}$	$\pm1.5/\pm0.7/\pm1.7$	76.27	7.75	0.79	−4.3	0.00
127.0	80.54	$^{+2.9}_{-2.5}$	$\pm1.5/\pm0.7/\pm1.7$	75.29	7.71	0.78	−4.3	0.00
127.5	79.60	$^{+2.8}_{-2.6}$	$\pm1.5/\pm0.7/\pm1.7$	74.36	7.67	0.78	−4.3	0.00
128.0	78.67	$^{+2.9}_{-2.6}$	$\pm1.5/\pm0.7/\pm1.7$	73.44	7.63	0.77	−4.3	0.00
128.5	77.63	$^{+3.0}_{-2.5}$	$\pm1.5/\pm0.7/\pm1.7$	72.45	7.57	0.76	−4.3	0.00
129.0	76.75	$^{+2.9}_{-2.6}$	$\pm1.5/\pm0.7/\pm1.7$	71.57	7.54	0.75	−4.3	0.00
129.5	75.82	$^{+2.9}_{-2.6}$	$\pm1.5/\pm0.7/\pm1.7$	70.66	7.49	0.74	−4.3	0.00
130.0	74.90	$^{+3.0}_{-2.6}$	$\pm1.5/\pm0.7/\pm1.7$	69.77	7.43	0.73	−4.4	0.00

Table 221: Total $Z(\to\nu\bar{\nu})H$ cross sections including QCD and EW corrections and their uncertainties for a proton–proton collision energy $\sqrt{s} = 13$ TeV.

M_H [GeV]	σ [fb]	Δ_{scale} [%]	$\Delta_{PDF/\alpha_s/PDF\oplus\alpha_s}$ [%]	$\sigma^{DY}_{NNLOQCD}$ [fb]	$\sigma^{ggZH}_{NLO+NLL}$ [fb]	$\sigma_{t\text{-loop}}$ [fb]	δ_{EW} [%]	σ_γ [fb]
120.0	199.71	$^{+3.4}_{-3.0}$	$\pm1.3/\pm1.0/\pm1.6$	179.34	26.00	2.07	−4.3	0.00
120.5	197.49	$^{+3.4}_{-3.0}$	$\pm1.3/\pm1.0/\pm1.6$	177.22	25.85	2.04	−4.3	0.00
121.0	195.02	$^{+3.5}_{-3.0}$	$\pm1.3/\pm1.0/\pm1.6$	174.89	25.64	2.02	−4.3	0.00
121.5	192.73	$^{+3.6}_{-3.0}$	$\pm1.3/\pm1.0/\pm1.6$	172.77	25.40	2.01	−4.3	0.00
122.0	190.57	$^{+3.6}_{-3.0}$	$\pm1.3/\pm1.0/\pm1.6$	170.51	25.45	1.98	−4.3	0.00
122.5	188.29	$^{+3.6}_{-3.0}$	$\pm1.3/\pm0.9/\pm1.6$	168.30	25.31	1.97	−4.3	0.00
123.0	186.15	$^{+3.6}_{-3.1}$	$\pm1.3/\pm0.9/\pm1.6$	166.32	25.10	1.93	−4.3	0.00
123.5	184.00	$^{+3.5}_{-3.1}$	$\pm1.3/\pm0.9/\pm1.6$	164.18	25.02	1.93	−4.3	0.00
124.0	181.88	$^{+3.6}_{-3.1}$	$\pm1.3/\pm0.9/\pm1.6$	162.15	24.86	1.92	−4.3	0.00
124.1	181.59	$^{+3.7}_{-3.2}$	$\pm1.3/\pm0.9/\pm1.6$	161.86	24.87	1.91	−4.4	0.00
124.2	181.01	$^{+3.8}_{-3.0}$	$\pm1.3/\pm0.9/\pm1.6$	161.32	24.82	1.89	−4.4	0.00
124.3	180.60	$^{+3.7}_{-3.1}$	$\pm1.3/\pm0.9/\pm1.6$	160.91	24.80	1.89	−4.4	0.00
124.4	180.13	$^{+3.7}_{-3.0}$	$\pm1.3/\pm0.9/\pm1.6$	160.49	24.74	1.89	−4.4	0.00
124.5	179.72	$^{+3.8}_{-3.0}$	$\pm1.3/\pm0.9/\pm1.6$	160.10	24.71	1.89	−4.4	0.00
124.6	179.27	$^{+3.8}_{-3.0}$	$\pm1.3/\pm0.9/\pm1.6$	159.68	24.67	1.88	−4.4	0.00
124.7	178.90	$^{+3.8}_{-3.1}$	$\pm1.3/\pm0.9/\pm1.6$	159.26	24.70	1.88	−4.4	0.00
124.8	178.51	$^{+3.7}_{-3.1}$	$\pm1.3/\pm0.9/\pm1.6$	158.96	24.61	1.88	−4.4	0.00
124.9	178.00	$^{+3.9}_{-3.1}$	$\pm1.3/\pm0.9/\pm1.6$	158.47	24.58	1.86	−4.4	0.00
125.0	177.62	$^{+3.8}_{-3.1}$	$\pm1.3/\pm0.9/\pm1.6$	158.10	24.57	1.85	−4.4	0.00
125.09	177.30	$^{+3.8}_{-3.0}$	$\pm1.3/\pm0.9/\pm1.6$	157.77	24.55	1.86	−4.4	0.00
125.1	177.22	$^{+3.9}_{-3.0}$	$\pm1.3/\pm0.9/\pm1.6$	157.70	24.54	1.87	−4.4	0.00
125.2	176.81	$^{+3.8}_{-3.1}$	$\pm1.3/\pm0.9/\pm1.6$	157.34	24.47	1.87	−4.4	0.00
125.3	176.48	$^{+3.8}_{-3.1}$	$\pm1.3/\pm0.9/\pm1.6$	157.00	24.48	1.86	−4.4	0.00
125.4	176.15	$^{+3.8}_{-3.1}$	$\pm1.3/\pm0.9/\pm1.6$	156.67	24.46	1.87	−4.4	0.00
125.5	175.68	$^{+3.7}_{-3.1}$	$\pm1.3/\pm0.9/\pm1.6$	156.21	24.44	1.86	−4.4	0.00
125.6	175.36	$^{+3.8}_{-3.1}$	$\pm1.3/\pm0.9/\pm1.6$	155.85	24.48	1.85	−4.4	0.00
125.7	174.88	$^{+3.8}_{-3.0}$	$\pm1.3/\pm0.9/\pm1.6$	155.47	24.36	1.85	−4.4	0.00
125.8	174.63	$^{+3.7}_{-3.2}$	$\pm1.3/\pm0.9/\pm1.6$	155.18	24.40	1.85	−4.4	0.00
125.9	174.16	$^{+3.8}_{-3.1}$	$\pm1.3/\pm0.9/\pm1.6$	154.74	24.36	1.83	−4.4	0.00
126.0	173.80	$^{+3.8}_{-3.1}$	$\pm1.3/\pm0.9/\pm1.6$	154.36	24.37	1.83	−4.4	0.00
126.5	171.76	$^{+3.7}_{-3.2}$	$\pm1.3/\pm0.9/\pm1.6$	152.40	24.23	1.81	−4.4	0.00
127.0	169.73	$^{+3.7}_{-3.2}$	$\pm1.3/\pm0.9/\pm1.6$	150.49	24.07	1.79	−4.4	0.00
127.5	167.75	$^{+3.8}_{-3.2}$	$\pm1.3/\pm0.9/\pm1.6$	148.56	23.94	1.78	−4.4	0.00
128.0	165.85	$^{+3.9}_{-3.1}$	$\pm1.3/\pm0.9/\pm1.6$	146.74	23.81	1.77	−4.4	0.00
128.5	164.02	$^{+3.9}_{-3.2}$	$\pm1.3/\pm0.9/\pm1.6$	145.06	23.62	1.75	−4.4	0.00
129.0	162.22	$^{+3.8}_{-3.2}$	$\pm1.3/\pm0.9/\pm1.6$	143.28	23.55	1.73	−4.4	0.00
129.5	160.33	$^{+3.9}_{-3.2}$	$\pm1.3/\pm0.9/\pm1.6$	141.45	23.44	1.72	−4.4	0.00
130.0	158.65	$^{+3.9}_{-3.2}$	$\pm1.3/\pm0.9/\pm1.6$	139.88	23.29	1.70	−4.4	0.00

Table 222: Total $Z(\to\nu\bar{\nu})H$ cross sections including QCD and EW corrections and their uncertainties for a proton–proton collision energy $\sqrt{s} = 14$ TeV.

M_H	σ	Δ_{scale}	$\Delta_{PDF/\alpha_s/PDF\oplus\alpha_s}$	$\sigma^{DY}_{NNLOQCD}$	$\sigma^{ggZH}_{NLO+NLL}$	$\sigma_{t\text{-loop}}$	δ_{EW}	σ_γ
[GeV]	[fb]	[%]	[%]	[fb]	[fb]	[fb]	[%]	[fb]
120.0	222.28	$^{+3.6}_{-3.0}$	$\pm1.3/\pm1.0/\pm1.7$	198.00	30.48	2.33	−4.3	0.00
120.5	219.82	$^{+3.7}_{-3.1}$	$\pm1.3/\pm1.0/\pm1.7$	195.63	30.34	2.29	−4.3	0.00
121.0	217.19	$^{+3.6}_{-3.1}$	$\pm1.3/\pm1.0/\pm1.7$	193.16	30.10	2.27	−4.3	0.00
121.5	214.80	$^{+3.5}_{-3.1}$	$\pm1.3/\pm1.0/\pm1.7$	190.76	30.04	2.25	−4.3	0.00
122.0	212.29	$^{+3.6}_{-3.1}$	$\pm1.3/\pm1.0/\pm1.7$	188.38	29.84	2.23	−4.3	0.00
122.5	209.94	$^{+3.6}_{-3.2}$	$\pm1.3/\pm1.0/\pm1.7$	186.16	29.64	2.22	−4.3	0.00
123.0	207.36	$^{+3.8}_{-3.1}$	$\pm1.3/\pm1.0/\pm1.6$	183.66	29.50	2.19	−4.3	0.00
123.5	204.93	$^{+3.7}_{-3.1}$	$\pm1.3/\pm1.0/\pm1.6$	181.35	29.29	2.19	−4.4	0.00
124.0	202.68	$^{+3.8}_{-3.2}$	$\pm1.3/\pm1.0/\pm1.6$	179.10	29.24	2.15	−4.4	0.00
124.1	202.20	$^{+3.7}_{-3.2}$	$\pm1.3/\pm1.0/\pm1.6$	178.68	29.16	2.15	−4.4	0.00
124.2	201.67	$^{+3.7}_{-3.1}$	$\pm1.3/\pm1.0/\pm1.6$	178.16	29.13	2.15	−4.4	0.00
124.3	201.31	$^{+3.7}_{-3.2}$	$\pm1.3/\pm1.0/\pm1.6$	177.75	29.18	2.13	−4.4	0.00
124.4	200.70	$^{+3.8}_{-3.2}$	$\pm1.3/\pm1.0/\pm1.6$	177.24	29.06	2.13	−4.4	0.00
124.5	200.38	$^{+3.7}_{-3.3}$	$\pm1.3/\pm1.0/\pm1.6$	176.93	29.04	2.14	−4.4	0.00
124.6	199.83	$^{+3.8}_{-3.2}$	$\pm1.3/\pm1.0/\pm1.6$	176.43	28.98	2.12	−4.4	0.00
124.7	199.45	$^{+3.8}_{-3.3}$	$\pm1.3/\pm1.0/\pm1.6$	176.03	29.00	2.12	−4.4	0.00
124.8	198.90	$^{+3.8}_{-3.2}$	$\pm1.3/\pm1.0/\pm1.6$	175.57	28.90	2.11	−4.4	0.00
124.9	198.43	$^{+3.8}_{-3.2}$	$\pm1.3/\pm1.0/\pm1.6$	175.07	28.91	2.12	−4.4	0.00
125.0	198.12	$^{+3.8}_{-3.3}$	$\pm1.3/\pm1.0/\pm1.6$	174.77	28.88	2.11	−4.4	0.00
125.09	197.64	$^{+3.8}_{-3.2}$	$\pm1.3/\pm1.0/\pm1.6$	174.28	28.86	2.12	−4.4	0.00
125.1	197.58	$^{+3.9}_{-3.3}$	$\pm1.3/\pm1.0/\pm1.6$	174.25	28.85	2.11	−4.4	0.00
125.2	197.16	$^{+3.8}_{-3.2}$	$\pm1.3/\pm1.0/\pm1.6$	173.81	28.86	2.10	−4.4	0.00
125.3	196.76	$^{+3.8}_{-3.3}$	$\pm1.3/\pm1.0/\pm1.6$	173.44	28.82	2.10	−4.4	0.00
125.4	196.26	$^{+3.9}_{-3.2}$	$\pm1.3/\pm1.0/\pm1.6$	172.97	28.77	2.09	−4.4	0.00
125.5	195.81	$^{+3.9}_{-3.2}$	$\pm1.3/\pm1.0/\pm1.6$	172.56	28.72	2.10	−4.4	0.00
125.6	195.44	$^{+3.8}_{-3.3}$	$\pm1.3/\pm1.0/\pm1.6$	172.22	28.68	2.09	−4.4	0.00
125.7	194.93	$^{+3.9}_{-3.3}$	$\pm1.3/\pm1.0/\pm1.6$	171.70	28.68	2.08	−4.4	0.00
125.8	194.42	$^{+3.9}_{-3.2}$	$\pm1.3/\pm1.0/\pm1.6$	171.22	28.63	2.08	−4.4	0.00
125.9	194.00	$^{+3.9}_{-3.2}$	$\pm1.3/\pm1.0/\pm1.6$	170.82	28.60	2.08	−4.4	0.00
126.0	193.44	$^{+4.0}_{-3.2}$	$\pm1.3/\pm1.0/\pm1.6$	170.28	28.56	2.08	−4.4	0.00
126.5	191.38	$^{+4.0}_{-3.3}$	$\pm1.3/\pm1.0/\pm1.6$	168.33	28.40	2.05	−4.4	0.00
127.0	189.28	$^{+4.1}_{-3.3}$	$\pm1.3/\pm1.0/\pm1.6$	166.30	28.28	2.03	−4.4	0.00
127.5	187.21	$^{+4.0}_{-3.3}$	$\pm1.3/\pm1.0/\pm1.6$	164.34	28.10	2.02	−4.4	0.00
128.0	185.00	$^{+4.1}_{-3.2}$	$\pm1.3/\pm1.0/\pm1.6$	162.26	27.92	2.00	−4.4	0.00
128.5	183.14	$^{+4.0}_{-3.4}$	$\pm1.3/\pm1.0/\pm1.6$	160.44	27.82	1.99	−4.4	0.00
129.0	181.22	$^{+3.9}_{-3.4}$	$\pm1.3/\pm1.0/\pm1.6$	158.65	27.66	1.95	−4.4	0.00
129.5	179.09	$^{+3.9}_{-3.4}$	$\pm1.3/\pm1.0/\pm1.6$	156.62	27.50	1.94	−4.4	0.00
130.0	176.91	$^{+4.1}_{-3.4}$	$\pm1.3/\pm1.0/\pm1.6$	154.61	27.27	1.92	−4.5	0.00

Table 223: Energy scan of Inclusive WH cross sections including QCD and EW corrections for a Higgs boson mass of 125 GeV, together with their corresponding uncertainties.

$\sqrt{s}$ [TeV]	σ^{WH}[fb]	Δ_{scale} [%]	PDF $\oplus$ α_{s}[%]	PDF [%]	α_{s}[%]	σ^{W^+H}[fb]	σ^{W^-H}[fb]
6.0	456.00	$^{+0.7}_{-1.0}$	$\pm$2.2	$\pm$2.1	$\pm$0.6	295.80	160.20
6.5	515.90	$^{+0.7}_{-0.9}$	$\pm$2.2	$\pm$2.1	$\pm$0.6	332.40	183.50
7.0	577.30	$^{+0.7}_{-0.9}$	$\pm$2.1	$\pm$2.0	$\pm$0.6	369.60	207.70
7.5	639.40	$^{+0.6}_{-0.9}$	$\pm$2.1	$\pm$2.0	$\pm$0.7	407.20	232.20
8.0	702.50	$^{+0.6}_{-0.9}$	$\pm$2.0	$\pm$1.9	$\pm$0.7	445.30	257.20
8.5	766.40	$^{+0.6}_{-0.8}$	$\pm$2.0	$\pm$1.9	$\pm$0.7	483.20	283.20
9.0	831.50	$^{+0.5}_{-0.8}$	$\pm$2.0	$\pm$1.9	$\pm$0.7	522.10	309.50
9.5	897.20	$^{+0.5}_{-0.8}$	$\pm$2.0	$\pm$1.8	$\pm$0.8	561.10	336.10
10.0	963.10	$^{+0.5}_{-0.8}$	$\pm$2.0	$\pm$1.8	$\pm$0.8	599.90	363.10
10.5	1030.00	$^{+0.6}_{-0.7}$	$\pm$2.0	$\pm$1.8	$\pm$0.8	639.30	390.30
11.0	1097.00	$^{+0.5}_{-0.7}$	$\pm$1.9	$\pm$1.8	$\pm$0.8	678.90	418.60
11.5	1166.00	$^{+0.4}_{-0.7}$	$\pm$1.9	$\pm$1.7	$\pm$0.8	719.00	446.80
12.0	1235.00	$^{+0.4}_{-0.7}$	$\pm$1.9	$\pm$1.7	$\pm$0.8	759.80	475.40
12.5	1304.00	$^{+0.5}_{-0.7}$	$\pm$1.9	$\pm$1.7	$\pm$0.9	800.00	504.10
13.0	1373.00	$^{+0.5}_{-0.7}$	$\pm$1.9	$\pm$1.7	$\pm$0.9	840.20	532.50
13.5	1443.00	$^{+0.4}_{-0.7}$	$\pm$1.8	$\pm$1.6	$\pm$0.9	881.90	561.40
14.0	1514.00	$^{+0.4}_{-0.7}$	$\pm$1.8	$\pm$1.6	$\pm$0.9	922.40	591.10
14.5	1583.00	$^{+0.5}_{-0.6}$	$\pm$1.8	$\pm$1.6	$\pm$0.9	961.80	621.30
15.0	1656.00	$^{+0.4}_{-0.7}$	$\pm$1.8	$\pm$1.6	$\pm$0.8	1004.00	652.30

Table 224: Energy scan of Inclusive WH cross sections including QCD and EW corrections for a Higgs boson mass of 125.09 GeV, together with their corresponding uncertainties.

$\sqrt{s}$ [TeV]	σ^{WH}[fb]	Δ_{scale} [%]	PDF $\oplus$ α_{s}[%]	PDF [%]	α_{s}[%]	σ^{W^+H}[fb]	σ^{W^-H}[fb]
6.0	454.90	$^{+0.7}_{-1.0}$	$\pm$2.2	$\pm$2.1	$\pm$0.6	295.20	159.70
6.5	514.70	$^{+0.7}_{-0.9}$	$\pm$2.2	$\pm$2.1	$\pm$0.6	331.70	183.10
7.0	575.90	$^{+0.7}_{-0.8}$	$\pm$2.1	$\pm$2.0	$\pm$0.6	368.70	207.10
7.5	637.50	$^{+0.6}_{-0.9}$	$\pm$2.1	$\pm$2.0	$\pm$0.7	405.90	231.60
8.0	700.80	$^{+0.6}_{-0.8}$	$\pm$2.0	$\pm$1.9	$\pm$0.7	444.20	256.60
8.5	764.60	$^{+0.6}_{-0.8}$	$\pm$2.0	$\pm$1.9	$\pm$0.7	482.00	282.60
9.0	829.40	$^{+0.6}_{-0.8}$	$\pm$2.0	$\pm$1.9	$\pm$0.7	520.70	308.70
9.5	895.40	$^{+0.5}_{-0.8}$	$\pm$2.0	$\pm$1.8	$\pm$0.8	559.90	335.50
10.0	960.90	$^{+0.5}_{-0.8}$	$\pm$2.0	$\pm$1.8	$\pm$0.8	598.50	362.40
10.5	1028.00	$^{+0.5}_{-0.8}$	$\pm$2.0	$\pm$1.8	$\pm$0.8	638.20	389.70
11.0	1095.00	$^{+0.6}_{-0.7}$	$\pm$1.9	$\pm$1.8	$\pm$0.8	677.20	417.50
11.5	1163.00	$^{+0.5}_{-0.7}$	$\pm$1.9	$\pm$1.7	$\pm$0.8	717.40	445.80
12.0	1233.00	$^{+0.4}_{-0.8}$	$\pm$1.9	$\pm$1.7	$\pm$0.8	758.30	474.40
12.5	1302.00	$^{+0.5}_{-0.8}$	$\pm$1.9	$\pm$1.7	$\pm$0.9	798.40	503.10
13.0	1370.00	$^{+0.5}_{-0.7}$	$\pm$1.9	$\pm$1.7	$\pm$0.9	838.20	531.60
13.5	1439.00	$^{+0.5}_{-0.7}$	$\pm$1.8	$\pm$1.6	$\pm$0.9	879.40	559.90
14.0	1510.00	$^{+0.4}_{-0.7}$	$\pm$1.8	$\pm$1.6	$\pm$0.9	920.40	589.60
14.5	1580.00	$^{+0.4}_{-0.6}$	$\pm$1.8	$\pm$1.6	$\pm$0.9	959.80	620.00
15.0	1653.00	$^{+0.5}_{-0.7}$	$\pm$1.8	$\pm$1.6	$\pm$0.8	1002.00	650.50

Table 225: Energy scan of Inclusive ZH cross sections including QCD and EW corrections for a Higgs boson mass of 125 GeV, together with their corresponding uncertainties.

$\sqrt{s}$ [TeV]	σ^{ZH}[fb]	Δ_{scale} [%]	PDF $\oplus$ α_{s}[%]	PDF [%]	α_{s}[%]	σ^{ggZH}[fb]
6.0	262.50	$^{+2.3}_{-2.2}$	$\pm$1.7	$\pm$1.6	$\pm$0.6	18.53
6.5	300.30	$^{+2.5}_{-2.2}$	$\pm$1.7	$\pm$1.6	$\pm$0.6	23.08
7.0	339.10	$^{+2.6}_{-2.4}$	$\pm$1.7	$\pm$1.6	$\pm$0.7	28.08
7.5	379.50	$^{+2.7}_{-2.4}$	$\pm$1.7	$\pm$1.6	$\pm$0.7	33.58
8.0	420.70	$^{+2.9}_{-2.4}$	$\pm$1.7	$\pm$1.5	$\pm$0.8	39.62
8.5	463.10	$^{+2.9}_{-2.5}$	$\pm$1.7	$\pm$1.5	$\pm$0.8	46.08
9.0	507.00	$^{+3.0}_{-2.6}$	$\pm$1.7	$\pm$1.5	$\pm$0.8	52.96
9.5	551.00	$^{+3.2}_{-2.6}$	$\pm$1.7	$\pm$1.5	$\pm$0.8	60.23
10.0	596.20	$^{+3.3}_{-2.7}$	$\pm$1.7	$\pm$1.4	$\pm$0.8	68.12
10.5	642.30	$^{+3.4}_{-2.7}$	$\pm$1.6	$\pm$1.4	$\pm$0.8	76.36
11.0	689.70	$^{+3.4}_{-2.9}$	$\pm$1.6	$\pm$1.4	$\pm$0.9	84.92
11.5	736.80	$^{+3.6}_{-2.9}$	$\pm$1.6	$\pm$1.4	$\pm$0.9	93.95
12.0	785.30	$^{+3.6}_{-3.0}$	$\pm$1.6	$\pm$1.3	$\pm$0.9	103.40
12.5	834.10	$^{+3.6}_{-3.0}$	$\pm$1.6	$\pm$1.3	$\pm$0.9	113.50
13.0	883.70	$^{+3.8}_{-3.1}$	$\pm$1.6	$\pm$1.3	$\pm$0.9	123.30
13.5	934.60	$^{+3.7}_{-3.2}$	$\pm$1.6	$\pm$1.3	$\pm$0.9	134.10
14.0	985.80	$^{+3.8}_{-3.3}$	$\pm$1.6	$\pm$1.3	$\pm$1.0	145.00
14.5	1037.00	$^{+3.9}_{-3.3}$	$\pm$1.6	$\pm$1.3	$\pm$1.0	156.30
15.0	1088.00	$^{+4.1}_{-3.3}$	$\pm$1.6	$\pm$1.3	$\pm$1.0	167.80

Table 226: Energy scan of Inclusive ZH cross sections including QCD and EW corrections for a Higgs boson mass of 125.09 GeV, together with their corresponding uncertainties.

$\sqrt{s}$ [TeV]	σ^{ZH}[fb]	Δ_{scale} [%]	PDF $\oplus$ α_{s}[%]	PDF [%]	α_{s}[%]	σ^{ggZH}[fb]
6.0	261.80	$^{+2.3}_{-2.2}$	±1.7	±1.6	±0.6	18.51
6.5	299.60	$^{+2.5}_{-2.3}$	±1.7	±1.6	±0.6	23.04
7.0	338.30	$^{+2.6}_{-2.3}$	±1.7	±1.6	±0.7	28.08
7.5	378.40	$^{+2.7}_{-2.4}$	±1.7	±1.6	±0.7	33.53
8.0	419.90	$^{+2.8}_{-2.4}$	±1.7	±1.5	±0.8	39.58
8.5	462.30	$^{+2.9}_{-2.5}$	±1.7	±1.5	±0.8	46.08
9.0	505.90	$^{+3.0}_{-2.6}$	±1.7	±1.5	±0.8	52.94
9.5	550.00	$^{+3.1}_{-2.7}$	±1.7	±1.5	±0.8	60.19
10.0	595.20	$^{+3.2}_{-2.8}$	±1.7	±1.4	±0.8	68.15
10.5	641.00	$^{+3.4}_{-2.8}$	±1.6	±1.4	±0.8	76.26
11.0	687.80	$^{+3.4}_{-2.9}$	±1.6	±1.4	±0.9	84.80
11.5	735.40	$^{+3.5}_{-2.9}$	±1.6	±1.4	±0.9	93.84
12.0	783.10	$^{+3.6}_{-2.9}$	±1.6	±1.3	±0.9	103.30
12.5	832.90	$^{+3.6}_{-3.0}$	±1.6	±1.3	±0.9	113.30
13.0	882.10	$^{+3.8}_{-3.0}$	±1.6	±1.3	±0.9	123.20
13.5	933.10	$^{+3.8}_{-3.2}$	±1.6	±1.3	±0.9	133.90
14.0	983.50	$^{+3.8}_{-3.2}$	±1.6	±1.3	±1.0	144.90
14.5	1035.00	$^{+4.0}_{-3.3}$	±1.6	±1.3	±1.0	156.00
15.0	1087.00	$^{+4.0}_{-3.3}$	±1.6	±1.3	±1.0	168.00

Appendix E

$t\bar{t}H$ and tH cross sections

In this appendix the cross-sections for $t\bar{t}H$ and tH productions are expanded to a scan over SM Higgs boson masses.

Table 227: SM-like $t\bar{t}H$ cross section at the LHC with $\sqrt{s} = 7$ TeV.

$M_{\rm H}$[GeV]	$\sigma^{\rm NLO}_{\rm QCD}$[fb]	$\sigma^{\rm NLO}_{\rm QCD+EW}$[fb]	$K_{\rm QCD}$	$\delta_{\rm EW}$[%]	Scale[%]	$\alpha_{\rm s}$[%]	PDF[%]	PDF+$\alpha_{\rm s}$[%]
120.0	97.69	100.54	1.19	2.9	+ 3.6 - 9.3	±2.2	±3.9	±4.5
120.5	96.54	99.36	1.19	2.9	+ 3.6 - 9.3	±2.2	±3.9	±4.5
121.0	95.22	98.00	1.19	2.9	+ 3.6 - 9.3	±2.2	±3.9	±4.5
121.5	94.05	96.79	1.19	2.9	+ 3.5 - 9.2	±2.2	±3.9	±4.5
122.0	93.00	95.72	1.19	2.9	+ 3.5 - 9.2	±2.2	±3.9	±4.5
122.5	91.86	94.55	1.19	2.9	+ 3.5 - 9.2	±2.2	±3.9	±4.5
123.0	90.71	93.35	1.19	2.9	+ 3.5 - 9.2	±2.2	±3.9	±4.5
123.5	89.57	92.16	1.19	2.9	+ 3.5 - 9.2	±2.2	±3.9	±4.5
124.0	88.51	91.07	1.19	2.9	+ 3.5 - 9.2	±2.2	±3.9	±4.5
124.1	88.27	90.84	1.19	2.9	+ 3.4 - 9.2	±2.2	±3.9	±4.5
124.2	88.03	90.60	1.19	2.9	+ 3.5 - 9.2	±2.2	±3.9	±4.5
124.3	87.86	90.42	1.19	2.9	+ 3.5 - 9.2	±2.2	±3.9	±4.5
124.4	87.64	90.18	1.19	2.9	+ 3.5 - 9.2	±2.2	±3.9	±4.5
124.5	87.54	90.07	1.19	2.9	+ 3.5 - 9.2	±2.2	±3.9	±4.5
124.6	87.19	89.72	1.19	2.9	+ 3.5 - 9.2	±2.2	±3.9	±4.5
124.7	87.05	89.57	1.19	2.9	+ 3.5 - 9.2	±2.2	±3.9	±4.5
124.8	86.78	89.30	1.19	2.9	+ 3.5 - 9.2	±2.2	±3.9	±4.5
124.9	86.61	89.12	1.19	2.9	+ 3.5 - 9.2	±2.2	±3.9	±4.5
125.0	86.29	88.78	1.19	2.9	+ 3.4 - 9.2	±2.2	±3.9	±4.5
125.09	86.15	88.64	1.19	2.9	+ 3.5 - 9.2	±2.2	±3.9	±4.5
125.1	86.25	88.73	1.19	2.9	+ 3.5 - 9.2	±2.2	±3.9	±4.5
125.2	85.94	88.41	1.19	2.9	+ 3.5 - 9.2	±2.2	±3.9	±4.5
125.3	85.76	88.25	1.19	2.9	+ 3.4 - 9.2	±2.2	±3.9	±4.5
125.4	85.47	87.94	1.19	2.9	+ 3.5 - 9.2	±2.2	±3.9	±4.5
125.5	85.37	87.83	1.19	2.9	+ 3.4 - 9.2	±2.2	±3.9	±4.5
125.6	85.18	87.61	1.19	2.9	+ 3.5 - 9.2	±2.2	±3.9	±4.5
125.7	84.97	87.42	1.19	2.9	+ 3.5 - 9.2	±2.2	±3.9	±4.5
125.8	84.69	87.14	1.19	2.9	+ 3.4 - 9.2	±2.2	±3.9	±4.5
125.9	84.59	87.03	1.19	2.9	+ 3.5 - 9.2	±2.2	±3.9	±4.5
126.0	84.30	86.74	1.19	2.9	+ 3.5 - 9.2	±2.2	±3.9	±4.5
126.5	83.31	85.71	1.19	2.9	+ 3.4 - 9.2	±2.2	±3.9	±4.5
127.0	82.41	84.77	1.19	2.9	+ 3.5 - 9.2	±2.2	±3.9	±4.5
127.5	81.36	83.69	1.19	2.9	+ 3.5 - 9.2	±2.2	±3.9	±4.5
128.0	80.34	82.62	1.19	2.8	+ 3.5 - 9.2	±2.2	±3.9	±4.5
128.5	79.41	81.67	1.19	2.8	+ 3.4 - 9.2	±2.2	±3.9	±4.5
129.0	78.50	80.73	1.19	2.8	+ 3.4 - 9.2	±2.2	±3.9	±4.5
129.5	77.53	79.73	1.19	2.8	+ 3.4 - 9.2	±2.2	±3.9	±4.5
130.0	76.67	78.82	1.19	2.8	+ 3.4 - 9.2	±2.2	±3.9	±4.5

Table 228: SM-like $t\bar{t}H$ cross section at the LHC with $\sqrt{s} = 8$ TeV.

M_{H}[GeV]	$\sigma^{\mathrm{NLO}}_{\mathrm{QCD}}$[fb]	$\sigma^{\mathrm{NLO}}_{\mathrm{QCD+EW}}$[fb]	K_{QCD}	δ_{EW}[%]	Scale[%]	α_{s}[%]	PDF[%]	PDF+α_{s}[%]
120.0	146.1	150.1	1.20	2.7	+ 4.1 - 9.2	±2.1	±3.7	±4.3
120.5	144.6	148.5	1.20	2.7	+ 4.1 - 9.2	±2.1	±3.7	±4.3
121.0	142.6	146.5	1.20	2.7	+ 4.1 - 9.3	±2.1	±3.7	±4.3
121.5	140.9	144.7	1.20	2.7	+ 4.0 - 9.2	±2.1	±3.7	±4.3
122.0	139.3	143.1	1.20	2.7	+ 4.1 - 9.2	±2.1	±3.7	±4.3
122.5	137.6	141.3	1.20	2.7	+ 4.1 - 9.2	±2.1	±3.7	±4.3
123.0	135.8	139.5	1.20	2.7	+ 4.0 - 9.2	±2.1	±3.7	±4.3
123.5	134.3	137.9	1.20	2.7	+ 4.0 - 9.2	±2.1	±3.7	±4.3
124.0	132.8	136.3	1.20	2.7	+ 4.0 - 9.2	±2.1	±3.7	±4.3
124.1	132.6	136.1	1.20	2.6	+ 4.0 - 9.2	±2.1	±3.7	±4.3
124.2	132.0	135.5	1.20	2.7	+ 4.0 - 9.2	±2.1	±3.7	±4.3
124.3	131.7	135.2	1.20	2.7	+ 4.0 - 9.2	±2.1	±3.7	±4.3
124.4	131.4	134.9	1.20	2.6	+ 4.0 - 9.2	±2.1	±3.7	±4.3
124.5	131.1	134.6	1.20	2.7	+ 4.0 - 9.2	±2.1	±3.7	±4.3
124.6	130.8	134.3	1.20	2.6	+ 4.0 - 9.2	±2.1	±3.7	±4.3
124.7	130.5	133.9	1.20	2.6	+ 4.0 - 9.2	±2.1	±3.7	±4.3
124.8	130.1	133.6	1.20	2.6	+ 4.0 - 9.2	±2.1	±3.7	±4.3
124.9	130.0	133.4	1.20	2.6	+ 4.0 - 9.2	±2.1	±3.7	±4.3
125.0	129.6	133.0	1.20	2.6	+ 4.1 - 9.2	±2.1	±3.7	±4.3
125.09	129.1	132.6	1.20	2.6	+ 4.0 - 9.2	±2.1	±3.7	±4.3
125.1	129.2	132.7	1.20	2.6	+ 4.0 - 9.2	±2.1	±3.7	±4.3
125.2	129.0	132.4	1.20	2.6	+ 4.1 - 9.2	±2.1	±3.7	±4.3
125.3	128.7	132.1	1.20	2.6	+ 4.0 - 9.2	±2.1	±3.7	±4.3
125.4	128.3	131.6	1.20	2.6	+ 4.0 - 9.2	±2.1	±3.7	±4.3
125.5	128.0	131.4	1.20	2.6	+ 4.0 - 9.2	±2.1	±3.7	±4.3
125.6	127.6	131.0	1.20	2.6	+ 4.0 - 9.2	±2.1	±3.7	±4.3
125.7	127.3	130.6	1.20	2.6	+ 4.0 - 9.2	±2.1	±3.7	±4.3
125.8	127.1	130.5	1.20	2.6	+ 4.0 - 9.2	±2.1	±3.7	±4.3
125.9	126.8	130.2	1.20	2.6	+ 4.0 - 9.2	±2.1	±3.7	±4.3
126.0	126.6	129.9	1.20	2.6	+ 4.0 - 9.2	±2.1	±3.7	±4.3
126.5	125.0	128.2	1.20	2.6	+ 4.0 - 9.2	±2.1	±3.7	±4.3
127.0	123.5	126.6	1.20	2.6	+ 4.0 - 9.2	±2.1	±3.7	±4.3
127.5	122.1	125.3	1.20	2.6	+ 4.0 - 9.2	±2.1	±3.7	±4.3
128.0	120.6	123.7	1.20	2.6	+ 4.0 - 9.2	±2.1	±3.7	±4.3
128.5	119.3	122.4	1.20	2.6	+ 4.0 - 9.2	±2.1	±3.7	±4.3
129.0	117.8	120.8	1.20	2.5	+ 4.0 - 9.2	±2.1	±3.7	±4.3
129.5	116.4	119.4	1.20	2.5	+ 3.9 - 9.2	±2.1	±3.7	±4.3
130.0	115.2	118.1	1.20	2.5	+ 4.0 - 9.2	±2.2	±3.7	±4.3

Table 229: SM-like $t\bar{t}H$ cross section at the LHC with $\sqrt{s} = 13$ TeV.

$M_{\rm H}$[GeV]	$\sigma^{\rm NLO}_{\rm QCD}$[fb]	$\sigma^{\rm NLO}_{\rm QCD+EW}$[fb]	$K_{\rm QCD}$	$\delta_{\rm EW}$[%]	Scale[%]	$\alpha_{\rm s}$[%]	PDF[%]	PDF+$\alpha_{\rm s}$[%]
120.0	559.8	569.7	1.25	1.8	+ 5.9 - 9.3	±2.0	±3.0	±3.6
120.5	552.9	562.5	1.25	1.8	+ 5.8 - 9.2	±2.0	±3.0	±3.6
121.0	547.2	556.8	1.25	1.8	+ 5.9 - 9.3	±2.0	±3.0	±3.6
121.5	540.8	550.2	1.25	1.7	+ 5.9 - 9.3	±2.0	±3.0	±3.6
122.0	534.5	543.8	1.25	1.7	+ 5.9 - 9.3	±2.0	±3.0	±3.6
122.5	528.3	537.5	1.25	1.7	+ 5.8 - 9.2	±2.0	±3.0	±3.6
123.0	522.4	531.5	1.25	1.7	+ 5.8 - 9.2	±2.0	±3.0	±3.6
123.5	517.0	525.9	1.25	1.7	+ 5.9 - 9.2	±2.0	±3.0	±3.6
124.0	510.6	519.3	1.25	1.7	+ 5.9 - 9.2	±2.0	±3.0	±3.6
124.1	509.2	517.9	1.25	1.7	+ 5.8 - 9.2	±2.0	±3.0	±3.6
124.2	508.1	516.7	1.25	1.7	+ 5.8 - 9.2	±2.0	±3.0	±3.6
124.3	507.4	516.1	1.25	1.7	+ 5.9 - 9.3	±2.0	±3.0	±3.6
124.4	505.7	514.3	1.25	1.7	+ 5.8 - 9.2	±2.0	±3.0	±3.6
124.5	504.6	513.2	1.25	1.7	+ 5.8 - 9.2	±2.0	±3.0	±3.6
124.6	503.7	512.2	1.25	1.7	+ 5.8 - 9.2	±2.0	±3.0	±3.6
124.7	503.0	511.5	1.25	1.7	+ 5.9 - 9.3	±2.0	±3.0	±3.6
124.8	501.4	510.0	1.25	1.7	+ 5.9 - 9.3	±2.0	±3.0	±3.6
124.9	500.1	508.6	1.25	1.7	+ 5.8 - 9.2	±2.0	±3.0	±3.6
125.0	498.7	507.1	1.25	1.7	+ 5.8 - 9.2	±2.0	±3.0	±3.6
125.09	498.0	506.5	1.25	1.7	+ 5.8 - 9.2	±2.0	±3.0	±3.6
125.1	497.6	506.0	1.25	1.7	+ 5.9 - 9.3	±2.0	±3.0	±3.6
125.2	496.8	505.2	1.25	1.7	+ 5.8 - 9.2	±2.0	±3.0	±3.6
125.3	495.9	504.3	1.25	1.7	+ 5.8 - 9.2	±2.0	±3.0	±3.6
125.4	494.9	503.3	1.25	1.7	+ 5.9 - 9.3	±2.0	±3.0	±3.6
125.5	493.9	502.3	1.25	1.7	+ 5.9 - 9.3	±2.0	±3.0	±3.6
125.6	492.3	500.7	1.25	1.7	+ 5.8 - 9.2	±2.0	±3.0	±3.6
125.7	491.0	499.3	1.25	1.7	+ 5.8 - 9.2	±2.0	±3.0	±3.6
125.8	489.9	498.2	1.25	1.7	+ 5.8 - 9.2	±2.0	±3.0	±3.6
125.9	488.9	497.1	1.25	1.7	+ 5.9 - 9.3	±2.0	±3.0	±3.6
126.0	488.2	496.4	1.25	1.7	+ 5.8 - 9.2	±2.0	±3.0	±3.6
126.5	482.7	490.9	1.25	1.7	+ 5.8 - 9.2	±2.0	±3.0	±3.6
127.0	477.0	485.1	1.25	1.7	+ 5.8 - 9.2	±2.0	±3.0	±3.6
127.5	471.9	479.9	1.25	1.7	+ 5.8 - 9.2	±2.0	±3.0	±3.6
128.0	466.4	474.2	1.25	1.7	+ 5.8 - 9.2	±2.0	±3.0	±3.6
128.5	461.2	468.9	1.25	1.7	+ 5.8 - 9.2	±2.0	±3.0	±3.6
129.0	456.3	463.9	1.25	1.7	+ 5.8 - 9.3	±2.0	±3.0	±3.6
129.5	451.1	458.6	1.25	1.7	+ 5.8 - 9.2	±2.0	±3.0	±3.6
130.0	446.5	453.9	1.25	1.7	+ 5.8 - 9.3	±2.0	±3.0	±3.6

Table 230: SM-like $t\bar{t}H$ cross section at the LHC with $\sqrt{s} = 14$ TeV.

M_{H}[GeV]	$\sigma^{\mathrm{NLO}}_{\mathrm{QCD}}$[fb]	$\sigma^{\mathrm{NLO}}_{\mathrm{QCD+EW}}$[fb]	K_{QCD}	δ_{EW}[%]	Scale[%]	α_{s}[%]	PDF[%]	PDF+α_{s}[%]
120.0	677.4	688.8	1.26	1.7	+ 6.1 - 9.2	±1.9	±2.9	±3.5
120.5	669.8	681.2	1.26	1.7	+ 6.1 - 9.2	±1.9	±2.9	±3.5
121.0	661.1	672.2	1.26	1.7	+ 6.1 - 9.2	±1.9	±2.9	±3.5
121.5	654.4	665.6	1.26	1.7	+ 6.1 - 9.2	±1.9	±2.9	±3.5
122.0	647.6	658.4	1.26	1.7	+ 6.1 - 9.3	±1.9	±2.9	±3.5
122.5	640.0	650.8	1.26	1.7	+ 6.1 - 9.3	±1.9	±3.0	±3.5
123.0	632.1	642.6	1.26	1.7	+ 6.1 - 9.2	±1.9	±2.9	±3.5
123.5	624.9	635.3	1.26	1.7	+ 6.1 - 9.2	±1.9	±2.9	±3.5
124.0	617.7	627.9	1.26	1.7	+ 6.1 - 9.2	±1.9	±2.9	±3.5
124.1	616.7	626.8	1.26	1.6	+ 6.1 - 9.2	±1.9	±2.9	±3.5
124.2	615.7	625.8	1.26	1.6	+ 6.2 - 9.3	±1.9	±2.9	±3.5
124.3	614.8	625.0	1.26	1.7	+ 6.1 - 9.2	±1.9	±2.9	±3.5
124.4	612.9	623.0	1.26	1.6	+ 6.1 - 9.3	±1.9	±2.9	±3.5
124.5	611.6	621.7	1.26	1.6	+ 6.1 - 9.3	±1.9	±2.9	±3.5
124.6	609.3	619.3	1.26	1.6	+ 6.1 - 9.2	±1.9	±2.9	±3.5
124.7	608.5	618.6	1.26	1.7	+ 6.1 - 9.2	±1.9	±2.9	±3.5
124.8	606.9	616.9	1.26	1.6	+ 6.1 - 9.2	±1.9	±2.9	±3.5
124.9	605.3	615.2	1.26	1.6	+ 6.1 - 9.2	±1.9	±2.9	±3.5
125.0	603.7	613.7	1.26	1.7	+ 6.0 - 9.2	±1.9	±2.9	±3.5
125.09	603.0	612.8	1.26	1.6	+ 6.0 - 9.2	±1.9	±2.9	±3.5
125.1	602.8	612.7	1.26	1.6	+ 6.1 - 9.3	±1.9	±2.9	±3.5
125.2	602.2	612.1	1.26	1.6	+ 6.1 - 9.3	±1.9	±2.9	±3.5
125.3	600.2	610.0	1.26	1.6	+ 6.1 - 9.2	±1.9	±2.9	±3.5
125.4	599.1	608.9	1.26	1.6	+ 6.1 - 9.2	±1.9	±2.9	±3.5
125.5	597.8	607.5	1.26	1.6	+ 6.1 - 9.2	±1.9	±2.9	±3.5
125.6	595.9	605.6	1.26	1.6	+ 6.1 - 9.2	±1.9	±2.9	±3.5
125.7	594.7	604.4	1.26	1.6	+ 6.1 - 9.3	±1.9	±2.9	±3.5
125.8	593.9	603.5	1.26	1.6	+ 6.1 - 9.3	±1.9	±2.9	±3.5
125.9	592.5	602.2	1.26	1.6	+ 6.1 - 9.2	±1.9	±2.9	±3.5
126.0	591.2	600.9	1.26	1.6	+ 6.1 - 9.2	±1.9	±2.9	±3.5
126.5	584.4	593.8	1.26	1.6	+ 6.1 - 9.2	±1.9	±2.9	±3.5
127.0	578.2	587.4	1.26	1.6	+ 6.1 - 9.2	±1.9	±2.9	±3.5
127.5	571.5	580.7	1.26	1.6	+ 6.0 - 9.2	±1.9	±2.9	±3.5
128.0	565.9	574.8	1.26	1.6	+ 6.1 - 9.2	±1.9	±2.9	±3.5
128.5	558.6	567.3	1.26	1.6	+ 6.1 - 9.2	±1.9	±2.9	±3.5
129.0	552.9	561.3	1.26	1.5	+ 6.1 - 9.2	±1.9	±2.9	±3.5
129.5	546.8	555.1	1.26	1.5	+ 6.1 - 9.2	±1.9	±2.9	±3.5
130.0	540.5	548.6	1.26	1.5	+ 6.1 - 9.2	±1.9	±2.9	±3.5

Table 231: $t\bar{t}H$ cross section for $M_{\rm H} = 125$ GeV and different collider energies.

$\sqrt{s}$ [TeV]	$\sigma_{\rm QCD}$ [fb]	$\sigma_{\rm REF}$ [fb]	$K_{\rm QCD}$	$\delta_{\rm EW}$[%]	Scale[%]	$\alpha_{\rm s}$[%]	PDF	PDF+$\alpha_{\rm s}$[%]
6.0	52.86	55.58	1.18	3.5	+ 3.1 - 9.2	$\pm$2.3	$\pm$4.2	$\pm$4.7
6.5	68.49	70.97	1.18	3.2	+ 3.3 - 9.2	$\pm$2.2	$\pm$4.0	$\pm$4.6
7.0	86.29	88.78	1.19	2.9	+ 3.4 - 9.2	$\pm$2.2	$\pm$3.9	$\pm$4.5
7.5	106.7	109.5	1.19	2.8	+ 3.7 - 9.2	$\pm$2.2	$\pm$3.8	$\pm$4.4
8.0	129.5	133.0	1.20	2.6	+ 4.1 - 9.2	$\pm$2.1	$\pm$3.7	$\pm$4.3
8.5	154.9	158.5	1.21	2.4	+ 4.2 - 9.2	$\pm$2.1	$\pm$3.6	$\pm$4.2
9.0	182.7	186.9	1.21	2.3	+ 4.5 - 9.2	$\pm$2.1	$\pm$3.5	$\pm$4.1
9.5	213.0	217.9	1.22	2.2	+ 4.6 - 9.2	$\pm$2.1	$\pm$3.5	$\pm$4.0
10.0	246.3	251.4	1.22	2.1	+ 4.9 - 9.3	$\pm$2.1	$\pm$3.4	$\pm$4.0
10.5	282.0	287.6	1.23	2.0	+ 5.1 - 9.3	$\pm$2.0	$\pm$3.3	$\pm$3.9
11.0	320.1	326.4	1.23	1.9	+ 5.2 - 9.2	$\pm$2.0	$\pm$3.3	$\pm$3.8
11.5	360.9	367.7	1.24	1.9	+ 5.4 - 9.2	$\pm$2.0	$\pm$3.2	$\pm$3.8
12.0	404.6	411.7	1.24	1.8	+ 5.6 - 9.2	$\pm$2.0	$\pm$3.1	$\pm$3.7
12.5	450.7	458.2	1.25	1.8	+ 5.7 - 9.3	$\pm$2.0	$\pm$3.1	$\pm$3.6
13.0	498.7	507.2	1.25	1.7	+ 5.8 - 9.2	$\pm$2.0	$\pm$3.0	$\pm$3.6
13.5	550.5	559.2	1.26	1.7	+ 6.0 - 9.3	$\pm$2.0	$\pm$3.0	$\pm$3.5
14.0	603.7	613.7	1.26	1.7	+ 6.0 - 9.2	$\pm$1.9	$\pm$2.9	$\pm$3.5
14.5	660.8	670.5	1.26	1.6	+ 6.2 - 9.2	$\pm$1.9	$\pm$2.9	$\pm$3.5
15.0	719.5	730.0	1.27	1.6	+ 6.2 - 9.2	$\pm$1.9	$\pm$2.8	$\pm$3.4

Table 232: $t\bar{t}H$ cross section for $M_{\mathrm{H}} = 125.09$ GeV and different collider energies.

$\sqrt{s}$ [TeV]	σ_{QCD}[fb]	σ_{REF}[fb]	K_{QCD}	δ_{EW}[%]	Scale[%]	α_{s}[%]	PDF	PDF+α_{s}[%]
6.0	52.76	55.49	1.18	3.3	+ 3.1 - 9.2	±2.3	±4.2	±4.7
6.5	68.30	70.82	1.18	3.1	+ 3.2 - 9.2	±2.2	±4.0	±4.6
7.0	86.15	88.64	1.19	2.9	+ 3.5 - 9.2	±2.2	±3.9	±4.5
7.5	106.6	109.3	1.20	2.8	+ 3.8 - 9.2	±2.2	±3.8	±4.4
8.0	129.1	132.6	1.20	2.6	+ 4.0 - 9.2	±2.1	±3.7	±4.3
8.5	154.5	158.1	1.21	2.5	+ 4.2 - 9.2	±2.1	±3.6	±4.2
9.0	182.2	186.5	1.21	2.3	+ 4.5 - 9.2	±2.1	±3.5	±4.1
9.5	212.6	217.4	1.22	2.2	+ 4.6 - 9.2	±2.1	±3.5	±4.0
10.0	245.7	250.9	1.22	2.1	+ 4.9 - 9.2	±2.1	±3.4	±4.0
10.5	281.3	287.0	1.23	2.0	+ 5.1 - 9.3	±2.0	±3.3	±3.9
11.0	319.6	325.8	1.23	2.0	+ 5.3 - 9.2	±2.0	±3.3	±3.8
11.5	360.2	367.1	1.24	1.9	+ 5.4 - 9.2	±2.0	±3.2	±3.8
12.0	403.7	411.0	1.24	1.8	+ 5.5 - 9.2	±2.0	±3.1	±3.7
12.5	449.5	457.5	1.25	1.8	+ 5.7 - 9.3	±2.0	±3.1	±3.6
13.0	498.0	506.5	1.25	1.7	+ 5.8 - 9.2	±2.0	±3.0	±3.6
13.5	549.5	558.4	1.26	1.7	+ 6.0 - 9.3	±2.0	±3.0	±3.5
14.0	603.0	612.8	1.26	1.6	+ 6.0 - 9.2	±1.9	±2.9	±3.5
14.5	659.1	669.7	1.26	1.6	+ 6.2 - 9.2	±1.9	±2.9	±3.5
15.0	719.0	729.2	1.27	1.5	+ 6.3 - 9.2	±1.9	±2.8	±3.4

Table 233: Cross sections for t-channel tH and $\bar{t}H$ production at the 7 TeV LHC.

M_{H}[GeV]	$\sigma_{tH+\bar{t}H}$[fb]	K_{QCD}	Scale+FS [%]	α_S [%]	PDF [%]	PDF+α_S [%]	σ_{tH}[fb]	$\sigma_{\bar{t}H}$[fb]
120.0	12.89	1.12	$+7.6\ -16.6$	±1.5	±4.7	±4.9	8.88	4.00
120.5	12.81	1.12	$+7.5\ -16.5$	±1.5	±4.7	±4.9	8.83	3.97
121.0	12.73	1.12	$+7.6\ -16.5$	±1.5	±4.7	±4.9	8.78	3.95
121.5	12.67	1.13	$+7.5\ -16.6$	±1.5	±4.7	±4.9	8.73	3.93
122.0	12.60	1.13	$+7.5\ -16.6$	±1.5	±4.7	±4.9	8.69	3.92
122.5	12.54	1.13	$+7.5\ -16.8$	±1.5	±4.7	±4.9	8.63	3.89
123.0	12.47	1.13	$+7.5\ -16.7$	±1.5	±4.7	±4.9	8.60	3.88
123.5	12.41	1.13	$+7.4\ -16.8$	±1.5	±4.7	±4.9	8.55	3.86
124.0	12.36	1.13	$+7.4\ -17.0$	±1.5	±4.7	±4.9	8.51	3.84
124.1	12.35	1.13	$+7.4\ -16.9$	±1.5	±4.7	±4.9	8.51	3.84
124.2	12.35	1.13	$+7.4\ -17.0$	±1.5	±4.7	±4.9	8.50	3.83
124.3	12.33	1.13	$+7.4\ -17.0$	±1.5	±4.7	±4.9	8.50	3.83
124.4	12.31	1.13	$+7.4\ -17.0$	±1.5	±4.7	±4.9	8.50	3.83
124.5	12.28	1.13	$+7.4\ -16.9$	±1.5	±4.7	±4.9	8.46	3.82
124.6	12.28	1.13	$+7.4\ -16.8$	±1.5	±4.7	±4.9	8.47	3.82
124.7	12.26	1.13	$+7.4\ -16.8$	±1.5	±4.7	±4.9	8.47	3.81
124.8	12.25	1.13	$+7.4\ -16.8$	±1.5	±4.7	±4.9	8.44	3.81
124.9	12.23	1.13	$+7.4\ -16.8$	±1.5	±4.7	±4.9	8.43	3.80
125.0	12.26	1.14	$+7.3\ -17.2$	±1.5	±4.7	±4.9	8.43	3.80
125.09	12.23	1.13	$+7.4\ -17.0$	±1.5	±4.7	±5.0	8.42	3.80
125.1	12.23	1.13	$+7.4\ -17.0$	±1.5	±4.7	±5.0	8.42	3.80
125.2	12.22	1.13	$+7.3\ -16.9$	±1.5	±4.7	±5.0	8.41	3.80
125.3	12.21	1.13	$+7.4\ -16.9$	±1.5	±4.7	±5.0	8.41	3.79
125.4	12.17	1.13	$+7.4\ -16.8$	±1.5	±4.7	±5.0	8.40	3.79
125.5	12.19	1.14	$+7.4\ -17.0$	±1.5	±4.7	±5.0	8.40	3.79
125.6	12.18	1.14	$+7.3\ -17.1$	±1.5	±4.7	±5.0	8.39	3.78
125.7	12.16	1.13	$+7.3\ -17.0$	±1.5	±4.7	±5.0	8.38	3.78
125.8	12.14	1.13	$+7.4\ -16.8$	±1.5	±4.7	±5.0	8.36	3.78
125.9	12.13	1.13	$+7.3\ -17.0$	±1.5	±4.7	±5.0	8.35	3.77
126.0	12.13	1.14	$+7.3\ -17.0$	±1.5	±4.7	±5.0	8.34	3.77
126.5	12.07	1.14	$+7.3\ -17.1$	±1.5	±4.7	±5.0	8.32	3.75
127.0	11.99	1.14	$+7.3\ -17.1$	±1.5	±4.7	±5.0	8.27	3.74
127.5	11.97	1.14	$+7.3\ -17.1$	±1.5	±4.7	±5.0	8.24	3.72
128.0	11.90	1.14	$+7.2\ -17.2$	±1.5	±4.7	±5.0	8.20	3.70
128.5	11.85	1.14	$+7.2\ -17.5$	±1.5	±4.8	±5.0	8.16	3.69
129.0	11.78	1.14	$+7.3\ -17.2$	±1.5	±4.8	±5.0	8.12	3.67
129.5	11.74	1.14	$+7.2\ -17.4$	±1.5	±4.8	±5.0	8.08	3.66
130.0	11.67	1.14	$+7.2\ -17.4$	±1.5	±4.8	±5.0	8.04	3.65

Table 234: Cross sections for t-channel tH and $\bar{t}H$ production at the 8 TeV LHC.

M_{H}[GeV]	$\sigma_{tH+\bar{t}H}$[fb]	K_{QCD}	Scale+FS [%]	α_S [%]	PDF [%]	PDF+α_S [%]	σ_{tH}[fb]	$\sigma_{\bar{t}H}$[fb]
120.0	19.59	1.14	$+7.4\ -16.0$	±1.4	±4.4	±4.6	13.37	6.22
120.5	19.49	1.14	$+7.4\ -16.0$	±1.4	±4.4	±4.6	13.30	6.19
121.0	19.38	1.14	$+7.4\ -16.0$	±1.4	±4.4	±4.6	13.25	6.16
121.5	19.29	1.14	$+7.4\ -16.1$	±1.4	±4.4	±4.6	13.15	6.13
122.0	19.21	1.14	$+7.4\ -16.1$	±1.4	±4.4	±4.6	13.10	6.11
122.5	19.11	1.14	$+7.4\ -16.3$	±1.4	±4.4	±4.6	13.02	6.08
123.0	19.02	1.14	$+7.3\ -16.3$	±1.4	±4.4	±4.6	12.99	6.05
123.5	18.92	1.14	$+7.3\ -16.2$	±1.4	±4.4	±4.6	12.93	6.03
124.0	18.87	1.15	$+7.3\ -16.4$	±1.4	±4.4	±4.6	12.86	5.99
124.1	18.82	1.15	$+7.3\ -16.3$	±1.4	±4.4	±4.6	12.84	5.99
124.2	18.81	1.15	$+7.3\ -16.4$	±1.4	±4.4	±4.6	12.85	6.00
124.3	18.78	1.15	$+7.3\ -16.4$	±1.4	±4.4	±4.6	12.84	5.99
124.4	18.76	1.15	$+7.3\ -16.3$	±1.4	±4.4	±4.6	12.82	5.97
124.5	18.78	1.15	$+7.2\ -16.4$	±1.4	±4.4	±4.6	12.81	5.97
124.6	18.75	1.15	$+7.3\ -16.4$	±1.4	±4.4	±4.6	12.78	5.97
124.7	18.75	1.15	$+7.3\ -16.5$	±1.4	±4.4	±4.6	12.78	5.96
124.8	18.71	1.15	$+7.2\ -16.5$	±1.4	±4.4	±4.6	12.76	5.95
124.9	18.70	1.15	$+7.2\ -16.5$	±1.4	±4.4	±4.6	12.77	5.95
125.0	18.69	1.15	$+7.3\ -16.5$	±1.4	±4.4	±4.6	12.73	5.95
125.09	18.66	1.15	$+7.3\ -16.6$	±1.4	±4.4	±4.6	12.72	5.95
125.1	18.66	1.15	$+7.3\ -16.6$	±1.4	±4.4	±4.6	12.72	5.95
125.2	18.66	1.15	$+7.3\ -16.6$	±1.4	±4.4	±4.6	12.74	5.94
125.3	18.64	1.15	$+7.2\ -16.5$	±1.4	±4.4	±4.6	12.70	5.92
125.4	18.62	1.15	$+7.2\ -16.5$	±1.4	±4.4	±4.6	12.69	5.93
125.5	18.62	1.15	$+7.2\ -16.6$	±1.4	±4.4	±4.6	12.68	5.92
125.6	18.57	1.15	$+7.2\ -16.6$	±1.4	±4.4	±4.6	12.66	5.92
125.7	18.55	1.15	$+7.2\ -16.5$	±1.4	±4.4	±4.6	12.66	5.91
125.8	18.56	1.15	$+7.2\ -16.5$	±1.4	±4.4	±4.6	12.64	5.90
125.9	18.54	1.15	$+7.2\ -16.5$	±1.4	±4.4	±4.6	12.65	5.90
126.0	18.52	1.15	$+7.2\ -16.6$	±1.4	±4.4	±4.7	12.62	5.90
126.5	18.44	1.15	$+7.2\ -16.8$	±1.4	±4.4	±4.7	12.56	5.87
127.0	18.36	1.15	$+7.2\ -16.4$	±1.4	±4.4	±4.7	12.49	5.85
127.5	18.28	1.15	$+7.1\ -16.8$	±1.4	±4.4	±4.7	12.45	5.82
128.0	18.20	1.15	$+7.1\ -16.8$	±1.4	±4.4	±4.7	12.42	5.79
128.5	18.13	1.16	$+7.1\ -16.8$	±1.4	±4.5	±4.7	12.36	5.79
129.0	18.04	1.16	$+7.1\ -16.8$	±1.4	±4.5	±4.7	12.30	5.75
129.5	17.96	1.16	$+7.1\ -16.8$	±1.4	±4.5	±4.7	12.26	5.72
130.0	17.87	1.16	$+7.1\ -16.9$	±1.4	±4.5	±4.7	12.19	5.71

Table 235: Cross sections for t-channel tH and $\bar{t}H$ production at the 13 TeV LHC.

M_{H}[GeV]	$\sigma_{tH+\bar{t}H}$[fb]	K_{QCD}	Scale+FS [%]	α_S [%]	PDF [%]	PDF+α_S [%]	σ_{tH}[fb]	$\sigma_{\bar{t}H}$[fb]
120.0	77.31	1.19	$+6.7$ -14.6	±1.2	±3.5	±3.7	50.86	26.43
120.5	77.11	1.19	$+6.7$ -14.8	±1.2	±3.5	±3.7	50.71	26.33
121.0	76.84	1.19	$+6.7$ -14.7	±1.2	±3.5	±3.7	50.47	26.23
121.5	76.48	1.19	$+6.6$ -14.7	±1.2	±3.5	±3.7	50.24	26.13
122.0	76.14	1.19	$+6.7$ -14.7	±1.2	±3.5	±3.7	50.11	26.02
122.5	75.81	1.19	$+6.6$ -14.6	±1.2	±3.5	±3.7	49.85	25.90
123.0	75.52	1.19	$+6.6$ -14.8	±1.2	±3.5	±3.7	49.72	25.84
123.5	75.23	1.19	$+6.6$ -14.9	±1.2	±3.5	±3.7	49.47	25.75
124.0	74.99	1.19	$+6.6$ -15.1	±1.2	±3.5	±3.7	49.30	25.60
124.1	74.71	1.19	$+6.6$ -14.6	±1.2	±3.5	±3.7	49.35	25.59
124.2	74.77	1.19	$+6.6$ -14.7	±1.2	±3.5	±3.7	49.25	25.58
124.3	74.81	1.19	$+6.5$ -14.9	±1.2	±3.5	±3.7	49.15	25.56
124.4	74.77	1.20	$+6.6$ -14.9	±1.2	±3.5	±3.7	49.18	25.57
124.5	74.59	1.19	$+6.6$ -14.9	±1.2	±3.5	±3.7	49.14	25.53
124.6	74.52	1.19	$+6.6$ -14.7	±1.2	±3.5	±3.7	49.04	25.49
124.7	74.48	1.19	$+6.6$ -14.8	±1.2	±3.5	±3.7	49.01	25.49
124.8	74.48	1.20	$+6.6$ -14.9	±1.2	±3.5	±3.7	48.98	25.46
124.9	74.47	1.20	$+6.6$ -15.1	±1.2	±3.6	±3.7	48.94	25.42
125.0	74.25	1.20	$+6.5$ -14.9	±1.2	±3.5	±3.7	48.89	25.42
125.09	74.26	1.19	$+6.5$ -14.7	±1.2	±3.5	±3.7	48.89	25.40
125.1	74.26	1.19	$+6.5$ -14.7	±1.2	±3.5	±3.7	48.89	25.40
125.2	74.32	1.20	$+6.5$ -15.0	±1.2	±3.5	±3.7	48.87	25.40
125.3	74.30	1.20	$+6.6$ -14.9	±1.2	±3.6	±3.8	48.81	25.38
125.4	74.14	1.20	$+6.6$ -14.9	±1.2	±3.6	±3.7	48.79	25.34
125.5	74.07	1.20	$+6.6$ -15.0	±1.2	±3.5	±3.7	48.77	25.34
125.6	74.09	1.20	$+6.5$ -15.2	±1.2	±3.6	±3.7	48.75	25.32
125.7	74.01	1.20	$+6.5$ -15.0	±1.2	±3.6	±3.7	48.70	25.31
125.8	73.90	1.20	$+6.5$ -15.0	±1.2	±3.6	±3.7	48.65	25.30
125.9	73.70	1.20	$+6.6$ -14.8	±1.2	±3.5	±3.7	48.57	25.30
126.0	73.75	1.19	$+6.5$ -15.0	±1.2	±3.6	±3.7	48.58	25.27
126.5	73.53	1.20	$+6.5$ -14.9	±1.2	±3.6	±3.8	48.37	25.16
127.0	73.29	1.20	$+6.5$ -15.1	±1.2	±3.6	±3.8	48.20	25.11
127.5	73.04	1.20	$+6.5$ -15.1	±1.2	±3.6	±3.8	48.07	24.99
128.0	72.77	1.20	$+6.5$ -15.1	±1.2	±3.6	±3.8	47.93	24.91
128.5	72.44	1.20	$+6.4$ -15.0	±1.2	±3.6	±3.8	47.65	24.81
129.0	72.23	1.20	$+6.4$ -15.1	±1.2	±3.6	±3.8	47.55	24.74
129.5	72.03	1.20	$+6.4$ -15.2	±1.2	±3.6	±3.8	47.34	24.66
130.0	71.84	1.20	$+6.4$ -15.3	±1.2	±3.6	±3.8	47.23	24.59

Table 236: Cross sections for t-channel tH and $\bar{t}H$ production at the 14 TeV LHC.

M_{H}[GeV]	$\sigma_{tH+\bar{t}H}$[fb]	K_{QCD}	Scale+FS [%]	α_S [%]	PDF [%]	PDF+α_S [%]	σ_{tH}[fb]	$\sigma_{\bar{t}H}$[fb]
120.0	93.64	1.20	$+6.6\ -14.4$	±1.2	±3.4	±3.6	61.29	32.31
120.5	93.30	1.20	$+6.6\ -14.4$	±1.2	±3.4	±3.6	61.10	32.17
121.0	92.98	1.20	$+6.5\ -14.4$	±1.2	±3.4	±3.6	60.80	32.07
121.5	92.39	1.20	$+6.5\ -14.3$	±1.2	±3.4	±3.6	60.56	31.92
122.0	92.26	1.20	$+6.5\ -14.4$	±1.2	±3.4	±3.6	60.28	31.83
122.5	91.78	1.20	$+6.5\ -14.4$	±1.2	±3.4	±3.6	60.04	31.69
123.0	91.48	1.20	$+6.5\ -14.3$	±1.2	±3.4	±3.6	59.86	31.60
123.5	90.94	1.20	$+6.5\ -14.4$	±1.2	±3.4	±3.6	59.72	31.49
124.0	90.83	1.20	$+6.5\ -14.6$	±1.2	±3.4	±3.6	59.43	31.34
124.1	90.81	1.20	$+6.5\ -14.6$	±1.2	±3.4	±3.6	59.34	31.35
124.2	90.62	1.20	$+6.5\ -14.6$	±1.2	±3.4	±3.6	59.35	31.33
124.3	90.54	1.20	$+6.4\ -14.6$	±1.2	±3.4	±3.6	59.27	31.30
124.4	90.55	1.20	$+6.5\ -14.8$	±1.2	±3.4	±3.6	59.23	31.24
124.5	90.38	1.20	$+6.4\ -14.4$	±1.2	±3.4	±3.6	59.18	31.22
124.6	90.35	1.20	$+6.4\ -14.6$	±1.2	±3.4	±3.6	59.15	31.21
124.7	90.38	1.20	$+6.5\ -14.6$	±1.2	±3.4	±3.6	59.17	31.20
124.8	90.29	1.20	$+6.4\ -14.7$	±1.2	±3.4	±3.6	59.07	31.17
124.9	90.21	1.20	$+6.5\ -14.7$	±1.2	±3.4	±3.6	59.11	31.11
125.0	90.10	1.20	$+6.4\ -14.7$	±1.2	±3.4	±3.6	59.07	31.12
125.09	90.12	1.20	$+6.4\ -14.7$	±1.2	±3.4	±3.6	58.96	31.11
125.1	90.12	1.20	$+6.4\ -14.7$	±1.2	±3.4	±3.6	58.96	31.11
125.2	89.98	1.20	$+6.4\ -14.6$	±1.2	±3.4	±3.6	58.92	31.09
125.3	89.94	1.20	$+6.4\ -14.6$	±1.2	±3.4	±3.6	58.83	31.07
125.4	89.88	1.20	$+6.4\ -14.7$	±1.2	±3.4	±3.6	58.98	31.02
125.5	89.76	1.20	$+6.4\ -14.6$	±1.2	±3.4	±3.6	58.81	31.04
125.6	89.72	1.20	$+6.4\ -14.8$	±1.2	±3.4	±3.6	58.70	31.00
125.7	89.73	1.20	$+6.4\ -14.7$	±1.2	±3.4	±3.6	58.78	30.99
125.8	89.62	1.20	$+6.4\ -14.7$	±1.2	±3.4	±3.6	58.72	30.93
125.9	89.58	1.20	$+6.4\ -14.7$	±1.2	±3.4	±3.6	58.66	30.96
126.0	89.50	1.20	$+6.4\ -14.7$	±1.2	±3.4	±3.6	58.59	30.95
126.5	89.11	1.20	$+6.4\ -14.8$	±1.2	±3.4	±3.6	58.38	30.83
127.0	88.86	1.20	$+6.4\ -14.8$	±1.2	±3.5	±3.7	58.19	30.72
127.5	88.44	1.20	$+6.4\ -14.5$	±1.2	±3.4	±3.6	57.94	30.62
128.0	88.28	1.20	$+6.4\ -14.9$	±1.2	±3.4	±3.6	57.76	30.51
128.5	87.91	1.20	$+6.3\ -14.8$	±1.2	±3.5	±3.6	57.52	30.42
129.0	87.62	1.21	$+6.3\ -14.8$	±1.2	±3.5	±3.6	57.35	30.28
129.5	87.44	1.21	$+6.3\ -15.1$	±1.2	±3.5	±3.7	57.17	30.17
130.0	87.10	1.21	$+6.3\ -14.9$	±1.2	±3.5	±3.7	56.92	30.06

Table 237: Cross sections for t-channel tH and $\bar{t}H$ production for a Higgs boson mass of 125 GeV and 6 TeV $\leq \sqrt{s} \leq$ 15 TeV.

$\sqrt{s}$ [TeV]	$\sigma_{tH+\bar{t}H}$[fb]	K_{QCD}	Scale+FS [%]	α_S [%]	PDF [%]	PDF+α_S [%]	σ_{tH}[fb]	$\sigma_{\bar{t}H}$[fb]
6.0	7.31	1.12	$+7.5$ -17.5	±1.6	±5.1	±5.4	5.10	2.20
6.5	9.58	1.12	$+7.4$ -17.3	±1.5	±4.9	±5.1	6.64	2.94
7.0	12.26	1.14	$+7.3$ -17.2	±1.5	±4.7	±4.9	8.43	3.80
7.5	15.26	1.14	$+7.3$ -16.7	±1.4	±4.6	±4.8	10.46	4.80
8.0	18.69	1.15	$+7.3$ -16.5	±1.4	±4.4	±4.6	12.73	5.95
8.5	22.47	1.15	$+7.2$ -16.3	±1.4	±4.3	±4.5	15.26	7.23
9.0	26.71	1.16	$+7.1$ -16.2	±1.3	±4.2	±4.4	18.02	8.66
9.5	31.28	1.17	$+7.1$ -16.0	±1.3	±4.1	±4.3	21.05	10.23
10.0	36.28	1.17	$+6.9$ -15.8	±1.3	±4.0	±4.2	24.32	11.94
10.5	41.62	1.18	$+6.9$ -15.6	±1.3	±3.9	±4.1	27.82	13.85
11.0	47.47	1.18	$+6.8$ -15.5	±1.2	±3.8	±4.0	31.57	15.88
11.5	53.55	1.18	$+6.8$ -15.2	±1.2	±3.7	±3.9	35.54	18.01
12.0	60.08	1.19	$+6.7$ -15.2	±1.2	±3.7	±3.9	39.80	20.38
12.5	67.08	1.19	$+6.6$ -15.1	±1.2	±3.6	±3.8	44.26	22.85
13.0	74.25	1.20	$+6.5$ -14.9	±1.2	±3.5	±3.7	48.89	25.42
13.5	82.03	1.20	$+6.5$ -14.8	±1.2	±3.5	±3.7	53.83	28.20
14.0	90.10	1.20	$+6.4$ -14.7	±1.2	±3.4	±3.6	59.07	31.12
14.5	98.65	1.21	$+6.4$ -14.8	±1.2	±3.4	±3.6	64.32	34.20
15.0	107.2	1.21	$+6.3$ -14.4	±1.1	±3.3	±3.5	69.98	37.41

Table 238: Cross sections for s-channel tH and $\bar{t}H$ production at the 7 TeV LHC.

M_{H}[GeV]	$\sigma_{tH+\bar{t}H}$[fb]	K_{QCD}	Scale [%]	α_S [%]	PDF [%]	PDF+α_S [%]	σ_{tH}[fb]	$\sigma_{\bar{t}H}$[fb]
120.0	1.028	1.19	$+2.9\ -2.5$	±0.0	±3.0	±3.0	0.709	0.319
120.5	1.018	1.19	$+2.9\ -2.5$	±0.0	±3.0	±3.0	0.703	0.315
121.0	1.008	1.19	$+2.9\ -2.5$	±0.0	±3.0	±3.0	0.696	0.311
121.5	1.000	1.19	$+2.9\ -2.6$	±0.0	±3.0	±3.0	0.689	0.309
122.0	0.987	1.19	$+2.9\ -2.5$	±0.0	±3.0	±3.0	0.682	0.305
122.5	0.978	1.19	$+2.8\ -2.5$	±0.0	±3.0	±3.0	0.676	0.302
123.0	0.969	1.19	$+2.9\ -2.5$	±0.0	±3.0	±3.0	0.669	0.299
123.5	0.960	1.19	$+2.9\ -2.5$	±0.0	±3.0	±3.0	0.663	0.296
124.0	0.949	1.19	$+2.9\ -2.5$	±0.0	±3.0	±3.0	0.655	0.293
124.1	0.947	1.19	$+2.9\ -2.6$	±0.0	±3.0	±3.0	0.654	0.292
124.2	0.943	1.19	$+2.8\ -2.5$	±0.0	±3.0	±3.0	0.653	0.291
124.3	0.943	1.19	$+2.9\ -2.6$	±0.0	±3.0	±3.0	0.652	0.291
124.4	0.941	1.19	$+2.9\ -2.6$	±0.0	±3.0	±3.0	0.651	0.290
124.5	0.939	1.19	$+2.9\ -2.5$	±0.0	±3.0	±3.0	0.650	0.290
124.6	0.937	1.19	$+2.9\ -2.5$	±0.0	±3.0	±3.0	0.648	0.289
124.7	0.935	1.19	$+2.9\ -2.6$	±0.0	±3.0	±3.0	0.647	0.288
124.8	0.934	1.19	$+2.9\ -2.5$	±0.0	±3.0	±3.0	0.645	0.288
124.9	0.933	1.19	$+2.9\ -2.6$	±0.0	±3.0	±3.0	0.644	0.287
125.0	0.930	1.19	$+2.9\ -2.5$	±0.0	±3.0	±3.0	0.642	0.287
125.09	0.929	1.19	$+2.9\ -2.6$	±0.0	±3.0	±3.0	0.642	0.286
125.1	0.929	1.19	$+2.9\ -2.6$	±0.0	±3.0	±3.0	0.642	0.286
125.2	0.925	1.19	$+2.8\ -2.5$	±0.0	±3.0	±3.0	0.641	0.285
125.3	0.925	1.19	$+2.9\ -2.6$	±0.0	±3.0	±3.0	0.640	0.285
125.4	0.922	1.19	$+2.9\ -2.6$	±0.0	±3.0	±3.0	0.638	0.284
125.5	0.921	1.19	$+2.9\ -2.6$	±0.0	±3.0	±3.0	0.638	0.284
125.6	0.919	1.19	$+2.9\ -2.6$	±0.0	±3.0	±3.0	0.636	0.283
125.7	0.917	1.19	$+2.9\ -2.6$	±0.0	±3.0	±3.0	0.634	0.283
125.8	0.916	1.19	$+2.9\ -2.5$	±0.0	±3.0	±3.0	0.633	0.282
125.9	0.914	1.19	$+2.9\ -2.6$	±0.0	±3.0	±3.0	0.632	0.281
126.0	0.912	1.19	$+2.9\ -2.5$	±0.0	±3.0	±3.0	0.630	0.280
126.5	0.903	1.19	$+2.9\ -2.6$	±0.0	±3.0	±3.0	0.625	0.278
127.0	0.894	1.19	$+2.9\ -2.6$	±0.0	±3.0	±3.0	0.619	0.275
127.5	0.885	1.19	$+2.9\ -2.6$	±0.0	±3.0	±3.0	0.613	0.272
128.0	0.875	1.19	$+2.9\ -2.5$	±0.0	±3.1	±3.1	0.607	0.270
128.5	0.869	1.19	$+2.9\ -2.6$	±0.0	±3.1	±3.1	0.601	0.267
129.0	0.860	1.19	$+2.9\ -2.6$	±0.0	±3.1	±3.1	0.595	0.264
129.5	0.852	1.19	$+2.9\ -2.6$	±0.0	±3.1	±3.1	0.589	0.262
130.0	0.843	1.19	$+2.9\ -2.6$	±0.0	±3.1	±3.1	0.585	0.259

Table 239: Cross sections for s-channel tH and $\bar{t}H$ production at the 8 TeV LHC.

$M_{\rm H}$[GeV]	$\sigma_{tH+\bar{t}H}$[fb]	$K_{\rm QCD}$	Scale [%]	α_S [%]	PDF [%]	PDF+α_S [%]	σ_{tH}[fb]	$\sigma_{\bar{t}H}$[fb]
120.0	1.339	1.19	$+2.8$ -2.4	±0.1	±2.8	±2.8	0.913	0.426
120.5	1.326	1.19	$+2.8$ -2.4	±0.0	±2.8	±2.8	0.903	0.422
121.0	1.313	1.19	$+2.8$ -2.3	±0.0	±2.8	±2.8	0.895	0.418
121.5	1.301	1.19	$+2.8$ -2.4	±0.0	±2.8	±2.8	0.887	0.413
122.0	1.287	1.19	$+2.8$ -2.4	±0.0	±2.8	±2.8	0.878	0.409
122.5	1.274	1.19	$+2.8$ -2.4	±0.0	±2.8	±2.8	0.870	0.405
123.0	1.263	1.19	$+2.8$ -2.4	±0.0	±2.8	±2.8	0.862	0.401
123.5	1.251	1.19	$+2.8$ -2.4	±0.0	±2.8	±2.8	0.854	0.397
124.0	1.238	1.19	$+2.7$ -2.3	±0.0	±2.8	±2.8	0.845	0.393
124.1	1.235	1.19	$+2.8$ -2.4	±0.0	±2.8	±2.8	0.843	0.392
124.2	1.233	1.19	$+2.8$ -2.4	±0.0	±2.8	±2.8	0.842	0.391
124.3	1.232	1.19	$+2.8$ -2.4	±0.0	±2.8	±2.8	0.841	0.390
124.4	1.228	1.19	$+2.8$ -2.4	±0.0	±2.8	±2.8	0.839	0.390
124.5	1.225	1.19	$+2.8$ -2.4	±0.0	±2.8	±2.8	0.838	0.388
124.6	1.224	1.19	$+2.7$ -2.4	±0.0	±2.8	±2.8	0.836	0.388
124.7	1.221	1.19	$+2.8$ -2.4	±0.0	±2.8	±2.8	0.834	0.387
124.8	1.219	1.19	$+2.8$ -2.4	±0.0	±2.8	±2.8	0.832	0.386
124.9	1.216	1.19	$+2.8$ -2.4	±0.0	±2.8	±2.8	0.831	0.385
125.0	1.214	1.19	$+2.8$ -2.4	±0.0	±2.8	±2.8	0.829	0.385
125.09	1.211	1.19	$+2.8$ -2.4	±0.0	±2.8	±2.8	0.828	0.384
125.1	1.211	1.19	$+2.8$ -2.4	±0.0	±2.8	±2.8	0.828	0.384
125.2	1.209	1.19	$+2.8$ -2.4	±0.0	±2.8	±2.8	0.827	0.383
125.3	1.208	1.19	$+2.8$ -2.4	±0.0	±2.8	±2.8	0.825	0.383
125.4	1.204	1.19	$+2.8$ -2.4	±0.0	±2.8	±2.8	0.824	0.381
125.5	1.202	1.19	$+2.8$ -2.4	±0.0	±2.8	±2.8	0.822	0.381
125.6	1.200	1.19	$+2.8$ -2.4	±0.0	±2.8	±2.8	0.820	0.380
125.7	1.198	1.19	$+2.8$ -2.4	±0.0	±2.8	±2.8	0.818	0.379
125.8	1.195	1.19	$+2.8$ -2.4	±0.0	±2.8	±2.8	0.817	0.379
125.9	1.193	1.19	$+2.8$ -2.4	±0.0	±2.8	±2.8	0.815	0.378
126.0	1.191	1.19	$+2.8$ -2.4	±0.0	±2.8	±2.8	0.814	0.377
126.5	1.179	1.19	$+2.8$ -2.4	±0.0	±2.8	±2.8	0.806	0.373
127.0	1.167	1.19	$+2.8$ -2.4	±0.0	±2.8	±2.8	0.798	0.370
127.5	1.158	1.19	$+2.7$ -2.3	±0.0	±2.8	±2.8	0.791	0.366
128.0	1.146	1.19	$+2.8$ -2.4	±0.0	±2.8	±2.8	0.784	0.363
128.5	1.134	1.19	$+2.8$ -2.4	±0.0	±2.8	±2.8	0.777	0.359
129.0	1.126	1.19	$+2.8$ -2.4	±0.0	±2.8	±2.8	0.770	0.356
129.5	1.115	1.19	$+2.8$ -2.4	±0.0	±2.8	±2.8	0.763	0.352
130.0	1.103	1.19	$+2.8$ -2.4	±0.0	±2.8	±2.8	0.755	0.348

Table 240: Cross sections for s-channel tH and $\bar{t}H$ production at the 13 TeV LHC.

M_{H}[GeV]	$\sigma_{tH+\bar{t}H}$[fb]	K_{QCD}	Scale [%]	α_S [%]	PDF [%]	PDF+α_S [%]	σ_{tH}[fb]	$\sigma_{\bar{t}H}$[fb]
120.0	3.158	1.21	$+2.4\ -1.8$	±0.3	±2.2	±2.2	2.060	1.095
120.5	3.124	1.20	$+2.4\ -1.8$	±0.3	±2.2	±2.2	2.042	1.083
121.0	3.101	1.21	$+2.4\ -1.8$	±0.3	±2.2	±2.2	2.022	1.073
121.5	3.068	1.20	$+2.4\ -1.8$	±0.3	±2.2	±2.2	2.006	1.063
122.0	3.045	1.21	$+2.4\ -1.8$	±0.3	±2.2	±2.2	1.989	1.052
122.5	3.007	1.20	$+2.4\ -1.8$	±0.3	±2.2	±2.2	1.971	1.043
123.0	2.988	1.20	$+2.4\ -1.8$	±0.3	±2.2	±2.2	1.953	1.033
123.5	2.960	1.20	$+2.4\ -1.8$	±0.2	±2.2	±2.2	1.935	1.023
124.0	2.932	1.20	$+2.4\ -1.8$	±0.2	±2.2	±2.2	1.915	1.014
124.1	2.928	1.20	$+2.4\ -1.8$	±0.2	±2.2	±2.2	1.916	1.012
124.2	2.920	1.20	$+2.4\ -1.8$	±0.2	±2.2	±2.2	1.912	1.010
124.3	2.918	1.20	$+2.4\ -1.8$	±0.2	±2.2	±2.2	1.906	1.008
124.4	2.908	1.20	$+2.4\ -1.8$	±0.2	±2.2	±2.2	1.904	1.006
124.5	2.907	1.20	$+2.4\ -1.8$	±0.2	±2.2	±2.2	1.902	1.004
124.6	2.901	1.20	$+2.4\ -1.8$	±0.2	±2.2	±2.2	1.897	1.003
124.7	2.900	1.21	$+2.4\ -1.8$	±0.2	±2.2	±2.2	1.892	1.000
124.8	2.895	1.20	$+2.4\ -1.8$	±0.2	±2.2	±2.2	1.891	0.998
124.9	2.886	1.20	$+2.4\ -1.8$	±0.2	±2.2	±2.2	1.888	0.996
125.0	2.879	1.20	$+2.4\ -1.8$	±0.2	±2.2	±2.2	1.882	0.996
125.09	2.875	1.20	$+2.4\ -1.8$	±0.2	±2.2	±2.2	1.881	0.993
125.1	2.875	1.20	$+2.4\ -1.8$	±0.2	±2.2	±2.2	1.881	0.993
125.2	2.871	1.20	$+2.4\ -1.8$	±0.2	±2.2	±2.2	1.876	0.991
125.3	2.861	1.20	$+2.4\ -1.8$	±0.2	±2.2	±2.2	1.874	0.989
125.4	2.860	1.20	$+2.4\ -1.8$	±0.2	±2.2	±2.2	1.871	0.988
125.5	2.857	1.20	$+2.4\ -1.8$	±0.2	±2.2	±2.2	1.868	0.987
125.6	2.851	1.20	$+2.4\ -1.8$	±0.2	±2.2	±2.2	1.863	0.983
125.7	2.845	1.20	$+2.4\ -1.8$	±0.2	±2.2	±2.2	1.859	0.982
125.8	2.842	1.20	$+2.4\ -1.8$	±0.2	±2.2	±2.2	1.858	0.980
125.9	2.835	1.20	$+2.4\ -1.8$	±0.2	±2.2	±2.2	1.855	0.979
126.0	2.826	1.20	$+2.4\ -1.8$	±0.2	±2.2	±2.2	1.849	0.977
126.5	2.802	1.20	$+2.4\ -1.8$	±0.2	±2.2	±2.2	1.837	0.967
127.0	2.780	1.20	$+2.4\ -1.8$	±0.2	±2.2	±2.2	1.820	0.959
127.5	2.752	1.20	$+2.4\ -1.8$	±0.2	±2.2	±2.2	1.804	0.950
128.0	2.726	1.20	$+2.4\ -1.8$	±0.2	±2.2	±2.2	1.788	0.941
128.5	2.705	1.20	$+2.4\ -1.8$	±0.2	±2.2	±2.2	1.771	0.933
129.0	2.683	1.20	$+2.4\ -1.8$	±0.2	±2.2	±2.2	1.755	0.924
129.5	2.657	1.20	$+2.4\ -1.8$	±0.2	±2.2	±2.2	1.742	0.916
130.0	2.633	1.20	$+2.4\ -1.8$	±0.2	±2.2	±2.2	1.728	0.908

Table 241: Cross sections for s-channel tH and $\bar{t}H$ production at the 14 TeV LHC.

$M_{\rm H}$[GeV]	$\sigma_{tH+\bar{t}H}$[fb]	$K_{\rm QCD}$	Scale [%]	α_S [%]	PDF [%]	PDF+α_S [%]	σ_{tH}[fb]	$\sigma_{\bar{t}H}$[fb]
120.0	3.558	1.21	$+2.3$ -1.7	±0.3	±2.1	±2.1	2.310	1.248
120.5	3.523	1.21	$+2.3$ -1.7	±0.3	±2.1	±2.1	2.289	1.235
121.0	3.490	1.21	$+2.3$ -1.7	±0.3	±2.1	±2.1	2.267	1.225
121.5	3.457	1.21	$+2.3$ -1.7	±0.3	±2.1	±2.1	2.246	1.213
122.0	3.429	1.21	$+2.3$ -1.7	±0.3	±2.1	±2.1	2.226	1.201
122.5	3.395	1.21	$+2.3$ -1.7	±0.3	±2.1	±2.1	2.206	1.190
123.0	3.363	1.21	$+2.3$ -1.7	±0.3	±2.1	±2.1	2.188	1.179
123.5	3.335	1.21	$+2.3$ -1.7	±0.3	±2.1	±2.1	2.168	1.168
124.0	3.307	1.21	$+2.3$ -1.7	±0.3	±2.1	±2.1	2.148	1.159
124.1	3.298	1.20	$+2.3$ -1.7	±0.3	±2.1	±2.1	2.146	1.154
124.2	3.294	1.21	$+2.3$ -1.7	±0.3	±2.1	±2.1	2.138	1.153
124.3	3.286	1.20	$+2.3$ -1.7	±0.3	±2.1	±2.1	2.136	1.149
124.4	3.280	1.20	$+2.3$ -1.7	±0.3	±2.1	±2.1	2.136	1.148
124.5	3.274	1.20	$+2.3$ -1.7	±0.3	±2.1	±2.1	2.131	1.147
124.6	3.273	1.21	$+2.3$ -1.7	±0.3	±2.1	±2.1	2.128	1.145
124.7	3.261	1.20	$+2.3$ -1.7	±0.3	±2.1	±2.1	2.122	1.143
124.8	3.261	1.21	$+2.3$ -1.7	±0.3	±2.1	±2.1	2.119	1.141
124.9	3.251	1.21	$+2.3$ -1.7	±0.3	±2.1	±2.1	2.117	1.138
125.0	3.249	1.21	$+2.3$ -1.7	±0.3	±2.1	±2.1	2.110	1.137
125.09	3.240	1.20	$+2.3$ -1.7	±0.3	±2.1	±2.1	2.104	1.134
125.1	3.240	1.20	$+2.3$ -1.7	±0.3	±2.1	±2.1	2.104	1.134
125.2	3.234	1.20	$+2.3$ -1.7	±0.3	±2.1	±2.1	2.102	1.130
125.3	3.227	1.20	$+2.3$ -1.7	±0.3	±2.1	±2.1	2.102	1.129
125.4	3.222	1.20	$+2.3$ -1.7	±0.3	±2.1	±2.1	2.098	1.128
125.5	3.219	1.21	$+2.3$ -1.7	±0.3	±2.1	±2.1	2.094	1.126
125.6	3.215	1.21	$+2.4$ -1.7	±0.3	±2.1	±2.1	2.091	1.124
125.7	3.205	1.20	$+2.3$ -1.7	±0.3	±2.1	±2.1	2.086	1.122
125.8	3.202	1.21	$+2.3$ -1.7	±0.3	±2.1	±2.1	2.083	1.119
125.9	3.195	1.21	$+2.3$ -1.7	±0.3	±2.1	±2.1	2.080	1.118
126.0	3.191	1.21	$+2.3$ -1.7	±0.3	±2.1	±2.1	2.074	1.115
126.5	3.160	1.20	$+2.3$ -1.7	±0.3	±2.1	±2.1	2.058	1.106
127.0	3.133	1.20	$+2.3$ -1.7	±0.3	±2.1	±2.1	2.040	1.095
127.5	3.104	1.20	$+2.4$ -1.7	±0.3	±2.1	±2.1	2.023	1.085
128.0	3.079	1.20	$+2.3$ -1.7	±0.3	±2.1	±2.1	2.001	1.073
128.5	3.053	1.20	$+2.4$ -1.7	±0.3	±2.1	±2.1	1.987	1.065
129.0	3.025	1.20	$+2.3$ -1.7	±0.3	±2.1	±2.2	1.969	1.054
129.5	2.998	1.20	$+2.3$ -1.7	±0.3	±2.1	±2.2	1.953	1.047
130.0	2.971	1.20	$+2.3$ -1.7	±0.3	±2.1	±2.2	1.937	1.037

Table 242: Cross sections for s-channel tH and $\bar{t}H$ production for a Higgs boson mass of 125 GeV and 6 TeV $\leq \sqrt{s} \leq$ 15 TeV.

$\sqrt{s}$ [TeV]	$\sigma_{tH+\bar{t}H}$[fb]	K_{QCD}	Scale [%]	α_S [%]	PDF [%]	PDF+α_S [%]	σ_{tH}[fb]	$\sigma_{\bar{t}H}$[fb]
6.0	0.669	1.19	$+3.0$ -2.8	±0.1	±3.3	±3.3	0.470	0.200
6.5	0.796	1.19	$+2.9$ -2.7	±0.1	±3.2	±3.2	0.555	0.242
7.0	0.930	1.19	$+2.9$ -2.5	±0.0	±3.0	±3.0	0.642	0.287
7.5	1.070	1.19	$+2.8$ -2.5	±0.0	±2.9	±2.9	0.735	0.334
8.0	1.214	1.19	$+2.8$ -2.4	±0.0	±2.8	±2.8	0.829	0.385
8.5	1.363	1.19	$+2.7$ -2.3	±0.1	±2.7	±2.7	0.927	0.437
9.0	1.517	1.19	$+2.7$ -2.2	±0.1	±2.6	±2.6	1.025	0.492
9.5	1.676	1.19	$+2.7$ -2.2	±0.1	±2.6	±2.6	1.127	0.549
10.0	1.838	1.19	$+2.6$ -2.1	±0.1	±2.5	±2.5	1.231	0.608
10.5	2.004	1.19	$+2.6$ -2.0	±0.2	±2.4	±2.4	1.338	0.668
11.0	2.173	1.20	$+2.5$ -2.0	±0.2	±2.4	±2.4	1.444	0.731
11.5	2.345	1.20	$+2.5$ -1.9	±0.2	±2.3	±2.3	1.550	0.794
12.0	2.519	1.20	$+2.5$ -1.9	±0.2	±2.3	±2.3	1.661	0.859
12.5	2.703	1.20	$+2.4$ -1.8	±0.2	±2.2	±2.2	1.772	0.928
13.0	2.879	1.20	$+2.4$ -1.8	±0.2	±2.2	±2.2	1.882	0.996
13.5	3.060	1.20	$+2.4$ -1.7	±0.3	±2.2	±2.2	1.997	1.065
14.0	3.249	1.21	$+2.3$ -1.7	±0.3	±2.1	±2.1	2.110	1.137
14.5	3.439	1.21	$+2.3$ -1.7	±0.3	±2.1	±2.1	2.227	1.207
15.0	3.623	1.21	$+2.3$ -1.6	±0.3	±2.1	±2.1	2.343	1.281

Appendix F

$b\bar{b}$H cross sections

In this appendix the cross-sections for $b\bar{b}$H production are expanded to a scan over SM Higgs boson masses as discussed in Section IV.2.2.

Table 243: Inclusive bbH cross sections for a LHC CM energy of $\sqrt{s} = 7$ TeV, obtained using Santander Matching with 5FS (NNLO) and 4FS (NLO), together with their total uncertainties.

M_{H}[GeV]	σ^{bbH}[fb]	$+\mathrm{QCD\,scale} \oplus \mathrm{PDF} \oplus \alpha_{\mathrm{s}}$[%]	$-\mathrm{QCD\,scale} \oplus \mathrm{PDF} \oplus \alpha_{\mathrm{s}}$[%]
120.0	178.20	+21.0	−22.8
120.5	176.20	+21.0	−22.8
121.0	173.50	+20.9	−22.7
121.5	171.00	+20.9	−22.7
122.0	168.80	+20.9	−22.7
122.5	166.30	+20.8	−22.6
123.0	163.40	+20.7	−22.5
123.5	161.90	+20.7	−22.5
124.0	159.70	+20.8	−22.6
124.1	159.10	+20.8	−22.6
124.2	158.60	+20.8	−22.6
124.3	158.30	+20.8	−22.7
124.4	157.90	+20.9	−22.7
124.5	157.30	+20.7	−22.5
124.6	157.20	+20.8	−22.5
124.7	156.40	+20.8	−22.5
124.8	155.70	+20.8	−22.6
124.9	155.50	+20.8	−22.6
125.0	155.20	+20.7	−22.4
125.1	154.50	+20.7	−22.5
125.09	154.70	+20.8	−22.5
125.2	154.30	+20.8	−22.5
125.3	153.80	+20.8	−22.5
125.4	153.20	+20.8	−22.6
125.5	152.70	+20.7	−22.4
125.6	152.40	+20.6	−22.4
125.7	152.10	+20.7	−22.5
125.8	151.40	+20.7	−22.5
125.9	151.00	+20.8	−22.5
126.0	150.80	+20.7	−22.3
126.5	148.60	+20.6	−22.3
127.0	146.70	+20.6	−22.3
127.5	144.60	+20.5	−22.2
128.0	142.50	+20.4	−22.2
128.5	140.60	+20.4	−22.2
129.0	138.90	+20.4	−22.1
129.5	137.00	+20.4	−22.1
130.0	135.10	+20.3	−22.1

Table 244: Inclusive bbH cross sections for a LHC CM energy of $\sqrt{s} = 8$ TeV, obtained using Santander Matching with 5FS (NNLO) and 4FS (NLO), together with their total uncertainties.

M_{H}[GeV]	σ^{bbH}[fb]	$+\mathrm{QCD\,scale} \oplus \mathrm{PDF} \oplus \alpha_{\mathrm{s}}$[%]	$-\mathrm{QCD\,scale} \oplus \mathrm{PDF} \oplus \alpha_{\mathrm{s}}$[%]
120.0	231.50	+20.8	−22.8
120.5	228.90	+20.8	−22.8
121.0	225.00	+20.7	−22.7
121.5	222.40	+20.8	−22.7
122.0	219.00	+20.6	−22.6
122.5	216.10	+20.7	−22.5
123.0	213.20	+20.7	−22.5
123.5	210.40	+20.7	−22.4
124.0	207.10	+20.6	−22.4
124.1	206.90	+20.7	−22.4
124.2	206.20	+20.6	−22.5
124.3	205.60	+20.7	−22.6
124.4	205.20	+20.8	−22.6
124.5	204.50	+20.6	−22.4
124.6	204.30	+20.7	−22.5
124.7	203.60	+20.7	−22.5
124.8	202.80	+20.6	−22.5
124.9	202.40	+20.7	−22.5
125.0	202.10	+20.7	−22.3
125.1	201.50	+20.6	−22.4
125.09	200.80	+20.6	−22.3
125.2	200.80	+20.7	−22.4
125.3	200.50	+20.7	−22.4
125.4	199.80	+20.7	−22.5
125.5	199.30	+20.6	−22.3
125.6	199.30	+20.6	−22.3
125.7	198.80	+20.7	−22.4
125.8	198.20	+20.7	−22.4
125.9	197.40	+20.8	−22.5
126.0	196.80	+20.6	−22.3
126.5	193.60	+20.6	−22.1
127.0	191.40	+20.5	−22.2
127.5	188.20	+20.4	−22.1
128.0	186.40	+20.4	−22.1
128.5	183.30	+20.3	−22.0
129.0	181.10	+20.3	−22.0
129.5	178.60	+20.4	−22.0
130.0	176.30	+20.3	−21.9

Table 245: Inclusive bbH cross sections for a LHC CM energy of $\sqrt{s} = 13$ TeV, obtained using Santander Matching with 5FS (NNLO) and 4FS (NLO), together with their total uncertainties.

M_{H}[GeV]	σ^{bbH}[fb]	$+\mathrm{QCD\,scale} \oplus \mathrm{PDF} \oplus \alpha_{\mathrm{s}}$[%]	$-\mathrm{QCD\,scale} \oplus \mathrm{PDF} \oplus \alpha_{\mathrm{s}}$[%]
120.0	553.40	+20.3	−24.4
120.5	547.10	+20.3	−24.4
121.0	541.40	+20.4	−24.3
121.5	534.30	+20.5	−24.3
122.0	526.80	+20.4	−24.3
122.5	520.00	+20.2	−24.2
123.0	512.40	+21.2	−24.1
123.5	506.60	+20.1	−24.0
124.0	499.90	+20.1	−24.0
124.1	498.50	+20.1	−24.0
124.2	497.60	+20.3	−24.1
124.3	495.50	+20.2	−24.1
124.4	495.00	+20.3	−24.1
124.5	493.00	+20.0	−23.9
124.6	491.80	+20.1	−24.0
124.7	491.90	+20.6	−24.1
124.8	489.90	+20.2	−24.0
124.9	489.10	+20.3	−24.1
125.0	488.00	+20.2	−23.9
125.1	486.30	+20.1	−23.9
125.09	486.00	+20.5	−23.9
125.2	485.00	+20.1	−24.0
125.3	483.30	+20.1	−24.0
125.4	482.20	+20.2	−24.0
125.5	480.90	+20.1	−23.8
125.6	479.20	+20.1	−23.9
125.7	478.90	+20.1	−23.9
125.8	476.80	+20.1	−23.9
125.9	475.70	+20.2	−24.0
126.0	476.00	+20.2	−23.8
126.5	469.50	+20.0	−23.7
127.0	463.50	+20.0	−23.7
127.5	458.00	+20.0	−23.6
128.0	451.30	+19.9	−23.6
128.5	446.30	+19.9	−23.5
129.0	441.60	+20.0	−23.4
129.5	435.80	+19.9	−23.4
130.0	430.40	+19.9	−23.3

Table 246: Inclusive bbH cross sections for a LHC CM energy of $\sqrt{s} = 14$ TeV, obtained using Santander Matching with 5FS (NNLO) and 4FS (NLO), together with their total uncertainties.

M_{H}[GeV]	σ^{bbH}[fb]	$+$QCD scale $\oplus$ PDF $\oplus$ α_{s}[%]	$-$QCD scale $\oplus$ PDF $\oplus$ α_{s}[%]
120.0	628.80	$+20.4$	-24.7
120.5	620.40	$+20.3$	-24.6
121.0	610.50	$+20.2$	-24.5
121.5	603.20	$+20.2$	-24.4
122.0	596.10	$+20.2$	-24.4
122.5	588.40	$+20.2$	-24.3
123.0	580.10	$+20.0$	-24.2
123.5	574.50	$+20.1$	-24.2
124.0	567.20	$+23.4$	-24.2
124.1	565.60	$+20.1$	-24.2
124.2	564.20	$+20.1$	-24.2
124.3	562.10	$+20.1$	-24.2
124.4	560.80	$+20.1$	-24.3
124.5	559.60	$+20.1$	-24.1
124.6	557.70	$+20.0$	-24.1
124.7	556.30	$+20.1$	-24.2
124.8	555.10	$+20.2$	-24.2
124.9	554.50	$+20.3$	-24.2
125.0	552.90	$+20.0$	-24.0
125.1	552.20	$+20.1$	-24.1
125.09	552.10	$+20.2$	-24.1
125.2	550.10	$+23.0$	-24.0
125.3	548.10	$+20.1$	-24.2
125.4	547.40	$+20.6$	-24.1
125.5	545.30	$+19.9$	-24.0
125.6	544.80	$+20.6$	-24.0
125.7	542.20	$+20.0$	-24.0
125.8	541.50	$+20.8$	-24.1
125.9	539.80	$+20.0$	-24.1
126.0	538.40	$+19.9$	-23.9
126.5	534.20	$+20.0$	-23.9
127.0	526.00	$+19.9$	-23.8
127.5	520.00	$+19.8$	-23.7
128.0	512.40	$+19.8$	-23.7
128.5	506.20	$+19.8$	-23.7
129.0	500.20	$+19.7$	-23.6
129.5	494.30	$+19.7$	-23.6
130.0	487.80	$+21.4$	-23.5

Table 247: Energy scan of Inclusive bbH cross sections for a Higgs boson mass of 125 GeV, obtained using Santander Matching with 5FS (NNLO) and 4FS (NLO), together with their total uncertainties.

$\sqrt{s}$ [TeV]	σ^{bbH}[fb]	$+$QCD scale $\oplus$ PDF $\oplus$ α_s[%]	$-$QCD scale $\oplus$ PDF $\oplus$ α_s[%]
6.0	112.70	$+20.9$	-22.5
6.5	133.50	$+20.8$	-22.5
7.0	155.20	$+20.7$	-22.4
7.5	177.90	$+20.6$	-22.4
8.0	202.10	$+20.7$	-22.3
8.5	226.70	$+20.5$	-22.3
9.0	252.50	$+20.4$	-22.5
9.5	280.00	$+20.5$	-22.7
10.0	306.90	$+20.4$	-22.8
10.5	335.60	$+20.4$	-23.0
11.0	363.90	$+20.2$	-23.1
11.5	394.40	$+20.3$	-23.2
12.0	424.30	$+20.2$	-23.4
12.5	455.70	$+20.1$	-23.6
13.0	488.00	$+20.2$	-23.9
13.5	520.00	$+20.1$	-24.0
14.0	552.90	$+20.0$	-24.0
14.5	588.00	$+20.1$	-24.2
15.0	620.30	$+20.0$	-24.4

Table 248: Energy scan of Inclusive bbH cross sections for a Higgs boson mass of 125.09 GeV, obtained using Santander Matching with 5FS (NNLO) and 4FS (NLO), together with their total uncertainties.

$\sqrt{s}$ [TeV]	σ^{bbH}[fb]	$+$QCD scale $\oplus$ PDF $\oplus$ α_s[%]	$-$QCD scale $\oplus$ PDF $\oplus$ α_s[%]
6.0	112.50	$+20.8$	-22.5
6.5	133.40	$+20.8$	-22.5
7.0	154.50	$+20.7$	-22.5
7.5	177.40	$+20.6$	-22.4
8.0	201.50	$+20.6$	-22.4
8.5	226.30	$+20.5$	-22.4
9.0	252.00	$+20.4$	-22.5
9.5	279.20	$+20.5$	-22.7
10.0	306.60	$+20.4$	-22.8
10.5	334.60	$+20.4$	-23.0
11.0	362.80	$+20.3$	-23.1
11.5	393.00	$+20.3$	-23.2
12.0	423.50	$+20.2$	-23.4
12.5	454.30	$+20.1$	-23.5
13.0	486.30	$+20.1$	-23.9
13.5	518.30	$+20.1$	-24.0
14.0	552.20	$+20.1$	-24.1
14.5	584.80	$+20.0$	-24.2
15.0	618.60	$+19.8$	-24.4

References

[1] ATLAS Collaboration, G. Aad et al., *Observation of a new particle in the search for the Standard Model Higgs boson with the ATLAS detector at the LHC*, Phys. Lett. **B716** (2012) 1–29, arXiv:1207.7214 [hep-ex]. (1, 21, 49, 264, 373, 492)

[2] CMS Collaboration, S. Chatrchyan et al., *Observation of a new boson at a mass of 125 GeV with the CMS experiment at the LHC*, Phys. Lett. **B716** (2012) 30–61, arXiv:1207.7235 [hep-ex]. (1, 21, 49, 373, 386, 492)

[3] ATLAS Collaboration, G. Aad et al., *Evidence for the spin-0 nature of the Higgs boson using ATLAS data*, Phys. Lett. **B726** (2013) 120–144, arXiv:1307.1432 [hep-ex]. (1, 386)

[4] CMS Collaboration, S. Chatrchyan et al., *Study of the Mass and Spin-Parity of the Higgs Boson Candidate Via Its Decays to Z Boson Pairs*, Phys. Rev. Lett. **110** (2013) 081803, arXiv:1212.6639 [hep-ex]. (1, 386)

[5] ATLAS, CMS Collaboration, G. Aad et al., *Combined Measurement of the Higgs Boson Mass in pp Collisions at $\sqrt{s} = 7$ and 8 TeV with the ATLAS and CMS Experiments*, Phys. Rev. Lett. **114** (2015) 191803, arXiv:1503.07589 [hep-ex]. (1, 7, 394, 492, 591)

[6] ATLAS, CMS Collaboration, G. Aad et al., *Measurements of the Higgs boson production and decay rates and constraints on its couplings from a combined ATLAS and CMS analysis of the LHC pp collision data at $\sqrt{s} = 7$ and 8 TeV*, JHEP **08** (2016) 045, arXiv:1606.02266 [hep-ex]. (1, 2, 303, 341, 394, 492, 590, 621, 629)

[7] LHC Higgs Cross Section Working Group, S. Dittmaier, C. Mariotti, G. Passarino, and R. Tanaka (Eds.), *Handbook of LHC Higgs Cross Sections: 1. Inclusive Observables*, CERN-2011-002 (CERN, Geneva, 2011) , arXiv:1101.0593 [hep-ph]. (1, 9, 21, 25, 43, 85, 419, 607)

[8] LHC Higgs Cross Section Working Group, S. Dittmaier, C. Mariotti, G. Passarino, and R. Tanaka (Eds.), *Handbook of LHC Higgs Cross Sections: 2. Differential Distributions*, CERN-2012-002 (CERN, Geneva, 2012) , arXiv:1201.3084 [hep-ph]. (1, 9, 21, 23, 27, 28, 47, 85, 124, 419, 607)

[9] LHC Higgs Cross Section Working Group, S. Heinemeyer, C. Mariotti, G. Passarino, and R. Tanaka (Eds.), *Handbook of LHC Higgs Cross Sections: 3. Higgs Properties*, CERN-2013-004 (CERN, Geneva, 2013) , arXiv:1307.1347 [hep-ph]. (1, 9, 17, 21, 23, 25, 27, 28, 47, 60, 72, 85, 126, 230, 303, 327, 346, 401, 402, 403, 404, 405, 419, 458, 483, 497, 498, 540, 580, 607, 608, 621, 625)

[10] LHC Higgs Cross Section Working Group Collaboration, A. David, A. Denner, M. Duehrssen, M. Grazzini, C. Grojean, G. Passarino, M. Schumacher, M. Spira, G. Weiglein, and M. Zanetti, *LHC HXSWG interim recommendations to explore the coupling structure of a Higgs-like particle*, arXiv:1209.0040 [hep-ph]. (1, 336, 339, 380, 401)

[11] Particle Data Group Collaboration, K. Olive et al., *Review of Particle Physics*, Chin. Phys. **C38** (2014) 090001. (5, 7, 50, 126, 330, 409, 410)

[12] T. van Ritbergen, J. A. M. Vermaseren, and S. A. Larin, *The Four loop beta function in quantum chromodynamics*, Phys. Lett. **B400** (1997) 379–384, arXiv:hep-ph/9701390 [hep-ph]. (5)

[13] M. Czakon, *The Four-loop QCD beta-function and anomalous dimensions*, Nucl. Phys. **B710** (2005) 485–498, arXiv:hep-ph/0411261 [hep-ph]. (5)

[14] P. A. Baikov, K. G. Chetyrkin, and J. H. Kühn, *Quark Mass and Field Anomalous Dimensions to $\mathcal{O}(\alpha_s^5)$*, JHEP **10** (2014) 076, arXiv:1402.6611 [hep-ph]. (5)

[15] S. Moch, J. A. M. Vermaseren, and A. Vogt, *The Three loop splitting functions in QCD: The Nonsinglet case*, Nucl. Phys. **B688** (2004) 101–134, arXiv:hep-ph/0403192 [hep-ph]. (6)

[16] A. Vogt, S. Moch, and J. A. M. Vermaseren, *The Three-loop splitting functions in QCD: The*

Singlet case, Nucl. Phys. **B691** (2004) 129–181, arXiv:hep-ph/0404111 [hep-ph]. (6)

[17] P. Marquard, A. V. Smirnov, V. A. Smirnov, and M. Steinhauser, *Quark Mass Relations to Four-Loop Order in Perturbative QCD*, Phys. Rev. Lett. **114** (2015) 142002, arXiv:1502.01030 [hep-ph]. (6, 7, 34)

[18] CMS Collaboration, V. Khachatryan et al., *Measurement of the top quark mass using proton-proton data at $\sqrt{s} = 7$ and 8 TeV*, Phys. Rev. **D93** (2016) 072004, arXiv:1509.04044 [hep-ex]. (6)

[19] M. Jezabek and J. H. Kühn, *The Top width: Theoretical update*, Phys. Rev. **D48** (1993) 1910–1913, arXiv:hep-ph/9302295 [hep-ph]. [Erratum-ibid. **D49** (1994) 4970]. (6)

[20] A. Czarnecki and K. Melnikov, *Two loop QCD corrections to top quark width*, Nucl. Phys. **B544** (1999) 520–531, arXiv:hep-ph/9806244 [hep-ph]. (6)

[21] K. G. Chetyrkin, R. Harlander, T. Seidensticker, and M. Steinhauser, *Second order QCD corrections to $\Gamma(t \to Wb)$*, Phys. Rev. **D60** (1999) 114015, arXiv:hep-ph/9906273 [hep-ph]. (6)

[22] I. R. Blokland, A. Czarnecki, M. Slusarczyk, and F. Tkachov, *Heavy to light decays with a two loop accuracy*, Phys. Rev. Lett. **93** (2004) 062001, arXiv:hep-ph/0403221 [hep-ph]. (6)

[23] I. R. Blokland, A. Czarnecki, M. Slusarczyk, and F. Tkachov, *Next-to-next-to-leading order calculations for heavy-to-light decays*, Phys. Rev. **D71** (2005) 054004, arXiv:hep-ph/0503039 [hep-ph]. [Erratum-ibid. **D79** (2009) 019901]. (6)

[24] J. Gao, C. S. Li, and H. X. Zhu, *Top Quark Decay at Next-to-Next-to Leading Order in QCD*, Phys. Rev. Lett. **110** (2013) 042001, arXiv:1210.2808 [hep-ph]. (6)

[25] M. Brucherseifer, F. Caola, and K. Melnikov, *$\mathcal{O}(\alpha_s^2)$ corrections to fully-differential top quark decays*, JHEP **04** (2013) 059, arXiv:1301.7133 [hep-ph]. (6)

[26] K. G. Chetyrkin, J. H. Kühn, A. Maier, P. Maierhöfer, P. Marquard, M. Steinhauser, and C. Sturm, *Charm and Bottom Quark Masses: An Update*, Phys. Rev. **D80** (2009) 074010, arXiv:0907.2110 [hep-ph]. (7)

[27] C. W. Bauer, Z. Ligeti, M. Luke, A. V. Manohar, and M. Trott, *Global analysis of inclusive B decays*, Phys. Rev. **D70** (2004) 094017, arXiv:hep-ph/0408002 [hep-ph]. (7, 15, 328)

[28] M. Botje et al., *The PDF4LHC Working Group Interim Recommendations*, arXiv:1101.0538 [hep-ph]. (9, 13, 483)

[29] H.-L. Lai, M. Guzzi, J. Huston, Z. Li, P. M. Nadolsky, et al., *New parton distributions for collider physics*, Phys. Rev. D **82** (2010) 074024, arXiv:1007.2241 [hep-ph]. (9, 108, 644)

[30] A. D. Martin, W. J. Stirling, R. S. Thorne, and G. Watt, *Parton distributions for the LHC*, Eur. Phys. J. **C63** (2009) 189, arXiv:0901.0002 [hep-ph]. (9, 242, 498)

[31] R. D. Ball et al., *Parton distributions with LHC data*, Nucl. Phys. **B867** (2013) 244, arXiv:1207.1303 [hep-ph]. (9, 242, 385)

[32] ZEUS, H1 Collaboration, H. Abramowicz et al., *Combination of measurements of inclusive deep inelastic $e^{\pm}p$ scattering cross sections and QCD analysis of HERA data*, Eur. Phys. J. **C75** (2015) 580, arXiv:1506.06042 [hep-ex]. (9, 13, 36)

[33] J. R. Andersen et al., *Les Houches 2013: Physics at TeV Colliders: Standard Model Working Group Report*, 2014. arXiv:1405.1067 [hep-ph]. (9, 14, 124, 125)

[34] J. Rojo et al., *The PDF4LHC report on PDFs and LHC data: Results from Run I and preparation for Run II*, J. Phys. **G42** (2015) 103103, arXiv:1507.00556 [hep-ph]. (9)

[35] J. Butterworth et al., *PDF4LHC recommendations for LHC Run II*, J. Phys. **G43** (2016) 023001, arXiv:1510.03865 [hep-ph]. (9, 12, 19, 36, 37, 38, 43, 64, 68, 88, 89, 122, 125, 145, 152, 156, 163, 167, 188, 222, 223, 458, 516, 544, 580)

[36] S. Dulat, T.-J. Hou, J. Gao, M. Guzzi, J. Huston, P. Nadolsky, J. Pumplin, C. Schmidt,

D. Stump, and C. P. Yuan, *New parton distribution functions from a global analysis of quantum chromodynamics*, Phys. Rev. **D93** (2016) 033006, arXiv:1506.07443 [hep-ph]. (9, 38, 223)

[37] L. A. Harland-Lang, A. D. Martin, P. Motylinski, and R. S. Thorne, *Parton distributions in the LHC era: MMHT 2014 PDFs*, Eur. Phys. J. **C75** (2015) 204, arXiv:1412.3989 [hep-ph]. (9, 38, 116, 145, 468)

[38] NNPDF Collaboration, R. D. Ball et al., *Parton distributions for the LHC Run II*, JHEP **04** (2015) 040, arXiv:1410.8849 [hep-ph]. (9, 38, 109)

[39] A. Accardi et al., *A Critical Appraisal and Evaluation of Modern PDFs*, Eur. Phys. J. **C76** (2016) 471, arXiv:1603.08906 [hep-ph]. (9)

[40] S. Alekhin, J. Bluemlein, and S. Moch, *The ABM parton distributions tuned to LHC data*, Phys. Rev. **D89** (2014) 054028, arXiv:1310.3059 [hep-ph]. (9, 13, 36)

[41] A. Accardi, L. T. Brady, W. Melnitchouk, J. F. Owens, and N. Sato, *Constraints on large-x parton distributions from new weak boson production and deep-inelastic scattering data*, Phys. Rev. **D93** (2016) 114017, arXiv:1602.03154 [hep-ph]. (9)

[42] P. Jimenez-Delgado and E. Reya, *Delineating parton distributions and the strong coupling*, Phys. Rev. **D89** (2014) 074049, arXiv:1403.1852 [hep-ph]. (9, 13, 36)

[43] A. Buckley, J. Ferrando, S. Lloyd, K. Nordström, B. Page, et al., *LHAPDF6: parton density access in the LHC precision era*, Eur. Phys. J. **C75** (2015) 132, arXiv:1412.7420 [hep-ph]. (9, 19, 540)

[44] NNPDF Collaboration, L. Del Debbio, S. Forte, J. I. Latorre, A. Piccione, and J. Rojo, *Unbiased determination of the proton structure function F_2^p with faithful uncertainty estimation*, JHEP **03** (2005) 080, arXiv:hep-ph/0501067 [hep-ph]. (9)

[45] NNPDF Collaboration, L. Del Debbio, S. Forte, J. I. Latorre, A. Piccione, and J. Rojo, *Neural network determination of parton distributions: The Nonsinglet case*, JHEP **03** (2007) 039, arXiv:hep-ph/0701127 [hep-ph]. (9)

[46] J. Pumplin et al., *Uncertainties of predictions from parton distribution functions. 2. The Hessian method*, Phys. Rev. **D65** (2001) 014013, arXiv:hep-ph/0101032. (9)

[47] G. Watt and R. S. Thorne, *Study of Monte Carlo approach to experimental uncertainty propagation with MSTW 2008 PDFs*, JHEP **08** (2012) 052, arXiv:1205.4024 [hep-ph]. (9)

[48] J. Gao and P. Nadolsky, *A meta-analysis of parton distribution functions*, JHEP **07** (2014) 035, arXiv:1401.0013 [hep-ph]. (9, 11)

[49] S. Carrazza, S. Forte, Z. Kassabov, J. I. Latorre, and J. Rojo, *An Unbiased Hessian Representation for Monte Carlo PDFs*, Eur. Phys. J. **C75** (2015) 369, arXiv:1505.06736 [hep-ph]. (9, 12, 38)

[50] S. Carrazza, J. I. Latorre, J. Rojo, and G. Watt, *A compression algorithm for the combination of PDF sets*, Eur. Phys. J. **C75** (2015) 474, arXiv:1504.06469 [hep-ph]. (11)

[51] A. D. Martin, W. J. Stirling, R. S. Thorne, and G. Watt, *Uncertainties on α_S in global PDF analyses*, Eur. Phys. J. **C64** (2009) 653–680, arXiv:0905.3531 [hep-ph]. (12)

[52] F. Demartin, S. Forte, E. Mariani, J. Rojo, and A. Vicini, *The impact of PDF and α_s uncertainties on Higgs Production in gluon fusion at hadron colliders*, Phys. Rev. **D82** (2010) 014002, arXiv:1004.0962 [hep-ph]. (12)

[53] H.-L. Lai et al., *Uncertainty induced by QCD coupling in the CTEQ global analysis of parton distributions*, Phys. Rev. **D82** (2010) 054021, arXiv:1004.4624 [hep-ph]. (12)

[54] J. Alwall, R. Frederix, S. Frixione, V. Hirschi, F. Maltoni, O. Mattelaer, H. S. Shao, T. Stelzer, P. Torrielli, and M. Zaro, *The automated computation of tree-level and next-to-leading order differential cross sections, and their matching to parton shower simulations*, JHEP **07** (2014) 079, arXiv:1405.0301 [hep-ph]. (13, 69, 86, 93, 109, 123, 125, 127, 145, 147, 149, 152,

160, 162, 167, 171, 173, 197, 200, 223, 381, 383, 388, 415, 468, 469, 492, 525, 526, 540, 543, 576, 644)

[55] V. Bertone, R. Frederix, S. Frixione, J. Rojo, and M. Sutton, *aMCfast: automation of fast NLO computations for PDF fits*, JHEP **08** (2014) 166, arXiv:1406.7693 [hep-ph]. (13)

[56] T. Carli et al., *A posteriori inclusion of parton density functions in NLO QCD final-state calculations at hadron colliders: The APPLGRID Project*, Eur. Phys. J. **C66** (2010) 503, arXiv:0911.2985 [hep-ph]. (13)

[57] J. Rojo et al., *The Les Houches benchmarks for GM-VFN heavy quark schemes in deep-inelastic scattering*, in *J. R. Andersen et al., "The SM and NLO multileg working group: Summary report"*. 2010. arXiv:1003.1241 [hep-ph]. (14)

[58] M. Guzzi, P. M. Nadolsky, H.-L. Lai, and C.-P. Yuan, *General-Mass Treatment for Deep Inelastic Scattering at Two-Loop Accuracy*, Phys. Rev. **D86** (2012) 053005, arXiv:1108.5112 [hep-ph]. (14)

[59] R. Thorne, *Effect of changes of variable flavor number scheme on parton distribution functions and predicted cross sections*, Phys. Rev. **D86** (2012) 074017, arXiv:1201.6180 [hep-ph]. (14)

[60] J. Gao, M. Guzzi, and P. M. Nadolsky, *Charm quark mass dependence in a global QCD analysis*, Eur. Phys. J. **C73** (2013) 2541, arXiv:1304.3494 [hep-ph]. (14, 15)

[61] A. H. Hoang and A. V. Manohar, *Charm quark mass from inclusive semileptonic B decays*, Phys. Lett. **B633** (2006) 526–532, arXiv:hep-ph/0509195 [hep-ph]. (15)

[62] A. D. Martin, W. J. Stirling, R. S. Thorne, and G. Watt, *Heavy-quark mass dependence in global PDF analyses and 3- and 4-flavour parton distributions*, Eur. Phys. J. **C70** (2010) 51–72, arXiv:1007.2624 [hep-ph]. (15)

[63] V. Bertone, S. Carrazza, and J. Rojo, *Doped Parton Distributions*, in *27th Rencontres de Blois on Particle Physics and Cosmology Blois, France, May 31-June 5, 2015*. 2015. arXiv:1509.04022 [hep-ph]. (15)

[64] L. A. Harland-Lang, A. D. Martin, P. Motylinski, and R. S. Thorne, *Charm and beauty quark masses in the MMHT2014 global PDF analysis*, Eur. Phys. J. **C76** (2016) 10, arXiv:1510.02332 [hep-ph]. (15, 515)

[65] R. D. Ball, V. Bertone, F. Cerutti, L. Del Debbio, S. Forte, A. Guffanti, J. I. Latorre, J. Rojo, and M. Ubiali, *Impact of Heavy Quark Masses on Parton Distributions and LHC Phenomenology*, Nucl. Phys. **B849** (2011) 296–363, arXiv:1101.1300 [hep-ph]. (15)

[66] S. Alekhin and S. Moch, *Heavy-quark deep-inelastic scattering with a running mass*, Phys. Lett. **B699** (2011) 345–353, arXiv:1011.5790 [hep-ph]. (16)

[67] K. G. Chetyrkin, J. H. Kühn, and C. Sturm, *QCD decoupling at four loops*, Nucl. Phys. **B744** (2006) 121–135, arXiv:hep-ph/0512060 [hep-ph]. (16, 380, 606)

[68] A. Denner, S. Heinemeyer, I. Puljak, D. Rebuzzi, and M. Spira, *Standard Model Higgs-Boson Branching Ratios with Uncertainties*, Eur. Phys. J. **C71** (2011) 1753, arXiv:1107.5909 [hep-ph]. (21)

[69] A. Djouadi, J. Kalinowski, and M. Spira, HDECAY*: A Program for Higgs boson decays in the standard model and its supersymmetric extension*, Comput. Phys. Commun. **108** (1998) 56–74, arXiv:hep-ph/9704448 [hep-ph]. http://tiger.web.psi.ch/hdecay/. (21, 27, 94, 223, 376, 378, 499, 554, 585, 591, 605, 606, 657)

[70] M. Spira, *QCD effects in Higgs physics*, Fortsch. Phys. **46** (1998) 203–284, arXiv:hep-ph/9705337 [hep-ph]. (21, 27, 374, 491, 499, 606)

[71] A. Djouadi, M. M. Mühlleitner, and M. Spira, *Decays of supersymmetric particles: The Program SUSY-HIT (SUspect-SdecaY-Hdecay-InTerface)*, Acta Phys. Polon. **B38** (2007)

635–644, arXiv:hep-ph/0609292 [hep-ph]. (21, 27, 376, 378, 499, 554, 591, 606)

[72] A. Bredenstein, A. Denner, S. Dittmaier, and M. Weber, *Precise predictions for the Higgs-boson decay $H \to WW/ZZ \to 4$ leptons*, Phys. Rev. **D74** (2006) 013004, arXiv:hep-ph/0604011 [hep-ph]. (21, 491, 499, 585)

[73] A. Bredenstein, A. Denner, S. Dittmaier, and M. Weber, *Radiative corrections to the semileptonic and hadronic Higgs-boson decays $H \to WW/ZZ \to 4$ fermions*, JHEP **02** (2007) 080, arXiv:hep-ph/0611234 [hep-ph]. (21, 491, 499)

[74] A. Bredenstein, A. Denner, S. Dittmaier, A. Mück, and M. M. Weber, `Prophecy4f`*: A Monte Carlo generator for a proper description of the Higgs decay into 4 fermions*, http://prophecy4f.hepforge.org/, 2010. (21)

[75] L. Mihaila, B. Schmidt, and M. Steinhauser, *$\Gamma(H \to b\bar{b})$ to order $\alpha\alpha_s$*, Phys. Lett. **B751** (2015) 442–447, arXiv:1509.02294 [hep-ph]. (21)

[76] S. Boselli, C. M. C. Calame, G. Montagna, O. Nicrosini, and F. Piccinini, *Higgs boson decay into four leptons at NLOPS electroweak accuracy*, JHEP **06** (2015) 023, arXiv:1503.07394 [hep-ph]. (26, 27)

[77] S. Boselli, C. M. C. Calame, G. Montagna, O. Nicrosini, and F. Piccinini, `Hto4l`*: An event generator for SM Higgs decay into 4 charged leptons at NLOPS EW accuracy*, http:www.pv.infn.it/hepcomplex/hto4l.html, 2015. (26)

[78] A. Bredenstein, A. Denner, S. Dittmaier, and M. M. Weber, *Precision calculations for the Higgs decays $H \to ZZ/WW \to 4$ leptons*, in *Proceedings, 8th DESY Workshop on Elementary Particle Theory: Loops and Legs in Quantum Field Theory: Eisenach, Germany, 23-28 April 2006*, vol. 160, pp. 131–135. 2006. arXiv:hep-ph/0607060 [hep-ph]. (26)

[79] A. Bredenstein, A. Denner, S. Dittmaier, and M. M. Weber, *Precision calculations for $H \to WW/ZZ \to 4$fermions with PROPHECY4f*, arXiv:0708.4123 [hep-ph]. (26)

[80] S. Alioli, P. Nason, C. Oleari, and E. Re, *NLO Higgs boson production via gluon fusion matched with shower in POWHEG*, JHEP **04** (2009) 002, arXiv:0812.0578 [hep-ph]. (27, 240)

[81] S. Alioli, P. Nason, C. Oleari, and E. Re, *A general framework for implementing NLO calculations in shower Monte Carlo programs: the POWHEG BOX*, JHEP **06** (2010) 043, arXiv:1002.2581 [hep-ph]. (27, 69, 123, 125, 162, 492, 506, 526, 609, 643, 644)

[82] S. Heinemeyer, W. Hollik, and G. Weiglein, *FeynHiggs: A Program for the calculation of the masses of the neutral CP even Higgs bosons in the MSSM*, Comput. Phys. Commun. **124** (2000) 76–89, arXiv:hep-ph/9812320 [hep-ph]. (27, 493, 495)

[83] S. Heinemeyer, W. Hollik, and G. Weiglein, *The Masses of the neutral CP - even Higgs bosons in the MSSM: Accurate analysis at the two loop level*, Eur. Phys. J. **C9** (1999) 343–366, arXiv:hep-ph/9812472 [hep-ph]. (27, 490, 493, 495)

[84] G. Degrassi, S. Heinemeyer, W. Hollik, P. Slavich, and G. Weiglein, *Towards high precision predictions for the MSSM Higgs sector*, Eur. Phys. J. **C28** (2003) 133–143, arXiv:hep-ph/0212020 [hep-ph]. (27, 492, 493, 495)

[85] M. Frank, T. Hahn, S. Heinemeyer, W. Hollik, H. Rzehak, et al., *The Higgs Boson Masses and Mixings of the Complex MSSM in the Feynman-Diagrammatic Approach*, JHEP **02** (2007) 047, arXiv:hep-ph/0611326 [hep-ph]. (27, 491, 493, 495)

[86] T. Hahn, S. Heinemeyer, W. Hollik, H. Rzehak, and G. Weiglein, *FeynHiggs: A program for the calculation of MSSM Higgs-boson observables - Version 2.6.5*, Comput. Phys. Commun. **180** (2009) 1426–1427. (27)

[87] T. Hahn, S. Heinemeyer, W. Hollik, H. Rzehak, and G. Weiglein, *High-Precision Predictions for the Light CP -Even Higgs Boson Mass of the Minimal Supersymmetric Standard Model*, Phys. Rev. Lett. **112** (2014) 141801, arXiv:1312.4937 [hep-ph]. (27, 490, 493, 495)

[88] P. Z. Skands et al., *SUSY Les Houches accord: Interfacing SUSY spectrum calculators, decay packages, and event generators*, JHEP **07** (2004) 036, arXiv:hep-ph/0311123 [hep-ph]. (27, 393)

[89] B. C. Allanach et al., *SUSY Les Houches Accord 2*, Comput. Phys. Commun. **180** (2009) 8–25, arXiv:0801.0045 [hep-ph]. (27, 393)

[90] E. Accomando, G. Chachamis, F. Fugel, M. Spira, and M. Walser, *Neutral Higgs Boson Decays to Squark Pairs reanalyzed*, Phys. Rev. **D85** (2012) 015004, arXiv:1103.4283 [hep-ph]. (27, 491, 606)

[91] M. Carena, S. Heinemeyer, O. Stål, C. E. M. Wagner, and G. Weiglein, *MSSM Higgs Boson Searches at the LHC: Benchmark Scenarios after the Discovery of a Higgs-like Particle*, Eur. Phys. J. **C73** (2013) 2552, arXiv:1302.7033 [hep-ph]. (28, 493, 497, 498, 665)

[92] LHC Higgs Cross Section Working Group, BR subgroup. https://twiki.cern.ch/twiki/bin/view/LHCPhysics/LHCHXSWGBRs. (28)

[93] C. Anastasiou, C. Duhr, F. Dulat, E. Furlan, T. Gehrmann, F. Herzog, A. Lazopoulos, and B. Mistlberger, *High precision determination of the gluon fusion Higgs boson cross-section at the LHC*, JHEP **05** (2016) 058, arXiv:1602.00695 [hep-ph]. (29, 31, 37, 38, 39, 41, 42, 43, 44, 45, 67, 255)

[94] C. Anastasiou, C. Duhr, F. Dulat, E. Furlan, T. Gehrmann, F. Herzog, and B. Mistlberger, *Higgs boson gluon-fusion production beyond threshold in N^3LO QCD*, JHEP **03** (2015) 091, arXiv:1411.3584 [hep-ph]. (29, 38, 491, 607)

[95] C. Anastasiou, C. Duhr, F. Dulat, E. Furlan, T. Gehrmann, et al., *Higgs boson gluon–fusion production at threshold in $N^3LO\ QCD$*, Phys. Lett. **B737** (2014) 325, arXiv:1403.4616 [hep-ph]. (29, 38, 491, 607)

[96] C. Anastasiou, C. Duhr, F. Dulat, F. Herzog, and B. Mistlberger, *Higgs Boson Gluon-Fusion Production in QCD at Three Loops*, Phys. Rev. Lett. **114** (2015) 212001, arXiv:1503.06056 [hep-ph]. (29, 38, 58, 59, 63, 67, 252)

[97] S. Dawson, *Radiative corrections to Higgs boson production*, Nucl. Phys. **B359** (1991) 283–300. (29, 374, 491, 607)

[98] D. Graudenz, M. Spira, and P. M. Zerwas, *QCD corrections to Higgs boson production at proton proton colliders*, Phys. Rev. Lett. **70** (1993) 1372–1375. (29, 36, 374, 491)

[99] A. Djouadi, M. Spira, and P. M. Zerwas, *Production of Higgs bosons in proton colliders: QCD corrections*, Phys. Lett. **B264** (1991) 440–446. (29, 252, 374, 380, 491, 606, 607)

[100] C. Anastasiou and K. Melnikov, *Higgs boson production at hadron colliders in NNLO QCD*, Nucl. Phys. **B646** (2002) 220–256, arXiv:hep-ph/0207004 [hep-ph]. (29, 36, 252, 255, 374, 491, 607)

[101] R. V. Harlander and W. B. Kilgore, *Next-to-next-to-leading order Higgs production at hadron colliders*, Phys. Rev. Lett. **88** (2002) 201801, arXiv:hep-ph/0201206 [hep-ph]. (29, 36, 374, 491, 498, 607)

[102] V. Ravindran, J. Smith, and W. L. van Neerven, *NNLO corrections to the total cross-section for Higgs boson production in hadron hadron collisions*, Nucl. Phys. **B665** (2003) 325–366, arXiv:hep-ph/0302135 [hep-ph]. (29, 36, 252, 374, 491, 607)

[103] R. V. Harlander and K. J. Ozeren, *Finite top mass effects for hadronic Higgs production at next-to-next-to-leading order*, JHEP **11** (2009) 088, arXiv:0909.3420 [hep-ph]. (30, 43, 79, 491, 607)

[104] A. Pak, M. Rogal, and M. Steinhauser, *Finite top quark mass effects in NNLO Higgs boson production at LHC*, JHEP **02** (2010) 025, arXiv:0911.4662 [hep-ph]. (30, 34, 79, 252, 256, 491, 607)

[105] R. V. Harlander and K. J. Ozeren, *Top mass effects in Higgs production at next-to-next-to-leading order QCD: Virtual corrections*, Phys. Lett. **B679** (2009) 467–472, arXiv:0907.2997 [hep-ph]. (30, 43, 79, 491, 607)

[106] R. V. Harlander, H. Mantler, S. Marzani, and K. J. Ozeren, *Higgs production in gluon fusion at next-to-next-to-leading order QCD for finite top mass*, Eur. Phys. J. **C66** (2010) 359–372, arXiv:0912.2104 [hep-ph]. (30, 34, 43, 79, 252, 256, 491, 607)

[107] U. Aglietti, R. Bonciani, G. Degrassi, and A. Vicini, *Two loop light fermion contribution to Higgs production and decays*, Phys. Lett. **B595** (2004) 432–441, arXiv:hep-ph/0404071 [hep-ph]. (30, 36, 374, 380, 491, 498, 608)

[108] S. Actis, G. Passarino, C. Sturm, and S. Uccirati, *NLO Electroweak Corrections to Higgs Boson Production at Hadron Colliders*, Phys. Lett. **B670** (2008) 12–17, arXiv:0809.1301 [hep-ph]. (30, 36, 43, 374, 380, 608)

[109] S. Actis, G. Passarino, C. Sturm, and S. Uccirati, *NNLO Computational Techniques: The Cases $H \to \gamma\gamma$ and $H \to gg$*, Nucl. Phys. **B811** (2009) 182–273, arXiv:0809.3667 [hep-ph]. (30, 36, 43, 374, 380)

[110] C. Anastasiou, R. Boughezal, and F. Petriello, *Mixed QCD-electroweak corrections to Higgs boson production in gluon fusion*, JHEP **04** (2009) 003, arXiv:0811.3458 [hep-ph]. (30, 44, 374)

[111] J. A. M. Vermaseren, A. Vogt, and S. Moch, *The third-order QCD corrections to deep-inelastic scattering by photon exchange*, Nucl. Phys. **B724** (2005) 3, arXiv:hep-ph/0504242. (32)

[112] G. Soar, S. Moch, J. A. M. Vermaseren, and A. Vogt, *On Higgs-exchange DIS, physical evolution kernels and fourth-order splitting functions at large x*, Nucl. Phys. **B832** (2010) 152–227, arXiv:0912.0369 [hep-ph]. (32)

[113] S. Frixione, Z. Kunszt, and A. Signer, *Three jet cross-sections to next-to-leading order*, Nucl. Phys. **B467** (1996) 399–442, arXiv:hep-ph/9512328 [hep-ph]. (33, 125, 162, 163, 525)

[114] P. Marquard, A. V. Smirnov, V. A. Smirnov, and M. Steinhauser, *Four-loop relation between the $\overline{\text{MS}}$ and on-shell quark mass*, in *Proceedings, 12th International Symposium on Radiative Corrections (Radcor 2015) and LoopFest XIV (Radiative Corrections for the LHC and Future Colliders)*. 2016. arXiv:1601.03748 [hep-ph]. (34)

[115] M. Krämer, E. Laenen, and M. Spira, *Soft gluon radiation in Higgs boson production at the LHC*, Nucl. Phys. **B511** (1998) 523–549, arXiv:hep-ph/9611272 [hep-ph]. (34, 35, 374, 380, 491, 606)

[116] S. Catani, D. de Florian, M. Grazzini, and P. Nason, *Soft gluon resummation for Higgs boson production at hadron colliders*, JHEP **07** (2003) 028, arXiv:hep-ph/0306211 [hep-ph]. (34, 35, 491, 608)

[117] S. Moch and A. Vogt, *Higher-order soft corrections to lepton pair and Higgs boson production*, Phys. Lett. **B631** (2005) 48–57, arXiv:hep-ph/0508265 [hep-ph]. (34, 491, 607, 608)

[118] V. Ravindran, *On Sudakov and soft resummations in QCD*, Nucl. Phys. **B746** (2006) 58–76, arXiv:hep-ph/0512249 [hep-ph]. (34, 608)

[119] V. Ravindran, *Higher-order threshold effects to inclusive processes in QCD*, Nucl. Phys. **B752** (2006) 173–196, arXiv:hep-ph/0603041 [hep-ph]. (34, 491, 607)

[120] D. de Florian and M. Grazzini, *Higgs production through gluon fusion: Updated cross sections at the Tevatron and the LHC*, Phys. Lett. **B674** (2009) 291–294, arXiv:0901.2427 [hep-ph]. (34)

[121] D. de Florian and M. Grazzini, *Higgs production at the LHC: updated cross sections at $\sqrt{s} = 8$ TeV*, Phys. Lett. **B718** (2012) 117–120, arXiv:1206.4133 [hep-ph]. (34)

[122] M. Bonvini and S. Marzani, *Resummed Higgs cross section at N^3LL*, JHEP **09** (2014) 007,

arXiv:1405.3654 [hep-ph]. (34, 38, 42)

[123] M. Bonvini, S. Marzani, C. Muselli, and L. Rottoli, *On the Higgs cross section at N^3LO+N^3LL and its uncertainty*, JHEP **08** (2016) 105, arXiv:1603.08000 [hep-ph]. (34, 38, 39, 42, 44)

[124] A. Vogt, *Next-to-next-to-leading logarithmic threshold resummation for deep inelastic scattering and the Drell-Yan process*, Phys. Lett. **B497** (2001) 228–234, arXiv:hep-ph/0010146 [hep-ph]. (35)

[125] S. Moch, J. A. M. Vermaseren, and A. Vogt, *Higher-order corrections in threshold resummation*, Nucl. Phys. **B726** (2005) 317–335, arXiv:hep-ph/0506288 [hep-ph]. (35)

[126] E. Laenen and L. Magnea, *Threshold resummation for electroweak annihilation from DIS data*, Phys. Lett. **B632** (2006) 270–276, arXiv:hep-ph/0508284 [hep-ph]. (35)

[127] S. Catani, D. de Florian, and M. Grazzini, *Higgs production in hadron collisions: Soft and virtual QCD corrections at NNLO*, JHEP **05** (2001) 025, arXiv:hep-ph/0102227 [hep-ph]. (35, 374, 491)

[128] T. Schmidt and M. Spira, *Higgs Boson Production via Gluon Fusion: Soft-Gluon Resummation including Mass Effects*, Phys. Rev. **D93** (2016) 014022, arXiv:1509.00195 [hep-ph]. (35, 36, 38, 42)

[129] S. Catani, M. L. Mangano, P. Nason, and L. Trentadue, *The Top cross-section in hadronic collisions*, Phys. Lett. **B378** (1996) 329–336, arXiv:hep-ph/9602208 [hep-ph]. (35)

[130] S. Catani, M. L. Mangano, P. Nason, and L. Trentadue, *The Resummation of soft gluons in hadronic collisions*, Nucl. Phys. **B478** (1996) 273–310, arXiv:hep-ph/9604351 [hep-ph]. (35, 145)

[131] S. Forte, A. Isgrò, and G. Vita, *Do we need N^3LO Parton Distributions?*, Phys. Lett. **B731** (2014) 136–140, arXiv:1312.6688 [hep-ph]. (36, 42)

[132] M. Bonvini, S. Marzani, J. Rojo, L. Rottoli, M. Ubiali, R. D. Ball, V. Bertone, S. Carrazza, and N. P. Hartland, *Parton distributions with threshold resummation*, JHEP **09** (2015) 191, arXiv:1507.01006 [hep-ph]. (36)

[133] M. Spira, HIGLU*: A program for the calculation of the total Higgs production cross-section at hadron colliders via gluon fusion including QCD corrections*, arXiv:hep-ph/9510347 [hep-ph]. http://tiger.web.psi.ch/higlu/. (36, 374, 554, 591, 608)

[134] M. Spira, *HIGLU and HDECAY: Programs for Higgs boson production at the LHC and Higgs boson decay widths*, in *New computing techniques in physics research V. Proceedings, 5th International Workshop, AIHENP '96, Lausanne, Switzerland, September 2-6, 1996*, vol. A389, pp. 357–360. 1997. arXiv:hep-ph/9610350 [hep-ph]. (36, 374)

[135] R. V. Harlander, S. Liebler, and H. Mantler, *SusHi: A program for the calculation of Higgs production in gluon fusion and bottom-quark annihilation in the Standard Model and the MSSM*, Comput. Phys. Commun. **184** (2013) 1605–1617, arXiv:1212.3249 [hep-ph]. (36, 492, 498, 516, 536, 554, 591, 608)

[136] M. Spira, A. Djouadi, D. Graudenz, and P. Zerwas, *Higgs boson production at the LHC*, Nucl. Phys. **B453** (1995) 17–82, arXiv:hep-ph/9504378 [hep-ph]. (36, 63, 252, 374, 380, 491, 498, 606, 607, 608)

[137] M. I. Kotsky and O. I. Yakovlev, *On the resummation of double logarithms in the process $H \to \gamma\gamma$*, Phys. Lett. **B418** (1998) 335–344, arXiv:hep-ph/9708485 [hep-ph]. (36)

[138] R. Akhoury, H. Wang, and O. I. Yakovlev, *On the Resummation of large QCD logarithms in $H \to \gamma\gamma$ decay*, Phys. Rev. **D64** (2001) 113008, arXiv:hep-ph/0102105 [hep-ph]. (36)

[139] K. Melnikov and A. Penin, *On the light quark mass effects in Higgs boson production in gluon fusion*, JHEP **05** (2016) 172, arXiv:1602.09020 [hep-ph]. (36)

[140] R. Harlander and P. Kant, *Higgs production and decay: Analytic results at next-to-leading order*

QCD, JHEP **12** (2005) 015, arXiv:hep-ph/0509189 [hep-ph]. (36, 374, 491, 498, 607, 608)

[141] C. Anastasiou, S. Bucherer, and Z. Kunszt, *HPro: A NLO Monte-Carlo for Higgs production via gluon fusion with finite heavy quark masses*, JHEP **10** (2009) 068, arXiv:0907.2362 [hep-ph]. (36, 79, 374)

[142] C. Anastasiou, S. Beerli, S. Bucherer, A. Daleo, and Z. Kunszt, *Two-loop amplitudes and master integrals for the production of a Higgs boson via a massive quark and a scalar-quark loop*, JHEP **01** (2007) 082, arXiv:hep-ph/0611236 [hep-ph]. (36, 374, 491, 608)

[143] U. Aglietti, R. Bonciani, G. Degrassi, and A. Vicini, *Analytic results for virtual QCD corrections to Higgs production and decay*, JHEP **01** (2007) 021, arXiv:hep-ph/0611266. (36, 374, 491, 608)

[144] A. Denner, S. Dittmaier, M. Grazzini, R. Harlander, R. Thorne, M. Spira, and M. Steinhauser, *Standard Model input parameters for Higgs physics*, LHCHXSWG-INT-2015-006, 2015. (36, 122, 125, 145, 152, 153, 156, 163, 167, 222, 380, 499, 613)

[145] A. Djouadi and P. Gambino, *Leading electroweak correction to Higgs boson production at proton colliders*, Phys. Rev. Lett. **73** (1994) 2528–2531, arXiv:hep-ph/9406432 [hep-ph]. (36, 374, 380, 608)

[146] K. G. Chetyrkin, B. A. Kniehl, and M. Steinhauser, *Virtual top quark effects on the $H \to b\bar{b}$ decay at next-to-leading order in QCD*, Phys. Rev. Lett. **78** (1997) 594–597, arXiv:hep-ph/9610456 [hep-ph]. (36, 374, 380)

[147] K. G. Chetyrkin, B. A. Kniehl, and M. Steinhauser, *Three loop $\mathcal{O}(\alpha_s^2 G_F M_t^2)$ corrections to hadronic Higgs decays*, Nucl. Phys. **B490** (1997) 19–39, arXiv:hep-ph/9701277 [hep-ph]. (36, 374, 380)

[148] U. Aglietti, R. Bonciani, G. Degrassi, and A. Vicini, *Two-loop electroweak corrections to Higgs production in proton-proton collisions*, in *TeV4LHC Workshop: 2nd Meeting Brookhaven, Upton, New York, February 3-5, 2005*. 2006. arXiv:hep-ph/0610033 [hep-ph]. (36, 374, 380)

[149] G. Degrassi and F. Maltoni, *Two-loop electroweak corrections to Higgs production at hadron colliders*, Phys. Lett. **B600** (2004) 255–260, arXiv:hep-ph/0407249 [hep-ph]. (36, 374, 380, 608)

[150] D. de Florian and J. Zurita, *Soft-gluon resummation for pseudoscalar Higgs boson production at hadron colliders*, Phys. Lett. **B659** (2008) 813–820, arXiv:0711.1916 [hep-ph]. (38)

[151] S. Catani, L. Cieri, D. de Florian, G. Ferrera, and M. Grazzini, *Threshold resummation at N^3LL accuracy and soft-virtual cross sections at N^3LO*, Nucl. Phys. **B888** (2014) 75–91, arXiv:1405.4827 [hep-ph]. (38)

[152] M. Bonvini and L. Rottoli, *Three loop soft function for N^3LL' gluon fusion Higgs production in soft-collinear effective theory*, Phys. Rev. **D91** (2015) 051301, arXiv:1412.3791 [hep-ph]. (38)

[153] M. Bonvini and L. Rottoli, TROLL, http://www.ge.infn.it/~bonvini/troll/. (38)

[154] M. Bonvini, ggHiggs, http://www.ge.infn.it/~bonvini/higgs/. (38)

[155] R. D. Ball, M. Bonvini, S. Forte, S. Marzani, and G. Ridolfi, *Higgs production in gluon fusion beyond NNLO*, Nucl. Phys. **B874** (2013) 746, arXiv:1303.3590 [hep-ph]. (38, 491, 607)

[156] G. Altarelli, *Partons in Quantum Chromodynamics*, Phys. Rept. **81** (1982) 1. (38)

[157] V. Ahrens, T. Becher, M. Neubert, and L. L. Yang, *Origin of the Large Perturbative Corrections to Higgs Production at Hadron Colliders*, Phys. Rev. **D79** (2009) 033013, arXiv:0808.3008 [hep-ph]. (38)

[158] C. F. Berger, C. Marcantonini, I. W. Stewart, F. J. Tackmann, and W. J. Waalewijn, *Higgs Production with a Central Jet Veto at NNLL+NNLO*, JHEP **04** (2011) 092, arXiv:1012.4480

[hep-ph]. (38, 46, 56)

[159] I. W. Stewart, F. J. Tackmann, J. R. Walsh, and S. Zuberi, *Jet p_T resummation in Higgs production at NNLL′+NNLO*, Phys. Rev. **D89** (2014) 054001, arXiv:1307.1808. (38, 45, 55, 56, 60, 61, 63, 468)

[160] M. Cacciari and N. Houdeau, *Meaningful characterisation of perturbative theoretical uncertainties*, JHEP **09** (2011) 039, arXiv:1105.5152 [hep-ph]. (42, 330, 425)

[161] E. Bagnaschi, M. Cacciari, A. Guffanti, and L. Jenniches, *An extensive survey of the estimation of uncertainties from missing higher orders in perturbative calculations*, JHEP **02** (2015) 133, arXiv:1409.5036 [hep-ph]. (42)

[162] A. David and G. Passarino, *How well can we guess theoretical uncertainties?*, Phys. Lett. **B726** (2013) 266–272, arXiv:1307.1843. (42, 327, 330, 425)

[163] A. Banfi, P. F. Monni, G. P. Salam, and G. Zanderighi, *Higgs and Z-boson production with a jet veto*, Phys. Rev. Lett. **109** (2012) 202001, arXiv:1206.4998 [hep-ph]. (45, 49, 51, 63, 64)

[164] T. Becher and M. Neubert, *Factorization and NNLL Resummation for Higgs Production with a Jet Veto*, JHEP **07** (2012) 108, arXiv:1205.3806 [hep-ph]. (45, 56)

[165] I. W. Stewart and F. J. Tackmann, *Theory Uncertainties for Higgs and Other Searches Using Jet Bins*, Phys. Rev. **D85** (2012) 034011, arXiv:1107.2117 [hep-ph]. (45, 46, 47, 49)

[166] A. Banfi, P. F. Monni, and G. Zanderighi, *Quark masses in Higgs production with a jet veto*, JHEP **01** (2014) 097, arXiv:1308.4634 [hep-ph]. (45, 63)

[167] P. F. Monni, E. Re, and P. Torrielli, *Higgs Transverse-Momentum Resummation in Direct Space*, Phys. Rev. Lett. **116** (2016) 242001, arXiv:1604.02191 [hep-ph]. (45, 67, 68, 69)

[168] F. J. Tackmann, J. R. Walsh, and S. Zuberi, *Resummation Properties of Jet Vetoes at the LHC*, Phys. Rev. **D86** (2012) 053011, arXiv:1206.4312 [hep-ph]. (46, 56)

[169] S. Gangal and F. J. Tackmann, *Next-to-leading-order uncertainties in Higgs+2 jets from gluon fusion*, Phys. Rev. **D87** (2013) 093008, arXiv:1302.5437 [hep-ph]. (46, 47)

[170] A. Banfi, G. P. Salam, and G. Zanderighi, *NLL+NNLO predictions for jet-veto efficiencies in Higgs-boson and Drell-Yan production*, JHEP **06** (2012) 159, arXiv:1203.5773 [hep-ph]. (47, 64)

[171] ATLAS Collaboration, G. Aad et al., *Observation and measurement of Higgs boson decays to WW^* with the ATLAS detector*, Phys. Rev. **D92** (2015) 012006, arXiv:1412.2641 [hep-ex]. (49, 54)

[172] S. Catani and M. Grazzini, *An NNLO subtraction formalism in hadron collisions and its application to Higgs boson production at the LHC*, Phys. Rev. Lett. **98** (2007) 222002, arXiv:hep-ph/0703012 [hep-ph]. (49, 246, 458, 464)

[173] J. M. Campbell, R. K. Ellis, and G. Zanderighi, *Next-to-Leading order Higgs + 2 jet production via gluon fusion*, JHEP **10** (2006) 028, arXiv:hep-ph/0608194 [hep-ph]. (50)

[174] F. Caola, K. Melnikov, and M. Schulze, *Fiducial cross sections for Higgs boson production in association with a jet at next-to-next-to-leading order in QCD*, Phys. Rev. **D92** (2015) 074032, arXiv:1508.02684 [hep-ph]. (54, 58, 59, 63, 65, 67, 70, 72, 460, 461)

[175] C. W. Bauer, S. Fleming, and M. E. Luke, *Summing Sudakov logarithms in $B \to X_s\gamma$ in effective field theory*, Phys. Rev. **D63** (2000) 014006, arXiv:hep-ph/0005275 [hep-ph]. (56)

[176] C. W. Bauer, S. Fleming, D. Pirjol, and I. W. Stewart, *An Effective field theory for collinear and soft gluons: Heavy to light decays*, Phys. Rev. **D63** (2001) 114020, arXiv:hep-ph/0011336 [hep-ph]. (56)

[177] C. W. Bauer and I. W. Stewart, *Invariant operators in collinear effective theory*, Phys. Lett. **B516** (2001) 134–142, arXiv:hep-ph/0107001 [hep-ph]. (56)

[178] C. W. Bauer, D. Pirjol, and I. W. Stewart, *Soft collinear factorization in effective field theory*, Phys. Rev. **D65** (2002) 054022, arXiv:hep-ph/0109045 [hep-ph]. (56)

[179] I. W. Stewart, F. J. Tackmann, and W. J. Waalewijn, *Factorization at the LHC: From PDFs to Initial State Jets*, Phys. Rev. **D81** (2010) 094035, arXiv:0910.0467 [hep-ph]. (56)

[180] Z. Ligeti, I. W. Stewart, and F. J. Tackmann, *Treating the b quark distribution function with reliable uncertainties*, Phys. Rev. **D78** (2008) 114014, arXiv:0807.1926 [hep-ph]. (56)

[181] R. Abbate, M. Fickinger, A. H. Hoang, V. Mateu, and I. W. Stewart, *Thrust at N^3LL with Power Corrections and a Precision Global Fit for $\alpha_s(m_Z)$*, Phys. Rev. **D83** (2011) 074021, arXiv:1006.3080 [hep-ph]. (56)

[182] R. Boughezal, F. Caola, K. Melnikov, F. Petriello, and M. Schulze, *Higgs boson production in association with a jet at next-to-next-to-leading order*, Phys. Rev. Lett. **115** (2015) 082003, arXiv:1504.07922 [hep-ph]. (59, 63, 65, 67, 461, 468)

[183] R. Boughezal, C. Focke, W. Giele, X. Liu, and F. Petriello, *Higgs boson production in association with a jet at NNLO using jettiness subtraction*, Phys. Lett. **B748** (2015) 5–8, arXiv:1505.03893 [hep-ph]. (59, 63, 65, 67, 72, 94, 468)

[184] R. Boughezal, X. Liu, F. Petriello, F. J. Tackmann, and J. R. Walsh, *Combining Resummed Higgs Predictions Across Jet Bins*, Phys. Rev. **D89** (2014) 074044, arXiv:1312.4535 [hep-ph]. (60, 61)

[185] X. Liu and F. Petriello, *Resummation of jet-veto logarithms in hadronic processes containing jets*, Phys. Rev. **D87** (2013) 014018, arXiv:1210.1906 [hep-ph]. (60, 61)

[186] X. Liu and F. Petriello, *Reducing theoretical uncertainties for exclusive Higgs-boson plus one-jet production at the LHC*, Phys. Rev. **D87** (2013) 094027, arXiv:1303.4405 [hep-ph]. (60, 61, 62)

[187] T. Becher, M. Neubert, and L. Rothen, *Factorization and N^3LL_p+NNLO predictions for the Higgs cross section with a jet veto*, JHEP **10** (2013) 125, arXiv:1307.0025 [hep-ph]. (63)

[188] M. Dasgupta, F. Dreyer, G. P. Salam, and G. Soyez, *Small-radius jets to all orders in QCD*, JHEP **04** (2015) 039, arXiv:1411.5182 [hep-ph]. (63)

[189] A. Banfi, F. Caola, F. A. Dreyer, P. F. Monni, G. P. Salam, G. Zanderighi, and F. Dulat, *Jet-vetoed Higgs cross section in gluon fusion at N^3LO+NNLL with small-R resummation*, JHEP **04** (2016) 049, arXiv:1511.02886 [hep-ph]. (63, 64, 65, 72, 461)

[190] JetVHeto, http://jetvheto.hepforge.org. (63)

[191] M. Cacciari, G. P. Salam, and G. Soyez, *The anti-k_t jet clustering algorithm*, JHEP **04** (2008) 063, arXiv:0802.1189 [hep-ph]. (64, 88, 96, 116, 134, 456, 457, 469, 528, 529)

[192] M. Cacciari, G. P. Salam, and G. Soyez, *FastJet User Manual*, Eur. Phys. J. **C72** (2012) 1896, arXiv:1111.6097 [hep-ph]. (64, 109, 116)

[193] G. Bozzi, S. Catani, D. de Florian, and M. Grazzini, *The q_T spectrum of the Higgs boson at the LHC in QCD perturbation theory*, Phys. Lett. **B564** (2003) 65–72, arXiv:hep-ph/0302104 [hep-ph]. (67)

[194] G. Bozzi, S. Catani, D. de Florian, and M. Grazzini, *Transverse-momentum resummation and the spectrum of the Higgs boson at the LHC*, Nucl. Phys. **B737** (2006) 73–120, arXiv:hep-ph/0508068 [hep-ph]. (67, 69, 464, 468, 492, 506)

[195] J. C. Collins, D. E. Soper, and G. F. Sterman, *Transverse Momentum Distribution in Drell-Yan Pair and W and Z Boson Production*, Nucl. Phys. **B250** (1985) 199–224. (67, 492, 506)

[196] S. Catani, D. de Florian, and M. Grazzini, *Universality of nonleading logarithmic contributions in transverse momentum distributions*, Nucl. Phys. **B596** (2001) 299–312, arXiv:hep-ph/0008184 [hep-ph]. (67, 457, 458)

[197] T. Becher and M. Neubert, *Drell-Yan Production at Small q_T, Transverse Parton Distributions*

and the Collinear Anomaly, Eur. Phys. J. **C71** (2011) 1665, arXiv:1007.4005 [hep-ph]. (67)

[198] X. Chen, J. Cruz-Martinez, T. Gehrmann, E. W. N. Glover, and M. Jaquier, *NNLO QCD corrections to Higgs boson production at large transverse momentum*, JHEP **10** (2016) 066, arXiv:1607.08817 [hep-ph]. (67, 70, 72)

[199] Y. L. Dokshitzer, D. Diakonov, and S. I. Troian, *On the Transverse Momentum Distribution of Massive Lepton Pairs*, Phys. Lett. **B79** (1978) 269–272. (67)

[200] G. Parisi and R. Petronzio, *Small Transverse Momentum Distributions in Hard Processes*, Nucl. Phys. **B154** (1979) 427–440. (67, 68)

[201] S. Frixione, P. Nason, and G. Ridolfi, *Problems in the resummation of soft gluon effects in the transverse momentum distributions of massive vector bosons in hadronic collisions*, Nucl. Phys. **B542** (1999) 311–328, arXiv:hep-ph/9809367 [hep-ph]. (67)

[202] A. Banfi, G. P. Salam, and G. Zanderighi, *Principles of general final-state resummation and automated implementation*, JHEP **03** (2005) 073, arXiv:hep-ph/0407286 [hep-ph]. (67, 68)

[203] A. Banfi, H. McAslan, P. F. Monni, and G. Zanderighi, *A general method for the resummation of event-shape distributions in e^+e^- annihilation*, JHEP **05** (2015) 102, arXiv:1412.2126 [hep-ph]. (67)

[204] D. de Florian, G. Ferrera, M. Grazzini, and D. Tommasini, *Transverse-momentum resummation: Higgs boson production at the Tevatron and the LHC*, JHEP **11** (2011) 064, arXiv:1109.2109 [hep-ph]. (69, 468)

[205] K. Hamilton, P. Nason, C. Oleari, and G. Zanderighi, *Merging H/W/Z + 0 and 1 jet at NLO with no merging scale: a path to parton shower + NNLO matching*, JHEP **05** (2013) 082, arXiv:1212.4504 [hep-ph]. (69, 109)

[206] R. Frederix and S. Frixione, *Merging meets matching in MC@NLO*, JHEP **12** (2012) 061, arXiv:1209.6215 [hep-ph]. (69, 93, 94, 109, 170, 468)

[207] T. Sjöstrand, S. Ask, J. R. Christiansen, R. Corke, N. Desai, P. Ilten, S. Mrenna, S. Prestel, C. O. Rasmussen, and P. Z. Skands, *An Introduction to PYTHIA 8.2*, Comput. Phys. Commun. **191** (2015) 159–177, arXiv:1410.3012 [hep-ph]. (69, 123, 171, 468)

[208] K. Hamilton, P. Nason, E. Re, and G. Zanderighi, *NNLOPS simulation of Higgs boson production*, JHEP **10** (2013) 222, arXiv:1309.0017 [hep-ph]. (69, 113, 468)

[209] V. Del Duca, A. Frizzo, and F. Maltoni, *Higgs boson production in association with three jets*, JHEP **05** (2004) 064, arXiv:hep-ph/0404013 [hep-ph]. (70)

[210] L. J. Dixon, E. W. N. Glover, and V. V. Khoze, *MHV rules for Higgs plus multi-gluon amplitudes*, JHEP **12** (2004) 015, arXiv:hep-th/0411092 [hep-th]. (70)

[211] S. D. Badger, E. W. N. Glover, and V. V. Khoze, *MHV rules for Higgs plus multi-parton amplitudes*, JHEP **03** (2005) 023, arXiv:hep-th/0412275 [hep-th]. (70)

[212] L. J. Dixon and Y. Sofianatos, *Analytic one-loop amplitudes for a Higgs boson plus four partons*, JHEP **08** (2009) 058, arXiv:0906.0008 [hep-ph]. (70)

[213] S. Badger, E. W. Nigel Glover, P. Mastrolia, and C. Williams, *One-loop Higgs plus four gluon amplitudes: Full analytic results*, JHEP **01** (2010) 036, arXiv:0909.4475 [hep-ph]. (70)

[214] S. Badger, J. M. Campbell, R. K. Ellis, and C. Williams, *Analytic results for the one-loop NMHV Hqqgg amplitude*, JHEP **12** (2009) 035, arXiv:0910.4481 [hep-ph]. (70)

[215] T. Gehrmann, M. Jaquier, E. W. N. Glover, and A. Koukoutsakis, *Two-Loop QCD Corrections to the Helicity Amplitudes for $H \to 3$ partons*, JHEP **02** (2012) 056, arXiv:1112.3554 [hep-ph]. (70)

[216] A. Gehrmann-De Ridder, T. Gehrmann, and E. W. N. Glover, *Antenna subtraction at NNLO*, JHEP **09** (2005) 056, arXiv:hep-ph/0505111 [hep-ph]. (70)

[217] A. Daleo, T. Gehrmann, and D. Maitre, *Antenna subtraction with hadronic initial states*, JHEP **04** (2007) 016, arXiv:hep-ph/0612257 [hep-ph]. (70)

[218] J. Currie, E. W. N. Glover, and S. Wells, *Infrared Structure at NNLO Using Antenna Subtraction*, JHEP **04** (2013) 066, arXiv:1301.4693 [hep-ph]. (70)

[219] X. Chen, T. Gehrmann, E. W. N. Glover, and M. Jaquier, *Precise QCD predictions for the production of Higgs + jet final states*, Phys. Lett. **B740** (2015) 147–150, arXiv:1408.5325 [hep-ph]. (70)

[220] A. Gehrmann-De Ridder, T. Gehrmann, E. W. N. Glover, A. Huss, and T. A. Morgan, *Precise QCD predictions for the production of a Z boson in association with a hadronic jet*, Phys. Rev. Lett. **117** (2016) 022001, arXiv:1507.02850 [hep-ph]. (70)

[221] A. Gehrmann-De Ridder, T. Gehrmann, E. W. N. Glover, A. Huss, and T. A. Morgan, *NNLO QCD corrections for Z boson plus jet production*, in *Proceedings, 12th International Symposium on Radiative Corrections (Radcor 2015) and LoopFest XIV (Radiative Corrections for the LHC and Future Colliders)*. 2016. arXiv:1601.04569 [hep-ph]. (70)

[222] A. Gehrmann-De Ridder, T. Gehrmann, E. W. N. Glover, A. Huss, and T. A. Morgan, *The NNLO QCD corrections to Z boson production at large transverse momentum*, JHEP **07** (2016) 133, arXiv:1605.04295 [hep-ph]. (70)

[223] D. de Florian, G. Ferrera, M. Grazzini, and D. Tommasini, *Higgs boson production at the LHC: transverse momentum resummation effects in the H-$\to 2\gamma$, H$\to$WW$\to \ell\nu\ell\nu$ and H$\to$ ZZ$\to 4\ell$ decay modes*, JHEP **06** (2012) 132, arXiv:1203.6321 [hep-ph]. (71, 240, 267, 271, 457)

[224] M. Grazzini and H. Sargsyan, *Heavy-quark mass effects in Higgs boson production at the LHC*, JHEP **09** (2013) 129, arXiv:1306.4581 [hep-ph]. (71, 79, 81, 82, 246, 457, 491, 504)

[225] T. Becher, M. Neubert, and D. Wilhelm, *Higgs-Boson Production at Small Transverse Momentum*, JHEP **05** (2013) 110, arXiv:1212.2621 [hep-ph]. (72)

[226] D. Neill, I. Z. Rothstein, and V. Vaidya, *The Higgs Transverse Momentum Distribution at NNLL and its Theoretical Errors*, JHEP **12** (2015) 097, arXiv:1503.00005 [hep-ph]. (72)

[227] G. Cullen, N. Greiner, G. Heinrich, G. Luisoni, P. Mastrolia, G. Ossola, T. Reiter, and F. Tramontano, *Automated One-Loop Calculations with GoSam*, Eur. Phys. J. **C72** (2012) 1889, arXiv:1111.2034 [hep-ph]. (72, 146, 246, 248, 468)

[228] G. Cullen et al., *GOSAM-2.0: a tool for automated one-loop calculations within the Standard Model and beyond*, Eur. Phys. J. **C74** (2014) 3001, arXiv:1404.7096 [hep-ph]. (72, 146, 246, 248, 468)

[229] T. Gleisberg et al., *Event generation with SHERPA 1.1*, JHEP **02** (2009) 007, arXiv:0811.4622 [hep-ph]. (72, 123, 171, 234, 240, 382, 420, 468, 527)

[230] N. Greiner, S. Höche, G. Luisoni, M. Schönherr, J.-C. Winter, and V. Yundin, *Phenomenological analysis of Higgs boson production through gluon fusion in association with jets*, JHEP **01** (2016) 169, arXiv:1506.01016 [hep-ph]. (72, 78, 246, 468)

[231] R. V. Harlander, H. Mantler, and M. Wiesemann, *Transverse momentum resummation for Higgs production via gluon fusion in the MSSM*, JHEP **11** (2014) 116, arXiv:1409.0531 [hep-ph]. (73, 82, 491, 492, 504, 506, 609)

[232] R. Frederix, S. Frixione, E. Vryonidou, and M. Wiesemann, *Heavy-quark mass effects in Higgs plus jets production*, JHEP **08** (2016) 006, arXiv:1604.03017 [hep-ph]. (73)

[233] K. Hamilton, P. Nason, and G. Zanderighi, *Finite quark-mass effects in the NNLOPS POWHEG+MiNLO Higgs generator*, JHEP **05** (2015) 140, arXiv:1501.04637 [hep-ph]. (73)

[234] S. Marzani, R. D. Ball, V. Del Duca, S. Forte, and A. Vicini, *Higgs production via gluon-gluon fusion with finite top mass beyond next-to-leading order*, Nucl. Phys. **B800** (2008) 127–145,

arXiv:0801.2544 [hep-ph]. (79, 252, 491, 607)

[235] A. Pak, M. Rogal, and M. Steinhauser, *Virtual three-loop corrections to Higgs boson production in gluon fusion for finite top quark mass*, Phys. Lett. **B679** (2009) 473–477, arXiv:0907.2998 [hep-ph]. (79, 491, 607)

[236] U. Baur and E. W. N. Glover, *Higgs Boson Production at Large Transverse Momentum in Hadronic Collisions*, Nucl. Phys. **B339** (1990) 38–66. (79, 460)

[237] R. K. Ellis, I. Hinchliffe, M. Soldate, and J. J. van der Bij, *Higgs Decay to $\tau^+\tau^-$: A Possible Signature of Intermediate Mass Higgs Bosons at the SSC*, Nucl. Phys. **B297** (1988) 221–243. (79, 81, 460)

[238] W.-Y. Keung and F. J. Petriello, *Electroweak and finite quark-mass effects on the Higgs boson transverse momentum distribution*, Phys. Rev. **D80** (2009) 013007, arXiv:0905.2775 [hep-ph]. (79, 81)

[239] U. Langenegger, M. Spira, A. Starodumov, and P. Trueb, *SM and MSSM Higgs Boson Production: Spectra at large transverse Momentum*, JHEP **06** (2006) 035, arXiv:hep-ph/0604156 [hep-ph]. (79, 491)

[240] E. Bagnaschi, G. Degrassi, P. Slavich, and A. Vicini, *Higgs production via gluon fusion in the POWHEG approach in the SM and in the MSSM*, JHEP **02** (2012) 088, arXiv:1111.2854 [hep-ph]. (79, 491, 492, 504, 506, 609)

[241] S. Höche, F. Krauss, M. Schönherr, and F. Siegert, *QCD matrix elements + parton showers: The NLO case*, JHEP **04** (2013) 027, arXiv:1207.5030 [hep-ph]. (79, 80, 170, 468, 527)

[242] S. Catani, F. Krauss, R. Kuhn, and B. R. Webber, *QCD matrix elements + parton showers*, JHEP **11** (2001) 063, arXiv:hep-ph/0109231 [hep-ph]. (79, 83, 234, 527)

[243] F. Krauss, *Matrix elements and parton showers in hadronic interactions*, JHEP **08** (2002) 015, arXiv:hep-ph/0205283 [hep-ph]. (79)

[244] L. Lönnblad, *Correcting the color dipole cascade model with fixed order matrix elements*, JHEP **05** (2002) 046, arXiv:hep-ph/0112284 [hep-ph]. (79)

[245] J. Alwall, Q. Li, and F. Maltoni, *Matched predictions for Higgs production via heavy-quark loops in the SM and beyond*, Phys. Rev. **D85** (2012) 014031, arXiv:1110.1728 [hep-ph]. (79)

[246] F. Krauss, R. Kühn, and G. Soff, *AMEGIC++ 1.0: A Matrix element generator in C++*, JHEP **02** (2002) 044, arXiv:hep-ph/0109036 [hep-ph]. (80, 527)

[247] F. Cascioli, P. Maierhöfer, and S. Pozzorini, *Scattering Amplitudes with Open Loops*, Phys. Rev. Lett. **108** (2012) 111601, arXiv:1111.5206 [hep-ph]. (80, 123, 125, 146, 162, 171, 200, 234, 240, 253, 387, 420, 464, 469, 525, 527)

[248] A. Denner, S. Dittmaier, and L. Hofer, *COLLIER – A fortran-library for one-loop integrals*, PoS **LL2014** (2014) 071, arXiv:1407.0087 [hep-ph]. (80, 127, 146, 234)

[249] S. Catani and M. H. Seymour, *A General algorithm for calculating jet cross-sections in NLO QCD*, Nucl. Phys. **B485** (1997) 291–419, arXiv:hep-ph/9605323 [hep-ph]. [Erratum-ibid. **B510** (1998) 503]. (80, 125, 127, 162, 264, 464, 527)

[250] E. Bagnaschi, R. V. Harlander, H. Mantler, A. Vicini, and M. Wiesemann, *Resummation ambiguities in the Higgs transverse-momentum spectrum in the Standard Model and beyond*, JHEP **01** (2016) 090, arXiv:1510.08850 [hep-ph]. (80, 82, 492, 504, 506, 507)

[251] M. Buschmann, C. Englert, D. Goncalves, T. Plehn, and M. Spannowsky, *Resolving the Higgs-Gluon Coupling with Jets*, Phys. Rev. **D90** (2014) 013010, arXiv:1405.7651 [hep-ph]. (81, 357, 472)

[252] E. Bagnaschi and A. Vicini, *The Higgs transverse momentum distribution in gluon fusion as a multiscale problem*, JHEP **01** (2016) 056, arXiv:1505.00735 [hep-ph]. (82, 491, 492, 504,

506)

[253] S. Höeche, F. Krauss, S. Schumann, and F. Siegert, *QCD matrix elements and truncated showers*, JHEP **05** (2009) 053, arXiv:0903.1219 [hep-ph]. (83)

[254] A. Denner, S. Dittmaier, S. Kallweit, and A. Mück, *HAWK 2.0: A Monte Carlo program for Higgs production in vector-boson fusion and Higgs strahlung at hadron colliders*, Comput. Phys. Commun. **195** (2015) 161–171, arXiv:1412.5390 [hep-ph]. (85, 93, 376, 420)

[255] A. Denner, S. Dittmaier, and A. Mück, HAWK*: A Monte Carlo generator for the production of Higgs bosons Attached to WeaK bosons at hadron colliders*, http://hawk.hepforge.org/, 2010. (85, 93)

[256] M. Ciccolini, A. Denner, and S. Dittmaier, *Strong and electroweak corrections to the production of Higgs + 2jets via weak interactions at the LHC*, Phys. Rev. Lett. **99** (2007) 161803, arXiv:0707.0381 [hep-ph]. (85, 88, 93, 376, 580)

[257] M. Ciccolini, A. Denner, and S. Dittmaier, *Electroweak and QCD corrections to Higgs production via vector-boson fusion at the LHC*, Phys. Rev. **D77** (2008) 013002, arXiv:0710.4749 [hep-ph]. (85, 88, 93, 376, 420, 580)

[258] A. Denner, S. Dittmaier, S. Kallweit, and A. Mück, *Electroweak corrections to Higgs-strahlung off W/Z bosons at the Tevatron and the LHC with HAWK*, JHEP **03** (2012) 075, arXiv:1112.5142 [hep-ph]. (85, 93, 96, 376, 420)

[259] S. Frixione, P. Torrielli, and M. Zaro, *Higgs production through vector-boson fusion at the NLO matched with parton showers*, Phys. Lett. **B726** (2013) 273–282, arXiv:1304.7927 [hep-ph]. (86)

[260] P. Nason and C. Oleari, *NLO Higgs boson production via vector-boson fusion matched with shower in POWHEG*, JHEP **02** (2010) 037, arXiv:0911.5299 [hep-ph]. (86)

[261] T. Figy, V. Hankele, and D. Zeppenfeld, *Next-to-leading order QCD corrections to Higgs plus three jet production in vector-boson fusion*, JHEP **02** (2008) 076, arXiv:0710.5621 [hep-ph]. (86, 87, 107, 580)

[262] B. Jäger, F. Schissler, and D. Zeppenfeld, *Parton-shower effects on Higgs boson production via vector-boson fusion in association with three jets*, JHEP **07** (2014) 125, arXiv:1405.6950 [hep-ph]. (86, 87, 107)

[263] P. Bolzoni, F. Maltoni, S.-O. Moch, and M. Zaro, *Higgs production via vector-boson fusion at NNLO in QCD*, Phys. Rev. Lett. **105** (2010) 011801, arXiv:1003.4451 [hep-ph]. (86, 87, 261, 419, 575, 580)

[264] P. Bolzoni, F. Maltoni, S.-O. Moch, and M. Zaro, *Vector boson fusion at NNLO in QCD: SM Higgs and beyond*, Phys. Rev. **D85** (2012) 035002, arXiv:1109.3717 [hep-ph]. (86, 87, 419, 575, 578, 580)

[265] T. Han, G. Valencia, and S. Willenbrock, *Structure function approach to vector boson scattering in p p collisions*, Phys. Rev. Lett. **69** (1992) 3274–3277, arXiv:hep-ph/9206246 [hep-ph]. (86, 419, 580)

[266] W. A. Bardeen, A. J. Buras, D. W. Duke, and T. Muta, *Deep Inelastic Scattering Beyond the Leading Order in Asymptotically Free Gauge Theories*, Phys. Rev. **D18** (1978) 3998. (87, 580)

[267] D. I. Kazakov, A. V. Kotikov, G. Parente, O. A. Sampayo, and J. Sanchez Guillen, *Complete quartic (α_s^2) correction to the deep inelastic longitudinal structure function F_L in QCD*, Phys. Rev. Lett. **65** (1990) 1535–1538. [Erratum-ibid. **65** (1990) 2921]. (87, 580)

[268] E. B. Zijlstra and W. L. van Neerven, *Order α_s^2 correction to the structure function $F_3(x, Q^2)$ in deep inelastic neutrino - hadron scattering*, Phys. Lett. **B297** (1992) 377–384. (87, 580)

[269] E. B. Zijlstra and W. L. van Neerven, *Order α_s^2 QCD corrections to the deep inelastic proton structure functions F_2 and F_L*, Nucl. Phys. **B383** (1992) 525–574. (87, 580)

[270] S. Moch and J. A. M. Vermaseren, *Deep inelastic structure functions at two loops*, Nucl. Phys. **B573** (2000) 853–907, arXiv:hep-ph/9912355 [hep-ph]. (87, 580)

[271] W. L. van Neerven and J. A. M. Vermaseren, *The Role of the Five Point Function in Radiative Corrections to Two Photon Physics*, Phys. Lett. **B142** (1984) 80. (87, 580)

[272] J. Blumlein, G. J. van Oldenborgh, and R. Ruckl, *QCD and QED corrections to Higgs boson production in charged current ep scattering*, Nucl. Phys. **B395** (1993) 35–59, arXiv:hep-ph/9209219 [hep-ph]. (87, 580)

[273] R. V. Harlander, J. Vollinga, and M. M. Weber, *Gluon-Induced Weak Boson Fusion*, Phys. Rev. **D77** (2008) 053010, arXiv:0801.3355 [hep-ph]. (87, 580)

[274] M. Cacciari, F. A. Dreyer, A. Karlberg, G. P. Salam, and G. Zanderighi, *Fully Differential Vector-Boson-Fusion Higgs Production at Next-to-Next-to-Leading Order*, Phys. Rev. Lett. **115** (2015) 082002, arXiv:1506.02660 [hep-ph]. (87, 88, 419)

[275] K. Arnold et al., *VBFNLO: A Parton level Monte Carlo for processes with electroweak bosons*, Comput. Phys. Commun. **180** (2009) 1661–1670, arXiv:0811.4559 [hep-ph]. (87, 226, 232, 388)

[276] T. Figy, C. Oleari, and D. Zeppenfeld, *Next-to-leading order jet distributions for Higgs boson production via weak boson fusion*, Phys. Rev. **D68** (2003) 073005, arXiv:hep-ph/0306109 [hep-ph]. (87, 419)

[277] V. Hankele, G. Klamke, D. Zeppenfeld, and T. Figy, *Anomalous Higgs boson couplings in vector boson fusion at the CERN LHC*, Phys. Rev. **D74** (2006) 095001, arXiv:hep-ph/0609075 [hep-ph]. (87, 376, 390)

[278] T. Figy, S. Palmer, and G. Weiglein, *Higgs Production via Weak Boson Fusion in the Standard Model and the MSSM*, JHEP **02** (2012) 105, arXiv:1012.4789 [hep-ph]. (87)

[279] NNPDF Collaboration, R. D. Ball et al., *Parton distributions with QED corrections*, Nucl. Phys. **B877** (2013) 290–320, arXiv:1308.0598 [hep-ph]. (88, 96, 122, 156)

[280] A. Manohar, P. Nason, G. P. Salam, and G. Zanderighi, *How bright is the proton? A precise determination of the photon PDF*, arXiv:1607.04266 [hep-ph]. (93, 96)

[281] R. Frederix, S. Frixione, A. Papaefstathiou, S. Prestel, and P. Torrielli, *A study of multi-jet production in association with an electroweak vector boson*, JHEP **02** (2016) 131, arXiv:1511.00847 [hep-ph]. (94, 109)

[282] G. Ferrera, M. Grazzini, and F. Tramontano, *Higher-order QCD effects for associated WH production and decay at the LHC*, JHEP **04** (2014) 039, arXiv:1312.1669 [hep-ph]. (94, 95, 103, 116, 419)

[283] G. Ferrera, M. Grazzini, and F. Tramontano, *Associated ZH production at hadron colliders: the fully differential NNLO QCD calculation*, Phys. Lett. **B740** (2015) 51–55, arXiv:1407.4747 [hep-ph]. (94, 95, 103, 419)

[284] J. Gaunt, M. Stahlhofen, F. J. Tackmann, and J. R. Walsh, *N-jettiness Subtractions for NNLO QCD Calculations*, JHEP **09** (2015) 058, arXiv:1505.04794 [hep-ph]. (94)

[285] R. Boughezal, C. Focke, X. Liu, and F. Petriello, *W-boson production in association with a jet at next-to-next-to-leading order in perturbative QCD*, Phys. Rev. Lett. **115** (2015) 062002, arXiv:1504.02131 [hep-ph]. (94)

[286] R. Boughezal, J. M. Campbell, R. K. Ellis, C. Focke, W. T. Giele, X. Liu, and F. Petriello, *Z-boson production in association with a jet at next-to-next-to-leading order in perturbative QCD*, Phys. Rev. Lett. **116** (2016) 152001, arXiv:1512.01291 [hep-ph]. (94)

[287] J. M. Campbell and R. K. Ellis, *An Update on vector boson pair production at hadron colliders*, Phys. Rev. **D60** (1999) 113006, arXiv:hep-ph/9905386 [hep-ph]. (94)

[288] J. M. Campbell, R. K. Ellis, and C. Williams, *Vector boson pair production at the LHC*, JHEP

07 (2011) 018, arXiv:1105.0020 [hep-ph]. (94, 244, 386, 649)

[289] J. M. Campbell, R. K. Ellis, and W. T. Giele, *A Multi-Threaded Version of MCFM*, Eur. Phys. J. **C75** (2015) 246, arXiv:1503.06182 [physics.comp-ph]. (94)

[290] J. M. Campbell, R. K. Ellis, and C. Williams, *Associated production of a Higgs boson at NNLO*, JHEP **06** (2016) 179, arXiv:1601.00658 [hep-ph]. (94, 103, 471, 472)

[291] G. Ferrera, M. Grazzini, and F. Tramontano, *Associated WH production at hadron colliders: a fully exclusive QCD calculation at NNLO*, Phys. Rev. Lett. **107** (2011) 152003, arXiv:1107.1164 [hep-ph]. (95, 116, 419)

[292] O. Brein, R. V. Harlander, and T. J. Zirke, *vh@nnlo - Higgs Strahlung at hadron colliders*, arXiv:1210.5347 [hep-ph]. (95, 98, 248)

[293] R. V. Harlander, S. Liebler, and T. Zirke, *Higgs Strahlung at the Large Hadron Collider in the 2-Higgs-Doublet Model*, JHEP **02** (2014) 023, arXiv:1307.8122 [hep-ph]. (95, 98, 248)

[294] R. Hamberg, W. L. van Neerven, and T. Matsuura, *A Complete calculation of the order α_s^2 correction to the Drell-Yan K factor*, Nucl. Phys. **B359** (1991) 343–405. [Erratum-ibid. **B644** (2002) 403]. (95)

[295] O. Brein, A. Djouadi, and R. Harlander, *NNLO QCD corrections to the Higgs-strahlung processes a hadron collider*, Phys. Lett. **B579** (2004) 149–156, arXiv:hep-ph/0307206 [hep-ph]. (95, 98)

[296] O. Brein, R. Harlander, M. Wiesemann, and T. Zirke, *Top-Quark Mediated Effects in Hadronic Higgs-Strahlung*, Eur. Phys. J. **C72** (2012) 1868, arXiv:1111.0761 [hep-ph]. (95)

[297] B. A. Kniehl, *Elastic ep scattering and the Weizsäcker-Williams approximation*, Phys. Lett. **B254** (1991) 267–273. (95)

[298] D. A. Dicus and C. Kao, *Higgs Boson - Z^0 Production From Gluon Fusion*, Phys. Rev. **D38** (1988) 1008. [Erratum-ibid. **D42** (1990) 2412]. (95)

[299] B. A. Kniehl and C. P. Palisoc, *Associated production of Z and neutral Higgs bosons at the CERN Large Hadron Collider*, Phys. Rev. **D85** (2012) 075027, arXiv:1112.1575 [hep-ph]. (95)

[300] L. Altenkamp, S. Dittmaier, R. V. Harlander, H. Rzehak, and T. J. E. Zirke, *Gluon-induced Higgs-strahlung at next-to-leading order QCD*, JHEP **02** (2013) 078, arXiv:1211.5015 [hep-ph]. (95, 98, 608)

[301] R. V. Harlander, A. Kulesza, V. Theeuwes, and T. Zirke, *Soft gluon resummation for gluon-induced Higgs Strahlung*, JHEP **11** (2014) 082, arXiv:1410.0217 [hep-ph]. (95, 98)

[302] A. D. Martin, R. G. Roberts, W. J. Stirling, and R. S. Thorne, *Parton distributions incorporating QED contributions*, Eur. Phys. J. **C39** (2005) 155, arXiv:hep-ph/0411040. (96)

[303] S. Carrazza, S. Forte, Z. Kassabov, and J. Rojo, *Specialized minimal PDFs for optimized LHC calculations*, Eur. Phys. J. **C76** (2016) 205, arXiv:1602.00005 [hep-ph]. (99)

[304] F. Campanario, T. M. Figy, S. Plätzer, and M. Sjödahl, *Electroweak Higgs Boson Plus Three Jet Production at Next-to-Leading-Order QCD*, Phys. Rev. Lett. **111** (2013) 211802, arXiv:1308.2932 [hep-ph]. (107)

[305] F. Campanario, *Towards $pp \to VVjj$ at NLO QCD: Bosonic contributions to triple vector boson production plus jet*, JHEP **10** (2011) 070, arXiv:1105.0920 [hep-ph]. (107)

[306] J. Bellm et al., *Herwig 7.0/Herwig++ 3.0 release note*, Eur. Phys. J. **C76** (2016) 196, arXiv:1512.01178 [hep-ph]. (107, 111, 123, 125, 200, 387, 389, 468)

[307] S. Plätzer and S. Gieseke, *Dipole Showers and Automated NLO Matching in Herwig++*, Eur. Phys. J. **C72** (2012) 2187, arXiv:1109.6256 [hep-ph]. (107, 125)

[308] G. Luisoni, P. Nason, C. Oleari, and F. Tramontano, *$HW^{\pm}$/HZ + 0 and 1 jet at NLO with the POWHEG BOX interfaced to GoSam and their merging within MiNLO*, JHEP **10** (2013) 083,

arXiv:1306.2542 [hep-ph]. (109, 113, 116)

[309] B. Hespel, F. Maltoni, and E. Vryonidou, *Higgs and Z boson associated production via gluon fusion in the SM and the 2HDM*, JHEP **06** (2015) 065, arXiv:1503.01656 [hep-ph]. (109, 386)

[310] Rivet, http://rivet.hepforge.org/analyses. (109, 453, 484)

[311] ATLAS Collaboration, G. Aad et al., *Search for the $b\bar{b}$ decay of the Standard Model Higgs boson in associated $(W/Z)H$ production with the ATLAS detector*, JHEP **01** (2015) 069, arXiv:1409.6212 [hep-ex]. (109, 639)

[312] CMS Collaboration, S. Chatrchyan et al., *Search for the standard model Higgs boson produced in association with a W or a Z boson and decaying to bottom quarks*, Phys. Rev. **D89** (2014) 012003, arXiv:1310.3687 [hep-ex]. (109, 639)

[313] M. Bahr et al., *Herwig++ Physics and Manual*, Eur. Phys. J. **C58** (2008) 639–707, arXiv:0803.0883 [hep-ph]. (111, 123, 200, 387, 389, 543)

[314] W. Astill, W. Bizon, E. Re, and G. Zanderighi, *NNLOPS accurate associated HW production*, JHEP **06** (2016) 154, arXiv:1603.01620 [hep-ph]. (113, 116)

[315] A. Karlberg, E. Re, and G. Zanderighi, *NNLOPS accurate Drell-Yan production*, JHEP **09** (2014) 134, arXiv:1407.2940 [hep-ph]. (113)

[316] J. C. Collins and D. E. Soper, *Angular Distribution of Dileptons in High-Energy Hadron Collisions*, Phys. Rev. **D16** (1977) 2219. (115)

[317] M. Cacciari and G. P. Salam, *Dispelling the N^3 myth for the k_t jet-finder*, Phys. Lett. **B641** (2006) 57–61, arXiv:hep-ph/0512210 [hep-ph]. (116)

[318] T. Sjostrand, S. Mrenna, and P. Z. Skands, *A Brief Introduction to PYTHIA 8.1*, Comput. Phys. Commun. **178** (2008) 852–867, arXiv:0710.3820 [hep-ph]. (116, 123, 239, 382, 528, 543, 642, 648)

[319] P. Skands, S. Carrazza, and J. Rojo, *Tuning PYTHIA 8.1: the Monash 2013 Tune*, European Physical Journal **74** (2014) 3024, arXiv:1404.5630 [hep-ph]. (116, 123, 171)

[320] P. Nason and C. Oleari, *Generation cuts and Born suppression in POWHEG*, arXiv:1303.3922 [hep-ph]. (116)

[321] L. Reina and S. Dawson, *Next-to-leading order results for $t\bar{t}H$ production at the Tevatron*, Phys. Rev. Lett. **87** (2001) 201804, arXiv:hep-ph/0107101 [hep-ph]. (121, 125, 144, 147)

[322] S. Dawson, L. Orr, L. Reina, and D. Wackeroth, *Associated top quark Higgs boson production at the LHC*, Phys. Rev. **D67** (2003) 071503, arXiv:hep-ph/0211438 [hep-ph]. (121, 125, 144, 147)

[323] S. Dawson, C. Jackson, L. Orr, L. Reina, and D. Wackeroth, *Associated Higgs production with top quarks at the large hadron collider: NLO QCD corrections*, Phys. Rev. **D68** (2003) 034022, arXiv:hep-ph/0305087 [hep-ph]. (121, 125, 144, 147, 148)

[324] W. Beenakker, S. Dittmaier, M. Krämer, B. Plümper, M. Spira, et al., *Higgs radiation off top quarks at the Tevatron and the LHC*, Phys. Rev. Lett. **87** (2001) 201805, arXiv:hep-ph/0107081 [hep-ph]. (121, 147, 148)

[325] W. Beenakker, S. Dittmaier, M. Krämer, B. Plümper, M. Spira, et al., *NLO QCD corrections to $t\bar{t}H$ production in hadron collisions*, Nucl. Phys. **B653** (2003) 151–203, arXiv:hep-ph/0211352 [hep-ph]. (121, 134, 138, 147, 148)

[326] Z. Yu, M. Wen-Gan, Z. Ren-You, C. Chong, and G. Lei, *QCD NLO and EW NLO corrections to $t\bar{t}H$ production with top quark decays at hadron collider*, Phys. Lett. **B738** (2014) 1–5, arXiv:1407.1110 [hep-ph]. (121)

[327] S. Frixione, V. Hirschi, D. Pagani, H. S. Shao, and M. Zaro, *Weak corrections to Higgs hadroproduction in association with a top-quark pair*, JHEP **09** (2014) 065, arXiv:1407.0823

[hep-ph]. (121, 123)

[328] S. Frixione, V. Hirschi, D. Pagani, H. S. Shao, and M. Zaro, *Electroweak and QCD corrections to top-pair hadroproduction in association with heavy bosons*, JHEP **06** (2015) 184, arXiv:1504.03446 [hep-ph]. (121, 123, 156, 158, 170)

[329] P. Ciafaloni and D. Comelli, *Sudakov enhancement of electroweak corrections*, Phys. Lett. **B446** (1999) 278–284, arXiv:hep-ph/9809321 [hep-ph]. (121)

[330] M. Ciafaloni, P. Ciafaloni, and D. Comelli, *Bloch-Nordsieck violating electroweak corrections to inclusive TeV scale hard processes*, Phys. Rev. Lett. **84** (2000) 4810–4813, arXiv:hep-ph/0001142 [hep-ph]. (121)

[331] A. Denner and S. Pozzorini, *One loop leading logarithms in electroweak radiative corrections. 1. Results*, Eur. Phys. J. **C18** (2001) 461–480, arXiv:hep-ph/0010201 [hep-ph]. (121)

[332] A. Denner and S. Pozzorini, *One loop leading logarithms in electroweak radiative corrections. 2. Factorization of collinear singularities*, Eur. Phys. J. **C21** (2001) 63–79, arXiv:hep-ph/0104127 [hep-ph]. (121)

[333] J. M. Butterworth, A. R. Davison, M. Rubin, and G. P. Salam, *Jet substructure as a new Higgs search channel at the LHC*, Phys. Rev. Lett. **100** (2008) 242001, arXiv:0802.2470 [hep-ph]. (122)

[334] T. Plehn, G. P. Salam, and M. Spannowsky, *Fat Jets for a Light Higgs*, Phys. Rev. Lett. **104** (2010) 111801, arXiv:0910.5472 [hep-ph]. (122)

[335] M. R. Buckley, T. Plehn, T. Schell, and M. Takeuchi, *Buckets of Higgs and Tops*, JHEP **02** (2014) 130, arXiv:1310.6034 [hep-ph]. (122)

[336] S. Kallweit, J. M. Lindert, P. Maierhöfer, S. Pozzorini, and M. Schönherr, *NLO electroweak automation and precise predictions for W+multijet production at the LHC*, JHEP **04** (2015) 012, arXiv:1412.5157 [hep-ph]. (123, 160)

[337] G. Marchesini, B. Webber, G. Abbiendi, I. Knowles, M. Seymour, et al., *HERWIG: A Monte Carlo event generator for simulating hadron emission reactions with interfering gluons. Version 5.1 - April 1991*, Comput. Phys. Commun. **67** (1992) 465–508. (123)

[338] G. Corcella, I. G. Knowles, G. Marchesini, S. Moretti, K. Odagiri, P. Richardson, M. H. Seymour, and B. R. Webber, *HERWIG 6: An Event generator for hadron emission reactions with interfering gluons (including supersymmetric processes)*, JHEP **01** (2001) 010, arXiv:hep-ph/0011363 [hep-ph]. (123, 240)

[339] T. Sjostrand, S. Mrenna, and P. Z. Skands, *PYTHIA 6.4 Physics and Manual*, JHEP **05** (2006) 026, arXiv:hep-ph/0603175 [hep-ph]. (123, 644)

[340] S. Frixione and B. R. Webber, *Matching NLO QCD computations and parton shower simulations*, JHEP **06** (2002) 029, arXiv:hep-ph/0204244 [hep-ph]. (123, 125, 171, 492, 506, 524, 525, 527)

[341] S. Frixione, P. Nason, and B. R. Webber, *Matching NLO QCD and parton showers in heavy flavor production*, JHEP **08** (2003) 007, arXiv:hep-ph/0305252 [hep-ph]. (123, 125, 171)

[342] P. Nason, *A New method for combining NLO QCD with shower Monte Carlo algorithms*, JHEP **11** (2004) 040, arXiv:hep-ph/0409146 [hep-ph]. (123, 125, 162, 171, 492, 506, 524, 526, 643, 644)

[343] S. Frixione, P. Nason, and C. Oleari, *Matching NLO QCD computations with Parton Shower simulations: the POWHEG method*, JHEP **11** (2007) 070, arXiv:0709.2092 [hep-ph]. (123, 125, 162, 171, 386, 506, 524, 526, 643, 644)

[344] S. Frixione, P. Nason, and G. Ridolfi, *A Positive-weight next-to-leading-order Monte Carlo for heavy flavour hadroproduction*, JHEP **09** (2007) 126, arXiv:0707.3088 [hep-ph]. (123, 125, 644)

[345] S. Höche, F. Krauss, M. Schönherr, and F. Siegert, *A critical appraisal of NLO+PS matching methods*, JHEP **09** (2012) 049, arXiv:1111.1220 [hep-ph]. (123, 125, 162, 171, 468, 527)

[346] S. Höche, F. Krauss, M. Schönherr, and F. Siegert, *W+ n-Jet predictions at the Large Hadron Collider at next-to-leading order matched with a parton shower*, Phys. Rev. Lett. **110** (2013) 052001, arXiv:1201.5882 [hep-ph]. (123)

[347] R. Frederix, S. Frixione, V. Hirschi, F. Maltoni, R. Pittau, et al., *Scalar and pseudoscalar Higgs production in association with a top-antitop pair*, Phys. Lett. **B701** (2011) 427–433, arXiv:1104.5613 [hep-ph]. (123, 134)

[348] V. Hirschi, R. Frederix, S. Frixione, M. V. Garzelli, F. Maltoni, and R. Pittau, *Automation of one-loop QCD corrections*, JHEP **05** (2011) 044, arXiv:1103.0621 [hep-ph]. (123, 125, 144, 146, 162, 171, 525)

[349] G. Bevilacqua et al., *HELAC-NLO*, arXiv:1110.1499 [hep-ph]. (123, 125, 162, 171)

[350] M. Garzelli, A. Kardos, C. Papadopoulos, and Z. Trócsányi, *Standard Model Higgs boson production in association with a top anti-top pair at NLO with parton showering*, Europhys.Lett. **96** (2011) 11001, arXiv:1108.0387 [hep-ph]. (123, 125)

[351] H. B. Hartanto, B. Jäger, L. Reina, and D. Wackeroth, *Higgs boson production in association with top quarks in the POWHEG BOX*, Phys. Rev. **D91** (2015) 094003, arXiv:1501.04498 [hep-ph]. (123, 144)

[352] F. Cascioli, S. Höche, F. Krauss, P. Maierhöfer, S. Pozzorini, and F. Siegert, *Precise Higgs-background predictions: merging NLO QCD and squared quark-loop corrections to four-lepton + 0,1 jet production*, JHEP **01** (2014) 046, arXiv:1309.0500 [hep-ph]. (123, 171, 234, 253)

[353] G. Ossola, C. G. Papadopoulos, and R. Pittau, *CutTools: A Program implementing the OPP reduction method to compute one-loop amplitudes*, JHEP **03** (2008) 042, arXiv:0711.3596 [hep-ph]. (125, 162, 525)

[354] S. Catani, S. Dittmaier, M. H. Seymour, and Z. Trócsányi, *The Dipole formalism for next-to-leading order QCD calculations with massive partons*, Nucl. Phys. **B627** (2002) 189–265, arXiv:hep-ph/0201036 [hep-ph]. (125, 127, 162, 527)

[355] S. Schumann and F. Krauss, *A Parton shower algorithm based on Catani-Seymour dipole factorisation*, JHEP **03** (2008) 038, arXiv:0709.1027 [hep-ph]. (125, 162, 234, 267, 527)

[356] S. Höche and M. Schönherr, *Uncertainties in next-to-leading order plus parton shower matched simulations of inclusive jet and dijet production*, Phys. Rev. **D86** (2012) 094042, arXiv:1208.2815 [hep-ph]. (125, 162, 171, 468)

[357] S. Frixione, *A General approach to jet cross-sections in QCD*, Nucl. Phys. **B507** (1997) 295–314, arXiv:hep-ph/9706545 [hep-ph]. (125, 162, 163, 525)

[358] R. Frederix, S. Frixione, F. Maltoni, and T. Stelzer, *Automation of next-to-leading order computations in QCD: The FKS subtraction*, JHEP **10** (2009) 003, arXiv:0908.4272 [hep-ph]. (125, 162, 525)

[359] G. Ossola, C. G. Papadopoulos, and R. Pittau, *Reducing full one-loop amplitudes to scalar integrals at the integrand level*, Nucl. Phys. **B763** (2007) 147–169, arXiv:hep-ph/0609007 [hep-ph]. (125, 162, 246, 525)

[360] T. Binoth, F. Boudjema, G. Dissertori, A. Lazopoulos, A. Denner, et al., *A Proposal for a standard interface between Monte Carlo tools and one-loop programs*, Comput. Phys. Commun. **181** (2010) 1612–1622, arXiv:1001.1307 [hep-ph]. (125, 246, 334, 389)

[361] S. Alioli, S. Badger, J. Bellm, B. Biedermann, F. Boudjema, et al., *Update of the Binoth Les Houches Accord for a standard interface between Monte Carlo tools and one-loop programs*, Comput. Phys. Commun. **185** (2014) 560–571, arXiv:1308.3462 [hep-ph]. (125, 246, 389)

[362] M. Sjodahl, *ColorFull – a C++ library for calculations in SU(Nc) color space*, Eur. Phys. J. **C75** (2015) 236, arXiv:1412.3967 [hep-ph]. (125)

[363] S. Plätzer, *Summing Large-N Towers in Colour Flow Evolution*, Eur. Phys. J. **C74** (2014) 2907, arXiv:1312.2448 [hep-ph]. (125)

[364] J. Alwall, M. Herquet, F. Maltoni, O. Mattelaer, and T. Stelzer, *MadGraph 5 : Going Beyond*, JHEP **06** (2011) 128, arXiv:1106.0522 [hep-ph]. (125, 200, 302, 554, 642, 643, 648)

[365] F. Cascioli, S. Höche, F. Krauss, P. Maierhöfer, S. Pozzorini, and F. Siegert, *Automatic one-loop calculations with Sherpa+OpenLoops*, in *Proceedings, 15th International Workshop on Advanced Computing and Analysis Techniques in Physics Research (ACAT 2013)*, vol. 523, p. 012058. 2014. (125, 527)

[366] S. Gieseke, P. Stephens, and B. Webber, *New formalism for QCD parton showers*, JHEP **12** (2003) 045, arXiv:hep-ph/0310083 [hep-ph]. (125)

[367] S. Plätzer and S. Gieseke, *Coherent Parton Showers with Local Recoils*, JHEP **01** (2011) 024, arXiv:0909.5593 [hep-ph]. (125, 468)

[368] P. Artoisenet, R. Frederix, O. Mattelaer, and R. Rietkerk, *Automatic spin-entangled decays of heavy resonances in Monte Carlo simulations*, JHEP **03** (2013) 015, arXiv:1212.3460 [hep-ph]. (126, 152, 382, 385)

[369] M. V. Garzelli, A. Kardos, and Z. Trócsányi, *Hadroproduction of $W^+W^-b\bar{b}$ at NLO accuracy matched with shower Monte Carlo programs*, JHEP **08** (2014) 069, arXiv:1405.5859 [hep-ph]. (126)

[370] S. Frixione, E. Laenen, P. Motylinski, and B. R. Webber, *Angular correlations of lepton pairs from vector boson and top quark decays in Monte Carlo simulations*, JHEP **04** (2007) 081, arXiv:hep-ph/0702198 [HEP-PH]. (126, 385)

[371] A. Denner and R. Feger, *NLO QCD corrections to off-shell top-antitop production with leptonic decays in association with a Higgs boson at the LHC*, JHEP **11** (2015) 209, arXiv:1506.07448 [hep-ph]. (127, 136)

[372] S. Actis, A. Denner, L. Hofer, A. Scharf, and S. Uccirati, *Recursive generation of one-loop amplitudes in the Standard Model*, JHEP **04** (2013) 037, arXiv:1211.6316 [hep-ph]. (127, 137)

[373] A. Denner, S. Dittmaier, M. Roth, and D. Wackeroth, *Predictions for all processes $e^+e^- \to 4$ fermions $+\gamma$*, Nucl. Phys. **B560** (1999) 33–65, arXiv:hep-ph/9904472 [hep-ph]. (127, 137)

[374] A. Denner, S. Dittmaier, M. Roth, and L. Wieders, *Electroweak corrections to charged-current $e^+e^- \to 4$ fermion processes: Technical details and further results*, Nucl. Phys. **B724** (2005) 247–294, arXiv:hep-ph/0505042 [hep-ph]. Erratum-ibid. **B854** (2012) 504–507. (127, 137, 246)

[375] A. Denner and S. Dittmaier, *The Complex-mass scheme for perturbative calculations with unstable particles*, Nucl. Phys. Proc. Suppl. **160** (2006) 22–26, arXiv:hep-ph/0605312 [hep-ph]. (127, 137)

[376] A. Denner, S. Dittmaier, and L. Hofer, *Collier: a fortran-based Complex One-Loop LIbrary in Extended Regularizations*, arXiv:1604.06792 [hep-ph]. (127)

[377] G. 't Hooft and M. J. G. Veltman, *Scalar One Loop Integrals*, Nucl. Phys. **B153** (1979) 365–401. (127, 331)

[378] W. Beenakker and A. Denner, *Infrared divergent scalar box integrals with applications in the electroweak standard model*, Nucl. Phys. **B338** (1990) 349–370. (127)

[379] S. Dittmaier, *Separation of soft and collinear singularities from one-loop N-point integrals*, Nucl. Phys. **B675** (2003) 447–466, arXiv:hep-ph/0308246. (127)

[380] A. Denner and S. Dittmaier, *Scalar one-loop 4-point integrals*, Nucl. Phys. **B844** (2011) 199–242, arXiv:1005.2076 [hep-ph]. (127, 146)

[381] G. Passarino and M. J. G. Veltman, *One Loop Corrections for e^+e^- Annihilation Into $\mu^+\mu^-$ in the Weinberg Model*, Nucl. Phys. **B160** (1979) 151. (127, 331, 390)

[382] A. Denner and S. Dittmaier, *Reduction of one loop tensor 5-point integrals*, Nucl. Phys. **B658** (2003) 175–202, arXiv:hep-ph/0212259 [hep-ph]. (127, 146)

[383] A. Denner and S. Dittmaier, *Reduction schemes for one-loop tensor integrals*, Nucl. Phys. **B734** (2006) 62–115, arXiv:hep-ph/0509141 [hep-ph]. (127, 146)

[384] M. Jezabek and J. H. Kühn, *QCD Corrections to Semileptonic Decays of Heavy Quarks*, Nucl. Phys. **B314** (1989) 1–6. (134, 137)

[385] A. Denner, S. Dittmaier, S. Kallweit, and S. Pozzorini, *NLO QCD corrections to off-shell top-antitop production with leptonic decays at hadron colliders*, JHEP **10** (2012) 110, arXiv:1207.5018 [hep-ph]. (137)

[386] A. Denner, R. Feger, and A. Scharf, *Irreducible background and interference effects for Higgs-boson production in association with a top-quark pair*, JHEP **04** (2015) 008, arXiv:1412.5290 [hep-ph]. (137, 142)

[387] R. Kleiss and W. J. Stirling, *Top quark production at hadron colliders: some useful formulae*, Z. Phys. **C40** (1988) 419–423. (137)

[388] R. G. Stuart, *Gauge invariance, analyticity and physical observables at the Z0 resonance*, Phys. Lett. **B262** (1991) 113–119. (137)

[389] A. Aeppli, G. J. van Oldenborgh, and D. Wyler, *Unstable particles in one loop calculations*, Nucl. Phys. **B428** (1994) 126–146, arXiv:hep-ph/9312212 [hep-ph]. (137)

[390] A. Bredenstein, A. Denner, S. Dittmaier, and S. Pozzorini, *NLO QCD Corrections to $t\bar{t}b\bar{b}$ Production at the LHC: 2. full hadronic results*, JHEP **03** (2010) 021, arXiv:1001.4006 [hep-ph]. (138, 170)

[391] ATLAS Collaboration, *Search for the Standard Model Higgs boson produced in association with top quarks in proton-proton collisions at $\sqrt{s} = 7$ TeV using the ATLAS detector*, ATLAS-CONF-2012-135, 2012. (140)

[392] A. Kulesza, L. Motyka, T. Stebel, and V. Theeuwes, *Soft gluon resummation for associated $t\bar{t}H$ production at the LHC*, JHEP **03** (2016) 065, arXiv:1509.02780 [hep-ph]. (142, 143, 144)

[393] A. Broggio, A. Ferroglia, B. D. Pecjak, A. Signer, and L. L. Yang, *Associated production of a top pair and a Higgs boson beyond NLO*, JHEP **03** (2016) 124, arXiv:1510.01914 [hep-ph]. (142, 143, 146, 147, 148, 149, 150, 151)

[394] R. Bonciani, S. Catani, M. L. Mangano, and P. Nason, *Sudakov resummation of multiparton QCD cross-sections*, Phys. Lett. **B575** (2003) 268–278, arXiv:hep-ph/0307035 [hep-ph]. (143)

[395] S. M. Aybat, L. J. Dixon, and G. F. Sterman, *The Two-loop anomalous dimension matrix for soft gluon exchange*, Phys. Rev. Lett. **97** (2006) 072001, arXiv:hep-ph/0606254 [hep-ph]. (143)

[396] N. Kidonakis and G. F. Sterman, *Subleading logarithms in QCD hard scattering*, Phys. Lett. **B387** (1996) 867–874. (144)

[397] R. Bonciani, S. Catani, M. L. Mangano, and P. Nason, *NLL resummation of the heavy quark hadroproduction cross-section*, Nucl. Phys. **B529** (1998) 424–450, arXiv:hep-ph/9801375 [hep-ph]. [Erratum-ibid. **B803** (2008) 234]. (144)

[398] W. Beenakker, S. Brensing, M. Krämer, A. Kulesza, E. Laenen, and I. Niessen, *NNLL resummation for squark-antisquark pair production at the LHC*, JHEP **01** (2012) 076, arXiv:1110.2446 [hep-ph]. (144)

[399] W. Beenakker, T. Janssen, S. Lepoeter, M. Krämer, A. Kulesza, E. Laenen, I. Niessen, S. Thewes, and T. Van Daal, *Towards NNLL resummation: hard matching coefficients for squark and gluino hadroproduction*, JHEP **10** (2013) 120, arXiv:1304.6354 [hep-ph]. (144)

[400] V. Ahrens, A. Ferroglia, M. Neubert, B. D. Pecjak, and L. L. Yang, *Renormalization-Group Improved Predictions for Top-Quark Pair Production at Hadron Colliders*, JHEP **09** (2010) 097, arXiv:1003.5827 [hep-ph]. (146, 147, 148)

[401] T. Becher, A. Broggio, and A. Ferroglia, *Introduction to Soft-Collinear Effective Theory*, vol. 896 of *Lect. Notes Phys.* Springer-Verlag Berlin Heidelberg, Germany, 206 p, 2015. arXiv:1410.1892 [hep-ph]. (146)

[402] H. T. Li, C. S. Li, and S. A. Li, *Renormalization group improved predictions for $t\bar{t}W^{\pm}$ production at hadron colliders*, Phys. Rev. **D90** (2014) 094009, arXiv:1409.1460 [hep-ph]. (146)

[403] A. Ferroglia, M. Neubert, B. D. Pecjak, and L. L. Yang, *Two-loop divergences of scattering amplitudes with massive partons*, Phys. Rev. Lett. **103** (2009) 201601, arXiv:0907.4791 [hep-ph]. (146)

[404] A. Ferroglia, M. Neubert, B. D. Pecjak, and L. L. Yang, *Two-loop divergences of massive scattering amplitudes in non-abelian gauge theories*, JHEP **11** (2009) 062, arXiv:0908.3676 [hep-ph]. (146)

[405] T. Becher, M. Neubert, and G. Xu, *Dynamical Threshold Enhancement and Resummation in Drell-Yan Production*, JHEP **07** (2008) 030, arXiv:0710.0680 [hep-ph]. (147, 148)

[406] L. Reina, S. Dawson, and D. Wackeroth, *QCD corrections to associated $t\bar{t}h$ production at the Tevatron*, Phys. Rev. **D65** (2002) 053017, arXiv:hep-ph/0109066 [hep-ph]. (147)

[407] A. Broggio, A. S. Papanastasiou, and A. Signer, *Renormalization-group improved fully differential cross sections for top pair production*, JHEP **10** (2014) 98, arXiv:1407.2532 [hep-ph]. (147)

[408] V. Ahrens, A. Ferroglia, M. Neubert, B. D. Pecjak, and L.-L. Yang, *RG-improved single-particle inclusive cross sections and forward-backward asymmetry in $t\bar{t}$ production at hadron colliders*, JHEP **09** (2011) 070, arXiv:1103.0550 [hep-ph]. (147)

[409] A. Broggio, A. Ferroglia, M. Neubert, L. Vernazza, and L. L. Yang, *Approximate NNLO Predictions for the Stop-Pair Production Cross Section at the LHC*, JHEP **07** (2013) 042, arXiv:1304.2411 [hep-ph]. (147)

[410] F. Demartin, F. Maltoni, K. Mawatari, and M. Zaro, *Higgs production in association with a single top quark at the LHC*, Eur. Phys. J. **C75** (2015) 267, arXiv:1504.00611 [hep-ph]. (151, 152, 153, 154, 155, 383)

[411] F. Demartin, B. Maier, F. Maltoni, K. Mawatari, and M. Zaro, *tWH associated production at the LHC*, arXiv:1607.05862 [hep-ph]. (151)

[412] F. Maltoni, G. Ridolfi, and M. Ubiali, *b-initiated processes at the LHC: a reappraisal*, JHEP **07** (2012) 022, arXiv:1203.6393 [hep-ph]. [Erratum-ibid. **04** (2013) 095]. (153, 512, 540)

[413] ATLAS Collaboration, G. Aad et al., *Search for $H \to \gamma\gamma$ produced in association with top quarks and constraints on the Yukawa coupling between the top quark and the Higgs boson using data taken at 7 TeV and 8 TeV with the ATLAS detector*, Phys. Lett. **B740** (2015) 222–242, arXiv:1409.3122 [hep-ex]. (154)

[414] CMS Collaboration, V. Khachatryan et al., *Search for the associated production of a Higgs boson with a single top quark in proton-proton collisions at $\sqrt{s} = 8$ TeV*, JHEP **06** (2016) 177, arXiv:1509.08159 [hep-ex]. (154)

[415] A. Lazopoulos, T. McElmurry, K. Melnikov, and F. Petriello, *Next-to-leading order QCD corrections to $t\bar{t}Z$ production at the LHC*, Phys. Lett. **B666** (2008) 62–65, arXiv:0804.2220 [hep-ph]. (156)

[416] A. Kardos, Z. Trócsányi, and C. Papadopoulos, *Top quark pair production in association with a Z-boson at NLO accuracy*, Phys. Rev. **D85** (2012) 054015, arXiv:1111.0610 [hep-ph]. (156)

[417] J. M. Campbell and R. K. Ellis, $t\bar{t}W^{\pm}$ *production and decay at NLO*, JHEP **07** (2012) 052, arXiv:1204.5678 [hep-ph]. (156)

[418] M. V. Garzelli, A. Kardos, C. G. Papadopoulos, and Z. Trócsányi, Z^0 *- boson production in association with a* $t\bar{t}$ *pair at NLO accuracy with parton shower effects*, Phys. Rev. **D85** (2012) 074022, arXiv:1111.1444 [hep-ph]. (156)

[419] M. V. Garzelli, A. Kardos, C. G. Papadopoulos, and Z. Trócsányi, $t\bar{t}W^{\pm} + t\bar{t}Z$ *Hadroproduction at NLO accuracy in QCD with Parton Shower and Hadronization effects*, JHEP **11** (2012) 056, arXiv:1208.2665 [hep-ph]. (156, 162)

[420] F. Maltoni, D. Pagani, and I. Tsinikos, *Associated production of a top-quark pair with vector bosons at NLO in QCD: impact on* $t\bar{t}H$ *searches at the LHC*, JHEP **02** (2016) 113, arXiv:1507.05640 [hep-ph]. (167)

[421] A. Bredenstein, A. Denner, S. Dittmaier, and S. Pozzorini, *NLO QCD corrections to* $pp \to t\bar{t}b\bar{b} + X$ *at the LHC*, Phys. Rev. Lett. **103** (2009) 012002, arXiv:0905.0110 [hep-ph]. (170)

[422] G. Bevilacqua, M. Czakon, C. Papadopoulos, R. Pittau, and M. Worek, *Assault on the NLO Wishlist:* $pp \to t\bar{t}b\bar{b}$, JHEP **09** (2009) 109, arXiv:0907.4723 [hep-ph]. (170)

[423] M. V. Garzelli, A. Kardos, and Z. Trócsányi, $t\bar{t}b\bar{b}$ *hadroproduction at NLO accuracy matched with parton shower*, in *Proceedings, 2013 European Physical Society Conference on High Energy Physics (EPS-HEP 2013): Stockholm, Sweden, July 18-24, 2013*, p. 253. 2013. (170)

[424] M. V. Garzelli, A. Kardos, and Z. Trócsányi, *Hadroproduction of* $t\bar{t}b\bar{b}$ *final states at LHC: predictions at NLO accuracy matched with Parton Shower*, JHEP **03** (2015) 083, arXiv:1408.0266 [hep-ph]. (170)

[425] F. Cascioli, P. Maierhoefer, N. Moretti, S. Pozzorini, and F. Siegert, *NLO matching for ttbb production with massive b-quarks*, arXiv:1309.5912 [hep-ph]. (170, 171, 173, 175, 176)

[426] L. Lönnblad and S. Prestel, *Merging Multi-leg NLO Matrix Elements with Parton Showers*, JHEP **03** (2013) 166, arXiv:1211.7278 [hep-ph]. (170, 468)

[427] S. Höche, F. Krauss, P. Maierhöfer, S. Pozzorini, M. Schönherr, and F. Siegert, *Next-to-leading order QCD predictions for top-quark pair production with up to two jets merged with a parton shower*, Phys. Lett. **B748** (2015) 74–78, arXiv:1402.6293 [hep-ph]. (170)

[428] N. Moretti, P. Petrov, S. Pozzorini, and M. Spannowsky, *Measuring the signal strength in* $t\bar{t}H$ *with* $H \to b\bar{b}$, Phys. Rev. **D93** (2016) 014019, arXiv:1510.08468 [hep-ph]. (171)

[429] A. Kardos and Z. Trócsányi, *Hadroproduction of t anti-t pair with a b anti-b pair using PowHel*, J. Phys. **G41** (2014) 075005, arXiv:1303.6291 [hep-ph]. (171)

[430] S. Catani, B. R. Webber, and G. Marchesini, *QCD coherent branching and semiinclusive processes at large x*, Nucl. Phys. **B349** (1991) 635–654. (172)

[431] M. Wiesemann, R. Frederix, S. Frixione, V. Hirschi, F. Maltoni, and P. Torrielli, *Higgs production in association with bottom quarks*, JHEP **02** (2015) 132, arXiv:1409.5301 [hep-ph]. (173, 514, 516, 524, 525, 526, 527, 529, 533)

[432] T. Plehn, M. Spira, and P. M. Zerwas, *Pair production of neutral Higgs particles in gluon-gluon collisions*, Nucl. Phys. **B479** (1996) 46–64, arXiv:hep-ph/9603205 [hep-ph]. [Erratum-ibid. **B531** (1998) 655]. (187, 377)

[433] A. Djouadi, W. Kilian, M. Mühlleitner, and P. M. Zerwas, *Production of neutral Higgs boson pairs at LHC*, Eur. Phys. J. **C10** (1999) 45–49, arXiv:hep-ph/9904287 [hep-ph]. (187)

[434] E. W. N. Glover and J. J. van der Bij, *Higgs boson pair production via gluon fusion*, Nucl. Phys.

B309 (1988) 282. (187, 377)

[435] S. Dawson, S. Dittmaier, and M. Spira, *Neutral Higgs boson pair production at hadron colliders: QCD corrections*, Phys. Rev. **D58** (1998) 115012, arXiv:hep-ph/9805244 [hep-ph]. (188, 189, 192, 377, 387)

[436] D. de Florian and J. Mazzitelli, *Higgs Boson Pair Production at Next-to-Next-to-Leading Order in QCD*, Phys. Rev. Lett. **111** (2013) 201801, arXiv:1309.6594 [hep-ph]. (188, 189, 192, 377)

[437] S. Borowka, N. Greiner, G. Heinrich, S. Jones, M. Kerner, J. Schlenk, U. Schubert, and T. Zirke, *Higgs Boson Pair Production in Gluon Fusion at Next-to-Leading Order with Full Top-Quark Mass Dependence*, Phys. Rev. Lett. **117** (2016) 012001, arXiv:1604.06447 [hep-ph]. [Erratum-ibid. **117** (2016) 079901]. (188, 190, 191, 197, 200, 202)

[438] S. Borowka, N. Greiner, G. Heinrich, S. P. Jones, M. Kerner, J. Schlenk, and T. Zirke, *Full top quark mass dependence in Higgs boson pair production at NLO*, arXiv:1608.04798 [hep-ph]. (188, 197, 201)

[439] D. de Florian and J. Mazzitelli, *Higgs pair production at next-to-next-to-leading logarithmic accuracy at the LHC*, JHEP **09** (2015) 053, arXiv:1505.07122 [hep-ph]. (188, 189, 190, 191, 197, 205, 207, 377)

[440] G. Degrassi, P. P. Giardino, and R. Gröber, *On the two-loop virtual QCD corrections to Higgs boson pair production in the Standard Model*, Eur. Phys. J. **C76** (2016) 411, arXiv:1603.00385 [hep-ph]. (188)

[441] J. Grigo, J. Hoff, and M. Steinhauser, *Higgs boson pair production: top quark mass effects at NLO and NNLO*, Nucl. Phys. **B900** (2015) 412–430, arXiv:1508.00909 [hep-ph]. (188, 377)

[442] J. Grigo, K. Melnikov, and M. Steinhauser, *Virtual corrections to Higgs boson pair production in the large top quark mass limit*, Nucl. Phys. **B888** (2014) 17–29, arXiv:1408.2422 [hep-ph]. (188, 377)

[443] J. Grigo, J. Hoff, K. Melnikov, and M. Steinhauser, *On the Higgs boson pair production at the LHC*, Nucl. Phys. **B875** (2013) 1–17, arXiv:1305.7340 [hep-ph]. (188, 377)

[444] R. Frederix, S. Frixione, V. Hirschi, F. Maltoni, O. Mattelaer, et al., *Higgs pair production at the LHC with NLO and parton-shower effects*, Phys. Lett. **B732** (2014) 142, arXiv:1401.7340 [hep-ph]. (188, 190, 192, 193, 195, 196, 197, 377)

[445] F. Maltoni, E. Vryonidou, and M. Zaro, *Top-quark mass effects in double and triple Higgs production in gluon-gluon fusion at NLO*, JHEP **11** (2014) 079, arXiv:1408.6542 [hep-ph]. (188, 192, 193, 196, 200, 377)

[446] J. Baglio, A. Djouadi, R. Gröber, M. M. Mühlleitner, J. Quevillon, and M. Spira, *The measurement of the Higgs self-coupling at the LHC: theoretical status*, JHEP **04** (2013) 151, arXiv:1212.5581 [hep-ph]. (190, 193, 194, 195)

[447] L.-S. Ling, R.-Y. Zhang, W.-G. Ma, L. Guo, W.-H. Li, and X.-Z. Li, *NNLO QCD corrections to Higgs pair production via vector boson fusion at hadron colliders*, Phys. Rev. **D89** (2014) 073001, arXiv:1401.7754 [hep-ph]. (193)

[448] M. J. Dolan, C. Englert, N. Greiner, K. Nordstrom, and M. Spannowsky, *$hhjj$ production at the LHC*, Eur. Phys. J. **C75** (2015) 387, arXiv:1506.08008 [hep-ph]. (193, 246)

[449] M. J. Dolan, C. Englert, N. Greiner, and M. Spannowsky, *Further on up the road: $hhjj$ production at the LHC*, Phys. Rev. Lett. **112** (2014) 101802, arXiv:1310.1084 [hep-ph]. (193)

[450] C. Englert, F. Krauss, M. Spannowsky, and J. Thompson, *Di-Higgs phenomenology in $t\bar{t}hh$: The forgotten channel*, Phys. Lett. **B743** (2015) 93–97, arXiv:1409.8074 [hep-ph]. (193)

[451] M. J. Dolan, C. Englert, and M. Spannowsky, *Higgs self-coupling measurements at the LHC*, JHEP **10** (2012) 112, arXiv:1206.5001 [hep-ph]. (197)

[452] M. Gouzevitch, A. Oliveira, J. Rojo, R. Rosenfeld, G. P. Salam, and V. Sanz, *Scale-invariant resonance tagging in multijet events and new physics in Higgs pair production*, JHEP **07** (2013) 148, arXiv:1303.6636 [hep-ph]. (197)

[453] A. Papaefstathiou, L. L. Yang, and J. Zurita, *Higgs boson pair production at the LHC in the $b\bar{b}W^+W^-$ channel*, Phys. Rev. **D87** (2013) 011301, arXiv:1209.1489 [hep-ph]. (197)

[454] J. K. Behr, D. Bortoletto, J. A. Frost, N. P. Hartland, C. Issever, and J. Rojo, *Boosting Higgs pair production in the $b\bar{b}b\bar{b}$ final state with multivariate techniques*, Eur. Phys. J. **C76** (2016) 386, arXiv:1512.08928 [hep-ph]. (197)

[455] G. Ferrera and J. Pires, *Transverse-momentum resummation for Higgs boson pair production at the LHC with top-quark mass effects*, arXiv:1609.01691 [hep-ph]. (200)

[456] P. Maierhöfer and A. Papaefstathiou, *Higgs Boson pair production merged to one jet*, JHEP **03** (2014) 126, arXiv:1401.0007 [hep-ph]. (200, 388)

[457] S. Gieseke et al., *Herwig++ 2.5 Release Note*, arXiv:1102.1672 [hep-ph]. (200, 387)

[458] K. Arnold et al., *Herwig++ 2.6 Release Note*, arXiv:1205.4902 [hep-ph]. (200, 387)

[459] J. Bellm et al., *Herwig++ 2.7 Release Note*, arXiv:1310.6877 [hep-ph]. (200, 387)

[460] M. J. Dolan, C. Englert, and M. Spannowsky, *New Physics in LHC Higgs boson pair production*, Phys. Rev. **D87** (2013) 055002, arXiv:1210.8166 [hep-ph]. (202)

[461] J. Baglio, O. Eberhardt, U. Nierste, and M. Wiebusch, *Benchmarks for Higgs Pair Production and Heavy Higgs boson Searches in the Two-Higgs-Doublet Model of Type II*, Phys. Rev. **D90** (2014) 015008, arXiv:1403.1264 [hep-ph]. (202, 211)

[462] B. Hespel, D. Lopez-Val, and E. Vryonidou, *Higgs pair production via gluon fusion in the Two-Higgs-Doublet Model*, JHEP **09** (2014) 124, arXiv:1407.0281 [hep-ph]. (202, 211, 212, 218, 386, 567)

[463] A. Falkowski, *Effective field theory approach to LHC Higgs data*, Pramana **87** (2016) 39, arXiv:1505.00046 [hep-ph]. (202, 285, 361)

[464] R. Contino, M. Ghezzi, C. Grojean, M. Mühlleitner, and M. Spira, *Effective Lagrangian for a light Higgs-like scalar*, JHEP **07** (2013) 035, arXiv:1303.3876 [hep-ph]. (203, 287, 299, 302, 317, 383, 392, 393)

[465] B. Dumont, S. Fichet, and G. von Gersdorff, *A Bayesian view of the Higgs sector with higher dimensional operators*, JHEP **07** (2013) 065, arXiv:1304.3369 [hep-ph]. (203, 293)

[466] S. Dawson, E. Furlan, and I. Lewis, *Unravelling an extended quark sector through multiple Higgs production?*, Phys. Rev. **D87** (2013) 014007, arXiv:1210.6663 [hep-ph]. (203)

[467] F. Goertz, A. Papaefstathiou, L. L. Yang, and J. Zurita, *Higgs boson pair production in the D=6 extension of the SM*, JHEP **04** (2015) 167, arXiv:1410.3471 [hep-ph]. (204, 295, 388)

[468] A. Azatov, R. Contino, G. Panico, and M. Son, *Effective field theory analysis of double Higgs boson production via gluon fusion*, Phys. Rev. **D92** (2015) 035001, arXiv:1502.00539 [hep-ph]. (204, 205)

[469] M. Gillioz, R. Gröber, C. Grojean, M. Mühlleitner, and E. Salvioni, *Higgs Low-Energy Theorem (and its corrections) in Composite Models*, JHEP **10** (2012) 004, arXiv:1206.7120 [hep-ph]. (204, 636)

[470] C.-Y. Chen, S. Dawson, and I. M. Lewis, *Top Partners and Higgs Boson Production*, Phys. Rev. **D90** (2014) 035016, arXiv:1406.3349 [hep-ph]. (204)

[471] A. Carvalho, M. Dall'Osso, P. De Castro Manzano, T. Dorigo, F. Goertz, M. Gouzevich, and M. Tosi, *Analytical parametrization and shape classification of anomalous HH production in the EFT approach*, LHCHXSWG-2016-001, arXiv:1608.06578 [hep-ph]. (205, 206)

[472] R. Gröber, M. Mühlleitner, M. Spira, and J. Streicher, *NLO QCD Corrections to Higgs Pair Production including Dimension-6 Operators*, JHEP **09** (2015) 092, arXiv:1504.06577 [hep-ph]. (205, 206, 303, 335, 349, 377)

[473] A. Carvalho, M. Dall'Osso, T. Dorigo, F. Goertz, C. A. Gottardo, and M. Tosi, *Higgs Pair Production: Choosing Benchmarks With Cluster Analysis*, JHEP **04** (2016) 126, arXiv:1507.02245 [hep-ph]. (205)

[474] T. Binoth and J. J. van der Bij, *Influence of strongly coupled, hidden scalars on Higgs signals*, Z. Phys. **C75** (1997) 17–25, arXiv:hep-ph/9608245 [hep-ph]. (206)

[475] R. Schabinger and J. D. Wells, *A Minimal spontaneously broken hidden sector and its impact on Higgs boson physics at the large hadron collider*, Phys. Rev. **D72** (2005) 093007, arXiv:hep-ph/0509209 [hep-ph]. (206, 585)

[476] B. Patt and F. Wilczek, *Higgs-field portal into hidden sectors*, arXiv:hep-ph/0605188 [hep-ph]. (206)

[477] F. Bojarski, G. Chalons, D. Lopez-Val, and T. Robens, *Heavy to light Higgs boson decays at NLO in the Singlet Extension of the Standard Model*, JHEP **02** (2016) 147, arXiv:1511.08120 [hep-ph]. (207, 589)

[478] S. Y. Choi, C. Englert, and P. M. Zerwas, *Multiple Higgs-Portal and Gauge-Kinetic Mixings*, Eur. Phys. J. **C73** (2013) 2643, arXiv:1308.5784 [hep-ph]. (207)

[479] ATLAS Collaboration, G. Aad et al., *Constraints on new phenomena via Higgs boson couplings and invisible decays with the ATLAS detector*, JHEP **11** (2015) 206, arXiv:1509.00672 [hep-ex]. (207, 211)

[480] T. Robens and T. Stefaniak, *Status of the Higgs Singlet Extension of the Standard Model after LHC Run 1*, Eur. Phys. J. **C75** (2015) 104, arXiv:1501.02234 [hep-ph]. (207, 208, 590)

[481] D. López-Val and T. Robens, *Δr and the W-boson mass in the singlet extension of the standard model*, Phys. Rev. **D90** (2014) 114018, arXiv:1406.1043 [hep-ph]. (207, 590)

[482] T. Robens and T. Stefaniak, *LHC Benchmark Scenarios for the Real Higgs Singlet Extension of the Standard Model*, Eur. Phys. J. **C76** (2016) 268, arXiv:1601.07880 [hep-ph]. (208, 214, 215, 216, 217, 590, 594)

[483] S. Dawson and I. M. Lewis, *NLO corrections to double Higgs boson production in the Higgs singlet model*, Phys. Rev. **D92** (2015) 094023, arXiv:1508.05397 [hep-ph]. (208, 210, 211, 212, 213, 589)

[484] R. Costa, M. Mühlleitner, M. O. P. Sampaio, and R. Santos, *Singlet Extensions of the Standard Model at LHC Run 2: Benchmarks and Comparison with the NMSSM*, JHEP **06** (2016) 034, arXiv:1512.05355 [hep-ph]. (209, 589, 591, 592, 599, 601, 602)

[485] G. Branco, P. Ferreira, L. Lavoura, M. Rebelo, M. Sher, et al., *Theory and phenomenology of two-Higgs-doublet models*, Phys.Rept. **516** (2012) 1–102, arXiv:1106.0034 [hep-ph]. (210, 247, 542, 549, 551)

[486] H. E. Haber and O. Stål, *New LHC benchmarks for the $\mathcal{CP}$-conserving two-Higgs-doublet model*, Eur. Phys. J. **C75** (2015) 491, arXiv:1507.04281 [hep-ph]. [Erratum-ibid. **C76** (2016) 312]. (211, 633)

[487] ATLAS Collaboration, G. Aad et al., *Search for Higgs boson pair production in the $b\bar{b}b\bar{b}$ final state from pp collisions at $\sqrt{s} = 8$ TeVwith the ATLAS detector*, Eur. Phys. J. **C75** (2015) 412, arXiv:1506.00285 [hep-ex]. (219)

[488] CMS Collaboration, V. Khachatryan et al., *Search for resonant pair production of Higgs bosons decaying to two bottom quark–antiquark pairs in proton–proton collisions at 8 TeV*, Phys. Lett. **B749** (2015) 560–582, arXiv:1503.04114 [hep-ex]. (219, 220)

[489] ATLAS Collaboration, G. Aad et al., *Search For Higgs Boson Pair Production in the $\gamma\gamma b\bar{b}$ Final*

State using pp Collision Data at $\sqrt{s} = 8$ TeV from the ATLAS Detector, Phys. Rev. Lett. **114** (2015) 081802, arXiv:1406.5053 [hep-ex]. (219)

[490] ATLAS Collaboration, G. Aad et al., *Searches for Higgs boson pair production in the $hh \to bb\tau\tau, \gamma\gamma WW^*, \gamma\gamma bb, bbbb$ channels with the ATLAS detector*, Phys. Rev. **D92** (2015) 092004, arXiv:1509.04670 [hep-ex]. (219, 220)

[491] CMS Collaboration, V. Khachatryan et al., *Search for two Higgs bosons in final states containing two photons and two bottom quarks in proton-proton collisions at 8 TeV*, Phys. Rev. **D94** (2016) 052012, arXiv:1603.06896 [hep-ex]. (219, 220)

[492] CMS Collaboration, V. Khachatryan et al., *Searches for a heavy scalar boson H decaying to a pair of 125 GeV Higgs bosons hh or for a heavy pseudoscalar boson A decaying to Zh, in the final states with $h \to \tau\tau$*, Phys. Lett. **B755** (2016) 217–244, arXiv:1510.01181 [hep-ex]. (219, 220)

[493] CMS Collaboration, *Model independent search for Higgs boson pair production in the $\mathrm{b\bar{b}}\tau^+\tau^-$ final state*, CMS-PAS-HIG-15-013, 2016. (219, 220)

[494] CMS Collaboration, *Search for Resonant Pair Production of Higgs Bosons Decaying to $b\bar{b}$ and $\tau^+\tau^-$ in Proton-Proton Collisions at $\sqrt{s} = 8$ TeV*, CMS-PAS-EXO-15-008, 2015. (219, 220)

[495] CMS Collaboration, V. Khachatryan et al., *Search for heavy resonances decaying to two Higgs bosons in final states containing four b quarks*, Eur. Phys. J. C **76** (2016) 371, arXiv:1602.08762 [hep-ex]. (219, 220)

[496] ATLAS Collaboration, *Prospects for measuring Higgs pair production in the channel $H(\to \gamma\gamma)H(\to b\bar{b})$ using the ATLAS detector at the HL-LHC*, ATL-PHYS-PUB-2014-019, 2014. (220)

[497] ATLAS Collaboration, *Higgs Pair Production in the $H(\to \tau\tau)H(\to b\bar{b})$ channel at the High-Luminosity LHC*, ATL-PHYS-PUB-2015-046, 2015. (220)

[498] CMS Collaboration, J. Butler, D. Contardo, M. Klute, J. Mans, and L. Silvestris (Eds), *Technical Proposal for the Phase-II Upgrade of the CMS Detector*, Tech. Rep. CERN-LHCC-2015-010. LHCC-P-008, CERN, Geneva, Jun, 2015. http://cds.cern.ch/record/2020886. (220)

[499] N. Kauer and G. Passarino, *Inadequacy of zero-width approximation for a light Higgs boson signal*, JHEP **08** (2012) 116, arXiv:1206.4803 [hep-ph]. (221, 223, 232, 260, 425, 461, 470, 478, 627)

[500] F. Caola and K. Melnikov, *Constraining the Higgs boson width with ZZ production at the LHC*, Phys. Rev. **D88** (2013) 054024, arXiv:1307.4935 [hep-ph]. (221, 470, 627)

[501] J. M. Campbell, R. K. Ellis, and C. Williams, *Bounding the Higgs width at the LHC using full analytic results for $gg \to e^-e^+\mu^-\mu^+$*, JHEP **04** (2014) 060, arXiv:1311.3589 [hep-ph]. (221, 238, 244, 249, 386, 627)

[502] C. Englert and M. Spannowsky, *Limitations and Opportunities of Off-Shell Coupling Measurements*, Phys. Rev. **D90** (2014) 053003, arXiv:1405.0285 [hep-ph]. (221, 627)

[503] H. E. Logan, *Hiding a Higgs width enhancement from off-shell $gg(\to h^*) \to ZZ$ measurements*, Phys. Rev. **D92** (2015) 075038, arXiv:1412.7577 [hep-ph]. (221)

[504] J. S. Gainer, J. Lykken, K. T. Matchev, S. Mrenna, and M. Park, *Beyond Geolocating: Constraining Higher Dimensional Operators in $H \to 4\ell$ with Off-Shell Production and More*, Phys. Rev. **D91** (2015) 035011, arXiv:1403.4951 [hep-ph]. (221)

[505] A. Azatov, C. Grojean, A. Paul, and E. Salvioni, *Taming the off-shell Higgs boson*, Zh. Eksp. Teor. Fiz. **147** (2015) 410–425, arXiv:1406.6338 [hep-ph]. [J. Exp. Theor. Phys.120,354(2015)]. (221)

[506] CMS Collaboration, V. Khachatryan et al., *Constraints on the Higgs boson width from off-shell production and decay to Z-boson pairs*, Phys. Lett. **B736** (2014) 64–85, arXiv:1405.3455

[hep-ex]. (221, 223, 386, 627)

[507] ATLAS Collaboration, G. Aad et al., *Constraints on the off-shell Higgs boson signal strength in the high-mass ZZ and WW final states with the ATLAS detector*, Eur. Phys. J. **C75** (2015) 335, arXiv:1503.01060 [hep-ex]. (221, 223, 238, 239, 240, 241, 244, 627)

[508] CMS Collaboration, V. Khachatryan et al., *Search for Higgs boson off-shell production in proton-proton collisions at 7 and 8 TeV and derivation of constraints on its total decay width*, JHEP **09** (2016) 051, arXiv:1605.02329 [hep-ex]. (221, 222)

[509] S. P. Martin, *Shift in the LHC Higgs diphoton mass peak from interference with background*, Phys. Rev. **D86** (2012) 073016, arXiv:1208.1533 [hep-ph]. (222, 257, 258)

[510] L. J. Dixon and Y. Li, *Bounding the Higgs Boson Width Through Interferometry*, Phys. Rev. Lett. **111** (2013) 111802, arXiv:1305.3854 [hep-ph]. (222, 257, 258, 259, 260, 263, 264, 271)

[511] T. Binoth, M. Ciccolini, N. Kauer, and M. Krämer, *Gluon-induced WW background to Higgs boson searches at the LHC*, JHEP **03** (2005) 065, arXiv:hep-ph/0503094 [hep-ph]. (223)

[512] T. Binoth, M. Ciccolini, N. Kauer, and M. Krämer, *Gluon-induced W-boson pair production at the LHC*, JHEP **12** (2006) 046, arXiv:hep-ph/0611170 [hep-ph]. (223)

[513] N. Kauer, *Interference effects for $H \to WW/ZZ \to \ell\bar{\nu}_\ell\bar{\ell}\nu_\ell$ searches in gluon fusion at the LHC*, JHEP **12** (2013) 082, arXiv:1310.7011 [hep-ph]. (223, 238)

[514] N. Kauer, C. O'Brien, and E. Vryonidou, *Interference effects for $H \to WW \to \ell\nu q\bar{q}'$ and $H \to ZZ \to \ell\bar{\ell}q\bar{q}$ searches in gluon fusion at the LHC*, JHEP **10** (2015) 074, arXiv:1506.01694 [hep-ph]. (223, 224, 229)

[515] V. Hirschi and O. Mattelaer, *Automated event generation for loop-induced processes*, JHEP **10** (2015) 146, arXiv:1507.00020 [hep-ph]. (223)

[516] A. Ballestrero, A. Belhouari, G. Bevilacqua, V. Kashkan, and E. Maina, *PHANTOM: A Monte Carlo event generator for six parton final states at high energy colliders*, Comput. Phys. Commun. **180** (2009) 401–417, arXiv:0801.3359 [hep-ph]. (226, 232)

[517] A. Ballestrero and E. Maina, *Interference Effects in Higgs production through Vector Boson Fusion in the Standard Model and its Singlet Extension*, JHEP **01** (2016) 045, arXiv:1506.02257 [hep-ph]. (226, 232)

[518] J. Baglio et al., *Release Note - VBFNLO 2.7.0*, arXiv:1404.3940 [hep-ph]. (226, 232, 388)

[519] B. Jager, C. Oleari, and D. Zeppenfeld, *Next-to-leading order QCD corrections to W^+W^- production via vector-boson fusion*, JHEP **07** (2006) 015, arXiv:hep-ph/0603177 [hep-ph]. (226, 232)

[520] B. Jager, C. Oleari, and D. Zeppenfeld, *Next-to-leading order QCD corrections to Z boson pair production via vector-boson fusion*, Phys. Rev. **D73** (2006) 113006, arXiv:hep-ph/0604200 [hep-ph]. (226, 232)

[521] G. Bozzi, B. Jager, C. Oleari, and D. Zeppenfeld, *Next-to-leading order QCD corrections to W^+Z and W^-Z production via vector-boson fusion*, Phys. Rev. **D75** (2007) 073004, arXiv:hep-ph/0701105 [hep-ph]. (226, 232)

[522] B. Jager, C. Oleari, and D. Zeppenfeld, *Next-to-leading order QCD corrections to W^+W^+jj and W^-W^-jj production via weak-boson fusion*, Phys. Rev. **D80** (2009) 034022, arXiv:0907.0580 [hep-ph]. (226, 232)

[523] B. Feigl, *Electroweak Processes in the Standard Model and Beyond: Backgrounds to Higgs Physics and Semileptonic Decay Modes*. PhD thesis, KIT, Karlsruhe, TP, 2013. http://digbib.ubka.uni-karlsruhe.de/volltexte/1000037298. (226, 232)

[524] A. Alloul, N. D. Christensen, C. Degrande, C. Duhr, and B. Fuks, *FeynRules 2.0 - A complete toolbox for tree-level phenomenology*, Comput. Phys. Commun. **185** (2014) 2250–2300,

arXiv:1310.1921 [hep-ph]. (232, 381, 383, 393)

[525] N. Kauer and C. O'Brien, *Heavy Higgs signal background interference in $gg \to VV$ in the Standard Model plus real singlet*, Eur. Phys. J. **C75** (2015) 374, arXiv:1502.04113 [hep-ph]. (232, 249, 589)

[526] E. Maina, *Interference effects in Heavy Higgs production via gluon fusion in the Singlet Extension of the Standard Model*, JHEP **06** (2015) 004, arXiv:1501.02139 [hep-ph]. (232, 589)

[527] F. Caola, K. Melnikov, R. Roentsch, and L. Tancredi, *QCD corrections to ZZ production in gluon fusion at the LHC*, Phys. Rev. **D92** (2015) 094028, arXiv:1509.06734 [hep-ph]. (239, 246, 253, 254, 256)

[528] ATLAS Collaboration, *Determination of the off-shell Higgs boson signal strength in the high-mass ZZ final state with the ATLAS detector*, ATLAS-CONF-2014-042, 2014. (239, 240)

[529] J. Gao et al., *CT10 next-to-next-to-leading order global analysis of QCD*, Phys. Rev. **D89** (2014) 033009, arXiv:1302.6246 [hep-ph]. (242, 249)

[530] Y. Gao, A. V. Gritsan, Z. Guo, K. Melnikov, M. Schulze, and N. V. Tran, *Spin determination of single-produced resonances at hadron colliders*, Phys. Rev. **D81** (2010) 075022, arXiv:1001.3396 [hep-ph]. (244, 245, 386, 387)

[531] S. Bolognesi, Y. Gao, A. V. Gritsan, K. Melnikov, M. Schulze, N. V. Tran, and A. Whitbeck, *On the spin and parity of a single-produced resonance at the LHC*, Phys. Rev. **D86** (2012) 095031, arXiv:1208.4018 [hep-ph]. (244, 245, 386, 387)

[532] I. Anderson et al., *Constraining anomalous HVV interactions at proton and lepton colliders*, Phys. Rev. **D89** (2014) 035007, arXiv:1309.4819 [hep-ph]. (244, 245, 386, 387)

[533] J. M. Campbell and R. K. Ellis, *MCFM for the Tevatron and the LHC*, in *Proceedings, 10th DESY Workshop on Elementary Particle Theory: Loops and Legs in Quantum Field Theory*, vol. 205-206, pp. 10–15. 2010. arXiv:1007.3492 [hep-ph]. (244, 386, 649)

[534] CMS Collaboration, V. Khachatryan et al., *Constraints on the spin-parity and anomalous HVV couplings of the Higgs boson in proton collisions at 7 and 8 TeV*, Phys. Rev. **D92** (2015) 012004, arXiv:1411.3441 [hep-ex]. (245, 246, 386, 387, 394)

[535] CMS Collaboration, V. Khachatryan et al., *Limits on the Higgs boson lifetime and width from its decay to four charged leptons*, Phys. Rev. **D92** (2015) 072010, arXiv:1507.06656 [hep-ex]. (245, 246, 386)

[536] M. Grazzini, *NNLO predictions for the Higgs boson signal in the $H \to WW \to \ell\nu\ell\nu$ and $H \to ZZ \to 4\ell$ decay channels*, JHEP **02** (2008) 043, arXiv:0801.3232 [hep-ph]. (246)

[537] K. Melnikov and M. Dowling, *Production of two Z-bosons in gluon fusion in the heavy top quark approximation*, Phys. Lett. **B744** (2015) 43–47, arXiv:1503.01274 [hep-ph]. (246, 253, 254, 255, 256)

[538] R. Ellis, W. T. Giele, Z. Kunszt, and K. Melnikov, *Masses, fermions and generalized D-dimensional unitarity*, Nucl. Phys. **B822** (2009) 270–282, arXiv:0806.3467 [hep-ph]. (246)

[539] P. Mastrolia, G. Ossola, C. Papadopoulos, and R. Pittau, *Optimizing the Reduction of One-Loop Amplitudes*, JHEP **06** (2008) 030, arXiv:0803.3964 [hep-ph]. (246)

[540] P. Mastrolia, G. Ossola, T. Reiter, and F. Tramontano, *Scattering AMplitudes from Unitarity-based Reduction Algorithm at the Integrand-level*, JHEP **08** (2010) 080, arXiv:1006.0710 [hep-ph]. (246)

[541] H. van Deurzen, *Associated Higgs Production at NLO with GoSam*, Acta Phys.Polon. **B44** (2013) 2223–2230. (246)

[542] H. van Deurzen, G. Luisoni, P. Mastrolia, E. Mirabella, G. Ossola, and T. Peraro, *Multi-leg*

One-loop Massive Amplitudes from Integrand Reduction via Laurent Expansion, JHEP **03** (2014) 115, arXiv:1312.6678 [hep-ph]. (246)

[543] T. Peraro, *Ninja: Automated Integrand Reduction via Laurent Expansion for One-Loop Amplitudes*, Comput. Phys. Commun. **185** (2014) 2771–2797, arXiv:1403.1229 [hep-ph]. (246)

[544] G. Heinrich, G. Ossola, T. Reiter, and F. Tramontano, *Tensorial Reconstruction at the Integrand Level*, JHEP **10** (2010) 105, arXiv:1008.2441 [hep-ph]. (246)

[545] T. Binoth, J.-P. Guillet, G. Heinrich, E. Pilon, and T. Reiter, *Golem95: A Numerical program to calculate one-loop tensor integrals with up to six external legs*, Comput. Phys. Commun. **180** (2009) 2317–2330, arXiv:0810.0992 [hep-ph]. (246)

[546] G. Cullen, J. Guillet, G. Heinrich, T. Kleinschmidt, E. Pilon, et al., *Golem95C: A library for one-loop integrals with complex masses*, Comput. Phys. Commun. **182** (2011) 2276–2284, arXiv:1101.5595 [hep-ph]. (246)

[547] J. P. Guillet, G. Heinrich, and J. F. von Soden-Fraunhofen, *Tools for NLO automation: extension of the golem95C integral library*, Comput. Phys. Commun. **185** (2014) 1828–1834, arXiv:1312.3887 [hep-ph]. (246)

[548] A. van Hameren, *OneLOop: For the evaluation of one-loop scalar functions*, Comput. Phys. Commun. **182** (2011) 2427–2438, arXiv:1007.4716 [hep-ph]. (246)

[549] R. K. Ellis and G. Zanderighi, *Scalar one-loop integrals for QCD*, JHEP **02** (2008) 002, arXiv:0712.1851 [hep-ph]. (246)

[550] M. Chiesa, N. Greiner, and F. Tramontano, *Automation of electroweak corrections for LHC processes*, J. Phys. **G43** (2016) 013002, arXiv:1507.08579 [hep-ph]. (246)

[551] G. Cullen, H. van Deurzen, N. Greiner, G. Luisoni, P. Mastrolia, E. Mirabella, G. Ossola, T. Peraro, and F. Tramontano, *Next-to-Leading-Order QCD Corrections to Higgs Boson Production Plus Three Jets in Gluon Fusion*, Phys. Rev. Lett. **111** (2013) 131801, arXiv:1307.4737 [hep-ph]. (246, 468)

[552] C. Degrande, C. Duhr, B. Fuks, D. Grellscheid, O. Mattelaer, et al., *UFO - The Universal FeynRules Output*, Comput. Phys. Commun. **183** (2012) 1201–1214, arXiv:1108.2040 [hep-ph]. (246, 381, 383)

[553] C. Degrande, *Automatic evaluation of UV and R2 terms for beyond the Standard Model Lagrangians: a proof-of-principle*, Comput. Phys. Commun. **197** (2015) 239–262, arXiv:1406.3030 [hep-ph]. (246, 576)

[554] N. Greiner, G. Heinrich, J. Reichel, and J. F. von Soden-Fraunhofen, *NLO QCD corrections to diphoton plus jet production through graviton exchange*, JHEP **11** (2013) 028, arXiv:1308.2194 [hep-ph]. (246)

[555] G. Cullen, N. Greiner, and G. Heinrich, *Susy-QCD corrections to neutralino pair production in association with a jet*, Eur. Phys. J. **C73** (2013) 2388, arXiv:1212.5154 [hep-ph]. (246)

[556] T. Hahn, *Generating Feynman diagrams and amplitudes with FeynArts 3*, Comput. Phys. Commun. **140** (2001) 418–431, arXiv:hep-ph/0012260 [hep-ph]. (248)

[557] T. Hahn and M. Perez-Victoria, *Automatized one-loop calculations in four and D dimensions*, Comput. Phys. Commun. **118** (1999) 153–165, arXiv:hep-ph/9807565. (248)

[558] D. Eriksson, J. Rathsman, and O. Stal, *2HDMC: Two-Higgs-Doublet Model Calculator Physics and Manual*, Comput. Phys. Commun. **181** (2010) 189–205, arXiv:0902.0851 [hep-ph]. (248, 552, 554)

[559] F. Maltoni and T. Stelzer, *MadEvent: Automatic event generation with MadGraph*, JHEP **02** (2003) 027, arXiv:hep-ph/0208156 [hep-ph]. (248)

[560] J. Alwall, P. Demin, S. de Visscher, R. Frederix, M. Herquet, F. Maltoni, T. Plehn, D. L.

Rainwater, and T. Stelzer, *MadGraph/MadEvent v4: The New Web Generation*, JHEP **09** (2007) 028, arXiv:0706.2334 [hep-ph]. (248, 526)

[561] N. Kauer, *Signal-background interference in $gg \to H \to VV$*, in *Proceedings, 10th International Symposium on Radiative Corrections: Applications of Quantum Field Theory to Phenomenology (RADCOR 2011): Mamallapuram, Tamil Nadu, India, September 26-30, 2011*. 2012. arXiv:1201.1667 [hep-ph]. (249)

[562] ATLAS Collaboration, G. Aad et al., *Search for an additional, heavy Higgs boson in the $H \to ZZ$ decay channel at $\sqrt{s} = 8$ TeV in pp collision data with the ATLAS detector*, Eur. Phys. J. **C76** (2016) 45, arXiv:1507.05930 [hep-ex]. (249)

[563] ATLAS Collaboration, G. Aad et al., *Search for a high-mass Higgs boson decaying to a W boson pair in pp collisions at $\sqrt{s} = 8$ TeV with the ATLAS detector*, JHEP **01** (2016) 032, arXiv:1509.00389 [hep-ex]. (249)

[564] N. Greiner, S. Liebler, and G. Weiglein, *Interference contributions to gluon initiated heavy Higgs production in the Two-Higgs-Doublet Model*, Eur. Phys. J. **C76** (2016) 118, arXiv:1512.07232 [hep-ph]. (250, 251)

[565] R. V. Harlander and W. B. Kilgore, *Higgs boson production in bottom quark fusion at next-to-next-to-leading order*, Phys. Rev. **D68** (2003) 013001, arXiv:hep-ph/0304035. (252, 491, 498, 512, 514, 516, 519, 608)

[566] F. Cascioli, T. Gehrmann, M. Grazzini, S. Kallweit, P. Maierhoefer, A. von Manteuffel, S. Pozzorini, D. Rathlev, L. Tancredi, and E. Weihs, *ZZ production at hadron colliders in NNLO QCD*, Phys. Lett. **B735** (2014) 311–313, arXiv:1405.2219 [hep-ph]. (252, 256)

[567] T. Gehrmann, M. Grazzini, S. Kallweit, P. Maierhöfer, A. von Manteuffel, S. Pozzorini, D. Rathlev, and L. Tancredi, *W^+W^- Production at Hadron Colliders in Next to Next to Leading Order QCD*, Phys. Rev. Lett. **113** (2014) 212001, arXiv:1408.5243 [hep-ph]. (252, 256)

[568] F. Caola, K. Melnikov, R. Roentsch, and L. Tancredi, *QCD corrections to W^+W^- production through gluon fusion*, Phys. Lett. **B754** (2016) 275–280, arXiv:1511.08617 [hep-ph]. (253, 254)

[569] F. Caola, J. M. Henn, K. Melnikov, A. V. Smirnov, and V. A. Smirnov, *Two-loop helicity amplitudes for the production of two off-shell electroweak bosons in gluon fusion*, JHEP **06** (2015) 129, arXiv:1503.08759 [hep-ph]. (253)

[570] A. von Manteuffel and L. Tancredi, *The two-loop helicity amplitudes for $gg \to V_1V_2 \to 4$ leptons*, JHEP **06** (2015) 197, arXiv:1503.08835 [hep-ph]. (253)

[571] R. K. Ellis, W. T. Giele, and Z. Kunszt, *A Numerical Unitarity Formalism for Evaluating One-Loop Amplitudes*, JHEP **03** (2008) 003, arXiv:0708.2398 [hep-ph]. (253)

[572] S. D. Badger, *Direct Extraction Of One Loop Rational Terms*, JHEP **01** (2009) 049, arXiv:0806.4600 [hep-ph]. (253)

[573] M. Bonvini, F. Caola, S. Forte, K. Melnikov, and G. Ridolfi, *Signal-background interference effects for $gg \to H \to W^+W^-$ beyond leading order*, Phys. Rev. **D88** (2013) 034032, arXiv:1304.3053 [hep-ph]. (255, 256)

[574] J. M. Campbell, R. K. Ellis, M. Czakon, and S. Kirchner, *Two loop correction to interference in $gg \to ZZ$*, JHEP **08** (2016) 011, arXiv:1605.01380 [hep-ph]. (257)

[575] F. Caola, M. Dowling, K. Melnikov, R. Röntsch, and L. Tancredi, *QCD corrections to vector boson pair production in gluon fusion including interference effects with off-shell Higgs at the LHC*, JHEP **07** (2016) 087, arXiv:1605.04610 [hep-ph]. (257)

[576] V. Barger, M. Ishida, and W.-Y. Keung, *Total Width of 125 GeV Higgs Boson*, Phys. Rev. Lett. **108** (2012) 261801, arXiv:1203.3456 [hep-ph]. (257)

[577] L. J. Dixon and M. S. Siu, *Resonance continuum interference in the diphoton Higgs signal at the LHC*, Phys. Rev. Lett. **90** (2003) 252001, arXiv:hep-ph/0302233 [hep-ph]. (258, 259)

[578] D. A. Dicus and S. S. Willenbrock, *Photon Pair Production and the Intermediate Mass Higgs Boson*, Phys. Rev. **D37** (1988) 1801. (258)

[579] D. de Florian, N. Fidanza, R. Hernández-Pinto, J. Mazzitelli, Y. Rotstein Habarnau, and G. Sborlini, *A complete $\mathcal{O}(\alpha_S^2)$ calculation of the signal-background interference for the Higgs diphoton decay channel*, Eur. Phys. J. **C73** (2013) 2387, arXiv:1303.1397 [hep-ph]. (258)

[580] S. P. Martin, *Interference of Higgs diphoton signal and background in production with a jet at the LHC*, Phys. Rev. **D88** (2013) 013004, arXiv:1303.3342 [hep-ph]. (260)

[581] B. A. Dobrescu and J. D. Lykken, *Coupling spans of the Higgs-like boson*, JHEP **02** (2013) 073, arXiv:1210.3342 [hep-ph]. (260)

[582] A. Djouadi and G. Moreau, *The couplings of the Higgs boson and its CP properties from fits of the signal strengths and their ratios at the 7+8 TeV LHC*, Eur. Phys. J. **C73** (2013) 2512, arXiv:1303.6591 [hep-ph]. (260)

[583] CMS Collaboration, *Combination of standard model Higgs boson searches and measurements of the properties of the new boson with a mass near 125 GeV*, CMS-PAS-HIG-13-005, 2013. (260)

[584] F. Richard and P. Bambade, *Strategy to measure the Higgs mass, width and invisible decays at ILC*, in *International Linear Colliders (ILC) Workshop Valencia, Spain, November 6-10, 2006*. 2007. arXiv:hep-ph/0703173 [HEP-PH]. (260)

[585] M. E. Peskin, *Comparison of LHC and ILC Capabilities for Higgs Boson Coupling Measurements*, arXiv:1207.2516 [hep-ph]. (260)

[586] T. Han and Z. Liu, *Potential precision of a direct measurement of the Higgs boson total width at a muon collider*, Phys. Rev. **D87** (2013) 033007, arXiv:1210.7803 [hep-ph]. (260)

[587] A. Conway and H. Wenzel, *Higgs Measurements at a Muon Collider*, arXiv:1304.5270 [hep-ex]. (260)

[588] F. Coradeschi, D. de Florian, L. J. Dixon, N. Fidanza, S. Höche, H. Ita, Y. Li, and J. Mazzitelli, *Interference effects in the $H(\to \gamma\gamma) + 2$ jets channel at the LHC*, Phys. Rev. **D92** (2015) 013004, arXiv:1504.05215 [hep-ph]. (261, 263, 264)

[589] B. R. Webber, *Monte Carlo Simulation of Hard Hadronic Processes*, Ann. Rev. Nucl. Part. Sci. **36** (1986) 253–286. (264)

[590] A. Buckley et al., *General-purpose event generators for LHC physics*, Phys. Rept. **504** (2011) 145–233, arXiv:1101.2599 [hep-ph]. (264)

[591] S. Höche and S. Prestel, *The midpoint between dipole and parton showers*, Eur. Phys. J. **C75** (2015) 461, arXiv:1506.05057 [hep-ph]. (264)

[592] G. Gustafson, *Dual Description of a Confined Color Field*, Phys. Lett. **B175** (1986) 453. (264)

[593] G. Gustafson and U. Pettersson, *Dipole Formulation of QCD Cascades*, Nucl. Phys. **B306** (1988) 746. (264)

[594] L. Lönnblad, *ARIADNE version 4: A Program for simulation of QCD cascades implementing the color dipole model*, Comput. Phys. Commun. **71** (1992) 15–31. (264)

[595] H. Kharraziha and L. Lönnblad, *The Linked dipole chain Monte Carlo*, JHEP **03** (1998) 006, arXiv:hep-ph/9709424 [hep-ph]. (264)

[596] CMS Collaboration, V. Khachatryan et al., *Observation of the diphoton decay of the Higgs boson and measurement of its properties*, Eur. Phys. J. **C74** (2014) 3076, arXiv:1407.0558 [hep-ex]. (264, 386)

[597] ATLAS Collaboration, *Estimate of the m_H shift due to interference between signal and background processes in the $H \to \gamma\gamma$ channel, for the $\sqrt{s} = 8$ TeV dataset recorded by ATLAS*,

ATL-PHYS-PUB-2016-009, 2016. (266, 271)

[598] ATLAS Collaboration, G. Aad et al., *Measurement of the Higgs boson mass from the $H \to \gamma\gamma$ and $H \to ZZ^* \to 4\ell$ channels with the ATLAS detector using 25 fb^{-1} of pp collision data*, Phys. Rev. **D90** (2014) 052004, arXiv:1406.3827 [hep-ex]. (266, 267, 270)

[599] G. Cowan, K. Cranmer, E. Gross, and O. Vitells, *Asymptotic formulae for likelihood-based tests of new physics*, Eur. Phys. J. **C71** (2011) 1554, arXiv:1007.1727 [physics.data-an]. [Erratum-ibid. **C73** (2013) 2501]. (270)

[600] Z. Bern, L. J. Dixon, and C. Schmidt, *Isolating a light Higgs boson from the diphoton background at the CERN LHC*, Phys. Rev. **D66** (2002) 074018, arXiv:hep-ph/0206194 [hep-ph]. (271)

[601] A. V. Manohar, *Effective field theories*, in *Perturbative and nonperturbative aspects of quantum field theory. Proceedings, 35. Internationale Universitätswochen für Kern- und Teilchenphysik*, vol. 479, pp. 311–362. 1997. arXiv:hep-ph/9606222 [hep-ph]. (285, 316, 317, 331)

[602] I. Z. Rothstein, *TASI lectures on effective field theories*, in *the 2002 Theoretical Advanced Study Institute (TASI-02)*. University of Colorado campus in Boulder, CO, USA, June 3–28, 2002. arXiv:hep-ph/0308266 [hep-ph]. (285, 316, 317)

[603] D. B. Kaplan, *Five lectures on effective field theory*, in *the 17th National Nuclear Physics Summer School*. Berkeley, CA, USA, June 6-17, 2005. arXiv:nucl-th/0510023 [nucl-th]. (285)

[604] C. P. Burgess, *Introduction to Effective Field Theory*, Ann. Rev. Nucl. Part. Sci. **57** (2007) 329–362, arXiv:hep-th/0701053 [hep-th]. (285, 316, 317)

[605] S. Weinberg, *Effective Field Theory, Past and Future*, in *Proceedings, 6th International Workshop on Chiral dymamics*, vol. CD09, p. 001. 2009. arXiv:0908.1964 [hep-th]. (285)

[606] S. Willenbrock and C. Zhang, *Effective Field Theory Beyond the Standard Model*, Ann. Rev. Nucl. Part. Sci. **64** (2014) 83–100, arXiv:1401.0470 [hep-ph]. (285, 308)

[607] E. Masso, *An Effective Guide to Beyond the Standard Model Physics*, JHEP **10** (2014) 128, arXiv:1406.6376 [hep-ph]. (285, 293, 392)

[608] A. Pomarol, *Higgs Physics*, in *2014 European School of High-Energy Physics (ESHEP 2014) Garderen, The Netherlands, June 18-July 1, 2014*. 2014. arXiv:1412.4410 [hep-ph]. (285, 316, 392)

[609] B. Henning, X. Lu, and H. Murayama, *How to use the Standard Model effective field theory*, JHEP **01** (2016) 023, arXiv:1412.1837 [hep-ph]. (285, 308, 335, 394)

[610] A. David and G. Passarino, *Through precision straits to next standard model heights*, Rev. Phys. **1** (2016) 13–28, arXiv:1510.00414 [hep-ph]. (285, 327, 329, 331, 332, 338, 401, 427, 433, 434)

[611] R. Contino, A. Falkowski, F. Goertz, C. Grojean, and F. Riva, *On the Validity of the Effective Field Theory Approach to SM Precision Tests*, JHEP **07** (2016) 144, arXiv:1604.06444 [hep-ph]. (285, 306, 311, 419)

[612] A. Biekötter, A. Knochel, M. Krämer, D. Liu, and F. Riva, *Vices and virtues of Higgs effective field theories at large energy*, Phys. Rev. **D91** (2015) 055029, arXiv:1406.7320 [hep-ph]. (285, 307, 308, 309, 337)

[613] S. Weinberg, *Baryon and Lepton Nonconserving Processes*, Phys. Rev. Lett. **43** (1979) 1566–1570. (285, 314)

[614] B. Grzadkowski, M. Iskrzynski, M. Misiak, and J. Rosiek, *Dimension-Six Terms in the Standard Model Lagrangian*, JHEP **10** (2010) 085, arXiv:1008.4884 [hep-ph]. (285, 287, 289, 302, 314, 316, 317, 319, 346, 383, 391, 392, 425)

[615] L. Lehman, *Extending the Standard Model Effective Field Theory with the Complete Set of*

Dimension-7 Operators, Phys. Rev. **D90** (2014) 125023, arXiv:1410.4193 [hep-ph]. (285, 314, 335)

[616] B. Henning, X. Lu, T. Melia, and H. Murayama, *2, 84, 30, 993, 560, 15456, 11962, 261485, ...: Higher dimension operators in the SM EFT*, arXiv:1512.03433 [hep-ph]. (285, 314, 335)

[617] L. Lehman and A. Martin, *Low-derivative operators of the Standard Model effective field theory via Hilbert series methods*, JHEP **02** (2016) 081, arXiv:1510.00372 [hep-ph]. (285, 335)

[618] A. de Gouvea, J. Herrero-Garcia, and A. Kobach, *Neutrino Masses, Grand Unification, and Baryon Number Violation*, Phys. Rev. **D90** (2014) 016011, arXiv:1404.4057 [hep-ph]. (285)

[619] F. F. Deppisch, J. Harz, M. Hirsch, W.-C. Huang, and H. Päs, *Falsifying High-Scale Baryogenesis with Neutrinoless Double Beta Decay and Lepton Flavor Violation*, Phys. Rev. **D92** (2015) 036005, arXiv:1503.04825 [hep-ph]. (285)

[620] W. Buchmuller and D. Wyler, *Effective Lagrangian Analysis of New Interactions and Flavor Conservation*, Nucl. Phys. **B268** (1986) 621–653. (286, 314, 316, 346, 355, 389)

[621] A. Falkowski, *Higgs Basis: Proposal for an EFT basis choice for LHC HXSWG*, LHCHXSWG-INT-2015-001, 2015. (287, 288, 290, 291, 297, 302, 304)

[622] P. Artoisenet, P. de Aquino, F. Demartin, R. Frederix, S. Frixione, et al., *A framework for Higgs characterisation*, JHEP **11** (2013) 043, arXiv:1306.6464 [hep-ph]. (290, 304, 335, 382)

[623] A. Pomarol and F. Riva, *Towards the Ultimate SM Fit to Close in on Higgs Physics*, JHEP **01** (2014) 151, arXiv:1308.2803 [hep-ph]. (293, 301, 312, 326)

[624] T. Corbett, O. J. P. Éboli, J. Gonzalez-Fraile, and M. C. Gonzalez-Garcia, *Determining Triple Gauge Boson Couplings from Higgs Data*, Phys. Rev. Lett. **111** (2013) 011801, arXiv:1304.1151 [hep-ph]. (293)

[625] J. Ellis, V. Sanz, and T. You, *The Effective Standard Model after LHC Run I*, JHEP **03** (2015) 157, arXiv:1410.7703 [hep-ph]. (293, 301, 360)

[626] A. Falkowski, M. Gonzalez-Alonso, A. Greljo, and D. Marzocca, *Global constraints on anomalous triple gauge couplings in effective field theory approach*, Phys. Rev. Lett. **116** (2016) 011801, arXiv:1508.00581 [hep-ph]. (293, 302, 312)

[627] A. Butter, O. J. P. Éboli, J. Gonzalez-Fraile, M. C. Gonzalez-Garcia, T. Plehn, and M. Rauch, *The Gauge-Higgs Legacy of the LHC Run I*, JHEP **07** (2016) 152, arXiv:1604.03105 [hep-ph]. (293, 312, 360)

[628] K. Hagiwara, S. Ishihara, R. Szalapski, and D. Zeppenfeld, *Low-energy effects of new interactions in the electroweak boson sector*, Phys. Rev. **D48** (1993) 2182–2203. (293, 302, 329, 358, 389)

[629] R. Contino, C. Grojean, M. Moretti, F. Piccinini, and R. Rattazzi, *Strong Double Higgs Production at the LHC*, JHEP **05** (2010) 089, arXiv:1002.1011 [hep-ph]. (295, 347, 354)

[630] R. S. Gupta, A. Pomarol, and F. Riva, *BSM Primary Effects*, Phys. Rev. **D91** (2015) 035001, arXiv:1405.0181 [hep-ph]. (297, 392)

[631] R. Alonso, E. E. Jenkins, A. V. Manohar, and M. Trott, *Renormalization Group Evolution of the Standard Model Dimension Six Operators III: Gauge Coupling Dependence and Phenomenology*, JHEP **04** (2014) 159, arXiv:1312.2014 [hep-ph]. (298, 301, 303, 314, 317, 318, 324, 332, 335, 337, 394)

[632] A. Falkowski and F. Riva, *Model-independent precision constraints on dimension-6 operators*, JHEP **02** (2015) 039, arXiv:1411.0669 [hep-ph]. (301, 312)

[633] L. Berthier and M. Trott, *Consistent constraints on the Standard Model Effective Field Theory*, JHEP **02** (2016) 069, arXiv:1508.05060 [hep-ph]. (301, 326, 327, 328, 329, 330, 331)

[634] A. Efrati, A. Falkowski, and Y. Soreq, *Electroweak constraints on flavorful effective theories*,

JHEP **07** (2015) 018, arXiv:1503.07872 [hep-ph]. (301)

[635] J. Brod, U. Haisch, and J. Zupan, *Constraints on CP-violating Higgs couplings to the third generation*, JHEP **11** (2013) 180, arXiv:1310.1385 [hep-ph]. (302, 625, 631)

[636] W. Altmannshofer, J. Brod, and M. Schmaltz, *Experimental constraints on the coupling of the Higgs boson to electrons*, JHEP **05** (2015) 125, arXiv:1503.04830 [hep-ph]. (302, 631, 639)

[637] Y. T. Chien, V. Cirigliano, W. Dekens, J. de Vries, and E. Mereghetti, *Direct and indirect constraints on CP-violating Higgs-quark and Higgs-gluon interactions*, JHEP **02** (2016) 011, arXiv:1510.00725 [hep-ph]. (302, 631)

[638] V. Cirigliano, W. Dekens, J. de Vries, and E. Mereghetti, *Is there room for CP violation in the top-Higgs sector?*, Phys. Rev. **D94** (2016) 016002, arXiv:1603.03049 [hep-ph]. (302)

[639] A. Falkowski, B. Fuks, K. Mawatari, K. Mimasu, F. Riva, and V. sanz, *Rosetta: an operator basis translator for Standard Model effective field theory*, Eur. Phys. J. **C75** (2015) 583, arXiv:1508.05895 [hep-ph]. (302, 304, 383, 393, 394)

[640] J. Elias-Miró, J. R. Espinosa, E. Masso, and A. Pomarol, *Renormalization of dimension-six operators relevant for the Higgs decays $h \to \gamma\gamma, \gamma Z$*, JHEP **08** (2013) 033, arXiv:1302.5661 [hep-ph]. (303)

[641] J. Elias-Miró, J. R. Espinosa, E. Masso, and A. Pomarol, *Higgs windows to new physics through d=6 operators: constraints and one-loop anomalous dimensions*, JHEP **11** (2013) 066, arXiv:1308.1879 [hep-ph]. (303, 335)

[642] R. Contino, M. Ghezzi, C. Grojean, M. Mühlleitner, and M. Spira, *eHDECAY: an Implementation of the Higgs Effective Lagrangian into HDECAY*, Comput. Phys. Commun. **185** (2014) 3412–3423, arXiv:1403.3381 [hep-ph]. (303, 378)

[643] M. Grazzini, A. Ilnicka, M. Spira, and M. Wiesemann, *BSM effects on the Higgs transverse-momentum spectrum in an EFT approach*, in *Proceedings, 2015 European Physical Society Conference on High Energy Physics (EPS-HEP 2015): Vienna, Austria, July 22-29, 2015*, p. 144. 2015. arXiv:1511.08059 [hep-ph]. (303)

[644] K. Mimasu, V. Sanz, and C. Williams, *Higher Order QCD predictions for Associated Higgs production with anomalous couplings to gauge bosons*, JHEP **08** (2016) 039, arXiv:1512.02572 [hep-ph]. (303, 335, 472, 473)

[645] C. Grojean, E. E. Jenkins, A. V. Manohar, and M. Trott, *Renormalization Group Scaling of Higgs Operators and $\Gamma(h \to \gamma\gamma)$*, JHEP **04** (2013) 016, arXiv:1301.2588 [hep-ph]. (303, 318, 329, 332, 335)

[646] E. E. Jenkins, A. V. Manohar, and M. Trott, *Renormalization Group Evolution of the Standard Model Dimension Six Operators I: Formalism and lambda Dependence*, JHEP **10** (2013) 087, arXiv:1308.2627 [hep-ph]. (303, 318, 329, 332, 335, 394)

[647] E. E. Jenkins, A. V. Manohar, and M. Trott, *Renormalization Group Evolution of the Standard Model Dimension Six Operators II: Yukawa Dependence*, JHEP **01** (2014) 035, arXiv:1310.4838 [hep-ph]. (303, 318, 332, 335, 394)

[648] M. Ghezzi, R. Gomez-Ambrosio, G. Passarino, and S. Uccirati, *NLO Higgs effective field theory and κ-framework*, JHEP **07** (2015) 175, arXiv:1505.03706 [hep-ph]. (303, 329, 331, 332, 335, 337, 401, 426)

[649] C. Hartmann and M. Trott, *Higgs Decay to Two Photons at One Loop in the Standard Model Effective Field Theory*, Phys. Rev. Lett. **115** (2015) 191801, arXiv:1507.03568 [hep-ph]. (303, 329, 335, 426)

[650] R. Gauld, B. D. Pecjak, and D. J. Scott, *One-loop corrections to $h \to b\bar{b}$ and $h \to \tau\bar{\tau}$ decays in the Standard Model Dimension-6 EFT: four-fermion operators and the large-m_t limit*, JHEP **05** (2016) 080, arXiv:1512.02508 [hep-ph]. (303, 329, 332, 335)

[651] M. Gonzalez-Alonso, A. Greljo, G. Isidori, and D. Marzocca, *Pseudo-observables in Higgs decays*, Eur. Phys. J. **C75** (2015) 128, arXiv:1412.6038 [hep-ph]. (303, 332, 338, 380, 381, 382, 401, 406, 407, 422)

[652] A. Greljo, G. Isidori, J. M. Lindert, and D. Marzocca, *Pseudo-observables in electroweak Higgs production*, Eur. Phys. J. **C76** (2016) 158, arXiv:1512.06135 [hep-ph]. (303, 380, 381, 382, 401, 412, 415, 416, 417, 418, 419, 422)

[653] G. F. Giudice, C. Grojean, A. Pomarol, and R. Rattazzi, *The Strongly-Interacting Light Higgs*, JHEP **06** (2007) 045, arXiv:hep-ph/0703164 [hep-ph]. (304, 307, 309, 343, 348, 375, 378, 383, 392)

[654] A. Manohar and H. Georgi, *Chiral Quarks and the Nonrelativistic Quark Model*, Nucl. Phys. **B234** (1984) 189. (304, 307, 316, 317, 606)

[655] S. Weinberg, *The Quantum theory of fields, Vol. 1: Foundations*. Cambridge University Press, UK, 609 p, 2005. (306)

[656] D. Racco, A. Wulzer, and F. Zwirner, *Robust collider limits on heavy-mediator Dark Matter*, JHEP **05** (2015) 009, arXiv:1502.04701 [hep-ph]. (307)

[657] A. G. Cohen, D. B. Kaplan, and A. E. Nelson, *Counting 4 pis in strongly coupled supersymmetry*, Phys. Lett. **B412** (1997) 301–308, arXiv:hep-ph/9706275 [hep-ph]. (307, 316, 317)

[658] K. Agashe, R. Contino, and A. Pomarol, *The Minimal composite Higgs model*, Nucl. Phys. **B719** (2005) 165–187, arXiv:hep-ph/0412089 [hep-ph]. (307, 342, 343, 378)

[659] J. A. Dror, M. Farina, E. Salvioni, and J. Serra, *Strong tW Scattering at the LHC*, JHEP **01** (2016) 071, arXiv:1511.03674 [hep-ph]. (308)

[660] O. Bessidskaia Bylund, F. Maltoni, I. Tsinikos, E. Vryonidou, and C. Zhang, *Probing top quark neutral couplings in the Standard Model Effective Field Theory at NLO in QCD*, JHEP **05** (2016) 052, arXiv:1601.08193 [hep-ph]. (308)

[661] A. Biekötter, J. Brehmer, and T. Plehn, *Extending the limits of Higgs effective theory*, Phys. Rev. **D94** (2016) 055032, arXiv:1602.05202 [hep-ph]. (308, 368, 472, 474)

[662] O. Domenech, A. Pomarol, and J. Serra, *Probing the SM with Dijets at the LHC*, Phys. Rev. **D85** (2012) 074030, arXiv:1201.6510 [hep-ph]. (308)

[663] G. Durieux, F. Maltoni, and C. Zhang, *Global approach to top-quark flavor-changing interactions*, Phys. Rev. **D91** (2015) 074017, arXiv:1412.7166 [hep-ph]. (308)

[664] R. Barbieri, B. Bellazzini, V. S. Rychkov, and A. Varagnolo, *The Higgs boson from an extended symmetry*, Phys. Rev. **D76** (2007) 115008, arXiv:0706.0432 [hep-ph]. (308)

[665] J. Elias-Miró, C. Grojean, R. S. Gupta, and D. Marzocca, *Scaling and tuning of EW and Higgs observables*, JHEP **05** (2014) 019, arXiv:1312.2928 [hep-ph]. (308, 335)

[666] B. Henning, X. Lu, and H. Murayama, *What do precision Higgs measurements buy us?*, arXiv:1404.1058 [hep-ph]. (308)

[667] D. Liu, A. Pomarol, R. Rattazzi, and F. Riva, *Patterns of Strong Coupling for LHC Searches*, arXiv:1603.03064 [hep-ph]. (309)

[668] I. Low, R. Rattazzi, and A. Vichi, *Theoretical Constraints on the Higgs Effective Couplings*, JHEP **04** (2010) 126, arXiv:0907.5413 [hep-ph]. (309)

[669] J. de Blas, J. M. Lizana, and M. Perez-Victoria, *Combining searches of Z' and W' bosons*, JHEP **01** (2013) 166, arXiv:1211.2229 [hep-ph]. (309)

[670] D. Pappadopulo, A. Thamm, R. Torre, and A. Wulzer, *Heavy Vector Triplets: Bridging Theory and Data*, JHEP **09** (2014) 060, arXiv:1402.4431 [hep-ph]. (309)

[671] S. Weinberg, *Effective Gauge Theories*, Phys. Lett. **B91** (1980) 51–55. (313, 316, 317)

[672] S. R. Coleman, J. Wess, and B. Zumino, *Structure of phenomenological Lagrangians. 1.*, Phys.

Rev. **177** (1969) 2239–2247. (313, 316, 317)

[673] C. G. Callan, Jr., S. R. Coleman, J. Wess, and B. Zumino, *Structure of phenomenological Lagrangians. 2.*, Phys. Rev. **177** (1969) 2247–2250. (313, 316, 317)

[674] L. F. Abbott and M. B. Wise, *The Effective Hamiltonian for Nucleon Decay*, Phys. Rev. **D22** (1980) 2208. (314)

[675] H. Georgi, *Effective field theory*, Ann. Rev. Nucl. Part. Sci. **43** (1993) 209–252. (316, 317)

[676] D. B. Kaplan, *Effective field theories*, in *Beyond the standard model 5. Proceedings, 5th Conference, Balholm, Norway, April 29-May 4, 1997*. 1995. arXiv:nucl-th/9506035 [nucl-th]. (316, 317)

[677] M. A. Luty, *Naive dimensional analysis and supersymmetry*, Phys. Rev. **D57** (1998) 1531–1538, arXiv:hep-ph/9706235 [hep-ph]. (316, 317)

[678] J. Polchinski, *Effective field theory and the Fermi surface*, in *Theoretical Advanced Study Institute (TASI 92): From Black Holes and Strings to Particles* . Boulder, Colorado, USA, June 3–28, 1992. arXiv:hep-th/9210046 [hep-th]. (316, 317)

[679] W. Skiba, *Effective Field Theory and Precision Electroweak Measurements*, in *Physics of the large and the small, TASI 09, proceedings of the Theoretical Advanced Study Institute in Elementary Particle Physics*, pp. 5–70. Boulder, Colorado, USA, 1–26 June, 2009. arXiv:1006.2142 [hep-ph]. (316, 317)

[680] E. E. Jenkins, A. V. Manohar, and M. Trott, *On Gauge Invariance and Minimal Coupling*, JHEP **09** (2013) 063, arXiv:1305.0017 [hep-ph]. (316, 317)

[681] E. E. Jenkins, A. V. Manohar, and M. Trott, *Naive Dimensional Analysis Counting of Gauge Theory Amplitudes and Anomalous Dimensions*, Phys. Lett. **B726** (2013) 697–702, arXiv:1309.0819 [hep-ph]. (316, 317)

[682] G. Buchalla, O. Catá, and C. Krause, *A Systematic Approach to the SILH Lagrangian*, Nucl. Phys. **B894** (2015) 602–620, arXiv:1412.6356 [hep-ph]. (316, 317, 346, 347, 348)

[683] G. Buchalla, O. Catá, and C. Krause, *On the Power Counting in Effective Field Theories*, Phys. Lett. **B731** (2014) 80–86, arXiv:1312.5624 [hep-ph]. (316, 317, 342, 343)

[684] B. M. Gavela, E. E. Jenkins, A. V. Manohar, and L. Merlo, *Analysis of General Power Counting Rules in Effective Field Theory*, Eur. Phys. J. **C76** (2016) 485, arXiv:1601.07551 [hep-ph]. (316, 317)

[685] C. Arzt, M. B. Einhorn, and J. Wudka, *Patterns of deviation from the standard model*, Nucl. Phys. **B433** (1995) 41–66, arXiv:hep-ph/9405214 [hep-ph]. (316, 337, 424)

[686] M. B. Einhorn and J. Wudka, *The Bases of Effective Field Theories*, Nucl. Phys. **B876** (2013) 556–574, arXiv:1307.0478 [hep-ph]. (316, 337, 424)

[687] G. Panico and A. Wulzer, *The Composite Nambu-Goldstone Higgs*, Lect. Notes Phys. **913** (2016) pp.1–316, arXiv:1506.01961 [hep-ph]. (316, 636)

[688] R. E. Kallosh and I. V. Tyutin, *The Equivalence theorem and gauge invariance in renormalizable theories*, Yad. Fiz. **17** (1973) 190–209. [Sov. J. Nucl. Phys. **17** (1973) 98]. (317)

[689] G. 't Hooft and M. J. G. Veltman, *Combinatorics of gauge fields*, Nucl. Phys. **B50** (1972) 318–353. (317, 331)

[690] H. D. Politzer, *Power Corrections at Short Distances*, Nucl. Phys. **B172** (1980) 349–382. (317)

[691] G. Sanchez-Colon and J. Wudka, *Effective operator contributions to the oblique parameters*, Phys. Lett. **B432** (1998) 383–389, arXiv:hep-ph/9805366 [hep-ph]. (317)

[692] W. Kilian and J. Reuter, *The Low-energy structure of little Higgs models*, Phys. Rev. **D70** (2004) 015004, arXiv:hep-ph/0311095 [hep-ph]. (317)

[693] C. Grojean, W. Skiba, and J. Terning, *Disguising the oblique parameters*, Phys. Rev. **D73** (2006) 075008, arXiv:hep-ph/0602154 [hep-ph]. (317)

[694] M. Trott, *On the consistent use of Constructed Observables*, JHEP **02** (2015) 046, arXiv:1409.7605 [hep-ph]. (317, 426)

[695] B. Grinstein and M. B. Wise, *Operator analysis for precision electroweak physics*, Phys. Lett. **B265** (1991) 326–334. (321, 326)

[696] A. V. Manohar and M. B. Wise, *Modifications to the properties of the Higgs boson*, Phys. Lett. **B636** (2006) 107–113, arXiv:hep-ph/0601212 [hep-ph]. (322)

[697] R. S. Chivukula and H. Georgi, *Composite Technicolor Standard Model*, Phys. Lett. **B188** (1987) 99. (324, 325, 631)

[698] G. D'Ambrosio, G. F. Giudice, G. Isidori, and A. Strumia, *Minimal flavor violation: An Effective field theory approach*, Nucl. Phys. **B645** (2002) 155–187, arXiv:hep-ph/0207036 [hep-ph]. (324, 325, 394, 631)

[699] V. Cirigliano, B. Grinstein, G. Isidori, and M. B. Wise, *Minimal flavor violation in the lepton sector*, Nucl. Phys. **B728** (2005) 121–134, arXiv:hep-ph/0507001 [hep-ph]. (324, 325, 632)

[700] T. van Ritbergen and R. G. Stuart, *On the precise determination of the Fermi coupling constant from the muon lifetime*, Nucl. Phys. **B564** (2000) 343–390, arXiv:hep-ph/9904240 [hep-ph]. (325)

[701] Z. Han and W. Skiba, *Effective theory analysis of precision electroweak data*, Phys. Rev. **D71** (2005) 075009, arXiv:hep-ph/0412166 [hep-ph]. (326)

[702] C. P. Burgess, S. Godfrey, H. Konig, D. London, and I. Maksymyk, *Model independent global constraints on new physics*, Phys. Rev. **D49** (1994) 6115–6147, arXiv:hep-ph/9312291 [hep-ph]. (326)

[703] P. Bamert, C. P. Burgess, J. M. Cline, D. London, and E. Nardi, *R(b) and new physics: A Comprehensive analysis*, Phys. Rev. **D54** (1996) 4275–4300, arXiv:hep-ph/9602438 [hep-ph]. (326)

[704] C. P. Burgess, S. Godfrey, H. Konig, D. London, and I. Maksymyk, *Bounding anomalous gauge boson couplings*, Phys. Rev. **D50** (1994) 7011–7024, arXiv:hep-ph/9307223 [hep-ph]. (326)

[705] L. Berthier and M. Trott, *Towards consistent Electroweak Precision Data constraints in the SMEFT*, JHEP **05** (2015) 024, arXiv:1502.02570 [hep-ph]. (326, 327, 328, 329, 330, 331, 426)

[706] D. Yu. Bardin, M. Grunewald, and G. Passarino, *Precision calculation project report*, arXiv:hep-ph/9902452 [hep-ph]. (328, 401, 425)

[707] A. V. Manohar and P. Ruiz-Femenía, *The Orthopositronium decay spectrum using NRQED*, Phys. Rev. **D69** (2004) 053003, arXiv:hep-ph/0311002 [hep-ph]. (328)

[708] W. E. Caswell and G. P. Lepage, *Effective Lagrangians for Bound State Problems in QED, QCD, and Other Field Theories*, Phys. Lett. **B167** (1986) 437–442. (328)

[709] G. T. Bodwin, E. Braaten, and G. P. Lepage, *Rigorous QCD analysis of inclusive annihilation and production of heavy quarkonium*, Phys. Rev. **D51** (1995) 1125–1171, arXiv:hep-ph/9407339 [hep-ph]. [Erratum-ibid. **D55** (1997) 5853]. (328, 624)

[710] M. E. Luke, A. V. Manohar, and I. Z. Rothstein, *Renormalization group scaling in nonrelativistic QCD*, Phys. Rev. **D61** (2000) 074025, arXiv:hep-ph/9910209 [hep-ph]. (328)

[711] A. Pineda and J. Soto, *Potential NRQED: The Positronium case*, Phys. Rev. **D59** (1999) 016005, arXiv:hep-ph/9805424 [hep-ph]. (328)

[712] B. Grinstein and I. Z. Rothstein, *Effective field theory and matching in nonrelativistic gauge theories*, Phys. Rev. **D57** (1998) 78–82, arXiv:hep-ph/9703298 [hep-ph]. (328)

[713] C. Englert and M. Spannowsky, *Effective Theories and Measurements at Colliders*, Phys. Lett. **B740** (2015) 8–15, arXiv:1408.5147 [hep-ph]. (329)

[714] K. Hagiwara, R. Szalapski, and D. Zeppenfeld, *Anomalous Higgs boson production and decay*, Phys. Lett. **B318** (1993) 155–162, arXiv:hep-ph/9308347 [hep-ph]. (329, 355, 389)

[715] S. Alam, S. Dawson, and R. Szalapski, *Low-energy constraints on new physics revisited*, Phys. Rev. **D57** (1998) 1577–1590, arXiv:hep-ph/9706542 [hep-ph]. (329)

[716] G. Passarino, *NLO Inspired Effective Lagrangians for Higgs Physics*, Nucl. Phys. **B868** (2013) 416–458, arXiv:1209.5538 [hep-ph]. (329, 331, 332, 335, 426)

[717] J. D. Wells and Z. Zhang, *Renormalization group evolution of the universal theories EFT*, JHEP **06** (2016) 122, arXiv:1512.03056 [hep-ph]. (329, 335)

[718] C. Hartmann and M. Trott, *On one-loop corrections in the standard model effective field theory; the $\Gamma(h \to \gamma\gamma)$ case*, JHEP **07** (2015) 151, arXiv:1505.02646 [hep-ph]. (329, 335, 426)

[719] D. Hanneke, S. Fogwell, and G. Gabrielse, *New Measurement of the Electron Magnetic Moment and the Fine Structure Constant*, Phys. Rev. Lett. **100** (2008) 120801, arXiv:0801.1134 [physics.atom-ph]. (329, 330)

[720] A. Wicht, J. M. Hensley, E. Sarajlic, and S. Chu, *A Preliminary Measurement of the Fine Structure Constant Based on Atom Interferometry*, Physica Scripta **T102** (2002) 82–88. (329)

[721] SLD Electroweak Group, DELPHI, ALEPH, SLD, SLD Heavy Flavour Group, OPAL, LEP Electroweak Working Group, L3 Collaboration, S. Schael et al., *Precision electroweak measurements on the Z resonance*, Phys. Rept. **427** (2006) 257–454, arXiv:hep-ex/0509008 [hep-ex]. (330, 341, 407)

[722] P. J. Mohr, B. N. Taylor, and D. B. Newell, *CODATA Recommended Values of the Fundamental Physical Constants: 2010*, Rev. Mod. Phys. **84** (2012) 1527–1605, arXiv:1203.5425 [physics.atom-ph]. (330)

[723] R. Bouchendira, P. Clade, S. Guellati-Khelifa, F. Nez, and F. Biraben, *New determination of the fine structure constant and test of the quantum electrodynamics*, Phys. Rev. Lett. **106** (2011) 080801, arXiv:1012.3627 [physics.atom-ph]. (330)

[724] CMS Collaboration, *Projected Performance of an Upgraded CMS Detector at the LHC and HL-LHC: Contribution to the Snowmass Process*, in *Proceedings, Community Summer Study 2013: Snowmass on the Mississippi (CSS2013)*. Minneapolis, MN, USA, July 29 – August 6, 2013. arXiv:1307.7135. (331, 336, 341)

[725] ATLAS, CMS Collaboration, M. Flechl, *Higgs physics: Review of recent results and prospects from ATLAS and CMS*, in *Proceedings, 4th Symposium on Prospects in the Physics of Discrete Symmetries (DISCRETE 2014): London, UK, December 2-6, 2014*, vol. 631, p. 012028. 2015. arXiv:1503.00632 [hep-ex]. (331, 336)

[726] G. 't Hooft and M. J. G. Veltman, *Regularization and Renormalization of Gauge Fields*, Nucl. Phys. **B44** (1972) 189–213. (331)

[727] P. A. Grassi, B. A. Kniehl, and A. Sirlin, *Width and partial widths of unstable particles*, Phys. Rev. Lett. **86** (2001) 389–392, arXiv:hep-th/0005149 [hep-th]. (332, 427)

[728] B. A. Kniehl and A. Sirlin, *On the field renormalization constant for unstable particles*, Phys. Lett. **B530** (2002) 129–132, arXiv:hep-ph/0110296 [hep-ph]. (332)

[729] S. Goria, G. Passarino, and D. Rosco, *The Higgs Boson Lineshape*, Nucl. Phys. **B864** (2012) 530–579, arXiv:1112.5517 [hep-ph]. (332, 427, 430, 434)

[730] P. A. Grassi, B. A. Kniehl, and A. Sirlin, *Width and partial widths of unstable particles in the light of the Nielsen identities*, Phys. Rev. **D65** (2002) 085001, arXiv:hep-ph/0109228 [hep-ph]. (332)

[731] G. Passarino, C. Sturm, and S. Uccirati, *Higgs Pseudo-Observables, Second Riemann Sheet and*

All That, Nucl. Phys. **B834** (2010) 77–115, arXiv:1001.3360 [hep-ph]. (332, 338, 401)

[732] H. A. Weldon, *The Description of Unstable Particles in Quantum Field Theory*, Phys. Rev. **D14** (1976) 2030. (332, 427)

[733] J. C. Ward, *An Identity in Quantum Electrodynamics*, Phys. Rev. **78** (1950) 182. (332)

[734] A. A. Slavnov, *Ward Identities in Gauge Theories*, Theor. Math. Phys. **10** (1972) 99–107. [Teor. Mat. Fiz. **10** (1972) 153]. (332)

[735] J. C. Taylor, *Ward Identities and Charge Renormalization of the Yang-Mills Field*, Nucl. Phys. **B33** (1971) 436–444. (332)

[736] A. Denner, G. Weiglein, and S. Dittmaier, *Application of the background field method to the electroweak standard model*, Nucl. Phys. **B440** (1995) 95–128, arXiv:hep-ph/9410338 [hep-ph]. (333, 334)

[737] A. Denner, *Techniques for calculation of electroweak radiative corrections at the one loop level and results for W physics at LEP-200*, Fortsch. Phys. **41** (1993) 307–420, arXiv:0709.1075 [hep-ph]. (333)

[738] M. E. Peskin and T. Takeuchi, *A New constraint on a strongly interacting Higgs sector*, Phys. Rev. Lett. **65** (1990) 964–967. (334, 344)

[739] G. Leibbrandt, *Introduction to Noncovariant Gauges*, Rev. Mod. Phys. **59** (1987) 1067. (334)

[740] B. S. DeWitt, *Quantum Theory of Gravity. 2. The Manifestly Covariant Theory*, Phys. Rev. **162** (1967) 1195–1239. (334)

[741] L. F. Abbott, *Introduction to the Background Field Method*, Acta Phys. Polon. **B13** (1982) 33. (334)

[742] M. B. Einhorn and J. Wudka, *Screening of Heavy Higgs Radiative Effects*, Phys. Rev. **D39** (1989) 2758. (334)

[743] J. de Blas, M. Chala, and J. Santiago, *Renormalization Group Constraints on New Top Interactions from Electroweak Precision Data*, JHEP **09** (2015) 189, arXiv:1507.00757 [hep-ph]. (335)

[744] O. Cheyette, *Derivative Expansion of the Effective Action*, Phys. Rev. Lett. **55** (1985) 2394. (335)

[745] O. Cheyette, *Effective Action for the Standard Model With Large Higgs Mass*, Nucl. Phys. **B297** (1988) 183–204. (335)

[746] M. K. Gaillard, *The Effective One Loop Lagrangian With Derivative Couplings*, Nucl. Phys. **B268** (1986) 669–692. (335)

[747] A. Drozd, J. Ellis, J. Quevillon, and T. You, *Comparing EFT and Exact One-Loop Analyses of Non-Degenerate Stops*, JHEP **06** (2015) 028, arXiv:1504.02409 [hep-ph]. (335)

[748] A. Drozd, J. Ellis, J. Quevillon, and T. You, *The Universal One-Loop Effective Action*, JHEP **03** (2016) 180, arXiv:1512.03003 [hep-ph]. (335)

[749] J. Brehmer, A. Freitas, D. Lopez-Val, and T. Plehn, *Pushing Higgs Effective Theory to its Limits*, Phys. Rev. **D93** (2016) 075014, arXiv:1510.03443 [hep-ph]. (335, 361, 363, 364, 365, 366, 367, 368)

[750] F. del Aguila, Z. Kunszt, and J. Santiago, *One-loop effective lagrangians after matching*, Eur. Phys. J. **C76** (2016) 244, arXiv:1602.00126 [hep-ph]. (335)

[751] L. Lehman and A. Martin, *Hilbert Series for Constructing Lagrangians: expanding the phenomenologist's toolbox*, Phys. Rev. **D91** (2015) 105014, arXiv:1503.07537 [hep-ph]. (335)

[752] B. Henning, X. Lu, T. Melia, and H. Murayama, *Hilbert series and operator bases with derivatives in effective field theories*, Commun. Math. Phys. **347** (2016) 363–388, arXiv:1507.07240 [hep-th]. (335)

[753] G. M. Pruna and A. Signer, *The $\mu \to e\gamma$ decay in a systematic effective field theory approach with dimension 6 operators*, JHEP **10** (2014) 014, arXiv:1408.3565 [hep-ph]. (335)

[754] ATLAS Collaboration, G. Aad et al., *Measurements of the Higgs boson production and decay rates and coupling strengths using pp collision data at $\sqrt{s} = 7$ and 8 TeV in the ATLAS experiment*, Eur. Phys. J. **C76** (2016) 6, arXiv:1507.04548 [hep-ex]. (335, 492, 496, 626, 639)

[755] CMS Collaboration, V. Khachatryan et al., *Precise determination of the mass of the Higgs boson and tests of compatibility of its couplings with the standard model predictions using proton collisions at 7 and 8 TeV*, Eur. Phys. J. **C75** (2015) 212, arXiv:1412.8662 [hep-ex]. (336, 492, 496, 626)

[756] S. Dawson et al., *Working Group Report: Higgs Boson*, in *Proceedings, Community Summer Study 2013: Snowmass on the Mississippi (CSS2013): Minneapolis, MN, USA, July 29-August 6, 2013*. 2013. arXiv:1310.8361 [hep-ex]. (336)

[757] C. Englert, M. McCullough, and M. Spannowsky, *Combining LEP and LHC to bound the Higgs Width*, Nucl. Phys. **B902** (2016) 440–457, arXiv:1504.02458 [hep-ph]. (336, 425)

[758] C. Englert, I. Low, and M. Spannowsky, *On-shell interference effects in Higgs boson final states*, Phys. Rev. **D91** (2015) 074029, arXiv:1502.04678 [hep-ph]. (336)

[759] M. Ghezzi, G. Passarino, and S. Uccirati, *Bounding the Higgs Width Using Effective Field Theory*, in *Proceedings, 12th DESY Workshop on Elementary Particle Physics: Loops and Legs in Quantum Field Theory (LL2014)*, vol. LL2014, p. 072. 2014. arXiv:1405.1925 [hep-ph]. (336, 425)

[760] A. Azatov, R. Contino, and J. Galloway, *Model-Independent Bounds on a Light Higgs*, JHEP **04** (2012) 127, arXiv:1202.3415 [hep-ph]. [Erratum-ibid. **04** (2013) 140]. (336)

[761] J. R. Espinosa, C. Grojean, M. Mühlleitner, and M. Trott, *Fingerprinting Higgs Suspects at the LHC*, JHEP **05** (2012) 097, arXiv:1202.3697 [hep-ph]. (336)

[762] D. Carmi, A. Falkowski, E. Kuflik, and T. Volansky, *Interpreting LHC Higgs Results from Natural New Physics Perspective*, JHEP **07** (2012) 136, arXiv:1202.3144 [hep-ph]. (336)

[763] J. Ellis, D. S. Hwang, V. Sanz, and T. You, *A Fast Track towards the 'Higgs' Spin and Parity*, JHEP **11** (2012) 134, arXiv:1208.6002 [hep-ph]. (337, 472)

[764] G. Isidori and M. Trott, *Higgs form factors in Associated Production*, JHEP **02** (2014) 082, arXiv:1307.4051 [hep-ph]. (337, 338, 352)

[765] G. Isidori, A. V. Manohar, and M. Trott, *Probing the nature of the Higgs-like Boson via $h \to V\mathcal{F}$ decays*, Phys. Lett. **B728** (2014) 131–135, arXiv:1305.0663 [hep-ph]. (338, 627)

[766] D. B. Kaplan and H. Georgi, *SU(2) x U(1) breaking by vacuum misalignment*, Phys. Lett. **B136** (1984) 183. (342, 631, 636)

[767] D. B. Kaplan, H. Georgi, and S. Dimopoulos, *Composite Higgs Scalars*, Phys. Lett. **B136** (1984) 187. (342, 631, 636)

[768] T. Banks, *Constraints on $SU_2 \times U_1$ breaking by vacuum misalignment*, Nucl. Phys. **B243** (1984) 125–130. (342)

[769] M. J. Dugan, H. Georgi, and D. B. Kaplan, *Anatomy of a Composite Higgs Model*, Nucl. Phys. **B254** (1985) 299. (342, 631, 636)

[770] R. Contino, L. Da Rold, and A. Pomarol, *Light custodians in natural composite Higgs models*, Phys. Rev. **D75** (2007) 055014, arXiv:hep-ph/0612048 [hep-ph]. (342, 343, 378)

[771] R. Contino, *The Higgs as a Composite Nambu-Goldstone Boson*, in *Physics of the large and the small, TASI 09, proceedings of the Theoretical Advanced Study Institute in Elementary Particle Physics*, pp. 235–306. Boulder, Colorado, USA, June 1–26, 2009. arXiv:1005.4269 [hep-ph]. (342, 343)

[772] A. Falkowski, *Pseudo-goldstone Higgs production via gluon fusion*, Phys. Rev. **D77** (2008) 055018, arXiv:0711.0828 [hep-ph]. (342, 343)

[773] M. Carena, L. Da Rold, and E. Pontón, *Minimal Composite Higgs Models at the LHC*, JHEP **06** (2014) 159, arXiv:1402.2987 [hep-ph]. (342, 343)

[774] R. Alonso, I. Brivio, B. Gavela, L. Merlo, and S. Rigolin, *Sigma Decomposition*, JHEP **12** (2014) 034, arXiv:1409.1589 [hep-ph]. (342)

[775] I. M. Hierro, L. Merlo, and S. Rigolin, *Sigma Decomposition: The CP-Odd Lagrangian*, JHEP **04** (2016) 016, arXiv:1510.07899 [hep-ph]. (342)

[776] S. Weinberg, *Phenomenological Lagrangians*, Physica **A96** (1979) 327–340. (342, 346)

[777] T. Appelquist and C. W. Bernard, *Strongly Interacting Higgs Bosons*, Phys. Rev. **D22** (1980) 200. (342)

[778] A. C. Longhitano, *Heavy Higgs Bosons in the Weinberg-Salam Model*, Phys. Rev. **D22** (1980) 1166. (342)

[779] T. Appelquist, M. J. Bowick, E. Cohler, and A. I. Hauser, *The Breaking of Isospin Symmetry in Theories With a Dynamical Higgs Mechanism*, Phys. Rev. **D31** (1985) 1676. (342)

[780] G. Cvetic and R. Kogerler, *Fermionic Couplings in an Electroweak Theory With Nonlinear Spontaneous Symmetry Breaking*, Nucl. Phys. **B328** (1989) 342–374. (342)

[781] A. Dobado and M. J. Herrero, *Phenomenological Lagrangian Approach to the Symmetry Breaking Sector of the Standard Model*, Phys. Lett. **B228** (1989) 495–502. (342)

[782] A. Dobado and M. J. Herrero, *Testing the Hypothesis of Strongly Interacting Longitudinal Weak Bosons in Electron - Positron Collisions at Tev Energies*, Phys. Lett. **B233** (1989) 505–511. (342)

[783] A. Dobado, M. J. Herrero, and T. N. Truong, *Study of the Strongly Interacting Higgs Sector*, Phys. Lett. **B235** (1990) 129. (342)

[784] A. Dobado, M. J. Herrero, and J. Terron, *The Role of Chiral Lagrangians in Strongly Interacting $W_L W_L$ Signals at pp Supercolliders*, Z. Phys. **C50** (1991) 205–219. (342)

[785] F. Feruglio, *The Chiral approach to the electroweak interactions*, Int. J. Mod. Phys. **A8** (1993) 4937–4972, arXiv:hep-ph/9301281 [hep-ph]. (342)

[786] A. Dobado, M. J. Herrero, J. R. Pelaez, E. Ruiz Morales, and M. T. Urdiales, *Learning about the strongly interacting symmetry breaking sector at LHC*, Phys. Lett. **B352** (1995) 400–410, arXiv:hep-ph/9502309 [hep-ph]. (342)

[787] A. Dobado, M. J. Herrero, J. R. Pelaez, and E. Ruiz Morales, *CERN LHC sensitivity to the resonance spectrum of a minimal strongly interacting electroweak symmetry breaking sector*, Phys. Rev. **D62** (2000) 055011, arXiv:hep-ph/9912224 [hep-ph]. (342, 344)

[788] A. Dobado, D. Espriu, and M. J. Herrero, *Chiral Lagrangians as a tool to probe the symmetry breaking sector of the SM at LEP*, Phys. Lett. **B255** (1991) 405–414. (342)

[789] D. Espriu and M. J. Herrero, *Chiral Lagrangians and precision tests of the symmetry breaking sector of the Standard Model*, Nucl. Phys. **B373** (1992) 117–168. (342)

[790] D. Espriu and J. Manzano, *CP violation and family mixing in the effective electroweak Lagrangian*, Phys. Rev. **D63** (2001) 073008, arXiv:hep-ph/0011036 [hep-ph]. (342)

[791] R. Alonso, M. B. Gavela, L. Merlo, S. Rigolin, and J. Yepes, *Minimal Flavour Violation with Strong Higgs Dynamics*, JHEP **06** (2012) 076, arXiv:1201.1511 [hep-ph]. (342)

[792] G. Buchalla and O. Catá, *Effective Theory of a Dynamically Broken Electroweak Standard Model at NLO*, JHEP **07** (2012) 101, arXiv:1203.6510 [hep-ph]. (342)

[793] G. Buchalla, O. Catá, R. Rahn, and M. Schlaffer, *Effective Field Theory Analysis of New Physics in $e^+e^- \to W^+W^-$ at a Linear Collider*, Eur. Phys. J. **C73** (2013) 2589, arXiv:1302.6481 [hep-ph]. (342)

[794] J. Bagger, V. D. Barger, K.-m. Cheung, J. F. Gunion, T. Han, G. A. Ladinsky, R. Rosenfeld, and C. P. Yuan, *The Strongly interacting WW system: Gold plated modes*, Phys. Rev. **D49** (1994) 1246–1264, arXiv:hep-ph/9306256 [hep-ph]. (342)

[795] V. Koulovassilopoulos and R. S. Chivukula, *The Phenomenology of a nonstandard Higgs boson in W_LW_L scattering*, Phys. Rev. **D50** (1994) 3218–3234, arXiv:hep-ph/9312317 [hep-ph]. (342)

[796] C. P. Burgess, J. Matias, and M. Pospelov, *A Higgs or not a Higgs? What to do if you discover a new scalar particle*, Int. J. Mod. Phys. **A17** (2002) 1841–1918, arXiv:hep-ph/9912459 [hep-ph]. (342)

[797] L.-M. Wang and Q. Wang, *Electroweak chiral Lagrangian for neutral Higgs boson*, Chin. Phys. Lett. **25** (2008) 1984, arXiv:hep-ph/0605104 [hep-ph]. (342)

[798] B. Grinstein and M. Trott, *A Higgs-Higgs bound state due to new physics at a TeV*, Phys. Rev. **D76** (2007) 073002, arXiv:0704.1505 [hep-ph]. (342)

[799] R. Alonso, M. B. Gavela, L. Merlo, S. Rigolin, and J. Yepes, *The Effective Chiral Lagrangian for a Light Dynamical "Higgs Particle"*, Phys. Lett. **B722** (2013) 330–335, arXiv:1212.3305 [hep-ph]. [Erratum-ibid. **B726** (2013) 926]. (342, 343)

[800] D. Espriu, F. Mescia, and B. Yencho, *Radiative corrections to W_LW_L scattering in composite Higgs models*, Phys. Rev. **D88** (2013) 055002, arXiv:1307.2400 [hep-ph]. (342, 343, 344, 347, 354)

[801] G. Buchalla, O. Catá, and C. Krause, *Complete Electroweak Chiral Lagrangian with a Light Higgs at NLO*, Nucl. Phys. **B880** (2014) 552–573, arXiv:1307.5017 [hep-ph]. (342, 343, 344)

[802] I. Brivio, T. Corbett, O. J. P. Éboli, M. B. Gavela, J. Gonzalez-Fraile, M. C. Gonzalez-Garcia, L. Merlo, and S. Rigolin, *Disentangling a dynamical Higgs*, JHEP **03** (2014) 024, arXiv:1311.1823 [hep-ph]. (342, 347)

[803] R. L. Delgado, A. Dobado, and F. J. Llanes-Estrada, *One-loop W_LW_L and Z_LZ_L scattering from the electroweak Chiral Lagrangian with a light Higgs-like scalar*, JHEP **02** (2014) 121, arXiv:1311.5993 [hep-ph]. (342)

[804] M. B. Gavela, J. Gonzalez-Fraile, M. C. Gonzalez-Garcia, L. Merlo, S. Rigolin, and J. Yepes, *CP violation with a dynamical Higgs*, JHEP **10** (2014) 044, arXiv:1406.6367 [hep-ph]. (342)

[805] R. Urech, *Virtual photons in chiral perturbation theory*, Nucl. Phys. **B433** (1995) 234–254, arXiv:hep-ph/9405341 [hep-ph]. (342)

[806] M. Knecht, H. Neufeld, H. Rupertsberger, and P. Talavera, *Chiral perturbation theory with virtual photons and leptons*, Eur. Phys. J. **C12** (2000) 469–478, arXiv:hep-ph/9909284 [hep-ph]. (342)

[807] A. Nyffeler and A. Schenk, *The Electroweak chiral Lagrangian reanalyzed*, Phys. Rev. **D62** (2000) 113006, arXiv:hep-ph/9907294 [hep-ph]. (342)

[808] J. Hirn and J. Stern, *The Role of spurions in Higgsless electroweak effective theories*, Eur. Phys. J. **C34** (2004) 447–475, arXiv:hep-ph/0401032 [hep-ph]. (342)

[809] M. Herrero and E. Ruiz-Morales, *Study of $\gamma\gamma \to W^+W^-_L$ and $\gamma\gamma \to Z_LZ_L$ reactions with chiral Lagrangians*, Phys. Lett. **B296** (1992) 397–407, arXiv:hep-ph/9208220 [hep-ph]. (343)

[810] M. J. Herrero and E. Ruiz Morales, *The Electroweak chiral Lagrangian for the Standard Model with a heavy Higgs*, Nucl. Phys. **B418** (1994) 431–455, arXiv:hep-ph/9308276 [hep-ph]. (343)

[811] M. J. Herrero and E. Ruiz Morales, *Nondecoupling effects of the SM higgs boson to one loop*,

Nucl. Phys. **B437** (1995) 319–355, arXiv:hep-ph/9411207 [hep-ph]. (343)

[812] S. Dittmaier and C. Grosse-Knetter, *Deriving nondecoupling effects of heavy fields from the path integral: A Heavy Higgs field in an SU(2) gauge theory*, Phys. Rev. **D52** (1995) 7276–7293, arXiv:hep-ph/9501285 [hep-ph]. (343)

[813] S. Dittmaier and C. Grosse-Knetter, *Integrating out the standard Higgs field in the path integral*, Nucl. Phys. **B459** (1996) 497–536, arXiv:hep-ph/9505266 [hep-ph]. (343)

[814] R. L. Delgado, A. Dobado, and F. J. Llanes-Estrada, *Light 'Higgs', yet strong interactions*, J. Phys. **G41** (2014) 025002, arXiv:1308.1629 [hep-ph]. (343, 344, 347)

[815] R. L. Delgado, A. Dobado, M. J. Herrero, and J. J. Sanz-Cillero, *One-loop $\gamma\gamma \to W_L^+ W_L^-$ and $\gamma\gamma \to Z_L Z_L$ from the Electroweak Chiral Lagrangian with a light Higgs-like scalar*, JHEP **07** (2014) 149, arXiv:1404.2866 [hep-ph]. (343, 344, 347, 350, 351, 352)

[816] M. B. Gavela, K. Kanshin, P. A. N. Machado, and S. Saa, *On the renormalization of the electroweak chiral Lagrangian with a Higgs*, JHEP **03** (2015) 043, arXiv:1409.1571 [hep-ph]. (343)

[817] F.-K. Guo, P. Ruiz-Femenía, and J. J. Sanz-Cillero, *One loop renormalization of the electroweak chiral Lagrangian with a light Higgs boson*, Phys. Rev. **D92** (2015) 074005, arXiv:1506.04204 [hep-ph]. (343)

[818] R. Alonso, E. E. Jenkins, and A. V. Manohar, *A Geometric Formulation of Higgs Effective Field Theory: Measuring the Curvature of Scalar Field Space*, Phys. Lett. **B754** (2016) 335–342, arXiv:1511.00724 [hep-ph]. (343)

[819] A. Pich, I. Rosell, and J. J. Sanz-Cillero, *Oblique S and T Constraints on Electroweak Strongly-Coupled Models with a Light Higgs*, JHEP **01** (2014) 157, arXiv:1310.3121 [hep-ph]. (343, 344)

[820] O. Catá, *Lurking pseudovectors below the TeV scale*, Eur. Phys. J. **C74** (2014) 2991, arXiv:1402.4990 [hep-ph]. (343)

[821] A. Pich, I. Rosell, J. Santos, and J. J. Sanz-Cillero, *Low-energy signals of strongly-coupled electroweak symmetry-breaking scenarios*, Phys. Rev. **D93** (2016) 055041, arXiv:1510.03114 [hep-ph]. (343)

[822] R. Alonso, M. B. Gavela, L. Merlo, S. Rigolin, and J. Yepes, *Flavor with a light dynamical "Higgs particle"*, Phys. Rev. **D87** (2013) 055019, arXiv:1212.3307 [hep-ph]. (343)

[823] G. Buchalla, O. Catá, A. Celis, and C. Krause, *Fitting Higgs Data with Nonlinear Effective Theory*, Eur. Phys. J. **C76** (2016) 233, arXiv:1511.00988 [hep-ph]. (345, 346, 348)

[824] G. Buchalla, O. Catá, A. Celis, and C. Krause, *Note on Anomalous Higgs-Boson Couplings in Effective Field Theory*, Phys. Lett. **B750** (2015) 298–301, arXiv:1504.01707 [hep-ph]. (346)

[825] G. Buchalla, O. Catá, and G. D'Ambrosio, *Nonstandard Higgs couplings from angular distributions in $h \to Z\ell^+\ell^-$*, Eur. Phys. J. **C74** (2014) 2798, arXiv:1310.2574 [hep-ph]. (348)

[826] C. Grojean, E. Salvioni, M. Schlaffer, and A. Weiler, *Very boosted Higgs in gluon fusion*, JHEP **05** (2014) 022, arXiv:1312.3317 [hep-ph]. (348, 472, 491)

[827] R. Contino, M. Ghezzi, M. Moretti, G. Panico, F. Piccinini, and A. Wulzer, *Anomalous Couplings in Double Higgs Production*, JHEP **08** (2012) 154, arXiv:1205.5444 [hep-ph]. (349)

[828] CMS Collaboration, S. Chatrchyan et al., *Study of exclusive two-photon production of W^+W^- in pp collisions at $\sqrt{s} = 7$ TeV and constraints on anomalous quartic gauge couplings*, JHEP **07** (2013) 116, arXiv:1305.5596 [hep-ex]. (350)

[829] CMS Collaboration, *Evidence for exclusive gamma-gamma to W^+W^- production and*

constraints on Anomalous Quartic Gauge Couplings at $\sqrt{s} = 8$ *TeV*, CMS-PAS-FSQ-13-008, 2015. (350)

[830] CMS and TOTEM diffractive and forward physics working Group Collaboration, M. Albrow et al., *Prospects for Diffractive and Forward Physics at the LHC*, Tech. Rep. CERN-CMS-Note-2007-002, CERN-LHCC-2006-039-G-124, CMS-Note-2007-002, TOTEM-Note-2006-005, LHCC-G-124, CERN-TOTEM-Note-2006-005, CERN, Geneva, 2006. (350, 352)

[831] FP420 R, D Collaboration, M. G. Albrow et al., *The FP420 & Project: Higgs and New Physics with forward protons at the LHC*, JINST **4** (2009) T10001, arXiv:0806.0302 [hep-ex]. (350, 352)

[832] RP220 Collaboration, C. Royon, *Project to install roman pot detectors at 220 m in ATLAS*, in *Proceedings, 15th International Workshop on Deep-inelastic scattering and related subjects (DIS 2007). Vol. 1 and 2*, pp. 759–763. 2007. arXiv:0706.1796 [physics.ins-det]. (350, 352)

[833] A. Dobado and J. Morales, *A Note on the* $\gamma\gamma \to \pi^0\pi^0$ *reaction in the* $1/N$ *expansion of* χPT, Phys. Lett. **B365** (1996) 264–274, arXiv:hep-ph/9511244 [hep-ph]. (350)

[834] J. Bijnens, S. Dawson, and G. Valencia, $\gamma\gamma \to \pi^0\pi^0$ *and* $K_L \to \pi^0\gamma\gamma$ *in the chiral quark model*, Phys. Rev. **D44** (1991) 3555–3561. (350)

[835] J. Bijnens and F. Cornet, *Two Pion Production in Photon-Photon Collisions*, Nucl. Phys. **B296** (1988) 557–568. (350)

[836] U. Burgi, *Charged pion pair production and pion polarizabilities to two loops*, Nucl. Phys. **B479** (1996) 392–426, arXiv:hep-ph/9602429 [hep-ph]. (350)

[837] N. Watanabe, Y. Kurihara, K. Sasaki, and T. Uematsu, *Higgs Production in Two-Photon Process and Transition Form Factor*, Phys. Lett. **B728** (2014) 202–205, arXiv:1311.1601 [hep-ph]. (352)

[838] A. Alloul, B. Fuks, and V. Sanz, *Phenomenology of the Higgs Effective Lagrangian via FEYNRULES*, JHEP **04** (2014) 110, arXiv:1310.5150 [hep-ph]. (352, 383, 475)

[839] R. L. Delgado, A. Dobado, and F. J. Llanes-Estrada, *Possible new resonance from* W_LW_L*-*hh *interchannel coupling*, Phys. Rev. Lett. **114** (2015) 221803, arXiv:1408.1193 [hep-ph]. (352, 353, 354)

[840] R. L. Delgado, A. Dobado, and F. J. Llanes-Estrada, *Unitarity, analyticity, dispersion relations, and resonances in strongly interacting* W_LW_L*,* Z_LZ_L*, and* hh *scattering*, Phys. Rev. **D91** (2015) 075017, arXiv:1502.04841 [hep-ph]. (352, 353, 354)

[841] A. Dobado, F.-K. Guo, and F. J. Llanes-Estrada, *Production cross section estimates for strongly-interacting Electroweak Symmetry Breaking Sector resonances at particle colliders*, Commun. Theor. Phys. **64** (2015) 701–709, arXiv:1508.03544 [hep-ph]. (353, 354)

[842] C. N. Leung, S. T. Love, and S. Rao, *Low-Energy Manifestations of a New Interaction Scale: Operator Analysis*, Z. Phys. **C31** (1986) 433. (355)

[843] A. De Rujula, M. B. Gavela, P. Hernandez, and E. Masso, *The Selfcouplings of vector bosons: Does LEP-1 obviate LEP-2?*, Nucl. Phys. **B384** (1992) 3–58. (355)

[844] K. Hagiwara, S. Matsumoto, and R. Szalapski, *Constraints on new physics in the electroweak bosonic sector from current data and future experiments*, Phys. Lett. **B357** (1995) 411–418, arXiv:hep-ph/9505322 [hep-ph]. (355)

[845] M. C. Gonzalez-Garcia, *Anomalous Higgs couplings*, Int. J. Mod. Phys. **A14** (1999) 3121–3156, arXiv:hep-ph/9902321 [hep-ph]. (355)

[846] M. Duhrssen, S. Heinemeyer, H. Logan, D. Rainwater, G. Weiglein, and D. Zeppenfeld, *Extracting Higgs boson couplings from CERN LHC data*, Phys. Rev. **D70** (2004) 113009,

arXiv:hep-ph/0406323 [hep-ph]. (355)

[847] R. Lafaye, T. Plehn, M. Rauch, D. Zerwas, and M. Duhrssen, *Measuring the Higgs Sector*, JHEP **08** (2009) 009, arXiv:0904.3866 [hep-ph]. (355)

[848] C. Englert, R. Kogler, H. Schulz, and M. Spannowsky, *Higgs coupling measurements at the LHC*, Eur. Phys. J. **C76** (2016) 393, arXiv:1511.05170 [hep-ph]. (356, 357, 358)

[849] T. Corbett, O. J. P. Éboli, D. Goncalves, J. Gonzalez-Fraile, T. Plehn, and M. Rauch, *The Higgs Legacy of the LHC Run I*, JHEP **08** (2015) 156, arXiv:1505.05516 [hep-ph]. (356, 358, 359, 360, 472)

[850] A. Banfi, A. Martin, and V. Sanz, *Probing top-partners in Higgs+jets*, JHEP **08** (2014) 053, arXiv:1308.4771 [hep-ph]. (357, 472, 473, 491)

[851] M. Buschmann, D. Goncalves, S. Kuttimalai, M. Schönherr, F. Krauss, and T. Plehn, *Mass Effects in the Higgs-Gluon Coupling: Boosted vs Off-Shell Production*, JHEP **02** (2015) 038, arXiv:1410.5806 [hep-ph]. (357, 471, 472)

[852] T. Corbett, O. J. P. Éboli, J. Gonzalez-Fraile, and M. C. Gonzalez-Garcia, *Robust Determination of the Higgs Couplings: Power to the Data*, Phys. Rev. **D87** (2013) 015022, arXiv:1211.4580 [hep-ph]. (358)

[853] K. Cranmer, S. Kreiss, D. Lopez-Val, and T. Plehn, *Decoupling Theoretical Uncertainties from Measurements of the Higgs Boson*, Phys. Rev. **D91** (2015) 054032, arXiv:1401.0080 [hep-ph]. (359)

[854] T. Corbett, O. J. P. Éboli, D. Goncalves, J. Gonzalez-Fraile, T. Plehn, and M. Rauch, *The Non-Linear Higgs Legacy of the LHC Run I*, arXiv:1511.08188 [hep-ph]. (360)

[855] J. Ellis, V. Sanz, and T. You, *Complete Higgs Sector Constraints on Dimension-6 Operators*, JHEP **07** (2014) 036, arXiv:1404.3667 [hep-ph]. (360, 472)

[856] W. Kilian, *Electroweak symmetry breaking: The bottom-up approach*, Springer Tracts Mod. Phys. **198** (2003) 1–113. (361)

[857] C. Englert, A. Freitas, M. M. Mühlleitner, T. Plehn, M. Rauch, M. Spira, and K. Walz, *Precision Measurements of Higgs Couplings: Implications for New Physics Scales*, J. Phys. **G41** (2014) 113001, arXiv:1403.7191 [hep-ph]. (361)

[858] M. Gorbahn, J. M. No, and V. Sanz, *Benchmarks for Higgs Effective Theory: Extended Higgs Sectors*, JHEP **10** (2015) 036, arXiv:1502.07352 [hep-ph]. (363, 364)

[859] R. V. Harlander and W. B. Kilgore, *Soft and virtual corrections to $pp \to H + X$ at NNLO*, Phys. Rev. **D64** (2001) 013015, arXiv:hep-ph/0102241 [hep-ph]. (374, 491)

[860] R. P. Kauffman and W. Schaffer, *QCD corrections to production of Higgs pseudoscalars*, Phys. Rev. **D49** (1994) 551–554, arXiv:hep-ph/9305279 [hep-ph]. (374)

[861] A. Djouadi, M. Spira, and P. M. Zerwas, *Two photon decay widths of Higgs particles*, Phys. Lett. **B311** (1993) 255–260, arXiv:hep-ph/9305335 [hep-ph]. (374, 606)

[862] M. Spira, A. Djouadi, D. Graudenz, and P. M. Zerwas, *SUSY Higgs production at proton colliders*, Phys. Lett. **B318** (1993) 347–353. (374, 491, 606)

[863] S. Dawson, A. Djouadi, and M. Spira, *QCD corrections to SUSY Higgs production: The Role of squark loops*, Phys. Rev. Lett. **77** (1996) 16–19, arXiv:hep-ph/9603423 [hep-ph]. (374, 491, 606)

[864] M. Mühlleitner and M. Spira, *Higgs Boson Production via Gluon Fusion: Squark Loops at NLO QCD*, Nucl. Phys. **B790** (2008) 1–27, arXiv:hep-ph/0612254 [hep-ph]. (374, 491, 606, 608)

[865] R. Bonciani, G. Degrassi, and A. Vicini, *Scalar Particle Contribution to Higgs Production via Gluon Fusion at NLO*, JHEP **11** (2007) 095, arXiv:0709.4227 [hep-ph]. (374, 491)

[866] R. V. Harlander and W. B. Kilgore, *Production of a pseudoscalar Higgs boson at hadron*

colliders at next-to-next-to leading order, JHEP **10** (2002) 017, arXiv:hep-ph/0208096 [hep-ph]. (374, 491, 498, 607)

[867] C. Anastasiou and K. Melnikov, *Pseudoscalar Higgs boson production at hadron colliders in NNLO QCD*, Phys. Rev. **D67** (2003) 037501, arXiv:hep-ph/0208115 [hep-ph]. (374, 491, 607)

[868] R. V. Harlander and M. Steinhauser, *Hadronic Higgs production and decay in supersymmetry at next-to-leading order*, Phys. Lett. **B574** (2003) 258–268, arXiv:hep-ph/0307346 [hep-ph]. (374, 491, 498)

[869] R. Harlander and M. Steinhauser, *Effects of SUSY QCD in hadronic Higgs production at next-to-next-to-leading order*, Phys. Rev. **D68** (2003) 111701, arXiv:hep-ph/0308210 [hep-ph]. (374, 491)

[870] R. V. Harlander and M. Steinhauser, *Supersymmetric Higgs production in gluon fusion at next-to-leading order*, JHEP **09** (2004) 066, arXiv:hep-ph/0409010 [hep-ph]. (374, 491, 498)

[871] R. V. Harlander and F. Hofmann, *Pseudo-scalar Higgs production at next-to-leading order SUSY-QCD*, JHEP **03** (2006) 050, arXiv:hep-ph/0507041 [hep-ph]. (374, 491, 498, 608)

[872] G. Degrassi and P. Slavich, *On the NLO QCD corrections to Higgs production and decay in the MSSM*, Nucl. Phys. **B805** (2008) 267–286, arXiv:0806.1495 [hep-ph]. (374, 491)

[873] G. Degrassi and P. Slavich, *NLO QCD bottom corrections to Higgs boson production in the MSSM*, JHEP **11** (2010) 044, arXiv:1007.3465 [hep-ph]. (374, 491, 498)

[874] G. Degrassi, S. Di Vita, and P. Slavich, *NLO QCD corrections to pseudoscalar Higgs production in the MSSM*, JHEP **08** (2011) 128, arXiv:1107.0914 [hep-ph]. (374, 491, 498, 608)

[875] G. Degrassi, S. Di Vita, and P. Slavich, *On the NLO QCD Corrections to the Production of the Heaviest Neutral Higgs Scalar in the MSSM*, Eur. Phys. J. **C72** (2012) 2032, arXiv:1204.1016 [hep-ph]. (374, 491, 498, 608)

[876] C. Anastasiou, S. Beerli, and A. Daleo, *The Two-loop QCD amplitude $gg \to h, H$ in the Minimal Supersymmetric Standard Model*, Phys. Rev. Lett. **100** (2008) 241806, arXiv:0803.3065 [hep-ph]. (374, 491)

[877] M. Mühlleitner, H. Rzehak, and M. Spira, *SUSY-QCD Corrections to MSSM Higgs Boson Production via Gluon fusion*, in *Proceedings, 9th International Symposium on Radiative Corrections: Applications of quantum field theory to phenomenology. (RADCOR 2009): Ascona, Switzerland, October 25-30, 2009*, vol. RADCOR2009, p. 043. 2010. arXiv:1001.3214 [hep-ph]. (374, 491)

[878] M. Mühlleitner, H. Rzehak, and M. Spira, *MSSM Higgs boson production via gluon fusion*, in *Physics at the LHC2010. Proceedings, 5th Conference, PLHC2010, Hamburg, Germany, June 7-12, 2010*, pp. 415–417. 2010. (374)

[879] K. G. Chetyrkin, B. A. Kniehl, and M. Steinhauser, *Strong coupling constant with flavor thresholds at four loops in the MS scheme*, Phys. Rev. Lett. **79** (1997) 2184–2187, arXiv:hep-ph/9706430 [hep-ph]. (374, 491)

[880] K. G. Chetyrkin, B. A. Kniehl, and M. Steinhauser, *Decoupling relations to $\mathcal{O}(\alpha_s^3)$ and their connection to low-energy theorems*, Nucl. Phys. **B510** (1998) 61–87, arXiv:hep-ph/9708255 [hep-ph]. (374, 380, 491, 606)

[881] D. Choudhury and P. Saha, *Higgs production as a probe of anomalous top couplings*, JHEP **08** (2012) 144, arXiv:1201.4130 [hep-ph]. (374)

[882] C. Degrande, J. M. Gerard, C. Grojean, F. Maltoni, and G. Servant, *Probing Top-Higgs Non-Standard Interactions at the LHC*, JHEP **07** (2012) 036, arXiv:1205.1065 [hep-ph]. [Erratum-ibid. **03** (2013) 032]. (374)

[883] C. G. Callan, Jr., *Broken scale invariance in scalar field theory*, Phys. Rev. **D2** (1970) 1541–1547. (375)

[884] K. Symanzik, *Small distance behavior in field theory and power counting*, Commun. Math. Phys. **18** (1970) 227–246. (375)

[885] S. R. Coleman and R. Jackiw, *Why dilatation generators do not generate dilatations?*, Annals Phys. **67** (1971) 552–598. (375)

[886] R. J. Crewther, *Nonperturbative evaluation of the anomalies in low-energy theorems*, Phys. Rev. Lett. **28** (1972) 1421. (375)

[887] M. S. Chanowitz and J. R. Ellis, *Canonical Anomalies and Broken Scale Invariance*, Phys. Lett. **B40** (1972) 397–400. (375)

[888] M. S. Chanowitz and J. R. Ellis, *Canonical Trace Anomalies*, Phys. Rev. **D7** (1973) 2490–2506. (375)

[889] ATLAS Collaboration, G. Aad et al., *Test of CP Invariance in vector-boson fusion production of the Higgs boson using the Optimal Observable method in the ditau decay channel with the ATLAS detector*, arXiv:1602.04516 [hep-ex]. (376)

[890] A. Agostini, G. Degrassi, R. Gröber, and P. Slavich, *NLO-QCD corrections to Higgs pair production in the MSSM*, JHEP **04** (2016) 106, arXiv:1601.03671 [hep-ph]. (377)

[891] Y. Schroder and M. Steinhauser, *Four-loop decoupling relations for the strong coupling*, JHEP **01** (2006) 051, arXiv:hep-ph/0512058 [hep-ph]. (380, 606)

[892] P. A. Baikov and K. G. Chetyrkin, *Top Quark Mediated Higgs Boson Decay into Hadrons to Order α_s^5*, Phys. Rev. Lett. **97** (2006) 061803, arXiv:hep-ph/0604194 [hep-ph]. (380, 606)

[893] T. Inami, T. Kubota, and Y. Okada, *Effective Gauge Theory and the Effect of Heavy Quarks in Higgs Boson Decays*, Z. Phys. **C18** (1983) 69. (380, 606)

[894] K. G. Chetyrkin, B. A. Kniehl, and M. Steinhauser, *Hadronic Higgs decay to order α_s^4*, Phys. Rev. Lett. **79** (1997) 353–356, arXiv:hep-ph/9705240 [hep-ph]. (380, 606)

[895] J. R. Ellis, M. K. Gaillard, and D. V. Nanopoulos, *A Phenomenological Profile of the Higgs Boson*, Nucl. Phys. **B106** (1976) 292. (380, 472)

[896] M. A. Shifman, A. I. Vainshtein, M. B. Voloshin, and V. I. Zakharov, *Low-Energy Theorems for Higgs Boson Couplings to Photons*, Sov. J. Nucl. Phys. **30** (1979) 711–716. [Yad. Fiz.30,1368(1979)]. (380, 472)

[897] B. A. Kniehl and M. Spira, *Low-energy theorems in Higgs physics*, Z. Phys. **C69** (1995) 77–88, arXiv:hep-ph/9505225 [hep-ph]. (380, 472)

[898] J. S. Gainer, J. Lykken, K. T. Matchev, S. Mrenna, and M. Park, *The Matrix Element Method: Past, Present, and Future*, in *Proceedings, Community Summer Study 2013: Snowmass on the Mississippi (CSS2013)*. Minneapolis, MN, USA, July 29 – August 6, 2013. arXiv:1307.3546 [hep-ph]. (381)

[899] M. Bordone, A. Greljo, G. Isidori, D. Marzocca, and A. Pattori, *Higgs Pseudo Observables and Radiative Corrections*, Eur. Phys. J. **C75** (2015) 385, arXiv:1507.02555 [hep-ph]. (381, 382, 409)

[900] N. D. Christensen, P. de Aquino, C. Degrande, C. Duhr, B. Fuks, M. Herquet, F. Maltoni, and S. Schumann, *A Comprehensive approach to new physics simulations*, Eur. Phys. J. **C71** (2011) 1541, arXiv:0906.2474 [hep-ph]. (382)

[901] P. de Aquino, W. Link, F. Maltoni, O. Mattelaer, and T. Stelzer, *ALOHA: Automatic Libraries Of Helicity Amplitudes for Feynman Diagram Computations*, Comput. Phys. Commun. **183** (2012) 2254–2263, arXiv:1108.2041 [hep-ph]. (383)

[902] F. Maltoni, K. Mawatari, and M. Zaro, *Higgs characterisation via vector-boson fusion and associated production: NLO and parton-shower effects*, Eur. Phys. J. **C74** (2014) 2710,

arXiv:1311.1829 [hep-ph]. (383)

[903] F. Demartin, F. Maltoni, K. Mawatari, B. Page, and M. Zaro, *Higgs characterisation at NLO in QCD: CP properties of the top-quark Yukawa interaction*, Eur. Phys. J. **C74** (2014) 3065, arXiv:1407.5089 [hep-ph]. (383)

[904] J. Alwall et al., *A Standard format for Les Houches event files*, Comput. Phys. Commun. **176** (2007) 300–304, arXiv:hep-ph/0609017 [hep-ph]. (386)

[905] CMS Collaboration, S. Chatrchyan et al., *Measurement of the properties of a Higgs boson in the four-lepton final state*, Phys. Rev. **D89** (2014) 092007, arXiv:1312.5353 [hep-ex]. (386)

[906] CMS Collaboration, S. Chatrchyan et al., *Measurement of Higgs boson production and properties in the WW decay channel with leptonic final states*, JHEP **01** (2014) 096, arXiv:1312.1129 [hep-ex]. (386)

[907] CMS Collaboration, V. Khachatryan et al., *Combined search for anomalous pseudoscalar HVV couplings in VH($H \to b\bar{b}$) production and $H \to VV$ decay*, Phys. Lett. **B759** (2016) 672–696, arXiv:1602.04305 [hep-ex]. (386)

[908] ATLAS Collaboration, G. Aad et al., *Study of the spin and parity of the Higgs boson in diboson decays with the ATLAS detector*, Eur. Phys. J. **C75** (2015) 476, arXiv:1506.05669 [hep-ex]. [Erratum-ibid. **C76** (2016) 152]. (386, 394)

[909] T. Plehn and M. Rauch, *The quartic higgs coupling at hadron colliders*, Phys. Rev. **D72** (2005) 053008, arXiv:hep-ph/0507321 [hep-ph]. (387)

[910] O. J. P. Éboli, M. C. Gonzalez-Garcia, and J. K. Mizukoshi, *$pp \to jje^{\pm}\mu^{\pm}\nu\nu$ and $jje^{\pm}\mu^{\mp}\nu\nu$ at $\mathcal{O}(\alpha_{\rm em}^6)$ and $\mathcal{O}(\alpha_{em}^4\alpha_s^2)$ for the study of the quartic electroweak gauge boson vertex at CERN LHC*, Phys. Rev. **D74** (2006) 073005, arXiv:hep-ph/0606118 [hep-ph]. (389)

[911] C. Degrande, O. Éboli, B. Feigl, B. Jäger, W. Kilian, O. Mattelaer, M. Rauch, J. Reuter, M. Sekulla, and D. Wackeroth, *Monte Carlo tools for studies of non-standard electroweak gauge boson interactions in multi-boson processes: A Snowmass White Paper*, in *Proceedings, Community Summer Study 2013: Snowmass on the Mississippi (CSS2013)*. Minneapolis, MN, USA, July 29 – August 6, 2013. arXiv:1309.7890 [hep-ph]. (389, 390)

[912] K. Arnold et al., *VBFNLO: A Parton Level Monte Carlo for Processes with Electroweak Bosons – Manual for Version 2.5.0*, arXiv:1107.4038 [hep-ph]. (389)

[913] L3 Collaboration, P. Achard et al., *Search for anomalous couplings in the Higgs sector at LEP*, Phys. Lett. **B589** (2004) 89–102, arXiv:hep-ex/0403037 [hep-ex]. (390)

[914] T. Figy and D. Zeppenfeld, *QCD corrections to jet correlations in weak boson fusion*, Phys. Lett. **B591** (2004) 297–303, arXiv:hep-ph/0403297 [hep-ph]. (390)

[915] V. D. Barger, K. Cheung, T. Han, and R. J. N. Phillips, *Strong W^+W^+ scattering signals at pp supercolliders*, Phys. Rev. **D42** (1990) 3052–3077. (390)

[916] G. J. Gounaris, J. Layssac, and F. M. Renard, *Unitarity constraints for transverse gauge bosons at LEP and supercolliders*, Phys. Lett. **B332** (1994) 146–152, arXiv:hep-ph/9311370 [hep-ph]. (390)

[917] A. Alboteanu, W. Kilian, and J. Reuter, *Resonances and Unitarity in Weak Boson Scattering at the LHC*, JHEP **11** (2008) 010, arXiv:0806.4145 [hep-ph]. (390, 391)

[918] W. Kilian, T. Ohl, J. Reuter, and M. Sekulla, *High-Energy Vector Boson Scattering after the Higgs Discovery*, Phys. Rev. **D91** (2015) 096007, arXiv:1408.6207 [hep-ph]. (390, 391, 474)

[919] W. Kilian, T. Ohl, and J. Reuter, *WHIZARD: Simulating Multi-Particle Processes at LHC and ILC*, Eur. Phys. J. **C71** (2011) 1742, arXiv:0708.4233 [hep-ph]. (390)

[920] M. Moretti, T. Ohl, and J. Reuter, *O'Mega: An Optimizing matrix element generator*, arXiv:hep-ph/0102195 [hep-ph]. (390)

[921] W. Kilian, T. Ohl, J. Reuter, and C. Speckner, *QCD in the Color-Flow Representation*, JHEP **10** (2012) 022, arXiv:1206.3700 [hep-ph]. (390)

[922] W. Kilian, J. Reuter, S. Schmidt, and D. Wiesler, *An Analytic Initial-State Parton Shower*, JHEP **04** (2012) 013, arXiv:1112.1039 [hep-ph]. (391)

[923] C. Weiss, B. Chokoufe Nejad, W. Kilian, and J. Reuter, *Automated NLO QCD Corrections with WHIZARD*, in *Proceedings, 2015 European Physical Society Conference on High Energy Physics (EPS-HEP 2015): Vienna, Austria, July 22-29, 2015*, p. 466. 2015. arXiv:1510.02666 [hep-ph]. (391)

[924] B. Chokoufe Nejad, W. Kilian, J. Reuter, and C. Weiss, *Matching NLO QCD Corrections in WHIZARD with the POWHEG scheme*, in *Proceedings, 2015 European Physical Society Conference on High Energy Physics (EPS-HEP 2015): Vienna, Austria, July 22-29, 2015*, p. 317. 2015. arXiv:1510.02739 [hep-ph]. (391)

[925] N. D. Christensen, C. Duhr, B. Fuks, J. Reuter, and C. Speckner, *Introducing an interface between WHIZARD and FeynRules*, Eur. Phys. J. **C72** (2012) 1990, arXiv:1010.3251 [hep-ph]. (391)

[926] W. Kilian, T. Ohl, J. Reuter, and M. Sekulla, *Resonances at the LHC beyond the Higgs boson: The scalar/tensor case*, Phys. Rev. **D93** (2016) 036004, arXiv:1511.00022 [hep-ph]. (391)

[927] O. J. P. Éboli, M. C. Gonzalez-Garcia, and S. M. Lietti, *Bosonic quartic couplings at CERN LHC*, Phys. Rev. **D69** (2004) 095005, arXiv:hep-ph/0310141 [hep-ph]. (391)

[928] F. Bach and T. Ohl, *Anomalous Top Couplings at Hadron Colliders Revisited*, Phys. Rev. **D86** (2012) 114026, arXiv:1209.4564 [hep-ph]. (392)

[929] F. Bach and T. Ohl, *Anomalous top charged-current contact interactions in single top production at the LHC*, Phys. Rev. **D90** (2014) 074022, arXiv:1407.2546 [hep-ph]. (392)

[930] A. Caldwell, D. Kollar, and K. Kroninger, *BAT: The Bayesian Analysis Toolkit*, Comput. Phys. Commun. **180** (2009) 2197–2209, arXiv:0808.2552 [physics.data-an]. (392)

[931] The HEPfit collaboration, HEPfit*: a Code for the Combination of Indirect and Direct Constraints on High Energy Physics Models*, in preparation. (392)

[932] The HEPfit collaboration. http://hepfit.roma1.infn.it. (392)

[933] J. de Blas, M. Ciuchini, E. Franco, D. Ghosh, S. Mishima, M. Pierini, L. Reina, and L. Silvestrini, *Global Bayesian Analysis of the Higgs-boson Couplings*, in *Proceedings, 37th International Conference on High Energy Physics (ICHEP 2014): Valencia, Spain, July 2-9, 2014*, vol. 273-275, pp. 834–840. 2016. arXiv:1410.4204 [hep-ph]. (392)

[934] M. Ciuchini, E. Franco, S. Mishima, M. Pierini, L. Reina, and L. Silvestrini, *Update of the electroweak precision fit, interplay with Higgs-boson signal strengths and model-independent constraints on new physics*, in *Proceedings, 37th International Conference on High Energy Physics (ICHEP 2014)*. Valencia, Spain, July 2–9, 2014. arXiv:1410.6940 [hep-ph]. (392)

[935] J. de Blas, M. Ciuchini, E. Franco, D. Ghosh, S. Mishima, M. Pierini, L. Reina, and L. Silvestrini, *Updates on fits to electroweak parameters*, in *International Symposium on Lepton Photon Interactions at High Energies (LP 2015) Ljubljana, Slovenia, August 17-22, 2015*. to appear in the LP 2015 Proceedings. (392)

[936] J. de Blas, M. Ciuchini, E. Franco, S. Mishima, M. Pierini, L. Reina, and L. Silvestrini, *Electroweak precision observables and Higgs-boson signal strengths in the Standard Model and beyond: present and future*, arXiv:1608.01509 [hep-ph]. (392)

[937] C. Degrande, B. Fuks, K. Mawatari, K. Mimasu, and V. Sanz, *Electroweak Higgs boson production in the standard model effective field theory beyond leading order in QCD*, arXiv:1609.04833 [hep-ph]. (394)

[938] M. Boggia, R. Gomez-Ambrosio, and G. Passarino, *Low energy behaviour of standard model*

extensions, JHEP **05** (2016) 162, arXiv:1603.03660 [hep-ph]. (394)

[939] L. Brenner, N. Belyaev, V. Bortolotto, C. D. Burgard, M. Duehrssen-Debling, K. M. Ecker, S. Gadatsch, D. S. Gray, A. Kaluza, K. Koeneke, R. Konoplich, S. Kortner, K. Prokofiev, C. Schmitt, and W. Verkerke, *A morphing technique for signal modelling in a multidimensional space of coupling parameters*, LHCHXSWG-INT-2016-004, 2016. (395, 398)

[940] M. Baak, S. Gadatsch, R. Harrington, and W. Verkerke, *Interpolation between multi-dimensional histograms using a new non-linear moment morphing method*, Nucl. Instrum. Meth. **A771** (2015) 39–48, arXiv:1410.7388 [physics.data-an]. (395)

[941] W. Verkerke and D. P. Kirkby, *The RooFit toolkit for data modeling*, in *Statistical Problems in Particle Physics, Astrophysics and Cosmology (PHYSTAT 05): Proceedings, Oxford, UK, September 12-15, 2005*, vol. C0303241, p. MOLT007. 2003. arXiv:physics/0306116 [physics]. (395)

[942] ROOT Collaboration, K. Cranmer, G. Lewis, L. Moneta, A. Shibata, and W. Verkerke, *HistFactory: A tool for creating statistical models for use with RooFit and RooStats*, CERN-OPEN-2012-016, 2012. (395)

[943] M. Gonzalez-Alonso, A. Greljo, G. Isidori, and D. Marzocca, *Electroweak bounds on Higgs pseudo-observables and $h \to 4\ell$ decays*, Eur. Phys. J. **C75** (2015) 341, arXiv:1504.04018 [hep-ph]. (401, 408)

[944] A. Greljo, G. Isidori, and D. Marzocca, `Higgs PO`, http://www.physik.uzh.ch/data/HiggsPO. (402)

[945] W. Bernreuther and A. Brandenburg, *Signatures of Higgs sector CP violation in top quark pair production at proton proton supercolliders*, Phys. Lett. **B314** (1993) 104–111. (403)

[946] S. Berge, W. Bernreuther, and J. Ziethe, *Determining the CP parity of Higgs bosons at the LHC in their tau decay channels*, Phys. Rev. Lett. **100** (2008) 171605, arXiv:0801.2297 [hep-ph]. (403)

[947] F. Bishara, Y. Grossman, R. Harnik, D. J. Robinson, J. Shu, and J. Zupan, *Probing CP Violation in $h \to \gamma\gamma$ with Converted Photons*, JHEP **04** (2014) 084, arXiv:1312.2955 [hep-ph]. (404)

[948] M. Gonzalez-Alonso and G. Isidori, *The $h \to 4l$ spectrum at low m_{34}: Standard Model vs. light New Physics*, Phys. Lett. **B733** (2014) 359–365, arXiv:1403.2648 [hep-ph]. (405, 628)

[949] N. Davidson, T. Przedzinski, and Z. Was, *PHOTOS Interface in C++: Technical and Physics Documentation*, Comput. Phys. Commun. **199** (2016) 86–101, arXiv:1011.0937 [hep-ph]. (409)

[950] W. Murray, *The sensitivity of the Higgs boson branching ratios to the W boson width*, Phys. Lett. **B758** (2016) 98–100, arXiv:1604.01665 [hep-ph]. (410)

[951] T. Gleisberg and F. Krauss, *Automating dipole subtraction for QCD NLO calculations*, Eur. Phys. J. **C53** (2008) 501–523, arXiv:0709.2881 [hep-ph]. (420, 527)

[952] F. Cascioli, J. Lindert, P. Maierhöfer, and S. Pozzorini, `OpenLoops`, http://openloops.hepforge.org. (420)

[953] S. Höche, S. Kuttimalai, S. Schumann, and F. Siegert, *Beyond Standard Model calculations with Sherpa*, Eur. Phys. J. **C75** (2015) 135, arXiv:1412.6478 [hep-ph]. (420)

[954] J. M. Campbell, R. K. Ellis, and C. Williams, *Bounding the Higgs Width at the LHC*, in *Proceedings, 12th DESY Workshop on Elementary Particle Physics: Loops and Legs in Quantum Field Theory (LL2014)*, p. 008. 2014. arXiv:1408.1723 [hep-ph]. (425)

[955] A. Denner, S. Dittmaier, M. Roth, and L. H. Wieders, *Complete electroweak $\mathcal{O}(\alpha)$ corrections to charged-current $e^+e^- \to 4$ fermion processes*, Phys. Lett. **B612** (2005) 223–232, arXiv:hep-ph/0502063 [hep-ph]. [Erratum-ibid. **B704** (2011) 667]. (430)

[956] D. Yu. Bardin and G. Passarino, *The standard model in the making: Precision study of the*

electroweak interactions. Clarendon Press, Oxford, UK, 685 p, 1999. (432)

[957] C. F. Uhlemann and N. Kauer, *Narrow-width approximation accuracy*, Nucl. Phys. **B814** (2009) 195–211, arXiv:0807.4112 [hep-ph]. (434)

[958] M. L. Nekrasov, *Modified perturbation theory for pair production and decay of fundamental unstable particles*, Int. J. Mod. Phys. **A24** (2009) 6071–6103, arXiv:0709.3046 [hep-ph]. (434)

[959] F. V. Tkachov, *On the structure of systematic perturbation theory with unstable fields*, in *High energy physics and quantum field theory. Proceedings, 14th International Workshop, QFTHEP'99, Moscow, Russia, May 27-June 2, 1999*, pp. 641–645. 1999. arXiv:hep-ph/0001220 [hep-ph]. (434)

[960] G. Passarino, *Higgs Boson Production and Decay: Dalitz Sector*, Phys. Lett. **B727** (2013) 424–431, arXiv:1308.0422 [hep-ph]. (434)

[961] D. Gillberg and J. Lacey. https://svnweb.cern.ch/cern/wsvn/lhchiggsxs/repository/TemplateXS. (450)

[962] ATLAS Collaboration, G. Aad et al., *Measurements of fiducial and differential cross sections for Higgs boson production in the diphoton decay channel at $\sqrt{s} = 8$ TeV with ATLAS*, JHEP **09** (2014) 112, arXiv:1407.4222 [hep-ex]. (452, 453, 482, 486)

[963] CMS Collaboration, V. Khachatryan et al., *Measurement of differential cross sections for Higgs boson production in the diphoton decay channel in pp collisions at $\sqrt{s} = 8$ TeV*, Eur. Phys. J. **C76** (2016) 13, arXiv:1508.07819 [hep-ex]. (452, 453, 482)

[964] ATLAS Collaboration, G. Aad et al., *Fiducial and differential cross sections of Higgs boson production measured in the four-lepton decay channel in pp collisions at $\sqrt{s}$=8 TeV with the ATLAS detector*, Phys. Lett. **B738** (2014) 234–253, arXiv:1408.3226 [hep-ex]. (452, 453, 476, 477, 482, 483)

[965] CMS Collaboration, V. Khachatryan et al., *Measurement of differential and integrated fiducial cross sections for Higgs boson production in the four-lepton decay channel in pp collisions at $\sqrt{s} = 7$ and 8 TeV*, JHEP **04** (2016) 005, arXiv:1512.08377 [hep-ex]. (452, 453, 476, 477, 482)

[966] CMS Collaboration, *Measurement of the transverse momentum spectrum of the Higgs boson produced in pp collisions at $\sqrt{s} = 8$ TeV using the $H \to WW$ decays*, CMS-PAS-HIG-15-010. (452, 453, 478, 482)

[967] ATLAS Collaboration, G. Aad et al., *Measurements of the Total and Differential Higgs Boson Production Cross Sections Combining the $H \to \gamma\gamma$ and $H \to ZZ^* \to 4\ell$ Decay Channels at $\sqrt{s}$=8 TeV with the ATLAS Detector*, Phys. Rev. Lett. **115** (2015) 091801, arXiv:1504.05833 [hep-ex]. (452, 455, 482, 483, 485)

[968] HepData Collaboration. http://hepdata.cedar.ac.uk/. (453, 484)

[969] ATLAS Collaboration, G. Aad et al., *Constraints on non-Standard Model Higgs boson interactions in an effective Lagrangian using differential cross sections measured in the $H \to \gamma\gamma$ decay channel at $\sqrt{s} = 8$ TeV with the ATLAS detector*, Phys. Lett. **B753** (2016) 69–85, arXiv:1508.02507 [hep-ex]. (453)

[970] ATLAS Collaboration, G. Aad et al., *Measurements of four-lepton production in pp collisions at $\sqrt{s} = 8$ TeV with the ATLAS detector*, Phys. Lett. **B753** (2016) 552–572, arXiv:1509.07844 [hep-ex]. (453, 471, 485)

[971] ATLAS Collaboration, *Measurement of the Higgs boson production cross section at 7, 8 and 13 TeV center-of-mass energies in the $H \to \gamma\gamma$ channel with the ATLAS detector*, ATLAS-CONF-2015-060, 2015. (453)

[972] CMS Collaboration, *Studies of Higgs boson production in the four-lepton final state at $\sqrt{s} = 13$ TeV*, CMS-PAS-HIG-15-004, 2016. (453)

[973] J. R. Andersen et al., *Les Houches 2015: Physics at TeV Colliders Standard Model Working Group Report*, in *9th Les Houches Workshop on Physics at TeV Colliders (PhysTeV 2015) Les Houches, France, June 1-19, 2015*. 2016. arXiv:1605.04692 [hep-ph]. (455, 466, 469, 485)

[974] M. Grazzini, HRes, http://theory.fi.infn.it/grazzini/codes.html. (457)

[975] R. V. Harlander, T. Neumann, K. J. Ozeren, and M. Wiesemann, *Top-mass effects in differential Higgs production through gluon fusion at order α_s^4*, JHEP **08** (2012) 139, arXiv:1206.0157 [hep-ph]. (460)

[976] M. Grazzini, S. Kallweit, and D. Rathlev, *ZZ production at the LHC: fiducial cross sections and distributions in NNLO QCD*, Phys. Lett. **B750** (2015) 407–410, arXiv:1507.06257 [hep-ph]. (463, 466)

[977] S. Kallweit, MUNICH *is the abbreviation of "MUlti-chaNnel Integrator at Swiss (CH) precision" — an automated parton level NLO generator*, In preparation. (464)

[978] S. Catani and M. H. Seymour, *The Dipole formalism for the calculation of QCD jet cross-sections at next-to-leading order*, Phys. Lett. **B378** (1996) 287–301, arXiv:hep-ph/9602277 [hep-ph]. (464)

[979] F. Caola, J. M. Henn, K. Melnikov, A. V. Smirnov, and V. A. Smirnov, *Two-loop helicity amplitudes for the production of two off-shell electroweak bosons in quark-antiquark collisions*, JHEP **11** (2014) 041, arXiv:1408.6409 [hep-ph]. (465)

[980] T. Gehrmann, A. von Manteuffel, and L. Tancredi, *The two-loop helicity amplitudes for $q\overline{q}' \to V_1 V_2 \to 4$ leptons*, JHEP **09** (2015) 128, arXiv:1503.04812 [hep-ph]. (465)

[981] J. Wang, C. S. Li, Z. Li, C. P. Yuan, and H. T. Li, *Improved Resummation Prediction on Higgs Production at Hadron Colliders*, Phys. Rev. **D86** (2012) 094026, arXiv:1205.4311 [hep-ph]. (468)

[982] P. Sun, J. Isaacson, C. P. Yuan, and F. Yuan, *Resummation of High Order Corrections in Higgs Boson Plus Jet Production at the LHC*, arXiv:1602.08133 [hep-ph]. (468)

[983] S. Höche, Y. Li, and S. Prestel, *Higgs-boson production through gluon fusion at NNLO QCD with parton showers*, Phys. Rev. **D90** (2014) 054011, arXiv:1407.3773 [hep-ph]. (468)

[984] T. Gleisberg and S. Höeche, *Comix, a new matrix element generator*, JHEP **12** (2008) 039, arXiv:0808.3674 [hep-ph]. (468, 527)

[985] K. Hamilton, P. Nason, and G. Zanderighi, *MINLO: Multi-Scale Improved NLO*, JHEP **10** (2012) 155, arXiv:1206.3572 [hep-ph]. (468)

[986] M. Rubin, G. P. Salam, and S. Sapeta, *Giant QCD K-factors beyond NLO*, JHEP **09** (2010) 084, arXiv:1006.2144 [hep-ph]. (468)

[987] S. Höche, F. Krauss, and M. Schönherr, *Uncertainties in MEPS@NLO calculations of h+jets*, Phys. Rev. **D90** (2014) 014012, arXiv:1401.7971 [hep-ph]. (468)

[988] S. Plätzer, *Controlling inclusive cross sections in parton shower + matrix element merging*, JHEP **08** (2013) 114, arXiv:1211.5467 [hep-ph]. (468)

[989] J. R. Andersen and J. M. Smillie, *Constructing All-Order Corrections to Multi-Jet Rates*, JHEP **01** (2010) 039, arXiv:0908.2786 [hep-ph]. (469)

[990] J. R. Andersen and J. M. Smillie, *Multiple Jets at the LHC with High Energy Jets*, JHEP **06** (2011) 010, arXiv:1101.5394 [hep-ph]. (469)

[991] J. R. Andersen and C. D. White, *A New Framework for Multijet Predictions and its application to Higgs Boson production at the LHC*, Phys. Rev. **D78** (2008) 051501, arXiv:0802.2858 [hep-ph]. (469)

[992] A. Buckley, J. Butterworth, L. Lönnblad, D. Grellscheid, H. Hoeth, et al., *Rivet user manual*, Comput. Phys. Commun. **184** (2013) 2803–2819, arXiv:1003.0694 [hep-ph]. (469)

[993] J. M. Campbell, R. K. Ellis, and C. Williams, *Gluon-Gluon Contributions to W^+W^- Production and Higgs Interference Effects*, JHEP **10** (2011) 005, arXiv:1107.5569 [hep-ph]. (470)

[994] A. Azatov and A. Paul, *Probing Higgs couplings with high p_T Higgs production*, JHEP **01** (2014) 014, arXiv:1309.5273 [hep-ph]. (472, 491)

[995] J. R. Espinosa, C. Grojean, V. Sanz, and M. Trott, *NSUSY fits*, JHEP **12** (2012) 077, arXiv:1207.7355 [hep-ph]. (472)

[996] J. Ellis, V. Sanz, and T. You, *Associated Production Evidence against Higgs Impostors and Anomalous Couplings*, Eur. Phys. J. **C73** (2013) 2507, arXiv:1303.0208 [hep-ph]. (472)

[997] CMS Collaboration, S. Chatrchyan et al., *Measurement of the W^+W^- Cross section in pp Collisions at $\sqrt{s} = 7$ TeV and Limits on Anomalous $WW\gamma$ and WWZ couplings*, Eur. Phys. J. **C73** (2013) 2610, arXiv:1306.1126 [hep-ex]. (472)

[998] CMS Collaboration, S. Chatrchyan et al., *Measurement of W^+W^- and ZZ production cross sections in pp collisions at $\sqrt{s}$ = 8 TeV*, Phys. Lett. **B721** (2013) 190, arXiv:1301.4698 [hep-ex]. (472)

[999] ATLAS Collaboration, G. Aad et al., *Measurement of total and differential W^+W^- production cross sections in proton-proton collisions at $\sqrt{s} = 8$ TeV with the ATLAS detector and limits on anomalous triple-gauge-boson couplings*, JHEP **09** (2016) 029, arXiv:1603.01702 [hep-ex]. (472)

[1000] T. Plehn, D. L. Rainwater, and D. Zeppenfeld, *Determining the structure of Higgs couplings at the LHC*, Phys. Rev. Lett. **88** (2002) 051801, arXiv:hep-ph/0105325 [hep-ph]. (473)

[1001] J. Brehmer, J. Jaeckel, and T. Plehn, *Polarized WW Scattering on the Higgs Pole*, Phys. Rev. **D90** (2014) 054023, arXiv:1404.5951 [hep-ph]. (473, 474)

[1002] S. Dawson, *The Effective W Approximation*, Nucl. Phys. **B249** (1985) 42–60. (473)

[1003] K. Hagiwara, Q. Li, and K. Mawatari, *Jet angular correlation in vector-boson fusion processes at hadron colliders*, JHEP **07** (2009) 101, arXiv:0905.4314 [hep-ph]. (473)

[1004] C. Englert, D. Goncalves-Netto, K. Mawatari, and T. Plehn, *Higgs Quantum Numbers in Weak Boson Fusion*, JHEP **01** (2013) 148, arXiv:1212.0843 [hep-ph]. (473, 474)

[1005] A. Djouadi, R. M. Godbole, B. Mellado, and K. Mohan, *Probing the spin-parity of the Higgs boson via jet kinematics in vector boson fusion*, Phys. Lett. **B723** (2013) 307–313, arXiv:1301.4965 [hep-ph]. (473)

[1006] T. Han, D. Krohn, L.-T. Wang, and W. Zhu, *New Physics Signals in Longitudinal Gauge Boson Scattering at the LHC*, JHEP **03** (2010) 082, arXiv:0911.3656 [hep-ph]. (474)

[1007] A. Djouadi, O. Lebedev, Y. Mambrini, and J. Quevillon, *Implications of LHC searches for Higgs–portal dark matter*, Phys. Lett. **B709** (2012) 65–69, arXiv:1112.3299 [hep-ph]. (474)

[1008] A. Butter, T. Plehn, M. Rauch, D. Zerwas, S. Henrot-Versillé, and R. Lafaye, *Invisible Higgs Decays to Hooperons in the NMSSM*, Phys. Rev. **D93** (2016) 015011, arXiv:1507.02288 [hep-ph]. (474)

[1009] O. J. P. Éboli and D. Zeppenfeld, *Observing an invisible Higgs boson*, Phys. Lett. **B495** (2000) 147–154, arXiv:hep-ph/0009158 [hep-ph]. (474)

[1010] B. Mellado, W. Quayle, and S. L. Wu, *Prospects for the observation of a Higgs boson with $H \to \tau^+\tau^- \to \ell^+\ell^- \not{p}_T$ associated with one jet at the LHC*, Phys. Lett. **B611** (2005) 60–65, arXiv:hep-ph/0406095 [hep-ph]. (474)

[1011] C. Bernaciak, T. Plehn, P. Schichtel, and J. Tattersall, *Spying an invisible Higgs boson*, Phys. Rev. **D91** (2015) 035024, arXiv:1411.7699 [hep-ph]. (475)

[1012] ATLAS Collaboration, G. Aad et al., *Search for Dark Matter in Events with Missing Transverse*

Momentum and a Higgs Boson Decaying to Two Photons in pp Collisions at $\sqrt{s} = 8$ TeV with the ATLAS Detector, Phys. Rev. Lett. **115** (2015) 131801, arXiv:1506.01081 [hep-ex]. (475)

[1013] I. Brivio, M. B. Gavela, L. Merlo, K. Mimasu, J. M. No, R. del Rey, and V. Sanz, *Non-linear Higgs portal to Dark Matter*, JHEP **04** (2016) 141, arXiv:1511.01099 [hep-ph]. (475)

[1014] G. Cowan, *A survey of unfolding methods for particle physics*, in *Advanced Statistical Techniques in Particle Physics. Proceedings, Conference, Durham, UK, March 18-22, 2002*, vol. C0203181, pp. 248–257. 2002. (478, 479)

[1015] A. Höcker and V. Kartvelishvili, *SVD approach to data unfolding*, Nucl. Instrum. Meth. **A372** (1996) 469–481, arXiv:hep-ph/9509307 [hep-ph]. (480)

[1016] G. D'Agostini, *A Multidimensional unfolding method based on Bayes' theorem*, Nucl. Instrum. Meth. **A362** (1995) 487–498. (480)

[1017] ATLAS Collaboration, *Further ATLAS tunes of PYTHIA6 and Pythia 8*, ATL-PHYS-PUB-2011-014, 2011. (482, 483)

[1018] ATLAS Collaboration, *New ATLAS event generator tunes to 2010 data*, ATL-PHYS-PUB-2011-008, 2011. (482)

[1019] ATLAS Collaboration, *ATLAS tunes of PYTHIA 6 and Pythia 8 for MC11*, ATL-PHYS-PUB-2011-009, 2011. (482)

[1020] ATLAS Collaboration, *Proposal for truth particle observable definitions in physics measurements*, ATL-PHYS-PUB-2015-013. (482)

[1021] ATLAS Collaboration, G. Aad et al., *Measurement of fiducial differential cross sections of gluon-fusion production of Higgs bosons decaying to $WW^* \to e\nu\mu\nu$ with the ATLAS detector at $\sqrt{s} = 8$ TeV*, JHEP **08** (2016) 104, arXiv:1604.02997 [hep-ex]. (485)

[1022] Y. Okada, M. Yamaguchi, and T. Yanagida, *Upper bound of the lightest Higgs boson mass in the minimal supersymmetric standard model*, Prog. Theor. Phys. **85** (1991) 1–6. (490)

[1023] Y. Okada, M. Yamaguchi, and T. Yanagida, *Renormalization group analysis on the Higgs mass in the softly broken supersymmetric standard model*, Phys. Lett. **B262** (1991) 54–58. (490)

[1024] J. R. Ellis, G. Ridolfi, and F. Zwirner, *Radiative corrections to the masses of supersymmetric Higgs bosons*, Phys. Lett. **B257** (1991) 83–91. (490)

[1025] J. R. Ellis, G. Ridolfi, and F. Zwirner, *On radiative corrections to supersymmetric Higgs boson masses and their implications for LEP searches*, Phys. Lett. **B262** (1991) 477–484. (490)

[1026] A. Brignole, J. R. Ellis, G. Ridolfi, and F. Zwirner, *The Supersymmetric charged Higgs boson mass and LEP phenomenology*, Phys. Lett. **B271** (1991) 123–132. (490)

[1027] H. E. Haber and R. Hempfling, *Can the mass of the lightest Higgs boson of the minimal supersymmetric model be larger than m_Z?*, Phys. Rev. Lett. **66** (1991) 1815–1818. (490)

[1028] P. H. Chankowski, S. Pokorski, and J. Rosiek, *Charged and neutral supersymmetric Higgs boson masses: Complete one loop analysis*, Phys. Lett. **B274** (1992) 191–198. (490)

[1029] P. H. Chankowski, S. Pokorski, and J. Rosiek, *Complete on-shell renormalization scheme for the minimal supersymmetric Higgs sector*, Nucl. Phys. **B423** (1994) 437–496, arXiv:hep-ph/9303309 [hep-ph]. (490)

[1030] A. Brignole, *Radiative corrections to the supersymmetric charged Higgs boson mass*, Phys. Lett. **B277** (1992) 313–323. (490)

[1031] A. Brignole, *Radiative corrections to the supersymmetric neutral Higgs boson masses*, Phys. Lett. **B281** (1992) 284–294. (490)

[1032] A. Dabelstein, *The One loop renormalization of the MSSM Higgs sector and its application to the neutral scalar Higgs masses*, Z. Phys. **C67** (1995) 495–512, arXiv:hep-ph/9409375 [hep-ph]. (490)

[1033] D. M. Pierce, J. A. Bagger, K. T. Matchev, and R.-j. Zhang, *Precision corrections in the minimal supersymmetric standard model*, Nucl. Phys. **B491** (1997) 3–67, arXiv:hep-ph/9606211 [hep-ph]. (490, 540, 606)

[1034] R. Barbieri, M. Frigeni, and F. Caravaglios, *The Supersymmetric Higgs for heavy superpartners*, Phys. Lett. **B258** (1991) 167–170. (490)

[1035] J. R. Espinosa and M. Quiros, *Two loop radiative corrections to the mass of the lightest Higgs boson in supersymmetric standard models*, Phys. Lett. **B266** (1991) 389–396. (490)

[1036] H. E. Haber and R. Hempfling, *The Renormalization group improved Higgs sector of the minimal supersymmetric model*, Phys. Rev. **D48** (1993) 4280–4309, arXiv:hep-ph/9307201 [hep-ph]. (490)

[1037] J. A. Casas, J. R. Espinosa, M. Quiros, and A. Riotto, *The Lightest Higgs boson mass in the minimal supersymmetric standard model*, Nucl. Phys. **B436** (1995) 3–29, arXiv:hep-ph/9407389 [hep-ph]. [Erratum-ibid. **B439** (1995) 466]. (490)

[1038] M. Carena, J. R. Espinosa, M. Quiros, and C. E. M. Wagner, *Analytical expressions for radiatively corrected Higgs masses and couplings in the MSSM*, Phys. Lett. **B355** (1995) 209–221, arXiv:hep-ph/9504316 [hep-ph]. (490)

[1039] M. Carena, M. Quiros, and C. E. M. Wagner, *Effective potential methods and the Higgs mass spectrum in the MSSM*, Nucl. Phys. **B461** (1996) 407–436, arXiv:hep-ph/9508343 [hep-ph]. (490)

[1040] H. E. Haber, R. Hempfling, and A. H. Hoang, *Approximating the radiatively corrected Higgs mass in the minimal supersymmetric model*, Z. Phys. **C75** (1997) 539–554, arXiv:hep-ph/9609331 [hep-ph]. (490)

[1041] J. R. Espinosa and I. Navarro, *Radiative corrections to the Higgs boson mass for a hierarchical stop spectrum*, Nucl. Phys. **B615** (2001) 82–116, arXiv:hep-ph/0104047 [hep-ph]. (490)

[1042] R. Hempfling and A. H. Hoang, *Two loop radiative corrections to the upper limit of the lightest Higgs boson mass in the minimal supersymmetric model*, Phys. Lett. **B331** (1994) 99–106, arXiv:hep-ph/9401219 [hep-ph]. (490)

[1043] S. Heinemeyer, W. Hollik, and G. Weiglein, *QCD corrections to the masses of the neutral CP - even Higgs bosons in the MSSM*, Phys. Rev. **D58** (1998) 091701, arXiv:hep-ph/9803277 [hep-ph]. (490)

[1044] S. Heinemeyer, W. Hollik, and G. Weiglein, *Precise prediction for the mass of the lightest Higgs boson in the MSSM*, Phys. Lett. **B440** (1998) 296–304, arXiv:hep-ph/9807423 [hep-ph]. (490)

[1045] M. Carena, H. E. Haber, S. Heinemeyer, W. Hollik, C. E. M. Wagner, and G. Weiglein, *Reconciling the two loop diagrammatic and effective field theory computations of the mass of the lightest CP - even Higgs boson in the MSSM*, Nucl. Phys. **B580** (2000) 29–57, arXiv:hep-ph/0001002 [hep-ph]. (490)

[1046] S. Heinemeyer, W. Hollik, H. Rzehak, and G. Weiglein, *High-precision predictions for the MSSM Higgs sector at $\mathcal{O}(\alpha_b\alpha_s)$*, Eur. Phys. J. **C39** (2005) 465–481, arXiv:hep-ph/0411114 [hep-ph]. (490)

[1047] R.-J. Zhang, *Two loop effective potential calculation of the lightest CP even Higgs boson mass in the MSSM*, Phys. Lett. **B447** (1999) 89–97, arXiv:hep-ph/9808299 [hep-ph]. (490)

[1048] J. R. Espinosa and R.-J. Zhang, *MSSM lightest CP even Higgs boson mass to $\mathcal{O}(\alpha_s\alpha_t)$: The Effective potential approach*, JHEP **03** (2000) 026, arXiv:hep-ph/9912236 [hep-ph]. (490)

[1049] J. R. Espinosa and R.-J. Zhang, *Complete two loop dominant corrections to the mass of the lightest CP even Higgs boson in the minimal supersymmetric standard model*, Nucl. Phys. **B586** (2000) 3–38, arXiv:hep-ph/0003246 [hep-ph]. (490)

[1050] G. Degrassi, P. Slavich, and F. Zwirner, *On the neutral Higgs boson masses in the MSSM for arbitrary stop mixing*, Nucl. Phys. **B611** (2001) 403–422, arXiv:hep-ph/0105096 [hep-ph]. (490, 605, 606)

[1051] A. Brignole, G. Degrassi, P. Slavich, and F. Zwirner, *On the $\mathcal{O}(\alpha_t^2)$ two loop corrections to the neutral Higgs boson masses in the MSSM*, Nucl. Phys. **B631** (2002) 195–218, arXiv:hep-ph/0112177 [hep-ph]. (490, 605, 606)

[1052] A. Brignole, G. Degrassi, P. Slavich, and F. Zwirner, *On the two loop sbottom corrections to the neutral Higgs boson masses in the MSSM*, Nucl. Phys. **B643** (2002) 79–92, arXiv:hep-ph/0206101 [hep-ph]. (490, 605, 606)

[1053] A. Dedes, G. Degrassi, and P. Slavich, *On the two loop Yukawa corrections to the MSSM Higgs boson masses at large tan beta*, Nucl. Phys. **B672** (2003) 144–162, arXiv:hep-ph/0305127 [hep-ph]. (490, 605, 606)

[1054] S. P. Martin, *Two loop effective potential for the minimal supersymmetric standard model*, Phys. Rev. **D66** (2002) 096001, arXiv:hep-ph/0206136 [hep-ph]. (490)

[1055] S. P. Martin, *Complete two loop effective potential approximation to the lightest Higgs scalar boson mass in supersymmetry*, Phys. Rev. **D67** (2003) 095012, arXiv:hep-ph/0211366 [hep-ph]. (490)

[1056] S. P. Martin, *Strong and Yukawa two-loop contributions to Higgs scalar boson self-energies and pole masses in supersymmetry*, Phys. Rev. **D71** (2005) 016012, arXiv:hep-ph/0405022 [hep-ph]. (490)

[1057] S. Borowka, T. Hahn, S. Heinemeyer, G. Heinrich, and W. Hollik, *Momentum-dependent two-loop QCD corrections to the neutral Higgs-boson masses in the MSSM*, Eur. Phys. J. **C74** (2014) 2994, arXiv:1404.7074 [hep-ph]. (490)

[1058] S. Borowka, T. Hahn, S. Heinemeyer, G. Heinrich, and W. Hollik, *Renormalization scheme dependence of the two-loop QCD corrections to the neutral Higgs-boson masses in the MSSM*, Eur. Phys. J. **C75** (2015) 424, arXiv:1505.03133 [hep-ph]. (490)

[1059] G. Degrassi, S. Di Vita, and P. Slavich, *Two-loop QCD corrections to the MSSM Higgs masses beyond the effective-potential approximation*, Eur. Phys. J. **C75** (2015) 61, arXiv:1410.3432 [hep-ph]. (490)

[1060] S. P. Martin, *Three-loop corrections to the lightest Higgs scalar boson mass in supersymmetry*, Phys. Rev. **D75** (2007) 055005, arXiv:hep-ph/0701051 [hep-ph]. (490)

[1061] P. Draper, G. Lee, and C. E. M. Wagner, *Precise estimates of the Higgs mass in heavy supersymmetry*, Phys. Rev. **D89** (2014) 055023, arXiv:1312.5743 [hep-ph]. (490, 493)

[1062] R. V. Harlander, P. Kant, L. Mihaila, and M. Steinhauser, *Higgs boson mass in supersymmetry to three loops*, Phys. Rev. Lett. **100** (2008) 191602, arXiv:0803.0672 [hep-ph]. [Phys. Rev. Lett.101,039901(2008)]. (490)

[1063] P. Kant, R. V. Harlander, L. Mihaila, and M. Steinhauser, *Light MSSM Higgs boson mass to three-loop accuracy*, JHEP **08** (2010) 104, arXiv:1005.5709 [hep-ph]. (490)

[1064] H. M. Georgi, S. L. Glashow, M. E. Machacek, and D. V. Nanopoulos, *Higgs Bosons from Two Gluon Annihilation in Proton Proton Collisions*, Phys. Rev. Lett. **40** (1978) 692. (490, 607)

[1065] K. G. Chetyrkin, B. A. Kniehl, M. Steinhauser, and W. A. Bardeen, *Effective QCD interactions of CP odd Higgs bosons at three loops*, Nucl. Phys. **B535** (1998) 3–18, arXiv:hep-ph/9807241 [hep-ph]. (491)

[1066] R. V. Harlander, *Virtual corrections to $gg \to H$ to two loops in the heavy top limit*, Phys. Lett. **B492** (2000) 74–80, arXiv:hep-ph/0007289 [hep-ph]. (491)

[1067] A. Pak, M. Rogal, and M. Steinhauser, *Production of scalar and pseudo-scalar Higgs bosons to next-to-next-to-leading order at hadron colliders*, JHEP **09** (2011) 088, arXiv:1107.3391

[hep-ph]. (491, 607)

[1068] F. Caola and S. Marzani, *Finite fermion mass effects in pseudoscalar Higgs production via gluon-gluon fusion*, Phys. Lett. **B698** (2011) 275–283, arXiv:1101.3975 [hep-ph]. (491, 607)

[1069] S. Buehler and A. Lazopoulos, *Scale dependence and collinear subtraction terms for Higgs production in gluon fusion at N3LO*, JHEP **10** (2013) 096, arXiv:1306.2223 [hep-ph]. (491, 607)

[1070] A. Idilbi, X.-d. Ji, J.-P. Ma, and F. Yuan, *Threshold resummation for Higgs production in effective field theory*, Phys. Rev. **D73** (2006) 077501, arXiv:hep-ph/0509294 [hep-ph]. (491)

[1071] A. Idilbi, X.-d. Ji, and F. Yuan, *Resummation of threshold logarithms in effective field theory for DIS, Drell-Yan and Higgs production*, Nucl. Phys. **B753** (2006) 42–68, arXiv:hep-ph/0605068 [hep-ph]. (491)

[1072] V. Ahrens, T. Becher, M. Neubert, and L. L. Yang, *Renormalization-Group Improved Prediction for Higgs Production at Hadron Colliders*, Eur. Phys. J. **C62** (2009) 333–353, arXiv:0809.4283 [hep-ph]. (491)

[1073] R. V. Harlander, F. Hofmann, and H. Mantler, *Supersymmetric Higgs production in gluon fusion*, JHEP **02** (2011) 055, arXiv:1012.3361 [hep-ph]. (491)

[1074] A. Pak, M. Steinhauser, and N. Zerf, *Towards Higgs boson production in gluon fusion to NNLO in the MSSM*, Eur. Phys. J. **C71** (2011) 1602, arXiv:1012.0639 [hep-ph]. [Erratum-ibid. **C72** (2012) 2182]. (491)

[1075] A. Pak, M. Steinhauser, and N. Zerf, *Supersymmetric next-to-next-to-leading order corrections to Higgs boson production in gluon fusion*, JHEP **09** (2012) 118, arXiv:1208.1588 [hep-ph]. (491)

[1076] R. Hempfling, *Yukawa coupling unification with supersymmetric threshold corrections*, Phys. Rev. **D49** (1994) 6168–6172. (491, 540, 606)

[1077] L. J. Hall, R. Rattazzi, and U. Sarid, *The Top quark mass in supersymmetric SO(10) unification*, Phys. Rev. **D50** (1994) 7048–7065, arXiv:hep-ph/9306309 [hep-ph]. (491, 606)

[1078] M. Carena, M. Olechowski, S. Pokorski, and C. E. M. Wagner, *Electroweak symmetry breaking and bottom - top Yukawa unification*, Nucl. Phys. **B426** (1994) 269–300, arXiv:hep-ph/9402253 [hep-ph]. (491, 606)

[1079] M. Carena, D. Garcia, U. Nierste, and C. E. M. Wagner, *Effective Lagrangian for the $\bar{t}bH^+$ interaction in the MSSM and charged Higgs phenomenology*, Nucl. Phys. **B577** (2000) 88–120, arXiv:hep-ph/9912516 [hep-ph]. (491, 606, 607)

[1080] J. Guasch, P. Hafliger, and M. Spira, *MSSM Higgs decays to bottom quark pairs revisited*, Phys. Rev. **D68** (2003) 115001, arXiv:hep-ph/0305101 [hep-ph]. (491, 540, 606, 607)

[1081] D. Noth and M. Spira, *Higgs Boson Couplings to Bottom Quarks: Two-Loop Supersymmetry-QCD Corrections*, Phys. Rev. Lett. **101** (2008) 181801, arXiv:0808.0087 [hep-ph]. (491, 540, 606, 607)

[1082] D. Noth and M. Spira, *Supersymmetric Higgs Yukawa Couplings to Bottom Quarks at next-to-next-to-leading Order*, JHEP **06** (2011) 084, arXiv:1001.1935 [hep-ph]. (491, 540, 606, 607)

[1083] L. Mihaila and C. Reisser, *$\mathcal{O}(\alpha_s^2)$ corrections to fermionic Higgs decays in the MSSM*, JHEP **08** (2010) 021, arXiv:1007.0693 [hep-ph]. (491, 540, 606, 607)

[1084] R. Bonciani, G. Degrassi, and A. Vicini, *On the Generalized Harmonic Polylogarithms of One Complex Variable*, Comput. Phys. Commun. **182** (2011) 1253–1264, arXiv:1007.1891 [hep-ph]. (491, 498, 608)

[1085] S. Dittmaier, M. Krämer, 1, and M. Spira, *Higgs radiation off bottom quarks at the Tevatron and the CERN LHC*, Phys. Rev. **D70** (2004) 074010, arXiv:hep-ph/0309204 [hep-ph]. (491, 498, 514, 516, 519, 524, 526, 608)

[1086] S. Dawson, C. B. Jackson, L. Reina, and D. Wackeroth, *Exclusive Higgs boson production with bottom quarks at hadron colliders*, Phys. Rev. **D69** (2004) 074027, arXiv:hep-ph/0311067 [hep-ph]. (491, 498, 514, 516, 519, 524, 526, 608)

[1087] D. Dicus, T. Stelzer, Z. Sullivan, and S. Willenbrock, *Higgs boson production in association with bottom quarks at next-to-leading order*, Phys. Rev. **D59** (1999) 094016, arXiv:hep-ph/9811492 [hep-ph]. (491, 514, 608)

[1088] F. Maltoni, Z. Sullivan, and S. Willenbrock, *Higgs-boson production via bottom-quark fusion*, Phys. Rev. **D67** (2003) 093005, arXiv:hep-ph/0301033. (491, 512, 516)

[1089] S. Dittmaier, M. Krämer, 1, A. Mück, and T. Schluter, *MSSM Higgs-boson production in bottom-quark fusion: Electroweak radiative corrections*, JHEP **03** (2007) 114, arXiv:hep-ph/0611353 [hep-ph]. (491, 511)

[1090] S. Dawson, C. B. Jackson, and P. Jaiswal, *SUSY QCD Corrections to Higgs-b Production : Is the Δ_b Approximation Accurate?*, Phys. Rev. **D83** (2011) 115007, arXiv:1104.1631 [hep-ph]. (491, 511)

[1091] S. Dittmaier, P. Häfliger, M. Krämer, M. Spira, and M. Walser, *Neutral MSSM Higgs-boson production with heavy quarks: NLO supersymmetric QCD corrections*, Phys. Rev. **D90** (2014) 035010, arXiv:1406.5307 [hep-ph]. (491, 511, 514)

[1092] O. Brein and W. Hollik, *Distributions for MSSM Higgs boson + jet production at hadron colliders*, Phys. Rev. **D76** (2007) 035002, arXiv:0705.2744 [hep-ph]. (491)

[1093] R. V. Harlander and T. Neumann, *Probing the nature of the Higgs-gluon coupling*, Phys. Rev. **D88** (2013) 074015, arXiv:1308.2225 [hep-ph]. (491)

[1094] S. Dawson, I. M. Lewis, and M. Zeng, *Effective field theory for Higgs boson plus jet production*, Phys. Rev. **D90** (2014) 093007, arXiv:1409.6299 [hep-ph]. (491)

[1095] U. Langenegger, M. Spira, and I. Strebel, *Testing the Higgs Boson Coupling to Gluons*, arXiv:1507.01373 [hep-ph]. (491)

[1096] E. Bagnaschi, R. V. Harlander, S. Liebler, H. Mantler, P. Slavich, and A. Vicini, *Towards precise predictions for Higgs-boson production in the MSSM*, JHEP **06** (2014) 167, arXiv:1404.0327 [hep-ph]. (491, 608)

[1097] A. Dabelstein, *Fermionic decays of neutral MSSM Higgs bosons at the one loop level*, Nucl. Phys. **B456** (1995) 25–56, arXiv:hep-ph/9503443 [hep-ph]. (491)

[1098] K. E. Williams, H. Rzehak, and G. Weiglein, *Higher order corrections to Higgs boson decays in the MSSM with complex parameters*, Eur. Phys. J. **C71** (2011) 1669, arXiv:1103.1335 [hep-ph]. (491, 499)

[1099] S. Heinemeyer, W. Hollik, and G. Weiglein, *Decay widths of the neutral CP even MSSM Higgs bosons in the Feynman diagrammatic approach*, Eur. Phys. J. **C16** (2000) 139–153, arXiv:hep-ph/0003022 [hep-ph]. (491)

[1100] A. Brignole and F. Zwirner, *Radiative corrections to the decay $H \to hh$ in the minimal supersymmetric standard model*, Phys. Lett. **B299** (1993) 72–82, arXiv:hep-ph/9210266 [hep-ph]. (491)

[1101] V. D. Barger, M. S. Berger, A. L. Stange, and R. J. N. Phillips, *Supersymmetric Higgs boson hadroproduction and decays including radiative corrections*, Phys. Rev. **D45** (1992) 4128–4147. (491)

[1102] S. Heinemeyer and W. Hollik, *The Decay $h^0 \to A^0 \to A^0 A^0$: a Complete one loop calculation in the MSSM*, Nucl. Phys. **B474** (1996) 32–56, arXiv:hep-ph/9602318 [hep-ph]. (491)

[1103] W. Hollik and J.-H. Zhang, *Radiative Corrections to $H^0 \to WW/ZZ$ in the MSSM*, Phys. Rev. **D84** (2011) 055022, arXiv:1109.4781 [hep-ph]. (491)

[1104] H. Goldberg, *Constraint on the Photino Mass from Cosmology*, Phys. Rev. Lett. **50** (1983) 1419. [Erratum-ibid. **103** (2009) 099905]. (491)

[1105] J. R. Ellis, J. S. Hagelin, D. V. Nanopoulos, K. A. Olive, and M. Srednicki, *Supersymmetric Relics from the Big Bang*, in *BATAVIA 1984, Proceedings, Inner Space/Outer Space, 458-459., In Srednicki, M.A. (ed.): Particle physics and cosmology, 223-246*, vol. B238, pp. 453–476. 1984. (491)

[1106] C. Weber, H. Eberl, and W. Majerotto, *Improved full one loop corrections to $A^0 \to f_1 \bar{f}_2$ and $f_2 \to f_1 A^0$*, Phys. Rev. **D68** (2003) 093011, arXiv:hep-ph/0308146 [hep-ph]. (491)

[1107] S. Heinemeyer and C. Schappacher, *Heavy Higgs Decays into Sfermions in the Complex MSSM: A Full One-Loop Analysis*, Eur. Phys. J. **C75** (2015) 198, arXiv:1410.2787 [hep-ph]. (491)

[1108] A. Bharucha, A. Fowler, G. Moortgat-Pick, and G. Weiglein, *Consistent on shell renormalisation of electroweakinos in the complex MSSM: LHC and LC predictions*, JHEP **05** (2013) 053, arXiv:1211.3134 [hep-ph]. (491)

[1109] H. Eberl, W. Majerotto, and Y. Yamada, *Full one-loop corrections to SUSY Higgs boson decays into charginos*, Phys. Lett. **B597** (2004) 275–284, arXiv:hep-ph/0405187 [hep-ph]. (491)

[1110] S. Heinemeyer and C. Schappacher, *Higgs Decays into Charginos and Neutralinos in the Complex MSSM: A Full One-Loop Analysis*, Eur. Phys. J. **C75** (2015) 230, arXiv:1503.02996 [hep-ph]. (491)

[1111] A. Djouadi and J. Quevillon, *The MSSM Higgs sector at a high M_{SUSY}: reopening the low tanβ regime and heavy Higgs searches*, JHEP **10** (2013) 028, arXiv:1304.1787 [hep-ph]. (492, 493, 497)

[1112] L. Maiani, A. Polosa, and V. Riquer, *Bounds to the Higgs Sector Masses in Minimal Supersymmetry from LHC Data*, Phys. Lett. **B724** (2013) 274–277, arXiv:1305.2172 [hep-ph]. (492, 493, 497)

[1113] A. Djouadi, L. Maiani, G. Moreau, A. Polosa, J. Quevillon, et al., *The post-Higgs MSSM scenario: Habemus MSSM?*, Eur. Phys. J. **C73** (2013) 2650, arXiv:1307.5205 [hep-ph]. (492, 493, 494, 495, 497)

[1114] A. Djouadi, L. Maiani, A. Polosa, J. Quevillon, and V. Riquer, *Fully covering the MSSM Higgs sector at the LHC*, JHEP **06** (2015) 168, arXiv:1502.05653 [hep-ph]. (492, 493, 494, 495, 497)

[1115] S. Heinemeyer, *Benchmark Scenario for low $\tan\beta$ in the MSSM: First preliminary interim recommendation/suggestion*, LHCHXSWG-2014-LL, 2014. (492, 493, 495)

[1116] G. Lee and C. E. M. Wagner, *Higgs bosons in heavy supersymmetry with an intermediate m_A*, Phys. Rev. **D92** (2015) 075032, arXiv:1508.00576 [hep-ph]. (492, 493, 495, 496)

[1117] H. Mantler and M. Wiesemann, *Hadronic Higgs production through NLO + PS in the SM, the 2HDM and the MSSM*, Eur. Phys. J. **C75** (2015) 257, arXiv:1504.06625 [hep-ph]. (492, 506, 609)

[1118] H. Mantler, M. Wiesemann, and S. Liebler, aMCSusHi, https://cp3.irmp.ucl.ac.be/projects/madgraph/wiki/aMCSushi, 2015. (492, 506)

[1119] S. Alioli, K. Hamilton, P. Nason, C. Oleari, E. Re, and G. Zanderighi, POWHEG-BOX, http://powhegbox.mib.infn.it/, 2015. (492, 506)

[1120] H. Mantler and M. Wiesemann, *Top- and bottom-mass effects in hadronic Higgs production at small transverse momenta through LO+NLL*, Eur. Phys. J. **C73** (2013) 2467, arXiv:1210.8263 [hep-ph]. (492, 504, 506, 609)

[1121] H. Mantler and M. Wiesemann, MoRe-SusHi,

http://sushi.hepforge.org/moresushi.html, 2015. (492, 506)

[1122] E. Bagnaschi et al., *Benchmark scenarios for low* $\tan\beta$ *in the MSSM*, LHCHXSWG-2015-002, 2015. (492, 497)

[1123] CMS Collaboration, V. Khachatryan et al., *Search for neutral MSSM Higgs bosons decaying to a pair of tau leptons in pp collisions*, JHEP **10** (2014) 160, arXiv:1408.3316 [hep-ex]. (492)

[1124] ATLAS Collaboration, G. Aad et al., *Search for neutral Higgs bosons of the minimal supersymmetric standard model in pp collisions at* $\sqrt{s}$ *= 8 TeV with the ATLAS detector*, JHEP **11** (2014) 056, arXiv:1409.6064 [hep-ex]. (492)

[1125] CMS Collaboration, *Search for charged Higgs bosons with the* $H^+ \to \tau^+\nu_\tau$ *decay channel in the fully hadronic final state at* $\sqrt{s} = 8$ *TeV*, CMS-PAS-HIG-14-020, 2014. (492)

[1126] ATLAS Collaboration, G. Aad et al., *Search for charged Higgs bosons decaying via* $H^\pm \to \tau^\pm\nu$ *in fully hadronic final states using pp collision data at* $\sqrt{s} = 8$ *TeV with the ATLAS detector*, JHEP **03** (2015) 088, arXiv:1412.6663 [hep-ex]. (492, 539)

[1127] B. Allanach, A. Djouadi, J. Kneur, W. Porod, and P. Slavich, *Precise determination of the neutral Higgs boson masses in the MSSM*, JHEP **09** (2004) 044, arXiv:hep-ph/0406166 [hep-ph]. (492)

[1128] A. Arbey, M. Battaglia, and F. Mahmoudi, *Supersymmetric Heavy Higgs Bosons at the LHC*, Phys. Rev. **D88** (2013) 015007, arXiv:1303.7450 [hep-ph]. (493)

[1129] A. Djouadi, J.-L. Kneur, and G. Moultaka, *SuSpect: A Fortran code for the supersymmetric and Higgs particle spectrum in the MSSM*, Comput. Phys. Commun. **176** (2007) 426–455, arXiv:hep-ph/0211331 [hep-ph]. (495)

[1130] LHC Higgs Cross Section Working Group, MSSM subgroup. https://twiki.cern.ch/twiki/bin/view/LHCPhysics/LHCHXSWGMSSMNeutral. (497)

[1131] R. Harlander, M. Krämer, and M. Schumacher, *Bottom-quark associated Higgs-boson production: reconciling the four- and five-flavour scheme approach*, arXiv:1112.3478 [hep-ph]. (498, 514, 516, 540, 541)

[1132] PDF4LHC Working Group. http://www.hep.ucl.ac.uk/pdf4lhc/PDF4LHC_practical_guide.pdf. (498)

[1133] E. Braaten and J. Leveille, *Higgs Boson Decay and the Running Mass*, Phys. Rev. **D22** (1980) 715. (499, 525, 606)

[1134] N. Sakai, *Perturbative QCD Corrections to the Hadronic Decay Width of the Higgs Boson*, Phys. Rev. **D22** (1980) 2220. (499, 606)

[1135] T. Inami and T. Kubota, *Renormalization Group Estimate of the Hadronic Decay Width of the Higgs Boson*, Nucl. Phys. **B179** (1981) 171. (499, 606)

[1136] M. Drees and K.-i. Hikasa, *Heavy Quark Thresholds in Higgs Physics*, Phys. Rev. **D41** (1990) 1547. (499, 606)

[1137] M. Drees and K.-i. Hikasa, *Note on QCD corrections to hadronic Higgs decay*, Phys. Lett. **B240** (1990) 455. (499, 606)

[1138] S. Gorishnii, A. Kataev, S. Larin, and L. Surguladze, *Corrected Three Loop QCD Correction to the Correlator of the Quark Scalar Currents and* $\Gamma_{\rm tot}(H^0 \to \text{Hadrons})$, Mod. Phys. Lett. **A5** (1990) 2703–2712. (499, 606)

[1139] S. Gorishnii, A. Kataev, S. Larin, and L. Surguladze, *Scheme dependence of the next to next-to-leading QCD corrections to* $\Gamma_{\rm tot}(H^0 \to \text{hadrons})$ *and the spurious QCD infrared fixed point*, Phys. Rev. **D43** (1991) 1633–1640. (499, 606)

[1140] A. L. Kataev and V. T. Kim, *The Effects of the QCD corrections to* $\Gamma_{\rm tot}(H^0 \to b\bar{b})$, Mod. Phys. Lett. **A9** (1994) 1309–1326. (499, 606)

[1141] S. Gorishnii, A. Kataev, and S. Larin, *The Width of Higgs Boson Decay Into Hadrons: Three Loop Corrections of Strong Interactions*, Sov. J. Nucl. Phys. **40** (1984) 329–334. (499, 606)

[1142] L. R. Surguladze, *Quark mass effects in fermionic decays of the Higgs boson in $\mathcal{O}(\alpha_s^2)$ perturbative QCD*, Phys. Lett. **B341** (1994) 60–72, arXiv:hep-ph/9405325 [hep-ph]. (499, 606)

[1143] S. Larin, T. van Ritbergen, and J. Vermaseren, *The Large top quark mass expansion for Higgs boson decays into bottom quarks and into gluons*, Phys. Lett. **B362** (1995) 134–140, arXiv:hep-ph/9506465 [hep-ph]. (499, 606)

[1144] K. Chetyrkin and A. Kwiatkowski, *Second order QCD corrections to scalar and pseudoscalar Higgs decays into massive bottom quarks*, Nucl. Phys. **B461** (1996) 3–18, arXiv:hep-ph/9505358 [hep-ph]. (499, 606)

[1145] K. Chetyrkin, *Correlator of the quark scalar currents and $\Gamma_{tot}(H \to \text{hadrons})$ at $\mathcal{O}(\alpha_s^3)$ in pQCD*, Phys. Lett. **B390** (1997) 309–317, arXiv:hep-ph/9608318 [hep-ph]. (499, 606)

[1146] P. Baikov, K. Chetyrkin, and J. H. Kühn, *Scalar correlator at $\mathcal{O}(\alpha_s^4)$, Higgs decay into b-quarks and bounds on the light quark masses*, Phys. Rev. Lett. **96** (2006) 012003, arXiv:hep-ph/0511063 [hep-ph]. (499, 606)

[1147] E. Boos and T. Plehn, *Higgs boson production induced by bottom quarks*, Phys. Rev. **D69** (2004) 094005, arXiv:hep-ph/0304034 [hep-ph]. (512, 516)

[1148] D. L. Rainwater, M. Spira, and D. Zeppenfeld, *Higgs boson production at hadron colliders: Signal and background processes*, in *Physics at TeV colliders. Proceedings, Euro Summer School*. Les Houches, France, May 21-June 1, 2001. arXiv:hep-ph/0203187 [hep-ph]. (512, 516)

[1149] S. Dawson, C. B. Jackson, L. Reina, and D. Wackeroth, *Higgs production in association with bottom quarks at hadron colliders*, Mod. Phys. Lett. **A21** (2006) 89–110, arXiv:hep-ph/0508293 [hep-ph]. (514, 526)

[1150] N. Liu, L. Wu, P. W. Wu, and J. M. Yang, *Complete one-loop effects of SUSY QCD in $b\bar{b}h$ production at the LHC under current experimental constraints*, JHEP **01** (2013) 161, arXiv:1208.3413 [hep-ph]. (514)

[1151] C. Balazs, H.-J. He, and C. P. Yuan, *QCD corrections to scalar production via heavy quark fusion at hadron colliders*, Phys. Rev. **D60** (1999) 114001, arXiv:hep-ph/9812263 [hep-ph]. (514, 608)

[1152] T. Ahmed, M. Mahakhud, P. Mathews, N. Rana, and V. Ravindran, *Two-loop QCD corrections to Higgs $\to b + \bar{b} + g$ amplitude*, JHEP **08** (2014) 075, arXiv:1405.2324 [hep-ph]. (514)

[1153] T. Gehrmann and D. Kara, *The $Hb\bar{b}$ form factor to three loops in QCD*, JHEP **09** (2014) 174, arXiv:1407.8114 [hep-ph]. (514)

[1154] M. Bonvini, A. S. Papanastasiou, and F. J. Tackmann, *Resummation and matching of b-quark mass effects in $b\bar{b}H$ production*, JHEP **11** (2015) 196, arXiv:1508.03288 [hep-ph]. (514, 515, 517, 518, 519, 520, 540)

[1155] S. Forte, D. Napoletano, and M. Ubiali, *Higgs production in bottom-quark fusion in a matched scheme*, Phys. Lett. **B751** (2015) 331–337, arXiv:1508.01529 [hep-ph]. (514, 515, 519, 521, 540, 541)

[1156] R. D. Ball, M. Bonvini, and L. Rottoli, *Charm in Deep-Inelastic Scattering*, JHEP **11** (2015) 122, arXiv:1510.02491 [hep-ph]. (514)

[1157] M. Buza, Y. Matiounine, J. Smith, and W. L. van Neerven, *Charm electroproduction viewed in the variable flavor number scheme versus fixed order perturbation theory*, Eur. Phys. J. **C1** (1998) 301–320, arXiv:hep-ph/9612398 [hep-ph]. (514)

[1158] I. Bierenbaum, J. Blumlein, and S. Klein, *The Gluonic Operator Matrix Elements at $\mathcal{O}(\alpha_s^2)$ for*

DIS Heavy Flavor Production, Phys. Lett. **B672** (2009) 401–406, arXiv:0901.0669 [hep-ph]. (514)

[1159] J. Ablinger, J. Blumlein, S. Klein, C. Schneider, and F. Wissbrock, *The $\mathcal{O}(\alpha_s^3)$ Massive Operator Matrix Elements of $O(n_f)$ for the Structure Function $F_2(x, Q^2)$ and Transversity*, Nucl. Phys. **B844** (2011) 26–54, arXiv:1008.3347 [hep-ph]. (514)

[1160] J. Ablinger, J. Blümlein, A. De Freitas, A. Hasselhuhn, A. von Manteuffel, M. Round, C. Schneider, and F. Wißbrock, *The Transition Matrix Element $A_{gq}(N)$ of the Variable Flavor Number Scheme at $\mathcal{O}(\alpha_s^3)$*, Nucl. Phys. **B882** (2014) 263–288, arXiv:1402.0359 [hep-ph]. (514)

[1161] J. Ablinger, A. Behring, J. Blümlein, A. De Freitas, A. Hasselhuhn, A. von Manteuffel, M. Round, C. Schneider, and F. Wißbrock, *The 3-Loop Non-Singlet Heavy Flavor Contributions and Anomalous Dimensions for the Structure Function $F_2(x, Q^2)$ and Transversity*, Nucl. Phys. **B886** (2014) 733–823, arXiv:1406.4654 [hep-ph]. (514)

[1162] J. Ablinger, A. Behring, J. Blümlein, A. De Freitas, A. von Manteuffel, and C. Schneider, *The 3-loop pure singlet heavy flavor contributions to the structure function $F_2(x, Q^2)$ and the anomalous dimension*, Nucl. Phys. **B890** (2014) 48–151, arXiv:1409.1135 [hep-ph]. (514)

[1163] M. Beneke and V. M. Braun, *Heavy quark effective theory beyond perturbation theory: Renormalons, the pole mass and the residual mass term*, Nucl. Phys. **B426** (1994) 301–343, arXiv:hep-ph/9402364 [hep-ph]. (515)

[1164] M. Beneke, *Renormalons*, Phys. Rept. **317** (1999) 1–142, arXiv:hep-ph/9807443 [hep-ph]. (515)

[1165] V. Bertone, S. Carrazza, and J. Rojo, *APFEL: A PDF Evolution Library with QED corrections*, Comput. Phys. Commun. **185** (2014) 1647, arXiv:1310.1394 [hep-ph]. (515)

[1166] M. Bonvini, A. S. Papanastasiou, and F. J. Tackmann, *Matched predictions for the $b\bar{b}H$ cross section at the 13 TeV LHC*, arXiv:1605.01733 [hep-ph]. (517, 519, 520, 521)

[1167] S. Bühler, F. Herzog, A. Lazopoulos, and R. Müller, *The fully differential hadronic production of a Higgs boson via bottom quark fusion at NNLO*, JHEP **07** (2012) 115, arXiv:1204.4415 [hep-ph]. (519, 524)

[1168] S. Forte, D. Napoletano, and M. Ubiali, *Higgs production in bottom-quark fusion: matching beyond leading order*, arXiv:1607.00389 [hep-ph]. (521)

[1169] B. Jager, L. Reina, and D. Wackeroth, *Higgs boson production in association with b jets in the POWHEG BOX*, Phys. Rev. **D93** (2016) 014030, arXiv:1509.05843 [hep-ph]. (524, 526)

[1170] J. M. Campbell, R. K. Ellis, F. Maltoni, and S. Willenbrock, *Higgs-Boson production in association with a single bottom quark*, Phys. Rev. **D67** (2003) 095002, arXiv:hep-ph/0204093 [hep-ph]. (524)

[1171] R. V. Harlander, K. J. Ozeren, and M. Wiesemann, *Higgs plus jet production in bottom quark annihilation at next-to-leading order*, Phys. Lett. **B693** (2010) 269–273, arXiv:1007.5411 [hep-ph]. (524)

[1172] R. Harlander and M. Wiesemann, *Jet-veto in bottom-quark induced Higgs production at next-to-next-to-leading order*, JHEP **04** (2012) 066, arXiv:1111.2182 [hep-ph]. (524)

[1173] K. J. Ozeren, *Analytic Results for Higgs Production in Bottom Fusion*, JHEP **11** (2010) 084, arXiv:1010.2977 [hep-ph]. (524)

[1174] A. Belyaev, P. M. Nadolsky, and C. P. Yuan, *Transverse momentum resummation for Higgs boson produced via b anti-b fusion at hadron colliders*, JHEP **04** (2006) 004, arXiv:hep-ph/0509100 [hep-ph]. (524)

[1175] R. V. Harlander, A. Tripathi, and M. Wiesemann, *Higgs production in bottom quark annihilation: Transverse momentum distribution at NNLO+NNLL*, Phys. Rev. **D90** (2014)

015017, arXiv:1403.7196 [hep-ph]. (524)

[1176] T. Stelzer and W. F. Long, *Automatic generation of tree level helicity amplitudes*, Comput. Phys. Commun. **81** (1994) 357–371, arXiv:hep-ph/9401258 [hep-ph]. (526)

[1177] R. V. Harlander, *Higgs production in heavy quark annihilation through next-to-next-to-leading order QCD*, Eur. Phys. J. **C76** (2016) 252, arXiv:1512.04901 [hep-ph]. (535)

[1178] CMS Collaboration, V. Khachatryan et al., *Search for a charged Higgs boson in pp collisions at* $\sqrt{s} = 8\,TeV$, JHEP **11** (2015) 018, arXiv:1508.07774 [hep-ex]. (539)

[1179] C. Degrande, R. Frederix, V. Hirschi, M. Ubiali, M. Wiesemann, and M. Zaro, *Accurate predictions for charged Higgs production: closing the* $m_{H^\pm} \sim m_t$ *window*, arXiv:1607.05291 [hep-ph]. (539)

[1180] M. Flechl, R. Klees, M. Krämer, M. Spira, and M. Ubiali, *Improved cross-section predictions for heavy charged Higgs boson production at the LHC*, Phys. Rev. **D91** (2015) 075015, arXiv:1409.5615 [hep-ph]. (539, 540, 541)

[1181] C. Degrande, M. Ubiali, M. Wiesemann, and M. Zaro, *Heavy charged Higgs boson production at the LHC*, JHEP **10** (2015) 145, arXiv:1507.02549 [hep-ph]. (540, 543, 544, 546)

[1182] M. Carena, M. Olechowski, S. Pokorski, and C. E. M. Wagner, *Radiative electroweak symmetry breaking and the infrared fixed point of the top quark mass*, Nucl. Phys. **B419** (1994) 213–239, arXiv:hep-ph/9311222 [hep-ph]. (540)

[1183] S. Dittmaier, M. Krämer, M. Spira, and M. Walser, *Charged-Higgs-boson production at the LHC: NLO supersymmetric QCD corrections*, Phys. Rev. D **83** (2011) 055005, arXiv:0906.2648 [hep-ph]. (540)

[1184] D. Bourilkov, R. C. Group, and M. R. Whalley, *LHAPDF: PDF use from the Tevatron to the LHC*, arXiv:hep-ph/0605240. (540)

[1185] T. Plehn, *Charged Higgs boson production in bottom gluon fusion*, Phys. Rev. D **67** (2003) 014018, arXiv:hep-ph/0206121. (540)

[1186] C. Weydert, S. Frixione, M. Herquet, M. Klasen, E. Laenen, T. Plehn, G. Stavenga, and C. D. White, *Charged Higgs boson production in association with a top quark in MC@NLO*, Eur. Phys. J. **C67** (2010) 617–636, arXiv:0912.3430 [hep-ph]. (543)

[1187] M. Klasen, K. Kovarik, P. Nason, and C. Weydert, *Associated production of charged Higgs bosons and top quarks with POWHEG*, Eur. Phys. J. **C72** (2012) 2088, arXiv:1203.1341 [hep-ph]. (543)

[1188] T. D. Lee, *A Theory of Spontaneous T Violation*, Phys. Rev. **D8** (1973) 1226–1239. (549)

[1189] J. F. Gunion, H. E. Haber, G. L. Kane, and S. Dawson, *The Higgs Hunter's Guide*. Westview Press, USA, 448 p, 2000. (549, 578)

[1190] I. F. Ginzburg, M. Krawczyk, and P. Osland, *Two Higgs doublet models with CP violation*, in *Linear colliders. Proceedings, International Workshop on physics and experiments with future electron-positron linear colliders, LCWS 2002*. Seogwipo, Jeju Island, Korea, August 26-30, 2002. arXiv:hep-ph/0211371 [hep-ph]. (549)

[1191] S. L. Glashow and S. Weinberg, *Natural Conservation Laws for Neutral Currents*, Phys. Rev. **D15** (1977) 1958. (550, 631, 632)

[1192] E. A. Paschos, *Diagonal Neutral Currents*, Phys. Rev. **D15** (1977) 1966. (550, 631, 632)

[1193] V. D. Barger, J. L. Hewett, and R. J. N. Phillips, *New Constraints on the Charged Higgs Sector in Two Higgs Doublet Models*, Phys. Rev. **D41** (1990) 3421–3441. (550)

[1194] D. Fontes, J. C. Romão, R. Santos, and J. a. P. Silva, *Large pseudoscalar Yukawa couplings in the complex 2HDM*, JHEP **06** (2015) 060, arXiv:1502.01720 [hep-ph]. (550)

[1195] J. F. Gunion and H. E. Haber, *The CP conserving two Higgs doublet model: The Approach to the decoupling limit*, Phys. Rev. **D67** (2003) 075019, arXiv:hep-ph/0207010 [hep-ph].

(550, 633)

[1196] I. F. Ginzburg, M. Krawczyk, and P. Osland, *Resolving SM like scenarios via Higgs boson production at a photon collider. 1. 2HDM versus SM*, arXiv:hep-ph/0101208 [hep-ph]. (550)

[1197] P. M. Ferreira, J. F. Gunion, H. E. Haber, and R. Santos, *Probing wrong-sign Yukawa couplings at the LHC and a future linear collider*, Phys. Rev. **D89** (2014) 115003, arXiv:1403.4736 [hep-ph]. (550)

[1198] P. M. Ferreira, R. Guedes, M. O. P. Sampaio, and R. Santos, *Wrong sign and symmetric limits and non-decoupling in 2HDMs*, JHEP **12** (2014) 067, arXiv:1409.6723 [hep-ph]. (550, 552)

[1199] N. G. Deshpande and E. Ma, *Pattern of Symmetry Breaking with Two Higgs Doublets*, Phys. Rev. **D18** (1978) 2574. (550, 553)

[1200] Q.-H. Cao, E. Ma, and G. Rajasekaran, *Observing the Dark Scalar Doublet and its Impact on the Standard-Model Higgs Boson at Colliders*, Phys. Rev. **D76** (2007) 095011, arXiv:0708.2939 [hep-ph]. (550)

[1201] R. Barbieri, L. J. Hall, and V. S. Rychkov, *Improved naturalness with a heavy Higgs: An Alternative road to LHC physics*, Phys. Rev. **D74** (2006) 015007, arXiv:hep-ph/0603188 [hep-ph]. (550)

[1202] L. Lopez Honorez, E. Nezri, J. F. Oliver, and M. H. Tytgat, *The Inert Doublet Model: An Archetype for Dark Matter*, JCAP **02** (2007) 028, arXiv:hep-ph/0612275 [hep-ph]. (550)

[1203] A. Ilnicka, M. Krawczyk, and T. Robens, *Inert Doublet Model in light of LHC Run I and astrophysical data*, Phys. Rev. **D93** (2016) 055026, arXiv:1508.01671 [hep-ph]. (550, 554, 565)

[1204] A. Arhrib, Y.-L. S. Tsai, Q. Yuan, and T.-C. Yuan, *An Updated Analysis of Inert Higgs Doublet Model in light of the Recent Results from LUX, PLANCK, AMS-02 and LHC*, JCAP **1406** (2014) 030, arXiv:1310.0358 [hep-ph]. (550)

[1205] E. Dolle, X. Miao, S. Su, and B. Thomas, *Dilepton Signals in the Inert Doublet Model*, Phys. Rev. **D81** (2010) 035003, arXiv:0909.3094 [hep-ph]. (550)

[1206] E. M. Dolle and S. Su, *The Inert Dark Matter*, Phys. Rev. **D80** (2009) 055012, arXiv:0906.1609 [hep-ph]. (550)

[1207] M. Gustafsson, S. Rydbeck, L. Lopez-Honorez, and E. Lundstrom, *Status of the Inert Doublet Model and the Role of multileptons at the LHC*, Phys. Rev. **D86** (2012) 075019, arXiv:1206.6316 [hep-ph]. (550)

[1208] I. Ginzburg, K. Kanishev, M. Krawczyk, and D. Sokolowska, *Evolution of Universe to the present inert phase*, Phys. Rev. **D82** (2010) 123533, arXiv:1009.4593 [hep-ph]. (550)

[1209] V. D. Barger, N. G. Deshpande, J. L. Hewett, and T. G. Rizzo, *A Separate Higgs?*, in *Workshop on Physics at Current Accelerators and the Supercollider*. Argonne, Illinois, June 2–5, 1993. arXiv:hep-ph/9211234 [hep-ph]. (550)

[1210] M. A. Diaz and T. J. Weiler, *Decays of a fermiophobic Higgs*, in *the 3rd Annual Southern Association for High-energy Physics Meeting*. Gulf Shores, Alabama, USA, January 3-5, 1994. arXiv:hep-ph/9401259 [hep-ph]. (550)

[1211] L. Brucher and R. Santos, *Experimental signatures of fermiophobic Higgs bosons*, Eur. Phys. J. **C12** (2000) 87–98, arXiv:hep-ph/9907434 [hep-ph]. (550)

[1212] R. Santos, *Interpretation of the LHC run-1 Higgs results (2HDM)*, in *Proceedings, 5th International Workshop on Prospects for Charged Higgs Discovery at Colliders (CHARGED 2014): Uppsala, Sweden, September 16-18, 2014*, p. 016. 2015. (551)

[1213] P. M. Ferreira, L. Lavoura, and J. P. Silva, *Renormalization-group constraints on Yukawa*

alignment in multi-Higgs-doublet models, Phys. Lett. **B688** (2010) 341–344, arXiv:1001.2561 [hep-ph]. (551)

[1214] G. C. Branco, W. Grimus, and L. Lavoura, *Relating the scalar flavor changing neutral couplings to the CKM matrix*, Phys. Lett. **B380** (1996) 119–126, arXiv:hep-ph/9601383 [hep-ph]. (551)

[1215] F. J. Botella, G. C. Branco, and M. N. Rebelo, *Minimal Flavour Violation and Multi-Higgs Models*, Phys. Lett. **B687** (2010) 194–200, arXiv:0911.1753 [hep-ph]. (551)

[1216] F. J. Botella, G. C. Branco, M. Nebot, and M. N. Rebelo, *Two-Higgs Leptonic Minimal Flavour Violation*, JHEP **10** (2011) 037, arXiv:1102.0520 [hep-ph]. (551)

[1217] D. Eriksson, J. Rathsman, and O. Stal, *2HDMC: Two-Higgs-doublet model calculator*, Comput. Phys. Commun. **181** (2010) 833–834. (552, 554)

[1218] R. Coimbra, M. O. P. Sampaio, and R. Santos, *ScannerS: Constraining the phase diagram of a complex scalar singlet at the LHC*, Eur. Phys. J. **C73** (2013) 2428, arXiv:1301.2599 [hep-ph]. (552, 588, 590, 591)

[1219] R. Harlander, M. Mühlleitner, J. Rathsman, M. Spira, and O. Stål, *Interim recommendations for the evaluation of Higgs production cross sections and branching ratios at the LHC in the Two-Higgs-Doublet Model*, arXiv:1312.5571 [hep-ph]. (552, 554)

[1220] P. M. Ferreira, R. Santos, and A. Barroso, *Stability of the tree-level vacuum in two Higgs doublet models against charge or CP spontaneous violation*, Phys. Lett. **B603** (2004) 219–229, arXiv:hep-ph/0406231 [hep-ph]. [Erratum-ibid. **B629** (2005) 114]. (553)

[1221] A. Barroso, P. M. Ferreira, and R. Santos, *Charge and CP symmetry breaking in two Higgs doublet models*, Phys. Lett. **B632** (2006) 684–687, arXiv:hep-ph/0507224 [hep-ph]. (553)

[1222] A. Barroso, P. M. Ferreira, and R. Santos, *Neutral minima in two-Higgs doublet models*, Phys. Lett. **B652** (2007) 181–193, arXiv:hep-ph/0702098 [HEP-PH]. (553)

[1223] I. P. Ivanov, *Minkowski space structure of the Higgs potential in 2HDM*, Phys. Rev. **D75** (2007) 035001, arXiv:hep-ph/0609018 [hep-ph]. [Erratum-ibid. **D76** (2007) 039902]. (553)

[1224] I. P. Ivanov, *Minkowski space structure of the Higgs potential in 2HDM. II. Minima, symmetries, and topology*, Phys. Rev. **D77** (2008) 015017, arXiv:0710.3490 [hep-ph]. (553)

[1225] M. Maniatis, A. von Manteuffel, O. Nachtmann, and F. Nagel, *Stability and symmetry breaking in the general two-Higgs-doublet model*, Eur. Phys. J. **C48** (2006) 805–823, arXiv:hep-ph/0605184 [hep-ph]. (553)

[1226] A. Barroso, P. M. Ferreira, I. P. Ivanov, and R. Santos, *Metastability bounds on the two Higgs doublet model*, JHEP **06** (2013) 045, arXiv:1303.5098 [hep-ph]. (553)

[1227] I. P. Ivanov, *General two-order-parameter Ginzburg-Landau model with quadratic and quartic interactions*, Phys. Rev. **E79** (2009) 021116, arXiv:0802.2107 [cond-mat.other]. (553)

[1228] S. Kanemura, T. Kubota, and E. Takasugi, *Lee-Quigg-Thacker bounds for Higgs boson masses in a two doublet model*, Phys. Lett. **B313** (1993) 155–160, arXiv:hep-ph/9303263 [hep-ph]. (553)

[1229] A. G. Akeroyd, A. Arhrib, and E.-M. Naimi, *Note on tree level unitarity in the general two Higgs doublet model*, Phys. Lett. **B490** (2000) 119–124, arXiv:hep-ph/0006035 [hep-ph]. (553)

[1230] B. W. Lee, C. Quigg, and H. B. Thacker, *Weak Interactions at Very High-Energies: The Role of the Higgs Boson Mass*, Phys. Rev. **D16** (1977) 1519. (553)

[1231] M. E. Peskin and T. Takeuchi, *Estimation of oblique electroweak corrections*, Phys. Rev. **D46** (1992) 381–409. (553, 590)

[1232] C. D. Froggatt, R. G. Moorhouse, and I. G. Knowles, *Leading radiative corrections in two scalar doublet models*, Phys. Rev. **D45** (1992) 2471–2481. (553)

[1233] W. Grimus, L. Lavoura, O. M. Ogreid, and P. Osland, *The Oblique parameters in multi-Higgs-doublet models*, Nucl. Phys. **B801** (2008) 81–96, arXiv:0802.4353 [hep-ph]. (553)

[1234] H. E. Haber and D. O'Neil, *Basis-independent methods for the two-Higgs-doublet model III: The CP-conserving limit, custodial symmetry, and the oblique parameters S, T, U*, Phys. Rev. **D83** (2011) 055017, arXiv:1011.6188 [hep-ph]. (553)

[1235] M. Baak, M. Goebel, J. Haller, A. Hoecker, D. Ludwig, K. Moenig, M. Schott, and J. Stelzer, *Updated Status of the Global Electroweak Fit and Constraints on New Physics*, Eur. Phys. J. **C72** (2012) 2003, arXiv:1107.0975 [hep-ph]. (553)

[1236] Tevatron Electroweak Working Group, CDF, DELPHI, SLD Electroweak and Heavy Flavour Groups, ALEPH, LEP Electroweak Working Group, SLD, OPAL, D0, L3 Collaboration, L. E. W. Group, *Precision Electroweak Measurements and Constraints on the Standard Model*, arXiv:1012.2367 [hep-ex]. (553)

[1237] P. Bechtle, O. Brein, S. Heinemeyer, O. Stål, T. Stefaniak, G. Weiglein, and K. E. Williams, HiggsBounds*-4: Improved Tests of Extended Higgs Sectors against Exclusion Bounds from LEP, the Tevatron and the LHC*, Eur. Phys. J. **C74** (2014) 2693, arXiv:1311.0055 [hep-ph]. http://higgsbounds.hepforge.org. (553, 590, 605)

[1238] P. Bechtle, S. Heinemeyer, O. Stål, T. Stefaniak, and G. Weiglein, HiggsSignals*: Confronting arbitrary Higgs sectors with measurements at the Tevatron and the LHC*, Eur. Phys. J. **C74** (2014) 2711, arXiv:1305.1933 [hep-ph]. http://higgsbounds.hepforge.org. (553, 590, 606)

[1239] LEP, DELPHI, OPAL, ALEPH, L3 Collaboration, G. Abbiendi et al., *Search for Charged Higgs bosons: Combined Results Using LEP Data*, Eur. Phys. J. **C73** (2013) 2463, arXiv:1301.6065 [hep-ex]. (553)

[1240] A. Wahab El Kaffas, P. Osland, and O. M. Ogreid, *Constraining the Two-Higgs-Doublet-Model parameter space*, Phys. Rev. **D76** (2007) 095001, arXiv:0706.2997 [hep-ph]. (553)

[1241] M. Aoki, S. Kanemura, K. Tsumura, and K. Yagyu, *Models of Yukawa interaction in the two Higgs doublet model, and their collider phenomenology*, Phys. Rev. **D80** (2009) 015017, arXiv:0902.4665 [hep-ph]. (553)

[1242] S. Su and B. Thomas, *The LHC Discovery Potential of a Leptophilic Higgs*, Phys. Rev. **D79** (2009) 095014, arXiv:0903.0667 [hep-ph]. (553)

[1243] F. Mahmoudi and O. Stal, *Flavor constraints on the two-Higgs-doublet model with general Yukawa couplings*, Phys. Rev. **D81** (2010) 035016, arXiv:0907.1791 [hep-ph]. (553)

[1244] O. Deschamps, S. Descotes-Genon, S. Monteil, V. Niess, S. T'Jampens, and V. Tisserand, *The Two Higgs Doublet of Type II facing flavour physics data*, Phys. Rev. **D82** (2010) 073012, arXiv:0907.5135 [hep-ph]. (553)

[1245] A. Denner, R. J. Guth, W. Hollik, and J. H. Kühn, *The Z width in the two Higgs doublet model*, Z. Phys. **C51** (1991) 695–705. (553)

[1246] H. E. Haber and H. E. Logan, *Radiative corrections to the Z b anti-b vertex and constraints on extended Higgs sectors*, Phys. Rev. **D62** (2000) 015011, arXiv:hep-ph/9909335 [hep-ph]. (553)

[1247] A. Freitas and Y.-C. Huang, *Electroweak two-loop corrections to $sin^2\theta^{b\bar{b}}_{eff}$ and R_b using numerical Mellin-Barnes integrals*, JHEP **08** (2012) 050, arXiv:1205.0299 [hep-ph]. [Erratum-ibid. **10** (2013) 044]. (553)

[1248] M. Misiak et al., *Updated NNLO QCD predictions for the weak radiative B-meson decays*, Phys. Rev. Lett. **114** (2015) 221801, arXiv:1503.01789 [hep-ph]. (553)

[1249] CMS Collaboration, S. Chatrchyan et al., *Search for a light charged Higgs boson in top quark decays in pp collisions at $\sqrt{s} = 7$ TeV*, JHEP **07** (2012) 143, arXiv:1205.5736 [hep-ex].

(553)

[1250] ATLAS Collaboration, G. Aad et al., *Search for charged Higgs bosons decaying via $H^+ \to \tau\nu$ in top quark pair events using pp collision data at $\sqrt{s} = 7$ TeV with the ATLAS detector*, JHEP **06** (2012) 039, arXiv:1204.2760 [hep-ex]. (553)

[1251] S. Inoue, M. J. Ramsey-Musolf, and Y. Zhang, *CP-violating phenomenology of flavor conserving two Higgs doublet models*, Phys. Rev. **D89** (2014) 115023, arXiv:1403.4257 [hep-ph]. (553)

[1252] ACME Collaboration, J. Baron et al., *Order of Magnitude Smaller Limit on the Electric Dipole Moment of the Electron*, Science **343** (2014) 269–272, arXiv:1310.7534 [physics.atom-ph]. (553, 606)

[1253] M. Jung and A. Pich, *Electric Dipole Moments in Two-Higgs-Doublet Models*, JHEP **04** (2014) 076, arXiv:1308.6283 [hep-ph]. (554)

[1254] J. Shu and Y. Zhang, *Impact of a CP Violating Higgs Sector: From LHC to Baryogenesis*, Phys. Rev. Lett. **111** (2013) 091801, arXiv:1304.0773 [hep-ph]. (554)

[1255] Planck Collaboration, P. A. R. Ade et al., *Planck 2015 results. XIII. Cosmological parameters*, Astron. Astrophys. **594** (2016) A13, arXiv:1502.01589 [astro-ph.CO]. (554)

[1256] LUX Collaboration, D. Akerib et al., *First results from the LUX dark matter experiment at the Sanford Underground Research Facility*, Phys. Rev. Lett. **112** (2014) 091303, arXiv:1310.8214 [astro-ph.CO]. (554, 590)

[1257] G. Belanger, F. Boudjema, A. Pukhov, and A. Semenov, micrOMEGAs_*3: A program for calculating dark matter observables*, Comput. Phys. Commun. **185** (2014) 960–985, arXiv:1305.0237 [hep-ph]. (554)

[1258] G. Belanger, F. Boudjema, A. Pukhov, and A. Semenov, *Dark matter direct detection rate in a generic model with* micrOMEGAs *2.2*, Comput. Phys. Commun. **180** (2009) 747–767, arXiv:0803.2360 [hep-ph]. (554)

[1259] F. Kling, J. M. No, and S. Su, *Anatomy of Exotic Higgs Decays in 2HDM*, JHEP **09** (2016) 093, arXiv:1604.01406 [hep-ph]. (559)

[1260] G. C. Dorsch, S. J. Huber, K. Mimasu, and J. M. No, *Echoes of the Electroweak Phase Transition: Discovering a second Higgs doublet through $A_0 \to Z H_0$*, Phys. Rev. Lett. **113** (2014) 211802, arXiv:1405.5537 [hep-ph]. (563)

[1261] CMS Collaboration, *Search for H/A decaying into Z and A/H, with $Z \to \ell\ell$ and $A/H \to bb$ or $A/H \to \tau\tau$*, CMS-PAS-HIG-15-001, 2015. (575)

[1262] G. C. Branco, L. Lavoura, and J. P. Silva, *CP Violation*, vol. 103 of *Int. Ser. Monogr. Phys.* Oxford Science Publications, UK, 536 p, 1999. (568)

[1263] D. Fontes, J. C. Romão, R. Santos, and J. P. Silva, *Undoubtable signs of CP-violation in Higgs boson decays at the LHC run 2*, Phys. Rev. **D92** (2015) 055014, arXiv:1506.06755 [hep-ph]. (568)

[1264] A. Arhrib and R. Benbrik, *Searching for a CP-odd Higgs via a pair of gauge bosons at the LHC*, arXiv:hep-ph/0610184 [hep-ph]. (568)

[1265] D. Fontes, J. C. Romão, and J. a. P. Silva, *$h \to Z\gamma$ in the complex two Higgs doublet model*, JHEP **12** (2014) 043, arXiv:1408.2534 [hep-ph]. (568, 569, 570, 571, 572)

[1266] F. J. Botella, G. C. Branco, M. Nebot, and M. N. Rebelo, *Flavour Changing Higgs Couplings in a Class of Two Higgs Doublet Models*, Eur. Phys. J. **C76** (2016) 161, arXiv:1508.05101 [hep-ph]. (573)

[1267] A. Falkowski, S. Rychkov, and A. Urbano, *What if the Higgs couplings to W and Z bosons are larger than in the Standard Model?*, JHEP **04** (2012) 073, arXiv:1202.1532 [hep-ph]. (574)

[1268] B. Grinstein, C. W. Murphy, D. Pirtskhalava, and P. Uttayarat, *Theoretical Constraints on*

Additional Higgs Bosons in Light of the 126 GeV Higgs, JHEP **05** (2014) 083, arXiv:1401.0070 [hep-ph]. (574)

[1269] B. Bellazzini, L. Martucci, and R. Torre, *Symmetries, Sum Rules and Constraints on Effective Field Theories*, JHEP **09** (2014) 100, arXiv:1405.2960 [hep-th]. (574)

[1270] ATLAS Collaboration, G. Aad et al., *Search for a Charged Higgs Boson Produced in the Vector-Boson Fusion Mode with Decay $H^{\pm} \to W^{\pm}Z$ using pp Collisions at $\sqrt{s} = 8$ TeV with the ATLAS Experiment*, Phys. Rev. Lett. **114** (2015) 231801, arXiv:1503.04233 [hep-ex]. (575)

[1271] H. Georgi and M. Machacek, *Doubly Charged Higgs Bosons*, Nucl. Phys. **B262** (1985) 463. (575, 576)

[1272] M. S. Chanowitz and M. Golden, *Higgs Boson Triplets with $M_W = M_Z \cos\theta_W$*, Phys. Lett. **B165** (1985) 105. (575, 576)

[1273] S. Godfrey and K. Moats, *Exploring Higgs Triplet Models via Vector Boson Scattering at the LHC*, Phys. Rev. **D81** (2010) 075026, arXiv:1003.3033 [hep-ph]. (575, 578)

[1274] K. Hartling, K. Kumar, and H. E. Logan, *GMCALC: a calculator for the Georgi-Machacek model*, arXiv:1412.7387 [hep-ph]. (575, 579, 585)

[1275] C. Degrande, K. Hartling, H. E. Logan, A. D. Peterson, and M. Zaro, *Automatic predictions in the Georgi-Machacek model at next-to-leading order accuracy*, Phys. Rev. **D93** (2016) 035004, arXiv:1512.01243 [hep-ph]. (576)

[1276] K. Hartling, K. Kumar, and H. E. Logan, *The decoupling limit in the Georgi-Machacek model*, Phys. Rev. **D90** (2014) 015007, arXiv:1404.2640 [hep-ph]. (576, 578, 579)

[1277] M. Aoki and S. Kanemura, *Unitarity bounds in the Higgs model including triplet fields with custodial symmetry*, Phys. Rev. **D77** (2008) 095009, arXiv:0712.4053 [hep-ph]. [Erratum-ibid. **D89** (2014) 059902]. (577, 579)

[1278] H. E. Logan and V. Rentala, *All the generalized Georgi-Machacek models*, Phys. Rev. **D92** (2015) 075011, arXiv:1502.01275 [hep-ph]. (579)

[1279] C.-W. Chiang, S. Kanemura, and K. Yagyu, *Novel constraint on the parameter space of the Georgi-Machacek model with current LHC data*, Phys. Rev. **D90** (2014) 115025, arXiv:1407.5053 [hep-ph]. (579)

[1280] K. Hartling, K. Kumar, and H. E. Logan, *Indirect constraints on the Georgi-Machacek model and implications for Higgs boson couplings*, Phys. Rev. **D91** (2015) 015013, arXiv:1410.5538 [hep-ph]. (579)

[1281] M. Zaro, P. Bolzoni, F. Maltoni, and S.-O. Moch, *Charged Higgs production via vector-boson fusion at NNLO in QCD*, in *Proceedings, 3rd International Workshop on Prospects for charged Higgs discovery at colliders (CHARGED 2010): Uppsala, Sweden, September 27-30, 2010*, vol. CHARGED2010, p. 028. 2010. arXiv:1012.1806 [hep-ph]. (580)

[1282] V. Silveira and A. Zee, *Scalar Phantoms*, Phys. Lett. **B161** (1985) 136. (585, 621, 643)

[1283] J. McDonald, *Gauge singlet scalars as cold dark matter*, Phys. Rev. **D50** (1994) 3637–3649, arXiv:hep-ph/0702143 [HEP-PH]. (585)

[1284] C. Burgess, M. Pospelov, and T. ter Veldhuis, *The Minimal model of nonbaryonic dark matter: A Singlet scalar*, Nucl. Phys. **B619** (2001) 709–728, arXiv:hep-ph/0011335 [hep-ph]. (585)

[1285] M. C. Bento, O. Bertolami, R. Rosenfeld, and L. Teodoro, *Selfinteracting dark matter and invisibly decaying Higgs*, Phys. Rev. **D62** (2000) 041302, arXiv:astro-ph/0003350 [astro-ph]. (585)

[1286] H. Davoudiasl, R. Kitano, T. Li, and H. Murayama, *The New minimal standard model*, Phys. Lett. **B609** (2005) 117–123, arXiv:hep-ph/0405097 [hep-ph]. (585)

[1287] A. Kusenko, *Sterile neutrinos, dark matter, and the pulsar velocities in models with a Higgs singlet*, Phys. Rev. Lett. **97** (2006) 241301, arXiv:hep-ph/0609081 [hep-ph]. (585)

[1288] J. J. van der Bij, *The Minimal non-minimal standard model*, Phys. Lett. **B636** (2006) 56–59, arXiv:hep-ph/0603082 [hep-ph]. (585)

[1289] X.-G. He, T. Li, X.-Q. Li, J. Tandean, and H.-C. Tsai, *Constraints on Scalar Dark Matter from Direct Experimental Searches*, Phys. Rev. **D79** (2009) 023521, arXiv:0811.0658 [hep-ph]. (585)

[1290] M. Gonderinger, Y. Li, H. Patel, and M. J. Ramsey-Musolf, *Vacuum Stability, Perturbativity, and Scalar Singlet Dark Matter*, JHEP **01** (2010) 053, arXiv:0910.3167 [hep-ph]. (585)

[1291] Y. Mambrini, *Higgs searches and singlet scalar dark matter: Combined constraints from XENON 100 and the LHC*, Phys. Rev. **D84** (2011) 115017, arXiv:1108.0671 [hep-ph]. (585)

[1292] X.-G. He, B. Ren, and J. Tandean, *Hints of Standard Model Higgs Boson at the LHC and Light Dark Matter Searches*, Phys. Rev. **D85** (2012) 093019, arXiv:1112.6364 [hep-ph]. (585)

[1293] A. Menon, D. Morrissey, and C. Wagner, *Electroweak baryogenesis and dark matter in the nMSSM*, Phys. Rev. **D70** (2004) 035005, arXiv:hep-ph/0404184 [hep-ph]. (585)

[1294] S. J. Huber, T. Konstandin, T. Prokopec, and M. G. Schmidt, *Electroweak Phase Transition and Baryogenesis in the nMSSM*, Nucl. Phys. **B757** (2006) 172–196, arXiv:hep-ph/0606298 [hep-ph]. (585)

[1295] S. Profumo, M. J. Ramsey-Musolf, and G. Shaughnessy, *Singlet Higgs phenomenology and the electroweak phase transition*, JHEP **08** (2007) 010, arXiv:0705.2425 [hep-ph]. (585, 621, 643)

[1296] V. Barger, D. J. H. Chung, A. J. Long, and L.-T. Wang, *Strongly First Order Phase Transitions Near an Enhanced Discrete Symmetry Point*, Phys. Lett. **B710** (2012) 1–7, arXiv:1112.5460 [hep-ph]. (585)

[1297] J. R. Espinosa, T. Konstandin, and F. Riva, *Strong Electroweak Phase Transitions in the Standard Model with a Singlet*, Nucl. Phys. **B854** (2012) 592–630, arXiv:1107.5441 [hep-ph]. (585)

[1298] A. Datta and A. Raychaudhuri, *Next-to-minimal Higgs: Mass bounds and search prospects*, Phys. Rev. **D57** (1998) 2940–2948, arXiv:hep-ph/9708444 [hep-ph]. (585)

[1299] O. Bahat-Treidel, Y. Grossman, and Y. Rozen, *Hiding the Higgs at the LHC*, JHEP **05** (2007) 022, arXiv:hep-ph/0611162 [hep-ph]. (585)

[1300] V. Barger, P. Langacker, and G. Shaughnessy, *Collider Signatures of Singlet Extended Higgs Sectors*, Phys. Rev. **D75** (2007) 055013, arXiv:hep-ph/0611239 [hep-ph]. (585)

[1301] V. Barger, P. Langacker, M. McCaskey, M. J. Ramsey-Musolf, and G. Shaughnessy, *LHC Phenomenology of an Extended Standard Model with a Real Scalar Singlet*, Phys. Rev. **D77** (2008) 035005, arXiv:0706.4311 [hep-ph]. (585)

[1302] V. Barger, P. Langacker, M. McCaskey, M. Ramsey-Musolf, and G. Shaughnessy, *Complex Singlet Extension of the Standard Model*, Phys. Rev. **D79** (2009) 015018, arXiv:0811.0393 [hep-ph]. (585)

[1303] D. O'Connell, M. J. Ramsey-Musolf, and M. B. Wise, *Minimal Extension of the Standard Model Scalar Sector*, Phys. Rev. **D75** (2007) 037701, arXiv:hep-ph/0611014 [hep-ph]. (585)

[1304] R. S. Gupta and J. D. Wells, *Higgs boson search significance deformations due to mixed-in scalars*, Phys. Lett. **B710** (2012) 154–158, arXiv:1110.0824 [hep-ph]. (585)

[1305] S. Kanemura, M. Kikuchi, and K. Yagyu, *Radiative corrections to the Higgs boson couplings in the model with an additional real singlet scalar field*, Nucl. Phys. **B907** (2016) 286–322, arXiv:1511.06211 [hep-ph]. (589)

[1306] G. M. Pruna and T. Robens, *Higgs singlet extension parameter space in the light of the LHC discovery*, Phys. Rev. **D88** (2013) 115012, arXiv:1303.1150 [hep-ph]. (590)

[1307] R. Costa, A. P. Morais, M. O. P. Sampaio, and R. Santos, *Two-loop stability of a complex singlet extended Standard Model*, Phys. Rev. **D92** (2015) 025024, arXiv:1411.4048 [hep-ph]. (590, 592, 599, 601)

[1308] R. N. Lerner and J. McDonald, *Gauge singlet scalar as inflaton and thermal relic dark matter*, Phys. Rev. **D80** (2009) 123507, arXiv:0909.0520 [hep-ph]. (590)

[1309] G. Belanger, F. Boudjema, and A. Pukhov, micrOMEGAs*: a code for the calculation of Dark Matter properties in generic models of particle interaction*, arXiv:1402.0787 [hep-ph]. https://lapth.cnrs.fr/micromegas/. (590)

[1310] Planck Collaboration, P. Ade et al., *Planck 2013 results. XVI. Cosmological parameters*, Astron. Astrophys. (2014) , arXiv:1303.5076 [astro-ph.CO]. (590)

[1311] WMAP Collaboration, G. Hinshaw et al., *Nine-Year Wilkinson Microwave Anisotropy Probe (WMAP) Observations: Cosmological Parameter Results*, Astrophys. J. Suppl. **208** (2013) 19, arXiv:1212.5226 [astro-ph.CO]. (590)

[1312] I. Maksymyk, C. P. Burgess, and D. London, *Beyond S, T and U*, Phys. Rev. **D50** (1994) 529–535, arXiv:hep-ph/9306267 [hep-ph]. (590)

[1313] P. Bechtle, O. Brein, S. Heinemeyer, G. Weiglein, and K. E. Williams, *HiggsBounds: Confronting Arbitrary Higgs Sectors with Exclusion Bounds from LEP and the Tevatron*, Comput. Phys. Commun. **181** (2010) 138–167, arXiv:0811.4169 [hep-ph]. (590, 605)

[1314] P. Bechtle, O. Brein, S. Heinemeyer, G. Weiglein, and K. E. Williams, *HiggsBounds 2.0.0: Confronting Neutral and Charged Higgs Sector Predictions with Exclusion Bounds from LEP and the Tevatron*, Comput. Phys. Commun. **182** (2011) 2605–2631, arXiv:1102.1898 [hep-ph]. (590, 605)

[1315] P. Bechtle, S. Heinemeyer, O. Stål, T. Stefaniak, and G. Weiglein, *Applying Exclusion Likelihoods from LHC Searches to Extended Higgs Sectors*, Eur. Phys. J. **C75** (2015) 421, arXiv:1507.06706 [hep-ph]. (590)

[1316] R. Costa, R. Guedes, M. O. P. Sampaio, and R. Santos, ScannerS, http://scanners.hepforge.org, 2014. (591)

[1317] P. Fayet, *Supergauge Invariant Extension of the Higgs Mechanism and a Model for the electron and Its Neutrino*, Nucl. Phys. **B90** (1975) 104–124. (603)

[1318] M. Dine, W. Fischler, and M. Srednicki, *A Simple Solution to the Strong CP Problem with a Harmless Axion*, Phys. Lett. **B104** (1981) 199. (603)

[1319] H. P. Nilles, M. Srednicki, and D. Wyler, *Weak Interaction Breakdown Induced by Supergravity*, Phys. Lett. **B120** (1983) 346. (603)

[1320] J. Derendinger and C. A. Savoy, *Quantum Effects and SU(2) x U(1) Breaking in Supergravity Gauge Theories*, Nucl. Phys. **B237** (1984) 307. (603)

[1321] J. Frere, D. Jones, and S. Raby, *Fermion Masses and Induction of the Weak Scale by Supergravity*, Nucl. Phys. **B222** (1983) 11. (603)

[1322] A. I. Veselov, M. I. Vysotsky, and K. A. Ter-Martirosian, *Low-Energy Supergravity and the Light t Quark*, Sov. Phys. JETP **63** (1986) 489. [Zh. Eksp. Teor. Fiz. **90** (1986) 838-858]. (603)

[1323] J. R. Ellis, J. Gunion, H. E. Haber, L. Roszkowski, and F. Zwirner, *Higgs Bosons in a Nonminimal Supersymmetric Model*, Phys. Rev. **D39** (1989) 844. (603)

[1324] U. Ellwanger, M. Rausch de Traubenberg, and C. A. Savoy, *Particle spectrum in supersymmetric models with a gauge singlet*, Phys. Lett. **B315** (1993) 331–337, arXiv:hep-ph/9307322 [hep-ph]. (603)

[1325] S. King and P. White, *Resolving the constrained minimal and next-to-minimal supersymmetric*

standard models, Phys. Rev. **D52** (1995) 4183–4216, arXiv:hep-ph/9505326 [hep-ph]. (603)

[1326] U. Ellwanger, M. Rausch de Traubenberg, and C. A. Savoy, *Phenomenology of supersymmetric models with a singlet*, Nucl. Phys. **B492** (1997) 21–50, arXiv:hep-ph/9611251 [hep-ph]. (603)

[1327] F. Franke and H. Fraas, *Neutralinos and Higgs bosons in the next-to-minimal supersymmetric standard model*, Int. J. Mod. Phys. **A12** (1997) 479–534, arXiv:hep-ph/9512366 [hep-ph]. (603)

[1328] B. Ananthanarayan and P. N. Pandita, *The Nonminimal supersymmetric standard model at large tan beta*, Int. J. Mod. Phys. **A12** (1997) 2321–2342, arXiv:hep-ph/9601372 [hep-ph]. (603)

[1329] U. Ellwanger and C. Hugonie, *Masses and couplings of the lightest Higgs bosons in the (M+1) SSM*, Eur. Phys. J. **C25** (2002) 297–305, arXiv:hep-ph/9909260 [hep-ph]. (603)

[1330] U. Ellwanger, C. Hugonie, and A. M. Teixeira, *The Next-to-Minimal Supersymmetric Standard Model*, Phys.Rept. **496** (2010) 1–77, arXiv:0910.1785 [hep-ph]. (603, 604)

[1331] M. Maniatis, *The Next-to-Minimal Supersymmetric extension of the Standard Model reviewed*, Int. J. Mod. Phys. **A25** (2010) 3505–3602, arXiv:0906.0777 [hep-ph]. (603)

[1332] J. E. Kim and H. P. Nilles, *The mu Problem and the Strong CP Problem*, Phys. Lett. **B138** (1984) 150. (603)

[1333] M. Bastero-Gil, C. Hugonie, S. F. King, D. P. Roy, and S. Vempati, *Does LEP prefer the NMSSM?*, Phys. Lett. **B489** (2000) 359–366, arXiv:hep-ph/0006198 [hep-ph]. (603)

[1334] R. Dermisek and J. F. Gunion, *Consistency of LEP event excesses with an $h \to aa$ decay scenario and low-fine-tuning NMSSM models*, Phys. Rev. **D73** (2006) 111701, arXiv:hep-ph/0510322 [hep-ph]. (603)

[1335] U. Ellwanger, G. Espitalier-Noel, and C. Hugonie, *Naturalness and Fine Tuning in the NMSSM: Implications of Early LHC Results*, JHEP **09** (2011) 105, arXiv:1107.2472 [hep-ph]. (603)

[1336] G. G. Ross and K. Schmidt-Hoberg, *The Fine-Tuning of the Generalised NMSSM*, Nucl. Phys. **B862** (2012) 710–719, arXiv:1108.1284 [hep-ph]. (603)

[1337] G. G. Ross, K. Schmidt-Hoberg, and F. Staub, *The Generalised NMSSM at One Loop: Fine Tuning and Phenomenology*, JHEP **08** (2012) 074, arXiv:1205.1509 [hep-ph]. (603)

[1338] T. Gherghetta, B. von Harling, A. D. Medina, and M. A. Schmidt, *The Scale-Invariant NMSSM and the 126 GeV Higgs Boson*, JHEP **02** (2013) 032, arXiv:1212.5243 [hep-ph]. (603)

[1339] M. Perelstein and B. Shakya, *XENON100 implications for naturalness in the MSSM, NMSSM, and λ-supersymmetry model*, Phys. Rev. **D88** (2013) 075003, arXiv:1208.0833 [hep-ph]. (603)

[1340] S. F. King, M. Mühlleitner, R. Nevzorov, and K. Walz, *Natural NMSSM Higgs Bosons*, Nucl. Phys. **B870** (2013) 323–352, arXiv:1211.5074 [hep-ph]. (603, 608, 617)

[1341] D. Kim, P. Athron, C. Balázs, B. Farmer, and E. Hutchison, *Bayesian naturalness of the CMSSM and CNMSSM*, Phys. Rev. **D90** (2014) 055008, arXiv:1312.4150 [hep-ph]. (603)

[1342] A. Kaminska, G. G. Ross, K. Schmidt-Hoberg, and F. Staub, *A precision study of the fine tuning in the DiracNMSSM*, JHEP **06** (2014) 153, arXiv:1401.1816 [hep-ph]. (603)

[1343] M. Y. Binjonaid and S. F. King, *Naturalness of scale-invariant NMSSMs with and without extra matter*, Phys. Rev. **D90** (2014) 055020, arXiv:1403.2088 [hep-ph]. [Erratum-ibid. **D90** (2014) 079903]. (603)

[1344] U. Ellwanger and A. M. Teixeira, *NMSSM with a singlino LSP: possible challenges for searches for supersymmetry at the LHC*, JHEP **10** (2014) 113, arXiv:1406.7221 [hep-ph]. (603, 615)

[1345] H. K. Dreiner, F. Staub, and A. Vicente, *General NMSSM signatures at the LHC*, Phys. Rev.

D87 (2013) 035009, arXiv:1211.6987 [hep-ph]. (604)

[1346] S. King, M. Mühlleitner, R. Nevzorov, and K. Walz, *Discovery Prospects for NMSSM Higgs Bosons at the High-Energy Large Hadron Collider*, Phys. Rev. **D90** (2014) 095014, arXiv:1408.1120 [hep-ph]. (604, 608, 617)

[1347] G. Degrassi and P. Slavich, *On the radiative corrections to the neutral Higgs boson masses in the NMSSM*, Nucl. Phys. **B825** (2010) 119–150, arXiv:0907.4682 [hep-ph]. (605, 606, 607)

[1348] F. Staub, W. Porod, and B. Herrmann, *The Electroweak sector of the NMSSM at the one-loop level*, JHEP **10** (2010) 040, arXiv:1007.4049 [hep-ph]. (605, 606)

[1349] K. Ender, T. Graf, M. Mühlleitner, and H. Rzehak, *Analysis of the NMSSM Higgs Boson Masses at One-Loop Level*, Phys. Rev. **D85** (2012) 075024, arXiv:1111.4952 [hep-ph]. (605, 606)

[1350] T. Graf, R. Gröber, M. Mühlleitner, H. Rzehak, and K. Walz, *Higgs Boson Masses in the Complex NMSSM at One-Loop Level*, JHEP **10** (2012) 122, arXiv:1206.6806 [hep-ph]. (605, 606)

[1351] P. Drechsel, L. Galeta, S. Heinemeyer, and G. Weiglein, *Precise Predictions for the Higgs-Boson Masses in the NMSSM*, arXiv:1601.08100 [hep-ph]. (605)

[1352] M. Mühlleitner, D. T. Nhung, H. Rzehak, and K. Walz, *Two-loop contributions of the order $\mathcal{O}(\alpha_t\alpha_s)$ to the masses of the Higgs bosons in the CP-violating NMSSM*, JHEP **05** (2015) 128, arXiv:1412.0918 [hep-ph]. (605, 606)

[1353] M. D. Goodsell, K. Nickel, and F. Staub, *Two-loop corrections to the Higgs masses in the NMSSM*, Phys. Rev. **D91** (2015) 035021, arXiv:1411.4665 [hep-ph]. (605)

[1354] F. Staub, P. Athron, U. Ellwanger, R. Gröber, M. Mühlleitner, P. Slavich, and A. Voigt, *Higgs mass predictions of public NMSSM spectrum generators*, Comput. Phys. Commun. **202** (2016) 113–130, arXiv:1507.05093 [hep-ph]. (605)

[1355] U. Ellwanger, J. F. Gunion, and C. Hugonie, *NMHDECAY: A Fortran code for the Higgs masses, couplings and decay widths in the NMSSM*, JHEP **02** (2005) 066, arXiv:hep-ph/0406215 [hep-ph]. (605, 606)

[1356] U. Ellwanger and C. Hugonie, *NMHDECAY 2.0: An Updated program for sparticle masses, Higgs masses, couplings and decay widths in the NMSSM*, Comput. Phys. Commun. **175** (2006) 290–303, arXiv:hep-ph/0508022 [hep-ph]. (605, 606)

[1357] U. Ellwanger and C. Hugonie, *NMSPEC: A Fortran code for the sparticle and Higgs masses in the NMSSM with GUT scale boundary conditions*, Comput. Phys. Commun. **177** (2007) 399–407, arXiv:hep-ph/0612134 [hep-ph]. (605)

[1358] F. Domingo, *A New Tool for the study of the CP-violating NMSSM*, JHEP **06** (2015) 052, arXiv:1503.07087 [hep-ph]. (605)

[1359] A. Dedes and P. Slavich, *Two loop corrections to radiative electroweak symmetry breaking in the MSSM*, Nucl. Phys. **B657** (2003) 333–354, arXiv:hep-ph/0212132 [hep-ph]. (605, 606)

[1360] D. Das, U. Ellwanger, and A. M. Teixeira, *NMSDECAY: A Fortran Code for Supersymmetric Particle Decays in the Next-to-Minimal Supersymmetric Standard Model*, Comput. Phys. Commun. **183** (2012) 774–779, arXiv:1106.5633 [hep-ph]. (605, 606)

[1361] M. Mühlleitner, A. Djouadi, and Y. Mambrini, *SDECAY: A Fortran code for the decays of the supersymmetric particles in the MSSM*, Comput. Phys. Commun. **168** (2005) 46–70, arXiv:hep-ph/0311167 [hep-ph]. (605, 606)

[1362] F. Domingo and U. Ellwanger, *Updated Constraints from B Physics on the MSSM and the NMSSM*, JHEP **12** (2007) 090, arXiv:0710.3714 [hep-ph]. (605)

[1363] F. Domingo and U. Ellwanger, *Constraints from the Muon g-2 on the Parameter Space of the*

NMSSM, JHEP **07** (2008) 079, arXiv:0806.0733 [hep-ph]. (605)

[1364] G. Belanger, F. Boudjema, C. Hugonie, A. Pukhov, and A. Semenov, *Relic density of dark matter in the NMSSM*, JCAP **0509** (2005) 001, arXiv:hep-ph/0505142 [hep-ph]. (605)

[1365] DELPHI, OPAL, ALEPH, LEP Working Group for Higgs Boson Searches, L3 Collaboration, S. Schael et al., *Search for neutral MSSM Higgs bosons at LEP*, Eur. Phys. J. **C47** (2006) 547–587, arXiv:hep-ex/0602042 [hep-ex]. (605)

[1366] J. Bernon, B. Dumont, and S. Kraml, *Status of Higgs couplings after run 1 of the LHC*, Phys. Rev. **D90** (2014) 071301, arXiv:1409.1588 [hep-ph]. (605)

[1367] W. Porod, *SPheno, a program for calculating supersymmetric spectra, SUSY particle decays and SUSY particle production at e^+e^- colliders*, Comput. Phys. Commun. **153** (2003) 275–315, arXiv:hep-ph/0301101 [hep-ph]. (605)

[1368] W. Porod and F. Staub, *SPheno 3.1: Extensions including flavour, CP-phases and models beyond the MSSM*, Comput. Phys. Commun. **183** (2012) 2458–2469, arXiv:1104.1573 [hep-ph]. (605)

[1369] F. Staub, *Sarah*, arXiv:0806.0538 [hep-ph]. (605)

[1370] F. Staub, *From Superpotential to Model Files for FeynArts and CalcHep/CompHep*, Comput. Phys. Commun. **181** (2010) 1077–1086, arXiv:0909.2863 [hep-ph]. (605)

[1371] F. Staub, *Automatic Calculation of supersymmetric Renormalization Group Equations and Self Energies*, Comput. Phys. Commun. **182** (2011) 808–833, arXiv:1002.0840 [hep-ph]. (605)

[1372] F. Staub, SARAH *3.2: Dirac Gauginos, UFO output, and more*, Comput. Phys. Commun. **184** (2013) 1792–1809, arXiv:1207.0906 [hep-ph]. (605)

[1373] F. Staub, SARAH *4: A tool for (not only SUSY) model builders*, Comput. Phys. Commun. **185** (2014) 1773–1790, arXiv:1309.7223 [hep-ph]. (605)

[1374] M. D. Goodsell, K. Nickel, and F. Staub, *Two-Loop Higgs mass calculations in supersymmetric models beyond the MSSM with SARAH and SPheno*, Eur. Phys. J. **C75** (2015) 32, arXiv:1411.0675 [hep-ph]. (605)

[1375] M. Goodsell, K. Nickel, and F. Staub, *Generic two-loop Higgs mass calculation from a diagrammatic approach*, Eur. Phys. J. **C75** (2015) 290, arXiv:1503.03098 [hep-ph]. (605)

[1376] M. D. Goodsell and F. Staub, *The Higgs mass in the CP violating MSSM, NMSSM, and beyond*, arXiv:1604.05335 [hep-ph]. (605)

[1377] W. Porod, F. Staub, and A. Vicente, *A Flavor Kit for BSM models*, Eur. Phys. J. **C74** (2014) 2992, arXiv:1405.1434 [hep-ph]. (605)

[1378] J. Baglio, R. Gröber, M. Mülleitner, D. T. Nhung, H. Rzehak, M. Spira, J. Streicher, and K. Walz, *NMSSMCALC: A Program Package for the Calculation of Loop-Corrected Higgs Boson Masses and Decay Widths in the (Complex) NMSSM*, Comput. Phys. Commun. **185** (2014) 3372–3391, arXiv:1312.4788 [hep-ph]. (606, 607)

[1379] J. M. Butterworth et al., *The Tools and Monte Carlo Working Group Summary Report from the Les Houches 2009 Workshop on TeV Colliders*, in *Physics at TeV colliders. Proceedings, 6th Workshop, dedicated to Thomas Binoth, Les Houches, France, June 8-26, 2009*. 2010. arXiv:1003.1643 [hep-ph]. (606)

[1380] A. Mendez and A. Pomarol, *QCD corrections to the charged Higgs boson hadronic width*, Phys. Lett. **B252** (1990) 461–466. (606)

[1381] C.-S. Li and R. J. Oakes, *QCD corrections to the hadronic decay width of a charged Higgs boson*, Phys. Rev. **D43** (1991) 855–859. (606)

[1382] A. Djouadi and P. Gambino, *QCD corrections to Higgs boson selfenergies and fermionic decay widths*, Phys. Rev. **D51** (1995) 218–228, arXiv:hep-ph/9406431 [hep-ph]. [Erratum-ibid. **D53** (1996) 4111]. (606)

[1383] M. Carena, S. Mrenna, and C. E. M. Wagner, *MSSM Higgs boson phenomenology at the Tevatron collider*, Phys. Rev. **D60** (1999) 075010, arXiv:hep-ph/9808312 [hep-ph]. (606)

[1384] M. Carena, J. R. Ellis, S. Mrenna, A. Pilaftsis, and C. E. M. Wagner, *Collider probes of the MSSM Higgs sector with explicit CP violation*, Nucl. Phys. **B659** (2003) 145–178, arXiv:hep-ph/0211467 [hep-ph]. (606)

[1385] A. Djouadi, V. Driesen, W. Hollik, and J. I. Illana, *The Coupling of the lightest SUSY Higgs boson to two photons in the decoupling regime*, Eur. Phys. J. **C1** (1998) 149–162, arXiv:hep-ph/9612362 [hep-ph]. (606)

[1386] H.-Q. Zheng and D.-D. Wu, *First order QCD corrections to the decay of the Higgs boson into two photons*, Phys. Rev. **D42** (1990) 3760–3763. (606)

[1387] A. Djouadi, M. Spira, J. J. van der Bij, and P. M. Zerwas, *QCD corrections to gamma gamma decays of Higgs particles in the intermediate mass range*, Phys. Lett. **B257** (1991) 187–190. (606)

[1388] S. Dawson and R. P. Kauffman, *QCD corrections to $H \to \gamma\gamma$*, Phys. Rev. **D47** (1993) 1264–1267. (606)

[1389] K. Melnikov and O. I. Yakovlev, *Higgs-two-photon interaction in the standard model. The QCD radiative correction*, Phys. Lett. **B312** (1993) 179–183, arXiv:hep-ph/9302281 [hep-ph]. (606)

[1390] M. Inoue, R. Najima, T. Oka, and J. Saito, *QCD corrections to two photon decay of the Higgs boson and its reverse process*, Mod. Phys. Lett. **A9** (1994) 1189–1194. (606)

[1391] A. Djouadi, J. Kalinowski, P. Ohmann, and P. M. Zerwas, *Heavy SUSY Higgs bosons at e^+e^- linear colliders*, Z. Phys. **C74** (1997) 93–111, arXiv:hep-ph/9605339 [hep-ph]. (606)

[1392] A. Djouadi, P. Janot, J. Kalinowski, and P. M. Zerwas, *SUSY decays of Higgs particles*, Phys. Lett. **B376** (1996) 220–226, arXiv:hep-ph/9603368 [hep-ph]. (606)

[1393] A. Bartl, H. Eberl, K. Hidaka, T. Kon, W. Majerotto, and Y. Yamada, *QCD corrections to Higgs boson decays into squarks in the minimal supersymmetric standard model*, Phys. Lett. **B402** (1997) 303–313, arXiv:hep-ph/9701398 [hep-ph]. (606)

[1394] A. Arhrib, A. Djouadi, W. Hollik, and C. Junger, *SUSY Higgs boson decays into scalar quarks: QCD corrections*, Phys. Rev. **D57** (1998) 5860–5870, arXiv:hep-ph/9702426 [hep-ph]. (606)

[1395] H. Eberl, K. Hidaka, S. Kraml, W. Majerotto, and Y. Yamada, *Improved SUSY QCD corrections to Higgs boson decays into quarks and squarks*, Phys. Rev. **D62** (2000) 055006, arXiv:hep-ph/9912463 [hep-ph]. (606)

[1396] J. Baglio, C. O. Krauss, M. Mühlleitner, and K. Walz, *Next-to-Leading Order NMSSM Decays with CP-odd Higgs Bosons and Stops*, JHEP **10** (2015) 024, arXiv:1505.07125 [hep-ph]. (606)

[1397] R. N. Cahn, *The Higgs Boson*, Rept. Prog. Phys. **52** (1989) 389. (606)

[1398] A. Djouadi, J. Kalinowski, and P. M. Zerwas, *Two and three-body decay modes of SUSY Higgs particles*, Z. Phys. **C70** (1996) 435–448, arXiv:hep-ph/9511342 [hep-ph]. (606)

[1399] S. Moretti and W. J. Stirling, *Contributions of below threshold decays to MSSM Higgs branching ratios*, Phys. Lett. **B347** (1995) 291–299, arXiv:hep-ph/9412209 [hep-ph]. [Erratum-ibid. **B366** (1996) 451]. (606)

[1400] A. Djouadi, *The Anatomy of electro-weak symmetry breaking. II. The Higgs bosons in the minimal supersymmetric model*, Phys. Rept. **459** (2008) 1–241, arXiv:hep-ph/0503173 [hep-ph]. (606)

[1401] R. L. Arnowitt, J. L. Lopez, and D. V. Nanopoulos, *Keeping the Demon of SUSY at Bay*, Phys. Rev. **D42** (1990) 2423–2426. (606)

[1402] J. R. Ellis and R. A. Flores, *Implications of the strange spin of the nucleon for the neutron electric dipole moment in supersymmetric theories*, Phys. Lett. **B377** (1996) 83–88, arXiv:hep-ph/9602211 [hep-ph]. (606)

[1403] S. Weinberg, *Larger Higgs Exchange Terms in the Neutron Electric Dipole Moment*, Phys. Rev. Lett. **63** (1989) 2333. (606)

[1404] D. A. Dicus, *Neutron Electric Dipole Moment From Charged Higgs Exchange*, Phys. Rev. **D41** (1990) 999. (606)

[1405] J. Dai, H. Dykstra, R. G. Leigh, S. Paban, and D. Dicus, *CP Violation From Three Gluon Operators in the Supersymmetric Standard Model*, Phys. Lett. **B237** (1990) 216. [Erratum-ibid. **B242** (1990) 547]. (606)

[1406] I. B. Khriplovich and S. K. Lamoreaux, *CP violation without strangeness: Electric dipole moments of particles, atoms, and molecules*. Springer-Verlag Berlin Heidelberg, Germany, 230 p, 1997. (606)

[1407] M. Pospelov and A. Ritz, *Theta induced electric dipole moment of the neutron via QCD sum rules*, Phys. Rev. Lett. **83** (1999) 2526–2529, arXiv:hep-ph/9904483 [hep-ph]. (606)

[1408] M. Pospelov and A. Ritz, *Theta vacua, QCD sum rules, and the neutron electric dipole moment*, Nucl. Phys. **B573** (2000) 177–200, arXiv:hep-ph/9908508 [hep-ph]. (606)

[1409] M. Pospelov and A. Ritz, *Neutron EDM from electric and chromoelectric dipole moments of quarks*, Phys. Rev. **D63** (2001) 073015, arXiv:hep-ph/0010037 [hep-ph]. (606)

[1410] D. A. Demir, M. Pospelov, and A. Ritz, *Hadronic EDMs, the Weinberg operator, and light gluinos*, Phys. Rev. **D67** (2003) 015007, arXiv:hep-ph/0208257 [hep-ph]. (606)

[1411] D. A. Demir, O. Lebedev, K. A. Olive, M. Pospelov, and A. Ritz, *Electric dipole moments in the MSSM at large tan beta*, Nucl. Phys. **B680** (2004) 339–374, arXiv:hep-ph/0311314 [hep-ph]. (606)

[1412] M. Pospelov and A. Ritz, *Electric dipole moments as probes of new physics*, Annals Phys. **318** (2005) 119–169, arXiv:hep-ph/0504231 [hep-ph]. (606)

[1413] K. A. Olive, M. Pospelov, A. Ritz, and Y. Santoso, *CP-odd phase correlations and electric dipole moments*, Phys. Rev. **D72** (2005) 075001, arXiv:hep-ph/0506106 [hep-ph]. (606)

[1414] G. F. Giudice and A. Romanino, *Electric dipole moments in split supersymmetry*, Phys. Lett. **B634** (2006) 307–314, arXiv:hep-ph/0510197 [hep-ph]. (606)

[1415] J. R. Ellis, J. S. Lee, and A. Pilaftsis, *Electric Dipole Moments in the MSSM Reloaded*, JHEP **10** (2008) 049, arXiv:0808.1819 [hep-ph]. (606)

[1416] Y. Li, S. Profumo, and M. Ramsey-Musolf, *Higgs-Higgsino-Gaugino Induced Two Loop Electric Dipole Moments*, Phys. Rev. **D78** (2008) 075009, arXiv:0806.2693 [hep-ph]. (606)

[1417] J. Ellis, J. S. Lee, and A. Pilaftsis, *A Geometric Approach to CP Violation: Applications to the MCPMFV SUSY Model*, JHEP **10** (2010) 049, arXiv:1006.3087 [hep-ph]. (606)

[1418] K. Cheung, T.-J. Hou, J. S. Lee, and E. Senaha, *Higgs Mediated EDMs in the Next-to-MSSM: An Application to Electroweak Baryogenesis*, Phys. Rev. **D84** (2011) 015002, arXiv:1102.5679 [hep-ph]. (606)

[1419] S. F. King, M. Mühlleitner, R. Nevzorov, and K. Walz, *Exploring the CP-violating NMSSM: EDM Constraints and Phenomenology*, Nucl. Phys. **B901** (2015) 526–555, arXiv:1508.03255 [hep-ph]. (606)

[1420] B. C. Regan, E. D. Commins, C. J. Schmidt, and D. DeMille, *New limit on the electron electric dipole moment*, Phys. Rev. Lett. **88** (2002) 071805. (606)

[1421] C. A. Baker et al., *An Improved experimental limit on the electric dipole moment of the neutron*, Phys. Rev. Lett. **97** (2006) 131801, arXiv:hep-ex/0602020 [hep-ex]. (606)

[1422] W. C. Griffith, M. D. Swallows, T. H. Loftus, M. V. Romalis, B. R. Heckel, and E. N. Fortson,

Improved Limit on the Permanent Electric Dipole Moment of Hg-199, Phys. Rev. Lett. **102** (2009) 101601. (606)

[1423] P. Athron, J.-h. Park, D. Stöckinger, and A. Voigt, *FlexibleSUSY - A spectrum generator generator for supersymmetric models*, Comput. Phys. Commun. **190** (2015) 139–172, arXiv:1406.2319 [hep-ph]. (607)

[1424] J. E. Camargo-Molina, B. O'Leary, W. Porod, and F. Staub, *Stability of the CMSSM against sfermion VEVs*, JHEP **12** (2013) 103, arXiv:1309.7212 [hep-ph]. (607)

[1425] N. Blinov and D. E. Morrissey, *Vacuum Stability and the MSSM Higgs Mass*, JHEP **03** (2014) 106, arXiv:1310.4174 [hep-ph]. (607)

[1426] D. Chowdhury, R. M. Godbole, K. A. Mohan, and S. K. Vempati, *Charge and Color Breaking Constraints in MSSM after the Higgs Discovery at LHC*, JHEP **02** (2014) 110, arXiv:1310.1932 [hep-ph]. (607)

[1427] J. E. Camargo-Molina, B. Garbrecht, B. O'Leary, W. Porod, and F. Staub, *Constraining the Natural MSSM through tunneling to color-breaking vacua at zero and non-zero temperature*, Phys. Lett. **B737** (2014) 156–161, arXiv:1405.7376 [hep-ph]. (607)

[1428] U. Chattopadhyay and A. Dey, *Exploring MSSM for Charge and Color Breaking and Other Constraints in the Context of Higgs@125 GeV*, JHEP **11** (2014) 161, arXiv:1409.0611 [hep-ph]. (607)

[1429] U. Ellwanger and C. Hugonie, *Constraints from charge and color breaking minima in the (M+1)SSM*, Phys. Lett. **B457** (1999) 299–306, arXiv:hep-ph/9902401 [hep-ph]. (607)

[1430] Y. Kanehata, T. Kobayashi, Y. Konishi, O. Seto, and T. Shimomura, *Constraints from Unrealistic Vacua in the Next-to-Minimal Supersymmetric Standard Model*, Prog. Theor. Phys. **126** (2011) 1051–1076, arXiv:1103.5109 [hep-ph]. (607)

[1431] T. Kobayashi, T. Shimomura, and T. Takahashi, *Constraining the Higgs sector from False Vacua in the Next-to-Minimal Supersymmetric Standard Model*, Phys. Rev. **D86** (2012) 015029, arXiv:1203.4328 [hep-ph]. (607)

[1432] J. E. Camargo-Molina, B. O'Leary, W. Porod, and F. Staub, **Vevacious***: A Tool For Finding The Global Minima Of One-Loop Effective Potentials With Many Scalars*, Eur. Phys. J. **C73** (2013) 2588, arXiv:1307.1477 [hep-ph]. (607)

[1433] C. L. Wainwright, *CosmoTransitions: Computing Cosmological Phase Transition Temperatures and Bubble Profiles with Multiple Fields*, Comput. Phys. Commun. **183** (2012) 2006–2013, arXiv:1109.4189 [hep-ph]. (607)

[1434] S. Liebler, *Neutral Higgs production at proton colliders in the CP-conserving NMSSM*, Eur. Phys. J. **C75** (2015) 210, arXiv:1502.07972 [hep-ph]. (608)

[1435] R. N. Cahn and S. Dawson, *Production of Very Massive Higgs Bosons*, Phys. Lett. **B136** (1984) 196. [Erratum-ibid. **B138** (1984) 464]. (608)

[1436] K.-i. Hikasa, *Heavy Higgs Production in e^+e^- and e^-e^- Collisions*, Phys. Lett. **B164** (1985) 385. [Erratum-ibid. **B195** (1987) 623]. (608)

[1437] G. Altarelli, B. Mele, and F. Pitolli, *Heavy Higgs Production at Future Colliders*, Nucl. Phys. **B287** (1987) 205–224. (608)

[1438] R. Raitio and W. W. Wada, *Higgs Boson Production at Large Transverse Momentum in QCD*, Phys. Rev. **D19** (1979) 941. (608)

[1439] J. N. Ng and P. Zakarauskas, *A QCD Parton Calculation of Conjoined Production of Higgs Bosons and Heavy Flavors in $p\bar{p}$ Collision*, Phys. Rev. **D29** (1984) 876. (608)

[1440] Z. Kunszt, *Associated Production of Heavy Higgs Boson with Top Quarks*, Nucl. Phys. **B247** (1984) 339. (608)

[1441] J. F. Gunion, *Associated top-anti-top-Higgs production as a large source of WH events:*

implications for Higgs detection in the $\ell\nu\gamma\gamma$ final state, Phys. Lett. **B261** (1991) 510–517. (608)

[1442] W. J. Marciano and F. E. Paige, *Associated production of Higgs bosons with $t\bar{t}$ pairs*, Phys. Rev. Lett. **66** (1991) 2433–2435. (608)

[1443] A. Djouadi and M. Spira, *SUSY - QCD corrections to Higgs boson production at hadron colliders*, Phys. Rev. **D62** (2000) 014004, arXiv:hep-ph/9912476 [hep-ph]. (608)

[1444] W. Hollik, T. Plehn, M. Rauch, and H. Rzehak, *Supersymmetric Higgs Bosons in Weak Boson Fusion*, Phys. Rev. Lett. **102** (2009) 091802, arXiv:0804.2676 [hep-ph]. (608)

[1445] W. Peng, M. Wen-Gan, H. Hong-Sheng, Z. Ren-You, H. Liang, and J. Yi, *NLO supersymmetric QCD corrections to $t\bar{t}h^0$ associated production at hadron colliders*, arXiv:hep-ph/0505086 [hep-ph]. (608)

[1446] W. Hollik and M. Rauch, *Higgs-Boson production in association with heavy quarks*, in *Supersymmetry and the unification of fundamental interactions. Proceedings, 14th International Conference, SUSY 2006, Irvine, USA, June 12–17, 2006*, vol. 903, pp. 117–120. 2007. arXiv:hep-ph/0610340 [hep-ph]. (608)

[1447] P. Häfliger, *Associated MSSM Higgs production with heavy quarks: SUSY-QCD corrections and impact of A_0 on the mSUGRA parameter space*. PhD thesis, Zurich, ETH, 2006. http://e-collection.library.ethz.ch/view/eth:29320. (608)

[1448] M. Walser, *NLO QCD and SUSY-QCD corrections to associated MSSM Higgs production with heavy quarks at hadron colliders*. PhD thesis, Zurich, ETH, 2008. http://e-collection.library.ethz.ch/view/eth:30494. (608)

[1449] S. L. Glashow, D. V. Nanopoulos, and A. Yildiz, *Associated Production of Higgs Bosons and Z Particles*, Phys. Rev. **D18** (1978) 1724–1727. (608)

[1450] Z. Kunszt, Z. Trócsányi, and W. J. Stirling, *Clear signal of intermediate mass Higgs boson production at LHC and SSC*, Phys. Lett. **B271** (1991) 247–255. (608)

[1451] B. Allanach, M. Badziak, C. Hugonie, and R. Ziegler, *Light Sparticles from a Light Singlet in Gauge Mediation*, Phys. Rev. **D92** (2015) 015006, arXiv:1502.05836 [hep-ph]. (613)

[1452] N.-E. Bomark, S. Moretti, S. Munir, and L. Roszkowski, *A light NMSSM pseudoscalar Higgs boson at the LHC redux*, JHEP **02** (2015) 044, arXiv:1409.8393 [hep-ph]. (614)

[1453] N.-E. Bomark, S. Moretti, and L. Roszkowski, *Detection prospects of light NMSSM Higgs pseudoscalar via cascades of heavier scalars from vector boson fusion and Higgs-strahlung*, J. Phys. **G43** (2016) 105003, arXiv:1503.04228 [hep-ph]. (614)

[1454] C. T. Potter, *Natural NMSSM with a Light Singlet Higgs and Singlino LSP*, Eur. Phys. J. **C76** (2016) 44, arXiv:1505.05554 [hep-ph]. (614)

[1455] D. Barducci, G. Bélanger, C. Hugonie, and A. Pukhov, *Status and prospects of the nMSSM after LHC Run-1*, JHEP **01** (2016) 050, arXiv:1510.00246 [hep-ph]. (615)

[1456] U. Ellwanger and A. M. Teixeira, *Excessive Higgs pair production with little MET from squarks and gluinos in the NMSSM*, JHEP **04** (2015) 172, arXiv:1412.6394 [hep-ph]. (615)

[1457] C. Han, D. Kim, S. Munir, and M. Park, *$\mathcal{O}(1)$ GeV dark matter in SUSY and a very light pseudoscalar at the LHC*, JHEP **07** (2015) 002, arXiv:1504.05085 [hep-ph]. (616)

[1458] C. Beskidt, W. de Boer, D. I. Kazakov, and S. Wayand, *Higgs branching ratios in constrained minimal and next-to-minimal supersymmetry scenarios surveyed*, Phys. Lett. **B759** (2016) 141–148, arXiv:1602.08707 [hep-ph]. (618)

[1459] N. D. Christensen, T. Han, Z. Liu, and S. Su, *Low-Mass Higgs Bosons in the NMSSM and Their LHC Implications*, JHEP **08** (2013) 019, arXiv:1303.2113 [hep-ph]. (619)

[1460] T. Han, Z. Liu, and S. Su, *Light Neutralino Dark Matter: Direct/Indirect Detection and Collider Searches*, JHEP **08** (2014) 093, arXiv:1406.1181 [hep-ph]. (619)

[1461] ATLAS Collaboration, G. Aad et al., *Search for Higgs and Z Boson Decays to J/$\psi\,\gamma$ and Υ*

(nS),γ with the ATLAS Detector, Phys. Rev. Lett. **114** (2015) 121801, arXiv:1501.03276 [hep-ex]. (621, 629, 639, 640)

[1462] CMS Collaboration, V. Khachatryan et al., *Search for a Higgs boson decaying into $\gamma^*\gamma \to \ell\ell\gamma$ with low dilepton mass in pp collisions at $\sqrt{s} = 8$ TeV*, Phys. Lett. **B753** (2016) 341–362, arXiv:1507.03031 [hep-ex]. (621, 639)

[1463] G. Perez, Y. Soreq, E. Stamou, and K. Tobioka, *Constraining the charm Yukawa and Higgs-quark coupling universality*, Phys. Rev. **D92** (2015) 033016, arXiv:1503.00290 [hep-ph]. (621, 629)

[1464] B. A. Dobrescu and K. T. Matchev, *Light axion within the next-to-minimal supersymmetric standard model*, JHEP **09** (2000) 031, arXiv:hep-ph/0008192 [hep-ph]. (621, 643)

[1465] U. Ellwanger, J. F. Gunion, C. Hugonie, and S. Moretti, *Towards a no lose theorem for NMSSM Higgs discovery at the LHC*, arXiv:hep-ph/0305109 [hep-ph]. (621, 643)

[1466] R. Dermisek and J. F. Gunion, *Escaping the large fine tuning and little hierarchy problems in the next to minimal supersymmetric model and $h \to aa$ decays*, Phys. Rev. Lett. **95** (2005) 041801, arXiv:hep-ph/0502105 [hep-ph]. (621, 643, 655)

[1467] S. Chang, R. Dermisek, J. F. Gunion, and N. Weiner, *Nonstandard Higgs Boson Decays*, Ann. Rev. Nucl. Part. Sci. **58** (2008) 75–98, arXiv:0801.4554 [hep-ph]. (621)

[1468] D. E. Morrissey and A. Pierce, *Modified Higgs Boson Phenomenology from Gauge or Gaugino Mediation in the NMSSM*, Phys. Rev. **D78** (2008) 075029, arXiv:0807.2259 [hep-ph]. (621, 643, 655)

[1469] A. Belyaev, J. Pivarski, A. Safonov, S. Senkin, and A. Tatarinov, *LHC discovery potential of the lightest NMSSM Higgs in the $h_1 \to a_1 a_1 \to 4\mu$ channel*, Phys. Rev. **D81** (2010) 075021, arXiv:1002.1956 [hep-ph]. (621, 643)

[1470] N. Blinov, J. Kozaczuk, D. E. Morrissey, and C. Tamarit, *Electroweak Baryogenesis from Exotic Electroweak Symmetry Breaking*, Phys. Rev. **D92** (2015) 035012, arXiv:1504.05195 [hep-ph]. (621, 643)

[1471] M. Pospelov, A. Ritz, and M. B. Voloshin, *Secluded WIMP Dark Matter*, Phys. Lett. **B662** (2008) 53–61, arXiv:0711.4866 [hep-ph]. (621, 643)

[1472] P. Draper, T. Liu, C. E. M. Wagner, L.-T. Wang, and H. Zhang, *Dark Light Higgs*, Phys. Rev. Lett. **106** (2011) 121805, arXiv:1009.3963 [hep-ph]. (621)

[1473] S. Ipek, D. McKeen, and A. E. Nelson, *A Renormalizable Model for the Galactic Center Gamma Ray Excess from Dark Matter Annihilation*, Phys. Rev. **D90** (2014) 055021, arXiv:1404.3716 [hep-ph]. (621, 643)

[1474] A. Martin, J. Shelton, and J. Unwin, *Fitting the Galactic Center Gamma-Ray Excess with Cascade Annihilations*, Phys. Rev. **D90** (2014) 103513, arXiv:1405.0272 [hep-ph]. (621, 643)

[1475] G. Burdman, Z. Chacko, H.-S. Goh, and R. Harnik, *Folded supersymmetry and the LEP paradox*, JHEP **02** (2007) 009, arXiv:hep-ph/0609152 [hep-ph]. (621, 655, 657)

[1476] N. Craig, A. Katz, M. Strassler, and R. Sundrum, *Naturalness in the Dark at the LHC*, JHEP **07** (2015) 105, arXiv:1501.05310 [hep-ph]. (621, 655, 657, 658, 661)

[1477] D. Curtin and C. B. Verhaaren, *Discovering Uncolored Naturalness in Exotic Higgs Decays*, JHEP **12** (2015) 072, arXiv:1506.06141 [hep-ph]. (621, 657, 658, 659, 661, 662)

[1478] M. J. Strassler and K. M. Zurek, *Discovering the Higgs through highly-displaced vertices*, Phys. Lett. **B661** (2008) 263–267, arXiv:hep-ph/0605193 [hep-ph]. (621, 648, 655)

[1479] D. Curtin, R. Essig, S. Gori, P. Jaiswal, A. Katz, et al., *Exotic decays of the 125 GeV Higgs boson*, Phys. Rev. **D90** (2014) 075004, arXiv:1312.4992 [hep-ph]. (621, 642, 643, 644, 647, 653)

[1480] G. Perez, Y. Soreq, E. Stamou, and K. Tobioka, *Prospects for measuring the Higgs boson coupling to light quarks*, Phys. Rev. **D93** (2016) 013001, arXiv:1505.06689 [hep-ph]. (622, 629, 639)

[1481] M. Bander and A. Soni, *Decays of Higgs Scalars Into Vector Mesons and Photons*, Phys. Lett. **B82** (1979) 411. (622, 639)

[1482] W.-Y. Keung, *Decay of the Higgs boson into heavy-quarkonium states*, Phys. Rev. **D27** (1983) 2762. (622)

[1483] G. T. Bodwin, F. Petriello, S. Stoynev, and M. Velasco, *Higgs boson decays to quarkonia and the $H\bar{c}c$ coupling*, Phys. Rev. **D88** (2013) 053003, arXiv:1306.5770 [hep-ph]. (622, 628, 629)

[1484] A. L. Kagan, G. Perez, F. Petriello, Y. Soreq, S. Stoynev, and J. Zupan, *Exclusive Window onto Higgs Yukawa Couplings*, Phys. Rev. Lett. **114** (2015) 101802, arXiv:1406.1722 [hep-ph]. (622, 624, 625, 629)

[1485] G. T. Bodwin, H. S. Chung, J.-H. Ee, J. Lee, and F. Petriello, *Relativistic corrections to Higgs boson decays to quarkonia*, Phys. Rev. **D90** (2014) 113010, arXiv:1407.6695 [hep-ph]. (622, 624, 625, 629)

[1486] Y. Grossman, M. König, and M. Neubert, *Exclusive radiative decays of W and Z bosons in QCD factorization*, JHEP **04** (2015) 101, arXiv:1501.06569 [hep-ph]. (622, 639)

[1487] M. Koenig and M. Neubert, *Exclusive Radiative Higgs Decays as Probes of Light-Quark Yukawa Couplings*, JHEP **08** (2015) 012, arXiv:1505.03870 [hep-ph]. (622, 623, 624, 625, 629)

[1488] R. Harnik, J. Kopp, and J. Zupan, *Flavor Violating Higgs Decays*, JHEP **03** (2013) 026, arXiv:1209.1397 [hep-ph]. (623, 631, 637, 639)

[1489] G. Degrassi and F. Maltoni, *Two-loop electroweak corrections to the Higgs-boson decay $H \to$ gamma gamma*, Nucl. Phys. **B724** (2005) 183–196, arXiv:hep-ph/0504137 [hep-ph]. (623)

[1490] G. P. Lepage and S. J. Brodsky, *Exclusive Processes in Perturbative Quantum Chromodynamics*, Phys. Rev. **D22** (1980) 2157. (624)

[1491] A. V. Efremov and A. V. Radyushkin, *Factorization and Asymptotical Behavior of Pion Form-Factor in QCD*, Phys. Lett. **B94** (1980) 245–250. (624)

[1492] D.-N. Gao, *A note on Higgs decays into Z boson and $J/\psi(\Upsilon)$*, Phys. Lett. **B737** (2014) 366–368, arXiv:1406.7102 [hep-ph]. (628)

[1493] S. Alte, M. König, and M. Neubert, *Exclusive Weak Radiative Higgs Decays in the Standard Model and Beyond*, arXiv:1609.06310 [hep-ph]. (628)

[1494] A. Yu. Korchin and V. A. Kovalchuk, *Polarization effects in the Higgs boson decay to γZ and test of CP and CPT symmetries*, Phys. Rev. **D88** (2013) 036009, arXiv:1303.0365 [hep-ph]. (628)

[1495] Particle Data Group Collaboration, J. Beringer et al., *Review of Particle Physics (RPP)*, Phys. Rev. **D86** (2012) 010001. (629, 630)

[1496] G. Colangelo et al., *Review of lattice results concerning low energy particle physics*, Eur. Phys. J. **C71** (2011) 1695, arXiv:1011.4408 [hep-lat]. (630)

[1497] C. T. H. Davies, C. McNeile, E. Follana, G. P. Lepage, H. Na, and J. Shigemitsu, *Update: Precision D_s decay constant from full lattice QCD using very fine lattices*, Phys. Rev. **D82** (2010) 114504, arXiv:1008.4018 [hep-lat]. (630)

[1498] P. Gelhausen, A. Khodjamirian, A. A. Pivovarov, and D. Rosenthal, *Decay constants of heavy-light vector mesons from QCD sum rules*, Phys. Rev. **D88** (2013) 014015, arXiv:1305.5432 [hep-ph]. [Erratum-ibid. **D91** (2015) 099901]. (630)

[1499] Y. Chen, A. Alexandru, T. Draper, K.-F. Liu, Z. Liu, and Y.-B. Yang, *Leptonic Decay Constant of ρ at Physical Point*, arXiv:1507.02541 [hep-ph]. (630)

[1500] D. Becirevic, V. Lubicz, F. Mescia, and C. Tarantino, *Coupling of the light vector meson to the vector and to the tensor current*, JHEP **05** (2003) 007, arXiv:hep-lat/0301020 [hep-lat]. (630)

[1501] I. Brivio, F. Goertz, and G. Isidori, *Probing the Charm Quark Yukawa Coupling in Higgs+Charm Production*, Phys. Rev. Lett. **115** (2015) 211801, arXiv:1507.02916 [hep-ph]. (629, 639)

[1502] G. Blankenburg, J. Ellis, and G. Isidori, *Flavour-Changing Decays of a 125 GeV Higgs-like Particle*, Phys. Lett. **B712** (2012) 386–390, arXiv:1202.5704 [hep-ph]. (631, 637, 639)

[1503] M. Gorbahn and U. Haisch, *Searching for $t \to c(u)h$ with dipole moments*, JHEP **06** (2014) 033, arXiv:1404.4873 [hep-ph]. (631)

[1504] CMS Collaboration, *Search for lepton flavour violating decays of the Higgs boson to $e\tau$ and $e\mu$ in proton-proton collisions at $\sqrt{s} = 8$ TeV*, CMS-PAS-HIG-14-040, 2015. (631, 637)

[1505] ATLAS Collaboration, G. Aad et al., *Search for lepton-flavour-violating $H \to \mu\tau$ decays of the Higgs boson with the ATLAS detector*, JHEP **11** (2015) 211, arXiv:1508.03372 [hep-ex]. (631, 637, 639)

[1506] CMS Collaboration, V. Khachatryan et al., *Search for Lepton-Flavour-Violating Decays of the Higgs Boson*, Phys. Lett. **B749** (2015) 337–362, arXiv:1502.07400 [hep-ex]. (631, 637, 639)

[1507] F. Bishara, J. Brod, P. Uttayarat, and J. Zupan, *Nonstandard Yukawa Couplings and Higgs Portal Dark Matter*, JHEP **01** (2016) 010, arXiv:1504.04022 [hep-ph]. (631, 635)

[1508] A. Dery, A. Efrati, Y. Nir, Y. Soreq, and V. Susic, *Model building for flavor changing Higgs couplings*, Phys. Rev. **D90** (2014) 115022, arXiv:1408.1371 [hep-ph]. (631, 634)

[1509] A. Dery, A. Efrati, G. Hiller, Y. Hochberg, and Y. Nir, *Higgs couplings to fermions: 2HDM with MFV*, JHEP **08** (2013) 006, arXiv:1304.6727 [hep-ph]. (631)

[1510] A. Dery, A. Efrati, Y. Hochberg, and Y. Nir, *What if $BR(h \to \mu\mu)/BR(h \to \tau\tau)$ does not equal m_μ^2/m_τ^2?*, JHEP **05** (2013) 039, arXiv:1302.3229 [hep-ph]. (631, 632, 634)

[1511] M. Bauer, M. Carena, and K. Gemmler, *Creating the Fermion Mass Hierarchies with Multiple Higgs Bosons*, arXiv:1512.03458 [hep-ph]. (631, 635)

[1512] C. D. Froggatt and H. B. Nielsen, *Hierarchy of Quark Masses, Cabibbo Angles and CP Violation*, Nucl. Phys. **B147** (1979) 277. (631, 634)

[1513] G. F. Giudice and O. Lebedev, *Higgs-dependent Yukawa couplings*, Phys. Lett. **B665** (2008) 79–85, arXiv:0804.1753 [hep-ph]. (631, 635)

[1514] L. Randall and R. Sundrum, *A Large mass hierarchy from a small extra dimension*, Phys. Rev. Lett. **83** (1999) 3370–3373, arXiv:hep-ph/9905221 [hep-ph]. (631, 635)

[1515] H. Georgi, D. B. Kaplan, and P. Galison, *Calculation of the Composite Higgs Mass*, Phys. Lett. **B143** (1984) 152. (631, 636)

[1516] J. A. Aguilar-Saavedra, *A Minimal set of top-Higgs anomalous couplings*, Nucl. Phys. **B821** (2009) 215–227, arXiv:0904.2387 [hep-ph]. (631)

[1517] E. Gabrielli and G. F. Giudice, *Supersymmetric corrections to epsilon prime / epsilon at the leading order in QCD and QED*, Nucl. Phys. **B433** (1995) 3–25, arXiv:hep-lat/9407029 [hep-lat]. [Erratum-ibid. **B507** (1997) 549]. (631)

[1518] A. Ali and D. London, *Profiles of the unitarity triangle and CP violating phases in the standard model and supersymmetric theories*, Eur. Phys. J. **C9** (1999) 687–703, arXiv:hep-ph/9903535 [hep-ph]. (631)

[1519] A. J. Buras, P. Gambino, M. Gorbahn, S. Jager, and L. Silvestrini, *Universal unitarity triangle*

and physics beyond the standard model, Phys. Lett. **B500** (2001) 161–167, arXiv:hep-ph/0007085 [hep-ph]. (631)

[1520] A. J. Buras, *Minimal flavor violation*, in *Theoretical physics. Proceedings, 43rd Cracow School, Zakopane, Poland, May 30-June 8, 2003*, vol. B34, pp. 5615–5668. 2003. arXiv:hep-ph/0310208 [hep-ph]. (631)

[1521] A. L. Kagan, G. Perez, T. Volansky, and J. Zupan, *General Minimal Flavor Violation*, Phys. Rev. **D80** (2009) 076002, arXiv:0903.1794 [hep-ph]. (631)

[1522] H. E. Haber and G. L. Kane, *The Search for Supersymmetry: Probing Physics Beyond the Standard Model*, Phys. Rept. **117** (1985) 75–263. (633)

[1523] D. Aloni, Y. Nir, and E. Stamou, *Large BR($h \to \tau\mu$) in the MSSM?*, JHEP **04** (2016) 162, arXiv:1511.00979 [hep-ph]. (633, 638)

[1524] M. Carena, I. Low, N. R. Shah, and C. E. M. Wagner, *Impersonating the Standard Model Higgs Boson: Alignment without Decoupling*, JHEP **04** (2014) 015, arXiv:1310.2248 [hep-ph]. (633, 634)

[1525] P. S. B. Dev and A. Pilaftsis, *Maximally Symmetric Two Higgs Doublet Model with Natural Standard Model Alignment*, JHEP **12** (2014) 024, arXiv:1408.3405 [hep-ph]. (633)

[1526] M. Carena, H. E. Haber, I. Low, N. R. Shah, and C. E. M. Wagner, *Complementarity between Nonstandard Higgs Boson Searches and Precision Higgs Boson Measurements in the MSSM*, Phys. Rev. **D91** (2015) 035003, arXiv:1410.4969 [hep-ph]. (633)

[1527] P. S. B. Dev and A. Pilaftsis, *Natural Standard Model Alignment in the Two Higgs Doublet Model*, in *Proceedings, 4th Symposium on Prospects in the Physics of Discrete Symmetries (DISCRETE 2014)*, vol. 631, p. 012030. 2015. arXiv:1503.09140 [hep-ph]. (633)

[1528] M. Carena, H. E. Haber, I. Low, N. R. Shah, and C. E. M. Wagner, *Alignment limit of the NMSSM Higgs sector*, Phys. Rev. **D93** (2016) 035013, arXiv:1510.09137 [hep-ph]. (633)

[1529] D. Carmi, A. Falkowski, E. Kuflik, T. Volansky, and J. Zupan, *Higgs After the Discovery: A Status Report*, JHEP **10** (2012) 196, arXiv:1207.1718 [hep-ph]. (634)

[1530] A. Falkowski, F. Riva, and A. Urbano, *Higgs at last*, JHEP **11** (2013) 111, arXiv:1303.1812 [hep-ph]. (634)

[1531] B. Grinstein and P. Uttayarat, *Carving Out Parameter Space in Type-II Two Higgs Doublets Model*, JHEP **06** (2013) 094, arXiv:1304.0028 [hep-ph]. [Erratum-ibid. **09** (2013) 110]. (634)

[1532] M. Leurer, Y. Nir, and N. Seiberg, *Mass matrix models: The Sequel*, Nucl. Phys. **B420** (1994) 468–504, arXiv:hep-ph/9310320 [hep-ph]. (634)

[1533] Y. Grossman and Y. Nir, *Lepton mass matrix models*, Nucl. Phys. **B448** (1995) 30–50, arXiv:hep-ph/9502418 [hep-ph]. (634)

[1534] M. Bauer, M. Carena, and K. Gemmler, *Flavor from the Electroweak Scale*, JHEP **11** (2015) 016, arXiv:1506.01719 [hep-ph]. (635)

[1535] T. Gherghetta and A. Pomarol, *Bulk fields and supersymmetry in a slice of AdS*, Nucl. Phys. **B586** (2000) 141–162, arXiv:hep-ph/0003129 [hep-ph]. (635)

[1536] Y. Grossman and M. Neubert, *Neutrino masses and mixings in nonfactorizable geometry*, Phys. Lett. **B474** (2000) 361–371, arXiv:hep-ph/9912408 [hep-ph]. (635)

[1537] S. J. Huber and Q. Shafi, *Fermion masses, mixings and proton decay in a Randall-Sundrum model*, Phys. Lett. **B498** (2001) 256–262, arXiv:hep-ph/0010195 [hep-ph]. (635)

[1538] S. J. Huber, *Flavor violation and warped geometry*, Nucl. Phys. **B666** (2003) 269–288, arXiv:hep-ph/0303183 [hep-ph]. (635)

[1539] A. Azatov, M. Toharia, and L. Zhu, *Higgs Mediated FCNC's in Warped Extra Dimensions*, Phys. Rev. **D80** (2009) 035016, arXiv:0906.1990 [hep-ph]. (635, 636)

[1540] S. Casagrande, F. Goertz, U. Haisch, M. Neubert, and T. Pfoh, *Flavor Physics in the Randall-Sundrum Model: I. Theoretical Setup and Electroweak Precision Tests*, JHEP **10** (2008) 094, arXiv:0807.4937 [hep-ph]. (635)

[1541] M. Bauer, S. Casagrande, U. Haisch, and M. Neubert, *Flavor Physics in the Randall-Sundrum Model: II. Tree-Level Weak-Interaction Processes*, JHEP **09** (2010) 017, arXiv:0912.1625 [hep-ph]. (635)

[1542] R. Malm, M. Neubert, K. Novotny, and C. Schmell, *5D Perspective on Higgs Production at the Boundary of a Warped Extra Dimension*, JHEP **01** (2014) 173, arXiv:1303.5702 [hep-ph]. (635)

[1543] P. R. Archer, M. Carena, A. Carmona, and M. Neubert, *Higgs Production and Decay in Models of a Warped Extra Dimension with a Bulk Higgs*, JHEP **01** (2015) 060, arXiv:1408.5406 [hep-ph]. (635)

[1544] M. Blanke, A. J. Buras, B. Duling, S. Gori, and A. Weiler, Δ *F=2 Observables and Fine-Tuning in a Warped Extra Dimension with Custodial Protection*, JHEP **03** (2009) 001, arXiv:0809.1073 [hep-ph]. (635)

[1545] M. Blanke, A. J. Buras, B. Duling, K. Gemmler, and S. Gori, *Rare K and B Decays in a Warped Extra Dimension with Custodial Protection*, JHEP **03** (2009) 108, arXiv:0812.3803 [hep-ph]. (635)

[1546] M. E. Albrecht, M. Blanke, A. J. Buras, B. Duling, and K. Gemmler, *Electroweak and Flavour Structure of a Warped Extra Dimension with Custodial Protection*, JHEP **09** (2009) 064, arXiv:0903.2415 [hep-ph]. (635)

[1547] K. Agashe, G. Perez, and A. Soni, *Collider Signals of Top Quark Flavor Violation from a Warped Extra Dimension*, Phys. Rev. **D75** (2007) 015002, arXiv:hep-ph/0606293 [hep-ph]. (635)

[1548] K. Agashe, A. Azatov, Y. Cui, L. Randall, and M. Son, *Warped Dipole Completed, with a Tower of Higgs Bosons*, JHEP **06** (2015) 196, arXiv:1412.6468 [hep-ph]. (635)

[1549] B. M. Dillon and S. J. Huber, *Non-Custodial Warped Extra Dimensions at the LHC?*, JHEP **06** (2015) 066, arXiv:1410.7345 [hep-ph]. (635)

[1550] G. Cacciapaglia, C. Csaki, J. Galloway, G. Marandella, J. Terning, and A. Weiler, *A GIM Mechanism from Extra Dimensions*, JHEP **04** (2008) 006, arXiv:0709.1714 [hep-ph]. (635)

[1551] K. Agashe, G. Perez, and A. Soni, *Flavor structure of warped extra dimension models*, Phys. Rev. **D71** (2005) 016002, arXiv:hep-ph/0408134 [hep-ph]. (635)

[1552] K. Agashe, G. Perez, and A. Soni, *B-factory signals for a warped extra dimension*, Phys. Rev. Lett. **93** (2004) 201804, arXiv:hep-ph/0406101 [hep-ph]. (635)

[1553] ATLAS Collaboration, G. Aad et al., *A search for $t\bar{t}$ resonances using lepton-plus-jets events in proton-proton collisions at $\sqrt{s} = 8$ TeV with the ATLAS detector*, JHEP **08** (2015) 148, arXiv:1505.07018 [hep-ex]. (636)

[1554] D. B. Kaplan, *Flavor at SSC energies: A New mechanism for dynamically generated fermion masses*, Nucl. Phys. **B365** (1991) 259–278. (636)

[1555] K. Agashe and R. Contino, *Composite Higgs-Mediated FCNC*, Phys. Rev. **D80** (2009) 075016, arXiv:0906.1542 [hep-ph]. (636)

[1556] C. Delaunay, C. Grojean, and G. Perez, *Modified Higgs Physics from Composite Light Flavors*, JHEP **09** (2013) 090, arXiv:1303.5701 [hep-ph]. (636, 637)

[1557] A. Azatov, G. Panico, G. Perez, and Y. Soreq, *On the Flavor Structure of Natural Composite Higgs Models & Top Flavor Violation*, JHEP **12** (2014) 082, arXiv:1408.4525 [hep-ph]. (636)

[1558] A. Pomarol and F. Riva, *The Composite Higgs and Light Resonance Connection*, JHEP **08**

(2012) 135, arXiv:1205.6434 [hep-ph]. (636)

[1559] C. Delaunay, T. Golling, G. Perez, and Y. Soreq, *Enhanced Higgs boson coupling to charm pairs*, Phys. Rev. **D89** (2014) 033014. (636, 639)

[1560] M. Redi and A. Weiler, *Flavor and CP Invariant Composite Higgs Models*, JHEP **11** (2011) 108, arXiv:1106.6357 [hep-ph]. (637)

[1561] M. Redi, *Composite MFV and Beyond*, Eur. Phys. J. **C72** (2012) 2030, arXiv:1203.4220 [hep-ph]. (637)

[1562] M. Redi, *Leptons in Composite MFV*, JHEP **09** (2013) 060, arXiv:1306.1525 [hep-ph]. (637)

[1563] C. Csaki, C. Delaunay, C. Grojean, and Y. Grossman, *A Model of Lepton Masses from a Warped Extra Dimension*, JHEP **10** (2008) 055, arXiv:0806.0356 [hep-ph]. (637)

[1564] F. del Aguila, A. Carmona, and J. Santiago, *Neutrino Masses from an A4 Symmetry in Holographic Composite Higgs Models*, JHEP **08** (2010) 127, arXiv:1001.5151 [hep-ph]. (637)

[1565] C. Hagedorn and M. Serone, *Leptons in Holographic Composite Higgs Models with Non-Abelian Discrete Symmetries*, JHEP **10** (2011) 083, arXiv:1106.4021 [hep-ph]. (637)

[1566] C. Hagedorn and M. Serone, *General Lepton Mixing in Holographic Composite Higgs Models*, JHEP **02** (2012) 077, arXiv:1110.4612 [hep-ph]. (637)

[1567] ATLAS Collaboration, G. Aad et al., *Search for flavour-changing neutral current top quark decays $t \to Hq$ in pp collisions at $\sqrt{s} = 8$ TeV with the ATLAS detector*, JHEP **12** (2015) 061, arXiv:1509.06047 [hep-ex]. (637, 639)

[1568] CMS Collaboration, *Search for the Flavor-Changing Neutral Current Decay $t \to qH$ Where the Higgs Decays to $b\bar{b}$ Pairs at $\sqrt{s} = 8$ TeV*, CMS-PAS-TOP-14-020, 2015. (637)

[1569] CMS Collaboration, *Search for top quark decays via Higgs-boson-mediated flavor changing neutral currents in pp collisions at $\sqrt{s} = 8$ TeV*, CMS-PAS-TOP-13-017, 2015. (637)

[1570] I. Doršner, S. Fajfer, A. Greljo, J. F. Kamenik, N. Košnik, and I. Nišandžić, *New Physics Models Facing Lepton Flavor Violating Higgs Decays at the Percent Level*, JHEP **06** (2015) 108, arXiv:1502.07784 [hep-ph]. (637, 638)

[1571] MEG Collaboration, J. Adam et al., *New constraint on the existence of the $\mu^+ \to e^+\gamma$ decay*, Phys. Rev. Lett. **110** (2013) 201801, arXiv:1303.0754 [hep-ex]. (637)

[1572] SINDRUM II Collaboration, W. H. Bertl et al., *A Search for muon to electron conversion in muonic gold*, Eur. Phys. J. **C47** (2006) 337–346. (637)

[1573] W. Altmannshofer, S. Gori, A. L. Kagan, L. Silvestrini, and J. Zupan, *Uncovering Mass Generation Through Higgs Flavor Violation*, Phys. Rev. **D93** (2016) 031301, arXiv:1507.07927 [hep-ph]. (638)

[1574] D. Ghosh, R. S. Gupta, and G. Perez, *Is the Higgs Mechanism of Fermion Mass Generation a Fact? A Yukawa-less First-Two-Generation Model*, Phys. Lett. **B755** (2016) 504–508, arXiv:1508.01501 [hep-ph]. (638)

[1575] A. Crivellin, G. D'Ambrosio, and J. Heeck, *Addressing the LHC flavor anomalies with horizontal gauge symmetries*, Phys. Rev. **D91** (2015) 075006, arXiv:1503.03477 [hep-ph]. (638)

[1576] A. Crivellin, G. D'Ambrosio, and J. Heeck, *Explaining $h \to \mu^\pm\tau^\mp$, $B \to K^*\mu^+\mu^-$ and $B \to K\mu^+\mu^-/B \to Ke^+e^-$ in a two-Higgs-doublet model with gauged $L_\mu - L_\tau$*, Phys. Rev. Lett. **114** (2015) 151801, arXiv:1501.00993 [hep-ph]. (638)

[1577] M. D. Campos, A. E. C. Hernandez, H. Pas, and E. Schumacher, *Higgs $\to \mu\tau$ as an indication for S_4 flavor symmetry*, Phys. Rev. **D91** (2015) 116011, arXiv:1408.1652 [hep-ph]. (638)

[1578] I. de Medeiros Varzielas and G. Hiller, *Clues for flavor from rare lepton and quark decays*,

JHEP **06** (2015) 072, arXiv:1503.01084 [hep-ph]. (638)

[1579] ATLAS Collaboration, G. Aad et al., *Evidence for the Higgs-boson Yukawa coupling to tau leptons with the ATLAS detector*, JHEP **04** (2015) 117, arXiv:1501.04943 [hep-ex]. (639)

[1580] CMS Collaboration, S. Chatrchyan et al., *Evidence for the 125 GeV Higgs boson decaying to a pair of τ leptons*, JHEP **05** (2014) 104, arXiv:1401.5041 [hep-ex]. (639)

[1581] CDF, D0 Collaboration, T. Aaltonen et al., *Evidence for a particle produced in association with weak bosons and decaying to a bottom-antibottom quark pair in Higgs boson searches at the Tevatron*, Phys. Rev. Lett. **109** (2012) 071804, arXiv:1207.6436 [hep-ex]. (639)

[1582] CMS Collaboration, S. Chatrchyan et al., *Evidence for the direct decay of the 125 GeV Higgs boson to fermions*, Nature Phys. **10** (2014) 557–560, arXiv:1401.6527 [hep-ex]. (639)

[1583] CMS Collaboration, V. Khachatryan et al., *Search for the associated production of the Higgs boson with a top-quark pair*, JHEP **09** (2014) 087, arXiv:1408.1682 [hep-ex]. [Erratum-ibid. **10** (2014) 106]. (639)

[1584] ATLAS Collaboration, G. Aad et al., *Search for the Standard Model Higgs boson decay to $\mu^+\mu^-$ with the ATLAS detector*, Phys. Lett. **B738** (2014) 68–86, arXiv:1406.7663 [hep-ex]. (639)

[1585] CMS Collaboration, V. Khachatryan et al., *Search for a standard model-like Higgs boson in the $\mu^+\mu^-$ and e^+e^- decay channels at the LHC*, Phys. Lett. **B744** (2015) 184–207, arXiv:1410.6679 [hep-ex]. (639)

[1586] CMS Collaboration, V. Khachatryan et al., *Searches for heavy Higgs bosons in two-Higgs-doublet models and for $t \to ch$ decay using multilepton and diphoton final states in pp collisions at 8 TeV*, Phys. Rev. **D90** (2014) 112013, arXiv:1410.2751 [hep-ex]. (639)

[1587] ATLAS Collaboration, G. Aad et al., *Search for Scalar Charm Quark Pair Production in pp Collisions at $\sqrt{s} = 8$ TeV with the ATLAS Detector*, Phys. Rev. Lett. **114** (2015) 161801, arXiv:1501.01325 [hep-ex]. (639)

[1588] T.-C. Huang and F. Petriello, *Rare exclusive decays of the Z-boson revisited*, Phys. Rev. **D92** (2015) 014007, arXiv:1411.5924 [hep-ph]. (639)

[1589] N. N. Achasov, *The $Z \to c\bar{c} \to \gamma\gamma^*$, $Z \to b\bar{b} \to \gamma\gamma^*$ triangle diagrams and the $Z \to \gamma\psi$, $Z \to \gamma\Upsilon$ decays*, Theor. Math. Phys. **170** (2012) 39–51. [Teor. Mat. Fiz. **170** (2012) 49]. (639)

[1590] ATLAS Collaboration, *Search for the Standard Model Higgs and Z Boson decays to $J\psi\,\gamma$: HL-LHC projections*, ATL-PHYS-PUB-2015-043, 2015. (640)

[1591] A. Chisholm and K. Nikolopoulos. Private communication. (640)

[1592] ATLAS Collaboration, M. Shochet, L. Tompkins, V. Cavaliere, P. Giannetti, A. Annovi, and G. Volpi (Eds.), *Fast TracKer (FTK) Technical Design Report*, Tech. Rep. CERN-LHCC-2013-007, ATLAS-TDR-021, CERN, Geneva, Jun., 2013. (640)

[1593] ATLAS Collaboration, G. Aad et al., *Measurement of the production of a W boson in association with a charm quark in pp collisions at $\sqrt{s} = 7$ TeV with the ATLAS detector*, JHEP **05** (2014) 068, arXiv:1402.6263 [hep-ex]. (641)

[1594] CMS Collaboration, S. Chatrchyan et al., *Measurement of associated W + charm production in pp collisions at $\sqrt{s}$ = 7 TeV*, JHEP **02** (2014) 013, arXiv:1310.1138 [hep-ex]. (641)

[1595] D. Curtin, R. Essig, and Y.-M. Zhong, *Uncovering light scalars with exotic Higgs decays to $b\bar{b}\mu^+\mu^-$*, JHEP **06** (2015) 025, arXiv:1412.4779 [hep-ph]. (642, 655)

[1596] B. A. Dobrescu, G. L. Landsberg, and K. T. Matchev, *Higgs boson decays to CP odd scalars at the Tevatron and beyond*, Phys. Rev. **D63** (2001) 075003, arXiv:hep-ph/0005308 [hep-ph]. (643)

[1597] S. Chang, P. J. Fox, and N. Weiner, *Visible Cascade Higgs Decays to Four Photons at Hadron*

Colliders, Phys. Rev. Lett. **98** (2007) 111802, arXiv:hep-ph/0608310 [hep-ph]. (643)

[1598] B. Bellazzini, C. Csaki, A. Falkowski, and A. Weiler, *Buried Higgs*, Phys. Rev. **D80** (2009) 075008, arXiv:0906.3026 [hep-ph]. (643)

[1599] C.-R. Chen, M. M. Nojiri, and W. Sreethawong, *Search for the Elusive Higgs Boson Using Jet Structure at LHC*, JHEP **11** (2010) 012, arXiv:1006.1151 [hep-ph]. (643)

[1600] A. Falkowski, D. Krohn, L.-T. Wang, J. Shelton, and A. Thalapillil, *Unburied Higgs boson: Jet substructure techniques for searching for Higgs' decay into gluons*, Phys. Rev. **D84** (2011) 074022, arXiv:1006.1650 [hep-ph]. (643)

[1601] B. Holdom, *Two U(1)'s and Epsilon Charge Shifts*, Phys. Lett. **B166** (1986) 196. (643)

[1602] P. Galison and A. Manohar, *Two Z's or not two Z's?*, Phys. Lett. **B136** (1984) 279. (643)

[1603] K. R. Dienes, C. F. Kolda, and J. March-Russell, *Kinetic mixing and the supersymmetric gauge hierarchy*, Nucl. Phys. **B492** (1997) 104–118, arXiv:hep-ph/9610479 [hep-ph]. (643)

[1604] S. Gopalakrishna, S. Jung, and J. D. Wells, *Higgs boson decays to four fermions through an abelian hidden sector*, Phys. Rev. **D78** (2008) 055002, arXiv:0801.3456 [hep-ph]. (643)

[1605] A. Martin and T. S. Roy, *The Gold-Plated Channel for Supersymmetric Higgs via Higgsphilic Z'*, arXiv:1103.3504 [hep-ph]. (643)

[1606] C.-F. Chang, E. Ma, and T.-C. Yuan, *Multilepton Higgs Decays through the Dark Portal*, JHEP **03** (2014) 054, arXiv:1308.6071 [hep-ph]. (643)

[1607] H. Davoudiasl, H.-S. Lee, I. Lewis, and W. J. Marciano, *Higgs Decays as a Window into the Dark Sector*, Phys. Rev. **D88** (2013) 015022, arXiv:1304.4935 [hep-ph]. (643)

[1608] D. Curtin, R. Essig, S. Gori, and J. Shelton, *Illuminating Dark Photons with High-Energy Colliders*, JHEP **02** (2015) 157, arXiv:1412.0018 [hep-ph]. (643, 655, 656)

[1609] D. Stump, J. Huston, J. Pumplin, W.-K. Tung, H. L. Lai, S. Kuhlmann, and J. F. Owens, *Inclusive jet production, parton distributions, and the search for new physics*, JHEP **10** (2003) 046, arXiv:hep-ph/0303013 [hep-ph]. (644)

[1610] J. Alwall et al., *Comparative study of various algorithms for the merging of parton showers and matrix elements in hadronic collisions*, Eur. Phys. J. **C53** (2008) 473–500, arXiv:0706.2569 [hep-ph]. (644)

[1611] A. Djouadi and M. Drees, *Higgs boson decays into light gravitinos*, Phys. Lett. **B407** (1997) 243–249, arXiv:hep-ph/9703452 [hep-ph]. (648)

[1612] J. D. Mason, D. E. Morrissey, and D. Poland, *Higgs Boson Decays to Neutralinos in Low-Scale Gauge Mediation*, Phys. Rev. **D80** (2009) 115015, arXiv:0909.3523 [hep-ph]. (648, 655, 664)

[1613] C. Petersson, A. Romagnoni, and R. Torre, *Higgs Decay with Monophoton + MET Signature from Low Scale Supersymmetry Breaking*, JHEP **10** (2012) 016, arXiv:1203.4563 [hep-ph]. (648, 649)

[1614] CMS Collaboration, V. Khachatryan et al., *Search for exotic decays of a Higgs boson into undetectable particles and one or more photons*, Phys. Lett. **B753** (2016) 363–388, arXiv:1507.00359 [hep-ex]. (648, 649, 651)

[1615] ATLAS Collaboration, *Search for exotic Higgs-boson decays in events with at least one photon, missing transverse momentum, and two forward jets produced in $\sqrt{s}$ = 8 TeV pp collisions with the ATLAS detector*, ATLAS-CONF-2015-001, 2015. (648)

[1616] DELPHES 3 Collaboration, J. de Favereau et al., *DELPHES 3, A modular framework for fast simulation of a generic collider experiment*, JHEP **02** (2014) 057, arXiv:1307.6346 [hep-ex]. (648)

[1617] N. D. Christensen, P. de Aquino, N. Deutschmann, C. Duhr, B. Fuks, C. Garcia-Cely, O. Mattelaer, K. Mawatari, B. Oexl, and Y. Takaesu, *Simulating spin-$\frac{3}{2}$ particles at colliders*,

Eur. Phys. J. **C73** (2013) 2580, arXiv:1308.1668 [hep-ph]. (649)

[1618] J. Anderson, A. Avetisyan, R. Brock, S. Chekanov, T. Cohen, et al., *Snowmass Energy Frontier Simulations*, arXiv:1309.1057 [hep-ex]. (649)

[1619] M. J. Strassler and K. M. Zurek, *Echoes of a hidden valley at hadron colliders*, Phys. Lett. **B651** (2007) 374–379, arXiv:hep-ph/0604261 [hep-ph]. (655)

[1620] M. J. Strassler, *Possible effects of a hidden valley on supersymmetric phenomenology*, arXiv:hep-ph/0607160 [hep-ph]. (655)

[1621] T. Han, Z. Si, K. M. Zurek, and M. J. Strassler, *Phenomenology of hidden valleys at hadron colliders*, JHEP **07** (2008) 008, arXiv:0712.2041 [hep-ph]. (655)

[1622] CMS Collaboration, V. Khachatryan et al., *Search for long-lived particles that decay into final states containing two electrons or two muons in proton-proton collisions at* $\sqrt{s} = 8$ *TeV*, Phys. Rev. **D91** (2015) 052012, arXiv:1411.6977 [hep-ex]. (655)

[1623] ATLAS Collaboration, G. Aad et al., *Search for long-lived neutral particles decaying into lepton jets in proton-proton collisions at* $\sqrt{s} = 8$ *TeV with the ATLAS detector*, JHEP **11** (2014) 088, arXiv:1409.0746 [hep-ex]. (655, 663)

[1624] M. L. Graesser, *Broadening the Higgs boson with right-handed neutrinos and a higher dimension operator at the electroweak scale*, Phys. Rev. **D76** (2007) 075006, arXiv:0704.0438 [hep-ph]. (655)

[1625] M. L. Graesser, *Experimental Constraints on Higgs Boson Decays to TeV-scale Right-Handed Neutrinos*, arXiv:0705.2190 [hep-ph]. (655)

[1626] W.-Y. Keung and P. Schwaller, *Long Lived Fourth Generation and the Higgs*, JHEP **06** (2011) 054, arXiv:1103.3765 [hep-ph]. (655)

[1627] A. Maiezza, M. Nemevsek, and F. Nesti, *Lepton Number Violation in Higgs Decay at LHC*, Phys. Rev. Lett. **115** (2015) 081802, arXiv:1503.06834 [hep-ph]. (655)

[1628] L. M. Carpenter, D. E. Kaplan, and E.-J. Rhee, *Reduced fine-tuning in supersymmetry with R-parity violation*, Phys. Rev. Lett. **99** (2007) 211801, arXiv:hep-ph/0607204 [hep-ph]. (655)

[1629] D. Aristizabal Sierra, W. Porod, D. Restrepo, and C. E. Yaguna, *Novel Higgs decay signals in R-parity violating models*, Phys. Rev. **D78** (2008) 015015, arXiv:0804.1907 [hep-ph]. (655)

[1630] ATLAS Collaboration, G. Aad et al., *Search for pair-produced long-lived neutral particles decaying in the ATLAS hadronic calorimeter in pp collisions at* $\sqrt{s} = 8$ *TeV*, Phys. Lett. **B743** (2015) 15–34, arXiv:1501.04020 [hep-ex]. (655, 660, 662, 663)

[1631] ATLAS Collaboration, G. Aad et al., *Search for long-lived, weakly interacting particles that decay to displaced hadronic jets in proton-proton collisions at* $\sqrt{s} = 8$ *TeV with the ATLAS detector*, Phys. Rev. **D92** (2015) 012010, arXiv:1504.03634 [hep-ex]. (655, 660, 662, 663)

[1632] Z. Chacko, H.-S. Goh, and R. Harnik, *The Twin Higgs: Natural electroweak breaking from mirror symmetry*, Phys. Rev. Lett. **96** (2006) 231802, arXiv:hep-ph/0506256 [hep-ph]. (657)

[1633] C. Csaki, E. Kuflik, S. Lombardo, and O. Slone, *Searching for displaced Higgs boson decays*, Phys. Rev. **D92** (2015) 073008, arXiv:1508.01522 [hep-ph]. (657, 660, 661, 662, 663)

[1634] C. J. Morningstar and M. J. Peardon, *The Glueball spectrum from an anisotropic lattice study*, Phys. Rev. **D60** (1999) 034509, arXiv:hep-lat/9901004 [hep-lat]. (657)

[1635] J. E. Juknevich, *Pure-glue hidden valleys through the Higgs portal*, JHEP **08** (2010) 121, arXiv:0911.5616 [hep-ph]. (657)

[1636] D. Curtin and A. Katz. In preparation, 2016. (658)

[1637] CMS Collaboration, V. Khachatryan et al., *Search for Long-Lived Neutral Particles Decaying to*

Quark-Antiquark Pairs in Proton-Proton Collisions at $\sqrt{s} = 8$ TeV, Phys. Rev. **D91** (2015) 012007, arXiv:1411.6530 [hep-ex]. (660, 662)

[1638] A. Coccaro, D. Curtin, H. J. Lubatti, H. Russell, and J. Shelton, *Data-driven Model-independent Searches for Long-lived Particles at the LHC*, arXiv:1605.02742 [hep-ph]. (661)

[1639] P. Ilten, J. Thaler, M. Williams, and W. Xue, *Dark photons from charm mesons at LHCb*, Phys. Rev. **D92** (2015) 115017, arXiv:1509.06765 [hep-ph]. (663)

[1640] ATLAS Collaboration, G. Aad et al., *Search for direct production of charginos and neutralinos in events with three leptons and missing transverse momentum in $\sqrt{s} = 8$ TeV pp collisions with the ATLAS detector*, JHEP **04** (2014) 169, arXiv:1402.7029 [hep-ex]. (665)

[1641] ATLAS Collaboration, G. Aad et al., *Search for the electroweak production of supersymmetric particles in $\sqrt{s}$=8 TeV pp collisions with the ATLAS detector*, Phys. Rev. **D93** (2016) 052002, arXiv:1509.07152 [hep-ex]. (665)

[1642] CMS Collaboration, V. Khachatryan et al., *Search for supersymmetry in events with soft leptons, low jet multiplicity, and missing transverse energy in proton-proton collisions at $\sqrt{s} = 8$ TeV*, Phys. Lett. **B759** (2016) 9–35, arXiv:1512.08002 [hep-ex]. (665)